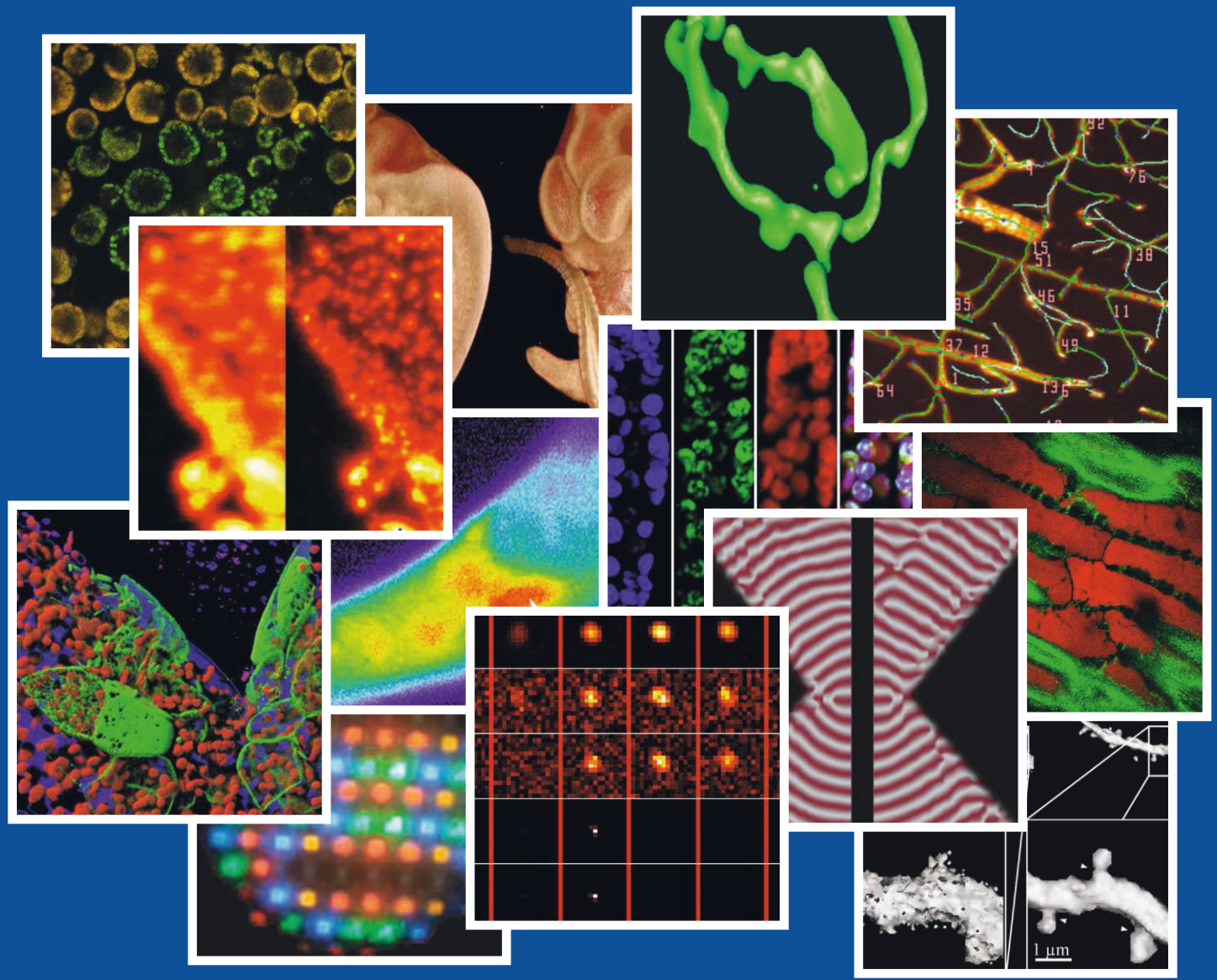
Handbook of Biological Confocal Microscopy

THIRD EDITION



James B. Pawley

Editor

HANDBOOK OF BIOLOGICAL CONFOCAL MICROSCOPY

THIRD EDITION

HANDBOOK OF BIOLOGICAL CONFOCAL MICROSCOPY

THIRD EDITION

Editor

James B. Pawley

Department of Zoology
University of Wisconsin
Madison, Wisconsin

Springer

James B. Pawley
Department of Zoology
University of Wisconsin
Madison, WI 53706
USA

Library of Congress Control Number: 2005926334

ISBN 10: 0-387-25921-X
ISBN 13: 987-0-387-25921-5

Printed on acid-free paper.

© 2006, 1995, 1989 Springer Science+Business Media, LLC
All rights reserved. This work may not be translated or copied in whole or in part without the written permission of the publisher (Springer Science+Business Media, LLC, 233 Spring Street, New York, NY 10013, USA), except for brief excerpts in connection with reviews or scholarly analysis. Use in connection with any form of information storage and retrieval, electronic adaptation, computer software, or by similar or dissimilar methodology now known or hereafter developed is forbidden.
The use in this publication of trade names, trademarks, service marks, and similar terms, even if they are not identified as such, is not to be taken as an expression of opinion as to whether or not they are subject to proprietary rights.

9 8 7 6 5 (Corrected at 5th printing)

springer.com

To my wonderful wife, Christine, who is hoping that
we still get along once she begins to see me more often,
and to the friends and partners of all the 123 authors, similarly oppressed.

Preface to the Third Edition

Once the second edition was safely off to the printer, the 110 authors breathed a sigh of relief and relaxed, secure in the belief that they would "never have to do that again." That lasted for 10 years. When we finally awoke, it seemed that a lot had happened. In particular, people were trying to use the *Handbook* as a textbook even though it lacked the practical chapters needed. There had been tremendous progress in lasers and fiber-optics and in our understanding of the mechanisms underlying photobleaching and phototoxicity. It was time for a new book. I contacted "the usual suspects" and almost all agreed as long as the deadline was still a year away.

That was in 2002. Three years later, most of the old chapters have been substantially or totally rewritten. Although 12 of the chapters are on topics that have either been rendered obsolete by improvements in instrumentation or changes in research interest have been dropped, some have been replaced by chapters on similar topics. To make the *Handbook* of more use as a textbook, we have added an extended appendix about practical multiphoton imaging and another describing the operation of CCD cameras in some detail. There is a new series of practical chapters on confocal microscopy and the selection of dyes, as well as on ion imaging, and on methods for studying brain slices, embryos, biofilms and plants (two). There is also a new chapter describing in some detail how such components as interference filters, acousto-optical devices, and galvanometers are made and what parameters limit their performance. The single chapter on 3D image analysis now has the company of two more on automated 3D image analysis and a third on high-content screening and a fourth on database management. Chapters have been added describing techniques that have only recently come to the fore, such as patterned-illumination fluorescence microscopy, fluorescence resonance energy transfer (FRET) and the generation and detection of second- and third-harmonic signals. In addition, new imaging techniques such as stimulated emission depletion (STED), coherent anti-Stokes Raman (CARS) imaging and selected plane illumination (SPIM) now have their own chapters and there are also chapters that connect the world of 3D light microscopy to the larger world of micro-CT and micro-MRI and the smaller world revealed by the scanning and transmission electron microscopes. To round out the story we even have a chapter on what PowerPoint does to the results, and the annotated bibliography has been updated and extended.

As with the previous editions, the editor enjoyed a tremendous amount of good will and cooperation from the 124 authors involved. Both I, and the light microscopy community in general, owe them all a great debt of gratitude. On a more personal note, I would like to thank Kathy Lyons and her associates at Springer for their unstinting support on one of the biggest books they have done in microscopy and the assistance of her co-workers at Chernow Editorial Services, Barbara Chernow and Kathy Cleghorn. Helen Noeldner was again willing to work long hours to keep all the manuscripts straight in spite of my best effort to confuse them. Thanks are also due to Bill Feeny, the Zoology Department artist, for the innumerable figures that he rescued, reconstructed and otherwise returned to life.

If the hidden agenda of the first edition was photon efficiency, and of the second, spherical aberration, the message of the third edition is definitely that all raw, 3D data sets should be deconvolved (or at least 3D-Gaussian filtered) before being viewed or measured. Not only is this required to meet the Nyquist reconstruction criterion, it also greatly reduces the apparent effects of Poisson Noise by effectively averaging the signal over the 50–100 voxels needed to make a Nyquist-sampled, 3D image of a single point object. This last factor allows one to obtain acceptable images using much less excitation, thereby reducing the chance that studies of living cells will be compromised by artifacts caused by phototoxicity. As evermore studies in 3D light microscopy are carried out on living cells, nothing is more important. Now we need dyes that produce less toxicity because they do not cross to the triplet state and photodetectors that operate with lower noise and higher quantum efficiency! That will take another book.

James B. Pawley
January 2006

Preface to the Second Edition

Confocal microscopy is a good idea that was invented, forgotten and then reinvented about once every decade in the years between 1957 and 1985. However, when White and Amos demonstrated an instrument that was sufficiently user-friendly to become the ideal tool for the 3D localization of specific, fluorescent labels in biological specimens, the field finally took off. Soon after the publication of their 1985 article in the *Journal of Cell Biology*, requests to fund the purchase of similar equipment increased at such a rate that, in the fall of 1988, the U.S. National Science Foundation (NSF) realized that it needed some hard information about the capabilities of this new technique. They funded a two-day symposium on the subject as part of the August 1989 annual meeting of the Electron Microscope Society of America and also financed the publication of 18 papers by the participants as *The Handbook of Biological Confocal Microscopy* for free distribution at the meeting.

This first edition of the *Handbook* differed from most of the many other compiled volumes on the subject in that, rather than each author concentrating on his or her own work, an outline for the entire book was written first, and then authors were solicited to cover particular aspects of the instrumentation or its use. Although the necessity of having a volume ready for distribution by August 1989 imposed stringent deadlines on the authors and required the typography and printing to be done locally, every effort was made to try to edit the chapters so that they fit together to form a cohesive whole. The success of the project was due almost entirely to the enthusiasm the authors had for sharing their knowledge of this fascinating subject with a wider audience. Manuscripts originally expected to be 10 pages in length ended up being more than twice this length, and several were more that 50 pages long.

The resulting volume included chapters that described and compared each of the component parts of the microscope itself (laser and conventional light sources, intermediate optics, alternative scanning systems, objectives, pinholes, detectors, and antecedent and related optical techniques), chapters that discussed the digital aspects of data acquisition (pixelation, digitization, and display and measurement of 3D data sets) and chapters that reviewed the properties of fluorescent dyes, the techniques of 3D specimen preparation, and the fundamental limitations and practical complexities of quantitative confocal fluorescence imaging. An annotated bibliography of the field was also included.

If this first book had any underlying theme, it was probably the importance of photon efficiency. This came about because, as the chapters came together, it became clear that technical limitations of the early instruments, in combination with suboptimal operating techniques, often had an effect such that the signal actually recorded was only about 1% of the expected signal. The *Handbook* included several concrete suggestions for increasing this fraction, and it is a pleasure to report that instruments incorporating many of these improvements now demonstrate an efficiency figure that is closer to 10–20%.

Because of the widespread acceptance of the NSF-sponsored volume by users of the confocal microscope, a revised edition (the "red book") was published by Plenum in 1990. Although this hardcover version included over 40 new figures, updated tabular information and over 1,400 typographical improvements, it was otherwise generally very similar to the initial offering.

However, the past five years has seen a virtual explosion in the field of biological confocal microscopy. As it became more and more evident that the original *Handbook* could no longer claim to cover the entire field, I contacted the original set of authors about producing an updated edition. Remembering the frantic urgency that had typified the production of the first edition, I did this with some trepidation; but I need not have worried. The response was uniformly enthusiastic, and several authors were not only willing to completely revise their original chapters but also volunteered to write additional chapters describing several new areas. The response from the 17 new authors was similarly enthusiastic.

The final product includes 37 chapters (15 updated from the first edition, 21 new ones, and an annotated bibliography) and is almost three times as long as the original. Chapters covering confocal operation in the UV, in the transmission mode, and when scanning at video rates using a variety of either point-scanning or line-scanning techniques have been added. The use of pulsed laser sources for both two-photon excitation and fluorescence-lifetime imaging is covered in depth, and there is an entire chapter on the functional principles of modern fiberoptic components and the manifold ways that these can be applied to confocal microscopy. In addition, chapters on the joys and perils of observing living specimens in the confocal microscope and on the detection of gold-conjugated labels now complement a revised version of the earlier chapter describing the preparation of dead specimens.

No less than 3 of the new chapters address the comparative advantages of the confocal and widefield/deconvolution methods of obtaining 3D data sets from biological specimens with the minimum possible damage. Although each of these chapters proceeds from a very different perspective (algebraic optics, actual measurements, and minimum-entrope image processing), I believe that together they give a balanced view of this complex and important subject and make it clear that the confocal microscope could still be improved if the present photodetector were replaced with one having a higher quantum efficiency. The longest chapter in the book describes the inner workings of the 17 currently available systems applicable to the analysis and display of 3D digital image data, and there is now also a chapter describing the features of all of the current hardware systems for the storage, display, and hard-copy output of 3D and 4D image data sets.

The subtext of this second edition is probably an increased recognition of the extent to which the resolution and signal strength of confocal images can be degraded by spherical aberration introduced whenever there is a refractive-index mismatch, such as that occurring when an oil-immersion objective is used with an aqueous specimen. Not only is an entirely new chapter devoted to the subject, but many other authors emphasize the same point in their chapters. Again, the manufacturers have responded with the introduction of a number of superb new water-immersion objectives to simplify confocal observations of living specimens; these are also described.

On the subject of optics there are also two chapters on real-time 3D imaging. In one, the approach is to combine a high speed slit scanner with rapid motion of the focus plane, while the other demonstrates the truth of the almost paradoxical premise that it can be useful to actually increase the chromatic aberration of an objective if it is to be used to examine surface height in the back-scattered light mode with "white" light. Of more interest to those wishing to improve axial resolution in the fluorescent mode is the chapter describing new, high-resolution techniques that combine either two or even three confocal objectives with two-photon excitation to improve resolution to a level heretofore believed to be impossible.

Finally, there is a tutorial chapter intended for the novice user, as well as two appendixes. The first appendix describes the relationship between real-space and optical coordinates, while the second provides a compilation of the optical path layouts of the major commercial confocal instruments.

The topics in this book cover a very wide range of disciplines. While this is good in that it shows the integrating nature of the field, it can lead to problems with notation when optical physicists, experts on information theory, microscope designers, and just plain biologists have to try to agree on a common system of notation. In the first edition, we did not even try to overcome this problem. Although this led to some confusion, I must confess that my efforts to remedy the problem in the present volume have not been totally successful. Index of refraction has been rendered as η, so that **n** can be reserved for the number of quantum events; where *t* has been used for thickness, we have tried to use italics, so that **t** could be used for time as a variable and T for temperature, while specific times (lifetimes, pulse times) are shown as T or τ; wherever *x*, *y* and *z* are used as directions, we have italicized them, while we have tried to keep r as actual dimensions in the *x*–*y* plane (r_p = pinhole radius, r_s = slit width, r_d = detector diameter, etc.); and numerical aperture appears almost everywhere as NA but becomes A_{NA} in some equations. Perhaps most debatable was my decision to try to save space by replacing the word "wavelength" with λ in the body of the text. On reflection, this change probably did not repay, in space, the interruption of the reader that it produces, but, unfortunately, by the time this became evident, it was too late to change it. In spite of our best efforts, problems arose because, while authors wanted to fit in with the book as whole, they also, understandably, wished to remain consistent with their previous publications. I would like to thank them all for their cooperation on this complex issue, and I hope that our efforts at consistency have not introduced any errors into the text.

This brings us to the Index. There was not enough time to prepare an index for the NSF version. One was put together for the "red book," but it was somewhat less extensive than one might have wished for a handbook. This time, when faced with the need to do it all again, and also having all of the text in electronic form, I was mindful of the two opposing indexing concepts currently pervasive in the popular culture. What one might call the minimalist view of indexing comes from the Douglas Adams book *The Hitchhiker's Guide to the Galaxy*, where the original entry for Earth is "Harmless;" this is only slightly improved later by being updated to "Mostly Harmless." The opposing view was crystallized by Barry Commoner as: "Everything is connected to everything else" — a concept amply demonstrated within the field of confocal microscopy. Trying to steer a middle course between these two extremes, I have concocted a new Index that is over twelve times the size of the previous one (now with nearly 7,000 topics and about twice that many page listings), while the book itself has almost tripled. This Index contains entries for almost every diagram, plot, image, and table in the book. It also lists under "Summaries" the pages of the summary sections that conclude most chapters and contain their "take-home lessons." The listing "chapter" refers to an entire chapter starting on the page noted and dealing predominantly with the listed topic. Although subjects in the text are extensively cross-indexed, literally "connecting everything to everything else" would have required another book. I settled for making sure that each text topic appeared at least once under all of the Index topics that seemed appropriate, but I did not attempt to list all the pages in each chapter on which a term was mentioned. As a result, the reader would probably be well-advised to look for additional information on the pages adjacent to (usually following) those pages listed in the Index. I beg indulgence for all of the "inevitable omissions."

Confocal microscopy is not the only technology to have developed over the last five years. Constant improvements in the international digital communication network have brought e-mail and electronic file transfer into the normal working lives of most of the authors, and this made the editing of the present edition much more of a two-way process. Chapters could be modified to fit better with their neighbors, returned, checked, and resubmitted all in a matter of days, even when the authors concerned were in Australia, Taiwan, and Europe. Although this process added a welcome level of flexibility not present for the earlier book, it also imposed an additional strain on the authors, who often were just congratulating themselves on finally getting their chapter "out the door" only to have them reappear with a lot of suggested changes and requests for expansion to cover additional areas. Again, the authors responded to this challenge in the most positive manner possible, and this seems the most appropriate place to record my sincere thanks to them for the cooperative spirit that they invariably displayed. Thanks are also due to Helen Noeldner, who provided the order and secretarial assistance without which we could not have succeeded; to Mary Born, my editor at Plenum, whose kind voice prevented me from jumping out of my twelfth-floor window on several occasions; to those manufacturers who provided support for publishing some of the color figures and to their representatives for providing the diagrams and other information included in Appendix 2; to NSF, which provided me with grant DIR-90-17534, to my wife; Christine, who toiled many late nights on the Index; and to my family (and doubtless the families of the authors), who gave me their precious time to help get this project finished.

All of these contributed everything that they could in an effort to make this the most comprehensive, accurate, and useful volume on the subject possible. We all hope that you will think we have succeeded.

James B. Pawley
January 1995

Contents

Preface to the Third Edition vii
Preface to the Second Edition ix
Contributors xxv

CHAPTER 1: FOUNDATIONS OF CONFOCAL SCANNED IMAGING IN LIGHT MICROSCOPY

Shinya Inoué

Light Microscopy 1
Lateral Resolution 1
Axial Resolution 3
Depth of Field 4
Confocal Imaging 4
Impact of Video 5
Nipkow Disk 5
Electron-Beam-Scanning Television 6
Impact of Modern Video 7
Lasers and Microscopy 7
Holography 7
Laser Illumination 8
Laser-Illuminated Confocal Microscopes 9
Confocal Laser-Scanning Microscope 9
Two- and Multi-Photon Microscopy 10
Is Laser-Scanning Confocal Microsopy a Cure-All? 11
Speed of Image or Data Acquisition 11
Yokogawa Disk-Scanning Confocal System 12
Depth of Field in Phase-Dependent Imaging 13
Other Optical and Mechanical Factors Affecting Confocal Microscopy 13
Lens Aberration 13
Unintentional Beam Deviation 15
Contrast Transfer and Resolution in Confocal Versus Non-Confocal Microscopy 16
Summary 16

CHAPTER 2: FUNDAMENTAL LIMITS IN CONFOCAL MICROSCOPY

James B. Pawley

Introduction 20
What Limits? 20
Counting Statistics: The Importance of n 20
Source Brightness 21
Specimen Response: Dye Saturation 21
A Typical Problem 24
Practical Photon Efficiency 24
Losses in the Optical System 25
Detection and Measurement Losses 28
Where Have All the Photons Gone? 33
Resolution: How Much Is Enough? 36
Can Resolution Be Too High? 36
Limitations Imposed by Spatial and Temporal Quantization 37
Practical Considerations Relating Resolution to Distortion 39
Conclusion 41

CHAPTER 3: SPECIAL OPTICAL ELEMENTS

Jens Rietdorf and Ernst H.K. Stelzer

Introduction 43
Regulating the Intensity 43
Wavelength Selective Filtering Devices 43
Selecting the Wavelength of the Illumination and the Detected Light 44
Separating the Light Paths 44
Conventional Filters 45
Interference Filters 45
Dichroic and Polarizing Beam-Splitters 50
Filters and Dispersive Elements for Multi-Channel Detection 51
Mechanical Scanners 51
Galvanometer Scanners 52
General Specifications 54
Acousto-Optical Components 54
Acousto-Optical Deflectors 56
Acousto-Optical Modulators 56
Acousto-Optical Tunable Filters 56
Acousto-Optical Beam-Splitters 56
Electro-Optical Modulators 57
Piezoelectric Scanners 57
Polarizing Elements 57
Removing Excess Light 58

CHAPTER 4: POINTS, PIXELS, AND GRAY LEVELS: DIGITIZING IMAGE DATA

James B. Pawley

Contrast Transfer Function, Points, and Pixels 59
Pixels, Images, and the Contrast Transfer Function . . . 59
Digitization and Pixels 62
Digitization of Images 62
How Big Should a Pixel Be? Sampling and Quantum Noise 63
The Nyquist Criterion 64
Estimating the Expected Resolution of an Image 65
The Story So Far 68
Reality Check? 68
Is Over-Sampling Ever Wise? 68
Under-Sampling? 68
Digitizing Trade-Offs 68

Nyquist Reconstruction: "Deconvolution Lite" 68
Some Special Cases 70
Gray Levels, "Noise," and Photodetector Performance 71
Optical Density 71
The Zone System: Quantified Photography 71
Linearity: Do We Need It? 72
Gray Levels in Images Recorded Using Charge-Coupled Devices: The Intensity Spread Function 74
What Counts as Noise? 74
Measuring the Intensity Spread Function 75
Calibrating a Charge-Coupled Device to Measure the ISF 75
"Fixed-Pattern" Noise 76
Gain-Register Charge-Coupled Devices 76
Multiplicative Noise 77
Trade-Offs 79

CHAPTER 5: LASER SOURCES FOR CONFOCAL MICROSCOPY

Enrico Gratton and Martin J. vandeVen

Introduction 80
Laser Power Requirements 80
The Basic Laser 81
Principle of Operation 82
Pumping Power Requirements 82
Laser Modes: Longitudinal (Axial) and Transverse 82
Polarization 83
Coherent Properties of Laser Light 83
Phase Randomization: Scrambling the Coherence Properties of Laser Light 84
Measures to Reduce the Coherence Length of Laser Light 84
Heat Removal 84
Other Installation Requirements 85
Attenuation of Laser Beams 85
Stabilization of Intensity, Wavelength, and Beam Position in Lasers 85
Sources of Noise in Lasers 85
Spatial Beam Characteristics 89
Laser Requirements for Biological Confocal Laser Scanning Microscopy-Related Techniques 89
Optical Tweezers 89
Total Internal Reflection Microscopy 89
Confocal Raman Confocal Laser Scanning Microscopy for Chemical Imaging 90
Non-Linear Confocal Microscopy 90
Nanosurgery and Microdissection 90
Types of Lasers 90
Continuous Wave Lasers 90
Gas Lasers 90
Dye Lasers 103
Solid-State Lasers 103
Thin Disk Lasers 109
Pulsed Lasers 110
Classification of Pulsed Laser Systems 111
Nitrogen Lasers 112
Excimer Lasers 112
Metal Vapor Lasers 112
Dye Lasers 112
Modulated Diode Lasers 112
Diode Pumped Solid State Laser in Pulsed Mode 112
Ultrafast Diode Pumped Solid State Lasers 112
Titanium-Sapphire and Related Ultrafast Lasers 112
White Light Continuum Lasers 113
Ultrafast Fiber Lasers 113
Wavelength Expansion Through Non-Linear Techniques 114
Second and Higher Harmonic Generation: SHG, THG, FHG Label-Free Microscopy 114
Sum or Difference Mixing 114
Optical Parametric Oscillators and Optical Parametric Amplifiers 114
Pulse Length Measurement 115
Maintenance 115
Maintenance of Active Laser Media 115
Maintenance of Pumping Media 116
Maintenance of the Optical Resonator 116
Maintenance of Other System Components 116
Troubleshooting 117
Safety Precautions 117
Beam Stops 118
Curtains 118
Laser Goggles 118
Screens 118
Exposure Effects, Warning Signs, and Interlocks 118
Infrared Paper 118
Conclusion 118

CHAPTER 6: NON-LASER LIGHT SOURCES FOR THREE-DIMENSIONAL MICROSCOPY

Andreas Nolte, James B. Pawley, and Lutz Höring

Introduction 126
General Remarks on Choice of Excitation Light Sources 126
Scrambling and Filtering the Light 131
Types of Sources and Their Features 132
Structure 132
Wavelength 135
Stability in Time and Wavelength 136
Radiance 137
Control 138
Measuring What Comes Through the Illumination System 139
The Bare Minimum 139
Types of Confocal Microscopes That Can Use Non-Laser Light Sources 141
Tandem Scanning: Basic Description 141
Single-Sided Disk Scanning: Basic Description 141
Exposure Time and Source Brightness 141
Future Trends 143

CHAPTER 7: OBJECTIVE LENSES FOR CONFOCAL MICROSCOPY

H. Ernst Keller

Introduction 145
Aberrations of Refractive Systems 146
Defocusing 146
Monochromatic Aberrations 147
Chromatic Aberrations 152

Finite Versus Infinity Optics . . . 156
Working Distance . . . 157
Optical Materials . . . 158
Anti-Reflection Coatings . . . 158
Transmission of Microscope Objectives . . . 158
Conclusion . . . 160

CHAPTER 8: THE CONTRAST FORMATION IN OPTICAL MICROSCOPY

Ping-Chin Cheng

Introduction . . . 162
Sources of Contrast . . . 163
Absorption Contrast . . . 163
Scattering and Reflection Contrast . . . 167
Phase Contrast . . . 171
Fluorescence Contrast . . . 172
Contrast Related to Excitation Wavelength Change . . . 173
Negative Contrast . . . 173
Special Concerns in Ultraviolet and Near-Infrared Range Confocal Microscopy . . . 174
Total Internal Reflection Contrast . . . 177
Harmonic Generation Contrast . . . 179
Geometric Contrast . . . 180
z-Contrast in Confocal Microscopy . . . 180
Total Internal Refraction Fluorescence Contrast . . . 180
Fluorescence Resonant Energy Transfer . . . 184
Fluorescence Recovery After Photobleaching (FRAP and FLIP) . . . 187
Structural Contrast . . . 188
Harmonic Generation Contrast . . . 188
Birefringence Contrast . . . 188
Derived Contrast (Synthetic Contrast) . . . 188
Ratiometric . . . 189
Deconvolution . . . 189
Movement Contrast (Subtraction of Previous Image) . . . 190
Spectral Unmixing and Color Reassignment . . . 190
Effects of the Specimen: Spherical Aberration and Optical Heterogeneity . . . 192
Mounting Medium Selection . . . 198
Artificial Contrast . . . 201
Contrast Resulting from Instrument Vibration and Ambient Lighting . . . 201
Contrast Resulting from Interference of Cover Glass Surfaces . . . 201
Background Level and Ghost Images from the Transmission Illuminator . . . 201
Contrast Resulting from Differences in Photobleaching Dynamics . . . 202
Effect of Spectral Leakage and Signal Imbalance Between Different Channels . . . 203
New Contrasts: Fluorescence Lifetime and Coherent Antistokes Raman Spectroscopy . . . 204
Summary . . . 204

CHAPTER 9: THE INTERMEDIATE OPTICAL SYSTEM OF LASER-SCANNING CONFOCAL MICROSCOPES

Ernst H.K. Stelzer

Introduction . . . 207
Design Principles . . . 207
Overview . . . 207
Telecentricity . . . 207
The Scanning System . . . 208
The Back-Focal Planes . . . 210
Practical Requirements . . . 210
Diffraction Limit . . . 210
Geometric Distortion . . . 211
Evaluation of the Illumination and Detection Systems . . . 211
Influence of Optical Elements . . . 211
Errors . . . 211
Evaluation of Optical Arrangements . . . 212
Evaluation of Scanner Arrangements . . . 213
Scanners . . . 215
Attachment to Microscopes . . . 217
Merit Functions . . . 217
Multi-Fluorescence . . . 217
Special Setups . . . 218
Setups for Fluorescence Recovery After Photobleaching Experiments . . . 218
Setups for Fluorescence Resonance Energy Transfer Experiments . . . 218
Setups for the Integration of Optical Tweezers . . . 218
Setups for the Integration of Laser Cutters . . . 218
Setups for the Observation of Living Specimens . . . 219
Miniaturization and Computer Control . . . 219
Thermal Stability . . . 219
Vibration Isolation . . . 219
Conclusions and Future Prospects . . . 219

CHAPTER 10: DISK-SCANNING CONFOCAL MICROSCOPY

Derek Toomre and James B. Pawley

Introduction . . . 221
Background . . . 221
Living Cell Imaging: Probing the Future . . . 221
A Need for Speed and Less Photobleaching . . . 222
Advantages and Limitations of Confocal Laser-Scanning Microscopes . . . 222
Other Imaging and Deconvolution . . . 223
Confocal Disk-Scanning Microscopy . . . 223
Nipkow Disk — An Innovation . . . 223
A Renaissance — Advantages of Disk-Scanning Confocal Imaging . . . 223
Disadvantages . . . 224
Critical Parameters in Pinhole and Slit Disks . . . 224
Fill Factor and Spacing Interval F . . . 224
Lateral Resolution . . . 225
Pinhole/Slit Size . . . 225
Axial Resolution . . . 225
Types of Disk-Scanning Confocals . . . 228
General Considerations . . . 228
Disk Scanners for Backscattered Light Imaging . . . 228
CARV, DSU, and Other Disk-Scanning Confocal Microscopes . . . 229
The Yokogawa Microlens — An Illuminating Approach . . . 231
New Fast Slit Scanner — Zeiss LSM510 LIVE . . . 231
New Detectors — A Critical Component . . . 232
Image Intensifiers . . . 232
On-Chip Electron Multiplying Charge-Coupled Device . . . 233

Electron Multiplication Charge-Coupled Devices and Disk Scanners . . . 234
Applications and Examples of Confocal Disk-Scanning Microscopes . . . 235
Comparison with Epi-Fluorescence Imaging . . . 235
Fast 3D/4D Imaging . . . 235
Blazingly Fast Confocal Imaging . . . 235
Future Developments? . . . 236
Summary . . . 237

CHAPTER 11: MEASURING THE REAL POINT SPREAD FUNCTION OF HIGH NUMERICAL APERTURE MICROSCOPE OBJECTIVE LENSES

Rimas Juškaitis

Introduction . . . 239
Measuring Point Spread Function . . . 240
Fiber-Optic Interferometer . . . 240
Point Spread Function Measurements . . . 241
Chromatic Aberrations . . . 242
Apparatus . . . 243
Axial Shift . . . 243
Pupil Function . . . 245
Phase-Shifting Interferometry . . . 245
Zernike Polynomial Fit . . . 245
Restoration of a 3D Point Spread Function . . . 247
Empty Aperture . . . 248
Miscellanea . . . 248
Temperature Variations . . . 248
Polarization Effects . . . 249
Apodization . . . 250
Conclusion . . . 250

CHAPTER 12: PHOTON DETECTORS FOR CONFOCAL MICROSCOPY

Jonathan Art

Introduction . . . 251
The Quantal Nature of Light . . . 251
Interaction of Photons with Materials . . . 252
Thermal Effects . . . 252
Direct Effects . . . 252
Photoconductivity . . . 252
Photovoltaic . . . 252
Photoemissive . . . 254
Comparison of Detectors . . . 255
Noise Internal to Detectors . . . 256
Noise in Internal Detectors . . . 256
Noise in Photoemissive Devices . . . 256
Statistics of Photon Flux and Detectors . . . 257
Representing the Pixel Value . . . 258
Conversion Techniques . . . 259
Assessment of Devices . . . 260
Point Detection Assessment and Optimization . . . 260
Field Detection Assessment and Optimization . . . 261
Detectors Present and Future . . . 262

CHAPTER 13: STRUCTURED ILLUMINATION METHODS

Rainer Heintzmann

Introduction . . . 265
Experimental Considerations . . . 265
Pattern Generation . . . 266
Computing Optical Sections from Structured-Illumination Data . . . 268
Resolution Improvement by Structured Illumination . . . 270
Nonlinear Structured Illumination . . . 276
Summary . . . 276

CHAPTER 14: VISUALIZATION SYSTEMS FOR MULTI-DIMENSIONAL MICROSCOPY IMAGES

N.S. White

Introduction . . . 280
Definitions . . . 280
What Is the Microscopist Trying to Achieve? . . . 280
Criteria for Choosing a Visualization System . . . 281
Why Do We Want to Visualize Multi-Dimensional Laser-Scanning Microscopy Data? . . . 281
Data and Dimensional Reduction . . . 281
Objective or Subjective Visualization? . . . 281
Prefiltering . . . 281
Identifying Unknown Structures . . . 281
Highlighting Previously Elucidated Structures . . . 284
Visualization for Multi-Dimensional Measurements . . . 284
What Confocal Laser Scanning Microscopy Images Can the Visualization System Handle? . . . 286
Image Data: How Are Image Values Represented in the Program? . . . 286
What Dimensions Can the Images and Views Have? . . . 286
Standard File Formats for Calibration and Interpretation . . . 288
How Will the System Generate the Reconstructed Views? . . . 290
Assessing the Four Basic Steps in the Generation of Reconstructed Views . . . 290
Loading the Image Subregion . . . 290
Choosing a View: The 5D Image Display Space . . . 291
Mapping the Image Space into the Display Space . . . 294
How Do 3D Visualizations Retain the *z*-Information? . . . 296
Mapping the Data Values into the Display . . . 300
How Can Intensities Be Used to Retain *z*-Information? . . . 304
Hidden-Object Removal . . . 304
Adding Realism to the View . . . 306
How Can I Make Measurements Using the Reconstructed Views? . . . 312
Conclusion . . . 312

CHAPTER 15: AUTOMATED THREE-DIMENSIONAL IMAGE ANALYSIS METHODS FOR CONFOCAL MICROSCOPY

Badrinath Roysam, Gang Lin, Muhammad-Amri Abdul-Karim, Omar Al-Kofahi, Khalid Al-Kofahi, William Shain, Donald H. Szarowsk, and James N. Turner

Introduction . . . 316
Types of Automated Image Analysis Studies . . . 318

Common Types of Biological Image Objects 319
Specimen Preparation and Image Preprocessing Methods 319
Data Collection Guidelines for Image Analysis Purposes 319
Image Preprocessing Methods 320
General Segmentation Methods Applicable to Confocal Data 321
Bottom-Up Segmentation Methods 321
Top-Down Segmentation Methods 322
Hybrid Segmentation Methods Combining Bottom-Up and Top-Down Processing 322
Example Illustrating Blob Segmentation 322
Model-Based Object Merging 323
Example Illustrating Segmentation of Tube-Like Objects 324
Skeletonization Methods 324
Vectorization Methods 324
Example Combining Tube and Blob Segmentation 328
Registration and Montage Synthesis Methods 328
Methods for Quantitative Morphometry 331
Methods for Validating the Segmentation and Making Corrections 333
Analysis of Morphometric Data 334
Discussion, Conclusion, and Future Directions 335

CHAPTER 16: FLUOROPHORES FOR CONFOCAL MICROSCOPY: PHOTOPHYSICS AND PHOTOCHEMISTRY

Roger Y. Tsien, Lauren Ernst, and Alan Waggoner

Introduction 338
Photophysical Problems Related to High Intensity Excitation 338
Singlet State Saturation 338
Triplet State Saturation 339
Contaminating Background Signals 339
What Is the Optimal Intensity? 340
Photodestruction of Fluorophores and Biological Specimens 340
Dependency on Intensity or Its Time Integral? 340
Strategies for Signal Optimization in the Face of Photobleaching 341
Light Collection Efficiency 341
Spatial Resolution 341
Protective Agents 341
Fluorophore Concentration 342
Choice of Fluorophore 342
Fluorescent Labels for Antibodies, Other Proteins, and DNA Probes 342
Fluorescent Organic Dyes 342
Phycobiliproteins 343
DNA Probes 343
Luminescent Nanocrystals 343
Fluorescent Lanthanide Chelates 345
Fluorescent Indicators for Dynamic Intracellular Parameters 346
Membrane Potentials 346
Ion Concentrations 346
pH Indicators 346
Ca^{2+} Indicators 346
Oxygen Sensor 347
cAMP Indicators 347
Fatty Acid Indicator 347
Genetically Expressed Intracellular Fluorescent Indicators 348
Green Fluorescent Protein 348
Ligand-Binding Modules 348
Ion Indicators 348
Future Developments 348

CHAPTER 17: PRACTICAL CONSIDERATIONS IN THE SELECTION AND APPLICATION OF FLUORESCENT PROBES

Iain D. Johnson

Introduction 353
Selection Criteria for Dyes and Probes 353
Organic Dyes 353
Fluorescent Proteins: Green Fluorescent Protein and Phycobiliproteins 356
Quantum Dots 357
Multi-Photon Excitation 357
Introducing the Probe to the Specimen 358
Loading Methods 358
Target Abundance and Autofluorescence Considerations 360
Interactions of Probes and Specimens 361
Localization and Metabolism 361
Perturbation and Cytotoxicity 362
Under the Microscope 362
Photobleaching 362
Phototoxicity 363
Summary 364

CHAPTER 18: GUIDING PRINCIPLES OF SPECIMEN PRESERVATION FOR CONFOCAL FLUORESCENCE MICROSCOPY

Robert Bacallao, Sadaf Sohrab, and Carrie Phillips

Introduction 368
Characteristics of Fixatives 368
Glutaraldehyde 369
Formaldehyde 369
Fixation Staining and Mounting Methods 370
Glutaraldehyde Fixation 370
pH Shift/Formaldehyde Fixation 370
Immunofluorescence Staining 371
Mounting the Specimen 371
Critical Evaluation of Light Microscopy Fixation and Mounting Methods 371
Use of the Cell Height to Evaluate the Fixation Method 372
Use of Cell Height to Evaluate Mounting Media 373
Well-Defined Structures Can Be Used to Evaluate Fixation Methods 373
Comparison of *In Vivo* Labeled Cell Organelles with Immunolabeled Cell Organelles 374
General Notes 374
Labeling Samples with Two or More Probes 375

Triple Labeling 375
Preparation of Tissue Specimens 376
Labeling Thick Sections 376
Refractive Index Mismatch 377
Screening Antibodies on Glutaraldehyde-Fixed Specimens 377
Microwave Fixation 377
Conclusion 378

CHAPTER 19: CONFOCAL MICROSCOPY OF LIVING CELLS

Michael E. Dailey, Erik Manders, David R. Soll, and Mark Terasaki

Introduction 381
Overview of Living-Cell Confocal Imaging Techniques 382
Time-Lapse Fluorescence Imaging 382
Multi-Channel Time-Lapse Fluorescence Imaging . . . 382
Spectral Imaging and Linear Unmixing 382
Fluorescence Recovery After Photobleaching 382
Fluorescence Loss in Photobleaching 382
Fluorescence Resonance Energy Transfer 382
Fluorescence Lifetime Imaging 382
Fluorescence Correlation Spectroscopy 383
Fluorescence Speckle Microscopy 383
Photo-Uncaging/Photoactivation 383
Optical Tweezers/Laser Trapping 383
Physiological Fluorescence Imaging 383
Combining Fluorescence and Other Imaging Modalities 383
General Considerations for Confocal Microscopy of Living Cells 386
Maintenance of Living Cells and Tissue Preparations 387
Fluorescent Probes 387
Minimizing Photodynamic Damage 389
The Online Confocal Community 390
A Convenient Test Specimen 390
Specific Example I: Visualizing Chromatin Dynamics Using Very Low Light Levels 390
Phototoxicity 390
Reduction of Phototoxicity 391
Improving Image Quality in Low-Dose Microscopy 391
Low-Dose Imaging Conclusion 391
Specific Example II: Multi-Dimensional Imaging of Microglial Cell Behaviors in Live Rodent Brain Slices 392
Preparation of Central Nervous System Tissue Slices 393
Fluorescent Staining 393
Maintaining Tissue Health on the Microscope Stage 393
Imaging Methods 394
Imaging Deep Within Tissue 395
Keeping Cells in Focus 395
Handling the Data 395
Results 396
Conclusion 396
Future Directions 398

CHAPTER 20: ABBERATIONS IN CONFOCAL AND MULTI-PHOTON FLUORESCENCE MICROSCOPY INDUCED BY REFRACTIVE INDEX MISMATCH

Alexander Egner and Stefan W. Hell

Introduction 404
The Situation 404
Theory 404
Results of Theoretical Calculations 407
Experiments 409
Other Considerations 410
Dry Objectives 410
Refractive Index, Wavelength, and Temperature 411
Spherical Aberration Correction 411
Conclusion 412
Consequences 412
Practical Strategies to Reduce Refractive Index Mismatch 412

CHAPTER 21: INTERACTION OF LIGHT WITH BOTANICAL SPECIMENS

Ping-Chin Cheng

Introduction 414
Light Attenuation in Plant Tissue 414
Linear Absorption 414
Nonlinear Absorption 416
Scattering 417
Refractive Index Heterogeneity 418
Birefringent Structures in Plant Cells 420
Fluorescence Properties of Plants 421
Changes in Emission Spectra Depending on One- Versus Two-Photon Excitation 421
Microspectroscopy 421
Light–Specimen Interaction (Fluorescence Emission) 425
Harmonic Generation Properties 428
The Effect of Fixation on the Optical Properties of Plants 428
Living Plant Cells 429
Callus, Suspension Culture Cells and Protoplasts 429
Meristem 430
Stem and Root 430
Microspores and Pollen Grains 431
Cuticles, Hairs, and Waxes 434
Storage Structures 435
Mineral Deposits 436
Primary and Secondary Cell Walls 438
Fungi 438
Conclusion 439

CHAPTER 22: SIGNAL-TO-NOISE RATIO IN CONFOCAL MICROSCOPES

Colin J.R. Sheppard, Xiaosong Gan, Min Gu, and Maitreyee Roy

Introduction 442
Sources of Noise 442
Shot Noise and Quantum Efficiency 442
Background Noise 443

Signal Level in Confocal Microscopes 444
Signal-to-Noise Ratio for Confocal Microscopes 445
Q_E, N1, and Stain Level 445
N2 and Detectability 446
Multi-Photon Fluorescence Microscopy 447
Designs of Confocal Microscopes 447
Sampling 448
Comparative Performance of Fluorescence Microscopes 448
Bleaching-Limited Performance 448
Saturation-Limited Performance 450
Effects of Scanning Speed 450
3D Imaging 451
Summary 451

CHAPTER 23: COMPARISON OF WIDEFIELD/DECONVOLUTION AND CONFOCAL MICROSCOPY FOR THREE-DIMENSIONAL IMAGING

Peter J. Shaw

Introduction 453
The Point Spread Function: Imaging as a Convolution 453
Limits to Linearity and Shift Invariance 457
Deconvolution 457
Practical Differences 458
Temporal Resolution 458
Combination of Charged-Coupled Device and Confocal Imaging 458
Integration of Fluorescence Intensity 459
Resolution, Sensitivity, and Noise 459
Fluorescence Excitation 459
Fluorescent Light Detection 459
Gain Register Charge-Coupled Devices 460
Out-of-Focus Light 461
Model Specimens 461
The Best Solution: Deconvolving Confocal Data 461
Practical Comparisons 463
Conclusion 466
Summary 467

CHAPTER 24: BLIND DECONVOLUTION

Timothy J. Holmes, David Biggs, and Asad Abu-Tarif

Introduction 468
Purposes of Deconvolution 468
Advantages and Limitations 468
Principles 472
Data Collection Model 472
Maximum Likelihood Estimation 472
Algorithms 472
Different Approaches 475
3D 475
2D Image Filtering 476
Data Corrections 477
Light Source and Optics Alignment 477
Newest Developments 478
Subpixel 478
Polarized Light 479
Live Imaging 480
More Examples 480
Blind Deconvolution and Spherical Aberration 480
Widefield Fluorescence Simulation 481
Spinning-Disk Confocal 481
Two Photon 481
Speed 482
Future Directions 483
Summary of Main Points 483

CHAPTER 25: IMAGE ENHANCEMENT BY DECONVOLUTION

Mark B. Cannell, Angus McMorland, and Christian Soeller

Introduction 488
Background 488
Image Formation 489
Forwards: Convolution and the Imaging System . . . 490
Properties of the Point Spread Function 492
Quantifying the Point Spread Function 492
The Missing Cone Problem 494
Noise 495
Deconvolution Algorithms 495
Nearest-Neighbor Deconvolution 495
Wiener Filtering 496
Nonlinear Constrained Iterative Deconvolution Algorithms 496
Comparison of Methods 497

CHAPTER 26: FIBER-OPTICS IN SCANNING OPTICAL MICROSCOPY

Peter Delaney and Martin Harris

Introduction 501
Key Fiber Technologies Relevant to Scanning Microscopy 501
Glass Made from Gas and Its Transmission Properties 501
Step Index and Gradient Index Optical Fibers 501
Modes in Optical Fibers 502
Evanescent Wave and Polarization Effects in Optical Fibers 503
Polarization-Maintaining Fibers 503
Fused Biconical Taper Couplers: Fiber-Optic Beam-Splitters 503
Microstructure Fibers 504
Fiber Image Transfer Bundles 504
Key Functions of Fibers in Optical Microscopes . . . 505
Optical Fiber for Delivering Light 505
Optical Fiber as a Detection Aperture 506
Same Fiber for Both Source and Confocal Detection 506
Fiber Delivery for Nonlinear Microscopy with Femtosecond Lasers 507
Large Core Fibers as Source or Detection Apertures 507
Benchtop Scanning Microscopes Exploiting Fiber Components 507
Miniaturized Scanning Confocal Microscope Imaging Heads 508
Miniature Confocal Imaging Heads Based on Coherent Imaging Bundles 508

Resolution and Optical Efficiency of Bundles 509
Bundle Imagers for *In Vivo* Studies in Animals 509
Scan Heads Based on Single Fibers with Miniature Scanning Mechanisms 510
Vibrating the Fiber Tip 510
Vibrating the Lens and Fiber 510
Scanning with Micromirrors 511
Scanning Fiber Confocal Microscopes for *In Vivo* Imaging in Animals 512
Implementations for Clinical Endomicroscopy 513
Summary 513

CHAPTER 27: FLUORESCENCE LIFETIME IMAGING IN SCANNING MICROSCOPY

H.C. Gerritsen, A. Draaijer, D.J. van den Heuvel, and A.V. Agronskaia

Introduction 516
Fluorescence, Lifetime, and Quantum Efficiency 516
Fluorescence Lifetime Spectroscopy 516
Fluorescence Lifetime Imaging Applications 516
Fluorescence Resonance Energy Transfer 517
Fluorescence Lifetime Imaging Methods 518
Introduction 518
Lifetime Sensing in the Frequency Domain 518
Fluorescence Lifetime Sensing in the Time Domain 520
Comparison of Confocal Fluorescence Lifetime Imaging Methods 523
Applications 527
Multi-Labeling and Segmentation 527
Ion-Concentration Determination 528
Probes for Fluorescence Lifetime Microscopy 530
Summary 532

CHAPTER 28: MULTI-PHOTON MOLECULAR EXCITATION IN LASER-SCANNING MICROSCOPY

Winfried Denk, David W. Piston, and Watt W. Webb

Introduction 535
Physical Principles of Multi-Photon Excitation and Their Implications for Image Formation 535
Physics of Multi-Photon Excitation 535
Optical Pulse Length 537
Excitation Localization 538
Detection 538
Wavelengths 538
Resolution 539
Photodamage: Heating and Bleaching 539
Instrumentation 540
Lasers and the Choice of Excitation Wavelengths 540
Detection 541
Optical Aberrations 542
Pulse Spreading Due to Group Delay Dispersion 543
Control of Laser Power 543
Resonance and Non-Mechanical Scanning 543
Chromophores (Fluorophores and Caged Compounds) 543
Two-Photon Absorption Cross-Sections 543
Caged Compounds 544
Cell Viability During Imaging 544
Applications 545
Calcium Imaging 545
Uncaging and Photobleaching 545
Autofluorescence 545
Developmental Biology 545
In Vivo (Intact Animal) Imaging 545
Outlook 545

CHAPTER 29: MULTIFOCAL MULTI-PHOTON MICROSCOPY

Jörg Bewersdorf, Alexander Egner, and Stefan W. Hell

Introduction 550
Background 550
Determination of the Optimum Degree of Parallelization 550
Experimental Realization 551
A Multi-Focal Multi-Photon Microscopy Setup Using a Nipkow-Type Microlens Array 551
Resolution 552
Time Multiplexing as a Solution to Interfocal Crosstalk 553
Alternative Realizations 554
Advanced Variants of Multi-Focal Multi-Photon Microscopy 555
Space Multiplexing 555
Fluorescence Lifetime Imaging 555
Second Harmonic Generation Multi-Focal Multi-Photon Microscopy 556
Multi-Focal Multi-Photon Microscopy-4Pi Microscopy 556
Imaging Applications 556
Limitations 556
Current Developments 558
Summary 559

CHAPTER 30: 4Pi MICROSCOPY

Jörg Bewersdorf, Alexander Egner, and Stefan W. Hell

Introduction 561
Theoretical Background 562
The Point Spread Function 562
The z-Response and the Axial Resolution 563
The Optical Transfer Function 563
Multi-Focal Multi-Photon Microscopy–4Pi Microscopy 563
Space Invariance of the Point Spread Function 564
Live Mammalian Cell 4Pi Imaging 564
Type C 4Pi Microscopy with the Leica TCS 4PI 565
Resolution 567
Type C 4Pi Imaging in Living Cells 568
Summary and Outlook 568

CHAPTER 31: NANOSCALE RESOLUTION WITH FOCUSED LIGHT: STIMULATED EMISSION DEPLETION AND OTHER REVERSIBLE SATURABLE OPTICAL FLUORESCENCE TRANSITIONS MICROSCOPY CONCEPTS

Stefan W. Hell, Katrin I. Willig, Marcus Dyba, Stefan Jakobs, Lars Kastrup, and Volker Westphal

The Resolution Issue . . . 571
Breaking the Diffraction Barrier: The Concept of Reversible Saturable Optical Fluorescence Transitions . . . 571
Different Approaches of Reversible Saturable Optical Fluorescence Transitions Microscopy . . . 573
Stimulated Emission Depletion Microscopy . . . 574
Challenges and Outlook . . . 577

CHAPTER 32: MASS STORAGE, DISPLAY, AND HARD COPY

Guy Cox

Introduction . . . 580
Mass Storage . . . 580
- Data Compression . . . 580
- Removable Storage Media . . . 585
- Random-Access Devices . . . 586
- Solid State Devices . . . 588

Display . . . 588
- Monitors . . . 588
- Liquid Crystal Displays . . . 589
- Data Projectors . . . 590

Hard Copy . . . 590
- Photographic Systems . . . 590
- Digital Printers . . . 591

Conclusion . . . 593
Summary . . . 593
- Bulk Storage . . . 593
- Display . . . 594
- Hard Copy . . . 594

CHAPTER 33: COHERENT ANTI-STOKES RAMAN SCATTERING MICROSCOPY

X. Sunney Xie, Ji-Xin Cheng, and Eric Potma

Introduction . . . 595
Unique Features of Coherent Anti-Stokes Raman Scattering Under the Tight-Focusing Condition . . . 596
Forward and Backward Detected Coherent Anti-Stokes Raman Scattering . . . 597
Optimal Laser Sources for Coherent Anti-Stokes Raman Scattering Microscopy . . . 599
Suppression of the Non-Resonant Background . . . 600
- Use of Picosecond Instead of Femtosecond Pulses . . . 600
- Epi-Detection . . . 600
- Polarization-Sensitive Detection . . . 600
- Time-Resolved Coherent Anti-Stokes Raman Scattering Detection . . . 600
- Phase Control of Excitation Pulses . . . 600

Multiplex Coherent Anti-Stokes Raman Scattering Microspectroscopy . . . 602
Coherent Anti-Stokes Raman Scattering Correlation Spectroscopy . . . 602
Coherent Anti-Stokes Raman Scattering Microscopy Imaging of Biological Samples . . . 603
Conclusions and Perspectives . . . 604

CHAPTER 34: RELATED METHODS FOR THREE-DIMENSIONAL IMAGING

J. Michael Tyszka, Seth W. Ruffins, Jamey P. Weichert, Michael J. Paulus, and Scott E. Fraser

Introduction . . . 607
Surface Imaging Microscopy and Episcopic Fluorescence Image Capture . . . 607
Optical Coherence Tomography . . . 609
Optical Projection Tomography . . . 610
Light Sheet Microscopy . . . 613
- Optical Setup . . . 613

Micro-Computerized Tomography Imaging . . . 614
- Operating Principle . . . 614
- Contrast and Dose . . . 614
- Computed Tomography Scanning Systems . . . 615

Magnetic Resonance Microscopy . . . 618
- Basic Principles of Nuclear Magnetic Resonance . . . 618
- Magnetic Resonance Image Formation . . . 619
- Magnetic Resonance Microscopy Hardware . . . 622
- Strengths and Limitations of Magnetic Resonance Microscopy . . . 622
- Image Contrast in Magnetic Resonance Microscopy . . . 622
- Magnetic Resonance Microscopy Applications . . . 623
- Future Development of Magnetic Resonance Microscopy . . . 624

Conclusion . . . 624

CHAPTER 35: TUTORIAL ON PRACTICAL CONFOCAL MICROSCOPY AND USE OF THE CONFOCAL TEST SPECIMEN

Victoria Centonze and James B. Pawley

Introduction . . . 627
- Getting Started . . . 627
- Bleaching — The Only Thing That Really Matters . . . 627

Getting a Good Confocal Image . . . 629
- Simultaneous Detection of Backscattered Light and Fluorescence . . . 631

New Controls . . . 631
- Photon Efficiency . . . 631
- Pinhole Size . . . 631
- Stray Light . . . 632
- Is the Back-Focal Plane Filled? . . . 633
- Pinhole Summary . . . 633
- Statistical Considerations in Confocal Microscopy . . . 633
- The Importance of Pixel Size . . . 634
- Measuring Pixel Size . . . 635
- Over-Sampling and Under-Sampling . . . 635
- Nyquist Reconstruction and Deconvolution . . . 635
- Pixel Size Summary . . . 636

Using a Test Specimen 636
Why Use a Test Specimen? 636
Description of the Test Specimen 636
Using the Test Specimen 637
The Diatom: A Natural 3D Test Specimen 638
Reasons for Poor Performance 640
Sampling Problems 640
Optical Problems 640
Imaging Depth 643
Singlet-State Saturation 643
Which 3D Method Is Best? 644
Optimal 3D Light Microscopy Summary 646
Things to Remember About Deconvolution 646
Decision Time 646
Multi-Photon Versus Single-Photon Excitation 646
Widefield Versus Beam Scanning 647
Summary 647

CHAPTER 36: PRACTICAL CONFOCAL MICROSCOPY

Alan R. Hibbs, Glen MacDonald, and Karl Garsha

The Art of Imaging by Confocal Microscopy 650
Balancing Multiple Parameters 650
Monitoring Instrument Performance 650
Illumination Source 650
Scan Raster and Focus Positioning 651
Optical Performance and Objective Lenses 652
Signal Detection 660
Optimizing Multi-Labeling Applications 663
Control Samples Establish the Limits 663
Separation of Fluorescence into Spectral Regions 664
Sequential Channel Collection to Minimize Bleed-Through 664
Spectral Unmixing 664
Colocalization 667
Image Collection for Colocalization 667
Quantifying Colocalization 668
Spatial Deconvolution in Colocalization Studies 668
Discussion 670

CHAPTER 37: SELECTIVE PLANE ILLUMINATION MICROSCOPY

Jan Huisken, Jim Swoger, Steffen Lindek, and Ernst H.K. Stelzer

Introduction 672
Combining Light Sheet Illumination and Orthogonal Detection 672
Selective Plane Illumination Microscopy Setup 673
Lateral Resolution 674
Light Sheet Thickness and Axial Resolution 674
Applications 675
Processing Selective Plane Illumination Microscopy Images/Multi-View Reconstruction 675
Summary 678

CHAPTER 38: CELL DAMAGE DURING MULTI-PHOTON MICROSCOPY

Karsten König

Introduction 680
Photochemical Damage in Multi-Photon Microscopes 682
Absorbers and Targets in Biological Specimens 682
Laser Exposure Parameters 682
Evidence for Near Infrared-Induced Reactive Oxygen Species Formation 683
Evidence for Near Infrared-Induced DNA Strand Breaks 684
Photodynamic-Induced Effects 684
Photothermal Damage 685
Damage by Optical Breakdown 685
Modifications of Ultrastructure 685
Influence of Ultrashort Near Infrared Pulses on Reproductive Behavior 686
Nanosurgery 686
Conclusion 687

CHAPTER 39: PHOTOBLEACHING

Alberto Diaspro, Giuseppe Chirico, Cesare Usai, Paola Ramoino, and Jurek Dobrucki

Introduction 690
Photobleaching 691
Photobleaching Mechanisms 691
Reducing Photobleaching 693
Photobleaching at the Single-Molecule Level 696
Photobleaching of Single Molecules 697
Photobleaching and Photocycling of Single Fluorescent Proteins 698
Bleaching and Autofluorescence 698
Other Fluorescent Proteins 698
Conclusion 699

CHAPTER 40: NONLINEAR (HARMONIC GENERATION) OPTICAL MICROSCOPY

Ping-Chin Cheng and C.K. Sun

Introduction 703
Harmonic Generation 704
Second Harmonic Generation 704
Third Harmonic Generation 705
Multi-Photon Absorption and Fluorescence 705
Light Sources and Detectors for Second Harmonic Generation and Third Harmonic Generation Imaging 706
Nonlinear Optical Microscopy Setup 708
Optically Active Biological Structures 710
Optically Active Structures in Plants 710
Optically Active Structures in Animal Tissues 714
Polarization Dependence of Second Harmonic Generation 717
Summary 719

CHAPTER 41: IMAGING BRAIN SLICES

Ayumu Tashiro, Gloster Aaron, Dmitriy Aronov, Rosa Cossart, Daniella Dumitriu, Vivian Fenstermaker, Jesse Goldberg, Farid Hamzei-Sichani, Yuji Ikegaya, Sıla Konur, Jason MacLean, Boaz Nemet, Volodymyr Nikolenko, Carlos Portera-Cailliau, and Rafael Yuste

Introduction 722

Making Brain Slices . . . 722
Acute Slices . . . 722
Cultured Slices . . . 724
Labeling Cells . . . 724
Biolistic Transfection . . . 724
Genetic Manipulation with Dominant-Negative and Constitutively Active Mutants . . . 725
Diolistics and Calistics . . . 726
Dye Injection with Whole-Cell Patch Clamp . . . 726
Slice Loading and "Painting" with Acetoxymethyl Ester Indicators . . . 726
Green Fluorescent Protein Transgenic Mice . . . 727
Imaging Slices . . . 727
Two-Photon Imaging of Slices . . . 727
Slice Chamber Protocol . . . 727
Choice of Objectives . . . 727
Beam Collimation and Pulse Broadening . . . 728
Image Production, Resolution, and *z*-Sectioning . . . 729
Choice of Indicators for Two-Photon Imaging of Calcium . . . 729
Photodamage . . . 729
Second Harmonic Imaging . . . 729
Silicon-Intensified Target Camera Imaging . . . 730
Morphological Processing and Analysis . . . 730
Biocytin Protocol . . . 730
Anatomy with a Two-Photon/Neurolucida System . . . 731
Correlated Electron Microscopy . . . 731
Morphological Classification of Neurons Using Cluster Analysis . . . 731
Image Processing . . . 732
Compensation for the Drift and the Vibration of the Slices . . . 732
Alignment Based on the Overlap Between Images . . . 732
Alignment Based on the Center of Mass . . . 732
Online Cell Detection of Neurons . . . 733
Image De-Noising Using Wavelets . . . 734
Summary . . . 734

CHAPTER 42: FLUORESCENT ION MEASUREMENT

Mark B. Cannell and Stephen H. Cody

Introduction . . . 736
The Limiting Case . . . 736
Choice of Indicator . . . 737
Introducing the Indicators into Cells . . . 738
Care of Fluorescent Probes . . . 739
Interpretation of Measurements . . . 740
Kinetics . . . 741
Calibration . . . 742
Conclusion . . . 745

CHAPTER 43: CONFOCAL AND MULTI-PHOTON IMAGING OF LIVING EMBRYOS

Jeff Hardin

Introduction . . . 746
Into the Depths: Embryos Are Thick, Refractile, and Susceptible to Photodamage . . . 746
Imaging Embryos Often Requires "4D" Imaging . . . 746
The Quest for Better Resolution: Aberration and the Challenge of Imaging Thick Embryos . . . 747
Embryos Are Highly Scattering and Refractile Specimens . . . 747
Imaging Embryos Involves Inherent Trade-Offs . . . 747
Common Themes in Living Embryo Imaging Have System-Specific Solutions . . . 748
Dealing with Depth: Strategies for Imaging Thick Specimens . . . 748
Avoiding the Thickness Dilemma: Going Small . . . 748
Grazing the Surface: Superficial Optical Sections Are Often Sufficient . . . 748
Up from the Deep: Explants Can Reduce the Thickness of Specimens Dramatically . . . 748
Multi-Photon Microscopy Can Penetrate More Deeply into Specimens . . . 749
Selective Plane Illumination Can Provide Optical Sectioning in Very Thick Specimens . . . 751
Deconvolution and Other Post-Acquisition Processing . . . 751
Striving for Speed: Strategies for Reducing Specimen Exposure . . . 753
Simple Solutions: Reducing Image Dimensions, Increasing Slice Spacing, and Scan Speed . . . 753
Disk-Scanning Confocal Microscopy Allows High-Speed Acquisition . . . 754
Additional Hardware Improvements Can Increase Acquisition Speed . . . 754
Localizing Label: Strategies for Increasing Effective Contrast in Thick Specimens . . . 755
Addition of Labeled Proteins to Embryos . . . 756
Expressing Green Fluorescent Protein and mRFP Constructs in Embryos Allows Dynamic Analysis of Embryos at Multiple Wavelengths . . . 756
Using Selective Labeling to Reduce the Number of Labeled Structures . . . 757
Bulk Vital Labeling Can Enhance Contrast . . . 760
Seeing in Space: Strategies for 4D Visualization . . . 761
Depicting Embryos in Time and Space: 2D + Time Versus 3D + Time . . . 762
Other Uses for Confocal and Multi-Photon Microscopy in Imaging and Manipulating Embryos . . . 764
Multi-Photon–Based Ablation . . . 764
Fluorescence Resonance Energy Transfer . . . 764
Conclusions: A Bright Future for 3D Imaging of Living Embryos . . . 766

CHAPTER 44: IMAGING PLANT CELLS

Nuno Moreno, Susan Bougourd, Jim Haseloff, and José A. Feijó

Introduction . . . 769
The Ever Present Problem of Autofluorescence . . . 770
Single-Photon Confocal Microscopy . . . 772
Staining Plant Tissues . . . 774
Clearing Intact Plant Material . . . 774
3D Reconstruction . . . 775
3D Segmentation . . . 776
Two-Photon Excitation: Are Two Better Than One? . . . 778
Improved Signal-to-Noise Ratio and Dynamic Range . . . 778

Imaging Thick/Opaque Specimens 779
Fading, Vital Imaging, and Cell Viability 779
Two-Photon Imaging of Plant Cells and Organelles 782
Two-Photon Excitation Imaging of Green Fluorescent Protein 782
Dynamic Imaging 783
Deconvolution 784
Conclusion 785

CHAPTER 45: PRACTICAL FLUORESCENCE RESONANCE ENERGY TRANSFER OR MOLECULAR NANOBIOSCOPY OF LIVING CELLS

Irina Majoul, Yiwei Jia, and Rainer Duden

Introduction 788
How to Make a Good Science 788
Beauty, Functionality, Cell Cycle, and Living-Cell Imaging 790
Fluorescence Resonance Energy Transfer Theory . . . 790
Fluorescent Proteins and Fluorescence Resonance Energy Transfer 794
Qualitative Analysis 795
Preparation 795
Nanobioscopy of Protein-Protein Interactions with Fluorescence Resonance Energy Transfer . . . 795
Methods of Fluorescence Resonance Energy Transfer Measurement 795
Sensitized Emission of Acceptor 795
Donor Fluorescence 796
Acceptor Bleach 797
Fluorescent Proteins as Fluorescence Resonance Energy Transfer Pairs 798
Cyan Fluorescent Protein and Yellow Fluorescent Protein — The Commonly Used Fluorescence Resonance Energy Transfer Pair 798
Cyan Fluorescent Protein or Green Fluorescent Protein Forms a Fluorescence Resonance Energy Transfer Pair with mRFP1 798
Fluorescence Resonance Energy Transfer-Based Sensors 798
Fluorescence Resonance Energy Transfer and Other Complementary Methods 799
Fluorescence Resonance Energy Transfer and Fluorescence Lifetime Imaging Microscope 799
Fluorescence Recovery After Photobleaching and Fluorescence Loss in Photobleaching 801
Fluorescence Resonance Energy Transfer and Fluorescence Correlation Spectroscopy 801
Fluorescence Resonance Energy Transfer and Total Internal Reflection Fluorescence 801
Quantum Dots and Fluorescence Resonance Energy Transfer 801
Cloning and Expression of Fluorescent Constructs for Fluorescence Resonance Energy Transfer 801
Cloning of Fluorescent Chimeras 801
Functional Activity of Expressed Constructs 802
Expression and Over-Expression 802
Methods for Introducing Chromophores into Living Cells 803
Electroporation 803
Transfection Reagents 803
Microinjection 803
Future Perspectives: 3D Microscopy, Biological Complexity, and *In Vivo* Molecular Imaging 804
***In Vivo* Molecular Imaging** 806

CHAPTER 46: AUTOMATED CONFOCAL IMAGING AND HIGH-CONTENT SCREENING FOR CYTOMICS

Maria A. DeBernardi, Stephen M. Hewitt, and Andres Kriete

Introduction 809
Platforms Used for Automated Confocal Imaging 810
Types of Assays 811
3D Cell Microarray Assays 815
Data Management and Image Informatics 816
Conclusion 817

CHAPTER 47: AUTOMATED INTERPRETATION OF SUBCELLULAR LOCATION PATTERNS FROM THREE DIMENSIONAL CONFOCAL MICROSCOPY

Ting Zhao and Robert F. Murphy

Introduction 818
Protein Subcellular Location 818
Overview of 2D Dataset Analysis 818
High-Resolution 3D Datasets 820
3DHeLa 820
3D3T3 820
Image Acquisition Considerations When Using Automated Analysis 821
Image Processing and Analysis 822
Segmentation of Multi-Cell Images and Preprocessing 822
3D Subcellular Location Features 822
Automated Classification of Location Patterns 824
Classification of 3DHeLa Dataset 824
Downsampled Images with Different Gray Scales 824
Clustering of Location Patterns: Location Proteomics 825
Exclusion of Outliers 825
Determination of Optimal Clustering 825
Statistical Comparison of Location Patterns 826
Image Database Systems 827
Future Directions 827

CHAPTER 48: DISPLAY AND PRESENTATION SOFTWARE

Felix Margadant

Introduction 829
Testing 830
"Static" Image Performance 831
Brightness 832
Resolution: Changing the Display Size of Your Images 832
Compression 835
Motion Pictures 836
Coding Limitations 838

Up-Sampling or Frame Rate Matching 838
Motion Picture Artifacts 839
The MPEG Formats 840
MPEG Display Formats 840
Very High Resolutions 841
Movie Compression and Entropy 841
Performance Benchmark 841
Storing Your Presentation for Remote Use 842
Taking Your Presentation on the Road: Digital Rights Management and Overlaying 844

CHAPTER 49: WHEN LIGHT MICROSCOPE RESOLUTION IS NOT ENOUGH: CORRELATIONAL LIGHT MICROSCOPY AND ELECTRON MICROSCOPY

Paul Sims, Ralph Albrecht, James B. Pawley, Victoria Centonze, Thomas Deerinck, and Jeff Hardin

Introduction 846
Early Correlative Microscopy 846
Early 4D Microscopy 846
Correlative Light Microscope/Electron Microscope Today 846
Light Microscope and Electron Microscope Have Different Requirements 846
Finding the Same Cell Structure in Two Different Types of Microscope: Light Microscope/Scanning Electron Microscope 850
Finding the Same Cell Structure in Two Different Types of Microscope: Light Microscope/Transmission Electron Microscope 852
Cryo-Immobilization Followed by Post-Embedding Confocal Laser Scanning Microscopy on Thin Sections 856
Tiled Montage Transmission Electron Microscope Images Aid Correlation 858
Conclusion 860

CHAPTER 50: DATABASES FOR TWO- AND THREE-DIMENSIONAL MICROSCOPICAL IMAGES IN BIOLOGY

Steffen Lindek, Nicholas J. Salmon, and Ernst H.K. Stelzer

Introduction 861
Data and Metadata Management in Microscopes 861
Recent Developments 861
Image Information Management 862
The Aims of Modern Microscope System Design . . . 862
Instrument Database Model 864
System Requirements 864
Image Database Model 864
Selected Projects 865
BioImage 865
Biomedical Image Library 866
Scientific Image DataBase 866
Other Projects 866
Criteria and Requirements for Microscopy Databases 866
User Interface 866
Query by Content 866
Metadata Structure 867
Digital Rights Management 867
Future Prospects 867

CHAPTER 51: CONFOCAL MICROSCOPY OF BIOFILMS — SPATIOTEMPORAL APPROACHES

R.J. Palmer, Jr., Janus A.J. Haagensen, Thomas R. Neu, and Claus Sternberg

Introduction 870
Sample Presentation 870
Flowcells and Other Perfusion Chambers 870
Water-Immersible Lenses 872
Upright Versus Inverted Microscopes 872
Setup of a Flow Chamber System Setup — A Practical Example 872
Making Bacteria Fluorescent 873
Fluorescent Proteins 873
Stains 874
Nucleic Acid Stains 874
Live/Dead Stain 875
Fluorescence *In Situ* Hybridization 875
General Procedure for Embedding of Flowcell-Grown Biofilms for Fluorescence *In Situ* Hybridization . . . 876
Antibodies 877
Preparation of Labeled Primary Antibodies 878
Imaging Bacteria Without Fluorescence 879
Imaging Extracellular Polymeric Substances in Biofilms 879
Application of Two-Photon Laser-Scanning Microscopy for Biofilm Analysis 882
Limitations of Confocal Laser Scanning Microscopy and Two-Photon Laser-Scanning Microscopy in Biofilm Analysis 884
Temporal Experiments 885
Time-Lapse Confocal Imaging 885
Summary and Future Directions 887

CHAPTER 52: BIBLIOGRAPHY OF CONFOCAL MICROSCOPY

Robert H. Webb

A. Book and Review Articles 889
B. Historical Interest 889
C. Theory (Mostly) 890
D. Technical 891
E. General 891
F. Adaptive Optics 892
G. Differential 892
H. Display 892
I. Fiber-Optic Confocal Microscopes 893
J. Index Mismatch 893
K. Multiplex 894
L. Nonlinear 894
M. Polarization 894
N. Profilometry 895
O. Point Spread Function 895
P. Pupil Engineering 896
Q. Thickness 896
R. Turbidity 896
S. Variants on the Main Theme 897

APPENDIX 1: PRACTICAL TIPS FOR TWO-PHOTON MICROSCOPY

Mark B. Cannell, Angus McMorland, and Christian Soeller

Introduction . . . 900
Laser Safety . . . 900
Laser Alignment . . . 900
Testing Alignment and System Performance . . . 900
Laser Settings and Operation . . . 901
Monitoring Laser Performance . . . 901
Power Levels and Trouble-Shooting . . . 903
Choice of Pulse Length . . . 903
Controlling Laser Power . . . 903
Am I Seeing Two-Photon Excited Fluorescence or 904
Stray Light and Non-Descanned Detection . . . 904
Laser Power Adjustment for Imaging at Depth . . . 904
Simultaneous Imaging of Multiple Labels . . . 904
Minimize Exposure During Orientation and Parameter Setting . . . 905
Ultraviolet-Excited Fluorochromes . . . 905

APPENDIX 2: LIGHT PATHS OF THE CURRENT COMMERCIAL CONFOCAL LIGHT MICROSCOPES USED IN BIOLOGY

James B. Pawley

Introduction . . . 906
BD-CARV II . . . 907
LaVision-BioTec TriM-Scope . . . 907
Leica TCS SP2 AOBS-MPRS . . . 910
Nikon C1si . . . 911
Olympus Fluoview 1000-DSU . . . 912
Visitech VT Infinity-VT-eye . . . 914
Yokogawa CSU 22 . . . 915
Zeiss LSM-5-LIVE Fast Slit Scanner–LSM 510 META–FCS . . . 916

APPENDIX 3: MORE THAN YOU EVER REALLY WANTED TO KNOW ABOUT CHARGE-COUPLED DEVICES

James B. Pawley

Introduction . . . 919
Part I: How Charge-Coupled Devices Work . . . 919
Charge Coupling . . . 919
Readout Methods . . . 920
What Could Go Wrong? . . . 920
Quantum Efficiency . . . 920
Edge Effects . . . 921
Charge Loss . . . 921
Leakage or "Dark Charge" . . . 921
Blooming . . . 921
Incomplete Charge Transfer . . . 923
Charge Amplifiers . . . 923
What Is a Charge Amplifier? . . . 923
FET Amplifier Performance . . . 924
Noise Sources in the Charge-Coupled Device . . . 924
Fixed Pattern Noise . . . 924
Noise from the Charge Amplifier . . . 925
Where Is Zero? . . . 925
A New Idea: The Gain Register Amplifier!! . . . 925
Of Course, There Is One Snag! . . . 926
Part II: Evaluating a Charge-Coupled Device . . . 927
A. Important Charge-Coupled Device Specs for Live-Cell Stuff! . . . 927
B. Things That Are (Almost!) Irrelevant When Choosing a Charge-Coupled Device for Live-Cell Microscopy . . . 929
C. A Test You Can Do Yourself!!! . . . 930
D. Intensified Charge-Coupled Devices . . . 930

Index . . . 933

Contributors

Gloster Aaron
Department of Biological Sciences, Columbia University, New York, NY 10027, USA

Muhammad-Amri Abdul-Karim
Center for Subsurface Sensing and Imaging Systems, Rensselaer Polytechnic Institute, Troy, NY 12180, USA

Asad Abu-Tarif
AutoQuant Imaging, Inc., Watervliet, NY 12189, USA

A.V. Agronskaia
Department of Molecular Biophysics, Utrecht University, The Netherlands

Ralph Albrecht
Department of Animal Sciences, University of Wisconsin-Madison, Madison, WI, 53706, USA

Khalid Al-Kofahi
Center for Subsurface Sensing and Imaging Systems, Rensselaer Polytechnic Institute, Troy, NY 12180, USA

Omar Al-Kofahi
Center for Subsurface Sensing and Imaging Systems, Rensselaer Polytechnic Institute, Troy, NY 12180, USA

Dmitriy Aronov
Department of Biological Sciences, Columbia University, New York, NY 10027, USA

Jonathan Art
Department of Anatomy and Cell Biology, University of Illinois College of Medicine, Chicago, IL 60612, USA

Robert Bacallao
Division of Nephrology, Indiana University School of Medicine, Indianapolis, IN 40202, USA

Jörg Bewersdorf
Department of NanoBiophotonics, Max Planck Institute for Biophysical Chemistry, 37070 Göttingen, Germany

David Biggs
AutoQuant Imaging, Inc., Watervliet, NY 12189, USA

Susan Bougourd
Department of Biology, University of York, York YO10 5YW, UK

Mark B. Cannell
School of Medicine and Health Sciences, University of Auckland, New Zealand

Victoria Centonze
Department of Cellular and Structural Biology, Optical Imaging Facility, University of Texas Health Science Center at San Antonio, San Antonio, TX 78229, USA

Ji-Xin Cheng
Department of Chemistry and Chemical Biology, Harvard University, Cambridge, MA 02138, USA and Department of Biomedical Engineering, Purdue University, West Lafayette, IN 47907, USA

Ping-Chin Cheng
Department of Electrical Engineering, Advanced Microscopy and Imaging Laboratory, State University of New York, Buffalo, NY 14260, USA and Department of Biological Sciences, National University of Singapore, Singapore

Giuseppe Chirico
Department of Physics, University of Milano Bicocca, Milan, Italy and INFM, The National Institute for the Physics of Matter, Italy

Stephen H. Cody
Central Resource for Advanced Microscopy, Ludwig Institute for Cancer Research, PO Royal Melbourne Hospital, Parkville Victoria, 3050, Australia

Rosa Cossart
Department of Biological Sciences, Columbia University, New York, NY 10027, USA

Guy Cox
Electron Microscope Unit, University of Sydney, NSW 2006, Australia

Michael E. Dailey
Department of Biological Sciences, University of Iowa, Iowa City, IA 52242, USA

Maria A. DeBernardi
Department of Biology, The Johns Hopkins University, Baltimore, MD 20850, USA

Thomas Deerinck
National Center for Microscopy and Imaging Research, University of California-San Diego, La Jolla, CA 92093, USA

Peter Delaney
Optiscan Pty. Ltd., Mount Waverley MDC, Victoria, 3149, Australia

Winfried Denk
Max-Planck Institute for Medical Research, Heidelberg, Germany

Alberto Diaspro
Department of Physics, IFOM, LAMBS-MicroScoBio Research Center, University of Genoa, Genoa, Italy and INFM, The National Institute for the Physics of Matter, Italy

Jurek Dobrucki
Department of Biophysics, Laboratory of Confocal Microscopy and Image Analysis, Jagiellonian University, Kraków, Poland

A. Draaijer
Department of Analytical Sciences, TNO-Voeding, Utrechtseweg 48, 3704 HE Utrecht, The Netherlands

Rainer Duden
Royal Holloway University of London, School of Biological Sciences, Egham TW20 0WEX, UK

Daniella Dumitriu
Department of Biological Sciences, Columbia University, New York, NY 10027, USA

Marcus Dyba
Department of NanoBiophotonics, Max Planck Institute for Biophysical Chemistry, D-37018 Goettigen, Germany

Alexander Egner
Department of NanoBiophotonics, Max Planck Institute for Biophysical Chemistry, 37070 Göttingen, Germany

Lauren Ernst
Department of Biological Sciences and Molecular Biosensors and Imaging Center, Carnegie Mellon University, Pittsburgh, PA 15213, USA

José A. Feijó
Department Biologia Vegetal, Universidade de Lisboa, Faculdade de Ciências, Campo Grande, C2, PT-1749-016 Lisboa, Portugal

Vivian Fenstermaker
Department of Biological Sciences, Columbia University, New York, NY 10027, USA

Scott E. Fraser
Division of Biology, Beckman Institute (139–74), California Institute of Technology, Pasadena, CA 91125, USA

Xiaosong Gan
Centre for Microphotonics, Swinburne University, Australia

Karl Garsha
Imaging Technology Gray, Beckman Institute for Advanced Science Techology, Universtiy of Illinois at Urbana–Champaign, IL 61801, USA

H.C. Gerritsen
Department of Molecular Biophysics, Utrecht University, 3508 TA Utrecht, The Netherlands

Jesse Goldberg
Department of Biological Sciences, Columbia University, New York, NY 10027, USA

Enrico Gratton
Department of Physics, University of Illinois at Urbana-Champaign, Laboratory for Fluorescence Dynamics, Urbana, IL 61801, USA

Min Gu
Centre for Microphotonics, Swinburne University, Australia

Janus A.J. Haagensen
Center for Biomedical Microbiology, BioCentrum, Technical University of Denmark, 2800, Lyngby, Denmark

Farid Hamzei-Sichani
Department of Biological Sciences, Columbia University, New York, NY 10027, USA

Jeff Hardin
Department of Zoology, University of Wisconsin–Madison, Madison, WI 53706, USA

Martin Harris
Optiscan Pty. Ltd., Mount Waverley MDC, Victoria, 3149, Australia

Jim Haseloff
Department of Plant Sciences, University of Cambridge, Cambridge CB2 3EA, UK

Rainer Heintzmann
Randall Division, King's College London, London SE1 1UL, UK

Stefan W. Hell
Department of NanoBiophotonics, Max Planck Institute for Biophysical Chemistry, D-37018 Goettigen, Germany

Stephen M. Hewitt
Tissue Array Research Program, Laboratory of Pathology, Center for Cancer Research, National Cancer Institute, National Institutes of Health, Bethesda, MD 20886, USA

Alan R. Hibbs
Biocon, 2 Vista Court, Melbourne, VIC 3135, Australia

Timothy J. Holmes
AutoQuant Imaging, Inc., Watervliet, NY 12189, USA and Rensselaer Polytechnic Institute, Troy, NY 12180, USA

Lutz Höring
Carl Zeiss AG, 73447 Oberkochen, Germany

Jan Huisken
Light Microscopy Group, European Molecular Biology Laboratory (EMBL), 69012 Heidelberg, Germany

Yuji Ikegaya
Department of Biological Sciences, Columbia University, New York, NY 10027, USA

Shinya Inoué
Marine Biological Laboratory, Woods Hole, MA 02543, USA

Stefan Jakobs
Department of NanoBiophotonics, Max Planck Institute for Biophysical Chemistry, D-37108 Göttigen, Germany

Yiwei Jia
SEG, Olympus America Inc., Melville, NY 11747, USA

Iain D. Johnson
Molecular Probes, Inc., Eugene, OR 97402, USA

Rimas Juškaitis
Department of Engineering Science, University of Oxford, Oxford OX1 3PJ, UK

Lars Kastrup
Department of NanoBiophotonics, Max Planck Institute for Biophysical Chemistry, D-37108 Göttigen, Germany

H. Ernst Keller
Carl Zeiss, Inc., Thornwood, NY 10594, USA

Karsten König
Fraunhofer Institute of Biomedical Technology, D-661119 Saarbrücken, Germany

Sila Konur
Department of Biological Sciences, Columbia University, New York, NY 10027, USA

Andres Kriete
Coriell Institute for Medical Research and Drexel University, Philadelphia, PA 19104, USA

Gang Lin
Center for Subsurface Sensing and Imaging Systems, Rensselaer Polytechnic Institute, Troy, NY 12180, USA

Steffen Lindek
Light Microscopy Group, European Molecular Biology Laboratory (EMBL), 69012 Heidelberg, Germany

Glen MacDonald
V.M. Bloedel Hearing Research Center, University of Washington, Seattle, WA 98195, USA

Jason MacLean
Department of Biological Sciences, Columbia University, New York, NY 10027, USA

Irina Majoul
Royal Holloway University of London, School of Biological Sciences, Egham TW20 0WEX, UK

Erik Manders
Centre for Advanced Microscopy, Section of Molecular Cytology, Swammerdam Institute for Life Sciences, Faculty of Science, University of Amsterdam, 1090 GB Amsterdam, The Netherlands

Felix Margadant
Zurich, Switzerland

Angus McMorland
School of Medicine and Health Sciences, University of Auckland, New Zealand

Nuno Moreno
Centro de Biologia do Desenvolvimento, Instituto Gulbenkian de Ciência, PT-2780-156 Oeiras, Portugal

Robert F. Murphy
Departments of Biomedical Engineering and Biological Sciences and Center for Bioimage Informatics, Carnegie Mellon University, Pittsburgh, PA 15213, USA

Boaz Nemet
Department of Biological Sciences, Columbia University, New York, NY 10027, USA

Thomas R. Neu
Department of River Ecology, UFZ Center for Environmental Research Leipzig-Halle, 39114, Magdeburg, Germany

Volodymyr Nikolenko
Department of Biological Sciences, Columbia University, New York, NY 10027, USA

Andreas Nolte
Carl Zeiss MicroImaging GmbH, 37081, Goettingen, Germany

R.J. Palmer, Jr.
Oral Infection and Immunity Branch, National Institute of Dental and Craniofacial Research, National Institutes of Health, Bethesda, MD 20886, USA

Michael J. Paulus
ORNL and CTI-Concorde Microsystems, LLC, Knoxville, TN 37932, USA

James B. Pawley
Department of Zoology, University of Wisconsin–Madison, Madison, WI 53706, USA

Carrie Phillips
Division of Nephrology, Indianapolis, IN 40202, USA

David W. Piston
Vanderbilt University, Nashville, TN 37232, USA

Carlos Portera-Cailliau
Department of Biological Sciences, Columbia University, New York, NY 10027, USA

Eric Potma
Department of Chemistry and Chemical Biology, Harvard University, Cambridge, MA 02138, USA

Paola Ramoino
Department for the Study of the Territory and Its Resources, University of Genoa, Italy

Jens Rietdorf
Light Microscopy Group, European Molecular Biology Laboratory, 69012 Heidelberg, Germany

Maitreyee Roy
Department of Physical Optics, School of Physics, University of Sydney, NSW 2006, Australia

Badrinath Roysam
Center for Subsurface Sensing and Imaging Systems, Rensselaer Polytechnic Institute, Troy, NY 12180, USA

Seth W. Ruffins
Division of Biology, Beckman Institute (139–74), California Institute of Technology, Pasadena, CA 91125, USA

Nicholas J. Salmon
SLS Software Technologies GmbH, Heidelberg, Germany

William Shain
New York State Department of Health, The Wadsworth Center, Albany, NY 12201, USA

Peter J. Shaw
Department of Cell and Developmental Biology, John Innes Centre, Colney, Norwich NR4 7UH, UK

Colin J.R. Sheppard
Division of Bioengineering, National University of Singapore, Singapore 117576, and Department of Diagnostic Radiology, National University of Singapore, 119074, Singapore

Paul Sims
Department of Zoology, University of Wisconsin–Madison, Madison, WI 53706, USA

Christian Soeller
School of Medicine and Health Sciences, University of Auckland, New Zealand

Sadaf Sohrab
Division of Nephrology, Indianapolis, IN 40202, USA

David R. Soll
Carver/Emil Witschi Professor in the Biological Sciences and Director, W.M. Keck Dynamic Image Analysis Facility, Department of Biological Sciences, University of Iowa, Iowa City, IA 52242, USA

Ernst H.K. Stelzer
Light Microscopy Group, European Molecular Biology Laboratory 69012 Heidelberg, Germany

Claus Sternberg
Center for Biomedical Microbiology, BioCentrum, Technical University of Denmark, 2800, Lyngby, Denmark

C.K. Sun
Department of Electrical Engineering, National Taiwan University, Taipei, Taiwan, Republic of China

Jim Swoger
Light Microscopy Group, European Molecular Biology Laboratory 69012 Heidelberg, Germany

Donald H. Szarowsk
New York State Department of Health, The Wadsworth Center, Albany, NY 12201, USA

Ayumu Tashiro
Department of Biological Sciences, Columbia University, New York, NY 10027, USA

Mark Terasaki
Department of Physiology, University of Connecticut Health Center, Farmington, CT 06032, USA

Derek Toomre
Department of Cell Biology, Yale University School of Medicine, New Haven, CT 06520, USA

Roger Y. Tsien
Department of Pharmacology 0647, School of Medicine, University of California, San Diego, CA 92093, USA

James N. Turner
New York State Department of Health, The Wadsworth Center, Albany, NY 12201, USA

J. Michael Tyszka
Division of Biology, Beckman Institute (139–74), California Institute of Technology, Pasadena, CA 91125, USA

Cesare Usai
Institute of Biophysics, National Research Council, Genoa, Italy

D.J. van den Heuvel
Department of Molecular Biophysics, Utrecht University, 3508 TA Utrecht, The Netherlands

Martin J. vandeVen
Department of Cell Physiology, Microfluorimetry Section, Biomedical Institute, Limburg University Center and Trans National University Limburg, University Campus Building D, and Institute for Materials Research IMO/IMOMEC, Wetenschapspark 1, Diepenbeek, Belgium

Alan Waggoner
Department of Biological Sciences and Molecular Biosensors and Imaging Center, Carnegie Mellon University, Pittsburgh, PA 15213, USA

Robert H. Webb
Schepens Eye Research Institute and Wellman Center for Photomedicine, Boston, MA 02114, USA

Watt W. Webb
School of Applied and Engineering Physics, Cornell University, Ithaca, NY 14853, USA

Jamey P. Weichert
Radiology Department, University of Wisconsin–Madison, BX 3252 Clinical Science Center, Madison, WI 53792, USA

Volker Westphal
Department of NanoBiophotonics, Max Planck Institute for Biophysical Chemistry, D-37018 Göttigen, Germany

N.S. White
Sir William Dunn School of Pathology, University of Oxford, Oxford OX1 3RE, UK

Katrin I. Willig
Department of NanoBiophotonics, Max Planck Institute for Biophysical Chemistry, D-37018 Göttigen, Germany

X. Sunney Xie
Department of Chemistry and Chemical Biology, Harvard University, Cambridge, MA 02138, USA

Rafael Yuste
Department of Biological Sciences, Columbia University, New York, NY 10027, USA

Ting Zhao
Departments of Biomedical Engineering and Biological Sciences and Center for Bioimage Informatics, Carnegie Mellon University, Pittsburgh, PA 15213, USA

1

Foundations of Confocal Scanned Imaging in Light Microscopy

Shinya Inoué

Seldom has the introduction of a new instrument generated as instant an excitement among biologists as the laser-scanning confocal microscope. With the new microscope, one can slice incredibly clean, thin optical sections out of thick fluorescent specimens; view specimens in planes tilted to, and even running parallel to, the line of sight; penetrate deep into light-scattering tissues; gain impressive three-dimensional (3D) views at very high resolution; obtain differential interference or phase-contrast images in exact register with confocal fluorescence images; and improve the precision of microphotometry.

While the instrument that engendered such excitement became commercially available first in 1987, the optical and electronic theory and the technology that led to this sudden emergence had been brewing for several decades. The development of this microscope stems from several roots, including light microscopy, confocal imaging, video and scanning microscopy, and coherent or laser-illuminated optics (see historic overview in Table 1.1). In this chapter, I will first discuss some basic principles relating to lateral and axial resolution as well as depth of field in light microscopy, highlight some history that lays a foundation to the development of laser-scanning confocal microscopy, and end with some general remarks regarding the new microscopes, including a disk-scanning confocal system.

LIGHT MICROSCOPY

Lateral Resolution[1]

The foundations of modern light microscopy were established a century ago by Ernst Abbe (1873, 1884). He demonstrated how the diffraction of light by the specimen, and by the objective lens, determined image resolution; defined the conditions needed to design a lens whose resolution was diffraction limited (rather than limited by chromatic and spherical aberrations); and established the role of the objective and condenser numerical apertures (NA) on image resolution (Eq. 1). Thus,

$$d_{\min} = \frac{1.22\lambda_o}{\mathrm{NA}_{obj} + \mathrm{NA}_{cond}} \qquad \textbf{(1)}$$

where $d_{\min}$ is the minimum spacing *in a periodic grating* that can just be resolved. $d_{\min}$ is expressed as lateral distance in the specimen space; λ_o is the wavelength of light in vacuum; and NA_{obj} and NA_{cond} are the numerical apertures of the objective and condenser lenses, respectively. The NA is the product of the sine of the half-angle (α) of the cone of light either acceptable by the objective lens or emerging from the condenser lens and the refractive indexes (η) of the imbibing medium between the specimen and the objective or condenser lens, respectively.

Equation 1 demonstrates that, in addition to the wavelength and the NA of the objective lens, the condenser NA also affects image resolution in the microscope. For objects that are illuminated fully coherently (a condition that pertains when NA_{cond} approaches 0, namely when the condenser iris is closed down to a pinhole), the minimum resolvable lateral spacing **increases** (i.e., **the resolution decreases**) by a factor of 2 compared to the case when the condenser iris is opened so that $NA_{cond} = NA_{obj}$. As the condenser iris is opened and NA_{cond} becomes larger, the illumination becomes progressively less coherent and resolution increases. [Note, however, that laser beams tend to illuminate objects coherently even when the condenser iris is not closed down (see Chapter 5, *this volume*).]

Equation 1 describes the relation between NA and resolution for line-grating objects. A complementary method of defining the limit of resolution uses point objects instead of line gratings. The image, in focus, of an infinitely small luminous object point is itself not infinitely small, but is a circular Airy diffraction image with a central bright disk and progressively weaker concentric dark and bright rings. The radius r_{Airy} of the first dark ring around the central disk of the Airy diffraction image depends on λ and the NA of the objective:

$$r_{Airy} = 0.61\frac{\lambda_o}{\mathrm{NA}_{obj}} \qquad \textbf{(2)}$$

where r_{Airy} is expressed as distance in the specimen plane.

When there exist two points of light separated by a small distance d in the specimen plane, their diffraction images lie side by side in the image plane. The images of two equally bright spots are said to be resolved if d is larger or equal to the radius of the Airy disk. This is the Rayleigh criterion, and it relies on the assumption that the two point sources radiate incoherently. If the two point sources emit light coherently, their amplitude rather than

[1] For extensive discussions on modern microscope lens design and aberrations and a more rigorous treatment of the optical principles and applications of light microscopy than is appropriate for this revised chapter, refer to complementary chapters in *Handbook of Optics* (e.g., Inoué and Oldenbourg, 1994) and in *Video Microscopy*, *2nd edition* (Inoué and Spring, 1997).

Shinya Inoué • Marine Biological Laboratory, Woods Hole, Massachusetts 02543

TABLE 1.1. Historic Overview[a]

Confocal Microscopy	Microscopy	Video (Microscopy)
	Abbe (1873, 1884)[a,c]	Nipkow (1884)
	Berek (1927)[d]	
		Zworykin (1934)
	Zernicke (1935)[a,c]	
	Gabor (1948)[a]	
	Hopkins (1951)[a]	Flory (1951)
		Young and Roberts (1951)
		Flying spot[c]
	Linfoot and Wolf (1953)	
	3D diffraction by annul. apert.[a,d]	
	Tolardo di Francia (1955)	
	Limited field[b]	
	Nomarski (1955)[a]	
	Linfoot and Wolf (1956)	Montgomery *et al*. (1956)
	3D diffraction pattern[a,d]	Flying spot UV[c]
	Ingelstam (1956)	
	Resolution and info. theory[a]	
Minsky Patent (1957)		
Insight[a,b,c,d]		
Stage scanning[f]		
	Kubota and Inoué (1959)[a,c]	
	Smith and Osterberg (1961)[a]	
		Freed and Engle (1962)
		Flying spot[c]
	Harris (1964)[a,b]	
	Ellis (1966)	
	Holomicrography[a]	
Petráň *et al.* (1968)		
Tandem scanning[d,g]		
Davidovits and Egger (1971)		
Laser illumination		
Lens scanning[d]		
	Hellwarth and Christensen (1974)	
	Second harmonic generation[c,d]	
	Hoffman and Gross (1975)	
	Modulation contrast[c]	
Sheppard and Choudhury (1977)		
Theory[a,b,d]		
Sheppard *et al.* (1978)	Ellis (1978)	
Stage scanning[c,d,e,f]	Single sideband edge enhancement microscopy[c,d]	
Cremer and Cremer (1978)		
Auto-focus stage scanning[d]		
"4-π-point illumination"[a,b,d]		
Brakenhoff *et al.* (1979)		Castleman (1979)
Specimen scan[a,b,d,e]		Digital image processing[a,c,e]
Koester (1980)	Quate (1980)	
Scanning mirror[d]	Acoustic microscopy[a,c]	
		Inoué (1981)[a,c]
		Allen *et al.* (1981a,b)[a,c]
		Fuchs *et al.* (1982)[f]
		Agard and Sedat (1983)[a,c,d]
Cox and Sheppard (1983)		
Digital recording[d,e]		
Åslund *et al.* (1983)		
2-mirror laser scanning[d]		
Hamilton *et al.* (1984)		
Differential phase[c,d]		
Wilson and Sheppard (1984)		
Extended depth of field[c,d,e,f]		
Boyde (1985a)	Ellis (1985)	Sher and Barry (1985)[f]
Nipkow type[d,e]	Light scrambler[d]	Fay *et al.* (1985)[a,c,d]
Carlsson *et al.* (1985)		
Laser scan, Stacks of confocal images[d,e]		
Wijnaendts van Resandt *et al.* (1985)		
xz-view[d,e]		

TABLE 1.1. (*Continued*)

Confocal Microscopy	Microscopy	Video (Microscopy)
Suzuki-Horikawa (1986)	Cox and Sheppard (1986)	Inoué (1986)
Video-rate laser scan[g]		Overview, How to[a,c,e,f]
Acousto-optical modulator		
No exit pinhole		
Xiao and Kino (1987)		Castleman (1987)[a]
Nipkow type[d]		
Amos et al. (1987)[c,d,e]		
McCarthy and Walker (1988)	Ellis (1988)	
Nipkow type[d]	Scanned aperture phase contrast[a,c,d]	
Denk *et al.* (1990)		
Two photon[a,c,d,f]		
Hell and Wichmann (1994)		
PSF reduction by stimulated emission depletion[a,b,d]		
		Oldenbourg and Mei (1995)
		LC-pol system[c,d]
Ichihara *et al.* (1996)		
High-throughput spinning disk[d,f,g]		
		Conchello *et al.* (1997)
		Aperture scanning[a,b,c,d,f]
	Gustaffson *et al.* (2000)	
	Structured illumination[a,b,c,d]	
	Volkmer *et al.* (2001)	Inoué *et al.* (2001a,b)
	Coherent anti-stokes raman[c]	Centrifuge pol scope[c,g]
	Inoué *et al.* (2002)	
	Fluorescence pol[c]	

[a] Diffraction theory.
[b] Superresolution.
[c] Contrast modes.
[d] Optical sectioning/depth of field.
[e] Stereo.
[f] 3D in objective space.
[g] High speed.

their intensity distribution in the image must be considered, and resolution generally decreases. The impact of the quality and NA of the condenser on the lateral resolution of point objects was considered by Hopkins and Barham (1950). Their results are similar to, but not strictly identical with, the case of line-grating objects (see Born and Wolf, 1980).

It is important to realize that these resolution criteria apply only to objective lenses used under conditions in which the image is free from significant aberrations (see Chapters 6, 7, 8, 9, 11, and 22, *this volume*; Inoué and Oldenbourg, 1994; Chapters 2 and 3 in Inoué and Spring, 1997). This implies several things:

- A well-corrected clean objective lens is used within the wavelengths of light and diameter of field for which the lens was designed (commonly in conjunction with specific oculars and/or tube lenses).
- The refractive index, dispersion, and thickness of the coverslip and immersion media are those specified for the particular objective lens.
- The correct tube length and ancillary optics are used and the optics are axially aligned.
- The full complement of image-forming rays and light waves leaving all points of the objective-lens aperture converge to the image plane without obstruction.
- The condenser aperture is homogeneously and fully illuminated.
- The condenser is properly focused to produce Köhler illumination.

These considerations for resolution assume that the specimen is viewed in conventional widefield (WF) microscopy. When the (instantaneous) field of view becomes extremely small, as in confocal microscopy, the resolution can in fact be greater than when the field of view is not so limited. We shall return to this point later.[2]

Axial Resolution

We now turn to the axial (z-axis) resolution, measured along the optical axis of the microscope, that is, perpendicular to the plane of focus in which the lateral resolution was considered.

To define axial resolution, it is customary to use the 3D diffraction image of a point source that is formed near the focal plane. In the case of lateral resolution, that is, the resolution in the plane of focus, the Rayleigh criterion makes use of the infocus diffraction images (the central cross-section of the 3D diffraction pattern) of two point sources and the minimum distance that they can approach each other laterally, yet still be distinguished as two. Similarly, axial resolution can be defined by the minimum distance

[2] Note also that one's ability to determine the **location** of an object is not determined by the resolution limit of the system. In fact, the location of an object (diffraction pattern) can be determined under a microscope with precisions that are many times, or even orders of magnitude, greater than the resolution limit (e.g., Denk and Webb, 1987; also see Inoué, 1989).

that the diffraction images of two points can approach each other along the axis of the microscope, yet still be seen as two. To define this minimum distance, we use again the diffraction image of an infinitely small point object and ask for the location of the first minimum along the axis of the microscope.

The precise distribution of energy in the image-forming light above and below focus, especially for high NA objective lenses, cannot be deduced by geometric ray tracing but must be derived from wave optics. The wave optical studies of Linfoot and Wolf (1956) show that the image of a point source produced by a diffraction-limited optical system (e.g., a well-designed and properly used light microscope) is not only periodic around the point of focus in the focal plane, but is also periodic above and below the focal plane along the axis of the microscope. [Such 3D diffraction images (including those produced in the presence of lens aberrations) are presented photographically by Cagnet *et al*. (1962; also see Chapter 7, *this volume*, Fig. 7.4). The intensity distribution calculated by Linfoot and Wolf for an aberration-free system is reproduced in Born and Wolf (1980) and also in Inoué and Spring (1997, Fig. 2-30). The 3D pattern of a point source formed by a lens possessing an annular aperture was calculated by Linfoot and Wolf (1953).]

The distance from the center of the 3D diffraction pattern to the first axial minimum (in object space dimensions) is given by

$$z_{\min} = \frac{2\lambda_o \eta}{(NA_{obj})^2} \qquad \textbf{(3)}$$

where η is the refractive index of the object medium. $z_{\min}$ corresponds to the distance by which we have to raise the microscope objective in order to focus the first intensity minimum observed along the axis of the 3D diffraction pattern instead of the central maximum.[3]

As with the lateral resolution limit, we can use $z_{\min}$ as a measure of the limit of axial resolution of the microscope optics. Note, however, that $z_{\min}$ shrinks inversely proportionally with the *square* of the NA_{obj}, in contrast to the lateral resolution limit which shrinks with the first power of the NA_{obj}. Thus, the ratio of axial-to-lateral resolution ($z_{\min}/r_{Airy} = 3.28\eta/NA_{obj}$) is substantially larger than λ and is inversely proportional to the NA of the objective lens.

Depth of Field

The depth of field of a microscope is the depth of the image (measured along the microscope axis translated into distances in the specimen space) that appears to be sharply in focus at one setting of the fine-focus adjustment. In brightfield microscopy, this depth should be approximately equal to the axial resolution, at least in theory. The actual depth of field has been determined experimentally, and the contribution of various factors that affect the measurement have been explored by Berek (1927).

According to Berek, the depth of field is affected by (1) the geometric and diffraction-limited spreading, above and below the plane of focus, of the light beam that arose from a single point in the specimen; (2) the accommodation of the observer's eye; and (3) the final magnification of the image. The second factor becomes irrelevant when the image is not viewed directly through the ocular but is instead focused onto a thin detector (as in video microscopy or confocal microscopy with a minute exit pinhole). The third factor should also disappear once the total magnification is raised sufficiently, so that the unit diffraction image becomes significantly larger than the resolution element of the detector (e.g., Hansen in Inoué, 1986; Castleman, 1987, 1993; Schotten, 1993; Inoué and Spring, 1997, Section 12.2).

When the detector can be considered to be infinitely thin and made up of resolution elements spaced sufficiently (at least 2-fold) finer than the Airy disk radius, then one need only to consider the diffraction-limited depth of field. In that case, the depth of field is taken to be

$$\delta = \frac{1}{4}(z_{\min^+} - z_{\min^-}) \qquad \textbf{(4)}$$

that is, one quarter of the distance between the first axial minima above ($z_{\min^+}$) and below ($z_{\min^-}$) the central maximum in the 3D Airy pattern converted to distances in specimen space (see Eq. 3; $z_{\min^+}$ and $z_{\min^-}$ correspond to Z1 and −Z1 in Chapter 7, Fig. 7.4, *this volume*).

In conventional fluorescence and darkfield microscopy, the light arising from each image point produces significant intensity within a solid cone that reaches a considerable distance above and below focus (as seen in the point-spread functions for these modes of microscopy; e.g., Streibl, 1985; also Chapters 11 and 23, *this volume*). Therefore, fluorescent (or light-scattering) objects that are out of focus produce unwanted light that is collected by the objective and reduces the contrast of the signal from the region in focus.

For these reasons, the depth of field may be difficult to measure or even to define precisely in conventional fluorescence and darkfield microscopy. Put another way, one could say that when objects that are not infinitely thin are observed in conventional fluorescence or darkfield microscopy, the apparent depth of field is very much greater than the axial resolution.

The unwanted light that expands the apparent depth of field is exactly what confocal imaging eliminates. Thus, we can view only those fluorescent and light-scattering objects that lie within the depth that is given by the axial resolution of the microscope and attain the desired shallow depth of field.

As mentioned earlier, the lateral resolution of a microscope is also a function of the size of the field observed at any one instant. Tolardo di Francia (1955) suggested, and Ingelstam (1956) argued on the basis of information theory, that one gains lateral resolution by a factor of $\sqrt{2}$ as the field of view becomes vanishingly small. These theoretical considerations set the stage for the development of confocal imaging.

CONFOCAL IMAGING

As a young postdoctoral fellow at Harvard University in 1957, Marvin Minsky applied for a patent for a microscope that used a stage-scanning confocal optical system. Not only was the conception farsighted, but his insight into the potential application and significance of confocal microscopy was nothing short of remarkable. [See the delightful article by Minsky (1988) that shows even greater insight into the significance of confocal imaging than do the following extracts culled from his patent application.]

In Minsky's embodiment of the confocal microscope, the conventional microscope condenser is replaced by a lens identical to the objective lens. The field of illumination is limited by a pinhole, positioned on the microscope axis. A reduced image of this pinhole

[3] As discussed later, the distance $z_{\min}$ can be reduced significantly below the classical limit given by Eq. 1.3, for example, by reducing the effective point-spread function by special use of two-photon confocal imaging.

is projected onto the specimen by the "condenser." The field of view is also restricted by a second (or exit) pinhole in the image plane placed confocally to the illuminated spot in the specimen and to the first pinhole (Fig. 1.1). Instead of trans-illuminating the specimen with a separate "condenser" and objective lens, the confocal microscope could also be used in the epi-illuminating mode, making a single objective lens serve as both the condenser and the objective lens (Fig. 1.2).

Using either transmitted or epi-illumination, the specimen is scanned with a point of light by moving the specimen over short distances in a raster pattern. (The specimen stage was supported on two orthogonally vibrating tuning forks driven by electromagnets at 60 and 6000 Hz.) The variation in the amount of light, modulated by the specimen and passing the second pinhole, is captured by a photoelectric cell. The photoelectric current is amplified and modulates the beam intensity of a long-persistence cathode-ray tube (CRT) scanned in synchrony with the tuning forks. As a result, the image of the specimen is displayed on the CRT. The ratio of scanning distances between the electron beam and the specimen provides image magnification, which is variable and can be very large.

With this stage-scanning confocal microscope, Minsky says, light scattered from parts other than the illuminated point on the specimen is rejected from the optical system (by the exit pinhole) to an extent never before realized. As pointed out in the patent application, there are several advantages to such an optical system:

- Reduced blurring of the image from light scattering
- Increased effective resolution
- Improved signal-to-noise ratio
- Permits unusually clear examination of thick, light-scattering objects
- *xy*-scan possible over wide areas of the specimen
- Inclusion of a *z*-scan is possible
- Electronic adjustment of magnification

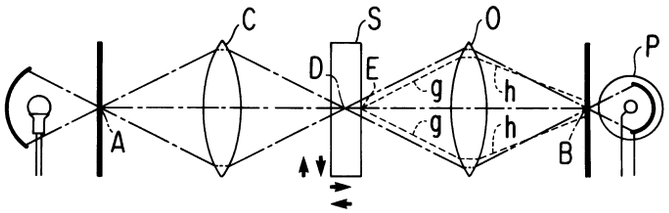


FIGURE 1.1. Optical path in simple confocal microscope. The condenser lens, C, forms an image of the first pinhole, A, onto a confocal spot, D, in the specimen, S. The objective lens, O, forms an image of D onto the second (exit) pinhole, B, which is confocal with D and A. Another point, such as E in the specimen, would not be in focus with A, so that the illumination would be less. In addition, most of the light, g–h, scattered from E would not pass the second pinhole, B. The light reaching the phototube, P, from E is thus greatly attenuated compared to that from the confocal point, D. In addition, the exit pinhole can be made small enough to exclude the diffraction rings in the image of D, so that the resolving power of the microscope is improved. As the specimen is scanned, the phototube provides a signal of the light passing through sequential specimen points D_1, D_2, D_3, etc. (not shown). D_1, D_2, D_3, etc., can lie in the focal plane as in conventional microscopy or perpendicular to it, or at any angle defined by the scanning pattern, so that optical sections can be made in or at angles tilted from the conventional image plane. Because, in the stage-scanning system, the small scanning spot, D, lies exactly on the axis of the microscope, the lenses C and O can be considerably less sophisticated than conventional microscope lenses, which must form images from points some distance away from the lens axis. (After Minsky, 1957.)

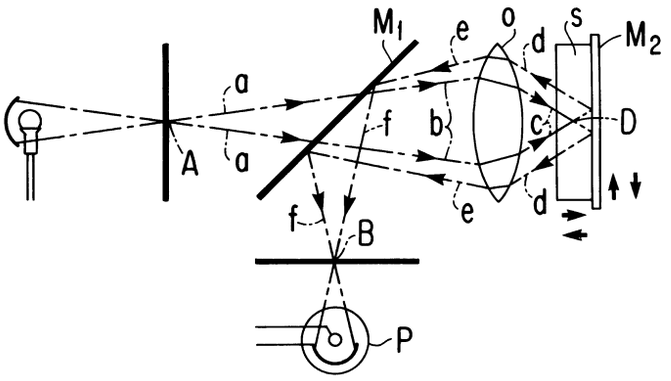


FIGURE 1.2. Optical path in epi-illuminated confocal microscope. The entrance pinhole, A, point D in the specimen, S, and exit pinhole, B, are confocal points as in Figure 1.1. A partial, or dichromatic, mirror, M_1, transmits the illuminating beam a–b–c and reflects the beam d–e which passed D and was reflected by the mirror, M_2, on which the specimen is lying. Only the reflected beam that passes point D focuses onto the detector pinhole and reaches the photocell, P. A single lens, O, replaces the condenser and objective lenses in Figure 1.1. (After Minsky, 1957.)

- Especially well suited for making quantitative studies of the optical properties of the specimen
- An infinite number of aperture planes in the microscope are potentially available for modulating the aperture with darkfield stops, annuli, phase plates, etc.
- Complex contrast effects can be provided with comparatively simple equipment
- Permits use of less complex objective lenses, including those for long working distance, ultraviolet (UV), or infrared imaging, as they need to be corrected only for a single axial point.

The high-resolution acoustic microscope developed by Quate and co-workers (Quate, 1980) and the laser disk, video, and audio recorder/players are object-scanning-type confocal microscopes. The designers of these instruments take advantage of the fact that only a single axial point is focused or scanned (see, e.g., Inoué and Spring, 1997, Sect. 11.10).

IMPACT OF VIDEO

Nipkow Disk

Just about the same time that Abbe in Jena laid the foundation for modern light microscopy, a young student in Berlin, Paul Nipkow (1884), figured out how to convert a two-dimensional (2D) optical image into an electrical signal that could be transmitted as a one-dimensional (1D), or serial, time-dependent signal, over a single cable (as in a Morse code). Prior to Nipkow, most attempts at the electrical transmission of optical images involved the use of multiple detectors and as many cables.

Nipkow dissected the image by scanning over it in a raster pattern, using a spinning opaque wheel perforated by a series of rectangular holes. The successive holes, placed a constant angle apart around the center of the disk but on constantly decreasing radii (i.e., arranged as an Archimedes spiral), generated the raster-scanning pattern (Fig. 1.3). The brightness of each image element, thus scanned by the raster, was picked up by a photocell. The

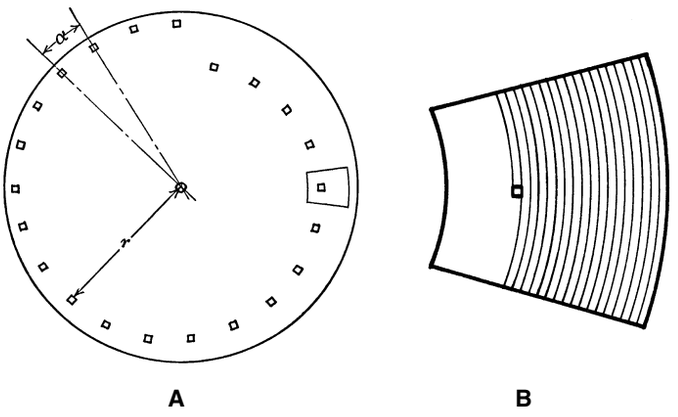


FIGURE 1.3. Nipkow disk. The perforations in the opaque disk, A, which is rotating at a constant velocity, scan the image in a raster pattern as shown in B. (After Zworykin and Morton, 1954.)

output of the photocell reflected the brightness of the sequentially scanned image elements and drove a neon bulb that, viewed through another (part of the) Nipkow disk, reproduced the desired picture.

A similar type of scanner disk, but with multiple, centrosymmetric sets of spirally placed holes, was used by Mojmir Petráň and co-workers at Prague and New Haven to develop their epi-illuminated tandem-scanning confocal microscope (TSM) (Egger and Petráň, 1967; Petráň *et al*., 1968). In Petráň's microscope, holes on a portion of the spinning disk placed in front of the light-source collector lens are imaged onto the specimen by the objective lens. Each point of light reflected or scattered by the specimen is focused by the same objective lens back onto the centrosymmetric portion of the Nipkow disk. The pinholes at this region exclude the light originating from points in the specimen not illuminated by the first set of pinholes, giving rise to confocal operation (Chapter 10, *this volume*).

As with Nipkow's initial attempt at television, this TSM tends to suffer from the low fraction (1%–2%) of light that is transmitted through the source pinholes. Also, very high mechanical precision is required for fabricating the symmetrical Nipkow disk and for spinning it exactly on axis. In addition, some of the advantages pointed out by Minsky for the stage-scanning type confocal optics are lost because the objective lenses are no longer focusing a single axial point of light.

However, for biological applications, the tandem-scanning system provides the decided advantage that the specimen remains stationary. As a result, the speed of the raster scan is not limited by the mass of the specimen support as it is in stage scanning, and the scanning system is unlikely to introduce any geometrical distortion. Thus, with a TSM, one can observe objects that reflect or scatter light moderately strongly, in real time, either by using a television or photographic camera or by observing the image directly through the eyepiece.

In addition to Petráň and co-workers, Alan Boyde (1985a) in London took advantage of the good axial discrimination and light-penetrating capability of the tandem scanning confocal microscope and pioneered its use for viewing biological objects. In particular, he used it for imaging below the surface of hard tissue such as bone and teeth to visualize the cells and lacunae found there (see Lewin, 1985). Boyde also provides striking stereoscopic images obtained with the tandem-scanning confocal microscope (Boyde, 1985b, 1987).

Gordon Kino and co-workers at Stanford University have designed a confocal microscope using a Nipkow disk in a manner that differs somewhat from the Petráň type (Xiao and Kino, 1987; also see Chapter 10, *this volume*). In the Kino type, the rays illuminating the specimen and those scattered by the specimen traverse the *same* set of pinholes on the spinning Nipkow disk rather than those that are centrosymmetrical. By using a special low-reflection Nipkow disk, tilted somewhat to the optic axis of the microscope, and by employing crossed polarizers and a quarter-wave birefringent plate to further reduce the spurious reflections from the disk, they are able to use only one side of it, thus alleviating some of the alignment difficulties of the Petráň type.

More recently, spinning-disk confocal units have been vastly improved by adding microlenses to the pinholes. As described later (see "Yokogawa Disk-Scanning Confocal System" below), the microlens-equipped disk-scanning systems effectively provide video-rate and faster confocal full-frame imaging and in real color. While in part depending on older technology, the confocal-scanning unit (CSU) systems turn out to have certain advantages not achievable with point-scanning confocal systems.

Electron-Beam-Scanning Television

While Nipkow's invention laid the conceptual groundwork for television, raster scanning based on a mechanical device was simply too inefficient for practical television. Thus, it was not until five decades after Nipkow, following the advent of vacuum tube and electronic technology, that Zworykin (1934) and his colleagues at RCA were able to devise a practical television system. These workers developed the image iconoscope, an image-storage-type electron-beam-scanning image pickup tube. The image iconoscope, coupled with a CRT for picture display, permitted very rapid, "inertialess" switching and scanning of the image and picture elements. With these major breakthroughs, television not only became practical for broadcasting but emerged as a tool that could be applied to microscopy (see Inoué and Spring, 1997, Sects. 1.1 and 1.2).

An early application of video (the picture portion of television) was the flying spot UV microscope of Young and Roberts (1951). With this microscope, the specimen remains stationary and single object points are scanned serially in a raster pattern by a moving spot of UV light emitted by the face of a special high-intensity UV-CRT. The optical elements (condenser) of the microscope demagnify this moving spot onto the specimen, which modulates its brightness. The modulated UV light is then picked up by a phototube and amplified electronically before being displayed on a visible-light CRT scanned in synchrony with the UV-CRT.

Young and Roberts point out that by illuminating only a single specimen point at a time with a flying-spot microscope, flare is reduced and the image becomes a closer rendition of the specimen's optical properties than that obtained with a non-scanning microscope. They also point out that for these same reasons — and because a photoelectric detector can provide a sequential, linear output of the brightness of each specimen point — quantitative analysis becomes possible with a flying-spot microscope. In addition, they note that the electronic photodetector raises the sensitivity of image capture by perhaps two orders of magnitude compared to photography.

It should be noted that the flare which would otherwise arise from the unilluminated parts of the specimen is significantly

reduced with a flying-spot microscope (see Sheppard and Choudhury, 1977), even though the exit pinhole used in a confocal microscope is not present. Thus, for example, Wilke *et al*. (1983) and Suzuki and Hirokawa (1986) developed laser-scanning flying-spot microscopes (coupled with digital image processors) to raise image contrast (at video rate) in fluorescence, differential-interference-contrast (DIC), and brightfield microscopy. Naturally, the exit pinhole in a confocal system is very much more effective at excluding unwanted light arising from different layers or portions of the specimen not currently illuminated by the source "pinhole," but it does so at the cost of reduced image brightness, lower scanning speed, and increased instrumental complexity and price.

While the flying-spot, or beam-scanning, microscope was developed and applied in UV microscopy for about a decade after its introduction, its further development as an imaging device was eclipsed for some time by the need and the opportunity to develop automated microscopy for rapid cell sorting and diagnosis. Here, the aim was not the imaging of cell structures as such but rather the rapid and efficient classification of cells based on their biochemical characteristics, taking advantage of the emerging power of high-speed digital computers. The size, shape, absorbance, light scattering, or light emission of cells (labeled with specific fluorescent markers) was used either to classify the cells by scanning the slide under a microscope or to sort the cells at very high rates as the cells traversed a monitoring laser beam in a flow cell or a Coulter-type cell separator.

Impact of Modern Video

Meanwhile, starting in the late 1970s, the introduction of new solid state devices, especially large-scale integrated circuits and related technology, led to dramatic improvements in the performance and availability, and reduction in price, of industrial-grade video cameras, video tape recorders, and display devices. Concurrently, ever more compact and powerful digital computers and image-processing systems appeared in rapid succession. These advances led to the birth of modern video microscopy, which in turn brought about a revitalized interest in the power and use of the light microscope (for reviews see Allen *et al*., 1981a,b; Inoué, 1981, 1989; Allen, 1985; Inoué and Spring, 1997).

In brief, dynamic structures in living cells could now be visualized with a clarity, speed, and resolution never achieved before in DIC, fluorescence, polarized-light, darkfield, and other modes of microscopy; the growth and shortening of individual molecular filaments of tubulin and f-actin, and their gliding motion and interaction with motor molecules, could be followed in real time directly on the monitor screen; and the changing concentration and distribution of ions and specific protein molecules tagged with fluorescent reporter molecules could be followed, moment by moment, in physiologically active cells (Chapters 19, 29, and 42, *this volume*).

In addition to its immediate impact on cellular and molecular biology, video microscopy and digital image processing also stimulated the exploration of other new approaches in light microscopy along several fronts. These include the development of ratio imaging and new reporter dyes for quantitative measurement of local intracellular pH, calcium ion concentration, etc. (Tanasugarn *et al*., 1984; Bright *et al*., 1989; Tsien, 1989; Chapters 16, 19, and 29, *this volume*); the computational extraction of pure optical sections from whole-mount specimens in fluorescence microscopy (based on deconvolution of multi-layered images utilizing knowledge of the microscope's point-spread function; Agard and Sedat, 1983; Agard *et al*., 1989; see also Chapters 23, 24, and 25, *this volume*); 3D imaging including stereoscopy (Brakenhoff *et al*., 1986, 1989; Inoué and Inoué, 1986; Åslund *et al*., 1987; Stevens *et al*., 1994; Inoué and Spring, 1997, Sect. 12.7.7); and, finally, the further development of laser-scanning microscopy and confocal microscopy.

LASERS AND MICROSCOPY

Holography

In 1960, Maiman announced the development of the first operating laser. However, "his initial paper, which would have made his findings known in a more traditional fashion, was rejected for publication by the editors of *Physical Review Letters* — this to their everlasting chagrin." (For historic accounts including this quotation and a comprehensive discussion of the principles and application of lasers and holography, see Sects. 14.2 and 14.3 in Hecht, 1987; see also Chapter 5, *this volume*.) Shortly thereafter, two types of applications of lasers were sought in microscopy. One took advantage of the high degree of monochromaticity and the attendant long coherence length. Coherence length is the distance over which the laser waves could be shifted in path and still remain coherent enough to display clear interference phenomena (note that, in fact, this reflects a very high degree of temporal coherence). These characteristics made the laser an ideal source for holography (Leith and Upatnieks, 1963, 1964).

To explore the use of holography with the microscope, Ellis (1966) introduced a conventional light microscope into one of two beams split from a laser. When this beam was combined with the other beam passing outside of the microscope, the two beams could be made to interfere in a plane above the ocular. The closely spaced interference fringes were recorded on very fine-grained photographic film to produce the hologram.

What Ellis found was that the coherence length of the laser beam was so long that the hologram constructed as described above could be viewed not only to reconstruct an image of the specimen being magnified by the microscope, but also to reconstruct images of the inside of the microscope. Indeed, in the hologram one could see the whole optical train and interior of the microscope, starting with the substage condenser assembly, the specimen, the objective lens and its back aperture, the interior of the body tube up to the ocular, and even the light shield placed above it! This made it possible for Ellis to view the hologram through appropriately positioned stops, phase plates, etc., and to generate contrast from the specimen in imaging modes such as darkfield or oblique illumination, phase contrast, etc., *after* the hologram itself had been recorded. In other words, the state of the specimen at a given point of time could be reconstructed and viewed after the fact in contrast modes different from the one present when the hologram was recorded.

In principle, holomicrography presents many intriguing possibilities including 3D imaging. But the very virtue of the long coherence length of the laser beam means that the hologram also registers all the defects and dirt in the microscope. Without laser illumination, the optical noise produced by these defects would be far out of focus. With a laser illuminating the whole field of view of the microscope, the interference fringes from these out-of-focus defects intrude into the holographic image of the specimen where they are prominently superimposed. Because of this problem, holomicrography has so far not been widely used. [However, see

Sharnoff *et al*. (1986), who have figured out how to obtain holomicrograms that display only the *changes* taking place in the specimen (contracting muscle striations) over an interval of time and thus eliminate the fixed-patterned optical noise.]

Laser Illumination

Another practical application of lasers in microscopy is its use as an intense, monochromatic light source. Lasers can produce light beams with a very high degree of monochromaticity and polarization, implying a high degree of coherence. Some lasers also generate beams with very high intensity. Thus, an appropriate laser could serve as a valuable light source in those modes of microscopy where monochromaticity, high intensity, and a high degree of coherence and polarization are important.

To use the laser as an effective light source for microscopy, three conditions must be satisfied:

- Both the microscope's field of view and the condenser aperture must appropriately be filled.
- The coherence length of the laser beam (i.e., the temporal coherence) must be reduced to eliminate interference from out-of-focus defects.
- The coherence at the image plane must be reduced to eliminate laser "speckle" and to maximize image resolution.

In fact, these three conditions are not totally independent, but they do specify the conditions that must be met.

One of the following five approaches can be used to fulfill these conditions (see also Chapter 6, *this volume*).

Spinning-Disk Scrambler

The laser beam, expanded to fill the desired field, is passed through a spinning ground-glass diffuser placed in front of the beam expander lens (Hard *et al*., 1977). The ground glass diffuses the light so that the condenser aperture is automatically filled. However, if the ground glass were not moving, small regions of its irregular surface would act as coherent scatterers and the image field would still be filled with laser speckle. Spinning or vibrating the ground glass reduces the temporal coherence of each of the coherent scattering points to a period shorter than the integration time of the image sensor. Thus, when averaged over the period of the motion, the field also becomes uniformly illuminated. This approach, while simple to understand, can result in considerable light loss at the diffuser. Also, inhomogeneity of the diffuser's texture can give rise to concentric rings of varying brightnesses which traverse the field.

Oscillating-Fiber Scrambler

The laser beam is focused onto the entrance end of a single-stranded multi-mode optical fiber whose output end lies at the focal point of a beam-expanding lens. This lens projects an enlarged image of the fiber tip to fill the condenser aperture. The fiber, which is fixed at both ends, is vibrated at some point along its length. The field and aperture are then uniformly filled with incoherent light with little loss of intensity (Ellis, 1979). If the fiber were not vibrated, the simple fact that the light beam is transmitted through the fiber could make the laser beam highly multi-modal. That would reduce the lateral coherence of the beam at the aperture plane, but the image would still be filled with speckle. Vibration that reduces the temporal coherence of the beam below the integration time of the image sensor integrates out the speckle without loss of light (see also Chapter 6, *this volume*).

Multi-Length Fiber Scrambler

None of the mechanical scramblers mentioned above can be used where speckles have to be removed within extremely brief time periods. For example, in a centrifuge polarizing microscope, the laser output must be made spatially incoherent within the few nanoseconds required to freeze the image of the specimen flying through the field of the objective lens at speeds up to 100 m/s (Inoué *et al*., 2001b). Our solution for reducing the coherence of the laser pulse was to introduce a fiber bundle made up of up to 100 fibers of multiple lengths between two multi-mode single-fiber scramblers. The first multi-mode fiber introduced some phase randomizing effects, while the multi-length fibers provided a fiber bundle output whose phase varied depending on the length of the fiber. However, the intensities of the fiber output varied depending on their location in the bundle. The final multi-mode fiber made the non-uniform brightness of the bundle output homogeneous, so that the microscope condenser received uniform illumination. Thus, without using any mechanically moving parts, the phase of the monochromatic laser beam is randomized, and speckles are eliminated from the field image, while the whole condenser aperture is filled uniformly.

Field Scanning

The field is scanned by a minute focused spot (the diffraction image) of a single-mode laser beam that has been expanded to fill the condenser aperture (as in a laser-scanning confocal microscope). Thus, the specimen is scanned point by point, and the signal light reflected, transmitted, or emitted by the specimen is collected and focused by the objective lens. This imaging mode avoids the generation of speckle from laser-illuminated specimens because speckle arises from the interference between the coherent light waves scattered from different parts of a specimen. (This optical setup is less effective at removing speckle when a smooth reflecting surface is presented slightly away from the plane of focus.)

This fourth approach leads to field-scanning microscopy. A focused spot of laser light can be made to scan the field as in a flying-spot microscope, or the specimen can be moved and scanned through a fixed focus point. Alternatively, an exit pinhole and beam scanners can be added to generate a laser-scanning confocal microscope.

Aperture Scanning

The minute diffraction image of a single-mode laser is focused by a beam expander onto an off-axis point on the condenser aperture. The small spot is scanned (made to precess) over the condenser aperture in such a way that the field is uniformly illuminated. At any instant of time, the specimen is illuminated by a tilted collimated beam of light emerging from the condenser and originating from the illuminated aperture point. Selected regions of the aperture are filled in rapid succession by scanning the spot, so that the whole field is illuminated by collimated, coherent beams at successively changing azimuth angles. The rapid scanning of the source reduces the temporal coherence of illumination at the object plane to less than the response time of the image detector. Nevertheless, the lateral coherence is maintained for each instantaneous beam that illuminates the specimen (Ellis, 1988).

Ellis has argued the theoretical advantage provided by this fifth approach and has demonstrated its practical attractiveness. With aperture scanning, one gains new degrees of freedom for optical image processing because the aperture function (which controls the image transfer function of the microscope) can be regulated dynamically for each point of the aperture. The image resolution

and the shallow depth of field that can be achieved with aperture-scanning phase-contrast microscopy is most impressive (see, e.g., Inoué and Spring, 1997, Fig. 2-47).

Laser-Illuminated Confocal Microscopes

During the early 1970s, Egger and co-workers at Yale University developed a laser-illuminated confocal microscope in which the objective lens was oscillated in order to scan the beam over the specimen. Davidovits and Egger obtained a U.S. patent on this microscope (1972; see review by Egger, 1989).

A few years later, Sheppard and Choudhury (1977) provided a thorough theoretical analysis on various modes of confocal and laser-scanning microscopy. The following year, Sheppard *et al*. (1978) and Wilson *et al*. (1980) described an epi-illuminating confocal microscope of the stage-scanning type, equipped with a laser source and a photomultiplier tube (PMT) as the detector, using a novel specimen holder. The specimen holder, supported on four taut steel wires running parallel to the optical axis, allowed precise *z*-axis positioning as well as fairly rapid voice-coil-actuated scanning of the specimen in the *xy*-plane. Using this instrument, Sheppard *et al*. demonstrated the value of the confocal system particularly for examining integrated circuit chips. With stage-scanning confocal imaging, optical sections and profile images could be displayed on a slow-scan monitor over areas very much *larger* than can be contained within the field of view of any given objective lens by conventional microscopy.

These authors capitalized on the fact that the confocal signal falls off extremely sharply with depth, and the image is therefore completely dark for regions of the specimen that are not near the confocal focus plane. For example, with a tilted integrated circuit chip, only the portion of the surface within the shallow depth of field (at any selected *z*-value) could be displayed, as a strip-shaped region elongated parallel to the chip's axis of tilt. Other areas of the image were dark and devoid of structure. Conversely, by combining all the *xy*-scan images made during a slow *z*-scan, they could produce a final "extended focus" image of the whole tilted surface, which demonstrated maximum spatial resolution on all features throughout the focus range (Wilson and Sheppard, 1984; Wilson, 1985) (Chapter 22, *this volume*).

This could be done even when the specimen surface was not a single tilted plane but was wavy or consisted of complex surfaces. In their monograph *Scanning Optical Microscopy*, Wilson and Sheppard (1984) show shallow optical sections of insect antennae shining on a dark background. They also show stereo-pair images of the same object consisting of two "extended focus" images made by focusing along two focal axes that were tilted by several degrees relative to the optical axis. Extended-focus images demonstrate that *the confocal system can either decrease or increase the effective depth of field without loss of resolution*.

As described in the final section of this article, the lateral resolution that is practically attainable can be improved by using confocal optics. In addition, the removal of the extraneous light contributed by out-of-focus objects dramatically improves the contrast and gives rise to a brilliantly sharp image.

Sheppard *et al*. also managed to display different regions on the surface of an integrated circuit chip with varying intensity or pseudocolor corresponding to the height of the region. This is possible because the amount of light reflected by an (untilted) step on the surface of the chip and passing the second pinhole varies with the distance of the reflecting surface from the focal plane. The authors also showed that, by processing the photoelectric signal electronically, the edges of the steps alone could be outlined or the gradient of the steps could be displayed in a DIC-like image (Hamilton and Wilson, 1984). [For the basics of digital image processing, see Castleman (1979), Baxes (1984), Gonzales and Wintz (1987), Chapter 12 in Inoué and Spring (1997), and Chapter 14, *this volume*.]

The integrated circuit chip could also be displayed with contrast reflecting the status of the local circuit elements, for example, reflecting its temperature or the amount of photo-induced current flowing through the circuit, superimposed on the confocal image of the chip made with reflected light (Wilson and Sheppard, 1984).

In addition to the Oxford group, the brothers Cremer and Cremer (1978) of Heidelberg designed a specimen-scanning laser-illuminated confocal microscope. This epi-fluorescence system was equipped with (1) a circular exit pinhole, in front of the first PMT, whose diameter was equal to the principal maximum of the diffraction pattern; and (2) an annular aperture, in front of a second PMT, whose opening corresponded to the first subsidiary maximum of the diffraction pattern. The output of the two PMTs was used to provide autofocus as well as displays of surface contour and fluorescent intensity distribution.

In the 1978 article, the Cremers also discussed the possibility of laser spot illumination using a "4π-point hologram" that could, at least in principle, provide long working distance relative to the small spot size that could be produced.

CONFOCAL LASER-SCANNING MICROSCOPE

In addition to those already mentioned, the pioneering work of the Oxford electrical engineering group was followed in several European laboratories by Brakenhoff *et al*. (1979, 1985), Wijnaendts van Resandt *et al*. (1985), and Carlsson *et al*. (1985). These investigators respectively developed the stage-scanning confocal microscope further, verified the theory of confocal imaging, and expanded its application into cell biology. I shall defer further discussions on these important contributions to authors of other chapters in this volume. In the meantime, video microscopy and digital image processing were also advancing at a rapid rate.

These circumstances culminated in the development of the confocal laser-scanning microscope (CLSM, Figs. 1.4, 1.5; Åslund *et al*., 1983, 1987) and publication of its biological application by Carlsson *et al*. (1985), Amos *et al*. (1987), and White *et al*. (1987). The publications were followed shortly by introduction of laser-scanning confocal microscopes to the market by Sarastro, Bio-Rad, Olympus, Zeiss, and Leitz. It was White, Amos, and Fordham of the Cambridge group that first enraptured the world's biological community with their exquisite and convincing illustrations of the power of the CLSM. Here at last was a microscope that could generate clear, thin optical sectioned images, totally free of out-of-focus fluorescence, from whole embryos or cells and at NAs as high as 1.4. Not only could one obtain such remarkable optical-sectioned fluorescence images in a matter of seconds, but *x-z* sections (providing views at right angles to the normal direction of observation) could also be captured and rapidly displayed on the monitor. A series of optical sections (stored in the memory of the built-in or add-on digital image processor) could be converted into 3D images or displayed as stereo pairs. The confocal fluorescent optical sections could also be displayed side by side with non-confocal brightfield or phase-contrast images, acquired concurrently using the transmitted portion of the scanning laser beam. These images could also be displayed superimposed on top of each other, for example, with each image coded in different pseudocolor, but unlike similar image pairs produced by conventional

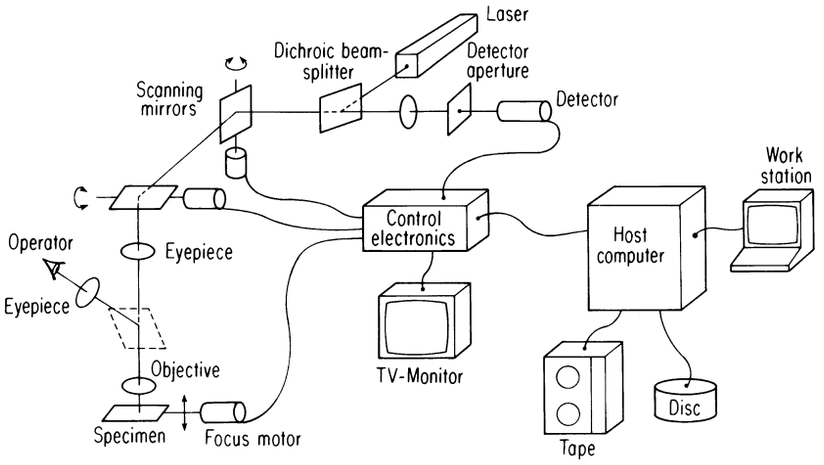


FIGURE 1.4. Schematic of laser-scanning confocal microscope. (From Åslund *et al*., 1987.)

microscopes, the two images were in exact register and showed no parallax as each was generated by the same scanning spot.

Most of the laser-scanning systems discussed in this section employed epi-illumination using some form of mechanical scanning devices. They could not readily be applied to confocal imaging of transmitted light, for example, for high-extinction polarization or DIC microscopy. Nevertheless, Goldstein *et al*. (1990) developed a system using an Image Dissector Tube which, in principle, should be able to provide confocal imaging in the trans-illumination mode. Such an approach may eventually lead to workable transmission laser-scanning confocal microscopes with multiple contrast modes.

TWO- AND MULTI-PHOTON MICROSCOPY

As noted, conventional point-scanning confocal microscopes dramatically reduce the contribution of fluorescence from out-of-focus regions of the specimen. Nevertheless, regions of the specimen above and below the focal plane are exposed to the full cones of intense excitation light, converging and diverging from the illuminated spot. Thus, with conventional confocal microscopy, biological specimens tend to suffer from photon-induced damage and rapid bleaching of fluorescence, while the fraction of the short wavelength excitation beam that reaches the focal plane is reduced by absorption in the intervening material. Many of these shortcomings are circumvented by two- and multi-photon microscopy.

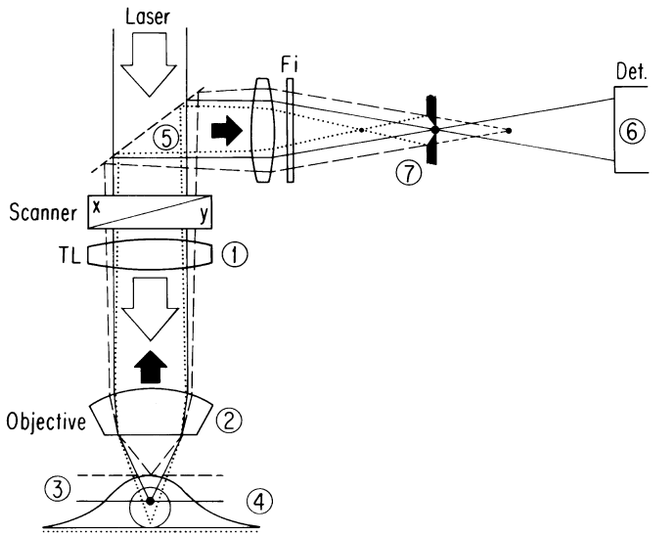


FIGURE 1.5. Depth discrimination in a laser-scanning confocal fluorescent microscope. Compare with Figure 1.2. (Courtesy of Dr. H. Kapitza, Carl Zeiss, Oberkochen.)

By focusing a pulse of very intense laser beam with twice the wavelength (half the frequency) of the standard short wavelength excitation beam, and within a period shorter than the fluorescence decay time of the fluorophore, the coherently interfering photons can excite molecules at half the wavelength of the long wavelength laser, and do so *selectively* in the focused spot. In other words, the output of an intense near-infrared (IR) laser induces fluorescence in a blue or UV excitable fluorophore at, and only at, the focused spot where the coherent electromagnetic field strength is so high (within the required brief period) that it acts nonlinearly to excite the chromophores at twice the frequency of the IR field. The fluorophores in the cone of the illuminating light above and below focus do not experience the two-photon effect and, therefore, are not excited or damaged. Additionally, in contrast to conventional confocal microscopy, two-photon laser scanning systems do not require an exit pinhole or an image-forming objective lens. This is because the minute two-photon excited fluorescent spot is totally isolated in space and is free of "parasitic" fluorescence in the *xy*-plane as well as along the *z*-axis. Therefore, the fluorescence emission needs only to be collected by an efficient photodetector as the excitation spot is being scanned (see Chapter 28, *this volume*).

Thus, compared to conventional confocal microscopy, two-photon microscopy permits confocal imaging of planes much deeper in the tissue, and with considerably higher light-gathering efficiency, as well as with less fluorescence bleaching and specimen damage outside of the focal plane. Denk *et al*. (1990) and Squirrel *et al*. (1999) have made extended time-lapse recordings of dividing tissue-cultured cells and mammalian embryos in two-photon microscopy.

In another interesting and ingenious application of two-photon microscopy, the fluorescence excitation volume (point-spread function) has been reduced considerably below that defined by wave optics by use of two partially overlapping excitation volumes. The first excites fluorescence in the standard two-photon volume, while the second volume, concurrently generated by a somewhat longer wavelength, quenches the fluorescence (by stim-

ulated emission depletion) in the zone where the two volumes overlap each other. A phase plate in the depletion beam path has the effect that this beam is almost the inverse of the Airy disk and has a null at the focus. Thus, the volume of region actually fluorescing is carved smaller than the standard two-photon excitation volume, and, in fact, Hell and Wichmann (1994) report having reduced the height of the point-spread function (PSF) by as much as a factor of five (see also Klar *et al.*, 2000, Chapter 31, *this volume*).

IS LASER-SCANNING CONFOCAL MICROSCOPY A CURE-ALL?

With the impressively thin and clean optical sections that are obtainable, and the *x*-*z* sections and stereoscopic images that can neatly be displayed or reconstructed, one can be tempted to treat the CLSM as a cure-all. One may even think of the instrument as the single microscope that should be used for all modern cell biology or embryology. How valid is such a statement and what, in fact, are the limitations of the current instruments beyond their high costs?

The fundamental limits of confocal imaging will be covered in the next chapter. Here I will comment on three topics: the speed of image or data acquisition, comparison with the depth of field in phase-dependent imaging, and some optical and mechanical factors affecting confocal microscopy.

Speed of Image or Data Acquisition

Several factors affect the time needed to acquire a usable image with a confocal microscope. These include (1) the type of confocal system used; (2) the optical magnification and numerical aperture of the system; (3) the desired area covered; (4) required quality of the image (e.g., lateral and axial resolution, levels of image gray scale, degree of freedom from graininess); and (5) the amount of light reaching the sensor. Here we will survey a few general points relating to the choice of instruments, specifically as applied to biology.

Among the different confocal systems, the stage-scanning type requires the longest time (~10 s) to acquire a single image because the specimen support has to be translated (vibrated) very precisely. Biological specimens are often bathed in a liquid medium, and for these, any movement presents a problem. Even if the specimen chamber is completely sealed and the gas phase excluded to minimize the inertial effects of stage scanning, specimen motion still can occur during stage scanning. The alternative lens-scanning system can encounter worse problems when oil-immersion lenses are used. Very often structures in biological specimens are moving or changing dynamically at rates incompatible with very slow scan rates. Thus, despite the many virtues of the stage-scanning system recognized by Minsky (1957) and by Wilson and Sheppard (1984), there is little chance that the stage-scanning microscope will be widely used in biology. An exception might be for large-area 3D scanning of fixed and permanently mounted specimens. Such specimens require, or can take advantage of, those virtues of the stage-scanning system that cannot be duplicated by other confocal designs.

In the Petráň-type TSM or the Kino-type confocal microscope, the disk can be spun rapidly enough to provide images at video rate (30 frames/s). When speed of image acquisition is of paramount importance, as in the study of moving cells, living cells at high magnification, or microtubules growing *in vitro*, the type of speed provided by the Nipkow disk system may be indispensable. For example, at the ~10,000× magnification needed for clear visualization, the Brownian motion of microtubules (even those many micrometers long) is so great that an image acquisition time of >0.1 s blurs the image beyond use.

As discussed earlier, the downside of the classical Nipkow disk-type system is that the efficiency of light transmission is low, light reflected by the spinning disk reduces image contrast, and the image may suffer from intrusive scan lines. Also, observation is usually by direct viewing through the ocular, or via some photographic or video imaging device, rather than using a PMT. While video imaging does have its own advantages, video sensors other than cooled charge-coupled devices (CCDs) and special return-beam-type pickup tubes operate over a limited dynamic range. Conventional video pickup tubes seldom respond linearly over a range of >100 : 1 (more commonly somewhat less; see Inoué and Spring, 1997), and they have relatively high measurement noise. By contrast, a PMT can have a dynamic range of $\geq 10^6$. When exceedingly weak signals need to be detected from among strong signals, or when image photometry demands dynamic range and precision beyond those attainable with standard video cameras, an imaging system using a cooled CCD or a PMT detector may be required. Modern stage-scanning- and laser-scanning-type confocal microscopes use such detectors (Chapter 12, *this volume*). Nevertheless, for some applications improved versions of the Nipkow-disk-type confocal instruments may provide optical sections with better signal and image quality than with CLSMs as discussed below under "Yokogawa Disk-Scanning Confocal System."

The frame-scanning rate of the CLSM falls somewhere between that of the stage- and tandem-scanning types, normally about 1 to 2 s/frames. This rate is the minimum time required by the mirror galvanometers (that are used to scan the illuminating and return beams) to produce an image of, say, 512×768 picture elements. This limitation in scanning speed relates to the absolute time required to scan along the fastest axis (usually the *x*, or horizontal, scan). The scanning speed cannot be increased without affecting image resolution or confocal discrimination (Chapters 3, 21, and 25, *this volume*).

The *x*-scanning speed can be increased by using a resonance galvanometer, a spinning mirror, or an acousto-optical modulator instead of the mirror galvanometers (Chapters 3, 9, and 29, *this volume*). However, doing so may reduce both scan flexibility (i.e., no optical "zoom" magnification) and inefficient use of the duty cycle. Furthermore, in a scanning confocal system used for fluorescence microscopy, one cannot use the same acousto-optical device (or other diffraction-based electro-optical modulator) to both scan the exciting beam and de-scan the emitted beam because the modulator would deviate the two beams by different amounts based on their λ.

Of even greater importance, the image captured by a CLSM in a single, 1- to 2-s scan time is commonly too noisy because the image-forming signal is simply not made up of enough photons. The image generally must be integrated electronically over several frame times to reduce the noise, just as when one is using a high-sensitivity video camera. Thus, with a CLSM, it often requires several, or many, seconds to acquire a well-resolved, high-quality fluorescence image.

If, in an attempt to reduce the number of frames that must be integrated, one tries to increase the signal reaching the PMT by raising the source brightness, by opening up the exit pinhole, or by increasing the concentration of fluorochrome, each alteration introduces new problems of its own. In fact, in CLSMs used for fluorescence imaging, if anything, one wants to reduce the light

reaching the specimen in order to avoid saturation of the fluorophores, significant bleaching, and other excitation-induced damage. There is almost an indeterminacy principle operating here: One simply cannot simultaneously achieve high temporal resolution, high spatial resolution, large pixel numbers, and a wide gray scale simultaneously. This speed limitation must be seen as a disadvantage of the CLSM.

As already discussed, two-photon confocal fluorescence microscopy (Chapter 28, *this volume*) is a promising new approach that may reduce the effect of some of these limitations in addition to providing excellent lateral and axial resolution. However, because the time between pulses is long (10–12 s) compared to the fluorescence time of organic dyes, it only produces signal 10% to 20% of the time. This low-duty cycle exacerbates the data rate limit.

While the sampling rate for obtaining whole images with the CLSM is limited, this does not imply that the temporal resolution of the detector system is inherently low. For example, one can measure relatively high-speed events with the CLSM, if one decides to sacrifice pixel numbers by reducing the size of the scanned area or even by using a single, or a few, line scan(s). In addition to the high temporal resolution, the bleaching of diffusible fluorochromes and photodynamic damage to the cell are reported to be significantly reduced when the scan is restricted to a single line (Chapter 19, *this volume*).

Another alternative for gaining speed is to use a slit instead of a pinhole for confocal scanning. This approach, although somewhat less effective than confocal imaging with small round pinholes, is surprisingly effective in suppressing the contribution of out-of-focus features. Several manufacturers have produced laser-illuminated, slit-scanning confocal microscopes that provide video-rate or direct-view imaging systems that are quite easy to operate, at a fraction of the price of the normal CLSM. However, the rapid bleaching of fluorescent dyes encountered with the slit-scanning system has been a disappointment for those hoping to gain confocal scanning speed for studies on living cells.

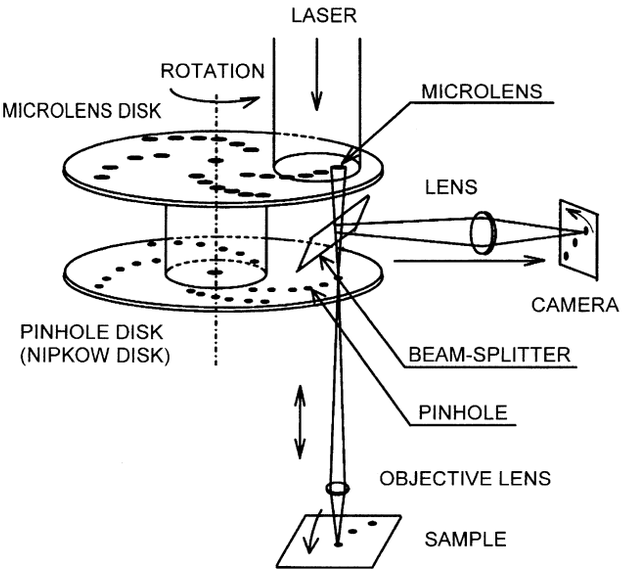


FIGURE 1.6. Schematic of optics in the CSU-10. The expanded and collimated laser beam illuminates the active portion of the upper Nipkow disk containing some 20,000 microlenses. Each microlens focuses the laser beam (through the dichromatic filter cube) onto its corresponding pinhole, thus significantly raising the fraction of the illuminating beam that is transmitted by the main Nipkow disk containing the pinhole array. From the pinholes, the beams progress down to fill the aperture of the objective lens. The objective lens generates a reduced image of the pinholes in the focal plane of the specimen.

Fluorescence given off by the illuminated points in the specimen is captured by the objective lens and focused back onto the Nipkow disk containing the pinhole array. Each pinhole now acts as its own confocal exit pinhole and eliminates fluorescence from out-of-focus regions, thus selectively transmitting fluorescence that originated from the specimen points illuminated by that particular pinhole. (However, for specimens with fluorescence distributed over large depths, some out-of-focus fluorescence can leak through adjacent pinholes in multiple pinhole systems such as the CSU-10; see text.) The rays transmitted by the exit pinholes are deflected by the dichromatic beam splitter, located between the two Nipkow disks, and proceed to the image plane. (Figure courtesy of Yokogawa Electric Corporation.)

Yokogawa Disk-Scanning Confocal System

A new confocal disk-scanning unit (CSU-10 and CSU-21) designed by Yokogawa Electric Corporation provides video-rate and faster confocal imaging with several advantages while overcoming the two major factors that had limited earlier TSM systems. The new system uses two Nipkow-type disks located one above the other with precisely aligned perforations. In place of pinholes, the first disk contains some 10,000 microlenses, each of which focuses the collimated laser beam onto a corresponding pinhole on the second disk. The microlenses increase the throughput of excitation laser from a scant 1% to 2% of conventional Nipkow disks to nearly 50%. At the same time, a dichromatic filter cube is placed between the two disks, so that light reflected or scattered from the initial disk no longer contributes unwanted background to the fluorescence signal received by the detector (Fig. 1.6). These confocal scanning units can be attached to any upright or inverted research-grade light microscope. The 1000 or so pinholes that scan the specimen in parallel at any instant of time are arranged in a unique geometrical pattern. The unique pattern reduces image streaking (found with conventional Nipkow disks) and provides uniform illumination of the whole field of view (Inoué and Inoué, 2002).

With any multiple-pinhole- (or slit-) scanning system, some light originating from outside the focal plane is transmitted through "neighboring" pinholes, so that focal discrimination is not as effective as, or the confocal stringency does not match that of, a point-scanning confocal system. Nevertheless, the Yokogawa system provides very effective focal discrimination and capability for providing striking optical sections in real time, either for direct observation through the eyepiece or captured on a video or photographic camera or a CCD. The residual out-of-focus contribution can be rapidly and effectively reduced by "unsharp masking" or "neighborhood deconvolution" digital processing. (Several examples of the dynamic cellular changes captured with the CSU-10, as well as the effectiveness of postprocessing, are illustrated in Inoué and Inoué, 2002. See also Chapter 10, *this volume*.)

In addition to the effective, real-time and faster-than-video-rate confocal fluorescence imaging in real color (which can be viewed superimposed with the brightfield or DIC image of the specimen), several observers have been impressed by the significantly slower fluorescence bleaching rate and much longer survival time for living cells observed with the CSU-10 (coupled to low-noise CCD or video cameras) compared to imaging of the same objects with point-scanning confocal systems. For example, CSU-10 imaging was found indispensable for capturing the dynamic growth, motion, and gliding of GFP-expressing microtubules in yeast cells

as well as speckle images of tubulin flux in pTk-1 tissue cells and in the thick spindles undergoing mitosis in *Xenopus* egg extracts (Waterman-Storer and Salmon, 1997; Grego *et al*., 2001; Tran *et al*., 2001; Maddox *et al*., 2002). The reasons for low-fluorescence bleaching and extended cell survival are discussed in Inoué and Inoué (2002 and in Chapter 38, *this volume*.)

The advantage of the real-time, direct-view confocal system extends beyond capturing sharp images of moving or dynamically changing objects, whose images would be blurred or distorted by the slow frame-capture rate of conventional CLSMs. For example, with a CLSM it is difficult to visualize, or even to find, minute fluorescent objects that are sparsely distributed in three dimensions. With an image intensifier CCD camera coupled to a direct-view system, the signal from such sparsely distributed objects is readily found in real time as one focuses through the specimen.

Depth of Field in Phase-Dependent Imaging

The *z*-axis resolution measured in epi-fluorescence imaging with a confocal laser scanning microscope is reported to be 1.5 µm with an NA 0.75 objective lens (Cox and Sheppard, 1993) and 0.48 µm with an NA 1.3 objective lens (Hell *et al*., 1993) at a wavelength of 514 nm. Kino reports a depth of field of 0.35 µm for NA 1.4 confocal optics, when imaging point-like reflecting objects. These numbers are in good agreement with Eqs. 2 and 3, and the height of the 3D diffraction pattern of a point object discussed earlier. In addition, Stephan Hell, as described above, has achieved even shallower field depths by superimposing two 3D diffraction spots of differing wavelengths in stimulated depletion point-scanning confocal microscopy.

How do these shallow depth of fields attainable with a confocal microscope compare with those obtainable in the absence of confocal imaging? While I could come up with no hard numbers for fluorescence microscopy without confocal imaging (except where 3D deconvolution is employed, see Chapters 23, 24, and 25, *this volume*), it is well known that the fluorescence from out-of-focus objects substantially blurs the in-focus image. On the other hand, for contrast generated by phase-dependent methods such as phase-contrast, DIC, and polarized-light microscopy, Gordon Ellis and I have obtained data that show remarkably thin optical sections in the absence of confocal imaging.

Thus, using a 100× NA 1.4 Nikon PlanApo objective lens, combined with an NA 1.35 rectified condenser whose full aperture was uniformly illuminated through a light scrambler with 546-nm light from a 100-W high-pressure Hg arc source (as described in Ellis, 1985, and in Inoué, 1986, Appendix 3), I obtained depth of fields of *ca.* 0.2, 0.25, and 0.15 µm, respectively, for phase-contrast, rectified DIC, and rectified polarized-light microscopy.

These values were obtained by examining video images of surface ridges on a tilted portion of a human buccal epithelial cell. The video signal was contrast enhanced digitally but without spatial filtration. The change in image detail that appeared with each 0.2-µm shift of focus (brought about by incrementing a calibrated stepper motor) was inspected in the image and enlarged to ~10,000× on a high-resolution video monitor. As shown in Figure 1.7, the fine ridges on the cell surface are not contiguous in the succeeding images stepped 0.2 µm apart in the polarized-light and phase-contrast images, but they are just contiguous in the DIC images. From these observations, the depth of field in the rectified polarized-light image is estimated to be somewhat below, and the DIC image just above, the 0.2-µm step height. [The phase-contrast images here should not be compared literally with the images in the two other contrast modes because the diameter of the commercially available phase annulus was rather small, and out-of-focus regions intruded obtrusively into the image. With Ellis' aperture-scanning phase-contrast microscope, the illuminating rays, and the correspondingly minute phase absorber spot, scan the outermost rim of the objective lens aperture in synchrony. Therefore, essentially the full NA of the objective lens is available to transmit the waves diffracted by the specimen. Under these conditions, the *z*-axis resolution of the optical section in phase-contrast appears to be even higher than that of the two other contrast modes shown here (Ellis, 1988; Inoué, 1994).]

For polarization microscopy of specimens with low retardances, the LC-Pol scope system devised by Oldenbourg and Mei (1995; see also Oldenbourg, 1996) also provides effective optical sectioning. The LC-Pol scope generates an image (retardance map) whose pixel brightness is proportional to the retardance of the specimen at each pixel, independent of the specimen's azimuth orientation, while the algorithm used to compute the retardance map also reduces the polarization aberrations introduced by the optics (that otherwise degrade the image; Shribak *et al*., 2002). Thus, with the LC-Pol scope system, objective lenses with NA as high as 1.4 can be used at their full aperture to detect retardances as low as 0.03 nm. The use of the high NA lenses at full aperture then provides the shallow depth of field (of less than 1-µm thickness) as illustrated in Figure 1.8. In fact, the LC-Pol scope can individually resolve two flagellar axonemes that cross each other and are separated by no more than their diameter of about 0.2 µm (Oldenbourg *et al*., 1998).

We do not yet quite understand why the depth of field of the non-confocal phase-dependent images should be so thin. It may well be that contrast generation in phase-dependent imaging involves partial coherence even at very high NAs, and that an effect similar to the one proposed elsewhere for half-wave masks (Inoué, 1989) is giving us increased lateral as well as axial resolution. Whatever the theoretical explanation turns out to be, our observations show that for phase-dependent imaging of relatively transparent objects, even in the absence of confocal optics, optical sections can be obtained (at video rate) that appear to be somewhat thinner than for fluorescence imaging in the presence of confocal optics. Moreover, they perform this function without requiring that energy be deposited in the specimen, i.e., without producing photodamage.

OTHER OPTICAL AND MECHANICAL FACTORS AFFECTING CONFOCAL MICROSCOPY

Lens Aberration

With stage- or object-scanning confocal microscopes, we saw earlier that high NA lenses with simplified design and long working distances could be used because the confocal image points (source pinhole, illuminated specimen point, and detector pinhole) all lie exactly on the optical axis of the microscope. This same principle is now used widely in the design of optical disk recorder/players.

In contrast, with TSM and CLSM sharp images of the source "pinhole(s)" must be focused over a relatively large area away from the lens axis. In addition, the objective lens and the scanner must bring images of the illuminated spot(s) and the source pinhole(s) into exact register with the exit pinhole(s), and for fluorescence microscopy, do so at different wavelengths. Thus, for these systems to function efficiently, the microscope objective lens has to be exceptionally well corrected. The field must be flat over an

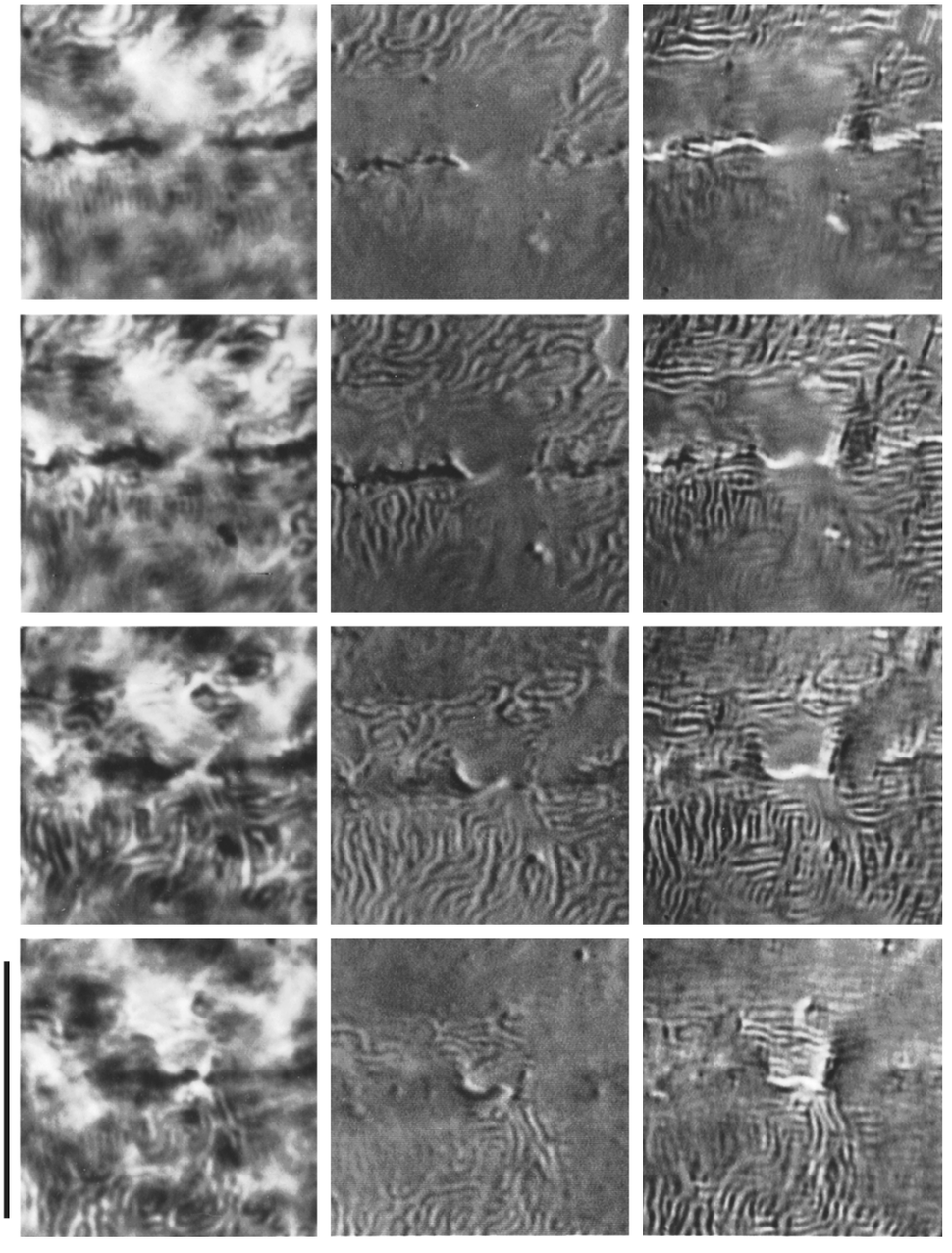


FIGURE 1.7. Optical sections of surface ridges on an oral epithelial cell. These ultrathin optical sections were obtained without confocal imaging in phase-contrast (left), rectified DIC (middle), and rectified polarized-light microscopy (right). The focus planes for the successive frames in each contrast mode were incremented 0.2 μm. Scale bar 10 μm. (See text and original article for details. From Inoué, 1988.)

appreciable area, axial and off-axis aberrations must be corrected over the field used, and lateral and longitudinal chromatic aberrations must be well corrected for both the emission *and* illuminating wavelengths. As far as is possible, the aberrations should be corrected within the objective lens without the need to use a complimentary ocular. [For details of these subjects and design of modern lenses to overcome the aberrations, see Inoué and Oldenbourg (1994), Shimizu and Takenaka (1994), and Chapter 7, *this volume*.] Finally, the lens and other optical components must have good transmission over the needed wavelength range.

These combined conditions place a strenuous requirement on the design of the objective lens. Fortunately, with the availability of modern glass stocks and high-speed computer-optimized design, a series of excellent-quality, high-NA, PlanApo, and high-UV-transmitting lenses have appeared from all four major microscope manufacturers (Leitz, Nikon, Olympus, Zeiss) during the past decade.

Even with excellent lenses, however, the image loses its sharpness when one focuses into a transparent, live, or wet specimen by more than a few micrometers from the inside surface of the coverslip. The problem here is that oil-immersion microscope objectives are designed to be used under rather stringent optical conditions, namely homogeneous immersion of everything, including the specimen itself, in a medium of $\eta = 1.52$. When such a lens is used on live or wet specimens immersed in water or physiological saline solution, even with the coverslip properly oil con-

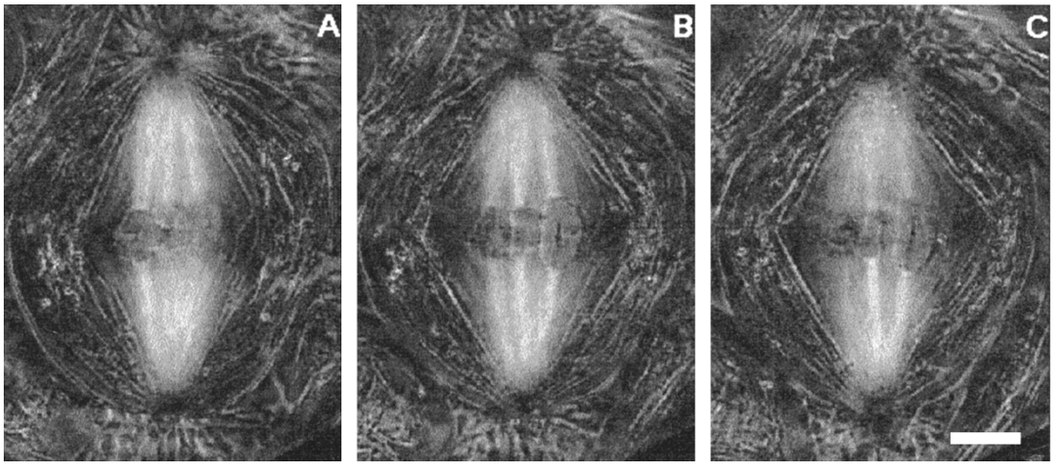


FIGURE 1.8. Optical sections of meiosis-I metaphase spindle in live spermatocyte of a crane fly *Nephrotoma sturalis* observed with the LC-Pol scope. In focus are: (A) the upper kinetochores (Ks) and their two K-fibers for the left bivalent chromosome; (B) upper Ks and fibers for the middle and right bivalents; (C) lower Ks and fibers for the middle and right bivalents. The birefringence retardation of the K-fibers, made up of a dense bundle of microtubules, is *ca.* 1 nm greater than that due to the background array of spindle microtubules. The effect of optical sectioning is more obvious in the mitochondrial threads (which are much thinner than the K-fibers and free of background birefringence) that surround the spindle. Imaged with 546-nm illumination in LC-Pol scope with Nikon 60×/1.4 NA "DIC" PlanApo objective lens combined with condenser NA at 1.0. The fine focus control was shifted 1.2 µm between (A) and (B), and 0.9 µm between (B) and (C). White = 3.0 nm retardance. Scale bar = 5 µm.

tacted to the objective lens, aberrations are no longer properly corrected once the image-forming rays traverse a significant distance in the η = 1.33 aqueous medium. Doing so distorts the unit diffraction image and alters the shape (and even the location of) the point-spread function, and does so to varying degrees as one focuses to different depths into the aqueous medium.[4] This important topic is discussed in detail in Chapters 7 and 20 (*this volume*) and in Inoué and Spring (1997, Sect. 2.5).

The same holds true also for high-NA dry objectives because they are designed under the assumption that (unless embedded in a η = 1.52 medium) the specimen lies in an infinitely thin layer placed directly against a coverslip whose thickness (generally 0.17 mm), refractive index, and dispersion conform to specification.

One approach to overcoming these problems is to switch to a water-immersion objective lens. Then the cumulative depth of the water layer between the objective lens and the focused portion of the specimen should remain unchanged with focus. Whether the objective lens is designed for homogeneous water immersion or for use in the presence of a coverslip does not matter, so long as, in the latter case, a coverslip with the proper specifications is used. In fact, however, even the small difference in η between physiological solutions, seawater, tissue, and pure water must be taken into account. While this approach does overcome some of the aberration problems, water-immersion lenses cannot be made with NAs of much above 1.25 (because of the 1.33 refractive index of water). Several manufacturers now produce high-NA water-immersion objectives with excellent correction, some with high transmissions for UV down to wavelengths of 340 nm. In our experience, the Nikon 60× 1.2 NA Plan Apochromatic, correction-collar-equipped water-immersion objective gave an impressive DIC image of diatom frustule through a 220-µm-thick layer of water between specimen and coverslip. Adjustment of the collar, as in dry- or variable-immersion objective lenses, compensates for the relative thickness of layers having higher or lower η. With the increasing use of electronic and electro-mechanical controls in confocal and conventional microscopes, it is now possible to design a superior high-NA lens with an auto-compensating correction device (possibly built outside of the objective lens) that is electronically linked to the fine focus control.

A (motor-driven) optical-correcting unit, such as the In-Focus system (Infinity Photo-Optical Company, Boulder, CO), placed in the parallel-beam region of a microscope can be used to change the focal level and/or correct for residual spherical aberration without displacing the objective lens. In fact we find that the unit can often improve the point-spread function, so that the *z*-axis distribution of the 3D diffraction pattern becomes more symmetric, even for "highly corrected" Plan Apochromatic objective lenses used following the manufacturer's exact specifications (see Chapters 7 and 9, *this volume*). Conversely, by appropriately linking the In-Focus drive with the objective (and condenser) lens motor drive(s), one can now substantially improve the point-spread function even when focusing deeper, for example, into a specimen residing in an aqueous medium.

Unintentional Beam Deviation

The intensity of each point in the final image from a confocal microscope is designed to measure the amount of light transmitted by the detector pinhole for the corresponding point in the specimen as it is being scanned. However, if the amount of light transmitted by the detector pinhole is modulated by factors not related to the interaction of the illuminating point of light and the specimen at that raster point, or if the confocality between the entrance pinhole, the illuminated specimen point, and the detector pinhole were to be transiently lost for any reason, one would obtain a false reading of the brightness at that point.

One such error could be introduced if a localized, lens- or prism-shaped region having a η different from that of the sur-

[4] Note also that the refractive index and dispersion of the immersion media could also be significantly affected by temperature. Some high NA immersion lenses are thus equipped with correction collars to compensate for these variations in addition to the thickness of the coverslip.

roundings were present in the path of the scanning or imaging beam. The scanning or imaging beam would then be refracted or deviated and the intensity of light reaching the detector falsely modified. Such a false signal could be difficult to distinguish from variations in a genuine signal arising from a specimen point in the focus plane. The plane of focus may also be distorted by the presence of such refracting regions (Pawley, 2002), so that one may no longer be scanning a flat optical section through the specimen (Chapter 17, *this volume*). Moreover, as discussed in the previous section, the diffraction pattern of each image point formed by an oil-immersion lens can be distorted and displaced along the *z*-axis even when a layer of optically homogeneous aqueous medium is present between the specimen and the coverslip [see Fig. 2–40 (after Gibson and Lanni, 1991) in Inoué and Spring, 1997]. Attempts to correct some beam deviations by interferometric measurements of the specimen have been published (Kam *et al*., 2001).

Clearly, vibration of the microscope, and even minor distortions of the mechanical components that support the optics or the specimen, may introduce misalignment between the two pinholes and what was supposed to be the confocal point in the specimen. This could lead to short-term periodic errors or longer-term drift. Antivibration tables that isolate the instrument from building and floor vibrations are commonly used to support confocal microscopes. While such a support is useful and may be essential in some building locations, it does not eliminate the influence of airborne vibration, which can in fact raise major havoc in microscopy (G.W. Ellis, personal communication, 1966). Nor does it eliminate the influence of thermal drift or vibration arising from the operation of the instrument.

Given the need to precisely maintain the confocal alignment and to use some form of mechano-optical scanning within the instrument, a confocal microscope is especially susceptible to vibration and problems of mechanical distortion. Indeed, once the complex optical, electro-optical, mechanical, and electronic systems have been appropriately designed, the success of one confocal instrument over another may well depend on its immunity to vibration, in addition to the friendliness of its user interface. Yokogawa's disk-scanning system, while with somewhat reduced confocal stringency, turns out to be remarkably immune to vibration problems.

CONTRAST TRANSFER AND RESOLUTION IN CONFOCAL VERSUS NON-CONFOCAL MICROSCOPY

In addition to designing and successfully demonstrating the power of stage-scanning confocal microscopy, Wilson and colleagues have extensively analyzed the theoretical foundations of confocal microscope imaging (see Wilson and Sheppard, 1984; Wilson, 1990; Chapters 11, 22, and 23, *this volume*). Their mathematical treatment leads to the somewhat surprising conclusion that the ultimate limit of resolution (i.e., the cut-off spatial frequency or spacing at which image contrast of periodic objects drops to zero) obtainable with *coherent confocal* microscopy is identical with that for *incoherent non-confocal* microscopy. However, compared to incoherent non-confocal optics, image contrast should rise much more sharply with coherent confocal optics as the spatial period is increased. Therefore, the practical resolution attained at threshold contrast (i.e., the minimum contrast required for the spacing to be detected) was expected to be significantly greater with confocal optics than with conventional non-confocal optics.

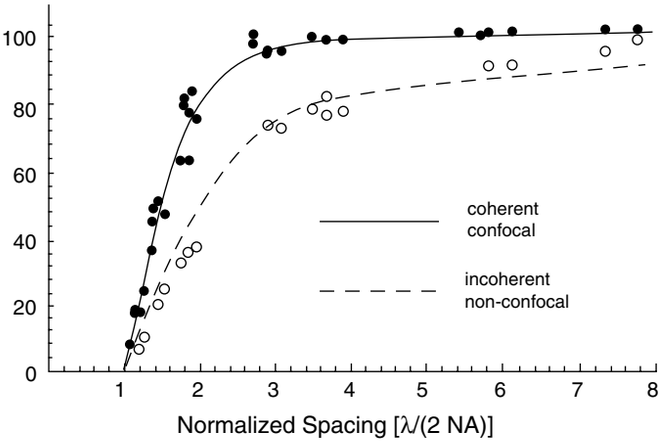


FIGURE 1.9. Experimental contrast transfer values measured as a function of the spatial period of line gratings using a laser beam-scanning microscope in the confocal reflection mode (solid points) and in the non-confocal transmission mode (circles). In both imaging modes, PlanApo objective lenses (Nikon Inc., Melville, NY) with numerical apertures (NAs) ranging from 0.45 to 1.4 and laser wavelengths (λ) of 514.5 nm or 488 nm were used. Spatial periods are expressed in units of the limiting wavelength, λ/2(NA), to normalize the data taken with different laser λ and lenses of different NA. We call data presented in this fashion the contrast transfer characteristic (CTC).

Continuous lines are theoretical curves displaying calculated CTCs for the coherent confocal and the incoherent non-confocal imaging modes. Comparison of the two CTC curves shows that, while the limiting resolutions are identical for both imaging modes, the contrast due to fine detail in the specimen is maintained much better with confocal optics. (The microscope was a prototype built by Hamamatsu Photonics Kabushiki Kaisha, Japan. It was used with the detector pinhole diameter reduced to a small fraction of the Airy disk diameter. From Oldenbourg *et al*., 1993.)

We have confirmed these predictions by direct measurement on test gratings that we fabricated by electron lithography with spacings down to 0.1 µm. Indeed, with confocal optics equipped with a small exit pinhole, the contrast transfer efficiency rose to 80% at twice (and reached 100% at three times) the cut-off spacing. With incoherent non-confocal imaging, 80% contrast transfer was not attained until four times and did not even reach the 100% transfer rate at eight times the cut-off spacing (Fig. 1.9)!

SUMMARY

- The limiting resolution of all microscopes depends on the λ of the light used and the NA of the objective and condenser lenses. Dirty or misaligned optics or vibration, or both, can reduce the achieved resolution. Test resolution regularly, and especially pay attention to the iris setting and full illumination of the condenser aperture, to assure optimal performance.
- A small detector pinhole in the confocal microscope is essential if the maximum optical sectioning capability and resolution of the instrument are to be realized concurrently. Correct alignment and use of this control is very important. However, a larger pinhole may be required to improve the signal when there is limited light level, motion in the specimen, or fading of fluorescence.
- By opening the confocal exit pinhole (to not much greater than the Airy disk diameter), one loses the advantage of higher X–Y resolution in fluorescence microscopy but retains much of the capability for rejecting out-of-focus information while also gaining in the fluorescence signal.

- The ultimate resolution limit of a CLSM in the reflection mode is the same as that of a conventional light microscope, but the contrast that it produces from features is higher. For fluorescence imaging, the resolution in a confocal microscope can be $\sim\sqrt{2}$ greater than with conventional microscopy, but only *if* the confocal detector pinhole is appreciably smaller than the Airy disk produced by a point fluorescent object.
- CLSM is not a cure-all for all biological studies. Its sampling speed is limited, and it does not lend itself to using either interference effects to produce contrast, such as phase or DIC, which have been found to be relatively innocuous to living cells, or polarization contrast that can reveal fine structural dynamics noninvasively.
- Video microscopy can take advantage of the various types of interference and polarizing contrast not easily implemented in the CLSM. Therefore, it is ideal for dynamic, high-resolution observations of living specimens and for tracking the behavior of macromolecular assemblies.
- Holographic microscopy is a field with intriguing promise that is so far beset by practical difficulties.
- Two-photon microscopy and CLSMs provide high-confocal stringency and, in general, are methods of choice for obtaining clear, high-resolution optical sections of the fluorescence distribution in 3D fluorescent specimens. However, for capturing well-resolved optical sections of highly dynamic specimens, or for detection of sparsely distributed minute fluorescent objects, the newer disk-scanning confocal systems employing microlenses on the pinholes may well be the system of choice.

ACKNOWLEDGMENT

This chapter is an updated version of the chapter in the first and second editions. We thank the staff of Yokogawa Electric Corporation for Figure 1.6 and Drs. James LaFountain and Rudolf Oldenbourg for making available the yet unpublished source material for Figure 1.8. We are most grateful to Professor Yoshinori Fujiyoshi of Kyoto University, whose support made the preparation of this chapter possible.

REFERENCES

Abbe, E., 1873, Beiträge zur Theorie des Mikroskops und der mikroskopischen Wahrnehmung, *Schultzes Arc. f. Mikr. Anat.* 9:413–468.

Abbe, E., 1884, Note on the proper definition of the amplifying power of a lens or a lens-system, *J. Royal Microsc. Soc.* 4:348–351.

Agard, D.A., and Sedat, J.W., 1983, Three dimensional architecture of a polytene nucleus, *Nature* 302:676–681.

Agard, D.A., Hiraoka, Y., Shaw, P., and Sedat, J.W., 1989, Fluorescence microscopy in three dimensions, *Methods Cell Biol.* 30: 353–377.

Allen, R.D., 1985, New observations on cell architecture and dynamics by video-enhanced contrast optical microscopy, *Annu. Rev. Biophys. Biophysical Chem.* 14:265–290.

Allen, R.D., Travis, J.L., Allen, N.S., and Yilmaz, H., 1981a, Video-enhanced contrast polarization (AVEC-POL) microscopy: A new method applied to the detection of birefringence in the motile reticulopodial network of *Allogromia laticollaris*, *Cell Motil.* 1:275–289.

Allen, R.D., Allen, N.S., and Travis, J.L., 1981b, Video-enhanced contrast, differential interference contrast (AVEC-DIC) microscopy: A new method capable of analyzing microtubule-related motility in the reticulopodial network of *Allogromia laticollaris*, *Cell Motil.* 1:291–302.

Amos, W.B., White, J.G., and Fordham, M., 1987, Use of confocal imaging in the study of biological structures, *Appl. Opt.* 26:3239–3243.

Åslund, N., Carlsson, K., Liljeborg, A., and Majlof, L., 1983, PHOIBOS, a microscope scanner designed for micro-fluorometric applications, using laser induced fluorescence. In: *Proceedings of the Third Scandinavian Conference on Image Analysis, Studentliteratur*, Lund, p. 338.

Åslund, N., Liljeborg, A., Forsgren, P.-O., and Wahlsten, S., 1987, Three dimensional digital microscopy using the PHOIBOS scanner, *Scanning* 9:227–235.

Baxes, G.A., 1984, *Digital Image Processing: A Practical Primer*, Prentice-Hall, Englewood Cliffs, New Jersey.

Berek, M., 1927, Grundlagen der Tiefenwahrnehmung im Mikroskop, *Marburg Sitzungs Ber.* 62:189–223.

Born, M., and Wolf, E., 1980, *Principles of Optics*, 6th ed., Pergamon Press, Oxford, England.

Boyde, A., 1985a, Tandem scanning reflected light microscopy (TSRLM), Part 2: Pre-MICRO 84 applications at UCL, *Proc. Royal Microsc. Soc.* 20:131–139.

Boyde, A., 1985b, Stereoscopic images in confocal (tandem scanning) microscopy, *Science* 230:1270–1272.

Boyde, A., 1987, Colour-coded stereo images from the tandem scanning reflected light microscope (TSRLM), *J. Microsc.* 146:137–142.

Brakenhoff, G.J., Blom, P., and Barends, P., 1979, Confocal scanning light microscopy with high aperture immersion lenses, *J. Microsc.* 117:219–232.

Brakenhoff, G.J., van der Voort, H.T.M., van Spronsen, E.A., Linnemans, W.A.M., and Nanninga, N., 1985, Three dimensional chromatin distribution in neuroblastoma nuclei shown by confocal scanning laser microscopy, *Nature* 317:748–749.

Brakenhoff, G.J., van der Voort, H.T.M., van Spronsen, E.A., and Nanninga, N., 1986, Three dimensional imaging by confocal scanning fluorescence microscopy. In: *Recent Advances in Electron and Light Optical Imaging in Biology and Medicine*, Vol. 483 (A. Somlyo, ed.), Ann. N.Y. Acad. Sci., New York, pp. 405–414.

Brakenhoff, G.J., van Spronsen, E.A., van der Voort, H.T.M., and Nanninga, N., 1989, Three dimensional confocal fluorescence microscopy, *Methods Cell Biol.* 30:379–398.

Bright, G.R., Fisher, G.W., Rogowska, J., and Taylor, D.L., 1989, Fluorescence ratio imaging microscopy, *Methods Cell Biol.* 30:157–192.

Cagnet M., Françon, M., and Thrierr, J.C., 1962, *Atlas of Optical Phenomena*, Springer-Verlag, Berlin.

Carlsson, K., Danielsson, P., Lenz, R., Liljeborg, A., Majlof, L., and Åslund, N., 1985, Three-dimensional microscopy using a confocal laser scanning microscope, *Opt. Lett.* 10:53–55.

Castleman, K.R., 1979, *Digital Image Processing*, Prentice-Hall, Englewood Cliffs, New Jersey.

Castleman, K.R., 1987, Spatial and photometric resolution and calibration requirements for cell image analysis instruments, *Appl. Opt.* 26:3338–3342.

Castleman, K.R., 1993, Resolution and sampling requirements for digital image processing, analysis, and display. In: *Electronic Light Microscopy* (D. Shotton, ed.), Wiley-Liss Inc., New York, pp. 71–94.

Conchello, J.-A., Heym, J.P., Wei, J.L., and Lichtman, J.W., 1997, NOVEL reflected light confocal profilometer, *Proc. SPIE Conf.* 2984:101–112.

Cox, G., and Sheppard, C., 1993, Effects of image deconvolution on optical sectioning in conventional and confocal microscopes, *Bioimaging* 1:82–95.

Cox, I.J., and Sheppard, C.J.R., 1983, Scanning optical microscope incorporating a digital framestore and microcomputer, *Appl. Opt.* 22:1474–1478.

Cox, I.J., and Sheppard, C.J.R., 1986, Information capacity and resolution in an optical system, *J. Opt. Soc. Am.* 3:1152–1158.

Cremer, C., and Cremer, T. 1978, Considerations on a laser-scanning-microscope with high resolution and depth of field, *Microsc. Acta* 81:31–44.

Davidovits, P., and Egger, M.D., 1971, Scanning laser microscope for biological investigations, *Appl. Opt.* 10:1615–1619.

Davidovits, P., and Egger, M.D., 1972, U.S. Patent #3,643,015, Scanning Optical Microscope.

Denk, W., and Webb, W.W., 1987, Displacement fluctuation spectroscopy of the sensory hair bundles of mechanosensitive cells of the inner ear, *Bull. Am. Phys. Soc.* 32:645.

Denk, W., Strickler, J.H., and Webb, W.W., 1990, Two-photon laser scanning fluorescence microscopy, *Science* 248:73–76.

Egger, M.D., 1989, The development of confocal microscopy, *Trends Neurosci.* 12:11.

Egger, M.D., and Petráň, M., 1967, New reflected-light microscope for viewing unstained brain and ganglion cells, *Science* 157:305–307.

Ellis, G.W., 1966, Holomicrography: Transformation of image during reconstruction a posteriori, *Science* 154:1195–1196.

Ellis, G.W., 1978, Advances in visualization of mitosis *in vivo*. In: *Cell Reproduction, in Honor of Daniel Mazia* (E. Dirksen, D. Prescott, and C.F. Fox, eds.), Academic Press, New York, pp. 465–476.

Ellis, G.W., 1979, A fiber-optic phase-randomizer for microscope illumination by laser, *J. Cell Biol.* 83:303a.

Ellis, G.W., 1985, Microscope illuminator with fiber-optic source integrator, *J. Cell Biol.* 101:83a.

Ellis, G.W., 1988, Scanned aperture light microscopy In: *Proceedings of the Forty-sixth Annual Meeting of EMSA*, San Francisco Press, San Francisco, pp. 48–49.

Fay, F.S., Fogarty, K.E., and Coggins, J.M., 1985, Analysis of molecular distribution in single cells using a digital imaging microscope. In: *Optical Methods in Cell Physiology* (P. De Weer and B.M. Salzberg, eds.), John Wiley & Sons, New York.

Flory, L.E., 1951, The television microscope, *Cold Spring Harbor Symp. Quant. Biol.* 16:505–509.

Freed, J.J., and Engle, J.L. 1962, Development of the vibrating-mirror flying spot microscope for ultraviolet spectrophotometry, *Ann. N.Y. Acad. Sci.* 97:412–448.

Fuchs, H., Pizer, S.M., Heinz, E.R., Bloomberg, S.H., Tsai, L-C., and Strickland, D.C., 1982, Design and image editing with a space-filling 3D display based on a standard raster graphics system, *Proc. Soc. Photo. Opt. Instrum. Eng.* 367:117–127.

Gibson, S.F., and Lanni, F., 1991. Experimental test of an analytical model of aberration in an oil-immersion objective lens used in three-dimensional light microscopy, *J. Opt. Soc. Am.* A 8:1601–1613.

Goldstein, S.R., Hubin, T., Rosenthal, S., and Washburn, C., 1990, The VRIDICOM: a video rate image dissector confocal microscope. In: *Optical Microscopy for Biology* (B. Herman and K. Jacobson, eds.), Wiley-Liss, Inc., New York, pp. 59–72.

Gonzales, R.C., and Wintz, P., 1987, *Digital Image Processing*, 2nd ed., Addison-Wesley, Reading, Massachusetts.

Grego, S., Cantillana, V., and Salmon, E.D., 2001, Microtubule treadmilling in vitro investigated by fluorescence speckle and confocal microscopy, *Biophys. J.* 81:66–78.

Gustafsson, M.G.L., 2000, Surpassing the lateral resolution limit by a factor of two using structured illumination microscopy, *J. Microsc.* 198:82–87.

Hamilton, D.K., and Wilson, T. 1984, Two-dimensional phase imaging in the scanning optical microscope, *Appl. Opt.* 23:348–352.

Hansen, E.W., 1986, Appendix II. In: *Video Microscopy* (S. Inoué, ed.), Plenum Press, New York, pp. 467–475.

Hard, R., Zeh, R., and Allen, R.D., 1977, Phase-randomized laser illumination for microscopy, *J. Cell Sci.* 23:335–343.

Harris, J.L., 1964, Diffraction and resolving power, *J. Opt. Soc. Am.* 54:931–936.

Hecht, E., 1987, *Optics*, 2nd ed., Addison-Wesley, Reading, Massachusetts.

Hell, S.W., and Wichmann, J., 1994, Breaking the diffraction resolution limit by stimulated emission: stimulated-emission-depletion fluorescence microscopy, *Opt. Lett.* 19:780–782.

Hell, S.W., Reiner, G., Cremer, C., and Stelzer, E.H.K., 1993, Aberrations in confocal fluorescence microscopy induced by mismatches in refractive index, *J. Microsc.* 169:391–405.

Hellwarth, R., and Christensen, P., 1974, Nonlinear optical microscopic examination of structure in polycrystalline ZnSe, *Optics Comm.* 12:318–322.

Hoffman, R., and Gross, L., 1975, Modulation contrast microscopy, *Appl. Opt.* 14:1169–1176.

Hopkins, H.H., 1951, The concept of partial coherence in optics, *Proc. Royal Soc. Lond.* 208A:263.

Hopkins, H.H., and Barham, P.M., 1950, The influence of the condenser on microscopic resolution, *Proc. Royal Soc. Lond.* 63B:737–744.

Ichihara, A., Tanaami, T., Isozaki, K., Sugiyama, Y., Kosugi, Y., Mikuriya, K., Abe, M., and Uemura, I., 1996, High-speed confocal fluorescence microscopy using a Nipkow scanner with microlenses — for 3-D imaging of single fluorescent molecule in real-time, *Bioimages* 4:57–62.

Ingelstam, E., 1956, Different forms of optical information and some interrelations between them. In: *Problem in Contemporary Optics*, Istituto Nazionale di Ottica, Arcetri-Firenze, pp. 128–143.

Inoué, S., 1981, Video image processing greatly enhances contrast, quality, and speed in polarization based microscopy, *J. Cell Biol.* 89:346–356.

Inoué, S., 1986, *Video Microscopy*, Plenum Press, New York.

Inoué, S., 1988, Progress in video microscopy, *Cell Motil. Cytoskel.* 10:13–17.

Inoué S., 1989, Imaging of unresolved objects, superresolution, and precision of distance measurement, with video microscopy, *Methods Cell Biol.* 30:85–112.

Inoué S., 1994, Ultra-thin optical sectioning and dynamic volume investigation with conventional light microscopy. In: *Three-Dimensional Confocal Microscopy* (J.K. Stevens, L.R. Mills, and J. Trogadis, eds.), Academic Press, San Diego, pp. 397–419.

Inoué, S., and Inoué, T.D., 1986, Computer-aided stereoscopic video reconstruction and serial display from high-resolution light-microscope optical sections. In: *Recent Advances in Electron and Light Optical Imaging in Biology and Medicine*, Vol. 483 (A. Somlyo, ed.), Ann. N.Y. Acad. Sci., New York, pp. 392–404.

Inoué, S., and Inoué, T.D., 2002, Direct-view high-speed confocal scanner — the CSU-10. In: *Cell Biological Applications of Confocal Microscopy*, 2nd ed. (B. Matsumoto, ed.), Academic Press, San Diego, pp. 87–123.

Inoué, S., and Oldenbourg, R., 1995, Optical instruments: Microscopes. In: *Handbook of Optics*, 2nd ed., Vol. 2 (M. Bass, ed.), McGraw-Hill, New York, pp. 17.1–17.52.

Inoué, S., and Spring, K., 1997, *Video Microscopy*, 2nd ed., Plenum Press, New York.

Inoué, S., Goda, M., and Knudson, R.A., 2001a, Centrifuge polarizing microscope. II. Sample biological applications, *J. Microsc.* 201:357–367.

Inoué, S., Knudson, R.A., Goda, M., Suzuki, K., Nagano, C., Okada, N., Takahashi, H., Ichie, K., Iida, M., and Yamanaka, K., 2001b, Centrifuge polarizing microscope. I. Rationale, design, and instrument performance, *J. Microsc.* 201:341–356.

Inoué, S., Shimomura, O., Goda, M., Shribak, M., and Tran, P.T., 2002, Fluorescence polarization of green fluorescent protein (GFP), *Proc. Natl. Acad. Sci.* 99:4272–4277.

Kam, Z., Hanser, B., Gustafsson, M.G.L., Agard, D.A., and Sedat, J.W., 2001, Computational adaptive optics for live three-dimensional biological imaging, *Proc. Natl. Acad. Sci.* 98:3790–3795.

Klar, T.A., Jacobs, S., Dyba, M., Egner, A., and Hell, S.W., 2000, Fluorescence microscopy with diffraction resolution barrier broken by stimulated emission, *Proc. Natl. Acad. Sci.* 97:8206–8210.

Koester, C.J., 1980, Scanning mirror microscope with optical sectioning characteristics: Applications in ophthalmology, *Appl. Opt.* 19:1749–1757.

Kubota, H., and Inoué, S., 1959, Diffraction images in the polarizing microscope, *J. Opt. Soc. Am.* 49:191–198.

Leith, E.N., and Upatnieks, J., 1963, Wavefront reconstruction with continuous-tone objects, *J. Opt. Soc. Am.* 53:1377–1381.

Leith, E.N., and Upatnieks, J., 1964, Wavefront reconstruction with diffused illumination and 3D objects, *J. Opt. Soc. Am.* 54:1295–1301.

Lewin, R., 1985, New horizons for light microscopy, *Science* 230:1258–1262.

Linfoot, E.H., and Wolf, E., 1953, Diffraction images in systems with an annular aperture, *Proc. Phys. Soc. B* 66:145–149.

Linfoot, E.H., and Wolf, E., 1956, Phase distribution near focus in an aberration-free diffraction image, *Proc. Phys. Soc. B* 69:823–832.

Maddox, P., Desai, A., Oegema, K., Mitchison, T.J., and Salmon, E.D., 2002, Poleward microtubule flux is a major component of spindle dynamics and anaphase A in mitotic *Drosophila* embryos, *Curr. Biol.* 12:1670–1674.

McCarthy, J.J., and Walker, J.S., 1988, Scanning confocal optical microscopy, *EMSA Bull.* 18:75–79.

Minsky, M., 1957, U.S. Patent #3013467, Microscopy Apparatus.

Minsky, M., 1988, Memoir on inventing the confocal scanning microscope, *Scanning* 10:128–138.

Montgomery, P.O., Roberts, F., and Bonner, W., 1956, The flying-spot monochromatic ultra-violet television microscope, *Nature* 177:1172.

Nipkow, P., 1884, German Patent #30,105.

Nomarski, G., 1955, Microinterférométre différentiel à ondes polarisées, *J. Phys. Radium* 16:S9–S13.

Oldenbourg, R., 1996, A new view on polarization microscopy, *Nature* 381:811–812.

Oldenbourg, R., and Mei, G., 1995, New polarized light microscope with precision universal compensator, *J. Microsc.* 180:140–147.

Oldenbourg, R., Salmon, E.D., and Tran, P.T., 1998, Birefringence of single and bundled microtubules, *Biophys. J.* 74:645–654.

Oldenbourg, R., Terada, H., Tiberio, R., and Inoué, S., 1993, Image sharpness and contrast transfer in coherent confocal microscopy, *J. Microsc.* 172:31–39.

Pawley, J.B., 2002, Limitations on optical sectioning in live-cell confocal microscopy, *Scanning* 21:241–246.

Petráň, M., Hadravsky, M., Egger, D., and Galambos, R., 1968, Tandem-scanning reflected-light microscope, *J. Opt. Soc. Am.* 58:661–664.

Quate, C.F., 1980, Microwaves, acoustic and scanning microscopy. In: *Scanned Image Microscopy* (E.A. Ash, ed.), Academic Press, San Diego, pp. 23–55.

Sharnoff, M., Brehm, L., and Henry, R., 1986, Dynamic structures through microdifferential holography, *Biophys. J.* 49:281–291.

Sheppard, C.J.R., and Choudhury, A., 1977, Image formation in the scanning microscope, *Optica* 24:1051.

Sheppard, C.J.R., Gannaway, J.N., Walsh, D., and Wilson, T., 1978, *Scanning Optical Microscope for the Inspection of Electronic Devices*, Microcircuit Engineering Conference, Cambridge.

Sher, L.D., and Barry, C.D., 1985, The use of an oscillating mirror for 3D displays. In: *New Methodologies in Studies of Protein Configuration* (T.T. Wu, ed.), Van Nostrand-Reinhold, Princeton, New Jersey.

Shimizu, Y., and Takenaka, H., 1994, Microscope objective design. In: *Advances in Optical and Electron Microscopy*, Vol. 14 (C. Sheppard and T. Mulvey, eds.), Academic Press, San Diego, pp. 249–334.

Shotten, D., ed., 1993, *Electronic Light Microscopy: The Principles and Practice of Video-enhanced Contrast, Digital Intensified Fluorescence, and Confocal Scanning Light Microscopy*, John Wiley & Sons, New York.

Shribak, M., Inoué, S., and Oldenbourg, R., 2002, Polarization aberrations caused by differential transmission and phase shift in high-numerical-aperture lenses: theory, measurement, and rectification, *Opt. Eng.* 41:943–954.

Smith, L.W., and Osterberg, H., 1961, Diffraction images of circular self-radiant disks, *J. Opt. Soc. Am.* 51:412–414.

Squirrel, J.M., Wokosin, D.L., White, J.G., and Bavister, B.D., 1999, Long-term two-photon fluorescence imaging of mammalian embryos without compromising viability, *Nature Biotech.* 17:763–767.

Stevens, J.K., Mills, L.R., and Trogadis, J., 1994, *Three-Dimensional Confocal Microscopy*, Academic Press, San Diego.

Streibl, N., 1985, Three dimensional imaging by a microscope, *J. Opt. Soc. Am.* A 2:121–127.

Suzuki, T., and Hirokawa, Y., 1986, Development of a real-time scanning laser microscope for biological use, *Appl. Opt.* 25:4115–4121.

Tanasugarn, L., McNeil, P., Reynolds, G.T., and Taylor, D.L., 1984, Microspectrofluorometry by digital image processing: Measurement of cytoplasmic pH, *J. Cell Biol.* 89:717–724.

Tolardo di Francia, G., 1955, Resolving power and information, *J. Opt. Soc. Am.* 45:497–501.

Tran, P.T., Marsh, L., Doye, V., Inoué, S., and Chang, F., 2001, A mechanism for nuclear positioning in fission yeast based on microtubule pushing, *J. Cell Biol.* 153:397–411.

Tsien, R.Y., 1989, Fluorescent indicators of ion concentration, *Methods Cell Biol.* 30:127–156.

Volkmer, A., Cheng, J.-X., and Xie, X. S., 2001, Vibrational imaging with high sensitivity via epidetected coherent anti-Stokes Raman scattering microscopy, *Phys. Rev. Lett.* 87:023901-1–023901-4.

Waterman-Storer, C.M., and Salmon, E.D., 1997, Actomyosin-based retrograde flow of microtubules in the lamella of migrating epithelial cells influences microtubule dynamic instability and turnover and is associated with microtubule breakage and treadmilling, *J. Cell Biol.* 139:417–434.

White, J.G., Amos, W.B., and Fordham, M., 1987, An evaluation of confocal versus conventional imaging of biological structures by fluorescence light microscopy, *J. Cell Biol.* 105:41–48.

Wijnaendts van Resandt, R.W., Marsman, H.J.B., Kaplan, R., Davoust, J., Stelzer, E.H.K., and Strickler, R., 1985, Optical fluorescence microscopy in three dimensions: Microtomoscopy, *J. Microsc.* 138:29–34.

Wilke, V., Gödecke, U., and Seidel, P., 1983, Laser-scan-mikroskop, *Laser and Optoelecktron* 15:93–101.

Wilson, T., 1985, Scanning optical microscopy, *Scanning* 7:79–87.

Wilson, T., 1990, *Confocal Microscopy*, Academic Press, London.

Wilson, T., and Sheppard, C., 1984, *Theory and Practice of Scanning Optical Microscopy*, Academic Press, London.

Wilson, T., Gannaway, J.N., and Johnson, P., 1980, A scanning optical microscope for the inspection of semiconductor materials and devices, *J. Microsc.* 118:390–314.

Xiao, G.Q., and Kino, G.S., 1987, A real-time confocal scanning optical microscope. In: *Proceedings of SPIE*, Vol. 809, *Scanning Imaging Technology* (T. Wilson and L. Balk, eds.), pp. 107–113.

Young, J.Z., and Roberts, F., 1951, A flying-spot microscope, *Nature* 167: 231.

Zernicke, V.F., 1935, Das Phasenkontrastverfahren bei der mikroskopischen Beobachtung, *Z. Tech. Phys.* 16:454–457.

Zworykin, V.K., 1934, The iconoscope — a modern version of the electric eye, *Proceedings of IRE* 22:16–32.

Zworykin, V.K., and Morton, G.A., 1954, *Television: The Electronics of Image Transmission in Color and Monochrome*, 2nd ed., John Wiley & Sons, New York.

2

Fundamental Limits in Confocal Microscopy

James B. Pawley

INTRODUCTION

The previous chapter described how the confocal approach developed from conventional light microscopy and outlined the basic advantages gained by the use of confocal sampling techniques, primarily that the exclusion of light by the confocal pinhole makes it possible to record data from optical sections. This chapter will discuss the fundamental considerations that limit the performance of all confocal microscopes. Though at present no commercially available equipment approaches these limits, some simple tests will be described to help the user assess how well a given instrument performs. Additional information to help the user to operate the confocal microscope in an optimal manner can be found in Chapter 35, "A Tutorial on Confocal Microscopy," and Chapter 36, "Practical Confocal Microscopy." These also include methods for measuring resolution and other useful parameters.

What Limits?

The task of the confocal light microscope is to measure optical or fluorescent properties within a number of small, contiguous subvolumes of the specimen (Fig. 2.1; Pawley and Centonze, 1994). The fundamental limits on this process, therefore, are related to the quantitative accuracy with which these measurements can be made, a factor that depends on the number of photons that pass into n_1 and out of, n_2, the sub-volume; its size (δx, δy, δz); and its position (x, y, z). Additional limitations are imposed on the rate at which these measurements can be made by the effects of photodamage to the specimen, finite source brightness, and fluorescence saturation. Finally, limitations are imposed by the fact that the continuous specimen must be measured in terms of discrete volume elements called voxels [a voxel is the three-dimensional (3D) equivalent of a pixel, which is the smallest element of a two-dimensional (2D) digital image]. This chapter will try to define the factors that ultimately limit the accuracy with which these measurements can be made. As such, it will serve as an introduction to many of the chapters that follow in which the practical and theoretical aspects of these problems are discussed in greater detail. The discussion should be applicable to the consideration of any type of confocal microscope, though here, as elsewhere in this volume, microscopes in which scanning is accomplished by moving the light beam(s) rather than the specimen will be emphasized because they are more easily applied to living specimens. Most of the discussion will focus on the performance of the confocal laser scanning microscope (CLSM), but in some cases, differences between the mirror-scanning and disk-scanning instruments (including both tandem and single-sided disks) will dictate a separate consideration.

The data recorded from a confocal microscope will, in the simplest case, be a set of intensity values (usually representing the concentration of fluorophore) for every voxel throughout a 3D volume within the specimen. Though these data may often be displayed as an image, it should always be remembered that the single-beam confocal microscope is intrinsically a serial or sampling instrument, not a parallel-imaging instrument. While it is true that one may choose to sample a plane by sequentially scanning the illumination over a large number of overlapping sub-volumes that cover the focus plane and that by doing so, one may produce a 2D image, given sufficiently flexible equipment, one could also use the same total sampling (imaging) time to measure a single point at a great many different times, a smaller volume within the sample or, indeed, any other small collection of points within the specimen a great many times.

The distinction between sampling and imaging is, of course, not absolute; after all, most of us will view the final result as some sort of image. However, the distinction is still useful because it requires one to explicitly confront many problems that are not always so obvious when microscope images are viewed directly by eye or after photographic recording.

The sampling approach, which is covered in more detail in Chapter 4, allows an image to be built up from a number of individual measurements, each of which reflect properties within a specific region of the sample. If the measured properties are optical, the measurements involve counting photons, and this process itself implies limits on both the data rate and the statistical accuracy that are often ignored in normal widefield (WF) microscopy. These limitations are associated with factors such as counting statistics, source brightness, and specimen response, and are discussed next.

Although the points raised so far constitute a fairly complete list of the **physical limits** on the accuracy and completeness of the data stored in the image memory of a confocal microscope, they say nothing about factors affecting the response of either the dye molecules in the specimen or the response of these molecules to the excitation. A more complete understanding of these and other important variables can be found outlined in Pawley (2000) and in greater detail throughout the other chapters of this book.

Counting Statistics: The Importance of *n*

The accuracy of any particular measurement involving fundamental, quantum interactions (such as counting photons) is limited by Poisson statistics. Without going into the details, this means that if the same measurement is made repeatedly, and the average result of these measurements is n photons/measurement, the chance that any specific measurement is in the range between $\mathbf{n} + \sqrt{\mathbf{n}}$ and n

James B. Pawley • University of Wisconsin, Madison, Wisconsin 53706

 Handbook of Biological Confocal Microscopy, Third Edition, edited by James B. Pawley, Springer Science+Business Media, LLC, New York, 2006.

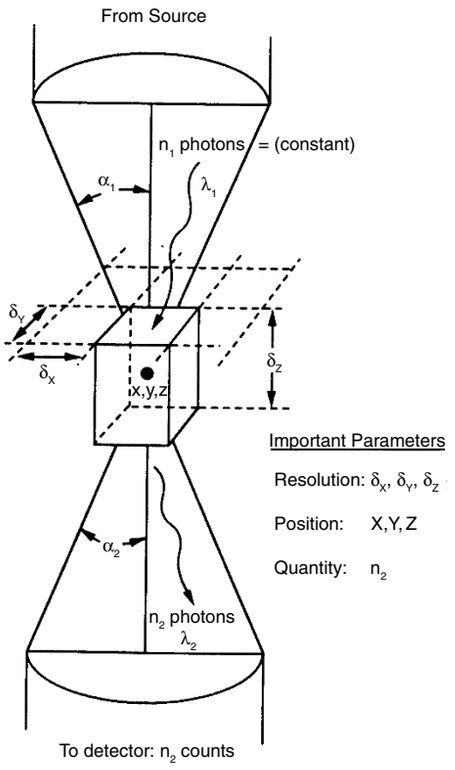


FIGURE 2.1. Parameters related to the fundamental limitations of confocal microscopy.

$-\sqrt{n}$ is only 63%. For example, if n is 100 photons, 63% of the measurements will be in the range from $100-\sqrt{100}$ to $100+\sqrt{100}$ or between 90 and 110. Such a measurement is said to have 10% statistics. It can be seen that increasing the precision to 1% requires that n be increased to $(100)^2$ or 10,000 photons. While similar considerations limit the performance of all types of image measurements, they are more explicit in their effect on confocal microscopy where photons are routinely counted individually. It might help to have a better idea about the numbers of photons involved. Figure 2.2 shows how a 1 mW laser beam composed of 10^{15} photon/s becomes a detected signal of only 10–100 photons/pixel.

The uncertainty associated with counting quantum-mechanical events is often spoken of in terms of it being the source of **intrinsic** or **statistical** noise, and this usage is the basis of the common belief that, while a single-scan image is "noisy," the "noise" can be "reduced" by summing or Kalman-averaging the data from many frames. This usage is accurate to the extent that because the summed image contains more data, it is better statistically determined and appears less noisy. However, it is important to keep intrinsic noise separate in one's mind from **extrinsic** noise such as that introduced by detector dark-current or electronic noise, or that produced by stray or out-of-focus light[1] because, unlike intrinsic noise, these factors are susceptible to being reduced by careful technique and technological improvements. Furthermore, in the case of fixed pattern noise, the effect may not be reduced by averaging many frames.

[1] A simple test for stray is to collect a frame with the room lights on but the laser turned off. If the average brightness of this frame or one with the laser on but no specimen in place, is higher than that with the laser and room lights off, you may have a stray light problem.

While it is misleading to think that the **only** way to reduce "noise" is to average more data, it is also true that in a well-designed CLSM, the major noise source is intrinsic noise. This fact highlights the importance of making sure that as many as possible of the available photons are recorded as part of the signal. Photon efficiency is discussed later.

Source Brightness

A fundamental law of optics states that the brightness of light in the image (measured in watts/cm^2/steradian) can never be greater than it was in the object (or source). In the case of laser-scanning microscopes, the intrinsic brightness of the laser source is so high that this law does not present a practical limitation on performance (though photodamage of the specimen may do so). However, it does pose a limitation on the performance of disk-scanning confocal instruments, many of which currently use mercury arc sources that lose 90% to 98% of their intensity in passing through the disk (Chapters 6, 10, *this volume*). In the latter case, the source brightness and the optical design of the illuminating optics are crucial to being able to detect enough photons to produce a statistically well-defined fluorescence image in a reasonable amount of time. At present, the total power of the narrow-band illumination needed to excite fluorescence that emerges from the best disk-scanning instruments is at least an order of magnitude less than that commonly used with the laser instruments. However, improved non-laser sources are constantly being developed (Chapter 6, *this volume*) and, in addition, the laser-powered disk-scanning microscopes are beginning to take over some of the fast-scanning market previously dominated by the arc-illuminated disk scanners (Chapter 10, *this volume*).

Specimen Response: Dye Saturation

In normal, widefield (WF) microscopy, it is safe to assume that photons interact with the specimen in a manner that is independent of the illumination intensity. However, this linear response is not characteristic of laser-based confocal microscopes operated at effective laser power levels of >1 mW. Conceivable departures include the possibility that absorption in the specimen may cause sufficient warming to produce damage or that the electric field strength may become sufficient to produce a nonlinear response (such as 2-photon excitation, Chapters 28 and 37, *this volume*). However, the most obvious complication is the phenomenon of singlet-state fluorescence saturation.

This phenomenon occurs when the flux of exciting illumination is so intense that, at any instant, a significant fraction of the fluorescent molecules in the illuminated area are already in the singlet-excited state. As excited molecules no longer absorb light at the usual wavelength (λ), this has the effect of lowering the effective dye concentration. This saturation threshold can easily be reached at flux levels around 10^6 W/m^2 such as are found in CLSMs (see Chapters 16, 17, and 39, *this volume*). The problem is more severe when using dye molecules with high absorption crossections, or long fluorescent decay times especially when the dye must be used at low concentration.

Effects of Saturation

Because fluorescence saturation is a property of the beam, it affects **all** dye molecules equally, so those in "bright" pixels are affected the same as those in "dim" pixels. As a result, the contrast of the final image seems unaffected: bright areas are bright, dark areas, dark. In other words, an image recorded with a beam intense

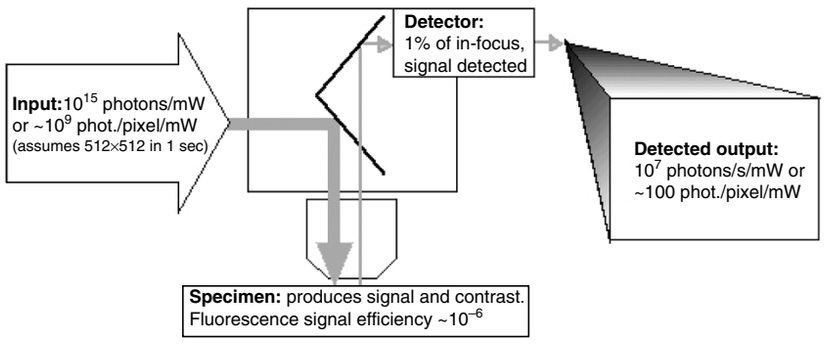


FIGURE 2.2. Schematic diagram showing photon numbers at various stages of fluorescence microscopy.

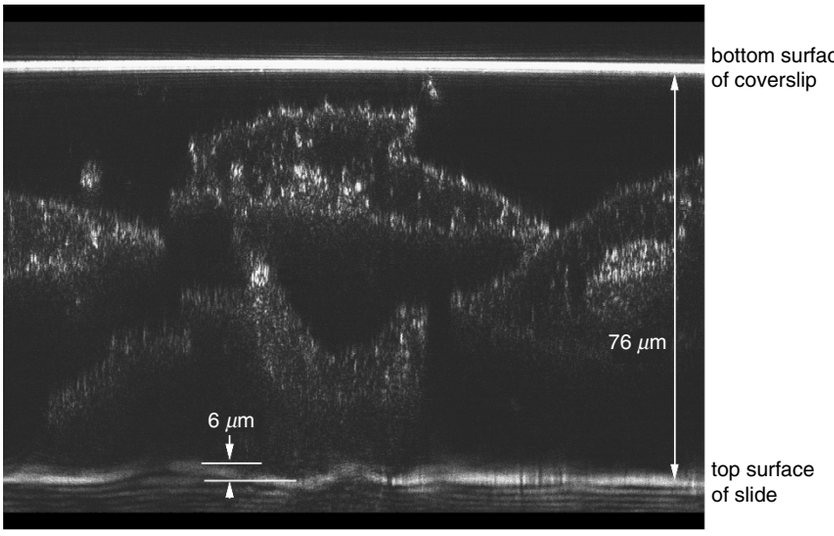


FIGURE 2.3. Confocal XZ, backscattered light image of cheek cells in a chamber made of a coverslip held away from the microscope slide by dots of dried nail polish. The image of the upper glass/water interface is straight and smooth. The lower one is not. This is an indication that the optical properties of the cheek cells have distorted the optical section. Bio-Rad MRC-600 confocal mounted on a Nikon upright microscope with a 60× NA 1.4 Plan-Apo oil-immersion objective.

enough to cause saturation does not look "clipped" in intensity in the same way that an overexposed photograph does. However, the danger of fluorescence saturation is that in its presence, the signal from **any particular** pixel becomes a function of variables other than dye concentration. These variables include the local fluorescent decay time constant, which can depend strongly on the molecular environment, and local defocus effects that may affect the peak intensity in the focused spot and hence the degree of saturation. It follows from this last point that, as saturation occurs mainly at the center of the focused spot, relatively more signal will be produced from **adjacent** planes when one operates near saturation, an effect that marginally reduces *z*-resolution.

Finally, although the mechanisms of photodegradation are as yet imperfectly understood (see Chapters 16 and 39, *this volume*), it now seems likely that the absorption of a second photon by a molecule still in the singlet-excited state may turn out to be a common bleaching mechanism. If high levels of light flux increase the **rate** at which fluorescent dye is bleached (per illuminating photon), operation near saturation may increase the bleach rate.

This fundamental limitation on the rate of fluorescent data acquisition can be side-stepped if the light illuminates more than one focused spot on the specimen. However, to preserve confocal conditions, a separate excitation and detection pinhole must be used for each spot, a condition that is only present in the disk-scanning and line-scanning instruments at this time.

The Effect of Refractile Cellular Structures

As is diagramed in countless textbooks, the pinhole of the confocal optical system excludes light emitted or scattered from features that are above or below the focus plane, creating the "optical section." However, all these diagrams assume that the specimen is optically uniform. While this assumption may be met for fixed specimens that are embedded in a mounting media having a high refractive index (RI), it is less accurate in describing the optics of living cells. The fact that living cells produce high-contrast images when viewed using phase-contrast or differential-interference contrast optics, is a clear indication that the RI of many cellular structures is substantially different from that of water. Figure 2.3 is an *xz*-image of a clump of cheek cells mounted between the coverslip (top) and the slide (bottom) made using **backscattered light** (BSL).[2] As it should be, the flat surface of the coverslip is imaged as a thin horizontal white line. However, because of the presence of the cheek cells, the equally flat surface of the glass slide is rendered as a fuzzy line that undulates up and down by as much as

[2] Backscattered light is a more general term for what is often referred to as "reflected light." It is recommended that the term "reflected" be reserved to describe light scattered by features sufficiently large and smooth so that "the angle of incidence equals the angle of reflection." Most cells produce much more backscattered light than reflected light.

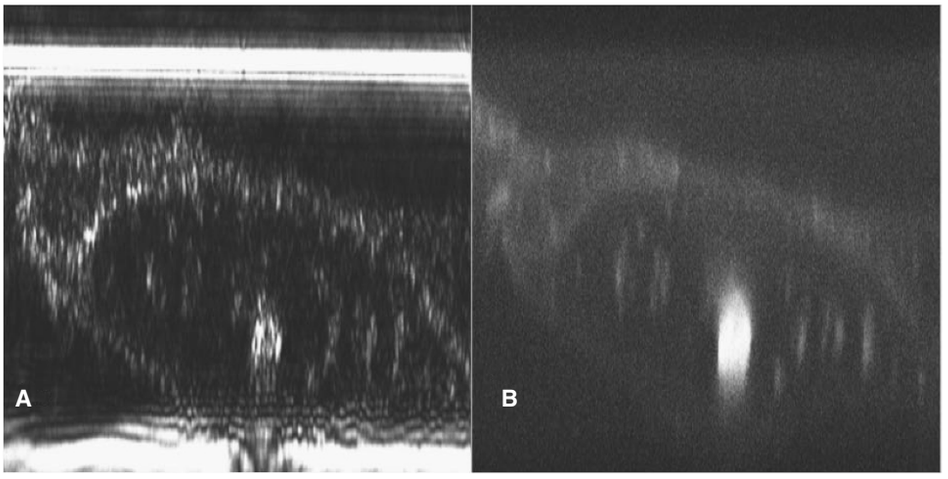


FIGURE 2.4. (A) Confocal XZ, backscattered light image of cheek cells in a chamber made of a coverslip held away from the microscope slide by dots of dried nail polish. (B) Acridine orange fluorescence image of the same specimen as in (A). It is easy to see how the presence of the nucleus (the large blob in the fluorescence image) has displaced the BSL image of the top surface of the slide. Optical system the same as in Figure 2.3. Field width, 50 μm; field height, ~60 μm.

6 μm. Figures 2.4 and 2.5 make clear the role that the nuclei in some cells can play in distorting the "plane of focus." In this case, the "surface of best focus" is clearly not a plane (Pawley, 2002).

The idea that the RI anomalies caused by common cellular structures, such as nuclei, are sufficiently severe to displace the location of any optical section on their far side by distances on the order of micrometers is deeply disturbing. As living cells necessarily have nuclei and other refractive organelles, it is hard to see how, or even if, we can compensate for the sequellae of their optical properties. Although one might imagine computer calculations that would model these optical effects and thereby improve matters, such calculations will be immensely complex and therefore take time: time seldom available when viewing living cells. In general, it seems that we must accustom ourselves to more modest performance when viewing living specimens in a 3D light microscope.

Given the distortion noted above, it seems inevitable that these RI anomalies must also deform the point-spread-function (PSF) of the microscope in nearby regions. This raises questions about the confidence one can have in images produced by widefield/image-deconvolution of living specimens. It is not that deconvolution will not produce a sharper image. The problem is, does this sharper image accurately represent the 3D structure of the specimen?

In some tissues, cellular structures are naturally less optically disruptive: cornea and lens come to mind. For other living tissues, it seems that one must be mindful that the visibility of peri-nuclear structures may depend not only on their presence or absence but also on whether these structures are located on the near or far side of the nucleus. When they are located on the far side, mounting the specimen between two coverslips so that it can be flipped over may be worthwhile (see Chapter 15, *this volume*).

When looking far below the surface of a tissue, it may be worth the effort to try to orient the specimen so that the foreground contains as few nuclei as possible.

A first approximation of how serious this problem is on any particular specimen can be obtained by viewing the specimen using phase-contrast or darkfield optics. Contrast in both of these imaging modes is proportional to changes in local RI.

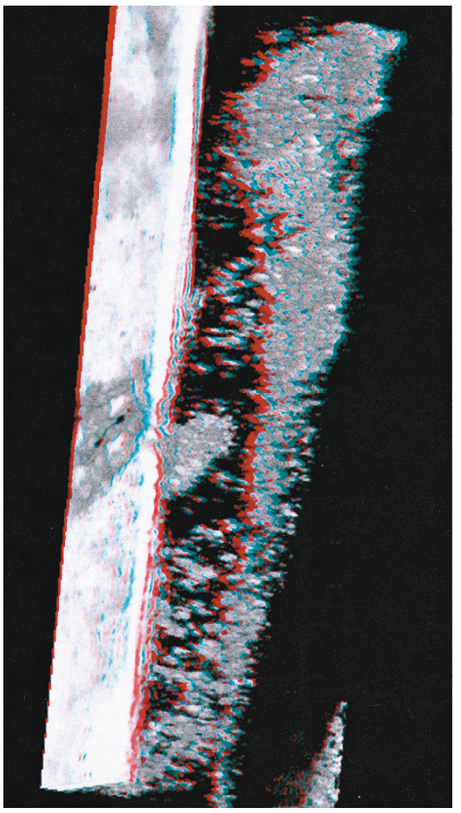


FIGURE 2.5. Stereo view from part of a z-stack of 128, 512 × 512 BSL images of a cheek cell specimen. The projection orientation was chosen to emphasize the spatial relationship between the nucleus (central blob) and the distorted area of the image of the water/slide interface originally located below it. The four-way symmetry of the "distortion" image is caused by the interaction of the nucleus and the polarized laser beam and modified by the fact that high-NA light is more likely to reflect from the slide interface. Bio-Rad Radiance confocal mounted on a Zeiss Axiophot upright microscope with a 40× NA 1.2 C-PlanApo water-immersion objective. To obtain stereo effect, view through red/blue or red/green glasses.

A Typical Problem

The many limits on CLSM performance do not act alone but can combine in complex and subtle ways. To highlight the interactions between counting statistics and more widely recognized limits such as spatial resolution, let us define a characteristic microscopical problem shown schematically in Figure 2.6. The specimen is a cell in which some of the protein sub-units making up the cytoskeletal fibers have been replaced with fluorescent analogs. These fibers are very small, about 10 times smaller than the *x,y*-resolution limit of light optics, and excitation of the fluorescent dye causes it to bleach, a process that is probably toxic to the cell. Because the object is to observe the formation and movement of the linear cytoskeletal elements within the living cell, one cannot take advantage of the higher spatial resolution of the electron microscope because this instrument cannot be used on living cells.

This example, though perhaps overly specific, is not uncharacteristic, and it has the advantage of highlighting interactions between many of the fundamental limitations. The important features of this example are as follows:

- The observer would benefit from high spatial resolution in all three dimensions.
- Accuracy in measuring intensity-of-stain/unit-length will be important, because doing so may permit determination of the number of sub-resolution, linear polymers bundled together to make up each visible fiber.
- A number of images must be recorded at different times in order to show change/motion.
- Each measurement will cause bleaching and cellular toxicity.

Clearly, these conditions contain an inherent contradiction: to obtain more quantitative temporal or spatial accuracy, more light must pass through the sample but this will produce more fading and cytotoxicity. As a result, the improved images may be of a dying cell rather than a living one, and, therefore, the **biological reliability** of the measurement may be inversely proportional to the **physical accuracy** set by counting statistics.

Other interactions between these parameters are also possible. High spatial resolution implies that the micro-volumes (pixels) excited by the beam and sampled by the detector must be very close together (actually the spacing between lines is less than one quarter the diameter of the Airy disk). The measurement at each pixel is really the detection of the small fraction (<1%) of the fluorescent excitations excited by the beam that actually produces signal in the detector while this pixel is illuminated.

Higher spatial resolution implies smaller pixels and, hence, the need to count more photons from any given volume of the specimen. The increases in detected signal implied by improved resolution are not insignificant: maintaining the statistical accuracy of the measurements when the resolution increases by a factor of 2 requires four times more signal in order to image a single plane and eight times more if a 3D volume is to be sampled. Fortunately, the only way to actually increase the resolution by 2× is to increase the numerical aperture (NA) by 2×, and doing so increases the fraction of the photons emitted from the specimen that are captured by the lens by a factor of $(\Delta NA)^2$ or 4×. As a result, some of the improved image quality can sometimes be retained by collecting a larger fraction of the emitted light rather than simply by exposing the specimen to increased illumination.[3]

This interaction emphasizes the importance of keeping the pixel size appropriate to the operating resolution. Those who usually use WF microscopes to record images on film may be less familiar with the idea that pixel size is an explicit experimental variable.[4] It is important to understand that the "zoom" magnification factor used to change the size of the area scanned on the specimen on most commercial CLSMs usually does so by changing the pixel size (referred to the specimen). Therefore, although the ability to vary the display magnification by a factor of about 10 : 1 may seem to be great convenience, **with a given λ and NA, only one zoom setting provides optimal Nyquist sampling** of the optical image data. All other zoom settings must necessarily either over- or under-sample the data and either produce more beam damage or record less resolution than they should. (See Chapter 4, *this volume*, for how to choose the optimal zoom setting.)

Given the interrelated constraints highlighted by these examples, the two features needed for a confocal microscope to approach its ultimate performance are:

- *Photon Efficiency:* The system must count as many as possible of the photons transmitted or emitted by the sample at the plane of focus.
- *Spatial and Temporal Resolution:* Generally one should focus the laser into a spot that is as small as possible though, on occasion, it may be advantageous to make this volume somewhat larger to avoid saturation or photodamage effects.

These two topics will now be discussed in more detail.

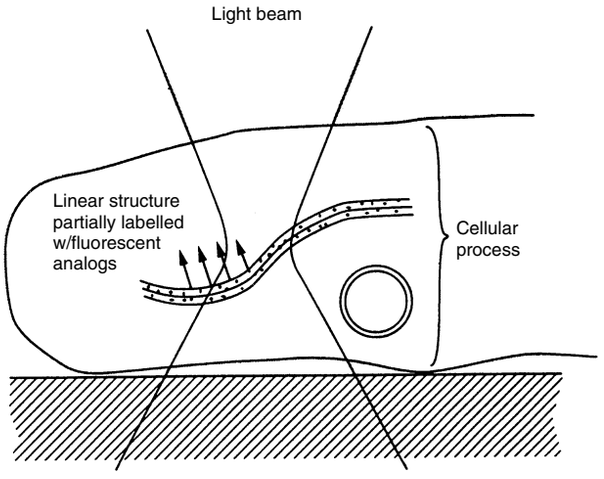


FIGURE 2.6. Diagram of a notional specimen: a living cell process containing a filamentous structure smaller than the resolution limit and sparsely stained with fluorescent analog molecules.

PRACTICAL PHOTON EFFICIENCY

Photon efficiency (γ) is a measure of the fraction of the signal photons generated by the action of the laser beam on the specimen that are actually represented in the final image data set stored in the computer. Although photons can be lost both between the light source and the specimen and between the specimen and the detector, those lost before reaching the sample can usually be "replaced"

[3] Although this reciprocity works in the *xy*-plane, it doesn't compensate in the *z*-direction because *z*-resolution is proportional to $1/(NA)^2$.

[4] These problems are strictly analogous if we relate pixel size to the size of the film grain. To record faint fluorescence, we choose a "fast" grainy film with a high ISO rating only to discover that it does not record details as small as those visible when using a film with a lower ISO rating.

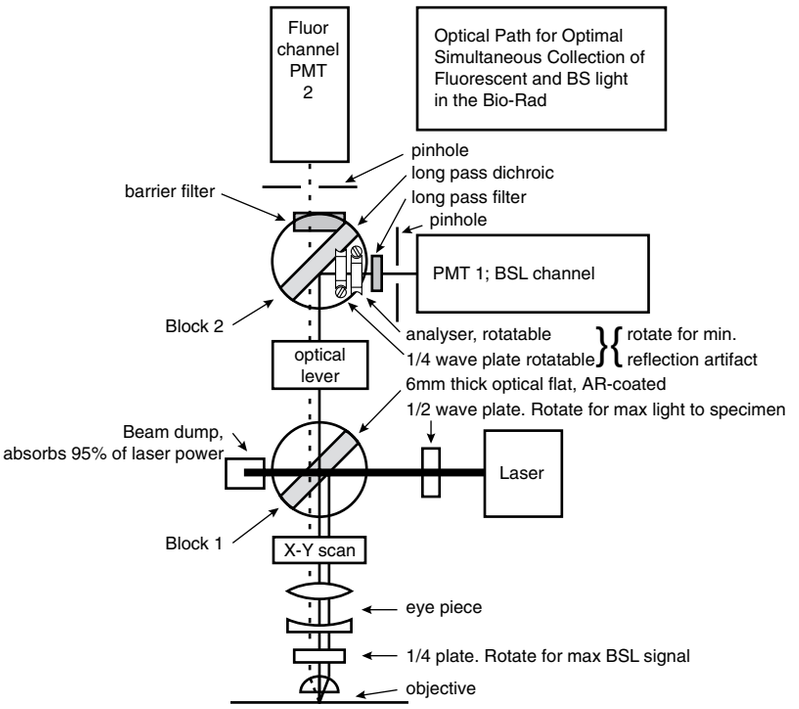


FIGURE 2.7. A system of two filter blocks for use with the Bio-Rad MRC-500–1024 which permits optimal removal of specular reflection artifacts and the simultaneous collection of BSL and fluorescence signals. Block I contains a beam-splitter consisting of a 6-mm-thick Pyrex optical flat, anti-reflection coated on its rear (upper) side. A 1/2-wave plate after the laser is used to rotate the laser polarization so that 0.8% to 5% of the laser light is reflected down the optic axis and through a 1/4-wave plate between the ocular and the objective. Almost all of the returning BSL and fluorescent light passes through the beam-splitter to Block II, where the two signals are separated with a dichroic mirror. The long λ signal passes to PMT 1 via an emission filter. Signal at the excitation wavelength passes through a second 1/4-wave plate and analyzer (both rotatable) and a laser line filter to PMT 2. The orientation of the 1/2-wave plate is adjusted to give maximum light from the objective, then the rotatable elements in Block II are adjusted to eliminate spurious reflections. Finally, the 1/4-wave plate in the microscope body is rotated to produce the maximum BSL signal from a living cell.

with relative ease by an increase in laser power.[5] However, photons lost after leaving the sample represent a more fundamental loss: they carry information obtained at the expense of radiation damage to the specimen.

Current instruments waste photons in a number of straightforward ways, some of which are discussed later in this section. Two somewhat less obvious cases of photon inefficiency that can be grouped under the heading "wasted light" are worthy of mention here.

Whenever the laser beam passes from a region having one RI to another region having a different RI, some light is scattered back towards the source. As a result, almost any biological specimen, particularly a living one, produces BSL. In most current instruments used in the fluorescent mode, the BSL is reflected back to the source by the dichroic beam-splitter and thereby wasted. As is also pointed out in Chapter 9, it is possible to design the confocal microscope in such a way that both the BSL and the fluorescent signal can be detected separately and in a totally non-interfering manner to produce a BSL image that is perfectly aligned with the fluorescent image (Pawley *et al.*, 1993a, Pawley, 2002). This image provides information on the optical inhomogeneities in the cell at no additional cost in terms of radiation damage to the specimen (Fig. 2.7).

The second example of wasted light is that which is elicited by the laser during line retrace in raster-scanning instruments. As photons excited from the specimen by this light are not detected, it represents a significant (30% for 1s scans, 10% for 4s scans) and unnecessary assault on the specimen. Fortunately, it can be eliminated by gating the light source during retrace using a Pockels Cell or the acousto-optical deflector (AOD), now available on most commercial instruments. Early video-rate scanners using resonant galvanometer scanning employed a system of blades to mask the sides of the raster so that light did not reach the specimen as the beam slowed down before turning around at either end of the sinusoidal motion.

Light generated inside the specimen can be lost through several mechanisms:

1. Absorption or scattering in either the objective lens or the medium that couples it to the specimen, or by the fixed and/or moving mirrors and transfer optics needed to "de-scan" the beam (see also Chapters 7 and 9, *this volume*).
2. Incorrect alignment of the optical system resulting in the improper placement or orientation of the pinhole or slit (see also Chapters 3, 8, 11, 22, 35, and 36, *this volume*).
3. Low quantum efficiency (QE) of the photon detector (see also Chapter 12, *this volume*).
4. Imprecise digitization of the output of the photon detector (see also Chapter 12, *this volume*).

While these subjects will be covered in much more detail in the chapters noted above, a few points will be made here as a background to descriptions of the practical tests of performance to be described later.

Losses in the Optical System

Objectives

To a first approximation, fluorescent light proceeds from the site of its generation in all directions equally. As a result, only a small fraction even strikes the objective lens: ~30% of the total for NA 1.4 and this fraction decreases with $1/(NA)^2$. The fraction of this light that emerges from the other side of the objective depends on its transmittance. Although measuring the absolute transmittance of an objective lens at full NA is far from easy (see Chapter 7, *this volume*, for details), useful measurements comparing the effective

[5] As noted above, such an increase is more difficult when using the arc sources commonly employed in the disk-scanning approach.

transmission of individual objectives can be made on epi-illuminated instruments with significantly less trouble. All that is needed is a photodiode light sensor (one **without** an air space between it and any clear glass "window") linked to a sensitive current meter (or better, a basic photometer) and a front-surfaced mirror. After adjusting the instrument to measure BSL and fitting objective lens A, align the instrument if necessary, then switch to a high zoom setting and measure the light emerging **from** the objective with the sensor (be sure to exclude stray light from the room and couple the lens to the sensor with immersion oil if it is an oil-immersion lens). Call this light reading I_a. Now place a front-surfaced mirror, slightly tilted, on the specimen stage and set up the microscope to image the reflecting surface using the BSL signal. Be careful to keep the illumination level very low so as not to damage the photomultiplier tube (PMT) in the microscope (and to realign the instrument if reducing the illumination requires the addition of ND filters in front of the laser, see Chapter 35, *this volume*). Focus on some dust on the mirror. Because of the slight tilt, the surface will only be near focus (bright) along a broad band. Use the computer controls to measure the peak brightness (B_a) of this band and that of some dark area (b_a) well away from the bright band (or better yet, with the laser obscured). This second, background reading is to compensate for non-specific reflections in the optical system, poor DC balance in the PMT head amplifier, and the Brightness or Black-level offset setting, etc. The reading should be slightly positive to ensure that "zero signal" is within the linear range of the digitizer.

Some microscopes produce severe specular reflection artifacts when used in the BSL mode: make measurements in a part of the image field unaffected by these reflections. Also be sure to adjust the PMT gain so that at a single setting, the signal remains well within the linear region of the digitizing system (about "three-quarters-full" or 192 counts/pixel in an 8-bit system) throughout the entire procedure.

Now change lenses, realign, and make a second set of measurements I_b, B_b, and b_b without changing the PMT gain.

To a reasonable approximation, the comparative transmission (T_{comp}) of the first lens as a fraction of the second will be the following:

$$T_{comp} = \frac{I_b(B_a - b_a)}{I_a(B_b - b_b)}100\% \quad \textbf{(1)}$$

(Transmission specifications for a number of common objectives can be found in tables in Chapter 7, *this volume*.)

Mirrors

On some scanners, a similar setup can be used to test the performance of the internal mirrors. Again, the light intensity leaving the objective, I_a, is measured. Then the beam is stopped (or made to scan a very small raster) at the part of the scan when it is focused on the mirror surface (brightest). After turning off the PMT(!), a second reading is made (P_a) with the same photodiode placed just in front of the pinhole, making sure that **all** of the light strikes the sensitive part of the sensor.

The P_a/I_a ratio will usually be depressingly small (~10%–20%), but the difference covers reflection losses at the various mirror and filter surfaces, including the beam-splitter (50%–60% loss on each pass) as well as those at the scan lens, the various transfer lenses and the objective. (A method for making a similar measurement that does not require placing the photodiode in front of the pinhole is given in the section "Measuring Photon Efficiency.")

Though indirect and somewhat cumbersome, such measurements can be useful for two reasons: (1) as a rough method of comparing the performance of different instruments (or different types of mirrors fitted to the same type of instrument) and (2) to monitor performance of a specific instrument over time. Performance degrades as dust and/or hydrocarbon or other atmospheric vapors condense onto the surfaces of mirrors and other optical components. In instruments having up to 11 reflective surfaces in the detector chain, a change in reflectance of even 1% can have marked effects on photon efficiency (see Chapter 7, *this volume*).

Pinhole

Is the Confocal Pinhole a "Good Thing"?

It is argued by some that the pinhole is the Achilles' heel of the confocal approach because it excludes photons that, while not originating from the plane of focus, do still carry relevant information regarding other planes because of the non-point nature of the focused optical probe. The process of "deconvolution" will "put the photons back where they came from" and all will be well (see Chapters 23, 24, and 25, *this volume*). Elaborate and authoritative mathematical analyses seem to support an argument that can be summarized, not too unfairly, as suggesting that, "as all measured photons are good, excluding photons must be bad." The problem is that the mathematics that describe so well the actions of light waves, generally has more trouble accounting for the behavior of photons, or more particularly of the errors in counting them caused by Poisson noise.

Leaving aside possible modifications to the confocal detector (noted in the next segment) that would allow photons from nearby planes-of-focus to be separately collected in a confocal instrument, the contention that light from out-of-focus planes contains information deserves some consideration. In the discussion that follows, all non-confocal (WF) images will be composed of light from both in-focus and out-of-focus planes while confocal images consist of light from **only** in-focus planes. The argument turns on the relative quantum efficiency (QE) of the detectors normally used with each technique [cooled charged-coupled device (CCD) vs. PMT] and on when and to what extent the out-of-focus light can yield information regarding a 3D structure **beyond t**hat contained in the in-focus light. This matter is covered in more detail in the appendix to Chapter 13, and also in Chapters 22, 23, and 24 and in Pawley (1994).

Let us take some examples. All will agree that an out-of-focus WF image of an isolated point object will be a larger and less intense image than an in-focus one (Fig. 2.8) and, furthermore, that a knowledge of the optical-transfer-function of the system, together with information from other adjacent planes as to whether the current plane of focus is above or below the plane containing the point object, will allow us to use computer image-processing techniques to gain some information from this out-of-focus data. Supposing then that only out-of-focus images were available, one would be justified in saying that, from an analysis of out-of-focus data, information had been gained as to the actual location of the object (i.e., in-focus information). But beyond that, would one be justified in saying that this would be a significant addition to the information present in an image of the plane containing the object (the in-focus image)? In other words, is the out-of-focus information "useful" only because in-focus information is lacking?

Another aspect of a measurement in which WF techniques will give a more accurate estimate is, for instance, a measurement of the total fluorescence from an entire specimen (say, all of the chromosomes in a nucleus). For a given dose to the specimen, the WF

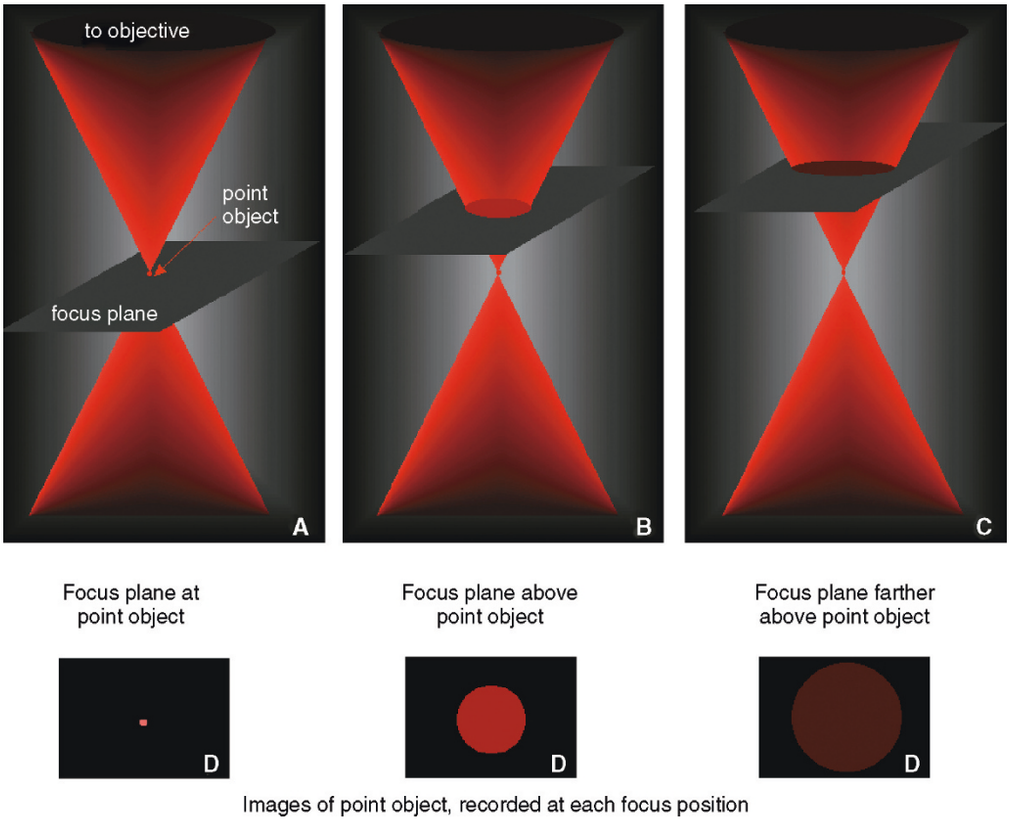


FIGURE 2.8. Image geometry. A schematic diagram showing how the cone of light leaving a point object at angles that will be accepted by the objective, looking at different focus planes.

technique can be more accurate simply because it will detect more total photons.

On the other hand, there must be some limit to the extent that light from sources remote from the in-focus plane can provide more information about that plane than it obscures (Chapter 10, *this volume*, Appendix). For instance, suppose the specimen consists of a small, 0.2-µm feature in the plane of focus and a larger and 10× brighter feature 1 µm above it. Let us also suppose that the point-spread function (PSF) of the optical system is such that, in the WF image focused on the plane containing the small object, 75% of the light reaching the pixels centered on this feature originates from the larger, brighter out-of-focus feature. As this extra signal will double the statistical noise associated with intensities measured in these pixels, it is hard to see how the WF measurement could be better than a confocal measurement that senses the in-focus feature but excludes most of the out-of-focus light before it reaches the detector.

As a more complex example, consider a BSL image of a tooth in which virtually every voxel scatters light. In such a thick "dense" specimen, the fraction of the WF signal originating from the in-focus plane is so small and so uniform that even detecting it using WF imaging and signal processing would be extremely difficult, and the suggestion that the out-of-focus signal actually contributes information **beyond** that available in the in-focus or confocal image seems difficult to support.

Somewhere in between these extremes might be the more realistic situations defined by the two, vertical "sight lines" labeled A and B, in Figure 2.9.

The question then becomes: Up to what level of 3D staining density (or sparsity) can **information** about the specimen (as distinct from **signal** defined as "output for the detector") be gained from out-of-focus light? The answer will not be a simple one, as it depends on a number of practical factors apart from the sparsity of the staining, such as (1) how well one knows the optical response function of the microscope and how it changes with z or, (2) the relative amounts of specific and non-specific staining and the exact effects of applying nonlinear image processing algorithms such as non-negativity or "maximum entropy" (see Chapters 23 and 24, particularly the Appendix, *this volume*).

Excellent results from the WF/image-processing approach are also shown in these chapters and elsewhere, but, because of the difficulty of producing fluorescent specimens that have an interesting 3D geometry but which do not bleach when they are looked at using first one method and then the other, no meaningful side-by-side comparison has yet been performed although there have been some computer simulations. More sophisticated comparisons are described in (Chapters 13 and 24, *this volume*), but it becomes clear that, to be both realistic and useful, any comparisons are likely to be complex as they must include differences in the QEs of the respective detectors (3–10× higher for WF) as well as the details of the optics, the geometry of the stained features in the specimen, and differences in the response of the dye to the much more intense light that must be used in any scanning technique.

The important parameters characterizing the three most popular methods of obtaining 3D images from fluorescent bio-

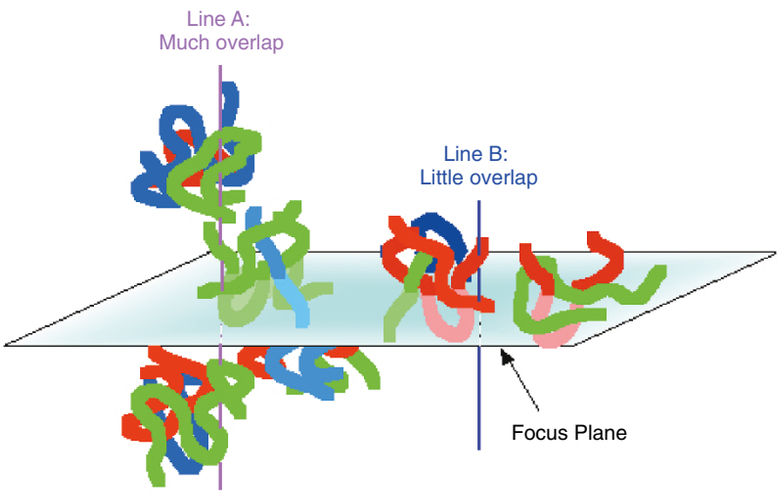


FIGURE 2.9. Schematic diagram showing areas of an imaginary fluorescent structure to illustrate how local variations in stain density change the levels of out-of-focus light detected.

logical specimens are summarized and compared in Chapter 35, Table 35.1 and 35.2.

Proper Use of the Confocal Pinhole

In a confocal microscope, the pinhole is present to prevent light originating from anywhere but the plane of focus from reaching the detector. It is mounted in an image plane, and, if it is misaligned or if its size is reduced beyond that corresponding to a diffraction-limited spot on the sample (i.e., a pinhole diameter of 0.7–1.5 Airy units), then it will severely reduce the number of photons reaching the detector while producing only a marginal improvement in *xy*- or *z*-resolution. Making the pinhole larger than the diameter of the diffraction-limited spot allows more photons to be detected but, as ~80% of those originating **from** the plane of focus were already being collected, **most of the additional signal comes from adjacent planes**,[6] reducing the *z*-resolution. Choice of the proper size and shape for the pinhole is a sensitive function of λ, and the objective lens NA and magnification. However, even an "optimum" 1 Airy aperture will exclude at least some photons (the ~20% present in the outer rings of the Airy disk), and this represents a fundamental cost of using the confocal pinhole.

Given these uncertainties, it seems unlikely that little, if any, additional, useful information will be gained from the out-of-focus light as long as:

- The "bright" voxels are stained at least 10× more intensely than background voxels and are each capable of producing at least **20 detectable photons/pixel** when present in the focus plane of a confocal instrument.
- The confocal detector pinhole is kept at 1 to 2 Airy units, the size needed to demonstrate a lateral resolution equal to that of a WF instrument with the same NA, λ, etc.
- Both instruments are designed and adjusted in accordance with the sampling and photon-efficiency criteria proposed in this book.
- The advantage of the confocal approach will increase as the total number of planes sampled (or imaged) is reduced.

[6] Assuming that fluorescent dye is located there.

Detection and Measurement Losses

The Detector

The detector characteristics of importance to 3D microscopy have been reviewed by several authors (Pawley, 1994; Sheppard *et al.*, 1992; Sandison *et al.*, 1994). The characteristics of most importance to photon efficiency are:

- *Effective quantum efficiency* (QE_{eff})*:* The proportion of the photons arriving at the detector that actually contribute to an output signal that is linearly proportional to the photon input. (QE is often a strong function of the λ of the detected photons, Fig. 2.10.)
- *Noise level:* This includes both additive noise, in the form of PMT or CCD dark current noise or electronic amplifier noise, and multiplicative noise in the form of random variations in size of the actual PMT output pulses derived from identical input photons.

The Photomultiplier Tube

Although the PMT is the most common detector used in the CLSM, it is not necessarily the ideal detector. While the raw QE of the most modern PMTs may be as high as 30%, this still means that 70% of the photons produce no signal. At 565 nm, only about 15% photons striking the outer surface of a selected, end-window PMT with an S-20 multi-alkali photocathode are absorbed in the thin photocathode (PC) layer evaporated onto the inner surface of the window (Fig. 2.10). The remaining 85% are either transmitted or reflected. As only those photons that are absorbed can produce photoelectrons (PE) for subsequent amplification in the multiplier section of the PMT, it is clear that any mechanism that reduces transmission or reflection losses may substantially improve PMT QE. This can be done by introducing the light into the end window of the PMT at an angle such that it is totally internally reflected by the PC (Gunter *et al.*, 1970). The light not absorbed in the PC then totally reflects off the outer surface of the window and strikes the PC again. This process continues until the light is either absorbed or it reaches the far side of the PC. Using such an optical enhancer, we have reported an **increase** in QE of 60% at 520 nm, 180% at 690 nm, and 220% at 820 nm (Pawley *et al.*, 1993).

Transmission losses can also be decreased by employing a new GaAs and GaAsP photocathode or using an opaque photocathode,

as is found in side-window PMTs (Fig. 2.10). These have markedly higher QE, especially in the red. On the other hand, it is important to remember that published QE curves tend to represent the very best performance measured and, especially on end-window tubes, there is lot of tube-to-tube variation. In addition, published QE curves only show the fraction of photons producing photoelectrons, not the fraction that actually reach the first dynode and start a cascade.

Though a significant achievement, improved PC performance in the red is usually accompanied by significantly higher dark-count rates. Although the dark current of a PMT is usually low (0.1 count/pixel), it is a strong function of the temperature (Fig. 2.11). In the heated confines of some commercial instruments, it may not always be small compared to the signal level of a weakly fluorescent sample, and this is especially true if excitation levels have been reduced to permit photon-counting without pulse-pileup. The fact that dark count rate is proportional to PC size explains the trend to PMTs with 10-mm PC diameters rather than the 25-mm tubes previously common. Dark current can also be reduced by cooling the PC.

Of more concern is the fact that PMT output pulses produced by single PEs vary in size by an order of magnitude because of statistical variations in the small number of particles present in the early stages of the electron multiplier [Fig. 2.12(A)]. The distribution in the height of these single PE pulses is shown in Figure 2.12(B) for several representative types of PMTs. Clearly, if one merely sums the output pulses, some electrons will count more than others. This produces multiplicative noise and the value sensed by integrating the pulses and recording the sum in the computer will have more uncertainty than had the photon pulses been counted directly.

As most of the scatter in the pulse-height distribution reflects Poisson noise applied to the small number of secondary electrons generated at the first dynode, it is important to keep this number as high as possible. Figure 2.13 shows that first-dynode gain can be as high as 20 on average but only if a relatively high voltage (600 V) is placed on the first stage of the voltage divider. Current commercial confocals are more likely to use less than half this voltage, leading to a likely gain of 10. Clearly, this will introduce an additional uncertainty in the process of trying to determine how many photons were detected in each pixel. Thirty percent multiplicative noise can only be overcome by collecting about 60% more signal.[7] In this way multiplicative noise reduces the effective QE well below that of the published graphs. Indeed, when one includes the "optimism" that often characterizes photocathode QE curves, the signal lost because some photoelectrons fail to propagate at the first dynode, and the effect of multiplicative noise, the **effective QE** of the entire PMT is usually less than 50% of what one would have predicted from the published curves alone.

There are some reasons for hope. Hybrid PMTs amplify photoelectrons by accelerating them directly onto a silicon photodiode [Fig. 2.14(A)]. By using an acceleration of tens of kilovolts, the electrons arrive at the diode with enough energy to make thousands of electron-hole (e-h) pairs. This extremely high "first-stage gain" substantially reduces multiplicative noise, as can be seen in Figure 2.14(B), which shows the pulse-height distribution from a hybrid PMT exposed to about 6 ± 2.5 photoelectrons. Because every photoelectron produces a nearly identical number of e-h pairs in the silicon, pixels in which, for instance, eight arrive, produce integrated output pulses that are clearly different in size from those made by either seven or nine photoelectrons. This pro-

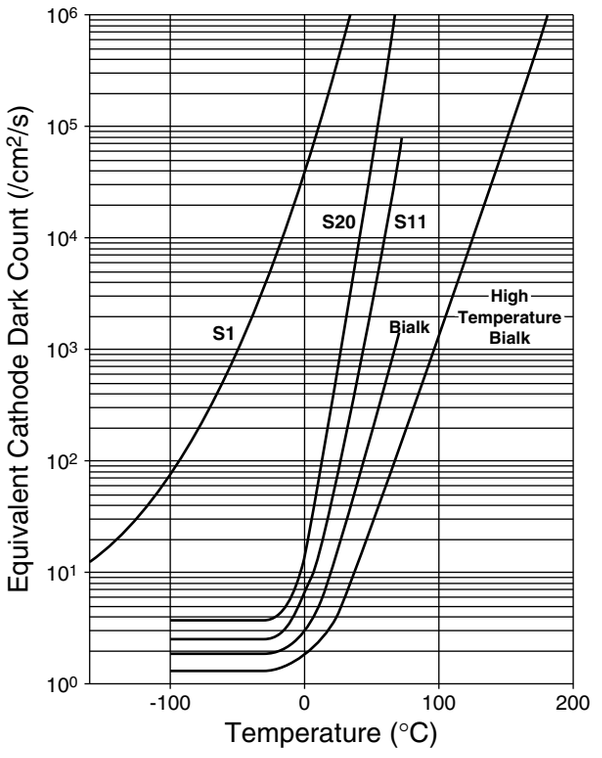


FIGURE 2.11. Variation of PMT dark current with photocathode temperature for a number of photocathode materials. The S1 curve represents performance of the only classical photocathode material with significant response in the near-IR. As the modern replacement of S1, GaAs, also has high dark current and is often used with a cooled photocathode. Please note that the vertical axis is logarithmic.

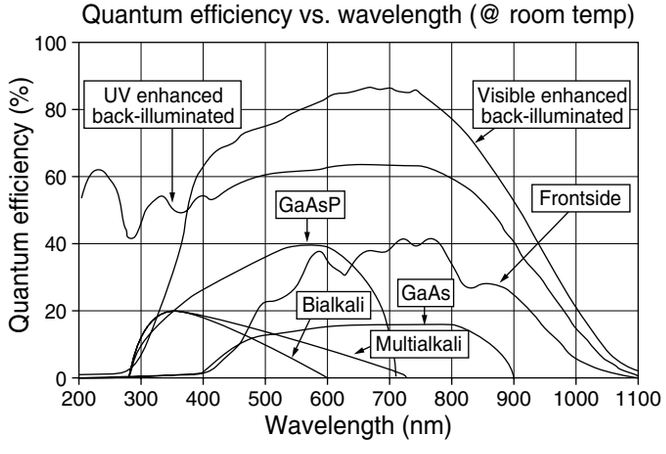


FIGURE 2.10. Variation of quantum efficiency with wavelength of some representative PMT photocathode materials and different types of CCDs. Unless they are thinned and rear-illuminated, the performance of the Si sensors in a CCD is substantially (50%) less in the green and blue because of absorption and scattering in the overlying polysilicon charge-transfer electrodes. Curves for the bialkyli, multialkyli, GaAs, and GaAsP photocathodes are "raw" figures of the photolelectrons leaving the photocathode, and do not take into account the ~30% of these that fail to multiply at the first dynode.

[7] Or by photon counting, an ability lost to the confocal world when Bio-Rad ceased making confocal microscopes.

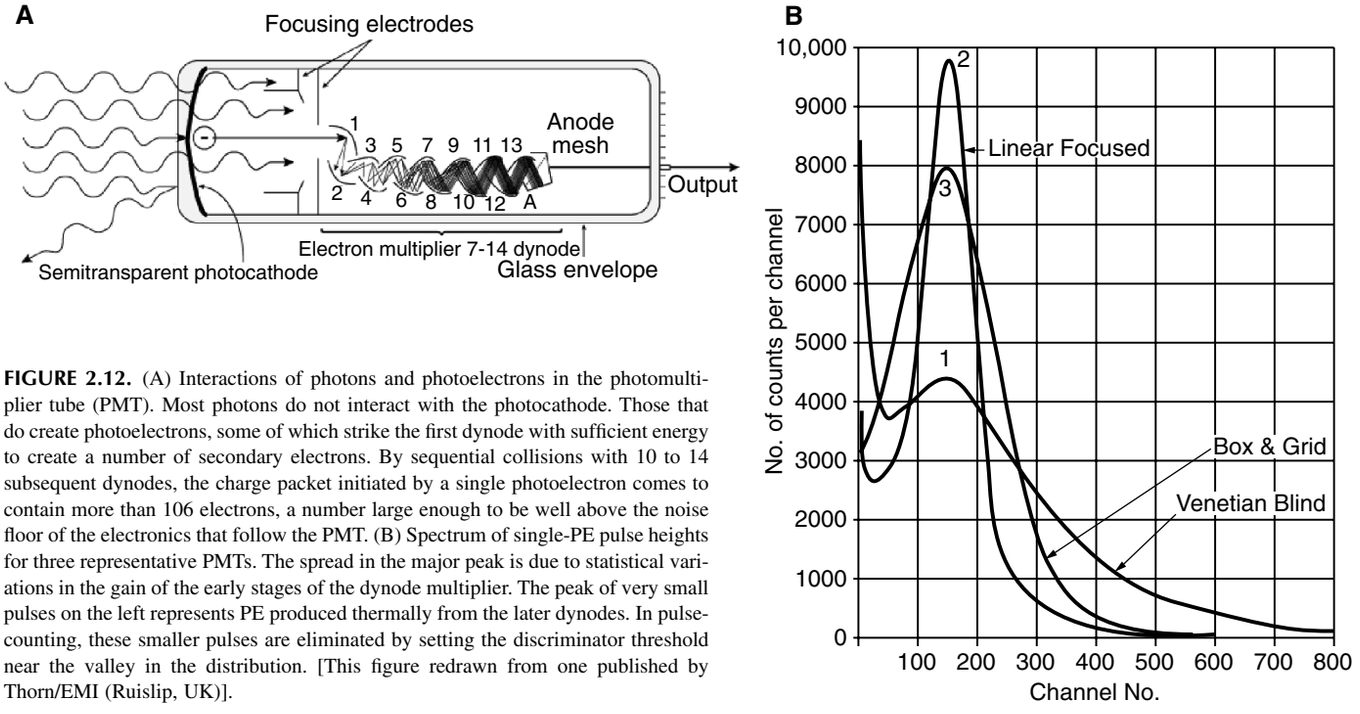


FIGURE 2.12. (A) Interactions of photons and photoelectrons in the photomultiplier tube (PMT). Most photons do not interact with the photocathode. Those that do create photoelectrons, some of which strike the first dynode with sufficient energy to create a number of secondary electrons. By sequential collisions with 10 to 14 subsequent dynodes, the charge packet initiated by a single photoelectron comes to contain more than 106 electrons, a number large enough to be well above the noise floor of the electronics that follow the PMT. (B) Spectrum of single-PE pulse heights for three representative PMTs. The spread in the major peak is due to statistical variations in the gain of the early stages of the dynode multiplier. The peak of very small pulses on the left represents PE produced thermally from the later dynodes. In pulse-counting, these smaller pulses are eliminated by setting the discriminator threshold near the valley in the distribution. [This figure redrawn from one published by Thorn/EMI (Ruislip, UK)].

vides the advantages of photon counting without the danger of saturation due to pulse pileup. The problem at present is high cost, relatively short lifetime and sensitivity to damage from overexposure.

Finally, as the PMT is a single-channel device, it can provide a measure of only those photons that pass through the pinhole mask. This makes the proper setting of this parameter very important. One cannot decide later that it should have been bigger or smaller.

The Cooled Charge-Coupled Device

The only practical alternative to the PMT is the solid-state detector of which the cooled charge-coupled device (CCD) is the optimal example. This detector has both different capabilities and different problems (see Chapter 12 and Appendix 3, *this volume*). The QE can be very high (70%–80%) and extends well into the infrared (Fig. 2.10). Furthermore, as each photon is recorded as an identical amount of current, there is no multiplicative noise. Unfortunately, to keep the noise level acceptably low (±5 photoelectron/measurement), this detector must be cooled to –40 to 80°C and read out at the relatively low rate of 100,000 pixels/s (vs. 400,000 pixels/s for a normal CLSM). This noise level is clearly too high if the **peak** signal level is only 10 photons/pixel, as it can be on many CLSMs.[8] It is less serious when the signal from the **darkest** pixel is >25 photoelectrons because then statistical variations in this number (i.e., $\sqrt{25} = 5$) are similar in size to the measurement noise. These features make the cooled CCD detector more suitable for slowly scanned images (10–100 s/frame) producing relatively high signal levels. (See discussion of this subject in Chapters 10, 12, and 23, *this volume*.)

In the disk-scanning and line-scanning confocal microscopes, the image data emerges as a real image rather than as a time sequence of intensity values from a single detector. Although this real image can be detected photographically or by eye, both of these sensors have fairly low QE. However, these confocal microscopes can approach the photon efficiency of the CLSM if they incorporate a cooled CCD sensor having detection performance similar to that described in the last paragraph. This combination is now implemented in several commercial instruments.

Of even more importance is the recent introduction of the electron multiplier CCD (EM-CCD). In the EM-CCD, a gain register is introduced between the end of the horizontal register and the read amplifier. The gain register consists of ~500 charge-coupled elements in which one of the three charge transfer voltages is much higher than normal. When exposed to this higher voltage, each electron in the charge pocket has about a 1% chance[9] of multiplying by collision with covalent electrons from the silicon lattice. This process produces two electrons and when repeated ~500 times, the average gain can be over 1000×, which is sufficient to lift the signal from even one signal electron well above the read noise of the output field effect transistor (FET) amplifier.

This produces an image detector with the QE of silicon and the noise characteristics of a PMT. There is a snag, of course: the random nature of the electron multiplication process produces

[8] Many users may find it hard to accept that the **brightest pixel** in their confocal images represents a signal of only 8–12 photons. Indeed, they may point to a histogram of such an image and note that there are some pixels present with every possible value from 0–255. Surely, if there are 256 possible values, the brightest must correspond to 255 photons. In fact, the relationship between photon signal level and digital value stored in the image memory is arbitrarily determined by the particular PMT gain and black-level setting chosen. The reason that a signal representing at most 8 photons is not displayed as a posterized image containing only 8 possible gray levels is that multiplicative **noise** in the PMT blends these 8 levels into each other so that the transitions are not apparent. Quite simply, some photoelectrons are counted as "more equal than others."

[9] The useful range is 0.5% to 1.5% and depends on how high the voltage on the transfer electrode is.

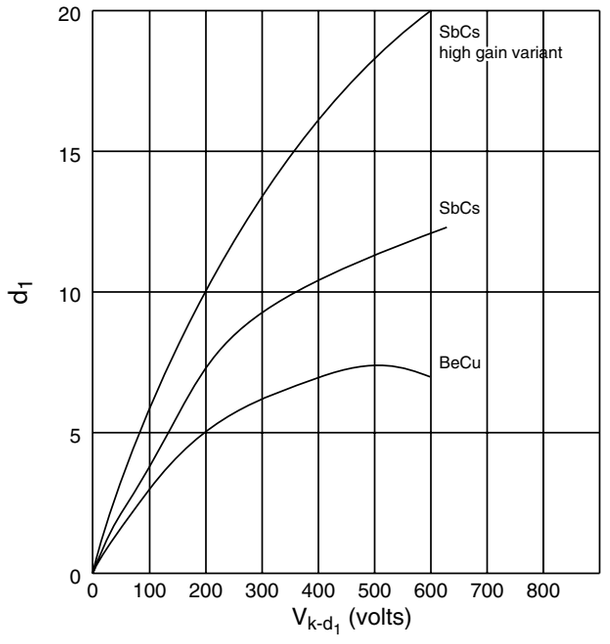


FIGURE 2.13. Variation of the gain from collisions that occur at the first dynode with cathode/first-dynode voltage.

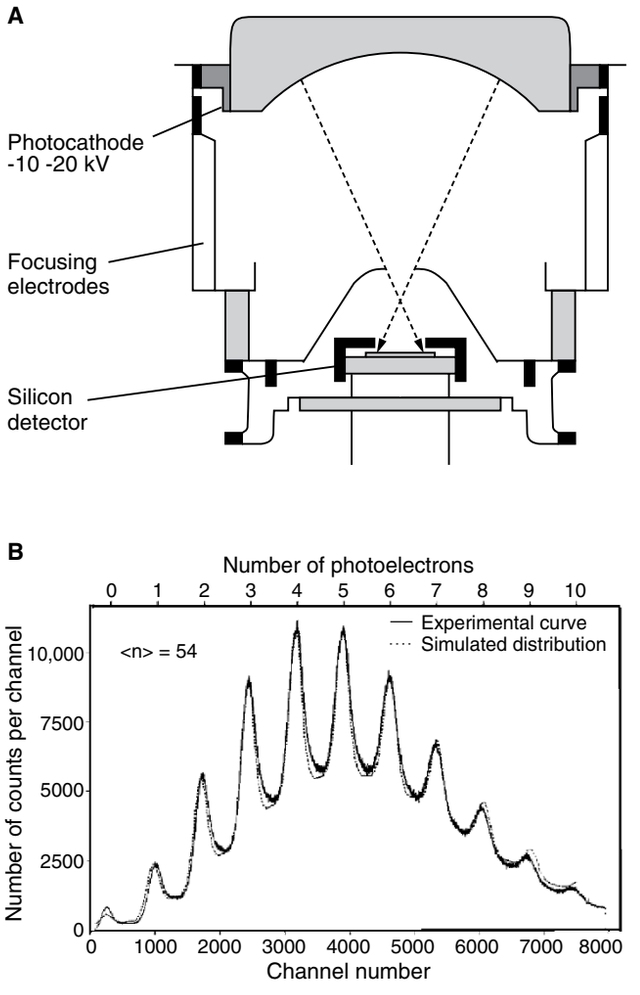


FIGURE 2.14. Hybrid PMTs. (A) Diagram of hybrid PMT layout. Photoelectrons leaving the photocathode are accelerated onto a silicon photodiode (or an array of such diodes) with sufficient energy to produce thousands of electron-hole pairs in the silicon. The very high gain of the first (and only) stage greatly reduces the effect of multiplicative noise. (B) A plot of single-pixel signal levels obtained from such a hybrid PMT under conditions where the photocathode was emitting on average, about 6 photoelectrons/pixel. The clearly defined peaks represent signal levels of from 1 to 11 photoelectrons/pixel.

even more multiplicative noise than is present in a good PMT. As a result, the output signal has about 1.4× more noise than can be attributed to Poisson noise alone. As this can only be reduced by counting 2× more photons, the easiest way to think of the EM-CCD is that it has no read noise, but the QE_{eff} is only 50% as great as it would have been in the absence of the multiplicative noise (i.e., a back-illuminated CCD detector having a QE of 80% would have an effective QE of only 40% if it were read out by an EM-CCD amplifier). This means that the EM-CCD is only optimal in the 0 to 20 PE/pixel signal range — just where the disk-scanning confocals operate[10] (see Chapters 10 and 43, *this volume*).

In addition to high QE, Si photon detectors have a variety of other practical advantages. As the sensitive element in such a detector is typically very small (5–30 µm on a side), selective use of only a few elements in a small, planar, 2D array could permit it to operate in the CLSM as a combination pinhole and detector. Figure 2.15 is a sketch of what such a detector might look like. After each pixel interval of the microscope, the charge pattern in the 5 × 5 sensor array at the top would be transferred to the read register and then the signal in all 25 pixels would be read out sequentially at about 35 MHz. These 25 values could then be "decoded" in a number of possible ways, the most straightforward of which would be to provide three separate signals corresponding to the summed signals from the brown, orange, and red areas of the sensor array. In this way, it would be possible to collect signal simultaneously at three different pinhole sizes.

With such a detector, pinhole alignment could be done electronically simply by searching for the detector element producing the most signal from a planar specimen and misalignment could be detected on the fly by comparing, for example, summed output from the 5 pixels on the left with the 5 on the right (Pawley, 1996).

Digitization

In the simplest CLSM system, the output of the PMT head amplifier is passed directly to the analog-to-digital converter (ADC), which samples the voltage for a few nanoseconds during the time of each pixel (t_p) and turns the sensed voltage into a digital number. As t_p is usually a few microseconds, it is important to ensure that the voltage present during the much shorter sampling time is a

[10] On first hearing, 20 c/pixel may sound like a very low level of signal. In fact, however, considerable experience shows that much fluorescence confocal microscopy is performed at much lower signal levels. The next section gives methods for those with instruments capable of fast-photon counting to calibrate their PMT gain controls. Those who follow this procedure may be surprised to find that when they are using "normal" PMT gain (8.00 and above on recent Bio-Rads), 256 stored in the memory corresponds to ~10 photons or less.

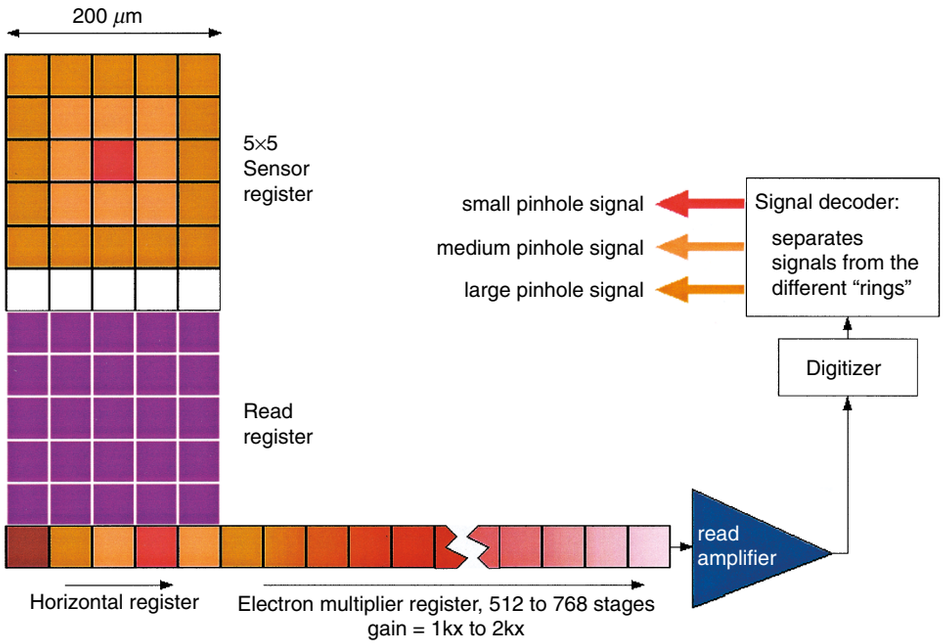


FIGURE 2.15. Schematic diagram showing a proposed solid-state detector that could be used to replace the PMT used in confocal microscopes. The detector uses an electron-multiplier register to reduce the read noise below 0.01 electron/pixel. By reading out all 25 pixels in the sensor array at each pixel of the confocal raster and then apportioning the signal to the three concentric areas of the sensor, this device would allow one to simultaneously collect signal at three different effective pixel sizes.

good measure of the average signal level during t_p. This is usually accomplished by limiting the bandwidth of the amplifier immediately preceding the ADC by giving it a time-constant of $t_p/4$. This approach is simple and effectively expands the sampling time from ~$t_p/1000$ to $t_p/4$ without excessively blending the signal from each pixel with that of its neighbors. However, this still means that the system is only "counting" about 25% of the time.

The situation can be improved if, as mentioned above, the system adjusts the electronic bandwidth to coincide with the optical bandwidth of the microscope and changes the pre-amp time constant to compensate for changes in optical resolution, scan speed (in μm/s as the focus plane) and t_p (see also Chapter 4, *this volume*).

Alternatively, it can also be improved if the CLSM uses a digitizer employing full integration. Such a system can be implemented in two ways. As first used by Sarastro/Molecular Dynamics and later by Bio-Rad, the output of the PMT is integrated by feeding a proportional current into a capacitor, then reading the capacitor voltage out to an ADC and finally resetting the capacitor voltage back to 0 (Fig. 2.16, lower left). The Bio-Rad MRC-600 and later instruments incorporate three circuits of this type in each digitizing channel: one accumulating, the second being read out, and the third being reset.

The second method of implementing full integration is to feed the output from a high-bandwidth ($t_p/20$) head amplifier into a high speed ADC running at, say, 10× the pixel rate and then utilizing fast digital circuitry to average the 10 successive digital readings needed to produce the single value actually stored for each pixel.

Compared to $t_p/4$ bandwidth limiting, either method of full integration effectively provides 4× more useful signal without any more light being detected.

Photon Counting

Obtaining a digital representation of optical data is ultimately a question of counting photons. Ideally, this means not only using a high-QE detector but also using a signal to which the contribution of each photon is equal. In the case of the solid-state sensors, the uniformity condition is automatically met by the sensing process (1 photon = 1 PE) but this condition can also be met by the PMT if it is operated in a pulse-counting mode.

In pulse-counting, the goal is not to measure the average level of the output current during the T_p but rather attempts to eliminate the effects of multiplicative noise by discriminating, and then counting, the individual output pulses resulting from the emission of individual PEs from the PC of the PMT. To reduce the effect of small noise pulses generated from the dynodes of the PMT, photon pulses are passed through a discriminator set to trigger on pulses larger than those at the bottom of the "valley" seen near the left edge of the pulse-height plot in Figure 2.12(B). Each time the PMT output goes above this preset threshold, one pulse is counted (Fig. 2.16).

Unfortunately, problems arise when large numbers of photons must be counted in a short time because the output of the PMT preamp does not immediately return to zero after each pulse. If a second pulse arrives before the first one is over, the second, or piled-up, pulse will be missed. Beyond the problem of pile-up is

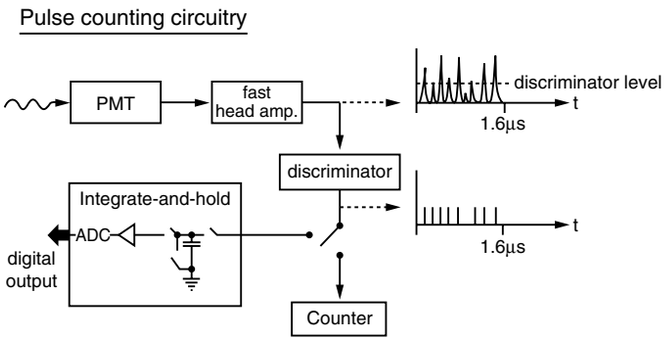


FIGURE 2.16. Two alternative approaches to counting single-photon pulses. In both, the signal from a fast head amplifier is passed to a discriminator. Uniform pulses from the discriminator can either be counted with digital circuitry or integrated in a capacitor and then read out through an analog-to-digital converter (ADC).

the difficulty of actually counting the output from the discriminator at very high asynchronous count rates.

Suppose a laser-scanning instrument scans a 512×512 raster in 1 s and 25% of this time is used for retrace. That leaves T_p = ~3 µs/pixel. If each photon pulse occupies 30 ns (t_p), the maximum number of pulses that one could possibly count in each pixel would be 100 but, because the photons arrive at random times, even at one tenth of this rate (i.e., 10 counts/pixel), 10% of the photons will still arrive when the circuit is already busy.

In general, the rate that pulses are recorded R_{rec} is given by

$$R_{rec} = T_p / t_p \left(1 - e^{-R_{input} t_p / T_p}\right) \quad \textbf{(2)}$$

The Bio-Rad MRC-1024 had a maximum count rate of 58 counts/pixel and its response was fairly linear up to about 15 counts/pixel. This instrument (and its successors) was unusual for allowing the user to switch to the photon-counting mode without any complicated adjustments. This ability made it fairly easy to occasionally switch modes, just to determine the number of photons/pixel that were actually being detected. On first hearing, 10 counts/pixel may sound like a very low level of signal. In fact, however, considerable experience with just this sort of mode switching shows that much fluorescence confocal microscopy is performed at much lower peak signal levels. Although one should be concerned about the signal saturation that occurs when one exceeds the linear range of the fast-photon counting circuitry, it is also important to remember that, to some degree, one can correct for piled-up losses with a simple look-up table.[11] Furthermore, such losses need not be reduced to zero but merely made small compared to the intrinsic statistical noise. Pile-up losses will become less important if more manufacturers switch to pulse-counting PMTs and use faster head amplifiers and counters.

With regard to the latter, digital counters are not strictly mandatory. All that must be done in order to remove PMT multiplicative noise is to clip all the single-PE pulses to a uniform size and feed them to a fully integrating ADC (Fig. 2.16). In fact, in some commercial instruments, much of the **beneficial effect of photon-counting** is incorporated into the **analog** digitization system by the simple expedient of arranging the electronic and PMT gain so that the single-PE pulses saturate a fast, high-gain amplifier installed between the PMT and the slower amplifier stage that leads to the ADC. Because this saturable amplifier is fast, each pulse is separately clipped to a uniform height, thereby meeting the criterion that each photon contribute equally to the final number recorded.

Where Have All the Photons Gone?

All present instruments embody design compromises that prevent them from obtaining the ultimate in photon efficiency throughout the four processes discussed above. Many systems employ more refractive optics than is absolutely necessary and most suffer transmission losses in the range of 30% to 65% (transmission figures as a function of λ for a number of modern objectives are given in Table 7.3, *this volume*). Although the metal mirrors that produced **losses of 85%** in early confocal instruments have now been replaced with broadband, dielectric-multilayer mirrors that reflect 98% of in-bandwidth light, the loss at each surface is multiplicative. The main culprit is often the triple dichroic beam splitter. Far from just reflecting at laser lines, this component often sends as much as 40% of the light between the laser lines back towards the laser. The use of an acousto-optical device as a beam-splitter (AOBS) by Leica has made a significant contribution to alleviating this problem (see Figs. 3.10 and 3.23, *this volume*).

Insufficient attention is often paid to the selection and adjustment of the PMT itself. While many recognize that any specific tube will operate best over only a narrow range of accelerating voltages and that those with bialkali photocathodes have lower noise and higher QE in the green, while those with S-20, multialkali, photocathodes are better in the red and near-infrared, it is usually forgotten that the performance of individual tubes often varies from the mean for their type by more than a factor of 2. In addition, the new side-window PMTs that are used in a number of systems have a response in the red that is almost 3× that of traditional end-window tubes. While this performance also implies a substantial increase in dark current, cooled versions are now available.

Additional degradation is imposed on the data by multiplicative noise and poor digitizing circuitry. Finally, signal is often lost because of poor alignment, and the improper choice of pinhole diameter may exclude as much as 90% of the useful signal from the detector in a vain attempt to extract an "imaginary" improvement in resolution (imaginary because the low signal levels prevent useful information from being obtained before the specimen is destroyed).

Taken together, all of these factors can add up to a factor of 100× or more in photon efficiency between state-of-the-art and sloppy operation on poorly chosen equipment. Every action that results in more efficient use of the photons generated within the specimen should be thought of as being directly responsible for making it possible to collect a proportionally larger number of images (or images with better statistics) before the specimen is damaged.

Measuring Photon Efficiency

The PMT output signal is the only source of readily available data with which to try to measure the photon efficiency. Unfortunately,

[11] If 10 were counted and this is known to cause 10% dead time, record 11.

a large number of parameters can have a major effect on this single measurement (Pawley, 2002). Those discussed above include:

- Laser power, which is a function of temperature, cavity gain, precision of stabilizing circuit, etc.
- The transmission of ND and other filters used at a particular λ.
- Proper alignment of the optics launching the light into the fiber.
- The NA and transmission of the objective lens and other optics.
- Reflectivity of the mirrors for the particular λ and polarization in use.
- The fraction of the laser beam that is actually accepted by the objective back entrance pupil (varies with NA/magnification).
- Pinhole diameter and alignment.
- PMT voltage and black-level setting.
- Staining density and type of dye.
- Focus level and RI of embedding media.

The number and diversity of these parameters make it difficult to obtain a measure of the fraction of the photons leaving the focused spot that are actually counted as part of the stored image data.

What is needed is a stable point-source of light of known intensity that can be mounted conveniently below the objective. One way to make such a source is by allowing a known amount of laser light to strike a stable phosphor. One first measures the light **emerging** from the objective (as noted above) and adjusts it to some standard amount. Specimens that maintain a constant level of fluorescent efficiency (i.e., ones that do not bleach or change with time) include such inorganic phosphors as single crystals of CaF_2–Eu or YAG–Ce and uranyl glass. Unfortunately, although these materials are very stable under intense laser illumination, they also have very high RI. Consequently, high NA objectives are unable to form an aberration-free focus within them, and because of this the signal that they generate at the PMT decreases rapidly as the focus plane moves into the material. However, they can be useful to those who normally use objectives of lower NA where spherical aberration effects are a less serious factor. Cubes of fluorescent plastic or uranyl glass also offer a convenient way of demonstrating correct alignment of the laser with the objective back-focal plane (BFP; see Chapter 36, *this volume*). An alternative fluorescence standard can be fabricated by dissolving dye in immersion oil or water (depending on the correction of the objective), but such specimens are not always as stable over time as one might wish.

A more direct approach to measuring photon efficiency involves using the microscope simply to image a small light source such as a light-emitting diode (LED) specimen, or the light formed by the microscope's normal transmission illumination system set up for Köhler illumination (Fig. 2.17). The arc or incandescent transmission source must be provided with a known and constant power supply. Once this has been set up, the only major variables remaining are the amount of metal deposited on the inside of the glass envelope surrounding the source, the bandpass effects of any filters that remain in the light path, the pinhole diameter, and the PMT voltage. In many instruments, it is relatively easy to remove all of the dichroic and bandpass filters and let the light from the image plane pass directly to the PMT. Under these conditions, one should get a standard reading with a given objective, pinhole size, and lamp power. Although the microscope is now a flying spot detector and only collects photons from one pixel at a time with the result that the effective signal intensity is about 250,000× less than if the PMT were measuring the entire field, it will often still be necessary to place ND filters between the source and the condenser lens to permit the PMT to be operated at a voltage similar to that normally used. Line-frequency variations in the filament heating current may be visible in the data as will any instability in the plasma of arc sources. For this reason, it may be more convenient to measure the PMT output with an analog DC voltmeter than with the ADC and image memory (see Chapter 36, *this volume*).

With such a setup, one can also calibrate the actual effective size of the pinhole. To do this, record the PMT signal level (I_s) as a function of the pinhole setting. I_s should vary as the square of the pinhole diameter, and a plot of $\sqrt{I_s}$ versus pinhole diameter should be a straight line passing through the origin. Departures from linearity may indicate that dust is obscuring part of the aperture or that the pinhole control does not give a very accurate estimate of pinhole diameter.

By introducing ND filters below the stage, it is possible to reduce the intensity of the light to the level at which photon-counting is appropriate. On those instruments that have this ability, one can easily make measurements to determine a rough ratio between the actual number of photons being detected (using photon-counting) and analog-intensity-values stored in the memory at the same PMT gain settings. This is done by recording the same brightfield "image" in both analog and photon-counting modes. Such information should be used to reach a rational deci-

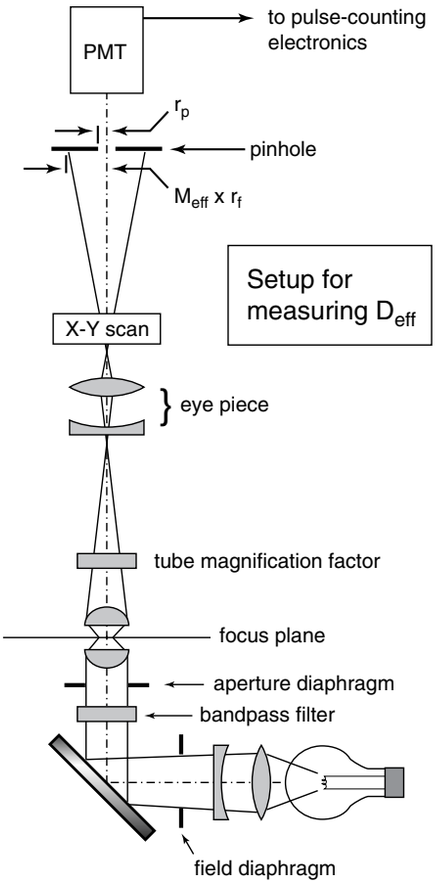


FIGURE 2.17. Optical setup for measuring the detection efficiency or the effective size of the pinhole using the internal transmitted illumination system of the microscope as a standard light source.

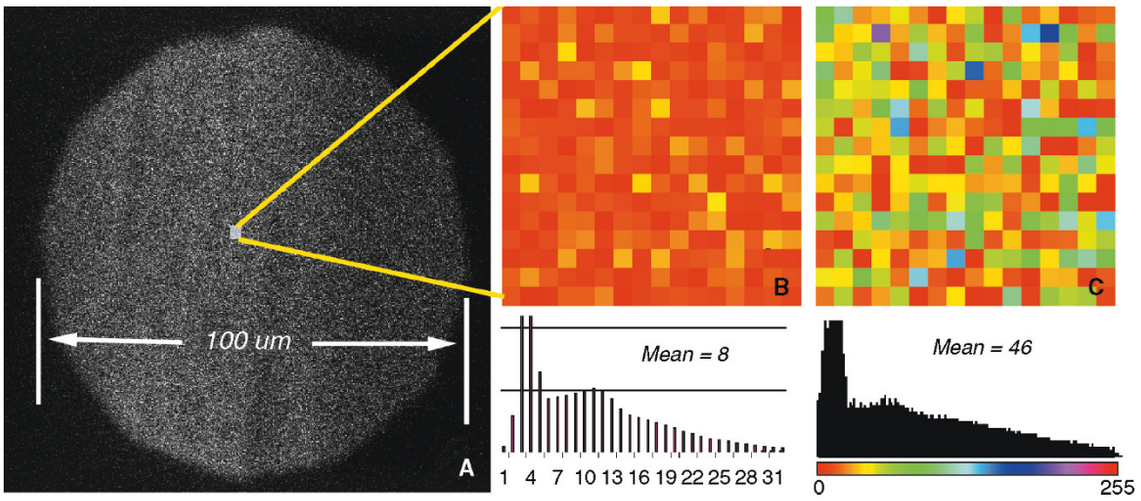


FIGURE 2.18. Effect of photon counting. The two images were made using the confocal detection system as a flying-spot scanner to record the light from the internal transmitted-light illumination system set up for Köhler illumination. Both images were recorded with a PMT setting of 8.00 but (A) was recorded in the analog mode while (B) was recorded using the fast-photon-counting mode (and the contrast was subsequently stretched as the brightest pixel had only 12 counts recorded in it).

sion about when one can use photon-counting without fear of pulse pile-up (i.e., that if the PMT gain is above XX, the signal level registering as 255 in the image memory is only "*x*" photons/pixel and so one can switch to photon-counting for lower multiplicative noise without any worry of pile-up losses). Figure 2.18 shows two such images with their accompanying histograms. The circle is formed by the field diaphragm that has been partially closed to provide a "zero-signal" reference. Different output look-up tables had to be used to display the two images because the photon-counting image had only 12 counts in the brightest pixel.

Finally, if a calibrated radiometer is available, it is possible to use this setup to measure the actual detection efficiency of the instrument, D_{eff}. From an image such as that in Figure 2.19(B), it is easy to measure the actual radius (r_f) of the field diaphragm in the focus plane in micrometers. If one can then measure the total light power (P) passing through this plane by placing the sensor of a photometer calibrated to measure milliwatts and one can specify the λ of these photons by placing a narrow-band filter in the illumination light path, one can then calculate the flux of photons passing through this plane in photons/μm^2, (F).

The energy of a single photon is $h\nu = hc/\lambda$, where c is the speed of light and h is Planck's constant, so the total number of photons having wavelength λ coming through the condenser and into the sensor of the photometer is $n = P\lambda/hc$ (photons/s). The fraction of those that should then reach the PMT is simply the ratio of the effective area of the pinhole (πr_o^2) to the effective area of the field diaphragm. The effective radius of the pinhole is its physical size (r_p) divided by the total magnification between it and the focus plane (M_{eff}). In the Bio-Rad, $r_p = 8$ mm with the pinhole all the way open and $M_{\text{eff}} = 53(M_{\text{tube}})(M_{\text{obj}})$. With a 10× lens and a $M_{\text{tube}} = 1.5$ (assuming 1.25× for the fluorescence attachment and 1.25× for the differential interference contrast (DIC) attachment. For modern, infinity-conjugate microscopes, $M_{\text{tube}} = 1$), $r_o = 5\,\mu$m. (Values of M_{eff} for a number of confocal instruments are tabulated in Appendix 2.)

If the radius of the field diaphragm is set to $r_f = 500\,\mu$m in the focus plane, then the fraction of the light from this plane entering the detector pinhole is $(r_o/r_f)^2 = (5/500)^2 = 0.01\%$, and the total number of photons striking the PMT, n_{PMT}, in sampling time t_s(s) will be

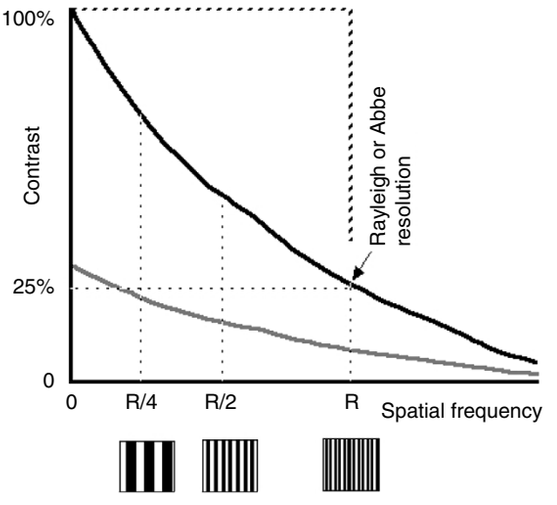


FIGURE 2.19. Contrast transfer function (CTF) of a microscope optical system. The black line shows how the contrast in the image of a high-contrast bar pattern varies with the spatial frequency of the pattern (spacings/μm). The gray line represents the response measured if the dark bars in the test target reflect (or transmit) 70% of the incident light rather than 0%. The dashed line represents the imaginary situation of a CTF in which all spatial frequencies up to the "resolution limit" really have equal contrast. The diagram makes clear why high frequency features of a test object are more likely to remain visible above any arbitrary noise level (5% of 26.5% shown) if they have 100% contrast rather than 30%.

$$n_{PMT} = \frac{D_{eff} N \, r_o^2}{r_f^2} t_s = \frac{D_{eff} P \lambda}{h \, c} t_s \frac{r_o^2}{r_f^2} = K D_{eff} P \qquad (3)$$

where D_{eff} is the transmission efficiency of the optical system and K is a constant that relates the power measured coming out of the condenser P, to D_{eff} and the number of photons counted in the PMT. For a Bio-Rad setup as noted above and with P measured in nanowatts and λ = 546 nm, K = 0.04 photons/pixel/nW. The comparison between photons/pixel measured at the image plane with those detected by photon-counting is a worthwhile, though sobering, exercise.

Nothing increases the probability that normal operating procedures are optimal as much as practicing these techniques under test conditions because, in this case, one knows if one is getting the correct answer (see Chapters 35 and 36, *this volume*, for additional performance tests).

RESOLUTION: HOW MUCH IS ENOUGH?

A peculiar feature of any properly aligned confocal microscope is that it is always "in focus," in that the exciting and detecting light paths are always focused into the same diffraction-limited spot. Details of the size and shape of the volume sampled in this way are dependent almost entirely on the design of the optical system (especially the NA of the objective lens and the RI of the medium surrounding the specimen as formulated in the Abbe equation). In broad terms, the effective *xy*-resolution in biological confocal fluorescence microscopy is essentially the same as it is in widefield,[12] while the *z*-resolution is about 3× worse at NA 1.4 and 4× worse at NA 1.2. A more detailed analysis can be found in Chapters 1, 7, and 8. In addition, there is the important trade-off between spatial resolution, statistical accuracy, and radiation damage, as outlined above and related to the setting of the pinhole diameter.

Rather than repeat the straightforward aspects of theoretical resolution again here, this section will discuss three other aspects that are perhaps less obvious but which are both characteristic of confocal microscopy and that fundamentally limit the ability of the instrument to solve biological problems. These topics are:

- Circumstances under which it may be desirable to reduce resolution.
- The effect of image digitization on spatial and temporal resolution.
- Practical considerations that may degrade resolution or produce distortion.

Can Resolution Be Too High?

Normally, the microscopist makes every effort to obtain the highest possible spatial resolution, and, to the extent that the specimen is not degraded by being so observed, this is entirely proper. Although, in the case of biological samples, the condition of non-degradation is never entirely met, such samples can be rendered very robust by treatment with anti-bleaching agents and fade-resistant dyes (Chapters 16, 18, and 39, *this volume*). However, such fixed and chemically protected structures cannot be considered the general case. Recently, significant improvements in the photon efficiency of confocal instruments has led to them being used increasingly for viewing living specimens (Chapter 19, *this volume*). Indeed, experiments in which thousands of images have been recorded from particularly hardy cell lines are no longer unusual.

To determine when it may be advisable to intentionally reduce spatial resolution, it will be helpful to consider a second specimen type: a living cell that has been micro-injected with a fluorescent substance that changes its absorption spectrum in response to the local concentration of certain ionic species, a concentration expected to change on the scale of a few micrometers. The object of the experiment is to monitor changes in the concentration of this ion as a function of time and experimental conditions. The major complication is that the dye is cytotoxic, and this is especially true when it is excited by light. Furthermore, the fluorescence must be measured accurately at two different exciting wavelengths to determine the ionic concentration by ratioing the results. Because of diffusion, significant changes in ion concentration are not expected to occur on the scales smaller than 1 µm.

How does one optimize an instrument to perform this experiment? Clearly the cytotoxicity problem implies:

- Using a water-immersion lens of large NA to collect as much light as possible.
- Using the lowest dye concentration consistent with the statistical accuracy required.
- Using a magnification such that, when referred to the specimen, a pixel is on the order of 1 µm^2.

The amount of illuminating light that should be used must be determined on the basis of the number and accuracy of the measurements that are to be made. As it is important to measure changes in ionic concentration, it can be assumed that the time available for each measurement is a constant, probably set by the maximum scan speed of the galvanometers, although the intensity of the illumination used to make the images need not be. Both statistical accuracy and toxicity will increase with the intensity of the exciting beam. As "biological accuracy" cannot be sacrificed to obtain better statistical accuracy, conditions must be adjusted to maximize the number of measurements that can be made before the cell is damaged. Considering this problem from the point of view of a single-beam confocal will highlight the effect of fluorescence saturation.

The need for ratio imaging implies a fairly short scan-time to avoid changes in the specimen between the two component images. The need for statistical accuracy implies an intensely illuminated spot to produce many countable photons but, in single-beam confocal systems, saturation puts a limit on the maximum useful flux that can be used. Fortunately, the low spatial resolution required provides some flexibility. The flux of exciting illumination is highest at the neck of the cone of illumination formed by the objective lens, and the diameter of this cone will be smaller (and the flux higher) when the lens used to form it is operated at full NA. In the example described, however, the large NA was chosen to provide high collection efficiency, not high resolution. As the pixel size is to be 1 µm, there is no need to focus the entire beam into a 0.2-µm spot because this will produce a maximum flux density 25 times greater than that present in a 1-µm spot and incur a proportionally greater risk of dye saturation. (Note: To insure that the signal is collected from the entire area of the larger spot, a 5× larger pinhole diameter must be used.)

[12] Although other chapters in this volume note that the ultimate *xy*-resolution in confocal is 1.4x smaller than that in widefield, this assumes the use of a very small pinhole. Given the low signal levels that characterize stained biological specimens one virtually never uses such a small pinhole. The statement above assumes a pinhole diameter of 2 Airy units.

When using coherent laser illumination, the only way to make the spot larger is to under-fill the BFP of the objective lens, thereby reducing its effective NA. However, if one is using a more diffuse source such as an Hg arc, one can use a larger source "pinhole" in the intermediate image plane. Although under-filling the objective reduces the *z*-resolution, considerable depth discrimination remains, and the confocal microscope retains all of the other desirable features, such as quantitative measurement accuracy, and the ability to scan a plane within a larger specimen often makes it ideal for studies of this kind.

The lesson here, then, is that because of the twin considerations of dye diffusion and saturation, it is often important to be able to adjust the image-forming properties of the instrument to produce a spot size appropriate to the experiment at hand. The ability to intentionally under-fill a high-NA objective is poorly implemented on current commercial instruments.

Limitations Imposed by Spatial and Temporal Quantization

Although the image viewed in a disk-scanning or slit-scanning confocal microscope is, in principle, as continuous as that from a WF microscope, this distinction is lost when the image is finally sensed using a cooled CCD or a digital-video image sensor. The fact that all digital confocal images must be recorded and treated in terms of measurements made within discrete pixels can limit the effective resolution of the instrument in ways that may not be familiar to some who approach digital microscopy for the first time. In a sense, these limits are more practical than fundamental because, if the microscope operation follows the rules of Nyquist sampling theory as discussed below (and in greater detail in Chapter 4, *this volume*), these limits should present no obstacle to recording good images. However, because incautious use of the "zoom" magnification control found on all commercial CLSMs makes it relatively easy to operate these instruments outside the Nyquist conditions, a brief discussion of sampling theory is also included here. It is mentioned under the heading "Resolution" because it involves the ability to **record** "the separation of two closely spaced objects."

Spatial Frequencies and the Contrast Transfer Function

Sampling theory, like resolution itself, is often easier to think about accurately in the "**spatial frequency domain**" where one considers not the size of objects themselves but the inverse of their size: "How many objects are visible per millimeter?" In the spatial frequency domain, an image is seen as being composed of the **spacings** between features rather than the features themselves. The reason for using this seemingly obscure mental construct is that the ability of an optical system to transmit information depends entirely on the spatial frequency of this information. More specifically, all optical systems reduce the contrast of the high spatial frequencies (representing smaller spacings) more than they do lower spatial frequencies (representing larger features). This fact is made evident when one plots the contrast transfer function (CTF) of an optical system by measuring the contrast present in an image of a test object made up of regular arrays of black-and-white bars each having a specific spacing or frequency (Oldenbourg *et al.*, 1993; Chapter 1 and Figures 35.6–35.11 in Chapter 35, *this volume*). Such a CTF is shown by the black line in Figure 2.19 and the gray line below it represents the image contrast produced by a test target that is 100% white and 70% gray (i.e., one with only 30% contrast).

Contrast Transfer Function and Resolution

Although in common parlance the word "resolution" is often used as though it were an independent parameter, Figure 2.19 makes it clear that the number chosen to represent the "resolution" is really somewhat arbitrary. It refers to the highest spatial frequency at which the contrast is above some given value. For instance, the Rayleigh/Abbe criterion for bright, point-objects on a black background (i.e., stars on a clear night) really assumes that the minimum visible contrast is 25%. The problem with this simplistic attitude to resolution is that it can give one the idea that, no matter what their original contrast (i.e., the staining specificity) in the object, all spatial frequencies up to "the resolution" are equally visible as is implied by the upper dashed line in Figure 2.19. In fact, the most important message from Figure 2.19 is that the contrast-in-the-image is proportional to contrast-in-the-object as degraded by the CTF of the imaging system, and in particular, **the contrast of small features just within the "resolution limit" is much lower than that of larger features**.

Visibility, Resolution, and the Rose Criterion

The reciprocal relationship between contrast and resolution is important because usually what one is actually interested in is not resolution *per se* but **visibility**: the ability of an observer to recognize two closely spaced features as being separate. Visibility is a much more slippery concept because it depends not only on the calculable aspects of diffraction theory but on the higher functions that our visual system uses to determine how a particular pattern of light intensity should be interpreted. As a result, there are few standard methods for measuring visibility.

On the other hand, visibility has the advantage of requiring us to consider another important parameter of the image data: its signal-to-noise ratio (S/N). The Rose Criterion states that, to be visible, a dark feature that is a single pixel in size must have an intensity that differs from that of a white background by at least 5 times the noise level of the background[13] (Rose, 1948). Although the factor 5 is somewhat lower for lines and other geometrical features, the point is that visibility depends on more than geometrical optics and the CTF. Assuming that the contrast is measured in units that are proportional to the statistical precision with which each signal level is known, visibility also depends on both the absolute and the relative difference between the signal levels of the feature and the background. In the case of being able to resolve two point features, the Rose Criterion requires that the noise be low enough and the contrast be high enough that one can discriminate the lower intensity of the pixel between the two features as being different from that of the peaks. A number of authors have pointed out that, in fluorescence confocal microscopy, one seldom counts enough photons for the 25% contrast of the Abbe resolution to be visible with any degree of confidence.

As with the CTF curve, where resolution is defined in terms of contrast in the final image, visibility requires that, as smaller objects have lower contrast, more photons will have to be counted to reduce the Poisson noise of the measurement well below the low contrast of the features.

The reader can see that visibility brings together the contrast of the object (as embodied in its staining characteristics), the focus-

[13] The choice of a dark feature on a white ground is not arbitrary. A white signal has significant but measurable Poisson noise. A truly black background does not.

ing properties of the optical system as defined by the CTF and the statistical requirements of the Rose Criterion. However, there is still one other process that can limit whether or not a feature is visible in the final image and that is how the signal is digitized.

Digitization and the Nyquist Criterion

To convert any continuous, analog signal into a digital representation, it is sampled by measuring its intensity at regular intervals in time (or space). Suppose that one is recording the air temperature at a particular location over time. How often should one make such measurements? Clearly the answer depends on the rate of change of the "features" of the temperature record that are of interest. These might be the effects of breezes or thermals that may change over seconds or less, or they might be climatic changes that might only be noticeable over centuries or millennia. Nyquist's crucial insight was that there is a fixed relationship between the highest temporal (or spatial) frequency of interest in the data set and the minimum rate at which samples must be taken if they are to record all the possible significant variations in that signal accurately. Specifically, for non-periodic data, the sampling frequency should be at least 2.4× higher than the highest frequency in the data. Consequently, to preserve all of the information that could be recorded using a CTF such as that shown in Figure 2.19, it will be necessary to have the pixels smaller than 1/2.4 F_c where F_c is the cut-off frequency.[14] This means that the Airy figure image of a point object should be at least 4 to 5 pixels across the diameter of its first dark ring.

The practical problem that arises in CLSM is that, although changing the "zoom" magnification changes the area scanned on the specimen, it does not normally do so by varying the number of pixels, and consequently, pixel size is inversely proportional to the zoom factor. However, this does not change the fact that, for a given optical system, only one pixel size (and one zoom factor!) matches the Nyquist criterion. At zoom settings that provide smaller pixels, the data will be over-sampled with the result that it will be bleached more than necessary and only a smaller field of view can be scanned in a given period. It is becoming more common for manufacturers to display the pixel size as part of the setup display, but if this is not done, it is not difficult to calculate if one has a knowledge of the length of some feature in the image in both pixels and micrometers.

On the other hand, at lower zoom settings where the pixels are larger than those prescribed by Nyquist, not only may some smaller features be missed entirely but features not present in the object may "appear" in the data because of a phenomenon called aliasing.

One can understand aliasing by returning to the temperature analogy. Assume that the thermometer is capable of responding to changes in temperature on the order of minutes but that only annual changes are of interest. Nyquist would seem to say that one can find out the average yearly temperature by making on average 2.4 measurements/year. However, there could clearly be problems if one sample is made at 6 AM in December and the next at 11 AM in May! Large day-to-day and time-of-day variations will swamp out small changes in the average annual temperature. Nyquist can only work if the response time of the sensor is reduced until it is about 2.4× our sampling interval. This could be accomplished by burying the thermometer a few meters in the earth where the temperature changes much more slowly (Pollock and Chapman, 1993).

An analogous situation occurs in a CLSM operated at a low zoom setting. When images are recorded on a "continuous" medium, there is no possibility that small but bright objects will be entirely missed. However, this is not true of sampling systems. When pixels are large compared with the optical resolution (i.e., low zoom setting), it is possible that small features will be missed altogether (so-called "blind spots"). Blind spots only occur because Nyquist sampling conditions are not met and small features lying between scan lines are not sampled. However, on instruments that employ $T_p/4$ integration rather than full-integration in their digitizing circuitry, small features that the scanning beam passes during the dead time of the digitizer may be recorded with lower contrast or not at all.

Aliasing may cause features to appear larger, smaller, or in different locations from where they should be. Like aliasing, blind spots are only a problem when the pixel size is much larger than the spot size and where the object contains a lot of small features (see Chapters 4 and 35, *this volume*, for a more complete analysis).

There are two strategies for reducing these problems (both discussed in the previous sections): increasing the size of the focal spot and using a fully integrating digitization system. However, the latter approach only avoids blind spots in the horizontal direction.

The Nyquist sampling rule is often flaunted by practicing microscopists but the errors produced by this practice usually pass unnoticed for two reasons:

- Working images that are somewhat over-sampled tend to be more pleasant to view on the display screen. As the size of the individual pixels (referred to the sample) is considerably smaller than the Nyquist limit, the data looks "as it should" but the radiation dose needed to record it was higher than necessary.
- The pixel intensities making up the images involve so few quanta that statistical variations in the signal pose a greater limitation to defining the position of the edge of a feature than does the quantization of the image in space. This is less of a limitation if one uses more photons, which happens when one uses more pixels.

Nevertheless, as applications of confocal technology more closely approach the absolute limits (e.g., by more closely matching the pixel size to that of the data of interest and improving the photon efficiency so that the statistical noise is reduced) the costs of incorrect spatial (and temporal) quantizing will become more apparent.

Fortunately, a technique is available to help solve the noise problem. Because Poisson noise affects the measurement of intensity in each pixel independently, positive noise excursions can appear to be small bright features that are only one pixel wide. These can be eliminated by adhering to the second aspect of Nyquist sampling, the part related to **reconstructing** an analog image from the digital data. Nyquist mandates that the reconstructed signal be passed though an "amplifier" having the same bandwidth as that from which the original signal was obtained. In the case of microscopy, the input "bandwidth" in question is

[14] The original Nyquist theory related to 1-dimensional data. As 2D images may contain spatial frequencies at any angle to the raster axes, it might seem logical to increase the sampling frequency by 1.4 to account for features running at 45° to these axes. However, as is shown in Fig. 4.10, adjacent rows of pixels fill in this data. In addition, because the low S/N of most confocal data limits the effective resolution of final data more severely than does the Abbe criterion, the rule that pixels should be 2× smaller than the Abbe resolution limit works well.

defined by the CTF of the optics. As single-pixel noise includes spatial frequencies that are at least 4× higher than the Abbe limit, no information is lost by passing the recorded data through an "amplifier" having the same 3D bandwidth as the microscope. The simplest way of doing this is to deconvolve it.

This point bears repeating. Although deconvolution and confocal imaging are often seen as competing methods aimed at the same goal, namely producing images of 3D stain distributions, in fact, they are not exclusive, and there is much to be said for combining them. Not only does deconvolution suppress the "single-pixel" features created by Poisson noise, it also effectively averages the signal over 16 to 25 pixels in 2D and 64 to 125 voxels in 3D because this is the number of pixel/voxels that carry appreciable signal in the Nyquist-sampled image of a point object (Fig. 2.20). **In other words, it has the same effect of reducing the uncertainty in the estimate of the brightness in individual voxels as Kalman averaging for 64 to 125 frames.**[15] This point is so important that the present edition of this volume devotes an entire chapter to it: Chapter 25.

Figure 2.21 shows what can be accomplished. This example was kindly provided by Hans vander Voort of SVI, Delft, NE. The top row shows a through-focus series of an actual Nyquist-sampled PSF. The next two rows show two simulated through-focus series in which Poisson noise has been added as though the brightest pixel recorded only 25 photons, and the remainder proportionally less. Although the noise is different in each column, when they are deconvolved, the results (seen in the two bottom rows), are almost identical.

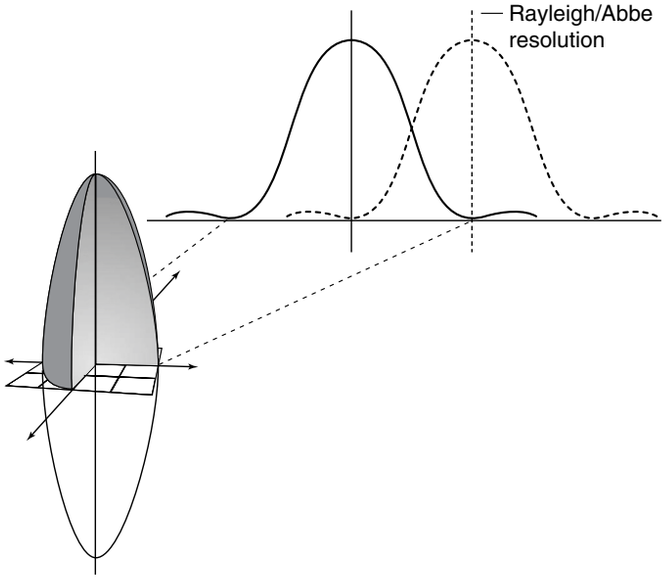


FIGURE 2.20. Relationship between the Rayleigh-criterion resolution, the point-spread function (PSF), and Nyquist sampling. If the PSF is sampled at the Nyquist level, each pixel will be less than 1/4 of the distance from one side of it to the other and ~16 pixels will have significant signal in them in each *xy*-plane.

Because the confocal PSF is so much more confined than that of WF data, it takes much less time to deconvolve confocal data. Indeed it is quite reasonable to approximate the process by a 3D Gaussian blur (see Fig. 19.2, *this volume*).

There are two other matters about sampling that should be considered:

- *Temporal aliasing effects*: The accuracy with which temporal changes can be imaged is limited by the frame-scan rate. Failure to sample sufficiently often can create artifacts such as the "back-rotating wagon-wheel effect" familiar from the movies. In the CLSM, temporal aliasing not only limits the ability to follow motion, it also has a resolution component in terms of the imprecision of the measurement of the location (or motion) of objects. Specifically, because the pixel time is short while the frame time is long, motion of the specimen produces distortion rather than the directional blurring that would occur if the whole field was recorded continuously over the same period of time.
- *Mismatch of probe and pixel shape*: There is a mismatch in shape between the circular shape of the moving Airy disk and the "hard-edged" square shape of a pixel on the liquid-crystal display (LCD), a difference made more pronounced by the innate tendency of the human visual system to emphasize edges.

In the case of a signal recorded by a cooled CCD detector on a disk-scanning confocal system, the CCD detector spatially quantizes the signal in a manner entirely determined by its sensor geometry and the total optical magnification. However, because the scanning mirrors in the CLSM follow ballistic rather than stepped trajectories, the output from the PMT of these instruments is, in principle, continuous in the horizontal direction. As a result, averaged over the digitizing time, the Airy disk is not round but is slightly more blurred in the horizontal direction.

Practical Considerations Relating Resolution to Distortion

To obtain the theoretical spatial resolution of a confocal microscope, it is, of course, necessary to have a diffraction-limited optical system, but this is not sufficient. Leaving the practical aspects of alignment and optical quality for Chapters 7 through 11, 22, and 35, this section discusses the limitations imposed by mechanical stability and the repeatability of the scanning system, a topic that highlights one of the most important differences between disk-scanning and laser-scanning instruments.

In disk-scanning instruments, the image is real and, therefore, cannot be distorted by the scanning system.[16] If a CCD sensor is used to detect it, geometrical distortion in the digitized image is extremely low, and because of the inherent mechanical stability of the sensor, any distortion that remains from the optics is stable and can be corrected by minor digital image processing. The mechanical problems of this instrument are, therefore, confined to the effects of vibration and the relative motion of the stage and lens.

In all confocal instruments, it is vital that relative motion between the objective and the specimen be kept to less than 10% of the resolution limit in *x*, *y*, and *z*. In tandem disk-scanning

[15] Although such filtering **will** reduce image contrast, the contrast can be increased arbitrarily by changing the display look-up table, a process that **does not** decrease the S/N.

[16] Although it can be distorted by any barrel or pincushion distortion present in the optics.

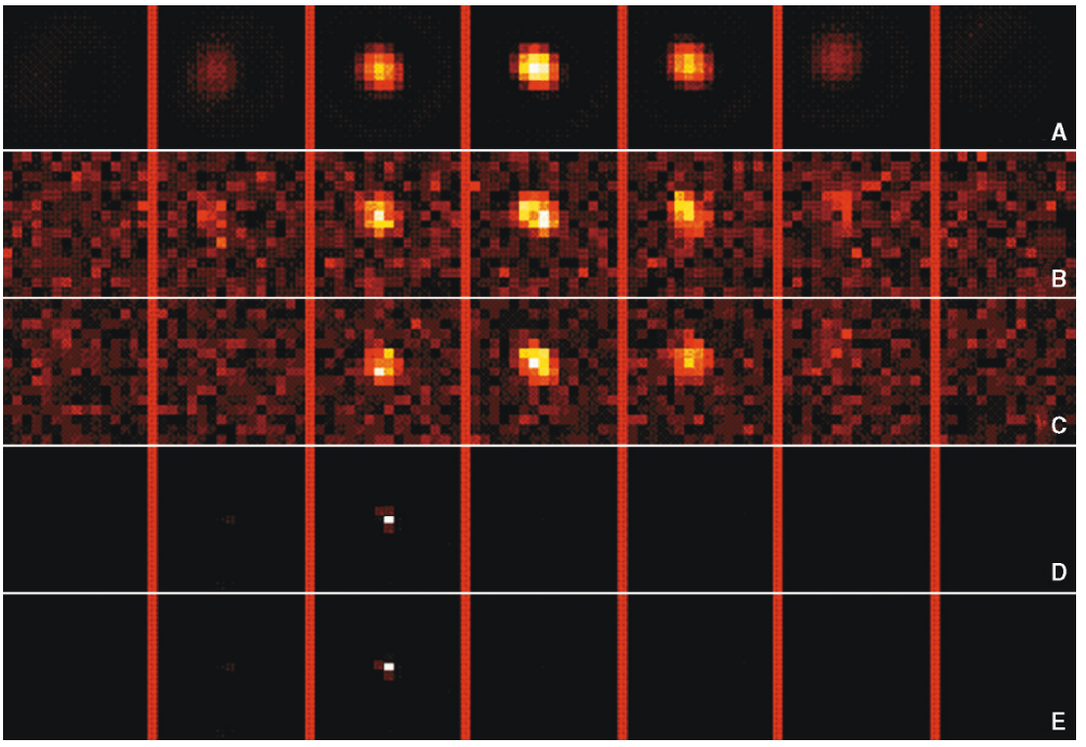


FIGURE 2.21. Deconvolution of simulated confocal data improves S/N and resolution. (A) shows a through-focus series of an actual Nyquist-sampled PSF. (B) and (C) show simulated images in which Poisson noise has been added as though the brightest pixel recorded only 25 photons. Although the noise is different in each column, when they are deconvolved, the results (D) and (E) are almost identical. (This example was kindly provided by Hans vander Voort of SVI, Delft, NE.)

instruments, both the rotating disk and the cooling system of the often-large illumination sources represent potential sources of vibration in addition to those normally present in the environment. All vibrations must be reduced below the tolerance levels or resolution will be degraded in a fairly straightforward manner. In this regard, it is not sufficient to mechanically isolate the microscope on some sort of isolation table because laser-cooling fans, spinning disks, scanning galvanometers, etc. can all **introduce** vibration into the isolated system.

Not so straightforward is the effect of vibration, and possibly stray electrical and magnetic fields acting either directly on the galvanometers or introducing spurious signals into the current amplifiers that control them. In these instruments, accurate imaging depends on the mirrors causing the beam to scan over the sample in a precise pattern duplicating the mathematically perfect raster represented by the data locations in the image memory. Failure to duplicate this raster has the result that data will be displayed in the wrong pixel, producing distortion. On a system with a 1000-line raster and a 10 : 1 zooming ratio, keeping beam placement to within 0.1 of a pixel requires accuracy of one part in 10^5. The electromechanical properties of the galvanometers (mass, spring constant, frequency response, overshoot, resonant frequency, bearing tolerance, rigidity, etc.) produce additional errors (Chapter 3, *this volume*). Image distortions produced by these errors are often masked by the paucity of test samples having an accurately defined geometry (Pawley *et al.*, 1993) and by the fact that, at high zoom, current instruments greatly over-sample the image so the smallest, visible structural features are many pixels wide.

This problem merits mention here because it is possible to measure the x, y, z **position of the centroid** of an object in a digital image to an accuracy that is **much smaller than the spatial resolution limit**. Indeed, WF light microscopy techniques have been used to measure motion on the order of 1 nm (Gelles *et al.*, 1988). However, due to the random imprecision in the systems used to position the mirrors, it is unlikely that measurements of similar reliability could be made on any present CLSM. In this context, then, the accuracy and precision with which mirror position can be controlled is a fundamental limitation on the ability of CLSM to determine position.

The presence of scan instability can be detected either by visually comparing sequential **single-scan** images of a diagonal knife-edge viewed at the highest possible magnification, contrast and signal level or, alternatively, by computing the apparent motion of the centroids of two fixed objects, each covering 100 to 200 pixels as they are recorded on a number of sequential scans. The variations measured by the second method should decrease rapidly with increasing illumination intensity because of improved statistical accuracy, although they may then begin to measure stage drift.

However, before all position errors are blamed on the galvanometers, it is important that living cells are far from the innocuous transparent objects often assumed in articles on microscope optics. As noted above the pronounced variations in RI that allow

TABLE 2.1. Fundamental Limits in Confocal Microscopy

Parameter	Theoretical	Practical
Resolution	Spatial: Y $\lambda_1, \lambda_2, \alpha_1, \alpha_2$	Alignment Off-axis aberrations
	X $\lambda_1, \lambda_2, \alpha_1, \alpha_2$	Alignment Off-axis aberrations Bandwidth Ballistic scan
	Z $\lambda_1, \lambda_2, \alpha_1, \alpha_2$ Pinhole diam.	Alignment Off-axis aberrations Δ tube length
	Temporal: Scan speed Signal decay times	Quantization of t
Position	Objective lens distortion Pixellation limitations Sampling time	Mirror accuracy Vibration
Quantitative measurement	Poisson statistics	Mirror and digitizing losses Detector QE and noise Bleaching/photodamage Saturation Source brightness

us to image cellular organelles in phase-contrast or differential-interference contrast microscopy can also profoundly distort the focus plane in the *z*-direction.

CONCLUSION

I have attempted to highlight some aspects of confocal instrumentation that must be addressed in order to attain performance limited only by fundamental considerations (Table 2.1). Although the constituent aspects of both photon efficiency and resolution have been addressed separately, I have tried to emphasize that the effects of both of these factors overlap and interact in a fairly complex manner. To summarize:

- Although resolution in the confocal microscope is primarily a function of the NA of the optical system and the λ of the light, it can also be further limited if the signal level represents so few quanta that the detected signal lacks the statistical precision to produce a "visible" feature or if the data are not correctly sampled because the pixels are too large.
- To improve the statistical precision of the signal, every effort should be made to count as many of the photons emerging from the specimen as possible:
  - — Reduce optical losses.
  - — Select the best type of PMT for the signal to be detected. New photodetectors may soon become available.
  - — Use photon-counting when appropriate.
  - — Check alignment often.
  - — Routinely check performance by making and analyzing images of test objects.
- To remove "single-pixel noise features" and provide the advantages of multi-voxel averaging, all Nyquist-sampled, 3D confocal results should be deconvolved (or at least 3D Gaussian filtered) before being viewed. Likewise, Nyquist-sampled 2D data should be filtered.
- The effects of image quantization should not be ignored. Only one pixel size (zoom setting?) is really optimal for each λ, NA, and lens magnification.
- Care should be taken to keep the pinhole diameter larger than that of the Airy disk at its half-power points (0.5 Airy unit). This setting will change with λ, NA, and lens magnification.
- Special circumstances may dictate breaking sampling and pinhole "rules," but they should still be recognized and acknowledged.
- It should be possible to operate the system both at its diffraction-limited resolution and at larger spot sizes.
- In laser-scanned instruments, imperfect scanning precision can introduce distortion.
- Fluorescence saturation places unexpected limits on the speed with which experiments can be performed with laser-scanning microscopes.

ACKNOWLEDGMENT

This chapter has benefited greatly from my conversations with Sam Wells (Cornell University) and Jon Art (University of Chicago). Thanks to Nick Doe (Bio-Rad, Hemel Hempstead, UK), who assisted with measurements of the digitization circuitry on the MRC-1000 and 1024. Figures 2.3, 2.4, and 2.5 were made while the author was a guest of the Key Centre for Microscopy and Microanalysis at the University of Sydney, in Sydney, Australia, supported by the Sabbatical Fund of the University of Wisconsin and by NSF grant # 9724515. I thank Guy Cox and other members of the Center for their patience, generosity, and assistance. The data for Figure 2.10 were obtained from Hamamatsu and data for Figure 2.14 were obtained Delft Photonics, Delft, NE. Figure 2.21 was kindly provided by Hans vander Voort of Scientific Volume Imaging, Delft, NE. Figure 2.18 was provided by P. Sims, University of Wisconsin, Zoology Department. Cheryle Hughes and Bill Feeney, artists in the Zoology Department, University of Wisconsin-Madison, made the other drawings. This work was supported by grant DIR-90–17534 from the US National Science Foundation (JP) and grant DRR-570 from the US National Institutes of Health to the Integrated Microscopy Laboratory, Madison, Wisconsin.

REFERENCES

Gelles, J., Schnapp, B.J., Steur, E., and Scheetz, M.P., 1988, Nanometer scale motion analysis of microtubule-based motor enzymes, *Proc. EMSA* 46:68–69.

Gunter, W.D. Jr., Grant, G.R., and Shaw, S., 1970, Optical devices to increase photocathode quantum efficiency. *Appl. Opt.* 9:251–257.

Oldenbourg, R., Terada, H., Tiberio, R., Inoué, S., 1993, Image sharpness and contrast transfer in coherent confocal microscopy. *J. Microscopy* 172:31–39.

Pawley, J.B., 1994, The sources of noise in three-dimensional microscopical data sets. In: *Three Dimensional Confocal Microscopy: Volume Investigation of Biological Specimens* (J. Stevens, ed.), Academic Press, New York, pp. 47–94.

Pawley, J.B., 2000, The 39 steps: A cautionary tale about "quantitative" 3D fluorescence microscopy, *BioTechniques*, 28:884.

Pawley, J.B., 2002, Limitations on optical sectioning in live-cell confocal microscopy, *Scanning*, 21:241–246.

Pawley, J.B., and Centonze, V., 1998, Practical laser-scanning confocal light microscopy: Obtaining optimal performance from your instrument. In: *Cell Biology: A Laboratory Handbook* (J.E. Celis, ed.) Academic Press, New York, pp. 149–169.

Pawley, J.B., Amos, W.B., Dixon, A., and Brelje, T.C., 1993a, Simultaneous, non-interfering, collection of optimal fluorescent and backscattered light signals on the MRC-500/600. *Proc. Microsc. Soc. Am.* 51:156–157.

Pawley, J., Blouke, M., and Janesick, J., 1996, The CCDiode: An optimal detector for laser confocal microscopes, *Proc. SPIE* 2655:125–129.

Pawley, J.B., Hasko, D., and Cleaver, J., 1993, A standard test and calibration specimen for confocal microscopy II. In: *Proceedings of the 1993 International Conference on Confocal Microscopy and 3-D Image Processing* (C.J.R. Sheppard, ed). Sydney, Australia, p. 35.

Pollock, H.N., and Chapman, D.S., 1993, Underground records of changing climate, *Sci. Am*. 68:44–50.

Rose, A., 1948, Television pickup tubes and the problem of noise. *Adv. Electron* 1:131.

Sandison, D.R., Piston, D.W., Williams, M., Webb, W.W., 1994, Quantitative comparison of background rejection, signal-to-noise ratio, and resolution in confocal and fullfield laser scanning microscopes. *Appl. Opt.* 1994: 3576–3588.

Sheppard, J.R., Gu, M., and Roy, M., 1992, Signal-to-noise ratio in confocal microscope systems. *J. Microsc.* 168:209–218.

3

Special Optical Elements

Jens Rietdorf and Ernst H.K. Stelzer

INTRODUCTION

The amazing array of microscopic instrumentation for generating three-dimensional images of biological specimens that are described elsewhere in this volume rely on a relatively small number of optical and mechanical components. Although most biologists have a general idea of their function and how to operate them, some mysteries remain.

It is the purpose of this chapter to provide the reader with a description of how components are specified, which components are used in commercially available equipment, and how they operate, along with some insight in terms of their specific applications to confocal or multi-photon microscopy. We will try to emphasize those specifications and limitations that impinge directly on the performance of the entire instrument so that the reader can understand the various trade-offs and raise sensible questions during the purchasing process. Those wishing to make their own confocal from scratch will need to consult more detailed sources.

The comments provide insights developed over many years during which we designed, built, and used a large number of different confocal microscopes. Our comments are meant to improve the understanding of the fine points of microscope operation among users, and should not be construed as recommendations either in favor of or against any particular brand. If some of our remarks seem vague or inconclusive this may reflect the fact that some elements make sense in this but not in that design. Parts that might have been important in the past often become less important due to technical improvements in other areas.

The best approach to optical design is: "Efficiency through simplicity." Use as few optical elements as are absolutely necessary to achieve a certain goal and place them in the optimal location along the optical path. In general, flat surfaces are more easily manufactured and easier and less expensive to coat than curved surfaces. Lenses with long focal lengths usually have fewer aberrations and are less expensive than those with short focal lengths. Additionally, the actual performance of an optical instrument always seems to reflect engineering and financial compromises.

This chapter describes the operation of some of the important components used in confocal microscopes: filters, scanners, acousto-optical devices, electro-optical modulators, and polarizers. It complements in particular Chapter 9, which discusses the intermediate optics of confocal microscopes.

REGULATING THE INTENSITY

In modern laser confocal microscopes, the intensity of the light is typically regulated using acousto-optical tunable filters (AOTFs; see below), combinations of several AOTFs, or combinations of AOTFs and neutral-density (ND) filters. A polarizer can also serve as a continuously variable attenuator as most lasers emit polarized light (Callamaras and Parker, 1999). However, if the polarization axis needs to be preserved [e.g., to maintain proper differential interference contrast (DIC) operation] a second polarizer must be included and adjusted to pass the original beam. Neutral-density filters are either absorptive gray glass filters (for low-power applications) or reflective metallic filters (for high-power applications) that attenuate the intensity of the transmitted light independent of the wavelength (λ). Circular, neutral-density filters, which have a band of optical density around their perimeter that increase linearly or logarithmically with the angle, also allow one to control the intensity continuously, but the intensity profile of a large beam passing such a filter becomes slightly inhomogeneous.

Because most lasers used in confocal microscopy produce only milliwatts of power, there is little danger of overheating the ND filter. However, this does not apply to filters used with arc sources or lasers for multiphoton excitation, where the beam power may reach several watts. ND filters come in two general types, those made of darkened glass that absorbs light and those coated with a metal film that reflects light. The former are more likely to overheat and the latter more likely to produce stray light or to deflect potentially damaging power elsewhere.

WAVELENGTH SELECTIVE FILTERING DEVICES

The following sections discuss the different filter types available for use as excitation or emission filters or as dichroic mirrors. In fluorescence microscopy, filtering devices (e.g., Melles Griot Catalog, Chapter 13) are used to separate light beams on the basis of their wavelengths. Four different types of filters are used to selectively transmit or block a desired range of wavelengths (Fig. 3.1): (a) short-pass filters (blue line) that cut-off wavelengths longer than a certain wavelength (λ_0) — heat filters are used to exclude infrared light to reduce specimen heating by the illumination; (b) long-pass filters (red line) that only transmit light longer than a certain wavelength — fluorescence emission filters are often long-pass filters used to prevent the excitation light from reaching the detector; (c) bandpass filters (light green line) that only trans-

Jens Rietdorf and Ernst H.K. Stelzer • Advanced Light Microscopy Facility and Light Microscopy Group, European Molecular Biology Laboratory (EMBL), Heidelberg, Germany

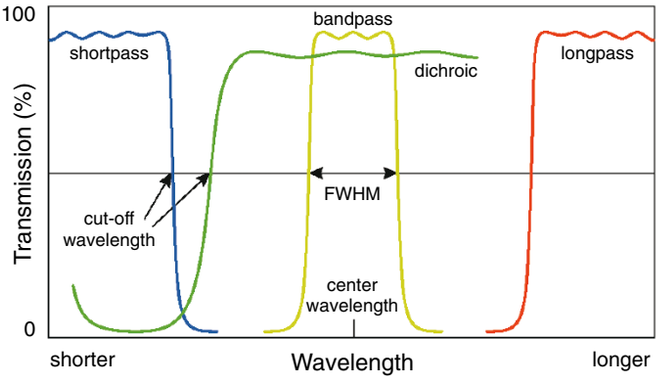


FIGURE 3.1. Types of filters. Filters are flat optical components designed only to transmit light of certain wavelengths. There are four general types: short-pass (dark blue), long-pass dichroic (dark green), bandpass (yellow-green), and long-pass (red).

mit light between a cut-on and a cut-off wavelength — these may be used to select either excitation or emission wavelengths especially when one is trying to image signals from more than one fluorophore simultaneously; and (d) dichroic mirrors (dark green line) that separate the emitted light from the excitation light. In fluorescence microscopy, dichroic mirrors are long-pass filters designed to operate when oriented at 45° to the optical axis.

Note that active optical devices such as acousto-optical (AO) elements can also fulfill these functions (see description of AODs and AOBSs below) and some confocal systems have now replaced all filter components by AO devices and dispersive elements (e.g., Leica AOBS SP2 and RS).

Selecting the Wavelength of the Illumination and the Detected Light

While filament-based lamps emit a continuous spectrum of light that is very similar to black-body radiation, high-pressure, plasma-based light sources emit a large number of distinct lines on top of a black-body radiation background (see Chapter 6, *this volume*). Lasers come in various types and may emit one or a number of lines, each with an extremely narrow bandwidth (see Chapter 5, *this volume*). Finally, femtosecond pulsed lasers emit bands that can be up to several tens of nanometers wide.

The spectral problems posed by epi-fluorescence microscopy can be understood by looking at Figure 3.2, which shows the important variables schematically. The excitation spectrum of a fluorophore (blue) is skewed so that the peak is towards its long-λ side while the emission spectrum (green) is peaked near its short-λ side. The difference in nanometers between the peaks of these spectra is referred to as the Stokes shift. A large Stokes shift has the advantage that it is relatively easy to separate the excitation light from the much fainter signal light, but it also "uses up" more of the spectrum, making it more difficult to excite and record signal from two or more dyes at the same time.

The object is to excite the dye as efficiently as possible while collecting as much of the emitted light as possible without transmitting any excitation light into the detection channel, a task complicated by the fact that the excitation light is usually about 10^5 to 10^6 times brighter than the fluorescence emission.

Ideally, one should illuminate with a narrow wavelength band that matches the peak excitation wavelength of a fluorophore selected. This requires both that the excitation filter pass only this band and that the dichroic beam-splitter reflect it. Although this can work well if one has a laser line that coincides with the peak of the excitation spectrum, more commonly, the excitation is from a Hg or Xe arc. As such sources are far less bright than lasers, in terms of being able to concentrate a lot of photons onto a single point in the specimen (see also Chapter 6, *this volume*), one normally chooses to excite the dye over a band of wavelengths that matches the "half-power" points of the excitation spectrum. Although this allows more photons to strike the dye, it also means that the window of wavelengths available for detecting the fluorescent light must now start at a slightly longer wavelength if it is to exclude all the excitation light.

On the other hand, no matter what the bandwidth of the excitation, fluorophores emit light over a spectral band and the wider the detection bandwidth, the more signal will be recorded.[1] An emission filter (sometimes called a barrier or rejection filter), is necessary to block any excitation light from reaching the detector. This filter is at least a long-pass filter, but may be a bandpass filter if this is needed to block undesired autofluorescence or when the emission from two or more fluorophores must be discriminated.

Generally speaking, each fluorophore requires different illumination and detection filters, and yet other filter packages when two or more fluorophores are present in the same specimen. Although total signal is maximized when large filter bandwidths are used, spectral discrimination is enhanced if the filters are chosen to provide a good separation of the bands. In addition, narrowing the illumination spectrum to match the excitation peak will increase the excitation efficiency while reducing the bleaching and excitation of non-specific fluorescence, by avoiding wavelengths that excite the fluorophore less efficiently (Kramer, 1999).

Separating the Light Paths

In fluorescence microscopes, part of the light path is used by both the excitation and the fluorescent light and these two components must be separated, based on their spectral properties and their

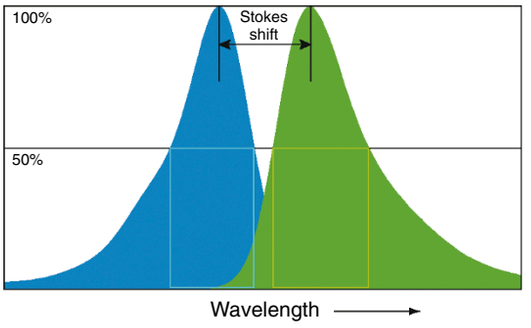


FIGURE 3.2. Fluorescence parameters. To a first approximation, the excitation and emission spectra are mirror images of each other. The wavelength difference between their peaks is called the Stokes shift and varies with the dye and its environment. The bandwidth (light blue and light green rectangles) is a measure of the width of each spectrum, defined as the wavelength difference between the half-power points of each spectrum.

[1] The fact that all common photodetectors cease to respond once the energy of each photon drops below a fixed level, places a practical limit on the long-λ end of the detection bandwidth.

direction of propagation. This separation is produced either by dichroic mirrors, which transmit one part of the spectrum and reflect the other part when placed at 45° in the light path, or by acousto-optical beam-splitters (see AOBS below). For single fluorophores, a long-pass dichroic that reflects the short-λ illumination light and transmits the fluorescent light is generally chosen. Note that, in a two-photon microscope, the fluorescent light has a shorter λ than the excitation light. Therefore, if a single-photon setup is also used for two-photon excitation, the long-pass dichroic must be replaced by a short-pass dichroic.

Common fluorophores usually have a Stokes shift of 20 to 100 nm, that is, the peak of the emission spectrum occurs at a λ that is 20 to 100 nm longer than that of the absorption peak (e.g., Molecular Probes, 2002, pp. 903–905; Chapter 16, *this volume*). Therefore, in order to transmit most of the short-λ part of the fluorescence to the detector, dichroic mirrors must have a very sharp edge between their reflection and transmission bands. While a loss of illumination intensity due to reduced reflection by the dichroic mirror can often be compensated for by increasing the intensity of the light source, fluorescence mistakenly reflected towards the source rather than proceeding to the detector represents a loss that cannot be remedied without subjecting the specimen to more light.

Modern confocal microscopes may have several detectors to allow the simultaneous detection of signals in different wavebands.

Conventional Filters

Conventional filters generally consist of colored glass, metallic films, or polymers that absorb unwanted wavelengths. Colored glass filters are relatively inexpensive and easy to handle, but have some disadvantages (Reichman, 2000, p. 11): the cut-off between the transmission and absorptions bands is rather gradual and the peak transmittance is usually low. Additionally, because they absorb light, they may overheat and crack if subjected to high light intensities (i.e., in the illumination path). In addition, many of the glasses involved are autofluorescent. In recent years, advances in the manufacture of interference filters have made them the λ-selective components of choice for all filter-based microscopes.

Interference Filters

It is not an overstatement to say that the development of epifluorescence microscopy owed more to the perfection of interference filters, and more particularly of dichroic beam-splitters, than to that of any other optical component.

When light passes from a smooth medium having a refractive index (RI) of n_1 to a second medium with an RI = n_2, an amount of the light proportional to $(n_1 - n_2)^2$, is reflected [Fig. 3.3(A)]. When light strikes a thin layer of high-RI material covering a substrate of low-RI, optical-grade glass or fused silica/quartz, some light reflects back from each interface. If the thickness of the layer is such that the light reflected by the top surface is out-of-phase with the light reflected from the next surface down (i.e., the layer is λ/4 (or 3λ/4, 5λ/4 . . .) thick,[2] these two beams will be out of phase and will tend to cancel each other out, with the result that less total light will be reflected [Fig. 3.3(B)]. Alternatively, if either λ or the thickness of the layer is changed so that the two reflected waves are now in phase (i.e., the layer is λ2 thick), then the total reflectivity at this wavelength is increased, although still quite low [about 10% from only two surfaces, Fig. 3.3(C,D)]. The total reflectivity can be increased almost arbitrarily by adding more layers of alternating high- and low-RI materials (Fig. 3.4).

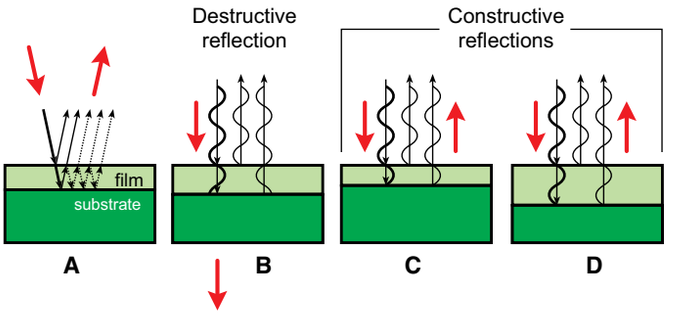


FIGURE 3.3. Interference filtering. (A) When light strikes a transparent surface covered by a thin transparent film having a different refractive index, some light is reflected by each interface. (B) If the thickness of the film is such that these two wave-trains are out-of-phase as they leave the surface, they will tend to cancel out, reducing the overall reflectivity (and increasing transmission). (C, D) On the other hand, for light with a wavelength such that the waves leaving the surface are in phase, the total reflectivity will be increased. (These diagrams modified from originals kindly provided by Turan Erdogan, Semrock, Rochester, NY.)

Traditionally, the materials used for the high-index layers were zinc sulfide (RI = 2.35), zinc selenide (RI = 2.67), and sodium aluminum fluoride, or cryolite, was used for the low-index material. Because these materials are both soft and hygroscopic, they must be protected, usually by sticking the coated sides of two glass substrates together with epoxy [Fig. 3.5(A)]. This has the disadvantage of making it very difficult to make all the flat surfaces parallel with the result that most such filters suffer from "wedge-error" and light passing through them is deflected at a slight angle.

More recently, these coating materials have been replaced by semi-transparent layers of metal oxides. Although more complex and time-consuming to deposit,[3] these so-called **hard coatings**, are unaffected by water, temperature changes, or normal, careful handling, and because they deposit as denser, more uniform layers, the interfaces are more uniform and hence scatter less light. As a result, more light is transmitted. Best of all, because they are deposited on a single piece of glass [Fig. 3.5(B)], both the wedge error and wavefront error ("flatness") can be reduced substantially (respectively to <0.1 minute of arc and <λ/inch of surface), and this reduces pixel shift when the filters (or dichroics) must be changed for sequentially recording several dyes in a single specimen.

[2] One must remember that, when measuring film thickness in terms of wavelength, we are referring to optical thickness (i.e., geometric thickness × RI) but that, as RI changes with wavelength, some subtlety is needed in determining the correct actual thickness. In practice this is accomplished by actually monitoring the transmission of the filter as each layer is deposited.

[3] The process involves ion-assisted deposition, a recent modification of evaporation methods that utilizes either direct thermal or electron beam to vaporize source materials and an energetic ion source that ionizes the evaporated materials and then bombards the substrate with them. This process increases the packing density in the film layers, which increases the RI and improves the mechanical characteristics of the coat. Fewer voids reduces water absorption, a common cause of mechanical failure and unstable optical properties. Depending on the films being deposited, various ion species may be employed, including oxygen or inert gases such as argon.

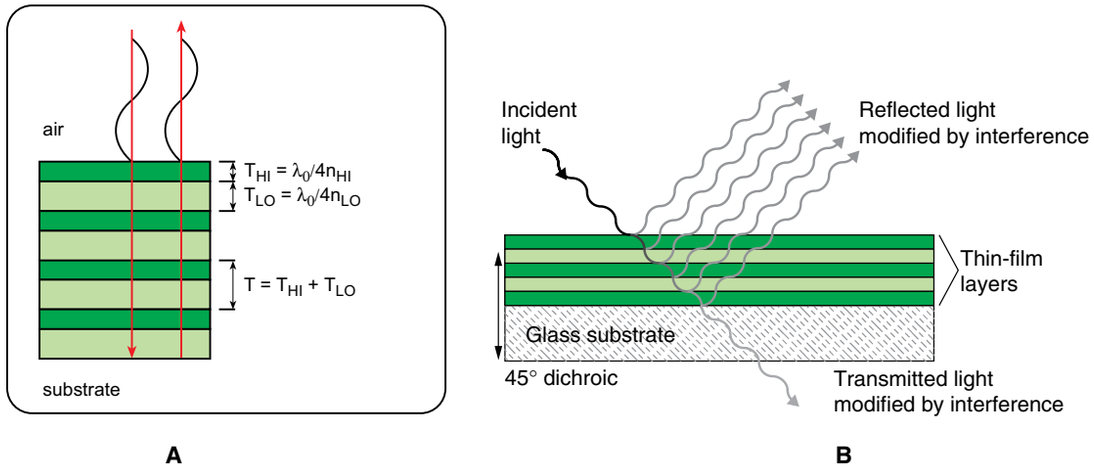


FIGURE 3.4. Interference mirrors. (A) Light impinging on a stack of transparent layers of alternating high and low refractive index, will be highly reflected if each layer is λ/4 of a wavelength in thickness. (B) This also applies to surfaces struck at an angle of 45°, although in this case, shorter wavelengths will be reflected for a given layer thickness.

Traditional dielectric coatings are often stacked into units called **cavities**, which are constructed of groups of alternating layers separated by a wider layer of one of the materials called a **spacer** (see Fig. 3.6). The spacers are produced with a thickness that corresponds to even multiples of a half wavelength in order to reflect or transmit light in registration with the dielectric layers. Increasing the number of cavities utilized to build an interference filter produces a proportional increase in the slope of the cut-on and cut-off wavelength transmission boundaries. Conventional interference filters featuring up to 15 stacked cavities can have a total of over 75 individual dielectric layers and provide a bandwidth only a few nanometers wide. However, because the surfaces of soft, evaporated films are not perfectly smooth, they produce incoherent scattering that reduces peak transmission substantially when many layers are used. Because the surfaces formed by the hard coating materials are smoother [Fig. 3.6(C)] and can be deposited more precisely, it is possible to deposit more than 200 of them without reducing peak transmission substantially and while restricting cumulative thickness errors so that the order of the array is maintained.

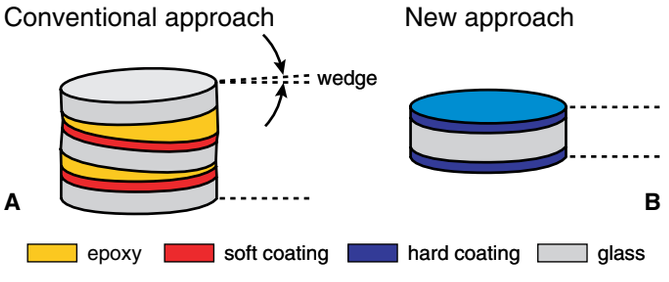


FIGURE 3.5. Fabrication methods. (A) As the materials conventionally used for the thin films that make up interference filters are both soft and hygroscopic, they must be protected from the environment by placing them on the inside of a filter assembly composed of at least two pieces of glass held together with epoxy. (B) As the coatings used on more modern filters are hard enough to be applied to the outside of a single glass blank, the assembly can both be thinner and have surfaces that are more parallel. (These diagrams modified from originals kindly provided by Turan Erdogan, Semrock, Rochester, NY.)

Types of Interference Filters

Virtually any type of filter can be designed and constructed with thin-film interference coating technology, including bandpass, short-pass, long-pass, dichroic beam-splitters, neutral density, and a variety of mirrors, including those used to confine laser cavities (Fig. 3.1). We will start by considering a **long-pass cut-off beam-splitter** (Fig. 3.7)[4] that reflects all light $<\lambda_0$. Clearly, this could be made by depositing onto the substrate a stack of cavities, each with λ/2-thick layers tuned to different wavebands longer than λ_0. Those cavities reflecting light near to λ_0 must have steeper cut-offs (i.e., more layers) than those centered farther away but the result is that **only wavelengths shorter than λ_0 will be reflected**. It is important to remember that, as any light that is not transmitted by an interference filter is reflected rather than absorbed or scattered, provision must be made to absorb it lest it become a source of stray light.

A **short-pass filter** is made using the reverse logic (**reflect λ longer than λ_0**), while a bandpass filter could be made by essentially coupling a short-pass and a long-pass filter. Alternatively, one can deposit λ/4 layers for the wavelengths that one does want to transmit with the assumption that other wavelengths will be reflected. As the latter approach involves thinner layers that take less time to deposit, it is therefore more commonly used. Figure 3.8 shows the performance of both "hard" and "soft" bandpass filters as might be used as the excitation and emission filters for a fluorescein cube. When the "hard" curves are combined with the filter shown in Figure 3.7 (now used as a beam-splitter), the performance of the resulting set can be seen in Figure 3.9.

Although in fact most filters are made using film-thickness patterns considerably more complex than those just described, state-of-the-art methods now allow one to fabricate a component as complex as the triple-dichroic beam-splitter designed to reflect 364, 488, and 633 nm light so accurately that the measured performance closely approximates the theory (Fig. 3.10). One can see

[4] Because they have been a leader in introducing this new technology to microscopy, this chapter uses many illustrations provided by Semrock, Inc. (Rochester, NY). However, it seems likely that, by the time you read this text, other filter companies will also be offering similar products fabricated using the new hard-coating techniques.

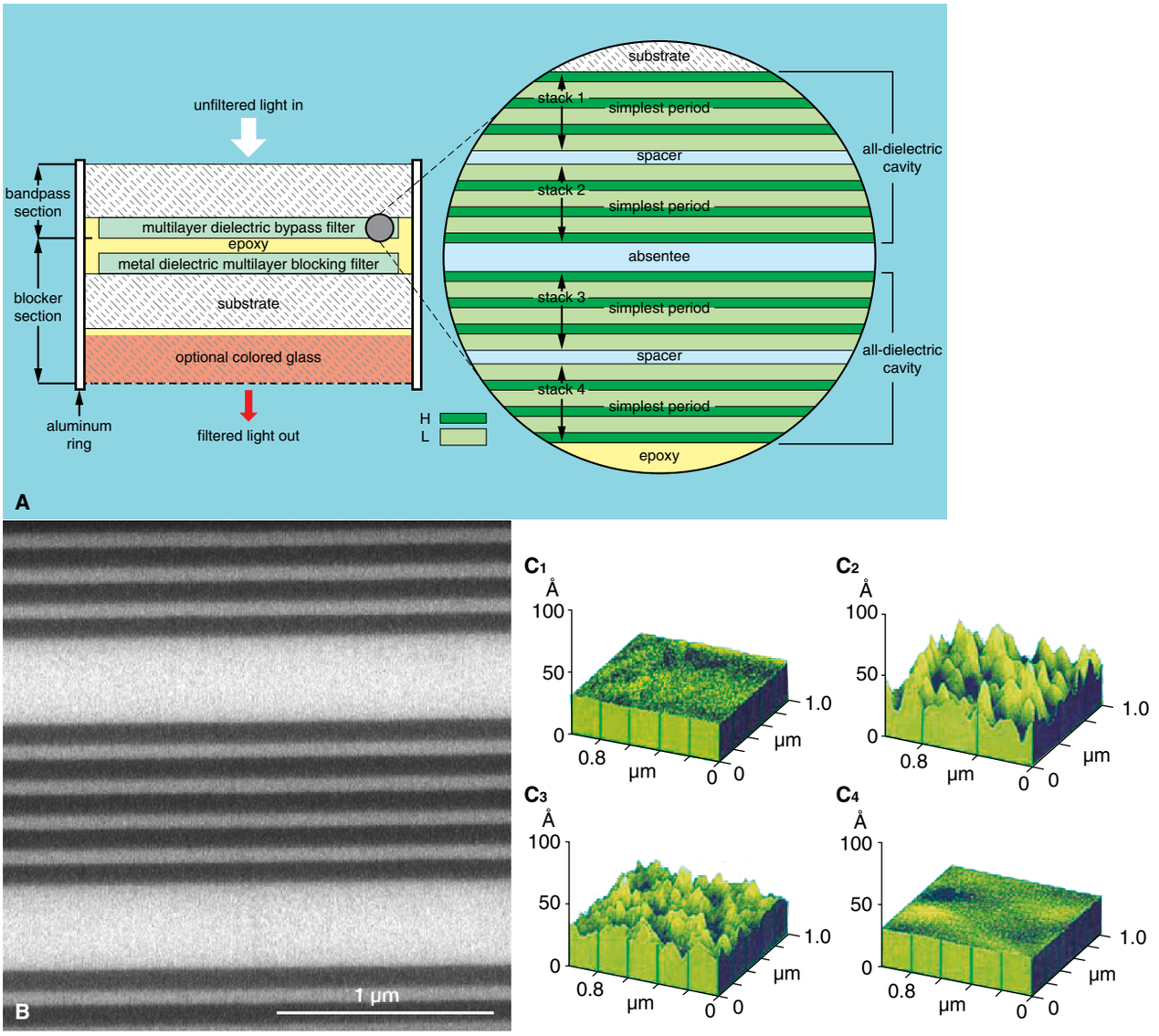


FIGURE 3.6. Layers, cavities, filters and surfaces. (A) Most interference filters use tens or even hundreds of layers. These layers are often grouped in sets of 5, with a thicker spacer layer between them. Larger sets are referred to as cavities. (B) Scanning electron microscope image of the edge-view of a part of a stack of layers. The lighter layers are thinner and have a higher refractive index. (C) Atomic force micrographs of the surface of a variety of optical surfaces: (C1) "super-polished" substrate with a surface quality of 0.5Å rms; (C2) same substrate with a 25-layer, mirror coating deposited by electron-beam (EB) evaporation, 10 Å surface quality; (C3) same substrate with a 25-layer, mirror coating deposited by continuous, plasma-enhanced or ion-assisted EB coating, 4 Å surface quality; (C4) same substrate with a 50-layer, ion-beam-sputtered coating, 0.5 Å surface quality. The improvement in surface roughness is clear and this results in lower inter-layer and overall scattering. (The diagram modified from an original kindly provided by Melles Griot, Rochester, NY. The micrograph is from Turan Erdogan, Semrock, Rochester, NY.)

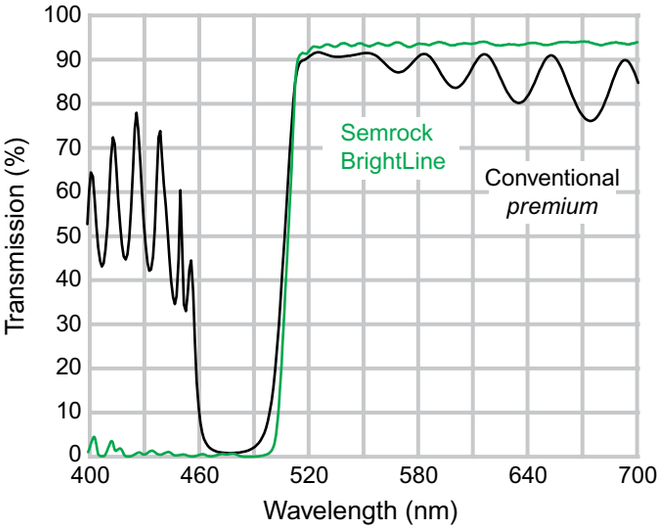


FIGURE 3.7. Performance of a 45° beam-splitter. The black line represents the transmission characteristics of a traditional, high-quality dichroic beam-splitter. The green line represents the performance of a newer, hard-coated filter. The superior optical properties of the hard coatings allow one to use more layers to produce steeper cut-offs while still maintaining very high peak transmission. (This diagram modified from an original kindly provided by Turan Erdogan, Semrock, Rochester, NY.)

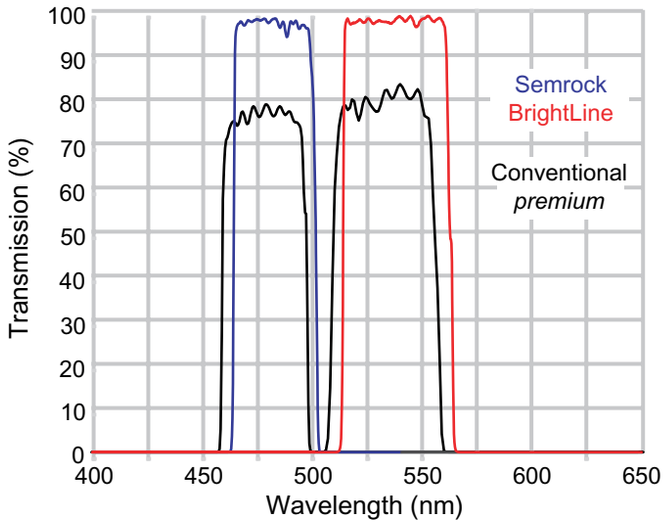


FIGURE 3.8. Excitation and emission bandpass filters. The difference in performance between the older "soft" coatings and the newer "hard" ones is evident. (This diagram modified from an original kindly provided by Turan Erdogan, Semrock, Rochester, NY.)

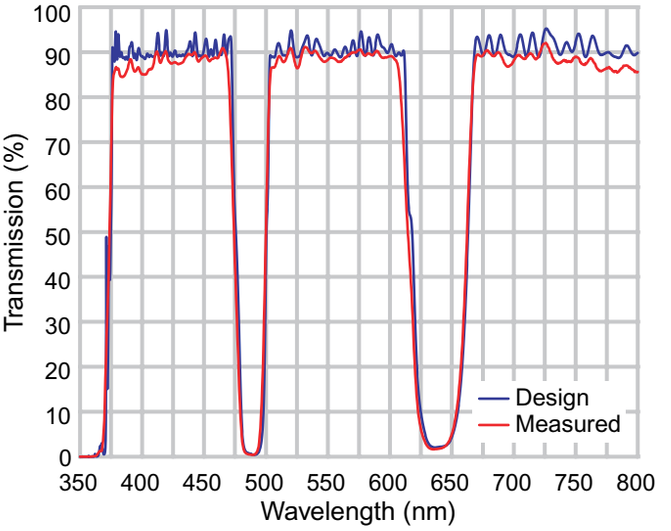


FIGURE 3.10. Theory and practice in filter design. The hard optical coating performance is so predictable that theoretical and actual performance can be very similar, even on a component as complex as a triple-bandpass dichroic. (This diagram modified from an original kindly provided by Turan Erdogan, Semrock, Rochester, NY.)

the close agreement between designed and measured performance that is possible when using the new hard coatings.

Although the average biological microscopist is unlikely to try to manufacture an interference filter, one factor worth remembering is that "reflections add." In other words, cavities shape the spectral properties of the incident light by subtraction: by reflecting unwanted wavelengths. Once these wavelengths have been removed from the beam, they cannot be "restored" merely by depositing a subsequent layer that would have transmitted them. In practice, this means that it is easier to make a filter that transmits only one specific wavelength.

The number of layers and cavities deposited is the variable used to control the nominal wavelength, bandwidth, and blocking level of the filter with very high precision. Figure 3.11 shows the performance of a pair of "hard" filters made for use in Raman spectroscopy. In this technique, photons scattered by individual molecules in a transparent specimen (or even in the optics!), are found to have lost very small amounts of energy, and the amount of this loss is related to the electronic structure of the scattering material. As a result, the scattered light contains spectral data that allows one to identify the scattering molecules. Because Raman scattering is produced by every element in the optical system and

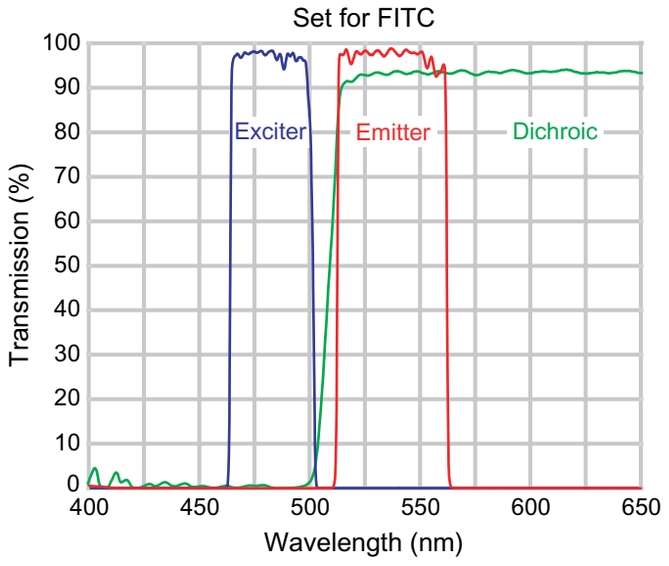


FIGURE 3.9. Filter cube for FITC. Combined performance of the filters diagramed in Figures 3.7 and 3.8. (This diagram modified from an original kindly provided by Turan Erdogan, Semrock, Rochester, NY.)

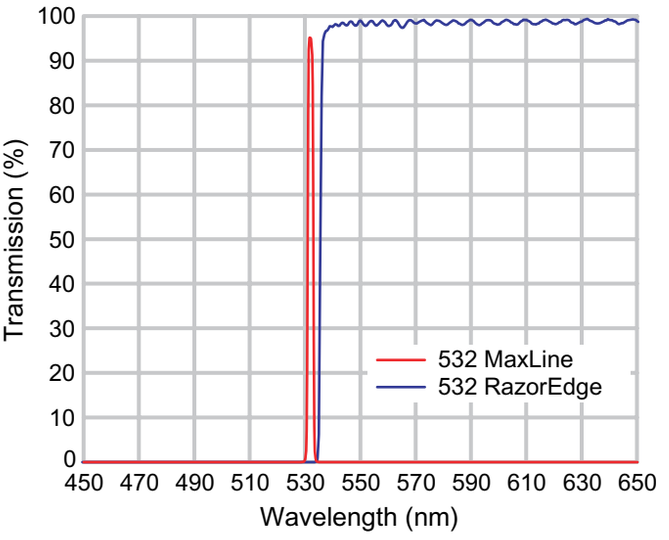


FIGURE 3.11. Laser-line mirrors. Modern hard-coating mirrors can be made with enough layers to produce very narrow reflection bands (red line), and long-pass filters with extremely steep cut-offs (blue line). (This diagram modified from an original kindly provided by Semrock, Rochester, NY.)

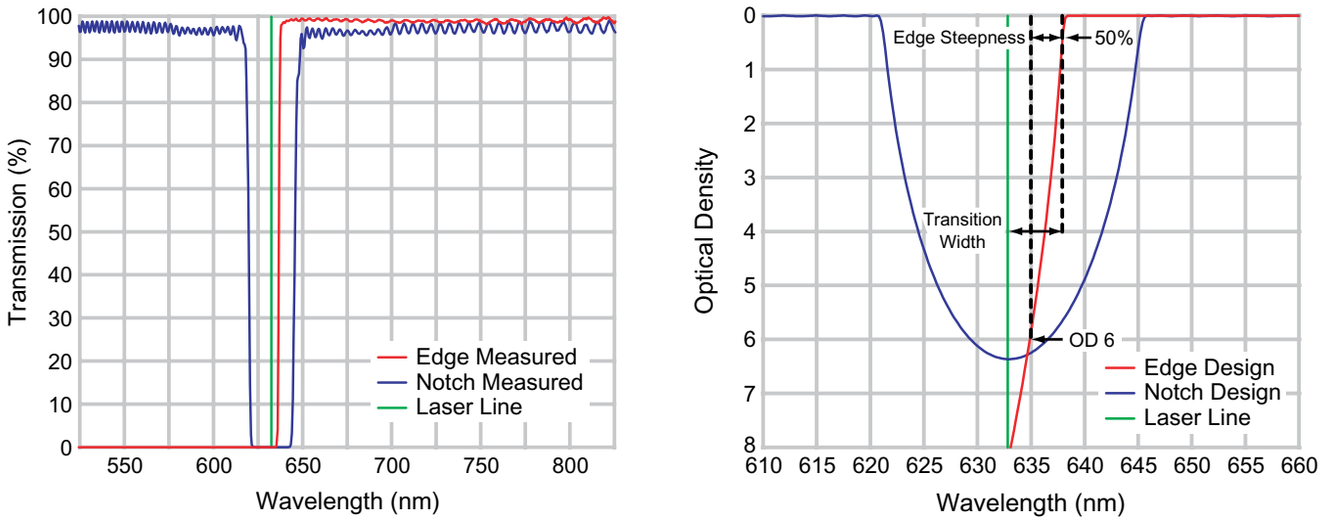


FIGURE 3.12. Linear versus logarithmic plots of transmission. Although transmission graphs (left) are easy to understand, they don't give the whole story because one can only read them to about 1% transmission. As the emitted light is about one million times dimmer than the excitation, great effort is required to produce dichroic and barrier filters with sufficient "blocking" to prevent any excitation light from reaching the detector. As a result, one can only usefully estimate filter suitability if one views a transmission plot displayed in logarithmic, "optical density units" (OD, right). Here one can see that a laser-line "notch" filter with a transmission bandwidth of ±12 nm has a transmission ratio of $>10^6$, and that the cut-off of the long-pass barrier is similarly steep. (These diagrams modified from originals kindly provided by Turan Erdogan, Semrock, Rochester, NY.)

because the specimen itself produces very little Raman-scattered light, filters such as those shown in Figure 3.11 are needed to ensure that the light striking the specimen is uncontaminated with Raman wavelengths picked up "in-transit" (red line), using a "laser-line" filter composed of a very large number of λ/4 layers that effectively transmits only the laser light. A steep-cut-off, long-pass filter is used so that only light with $\lambda > \lambda_{laser}$ can reach the spectrometer (blue line).

If the optical configuration requires that the filter pass the laser line rather than block it, a notch filter is used. Figure 3.12 shows the performance of this combination in two different ways: (a) as a linear plot (as is the case in all the other figures so far) and (b) with the vertical scale in optical density (OD) units. As OD units are logarithmic, the figure shows that the blocking level of this filter at its center wavelength is $>10^6\times$. Such a filter (or at least one centered at a longer wavelength!) could be used to block near-IR from a pulsed laser from reaching a transmitted light detector set up to measure the second- or third-harmonic signal (see Chapter 40, *this volume*). More generally, because the fluorescence signal is commonly $10^6\times$ less intense than the excitation, it is often even more important that emission filters have good blocking than that they have a sharp cut-off, because without this feature, a lot of stray, reflected excitation light may reach the detector, effectively reducing image contrast.

Because light striking a thin film at an angle will need to have a slightly shorter wavelength in order for the next interface to be encountered in exactly λ/2 or λ/4, the spectral properties of interference filters and beam-splitters vary with incidence angle. Figure 3.13(A) shows both how $\lambda_{cut\text{-}off}$ of a short-pass filter changes by about 10% as the incidence angle increases to 45° and also how this effect depends on the polarization direction of the incident light. At angles greater than normal incidence, light waves undulating parallel to the plane containing the incident and reflected rays (*p*-polarization) exhibit a different transmission profile from waves undulating perpendicular to the plane of incidence and reflection (*s*-polarization). Except when performing anisotropy measurements, it is usually desirable to reduce the polarization-dependent behavior of filters in the detection path because light emanating from the sample is typically less polarized. However, in the excitation light path this pol-dependence can be exploited to achieve a higher reflectance for polarized excitation laser light.

Figure 3.13(A) makes clear how the intensity of the beam striking the specimen in a single-beam, confocal microscope can vary substantially if the light emerging from the (supposedly) polarization-preserving fiber connecting the scan head to the laser skips between modes. Changing the pol-direction of the fiber output changes the amount of this light that is reflected by the 45° dichroic[5] and proceeds to the objective (see Chapter 26, *this volume*).

Figure 3.13(B) shows how this angle dependence can be utilized intentionally to tune the bandpass of a narrow, notch filter, or other high cut-off component, by tilting it up to 14° from normal incidence.

It is widely understood that the prime advantage of using infinity-conjugate objectives is that, in the space between the objective and the tube lens, light rays originating at the front focus plane will be parallel to the optical axis and therefore, that such rays will strike any filter or dichroic introduced into this region at a fixed angle. However, as light rays originating from above or below the plane-of-focus will not be parallel to the optical axis in this space, the effective cut-off wavelength of these components may shift slightly when applied to such light. Although such light is excluded by the pinhole in a confocal microscope, it can reach the detector in the widefield microscope.

[5] A dichroic beam-splitter is very similar to an interference filter except that the reflective, interference layers are deposited only on a single outside surface and the substrate is often thinner. The "back" side of the substrate is often coated with a broadband, anti-reflection coating.

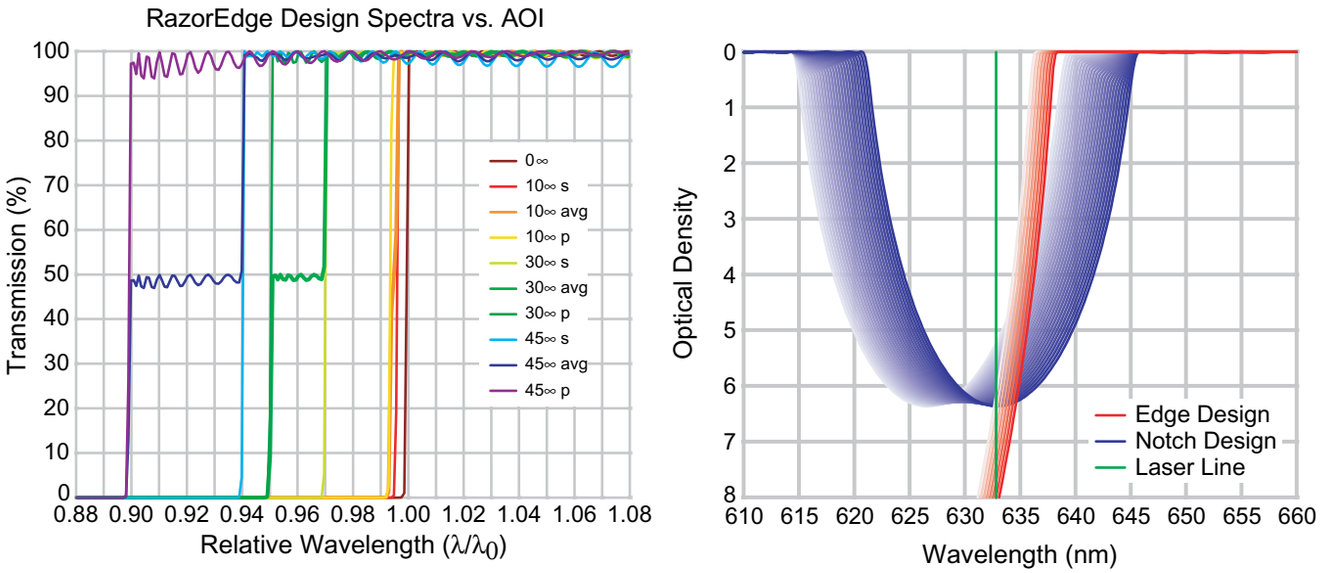


FIGURE 3.13. Reflectivity and incidence angle. As the angle at which the incident light strikes the filter becomes less than 90°, the cut-off wavelength becomes shorter (left). The change in wavelength is about 10% at 45° although the exact amount depends strongly on the polarization of the incident light (6% vs. 10%). This angular dependence can be used to 'tune' the cut-off wavelengths of notch and edge filters (right). (These diagrams modified from originals kindly provided by Turan Erdogan, Semrock, Rochester, NY.)

Dichroic and Polarizing Beam-Splitters

Dichroic mirrors or beam-splitters are special interference filters that reflect light in defined bands while transmitting light in other bands when placed at an angle in a light path (in distinction to dichroic filters, dichroic mirrors are placed at an angle to the incident light and their reflective properties are just as important as their transmission). To insure that the image made with one dichroic is aligned with that made with others, the glass blanks (substrates) used to produce them must be polished to very fine tolerances for thickness and parallelism (see above). This is necessary because, in epi-fluorescence microscopy, the imaging rays pass through a beam-splitter oriented at 45°, and the position of the transmitted light bundle is displaced by an amount proportional to the thickness and RI of the substrate on which the interference layers are deposited. If the thickness is reduced much below 3 mm, the flatness of the substrate may be compromised and, of course, the refractive index (RI) of glass is a function of the wavelength: for BK7 glass RI = 1.507 @ 1060 nm but RI = 1.536 @ 365 nm. This difference is so large that the variation in offset will be very noticeable in any design that covers a range from the ultraviolet to the near-infrared. Instead of ignoring these effects, it is probably wise to work with them and for example, to use a thicker piece of glass instead of a thin glass plate and create shifts that are so large that secondary or ghost images are easily removable with a regular aperture.[6]

To circumvent the spectral problems of interference-based beam-splitters, it is possible to use a polarizing beam-splitter that reflects half of the light polarized in one direction and transmits all the light polarized in the other direction (Cox, 2002). About 80% of the fluorescent light is transmitted for all visible wavelengths. There is no spectral distortion because the transmittance is independent of the wavelength, and the beam-splitter does not need to be changed, simplifying alignment.

The beam-splitter in the LSM 5-Live line-scanning confocal microscope (Carl Zeiss, Jena, DE) uses a linear mirror in the center of a glass blank located in an optical plane corresponding to the back-focal plane and placed to only reflect a narrow "line" of laser illumination (Fig. 3.14). As only a small fraction of the blank is coated as a mirror, more than 95% of the entire bundle of fluores-

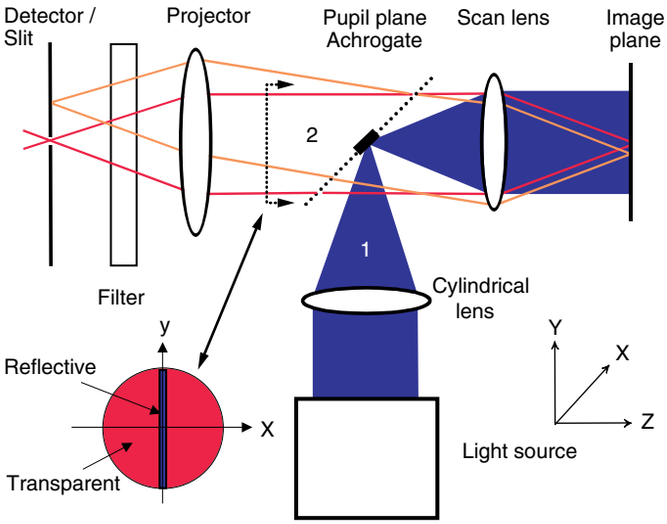


FIGURE 3.14. Operation of the "Acrogate." The beam-splitter in the Zeiss 5-Live takes advantage of the fact that, in a line-scanner, only a line of illumination exists in the back-focal plane. Consequently, a piece of glass with a high-reflectivity linear mirror across the center will reflect all of a line of coherent laser light down to the specimen but obstruct only about 5% of the returning fluorescent light, and this performance is not affected by wavelength.

[6] Indeed, a very useful achromatic beam-splitter can be made by using such a piece of glass with no coating on the near surface. Such a surface will reflect about 5% of all light impinging at 45°. Although, this "wastes" laser power, there is usually more than one needs of this in any case. Care must be taken that any excitation light not reflected is absorbed before it can become stray light.

cent light returning from the objective can be transmitted (see also Chapter 10, *this volume*).

Filters and Dispersive Elements for Multi-Channel Detection

As light emitted by fluorophores in the sample is mainly unpolarized, polarization-sensitive beam-splitters can only separate half of it from the polarized excitation light. Instead, the emitted light is either sequentially split by a combination of short-pass and long-pass dichroic mirrors before being passed through a bandpass or long-pass emission filter to the detector (see Fig. 3.9), or it strikes a dispersive element (e.g., a grating or a prism). Light split by a dispersive element can either be projected directly onto a fixed array of mini-photomultiplier tubes (PMT) from which a relatively continuous spectrum is recorded (Fig. 3.15, as in the Zeiss META), or the light passes through a system of slits and/or mirrors that can be adjusted to pre-select the segments of the spectrum directed to each detector (Fig. 3.16, as in the Leica TCS SP II). The former system has the advantage of more channels (32 vs. 4 detectors, 8 vs. 4 channels digitized simultaneously) but the disadvantages that the width of each spectral channel is quantized by the spacing of the PMTs, that some signal is lost in the dead zone between photocathodes and because mini-PMTs have lower quantum efficiency and more multiplicative noise than the more conventional PMT. In both systems, optimal spectral resolution requires that the light passed by the pinhole originate from a very small area of the specimen (i.e., it must be collimated light: opening the pinhole reduces spectral resolution), a factor that is not important for systems that use interference filters to separate the light. More details about these detectors and tests that can be applied to validate their performance can be found in Chapter 36 (*this volume*; Lerner and Zucker, 2004).

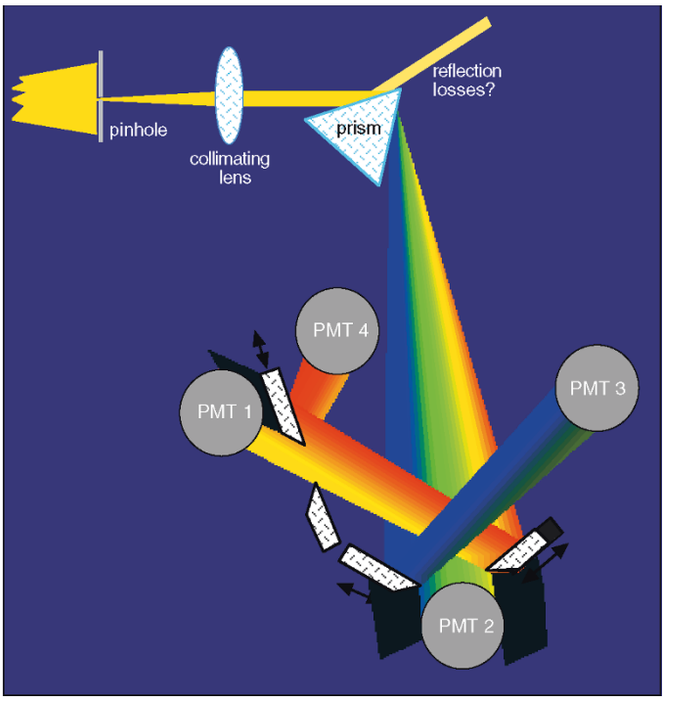


FIGURE 3.16. Schematic diagram of the spectral detector in the Leica TCS SP II. Light passing through the pinhole is made parallel by a collimating lens and refracted by a prism. Light of different colors is reflected to one of four photomultiplier tubes (PMTs) by a series of movable mirrors that can also be arranged to form shutters or slits. Up to four signals can be digitized from the four PMTs.

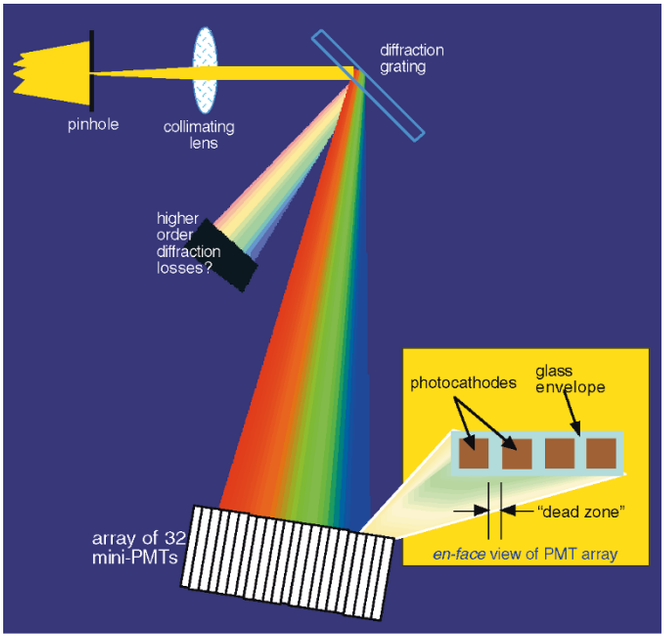


FIGURE 3.15. Schematic diagram of spectral detector in a Zeiss META confocal head. Light passing through the pinhole is made parallel by a collimating lens and diffracted by a diffraction grating. Light of different colors strikes different segments of a 32-channel mini-PMT array. Light that strikes the active area of one of the photocathodes produces photoelectrons that are amplified by the adjoining electron-multiplier section. Up to eight signals can be digitized from eight sets of adjacent PMT channels. Metal pins are placed in front of the PMT array to prevent light at laser wavelength from reaching the detector.

MECHANICAL SCANNERS

In most of the commercial confocal microscopes used in biology, the beam scans, not the specimen. The laser light is scanned over the image plane by changing the angle at which the laser beam passes through the back-focal plane (BFP) of the objective. If the rotational axis of a scan mirror coincides with both its own surface and the optical axis at a telecentric plane (i.e., any plane that is conjugate to the back-focal plane of the microscope objective lens), rotation of the mirror moves the focused spot across the focus plane in a straight line (Fig. 3.17). The devices used to tilt the mirror in a rapid and precise manner are called galvanometers.

While the first generation of scanning microscopes could only scan the beam over rectangular areas of the specimen using lines running in a fixed orientation, modern instruments are equipped with scanners that allow one to rotate the scanned rectangle or even scan arbitrarily shaped areas. The scan angle can be rotated by apportioning some of the x-scan signal to the y-galvo and vice versa. Scanning an arbitrary area is particularly useful for experiments involving FRAP or the release of caged compounds, where the high-intensity illumination area can be precisely matched to a region of interest defined using biological criteria applied to the recorded image.

Flexible scanning, integrated to a system to shift excitation and emission wavelengths rapidly, allows a much greater flexibility

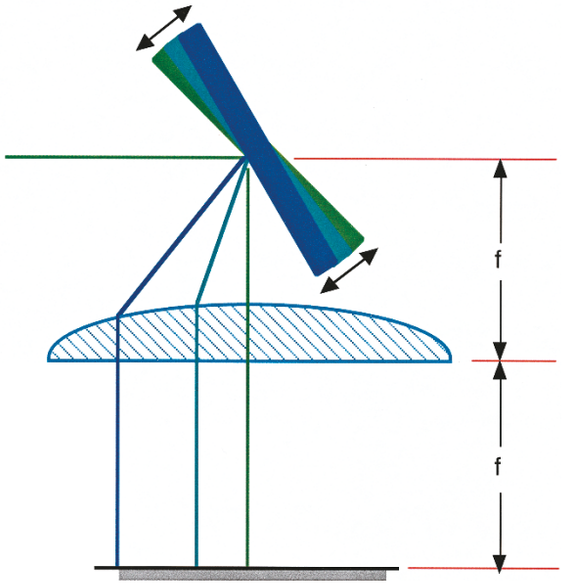


FIGURE 3.17. How rotation of a mirror in an aperture plane causes the linear motion of the focused spot. Rotation of the mirror changes the angle at which light leaves the focal point. The green line at 45° represents the neutral mirror position. Light blue and dark blue lines show the effect of rotating the mirror clockwise by one half of the total deflection angle. Because it is not possible to mount the galvanometer at the actual back-focal plane of the objective, a scan lens is used to image this plane to a more convenient location. Because this lens has some magnification (M), the angles actually scanned by the galvanometer mirror are less than those implied by this diagram by a factor of 1/M. f, focal length.

regarding the sequential acquisition of signals from different labels (line-by-line or frame-by-frame). This section describes the different scanner types. More detailed information can be found on the Web pages of Cambridge Technology (Cambridge, MA) and GSI-Lumonics (formerly, General Scanning, Bellerica, ME).

Galvanometer Scanners

Beam scanning is generally implemented using mirrors mounted on galvanometer "motors" (see Chapter 9, *this volume*). The mirror surface is deposited on a substrate of silicon, fused quartz, or, for highest performance and cost, beryllium. Such a rotating mirror device can control the scan angle with exquisite accuracy and has the additional advantage that the scanning angle is insensitive to wavelength, something not true of the faster acousto-optical scanners.

Like a motor, the actuator in a galvanometer has a rotor and a stator and currents circulating in coils in one or the other interact with the magnetic field of a permanent magnet in the other to produce the forces that move the rotor (Fig. 3.18). The responsiveness of the actuator depends on the torque/inertia ratio. In general, moving-coil actuators have a lower moment of inertia (I), lower torque, and better positioning accuracy than moving-magnet actuators, while the latter can move faster because of their superior stiffness. Consequently, they are the type most often used in confocal microscopes.

Although some cheap scanners achieve high scan speed by rotating continuously (rotating multi-mirror scanners), the angular scanning range of such scanners is fixed and consequently, the scanned area cannot be "zoomed." In addition, the scan motion is not linear and it is difficult to fabricate and mount a multi-segment mirror in which all the facets are an equal distance from the axis. To avoid these limitations, the scanners used in confocal microscopes oscillate around a fixed neutral position. Such galvanometers come in two flavors: resonant scanners that vibrate at a fixed frequency and in which much of the force needed to oscillate the mirror is provided by energy stored in a torsion spring, and linear galvanometers that operate at lower but variable frequencies and in which the spring is much weaker or absent.[7] In both cases, the required scan forces increase with the square of both the scan frequency and the scan angle and the limit on both is usually set by the amount of power that can be dissipated by the actuators. The important difference is that, as a resonant actuator requires far less power than a linear one at a given scan frequency and scan angle, it can attain more of either (or both) of these before overheating.

Resonant galvanometers usually operate at 4 kHz and above, often near to a fractional multiple of the horizontal scan frequencies of the NTSC video standard. The mirror angle varies in a sinusoidal manner at a frequency determined by the mechanical resonance of the device. This in turn is determined by the spring constant k and the moment of inertia I of the rotor/mirror assembly: larger mirror or higher I, lower frequency; stiffer spring, higher frequency but smaller scan angle.

The Olympus SIM scanner runs sinusoidally in "tornado" mode. The Leica RS uses a resonant scanner but drives it with a sawtoothlike waveform. However, the angular velocity of a resonant galvanometer varies, reaching a maximum at a phase angle of 0° and a minimum at ±90°, where the scan direction changes. As the signal intensity per pixel is inversely proportional to scanner speed, in order to keep geometrical scan nonlinearity to <4%, recording is restricted to the two ±30° intervals of the total 360° waveform. As sin 30° = 0.5, the actual amplitude of the mirror motion has to be twice as large as is actually required to scan the field being digitized and, because of the time lost in turnaround, signal can only be collected 15% to 30% of the time. To avoid

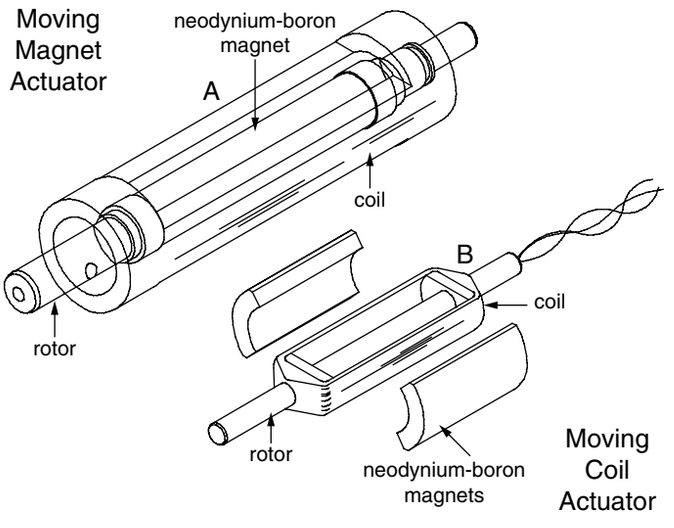


FIGURE 3.18. Two types of galvanometer actuator. Although moving-magnet actuators (A) are smaller and more rigid, moving-coil actuators (B) are more precise. (These diagrams modified from originals kindly provided by R. Aylward, Cambridge Technologies, Cambridge, MA.)

[7] Mechanical stops of some kind must be used to restrict rotor movement to <1 rotation.

bleaching outside the recorded area during the remainder of the waveform, stops are inserted at an image plane to exclude light that would otherwise land outside the digitized area.

The effective scanning speed can be increased by collecting data during both the forward and the backward movements of the mirror. However, because the backward movement also reverses the direction in which pixels are recorded, additional electronics or appropriate software is needed to repackage the data into a standard image format. This alignment process is seldom totally successful, especially when used to perform confocal imaging at video rate, and the result is that every other line is displaced slightly sideways with respect to its neighbor.

Here at the EMBL, two high-resolution methods have been implemented to solve this problem: use of a position signal from the galvanometer to detect the zero-crossing voltage line. This event starts a counter. By running the galvanometer symmetrically and using two independently adjusted counters, the forward and backward movements can be accurately synchronized, although special software is still needed to rearrange the pixel order. However, even this trick does not overcome the fact that sinusoidal bidirectional scanning permits one to record quasi-linear data during only ~33% of the scan time.[8]

For example, the galvo inside the Leica TCS SP2 RS runs at 4000 lines/s (8000 in bidirectional mode) and this translates into 150 fps @ 32 × 512 pixel @ zoom 1. Using a galvanometer from Cambridge Technology, Olympus claims 4000 lines or 16 fps @ 256 × 256 for both their confocal microscopes in the Fluoview 1000.

Resonant scanners accelerate fast enough to actually cause the mirror to bend or flex. This has two negative effects: (a) the wavefront can become distorted, reducing the resolution of the instrument and (b) if a high-reflectivity coating is used, it may age more rapidly than on a mirror at rest. The latter problem can be avoided by using the less-efficient "enhanced full-metal" coatings.

Note that flexing is more of a problem for large mirrors so choosing a mirror is always a compromise between rigidity/scan speed and the mirror size required to reflect a beam large enough to fill the BFP of all the objective lenses used. Clearly these requirements can interact in that a mirror big enough to reflect the entire ray bundle may also flex enough to negate the resolution improvement obtained by so doing. In this case it is important to remember that, at a given NA, the ray bundle required will be smaller when using an objective with a higher magnification.

In a linear galvanometer, almost all of the torque needed to move the mirror is provided by the magnetic forces produced by currents flowing in coils. The maximum speed is limited by the amount of RMS power the galvo can dissipate without the permanent magnet being heated beyond its Curie point (100–110°C) where it becomes demagnetized. Although linear galvanometers try to follow a distorted sawtooth waveform, in this electro-mechanical system, much more time is lost to overscan than is common in the electron-magnetic systems used to scan the electron beam in a cathode-ray tube (CRT).[9] Time lost in retrace is one of the reasons that, assuming that the microscope is designed properly, one should get better results recording signal from a single, 3-s scan than by Kalman-averaging three, 1-s scans.[10] If the mirror is driven with a triangular wave and the signal collected in both directions, it is possible to increase both the "usable/unusable" duty cycle and the line-scan rate, as long as provision is made for inverting the pixel order and aligning the two sets of scans (see above).

In contrast to resonant galvanometers, linear galvanometers follow the input signal at any drive frequency although with a phase delay that is not negligible under normal operating conditions. Ideally, a sawtooth motion produces a relatively slow, linear recording line followed by a fast retrace (mono-directional scans). Problems occur because of the high angular acceleration needed during the transition between the end of one line to the beginning of the next (i.e., the retrace). The disparity between the linear sawtooth or triangular-wave input and the actual motion of the mirror is best reduced by using closed-loop negative feedback: the universal engineering prescription for "distortion" (Aylward, 1999, 2003). This requires a means by which the position of the rotor can be measured and the information fed back to the control circuitry driving the coils.

Figure 3.19 diagrams four methods of detecting rotor position: two involving changes in capacitance between fixed and moving

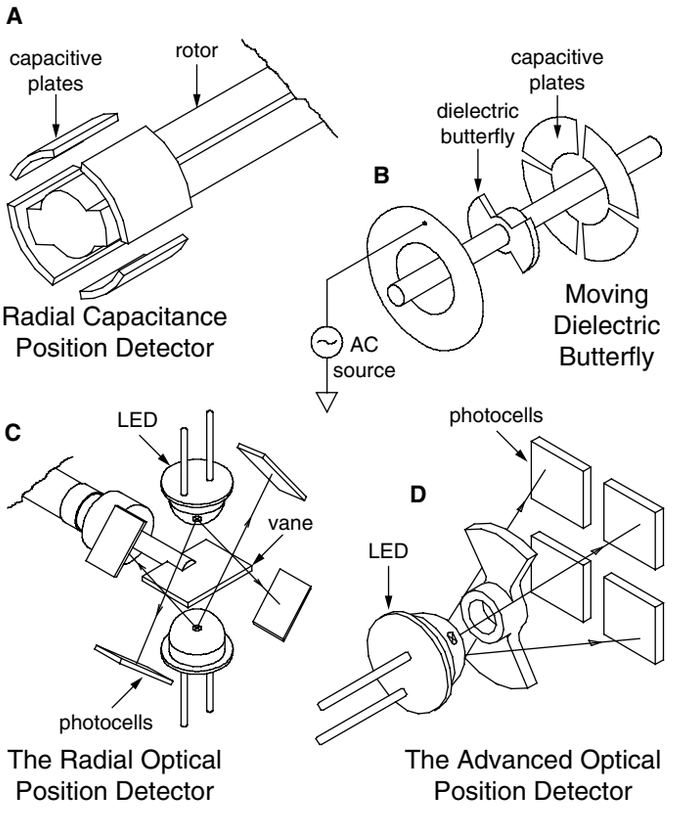


FIGURE 3.19. Four types of galvanometer position sensor. Rotor position can be determined by ascertaining changes in the capacitance between structures attached to it and other electrodes mounted on the stator. The dielectric butterfly design (B) is more precise than that shown in (A) because it is easier to align. [Note that in (B), the electrode spacings have been exploded for clarity.] (These diagrams modified from originals kindly provided by R. Aylward, Cambridge Technologies, Cambridge, MA.)

[8] Two ± 30° scans cover 120°, or 33% of the 360° sine-wave cycle.

[9] In other words, when you use a higher line rate, a significant fraction (20%–50%) of your collection time can be wasted by retrace. This reduces the signal-to-noise ratio (S/N) of the data beyond that which comes about merely because the beam spends less time in each pixel and therefore excites fewer photons.

[10] On the other hand, from the sampling point of view, if one is recording three-dimensional data, it is better to record three 1-s scans at slightly different defocus positions, if doing so is needed to meet Nyquist conditions in the *z*-direction.

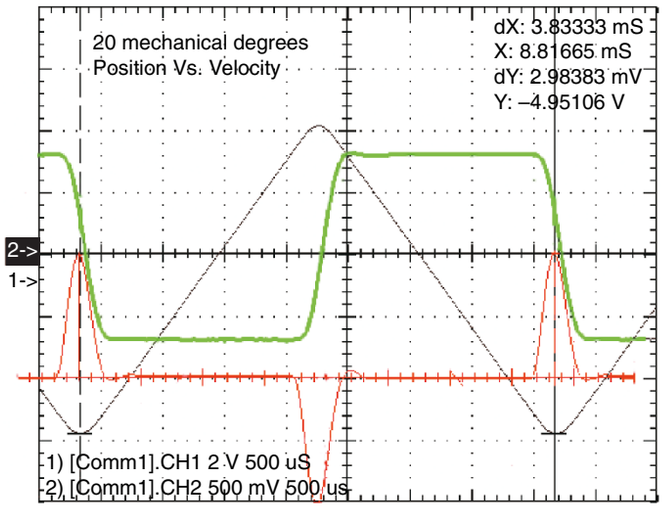


FIGURE 3.20. Galvanometer mirror performance. Measured plots of mirror position (black), angular velocity (green), and drive current (red). (These diagrams modified from originals kindly provided by Steven Sequeira, Cambridge Technologies, Cambridge, MA.)

electrodes and two involving the modulation of light from a light-emitting diode (LED) by the action of a shutter attached to the rotor. Of the capacitance methods, the newer "dielectric butterfly" method provides repeatability of 1 micro-radian (i.e., 1 mm at a range of 1 km). Although the LED methods are less precise, they are also much smaller and less expensive. In its efforts to make the actual motion of the mirror mimic the sawtooth waveform, the feedback circuit produces a current acceleration/deceleration waveform that hardly resembles a "sawtooth" at all (Fig. 3.20 red line).

As useful signals cannot be recorded during retrace, the beam should be blanked to avoid unnecessary bleaching and this can be implemented using mechanical stops such as those mentioned above or by using laser-blanking systems utilizing an AOD or a Pockels Cell (see below). Not only do these devices reduce the average light dose to the sample by 10% to 20%, they also eliminate the high-dose damage done in the region to either side of the raster where the beam slows down, stops, and re-accelerates. As this process may deposit 10 to 20 times more photons/μm^2 in these localized areas, it is wise to ensure that living cells do not extend beyond the side borders of the recorded area if appropriate beam-blanking is not available.

An advantage of using linear actuators responding to sawtooth drive signals is that the actual recording time can be 2 to 2.5 times higher than the 33% mentioned above. The advantages of one type of galvanometer over the other in terms of stability and long-term performance are not known.

Olympus drives their optional SIM scanner in a special "tornado" mode in which a damped, sinusoidal signal is applied to both scanners, producing a spiral, Lissajous pattern. This pattern is used to generate a circular bleaching spot without wasting any time turning the scanner around, as happens when it is driven with sawtooth signals. However, because the beam paths overlap in the center of this circle, more energy is deposited there, creating a non-uniform bleach.

General Specifications

Scanners wobble above and below the scan line and jitter as they go along it. The wobble specification tells how well a scanner remains on the line and the jitter how accurately the scanner returns to a specific pixel of that line at a given instant of the scan cycle. In both cases, performance depends on the quality of the bearings and the care with which the moving mass has been mass balanced.[11] In a scanning microscope, these specifications can affect the resolution limit of the microscope.

Let us assume an optical scan angle of ± 3° in a beam scanner (i.e., a complete mechanical scan of 6° or 100 mrad). If there are 2500 pixels/line, the jitter (and the wobble) must be lower than 40 µrad (100 mrad/2500), which is about four times more than the 5 to 10 µrad specification for the Cambridge Technology 6210H [with advanced optical feedback, Figure 3.16(D), used in many confocal microscopes. Cambridge Technology scanners have 15 µrad drift per °C]. Fortunately, common experience has shown that the scanner specifications tend to be conservative and their actual performance is good enough that it does not limit microscope performance. The actual test is to use the galvanometers at the very small scan angles appropriate to high-NA, low-magnification lenses. The minimal scan angle of the instruments built at EMBL is ~20 µrad/line, but even here, the stability is so good that an indicator must be used to tell the user that the scanner is operating. More recent scanners have even better specifications and use even larger mirrors, a factor that allows designers to use simpler scanning lenses.

Current devices represent a highly optimized product that is the culmination of intensive research over many years. Commercial units perform at or near the limits imposed by physics (e.g., galvo mass vs. planarity, mirror diameter, drive power vs. overheating) and materials properties (density vs. stiffness). In spite of this long development history, last year Cambridge Technology introduced the 6215H galvanometer with scan rates 50% to 100% higher (1.5 kHz triangular wave @ ± 3°) than the previous model.

The situation is less settled in the field of resonant galvanometers where the number of applications for very fast scanners is increasing rapidly and not all of the requirements can be fulfilled using electro-optic or acousto-optic devices. With resonant scanners, one-directional line scanning can now be performed at up to 8000 Hz with present commercial scanners but research scanners have gone faster. However, resonant scanners have the disadvantage that their scan speed is fixed and their duty cycle short. To improve the signal-to-noise ratio of weak fluorescence signals, one can only line average, and this process accumulates readout noise. Finally, there is also no simple way to move the beam within a specific region or along a line that isn't horizontal. For FRAP experiments, one must bypass the laser light around the resonant scanner to a second linear scanner.

ACOUSTO-OPTICAL COMPONENTS

The performance of acousto-optical components is based on the optical effects of acoustic fields on birefringent crystals. The acoustic field is generated and controlled by a piezoelectric

[11] Mass balancing is both crucially important to reduce vibration and difficult to achieve if one adheres to the optical requirement that the axis-of-rotation pass through the plane of the mirror. If the mirror surface is on the axis, it follows that the material making up the mirror assembly can only be distributed symmetrically on both sides of the axis if additional structures are added solely to counterbalance it. Such additions lead in turn to complex mirror geometries that increase both *I* and the chance that the mirror will flex. As a result, the scanners used in confocals are likely to have silicon mirrors about 1-mm thick mounted symmetrically (i.e., with the axis going up the middle of the silicon). Moral: One pays in many ways for trying to scan fast. Do not do it unless you need to.

crystal, excited at 50 to 150 MHz, attached to one side of the crystal and a vibration absorber attached to the facing side. At a specific frequency of the acoustic wave, the periodic pattern of compression and rarefaction associated with it affects the local density, and therefore the RI, of the crystal to form a three-dimensional periodic diffractor. Light passing through the crystal is diffracted at an angle (θ) that depends on the frequency (and hence the wavelength) of the acoustic wave and on the wavelength of the light[12] and is defined by the equation:

$$\theta = \lambda f_a / V_a$$

where λ is the optical wavelength in air, V_a is the acoustical velocity of the material, and f_a is the acoustic frequency. In a TeO_2 crystal excited at 100 MHz, the diffraction angle for 500 nm light is ~4.3°.

Normally the crystal is shaped like a rhombus, with the undiffracted beam entering and leaving normal to the two sides and the piezo generating plane waves that are parallel to the other two sides (Fig. 3.21). The waves are tilted with respect to the laser beam by an angle that is roughly half of the expected diffraction angle.

Although fused and crystalline quartz can be used as the active material, the preferred AO material is TeO_2. Most AO materials operate well only over a limited wavelength range: generally less than 400 nm (Chang, 1995). They also affect the polarization of the light. Light passing through a TeO_2 AOD, along the "slow" direction, will emerge with its polarization direction rotated by 90°.

By sweeping the drive frequency of the pressure waves, an acousto-optical deflector (AOD) will deflect a beam of monochromatic light over a range of angles, making it useful as a scanning device. Acousto-optical modulators (AOM) are used to blank a monochromatic light beam intermittently, to create a new beam with a lower (time-averaged) intensity. In an acousto-optical tunable filter (AOTF), the pressure wave pattern in the crystal is used to spectrally filter the light. An acousto-optical beam-splitter (AOBS) is really just an AOTF used to spectrally combine or separate the light at specific laser wavelengths from all other light.

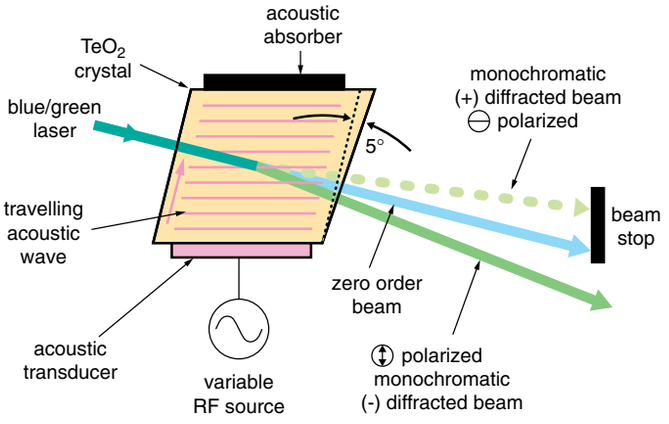


FIGURE 3.21. Schematic diagram of acousto-optical device. Light entering from the left strikes the surface of the TeO_2 crystal at normal incidence. Acoustic waves propagating upwards from the piezoelectric transducer diffract the light beam, either up or down, depending on the polarization of the light beam. Because diffracted light would suffer dispersion on leaving the crystal, the far face is cut at a steeper angle than would be needed if it were a rhombus. Therefore, the device shown would work optimally only with light polarized parallel to an acoustic beam that diffracts into the 1st order.

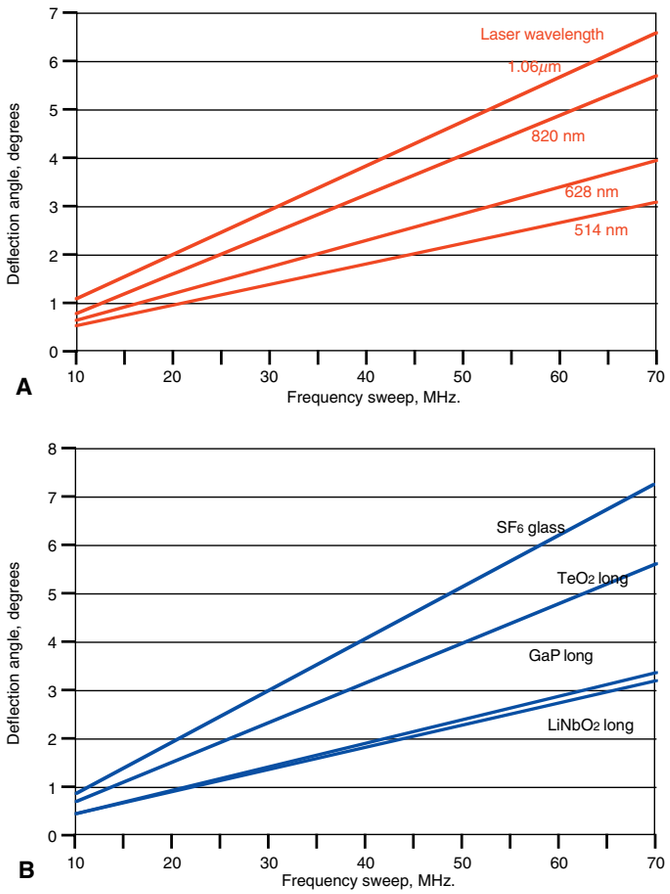


FIGURE 3.22. AOD performance. The amount of deflection produced by an AOD varies with the amount of change in the acoustic frequency, the wavelength of the incoming light (A), and the material in which the deflection takes place (B).

As the frequency of the acoustic wave can be changed on the microsecond time scale, acousto-optical components can change their deflection properties much faster than when using mechanical parts. For a given frequency sweep, the amount of deflection depends on the type of material used in the AOD and the wavelength of the incident light (Fig. 3.22). The response time is limited by the time it takes for a new acoustic wave field to propagate across the width of the crystal and, therefore, depends linearly on the width of the light beam that has to be modulated. Typical rates are ~150 ns/mm of beam width. Only a narrow band of wavelengths are diffracted and out-of-band contributions are reduced, a feature that is especially suitable for filtering devices. Also, as acousto-optical components do not have any moving parts, they require little maintenance.

At root, all AO components are very similar. They use the same crystals, operating at the same acoustic frequencies and diffract over similar angles. As AOTFs and AOBSs operate on smaller beams, they can be faster and because they operate at fixed input and output angles, the crystals are smaller and less expensive. As AODs operate at a fixed input angle but a variable output angle, they must be larger, slower, and more expensive. Otherwise they are just AOTFs operating with a swept acoustic frequency. Increas-

[12] In TeO_2, the crystal most commonly used, the speed of sound is 660 m/s. As a result, a 100 MHz wave will have a period of about 6.6 μm, about 10 to 15 time greater than the wavelength of the light being diffracted.

ing the acoustic frequency increases the deflection angle: increasing the acoustic power increases the fraction of the light that is deflected from the incident beam. The preferred crystal, TeO_2, gives the most deflection for a given input wavelength and acoustic power level. It is only replaced by one of the other materials when deflecting high-power laser beams[13] or when it cannot be cooled sufficiently well.

Acousto-Optical Deflectors

Acousto-optical deflectors (AOD) can scan a laser beam at up to 100 kHz, compared to about 500 to 1000 Hz for linear galvanometer scanners and about 4 to 8 kHz for resonant galvanometers. In addition, they allow zooming and varying the scan speed. As they do not have the momentum associated with moving parts, they require little retrace time and are capable of rapidly accessing random scan areas.

However, one cannot simply replace the faster of the two scanners in your confocal (as described in Chapter 9, *this volume*) with an AOD because, as the deflection is produced by diffraction, the scan angle depends on the wavelength of the light beam. As a result, the longer wavelength fluorescent light will be deflected by a different amount on its way back through the crystal and will therefore fail to pass through the pinhole. Although this dispersion effect can be theoretically compensated for by a chromatic correction system, such systems involve so many additional expensive, lossy elements, they are not practical for confocal use. AOD dispersion is an even more serious problem when working with pulsed radiation in a multi-photon microscope (Lechleiter *et al.*, 2002).

A workable AOD scan system can be developed for confocal fluorescence microscopy if the incident laser beam is first *x*-deflected by the AOD and then, after passing the dichroic mirror, *y*-deflected by a slower, galvanometer scanner. As the returning fluorescence emission is deflected by the slower scanner and reflected by the dichroic mirror in the direction of a linear detector, it does not reach the AOD. A lens focuses light from the dichroic onto a detector slit, which must be used because the movement along the fast axis is not being descanned. Although a linear CCD detector behind the slit might be used to "track" the moving signal spot, this solution is still confocal only along one axis. However, it gives better sectioning than slit-illumination/slit-detection systems, such as the Zeiss LSM-5Live and in practice it seems to work quite well (Draaijer and Houpt, 1988; Tsien and Bacskai, 1995).

Compared to galvanometers, AODs provide small deflection angles (<3.5° vs. ~6° needed for most objectives), a limited angular resolution,[14] a non-circular aperture, and a low "reflection" efficiency (<70%, i.e., only 0%–70% of the incident beam is deflected vs. 95%–99% for a mirror). These parameters depend on each other. A higher angular resolution can be achieved, but only at the expense of a spatial variation in the diffraction efficiency (10% at 2000 lines). Finally, the drive signals fed to an AOD must be readjusted for each excitation wavelength. Although this can be arranged for a small number of discrete laser lines, it cannot be used to deflect "white" light in a useful manner.

Acousto-Optical Modulators

Acousto-optical modulators (AOM) are used to modulate the intensity of a beam and can thus also function as laser-line selectors. In FRAP experiments, for example, they are used to switch the laser on and off rapidly (Flamion *et al.*, 1991). It is common to choose the deflected beam as the one that is used by the optical system because it can be switched on and off with high extinction ratio (typically >40 dB or 100 : 1) and its intensity can be varied from zero to more than 85% of the incident beam (Fig. 3.17).

Acousto-Optical Tunable Filters

Acousto-optical deflection causes light of different wavelengths to exit the crystal at different angles. In an optical system designed so that input light strikes the crystal at only one angle and diffracted light re-enters the optical system only at one diffraction angle, then one can choose the wavelength of the light diffracted at this angle by varying the frequency of the acoustic wave. This makes it a "tunable filter." Because it is not possible to diffract all the light (and therefore turn off the input beam), the acousto-optical tunable filters (AOTF) is usually configured so that one uses the light in the diffracted beam.

As temperature affects both the RI of the crystal and the speed of sound, it also affects the wavelengths of both the light and the acoustic waves. Therefore, it also affects the diffraction angle. If the angle changes enough so that the diffracted beam "misses" the entrance of the optical system (i.e., wanders off the input pupil of the optical fiber), this will result in a large reduction in the signal entering the fiber (and finally striking the specimen).

Because the diffraction properties of acousto-optical filters (Harris and Wallace, 1969) can be switched within microseconds, they are a tremendous improvement over using filter wheels to choose excitation wavelengths (Nitschke *et al.*, 1997). AOTFs can be used to select the illumination waveband when working with either a broadband light source (Lewis *et al.*, 1992) or a multi-line laser (Wachman *et al.*, 1997). They can also be used to select a light detection band (Wachman *et al.*, 1997).

When one has signals from two or more fluorophores, it is easier to separate them if they are excited individually and sequentially. To accomplish this, the AOTF can be used to change the laser lines after each line scan, that is, each line is scanned several times, sequentially — once for each of the excitation wavelengths needed. However, one can only take full advantage of this high-speed switching of the excitation if the other components in the light paths can also be adapted to operate with similar speed and flexibility.

AOTFs are also used for switching off the illumination light during retrace (see above).

Acousto-Optical Beam-Splitters

The acousto-optical beam-splitter (AOBS) is actually an AOTF used in an imaginative manner by Leica to replace the dichroic mirror usually used to separate the illumination and detections paths in a confocal fluorescence microscope (Engelhardt *et al.*, 1999; Birk *et al.*, 2002; it is implemented in Leica's Spectral Confocal Microscopes, TCS SP2 AOBS). In practice, the AOBS is programmed so that it leaves most (90%–95%) of the fluorescent light undeflected, and only deflects light at specific laser lines.

[13] Such as those used for laser light shows.

[14] About 500–1500 lines. This is set by time-bandwidth product of the crystal: faster scans have less precision and hence fewer distinct lines in the raster. This occurs because if the acoustic frequency varies too rapidly, the acoustic wavelength will be different on the near and far sides of the light beam, diffracting these rays differently.

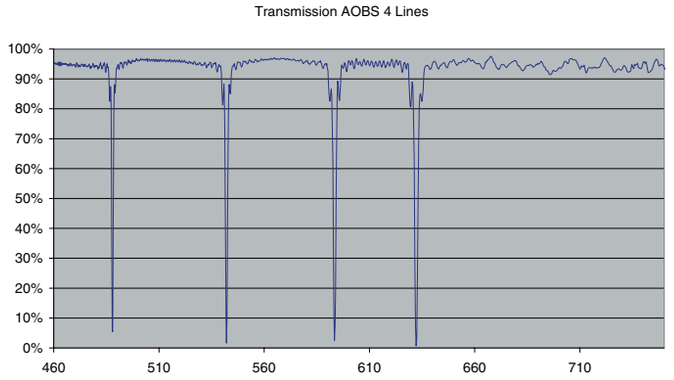


FIGURE 3.23. Transmission of Leica acousto-optical beam-splitter (AOBS). This plot shows the transmission of the beam-splitter to light originating from a point in the specimen. The notches in the transmission at 488, 542, 593, and 623 nm show that the AOBS has been adjusted to diffract these wavelengths of laser light into the beam and, consequently, remove then on the return trip. The position of these bands can be adjusted to suit any visible laser that might be used.

Because it is possible to excite the piezo with a signal that is the sum of several specific frequencies, and because the resulting pressure field then diffracts several wavelengths simultaneously, the AOBS allows efficient, simultaneous deflection of up to 8 laser lines towards the sample, while the average transmission of the crystal (away from the reflection bands) is about 95% (Fig. 3.23). The intensity of each line can be controlled independently over a range of more than 20 : 1.

The advantages of the AOBS over systems that use several, multi-band, dichroic mirrors as the main beam-splitter are its high efficiency, its lack of moving parts, and its flexibility in terms of being able to set up the system to use new laser lines simply by changing the software. On the other hand, because the proper operation of the AOBS depends on the light input being parallel as it passes through the crystal, light originating above or below the plane-of-focus may see slightly different transmission characteristics. Fortunately, in confocal operations, most out-of-focus light is removed at the pinhole.

ELECTRO-OPTICAL MODULATORS

Electro-optical modulators (EOM) are crystals utilizing the Pockels effect to modulate the polarization, the intensity, the phase, the frequency, or the direction of propagation of laser beams. They are faster (1 GHz) than acousto-optical devices but they not only are sensitive to electro-magnetic interference but they also generate quite a lot of it (Draaijer *et al*., 1996). In addition, they have a lower extinction ratio and are more sensitive to temperature changes (Chang, 1995). EOMs can be used to modify the polarization (Hofkens *et al*., 1998) and the intensity or the frequency of laser beams (Helm *et al*., 2001). Although, in principle they can also be used as scanners, they are generally not used as such in microscopes. They are usually optimized for performance at a single wavelength (Maldonado, 1995).

Piezoelectric Scanners

Piezoelectric scanners are mostly used to move the objective lens axially for three-dimensional imaging (Callamaras and Parker, 1999) or to move the object, either up and down or in all three directions (in a stage-scanning microscope).* Because massive objects are being scanned, settling times are in the millisecond range and horizontal scan speeds are limited to 10 to 100 Hz. Piezoelectric scanners utilize the piezoelectric effect: the generation of a voltage across some crystals when they are compressed or alternatively, the deformation of a crystal when a voltage is applied. In piezoelectric scanners, voltages are applied to electrodes on a tube piezoelectric ceramic and this elongates and moves an object fixed to the end of the tube. Typically, extensions of about 100 to 200 µm are possible with a resolution in the order of 1 nm (sub-nanometer resolution can be achieved if smaller travel ranges are acceptable). Like galvanometer scanners, piezoelectric scanners can be driven in a resonant mode with frequencies in the kilohertz range.

Piezoelectric scanners suffer from two problems: hysteresis, in which a given voltage produces a different displacement when approached from a lower voltage than when approached from a higher voltage (i.e., the position does not track when reversing the scanning direction), and creep, in which the position changes with time, even though the applied voltage remains fixed. As a result, piezoelectric elements are best used in conjunction with an element that measures the position, such as a capacitance-based translation/rotation sensor. In addition, hysteresis effects are easily avoided by always approaching the final position from only one direction, rather than moving the system back and forth. In this case the illumination is best switched off when driving the objective back towards the start position. Position drifts with time are seldom a serious limitation for most scanning light microscopy applications.

POLARIZING ELEMENTS

The combination of a polarizing beam-splitter and a quarter-wave plate is very useful in confocal reflection microscopy because it provides access to a backscattered (reflected) light signal without any loss of photon efficiency (Pawley *et al*., 1993). A horizontally polarized beam is reflected by a polarizing beam-splitter and then circularly polarized with the quarter-wave plate before being focused into the sample. The light scattered back from inhomogeneities is rotated by another 45° when passing the quarter-wave plate on the return journey and, now vertically polarized, deflected by the polarizing beam-splitter. This beam can be used to generate backscattered light contrast.

It should not be forgotten that the signal derived from small features in a biological specimen is usually incoherently backscattered and not coherently reflected. From a physical point of view, backscattered and reflected light have different properties. The detection system described above will only produce a useful signal if the process of contrast generation preserves the polarization of the incident light. The arrangement does not reduce the efficiency of the fluorescence detection path, and there are good reasons to believe that a circularly polarized beam is better focused by standard objective lenses than is a linearly polarized beam (van der Voort and Brakenhoff, 1989).

* Recently piezo activators have been used to provide small deflections of the galvo mirror along an axis perpendicular to the galvo axis. This is used to provide rapid XY scanning in multi-beam scanners using a single galvo.

REMOVING EXCESS LIGHT

It is always a good idea to introduce adjustable apertures (e.g., irises) into the optical path. The best locations for these are, of course, at conjugates of the aperture and field planes. On one hand these apertures can be used to adjust the beam because they essentially define the optical paths in the instrument (i.e., NA and field of view). On the other hand, once the instrument is aligned for Köhler illumination (see the Appendix of Chapter 36, *this volume*), these apertures should be closed as far as possible so that stray light is reduced, preventing any light from entering the optical system beyond that needed (1) to fill the back-focal plane and (2) to fill the field-of-view.

Some optical elements require more effective care of unwanted light. Good examples are AOMs and AOTFs. These components control not only the laser light intensity, they also "switch" laser light sources on and off by deflecting the beam. However, light deflected so that it does **not** enter the optical path is likely to reflect to places where it is unwanted unless steps are taken to absorb it.

Flip mirrors can also be used to keep a laser from entering an optical device. Particularly, when lasers in excess of a few tens of milliwatts are used, any deflected beam should be guided towards a strong absorber. A blackened surface on the inner endplate of a tube works very well for lower laser powers, while a 20-mm high stack of razor blades whose cutting edges are oriented towards the beam will do an excellent job for higher laser powers. Powers above 1 W are rarely used in microscopy but if they are, acousto- and electro-optical devices may start having problems and beam dumps will require extra cooling (improved air circulation and even water cooling).

SOME USEFUL LINKS

http://www.cambridgetechnology.com/news/Choosing%20A%20Galvanometer.html
http://www.brimrose.com
http://www.gsilumonics.com/
http://micro.magnet.fsu.edu/primer/techniques/fluorescence/interferencefilterintro.html
http://www.neostech.com/new_content.asp?content=AO_Introduction
http://www.semrock.com

ACKNOWLEDGMENTS

We thank Turan Erdogan of Semrock (Rochester, NY), for information on their hard-coated intereference filters and for the plots used in Figures 3.1 to 3.5 and Figures 3.7 to 3.13. We thank Redmond Aylward and Steven Sequeira of Cambridge Technologies (Cambridge, MA) for discussions and suggestions regarding the operation of galvanometers and for permission to use Figures 3.18 to 3.20. We thank Warren Seale of Neos Technologies (Melbourne, FL) for helpful suggestions to improve the text explaining AO devices and Leica Microsystems (Heidelberg, Germany) for disclosing data on the transmission of their AOBS beam-splitter used in Figure 3.23. We thank Timo Zimmermann for valuable discussions and help with drawing of figures. The authors are also particularly grateful to Steffen Lindek for the various comments on and contributions to the manuscript. Without the skilled assistance of Bill Feeny, the artist at the Department of Zoology, of the University of Wisconsin, most of the figures in this chapter would only be ideas. We thank Carl Zeiss, Leica Microsystems, and Olympus Europe for their permanent support of the Advanced Light Microscopy Facility at EMBL.

REFERENCES

Aylward, R.P., 1999, The advances and technologies of galvanometer-based optical scanners, *SPIE Int. Soc. Opt. Eng*. 3787:158–164.

Aylward, R.P., 2003, Advanced galvanometer-based optical scanner design, *Sensor Rev*. 23:216–222.

Birk, H., Engelhardt, J., Storz, R., Hartmann, N., Bradl, J., and Ulrich, H., 2002, Programmable beam-splitter for confocal laser scanning microscopy, *SPIE Proc.* 4621:16–27.

Callamaras, N., and Parker, I., 1999, Construction of a confocal microscope for real-time x-y and x-z imaging. *Cell Calcium*, 26:271–279.

Chang, I.C., 1995, Acousto-optic devices and applications. In: *Handbook of Optics*, Vol. II (M. Bass, ed.), McGraw-Hill, New York, pp. 12.1–12.54.

Cox, G., 2002, Biological confocal microscopy, *Mater. Today*, March:34–41.

Draaijer, A., and Houpt, P. M., 1988, A standard video-rate confocal laser-scanning reflection and fluorescence microscope, *Scanning* 10:139–145.

Draaijer, A., Gerritsen, H.C., and Sanders, R., 1996, Time-domain confocal fluorescence lifetime imaging. Instrumentation, *Scanning* 18:56–57.

Engelhardt, J., Ulrich, H., and Bradl, J., 1999, Optische Anordnung. German patent application DE 199 06 757 A1.

Flamion, B., Bungay, P.M., Gibson, C.C., and Spring, K.R., 1991, Flow-rate measurements in isolated perfused kidney-tubules by fluorescence photobleaching recovery, *Biophys. J.* 60:1229–1242.

Harris, S.E., and Wallace, R.W., 1969, Acousto-optic tunable filter, *J. Opt. Soc. Am.* 59:744–747.

Helm, J.P., Haug, F.M.S., Storm, J.F., and Ottersen, O.P., 2001, Design and installation of a multimode microscopy system, *SPIE Proc.* 4262:396–406.

Hofkens, J., Verheijen, W., Shukla, R., Dehaen, W., and De Schryver, F.C., 1998, Detection of a single dendrimer macromolecule with a fluorescent dihydropyrrolopurroledione (DPP) core embedded in a thin polystyrene polymer film, *Macromolecules* 31:4493–4497.

Kramer, J., 1999, The right filter set gets the most out of a microscope, *Biophotonics Intl.* 6:54–58.

Lechleiter, J.D., Lin, D.T., and Sieneart, I., 2002, Multi-photon laser scanning microscopy using an acoustic optical deflector, *Biophys. J*. 83:2292–2299.

Lerner J.L., and Zucker, R.M., 2004, Calibration and validation of confocal spectroscopic imaging systems, *Cytometry* 62A:8–34.

Lewis, E.N., Treado, P.J., and Levin, I.W., 1992, Visible/near-infrared imaging spectrometry — applications of an acousto-optic tunable filter (AOTF) to biological microscopy, *FASEB J.* 6: A34.

Maldonado, T.A., 1995, Electro-optic modulators. In: *Handbook of Optics*, Vol. II (M. Bass, ed.), McGraw-Hill, New York, pp. 13.1–13.35.

Melles Griot, 1999, *The Practical Application of Light*, Melles Griot, Irvine, CA. The Melles Griot catalogue is very informative and contains numerous excellent comments on optical elements and performance characteristics.

Molecular Probes, 2002, *Handbook of Fluorescent Probes and Research Products*, Molecular Probes, Eugene, Oregon.

Nitschke, R., Wilhelm, S., Borlinghaus, R., Leipziger, J., Bindels, R., and Greger, R., 1997, A modified confocal laser scanning microscope allows fast ultraviolet ratio imaging of intracellular Ca^{2+} activity using Fura-2, *Pflug. Arch. Eur. J. Phy.* 433:653–663.

Pawley, J.B., Amos, W.B., Dixon, A., and Brelje, T.C., 1993, Simultaneous, non-interfering, collection of optimal fluorescent and backscattered light signals on the MRC-500/600, *Proc. Microsc. Soc. Am.* 51:156–157.

Reichman, J., 2000, *Handbook of Optical Filters for Fluorescence Microscopy*, Chroma Technology Corp., Brattleboro, Vermont.

Tsien, R.Y., and Bacskai, B.J., 1995, Video-rate confocal microscopy. In: *Handbook of Biological Confocal Microscopy*, 2nd ed., (J.B. Pawley, ed.), Plenum Press, New York.

van der Voort, H.T.M., and Brakenhoff, G.J., 1989, Modeling of 3D confocal imaging at high numerical aperture in fluorescence, *SPIE Proc.* 1028:39–44.

Wachman, E.S., Niu, W., and Farkas, D.L., 1997, AOTF microscope for imaging with increased speed and spectral versatility, *Biophys. J.* 73:1215–1222.

4

Points, Pixels, and Gray Levels: Digitizing Image Data

James B. Pawley

CONTRAST TRANSFER FUNCTION, POINTS, AND PIXELS

Microscopical images are now almost always recorded digitally. To accomplish this, the flux of photons that forms the final image must be divided into small geometrical subunits called pixels. The light intensity in each pixel will be stored as a single number. Changing the objective magnification, the zoom magnification on your confocal control panel, or choosing another coupling tube magnification for your charge-coupled device (CCD) camera changes the size of the area on the object that is represented by one pixel. If you can arrange matters so that the smallest feature recorded in your image data is at least 4 to 5 pixels wide in each direction, then all is well.

This process is diagrammed for a laser-scanning confocal in Figure 4.1, where the diameter of the scanning beam is shown to be at least four times the interline spacing of the scanning raster. This means that any individual fluorescent molecule should be excited by at least four overlapping, adjacent scan lines and that, along each scan line, it will contribute signal to at least four sequential pixels. Finally, it is important to remember that information stored following these rules will only properly resemble the original light pattern if it is first spatially filtered to remove noise signals that are beyond the spatial bandwidth of the imaging system. Image deconvolution is the most accurate way of imposing this reconstruction condition and this applies equally to data that have been collected by widefield or scanning techniques. If you do this right, your image should look like that in Figure 4.2.

If you are already convinced of this, jump to page 71 for the second half of this chapter, on gray levels. But if it all seems to be irrelevant mumbo-jumbo, read on. Incorrect digitization can destroy data.

Pixels, Images, and the Contrast Transfer Function

If microscopy is the science of making magnified images, a proper discussion of the process of digitizing these images must involve some consideration of the images themselves. Unfortunately, microscopic images are a very diverse breed and it is hard to say much about them that is both useful and specific. For the purposes of discussion, we assume that any microscopic image is just the sum of the blurred images the individual "point objects" that make up the object.

But what is a point object? How big is it? Is it the size of a cell, an organelle, or a molecule? Fortunately, we don't have to answer this question directly because we aren't so much interested in a point on the object itself as the image of such an object. As should be clear from Chapters 1 and 2, our ability to image small features in a microscope is limited at the very least by the action of diffraction.[1]

So point objects can be thought of as features smaller than the smallest details that can be transmitted by the optical system. The final image is merely the sum of all the point images. Although the images themselves may be varied in the extreme, all are composed of mini-images of points on the object.

By accepting this simplification, we can limit our discussion to how best to record the data in images of points. Of course, we need more than the ability to divide the image flux into point measurements: the intensity so recorded must tell us something about microscopical **structure**. In order for an image to be perceivable by the human eye and mind, the array of point images must display **contrast**. Something about the specimen must produce changes in the intensity recorded at different image points. At its simplest, transmission contrast may be due to structures that are partially or fully opaque. More often in biology, structural features merely affect the phase of the light passing through them, or become self-luminous under fluorescent excitation. No matter what the mechanism, no contrast, no image. And the amount of contrast present in the image determines the accuracy with which we must know the intensity value at each pixel.

Contrast can be defined in many ways but usually it involves a measure of the variation of image signal intensity divided by its average value:

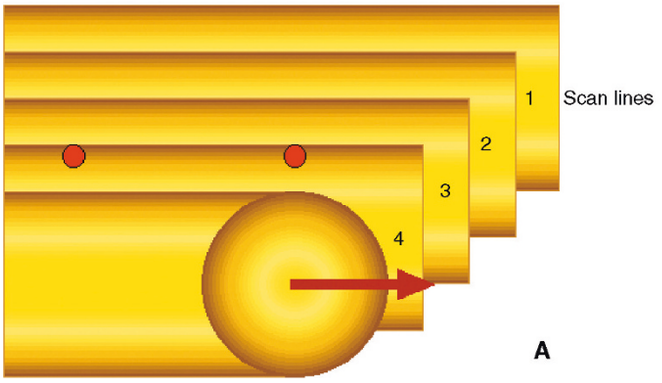
$$C = \frac{\Delta I}{\bar{I}}$$

Contrast is just as essential to the production of an image as "resolution." Indeed, the two concepts can only be thought of in terms of each other. They are linked by a concept called the contrast transfer function (CTF), an example of which is shown in Figure 4.3.

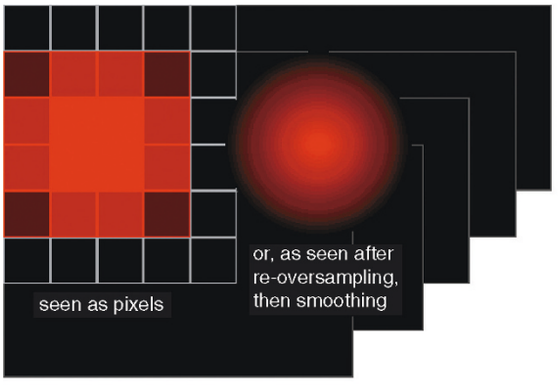
The CTF (or power spectrum) is the most fundamental and useful measure for characterizing the information transmission capability of any optical imaging system. Quite simply, it is a graph that plots the contrast that features produce in the image as a function of their size, or rather of the inverse of their size: their spatial frequency. Periodic features spaced 1 mm apart can also be thought of as having a spatial frequency of 1000 periods/m, or 1 period/mm or 1/1000 of a period/μm. Although we don't often view periodic objects in biological microscopy (diatom frustules, bluebird feathers or butterfly wing scales might be exceptions), any image can be thought of not just as an array of points having different intensities, but also as a collection of "spacings" and orientations.

[1] It is usually limited even more severely by the presence of aberrations.

James B. Pawley • University of Wisconsin, Madison, Wisconsin 53706



The geometry of the beam scannning the specimen



The pixels as they appear in red channel of the display CRT B

FIGURE 4.1. What Nyquist sampling really means: the smallest feature should be at least 4 pixels wide. In (A), a yellow beam scans over two red point features. Because the "resolution" of the micrograph is defined, by the Abbe/Rayleigh criterion, as the distance from the center to the edge of the beam while Nyquist sampling says that pixels should be one half this size, pixels are one quarter of the beam diameter. From this, it follows that, at the end of each line, the beam will move down the raster only 25% of its diameter (i.e., it will scan over each feature at least four times). In (B) we see how such a signal will be displayed as a "blocky" blob on the screen, about 4 pixels in diameter. Because our eyes are designed to concentrate on the edges of each pixel, the screen representation doesn't look like an Airy disk (and would look even worse were we to add the normal amount of Poisson noise). We can get an "accurate" impression of the image of a point object only if we resample the 4×4 array into a much larger array and apportion the detected signal among these smaller, less distinct, pixels to form an image that looks like the circular blob on the lower right.

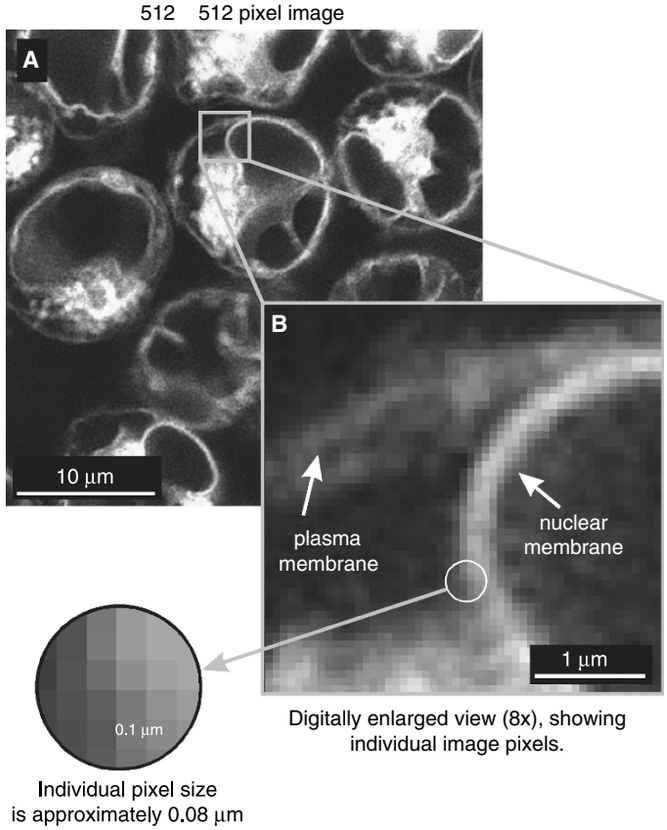


FIGURE 4.2. A properly sampled 2D image. When your image is recorded with Nyquist-sized pixels then the smallest features will be 4 to 5 pixels across. (This figure kindly provided by Dr. Alan Hibbs of BioCon, Melbourne, Australia.)

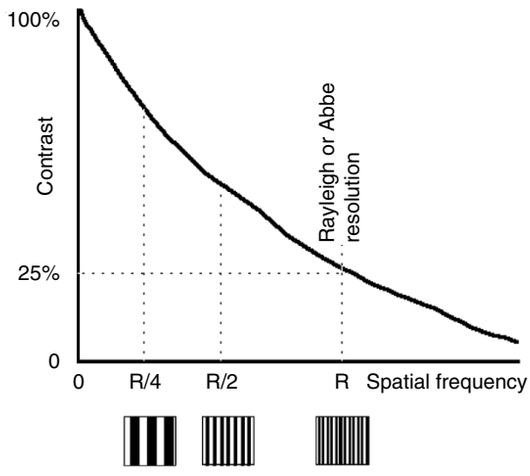


FIGURE 4.3. Contrast transfer function (CTF). This graph relates how the contrast of a feature in the image is inversely related to its size. Smaller "spacings" (see boxes below graph) have higher "spatial frequency" and will appear in the image with much lower contrast than they had in the object. Although the Rayleigh/Abbe resolution is conventionally set at the point where the CTF has dropped to 25%, even features that are twice this large (i.e., have one half the spatial frequency, R/2) are still represented in the image with only about half of their original contrast.

An image of a preparation of circular nuclei 7 µm in diameter has spacings of all possible orientations that are equal to the diameter of the nuclei in micrometers. The inverse of this diameter, in features/µm, would be the spatial frequency of the nuclei (in this case, about 150/mm).

The intensity of the CTF at zero spatial frequency is a measure of the average brightness of the entire image. The CTF graphs the image contrast assuming that the object itself has 100% contrast (i.e., that it is composed of alternating black and white bars having a variety of different periodicities; as few biological specimens have contrast this high, contrast in microscope images will be correspondingly lower). Because of the limitations imposed by diffraction, the contrast of the widest bars (spatial frequency near zero) will be almost 100% while bars that are closer together (i.e., have a spatial frequency nearer the diffraction limit) will be recorded with lower contrast in the image.

From Figure 4.3, one can see that the Rayleigh-criterion resolution is not really a hard-and-fast resolution limit but merely the spatial frequency at which the CTF of the optical system has dropped to about 25%. In general, features twice as big as the Rayleigh limit (i.e., R/2, half the spatial frequency) will be transmitted with a bit less than twice this contrast (i.e., ~50%), and so on for progressively larger features (although the image contrast can never be more than 100%).

One of the reasons that the CTF is such a useful guide to optical performance is that it emphasizes the performance for imaging small features. If we assume for a moment that we are using a high numerical aperture (NA) objective (NA 1.4) producing a Rayleigh resolution (R, in a microscope, this is often called the Abbe limit) of ~0.25 µm, then the part of the graph to the left of the R/4 marking describes the way that the optical system will transmit all the features larger than 1.0 µm (or R/4). All of the plot to the right of the R/4 mark refers to its transmission of features smaller than 1.0 µm. This is the part of the plot where problems are likely to occur. In addition, it reminds us that diffraction affects the appearance of features that are larger than the Abbe limit. In the end, resolution can only be defined in terms of contrast. It is NOT the case that everything works perfectly up to the Abbe limit and then nothing works at all.

The reason that the CTF is particularly useful in microscopy is that, if everything goes right (i.e., proper illumination, optically uniform specimen, no lens aberrations), its shape is entirely determined by the process of diffraction. If this is true, then the curve is directly analogous to what we can see in the back-focal plane (BFP) of the objective lens. You may recall that, when illuminated by axial illumination, large features (which have low spatial frequencies) diffract light near the axis while smaller features diffract light at larger angles. If you imagine that the left axis of the CTF plot (zero spatial frequency) is located at the exact center of the BFP, then the sloping part of the CFT curve can be thought of as representing a radial plot of the light intensity passing through the rest of the BFP.[2]

Light passing near the axis has been diffracted by large features. As many diffraction orders from these features will be accepted by the NA of the objective, they will be represented in the image with high contrast (Fig. 4.4).[3] Light out at the edge of the BFP consists of high-order diffraction from large features plus low-order diffraction from smaller features. The smallest features visible at this NA will diffract light at an angle that is almost equal to the NA of the objective, as defined by the outer border of the BFP. As only one diffraction order from these features will be accepted by the objective, the features that diffract at this angle will be represented in the image with low contrast.

As a result, one can "see" important aspects of the CTF, simply by viewing the BFP, for example, using a phase telescope or Bertrand lens. For example, when using a phase lens for fluorescent imaging, the phase ring present in the BFP of the objective partially obscures (50%–90% opacity) and shifts the phase of any rays passing through it. Therefore, features in the object that are the correct size to diffract at the angles obscured by the ring will be less well represented in the image data recorded.

Finally, the CTF is useful because it is universal. Assuming that you normalize the spatial frequency axis of the CTF plot in Figure 4.3 for the NA and λ in use (i.e., the spatial frequency under the 25% contrast point on the curve should be the reciprocal of the Abbe resolution), it is a reasonable approximation of the CTF of any diffraction-limited optical system. As such it defines the best we can hope for in terms of direct imaging (i.e., without non-linear image processing such as deconvolution to be discussed later, or the use of clever tricks like STED as discussed in Chapter 31, *this volume*).

The CTF can be used to characterize the performance of every part of the imaging system: not only the optical system but also the image detector (film or video camera), the image storage system (film or digital storage), the system used to display or make hardcopy of the stored result, even the performance of your eyes/glasses!

The performance of the entire imaging chain is merely the product of the CTF curves defining all the individual processes. Because the CTF always drops at higher spatial frequencies, the CTF of an image having passed two processes will always be lower than that for either process by itself (Fig. 4.5). In other words, small features that have low contrast become even less apparent as they pass through each successive stage from structures in the object to an image on the retina of the viewer.

As can be seen from Figure 4.5, the steps with the lowest CTF are usually the objective and the video camera. A digital CCD camera (i.e., a CCD camera in which each square pixel reads out directly into a specific memory location) would produce better results than the video-rate television camera/digitizer combination shown in Figure 4.5 because the latter digitizes the data twice, a process that can reduce the contrast of fine, vertical lines that are sampled in the horizontal direction by a factor of 2. The performance of all of the steps past the ocular can be "improved" by

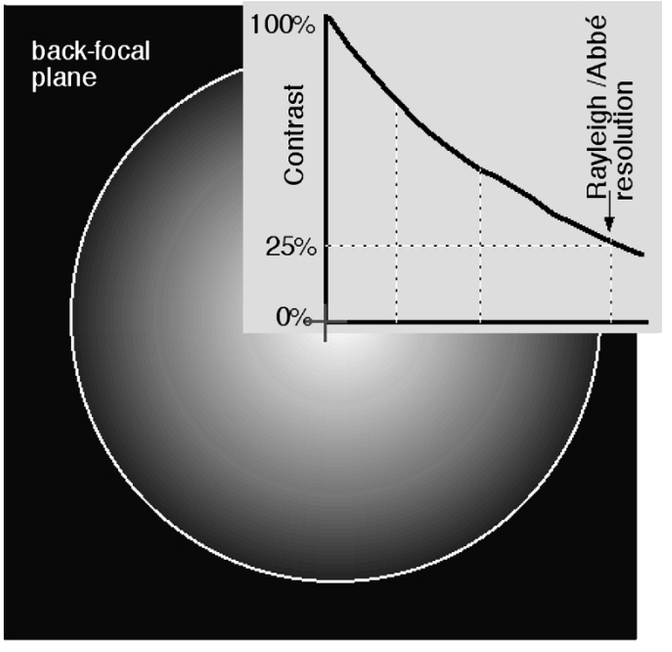


FIGURE 4.4. Relationship between the CTF and the position in the back-focal plane of the objective lens that axial light will diffract from features of different spatial frequencies.

[2] It is uncommon to image using only axial illumination, at least in part because filling the condenser BFP increases the number of diffraction orders that can pass through the objective, thereby doubling the resolution. It is assumed here only for illustrative purposes.

[3] Strictly speaking, the following analysis is only accurate for axial illumination. However, even for the convergent illumination used to get the highest resolution in transmission imaging, the general point is correct: light rays carrying information about smaller features are more likely to be represented by rays that pass near the edges of the back-focal plane.

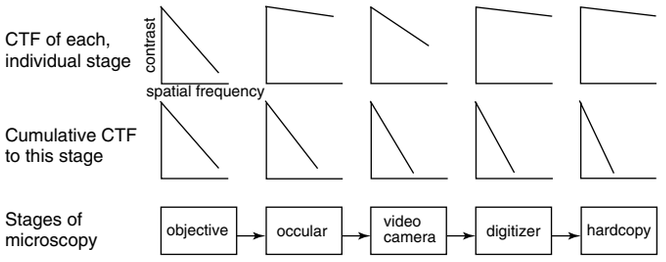


FIGURE 4.5. The CTF of each component in the microscope system affects the final result. Every optical component and digital process can be characterized by a CTF. The effects of a series of steps can be determined by multiplying together the CTFs of all the steps.

working at higher magnification: if the pattern of light presented to the camera (or eye) contains larger features, their contrast will be reduced less by imperfections in the camera (or eye) itself. However, this approach also has limitations. Working at higher magnification requires either a larger image sensor or a smaller field of view. Much of the remainder of this chapter is concerned with making the most appropriate choice of "magnification," although the discussion is usually in terms of "How large should a pixel be, referred to the object?"

Once the information is digitally encoded, further CTF degradation can be minimized as long as certain rules are obeyed (as discussed below and in Chapter 48, *this volume*).

The lessons so far are

- No matter how high the contrast of the optical process defining a feature in the object, smaller features are always depicted in the final image with less contrast than larger features.
- Features that have low intrinsic contrast in the object will have even lower contrast in the image.

On the other hand, remember that Figure 4.3 shows the best for which we can hope. It is not at all hard to end up with system performance that is substantially (~50%) worse than that described by Figure 4.3. This means that while one can no longer see the smallest features, one now might just as well use larger pixels.

In this chapter, we will assume that Figure 4.3 really does describe optical system performance, and go on to consider the other factors important to ensure that image data is digitally recorded in an optimal manner.

DIGITIZATION AND PIXELS

Image digitization refers to the process whereby an apparently continuous analog image is recorded as discrete intensity values at equally spaced locations on an *xy*-grid over the image field. This grid is called a raster.

Typically the image area is divided into an array of rows and columns in much the same way as a television image. In North and South America and Japan, the television image is composed of 483 lines covering a rectangular area having proportions that are 3 units high by 4 units wide. If each line in such an image is divided into about 640 equal picture elements or pixels, then each pixel will be square if you discard three lines and record a raster of 640 × 480 pixels.

Newer computer-based CCD image digitization systems do not rely on any broadcast television standard, and are more likely to use rasters of 512 × 512 or 1024 × 1024 pixels, although other dimensions are not uncommon. In scientific imaging, it is advisable to avoid digitizing schemes involving pixels that do not represent **square** subunits of the image plane (for example, those produced by digitizing each line from a television image into only 512 pixels rather than 640 pixels) as there is little support for displaying or printing such images directly.

Digitization of Images

The actual process by which the signal from the image detector is converted into the intensity values stored in the computer memory for each pixel depends on the type of microscope involved.

CCD cameras: Typically, a widefield or disk-scanning confocal microscope uses a camera incorporating a CCD image sensor. Although we will not describe in detail the operation of these sensors (see Chapter 12 and Appendix 3, *this volume*), the camera operates by reading out a voltage proportional to the number of photons absorbed within a small square area of the sensor surface during the exposure time. As long as the intensity value readout is stored directly into the computer, this small area on the CCD defines the pixel size for the remainder of the imaging system.[4]

As far as the user is concerned, the most important parameters involved in attaching the CCD to the microscope are the NA of the objective, the wavelength, and the total magnification up to the surface of the sensor. Together these parameters determine both the proper size of a pixel referred to the plane imaged in the specimen, and also the optimal pixel size for the CCD. For example, if a CCD camera with 8 × 8 µm pixels is coupled to a microscope with a 40 × 1.3 NA objective via a 1× coupling tube, each sensor pixel will cover 8/40 = 0.2 µm. The same camera and coupling will produce "0.08 µm pixels" when used with a 100× objective, but the number of photons striking each pixel during a given exposure time will now be 2.5 × 2.5 = 6.25× less because signal intensity goes down with the square of the magnification.

Photomultiplier tubes (PMTs): On a laser confocal microscope, signal photons strike the photocathode of a PMT where some small fraction of them each produce a single photoelectron (PE). These PE are then amplified about a million times by charge multiplication. The signal current emerging from the PMT is digitized under the control of a pixel clock which also controls how the scanning mirrors sweep over a rectangular raster on the specimen. This clock divides the time taken to scan one line into the appropriate number of intervals, so that each time interval represents a square area of the image (i.e., each time interval represents the same distance along the scan line as the spacing between adjacent lines). As the PMT signal is digitized for each interval, or pixel, the pixel value represents the signal intensity of a small square area of the final image.

Because the shape of the raster in a laser confocal microscope is defined by the size of the electronic signals sent to the scan mirrors (Fig. 4.6) rather than by the fixed array of electrodes on the surface of the CCD, there is much more flexibility in terms of the size and shape of the rasters that can be scanned.

[4] This is not true if the CCD is read out to form an analog "composite video" signal which is then redigitized into the computer. Such uncorrelated redigitization can reduce the effective horizontal resolution of the data by almost a factor of 2 and should be avoided. Likewise, one should be careful when "resizing" images using image processing programs because, unless it is done in integer multiples, this process also involves resampling, a process that reduces image contrast.

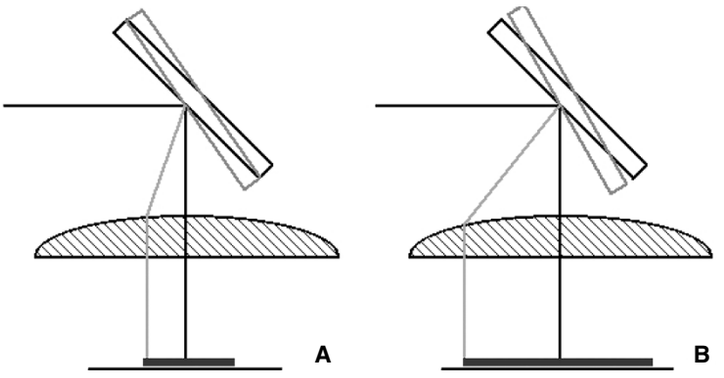


FIGURE 4.6. Mirror scan angle and magnification. The galvanometer mirror scans the laser beam across the focus plane of the objective by effectively changing the angle at which the laser beam passes through the back-focal point of the objective lens. A larger deflection of the mirror scans the light over a longer line on the specimen (B). As the data from this longer line are finally displayed on the same sized computer monitor, the effect is to lower the overall magnification of the image. If the number of pixels digitized along each line remains constant, a longer line on the specimen implies larger pixels.

In particular, a combination of the magnification of the objective and the zoom magnification on the scan control panel defines the dimensions of the raster at the object plane in the specimen. If more current is sent to the scanning mirrors (low zoom magnification), they will drive the scanning beam over a larger area of the specimen and, assuming a fixed raster size (e.g., 512 × 512 pixels), this means that each pixel will now represent a larger area of the specimen (Fig. 4.7, darkest square). Conversely, higher zoom magnification will send smaller currents to the scan mirrors. This will make the raster scan over a smaller area on the specimen, and make the area represented by a single pixel proportionally smaller (Fig. 4.7, lightest square). As a result, and unlike the CCD case, pixel size is under continuous control as the user changes raster shape/size and zoom magnification settings. However, your control panel should constantly display the current pixel dimensions.

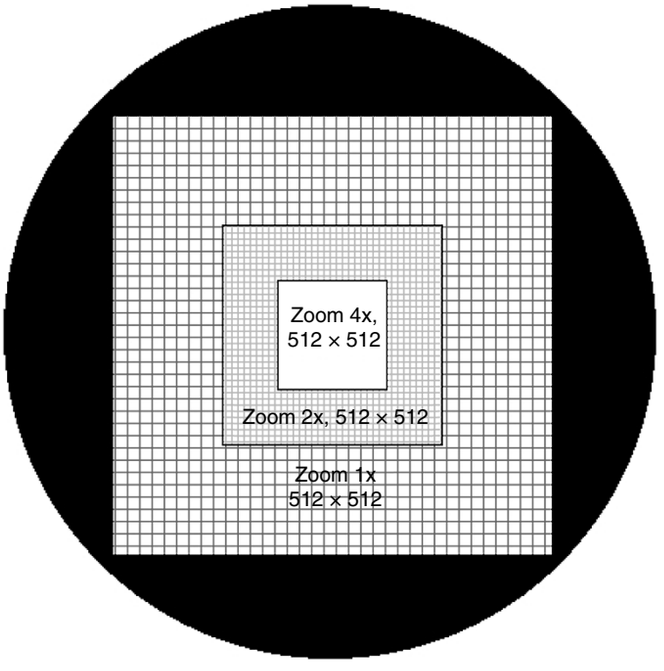


FIGURE 4.7. Relationship between zoom setting and area scanned on the specimen. A higher zoom magnification setting scans the beam over a smaller area of the sample. As each pixel now represents a smaller area on the specimen, we say that the pixels are "smaller." The important thing is to adjust the zoom magnification so that the pixel size is about 50% of the Abbe resolution for the NA and wavelength in use.

HOW BIG SHOULD A PIXEL BE? SAMPLING AND QUANTUM NOISE

Clearly, it is not possible to represent features spaced, say, 1 µm apart if the pixel dimensions are 2 × 2 µm. Having smaller pixels will increase the chance that small features of the specimen are adequately sampled. However, having smaller pixels also has disadvantages. It means either imaging a smaller area of the specimen or using a larger raster size [1024 × 1024 rather than 512 × 512; Fig. 4.8(A)]. If you choose a larger raster, you must store and analyze more data. You must also either collect fewer signal photons from each pixel [Fig. 4.8(B)] or take longer to scan the larger raster. Longer counts require you to expose the specimen to more light [Fig. 4.8(C)], a process that may be deleterious, especially to living specimens.

Settling for less signal in each pixel is also not without problems. The signal that is being counted is not continuous but is composed of photons, sometimes quite small numbers of photons. In fact, it is not uncommon for the signal from a single pixel in the bright area of a fluorescent confocal specimen to represent the detection of only 9 to 16 photons.

As the detection of a photon is a quantum mechanical event, there is an intrinsic uncertainty in the number actually detected on any given trial. This uncertainty is referred to as Poisson, or statistical, noise and is equal to the square root of the number of events (photons) detected. Therefore, reading 16 photons really means detecting 16 ± 4 events.[5] **Like diffraction, Poisson noise is a rigid physical limitation**. The **only** way to reduce the relative uncertainty that it causes is to count more events.

If we increase the zoom magnification by a factor of 2, there will be 4× as many pixels covering any given scanned area of a two-dimensional (2D) specimen. If, at the same time, we also reduce the laser power by a factor of 4, the same total amount of signal/µm^2 will emerge from the reduced area now being scanned, producing the same bleaching or other photo damage but the average signal level in each bright pixel will now be not 16 photons, but only 4 ± 2 photons. The uncertainty of each measurement is now 50%. In other words, when photons are scarce, one seldom wants to use pixels smaller than are absolutely necessary to record the information in the image.

It is simply a case of "winning on the swings what you lose on the roundabouts." Either scenario has advantages and dis-

[5] That is, 67% of a series of measurements of this intensity would be in the range of 12 to 20 photons and 33% of such measurements will be outside even this range. In other words, if you detect 10 photons you really have very little idea about what the signal intensity really "should have been."

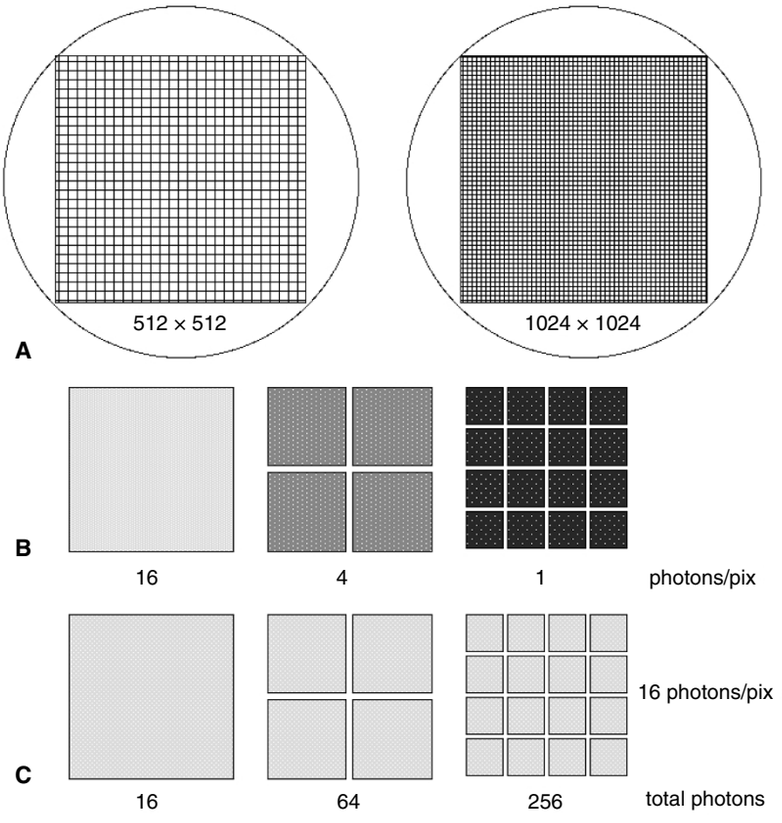


FIGURE 4.8. Relationship between raster size, pixel size, and "light dose." (A) If a microscope scanning at a zoom setting of 1 is switched from a 512 × 512 raster to one of 1024 × 1024 pixels, the dimensions of each pixel on the specimen will drop by 50%. (B) If the same amount of signal is split between more pixels, the signal level from each one goes down (and the Poisson noise goes up), but if the beam scans more slowly or is made more intense so that the same amount of signal is still collected from each pixel, (C), then the amount of damage/pixel increases. There is no free lunch!

advantages. Surely there must be a "best" strategy for setting the zoom correctly to produce the best pixel size.

Fortunately there is!

THE NYQUIST CRITERION

It was not until 1929 that Harry Nyquist, who worked for the telegraph company, gave much thought to the optimal strategy for digitally sampling an analog signal (Nyquist, 1928). When such sampling first became technically possible, the signal in question was electronic, perhaps the audio signal of a radio program. The process envisioned, as diagramed in Figure 4.9, requires six components: a **pre-amplifier** feeding the signal to the **analog-to-digital converter** (ADC), a **digital memory** system for storing the digital data from the ADC, **a digital-to-analog converter** (DAC) that reassembles the digital information into a continuous analog signal that can be passed to the **output amplifier,** and, finally, a **clock** to synchronize the whole process. The clock determines the time interval between samples (i.e., the sampling frequency, in samples/s).

The information content of any electronic signal is limited by the electronic bandwidth of the amplifier used to transmit it.[6] In 1949, Claude Shannon was able to prove Nyquist's theorem and show that, if the interval between the intensity measurements is less than half the period of the highest frequency in the signal, it will then be possible to faithfully reconstruct the original signal from the digital values recorded (Shannon, 1949). **The Shannon sampling frequency,** which is the inverse of the Shannon sampling interval, is also known as the **Nyquist frequency, especially in the imaging community**.

It is often forgotten that there is a second part of the Shannon/Nyquist theorem: the part about reconstructing the original data. The theorem states that the output "amplifier" through which you play back the reconstructed signal from the DAC must have the same bandwidth as the pre-amplifier that originally fed the signal to the ADC. This is an important condition, one that is often not satisfied in current confocal microscopes unless their images are deconvolved before presentation (as will be discussed later).

Attempting to apply Nyquist sampling to 2D or three-dimensional (3D) images gives rise to the question: How do we measure the "bandwidth" of the "amplifiers" when faced with the problem of digitizing 2D or 3D microscopical image data?

Electronic bandwidth is not a simple concept. The frequency response of any real amplifier does not remain flat until some frequency and then go abruptly to zero at any higher frequency. Rather, limitations imposed by the components of which the circuit is made cause its power response to decrease gradually as the frequency increases, usually dropping to one half or one quarter the original output power as the frequency goes up each octave above

[6] Think of this as the frequency response of your stereo system. Good high frequency response will let you hear your music more accurately. The frequency response of your stereo is usually plotted in decibels (a measure of relative power) on the *y*-axis against the log of the frequency on the *x*-axis. Note the similarities to Figure 4.1.

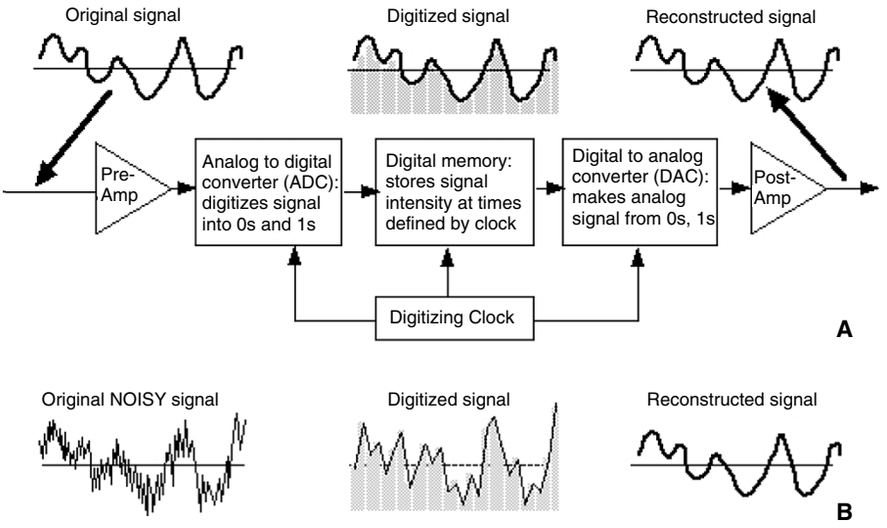


FIGURE 4.9. The components needed to digitize and reconstruct an analog signal. The "post-amp" is essential to remove the "single-pixel noise" that is added to the original analog signal by Poisson statistics. Because real, Nyquist-sampled data can never have features smaller than 4 pixels across, single-pixel noise can be removed by limiting the bandwidth of the post-amplifier. In microscopy, this limiting function is implemented by either Gaussian filtering or deconvolving the raw 3D data.

some "cut-off frequency."[7] As in optical systems, higher electronic frequencies are still transmitted, but at lower intensity. In electronics, the convention is to define the bandwidth by the frequency at which the power response drops to 50% of the linear response, a frequency called the "3 dB point." This defines the bandwidth Shannon used. In optical terms, we usually think of the image being useful until it drops to about 25% of its peak contrast (i.e., the Abbe criterion noted above), although this too is an arbitrary choice.

If we think of an analog electronic signal as a one-dimensional image, it is not hard to think of an image as a 2D (or 3D) version. Except that image data varies in space rather than time, the rest of the analysis applies. The "bandwidth" of an image must be somehow related to its "sharpness," and this is related to the highest spatial frequencies it contains.

Now if we were applying this analysis to the CCD sensor used in a consumer snapshot camera, we would have a problem. Although the "world" out there may be composed of objects of every size, we really have little knowledge of the CTF of the lens, let alone whether or not it is focused correctly or whether you are capable of holding it motionless during the exposure period. As a result, we really don't know the bandwidth of the data and consequently we don't know whether or not the pixels are small enough to meet the Nyquist criterion. "More is better" is the slogan that sells.

Fortunately, this is not the case in microscopy. Here we do know that, at the very least, diffraction limits the maximum sharpness of the data that can be recorded, and that the "spatial frequency response" of the microscope can be defined by a suitably calibrated version of Figure 4.3.

Therefore, the convention is to choose the size of the pixel to be equal to one half of the Abbe criterion resolution of the optical system.

There are some caveats. The structural features of a 1D image can only vary in that dimension. The structural features of a 2D image can vary in more than two possible directions. Although signals defining features such as vertical or horizontal lines, vary in only the *x*- or *y*-directions, respectively, what about a set of lines oriented at 45° to these axes? It would seem that sampling points along a 45° line would be spaced 1.41× as far apart as sampling points along features that vary along the *x*- or *y*-axes. Pixels just small enough to sample a given small spacing when it is oriented vertically or horizontally would be 1.41× too big to sample this same structure were it to be oriented at 45°. However, this analysis neglects the fact that all image "features" extend in 2D. As a result, lines running at 45° will also be sampled by other pixels in the array and if we count all the pixels that sample the blurred features along a line at 45°, one finds that the sampling interval isn't 1.41× larger but in fact only 0.707 as large as the sampling interval in the *x*- or *y*-directions (Fig. 4.10). Clearly we want to be able to see structures oriented in any direction. To be on the safe side, it may be better to use pixels ~2.8× smaller than the finest spacing you expect to record in your image.[8]

Estimating the Expected Resolution of an Image

Assuming that the shape of the CTF curve describing the optics of the microscope depends only on the NA and the wavelength, it is also a plot of power level versus the logarithm of the frequency, just like the frequency response curve of a stereo. Although the CTF defines the best that one can hope for, it does not guarantee it.

Performance can be worse, and if, in fact, it is worse, does it make sense to use smaller pixels than we need?

Let us take some concrete examples. The calculation of the Abbe criterion resolution assumes that **two point objects of similar intensity** are represented in the image as Airy disks, spaced so that the peak of each is located over the first dark ring of the other. If we sum the light intensity of these two Airy disks, there will be a valley between the two peaks in the summed image. At the exact mathematical bottom of this valley, the intensity is

[7] As in music, an octave represents a factor of 2 in signal frequency.

[8] A similar line of argument could be used to suggest that one use even smaller pixels when sampling 3D data because the diagonal of a cube is 1.732x longer than its side. However, we will soon see that, as the *z*-resolution of the confocal microscope is always at least 3x lower than the *xy*-resolution, ignoring this factor does not cause any problem in practice.

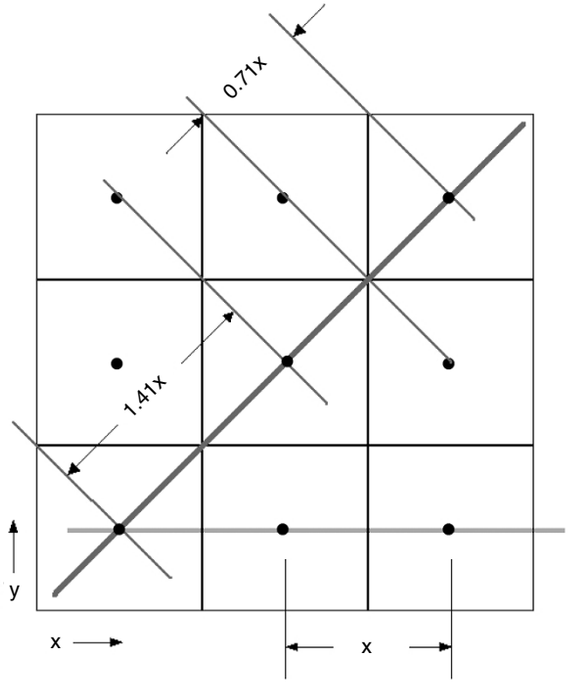


FIGURE 4.10. Spatial frequency and geometry. The 3 × 3 array of squares represents a small raster and the dots in the center of each represent the sampling points. Although one might be tempted to think that these sampling points would be too far apart along the diagonal to be able to properly sample any signal that just meets the Nyquist sampling criterion when oriented either horizontally or vertically, this is not so because the sampling points of the adjacent diagonal rows of pixels actually sample at 0.71 of the *x*- or *y*-raster pitch.

about 25% lower than the intensity of either peak. This is the basis of the idea that 25% contrast is equal to the Abbe criterion resolution (Fig. 4.11).

Under these circumstances, the smallest resolvable spacing is defined as the distance between the center of an Airy disk and the center of its first dark ring. To be properly sampled, pixels should be less than one half this distance in size.[9]

Suppose that, along a line joining centers of the images of the two points, one pixel just happens to be centered on the brightest part of one Airy disk. The adjacent pixel would then be centered over the valley between the peaks and the third pixel will be over the second Airy peak. If we sample the brightness at the center of these three pixels, the digital data will reflect the trough in intensity between them.

On the other hand, if the "valley pixel" has a value proportional not to the intensity at the exact center of the pixel but to the average intensity over the whole pixel,[10] the value stored for the center pixel will be much more than 75% of the peak intensity:

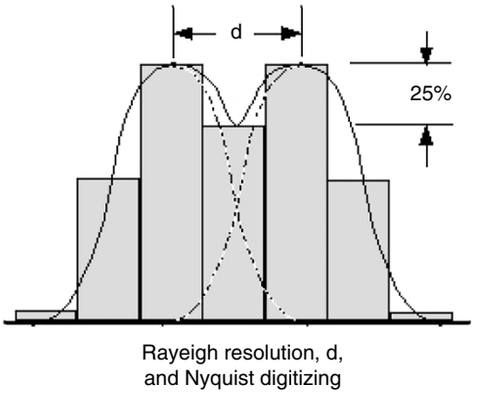


FIGURE 4.11. Nyquist sampling of an image of two points separated by the Rayleigh resolution.

that is, the contrast recorded between the three pixels will now be much lower than 25% (Fig. 4.12).

If the two features that produced the two Airy disk images are not of equal brightness (surely the more likely occurrence) then the contrast along a line joining the peaks will again be much less than 25%.

Worse still, what if the peaks are uncooperative and are not squarely centered on two pixels, nicely spaced on either side of the central, darker pixel? If the value recorded at each pixel is the average of the intensity across the pixel, the contrast along a line between the features can be substantially reduced or even eliminated (Fig. 4.13).

Now it is fair to say that while these considerations are problems, to some extent, they only represent a serious problem if we ignore the second part of the Nyquist sampling theorem, the part having to do with reconstruction. If the image is properly reconstructed (deconvolved), in most cases, information from adjoining pixels (those in the rows in front or behind the printed page in Fig. 4.13) will allow one to smooth the image to form a good estimate of the structure of the original object as is discussed later in the chapter.[11]

Deconvolving or filtering the image data eliminates high spatial frequencies. Effectively, such filtering causes the signal to overshoot the contrast present in the digital signal. This process substantially reverses the apparent reduction in contrast that occurs on digitization.

[9] Or perhaps a bit less if we use the 2.3 or 2.8 samples/resolvable element (resel) suggested above. For simplicity, I will stick to 2 samples/resel in this discussion, because, as discussed below, in the case of the fluorescent images of most interest, lack of signal usually prevents one from realizing Abbe criterion resolution and consequently the "actual" resolution is lower than Abbe and using somewhat fewer/larger pixels is appropriate.

[10] In microscopy terms, the CCD samples the average value of a pixel while the ADC sampling the PMT signal in most single-beam confocals acts more as the center-sampling device.

[11] Periodic structures having a size near the resolution limit also present sampling problems. Suppose that the object is a sinusoidally varying structure with a period equal to the Abbe spacing. If the two samples required by Nyquist coincide with the plus and minus excursions of the sine wave, then we will have some measure of its magnitude and the position of its zero-crossing [Fig. 4.5(B)]. However, if the two samples happen to be taken as the sine wave crosses its origin, all the sampled values will be zero and hence can contain no information about the sine wave [Fig. 4.5(C)]. This apparent exception to Nyquist sampling success is not actually an exception in terms of the original application of the theorem: information theory. According to information theory, a sine wave contains no information beyond its frequency and magnitude. As long as you have slightly more than two samples/period, the sampling intervals will "beat" with the data to create a sort of moiré effect, from which one can estimate the magnitude and period of the sine-wave object. All this does not change the fact that an image of a periodic object must be at least 2x over-sampled if it is to be recorded with reasonable fidelity [Fig. 4.5(A)]. This is particularly important when imaging the regular patterns found on resolution test targets.

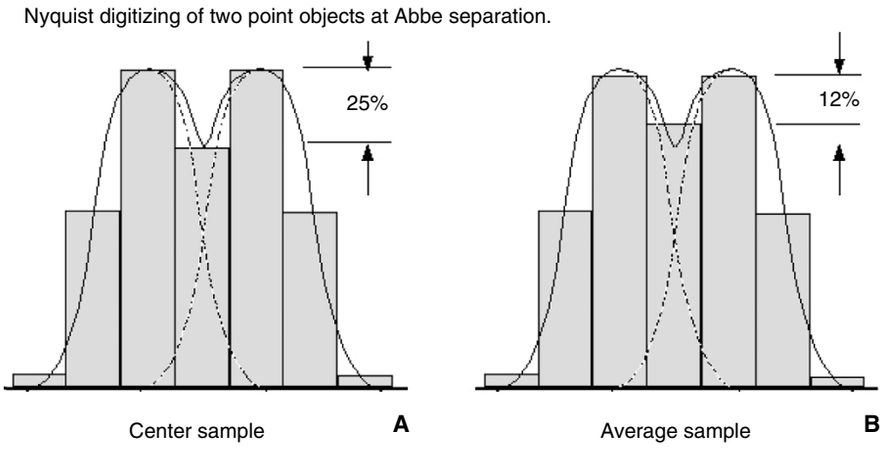


FIGURE 4.12. Two methods of sampling: at the center point and as the average value.

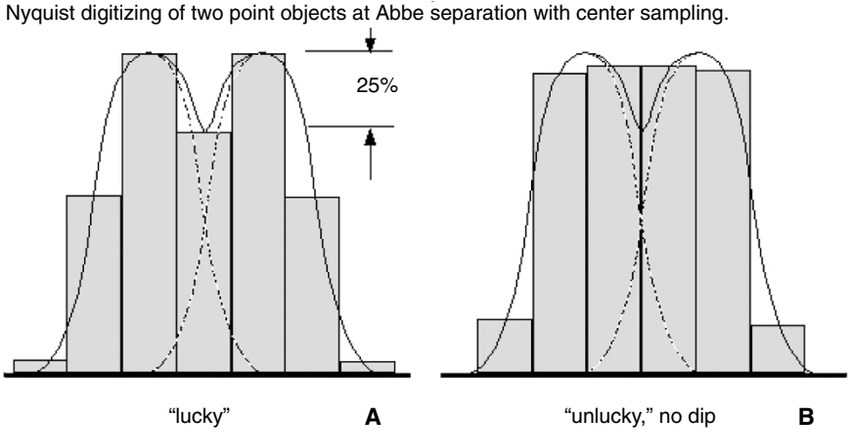


FIGURE 4.13. How can this possibly work? "Lucky" and "unlucky" Nyquist sampling of the image of two points separated by one Rayleigh resolution.

On the other hand, this reduction in contrast is entirely relevant if one tries to assess raw digital image data from a Nyquist-sampled confocal microscope directly from the cathode-ray tube (CRT) or liquid-crystal display (LCD) screen or when viewing unprocessed data as a hardcopy from a digital printer.

There is another problem that even proper reconstruction will not solve. Recall the example above in which a "bright" signal (perhaps the peak of an Airy disk?) was only 16 ± 4 photons. Clearly the ±4 represents a 25% average error, that is the same order of uncertainty as the maximum expected contrast we hope to see between the peaks (Fig. 4.14). In other words, even though diffraction theory says that we should record a lower signal in the pixel between two peaks of equal intensity, at these low signal levels, Poisson statistics says that, about 30% of the time, the intervening pixel will actually be measured as brighter than at least one of the two peaks. [As each peak pixel is subject to its own independent statistical variations, in a given image, it is unlikely that all 3 pixels (or 9 pixels if we consider the 2D image) will be recorded as the same brightness.]

Artifactual "features" such as those diagramed in Figure 4.14(B) and produced by "single-pixel" Poisson noise, will be removed if the dataset is deconvolved or even 3D-Gaussian smoothed as discussed below.

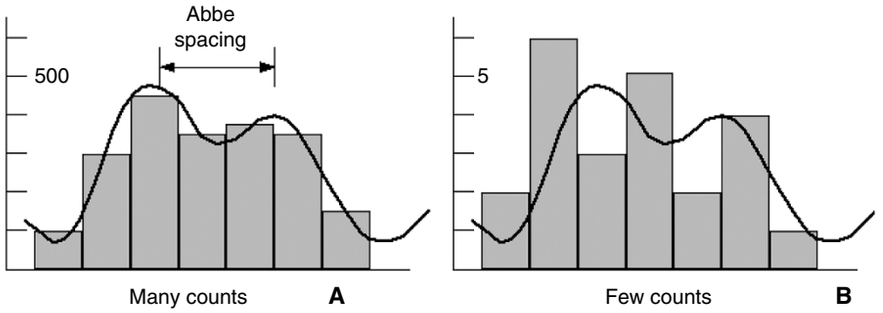


FIGURE 4.14. The effect of Poisson noise. While a Nyquist-sampled signal of Rayleigh-separated features seems to work well when the signal is composed of many photons and has little noise (A), when the number of photons counted drops by a factor of 100, and the signal-to-noise ratio (S/N) drops by a factor of 10, then random variations in the signal can play havoc with the data (B) allowing "single-pixel" noise features to masquerade as very small features.

The Story So Far

Once we know the size of the smallest data we hope to record, we can adjust the zoom magnification on a confocal microscope or the CCD camera coupling tube magnification on a widefield microscope to make the pixels the right size.

But is Figure 4.3 really a good way to estimate this maximum spatial frequency?

REALITY CHECK?

Are we kidding ourselves in thinking we will be able to **see individual point features separated by Abbe criterion resolution** when viewing faint, fluorescent specimens? In fact, under these conditions, we may be lucky to separate features that are even twice this far apart and we now recognize that we could record such data using pixels that were twice as big and 4× less numerous (in a 2D image; 8× fewer in a 3D image).

On the other hand, our human ability to "see" (recognize?) extended features, such as fibers or membranes, is enhanced by the ability of our mind to extract structural information from noisy data. We do this "magic" by integrating our visual analysis over many more pixels (100×?). While viewing noisy, extended objects doesn't improve the quality of the data, it allows the mind the illusion of averaging out the statistical noise over more pixels because each is an independent measurement. In this case, Nyquist/Abbe sampling may be more worthwhile after all.

Is Over-Sampling Ever Wise?

Yes! When viewing a specimen that is not damaged by interacting with light, over-sampling can improve visibility by recording more data and hence reducing the effect of Poisson noise. Video-enhanced contrast microscopy has been utilized to image isolated features much smaller than the Abbe limit. When imaging structures such as isolated microtubules, one often employs "empty magnification," sampling much more finely than is required by Nyquist. This is effective because such structures produce only a very small amount of image contrast.

As a simplified example, assume that the signal from the feature is only 1% greater than that from the gray background. Turning the light signal into an electronic signal permits one to adjust the contrast arbitrarily. However, if the electronic signal is too noisy, the result will just be more contrasty noise.

To detect a 1% difference using photons, we must ensure that the contrast produced by Poisson noise variations in the background gray are less than that between the background and the feature. At the minimum, this involves counting at least 10,000 photons/pixel because the Poisson noise is $\sqrt{10{,}000}$ and 100/10,000 = 1%. One could produce an even more easily interpretable image if the intensity of the feature differs from the background by more than one standard deviation. Recording 100,000 photons/pixel would make the 1% signal become 3× more than the Poisson noise.

As most image sensors saturate (become non-linear) when exposed to more than 100,000 photons/pixel, the only way to "see" such a low contrast feature is to make many different measurements (i.e., use more pixels). A single pixel might be bright because of statistics but it is less likely that four adjacent pixels will all be recorded as bright. Using more pixels produces even greater visibility by further separating the signal representing the feature from that representing the background.[12]

Under-Sampling?

In some cases, the useful resolution of the image is set by non-optical limits. An example might be a fluorescence image of a cell containing a dye that changes its properties in response to the concentration of certain ions. If the diffusion of ions and dye molecules precludes the existence of small-scale variations in the fluorescence signal from such a cell (i.e., no small features), there is no need to divide the data into small pixels. Measuring each of fewer, larger pixels for a longer time may give more accurate results, especially when the expected changes in ion concentration produce only small changes in the fluorescent properties of the dye used (i.e., a low-contrast image) or when two noisy images must be ratioed to obtain the final result.

In such specimens, high **spatial** resolution is impossible because of diffusion, while high **intensity** resolution is required to make small changes visible. In this case, it is particularly important to spatially filter the raw digital data before attempting to display or ratio the data (see Chapter 42, *this volume*).

DIGITIZING TRADE-OFFS

We have now discussed how most of the relevant factors: pixel size, optical resolution, and photon signal strength all interact. The best choice will almost always depend primarily on the robustness of your sample: Assuming careful adjustment of the optics, more counted photons will always give a better estimate of the distribution of fluorescent molecules within the specimen.

You must decide when the need for better spatial or intensity resolution justifies increasing the signal level and when it cannot be tolerated because to do so would reduce the "biological reliability" of the data (i.e., kill or injure the cells, see Chapters 38 and 39, *this volume*). Data with higher spatial resolution may not be useful if they represent structural features of a cell that is dead or dying.

NYQUIST RECONSTRUCTION: "DECONVOLUTION LITE"

Elsewhere in this volume the technique for recording 3D data sets of both point objects and fluorescent specimens using a widefield microscope and a CCD camera and then computer-processing the resulting data to produce 3D images much like those produced by the confocal microscope are discussed in detail (Chapters 23, 24, and 25). The most advanced form of this processing is called iterative, constrained 3D deconvolution and uses the image of the point object to determine the 3D point-spread function (PSF) for the imaging system. Here, I will discuss only one part of this process, a process that can be thought of as filtering or smoothing.

[12] It is important to state here that I am not talking about limitations in the image that could be overcome by resetting the "contrast" and "brightness" of the image display system in order to make any image contrast more visible to the observer. These are assumed to be set in the best possible manner for the individual concerned. The limitation on visibility discussed here relates solely to the fact that the data in the recorded image is insufficiently precise for any observer (or even a computer!) to determine the presence or absence of the structure. For more about visibility and the Rose criterion, see Chapters 2 and 8, *this volume*.

As noted above, sampling the analog data to produce the digital record was only half of the process. The second part involves "passing the reconstructed signal through an amplifier having the same bandwidth as that from which the original data was received."

To see why this is necessary it may help if we imagine a reconstruction of the digital data as being sort of a bar graph, in which each bar represents the intensity value stored for this pixel [Fig. 4.15(A)]. Clearly a "signal" represented by the boxy contour line going along the tops of the bars will generally change much more abruptly than the original data. As a result, it is not a faithful reconstruction of the original signal.

How can it be made more similar? In terms of Fourier optics a "square-wave object," such as a bar, can be thought of as being composed of the sum of a number of sine-wave objects, each having a periodicity that is an integer-multiple (harmonic) of the square wave frequency. The first sine term in this series converts each "square" of the square wave into a rounded curve. As subsequent terms are added, they add the "ears" to the hump that make the sum resemble the original boxy square wave ever more accurately (Fig. 4.16).

If we apply this logic to the top line of our bar graph, we can think of it as the sum of a lot of sine waves. If we leave out the higher harmonic terms before reconstructing the original line, the boxy corners will be rounded. Passing the boxy reconstruction through an amplifier of limited bandwidth prevents the higher order terms (higher frequencies) in the sine-wave series from being included in the reconstructed signal [Fig. 4.15(C)].

This is important when viewing a digital image because our eye/brain system is designed to emphasize the sharp edges that define the boundary of each pixel on the liquid-crystal display (LCD) screen and this is more likely to happen when a single noisy pixel stands out from a darker background.

The same thing is true when we reconstruct an image from digital data. However, in the case of fluorescence or other low-intensity data, there is an additional complication. The Nyquist theorem assumes that the signal digitized is continuous, that is, that

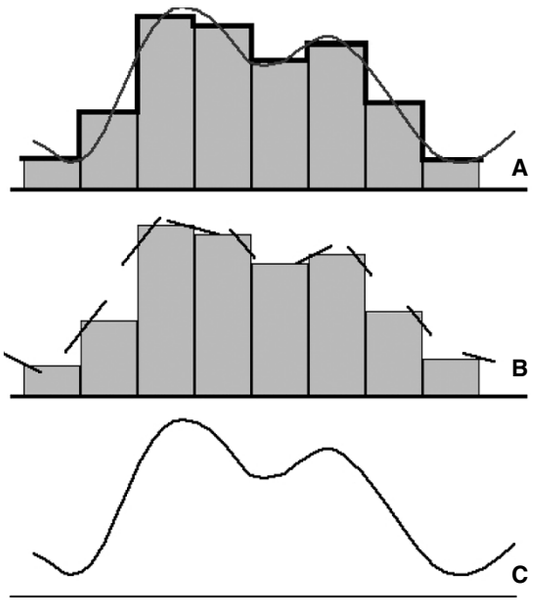


FIGURE 4.15. How "limiting the bandwidth of the output amplifier" smooths off the rough corners (B) and improves the reconstruction (C).

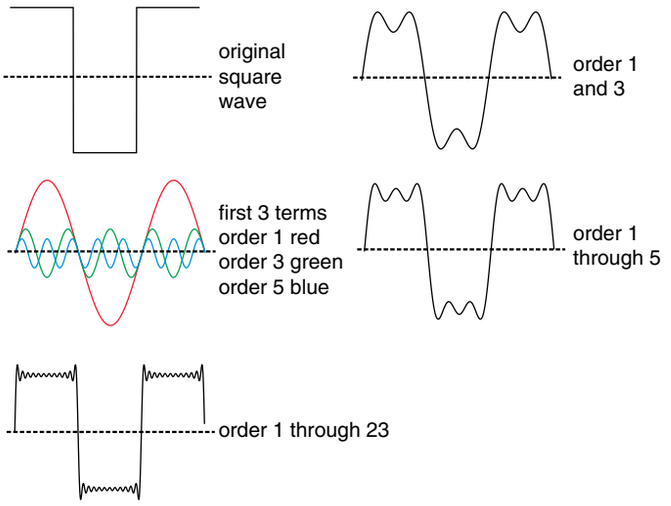


FIGURE 4.16. Fourier analysis. The Fourier theorem says that any periodic structure (such as the "square-wave" in the top left) can be represented as the sum of a number of sine waves, each of which is harmonic of the frequency of the structure. Think of these frequencies as the spatial frequencies introduced in Figure 4.2. As more components are added to the sum, the result looks more and more like the original. The same thing happens in microscopy, where using a lens with a higher NA allows more "terms" that are carrying high-frequency information (and therefore diffract at higher angles) to contribute to the image.

determining the intensity to be stored for each pixel does not involve measuring small numbers of quantum-mechanical events. A continuous signal is not capable of changing by a large amount from one pixel to the next because the pre-amplifier bandwidth was too narrow to permit such a rapid change.

In the microscopic case, the Abbe bandwidth limits the amount of change possible between adjacent Nyquist pixels. However, in the confocal, Poisson noise can effectively sneak past the "pre-amp"[13] and get digitized as part of the signal. As a result, such abrupt changes **can** be recorded.

Consider the following example: Suppose we record the image of a bright point object on a black background using Nyquist sampling. A one-dimensional (1D) transect across the center of this feature might include 5 pixels. If sampled many times, the **average** recorded intensities in the central pixels might represent 10 photons, 8 in the pixels on either sides, and 3 for the two pixels next farther out.

Had we recorded these averaged values, we would only have to worry about the "boxy corners" artifact noted above. However, if we only record a single set of values, Poisson noise introduces another factor. On any particular sampling of this line of data, we will generally not get the average values but something else. Were we to record not 3, 8, 10, 8, 3 but 2, 7, 13, 10, 4, the resulting reconstruction would now be very different. In particular, the center of the feature would have moved right and it would now appear narrower. The transients caused by the statistical nature of the signal have made a proper reconstruction more difficult.

In fact, one would be correct in saying that, as the accuracy of the values stored in the computer are always limited by the statistics involved in counting quantum mechanical events, we can never know their "true" intensity of any pixel and our efforts

[13] This is possible because, in this case, it is the microscope optics that limits the bandwidth rather than an electronic pre-amplifier.

to make a reconstruction of the object are doomed to be only approximate.

While this dismal analysis is correct, we would like at least to make this approximation as accurate as possible. We can do this by applying the second Nyquist constraint: treating the data stored in the image memory to make sure that they do not contain spatial frequencies that are higher than the optical system could have transmitted. Although the best way to do this is to subject the 3D data set to iterative 3D deconvolution, much benefit can be gained by applying a simple 2D or 3D Gaussian smoothing filter. The effect of such a filter is to make the intensity of every pixel depend to some extent on the intensity of 63 or 124 neighboring voxels (depending on whether a $4 \times 4 \times 4$ or a $5 \times 5 \times 5$ smoothing kernel is used). This filtering effect averages out much of the statistical noise, reducing it by an amount proportional to the number of voxels in the convolution kernel.

If we apply a smoothing filter that simply suppresses "impossible" spatial frequencies (i.e., those higher than the optical system is capable of producing), the contrast of small features that owe their (apparent) existence solely to the presence of quantum noise in the data will be greatly reduced.

It is important to note that applying such a filter will reduce the apparent contrast of the image data. Digital look-up tables can be used to increase the apparent contrast on the viewing screen and the resulting images will be just as contrasty and will show less statistical noise than the raw data.

MORAL: Your image is not suitable for viewing until it has been at least filtered to remove features that are smaller than the PSF, or, thought of the other way, to remove data having spatial frequencies beyond the maximum bandwidth of the optical system in use.

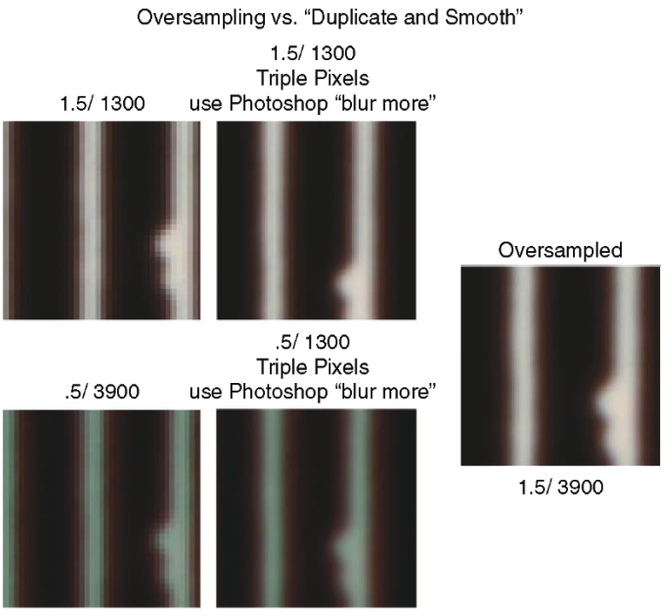


FIGURE 4.17. Wiggling the chip to increase the resolution. A number of CCD cameras increase their effective spatial resolution by adding together the information from a set of four (or nine) images, each of which is collected with the CCD displaced horizontally by one half (or one third) of a pixel, first in *x*, then in *y*, compared to the other members of the set. The image in the top left was made at a tube magnification of 1.5× with the camera readout normally, while that below it was made with 3× less optical magnification and 3× more "resolution" by moving the chip. Both look quite similar when they have been up-sampled and then blurred in Photoshop except that the "wiggled" result has a color caste caused by the fact that the color mask filters on the chip have a "pitch" that is twice the nominal pixel spacing. The up-sampled and blurred picture on the right is analogous to the round, red feature in Figure 4.1.

Some Special Cases

In classic sampling theory, the time (or space) taken to measure or sample the intensity in each pixel is very small compared to the inter-pixel sampling interval. Although this condition is met for the ADCs used in commercial confocal microscopes,[14] it is not met for the CCD camera, where it is common for the sensitive area of 1 pixel to be almost equal to the area it covers on the silicon surface. Clearly, this means that the space taken to sample the light flux is almost the same as the pixel size. The system works well enough as long as we stick to Nyquist sampling of a signal of known bandwidth (4–5 pixels/blob). In fact, some CCD manufacturers have gone even further and made an effort to increase the effective spatial resolution of a CCD by making a series of four or nine exposures, in which for each member of the series the sensor is offset from the previous one by one half or one third of a pixel in *x* and *y*, respectively.[15] While reasonable results can be obtained in this way, problems can develop when it is applied to color imaging systems that employ a color pattern mask on each pixel (Fig. 4.17).

Even in the confocal microscope, problems can occur because the zoom magnification control creates a variable relationship between the optical bandwidth of the signal and the electronic bandwidth which is set by the "time-constant" of the pre-amplifier just before the ADC. Not only that, but the optical bandwidth creates blurring in 2D while the pre-amplifier time constant only limits the signal bandwidth in the fast scan direction (usually horizontal). If the zoom is set to under-sample high-contrast optical data, then very large pixel-to-pixel variations are possible and the bandwidth should be wide. The reverse is true for over-sampling. In response to this problem, some commercial instruments estimate the optical resolution from the NA of the objective and the wavelength of the laser and then use this information to set the pre-amplifier to the optimal time constant (bandwidth) on the basis of the zoom setting. When such a system is functioning properly, the "apparent noisiness" of the signal recorded from a bright but relatively featureless object will become less as the zoom is increased: the signal/pixel remains the same but the longer time constants effectively averages this noisy signal over more pixels in the horizontal direction.

Starting with the MRC-600, all Bio-Rad scanners used full-integration digitizers. These were composed of three separate sections. At any instant, one is integrating the total DC signal current from the PMT during a pixel, the second is being read out, and the third is being set back to zero. This system effectively emulates the image digitizing system of the CCD. This approach works well for under-sampled data and was a great improvement on earlier systems that used a time constant that was fixed at (pixel time/4) and therefore let a lot of high-frequency noise through to the ADC.

If you don't want to worry about any of this, stick to Nyquist!

[14] Common values might be pixel period = 1 µs, sampling interval = 3 ns.
[15] For example, the Zeiss Axiocam.

GRAY LEVELS, "NOISE," AND PHOTODETECTOR PERFORMANCE

When an image is digitized it must be quantized in intensity as well as in location. The term **gray level** is the general term referring to the intensity of a particular pixel in the image. Beyond this general definition, things become more complicated. What kind of a measure? Linear? Logarithmic? What is **a gray level**? Let us begin at the beginning with a discussion of how these matters were handled by the first reliable method for recording image intensity: photography.

Optical Density

Early work on the quantification of image intensity was related to the performance of photographic materials. Developed photographic emulsions are darker where they have been exposed to more light. However, this darkening process is not linear because the individual grains of silver halide that make up the emulsion only become developable after absorbing, not one, but two light photons within a short space of time (~1s).[16] As a result, at low exposures the number of grains exposed is proportional to the square of the **light intensity**, a term we will use here to represent the number of photons per unit area per unit time at the detector.

The **photometric response** of photographic emulsions is quantified in terms of so-called HD curves. These plot the log of the light intensity (H) against the log of the darkening (D). Figure 4.18 shows the important features of such a curve. The darkening is measured as a ratio compared to a totally clear film, using logarithmic optical density (OD) units: OD = 0 implies no darkening and all the light is transmitted; OD = 1 means that the emulsion transmits 10% of the incident light; OD = 2 implies that it transmits 1% of the incident light, etc. The use of a log/log scale allows one to describe the HD response over 4 to 5 orders of magnitude on a single plot. However, it also obscures much of the quantitative complexity of the plot and parts of it that seem "linear" would not seem so on a linear plot.

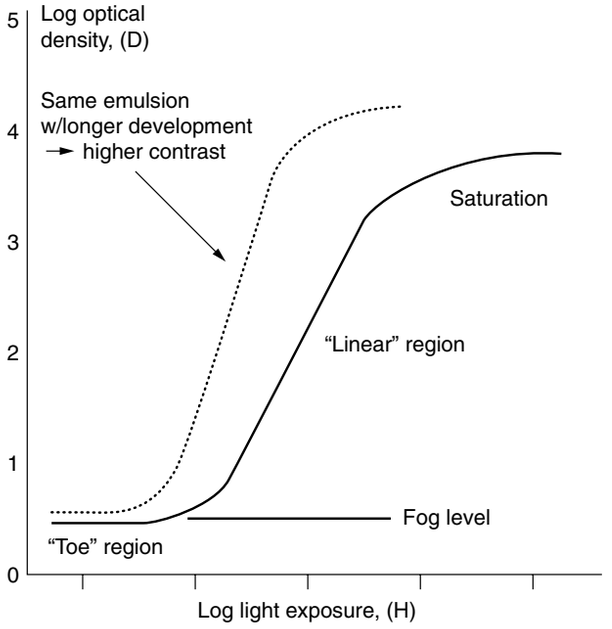


FIGURE 4.18. Photographic H–D curve.

Because there is always some background exposure of the emulsion, **D** is never "zero" but starts at the "fog" level. Small exposures produce almost no additional darkening because few grains receive two hits. Eventually, however, the log of darkening seems to become proportional to the log of exposure and the response curve enters its "linear" region. At high intensity, the response saturates for two reasons: as there are only a finite number of grains in each pixel, one cannot do more than develop all of them. In addition, as more grains are developed, they are more likely to be "behind" other developed grains and so each new grain contributes relatively less to the darkening of the emulsion. The presence of a background or noise-level signal and some sort of saturation effect at high exposure is not unique to photographic emulsions, but characterizes all types of photodetectors.

The response of a given emulsion will depend on the development conditions (type and concentration of developer, time, temperature) as well as the exposure level (light intensity × exposure time). The "linear" part of the curve becomes steeper (higher contrast) and starts at a lower exposure level if the development time or temperature is increased.

As the best photographic negatives are recorded using exposures representing H values below the center of the linear portion of the H–D curve, the transition region from the fog level to the linear region (called the "Toe" response) is of prime importance to the final result. In this region, the density is roughly proportional to the exposure squared. Of course, the photographic paper used to print the final result also has a photographic emulsion. Although print development conditions are more standardized, printing papers can be purchased in different contrasts.

In principle, one might suppose that the ideal situation would be for the paper to have an H–D response that just complemented that of the negative. The resulting print would represent a close approximation of the intensity values of the various parts of the image originally passing through the camera lens. In practice, a perfect match of these two square-law curves is very hard to achieve but this sort of compensation still occurs to some extent. For example, every camera lens transmits more light/unit area (and hence produces more darkening of the negative) in the center of the field than at the periphery. However, as this is also true of the optical system used to print the negative, the two non-linearities partially cancel out because the denser center of the negative serves as a sort of local neutral density filter.

The Zone System: Quantified Photography

Ansel Adams is justly famous not only for the beautiful images he recorded of nature but also for inventing **The Zone System** for quantifying photographic exposures and the response of various different emulsions. Each zone represents a brightness in the image being recorded that differs in intensity from neighboring zones by a factor of 2.

Adams believed that a good print could transmit information over a range of seven zones[17] and that it was important to match

[16] The response of photographic emulsions exposed to X rays, electrons, or other ionizing particles is quite linear.

[17] That is, that the brightest part of the print would reflect about $(2)^6 = 64$ times more than the darkest. This was a bit optimistic as a black print emulsion still reflects ~2%–3% and white only ~97%, a ratio of only about 1 : 30.

the range of brightness in the scene (which might be either more or less than seven zones) to the 64 : 1 range of brightness levels that could be seen in the print. This could be done by making a judicious choice of emulsion, exposure, and development conditions. While it is not appropriate here to go into all the details of this process, two aspects of this system deserve mention:

- The size of each inter-zone intensity steps relates to its neighbor logarithmically,[18] much like the eye/brain system (see below).
- The system is non-linear like the square-law response of a photographic emulsion exposed to light.[19]

Although this logarithmic response served well in photography, modern scientific imaging tends to prefer image recording systems with a linear response.

Linearity: Do We Need It?

There is obvious appeal to the idea that the intensity value detected in a given pixel should be linearly related to both the numerical value stored in the image memory and to the brightness of the same pixel when the image is finally displayed. It seems that this should be easy: most electronic photodetectors and ADCs are linear. It is also logical: how else could one represent what has been measured?

Although linearity does indeed have these advantages, there are some practical complications when applying it to electronic imaging, especially when viewing the sort of image data often encountered in fluoresecence microscopy. These complications have two sources:

1. Non-linearity is inherent in all the common methods whereby one can **view** digital image data: computer displays and grayscale or color hardcopy. In addition, there is the problem of how, or even if, one should try to account for the fact that the retinal/brain response of the eye is more logarithmic than linear.
2. Because of Poisson statistics, intensity values representing only a small number of photons are inherently imprecise; displaying as different tones, intensity steps that are smaller than this imprecision is pointless and can even be misleading. Worse still, the absolute imprecision is not constant but increases with the square-root of the intensity: the errors are greatest in the brightest parts of the image, "where the dye is."

The Goal

We start with the idea that the over-riding purpose of microscopy is to create in the mind of the observer the best possible estimate of the spatial distribution of the light intensities representing the structural features of the specimen. The question then arises as to whether or not one should bias the digitization or display processes away from "linearity" to compensate for the inherent statistical and physiological factors. We will try to answer this question with a **(very!)** quick review of some relevant aspects of human vision.

Problems Posed by Non-Linearity of the Visual System and Image Display Devices

Studies of the photometric response of the eye to light concentrate on the just noticeable difference (JND). It has been found that most people can recognize a feature that differs in brightness from its background by a fixed fraction of this background light intensity level, for example, 10%. Although there are some limitations on this response,[20] it can easily be seen to be inherently logarithmic. In addition, the number of "gray-levels" that a human eye can see is fixed by the size of the JND and the dynamic range of the image it is viewing.

Suppose that the background has 10 units of intensity, then if the feature is to be visible it will have to have either >9 or <11 units, a change of 10% or 1 unit. However, if the background is 100 units then the 10% JND step will be 10 units: 10 times bigger. No smaller increment or decrement will be visible to the eye.

How might you go about displaying the intensities 9, 10, 11, 90, 100, 110 units on a computer screen? Most computer video memories are 8 bits deep. This means that (notionally, at least) they can store and display a maximum of 2^8 or 256 different signal intensities.[21]

Suppose that we load our six intensity values into the video memory without change as the numbers 9, 10, 11, 90, 100, and 110. This will mean that the brightest part of our image uses less than half (110/256) of the numeric display range of which the display is capable. It also means that we do not utilize any of the memory levels between 11 and 89, 91 and 99 or 101 and 109, etc. Does this mean that we now have an image of 256 gray levels, of only the six levels of our object, or some other number?

Alternatively, to better utilize the dynamic range of the video memory, we might multiply the original numbers by ~2.3 before putting them into the video memory. The brightest patch would then be $2.3 \times 110 = 253$, almost at the top of the possible range. Do we now have an "8-bit" image?

What of the computer display itself? Is there a linear relationship between the number stored in the video memory and the number of photons/second emitted from the corresponding pixel of the CRT screen or LCD image display?

In a word: No! The exact relationship between these two is determined by the display manufacturer and the settings of the contrast, brightness, gamma, hue, and saturation controls. Although display standardization is possible for those working in the color printing industry, it is a very complex process seldom attempted by working microscopists, at least in part because it requires standardized room lighting. The fundamental problem for CRT displays is that, while the brightness of a pixel on the screen is directly

[18] The increment in darkening present between zones 6 and 7 represents the effect of recording 32 times more "additional photons/area" than the increment between zones 1 and 2.

[19] The steps in the brighter parts of the final image represent a larger increment of exposure than in the darker parts.

[20] We are very good at interpreting small changes in brightness at edges, but see the uniform areas on either side of the edge as shaded, even though they are not shaded. In fact, given the large number of recognized optical illusions, one must treat the eye/brain as more suitable for measuring contrast than intensity.

[21] In this discussion we will ignore the inconvenient fact that the performance of most display systems is itself limited by Poisson statistics. For instance, each "pixel" on the CRT contains only a small number of phosphor crystals, each of which may be more or less efficient at converting energy from the three beams of electrons into light. Only a very small fraction of these photons will pass through the pupil and be detected by the retina. How many actually do is subject to statistical variations. In addition, each of these three electron beams deposits only a small number (1000s?) of quantum-mechanical particles (electrons) into a small area of the tube surface during the "pixel-dwell" time. The exact number deposited is limited by Poisson statistics. Just because ignoring these complexities makes analysis easier does not mean that they are unimportant.

proportional to the amount of current in the electron beam during the time it is illuminated (i.e., the total charge deposited), this current is in turn proportional to the "3/2" power of the voltage applied to the control grid of the tube. Therefore, even if the digital number in the video memory is turned into a linearly proportional voltage at the grid of the CRT, changes in this value will produce a "more than proportional" brightness change from the phosphor.[22]

Cathode-ray tube manufacturers are aware of this problem and have developed a variety of countermeasures. The umbrella term for these efforts to introduce a compensating non-linearity in image brightness is **gamma**. In electronic imaging, gamma is a measure of the non-linearity of the relationship between stored intensity information (Fig. 4.19) and displayed brightness. It can be more or less than unity. Positive gamma stretches out changes in intensity occurring at the lower end of the intensity scale and compresses those occurring at the top of the scale. Negative gamma does the reverse. If nothing else, the presence of a gamma other than one means that shifting the average signal level up or down (using the black-level or "brightness" control) will also change the "gain" (or contrast) of the final result.

Given the uncertainty regarding the correction software used on a particular CRT, the setup adjustment of the individual electron guns themselves, not to mention differences introduced by user settings of the controls or the use of different phosphors on the face of the CRT, variations in the level and color of ambient lighting, the average user can have little confidence in the intensity linearity of most CRT displays.

The same situation is even more true for displays that incorporate LCDs, where viewing angle to the screen is an additional and important variable. Non-linearities also abound in all of the types of hard-copy renderings made using digital image printers:

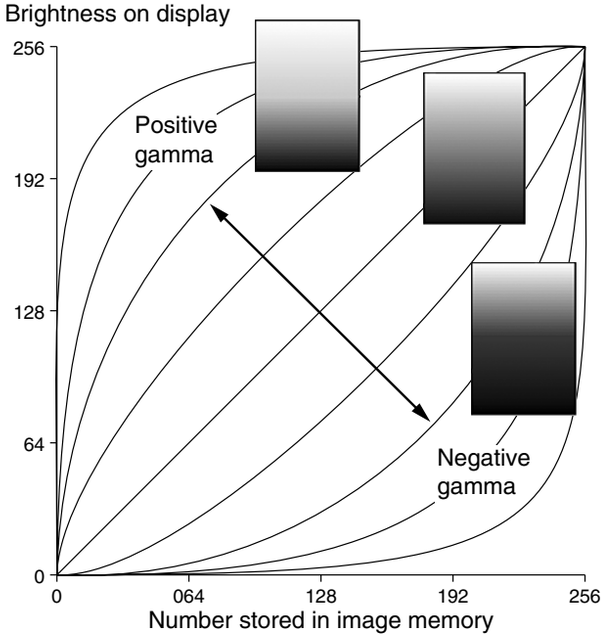


FIGURE 4.19. How the gamma control varies the relationship between input signal level and output brightness on the screen or the printed page.

[22] There are also other variables that affect pixel brightness: beam voltage (this may dip if the whole screen is bright vs. dark) or blooming (if the beam contains too much current, it will become larger, i.e., "bloom"). When this happens, central pixel brightness remains almost constant while adjacent pixels become brighter. This is not a complete list.

spectral properties of dyes, dither patterns, paper reflectance and dye absorption, etc. This topic is covered in more detail in Chapter 32.

Once one realizes that strict linearity is neither possible nor perhaps even desirable, one can move on to "distorting the gamma in a way that allows the observer to see the biological information that the image contains" while trying to be careful not to introduce irresponsible or misleading artifacts. Clearly, this is a hazy area in which much discretion is needed. The topic of responsibility when processing images is discussed in Chapter 14.

Matching the Gray Levels to the Information Content of the Image Data

When Ansel Adams developed the Zone System, no consideration was given to limitations on the recorded intensity other than the exposure conditions (exposure time and lens aperture), and the intrinsic illumination and reflectivity of object. This attitude was justified because the exposure of a single pixel on the large-format negatives he used involves the absorption of thousands of photons by a small fraction of the millions of silver-halide grains located there. As a result, statistical variations in this number (i.e., square root of the number of developed grains) were likely to be small compared to the 10% JND. The same was true of the printing papers.

In live-cell microscopy generally, and confocal fluorescence microscopy in particular, this condition is often not met. The fluorescence signal is inherently weak—about a million times less intense than the excitation light used to produce it. Although this limits the **rate** at which data can be produced, bleaching and phototoxicity may impose even more stringent limits to the total recorded intensity. **In other words, the imaging modality imposes absolute limits on the total number of photons that can be detected.** As a result, in biological fluorescence microscopy, we are usually starved for photons. In laser confocal microscopy, it is not uncommon to collect only 10 to 20 photons in the brightest pixels and zero or one photon in the unstained regions that often constitute a large majority (<99%) of the pixels in a particular scan.

Suppose that the signal in the **brightest pixel** of a confocal fluorescence image represents only **16 photons** (not an unusual figure). As we do not have negative photons, and even though we are collecting these data into an "8- or 12-bit" image memory having 256 or 4096 possible intensity intervals, respectively, one cannot imagine that an image in which the highest intensity was only 16 detected photons could possibly have more than 16 meaningful gray levels corresponding to 1, 2, 3, . . . 16 photons.

However, because the counting of photons is a quantum-mechanical event and hence limited by Poisson statistics, the number of "meaningful" intensity steps in this signal is even less. The brightest recorded signal is really 16 ± 4. The next dimmer signal level that can be discriminated from it by at least one standard deviation (σ), is 9 ± 3. With a 16-photon peak signal, we can discriminate only four "real" signal levels. These correspond to the levels 1 ± 1, 4 ± 2, 9 ± 3, and 16 ± 4.

This is really quite inconvenient. What can be done if the staining levels of our specimen, as modified by the CTF of our microscope, do not coincide with this square-law of statistical detectability? There is only one option: to collect more signal (more dye, longer exposure, etc.) or average the data in space over the <64 voxels that represent the whole, Nyquist-sampled, 3D PSF by **deconvolving** it as discussed above and, in more detail, in Chapter 25.

Beyond this, the only strategy is humility: Don't base great claims on the detected brightness of one or even a few pixels but on patterns visible in a number of images from many specimens.

GRAY LEVELS IN IMAGES RECORDED USING CHARGE-COUPLED DEVICES: THE INTENSITY SPREAD FUNCTION

The data recorded using CCD detectors for widefield /deconvolution are subject to similar limitations. Conventional CCDs have higher quantum efficiency (QE), but much higher readout noise, than the photomultiplier tube (PMT) detectors used in most single-beam confocals. The higher QE increases the number of detected photons (thereby reducing the effect of Poisson noise) but the presence of substantial read noise reduces the number of useful gray levels substantially below what one would estimate from Poisson noise alone. Read noise becomes even more important when excitation levels are lowered to reduce phototoxicity. Because both the sources and the form of the noise signals are quite different in each detector, it has been difficult to make comparisons that are both simple and informative and the recent introduction of the "electron multiplier" CCD readout amplifier (EM-CCD) has made comparisons even more complex. The discussion that follows describes an effort to define a suitable measure of overall photodetector performance.

What Counts as Noise?

Just what counts as "noise" in the context of fluorescence microscopy is far from settled. Should one count as noise the signal from non-specific staining? From stray or reflected light in the microscope? Fixed-pattern noise traceable to stray magnetic fields or electronic interference? Even among practicing microscopists, it is not uncommon for "noise" to become an umbrella term for anything that makes an image resemble the "snowy" output of a television receiver displaying the signal from a distant station. Although a variety of very different physical processes can produce such a "noisy" signal, only some of these can be related to defects in the performance of the detector/digitizer system. For example, it is common to hear that turning up the gain of the PMT makes the confocal image "noisier." It would be more proper to say that the fact that the PMT needs to be so high is an indication that the signal itself must be very weak and hence must contain a very high level of Poisson noise.[23]

In the discussion that follows, three types of noise will be considered:

- Poisson noise: the irreducible minimum uncertainty due to quantum mechanics.
- Readout noise: assumed to be random fluctuations in the electronics and virtually absent in the PMT and the EM-CCD.
- Quantum efficiency: Although many people think of QE as totally separate from noise, because it reduces the number of quantum mechanical events sensed, it increases the effect of Poisson noise.

One can define noise in any imaging system as that part of the electronic output of the detector that is not related to the number of photons detected per unit time and/or space. However, as the electronic signal from the PMT is digitized in a very different way from that of the CCD, it is much more useful to compare the performance of these detector systems not in terms of the signal from the detector but in terms of the number that is measured by the ADC and stored in the image memory to represent the brightness of a single pixel.

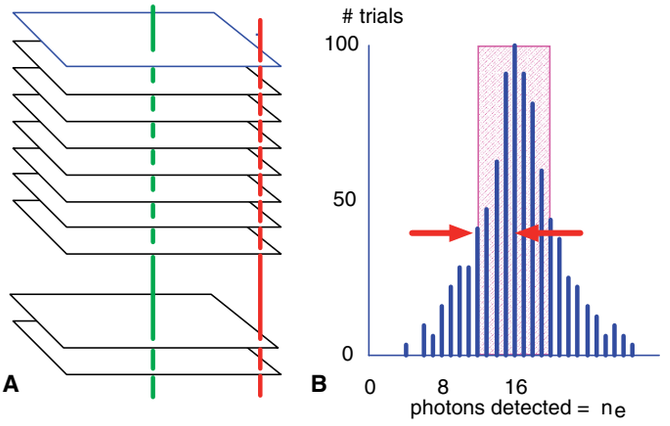


FIGURE 4.20. The ISF for a signal of 16 ± 4 photons/measurement. (A) About 700 identical exposures are acquired. The values collected at few particular pixels (red and green lines) are then converted from ADU units in the computer, to photoelectrons (n_e) and assembled to form a histogram (B). This example shows the number of photons absorbed at pixel p, assuming that, n_e, was 16 electrons/pixel and there is no read noise. Approximately 63% of the trials yield a value for n_e in the range of 16 ± 4 or between 12 to 20 (pink-shaded box). The halfwidth of this distribution (red arrows) equals the RMS noise of this measurement. The remaining 37% of trials yields a value outside this band.

Suppose that the average number of photons striking pixel, p, of a CCD during a number of identical exposure periods is n_p. This exposure will excite a number of electrons, n_e, into the valence band in the location of p, where n_e is smaller that than n_p because the QE is always less than 1. In fact:

$$\frac{n_e}{n_p} = \mathrm{QE} \qquad (1)$$

One might imagine that the best we can do is to measure n_e. However, as noted above, even this is impossible because the absorption of a photon is a quantum mechanical event and therefore the number absorbed on any given trial will not be constant but will vary according to Poisson statistics. If the average number of photons is 16, the histogram of numbers of photons actually absorbed on a given trial versus the number of times when this number was detected will look like Figure 4.20.

The hatched area denotes the ± 4 electrons band of values that corresponds to the $\pm\sqrt{16}$ imposed by Poisson statistics. On average, 63% of the trials should give values that lie within this band. Although only a small fraction of these trials (about 100) will yield what we have defined to be the average value (16), it is important to recognize that even a perfect photodetector (i.e., one with a QE = 1 and no measurement noise), could never record data any more accurate than this.[24]

[23] Unless, of course, the PMT is faulty and actually generates noise when high voltages are applied.

[24] The analysis also holds for a PMT used in the photon-counting mode and assuming that the number 16 refers to the average number of photons actually counted. As there is essentially no readout noise in such a PMT, the analysis stops here.

Other characteristics of the photodetector, such as the presence of measurement noise or imperfect digitization, can only move the distribution to the left and also widen it compared to its mean value. For example, if the QE were only 25% rather than 100%, the recorded values would cluster about four detected photons rather than 16 and the error bar would be ±2 photons — a 50% likely error that is twice that of the perfect detector (16 ± 4 represents a 25% error). Indeed, because the ratio of the peak value of this histogram to its width is a function of both the QE and the measurement noise, and also because it measures directly the accuracy of the detector in determining the number of photons associated with pixel p, this ratio of peak (also the mean) to its standard deviation (SD) provides a perfect metric for comparing the performance of the different types of photodetectors used in fluorescence light microscopy.

In analogy to the term point spread function (PSF), this metric is called the intensity spread function (ISF). Both concepts have an ideal result: the ideal PSF is the 3D Airy figure for a given NA and wavelength. The ideal ISF is the Poisson distribution for a given number of quantum events. In each case, it is easy to compare the actual result with the ideal.

The ISF is the ratio of the halfwidth at half maximum of the histogram of the intensities recorded from one pixel, Δn_p, on sequential "reads" of a constant signal, to the mean value of this signal, n_p, all calibrated in photoelectrons. The ratio of number of electrons actually counted is converted to photons using published QE curves.

$$\mathrm{ISF} = \frac{n_p}{\Delta n_p} \qquad (2)$$

MEASURING THE INTENSITY SPREAD FUNCTION

It is important to understand that the ISF is only a meaningful measure of detector performance if the graph is calibrated properly in terms of photoelectrons rather than arbitrary computer units. Only quantum mechanical events follow the Poisson distribution. This next section discusses how such calibration can be carried out.

Calibrating a Charge-Coupled Device to Measure the ISF

Because the readout noise of the conventional scientific CCDs used in microscopy is in the range of ± 3 electrons RMS to ± 15 electrons RMS, there is no way to discriminate the signal from a single real photoelectron from that of none. As a result, the gain of the amplifiers leading up to the ADC is usually adjusted so that the smallest digitizing interval (analog-digital unit or ADU) is equal to somewhere between half and all of the RMS noise value (sort of Nyquist sampling in "intensity space").[25] The specification defining #electron/ADU is called the gain setting. In other words, if the read noise is quoted as ±6 electrons RMS, then the gain setting should be in the range of 3 to 6 electrons/ADU. On the best cameras, this gain setting is measured quite accurately at the factory as part of the initial CCD setup process and is usually written on the inside cover of the user manual.

If this is not the case, a fair approximation of the gain setting can be calculated if one knows the full-well (maximum signal/pixel) of the CCD and the dynamic range, in bits, of the camera system as a whole. Suppose that the full-well signal is 40,000 electrons and the camera uses a 12-bit digitizing system. As 12-bits implies 4096 digitizing intervals, and, assuming that the pre-ADC, electronic, gain has been adjusted so that a 40,000 electron/ pixel signal will be stored as a value slightly less than 4096, one can see that the an increment of 1 ADU corresponds to ~10 electrons/ pixel (Fig. 4.21).[26]

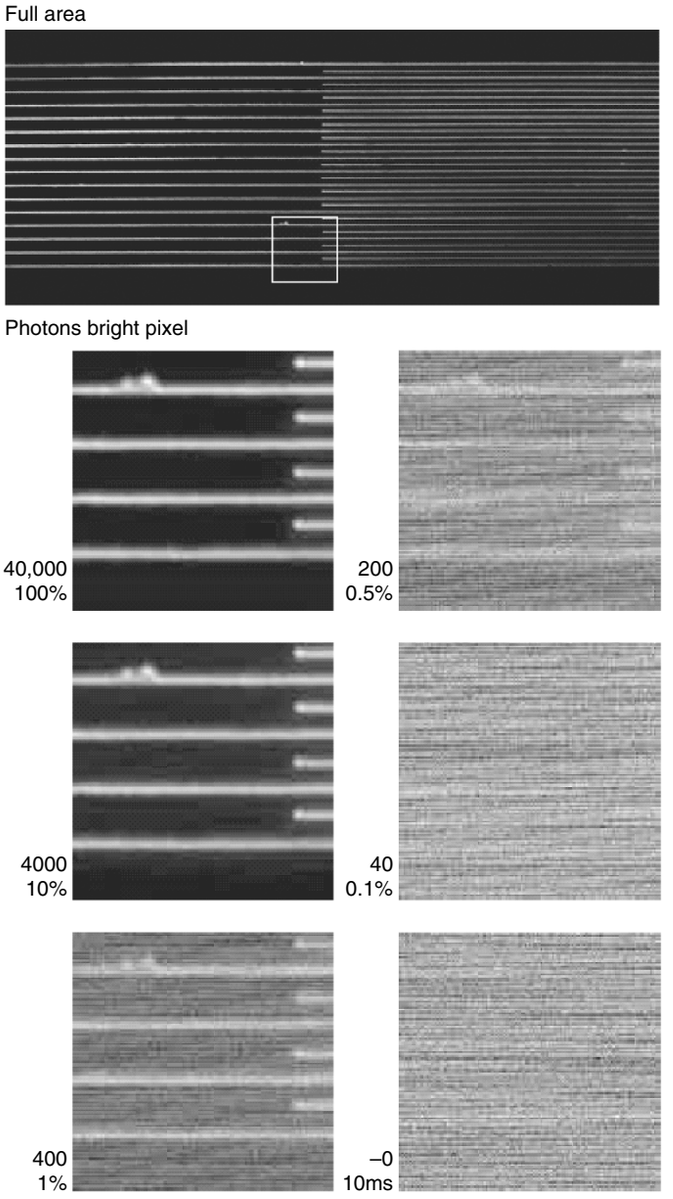


FIGURE 4.21. Bit depth and CCD camera performance. The top image was recorded using a "12-bit" CCD camera with a "full-well" (brightest) signal level of 40 k electrons/pixel. Subsequent images were recorded with the same light level but steadily shorter exposure times. Although one might expect the camera to have a S/N of about 4000 : 1 (i.e., 12-bits), the image disappears into the noise when the peak signal is reduced by a factor of only 1000 (10-bits).

[25] Another factor is that ADCs tend to be made with certain fixed levels of resolution, 12-bit, 14-bit, etc., and as this feature can be "sold," it is sometimes the case that the CCD noise level spans 8 or even 16 ADU.

[26] The uncertainty is due to the practice of setting up the system so that a zero-photon signal is recorded in the image memory not as zero but as some small positive value. This prevents lost data in the event that the zero signal level drifts downwards.

Once one knows the scaling factor between digitally recorded intensities and electrons, one merely has to acquire some image data and plot an intensity histogram, as shown in Figure 4.20. Continuing the example above, one can convert the digital image data to "electron data" by multiplying the value in every pixel by 10.

"Fixed-Pattern" Noise

Although one might assume that one could measure the read noise by calculating a histogram of all the pixel intensities (converted to electrons) in a single image made with no light striking the CCD, this is not so. All the pixels on a CCD are not equal. Charge packets from pixels on the corner of the array farthest from the read node must be transferred many more times than charge packets from pixels near the read node. More transfers take a longer time and this increases the dark current in far pixels versus near pixels. Variation in dark current is just one of a number of factors that can produce the fixed-pattern noise signal. Fixed-pattern noise differs from read noise in that its form is somewhat predictable over time and consequently it can be virtually eliminated by "flat-fielding." Flat-fielding is a digital normalization process that compensates for variations in the dark current (offset or dark level) and sensitivity on a pixel-by-pixel basis. For weak images, in which pixel-to-pixel sensitivity variations are small compared to Poisson noise, this can be accomplished by subtracting a dark image, made by averaging many dark fields, from each recorded image.

To generate the data needed to plot an ISF histogram similar to that in Figure 4.20, one should not use intensity values from all the pixels of a CCD exposed to a "uniform" light signal for two reasons. Not only is it very difficult to create such a uniform signal, but the fixed-pattern noise will usually produce much more spread in the ISF than the read noise. Therefore, one must make the ISF histogram using data from **sequential** brightness measurements obtained by reading a specific pixel many times in succession.

On a 3D deconvolution system, this can be accomplished by recording as a 3D data stack a long time-series (~100 frames) of "black" images, each using the shortest possible exposure time. To obtain the set of intensities recorded from a single pixel, extract the values along a "line" oriented in the time direction in the X, Y, T data stack. As no signal photons reached the detector during these exposures and the short exposure time keeps the dark current low, the signal is shown centered on zero intensity.[27] The horizontal scale has been calibrated using the value of 2.5 electrons/ACU provided by the manufacturer. The read noise specification for this camera is ±5 electrons and this tallies well with the width of the peak in the histogram. The bottom horizontal scale is calibrated in photons, using the quoted QE of this chip at this wavelength: 40%.

The histogram should vary only slightly as the *x*- and *y*-coordinates of the vertical line are varied. In general, the noise measured in this way will be lowest in the corner of the image closest to the read node (usually the top left corner of the image on the screen), and highest in the opposite corner.

As the ISF includes the effect of errors caused by both read noise and Poisson noise, it can be used to estimate the error at any signal level. Those interested in live-cell light microscopy often operate their system so that the maximum recorded signal is less that 10% of the CCD full-well capacity (i.e., only 4000 ± 63 electrons/pixel). Under these conditions, ISF performance at low signal levels becomes important. Those using a CCD camera to record the image from a disk-scanning confocal may have a peak signal of only 10 to 100 photoelectrons.

To simulate this situation, expose the camera to uniform illumination, sufficient to fill all the pixels with a signal that is (on average!) just 10 times the read noise level (50 photons or 20 ADU, in our example). This can be done by setting up a microscope for transmitted light illumination with a clear specimen and using ND filters and the CCD camera shutter control to reduce the recorded intensity sufficiently. This may require a darkened room and it is also important to use a regulated DC supply on the transmitted light source so that all the exposures in the series are exposed to a constant light level.

This second histogram should cluster around an intensity that is 50 electrons. At 2.5 electron/channel, this would be 20 channels to the right of the center of the zero-signal histogram. It should be wider than the first histogram because now it contains ±7 electrons of Poisson noise in addition to the read noise. To the extent that the read noise signal really is random or "white" (i.e., that it does **not** have some fixed pattern caused, for example, by flickering in the light source), these two RMS noise signals should be added as the square-root of the sum of their squares. Therefore, when scaled in electrons, the width of the distribution will now be $\sqrt{(25+49)}$ or about ±8.1 electrons (or ±3.2 channels).

Although it is not possible to use this setup to measure the QE directly, comparative measurements between different cameras are possible. As QE is a strong function of wavelength, one should use a narrow bandpass filter [such as the interference green filter used for critical differential-interference-contrast (DIC) imaging] in addition to the ND filters.[28] It is also necessary to compensate for the pixel dimensions: larger CCD pixels collect more photons, have higher full-well capacities, and somewhat higher read noise. However, as the CCD must be coupled to the focus plane in the object by an optical system having the magnification required to make the CCD pixels satisfy Nyquist, pixel size *per se* is not of fundamental importance. In general the QE curves published by the chip manufacturers are hard to improve on.

GAIN-REGISTER CHARGE-COUPLED DEVICES

In January 2001, Marconi introduced the CAM 65, a CCD camera incorporating a new type of charge amplifier (Lamontagne, 2004; Robbins and Hadwin, 2003).[29] The heart of this device is a new solid-state electron-multiplier amplifier. The electron multiplier is essentially a second horizontal register, located between the output of the normal serial (horizontal) register and the input of the charge amplifier. Because it has an extra, grounded phase between charge-transfer phases 1 and 2, and a higher and variable voltage (35–45 volts vs. the normal 5–15 volts) on phase 2, electrons must pass through a high field region when passing from phase 1 to phase 2. As a result, there is a small (~1%) chance that collision amplifi-

[27] CCD electronics are usually set up so that the "no-light" signal is centered on a value somewhat above zero, usually about 50 ADU. This assures that signal will not be lost even if amplifier drift were to cause the peak of this distribution to drift to a lower value.

[28] All these instructions assume use of a monochrome CCD. Because of the complex way that signals from adjacent pixels, each equipped with a different colored filter, are interpolated to produce the final color image, noise in single-chip color CCDs is quite complex. As a first approximation, one could expose a color CCD to one color at a time, and calculate the ISF for each one.

[29] More info at: http://e2vtechnologies.com/technologies/13vision.htm

cation will occur. Therefore, the electron multiplier operates as a series of 500 to 700 very-low-gain avalanche diodes.[30]

When the light signal is low, the phase 2 voltage can be increased to multiply each charge packet by from 200× to 4000×. This process increases the signal from even a single PE well above the noise floor of the normal FET read amplifier, and does so even this amplifier is operating at a very high readout speed (10 to 35 MHz).

Because the EM-CCD reads out fast without high read noise, it makes focusing and searching quick and easy. Because each charge packet always remains separated from all others, EM-CCDs have full spatial resolution, and as the gain of the register can be varied, the device "can be made as sensitive as needed." Of course, if one reads out fast, there may not be enough time to accumulate much signal but this cannot be blamed on the camera.

This system breaks the old rule that scientific CCDs have more readout noise when they read out faster.

There **is** one snag.

Multiplicative Noise

The charge amplification of the gain register is not quite "noise free" because the exact amount that each electron in the packet is amplified depends on probability.

The gain-per-charge-transfer is very low: about 1%/stage. A charge packet containing 100 electrons, would, on average, contain 101 electrons after one transfer. Big deal! Why bother? Because, after 500 or 600 transfers, the average total gain can reach more than 1000×. However, some electrons do not get amplified very much while others get amplified a lot (more like the stock market than a bank!!). This gives rise to "multiplicative noise." Given a series of charge packets, each containing only a single electron, the spectrum of pulse heights at the gain register output follows a decreasing exponential with many small pulses and fewer large ones (several useful, online references are available at: http://e2vtechnologies.com/technologies/l3vision.htm). (See Figure 4.22.)

The multiplicative noise generated by this type of pulse-height distribution has the same form and magnitude as Poisson noise. As RMS noise terms are added as the square-root of the sum of the squares, the output of the gain register has 1.41× the uncertainty present in the input PE signal. Because the only way to overcome this loss in precision is to count twice as much signal, one can think of the entire system **acting as if** the amplifier were noise-free but the sensor QE is only half its actual QE.[31]

The back-illuminated sensors now available have an intrinsic QE of about 85%, or effectively 42% when used in the EM-mode. This is still very good compared to the PMT, especially in the red end of the spectrum.

The 50% reduction in effective QE only occurs when the gain-register amplifier is used. If it is turned off, the CCD QE operates as advertised, but the read noise now depends on the FET amplifier and will increase with readout speed.

Multiplicative noise also occurs in the PMT because the gain experienced by each electron at each dynode is also subject to statistical noise. Suppose that an electron from the photocathode (PE)

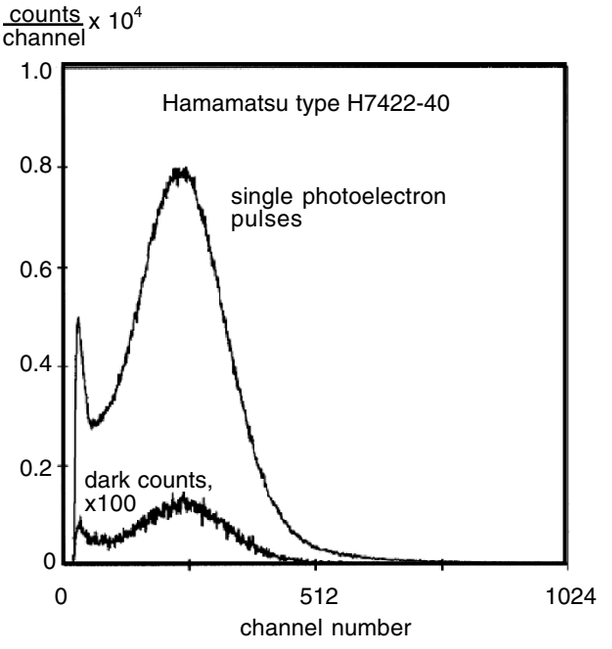


FIGURE 4.22. Single PE pulse-height spectrum.

produces an average of 16 secondary electrons (SE)/pixel on striking the first dynode. In fact, the number of SE arriving at the second dynode for a particular PE is governed by Poisson statistics: that is, it will be 16 ± 4. This uncertainty occurs at every dynode but it is most important at the first dynode because the number of quantum events is smallest there. Not surprisingly, after the pulse has propagated down the rest of the multiplier section, a PE that sent 20 SE to the second dynode is likely to produce a larger final pulse height than a PE that only produced 12 SE. The result is that single-PE pulses from the PMT may vary in size over a range of 10 : 1, although they will cluster around a mean value.[32] Because the gain/stage is much higher in a good PMT than in the gain register (more like 5×–10× than 1.01×), the single-PE pulse-height distribution has a distinct peak (Fig. 4.6). As a result, multiplicative noise adds only about 20% to the Poisson noise and the **effective QE** of a PMT is consequently reduced to about 70% (1/1.41) of that claimed by the manufacturer's QE curves.[33]

As used in the laser confocal, PMT multiplicative noise has another, more insidious, essentially psychological, effect. Although the histogram of the pixel intensities in a "normal" stored confocal image may show some pixels recorded at virtually every ADU level from 0 to 255, the image commonly represents a peak

[30] See Chapter 6 and Appendix 3 for definitions of phase I, etc.

[31] A more complete analysis of the noise produced by this detector can be found at http://www.marconitech.com/ccds/lllccd/technology.html. Try the third article: "Sub-Electron Read Noise at MHz Pixel Rates: University of Cambridge • Date: Jan 2001 • Filesize: 650 kb.

[32] PMT suppliers can provide a single PE pulse-height distribution graph for any type of tube. A good tube will have a "valley" between the single-PE peak and the electronic noise peak (near zero size) that is less than 33% of the peak height.

[33] Actually, it is worse than this, because the published QE curves are "best performance" not average performance, and they refer only to photoelectrons leaving the photocathode, per incoming photon, not photoelectrons that actually reach the first dynode and result in charge multiplication. About 30% of the electrons leaving the photocathode fail to reach the first dynode and propagate. This loss further reduces the effective QE.

TABLE 4.1. Theoretical Intensity Function (ISF) Values for Various Photon Signals to Compare Performance of a "Conventional" Scientific CCD, a "Gain-Register" CCD, and a PMT, Calculated as Per Discussion in Text. Bold Numbers Show Best Performance

	Slow Scientific CCD		Charge-Multiplier CCD (Optimal)		Charge-Multiplier CCD (Available)		PMT	
Signal (Photons)	Signal (PE)	ISF	Signal (PE)	ISF	Signal (PE)	ISF	Signal (PE)	ISF
5	4	.63	2		1	1	(0.5)	
10	8	1.2	4	**2**	2	1.41	1	1
20	16	2.2	8	**2.8**	4	2	2	1.41
45	36	**4.2**	18	**4.2**	9	3	4.5	2.1
80	64	**6.4**	32	5.7	16	4	8	2.8
100	80	**7.4**	40	6.3	20	4.5	10	3.1

signal of only about 10 photoelectrons. Were it not for the multiplicative noise in the PMT,[34] the operator would be alerted to the low signal level by the "posterizing" effect of having at most 10 gray levels displayed. The presence of multiplicative noise gives the illusion of a full gamut of "gray levels" when in fact the data are insufficient to define more than three or four levels at one-standard-deviation precision.

In large part, the ISF was developed to compare the photodetector performance of confocal microscopes employing EM-CCDs with those using PMTs.

At zero light level, the halfwidth of the ISF is equal to the read noise level. Although the ISF itself will vary with the signal level, a few standard signal levels could be chosen (say 10 or 100 photons/pixel) to specify detector performance.

Alternatively, as there seems to be a general trade-off between QE and read noise, one could calculate or measure the "crossover" signal level at which equal ISF performance should occur on two detectors. Given a 100 photon/pixel input, a perfect detector would have an ISF of 10 (i.e., QE = 1 and only Poisson noise, and ISF = $\sqrt{100}$). A real gain-register CCD with an effective QE of 40% and no read noise, would have an ISF of about $40/\sqrt{40}$, or 6.3. A conventional scientific CCD with a QE of 80% and a "white" read noise of ±6 electrons would have a Poisson noise of ±9 electrons, and an ISF of $(80/\sqrt{(36+80)} = 80/11$, or about 7.3. Other values are listed in Table 4.1, above.

Unless high read speed is important, Table 4.1 shows that a normal CCD with the parameters stated will yield more accurate data (higher ISF) for any signal greater than about 45 photons/pixel.

The situation is graphed in Figure 4.23 which shows a "mean-variance" plot of the noise of an EM-CCD camera operated with no gain, low-gain, and high gain (Janesick, 2001). It shows how the "noise" (as measured by the variance) varies with the signal level (in PE). The low-gain is the noisiest overall. The no-gain is least noisy above a signal level of ~20 PE (or ~45 photons) because the effective QE is higher with no EM amplification. However, below this level, the high-gain camera becomes increasingly superior as the signal level approaches zero. Because the EM-CCD effective QE is about three times higher than that of a PMT, this represents the high end (!) of the signal range of a confocal microscope.

Although this may sound like bad news for the EM-CCD, in fact, for a CCD camera on a disk-scanning confocal, the peak signal level may indeed be <45 photons/pixel/frame time (or indeed, less than 4!). Although 45 photons/pixel may not sound like much, remember that as long as the pixels (or voxels) are the correct size to meet the Nyquist sampling criterion (see Chapter 4, *this volume*), the 3D image of a single point object will produce significant counts in at least 64 to 125 voxels. Assuming proper digital filtering of the stored data before it is displayed, this means that at least 45 × 64 = 2880 photons will reach the photodetector from each "bright" point. Between 1152 and 2304 of these will be "detected," giving statistical accuracy in the 3% to 4% range.

In this simulation, the PMT never provides the highest ISF. In fact, it will do better than a gain-register CCD at very low **average** photon fluxes (~1 PE/ pixel) because its dark current and read noise is actually about 10× lower than the EM-CCD. Both the PMT and the EM-CCD are well-suited for confocal imaging because they measure zero light very accurately and this ability matches well with the fact that most voxels contain no stain.

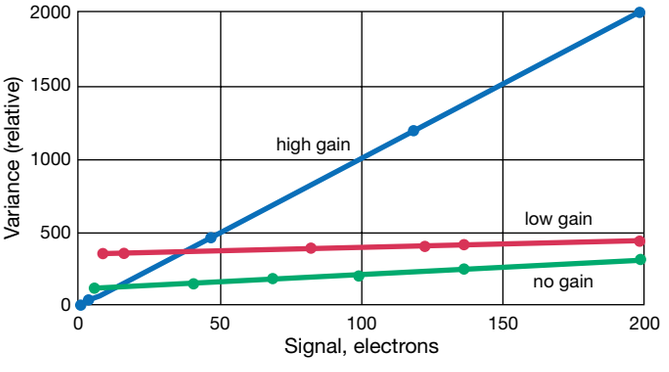


FIGURE 4.23. Mean-variance curves of an EM-CCD camera operated with no gain (green), low gain (red) and high gain (blue). The variance is a measure of the uncertaintly of the brightness measurement, obtained by subtracting two sequential CCD images of a flat "white" scene. The mean signal is the average value of the scene, calibrated in PE. One can easily see the greater accuracy provided by high-gain operation when detecting signal lower than ~20 PE. These plots kindly collected and provided by Colin Monks, Brian Bodensteiner and Pavani Korada (Intelligent Imaging Innovations, Denver, CO).

[34] Or if it were used in the photon-counting mode, which eliminates multiplicative noise by counting all single-PE pulses the same. Unfortunately, pulse-counting systems are usually by pulse-pileup limited to peak count rates of ~30 MHz. This means that in a 1 µs pixel time, 50% of a 15 counts/pixel signal would be lost to pileup.

TRADE-OFFS

Digital microscopy performance is dependent on three factors that have nothing directly to do with the specimen: optics/diffraction, photon statistics, and digitization. Unfortunately these three factors always interact. Although it is possible to make very poor digitization choices that substantially reduce the quality of the data collected (e.g., using less than Nyquist sampling or failing to count as much of the photon signal produced as possible), it is unfortunately the case that, even when one does everything right, there are still trade-offs. Assuming that the resolution is determined by the Abbe equation, this determines the pixel size needed to record data up to the Abbe resolution level. However, one will still not be able to visualize features separated by this distance unless the sample can provide enough photons. The intensities recorded in the pixels defining any small structure can only be determined approximately. If the false "contrast" produced by Poisson noise and read noise becomes comparable to the contrast of the image feature, the feature will become invisible. The only possible escape from this conundrum is ALWAYS to deconvolve 3D data and filter 2D data as this will eliminate artifactual "out-of-bandwidth" features and effectively average out the Poisson noise over the number of Nyquist voxels needed to define the central peak of the 3D Airy figure (see Chapter 25, *this volume*).

If low signal levels make seeing small details impossible, use bigger pixels (lower the zoom magnification, "bin" the CCD, or change its coupling tube magnification) and count more photons in each, bigger pixel. This will give you better statistical accuracy for the same damage level and it won't really reduce the spatial resolution because resolution is now limited more by counting statistics than by diffraction, or under-sampling. It will also have the added bonus of either a shorter scan time or a larger recorded field of view.

In live-cell microscopy, you can't have it all!!

ACKNOWLEDGMENTS

Thanks are due to Dr. Alan Hibbs of BioCon (Melbourne, Australia), who provided Figure 4.2, to Dr. Felix Mangadaut (Zurich) for Figure 4.16, to Zach Charlop-Powers (Madison) for Figure 4.21, to Dr. Stephen Gammie from the University of Wisconsin-Madison Zoology Department for letting me use his AxioCam to record the data used for Figure 4.21 and Colin Monks, Brian Bodensteiner and Pavani Korada (Intelligent Imaging Innovations, Denver, CO) for Figure 4.23.

REFERENCES

Janesick, J., 2001, Scientific Charge Coupled Devices, SPIE Press, Bellingham, WA. Vol. PM83 1–920 pages.

Lamontagne, N.D., 2004, Is it right for you? *Biophotonics International*, 11(1):38–42.

Nyquist, H., 1928, Certain topics in telegraph transmission theory. *Trans. AIEE* 47:617–644.

Robbins, M.S., and Hadwen, B.J., 2003, The Noise Performance of Electron Multiplying Charge Coupled Devices, *IEEE Trans. Elect. Dev.* 50(5): 1227–1232.

Shannon, C.E., 1949, Communication in the presence of noise, *Proc. Inst. Radio Eng.* 37:10–21.

5

Laser Sources for Confocal Microscopy

Enrico Gratton and Martin J. vandeVen

INTRODUCTION

Laser assisted confocal microscopy has made a lot of progress over the past few years. Laser systems have become more modular and compact. There is an ever-increasing number of available laser excitation lines as well as an improvement in user friendliness and ease of use. At the same time, expansion of Web resources has provided easy access to a wealth of information. Our goal is both to aid the experienced and novice microscopist in quickly locating and sorting through the relevant laser information and to provide a means of avoiding common problems and pitfalls in the use of laser excitation in the various fluorescence techniques such as fluorescence correlation spectroscopy (FCS), fluorescence lifetime imaging microscopy (FLIM), fluorescence loss in photobleaching (FLIP), fluorescence recovery after photobleaching (FRAP), optical coherence tomography (OCT), second harmonic generation (SHG), single molecule detection (SMD), and single particle tracking (SPT). In this chapter we describe the characteristic properties of a number of lasers commonly used in fluorescence microscopy. We concentrate on the characteristics of lasers in relation to their use as an illumination source for microscopy. Compared to other sources emitting electro-magnetic radiation, such as hot filaments, arc lamps, and light-emitting diodes (LEDs), lasers have a number of unique properties, which make them an almost ideal light source for use in confocal microscopy. These properties are:

- high degree of monochromaticity
- small divergence angle
- high brightness
- high degree of spatial and temporal coherence
- plane polarized emission (for many types)
- a Gaussian beam profile (in some cases this requires special optics).

In the 40 years since the realization of the first experimental laser, a wide and still rapidly expanding variety of lasers has been developed. Currently very rapid development of miniaturized, easy-to-use, tunable "pocket" lasers is taking place. These small convenient lasers are in the process of replacing many of the large laser systems still in use.

Available laser systems cover an extremely wide range, differing from each other in physical size, principle of operation, and optical, temporal, and mechanical properties, such as beam divergence, output power, polarization properties, duty cycle, stability of the beam, and vibration sensitivity. These characteristics are related to the mechanical design, emission wavelengths and tunability, ease of operation, maintenance costs, reliability, and safety aspects. This chapter introduces the microscopist to the operation of the laser, the most important laser parameters, their influence on the quality of the confocal image, and methods to create wavelength-tunable light sources. In addition, laser systems for second harmonic generation and optical tweezers are described.

LASER POWER REQUIREMENTS

First, we need an order of magnitude estimate of the emission intensity that can be obtained in fluorescence microscopy using 1 mW of input light. The amount of laser power needed depends crucially on the quantum efficiency of the contrast medium being studied. The most common contrast factors are sample fluorescence and backscatter.

It is convenient to express the quantities in terms of photons/(s $*$ pixel $*$ mW) of incident light at a given wavelength because the intrinsic dark noise of modern detectors is often specified in similar units. Also, expressing the flux per pixel provides a quantity that is independent of the illuminated area. The following are useful relationships:

- Energy of one photon: $h\nu = hc/\lambda = 4 \times 10^{-19}$J at $\lambda = 500$nm
- 1 mW of light intensity at 500 nm represents $2 \times 10^{+15}$ photons/s

On a widefield image of 1000×1000 pixels, 1 mW of incident light, uniformly distributed, is equivalent to

- flux per pixel = 2×10^9 photons/(s $*$ pixel $*$ mW) at 500 nm

There are two considerations. First, how many photons will be emitted per pixel? Secondly, how many photons can be tolerated per pixel before saturation of the fluorescent molecules occurs?

Let us analyze the first question. Using fluorescein, one of the most common probes, the molar extinction coefficient is about 100,000/cm of optical path. Assuming an effective optical path of about 1 µm (the depth of field), the molar extinction is about 10. The local concentration of fluorescein can vary, depending on the spatial location and the degree of labeling. Assuming that a

Enrico Gratton • University of Illinois at Urbana-Champaign, Department of Physics, Laboratory for Fluorescence Dynamics, Urbana, Illinois
Martin J. vandeVen • Department of Cell Physiology, Microfluorimetry Section, Biomedical Institute, Hasselt University and Trans National University Limburg, and Institute for Materials Research IMO/IMOMEC, Diepenbeek, Belgium

 Handbook of Biological Confocal Microscopy, Third Edition, edited by James B. Pawley, Springer Science+Business Media, LLC, New York, 2006.

concentration of $10^{-5}M$ is reasonable, the optical density (OD) of a 1 µm path length is ≈ 10^{-4}. The number of photons absorbed is then

$$\text{photons absorbed} = (\text{flux per pixel}) \times (\text{OD}) = 2 \times 10^5/(\text{s} * \text{pixel} * \text{mW}) \text{ at } 500\,\text{nm}.$$

Assuming a quantum yield of 0.8 and a collection efficiency of 10%, the detector receives

$$\text{photons at the detector} = 1.6 \times 10^4/(\text{s} * \text{pixel} * \text{mW of incident light}).$$

Given the quantum efficiency for a good detector (10% at 500 nm), the final detected photon flux should be about

$$\text{flux detected} = 1600 \text{ photons}/(\text{s} * \text{pixel} * \text{mW of light}).$$

This flux should be compared with the dark noise of most detectors, which can vary between 10 and 100 equivalent photons/(s ∗ pixel). In our estimation, the only quantities that can vary over a wide range are the power of the laser and the effective concentration of the probe. Lasers can have up to watts of power and the concentration of the probe can be higher than we have assumed. The efficiency of detection is usually smaller than we estimate and the noise can be larger. The purpose of our calculation is to give a rough idea of the kind of power that a laser must furnish to be usable for fluorescence detection in confocal laser scanning microscopy (CLSM). Tsien and Waggoner (Chapter 16, *this volume*) find an optimal power with the best signal-to-noise ratio (S/N) with respect to autofluorescence and elastic and inelastic scattering of 76 µW at 488 nm and 590 µW, as long as triplet formation is neglected. Therefore, a laser power of 1 to 2 mW spread over 10^6 pixels at the specimen position should be more than sufficient for most applications. Effectively, 10 to 100 µW is common in confocal. Assuming a 10% optical path efficiency a laserhead output power of >~1 mW suffices.

There are two different types of saturation effects. One is related to the number of molecules that can absorb light in a given area for a certain incident flux. In a given pixel, assuming a volume of 1 μm^3, the volume is 10^{-15} L. At a molar concentration of 10^{-5}, we should have approximately 6000 molecules/pixel. Since the number of photons absorbed per milliwatt of incident light is about $2.5 \times 10^{+5}$/s on a single pixel in widefield, each molecule is excited about 40 times per second. From the photophysical point of view, the decay of fluorescein (and in general any singlet single state decay) is very fast (4×10^{-9} s), so that the ground state should be repopulated very rapidly. However, in the confocal microscope for a pixel dwell time of about 1 µs, the 40 × 4 ns = 160 ns dead time represents 16% of the pixel period.

There are many possible photochemical processes that are either irreversible or have a cycle time of several milliseconds to seconds. In this latter case, even if the quantum yield for these effects is very low (below 0.001), and the exposure time is on the order of seconds, molecules lost to the long-lived state will severely limit the overall peak excitation intensity that can be used before the output loses its linear relationship with the input. For quantitative microscopy this is the most important limitation. Hess and Webb (2002) found that their FCS data implied a non-Gaussian three-dimensional (3D) volume and distortion of the calibration of the excitation volume at a power level of 10 to 100 µW at 488 nm, for one photon Rhodamine Green excitation and 5 to 10 mW at 980 nm, for the two-photon case (Rhodamine Green or Alexa 488, Molecular Probes).

Having discussed the power requirements, we continue with a concise description of the basic elements of a laser, its principle of operation, and other important practical aspects, such as heat removal and mechanical and optical stability.

In general, confocal microscopes work best at <1 mW of continuous wave (CW) beam power at the specimen and useful images of living cells have been made with <100 nW (see Chapter 19, *this volume*). When pulsed lasers are used for two-photon excitation it is important for the pulse frequency to be high enough (80–100 MHz) so that many pulses occur during the 1- to 4-µs pixel dwell time. The intensity instability of this light **when it reaches the specimen** must be small compared to the statistical uncertainty that will occur when the signal photons are detected; if the signal level is only 100 photons/pixel, then Poisson statistics will limit accuracy to 10%, while 10^4 detected photons will yield 1% accuracy.

THE BASIC LASER

The acronym *laser* stands for **l**ight **a**mplification by **s**timulated **e**mission of **r**adiation. Laser action, that is, the emission of coherent radiation, has been observed for a large number of different media, but all lasers have several features in common (see Fig. 5.1).

- **Active laser medium:** Atoms, molecules, and atomic ions in pure or mixed gases, vapors, liquids, or solids, confined to the gain medium volume where they can be excited by an external source of energy.
- **Excitation source:** An external source of energy used to pump the laser medium. This can be another laser, arc lamp or flash lamp, electron beam, proton beam, electrical current, electrical discharge or radio frequency (RF) excitation, etc. The choice of pump source is determined by the optical, thermal, and mechanical properties of the active medium and the wavelength region of interest.
- **Optical resonator:** The laser medium is enclosed between two parallel mirrors, which form a Fabry–Perot interferometer. The mirrors are placed at each end of the laser medium. One mirror, the high reflector (HR), totally reflects (R = 99.9%); the other mirror, the output coupler (OC), only partially reflects. To a first approximation, the ratio of these two reflectivities is the gain of the cavity that they form. For instance, if the reflectivity of the OC is 95%, on average a given photon will pass through it 1 time in 20 and, in the absence of other loss mechanisms, the cavity gain will be 20. In small semiconductor lasers the physical polished sides of the devices may act like

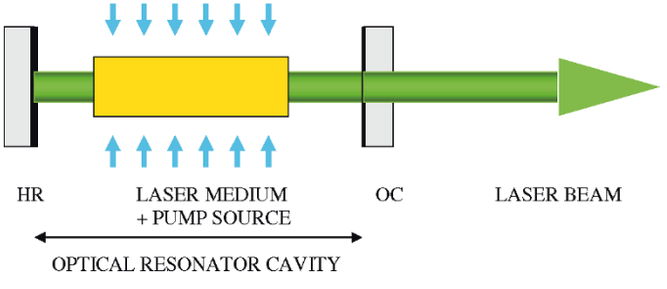


FIGURE 5.1. An optical resonator is formed between a highly reflective mirror (high reflector, R = 99.99%), HR, and a mirror with a reflectivity of, for example, 80%, the output coupler (OC). Within this resonator we find the active lasing medium (a crystal, semiconductor, liquid or gas) and its energy supply: the pump source, an arc lamp or flash lamp, another laser.

effective mirrors. Laser emission generated by electronic transitions that are relatively rare require cavities with higher gain.

Principle of Operation

A particle of the active laser gain medium becomes excited when it absorbs pump energy and goes to an excited level [Fig. 5.2(A)]. It then returns to the ground state via non-radiative relaxation processes and also by emission of radiation [Fig. 5.2(B)]. Under normal conditions, a Boltzmann equilibrium describes the population of the various energy levels: the higher the energy level the lower the population of that level. When an excited, metastable level with a long lifetime exists in the laser medium, energy will accumulate in this level. If the excitation is intense enough, the Boltzmann distribution normally present will "invert" for the population of this metastable state (i.e., there will be many more electons in the excited state than Boltzmann would predict). In the laser cavity, photons emitted from this energy level will strongly interact with the population of the metastable level [Fig. 5.2(C)], forcing it to release energy and return back to the lower level [Fig. 5.2(D)]. This process is called stimulated emission of radiation, that is, the interaction of the light with the excited particle increases the likelihood that the particle will return to the ground state. The stimulated emitted light has a high degree of monochromaticity, because emission occurs from a well-defined transition. In addition, the photon that results from this stimulated de-excitation process is in phase with the electromagnetic wave traveling in the laser medium. As a result, the emitted radiation has excellent spatial and temporal coherence and is highly directional.

A convenient way to let the electromagnetic radiation interact with the laser medium is a resonant cavity (Fig. 5.1). At optical wavelengths, this is achieved by a Fabry–Perot type interferometer. Two plane-parallel mirrors, one highly reflective, the other semi-transparent, are separated by a distance equal to an integral multiple of half the lasing wavelength. Because the electromagnetic radiation interacts repeatedly with the laser medium, this resonant cavity increases the probability of stimulating de-excitation. It also provides the necessary feedback to make the emission grow coherently. Because the emission of the first photon going in precisely the correct direction to reflect back and forth in the cavity is a low probability event, getting the laser to fire is a chaotic phenomenon that exhibits a threshold effect; lasers won't start or work stably below a certain output power level.

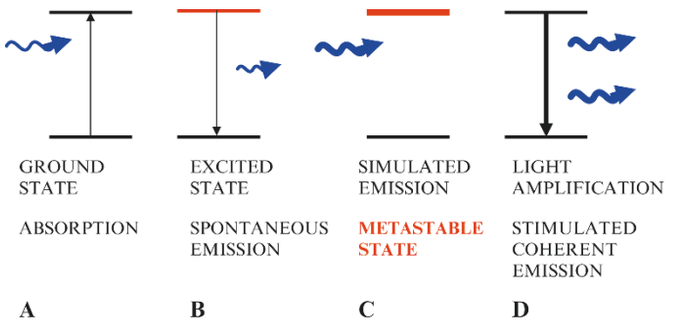


FIGURE 5.2. Optical (de)excitation processes. (A) Transition from ground state to excitated state upon absorption of a photon, an electron moves to a more outward shell, timescale < femtoseconds. (B) Relaxation to a lower level, for example, ground state under spontaneous emission of a photon, electron returns to a lower level, timescale nanoseconds. (C) Light driven interaction inside laser gain medium of a photon with electrons in excited metastable state with a long lifetime. (D) Stimulated coherent emission and light amplification.

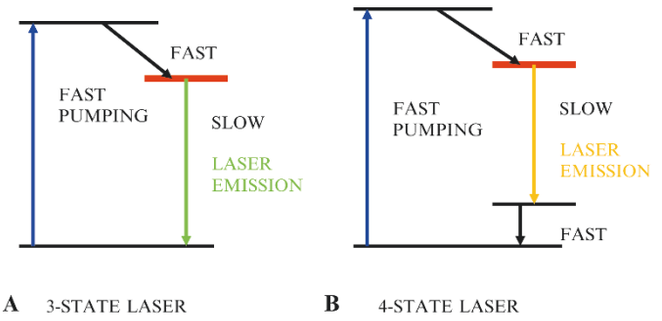


FIGURE 5.3. Fast non-radiative relaxation processes couple an excited state with a lower metastable energy level. Laser emission occurs in the gain medium from the metastable state. Dependent on the gain medium properties this laser process is described by a three-level or four-level lasing scheme.

So far we have only discussed a three-level laser, that is, ground-state, upper excited-state, and lower excited-state [Fig. 5.3(A)]. In a four-level laser [Fig 5.3(B)], as in the helium-neon (He-Ne) laser, the population inversion can be obtained more easily (Arecchi and Schultz-Dubois, 1972). The titanium–sapphire (Ti : Sa) vibronic laser is effectively also a four-level laser due to its broad energy bands (see later section). Other improvements relate to the replacement of the Fabry–Perot mirrors by corner cube reflectors or crossed-roof prisms to increase mechanical and thermal stability. For further information, see Arecchi and Schultz-Dubois, 1972; Stitch, 1979; Bertolotti, 1983; Bass and Stitch, 1985; Kudryashov and Weber, 1999; Webb and Jones, 2004; Hodgson and Weber, 2005.

An interesting approach is the increasing use of optical fibers that act as both lasing medium and cavity at the same time; a very compact design is described later in this chapter.

Pumping Power Requirements

In order to sustain laser action, the gain of the optical resonator needs to be larger than the losses due to resonator walls and other optical elements. The minimum necessary pumping power, P, is proportional to ν^3. This means that, as one shifts from the infrared (IR) through the visible (VIS) towards the ultraviolet (UV), an ever increasing amount of energy is needed to obtain laser action. This limits the possible pumping mechanisms.

Laser Modes: Longitudinal (Axial) and Transverse

- **Axial or longitudinal modes:** Separated by a distance, L, the two plane-parallel mirrors of the Fabry–Perot interferometer cavity form an optical resonator. This separation distance can be long (meters, as in big frame ion lasers) or very small (micrometers, as in very compact diode lasers). A number of standing wave patterns each consisting of an integer multiple, m, of half wavelengths, $\lambda/2$, exists in an optical cavity of length L: $m = L/(\lambda/2)$. The frequency, ν, for the mth vibration along the long axis of the laser is, therefore, $\nu = mc/2L$, where c is the speed of light in the laser cavity. The frequency spacing between adjacent longitudinal modes is $c/2L$, that is, the inverse of the laser cavity round-trip time. A very large number of longitudinal modes can exist in the laser cavity unless bandwidth-limiting devices such as Fabry–Perot etalons are installed in the cavity.

- **Transverse modes:** These modes vibrate perpendicular to the long axis of the laser and are known as transverse electromagnetic modes, TEM_{mn}, where m and n are integers describing the nodal points in the two directions perpendicular to the laser axis. For each transverse mode, many longitudinal modes can exist. (For an in-depth derivation, see laser handbooks by Arecchi and Schultz-Dubois, 1972; Stitch, 1979; Demtröder; 1996; Bass and Stitch; 1985; Hecht and Zajac, 2003; Silfvast, 2004). An adjustable diaphragm or pinhole inside the laser cavity is sometimes used to select the TEM_{00} lasing mode and control its intensity. No transverse modes exist in single (longitudinal) mode fiber lasers.

The TEM_{00} mode is desired for most light microscopy experiments. It has a Gaussian beam profile with no phase shifts across the beam. The maximum intensity is in the center of the beam, it has complete spatial coherence, and the smallest possible beam divergence. Only this mode can be focused to a diffraction-limited spot. Doughnut-shaped transverse modes TEM_{*01} (TEM_{10} in overlap with TEM_{01}), such as produced by some helium–cadmium (He-Cd) lasers operating at 325 nm, are not desirable because they possess no intensity in the center of the beam. In this case, spatial filtering is necessary (see later section).

Polarization

The output of many lasers is linearly polarized with the polarization vector vertical.

- **Lasers with Brewster surfaces:** A convenient and inexpensive way to minimize reflection losses and to generate linearly polarized light is the installation of a Brewster surface (i.e., one that is tilted so that the normal of the plane and the incoming beam form a specific angle, $\theta_{Brewster}$) at the end of the resonator. Horizontally polarized light incident on such a plane-parallel plate will be completely reflected. Vertically polarized light will be completely transmitted without any reflection losses (Fig. 5.4). In laser resonator cavities, this plate is usually a quartz or a fused-silica plate. In solid-state lasers, the semiconductor rod itself is sometimes cut at the Brewster angle to minimize reflection losses. In gas lasers, the exit windows are usually oriented at the Brewster angle to obtain vertically polarized light. Dust often collects on Brewster windows that point upward, damaging the coating. To operate properly, they must be kept absolutely clean using a dust cover and a slightly positive dry air or nitrogen pressure in the laser head. In the jet-stream dye laser, the jet is placed at Brewster angle in order to minimize losses due to reflection of the pumping beam, thereby maximizing the pumping efficiency. For the same reason, the tuning element of the dye laser is also placed at Brewster angle. Brewster surfaces can also be the origin of very dangerous reflections. Eye protection should always be worn when protective covers are removed from a laser.
- **Lasers built without Brewster windows** will still show some polarized output due to birefringence within several optical components. However, the plane of polarization may change with time and, even though the total intensity stays constant, should this light pass through a polarizer, large output intensity fluctuations may be observed.

Randomly polarized beams contain two orthogonal components but the phase and ratio of the two components vary rapidly in time, creating polarization noise. Dichroic mirrors, and, in fact, any mirror or lens surface, not at right angles with the incoming radiation will reflect vertically and horizontally polarized light differently (directions are taken with respect to the plane of incidence formed by the reflected and transmitted beams).

A convenient way to depolarize laser emission is to install a polarizer or polarizing beam-splitter and a l/4-wave plate. When placed at an angle of 45° with respect to the incoming linear polarization, this 1/4-wave plate converts linearly polarized light into circularly polarized light. These waveplates are usually designed for a specific wavelength. Achromatic retarders, such as Fresnel rhombs, are sometimes preferred, but are quite expensive (Driscoll and Vaughan, 1977; Hecht and Zajac, 2003). Another advantage of this arrangement in optical microscopy is that it prevents reflected or backscattered light from reaching the detector. The reflected light passes through the 1/4-wave plate in such a way that, on return, it is blocked by the input polarizer because its plane polarization is now orthogonal to the main transmission direction of the input polarizer. Phase randomizing will briefly be discussed in a later section. For an in-depth treatment see Chapter 31 by Harris and Delaney. In fiber lasers, optical isolators are inserted for the same reason, that is, to prevent backreflections. The polarization-independent isolator consists of a small cylindrical package containing a fiber pigtail, non-spherical collimating lenslet, a slightly wedged birefringent platelet, a magneto-optic Faraday rotator at 45°, exit birefringent platelet also at 45°, and refocusing lenslet followed by another fiber pigtail.

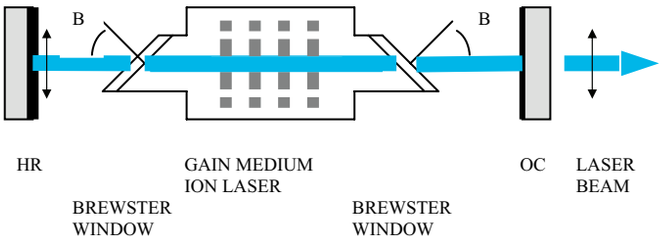


FIGURE 5.4. Emission of linearly (vertically) polarized laser light from an ion laser resonator cavity equipped with Brewster angle plasma-tube windows. Only vertically polarized light is amplified. It experiences no reflection losses at the Brewster angle: $B_{Brewster} = \tan^{-1} n$, with n the refractive index of the pure crystalline quartz window. Horizontally polarized light suffers reflection losses and stays below the lasing threshold. Windows normal to the optical axis of the laser would introduce reflection losses and could prevent the laser from operating at all or introduce a set of reduced length resonator cavities. Tungsten disks or BeO tubes with a central bore with or without focusing magnetic fields keep the lasing plasma volume centered in the cavity. Gas return paths are also provided in the disks. HR, highly reflecting mirror; OC, output coupling mirror.

Coherent Properties of Laser Light

Laser beams illuminate objects coherently. The process of stimulated emission imposes coherence effects on the emitted laser light waves. All parts of the electromagnetic wave reach a crest, that is, are in phase, at a given point in space at the same time. Spatial and temporal coherence is present. This coherence stretches for a certain distance and time and depends on the spectral width or pulse duration of the laser light. Beyond a certain distance or time interval synchronization differences arise. When a choice exists, a short coherence length laser should be used for CLSM or scrambling devices should be inserted into the optical path.

- **Temporal coherence:** The coherence time is the time interval during which light traveling over a certain distance maintains a phase difference of less than π (or 180°), $\tau_{coh.} = 1/\Delta\nu$.
- **Coherence length:** The path traveled by the wave during the coherence time is called the coherence length, $L_c \sim c/\Delta\omega$, where $\Delta\omega$ is the spectral width of the laser. Longitudinal coherence length $L_{coh.} = c/\Delta\nu$. Lateral coherence length, $l_{coh.} = \lambda/\phi$, with ϕ the beam divergence. For a typical gas laser, for example, a He-Ne laser with a bandwidth of 1.5 GHz, leads to L_{coh} of ~20 cm. In single-mode operation with $\Delta\omega \sim 1$ MHz, L_{coh} is ~50 m. A diode laser with a spectral width of 0.1 nm at 780 nm possesses a coherence length of 1 mm. Dye lasers equipped with tuning elements, diode lasers, and other lasers such as the Ti : Sa systems, usually have bandwidths on the order of tens of gigahertz and an L_{coh} of a few millimeters or less. Depending on the type of line narrowing element installed, L_{coh} can be increased by a factor of 10^3 to 10^6. For practical confocal microscopy, a shorter coherence length is preferred to eliminate the influence from out-of-focus defects. For example, dust on semi-transparent surfaces, lenses and mirrors creates interference fringes when a laser with long coherence length is used (Hell *et al.*, 1991). (See Tables 6.1 and 6.2 which contain columns with spectral width and pulse length, from which the coherence length follows.)
- **Spatial coherence:** Spatial coherence occurs when a constant, time-independent, phase difference exists for the optical field amplitude over a given distance at two different points in space.
- **Coherence surface:** The coherence surface is the region of space for which the absolute phase difference of the optical field is less than π. The well-known "speckle" pattern consisting of a pattern of darker and brighter light spots is visible when a matte wall surface is illuminated by a distant He-Ne laser. The interference effects caused by irregularities in the surface will be noticeable.
- **Coherence volume:** The coherence volume is the product of coherence length and the coherence surface. Interference between superimposed coherent waves will only be visible within this volume.

Phase Randomization: Scrambling the Coherence Properties of Laser Light

A long coherence length of lasers will cause laser speckles (i.e., interference effects) and scatter from out-of-focus particles and these will interfere with the image. Normally in a fluorescence CLSM, this scattered light is removed by the dichroic mirror as the emitted fluorescence has a different wavelength from the illuminating light source. However, a polarizing beam-splitter and l/4-wave retardation plate can be equally effective for the removal of light backscattered by dust or optical surfaces. The angular position of this 1/4-wave plate and the polarizer is important (Szarowski *et al.*, 1992). For generating circularly polarized light, it is only necessary that the incoming plane of polarization and the principal axis of the 1/4-wave plate be at a 45° angle. Light reflected or scattered from an illuminated dielectric surface has its direction of rotation reversed. On its return passage through the plate, the light becomes linearly polarized again, but its plane of polarization is now rotated by 90° and it is removed from the optical path by the polarizing beam-splitter.

Another method to reduce speckle comes from color confocal microscopy where one uses several lasers. As the coherence properties of the various laser light sources are not the same, averaging over the three wavelengths and over several planes will reduce the effect of the laser speckle (Cogwell *et al.*, 1992b).

Measures to Reduce the Coherence Length of Laser Light

Many applications work better and image quality improves if the coherence of the laser light is reduced. One way to achieve this is to place a rotating diffuser wedge in front of the beam expander (Hard *et al.*, 1977). Rotation or vibration of this wedge is essential to average out local diffuser properties. Alternatively, focusing the laser beam into a multi-mode optical fiber bounces the light around inside the fiber and mixes the various propagation modes to scramble the Gaussian intensity pattern (TEM_{00}) to a multi-mode pattern with a homogeneous spot intensity. This eliminates or reduces the coherence surface. A short focal length lens or graded index lens (GRIN) recollimates the light at the fiber exit.

To eliminate the speckle pattern due to temporal coherence properties, a piezoelectric driver can be used to induce vibrations in a section of the fiber (Ellis, 1979). In the context of medical imaging, Connor, Davenport and Gmitro (1992) used a rotating diffuser to eliminate the speckle pattern by coupling the laser beam into a bundle of small, multi-mode fibers. The latest method in this area is the introduction of ultra-thin single-mode image fibers. A fiber-optic bundle with a total diameter of 200 to 500 µm consisting of 2000 to 5000 micro image fibers, each with a core size of 1.0 to 1.4 µm (Kiat *et al.*, 1992), can be used as a phase randomizer in conjunction with a rotating diffuser. Although these ultra-thin fiber bundles propagate shorter wavelengths much more strongly than longer, leaky ones, this is not a problem as long as monochromatic laser light is used.

As light is scattered in all directions by most diffusers, they reduce the intensity of the laser light. However, holographic diffusers have been designed to carry strong forward intensity lobes. Among others, Lasiris, Inc. and Physical Optics Corp. (see Table 5.3) produce holographic laser beam homogenizers, having a conversion efficiency of 80% to 90% and low backscatter (Bains, 1993).

Laser coherence effects can also be eliminated by spot scanning the field of view with a tiny, focused, single-mode laser beam. Alternatively, the condenser plane can be scanned with the same tiny, focused, single-mode laser beam while illuminating the whole field of view. Coherence scrambling occurs because the laser spot rapidly scans the back-focal plane and the field is continuously illuminated with a mix of beam angles (Ellis, 1988).

Heat Removal

Most of the laser excitation energy is converted into heat. This must be removed to prevent thermal destruction of the active laser medium. Small laser systems can use convective air cooling, but larger laser systems need forced-air or water cooling. Especially for the largest systems, fans and turbulent water-flows may introduce vibrations in the system (microphonics). These unwanted mechanical vibrations are inevitably coupled to the mirror mounts of the resonator cavity, causing increased noise in the optical output. Pumps that recycle liquid laser-media are another source for vibration. In this case, the vibration is transferred via hoses to the active medium in the resonator. To minimize these effects, the hoses should be clamped or fastened to the support table as near as possible to the laser head.

The heat generated will also put thermal stress on the mechanical parts of the resonator. Poorly designed laser systems quickly lose their proper alignment or may need an unacceptably long warm-up time. The installation of a laser system in a room with large daily or annual temperature fluctuations or a ceiling fan continuously blowing cold, dusty, air directly onto a laser will also hamper operation and cause performance to deteriorate. The use of thermo-electrically (TEC) cooled diode lasers that are in thermal contact with their enclosures may create hot surfaces that should be labeled as such. Diode arrays may require water cooling. Because of their monolithic design, they are less susceptible to mechanical instabilities but thermal stress has to be avoided at all cost. The same is true for fiber lasers, which, due to the fiber length, are sensitive to temperature fluctuations unless countermeasures such as negeative temperature coefficient materials are used.

Other Installation Requirements

Manufacturers usually describe the electrical power requirements and flow rates for cooling water (Gibson, 1988, 1989; Rapp, 1988). Before installation of a laser system, adequate control of room temperature and air conditioning should be available. Walls should be painted to eliminate concrete dust from settling on delicate optical surfaces. For emergency situations, a master switch for the laser power should be installed with easy access at eye height and labeled as such. Heat from large fan-cooled laser power supplies can sometimes be plumbed directly into the intake of the air conditioning system, with backflow protection, if this is allowed. Similarly, acoustic noise can be very tiring and noisy power supplies should be placed outside the experiment room.

An exhaust for noxious fumes such as ozone or dye vapor should exist and backup systems should be established to prevent interruptions of power or coolant flow. Mechanical vibrations due to nearby traffic can be eliminated by installing the system on commercially available vibration-free, air-cushioned laser tables or on tables isolated using sand-filled containers, tennis balls, or motorcycle inner tubes. When equipment used for radio-frequency crystal-growth, nuclear magnetic resonance (NMR) equipment, building air-conditioning machines, large elevators, or other large laser systems are present, it is often wise to equip each laser with its own stabilized power line to prevent large voltage spikes from reaching laser power supplies. Hidden cables drawing a large current (for elevators, for example) in ducts near your facility may ruin a carefully planned sensitive system by disruptive induction currents. Stray magnetic fields may affect the flow of ions in gas lasers.

Movement of fiber-optic components changes the beam propagation properties of the fiber (bundle) and should be prevented for best stability (unless the device is used intentionally to scramble the laser light polarization and reduce the coherence length).

Attenuation of Laser Beams

Laser damage levels for materials are usually given in mW/cm^2 while laser output is given as total average power (mW) for a small, for example, 2-mm diameter beam. Although intensities in the milliwatt range can be attenuated with neutral density filters, high-power lasers will easily destroy this type of filter. The absorbed light may even bleach or heat them so much that they fracture or explode. Polaroid material can be used only for low light intensities but this material usually has a peak transmission of only 30% to 50%. For intensities above about 10 mW, better attenuators are Glan–Thompson polarizers. When a laser emits only polarized light, one rotatable polarizer, set at a proper angle will suffice. For randomly polarized lasers a set of two polarizers can be used. The first one passes 50% of the total intensity. The second polarizing analyzer transmits a continuously adjustable amount of light depending on its orientation angle. In all these cases one must be careful to ensure that light reflected from the various crystal surfaces is also absorbed by beam stops. Initial alignment should be done with only the lowest laser power available. If a polarizer is used to attenuate an initially randomly polarized laser beam, fluctuations in the intensity may be observed. These are due to the varying nature of the interaction between the cavity modes and therefore the polarization state inside the laser.

Glan–Thompson polarizers contain Canada balsam to hold them together. This material may absorb slightly, especially in the UV. Power levels above several watts (power = energy/time = area of pulse) will destroy this type of polarizer. For the highest expected power levels, air-spaced Glan–Taylor polarizers are strongly recommended. A new type of polarizing element is the Microwire polarizer commercialized by Moxtek Inc. (see Table 5.3). It fits in very tight spaces but is somewhat more fragile.

STABILIZATION OF INTENSITY, WAVELENGTH, AND BEAM POSITION IN LASERS

Sources of Noise in Lasers

Stability, both temporal and positional (beam pointing), is a very important aspect of any CLSM laser light source. As beam pointing affects the amount of light coupled into the delivery fiber, pointing instability can cause intensity instability. Other intensity instabilities are related to backreflections from the fiber that can be avoided (Cogwell *et al*., 1992a) by employing a wedged fiber input (e.g., Point Source, see Table 5.3). Figure 5.5 gives examples of noise in the output of several laser systems. The most stable are the diode laser and the forced-air cooled (fan) small-frame argon-ion laser. The argon-ion laser-pumped titanium : sapphire laser output was coupled into a fiber-optic attached to the detector. The average relative intensity fluctuations are defined as $N^{-1}\,\Sigma_i(|I_i - \langle I\rangle|/\langle I\rangle)$, where N is the number of points. For the diode laser this quantity is about 0.1% (Franceschini *et al*., 1994), and for the Ti : Sapphire laser at the fiber output, about 2%. Both would be acceptable for microcopical applications in which fewer than 50 photons were detected per pixel.

It is imperative to keep lasers well-aligned with very clean windows. Misaligned mirrors, a half-illuminated reference monitor diode, or a dust speck may create a very unstable output. As misalignment can cause unusual modes to appear, these laser lines will fluctuate independently, and the total output becomes unstable. For instance, the two UV lines of an old water-cooled argon-ion laser were observed to alternate between bright and dim with a period of a few seconds to a minute. Realignment helped but the tube had to be replaced. Transverse mode swapping is seen in He-Cd tubes that need replacement.

Noise in the optical output of a laser can be created by a variety of phenomena. Several factors produce high-frequency (noise) or slow variations (drift) in beam power. These include power-supply variations, thermal drift of the cavity, and mode competition. Examples include:

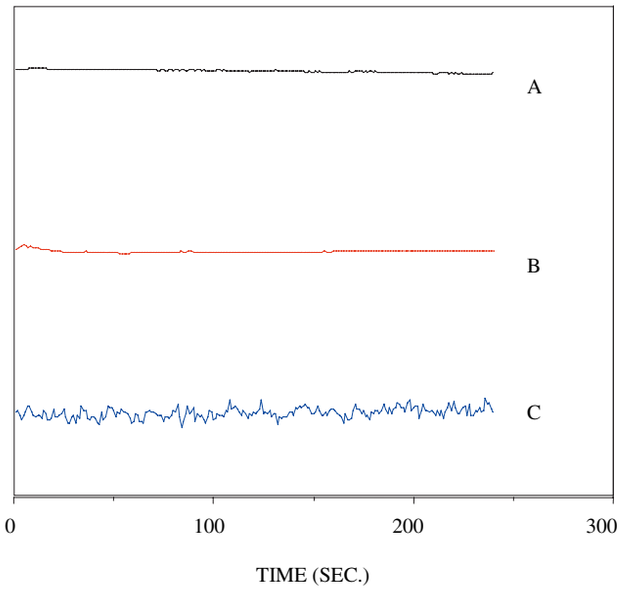


FIGURE 5.5. Measured laser emission stability (arbitrary units). Normalized and shifted intensities for (A) a diode laser (Sony SLD104AV, $\lambda = 780$ nm; *top* curve); (B) a forced-air cooled small frame argon-ion laser, Omnichrome model 532, running at 488 nm and 7 mW power (*center* curve); (C) Mira (Coherent) Ti:Sa laser running at 780 nm and 1.2 W (*bottom* curve). The normalized noise for the diode laser is 0.1% and for the Ti:Sa laser about 2%. The attenuated Ti:Sa laser was focused into a fiber-optic.

- **Dye lasers:** Noise and drift in dye lasers can be caused by air bubbles and inhomogeneity in the dye, the dye pump, and by the laser pump source.
- **Gas lasers:** A major source of noise comes from plasma oscillations and from microphonics generated by cooling water turbulence. Forced-air cooling for smaller lasers can avoid most microphonics, but the fan may introduce some new noise. Commercial confocals often mount the lasers on a heavy stone slab (Zeiss) or place them in a separate, shielded drawer (Leica). Also any optical pump source can introduce noise.
- **He-Cd lasers:** Strong plasma oscillation between 225 and 400 kHz may create an output variation of up to 12%.
- **Semiconductor or diode lasers:** Semiconductor laser diodes require a current source with the highest stability and the lowest electronic noise (Malzahn, 2004). Furthermore, temperature stability is imperative for adequate intensity and wavelength stability (Hodgson, 1994). Forward-biased semiconductor junctions are inherently thermally unstable; an increase in current increases the temperature, which, in turn, increases the current even more. Therefore, current supply design is very important and must be suited to the specific laser. Internal damage in laser diode junctions due to heat buildup ages the device, resulting in a reduced output and slope efficiency. 1/f noise is due to trapping of carriers in the device (Mooradian, 1993). Drive-current fluctuations also degrade the performance and will modulate the beam intensity. Mistreated fiber-optics can also increase the amount of noise. On the other hand, an imposed high frequency (MHz) modulation allows the laser to be used for time-resolved and frequency-domain imaging applications.
- **Solid-state lasers:** The important noise sources are microphonic noise and 1/f noise related to thermal fluctuations in the lasing rod. Furthermore the Ti : Sa rod temperature bath should be set at the correct temperature, for example, 18°C. Failing to do so creates condensation droplets on the pump surface. Fiber lasers should be kept in a stable temperature environment.

All lasers suffer from noise introduced by their power supplies. Switching-mode power supplies introduce switching ripple, typically at tens of kilohertz. This type of power supply was developed to take advantage of better transformer efficiencies and smaller physical sizes (Forrester, 1994a,b).

Planar optical elements and filters should be inserted at a small angle with respect to the optical axis to prevent beam reflections from returning to the laser cavity where they might increase the noise level of the laser (Cogswell *et al.*, 1992a).

Images created on commercial CLSM instruments may show a fine pattern of irregular vertical lines. Possible sources include resonances in the scanning mirror systems and high frequency ripple in the switching power supplies. However, sometimes the problem is not the light source but the detector system (French and Gratton, personal communication). Last but not least, the main laboratory power supply lines may be unstable.

Other sources of noise are caused by external influences: traffic vibrations, etc. A simple means to reduce its effect is a well-damped, stable support platform (see above).

Laser Beam Intensity Stabilization in Current- or Power-Control Mode

Continuous wave gas lasers can easily be intensity stabilized using either tube current stabilization or external modulation of the light intensity (Miller and Hoyt, 1986).

- **Constant-current mode:** An electronic feedback loop directly controls the tube current and minimizes current drift. As this system takes no account of how temperature may affect cavity gain, best results are obtained after the laser temperature stabilizes.
- **Constant output power mode:** The drive current is controlled via a signal obtained from a built-in monitor diode. The stabilization circuit typically consists of a beam-splitter–photodiode assembly mounted behind the output coupler. The monitor diode picks off a small amount of laser intensity. Changes in intensity are compensated for by opposing changes in the drive current. When not properly aligned, large intensity fluctuations may result. Multi-line lasing depends on an interplay of different gain and mode patterns especially when the bore holes in the internal BeO laser disks become larger with time (Fig. 5.4). A constant output power supply in combination with an aging plasma tube will increase in tube voltage and current supplied, damaging the tube further and even more rapidly. Both effects are even stronger in mixed gas lasers.

Even if the laser beam is stable, external noise can be introduced to the system by room dust, traffic vibrations, or movement of fiber-optic components and may still adversely affect intensity stability. The long-term stability of the largest argon-ion models is better than 1% in this control mode. But this light control mode does not work so well when multiple emission lines are monitored simultaneously (Brelje *et al.*, 1993).

Laser Beam Intensity Stabilization with External Pockels Cell Modulator

Some manufacturers provide special accessories to improve the intensity stability of CW lasers. These devices are external modulators incorporating a fast feedback system (Miller and Hoyt, 1986; Miller, 1991; see Fig. 5.6), and, of course, they reduce the total output power. Intensity fluctuations of up to 50% of the maximum power can be corrected in this way, but only with a 50% reduction in the total available power. Laser intensity stabilizers can regulate the output of CW and mode-locked lasers to within 0.025%, with a noise attenuation of 400 : 1 and a bandwidth from direct current (DC) to several megahertz in some systems.

Depending on the polarization state of the laser light, up to 80% transmission is obtained. In this system (Fig. 5.6), a photodiode is illuminated with a fraction of the laser light deflected by a beam-splitter. A servo-control unit compares the detector signal with a user-selected set point. The difference signal is amplified and drives an electro-optic (Pockels cell) modulator. The amplified electrical signal causes a rotation of the plane of polarization. Depending on the voltage applied, more or less light can pass through the modulator creating a variable beam attenuator. Ideally the laser beam should be stabilized as close as possible to the sample position rather than at the exit of the laser head. Otherwise, vibrations or dust may alter the stability of the beam after it leaves the source.

Stabilization units should be able to operate at a variety of wavelengths with UV capability when necessary. They should be protected against driver signals beyond a certain maximum, so that a runaway situation does not occur, for example, if the beam is blocked or temporarily interrupted. When the stabilizer is driven by an external control signal, complex intensity sequences may illuminate the sample. Commercial laser power controller (LPC) stabilizers can be obtained from BEOC and several other manufacturers (see Table 5.3).

When randomly polarized laser light has to be stabilized, the external Pockels cell modulator must be placed between two crossed polarizers. Unfortunately, such a modulator cannot work with low-repetition-rate pulsed lasers. Another simple way to remove laser noise is similar to that typically used in steady-state fluorescence spectroscopy. The effect of source fluctuations is cancelled by dividing the detected signal from the sample by a signal derived from the laser sampling monitor detector.

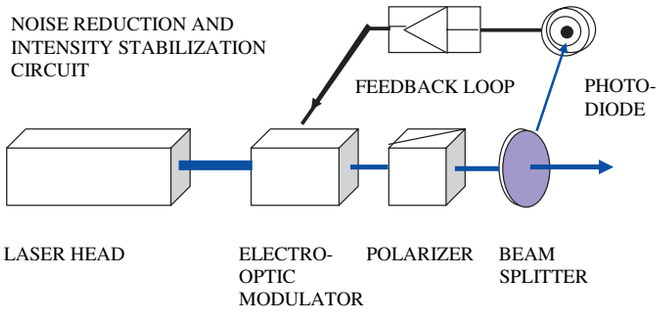


FIGURE 5.6. Example of a laser beam intensity stabilizer and laser noise suppressor. A beam-splitter delivers a fraction of the laser output beam to a fast photodiode detector. Electronic feedback loops for low- and high-frequency signals control the electro-optic modulator (EOM) intensity regulator. The rotated plane of polarization exiting from the EOM passes through an angle-adjustable Glan-Taylor polarizer. It defines a single plane of linear polarization. A detected intensity fluctuation alters the drive voltage to the crystal.

Diode Laser Intensity and Wavelength Stabilization

Incorporating a Fiber Bragg Reflector (FBR) or Grating (FBG) in a (pump) diode laser stabilizes wavelength, improves coupling efficiency, reduces unwanted reflections and the effects of temperature and drive current fluctuations, as well as simplifying manufacturing (Guy and Painchaud, 2004). The FBR consists of a stack of thin coating layers forming a bandpass reflectivity filter at either the high reflector or output coupler end. Even simpler is lens coupling the diode-laser output into a section of FBG fiber pigtail. A periodic or non-periodic (chirped) refractive index variation of the Bragg grating can be present in its core, creating a narrow band low-reflectivity filter that reflects a small fraction of the light from the diode laser back into it. However, due to interference effects, only a certain wavelength — the designed lasing wavelength — is actually fed back into the laser diode. All other wavelengths are out of phase and die off. In this way, the attachment of the proper FBG fiber pigtail creates a diode laser that is stabilized in wavelength and intensity. Naturally, if the FBG temperature or internal strain changes, the lasing wavelength will vary slightly. A typical temperature coefficient is 0.012 nm/°C. A temperature increase from 18°C to 40°C will cause the lasing wavelength to shift 0.26 nm, but in practice it may well be 5-fold larger. With temperature compensating packaging and a strain-inducing material with a negative temperature coefficient, this effect can be reduced to 0.001 nm/°C.

Beam Pointing Improvement Via Active Laser Cavity Stabilization

The mirror orientation changes when the laser cavity warms up. This causes the laser beam to wander and the beam intensity to vary. Active cavity stabilization corrects for misalignment of the resonator via a feedback mechanism (Peuse, 1988). The advantage is that the resonator structure becomes independent of changes in the environment, for example, temperature, and as a result provides an extremely short warm-up time (seconds), enabling hands-off operation. In addition, there is less chance that setting the power supply for a constant optical output will provide damaging power levels to a tube that has low gain because it is misaligned. Large frame ion lasers currently come standard with active resonator stabilization systems such as PowerTrack, ModeTrack and ModeTune (Coherent) or BeamLok Z-Lok (for mode-hop-free single-frequency operation) and J-Lok (for jitter reduction; Spectra Physics). These systems result in 1-min warm-up times, hands-off operation, and long-term intensity stability of better than 1%. Beam-pointing stability is obtained using a quadrant photodiode detector.

The horizontal and vertical positions of the high reflecting mirror are continuously tuned for optimum laser power with independent (magnetic or piezo) actuators. A small oscillation (dither signal) is superimposed on both actuators. A sensor photodiode signal reflects the power level of the beam. The filtered dither signal (lock-in detection) creates vertical and horizontal error signals. This oscillation is compared with a microprocessor-stored reference. The horizontal and vertical difference signals drive the mirror positions independently to obtain maximum power. The minimum detected oscillation (dither) signal corresponds with optimum alignment (Miller, 1991).

Beam Delivery and Positioning

Fiber-optic Coupling

Continous wave laser beams can be delivered to the scan head or microscope frame via single-mode, polarization-preserving, dual-

circular stress-rod design, fiber-optic (the so-called "Panda-eye pattern type," see Chapter 26, *this volume*). One should use fiber-optics whenever laser light has to be transported, eye-safe, over large distances, especially when the laser is located in a dusty environment (i.e., not a clean room). A single-mode fiber core typically has a diameter of 3 to 6 µm for VIS wavelengths. This creates a point-like excitation spot for confocal microscopy. Multi-mode fibers with core diameters ranging from 0.1 to 1 mm may also be used at times but beam characteristics such as beam width and polarization state are altered. However, fibers have been found less suitable for carrying UV light or for preserving the pulse width of femtosecond pulsed lasers. For femtosecond pulse lasers, the beam should be enclosed in a dust-free tube and reflected from dispersion controlling mirrors (e.g., from Newport Corp.). Picosecond systems are less affected (see Chapter 26, *this volume*). Handy beam couplers are available from many suppliers (OZ Optics Ltd., see Table 5.3). The Cell-viZio from Mauna Kea Technologies (see Table 5.3) uses a bundle of 30,000 fibers of 2 µm each.

Ultrafast pulses can currently be delivered by fiber-optic without dispersion using two methods: by pre-compensation or by photonic-bandgap fibers. Ultrafast pulses create non-linear effects in glass fibers and the fibers suffer from dispersion effects. Even at low pulse energies, a non-linear Brillouin and Raman background is generated. Pulse trains can only be transported without detrimental effects from chromatic dispersion under special conditions. By precompensating for the expected fiber pulse chirp with a dual prism or grating configuration (Fork *et al*., 1984; Zeek *et al*., 1999), the initial shape of the pulse can be preserved after it exits the fiber, but this adds to the complexity of the system and creates power loss. This precompensation uses the fact that a short pulse consists of many frequencies described by a Fourier sum, with proper amplitudes and phases.

In holey fiber coupling, single-mode, hollow-core (= air-filled) photonic-bandgap or crystal fibers (PCF), non-linear effects occur at a much higher threshold than in glass. As long as the zero-dispersion region of ~812 nm for the waveguide matches the laser wavelength, a perfect femtosecond pulse is transmitted without distortion (Tai *et al*., 2004). Tuning outside this range gives pulse broadening again (Hitz, 2004c). The spectral width of the 0 to 350 mW Ti : Sa laser stays unchanged at 812 nm after passing through a 1.5-m length of HC-800-01 bandgap fiber (Crystal Fibre A/S, see Table 5.3). Dunsby and colleagues (2004) describe an electronically tunable white light continuum, 435 to 1150 nm, generated by injecting 80 MHz 120 femtosecond light into a micro-structured fiber.

Direct Mirror Coupling and Pulse Width and Pulse Shape Control

Combinations of CW Lasers All commercial confocal systems these days offer facilities to combine the output of several lasers using dichroic mirrors and intensity-balancing neutral-density filters. A device for selecting wavelength and intensity, such as an acousto-optic tuning filter (AOTF) or acousto-optic beam splitter (AOBS), is then added. One of the advantages of having many separate lasers is that the intensity of each line is servo-controlled independently. In the competing Kr/Ar ion laser, it is only the total optical output that is stabilized. The portion of this total associated with each individual line can vary widely with time. For example, Cogswell and colleagues (1992a,b) combined a 632.8 nm He-Ne with a 532 nm frequency-doubled Nd-YAG laser and the 442-nm line from a He-Cd laser for true-color confocal reflection microscopy. Issues that may arise are spectral purity and polarization of the excitation.

Ultrafast Lasers Assuming the proper coatings, direct mirror coupling into the scan head can maintain the femtosecond pulse width and multi-photon intensity for ultrafast lasers such as Ti : Sa systems (Fermann *et al.*, 2002). On the other hand the dispersion material used in acousto-optic modulator (AOM) or acousto-optic deflector (AOD) devices or the glass in thick objectives may cause inappropriate pulse broadening due to group velocity dispersion (GVD). A GVD compensating prism or grating pair or a Gires–Tournois interferometer (GTI) can control the GVD and compensate the widening to some extent. Instead of prism and grating pairs, chirped mirrors could be used. These limit tunability but improve stability against environmental effects such as temperature changes and reduce high-frequency noise. In a chirped mirror, the Bragg wavelength increases with increasing penetration depth. Double-chirped mirrors that produce an additional chirp in the coupling of the incoming and reflected wave reach almost perfect dispersion compensation.

Multi-photon ultrafast (100 fs) lasers possess a phase that depends on the spectral region. To match the slightly different two-photon absorption properties of fluorophores in different environments one could tune the laser but this changes the beam properties such as intensity, phase distortions, etc. A better approach is to use a charge-coupled device (CCD) computer-assisted pulse shaper either to create a transform-limited flat phase across the spectrum or to modify the phases within the pulse via multi-photon intrapulse interference (MII), making selective excitation possible (Dantus, 2003; Dela Cruz, 2004). MII can also limit the amount of three-photon processes, thereby limiting deep UV damage to living cells.

Wavelength Selection and Intensity Control

Wavelength Selection

In commercial confocal systems, several laser beams are often combined via dichroic mirrors onto the same optical path leading towards an AOTF or AOBS (Chapter 3, *this volume*). Both allow very fast wavelength and intensity control on a microsecond timescale. We found, however, that the spectral purity of the AOTF–fiber combination is sometimes insufficient. When viewing mirror-like solid surfaces covered with labeled biosensor molecules excited at 488 nm, a little bit of 514-nm laser light was observed passing through the fiber-optic and masquerading as fluoroscein isothiocyanate (FITC) 509 nm emission. A thin 488 nm interference filter placed in front of the fiber-optic entrance in the AOTF module remedies this problem.

Intensity Control

Continuous wave laser beams can be deflected with acousto-optic devices/deflectors/modulators (AOD, AOM) for intensity and position control. The functioning and practical use of these devices has been discussed in great detail in Art and Goodman (1993). Draaijer and Houpt (1988) used these devices for video-rate scanning in confocal microscopy and their system was commercially available through Noran and still is supported by Visitech Intl. Ltd. and by Prairie Technologies, Inc. (see Table 5.3). Intensity control via an electro-optic modulator is described in Chapter 3. For use of polarizers to control laser intensity, see above under Attenuation of Laser Beams.

Polarization of the Laser Light

We measured a degree of polarization of the light entering the Zeiss AOFT at better than 1000 : 1. Using a compact home-built polarization sensitive power meter at the sample position the laser light was still very well polarized, better than 200 : 1 with the prin-

cipal axis 5° counterclockwise from the positive *x*-axis of the stage (i.e., left to right direction).

SPATIAL BEAM CHARACTERISTICS

Although lasers provide very small beam divergence, the uniformity of the intensity across the beam may be relatively poor. Fortunately, this is generally not a serious problem because the uniformity of illumination can be easily improved by spatial filtering. Filtering is very efficient when there is good spatial coherence of the beam.

Several devices are available for spatial filtering; the most common is the Gaussian spatial filter (Melles Griot, see Table 5.3), which consists of a focusing lens that converges the beam toward a very small pinhole. After this pinhole, a second lens, one focal length away, is used to regenerate a parallel beam. By choosing the focal lengths of the two lenses carefully, this configuration can also be used to expand or decrease the beam diameter but a pinhole is always essential for spatial filtering. Spatial filtering takes place because diffraction effects at the pinhole produce an out-going wavefront, which is the Fourier transform of the pinhole and is not affected by the spatial properties of the light impinging on the pinhole (Fig. 5.7). It should be noted that dust particles moving in the vicinity of the pinhole can modulate the transmitted intensity, so great care must be taken to ensure that this does not occur. For most practical purposes, a single-mode optical fiber functions as a spatial filter.

For large size beams from, for example, excimer lasers, an external beam homogenizer consisting of a prism/lens combination can be used. The optics recombine sections of the beam to produce a homogeneous rectangular shape (Austin *et al*., 1989).

Edge-emitting diode lasers typically require extensive astigmatic and anamorphic corrective optics to obtain a circular, parallel beam. Commercial packages are available to implement this (Ingeneric GmbH, see Table 5.3). However, the use of a spatial filter, a single-mode fiber-optic, or an overfilled back aperture plane can also produce a symmetric beam.

LASER REQUIREMENTS FOR BIOLOGICAL CONFOCAL LASER SCANNING MICROSCOPY-RELATED TECHNIQUES

Optical Tweezers

Single-cell manipulation is feasible by trapping the cell in an optical box formed by one or more focused laser beams. Each focal spot has a diameter of about 1 µm. Taken to the extreme, optical trapping can take place in a completely enclosed environment. Ashkin and colleagues (1987) reported the optical trapping of particles and viruses although the technique was also used decades earlier for levitation of particles in light-scattering experiments. A simple design is given, for example, in Smith and colleagues (1999). A beam power of 20 to 100 mW TEM_{00} at the specimen is sufficient. For biological specimens infrared light should be used. A careful choice of the trapping wavelength is essential to reduce optical damage to biological samples as much as possible. Shorter wavelengths are absorbed by the specimen, longer wavelengths by water. Therefore, traps commonly use a Nd-YAG (Hoffmann *et al*., 2000; Reichle *et al*., 2001) or a Nd-YLF 100 mW laser operating at 1064 nm. Other useful lasers may be a 632.8 nm, 25 mW He-Ne laser, or a diode laser beam. An improved design is given by Bechhoefer and Wilson (2002). Fiber lasers with their diffraction-limited output and excellent beam quality are also very suitable for laser tweezers applications (Woods, 2003).

Optical trapping of particles larger than the illumination wavelength can be explained with geometric optics. When a transparent spherical particle, having a refractive index larger than the surrounding medium, refracts a ray of light, a change in momentum of the refracted photon occurs. Due to the principle of conservation of momentum, the particle receives an equal but opposite change in momentum. This force pushes the particle away from the direction of the refracted photon.

When a particle, somewhat smaller than the focal spot of the laser beam, is suspended in the intensity gradient of a Gaussian beam profile, then the intensity of the light on one side of the particle is larger than on its opposite side. This makes the particle move to the side with the higher intensity (i.e., the center of the laser beam) and it seems as if the laser beam attracts the particle.

Heating and Damage Effects in the Cellular Environment

Cells attached to biosensor surfaces may suffer additional heating effects because of one-sided contact with a buffer solution and close contact with coated or absorbing semiconductor surfaces. Objects caught in an optical trap are also subjected to more severe heat stress. For instance, a 100 mW Nd-YVO_4 laser focused into watery media heats it by 0.8 K/100 mW, but, add a polystyrene bead in glycerol, and it jumps to 4 K/100 mW. Even when this amount of heat is not damaging to the cell, it influences the calibration of the trap, that is, the force–displacement relationship (Boas, 2003; Peterman, 2003). Several studies report cell damage conditions (König et al., 1996) of NIR multi-mode optical traps. Neumann (1999) shows that for the spectral region from 790 to 1064 nm, an oxygen-mediated, one-photon process is causing the damage. Wavelength and power level effects monitored over time by Leitz and colleagues (2002), indicate that the 700 to 760 nm spectral region is unsuitable due to induced photochemical effects, but that 810 nm is better because only photothermal effects occur. These can be controlled by reducing the trap energy to 36 mW. Cellular response to NIR light with varying pulse length is reported by König and colleagues (1999 and Chapter 38, *this volume*). Zhang and colleagues (1999) look at cell viability in CW Al : GaAs diode laser traps.

Total Internal Reflection Microscopy

For imaging cell adhesion and other biological processes such as vesicle transport and observing thin self-assembled layers

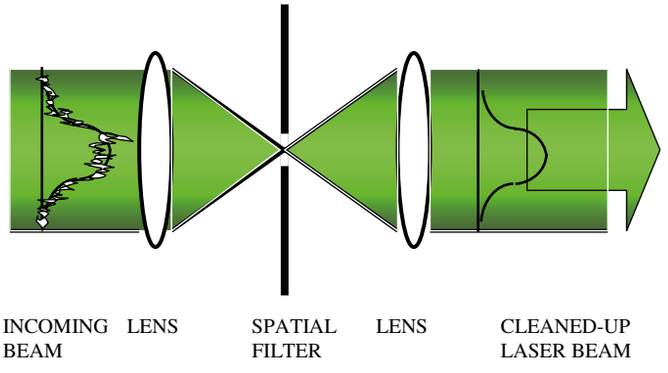


FIGURE 5.7. Diagram of a spatial filter by a pair of lenses and a small pinhole. High frequency noise is removed form the laser beam. The spatial intensity is cleaned up.

for biosensor applications, total internal reflection provides a background-free fluorescent imaging technique. Penetration of the evanescent wave beyond the boundary plane is limited to roughly 100 nm. Objects farther from the interface are not excited and stay dark. Two methods exist to create total internation reflection fluorescence (TIRF) conditions. One is to inject the light through a very high, ≥1.45, numerical aperture (NA) objective lens and the other utilizes an external prism coupling to the slide on the far side of the specimen. The through-the-objective lens method requires only 40 µW CW at 488 nm for green fluorescent protein (GFP) imaging with reduced bleaching effects. For the prism coupling technique, 20 mW CW was barely sufficient and would have benefitted from higher power. Other suitable lasers include 50 mW green 532 nm; 70 mW He-Ne laser, or 200 mW 488 water-cooled argon-ion lasers. It must be noted that, at these power levels, some published configurations of the external-beam prism method can be very hazardous to the eye.

Confocal Raman Confocal Laser Scanning Microscopy for Chemical Imaging

Raman spectroscopy and imaging is used in research on immobilized molecules and biosensor interfaces. It requires a mode-hop-free tuning range of several gigahertz, a narrow line width of 1 MHz, and output power of several hundred milliwatts. Cellular autofluorescence can present a large background. In order to reduce its influence, red excitation from a diode laser is a good choice. Stry and colleagues (2004) utilized a Tiger ECDL laser system (see Table 5.2), with grating tuning from 775 to 785 nm, and also from 730 to 1085 nm with 1 W output power.

Coherent anti-Stokes Raman scattering (CARS), complementary to CLSM, maps via vibrational contrast the intracellular water distribution. It uses the beat frequency of two lasers, preferably operating in the IR to avoid damage to cells as much as possible. Multi-photon lasers emitting picosecond pulses with widths of 2 to 5 ps are better for CARS because their spectral linewidth matches the typical Raman bandwidth of ~20 cm^{-1} much better than femtosecond pulses (Nan *et al*., 2004). They were able to visualize the CH_2 stretch vibrations from lipid tails (see also Chapter 33, *this volume*).

Non-Linear Confocal Microscopy

Second harmonic imaging is a very good method to probe external membranes of living cells. Laser system considerations and characteristics are given below under Wavelength Expansion Techniques. The SHG images show little speckle background and can be created with about the same laser intensity as used for fluorescence imaging. One can track microtubules with SHG and intracellular inhomogeneities with third harmonic generation (THG) (Hogan, 2004). Yang and Mertz (2002) used, for example, a mode-locked 860 nm Ti : Sa laser (see below) with a ~100 fs., 82 MHz optical pulse train that delivered 10 mW at the sample (see also Chapter 40, *this volume*).

Nanosurgery and Microdissection

Multi-photon imaging systems can be used for multi-photon ablation of cellular structures and tissue. It requires high (kHz) repetition rate lasers with 1 to 10 µJ pulse energies (Arrigoni, 2004a; also see Chapter 38, *this volume*).

TYPES OF LASERS

The earliest lasers were solid-state lasers using ruby as the active laser medium (Bertolotti, 1983). Subsequently, a wide variety of lasers were developed (Weast and Tuve, 1971; Arecchi, 1972; Brown, 1981; Bass and Stitch, 1985; Eden, 1988; Fermann *et al*., 2002; Silfvast, 2004; Webb and Jones, 2004). Essentially, all CW gas lasers (Bloom, 1968) and some solid-state lasers with emission in the visible part of the electromagnetic spectrum, meet the minimum intensity requirements estimated above for fluorescence microscopy. The list of available wavelengths continues to expand (Weber, 1999). For trapping and label-free SHG microscopy, IR wavelengths are the most suitable. Some other important parameters are the output power at each wavelength, efficiency, and stability. Table 5.1 lists the major types of CW lasers. Table 5.2 lists the major options for pulsed-laser systems.

CONTINUOUS WAVE LASERS

Continuous wave (CW) lasers can be divided into several classes:

- gas lasers
- dye lasers
- solid-state lasers.

Gas Lasers

Three major types of CW gas lasers are available (Bloom, 1968):

- argon-ion, krypton-ion, and a mixture of argon and krypton (mixed gas)
- helium–neon
- helium–cadmium
- alkali metallic vapor lasers.

The CO and CO_2 lasers that emit around 5 µm and at 10.6 µm are not discussed here. Commercially available, but not widely used and therefore also omitted from further discussion, are the neon laser that can emit 1 W of multi-line UV (CW) at 339.2 (0.3 W), 337.8 (0.2 W), and 332.4 nm (0.5 W) and the xenon laser emitting between 488 and 540 nm but usually only operated in pulsed mode. In general, krypton and helium–neon lasers are used only if red excitation is necessary, but the latter also now provide lines in yellow, green (GreNe), and orange (594 nm). With the increasing availability of red-absorbing dyes, their importance is growing. Several leading confocal microscope manufacturers still equip their systems with red and green helium–neon lasers emitting a few milliwatts and air-cooled argon-ion lasers. Argon–krypton mixed-gas ion lasers often form a cheaper alternative to the purchase of separate argon and krypton systems plus the additional requirements for power and beam-steering optics. It is worth realizing however, that the lifetime of a specific red laser line in a mixed gas laser may be much less than the stated lifetime of the strongest laser line (green, 514 nm).

Argon-ion

Because its emission wavelength matches the absorption peak of fluorescein and other popular dyes, the argon-ion laser is still by far the most common laser in microscopy. Lately, however, highly efficient 488 nm small-footprint, solid-state lasers have appeared.

TABLE 5.1. Continuous Wave Lasers

Tunable CW Dye lasers

Manufactory & Model	Pump Power	Wavel. Range	Spectral Width	CW Av. Power	Noise	Abs. Acc.	Wavel. Reset.	ASE	Conv. Eff.	Freq. Stab.	Beam Parameters			
											Diam.	Div.	Mode	Pol.
	mJ	nm	mW		rms, %	nm	nm	%	%	MHz/b	mm	mrad		%
Coherent 599[1]		390–930	20–401 60–100 500 GHz	200–1200	1/3-day						0.6	1.5	TEM_{00}	V
Radiant Dyes & CW Dye L.		560–650			2/h				<25		<1.3	<1.5		
Coherent 899[2]	5–15 W	370–1100	40–200 GHz	10–2000		0.1	0.1							
Radiant Dyes[3] & Dye		400–850	1/20 MHz		2.5	<0.03	<0.005	<0.5	12–32	100 Mhz/h		<0.5	TEM_{00}	V, >98
Ti:Sa		700–950	2 GHz											

Legends: Wavel(ength); CW: Continuous Wave; Av(erage), Power; Abs(olute) Acc(uracy); Wavel(ength) Reset(tability); ASE: Amplified Spontaneous Emission; Conv(ersion) Eff(iciency); Freq(uency) Stab(ility); Reset(ability); Beam Parameters Diam(eter) (e^{-2} = 13.5% intensity level), Div(ergence) (full angle), Mode, Pol(arization).

[1] Standing wave 3 mirror cavity dye laser, Invar bar temperature stabilized, Argon-ion and Verdi DPSS pump power 5 W UV or R, B, G, pump wavelength and output power depend on dye. 20–40, 60–100 and 500 GHz 1, 2 and 3 plate birefringent tuning, noise rated between 10 Hz and 100 kHz.

[2] Combined dye + TI:Sa resonator design, single frequency ring dye laser, accommodates both low (<8 W) and high power (>10 W) pump lasers, LiO_2 and KTP frequency doubling extends range down to 270 nm, Autoscan II complete automation. Example of costs for a second hand 899 system, without Ti:Sa: ~ 12,000 USD.

[3] Ti:Sa/Dye ring laser: Pumped with 308 nm excimer or 532 nm Nd:YAG; invar bar resonator, Linewidth for active/passive single frequency operation 1/20 MHz, broadband 3 plate birefringent filter 2 GHz, noise between 10 Hz and 1 MHz, Labview and C++ software control.

(*Continued*)

TABLE 5.1. Continuous Wave Lasers (*Continued*)

Manufactory & Model	Life & Power Cons.	Wave-length	CW Av. Pwr	CW Av. Pwr	CW Av. Pwr	Wave-length	CW Av. Pwr	Wave-length	CW Av. Pwr	Noise & Stabil.	Beam Parameters				
											Diam.	Div.	Mode	Pol.	Qual.
	(h) & (W)	(nm)	(mW)	(mW)	(mW)	(nm)	(mW)	(nm)	(mW)	(rms, %)	mm	mrad			M^2
Gas lasers: Argon- and Krypton-Ion Pure Gas and Mixed Laser Systems															
Coherent			70C-5	70C-K	70C-		300C-		Sabre						
Ion lasers[1]			Argon	Krypton	Spectral		308								
Small frame	>5,000 &	ML UV	50		50	351.1	250	275.4	180						
Water-cooled						363.8	250	302.4	380						
70C Innova[2]	<40 A/ph.	ML B.G	5,000			MLUV	750	334.5	500	0.5 light	1.5	0.5 (Ar)	TEM_0		
Series	3 phase	MM B.G	6,000			454.5	140	275.4–		reg.		0.8 (Kr)			
		457.9	300			457.9	560	305.5	1,600						
		465.8	70		30	465.8	180	300.3–		(3 long					
		472.2	100			472.2	240	335.8	3,000	term)					
		476.5	600		100	476.5	950	351.1	1,800	current					
		488.0	1,500		250	488.0	2,400	363.8	1,700	reg.					
		496.5	600			496.5	950	333.6–363.8							
		501.7	350			501.7	480		7,000						
300C-308	<55 A/ph	514.5	2,000		250	514.5	3,200			0.2	1.8 @*	0.4 @	TEM_0		
Small frame	3 phase	520.8			130	520.8		454.5	800		514.5	514.5			
Water-cooled		528.7	300			528.7	550	457.9	1,500						
		530.9			130			465.8	800		<2.6	<0.8			
Large frame	<70 A/ph	568.2			150	ML-VIS	8,000	472.2	1,300						
Water-cooled	3 phase	ML-VIS					8,000	476.5	3,000						
Sabre DBW25[3]	B							488.0	8,000						
Dual Brewster		ML Red		750				496.5	3,000						
Window (DBW)		ML white			2,500			501.7	1,800						
or Tunable		647.1		500	250			514.5	10,000						
Sealed Mirrors		676.4		120				528.7	1,800						
(TBM)		752.5			30			ML							
								VIS	25,000						
Coherent &	>5,000 h	457.9	80							<0.75	<1.3	<0.8	TEM_0	V	<1.2
Enterprise II	<31 A	488	200]							6 pp				100 : 1	
–610[4]	1 phase	514.5	350												
Water-cooled		ML VIS	1,000												
LASOS Laser		454.5–	40							<1	0.66	<1.05	TEM_{00}	V	<1.3
& Argon-ion[5]		514.5												500 : 1	
SpectraPhysics	<20 A	458	40 mW							<0.1	0.69	<0.95	TEM_{00}	V	<1.2
& Advantage[6]		488	all lines							<1 pp				100 : 1	
163Caircooled		514													

Gas lasers: Helium–Cadmium (He-Cd), Green/Yellow/Oramge/Red Helium–Neon (He–Ne)[7]									
Cooke Corp. &	n.a. &							H	
He–Cd, White +	<600–700	RGB	20–50	<0.5	1–2	0.5–1	Single/	100 : 1	
Black Knight[8]		325, 441.6	20–50	<0.5			Multi		
		RG, UV	30						
Melles Griot &	>50,000							V	
Green HeNe		543.5	1		0.88	0.81		500 : 1	
Yellow HeNe		591.1	1		0.75	0.92		random	
Orange HeNe		611.9	1		0.88	2.2			
Lasos Lasert &	>20,000								
Red HeNe		632.8	>10	0.5%	0.7	<1.4	TEM_{00}	500 : 1	<1.2

Legends: Lftm. (Lifetime); Pwr = Power; Cons(umption); FWHM (Full Width Half Maximum); Beam Parameters Diam(eter) (e^{-2} = 13.5% intensity level), Div(ergence) (full angle), Mode, Pol(arization); Qual(ity); ph(ase); ML Multiline; MM = Multi Mode; pp: peak-to-peak; reg(ulation), RGB: Red Green Blue, TBM: Tunable Bragg Mirror.

[1] Spectra-Physics produces similar water-cooled on lasers both in pure and mixed Argon/Krypton with Z-Lok automatic single frequency stabilization and J-Lok jitter reduction. Examples are the BeamLok 2060 and 2080 pure gas models and the Stabilite models 2017 and 2018-RM, as well as BeamLok 2060 mixed gas lasers.

[2] Innova Series V plasma tube, SuperInvar resonator, Model 70C: 3 phase with <40 A/phase, 8.51 cooling water flow rate/min., Model 300C: 3 phase with <55 A/phase, 9.6 l/min. cooling water, sealed mirrors, with PowerTrack, ModeTrack, ModeTune, modehop-free operation with etalon.

[3] 3 phase with <70 A/phase, SuperInvar stable resonator, with Sentry system management complete automation for wavelength selection, mode-control, search and tune, 5 min warm-up, NuTrack active cavity length stabilization for single frequency operation, Sabre Purelight Low Divergence beam diameter and beam divergence, noise level between 10 Hz and 2 MHz.

[4] Single phase and <31 A, SuperInvar resonator, 8 l/min. cooling water, Series V plasma tube, Single line and UV emitting systems also, Innova: Series V plasma tube, SuperInvar resonator, Model 70C: 3 phase with <40 A/phase, 8.51 cooling water flow rate/min., Model 300C: 3 phase with <55 A/phase, 9.6 l/min. cooling water, sealed mirrors, noise level with PowerTrack, ModeTrack, ModeTune; mode-hop-free with etalon.

[5] Warm-up time 15 min., stability <1% over 2 h., noise between 20 Hz and 2 MHz, beam pointing stability <30 µrad/3K.

[6] Advantage Model 163C–A 02, Noise level from 10 Hz–3 kHz, 0.3% from 10 Hz to 2 MHz.

[7] Many He-Ne suppliers exist. He-Cd are made by The Cooke Corporation, Melles Griot and Kimmon Electric, Vapor lasers. HeNe: Green 543 nm; Orange 594 nm; Red 633 nm Model LGK-7654-8 20 min warm-up time, noise between 30 Hz and 10 MHz, 5% power stability over 8 h.

[8] Black + White Knight RGB –450M, RGB 441.5/537.8/635.5 nm, other non-RGB version as indicated. Warm-up time 20 min., noise between 10 Hz and 10 MHz, stability 3%/2 h.

(*Continued*)

TABLE 5.1. Continuous Wave Lasers (*Continued*)

Diode lasers: Continuous Wave															
Manufactory & Model	Lifetime	Power Cons.	Wavel. & Spectr W.	CW Av. Power	Noise	Pointing Stab	Power Stab.	Mod. Freq.	Pulse Mod	Rise time	Beam Parameters				
											Diam.	Div.	Mode	Pol.	Qual.
	h	W	nm	mW	rms, %	µrad/°C	%	MHz	MHz	msec	mm	mrad			M^2
Blue Sky Res		<12	488 ±	25	<1%	<4	<2				0.7	<1		H	
& Chroma-			0.5 &											100 : 1	
Lase 488[1]			0.1												
Coherent[2] &			375 ± 5	8	<1	<0.6	<5	<5 Hz		<200	1 × 3	0.6 × 1	TEM_{00}	100 : 1	
Radius 375-8		<15	405 ± 5	50		<0.6	<5	<5 Hz		<200	4.7 × 1.6	0.7 × 0.3	TEM_{00}	100 : 1	
Radius 405-50	>10k		408	25											
Sapphire 460			460 ± 2	200	<0.5	<30	<2				0.7	<1.2	TEM_{00}	V100 : 1	<1.1
488-200[3]			488 ± 2	200	<0.5	<30	<2				0.7	<1.2	TEM_{00}	V100 : 1	<1.1
Radius 440-16	>20k	<15	440 ± 5	16	<0.5	<0.6	<5	<5 Hz		<200	1 × 3	0.7 × 0.3	TEM_{00}	100.1	
Radius 635-25			635 ± 7	25	<0.5	<0.6	<2	<100 Hz		<5	1	0.7 × 0.3	TEM_{00}	100 : 1	
Microlaser &			375 ± 5	6							6 stand.	<0.7	TEM_{00}	>100 : 1	
Lepton series			408 ± 10	36							or	<0.7	TEM_{00}	>100 : 1	
L4 xxx–xx–TE/			440 ± 10	12							1/2/4/	<0.7	TEM_{00}	>100 : 1	
			473 ± 10	3								<0.7	TEM_{00}	>100 : 1	
Novalux Inc.[4]	Twice that	<20	460 ± 2	5	<0.2	<30	<2				0.7	<1	TEM_{00}	V100 : 1	<1.2
& Protera	of argon ion	<20	488 ± 2	5–20	<0.2	<30					0.7	<1.2	TEM_{00}	V100 : 1	<1.2
xxx–x		<20	532 ± 2	5	0.2	<30	<2				0.7	<0.8	TEM_{00}	V100 : 1	<1.2
Power			375 ± 5	8				20–100	100 MHz		2.5 × 4	<0.5			
Technology			405 ± 10	50					dig. TTL		1.3	<0.5			
Inc.[5] &			440 ± 10	16							2.5 × 4	<0.5			
IQ series			473 ± 5	4							2.5 × 4	<0.5			
Toptica &			405 ± 10										TEM_{00}	100 : 1	
PVLS 500	>5000			3.5							2.1–4.3	<0.2			
PVLS 3000	>5000			50								<0.2			
Fiber Lasers															
Guided Color[6]			491	10	<1	<25								50 : 1 or	<1.3
& Fiber laser														random	
Lumics GmbH[7]			490 ± 3	>5	<0.5		<2						TEM_{00}		<1.1
National Laser		<15	490	10	<0.5	<30	<2				0.7	<1.2	TEM_{00}	random	<1.4
& LasNOVA[8]															
Unique-m.o.d.e	>10,000	5	491.5 &	5–10			<2				0.75	<1.2	TEM_{00}	random	<1.1
AG[9] &			<1		V 1										
UMFL491					<0.3										

Continuous Wave DPSS Lasers												
Cobolt AB &												
Blues[10]		<20	473	50	<0.5		3 (3 h)	0.1	<6	TEM_{00}	100 : 1	<1.2
Samba		<20	532	100	<0.5		3 (3 h)	0.1	<6	TEM_{00}		
INNOLIGHT[11]												
& Mephisto QTL			947	500	<0.1					TEM_{00}		<1.1
Mephisto Mephisto			1064	2000	<0.1					TEM_{00}		<1.1
YLF Mephisto E			1319	500	<0.1					TEM_{00}		<1.1
			1444 & 1 kHz	200	<0.1					TEM_{00}		<1.1
LaserQuantum & Torus 532			532	50–300	<1	<5	<1	2.5	0.5	TEM_{00}	V 100 : 1	<1.1
Melles Griot[12] &												
85 BTA			442 ± 3	5/8/10	<2 pp		~2.5	0.65	<1.1	TEM_{00}	V100 : 1	<1.2
85 BTC			442	45								
85 BCA[13]		<100	473 ± 5	5/10/15		<10 /h	~2.5	0.67		TEM_{00}	V100 : 1	<1.2
85 YCA		<60	561	>10	<2 pp <0.5 <3 pp			0.67	<1.2	TEM_{00}		<1.2
Rainbow Ph.[14] &												
BluePoint430		<60	430 ± 1	10	<0.5	<30	<2	0.4 × 0.3	<0.8	TEM_{00}	V100 : 1	<1.1
473 laser		<15	473	5–40	<1	<20	<2	0.25	3	TEM_{00}		<1.2
BluePoint488		<60	488 ± 1	5	<0.5	<30	<2	0.4 × 0.3	<0.8	TEM_{00}		<1.1
Toptica[15] &			605	50								
Eksel 110			evaluation									
TorsanaLas.[16] &	>10,000	<40	488 ±		<0.75	<40		0.7			V	
Starbright 488			0.3 & 0.1									
DPSS Kits												
ALPHALAS			1064	350			Q-Sw			TEM_{00}		
DPSS–[17]			532	15			IR + 532					

Legends: Pwr = power; Cons(umption); Wavel(ength); Spectr(al) W(idth) given as FWHM (Full Width Half Maximum); CW: Continuous Wave; Av(erage) Power; Pointing & Power Stab(ility); Mod(ulation) Freq(uency); Beam Parameters Diam(eter) (e^{-2} = 13.5% intensity level), Div(ergence)(full angle), Mode, Pol(arization), Beam Qual(ity). DPSS: Diode Pumped Solid State lasers.

[1] Noise between 20 Hz and 20 MHz, power stability over 8 h.

[2] Several models with varying output available, Model 375-8 CDRH; Model 405, noise between 210 Hz and 10 MHz, modulation may save tube life.

[3] Noise between 20 Hz and 2 MHz, power stability after 2 hours and ±3°C.

[4] Model 460-5; Model 488-15: Warm-up time <5 min, Spectral width <<0.01 nm, Noise between 20 Hz and 2 MHz typically only 0.03%, IR emission <0.1 mW, warm-up time 2 min.

[5] IQ series: Instrument Quality, beam circulization available as well as analog and digital modulation.

[6] Fiber Laser (Guided Color Technologies GmbH): noise level when stabilized otherwise >10%.

[7] Lumics LU0490F005.

[8] Noise level between 30 Hz and 100 MHz.

[9] Warm-up time <10 min, noise between 10 Hz and 10 MHz, optional single-mode fiber coupling.

[10] Noise level between 10 Hz–100 kHz pp, <3% between 100 kHz–5 MHz, <0.5% between 5–100 MHz, 3% long term (3 h) stability.

[11] Ring geometry DPSS, single frequency (1 kHz) with PZT over 20 GHz tuning range, noise eater option.

[12] Warm-up time 3 min, to beam-pointing stability 10–15 min, noise between 20 Hz and 10 MHz, TEC cooled.

[13] Warm-up time <3 min, Noise between 20 Hz and 10 MHz, pointing stability for ±2°C.

[14] Noise between 10 Hz and 10 MHz, power and pointing stability after 2 h, 473 nm laser data from CrystaLaser Inc., warm-up time 1 min.

[15] Evaluation kit for GaAsSb 5 W 808 nm pumped DPSS laser.

[16] Warm-up time <1 min, noise level between 20 Hz and 20 kHz.

[17] Kit comes complete with Nd:YVO4 or Nd:YAG crystal, pump diode, mirror sets, KTP doubling crystal, 670 nm alignment laser diode, IR — VIS converter.

TABLE 5.2. Pulsed Lasers

Manufactory & Model	Pump Power	Wavel. Range	Spectral Width	CW Av. Power	Noise	Abs. Accur.	Wavel. Reset.	ASE	Conv. Eff.	Freq. Stab.	Beam Parameters				
											Diam.	Div.	Mode	Pol.	Qual.
	mJ	nm	mW			nm	nm	%	%	$cm^{-1}/°C$	mm	mrad			M^2
Pulsed dye lasers															
LambdaPhysik & ScanMatePro[1]	<65@355 <150@53 2 @ 40 Hz	198–320 850	0.03, 0.07 –0.15 cm^{-1}		(rms) (%)			<0.5	28			0.5			
SpectraPhys.[2] & Duo	@1–30 Hz	360–950		1.5	6 pp						2 × 3	4			<1.1
SpectraPhys.[3] & Cobra	5–35 (gr) 5–80 (pr)	330–780	4 / 0.04 and		<0.5	<0.03	<0.005	<0.5	<20	<0.01 <0.05		<1.5		>98	
Cobra Stretch	8–150 (gr) 8–230 (pr)		0.02 cm^{-1}		<0.5	<0.03	<0.005	<0.5	<28	<0.01 <0.05		<1		>98	
PrecisionScan	50–650 (gr) @<100 Hz				<0.5	<0.03	<0.005	<0.5	<28	<0.01 <0.05		<0.5		>98	
Pulsed nitrogen lasers															
Manufactory & Model	Lifetime h	Power Cons. W	Wavel. & Spectr W nm & Mhz	CW Av. Power mW	Noise rms, %	Pointing Stab. µrad/C	Pk-Pk Stab. %	Rep. Rate MHz	Pulse Width ps	Pk Pwr & Pk E. mW & µJ	Beam Parameters				
											Diam. mm	Div. mrad	Mode	Pol. %	Qual. M^2
SpectraPhysics[4] & VSL337		337.1	0.1				<4 pp	1–20 Hz	4 k	30 kW & >120	3 × 7	3 × 8			
Pulsed excimer lasers															
Lambda-Physik & LPXPro		308 351		38 k 28 k			<0.0001 <0.0001		n.a. & 400 320						
TuiLaser AG & Excistar[5]		308 351		3.5 k 3.5 k		<2 <2	<0.0005 <0.0005	10,000 10,000	n.a & 8 8	3 × 6 3 × 6	<1 × 2 <1 × 2				
Pulsed diode lasers															
Becker-Hickl[6] & BDH series			375, 405, 475, 635, 680, 780	0.8, 2.4 0.9, 0.5, 10			<2	20 50 80	60, 60, 50, 50,	100–500					
Hamamatsu[7] & PLP-10		90	375, 405, 440, 470, 635, 650, 670, 780, 850 All ±10	70, 50, 20, 20, 30, 30, 30, 30, 50 pk power				2 Hz–100	100			15–34, 13–22, 10–35, 10–30, 12–32			

Pulsed diode laser									
PicoQuant[8] &		400, 635				0.1–1500			
MDL 300		670, 805							
PicoQuant &		375, 405,	1.0, 1.0,	<1			<70, 70,		>90
PDL LDH		440, 470	1.0, 1.0	3 pp			90, 90		>90
		& ±3	(wide)				narrow		
PicoQuant[9] &		635,	3.5,		<1%	40–80	<90,		>90
PDL LDH xxx		637, 655,	8.0, 6.0,		3% pp		100, 70,		>90
		660, 665,	8.0, 4.0				90, 90,		>90
		670, 690,	2.0, 8.0,				70, 70,		>90
		735, 757,	3.5, 6.0,				130, 90,		>90
		785, 806,	8.0, 10,				70, 120,		>90
		830, & ±7	4.0				100		>90
			(wide)				narrow		
PicoQuant[10] &		530 (SHG)	600				<50	600	
PicoTA		780–790,	160				<90	7000	
		1060.1065	150				<80	6000	
Pulsed vapor lasers									
Oxford		510.6					2.5 k to 3 3		
Lasers[11] &		578.2							
LS 10-10	<3 k		10 k		<5	0.01	40	4	
LS 20-10	<3 k		20 k		<5	0.01	80	4	
LS 20-50	<3 k		20 k		<2	0.01	80	4	
LS 35	<3 k		35 k		<3	0.01	140	4	

Legends: Power Cons(umption); Wavel(ength); Spectr(al) W(idth); CW: Continuous Wave; Av(erage) Power; Abs(olute) Accur(acy);Wavel(ength) Reset(tability); ASE: Asynchronous Spontaneous Emission; Conv(ersion) Eff(iciency); Freq(uency), Pointing, Power and Peak-to-Peak (pk-pk & pp) Stab(ility); Rep(itition) Rate; Peak Power (Pk Pwr) & Pulsek E(nergy); Beam Parameters Diam(eter) (e^{-2} = 13.5% intensity level), Div(ergence) (full angle), Mode, Pol(arization), (Beam) Qual(ality).

[1] Model ScanMatePro 2 pumped by both <40 Hz 308 nm Excimer and <50 Hz 355 as well as 532 nm Nd-Yag, 28% pump efficiency at 560 nm with Rhodamine 6G, frequency extension to 198 nm.

[2] Nitrogen laser pumped, pulse width >4 ns.

[3] Cobra series and PrecisionScan pumped by 355 nm and/or 532 nm at 10–100 Hz with Nd-Yag laser, LambdaLok (LLOck) frequency stability <0.01 cm^{-1} in Table LLock for PrecisionScan conversion efficiency at 570 nm, Labview and Sirah control software, SHG and THG packages available.

[4] Air-cooled VSL-337, int. and ext. trigger capabilities.

[5] Excistar S-500 suitable as pump source for cuvette type dye laser.

[6] Warm-up time 3 min., average power at 80 MHz pulse repetition rate, pulse width at 50 MHz @ 1 mW power, more red wavelengths available.

[7] Output peak power after fiber pigtail, wide pulse (listed) and narrow pulse operation.

[8] MDL: Modulated diode lasers, modulation frequency range 100 kHz–1.5 GHz.

[9] Repetition rate 80 MHz but other frequencies possible, pulse width with narrow pulse listed; with high power adjust pulse width is ~ <300 ps for wavelengths below 470 nm; above 470 nm pulse width in high power adjust mode <400 ps.(wide pulse listed), selected 50 ps devices , narrow distributed feedback bandwidth available, 440 nm also available with 3 mW average output.

[10] 80, 40, 20, 10 and 5 MHz pulse repetition rates and adjustable rates, ASE <50 mW @ 780 nm, <60 mW @ 1060 nm, fiber coupling passes <5% IR in multimode and <0.1% for single-mode fiber-optic, spectral linewidth 4 nm or 0.1 nm (narrow).

[11] Water consumption 2 l/min, 80% of plane-plane cavity output within 0.6 mrad, Timing jitter (ps): LS 10-10/20-10: 5 ps, LS 20-50: 2 ps, LS 35: 3 ps.

(*Continued*)

TABLE 5.2. Pulsed Lasers (*Continued*)

Manufactory & Model	Lifetime	Power Cons.	Wavel. & Spect W	Peak Energy	Jitter/ Noise	Pointing Stab.	Power Stab.	Mode lock	Pulse Width	Pulse Width	Beam Parameters				
											Diam.	Div.	Mode	Pol.	Qual.
	h	W	nm/Mhz	mJ	ns / %	µrad/C	%	MHz	ps	mW & µJ	Mm	mrad		Dir/%	M^2
Pulsed DPSS lasers															
Becker & Hickl[1] & BDL-405			405	0.3–1.3	<10 ps	20–50	20–50		20–8	>60					
Coherent[2] &	>10 k		527	15 k	12					200 ns	5		TEM_{00}	H	
Evolution with	(pump		527	30 k	20					200 ns	5		special	H	
Nd:YLF crystal	diode)		527	75 k	15					200 ns	7		version	H	
			527	90 k	18					200 ns	7			H	
Elektronik					0.04%				10 kHz		0.5	<0.7	TEM_{00}	H	<1.1
Laser System[3]			1,030	5–100 k					Q-sw						
& VersaDisk			515 / <5	2–15 k								<0.5		V/99	
GWU															<1.2
Lasertechnik[4] & simoLAS			1,064 ± 40	6 k											
Lumera Laser			1,064	16 k		n.a. & <1			160 ± 1	<10		<2	TEM_0	99	<1.1
& UPL-20			532	10 k											
SpectraPhysics[5]			527		3–20	n.a. & <1		<1	1–10 kHz		3		Multi-	H	
& Empower				30 k											
Spectra Physics[6]	>10 k	<700	532	2/5/6/8/		n.a. & 0.04	<2	1			2.3	<0.5	TEM_{00}	V/99	
& Millennia-Pro		<1.1 k		10 k											
Spectra Physics[7]	>10 k	<1 k	532	2000		n.a. & <1	25	<2	76 or 80	<12	1.4	<1	TEM_{00}	V/99	<1.3
& Vanguard	pump diode														
Coherent &		<1.3 k	532 &	2/5/6/8/		n.a. & <0.03	<2				2.25	<0.5		V/99	<1.1
Verdi			<5 MHz	10/18 k											
Kits															
ALPHALAS &		1,064/532							Q-sw.	Q-sw.		TEM_{00}			
Yag or YVO_4			500						5–15	10–30 k,					
			500						50–100 kHz	50–100 k					
Optronics[8]		1,064/532													

Pulsed lasers, ultrafast														
Amplitude Sys		1,030	1 k	n.a. &				50	<200					
& t-pulse				20 nJ										
Coherent[9] &	<2300	720–980	>1 k		n.a. &		2	90	<140	1.2		TEM_{00}	H/99.8	<1.1
ChameleonXR					<0.15									
Coherent		700–980	1.3 k		n.a. &		<3	76	<200	0.8	1.7	TEM_{00}	H	
Mira 900 fs[10], V			800		<0.1		<5		<3 k					
or Innova 310			1,400		<2		<5							
or Sabre 14 W			1.3 k		<2		<3							
Mira 900 ps, V			800		<0.1		<5							
or Innova 310		240–320	1.4 k		<2		<5							
or Sabre 14 W		350–500	2–15%		<2									
Doubling														
Coherent		800 ± 1			n.a &		1	80	<0.1			TEM_{00}	H/99	<1.2
Vitesse 800-2[11]			>200		<0.1					1.25	<1.2			
Vitesse 800-5			>650							1.45	<1.1			
DelMarVent&		1,230–1,270	180–250		n.a.				<65		<2	TEM_{00}	H	
SciCRF-65P					<2									
Femtolasers		800 & >50	880	1,600 &				11	<20	<2	2	TEM_{00}		<1.3
Productions				>80 nJ										
GmbH & FS														
Scientific XL[12]														
High Q Laser		800–900	>400				<1	75	<100			TEM_{00}	H	<1.2
& FemtoTrain[13]		1,064	>100–10 k				<1	60–1 k	7.5 k			TEM_{00}	H	<1.2
PicoTrain DPSS														
Quantronix &	3 phase	800 center		n.a & 1		<1.5%				10		near	V	<1.8
Integra-i[14]	50 A/ph											TEM_{00}		
SpectraPhysics[15]		710–990	1.5 k	150	n.a &	30 µrad/	<1	80	100	<2	<1	TEM_{00}	H	
& Mai-Tai					<0.1	100 nm							99.8	
SpectraPhysics					n.a &			80		<2	<1	TEM_{00}	500:1	
Tsunami fs[16]					<0.2									
w. MillenniaV		710–980	700	85					<130					
w. MillenniaX		700–1,000	1,400	170										
Tsunami ps														
w. MillenniaV		710–980	700						<2 k					
w. MillenniaX		700–1,000	1,500											
XL optics set		970–1,080												
Doubled fs sel				n.a &										
w. MillenniaV		345–540	>1.0	0.12 nJ										
w. MillenniaX		345–540	>1.8	0.22 nJ										
Doubled ps sel				n.a. &										
w. MillenniaV			>3.2	0.4 nJ										
w. MillenniaX			>6	0.75 nJ										
R&D Ultrafast		710–980												
Lasers Ltd &														
FemtoRose 100[17]									80–150					
FemtoRose 10									<10					
Time-Bandw&		780–860												
Tiger fs	<500		500				1%/°C	50–200	70			TEM_{00}		<1.1
Pallas ps	<500		500				1%/°C	75–200	–100 ps			TEM_{00}		<1.1

(*Continued*)

TABLE 5.2. Pulsed Lasers (*Continued*)

Manufactory & Model	Lifetime	Power Cons.	Wavel. & Spect W	Peak Energy	Jitter/ Noise, rms	Pointing Stab.	Power Stab.	Mode lock Freq.	Pulse Width	Pulse Width	Beam Parameters				
											Diam.	Div.	Mode	Pol.	Qual.
	h	W	nm/Mhz	mJ	ns / %	µrad/C	%	MHz	ps	mW & µJ	Mm	mrad		Dir/%	M^2
Pulse lasers: Ultrafast kits															
Avesta Project &						n.a. & <2						<2	TEM_{00}	H	
TIF-kit-xx			740–840	<250						<20					
			720–980	<1 k						<100					
CrF-kit-65P			1,240–1,270	<250						<65 s					
DelMarVentures			780–840,	250–1 k				<5	70–140		2–3	<2	TEM_{00}	H	
FemtoStart[18]			740–950,							20–200					
TISSA-20-100[19]			710–950												
Kapteyn-			780–810	400–450	n.a &				80–100	<15 fs	~1	~1	~	H	
Murnane Labs.			750–840		4.4–6.1					<25 fs			TEM_{00}		
& TS[20]			& >60 nm												

Legends: Power Cons(umption); Wavel(ength); Spectr(al) W(idth) at Full Width at Half maximum (FWHM); Av(erage) Power; T(iming) Jitter; Pointing and Energy Stab(ility); Rep(itition) Rate; Peak Power (Pk Pwr) & Pulsek E(nergy); Beam Parameters Diam(eter) (e^{-2} = 13.5% intensity level), Div(ergence)(full angle), Mode, Pol(arization), (Beam) Qual(ality).; fs: femtosecond, ps: picosecond, stabil(ity),V(erdi).

[1] Warm-up time 3 min., average power at 80 MHz pulse repetition rate, pulse width at 50 MHz @ 0.5 mW power, more red wavelengths available.

[2] Ti:Sa pump laser, pulse repetition rate 1–10 kHz,. Peak energy at 1 kHz pulse repetition rate, noise over 8 hours < 1% (rms).

[3] Noise level defined between 10 Hz to 1 GHz, consumes 600 W, linewidth without etalon < 1 GHz,, birefringent tuner for 1000–1060 nm region.

[4] Single-mode Nd:YVO4 ring laser.

[5] Nd:YLF pump laser for ultrafast amplifiers.

[6] Ti:Sa pump laser, noise between 10 Hz and 100 MHz, Quiet MultiAxial Mode doubling (QMAD), laserhead closed chiller cooled for 5, 6, 8 an 10 W versions.

[7] Model Vanguard 2000-HM-32, Nd:YVO4 lasing crystal, warm-up time 30 min, to full specifications 1 h., cooling air flow 300 cfm.

[8] Nd:YVO4 crystal, non-linear crystal, set of mirrors, Cr:YAG passive Q-switch, Glan-Taylor prism.

[9] Pumped by Verdi lasers, with Power Pulse automatic pulse width optimization, and Power Track active alignment, with MRU miniature air re-circulator unit for easy access to red wavelengths.

[10] V(erdi) model V8, Innova Argon-ion model 310-8 or V10 pump or Sabre ion laser 14 W pump laser, Optima version provides complete automated optimization, version S(imple) has manual starter, external Mira model 9300 harmonic generator with LBO crystal doubler with BBO frequency mixing crystal.

[11] Ti:Sa oscillator with built-in Verdi pump laser, noise between 10 Hz and 10 Mhz.

[12] (FemtoSource) Scientific SL.

[13] Ti:Sa model IC-xxx-400 many options w.r.t. crystals, pulse width, repetition rate, and PicoTrain, Nd:YVO4 crystal, output stability over 24 h.

[14] Pump source for OPA, includes Nd:YLF pump laser, stretcher, seed oscillator with multi-pass regenerative amplifier, compressor.

[15] Peak power at 800 nm, closed loop chiller, StabiLok beam pointing stability.

[16] Millennia V and X pump lasers, broadband optics, extra mirror set for wavelength range 970–1080 nm, average power at 970 nm, noise between 10 Hz and 2 MHz.

[17] Birefringent tuner.

[18] 5 W DPSS pump recommended, KLM mode-locking.

[19] 3–10 W DPSS or ion laser pump power.

[20] Pump power 6–10 W Ytterbium fiber pump, options available w.r.t. emission center, bandwidth and average power, FemtoRainbow 100 OPO KTP based delivers ~ 100 fs pulses.

Ultrafast fiber lasers

Manufactory & Model	Wavelength nm	CW Av. & Pk Power mW & kW	Time-jitter & Noise rms, ns/ %	Rep Ratel ML MHz	Pulse E & Width (FWHM) ML mJ & ps	Q-sw µJ & nsec	ML & Q-sw mJ & nsec	Beam Parameters Diam. mm	Div. mrad	Mode	Pol. Dir/%	Qual. M^2
IMRA & FemtoLiteA25	780	25		50	180 fs							
FemtoL.FX-10	800	10		50	120 fs							
Toptica[1] & FFS-F-C Sys	1,150–1,400	100			100 ± 10 ps					TEM_{00}	H	
Optical parametric oscillators (OPO)												
Coherent Mira-OPO[2] Ps and fs	525–665 KTP-ring-SHG 1050–1330 KTP linear/ ring-IR 1350–1600 CTA linear	>200–240 high power version	n.a. & <2 rates	76 MHz or other rep.	<1.2 ps <200			<1.25	<1.30	TEM_{00}	H >99	
Continuum & Sunlite EX[3]	222.5–450 445–1750 & <0.075		n.a. & ±10	10 Hz	350 mj @ 355 nm	50 mJ & 3–6 ns	50 mJ & 3–6 ns	~4–6	<1.5		V 99%	
GWU-Lasertechnik & Synchro fs[4]	870–1550 (s) 1570–5600 (i)	200(s)				n.a. & <250	n.a. & <250					
GWU-Lasertechnik & Synchro ps	1050–1510(s) 1590–3100(i)	250(s)				n.a. & <2 k	n.a. & <2 k					
Spectra-Physics[5] & OPAL 1.3	1100–1250	250	<5 stability	80 MHz	n.a. & <130 ps			<2.0	<1.0	TEM_{00}	H >99	
OPAL 1.5	1350–1600	200	<0.2		<130 ps							
Optical parametric amplifiers (OPA)												
Coherent[6] & OPA 9800/9850 Coherent[7] & OperA	1150–1600 (s) 1600–2630 (i) 400–1150 (SHG) 300–400 (FHG)		<2 (8 h)		>1 @ 800 nm 1 kHz	120 µJ @ 1.3 µm & <130	60 µJ @ 1.3 µm & <130 f				H(s) V (i)	
Quantronix[8] & TopasPlus Hep	417–2400				n.a. & 5–50 ps 80–150 ps	10–50	10–50					
Topas White	245–1700					10–50	10–50					
Spectra-Physics & Eclipse	1048 524	4 k 1.5 k		<7	n.a. <500 ps						99.9	

Legends: Av(erage) & Peak (Pk) Power; Rep(itition) rate; ML: Mode-Locked; Q-switched); Pulse E(nergy); Beam Parameters Diam(eter) (e^{-2} = 13.5% intensity level), Div(ergence) (full angle), Mode, Pol(arization), (Beam) Qual(ality);. i: idler; n.a.: not applicable; s: signal.

[1] FFS-F-C laser system: FemtoSecond Scientific Er doped fiber laser.

[2] 500 mW MIRA 900 pumping threshold, ring cavity version gives more output power, active length stabilization, sealed and purgeable, intracavity doubling for VIS range, NCPM crystal.

[3] Precision II models 355 nm pump laser, temperature stabilized, narrow bandwidth related replacement for a dye laser.

[4] 720–800 nm 1.2 W 100 fs pump at 1200 nm.

[5] Millennia X pump, LBO crystal, active stabilization, frequency doubler for visible, automated.

[6] OPA 9400/9450 and 9800/9850: RegA wavelength extension for Vis (blue) – NIR; RegA wavelength extension for NIR — MIR. RegA 9000/9500: High repetoition rate, < 260 kHz, ultrafast amplifiers, high spatial beam quality, one RegA can pump two OPAs. Other systems are: Hidra: custom high energy; Legend: Flexible Ti:Sa regenerative amplifier; Libra: One box, ultrafast Ti:Sa amplifier.

[7] gap free tuning from UV < 300 nm — MIR for wavelength extension of Legend and Libra, fs, lowest optical noise, automated, white light initiated OPA.

[8] Traveling Wave Optical Parametric Amplifier: femtesecond (listed) and picosecond pumped at e.g. 800 and 355 nm as well as 400 nm.

Their contrasting characteristics are described near the end of this section. As a pump source for Ti : Sa lasers, the argon-ion laser has been completely replaced by solid-state lasers.

In general, argon-ion laser stability is better than that of a krypton laser, with less gas slushing. The output power of krypton is at best about 30% that of argon under identical lasing conditions. Commercial systems provide a large variety of emission wavelengths and output powers (Fig. 5.8; Ginouves, 2002).

Fragile quartz plasma tubes have been replaced by versions with rugged metal/ceramic (beryllium oxide, BeO) envelopes for the small- and medium-frame lasers, which usually do not use a magnet to confine the plasma to the central core of the tube. External copper disks remove the heat.

Large systems with high output power use alumina (Al_2O_3) ceramic tubes with brazed tungsten/copper disks inside, crystalline quartz–coated windows, and quartz–metal hard seals (Fig. 5.4). This significantly increases their reliability. Other systems use rugged metal/ceramic BeO tubes. The central bore defines the laser beam. The plasma discharge pumps ions towards the cathode end of the tube, creating a pressure gradient between the anode and cathode. Return holes around the outer edge of the disks form an internal gas return path to maintain a uniform gas pressure along the length of the plasma tube. Typical gas pressure inside a gas laser is about 1 Torr.

The formation of color centers in the Brewster windows has been reduced by the use of better quality window materials, increasing the life span of this type of laser to 3000 to 10,000 h. However, tube lifetime may only reflect the life of the strongest laser line and not that of the weaker lines needed on a daily basis. The stability of these lasers, especially the small- and medium-sized models, is good because they can be cooled by convection (passive cooling) or forced air and their electric power requirements are modest. Some models are portable and easy to use. The larger frame lasers provide active resonator stabilization.

The wall-plug efficiency of large argon-ion models is very low (0.1% typical) and the heat generated must be removed with a large amount of cooling water. The turbulent flow causes some vibration in these systems while insufficient water flow may cause the cooling water to boil and lead to the destruction of the plasma tube. The large amount of heat generated also puts more strain on the resonator cavity. Longer warm-up times are necessary when no active stabilization is incorporated in the design. The operational lifetime of the higher power laser tubes is now well above 2000 h.

Using proper interference filters (inserted with their shiny side towards the laser head to prevent damage) or emission line selection by means of an AOTF or AOBS, single, strong laser lines can be selected. Dual line emitting argon-ion lasers simultaneously emitting at 454 to 457 nm and 514 nm are also offered (Table 5.1).

When the experiment requires a reliable, stable source of deep UV radiation at power levels of tens to hundreds of milliwatts, these ion laser systems provide a better alternative than any current solid-state UV laser system, as these require more steps to produce UV light. The area where the argon-ion laser was very valuable, as a 5 to 10 W pump source for solid-state Ti : Sa lasers, has been completely overtaken by solid-state lasers.

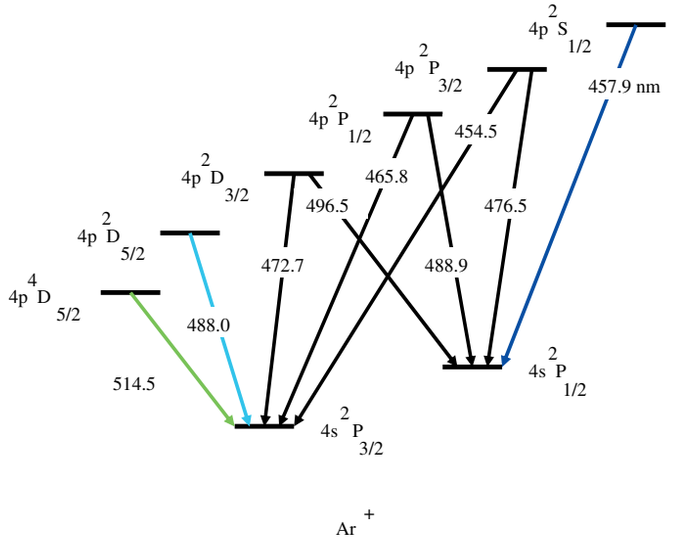


FIGURE 5.8. Schematic energy diagram for an argon-ion laser.

Argon-ion Laser Lines in the Ultraviolet

Commercially available argon lasers have emission wavelengths extending from 275 to 528 nm (Hecht, 1992). Higher discharge currents are necessary to populate the doubly-ionized argon levels sufficiently for deep UV emission. Wavelength selection is obtained by installation of an angle-tuned quartz prism or other appropriate optical elements. The wavelength range is extended down to 229 nm by inserting a frequency-doubling crystal in the laser cavity and thereby producing a CW intra-cavity frequency-doubled argon-ion laser system (FreD, Coherent, see Tables 5.1, 5.3). Reported power levels range from 40 mW at 228.9 nm to 1 W at 257 nm for the model Innova Sabre MotoFreD.

Argon-ion Laser Lines in the Visible Region of the Spectrum

The most common spectral region for lasers in microscopy is between 488 and 514 nm, although argon-ion laser emission can be obtained at 454.5, 457.9, 465.8, 472.7, 476.5, 488.0, 496.5, 503.7, 514.5, and 528.7 nm.

Krypton-ion

When strong red emission at 647.1 nm is needed to expand the spectral coverage of an argon-ion laser, a krypton laser is the system of choice (Brelje *et al*., 1993). Its stability is slightly less than that of a comparably sized argon-ion system and the gas retention in the graphite disks is slightly larger. However, with active stabilization now available and with ceramic tube technology firmly in place, both drawbacks have now been largely overcome. Based on the FreD argon-ion laser, see above, we may see the introduction of an intracavity frequency-doubled krypton-ion laser as a source for UV light at 376, 338, 323, 284, and 266 nm.

Mixed Gas Argon–Krypton

Combining the best properties of the argon and krypton ion lasers creates a reliable laser with stable output and the broad spectral coverage needed for multicolor CLSMs. Brelje and colleagues (1993) used an air-cooled 15 mW Kr-Ar ion laser for multicolor immunofluorescence microscopy and described a range of applications. Several companies produce systems delivering several tens of milliwatts, for example, Melles Griot (Table 5.3).

Helium–Neon

The use of these stable, inexpensive lasers in microscopy has been somewhat limited by their relatively low intensity and predominantly 632.8 nm red emission. Several manufacturers have recently

introduced He-Ne lasers with emission at 534, 594, 612, and 632.8 nm and lines in the infrared, for example, 1152 nm (Fig. 5.9). To better excite Texas Red, Alexa 594, and several other dyes, the red He-Ne at 632.8 nm and the green He-Ne (GreNe) at 543 nm have been joined by the orange He-Ne at 594 nm. Typical powers for the 632.8 nm line range from 0.5 to 10 mW with a maximum of 75 mW. Although increased competition is expected from solid-state, semiconductor, and diode lasers, the He-Ne laser still competes well thanks to its good beam quality, shorter wavelengths, and long lifetime. Invar-stabilized He-Ne frames are now available from Research Electro-Optics Inc. (Table 5.3). The 632.8 nm can be used to create an autofocus feedback circuitry that automatically adjusts for specimen vertical movement (ASI, Zeiss, Table 5.3).

Helium–Cadmium

Helium–cadmium (He-Cd) lasers have found several applications in microscopy. Usually they operate at three emission wavelengths: 325, 354, and 442 nm (Fig. 5.10), with power levels up to several hundred milliwatts (Hecht, 1993c). The shortest wavelength requires special optics and is very rarely used in fluorescence microscopy. Membrane probes such as Indo-1 and Fura-2 can be conveniently excited with the 354 nm line. The emission at 442 nm is ideal for excitation of cyan fluorescent protein, flavins, and other fluorescent molecules. The power available at 325 and 354 nm is generally on the order of a few to tens of milliwatts, while at 442 nm up to 150 mW is now available.

The stability of these lasers is substantially less than that of the argon-ion lasers. In the 325 nm region, intensity fluctuations of 10% to 20% are not uncommon but the emission tends to be more stable at 442 nm. Although most He-Cd systems had an operational life of 1 to 1.5 years (1000 to 2000 h), a new mirror technology has increased the lifetime of the coatings to >5000 h for 325 nm mirrors. The less powerful, smaller frame lasers, operating at 325 nm, may still have a limited life span. One manufacturer now supplies a sealed, multiple-wavelength version with up to 10,000 h lifetime (see Table 5.2).

The He-Cd laser experiences heavy competition from the numerous blue diode lasers coming to market in the wavelength region spanning roughly 400 to 450 nm.

Alkali Vapor Lasers

Diode–pumped, alkali lasers (DPAL) can generate blue laser emission by a two step up-conversion scheme (Beach et al., 2004; Krupke, 2004). Cesium and rubidium vapor CW lasers pumped by diode lasers either at 852 or 859 or with 876 or 921 nm (Cs) or at 780 or 795 or with 761 or 776 nm (Rb), emit at 455 or 459 (Cs) and 420 or 422 nm (Rb). With their low cost and compact design, potential 50% efficiency, high average power (>100 mW), easy scalability, and good beam quality, they will be competition for thin disk and fiber lasers and show a great potential.

Dye Lasers

As all dye lasers for confocal microscopy are optically pumped by other powerful lasers, they are not so much lasers as wavelength shifters. Suitable pump sources are excimer, ion, neodymium–yttrium aluminum garnet (Nd-YAG), neodymium–yttrium lithium fluoride (Nd-YLF), and metal vapor lasers. For CW operation, the dye is circulated to prevent heating and bleaching, to reduce the competing triplet-state population, and to remove dye molecule aggregates. Compared with gas lasers, the emission spectra are quite broad and this permits them to be tuned to lase over a fairly broad wavelength band. This band can be extended by changing dyes. Tuning of the laser is accomplished by a prism, a diffraction grating, and a stack of birefringent plates inserted at the Brewster angle or by etalons (Demtröder, 1996; Mollenauer and White, 1987). The laser medium is easy to handle, inexpensive, and consists of a fluorescent dye dissolved in a solvent. Because of so-called "forbidden transitions," the molecules tend to pile up in the first excited triplet state and thereby become unavailable for lasing. Rapid pumping or the use of a dye-jet stream reduces the population of this triplet state. In order to keep the quantum yield high, the dye is usually cooled to minimize competing processes, such as collisional and vibrational de-excitation. Intrinsic optical efficiencies as high as 20% or 30% can be obtained (not counting the efficiency of the pump laser) reaching an output power of several hundred milliwatts.

Operating a dye laser is sometimes rather cumbersome, involving bottles of spent laser dye and waste materials, dye spillage, and often large quantities of dye solvent that must be stored in a safe storage area. Cuvettes holding laser dye have to be cleaned regularly because the pumping beam bakes dye molecules onto the optical surfaces. Although solid-state lasers have largely replaced the dye laser, they still can fill several spectral gaps between 390 nm and the IR.

The intensity stability of dye lasers is lower than that of its lamp or laser pump source. Two percent to 5% intensity stability is considered good. Beam pointing stability is heavily influenced by the regular tuning done on these systems. Distances should be kept as short as possible or fiber-optic beam transport should be considered.

The spectral regions covered, tuning curves, and the output power offered can be found in the manufacturer's documentation.

Solid-State Lasers

An ever-growing number of power-efficient solid-state lasers is being offered for use in confocal microscopy. They are particularly successful in replacing inherently inefficient gas lasers. Their versatility and ease of operation either for use as CW or pulsed direct light sources or for use as pump sources for other lasers guarantees continued rapid development. There is a trend towards smaller more efficient all-in-one-box designs and a drive to increase total average power by creating laser arrays.

- **Semiconductor lasers:** Most are based on gallium mixtures, emit a single line in the red or NIR and can be pumped electrically with very high efficiency. SHG generation in an appropriate crystal creates UV, blue, and green emission. The number and versatility of these lasers increases daily.
- **Non-tunable solid-state laser:** Another class of laser is formed by the Nd-YAG, Nd-YLF, and neodymium–yttrium orthovanadate (Nd-YVO_4) systems operating at 1064, 1047, and 1064 nm, respectively. These can be used as a stand-alone light source or serve as a pump for dye-lasers and titanium : sapphire amplifier systems.
- **Tunable solid-state ultrafast lasers:** These are epitomized by the titanium : sapphire laser systems generating very short pulses down to a few to tens of femtosecond. They provide a very broad tuning range, comparable with that of dye lasers, but they are much easier to operate, generate a comparable or higher output, provide significantly better stability, and can be built in a range of configurations. They can also generate stable, high-power picosecond and femtosecond pulses as we will discuss later.

TABLE 5.3. Sample Listing of Manufacturers

ALPHALAS GmbH, Göttingen, Germany, +49-(0)551-770-6146, http://www.alphalas.com/
Amplitude Systemes, Talenc, France, +33-(0)5-4000-3447, http://www.amplitude-systemes.com
AVESTA PROJECTS Ltd., Troitsk/Moscow region, Russia, +7-(0)95-334-0078, http://www.avesta.ru/
ASI, Applied Scientific Instrum., Eugene, OR, (800)-706-2284, http://www.ASIimaging.com
BATOP GmbH, Weimar, Germany, +49-(0)172-3520029, http://www.batop.com/index.html
BEOC, Brocton Electro-Optics Corp., Brockton, MA, (508)-559-9958, http://www.brocktoneo.com/services.htm
Blue Sky Research, Miltipas, CA, (408) 941-6068, http://www.blueskyresearch.com/index.htm
Bromba GmbH, Münich, Germany, +49-(0)89-3266-8930, http://www.bromba.com/indicard.htm
Cambridge Laser Laboratories, Fremont, CA, (510)-651-0110, http://www.cambridgelasers.com/
CDP Inc. or Systems, represented by Edinburgh Instrum. Ltd. Inc, http://www.edinst.com/agencylaser.htm and PicoQuant GmbH.
Clark-MXR, Inc., Dexter, MI, (734)-426-2803, http://www.cmxr.com/gate.htm
Cobolt AB, Stockholm, Sweden, +46-(0)8-545-91-230, http://www.cobolt.se/
Coherent Inc., Laser Group, Santa Clara, CA, (800)-527-3786, http://www.cohr.com/ and http://search.coherentinc.com/cgi-bin/MsmFind.exe?RESMASK=MssRes.msk&CFGNAME=MssFind.cfg&QUERY=brochures
Continuum, Santa Clara, CA, A division of Excel Technology Comp., (888)-532-1064 http://www.continuumlasers.com/mainswf.html
The Cooke Corp., Auburn Hills, MI, (248)-276-8820, http://www.cookecorp.com/
CSK Optronics, Torrance, CA, (310)-574-8181, csk@usa.com
Crystal Fibre, A/S, Birkerød, Denmark, +45-(0)4348-2820, http://www.crystal-fibre.com/
CrystaLaser Inc., Reno, NV, (775)-348-4820, http://www.crystalaser.com/homenew.html
Del Mar Ventures, San Diego, CA, (858)-481-9523, http://www.femtosecondsystems.com/index.php
Edmund Optics Inc., Barrington, NJ, (800)-363-1992, http://www.edmundoptics.com/
Edmund Scientific, Tonawanda, NY, (800)-728-6999, http://scientificsonline.com/Default.asp?bhcd2=1099033491
Electronik Laser Systems GmbH, http://www.els.de/Products/vdisk.html
Electroi Optical Components, Inc., Santa Rosa, CA, (707)-568-1642, http://www.eoc-inc.com/ir_sensor_cards.htm
Evergreen Laser Corp., Durham, CT, (860)-349-1797, http://www.evergreenlaser.com/Default.htm
Excel/Quantronix Corp., East Setauket, NY, (631)-784-6100, http://www.quantron.com/
Femtolasers Productions GmbH, Vienna, Austria, +43-(0)1-503-70020, and Femtolasers Inc., Harvard, MA, (978)-456-9920, http://www.femtolasers.com/
Fianium Ltd., Southampton, UK, +44-(0)2380-458776, http://www.fianium.com
Guided Color Technologies GmbH, Jena, Germany, +49-(0)3641-675350, http://www.gc-tec.com/
GWU-Lasertechnik GmbH, Erftstadt, Germany, +49-(0)2235-955220, http://www.gwu-group.de/laser/index.html
High Q Laser, Hohenems, Austria, +43 (0)5576-43040, and High Q Laser (US) Inc., Watertown, MA, (617)-924-1441, http://www.highqlaser.at/ and http://www.HIGHQ-US.com/
Holo-Spectra Inc., Van Nuys, CA, (818)-994-9577, http://www.lasershs.com/index.html
IMRA America, Inc. (IMRA: Institut Minoru de Recherche Avancee, now IMRA Europe S.A.), Ann Arbor, MI, (734)-930-2590, http://www.imra.com/
Ingeneric Gmbh, Aachen, Germany, +49-(0)241-963-1343, http://www.ingeneric.com/
INNOLIGHT GmbH, Hannover, Germany, +49-(0)511-760-7270, http://www.innolight.de/products/start.htm
Kapteyn-Murnane Laboratories, Inc., Boulder, CO, (303)-544-9068, http://www.kmlabs.com/
Kimmon Electric USA., Englewood, CO, (303)-754-0401, Edinburgh Instrum. Ltd. rep http://www.edinst.com/agencylaser.htm
Lambda Physik AG (sub. of Coherent Inc.), Göttingen, Germany, +49-(0)551-69380, http://www.lambdaphysik.com/
Laser Diode, Inc. (part of Tyco Electronics Co.), Edison, NJ, (732)-549-9001, http://www.laserdiode.com/
Laser Innovations, Santa Paula, CA, (805)-933-0015, http://www.laserinnovations.com/coherent_lasers.htm
Laser Quantum Ltd, Stockport, Cheshire, UK, +44-(0)161-975-5300, http://www.laserquantum.com/
Laser Resale Inc., Sudbury, MA, (978)-443-8484, http://www.laserresale.com/
LaserMax Inc., Rochester, NY, (585)-272-5420, http://www.lasermax-inc.com/
Lasermet Ltd., Laser Safety Solutions, Bournemouth, UK, +44-(0)1202-770740, http://www.lasermet.com/
Lasiris Inc. (Div. of StockerYale), StockerYale Canada, Montreal, Quebec, Canada, (800)-814-9552
National Laser Corp., Salt Lake City, UT, (801)-467-3391, http://www.nationallaser.com
Lasos LaserTechnik GmbH, Jena, Germany, +49-(0)3641-29440, http://www.lasos.com/index.htm
Lexel Laser Inc. (div. of Cambridge Laser Laboratories), Fremont, CA, (510)-651-0110, http://www.lexellaser.com/
LFW, Laser Focus World Buyers Guide, PennWell Corp., 2004, Nashua, NH, (603)-819-0123, http://lfw.pennnet.com/home.cfm
LG Laser Technologies GmbH, Kleinostheim, Germany, +49-(0)6027-46620, http://www.lg-lasertechnologies.com/
LIA, Laser Institute of America, Orlando, FL, (800)-345-2737, http://www.laserinstitute.org/
Limo Lissotschenko Mikrooptik GmbH, Dortmund, Germany, +49-(0)231-222410, http://www.limo.de/
LUMERA LASER GmbH, Kaiserslautern, Germany, +49-(0)6301-703-181, http://www.lumera-laser.de/index2.html
Lumics GmbH, Berlin, Germany, +49-(0)30-6780-6760, http://www.lumics.de/
Lumitek Intl. Inc., Ijamsville, MD, (301)-831-1001, http://www.lumitek.com/Sensorcatalog.PDF
Mauna Kea Technologies, Paris, France, +33-(0)1-4824-0345, http://www.maunakeatech.com/
Melles Griot, Laser Div., Carlsbad, CA, (800)-645-2737, http://www.mellesgriot.com/contactus/default.asp
Micro Laser Systems, Garden Grove, CA, (714)-898-6001, http://www.microlaser.com/blueConfocal.html
MWK Industries, Corona, CA, (909)-278-0563, http://www.mwkindustries.com/
Newport Corp., Irvine, CA, (800)-222-6440, http://www.newport.com/
New Focus, Inc. (a division of Bookham), San Jose, CA, (408)-919-1500, http://www.newfocus.com/
Noran Instruments Inc., see Prairie Technologies, Inc.
Novalux Inc., Sunnyvale, CA, (408)-730-3800, http://www.novalux.com/contact.html
Oxford Lasers Inc., Littleton, MA, (978)-742-9000, http://www.oxfordlasers.com/
Optronics Technologies S.A., Athens, Greece, +30-(0)210-983-7121, http://www.optronics.gr/
OZ Optics, Ltd., Corp, Ontario, Canada, (800)-361-5415, http://www.ozoptics.com/

TABLE 5.3. (*Continued*)

P.A.L.M Microlaser Technologies AG, Bernried, Germany, +49-(0)8158)-99710, http://www.palm-microlaser.com/
Photonic Products Ltd., Bishops Storford, Hertfordshire, UK, +44-(0)1279-719190, http://www.photonic-products.com/company_ov.htm
Picoquant GmbH, Berlin, Germany, +49-(0)30-6392-6560, http://www.tcspc.com/
POC, Physical Optics Corp., Torrance, CA, (310)-320-3088, http://www.poc.com/
Point Source, Hamble, UK, +44-23-80-744500, http://www.point-source.com/products.asp
Power Technology Inc., Little Rock, AR, (501)-407-0712, http://www.powertechnology.com/pti/index.asp
Prairie Technologies Inc., services Noran microscopes, Middleton, WI, (608)-662-0022, http://www.prairie-technologies.com/index_files/page0005.htm
Quantronix (see Excel/Quantronix)
R&D Ultrafast Lasers Kft., Budapest, Hungary, +36-(0)1-392-2582, http://www.szipocs.com/products.php
Rainbow Photonics AG, Zürich, Switzerland, +41-0)1-445-2030, http://www.rainbowphotonics.com/
Research Electro-Optics, Boulder, CO, (303)-938-1960, http://www.reoinc.com/
Rockwell Laser Industries, Inc., Cincinnati, OH, (800)-945-2737, http://www.rli.com/
Roithner LaserTechnik, Vienna, Austria, +43-(0)1-586-52430, http://www.roithner-laser.com/
Sacher Lasertechnik Group, Marburg, Germany, +49-(0)6421-3040, http://www.sacher-laser.com/
Spectra-Physics Lasers and Photonics, Inc., Mountain View, CA, (800)-775-5273, http://www.spectra-physics.com/ and Darmstadt, Germany, +49-(0)6151-7080
StockerYale, Inc., Salem, NH, (603)-893-8778, http://www.stockeryale.com/i/lasers/index.htm
Teckhnoscan Laser Systems, Novosibirsk, Russia, +7 (0)3832-397224, http://www.tekhnoscan.com/english/index.htm
Toptica Photonics AG., Martinsried, Germany, +49-(0)8989-99690, http://www.toptica.com/index.php
Torsana Laser Technologies A/S, Skodborg, Denmark, +45-(0)4556-0056, http://www.torsanalaser.com/index.html
Time-Bandwidth Products, Inc. Zürich, Switzerland, +41 (0)44-445-3120, http://www.tbwp.com/Time_Bandwidth/Home/FrameSetHome.htm
TuiLaser AG, Germering/Münich, Germany, +49-(0)89-894070, http://www.tuilaser.com/products/lasers/index.htm
Uvex, Smithfield, RI, (800)-343-3411, http://www.uvex.com/
Visitech International Ltd., Sunderland, UK, +44-(0)191-516-6255, http://www.visitech.co.uk/index.html

Semiconductor or Diode Injection Lasers

Charge carriers in a semiconductor material can be pumped either optically or by an electric current (Fig. 5.11). Electron-beam–pumped semiconductor lasers can emit 3 to 5 W in the 480 to 650 nm range (Hobbs, 1993), but the most common excitation method simply starts with a diode not unlike that in a light-emitting diode (LED) and uses an externally applied current in the forward-biased direction. This process can have an efficiency as high as 80%. To do so, the electrons must be confined not to a bulk

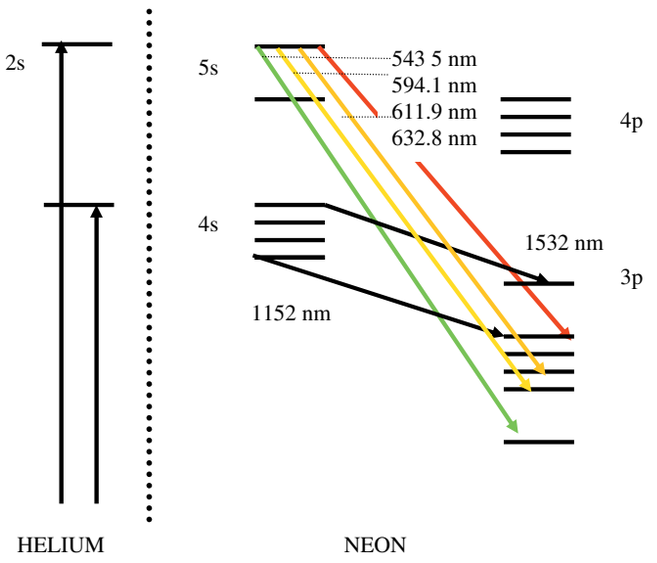


FIGURE 5.9. Schematic energy diagram for a helium–neon laser. Helium functions as a pump energy transferring buffer for neon.

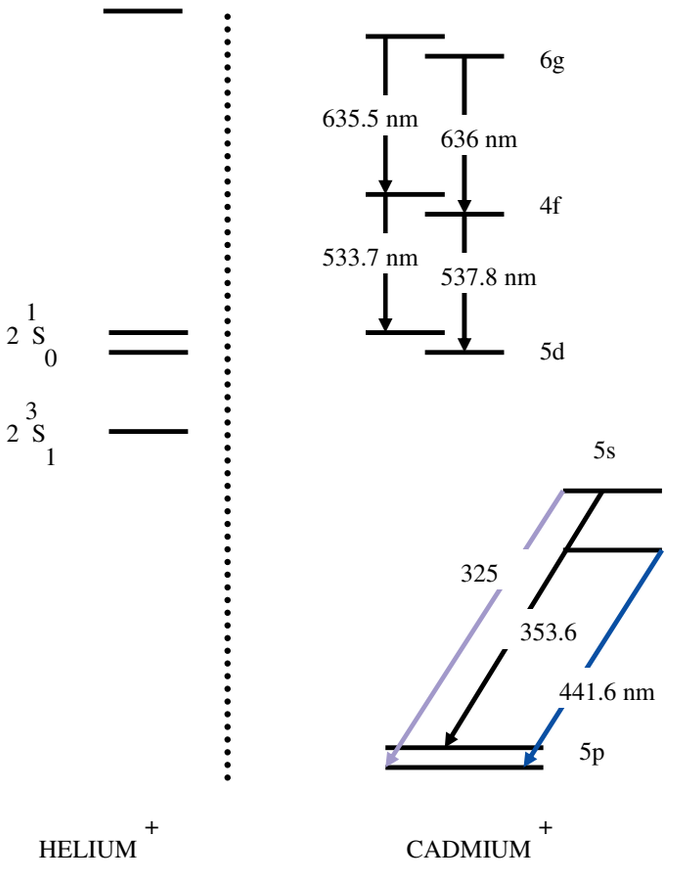


FIGURE 5.10. Schematic energy diagram for a helium–cadmium laser. Green and red emission is also possible but not commercialized.

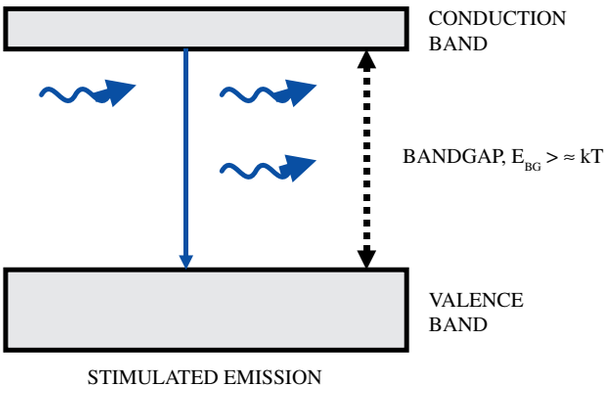


FIGURE 5.11. Schematic energy diagram for a semiconductor laser. It is based on laser emission from a forward biased *p-n* junction when driven by a well-regulated drive current.

volume (Fig. 5.12), but to a stack of very thin layers forming multiple quantum wells (MQW), or planes of quantum wires or dots (superlattice). Due to the small confined volume a high radiative efficiency exists as well as a low lasing threshold. Most devices still operate in NIR but the trend is to develop diode lasers using wide bandgap materials that have an output below the red. Blue diode lasers based either on ZnSe or doubling 860 nm light, emit at around 430 nm and are about to enter the commercial market. At higher power levels (Figueroa, 2002), direct frequency-doubling in the diode laser forms an alternative route to the blue region. For example, the D^3 (Direct Doubled Diode laser, Coherent) delivers 10 mW at 430 nm. When selecting a drive current source, it is important to select one with a low noise, good stability, and including a temperature controller on the diode laser head. Diode lasers can change their emission wavelength over a limited range (10–20 nm) by varying their drive current and junction temperature (Hodgson, 1994). The approximate tuning rate is about 0.1 nm /°C. Cooling brings the lasing wavelength down. Beam quality suffers from astigmatism that has to be optically corrected (Snyder and Cable, 1993). Edge emitters now provide high power, up to several watts CW in NIR.

Semiconductor lasers are very appealing because they are small [Fig. 5.13(B)], highly efficient, easy to use, and relatively cheap. Integrated fiber-optic output is another feature available from many manufacturers [Fig. 5.13(A)]. However, it should be stressed that this small package comes with important special requirements. The devices can be rapidly destroyed if both current transients or nanosecond current spikes at start-up and internal heating are not kept under control by the power supply electronics. Static discharges (SD) from a person or an ungrounded soldering iron, or the use of solder that is too hot or remains in contact for too long may instantly destroy the laser. A mechanical shunting device (Unger, 1994) may prevent SD damage during handling. Alternating current (AC) line filters are recommended (Hodgson, 1994). This market is strongly driven by the digital video disk (DVD) and audio compact disk (CD) industry where the goal is to increase information storage densities. Most, if not all, of the following examples are also wavelength stabilized by stacks of multi-layer coatings usually deposited at the HR side and producing bandpass filter reflectivity only for the lasing wavlength [Fig. 5.14(B,C)]. Combining a proper OC coating with a fiber pigtail having an inscribed Bragg grating has the same stabilizing effect.

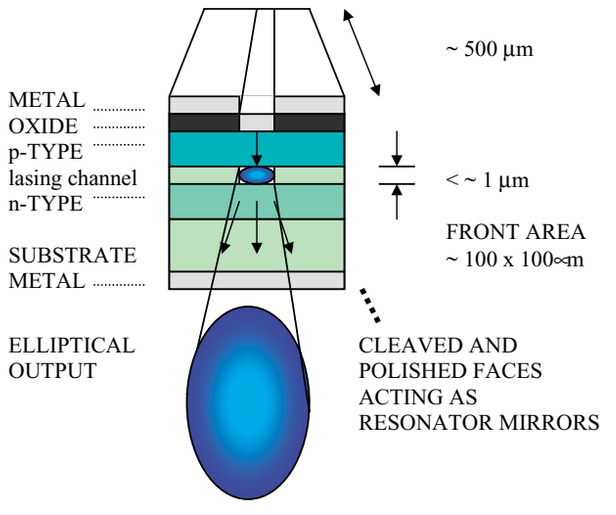


FIGURE 5.12. Dimensions and cross-section through an edge emitting diode laser. The polished sides act as highly reflecting mirror and output coupling mirror. Thermo-electric cooling to remove heat is required.

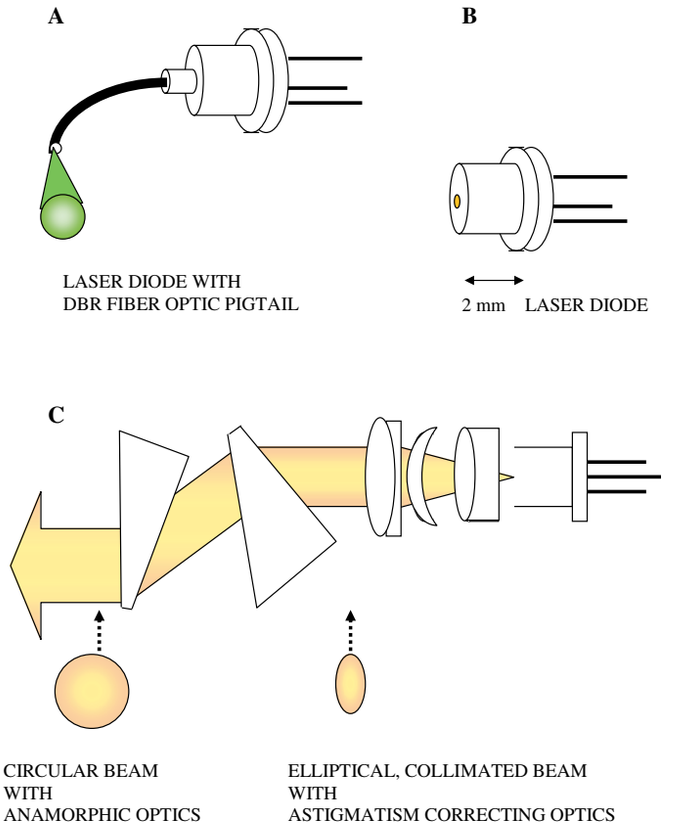


FIGURE 5.13. Example of (A) optional pigtail fiber-optics, (B) physical dimensions of a diode laser, and (C) corrective optics to create a circular beam profile.

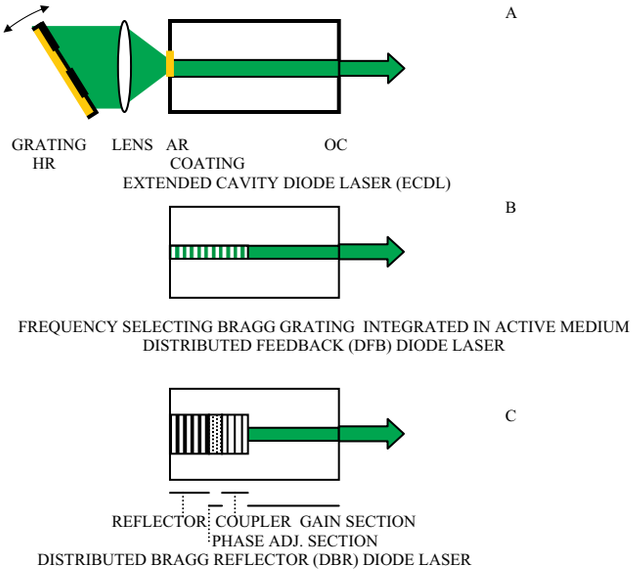


FIGURE 5.14. Diode lasers with wavelength tunability via an angle-adjustable grating in an extended cavity configuration (A); improved mechanical and thermal stability as well as wavelength and intensity control via a bandpass reflective filter formed by a stack of thin coating layers (Bragg grating). When the grating is incorporated into the gain medium the device is a distributed feedback (DFB) diode laser (B), otherwise it is a distributed Bragg reflector (DBR) diode laser. For ultrafast pulsed operation semiconductor saturable absorber (SESAM) layers can be added to the high reflecting mirror stack or to the saturable output coupler (SOC) to the output coupling face. Edge emitting diodes require corrective optics because the emission is elliptic.

Violet and Deep Blue Diode Lasers

Because these lasers produce 10 mW of deep blue emission (395–440 nm) from an input power of less than 10 W, they do not require water cooling. Compare this with an argon-ion laser producing the same 10 mW from 1 kW of electrical input, gallons of cooling water per minute, and filling a good part of a laser table. Most of the diode lasers have a single fixed-wavelength, which may vary somewhat (see above under FBG Wavelength Stabilization). Violet 405 nm (Photonic Products Ltd., Table 5.3) lasers efficiently couple into 3 µm core single-mode fibers. Diode lasers presently operate at 395 to 440 nm (LG Laser Technologies GmbH, Coherent; Table 5.3), 415 and 430 nm (Crystal Laser Inc.), 440 nm (PicoQuant model LDH 440, Power Technology Inc.), 457 nm (Melles Griot), and 473 nm (Crystal Laser Inc., Power Technology Inc.). But they are not nearly as cheap as laser-pointers! Prices range from a few thousand to US$25,000, depending on complexity and features such as thermo-electric cooling.

Visible and Red Diode Lasers

488 nm Diode Lasers An alternative to the argon-ion laser has appeared in the form of the Protera 488 system from Novalux Inc. (Table 5.3). Listed advantages over the argon-ion laser include twice the life expectancy (20,000 h), 1% of the power consumption, up to 20 mW output power, 2% of the size, 0.2% rms noise level, and built-in thermo-electric Peltier cooling with conductive heat removal via the enclosure. The ChromaLase 488 from Blue Sky Research has a typical power consumption of 2 W and output power from 1 to 25 mW output and creates 488 nm laser light by SHG doubling of ~980 nm IR light. Similar specifications are found for the Starbright 488, 10 mW pumped at 40 W (Torsana Laser Technologies A/S); the BluePoint 488 at 2 to 5 mW from Rainbow Photonics AG; and the tunable 488 nm laser from Toptica Photonics AG. Coherent introduced the Sapphire (NOT to be confused with a Ti : Sa system). It is a VECSEL GaAs diode laser consuming 30 to 60 W (mostly in the thermo-electric cooler), optically pumped at 976 nm, and intra-cavity frequency-doubled to provide 20 mW of electrical input.

The Novalux Inc. Protera is based on an ECSEL design with a three-mirror folded cavity for better mode control and uses a $KNbO_3$ doubling crystal inside the laser cavity.

491 nm Diode Lasers Some designs are based on up-conversion of a fiber laser to produce 10 mW at 491 nm (Guided Color Technologies and Lumics GmbH). Others use a different principle. The DPSS Dual Calypso laser (Nordborg and Karlsson, 2004) from Cobolt AB (Table 5.3) offers 491 nm at 20 mW and 532 nm at 50 mW simultaneously. It uses a periodically polled potassium titanium oxide phosphate (KTP) crystal, partly inside the laser cavity, for non-linear optical frequency conversion. The 491 nm line stems from sum frequency mixing of Nd : YVO_4 with the 1064 nm line from the Nd : YAG laser. Four hundred fifty-seven and 1340 nm lines can be added using similar methods. This laser has a noise level of <0.3% and can directly replace the argon-ion laser operating at 488 and 514 nm.

606 and 635 nm Diode Lasers The He-Ne 594 nm orange and the red 632.8 nm lines can be replaced by the 606 nm (orange) VECSEL Eksel 110 diode laser (Toptica Photonics AG; Häring and Gerster, 2003) and the ChromaLase 635 25 mW (Blue Sky Research). The Radius 635 nm CW 25 mW (Coherent) has a 16-h beam pointing stability of about 60 mrad compared with ~160 mrad for a 17 mW He-Ne. A 637 nm red diode laser He-Ne laser substitute has been incorporated into the Bio-Rad Radiance2100CLSM (currently Carl Zeiss CellScience Ltd.).

685 nm Diode Laser A 685 nm 30 mW CW diode laser is offered by Lasos Laser Technik GmbH.

Recent Developments in Diode Lasers

In this expanding field, many features are rapidly improving to the benefit of the user.

Emerging Tunability By incorporating a diode laser into an external cavity equipped with a tunable grating (a Littman-Metcalf cavity) wavelength tunability from 632.5 to 1630 nm within a 50–150 GHz bandwidth is now available (New Focus; Table 5.3; Scifres, 1994). These devices are listed as external or extended cavity diode lasers [ECDL; Fig. 5.14(A)]. A narrow-line width version has been described in Day and Dessau (1994). Although for the moment manufacturers seem to focus on single wavelength devices, mechanical and thermal stability should not be compromised.

Beam Quality and Delivery Diode lasers typically require extensive astigmatic and anamorphic corrective optics to obtain a circular, parallel beam [Fig. 5.13(C)]. Other methods include using a spatial filter or a single-mode fiber-optic as well as beam homogenizers, such as the monolithic V-step design by Ingeneric GmbH (Table 5.3), arrays of symmetrically arranged lenslets, the so-called "fly's-eye" lenses or light integrators (Homburg *et al.*, 2003), available, for example, from Limo Lissotschenko Mikroop-

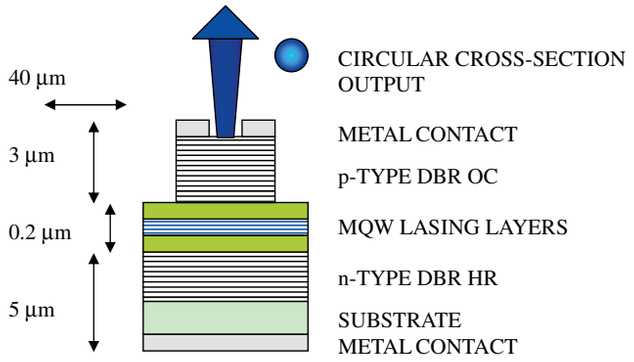


FIGURE 5.15. Dimensions and layout of a vertical cavity semiconductor diode laser (VCSEL). Stacks of thin coating layers form the distributed Bragg reflector (DBR) highly reflective mirror (HR) and the output coupling mirror (OC). The emission pattern is circular and can be near-Gaussian.

tik GmbH (Table 5.3). Optical elements, called graded index (GRIN) lenses, have also been introduced to eliminate spherical aberration in an elegant way (Carts, 1994). The vertical-cavity, surface-emitting semiconductor laser (VCSEL; Fig. 5.15), is a semiconductor laser with good circular-pattern beam quality (Cunningham, 1993). Power levels are now reaching 100 mW with a wall-plug efficiency of 20%, high temperature stability, and good beam quality.

Output Power and Cooling Output power has been increased by building diode lasers as banks or arrays but these often require additional water cooling that adds to their complexity. Quasi-CW output levels can reach 300 mJ and 1.5 kW peak power. Tens to 100 s of watts of CW power and long lifetimes are becoming common. Cooling requirements depend on the output power generated and they range from passive air cooling via thermo-electric (Peltier) cooling to water cooling, the latter often using microchannels for optimum control of the junction temperature.

Temperature Tuning There is no longer a need to have a large number of different diode lasers nor a large collection of emssion filters for CLSM. Sivers and colleagues (2004) showed that, with a 3 mW low-power superlattice (multi-quantum well) 635 nm diode laser attached to a Bio-Rad MRC600 CLSM, many cell stains that absorb in a broad range around 640 nm can be reached by cryogenically cooling the laser down to −196°C. This caused the emission wavelength to shift linearly ~25 nm down, while the output power went up about five times. For equal fluorescence signal, the noise level in the image caused by reflected laser light decreased five times because it was possible to optimize the laser wavelength to the optical filters more precisely.

Output Modulation Another important feature of semiconductor lasers is that their output can easily be modulated to well above 100 MHz and some can reach tens of gigahertz. This makes them prime candidates for use in frequency-domain fluorescence lifetime imaging microscopy (FLIM; see Chapter 27, *this volume*).

Diode- and Lamp-Pumped Solid-State Lasers

A second class of solid-state lasers includes those using neodymium yttrium aluminum garnet (Nd-YAG) and lasing in the IR at 1064.2 nm with very high fracture resistivity and good thermal conductance (Fig. 5.16); Yttrium lithium fluoride (Nd-YLF) with low thermal lensing (Arrigoni, 2004b); Nd-BaYF with better subpicosecond generation and amplification properties; yttrium orthovanadate lasing at 1064.3 nm having a lower lasing threshold than Nd-YAG (Kaminskii, 1981); $GdVO_4$ lasers and $Nd:LuVO_4$, also having a lower lasing threshold. All of the materials listed above are pumped by FBG diode lasers [Fig. 5.14(C)]. Nd-YAG and Nd-YLF provide high overall efficiency and the good beam quality necessary for frequency doubling to the visible producing lines at 532 and 523 nm. Microchip lasers are formed by sandwiching laser and frequency doubling crystals into a millimeter size compact structure. Due to their small size they benefit from ceramic laser materials with high thermal conductivity (Wisdom and Digonnet, 2004).

A simpler design is possible with ytterbium tungstate (Yb:KGW) absorbing between 900 and 1000 nm that can be directly pumped by a red diode laser.

Early models used flash lamp or CW krypton lamp pump sources but the latest models tend to be equipped with a diode laser [diode-pumped solid-state lasers (DPSS); Hobbs, 1994]. The advantages of diode lasers over conventional pump sources, such as lamps, are reduced cooling requirements because of higher efficiencies due to a collimated and focused output, a perfect match of pump-source emission wavelength with the absorption spectrum of the lasing medium, and enhanced frequency stability (Baer, 1986). A typical improvement in electrical-optical conversion efficiency is from 0.5% (TEM_{00} mode) to 6%.

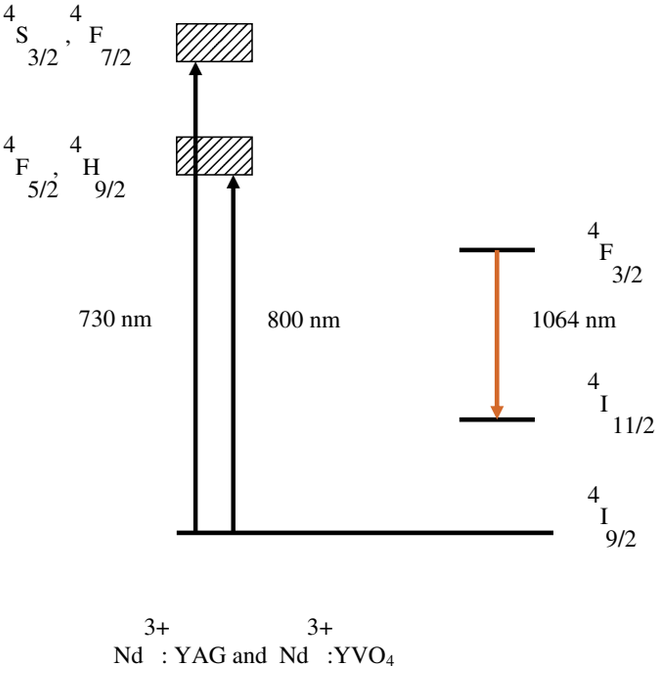


FIGURE 5.16. Schematic energy diagram for a neodymium–yttrium–aluminum garnet (Nd-YAG) laser and a neodymium–yttrium orthovanadate ($Nd:YVO_4$) laser.

The infrared output at 1064 (Nd-YAG) or 1054 nm (Nd-YLF) is easily frequency-doubled, tripled, or quadrupled with appropriate non-linear crystals such as lithium triborate (LBO) and beta barium borate (BBO) to provide radiation at 532 and 527 nm (SHG), 355 and 349 (THG), 266 and 262 nm [fourth harmonic generation (FHG)], respectively. BBO even allows generation of the fifth harmonic at 213 nm. The stability of these lasers is very good and the green emission wavelength is ideal for the excitation of rhodamine dyes or for pumping the *tunable* solid-state lasers described below. Nd-YAG also has lower-gain wavelengths at 1440, 1320, and 946 nm, which when doubled provide 720, 660, and 473 nm. Power levels sufficient to obtain frequency doubling create a blue laser suitable to replace the ion laser lines. Argon-ion 514 nm emission can be replaced with a frequency-doubled 532 nm DPSS design when the mode and beam characteristics are optimized. A 473 nm DPSS laser (CrystaLaser Inc. and National Laser Corp. with 5–10 mW, Table 5.3) is created by intracavity-$KNbO_3$ doubling the 946 nm IR light of a diode-pumped Nd:YAG laser. Typical cost is about US$8000.

As a pump source, the 514 nm line of a large frame argon-ion lasers may well be replaced with a frequency-doubled VersaDisk-515 laser from Electronik Laser Systems GmbH (Table 5.3) emitting, depending on the model, 2.5 to 15 W of 515 nm light in a small footprint without water cooling, and improving the Ti:Sa pump efficiency by 20% compared with the more common 532 nm DPSS pump source. Several companies now offer DPSS systems in kit form. Examples are the DPSS educational kit from Optronics Technologies S.A. and the Nd:YVO_4 and Nd:YAG kits with Cr:YAG SESAM from ALPHALAS GmbH. These lasers are extremely compact, stable, and efficient with good beam quality and offer turn-key operation. Electrical power requirements are low: tens of watts. Beam quality can be improved with Gaussian resonator mirrors and phase plates (Casperson, 1994).

Thin Disk Lasers

Very intense lines with much reduced thermal lensing and birefringence can be generated by thin disk lasers. Radial thermal effects are most severe in the rod-type lasing materials used in the original Nd-YAG designs. Slab-type designs largely lift this thermal problem. Scientific designs are profitting from Yb:YAG or similar based thin disk systems such as the VersaDisc by Electronik Laser Systems GmbH, which can attain tens to hundreds of watts of output power with minimal heating effects. It is based on a 100 µm thin disk of Nd:YAG, Yb:YAG, or other material bonded to a heat sink and optically pumped on the opposite side. Because the heat gradient is almost perfectly planar (i.e., parallel to the bonding surface), the thermal lensing strongly present in high-power, rod-type media is drastically reduced along with the amount of birefringence. Optical aberrations are not introduced. As the disk is small and thin, a special mechanical mirror arrangement makes the pumplight impinge on it many times. Lasers such as the VersaDisk currently deliver up to about 100 W CW at 1030 nm and about 15 W at 515 nm (Hitz, 2004a).

Tunable All Solid-State Laser

The release of the CW titanium-sapphire laser was an important event (Hammerling *et al.*, 1985). These lasers can be pumped by a CW ion, Nd-YLF, Nd-YAG, or diode laser. Because their vibrational-electronic levels are spread in a broad band, laser transitions can take place over a wide range, and, given the right mirrors, the tuning range extends from 700 to 1000 nm (Fig. 5.17). Power output is 3.5 W at 790 nm when pumped with an 18 W Nd-YVO_4 or 20 W all-line argon-ion laser. The Ti:Sa laser has virtually replaced the IR dye lasers; it is much easier to operate, no dyes have to be changed, and the long-term stability is better than 3% due to the elimination of flowing dye. The RMS noise between 10 Hz and 2 MHz is less than 2%, a factor of about 10 less than for dye lasers. The main characteristics of these systems are the generation of short pulses of about 100 fs (FWHM), and high peak power for frequency-doubling to the blue and near-UV spectral range and for use in two-photon CLSM. Several configurations have appeared resembling either CW ring or standing-wave dye lasers. To cover the complete spectral range of this laser, special mirror sets are required.

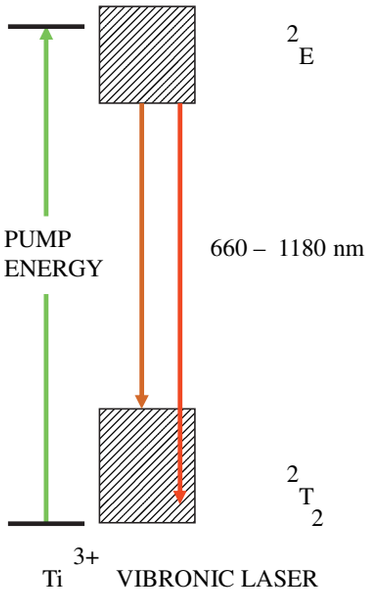


FIGURE 5.17. Schematic energy diagram for the Ti:Sa four-level vibronic laser.

A similar wide-tuning range and high average power is offered by the Alexandrite laser (Cr^{3+} in $BeAl_2O_4$ host), which covers the 730 to 826 nm region when pumped CW at room temperature. This laser can also be flash lamp pumped. The Forsterite laser (Cr^{4+} ions in a Mg_2SiO_4 host material) emits between 1167 and 1345 nm and can be used in the 1200 to 1250 nm tissue penetration window. Its three main pumping bands are centered around 350 to 550, 600 to 850, and 850 to 1200 nm. Both CW and pulsed models are available. Its second harmonic is tunable from 600 to 650 nm (Mortensen, 1994). Liu and colleagues (2001) report multi-photon femtosecond excitation of plant tissue at about 1250 nm with a Cr:forsterite laser (see also Chapter 21, *this volume)*. Potential members of this family of tunable solid-state lasers are the LiSAF laser (Cr in $LiSrAlF_6$) with a tuning range from 780 to 1060 nm and a peak emission at 825 nm (Perry *et al.*, 1993), and the LiCAF laser (Cr in $LiCaAlF_6$) tunable from 720 to 840 nm. Tunable UV could be created by Ce:LiSAF (Anderson, 1994b).

Continuous Wave Fiber Lasers and Up-Conversion

Confusingly, fiber-coupled lasers in which a fiber-optic merely guides the emission are also called fiber lasers. Although also capable of generating a white continuum, micro-structured photonic crystal fiber (PCF) laser delivery systems should not be classified as fiber lasers. Unlike single-mode fibers, highly multi-mode

core fibers are insensitive to twisting and bending but otherwise behave like single-mode fibers. PCF fibers designed to have better higher order dispersion compensation include the crystal fiber large mode area (LMA) PCF.

We will only use the term *fiber laser* for systems where the laser gain medium is the fiber itself. IMRA America (Table 5.3) shows that the design of a fiber laser can be very simple: Two resonator mirrors with the fiber-optic in between (Fig. 5.18). Double-clad fibers are preferred for fiber lasers because the pump light can be efficiently coupled into the high NA, ≥0.46, inner cladding while only a single, transverse-mode-doped core, having a low NA of about 0.06, is excited. They also possess excellent heat dissipation (Limpert *et al.*, 2004). Furthermore, using LMA double-clad fiber (for example, 20/400 µm core/outer cladding) reduces non-linear Brillouin and Raman effects (Galvanauskas and Samson, 2004). PCF fibers can accommodate high powers (Folkenberg and Broeng, 2004), with 260 W CW output from a short piece of 4 µm double-clad fiber, thereby also limiting non-linear effects.

Up-Conversion Fiber Lasers

Theses devices are based on excited state absoption of rare earth ions in fluoride "ZBLAN" glass fibers (Fig. 5.18). ZBLAN stands for zirconium, barium, lanthanum, aluminum, sodium fluoride. When pumped by a pair of diode lasers, each operating at a different red wavelength, several milliwatts of green light can be created (Piehler, 1993). In this typical up-conversion scheme, low-energy photons are sequentially absorbed and create a population inversion in the excited state (Chenard, 1994). By doping the fiber with more than one rare-earth material (Fig. 5.19), the spectral region longer than ~500 nm can be covered. Examples include doping with Er(bium) for 546 nm, with Pr(aseodymium) to obtain 491, 520, 605, 635, and 720 nm emission at 10 to 40 mW (Guided Color Technologies, GmbH; Table 5.3), with PrYb for 840 nm, with T(huliu)m for 482 and 800 nm as well as 470 nm and 1735 ± 1 nm from a single-frequency Tm-doped DFB fiber laser (Hitz, 2004b), with Tm for 980 nm, and with Yb for 1060 nm. One more example is the 700 blue fiber laser series from LasNova (Table 5.3).

Lumics GmbH has developed a fluorozirconate (ZBLAN glass) fiber laser that is a potential replacement for argon-ion lasers. The spectral linewidth of a fiber laser is typically very small, about 0.02 nm (Gabler, 2004). One notes that the exact wavelengths at times differ by 1 to 2 nm between various designs, a fact which may be related to doping and operating conditions.

In the IR, fluoride glass fiber can be doped with rare-earth ions, such as erbium, which emits at 1540 nm (Hecht, 1993a). The

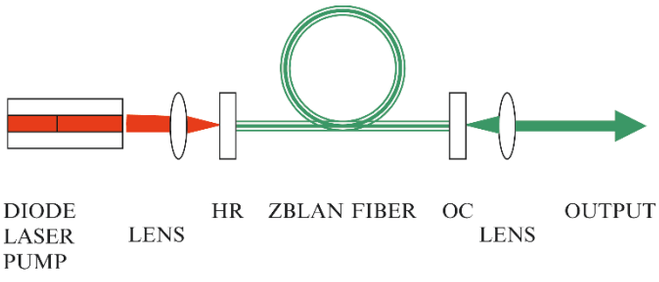


FIGURE 5.18. Schematic diagram of a dual ion doped CW ZBLAN up-conversion fiber laser. Pumped by a distributed feedback (DFB) diode laser emits visible laser light. The connectors contain the high reflecting mirror (HR) and the output coupling mirror (OC).

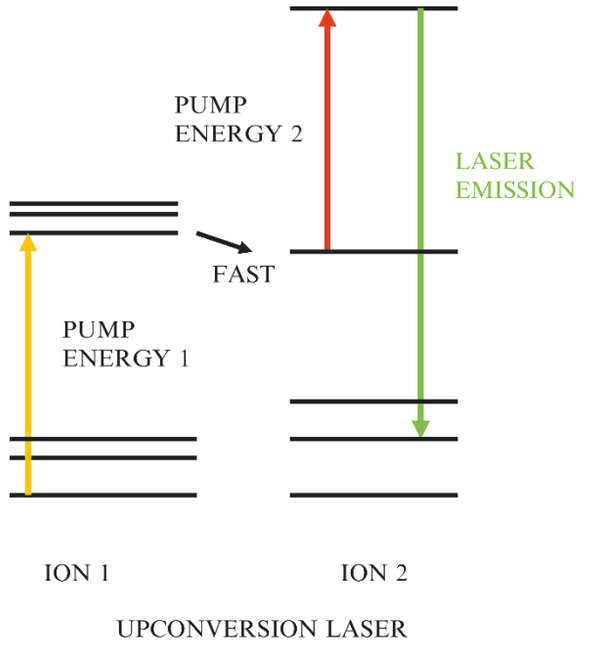


FIGURE 5.19. Schematic diagram for a dual ion doped up-conversion laser.

energy stored in the single-mode laser is about 500 µJ and, in a multi-mode laser, 10 mJ. The maximum optical peak power amounts to about 100 kW. Although initial tests were apparently carried out with an IMRA 775 nm 100 fs laser on a Zeiss microscope, no commercial system has yet been offered by Zeiss.

In a single-longitudinal-mode fiber laser with a fiber core of 2 to 4 µm, the interaction area is very small (a few square micrometers). The interaction length is very long, from millimeters to even kilometers. This results in a very high single-pass optical gain at very low threshold (sub-mW) pumping power levels with pumping efficiencies to 75%. Fibers consist of amorphous material that give very broad absorption bands (Chenard, 1994). The single-pass gain is practically unity. Output is always diffraction limited with excellent beam quality. In combination with an easily attainable average power level of a few watts this makes them very suitable for laser-tweezer applications. These advantages of a fiber laser were recognized as early as 1964. However, at that time there was little capacity to produce good quality, low-loss, single-axial-mode fiber.

PULSED LASERS

Why are pulsed lasers useful? The simple answer is higher peak power. Sufficiently powerful CW pump sources are often not available. Often the wavelength and intensity offered by available lasers are not appropriate. Therefore, wavelength conversion schemes have been developed and many of them are based on non-linear phenomena that occur only at very high intensity. Because of their high peak power, pulsed systems provide efficient wavelength conversion and tuning capabilities. In general terms, the peak intensity is greater than the average intensity by a factor that is the inverse of the duty cycle. The duty cycle is the ratio of pulse width to pulse interval and can often be 10^{-5}.

It is important to remember that pulsed lasers are only useful in scanned fluorescence microscopy if the pulses occur at a high

enough rate that many pulses occur in each digitizing period and intensity integration over the pixel period can provide a performance similar to a CW laser. Pulsed lasers are characterized by the high peak power (see Table 5.2).

Classification of Pulsed Laser Systems

A logical way to classify pulsed laser systems is according to their temporal pulse behavior. Four methods for pulsed operation exist: normal mode, Q-switching, mode-locking, and cavity-dumping.

- **Normal mode, free-running:** When observed with a fast diode and an oscilloscope, solid-state lasers generate a continuous train of random spikes with varying intensity caused by the interaction of various modes in their very small cavities. This type of operation is not very useful.
- **Q-switched lasers:** The term *Q-switched* is derived from the radio and microwave terminology, and it relates to a forced change in the quality factor, Q, of the resonant cavity (i.e., a bell is "high-Q," a lump of wet clay is "low Q"). A low Q resonator is one which hardly supports laser action. What is needed is a method of changing the gain, or resonance, of the laser cavity. A simple implementation of a Q-switching device is the installation of an optical shutter in the resonator. The sudden opening of the shutter releases all the energy stored in the excited electrons of the medium in one giant optical pulse.
- **Active, mode-locked:** In a resonant cavity, many simultaneously oscillating optical modes are present at the same time (Arecchi, 1972; Mollenauer and White, 1987). Usually these modes interact with each other in a random way and no phase relationship exists between them. The output power fluctuates randomly according to a time-dependent interaction between the various modes. Installation of an intra-cavity modulator (i.e., a high-speed shutter) with a resonance frequency exactly matching the round trip time, $2L/c$, in the laser resonator will lock all modes to that particular resonance frequency. A certain phase relationship is maintained. Throughout the cavity, a single, intra-cavity pulse is created at a pulse rate of 70 to 100 MHz. Mode-locking frequencies can be changed by using a crystal with different mode-locking frequency and simultaneously adjusting the laser cavity length. Thermal stability has to be excellent. Folded compact cavity design, further miniaturization, a one-box design strategy, direct IR diode pumping using ytterbium tungstate, and standard thermo-electric Peltier cooling help maintain proper mode-locking. For fiber lasers, smaller size $LiNbO_3$ Mach-Zehnder modulators are used because they possess a lower insertion loss and better control of chirp.
- **Passively mode-locked lasers:** In passive mode-locking a very high loss is introduced to interrupt CW operation.

Kerr Lens Mode-Locking

One way to generate short pulses from a solid-state Ti:Sa laser is using Kerr lens mode-locking. The Kerr effect refers to the quadratic non-linear dependence of the refractive index of a non-linear material on the applied electrical field. The intensity dependent refractive index induces a linear frequency sweep on any short optical pulse leading to spectral broadening. This effect can be compensated by sending the pulse through a few millimeters of glass or short piece of fiber-optic. High intensity optical pulses exert strong forces on the valence electrons of the laser medium. The transverse gradient in a Gaussian beam profile delivers the highest intensity near the center of the beam, less so near the perimeter. Kerr-induced refractive index effects cause the beam to contract producing self-focusing. This regular focusing pattern in the gain medium imposes a specific set of modes in the Ti:Sa laser and eliminates other non-matching modes. An important consequence is that the gain medium works like a master oscillator with its own set frequency. This method requires an intracavity slit or pinhole to suppress CW contributions and needs an active starter such as a noise spike created by tapping a mirror mount and otherwise perturbing the cavity.

Saturable Bragg Reflector and Semiconductor Saturable Absorber Mirrors

Creation of self-starting intense optical pulse trains in, for example, a Nd-YVO_4 or fiber laser running at a high frequency of, for example, 80 MHz, is implemented by introducing into the cavity a low-loss, superlattice, saturable-crystal absorber such as InGaAs. The material possesses a low reflectance for weak optical signals (such as noise) and a high reflectance for high power signals (such as optical pulses) and has a very short recovery time (saturable absorber mirror, SAM). It is incorporated into a high-reflectivity Bragg mirror. Quantum wells can be used in place of the InGaAs. The wider the spectral bandwidth of the gain medium, the shorter the optical pulse generated and, in addition, shorter pulses are created when a shorter rod is used because dispersion can be better compensated. For normal dispersion, red is ahead of blue light. For anomalous dispersion the opposite is true. Transparent materials usually possess normal dispersion. Because a Ti:Sa rod introduces normal dispersion, it must be compensated by inserting anomalous dispersion components such as prisms, grating pairs, or chirped mirrors into the cavity. In ultrafast Ti:Sa, Cr:LiSAF, or fiber lasers, pulse durations of a few tens of femtosecond can readily be created. Mode-locked oscillators such as an ultrafast Ti:Sa laser create nanojoule pulse energies.

The latest oscillator addition, Yb:KGW (tungstate), is directly pumped by two fiber-delivered high-power 940 or 980 nm IR diode pumps (Eclipse, Spectra Physics). No prism pair is required for compensation of the positive GVD because the cavity contains dispersion-compensating coatings. In addition, an saturable bragg reflector (SBR) Bragg high reflector provides self-starting and passive mode-locking. At 1048 nm, 100 mW average power is generated with a repetition rate of 80 MHz and a pulse width of 150 fs. Components are readily available (BATOP GmbH; Table 5.3). Similarly, a microchip Nd:YAG/Cr:YAG gain medium/absorber can be designed (Kraft, 2004).

Saturable Output Coupler

The SAM can be replaced by a saturable output coupler (SOC) incorporated into the cavity. A passively mode-locked DPSS laser creates a very simple design because the pump power can enter through the high reflector into the laser medium.

Cavity-Dumped Lasers

Cavity dumping is a common technique for reducing the laser repetition rate. For example, for frequency-domain fluorescence lifetime imaging microscopy (FLIM) the 80 or 76 MHz laser pulse repetition rate is too high. The repetition rate can be brought down to 2 or 4 MHz by applying a momentary radiofrequency (RF) signal to an appropriate modulator crystal. This allows more harmonics to be used for FLIM imaging and optimizes the system for the nanosecond or or picosecond lifetimes encountered.

Nitrogen Lasers

Among the more common pulsed lasers are nitrogen lasers. Because of their low pulse repetition rate (20–100 pps), nitrogen lasers are only used in microscopy for intentionally wounding cells (Burgess, 2004). The average power is between 1 mW to 1 W, and the emission wavelength is 337.1 nm (Hecht, 1993b). The pulse width of these lasers varies between a fraction of a microsecond to less than a nanosecond. The time characteristics of the pulsed nitrogen laser emission at 337 nm was exploited in fluorescence microscopy by Wang and colleagues (Wang, 1990; Wang *et al*., 1990, 1992). Their conclusion was, however, that the pulse-to-pulse intensity stability of this type of laser (500 ps FWHM pulse at 25 Hz) is not presently sufficient and long integration times were necessary. For this reason the nitrogen laser is unlikely to be useful in microscopy, particularly now that deep UV diode lasers (Crystal Laser Inc.; Table 5.3) possess much more favorable lasing characteristics. Bioeffects on living cells and tissues of UV laser irradiation can be severe but for microdissection applications the nitrogen 337 nm line is very suitable (Burgess, 2004).

Excimer Lasers

Although the vacuum-UV and UV output of these excimer lasers has given them a strong foothold in tissue ablation, this type of laser is not often used for CLSM. Air-cooled, compact models are available, such as *LEX*tra and COMpex models (Lambda Physik; Table 5.3). This company also introduced a metal–ceramic based NovaTube design, which lasts for 7×10^8 pulses on a single gas fill.

Metal Vapor Lasers

Metal vapor lasers (Lewis *et al*., 1988; Hecht, 1993d) are also extremely powerful and can be operated at much higher repetition rates than excimer lasers. The average power can exceed 100 W and the repetition rate can be as high as 20 to 50 kHz, which is still a bit slow for most microscope applications. Wall plug efficiencies reach 1%. Their characteristic emission wavelengths are also reported in Table 5.2.

Dye Lasers

In cancer treatment, high fluency rates are sometimes required. Real-time CLSM following the effects of high-energy 7.5 J/cm^2 585 nm pulsed dye laser irradiation on hyperplasia *in vivo* was reported by Aghassi and colleagues (2000). Otherwise, the need today for stable well-characterized tunable sources is largely filled by optical parametric oscillators (OPO) and optical parametric amplifiers (OPA; see below) in combination with solid-state pumping lasers. Not only is this technology far less messy than dye laser technology, it also adds IR coverage via difference frequency mixing (Radunsky, 2002).

Dye Laser with Intra-Cavity Absorber

Synchronously pumped dye lasers equipped with saturable absorbers have been used extensively in the past to obtain short pulses to cover the gap between 525 and 700 nm, which exists for Ti:Sa lasers (see below; Herrmann and Wilhelmi, 1987; Muckenheim *et al*., 1988).

Colliding-Pulse Dye Laser

Colliding-pulse mode-locked dye lasers can emit optical pulses of <100 fs pulse width at repetition rates of 100 MHz. They can produce an average power of 15 mW at 630 nm when pumped with at least a 4 W all-line argon-ion pump. Noise is less than 1% but this figure depends critically on pump laser performance. This type of laser was used by Denk and colleagues (1990) and Piston and colleagues (1992, 1994) for their first two-photon experiments. It has rather limited tunability. Thermal equilibrium is reached within 1 h after turning the system on. Ti:Sa lasers, which produce 100 fs pulses at 100× higher power, have replaced colliding-pulse mode-locked dye lasers.

Modulated Diode Lasers

A small current change makes a large change in the output intensity of the diode laser, allowing most CW diode lasers to be operated in pulsed mode. When the internal diode laser processes are fast enough and stray capacitance from leads, etc., is kept low, pulse repetition rates of several hundred megahertz can be obtained as long as the required average output power is moderate. To generate a crisp pulse train, the cut-on and cut-off slopes must be steep. A recent review by Landgraf (2001, 2003) lists a variety of diode lasers and their upper frequencies. Selected laser diodes have reached ~700 MHz, for use in determining fluorescence lifetime. With a trigger circuit, these devices could act as a poor man's Ti:Sa for FLIM.

Diode Pumped Solid State Laser in Pulsed Mode

Doubled or tripled output could be used in tissue ablation but otherwise the pulse repetition rate is too low and the high output power a waste for CLSM. Used as Ti:Sa pump laser, a dual rod, tandem cavity DPPS laser can now produce up to 90 W at 527 nm. An example of these systems producing 1 to 10 kHz optical pulse trains with a width of a few hundred nanoseconds are the Q-switched Evolution Nd:YLF family from Coherent Inc. (Arrigoni, 2004b) and the 30 W Empower series from Spectra Physics.

Ultrafast Diode Pumped Solid State Lasers

Many one-box compact and flexible solutions are appearing. Examples are the Pallas and Tiger compact picosecond/femtosecond laser systems from Time-Bandwidth (Table 5.3). Direct diode-pumped, passively mode-locked DPSS Nd-YLF lasers can make 70 fs pulses (Tiger-picosecond from High Q Laser Production) and 100 ps (Pallas) covering 780 to 860 nm, with a repetition rate of 50 to 200 MHz and an average output power of 500 mW.

Titanium-Sapphire and Related Ultrafast Lasers

This type of laser covers 660 (18 W pump) or 700 to 1100 nm (Duling, 1995; Fermann *et al*., 2002). It is an ideal source for two- and multi-photon microscopy. The long wavelength reduces scattering and allows it to penetrate farther into tissues than visible lasers. The fact that excitation occurs only at the focus plane improves the signal-to-background ratio and reduces phototoxity. Extensive overviews of multi-photon fluorescence microscopy and applications can be found at the excellent Molecular Expressions site (Florida University) and the Cornell site of DRBIO as well as in Chapters 28 and 37.

To cover the entire wavelength range, several sets of mirrors may be necessary. Most Ti:Sa systems are now pumped with low-

maintenance, highly efficient 5 to 10 W solid-state diode lasers. The self-mode-locking Kerr effect of the Ti:Sa lasing rod delivers 100 fs pulses at 80 to 100 MHz repetition rate. Modifications in design may lead to pulses as short as 20 fs or even 5 fs.[1] These very short pulses exhibit extreme pulse broadening as they pass through dispersive media. Measures to reduce or eliminate this effect are given above under beam delivery. The high average power combined with the short optical pulse width makes the Ti:Sa laser almost ideal for frequency doubling and tripling to the visible and 350 to 525 nm spectral regions. Following user demand, completely automated and tunable systems are now offered. These provide a somewhat limited tuning range to stay away from the edges of the gain curve. Examples are the Mai-Tai family from Spectra Physics and the Chameleon products from Coherent (Table 5.3). Gaussian profile and broadband mirrors are standard features.

On the other hand, several companies now offer kits to allow users to build their own ultrafast or CW Ti:Sa laser. These kits are much less expensive and also less complex. Still further simplification is under way by having all components on a small footprint in an all-in-one-box design. First, the Nd:YVO_4 green pump laser was upgraded with stronger pump diodes and higher efficiency doubling crystals. It now emits CW 18 W of 532 nm with low noise and in TEM_{00} mode. One pump diode suffices, halving replacement costs. Not only can the 532 nm output pump both the Ti:Sa oscillator and a regenerative Nd:YLF-based pulse amplifier, halving the number of green pump sources, but also the edges of the gain curve tuning range are more easily accessible. Thermal lensing gets worse with increased pump power but has been overcome by adjusting the focal length of the cavity mirrors. Nevertheless cryogenic cooling may be required if systems are scaled up further (Arrigoni, 2004b).

Heat dissipation and efficiency are areas where fiber and thin disk lasers have a clear edge. A further simplification is under way by using ytterbium oscillators, which can be pumped directly with IR diode lasers, bypassing the green pump step, but their pulse width, etc., is still not as short. Table 5.2 lists the specifications of several commercially available examples also in kit form. Most, if not all, use semiconductor saturable-absorber mirrors (SAMs or SESAMs, see above under mode-locking) to generate a self-starting, high-repetition-rate femtosecond or picosecond pulse train (Hogan, 2004).

White Light Continuum Lasers

A rather inexpensive source of quasi-white light is the CW He-Cd laser, which seems to the eye to emit white light. Some with a positive column discharge actually emit only three wavelengths simultaneously (325, 354, and 442 nm), while the hollow cathode design emits from UV to NIR. Selection of five lines creates an RGB white light laser emission (White Knight RGB Series, The Cooke Corp.; Table 5.3).

An elegant and wider supercontinuum white light source, with generation stretching from below 450 nm to above 950 nm, is feasible using a 1 m long photonic crystal fiber (PCF) with a 1.7 µm core diameter illuminated by the 3 to 5 ps 800 nm pulses from a 5 kW Ti:Sa laser (Espinase, 2004). This is an important step towards a white light femtosecond light source. A similar PCF white continuum source with a length of 38 cm was used by McConnell (2004) on a Bio-Rad 1024ES scan head. Coherent introduced a CW-pumped, cavity-dumped, regenerative amplifier with white light continuum generation at repetition rates up to 250 kHz and 100 fs pulses. However, even this much improved repetition rate is too slow for the usual CLSM applications. This problem is elegantly solved by a cavity dumped OPO, pumped by the second harmonic of a Ti:Sa laser. It delivers 30 fs pulses with a repetition rate of up to 4 MHz between 570 and 660 nm with a pulse energy of 13 nJ (Potma *et al.*, 1998).

Ultrafast Fiber Lasers

To generate short pulses with high peak power, a ring cavity can extract more energy from the pump. Bragg feedback (Friebele and Kersey, 1994) stabilizes the laser wavelength. Mode-locked single-mode fibers produce reliable, high repetition rate, short pulses with a small wavelength tuning capability (Duling, 1993; Smith and Lucek, 1993). Diode pumping and proper optics are necessary for best performance. The pump DFB diode laser, output, and amplifier stages are simply coupled by splicing devices (Fig. 5.20). This type of laser creates a very compact, efficient, and cheap alternative source for femtosecond pulses at gigahertz repetition rates and may soon replace the dye laser and some Ti:Sa systems. Hitz (2004d) reports a diode-laser-pumped Yb ultrafast fiber laser oscillator-amplifier system equipped with external grating compressor and generating 62 MHz, 100 fs with 25 W average power. Stability has to be improved against environmental changes caused by mechanical stress-induced birefringence and temperature variations. At the moment, a fiber laser is one fifth the size, has the same initial cost, but only one third the operational costs of a Nd-YAG or Nd-YVO_4 ultrafast system. The FemtoMaster1060, a passively mode-locked soliton fiber laser is offered by Fianium-

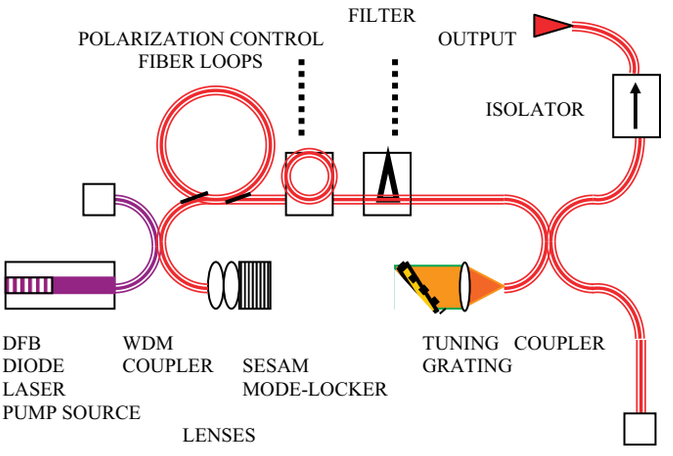


FIGURE 5.20. Schematic diagram for a femtosecond pulse mode-locked ultrafast diode laser. The emission of the fiber pigtailed distributed feedback (DFB) diode laser is coupled to the main laser gain medium fiber via a wavelength division multiplexer (WDM). Laser output exits from the laser resonator cavity in a similar way. The resonator consists of a lens-coupled high-reflecting mirror and a semicondcutor saturable absorber mirror (SESAM). The other end of the cavity contains the grating tuning element. For polarization, pulse width and dispersion control, extra elements are spliced in. Coupling the SESAM in a different way and lens coupling both gain medium fiber ends to the tuning grating would create a fiber-ring laser. In a flexible and compact way, diode-laser-pumped amplifier stages, pulse-width compressors, and frequency-doubling stages can be added.

[1] One can predict from the relationship $\Delta\tau.\Delta\nu > 1$ that for a spectral width of 200 nm one obtains a 10 fs pulse at 800 nm.

New Optics, Ltd., a company that has also developed mode-locked, tunable Yb and Nd fiber lasers. Typical specifications are tuning from 1040 to 1120 nm, 3 ps pulse width and 30 to 100 MHz repetition rate. With some further development, it may become a competitor for the Ti:Sa laser (Okhotnikov *et al*., 2003; Rusu *et al*., 2004). Pumped by a pigtailed diode laser, the mode-locked ultrafast Er fiber laser FemtoFiber Scientific (FFS) from Toptica Photonics AG (Table 5.3) produces pulses with a width of <100 fs at 100 ± 10 MHz, optional tunability over 1150 to 1400 nm and SHG doubling to 575 to 700 nm, 1550 nm is standard with 200 mW average and 18 kW peak power; the Femtolite family Er fiber laser and Yb-fiber based chirped pulsed amplifier FCPA μJewel series from IMRA America Inc.

WAVELENGTH EXPANSION THROUGH NON-LINEAR TECHNIQUES

The spectroscopist wishing to excite with laser light finds several gaps in the table of available wavelengths. Although dye lasers cover an extended portion of the spectrum, they require too much maintenance to be useful in standard confocal microscopy. Optically anisotropic crystals provide a good alternative towards tunable light as long as they are pumped with lasers having high (pulsed) peak power at a high repetition frequency.

Second and Higher Harmonic Generation: Second Harmonic Generation, Third Harmonic Generation, Fourth Harmonic Generation Label-Free Microscopy

Non-linear optical (NLO) effects occur in certain classes of optically anisotropic crystals (Lin and Chen, 1987; Tebo, 1988). Focusing intense laser light into these crystals generates radiation at half the wavelength or double the frequency. This process, therefore, is known as "frequency doubling" or "second harmonic generation" (e.g., Huth and Kuizenga, 1987; Higgins, 1992). The intensity of the frequency-doubled light output is proportional to the square of the incoming light intensity. A Cr:forsterite laser running at 1230 nm was used to create a very elegant second harmonic generation (SHG) and third harmonic generation (THG) system operating at 615 and 410 nm (respectively) with a pulse repetition rate of 110 MHz and a pulse width of 140 ps (Hogan, 2004; see also Chapter 40, *this volume*). When the incoming beam is very intense, even third, fourth, or fifth harmonics can be generated. However, the efficiency of harmonic generation decreases at higher orders. Most doubling crystals can be angle or temperature tuned. THG is very interesting for label-free monitoring of inhomogeneities at interfaces, for example, cell membranes (Moreaux *et al*., 2000). Yelin (2002) and Brocas and colleagues (2004) compare the THG performance of several systems: the Spectra Physics Tsunami-OPAL synchronously pumped OPO, which emits an 80 MHz 150 fs pulsetrain at around 1500 nm with an average power of 350 mW; and the T-pulse laser (Amplitude Systèmes) emitting 50 MHz 200 fs pulses at 1030 nm with 1.1 W of average power. THG reaches 500 and 343 nm, respectively, so UV transmitting optics may be required. A not-so-pleasant consequence of the doubling process is the doubling of the noise level. Pump lasers with excellent stability are a must. Higher peak powers and new, low-threshold materials require a careful reconsideration of design strategies (Beausoleil, 1992). CSK Optronics (Table 5.3) sells a line of compact doublers and triplers for Ti:Sa lasers. An important issue in this type of experiment is the amount of optical damage done to living cells and tissue by these powerful femtosecond pulses (Chu *et al*., 2003; and also see Chapter 38, *this volume*). THG peak intensities of 100 to 300 GW/cm^2 illumination (i.e., nJ/pulse) are not damaging.

Presently, it is also possible to combine less powerful tunable dye or semiconductor lasers to cover the wavelength range from 170 nm to 18 μm almost continuously.

Sum or Difference Mixing

Another technique for generating different wavelengths from certain basic laser wavelengths is sum or difference mixing. When two laser beams of high and low intensity and of frequency ω_1 and ω_2, respectively, are simultaneously focused into a non-linear optical crystal, a sum signal is generated. The intensity of the sum signal, $I_{(\omega 1+\omega 2)}$ is proportional to the product $I_{(\omega 1)} \times I_{(\omega 2)}$. The higher-intensity ω_1 laser helps in generating enhanced UV output I (ω_1 + ω_2) with an extended tuning range. In a similar way, difference mixing, $I_{(\omega 1-\omega 2)}$ leads to a tunable IR laser. (For examples, see Dunning, 1978; Adhav, 1986; Herrmann and Wilhelmi, 1987; Kaiser, 1988; Marshall, 1994; Demtröder, 1996)

Optical Parametric Oscillators and Optical Parametric Amplifiers

The highest repetition rate that can be obtained depends on pump energy storage. Potma and colleagues (1998) developed a cavity-dumped optical parametric oscillators (OPO) with 13 nJ pulses that reached a repetition rate of 4 MHz. These devices can generate a continuously tunable output by non-linear conversion of fixed wavelength high intensity CW or pulsed laser light (Butcher, 1994; Radunsky, 2002). OPOs are a reliable and easy-to-use means to cover spectral gaps left by dye or Ti:Sa lasers. Between the Ti:Sa fundamental, covering 700 to 1000 nm, and the second harmonic, covering 350 to 500 nm, a spectral gap also exists from 250 to 350 nm. This means that neither tryptophan, tyrosine, coumarine, or naphthalene nor the caged probes can be covered by a Ti:Sa. OPO efficiencies easily reach 40% to 60% (Anderson, 1993), and practical systems are available from many companies (Table 5.2). A continuously tunable output stretching from UV to IR is generated by non-linear conversion, that is, optical frequency mixing. Parametric frequency conversion creates two lower-energy photons (signal and idler) from each incoming photon. This process is the opposite of sum mixing.

There are two methods to overcome the low efficiency of the parametric generation: Method 1 — Parametric amplification in a non-linear BBO crystal pumped by the second harmonic of the Ti:Sa followed by pulse compression. Parametric down-conversion is incompatible with long pixel integration times, and high pulse energies may possibly be damaging, and instrumentationally, it is quite involved. Method 2 — Cavity-dumping a synchronously pumped OPO can produce pulse repetition rates up to 100 MHz. This allows FLIM imaging and reduces somewhat the average power delivered and cell damage. In addition, residual pump beams at 400 and 800 nm are available. Synchronous pumping means that the cavity lengths and, therefore, the pulse round-trip times are equal in both pump source and OPO (Potma *et al*., 1998).

Non-critical phase-matching (NCPM) in a crystal is preferred because it allows tight focusing of the pump beam and long interaction lengths, resulting in low OPO thresholds. Efficiency can be further increased by using periodically polled (PP) waveguides, which do not diffract a tightly focused beam as does bulk material, while at the same time they allow long interaction lengths with a good mode profile. For example, green output from a Q-switched

diode-pumped, frequency-doubled Nd-YAG laser pumps a non-linear crystal creating a broad tuning range and narrow bandwidth with 15 mW average power at around 670 nm. Typical oscillator and amplifier crystal combinations cover various spectral regions. Angle tuning a proper crystal will give a 405 to 2700 nm tuning range with 45% total (signal + idler) efficiency (QWU-Lasertechnik GmbH; Table 5.3). Continuum (Table 5.3) introduced the Sunlite OPO (Anderson, 1994a), which is currently the Sunlite EX OPO, with a very broad tuning range stretching from 222.5 to 1750 nm without a gap and providing line widths of 0.075 cm^{-1}. It is pumped with 100 to 160 mJ pulses at 355 nm from a Q-switched Nd:YAG. Such a system is a good replacement for pulsed dye lasers.

As mentioned above, there is a trend to create easy-to-operate automated all-in-one-box solutions. Spectra-Physics provides the LBO-based femtosecond synchronously pumped OPAL. Near the peak of the OPO tuning curve, it generates 200 to 250 mW and covers a wavelength range from 1100 to 2260 nm with pulse widths <130 fs. By frequency doubling, one covers the 550 nm gap left by the Ti:Sa systems. A further improvent with higher average power and repetition rates is obtained with ytterbium tungstate (Yb:KGW) employed in the Eclipse fs OPA (Spectra-Physics; Krueger and Féru, 2004).

Several OPO classes exist depending on the bandwidth narrowing optics used. The narrower the bandwidth, the less the gain. In addition, the number of passes through the crystal influences the gain. A single-pass device creates little gain for a 5 ns, 355 nm, 100 mJ pulse. Enclosure of the non-linear material in a resonant cavity gives optical feedback and adding a pulsed pump source creates extra gain. The complete design forms an optical parametric amplifier (OPA). The frequency stability of an OPO depends on the pump source stability and, with enough stability, single-resonant OPO (SRO), with feedback for idler or signal, or a double-resonant OPO (DRO) with feedback for signal and idler, can be built (Radunsky, 2002). OPOs as well as tunable CW dye lasers are often used as narrow bandwidth seed sources for OPAs. For example, by SHG doubling the 820 nm output from a Ti:Sa regenerative amplifier in a BBO crystal, one obtains 410 nm. This 410 nm pumps a second BBO crystal, the OPA. An 80-fold amplification is obtained resulting in 100 mJ pulses with narrow bandwidth. Changing the crystal angle (angle tuning) covers the wavelength range from 450 to 700 nm. These techniques can be adapted and implemented into fiber-optic OPO and OPA designs as well.

Pulse Length Measurement

Continuous on-line monitoring of the picosecond or femtosecond pulse shape immediately provides the feedback needed to align the cavity and perform other adjustments. Thermal drift may require cavity length retuning twice a day, even in a very large air-conditioned dedicated laboratory space. In a smaller space this may be required far more often. A pick-off signal from the monitoring diode is fed into an auto-correlator unit attached to a 400 MHz digital oscilloscope. Several designs exist but a computer-assisted background-free design is favored. A Web site explaining the operation of a background-free correlator is http://linac.ikp.physik.tu-darmstadt.de/fel/optical_pulse.html. Both time-dependent amplitude and phase must be known for many experimental procedures. Frequency-resolved optical gating (FROG) creates a two-dimensional function of the spectrally resolved autocorrelation at a range of correlation delays. Second harmonic-FROG in a non-collinear configuration is background free. Avesta (Del Mar Ventures; Table 5.3) offers a semiconductor-based design eliminating the non-linear crystal and the PMT detector. Created from a single pulse, the overlap of two identical, time-delayed pulses with different center frequencies generates a spectral interference pattern in spectral phase interferometry for direct electric-field reconstruction (SPIDER). Pulse spectrum and cross-correlations of a pulse with a pulse copy that has been altered by a dispersive plate or attenuator in one arm of the correlator are used for phase and intensity determination from correlation and spectrum only (PICASO).

MAINTENANCE

On delivery, most laser systems perform well above the guaranteed specifications given by the manufacturer. The consumable parts (i.e., laser tubes, lamps, dyes, and amplifier optics in solid-state lasers and attached fiber-optics) are usually not covered by the warranty. Depending on the type of laser used, these costs can be substantial.

A factor usually forgotten at the time of an initial laser purchase is the need to acquire peripheral equipment for proper maintenance. Extra dyes, filters, power meters, sampling oscilloscopes and sampling units, fast diodes, infrared viewers, spectrum analyzers, beam-dumps, radiation shields, warning signs, covers, laser goggles, explosion- and fire-proof cabinets for solvent storage, and hazardous waste disposal, etc., are often not included.

Maintenance of Active Laser Media

Laser Tubes

The plasma tubes in ion lasers must be replaced when the cathode sags or the bore of the tungsten disks or BeO tube corrodes to become too big. The "getter," always installed in the laser system to remove impurities in the gas, may become saturated. Cracks that form in cooling tubes usually lead to its immediate failure. The introduction of beryllium-oxide (BeO) tubes with superb heat conduction characteristics has significantly reduced the fragility of these laser systems and increased their reliability. Medium-power systems should last for 3000 to 5000 h (see Tables 5.1 and 5.2) and high-power systems for 2000 h.

Most laser systems come with 18-month warranties, but some self-contained, sealed systems carry a warranty for up to 5 years. The technology has significantly improved over the last few years to reduce the deposition of disk material and other contaminants on the inner surface of the Brewster windows. For the largest ion lasers, the aluminum oxide ceramic tube technology with brazed tungsten/copper disks has revolutionized deep UV output power levels and reliability. For He-Cd lasers, regular tube replacements are necessary after 1000 h of operation.

Tube Replacement and the Secondhand Laser Market

Several companies repair and resell worn laser tubes. Always ask for warranties and try-out. Old BeO tubes are considered hazardous material (HazMat) and can for a nominal amount be returned to the manufacturer.

What the User Can Do

To prolong the life of a tube, check mirror alignment so that the stabilized output can be attained with minimum excitation power to minimize tube component degradation. Check the water flow around the laser head for bad connections and look for internal deposits at least once a year. Keep dust out of laser systems; the laser should be connected to a permanent supply of clean, dry, room-temperature, oil-free air or nitrogen gas. A slight over-

pressure helps to prevent dust from entering the laser head. Commercial air filters that might introduce dry powders into the laser system should never be used. Synchronously pumped systems perform markedly better and the intensity stability improves when dust is absent. Do not run at the highest power unless necessary, keep a user log, and inform users on the cost per hour to prevent idling.

Dyes

Dye lasers pose a number of hidden costs. Rhodamine 6G is one of the least expensive dyes, and is the most stable with a lifetime of 2000 Wh for a typical 1-L reservoir (i.e., the output power of the dye is reduced to 50% when it is pumped for 1000 h at 2 W or 400 h when pumped at 5 W). Dye aggregates can be filtered out but evaporation of the solvents necessitates periodic refilling. When the dye pump inadvertently starts to suck in air, air bubbles are generated and cause immediate contamination of the optical mirror surfaces. This problem can be prevented by careful start-up. Any faint, sharp clicks at the nozzle position indicate air bubbles passing the nozzle opening. Operating the dye laser with the wrong solvent, for example, incorrect viscosity, may cause the dye to foam, which will quickly clog the system. In order to reduce downtime and contamination of dyes, it is recommended that every dye is run with its own pump module. This is more expensive, but results in a much faster hook-up. Used dye and leftover solvent should be discarded in a manner that does not pose a threat to humans or the environment. Dye nozzles should be cleaned regularly in a sonicator, especially when the system has not been used for a while. Non-laminar flow from the jet nozzle is an indication of nozzle problems.

Gases

Excimer lasers need regular gas changes. Ion lasers refill their gas from a ballast tank via a microcomputer-controlled valve system. This reduces the risk of overfilling the plasma tube and degrading the performance or losing laser power altogether.

Laser and Amplifier Rods

Solid-state media, at least for CW lasers, are quite robust. However, pulsed systems need a very good Gaussian beam quality, otherwise the rod coating will be damaged. Often one can hear this as sharp clicking sounds that indicate that the laser needs immediate attention. Improper Ti:Sa rod cooling leads to water condensation on the pump surface and produces instabilities. In the worst case, continued operation may damage the bulk of the laser rod (Soileau, 1987). Degradation of the surface layers of the medium, caused by the intense illumination from the pumping system and referred to as solarization, is less of a problem.

Diode Lasers

These devices are quite sensitive and can easily be damaged or destroyed. Damaged systems may show very weak output, a shift in emission wavelength, or a change in divergence or beam shape. Pigtail fiber-optics, normally attached in front of the laser diode, also are suspect when the output power drops significantly but the drive electronics should be checked as well (as we recently experienced!). The fiber-optics may have been pulled out of its socket or it may have broken. At high power levels damage to the fiber surface may also occur, especially with plastic fiber-optics. As discussed above, current transients (spikes) and electric discharges should be prevented at all times. Forward-biased semiconductor junctions are inherently thermally unstable; an increase in current increases the temperature, which, in turn, increases the current even more. Therefore, current supply design is important and must be suited to the specific laser.

Maintenance of Pumping Media

For CW or pulsed lasers, which are pumped by arc lamps, the lamp(s) must be replaced when the output power of the laser decreases. On the inside of the arc lamp, dark deposits may develop, which, over time, will cause an increase in absorption and catastrophic failure due to local heating. Defective lamps usually fail within the first 10 to 20 h after start-up (Smith, 1986; Littlechild and Mossler, 1988). Optical amplifier components can be shielded from damaging UV radiation by doping the quartz lamp envelope with cerium. Electrode sputtering can be reduced by using sintered tungsten doped material with a low-work function to create a more uniform cathode current and lower temperatures (Erlandson and Powell, 1991). In addition, longer flashlamp lifetime can be obtained by using mushroom-shaped cathodes.

Maintenance of the Optical Resonator

Dust is one of the major enemies of the laser and tobacco smoke should be kept out of any laser laboratory. Dust covers should be in place at all times and any dust on optical surfaces should be removed as soon as possible, for example, on wavelength tuning prisms, birefringent plates, mode locker or Pockels cell surfaces, or mirrors. As using the wrong solvent to clean optics can destroy the optical coating, use only the ultra-pure solvents recommended by the manufacturer and follow the proper procedure. When in doubt, first try it out on a test surface. Most laser manuals describe in detail the proper cleaning methods. Never use the same side of a cleaning wipe for more than one pass. A patterned movement should be used when cleaning optical surfaces.

The optical coatings on laser cavity mirrors and external mirrors or fibers cannot withstand prolonged exposure to UV radiation. Colored rings will appear on the coating surfaces or they may look hazy or foggy. The formation of color centers, which cause increased absorption, occurs in fused quartz materials: lenses, optical fibers, etc. Color centers are usually caused by included impurities. Resulting lattice defects are mostly single electrons bound to negative-ion vacancy sites: F-centers. Free electrons created by intense radiation become trapped in these sites. Excimer lasers with their high UV peak powers are particularly prone to creating color centers. At high power, too tight focusing, or self-focusing, conditions can produce mechanical damage (remember, lasers are used for machining!; Günther, 1993). Damaged parts must be replaced immediately to prevent the deteriorated beam from damaging other components. This is especially true for pulsed systems. Frequency-doubling elements should be inspected regularly or whenever laser intensity fluctuations occur. A microscope may be necessary to see damage to the coating. Heating of some crystals (e.g., KTP) seems to reduce these effects. Frequency-doubling and other hydroscopic crystals should be kept under optimum dry conditions at all times.

Maintenance of Other System Components

Cooling Water

A gradual decrease in laser power can be caused by the growth of algae in the cooling water. A small addition of sodium azide (NaN_3) prevents a reoccurrence of the growth. An annual check of the rubber rings in the cooling hoses is recommended. At least once a year the cooling circuitry should be checked for galvanic and other

types of corrosion (Schneider and Williams, 1993). Do not use tap water for cooling. Many laser and temperature bath manufacturers now offer closed-loop laser cooling systems. Heat removal with air-to-liquid cooling is also possible (Goldman, 1993). For proper operation of a Nd-YAG laser, the resistivity of the cooling water should be in the range recommended by the manufacturer. When the resistivity is too low, the lamps will not start. If it is too high, the plating on the inside of the elliptical resonator will dissolve and cause a decrease in laser power. Water filters and de-ionizing filters should be replaced regularly as demanded by the performance of the laser. Stacked diode laser arrays, small in size but with several tens of watts of optical output power, require liquid cooling with micro-channel technology or thermo-electric (Peltier) cooling.

External Optics

All optical surfaces should be kept as clean as possible. Mirror surfaces exposed to UV radiation will have to be replaced regularly, depending on the impinging power density. Coatings may peel off. Apertures in spatial filters should be inspected and replaced when damage (burn) occurs. Fiber-optics, especially the ones exposed to high-intensity UV light, may develop color centers, which result in increased absorption and, in the end, failure of the entrance section. High-intensity visible or infrared light may lead to overheating at the input fiber tip. Fortunately, the length of most fibers is sufficient to allow them to be cut back, repolished, and reconnectorized, though sometimes at substantial cost and time delays. If they are bent too tightly, fibers will break, causing a sudden loss of output power. Pigtail fibers attached to the main body of a laser diode may dislodge themselves. Due to the automated fabrication process, which includes angular positioning to optimize the output and to use the most intense emission spot, manual reattachment usually does not re-establish the original power level. Laser damage thresholds for dielectric mirrors and anti-reflective coatings are roughly 250 MW/cm^2 at 532 nm and 500 MW/cm^2 at 1064 nm, assuming surfaces are spotless and clean (Aubourg, 2002).

TROUBLESHOOTING

A very extensive and instructive body of information for gas, dye, and diode laser maintenance, including optics cleaning and repair, exists in Sam's Laser FAQ (see Web site listings).

SAFETY PRECAUTIONS

Laser hazards include thermal and fire, acoustic shockwave, and strongly wavelength-dependent photochemical damage. Types of beam exposure are direct exposure intrabeam, specular, and diffusion reflection effects. Eyes and skin are most commonly affected. Non-beam–related hazards include electrical shock, capacitors, hose leakage, water vapor condensation, air contaminants, fumes, aerosols with biological agents, cadmium and zinc telluride (that burns in the presence of high laser intensity and oxygen), radiation damage, fire, compressed gases, gas cylinders, earthquake damage, excimer gases, and laser dyes.

All lasers are generally divided into four classes:

Class 1. Embedded lasers and laser systems
Laser completely enclosed, radiation not accessible during use.

Class 1M. Lasers and laser systems:
CW = <40 μW blue and = <400 μW red.
Very low power: Safe for long-term intrabeam viewing.

Class 2. Low power visible lasers and laser systems:
CW = <1 mW.
Low power level. Safe for brief accidental naked eye direct exposure with blink and aversion response active.

Class 2M. Low-power visible lasers and laser systems.
Low-power visible collimated or divergent large beam diameters. Potential hazard with magnifiers

Class 3R. Visible. Low-power lasers and laser systems.
Accidental exposure usually not hazardous but eye injury possible upon intentional long-term viewing. Training required. Equivalent to Class IIIA "danger" [Center for Devices and Radiological Health (CDRH)] and ANSI 3a (USA).

Class 3R: Invisible. Low-power lasers and laser systems.
Wavelength dependent, limits are five times those of Class 1.

Class 3B. Medium-power lasers and laser systems:
CW = <500 mW.
Serious eye injury even for brief accidental exposure to direct beams possible. Training required.

Class 4. High-power lasers and laser systems.
Even diffuse and certainly direct-eye exposure will lead to serious eye and skin injury. Poses fire hazard as well. Training required.
with M: magnifying instruments and R: relaxed requirements. Limiting values for small point-like lasers with angular retinal spot size smaller than 1.5 mrad.

General safety precautions that become more stringent with increasing classification, must be followed when operating a laser [International Commission of Non-Ionizing Radiation Protection (ICNIRP) and International Electrotechnical Commission (IEC) 60825-1 guidelines, see revised ANSI-Z-136.3 1996 classification, safe use of lasers; Tozer, 2001; Schulmeister, 2003; Sliney, 1994; LIA and Rockwell Laser Industries Inc.; Table 5.3]. Separate photochemical and thermal retinal exposure limits, including limits for damage from ultrashort, <1 ns pulses, have been added as well as the *.M classes. Every laboratory should have a Laser Safety Officer (LSO) who should be consulted when necessary. This person should be responsible for the proper training of users of laser-assisted equipment. Safety training videos are available from LIA, OSHA, and Rockland Laser Industries (Table 5.3) and often also from your own local university. Outside the laser laboratory, a "laser in use" warning sign must be posted and a red warning light should be positioned at the entrance to the laser room.

Inside the laser laboratory, safety precautions are necessary even for users of enclosed systems attached to CLSMs whenever the system is opened or when the fiber-optics are aligned and exposure to a laser beam becomes a possibility.

A brief "Do and Don't" list:

- Inform everybody near the laser setup to be worked on. Check the sign-up agenda.
- Check and put all required accessory equipment on the ready.
- Have the entrance warning red light on when any laser is on.
- Remove everybody from the laser site whose presence is not required.
- Close the access doors.
- Close curtains.
- Remove rings, watches, and ties.
- Put safety goggles on.
- Never look directly into any laser beam.

- Align open laser heads with minimum power.
- Check for stray light and reflections with a hole-punched business or IR indicator card.
- Block beams not being attended.
- Disconnect electrical connections.
- Discharge large capacitors with a grounded large screwdriver with an insulated handle.

Beam Stops

Beam stops should be made out of anodized, flat black aluminum and positioned in such a way that no radiation is reflected back into the room. Stray reflections must be prevented; powerful IR or visible beams may easily start a fire on electrical cables or other flammable materials.

Curtains

Curtains should be made of special non-combustible material, preferably black in color. When a spot of 1 mm^2 is irradiated with approximately 1 MW/m^2 or more, the black side should emit a non-toxic smoke (that nevertheless may form damaging deposits on critical optical surfaces!) and may glow. See, for example, the Rockwell Laser Industries, Inc. and Lasermet Ltd. Web sites. Curtains are designed for low-power, 100 W/cm^2 or up to 1.2 kW/cm^2 lasers (MacMullin, 2004). Curtain shielding will prevent the accidental illumination of other people while aligning a laser or beam-splitter.

If a visual control is necessary from outside the room, a radiation-absorbing plastic window should be mounted in the door or wall. Tape should **not** be used to hold curtains together because this could allow the build-up of poisonous gases. Clothing is another possible source of trouble that is often disregarded. Famous are the stories of halved neckties.

Laser Goggles

A large range of eye protection devices is available (e.g., from LFW and Uvex; Table 5.3). A telling Ti:Sa fovea burn track is shown in Robinson (1998). It is important to realize that a 1 W/cm^2 irradiance level at the cornea can become a focused 100 kW/cm^2 retina spot of about 20 µm diameter.

Screens

Where possible, anodized, flat black aluminum pipes should be used to enclose all laser beams. These not only protect the operator, they also reduce dust in the beam line.

Exposure Effects, Warning Signs, and Interlocks

Each laser system must be equipped with the proper warning signs and interlocks. The listed references (Sliney and Wolbarsht, 1980; Rockwell, 1983, 1986; Winburn, 1985; Sliney, 1986) describe in detail electrical hazards and detrimental reflections from rings, watches, etc. Biological effects are also extensively covered, that is, thermal and photochemical effects upon exposure to CW and pulsed laser radiation, and the maximum permissible exposure to eyes and skin.

Chemical hazards may be caused by laser dyes, some of which are mutagenic. Dye solvents and laser gases must be properly handled. Basic protective measures include laser goggles (Burgin, 1988), cleanliness, and proper handling of chemicals. A sufficient number of eye protection devices should always be at hand when laser system components have to be repositioned or realigned. Naturally, one should reduce the power level as much as possible during alignment. Periodic training meetings and medical check-ups are recommended and can be used as a certificate of good laser usage conduct.

Infrared Paper

To safely find infrared beams, one can rely on infrared viewers but these are fairly expensive. An alternative is the use of IR indicator cards. These emit a visible luminescence via electron-trapped up-conversion. Suppliers include Bromba GmbH, Edmund Scientifics, Electro Optical Components, and Lumitek Intl. Inc. (Table 5.3).

CONCLUSION

In the previous sections, we have described the large number of lasers currently available for CLSM. These lasers vary widely in characteristic wavelengths, tunability, stability, output power, ease of use, and price. Rapidly expanding areas such as diode lasers, optical parametric amplification, and direct-doubling diode lasers would require an update every three months. Solid-state laser systems with wide tunability through the incorporation of optical parametric techniques and fiber lasers are areas showing rapid development.

Brelje and colleagues (1993) show a figure displaying the excitation wavelengths of various popular fluorophores with matching ion laser lines. This picture has certainly changed in the past years with the increase in power of solid-state and fiber lasers and the expansion of their range of tunability. For the moment we summarize several of the most often used lasers in Table 5.4. It is clear from this table that the ion lasers are being pushed out the door.

- For CLSM, a stable, TEM_{00} mode, easy-to-use laser with short coherence length is imperative.
- Wavelength tunable lasers require pulsed pump lasers with high peak power, good mode quality, and the best possible stability to reduce noise in the subsequent wavelength conversion and amplifier stages, as well as OPO, OPA, or master oscillator parametric amplifier (MOPA) optics. The best source is currently the tunable Ti:Sa laser. Excimer, nitrogen, and similar pulsed lasers and mode-locked solid-state lasers are still useful pump sources for tunable dye lasers if pulse repetition rates are sufficient for your purpose. The goal should be to each have a US$6000 modular, personal 2-photon source!
- Miniaturization and ease-of-operation via efficient, low-cost, low-noise, tunable semiconductor and fiber lasers is a reality now and these lasers are replacing big CW and pulsed laser systems. A trend exists towards modularity, efficiency, and small footprint.
- With the advent of completely automated, self-contained laser systems (Mai-Tai and Chameleon) the ideal turnkey system is almost present. Older, bigger, flexible laser systems cannot be considered turnkey systems and require constant attention from well-trained, qualified persons.
- Laser safety training is a must also for CLSM users and eye protection and other safety measures should be at hand as required.

TABLE 5.4. Lasers Often Used in LSCM

	Manufacturer and CLSM system						
Laser Type	Visitech international Vt-eye and Vt-Infinity	Leica TCP-SP2-AOBS *SP2*	Nikon Digital Eclipse C1 Plus	Olympus Fluoview FV1000 & *FV500*	Perkin-Elmer Ultraview	WITEC CRM200	Zeiss Axiovert 200M LSM 510 META
Fixed wavelength lasers							
HeCd							
UV 325 nm						10–30 mW	
Argon-ion							
UV 351 nm				*40 mW*		300 mW	
Argon-ion							
UV 364 nm						>20 mW	
Argon-ion							
UV 351, 364 nm		50 mW					80 mW Enterprise
Diode laser							
405 nm	6 mW	20 mW		6 mW (*25 mW*, opt)	7.5 mW		25 mW 50 mW (510 Live)
Diode laser							
408 nm			20 mW (mod.)				
Diode laser							
DPSS 430 nm		8 mW					
Diode laser							
440 nm			5 mW (mod.)	0.7 mW (*5 mW opt.)*	7 mW		16 mW (510 Live)
HeCd							
442 nm		20 mW		*6 mW*	20 mW	11 mW	
Argon-ion	458, 514 nm,						
Multi-line 458, 514 nm	25 mW	100 mW @ 457, 476, 488, 514 nm *65 mW*	40 mW	30 mW *40 mW* @ 457, 488, 515 nm	488, 514, 568, 7.5/15 mW each	25 mW @ 457–514.1 nm	30 mW 458, 477, 488, 514 nm
Blue only							
488 nm		+	10 mW	*10 mW*		+	
Laser diode							
488 nm							100 mW (510 Live)
DPSS							
532 nm							75 mW (510 Live)
Green HeNe							
543 nm	+	1.5 mW	1.5 mW	1 mW		1.25 mW	1 mW
Yellow DPSS							
561 nm							10 mW (510-META)
Krypton ion							
568 nm		25 mW		*10 mW*			
Krypton/Argon							
488, 568, 647 nm	20 mW	75 mW			+		
Orange HeNe							
594 nm		2 mW	2 mW				2 mW (510-META)
Red HeNe							
632.8 nm		10 mW	5 mW	10 mW		3.5 mW	5 mW
Diode laser						33 mW	
630 nm (ext. cavity)							
635 nm							35 mW(510 Live)
638 nm			10 mW (mod.)		640 7.8 mW		
NIR 750 nm				*2 mW CW*			
HeNe							
NIR 1152 nm						1 mW	

(*Continued*)

TABLE 5.4. Lasers Often Used in LSCM (*Continued*)

	Manufacturer and CLSM system						
Laser Type	Visitech international Vt-eye and Vt-Infinity	Leica TCP-SP2-AOBS *SP2*	Nikon Digital Eclipse C1 Plus	Olympus Fluoview FV1000 & *FV500*	Perkin-Elmer Ultraview	WITEC CRM200	Zeiss Axiovert 200M LSM 510 META
Broad-band tunable pulsed lasers							
Dye laser							
630 nm						3 mW	
Ti:Sa-Chameleon		1000 mW					1000 mW
720–930 nm		>1 ps					<100 fs
Ti:Sa-Mai-Tai		<1000 mW					<1000 mW
750–850 or 710–920 nm		>1 ps					<100 fs
Ti:Sa-Mira		100–700 mW					100–700 mW
690–1000 nm		>1 ps					<100 fs
Ti:Sa-Tsunami		100–700 mW					100–700 mW
680–1050 nm		>1 ps					<100–130 fs
NIR laser			1.2 ps, 1000 mW				
700–900 nm			720–1000 nm				

Mod.: modulated
Pp peak-to-peak
Visitech International, Inc, Sunderland, UK +44 (0)191 516 6255 http://www.visitech.co.uk/
Leica Microsystems, Mannheim, Germany, Ph. +49-(0)621-70280 http://www.leica-microsystems.com/website/lms.nsf
Nikon Inc., Melville, NY. Ph. (800)-526-4566, http://www.nikonusa.com/, http://www.nikon-instruments.jp/eng/
Olympus America, Melville, NY. Ph (631)-844-5000, http://microscope.olympus.com/, http://www.olympusamerica.com/seg_section/seg_home.asp and
Perkin-Elmer, Boston, MA, Ph. (800)-762-4000, http://las.perkinelmer.com/content/livecellimaging/index.asp
Carl Zeiss AG, Oberkochen, Germany, Ph. +49-(0)7364-200 http://www.zeiss.com/
WITec GmbH, Ulm, Germany, Ph. +49-(0)700-948-32366, http://www.WITec.de Confocal Raman microscope

ACKNOWLEDGMENT

This work was supported by National Institutes of Health grant PHS-1P41-RR03155.

REFERENCES

Adhav, R.S., 1986, Data sheet 714. Sum frequency mixing and second harmonic generation. Quantum Technology, Inc., Lake Mary, FL January: (407-323-7750).

Aghassi, D., Gonzalez, E., Anderson, R.R., Rajadhyaksha, M., and Gonzalez, S., 2000, Elucidating the pulsed dye laser treatment of sebaceous hyperplasia in vivo with real-time confocal scanning laser microscopy, *J. Am. Acad. Dermatol*. 43:49–53.

Anderson, S.G., 1993, Commercial OPO produces high-energy tunable output, *Laser Focus World* April:16–22.

Anderson, S.G., 1994a, Narrow-linewidth OPO uses extraordinary resonance, *Laser Focus World* April:15–18.

Anderson, S.G., 1994b, New material promises tunable UV output, *Laser Focus World* May:20–23.

ANSI Z-136.3-1993, ANSI Standard for the safe use of lasers. Laser Institute of America (LIA), Orlando, Florida.

Arecchi, F.T., and Schultz-Dubois, E.O., 1972, *Laser Handbook*, Vol. 1, North-Holland Publishing Co., Amsterdam.

Arrigoni, M., 2004a, Femtosecond laser pulses in biology: From microscopy to ablation and micromanipulation, *Biophotonics Intl*. June:48–51.

Arrigoni, M., 2004b, The power of the pump. *SPIE's oemagazine* October:29–30.

Austin, L., Scaggs, M., Sowada, U., and Kahlert, H-J., 1989, A UV beam-delivery system designed for excimers, *Photonics Spectra* May:89–96.

Art, J.J., and Goodman, M.B., 1993, Chapter 2 Rapid Scanning Confocal Microscopy, In: *Cell Biological Applications of Confocal Microscopy. Methods in Cell Biology*, (B. Matsumoto, ed.), Acad. Press, San Diego, pp. 53–58.

Ashkin, A., and Dziedzic, J.M., 1987, Optical trapping and manipulation of viruses and bacteria, *Science* 235:1517.

Aubourg, Ph., 2002, Laser damage: What is it?, *Europhotonics* June/July:46–47.

Baer, T.M., 1986, Diode Laser Pumping of Solid State Lasers, *Laser Focus/Electro Optics* June:82–92.

Bains, S., 1993, Holographic optics for when less is more, *Laser Focus World* April:151–154.

Bass, M., and Stitch, M.L., 1985, *Laser Handbook*, Vol. 5, North-Holland Publishing Co., Amsterdam.

Beach, R.J., Krupke, W.F., Kanz, V.K., Payne, S.A., Dubinskii, M.A., and Merkle, L.D., 2004, End-pumped continuous-wave alkali vapor lasers: experiment, model, and power scaling, *JOSA B*, 21:2151–2163.

Beausoleil, R.G., 1992, Highly efficient second harmonic generation, *Lasers & Optronics* May:17–21.

Bechhoefer, J., and Wilson, S., 2002, Faster, cheaper, safer optical tweezers for the undergraduate laboratory, *Am. J. Phys*. 70:393–400.

Bertolotti, M., 1983. *Masers and Lasers. An historical Approach*, Adam Hilger Ltd., Bristol.

Bloom. A.L., 1968. *Gas lasers*, John Wiley and Sons, New York.

Boas, G., 2003, Model pinpoints heating effects in optical tweezer experiments: Accurate measurements may improve calibration, *Biophotonics Intl*. April:59–60.

Brelje, T.C., Wessendorf, M.W., and Sorenson, R.L., 1993, Chapter 4, Multicolor Laser Scanning Confocal Immunofluorescence Microscopy: Practical Application and Limitations. In: *Cell Biological Applications of Confocal Microscopy. Methods in Cell Biology*, (B. Matsumoto, ed.), Academic Press, San Diego, pp. 120–123.

Brocas, A., Canioni, L., and Sarger, L., 2004, Efficient selection of focusing optics in non linear microscopy design through THG analysis, *Opt. Express*, 12:2317–2326.

Brown, D.C., 1981. High-Peak-Power Nd-Glass Laser Systems, In: *Springer Series in Optical Sciences*, Springer-Verlag, Berlin, Vol. 25 pp. 1–276.

Burgess, D.S., 2004, Laser microdissectionL Making inroads in research, *Biophotonics Intl.*, September:46–49.

Butcher, S. 1994, Optical parametric oscillators open new doors to researchers, *Photonics Spectra*, May:133–138.

Burgin, C.D., 1988. A guide for eyeware for protection from laser light, LLL-TB-87, LLNL, P.O. Box 808, Livermore, California.

Carts, Y.A., 1994, Gradient-index lens tames spherical aberrations, *Laser Focus World* January:142–143.

Casperson, L.W., 1994, How phase plates transform and control laser beams, *Laser Focus World* May:223–228.

Chenard, F., 1994, New applications abound for rare-earth doped fibers, *Photonics Spectra* May:124–130.

Chu, S.-W., Liu, T.-M, Sun, C.-K., Lin, C.-Y., and Tsai, H.-J., 2003, Real-time second-harmonic generation microscopy based on a 2 –GHz repetition rate Ti:sapphire laser, *OpticsExpress* 11:932–938.

Cogwell, C.J., Hamilton, D.K., and Sheppard, C.J.R., 1992a, True color confocal reflection microscope: 442 He-Cd, 532 of freq. doubled Nd-YAG with 633 nm from He-Ne laser, *J. Microscopy* 165:49–60.

Cogwell, C.J., Hamilton, D.K., and Sheppard, C.J.R., 1992b, Colour confocal reflection microscopy using red, green and blue lasers, *J. Microscopy* 165:103–117.

Connor Davenport, C.M., and Gmitro, A.F., 1992, Angioscopic fluorescence imaging system, in *Optical Fibers in Medicine VII*, Ed. A. Katzir, SPIE Proceedings, Los Angeles, California, *SPIE* 1649:192–202.

Cunningham, R., 1993, Vertical-cavity diode lasers, *Lasers & Optronics* December:19–20.

Dantus, M., 2003, Pulse shaping helps achieve selective two-photon excitation, *Biophotonics Intl*. September:61–62.

Day, T., and Li Dessau, K.D., 1994, Narrow band tunable external-cavity diode lasers offer new tools for researchers. *Photonics Spectra* March:99–103.

Dela Cruz, J.M., Pastrirk, I, Lozovoy, V.V., Walowicz, K.A., and Dantus, M., 2004, Multiphoton intrapulse interference 3: Probing microscopic chemical environments, *J. Phys. Chem. A*. 108:53–58.

Demtröder, W., 1996, Laser spectroscopy. Basic concepts and instrumentation. 2nd edition. In: *Springer Series in Chemical Physics*, Springer-Verlag, Berlin, Vol. 5, pp. 1–924.

Denk, W., Strickler, J.H., and Webb, W.W., 1990, Two-photon laser scanning fluorescence microscopy, *Science* 248:73–76.

Duling III, I.N., 1993, Compact fiber soliton lasers produce ultrashort pulses, *Laser Focus World* April:213–220.

Duling III, I.N., 1995, Compact sources of ultrashort pulses. Cambridge University Press, ISBN 0521461928.

Dunning, F.B., 1978, Tunable-ultraviolet generation by sum-frequency mixing, *Laser Focus Magazine* May:72–76.

Dunsby, C., Lanigan, P.M.P., McGinty, J., Elson, D.S., Requejo-Isidro, J., Munro, I., Galletly, N., McCann, F., Treanor, B., Önfet, B., Davis, D.M., Neil, M.A.A., and French, P.M.W., 2004, An electronically tunable ultrafast laser source applied to fluorescence imaging and fluorescence lifetime imaging microscopy, *J. Phys. D: Appl.Phys*. 37:3296–3303.

Draaijer, A., and Houpt, P.M., 1988, A standard video-rate confocal laser-scanning reflection and fluorescence microscope, *Scanning* 10:139–145.

Driscoll, W.G., and Vaughan W., 1977, *Handbook of Optics*, McGraw-Hill Book Co., New York.

Eden, J.G., 1988, UV and VUV lasers: Prospects and Applications, *Optics News* April:14–27.

Ellis, G.W. 1979, A fiber-optic phase-randomizer for microscope illumination by a laser. *J. Cell Biol*. 83:303a.

Ellis, G.W., 1988, Scanned aperture light microscopy, in *Proceedings of the 46th Annual Meeting of EMSA*. San Francisco Press Inc., San Francisco, pp. 48–49.

Espinase, Ph., 2004, Microstructured Fibers Enable Supercontinuum Generation, *SPIE OEMagazine*, August:11.

Erlandson, A.C., and Powell, H.T., 1991, Ten thousand flashlamps will drive the most-powerful laser, *Laser Focus World* August:95–100.

Fermann, M.E., Galvanauskas, A., and Sucha, G., 2002, Ultrafast lasers: Technology and applications, Marcel Dekker, Inc., New York.

Figueroa, J., 2002, High-power semiconductor lasers. The photonics design and applications handbook, H-219-H-222, Laurin Publ. Co. Inc., Pittsfield, Massachusetts.

Folkenberg, J.R., and Broeng, J., 2004, Photonic crystal fibers accommodate high powers. *Photonics Spectra* September:82–86.

Forrester, S., 1994a, DC/DC converters: Theory of operation, Part 1, *Sensors* January:28–35.

Forrester, S., 1994b, DC/DC converters: Theory of operation, Part 2, *Sensors* February:64–69.

Fork, R.L., Martinez, O.E., and Gordon, J.P., 1984, Negative dispersion using pairs of prisms, *Opt. Lett*. 9:150.

Franceschini, M.A., Fantini, S., and Gratton, E., 1994, LED's in frequency domain spectroscopy of tissues (J.R. Lacowicz). SPIE Proceedings. In: Advances in laser and light spectroscopy to diagnose cancer and other diseases (R.R. Alfano, ed.), Los Angeles, Vol. 2135, pp. 300–306.

Friebele, E.J., and Kersey, A.D., 1994, Fiberoptic sensors measure up for smart structures, *Laser Focus World* May:165–171.

Gabler, V., 2004, Miniature fibre lasers aim to modernize visible applications, *Europhotonics* August/September:28–29.

Galvanauskas, A., and Samson, B., 2004, Large-mode-area designs enhance fiber laser performance, *SPIE's oemagazine* July:15–17.

Gibson, J., 1988, Laser Cooling Water. The key to Improved Reliability, *Photonics Spectra* Nov:117–124.

Gibson, J., 1989, Laser water cooling loops deserve attention, *Laser Focus World* April:123–129.

Ginouves, P., 2002, Ion lasers, still a practical choice. The photonics design and applications handbook, H-206–208, Laurin Publ. Co. Inc., Pittsfield, Massachusetts.

Goldman, R.D., 1993, Air-to-liquid closed-loop cooling system meet the cost performance goals of today's laser market, *Laser and Optronics* February:15–17.

Günther, A.H., 1993, Optics damage constrains laser design and performance, *Laser Focus World* February:83–87.

Guy, M., and Painchaud, Y., 2004, Fiber Bragg gratings: A versatile approach to dispersion compensation, *Photonics Spectra* August:96–101.

Hammerling, P., Budgor, A.B., and Pinto, A., 1985, Tunable Solid-State Lasers, In: *Proceedings of the First International Conference*, La Jolla, California, June:13–15, 1984, Springer-Verlag, Berlin.

Hard, R., Zeh, R.D., and Allen, R.D., 1977, Phase-randomized laser illumination for microscopy, *J. Cell Sci*. 23:335–343.

Häring, R., and Gerster, E., 2003, Semiconductor laser system fills yellow-orange gap, *Europhotonics* August/September:38–39.

Hecht, E., and Zajac A., 2003, *Optics*, 4th Ed., Addison-Wesley Publishing Co., Reading, Pennsylvania.

Hecht, J., 1992, Ion lasers deliver power at visible and UV wavelengths, *Laser Focus World* December:97–105.

Hecht, J., 1993a, Laser action in fibers promises a revolution in communications, *Laser Focus World* February:75–81.

Hecht, J., 1993b, Nitrogen lasers produce ultraviolet light simply, *Laser Focus World* May:87–91.

Hecht, J., 1993c, HeCd lasers offer economical blue and ultraviolet light, *Laser Focus World* August:67–71.

Hecht, J., 1993d, Copper-vapor lasers find specialized applications, *Laser Focus World* October:99–103.

Hell, S., Witting, S., Schickfus, M.V., Wijnaendts van Resandt, A.W.; Hunklinger, S., Smolka, E., and Neiger M., 1991, A confocal beam scanning white-light microscope, *J. of Microscopy* 163:179–1876.

Herrmann, J., and Wilhelmi, B., 1987, Lasers for Ultrashort Light Pulses. North-Holland, Amsterdam.

Hess, S.T., and Webb, W.W., 2002, Focal volume optics and experimental artifacts in confocal fluorescence correlation spectroscopy, *Biophys. J.*, 60: 2900–2917.

Higgins, T.V.. 1992, Nonlinear crystals: where the colors of the rainbow begin, *Laser Focus World* January:125–133.

Hitz, B., 2004a, Something old, something new: German lab marries ring and disk, *Photonics Spectra* September:22–23.

Hitz, B., 2004b, Thulium laser enables single-frequency oscillation in new spectral region, *Photonics Spectra* September:28–303.

Hitz, B., 2004c, Hollow fiber delivers distortion-free femtosecond pulses, *Photonics Spectra* August:113–114.

Hitz, B., 2004d, Fiber laser system produces femtosecond pulses at 25 W of average power, *Photonics Spectra* November:88–89.

Hobbs, J.R., 1993, Semiconductor lasers diversify, *Laser Focus World* CLEO April:116.

Hobbs, J.R., 1994, Offset-plane mirrors transform laser beams, *Laser Focus World* May:46–50.

Hodgson, D.J., 1994, How power-supply selection can improve laser-diode performance. *Laser Focus World* January:129–137.

Hodgson, N., and Weber, H., 2005, Laser resonators and beam propagation. 2nd ed., Springer series in optical sciences, Vol. 108.

Hoffmann, A., Meyer zu Hörste, G., Pilarczyk, G., Monajembashi, S., Uhl, V., and Gruelich, K.O., 2000, Optical tweezers for confocal microscopy, *Appl. Phys. B*. 71:747–753.

Hogan, H., 2004, Imaging with three-part harmony, *Biophotonics Intl*. September:62–63.

Homburg, O., Finke, B., and Harten, P., 2003, High-precision homogenizers shape beams, *EuroPhotonics* August/September:34–35.

Huth, B.G., and Kuizenga, D., 1987, Green light from doubled Nd-YAG lasers, *Lasers & Optronics* October:59–61.

Kaiser, W., 1988, Ultrashort laser pulses and applications, Vol. 60, in *Topics in Applied Physics*, Springer-Verlag, Berlin.

Kaminskii, A.A., 1981, *Laser Crystals Their Physics and Properties* (translation; H.F. Ivey ed.), Vol. 14, *Springer Series in Optical Sciences*, Springer-Verlag, Berlin.

Kiat, L.S., Tanaka, K., Tsumanuma, T., and Sanada, K., 1992, Ultrathin single-mode imagefiber for medical usage, In: *Optical Fibers in Medicine VII*, (A. Katzir, ed,), SPIE Proceedings, Los Angeles, California. SPIE 1649:208–217.

König, K., Liang, H., Berns, M.W., and Tromberg, B.J., 1996, Cell damage in near-infrared multimode optical traps as a result of multipoint absorption, *Optics. Lett*. 1090–1092.

König, K., Becler, T.W., Fischer, P., Riemann, I., and Halbhuber, K.-J., 1999, Pulse-length dependence of cellular response to intense near-infrared laser pulses in multiphoton microscopes, *Optics Lett*. 24:113–115.

Kraft, T., 2004, Compact, robust lasers suit biotechnology applications, *Biophotonics Intl*. July: 44–46.

Krueger, A., and Féru, Ph., 2004, Ytterbium Tungstate revolutionizes the field of high-power ultrafast lasers, *Photonics Spectra* March:46–51.

Kudryashov, A.V., and Weber, H., 1999, Laser resonators: Novel design and development, *SPIE Monographs* PM67, pp. 1–317.

Krupke, W.F., 2004, Diode-pumped visible wavelength alkali laser, US Patent 6693942.

Landgraf, S., 2001, Application of semiconductor light sources for investigations of photochemical reactions, *Spectrochim. Acta A*, 57:2029–2048.

Landgraf, S., 2003, *Handbook of Luminescence, Display Materials and Devices*, Vol. 3, Chapter 9, pp. 371–398, ISBN:1–58883–032–2., American Scientific Publishers (ASP), Stevenson Ranch, California.

Leitz, G., Fallman, E., Tuck, S., and Axner, O., 2002, Stress Response in Caenorhabditis elegans Caused by Optical Tweezers: Wavelength, Power, and Time Dependence. *Biophys. J*. 82:2224–2231.

Lewis, R.R., Naylor, G.A., and Kearsley, A.J., 1988, Copper Vapor Lasers Reach High Power, *Laser Focus/Electro Optics* April;92–96.

Limpert, J., Liem, A., Schreiber, T., Röser, F., Zellmar, H., and Tünnermann, A., 2004, Scaling single-mode photonic crystal fiber lasers to kilowatts, *Photonics Spectra* May:54–63.

Lin, J.T., and Chen, C., 1987, Choosing a Non-linear Crystal, *Lasers & Optronics* November:59–63,

Liu, T.-M., Chu, S.-W., Sun, C.-K., Lin, B.-L., Cheng, P.-C., and Johnson, I., 2001. Multiphoton confocal microscopy using a femtosecond Cr:Forsterite laser, *J. Scanning Microscopies* 23:249–254.

Littlechild, J., and Mossler, D., 1988, Knowledge of Arc-Lamp Aging and Lifetime Effects Can Help to Avoid Unpleasant Surprises, *Laser Focus/Electro Optics* November:67–76.

MacMullin, T., 2004, Safety first, *SPIE's oemagazine* June:27–29.

Malzahn, U., 2004, Driving diode lasers is straightforward, *Europhotonics* August/September:22–23.

Marshall, L., 1994, Biological monitoring foreseen with ultraviolet light source, *Laser Focus World* April:83–87.

McConnell, G., 2004, Confocal laser scanning fluorescence microscopy with a visible continuum source, *OpticsExpress* 12:2844–2850.

Miller, P.J., 1991, Taming Laser Noise: Methods and Applications, *Photonics Spectra* April:183–187.

Miller, P., and Hoyt, C., 1986, Turning Down Laser Noise with Power Stabilizers, *Photonics Spectra* June:129–134.

Mollenauer, L.F., and White, J.C., 1987, Tunable Lasers, Vol. 59. *Topics in Applied Physics*, Springer-Verlag, Berlin.

Mooradian, A., 1993. External cavity tunable diode lasers, *Lasers & Optronics* May:35–37.

Moreaux, L., Sandre, O., and Mertz, J. 2000, Membrane imaging by second-harmonic generation microscopy, *JOSA B* 17:1685–1694.

Mortensen, P., 1994, Solid state lasers: Russians commercialize femtosecond laser, *Laser Focus World* April:36–38.

Muckenheim, W., Austin, L., and Basting, D., 1988, The pulsed dye Laser: Today's Technology, Today's Uses, *Photonics Spectra* June:79–84.

Nan, X., Yang, W.-Y., and Xie, X.S., 2004, CARS microscopy lights up lipids in living cells, *Biophotonics Intl*. August:44–47.

Neuman, C., Chadd, E.H., Liou, G.F., Bergman, K., and Block, S.M., 1999, Characterization of Photodamage to Escherichia coli in Optical Traps, *Biophys. J*. 77:2856–2863.

Nordborg, J., and Karlsson, H., 2004, Multi DPSS lasers — a true Ar-ion alternative, *Europhotonics* June/July:28–29.

Okhotnikov, O.G., Gomes, L.A., Xiang, N., Joukti, T., Chin, A.K., Singh, R., and Grudinin, A.B., 2003, 980-nm picosecond fiber laser, *IEEE Photonics Technol. Lett*. 15:1519–1521.

Perry, M.D., Payne, S.A., Ditmire, T., and Beach, R., 1993, Better materials trigger Cr:LiSAF laser development, *Laser Focus World* September:29:85–92.

Peterman, E.J.G., Gittes, F., and Schmidt, C.F., 2003, Laser induced heating in optical traps, *Biophys. J*. 84:1308–1316.

Peuse, B., 1988, Active stabilization of ion laser resonators. Active stabilization offers advantages in several areas, *Lasers & Optronics* November:61–65.

Piehler, D., 1993, Upconversion process creates compact blue/green lasers, *Laser Focus World* November:95–102.

Piston, D.W., Sandison, D.R., and Webb, W.W., 1992, Time-resolved fluorescence imaging and background rejection by two-photon excitation in laser scanning microscopy. In: *Time-Resolved Laser Spectroscopy in Biochemistry III* (J.R. Lakowicz, ed.), *SPIE Proceedings* Los Angeles, California, 1640:379–389.

Piston, D.W., Kirby, M., Cheng, H., Lederer, W.J., and Webb, W.W., 1994, Three dimensional imaging of intracellular calcium activity by two-photon excitation laser scanning microscopy, *Appl. Optics*. February:33:662–669.

Potma, E.O, de Boeij, W.P., Pshenichnikov, M.S., and Wiersman, D.A., 1998, A 30-fs cavity-dumped optical parametric oscillator, *Opt. Lett*. 23:1763–1765.

Radunsky, M.BV., 2002, The OPO: A research tool and more. The photonics design and applications handbook book 3, H-261–H264, Laurin Publ. Co. Inc., Pittsfield, Massachusetts.

Rapp, E.W., 1988, Design your cooling system for good laser performance, *Laser Focus/Electro Optics* September:65–70.

Reichle, C., Sparbier, K., Müller, T., Schnelle, Th., Walden, P., and Fuhr, G., 2001, Combined laser tweezers and dielectric field cage for the analysis of receptor-ligand interactions on single cells, *Electrophoresis* 22:272–282.

Robinson, K., 1998, Training and equipment help ensure laser safety, *Biophotonics Intl*. November/December:42–47.

Rockwell Associates Inc., 1983, *Laser Safety Training Manual*, 6th ed., Rockwell Associates Inc., Cincinnati, Ohio.

Rockwell, R.J. Jr., 1986, An introduction to exposure hazards and the evaluation of nominal hazard zones, *Lasers & Applications* May:97–103.

Rusu, M., Karirinne, S., Guina, M., Grudinin, A.B., and Okhotnikov, O.G., 2004, Femtosecond Neodymium-doped fiber laser operating in the 894–909-nm spectral range, *IEEE Photonics Technol. Lett*. 16:1029–1031.

Schneider, D.J., and Williams, D.C., 1993, Fighting corrosion in laser cooling systems, *Laser Focus World* December:110.

Schulmeister, K., 1994, Safety regulations changes, *Biophotonics Intl*. August:38–42.

Scifres, D.R., 1994, Diode lasers ride the wave of progress, *Photonics Spectra* 84–85.

Silfvast, W.T., 2004, *Laser Fundamentals*, 2nd ed. Cambridge University Press, New York.

Sivers, N.L., Van de Workeen, B.C., and Lee, S.M., 2004, Improving fluorescence confocal microscopy with cryogenically-cooled diode lasers, *Optics Express* 12:4157–4165.
Sliney, D.H., 1986, Laser Safety. The newest face on an old standard, *Photonics Spectra* April:83–96.
Sliney, D., and Wolbarsht, M., 1980, *Safety with lasers and other optical sources. A comprehensive handbook*, Plenum Press, New York.
Sliney, D.H., 1994, Laser safety concepts are changing, *Laser Focus World* May:185–192.
Smith, B., 1986, Lamps for Pumping Solid-state Lasers: Performance and Optimization, *Laser Focus/Electro Optics* September:58–73.
Smith, K., and Lucek, J.K., 1993, Modelocked fiber lasers promise high-speed data networks, *Laser Focus World* October:85–91.
Smith, S.P., Bhalotra, S.R., Brody, A.L., Brown, B.L., Boyda, E.K., and Prentiss, M., 1999, Inexpensive optical tweezers for undergraduate laboratories, *Am. J. Phys*. 67:26–35.
Snyder, J.J., and Cable, A.E., 1993, Cylindrical microlenses improve laser-diode beams, *Laser Focus World* February:97–100.
Soileau, M.J., 1987, Laser-Induced Damage, *Photonics Spectra* November:109–114.
Stry, S., Knispel, R., Hildebrandt, L., and Sacher, J., 2004, Tunable external cavity diode laser tackles high-power applications, *EuroPhotonics* February/March:26–27.
Stitch, M.L., 1979, *Laser Handbook*, Vol. 3, North-Holland Publishing Co., Amsterdam.
Szarowski, D.H., Smith, K.L, Herchenroder, A., Matuszek, G., Swann, J.W., and Turner, J.N., 1992, Optimized reflection imaging in laser confocal microscopy and its application to neurobiology, *Scanning* 14:104–111.
Tai, S.-P., Chan, M.-C., Tsai, T.-H., Guol, S.-H., Chen, L.-J., and Sun, C.-K., 2004, Two-photon fluorescence microscope with a hollow-core photonic crystal fiber, *Optics Express* 12:6122–6128.
Tebo, A.R., 1988, Scientists develop Useful Optical Materials, *Laser Focus/Electro Optics* August:103–110.
Tozer, B.A., 2001, Revised safety standards to benefit laser design and use, *Laser Focus World* March:81–82.
Unger, B., 1994, Device saves laser diodes from electrostatic-discharge damage. *Laser Focus World* May:238–240.
Wang, X.F., Kitajima, S., Uchida, T., Coleman, D.M., and Minami, S., 1990, Time-resolved fluorescence microscopy using multichannel photon counting, *Appl. Spectrosc*. 44:25–30.
Wang, X.F., 1990, Fundamental studies on time-resolved fluorescence image spectroscopy techniques. Dissertation, Osaka University.
Wang, X.F., Periasamy, A., Herman, B., and Coleman, D.M., 1992, Fluorescence lifetime imaging microscopy (FLIM): Instrumentation and applications. *Critical Reviews in Analytical Chem*. 23:369–395.
Weast, R.C., and Tuve, G.L., 1971, *Handbook of lasers with selected data on optical technology*, CRC Press. The Chemical Rubber Co., Cleveland, Ohio.
Webb, C.E., and Jones, J.D.C., 2004, *Handbook of laser technology and applications*. Vol.1, Principles, Vol. 2, Laser design and laser optics, Vol. 3, Applications, IOP Publ., Bristol, UK.
Weber, M.J., 1999, *Handbook of laser wavelengths*, CRC Press, New York.
Winburn, D.C., 1985, *Practical laser safety*, Marcel Dekker Inc., New York.
Wisdom, J., and Digonnet, M., 2004, Ceramic lasers: Ready for action, *Photonics Spectra* February:50–56.
Woods, S., 2003. Fiber lasers offer alternative for analytical applications, *Biophotonics Intl*. December:48.
Yang, C., and Mertz, J., 2003, Transmission confocal laser scanning microscopy with a virtual pinhole based on non-linear detection, *Optics Lett*. 28:224–226.
Yelin, D., Oron, D., Korkotian, E., Segal, M., and Silberberg, Y., 2002, Third-harmonic microscopy with a titanium-sapphire laser, *Appl. Phys. B*. 74:S97.
Zeek, E., Maginnis, K., Backus, S., Russek, U., Murmane, M., and Vdovin, G., 1999, Pulse compression by use of deformable mirrors, *Opt. Lett*. 24:493–495.
Zhang, Z.X., Sonek, G.J., Wei, X.B., Sun, C., Berns, M.W., and Tromberg, B.J., 1999, Cell viability and DNA measurements by two-photon fluorescence excitation in CW Al:GaAs diode laser optical traps, *J. Biomed. Optics* 4:256–259.

APPENDIX

LIST OF USEFUL WEB SITES AND TUTORIALS (NOT EXHAUSTIVE)

Books: Lists of General Reference Books on Lasers and Applications

http://micro.magnet.fsu.edu/primer/lightandcolor/lasersreferences.html
Spring, K.R., Parry-Hill, M.J., *et al*., *Molecular Expressions*, Florida State University, Tallahassee, Florida.
Dr. Rami Arieli, http://www.phys.ksu.edu/perg/vqm/laserweb/

Buyer's Guides

Photonics Laser Buyer's Guide, Laurin Publishing, http://www.photonics.com
Institute of Physics (IOP) Publishing Ltd., Temple Back, Bristol, UK, Ph. +44-(0)117–9297481- http://optics.org/buyers/

General References: Company Listings and Buyer's Guides

General

http://www.photonics.com/directory/bg/XQ/ASP/QX/index.htm
Laurin Publishing, 2002, *Photonics Directory, Buyer's Guide*. Brief, instructive chapters on optics, optical components, and comparison of developments for the various laser types in Book 3, *The Photonics Design and Applications Handbook*.

More Specific

Samual M. Goldwasser. Laser sales and services, http://www.repairfaq.org/sam/laserlps.htm#lpslss
Dr. Alexander N. Cartwright, http://www.ece.buffalo.edu/faculty/cartwright/links.html

Laser Information: Cleaning of Laser Optics

http://www.repairfaq.org/sam/laseratr.htm#atrcln

General Information with Many Links

http://resonator.physics.sunysb.edu/laser/laserlinks

History of the Laser

http://www.bell-labs.com/history/laser/
Schawlow and Townes biographies

Titanium–Sapphire Laser

http://www.drbio.cornell.edu/Infrastructure/Apparatus_WWW/Ti%20Sapphire%20Lasers.html
Evolution of Ti:Sa laser systems

Pulse Length Measurement by Optical Means

http://linac.ikp.physik.tu-darmstadt.de/fel/optical_pulse.html

Safety Issues

The health and safety committee at educational institutions should have Standard Operating Procedures (SOP) for laser operation and maintenance available. As examples may serve:
http://phantom.ehs.uiuc.edu/~rad/laser/
http://www2.umdnj.edu/eohssweb/aiha/technical/lasers.htm
http://web.princeton.edu/sites/ehs/laserguide/appendixC.htm
Laser safety self-audit checklist, http://www.microscopyu.com/articles/fluorescence/lasersafety.html
Spring, K.R., Parry-Hill, M.J., *et al*., *Molecular Expressions*, Florida State University, Tallahassee, Florida. Laser classifications, hazards, and bioeffects of various laser types, a brief and concise overview worth your attention.
http://stwi.weizmann.ac.il/Lasers/laserweb/ http://www.phys.ksu.edu/perg/vqm/laserweb/Misc/Apindex.htm
Dr. Rami Arieli, The Laser Adventure, Virtual school
Rockwell Laser Industries. Safety materials, regulations: laser safety standards organizations and products, e.g., Z136.1 ANSI document, laser accident database, access control measures, and courses, http://www.rli.com/
Rockwell Laser Industries safety issues and links laser bioeffects, manufacturers, standards, and laser user institutes and laboratories, http://www.rli.com/resources/links.asp?Link=3
http://repairfaq.ece.drexel.edu/sam/CORD/leot/
Laser Electro-Optics Technology (LEOT), Center For Occupational Research and Development (CORD), Waco, Texas, electrical safety issues.
Standards, hazards, and solutions, http://www.osha.gov/SLTC/laserhazards

Specific Lasers

Argon-Ion Laser

One page argon-ion laser basic construction and emission properties, one page overview of laser types and applications, basic level, http://www.rli.com/resources/argon.asp
Basic argon-ion laser, graph of relative laser line intensities, http://www.rli.com/resources/argon.asp

Advanced Level

Ionized gas spectra, construction characteristics, http://www.lexellaser.com/techinfo_gas-ion.htm
Laser wavelengths chart, http://www.lexellaser.com/techinfo_wavelengths.htm

Dye Laser

Commercial laser dye as well as CLSM companies have colorful wall charts and list dyes and matching laser lightsources on their sites.

Advanced Level

Dr. R. Alexander, http://members.aol.com/kpublish/Laser/Dye_Laser.html
Dr. Ladic site with excitation and emission spectrum maxima for dyes useful for CLSM, http://www.cs.ubc.ca/spider/ladic/images/fluoro.gif

Expert Level

Instructive site from LEOT, http://repairfaq.ece.drexel.edu/sam/CORD/leot/course03_mod10/mod03-10.html

Colliding Pulse Dye Laser

Expert Level

http://utol.ecen.ceat.okstate.edu/thz%20interactive%20tour/cpmlaser.htm

Fiber Lasers Tutorial

Construction, wavelengths, and optical characteristics, http://www.imra.com/lasers-tech-tut-frame-pdf.html

Titanium-Sapphire Laser

Basic Level

Evolution of Ti:Sa laser systems, http://www.drbio.cornell.edu/Infrastructure/Apparatus_WWW/Ti%20Sapphire%20Lasers.html

Advanced Level

http://micro.magnet.fsu.edu/primer/techniques/microscopylasers.html
Spring, K.R., Parry-Hill, M.J., *et al*., *Molecular Expressions*, Florida State University, Tallahassee, Florida. Beam divergence, beam expander, fiber-optic coupling (*), single and multiple mode fiber-optic, laser types.

Expert Level

Dr. Gavin D. Reid, Leeds University, and Klaas Wynne, University of Strathclyde, Glasgow, UK, Introduction to ultrafast laser systems and optical characterization, dispersion and its control, pulse broadening, amplification, optical Kerr effect, white light generation, OPA, auto and cross correlation,http://phys.strath.ac.uk/12-503B2/introduction/introduction.html
Construction of a fs mode-locked laser with a nice Ti:sa energy diagram, http://www.df.unipi.it/~fisapp/Gruppi/Metrologia/spiegazioni/boris.pdf

Troubleshooting

http://www.repairfaq.org/sam/laseratr.htm#atrcln

Tutorial Sites

Classification of sites:

- Basic level indicates many images, applets but no formulae.
- Advanced level with more thorough description of the issues supported often with applets.
- Expert level with equations and examples.

Basic Level

John Gormalli, stimulated emission explained, Web Science Resources Net (WSRNet), http://members.aol.com/WSRnet/tut/t1.htm
Stimulated emission explained, laser theory quiz, http://home.achilles.net/~ypvsj//quiz/index.html
Laser theory and applet on stimulated emission, http://www.point-source.com/LaserTheory.asp
Basic atom model, general laser classification and safety issues, http://www.howstuffworks.com/laser.htm
One page, ruby laser design and applications, http://home.achilles.net/~ypvsj//glossary/laser.html
Fraunhofer Institute's laser tutorial, http://www.ilt.fhg.de/ger/lasertutorial.html

Advanced Level

http://micro.magnet.fsu.edu/primer/lightandcolor/laserhome.html
Spring, K.R., Parry-Hill, M.J., *et al*., *Molecular Expressions*, Florida State University, Tallahassee, Florida. Laser fundamentals, safety issues, microscopy and lasers used, intensity modulation, references, many instructive applets worthwhile to visit.
http://www.olympusmicro.com/primer/lightandcolor/lasersintro.html
Samual M. Goldwasser's site, "A Practical Guide to Lasers for Experimenters and Hobbyists," Version 6.60, very extensive with safety issues, reference books and materials, schematics, construction, safety, repair issues, http://www.repairfaq.org/sam/laserfaq.htm
Dr. Alexander N. Cartwright, University of Buffalo, laser gain and pumping schemes, photonics educational applets, http://www.ece.buffalo.edu/faculty/cartwright/photonics/rateequations.html

Expert Level

Online educational resources for physics teachers http://www.ba.infn.it/www/didattica.html
Dr. Rami Arieli, The Laser Adventure, virtual school about lasers and their applications. Optics aspects, basic laser theory, laser cavities, lasing modes, fluorescence, laser line shape and width, laser beam properties, power, applets, applications, laser safety issues, questions, reference books, very extensive and useful also for course development, http://www.phys.ksu.edu/perg/vqm/laserweb/
Laser Electro-Optics Technology (LEOT), Center For Occupational Research and Development (CORD), Waco, Texas. Introduction to laser optics, electronics, components, systems, electrical safety issues, http://repairfaq.ece.drexel.edu/sam/CORD/leot/

Dr. P.L. Cross, Optical concepts, laser cavity design, laser operation, database of spectral properties of lasing materials, absorption and emission spectra, http://aesd.larc.nasa.gov/GL/tutorial/laser/las_out.htm

List Servers

http://www.msa.microscopy.com/MicroscopyListserver/MicroscopyArchives.html
Confocal microscopy list server for maintenance and trouble shooting. When there is a problem often it helps to look for similar experiences and solutions on the Web. A good site to start: http://listserv.acsu.buffalo.edu/archives/confocal.html

Microscopy Laboratory Sites

Dr. W. Webb, DRBIO, Cornell University, Ithaca, New York. Multi-photon excitation, physical principles, excitation cross-sections, fluorophore photostability, fluorescence techniques, e.g., FPR(photobleaching recovery), FCS, SPT, cell viability, resolution with an underfilled objective, real-time image acquisition. A lot of specialized information together for live cell imaging and spectroscopy, http://www.drbio.cornell.edu/Infrastructure/Infrastructure%20Index.html
Dr. Bruce Jenks, Nijmegen University, The Netherlands. Laser principle, optical scanner principle, optical sectioning, single and multi-photon illumination (dis)advantages, http://www.celanphy.sci.kun.nl/Bruce%20web/scanning%20microscopy.htm

Optics

Ultrafast optics, http://www.newport.com/Support/Tutorials/Optics/o4.asp

LIST OF ABBREVIATIONS

AC	Alternating Current
ASE	Amplified Spontaneous Emission
AOTF	Acousto-Optic Tuning Filter
AOBS	Acousto-Optic Beam Splitter
AOD	Acousto-Optic Deflector
AOM	Acousto-Optic Modulator
BBO	Beta Barium Borate
CCD	Charge-coupled Device
CDRH	Center for Devices and Radiological Health
CLSM	Confocal Laser Scanning Microscopy
CTA	Cesium Titanyl Arsenate
CW	Continuous Wave
DC	Direct Current
FBG	Fiber Bragg Grating
FCS	Fluorescence Correlation Spectroscopy
FHG	Fourth Harmonic Generation
FITC	Fluorescein IsoThioCyanate
FLIM	Fluorescence Lifetime Imaging Microscopy
FLIP	Fluorescence Loss in Photobleaching
FRAP	Fluorescence Recovery After Photobleaching
FROG	Frequency-Resolved Optical Gating
GFP	Green Fluorescent Protein
GreNe	Green Helium-Neon
GRIN	Graded Index Lens
GTI	Gires-Tournois Interferometer
GVD	Group Velocity Dispersion
He-Cd	Helium–Cadmium
He-Ne	Helium–Neon
HR	High Reflector Mirror
ICNIRP	International Commission on Non-Ionizing Radiation Protection
IEC	International Electrotechnical Commission
IR	Infrared
KLM	Kerr-Lens Mode-Locking
KTP	Potassium Titanium Oxide Phosphate
LASER	Light Amplification by Stimulated Emission of Radiation
LBO	Lithium TriBorate
LED	Light-Emitting Diode
LMA	Large Mode Area
LPC	Laser Power Controller
MII	Multi-Photon Intrapulse Interference
MOPA	Master Oscillator Parametric Amplifier
NA	Numerical Aperture
NCPM	Non Critical Phase Matching
Nd-YAG	Neodymium–Yttrium–Aluminum Garnet
Nd-YLF	Neodymium–Yttrium Lithium Fluoride
Nd-YVO_4	Neodymium–Yttrium Ortho Vanadate
NLO	Non-Linear Optical
NMR	Nuclear Magnetic Resonance
OC	Output Coupler Mirror
OCT	Optical Coherence Tomography
OD	Optical Density
OPA	Optical Parametric Amplifier
OPO	Optical Paramagnetic Oscillator
PCF	Photonic Crystal Fiber
PICASO	Phase and Intensity from Correlation and Spectrum Only
PZT	Piezo Tuning
Q-switch	Quality (of the laser resonator) switch
RF	Radio Frequency
SAM	Saturable Absorber Mirror
SBR	Saturable Bragg Reflector
SD	Static Discharge
SESAM	Semiconductor Saturable Absorber Mirror
SHG	Second Harmonic Generation
SMD	Single Molecule Detection
SOC	Saturable Output Coupler
SPIDER	Spectral Phase Interferometry for Direct Electric-field Reconstruction
SPT	Single Particle Tracking
TEC	Thermo-Electrically Cooled
TEM	Transverse electromagnetic
THG	Third Harmonic Generation
TIRFM	Total Internal Reflection Fluorescence Microscopy
UV	Ultraviolet
VECSEL	Vertical External Cavity Surface Emitting Laser
VIS	Visible

6

Non-Laser Light Sources for Three-Dimensional Microscopy

Andreas Nolte, James B. Pawley, and Lutz Höring

INTRODUCTION

General Remarks on Choice of Excitation Light Sources

The first light source used for microscopy was the sun and the second was a candle flame. Both are hot plasmas that emit essentially black-body radiation (Fig. 6.1) with the addition of a few elemental lines. The introduction of light sources powered by electricity, both arcs and incandescent filaments, added a new level of convenience and flexibility but required improvements in the light-harvesting optics needed to illuminate the imaged area with light that was both intense and uniform.

Brightness

Because the recorded intensity of the image drops with the square of the magnification, the most important characteristic of a source for microscope illumination is its **brightness or radiance**. In this case, **brightness** refers not just to the ability of the source to produce many photons/second but also to its ability to produce these photons from a small volume so that a fair share of them can be conveyed to the small area of the specimen that is being imaged.

A large diffuse source, such as the 40 W fluorescent tubes used for lighting houses,[1] produces about the same number of photons/second as does the 50 W, short arc HBO-50 bulb used in fluorescence microscopy. However, in the former case, the photons emerge from a phosphor surface approximately 0.1 m^2 in size, while a cross-section through the brightest part of the HBO-50 has an area about one million times smaller.

The laws of optics specify what fraction of the light leaving a source can be focused into an image of this source. In Figure 6.2, light leaving h_1 that does not strike the optical system clearly, will not be focused onto the image plane at h_2. Although some of this lost light can be reclaimed by placing a spherical reflecting mirror so that the focal point f is centered on the source, there are still limits on how bright the image will be. If the optical system makes an enlarged image h_2 of the source h_1 at the condenser back-focal plane (BFP, not shown), then the fixed number of photons from the source will be spread over a larger area and the image will not be so bright. If the optical system demagnifies the source, the image will be smaller, BUT it will not be brighter, because, as shown in Figure 6.2, to demagnify the source, it must be farther from the optical system than the image. As a result, the NA (aperture) of the optical system collecting light from the source will be smaller by exactly the same ratio as the image has been demagnified. In other words, no matter how many lenses are used, the ability of an optical system to make a smaller image of the source is inexorably tied to using a collector lens with a lower NA (as seen from the source) and this means that a smaller fraction of the light emitted by each point on the source is actually collected. One just cannot squeeze all the light into a smaller image.[2] The best one can do is to design an optical system that makes an image the same size as the source (magnification = 1).

The moral of this story is that the only way to have bright illumination on the specimen is to start with a small bright source. It follows that the fraction of the light from the HBO-50 that can be conveyed by any optical system to an area of the specimen that is, for example, 100 µm on a side is about one million times greater than could be achieved using the phosphor surface of a 40 W fluorescent lighting tube. Source brightness is measured in terms of photons/second/square centimeter/steradian (radiance), where the steradian is a measure of the solid angle into which the light projects.

Whether this level of illumination is sufficient for the needs of microscopy or not depends on the contrast method in use (fluorescence needs about $10^6\times$ more than bright field), on the time available to accumulate the image, on the contrast of the image, and on the accuracy with which one needs to measure this contrast. That said, although it is usually quite easy to reduce the brightness of a light source by introducing neutral density (ND) filters, making it brighter requires major redesign.

Considering just the standard configuration in bright-field microscopy, about 5 W of optical power is emitted by a 100 W halogen lamp at its rated power consumption. As the filament is 4.2×2.3 mm in size, its cross-section is about 10 mm^2. The aspherical collector lens can cover an aperture of NA = 0.7 (45° half angle) or about 0.15 of the full solid angle. Using a back reflector this can be increased to approximately 0.30. Because of the optical

[1] Really, a very diffuse Hg arc, surrounded by a coating of powdered, inorganic phosphor.

[2] Another line of argument is to point out that, for the image to be brighter than the source, one would have to move energy from a cooler source to a hotter image. This is forbidden by thermodynamics.

Andreas Nolte • Carl Zeiss AG, Goettingen, Germany
James B. Pawley • University of Wisconsin, Madison, Wisconsin 53706
Lutz Höring • Carl Zeiss AG, Oberkochen, Germany

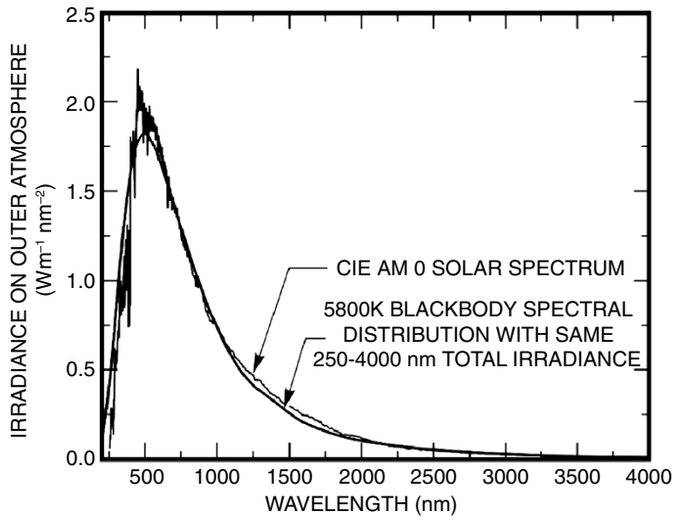


FIGURE 6.1. (A) CIE AM 0 Solar Spectrum**,** (B) 5800 K Blackbody spectral distribution with same 250 to 4000 nm total irradiance. (Spectra kindly provided by Oriel/Newport, Irvine, CA.)

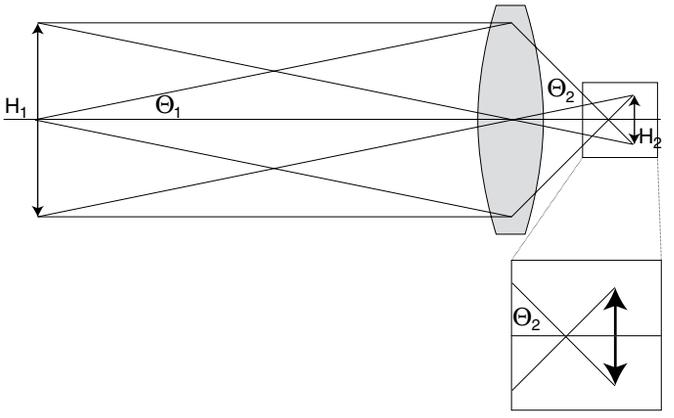


FIGURE 6.2. Relationship between demagnification and NA. When an optical system creates a demagnified image, h_2, the convergence angle, Θ_2, is larger than the divergence angle, Θ_1, leaving the source, h_1 and accepted by the optical system. Because the reduction in area caused by the demagnification is exactly compensated by the increase in NA^2, the image can never be brighter than the source.

rules mentioned above, even perfect optics can only transport about 0.001 of this optical power to illuminate a $100 \times 100\,\mu m$ area of the specimen.[3] This means that the power available to illuminate the field of a high magnification lens is less than $(5 \times 0.3 \times 0.001) = 0.0015\,W = 1.5\,mW$. Actual measurements of brightness at the focal plane are provided in Table 6.2 later in this chapter.

Assuming bright-field imaging for the moment, almost all of this light passes through the objective and intermediate optics and reaches the plane of a perfect charge-coupled device (CCD) camera, composed of a 1000×1000 array of $6\,\mu m$ pixels.[4] As such a sensor will be $6 \times 6\,mm$ in overall size; it will just match the size of the illuminated area on the specimen if a 60× lens is used. At this point, each pixel will intercept one millionth of the light at the specimen or 1.5 nW. As one watt of light corresponds to about 3×10^{18} photons/second and each $36\,\mu m^2$ CCD pixel can absorb about 20,000 photoelectrons before saturation, an exposure of 2×10^4 photons/$(1.5 \times 10^{-9}W) \times (3 \times 10^{18}$ photons/s/W$) = 3.7 \times 10^{-6}$ seconds. In other words, in the absence of other losses, even an exposure as short of $3\,\mu s$ would be enough to saturate the CCD (Inoué, 1997). Sadly, as the optical system just described focuses the filament into the focus plane, a blurred image of the filament will be present there to modulate whatever other contrast the specimen produces. Correcting this problem as described below and allowing for reflection and other losses will cut the signal by a factor of about 10. Adding an "interference green" filter and polarizer for optimal operation of monochrome differential-interference-contrast (DIC) imaging will cut the photon flux by another factor of 20. Should one decide instead to use this green light to excite fluorescence, the signal will likely be reduced by an additional factor of one million[5] and suddenly exposures of seconds or minutes are needed. The only solution is to use a brighter source.[6]

Uniformity

The second requirement of a light source for microscopy is **uniformity**; all parts of the imaged plane must receive the same illumination density. Initially this meant that the illumination level must be constant in any plane, a condition not too hard to arrange by focusing an image of a featureless source, such as the sun (lacking sunspots!) or a flame, directly onto the specimen. However, as the light-emitting area of arcs and most filaments cannot be called uniform, a new illumination system, **Köhler illumination**, was introduced, so that the non-uniformity was confined to aperture planes. While this optical solution does provide uniform intensity in the image planes, it means that there is still some non-uniformity in the angles at which light approaches each point of the focus plane.

The **Köhler illumination** system diagrammed in Figure 6.3 (Inoué, 1997) operates as follows: Light is collected from the near side of the source I using a high-aperture collector lens 1 while a spherical mirror returns light from the rear side of the source to form an image of the source to the side of the actual source (not shown in Fig. 6.3). This reflected light is also collected by the collector lens, increasing the apparent source size (Piller, 1977). The collector lens focuses the source at the back-focal plane of the condenser II (or of the objective in the case of epi-illumination III). Because of the reciprocal relationship of image and back-focal planes, anything that is in focus at one set of these planes is completely out of focus at the other. As a result, assuming that the condenser is correctly aligned and the source is planar, the focus plane in the specimen B is evenly illuminated. However, depending on the uniformity of the source and the aberrations of the optics, this light may not strike the specimen from all possible angles equally.[7]

The field aperture A lies in an intermediate image plane between the collector 1 and the condenser 2, from where it is

[3] As the most efficient optics operate at a magnification of 1 : 1, only the light emerging from a $100 \times 100\,\mu m$ area of the filament can be focused into an area of the same size on the specimen.

[4] The popular Sony ICX285AL chip has a pixel size of $6.45\,\mu m^2$.

[5] Of course, this factor depends strongly on the dye concentration, and distribution and the effective thickness of the sensed layer. Values in the range 10^{-3} to 10^{-9} would not be unusual.

[6] This discussion relates to low magnification operation where intensity is the main goal. At low magnification, it is necessary to illuminate a much larger area on the specimen. This involves exchanging optical elements to change the magnification between the plane of the field diaphragm and the plane of the specimen. This is possible because it is no longer important for the condenser to operate at high NA.

[7] Remember from diffraction theory that the highest resolution in transmission is only obtained when undiffracted light enters the objective from all angles up to that set by its NA.

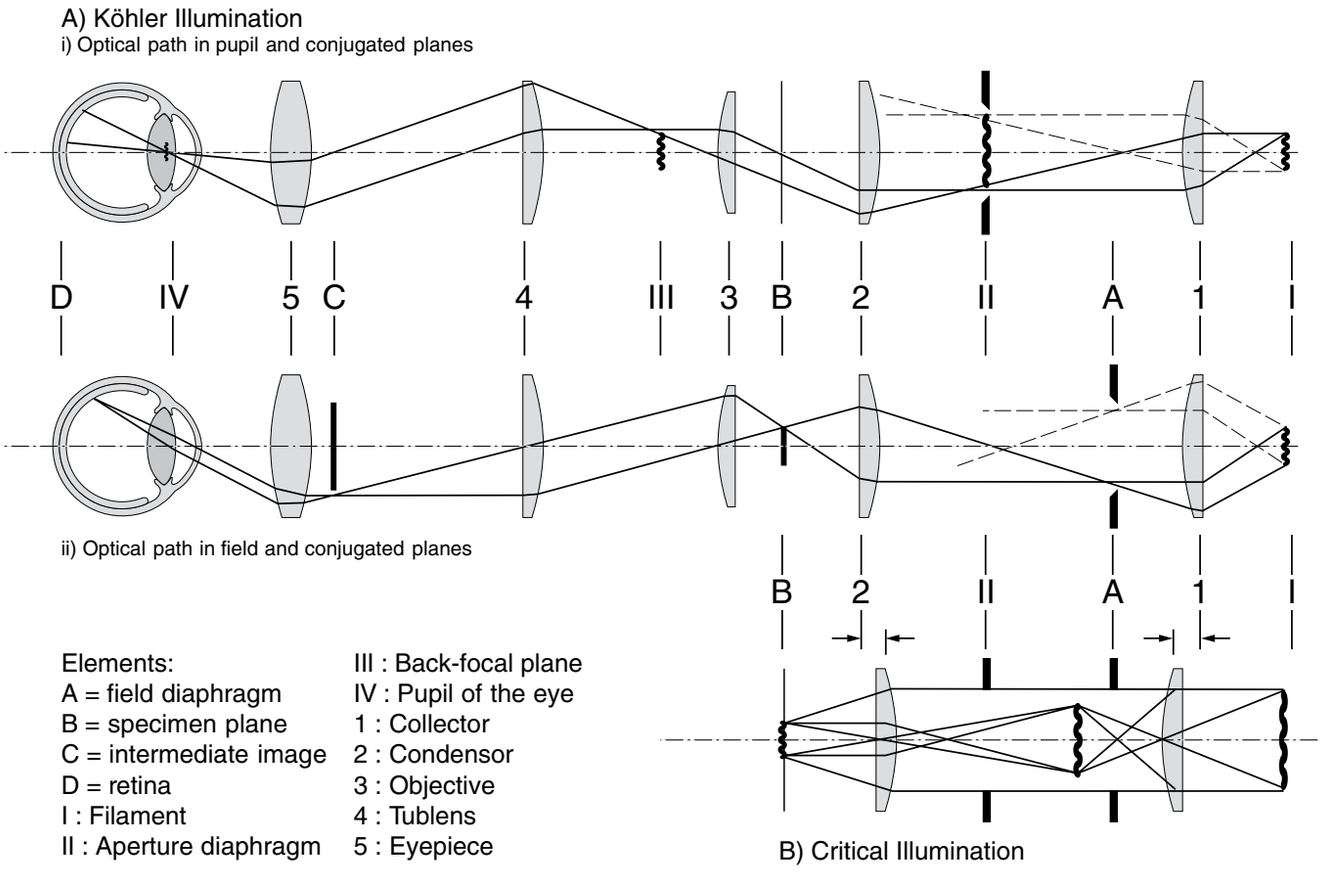


FIGURE 6.3. Köhler illumination with the optical elements: (1) collector, (2) condenser, (3) objective, (4) tube lens, and (5) eyepiece. (A.i) Ray paths focused on pupil and focal planes: (I) source, (II) aperture diaphragm, (III) back-focal plane of objective, (IV) eyepoint above ocular/pupil of the eye. (A.ii) Ray paths focusing on image planes: (A) field diaphragm, (B) focus plane in specimen, (C) intermediate image, (D) retina/CCD. (B) Critical illumination in which the source is focused directly on the focus plane in the specimen. This leads to more light striking the focus plane but precludes the use of the field diaphragm to limit excitation to the area of the specimen actually being imaged.

imaged at plane B in the specimen by the condenser. Its size can be adjusted to restrict the area illuminated to that being viewed without affecting the angle of the illuminating light.

Because it makes maximum use of neither the full surface of the source nor the full angular distribution of the emitted light, Köhler illumination is not very photon efficient. In addition, because the condenser lens should have the same NA as the objective, it must be focused with equal care if the field diaphragm is to remain properly focused into the image plane. Because, on most upright microscopes, the condenser and stage move together, moving the stage to change focus is a process that necessarily moves the condenser out of Köhler alignment. This, and the fact that microscope slides and coverslips are likely to vary in thickness by tens of micrometers, means that, ideally, one should readjust the condenser position whenever the specimen is changed or the focus plane substantially shifted.[8]

Of course, the Köhler illumination diagram has some hidden assumptions that are really not justified in practice. The chief of these is that the source is planar and that, therefore, light emerging from it can be focused by "perfect" lenses into other planes according to the geometric optics of the diagram. In fact, both arcs and most filament sources are approximately spherical in shape. Consequently, even if the optical system focuses light from a central plane of this sphere into the back-focal plane (BFP) of the condenser lens, many photons emerging from planes within the luminous sphere that are either in front of or behind the central plane will be proportionally out of focus at the condenser BFP, and at every other conjugate BFP in the diagram. The corollary of it being out-of-focus at the BFPs is that it will be partially in focus at the image plane and therefore, that in spite of our best efforts, the illumination will still have some structure at the focus plane.

Two more relevant variables of the illumination optics are the total magnification between the source and the BFP of the condenser and what might be termed its "length." All collector lenses have large NA to capture as many photons as possible, and a focal length short enough to keep the light source small without getting the glass so close to the source that the heat cracks it. However, as the need to dissipate the heat dictates that the source and collector be mounted at some distance from the condenser lens, a variety of optical arrangements are used to convey the light across the intervening space.

[8] The same argument also applies to inverted microscopes. Ideally, the objective and condenser would remain fixed to each other and only the stage would move.

At the other end of the illumination optics, the condenser lens should have an NA as large as that of the largest objective with which it will be used but its focal length is not specified.[9] A longer focal length implies a larger BFP and, if this is to be "filled" with an image of a filament, then the optics up to that point may have to form an enlarged image of the filament. Often epi-illumination Köhler optics are designed to make a relatively small image of the arc at the BFP of the objective so that this image is not truncated (and the light lost) by the relatively small BFP of, for example, a 100× NA 1.3 objective. However, this means that the larger BFP of a 40× NA 1.3 objective will be severely under-filled, a factor that reduces the rate at which excitation light diminishes above and below the focus plane and thereby affects the WF PSF (Hiraoka *et al.*, 1990).

The length is important because, although so-called telan lenses can be introduced to convey all the light from the focal point of the collector to the BFP of the condenser, light originating from planes in front of or behind this plane will "hit the wall" of the optical system and be lost or create reflections. The longer the optical conveyer system, the more it is true that the light reaching the condenser BFP will have originated near to the focal plane of the collector. This makes such light both more coherent and more structured because it conveys the image of the inhomogeneity of the filament at the focal plane of the collector.

To restore some semblance of order to the system, it is common to insert a flat, ground-glass surface just outside the collector lens, and let this planar surface become the effective source. This solves the out-of-focus light problem but substantially reduces (by >90%, depending on its roughness) the brightness of the source. For this reason, the ground glass is normally used only when imaging with coherent, transmitted light (phase contrast, DIC, etc.) and not when the main aim is just to get as many photons onto the specimen as possible (fluorescence, dark-field).

The alternative to **Köhler illumination** is **critical illumination**, a system that requires a highly uniform emitting surface I because this surface is focused directly into the imaged plane within the specimen B [Fig. 6.3(B)]. Because it images the entire source, a larger solid angle can be used than with Köhler illumination and therefore it can deliver more photons/second/square centimeter at the image plane. The downside is that any non-uniformity in the emitter will appear as a brightness change in the final image. The coherence of the illumination in this system is that of the source. If a large source is imaged, coherence is quite low. Flickering variations in brightness caused by convection within the plasma of the arc can make it tiring to view the specimen when the plasma is imaged directly onto the image plane, but a time-average of such an arc image is quite uniform. A solution to this brightness–coherence–uniformity conundrum was proposed by Gordon Ellis, who suggested that the image of the arc be focused on the entrance of a 1mm diameter multimode optical fiber that is then bent around two perpendicular axes. Mixing in the fiber scrambles the light so that the exit surface appears to be a uniformly illuminated circle. Illuminators of this type are discussed below in the section on light scrambling.

If the collection mirror used is elliptical or parabolic rather than spherical, and the arc tube is mounted axially (Fig. 6.4), it can collect up to 85% of the total emitted light. Unfortunately, the projected ray bundle has a dark central spot where rays are obscured by the end of the plasma tube. In addition, because arcs are more stable and uniform when the axis of the envelope is vertical, light sources using this type of collector usually project their output downwards.

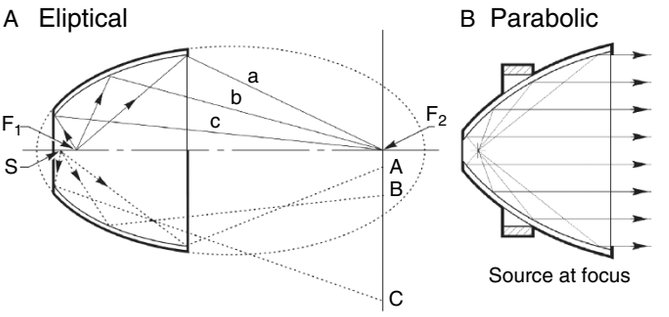


FIGURE 6.4. (A) Elliptical collector with both the focal points F_1 and F_2 and eccentricity $e < 1$, every ray (a–c) emitted from focal point F_1 will be imaged at focal point F_2. (B) Parabolic collector (eccentricity $e = 1$), with a source in the focal point. The source will be imaged into infinity (a parallel wave front). (Diagrams kindly provided by Oriel/Newport, Irvine, CA.)

The coatings on all collection mirrors should be dichroic to let heat wavelengths pass through. Reflectors designed for various wavelength bands are sold by Oriel Corp. (Stratford, CT) and Optical Radiation Company (Electroforming Division, Azusa, CA) among others, and sold as "cold mirrors" or "hot mirrors," depending on the wavelengths transmitted or reflected. If some scrambling is done and the source image is expanded, elliptical mirror sources can provide a Köhler illumination scheme suitable for disk-scanning instruments (see below), though a somewhat more uniform output can be produced if the elliptical surface is slightly deformed. These same companies and ICL Technologies (Sunnyvale, CA) make modules and lamp housings that utilize such aspheric reflectors. Many models are available for different arc lamps.

Wavelength

The third important variable is **wavelength**. Although the plasma and filament sources discussed so far have been "white light" sources with fairly uniform brightness across the visible wavelengths, the same is not true of arc sources. Photons are produced whenever an excited electron loses energy. They will be visible photons (i.e., photons having a wavelength of between 380 and 780 nm) if the amount of energy lost by the electron is in the range of 3.3 to 1.59 electron volts (eV). Excited electrons can be produced in many ways, but the traditional methods that produce them efficiently and from small volumes include heating the electrons in a tungsten filament to 3200 K or 3400 K, or heating a Hg or Xe plasma to a much higher temperature. These plasma sources also have specific emission bands that are defined by the specific energy levels of the atoms involved [Fig. 6.5(A,B)].[10]

From Figure 6.5(B), one can see that an Hg arc is almost 10× brighter at 365 nm than at 400 nm. Not surprisingly the 300 W Xe arc makes about 4× more total light than the 100 W Xe arc. However, because the brightest part of the image of the 300 W

[9] Except for the long working distance (LWD) condensers used on inverted microscopes to allow use with thick cells chambers or access to the specimen with micro-electrodes and the like.

[10] All irradiance spectra kindly provided by Newport Co. (Irvine, CA).

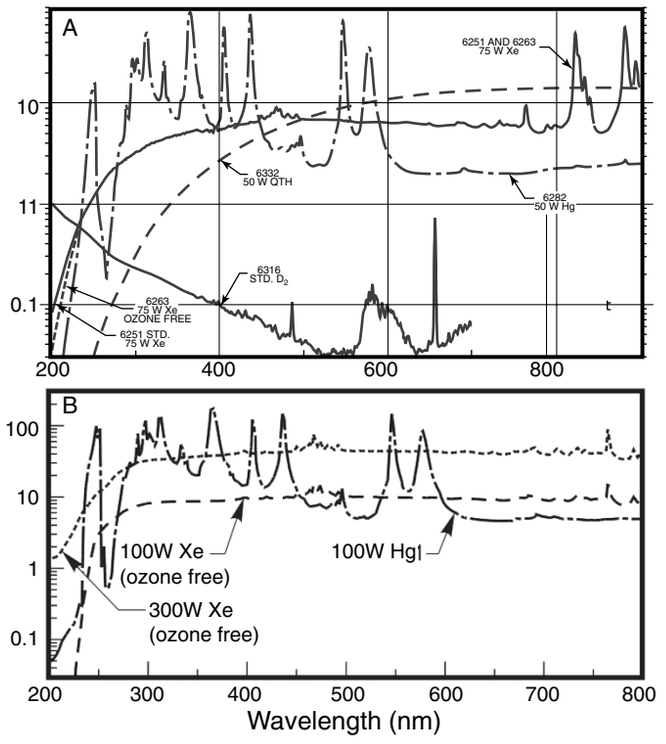


FIGURE 6.5. Wavelengths resolved irradiance of various light sources. (A) *Lower line*: 30 W deuterium arc lamp; *upper line*: 75 W xenon arc lamp; *dashed line*: 50 W halogen filament; *dashed/dotted line*: 50 W mercury arc lamp. (B) *Dashed line*: 100 W xenon arc lamp; *dashed/dotted drawn line*: 100 W mercury arc lamp; *dotted drawn line*: 300 W xenon arc lamp. (Spectra kindly provided by Oriel/Newport, Irvine, CA.)

source is almost 8× larger than the comparable area of the 100 W source, its brightness is only half as high.

Coherence

A fourth important source parameter is its **coherence**. Although coherence is closely related to brightness, in that bright sources are likely to also be highly coherent, the term *brightness* is more used to describe the ability of a source to focus a large number of photons into a small area, whereas *coherence* is more of a measure of the ability of wave functions that describe these photons to interfere with each other, either at the focus plane (good) or between the reflections from every dust particle and imperfection in the optical system (bad). In coherent light, a large fraction of the wave functions passing a given point are in-phase with each other.

Although light from a laser is extremely coherent, even here there are limitations. Laser light emerges not at a single wavelength but over a very narrow wavelength band. Consequently, even if all the photons started off in phase, after some distance (the coherence length) those with slightly longer wavelength will become out of phase with those of slightly shorter wavelength. What this means practically is that light scattered by a dust particle on one side of a piece of glass can only interfere with light scattered on the other side if the thickness of the glass is less than the coherence length.[11] Interference of this type is the source of "laser speckle," the pattern of random interferences that converts what should be a uniform beam into a pattern of black and white blobs. Because in microscopy it is preferable that the contrast seen in the image represent only the interference that occurred within the specimen, light sources of low coherence are preferred.

The process of light amplification by the stimulated emission of radiation that produces laser light (see Chapter 5, *this volume*) necessarily produces very coherent light. Although it is often assumed that coherent light can be produced in no other way, this is untrue. If one thinks of light as an oscillating electro-magnetic field that propagates in one direction, and chooses to measure this field at a particular instant and in a location of space that is smaller in dimensions than its wavelength, the wavefields of all the photons passing through this volume at any instant are added to produce a single electromagnetic wave vector; that is, the light emerging from this tiny volume is completely coherent. Were one to focus light from a filament onto a 0.2 μm diameter aperture, the light emerging from the hole would be coherent and all of it could be focused into a diffraction-limited spot.[12] The problem is that it would also be a very dim spot (about 6 nW of white light by extension of the calculations noted above). As the aperture gets bigger, the coherence is reduced.

Incoherent light, such as sunlight from a cloudy sky, and coherent light from a laser, are each limiting theoretical constructs. Even though, as presented in Chapter 1, using these limiting conditions simplifies the process of writing equations that describe the image formation process in the microscope, neither coherence condition can be realized in practical microscopy. In conventional microscopy, little attention is paid to the degree of coherence of the illuminating light except when considering diffraction and interference effects. Roughly speaking, light is considered to be incoherent when it does not produce speckle effects and coherent when it does.

Speckle is bright if the interference of light scattered by the feature is constructive with that from the background and it is dark if destructive interference occurs [Fig. 6.6(A); Briers, 1993]. The apparent size of the scattering feature and that of the individual speckles are related to the resolution limit (or NA) of the optics. In the case of incoherent illumination [Fig. 6.6(B)], overlap between speckle patterns having different wavelengths partially cancels them out to produce a lower contrast pattern. Because speckle is an interference phenomenon, any movement of the optical system or the specimen will result in a complex change of the speckle pattern in time.

Even in imaging situations that are well described by incoherent phenomena, coherent effects can often be detected if the results are examined with sufficient optical resolution (Reynolds *et al.*, 1989). In general microscopy, light with low coherence is desired for bright-field and reflection modes, while light with higher coherence is required for phase and interference modes. The process of fluorescent emission involves so many intermediate steps between excitation and emission that any coherence in the illuminating light is usually lost, and the light emitted from the specimen is basically incoherent.

If the coherence of the illuminating light is too high, microscopy in the reflected or backscattered light (BSL) mode[13] yields images with fringes caused by interference of the coherent

[11] The time required for light to move one coherence length is the coherence time.

[12] Conversely, the extent to which this is NOT possible is a good measure of incoherence.

[13] BSL is the more general term for reflected light, the term "reflected" should be reserved for the coherent scattering that occurs from smooth surfaces.

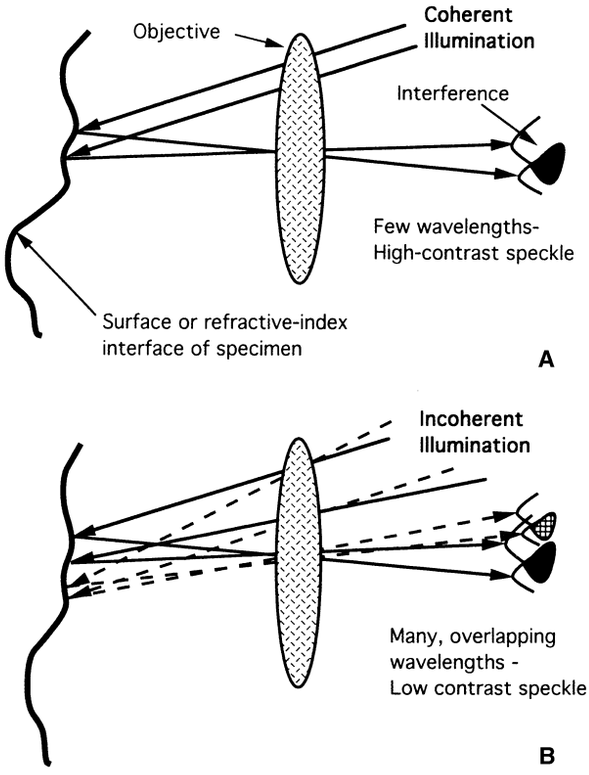


FIGURE 6.6. Speckle patterns. High-contrast patterns result from interference between two reflection maxima in a highly coherent system. (A) Low-contrast speckle results from the summation of interference intensity patterns in a system with incoherent illumination. (B) Speckle spot size is a function of system resolution.

light reflected from any of the optical surfaces: lenses, mirrors, dust windows, and, in particular, the coverslip surface. This complex interference can appear as defined rings, but more commonly, it appears as a high-contrast granular speckle superimposed upon the image, making real image details hard to interpret. Furthermore, when the specimen is transparent and has multi-layered microstructure, the speckle spots become even more complex figures.

The coherence of non-laser light sources can be modified by changing the magnification of the Köhler illumination system to reduce the effective source size. Doing so makes the light less intense but more suitable for interference microscopy.

While the sun is considered an incoherent source, under the imaging conditions of high-resolution microscopy, sunlight has enough coherence to impart speckle to the image. Tungsten ribbon lamps as well as light-emitting diode (LED)-based lamps have relatively low spatial coherence because of the large size of the emitter. Arc lamps have higher coherence unless a large area of the plasma is used as the source. As the short-arc Xe/I source mentioned below uses a plasma spot that, after demagnification, is one third the area of the Airy disk, as a source for a confocal microscope, the illumination is almost fully spatially coherent (Hell *et al.*, 1991). However, Hell and colleagues argue that because temporal coherence, associated with a bandwidth of 360 to 570 nm, corresponds to a frequency bandwidth of 3.07×10^8 MHz, to the extent that the intensity spectrum of the arc approximates a continuum, it is appropriate to use

$$\text{coherence length} \leq c/\text{frequency bandwidth}$$

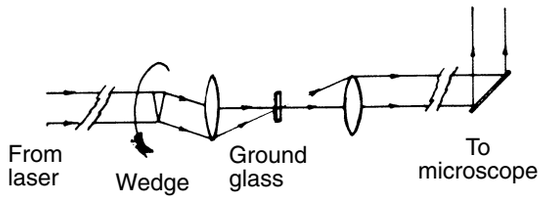


FIGURE 6.7. Phase randomization scheme for laser use. (After Hard, *et al.*, 1977.)

from Born and Wolf (1980). This yields an upper limit of coherence length of approximately 1 µm. Points in the specimen whose optical path difference are greater than 1 µm cannot interfere to give rise to noticeable interference artefacts in transparent microstructures.

A major function of Köhler illumination systems is to make the illumination homogeneous at the image planes and to control its coherence somewhat. However, it is essentially a coherent system and does not "scramble" light to any extent. Additional scrambling is sometimes needed to decrease spatial inhomogeneity, spatial coherence, or temporal coherence. Although most scramblers have been designed to work with highly coherent laser light, the same methods can also be used to reduce the coherence of light from other sources.

Scrambling and Filtering the Light

Three methods have been proposed to reduce coherence. Hard and colleagues (1977) proposed a method to phase-randomize laser light for illuminating a conventional microscope by inserting a rotating optical-wedge-and-ground-glass combination into the light path (Fig. 6.7). Because the wedge and the ground glass rotate, any remaining temporal coherence becomes cyclical. This method requires very stable placement and accurate alignment of the rotating device and the laser relative to the microscope (Reynolds *et al.*, 1989).

The second method to reduce coherence is to focus the laser light into a flexible length of single multi-mode optical fiber (Fig. 6.8). The internal reflections in the bent fiber are constantly changing because the fiber is vibrated at up to 100 kHz (Ellis, 1979) and this makes the exit beam appear uniform in intensity over time (rather than having the Gaussian profile characteristic of lasers). The phase is scrambled by the varying path lengths of the light passing through the fiber on different trajectories, but the high radiance and monochromaticity are preserved. Technical Video Ltd. (Woods Hole, MA) markets a non-vibrating version with a fixed, single quartz fiber segment bent to a specific radius in two perpendicular planes. Applied Precision Instruments (API, Issaquah,

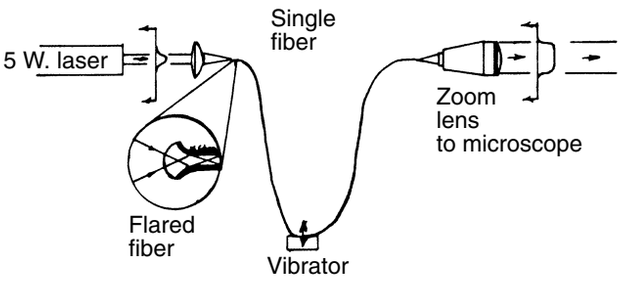


FIGURE 6.8. Phase randomization scheme for laser (after Ellis, 1979).

WA) also offers such a system as part of their Deltavision three-dimensional (3D) imaging system.

All these methods minimize speckle by making it change with time. Speckle is not apparent as long as the recording system records for a time period that is longer than the period of the scrambler. As the motorized system is quite slow, it is only suitable for photographic recordings. Although the fiber scrambler can be oscillated more rapidly, even this is too slow to cause a significant reduction in coherence over the 1.6μs pixel time that characterizes many beam-scanning confocal instruments.

As light scramblers can be damaged if subjected to a high total light flux, provision must be made to remove heat and other unwanted wavelengths before they enter the scrambler system. Ideally, only wavelengths critical to image formation should leave the source. Dichroics that reflect only specific wavelengths should be used to separate the useful light and allow the unwanted heat to escape. In single-sided disk scanners, this would not only reduce heating but also decrease flare and scattering from the top surface of the disk. Heat-absorbing glass is the most common heat filter, but a filter consisting of a chamber filled with a salt solution chosen to screen out infrared light has much higher heat capacity. Aside from heat removal, liquid filters can also be made to function as bandpass or cut-off filters by the careful choice of the salt used. An extensive description of useful solutions is described by Loveland (1970).

TYPES OF SOURCES AND THEIR FEATURES

The following section discusses the important parameters of various common non-laser light sources with respect to the goals of microscopy. In this sense "parameter" means a degree of freedom a user can change to optimize illumination for the application. Unfortunately these parameters are not independent of each other, and all components of an illumination system have to be treated together as a unit. Overall performance depends on the geometry of the source, the focal length, magnification and NA of the collecting optics, and these in turn depend on the shape and position of the mirrors and lenses. Much can be learned by removing the lamp housing and adjusting the controls used to position the source, the reflector, and the collector to project an image on the source on a distant wall. (When using arc sources, take care not to aim it in such a way that the direct light gives anyone a sunburn or strikes anyone in the eye.)

The important parameters of non-laser sources are:

1. Structure (spatial distribution, source geometry, coherence, alignment, collecting optics, etc.).
2. Available wavelengths.
3. Stability in time and wavelength.
4. Source radiance (brightness).
5. How source parameters such as intensity, color, and spatial distribution are controlled.

Structure

The Actual Source of the Light

Microscope sources are optimized to produce the maximum light intensity or brightness (photons/s/cm^2/steradian) from a tungsten ribbon or the arc of an electrical discharge. The filaments of halogen lamps are often bent to resemble disks or wide, flat bands to match the input aperture of the light-collection optics. Arc lamps generally generate light in a ball discharge at the tip of a pointed electrode (Fig. 6.9). The two electrodes in xenon arcs have different shapes. The anode has a bigger diameter and a flatter tip. As a result, the light will be most intense where electric flux lines are closest together near the point of the cathode [Fig. 6.9(B)]. As the pointed electrode erodes, the field at the tip decreases and the plasma ball becomes larger and therefore less intense.

These sources are geometrically similar but are different in size. The brightest part of the arc in a common HBO-100 arc lamp is about 0.3×0.5 mm in cross-section, the tungsten filament of a 100 W halogen lamp is about 4×2 mm wide. Both source dimensions are set by the manufacturer, and there is no option to vary them.

Electrons passing through the depletion region of any forward-biased semiconductor diode lose energy equal to eV_g, where V_g is the bandgap of the semiconductor. This energy is converted into a photon having an energy equal to the bandgap energy. Silicon diodes emit in the near-infrared (IR) region, but diodes made of other semiconductors emit in the visible and even the near ultraviolet (UV). When such a diode is configured primarily to produce light, it is called a light-emitting diode or LED (Schubert, 2003). Recently, technological developments have increased available power levels and now LEDs are used in applications where their long life and high efficiency are important, such as traffic lights. They are of interest to microscopists because they are compact and efficient light sources that can emit a high flux of quasi-monochromatic photons from a small area.

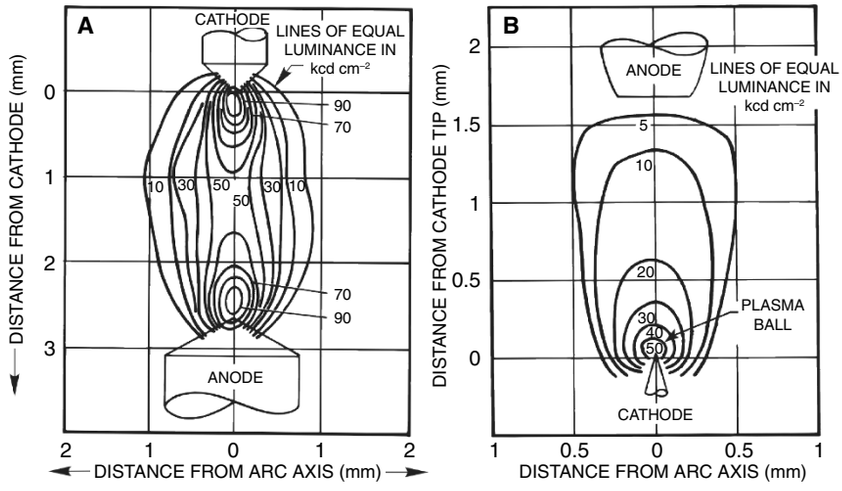


FIGURE 6.9. Iso-intensity plots from the discharge of a mercury arc lamp (A) and xenon arc lamp (B). Values in kcd/cm^{-2}. Note the different size scales and the fact that the Hg arc has two intense plasma balls while the xenon has only one, and this is smaller and less intense than the Hg. (Plots kindly provided by Oriel/Newport, Irvine, CA.)

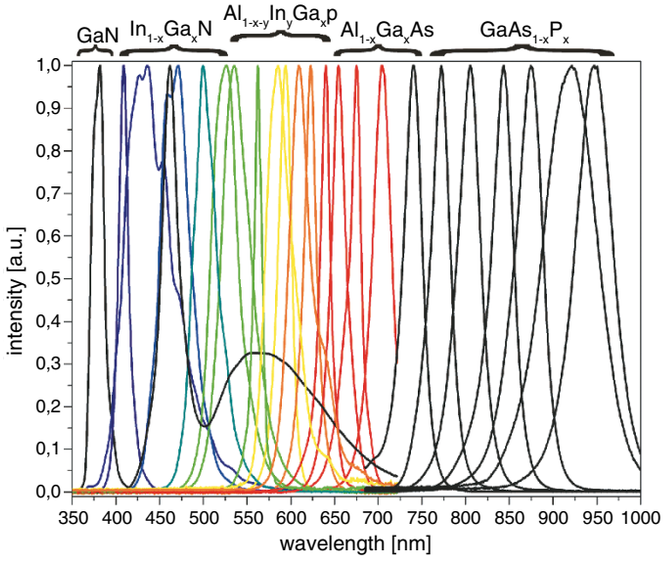


FIGURE 6.10. Spectral distributions of monochrome LEDs. The compounds used for the LED dies are shown above. The black line with a sharp peak at 460 nm and a smaller, wider peak at about 575 nm, is the emission curve of a so-called "white" LED — a blue emitter surrounded with a phosphor that absorbs at 575 nm and emits at longer wavelengths.

An LED source consists of an area of semiconductor crystal approximately 0.3 mm × 0.3 mm in size called a **die**. The most common crystals used are $Ga_{1-x}Al_xAs_{1-y}P_y$, GaN, and ZnSe and each emits in a different waveband (Fig. 6.10). Normally one or more dies are embedded in a larger LED structure for protection, light collection, and electrical and thermal handling. The advantage of LED technology is that one can combine these small units to build up a light source of the shape best suited to the needs of the application. Possible source geometries are limited only by heat dissipation and the permitted package density of the surface mount device (SMD) technology used to integrate a number of dies onto the printed circuit board. Very dense, bright, custom-designed sources can be fabricated in this way. Figure 6.11 shows the general structure of an LED and how they have changed over recent years (Steigerwald, 2002). Die dimensions up to 1.5 × 2 mm are now available.

How to Cope with the Heat?

The most important aspect of any microscopy light source is an efficient heat sink. Incandescent and the arc-based lamps produce a lot of heat because of their low optical conversion efficiency (5%–10%). The holders and housings of these lamps are made of a material resistant to high temperature and designed to dissipate ~100 W of heat. As a result, they cannot be mounted inside a microscope system. Although present LEDs have similar efficiency, all the photons produced are emitted over a narrow range of wavelengths (see below) and they operate at a **much** lower temperature. This means that less electrical power is needed for the same optical output and they can be more compact; for instance, they can be bonded to a small metal heat sink, cooled by a small, computer-controlled fan. This technology makes it possible to mount LED sources inside the microscope system, closer to the specimen, and avoid loss of light intensity in transit. Despite this flexibility, it is important to remember that LED-based sources do need an efficient heat sink because operating much above room temperature causes lower lifetime and a loss of optical output efficiency (Perduijn *et al.*, 2004; Fig. 9.12).

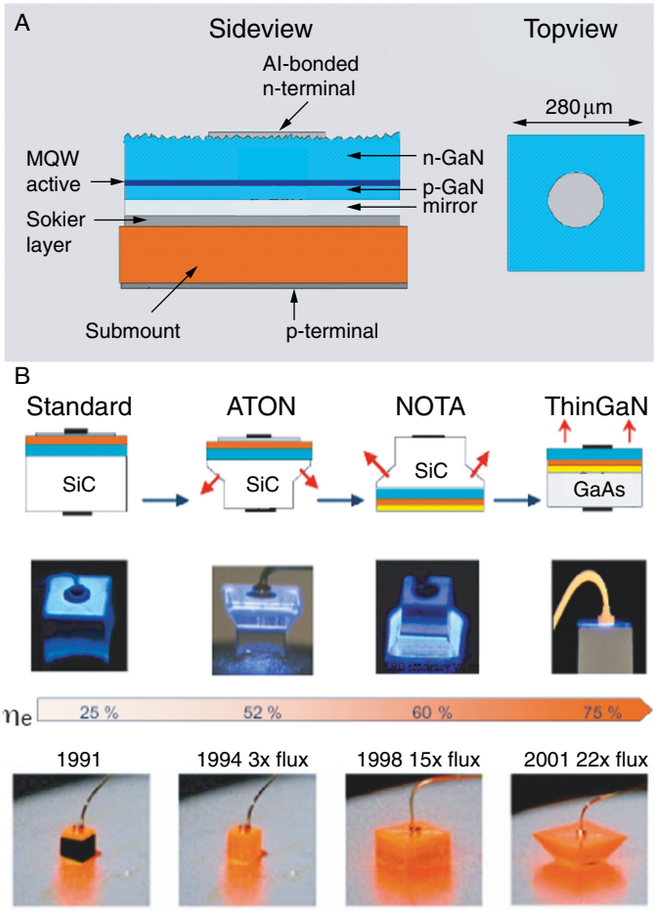


FIGURE 6.11. (A) General structure of an LED with the different layers marked. The mirror is used to reflect the back-emitted light to the right direction. The metal bond pad on the top is for the electrical contact. (B) Changes in the geometry of LED dies in recent years have led to larger dies and have increased the efficiency with which light is emitted. (With kind permission from OSRAM Optical Semiconductors, Regensburg, Germany.)

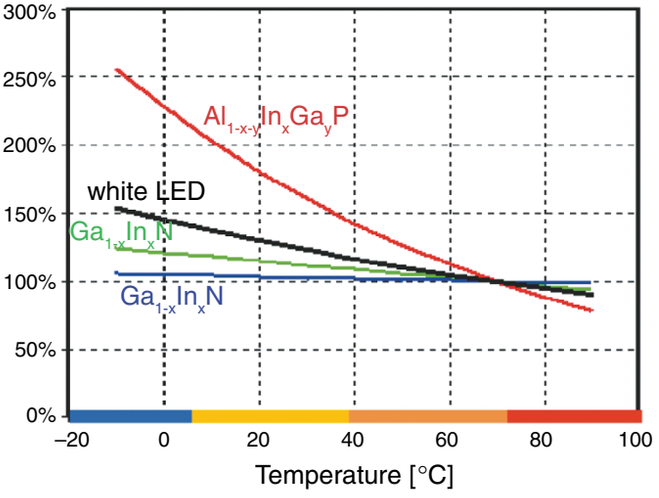


FIGURE 6.12. The dependence of light flux on LED temperature, standardized to 70°C for dies made using different types of LED crystals. Because dies emitting at longer wavelengths have a smaller bandgap energy, they are more affected by changes in temperature. Formulas for the compounds, note above.

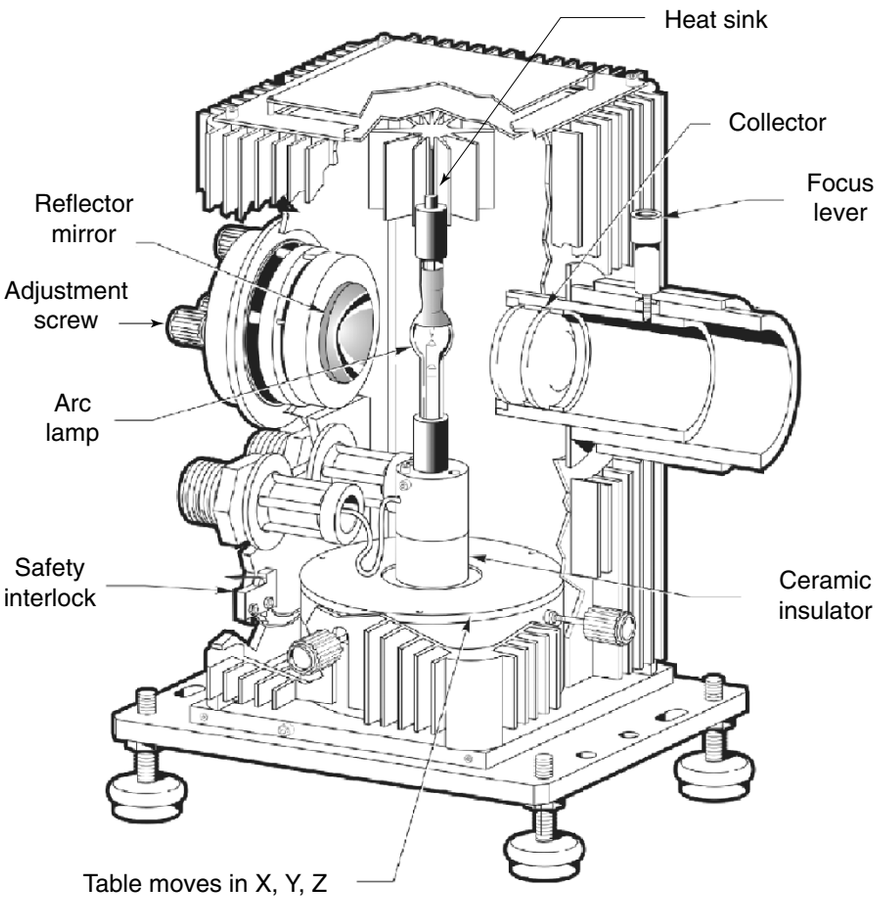


FIGURE 6.13. Diagram of lamp housing. The discharge of the arc is located at the focal points of the rear reflector and the first condenser lens, both of which can be moved in three directions to permit alignment with the optical system.

Reflecting and Collecting the Light: Source Optics

As incandescent and arc lamps are almost isotropic emitters that radiate equally in all directions, a spherical reflector can be placed behind the source to create the image of the source beside the actual arc. A collector lens is mounted so its focal point coincides with the center of the source; it catches a large fraction of the light and focuses it at the BFP of the condenser (Fig. 6.13). Due to the small source size and the desire for a short compact structure, collector lenses are usually aspheric and have high chromatic aberration.

LED-based sources use three different principles to reflect and collect the light generated inside the die. The first approach was to use the clear, molded plastic LED package itself to collect and focus the light. Although suitable for low-level bright-field applications, this method is rarely used in microscopy because of the limited optical power available from a single LED (e.g., the white light LED NEPW500, manufactured by Nichia with a $0.3\,mm^2$ die). The second approach is to work without a collector and print the LED dies directly onto the printed circuit board. The density of the packaging achievable in this way is only limited by the need to bond the single dies with the connecting wires and the ability to dissipate heat. The disadvantage is one loses any light that the LED die emits to the side (e.g., the monochrome arrays available from Laser2000 with 88 single $0.3\,mm^2$ dies packaged on a ceramic plate). The third possibility is to place the LED die into a mirrored well that acts as a reflector (e.g., the "Golden Dragon" manufactured by ORAM) and then arrange these units onto a printed circuit board. Because the reflectors are bigger than the dies, this results in a lower packing density.

As every die is a separate source, when an LED array is built up of several dies, one needs a different method to combine the light from them than one would use for a conventional lamp. The most efficient way to collect the emitted light is to use a microlens array placed the proper distance in front of the LED array. This array can be made of molded plastic or of glass and must be designed so that every LED die has its own collecting lens (Fig. 6.14). The main goal of this configuration is to catch as much light as possible and deliver it into the acceptance angle of the microscope illumination optics so that it fills the condenser aperture diaphragm with axial, parallel light as homogeneously as possible.

Source Alignment

The rule of thumb says the smaller the source, the more important it is to align it properly. For arc lamps and incandescent lamps, one must align the reflector and collector in such a way the source and its image from the reflector lie side by side and are centered in the aperture diaphragm of the illumination path. Only in this way will one be able to fill the aperture diaphragm approximately homogeneously (Fig. 6.15). Modern systems usually either incorporate special viewers so that one can check alignment or use self-aligning sources such as the self-aligning HBO-100 source available from Carl Zeiss (Fig. 6.16). The heart of the self-aligning source is a photodiode with four quadrants. Some of the light emitted by the arc in the direction towards the reflector passes through a small hole onto the optical axis where it is captured by

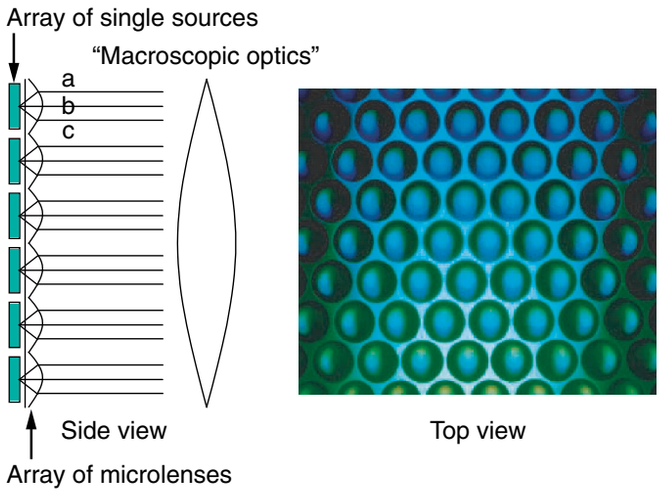


FIGURE 6.14. Principle of a micro-lens array. (A) Each mircro-lens efficiently couples the light from a single LED source to the macroscopic optics of the microscope. As a result, the macroscopic collector optics can have a lower aperture, and therefore, a larger focal length at a reasonable diameter. In addition, such optics have lower spherical and chromatic aberrations. (B) Hexagonal micro-lens array made of quartz glass. This example is normally used in telecommunication to couple two bundles of optical fibers together.

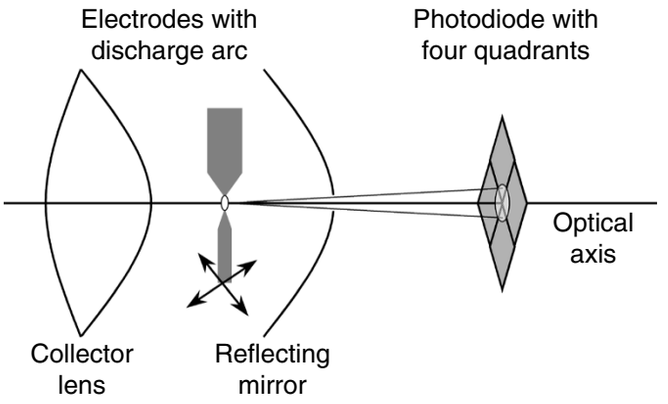


FIGURE 6.16. Components for a self-aligning source. Light passing through small hole in the reflector strikes a quadrant detector. Signals from this detector are used to move the arc in y and z until the output of all four diodes are equal.

the quadrants of the photodiode. A microcontroller measures the intensity of all four quadrants and moves the burner on an xy-stage until there is no difference between them. As the right reflector position depends on the particular optics of the microscope, the z-position of the reflector still has to be aligned manually.

For LED-based sources, alignment is simpler. In bright-field microscopy the main goal is to fill the aperture diaphragm as homogeneously as possible. This can be accomplished by mounting a large (5–10 mm) LED array just behind the aperture diaphragm. The problem in this case shifts to the alignment between the microlens array and the LED sources. As the focal length of the microlenses has to be relatively short and the LED sources are very small, the tolerance to a misalignment is also small.

Wavelength

Historically, many fluorophores were selected and used because they are excited by the intense lines of Hg arc lamps. This was not only because of the increased brightness but also because the narrow bandwidth made it more easy to design effective dichroic emission filters and beam-splitters. In addition, microscope objectives are often designed to give optimal correction at these wavelengths (Herman, 1998). As the laser wavelengths available seldom match these wavelengths, the microscopist using a laser confocal microscope must sometimes exchange familiar fluorochromes for new, less familiar ones that can be excited at laser wavelengths. Because histochemistry is complex enough without having to try entirely new stains and chemistry, it is important to have a light source flexible enough to excite the most suitable dye for each application.

The sun has very high brightness and the continuous spectrum of a black-body radiator with a surface temperature of 5800 K (Fig. 6.1). A clock-driven heliostat was used by Petran and colleagues (1985) to track it as a light source for confocal microscopy. The sun's broad continuous spectrum allows easy selection of wavelengths for difficult specimens.

Aside from the sun, only a synchrotron can provide as bright and continuous a spectrum (van der Oord, 1992; Gerritsen *et al.*, 1992, 1994). Although using the sun or a synchrotron as a light source might be ideal in many ways, the nuisance of having to depend on geography, season, cloudiness, and time of day led to the development of portable sources.

Incandescent lamps also emit essentially black-body radiation, the spectral shape of which depends on the temperature (Fig. 6.17). However, because the filament is only 3200 K or 3400 K, the light is less intense and has more red light than sunlight. Although it is possible to increase the blue component by raising the tempera-

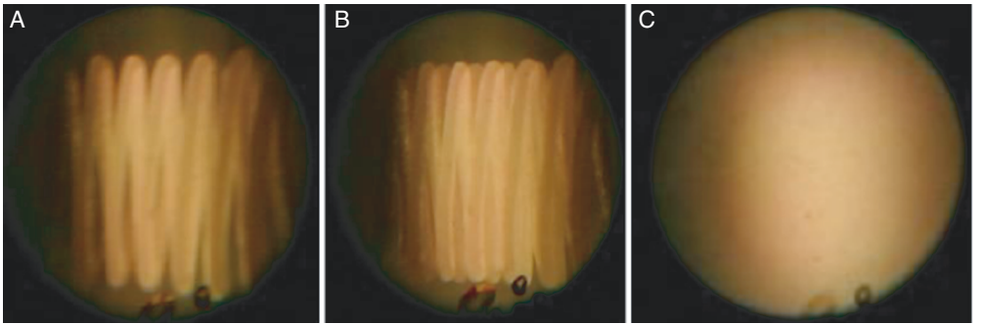


FIGURE 6.15. Image of the filament of a 100 W halogen source. (A) Image of filament and its reflection superimposed; (B) filament and its image side-by-side, right (C) after insertion of ground glass to randomize image of filament. The illumination optics do not magnify the image of the filament quite enough to fill the BFP completely. Even with the ground glass in place one can see a visible drop of intensity at the outer edges of the BFP.

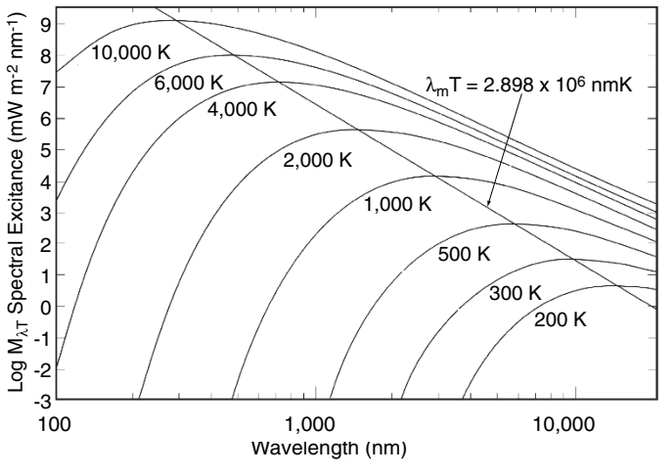


FIGURE 6.17. Spectral distribution of black-body radiation at various temperatures. Note that the vertical scale is logarithmic. The total luminosity of a black body varies with the fourth power of the temperature.

ture, doing so increases the rate at which the tungsten sublimes. The tungsten vapor condenses on the inside surface of the quartz envelope where it absorbs light from the source and heats the envelope. In addition, the filament becomes thinner until it fails.

The halogen gas in a quartz–halogen source interrupts this process by first reacting with the evaporating tungsten to form tungsten–halide compounds. These then decompose when they strike the hot filament, effectively returning the tungsten to the hottest (and thinnest) part of the filament. This permits the filament to be operated at a higher temperature with little darkening and a longer time before failure. Higher temperatures may also deform the filament structure, causing it to move from its correct location in the optical system.

The optimal wavelengths for exciting classic fluorescent dyes (436 nm, 546 nm, 579 nm, 365 nm, 405 nm) coincide with Hg arc emissions lines [Fig. 6.5(A)]. The carbon arc (not shown) has a single very intense line at 400 nm. Mixed-gas Hg-Xe arcs have many intense, useful spectral lines in the UV and visible. Xenon and zirconium arcs have spectral lines in the near IR.

The emission spectra of arc sources can be classified in three ways: (1) continuous, (2) line spectra, and (3) mix of lines and continuous spectra. Figure 6.5(A) shows the spectra of arcs using mercury and xenon, as well as a tungsten halogen incandescent source, plotted with the same horizontal scale.

The super-pressure xenon arc provides intense broadband illumination without prominent spectral lines in either the UV or the visible because the high pressure broadens the xenon spectral lines. Because the intensity of the continuum of a 75 W high-pressure xenon lamp is 2× higher than the continuum of a 100 W Hg arc lamp, the xenon lamp is better suited for low efficiency fluorophores not excited well by the prominent Hg lines. The availability of broadened spectral lines sometimes allows the simultaneous activation of several fluorochromes with differing emission wavelengths, including those in the UV.

The only disadvantage of the xenon lamp is the high pressure in the bulb (approximately 30 bar at room temperature and approximately 10× that at operating temperature). This makes it necessary to use protective gloves, goggles, and a shield to shelter the chest when changing a bulb in case it should explode.

The LED technology makes it possible to supply the right excitation wavelength for each fluorophore. Most wavelengths are now available from UV (365 nm) up to IR (>800 nm; Fig. 6.10) with intensities sufficient for widefield fluorescence. The FWHM of a quasi-monochrome LED varies from 20 to 40 nm, which is similar to the width of the excitation band of many fluorophores. Compared to laser light, the wider bandwidth of the LEDs make it easier to excite a variety of dyes, and compared to the continuous spectrum of an arc lamp they are cooler, smaller, and provide an easier way to choose the wavelength one wants and to do so rapidly. That said, one still needs to use excitation filters to remove the tails of their emission wavelength distribution.

Using conventional fluorescence microscopy as many as five different fluorescent labels have been imaged simultaneously in the same living cell (De Basio *et al.*, 1987).[14] This certainly could have been done as well using a disk-scanning confocal microscope having an efficiently configured arc source.

When imaging living cells, success requires using minimum light intensity at the specimen plane and choosing illumination wavelengths that interfere as little as possible with the life process under study. Using a continuous spectrum source, one can often make small wavelength changes that reduce specimen mortality. Because fluorophore excitation maxima are altered by their molecular environment, and because this is especially true for a fluorophore attached to a functioning macromolecule in a living cell, fine tuning the excitation wavelength can result in increased emission. Using strip- or wheel-type, continuously graded interference filters, such as those manufactured by Ocean Optics (Dunedin, FL), the microscopist can often precisely adjust the illuminating wavelength to minimize interference with the process under study and to maximize the excitation of a fluorophore in a particular cellular environment.

Stability in Time and Wavelength

Ramp-Up and Short-Time Stability

Everyone who has used an arc lamp knows the buzzing noise that occurs when the lamp is switched on and the plasma arc discharge is building up between the two electrodes. All sources based on plasma-discharge or incandescence need a considerable time to reach thermal stability.

Figure 6.18 shows typical intensity ramp-up curves for the various sources.[15] All lamps that produce significant heat show a dependence of the emission on the source temperature. This even applies to LED-based sources. It can take up to 1 h until the source is sufficiently stable to make reproducible measurements or to make a good time-lapse movie. Once operating temperature has been reached, the halogen lamp is the most stable source over time periods of a few milliseconds because of the high thermal inertia of the tungsten filament. LED-based sources react very fast (in a few microseconds) and, therefore, they are affected by any high-frequency instability in the power supply. In general, the most unstable source is the arc lamp. Not only is the arc itself a chaotic, flickering discharge but its light output can also be affected by ambient electromagnetic fields or an unstable power supply.

Stability can be increased by using the signal from a light sensor as a feedback signal to control the excitation power. The Oriel 68950 power supply controller (Newport, Inc., Irvine, CA)

[14] De Basio and colleagues measured five cell parameters: (fluorescent dye) nuclei (Hoechst 33342), mitochondria (diIC-[5]), endosomes (lissamine rhodamine), B-dextran, actin (fluorescein), cell volume (Cy7-dextran).

[15] These curves were measured with an upright microscope, using a source mounted in a common epi-illumination lamp housing. A 50/50 beam-splitter was used and a radiospectrometer placed at the BFP of the condenser.

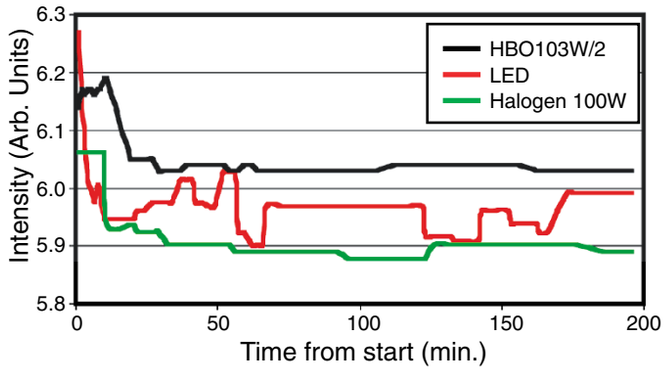


FIGURE 6.18. Ramp-up of brightness and long-term stability for various microscope light sources.

improves the stability of arc and halogen sources from 0.4% to 0.01% (Fig. 6.19). However, these figures are for total light output, and they cannot prevent local flickering in the particular region of the plasma that happens to be focused onto your specimen. Some suppliers of deconvolution systems, such as Applied Precision Instruments (Issaquah, WA), constantly monitor arc output during the CCD exposure time. They then use this information to normalize the CCD output for each plane of the *z*-stack.

Long-Time Stability, Degradation

When warmed up and powered by a regulated power supply, tungsten halogen sources are suitable for making photometric measurements.

Generally speaking, arcs are less stable than filament lamps because the points of the electrodes slowly erode. The larger radius of curvature that results reduces the concentration of current flow (and brightness) near the tip and also increases the power level needed to sustain the arc. Eventually the arc will not ignite. The intensity of the xenon arc can be deeply and rapidly modulated in time to keep the electrodes cool, as is the case for the electronic flash used for photography. Alternatively, the position of the arc plasma can be stabilized either by a periodic magnetic field imposed by a rotating permanent magnet or by the superimposition of a small, high frequency AC current on the main DC excitation current (Woodlee *et al.*, 1989).

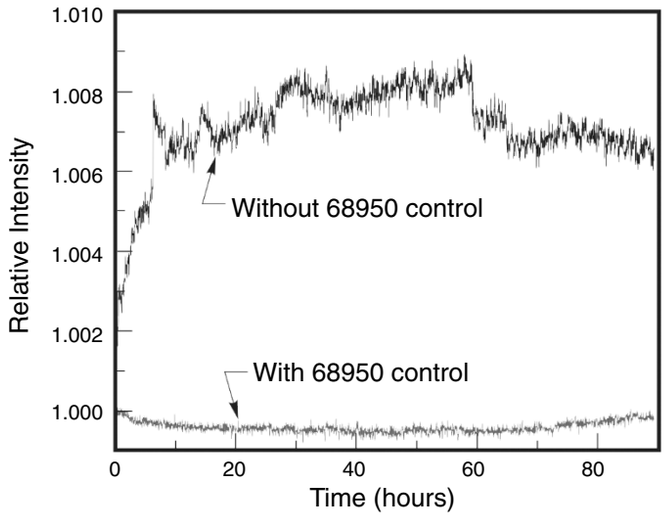


FIGURE 6.19. Stability plot of halogen source, with and without optical-feedback power stabilizing. Although quartz halogen sources are very stable, temperature rise increases output, and air-conditioning and other factors can produce transients. These can be compensated for by using the output from a monitor photodiode as the input to a negative feedback system controlling the power supplied to the lamp. (The plot was kindly provided by Oriel/Newport, Irvine, CA and reflects the performance of their 68950 power-supply controller.)

As the photoelectric effect is fully reversible, it is not surprising that the LED has the lowest operating temperature and, as a result, is the most stable source. In addition, as long as it is operated at the proper voltage/current, the LED has a much longer lifetime than all other sources. One usually has to change an arc about every 200 h and incandescent lamps about every 500 h, but the LED sources have lifetimes in the range of a few thousands hours without significant loss of intensity. Some manufacturers promise a lifetime of 100,000 h before the source intensity drops to 70%.

Stability in Wavelength

In the discharge of an arc lamp, the gas pressure affects the composition of the spectrum. As the pressure rises, the prominent lines broaden and the continuum rises [e.g., compare the continuum brightness of a mercury and a high-pressure xenon lamp in Fig 6.5(A)]. On the other hand, the peak wavelengths of prominent lines shift just a few nanometers (<5).

The continuous spectrum of an incandescent lamp depends only on the temperature of the filament (Planck's law) and on the gas present in the bulb (Fig. 6.17). At a fixed current, a change in color temperature can only occur if evaporated tungsten condenses on the glass bulb. A change in the current to an LED causes a shift of the emission peak similar in magnitude to that seen in lines of the arc lamps. This may be due to the LED die not being perfectly homogeneous. The size of the shift depends on the type and quality of the crystal material used.

As the shifts are small compared to the width of the lines, one can neglect the effect for arc lamps. For LEDs, one either has to calibrate the dependence of the wavelength on the operating current or operate the die in a different way (see sections on Radiance and Control).

Radiance

Arc lamps are several orders of magnitude more radiant than tungsten filament lamps [Fig. 6.5(A)]. The HBO-100 (100 W high-pressure mercury arc lamp) is the most radiant of the commonly used lamps, whatever the wattage, because it has a very small source size (compared to the HBO-200, for example). Because of the optics rule mentioned at the beginning of this chapter, the larger arcs are only useful to illuminate larger areas of the specimen rather than to illuminate a single spot with maximum intensity. The main limitation on arc radiance is that the electrode tips erode or even melt as the power level increases (Fig. 6.5).

New arc sources of very high radiance have been described by Steen and Sorensen (1993). In these sources, commercial Hg, Xe, or Hg/Xe arc lamps have been modified to permit direct water cooling of the electrodes and the superposition of large-amplitude short-duration (20 µs) current pulses on the DC operating current. Increases in output of up to 10-fold were observed during each pulse. Hell and colleagues (1991) describe a new generation of short arc lamps with extremely short electrode distances (0.5 mm) using a Xe/I fill and tungsten carbide electrodes in a quartz bulb. The tungsten iodide TlJ dopant gives rise to a radiating plasma spot only 150 µm in diameter. Over the 450 to 550 nm band, the radiance exceeded that of the conventional Xe short arc by a factor of 3 to 5 and that of an HBO-100 mercury lamp by 12. The new arc lamp

has useful radiance from 360 to 570 nm. These developments push the arc source radiance closer to the realm once thought available only from lasers. Tables of the radiance of various arcs and lasers can be found in the catalogues of Melles Griot (Rochester, NY) and Oriel Corp. (Stratford, CT, now a division of Newport Inc.).

When driven by a 120 Hz square wave, the modulated (Hg-I) arc lamp introduced by LTM Corp. (Sun Valley, CA) produces a very useful spectrum with an efficiency of 110 lumens/W, compared to 30 lumens/W for a normal xenon arc. The deep square-wave modulation of the Hg-I arc reduces average heat production, allowing the lamp housing to be compact enough for placement near the microscope.

As the bulk depletion region inside the LED die is an isotropic emitter (lambert), one might assume that the light leaving the front surface of the die would also be isotropic in all directions. However, as the light generated in the volume of the crystal must pass through the crystal/air interface, any rays that strike this surface at less than the critical angle will be reflected and reabsorbed by the crystal. Approximately 50% of the light generated internally is lost in this way and less light is emitted at bigger angles.

The radiance of the high-brightness LEDs available today is still far less than that of the prominent lines of the arc lamps (Fig. 6.20). In the continuous operation mode, the brightest 2×2 mm LED die (Luxeon, 5 W Emitter, Fa. Lumileds, San Jose, CA) today delivers around 50% of the continuum radiance of a 75 W XBO at the same wavelength, and is bright enough to get an acceptable fluorescent signal from a well-stained specimen (Braun and Merrin, 2003). Unfortunately these high-power dies are not yet very stable and because of the high thermal load they degenerate very fast. More to the point, they are still not available in all wavelengths. At present, better results are obtained using smaller emitters (1 W emitter, Luxeon) to build up a light source. With a proper heat sink these are now very stable.

In pulsed-mode operation (see subsection under Control), the available radiance can be a factor of 20 higher than for the same unit used in continuous mode. When grabbing fluorescence pictures quickly, this mode is the most suitable one, as one can trigger the camera with the light pulse to ensure efficient usage of the emitted light. This mode of operation is also now being used in the machine vision area of industry where LEDs have become a long-life substitute for xenon flash lamps for illuminating moving objects (see, e.g., available light sources at http://www.laser2000.de). For other manufacturers, see the links in Table 6.1.

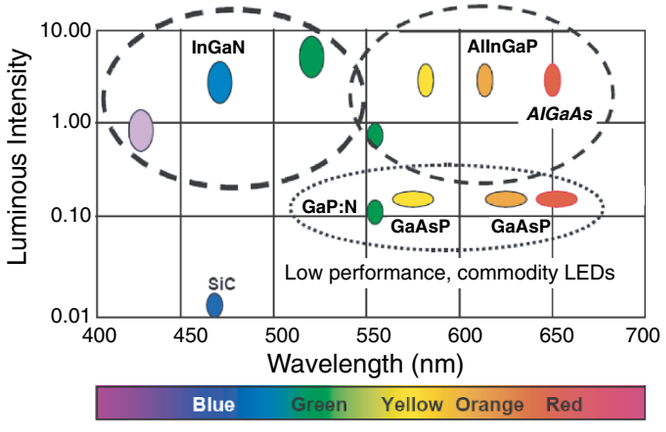


FIGURE 6.20. LED luminous intensity for various colors and dye compounds. Efficiency is measured in lumens/watt and refers to the efficiency with which electric power is converted into optical output.

TABLE 6.1. Useful Links

Microscopes, optics, and light sources
http://www.zeiss.com/
http://www.lot-oriel.com/
http://www.mellesgriot.com
http://www.chroma.com/
http://www.edmundoptics.com
http://www.optics.org/
http://www.wahl-optoparts.de/
http://www.oceanoptics.com
LEDs
http://www.luxeon.com/products/family.cfm?familyId=1
http://www.osram-os.com/
http://www.nichia.com/
http://we.home.agilent.com/USeng/nav/-11143.0/home.html
http://www.led.com/
http://www.optotech.com/
http://www.toyoda-gosei.com/led/index.html
http://www.stockeryale.com/
http://ledmuseum.home.att.net/ledleft.htm
http://www.laminaceramics.com
Basics and history
http://micro.magnet.fsu.edu/primer/
http://inventors.about.com/library/inventors/bllight.htm

Control

The quartz–halogen lamp is simply driven by a stabilized DC power supply converting the plug voltage into an adjustable voltage of 2 to 12 volts. Varying the voltage controls the temperature of the filament and thereby the spectral properties and intensity of the light.

Arc lamps are usually also driven by a current-stabilized power supply. The current can be decreased to 70% to lower the optical output and conserve the electrodes if one does not need the full optical power. Below 70% the plasma becomes unstable. Because of the decreasing temperature of the discharge, the vapor pressure drops and the discharge stops. Modern arc lamps have a heating filament wrapped around the bulb. This filament heats the bulb, restoring the vapor pressure, and allowing the current to be decreased down to 30% without stopping the discharge.

Neither arcs nor halogen lamps can be switched on rapidly. To change the emitting wavelength or intensity quickly one has to use mechanical shutters and filter wheels and switching times are usually longer than 100 ms.

The stabilizing circuitry of the arc power supply can stabilize the voltage, the current, or the total power (voltage × current). If the voltage is stabilized, the current (and the brightness) will slowly decrease as the electrodes become worn round. If the current is stabilized, the brightness will stay fairly constant[16] until the electrodes become too rounded for the arc to "strike." However, because an ever-higher voltage is required to maintain the fixed current, as the electrodes wear the power sent to the arc slowly increases. As a result, it can overheat and sometimes explode. Although power supplies that stabilize the total power level will avoid overheating, the light output will slowly drop with the current as the voltages needed to maintain the arc increases. All this suggests that it is best not to run an arc too long and that it might be a good idea to monitor the voltage across the arc to detect warning signs.

[16] The total light will stay about the same but it will be less concentrated at the tip of the electrode.

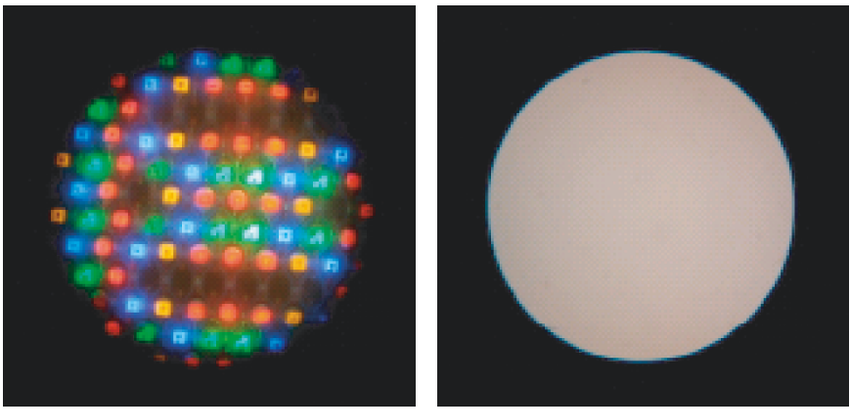


FIGURE 6.21. What an actual, functioning LED microscope source looks like. A close-packed array with four monochrome (470, 525, 590, 620 nm) colors on one matrix.

As each electron passing the depletion region emits one photon, LEDs can be controlled by any current-stabilized electrical source.[17] Depending on what is needed, the LED configuration as well as the control circuit can be easily changed. If only a single LED device is used (e.g., a "white" LED, usually one that couples a blue primary emission with red and green light from blue-excited phosphors), only a single-channel current source is needed and the intensity is controlled by changing the current flowing through the LED. It is more common to use more complex LED structures combining LED dies with different emission wavelengths to obtain either narrow-band light for multi fluorescence or "white light" in bright-field microscopy (Fig. 6.21). Such devices are controlled by a multi-channel current source. By rapidly switching these currents on and off, it is possible to change intensity or emission wavelength on a microsecond or even nanosecond scale. This is a very important feature for short-time scale methods such as fluorescence lifetime imaging measurements (FLIM; Hermann *et al.*, 2001). The switching on this timescale is called pulse mode.

Because the peak emission of a given type of a LED can be shifted by changing the current level, it is often more suitable to operate multi-LEDs in the pulse mode. One sets the peak current to produce the desired output wavelength and then changes the average source brightness by varying the pulse width at a fixed peak current. Although, compared to continuous mode, more total light is available in this way, using a higher current for more than a short pulse will lead to thermal damage. The "damage threshold" current pulse width must be evaluated for each LED.

The spectral output of the LED can be controlled very precisely in this way. The optical output follows the current pulse without significant delay. Pulse-modulation frequencies up to megahertz are possible.

MEASURING WHAT COMES THROUGH THE ILLUMINATION SYSTEM

The procedures for measuring the light throughput of any microscope with a photometer are thoroughly described in a step-by-step manner in the book *Photomicrography* (Loveland, 1970). He even describes making a photometer for such a purpose, but a useful substitute can be made by attaching almost any small photodiode (or even a small "solar cell") to an inexpensive digital voltmeter set on a sensitive current range. Using this, one can measure light in the most obscure locations within the microscope. "Photon bookkeeping" based on such measurements is the only way to pinpoint those parts of the light path where preventable loss is occurring.

Microscopists not interested in building a photometer can obtain one of the commercial units. World Precision Instruments (Sarasota, FL) markets a fiber-optic monochromator and photomultiplier subsystem that can be used to examine light at the intensities present at any location in a confocal optical system. A 50 µm fiber is standard with this system and other vendors are listed in Table 6.3.

Young (1989) described the use of a feedback-controlled LED to generate known amounts of light from small (5–50 µm) sources. Using this system in either the source plane or the image plane, he was able to calibrate the input–output characteristics of a microscope system over four orders of magnitude.

For a measurement of radiance resolved by angle and wavelength simultaneously one must use a professional radiospectrometer such as the CS-1000 made by Minolta. Such a device can provide very detailed information on the quality of an illumination source and the illumination path.

Selective light loss can occur anywhere along the optical path, heat filters, tilted interference filters, and dust windows, as well as obvious lens elements [consider that every lens surface causes the loss of at least 1% of the incident light despite anti-reflection (AR) coatings]. In the past, the transmission characteristics of objectives were seldom displayed in manuals, and even the general characteristics of UV versus non-UV lenses are still often hard to obtain (some figures are listed in Chapters 7, 27, and 29, *this volume*). Popular photography magazines often feature the color bias of various camera lenses, and these show that the color effect of a given AR coating is different for the large NA rays than for those near the optical axis, due to the quality and the optical properties of the lens coating. The AR coating on dust windows may block the transmission of UV or IR illumination. Epi-illumination requires broad transmission in both the illumination and the viewing direction.

The Bare Minimum

Even if one isn't inclined to be a full-time photon sleuth, it is wise at least to monitor the performance of the illumination system under a few commonly used standard conditions. For example, one should monitor how much light emerges from a favorite high-NA objective when it is set up for Köhler illumination with a particular filter cube and with the field diaphragm set to just illuminate the full field of this objective. This can be measured with a 1 cm^2 photometer paddle held in front of the objective. Assuming that one does not want to oil-couple the sensor to the objective, make

[17] On the other hand, use of a voltage-stabilized source will almost certainly damage these devices. At a fixed voltage the current increases with temperature, causing thermal runaway.

sure that the front of it is free from oil so that the fraction of the light escaping into the air is set only by total internal reflection from the flat front element (not an ideal situation but at least one that is repeatable). Then do the same with the most commonly used low magnification lens and maybe a couple of different filter cubes. Changes in these numbers will warn of misalignment, dust, aging arc bulbs, damaged filters, or help one determine the final resting place of that bit of paper that fell down inside.

An alternative to the photometer paddle is an Ulbricht sphere (also called an integrating sphere). Using an Ulbricht sphere, there is no problem with rays being reflected by the surface of the detector because the entrance of the detector is just a hole. Using this device, it is easy to measure what fraction of light reaches the specimen. On an upright microscope, remove the condenser and the *xy*-stage and mount the Ulbricht sphere below the objective with the entrance hole at the specimen plane. It may help to use the halogen lamp with the bright-field contrast in reflection to align the parts to each other. Mount the lamp of interest at the reflection port for illumination. All the light passing the objective is captured by the sphere. Table 6.2 shows the optical power delivered to the specimen plane measured in this way for various light sources and for two objectives with different fields of view.

TABLE 6.2. Optical Power of Different Light Sources in the Specimen Plane

Filterset No. Used	Excitation Wavelength (pass width) in nm	Examples for Fluorescence Dyes	HBO103W2	XBO75	LEDs	HAL100 (at 12 V)
			Optical Power [mW]			
Objective PlanNeoFluar 40×/0.75, field of view 0.625 mm diameter						
#2	365 (50)	DAPI, Hoechst33342	30.8	0.1	4.4 Nichia 3 W 365 nm	0
#47	436 (20)	CFP, ChromomycinA	10.5	3.5	1.4 Luxeon 3 W 450 nm	0.2
#9	450–490	GFP, Fluorescein	6.4	12.7	1.9 Luxeon 1 W 470 nm 4.8 Luxeon 3 W 470 nm 10.0 Luxeon 3 W 450 nm	3.2
#46	500 (20)	Calcium Green, YFP	1.6	4.4	0.4 Luxeon 1 W 505 nm 1.5 Luxeon 3 W 505 nm	1.5
#14	510–560	RhodamineB	20.2	12.7	1.3 Luxeon 1 W 530 nm 2.4 Luxeon 3 W 530 nm 0.1 Luxeon 1 W 505 nm	7.1
#20	546 (12)	Cy3, Rhodamine	11.1	2.8	☹	1.4
#26	575–625	Cy5	125.0	9.7	0.5 Luxeon 1 W 590 nm	8.3
Objective fluar 10×/0.5, field of view 2.5 mm diameter						
#2	365 (50)		61.4	3.4	8.5 Nichia 3 W 365 nm	0
#47	436 (20)		43.9	10.5	3.4 Luxeon 3 W 450 nm	1.8
#9	450–490		27.2	33.8	4.8 Luxeon 1 W 470 nm 11.1 Luxeon 3 W 470 nm 23.0 Luxeon 3 W 450 nm	11.1
#46	500 (20)		8.5	11.7	1.5 Luxeon 1 W 505 nm 4.3 Luxeon 3 W 505 nm	4.5
#14	510–560		79.0	36.7	2.8 Luxeon 1 W 530 nm 4.0 Luxeon 3 W 530 nm 0.9 Luxeon 1 W 505 nm	22.6
#20	546 (12)		44.2	8.3	☹	4.2
#26	575–625		243.1	30.1	2.7 Luxeon 1 W 590 nm	30.1

The different filter sets were chosen to show a representative profile of the optical power of the light sources at different wavelengths. The bandpasses of filter sets #9 and #46 lie between two prominent lines of the HBO103W2. The XBO75 is much more radiant. The optical power of the HAL100 is between one third and one half of the continuum of the HBO103W2. This is sufficient to excite the brightest dyes. We have made preliminary measurements of two examples for LED-based sources. In each case, a single 1 W Luxeon emitter was used with a single collector lens with no further alignment. This means that the values for the LEDs in Table 6.2 represent a minimum for the optical power at the specimen plane using only a single, 1 W die. With a more radiant emitter, or more individual dies and proper collecting optics, the optical power at the specimen plane can easily be increased by a factor of 4 to 8. This would put the LED radiance between the HAL100 and the arc sources.

TYPES OF CONFOCAL MICROSCOPES THAT CAN USE NON-LASER LIGHT SOURCES

The notion that confocal microscopes must use laser illumination is widespread because most commercial confocal microscopes are single-beam instruments (Leica, Nikon Real Time, Olympus, Zeiss), and these currently use only laser illumination. In fact, none of these microscopes even make a provision for the user to connect a non-laser light source for use in the confocal mode.

Nevertheless, it is not true that single-beam confocal microscopes **require** laser light. Minsky (the inventor of the first confocal microscope) used a zirconium arc illuminator in the functional prototype stage-scanning microscope he built in the 1950s (Minsky, 1988). Many current commercial disk-scanning confocal microscopes come only with non-laser sources because only such sources can provide the broad beam needed to simultaneously illuminate the many confocal apertures in the field of view.

Using a tandem-scanning confocal microscope with a high-NA water-immersion objective, transparent ciliate protozoa such as paramecium and vorticella can easily be viewed by eye swimming in water in the confocal BSL mode. BSL images are formed using the light that is scattered by the index of refraction difference between organelles and water. By carefully adjusting the rotation speed of the aperture disk, one can view the rapidly beating cilia with stroboscopic illumination. A field of beating cilia viewed *en face* appears as dots (cross-sections of the cilia) slowly moving in circles. Though easily viewed by eye, this motion is difficult to capture electronically or photographically because the brain is able to extract meaning out of successive images with the slight trailing-edge blur that renders electronically captured single images meaningless.

Tandem Scanning: Basic Description

The tandem-scanning mechanism consists of a symmetrical, spinning Nipkow aperture disk at the intermediate image plane of the objective. Thousands of apertures arranged in spirals both send beams to be focused on the object and sample the light returning to form the intermediate image. The double-sided optical system developed by Petran uniformly illuminates the excitation area of the disk that is to be imaged onto the object. Through a series of mirrors and beam-splitters, the image returning from the spots in the specimen is focused onto the lower surface of the opposite side of the disk where the in-focus light passes through a mirror image conjugate set of holes (Fig. 10.4, *this volume*). This series of mirrors and beam-splitters permits the illuminating and sensing apertures to be distinct, thereby preventing light reflected by the solid part of the disk on the illumination side from reaching the imaging side of the system.

The light-source optics must fulfill two functions. They must illuminate the area of the disk that will be utilized to form the final image (usually 1 to 2.5 cm diameter). In addition, this light must leave the disk with the correct angle of divergence to fill the BFP of the objective lens. On disks with very small holes, diffraction at the holes will usually ensure that the second condition is satisfied, so the problem becomes how to get the maximum amount of light incident on the active area of the disk. This is important because, as only 1% to 2% of the disk is open, the system is very wasteful of light. Careful matching of a large-NA collector lens and an optimized condenser is needed to ensure that sufficient light reaches the specimen to form an image in a reasonable time.

Single-Sided Disk Scanning: Basic Description

In a single-sided, disk-scanning optical system, the spinning Nipkow aperture disk is again located at the intermediate image plane of the objective but, because the beam-splitter is above the disk, the same apertures now serve as both sources and pinholes (Fig. 10.4, *this volume*). The aperture disk is tilted and covered with "black chrome" to reduce reflections of the source from reaching the eyepiece. Furthermore, a polarizer placed in the illumination path, a quarter waveplate above the objective, and an analyzer at the eyepiece form an "anti-flex" system to further reduce the effect of disk reflections.[18] Because it lacks any mirrors between the disk and the objective, the single-sided system is self-aligning.

Boyde and Petran (1990) directly tested the light budget in the two types of disk confocal systems and found little difference in light efficiency, though the tandem system appeared to have better contrast.

EXPOSURE TIME AND SOURCE BRIGHTNESS

In conventional microscopy, data for every point in the image is collected in parallel. This leads to a short capture time compared to any scanning process. The capture time is only limited by the time needed to fill the pixels in the CCD camera. Depending on the magnification, the fluorescent dye concentration, and the quality of the CCD itself, recording times vary from a few milliseconds to several seconds. Living cell observations with moving specimens are no problem. Figure 6.22 shows comparison pictures of cells taken with an HBO arc lamp and an LED-based source. Although the lower brightness of present LEDs required a recording time about four times longer than that needed with the HBO source, the quality of the images is comparable.

In scanning microscopy, the image is formed by scanning a point or a group of points over the surface to be imaged, and this scanning process takes a finite amount of time. If a raster scan is used, the image is completed when the raster is finished, and so the confocal microscope is a sampling system in both time and space. To view specimens that move or change accurately, the scan time must be short compared to the expected rate of change. This requires not just a fast scanning system but also a light source

[18] While at the same time, reducing light throughput by about two thirds.

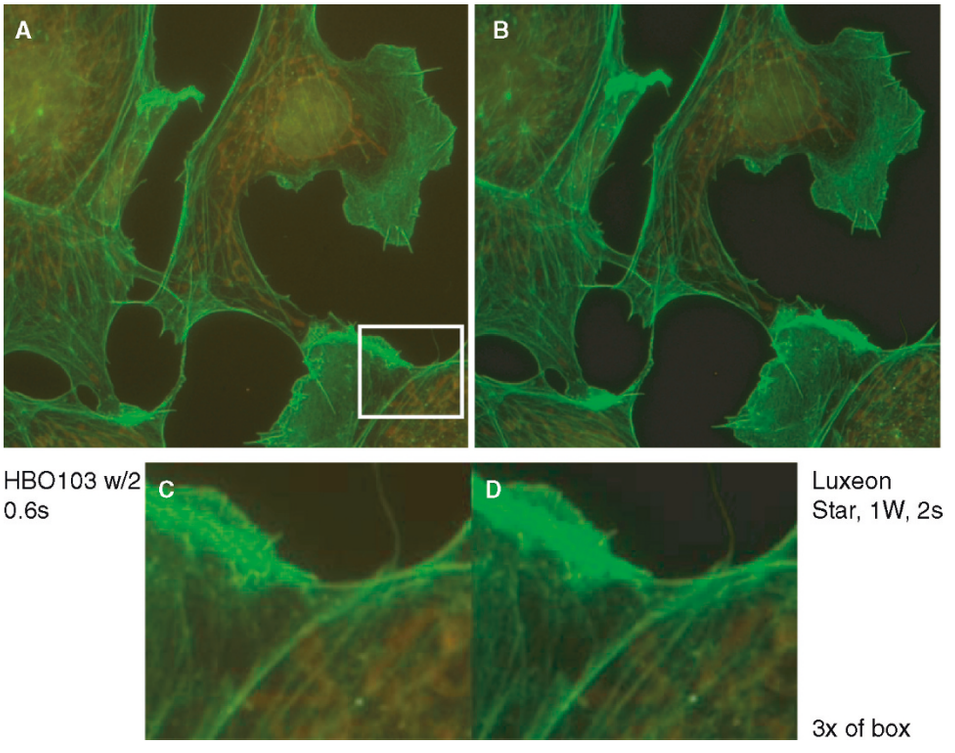


FIGURE 6.22. Fluorescent actin filaments imaged using HBO and LED sources. (A) HBO103W/2, exposure 600 ms, (B) Luxeon Star LED, 1 W, exposure 2 s. In the enlarged insets, one can see that some of the broadband light from the HBO gets past the excitation filter to excite the red MitoTracker Red dye as well as the Bodipy FL phallacidin, green dye, while the narrowband light from the LED does not do so. (Specimens are fixed BPAE cells stained on a Molecular Probes FluoCells prepared #1 slide. Imaged with an Axioplan 2, 63× /1.4 oil objective, Axiocam HrC, Filterset #9.)

bright enough to elicit from the specimen sufficient signal to make a usable image during the available scan time. In other words, shorter scan times need brighter sources. In practice, it has been the inability of arcs and LED-based sources to match the brightness of the laser that has prevented disk-scanning instruments from seriously challenging laser instruments for viewing low-intensity fluorescent specimens.

Because the rate at which signal can be derived from a fluorescent specimen depends fundamentally on the rate at which excitation photons impinge on the imaged area, some idea of the relative merits of the two approaches can be gained by measuring this quantity. When comparing disk- and laser-scanning data rates, it is important to normalize for the size of the area illuminated on the specimen from which data are being recorded because the former collects data in parallel while the latter collects only from one point at a time. Given comparable pinhole sizes and optical efficiencies, the crucial factor for a disk-scanning microscope is the rate at which the narrow-band, excitatory radiation strikes the area of the specimen that can be imaged by a high-quality imaging detector, such as a cooled CCD. A 512×512 CCD operating at the total magnification needed for proper Nyquist sampling of 0.25 µm resolution data (i.e., 0.1 µm pixels at the specimen; Chapter 4, *this volume*), images an area about $50 \times 50\,\mu m^2$ on the specimen.

In 1990, the illumination systems of the commercial, double-sided disk-scanning confocal microscopes could concentrate only 2 to 3 µW of narrow-band light into a 50×50 µm area, while the single-sided instruments could produce 6 µW (personal communication, V. Cejna, Technical Instruments, San Jose, CA). By contrast, the laser sources on the confocal laser-scanning microscope (CLSM) can easily deliver 100× more power (without producing significant singlet-state fluorescence saturation!) and can consequently produce data from (and bleaching of!) the specimen at a proportionally higher rate. This improvement is only partially offset by the fact that the CCD detector is about 3 to 6 times more quantum efficient than the photomultiplier tube used in the laser systems.

On the other hand, because disk-scanning instruments use many simultaneous apertures, the absolute limit on data acquisition presented by singlet-state fluorescence saturation (Chapters 2, 16, and 21, *this volume*) is far less of a limitation on these instruments. As a result, if higher radiance non-laser sources are developed and low-read-noise, electron-multiplier CCDs (EM-CCDs) replace the conventional CCDs now commonly used, the disk-scanning approach could eventually produce even higher useful frame rates than single-beam laser instruments and do so with the same number of photons from the specimen.

Another way to speed up the data rate is to use larger CCD sensors (1000^2). These would permit parallel detection of data from a larger area of the specimen while still maintaining the same pixel size. Although this strategy would increase the effective data acquisition rate by an amount proportional to the number of sensors in the detector, it would do so only at the price of viewing ever larger fields of the specimen. In other words, while it can be useful to survey larger fields in the same amount of time, it is not the same thing as increasing the source brightness or optical efficiency to permit imaging a particular cell more rapidly.

As current disk-scanning systems utilizing better illumination sources and improved optics claim power levels at the specimen that are 5 to 10 times higher than those measured in 1990, the balance may soon shift to the disk scanners.

FUTURE TRENDS

Viewed in one way, the arc lamps produce enough light right now to saturate or bleach common fluorescent dyes. The weak point of these sources is the difficulty of rapidly controlling operating parameters such as emitted intensity or spectral distribution. As these sources have been optimized over a period of many years, a quantum leap in performance is unlikely. On the other hand, arcs using different gas mixtures and electrode materials are constantly being developed and small improvements are likely to continue. The same is true for tungsten–halogen sources.

Viewed in another way, 100 years after the first use of Hg arcs in microscopy, and 40 years after the advent of the LED, microscopy has a new light source with many exciting possibilities. LEDs have all the features that arc lamps lack and they will soon be efficient enough to be run on a small battery. Although their weak point is still their marginal intensity, if one looks at the LED optical efficiency line over the last few years (Fig. 6.23), one notices a very interesting trend. LED brightness is projected to increase by about a factor of 3 in the next 5 years. Efforts are under way to use different growth mechanisms to produce LED die crystals with a geometry that decreases the loss of light through internal reflection. If this effort is successful, LEDs should be able to succeed in all fluorescence applications.

Improvements in the coupling between the LEDs and the microlens array and diffractive optical elements will increase the efficiency of the collection optics. Molded plastic technology is becoming ever more flexible in being formed to satisfy the requirements of this application. The brightness of a multi-color source mounted as a single flat array, such as that shown in Figure 6.21, could be increased by 3 or 4× by coupling together light from three to four planar sources, each emitting at a different wavelength, using an arrangement of dichroics and prisms similar to that used to separate R, G, and B light in a three-chip color CCD sensor. This would allow each LED color to be emitted at every location in the BFP. Three times as many dies would increase total light output by 300%.

Because LEDs have **no** emission at either 1/2 or 2× the design wavelength, it should be possible to develop more inexpensive and efficient light-source/filter sets for particular fluorescent dyes.

Somewhat farther over the horizon is the promise of organic LEDs (OLEDs). First developed in the early 1990s, OLEDs are built of organic molecules and light is generated by exciting the molecular orbitals of chromophore groups. Organic molecules sitting in a plastic lattice can be formed into almost any shape one can imagine. The brightness of these sources is now similar to that of conventional LEDs 20 years ago (Zhou, 2001). Although the operating lifetime of these sources is still very short, this technology is important as a potential area-display for consumer goods, such as video cellular phones, so substantial improvements may occur.

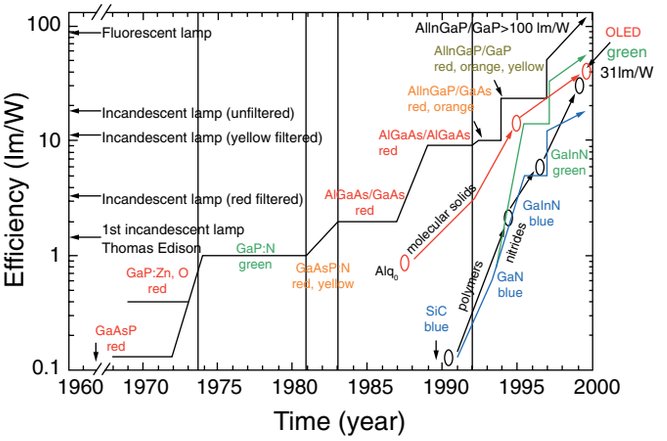


FIGURE 6.23. Development of the optical efficiency of LEDs in the last 40 years.

Significant improvements in arc sources (~10×) could be realized by using a modified elliptical collector (Luthjens *et al.*, 1990) with one of the newer Xe/I sources and by optimizing the magnification of the illumination optics to concentrate more light from the brightest part of this source into the 50 µm field covered by a 512 × 512 CCD.

Another development that should be mentioned is the emergence of a number of companies providing stand-alone light sources for use in microscopy (Table 6.3). Although initially these tended to be fiber-optic illuminators suitable for use with dissecting microscopes, more recently sources suitable for use in high-performance epifluorescence microscopy have been offered. Besides utilizing optimized arcs in elliptical collector mirrors and high-speed filters wheels for rapidly shifting the output wavelength, they also provide fiber-optic light scrambling.

TABLE 6.3. Companies Making Stand-Alone Microscopy Light Sources

Company	Model	Type of Source	Rapid λ Shifting?	Wavelength range, nm	Interfaces to . . .	URL
API	Uniform light source	HBO100/2	Yes	320–700	Sold only w/system	http://www.api.com/
Dolan-Jenner	Cold light sources	Arcs, e.g., metal halide	No	UV–VIS	Optical fiber	http://www.dolanjenner.com
EXFO	X-Cite 120PC	120 W metal halide	No	UV–VIS	Custom coupling optics	http://www.exfolifesciences.com
Illumination Technologies	Cold light sources	Halogen	No	VIS	Optical fiber	http://www.illuminationtech.com
Schott	Cold light sources	Arcs, e.g., metal halide	No	UV–VIS	Optical fiber	http://www.schott.com
StockerYale	Cold light sources	Halogen	No	VIS	Optical fiber	http://www.stockeryale.com
Sutter Inst	Lambda DG4	175 W XBO based	Yes, 1.2 ms	300–700	Optical fiber → flexible	http://www.sutter.com/
Till Photonics	Polycrome V	150 W XBO based	Yes, 400 nm/ms	320–680	Optical fiber → flexible	http://www.till-photonics.de
Technical Video Ltd	Fiber optic light scrambler	HBO100W/2	No	320–800	Optical fiber → All	http://www.technicalvideo.com

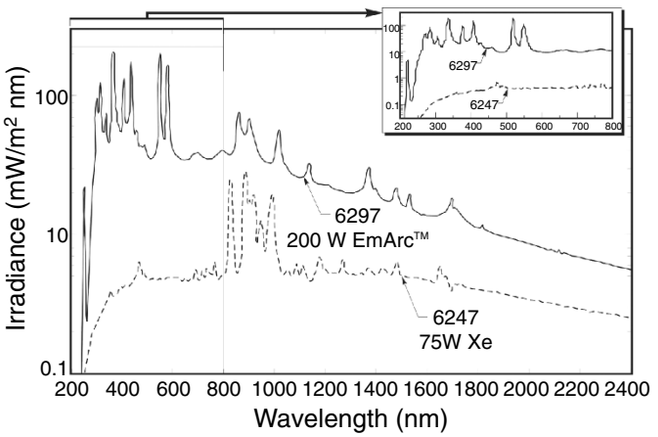


FIGURE 6.24. Spectral distribution of a 200 W EmArc, mercury–halide arc source and a 75 W xenon arc lamp (*dashed line*) 200 to 2400 nm. (Spectra kindly provided by Oriel/Newport, Irvine, CA.)

In a way, the really good news is that there is a great demand for high brightness light sources in areas of the economy that have considerably more market power than microscopy. Perusal of the Internet will show a wide variety of ingenious sources responding to both the general need to get more light for fewer watts of electric power and the more specific need to keep the source size small. The digital projectors used at scientific meetings are just the early scouts of a digital revolution about to overtake the movie industry. These projectors will need bright sources. Figure 6.24 shows the performance of one of the early candidates, a 200 W enhanced metal arc source that uses a mixture of gasses to produce an order of magnitude increase in light output in the visible, compared to a short arc 75 W Xe arc (USHIO, Inc. Cypress, CA). Although, at over US$2000 each, it is unlikely that many microscopists will use such sources immediately, there is every reason to think that eventually prices will come down.

ACKNOWLEDGMENTS

The authors thank Nancy Fernandez and Roger Milvid at the Oriel Division of Newport, Inc., for providing us with the spectra and diagrams used in Figures 6.1, 6.4, 6.5, 6.9, 6.13, 6.17, and 6.23; Volker Haerle at OSRAM Optical Semiconductors for permission to show Figure 6.11, and Anton Moffat at Carl Zeiss Jena, GmbH, for his support.

REFERENCES

Born, M., and Wolf, E., 1980, *Principles of Optics*, 6th ed., Pergamon Press, Oxford, England.

Boyde, A., and Petràň, M., 1990, Light budgets, light and heavy losses: One-or-two sided tandem scanning (real time, direct view, confocal microscopy), *J. Microsc*. 160:335–342.

Braun, D., and Merrin, J., 2003, Exciting brightfield fluorescence with power LEDs, Center for Studies in Physics and Biology, Rockefeller University, 1230 York Avenue, New York, NY, 10021, p. 22.

Briers, J.D., 1993, Speckle fluctuations and biomedical optics: Implications and applications, *Optical Eng*. 32:277–421.

De Basio, R., Bright, G.R., Ernst, L.A., Waggoner, A.S., and Taylor, D.L., 1987, Five-parameter fluorescence imaging: Wound healing of living Swiss 3T3 cells, *J. Cell Biol*. 105:1613–1622.

Ellis, G.W., 1979, A fiber-optic phase-randomizer laser for microscopy by laser, *J. Cell Biol*. 83:303a.

Gerritsen H.C., van der Oord, C., Levine, Y., Munro, I., Myring, W., Shaw, D., and Rommerts, F., 1992, Synchrotron radiation as a light source in confocal microscopy of biological processes. In: Time-Resolved Spectroscopy for Biochemistry III, Proc. SPIE 1640 (J.R. Lakowicz, ed.), SPIE—The International Society for Optical Engineering Press, Bellingham, Washington, pp. 754–760.

Hard, R., Zeh, R., and Allen, R.D., 1977, Phase-randomizer laser illuminator for microscopy, *J. Cell Sci*. 23:335.

Hell, S., Witting, S., Schickfus, M.V., Wijnaendts van Resandt, R.W., Hunklinger, S., Smolka, E., and Neiger, M., 1991, A confocal beam scanning white-light microscope, *J. Microsc*. 163:179–187.

Herman, B., 1998, *Fluorescence Microscopy*, 2nd ed., BIOS Scientific Publishers, Oxford, 1998.

Hermann, P., Maliwal, B.P., Lin, H.J., and Lakowicz, J.R., 2001, Frequency-domain fluorescence microscopy with LED as a light source, *J. Microsc.* 203:176–181.

Hiraoka, Y., Sedat, J.W., and Agard, D.A., 1990, Determination of the three-dimensional imaging properties of an optical microscope system: partial confocal behavior in epi-fluorescence microscopy. *Biophys. J.* 57:325–333.

Inoué, S., 1997, *Videomicroscopy, The Fundamentals*, 2nd ed., Plenum Press, New York.

Kam, Z., Jones, M.O., Chen, H., Agard, D., and Sedat, J.W., 1993, Design and construction of an optimal illumination system for quantitative widefield multi-dimensional microscopy. *Bioimaging* 1:71–81.

Loveland, L., 1970, *Photomicrography*, John Wiley and Sons, New York.

Luthjens, L.H., Hom, M.L., and Vermealen, M.J.W., 1990, Improved metal compound ellipsoidal-spherical mirror condenser for xenon short-arc lamp, *Rev. Sci. Inst*. 61:33–35.

Minsky, M., 1988, Memoir on inventing the confocal scanning microscopy, *Scanning* 10:128–138.

Perduijn, A., de Krijger, S., Claessens, J., Kaito, N., Yagi, T., Hsu, S.T., Sakakibara, M., Ito, T., Okada, S., 2004, Light output feedback solution for RGB LED backlight applications. (Application note available on the Lumiled home page.)

Petràň, M., Hadravsky, M., and Boyde, A., 1985, The tandem scanning reflected light microscope, *Scanning* 7:97–108.

Piller, H., 1977, Microscope Photometry, Springer-Verlag, New York, p. 253.

Reynolds, G.O., DeValis, J.B., Parrent, G.B. Jr., and Thompson, B.J., 1989, Parametric design of a conceptual high-resolution optical lithographic printer, In: *The New Physical Optics Notebook*, SPIE, The International Society for Optical Engineering Press, Bellingham, Washington, pp. 549–564.

Schubert, F., 2003, *Light-Emitting Diodes*, Cambridge University Press, New York.

Steen, H.B., and Sorensen, O.I., 1993, Pulse modulation of the excitation light source boosts the sensitivity of an arc lamp-based flow cytometer, *Cytometry* 14:115–122.

Steigerwald, D.A., Bhat, J.C., Collins, D., Fletcher, R.M., Holcomb, M.O., Ludowise, M.J., Martin, P.S., Rudaz, S.L., 2002, *IEEE Journal of Selected Topics in Quantum Electronics*, Lumileds Lighting, San Jose, California, 8:310–320.

van der Oord, C.J.R., 1992, Synchrotron radiation as a light source in confocal microscopy, *Rev. Sci. Instrum*. 63:632–633.

Woodlee, R.L., Fuh, M-R.S., Patonay, G., and Warner, I.M., 1989, Enhanced DC arc-lamp performance for spectroscopic application, *Rev. Sci. Instrum.* 60:3640–3642.

Young, I.T., 1989, Image fidelity: Characterizing the image transfer function, *Methods Cell. Biol*. 30:1–45.

Zhou, X., Pfeiffer, M., Huang, J.S., Blochwitz-Nimoth, J., Qin, D.S., Werner, A., Drechsel, J., Maennig, B., Leo, K., 2002, Low-voltage inverted transparent vacuum deposited organic light-emitting diodes using electrical doping, *Appl. Phys. Lett.* 81:922–924.

7

Objective Lenses for Confocal Microscopy

H. Ernst Keller

INTRODUCTION

No other component of the microscope is as instrumental in determining the information content of an image as the objective. The resolved detail, the contrast at which this detail is presented, the depth through the object from which useful information can be derived, and the diameter of the useful field are all limited by the performance of the objective. All other imaging components, such as relay optics, Telan systems, tube lenses and eyepieces, or projectives may have some corrective function but otherwise serve only to present the image generated by the objective to the detector in such a way that most of its information content can be recorded without degradation.

While this is true for any conventional microscope, it is particularly true for confocal scanning, where the objective becomes the condenser as well and needs to combine a high degree of optical correction with good throughput and a minimum of internal stray light or photon noise generation.

In general, the demands on the performance of the objective for confocal scanning are identical to the needs for demanding video microscopy, photomicroscopy, densitometry, photometry, spectrophotometry, and morphometry. However, this does not mean that confocal microscopy will not eventually call for special new lenses in which certain corrections may be sacrificed to enhance specific capabilities. In biological applications involving living cells, high photon efficiency is so important that it may be worth accepting a reduction in field size and chromatic correction in order to achieve the highest possible transmittance at a reasonable working distance by using a minimum number of lens elements. Another problem is the loss of correction for spherical aberration as an oil-immersion lens is focused deep into an aqueous specimen. High numerical aperture (NA) water-immersion objectives with correction collars for coverslip thickness variations, refractive index variations in the medium, or temperature-dependent index changes have become the lenses of choice for live-cell studies. Because of the difficulty manually rotating the correction collar while actually observing living specimens, correcting spherical aberration may require the addition of either deformable mirror correctors or motor-driven correction optics mounted later in the optical path (see also Chapter 20, *this volume*).

Because the critical demands of light microscopy and confocal scanning microscopy have increasingly forced the performance of objectives to approach their theoretical limits, a brief refresher on aberrations, design concepts, materials, etc., may be in order. An overview of optical aberrations in refractive systems — both inherent and induced by improper use of the microscope — and the basic performance characteristics of the different generic types of objectives will be presented.

The basic design concepts of microscope optics — finite versus infinite image distance, compensating versus fully corrected systems — need to be understood to properly match optical components and their properties for specific applications. Optical materials, cements, and anti-reflection coatings all influence the performance of the objective. Immersion liquids, the coverslip, and the mounting medium are all part of the optical train and can strongly affect the quality of the final image. We will try to put all of this into qualitative perspective, particularly as it pertains to confocal scanning. Additional information on the optics for microscopy can be found in a review paper by Inoué and Oldenbourg (1995) and in a review article on objective lens design by Shimizu and Takenaka (1994).

A detailed, quantitative comparison of the performance of different microscope objectives must be based on accepted criteria and precisely defined testing methods. Unfortunately, although the major microscope makers have developed their own proprietary methods, no independent, fully "objective" test procedure is readily accessible to users to quantify all performance data of an objective. (Juskaitis describes a sophisticated means for interferometric testing of objectives in Chapter 11, *this volume*.)

How, then, should the user of a confocal microscope judge the performance of an objective? Measurement and analysis of the real, not just theoretical, point spread function (PSF) of an objective, or better, of the complete imaging system, is critical for three-dimensional (3D) deconvolution. Observations of subresolution pinholes in an evaporated silver or aluminum coating are adequate to judge spherical aberration, astigmatism, coma, and flatness in transmitted light but do not work well in the epi-mode. Fluorescent beads in the 0.1 µm range are suitable replacements, but the fluorescence fades. Diatoms have long been a standard because of their precise and regular spacing and because they can be viewed in the backscattered (BSL, sometimes referred to as reflected) light mode or after embedment in fluorescent dye (Chapter 35, *this volume*). For example, how do we determine, at least qualitatively, how an image is degraded — by focusing deep into a specimen or by pairing optical components that are not matched? These are all challenges that are not yet fully resolved. They point to a need for detailed testing procedures that cover all aspects of the optics from source to detector.

Still, with our ability today to ray-trace lenses for their geometrical optical performance and to calculate wave-front aberrations, PSF, and intensity ratios through the Airy disk, most

H. Ernst Keller • Carl Zeiss, Inc., One Zeiss Drive, Thornwood, New York 10594

Handbook of Biological Confocal Microscopy, Third Edition, edited by James B. Pawley, Springer Science+Business Media, LLC, New York, 2006.

objectives now offered are close to diffraction limited, at least in the center of the image field. However, field size and optical performance at the periphery of the field are also especially important in beam-scanning confocal microscopy.

Long-term mechanical, thermal, and chemical stability of objectives used with lasers are a function of manufacturing tolerances and materials chosen. Submicron tolerances for the centration and spacing of lens elements in sophisticated, high-power objectives call for careful, gentle treatment by the user. A minor mechanical shock may generate enough stress on a lens element to seriously reduce the objective's performance in polarized light, in differential interference contrast (DIC), or in critical confocal scanning.

ABERRATIONS OF REFRACTIVE SYSTEMS

The ideal "diffraction-limited" objective generates a 3D PSF from an infinitely small object point. A cross-section perpendicular to the optical axis through the center of the PSF is the Airy disk, as shown in Figure 7.1(A). The diameter d_{Airy} of the first dark ring, generated by destructively interfering, diffracted wavefronts [Fig. 7.1(B)] is

$$d_{\text{Airy}} = \frac{1.22\lambda}{\eta \sin\alpha}$$

where λ is the wavelength of light, η is the refractive index of medium between the object and the objective, and α is the half-angle of the collected rays from the object point. The Rayleigh (or Abbe) criterion sets the limit for the smallest resolvable distance d between two points at one-half this diameter or,

$$r_{\text{Airy}} = \frac{1.22\lambda}{2\ \text{NA}}$$

or the radius of the Airy disk, where $\eta \sin\alpha$ is the NA. This point-to-point resolution for a given objective in turn determines the magnification required to enable any given detector to record all the resolvable details. Taking the spacing of the rods in the human retina as setting the limit, the total required magnification for visual observation — the so-called useful magnification — becomes about 500 to 1000 times the NA of the objective, while for digital recording we enlarge the Airy disk to 4 to 5 times the pixel dimension of the detector (Nyquist sampling, see Chapter 4, *this volume*).

Defocusing

Defocusing will change the size and intensity distribution of the unit image point (Fig. 7.2). Because defocusing and depth of field are closely related, let us take a look at the 3D PSF or "image body" of the "diffraction limited" objective (Chapter 1, *this volume*).

Figure 7.3 again shows a cross-section perpendicular to the optical axis in the optimally focused image/object plane, which is, of course, the intensity distribution of the Airy disk, while Figure 7.4 represents a section along the optical axis and its intensity distribution (actually, the log of the intensity, to make it more visible). Defocusing results in alternating bright and dark spots along the axis of the Airy disk (Fig. 7.2). The extension of the central bright body along the axis is $4\lambda/(\text{NA})^2$, but we can detect a change in the image with a defocus of only $\pm\lambda/(\text{NA})^2$ (the Rayleigh/Abbe unit in the z-direction). We call this the wave-optical depth of field (Figs. 7.3 and 7.4).

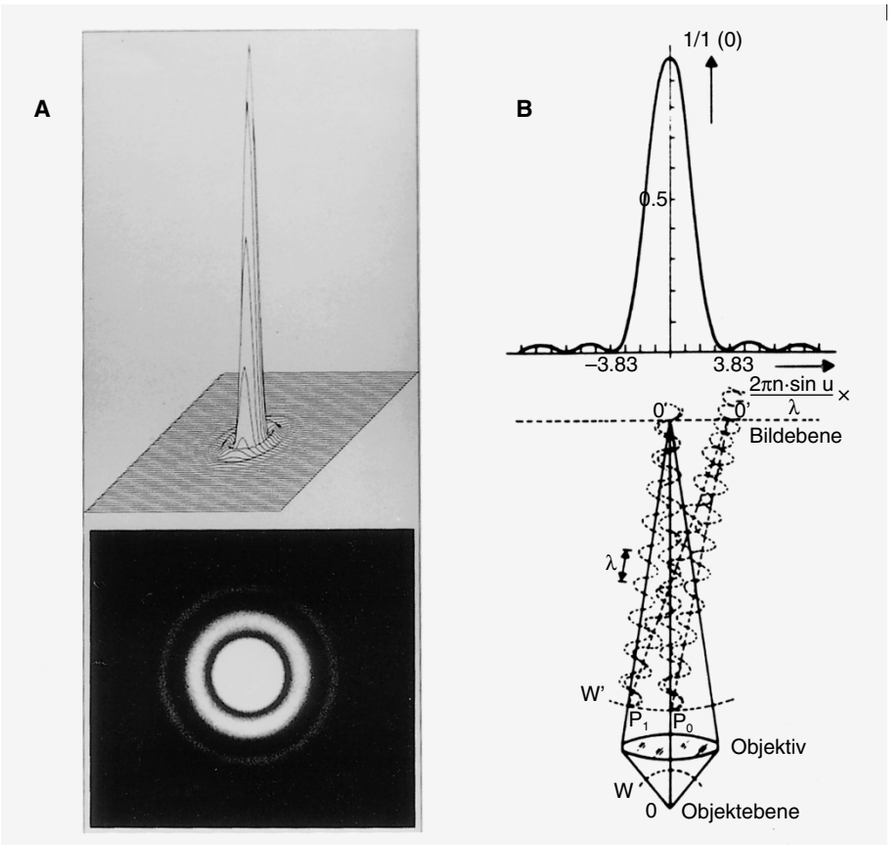


FIGURE 7.1. (A) Airy disk and its intensity distribution. (B) Generation diagram and profile of the Airy disk or unit image.

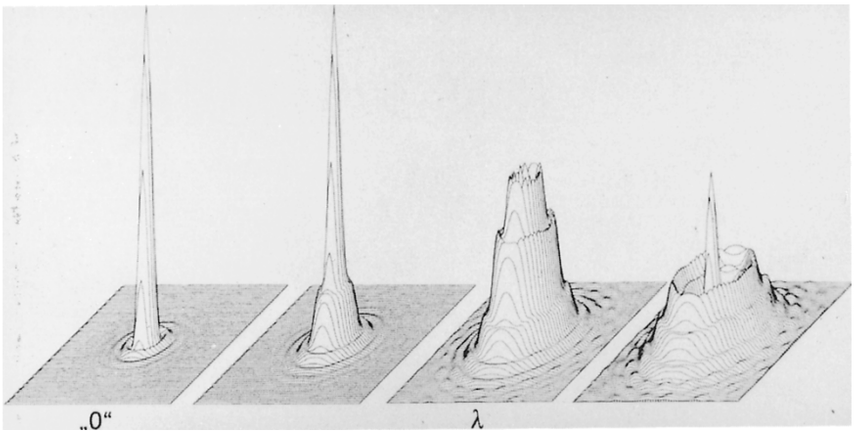


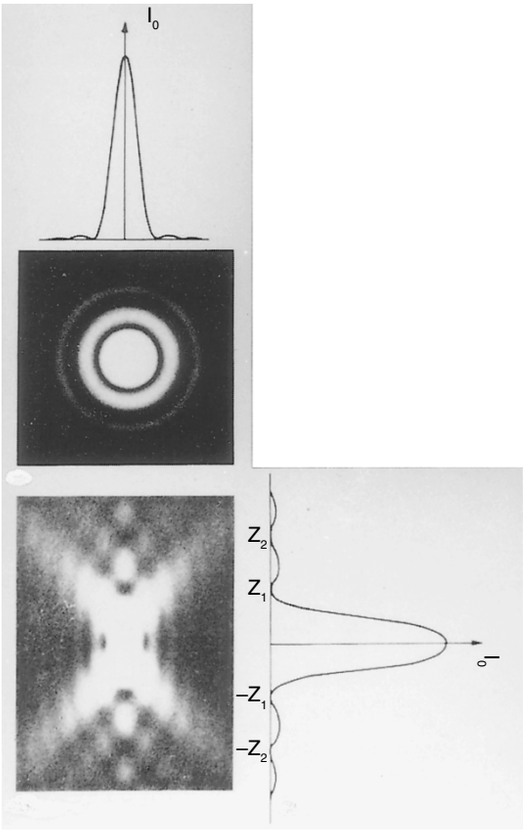
FIGURE 7.2. Changes in intensity distribution with focus changes.

Deviations from the "diffraction-limited" point image caused by lens aberrations can be grouped into either wavelength-independent (monochromatic) or chromatic aberrations.

Monochromatic Aberrations

Spherical Aberration

This axial aberration is generated by non-spherical wavefronts produced by the objective itself or by improper use of the objective, in particular, failure to use the correct coverglass thickness or maintain the designated tube length or the presence of substances between the objective and the focus plane having the wrong η (Chapter 20, *this volume*). Spherical aberration has the effect that paraxial rays have a different focal length from peripheral rays, and a blurring of the image body produces an asymmetrical intensity change when defocusing by $\pm\Delta Z$ (Fig. 7.5 and Fig. 20.3, *this volume*). Spherically ground and polished lenses have a shorter focal distance for peripheral rays than for paraxial rays.



FIGURES 7.3 and 7.4. Horizontal (focal plane) and vertical (optical axis) cross-section through unit image body.

Spherical aberration can be optimally corrected only for accurately specified object and image distances. It can, therefore, be easily induced by improper tube length caused by introduction of optical elements into the converging beam path of finitely designed systems or by the use of improper "windows," such as non-standard coverslips or immersion oil of non-specified refractive index between object and objective. Figure 7.6 shows the changes in size and intensity distribution through the image point with increasing penetration into an object in watery medium with a planapochromat 63×, NA 1.4 oil. The effect of this induced spherical aberration on the image point needs to be considered and either corrected for or at least understood before confocal microscopy can be applied optimally to 3D reconstruction (see Chapter 24, *this volume*). More specifically, let us consider how the image quality of another objective designed for diffraction-limited performance (the Plan-Neofluar 40×, NA 1.3 oil) deteriorates when focusing 10 µm into an aqueous medium.

At the water–coverslip interface, spherical aberration is generated, which shifts the focus of peripheral rays above the optimal focus of paraxial rays [Fig. 7.7(A,B)].

Figure 7.8 illustrates the change in intensity of a fluorescing object detected with a pinhole equal to the diameter of the Airy disk (1 Airy Unit) at 543 nm as a function of different penetration depths or focus changes, indicated in both micrometers and Rayleigh units (RE) into water. For depths of 0 µm, 5 µm, 10 µm, and 20 µm, the signal intensity at the pinhole detector drops dramatically along with deteriorating depth discrimination. Minor changes in refractive index are generated by changes in salt concentration, temperature, and differences in molecular structure. All these can induce positive or negative spherical aberration.

With increasing NA, changes in the thickness or the refractive index of the "window" between the object and the objective becomes critical, particularly with "dry" objectives. In the low-power, low-NA objective with relatively higher $NA_{\text{imageside}}$ where

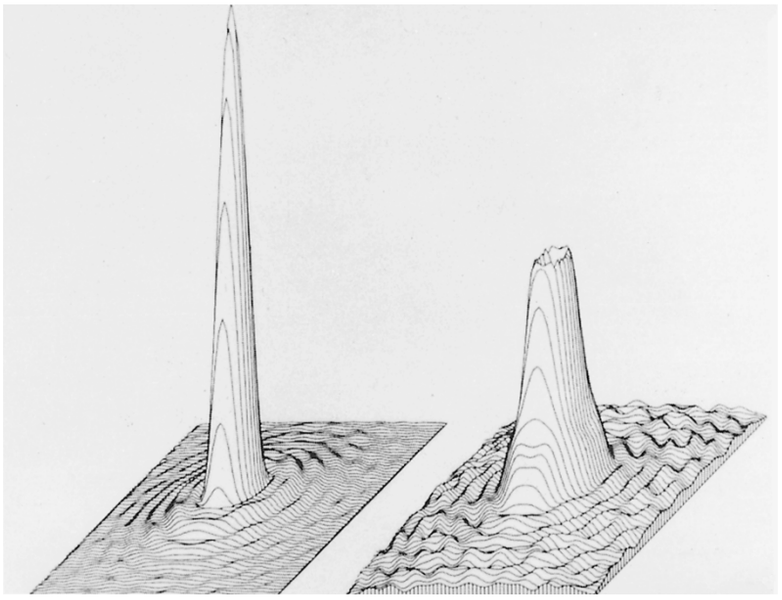


FIGURE 7.5. Nonsymmetrical change in the intensity distribution with focus change above (left) and below (right) best focus in a system limited by spherical aberration.

$$NA_{\text{imageside}} = \frac{NA_{\text{objectside}}}{\text{Magnification}}$$

small changes in tube length quickly lead to inferior images.

While the spherical aberration can be corrected to less-than-perceptible limits for visual observation for all types of objectives, this holds true only if all optical specifications for a given lens are fulfilled. For oil-immersion lenses with high NA, this usually means using a coverslip of 0.17 mm thickness, and $\eta = 1.518$ at 546 nm and 589 nm and an immersion oil with $\eta = 1.5180 \pm 0.0004$ at 546 nm or $\eta = 1.515$ at 589 nm, a condition complicated by the fact that, in all materials, η is a function of λ and temperature. If the exact properties of the coverslip and the oil are specified, then the manufacturer can correct spherical aberration for several values of λ: Zeiss achromats are corrected for 2 λs, neofluars for 3 λs, and planapochromats for 4 λs.

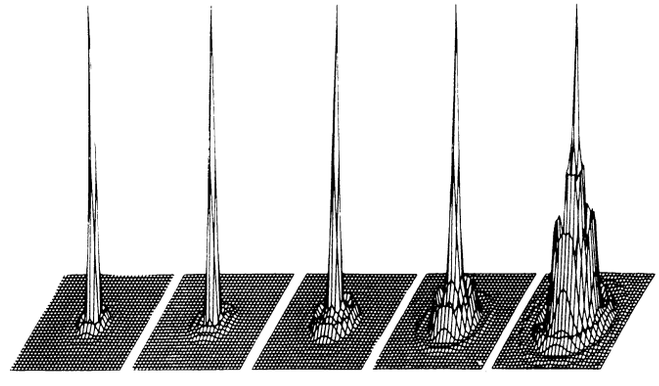


FIGURE 7.6. Change in the intensity distribution with increasing penetration into a watery medium with a planapochromat. Penetration depth from 0 to 4 µm. Note: In these plots, peak intensity has been normalized. In practice, it should decrease dramatically as the base of the intensity plot widens.

With high NA dry or water-immersion objectives, the thickness of the coverslip, standardized throughout the industry as 0.17 mm (# 1.5), is particularly important. Figure 7.9 shows the changes in the half-width of the intensity distribution curve with changes in coverslip thickness. With tolerances of ±10 µm for top-quality coverslips, the half-width can change by more than a factor of 2. With increasing NA (>0.5), particularly with dry and water-immersion lenses, selection of coverslips for correct thickness is particularly important. Even oil-immersion lenses such as the planapochromat

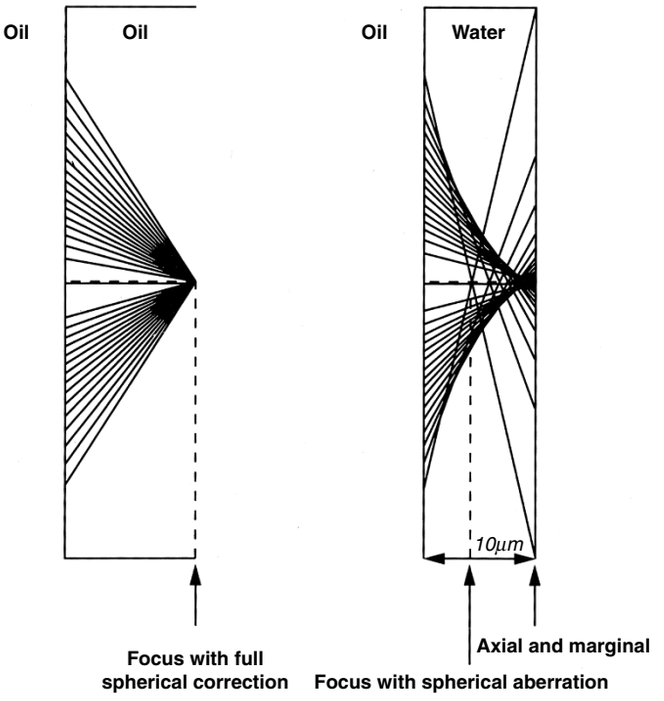


FIGURE 7.7. Ray diagram of an NA = 1.3 oil-immersion objective, focusing into oil (left) versus focus 10 µm in water (right).

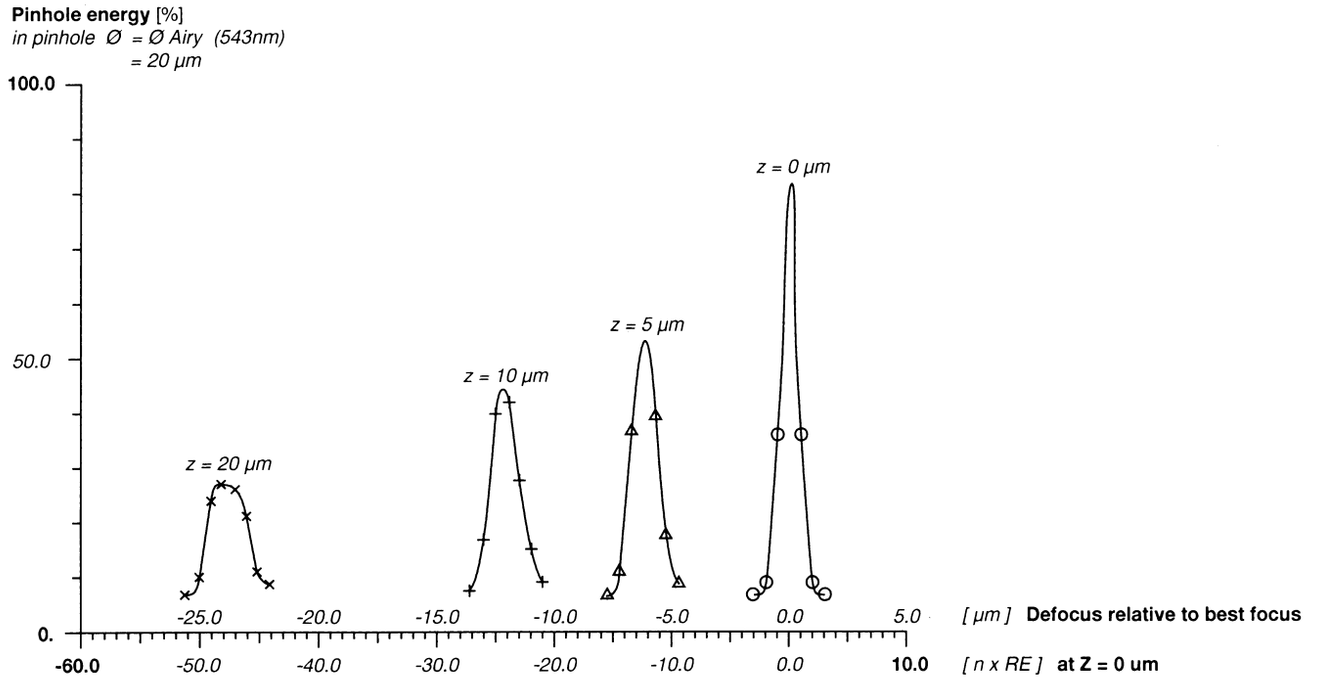


FIGURE 7.8. Pinhole energy measured through a 40×, NA 1.3 oil objective; as function of defocus and depth of penetration (Z) into water. As the thickness of the water layer increases from 0 and 50 µm, the resolution is reduced by about 3× and the intensity by a similar amount.

63×, NA 1.4 perform optimally only with a coverslip thickness of 0.17 mm (Chapter 8, *this volume*). Fortunately, electro-mechanical micrometers capable of reading coverslip thickness to an accuracy of ±1 µm are now available at relatively low cost.

The spherical aberration induced by non-specified coverslip thickness leads to loss of energy at the pinhole, reduced depth discrimination, and an axial shift of the best focus. This is shown in Figure 7.10 for a diffraction-limited, water-immersion 40×, NA 1.2 objective.

These examples underline the importance of maintaining the specified and computed optimal conditions for microscope objectives in order to achieve the full benefits of confocal microscopy.

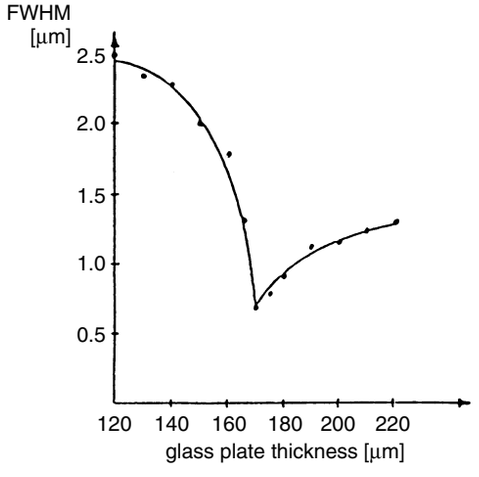


FIGURE 7.9. Changes in the half-width of the intensity distribution with changing coverslip thickness. Plan-Neofluar 63×, NA 1.2 water.

On high-NA, dry objectives or on multi-immersion objectives, eliminating induced spherical aberration requires that the correction collar be set exactly (±2 µm of glass-replaced-by-water at NA 1.2, see Figs. 7.9 and 20.3).

From the above, it becomes obvious that a water-immersion objective is the best choice to minimize induced spherical aberration when penetrating aqueous media. Unfortunately, the collection of 3D data requires moving the specimen with respect to the lens. If this is not to produce motion of the specimen, a coverslip must be used. Experiments have shown, however, that precise correction for coverslip thickness or even the use of "Cytop" (a new coverslip material with a refractive index of 1.34, which is almost that of water, developed by Olympus) will not suffice. The refractive differences in physiological media and in biological materials still require systems that permit adjustable correction for the spherical aberration induced by the specimen itself (see Figs. 2.3–2.5, *this volume*).

With the introduction of high-NA water-immersion objectives designed for coverglass use, some with working distances of 0.24 mm, microscopy on live cells or tissue has been greatly facilitated. Their correction collars not only allow one to compensate for variations in the coverglass thickness (after it has been measured with a micrometer or via the confocal software) but also allows one to compensate for refractive index changes due to temperature or concentration changes in the medium. Although these water-immersion objectives have nominally lower NAs than comparable oil lenses, keep in mind that the effective NA of the oil objective, when looking through water, is dictated by the refractive index of the water or of the medium of lowest refractive index between object and objective. For most aqueous specimens the water-immersion lens is clearly the preferred choice.

Not all experiments permit optimal imaging conditions, and the question arises whether objectives with lower NA or with a built-in iris would not sometimes yield better results. Figure 7.11 again plots

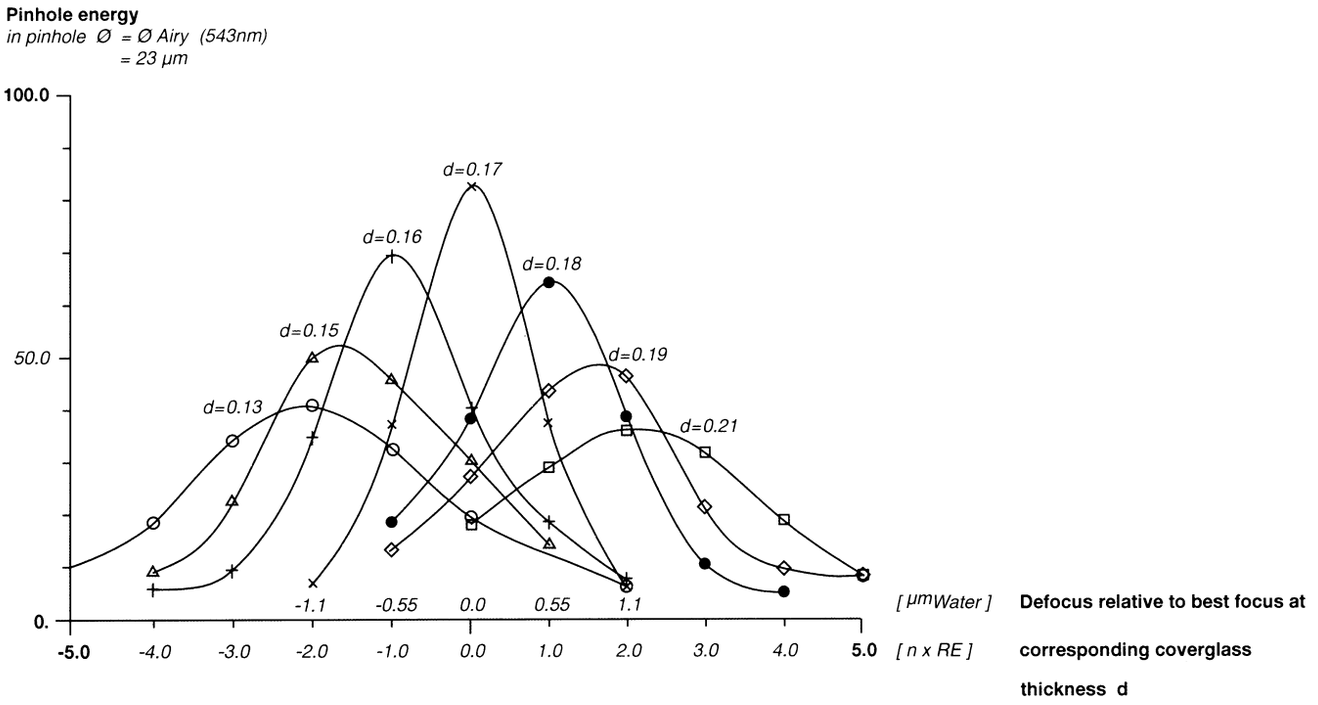


FIGURE 7.10. Pinhole energy as a function of defocus and coverslip thickness (d). Objective 40×, NA 1.2 water.

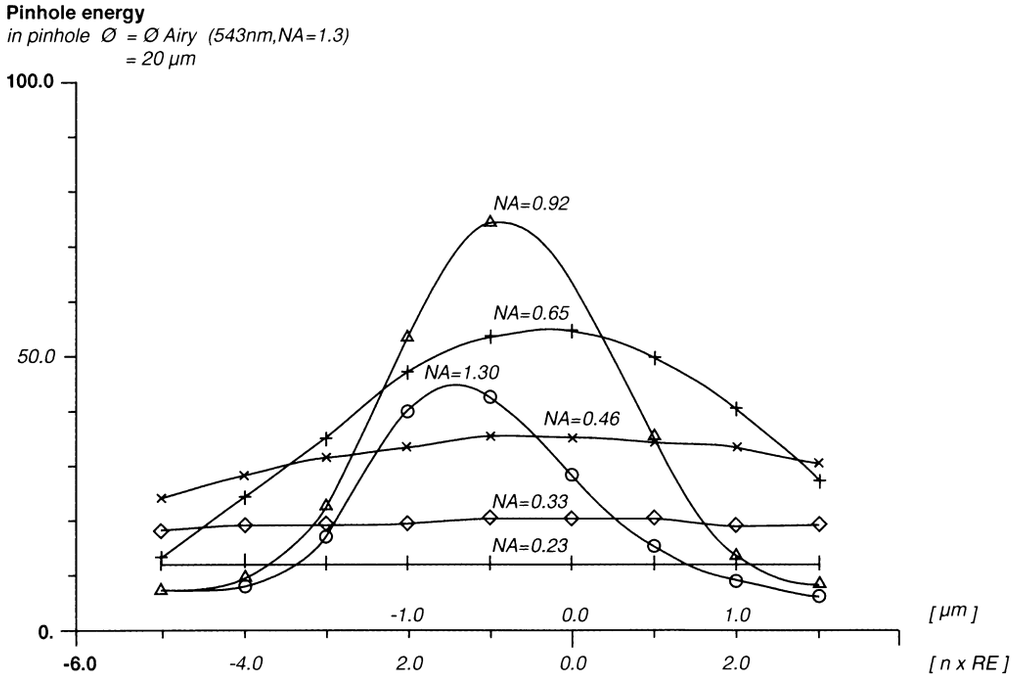


FIGURE 7.11. Pinhole energy as a function of defocus and NA: 40×, NA 1.3 objective with iris (variable aperture) penetrating 10 µm into water.

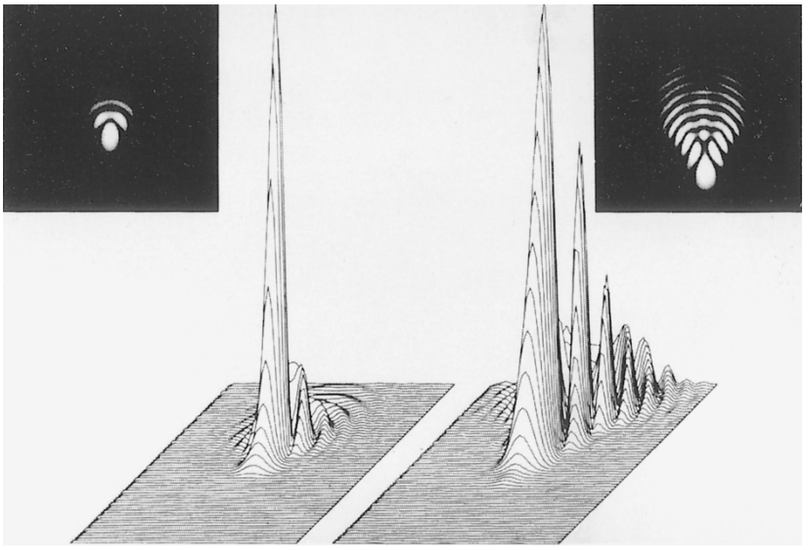


FIGURE 7.12. Intensity distribution in unit image with coma present: slight (left); serious (right).

detected pinhole energy as a function of focus change and NA for a 40× oil-immersion objective with variable NA. At the full NA of 1.3, penetrating 10 μm into a watery medium reduces pinhole energy to <50%, while reducing the NA to 0.92 actually puts more light through the pinhole if one compensates for the reduction in throughput by the lower aperture by increased light input. By reducing the effect of spherical aberration, a larger fraction of the energy reaches the pinhole. However, for NA ≤0.5, the Airy disk becomes significantly larger than the pinhole and the detected energy drops again (see Fig. 7.11). Here we also need to mention a very useful device, called InFocus, from Infinity PhotoOptical (Boulder, CO), which, by varying the effective tube length in a way that does not change the magnification, permits external compensation of spherical aberration to some degree. The system mounts between camera port and the camera (or confocal scan head) and can be motor driven by a computer that also moves the stage to compensate for the small focus changes that occur when the corrector is adjusted ("SAC," Intelligent Imaging Innovations, Denver, CO).

Coma

For object points away from the optical axis coma, a streaking, radial distortion of the image point is generated (Fig. 7.12). Fulfilling Abbe's sine condition,

$$r' \, \eta' \sin\beta' = r \, \eta \sin\beta$$

where r is the distance from the optical axis; η is the refractive index; and β is the viewing angle, all in image space ($'$) or object space (respectively), eliminates coma and produces an aplanatic system. Unfortunately, all factors with the potential to increase spherical aberration are also especially critical to coma.

As coma is only evident off-axis, it is not important in stage-scanning confocal microscopes. However, it can be important in beam-scanning systems, or when one scans off-axis (even at high zoom) to avoid on-axis specular reflections sometimes visible in the BSL mode.

Astigmatism

For off-axis points, two orthogonal cross-sections through the imaging wavefront (tangential and sagittal) can have different focal distances or radii. When this is the case and a perfectly symmetrical image point in the center of the field is moved off-axis, it becomes either radially or tangentially elongated, depending on the focus. The intensity ratio of the unit image will diminish, and definition, detail, and contrast are lost with increasing distance from the center.

Figure 7.13 shows the intensity distribution through one section of an astigmatic image point. A four-lobed Airy disk results when the focus is set at the compromise position between the radial and tangential extremes [Fig. 7.13(B)].

Poor lens centration in the objective or poor alignment between the objective, the intermediate optics, and the eyepiece increases both astigmatism and coma. Wedge-error in poor quality filters or dichroics can have the same effect.

Flatness of Field

A simple lens focuses image points from an extended flat object onto a spherical surface shaped like a shallow bowl or dish. Central and peripheral zones are not simultaneously in sharp focus. Prior to the advent of flat-field objectives by Zeiss in the late 1930s, the "usable" field at the intermediate image plane was only 10 to 12 mm. With present-day flat field or "Plan" objectives, ocular fields of 18, 20, and 25 mm exhibit sharp detail from center to edge; however, this improvement has been obtained at the expense of increases in complexity and cost and reduced transmission. In fact, it became practical only after the introduction of anti-reflection coatings.

In Figure 7.14, the field curvature for an achromat and a plan-apochromat are compared. Also shown is the astigmatism of the two orthogonal image spheres. Δ represents the depth-of-field unit

$$\Delta = \frac{\lambda}{\eta(\sin\alpha)^2}.$$

It needs to be mentioned here that the term Plan or "F" for flat field is no guarantee for a perfectly flat image with no astigmatism. No standards have been established. Also, the flatness in the final image may be affected by the correction of the eyepiece or other intermediate optics. The diameter of the field of view[1] over which all aberrations have been corrected and the field is flat is listed for a number of Zeiss objectives in Table 7.1.

[1] In the intermediate image plane.

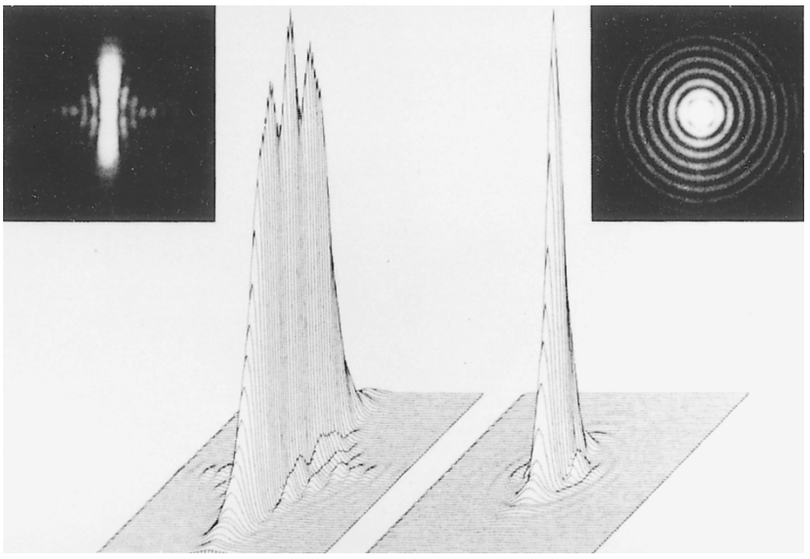


FIGURE 7.13. Intensity distribution in unit image with astigmatism: serious (left); slight (right).

In confocal scanning through thick materials, the dish-shaped section obtained with a non-plan objective may be of little consequence to the biologist, as long as there is no astigmatism or coma and one remains mindful of the distortion this aberration produces in 3D data sets. This is because the exact shape of most biological specimens is often more likely to be distorted by specimen preparation procedures than by optical problems, especially because, when the normal 512×512 image is scanned at Nyquist Zoom magnification, it usually covers only the small part of the field-of-view nearest the axis. The off-axis increase in astigmatism, coma, and field curvature is a good reason to use the "panning" controls, that shift the imaged area away from the optical axis, with caution. However, in materials science and for many critical applications, such as high-resolution imaging in semiconductor inspection, flatness of field is essential.

Distortion

Nonlinear magnification from center-to-edge of field puts the actual, off-axis image point either closer (barrel) or farther away (pincushion) from the axis than the true image point. Barrel or pincushion distortion results, and the true geometry of an object is no longer maintained in the image. Although less critical in biomedicine than in materials science, distortion is reduced to <1.5% of the radial distance from the axis in most objectives. It can be checked by imaging crossed grating lines, such as those found in hemocytometers, in the widefield mode. Ideally, the lines should be perfectly straight over the entire image field. A similar specimen can be useful to measure scan linearity in confocal laser-scanning microscopes, however, in this case distortion from nonlinearity of the scan is likely to be larger than that produced by the objective.

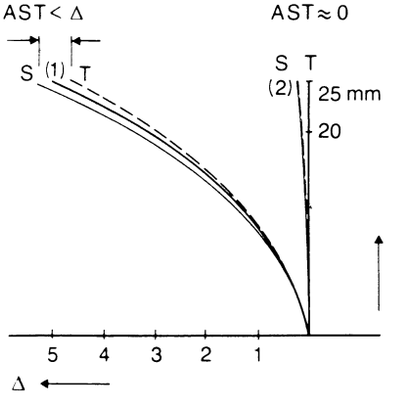


FIGURE 7.14. Flatness of field and astigmatism for (1) achromat and (2) planapochromat as a function of position in the intermediate image plane.

Chromatic Aberrations

Wavelength-dependent aberrations are caused by (1) the fact that the η of every optical glass varies with λ, a factor called dispersion; and (2) the fact that λ affects all the dimensions of the unit image point. This latter aberration, called diffraction-caused spreading, is usually barely noticeable in the center of the Airy disk but is more noticeable at the edges of the first fringe, where it influences the resolution. We will discuss this later.

Longitudinal Chromatic Aberration

This aberration is the result of changes in lens focal length, (Δf), with changing λ. In general, the image plane is in sharp focus for only one wavelength or for a narrow wave band. For other wavelengths, the image plane is slightly defocused. Figure 7.15 com-

TABLE 7.1. Diameter of Corrected Image for Some Zeiss Plan Objectives

	Flat Field of View	
Objective Conventional	Conventional	Confocal
Planapo 40×/1.2 water corr.	25	12
Achroplan 20×/0.5 water	24	25
Achroplan 100×/1.0 water	18	10

With best focus on the center, the "image disk" will not exceed the depth of field within the specified field; diameter in millimeters.

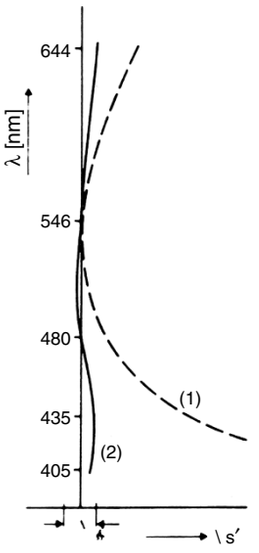


FIGURE 7.15. Longitudinal chromatic correction of (1) achromat and (2) apochromat.

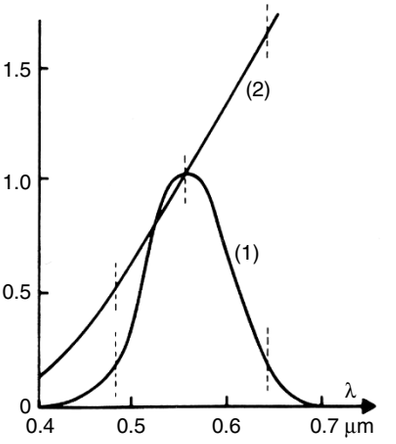


FIGURE 7.16. (1) Spectral sensitivity of the eye. (2) Spectral emission of a tungsten source.

pares the longitudinal chromatic correction of an achromat with that of an apochromat. In order to judge the influence of Δf on the image quality for a given lens, the spectral emission of the source as well as the spectral sensitivity of the detector need to be considered because both determine the effective brightness in the center of the disk (i.e., the energy that passes through the pinhole).

The peak sensitivity for the eye is at 550 nm, with a spectral range of ~400 to ~650 nm. Figure 7.16 shows the spectral emission of a typical light source and the spectral sensitivity of the eye. If we normalize the response at 550 nm to 100%, the sensitivity of the eye to an image of a sample illuminated by tungsten light is ~10% at 480 nm and ~30% at 640 nm. In confocal scanning, the emission spectrum of the source and the spectral sensitivity of the detector need to be considered along with the emission peak and bandwidth of the specific fluorophore.

Chromatic aberrations are both produced and corrected by utilizing the different dispersions of the glasses used. Glasses of "normal" dispersion have an almost linear decrease in η with increasing λ and are used for achromats. Only two wavelengths have the same focus, and the remaining "secondary spectrum" produces greenish or purple fringes on images of sharp edges.

For objectives with better chromatic correction, glasses of "abnormal" partial dispersion are needed. Here the refractive index changes more rapidly with wavelength in either the blue or red region.

Abbe used the crystal fluorite (CaF_2) to reduce the secondary spectrum, and more recently, glasses have become available with similar dispersion properties. By replacing any single lens with a doublet containing both a positive and a negative element, with each element having a different dispersion, it is possible to make the chromatic effects cancel out at two or more wavelengths. This has resulted in the high degree of chromatic correction for an apochromat (Fig. 7.15), where up to four or more wavelengths can have the same image location [see Fig. 15(A)].

With apochromat and semiapochromat or fluorite lenses, the "diffraction-caused spreading" of the intensity distribution, referred to above, can also be virtually eliminated, as Figure 7.17 illustrates. An achromat still has substantial intensity in the first fringe, while the apochromat approaches the theoretical resolution

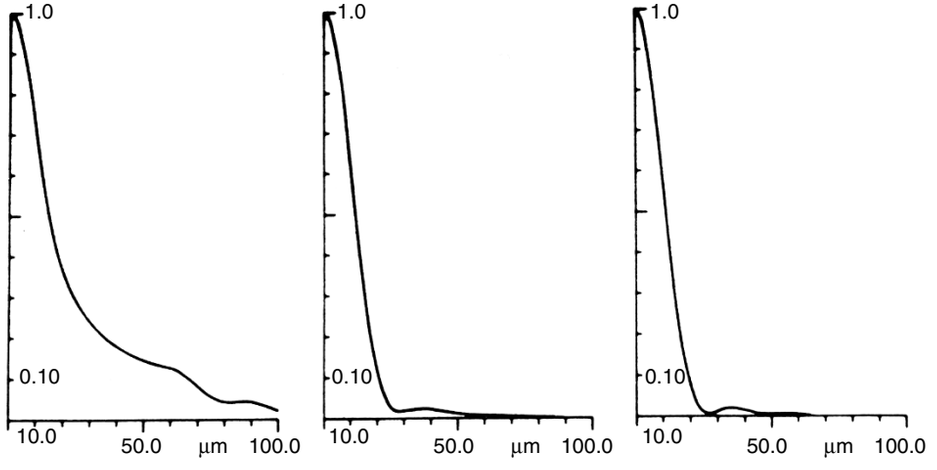


FIGURE 7.17. Intensity distribution in the image of a point object illuminated with white light for an achromat, plan-neofluar, and planapochromat.

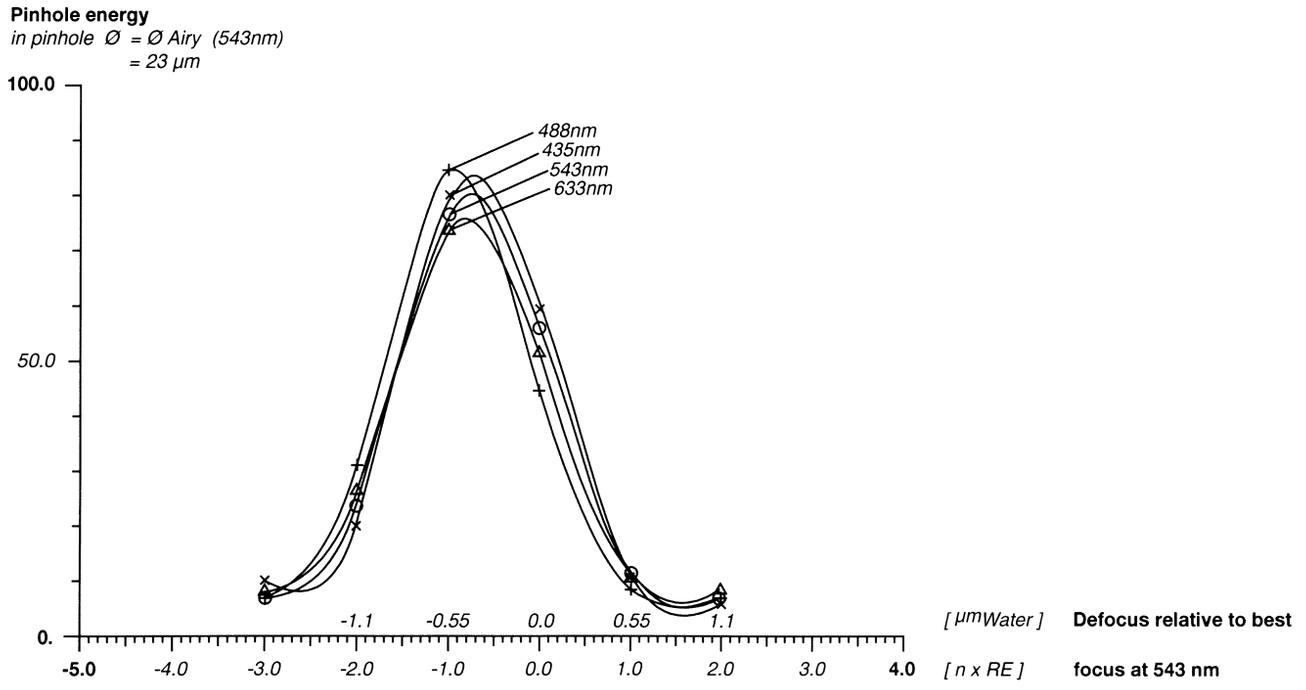


FIGURE 7.18. Pinhole energy as a function of defocus and wavelength: planapochromat 40×, NA 1.2 water, $d = 0.17$.

limit where the longitudinal chromatic aberration is $\leq\lambda/(\mathrm{NA})^2$, the wave-optical depth of field.

Because the apochromat requires elements of abnormal dispersion, their characteristics may not be ideal for some specific applications, such as fluorescence excitation in the near ultraviolet (UV) or polarizing microscopy. For this reason, a fluorite objective is often more suitable, and Figure 7.17 illustrates how close it comes to the performance of the apochromat.

For confocal scanning fluorescence images, it is important that the correction be as similar as possible at the excitation and emission wavelengths in order to produce the best results in terms of the signal transmission and resolution.

In UV-excited confocal fluorescence with emission in the visible range of the spectrum (e.g., 351 nm and 514 nm), even normal planapochromats will fail to assure precise parfocality. This will result in energy loss at the pinhole unless either one of the new "blue" objectives are employed[2] or the UV laser is specially adapted with its own optical interface to compensate for the objective's shortcomings. To accomplish the latter, the beam expander of the UV laser is adjusted to precisely parfocalize the excitation spot in the specimen with the image of the detection pinhole.

Some of the new water-immersion objectives designed for confocal imaging also specifically address the problem of UV excitation, not only by having a high degree of UV transmission, but also by extending the corrected waveband far enough to assure good confocality between UV-exciting and visible-emitted radiation. Specifically for near UV excitation, Nikon offers a CF Fluor 40×, NA 1.2 water lens with high transmission down to 340 nm and a working distance of 220 µm. Olympus now offers four UV-apochromats: 20×, NA 0.4; 40×, NA 0.9; 100×, NA 1.1 with working distances of 150 µm, 130 µm, and 130 µm, respectively. All are apochromatically corrected from 350 nm to 600 nm with excellent flatness over a 10 mm field. The Zeiss C-Apochromats 40×/1.2 water and 63×/1.2 water combine high, near-UV transmission with apochromatic color correction, flatness over a 14 mm field, and working distances of 0.24 mm. Figure 7.18 shows the pinhole energy as a function of focus and wavelength for such an objective.

An interesting and imaginative use for longitudinal chromatic aberration was described by Maly and Boyde (1994) as a means of implementing real-time, stereoscopic confocal microscopy (Boyde and Jones, 1995). They have developed special objectives with linear longitudinal chromatic dispersion (LLCD). When these lenses are used to detect the reflected light signal from a disk-scanning confocal microscope using "white" light illumination, discrete "strata" of the specimen surface appear in only those colors for which confocal conditions exist (i.e., different strata have different colors with the blue layer being closest to the objective and the red layer farthest). These spectral colors can then be either recorded with a color image sensor and converted directly into height by simple computer algorithms or used as the basis of a real-time stereoscopic imaging system. In the latter case, dispersive viewing elements (prisms) are used to change the different colors into a parallax shift that depends directly on the color and indirectly on the height. By mounting two such elements into the two sides of a binocular viewing head so that they have opposite horizontal dispersions, the viewer will perceive a striking, real-time stereoscopic confocal image. The special LLCD objectives described range from 10×/NA 0.3 to 120×/NA 1.0 (oil).

[2] These "blue" objectives have been designed to perform best in the near-UV blue end of the spectrum. Other manufacturers also now offer objectives optimized for best performance at near-IR-red wavelengths for using in multiphoton excitation microscopy.

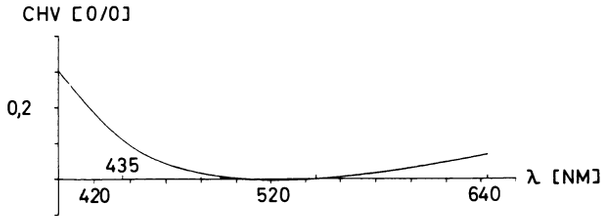


FIGURE 7.19. Lateral chromatic aberration for a Planapo 40×, NA 1.2 water.

Lateral Chromatic Aberration or Chromatic Magnification Difference

Because magnification is proportional to 1/f, the same change of f with λ that causes light of different λ to focus on different planes (producing axial chromatic aberration) also causes the magnification to change with λ, producing lateral chromatic aberration (LCA). If the magnification of an objective is different for different λ, images of sharp edges in the object will show blue or red fringes. In a non-corrected system, the blue component at 436 nm may be imaged 1.4% larger than the red component at 630 nm. Normally, the LCA is greater for objectives of short focal length and the magnification error can range from 1.1% to 1.9% of the radial distance from the optical axis.

In confocal scanning fluorescence, LCA can cause the excited light to return to a location nearer to, or farther from, the axis than the apparent location of the source (see Fig. 35.14, *this volume*). This results in intensity loss at the pinhole. Proper matching of all components is essential to assure full compensation of the LCA. In multi-channel fluorescence, poor registration of blue-, green-, and red-emitting markers can lead to possible errors in mapping their precise locations. A highly corrected lens such as the planapochromat 40×, NA 1.2 W keeps the LCA well within 0.2% over a wide wavelength range (Fig. 7.19).

In earlier, conventional microscope systems, all objectives were calculated to produce a constant amount of LCA, which was then compensated for by the eyepiece. This compensating system is illustrated in Figure 7.20. The modern, infinity-corrected microscope objectives are either fully LCA-corrected in the objective itself (Nikon, Olympus) or use a compensating tube lens for a full correction of the intermediate image.

The Zeiss ICS (Infinity Color-corrected System) optics are unusual among these tube-lens systems in that no correction for LCA takes place in the objective. The ICS tube lens is a single, spherical lens which fully compensates for LCA (range ≅ 1.1%–1.9%) in all objectives over the entire 25 mm intermediate image field (Fig. 7.21). This is possible because, although all off-axis imaging bundles pass through the exit pupil, the position of the exit pupil itself depends on the focal length of the objective (i.e., the magnification): the shorter the focal length, the closer the exit pupil is to the specimen. If we trace off-axis bundles from a short focal length objective to the tube lens, we find that they reach more peripheral zones of the tube lens, which compensate more strongly for the higher LCA present in high-magnification lenses. On the other hand, bundles from long focal-length objectives reach only the more axial zones that are appropriate for the lower LCA compensation needed in low-magnification objectives. Relieving the objective from LCA correction in this way means fewer elements in the objective and a choice of more suitable glass types, particularly for the Plan-Neofluars, where only one selected heavy flint glass and no fluorite is used. This virtually eliminates autofluorescence in the objective, improves extinction ratios for

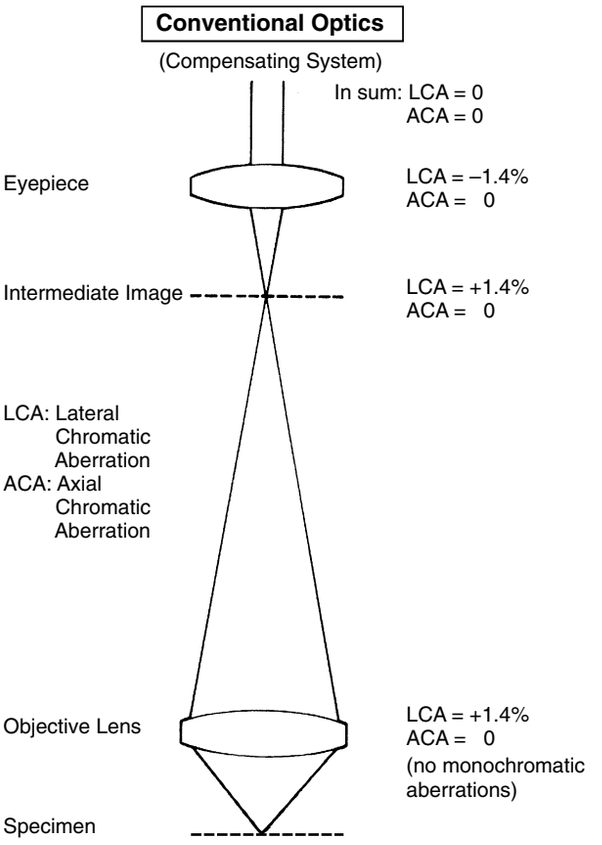


FIGURE 7.20. Correction of lateral chromatic aberration in conventional optics.

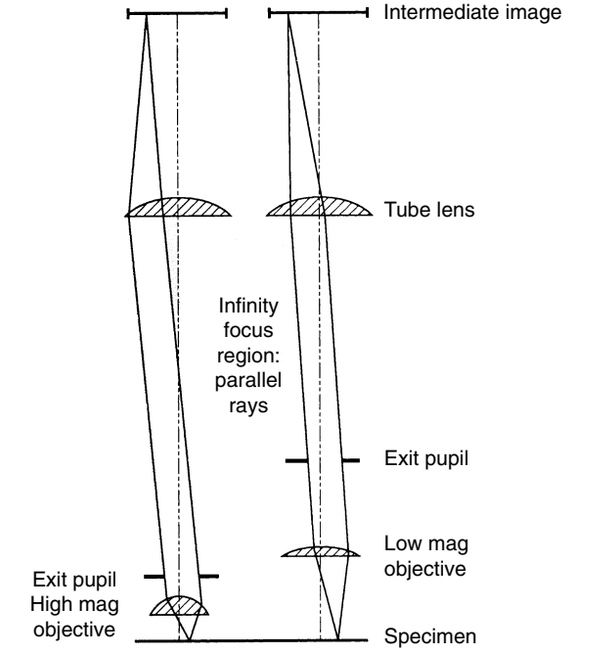


FIGURE 7.21. Zeiss's ICS optics operation. The same tube lens produces more chromatic correction for high magnification objectives than for low magnification objectives because the relative size and position of the exit pupils, and the optics of the infinity-focus objectives themselves, causes rays to pass through different parts of the tube lens (see text for more detail).

polarizing microscopy, and assures high light throughput and good contrast.

All off-axis aberrations can adversely affect the performance of beam-scanning systems. Potentially most critical is LCA in the confocal fluorescence mode, where the excited off-axis object point may be sufficiently shifted from the pinhole that a substantial signal loss may occur.

Example: A 100× oil objective may scan a 100 × 100 µm field in the object with 500 pixels per scan line. Assume that the position of a 0.2 µm diameter blue Airy disk of exciting light is shifted 1.9% of the distance from the center of the field compared to its corresponding red emission disk. Pixels that are 50 µm from the center will be displaced almost 1 µm or 5 pixel diameters away from the pinhole. Depending on the size of the pinhole, the severe loss of signal is obvious.

For confocal microscopy, the LCA — transferred to the specimen field — must be smaller than the pixel spacing on the periphery of the scanned field. For a raster scan of 512 × 512, this means an LCA of less than 0.19%, if we assume the ~1.4× resolution increase of confocal scanning. The LCA for a Planapo 40×, NA 1.2 W is shown in Figure 7.19. In more general terms, it means that Nikon CF objectives cannot be replaced by compensating objectives unless the rest of the system optics are also changed.

With the increasing interest in two-photon excitation, which requires optimal chromatic correction for the incoming infrared (IR) beam combined with efficient collection of the emitted photons, more and more lenses for that application have become available.

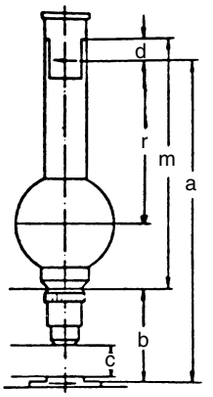
Reflecting Objectives

At first sight it might appear that a logical solution to the problem of chromatic aberration might be to use reflecting rather than refracting objectives. Reflection is insensitive to λ and, like the reflecting telescope, a reflecting microscope objective could offer excellent chromatic correction over a wide spectral range. In fact, some low and medium power reflecting objectives are routinely used particularly for far-IR microscopy. However, high resolution requires objectives with high NA and short focal length or even immersion systems. Though the diamond-turning lathe could produce the aspherical surfaces required with the necessary precision, such lenses cannot now be produced at reasonable cost. Furthermore, an inherent limitation of reflecting objectives is the elimination of paraxial imaging bundles with the corresponding loss of diffraction orders and effective NA.

FINITE VERSUS INFINITY OPTICS

Some conventinal microscopes still in use were built around the German DIN (now ISO) standard, which calls for the objective to form a real image at a tube length of 160 mm. The parfocal distance is set at 45 mm and the object-to-image distance is 195 mm (Fig. 7.22). This standard applies to many transmitted light techniques and has served us well for over 50 years.

Objectives with a finite image distance form a real, intermediate image directly. This intermediate image may either be corrected (Nikon) or it may have residual LCA to be compensated for by the eyepiece. Infinity-designed objectives require a tube lens to form this real, intermediate image. While this tube lens can also be employed to correct for residual aberrations, the intrinsic design advantage of infinite image distance (Fig. 7.23) is its relative insensitivity to optical components (such as filters, analyzers, compensators, DIC prisms, and reflectors) in the telescopic space between



m = mechanical tube length = 160 mm
a = object-to-image distance = 195 mm
b = object distance of objective = 45 mm
d = intermediate image distance of eyepiece = 10 mm
c = working distance of the objective
r = distance mounting shoulder monocular tube to intermediate image

FIGURE 7.22. Standard dimensions of DIN standard conventional microscope.

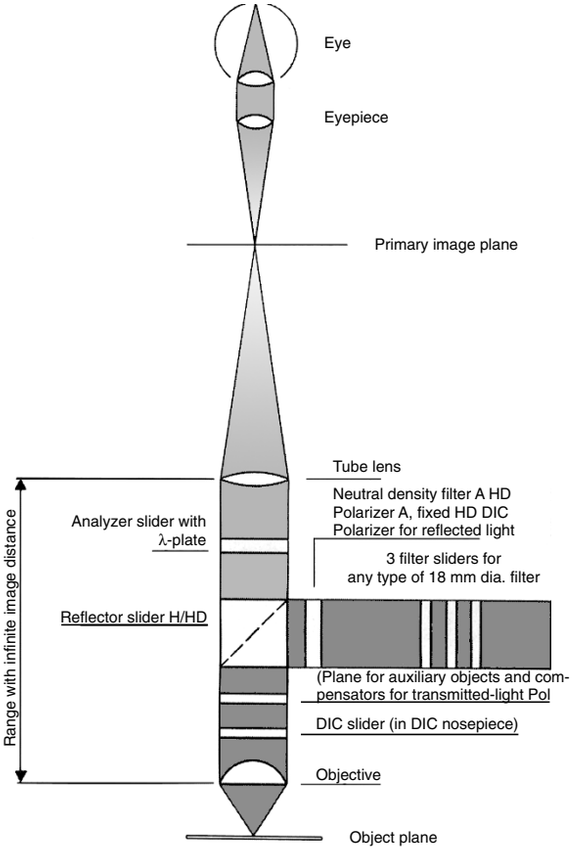


FIGURE 7.23. Advantage of using objectives with infinity correction. A number of accessories, such as the Wollaston prisms used for DIC and the filters for epi-fluorescence, can be introduced between the objective and the tube lens without affecting the image of the structure at the front focal plane.

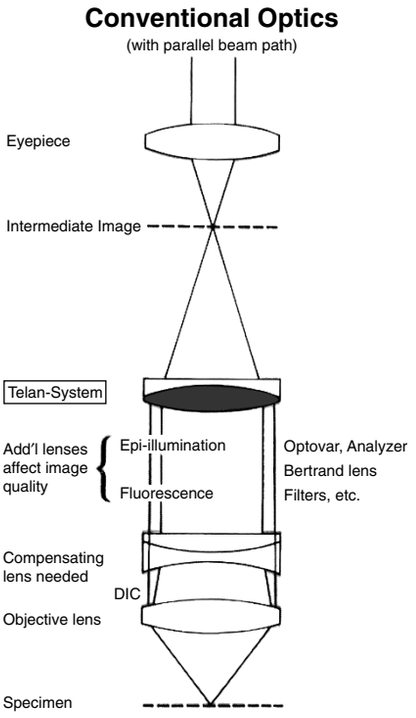


FIGURE 7.24. Conventional optics using Telan lenses. Requires more components that not only reduce resolution and cause reflection losses but also increase magnification.

objective and tube lens. Infinity or parallel beams are not affected by the thickness or η of such components as long as they are plane parallel. The location of the image point remains constant, both axially and laterally, as does the alignment between the objective and the tube lens.

Another advantage of infinity-corrected optics is that one can focus by moving the objective rather than having to move the stage, as is the case in most inverted and some upright microscopes.

In the converging beam path behind a 160 mm tube length objective, similar elements would cause axial, and possibly lateral, shift. This not only causes aberrations but makes it difficult to get good image registration in multi-parameter techniques (double or triple fluorescence). To avoid this, so-called Telan systems are added to generate an "infinity space" into which the "flat" components can be introduced. This eliminates the image shift and distortion but only at the cost of two additional optical elements — one negative and one positive — and with them some additional magnification (usually 1.25×) and the potential for more flare and stray light (Fig. 7.24).

The design concepts followed by major microscope manufacturers are summarized in Table 7.2.

WORKING DISTANCE

For reflected light objectives, the distance between the focus plane and the closest structural element of the objective is called the working distance (WD). For transmitted light lenses, the specified free working distance is the distance from the coverslip to the closest structural element of the lens. In a confocal microscope, the WD sets an absolute limit that the focus plane can be below the top surface of the coverslip. As an optical design parameter, WD can be varied over a considerable range, but, as can be seen from Table 7.3, it becomes decidedly shorter in objectives with higher NA and greater correction.

In oil lenses, the first refracting surface struck by a light ray is the far side of the first element of the objective. This surface is often a segment of a sphere that is large enough to encompass the full NA of the design. (The lens half-angle, α, is 74° at NA 1.4.) As the focus plane moves away from the glass, this sphere segment must become larger with the result that soon there is no longer sufficient space in which to install the other elements needed for chromatic and field corrections. These larger elements are also more expensive to produce.

When working with living materials, the matter of WD can have a second aspect because in such cases, it is often convenient to be able to change the z-position of the imaged plane in the object without actually moving either the position of the front surface of the objective or the specimen itself. This can occur when imaging the living eye where actual contact between the cornea and the objective is needed to reduce the effect of pulse-induced motion. To solve this problem, Petroll and colleagues (1993) have used an objective with internal focusing elements to permit changes in focus plane while maintaining mechanical contact.

The working distance is a critical issue for 3D imaging of thick samples or when manipulation or probing under the objective is required. However, we must also keep in mind that thick layers of medium between object and objective can easily create turbulence (e.g., when focusing) or inhomogeneities (such as air bubbles!) that can seriously impair image quality or signal intensity.

TABLE 7.2. Tube Length and Chromatic Corrections of the Major Microscope Manufacturers

Manufacturer	Mode	Fixed, Finite Tube Length (mm)	Infinite Tube Length Lens, f = mm	Chromatic Correction
Leica	Reflected	—	200	In-tube lens
	Transmit (older)	—	200	In-tube lens
		160	—	Leica correction
Nikon	Reflected (few) (most)	—	210	None required
		210	—	None required
	Transmit	160	—	None required
Olympus	Reflected	—	180	In-tube lens
	Transmit (some) (older)	—	180	In-tube lens
		160	—	Olympus correction
Zeiss	Reflected	—	160	Universal tube lens
	Transmit (older)	—	160	Universal tube lens
		160	—	Zeiss correction

TABLE 7.3. Working Distance of Some Zeiss Objectives

Objective	Immersion	Cover Glass	Working Distance
Epiplan 50×/0.5	Air	No	7 mm
Epiplan 100×/0.75	Air	No	0.98 mm
Epiplan-Neofluar 100×/0.9	Air	No (correction collar)	0.28–0.31 mm
LD Plan-Neofluar 40×/0.6	W/Gly	Yes (correction collar)	2.5–3.3 mm
Planapo 40×/0.95	Air	0.13–0.17 (Correction collar)	0.16 mm
Achroplan 40×/0.8	Water/dip	No	3.61 mm
Achroplan IR 63×/0.9	Water/dip	No	2.2 mm
Achroplan 100×/1.0	Water/dip	No	1.00 mm
c-Planapo 40×/1.2	Water	Yes	0.22 mm
Planapo 100×/1.4	Oil	Yes	0.17 mm

OPTICAL MATERIALS

More than 200 optical glasses are available to the optical designer. Their properties, such as refractive index, dispersion, transmission, contaminants, potential for auto-fluorescence, chemical and thermal resistance, and overall homogeneity are usually carefully selected to ensure superb optical performance. However, this may compromise other requirements, such as high transmission in the near-UV range or high extinction factors in polarizing microscopy. Some new materials, such as fluorocrown glass, approach the properties of natural fluorite while avoiding most of its drawbacks, such as the presence of organic contaminants and a crystalline structure that can seriously degrade performance in fluorescence and polarizing microscopy. Fully apochromatic correction, however, still requires both natural fluorite and glasses that have low transmission in near UV.

Therefore, the semi-apochromat is often the ideal compromise. It can be a true multi-purpose objective, combining excellent correction with good contrast, high NA, and high spectral throughput.

Even though their thickness is usually <10 µm, the cements between doublet or multiple lens elements can have spectral absorption properties that may render an objective unusable for specific applications.

The chemical and optical properties of optical glasses are usually proprietary. Decementation between lenses, caused by heat and different coefficients of expansion, is rare. Lasers of <100 mW energy in near-UV and visible range will cause no damage if their power is evenly distributed over the entire entrance pupil, however, damage can occur if a similar amount of light is brought to a focus on any optical surface having an appreciable absorption at that λ.

ANTI-REFLECTION COATINGS

As the sophistication of objectives increases, more elements are required, and this accentuates the need to eliminate internal reflections to produce higher transmission, better contrast, and less flare, particularly in incident- or reflected-light applications. Single-layer anti-reflection (AR) coatings dating back to the 1940s have since been refined and supplemented by multi-layer coatings, increasing the transmission in the visible spectral range through an air–glass interface from ~96% (not coated) to ~99% (single layer coating) to ~99.9% (multi-layer coating) (Figs. 7.25 and 7.26).

Coating materials can be magnesium fluoride and a multitude of proprietary materials (see Chapter 3, *this volume*), all of which have their own optical properties potentially affecting the transmission of the system in given spectral regions. In general, the interference characteristics of AR coatings are spectrally limited, and constructive interference for high transmission in the visible range means destructive interference in harmonically related frequencies outside the transmission band.

For specimens of very low reflectivity, the weak BSL signal may be overwhelmed by background light produced by internal reflections in the objective lens or other optical surfaces that reflect light that comes to a focus near an image plane. In this case, a so-called Antiflex system can have a great advantage. In this approach, we illuminate with polarized light and observe through an analyzer at 90° to the polarizer (Chapter 10, *this volume*). Because stray light produced by specular reflection from optical surfaces retains its direction of polarization, it can be blocked by the analyzer. If a 1/4 wave plate is incorporated into the front element of the objective with its vibration direction diagonal to both the polarizer and analyzer for a specific wavelength (usually 550 nm), this will generate circularly polarized light below the objective. The 1/4 wave plate rotates the plane of vibration of both the illumination and the returning BSL by 45° for a total of 90°, so light reflected from the object is now oriented parallel to the analyzer and can pass freely to the detector. This system is used for the so-called reflection contrast or reflection interference techniques but is also most effective in confocal studies of weakly scattering objects (Pawley *et al.*, 1993).

Transmission of Microscope Objectives

We have seen that a number of factors influence the spectral throughput of an objective: glasses, cements, coatings. However, these considerations must apply to not only the objective but to the whole system if it is to provide high transmission in the desired wavelength range.

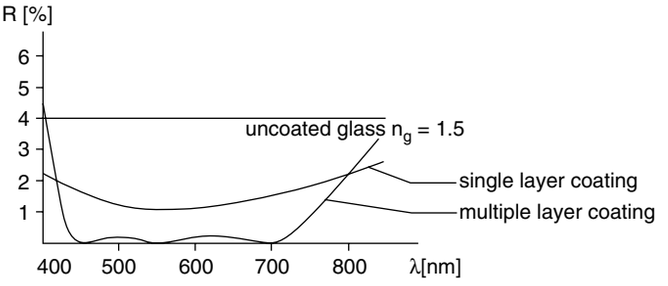


FIGURE 7.25. Reflectivity of glass surfaces covered with single- versus multi-layer coatings.

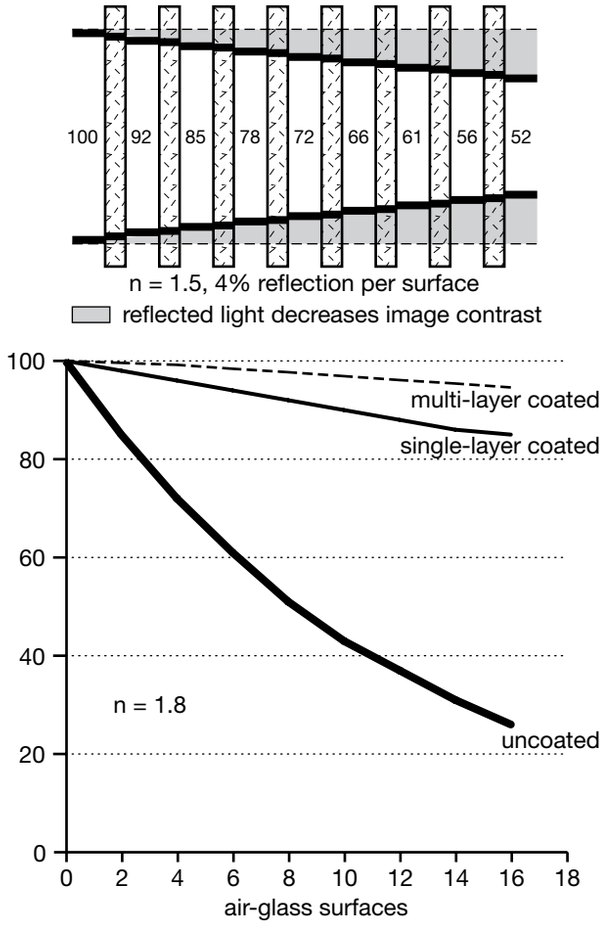


FIGURE 7.26. Reflections on surfaces of **n** = 1.5 (above) versus **n** = 1.8 (below). At **n** = 1.5, the eight elements with their 16 surfaces, each reflecting 4%, result in a throughput of only 52%. At **n** = 1.8, the 16 uncoated surfaces would pass only 26%. Single-layer anti-reflection coating increases total transmission to 85%, and multi-layer coating to 94.6%. This increase in throughput, and corresponding reduction in internal scatter and "noise," substantially enhances the contrast of the image because it both makes bright features brighter and dark features darker.

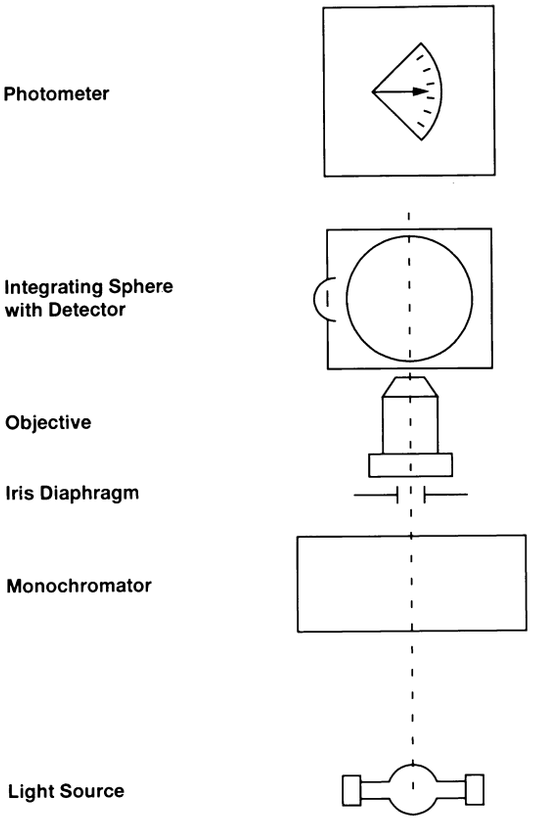


FIGURE 7.27. Setup to measure an objective's spectral transmission.

A typical arrangement to measure the spectral transmission of an objective is shown in Figure 7.27: light source (tungsten halogen and/or xenon) with monochromator and iris diaphragm fill the objective's back-aperture. A parallel light beam equal in diameter to the pupil of the objective strikes the rear of the objective and emerges through the front lens where it is collected by an integrating sphere and measured by a PMT with photometer read-out. The result is compared to a second measurement made with the objective removed.[3]

Table 7.4 shows the relative spectral transmission of several representative objectives that have been optimized for high transmission in the near-UV. With confocal fluorescence microscopy extending both towards the near UV as well as towards the IR, the spectral transmission of a total system needs to be looked at. The transmission curves for a number of objectives by Nikon, Leica, and Olympus are included in the Appendix at the end of this chapter. Keep in mind that these transmission curves are typical only for a given lens. Tolerances, particularly in the AR coating, can introduce significant variations, particularly at the cut-on and cut-off ends of the transmission curve.

Depending on the application, objectives can be chosen with high throughput in the near-UV or with extended IR transmission. Having good transmission in both the near-UV and the near-IR is not possible.

A number of new objectives, designed specifically for confocal microscopy, are either already available or in preparation. More detailed information on their performance and spectral throughput is best obtained directly from the manufacturers.

[3] The high-NA rays from an oil-immersion objective can only escape from the glass into the sphere if a small, planoconvex lens is attached to the front element with oil.

TABLE 7.4. Relative Transmission of Some Typical Objectives

		Wavelength (nm)				
Manufactuerer	Objective	320	350	400	500	600
Nikon	Fluor 40×/1.3 oil	16%	66%	80%	90%	91%
Olympus	UVSLM 40×/0.9 water	—	56%	—	88%	—
	UVSLM 100×/1.1 water	—	60%	—	90%	—
Zeiss	Fluar 40×/1.3 oil	29%	79%	88%	95%	99%
	Planapo 40×/1.2 water	20%	54%	86%	89%	92%
	Achropam 100×/1.0 water	—	605	90%	94%	90%

CONCLUSION

Many modern microscope objectives are well suited for confocal scanning as long as they are used within their design specifications. With the ever-wider use of confocal scanning microscopy for 3D live-cell imaging and with new microscope techniques emerging, new and improved objectives continue to appear. Often they are optimized for a specific application. This trend will continue. Just a few examples are the new highest-NA 60×/1.45 and 100×/1.45 oil-immersion lenses or the special objectives Olympus introduced for epi-illuminated total internal reflection fluorescence (TIRF) microscopy with an NA of 1.45 or 1.65. It follows from the discussion above that the latter NA requires a special immersion medium and rather costly high-index coverglasses.

In addition to the call for objectives with higher NAs, longer working distances, and maximum transmission in the visible and UV, this may be the place to "dream" about other exotic lens features. We might imagine a tunable objective, a lens whose chromatic correction can be "tuned" to the specific excitation and emission wavelengths actually in use to produce the best image quality with only a few elements and high transmission. If such tunability is impossible, perhaps special achromatic lenses will be designed for use with specific fluorophore/laser combinations, such as the "blue" objectives recently offered by Leica.

An even more exotic dream (included in the second edition of this volume) for a substantial increase in signal intensity realized by using two, matched lenses above and below the specimen, has now been commercially realized in the Leica 4Pi microscope (Chapter 30, *this volume*). On optically homogeneous specimens, equipping the "far" objective with a reflector to return the spot into itself, might not only increase photon efficiency but also might permit combining reflected and transmitted confocal scanning.

As mentioned earlier, two-photon excitation, will probably also spawn the development of special objectives, not only in terms of their spectral characteristics but with spherical and chromatic correction optimized for the IR, such as the recent "IR" objectives from Olympus.

For the study of live organisms, one needs water-immersion objectives that combine the long working distance needed for deep penetration, with the highest possible NA for better resolution and improved photon collection efficiency.

These are just a few thoughts on possible future developments in this area. No doubt, specialists in optical design will quickly return us to reality and make us do with less than our dreams.

ACKNOWLEDGMENTS

Many thanks to a number of scientists at Carl Zeiss, Germany, for their help in preparing this paper and for many of the illustrations. Special thanks to Mr. Franz Muchel, head of the mathematics group at Carl Zeiss, whose paper (Zeiss Information #100, 1/89, 20–27) on ICS optics has been particularly helpful, to Dr. Bernd Faltermeier for much support, and to Willi Ulrich, who provided many of the computer simulations and other valuable suggestions.

REFERENCES

Inoué, S., and Oldenbourg, R., 1995, Optical instruments: Microscopes, In: *Handbook of Optics* (M. Bass, ed.), 2nd ed., McGraw-Hill, New York, pp. 17.1–17.52.

Boyde, A., and Jones, S.S., 1995, Mapping and measuring surfaces using reflection confocal microscopy, In: *Handbook of Biological Confocal Microscopy*, 2nd ed., Plenum, New York, pp. 255–266.

Maly, M., and Boyde, A., 1994, Real-time stereoscopic confocal reflection confocal microscopy using objective lenses with linear longitudinal chromatic dispersion, *Scanning* 16:187–193.

Pawley, J.B., Amos, W.B., Dixon, A., and Brelje, T.C., 1993, Simultaneous, non-interfering collection of optimal fluorescent and backscattered light signals on the MRC 500/600. In: *Proceedings of the 51st Annual Meeting of the Microscopy Society of America*, San Francisco Press Inc., San Francisco, pp. 156–157.

Petroll, W.M., Cavanaugh, H.D., and Jester, J.V., 1993, Three dimensional imaging of corneal cells using in vivo confocal microscopy, *J. Microsc.* 170:213–219.

Shimizu, Y., and Takenaka, H., 1994, *Microscope Objective Design in Advances in Optical and Electron Microscopy* (C. Shepard and T. Mulvey, eds.) Academic Press, San Diego, pp. 249–334.

APPENDIX: LIGHT TRANSMISSION SPECIFICATIONS FOR A NUMBER OF MODERN OBJECTIVES MADE BY DIFFERENT MANUFACTURERS.[4]

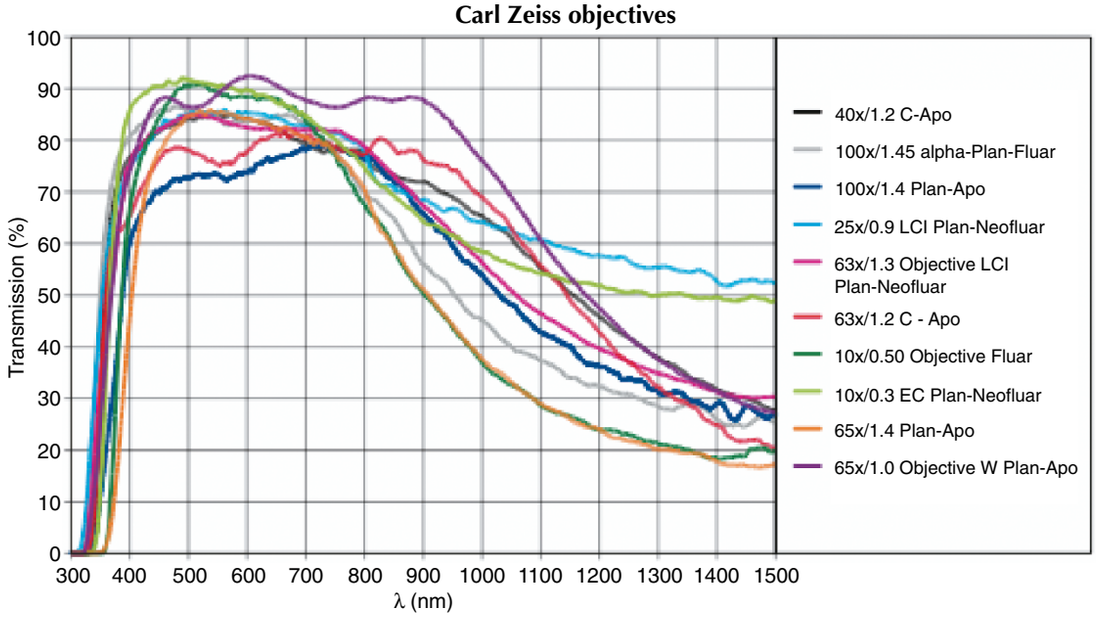
Leica objectives

Objective	Mag	NA	WD(μ)	T(350)%	T(546)%	T(900)%	Blue	Immersion
HC PL APO 10×/0.40 CS	10	0.40	2200	40	90	75		dry
APO L 20×/0.50 W UVI	20	0.50	3500	60	91	75		water
HC PL APO 20×/0.70, multi-imm, collar	20	0.70	260	40	87	71	•	water/glycerol/oil
HCX PL APO 63×/1.40-0.60 oil	63	1.40	100	20	82	63	•	oil
HCX PL APO 63×/1.30 glycerin collar	63	1.30	280	18	87	64		glycerol : water, 80 : 20
HCX PL APO 63×/1.2 W Corr	63	1.20	220	16	85	65		water

Blue = Blue variant available with color correction optimized in blue range for UV applications and GFPs with 405 or 430 excitation

[4] The specifications printed in this chapter are as supplied to the author by the manufacturers at the time that this book went to press (May 2005). The author and the editor have endeavored to insure that the printed versions of these specifications accurately reflect the reports that they received or that were available on the Internet. We make no other claim and readers are advised that improvements are to be expected and will doubtless be announced on the Internet.

Carl Zeiss objectives

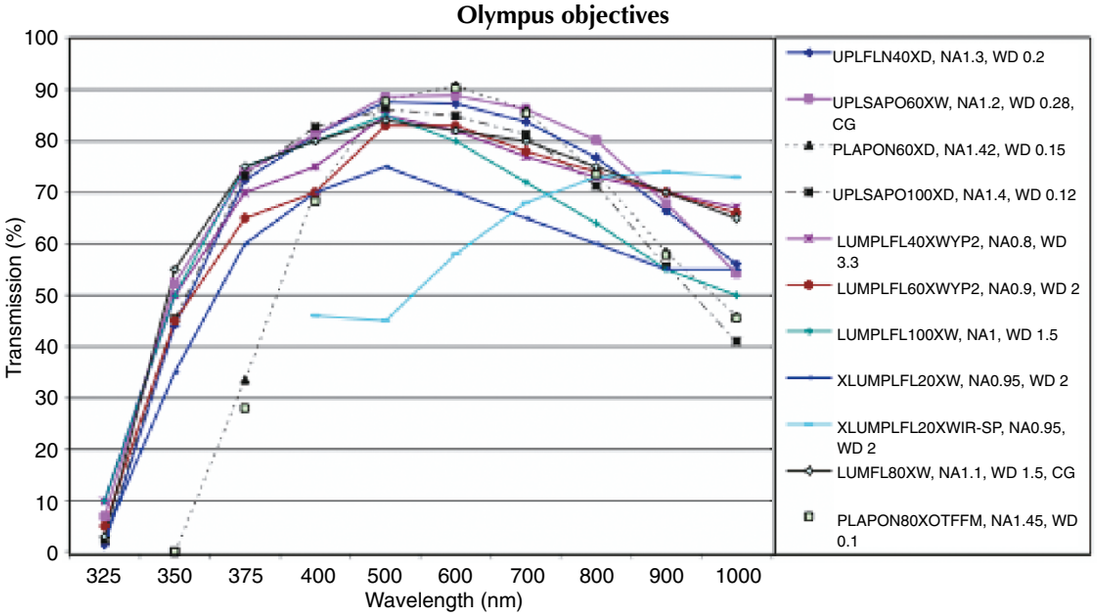


Nikon objectives

Objectives	N.A.	Coverglass (mm)	Working Distance (mm)	Trans % @350 nm*	Trans % @550 nm*	Trans % @900 nm*
CFI PLAN ACHROMAT 100× OIL	1.25	0.17	0.20	B	A	A
CFI PLAN APO 20×	0.75	0.17	1.00	E	A	B
CFI PLAN APO 40× w/collar,	0.95	0.17	.12–.16	E	A	B
CFI PLAN APO 60× A OIL IR	1.40	0.17	0.21	E	A	B
CFI PLAN APO 60× WI w/collar	1.20	0.15–0.18	0.22	E	A	B
CFI PLAN APO VC 60× WI	1.20	0.13–0.19	0.27	E	A	B
CFI PLAN FLUOR 20× mult-imm	0.75	0.17	.033–.035	B	A	A
CFI PLAN FLUOR 40×	0.75	0.17	0.72	A	A	A
CFI PLAN FLUOR 100× OIL	1.30	0.17	0.20	B	A	A
CFI SUPER FLUOR 40× w/collar	0.90	0.17	0.30	B	A	B
CFI SUPER FLUOR 40× OIL	1.30	0.17	0.22	B	A	A
CFI W FLUOR 60× dipping	1.00	n/a	2.00	B	A	A
CFI PLAN 100× dipping	1.10	n/a	2.50	E	A	A
CFI Plan Apo TIRF 60×H w/collar	1.45	0.17	0.13	E	A	B
CFI Plan Apo TIRF 100×H	1.45	0.17	0.13	E	A	B

Key: For transmission percentages: A = > 71%, B = 51–70%, C = 31–50%, D = 16–30%.

Olympus objectives



8

The Contrast Formation in Optical Microscopy

Ping-Chin Cheng

INTRODUCTION

In any form of microscopy, one needs not only an imaging system with enough resolution to delineate the fine details of the specimen but also a suitable contrast mechanism by which to "see" the shape of the structures of interest. Contrast is the difference between the signal in one pixel and that in another that conveys to the viewer information about the shape of the specimen. It is the difference between a blank screen and an image.

In photographic terms, contrast is the change in brightness of a negative or print. In other words, contrast is the difference in signal strength between various parts of an image or between details of interest and "background" (see also Chapter 4, *this volume*). The contrast (γ) is proportional to the intensity difference (ΔI) between two image areas, divided by the average image brightness $\bar{I}$.

$$\gamma = \frac{\Delta I}{\bar{I}}$$

In optical microscopy, contrast derives from differences in the way the various sub-volumes of the specimen (voxels) interact with the illumination. This interaction may include linear and nonlinear absorption, single- and multiple-photon fluorescence, Raman emission, fluorescence spectral shift, fluorescence lifetime, refraction, reflection, phase shift, scattering, changes in polarization, harmonic generation, etc. A contrast mechanism can thus be considered to be a special "filter" function by which specific types of spatial or temporal signals are selected to form a two-dimensional (2D) or three-dimensional (3D) image.

This chapter will provide an introduction to the contrast characteristics of those modalities that have been well investigated in confocal and nonlinear microscopy, including fluorescence and scattering contrast. It will also consider the deleterious influence on the confocal and multi-photon image of the absorptive, refractive, and reflective properties of structures that are between the plane-of-focus and the objective lens, of these topics are relevant to the operation of all epi-illuminated microscopes and some also apply to signals detected in transmission, particularly as used to detect second harmonic (SHG) and third harmonic (THG) signals.

In addition, this chapter will introduce ways in which the contrast present in the raw data from the microscope can be digitally modified before being presented in the final image. At various stages in this sequence, the signal may be ratioed, filtered, and corrupted and the contrast reduced by the addition of noise. In all these areas, this chapter serves as an introduction to other chapters in which individual contrast mechanisms are discussed in more depth.

Image contrast arises from the interaction of an incident light beam with the specimen. Various physical and digital "filters" can be used to select specific signals. For example, one can discriminate specific wavelengths using dichroic beam-splitters and barrier filters; the effective numerical aperture (NA) of the objective lens can produce topographic contrast from the geometric shape of specimen surfaces; polarized light can be used to obtain contrast caused by specimen birefringence; and fluorescence signals from ion-specific dyes in two different spectral channels can be ratioed to detect the concentration of ions such as $[Ca^{++}]$ and $[H^{+}]$.

The contrast that forms a microscopic image is determined by the number of physical, chemical, and biological phenomena. Contrast mechanisms can be subdivided into (a) optical contrast, (b) geometric contrast, (c) biological and chemical contrast, and (d) synthetic contrast. From the point of view of the specimen, the contrast mechanism can be intrinsic or extrinsic in nature. Although each of these contrast mechanisms will be discussed separately, it is not uncommon for more than one to be active at the same time and care must be taken to choose experimental parameters that emphasize the contrast that highlights the most informative of these interactions.

The interaction of an incident light beam with a sample is a complex event. Figure 8.1 shows a simplified version of such an interaction as well as some of the effects produced by the voxels above and below the voxel being sampled. These interactions give rise to the optical phenomena and the photochemical and biochemical effects that provide the bases of all the contrast.

When a beam of light with intensity I_0 is incident on a specimen, a number of physical phenomena may occur. These include the scattering of light due to Rayleigh, Mie, and Raman scattering (I_{S_R}, I_{S_M}, *and* I_{S_Raman}). Rayleigh scattering is caused by interactions with very small particles in the specimen (from the size of molecules up to ~10% of the wavelength) and its strength (I_{S_R}) is strongly wavelength dependent. It also depends on direction: scattering at right angles to the illumination is only half the forward intensity (I_{S_R}). Rayleigh scattering is elastic scattering because the scattered photons have the same energy as the incident photons.

By contrast, scattering in which the scattered photons have either a slightly higher or lower photon energy is called Raman scattering (I_{S_Raman}). This energy change usually involves either the excitation of some vibrational mode of the molecule (giving the scattered photon a lower energy), or the scattering of the photon off an excited vibrational state of a molecule (which adds its vibrational energy to the incident photon).

Cell organelles and other refractive structures larger than the wavelength of the illumination contribute to Mie scattering (I_{S_M}).

P.C. Cheng • State University of New York at Buffalo, Buffalo, New York 14260 and National University of Singapore, Singapore

 Handbook of Biological Confocal Microscopy, Third Edition, edited by James B. Pawley, Springer Science+Business Media, LLC, New York, 2006.

Mie scattering has a sharper and more intense forward lobe for larger particles than Rayleigh scattering (Fig. 8.2), is not wavelength dependent and is responsible for the almost white appearance of adipose and brain tissue. Such a scattering center can act as a secondary light source within the specimen.

In addition to these scattering events, refractive index (RI or **η**) differences between various biological structures can cause the incident ray to deviate from its original path, producing defocusing or sampling errors (i.e., imaging the signal from the "wrong" voxel). Reflection occurs at any interface separating regions of different RI.

The incident light can also be attenuated by absorption. Photon absorption occurs when the quantum energy of the photon matches the energy gap between the initial and final states of some electron in the specimen. If no pair of energy states exists such that the photon energy can elevate an electron from a lower to an upper state, then the matter is transparent to this radiation. In the absorption process, some of the absorbed energy can be re-emitted in the form of a fluorescent or phosphorescent photon. Biological molecules have specific absorption characteristics and the low effective absorbance of most tissue provides a relatively transparent "window" in the visible and near-infrared range (NIR). This window provides the working spectrum for all the optical microscopy (see Figs. 21.1 and 40.2, *this volume*). When the incident light intensity is very high, nonlinear optical phenomena such as nonlinear absorption, multi-photon fluorescence, and harmonic generation of incident light become prevalent (Fig. 8.1).

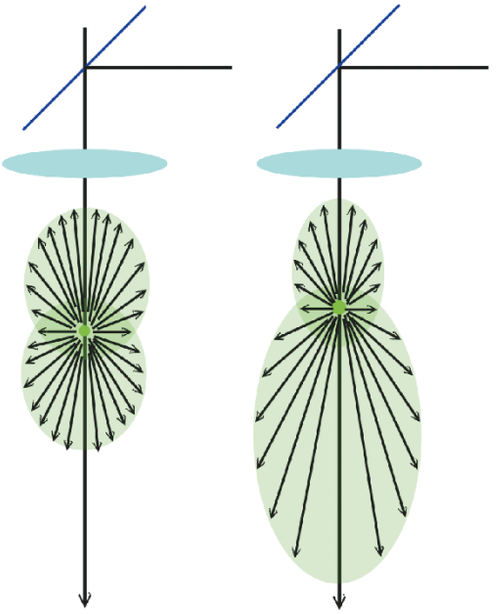


FIGURE 8.2. Rayleigh scattering (left) and Mie scattering (right). In Mie scattering, the forward lobe becomes larger as particles become larger. This is the reason that dark-field illumination produces more signal in transmission than in epi mode.

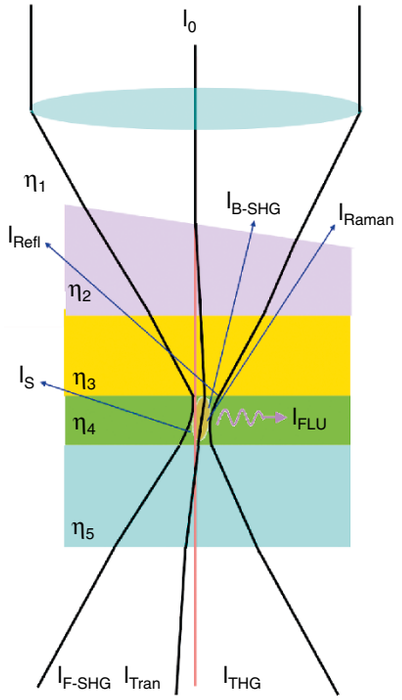


FIGURE 8.1. Interaction of light with a voxel of the specimen. The hypothetical specimen consists of four layers with different RIs (n2, n3, n4, n5) and the surface of the top layer is slanted with respect to the optical axis. The illuminating beam (I_0) is refracted by the surface of the top layer (pink) and subsequent layers with the result that the focal spot is not on the original optical axis (red line). Various signals, including fluorescence (I_{FLU}), scattering (I_S), reflection (I_{Refl}), Raman (I_{Raman}), second harmonic generation in both forward and backward direction ($I_{B\text{-}SHG}$ and $I_{F\text{-}SHG}$), and third harmonic generation (I_{THG}) may be produced when conditions are favorable. The pink spot at the focus indicates the volume where nonlinear phenomena prevail at high illumination intensity. Transmission intensity, I_{Tran}.

It is well known that different RIs can be associated with different crystallographic orientations of crystalline materials. For example, calcite crystals have indices of refraction for the o- and e-rays of 1.6584 and 1.4864, respectively. Mineral crystals showing two distinct indices of refraction are referred to as birefringent materials. Birefringence has to do with anisotropy in the binding forces between the atoms forming a crystal. A large number of quasi-crystalline biological materials also exhibit birefringence (Fig. 8.3).

SOURCES OF CONTRAST

Absorption Contrast

If the light–specimen interaction is predominantly photon absorption (as it is in the prepared tissue sections, stained with absorbing dyes), and the specimen has a uniform thickness [Fig. 8.4(A)], and if the incident light is I_0, then the transmitted intensity, I_1 and I_2 through structures 1 and 2 in the voxel being sampled is:

$$I_1 = I_0 e^{-\mu_1 x}$$

and

$$I_2 = I_0 e^{-\mu_2 x}$$

where μ_1 and μ_2 are the absorption coefficients of structures 1 and 2, respectively, and x is the length of the absorption path (the thickness of the voxel in this case). The contrast due to absorption (γ_{abs})

$$\gamma_{abs} = \frac{\Delta I}{\bar{I}} = \frac{I_1 - I_2}{\bar{I}}$$

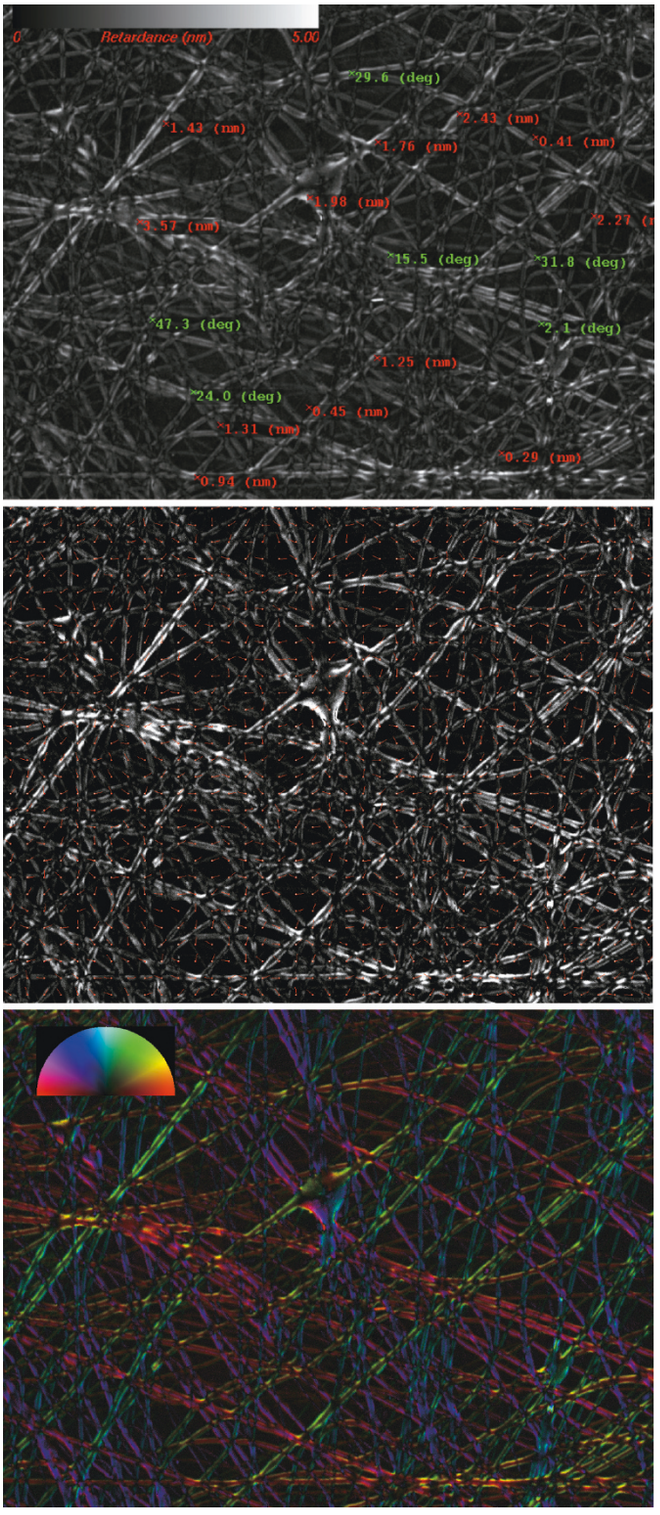


FIGURE 8.3. Birefringence of artificially reconstituted collagen fibers. (Upper) A retardance image of collagen fibers. (Middle) Orientation of the collagen fibers indicated by small arrows. (Lower) Orientation coded as color. [Images courtesy of Hanry Yu, Department of Physiology, National University of Singapore and made using a Polscope (Cambridge Research Inc., Cambridge, MA).]

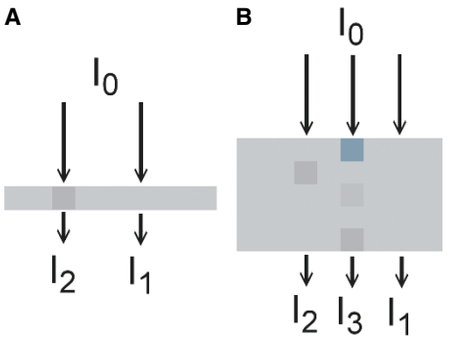


FIGURE 8.4. Hypothetical thin (A) and thick (B) specimens composed of a light-absorbing matrix with an absorption coefficient of μ_1 and containing small structures with an absorption coefficient of μ_2. The transmission intensities of the matrix and structure are I_1, I_2, and I_3, as marked.

However, in real specimens, the structure of interest is generally much smaller than the thickness of the specimen and therefore, it resembles the situation in Figure 8.4(B), the effective absorption coefficient μ_T for a given light path is:

$$\mu_T = \sum_{i=1}^{m} \mu_i$$

a term that describes an absorbing specimen composed of m different subunits, each having an absorption coefficient (μ_i), where μ_T is the absorption coefficient associated with the light attenuation along the specific light path.

For a sample with thickness x, and the effective absorption coefficients of an area of interest (μ_{T1} and μ_{T2}), the absorption contrast (γ_{abs}) is:

$$\gamma_{abs} = \frac{\Delta I}{\bar{I}} = \frac{I_1 - I_2}{\bar{I}} = I_0\left(e^{-\mu_{T_1}x} - e^{-\mu_{T_2}x}\right)\Big/ I_B$$

where $\bar{I} = \dfrac{\sum_{k=1}^{n} I_0 e^{-\mu_k x}}{n} = \dfrac{I_0 \sum_{k=1}^{n} e^{-\mu_k x}}{n} \approx I_B$ and n is the number of pixels in the image. The absorption contrast (γ_{abs}) between pixel 1 and 2 shown in Figure 8.4(B) is:

$$\gamma_{abs} = I_0\left(e^{-\mu_{T_1}x} - e^{-\mu_{T_2}x}\right) \cdot e^{\mu_B x}$$

The Rose criterion (Rose, 1948) relates contrast and noise to visibility. It states that, to be visible, the contrast between a feature and its surroundings must be 5 times the noise in the surroundings [signal-to-noise ratio (S/N) >5 : 1],

$$e^{(\mu_2 - \mu_1)x} \geq 5$$
$$(\mu_2 - \mu_1)x \geq \ln 5$$
$$\mu_2 - \mu_1 \geq \frac{\ln 5}{x}$$

Apart from the fact that the optical transfer function implies that small features will be rendered in the image with less contrast than large ones and that the Poisson noise associated with recording any image adds uncertainty to the measurement of contrast, large features will also have low contrast if the tissue is only lightly stained, and small, intensely stained structures will have less contrast when visualized inside a thick, stained region of the sample. Finally, unstained biological tissues contain few molecules that absorb in the visible and our ability to detect small changes in

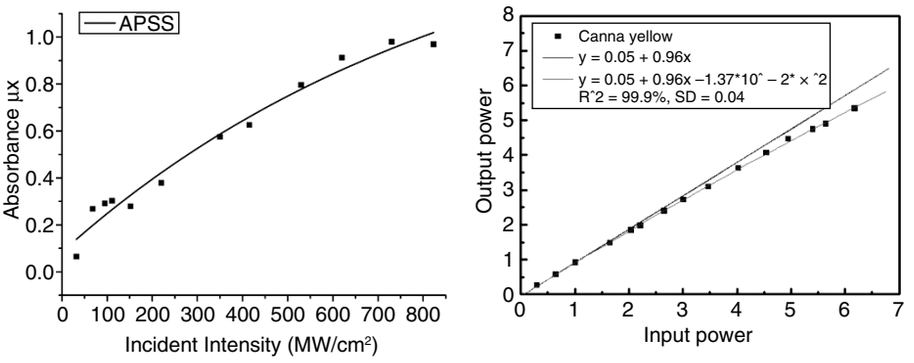


FIGURE 8.5. Nonlinear absorption of the up-converting dye, APSS, and of an ethanol extract of yellow petal of *Canna*, as a function of excitation light intensity.

absorbance by eye is poor. For all these reasons, linear absorbance contrast is used mainly on material that has been fixed and stained.

If one increases the incident intensity, the optical response of the specimen will eventually begin to show significant nonlinear components; in fact, the optical response can be described by the following power series [$\tilde{P}(t)$]:

$$\tilde{P}(t) = \varepsilon_0\chi^{(1)}\,\tilde{E}(t) + \varepsilon_0\chi^{(2)}\,\tilde{E}(t)^2 + \varepsilon_0\chi^{(3)}\,\tilde{E}(t)^3 + \ldots$$
$$\equiv \tilde{P}^{(1)}(t) + \tilde{P}^{(2)}(t) + \tilde{P}^{(3)}(t) + \ldots$$

where $\chi^{(1)}$ is the linear susceptibility, $\chi^{(2)}$ is the second-order nonlinear susceptibility, and $\chi^{(3)}$ is the third-order nonlinear susceptibility. The effective nonlinear absorption cross-section $\mu(I_0)_{eff}$ is a function of the incident intensity. The nonlinear transmission intensity,

$$I_{trans_nonlinear} = I_0 e^{-\mu(I_0)_{eff}\cdot x}$$

assuming the concentration of the pigment is relatively low, and that fluorescence is not a factor. Figure 8.5 shows the effective absorbance, $\mu(I_0)_{eff}\cdot x$, plotted against the incident illumination for a solution of the up-converting dye, APSS [Fig. 8.5(A)] and a methanol extract of yellow *Canna* petals [Fig. 8.5(B)], when illuminated with 780 nm NIR light from a Ti:sapphire mode-lock laser (85 MHz, 120 fs pulse). If, as in these cases, the absorber is a fluorophore, this nonlinear absorption may produce fluorescence.

The absorption properties of a specimen (color or opacity) can have a negative impact on image contrast in the backscattered light (BSL) mode. For example, the nearly opaque carbon particles in the polyethylene cable material, shown in Figure 8.6, cause a significant loss in signal intensity by attenuating both the illuminating beam and the BSL signal.

Although deep coloration in biological specimens, such as that caused by pigment granules and chloroplasts, can also have this

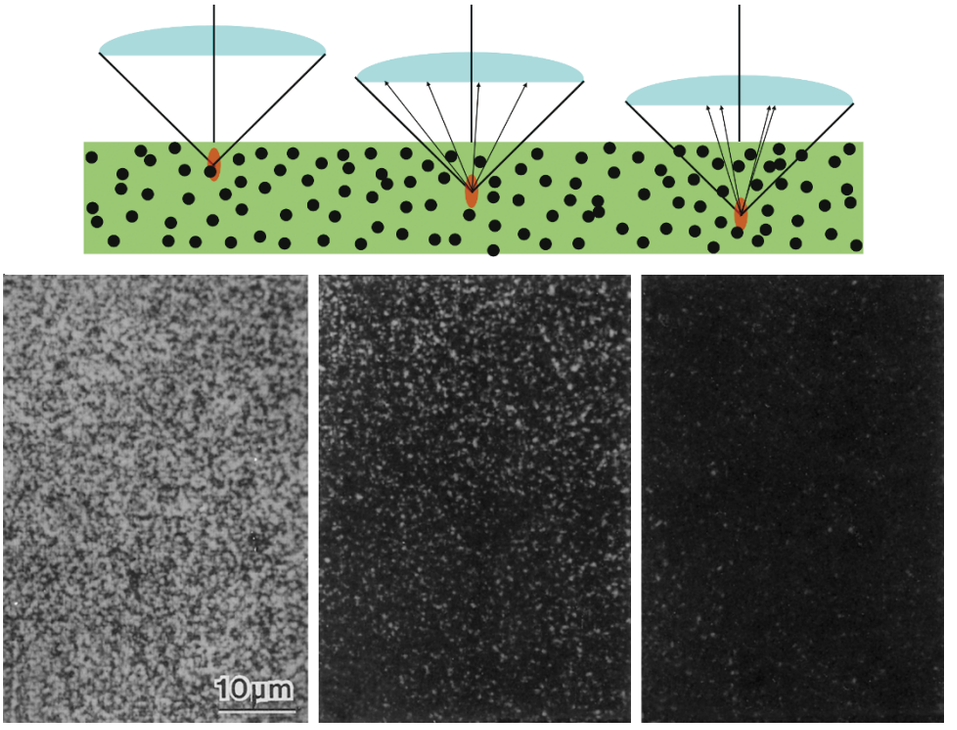


FIGURE 8.6. (Top) When the objective is focused into a particle-filled clear matrix, the scattered and reflected rays from the structure of interest are modulated by the particles located between the objective and focal plane. (Bottom) Diagram of self-shadowing.

effect, the problem can sometimes be minimized by selecting a λ that reduces absorption to a minimum. For example, when imaging plant cells, green illumination will be absorbed much less than blue or red. As many biological and polymeric specimens are very transparent to IR, it is sometimes worthwhile surrendering some resolution by using a longer λ in order to penetrate deeper into the specimen. For example, NIR (700–1200 nm) radiation can be used to study the internal structure of insects because insect cuticle is relatively translucent in this region of the IR spectrum. This improvement is due to lower absorbance and also to decreased Rayleigh scattering, which is proportional to λ^4. The other side of the equation is that objects of interest must now be somewhat larger to produce a detectable BSL signal.

Modern confocal microscopes are generally operated in an epi-illuminated configuration, both in fluorescence and BSL mode. However, it is also possible to operate the confocal microscope in the trans-illumination configuration to image absorption contrast (An *et al.*, 1990). The straightforward approach to designing a transmitted confocal microscope is to mount two opposed microscopes on a common optical axis with both objective lenses focused on a common point in a specimen. One serves as the light source and the other as the detector. Rastered images are obtained by scanning the specimen with an *xy* mechanical stage.

It is clear that such a design has some major drawbacks: (1) The stage scanning method is relatively slow and not suitable for most biological specimens because of the stage vibration involved. (2) In a beam-scanning system (either with a single laser beam or the multiple beams of a disk-scanning system), it is technically difficult to synchronize the scanning of separate illumination and detection systems perfectly. (3) Because of differences in the RI and optical path length within the specimen, a small translation of the specimen along the optical axis (*z*) can result in significant misalignment of the focal points of the two opposed objectives, reducing signal levels. Unfortunately, 3D sets of optical-section images can only be obtained by translation in *z* (Chapter 30, *this volume*).

Cheng and Lin (1990) demonstrated a simple trans-illuminated confocal design utilizing folded optics [Fig. 8.7(A)]. The design uses a second high-NA, infinity-corrected objective that is coaxial and confocal with the primary objective so that light transmitted through the specimen is captured by this second lens. A mirror normal to the optical axis and placed behind the second objective reflects the transmitted light back to the first objective along the same path, and a confocal configuration is maintained as long as the second objective remains confocal with the primary objective.

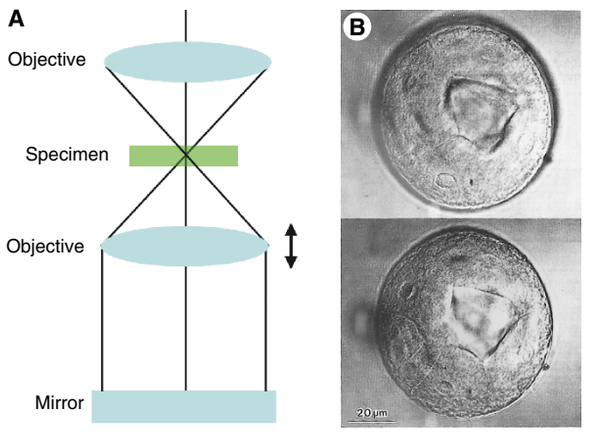


FIGURE 8.7. (A) Diagram of a double-pass, trans-illumination folded optical setup for trans-illuminated confocal light microscopy. (B) A set of trans-illuminated confocal images of a sea urchin embryo (*S. purpuratus*). The optical sections were obtained at 4 µm apart. The specimen was fixed in 3 : 1 (ethanol/acetic acid), stained by the Feulgen method, dehydrated, and cleared in methyl salicylate.

The problem is that any misalignment between the two objectives caused by moving an optically heterogeneous specimen in the *x*-, *y*-, or *z*-direction will cause a large reduction in signal, even in the absence of any absorptive dye. To avoid this, we have developed a computer-controlled, precision piezoelectric/mechanical system that allows precise positioning of the second objective lens by monitoring intensity changes in the captured image. Figure 8.7(B) shows two series of optical sections of a sea urchin embryo (*Strongylocentrotus purpuratus*) obtained in the transmitted, confocal mode using a laser scanning system. This set of images was obtained by realigning the folding optics after each focus change (4 µm total). Contrast in these images results primarily from absorption by the specimen summed over both passes, but there is also a small contribution from BSL and interference between the two beams. The effect of the BSL in the image can largely be removed by subtracting a pure BSL image from the absorption image.

Because the sensitivity for detecting absorptive tags is inherently low and because any optical misalignment caused by refractile organelles produces a signal reduction that can be confused with such absorption, transmitted confocal microscopy is unlikely to become an important imaging modality. However, this optical scheme can be used for forward-SHG detection in an epi-illumination setup.

With this basic transmitted optical system, a wide variety of interference contrast mechanisms can be implemented by adding the appropriate optical components into the back-focal plane of one or both objectives, or simply by using mirrors that cover only parts of these planes. Such images can, in principle, be collected in addition to, and independently of, any fluorescent signals (see Chapters 2, 9, and 30, *this volume*). For example, Cogswell (1994) demonstrated confocal imaging of both phase and amplitude objects. To optimize the optical conditions of both objectives, the specimen must be sandwiched between two coverslips instead of a microscope slide and a coverslip (Cheng *et al.*, 1994).

A bonus feature of this transmitted configuration is a small improvement in the signal strength when the microscope operates in epi-fluorescence mode. The folded optical path provides double excitation and, in addition, much of the fluorescent light captured by the lower objective lens is returned to the detector. Assuming that the dye is not close to singlet saturation and that the transmittance of the second objective is high, the system can increase fluorescence signal strength 2 to 3×. Although this approach may be of some use with disk-scanning microscopes where fluorescence image intensity is relatively low, problems related to maintaining alignment between the many beams used in such a system may restrict its use to prepared specimens that are embedded in a clearing medium. In addition, as the folded light path corresponds to operating in transmission fluorescence rather than epi-fluorescence, the barrier filter in front of the detector must be very efficient to exclude stray excitation light (see Chapter 3, *this volume*).

As harmonically generated signals propagate preferentially in the forward direction, the trans-detection configuration is the preferred detection layout. However, the double-pass method does permit simple, descanned SHG and THG detection when beam-

scanning. Sun and colleagues (2005) have demonstrated that certain biological specimens also generate backward SHG, meaning that conventional epi-detection can also be used.

Scattering and Reflection Contrast

Scattering includes Rayleigh, Mie, and Raman scattering. While the strongly wavelength-dependent Rayleigh scattering originates from molecules, Mie scattering primarily results from cellular structures such as organelles. On the other hand, because Raman scattering is a non-elastic event, the scattered photon either loses or gains energy from the vibrational state of the molecule involved, and consequently the scattered light carries information about the state of the molecule. When the structure is much larger than the wavelength of light and presents a smooth RI interface or metal surface, reflection results. Depending on the size and geometry of the feature in the specimen that causes it, the light signal that proceeds from the specimen toward the detector in an epi-illuminated, widefield, or confocal microscope is commonly either referred to as either BSL or reflected light.

The intensity of the Rayleigh-scattered light I varies inversely with the 4th power of the wavelength.

$$I = I_0 \frac{8\pi^4 N\alpha^2}{\lambda^4 R^2}(1+\cos^2\theta)$$

where N is the number of scatters, α is polarizability, and R is the distance from the scatterer.

Mie scattering is generated mainly by the organelles in the cell and is not strongly wavelength dependent, but the scattering intensity is proportional to the square of the ratio of the RI of the feature and the RI of the media. If scattered light is not a desired signal, it can be greatly reduced if the specimen is "cleared" by immersing it in an index-matched liquid. This allows one to image significantly deeper into the tissue (see Chapter 49, *this volume*).

When light is incident on a smooth interface separating materials with different RIs, such as the water/oil droplet, the reflected intensity depends on the incidence angle and the RI difference. In geometric optics, when light travels from one medium to another of different RI, the light separates into two components: the reflected ray and the refracted ray. The degree of reflection depends on the gradient of RI between the two media. The refracted ray changes its propagation angle (θ_r) with respect to the incident beam (θ_i) as described by Snell's law:

$$\frac{\sin\theta_i}{\sin\theta_r} = \eta_{21}$$

where constant η_{21} is the RI of the second medium relative to the first medium. It can be expressed in terms of the refractive indices of η_1 and η_2.

$$\eta_1 \sin\theta_1 = \eta_2 \sin\theta_r$$

If the incident angle (θ_i) is greater than the critical angle (θ_c), where

$$\sin\theta_c = \eta_{21}\ \eta_{21} < 1$$

then total reflection results. In reflected-light confocal microscopy, the reflectance (i.e., the ratio of illumination intensity to reflected intensity) of the specimen is one of the key factors determining signal strength. The reflectance is the ratio of the difference of the squares of the refractive indices of the two media.

$$\frac{I_{refl}}{I_0} = \left(\frac{\eta_1 - \eta_2}{\eta_1 + \eta_2}\right)^2$$

Therefore, the smaller the difference in RI between the two media, the lower the reflectance. In living biological specimens, the RIs of most cellular structures differ very little from that of the surrounding aqueous medium, and hence, structures inside biological specimens have much lower reflectance than most materials sciences specimens. For example, the reflectance of a gold-coated glass surface (a mirror or an integrated circuit chip) can be >95% and that of the metallic silver deposited in a Golgi-stained neuron may be −10%, but the typical reflectance of the surface of a maize leaf (surface cuticle interface with air) is ~0.03% and the reflectance of human bone imaged under a confocal microscope and that of living specimens, such as tissue culture cells, is even lower. Detection of reflection from a curved surface can produce image contrast related to the curvature and the NA of the objective lens used (Fig. 8.8). Despite the low reflectance, confocal images of tooth enamel prisms and Golgi-stained Purkinje cells have been obtained (Boyde, 1985). Watson (1989) demonstrated real-time imaging of an internal section of a tooth being abraded by a dental burr by using a tandem-scanning confocal microscope (TSM) operated in BSL mode.

When viewed with a multi-channel (or spectral) confocal microscope, colloidal-gold particles as small as 5 nm can be detected because they appear much brighter under green laser illumination than under blue or red. This is because the molecular resonance properties of gold particles cause them to Rayleigh scatter green light more strongly than other visible wavelengths (Born and Wolf, 1980). As a result, it is possible to ratio the images obtained from the blue and green channels to identify the colloidal gold specifically (Cogswell, 1994). This technique can be used to study the colloidal gold-labeled samples prior to fixation for EM study.

When light passes through matter, some of it is scattered in random directions with a small energy gain or loss due to Raman scattering. If the initial beam is sufficiently intense and very monochromatic, a threshold can be reached[1] beyond which light at the Raman frequencies is amplified and the output generally exhibits the characteristic of stimulated emission. Raman spectroscopy is a powerful analytical method in microscopy. As early as 1992, Sharonov and colleagues (1992) used it in confocal microscopy. Image contrast in a Raman confocal image can result either from intensity variations at a selected energy level or from variations in the Raman spectra obtained from different optical sections. In the latter case, the basic image unit in such an *xyk* image is referred to as "lambxel" (Cheng *et al.*, 1994).

Because light reflecting from inclined surfaces may be deflected away from the objective lens, BSL images of silver-impregnated nerve cells appear punctuate. Even though the dendrites are actually continuous structures, the silver grains with which they are decorated are not. Therefore, small "gaps" between nerve fibers seen in the confocal BSL images may not indicate a lack of continuity but only that the reflecting surface is tilted too steeply for the reflected light to reach the objective.

Golgi-stained Purkinje cells show strong contrast between the surface reflections from the silver-decorated cells and the weak scattering by the surrounding non-impregnated tissues. Golgi preparations are of interest primarily because the method stains only 1% to 5% of the neurons in the preparation (Barr and Kieman, 1988; Scheibel and Scheibel, 1970). This creates a clear image of the dendritic tree of a single neuron hundreds of micrometers in

[1] Something more likely to occur near the focus, where intensity is highest, a feature that gives the technique some z-resolution.

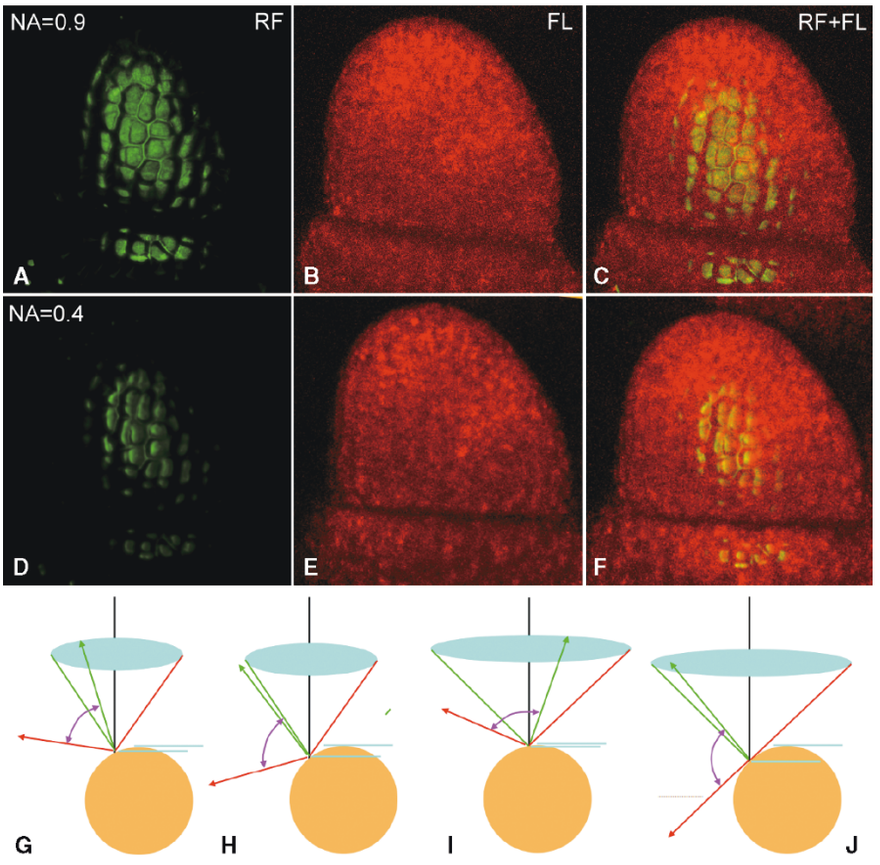


FIGURE 8.8. The effect of NA on the fraction of the light reflected from a sphere that is detected. A projection of confocal images made with reflected light (A) and autofluorescence (B), of the apical meristem of maize. (A–C) were made using an NA = 0.9 dry objective. (C) is a combined image. (D–F) The same, using an NA = 0.4 dry objective (magnification adjusted). Note that the region of detectable surface reflection is much smaller than that from which fluorescence can be detected and is lower with the low NA objective. (G–J) Diagrams that show how the NA and the height of the focus plane affects the fraction of a spherical surface from which reflected light can be collected by the objective lens (as defined by the red and green rays).

depth. If all the neurons stained, optical sectioning would be impossible because the high reflectivity would prevent light from penetrating much below the outer surface.

BSL images of living biological specimens present the same problems. Image contrast degrades as the objective lens focuses deeper into the tissue. Interfacial reflections from the various cellular components increasingly degrade the beam as it passes through more overlying cells. In addition, the deeper the microscope is focused into the specimen, the more heterogeneous the "medium" between the focal plane and the objective becomes, and the more that refraction produced by these inhomogeneities degrades the optical performance of the microscope. Figure 8.9 shows a BSL image of part of an amoebic pseudopod. The surface of the pseudopod, the mitochondria, vacuoles, and a number of other organelles and cytoplasmic crystals produce significant BSL. Chen and Cheng (1989) used the BSL mode to image the macronuclei of *Stentor coeruleus*.

Although the low reflectance of many living animal specimens makes is possible to see some distance into them, the low signal level that results complicates real-time BSL imaging of moving specimens. However, in plant cells, the interface reflections may be so strong that they bend the beam and produce "doubled" images in extended-focus (projection) views. This deflected illumination beam can also excite fluorophores to produce spurious fluorescent signals (Fig. 8.10, arrows).

When two reflective surfaces are in close proximity, interference fringes can occur. Although these fringes may be useful for measuring height, they also complicate image interpretation. Interference contrast can be used to study focal contacts (regions of close contact between the cell membrane with supporting substratum) in cultured animal cells. Figure 8.11 shows the interference fringes generated by the opposing surfaces of the plasma membrane of an amoeba and the cover glass.

In the materials sciences, Shinozald and colleagues (1991) used such interference fringes to study the delamination of a Cu thin film from an underlying polyimide substratum during a mechanical tensile test. This technique can also be used for detecting adhesion of transparent materials to the underlying support matrix. Figure 8.12 shows the delamination of a polyethylene film from glass in a micro-indenter test. Local detachment of the film from the underlying glass substratum results in pronounced interference fringes.

Figure 8.13 shows the surface of an ancient rice grain imaged by BSL confocal microscopy. The specimen is an artifact from an archeological site in southern Taiwan and contains mainly the carbonized skeleton of the endosperm. No trace of DNA was detectable in the grain. The double image of the surface actually represents separate images of the top and bottom surfaces of the cell wall (Fig. 8.13, *xz*- and *yz*-images). When imaging the interface of a dense block in a transparent medium, as shown in Figure 8.14, edge effects become prevalent. The vertical edge can be imaged in great depth but not the internal structures of the dense block. Figure 8.14(B) shows both the fluorescent and BS images of the edge of a maize stem (cross-section) mounted in water.

In disk-scanning confocal microscopes that utilize single-sided scanning, image contrast is reduced if light reflected by the disk surface is inadequately trapped. This increase in background signal level is particularly serious when the reflectance of the specimen is low. On-axis reflections of coherent light from optical surfaces are a serious problem when using a confocal microscope in the

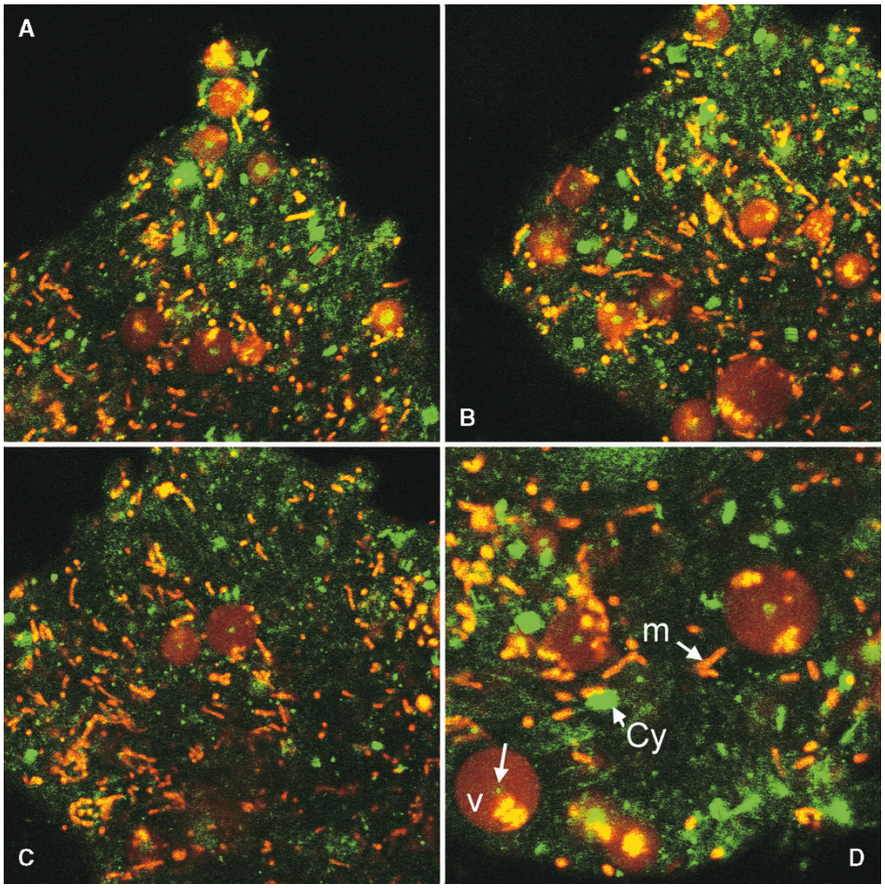


FIGURE 8.9. Two-channel confocal images of the pseudopod of an amoeba (*Chaos carolinense*) showing mitochrondria (m) and vacuoles in red fluorescence and backscattered light in green. The large, highly reflective structures are crystals (Cy) in the cytoplasm. A central scattering "core" (*arrow*) can be found in the spherical vacuoles (for an explanation, please see Fig. 8.19). (Images by Y. Deng, Z. Almshergi, and P.C. Cheng, Departments of Physiology and Biological Sciences, National University of Singapore.)

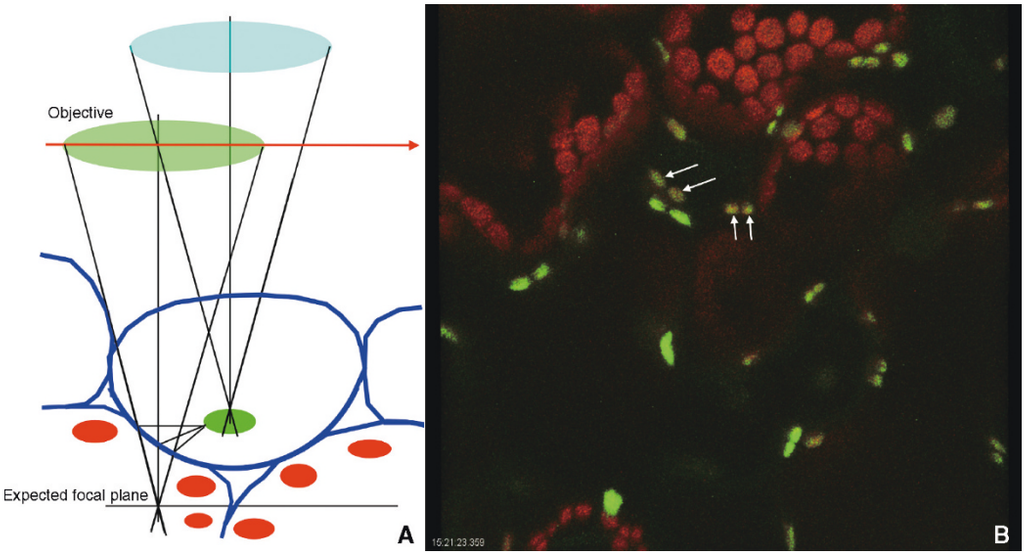


FIGURE 8.10. (A) Diagram of a possible situation that can generate a double image from a fluorescent organelle. In certain botanical specimens, the cytoplasm–cell membrane (cell wall) interface acts as an efficient reflective mirror, producing paired, mirror images of bright structures in an optical slice. In some cases, the position of the imaged organelle may be very different from the expected focal plane. (B) An extended focus (projection) view of an *A. thaliana* leaf. Note the double-imaged GFP organelles in the epidermal cells. The chloroplast-containing cells are mesophyll cells, situated below. (Image *courtesy of M. and D'A Weis, Agriculture Canada Laboratory, Summerland, BC.)

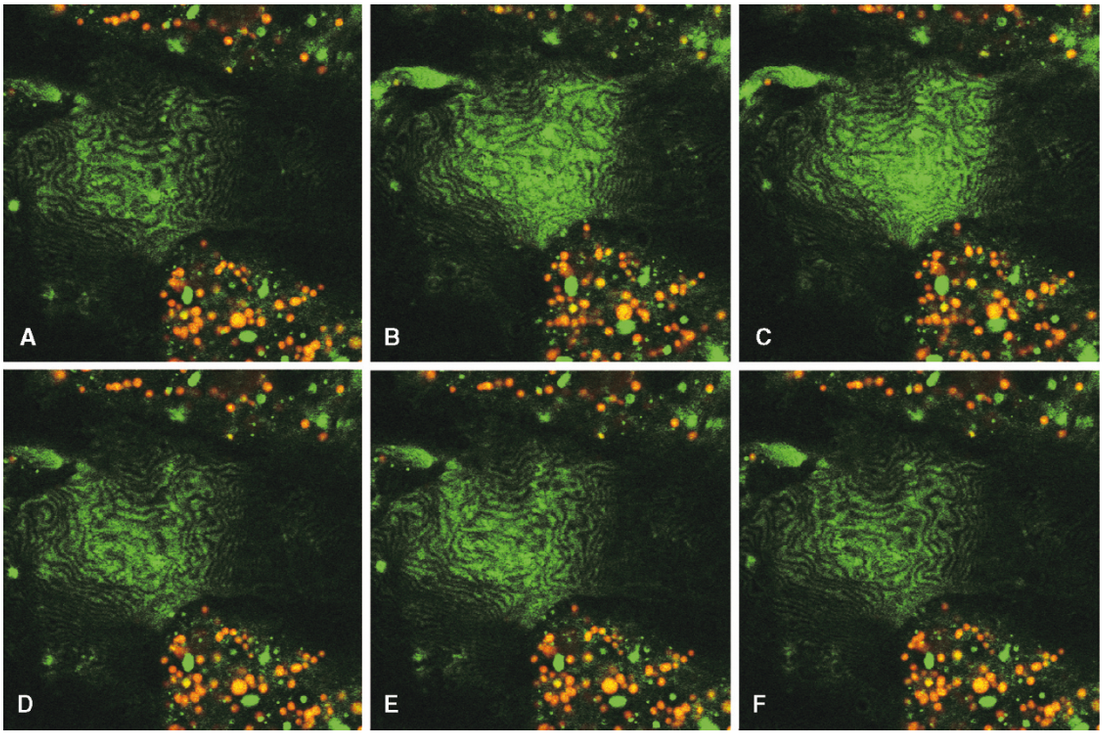


FIGURE 8.11. The separation between the plasma membrane of an amoeba and the coverslip can be monitored by the interference patterns generated by light reflected from these two surfaces. (A–F) time series showing movement of the plasma membrane. (*Green*, reflected/backscattered light; *red*, Mitotracker fluorescence.)

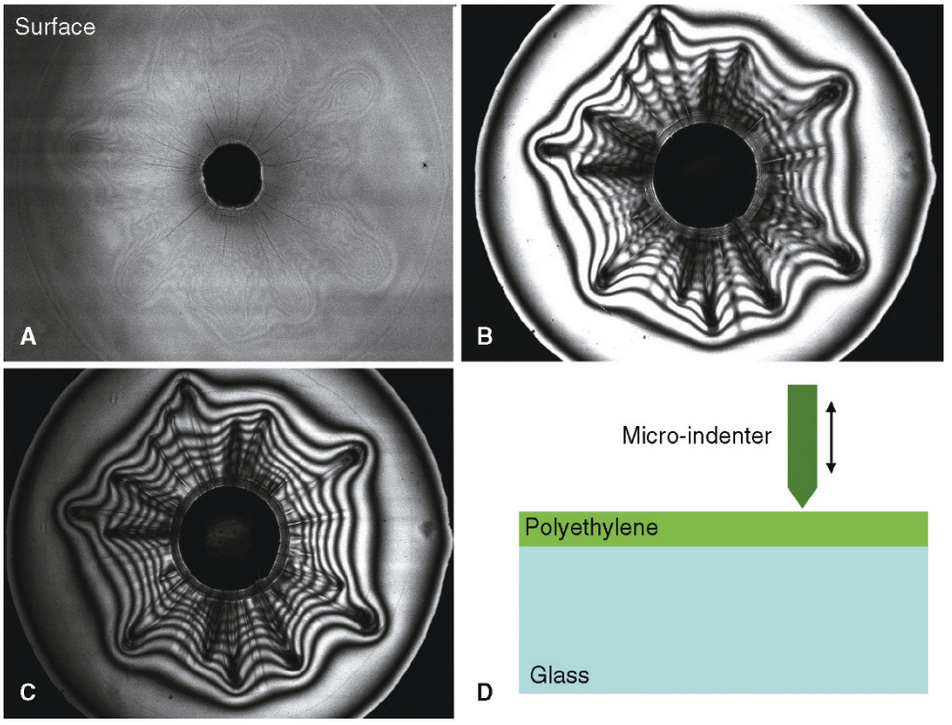


FIGURE 8.12. Delamination of plastic film from its substrate can be imaged by reflective confocal microscopy. (A) Focused near the surface of the polyethylene film, (B) and (C) focused near the plastic–glass interface. The interference patterns provide a good measure of the gap resulting from delamination. (D) Diagram of the experimental setup. A micro-indenter was used to deform the plastic, causing delamination. (Specimen courtesy of D.M. Shinozaki, Department of Mechanical Engineering, University of Western Ontario, London, Canada.)

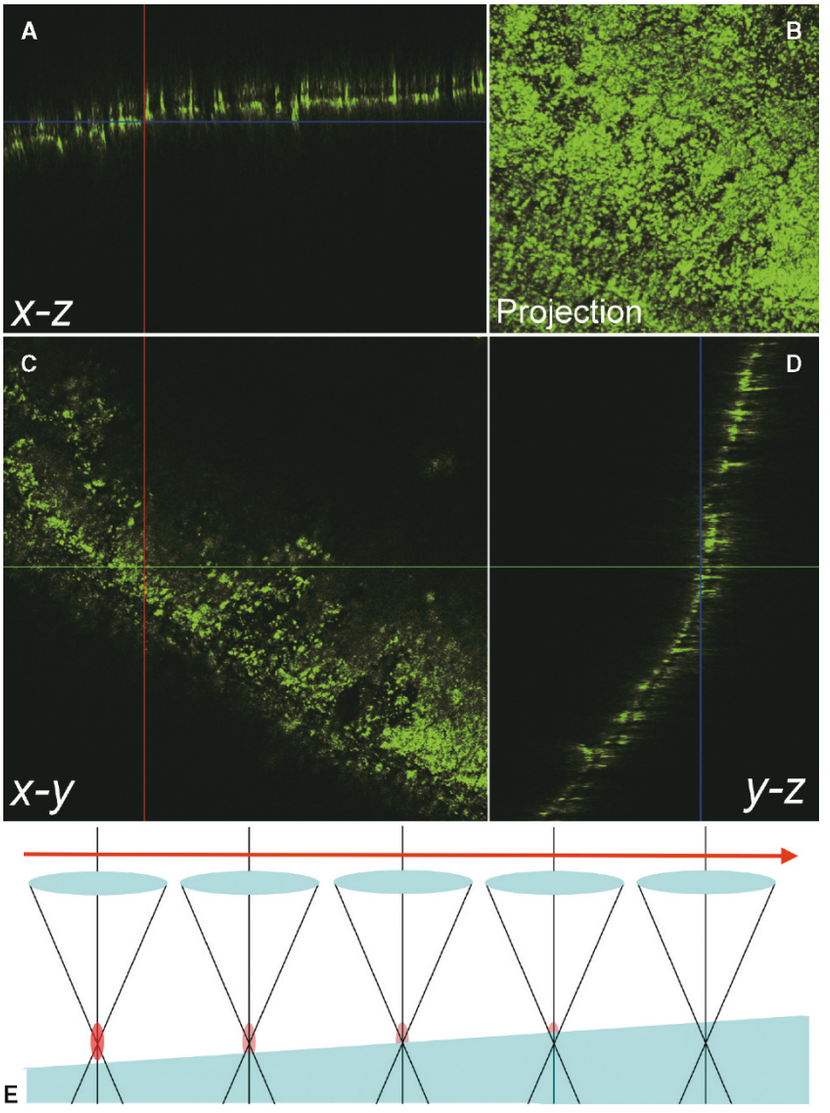


FIGURE 8.13. The surface of an ancient rice grain imaged by BSL confocal microscopy. The specimen is an artifact from a southern Taiwan archeological site and contains mainly the carbonized skeleton of the endosperm. (A) *xz* view, (B) extended focus view (projection view), (C) *xy* optical section, (D) *yz* view. Note the double-line in the *xz* and *yz* image. (E) Diagrammatic representation of the imaging condition. (Specimen kindly provided by Yue-Ie Caroline Hsing, Institute of Plant and Microbial Biology, Academia Sinica, Taipei, Taiwan.)

BSL mode. The result is a bright spot or a series of diffraction fringes in the center of the image (see Fig. 8.42, discussed later). Although this artifact can be avoided by panning the scanned area away from the optical axis, this approach sacrifices the field of view and degrades the image by using off-axis portions of the optical system in which the image is less well corrected (see Chapter 11, *this volume*).

In the single-sided confocal microscopes constructed by Kino (Xiao *et al.*, 1988) and by us (Cheng *et al.*, 1989), the light reflected from the surface of the spinning disk and from optical surfaces is removed by using a Glan–Taylor-type polarizer to achieve high polarization extinction (10^{-5}) of the illuminating laser beam, and adding a 1/4-wavelength retardation plate to the optical path just above the objective to convert the linearly polarized illuminating beam to circularly polarized light. With an analyzer placed just in front of the detector, this arrangement removes most unwanted reflections although there is still a small amount of reflection from the front surface of the objective lens.

Of greater concern is the fact that on-axis reflections from optical elements, or from the surface of the coverslip or the slide, can interrupt mode-locked operation of ultrafast lasers. This situation can be avoided by inserting a Faraday rotator and 1/4-wave plate into the illumination beam to prevent the reflected beam from re-entering the laser cavity (see also the discussion of Antiflex techniques in Figs. 2.7 and 10.5, *this volume*).

Phase Contrast

Because the human eye [or the charge-coupled device (CCD) camera] is sensitive only to changes in amplitude, phase variations produced by the specimen must be converted by the optical system into amplitude variations for them to become visible. For example, phase contrast and differential interference contrast (DIC) convert specimen-induced phase shifts of the illuminating light into amplitude contrast at the final image plane. Most biological specimens are 3D phase objects consisting of many compartments, each with a different RI. Apart from generating contrast, these structures also distort and shift the wavefront of the illuminating beam, resulting in complex interference patterns. Both phase and DIC are frequently used in conjunction with confocal microscopy to obtain the general morphology of the specimen. Because DIC has good *z* resolution, 3D digital image restoration of DIC image stacks is now commercially available (AutoQuant, Troy, NY; see also Chapters 2 and 24, *this volume*).

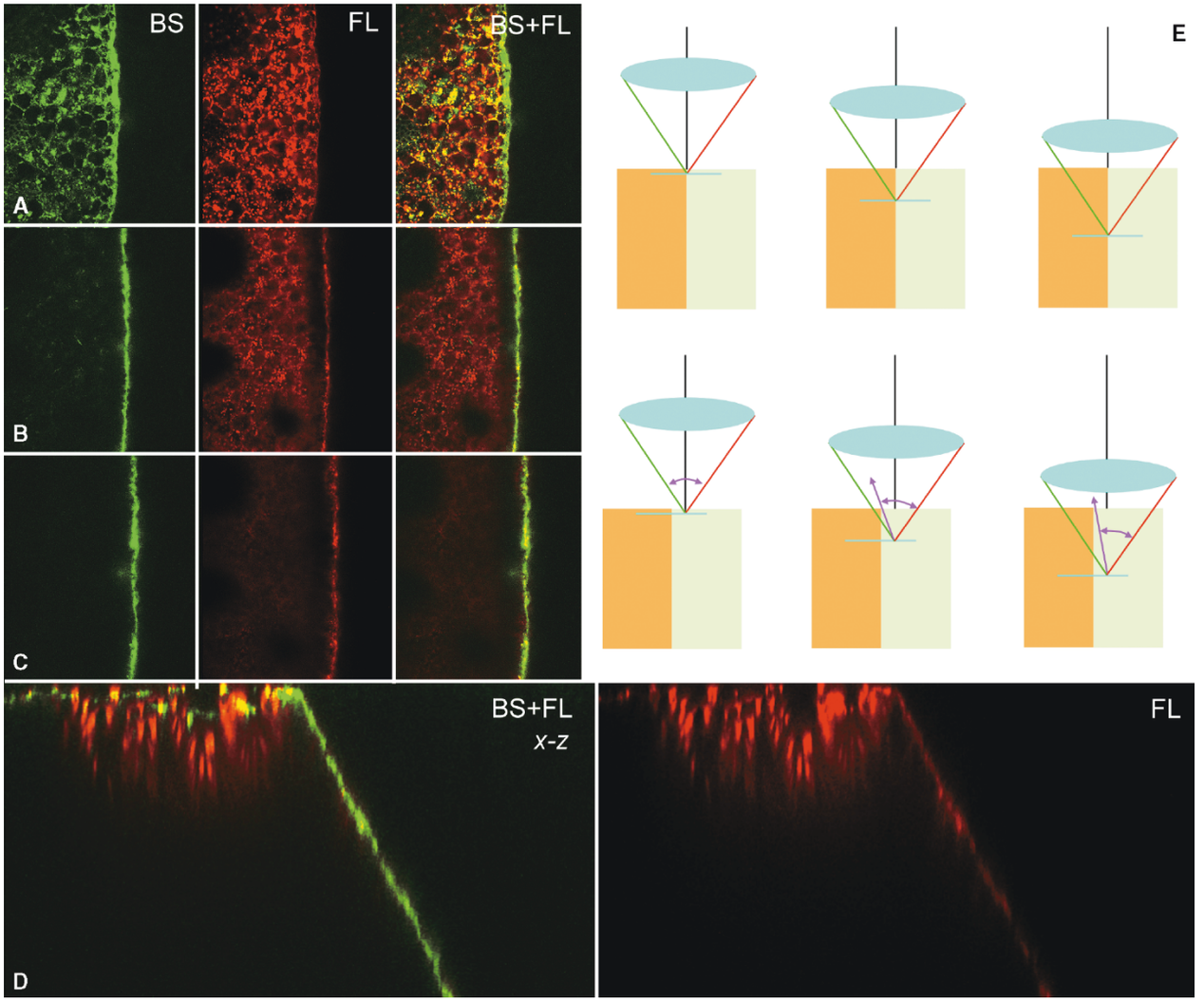


FIGURE 8.14. Edge effect. (A, B, C) Optical cross-sections (*xy*) of the edge of a maize stem at various depths. (D) *xz* section of the image stack showing the highlighted edge. Green, BS; red, autofluorescence (FL). (E) Diagram of the imaging situation. (Note the edge of the maize stem is actually tilted with respect to the optical axis although the diagram shows a vertical edge.)

Fluorescence Contrast

When one images emission signals, such as those produced by fluorescence microscopy, for a given ΔI, one can increase the contrast by lowering $\bar{I}$. In a typical epi-fluorescence microscopy, the background intensity from scattered illuminating light is removed by the dichroic beam-splitter and the barrier filter (see Chapter 3, *this volume*). In the absence of diffuse staining, this darkfield optical system produces a very low $\bar{I}$. This increases the contrast between the background and very weakly fluorescing structures, a feature that has ensured the popularity of this technique for the past 40 years.

The factors affecting the detectability of fluorescence from a voxel are the intensity of incident radiation, the intensity of the fluorescence (itself a function of the concentration of the fluorochrome, its absorption cross-section and its quantum yield (QY) at a given excitation wavelength), self-absorption within the voxel and between the voxel and objective, and the effective NA of the objective. Additional background signal may reach the detector because of imperfections in the dichroic elements and overlap between the absorption and emission spectra of the dyes involved (see Chapter 36, *this volume*).

In multi-photon fluorescence microscopy, the axial and transverse-contrast is the result of the 3D energy gradient at the focal point, the concentration and nonlinear QY of fluorophores, and background signal level under multi-photon excitation. Readers are kindly referred to Chapters 16, 28, and 40 for a detailed discussion of fluorescence imaging.

Because of its exquisite sensitivity and specificity, fluorescence microscopy is an extremely important tool in the biological sciences. In widefield fluorescence microscopy, the detected image data includes signal from both in-focus and out-of-focus subvolumes. This often produces an image that has excessive haze and lacks contrast. As this haze or flare is proportional to the thickness and stain density of the specimen, conventional, widefield epi-fluorescence works best when imaging thin specimens such as tissue culture cells. In confocal imaging, the signals from out-of-focus features are almost completely removed, resulting in an image with exceptionally high contrast (Fig. 8.15; Wijaendts van Resandt *et al.*, 1984; White *et al.*, 1987, Sheppard, 1993). In addition, modern

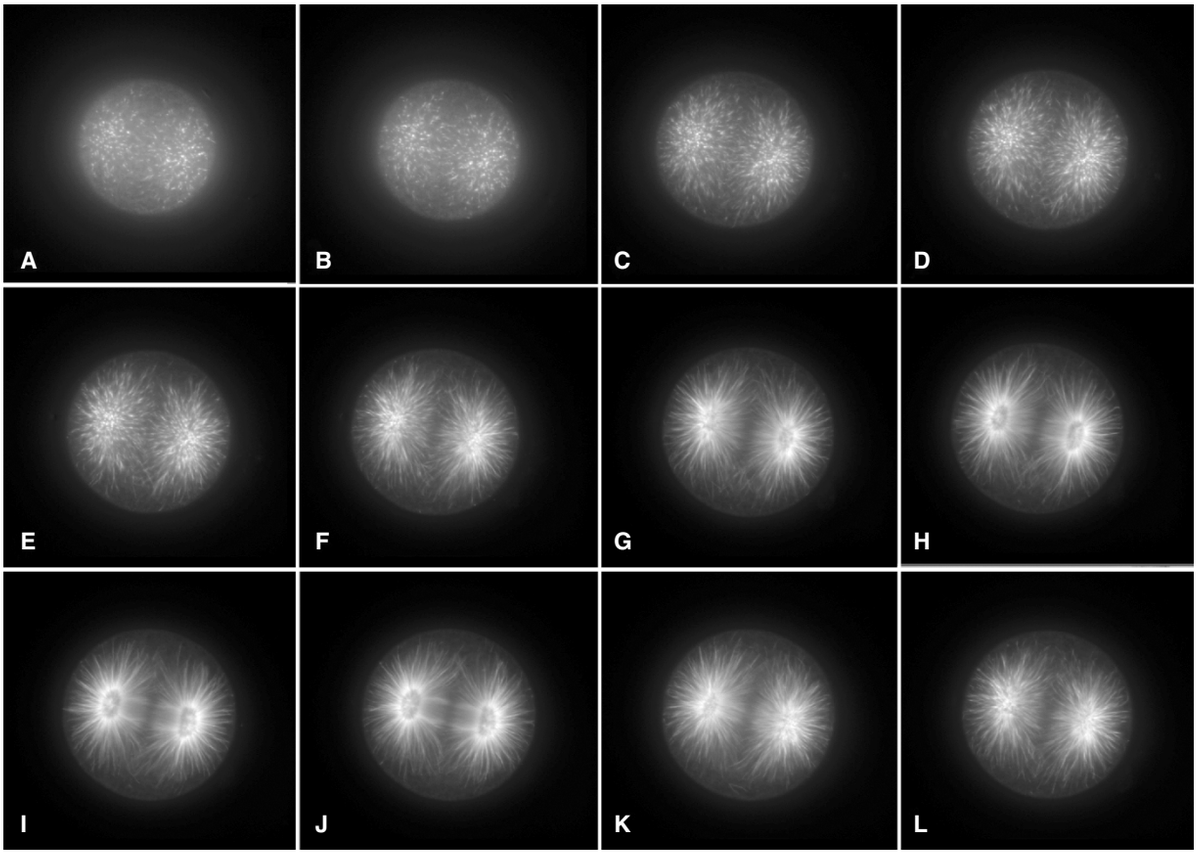


FIGURE 8.15. Series of confocal optical sections of the first mitotic division of a sea urchin embryo in which the microtubules have been labeled with a fluorescent dye.

3D image processing and restoration can further improve the S/N and contrast parameters of the image (see Fig. 8.40 in the Deconvolution section below).

Contrast Related to Excitation Wavelength Change

Biological specimens often naturally contain a large number of fluorescent molecules that produce autofluorescence. Because each fluorescent species has a unique absorption and emission spectra as well as a set QY, the total autofluorescence spectrum can vary with the excitation wavelength. Figure 21.13 shows the changes in the fluorescence spectra obtained from *Canna*, produced by using different excitation wavelengths from 350 nm to 514 nm. Figure 8.16 demonstrates this effect on the root tip of *Arabidopsis thaliana*. Although the signal levels are normalized in the 515 nm detection window, the fluorescence excited at 477 nm (yellow label) produces far less signal longer than 547 nm than does that excited using either 458 nm or 488 nm. The false-color images in Figure 8.16 clearly demonstrate the differences in signal level when the root tip is excited by various wavelengths.

When attempting to detect an exogenous fluorophore, one can often reduce the background level by picking exactly the right excitation wavelength. Therefore, to determine the optimal excitation and emission bandwidths, one must know the excitation spectrum of both the background autofluorescence and the tagged fluorescent probe(s). Figure 8.17 shows how images obtained in different emission bands can vary in appearance and contrast. The emission spectrum shown in Figure 8.16 indicated the presence of BSL and fluorescence from GFP and chlorophylls (Chl). Figure 8.18 is an extended-focus fluorescence image of an alga showing how using different emission filters [green bandpass (G) and red longpass (R)] changes the appearance of a chloroplast.

Negative Contrast

Small, isolated, non-fluorescent structures can be imaged with fluorescence confocal microscopy by filling the surrounding medium with a fluorescent solution. This dye-excluding technique was originally used in the study of polyethylene crystallites in xylene and can also be used to outline small crystal deposits and the extracellular compartment in biological specimens. Because dextrans are relatively inert and exhibit low toxicity, they are ideal markers to probe either extracellular or intracellular compartments. In the material sciences, dye-filling techniques are frequently used to provide contrast when studying micro-cavities (Harridose *et al.*, 1991; Shinozaki *et al.*, 1991; Cheng and Kriete, 1995).

Negative contrast can also be used in a number of biological applications. Figure 8.19 shows that the vacuoles in cells of the peony flower petal are sufficiently autofluorescent to reveal cytoplasmic strands traversing them as dark threads penetrating this fluorescent sea. After acquisition, the fluorescence image can be inverted for 3D reconstruction.

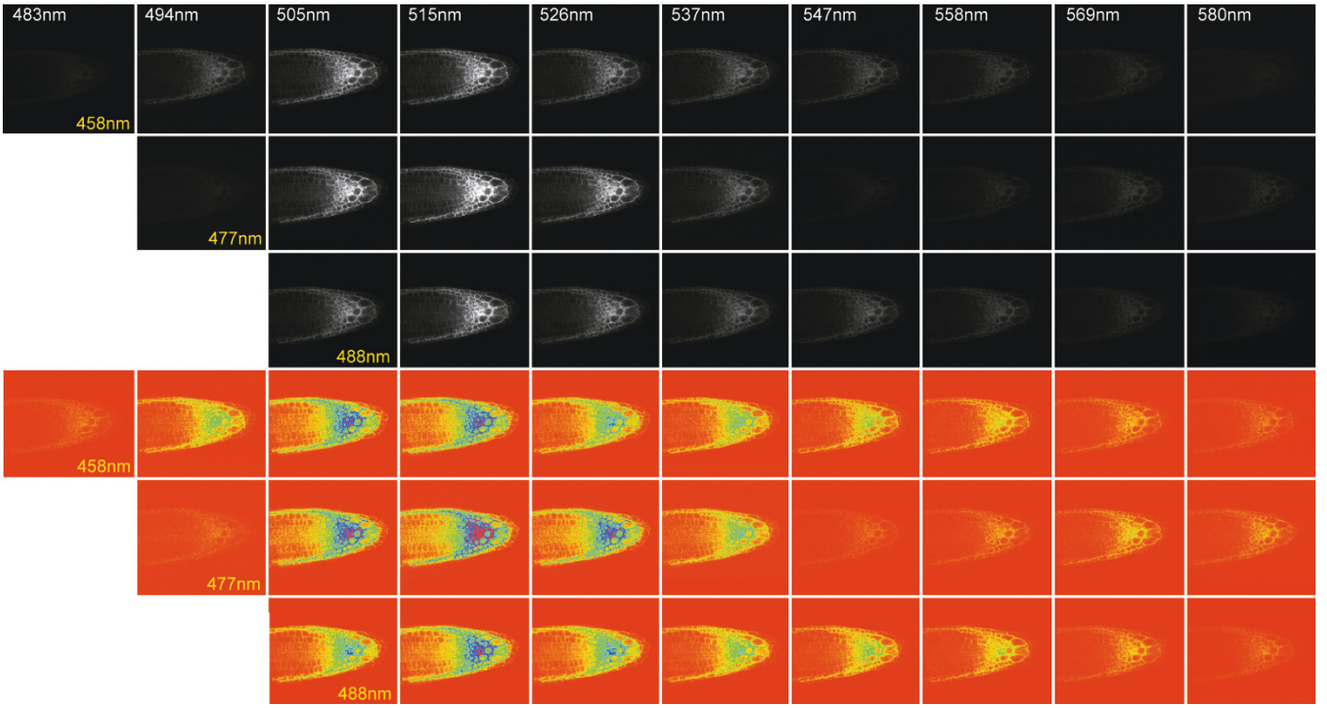


FIGURE 8.16. GFP in the root tip of *A. thaliana*, showing image contrast variation in response to different excitation wavelengths. For each excitation wavelength (*yellow labeling*) at 458 nm, 477 nm, and 488 nm, a series of spectral sections was obtained at 10 nm intervals using a Zeiss LSM510 Meta confocal microscope with the channel gain adjusted for normalized spectral response. The GFP emission peaks at 505 to 515 nm, and shows little variation between the three excitation wavelengths. However, the autofluorescence image (i.e., that at wavelengths >547 nm) shows significant variations at the different excitation wavelengths. The three color rows show the same images in false color to emphasize low-intensity signals. (Images obtained at the 2005 International Course on 3D Microscopy of Living Cells at the University of British Columbia, Vancouver, Canada.)

Figure 8.20(A) shows the fluorescence spectra (excited at different wavelengths) of a zebrafish expressing green fluorescent protein (GFP) and DsRed in its liver and pancreas. Using these spectra, we can understand the contrast and relative signal strength that will be produced when particular excitation wavelengths and filters are used. Figure 8.20(B) shows how the ratio of GFP signal to DsRed signal varies as a function of filter bandwidth. When the total fluorescence emission spectrum represents the sum of the overlapping spectra of a number of different types of fluorescent molecule (a situation typical of autofluorescence), the contrast may be improved by carefully selecting the excitation and detection wavelengths and bandwidths. The differences in photobleaching dynamics among different fluorophores may cause the contrast between two channels to vary during the course of a time-series image stack. Figure 8.21(A) shows the photobleaching spectra of a zebrafish expressing GFP (512 nm) and autofluorescence. In this case, both GFP and the autofluorescent species in the sample exhibit similar bleaching dynamics, resulting in a nearly constant intensity ratio (contrast) over the time course of the study [Fig. 8.21(B)]. Figure 8.22 shows an extended focus view of a zebrafish specimen showing green fluorescence from the pancreas and red fluorescence from the liver. In Figure 8.22(A) one can see that the liver is bisected into two lobes by the pigment cells [Fig. 8.22(B)]. This self-shadowing phenomenon is commonly observed in confocal optical sections [Fig. 8.22(C,D)].

Special Concerns in Ultraviolet and Near-Infrared Range Confocal Microscopy

A micrograph is a plot of the intensity of some signal versus position. Changes in this signal represent contrast. But what if there is an error in the position? If an optical system focuses two wavelengths from the same location on the object into two different locations in the image, then we have created some contrast that should not exist. This can happen if the optical system is not achromatic.

Although most objective lenses are properly corrected for chromatic errors in the visible spectrum, it is wise to check their performance (Fig. 8.23). Normally, the wavelength difference between the illumination and the detection only becomes a serious concern in epi-fluorescence confocal microscopy when one wavelength is outside the visible range. When the excitation wavelength is in the UV, one must use specially designed UV objective lenses that are both chromatically corrected and also transparent for both the excitation and emission wavelengths (Wells *et al.*, 1990; Cheng *et al.*, 1994). Similar conditions apply when detecting IR fluorescence.

The situation is a bit different in multi-photon fluorescence and harmonic generation microscopy where the fluorescence or harmonic signal intensity is proportional to the square of the illumination intensity. Assuming the fluorescence is not near saturation,

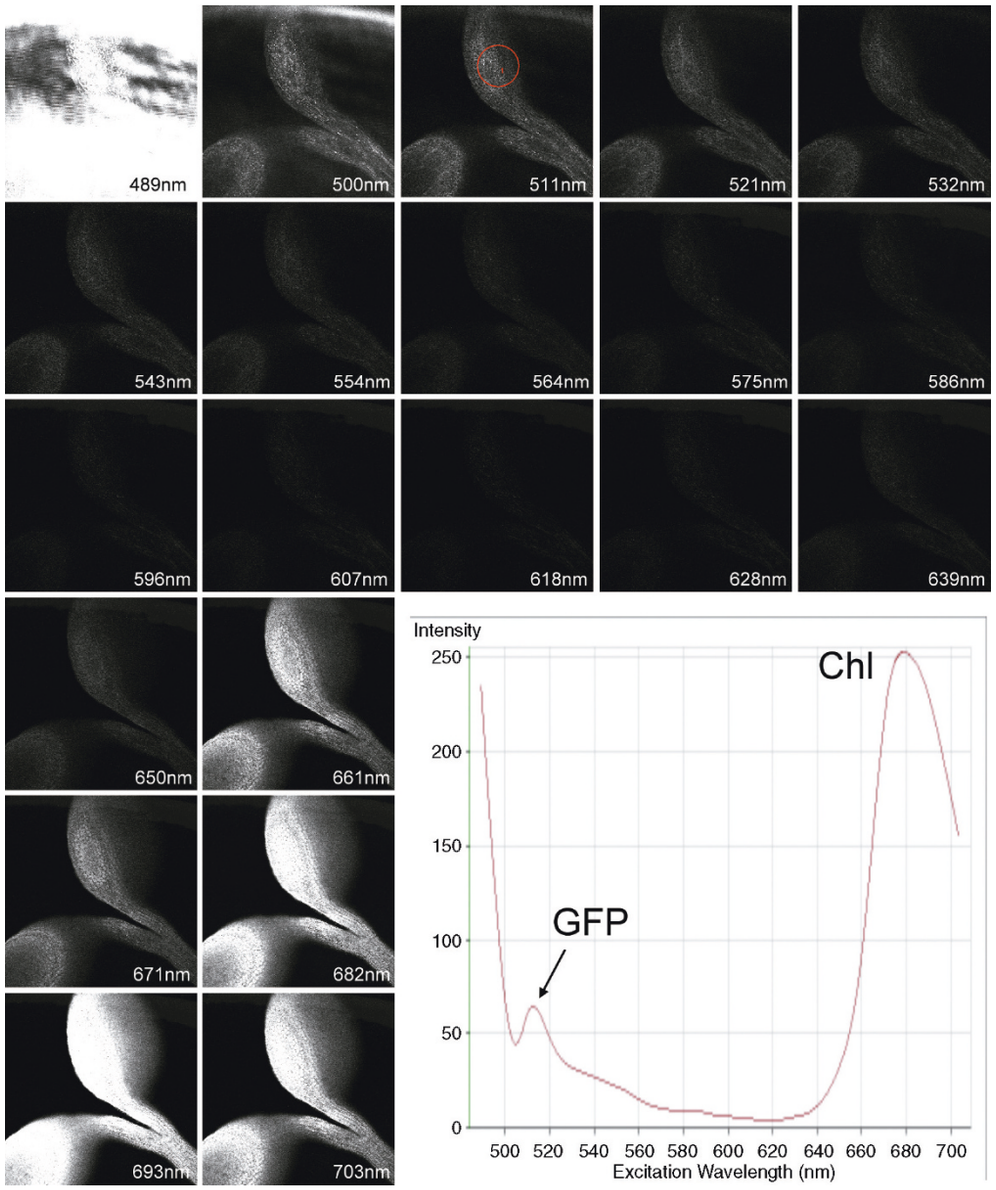


FIGURE 8.17. Spectral confocal image of a young seedling of *A. thaliana* showing GFP and autofluorescence from several chlorophylls. The specimen was excited at 488 nm. The spectrum was obtained from the circled region. The 489 nm image (saturated) represents reflections and scattering of the specimen and cover glass. Based on the spectrum, the 511 nm signal results from GFP while the other "green" fluorescence is the autofluorescence background. The image contrast for the chlorophyll autofluorescence depends on the wavelength of the detecting band (650 nm–703 nm). (Images obtained with a Zeiss 510 Meta. Specimen kindly provided by Shu-Hsing Wu, Institute of Plant and Microbial Biology, Academia Sinica, Taipei, Taiwan.)

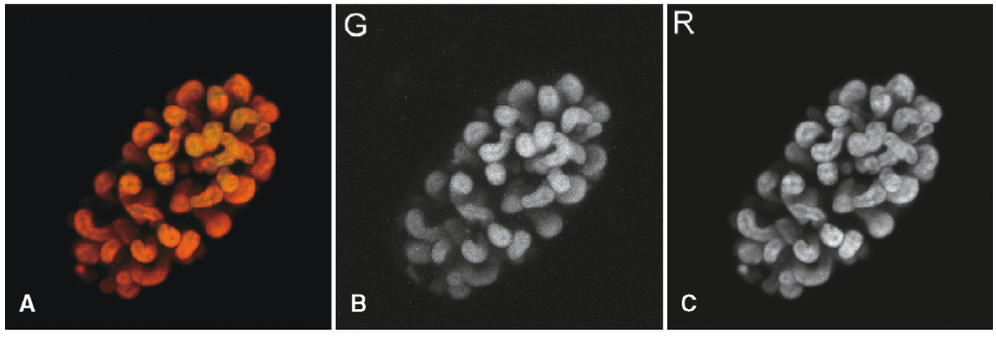


FIGURE 8.18. Autofluorescent image of the chloroplast of an alga. (A) Two-channel false-color image, (B) green channel (em: 540 nm bandpass), and (C) red channel (em: long-pass >600 nm). Note the difference in image contrast between (B) and (C).

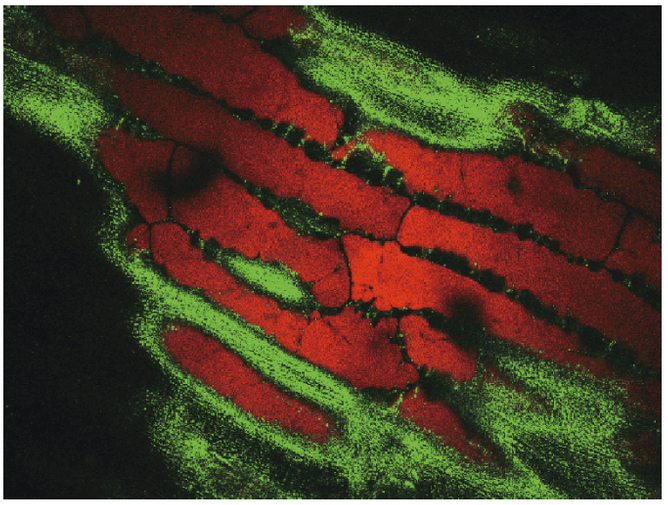


FIGURE 8.19. Two-channel confocal image of a peony petal. The strong autofluorescence of compounds in the vacuoles (*red*) allows one to image the fine (dark) cytoplasmic strands that traverse them, in negative contrast.

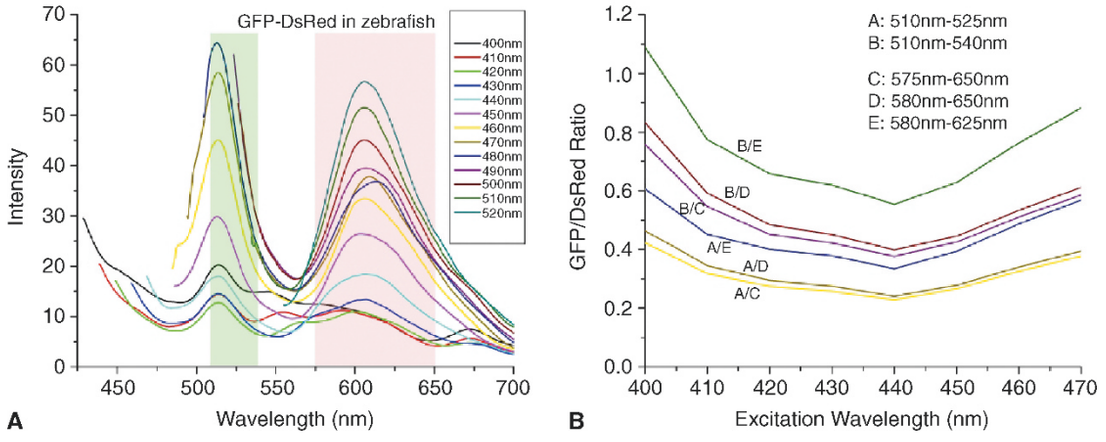


FIGURE 8.20. Emission spectra of GFP and DsRed in zebrafish (pancreas and liver, respectively) when excited at different wavelengths (ranging from 400 nm to 520 nm). Two hypotheical bandpass filters (green and pink bands) were used to separate the emission for imaging. In (B), the contrast ratio of these two channels are compared as a function of filter bandwidth.

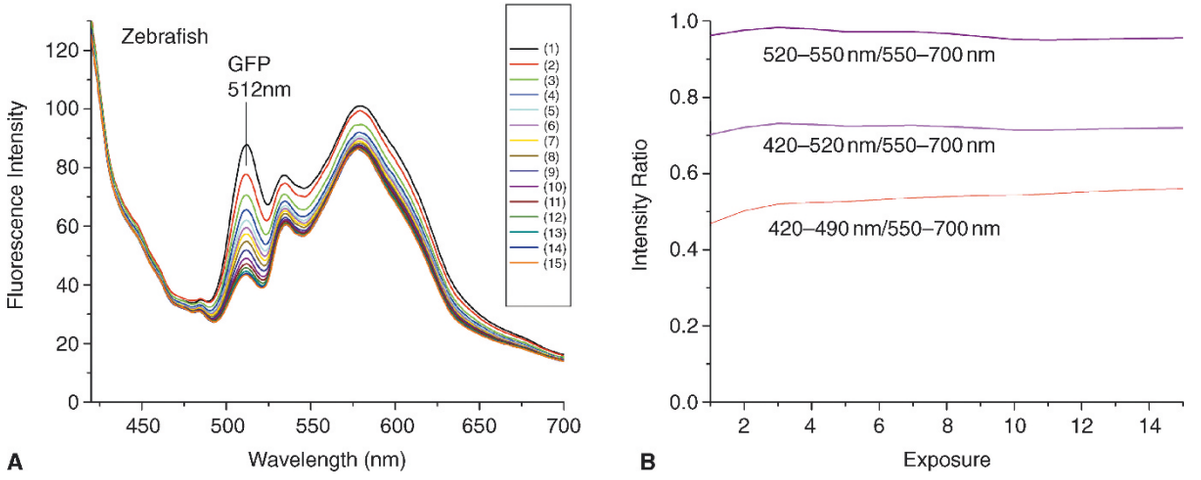


FIGURE 8.21. (A) Emission spectra of GFP (pancreas) and autofluorescence in zebrafish when excited using wavelengths from 400 nm to 520 nm. (B) Contrast ratios of the two channels when using filters having different passbands.

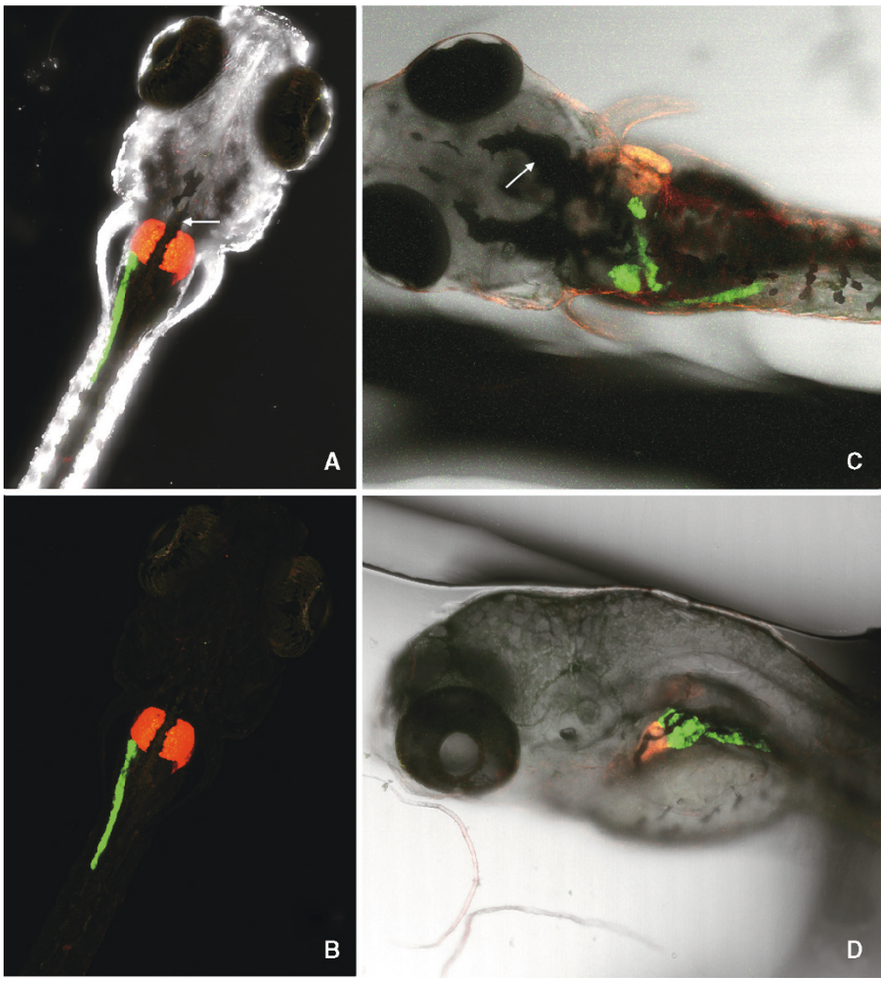


FIGURE 8.22. (A) Two-channel confocal projection images of zebrafish embryos, with a gray, non-confocal transmission image overlay, showing pancreas (GFP), liver (DsRed), and pigment cell (*arrow*). (B) The fluorescence images only. Note the liver is bisected into two lobes by the high absorption of the overlying pigment cells. (C) Embryo at a later stage, from above (D) imaging from the side can reduce the masking effect of the dorsally located pigment cells.

nonlinear signal generation is limited to the vicinity of the focal spot, and non-decanned detection can be used. In this case, chromatic correction from the excitation to the emission wavelength is superfluous because signal is only emitted from the focal region and therefore need not be focused. However, if one wishes to detect simultaneously several flurophores with large differences in QY, the fluorescence emission volume can be significantly different for each fluorophore.

If one uses a beam-scanning confocal unit with a detection pinhole to limit the size of the detection sub-volume, one must use an objective corrected for both the excitation and emission wavelengths but one can adjust the size and alignment of the pinholes for each detection channel to ensure that all signals are obtained from the same sub-volume. Such adjustments are particularly important in co-localization studies. Because the refractive index of the specimen (or medium) varies with wavelength, operation outside the waveband for which the objective is corrected can produce RI mismatches that can introduce spherical as well as chromatic aberration (Fig. 8.23).

Total Internal Reflection Contrast

The distance separating the flat surface of a glass plate (such as a coverslip) and a cellular structure having an RI higher than that of water and can be measured using total internal reflection microscopy (TIRM). Changes in this distance as small as 1 nm can be detected (Prieve and Walz, 1993). When a structure settles near a glass/water interface at which total internal reflection is occurring, some of the evanescent wave will be scattered by the structure, as diagrammed in Figure 8.24(A). This situation is called "frustrated" total internal reflection. Because of the non-uniform illumination of the water by the evanescent wave, the amount of light scattered by the structure is exquisitely sensitive to its proximity to the interface. This has been exploited to delineate focal contacts between cells and their substrates (Paddock, 1989).

When a scattering object is illuminated by an evanescent wave, the intensity of scattered light is a measure of the separation distance. The penetration depth (β^{-1}) of the evanescent wave is:

$$\beta = \frac{4\pi}{\lambda}\sqrt{(n_1 \sin\theta_i)^2 - n_2^2}$$

where λ is the wavelength of the incident light, η_1 and η_2 are the RIs of the coverslip and the fluid containing the particle, and θ_i is the angle of incidence of the illumination in the plate. The intensity of the light scattered by the cell, I, decays with the intensity of the evanescent wave. The scattered intensity $I(x)$ varies with the separation, x, as:

$$I(x) \approx I_0 e^{-\beta x}$$

Typically β^{-1} is about 100 nm when a glass coverslip is used as the "plate" and water is used for the bathing medium of a cellular "particle," having an RI of from 1.4 to 1.5 (proteins and lipids). Because of the exponential relationship, a very small change in x produces a measurable change in intensity. In a typical

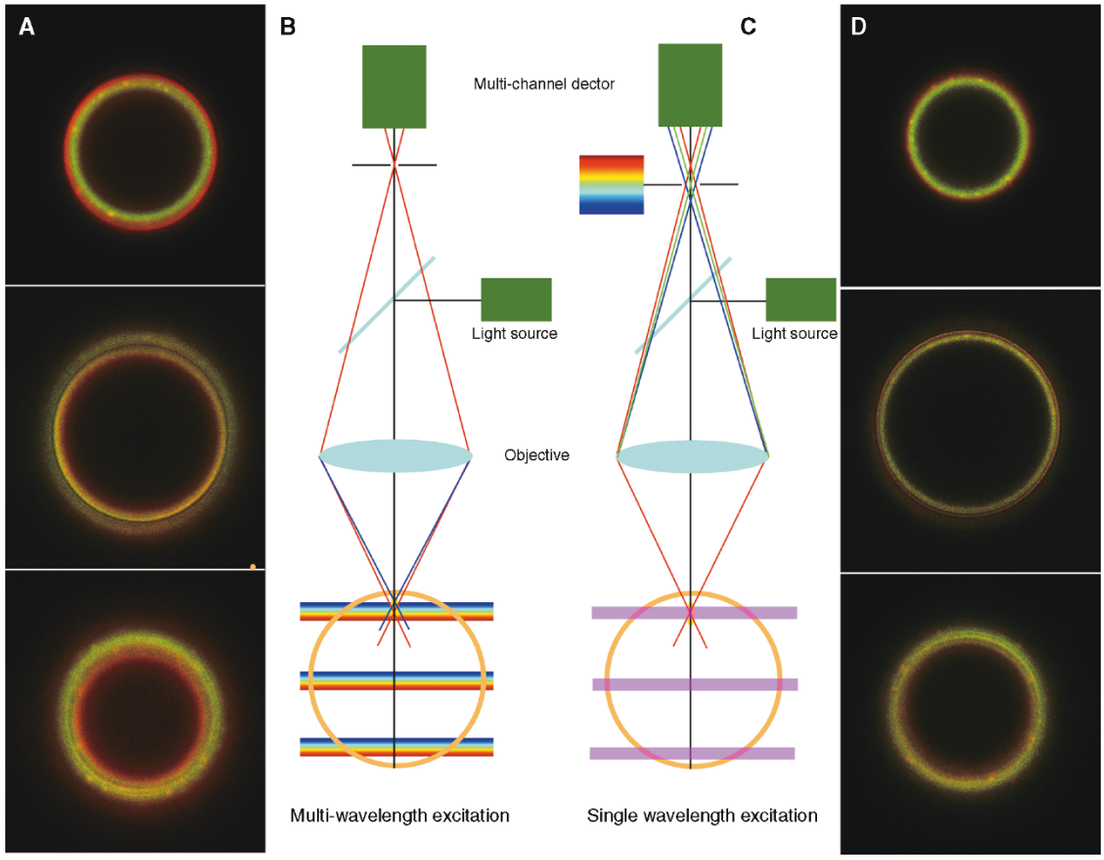


FIGURE 8.23. Chromatic aberration. (A) Optical sections of a latex bead with its shell labeled with fluorescent dyes (Tetra-spec, Molecular Probes). The image was obtained with two excitation wavelengths and recorded in two fluorescent channels. The separation of the "rings" in the images made at the three excitation wavelengths demonstrates that chromatic aberration is present. Note that, at the northern hemisphere, the red ring is outside the green ring, but that the order changes in the southern hemisphere. Although there is also significant chromatic separation at the equator, it is difficult to visualize in a single optical section because the aberrated rings are all about the same size. (B) Diagram of the imaging situation for (A). If only one excitation wavelength is used (C). Chromatic aberration primarily produces only misfocus at the detecting pinhole, resulting in signal loss of the "out-of-focus" rays. (D) The resulting images show less co-localization error. (Images obtained on a Leica confocal microscope with objective lens corrector collar intentionally set wrongly. M. Weis and P.C. Cheng, Agriculture Canada, Summerland, British Columbia, Canada, and State University of New York at Buffalo.)

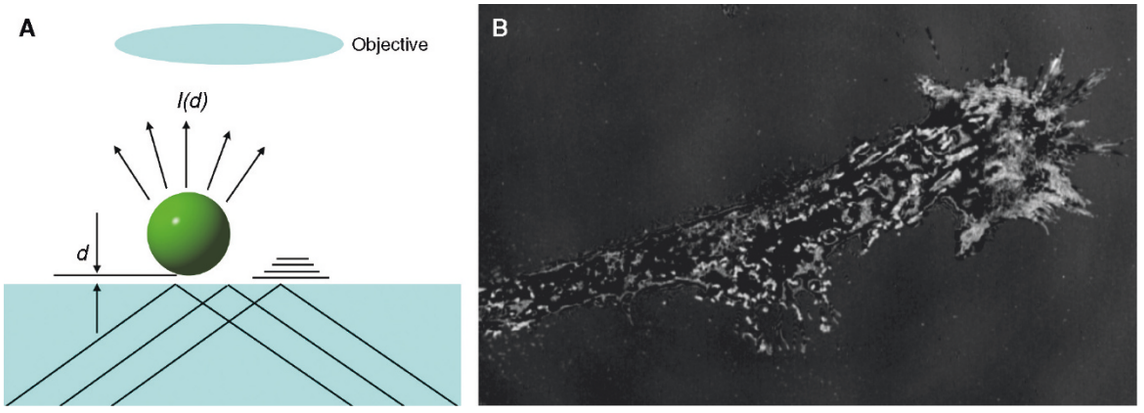


FIGURE 8.24. Total internal reflection microscopy (TIRM). (A) An evanescent wave generated at the glass/water surface can be scattered by particles near the surface. The scattering intensity I_d is a function of the distance between the surface and the particle. (B) TIRM image of a tissue-culture cell adhered to a coverslip.

biological imaging setup, $\eta_1 = 1.5$ (glass slide), and $\eta_2 = 1.33$ for the aqueous solution bathing the cell, a 1% change in signal intensity represents a 1 nm change in distance (x). It is important to note that the equation for $I(x)$ holds for all separations including the contact situation ($x = 0$). Figure 8.24(B) shows a TIRM image of a tissue-culture cell attached to a glass coverslip surface. The image intensity is a function of the separation between the cell membrane and the coverglass. Although interpreting TIRM images obtained from 3D scattering objects is often difficult (Van Labeke *et al.*, 1995; Carminati and Greffet, 1995a,b), recently, Carney and Schotland (2001) derived a theoretical foundation for three-dimensional TIRM.

Harmonic Generation Contrast

Recently, a number of new imaging modalities based on nonlinear optical phenomena have been developed (Cheng *et al*., 2001, 2002, 2003; Chu *et al*., 2001, 2003; Cheng *et al*., 2002). From the power series equation above, one can see that the second- and third-order nonlinear susceptibility, $\chi(2)$ and $\chi(3)$ (respectively) determine the contrast formation mechanism in nonlinear microscopy. Second harmonic generation can be considered to be an interaction involving the exchange of photons between the various frequency components of the electromagnetic field. In SHG, two photons of frequency ω are destroyed and, simultaneously, one photon of frequency 2ω (exactly) is created in a single, quantum mechanical process. As SHG is sensitive to the relative orientation between the polarization of the incident light and the symmetry condition of the material, the SHG signal can be used to provide information about crystal orientation and perfection, molecular structure, and regions where the centro-symmetry breaks down, such as surfaces and optical interfaces. It can also be induced either by structures that are organized on the sub-micron level or by a large, local residual electric field (e.g., a membrane potential).

Third harmonic generation involves three photons of frequency ω that are destroyed to create one photon of frequency 3ω. A nonlinear contribution to the polarization at the frequency of the incident field leads to a nonlinear contribution to the RI experienced by a wave at frequency ω. This is known as the Kerr effect.

Barad demonstrated that imaging with the third harmonic is possible and is especially suitable for imaging structures in transparent specimens with low intrinsic contrast. It is sensitive to changes in the nonlinear optical properties of the specimen such as interfaces between media of differing RI (Barad *et al.*, 1997).

Because harmonic generation and the Kerr effect involve only virtual state transitions that are related to the imaginary part of the nonlinear susceptibilities, no energy is deposited in the specimen and no damage can be produced. However, interactions involving real-level transitions, such as multi-photon absorption (that may lead to the generation of fluorescence, 2PF) do involve energy deposition and can induce photochemical responses such as photodamage or photo-induced polymerization. It is important to point out that both nonlinear absorption (fluorescence) and harmonic generation can occur simultaneously in the same specimen. Figure 8.25 shows a section of a maize leaf just below the epidermal cell using different excitation polarizations (THG, blue; SHG, green;

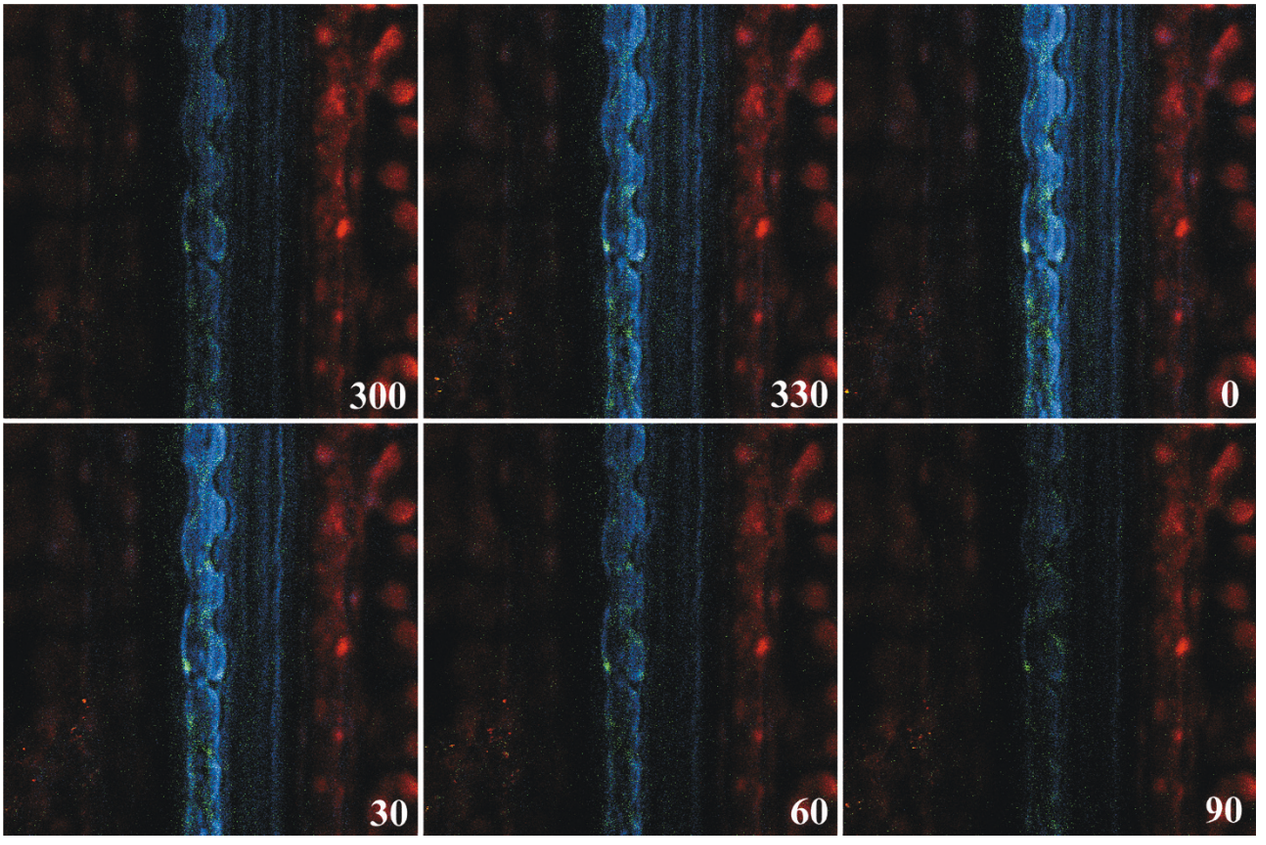


FIGURE 8.25. Nonlinear optical section of a maize leaf just below the epidermal cells at different illumination polarization (330°–90°). Note that, although there are few changes in two-photon fluorescence (red), there are significant changes in the THG signal intensity (blue). The optical section was obtained just tangential to the lower surface of silica cells, therefore, only high THG is observed from the interface. Very weak SHG (green) is detected from the silica cell at this optical section.

2PF, red). For a detailed discussion of these topics, the reader is kindly referred to Chapters 38, 39, and 40.

GEOMETRIC CONTRAST

z-Contrast in Confocal Microscopy

One of the basic properties of the confocal microscope is its ability to use a confocal aperture to reject out-of-focus signal. Therefore, confocal images are acquired from a narrow slice of the specimen. This optical sectioning capability gives the basic optical contrast mechanism of the confocal microscope and is commonly referred to as the *z*-contrast (axial contrast).

One can use this contrast mechanism when examining integrated circuits with reflected light confocal microscopy (Fig. 8.26). Although some image contrast results from differences in surface reflectivity and/or roughness, most of the contrast between adjacent circuit structures is due to the variation in the height of the surface. The surface topography of such specimens can be obtained by plotting the maximum intensity profile from a confocal *z*-stack.

The tilt of structural surfaces within a specimen also affects the reflection signal strength (Fig. 8.27). If the surface tilt is so high that no light reflects directly into the objective, then this part of the surface appears dark (or absent) in the image while a surface perpendicular to the optical axis will give a maximum signal. This type of image contrast is highly dependent on the NA of the objective: high-NA objectives reduce the amount of "surface angle" contrast (Fig. 8.8). On the other hand, such contrast can be increased if the detector is placed not directly behind the pinhole but in the diffraction plane of an auxiliary lens focused on the pinhole plane. A four-segment detector in this position gives independent signals proportional to the four possible different surface tilt directions (Fig. 8.28). Figure 8.29 shows a series of optical sections (reflective, RL; backscattered, BS; fluorescence, FL) of a fluorescent latex bead in water. The surface curvature determined the signal strength of the reflective signal. The center reflective core (arrow) in the bead is an artifact due to a lensing effect. When imaging a specimen consisting high absorbance features, such as a cross-section through the vasculature bundle of plant stem, the "effective" NA of the objective lens is limited by the fact that the surrounding secondary wall obscures the high-NA rays, resulting in a "pipe effect" (Fig. 8.30). As a result, the transverse and axial resolution decreases as one images deeper into this part of the tissue.

The field curvature of the objective lens can create artificial *z*-contrast when imaging a flat specimen because the spherical focus plane intersects only a ring-like area of the flat surface (Cheng and Kriete, 1994).

Total Internal Refraction Fluorescence Contrast

A light beam, incident on an interface separating regions of different RI, will be totally reflected if the incident angle exceeds a critical angle, θ_c. While "all" the light is reflected in the classic sense, quantum mechanics requires that a portion of the radiation penetrates into the distal phase. This radiation is called the evanescent wave and its strength decays exponentially.

Therefore, if a fluorescent structure is located in the second medium near the interface, a fluorescence signal can be excited and detected from it. The signal level is determined by the exponential decay function of the evanescent wave and by the QY and concentration of the fluorophore. This process creates a very thin optical section near the RI interface. The fluorescence intensity I_F is:

$$I_F(x) = QY[con] \cdot I_0 e^{-\beta x}$$

where QY is the quantum yield of a fluorophore, $[con]$ is its concentration, I_0 is the incident light intensity, and x is the separation distance between the dye molecule and the RI interface.

Figure 8.30 shows that total internal refraction fluorescence contrast (TIRF) can be used for measuring the $[Ca^{++}]$ in the subcellular cleft using the Fluo-3/Fura Red ratiometric system [Fig. 8.31(A)]. The calcium image in Figure 8.31(B) is superimposed on a TIRM image that shows the contact points of the cell from Figure 8.24. Figure 8.32 shows the cortical microtubule assembly near to the coverslip in a Vero cell. Figure 8.33 shows the

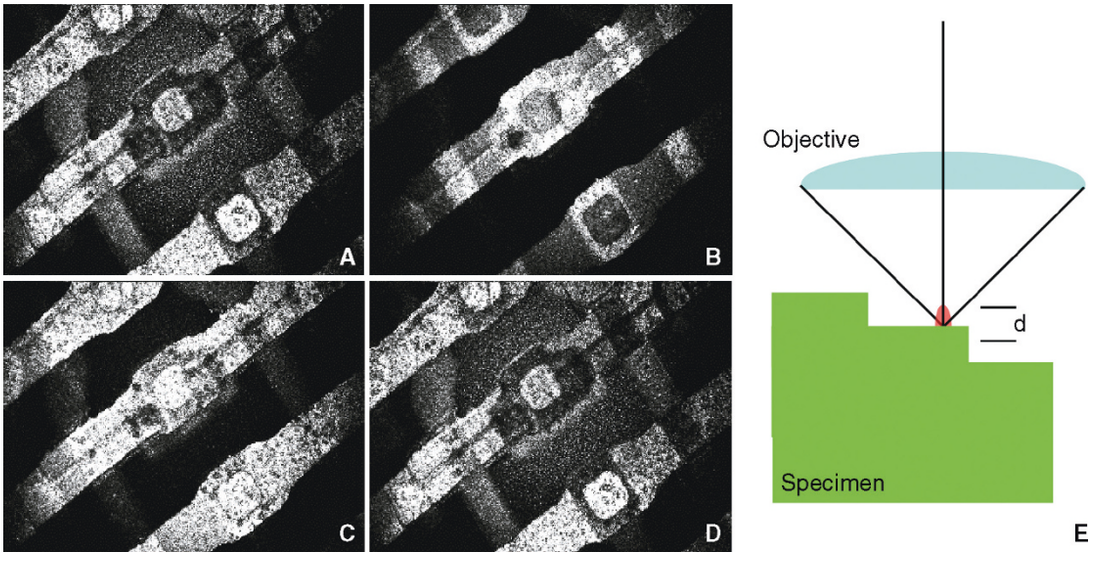


FIGURE 8.26. (A–D) Reflected-light confocal images of an integrated circuit at different focus levels. The image contrast is primarily the result of variations in the signal being focused through the pinhole between in-focus and out-of-focus structures. (E) Diagram representing confocal imaging of a stepped structure in which the steps are thicker than the thickness of the imaging plane (*shaded bar*).

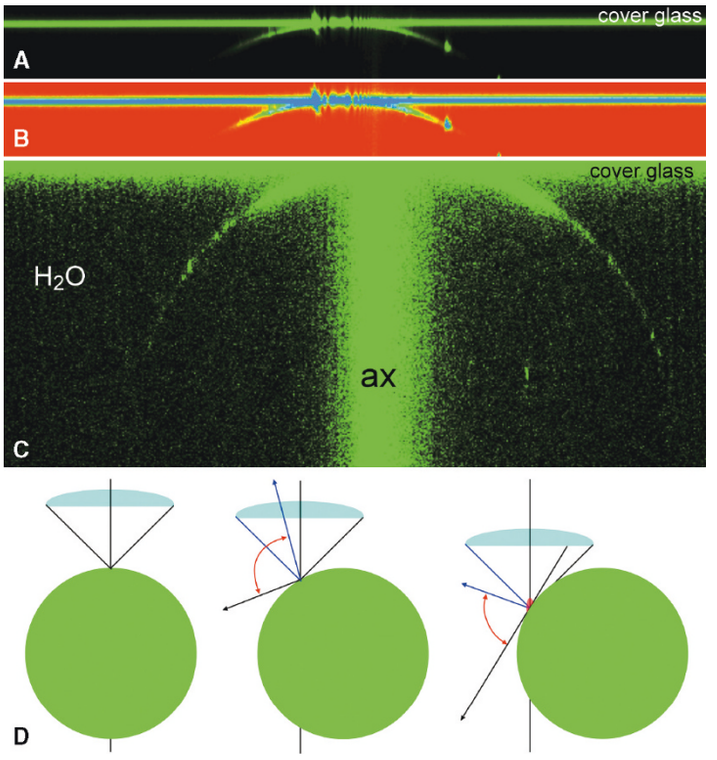


FIGURE 8.27. Reflected-light image of a glass bead, immersed in water and placed just under a cover glass. The bead was placed in the center of the microscope field, almost on the optical axis. (A) *xz* view shows the intensity "ripples" on the reflection signal from the coverslip surface caused by interference between the light reflected by the surface of the coverslip and that from the bead. (B) False color representation of (A); note the intensity fall-off from the "north pole" towards equator. (C) Same data with a higher detector gain setting to amplify weakly scattering signals such as the axial reflection (ax) from the microscope optics that is consequently visible at all *z*-positions. The surface of the sphere can be visualized down to ~30 degree north of the equator. (D) Diagram representing the relevant reflections.

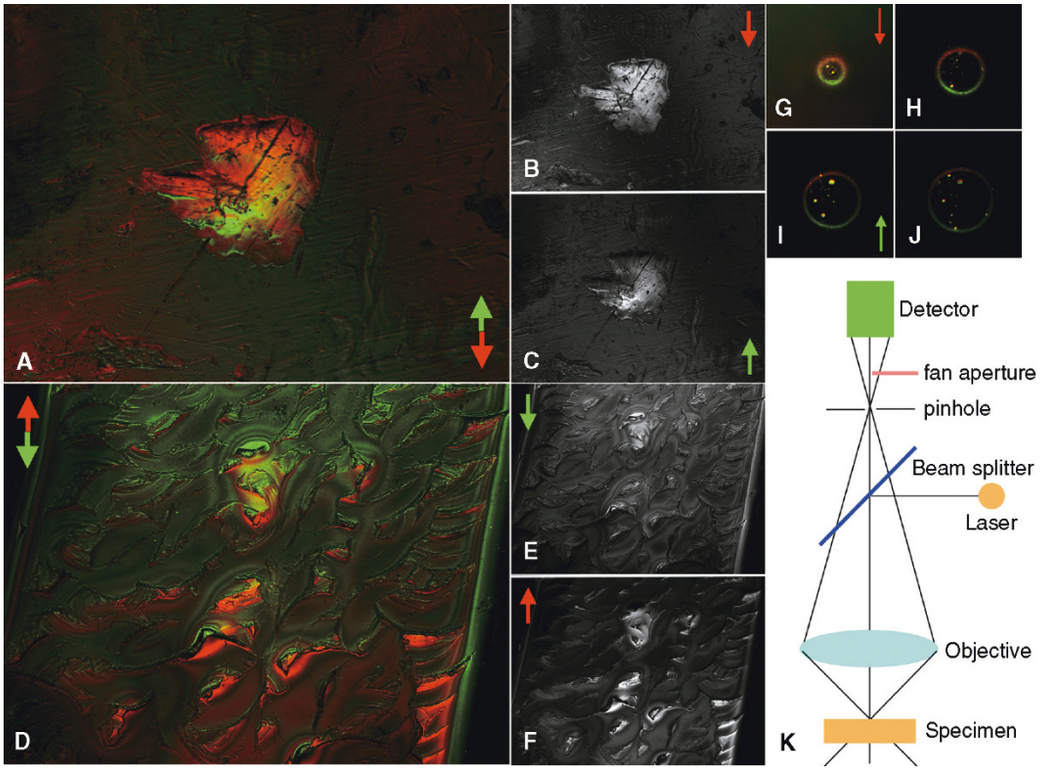


FIGURE 8.28. Surface orientation detection using reflected light imaging. (A) Color-coded surface orientation image of the surface features on a Singporian coin (*green and red arrows* show the orientation of surfaces). (B) and (C) are the individual images of the two surface orientations shown in (A). (D) Color-coded surface orientation image of a milled plastic surface showing cutting marks. (E, F) Corresponding orientation images shown in (D). (G–J) Color-coded surface orientation image of a glass bead. (K) Diagram of the microscope setup. Note how the use of a "fan aperture" obstructs signals from specific orientations. These effects were produced by introducing a two-position blade to obscure part of the "fan" of light behind the pinhole.

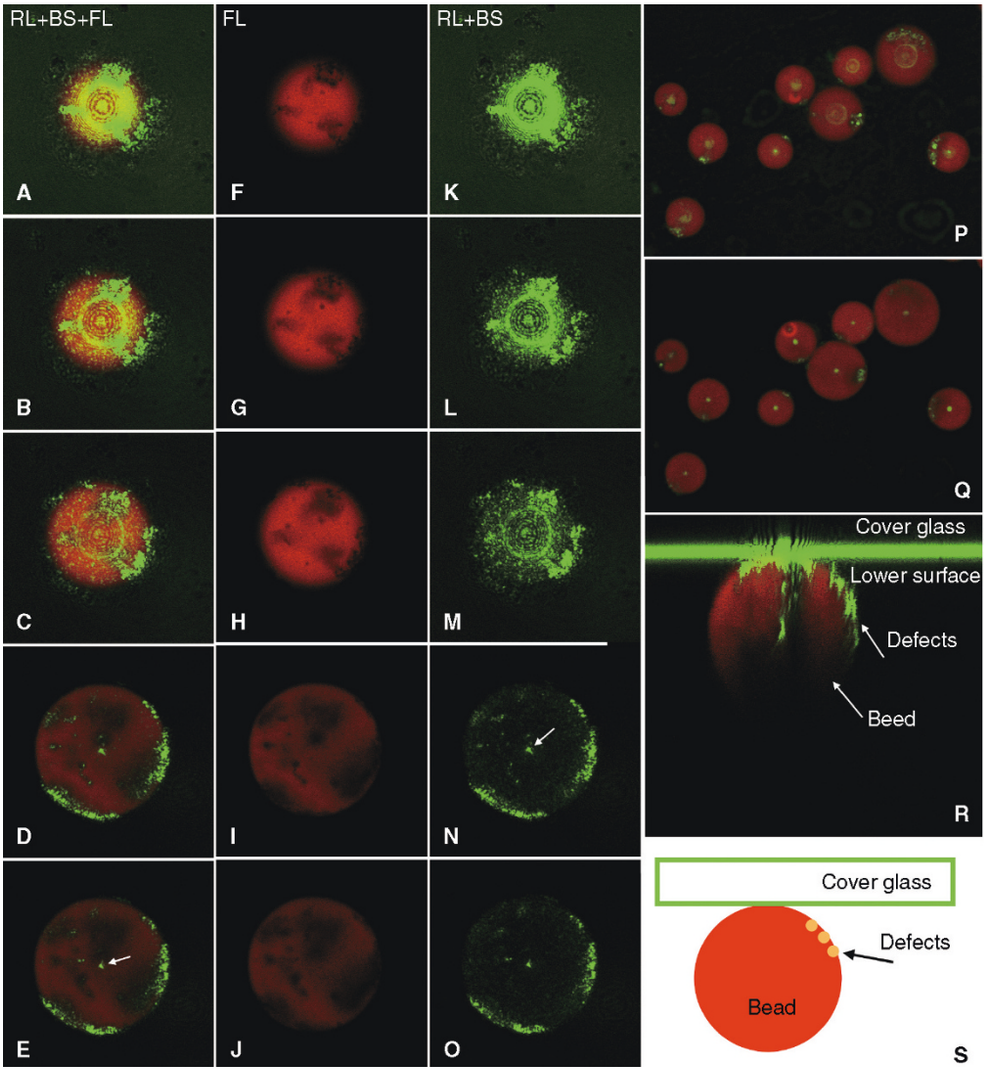


FIGURE 8.29. Confocal serial optical sections (A–E) of an 8 μm latex bead in water in fluorescence (F–J) and BSL (K–O) modes. (A–E) are combined images of fluorescence and BSL images. Note the axial reflection from the center of the bead and the "core" (*arrow*). The latex bead contains numerous "defects" that produce significant backscattered signal at various positions. (P, Q) Low magification optical sections of the beads showing the scatter "core" artifacts. (R) *xz* section of the bead shown in (A–E); (S) Diagrammatic representation of the imaging situation.

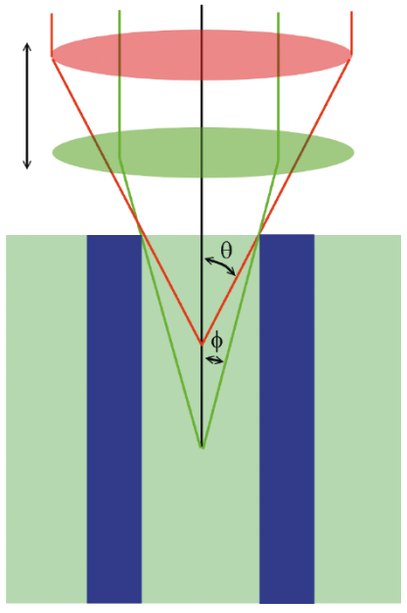


FIGURE 8.30. The "light piping" effect. When imaging features inside a highly absorbing tube-like structure (such as a vascular bundle in plants), the effective NA (or detection solid angle) decreases as the imaged plane moves deeper into the tissue (from θ to ϕ). This not only lowers the transverse and axial resolution of the microscope, but also decreases the signal intensity.

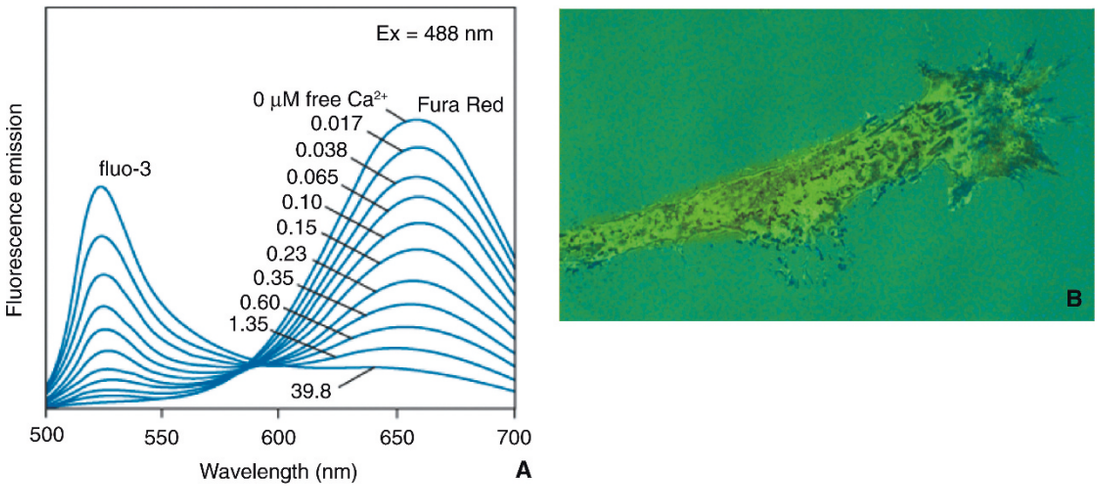


FIGURE 8.31. (A) The Fluo-3 and Fura Red indicator dye system allows ratiometric (Ca^{++}) determination using 488 nm excitation and detection at 520 nm and 660 nm. (B) Fluo-3/Fura Red used in TIRF to determine the (Ca^{++}) in the extracellular space between the cell membrane and the substrate.

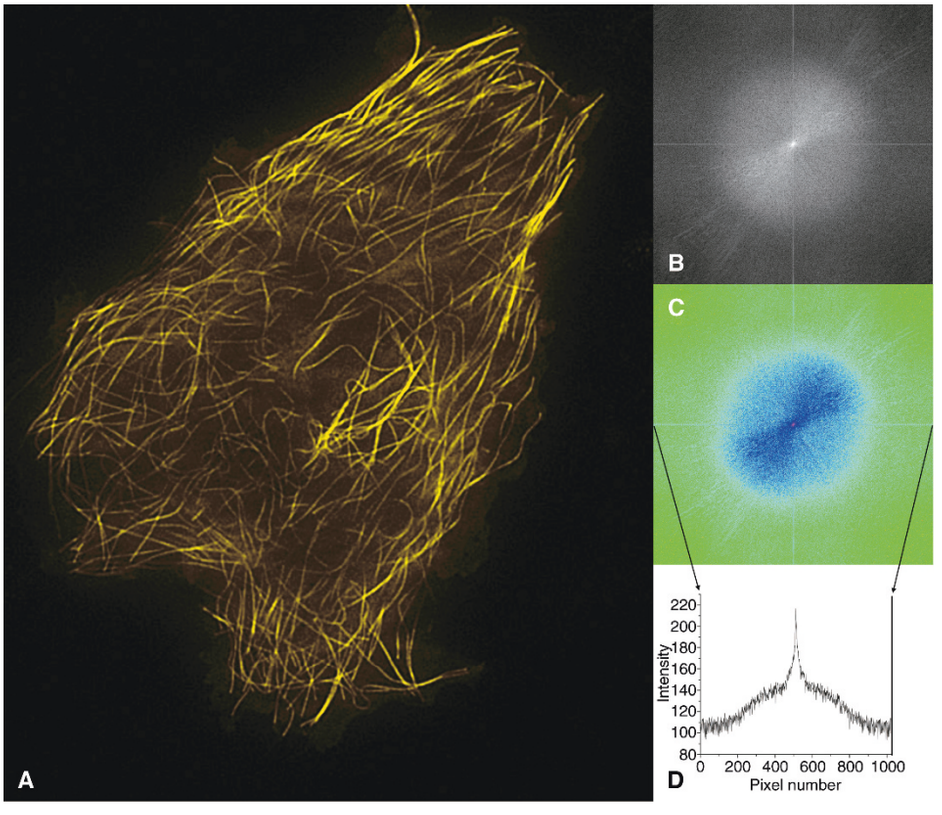


FIGURE 8.32. (A) TIRF micrograph of Vero cells transfected with EB3-GFP, a construct that marks microtubule plus ends, obtained with an Olympus TIRF microscope using an 60×/NA 1.42 oil-immersion objective and 488 nm excitation. (B) A fast Fourier transform (FFT) of the TIRF image; (C) false-color LUT of (B); (D) an intensity plot made horizontally across the diffraction pattern. (Images obtained at the 2005 International Course on 3D Microscopy of Living Cells at the University of British Columbia, Vancouver, Canada.)

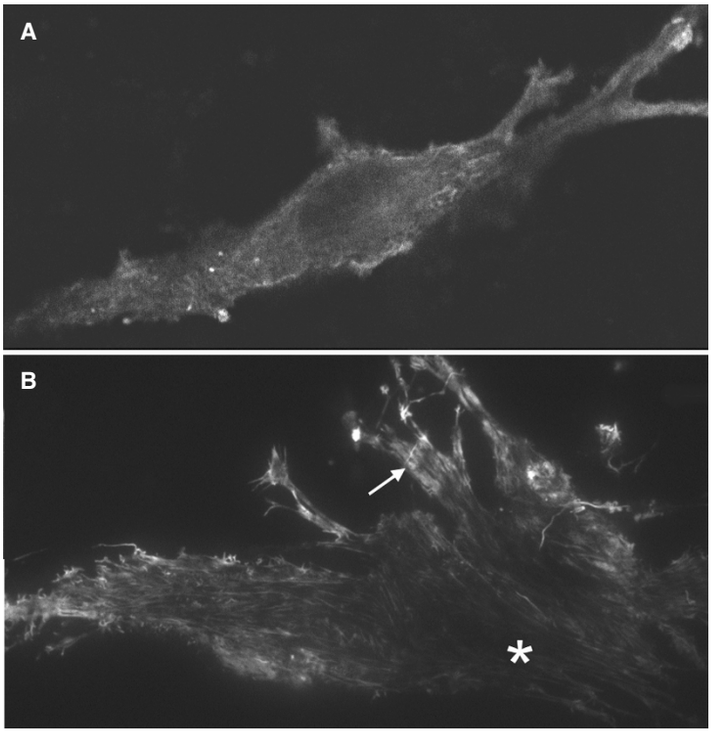


FIGURE 8.33. Comparison of confocal and TIRF Images of C2C12 cells transfected with GFP–MusculoTIRM, a novel TIRM family member specifically expressed only in skeletal and cardiac muscle cells. (A) Confocal image, collected with an Olympus Fluoview 1000 (60× NA 1.2/w objective) and deconvolved using AutoQuant AutoDeburr software. (B) TIRF image collected with Olympus TIRF system (60× NA 1.45/oil objective). Note the filamentous distribution near the plasma membrane is much clearer, and the trafficking of small particles can be observed better in the TIRF images. (Image courtesy of Zui Pan, Department of Physiology and Biophysics, UMDNJ-RWJMS, Piscataway, NJ. Image was taken at the 10th International Course on 3D Microscopy of Living Cells held at University of British Columbia, BC, Canada, 2005.)

comparison of confocal [Fig. 8.33(A)] and TIRF [Fig. 8.33(B)]. Images of C2C12 cells transfected with GFP–MusculoTIRM (a novel TIRM family member only specifically expressed in skeletal and cardiac muscle cells).

In TIRF imaging, whenever a high-RI cellular structure (e.g., an oil droplet) is in intimate contact with the coverglass, the incident ray will propagate into the droplet and become far-field illumination. "Leaked" light produced in this way can increase the background signal dramatically. In addition, TIRF excitation can occur not only at the defined glass–water interface, but also in a conventional epi-fluorescent microscopy wherever structural interfaces occur that have the proper RI and orientation to satisfy the TIRF condition. Consequently, most recorded fluorescence images are "contaminated" by a small but variable TIRF component.

Fluorescence Resonant Energy Transfer

Fluorescence resonance energy transfer (FRET) occurs when energy passes from one excited molecule (the donor) to a second molecule (the acceptor) because the emission spectra of the former overlaps the excitation spectra of the latter. However, the efficiency of this transfer is only significant if the two molecules are very close to each other (1–10 nm). As the efficiency of this energy transfer (E) varies inversely with the sixth power of the distance (r) between the donor and the acceptor, the ratio of the fluorescence intensity of the donor compared to that of the receptor is a measure of distance between them. Therefore, FRET can be a sensitive nonlinear measurement of inter-fluorophore distance, r, or of the rate of energy transfer,

$$E = R_0^6/(R_0^6 + r^6)$$

where E is the energy transfer efficiency and r is the distance between donor and acceptor. This leads to

$$E = 1 - (I_{DA}/I_D)$$

where I_D and I_{DA} is the intensity of the signal from the donor in the absence of, and the presence of, the acceptor, respectively.

The Förster distance R_0 is the distance, r, at which half the excitation energy of the donor is transferred to the acceptor while the other half is dissipated by all other processes, including light emission.

$$r = R_0\{(1/E) - 1\}^{1/6}$$

$$R_0 = 0.211\{K^2 n^{-4} Q_D J(\lambda)\}^{1/6}$$

where Q_D is the quantum yield for the donor, K_2 is a factor describing the relative dipole orientation between the two molecules, and $J(\lambda)$ is the overlap integral that accounts for the degree of spectral overlap between the donor emission and the acceptor absorption

$$J(\lambda) = \frac{\int_0^\infty f_D(\lambda)\varepsilon_A(\lambda)\lambda^4 d\lambda}{\int_0^\infty f_D(\lambda) d\lambda}$$

where $f_F(\lambda)$ is the corrected fluorescence intensity of the donor wavelength in the range λ and $\lambda + d\lambda$, with the total intensity normalized to unity, $\varepsilon_A(\lambda)$ is the extinction coefficient of the acceptor at λ, and is measured in units of $M^{-1}cm^{-1}$ (see also Chapter 45, *this volume*).

Figure 8.34 shows an intensity-based 2p-FRET data analysis that was used to localize the dimerization of C/EBPα proteins in the nuclei of GHFT1-5 cells. Figure 8.35 shows tissue FRET in traumatic axonal injury using BAD/Alexa 488 as the donor and Bcl-xL/Alexa 555 as the acceptor. The image demonstrates energy transfer consistent with BAD-Bcl-xL heterodimerization.

When the acceptor is bleached, the lifetime of the donor molecule increases because there are now fewer paths for excited donor molecules to lose their energy. Figure 8.36 combines FRET and fluorescence lifetime microscopy (FLIM, see below and also Chapter 27, *this volume*) to localize interacting protein molecules.

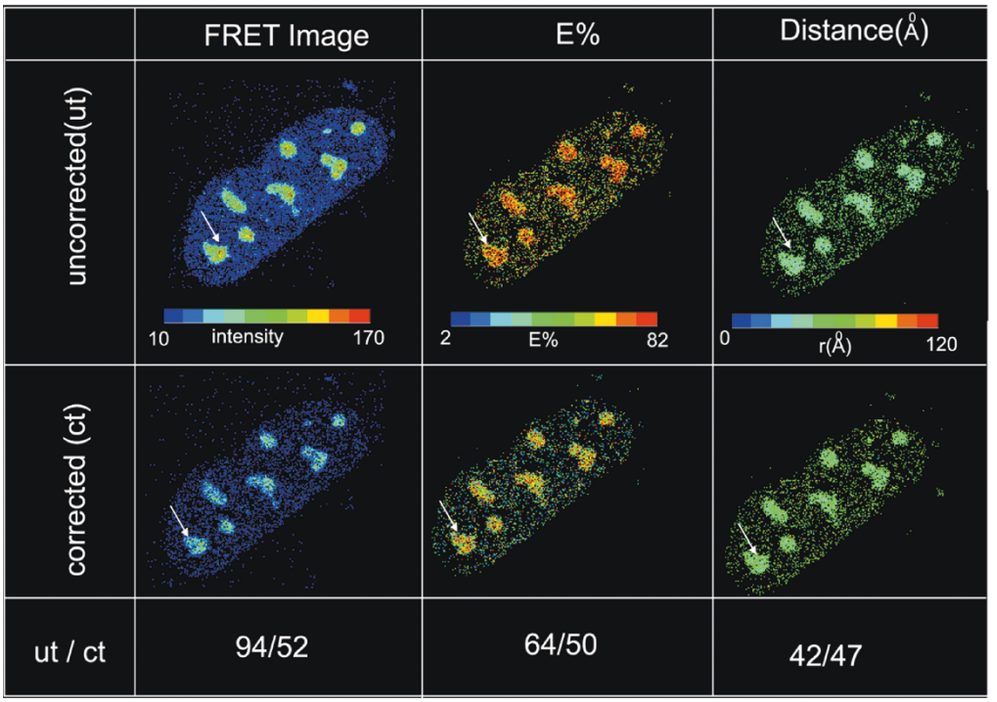


FIGURE 8.34. Intensity-based, quantitative 2p-FRET data analysis to localize the association of C/EBPα proteins in the nuclei of GHFT1–5 cells. Seven images were acquired using a Bio-Rad Radiance 2100 confocal/multiphoton microscopy as the data input for "precision-FRET" (PFRET, http://www.circusoft.com) imaging. The color bars clearly demonstrate the presence of acceptor and donor spectral bleedthrough (SBT) requiring correction. The top panel shows the uncorrected FRET, *E%*, and distance images and their respective color bars. The bottom panel shows the two-dimensional distribution of corrected FRET, *E%*, and the distance (*r*) images. For the protein complex marked with an arrow, the energy transfer efficiency, *E*, is 64% before correction and 50% after correction for Donor, and Acceptor spectral bleedthrough. The color image helps to identify the 2D distribution of distance between interacting protein molecules. (Images courtesy of A. Periasamy, University of Virginia, Charlottesville, Virginia.)

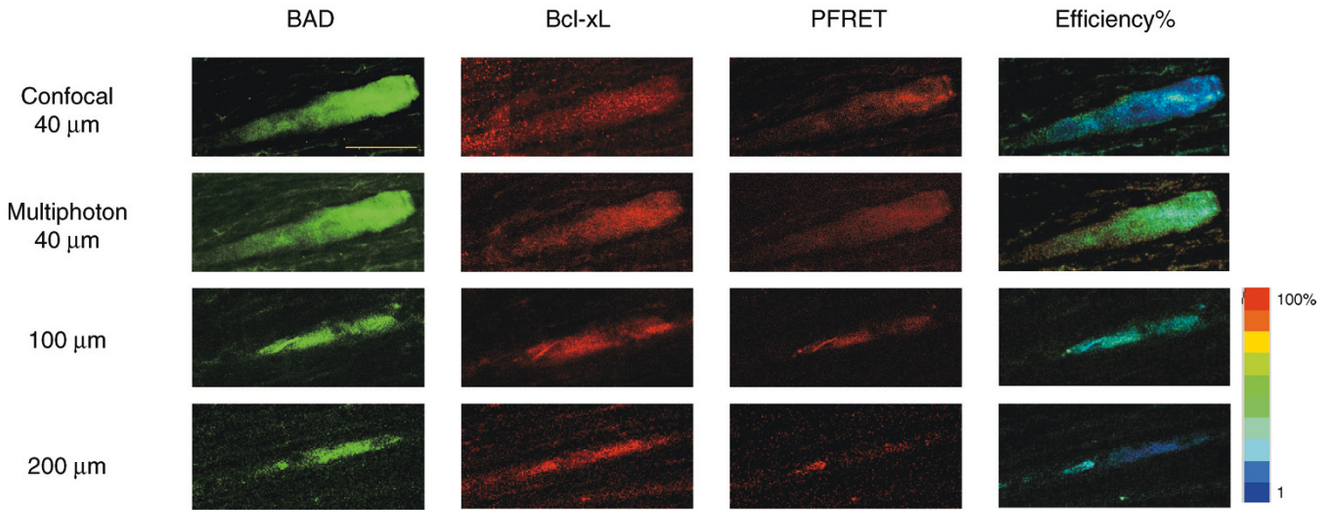


FIGURE 8.35. Tissue FRET in traumatic axonal injury. Six hours postinjury, the tissue was labeled with BAD/Alexa 488 (donor) and Bcl-xL/Alexa 555 (acceptor). These results show energy transfer consistent with BAD-Bcl-xL heterodimerization. The same tissue was used for both confocal-FRET and 2p-FRET imaging using a Bio-Rad Radiance 2100 confocal/multi-photon microscope. Although confocal "precision-FRET" (PFRET, http://www.circusoft.com) imaging was confined to the outer 40 µm of the specimen by low signal levels, 2p (or multi-photon) PFRET images provided useful data up to 200 µm into the tissue. This difference can be attributed to higher concentrations of the fluorophore deep inside the tissue and also to the fact that visible FRET signals scatter in the tissue and can only be detected with a non-descanned detector. Bar, 10 µm; 20× MIMM NA 0.75; Confocal-exD 488nm, emD 528/30, exA 543, emA 590/70; 2-photon-exD 790, exA 730. (Images courtesy of A. Periasamy, University of Virginia, Charlottesville, Virginia.)

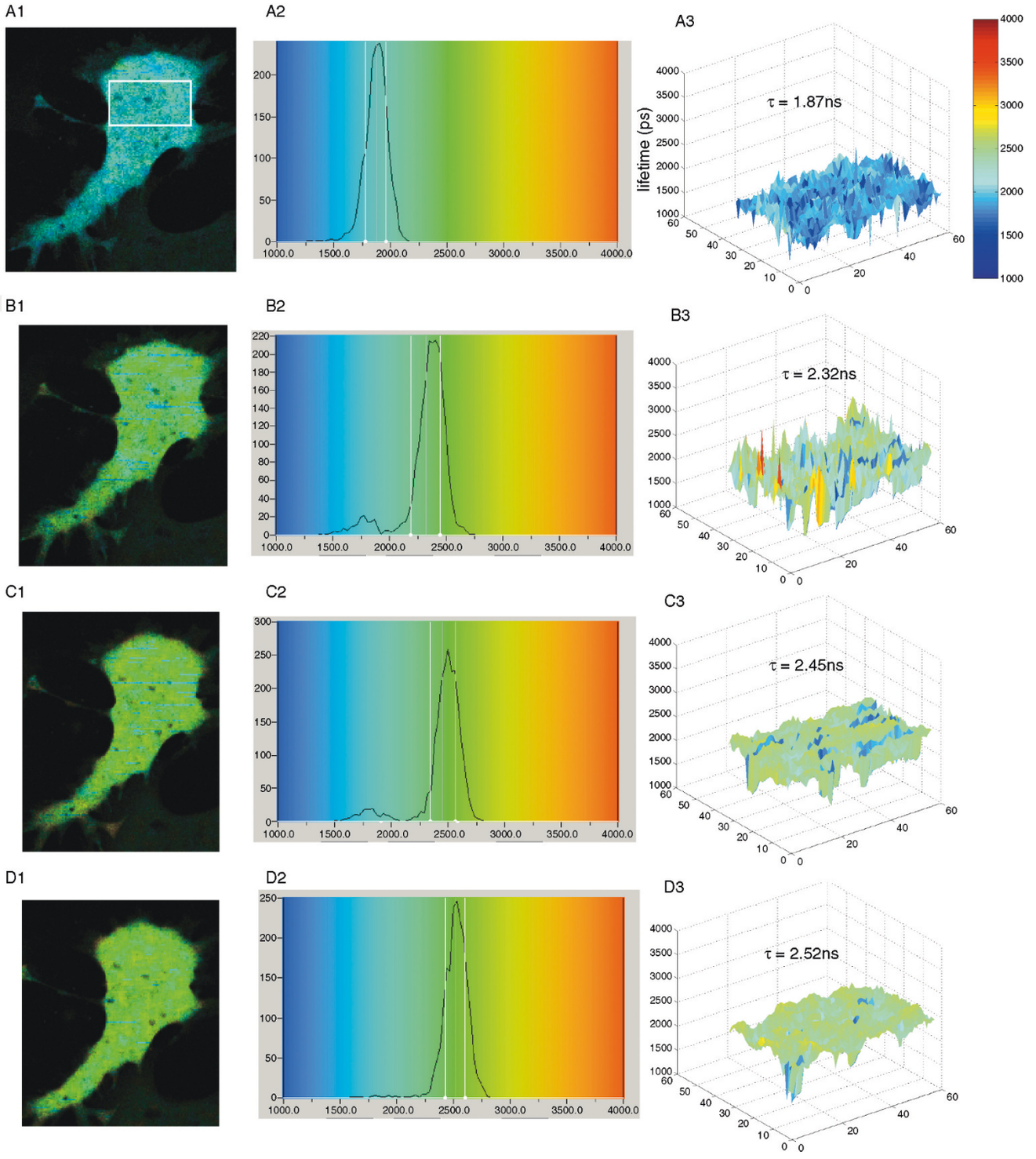


FIGURE 8.36. FRET-FLIM microscopy to localize interacting protein molecules. Images of cells expressing a FRET test molecule (eCFP coupled directly to eYFP through a 15 amino acid linker: eCFP-15aa-eYFP) were acquired and analyzed using time-correlated single-photon counting FRET-FLIM microscopy (TPSPC, Becker-Hickl, Berlin, Germany). The mean lifetime of the selected ROI was 1.87 ns in the presence of acceptor (A1 and A2) but the lifetime returned to 2.52 ns, the natural lifetime of eCFP (D1 and D2) after photobleaching of the acceptor molecule with 514 nm light, demonstrating that FRET had been occurring. As is illustrated in the 2D (A2–D2) and 3D (A3–D3) lifetime distribution, the average lifetime of the donor molecule steadily increases as more acceptor molecules are bleached. (Images courtesy of A. Periasamy, University of Virginia, Charlottesville, Virginia.)

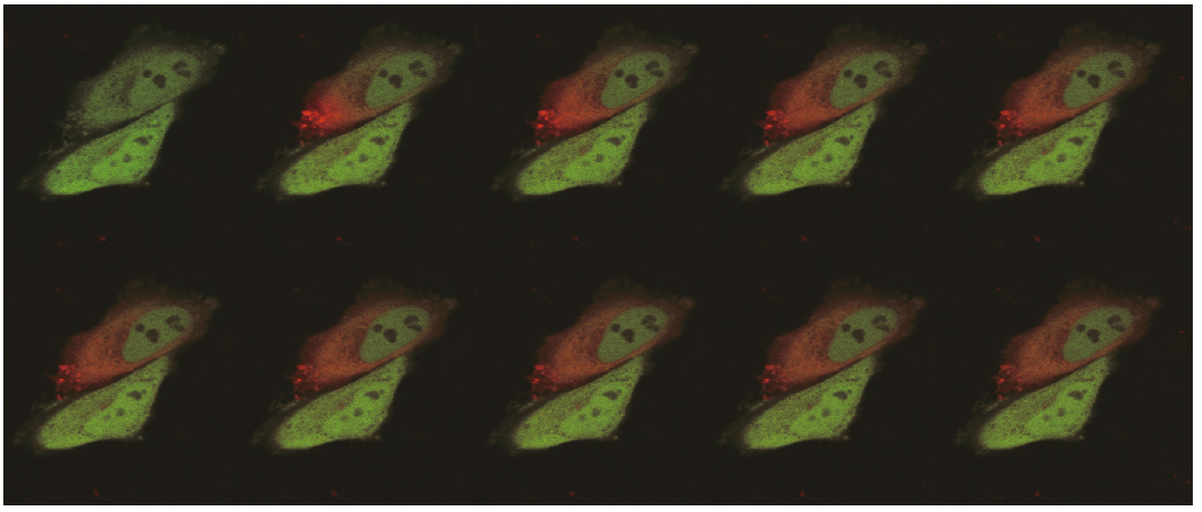


FIGURE 8.37. Fluorescence recovery after photobleaching (FRAP). Photobleaching of the fluorescent protein Kaede causes it to emit in the red, rather than the green. After bleaching between the first two images, the red fluorophores are slowly replaced by green ones.

Images of cells expressing a FRET test molecule (eCFP coupled directly to eYFP through a 15 amino acid linker: eCFP-15aa-eYFP) were acquired and analyzed using TCSPC (Becker-Hickl, Berlin, Germany) FRET-FLIM microscopy. The fact that the mean lifetime of the selected region of interest (ROI) was 1.87 ns in the presence of acceptor (A1 and A2), but returned to 2.52 ns, the "natural" lifetime of eCFP after the acceptor molecule was photobleached using 514 nm light (D1 and D2) shows that FRET had been occurring. This increase is illustrated in 2D (A2–D2) and 3D (A3–D3) lifetime distributions (Chen *et al.*, 2003).

Fluorescence Recovery After Photobleaching (FRAP and FLIP)

Fluorescence recovery after photobleaching (FRAP) has been used in biological research for more than three decades following the pioneering work of Webb (1976), who used it to study the lateral movement of Ach receptors in cell membranes. In this technique, a small region of interest is selectively photobleached with a high-intensity laser, and one then uses a low-intensity beam to monitor the recovery of the fluorescence intensity as unbleached molecules move back into the bleached region. The movement of the molecules can result from simple diffusion, from binding/dissociation, and/or from active transport, etc.

Analysis of the fluorescence recovery can be used to determine kinetic parameters of tagged proteins or other molecules, including their diffusion coefficients, pool fraction, transport rates, or binding/dissociation from other molecules.

In a typical FRAP experiment, the fluorescence in the region of interest is measured just before, ideally also during, and also after photobleaching. Figure 8.37 shows a pair of cells expressing the fluorescent protein Kaede, which changes its emission from green to red in response to photodamage. The sequence of eight images allows one to see the upper cell be "bleached" and then to follow the replacement of the damaged, "red" Kaede with undamaged green-emitting molecules.

From such images one may plot a recovery curve. Depending on the complexity of the interactions of the molecule of interest, the curve may have different shapes. From a simple, single exponential curve one can calculate the mobile fraction, R:

$$R = \frac{(F_\infty - F_0)}{(F_i - F_0)}$$

The $t_{1/2}$ is the time required for the fluorescence to recover half the way between the fluorescence level after bleaching (F_0) and that at the plateau level (F_∞). Although measuring the $t_{1/2}$ allows one to compare diffusion rates under different conditions, one must correct for the fact that the data-acquisition scans used to monitor fluorescence recovery may also produce some bleaching.

In the image, the difference between the bleached area and the surrounding un-bleached area provides bleaching contrast and this can be seen by simple image subtraction.

Following similar reasoning, one can monitor the continuity of cellular compartments with a technique called fluorescence loss in photobleaching (FLIP). In FLIP, a small region within a fluorescent cell is continuously photobleached while one images the whole cell. Over time, any cellular compartments connected to the area being bleached will gradually lose fluorescence as mobile molecules move into the bleached area, while the fluorescence in unconnected regions will be unaffected. In addition, FLIP can be used to assess whether the tagged molecules move freely between particular cellular compartments or if they undergo interactions that impede their motion. FLIP can also be used to reveal faint fluorescence in unconnected compartments that is obscured by bright fluorescence in the component being bleached.

A typical method for doing FRAP with a single-beam confocal or multi-photon microscope is to scan a small region of interest using a high-intensity illumination,[2] then use a low magnification setting and low beam power to scan a larger area. Some modern confocal microscopes, such as the Olympus Fluoview1000, are equipped with dual scanners: one for bleaching (and photoactivation), and the other for imaging. The FRAP data are typically either presented in *xyt* format or condensed into an intensity versus time plot (Reits and Neefjes, 2001; Patterson and Lippincott-Schwartz, 2002).

[2] Be careful not to use such a high power density that nonlinear damage mechanisms bias the outcome. See Chapters 38 and 49, *this volume*, for details.

STRUCTURAL CONTRAST

Harmonic Generation Contrast

At high illumination intensity, biological specimens exhibit a number of nonlinear optical responses; these include the emission of multi-photon fluorescence, nonlinear absorption that can lead to photodamage, and other photochemical responses (see Chapters 21 and 28, *this volume*). In addition, a number of biological structures, such as collagen fibers and plant cell walls, exhibit biophotonic properties capable of generating a SHG signal. Frequently, structures of this type are also birefringent.

The SHG signal provides information about features of the object that are composed of nano-scale crystalline structures that destroy optical centro-symmetry. On the other hand, optical interfaces in a cell or tissue provide the conditions needed to generate THG. Therefore, the THG signal represents optical interfaces such as those found at the cell membrane or at the surfaces of organelles. For a detailed discussion on harmonic signal generation, readers are kindly referred to Chapter 40.

Birefringence Contrast

A number of biological structures, including many of those important to cell motility, organization, and division, are birefringent. For example, microtubules, thin filaments, and myofibrils are all birefringent and can therefore be studied by using polarization microscopy (Fig. 8.38; also see Fig. 8.3, a set of polarization images of the collagen fiber orientation in an artificial 3D substrate used in tissue engineering). Conventional polarization microscopy uses two crossed polarizers above and below the specimen to achieved background extinction and make birefringent material appear as shades of gray on a black background. However, because obtaining a full understanding of the birefringence properties of the specimen using traditional polarization microscopy requires that the specimen be mounted on a centerable rotation stage, the technique was seldom used in biology. More recently, developments in liquid crystal technology have made it possible to implement dynamic polarization microscopy without mechanically rotating the specimen (Shribak and Oldenbourg, 2003). Liquid-crystal components permit one to change the orientation of polarizers, compensators, and analyzers rapidly and electronically, and to record three images, each made with the polarizing components in a different orientation, and then display a processed image in which the brightness of each pixel is proportional to the local retardance while its color codes the orientation of the structure (Oldenbourg, 2004). Figure 8.39 demonstrates variations in the retardance and orientation of the cell wall in plant tissues.

This technology has been used extensively in the study of the microtubule dynamics that drive cell movement. In addition, the technique has been used to identify the position and orientation of the first-division, mitotic apparatus in *in vitro* fertilization (IVF) procedures involving both human and endangered species (see Figs. 40.19 and 40.20, *this volume*).

Both the retardance and orientation of the birefringent structure can be calculated by simple algorithms from a set of three images obtained under different polarization conditions.

DERIVED CONTRAST (SYNTHETIC CONTRAST)

A combination of intrinsic and extrinsic factors can generate "synthetic" contrast. For example, images can show structural or spectral variations within a cell as a function of time, or indicate membrane potential or pH (ratio imaging). If fluorochrome-conjugated antibodies or fluorescent dyes are used to chemically tag specific molecules, these will fluoresce when the specimen is excited by a suitable light source, and create extrinsic contrast because the contrast depends on the binding specificity of fluorescent probes. This probe specificity is frequently used in conjunction with pulse-chase experiments to elucidate time-dependent events (in fact, such pulse-chase experiments can be considered another contrast mechanism).

To obtain a good confocal image, one must selectively combine extrinsic and intrinsic factors to emphasize the "image" signal and decrease the "background" signal. This can be done by improving the performance of the optics and by using special optical contrast methods. However, the prime factor determining the usefulness of an image is almost always the preparation of the specimen (Chapter 18, *this volume*). Because commercially available, multi-channel

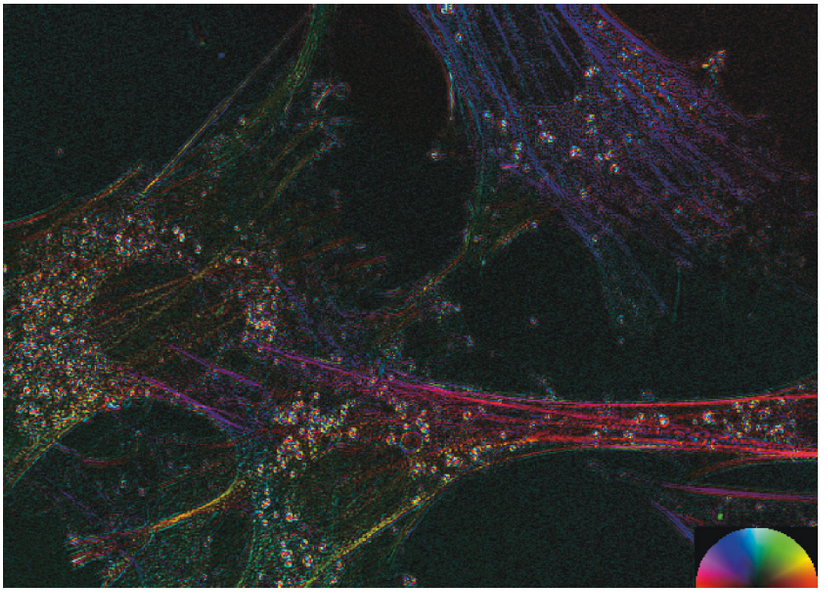


FIGURE 8.38. Polarization micrograph showing the orientation of cytoskeletal structures in a tissue-culture cell.

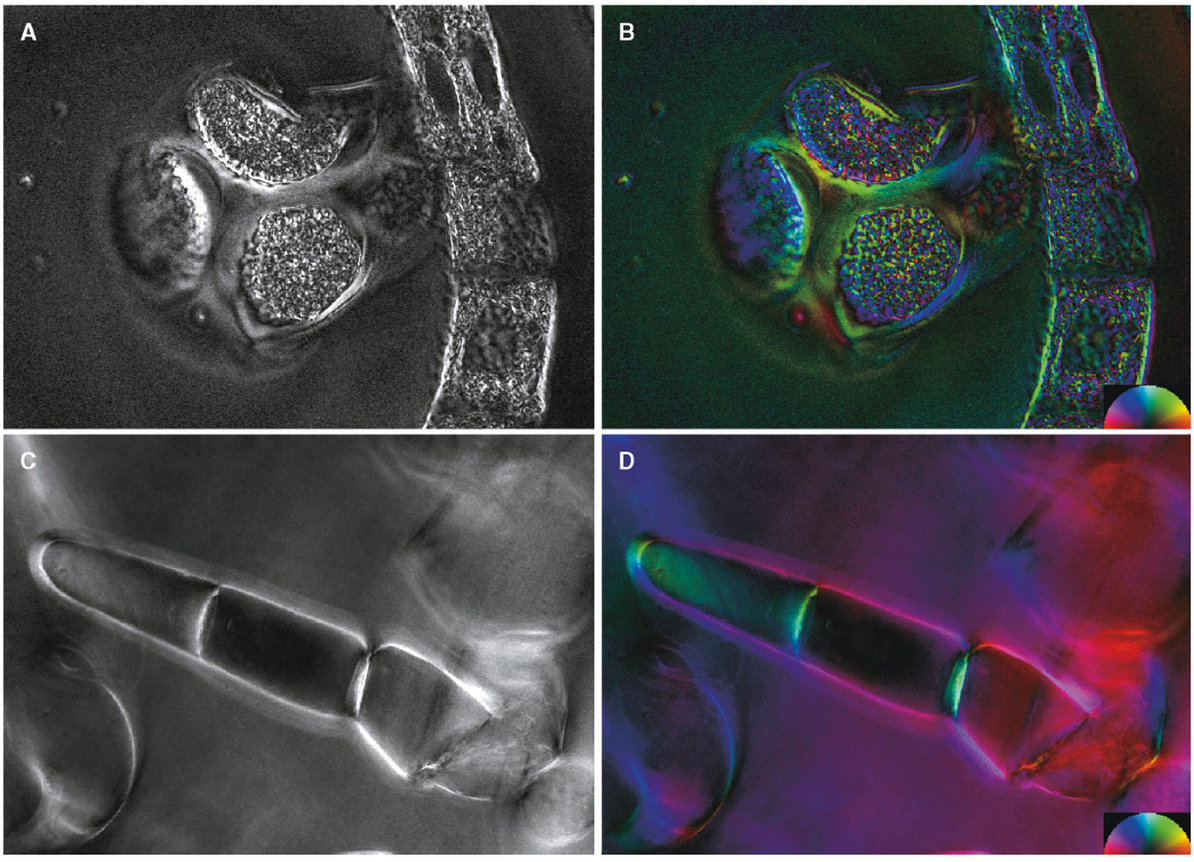


FIGURE 8.39. Birefringence images of developing microspores in *Cymbopetalum baillonii* (A, B) and in the cell wall of tobacco suspension-culture cells (C, D). (A) and (C) show retardance, (B) and (D) are color-coded for orientation. (Images courtesy of Chih-Hua Tsou and Hsing Yue-Ie Caroline of the Institute of Plant and Microbial Biology, Academia Sinica, Taipei, Taiwan.)

confocal microscopes can form images based on the detection of BSL and epi-fluorescence signals, we will discuss the various factors that affect the contrast of these images in more detail.

Ratiometric

In most fluorescence microscopy experiments, the intensity recorded in any pixel is proportional to the absorption cross-section, QY and concentration of the dye, and the size of the volume in the specimen recorded by this measurement (i.e., its *x*-, *y*-, *z*-resolution). These techniques depend on the fact that the spectral characteristics (absorption cross-section, QY), of some fluorophores (or combination of fluorophores) may change in response to the ionic or pH environment. However, these measurements can only be qualitative unless one can normalize for the concentration of the dye. As the concentration is difficult to control, it is often more convenient to normalize this number by making a ratio of two different measurements of the same molecules. Although the classic example involves the Ca^{++} indicator dyes, Indo-1 or Fura-2, other types of ratiometric imaging are also used to detecting ionic or pH changes in cells (see Chapters 16 and 42, *this volume*). By using a standard titration curve and ratioing the intensity of images obtained at two wavelengths, one can assign false colors in the resulting image to represent the actual ion concentrations or pH values. Figure 8.31 shows a typical fluorophore combination (Fluo3 and Fluro-red) used for detecting the Ca^{++} concentration (see also Fig. 21.33, *this volume*). Extensions of this technique can be applied to other situations; for example, in a photodamage experiment, images obtained at different time points can be ratioed to provide a contrast that shows the photodamage dynamics of various cellular compartments.

Deconvolution

In a widefield optical microscope, energy emitted by a point source is captured by the objective lens and imaged as a blurred set of diffraction fringes known as the point spread function (PSF). Thus, any image obtained from a microscope, $o(x, y, z)$, is actually the **convolution** of the function describing the actual light intensity distribution inside the original specimen in 3D $i(x, y, z)$ with the PSF $p(x, y, z)$,

$$o(x, y, z) = i(x, y, z) \otimes p(x, y, z)$$

Therefore, the PSF is the function that redistributes the original energy distribution from the specimen into the imaging space (Chapter 21, *this volume*). In the absence of noise, the mathematical operation of **deconvolution** reverses this process, creating a new 3D image data set that more closely approximates the structures of the specimen. It can increase the image contrast, reduce the effect of Poisson noise, and also decrease the effect of out-of-focus signals (Holmes and Cheng, 2005). Although in general, successful use of iterative deconvolution to improve 3D microscopical data requires that one know the PSF, so-called "blind" techniques can also be successful, as is explained in Chapter 24. However,

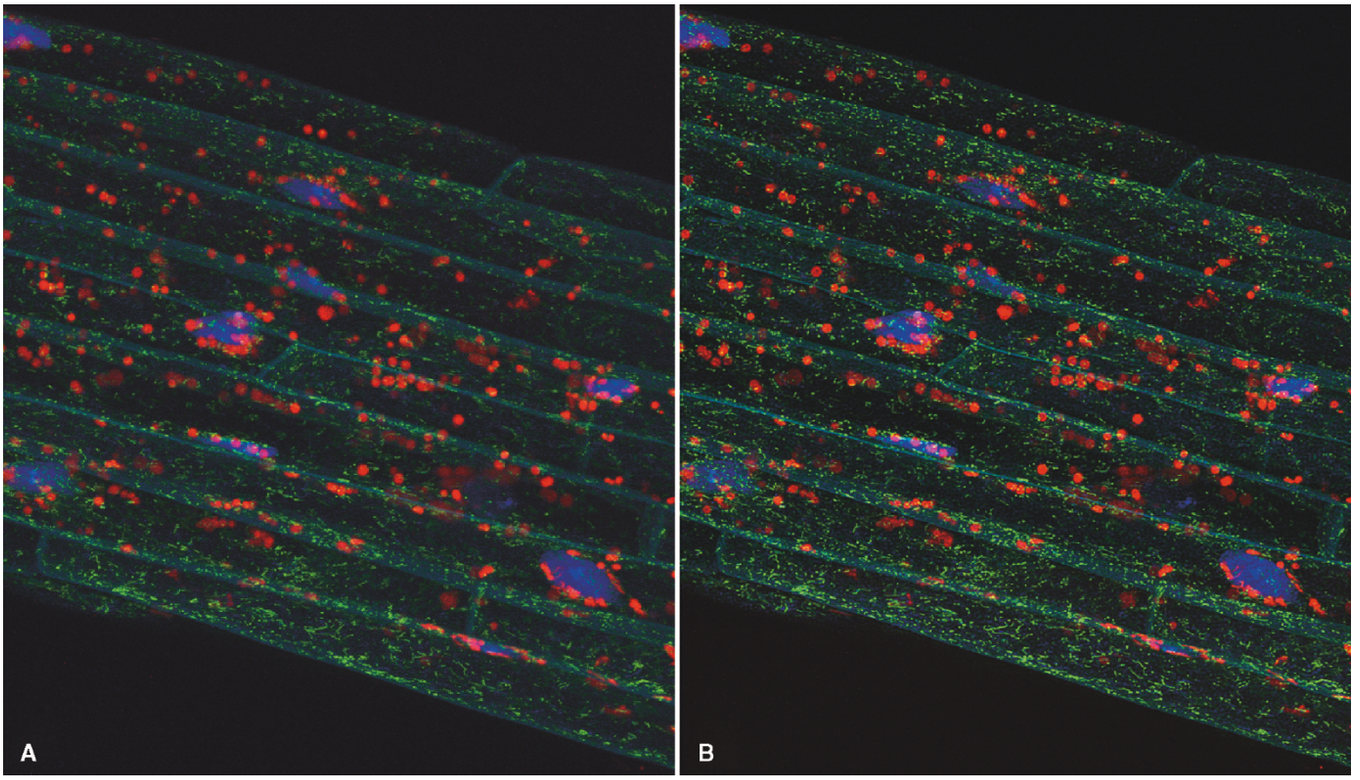


FIGURE 8.40. (A) Three-channel confocal microscopy of a 5-day-old, stable, transgenic seedling of *Arabidopsis thaliana*, simultaneously expressing four different recombinant proteins, ECFP-Gal4, EGFP-BDCaM53, EYFP-CoxIV, and DsRed2-RecA. ECFP-Gal4 accumulates in the nucleus and EGFP-BDCaM53 in the plasma membrane, EYFP-CoxIV accumulates in mitochondria and DsRed2-RecA in plastids. ECFP and EGFP can be excited and collected in a single channel because, as they are expressed in two distinct structures — namely, nucleus and plasma membrane — they are unlikely to be confused. (B) The same data, after blind deconvolution. (Images kindly provided by Naohiro Kato, Department of Biological Sciences, Louisiana State University, Baton Rouge, Louisiana, and obtained at the 2005 International Course on 3D Microscopy of Living Cells held at University of British Columbia, Vancouver, Canada.)

iterative techniques require that one be able to describe image quality in a mathematical and measurable fashion so that the results from one iteration can be compared with the previous one. For a detailed discussion on deconvolution operation, readers are kindly referred to Chapters 22, 23, 24, and 25.

The practical effect of deconvolution on contrast is that, on a basic level, deconvolution of confocal data acts as a nonlinear filter, something that reduces image contrast somewhat but also adaptively averages the signal over a large number of voxels, effectively eliminating the "single-pixel" noise features produced by Poisson noise (Fig. 8.40).

Movement Contrast (Subtraction of Previous Image)

Organelle movements within the cytoplasm or any other movements of the object can be emphasized and tracked by sequentially subtracting from each other images in a time series. For instance, subtracting an image of a culture cell obtained at time A from one obtained at time B can reveal small movements of organelles and/or the cytoskeleton; on the other hand, converting three consecutive time-sequenced images into RGB format can also effectively display structural movement (Fig. 8.41). This display technique emphasizes those structures that have moved between the two sampling times. Clearly, in order to obtain useful and reliable movement contrast, it is important that the sampling interval is small enough to faithfully record the movement. Otherwise, subtracting the resulting images can produce only nonsense.

Image movement due to specimen drift or a change in the water level of a water-immersion setup is a common problem. It is important to keep the specimen immobile while not exerting external forces that can deform it. Figure 8.42 shows a number of methods for holding the specimen and a simple apparatus to maintain immersion water levels for a prolonged period.

Spectral Unmixing and Color Reassignment

Using spectral unmixing techniques, one can characterize a pixel or an image region based on its spectral signature. Although such pixels may appear similar in RGB color to the naked eye [Fig. 8.43(A)], they may in fact have very different spectral signatures that only become visible when each one is assigned to a specific color. For example, Figure 8.43(B) shows a RGB image of a histological section of mouse intestine, stained with Syto Blue [Fig. 8.43(C)], Alexa Fluor 488 [Fig. 8.43(D)], Alexa Fluor 594 [Fig. 8.43(E)], and Alexa Fluor 647 [Fig. 8.43(F)], and also containing a significant amount of autofluorescence [Fig. 8.43(G)]. One can use spectral unmixing to separate the signals from the four fluorescent probes and the autofluorescence, and then generate a synthetic false-color image based on these four spectral categories. For other examples of spectral unmixing, see Figures 36.17 and 21.20.

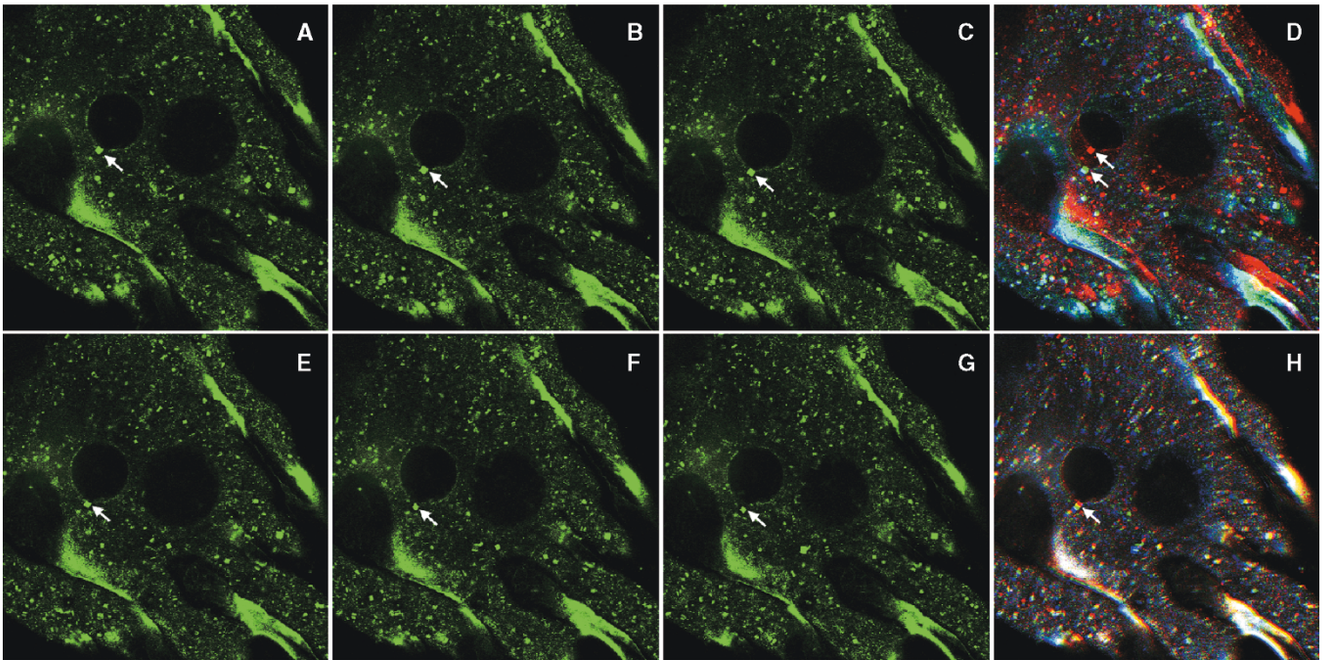


FIGURE 8.41. A time-lapse series of confocal optical sections was made using backscattered light to show movement of an amoeboid pseudopod. (A, B, C) and (E, F, G) are two time sequences of the pseudopod showing highly reflective crystals (*arrow*) and the plasma membrane. Note the scatter signal from the vacuole membrane. (D and H) are RGB merged images of (A, B, C) and (E, F, G), respectively, showing the organelle movement. The time interval is approximately 0.5 s.

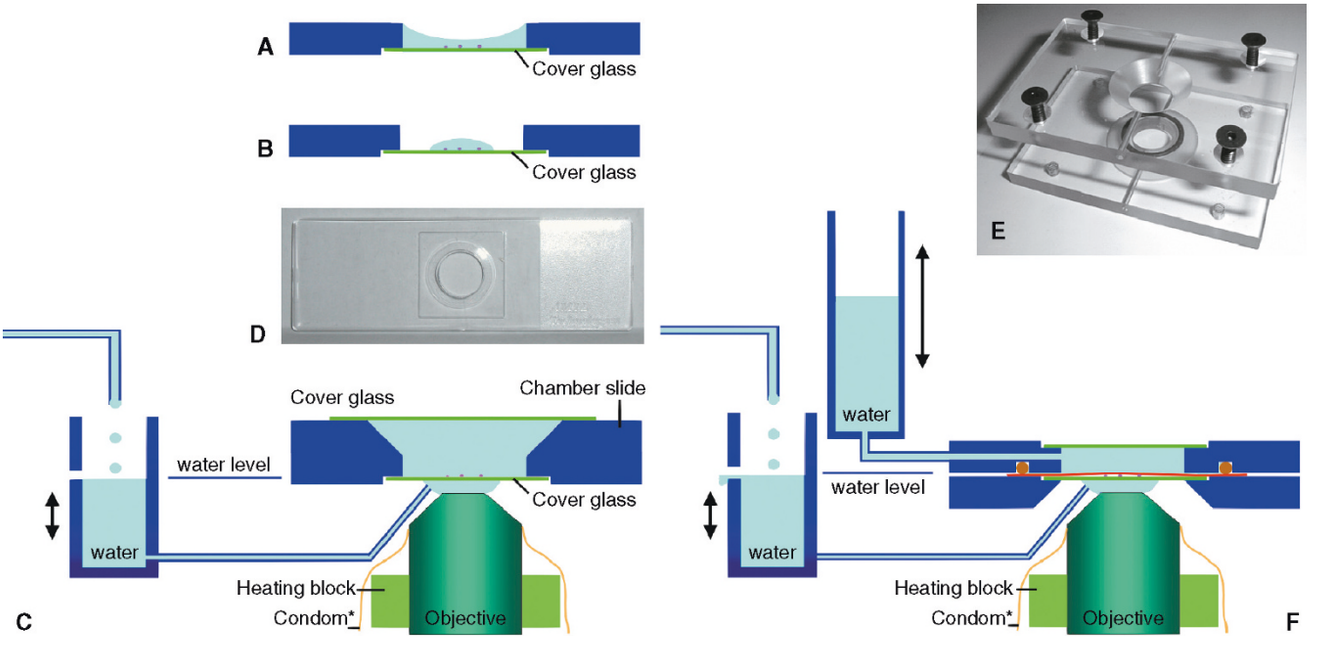


FIGURE 8.42. Various specimen chambers to handle small specimens. (A) and (B) chamber constructed using a slide with a center hole (C), the bottom of which is covered with a cover glass; the chamber can either be filled with liquid (A) or one can use a drop of medium (B) to create reflective meniscus, although this may introduce unwanted reflections. However, if an upper cover glass is used, the liquid meniscus problem is resolved (D). To prevent the immersion water from drying out (when using a water immersion objective), a water reservoir with overflow is used. By careful adjustment of the position of the overflow outlet, one can maintain the water level at the objective. A non-lubricated condom with its tip cut off is used to dress the objective lens to prevent water damage. (E) A specially made specimen chamber to handle small tissues (Cheng *et al.*, 1999). (F) Detailed diagram of the chamber shown in (E). The chamber consists of two compartments, the upper chamber connected to a water reservoir, maintaining a specific pressure on the red membrane (typically 10 µm Mylar), and this film then presses the small tissue fragment against the lower cover glass.

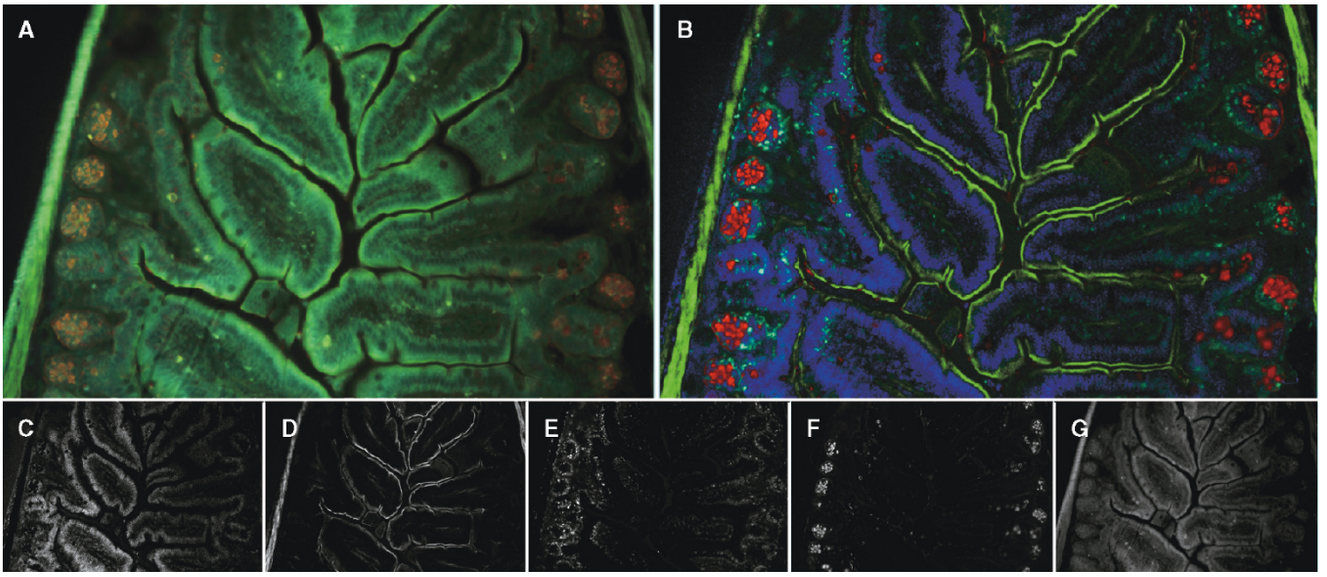


FIGURE 8.43. Mouse intestine specimen, labeled with Sytox Blue and Alexa Fluor 488, 594, and 647. (A) Conventional three-color image (B) composite of four component images extracted from the same data by "spectral unmixing." (C) Sytox Blue, (D) Alexa Fluor 488, (E) Alexa Fluor 594, (F) Alexa Fluor 647, and (G) autofluorescence. (The images were obtained using the Nuance imaging system of Cambridge Research Inc. (Cambridge, MA). Image courtesy of CRI.)

Effects of the Specimen: Spherical Aberration and Optical Heterogeneity

Although substantially transparent, biological specimens are seldom optically ideal. More often they are heterogeneous in structure, absorption, RI, and thickness. Because the specimen is part of the optical system, this heterogeneity can be particularly serious in a confocal microscope where each point is, in effect, imaged twice.

We can divide these effects into two categories: those that arise because the average RI of most biological specimens is not that for which the objective was designed and those caused by the fact the cells actually do not have one RI but many (i.e., they are optically lumpy and the lumps often have different RIs).

The first problem leads to spherical aberration, a topic that is discussed in many other chapters, particularly Chapter 20. Although, in general, spherical aberration can be avoided by scrupulous adherence to the recommendations of the manufacturer with regard to the RI and thickness of all layers between the objective and the focus plane, this is not always easy to do. Water objectives assume that the specimen is made of water and, as this is not true of living cells,[3] some degree of spherical aberration is usually present in images of living specimens. Indeed, spherical aberration is usually the main reason why the signal level drops as the focus plane moves into the specimen (Fig. 8.44).

Figure 8.45 clarifies the connection between reduced resolution and lower signal level. A dry objective was used to bleach planes into a piece of fluorescent plastic. Because the objective was designed to provide full spherical correction only on the far side of a 170μm coverslip, the best resolution (and highest light intensity) is found when the focus plane is some distance into the plastic. This figure confirms that the zone with the sharpest images [as seen in Fig. 8.45(B)] coincides with that having the highest signal [Fig. 8.45(C)]. Figure 8.46 drives the point home: *xy* images made of the same specimen, after it had been cut and polished to show the planes in edge view, show that the planes bleached in the "good" zone were indeed thinner than their neighbors and have the correct spacing. It is important to point out that the RI mismatch of the plastic specimen and the immersion medium (1.52) results in a change in the effective focal length that varies with focus plane position. This causes the spacing **between** the bleached planes to vary as a function of the depth.

On the horizon is a better solution: a stand-alone, motorized, computer-controlled spherical-aberration corrector is now available (Intelligent Imaging, Denver, CO) and one can imagine the day when a device with similar capabilities may become a standard microscope accessory.

However, such a device cannot correct for the optical problems caused by the optical heterogeneity of the specimen itself (see Figs. 2.3–2.5). As with the BSL imaging, reflection, refraction, and scattering of the illuminating beam by structures situated between the focal plane and objective lens produce a spot that is larger than it would have been if the optics were only limited by diffraction and this reduces the intensity of the exciting radiation reaching the fluorescent dye in each voxel being sampled.[4] This loss of excitation reduces the fluorescence yield from the focal spot in the specimen. Furthermore, the emitted fluorescent light will be attenuated by the same factors on its return to the detector pinhole. Whether these obstructing structures are the upper portion of the structure under study or something of little interest, this self-shadowing can significantly reduce the image contrast by lowering the signal strength. It is particularly pronounced when observing densely packed specimens. For example, Figure 8.47 shows a confocal autofluorescence image of the chloroplast of *Closterium*. This algal

[3] This is, after all, why cells produce phase contrast.

[4] In fact, the BSL signal level is a good measure of how much the ideal optical situation has been disturbed. It is not unexpected that tissues with particularly good transparency, such as the cornea, also give very low BSL signals.

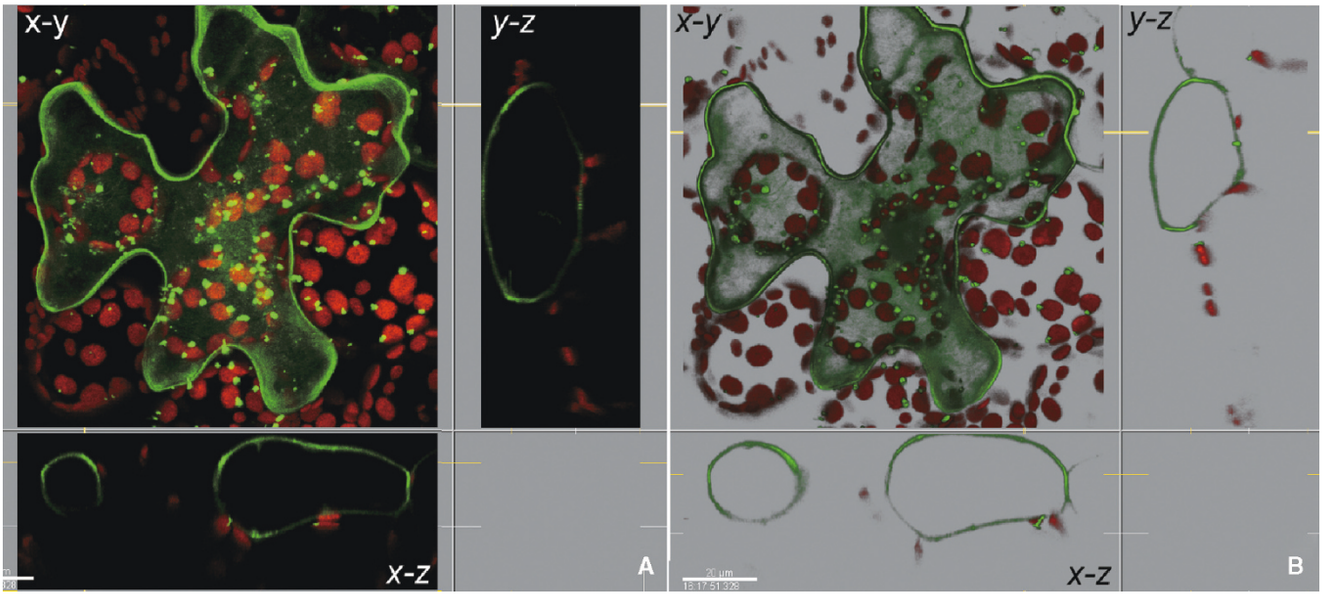


FIGURE 8.44. (A) Two-channel confocal image of epidermal cells and mesophyll cells of *A. thaliana*. The epidermal cell is GFP labeled. Note the intensity degradation in the deeper part of the tissue evident in the *xz* and *yz* sections. (B) Segmentation and α-blending can improve the visualization of the epidermal cell where it is in contact with the mesophyll cells (using Imaris software). Both *xy* projections have had top surface removed. (Image courtesy of Michael Weis, Yu Xiang, and D'Ann Rochon, Agriculture and Agri-Food Canada, PARC, Summerland, BC, Canada.)

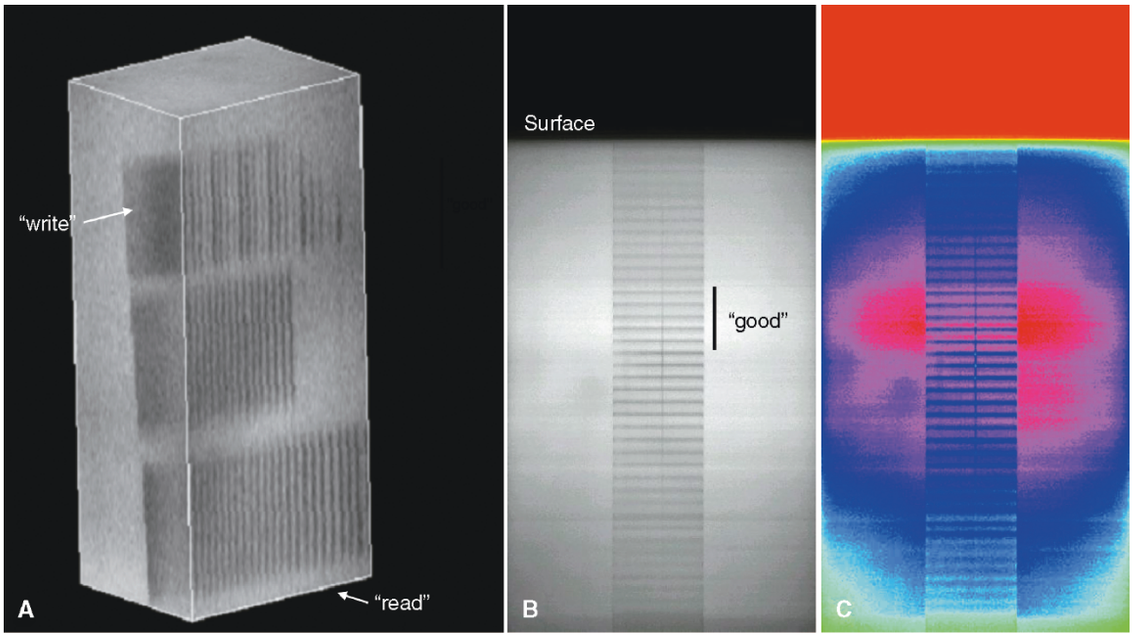


FIGURE 8.45. Two-photon bleach planes were written with equal spacing and equal intensity into a piece of fluorescent plastic (Chroma Scientific, Brattleboro, VT). After high-intensity writing, the block was re-scanned at a lower intensity to obtain an image of the photobleached pattern (A). Due to a mismatch between the RI of the plastic and the design condtions of the objective, the signal level and sharpness of the image varies significantly as a function of depth into the specimen. The best response is in the upper mid-range of the image labelled "good." At this depth, the spherical aberration caused by using this "dry" lens without a coverslip is almost compensated for by the thickness of the overlying plastic. As a result, this zone gives the best *z*-resolution (i.e., the sharpest photobleached planes) and also the highest signal intensity (B). (C) is a false-color version of (B). Although the spacing between the bleached planes seems to remain constant, this is only because, as both writing and imaging were done by the same setup, errors caused by SA-induced focal-length change cancel out (see Figs. 8.40 and 8.45).

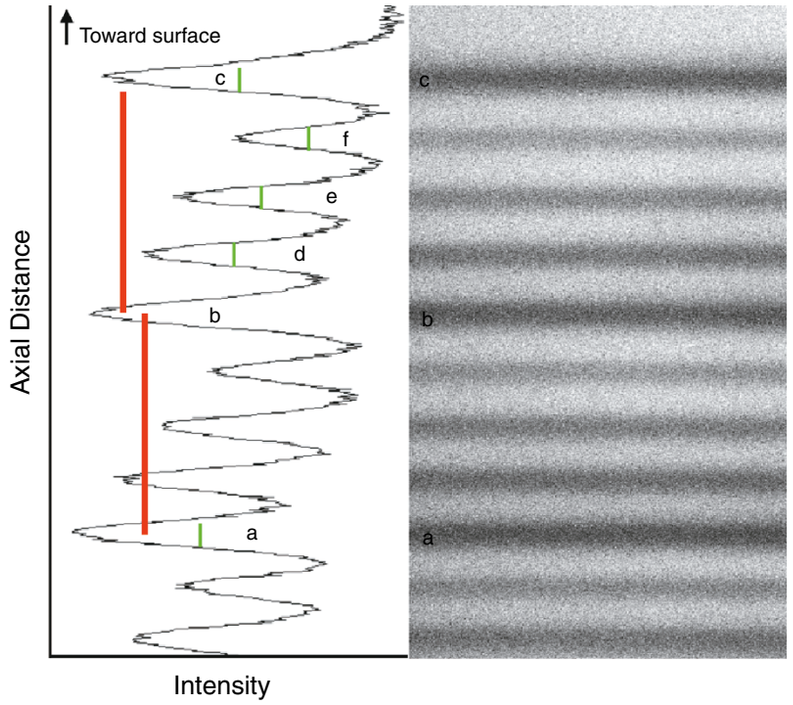


FIGURE 8.46. Two-photon bleach planes (equal *z*-spacing but with four different photobleaching intensities) were written into a fluorescent plastic block. After writing, the block was turned 90° and the surface trimmed with the glass knife on an ultramicrotome to expose the edges of the bleached planes. In a fluorescent image of this cut surface, one can see that the spacing of the bleached planes is not constant. At different depths the spacing varies because the focal length of the objective lens changes as the RI of the material between it and the focus plane changes. Compare the peak-to-peak distances between a-b and a-c, *red bars*). The FWHM of the bleached planes (i.e., the *z*-resolution) also varies (*green bars*).

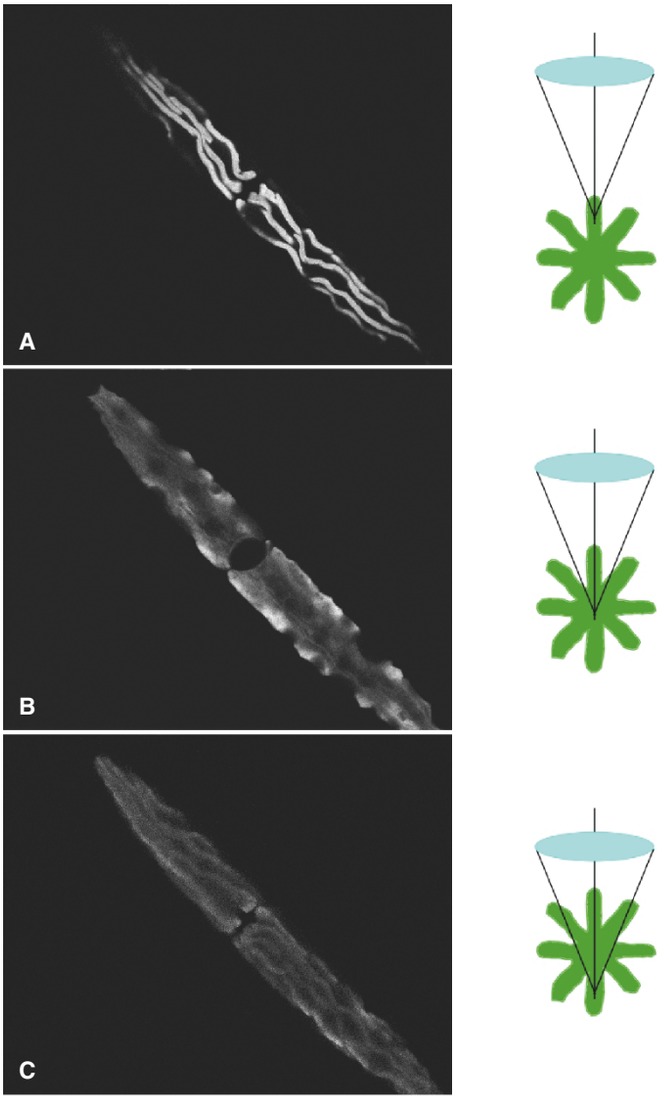


FIGURE 8.47. Self-shadowing phenomenon in epi-fluorescent mode. As the specimen attenuates both the excitation and the detected fluorescence, intensity is lower for structures located in deeper parts of the specimen. This phenomenon is particularly pronounced when the specimen is very densely stained or pigmented. (A, B, C) Epi-fluorescent confocal images of a living alga, *Closterium*. Three images were obtained under the same conditions. (A) Optical section showing chlorophyll autofluorescence near the top of the specimen, (B) from the middle of the specimen (35 µm from the top of the surface) and (C) from the bottom of the specimen (70 µm from the top of the surface). Note the reduction of the fluorescent signal (particularly in the center of the specimen where there is maximum shading).

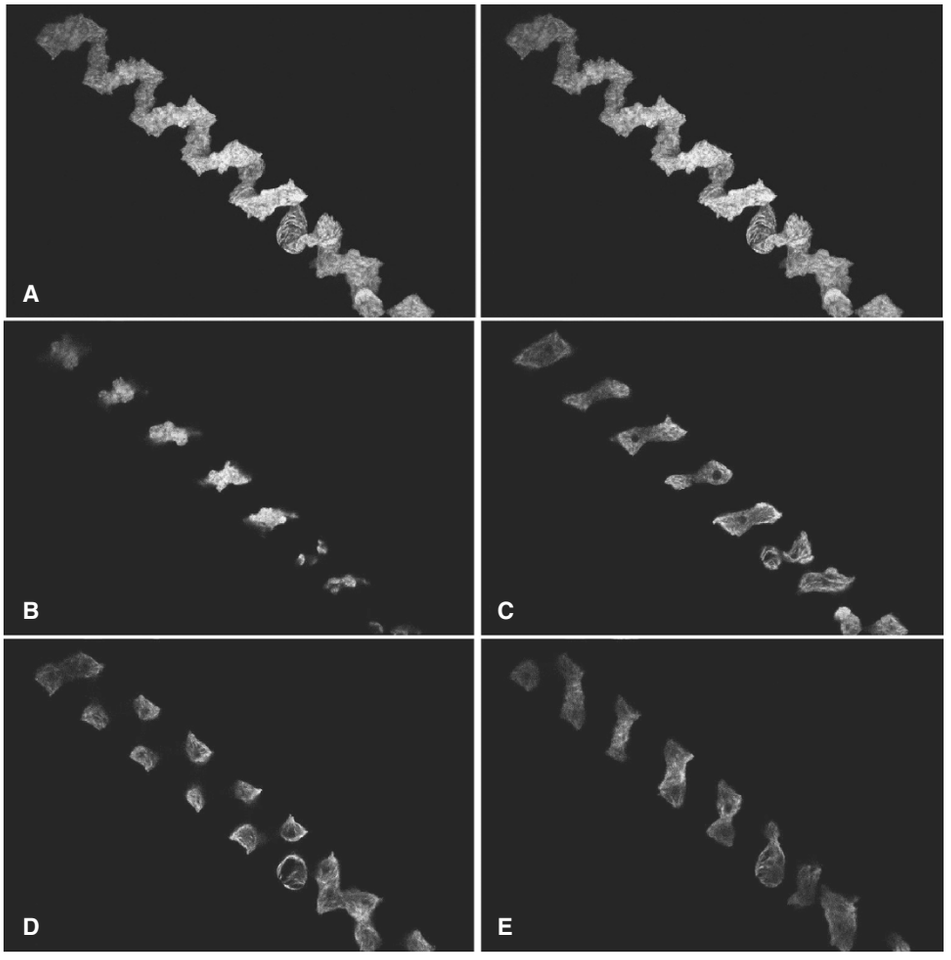


FIGURE 8.48. (A) A stereo-pair showing an epi-fluorescent confocal image of an algal cell (*Spirogyra*) with a loosely packed, autofluorescent spiral chloroplast. (B) Epi-fluorescent confocal image obtained from the top surface of the autofluorescent algal chloroplast. (C, D, E) Optical sections at various depths (20 μm, 40 μm, and 60 μm, respectively). Because of the loose packing of the chloroplasts, self-shadowing is much less than in Figure 8.41.

cell contains two chloroplasts with fin-like laminar projections that shield the lower portion of the chloroplast from excitation light [Fig. 8.46(C)]. Therefore, the images of the lower optical sections show a significant reduction in signal strength. In contrast, Figure 8.48 shows a similar auto-fluorescence image of *Spirogyra* where, because the spiral arrangement of the chloroplast minimizes self-shadowing, there is no significant drop in signal strength from the lower sections.

This self-shadowing phenomenon becomes particularly noticeable when imaging a spherical structure such as a pollen grain. Figure 8.49 is a demonstration of self-shadowing in a fluorescent latex bead. Note that both fluorescent and BS signals diminish toward the lower part of the bead. Figure 8.50 shows a mesophyll protoplast of *A. thaliana*; note the lower part of the cell cannot be imaged successively. Self-shadowing commonly occurs when imaging fixed plant tissue, as these frequently appear brown as a result of natural tannins or from the oxidized products of fixation. The absorption producing the coloration can significantly reduce the signal intensity and limit the effective optical section depth. It can often be removed by treating the tissue for 10 to 20 h in Stockwell's solution (Johansen, 1940).

Figure 8.51 shows that what should be a constant signal from a uniform fluorescent plastic is distorted by the presence of overlying material, in this case either a fluorescent 4 μm latex bead or a cell. Figure 8.52 shows that even the position at which a feature is recorded can be modified by the presence of such material (compare with and without a coverslip). In two-photon fluorescent microscopy, transparent objects that are embedded in the matrix can have similar effects (Fig. 8.53), but generally speaking, vertical shadowing is more severe with lenses of low NA than those of higher NA (Fig. 8.54) (Cheng and Cheng, 2001; Cheng *et al.*, 2002).

As biological materials such as proteins have a significantly higher absorption coefficient in the UV region than in visible light, a visually transparent specimen may pose a serious self-shadowing problem when imaged with a UV confocal microscope (Fig. 8.21 and Chapter 27, *this volume*). In contrast to tissue sections, it is important to note that, because of the absorbance and deflections produced by structures located between the lens and the focus plane, the optical sections obtained from confocal or nonlinear microscopy should not be considered to be uniformly sampled. It is important to remember this when the images are statistically analyzed.

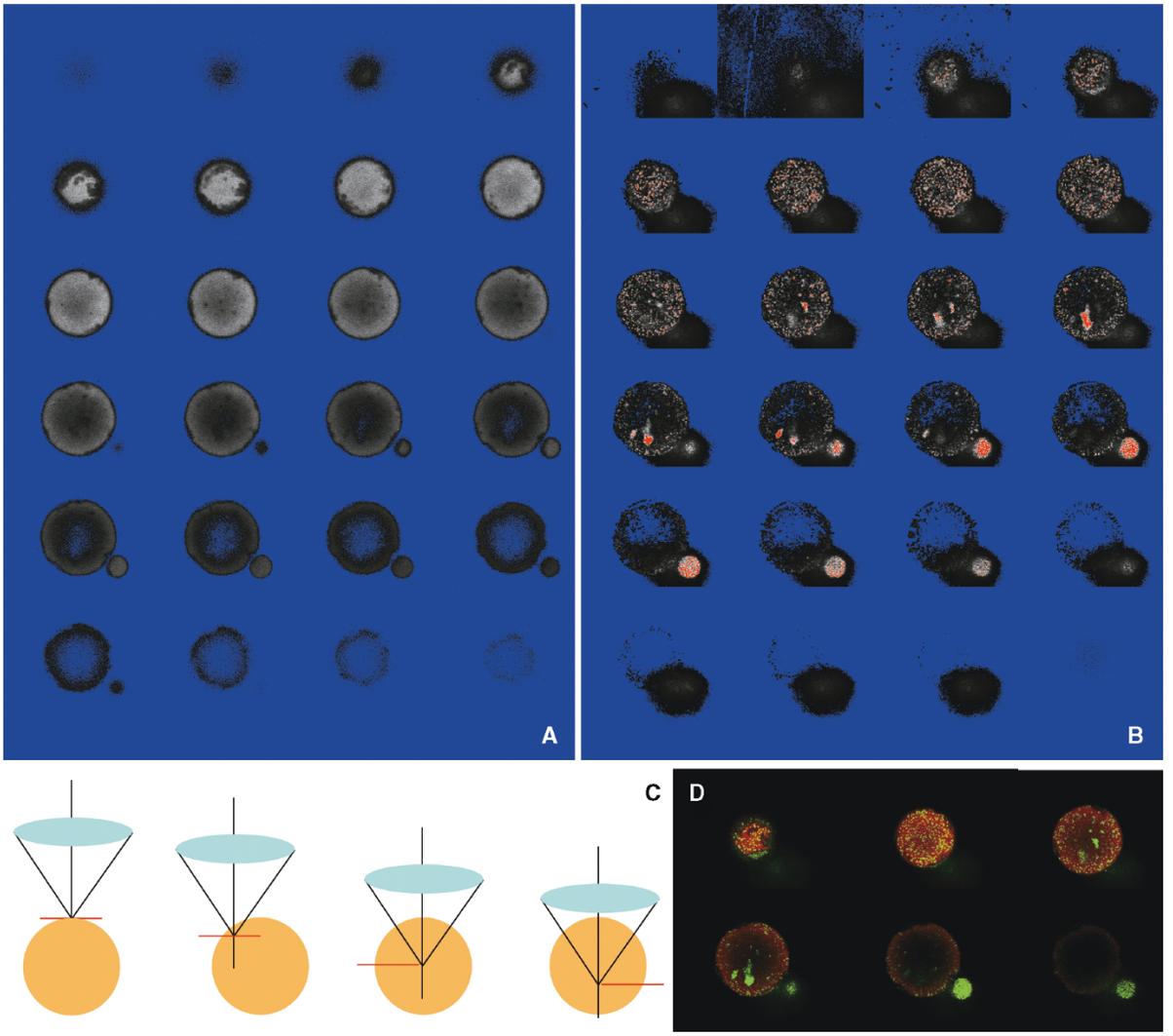


FIGURE 8.49. Fluorescence and BSL images of a latex bead. (A) Optical sections from the north hemisphere to the south hemisphere (in an upright microscope). Note the fluorescence intensity decreases as the section moves towards the southern hemisphere. The fluorescence intensity from the center of the bead also diminishes due to self-absorption of both excitation and emission light. (B) BSL image of the same bead shown in (A). The bead contains numerous "defects" that act as strong scattering centers. The color lookup table (LUT) for (A) and (B) are set as blue = 0 and 255 = red; this LUT allows one to see the base-line and saturation intensity regions in a printed document. (C) Diagrammatic representation of the geometry of the optical section series. (D) Two-channel optical sections of selective views of (A) and corresponding views in (B): green, BS image; red, fluorescent image.

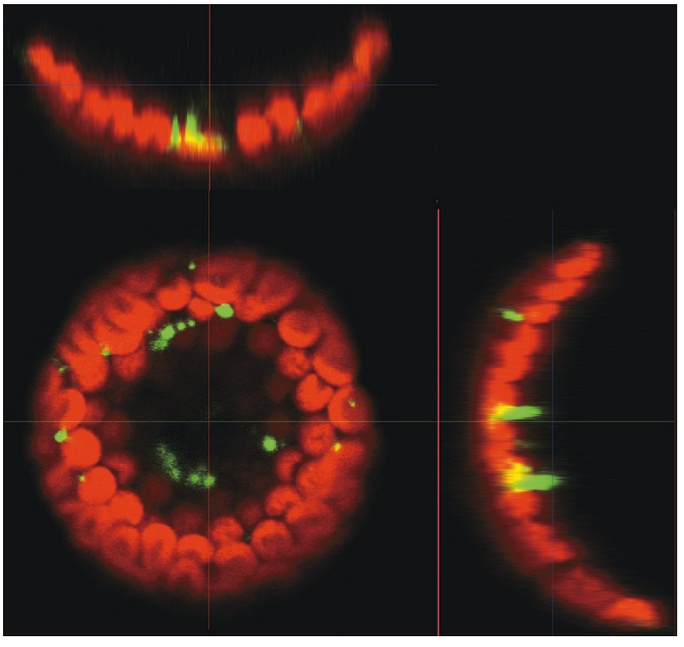


FIGURE 8.50. Confocal (*xy*) and *xz*, *yz* optical sections of a mesophyll protoplasts (*A. thaliana*) with pHBT95s::*AtTLP3*-GFP construct. Note that only half of the cell can be imaged as the self-shadowing is serious in this chloroplast-packed plant cell. (Image courtesy of Chih-Fu Yang and Jei-Fu Shaw, Institute of Plant and Microbial Biology, Academia Sinica, Taipei, Taiwan.)

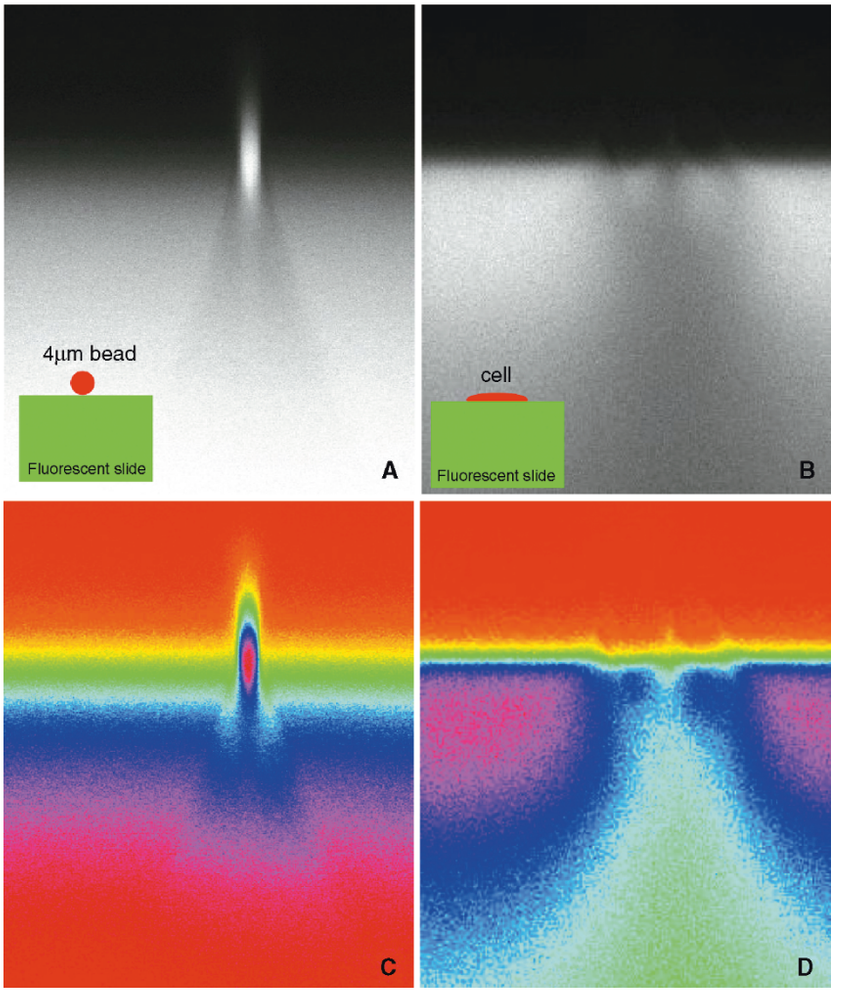


FIGURE 8.51. The effect of a latex bead and a cultured cell on the subsequent optical sections. A 4μm latex bead casts a shadow on the surface of a fluorescent slide (A), as does a cultured CHO cell (B). The inserts diagram the imaging situation in (A) and (B), respectively. (D) and (E) are false color versions of (A) and (B) that emphasize how surface structures can distort the image of the flat, plastic surface and also reduce the signal levels from locations below them.

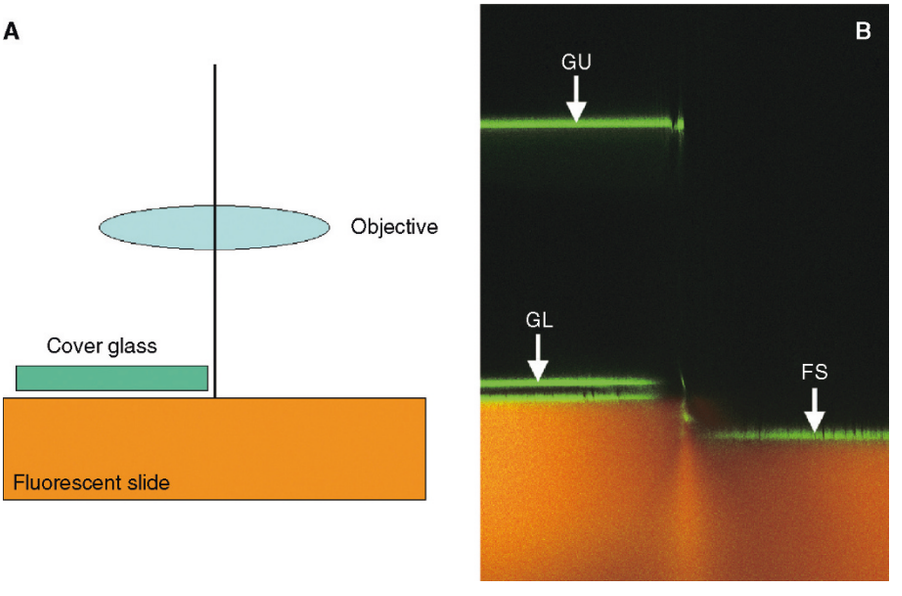


FIGURE 8.52. The effect of a coverslip on the focus position. (A) Diagram showing the imaging setup, (B) the upper and lower surfaces of the coverslip and the surface of the fluorescent plastic shows a strong reflective signal (*green*) and the fluorescent slide shows intense fluorescence (*orange*). Note the shift in focal position between the coverslip-covered and non-covered regions. The edge of the coverslip also casts a strong shadow into the plastic slide.

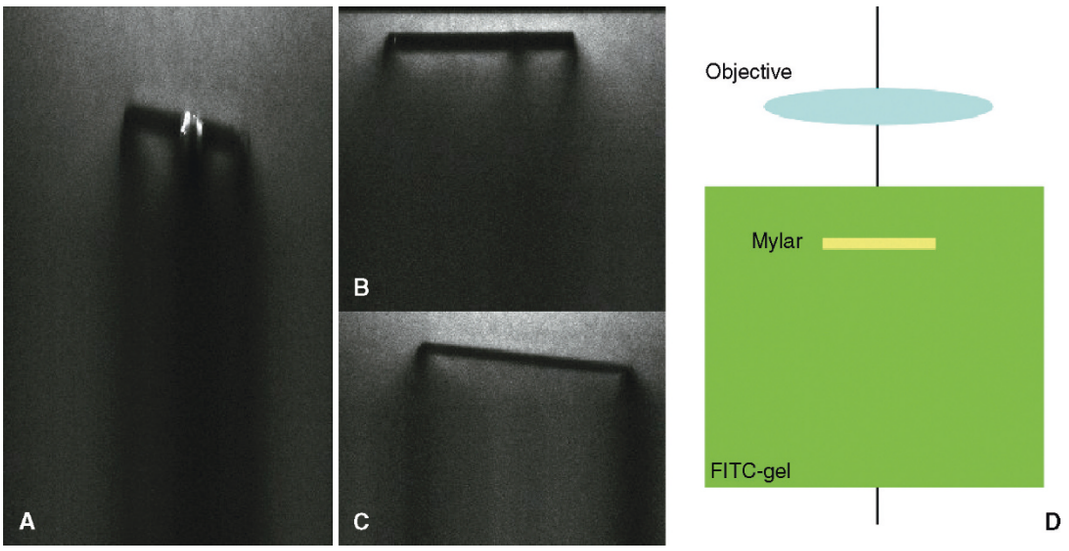


FIGURE 8.53. Self-shadowing due to RI mismatch. Minute pieces of transparent Mylar flakes suspended in a water-based FITC gel (FITC added to "Glitter," a type of cosmetic). (A–C) *xz* views of the fluorescent gel with Mylar flakes. Note the intensitity degradation under the Mylar flake, in particular near the edges. The white spots in the Mylar flake are caused by optical breakdown due to the high illumination intensity used (see also Chapter 38, *this volume*). All images are two-photon fluorescent images excited at 780 nm. (D) Diagram of the imaging situation.

Mounting Medium Selection

There is a general misconception that the confocal microscope is capable of obtaining optical sections as deep into a tissue as the working distance of the objective permits. This is seldom true, particularly if an oil-immersion lens is used to image living tissue immersed in water (Chapter 20, *this volume*, discusses this in depth). Figure 8.55 shows the degree of image degradation that can occur between optical sections obtained from the top and bottom of a glass bead. The top section is just beneath the coverslip and the bottom section is approximately 70 µm below the coverslip.

This sort of degradation is not only caused by specimens as atypical as glass beads. Figure 8.56 shows that image degradation can occur between optical sections obtained from the top and bottom of a sea urchin embryo. The top section is just beneath the coverslip and the bottom section is approximately 70 µm below the coverslip. Although this embryo had been cleared in glycerol and is very transparent, the loss of image definition is obvious in the lower section. For a detailed discussion of the media commonly used to mount plant tissue, see Cheng and colleagues (1994) and Chapter 21, and for animal tissue, see Chapter 17.

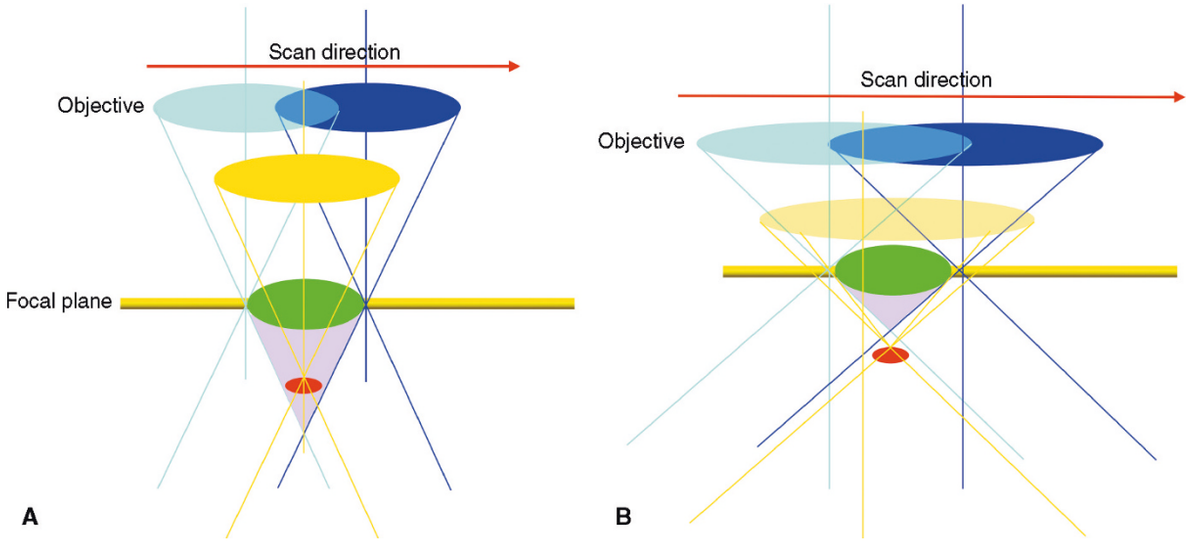


FIGURE 8.54. The effect of the NA of the objective lens on self-shadowing. (A) A small object (*red*) is included in the shadow (*magenta*) of the green object when a low-NA objective lens is used (scanning from light blue position to the dark blue position). The optical section is indicated by the yellow bar. When the objective is focused on the surface of the red object (by the yellow lens), the detecting solid-angle of the objective is not large enough to detect the fluorescence emitted. However, (B) the red object can be detected if a high NA objective is used (the yellow rays define the detectable cone of light).

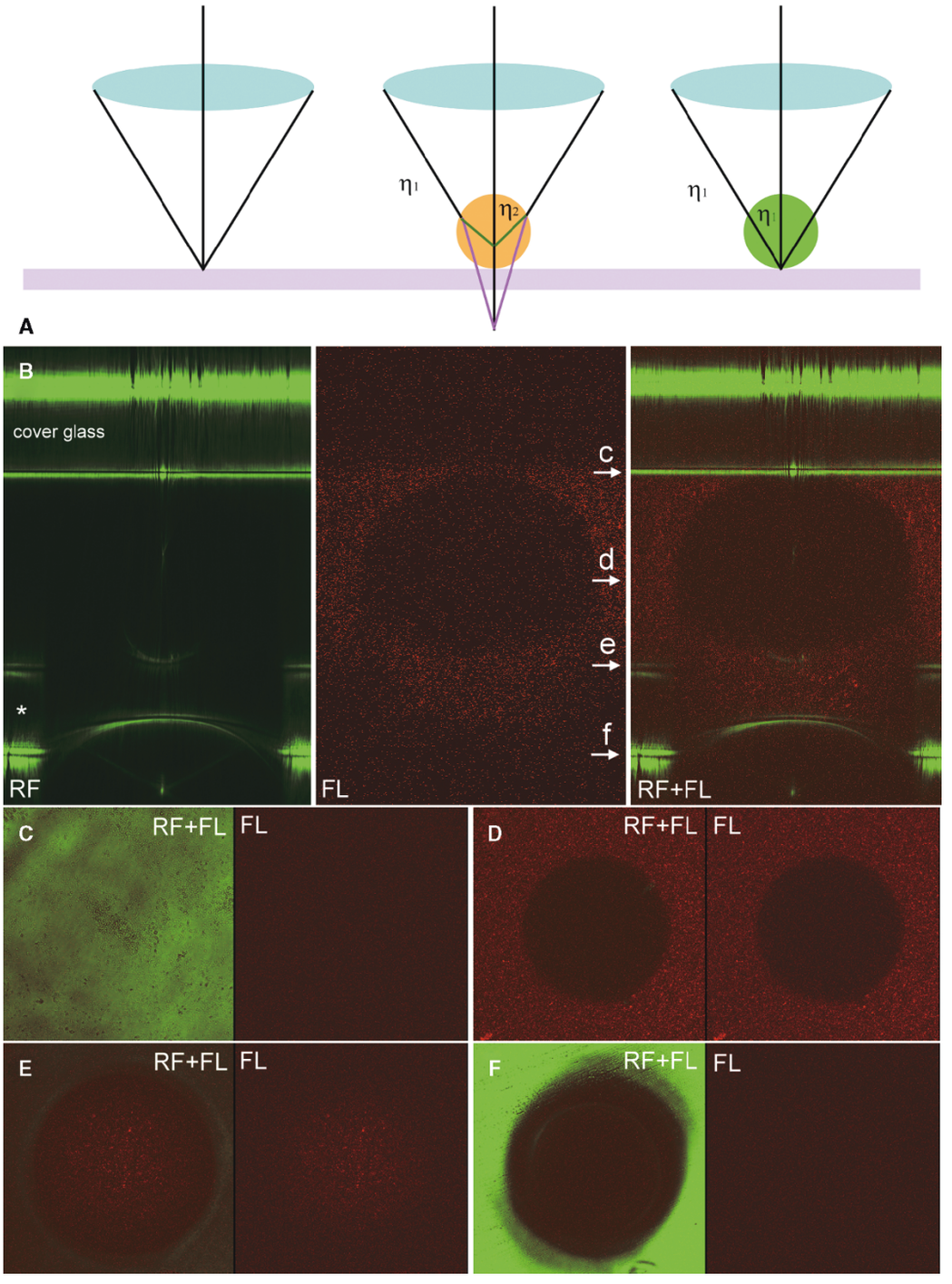


FIGURE 8.55. (A) Diagram showing the effects of a spherical structure situated between the objective lens and focal plane. (Left) The objective is focused onto a cover glass surface. (Middle) The focus plane of the objective is deviated if a spherical structure with an RI (η) different from that of the surrounding medium (η_1) is introduced into the optical path. The focus plane moves upward when $\eta > \eta_1$ (*green rays*) or downward when $\eta_- < \eta_1$ (*red rays*). (Right) When the refractive index of the spherical structure is the same as the surrounding medium (η_1), the focal plane of the objective remains on the mirror surface. (C) *xz* section showing the effect of the glass bead on the image of the lower cover glass surfaces. As an air objective lens corrected for 170 µm cover glass thickness was used, the image just below the top cover glass has the best resolution. (C–E) Series of confocal images of the surface of a cover glass on which a glass sphere ($\eta = 1.53$) was suspended in water ($\eta = 1.33$) with a trace of red fluorescent dye. [Green, reflective (RF); red, fluorescence (FL).] If the glass sphere is suspended in immersion oil ($\eta = 1.53$), the RIs of the glass bead and "mounting medium" now match, the glass surface under the glass bead remains in focus with the surrounding glass surface.

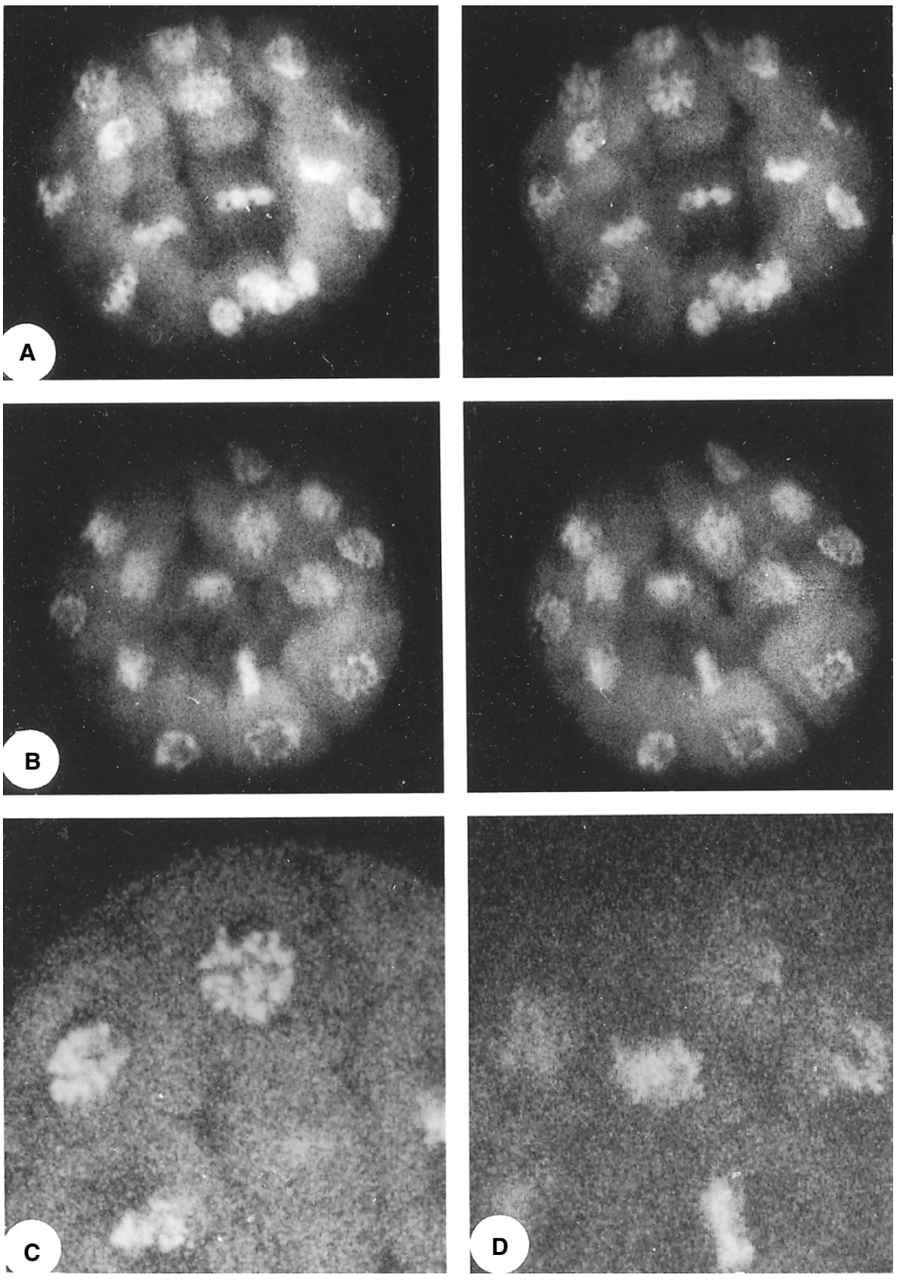


FIGURE 8.56. Two stereo-pairs showing the top half (A) and bottom half (B) of a sea urchin embryo (*Strongylocentrotus purpuratus*). Note the deterioration of image definition in the lower half. The specimen was Feulgen stained, cleared in glycerol, and scanned for 16 s on each of 15 sections using a Bio-Rad MRC 500 operating at 514 nm, full power with a Nikon 40×, NA 1.3 Fluor lens. The *S. purpuratus* embryo [80 µm diameter is less transparent than the species *Lytechinus variegatus* shown in Fig. 8.27(C)]. An optical section obtained from the top of the embryo (10 µm deep). (D) An optical section obtained from 70 µm deep. (Specimen courtesy of Dr. R. Summers, Department of Anatomical Sciences, State University of New York at Buffalo.)

ARTIFICIAL CONTRAST

Contrast Resulting from Instrument Vibration and Ambient Lighting

Vibrations resulting from the mechanical scanning systems of confocal microscopes and/or vibrations from external sources can have a serious negative effect on image contrast because they can alter the position of the specimen relative to the focal plane of the objective lens (Overington, 1976).

Interference from room light can also have a drastic effect on the recorded image. Room light scattered by the specimen and entering the detecting system can increase the DC background level as well as make moiré patterns between the AC component from the fluorescent lights and the pixel clock of the digitizer. Figure 8.57 shows the effect of AC components resulting from fluorescent room light. It is important to note that, especially when using an inverted microscope for either a widefield or multi-photon fluorescence with non-descanned detection, the specimen should be covered with a dark cup and the room should be kept in almost total darkness.

Vibration-induced variations in the relative positions of the pinholes can cause similar artifacts, degrading the effective resolution of the confocal imaging system. Figure 8.53 shows the effects of mechanical vibration on a confocal image of a dirty first-surface mirror. The image shows vibration contrast due to poor mechanical isolation from the building vibration (Fig. 8.58). An actively isolated optical bench can significantly improve the situation. Instability in the pointing direction of the laser (Chapter 5, *this volume*) can also contribute artificial contrast to the image, and laser intensity variations can introduce complex moiré patterns in signals recorded in a single-beam system.

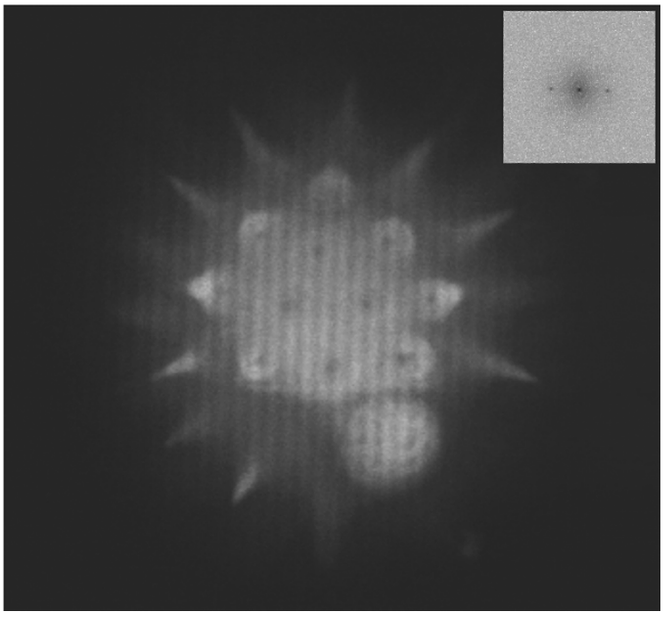


FIGURE 8.57. AC components in a confocal image resulting from fluorescent lights in the laboratory. Insert: Fourier power spectrum of the image showing spots related to the AC frequency.

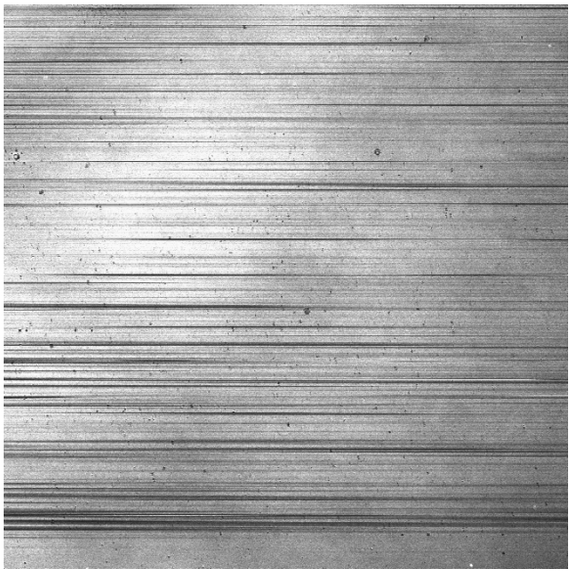


FIGURE 8.58. The effect of mechanical vibration on the confocal reflection image of a cover glass surface.

Contrast Resulting from Interference of Cover Glass Surfaces

Interference can also introduce spurious contrast into the recorded data. Figure 8.59 shows three confocal images (and their Fourier transforms) recorded from a focus plane located near the surface of a coverslip on which an *A. thaliana* seedling was resting. Patterns generated by the interference of light reflected from the two surfaces of the cover glass are clearly visible in the reflection image (489 nm) collected in a channel near the excitation wavelength (488 nm) [Fig. 8.59(A,D)]. However, this reflective light can still be detected in the 500 nm channel of the Zeiss 510 Meta system as shown in the Fourier transform of the fluorescence image [Fig. 8.59(B,E)]; since the cover glass surface reflection is much more intense than the fluorescence of the specimen, this signal is actually the scattered light leaking through the microscope monochrometer system. The spots are not visible in the image collected at 703 nm because the detecting channel is far away from the 489 nm [Fig. 8.59(C,F)]. Using the Fourier transform in this way provides a very sensitive test for the leakage of excitation light into the detector channels. One focuses the microscope on the surface of a cover glass to obtain an interference pattern and records the image in all the spectral channels in a normal way. Then examine the power spectrum of each image to determine if specific diffraction spots corresponding to the frequency of the interference pattern are present.

Background Level and Ghost Images from the Transmission Illuminator

Because the confocal microscope has high resolution along the *z*-axis, it can be very difficult to locate areas of interest if one searches in the confocal mode. Therefore, initial searching is generally done using conventional bright-field or widefield epi-fluorescence microscopy. Once an area of interest has been identified, one switches to confocal mode by redirecting the imaging path to the confocal scanning/detecting unit and by blocking the optical path from the trans-/epi-illuminator. However, if one

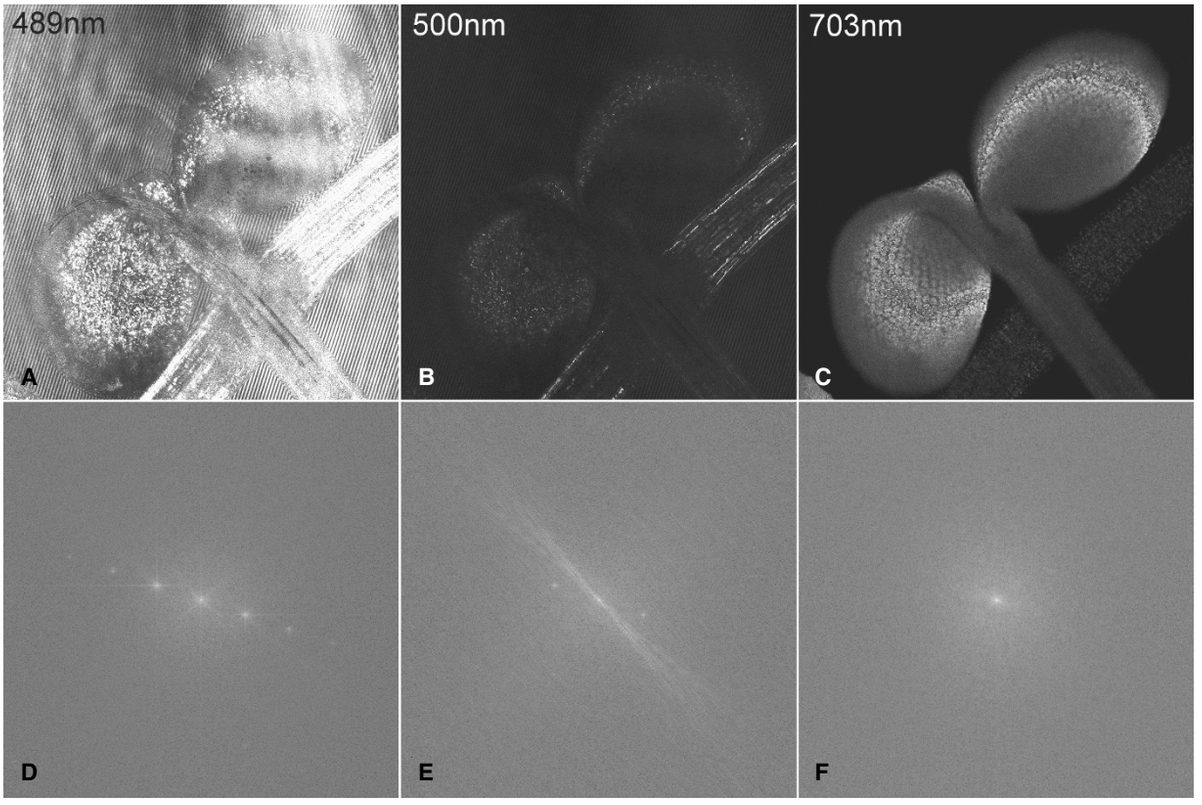


FIGURE 8.59. A young seeding of *A. thaliana* was placed in water under a cover glass and imaged at 488 nm using a Zeiss 510 META confocal microscope. (A) 489 nm channel shows strong backscattered light from the specimen and the surface of cover glass. Interference fringes are clearly visible. (B) 500 nm channel shows low intensity of autofluorescence. (C) 703 nm channel shows autofluorescence of chlorophylls. (D) Fast Fourier transform (FFT) of (A) shows the diffraction spots resulting from the interference fringes. (E) Even though there are no visible interference fringes in (B), its FFT indicates a significant amount of 488 nm illumination contamination in the image. (F) FFT of (C). (Specimen courtesy of Shu-Hsing Wu, Institute of Plant and Microbial Biology, Academia Sinica, Taipei, Taiwan.)

forgets to block the light from the conventional illuminator, some of it will reach the detector, producing excessive background. Depending on the spectral output of the illuminator, different fluorescence channels will record particular background levels. In an extreme case, when the specimen is relatively opaque, a ghost image may form.

Figure 8.60 shows a pollen grain of maize stained with periodic-acid Schiff (PAS) reagent for starch. The trans-illuminator was turned on at low intensity during the confocal scanning. The substage condenser was purposely misaligned off the optical axis to emphasize the ghost image effect. Note that the confocal fluorescence image of the pollen grain shows only the periphery of the pollen grain as a result of self-shadowing. However, the non-confocal transmitted-light ghost image (arrows) simply shows the shadow of the pollen grain. Therefore, it is important to turn off the trans-illuminator/epi-illuminator of the microscope during confocal observation as even a low glow can add significantly to the background level and produce complex image features that confuse interpretation.

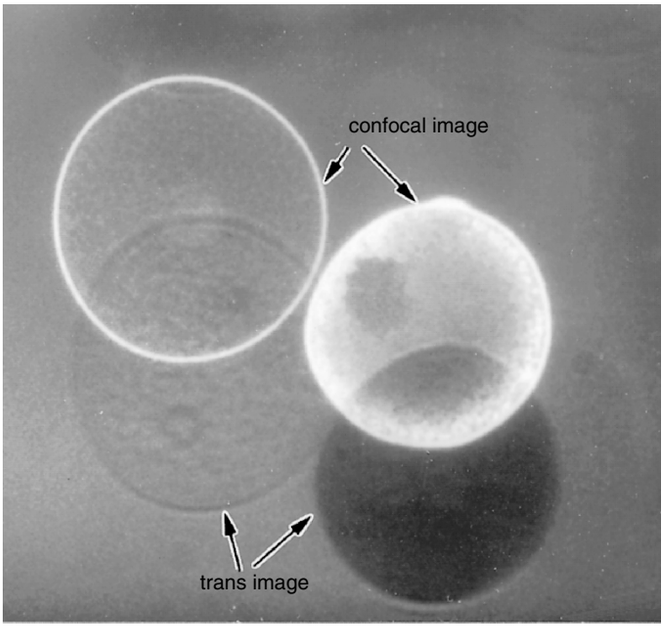


FIGURE 8.60. An epi-fluorescence confocal image of a pollen grain of maize stained with PAS. Due to the abundance of starch granules, the pollen was deeply stained. During the image acquisition, the substage illuminator was purposely turned on and misaligned to demonstrate the effect of a "ghost" image.

Contrast Resulting from Differences in Photobleaching Dynamics

Because different fluorophores in a multi-labeled specimen often photobleach at different rates, photobleaching that occurs while recording a series of optical sections can cause the first section to have a different spectral balance from the last. This complicates

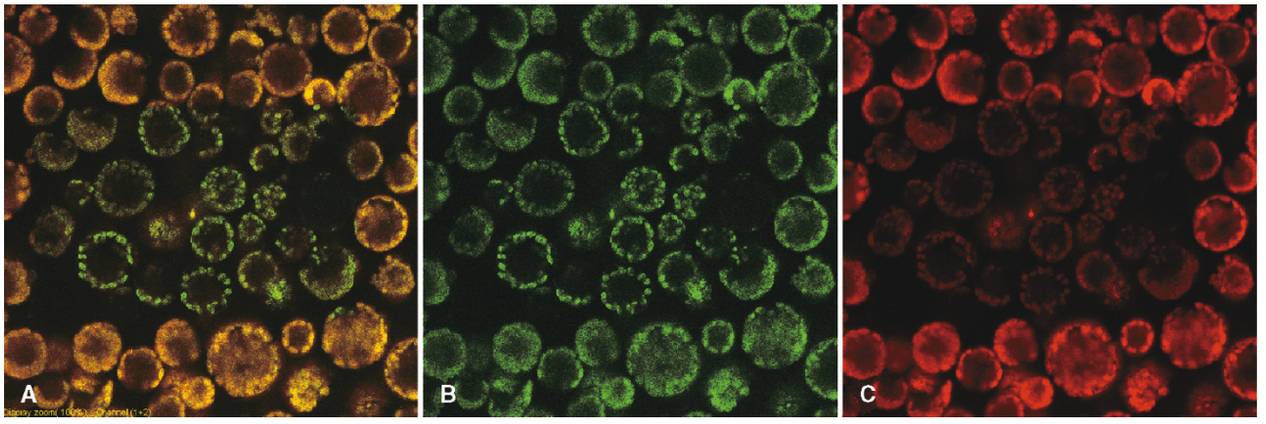


FIGURE 8.61. Photobleaching in the mesophyll protoplasts of *A. thaliana* by 780 nm NIR (A). Note that the green autofluorescence (B) bleaches more slowly than does the red autofluorescence (C) caused by chlorophyll.

any effort to correct for bleaching or for the signal loss that occurs as the *z*-stack penetrates farther into the specimen. Figure 8.61 is a dual-channel recording of mesophyll protoplasts of *A. thaliana*. It shows that the red fluorescence (chlorophylls) and the green autofluorescence photobleach at very different rates and, therefore, that bleach rate must be considered as a contrast parameter when imaging such specimens.

Effect of Spectral Leakage and Signal Imbalance Between Different Channels

The spectral resolution of the detection system is an important factor controlling image contrast in fluorescence microscopy. Poor spectral resolution, caused either by leakage and poor cut-off sharpness in the filter system (see Chapter 3, *this volume*), the spectral response of detector(s), or variations in the transmittance or properties of the optics can have a pronounced impact on image contrast and S/N.

A significant imbalance in image intensity among different detection channels in a multi-channel setup can have a serious impact on the spectral purity of the final image. If, in a typical specimen, labeled with fluoroscein-isothiocyanate and rhodamine (FITC-Rh), the concentration of FITC is significantly higher than that of Rh, then given equal excitation, the FITC will emit much more fluorescence than the Rh. Even 0.1% leakage of stray FITC light through the dichroic mirror and barrier filters into the Rh channel can contribute significantly to the detected signal. Clearly, any imbalance noted between two fluorescence channels may be due not to a difference in the concentration of the two fluorescent dyes but to an imbalance in their fluorescence efficiency with respect to the spectral bandwidth and blocking efficiency of the excitation and emission filters used. For example, attempts to view a specimen labeled with balanced amounts of FITC and Rh but excited using only the 488-nm line of an argon-ion laser will result in a very poor signal in the Rh channel. The use of dual excitation wavelengths (488 and 568 nm) from a krypton/argon laser can reduce this problem.

A simple plot of the pixel-by-pixel correlation between the intensity values detected in each channel can reveal possible cross-talk. Figure 8.62 shows such a plot between two fluorescence channels recorded from a FITC-labeled specimen, excited at 488 nm.

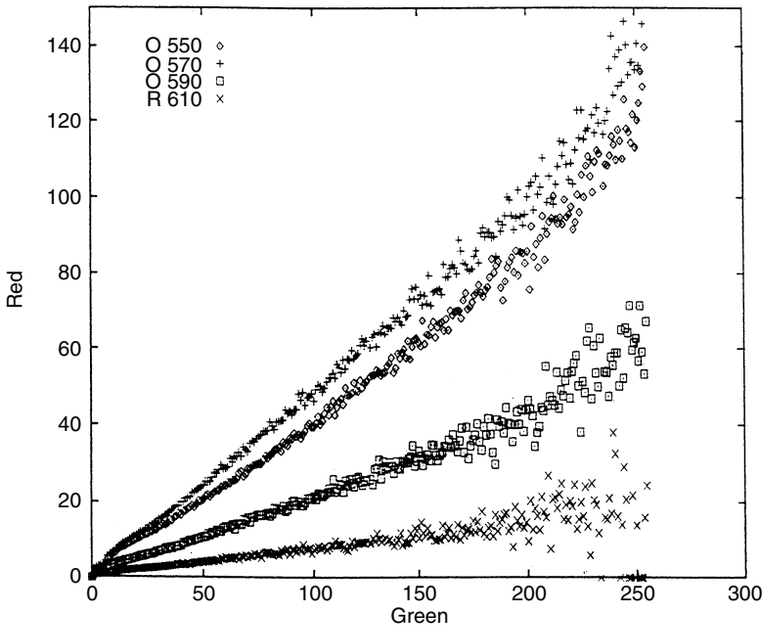


FIGURE 8.62. Spill-over from the FITC channel (*green*) to the rhodamine channel (*red*) for different low-pass filters.

The two channels were separated using a 570 nm dichroic beamsplitter; a 535 nm bandpass filter was used for channel 1 and various long-pass filters ranging from 570 to 610 nm were used for channel 2. Note that the correlation line decreases in slope as the cut-on wavelength of the barrier filter increases and the amount of excitation light reaching the detector is reduced.

NEW CONTRASTS: FLUORESCENCE LIFETIME AND COHERENT ANTISTOKES RAMAN SPECTROSCOPY

Since the second edition of the volume, the use of confocal contrast based on the fluorescence lifetime (FLIM) has become much more common. While this is partially because the equipment needed to record it is now commercially available, to an even greater extent it is because it seems that FLIM may be the best way to obtain a quantitative measure of FRET in living cells (Fig. 8.63). Chapter 27 explores this exciting new modality in more depth.

Although Raman microscopy had been available for some time, the chemical specificity it offers was only available at the cost of having to use relatively high illumination power while having to accept sensitivity so low that it was useless for detecting most biological molecules at the concentrations likely to be found in biological specimens. More recently, developments in laser technology have made coherent antistokes raman spectroscopy (CARS) a realistic contrast mode for 3D microscopy (Fig. 8.64). This new technique has better chemical sensitivity than normal Raman microscopy and requires less laser power to strike the specimen. Chapter 33 provides more details.

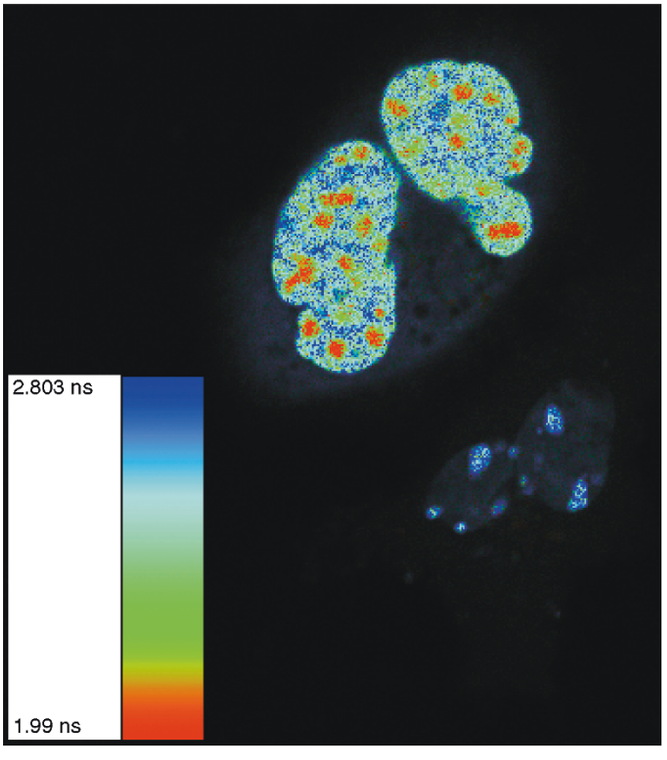


FIGURE 8.63. The FLIM images are color coded and overlaid on an intensity image. Blue represents short lifetime and red represents long lifetimes. The image was taken with an Olympus FV1000 with fiber output coupling to a PicoQuant FLIM system and a 405 nm pulsed laser was used for illumination. The sample is a living cell expressing cyan fluorescent protein (CFP) and yellow fluorescent protein (YFP). In the image, there are four cells. Two of them demonstrate FRET, as is shown by the blue color. (Image provided by Yiwei Jia of Olympus and Uwe Ortmann of PicoQuant; the image was taken at the University of Virginia FRET microscopy course.)

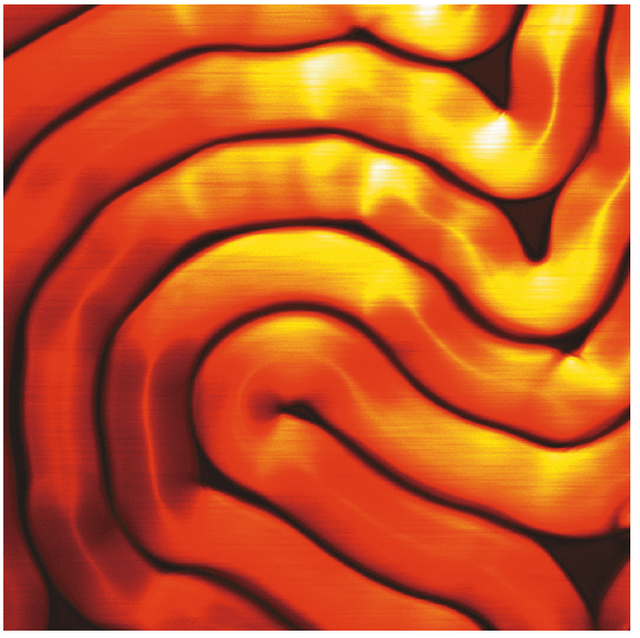


FIGURE 8.64. CARS Image of lecithin myelin figures using modified Olympus FV300 confocal system. ωp-ωs is tuned to the CH_2 symmetric stretch vibration at 2,838 cm^{-1}. This image shows that the myelin core is not composed of pure water but is enriched in lecithin. (Provided by Ji-Xin Cheng, Weldon School of Biomedical Engineering, Purdue University.)

Finally, although until recently, one usually viewed the electrical state of excitable cells indirectly by sensing Ca^{++}, there have long been membrane-incorporated or membrane-translocating fluorescent dyes that change their fluorescent output with membrane potential (Zochowski *et al.*, 2000). Recently, the combination of a disk-scanning microscope with an electron-multiplying CCD camera has provided the researcher with a method of detecting the electrical state directly and on a time scale almost fast enough to measure transients that are physiologically significant (Fig. 8.65).

SUMMARY

Image contrast mechanisms in confocal microscopy depend on a number of variables, many of which have been presented in this chapter. The acquisition parameters of the imaging system should be adjusted to emphasize to the signals carrying the information required and these adjustments must also take into account the characteristics of the specimen, and the image processing method to be used. To observe detailed structures with the appropriate contrast requires careful preparation of the specimen, and this depends in turn on an understanding of its chemical and physical properties.

In order to improve the visibility of structures in 3D while minimizing unwanted artifacts, the parameters needed for proper

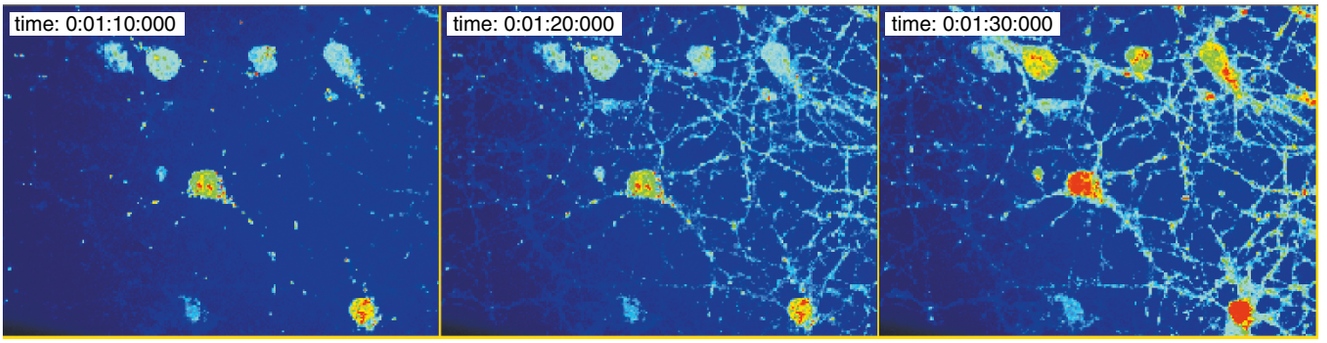


FIGURE 8.65. Cultured rat hippocampal neurons loaded with $DiSBAC_2(3)$, a voltage sensitive, membrane-translocating dye, and imaged with an Andor Revolution 488. Twenty 100 ms exposures on the iXon 887BV EM-CCD were obtained for each *z*-stack, using an EM Gain of 200. The last frame was taken almost simultaneously with the addition of 100 m*M* KCl, which depolarizes the cells and shows a near instantaneous rise in the $DiSBAC_2(3)$ signal. The change in signal is ~45%. (Image provided by Iain Johnson, Molecular Probes/Invitrogen, Eugene, Oregon, and Mark Browne, Andor, South Windsor, Connecticut.)

volume rendering must be properly selected (particularly, Nyquist sampling in *x*, *y*, *z*, and *t*). Improving the quality of the confocal data should always be the first goal. This includes maximizing the dynamic range of the recording system, the contrast between the structure of interest, and the background and the S/N of the recorded data.

ACKNOWLEDGMENTS

Most of the images presented in this chapter were obtained at the author's laboratories at the State University of New York at Buffalo and at the National University of Singapore (NUS) where he is a part-time professor of the Department of Biological Sciences (DBS). The author is grateful for the wonderful support and friendship from Professor Hew Choy Leong, Head of DBS-NUS and Professor Hanry Yu (Department of Physiology, NUS) during his 2003 and 2004 stay. The SHG work is a collaboration with Professor Chi-kuang Sun of the Department of Electrical Engineering, National Taiwan University, Taipei, Taiwan. Some of the images used in this chapter were obtained by the author in demonstration experiments at the International 3D Microscopy of Living Cell Course (organized by Professor J. Pawley) held annually at the University of British Columbia, Canada. Special thanks to Dr. T. Holmes at AutoQuant for providing the Auto-Deblur deconvolution software, to Drs. M. and D'A. Weis, Agriculture Canada, Summerland, British Columbia, Canada, for Figures 8.10 and 8.44, to Dr. A. Periasamy, University of Virginia, Charlottesville, Virginia, for Figures 8.34 through 8.36, and to Iain Johnson (Molecular Probes/Invitrogen, Eugene, OR) and M. Browne (Andor, South Windsor, CT) for Figure 8.65.

REFERENCES

An, J.J., Goodman, M.B., and Schwartz, E.A., 1990, Simultaneous fluorescent and transmission laser scanning confocal microscopy, *Biophys. J*. 59:155a.

Barad, Y., Eisenberg, H., Horowitz, M., and Silberberg, Y., 1997, Nonlinear scanning laser microscopy by third-harmonic generation, *App. Phys. Lett.* 70:922–924.

Barr, M.L., and Kieman, J.A., 1988, *The Human Nervous System — An Anatomical Viewpoint*, 5th ed., Lippincott, London, p. 17.

Born, M., and Wolf, E., 1980, *Principles of Optics*, 6th ed., Pergamon Press, Oxford.

Boyde, A., 1985, The tandem scanning reflected light microscope. Part II. Pre-Micro'84 application at UCL, *Proc. RMS* 20:131–139.

Carminati, R., and Greffet, J.J., 1995a, Two-dimensional numerical simulation of the photon scanning tunneling microscope. Concept of transfer function, *Opt. Commun.* 116:316–321.

Carminati, R., and Greffet, J., 1995b, Influence of dielectric contrast and topography on the near field scattered by an inhomogeneous surface: Boundary conditions for diffusion of light, *J. Opt. Soc. Am. A* 12:2716.

Carney, P., and Schotland, J., 2001, Three-dimensional total internal reflection microscopy, *Opt. Lett.* 26:1072.

Chen, I.-H., Chu, S.-W., Sun, C.-K., Lin, B.-L., and Cheng, P.C., 2002, Wavelength dependent damage in biological multi-photon confocal microscopy: A micro-spectroscopic comparison between femtosecond Ti:Sapphire and Cr:Forsterite laser sources, *Opt. Quantum.* 34(12):1251–1266.

Chen, V.K.-H., and Cheng, P.C., 1989, Real-time confocal imaging of Stentor coeruleus in epi-reflective mode by using a Tracer Northern Tandem scanning microscope, *Proc. 47th Annual Meeting EMSA* 47:138–139.

Chen, Y., Mills, J.D., and Periasamy, A., 2003, Protein interactions in cells and tissues using FLIM and FRET, *Differentiation.* 71:528–541.

Cheng, P.C., and Cheng, W.Y., 2001, Artifacts in confocal and multi-photon microscopy, *Microsc. Microanal*. 7:1018–1019.

Cheng, P.C., and Kriete, A., 1995, Image contrast in confocal light microscopy, In: *Handbook of Biological Confocal Microscopy* (J.B. Pawley, ed.), Plenum Press, New York, pp. 281–310.

Cheng, P.C., and Lin, T.H., 1990, The use of computer-controlled substage folding optics to enhance signal strength in fluorescent confocal microscopy, *Trans. Roy. Micros. Soc*. 1:459–642.

Cheng, P.C., Chen, V.H.-K., Kirn, H.G., and Pearson, R.E., 1989, An epi-fluorescent spinning-disk confocal microscope, *Proc. 47th Annual Meeting EMSA* 47:136–137.

Cheng, P.C., Hibbs, A.R., Yu, H., and Cheng, W.Y., 2002, An estimate of the contribution of spherical aberration and self-shadowing in confocal and multi-photon fluorescent microscopy, *Microsc. Microanal*. 8:1068–1069.

Cheng, P.C., Pareddy, D.R., Lin, T.H., Samarabandu, J.K., Acharya, R., Wang, G., and Liou, W.S., 1994, Confocal microscopy of botanical specimens, In: *Multidimensional Microscopy* (P.C. Cheng, T.H. Lin, W.L. Wu, and J.L. Wu, eds.), Springer-Verlag, Berlin, pp. 339–380.

Cheng, P.C., Sun, C.-K., Kao, F.-J, Lin, B.L., and Chu, S.-W., 2001, Nonlinear multi-modality spectro-microscopy: Multiphoton fluorescence, SHG and THG of biological specimen, *SPIE Proc*. 4262:98–103.

Cheng, P.C., Sun, C.K., Lin, B.L., Chu, S.W., Chen, I.S., Liu, T.M., Lee, S.P., Liu, H.L., Kuo, M.X., and Lin, D.J., 2002, Biological photonic crystals — Revealed by multi-photon nonlinear microscopy, *Microsc. Microanal.* 8:268–269.

Cheng, P.C., Sun, C.K., Cheng, W.Y., and Walden, D.B., 2003, Nonlinear biophotonic crystal effect of opaline silica deposits in maize, *J. Scanning Microsc.* 235:80–81.

Chu, S.W., Chen, I.S., Li, T.M., Lin, B.L., Cheng, P.C., and Sun, C.K., 2001, Multi-modality nonlinear spectral microscopy based on a femtosecond Cr:forsterite laser, *Opt. Lett.* 26:1909–1911.

Chu, S.W., Chen, I.-S., Liu, T.-M., Sun, C.-K., Lin, B.-L., Lee, S.-P., Cheng, P.C., Liu, H.-L., Kuo, M.-X., and Lin, D.-J., 2003, Nonlinear bio-photonic crystal effects revealed with multi-modal nonlinear microscopy, *J. Microsc.* 208:190–200.

Cogswell, C.J., 1994, High resolution confocal microscopy of phase and amplitude objects, In: *Multidimensional Microscopy* (P.C. Cheng, T.H. Lin, W.L. Wu, and J.L. Wu, eds.), Springer-Verlag, Berlin, pp. 87–102.

Deng, Y., Marko, M., Buttle, K.F., Leith, A., Mieczkowski, M., and Mannella, C.A., 1999, Cubic membrane structure in amoeba (*Chaos carolinesis*) mitochondria determined by electron microscopy tomography, *J. Struct. Biol.* 127:231–239.

Holmes, T., and Cheng, P.C., 2005, Basic principles of imaging, In: *Multi-Modality Microscopy* (H. Yu, P.C. Cheng, P.C. Lin, and F.J. Kao, eds.), World Scientific Publishing, in press.

Johansen, D.A., 1940, *Plant Microtechnique*, McGraw-Hill, New York.

Oldenbourg, R., 2004, Polarization microscopy with the LC-PolScope, In: *Live Cell Imaging: A Laboratory Manual* (D.L. Spector and R.D. Goldman, eds.), Cold Spring Harbor Laboratory Press, Cold Spring Harbor, New York, pp. 205–237.

Overington, J., 1976, *Vision and Acquisition*, Pentech Press, London.

Paddock, S.W., 1989, Tandem scanning reflected-light microscopy of cell-stratum adhesions and stress fibers in Swiss 3T3 cells, *J. Cell. Sci.* 93:143–146.

Patterson, G., and Lippincott-Schwartz, J., 2002, A photoactivatable GFP for selective photolabeling of proteins and cells, *Science.* 297:1873–1877.

Prieve, D.C., and Walz, J.Y., 1993, The scattering of an evanescent surface wave by a dielectric sphere in total internal reflection microscopy, *Appl. Opt*. 32:1629.

Reits, E.A., Neefjes, J.J., 2001, From fixed to FRAP: Measuring protein mobility and activity in living cells, *Nat. Cell Biol.* 3(6):E145–147.

Rose, A., 1948, Television pickup tubes and the problem of noise, *Adv. Electron* 1:131.

Scheibel, M.E., and Scheibel, A.B., 1970, The rapid Golgi method. Indian summer or renaissance? In: *Contemporary Research Methods in Neuroanatomy* (W.J.H. Nauta and S.O.E. Ebbeson, eds.), Springer-Verlag, New York, pp. 1–11.

Sharonov, S., Morjani, H., and Manfait, M., 1992, Confocal spectral imaging analysis: A new concept to study the drug distribution in single living cancer cell, *Anticancer Res*. 12:1804.

Sheppard, C.J.R., 1993, Confocal microscopy: Basic principles and system performance, In: *Multidimensional Microscopy* (P.C. Cheng, T.H. Lin, W.L. Wu, and J.L. Wu, eds.), Springer-Verlag, Berlin, pp. 1–31.

Shinozaki, D.M., Cheng, P.C., Haridoss, A., and Fenster, A., 1991, Three dimensional optical microscopy of water trees in polyethylene, *J. Mater. Sci.* 26:6151–6160.

Shinozald, D.M., Klauzner, A., and Cheng, P.C., 1991, Inelastic deformation of polyimide-copper thin films, *Mater. Sci. Eng. A* 142:135–144.

Shribak, M., and Oldenbourg, R., 2003, Techniques for fast and sensitive measurements of two-dimensional birefringence distributions, *Appl. Opt.* 42:3009–3017.

Sun, C.K., 2005, *Abstract of Focus on Microscopy*, Jena, Germany.

Sun, C.K., Huang, Y.C., Liu, H.C., Lin, B.L., and Cheng, P.C., 2001, Cell manipulation using diamond microparticles as optical tweezers handles, *J. Opt. Soc. Amer. B*, 18(10):1483–1489.

Tsou, C.-H., and Fu, Y.L., 2002, Pollen tetrad formation in *Annona* (Annonaceae): Proexine formation and binding mechanism, *Am. J. Botany* 89:734–747.

Van Labeke, D., Barchiesi, D., and Baida, F., 1995, Optical characterization of nanosources used in scanning near-field optical microscopy, *J. Opt. Soc. Am. A* 12(4):695–703.

Watson, T.F., 1989, Real-time confocal microscopy of high speed dental burr/tooth cutting interactions, *Abstracts of the 1st International Conference on Confocal Microscopy and the 2nd International Conference on 3D Image Processing in Microscopy*, Amsterdam, March 15–17, 1989.

Watson, T.F., Azzopardi, A., Etman, L.M., Cheng, P.C., and Sidhu, S.K., 2000, Confocal and mulit-photon microscopy of dental tissues and biomaterials, *Am. J. Dentistry* 13:19–24.

Webb, W.W., 1976, Perspectives on Cell Surface Mobility, In: *Measurement of Lateral Transport on Cell Surfaces* (V.T. Marchesi, ed.), Alan R. Liss, Inc., New York, pp. 276–278.

Wells, K.S., Sandison, D.R., Strickler, J.H., and Webb, W.W., 1990, Quantitative fluorescence imaging with laser scanning confocal microscopy, In: *Handbook of Biological Confocal Microscopy* (J. Pawley, ed.), Plenum Press, New York.

White, J.G., Amos, W.B., and Fordham, F., 1987, An evaluation of confocal vs. conventional imaging of biological structures by fluorescent light microscopy, *J. Cell Biol*. 105:41–48.

Wijaendts van Resandt, W., Marsman, H.J.B., Kaplan, R., Davoust, J., Stelzer, E.H.K., and Stricker, R., 1984, Optical fluorescence microscopy in three dimensions: Microtomoscopy, *J. Microsc.* 138:29–34.

Xiao, G.O., Corle, T.R., and Kino, G.S., 1988, Real-time confocal scanning microscope, *Appl. Phys. Lett*. 53:716–718.

Zochowski, M., Wachowiak, M., Falk, C.X., Cohen, L.B., Lam, Y.W., Antic, S., and Zecevic, D., 2000, Imaging membrane potential with voltage-sensitive dyes, *Biol. Bull*. 198:1–21.

9

The Intermediate Optical System of Laser-Scanning Confocal Microscopes

Ernst H.K. Stelzer

INTRODUCTION

This text explains some of the basics of intermediate optical systems in confocal microscopes. Important microscope components are discussed in more detail in other chapters: lasers (Chapter 5) and other light sources (Chapter 6), objective lenses (Chapter 7), special optical elements (Chapter 3), fibers (Chapter 26), and detectors (Chapter 12). Although this chapter concentrates on laser-based single-spot scanning instruments while other types of instruments are covered elsewhere (Chapters 10 and 29), remarks on different approaches will guide the interested reader.

DESIGN PRINCIPLES

Overview

The basic optical layout of a confocal fluorescence microscope is found in Figure 9.1. A laser beam is focused into a pinhole, which acts as a point-like light source. The spatially filtered light is deflected by a dichroic mirror and focused by an objective lens into the fluorescent specimen. The fluorescence light is emitted in all directions; a fraction of the fluorescence emission is collected by the objective lens and focused into a pinhole in front of a detector.

The lateral discrimination capability of the confocal fluorescence microscope occurs because light that is emitted in the focal plane at a distance Δx from the focus will miss the pinhole in front of the detector by a distance $M\Delta x$. The main advantage of a confocal microscope is, however, its axial discrimination capability. If the sample is flat, this property is not required, but in a thick sample, fluorophores located in front and behind the focal plane ($\Delta z \neq 0$) will also be excited by the incoming laser beam. However, their fluorescence emission will be focused either in front of or behind the image plane that includes the detection pinhole ($\Delta z' \neq 0$). Hence their images are expanded at the pinhole plane and only a fraction of the fluorescence light passes the pinhole to reach the detector. If one removes the pinhole, the axial discrimination is lost and such a laser-scanning system has the properties of a conventional fluorescence microscope.

A slightly different way to understand Figure 9.1 is to realize that the objective lens and the two tube lenses form images of both the illumination pinhole and the detection pinhole in the object. Ideally, both pinholes are located in conjugate image planes and on the optical axis. Therefore, their images will overlap perfectly in the object and define the volume element that is observable. This description emphasizes symmetry considerations.

Because a confocal microscope observes only one spot in the object at a time and the main interest is to form a two- or three-dimensional image, the sampling light spot must be either scanned through the object (beam scanner) or the object must be moved through the light spot (object scanner).

In most confocal microscopes the scan unit is attached to a conventional microscope, and the stage that positions the sample and the objective lens are part of the conventional instrument. This chapter discusses the other opto-mechanical elements, that is, the illumination and detection units and the confocal scanner. Essentially it provides a detailed description of how to build a beam scanning confocal fluorescence microscope.

Telecentricity

Figures 9.1 and 9.2 show the basic geometrical optics of a confocal microscope. Figure 9.1 outlines the major elements of the confocal microscope in terms of the objective lens and its image and object planes (a complete description is found in Chapter 7, *this volume*). In practice, the user of the microscope needs to know only the magnification and the numerical aperture (NA) of the lens. Most of the other properties (e.g., the diameter of the entrance aperture) can be easily calculated (see Tables 9.1 and 9.2). The sketch in Figure 9.1 show an ideal setup as it is well known from many papers on confocal microscopy (Bacallao and Stelzer, 1989). The microscope objective is, however, a multi-lens system, and the locations of its principal planes are usually provided by the manufacturer. The image and object distances must remain fixed if the full correction of the objective is to be exploited. This fixes the positions of the image and the object planes relative to the position of the objective (Table 9.1).

Ordinary photographic cameras use a single lens to form an image. This has the property that the magnification varies with the distance of the object from the lens. As a result, in pictures of high buildings taken from ground level, the edges are tilted towards the image's top center. This phenomenon is also known as the converging lines effect. A single lens is, therefore, of limited use when one intends to perform measurements in objects that have depth. A system that uses two lenses spaced the sum of their focal lengths apart has a magnification that depends only on the ratio of their respective focal lengths. Such systems are called telecentric.

All microscope objective lenses are corrected telecentrically (Fig. 9.2). A telecentric system is arranged like a Keplerian telescope with a stop in the common focal plane of the two lenses. The entrance and exit pupils are both at infinity in object and image space, respectively. Telecentric systems are space invariant and linear. Space invariance means that the lateral and longitudinal

Ernst H.K. Stelzer • Light Microscopy Group, European Molecular Biology Laboratory (EMBL), Heidelberg, Germany

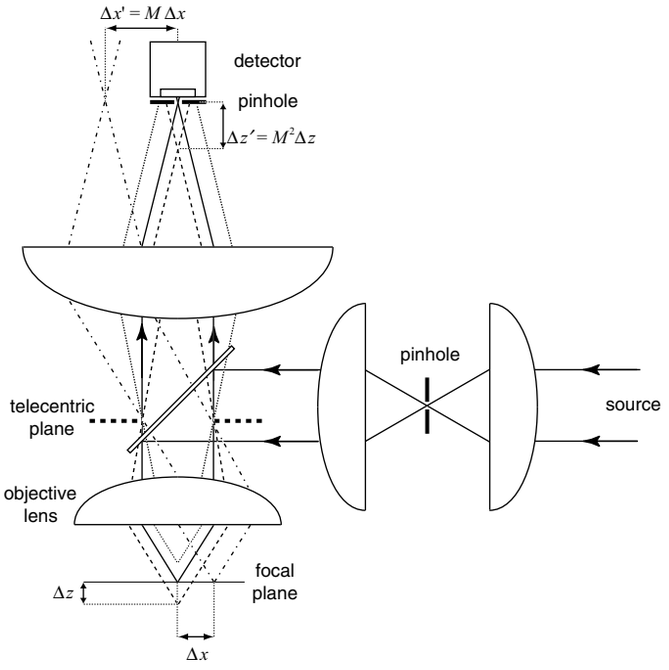


FIGURE 9.1. Principles of a confocal fluorescence microscope. The laser light of the excitation beam enters the instrument from the right-hand side. It is expanded by a telescope with the illumination pinhole in its center. A dichroic mirror deflects the laser beam towards the objective lens. The laser light excites the fluorophores in the focal plane. Some of the fluorescence emission is collected by the objective lens, passes the dichroic mirror, and is focused into the detection pinhole in front of a light detector.

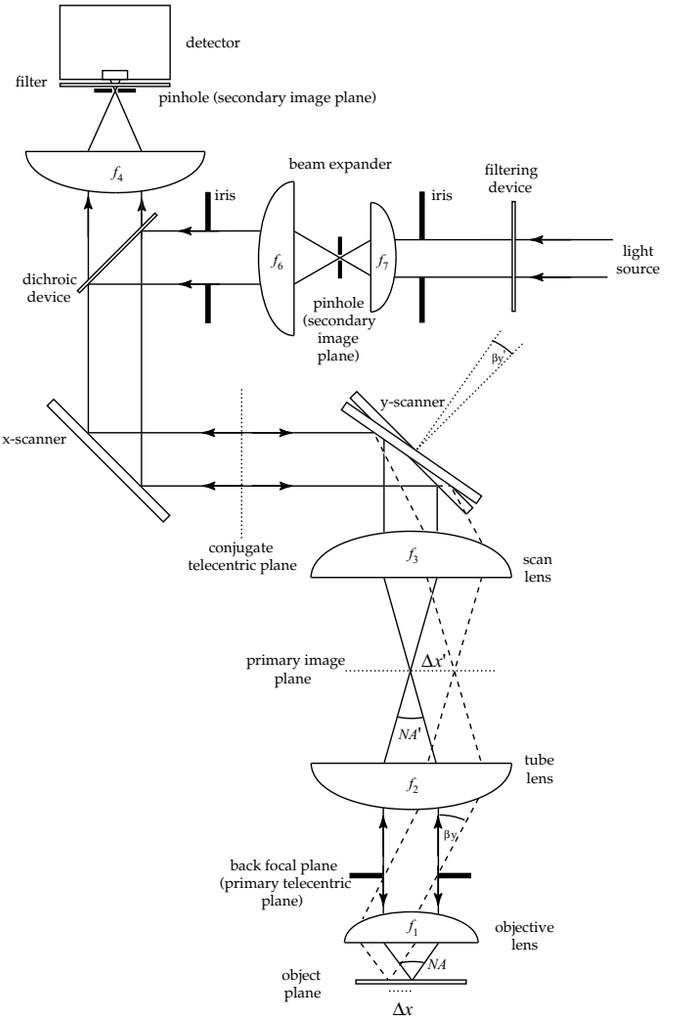


FIGURE 9.2. Simplified diagram of the components of a confocal fluorescence microscope. The light enters the instrument from the right-hand side. A filtering device selects at least one wavelength for the excitation of the fluorophores in the sample and also attenuates the light intensity to the required level. A beam expander adjusts the beam diameter to fit the diameter of the back-focal plane of the microscopes objective lens (Fig. 9.5). A dichroic mirror deflects the excitation light towards the scanner pair. Ideally both are located in conjugate telecentric planes of the microscope objective lens. By tilting the y-scanner by an angle β_y', a laser light spot is moved by $\Delta x'$ in the primary image plane of the microscope. The tube lens and the microscope objective lens form an image of the light spot in the object plane. The detected fluorescence light follows the same path backward and is descanned by the y-scanner. It passes the dichroic mirror and enters the pinhole. Filters in front of the detector pass at least one band from the sample response. The optical path is defined by irises that are also used to align the illumination and the detection paths. The two irises around the beam expander, which also remove any excess light that will not enter the sample anyway, and others (not shown) reduce stray light. Ideally they are located in telecentric planes, that is, always close by the focal plane of a lens. f_i are the focal lengths of the lenses (see Table 9.1).

magnifications of the optical system are constant throughout the whole space, and the shape of the point spread function (PSF) is independent of the absolute location of the point source. When observing two points near the focal plane of a microscope as the focal position is changed, the points become blurred, but their center–center distance does not change. Because of this particular property when defocusing, telecentricity is used in all optical measurement devices.

The most important feature of a telecentric system is that the magnification factor determines all the properties of the system. All beams pass the telecentric plane with an angle that is characteristic of the position of their focal point in the object plane. This property is very important, and the conjugate telecentric planes, like the conjugate image planes, are often shown in overviews of the optical paths of conventional microscopes. As we will notice later, it is important to know the positions of these planes if one wishes to extend optical paths.

The Scanning System

Because the position of the sampling light spot depends on the angle of the beam in the telecentric plane (Fig. 9.2, Table 9.1), the method of choice to scan the spot through the object plane is to change this angle. From the description above, it should be obvious that this can be achieved by placing a scanning mirror such that its pivot point (the center of the tilting movement) is in the center of a conjugate telecentric plane of the microscope objective. The stationary beam falling on this scanning mirror is reflected and, proportional to the tangent of the angle of the mirror, the spot moves to different positions in the object plane.

Any conjugate telecentric plane is an image of the telecentric plane of the microscope objective. An intermediate optical system forms an image of the scan mirror in the entrance aperture of the microscope objective. Not every arrangement is valid, however. As pointed out above, the microscope objective is designed to be used with fixed object and image distances. Otherwise it will not function correctly, in particular, spherical and chromatic aberration

TABLE 9.1. Mathematical Formulas

No.	Symbol/Equation	Description	Typical Value
	f_1	Focal length of microscope objective lens	1.9 mm
	f_2	Focal length of tube lens	160 mm
	f_3	Focal length of scan lens	50 mm
	f_4	Focal length of pinhole lens	50 mm
	$M = f_2/f_1$	Magnification of microscope objective lens	63
	NA	Numerical aperture of microscope objective lens	1.2
	$NA' = NA/M$	Numerical aperture of tube lens and scan lens	0.02
	n	Refractive index of immersion medium	1.33
	λ	Wavelength of light	
	λ_{ex}	Wavelength of excitation light (illumination path)	0.488 µm
	λ_{em}	Wavelength of emission light (detection path)	0.520 µm
	$\beta'_y = f_3/f_2 \cdot \beta$	Tilt angle of y-scanner	4°
	β_y	Tilt angle along y-axis in telecentric plane	11°
	$s_x \times s_y$	Size of first scan mirror	2 mm × 3 mm
	$\alpha = \sin^{-1} NA/n$	Angular aperture	64°
	$\Delta r = \frac{\lambda}{n\sqrt{3 - 2\cos\alpha - \cos 2\alpha}}$	Lateral resolution	0.22 µm
	$\Delta r_{img} = M \cdot \Delta r$	Lateral resolution in primary image plane	14 µm
	$\Delta z = \frac{\lambda}{n(1 - \cos\alpha)}$	Axial resolution	0.65 µm
	$\Delta r_{img} = M^2 \cdot \Delta z$	Axial resolution around primary image plane	2.6 mm
	$\Delta x = f_1 \cdot \tan\beta_y$	Field of view in object plane	0.4 mm
	$\Delta x' = \Delta x \cdot M$	Image size in primary image plane	24 mm
	$\phi_{BFP} = 320\ mm \cdot \frac{NA}{M}$	Diameter of back-focal plane of microscope objective lens	6.1 mm
	$\phi_{ill,ph} = \Delta r \cdot \frac{f_2}{f_1} \cdot \frac{f_4}{f_3} = \Delta r \cdot M \cdot \frac{f_4}{f_3}$	Diameter of illumination pinhole	23 µm
	$\phi_{det,ph} = \Delta r \cdot \frac{f_2}{f_1} \cdot \frac{f_6}{f_3} = \Delta r \cdot M \cdot \frac{f_6}{f_3}$	Diameter of pinhole in front of detector	30 µm

will no longer be properly corrected. If the (incident) light beam is collimated, the intermediate optical system must have its focal plane coincide with the image plane of the microscope objective (Fig. 9.2).

The imaging outlined so far can also be described as follows. Every point in the object plane has a conjugate point in the image plane. As the light spot is moved in the image plane, the conjugate light spot is moved in the object plane. To scan the object plane, light spots must be produced in the image plane. If the beam falling into the intermediate optical system is collimated, a spherically corrected beam will be achieved only if the focal plane of the lens and the image plane of the microscope objective coincide. The position of the light spot in the image plane then depends on the scan angle.

A single scan mirror will be fixed on a rotation axis and will, therefore, only be able to provide a motion of the focal point in one direction. However, this concept can be easily expanded to include more than one mirror and hence to scan along two perpendicular axes. As pointed out, the mirrors should be placed in conjugate telecentric planes. Any number of these planes may,

TABLE 9.2. Resolution of Different Objective Lenses in Conventional and Confocal Fluorescence Microscopy[a]

	Resolution[b] in Object Plane				Parameters in Image Plane			BFP
Lens[c]	Lateral (µm)	Lateral Conf. (µm)	Axial (µm)	Axial Conf. (µm)	Lateral Resolution[d] (µm)	Line Pairs/mm	Line Pairs/Image[e]	Diameter (mm)
100 × Oil/1.4	0.19	0.14	0.54	0.38	43.6	46	920	4.5
63 × Oil/1.4	0.19	0.14	0.54	0.38	27.5	73	1460	7.1
63 × W*/1.2	0.23	0.16	0.66	0.47	32	62	1250	6.1
40 × W*/1.2	0.23	0.16	0.66	0.47	20.3	98	1970	9.6
100 × W/1.0	0.28	0.20	1.10	0.78	61	33	660	3.2
63 × W/0.9	0.31	0.22	1.43	1.01	42.7	47	940	4.6
40 × W/0.8	0.35	0.25	1.87	1.32	30.5	66	1310	6.4
20 × /0.75	0.37	0.26	1.48	1.04	16.3	123	2460	12
20 × /0.6	0.47	0.33	2.50	1.77	20.3	98	1970	9.6

[a] For a wavelength of 500 nm. Refer to Table 9.1 for precise definitions and formulas.
[b] The resolution is the full width at half the maximum (FWHM).
[c] Oil refers to oil-immersion lens; W to water-immersion dipping lens; W* to a water-immersion lens corrected for usage with a cover glass.
[d] The resolution is given by $2M\ 0.61\ \lambda/NA$ (see Table 9.1).
[e] Assuming an intermediate image diameter of approximately 20 mm.

however, be easily generated by adding further optical elements. The image of a second mirror may then be formed on the first mirror. If the two mirrors move the beam in orthogonal directions, the object is scanned along orthogonal x and y axes.

What happens with the light emitted from the spot illuminated by the laser beam? As explained above, the images of the source and the detector pinholes overlap in a confocal microscope. The position of the illuminating light spot in the image plane is, therefore, linearly related to the position of the image of the light spot formed in the sample. Hence, the pinhole in front of the detector must be in a plane conjugate to all the image planes of the microscope (Fig. 9.2). In a scanning system, this means that we need an optical arrangement that will form an image of the image plane. The scan system will move this image across the pinhole, and the light from only one point in the object will enter the detector. If everything is set up correctly, this point will also be the point in the object that is illuminated by the laser. In most cases, the pinhole will be placed on the optical axis and in the focal plane of a lens. This detection lens and the intermediate optical system discussed above form a conjugate image plane.

The Back-Focal Planes

To work in the diffraction limit, the back-focal plane (BFP, also known as the entrance aperture or Fourier plane and defined by the stop in the telecentric plane) must be uniformly filled by a planar wave. Failing to do so results in a smaller effective NA and hence in a broader spot and in poorer resolution. As pointed out above, the BFP diameter of a lens is closely related to its resolution and its magnification (Table 9.2). The higher the resolution and the lower the magnification, the larger is the BFP diameter. This means that the diameter of the illumination pinhole must be matched to a specific lens, and the diameters of all optical elements throughout the illumination and detection paths must be large enough to transmit a beam of light this large without truncation. A microscope system with interchangeable objectives must either be adjustable or at least be usable with the lens having the largest BFP diameter. All other lenses will then be over-illuminated, which produces some stray reflections and involves some loss of illumination intensity. The best idea is actually to optimize the diameter for a set of lenses that have fairly similar M/NA ratios. Any design requires a decision regarding the specific lenses likely to be used and instrument performance in terms of illumination and detection efficiency. When working with lasers having a Gaussian beam profile, it is common to over-illuminate the BFP by a factor of 2, that is, the $1/e^2$ diameter of the Gaussian beam should be twice as large as the BFP diameter. This results in the beam transmitted having only about 70% of the light in the untruncated beam. Finally, the location of the BFPs on the optical axis varies by a few millimeters. Although in principle this causes vignetting, the effects can probably be neglected for all practical purposes in biology.

PRACTICAL REQUIREMENTS

Diffraction Limit

Illumination

The goal in confocal microscopy illumination is to make the light spot as small as possible. Its size should be determined only by the wavelength of the beam of laser light emerging from the single-mode fiber and the NA of the objective lens; that is, the system should be diffraction limited. According to Goodman (1968, p. 103), "An imaging system is said to be diffraction-limited if a diverging spherical wave, emanating from any point-source object, is converted by the system into a new wave, again spherical, that converges toward an ideal point in the image plane." The system, in our case, consists basically of the microscope objective lens and the tube lens. Because we have real elements, this requirement is never fulfilled. Every optical element will cause some degree of aberration that increases the spot size. The actual spot size Δr (Table 9.1) can be measured in the image plane of the microscope objective.

While Δr is approximately the full-width at half-maximum, $2\Delta r$ is approximately the diameter of the Airy disk in the image plane. In general, it should not be larger than the spot in the object plane times the magnification of the objective lens (e.g., an $M = 63$; NA = 1.2 lens at $\lambda = 488$ nm would have a Δr in the intermediate image plane of about 14 µm). Another important requirement to achieve the diffraction limit is that the aperture of the objective lens is uniformly filled with a planar light wave (if the objective lens is corrected for a finite distance, a spherical wave must fill its aperture).

Every optical element degrades the wavefront somewhat (a good description of aberrations introduced by optical elements is given in the Melles Griot catalogue (Chapter 1, 1999); the performance of real lenses is found in Melles Griot, Chapters 6 and 11, *this volume*). One goal of the optical system is to generate a light spot in the image plane that is smaller than actually required. This is equivalent to overfilling the microscope entrance aperture. Efficiency in the illumination path is often not of great importance, as lost light can be easily made up because most of the appropriate lasers have more power than is needed for fluorescence confocal microscopy. However, as applications such as fluorescence recovery after photobleaching (FRAP; Axelrod *et al.*, 1976) and other related techniques usually try to expose the sample to as much energy as possible within a short period of time, efficient light delivery has become a much more important issue.[1] Multiphoton microscopy (Denk *et al.*, 1990; Stelzer *et al.*, 1994; see also Chapter 28, *this volume*) is another field that requires an efficient illumination light path but has the additional requirement that group velocity dispersions should be under excellent control.

Detection

It is as important to achieve the diffraction limit in the detection path as it is in the illumination path. A pinhole that is somewhat larger than the ideal case produces only a modest reduction in the out-of-focus discrimination of the confocal setup (Wilson and Carlini, 1987; see also Chapter 22, *this volume*). Increasing the pinhole diameter is complementary to over-illuminating the entrance aperture of the microscope objective and can be used to correct the same errors mentioned above. If, however, the optical arrangement of the detection path is close to the ideal case, nothing can be gained in terms of detecting light from the focus plane by increasing the pinhole size beyond 1 or 2 Airy units. A particularly good test is that the intensity of the signal from a single point-like object (e.g., a 100-nm fluorescent latex bead or a non-resolvable concentration of some dye) should not increase by more than a factor of 3 as the pinhole diameter is increased. When one observes the image of a single point object that is in focus, a well-corrected

[1] In response, Olympus recently introduced a microscope incorporating an entirely separate intermediate optical system for use in FRAP and uncaging experiments.

confocal arrangement will collect at most (i.e., at the highest NA) 30% of the available light produced by the object and focus it at the pinhole.

Detection efficiency is always crucial in fluorescence microscopy. The basic rule is to have as few optical elements as possible in the detection path. Sticking as closely as possible to this rule helps avoid losses due to reflection or absorption and prevents unwanted degradation of the wave front. It is a particularly bad idea to place annular apertures into the detection path that obscure large fractions of the fluorescence light as is sometimes suggested to improve *z*-resolution (Martínez-Corral *et al.*, 2002). The light loss caused by such devices reduces detectability limits by increasing the effect of Poisson noise.

Because only the light emitted from the focal plane in the sample is collimated and properly focused into the detector pinhole, most stray light is excluded by the pinhole and is usually not a serious problem. However, any laser light that passes the dichroic beam-splitter should be captured in a simple beam stop to prevent it being returned and reflected up the axis from the back side of the dichroic. Exposed surfaces that could reflect light (especially laser light) should be covered with black paint, self-sticking velvet, or black anodized aluminum. The intensities are usually too low to cause heating.

Geometric Distortion

As geometric distortion is introduced by any inaccuracies in the scanning process, it is important to keep these as small as possible. Distortions can arise from deficiencies in either the mirror positioning system or the intermediate optics. The movement of the scanning mirror is known only approximately, and it was very common to run the horizontal galvanometers in a sine function that is linear to ± 4% only over a small part of the sine waveform (= ± 30%, see Chapter 3, *this volume*). The scanning system and the way it is used obviously define the geometric distortion to a very large degree. These factors also influence the efficiency of the illumination and the average energy penetrating a unit area. Much effort has been made to drive the scanners accurately, for example, by calculating sums of harmonics, changing the acceleration in a systematic manner, etc., in order to achieve a reasonably high duty cycle. The advent of DSP-controlled, lightweight ultra-precise galvanometers has made this task very easy. An essentially undistorted speed of more than 1 kHz even at large scanning angles is now readily available (see Chapter 3, *this volume*). Finally, great care must be taken when the intermediate lens is selected. The optimal solution is an f-theta lens.

EVALUATION OF THE ILLUMINATION AND DETECTION SYSTEMS

Influence of Optical Elements

All optical elements in the confocal microscope influence the characteristics of the light beam:

- its energy spectrum,
- its polarization,
- its modal distribution,
- its waist diameter,
- its divergence,
- its direction,
- its position relative to the optical axis.

In a fully corrected optical imaging system, all these parameters are considered, but in confocal microscopy this is usually not necessary. After all, a confocal microscope does not form an image, and the wavelength used at any time is only a small fraction of the total optical bandwidth.

Several rules govern the properties of the incoming beam (i.e., the beam entering the entrance aperture pupil of the objective lens), and another set of rules determines the properties of the beam entering the detector. The optical elements in either the illumination or the detection path are used to shape the beam, that is, to ensure that the beam will have the desired properties. The actual problem is that the optical elements are not perfect and that they influence to a varying degree more than one of the properties of the beam.

Errors

Beam Shift

The beam is shifted every time it traverses a flat optical component that is tilted relative to the optical axis or a lens that is not correctly centered. If the optical layout is designed for collimated beams, shifts can usually be compensated for in the detection path, but any shift in the illumination path can cause vignetting. On the other hand, in laser arrangements with collimated beams, flat surfaces are often purposely tilted by 0.5 to 1° to avoid interference effects caused by specular reflections. However, if these tilts are too large, refraction and dispersion can cause a visible wavelength-dependent shift of the beam. If the tilt is in the range of 1°, the shift is about 6 µm/mm of glass while, in the tilt range of 45° (as for a beam-splitter), the shift is about 330 µm/mm.

Angular Deflection

In the confocal microscope, any angular deflection of the beam is very critical and practically not correctable. Deflections are caused by flat optical components that have surfaces that are not parallel (i.e., they have wedge errors) or by lenses that are tilted relative to the optical axis. As pointed out above, in telecentric systems the angular deflection determines the position of the light spot in the object plane. Every deflection of the beam except that produced by the scanning system causes a shift of the observed area. The typical planarity achieved on a flat component is <1 second of arc. If the thickness varies 1 µm over a length of 25 mm, and the collimated beam is focused with a 90 mm lens, the axial shift at the focal plane is 2 µm. The amount of shift that is critical depends on the diameter of the pinhole, and an estimate of the tolerable wedge error depends to a large extent on the magnification of the objective lens. The dichroic mirror is in this respect the most critical part in a confocal fluorescence microscope. Even slight changes in its position cause the image of the source and detector pinholes not to overlap anymore. This is particularly important as most fluorescence microscopes operate with several excitation lines, and this means that, unless a multiband dichroic or an acousto-optical beam-splitter (AOBS, see Chapter 3, *this volume*) is used, the component must be frequently changed, a process that must not affect the angle of the beam. In addition, all the different dichroic mirrors must have similar surface characteristics (Fig. 9.2).

Polarization

The state of polarization does not seem to be very critical. However, a number of optical elements, especially the filters and beam-splitters with a dielectric coating, have a reflection coefficient that is polarization dependent as are the imaging characteristics of microscope objectives. Changing a dichroic mirror can

therefore have surprising effects on the image and on the amount of light that penetrates the sample. In fluorescence microscopy, it seems best to work with light that is either circularly polarized or phase randomized (Table 9.2).

Intensity Loss

Every element in the detection path causes some intensity loss. If the elements are coated (broadband, anti-reflection coating in transmission; broadband, high-reflection coating for mirrors), the energy losses can be as low as 0.5% per surface for wavelengths within the bandwidth.

The various filters cause the largest intensity losses. Filters come in three general types (Chapter 3, *this volume*): those made from absorbing/colored glass, interference filters made from transparent optical flats coated with several dielectric layers, and hybrids made from absorbing optical flats coated with dielectric layers. Dichroic filters are always of the interference type. An interesting alternative is to take advantage of the polarization dependence of the reflectivity of flat surfaces and to use an uncoated optical flat instead of a dichroic. At an incidence angle of 45°, an *s*-polarized beam can be reflected by 40% while the randomly polarized fluorescence emission may be transmitted up to 80%. A single reflective glass plate with an anti-reflection coated back will provide an excellent performance across a relatively large bandwidth with no need for substitutions that might produce misalignment. The Achrogate beam-splitter/scan-mirror found in the Zeiss LSM5 line scanner is a modification of this idea in which use is made of the fact that the diffraction pattern of a line is another line. Therefore, while a small silvered line in the center of the beam-splitter is sufficient to reflect the excitation line of any wavelength towards the objective, most of the returning signal bypasses it towards the detectors.

The narrow-band interference filters used to select a laser line transmit between 50% and 90%, depending on the batch, the manufacturing process, and the design bandwidth. Dichroic filters reflect 80% to 90% of a single laser line and should transmit more than 80% of the light 12 to 20 nm above the maximum reflection. Long-pass color filters transmit more than 90% of the light 12 to 20 nm above the 50% cut-off wavelength. Special dichroics can be designed that have a particularly high reflectance for the excitation laser line. In these cases the 50% cut-off can be pushed further and a difference of less than 15 nm can be achieved (see also Chapter 3, *this volume*).

Specifications of the most suitable filter depend on the excitation and emission spectra of the fluorophore and therefore on the laser line used. Thus, compromises can hardly be avoided, and carefully adapting the filters for any experiment involving more than one dye is worth both effort and time. For single-channel operation, the goal is to use a long-pass filter or a broadband interference filter that comes close to the emission maxima in the detection channels. If necessary, a change of the laser wavelength (Kr/Ar-ion lasers offer several lines between 458 nm and 647 nm) or a different dye should be considered. Note that dyes often change their spectral properties when coupled to antibodies or incorporated into the target cell (Chapters 16 and 17, *this volume*) and filters can age from prolonged exposure to intense light, particularly that from an Hg-arc lamp without an ultraviolet (UV) filter.

Evaluation of Optical Arrangements

This section discusses and evaluates different optical arrangements for confocal fluorescence microscopes, shows a drawing of the compact confocal camera built at EMBL, and shows the spectroscopic center of such an instrument, that is, the assembly that is used to separate the excitation from the emission light (Fig. 9.3).

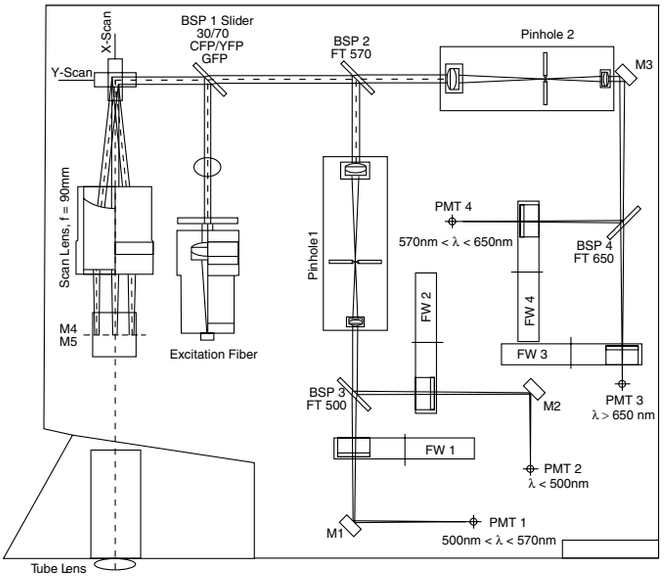


FIGURE 9.3. Schematic drawing of the compact confocal camera built at EMBL. Several lasers (not shown) provide light through an excitation fiber. The collimated beam is deflected by a dichroic mirror (BSP 1) towards the scan unit (upper left corner). The scan unit consists of two mirrors that deflect the beam in two orthogonal planes to scan it in the object plane. The fluorescence light emitted by the sample (not shown) is descanned by the scan unit, transmitted by the dichroic mirror BSP 1, and split into a short- and a long-wavelength component by another dichroic mirror (BSP 2). Each of the two beams is focused into a pinhole (pinholes 1 and 2). Behind the pinhole, each divergent beam is focused by a lens and split once more by a dichroic mirror (BSP 3 and 4). The resulting four convergent beams each pass a detection filter (filter wheels FW 1–4) and eventually hit a photomultiplier tube (PMT 1–4).

Class 1

In a class 1 system [Fig. 9.4(A)], the illumination pinhole is at the focal point of the first two lenses that spatially filter and expand the collimated laser beam. The expansion is determined by the ratio of the focal lengths of the two lenses and should be chosen to fill the entrance pupil of the objective lens. The spatially filtered beam is then deflected by the dichroic mirror in the direction of the scan unit. Fluorescence light emitted from the sample passes the dichroic mirror, and a lens focuses the beam into a pinhole in front of the detector (Fig. 9.4).

Refraction in the dichroic mirror causes the emission beam to shift as it passes through. This shift is intrinsic. But, because the light beams from the focal plane are collimated, any such shift can be corrected by displacing the detection lens and the detector by a similar amount. However, this arrangement cannot correct for any tilt produced by wedge error in the dichroic mirror, which must be carefully controlled. In order to obtain a backscattered light signal a polarizing beam-splitter and a quarter-wave plate can be placed between the beam expander and the dichroic mirror without decreasing the efficiency of the detection path. This setup is optimal, as it uses a small number of elements, guaranteeing high detection efficiency. Furthermore, it uses each optical element as it should be used; for example, a collimated beam passes the dichroic mirror and a planar wavefront enters an intermediate lens.

Class 2

In a class 2 system [Fig. 9.4(B)], the excitation light is focused into a pinhole that is at the focal point of two lenses arranged as

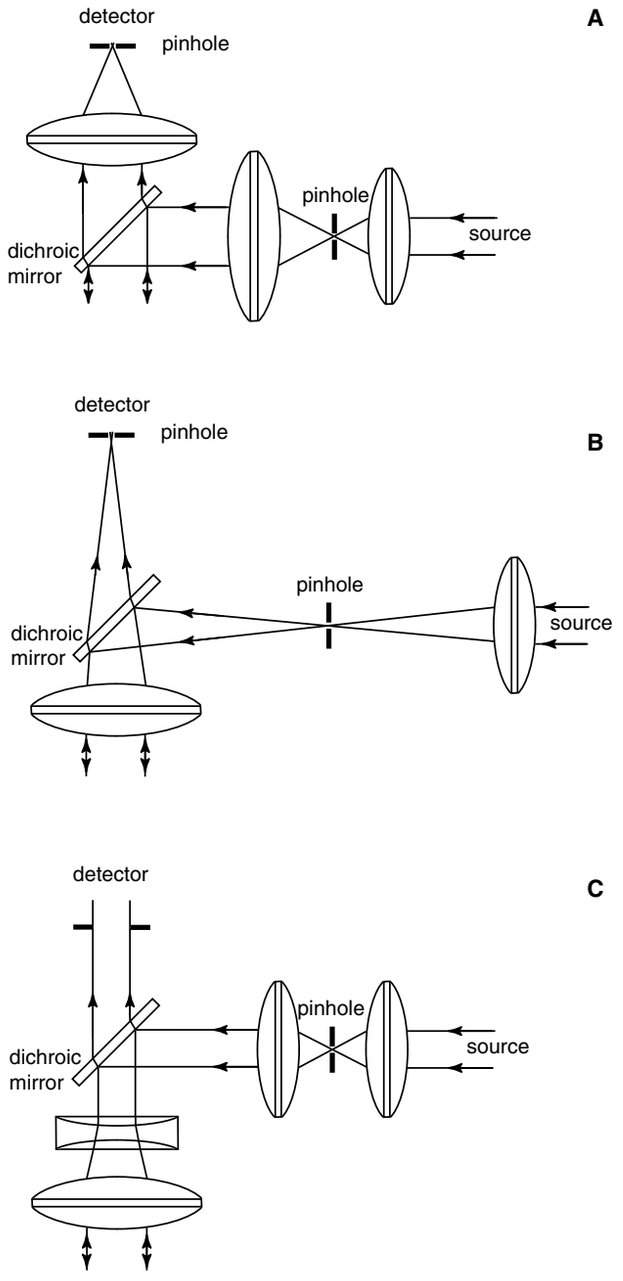


FIGURE 9.4. Three different optical arrangements. In all arrangements the laser beam comes in from the right-hand side, is spatially filtered by a pinhole, and deflected by a dichroic mirror in the direction of the tube lens (not shown). Note that refraction of the fluorescence light when passing the dichroic mirror causes a shift of the light path. The illumination and detection pinholes are placed in conjugate image planes. (A) In a Class 1 arrangement, the laser beam is expanded and collimated *before* it reaches the dichroic mirror. The collimated fluorescence light is focused into the detector pinhole by a separate lens *after* passing the dichroic mirror. This is the optically ideal arrangement. (B) In a Class 2 arrangement, the laser beam is expanded and collimated *after* it hits the dichroic mirror, so the beam is divergent at the dichroic mirror. The fluorescence light is focused into the detector pinhole by the same second lens of the beam expander *before* passing the dichroic mirror. (C) In a Class 3 arrangement, the laser beam is collimated before it reaches the dichroic mirror, and is expanded in the light path common to illumination and detection. Therefore, the beam expander (shown as a Galilean telescope) reduces the diameter of the fluorescence light beam that enters the detector placed at a long distance from the image plane.

a beam expander. However, the dichroic mirror is placed such that the divergent beam is deflected by its surface before being collimated. The second lens of the beam expander is also used to focus the fluorescence emission into the detector pinhole. A convergent detection beam therefore passes the dichroic mirror, which causes a shift and a reduced geometric focal length. This arrangement is, therefore, not able to correct for either a shift of the beam or a tilt of the beam at the dichroic mirror. It is also not possible to insert a beam-splitter arrangement to make use of the back-scattered or reflected light. The arrangement is sparse and, therefore, efficient but the dichroic mirror is placed in a convergent beam, which might cause trouble because the transmission/reflection properties of the dichroic mirror depend on the angle of incidence, and the spectral response will be different for axial and non-axial rays.

Class 3

In a class 3 system [Fig. 9.4(C)], the fluorescence light passes the dichroic mirror and enters a detector that is some distance away. The beam is shifted in the dichroic mirror. Any further shift of the beam can be corrected in this arrangement, whereas a tilt at the dichroic mirror cannot. The setup is obviously efficient, as it uses the minimal number of optical elements, and a collimated beam passes the dichroic mirror. Not having to use a detection lens reduces chromatic effects, but this must be balanced against the need for distances of more than 1 m before the beam can enter the photomultiplier tube (PMT). This "optical lever" is usually implemented by placing three, four, or more mirrors into the detection path, a process that makes the device, at least in principle, more sensitive to mechanical vibrations. However, to a first approximation, the distance between two conjugate image planes divided by the diameter of the detector is a constant, so the performance of this arrangement should be equivalent to that described as Class 1 [see Fig. 9.4(A)]. A detection lens will decrease the path length but, unless it is set up as a telescope, it also decreases the effective area of the detector and hence makes the introduction of a small pinhole necessary.

The advisability of using a beam expander [as shown in Figs. 9.4(A) and 9.4(B), but not in Fig. 9.4(C)] is debatable. The beam can, of course, be expanded elsewhere in the system (e.g., in a scan lens such as the eye-piece). It is, however, inefficient to spatially filter the beam in the common detection/illumination path. The main problem is that the laser may not run in TEM_{00} mode (Chapter 5, *this volume*). If it does not do so, it must be spatially filtered and then it may also be expanded in the same process. If the laser does run in TEM_{00} mode, the light need not be spatially filtered because it would all pass the filter anyway. A single-mode polarization preserving fiber can be regarded as a pinhole with a distinct entrance and a distinct exit. Thus it will always select the TEM_{00} mode of a laser.

Not shown in Figure 9.4 are filters and special equipment for double-fluorescence experiments. Although all could be placed in front of the second lens, it is better to put them behind the detector pinhole (see Fig. 9.3). It is, therefore, not necessary to include these parts in this discussion. A practical problem that may arise if a single pinhole is used for both channels is that one channel may receive less signal than the other. If two pinholes are used, one can be opened to increase the signal while the other remains set to the optimal size (Chapters 22 and 35, *this volume*).

Evaluation of Scanner Arrangements

The simplest of all confocal optical systems is exemplified by that used in the Optiscan confocal endoscope. In this system, light emerging from the end of a single-mode optical fiber is focused by an objective lens into a spot inside the specimen. Returning

light is picked up by the same fiber tip that also acts as the detector pinhole. Fluorescence light is separated from excitation light using interference filters mounted at the far laser end of the fiber. Scanning is accomplished by actually moving the fiber tip in an *xy*-raster using an electromagnetic drive. Although this system is extremely compact, the detector pinhole dimensions are fixed and there must always be some back-reflection from the scanning tip that will be added to any backscattered light signal from the specimen (see also Chapter 26, *this volume*).

However, conventional beam-scanning confocal microscopes use scan mirrors, and this section describes and evaluates four different arrangements of *xy*-scanners. Note that not all optical arrangements described above should be combined with all scanner arrangements.

The galvanometer mirrors used for confocal scanning microscopy must be custom-made for high efficiency in fluorescence applications. These mirrors have conflicting specifications: they should be small, lightweight, mechanically stable, and flat to a fraction of the wavelength, and the reflecting surface should be centered on the rotation axis of the scan unit. The compromise depends to a large degree on the application of the confocal fluorescence microscope and the arrangement of the scan unit. The emphasis should always be on efficiency and instruments that are tuned to perform best with high-NA high-magnification lenses. An excellent choice is currently the VM500 produced by GSI Lumonics. Its specifications meet essentially all requirements if one uses mirrors that are smaller, thicker, and flatter than the standard parts (see also Chapter 3, *this volume*).

The scan mirrors are effectively also aperture stops so their diameter must match the diameter of the conjugate BFP (see Table 9.2). Therefore, high NA and low magnification that requires a large beam diameter needs large scan mirrors to fill the BFP, a factor that limits horizontal (actually fast axis) scan speed (Fig. 9.5).

Two Scan Mirrors + Relay Optics

The two scanning mirrors rotate on perpendicular axes, so their combined movement produces an *xy*-movement of the light spot in the image plane [Fig. 9.5(A)]. As the relay optics form an image of the first mirror on the axis of the second mirror, both mirrors will be in conjugate telecentric planes of the microscope, as long as the axis of either mirror is in such a telecentric plane. This arrangement is optically perfect. The difficulty is that the requirements for the relay optics are very strict. They must produce perfect images over a broad range of wavelengths, and this is quite expensive and probably also not very efficient.

To have a well-corrected image across a widefield, one can also use two plane-scanning mirrors with two intermediate concave mirrors, as was done in some now obsolete Bio-Rad scan heads (e.g., Amos, 1991).

Two Closely Spaced Scan Mirrors

Two mirrors can also be used without any relay optics [Fig. 9.5(B)], as implemented, e.g., by Zeiss in the LSM 5 Series and more recently by Leica and almost all other companies). Again the mirrors rotate on perpendicular axes, but now they are placed as close together as possible with the telecentric plane located at the midpoint between them. The closer the two mirrors come together, the more this arrangement approximates perfect telecentricity. The actual error depends on the magnification of the intermediate optical system and is probably about 4 mm over 100 mm. In general, this will only have an effect at large scan angles (low zoom magnification) where optimal optical performance is less essential. The advantages of small size are obvious.

Center Pivot/Off-Axis Pivot

The arrangement described above can be improved by moving the axis of one mirror off the beam axis [Fig. 9.5(C), as implemented

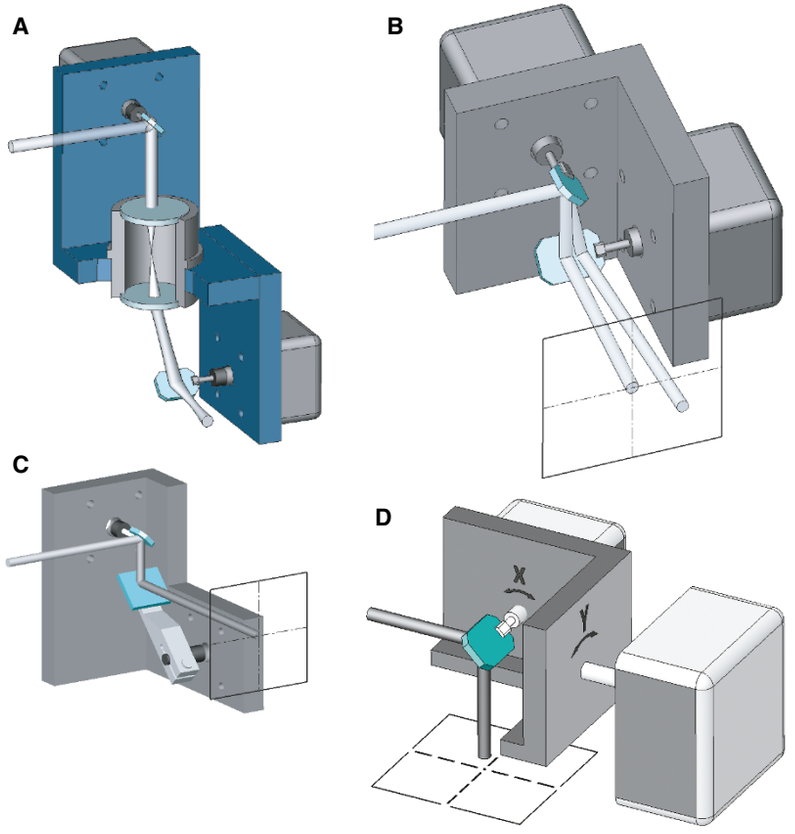


FIGURE 9.5. Four different scanner arrangements. (A) A system consisting of two scan units and intermediate imaging optics. Two mirrors are used to scan the beam along the *x* and *y* axes. The optical system is arranged such that an image of one scan mirror is formed on the other mirror. If either mirror is in a telecentric plane, both mirrors are in conjugate telecentric planes of the microscope. This is the basic and ideal optical arrangement. (B) The scan mirrors are placed as closely as possible and the geometric midpoint of the two mirrors is in a conjugate telecentric plane of the microscope. Both mirrors are, therefore, only approximately in a telecentric plane. (C) An arrangement with off-axis and on-axis scan units. While one mirror rotates around the center of its axis, the other has a pivot point that is off-axis. This latter movement compensates for the missing intermediate imaging optics. The two mirrors are, therefore, both in an approximate conjugate telecentric plane of the microscope. (D) A single scan mirror is used to scan the beam along both the *x* and *y* axes. This is accomplished by mounting the mirror on a fast galvanometer, which is itself mounted on a second, orthogonal scan unit whose center of rotation is in the center of the mirror.

initially by Molecular Dynamics]. The second mirror shifts as it rotates. The combined movement can reduce the apparent position error of the mirror by a factor of up to 25 (Carlsson and Liljeborg, 1989). It also changes the path length slightly as the *y*-scanner moves to the next line. This scanner arrangement may, therefore, not be used with the class 2 optical arrangement [see Fig. 9.4(B)].

Single Mirror/Double Tilt

The simplest solution is to use a single mirror that tilts around two orthogonal axes [Fig. 9.5(D), as implemented in the early Leica systems]. A small galvanometer is mounted on a larger, slow-scan unit. The galvanometer performs the fast movement and the scan unit provides the tilt along the slow axis. The center of the single mirror is easily placed in a telecentric plane of the microscope, and the efficiency is only limited by the reflection coefficient of this mirror (Stelzer *et al.*, 1988). However, this solution does not allow interchanging the *x* and *y* axes for scanning arbitrarily formed areas (Trepte, 1996).

Another possibility is to mount a single mirror on three linear translators. By appropriately driving the three devices one can tilt a mirror along any axis and can even place the point of rotation on the mirror surface. Such piezo-driven devices are available from a number of manufacturers. Although they currently lack either a sufficiently high speed or a large enough rotation angle, they are definitely an excellent choice if these issues are not critical and a compact device is anticipated.

Scanner arrangements can be evaluated on a number of criteria. The most important parameter for a confocal fluorescence microscope is photon efficiency. Other requirements might be the speed or precision with which the raster is scanned, the size and shape of the raster area, the size of the scan unit, *xy*-distortion, long-term stability/repeatability, and its flexibility in scanning nonstandard patterns.

Scanners

Z-Scanners

To get a three-dimensional image of a sample, it has to be scanned in three directions. Therefore, we need to discuss the options for scanning the sample axially, that is, up and down in a standard microscope. The two principal solutions are moving the beam while keeping the object stationary, and moving the object while keeping the beam stationary.

A movement of the focus by some special intermediate optics can be ruled out in microscopy. The reasoning is quite simple. In any telecentric system, the axial magnification M_z, is the square of the lateral magnification M. This relation tells us that, when using a 40× lens, an axial movement of the focus in the object by 10 µm produces a shift of the focus in the intermediate image plane of 16 mm![2] Therefore, it does not make sense to change focus position by moving, for example, the tube lens of the microscope or the scan lens along the optical axis. The required movement distances are by far too large. Therefore the only solution for beam scanning along the optical axis is the axial movement of the objective lens.

The most common method for producing *z*-motion is to drive the fine-focusing control of the microscope. Some manufacturers add an internal fixed reference for full control over the exact axial position. Another technique is to mount the lens (or the slide holder in case of object scanning) on a piezoelectric driver. This offers excellent, backlash-free operation over a range of ≤100 µm. Several manufacturers have mounted an extra galvanometer on a standard specimen stage. This moves the specimen by tilting a substage a few degrees.

The following points are to be considered: any movement along the optical axis affects the immersion-oil film. A rapid movement that increases the distance between the objective lens and the coverslip may cause the sample to "stick" to the lens or to break the film so that air bubbles penetrate the volume between the coverslip and the objective lens. All this could result in a shift of the absolute position of the object. If the absolute position of the object is important, one needs either a "hard" connection between the driving mechanism and the motor or an independent position feedback sensor. A potentiometer connected to the motor is insufficient.

The resolution of the *z*-axis motion must be determined according to the needs. A confocal fluorescence microscope for biological applications needs not be more precise than ±50 nm, whereas an instrument for confocal reflection microscopy should be able to determine axial position with a resolution better than ±4 nm.

Disk Scanners

As pointed out above, the pinholes in a beam-scanning device are located in the conjugate image planes of a conventional microscope. They can be placed directly into the first image plane. In the tandem scanner (Petráň *et al.*, 1968; see also Chapter 10, *this volume*) part of a rotating disk with holes that serve as both sources and detector pinholes is located in the intermediate image plane. The holes are arranged such that the object is uniformly covered by light passing through them as the disk rotates. The separation between adjacent holes guarantees little overlap between the detection and the illumination path when viewing specimens in which the dye is confined to a relatively thin layer. Atto Bioscience's CARV module, that converts a conventional fluorescence microscope into a real-time confocal system, uses a Nipkow disk with a set of spirally arranged pinholes to produce about 1000 beams in the field of view at one time. These can scan the entire field simultaneously at a rate of 400 to 1000 Hz. Because disk scanners form a real image, a charge-coupled device (CCD) camera is placed in an image plane of the microscope to detect the photons with a quantum efficiency that is 5 to 10 times better than that of a PMT. The main problems are the limited brightness of a conventional light source and the loss of 97% to 99% of the excitation light at the disk. Source brightness can easily be increased by using a higher-powered lamp or a laser as the light source, but eventually absorption by the disk causes it to overheat, limiting the effectiveness of this approach (see also Chapter 10, *this volume*).

There can also be a problem in matching the pinhole diameter to the specifications of the objective lens (e.g., 30 µm diameter for 63×/1.4 or 45 µm diameter for 100×/1.4). As a result, one disk is optimal for only a few lenses. In addition, if the disk resides in the intermediate image plane, the source and detector pinholes cannot be optimized independently (Chapter 11, *this volume*). Ideally, pinholes of this size should also be very thin, but this is in conflict with the mechanical stability of the disk.

However, the most challenging aspect of the intermediate optics of the tandem scanner is the difficulty of adjusting the various mirrors so that the returning pattern of points exactly coincides with the pattern of holes on the detector side of the disk. Assuming 40 µm holes and a 160 mm fixed conjugate objective lens, each hole in the field should be aligned with an accuracy of ±10 µm in *x* and *y* over a field of ~25 mm. Apart from the need to

[2] Some confocal endoscopes utilize special-purpose objectives that contain moveable elements capable of shifting the focus plane (see Chapter 26, *this volume*).

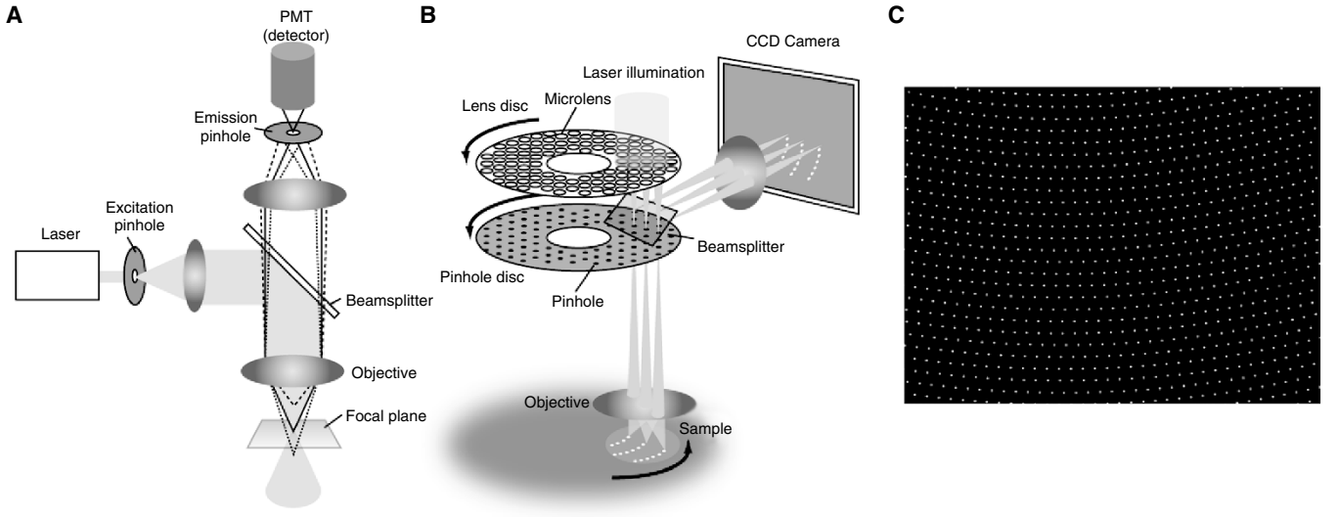


FIGURE 9.6. The optical system of the Yokogawa spinning disk microscope. An array of 20,000 microlenses is mounted on a disk. Approximately 1000 of them are illuminated at one time, and each of them focuses the light into a particular pinhole below it on a second disk. Both disks rotate synchronously at 30 Hz, and because 12 complete images are formed per rotation (a segment of 30° gives a complete image), an image acquisition rate of 360 Hz is achieved (Fukui *et al.*, 1999; Maddox *et al.*, 2003).

exactly orient the mirror angles so as not to distort the pattern of dots, the total length of the illumination and detection paths must match to about ±10 µm to prevent change in magnification from causing the outer spots to miss their holes. Not surprisingly, tandem scanners tend to use fairly large pinholes.

Some of the problems of the tandem scanner, such as disk thickness and alignment, are avoided by the single-sided disk scanner, which uses a tilted quartz disk coated with an opaque metal film except where the pinholes are located (Chapter 10, *this volume*). As the same area of the disk is used for both excitation and detection, there is almost no alignment problem, but there can be problems with the illumination light reflecting off the disk and obscuring the image data coming through the pinholes. Clever polarization techniques can reduce these reflections to a remarkable extent, and they are less of a problem when recording fluorescence images because then the light reflected from the disk can be excluded on the basis of its wavelength. However, it is still difficult to convey to the specimen sufficient light in a narrow waveband to permit high-resolution fluorescence images to be recorded in a reasonable time span.

The optical efficiency problem has been solved by Yokogawa in a design that is used by PerkinElmer, Solamere, Andor (Fig. 9.6), and others. A microlens array is mounted on a rotating disk. Each lens focuses the light from a laser into a particular pinhole located one focal length below it on a second disk, such that more than 40% of the light passes the pinholes (Tanaami *et al.*, 2002). The dichroic beam-splitter is placed between the disks, such that the detection light does not pass the microlenses (Fig. 9.6).

Object Scanners

The first operating confocal microscopes were stage scanners (Minsky, 1961; 1988; Brakenhoff *et al.*, 1979; Marsman *et al.*, 1983; Stelzer and Wijnaendts-van-Resandt, 1985), and those which scanned the beam by moving the objective lens (Wilke, 1985). One source and one detector pinhole are placed in conjugate image planes. The optical arrangement is stationary, and the object is scanned through a single beam that is located on the optical axis of the lens. Any geometrical distortion in the recorded image can come only from the imperfect control of the motion of the object. Object scanners, therefore, offer the highest quality image for data processing purposes and, because of their simplicity, they are very photon efficient. Disadvantages include a low scanning speed (10–150 lines/s) and the special specimen preparation techniques necessary to keep the moving mass low.

The two overriding considerations that have limited the use of this approach in biological confocal microscopy are that early instruments employing this technique did not permit the observer to switch to normal non-confocal operation easily, in order to scan the specimen and find the area of interest, and that biologists were concerned that mechanical resonance within the specimen would cause it to move relative to the stage, causing disruption of the cell and distortion of the image. Although the force on the specimen due to the scanner's acceleration is usually very low (about 1% of the gravity for an amplitude of 100 µm and a frequency of 10 Hz, but 1 G at 100 Hz), it can affect the behavior of living specimens suspended in viscous media (Fig. 9.7).

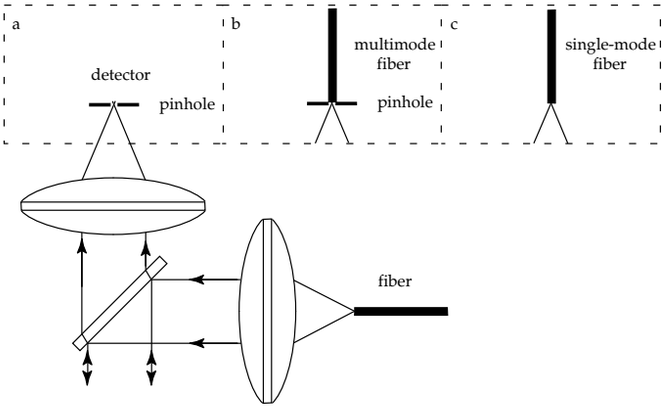


FIGURE 9.7. Optical arrangements using fibers. The arrangement of Class 1 uses illumination with an SMPP fiber, whose tip is in the focal point of a lens that collimates the beam. Complete plugs for laser-light delivery systems consist of the tip and a short-focus achromatic lens. The detection can be performed with a conventional system, employing a multi-mode fiber placed behind a detector pinhole, or using the same single-mode fiber used as the source.

Attachment to Microscopes

A conventional microscope offers several ports through which a confocal setup can be attached to it and through which the excitation beam can enter and the emission beam can leave the instrument. Commonly used are the video port, the ocular, or the port normally used for the photographic camera. Having mentioned efficiency as one of the main issues in confocal fluorescence microscopy, it should be obvious that it is preferable to use the port that causes the beam to pass the smallest number of optical elements. Many (but not all) inverted microscopes guide the detection light over long distances and many optical elements between the object and the ocular (or video port). If for some important reason such an inverted microscope is the system of choice, one should consider having the instrument modified to permit confocal operation using a simpler, separate path. Such modifications are now easier because both Nikon CF objectives and Zeiss ICS objective lenses (plus a tube lens) are fully chromatically corrected, and the attachment can be performed through the intermediate image plane without the need for any additional optics.

Among upright microscopes, the video port of the Zeiss Axioimager series provides direct access to the intermediate image plane. A confocal setup may be interfaced to this plane with no extra optical elements. Microscopes from other manufacturers also have this capability. The advantage of scanning through video ports and eyepieces is that no modification of the microscope is required.

Merit Functions

Functions that determine the performance of an instrument can be object dependent and object independent. An object-dependent merit function is the product of all transmission and all reflection coefficients weighted with the emission and absorption spectra of a particular fluorophore (Tables 9.3 and 9.4). The sum over all surface errors and the sums over all tilts, thickness variations, and deviations from planarity are object independent.

Object-dependent functions can be used to measure the performance of an instrument and to compare the data with those generated at later times or by other instruments.

This is not so easy with the other four merit functions that are more likely to be used in the design phase of an instrument to decide which development path should be followed. The sum over all surface errors should include all elements beyond the source pinhole. It determines how much the beam deviates from a perfect planar wave front, hence how well the beam can be focused and how much the objective lens must be over-illuminated. As a benchmark, it is important to remember that a wavefront error of only $\lambda/4$ reduces the contrast at the midpoint of the spatial frequency plot by almost 50%.

TABLE 9.3. Typical Intensity Losses in the Illumination Path

Element	Loss (%)	Remainder (%)
Laser		100
Mirror	1–3	98
1–3 dichroic mirrors for several lasers	3–10 per mirror	88
AOM	10–15	75
Fiber	25	56
Collimator/beam expander	4	54
Mirrors	1–3 per mirror	52
Polarizing beam-splitter and $\lambda/4$-plate	4	50
Dichroic mirror	10–20	42
Scanner	4	41
Relay lens	10	37
Inside microscope	10	33
BFP of objective lens	80	7
Total intensity entering the sample		7

TABLE 9.4. Typical Intensity Losses in the Detection Path

Element	Loss (%)	Remainder (%)
Sample emission		100
Collection by high-NA lens	75	25
Inside microscope	10	23
Relay lens	10	20
Scanner	4	19
Dichroic mirror	25–30	15
Collimator/beam expander	4	14
Dichroic mirror	20	11
Filter	40	7
Detector	85	1
Total intensity detected		1

MULTI-FLUORESCENCE

Multi-fluorescence experiments are those in which one observes specimens containing more than one fluorophore labeling different targets. Such experiments can be performed by observing each target separately or by observing two or more targets at the same time. In the first case, specific filter combinations would be selected for each fluorophore, matching the excitation line and the emission band. In the second case, one excitation line could excite emission from two or more fluorophores and this signal would have to be separated later in the detection path.

The main disadvantage of the first approach is the difficulty of inserting several different filter sets without changing the illumination or detection paths. Any change prevents the individual images from being properly aligned with each other. The amount of shift that can be tolerated depends on the resolution of the objective lens used. In addition, as was pointed out above, the images of the source and the detector pinholes must overlap in the object plane. If all the dichroic mirrors used do not have the same orientation and position, the signal will not fall into the pinhole and will be lost. On the other hand, observing each fluorophore separately does provide the necessary degrees of freedom needed for the optimal choice of filter sets to observe each dye.

Separating two emission bands for measurement after simultaneous excitation with a single line is possible only with a relatively low efficiency because the narrow bandpass of the two filter sets will cut off a lot of otherwise usable spectrum. In addition, if only a single excitation wavelength is used, one of the dyes will almost always be excited less efficiently than the other. However, the advantage of simultaneous excitation is that the corresponding pixels of the two images are definitely in register because a single spot of incident light is the source of both of them. If the color separation filters are placed behind the pinholes, this setup is also unaffected by changes of filter sets. A problem that cannot be dealt with so easily is the cross-talk between channels, caused by the limited spectral performance of the filters.

Another solution that also adds to the stability of the instrument is the use of double and triple dichroics, that is, dichroic mirrors that are designed to deflect several laser lines and let

several emission bands pass (or vice versa). They need not be moved in order to use different laser lines, whether these are used simultaneously or not, and they can even be used in combination with an acousto-optical element to switch laser lines on a pixel-by-pixel basis. The most critical element for the proper overlap of the illumination and the detection paths is the dichroic mirror, and therefore using such a double or triple dichroic is ideal for this purpose. The problem is that multiple dichroics (tri-chroics, tetra-chroics, . . .) have slightly reduced transmission between the reflection bands because of the design compromises needed to produce their complex spectral properties, and that they only match a small number of fluorophore combinations. As with every design, the user has to decide between efficiency and alignment.

The acousto-optical beam-splitter (AOBS, see Chapter 3) is a system recently invented by Leica (Birk *et al.*, 2002), which can replace the dichroic mirrors that usually separate the illumination and detections paths in confocal microscopes. The advantage of the AOBS is that it does not have fixed transmission and reflection bands, but that it can be programmed to adapt from single to multi-chromatic characteristics of any type. This adds flexibility for working with different combinations of laser lines and fluorophores. In practice, the AOBS is programmed such that it leaves most of the fluorescent light undeflected, while the laser lines are deflected by a fixed angle. In addition, the AOBS is more efficient in terms of transmittance and reflection. This allows one to work with less laser power and to detect with an improved signal-to-noise ratio. These benefits are particularly valuable when working with multiple detection channels.

An interesting option is the use of two-photon excitation (Denk *et al.*, 1990; Stelzer *et al.*, 1994; see also Chapters 28 and 37, *this volume*) to excite not only UV dyes but also practically any currently used visible dye (Fischer *et al.*, 1994). The required filter sets are of a very simple design and extremely efficient because excitation and emission lines are spectrally very far apart. It should be no real problem to use this technique in any of the existing confocal instruments in many implementations — however, because no fluorescence light is generated away from the plane of focus, the detector pinhole is unnecessary. Instruments used for a combination of single-photon and two-photon excitation should probably have provisions for both confocal and widefield (non-descanned) detection.

SPECIAL SETUPS

Setups for Fluorescence Recovery After Photobleaching Experiments

Bleaching experiments use lasers to bleach a spot, an area, or an arbitrary pattern into a fluorescent sample. Bleaching refers to the removal of the fluorescent response of the target, ideally without damaging the target itself. The experiment consists of the observation of time-dependent changes in the bleached pattern, that is, recording changes in the structure of the bleach patterns or recording the fluorescence intensity recovery in certain locations. The confocal beam scanner is in principle an ideal device for generating bleach patterns or for applying a laser light pulse of a well-defined intensity to a particular location. It is also quite well suited to observe those locations before and after the application of the bleaching light pulse. For the bleaching process, the main requirement is the capability to drive the scanners in a more or less arbitrary path across the sample and to control the laser power. Although bleaching occurs unavoidably during any observation process (excitation consumes a fluorophore with a certain probability) it is usually rather slow. For typical FRAP experiments one wishes to bleach fast. The whole pattern should be generated within much less than a second. This typically requires lasers that provide a higher power than those required for simply imaging (i.e., milliwatts, not microwatts). For FRAP experiments it also makes sense to provide for an efficient illumination path. So, apart from needing a higher-powered laser and appropriate software, all confocal beam-scanning fluorescence microscopes should be suited for FRAP experiments.

It should not be forgotten that single-photon bleaching occurs along the entire illumination path. Hence it is not restricted to the focal volume, but is more intense there if only a small area is exposed. Multi-photon excitation can be used to bleach in a well-defined three-dimensional location (Brown *et al.*, 1999; Chapters 28 and 35, *this volume*).

Setups for Fluorescence Resonance Energy Transfer Experiments

In a fluorescence resonance energy transfer experiment (Clegg, 1996), one tries to determine whether two fluorophores and hence two proteins are located within a few nanometers of each other. Under certain circumstances, an excited fluorophore can be quenched by a neighboring fluorophore if its own emission band overlaps the excitation band of the neighbor. In the spectral domain, this is, in principle, a multi-fluorescence experiment where only one fluorophore is excited directly by the laser light, and any confocal fluorescence microscope should be equipped to perform such experiments. In the temporal domain, one requires special equipment (not only software but also hardware) that controls the illumination and detection timing.

Setups for the Integration of Optical Tweezers

A particularly interesting application of lasers in biology is the use of focused beams to capture and move small objects such as cells or bacteria (Rohrbach and Stelzer, 2001; Rohrbach *et al.*, 2004). One usually employs lasers that provide powers in the milliwatt range. To reduce damage due to absorption and heating, these lasers operate in the near-infrared range (NIR, 800–1100 nm). Once again in principle, the beam-scanning confocals are equipped for such purposes. However, optical elements are optimized for the visible range of wavelengths (400–750 nm) and may fail to work well at the particularly important wavelength of Nd:YAG lasers, 1064 nm. It is, therefore, more appropriate to design a separate optical path with a separate scanner pair, optimized mirrors, well-adapted beam expanders, and an appropriate scan lens and to feed the NIR light into the system through a separate port.

Used in continuous mode, multi-photon lasers provide the right laser powers for optical tweezers. When operated in a slow scanning mode (<100 lines/s) they can move a lot of biological material towards the borders of the scan area.

Setups for the Integration of Laser Cutters

Pulsed UV laser beams and, to a certain extent, the pulsed NIR laser beams used for multi-photon microscopy, can be used to cut biological material (see Chapter 38, *this volume*). Once again being able to position the laser beam and to control its power are the

crucial aspects. However, the wavelength of the UV lasers (~355 nm) is outside the specifications of the visible path and a separate optimized path should be employed. A serious issue is that the axial foci of the UV as well as of the NIR beams can be several tens of micrometers away from the focal plane of the visible light. Using slightly divergent or convergent beams, respectively, is a mediocre solution. Much better is to refocus the beam during the cutting procedure, that usually lasts much less than a second, by placing the lens on a piezo-driven positioner.

Optical tweezers as well as laser cutters work very well with regular widefield microscopes. It makes perfect sense to use a beam steering device for either or both of these applications and to observe the effect in the considerably faster widefield video mode (Grill *et al.*, 2001; Grill *et al.*, 2003; Colombelli *et al.*, 2004).

Setups for the Observation of Living Specimens

The main issue in the observation of living specimens is to reduce the exposure of the sample to light as far as possible. The sample should only be illuminated when a signal that is relevant for the experiment is recorded or when the system is set up prior to the experiment. Hence, speed and precision of operation and ease of control are crucial elements of a high-quality instrument. An efficient light path, a precise control of the laser power, and the ability to turn off the laser beam during retrace or between frames are just a few of many effective procedures.

MINIATURIZATION AND COMPUTER CONTROL

Usually, confocal microscopes are built around a conventional microscope by attaching a new intermediate optical system to its body. However, because image acquisition in a confocal microscope is computer controlled, it is questionable whether this solution is appropriate. Utilizing the body and the basic mechanical and optical elements of a conventional microscope puts mechanical and physical constraints on the design of the optical system that are mostly dictated by anatomical considerations. Indeed, the size of the instrument (and thus the length of the optical paths) is adapted to the posture of the user. Optical corrections are performed to ensure that the image of the sample is well perceived through the observer's eyes. Because the most important issue in confocal fluorescence microscopy is efficiency, it seems reasonable to put these constraints aside and to start a new, computer-centered design, in which principles such as miniaturization and computer-delegation are put first. This also provides a number of other advantages such as higher precision and long-term stability, features that are required for high-resolution studies of living biological specimens. In addition, the state of the microscope at any point in time is known to the computer. Each setting is documented and therefore reproducible. Manual intervention other than placing the sample in the microscope is not necessary and not desirable.

Important points:

- Use of digital detectors/cameras
- Corrections made by software
- Instrument is not bigger than a pile of books
- Feasibility of quantitative microscopy
- Good temperature control due to small size
- Suitable for implementation of structured illumination (Gustafsson, 1999)

THERMAL STABILITY

The increasing use of confocal microscopes for the acquisition of large three-dimensional data sets and for time-lapse experiments generate a concern about the long-term thermal stability of the instruments. Recent systematic investigations (Adler and Pagakis, 2003, of the effect of temperature fluctuations) have shown that images are distorted due to movements of the microscope stage, in particular along the optical axis. For room temperature variations of several degrees, focal shifts of about 2 µm have been observed. This can result in a stretched or compressed image of the sample, depending on the direction of the shift. Such temperature variations can easily occur in laboratories with many heat sources (computers, lasers, lamps, etc.), or where the temperature is cooled down cyclically by air conditioning. For long time-lapse experiments that run during the night, one should remember that the heat load will inevitably be lower when the laboratory is less busy.

In addition to the large heat sources already mentioned, heaters close to the sample are obviously a concern, in particular sample chamber heaters, stage heaters, and objective lens heaters. Other temperature-sensitive parts that can be sources for thermal distortions of the image are the immersion oil, mounting liquids, the light sources, the acousto-optic tuning filter (AOTF), and fiber-optics (Swedlow *et al.*, 2002).

But, generally speaking, the thermal stability of modern commercial microscopes is quite well taken care of.

VIBRATION ISOLATION

Although, vibration-isolation tables just mechanically isolate the instrument from the environment, usually some more sophisticated versions can actively damp noise sources created by the instrument itself. The only real vibration sources in a confocal microscope are the scan mirrors and the cooling system of the laser head. The latter source can be eliminated if the laser head is not mounted on the same table as the microscope and the light is carried to the microscope by an optical fiber. Figure 9.7 shows how an arrangement of Class 1 uses illumination and detection with fibers (see also Chapter 26).

One should also remember that mechanical damping only works when all the optical elements, particularly heavy ones, are firmly fixed to the table. Otherwise the movement of the different elements will be independent and not in phase. Under any circumstances, damping mechanical vibration is a complicated task, and it is often fairly easy to do something that seems straightforward but that actually makes things worse.

CONCLUSIONS AND FUTURE PROSPECTS

The most important issue in any kind of light microscopy is photon efficiency, as this determines the gap between photo-damage and useful contrast in the recorded image. As long as the chosen optical arrangement maintains the necessary diffraction limit, the general rule is that the more sparse an optical path, the more efficient it will be. The scan system should be chosen in accordance with photon efficiency. Because a number of different scanning microscopes have been realized, each of them employing different optical and scanning arrangements, time should show which are the most efficient and the most versatile to use. My personal preferences are the optical arrangement shown in Figure 9.4(A) and the scanner arrangements shown in Figures 9.5(B) and 9.5(D).

Sparsity, relative simplicity, and good illumination efficiency are advantages of single-beam scanners over disk scanners. The disadvantage of single-beam scanners is that they have to use relatively inefficient PMT detectors to achieve high recording speeds. It is also a mistake to assume a technological standstill. The large number of companies and the short product lifetimes indicate that much can still be done. In the short term, major improvements are more likely to be found in the fluorescent dyes, in the biological application, or in other biochemical developments. Particularly useful alternatives are the disk scanning-devices. They offer an excellent compromise between speed and efficiency, and the new electron-multiplying charge-coupled device (EM-CCD) cameras give the disk scanners a detector that is very comparable to the PMT (see Chapters 10 and 12, *this volume*).

Ceterum censeo that conventional fluorescence microscopes are excellent, reliable, and easy-to-use optical instruments. A high-quality, conventional optical microscope should always be the first instrument of choice. Those scientists who do not achieve the expected image quality should consider attaching a high-quality, possibly cooled CCD camera (Hiraoka *et al.*, 1987) to their conventional widefield microscope. Using an efficient CCD camera, a powerful computer, and appropriate software to discriminate against out-of-focus light will in some cases be a simpler, and perhaps an even more efficient, solution to many relevant biological problems (Agard and Sedat, 1983; Fay et al., 1989; see also Chapters 23 and 24, *this volume*).

ACKNOWLEDGMENTS

I thank all my colleagues for interesting information that helped shaping the manuscript. I am particularly grateful to Steffen Lindek for his help in revising the text and the figures.

REFERENCES

Adler, J., and Pagakis, S.N., 2003, Reducing image distortions due to temperature-related microscope stage drift, *J. Microsc.* 210:131–137.

Agard, D., and Sedat, J., 1983, Three-dimensional architecture of a polytene nucleus, *Nature* 302:676–681.

Amos, W.B., 1991, Achromatic scanning system, US Patent 4,997,242.

Axelrod, D., Koppel, D.E., Schlessinger, J., Elson, E., and Webb, W.W., 1976, Mobility measurement by analysis of fluorescence photobleaching recovery kinetics, *Biophys. J.* 16:1055–1069.

Bacallao, R., and Stelzer, E.H.K., 1989, Preservation of biological specimens for observation in a confocal fluorescence microscope and operational principles of confocal fluorescence microscopy, *Methods Cell Biol.* 31:437–452.

Birk, H., Engelhardt, J., Storz, R., Hartmann, N., Bradl, J., and Ulrich, H., 2002, Programmable beam-splitter for confocal laser scanning microscopy, *SPIE Proc.* 4621:16–27.

Brakenhoff, G.J., Blom, P., and Barends, P., 1979, Confocal scanning light microscopy with high aperture immersion lenses, *J. Microsc*. 117:219–232.

Brown, E.B., Wu, E.S., Zipfel, W., and Webb, W.W., 1999, Measurement of molecular diffusion in solution by multiphoton fluorescence photobleaching recovery. *Biophys. J.* 77:2837–2849.

Carlsson, K., and Liljeborg, A., 1989, A confocal laser microscope scanner for digital recording of optical serial sections. *J. Microsc.* 153:171–180.

Clegg, R.M., 1996, Fluorescence resonance energy transfer, In: *Fluorescence Imaging Spectroscopy and Microscopy* (X.F. Wang and B. Herman, eds.), John Wiley and Sons, New York, p. 179–252.

Colombelli, J., Grill, S.W., and Stelzer, E.H.K., 2004, UV diffraction limited nanosurgery of live biological tissues, *Rev. Sci. Instrum*. 75:472–478.

Denk, W., Strickler, J.E., and Webb, W.W., 1990, Two-photon laser scanning fluorescence microscopy, *Science* 248:73–76.

Fay, F.S., Carrington, W., and Fogarty, K.E., 1989, Three-dimensional molecular distribution in single cells analysed using the digital imaging microscope, *J. Microsc.* 153:133–149.

Fischer, A., Cremer, C., and Stelzer, E.H.K., 1994, Fluorescence of coumarines and xanthenes after two-photon absorption with a pulsed titanium-sapphire laser, *Appl. Opt.* 345:1989–2003.

Fukui, Y., de Hostos, E., Yumura, S., Kitanishi-Yumura, T., and Inoue, S., 1999, Architectural dynamics of F-actin in eupodia suggests their role in invasive locomotion in *Dictyostelium*, *Exp. Cell Res.* 249:33–45.

Goodman, J.W., 1968, *Introduction to Fourier Optics*, McGraw-Hill: San Francisco.

Grill, S.W., Gönczy, P., Stelzer, E.H.K., and Hyman, A.A., 2001, Polarity controls forces governing asymmetric spindle positioning in the Caenorhabditis elegans embryo, *Nature* 409:630–633.

Grill, S.W., Howard, J., Schäffer, E., Stelzer, E.H.K., and Hyman, A.A., 2003, The distribution of active force generators controls mitotic spindle position, *Science* 301:518–521.

Gustafsson, M.G.L., 1999, Extended resolution fluorescence microscopy, *Curr. Opin. Struc. Biol.* 9:627–634.

Hiraoka, Y., Sedat, J.W., and Agard, D.A., 1987, The use of a charge-coupled device for quantitative optical microscopy of biological structures, *Science* 238:36–41.

Maddox, P.S., Moree, B., Canman, J.C., and Salmon, E.D., 2003, Spinning disk confocal microscope system for rapid high-resolution, multimode, fluorescence speckle microscopy and green fluorescent protein imaging in living cells, *Methods Enyzmol.* 360:597–617.

Marsman, H.J.B., Stricker, R., Wijnaendts-van-Resandt, R.W., Brakenhoff, G.J., and Blom, P., 1983, Mechanical scan system for microscopic applications, *Rev. Sci. Instrum.* 54:1047–1052.

Martínez-Corral, M., Caballero, M.T., Stelzer, E.H.K., and Swoger, J., 2002, Tailoring the axial shape of the point spread function using the Toraldo concept, *Opt. Express* 10:98–103.

Melles Griot, 1999, *The Practical Application of Light*, Irvine, CA, Melles Griot. (The Melles Griot catalogue is very informative and contains numerous excellent comments on optical elements and performance characteristics.)

Minsky, M., 1961, Microscopy Apparatus, US Patent 3,013,467.

Minsky, M., 1988, Memoir on inventing the confocal scanning microscope, *Scanning* 10:128–138.

Petráň, M., Hadravský, M., Egger, M.D., and Galambos, R., 1968, Tandem-scanning reflected-light microscope, *J. Opt. Soc. Am.* 58:661–664.

Rohrbach, A., and Stelzer, E.H.K., 2001, Optical trapping of dielectric particles in arbitrary fields. *J. Opt. Soc. Am. A* 18:839–853.

Rohrbach, A., Tischer, C., Neumayer, D., Florin, E.L., and Stelzer, E.H.K., 2004, Trapping and tracking a local probe with a photonic force microscope, *Rev. Sci. Instrum.* 75:2197–2210.

Stelzer, E.H.K., and Wijnaendts-van-Resandt, R.W., 1985, Applications of fluorescence microscopy in three dimensions — microtomoscopy, *SPIE Proc.* 602:63–70.

Stelzer, E.H.K., Hell, S., Lindek, S., Stricker, R., Pick, R., Storz, C., Ritter, G., and Salmon, N., 1994, Nonlinear absorption extends confocal fluorescence microscopy into the ultra-violet regime and confines the illumination volume, *Opt. Commun.* 104:223–228.

Stelzer, E.H.K., Stricker, R., Pick, R., Storz, C., and Hänninen, P., 1988, Confocal fluorescence microscopes for biological research, *SPIE Proc.* 1028:146–151.

Swedlow, J.R., Hu, J., Andrews, P.D., Roos, D.S., and Murray, J.M., 2002, Measuring tubulin content in *Toxoplasma gondii*: A comparison of laser-scanning confocal and widefield fluorescence microscopy, *Proc. Natl. Acad. Sci. USA* 99:2014–2019.

Tanaami, T., Otsuki, S., Tomosada, N., Kosugi, Y., Shimizu, M., and Ishida, H., 2002, High-speed 1-frame/ms scanning confocal microscope with a microlens and Nipkow disks, *Appl. Opt.* 411:4704–4708.

Trepte, O., 1996, Enhanced scanning control in a confocal scanning laser microscope, *Scanning* 18:356–361.

Wilke, V., 1985, Optical scanning microscopy — the laser scan microscope, *Scanning* 7:88–96.

Wilson, T., and Carlini, A.R., 1987, Size of the detector in confocal imaging systems, *Optik* 72:109–114.

10

Disk-Scanning Confocal Microscopy

Derek Toomre and James B. Pawley

INTRODUCTION

Rapid biological imaging of faint fluorophores in living cells — especially in four dimensions [three dimensions + time] — imposes different instrumentation challenges from slowly acquiring a single high-resolution confocal snapshot of fixed tissue. High acquisition speeds with acceptable contrast and minimal photobleaching suddenly become essential, all without losing the instantaneous optical sectioning that a confocal microscope affords. Of particular interest here, disk-scanning confocal microscopes are proving to be a powerful tool in rapid imaging of live cells in space and time. While the principle is relatively old, new instrument developments, both in optics and in novel ultra-sensitive charge-coupled device (CCD) cameras are greatly expanding the versatility and scope of this approach. However, knowing which system is best for a given question and understanding the inherent strengths and weaknesses is not easy, especially as many of the choices involve complex trade-offs between resolution, speed, sensitivity,[1] and signal-to-noise ratio (S/N). The goal of this chapter is to provide both a theoretical and a practical guide, with more emphasis on the latter especially when theoretical considerations are covered elsewhere (Chapters 22, 23, and 34, *this volume*). Here the relative merits, strengths, and weaknesses of using a disk-scanning confocal microscope for biological imaging will be examined and sample applications shown.

This chapter rests heavily on that written by G. S. Kino for the second edition, and many of his original figures and text have been retained or abridged. One notable distinction is that we have explicitly chosen to emphasize fluorescent, rather than reflected or backscattered light (BSL) imaging, as the former represents the most common use of this instrument in the biological sciences. We have also limited discussion on microscopes that are no longer in production (or are very rarely used by biologists) and instead have compared and contrasted the most prevalent current commercial disk-scanning confocal systems (Yokogawa, BD Bioscience, and Olympus) with conventional confocal light-scanning microscopy and with a new, fast confocal slit-scanning microscope from Zeiss. Finally, current limitations and new technological advances that in our opinion will markedly influence the power and popularity of this approach are discussed.

The reader is advised to pay special attention to other chapters in this volume that go into considerable depth about related subject areas: pinhole and slit detectors (Wilson and Sheppard, 1984; Wilson and Carlini, 1987; Chapters 25 and 34), signal-to-noise ratio (Chapters 22 and 23), multi-focal multi-photon microscopy (Chapter 29), photodetectors (Chapters 2 and 12), deconvolution (Chapters 23, 24, and 25), and visualization of three-dimensional (3D) datasets (Chapters 13 and 14).

BACKGROUND

Live Cell Imaging: Probing the Future

Since the publication of the second edition of this book in 1995, there has been a virtual explosion of live cell imaging papers. This is in no small part due to widespread use of genetically encoded tags, most notably green fluorescent protein (GFP) and now a literal rainbow of spectral mutants including CFP (cyan), YFP (yellow), RFP (red; monomeric and tetrameric), pH-(in)sensitive mutants, and fluorescence resonance energy transfer (FRET) probes (Miyawaki, 2003; Chapter 16, *this volume*). The immense popularity of these fluorophores derive from that fact that nearly any protein can be specifically tagged and followed in space and time. Illustrating their growing prevalence, in 1995, 2000, and 2003 there were respectively ~60, 1000, and 1600 citations of papers using "GFP." New categories of mixed chemical/genetic probes have been developed including FlAsH and ReAsH dyes which facilitate pulse-chase labeling and correlative light and electron microscopy (Gaietta *et al*., 2002). Of course, there is also a plethora of traditional vital dyes for measurements of cellular physiology (ion concentrations, membrane voltage, etc.), organelle dynamics (mitochondria, lysosomes, etc.), and fluorescently tagged ligands, lipids, and antibodies; the Molecular Probe catalogue (now Invitrogen) is an excellent reference, as are Chapters 17 and 36.[2] Very recently, small, semiconductor nanocrystals, also called "quantum dots," have been developed that are much brighter, more photostable, and have narrower emission spectra than traditional dyes (Lidke and Arndt-Jovin, 2004).[3]

What does all the progress in the probe development mean to the microscopist? As the floodgates of new specific fluorescent molecules and multi-spectral dyes have opened, there is an ever-increasing desire to **study the *dynamics* of molecules in living cells with *high spatial and temporal resolution***. The Holy Grail of such imaging is to study biochemistry at the **single molecule**

[1] Although sensitivity is a term that most people think that they understand, it lacks a specific technical meaning. We will use it here to represent a mixture of detector quantum efficiency and detector noise floor (including background). A "sensitive" detector is one suitable for discriminating a very weak light level from "black."

[2] See http://www.probes.com/.

[3] Nanocrystals have large absorption cross-sections and long decay times (τ ~10 ns). This makes them well suited for low-dose, 2-photon and confocal lifetime imaging, but can also cause singlet-state saturation at relatively low beam power.

Derek Toomre • Yale University School of Medicine, New Haven, Connecticut 06520-8002
James B. Pawley • University of Wisconsin-Madison, Madison, Wisconsin 53706

level in living cells. While this may sound like science fiction, the reality is that such scientific studies are being published using state-of-the-art probes and sophisticated microscopes (Sako and Yanagida, 2003).

A Need for Speed and Less Photobleaching

What are the **live cell** imaging needs of the biologist? There is no easy answer. Is it enough to see a single "snapshot" of a cell undergoing mitosis or is the process only revealed by time-lapse or four-dimensional (4D) imaging? Only the experimentalist can judge, but increasingly the desire to understand the complex and dynamic intra- and intercellular organization is pushing the trend towards larger multi-dimensional datasets, that include the following different spatial/temporal categories:[4]

- **2D/3D** imaging: A single two-dimenional (2D) snapshot or 3D "stack" or projection of many optical sections
- **2D + time**: Imaging of a single optical section over time. This varies from slow "**time-lapse**" (1 frame every s/min/h), to "**real-time**" (~30 frames/s), to the **ultrafast** (100–1000 frames/s).
- **4D (3D + time)**: Time-lapse (or real-time) imaging

Parameters that are generally important here are: adequate resolution (*xy*), *z*-axis optical sectioning, S/N, minimal photobleaching of fluorophores or phototoxicity to cells, and speed. How fast? This depends on the biological process being studied. For example, if studying microtubule dynamics, an acquisition of 0.1 to 1 frames per second (fps) may suffice. However, for fast processes such as calcium sparks or waves that happen in milliseconds, acquisition rates of 100 to 1000 fps may be needed.

One rule of thumb is to acquire images fast enough so that only minimal changes occur between frames (e.g., small changes in object intensity or position). In this way no action is missed and automated image analysis is facilitated. However, this "upper bound of the speed envelope" is often unrealistic, either because the imaging system cannot respond fast enough or because the sample bleaches too rapidly to obtain the desired information. This "rule" can be even more demanding when acquiring live 3D or 4D images as, in this case, each entire 3D stack must be acquired fast enough to essentially freeze the action. For example, if a vesicle is moving at 1 micron/s (a common speed) and one wishes to restrict object motion blur to ~0.25 microns, then ideally, the whole *z*-stack should be acquired in less than 250 ms. If this cell is 5 microns thick and one acquires a stack of 10 optical sections (500 nm *z*-steps), this means that each slice needs to be acquired in under 25 ms! This is not even considering the overhead time of fast (piezoelectric) focusing or the excitation of multiple dyes.

The other problem associated with 4D imaging is faster bleaching. For example, if a fluorescent sample were normally to bleach to 50% after 500 (2D) images, it would now photobleach after only 20 3D stacks of 25 planes each, or in 5 sec. if acquired at 4 stacks/s. Anyone who has attempted fluorescent time-lapse imaging, especially in 4D, knows all too well the problem of photobleaching and the proverbial proclamation that "every photon is sacred" and that 3D deconvolution reduces Poisson noise substantially by effectively averaging over ~100 voxels in Nyquist-sampled data (see Chapters 19 and 25, *this volume*).

[4] This is equally applicable for fixed cells, however, viewing living cells avoids fixation artifacts and can facilitate rapid screening of samples (e.g., GFP-based visual screens).

Advantages and Limitations of Confocal Laser-Scanning Microscopes

Why are confocal laser-scanning microscopes (LSM), so popular with the biological community in spite of their quarter to half million dollar expense? The single major advantage of the confocal LSM is the ability of its **spatial filter** (either a single pinhole or a slit) to reject out-of-focus light. This improves contrast-reducing background or haze, and provides better optical sectioning (and resolution) along the *z*-axis, although a ~30% increase in lateral (*xy*) resolution is possible if the pinhole is closed to about 0.05 Airy units[5] (Wilson and Sheppard, 1984). Given the many attributes of this mature technology, why should one use any other kind of light microscope for fluorescent imaging?

Alas, the source of its strength, the single confocal pinhole, is also its Achilles' heel, creating problems that while of little concern with bright, fixed cells, can be disadvantageous for fast or long-term imaging of living cells.[6] Let us start by considering the data rate. As is clearly demonstrated in Figure 35.19 (Chapter 35, *this volume*), the most important factor in obtaining a good, high-contrast image is to collect enough photons! Otherwise statistical noise in the signal makes the image grainy and smaller features become invisible. This means that both the collection of light (lens and intermediate optics) and its detection must be optimal. Most confocal LSM use **photomultiplier tubes (PMTs)** for detecting photons. Although they have a rapid response and good dynamic range, their **effective quantum efficiency (QE)** is low, typically only in the 6% to 15% range (in the 400–600 nm spectrum). This stands in stark contrast with the up to 90% QE achievable with a good back-illuminated, CCD camera (see Chapter 13, *this volume*).

Because the rate at which data can be derived from a fluorescent specimen depends directly on the number of excitation photons striking it, to image at the same frame rate, the intensity of the light in the single spot of an LSM must be about ~10^5 times higher than that used in a widefield (WF) system. This very intense excitation light can lead to **dye saturation** (see Chapters 2 and 16, *this volume*), a phenomenon that occurs when the excitation is so bright that most of the dye molecules are in the excited state. Using more laser power only raises the background because, as molecules away from the focus plane are now excited more strongly, but are still not saturated, they will produce relatively more out-of-focus light. It also increases photobleaching without increasing signal level (Chapters 38 and 39, *this volume*, discuss the relationship between bleaching and saturation). Saturation can only be minimized by using a dye with a faster singlet decay time or by using less intense light.

On the other hand, rapid fluorescent imaging requires more intense light so as to produce a similar number of emitted photons in a shorter time.[7] Clearly there is a theoretical maximum imaging speed set by the total **rate at which photons are generated**

[5] Rarely is this done when viewing live biological samples as signal level decreases approximately with the square of the pinhole diameter and low signal is much more a barrier than simple optics to seeing even the Abbe resolution.

[6] Note that when commercial single-beam confocal microscopes first appeared two decades ago, living cell fluorescent imaging was uncommon and a premium was put first on the optimization of resolution and later on multi-spectral excitation and detection, rather than on speed or sensitivity. Paradoxically, Zeiss' 2004 release of their LSM 510 LIVE confocal is based on a lower resolution slit scanner.

[7] An analogy can be drawn to filling up buckets with water, either drip-by-drip over hours or in a second with a fire hose.

(depending on the number of beams, the excitation intensity in each one, and the photoproperties and concentration of the dye) and the **photon efficiency** of the entire detector channel. Although one can increase signal level by using more dye, this can seldom be done without affecting functionality; for example, protein overexpression can cause misfolding or mislocalization.

One alternative is to scan a very small area of interest or even just a single line to gain frame speed. However, when sampling only a small region, information on a larger spatial scale is lost.[8] In fact, **weakly labeled samples are triple hit**; more intense light is needed to excite the dye to generate enough photons, leading to more background, phototoxicty, and increased photobleaching.

The second requirement for fast confocal imaging is that both the laser beam and the image of the pinhole must be raster-scanned over the sample — typically using linear galvanometers. The **mechanical properties of** linear galvanometers limit how fast a line can be scanned (low kilohertz, see Chapter 3, *this volume*). Although acousto-optical deflectors or resonant galvanometers can go faster, they have their own limitations (see Chapter 9, *this volume*). Finally, lasers are expensive and by definition only excite at very discrete "lines," limiting the fluorescent dyes that can be excited.

Other Imaging and Deconvolution

Is confocal imaging the only way to go? As mentioned above, the advantage of a (1-photon) confocal is to reduce background by rejecting out-of-focus **emission** light with a pinhole. Alternatively, one can make optical section images by limiting the **excitation** to a single optical plane or by using other microscopical techniques, for example, 2-photon excitation (Chapters 28, 29, and 37, *this volume*) or total internal reflection fluorescent microscopy (Toomre and Manstein, 2001). When imaging samples in which most or all of the dye is confined to a single optical plane (e.g., some *in vitro* assays), widefield (WF) epi-fluorescent imaging may suffice.

Alternatively, one may acquire a stack of WF epifluorescent images and use a measured, or theoretical, point spread function (PSF) to "deconvolve" the 3D image. The principle here is that at least some of the out-of-focus haze can be converted into useful information. While a detailed analysis of deconvolution is provided in Chapters 23 and 24, it is worth underscoring the following limitations of deconvolution:

- Deconvolution is time consuming (especially for 4D datasets) and does not give on-the-fly results.
- Small misalignment of the optics can prevent good deconvolution.

The quality of the deconvolution depends on the sample and the method of deconvolution (there are several). However, there is also some good news: deconvolution will also improve the image quality of confocal 3D datasets by suppressing out-of-bandwidth "features" caused by Poisson noise and effectively averaging signal levels over many voxels. In addition, because the confocal PSF is confined to a much smaller volume, the computer processing time is greatly reduced.

[8] Often one only determines *a posteriori* what region of an image was important.

CONFOCAL DISK-SCANNING MICROSCOPY

Nipkow Disk — An Innovation

The **Nipkow disk** that is central to the design of all modern disk-scanning confocal microscopes, was developed by Paul Nipkow in 1884 as a means of dissecting an image into a single continuous signal. Nipkow had the foresight to realize that if a series of pinholes (or squares) were arranged in an Archimedian spiral of constant pitch, then one revolution of the disk would be equivalent to scanning the object (see Fig. 1.3, *this volume*) and the light transmitted by the holes could be measured to record any image projected onto the disk. It was an early competitor of the television we know today. Apart from its mechanical complexity, its main weakness was that at any given time light is only detected (or transmitted) through a single small pinhole making it inefficient for detecting or displaying image information. This is why televisions no longer use Nipkow disks.

More recently, Petráň designed a new a new type of Nipkow disk, one having many more holes arranged in a series of nested spirals so that hundreds or thousands were present in the frame at any one time and in such a way that the entire pattern was axially symmetrical (Fig. 10.1).

A Renaissance — Advantages of Disk-Scanning Confocal Imaging

Disk-scanning imaging was reborn in 1967 in Egger and Petráň's first implementation of a **tandem scanning-disk confocal microscope**. The purpose of the Petráň disk was not to dissect the image (as in Nipkow's design) but to perform point-illumination/point-detection confocal imaging. Light transmission through a Petráň disk is hundreds to thousands of times higher than through a Nipkow disk.[9] New designs by both individuals (e.g., Kino, Xiao,

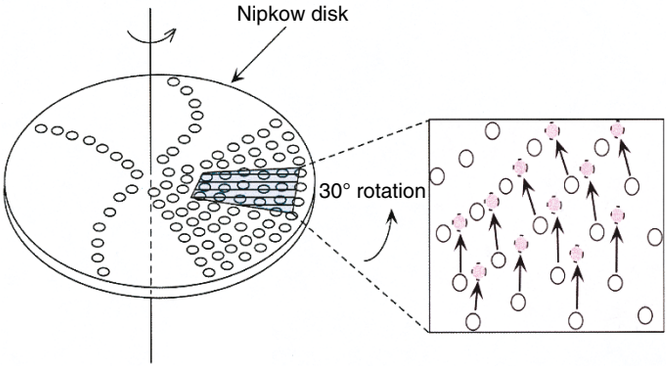


FIGURE 10.1. Schematic of a Nipkow/Petráň disk used in real-time disk-scanning confocal microscopy. Typically 20,000 to 200,000 pinholes are arranged in spirals of constant pitch (Archimedian) and a subregion (shown in blue) corresponding to about a thousand pinholes are illuminated and imaged. A partial rotation (e.g., 30° for the Yokogawa CSU10/22) of a rapidly disk-scanning (~1800–5000 rpm) scans the sample; arrows show how holes rotate to new positions (red). Images can be seen in real-time by eye or acquired using a camera that is synced with rotation of the disk. (Image adapted from H. Ishida *et al*., Department of Physiology, Tokai University.)

[9] Note on nomenclature: many people and companies call spinning confocal disks "Nipkow disks" even though the pinhole spacing and design may be radically different from the original Nipkow disk. Thus, a "Nipkow disk" merely denotes a **spinning disk** pinhole- (or slit-) based confocal system rather than a specific design.

TABLE 10.1. Comparison of Confocal LSM, Disk-Scanning, and Scanned Slit Microscopes

	Single-Beam Laser Scanning	Spinning Disk	Scanned Slit
Advantages	• High resolution • Excellent, adjustable *z*-resolution • FRAP/photoactivation • Simultaneous readout of several wavelength channels	• High speed • Good QE detector and sensitivity • Moderate cost[a] • Laser not required	• High speed • Good QE detector and sensitivity • Simultaneous readout of several wavelength channels
Disadvantages	• High cost • Slow to moderate speed • Low QE detector • High excitation intensity • More photobleaching • Requires lasers	• Lower resolution and *z*-resolution[b] • Fixed pinhole/slit • Low transmission of excitation[c]	• Lower resolution and *z*-resolution • Requires lasers • High cost • No FRAP

[a] Large price range from ~US$35,000 to US$300,000 (see Table 10.2).
[b] Depends on the pinhole/slit setting (see text and Fig. 10.4) and operationally on the light budget.
[c] An exception is the Yokogawa microlens design, which transmits more excitation light.

Boyde, Lichtman) and companies have further expanded the possibilities, however all disk scanners share common features. The optimal pinhole (or slit) size and spacing is important and will be discussed later and in Chapter 11.

The disk is located in a conjugate image plane and a partial rotation of the disk scans (see arrows) the specimen with thousands of beams of light that can cover the whole image plane in as little as 1 ms. While a single-beam confocal LSM illuminates and collects intensity information **serially**, multiple pinholes allow the specimen to be sampled in **parallel**. This produces a **multiplicative gain in potential scan speed** proportional to the number of pinholes present in the illumination/detection system.

As the Petráň microscope requires the illumination of a wide-field of pinholes, rather than a single small spot, a conventional "white" light source such as a mercury or xenon lamp can be used instead of a laser. Disk scanning is more rapid than the human visual flicker response rate (~18 Hz) and a **"real" confocal image** of the sample can be seen by eye or detected with a camera in true color.

Some of the earliest applications of disk-scanning confocal microscopes (e.g., Petráň, Kino, and colleagues) were to illuminate the sample with white light through the pinholes and collect light reflected from the confocal plane. When such a system employs objective lenses intentionally designed to have very high chromatic aberration, light of different wavelengths forms foci at different heights. The result is that images of opaque, reflective specimens are colored with each color representing features of a particular topographic elevation. By inserting diffraction gratings into the eyepieces of the microscope, such images can even be viewed as real-time stereo-pair images. As the gratings displace the location of features horizontally depending on their color, and as their color is coded for depth by orienting the gratings in opposite directions for each eye, a stereo-pair image is presented in which the actual 3D position of the specimen surface is both coded by color and made visible by stereo disparity (Chapter 15, *second edition*).

Advantages of disk-scanning include:

- **Up to 100- to 1000-fold gain of speed**: multiple points of light illuminate the sample and are detected **in parallel**, greatly reducing fluorophore saturation.
- Generating a **real image** that can be detected by eye or with a fast, high-QE CCD camera.
- **Less photobleaching** (due to lower local excitation intensity).
- **No** strict requirement for **laser** illumination, reducing cost and allowing more choices of excitation wavelengths.

Disadvantages

Several factors must be considered when using a disk-scanning confocal (see Table 10.1). First, light scattered or fluoresced by structures away from the focus plane can still reach the detector through an adjacent pinhole, decreasing the *z*-resolution of the system. Second, low transmission of light through the disk may hinder imaging of dim fluorescent samples. Although this can be compensated with longer exposure times, doing so negates the speed advantages that are sought. However, a high-QE detector may still give slow confocal imaging with less bleaching than a confocal LSM. Third, 90% to 99% of illumination light does not go through the disk and these reflections can cause high background, especially in single-sided bright-field spinning confocal microscopes. Field illumination may not be uniform and may require a correction lens and/or homogenization of the arc source (e.g., a liquid light guide). Finally, disk-scanning systems do not allow high power illumination of selected regions of interest for fluorescent recovery after photobleaching (FRAP) experiments. These disadvantages can be partially mitigated by judicious choice of intermediate optics, pinhole or slit size and spacing, detector type, and the addition of a separate bleaching system.

CRITICAL PARAMETERS IN PINHOLE AND SLIT DISKS

Fill Factor and Spacing Interval F

Although the present discussion has centered on confocal pinholes, the use of a confocal scanning disk with slit apertures can increase the transmitted light budget. Slits can either be arranged on the disk as spirals or in linear arrays. The main **trade-off between slit versus pinhole** is usually between **brighter illumination and higher signal with a slit design and better *z*-resolution with pinholes**. Slit-disk confocals have a larger percentage transmission (T), or fill factor, than pinholes when the ratio of the slit/pinhole diameter, D, to distance between slits/pinholes, S, is fixed:

$$T_{\text{slit}} = \left(\frac{D}{S}\right) \times 100 \qquad T_{\text{pinhole}} = \left(\frac{D}{S}\right)^2 \times 100 \qquad \textbf{(1)}$$

For example, if $D = 50$ microns and $S = 500$ microns, then 10% and 1% of the light will be transmitted by a disk with slits, and pinholes, respectively. The transmission of the pinhole disk can be increased by using a smaller pinhole spacing interval. However,

even if *D*/*S* is 1/5, only 4% of the light will be transmitted, and smaller *D* causes too much of the emitted light to return through neighboring pinholes, decreasing *z*-resolution,[10] as discussed below.

Other options are to increase the pinhole or slit diameter, however, this will decrease the axial resolution (see below). Alternatively, intermediate optics employing "microlenses," such as those used in the Yokogawa system, can focus more of the excitation light onto the pinholes but only if laser light is used. It is worth noting that when the slits are very close, this imaging system begins to resemble structured illumination (e.g., Zeiss Apo-tome; see Chapter 13, *this volume*) although there, signal detection is ***not*** confocal.

Lateral Resolution

The *xy*-resolution of the light microscope is described by the Abbe equation and is a function of the emission wavelength and numerical aperture of the objective:

$$r_{\text{Airy}} = 0.61\frac{\lambda_o}{NA_{\text{obj}}} \quad \textbf{(2)}$$

In biological fluorescence confocal microscopy, where overall performance drops rapidly because of poor signal statistics if *D* is reduced below one Airy unit, *xy*-resolution is essentially the same as that of the widefield instrument. This is particularly true for disk scanners having *D* that is more than 2 Airy units because, in this case, the CCD will record a mini-image from the light returning through each pinhole.[11]

Pinhole/Slit Size

What is the optimal pinhole size? Unlike confocal LSMs, which offer a diffraction-limited spot as the excitation pinhole and separate independently adjustable pinholes for each detection channel, disk-scanning confocals use the same pinhole for excitation and detection (or in tandem systems, one of identical size). While in both types of confocal, increasing *D* increases signal strength because light can now reach the detector from features farther from the focus plan, only in disk scanners does it also produce more signal because there is more excitation light striking the specimen in the larger excitation spot. This makes pinhole size important.

The **optimal diameter of a pinhole/slit**, D_{OPT}, sets it equal to the FWHM of the Airy figure and can be derived from the Fraunhofer formula (Goodman, 1968; Kino, 1987; Kino and Xiao, 1990) and expressed as the following approximate equation;[12]

$$D_{\text{opt}} = \frac{0.5\lambda h_1}{b} = \frac{0.5\lambda M}{NA} \quad \textbf{(4)}$$

where *M* and *NA* are, respectively, the magnification and numerical aperture of the objective lens. Assuming a 100× 1.4 NA oil-immersion lens, and λ = 560 nm, D_{OPT} is 20 µm but only 9.3 µm for a 40× 1.2 NA lens. Thus, one needs disks with different *D* values for objective lenses with different *M*/*NA* ratios. In commercial systems with a single disk (Yokogawa and CARV), the pinhole was designed for high magnification, high NA objectives, and even then the 50 to 70 micron pinhole diameter is excessively wide (Table 10.2).

The effects of pinholes (or slits) that are the wrong size are shown schematically in Figure 10.2. A small pinhole has decreased transmission due to its small area and also, because the illumination light diffracts at the aperture, the light from it overfills the pupil of the objective lens, wasting more light. On the detection side, an **overly small pinhole** rejects more light than necessary and decreases the S/N (identical to when one closes the pinhole too much in a confocal LSM). Alternatively, if the **pinhole is too big** then and the (non-laser) illumination is collimated rather than convergent, then it may not be diffracted adequately to fill the pupil of the objective, illuminating a larger spot at the focus plane.[13] Signal light from this larger spot will be imaged as a mini-image in the aperture of the disk. The emitted light is collected efficiently but the large pinhole makes the *z*-resolution worse. Some commercial systems allow one to change the slits to match the objective (DSU unit) while in others the pinholes are fixed (Yokogawa CSU series and CARV) and only the magnification of the objective or the tube can be adjusted to change the effective size of *D*.

Use of the ***same*** **pinhole or slit for both illumination and detection** causes the *z*-resolution of the non-laser disk-scanning confocals to fall off much more rapidly as *D* increases than occurs with single-beam confocals.[14] However, when the ***D*** **is optimal**, the curves for the single- and multi-beam scanners converge, as long as one ignores haze reaching the CCD through adjacent pinholes.

Axial Resolution

The **axial resolution**, *dz*, near the focal plane of slit and point scan confocal microscopes with very small pinhole/slit dimensions can be expressed by the equation

$$d = K\frac{\lambda}{n\left[1-\sqrt{1-\left(\frac{NA_z}{n}\right)^2}\right]} \quad \textbf{(3)}$$

where λ is the emission wavelength, *n* is the refractive index of the medium, *NA* is $n \sin\alpha$ (α is the acceptance angle of the objective of), and *K* is a scalar correction factor where for a slit disk K_{slit} = 0.95 and for a pinhole disk K_{pinhole} = 0.67. For example, if λ = 500 nm, NA = 1.2, and *n* = 1.33 then *d* would be 627 nm and 442 nm for a slit disk and pinhole disk, respectively. As long as *D* is the same for both pinholes and slits and also significantly smaller than the calculated Airy limit, slits will have ~1.4× worse optical sectioning than pinholes.

However, this statement really does not tell the whole story. If one were to make a *z*-scan through a thin, horizontal layer of dye,

[10] Also applies to slits (see graph in Fig. 10.9).

[11] This mini-image will have dimensions only a few pixels in size and the information it contains can only be recorded as long as the magnification of the camera lens is sufficient to match these pixels with the size of the pixels on the CCD.

[12] This sets the pinhole diameter at the full-width half-maximum of the Airy figure and lets through about 75% of the light in the central maximum. In biology, the pinhole/slit is often set at the first zero of the Airy figure, about twice as big.

[13] In laser-illuminated disk scanners, the high coherence of the source insures that the light is focused into an Airy figure no matter what the size of the aperture. However, the size of this figure depends on the extent to which light from each aperture fills the back-focal plane (BFP) of the objective, a factor that can be increased by the convergence angle of the light striking the disk.

[14] In laser-illuminated disk scanners, assuming that the divergence of the light leaving each pinhole is sufficient to fill the BFP of the objective, each excitation beamlet is focused into a single, diffraction-limited spot, regardless of the pinhole size. This occurs because of the extremely high coherence of laser light.

TABLE 10.2. Comparison of Some Different Microscope Specifications[a]

				Disk-Scanning Confocal		
Microscope Parameters	Epi-fluorescence	Confocal Point LSM	Confocal Line LSM	Yokogawa (CSU10/22)	CARV[b]	DSU
Supplier/Distributor	All major manufactures	Many: Zeiss, Leica, Olympus, Nikon . . .	Zeiss (LSM510 Live)	(Yokogawa) / PerkinElmer, Solamere Tech. McBain Instruments, Visitec[c]	Atto Bioscience	Olympus
Scan Type	No	Point scan	Line scan	Disk	Disk	Disk
Pinhole/Slit	None	Pinhole or slit	Slit	Microlens + pinhole	Pinhole	Slit
Adjustable pinhole/slit	n/a	Yes	Yes	No	No	Yes
Illumination	Hg or xenon arc lamp	Laser(s)	Lasers (diode)	Laser(s)	Hg or xenon arc lamp	Hg or xenon arc lamp
UV excitation	Yes	Yes, but need expensive laser	Yes (405 nm)	Only specified for 400–650 nm	Yes[d]	Yes
Pinhole or slit size/spacing diameter (μm)	n/a	Adjustable pinhole or slit	Adjustable slit	Pinhole 50/250	Pinhole 70/~250	Slits 13–38/140–400
Disk fill factor	n/a	n/a	n/a	4%	5%–7%	5%–10%
% Transmission pinhole/slit	~100%	~50%	> 90%	~40% with microlens	~5%–7%	5%–10%
Detector	CCD	PMT	Linear CCD	(EM) CCD	(EM) CCD	(EM) CCD
Detector: Max QE[e]	~50%–90%	~10%–20%	~50%–80%	~50%–90%	~50%–90%	~50%–90%
Full image scan rate[g]	n/a (no scan)	~1 fps (faster for ROI)	~120 fps @ 512 × 512	1000 fps	200 fps	~50 fps
Max. z-resolution	(Very poor)	Best	Moderate	Good	Good	Moderate
Cost	Inexpensive	Expensive ($200 K–$400 K)	Expensive (TBA)	Expensive ($100 K–$300 K)	~$50 K	~$35 K
Microscope compatibility	N/A	Usually sold with microscope	Zeiss	Many: inverted or upright	Many: inverted only	Olympus: inverted or upright
Relative space requirements	Small	Variable: medium/large	Medium	Large including laser	Medium	Small
Filter options; Exchangeable?	Standard; yes	Many internal filter options; no	Many internal filter options; no	1–3 filter cubes[f]	3 filter cubes; yes	6 filter cubes; yes

[a] Not an exclusive list and parameters may change.
[b] A CARV2 instrument will have 5× faster scanning and FRAP capacity.
[c] Supplied by Yokogawa (Japan) and distributed by PerkinElmer as part of the Ultraview microscope, Solamere Technology Group, McBain and Visitec as stand-alone or integrated units with lasers, integration software, etc.
[d] Post-disk intermediate optics do not transmit well in the lower UV (cutoff ~370 nm).
[e] Depend on camera/PMT model and spectral response curve (e.g., see Fig. 10.8).
[f] Acquisition speed may be limited by camera speed and/or number of photons collected. Note: When a line is scanned only once (maximum speed), it is possible that information may be lost or duplicated unless sychronization between disk position and camera exposure time is perfect.

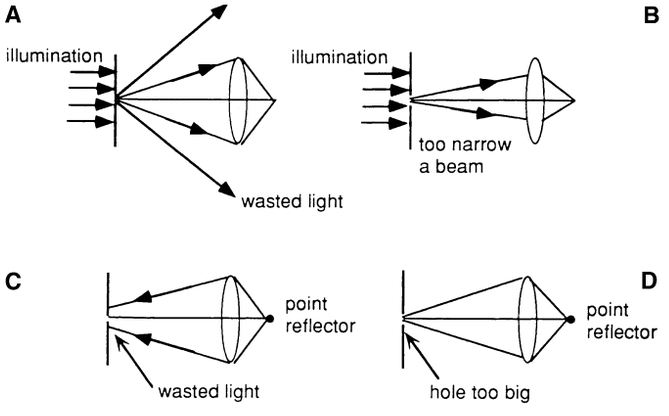


FIGURE 10.2. Ray paths with different pinhole sizes. (A) Pinhole too small wastes transmitted light with too wide a beam. (B) Pinhole too big yields a narrow beam and low effective aperture. (C) Pinhole too small wastes received light. (D) Pinhole too large gives poor definition.

there would be a peak as the focus plane coincided with the dye layer and Eq. 3 would describe the width of this peak. However, this peak would have a very long tail because an amount of light about equal to the square of the gross transmission of the disk would still reach the CCD through the wrong pinhole, even when the dye layer was very far out of focus. It is this tail of diffuse background haze that will limit overall performance whenever one observes specimens that are both thick and heavily stained and the amount of this background is proportional to the transmission of the disk.

Therefore, while Eq. 3 may provide a good estimate of the accuracy with which one can determine the surface height of a highly reflective semiconductor using a disk scanner with small pinholes placed on a sparse grid and a dry objective of relatively low NA, it fails to account for the many important practical matters that affect fluorescence imaging in transparent specimens. As the signal reflected from a semiconductor can easily be $10^5\times$ higher than that produced by a fluorescent specimen, D can be much less than one Airy unit. In addition, as the height variations of the semiconductor are both known and fairly small, it is possible to choose S large enough so that little light reflected from, for example, the highest feature, is sufficiently out of focus to pass through neighboring pinholes when the focus plane coincides with the lowest feature. Last but not least, as the structures of semiconductors tend to be relatively horizontal and opaque, one is usually more interested in determining the location of the outer surface (z-position, the height of peak reflection) than trying to see one feature below another (z-resolution).

However, in biological disk-scanning where the NA is high, the specimens are transparent and the signal levels are so low that $D/S > 0.1$, the fact that Eq. 3 takes no account of light coming through the wrong pinholes is a serious limitation. Let us call this light WP light (for wrong pinhole).

Clearly, the amount of WP light that reaches the detector depends on the staining pattern in the specimen. If the stain is confined to a horizontal plane that is thin in the manner defined above for a semiconductor, then there is little problem. However, because D and NA are now larger and S is smaller, the band of z-heights for which this is true is thinner. As the exact manner in which this plays out is both important to understand if one is to appreciate the optical sectioning properties of disk scanners and is also poorly conveyed by equations, we will attempt a more heuristic explanation.

Figure 10.3(A) shows a red fluorescent point object emitting light in all directions. We will not yet discuss how it is being excited except to note that the process follows exactly the same rules as are described below, except in reverse. Only some of the light leaving the point hits an objective lens having an acceptance half-angle of 45° (e.g., an NA 1.0 lens). The broken black horizontal line represents a disk with pinholes in it. Although the actual disk is located in the intermediate image plane on the other side of the objective, we can see its masking effect just as well in any image plane, including the focus plane in the specimen as shown here. In fact, it is rather instructive to imagine that the pinhole is sampling the light field near the focus plane.

In Figure 10.3(A), the point object is seen lying in the focus plane and, as we have assumed that D is 1 Airy unit in diameter (i.e., ~0.5 µm, when referred to the focus plane), and that essentially all of the light from the central maximum of the Airy disk that represents the point object goes through the pinhole and proceeds (via optics that are not shown) to the CCD. Figure 3(B) shows the layout of the disk viewed *en face*. The D/S is about 1/5, implying a S spacing of about 2.5 µm and a total transmission of ~4%, about normal for many disk scanners used in biology.

When the stage moves down, the point object drops below the focus plane, and the amount of light going through the central pinhole in the disk drops [Fig. 10.3(C)] because the light leaving the point object at any angle that the objective can accept now mostly strikes the bottom of the disk, as is represented by the pink disk in Figure 10.3(D).

When the point object is 2.5 µm from the focus plane of the NA 1 objective, the defocus equals S and some of the light from the point begins to pass through the first ring of neighboring pinholes, but not very much. In simple terms, 6× more light will now reach a CCD pixel that is focused on the wrong pinhole than reaches it through the proper pinhole. However, the light from the object that, at focus, was concentrated into a spot 0.5 µm in diameter is now spread over one with five times the diameter and 25× the area and, as the same diminution in intensity is occurring on the excitation side, the number of fluorescent photons/square centimeter at the plane of the disk is now 625× lower than it was at focus. As the pinholes are laid out as equilateral triangles, one can see from Figure 10.3(B) that only about D/S of the light striking the annulus with radius S and thickness D actually passes through the disk. This fraction would be much higher were we referring to an array of parallel slits.

As the point moves farther out of focus, the absolute number of photons reaching the CCD from the point continues to diminish until some light starts going through the ring of second neighbors, about 4 to 5 µm away from the focus plane.

We can see from Figure 10.3 that if the NA is higher, this same process will occur at lower defocus values, and vice versa.

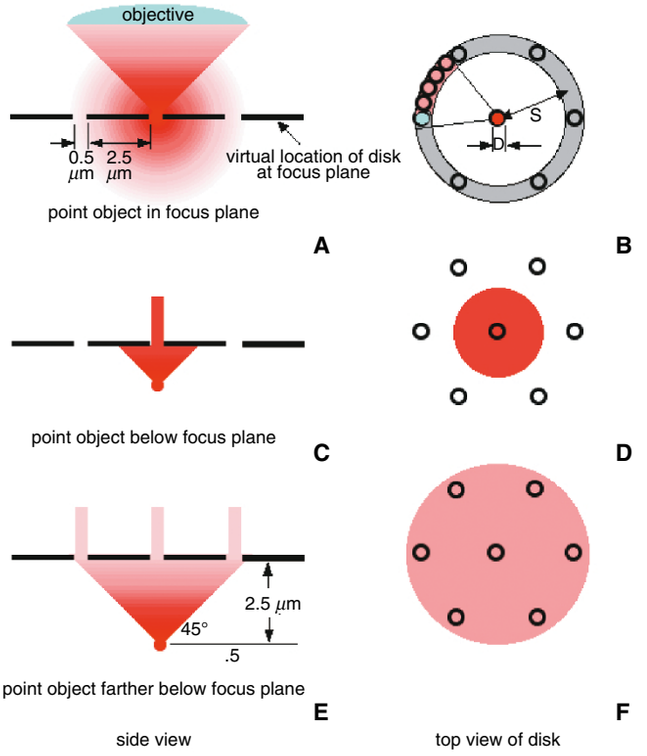


FIGURE 10.3. Diagrams showing how light originating from out-of-focus planes passes through adjoining pinholes to create a haze level and how this process is affected by the geometry of the pattern of the holes in the disk and the convergence angle of the objective, as described in the text.

So far so good. But what if instead of having a point object, we have an unpoint, a black hole in a sea of dye. When the unpoint is in the focus plane, a pinhole that should measure zero will not do so because other beams will be exciting dye above and below the specimen and some of this light will be out-of-focus enough to come through the pinhole that should be dark. Long before the dark point is distance S from focus, it will become invisible. The geometry that helped reduce the brightness of the out-of-focus point object by 625× no longer works because, beyond a defocus of $\pm D$, the diminution in intensity that occurs as the diameter of the cone of light from a single point is supplemented by brightness from the now-overlapping cones of fluorescent light from nearby holes.

Although Figure 10.3 discusses round apertures, similar reasoning can be applied to linear ones, with the exception that, when the defocus equals D, a larger fraction of the light will go through the next slit than went through the six nearest pinholes. This fact is often taken as evidence that "slit-scanners do a worse job of optical sectioning than point-scanners." However, if we keep the transmission of the two disks the same, the D/S of a slit disk will be smaller and, assuming that we choose the same D value based on the resolution of the objective, S will be larger and in the final situation stray light situation will be much the same as with pinholes. Yes, a greater fraction of the light goes through the next slit but now this will not happen until the defocus is greater and, consequently, the light intensity in photons/square centimeter, is lower. Indeed, as a slit scanner with a larger S value has a deeper band of z-values for which no overlap occurs, it could be said to provide better optical sectioning.

Clearly, any curves plotting the z-resolution of disk scanners inherently include assumptions about the stain distribution in the specimen, not only its thickness and pattern, but in the case of some line scanners, also its orientation in the xy-plane. In other words, any simple statements regarding the optical sectioning abilities of disk scanners that fail to discuss the nature of the specimen do not convey much useful information to the biologist.

Figure 10.3 shows that

- For specimens in which stained structures are confined to a thin layer, or for thicker specimens in which the stain is concentrated in clumps that represents only a small minority (say <1%) of voxels, disk scanners can approach the optical sectioning performance of single-beam confocals.
- Choosing a larger S increases the zone of best sectioning performance but also reduces signal levels.
- Specimens composed of heavily stained structures that extend over a range of depths will pose more problems.
- In the final analysis, optical sectioning performance has more to do with the transmission of the disk than with whether the apertures are slits or pinholes.

As will be discussed below in the section on electron multiplying CCD (EM-CCD), it is significant that all geometries will permit more light from objects that are far from the focus plane to reach the detector than would be the case with single-beam scanners.

TYPES OF DISK-SCANNING CONFOCALS

General Considerations

In disk-scanning microscopes, the scanning disk is positioned in an image plane. For all systems, but especially for those using reflected or backscattered light, it is important to prevent excitation light from reflecting off the disk and reaching the detector. Although most of the 90% to 99% of the light that does not pass through the disk (except the Yokogawa design) is absorbed by it, the amount reflected from even the blackest surface is immense compared with that returning from the specimen. This reflected light can be eliminated using barrier filters as long as the system is used to detect a fluorescent signal but other techniques must be used when the microscope is used to collect backscattered or reflected light. The disk-scanning units are often attached to the side port (camera) or back port (lamp) of the microscope and either a mercury/xenon arc lamp or laser fiber-optic (Yokogawa) is attached to the unit. A detailed comparison of the hardware specifications of common, commercial, epi-fluorescent, confocal LSM and disk-scanning microscopes is shown in Table 10.2.

Disk Scanners for Backscattered Light Imaging

The Tandem-Scanning Confocal Microscope

The earliest design of a disk-scanning confocal microscope used a tandem pinhole design (Petráň *et al*., 1968, 1985) in which pinholes arranged on the disk in a symmetric pattern of interleaved right- and left-handed Archimedian spirals, illumination and detection occur in tandem, through separate pinholes on opposite sides of the disk. The illumination entering one pinhole goes through the objective, and light reflected from the sample is optically rerouted via a set of mirrors and a pellicle beam-splitter to a second set of conjugate pinholes located on a diametrically opposed spiral (see Fig. 10.4). This convoluted light path was used to prevent glare reflected from the disk from reaching the ocular. This was a

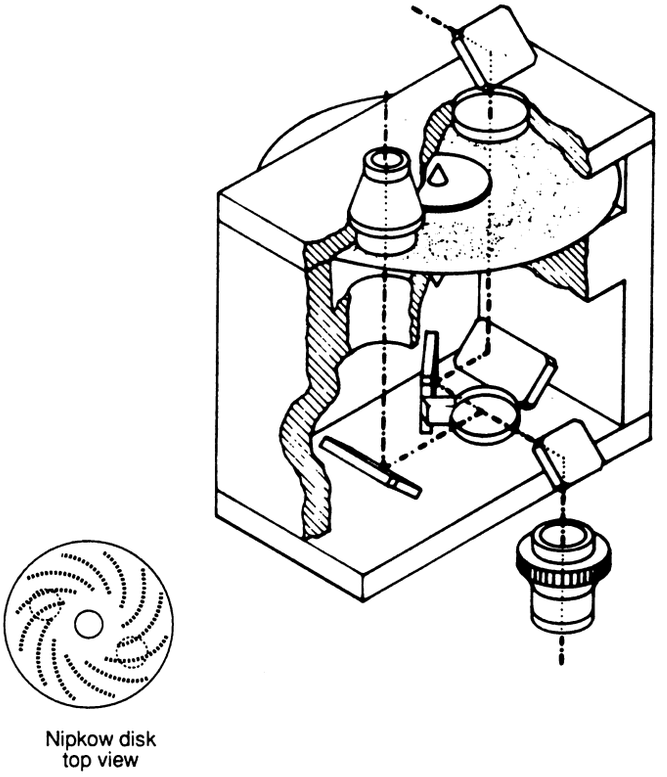


FIGURE 10.4. The tandem scanning reflected light microscope (Petráň *et al*., 1985).

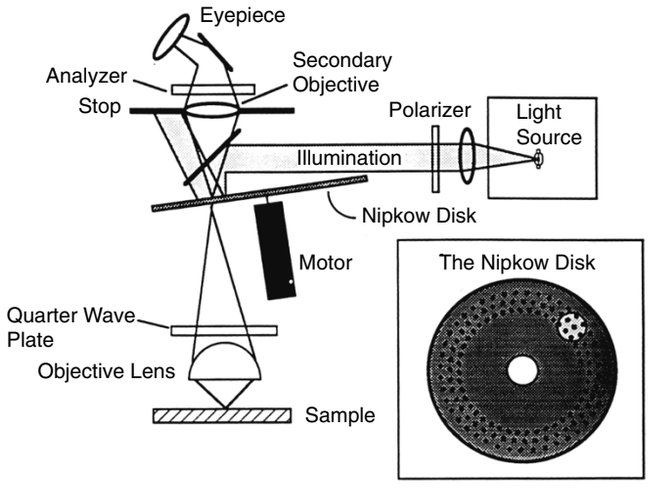


FIGURE 10.5. The single-sided scanning confocal light microscope (Xiao and Kino, 1990).

tremendous advantage when looking for weak backscattered-light signals but the difficulty of making and orienting a dichroic mirror on the surface of the pellicle beam-splitter made this design difficult to use for fluorescence. Not only was it hard to change the beam-splitter without ruining the alignment, but the intensity was so low that one still needed to make long exposures, thereby negating the advantages of the high scan speed. The other major limitation of this microscope was its mechanical complexity and the difficulty of properly translating the mirrors in three dimensions and tilting them along two axes. In fact, scan lines were always visible. A commercial version of this microscope using 40 to 70 micron square pinholes was produced by Noran (now Thermo-Noran, Middleton, WI, model TSM, now discontinued).

Single-Sided Disk Scanning Confocal Microscope

The single-sided disk-scanning confocal microscope designed by Gordon Kino (Xiao and Kino, 1987; Xiao *et al*., 1988; Lichtman *et al*., 1989) uses the same set of pinholes for illumination and detection (Fig. 10.5). It has a simple optical path that incorporates a number of features to minimize glare from the disk. The holes are etched in a polished black chrome coating evaporated onto a quartz disk and this disk is placed in the intermediate image plane at a slight angle so that excitation light is reflected off the optical axis to where it can be trapped by a beam stop. For BSL imaging, the input light is polarized and after being transmitted through the disk it passes through a quarter wave plate in front of the objective lens so as to produce circularly polarized light. Light reflected by the specimen undergoes the reverse effect and an analyzer placed in front of the eyepiece/camera selects against light reflected from the disk and passes light reflected from the specimen.

The disk on Kino's microscope contained ~200,000 pinholes of 25 micron diameter and spun at ~2000 rpm, giving a scanning speed of up to 700 frames/s. As the pinhole is near the optimal diameter for use with a high magnification, high NA lens, the resolving power of this system is similar to that of a single-beam confocal LSM, but much faster! Köhler illumination (Born and Wolf, 1998) is used so that standard epi-fluorescent (or bright-field) imaging can be achieved by removal of the disk. Important optimization parameters include adjusting the mercury (or xenon) arc so that illumination is uniform over the field of view. An aperture stop limits stray light and a field lens, positioned below the disk, decreases vignetting. For fluorescent imaging the 50/50 beam-splitter can be replaced by an appropriate fluorescent filter cube, as in epi-fluorescent microscopy.

Disk Scanner Designs for Use in Fluorescence

Because of its simplicity, the single-sided disk scanner is by far the most popular style of confocal disk-scanning microscope. Tricks such as tilting of the disk and the use of anti-flex techniques are unnecessary because modern dichroics and barrier filters can prevent almost all excitation light from reaching the CCD. Several commercial systems suitable for fluorescent imaging use variations of this design.

CARV, DSU, and Other Disk-Scanning Confocal Microscopes

Early commercial, fluorescent, single-sided disk systems were sold by Technical Instruments system (K2-Bio) and Newport Systems (VX100 confocal adaptor).[15] In the former, the upper part of a standard microscope was replaced with the disk and illumination system. The later system is based on an instrument developed by Jeff Lichtman (Lichtman *et al.*, 1989) and was sold as an attachment for an upright microscope. Briefly, a 4× low NA lens is used to image the disk scanner, mounted on a secondary external stage, onto the CCD. The secondary stage contains compact intermediate optics and a high NA main objective is used to image the specimen onto the disk. In both systems, the disk had separate tracks with different sized pinholes or slits so as to match the magnification of the objective or light budget of the application, but only the KCS Bio used normal, highly corrected microscope objectives under optimal optical conditions. The CARV (Boston, MA; Fig. 10.6; Table 10.2) uses a mercury arc lamp for excitation and mounts onto the left-side port of an inverted microscope. It uses 60 µm diameter pinholes at ~250 µm spacing, scans at 200 fps, and has ~5% to 8% transmission. As these pinholes are well above the Airy limit of even the highest magnification lens, *z*-resolution is moderate even when one utilizes the 1.5× auxiliary magnifier now found on some microscope stands to change a 100× objective into one with 150×. The user can see the live, confocal image through a second binocular head, but this system is relatively bulky and does not work with upright microscopes. The CARV2 with a faster scanning speed (1000 fps), automated filters, and the ability to do **FRAP** by switching the Nipkow disk with a photobleaching slit, has just been introduced.

A new disk-scanning unit, the **DSU** by Olympus (Figs. 10.7 and 10.8; Table 10.2) uses a **multi-slit** design in which half the slits are horizontal and the other half are vertical on the disk. The user can switch between five **different disks** (DSU1–5) each having a different fill factor (5% to 10%) and slit width (13 to 38 µm) for use with both low and high magnification objectives. The confocal head is compact, but as it attaches to the back Hg lamp port of either inverted or upright Olympus microscopes, direct viewing through the eyepiece is not possible. It has an adjustable field stop and, as the intermediate optics are part of the conventional illumination path, it is fully UV compatible. As shown in Figure 10.8 (bottom), $S > 8s$ (12.5% fill factor), otherwise the resolving power decreases substantially.

[15] See schematics in Appendix 2 of the second edition.

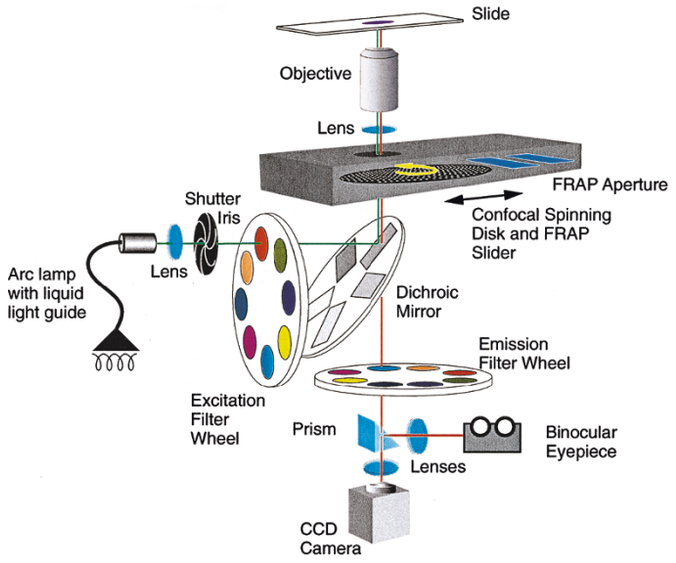
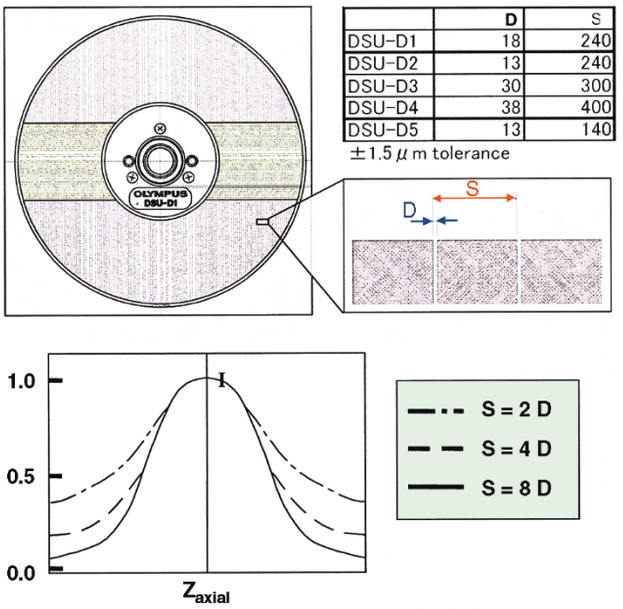


FIGURE 10.6. CARV (Atto Bioscience) disk-scanning confocal microscope. Schematic of the CARV2 optical path (BD Bioscience), a pinhole-based disk-scanning confocal system. (Image adapted from that provided by BD Bioscience.)



	D	S
DSU-D1	18	240
DSU-D2	13	240
DSU-D3	30	300
DSU-D4	38	400
DSU-D5	13	140

±1.5 μm tolerance

FIGURE 10.8. Characteristics of Olympus DSU slit-based confocal disk and importance of a low fill-factor for adequate axial resolution. (Top, left) Layout of the slit disk that is about the size of a CD. Approximately half the slits are horizontal (green) and half vertical (red) so that when rotated the lateral resolution is matched in the *x*- and *y*-axis. (Top, right) Blowup of a region of the disk. The slit width (*D*) and distance between slits (*S*) are indicated and a table shows the different *D* and *S* (in micrometers) of interchangeable disks. (Bottom) Plots show that axial resolution worsens as *S* decreases (for a fixed *D*) and in practice $S > 8D$ (12.5% fill factor). (Images and data adapted from those kindly provided by Olympus.)

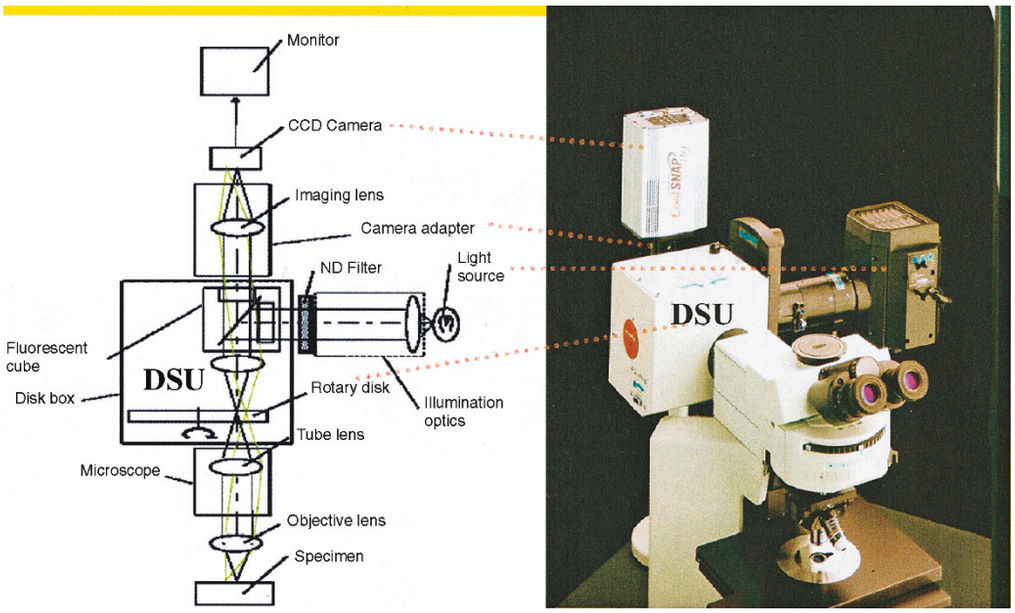


FIGURE 10.7. Olympus disk-scanning unit confocal instruments. (Left) Schematic of the optical path. (Right) Picture of the DSU (compact box) mounted on an upright microscope (can also be mounted on an inverted Olympus microscope). (Images adapted from those provided by Olympus USA.)

The Yokogawa Microlens — An Illuminating Approach

The **CSU10/22** disk-scanning head design by **Yokogawa** Electric (Japan) is an innovative twist on the single-sided disk-scanning fluorescence confocal microscope that greatly improves the excitation light budget (Fig. 10.9). Yokogawa focuses the light from a beam-expanded laser onto a disk containing **20,000 microlenses**. This disk is mounted on the same axis as the pinhole disk and in such a way that each lens focuses its light onto a different 50 µm diameter pinhole (Fig. 10.9, blue spindle). As the spacing interval between pinholes (pitch) is 250 microns, the excitation transmission would be only 4% without the microlens. With the microlens, the total **transmission through both disks is ~40%, an order of magnitude improvement** (Tanaami *et al.*, 2002). Thus, even for poorly stained samples there is adequate light.[16]

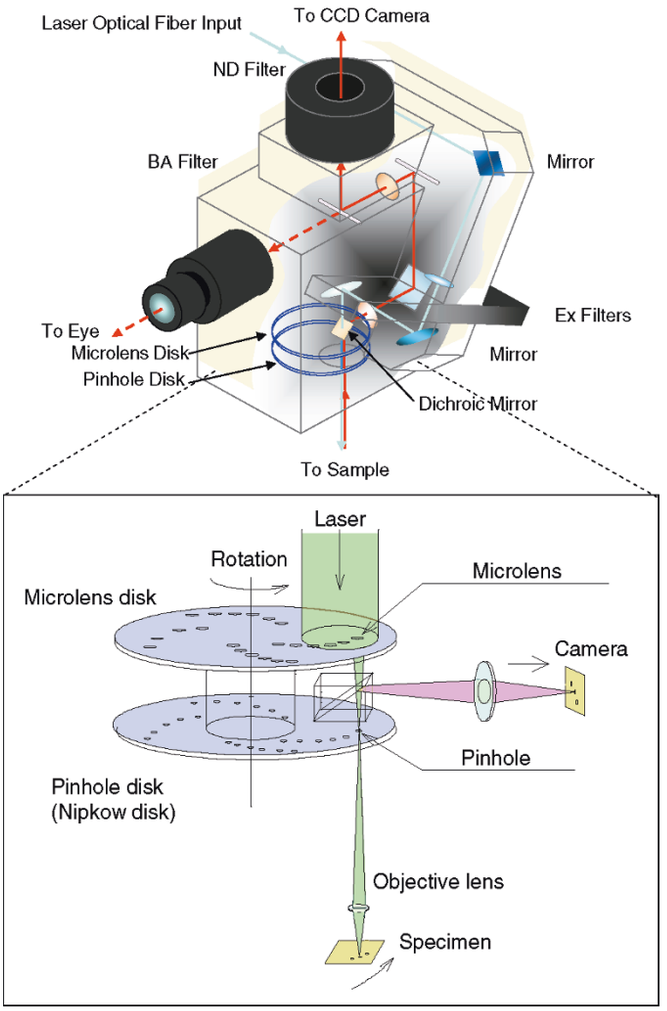


FIGURE 10.9. Schematic of Yokogawa CSU-10/22 spinning disk. Yokogawa has a microlens array top (blue disk) that focuses excitation laser light (green) onto 20,000 pinholes in a Nipkow disk located in an intermediate image plane, illuminating the sample. Emitted light (red) returns through the same pinhole and is reflected by a dichroic pellicle mirror positioned between the microlenses and the Nipkow disk and is then focused onto the camera. The positioning of the dichroic ensures that excitation light scattered by the disks is not detected. (Schematics adapted from those kindly provided by Yokogawa Electric Corporation, Japan.)

The disk rotates at 1800 to 5000 rpm, depending on the model (CSU-10 vs. CSU-21/22, respectively) and the hole pattern scans 12 frames in each rotation. This gives a theoretical maximum frame rate of 360 to 1000 fps, assuming that the camera will read out this fast and that enough signal can be produced in such a short period. In practice, operation at anything above 100 to 200 fps requires careful synchronization between the disk and the camera so that all holes move an integral number of frame crossings. Failure to do so will cause streaking in the image. Moiré effects can occur between the curved scan lines of the pinhole and the rectilinear layout of the CCD, especially at short exposure times, and this problem is worse when the CCD uses frame-transfer readout (Chong *et al.*, 2004).

At any one time ~1000 pinholes (6% of total) are illuminated. Direct viewing is possible through a monocular but laser safety concerns have eliminated this feature in some systems.[17]

A dichroic beam-splitter mounted between the two disks directs fluorescent light emerging from the pinholes to the CCD camera via a projection lens. The CSU-10 uses only a single filter cube that passes only up to three laser lines but this can be removed with some difficulty; the CSU-21/22 accommodates up to three dichroics and three emission filters but these must be installed at the factory and can not be changed. Current filters sold in the PerkinElmer version of the Yokogawa[18] system include GFP, CFP/YFP, GFP/Texas red/Cy5. Cross-talk can be an issue and thus an additional wheel of barrier filters is desirable. Several companies sell Yokogawa spinning disks units individually or as a complete package with hardware [lasers, acousto-optic modulator (AOM), cameras, *z*-piezodrivers, etc.] and software.[19]

New Fast Line Scanner — Zeiss LSM510 LIVE

Although not a disk-scanning system, the new Zeiss, LSM5 LIVE, line-scanning confocal microscope may soon emerge as a competitor to existing disk-scanning confocals. A schematic of the LSM5-LIVE is shown in Figure 10.10 and some parameters are included in Table 10.2. The largest departure from the popular point-scanning LSM510 is that the system scans a **line** of excitation over the focus plane and then detects the signal in parallel using a **1 × 512 pixel linear-array CCD**. The Gaussian beam from the laser is transformed into a plane of parallel light rays using anamorphic optics. This line of light reflects off a narrow, reflective patch in the center of an otherwise clear beam-splitter, called the Achrogate. The light sheet reflected by the Achrogate strikes a galvanometer scanning mirror located in an aperture plane, so that as it rotates, the line of light is scanned over the specimen in a direction perpendicular to its length. The objective focuses this line of light into another line, perpendicular to the first, at its focus plane. Light leaving the specimen at any angle that strikes the

[16] The total illumination power depends on the power of the laser line (e.g., 5–50 mW), its coupling efficiency to the single-mode fiber (~50%), and transmission through the beam expander, microlens, and pinhole (~40%). Light striking the 170 × 120 µm field covered by a 100× objective, should be in the range of 1–10 mW.

[17] PerkinElmer Ultraview 5-line instrument.

[18] We have extensively tested the Ultraview 5-laser line spinning disk system from PerkinElmer and, with exception of a few bugs in the file nomenclature, the hardware is well integrated and easy for new users to use. The system from Solamere offers more flexibility of setup configuration. If one integrates one's own system, attention should be paid to camera synchronization and the CSU/22 with a variable speed disk should facilitate this.

[19] Other purveyors include: Solamere Technologies, Salt Lake City, UT; Visitech, Sunderland, UK; Andor Technologies, Belfast, UK, etc.

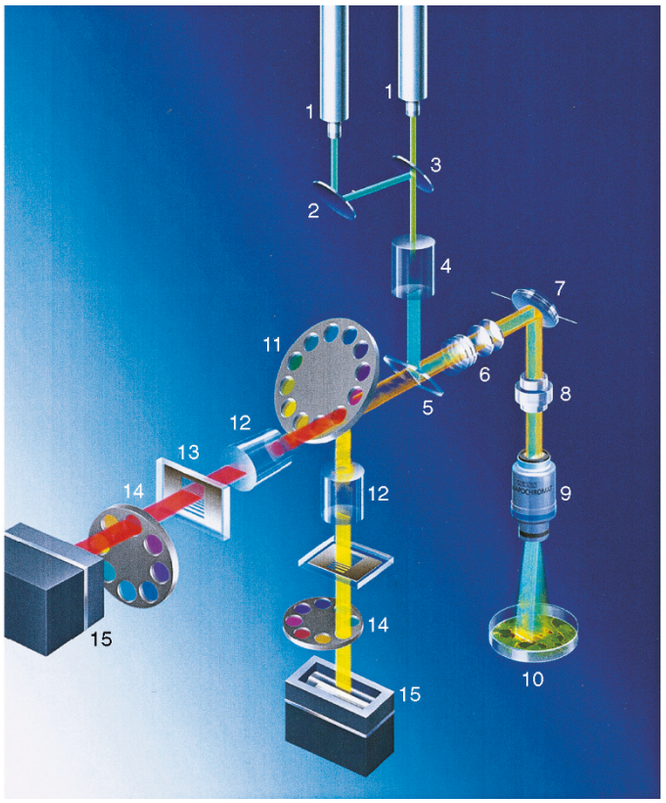


FIGURE 10.10. Schematic of Zeiss LSM5-LIVE, line-scanning confocal. 1, Laser fibers; 2–3, mirrors; 4, linear beam shaper; 5, Achrogate; 6, zoom lens; 7, scan mirror; 8, tube lens; 9, objective; 10, specimen; 11, dichroic wheel; 12, lens; 13, adjustable slit mask; 14, barrier filter; 15, linear 1 × 512 pixel, CCD. (Schematic kindly provided by Carl Zeiss Inc., Jena, DE.)

objective leaves it as a round beam, most of which does not strike the reflective patch and proceeds toward the detectors. It is then separated into two fluorescent channels by a dichroic beam-splitter and each channel passes through a "camera" lens that focuses the round beam to form an image of the illuminated line on the specimen at the surface of a glass aperture plate. The metallized reflective layer on the aperture plate is etched so as to form a number of slits having different widths. Normally, one would choose a slit having a width of 1 to 2 Airy units for the objective in use. Only the light passing the slit is transmitted to the linear CCD detector. The advantages of this system seem to be:

- Parallel illumination of 512 pixels increases the rate that data can be accumulated without reaching singlet-state saturation.
- Galvanometer scanning in a single direction increases the maximum frame rate to that set by the readout speed of the detector.
- The Achrogate reflects all the laser light, regardless of wavelength, but obstructs only about 5% of the returning signal.
- The detection slit can be adjusted independently of the illumination system to match the properties of the objective and the specimen.
- The linear CCD has a higher QE than any PMT and, if the present version is eventually replaced with an EM-CCD version (as discussed below), the noise level will be similar.

The trade-off in *xy*- and *z*-resolution is the same as for other laser-based slit-scanners. While the design is new and intriguing, more details on light efficiency and sensitivity are needed as is testing on dim fluorescent samples head-to-head with spinning disks.

NEW DETECTORS — A CRITICAL COMPONENT

A great benefit of disk-scanning confocals is their ability to produce a real-time, 2D **confocal image directly**. A PMT senses a signal that varies in time, not position, and requires a computer to assemble a viewable image. The ability to look down an eyepiece (depending on the model) and see a live image that permits you to select the best part of the specimen is a great convenience. Our eyes are exquisite detectors with an excellent dynamic range and ability to detect fine detail and motion. Although their spectral range is limited to ~400 to 600 nm and the QE is not very good (<10%), if the sample is bright enough, your eyes are the quickest way of finding a good region of the specimen.

Standard, front-illuminated **CCDs** have a QE of ~20% to 65% in the green, while with more expensive back-thinned CCD detectors, QE can approach **95%**, **far superior to a PMT**. Most standard, scientific CCDs have a 12 to 16 bit dynamic range and a noise floor of ± 5 to ± 15 electrons/pixel, depending on read speed and other design parameters. As a result, weak signals, such as those from very dim samples or single molecules, are lost in the readout noise.

A CCD camera can have good QE and still have poor noise performance; it turns photons into photoelectrons efficiently, but this signal is then obscured by the three sources of background noise: shot noise, dark charge noise, and electronic read-noise.[20] **Shot noise** is unavoidable and is due to the random Poisson statistics of collecting photons. **Dark noise** is the square root of the charge that leaks into the pixel during the exposure and depends exponentially on the CCD operating temperature (it is halved for every 8°C of cooling). **Electronic noise** increases with the capacitance (area) of the read node and the square root of the readout speed. The readout noise of a good scientific CCD is < ±10 electrons at a 1 MHz+ readout rate (see Table 10.3). This is much too high to detect single photons or the low light levels from a confocal scanner, where many pixels image voxels of the specimen contain no dye. (For more details about CCDs, see Appendix 3).

Image Intensifiers

For the last two decades, the detector of choice for fast imaging of low intensity dyes (e.g., single molecules) coupled an image intensifier with a CCD readout. In an image intensifier, photons strike a photocathode, releasing free electrons into a vacuum. Each electron is amplified usually by impact multiplication in a microchannel plate, producing a cloud of ~10^6 electrons that is then accelerated onto a phosphor layer where each one gives up its energy by producing an even larger number of photons. These photons are then conveyed to the CCD by a fiber-optics plate. The gain of the intensifier is so high that the signal in the CCD output corresponding to a single photoelectron is greater than the CCD readout noise.

The QE of an image intensifier is determined by the material used for the photocathode. The most modern cathodes use GaAsP and have an intrinsic QE of up to 30% to 40%, well into the red

[20] All detectors, including PMTs, suffer from this noise.

TABLE 10.3. Relative Parameters of CCD and EM-CCD Detectors

CCD and EM-CCD[a] Detectors	Traditional CCD: Orca ER[b]	EM-CCD: DV887BV	EM-CCD: DV860BI	EM-CCD: DV885VP
Chip: Front or back illuminated	Front	Back	Back	Front
Camera manufacturer and model	Hamamatsu (C4742-80-12AG)	Andor E2V CCD 87	Andor E2V CCD 60	Andor TI TC285
Active pixels	1344 × 1024	512 × 512	128 × 128	1000 × 1000
Pixel size[c]	6.45 µm	16 µm	24 µm	8 µm
Image area	8.67 × 6.6 mm	8.2 × 8.2 mm	3.1 × 3.1 mm	8.0 × 8.0 mm
Raw QE	70% @ 500 nm	92% @ 575 nm	92% @ 575 nm	>65% @ 600 nm
Readout speed	14.7 MHz	10, 5, 3, 1 MHz	10, 5, 3, 1 MHz	35, 27, 13, 5 MHz
Maximum cooling	–30°C	–90°C	–90°C	–90°C
Maximum EM gain (actual)	1	×1000	×1000	×1000
Dark current (minimum)	0.003 e/p/s	0.0035 e/p/s	0.004 e/p/s	0.001 e/p/s
Read noise (r.m.s.)[d]	8e @ 14.7 MHz	62e @ 10 MHz <1e with EM	60e @ 10 MHz <1e with EM	25e @ 35 MHz <1e with EM
CCD clocking	Multi-phase	Multi-phase	Multi-phase	Virtual phase
Vertical shift speed (per row)	Variable	3.4–6 µs variable	0.1–6 µs variable	0.1–6 µs variable
Maximum full frame rate	9 fps	>34 fps	>500 fps	>31 fps
Maximum frame rate (4 × 4)	>27 fps	>130 fps	>1300 fps	>100 fps
Binning	2 × 2, 4 × 4, 8 × 8	Full serial and parallel (vertical)	Full serial and parallel (vertical)	Full serial and parallel (vertical)
Fill factor	~75%	100%	100%	100%
Single pixel full well	18,000e	220,000e	200,000e	40,000e
Dynamic range of digitizer	2,250 : 1	12 bits @ 10 MHz >15 bits @ 1 MHz	12 bits @ 10 MHz >15 bits @ 1 MHz	12 bits @ 35 MHz 13 bits @ 5 MHz
A/D bit depth[e]	12 bits	14/16 bits	14/16 bits	14 bits
CCD type & mount	Progressive scan interline CCD with microlens: C-mount	Masked w/full frame transfer; C-mount	Masked w/full frame transfer; C-mount	Masked w/full frame transfer; C-mount

[a] EM-CCD cameras are sold by several companies including Andor (shown here), Hamamatsu, Roper, PCO, and others. Many use identical chips from E2V or Texas Instruments, however, other properties such as chip cooling temperature, vacuum and sealing, amplifier, hardware (e.g., TTL integration), software control and integration, internal shutters, etc., can vary considerably between manufactures and can strongly affect camera and versatility. Data kindly provided by Colin Coates at Andor Tech. (Belfast, Northern Ireland). All specifications based on manufacturers claims.
[b] This is a popular high readout speed, scientific CCD and chosen as a respective point of reference. There are hundreds of CCDs to choose from and specifications will vary considerably and are occasionally optimistic.
[c] Cameras with 18 µm pixels will require the use of a 2× phototube to produce Nyquist-sampled images with 40× and 60× high resolution objectives.
[d] Manufacture specifications; note often some of this bit depth is empty and the true dynamic range, which is determined by the ratio of the full well depth over the noise floor of the camera, is considerably smaller (e.g., if in the Orca ER 18,000e/8e = 2250, while $2^{12} = 4096$).

end of the spectrum. However, as good red performance often goes along with high dark current unless the photocathode is cooled, many intensifiers use the S-20 photocathode material commonly used in PMTs and having a QE at least 2× lower. In addition, as only about 50% of the photoelectrons reaching the micro-channel plate (MCP) are actually multiplied at all, and as the amount by which each of the remainder are actually amplified varies greatly (creating multiplicative noise), the effective QE is about half that of the photocathode itself. Finally, because both the MCP and the process of accelerating the charge onto the phosphor to make light, involve loss of spatial precision, the resolution of the entire camera is substantially less than would be indicated by the array size of the CCD.

On the other hand, the intensified CCD is the only common image sensor that can be **gated** on and off in nanoseconds,[21] permitting the extremely short acquisition bursts needed in specialty applications such as fluorescent lifetime imaging (FLIM).

Intensifier Advantages (+) and Disadvantages (–):

(+) Noise level very low; able to "see" signal from a single photoelectron.
(+) Fast gating possible.
(±) Effective QE of 10% to 25%.
(–) Pixel blooming of bright signals can occur.
(–) Scintillation or hot pixels can occur.
(–) Photocathode can be permanently damaged by brief overexposure to light.

On-Chip Electron Multiplying Charge-Coupled Device

Recently, the problem of increasing the signal from a single photoelectron above the noise level of the CCD-read amplifier has led to the perfection of on-chip **electron multiplication (EM)**. Although high-gain (10^8×), avalanche electron multiplication in a reverse-biased semiconductor photodiode has been used for some time to turn a single photoelectron into a current pulse large enough to be easily measured by electronics, efforts to apply this technique to the output of a CCD failed until recently.

The main distinction between an EM-CCD and a normal, scientific CCD is the **addition of a second horizontal register, called the gain register**, between the chip and the read amplifier (see Fig. 10.11, top). In the EM gain register, a higher voltage on one of the three sets of the charge-transfer electrodes sets up electric fields to produce, not the high gain impact multiplication found in the avalanche photodiode, but very low gain.[22] By then repeating the

[21] The camera readout time is much longer (e.g., <100 fps; Kindzelskii and Petty, 2003).

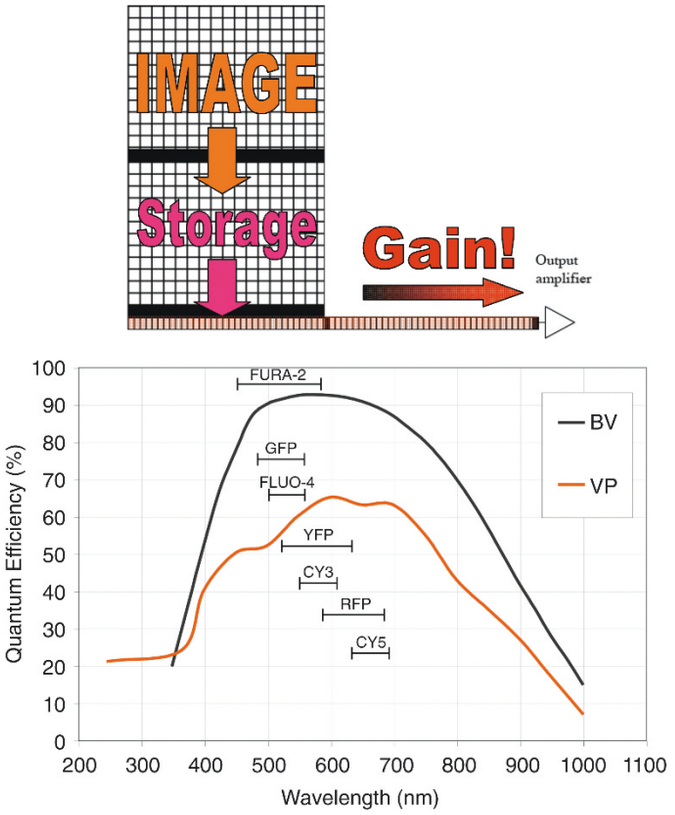


FIGURE 10.11. (Top) Anatomy of an electron multiplying CCD (EM-CCD) chip. Illumination of the imaging register (orange), read register (pink), and horizontal, readout register is to the same as any frame-transfer CCD chip. The main addition is an electron multiplying (EM) gain register (in red) before the output amplifier. (Bottom) Raw, spectral response curves of *back*-illuminated visible (*B*V) and *front*-illuminated visible (*F*V) EM-CCD chips. The emission wavelengths of some common dyes are indicated. (Data kindly provided by Colin Coates at Andor Tech.) When these chips are used with the EM register activated, the effective QE is only 50% of that shown.

process 500 or 1000 times over a line of many pixels, a gain of more than 1000 can be obtained. This makes the signal from even one photoelectron easily visible above the noise of the CCD read amplifier, even one operating at a very high read speed.[23]

With read noise effectively absent, the main remaining noise sources are dark current and clock-induced charge (CIC). Dark current can be substantially reduced by cooling the chip with a multi-stage Peltier cooler. At –80°C spurious dark current and CIC signals are reduced to about one count in 250 pixels. CIC is caused when lattice electrons are pulled into the valence band by the charge transfer process. Unmeasurable before the advent of the EM-CCD, CIC is now an important noise source that can be reduced somewhat by carefully shaping the charge transfer control pulses or made slightly worse by using back-thinned chips.

Amplifying the signal "on-chip" is appealing as it reduces the number of components and one can take advantage of the good QE of the CCD. As the signal from each pixel is amplified separately, the spatial resolution (MTF) of the EM-CCD is identical to that of the same CCD chip with the electron-multiplier turned off.

There is, of course, a price to pay and the price is increased multiplicative noise. While in a normal CCD, each photoelectron is counted the same, because of the statistical rules governing the impact ionization process in the EM-CCD, some electrons are amplified much more than others. As the noise term describing this process is of the same form as Poisson noise, and as such terms are "added" as the square root of the sum of the squares, the overall effect is to increase the "Poisson" noise level to 1.4× what it should be based on the number of photoelectrons actually produced. As the only way to reduce Poisson noise 1.4× is to count twice as many photoelectrons, it is perhaps easiest to think of the EM-CCD as having essentially no read noise but operating as though the effective QE were only 50% as high as it would be were the same CCD used without the electron multiplier. This fact must be remembered when viewing raw EM-CCD QE specifications.

Electron Multiplication Charge-Coupled Devices and Disk Scanners[24]

How do EM-CCDs improve disk-scanning confocal imaging? Good resolution and QE are important, but single-photon sensitivity means that the EM-CCD can detect very low signals when a normal CCD would only read noise. This is important not only because disk scanners without microlenses are light starved (e.g., it is like using a 95%–98% neutral density filter on your WF fluorescence system), but also because in a selectively stained specimen, by far the most common voxel intensity is zero and the EM-CCD measures zero very well.[25]

Figure 10.12 shows that even using a disk scanner and a back-thinned 90% primary QE EM-CCD, the exposure time for adequate S/N is significant (150 ms). Were a normal high quality CCD to be used instead, ~3- to 5-fold longer exposures would be needed for similar S/N. Even if one has enough light to use a normal CCD, using a more sensitive detector allows one to use less excitation and produce less photobleaching.

Currently, EM-CCD chips are manufactured by E2V (Enfield, UK) and Texas Instruments (Houston, TX) and are used in cameras from several companies: Andor, Hamamatsu, Roper, PCO, Red Shirt, and others. Several different EM-CCD chips exist and one should match the QE, pixel clock rate, pixel size, well depth, and total chip area to the biological process being investigated (see Table 10.3). For fast imaging, a smaller chip (e.g., 256 × 256 pixels) will provide increased frame rate. At present, all the available chips use full-frame transfer. While good for QE, the fact that the charge pattern moves past the image as it proceeds to the read register can cause some streaking and moiré effects with the scan lines of disk scanners even when fast vertical transfer is used (Chong *et al*., 2004). This can be avoided if EM-CCD chips incorporating interline transfer appear because such chips permit electronic shuttering at very high speed. However, unless such chips are also fitted with micro-lens arrays, these will pay a price in fill-factor and at least exhibit 2× lower effective QE.

Our tests of the Olympus DSU disk-scanning system have shown that EM-CCDs can make the difference between getting an acceptable image and seeing nothing because the signal level is below the noise threshold of our normal CCD. In addition, it

[22] The gain depends on the temperature and the exact voltage applied to a special set of charge transfer electrodes in the gain register, but is commonly about 1%/transfer, that is, a charge packet of 100 electrons would, on average, become 101 electrons after one transfer, or again on average, a single electron would become two electrons after about 100 transfers.

[23] The new chips will operate up to 35 MHz or 140 fps for a 512 × 512 array.

[24] See discussion at http://www.emccd.com.

[25] However, because of the reduction in effective QE the normal CCD begins to outperform the EM-CCD when the signal level gets much above about 100 photons/pixel. The exact crossover point depends on the read speed as this seriously changes the read noise of conventional CCDs.

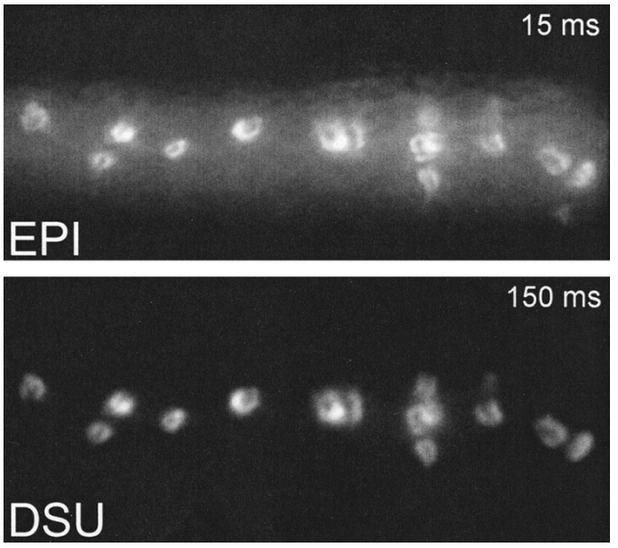


FIGURE 10.12. Disk-scanning slit confocal improves optical sectioning and S/N compared to epi-fluorescent, but requires longer exposure times. Lamprey neurons were microinjected with fluorescent-tagged phalloidin to label axons (ring-like structures). A single 15 ms exposure epi-fluorescent image was taken using an Olympus BX-51 microscope (1.1 NA 60× water-immersion objective) and an Andor 887, back-illuminated EM-CCD camera (top). After inserting the DSU disk #3 (10% transmission) a 150 ms image was acquired (same gain, bottom). In both images, the same number of photons struck the specimen. (Images kindly provided by Dr. Jennifer Morgan, Yale University Medical School.)

increased the number of high-quality images that could be acquired before photobleaching.[26]

EM-CCD Advantages (+) and Disadvantages (–):

(+) Like CCDs, EM-CCDs are photon efficient (good QE), have good contrast (MTF), are mechanically robust, and are not harmed by exposure to bright light.
(+) They have single-photon sensitivity.
(+) Ergo, they can greatly improve the speed or number of images acquired before photobleaching.
(–) No fast gating.
(–) Higher cost than normal CCD (roughly equivalent to an intensified CCD).

APPLICATIONS AND EXAMPLES OF CONFOCAL DISK-SCANNING MICROSCOPES

Comparison with Epi-Fluorescence Imaging

As discussed above, a simple disk-scanning confocal should have better optical sectioning but lower light throughput than a WF epi-fluorescence microscope. To demonstrate this we took images of the same specimen with both an epi-fluorescence setup and with an Olympus DSU spinning-slit system (10% transmission) using an Andor 512 × 512 BI EM-CCD camera. Ten times longer exposures were used with the disk in to compensate for reduced illumination striking the specimen. As seen in Figure 10.12 (processed identically), there is considerably less background fluorescence with the scanning disk in place.

Fast 3D/4D Imaging

The micro-lens–assisted spinning disks in the Yokogawa design transmit more illumination to the specimen, increasing the maximum imaging speed. Even with a traditional CCD such as the Hamamatsu Orca ER, one can record high resolution multi-color confocal stacks, as demonstrated in Figure 10.13. In ~20 s we acquired a 3D stack with 200 sections; a 3D reconstruction is shown in the lower panel. Using a single-beam confocal such as the Zeiss LSM510, acquisition of a data stack of similar size and quality would take ~5 min+. In the *xz* -views, one can see that *z*-resolution appears roughly on par with that of a good confocal LSM.

The ability to acquire confocal images rapidly allows fast 4D imaging. An example of such an application is shown in Figure 10.14 where 3D stacks of ~20 layers were each acquired in under 2.5 s and repeated over time. The scientific advantage of 4D imaging is that one gets a complete view of the process. In this example, clathrin dynamics can be seen on the upper cell surface, near the perinuclear Golgi region and also at the bottom of the cell; areas where dynamic changes occur are circled. The lower panel shows a single, 3D time point from a 4D stack of a double-labeled cell projected in space at two angles. As it is hard to convey in a static medium (this book) the visual power and the high level of biological contextual information available from looking at a 3D image over time from any angle. A movie made from this 3D data stack will be available on the Web site associated with this book http://www.springer.com/0-387-25921-X.

The challenge of how best to process and visualize large datasets will likely be an increasingly significant hurdle. It is worth commenting that while photobleaching is still a real limiting factor with a normal CCD, ultrasensitive cameras allow us to push this envelope as we enter the realm of the real-time 4D confocal imaging.

Blazingly Fast Confocal Imaging

Some biological processes can only be revealed (and understood) with high-speed imaging. Calcium sparks, flashes, and waves are examples. The 3D diffusion is so rapid that even a 1 ms exposure may not be fast enough and the process is definitely obscured in real-time (30 fps) or slower imaging.[27] Optical sectioning is needed both to improve S/N and also to sample a slice through the middle of a cell because such an image is less subject to volumetric changes in signal than is a normal epi-fluorescence image.

Maximum image acquisition speed is determined by four factors: the excitation power delivered to the sample, photophysical limits such as saturation, the disk scan speed, and the camera pixel clock and sensitivity. Because the read noise of a normal CCD rises rapidly with read speed while that of the EM-CCD does not, an ultrasensitive camera is essential. In Figure 10.15, the combination of a Yokogawa disk-scanning confocal and EM-CCD camera has permitted ~110 fps imaging of calcium sparks (top panel) or calcium waves induced by electrophysiological depolarization (bottom). These images are truly just the start of seeing life in the (ultra)fast lane.

[26] The same holds for image intensifiers, but lower QE and reduced resolution mitigate this benefit.

[27] Even current EM-CCDs may not be fast enough to fully visualize this process, as experiments with 50 ns time resolution made using a gated intensified camera (but ~30 ms repeat rates) show very fast initiation of the calcium spark (Kindzelskii and Petty, 2003).

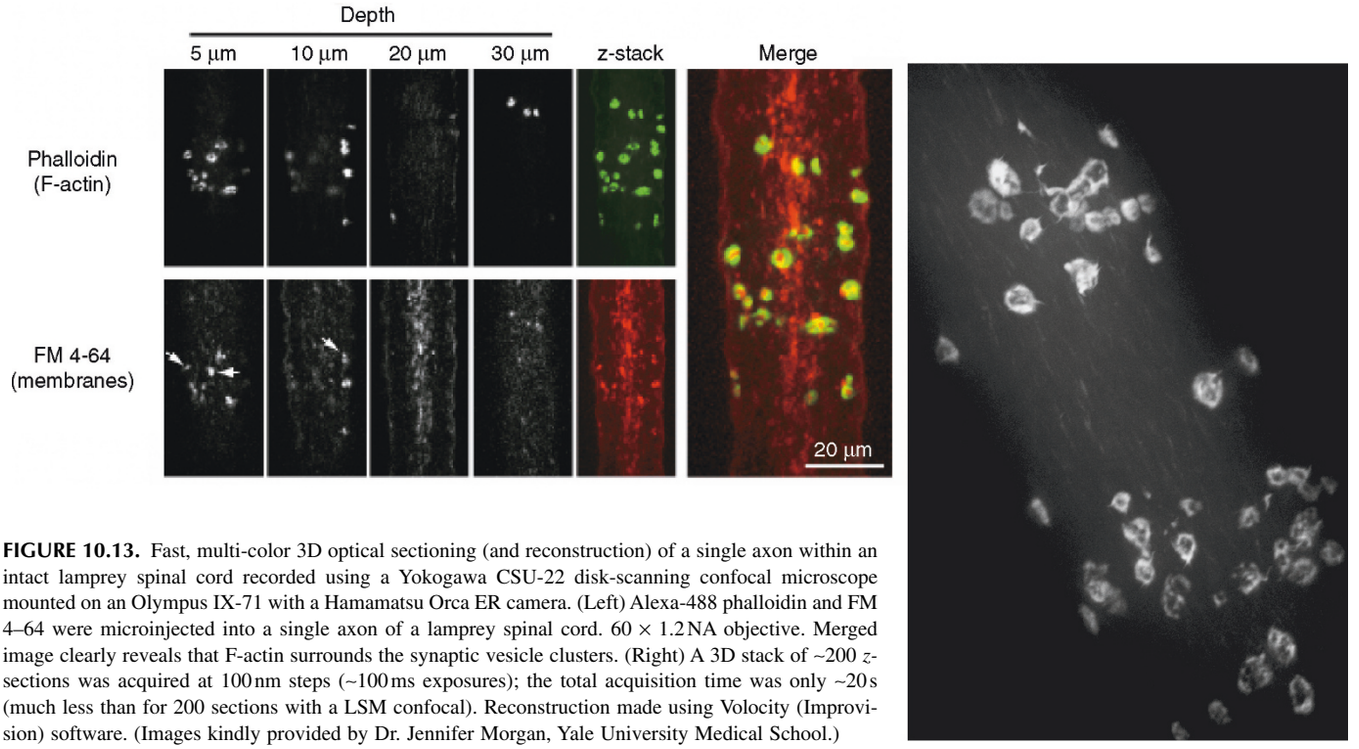


FIGURE 10.13. Fast, multi-color 3D optical sectioning (and reconstruction) of a single axon within an intact lamprey spinal cord recorded using a Yokogawa CSU-22 disk-scanning confocal microscope mounted on an Olympus IX-71 with a Hamamatsu Orca ER camera. (Left) Alexa-488 phalloidin and FM 4–64 were microinjected into a single axon of a lamprey spinal cord. 60 × 1.2 NA objective. Merged image clearly reveals that F-actin surrounds the synaptic vesicle clusters. (Right) A 3D stack of ~200 *z*-sections was acquired at 100 nm steps (~100 ms exposures); the total acquisition time was only ~20 s (much less than for 200 sections with a LSM confocal). Reconstruction made using Volocity (Improvision) software. (Images kindly provided by Dr. Jennifer Morgan, Yale University Medical School.)

FUTURE DEVELOPMENTS?

Although forecasting future development can be risky, it is always useful to consider what could be done better. One of the most challenging aspects of disk-scanning confocals is the low light budget for fluorescent excitation. The Yokogawa system avoids this at the cost of laser operation (limited wavelengths, high cost, high power/cooling. and large footprint). Two technological developments may mitigate this problem. Small, efficient **solid-state lasers** will doubtless become less expensive and even more con-

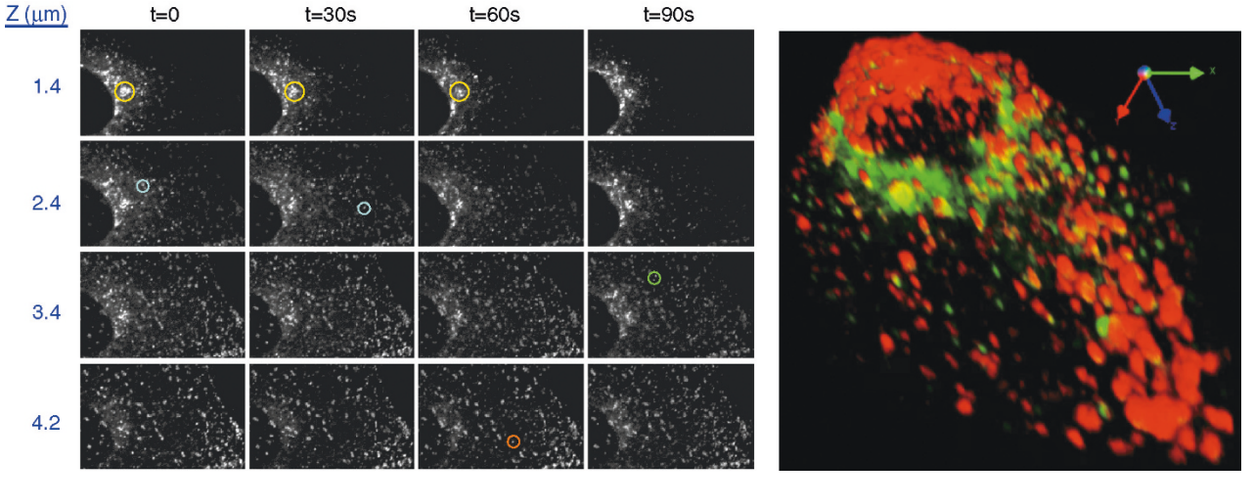


FIGURE 10.14. 3D/4D visualization of membrane trafficking with a disk-scanning confocal. (Left) 4D movie showing clathrin-GFP dynamics in PtK_2 cells imaged on an Ultraview PerkinElmer Yokogawa spinning disk system using a 60 × 1.2 NA water objective, Hamamatsu Orca ER CCD. Stacks of 21 *z*-slices were collected at 200 nm spacing, with exposure times of 100 ms/slice or <2.5 s/stack. 3D stacks were acquired at 30 s intervals. Some clathrin endosomal structures that changed over time are highlighted in different focal planes by colored circles. (Right) Living PtK_2 cells were labeled with clathrin-GFP (green) and transferrin (red) to label endosomes. A region of interest (~500 × 500 pixels × 10 slices), corresponding to 1 cell was very rapidly acquired in 4D at 1 s/stack and repeated over time (photobleaching occurred after ~50 stacks). (Images from R. Zoncu and D. Toomre, Yale University Medical School.)

venient.[28] High-intensity light-emitting diodes **(LED)** are becoming brighter and less expensive (see Chapter 6, *this volume*) and their lifespan is up to 100,000 h. In addition, they can be pulsed very rapidly, an ability that may make them useful for FLIM.

At the other end of the system, better detectors, such as microlens-equipped, interline-transfer EM-CCDs, would permit better coupling to present disk scanners. If interline-transfer chips turn out to be hard to develop, another solution to the smearing and moiré problems would be to turn off the illumination during fast vertical charge transfer. This could be implemented either by sending a blanking signal to the acousto-optical wavelength selector now used to select lines and power levels in most laser-based confocals, or by pulsing the power to an LED illumination system (see Chapter 6, *this volume*).

As camera performance improves (bigger chips, faster data transfer, better integration with system control software, etc.), new dyes are developed, and photobleaching becomes a less significant factor, HUGE amounts of data will be generated. Current cameras can read a full, 1 K × 1 chip at ~35 fps, or ~35 MB/s, or 126 GB/h! One may balk, but 4D imaging can easily require truly enormous datasets (see Chapters 32 and 50, *this volume*).

Better **data** integration, storage, visualization, and analysis are already extremely important areas that can easily become THE bottleneck in the system. More transparent data formats, such as those being used in the open microscopy environment (OME) may help.[29] This rapidly emerging problem will require companies to produce cameras that are highly integrated with acquisition, visualization, and analysis software to form a package that all works together. Both scientists and manufacturers have a vested interest here.

One may even ask the outrageous question: Will disk scanners start to replace single-beam confocals? Although it is hard to tell what will narrow the gap between disk-scanning confocals and single-beam LSMs, it should be noted that, because of their potential for high-speed imaging, CCD-equipped disk scanners are already being integrated into high content screening workstations for use in drug discovery and proteomics (outlined in Chapter 46, *this volume*).

While present disk scanners lack the ability to scan only a region of interest (ROI) to either photobleach (FRAP) or photoactivate probes, at least one manufacturer has already added a separate high-power, pulsed-laser system to a normal LSM for this purpose. There seems no reason why this could not also be done with a disk scanner.

Future disk scanners would benefit from better integration that allowed the system to make pixel-matched images using other contrast modalities such as brightfield, differential interference contrast (DIC), total internal reflection fluorescence microscopy (TIRFM), etc., and it seems quite likely that they might eventually be adapted to be sensitive to other photostates such as fluorescent lifetime and polarization. It will be of interest to many to see if this old approach to confocal imaging surges to the forefront.

SUMMARY

- Disk-scanning microscopes can produce back-scattered-light or fluorescent real-time color, confocal images.
- Disk-scanning confocals can scan 100 to 1000× faster than single-pinhole confocal LSMs.

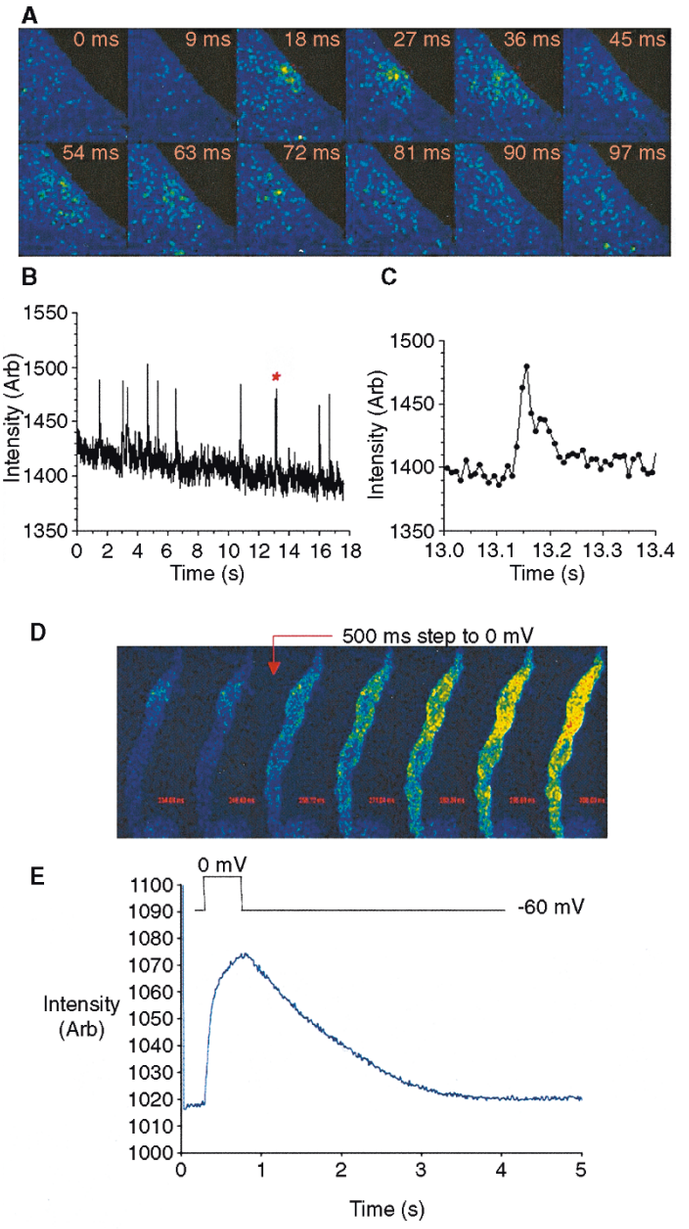


FIGURE 10.15. Very fast imaging of calcium with a Yokogawa disk-scanning confocal. (A–C) Images are from a guinea-pig bladder SMC recorded at 37°C at 113 fps (9 ms interval) on an Andor iXon camera with the 512 × 512 E2V EM-CCD (binned 2 × 2). The plots below each image show typical calcium sparks on a long timescale (B) and on an expanded timescale (C). (D, E) Images are from a rabbit urethral smooth muscle cell that was held at −60 mV and then depolarized to 0 mV for 500 ms. This experiment was recorded at 82 fps on the same camera and the montage in (D) shows false-colored consecutive images of changes in Ca^{2+} in response to the depolarization. (E) shows a record of whole cell fluorescence recorded over many seconds to demonstrate the stability of the signal and the S/N. To facilitate direct comparison with the raw video images often shown, the images, kindly provided by Dr. M. A. Hollywood, Smooth Muscle Group, Ireland (http://www.smoothmusclegroup.org), are shown magnified and unprocessed, rather than smoothed.

[28] As is evident in the Zeiss LSM5-Live slit scanner that only uses ~10 to 100 mW small solid-state lasers.
[29] http://www.openmicroscopy.org/.

- Quantum efficiency of detection can be an order of magnitude better than PMT-based LSM, reducing photobleaching and permitting the acquisition of long time series.
- Under optimum conditions, the lateral and axial resolution of a pinhole-based disk-scanning confocal is comparable to confocal LSMs. The *z*-resolution of a slit-based confocal is slightly lower.
- Pinhole/slit size must be matched to the magnification and NA of the objective lens.
- Both pinhole and slit disk designs have advantages. Compared to the disk using microlenses, the simpler slit disks are easier to interchange to properly match the slit width to the imaging conditions.
- In all cases, the fill factor of the disk limits the light throughput and, in general, greater throughput tracks with less effective optical sectioning.
- Low-noise, high QE EM-CCD cameras are critical for systems that have tight light budgets and require rapid image acquisition. Fortunately, they are now available.

As emphasized in Chapters 23, 24, and 25, image deconvolution of confocal data can be very powerful in overcoming the effects of bad imaging statistics attendant on low signal levels.

ACKNOWLEDGMENTS

Dr. G.S. Kino graciously provided many of the figures and much of the text is inspired and/or abridged from his previous versions. Olympus generously provided the DSU system for testing and Andor Tech kindly provided the EM-CCD cameras; both companies support the Yale CINEMA lab (Cellular Imaging using New Microscopy Approaches). Dr. Jennifer Morgan kindly did considerable testing with the Yokogawa and DSU cameras and provided several figures. We thank the following additional people for support and input: Dr. Charles Fangella, Dr. Chikara Abe, and Dr. Nicolas George at Olympus; Dr. Chris Calling, Dr. Colin Coates, and Dr. Mark Browne at Andor Tech.; Dr. Thomas Nicholson and Dr. Kay Mofford at PerkinElmer; Ms. Mizuho Shimizu (Yokogawa Electric Corp.); Dr. Mark A. Hollywood (Queen's University, Belfast, Ireland; Smooth Muscle Group, www.smoothmusclegroup.org); Dr. Sebastian Tille (Zeiss); Dr. Baggi Somasundaram (BD Bioscience). CINEMA lab and instrumentation are from the Ludwig Institute of Cancer Research (LICR) and a NSF-MRI instrumentation grant (DBI-0320840).

AFTERWORD

Other fast-scanning confocal designs are possible. Two instruments that are expected to come to the market soon are the "VT-infinity" instrument from Visitech (see Appendix 2) and the "LiveScan Swept Field," designed by Prairie Technologies (sold by Nikon). Both confocal heads use lasers for illumination, mirrors driven by piezoelectric elements and galvanometers to scan the sample and CCD cameras as efficient detectors. The VT-infinity system is somewhat reminiscent of the Yokogawa system in that it uses thousands of microlens and pinholes; these however are arranged as stationary arrays and scanning is achieved with galvo/piezo mirrors. The "Swept Field" system rapidly scans the sample (over 200 frames/sec) with either a slit or row of 32 pinholes (different sizes are available). In the return path a separate slit or row of pinholes is used; precise mechanical and optical alignment is likely essential for successful operation of this system. Both fast-scanning systems are intriguing in design and it will be interesting to see how they compare to spinning disk confocals counterparts.

REFERENCES

Born, M., and Wolf, E., 1980, *Principles of Optics*, 6th ed., Pergamon Press, Oxford, England.

Chong, F.K, Coates, C.G., Denvir, D.J., McHale, N., Thornbury, K., and Hollywood, M., 2004, Optimization of spinning disk confocal microscopy: Synchronization with the ultra-sensitive EMCCD, *SPIE Proc*. 5324:65.

Gaietta, G., Deerinck, T.J., Adams, S.R., Bouwer, J., Tour, O., Laird, D.W., Sosinsky, G.E., Tsien, R.Y., Ellisman, M.H., 2002, Multicolor and electron microscopic imaging of connexin trafficking, *Science* 296:503–507.

Goodman, J. W., 1968, *Introduction to Fourier Optics*, McGraw-Hill, New York.

Inoué, S., and Inoué, T., 2002, Direct-view high-speed confocal scanner: The CSU-10. Methods in Cell Biology, Vol. 70, pp. 87–127.

Kindzelskii, A.L., Petty, H.R., 2003, Intracellular calcium waves accompany neutrophil polarization, formylmethionylleucylphenylalanine stimulation, and phagocytosis: A high speed microscopy study, *J. Immunol*. 170:64–72.

Kino, G.S., 1987, *Acoustic Waves: Devices, Imaging, and Analog Signal Processing*, Prentice-Hall, New Jersey.

Kino, G.S., and Xiao, G.Q., 1990, Real-time scanning optical microscopes, In: *Scanning Optical Microscopes* (T. Wilson, ed.), Pergamon Press, Oxford, pp. 361–387.

Lichtman, J.W., Sunderland, W.J., and Wilkinson, R.S., 1989, High-resolution imaging of synaptic structure with a simple confocal microscope, *New Biologist* 1:75–82.

Lidke, D.S., Arndt-Jovin, D.J., 2004, Imaging takes a quantum leap, *Physiology (Bethesda)* 322–325.

Miyawaki, A., 2003, Fluorescence imaging of physiological activity in complex systems using GFP-based probes, *Curr. Opin. Neurobiol*. 5:591–596.

Petráň, M., Hadravsky, M., Egger, M.D., and Galambos, R., 1968, Tandem scanning reflected light microscope, *J. Opt. Soc. Am*. 58:661–664.

Petráň, M., Hadravsky, M., and Boyde, A., 1985, The tandem scanning reflected light microscope, *Scanning* 7:97–108.

Sako, Y., and Yanagida, T., 2003, Single-molecule visualization in cell biology, *Nat. Rev. Mol. Cell Biol*. Suppl:SS1–SS5.

Tanaami, T., Otsuki, S., Tomosada, N., Kosugi, Y., Shimizu, M., and Ishida, H., 2002, High-speed 1-frame/ms scanning confocal microscope with a microlens and Nipkow disks, *Appl. Opt*. 41:4704–4708.

Toomre, D., and Manstein, D.J., 2001, Lighting up the cell surface with evanescent wave microscopy, *Trends Cell Biol*. 11:298–303.

Wilson, T., 1990, Optical aspects of confocal microscopy, In *Confocal Microscopy* (T. Wilson, ed.), Pergamon Press, Oxford, 93–141.

Wilson, T., and Carlini, A.R., 1987, Size of the detector in confocal imaging systems, *Opt. Lett*. 12:227–229.

Wilson, T., and Sheppard, C.J.R., 1984, *Scanning Optical Microscopy,* Academic Press, New York.

Xiao, G.Q., and Kino, G.S., 1987, A real-time confocal scanning optical microscope, *SPIE Proc*. 809:107–113.

Xiao, G.Q., Corle, T.R., and Kino, G.S., 1988, Real-time confocal scanning optical microscope, *Appl. Phys. Lett.* 53:716–718.

Xiao, G.Q., Kino, G.S., and Masters, B.R., 1990, Observation of the rabbit cornea and lens with a new real-time confocal scanning optical microscope, *Scanning* 12:161–166.

11

Measuring the Real Point Spread Function of High Numerical Aperture Microscope Objective Lenses

Rimas Juškaitis

INTRODUCTION

Testing and characterization of high-quality lenses have been perfected into fine art with the advent of lasers, phase-shifting interferometers, charge-coupled device (CCD) cameras, and computers. A bewildering array of techniques is described in Malacara's classic reference book on the subject (Malacara, 1992). Several of these techniques, in particular the Twyman–Green interferometer and the star test, are applicable to testing of microscope objective lens.

Characterizing high numerical aperture (NA) objective lenses presents unique challenges. Many of the standard approaches, including Twyman–Green interferometry, are in fact comparative techniques. They require a reference object — an objective or a concave reflective surface — of the same or larger numerical aperture and of perfect (comparatively speaking) optical quality. This is problematic. Even if two lenses of the same type are available, a problem still remains of apportioning the measured aberrations to the individual lenses. The star test, which is absolute, hits a similar problem in that the Airy disk produced by the lens being tested is impossible to observe directly, and hence it has to be magnified by a lens with a similar or better resolution, that is, higher NA. Immersion lenses create further complications. All tests described in this chapter are free from these problems. They are absolute and use a small point scatterer or a flat mirror to create a reference wavefront against which the lens aberrations are checked. Together with advanced interferometric techniques and processing algorithms, this results in a range of techniques suitable for routine characterization of all available microscope objective lenses.

A few words have to be said regarding identity of the lenses used throughout this chapter. Although the principal data for the specimens used in our test is given, the name of their manufacturers is not. This is done for several reasons, not least to avoid accusations of not using most up-to-date lenses from company A to make it look worse than company B. As a university laboratory we rely on the stock of lenses which have accumulated over the years. A few people also brought their own lenses to test. Not all of these are necessarily the best in class. This work is about testing techniques and typical problems with high NA lenses, not about relative merits of individual lenses or their respective manufacturers.

Before describing specific lens testing techniques it might be useful to repeat here a few basic facts about microscope objective lenses in general. Modern objective lenses are invariably designed for infinite conjugate ratio, that is, the object of observation is placed in the front focal plane and its image is formed at infinity. In order to obtain a real intermediate image, a separate lens, called the tube lens, is used. The focal length of this lens F (which ranges from 165 mm for Zeiss and 180 mm for Olympus to 200 mm for Leica and Nikon) together with the magnification of the objective M gives the focal length of the objective $f = F/M$.

One of the basic postulates of aberration-free lens design is that it has to obey Abbe's sine condition. For a microscope objective treated as a thick lens, this can be interpreted as the fact that its front principal surface is actually a sphere of radius f centered at the front focus. Any ray leaving the focus at an angle α to the optical axis is intercepted by this surface at the height $d = f \sin\alpha$ and emerges from the back-focal plane parallel to the axis at the same height, as shown in Figure 11.1. For immersion lenses this has to be multiplied by the refractive index of the immersion fluid n.

In most high NA objective lenses, the back-focal plane, also called the pupil plane, is located inside the lens and is not, therefore, physically accessible. Fortunately, lens designers tend to put an aperture stop as close to this plane as possible, which greatly simplifies the task of identifying the pupil plane when re-imaging it using an auxiliary lens. Any extra elements, such as phase rings in phase contrast lenses or variable aperture iris diaphragms, will also be located in the back-focal plane.

The physical aperture of an objective lens D is related to its numerical aperture $n \sin\alpha$ via

$$D = \frac{2Fn \sin\alpha}{M}. \quad \textbf{(1)}$$

Ultimately it is limited by the size of the objective thread. For a modern low magnification high NA immersion lens with, say, $n \sin\alpha = 1$ and $M = 20$, D can be as large as 20 mm. This is one of the reasons why some lens manufacturers (notably Leica and Nikon) have now abandoned the former gold standard of the Royal Microscopical Society (RMS) thread and moved to larger thread sizes.

Every infinity-corrected lens needs a field lens to produce the intermediate image. Field lenses differ considerably between manufacturers and even between their various microscope ranges. Strictly speaking, one should test each objective lens together with its matching tube lens. We chose not to do this for several reasons. First, there is general movement to confine all aberration correction to the objective lens. The only aberration that is still sometimes corrected in the tube lens is the lateral color. This does not affect the results of our measurements. Moreover, there is a tendency to use objective lenses individually without their respective field lenses, especially in laboratory-built scanning systems. All this implies the importance of knowing imaging properties of high NA objective lenses as individual units.

Rimas Juškaitis • Department of Engineer Science, Parks Road, Oxford, United Kingdom OX1 3PJ.

Handbook of Biological Confocal Microscopy, Third Edition, edited by James B. Pawley, Springer Science+Business Media, LLC, New York, 2006.

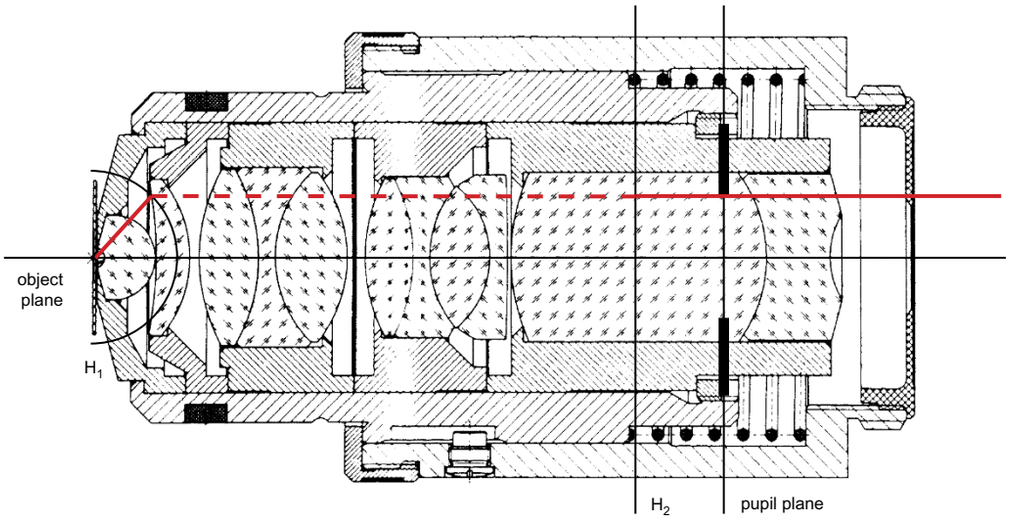


FIGURE 11.1. Schematic diagram of a typical high NA planapochromat objective lens. Principal surfaces, aperture stop, and marginal ray are indicated.

MEASURING POINT SPREAD FUNCTION

A perfect lens transforms a plane wave front into a converging spherical wave. If they are not too dramatic, any deviations from this ideal behavior can be described by introducing a complex Pupil Function $P(\rho, \theta)$, where ρ is the normalized radial coordinate in the pupil plane and μ is the azimuthal angle in the same plane. Both amplitude and phase aberrations can be present in a lens, but it is the latter that usually play the dominant role. The amplitude aberrations are typically limited to some apodization towards the edge of the pupil; these are discussed in more detail in the section "Apodization."

The optical field distribution produced by this (possibly aberrated) converging wave is termed the point spread function, or PSF, of the lens. This distribution can be obtained in its most elegant form if dimensionless optical coordinates in lateral

$$\upsilon = \frac{2\pi}{\lambda} n \sin\alpha \sqrt{x^2 + y^2} \qquad \textbf{(2)}$$

and axial

$$u = \frac{8\pi}{\lambda} n \sin^2\frac{\alpha}{2} z \qquad \textbf{(3)}$$

directions are used. In these coordinates the intensity distribution in the PSF is independent of the NA of the lens, and the surface $u = v$ corresponds to the edge of the geometric shadow. The actual focal field distribution in these newly defined cylindrical coordinates is given by (Born and Wolf, 1998):

$$h(u,\upsilon,\psi) = A \exp\left[\frac{iu}{4\sin^2\frac{\alpha}{2}}\right]\int_0^1\int_0^{2\pi} P(\rho,\theta)\times$$
$$\times \exp\left\{-i\left[\upsilon\rho\cos(\theta-\psi)+\frac{u\rho^2}{2}\right]\right\}\rho d\rho\, d\theta. \qquad \textbf{(4)}$$

The exponential term in front of the integral is nothing else than a standard phase factor of a plane wave $2\pi nz/\lambda$.

For the aberration-free case $P = 1$ and the integral over θ can be calculated analytically to give $2\pi J_0(v\rho)$. Equation 4 now simplifies to

$$h(u,\upsilon) = 2\pi\, A \exp\left[\frac{iu}{4\sin^2\frac{\alpha}{2}}\right]\int_0^1 \exp\left(-\frac{iu\rho^2}{2}\right) J_0(\upsilon\rho)\,\rho d\rho. \qquad \textbf{(5)}$$

This equation is readily calculated either numerically or using Lommel functions. The resulting intensity distributions are well known and can be found, for example, in Born and Wolf (1998). Not only that, but also PSFs subjected to various aberrations have been calculated countless times in the past and are instantly recognizable to most microscopists. It is precisely for this reason that a relatively straightforward measurement of the PSF can frequently provide an instant indication of what is wrong with a particular objective lens.

Equations 4 and 5 are, of course, scalar approximations. This approximation works remarkably well up to angular apertures of about 60°. Even above these angles the scalar approximation can be safely used as a qualitative tool. For those few lenses that seem to be beyond the scalar approach (and for the rigorous purists) there is always an option to use a well-developed vectorial theory (Richards and Wolf, 1959).

Fiber-Optic Interferometer

The requirement to measure both amplitude and phase of the PSF calls for an interferometer-based setup. The fiber-optic interferometer, Figure 11.2, that was eventually chosen for the task has several important advantages. It is an almost common-path system, which dramatically improves long-term stability. It is also a self-aligning system: light coupled from the fiber to the lens and scattered in the focal region is coupled back into the fiber with the same efficiency. For convenience, the whole setup is built around a single-mode fiber-optic beam-splitter, the second output of which is index-matched in order to remove the unwanted reflection. A helium–neon (He–Ne) laser operating at 633 nm is used as a light source. The whole setup bears cunning resemblance to a confocal microscope. In fact, it *is* a confocal microscope, or at least can be used as such (Wilson *et al.*, 1994). Provided that light emerging from the fiber overfills the pupil of the objective lens, the former acts as an effective pinhole ensuring spatial filtering of the backscattered light (see Chapter 26, *this volume*). Thus, if the

object can be regarded as a point scatterer, then the amplitude of the optical signal captured by the fiber

$$R \sim h^2 = |h|^2 \exp[2i \arg(h)] \quad \textbf{(6)}$$

that is, its magnitude is equal to the intensity of the PSF whereas the phase is twice the phase of the PSF. In order to measure both these parameters, light reflected back along the fiber from the tip is used as a reference beam r. Wavefronts of both signal and reference beams are perfectly matched in a single-mode fiber — this is the beauty of the fiber-optic interferometer. Furthermore, the fiber tip is dithered to introduce a time-varying phase shift between the interfering beams $\phi(t) = \phi_0 \cos \omega t$. The interference signal reaching the photodetector is now given by

$$I = |r+R|^2 = r^2 + |R|^2 + 2r[\mathrm{Re}(R)\cos(\phi_0 \cos \omega t) - \mathrm{Im}(R)\cos(\phi_0 \cos \omega t)], \quad \textbf{(7)}$$

where r was assumed to be real for simplicity. It is now a simple matter to extract both Re(R) and Im(R) from this signal by using lock-in detection technique. The signal of Eq. 7 is multiplied by $\cos \omega t$ and the result is low-pass filtered to give

$$I_1 = rJ_1(\phi_0)\mathrm{Im}(R), \quad \textbf{(8)}$$

whereas synchronous demodulation with $\cos 2\omega t$ yields

$$I_2 = rJ_0(\phi_0)\mathrm{Re}(R). \quad \textbf{(9)}$$

By appropriately adjusting the modulation amplitude ϕ_0, it is easy to achieve $J_1(\phi_0) = J_2(\phi_0)$ and, by substituting Eq. 6, to calculate

$$h \sim \sqrt{I_1^2 + I_2^2} \exp\left(\frac{i}{2} \arctan \frac{I_1}{I_2}\right). \quad \textbf{(10)}$$

Thus, the goal of obtaining both the amplitude and phase of the PSF of the objective lens has been achieved. Of course, in order to obtain full two- (2D) or three-dimensional (3D) PSF corresponding scanning of the object, the point scatterer is still required.

Point Spread Function Measurements

In order to demonstrate the effectiveness of this method in detecting small amounts of aberrations, it was tested on a special kind of objective lens. This 60 × 1.2 NA water-immersion plan-apochromat was developed for deconvolution applications and hence was specifically designed to have a well-corrected PSF. It was also equipped with a correction collar to compensate for cover glass thicknesses in the range 0.14 to 0.21 mm. One hundred nanometer colloidal gold beads mounted beneath a #1.5 coverslip of nominal thickness (0.17 mm) acted as point scatterers in this case. The coverslip was in turn mounted on a microscope slide and a gap between them was filled with immersion oil so as to eliminate reflection from the back surface of the coverslip. The size of the bead was carefully chosen experimentally in order to maximize the signal level without compromising the point-like behavior. Indeed, a control experiment using 40 nm beads yielded similar results to those presented below but with a vastly inferior signal-to-noise ratio.

In principle, this apparatus is capable of producing full 3D complex PSF data sets. It was found however that in most cases xz-cross–sections provided sufficient insight into the aberration properties of the lens without requiring too long acquisition times. Such results are shown in Figure 11.3 for two settings of the correction collar. In order to emphasize the side lobe structure, the magnitude of the PSF is displayed in decibels with the peak value taken to be 0 dB. It can be seen that a collar setting of 0.165 mm gives a near-perfect form to the PSF. The axial side lobes are symmetric with respect to the focal plane and the phase fronts away from this plane quickly assume the expected spherical shape. On the other hand, a small 10% deviation from the correct setting already has a quite pronounced effect on the PSF in the bottom row of Figure 11.3. The symmetry is broken, the axial extent of the PSF has increased by about 30%, and distinct phase singularities appeared on the phase fronts. Everything points towards a certain amount of uncompensated spherical aberration being present in the system. It is interesting to note that, as the phase map of the PSF seems to be more sensitive to the aberrations than the magnitude, this can be used as an early warning indicator of the trouble. It also underlines the importance of measuring both the magnitude and phase of the PSF.

Although so far the measured PSF has been described in purely qualitative terms, some useful quantitative information about the objective lens can also be extracted from these data. One parameter that can be readily verified is the objective's NA. Axial extent of the PSF is more sensitive to the NA than its lateral shape. Using

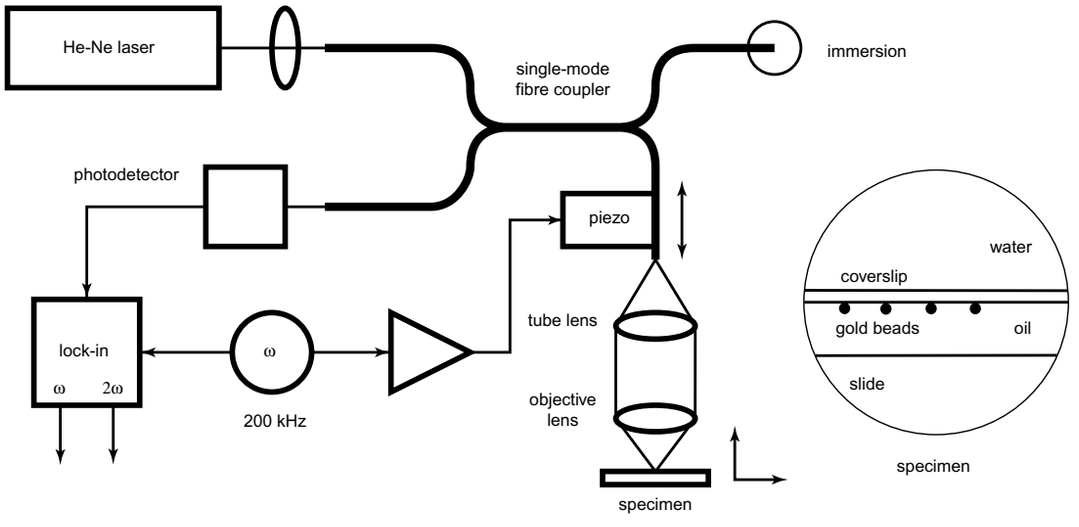


FIGURE 11.2. Schematic diagram of the fiber-optic interferometer–based setup for measuring objective PSFs.

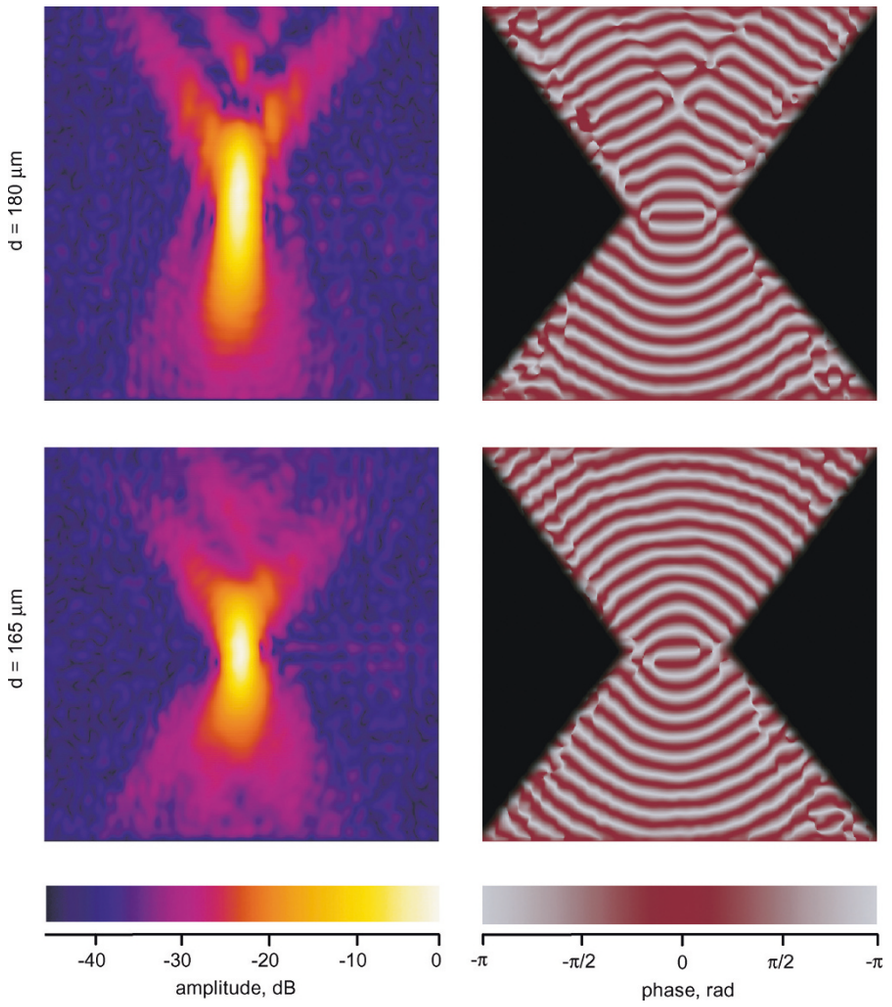


FIGURE 11.3. The amplitude and phase of the effective PSF for 60 × 1.2 NA water-immersion lens with correction collar. Results for two different collar settings are shown. Image size in both x (horizontal) and z (vertical) are 5 µm.

the axial section of the PSF is therefore the preferred method to determine the NA. Besides, the interference fringes present in the z-scan provide a natural calibration scale for the distance in z. The actual measurement was obtained by finding the best fit to the curve in Figure 11.4. A somewhat surprising result of this exercise was that the best fit corresponded to NA of 1.15, rather than the nominal value of 1.2. This is not a coincidence: such discrepancies were found with other high NA objective lenses as well. The reason for this kind of behavior will become clear in the section "Pupil Function."

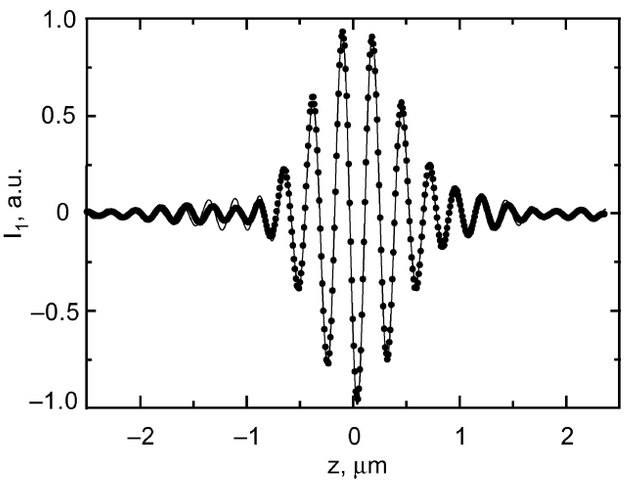


FIGURE 11.4. Measured (*dots*) and calculated (*line*) amplitude axial responses for the same lens.

CHROMATIC ABERRATIONS

Chromatic aberrations constitute another class of aberrations that can adversely affect the performance of any microscopy system. These aberrations are notoriously difficult to overcome in high NA objective lens design. The reason, at least in part, is the relative uniformity of dispersion properties of common glasses used in objective lenses. Ingenious solutions have been found at an expense of dramatic increase of the number of lens elements — typically to more than a dozen in apochromats. Even then, part of the correction may need to be carried out in the elements external to the objective.

Lateral and axial color, as they are called by lens designers, are usually treated as separate chromatic aberrations. The former, which manifests itself as the wavelength-dependent magnification, is easy to spot in conventional microscopes as coloring of the edges of high-contrast objects. Lateral chromatic aberration is also the more difficult of the two to correct. Traditionally this has been done by using the tube lens, or even the ocular, to offset the residual lateral color of the lens. Some of the latest designs claim

to have achieved full compensation within the objective lens itself — claims to be treated with caution. The correct testing procedure for the lateral color should include at least a matched tube lens. The simplest test would probably be to repeat the experiments described in the section "PSF Measurements" for several wavelengths at the edge of the field of view and record the shift of the lateral position of the point image.

In confocal microscopy, where the signal is determined by the overlap of the effective excitation and detection PSFs, the loss of register between them should lead to a reduction of signal towards the edge of the field of view. It has to be said, though, that in most confocal microscopes, almost always, only a small area around the optical axis is used for imaging, hence this apodization is hardly ever appreciable. Axial color, on the other hand, is rarely an issue in conventional microscopy, but it can be of serious consequence for confocal microscopy, especially when large wavelength shifts are involved, such as in multi-photon or second and third harmonic microscopy. Mismatch in axial positions of excitation and detection PSFs can easily lead to degradation or even complete loss of signal, even in the center of the field of view. Below we describe a test setup which uses this sensitivity of the confocal system to characterize axial chromatic aberration of high NA objective lenses.

Apparatus

Ideally, one could conceive an apparatus similar to that in Figure 11.2, whereby the laser is substituted with a broadband light source. One problem is immediately obvious: it is very difficult to couple any significant amount of power into a single-mode fiber from a broadband light source, such as an arc lamp. Using multiple lasers provides only a partial (and expensive) solution. Instead, it was decided to substitute the point scatterer with a plane reflector. Scanning the reflector axially produces the confocal signal (Wilson and Sheppard, 1984):

$$I = \left[\frac{\sin u/2}{u/2}\right]^2. \qquad \textbf{(11)}$$

The maximum signal is detected when the plane reflector lies in the focal plane. This will change with the wavelength if chromatic aberration is present. Using a mirror instead of a bead has another advantage: the resulting signal is one-dimensional, function of u only, and hence a dispersive element can be used to directly obtain 2D spectral axial responses without the necessity of acquiring multiple datasets at different wavelengths.

The resulting apparatus, depicted in Figure 11.5 and described in more detail in Juškaitis and Wilson (1999), is again based around a fiber-optic confocal microscope setup, but the interferometer part is now discarded. Instead, a monochromator prism made of SF4 glass is introduced to provide the spectral spread in the horizontal direction (i.e., in the image plane). Scanning in the vertical direction was introduced by a galvo-mirror moving in synchronism with the mirror in the focal region of the objective lens. The resulting 2D information is captured by a cooled 16-bit slow-scan CCD camera. A small-arc Xe lamp is used as a light source providing approximately 0.2 μW of broadband visible radiation in a single-mode fiber. This is sufficient to produce a spectral snapshot of a lens in about 10 s.

Axial Shift

Typical results obtained by the chromatic aberration measurement apparatus are shown in Figure 11.6. Because the raw images are not necessarily linear either in z or λ, a form of calibration procedure in both coordinates is required. To achieve this, the arc lamp light source was temporarily replaced by a He–Ne and a multi-line Ar^+ lasers. This gave enough laser lines to perform linearization in λ. As a bonus, coherent laser radiation also gave rise to interference fringes in the axial response with the reflection from the fiber tip acting as a reference beam, just as in the setup shown in Figure 11.2. When a usual high NA objective lens was substituted with a low NA version, these fringes covered the whole range of the z-scan and could be readily used to calibrate the axial coordinate. The traces shown in Figure 11.6 have been normalized to unity at each individual wavelength. The presence of longitudinal chromatic aberration is clearly seen in both plots. Their shapes are

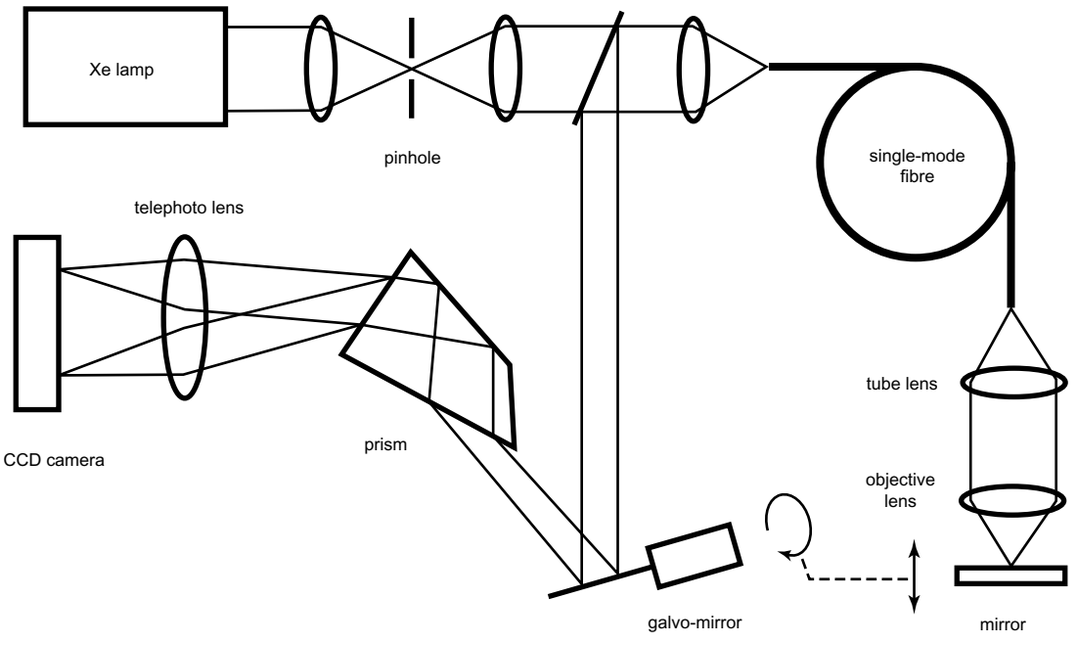


FIGURE 11.5. Experimental setup for measuring axial chromatic aberration of objective lenses.

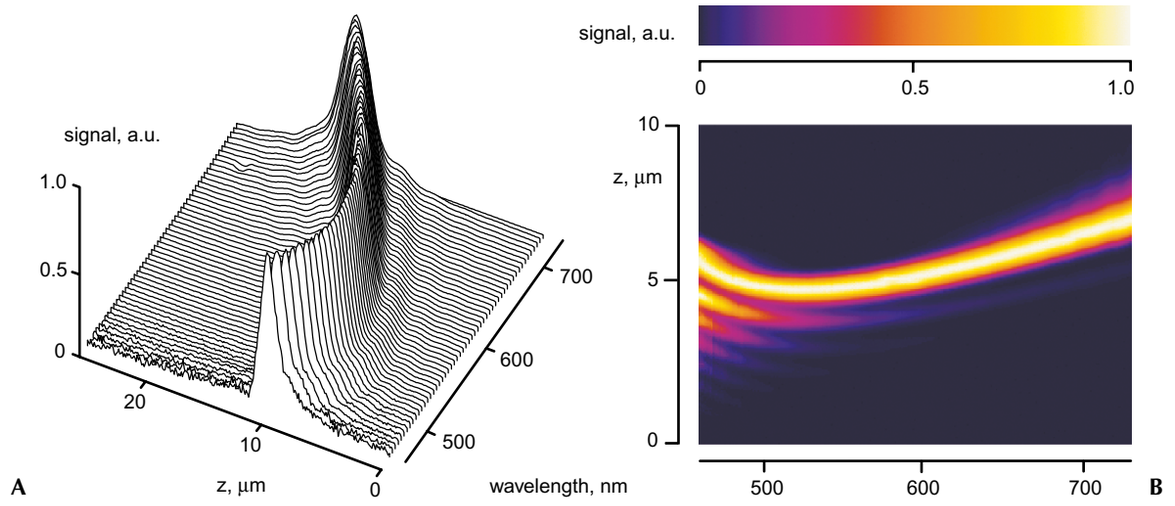


FIGURE 11.6. Experimental results from (A) 32×0.5 NA plan-achromat objective, displayed as 3D plot, and (B) 50×0.8 NA plan-achromat in pseudo-color representation. Note the change in z-scale.

characteristic for achromats in which the longitudinal color is corrected for two wavelengths only. It is interesting also to note the change of the shape of the axial response with the wavelength. This is noticeable for a 32×0.5 NA plan-achromat but it becomes particularly dramatic for a 50×0.8 NA plan-achromat [Fig. 11.6(b)]. Clearly the latter lens suffers from severe spherical aberration at wavelengths below 550 nm, which results in multiple secondary maxima at one side of the main peak of the axial response.

An interesting problem is posed by the tube lens in Figure 11.5. This lens may well contribute to the longitudinal chromatic aberration of the microscope as a whole and, therefore, it is desirable to use here a proper microscope tube lens matched to the objective. In fact it transpired that in some cases the tube lens exhibited significantly larger axial color aberration than the objective itself. This is hardly surprising: a typical tube lens is a simple triplet and, sometimes, even a singlet. Clearly, it is impossible to achieve any sophisticated color correction in such an element taken separately, therefore the objective lens would have to be designed to take this imperfection into account. Further information on this can be found in Chapter 7.

In this experiment, however, the main task was to evaluate the properties of the objective lens itself. A different approach was therefore adopted. The same achromatic doublet (Melles Griot 01 LAO 079) collimating lens was used with all objective lenses. Because the chromatic aberrations of this lens are well documented in the company literature, these effects could be easily removed from the final results presented in Figure 11.7. Figure 11.7(B) presents the same data but in a form more suited to confocal microscopy, whereby the chromatic shift is now expressed in optical units as defined in Eq. 3. The half width of the axial response to a plane mirror is then given by 2.78 optical units at all wavelengths and for all NAs. This region is also shown in the figure. The zero in the axial shift is arbitrarily set to correspond to $\lambda = 546$ nm for all the objectives tested.

As could be expected these results show improvement in performance of apochromats over achromats. They also show that none of the tested objectives (and this includes many more not shown in Figure 11.7 for fear of congestion) could meet the requirement of having a spectrally flat — to within the depth of field — axial behavior over the entire visible range. This was only

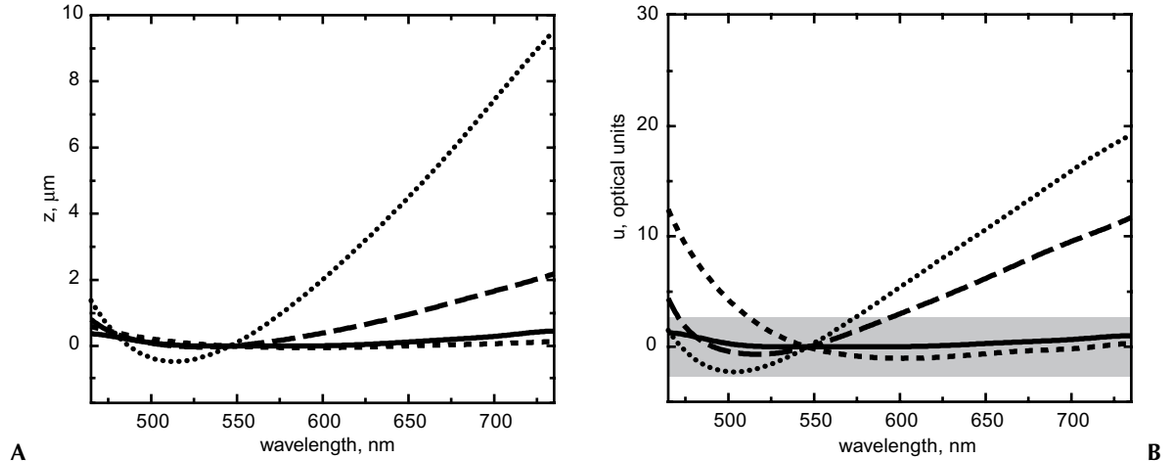


FIGURE 11.7. Wavelength dependence of the axial response maxima represented in physical (A) and optical (B) axial coordinates. The four traces correspond to: 32×0.5 NA plan-achromat (*dotted line*), 50×0.8 NA plan-achromat (*long dashes*), 100×1.4 NA plan-apochromat (*short dashes*), and the same lens stopped down to 0.7 NA (*solid line*).

possible to achieve by stopping down a 1.4 NA apochromat using a built-in aperture stop — the trick to be repeated several times again before this chapter expires.

PUPIL FUNCTION

Pupil function is the distribution of the phase and amplitude across the pupil plane when the lens is illuminated by a perfect spherical wave from the object side. It is related in scalar approximation to the PSF via a Fourier-like relationship (Eq. 4). It would appear, therefore, that they both carry the same information and therefore the choice between them should be a simple matter of convenience. Reality is a bit more complicated than that. Calculating the pupil function from the PSF is an ill-posed problem and therefore very sensitive to noise. Measurements of the pupil function provide direct and quantitative information about the aberrations of the lens — information that can only be inferred from the PSF measurements.

The trouble with mapping the pupil function is that a source of a perfect spherical wave is required. Such a thing does not exist but, fortunately, the dipole radiation approximates such a wave rather well, at least as far as phase is concerned. The approach described in this section is based on using small side-illuminated scatterers as sources of spherical waves. The actual pupil function measurement is then performed in a phase-shifting Mach–Zender interferometer in a rather traditional fashion.

Phase-Shifting Interferometry

The experimental setup depicted in Figure 11.8 comprised a frequency doubled Nd:YAG laser which illuminated a collection of 20 nm diameter gold beads deposited on the surface of a high refractive index glass prism acting as dipole scatterers (Juškaitis *et al.*, 1999). Because the laser light suffers total internal reflection at the surface of the prism, no direct illumination can enter the objective lens. The gold scatterers convert the evanescent field into the radiating spherical waves that were collected by the lens and converted into plane waves. These waves were then superimposed on a collimated reference wave. A 4-f lens system was then used to image the pupil plane of the lens onto a CCD camera. A pinhole in the middle of this projection system served to select a signal from a single scatterer. The size of this pinhole had to be carefully controlled so as not to introduce artifacts and degrade resolution in the image of the pupil function. A second CCD camera was employed to measure the PSF at the same time.

One of the mirrors in the reference arm of the interferometer was mounted on a piezoelectric drive and moved in synchronism with the CCD frame rate to produce successive interferograms of the pupil plane shifted by $2\pi/3$ rad

$$I_l \sim \left| r + P(\rho, \theta)\exp\left(i\frac{2\pi l}{3}\right)\right|^2, \qquad l = 0, 1, 2. \tag{12}$$

Using these three measurements the phase component of the pupil function was then calculated as

$$\arg[P(\rho, \theta)] = \arctan\frac{\sqrt{3}(I_1 - I_2)}{I_1 + I_2 - 2I_0}. \tag{13}$$

The lens, together with the prism, was mounted on a pivoting stage which could rotate the whole assembly around the axis aligned to an approximate location of the pupil plane. Thus, the off-axis as well as on-axis measurements of the pupil function could be obtained. A set of such measurements is presented in Figure 11.9, which clearly demonstrates how the performance of the lens degrades towards the edge of the field of view. Not only appreciable astigmatism and coma are introduced, but also vignetting becomes apparent. The presence of vignetting would be very difficult to deduce from direct measurements of the PSFs shown in Figure 11.10, as it could be easily mistaken for astigmatism. Not that such vignetting is necessarily an indication that something is wrong with the lens; it may well be deliberately introduced there by the lens designer to block off the most aberrated part of the pupil.

Zernike Polynomial Fit

Traditionally, the phase aberrations of the pupil functions are described quantitatively by expanding them using a Zernike circle polynomial set:

$$\arg[P(\rho, \theta)] = \sum_{i=1}^{\infty} a_i Z_i(\rho, \theta), \tag{14}$$

where a_i are aberration coefficients for corresponding Zernike polynomials $Z_i(\rho, \theta)$. Significant variations between different modifications of Zernike polynomials exist. In this work a set from Mahajan (1994) was used. The first 22 members of this set are listed in Table 11.1 together with their common names. This list can be further extended. In practice, however, expansion beyond the second-order spherical aberration is not very reliable due to experimental errors and noise in the measured image of $P(\rho, \theta)$.

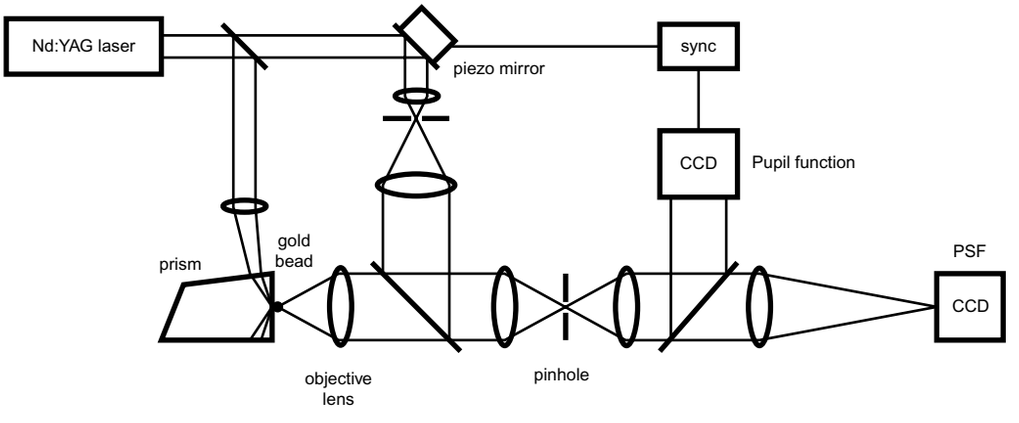


FIGURE 11.8. Phase-shifting Mach–Zehnder interferometer used for the pupil function measurements. Laser is frequency-doubled Nd:YAG laser.

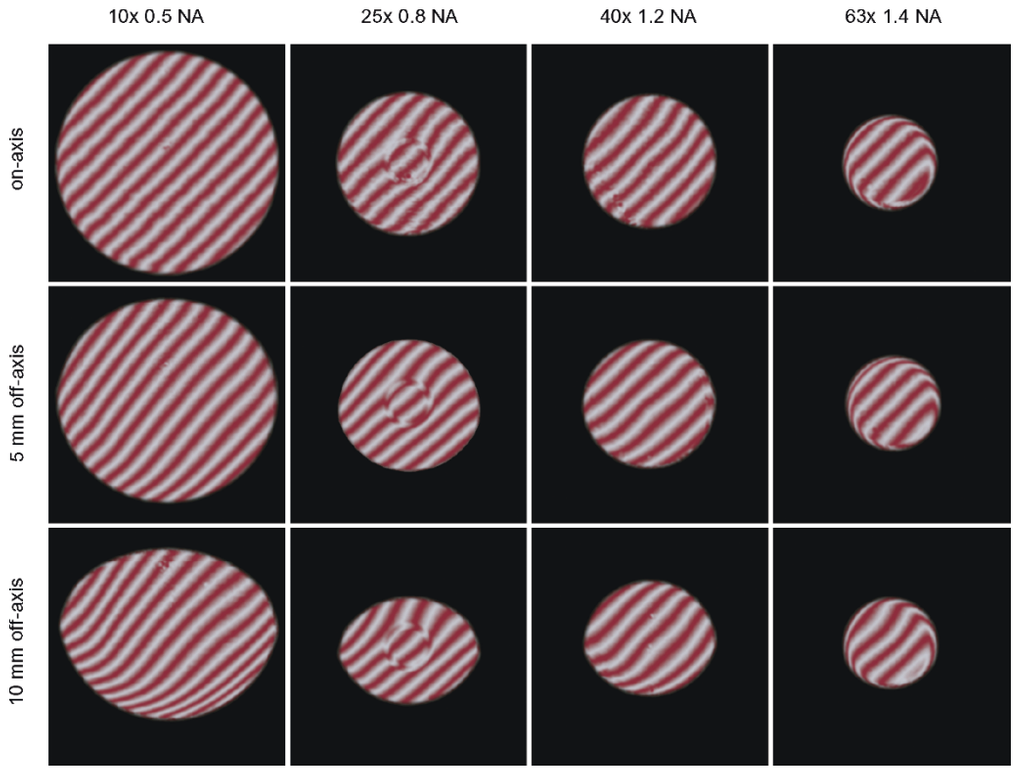


FIGURE 11.9. Phase distributions in the pupil plane of a representative range of objective lenses. Left to right: 10×0.5 NA, 25×0.8 NA multi-immersion, 40×1.2 NA water-immersion, and 63×1.4 NA oil-immersion objectives. Performance at the different positions in the field of view as measured in the intermediate image plane is shown. Regular phase tilt added to facilitate visualization.

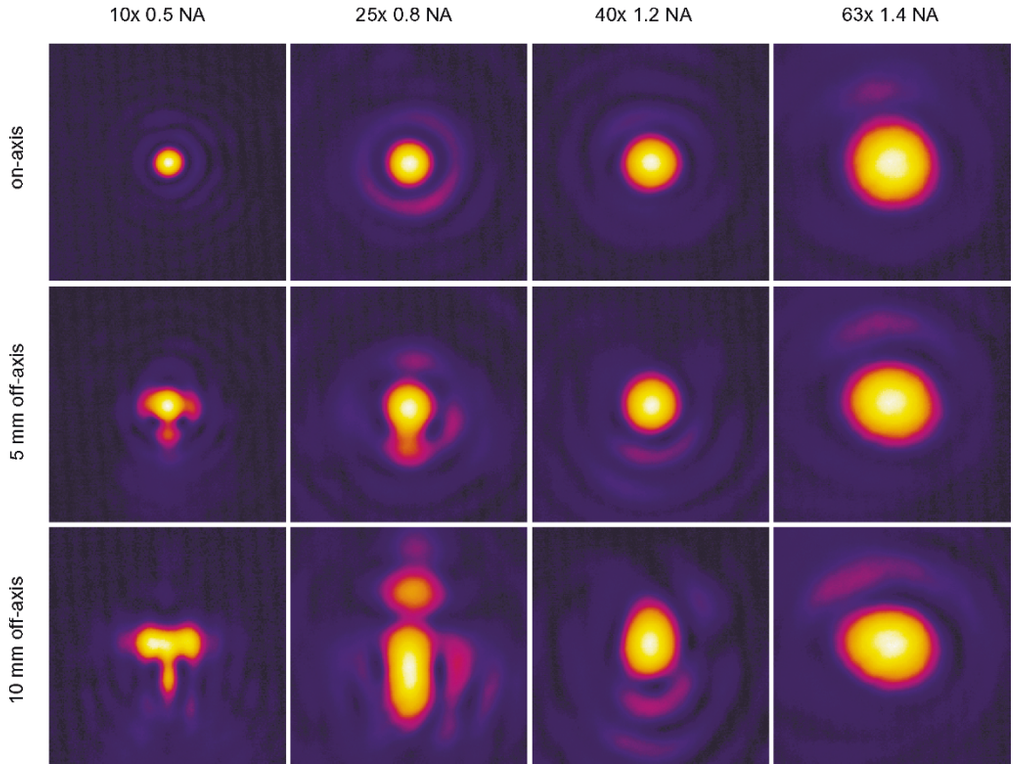


FIGURE 11.10. Point spread functions for the same lenses as in Figure 11.9.

TABLE 11.1. Orthonormal Zernike Circle Polynomials

i	n	m	$Z_i(r, \theta)$	Aberration Term
1	1	0	1	Piston
2	1	1	$2r\cos\theta$	Tilt
3	1	−1	$2r\sin\theta$	Tilt
4	2	0	$\sqrt{3}(2r^2 - 1)$	Defocus
5	2	2	$\sqrt{6}r^2\cos 2\theta$	Astigmatism
6	2	−2	$\sqrt{6}r^2\sin 2\theta$	Astigmatism
7	3	1	$2\sqrt{2}(3r^3 - 2r)\cos\theta$	Coma
8	3	−1	$2\sqrt{2}(3r^3 - 2r)\sin\theta$	Coma
9	3	3	$2\sqrt{2}r^3\cos 3\theta$	Trefoil
10	3	−3	$2\sqrt{2}r^3\sin 3\theta$	Trefoil
11	4	0	$\sqrt{5}(6r^4 - 6r^2 + 1)$	Primary spherical
12	4	2	$\sqrt{10}(4r^4 - 3r^2)\cos 2\theta$	
13	4	−2	$\sqrt{10}(4r^4 - 3r^2)\sin 2\theta$	
14	4	4	$\sqrt{10}r^4\cos 4\theta$	
15	4	−4	$\sqrt{10}r^4\sin 4\theta$	
16	5	1	$2\sqrt{3}(10r^5 - 12r^3 + 3r)\cos\theta$	
17	5	−1	$2\sqrt{3}(10r^5 - 12r^3 + 3r)\sin\theta$	
18	5	3	$2\sqrt{3}(5r^5 - 4r^3)\cos 3\theta$	
19	5	−3	$2\sqrt{3}(5r^5 - 4r^3)\sin 3\theta$	
20	5	5	$2\sqrt{3}r^5\cos 5\theta$	
21	5	−5	$2\sqrt{3}r^5\sin 5\theta$	
22	6	0	$\sqrt{7}(20r^6 - 30r^4 + 12r^2 - 1)$	Secondary spherical

The determination of the expansion coefficients a_i should, in principle, be a simple procedure, given that the Zernike polynomials are orthonormal. Multiplying the measured pupil function by a selected polynomial and integrating over the whole pupil area should directly yield the corresponding aberration coefficient. The real life is a bit more complicated, especially when processing the off-axis data, such as shown in Figure 11.9. One obstacle is vignetting: the standard Zernike set is no longer orthonormal over a non-circular pupil. Even without vignetting, the 2π phase ambiguity poses a problem. Before the expansion procedure can be applied, the phase of the pupil function has to be unwrapped — not necessarily a trivial procedure.

An entirely different expansion technique was developed to overcome these difficulties. This technique is based on a simulated, iterative wavefront correction routine, originally conceived to be used in adaptive optics applications together with a diffractive optics wavefront sensor (Neil *et al.*, 2000). The essence of the method is that small simulated amounts of individual Zernike aberrations are applied in turns to the measured pupil function. After each variation, the in-focus PSF is calculated and the whole process iteratively repeated until the Strehl ratio is maximized. The final magnitudes of the Zernike terms are then taken to be (with opposite signs) the values of the Zernike expansion coefficients of the experimentally measured, aberrated pupil function. This procedure is reasonably fast and sufficiently robust, provided that the initial circular aperture can still be restored from the vignetted pupil.

The power of this technique is demonstrated in Figure 11.11, where a 40 × 1.2 NA water-immersion lens was investigated at three different settings of the correction collar. As expected, adjusting the collar mainly changes the primary and secondary spherical aberration terms. Variations in the other terms are negligible. The optimum compensation is achieved close to $d = 0.15$ mm setting, where small amounts of both aberrations with opposite signs cancel each other. The usefulness of the Zernike expansion is further demonstrated by the fact that the main residual term in this case was the defocus, which, although not an aberration itself, could be easily mistaken for a spherical aberration upon visual inspection of the interference pattern.

Restoration of a 3D Point Spread Function

Nowhere is the power of the pupil function approach to the objective lens characterization more apparent than in cases when the full 3D shape of the PSF needs to be determined. Such need may arise, for example, when using deconvolution techniques to process images obtained with a confocal microscope.

As is clear from Eq. 4, it is not only possible to calculate an in-focus PSF from a measured pupil function, but the same can be done for any amount of defocus by choosing an appropriate value for the axial coordinate u. Repeating the process at regular steps in u yields a set of through-focus slices of the PSF. These can then be used to construct a 3D image of the PSF in much the same manner that 3D images are obtained in a confocal microscope. Compared to the direct measurement using a point scatterer, advantages of this approach are clear. A single measurement of the pupil function is sufficient and no scanning of the bead in three dimensions is required. Consequently, exposures per image pixel can be much longer. As a result, this method provides much improved signal-to-noise ratio in the final rendering of the PSF, allowing even the faintest sidelobes to be examined.

Obviously, presenting a complete 3D image on a flat page is always going to be a problem but, as Figure 11.12 shows, even just two meridional cross-sections of a 3D PSF provide infinitely more information than a plain 2D in-focus section of the same PSF at the bottom of Figure 11.9. Thus, for example, the yz-section clearly shows that the dominant aberration for this particular off-axis position is coma. Comparing the two sections it is also possible to note different convergence angles for the wavefronts in two directions — a direct consequence of vignetting.

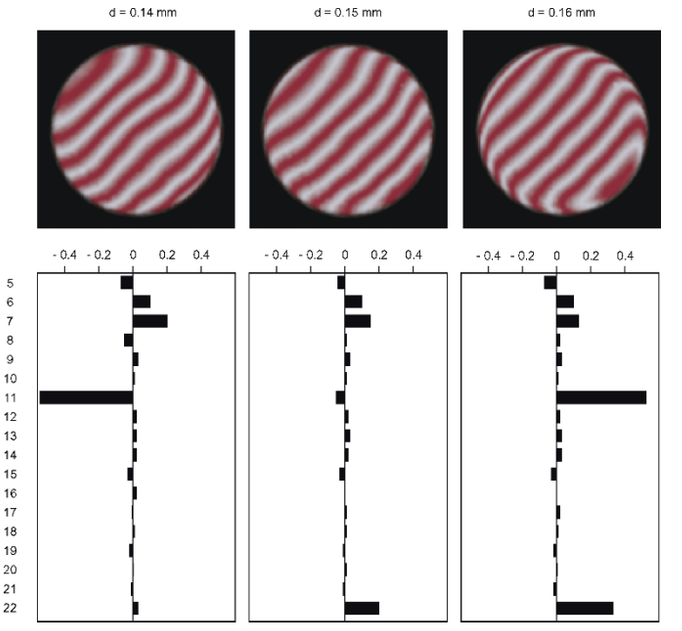


FIGURE 11.11. Variations in wavefront aberration function expressed via Zernike modes when correction collar of a water-immersion lens is adjusted.

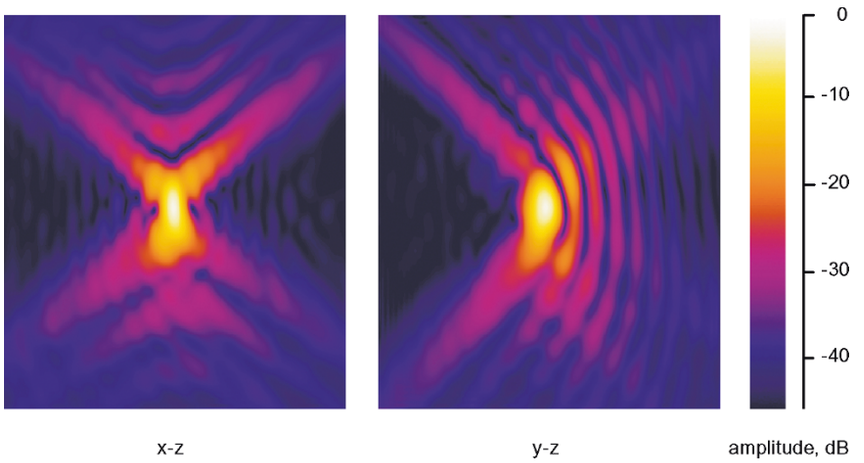


FIGURE 11.12. Three-dimensional PSF restored from pupil function data, shown here via two meridional sections.

Empty Aperture

Testing objective lenses with highest NAs (1.4 for oil, 1.2 for water immersion), one peculiar aberration pattern is often encountered. As shown in Figure 11.13, the lens is well corrected up to 90% to 95% of the aperture radius, but after that we see a runaway phase variation right to the edge. Speaking in Zernike terms, residual spherical aberration components of very high order are observed. Because of this high order, it appears unlikely that the aberrations are caused by improper immersion fluid or some other trivial reason. These would manifest themselves via low-order spherical as well. More realistically, this is a design flaw of the lens.

The portion of the lens affected by this feature varies from few to about 10%. For the lens in Figure 11.13, the line delimiting the effective aperture was somewhat arbitrarily drawn at NA = 1.3. What is undeniable is that the effect is not negligible. In all likelihood, this form of aberration is the reason for the somewhat mysterious phenomenon when a high NA lens exhibits a PSF that is perfect in all respects except for an apparently reduced NA. This was the case in "PSF Measurements" and also described by other researchers (Hell *et al.*, 1995).

It is quite clear that competitive pressures push the lens designers towards the boundary (and sometimes beyond the boundary) of the technical possibilities of the day. A few years ago no microscope lens manufacturer could be seen without a 1.4 NA oil-immersion lens when the Joneses next door were making one. The plot is likely to be repeated with the newly emerging 1.45 NA lenses. It is also true that a hefty premium is charged by the manufacturers for the last few tenths in the NA. It is quite possible that in many cases this is a very expensive *empty* aperture, which, although physically present, does not contribute to the resolving power of the lens.



FIGURE 11.13. Pupil function of 63 × 1.4 NA oil immersion lens with both nominal (outer ring) and effective working (inner ring) apertures indicated.

This discussion may seem to be slightly off the point because many users buy high NA lenses not because of their ultimate resolution, but because of their light gathering efficiency in fluorescence microscopy. This property is approximately proportional to NA^2 and therefore high NA lenses produce much brighter, higher contrast images. At first glance it may seem that the aberrated edge of the pupil will not affect this efficiency and hence buying a high NA lens, however aberrated, still makes sense. Unfortunately, this is not true. Because the phase variation at the edge is so rapid, the photons passing through it reach the image plane very far from the optical axis. They do not contribute to the main peak of the diffraction spot, instead they form distant sidelobes. In terms of real life images, it means that the brightness of the background, and not the image itself, is increased. Paradoxically, blocking the outermost portion of the pupil would in this case *improve* the image contrast!

The last statement may well be generalized in the following way: in the end, the only sure way of obtaining a near-perfect high NA objective lens is to acquire one with larger-than-required nominal NA and then stop it down. Incidentally, in certain situations this may be happening even without our deliberate intervention. Consider using an oil immersion lens on a water-based sample: no light at NA >1.33 can penetrate the sample anyway and hence the outer aperture of the lens is effectively blocked. Not that such use should be ever considered unless in dire need: see Chapter 20 for a graphic description of the Bad Things that will happen.

MISCELLANEA

In this section a few more results obtained with the pupil function evaluation apparatus are presented. These need not necessarily be of prime concern to most microscope users but might be of interest to connoisseurs and, indeed, could provide further insight into how modern objective lenses work.

Temperature Variations

Many microscopists should recall seeing 23°C on a bottle of immersion oil as a temperature at which the refractive index is

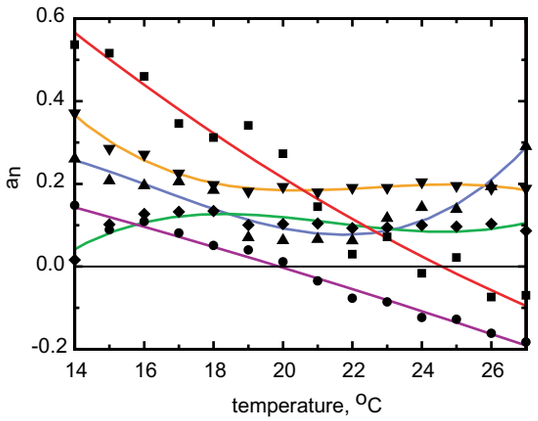


FIGURE 11.14. Temperature variation of primary (*red*) and secondary (*purple*) spherical aberrations as well as magnitudes of astigmatism (*blue*), coma (*orange*), and trefoil (*green*). The latter three were defined as $a = a = \sqrt{a_s^2 + a_c^2}$, where a_s^2 and a_s^2 are the sine and cosine components of the corresponding aberrations.

specified, typically $n = 1.518$ at $\lambda = 546\,\text{nm}$. But how important is this standard laboratory temperature to the performance of high NA lenses? In order to answer this question, the pupil function of a 100 × 1.4 NA oil-immersion lens was measured at a range of temperatures and the results were processed to obtain the variation of the primary aberration coefficients with the temperature.

The major factor in the degradation of the imaging qualities of the immersion lenses with temperature is the variation of the refractive index of the immersion oil, usually at the level of $dn/dT = 3 - 4 \times 10^{-4}$. The effect of this change is similar to that of introducing a layer of a refractive-index–mismatched material between the lens and the sample. The resulting aberrations are well understood, their exhaustive analysis can be found in Török and colleagues (1995). In short, spherical aberrations of various orders will be generated; the relative weight of higher-order terms rises dramatically with the NA of the lens. This is corroborated by the experimental data in Figure 11.14 which show steady, almost linear variation in both the primary and secondary spherical aberration terms with temperature. Less predictably, the same plot also registers significant variations in the other first-order aberrations: coma, astigmatism, and trefoil. Because of their asymmetry, these aberrations cannot be explained by the oil refractive index changes. They are probably caused by small irregular movements of individual elements within the objective lens itself.

Strictly speaking, aberrations caused by refractive index changes in the immersion fluid should not be regarded as lens aberrations. In practice, however, the lenses are designed for a particular set of layers of well-defined thicknesses and refractive indexes between the front of the lens and the specimen. Any change in these parameters upsets the fine optical phase balance in the system and results in aberrated PSF. This might be an argument why it makes sense to treat the immersion medium as being a part of the objective lens. The temperature effect depends dramatically on the type of the immersion fluid used. Water with $dn/dT \approx 8 \times 10^{-5}$ is far less sensitive; dry lenses, of course, are not affected at all. Long-working-distance lenses will be at a disadvantage too due to longer optical paths in the immersion fluid.

Closer analysis of Figure 11.14 reveals that the aberrations are indeed minimized around 23°C, where the combined primary and secondary spherical aberrations are close to their minimum. A small but noticeable hysteresis effect was also noted when, after a few temperature cycles, the aberration coefficients failed to return to their low initial values. It is tempting to connect this effect to the fact that the imaging properties of even the best of lenses always deteriorate with age — although accidental straining during experiments is still likely to remain the prevailing factor.

Polarization Effects

Polarization effects encountered when imaging a dipole with a high NA lens have been covered elsewhere (Wilson *et al.*, 1997). For the purposes of this investigation they are interesting inasmuch as the imperfections of the lens contribute to them. When an image of a small scatterer is viewed between the crossed polarizers, a characteristic "clover leaf" pattern emerges. An image of the pupil plane, Figure 11.15, is particularly telling. It shows that only the rays that travel very close to the edge of the pupil pass through the polarizer.

This happens because the polarization of light in these four segments is slightly rotated from its original *x*-direction. The reason for this rotation is 2-fold. First of all the radiation of a dipole is linearly polarized in the meridional plane, which can only be approximated by a uniformly polarized plane wave for small angles α. When this spherical wavefront is straightened by the lens and projected into the pupil plane, only light propagating in *xz* and *yz* possesses perfect *x*-polarization, the remainder is rotated to some degree. The degree of rotation increases dramatically with higher aperture angles. This effect is fundamentally geometrical; its close cousin is a well-known problem of how to comb a hairy ball.

The second reason for the polarization rotation is more prosaic: Fresnel losses. These tend to be higher for *s* than for *p* polarized

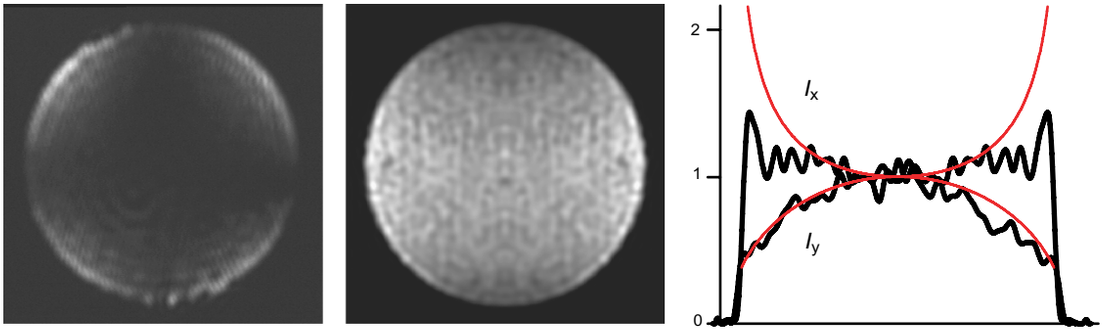


FIGURE 11.15. Polarization and apodization effects in a high NA lens. An image of a dipole scatterer viewed at the pupil plane of a 100 × 1.4 NA lens with crossed (left) and parallel (center) analyzers. Principal cross-sections, together with the theoretical predictions according to Eq. 15 (*red line*), are also shown.

light. For a beam travelling in a plane bisecting the *xz*- and *yz*-planes, the overall tendency would be to rotate the polarization towards the radial direction. Hence, this effect seems to work in the opposite direction to that caused by the geometric factor, which favors the azimuthal direction.

Apodization

So far the emphasis of this investigation has been on measuring the phase aberrations. This is justified by the fact that the phase deviations from an ideal spherical wavefront have considerably more impact on the shape of the PSF than similar imperfections in amplitude. Nevertheless, for completeness' sake it might be interesting now to have a closer look at the apodization effects occurring in high NA lenses. Using dipole radiation as a probe offers unique advantages in this task. Because the angular intensity distribution of the dipole radiation is well defined, any deviations from perfect lens behavior should be easy to spot.

Let's assume that the polarization vector of a dipole situated in the focus is aligned in the *x*-direction. Angular intensity distributions in the *xz*- and *yz*- (i.e., meridional and equatorial) planes will be given by, respectively, $I_x \sim \cos^2\alpha$ and $I_y = \text{const}$. Due to purely geometric reasons, these distributions will change when light propagates to the pupil plane even if the lens is perfect. With reference to Figure 11.11 and to the sine condition $d = nf\sin\alpha$, it is not too difficult to show that an extra factor of $\sec\alpha$ has to be introduced when going from the object to the pupil side of the objective in order to satisfy the energy conservation law. This factor has been well known since the early days of high NA lens theory (Richards and Wolf, 1959). Intensity distributions in the pupil plane should therefore look like $I_x \sim \cos\alpha$ and $I_y \sim \sec\alpha$ or, with the help of sine condition:

$$I_x \sim \frac{nf}{\sqrt{(nf)^2 - d^2}}, \qquad I_y \sim \frac{\sqrt{(nf)^2 - d^2}}{nf}. \tag{15}$$

An experiment to measure these distributions was carried out on the setup shown in Figure 11.8 by simply blocking the reference beam and capturing the pupil intensity image alone. To produce the results shown in Figure 11.15 images of eight individual scatterers were acquired and averaged in the computer. Intensity distributions in the two principal planes were then extracted. They follow the theoretical predictions rather well up to about half of the pupil radius. After that, apodization is apparent, and increases gradually, reaching about 30% to 50% towards the edge of the pupil.

The cause of this apodization in all likelihood is the Fresnel losses in the elements of the objective lens. Broadband antireflection coatings applied to these elements are less effective at the higher incidence angles that the high aperture rays are certain to encounter. Because of the nature of these losses, they are likely to be very individual for each particular type of objective lens. It is also worth noting a slight polarization dependence of the losses that contributes to polarization effects described in the previous section.

CONCLUSION

The range of experimental setups and techniques dedicated to the characterization of the high NA objective lenses could be continued. For example, the lateral chromatic aberration has not been considered thus far. One has to be practical, however, and draw a line at some point.

From the tests described in this chapter, the measurement of the pupil function provides the most detailed and insightful information about the capabilities of a particular lens. In many cases, two or three pupil functions measured across the field of view and, perhaps, tabulated in the form of Zernike coefficients, would be more than sufficient to predict the lens performance in most practical situations. It is disheartening to think of how much wasted time, frustration, and misunderstandings could be avoided if such information were to be supplied with the objective lenses by their manufacturers.

My overall conclusion is that the vast majority of currently designed objective lenses perform really well. Any imperfections visible in a microscope image are far more likely to be a result of a sloppy practice (e.g., tilted coverslip, incorrect immersion fluid, etc.) than of a fault of the lens itself. That said, cutting-edge designs are always going to be a problem and the very highest NA lenses should be approached with caution. It is also worth pointing out that elements of the microscope other than the objective lens may also be a factor in imaging quality. The tube lens is one such element of particular concern. Having evolved little over the last years, this lens simply has too few elements to achieve the aberration correction on par with that of an all-singing all-dancing objective lens. This situation is further exacerbated by the advent of a new breed of low magnification high NA objectives with their enormous back apertures.

ACKNOWLEDGMENT

I thank my colleagues M.A.A. Neil and T. Wilson for numerous contributions to this work.

REFERENCES

Born, M., and Wolf, M., 1998, *Principles of Optics*, Pergamon Press, Oxford.

Hell, S.W., Hanninen, P.E., Kuusisto, A., Schrader, M., and Soini, E., 1995, Annular aperture 2-photon excitation microscopy, *Opt. Commun.* 117:20–24.

Juškaitis, R., and Wilson, T., 1998, The measurement of the amplitude spread function of microscope objective lens, *J. Microsc.* 189:8–11.

Juškaitis, R., and Wilson, T., 1999, A method for characterizing longitudinal chromatic aberration of microscope objectives using a confocal optical system, *J. Microsc.* 195:17–22.

Juškaitis, R., Neil, M.A.A., and Wilson, T., 1999, Characterizing high quality microscope objectives: a new approach, *SPIE Proc*. 3605:140–145.

Mahajan, V.N., 1994, Zernike circle polynomials and optical aberrations of systems with circular pupils, *Appl. Optics* 33:8121–8124.

Malacara, D., 1992, *Optical Shop Testing*, John Wiley and Sons, New York.

Neil, M.A.A., Booth, M.J., and Wilson, T., 2000, New modal wave-front sensor: A theoretical analysis, *J. Opt. Soc. Am. A* 17:1098–1107.

Richards, B., and Wolf, E., 1959, Electromagnetic diffraction in optical systems II. Structure of the image field in an aplanatic system, *Proc. Roy. Soc. Lond. A* 253:358–379.

Török, P., Varga, P., and Németh, G., 1995, Analytical solution of the diffraction integrals and interpretation of wave-front distortion when light is focused through a planar interface between materials of mismatched refractive-indexes, *J. Opt. Soc. Am. A* 12:2660–2671.

Wilson, T., and Sheppard, C.J.R., 1984, *Theory and Practice of Scanning Optical Microscopy*, Academic Press, London.

Wilson, T., Juškaitis, R., Rea, N.P., and Hamilton, D.K., 1994, Fibre optic confocal and interference microscopy, *Opt. Commun.* 110:1–6.

Wilson, T., Juškaitis, R., and Higdon, P.D., 1997, The imaging of dielectric point scatterers in confocal and conventional polarisation microscopes, *Opt. Commun.* 141:298–313.

12

Photon Detectors for Confocal Microscopy

Jonathan Art

INTRODUCTION

In its most general form, confocal microscopy encompasses all optical techniques whose illumination and detection scheme examines each point in an object in the absence of interfering information from neighboring points. Recently the technique has expanded to encompass not only morphology but also disciplines as far afield as physiology, spectroscopy, fluorescence lifetime analysis, and even DNA sequencing. As a result, the requirements and design constraints on appropriate detection systems are as varied as the fields to which the technique is applied.

In the familiar case of fluorescent imaging, for example, confocal illumination and detection is used to reduce the background fluorescence from out-of-focus planes to obtain better image quality than that achieved in conventional fluorescence microscopy using Köhler illumination. For many confocal microscopes employing either disk (Petráň *et al.*, 1968) or line scan techniques, the primary detector is the human eye. It is attractive in terms of its quantum efficiency: roughly 16% of the photons incident on the cornea are perceived. The number and size of detector elements is high, on the order of 10^6, and this massive parallelism, joined with higher-order processing, results in the relatively rapid perception of an image. Any confocal technique using visible light that projects points in an object coherently onto conjugate points in an image plane can employ this detector. If the scanning is rapid enough, a stable, full-field image will be seen. When such microscopy is combined with focusing through the object, it is possible to readily identify and characterize its three-dimensional (3D) structure. Under relatively high illumination, such full-field confocal systems are in many ways the most general and suitable for a wide variety of tasks. The detection problem, if you will, has been solved for us over the last 10^9 years of evolution.

Under low-light conditions and for other more specialized tasks such as spectroscopy or fluorescent lifetime analysis, the eye is far from the perfect detector. Because it is highly adaptive and can work over nine log units of intensity, it is also less than ideal at quantitative comparisons of absolute intensity. Nor is the eye able to implement averaging and filtering techniques to enhance the signal-to-noise ratio (S/N) in the image. Finally, and often most significantly, some confocal systems have slow scanning rates or are designed to project points in the object plane back onto a single point, and it is impossible in such cases for the eye to perceive a coherent image.

For these reasons and others, it is necessary to develop techniques that approach, and in many respects surpass, the signal processing capabilities of the eye and that are amenable to further digital enhancement. The task is important because, at present, the design goal of achieving the highest S/N in a confocal image for a given dose to the specimen is often degraded by elements in the detection system. For example, when light levels are low (<20 photons/pixel), significant improvements in S/N can often be made by employing the greatest possible gain in the detector or by exploiting photon-counting, rather than analog measurement schemes. It should also be remembered that the particular detection scheme chosen is constrained not only by the detectors but also by the particular confocal technology employed, the levels of illumination that can be used, and limitations imposed by the nature specimen.

At the outset it should be noted that simple point detectors, such as photomultiplier tubes (PMT), are often used in conjunction with bandpass filters to quantify the number of photons at different wavelengths in a typical two- or three-channel laser scanning microscope. However, the recent interest in characterizing the full spectrum of dyes *in situ*, as well as a desire to separate labels whose wavelength of peak emission may differ by a few nanometers, has led to the development of sophisticated spectroscopic array detectors that divide the incident light into bands a few nanometers wide. In addition, continued improvements in multi-point or line-scanning confocal microscopy have resulted in the use of sophisticated array detectors that simultaneously accumulate data across the image plane. In all of these contexts, the overarching goal is to choose a detection scheme that yields the highest quantum efficiency, the lowest background levels, and the highest S/N.

In this chapter we will consider the quantal nature of light and the interaction of photons with materials. We will compare a number of possible detectors in terms of their quantum efficiency, responsivity, spectral response, inherent noise, response time, and linearity. We will then consider the design constraints in terms of the front-end circuitry that digitizes the data. The figures of merit for detection are usually that the estimate of the signal is limited either by the noise within the signal or by the background radiation. No physical detector can improve on these limits. Finally, we will suggest future directions toward more perfect detectors with signal processing capabilities limited only by the stochastic nature of the signal. We will begin by considering the kinetic energy of photons.

THE QUANTAL NATURE OF LIGHT

At very low light levels, two aspects of the quantal nature of light can be demonstrated. First, each particle, or photon, has an associated kinetic energy. An incident photon stream transfers kinetic energy to a material and gives rise to the variety of effects used in light detection. Second, at low light levels it is apparent that even

Jonathan Art • University of Illinois College of Medicine, Chicago, Illinois 60612

Handbook of Biological Confocal Microscopy, Third Edition, edited by James B. Pawley, Springer Science+Business Media, LLC, New York, 2006.

with perfect detection, the estimate of the intensity of a source is limited by the statistics of photon arrival at the detector. The statistical nature of photon flux will be considered in a later section.

First consider the kinetic energy of a photon incident on a detector. The classic frequency of electromagnetic radiation, ν (s^{-1}), is related to the quantum mechanical kinetic energy, $E(J)$, of an individual photon by $E = h\nu$, where h is Planck's constant (6.626×10^{-34} in Js). The relation between the frequency, ν, and the wavelength, λ (in m), is given by: $\nu = c/\lambda$, where c is the velocity of light (2.997×10^{8} m/s). Each photon in monochromatic green light, $\lambda = 550$ nm, has a kinetic energy of 3.58×10^{-19} J, or 2.25 electron volts (eV). The human eye is sensitive to light with λs roughly between 400 and 750 nm. In confocal microscopy, the range of molecular probes used in biological experiments will most likely fluoresce at λs that range from the ultraviolet to the near-infrared, say from 300 nm to 1200 nm. The associated photons will have kinetic energies between 4.16 and 1.03 eV. These modest energy levels will necessarily restrict the types of materials and the techniques that can be used for photon detection.

INTERACTION OF PHOTONS WITH MATERIALS

When metals or semiconductors are illuminated, the photons may be either reflected or absorbed. If they are absorbed, the kinetic energy (KE) of the photon is imparted to the structure. This energy may be transformed into a random motion as heat, or it may have a direct effect that changes the arrangement of charges in the crystal lattice of the material (Kittel, 1986). These direct effects are the bases of a number of internal and external techniques of photon detection.

Thermal Effects

Thermal effects do not depend on the photon nature of light, and the response of the material depends on the radiant power, not the spectral content of the radiation. Thermal effects are characterized by changes in properties of a material arising from an increase in its temperature due to the absorption of radiation. Heating and cooling of a macroscopic detector is slower than techniques in which photons interact directly with electrons in the material. Roughly speaking, thermal effects are on a millisecond time scale, and photon effects are on microsecond or nanosecond time scales. In confocal microscopy, the slow response and lower sensitivity of thermal detectors, as compared to direct photodetectors, would restrict their use as primary detectors. They could, however, be used to calibrate the system because their response is independent of the radiation λ. The performance of thermopiles, Golay cells, bolometers, and pyro-electric thermal detectors have been reviewed by Putley (1977) and will not be considered further here.

Direct Effects

In direct photodetection, the photons interact directly with electrons in the material. These electrons may either be free or bound to lattice or impurity atoms. For reasons of speed and sensitivity, the detectors used in confocal microscopy will generally be of the photon detection class. In metals and semiconductors, electrons are bound to their atoms within the material by electrostatic force. The average strength of this force is described by the material's ionization energy or work function. An electron with energy greater than this can escape from the atom. The smallest ionization energy for any elemental solid is ≈ 2.1 eV of metallic Cs. If an electron in solid Cs absorbs a photon with a KE ≥ 2.1 eV, a direct photoeffect can occur. The ionization energies of a number of materials are given in Table 12.1. Given the low KE of photons in the visible range, the materials employed for direct photodetection will almost always be semiconductors.

Direct photon effects can be divided into two classes, internal and external. Internal effects are those in which the electrons or holes stay within the material. Internal effects can be further subdivided in three ways: (1) those in which the incident photon interacts with a bound electron; (2) those in which the photon interacts with carriers that are already free; and (3) those in which the photon produces a localized excitation of an electron into a higher energy state within the atom. The external photoeffect, or photoemissive effect, is one in which the photon causes emission of an electron from the surface of the absorbing material known as the photocathode. External devices often charge-multiply this free electron, producing gain. Of all the possible direct detection methods, the most often used are the photoconductive, photovoltaic, and photoemissive.

Photoconductivity

In photodetectors exploiting the phenomenon of photoconductivity, a photon effect is manifested by an increase in the free electron or hole concentration of a material, causing an increase in its electrical conductivity. Intrinsic photoconductivity occurs if the photon has enough kinetic energy to produce an electron/hole pair [Fig. 12.1(A)]. Extrinsic photoconductivity occurs when an incident photon produces excitation at an impurity center in the form of either a free electron/bound hole or a free hole/bound electron [Fig. 12.1(B)]. In general, photoconductivity is a majority carrier phenomenon that corresponds to an increase in the number of electrons in an *n*-type semiconductor or an increase in the number of holes in a *p*-type material. The minority carriers will also contribute, but because of their shorter lifetimes, they contribute less. A circuit to detect the photoconductive effect is shown in Figure 12.2(A).

Photovoltaic

Unlike the photoconductive effect, the photovoltaic effect requires an internal potential barrier and field to separate the photoexcited hole–electron pair. This occurs at a simple *p–n* junction but can be observed in *p–i–n* diodes, Schottky barrier diodes, and avalanche diodes as well. The field-induced charge separation accompanying photoexcitation is shown in Figure 12.1(C). By definition, the photovoltaic effect is obtained at zero bias voltage, that is, the open

TABLE 12.1. Work Functions and Forbidden Energy Gaps for Common Materials Used in Direct Photodetectors

Metals	Work function, emission from bulk material, eV	Semiconductors	Forbidden energy gaps, eV
Be	3.67	CdS	2.40
Mg	3.66	CdSe	1.80
Ca	2.71	CdTe	1.50
Sr	2.24	GaP	2.24
Li	2.49	GaAs	1.35
Ba	2.38	Si	1.12
Na	2.29	Ge	0.67
K	2.24		
Rb	2.16		
Cs	2.14		

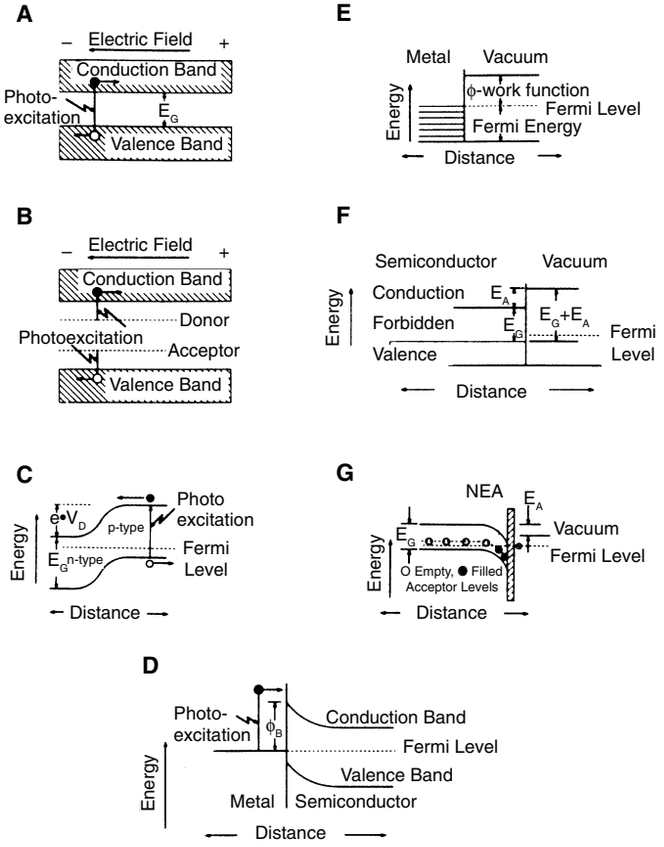


FIGURE 12.1. Direct photodetector energy-band models (energy vs. distance). (A) Energy profile of intrinsic photoconductivity producing an electron (*filled circle*) and a hole (*open circle*). (B) Energy profile of extrinsic photoconductivity producing either a free electron or a free hole. (C) Field-induced separation of charge in the photovoltaic effect. (D) Energy profile at the metal semiconductor interface of a Schottky diode. (E) Energy profile for emission from a classic photocathode material. (F) Energy profile for emission from semiconductor photocathodes. (G) Energy profile for emission from negative electron affinity photocathodes.

circuit voltage [Fig. 12.2(B)]. However, these detectors are frequently operated under reverse bias, so that the observed signal is actually a photocurrent (see, e.g., the following avalanche diode section) rather than a photovoltage [Fig. 12.2(C)]. In contrast to the photoconductive phenomenon, the photovoltaic effect is dependent on the minority carrier lifetime because the presence of both the majority and minority carriers is necessary for the intrinsic effect to be observed. Consequently, because the lifetimes of the minority carriers are less than those of majority carriers, the frequency response of photovoltaic detectors is higher than that of photoconductive devices.

p–i–n Diodes differ from *p–n* diodes in that a region of intrinsic material is incorporated between the two doped regions [Fig. 12.2(D)]. Absorption of incident radiation in the intrinsic region produces electron/hole pairs. Because of the high collection voltage and the small distance across the intrinsic material, the electron/hole pairs will drift rapidly through this region. As a consequence, the frequency response of a *p–i–n* diode will be higher than a comparable *p–n* diode (Mathur *et al.*, 1970).

The Schottky diode is formed at a metal–semiconductor interface [Fig. 12.1(D)]. Such an interface forms a potential barrier that causes separation of electrons and holes. These devices are especially useful at ultra-high frequencies and are often used as optical receivers operating in the GHz range (Sharpless, 1970).

Avalanche occurs in *p–n* diodes of moderate doping under reverse bias. Photoexcited or thermally excited electrons or holes are accelerated in the high-field region of the junction. As they are accelerated, they collide with the structure and free more electrons. Thus, as the name implies, an avalanche of electrons occurs in the high-field region. The advantage of the avalanche photodiode over other types of photodiodes is that it has internal gain. Under identical conditions, the response of such a diode is larger than that of the *p–n* diode. This internal gain cannot increase the S/N inherent in the detector, but it reduces the stringency of the noise and gain requirements of following stages. The high amplitude of the output and the speed of the response make avalanche diodes attractive for confocal microscopy, but the avalanche multiplication factor varies with the position of the initial photon absorption so the signal must be discriminated to remain a true measure of photon number. Additional difficulties with implementing avalanche diodes focus on the design of active drive circuits [Fig. 12.2(E)] that rapidly quench the avalanche response (Brown *et al.*, 1986, 1987). Because of their inherent speed and gain, avalanche diodes are often used in extremely rapid kinetic measurements performed at low repetition rates. Low repetition is necessary because the response to an incident photon must be quenched before the arrival of a subsequent one.

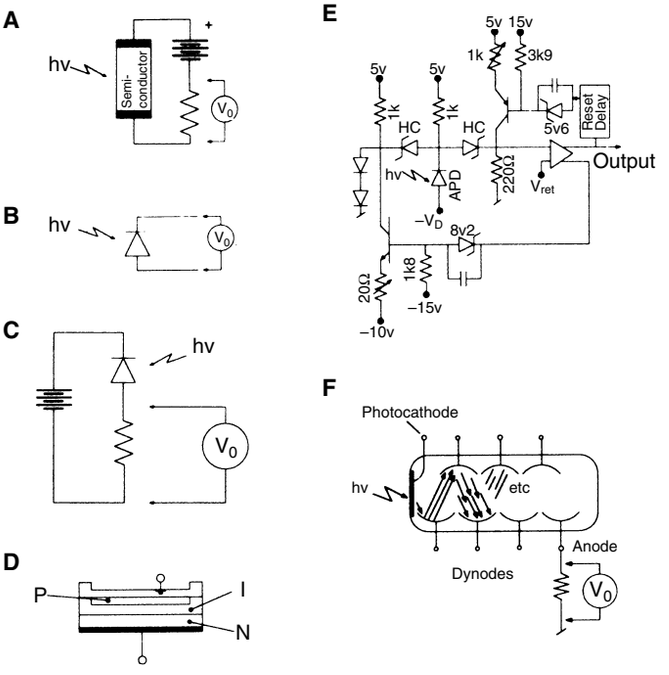


FIGURE 12.2. Direct photodetection circuits. (A) Photoconductivity measurement using a bias voltage and measuring the voltage drop across the series resistor. (B) Photovoltaic effect measures the potential difference generated across a simple *p–n* junction. (C) Measurement of the voltage drop across a series resistor produced by the photocurrent through a reverse biased photodiode. (D) Geometry of *p–i–n* photodiode with narrow intrinsic region between the *p* and *n* regions. (E) Active quenching circuit for an avalanche photodiode (Brown *et al.*, 1987). (F) Charge multiplication as photoelectrons are accelerated along a dynode chain by high potential between cathode and anode. Charge is converted to a potential difference across the load resistor at the anode.

Charge-Coupled Devices

Photoconductive or photovoltaic effects can be used to produce free carriers, which can then be injected into the transport structure of a charge-coupled device (CCD; Boyle and Smith, 1970). The metal–insulator–semiconductor and metal–oxide–semiconductor capacitors in these devices can be used to store photogenerated electrons [Fig. 12.3(A)]. Appropriate doping of the semiconductor substrate can be used to match the device to the λ of interest, and quantum efficiencies of greater than 85% can be achieved with commercially available devices when back-illuminated through the substrate (Fairchild, 1987). The maximum charge (in electrons) that each capacitor can store without overflowing into nearby pixels can be estimated by multiplying the pixel area (μm^2) by 600. Scientific CCD arrays range from 45 to $900\,\mu m^2$, corresponding to a maximum of 27,000 to 540,000 electrons/pixel.

Generally these devices are packaged as either linear (Coutures and Boucharlat, 1988) or two-dimensional (2D) arrays (Hier *et al.*, 1988; Mackay, 1988; McMullan, 1988) and are not available as simple elemental detectors. Because these devices have such high apparent quantum efficiency, they are suited to the low light requirements of confocal microscopy. For full-field, rotating disk, or line scan confocal microscopes, the 2D and one-dimensional (1D) arrays are a natural geometry, allowing the response of independent pixels to be integrated simultaneously. This is often an advantage at low light levels.

There are a number of ancillary considerations when using CCD arrays. First it should be noted that by their design [Fig. 12.3(B)], the 2D arrays will not have an available detector over the entire surface of the array. A percentage of the substrate will be occupied by the transport electronics and will be unavailable for primary imaging. Consequently, though the material may naturally have high quantum efficiency, a large fraction of the surface area of the device may be unavailable for photon capture. Second, because the difference in the number of electrons in each potential well represents the spatial variation of light incident on the detector, it is crucial that this variation be preserved as the packets of charge are transferred along the CCD to the output [Fig. 12.3(B2)]. Incomplete transfer of charge packets and the inability to transfer charge down the CCD structure in the absence of bias-, thermal- or photon-generated electrons in all the wells presently limited the utility of early devices in applications in which large expanses of the field are dark (Coutures and Boucharlat, 1988). Third, at low light levels the detection of the signal, the contrast, and the S/N are particularly dependent on the existence of low dark levels, and detectors that generate the fewest thermal electrons during photon capture and electron transport are to be preferred.

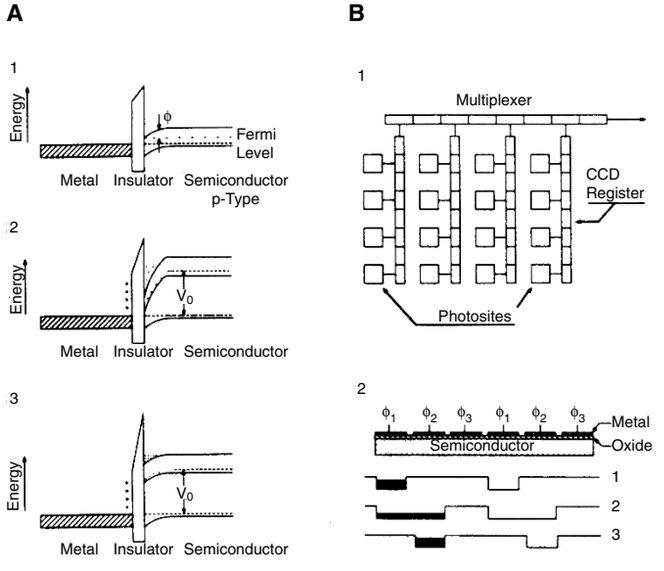


FIGURE 12.3. Charge-coupled devices used in photodetection. (A) Energy versus distance profile in metal–insulator–semiconductor *n*-channel structure. The initial bands (1) are changed after application of a gate voltage V_G (2) and charge builds up at the insulator–semiconductor interface until equilibrium is approached (3). (B) (1) Two-dimensional devices can be built from an array of discrete photosites and overlying CCD electrode arrays arranged to sequentially shift out and read the charge packets collected at each photosite. (2) Method of transfer of charge packet along MIS CCD structure. Overlapping clocks transfer charge between neighboring electrodes.

Photoemissive

The third direct photon detection technique is photoemissive, also known as the external photoeffect. The incident radiation causes the emission of an electron from the surface of the absorbing material (Einstein, 1905), the photocathode, into the surrounding space [(Fig. 12.1(E,F,G)], from whence it is collected by an anode. Photoemissive effects are used in simple vacuum phototubes composed of a simple cathode and anode. They are very fast. They are also found in devices that interpose gain, such as gas-filled phototubes that rely on the avalanche effect of photoelectrons striking the gas within the tube. In the familiar photomultiplier tube, the primary photoelectron strikes a series of emissive dynode surfaces interposed between the photocathode and the anode. At each surface, the number of electrons emitted is multiplied until, at the anode, millions of electrons may be collected for each photoelectron originally emitted from the photocathode [Fig. 12.2(F)].

Three special forms of photoemissive devices should be mentioned — the vacuum avalanche photodiode, the image dissector, and the microchannel plate. The first is a single gain-stage replacement for traditional PMTs that is particularly suited for photon counting. The latter two devices, in addition to the fast response, wide spectral sensitivity, and photon-counting capabilities of the usual types of PMTs, have position sensitivity and can be used as full-field detectors.

Vacuum Avalanche Photodiode

The vacuum avalanche photodiode (VAPD) combines an avalanche photodiode (APD) with a photocathode in a vacuum tube (Advanced Photonix). In the configuration shown in Figure 12.4(A), the electrons produced when photons are absorbed by the photocathode are accelerated by the large imposed electric field and bombard the underlying APD. A new electron is promoted for every 3.6 eV of incoming energy, and a typical 8k eV field would yield about 1800 new electrons striking the APD. These secondary electrons are subject to the internal APD field and will drift towards the junction and experience the gain inherent in the conventional avalanche phase. The total gain of such a device can be as much as 10^6, but because much of the gain is in the first stage, the noise figures are superior to conventional PMTs. Circuits suitable for single-photon counting or Raman spectroscopy are shown in Figure 12.4(B).

Image Dissector

The use of the image dissector tube in confocal microscopy (Goldstein, 1989) is a novel approach that combines the aperture and detection functions. The image dissector consists of the usual

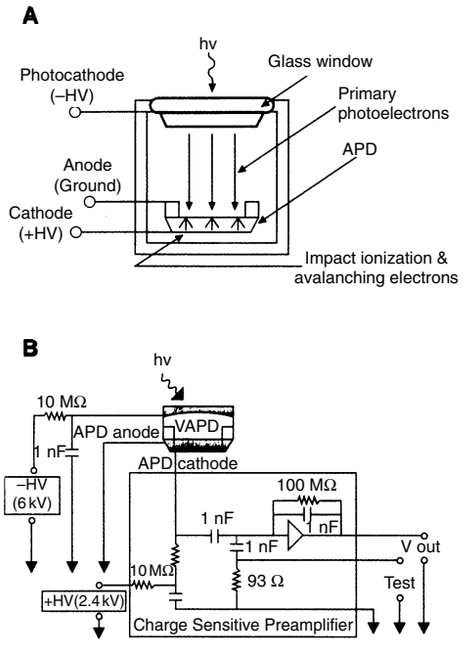


FIGURE 12.4. (A) Schematic of VAPD structure. Photons incident on the photocathode release photoelectrons that accelerate toward the underlying APD. (B) VAPD circuit suitable for photon and low-light-level spectroscopy.

photocathode and photomultiplier dynode chain. Between the two, an external magnetic field focuses the photoelectrons onto an image plane in which a small aperture is centered. Deflection coils sweep the image across the aperture, and only those electrons passing through the aperture undergo multiplication. All others are discarded. This type of field detector differs from normal vidicon tubes and CCD arrays in that integration does not take place in the detector between scans. Rather, it functions as a movable point detector and, in this capacity, can be used to track the illuminated spot in a confocal microscope electronically.

Microchannel Plate

The microchannel plate photomultiplier (MCP-PMT) differs from the usual PMT by replacing the chain of discrete dynodes with a channel of continuous photomultiplication. The MCPs are secondary multipliers consisting of an array of capillary tubes, or channels, fused together to form a plate. The tube diameter can be as small as a few micrometers, and the interior of each is coated with a photoemissive compound. A high-voltage electric field is imposed along the length of the tube. Photons entering one end of the tube at an angle strike the channel wall with sufficient energy to generate secondary electrons. These electrons are accelerated and in turn strike the wall farther down the tube, and the process is repeated. Gains of 10^4 to 10^6 can result from this series of collisions (Kume *et al*., 1988). The MCP can thus serve as an intermediate gain stage in front of lower sensitivity detectors.

Comparison of Detectors

Detectors vary widely in their response properties. A comparison of the quantum efficiency, responsivity, spectral response, response time, and linearity of direct photodetectors is given in Table 12.2. Unlike thermal detectors, the response of direct photodetectors depends on the photon nature of light. Therefore, the response of the detector varies with the λ of radiation. The direct detectors differ widely in their maximum sensitivity and quantum efficiency. Graphs of the spectral response for examples of direct detectors are given in Figure 12.5. PMTs with classic photocathode materials have greatest sensitivity in the blue to UV (QE $\leq$ 35%). The short λ limits are functions of the envelope materials rather than the photocathode materials and can be extended by using quartz and fluorite faceplates. Semiconductors are attractive photoemissive materials because they have high quantum efficiency at longer λs and can be designed with ionization energies or work functions that match the λ of interest. As such they will be useful either as negative electron affinity (NEA) emissive materials for cathodes and dynodes in PMTs or as solid-state detectors (QE $\leq$ 85%).

TABLE 12.2. Response Properties of Sample Direct Photodetectors

Type of detector	Quantum efficiency	Radiant sensitivity (A/W)	Spectral range	Response peak (nm)	Response (seconds)	Range	Type
Silicon		0.4	190–1000	720	5×10^{-7}	$10^{-11} - 10^{-3}$ W	Hamamatsu S 1227
photodiode	80.0%	0.5	190–1100	920	2×10^{-7}	$10^{-11} - 10^{-3}$ W	Hamamatsu S 1337
PIN silicon photodiode	83.0%	0.6	190–1060	900	3×10^{-9}	$10^{-11} - 10^{-2}$ W	Hamamatsu S 1721
GaAsP	—	0.18	190–680	610	1×10^{-6}	$10^{-13} - 10^{-13}$ W	Hamamatsu S 1025
photodiode (Schottky)		0.22	190–760	710	0.8×10^{-6}	$10^{-13} - 10^{-3}$ W	Hamamatsu S 1745
Avalanche photodiode	70.0%	—	350–1050	830	0.2×10^{-9}	2×10^6 cts/s	Hamamatsu S 2381
PMTs							
S-1	0.5%	2.5×10^{-3}	300–1100	800	15 ns (FWHM)	5×10^7 cts/s	Thorn-EMI-9684
S-20	23.0%	64.0×10^{-3}	300–850	420	25 ns (FWHM)	3.3×10^7 cts/s	Thorn-EMI-9890
GaAs:Cs-O	17.0%	120.0×10^{-3}	200–950	850			RCA-Type 60 ER
CCD linear	85.0%	4.5 V/mJ cm^{-2}	330–950	680 readout	50 ns/pixel	7500:1	Fairchild CCD-134
CCD Areal 488 × 380 elements	15.0%	0.08 V/mW cm^{-2}	500–1000	800 rate	@ 60 Hz field	1000:1	Fairchild CCD-222

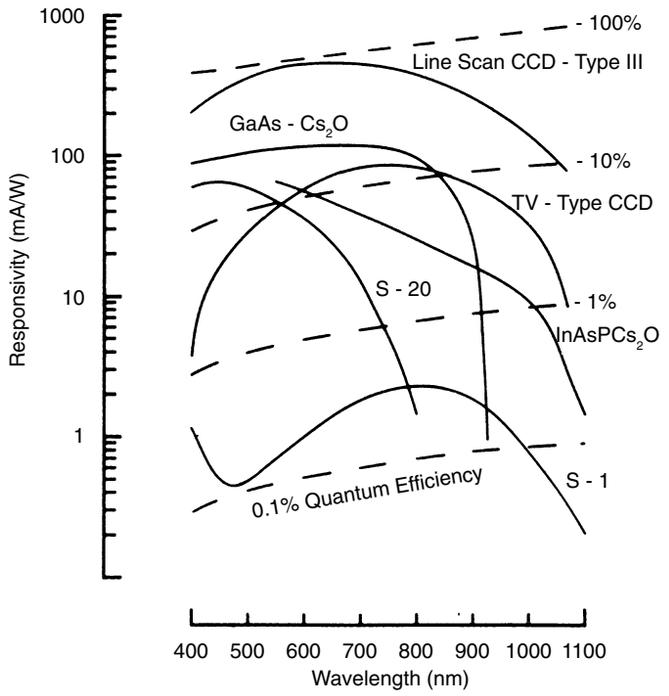


FIGURE 12.5. Typical spectral-response curves for internal and external direct photodetector materials.

NOISE INTERNAL TO DETECTORS

An ideal detector would be one in which detection is limited by the noise or background of the radiant source and no additional noise is added by the detector or subsequent amplification and conversion electronics. With present techniques, it is possible to design amplification and conversion stages with noise below that of the zero-signal output of the detector (Siliconix, 1986). Therefore, the detection scheme will generally be limited by the noise of the detector stage itself. All detectors are, in principle, in one of their two regimes. At very low light levels, their utility is limited by noise within the detector. At higher levels, the certainty in the estimate is limited by the statistics of photon flux. We will consider the noise inherent in both internal and external devices in turn. Formal expression of each noise contribution is given in Table 12.3 as the noise power obtained by summing the contributions of the independent noise sources in quadrature (Schwartz, 1970).

Noise in Internal Detectors

Internal detection with semiconductor devices is associated with two general classes of noise. The first is measurable in the absence of an applied bias voltage. It arises from the thermal motion of charge carriers within a material and is known as Johnson, Nyquist, or thermal noise. The second category of noise sources is only measurable in the presence of a bias voltage and is specific to the type of device and the variable measured in the photoconversion process. In photoconductors there also exists generation–recombination (g-r) noise, which is due to fluctuations in the rates of thermal generation and recombination of charge carriers, giving rise to a fluctuation in the average carrier concentration. This, in turn, is measured as a variation in average resistance. Complete analysis of g-r noise can be found in Van der Ziel (1959) and Burgess (1956). In diodes with an applied bias, shot noise is apparent. This noise is due to the quantal nature of current carriers and results in a statistical variation in the amplitude of the measured current. The final form of noise, which is not strictly amenable to analytic treatment, is 1/f noise, so named because the power varies more or less inversely with frequency.

Noise in Photoemissive Devices

For external photoemissive devices, the limit to detection is given by the dark current. This current has three origins: ohmic leakage, thermionic emission from the cathode and dynodes, and regenerative effects. Ohmic leakage is a breakdown between active leads

TABLE 12.3. Noise Currents in Direct Photodetectors[a]

Type of detector	Johnson noise[b]	Generation-recombination noise	Shot noise[c]	1/f Noise[d]	Multiplication noise	Value at which SNR = 1[e]
Extrinsic photo-detectors	Same	$I_{grn} = 2I_B\left(\frac{\tau B}{N}(1+\omega^2\tau^2)\right)^{1/2}$	Same	Same	N.A	
Intrinsic photo-detectors	Same	$i_{grn} = \frac{2IB}{N}\left(P_\tau \frac{B}{1+\omega^2\tau^2}\right)$	Same	Same	N.A	
Avalanche photodiodes	Same	N.A.	N.A.	Same	$i_M = M(2eIBM)^{1/2}$	10^{-14}
PMT alone	Same	N.A.	N.A.	N.A.	$i_2 = M(2eIB)^{1/2}\left(1+\frac{1}{\zeta-1}\right)^{1/2}$	-10^{-17}
I-V converter noise PMT and electronics	$(4kTgB(1 + R_{Lg} + (4\pi^{2/3})(R_{N/g})B^2C^2))^{1/2}$	N.A.	N.A.		Same	N.A.

[a] All sources considered to be independent, and total noise current is the square root of the sum of the squares of the contributing currents. Abbreviations: B, bandwidth of measurement; C, shunt capacitance of anode lead; d, dynode gain; e, charge on an electron f, frequency; g, shunt conductance of the anode lead; I, dark current; I_B, bias current; k, Boltzman's constant; K, multiplicative constant; M, charge multiplication or gain; N, number of electrons; P, number of holes R_L, load resistance; R_N, equivalent noise resistance of amplifier input; T, temperature in degrees Kelvin; carrier lifetime; angular frequency, NEP calculations are rough estimates for each class of detectors. Noise effects due to the noise-in-signal and that resulting from converter Q.E. I have not been included.
[b] $i_f = (4kTB/R_t)^{1/2}$ peak sensitivity (A/W) due to resistive components.
[c] $i_t = (2eIB)^{1/2}$ due to bias current.
[d] $i_F = (KI_B - {}^2B/f \sim {}^1)^{1/2}$ due to conjunctions with external conductors.
[e] NEP (W/Hz$^{-1/2}$ noise equivalent power).

along the insulating material of the tube. It can be identified at low acceleration voltages by the linear relation between the voltage and the measured current. At higher voltages the thermionic component, formally equivalent to shot noise, becomes apparent because thermally generated electrons from the cathode (or first dynode) undergo the same multiplication as do photoelectrons, and the amplitude of this component will increase in parallel with the amplitude of the PMT response under low light conditions. This component of the noise is dependent on temperature and can be reduced by cooling the tube.

At higher voltages, regenerative effects can come in and can include the glow of the dynodes under electron bombardment. Glowing of the glass envelope also occurs as photoelectrons impact the tube wall if it is not at the cathode potential. This effect can be eliminated either by keeping the envelope at a negative potential or by providing it with a shield at such a potential. Afterpulses can also occur. One type is the result of feedback from the dynodes to the photocathode (due to light given off from the dynode that impacts the photocathode and consequently gives off more electrons). This after-pulsing has a short delay (40–50 ns) after the initial pulse. A second type of after-pulse is due to the ionization of residual gases that are in the tube or are adsorbed in the envelope. Most prevalent are N^{2+} and H^{2+} ions that are accelerated back toward the negative cathode, giving rise to further electron emission. (The delay is somewhat longer, on the order of a few 100 ns.) Tubes that are run near a cooled helium environment will have troubles because the helium will permeate through the glass envelope and remain within the tube (RCA, 1980).

Further sources of noise arise from radioactive elements within the glass, such as $_{40}K$, or are due to cosmic rays. Additional noise is often produced after exposure of the tube to blue or near-ultraviolet (UV) light. Normally this is due to fluorescent room lights, though it is likely to be an increasing problem in experiments where near-UV light is used to stimulate the chromophors such as the Fura-2 and Indo-1 indicators used in the study of $[Ca^{2+}]$ (see Chapter 42, *this volume*).

The statistics of the effects of these noise sources will be considered next, along with the necessary probabilistic effect of the finite quantum efficiency of the original production of photoelectrons at the photocathode.

Statistics of Photon Flux and Detectors

Several of the parameters of direct photodetector behavior were given in Table 12.2. Many of the noise contributions for each detector are summarized in Table 12.3. In practice, the utility of the various detectors will be determined not only by the speed of the response necessary to represent the unique values at each pixel but also the absolute sensitivity of the device. In this section we will consider a figure of merit, the achievable S/N of the PMT, to demonstrate how the threshold sensitivity of a device is analyzed and predicted. This is not the only figure of merit that could be used for detectors. At the outset we suggested that confocal microscopy might examine light with λs from the UV to the near-infrared (IR). At the longer λs, the performance is limited by the background level of IR radiation. Comparisons of alternative figures of merit for detector function can be found in Seib and Aukerman (1973). In general, noise sources will either be additive or multiplicative. Additive noise, for example, is the noise added by the process of photoemission at the photocathode to the noise already present in the original photon flux. We can perform a straightforward analysis of the behavior of a detector in terms of the degradation of the S/N (Robben, 1971).

The detection process is limited at the front end by the S/N of photon flux. If the average rate of emission of photons is I_p, then during the observation interval τ the average observation is $n_p = I_p\tau$, and the variance is given by $\sigma_p^2 = I_p\tau = n_p$. The S/N is given by: $S/N = n_p/\sigma_p = (I_p\tau)^{1/2} = (n_p)^{1/2}$.

For any photon incident on the photocathode, the quantum efficiency (QE or Q_E) is the product of three probabilities. The first is the probability that a photon will be absorbed rather than transmitted or reflected. The second is the probability that this photon will produce a free electron. The third stands for the probability that the free electron will actually reach the surface of the material and escape. Therefore, for all real materials, QE < 1. Because the probability of release of a photoelectron per incident photon is related by the quantum efficiency, QE, then $n_{pe} = QE\ I_p\tau$. The variance of the number of photoelectrons, $\sigma_{pe}^2 = QE\ I_p\tau$. Consequently, at the stage of emission of photoelectrons from the photocathode, we can reduce the signal-to-noise ratio to $(S/N)_{pe} = (QE\ I_p\tau)^{1/2}$. The only way to improve on this S/N would be to use a material with the highest possible quantum efficiency, such as a NEA material.

During any recording period, τ, thermionic electrons will be emitted. The average number of these emissions is n_d, and their variance, $\sigma_{pe}^2 = n_d$. In all practical cases, the S/N of photoemission is determined from the total emission, which is a combination of the terms due to photoelectrons and thermionic electrons. The number of photoevents, $n_{pe} = n_c - n_d = QE\ I_p\tau$, where c and d indicate composite and dark terms, respectively. Because the photoevents and the thermal ones are independent, the square of the variances add, $\sigma_{pe}^2 = QE\ I\tau + n_d$. Thus, in the presence of dark noise, the S/N of a realizable PMT is given by $(S/N)_{pe} = (QE\ I_p\tau)/(QE\ I_p\tau + n_d)^{1/2}$.

Now consider what happens if we interpose j dynode stages all having identical gains, δ_j, and Poisson statistics of secondary emission. The gain seen at the anode will be $m = \delta 1 \cdot \delta 2 \ldots \delta j$. The anode variance, $\sigma_a^2 = QE\ n_p m^2[\{1 + 1/(\delta - 1)\} \cdot \{1 - (1/\delta j)\}]$. If, for example, we use negative affinity materials and in each stage the gain, δ, is large, then term $1/\delta j$ will be very small. Thus, $\sigma_a^2 \equiv QE\ n_{pm}^2\ [1 + 1/(\delta - 1)]$. The corresponding S/N is given by $S/N \equiv [QE\ n_p(\delta - 1)/\delta]^{1/2}$, which, if the gains are high, reduces to $S/N \equiv [QE\ n_p]^{1/2}$.

Thus, for any device with high gain at each stage, the performance will be dominated by the quantum efficiency of the first stage or perhaps by the photocathode and the statistics of the first dynode. In terms of current, the anode $(S/N)_a$ at the anode for a PMT is given for two cases in Table 12.3. The first is for the current alone, and the second includes the noise contributed by the output circuit noise in the amplifier. A complete analysis using generating functions to predict the total noise of a detector system based on additive and multiplicative noise sources is given in Jorgensen (1984) and Prescott (1966).

It should be noted that the implementation of spectroscopic imaging demanded the development of multi-channel detectors, and as is the case for the Zeiss 510 Meta, a multi-channel PMT. In array detectors such as the Hamamatsu H7260, 32 photomultiplier channels are arrayed in parallel within a single glass envelope. The face of each channel of the PMT is a scant 0.8 by 7 mm, on a 1 mm pitch, and the 10 dynodes occupy a linear array less than 15 mm in extent. As implemented, the accelerating voltage between photocathode and the first dynode is equal to the voltage drop between subsequent dynodes, so the QE and noise advantage obtained by having the greatest acceleration at the first stage between the cathode and dynode is lost. In more conventional single-channel PMTs, the acceleration voltage at this first stage is typically three times that of subsequent stages. Consequently, all

other things being equal, we would expect single-channel PMTs, to have better multiplicative noise performance than multi-channel arrays, if simply because the larger physical spacing between dynodes permits higher acceleration voltages at the initial stage.

A second issue concerning multi-channel arrays used for quantitative spectroscopy, while not concerning individual photon noise, *per se*, arises from possible cross-talk, and the variations in quantum efficiency, amplification, and noise characteristics between channels. When a single detector is used to characterize the spectrum of a fluorescent molecule, narrow filtering selects photons of different energies to play sequentially across the surface of the detector. Once the spectral characteristics of a given PMT are known, this information can be used to correct the experimentally determined spectra of interest. The requirements for multi-channel PMTs are no less exacting, and in principle the standard curve for each channel of the PMT needs to be determined. During manufacture variations on the order of 10% in the mean quantum efficiency and amplification are obtained. Obviously, because the photons in narrow energy bands will be directed to different detectors simultaneously in such a scheme, then to accurately determine the spectrum requires that the characteristics of each detector channel have been measured, and this information is used to normalize the raw data collected along the spectrum (see Chapter 36, *this volume*, for a simple test).

Representing the Pixel Value

In the majority of confocal microscopes, the image is constructed sequentially from the output of a point detector. Ideally, the digitized value at each pixel should reflect the average detector response during the time the beam dwells on a point in the field. Two problems must be considered. First, can we define a suitable means of sampling the response of the detector over the period used to estimate a pixel value? Second, because the goal of confocal microscopy is to achieve the maximum resolution, how do we avoid degrading the image with spurious correlation between the sampled values at neighboring pixels? Ideally the measure of intensity would be an average of the detector response over the time of interest. For ease of manufacture and implementation, however, such a scheme is often approximated by the use of a capacitive integration [Fig. 12.6(A)]. The time constant, τ, of such an integrator is often chosen to be 1/4 the pixel dwell-time. Such an integrator has the advantage that, in some sense, it represents a running average of the detector output. Unfortunately, it can be shown (Jones *et al*., 1971) that this form of integration results in a 2% correlation between neighboring pixels. (If the Nyquist bandwidth, as defined in Chapter 4, *this volume*, has been correctly chosen to be $1/2\pi\tau$, the signal will correlate between adjacent pixels by the same amount.) This correlation can be avoided by the use of true integration of the detector signal, whether this be in photon counting [Fig. 12.6(B,C)] or analog detection schemes [Fig. 12.6(D)]. Other advantages of full integration will be considered specifically with photon counting and with analog detection.

At low light levels ($\leq 10^8$ photons/s), direct photon-counting strategies have advantages over analog methods of light intensity estimation. The large gain inherent in most PMT designs is itself a distinct advantage in many photon-counting techniques because these tubes produce large pulses that are well above other sources of noise in the tube or in the subsequent electronics. In PMTs designed and selected for photon counting, the pulses produced by single-photon events are tightly distributed and widely separated from the amplitude of pulses produced by multiple photon events.

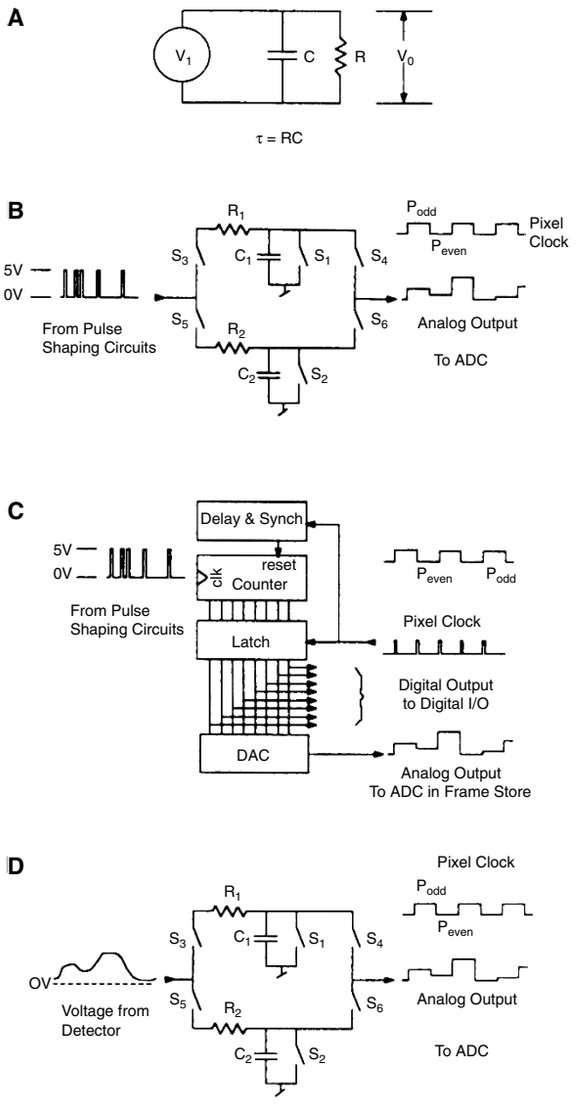


FIGURE 12.6. Methods of photon quantification. (A) RC integration. Charge or current from photodetector is changed into a voltage, and a running average is stored on a capacitor. The resistor in parallel should insure that the voltage across the capacitor decays with a time constant appropriate for the pixel dwell-time, but as this changes with scan zoom setting, the condition is not always met. (B) Analog method of photon counting. During alternate pixels, the upper and the lower half of the schematic circuit are used. During odd pixels, charge pulses generated by detected photons are stored on C_1. At the end of the pixel, S_3 is opened and the value on capacitor C_1 is converted to a digital word. This value is held for the duration of the pixel and then the capacitor is reset. While this conversion is taking place, the photon pulses for the next even pixel are accumulating on capacitor C_2, and the process is repeated. (C) Digital method of photon counting. ECL or TTL logic is used to count the photon pulses and output is by way of digital word or DAC conversion back to a video voltage. (D) Direct integration method used to store an analog output voltage. The circuit assumes that subsequent digital processing of the signal is used to normalize the response with respect to pixel dwell-time.

It is possible with modest acceleration voltages to produce well-defined charge packets that develop millivolt pulses of nanosecond duration across a 50Ω load. Further, removal of any variation in pulse amplitude at the load resistor can be accomplished by comparing the height of the pulse across the resistor with two well-defined thresholds. The lower threshold defines the minimum

height of a pulse considered to be due to a single photoelectron emitted from the photocathode, multiplied along the dynode chain, and collected by the anode. The upper threshold is greater than the pulse height produced by a majority of single photoelectron events, and pulses exceeding this height are likely to represent multiple photon events or other artifacts. The output of this two-stage detection scheme can be used to trigger a well-defined and tightly controlled pulse of known amplitude and duration. A minimum interval between pulses can be imposed to eliminate possible PMT artifacts such as those produced by correlated after-pulsing. Typically, pulses as short as 15 ns with a dead time between pulses of 5 ns can be used. Both Schottky transistor-transistor logic (TTL) and emitter-coupled logic (ECL) families are fast enough to count at the implied maximum rate of 50 MHz.

True integration of standard pulses can be accomplished as shown in Figure 12.6(B,C). In the analog method, pulses are directly integrated on a capacitor. Prior to integration, the capacitor is shorted to ground by a switch. During the integration, the shorting switch is open. In response to a series of input pulses, the voltage measured across the capacitor rises in a staircase fashion, with the rise at each step determined by the size of the capacitor and the magnitude and duration of the input pulses. At the end of the integration period, the final analog voltage is converted to a digital value using an analog-to-digital converter (ADC), and the capacitor is then reset. A duplicate capacitor and switch are arranged so that the capacitors integrate on alternate pixels, avoiding the loss of photon counts during ADC and capacitor resetting.

In the digital method, the pulses increment a TTL or ECL counter. At the end of the integration period, the count is latched in an output register. The counter is reset and begins accumulating counts for the next pixel. Additional logic can be configured to eliminate the loss of photon counts during output latching. The output of the digital latch can be used directly as an input for the image buffer, or the value can be converted back into a standard video voltage with a digital-to-analog converter (DAC). One attraction of the digital technique is that once the PMT pulses have been converted to logic levels, the process of integration with digital counters is immune to noise problems inherent in further analog processing. For either method of photon counting, with pixel dwell-times on the order of a microsecond, we would expect at most a few tens of photons to be counted. The small number of distinct signal levels represented by these photons could easily be converted to the range of standard video between 0 and 0.75 V and used as input to a typical 8-bit video ADC and frame grabber. Such a device would convert each voltage to a number between zero and 255.

For high light levels ($\geq 10^8$ photons/s) that might be typical of reflectance confocal microscopy as used in metallurgy or in the inspection of integrated circuits, the extreme measures needed to maximize the S/N under low light levels are unnecessary. A variety of different diode detectors with current-to-voltage converters can be used as, in these detectors, each photon absorbed deposits an identical amount of charge. In these examples, the output is continuous rather than discrete. Traditionally, low-pass filtering of the form of Figure 12.6(A) ($\tau = T/4$) is used to create a running average of the light intensity. The difficulty of pixel correlation remains whenever pixels are bigger than resels. It can be avoided by creating a technique similar to the analog method of integrating pulses in the photon detection scheme [Fig. 12.6(D)]. With the exception of the fact that the input to the capacitors is a continuous voltage rather than a series of discrete pulses, the technique and the process is identical to the previous case in Figure 12.6(B), though the results will be somewhat degraded by the fact that some photons contribute larger pulses to the total signal than others.

For either discrete or continuous estimates of luminance, the full integration technique is preferred over bandwidth limitation because it avoids the correlations inherent in using a running average. A second advantage is the ease with which different rates of confocal scanning can be implemented. With capacitive integration, the time constant of the integrator must be changed to match different rates of scan and pixel dwell-time and also to compensate for changes in the relative sizes of pixels and resels. With true integration, the match is automatic because the integration begins and ends at times defined by a pixel dwell-time. A third advantage of this technique is that the relative variance of the intensity estimate using full integration is half that obtained using capacitive integration with $\tau = T/4$ (Jones *et al.*, 1971). Consequently, for any desired level of precision, full integration will require 4× fewer frames for an average. This fact is important both in the speed of data acquisition and in minimizing photodamage to the sample.

CONVERSION TECHNIQUES

The resolution of the analog-to-digital conversion required for confocal microscopy is determined in part by the detector. For the photon-counting example above, all possible pixel values could be described uniquely with an 8-bit binary word. In full-field microscopy, however, a converter would need the resolution of a 14-bit binary word to take advantage of the linearity and large dynamic range of slow-scan CCD arrays. In essence, an ADC needs to have sufficient resolution to avoid degrading the S/N inherent in the conversion of the signal up to that point. The choice of converter is further restricted by the rate at which conversion is required. In general, confocal microscopy is characterized by a relatively high degree of resolution and high rates of digitization.

Of the types of converters available, only flash and successive approximation converters (Fig. 12.7) will be considered. The flash converter uses multiple comparators and simultaneously compares the analog input with all analog code levels. The speed of conversion is limited only by comparator speed and the propagation

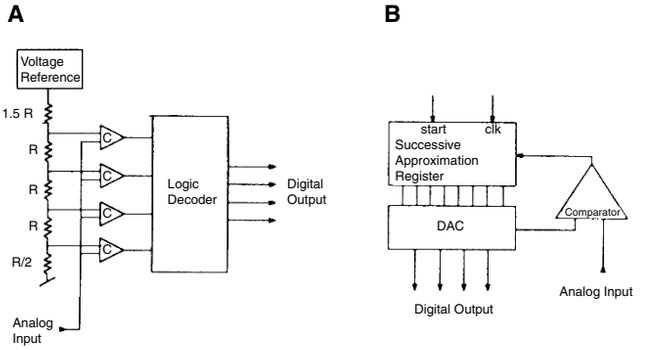


FIGURE 12.7. Converter types. (A) Parallel A/D converter in which the analog input is simultaneously compared with four reference levels. The delay through the system is determined by the logic delay, and conversion is very rapid. (B) Successive approximation A/D converter. On each clock cycle the digital input to the DAC is toggled starting with the most significant bit. The output of the DAC is compared with the analog input and if the DAC voltage is greater, the test bit is set to zero. The next significant bit is then tested in turn until, for an *n*-bit conversion, after *n* cycles the closest *n*-bit approximation to the analog input is found. Since *n* clock cycles are used, the time used with this method of conversion may be relatively long.

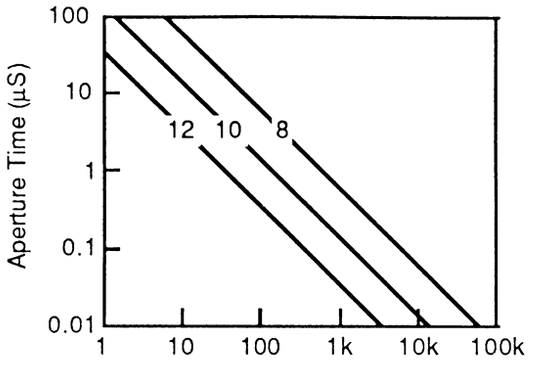


FIGURE 12.8. Aperture time versus frequency of a full-scale sinusoidal input for system accuracies to within one-half of one least-significant bit error.

delays through the logic. The successive approximation technique, on the other hand, operates on a feedback principle. The analog input and the output of a DAC are compared with a single comparator. The DAC is controlled by the output of a digital register whose bits are changed successively until the closest possible match is achieved between the DAC output and the analog input. This technique is relatively time consuming, and conversion often takes as much as a microsecond.

The rate of conversion and, therefore, the time window during which a conversion takes place, is of prime importance when choosing the method and resolution of the converter. During the time that the conversion is taking place, it is critical that the input change by less than the amount coded by the least significant bit. If the input changes by more than this amount, the conversion will be incorrect. This problem arises due to the uncertainty in the time aperture during which the conversion is performed. For the true integration schemes illustrated above, the problem does not arise because the output of the integrators is arranged to be constant for a large percentage of the pixel interval, and all that is required is that the conversion take place within this interval. For all the techniques that use a variant of the capacitive integration, the voltage will be changing during the period of conversion. In the capacitive integration we chose a τ equal to 1/4 the pixel dwell-time. For sampling periods of 1 µs, $\tau = 250$ ns, the integrator is equivalent to an RC filter with half-power bandwidth, or 3 dB point, of roughly 640 kHz. It is sobering to realize that to convert a sinusoidal voltage accurately to 8-bit resolution, at this frequency, the sampling aperture uncertainty would need to be shorter than 1 ns. The relationship between the desired resolution of the conversion, the frequency of a sinusoidal input, and the necessary sampling aperture is given in Figure 12.8.

To minimize problems created by the conversion aperture, either the converter must be extraordinarily fast or an additional component that samples and holds the input signal must be interposed between the detector and the converter. Such devices are similar to our integrator schemes in that they sample the analog input on a capacitor for a brief interval, and then the capacitor is disconnected from the input during the period that the conversion takes place. Consequently, the problems of rapidly sampling the input are transferred from the converter to the sampling-and-holding device. The ideal device for confocal microscopy must not only have a very short aperture uncertainty, but must also obtain the input voltage on the sampling capacitor to the desired resolution within a small fraction of the pixel dwell-time.

Because the output of this conversion is only certain to within 1/2 of a least significant bit, the converter can be viewed as an additional source of uncertainty or noise. With an 8-bit converter, this noise is relatively small compared to the sources mentioned previously. This is a necessary result of the finite resolution of the converter. In general, the dynamic range of the converter should be matched to the dynamic range of the detector. For example, if the S/N in the detector output is 1000, or 60 dB, then the converter output should be at least 10 bits to permit an equivalent resolution (see also Chapter 4, *this volume*).

ASSESSMENT OF DEVICES

Now that a number of laser-scanning and disk-scanning confocal microscopes have been reduced to practice and made available in the marketplace, it is proper to consider how well the implemented detection systems have been optimized. We shall consider one possible detector scheme for each type of microscope: the PMT for point detection and the CCD for full-field detection.

Point Detection Assessment and Optimization

Of current devices available for point detection, the PMT in photon-counting mode is the most suitable for low-light tasks with fluxes of fewer than 10^8 photons/s and $\lambda < 500$ nm. Most present microscopes using PMTs convert the anode current into a voltage and use this output as a measure of the incident illumination. Gain can be achieved in such a system by varying the acceleration voltage along the dynode chain, thereby increasing the photoelectron multiplication within the tube [Fig. 12.9(B)]. However, unfortunately, with progressively larger acceleration voltages, there is a tendency for the internal noise of the PMT to increase. This is particularly noticeable under low or absent light conditions when, with sufficient acceleration, the output of the headstage amplifier will display large-amplitude noise pulses. At lower voltages this noise source will be seen to disappear. This is a simple demonstration in the analog mode that the PMTs have a preferred operating range beyond which the noise of the device increases and the S/N decreases.

Most of the noise sources associated with anode current measurement can be avoided by using photon counting. In this mode, S/N is maximized by finding and using the optimal setting for the acceleration voltage. Ideally, such operations are performed using a pulse height analyzer to characterize the amplitude of pulses at the anode both in the dark and under low light conditions. Though such analyzers are rarely part of a typical microscopy laboratory, an alternate strategy can be employed. For pulse counting, the threshold detectors are first fixed at some nominal value, say 1 mV, for the lower detector. The output of the discriminator circuit can be counted digitally. Shown in Figure 12.9(A) is a comparison of the number of counts versus acceleration voltage acquired under no-light and two low-light conditions for the Bio-Rad MRC 500. In the dark with the laser off, the count rate rises gradually and then plateaus over an extended range (open boxes). Even at acceleration voltages in excess of 1 kV, there are fewer than 400 events detected by a Thorn C604 amplifier/discriminator. Under low light conditions with the laser on and without neutral density filters attenuating the beam, the count rate versus acceleration voltage was determined under two conditions. In the first case the count was taken without a specimen in the object plane (filled triangles). Ideally, in this case no light would be reflected back through the system and onto the PMT. Apparently, significant stray light is

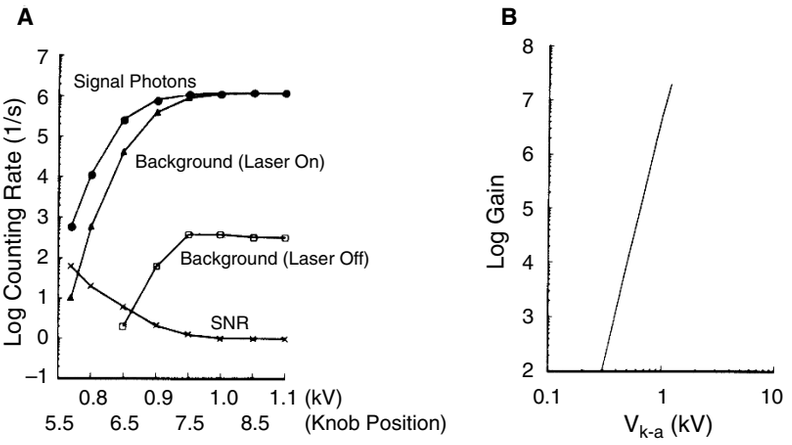


FIGURE 12.9. (A) Behavior of Bio-Rad PMT (Thorn 9828b) versus voltage. Confocal laser head mounted on a Zeiss UEM with a 40×, NA 0.75 water-immersion objective. A Thorn C604 head amplifier was used to generate and detect 1 mV pulses. The head amplifier output consisted of 15 ns ECL pulses with 5 ns deadtime. Responses were counted with the laser off, with the laser on and no object in the field, and with a FITC-stained specimen. Fewer than 400 events were counted in the dark. The number of events versus PMT acceleration voltage increased without an object in the plane of focus when the laser was energized and the beam entered the confocal head producing stray light. The number of counts increased again when a FITC-stained object was in the plane of focus. The maximum S/N of near 60 was achieved at PMT voltages between 750 and 850 V. On our Bio-Rad head, this corresponds to gain position between 5.5 and 6.5, but these exact readings may vary from instrument to instrument. (B) Gain versus acceleration voltage for PMT.

scattered back through the system and is detected even in the absence of a specimen. When a fluoroscein isothiocyanate (FITC)-stained specimen was placed in the object plane of the microscope, the number of signal photons detected (filled circles) was always greater than the background count. Perhaps because of the scattered light, the S/N of detection was a maximum of 60 at relatively low acceleration voltages between 750 and 850 V. The S/N dropped dramatically for higher accelerations near 1 kV. For most PMTs, the curve under low light conditions is similar to the curve recorded in the dark, but displaced towards higher counts. Therefore, in general there is a particular voltage for each photomultiplier for which the separation between the signal and the background noise is the greatest. The tube should be operated at this voltage. Operation at higher voltages will degrade the S/N and, in early models of the Bio-Rad 500, degradation of the S/N is compounded by the additional problem of scattered light within the confocal head. Figure 12.9(B) plots the gain versus the acceleration voltage. However, using a fixed, optimal PMT voltage produces a requirement for variable gain in the pre-ADC amplifier so that the signal output level matches the input of the ADC.

The output of the headstage PMT amplifier is often used as input to a video-rate frame-buffer running in a slow-scan mode. The transmission and digitization stage can often be another source of problems. In one commercial microscope, we noticed that in response to a step change from white to black, the detector/digitization system produced a series of damped oscillations or secondary bright levels. The problem could be eliminated by insuring that the transmission cable terminates with a matching impedance at the input of the video-board digitization stage.

As mentioned earlier, problems arise from using a capacitive integration technique and the consequent wide variation in output that occurs under certain conditions. Consider the difference in response that results when a photon is incident on the PMT at the beginning and at the end of a pixel dwell-time. Under full integration, the output in either case would be the same, and the result would be proportional to a single photon. Under capacitive integration, however, the voltage resulting from the photon that arrived at the beginning of the pixel dwell-period would have decayed to 2% of its value by the time that the pixel value was sampled. By comparison, the photon arriving just before the detector voltage was sampled would be at full amplitude. Consequently the output of such a detector/digitization scheme carries with it a random variation of the output dependent on the time of arrival of the incident photons during the integration period. This increase in noise will often prevent achieving a satisfactory S/N with an acceptable number of image scans.

The behavior of the PMT amplifier and conversion system can be tested directly by connecting a constant-current pulse generator capable of producing low-level steady currents and pulses comparable to those produced by the PMT with optimal acceleration voltage. If a series of pulses comparable to single photon events are produced at a constant rate near, but not equal to, the inverse of the pixel dwell-time, then capturing an image frame will reveal the method used to integrate during the pixel. If true integration is used, then the response can be one of three levels, with each pixel having a value equivalent to zero, one, or two pulses. Often it is convenient to map these values to, say, 0, 127, or 255 for an 8-bit frame grabber. On the other hand, if capacitive integration is used, the pixel values will assume all values between 0 and 255. Such a result would suggest that the detection and digitization scheme would converge more slowly towards an unbiased estimate of the luminance at the measured point than the full integration method.

Field Detection Assessment and Optimization

The line-scanning or field-scanning confocal microscopes require multi-element line or full-field detection systems rather than point detectors. As mentioned in the Introduction, the eye is often a suitable device but suffers under very low light conditions. Alternatively, one could use the normal types of field detectors currently used in video microscopy. A recent review of the field is available (Inoué and Spring, 1997). Many of the present-generation imaging devices are inappropriate due to the speed of the response. In addition, in many of the most sensitive tubes there is significant lag or carry-over between the image recorded during one frame scan and the next. Alternatively, a cooled CCD camera could be used as the detector, given its large dynamic range and extraordinarily high quantum efficiency. As noted above, the difficulty that arises with CCD devices is the generation of a noise-equivalent photoelectron signal due to thermal generation during the integration time, to variations in the charge-coupled transfer efficiency, or to random variations in the conversion at the output. To be sure, this noise can be minimized and, for some CCD chips with slow scan readout, the noise can be reduced to a few photon equivalents (rms). However, this still yields peak noise (5σ) readings of nearly 60 photon equivalents in the dark. Such a figure is not ideal under low light conditions. In older CCDs, a further problem arose from difficulties in transferring the signal through the charge-coupled

process when one of the detection sites contains too few photoelectrons. In this case, transfer along the device may be interrupted until sufficient charge accumulates from adjacent pixels in the column to permit transfer. This problem is likely to be exacerbated for fluorescent images in which there are likely to be large numbers of pixels without any photon hits during the integration period.

Because the distance between detector elements in a 2D CCD is on the order of 10 µm, it is possible in principle to add a gain stage by interposing a microchannel plate (such as the Hamamatsu HPK R2809, built with 6 µm elements) in front of the CCD (Kume *et al*., 1988). A modest gain of 100 would bring us clearly above the noise floor of the CCD and, because these CCDs can store as many as 5×10^5 electrons in a well, each would still be able to detect 5000 photoevents before becoming saturated. Unfortunately, because the MCP is manufactured with S1, multi-alkali, and bialkali photocathodes, the quantum efficiency of the composite device will be much less than that of the CCD. In addition, because of statistical variations in MCP gain, all photons will no longer deposit identical charge in the sensor. However, a benefit of such a strategy is that the MCP can be gated on and off and perhaps phased-locked to periods following an illuminating pulse. In this manner, the kinetics of the response to illumination could be followed on a nanosecond time scale. The response to such an experiment could be integrated simultaneously over the entire field, and after sufficient repetitions the value could be digitized in the usual fashion (see Chapter 27, *this volume*).

A more straightforward approach to providing gain and reducing the dark count in CCDs has resulted in cameras for full-field work that have high quantum efficiency, extremely low production of thermal electrons, and black levels reminiscent of PMTs. Such electron-multiplying CCDs, or EM-CCDs, have been commercially produced by both E2V (Chelmsford, UK), and Texas Instruments (Houston, TX, USA), under the names L3Vision and Impactron, respectively. These devices incorporate a silicon-based electron multiplication stage in addition to a conventional CCD structure. The electron multiplication is provided by the addition of a multiple-well gain register that is similar to the conventional shift register (see Figs. 2.15 and 10.11, *this volume*), except that the second phase electrode is replaced by two electrodes, one at a fixed potential, and the other clocked at a voltage of 40 to 50 V, a value much higher than necessary to transfer charge. The resulting intense electric field is sufficiently high to cause impact ionization as the electrons are transferred, and rather modest multiplication by a factor of 1.01 to 1.015 per stage can be achieved. Repeated over a few hundred wells, however, this multiplication is raised to the power of the number of wells in the register. The resulting gain in the Marconi device, with 591 wells, is on the order of 6600. Clearly, such gain is sufficient to overcome the readout noise that is the main noise factor at transfer rates greater than 1 MHz necessary for full-frame microscopy. Sufficient cooling is also used in these cameras to reduce the thermally generated background to a few electrons per frame, and the result is the creation of an image at low light levels that has the potential to combine the low background inherent in PMTs with the quantum efficiency possible with present generation CCDs.

There is one problem with this picture: the charge amplification process is very noisy in the sense that not all the electrons in the packet are amplified by the same amount. The multiplicative noise that this causes produces an uncertainty in the measurement of the signal in the charge packet that is very similar in magnitude and form to that caused by Poisson noise. As the two noise terms are added as the square root of the sum of the squares, the total noise becomes 1.4× greater than it would have been if each electron in the packet were amplified by the same amount; alternatively, the total noise is the same as if only 50% of the electrons in the original packet were counted perfectly. What this means practically is that the EM-CCD operates as though the read noise is essentially zero but the "effective QE" is only 50% of the actual QE.

A second less fundamental problem relates to the fact that all current EM-CCD chips use frame transfer readout. This means that, at the end of the exposures, the accumulated charge pattern is translated past the light field of its way to the read register, a process that can cause streaking unless the light is turned off, either by using a shutter or by turning off the microscope illumination.

As with all new devices, one expects a learning curve with respect to fully understanding the inherent noise. Two other sources of noise that became apparent only when the EM-CCD "abolished" read noise are those due to clocking and charge transfer. Even in conventional CCDs, spurious electrons are produced every 100 or so transfers, and clocking induced charge, or CIC, is rather low compared to read noise. In the EM-CCD special care must be taken with clock amplitudes and edges to minimize this effect, given the high acceleration voltages in the gain register. The other source of noise in the image results from the expected charge transfer efficiency (CTE) problems that result when wells are filled with 50,000 to 100,000 electrons and a small amount of charge is left behind during each transfer. This results in a streaking in the image, most apparent in fluorescent images where often one encounters high intensity pixels surrounded by black. Under such conditions the problem can be ameliorated by reducing the gain, because, at high pixel intensities, only modest gain is necessary to overcome either the thermal noise or that due to high-frequency readout.

DETECTORS PRESENT AND FUTURE

In conclusion, we will consider two general topics. The first is the means of optimizing the performance of this generation of confocal microscopes. The second is the specification of the qualities of the ideal detector to use in confocal microscopy. Our goal is to produce images with the least possible illumination of the specimen. In terms of constructing an image, this requires that the signal being recorded be limited only by the uncertainties of photon flux. From the analysis of the contributions of noise sources, the S/N is seen to be degraded at each step in the conversion process. As was shown in the section on the statistics of the photon flux and the detector, the first point of departure from the ideal when using a PMT as the detector is the fact that the quantum efficiency of realizable PMTs is much less than unity. Consequently, the emission of the photoelectron is itself a second probabilistic event in the cascade, and the S/N is reduced by $(QE)^{1/2}$, where QE is the quantum efficiency. The S/N could be enhanced simply by increasing the QE of the photocathode and the gain of the first dynode in the multiplication chain and, towards this goal, it is common (but sadly not universal) to place a zener diode between these electrodes so that the gain of this step is high regardless of the total PMT voltage used.

The S/N in PMTs could be enhanced further by cooling the tubes to reduce the effects of thermionic emission, by running the cathode at near ground potential to reduce the regenerative effects due to collisions between electrons and the tube wall, by reducing the effective cathode area and focusing of the photoelectron beam, and, finally, by reducing the number of stages in the dynode chain and increasing the gain at each stage. All of these argue for the use

of more efficient negative affinity materials, such as gallium-arsenide (GaAs) and gallium-arsenide-phosphide (GaAsP), a feature that would also move us towards the use of the less-damaging, longer λs. These maneuvers would also decrease the dispersion in the time-of-flight of the photoelectron cloud produced by a single incident photon, increasing the temporal resolution of the detector and making it easier to perform studies on fluorescence kinetics (Chapter 27, *this volume*).

Many present confocal microscopes use rather crude techniques to create a running average of the photon flux. Perhaps the two most straightforward improvements of the devices for use in biological or low-light measurements would be the following. First, one should eliminate the use of anode current measurements and the associated capacitive integration methods of pixel intensity estimation. Second, one should avoid the inappropriate use of the dynode acceleration voltage as a means of varying the intensity of the image. The S/N degradation produced by using these methods is too severe to warrant their continual use. The alternative to adjusting the gain in this way is to increase the incident light levels or to use variable digital or electronic gain. As other authors in this volume point out, increasing the light level can often result in severe photodamage to the specimen and bleaching of the photoprobe, again resulting in an inability to create a meaningful image in a minimum number of successive scans.

A convenient solution both to the problems of pixel convolution and to problems inherent in PMT operation can be implemented simply by using photon counting. The dark counts of photon-counting tubes are often below 100 photoelectrons/s, and in an image that has perhaps 10^6 pixels/s, this contribution is negligible. Thus, integrating over the pixel interval, the S/N will be limited by the photon statistics and the QE of the cathode material. The spurious noise due to regenerative effects and breakdown within the tube when run at high acceleration voltages can be eliminated. These effects can be demonstrated by comparing the averaged images collected under extremely low light conditions using the anode current measurement provided with the confocal microscope to a technique of direct photon counting. Figure 12.10 demonstrates the S/N problem viewed as a measurement task after the primary detector. In Figure 12.10(A), the signal is presumably buried somewhere within the extraordinary broadband noise in the trace. Because this is the input to the ADC stage, the signal will be sampled at the end of each pixel as an estimate of the pixel value. The result of averaging 512 frames acquired using this technique is shown in Figure 12.10(C). By comparison, the 16 levels from the photon-counting circuit are shown in Figure 12.10(B). The result of averaging 128 images acquired using only 10% as much illumination is shown in Figure 12.10(D). From the viewpoint of capturing a useful image, photon counting is to be pre-

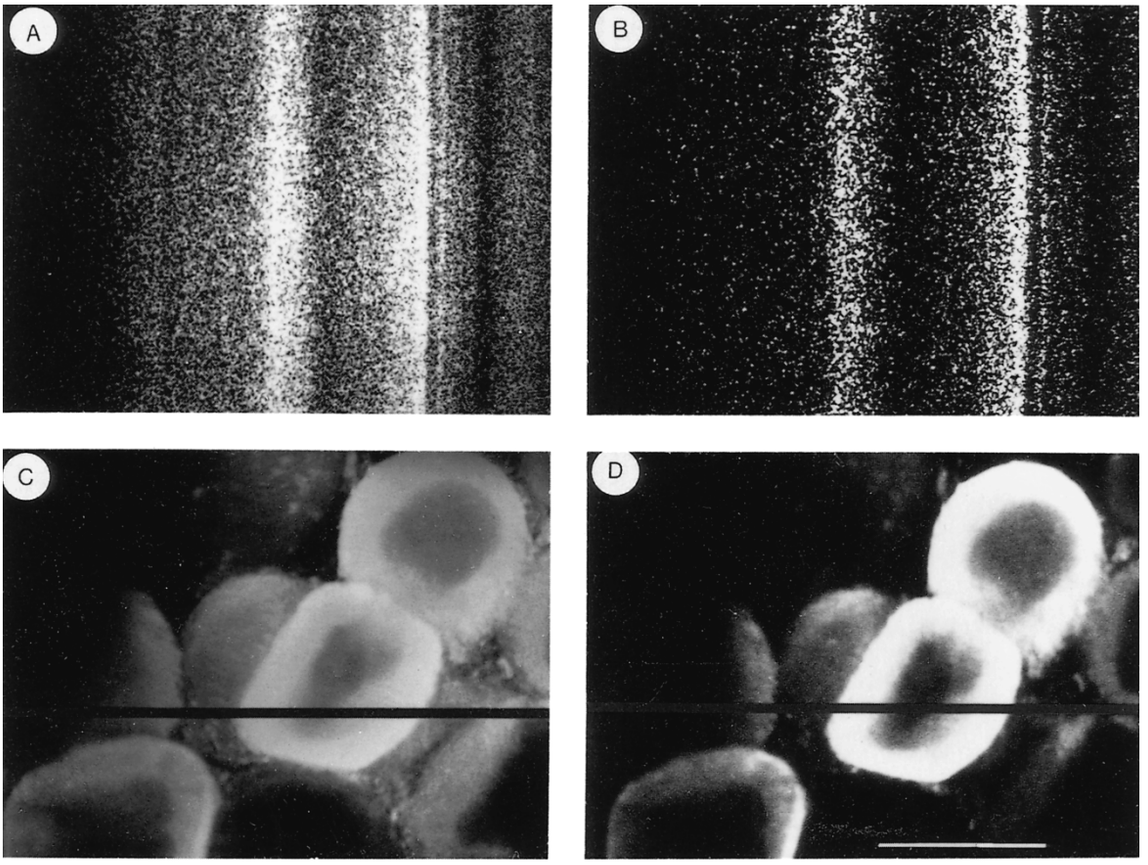


FIGURE 12.10. Comparison of the use of Bio-Rad MRC 500 confocal microscope in anode current measurement and photon-counting modes at low light levels. Pedal ganglion of *Aplysia* stained with antibody raised to pedal peptide (Pep) conjugated with FITC. (A) Background noise using anode current measurement apparent in the 512 scans of the single line indicated in (C). Successive scans displaced vertically. (B) Output of photon-counting circuit for the field line highlight in (D) demonstrating relatively noise-free operation. (C) Average of 512 fields using anode current measurement technique. Display restricted to values between 160 and 255 and expanded to the full dynamic range of the video memory before photographing. (D) Average of 128 fields, at 1/10th the light level of (C), using photon counting. Sixteen quantal levels expanded to the full dynamic range of the monitor before photographing. Scale bar = 100 μm.

ferred. Furthermore, because in this photon-counting unit the detection circuitry saturates at 10^7 photoelectrons/s (or 4×10^7 photons/s), the likelihood of bleaching the fluorescent probe is very low.

In the future, we should consider enhancing the quantum efficiency of the detectors. PMTs are presently limited to QE ≡ to levels near 35% for blue light but QE ≤ 3% for rhodamine. An alternative approach would be to examine further the feasibility of using the solid-state detectors normally used in CCD arrays as the primary detector. In the present generation CCD devices, QE approaches 80% well into the near IR, and this fact alone suggests that the solid-state direct photodetectors will ultimately come closest to achieving a S/N in the detected signal that is limited by the statistics of the photon flux. Presently, the sources of noise in realized devices are those due to thermal generation both in transfer along the readout registers and in resetting the readout capacitor. The second source of uncertainty is due to the readout noise. Because the readout of the voltage due to a packet of electrons can be made non-destructively, it is possible to shift each packet down a normal charge-coupled shift register and to make multiple readings along the register as the packet passes by. In this way, estimates of the pixel value would increase in precision with the square root of the number of estimates performed for each packet and with no apparent cost. Alternatively, the EM-CCD approach makes almost zero read noise available now, albeit at the cost of a 50% drop in QE.

REFERENCES

Brown, R.G.W., Jones, R., Rarity, J.G., and Ridley, K.D., 1987, Characterization of silicon avalanche photodiodes for photon correlation measurements. 2: Active quenching, *Appl. Opt*. 26:2383–2389.

Brown, R.G.W., Ridley, K.D., and Rarity, J.G., 1986, Characterization of silicon avalanche photodiodes for photon correlation measurements. 1: Passive quenching, *Appl. Opt*. 25:4122–4126.

Boyle, W.S., and Smith, G.E., 1970, Charge coupled semiconductor devices, *Bell Sys. Tech. J.* 49:587–593.

Burgess, R.E., 1956, The statistics of charge carrier fluctuations in semiconductors, *Proc. Phys. Soc*. B69:1020–1027.

Coutures, J.L., and Boucharlat, G., 1988, A 2 × 2048 pixel bilinear CCD array for spectroscopy (TH 7832 CDZ). *Adv. Electronics Electron Phys*. 74:173–179.

Einstein, A., 1905, Uber einen die Erzeugung und Verwandlung des Lichtes betreffenden heuristischen Gesichtspunkt, *Annalen der Physik* 17: 132–148.

Fairchild Weston Systems Inc., 1987, *CCD Imaging and Signal Processing Catalog and Applications Handbook*, Fairchild Weston Systems Inc. CCD Imaging Division, Sunnyvale, California.

Goldstein, S., 1989, A no-moving-parts video rate laser beam scanning type 2 confocal reflected/transmission microscope. *J. Microsc*. 153:RP1–RP2.

Hier, R.G., Zheng, W., Beaver, E.A., McIlwain, C.E., and Schmidt, G.W., 1988, Development of a CCD-digicon detector system, *Adv. Electronics Electron Phys*. 74:55–67.

Inoué, S., and Spring, K.R., 1997, *Video Microscopy: The Fundamentals*, Plenum Press, New York, pp, 1–741.

Jones, R., Oliver, C.J., and Pike, E.R., 1971, Experimental and theoretical comparison of photon-counting and current measurements of light intensity, *Appl. Opt*. 10:1673–1680.

Jorgensen, T. Jr., 1948, On probability generating functions, *Am. J. Phys*. 16:285–289.

Kittel, C., 1986, *Introduction to Solid State Physics*, 6th ed., John Wiley and Sons, New York, p. 646.

Kume, H., Koyama, K., Nakatsugawa, K., Suzuki, S., and Fatlowitz, D., 1986, Ultrafast microchannel plate photomultipliers, *Appl. Opt*. 27:1170–1178.

Lacaita, A., Cova, S., and Ghioni, M., 1988, Four-hundred-picosecond single-photon timing with commercially available avalanche photodiodes, *Rev. Sci. Instrum*. 59:1115–1121.

Mackay, C.D., 1988, Cooled CCD systems for biomedical and other applications, *Adv. Electronics Electron Phys*. 74:129–133.

McMullan, D., 1988, Image recording in electron microscopy, *Adv. Electronics Electron Phys*. 74:147–156.

Mathur, D.P., McIntyre, R.J., and Webb, P.P., 1970, A new germanium photodiode with extended long-wavelength response, *Appl. Opt*. 9:1842–1847.

Petráň, M., Hadravsky, M., Egger, M.D., and Galambos, R., 1968, Tandem scanning reflected-light microscope, *J. Opt. Soc. Am*. 58:661–664.

Prescott, J.R., 1966, A statistical model for photomultiplier single-electron statistics, *Nucl. Instrum. Methods* 39:173–179.

Putley, E.H., 1977, Thermal detectors, In: *Topics in Applied Physics, Vol. 19: Optical and Infrared Detectors* (R. J. Keyes, ed.), Springer-Verlag, Berlin, pp. 71–100.

RCA, 1980, *Photomultiplier Handbook*, RCA Solid State Division, Lancaster, Pennsylvania.

Robben, F., 1971, Noise in the measurement of light with photomultipliers, *Appl. Opt*. 10:776–796.

Schwartz, M., 1970, *Information Transmission, Modulation, and Noise*, 2nd ed., McGraw-Hill, New York, p. 672.

Seib, D.H., and Aukerman, L.W., 1973, Photodetectors for the 0.1 to 1.0 mm spectral region, *Adv. Electronics Electron Phys*. 34:95–221.

Siliconix Inc., 1986, *Small-Signal FET Data Book*, Siliconix Inc., Santa Clara, California.

Sharpless, W.M., 1970, Evaluation of a specially designed GaAs Schottky-barrier photodiode using 6328-nm radiation modulated at 4 GHz, *Appl. Opt*. 9:489–494.

Sommer, A.H., 1968, *Photoemissive Materials*, John Wiley and Sons, New York, p. 255.

Van der Ziel, A., 1959, *Fluctuation Phenomena in Semi-Conductors*, Academic Press, New York.

13

Structured Illumination Methods

Rainer Heintzmann

INTRODUCTION

In this chapter, I discuss methods of obtaining optical section data using methods other than standard confocal microscopy. These techniques have the potential of being more **light efficient**, **faster**, and of providing better **resolution** than standard, unprocessed confocal microscopy.

Confocal microscopy depends on an uneven distribution of the illumination on the sample, and this is accomplished by directing the beam to a single focus that is then scanned. The resulting signal is detected pointwise (voxel-by-voxel). In other systems, the focus is multiplexed and many points are scanned by a spinning disk (Petráň *et al.*, 1968; Bewersdorf *et al.,* 1998; Andresen *et al.*, 2001; Majoul *et al.*, 2002) or by the two-dimensional regular movement of a rectangular mask (Verveer *et al.*, 1998; Egner *et al.*, 2002).

Multiplexing takes advantage of the fact that many photodetectors operate in parallel to increase data throughput. In addition, by spreading the illumination over many pixels, parallel readout avoids problems, such as singlet-state fluorescence saturation, that can limit the data rate from single-beam confocal microscopes.

Multiplexed confocal systems operating with single photon excitation (Ichihara *et al.*, 1996; Verveer *et al.*, 1998) employ a structured mask (e.g., a pattern of linear or circular holes in a opaque plane or a pattern of microlenses on a rotating disk) for generating structured illumination as well as spatially filtering the fluorescent or scattered light emitted by the sample before it reaches the detector. The confocal signal is usually obtained by integrating this spatially filtered signal on the charge-coupled device (CCD) camera.

In contrast, the structured-illumination methods discussed here are based on the acquisition of a set[1] of individual images at a given focus plane, each made with a different position of an illumination mask, **but made with no mask in the detection beam path**, that is, widefield detection (Fig. 13.1). The detection pinholes can then be defined computationally in order to produce a confocal-like image from this set of images (as performed in Fig. 13.4). Other ways of processing the data to yield optically sectioned images are also presented below.

Some advantages and disadvantages of this strategy are:

1. Because a full image[2] is recorded for each position of the illumination mask, a much larger amount of data needs to be acquired per reconstructed slice. In this sense, patterned illumination with widefield detection also constitutes a "scanning" system and sample movement must be avoided during the acquisition time. Taking multiple images can be a disadvantage in speed, but as modern CCD cameras employ fast readout systems with negligible readout noise (e.g., with electron-multiplier amplification), this does not pose a major problem.

2. This large amount of data offers more flexibility for the treatment of the data. In contrast to standard confocal microscopy, it is unnecessary to choose a pinhole diameter during data acquisition with all the advantages and disadvantages of this choice. Once you have chosen the illumination pattern, the trade-off between sectioning strength (small hole) and better signal-to-noise ratio (large hole) can be dealt with after data acquisition (see Fig. 13.4) or be avoided entirely during data processing.

3. In most structured-illumination systems, the multi-spot approach distributes the power of the illumination light across multiple positions. In a single-spot confocal system, fluorescence saturation fundamentally limits the amount of collectable fluorescent light one can excite per unit/time and thus defines a minimum time required for the acquisition of an adequate fluorescence image. Given illumination sources of sufficient brightness, the simultaneous utilization of one thousand spots can potentially shorten the acquisition time substantially.[3]

4. An advantage of standard confocal scanning systems is that the scan is relatively localized. Thus, sample movement only causes major image distortion if the feature actually being scanned moves by an amount that is large compared to the beam size. In contrast, patterned illumination systems with widefield detection require that each part of the object be stable within the limits of the achievable resolution throughout the acquisition of an entire set of raw data images.

EXPERIMENTAL CONSIDERATIONS

For the sake of simplicity, an identical schematic setup (Fig. 13.1) will be assumed throughout this chapter. In this setup, the sample is illuminated through an illumination mask [e.g., Fig. 13.2(A–C)], which can be shifted by well-defined displacement to produce a set of regularly spaced light patterns. At each position of the illumination mask, an image of the sample is detected with a CCD camera at a conjugate image plane, usually maintaining a fixed, in-plane position with respect to the sample. The common features of all structured-illumination arrangements are that the sample is illuminated with structured light, and fluorescence or the scattered

[1] A set is a series of images made at one focus plane but with different illumination conditions.

[2] Or at least a substantial amount of signal originating from near the positions of the illumination spots.

[3] The amount by which the total acquisition time is shortened depends on how many images must be obtained at each plane, a factor that varies with the sparcity of the mask used.

Rainer Heintzmann • King's College London, London, United Kingdom

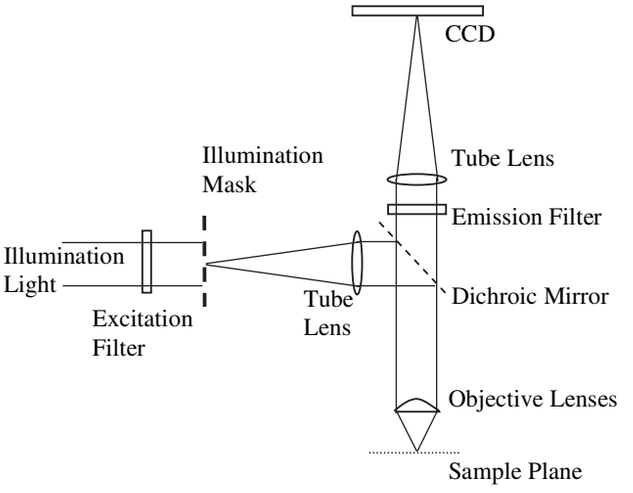


FIGURE 13.1. Possible experimental setup for acquiring structured-illumination data in the widefield fluorescence detection mode. The illumination mask is projected by the microscope optics onto the specimen in the sample plane, thereby defining the illumination pattern. The fluorescence light from the sample is, however, directly imaged onto the CCD camera without any mask in the detection path.

light is detected in a widefield–type arrangement without the use of any detection mask. The various structured-illumination methods differ greatly in how the pattern of light is generated (e.g., by interference patterns or even using a single-spot laser illumination) and also in the detection system [e.g., either widefield or descanning with detection of a small area near the illumination spot (Bertero *et al.*, 1984; Bertero *et al.*, 1989; Sheppard and Cogswell, 1990; Pawley *et al.*, 1996)]. Below, I describe different pattern generation techniques along with possible sources of errors.

Pattern Generation

Patterns of illumination can be generated by placing the illumination mask at the plane of the field stop in the illumination path of the microscope (Fig. 13.1). The mask can be a diffraction grating, or a spatial light modulator (SLM) such as a programmable liquid crystal, a digital mirror, or a liquid-crystal-on-silicon (LCOS) device, and can be illuminated either by incoherent light (Neil *et al.*, 1997; Heintzmann and Cremer, 1999a) or by a coherent laser (e.g., as in Lanni *et al.*, 1993 or Gustafsson, 2000).

For the optimal signal-to-noise ratio at the highest in-plane resolution, it is advantageous to produce the highest possible contrast (degree of modulation) of the light pattern in the sample plane. The

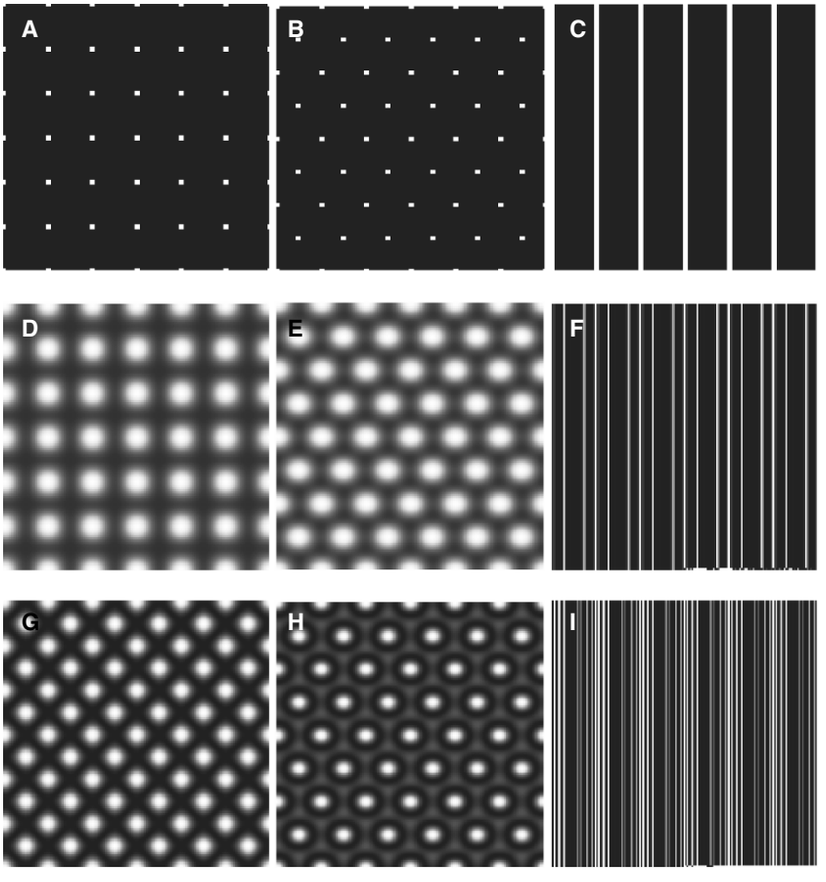


FIGURE 13.2. Different pattern masks (top row) along with the illumination patterns (rows below) generated in the plane of focus. (A) Regular spaced dots; (B) illumination dots placed on a hexagonal unit cell such as often used in spinning disk systems; (C) Line-grid. The unit-cell length D is indicated. (D–F) show the illumination pattern as generated by incoherent imaging of (A–C) at the sample plane. (G–I) correspond to coherent imaging with suppression of the zero-order in the diffraction pattern. Note the improved degree of modulation, yielding a darker background.

light diffracted from a coherently illuminated grid can be focused to well-defined diffraction orders. To achieve the maximum degree of modulation, it can be advantageous to block the zero diffraction order (stemming from non-diffracted light) with the help of a central beam stop at an appropriate position in the illumination path. It is also possible to generate illumination patterns by interfering beams of coherent light that have been separated by beam-splitters (Lanni *et al.*, 1986; Lanni *et al.*, 1993; Frohn *et al.*, 2000). However, in this case mechanical stability becomes a major concern because the relative length of the two beam paths formed by the splitter must remain stable to subwavelength precision during the time needed to record an entire set of images.

When working with microscopes that possess high aperture angles in the sample plane, it is important to keep the vector nature of light in mind (Fig. 13.3). Beams converging onto the focus plane at an angle of 90° with respect to each other do not generate an intensity interference pattern in *p*-polarization (meaning the polarization vector is in the plane defined by the two interfering beams), whereas the interference of *s*-polarized beams (polarization vector perpendicular to the plane that contains the two interfering beams) results in optimum mask contrast.[4] At a high numerical aperture, this consideration makes line-grid diffraction masks [e.g., Fig. 13.2(C)] with *s*-polarized illumination (polarization vector parallel to the lines) preferable to two-dimensionally structured masks.

The ideal source of this light is less clear. Because laser light is both polarized and very bright, it may seem an obvious choice. If a grating or SLM is used to generate an array of lines, the zero-order, undiffracted beam can be easily discriminated and removed to achieve the maximum possible modulation at the focus plane. Furthermore, laser light can be coupled into the microscope very efficiently even at high diffraction angles and, in combination with holographic techniques, it can be used to generate sparse patterns without a severe loss in total power. However, at present, laser light is only available at certain wavelengths and these do not always match the absorption spectra of the dyes of choice. In addition, the high lateral coherence of laser light can cause strong interference effects between the main beams generating the structure and light reflected by various optical surfaces, particularly the water–glass surfaces of the coverslip and the front surface of any non-immersion objective. Although lateral coherence can be scrambled in a number of ways (as discussed in Chapter 6, *this volume*), implementing these strategies adds so much complexity and cost that they have so far been used only in homemade systems.

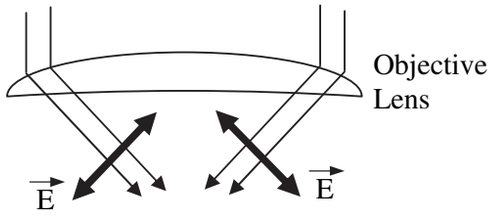


FIGURE 13.3. Influence of the vector nature (polarization/electric field) of light at high numerical aperture. The interfering electric field vectors (*bold arrows*) perpendicular to the light rays (*thin arrows*) can even be perpendicular to each other at *p*-polarization, and an aperture half-angle of 45°, as displayed here, leads to no intensity modulation in the sample plane. In contrast, *s*-polarization with the electric field vector pointing towards the reader would yield two parallel vectors and thus 100% contrast in the intensity pattern generated by constructive and destructive interference.

[4] Whereas *p*-polarized rays that converge at a relative angle of 40° are still capable of interfering well enough to produce 90% of full contrast.

Arc sources usually are less expensive, less coherent, and much less bright than laser sources (see Chapter 6, *this volume*). However, they emit over a very wide range of wavelengths and, particularly at the peaks of the Hg emission lines, they are bright enough for many studies. Because arcs can be considered as longitudinally and transversally incoherent, stray interference fringes are seldom a factor.

Their problem is insufficient brightness. If the illumination system is adjusted so that it only uses the light emerging from a small area of the source, the blocking of the zero order would still be possible. However, doing so reduces the intensity so much that long exposures are needed to maintain a decent signal-to-noise ratio in each image in the data set. To make matters worse, sparse illumination patterns can obstruct more than 90% of the incident light striking the pattern mask. Finally, as sheet polarizers transmit only about one third of the incident light, it is a matter of some interest as to whether or not, given a fixed exposure time, the increased contrast of the pattern is offset by the lower signal level caused by the use of the polarizer. As a rule of thumb, unless it is essential to collect data very rapidly, the 3× lower illumination intensity that occurs when you use a sheet polarizer is recommended for aqueous specimens whenever the objective numerical aperture (NA) is >0.4, using high spatial frequency gratings for in-plane resolution enhancement, or >0.8, when using lower spatial frequency gratings for optical-sectioning applications.

On the other hand, if one uses an arc source to project a pattern large enough so that its image is only marginally affected by diffraction, one can use an illumination system that utilizes light from a larger area of the source and the photon flux becomes sufficient for rapid optical sectioning using patterned illumination. Indeed, the Zeiss ApoTome is such a device. In the future, it may be possible to use an array of high-power, light-emitting diodes (LEDs) as a bright, incoherent source of patterned illumination.

The choice of the illumination pattern density very much depends on the type of sample as well as on the intended method of data processing. A comparably thick sample and/or a sample with volume-like staining is more difficult to process when using densely patterned illumination because the large amount of out-of-focus fluorescence will dominate the small amount of modulated fluorescence stemming from the focal plane (see Appendix, *this chapter*). Although using a sparse pattern reduces this signal-to-noise problem, it always requires the acquisition of more raw data images to produce a single set. This implies a longer image acquisition time. An elegant way to achieve sufficient flexibility and to optimize this trade-off between relatively noise-free sectioning and acquisition speed is to generate the pattern using a programmable array (Verveer *et al.*, 1998; Hanley *et al.*, 1999; Heintzmann *et al.*, 2001; Fukano and Miyawaki, 2003).

Out-of-focus-light can be reduced by closing the field diaphragm (Hiraoka *et al.*, 1990) and this technique may be very valuable. However, when using non-local reconstruction methods (e.g., the Fourier-space based approaches) the illumination pattern is assumed to be periodic at all out-of-focus positions. A small field diaphragm violates this assumption and may lead to problems during Fourier-based reconstruction.

The illumination pattern can be displaced relative to the sample by either translating the mask by a well-defined distance (Neil *et al.*, 1997; Gustafsson, 2000, 2005), by reprogramming the

pattern of a programmable diffraction (amplitude or phase) mask (Verveer *et al.*, 1998; Hanley *et al.*, 1999; Heintzmann *et al.*, 2001; Fukano and Miyawaki, 2003), by altering the relative phases of interfering beams (e.g., by splitting the beam and repositioning a piezo-actuated mirror in one of the beam paths) (Lanni *et al.*, 1993; Frohn *et al.*, 2000; Failla *et al.*, 2002), or by translating the sample past a fixed pattern, followed by a computational correction to account for this sample movement (Heintzmann and Cremer, 1999a). In the latter case appropriate interpolation kernels or Fourier-space based resampling approaches (leading to a sinc kernel) must be used to reduce interpolation-induced artifacts (Yaroslavsky, 2003) that occur as features on the object move across the pixels of the CCD.

Promising attempts to replace the confocal pinhole by a multiple element detector (Bertero *et al.*, 1984; Barth and Stelzer, 1994) with fast readout (Sheppard and Cogswell, 1990; Pawley *et al.*, 1996) also belong to the same category of structured illumination with somewhat widefield–like detection.[5] The data can thus be treated with methods similar to the descriptions given below, as long as the descanning is accounted for.

COMPUTING OPTICAL SECTIONS FROM STRUCTURED-ILLUMINATION DATA

The data acquired with a setup similar to the one shown in Figure 13.1 consists of a *z*-series of sets of images. Each set is taken at one focus position and each member of a set is taken at a different position of the illumination light pattern. The data from each set is first processed to yield an optically sectioned image using one of the methods described below.

Most methods for deriving an optical section from a set of structured-illumination images try to estimate the **degree of modulation** at each pixel. For simplicity, in the case of a one-dimensional grid [e.g., Fig. 13.2(C), top row in Fig. 13.7, p. 272, Fig. 13.11, p. 278] it is assumed that N images are acquired, each with the pattern shifted by $1/N$ with respect to the replicative unit cell.[6] In the top row of Figure 13.7, the interleaved positions of the three illumination patterns are indicated on the left side of each image for $N = 3$. As displayed in Figure 13.11, those parts of the sample that are out of focus are more homogeneously illuminated. Light emitted from these parts will undergo an additional blurring when imaged onto a detector conjugate to the in-focus plane. Thus, in contrast to the in-focus light, light from out-of-focus areas will exhibit very little modulation upon variation of the *x*-positions of the excitation pattern. Computing the degree of modulation over the multiple images, in a pixel-by-pixel fashion, will permit the discrimination of the non-modulated, out-of-focus from the modulated, in-focus information.

The degree of modulation can be calculated **locally**, considering only the modulation at a single pixel position over time, by various approaches:

1. Dodt (Dodt, 1990; Dodt and Becker, 2003) suggests emulating "synthetic pinholes" by summing up the thresholded images of a series of data acquired by transmission imaging with structured illumination. This technique has been successfully applied to the transmission infrared (IR) imaging of onion skin (Dodt and Becker, 2003) and 300 µm unstained, freshly prepared thick rat hippocampal slices in which single spines on dendrites could be resolved throughout the sample (40×, NA 0.8 objective at 780 nm, Dodt *et al.*, 2001). The advantage of this approach is that, while the optical aberrations induced by such samples render the operation of a standard confocal microscope in transmission close to impossible, the data processing strategy employed is very adaptive to optical aberrations and thus is able to yield a useful image containing information mainly from the focal slice.

2. Benedetti and co-workers (Benedetti *et al.*, 1996) determined the reconstructed slice I_{rec} by calculating the difference between maximum and minimum measured intensity I_i in each pixel i: [Eq. 1, see also Fig. 13.7(B)]. This approach[7] is robust with respect to various artifacts that often arise in imaging such as readout noise and especially fixed-pattern noise from the CCD. This noise, which usually does not vary systematically over time but rather randomly from pixel to pixel, is efficiently eliminated, as is scattered light from out-of-focus planes and from anywhere in the optical path. It is observed that this approach generates spurious patterns if the number of scanning steps is too low for the size of the illumination pattern as is seen by the residual horizontal stripes visible in Figure 13.7(B). However, it should be noted that the selected width for this pattern was extraordinarily wide and only three steps were chosen. For a denser pattern or an increased number of scanning steps, the visible performance of this method is similar to approach 3 [Fig. 13.7(C)], which is discussed below.

If the illumination pattern is sufficiently sparse [i.e., the spot-to-spot or line-to-line distance D in Figure 13.2(C) is large enough or, more generally, if the ratio of open to opaque area, the so-called mark/space ratio, is low], simply computing the maximum (Eq. 2) yields fairly good optical sections (Bendedetti *et al.*, 1996), albeit without the background suppression advantages of Eq. 1. These approaches have been applied to epi-fluorescence microscopy (Benedetti *et al.*, 1996) and transmission IR imaging (Dodt and Becker, 2003). By Eq. 3 (termed super-confocal), a further increase in optical sectioning quality is obtained. However, Eqs. 2 and 3 yield satisfying results only for data acquired using sparse illumination.

3. Other ways of determining the degree of modulation (Eqs. 4, 5) are described by Neil (Neil *et al.*, 1997). Equation 4 is based on square-law detection [Fig. 13.7(C)] and Eq. 5 emulates a homodyne detection scheme. Another possible approach is the computation of the absolute magnitude of the pixel-by-pixel Fourier-transform over each set of images (Ben-Levy and Peleg, 1995). For the case of three such images, this method is identical to Eq. 5. It should be noted that both of these methods would not be able to reconstruct the high *xy*-spatial frequency given in the moiré example discussed later [Fig. 13.5(A)], in which the Fourier-transform of the illumination grid has its peaks just outside the range of detectable spatial frequencies. This is the case when the highest possible fluorescent excitation spatial frequency is passed through the objective. Such light will consist of two beams passing through the edges of the back-focal plane. Because of the Stokes shift of the excited fluorescence light, this spatial frequency will

[5] For speed reasons, the suggested detector arrays are usually relatively small (e.g., 5 × 5 elements), yielding a confocal operation "bias" for thick specimens.

[6] The unit cell is defined as the smallest (vectorial) translation that can be applied to the pattern to reproduce its structure (e.g., the distance D indicated in C, Fig. 13.2).

[7] A system (ViCo) based on this and related concepts is marketed by Biomedica Mangoni s.n.c., Pisa, Italy.

not be imaged by the objective on the return trip. A similar situation occurs when employing grazing incidence illumination as in Frohn and colleagues (2000). Most strategies assume equally distributed phases between the images, but this is not a strict requirement. Fukano and Miyawaki (Fukano and Miyawaki, 2003) use a three-phase scheme with a relative phase of $2\pi/4$ between the three images, and a modified Eq. 4 for sectioning. With unequal phase approaches, care has to be taken (e.g., by shifting the 0-phase between series of images) to avoid bleaching illumination structure into the sample over time.

4. Scaled subtraction of the background is yet another way to process the raw images. Assuming that the nominal position and width of the illumination pattern is known, a pixel at the plane of focus is either illuminated or not in each of the images. First the value of each pixel is averaged over multiple images, each recorded at one of the positions of the illumination structure, that illuminates the in-focus parts of the sample in this pixel (ON). A second average is taken of all the pixel values where the pixel is nominally not irradiated (OFF) and subtracted from the first ON average. This technique estimates and removes the pinhole-to-pinhole background fluorescence, assuming that in-focus parts of the object do not yield fluorescence when not irradiated and out-of-focus parts fluoresce with equal brightness independent of the position of the illumination structure. It is termed "scaled subtraction" because only a scaled fraction of the sum of the pixel intensities in the non-illuminating frames has to be subtracted from the sum in the illuminating frames. Such a technique is commonly used for data where only these sums are acquired (conjugate and non-conjugate light) as in the programmable array microscope (Hanley *et al.*, 1999; Heintzmann *et al.*, 2001). The method and the scaling factor γ that is applied to the non-illuminated sum is covered by Eq. 6. Theoretically, such a scaled subtraction may yield negative results even in the totally noise-free limit, but these are so small that they can be neglected in practice. Note that even though Mask^{ON} and Mask^{OFF} in Eq. 6 were initially thought of as being binary masks, this technique of scaled subtraction can also be used with smooth masks [see Eq. 6(b)], in which case the binary mask is replaced by the spatially varying excitation probability in the computation. Equation 6(b) has been constructed in such a way that small spatial variations in mask intensity (e.g., due to moiré effects) are accounted for. If this is not an issue, β can be set to 1. The effect of Eq. 6(b) with β fixed to 1, is shown in Figure 13.4(C).

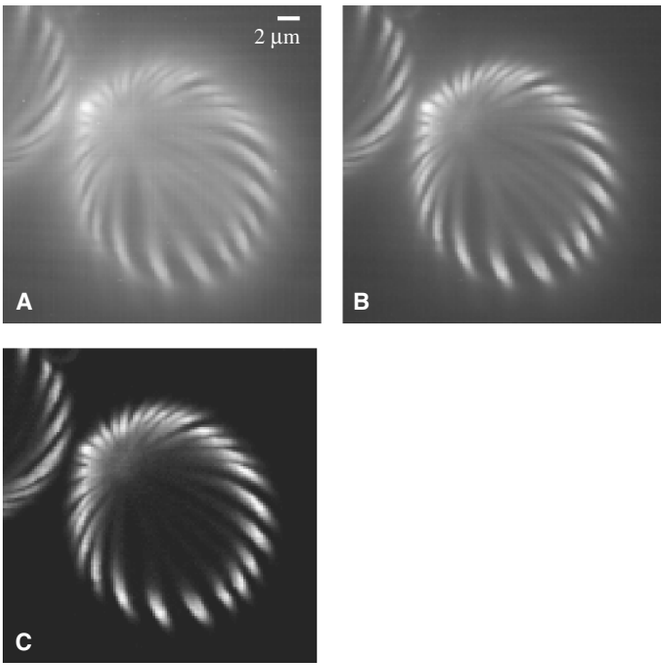


FIGURE 13.4. Confocal slices computed from structured-illumination data. (A) Virtual pinhole diameter chosen to be half the spot-to-spot distance. (B) Virtual pinhole selected as 0.15 of the spot-to-spot distance. (C) Scaled subtraction method with fixed $\beta = 1$ (see Eq. 6 in boxed list of equations) and illumination spot of Gaussian shape with width as in (B). [The experimental data for this figure was kindly provided by Pier Alberto Benedetti (pollen grain taken at 1.3 NA, ~450 nm excitation, ~550 nm emission, $6 \times 6 = 36$ patterned images acquired for this single slice, 200 nm pixel pitch in sample, spot-to-spot distance, 2.1 µm in sample).]

1. $$I_{rec}(x,y) = \underset{n=0\ldots N}{\text{Max}}\, I_n(x,y) - \underset{n=0\ldots N}{\text{Min}}\, I_n(x,y)$$

2. $$I_{rec}(x,y) = \underset{n=0\ldots N}{\text{Max}}\, I_n(x,y)$$

3. $$I_{rec}(x,y) = \underset{n=0\ldots N}{\text{Max}}\, I_n(x,y) + \underset{n=0\ldots N}{\text{Min}}\, I_n(x,y) - 2\underset{n=0\ldots N}{\text{Avg}}\, I_n(x,y)$$

4. $$I_{rec}(x,y) = \sqrt{\sum_{n=0}^{N} \left(I_n(x,y) - I_{(n+N \text{ div } 2) mod\, N}(x,y)\right)^2}$$

5. $$I_{rec}(x,y) = \left|\sum_{n=0}^{N} I_n(x,y)\, exp(2\pi i n/N)\right|$$

6a. $$I_{rec}(x,y) = \sum_{n=0}^{N} I_n(x,y) Mask_n^{on}(x,y) - \gamma \sum_{n=0}^{N} I_n(x,y) Mask_n^{off}(x,y)$$

$$\gamma = \frac{1}{MAR} - 1$$

6b. $$I_{rec}(x,y) = \beta \left[\frac{\sum_{n=0}^{N} I_n(x,y) Mask_n^{on}(x,y)}{\sum_{n=0}^{N} Mask_n^{on}(x,y)} - \frac{\sum_{n=0}^{N} I_n(x,y) Mask_n^{off}(x,y)}{\sum_{n=0}^{N} Mask_n^{off}(x,y)} \right]$$

$$\beta = \frac{N \sum_{n=0}^{N} Mask_n^{on}(x,y) - \left[\sum_{n=0}^{N} Mask_n^{on}(x,y)\right]^2}{N \sum_{n=0}^{N} \left(Mask_n^{on}(x,y)\right)^2 - \left[\sum_{n=0}^{N} Mask_n^{on}(x,y)\right]^2}$$

7a. $$\tilde{I}_{rec}(\vec{k}) = \frac{\sum_{l=-m}^{m} \frac{\alpha_l \tilde{\rho}_l(\vec{k} - \vec{s}_l)}{(\sigma_l \alpha_l)^2}}{\sum_{l=-m}^{m} \frac{1}{(\sigma_l \alpha_l)^2}}, \qquad \alpha_l = \frac{\tilde{h}_{goal}(\vec{k})}{\tilde{h}_{em,l}(\vec{k} + \vec{s}_l)}$$

7b. $$\tilde{\rho}_l(\vec{k}) = \sum_n (M^{-1})_{nl} \tilde{I}_n(\vec{k})$$

n: index of the acquired images (the grid position varies with n)
N: number of acquired images, *x*,*y*: in-plane positions in the image
i: imaginary constant, *l*: indexing the components (separated order)
$\underset{n=0\ldots N}{\text{Max}}$, $\underset{n=0\ldots N}{\text{Min}}$, $\underset{n=0\ldots N}{\text{Avg}}$: respective maximum, minimum or average value, computed at each pixel over all N successively acquired images.
$Mask_n^{on}$ and $Mask_n^{off} = 1 - Mask_n^{on}$ define which pixel was illuminated or not illuminated in a given frame *n*
MAR is the mark/area ratio describing the fraction of pixels considered to be illuminated

Note that, in contrast to filtering approaches, which consider information in neighboring pixels, this processing considers the multiframe data pixel by pixel. The optical sectioning visible in Figure 13.4 can thus not be explained as being the effect of a high-pass filter applied to the image data. It is a genuine method of optical sectioning obtained by processing images made at multiple illumination positions.

The scaled subtraction approach has also been used in a slightly different context of aperture correlation microscopy (Wilson *et al.*, 1996). In the first image, a mask with holes at random positions in it is scanned over the object and the image though the same mask is acquired. The second image consists of a, usually shorter, exposure with widefield illumination. Scaled subtraction of the two images serves to remove the remaining widefield information, which is present in the image acquired with illumination and detection through the random mask. A similar, yet more signal-to-noise effective approach, obviating the need for a separate widefield image, is to image the light rejected at the mask onto a separate detector (Hanley *et al.*, 1999; Heintzmann *et al.*, 2002) and also process the data by scaled subtraction.

All of the above techniques process the data **locally** by considering only a single pixel position in all the members of an image set for its own reconstruction and ignoring the intensities of neighboring pixels. Some of the above methods (Eqs. 1–5) are **nonlinear** in the sense that, during reconstruction, they employ at least one nonlinear operation such as thresholding, squaring, computing the absolute magnitude, or the maximum. In the absence of noise, they do remain linear with respect to the emitted light intensity. As long as the signal-to-noise ratio is high, the deviations from a linear treatment remains negligible and the resulting images can be used for quantification. However, in low-signal situations (e.g., high out-of-focus background) the deviation of the output from the true intensities in the sample will be severe. The nonlinear steps (absolute value, square root, maximum, minimum) statistically bias the result due to the influence of the noise, for example, when the true degree of modulation in a pixel should be zero but a high background is present in each of the images, methods based on taking the absolute value (Eqs. 4, 5) will yield a positive result just from the noise. They will not yield zero on average, whereas a linear method would be expected to do so.

The above evaluation techniques have the advantage of being fast and easy to compute. They do not require any knowledge of the absolute pattern position nor do they need to estimate this information from the measured data. Furthermore, they often show an inherent robustness to inexact pattern positioning. However, the results they produce are generally inferior to those achievable by approaches for the linear processing of structured-illumination data as outlined below.

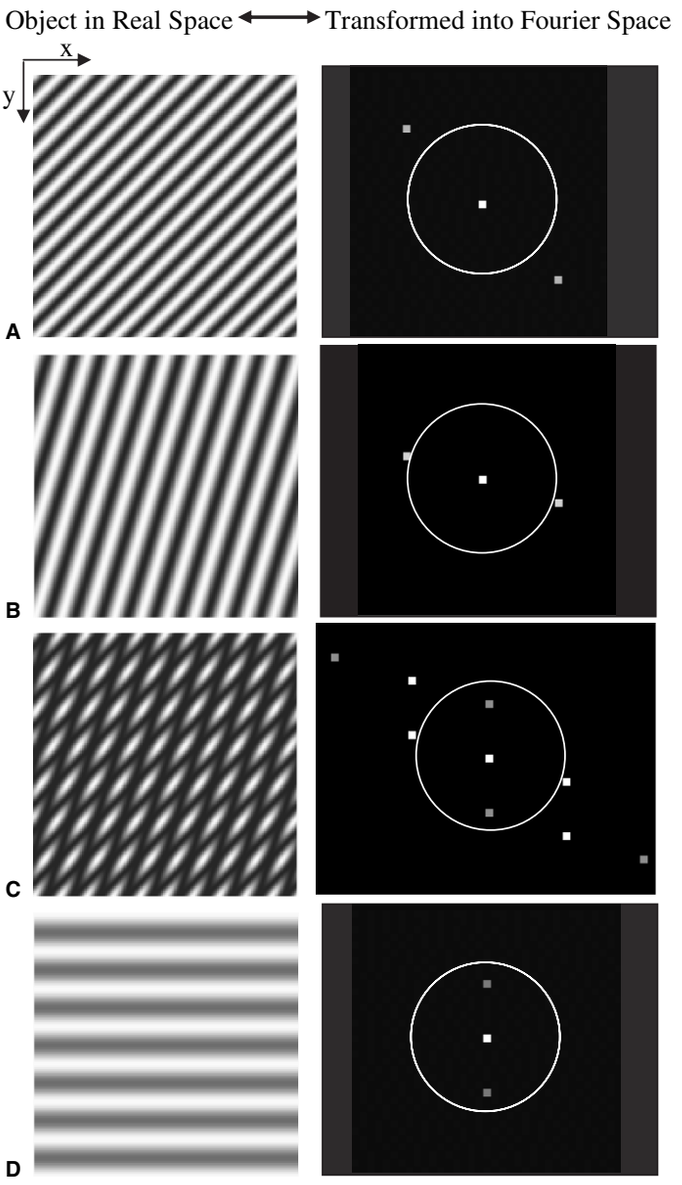


FIGURE 13.5. Moiré effect. A microscope can only detect information up to a maximal spatial frequency. In other words, a minimum distance between the maxima of a grid-like feature in the sample is required. The left column shows real-space features, whereas the right column shows the corresponding situation in Fourier-space. The circle indicates the limiting frequency (pass-band of the transfer function) up to which the microscope can detect information. In (A), a grid feature of the sample is shown that cannot be resolved with evenly distributed illumination, yielding equal fluorescence everywhere in the detected image. By illumination with another dense spatial grid (B), an aliased grid (C) is generated (moiré effect) that can then be partially detected (D). However, this detected grid (D) has "incorrect" spacing. Detailed knowledge about the moiré effect generated by the illumination pattern (B) can be used to reassign the detected spatial frequency to the correct place, thereby reconstructing (A).

RESOLUTION IMPROVEMENT BY STRUCTURED ILLUMINATION

In addition to achieving optical sectioning (Frohn *et al.*, 2001), structured illumination can also yield improved lateral resolution. The reason is that there is a moiré effect between the structured illumination pattern and the structure of the object, such that previously inaccessible spatial frequencies of the sample become detectable (Fig. 13.5). However, to yield a useful reconstruction, the illumination pattern must first be disentangled from the detected moiré fringes. This method was first conceived by Lucosz for the case of a rather dense line-grid illumination [Fig. 13.2(C)] and detection masks (Lucosz and Marchand, 1963) (the unit-cell distance in the sample coordinate system was on the order of the size of the point spread function) and also for two-dimensional grid [Fig. 13.2(A)] patterns (Lucosz, 1967). These arguments are based heavily on Fourier-space considerations and form the basis for all the computational unmixing systems used for data from widefield detectors recording images excited by structured illumination (as in Fig. 13.1).

FOURIER-SPACE — AN INTRODUCTION

Fourier-space is extremely useful in discussing optical imaging because the process of imaging can be modeled by simply multiplying the Fourier-transform of the sample distribution by the Fourier-transform of the point spread function of the microscope (the so-called optical transfer function); a process that is carried out in Fourier-space. To turn this result into a simulation of the image, this product must be "inverse-Fourier transformed" to bring it back into real space.

The concept of Fourier-space is based on the idea that any function in one-, two-, or three-dimensional space (e.g., a fluorophore distribution) can be represented as a sum of sinusoids varying in spatial frequency, direction, strength, and phase (position). The **spatial frequency** (or wave number) of a sine wave describes the number of bright maxima per distance (e.g., with the unit of meter^{-1}). Its component along the x-axis is indicated by k_x while the number of maxima counted along the y-axis is termed k_y. The right column of Figure 13.5 shows the magnitude of the Fourier-transformation of simple structures consisting of one (A, B, D) or only a small number of sine waves [Fig. 13.5(C)]. The displayed brightness is proportional to the magnitude of the transform at each location in Fourier-space (also called reciprocal space, frequency space, or k space). Such a plot shows only the strength of the sine wave, its direction, and spatial frequency. The exact phase (defining the position of the first maximum) is not displayed. The center in Fourier-space is located in the middle of each image. This position of zero spatial frequency corresponds to a uniform brightness in real space. The intensities away from the origin represent smaller and smaller spacings the farther out that they are.

As is apparent from Figure 13.5(A,B,D), a sinusoid shifted to all-positive values (by adding a constant), for example, the emitted sample intensity, yields three peaks in its Fourier-transformation. The central, zero-frequency peak represents the added constant and the two other peaks, taken together form the remaining sine wave in real space. Each individual peak in Fourier-space actually forms a complex-valued wave $\exp(i2\pi\mathbf{kr})$ with the respective $\mathbf{k}$ vector in positive/negative directions. As a sum these constitute the sine in real space: $2\sin(2\pi\mathbf{kr})$.

For a preliminary understanding of Fourier-space, it is sufficient to know that the values at two opposing positions in k space are complex conjugates to each other and when combined always form a sine wave in real space. Note that the small features of a sample are represented by sums of sine waves with high spatial frequency (small distance between successive wave maxima), such as is indicated in Figure 13.5(A). A coarser sinusoid [e.g., Fig. 13.5(D) as compared to Fig. 13.5(A)] has a $\mathbf{k}$ vector closer to the origin of Fourier-space.

The process of imaging is represented as a modification of the Fourier-transform of the sample distribution caused by multiplying it by the optical transfer function in Fourier-space. This function decays smoothly and amounts to zero everywhere beyond a certain maximum spatial frequency. This position, beyond which no information can be transferred, is indicated by the white circles in Figure 13.5. The decaying optical transfer function of a widefield microscope is also indicated by the dotted line in Figure 13.6. For a widefield microscope this in-plane cut-off frequency, when translated into a peak-to-peak distance of a sinusoid corresponds to the equation $d = \lambda/(2NA)$, with the vacuum wavelength λ and the numerical aperture NA.

To properly measure a sample feature (sinusoid) of this frequency, the observer needs to measure at a pixels-to-pixel spacing of below half this distance to avoid misinterpretation (aliasing) of the result. This required maximal pixel-to-pixel distance is called the Nyquist distance $d_{Nq} = \lambda/(4NA)$. For a different introduction to Fourier space, see the Appendix to Chapter 24, *this volume*.

Imaging can be treated elegantly in Fourier-space (see box "Fourier-Space — An Introduction") because a microscope essentially acts as a Fourier-filter. The periodic pattern introduced in the illumination path of the microscope yields a modification of the incident and thus of the emitted light. For fluorescence or reflection-type microscopy, the emitted light can be described as a multiplication of the sample structure times the illumination intensity or amplitude structure, respectively. This multiplication in real-space translates into a convolution in Fourier-space. Due to the periodicity of the illumination distribution, its Fourier-transform is a number of (delta) peaks at the reciprocal grid positions. The pattern of emitted light is a multiplication (in real space) of the illumination intensity distribution with the Fourier-transformed object, thus its Fourier-transformation is a sum of multiple Fourier-transformed objects (termed object components). These object components have their zero-frequency displaced to align with the reciprocal grating of the illumination distribution [Fig. 13.6(A), Fig. 13.8(C)]. The position and shape of the illumination structure in real space determines the individual position, strength, and phase of the multiple overlapping object components in Fourier-space.

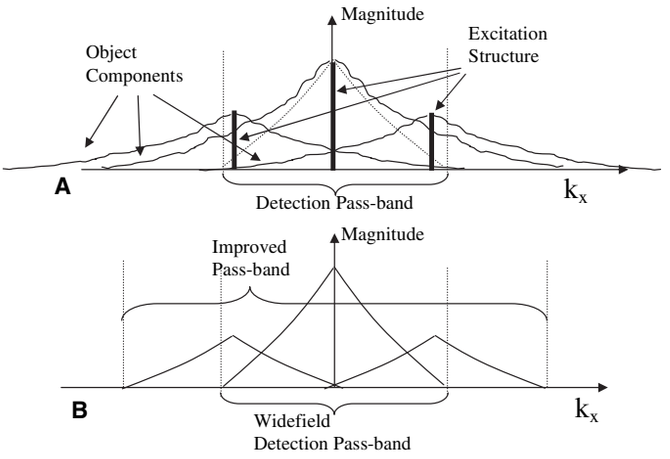


FIGURE 13.6. Scheme of the linear image reconstruction. (A) Fourier-transform of the structure of the emitted light. The optical transfer function defining the range of detectable special frequencies is indicated by the dotted line. (B) Detection sensitivity for the various reconstructed orders with their zero-frequency relocated to the origin.

The imaging of this emission intensity distribution is then described in Fourier-space by a multiplication with the optical transfer function. It is possible to computationally unmix the sum of the displaced copies of the object [Fig. 13.8(D)] by inversion (or pseudo-inverse) of the mixing matrix M, which mathematically describes the linear superposition of displaced object components and their relative phases [Eq. 7(b); see also Gustafsson, 2000; Heintzmann, 2003] and to shift the displaced position of their zero object frequency back to the real zero frequency. This shifting makes it obvious that, in comparison to flat-illuminated widefield microscopy, the pass-band of the microscope has then been increased by this moiré effect [Figs. 13.6(B), 13.8(E)]. Note that as opposed to the previously described methods (paragraphs 1–4), such resolution increase is even possible when the spatial modulation frequency falls outside the pass-band and is thus not imaged.

Acquiring a set of images (similar to the top row in Fig. 13.7), makes it possible to unmix the overlapping displaced object components [Fig. 13.8(C)]. An equation system for this unmixing can be constructed [Eq. 7(b)] by using the unique dependence of the complex phase of each object component on the position of the illumination structure. In a last step of image reconstruction, the individual unmixed object components [e.g., Fig. 13.8(D)] are shifted to their proper positions in Fourier-space, and multiple components that are present at the same frequency are averaged with frequency dependent weights (e.g., with the inverse variances

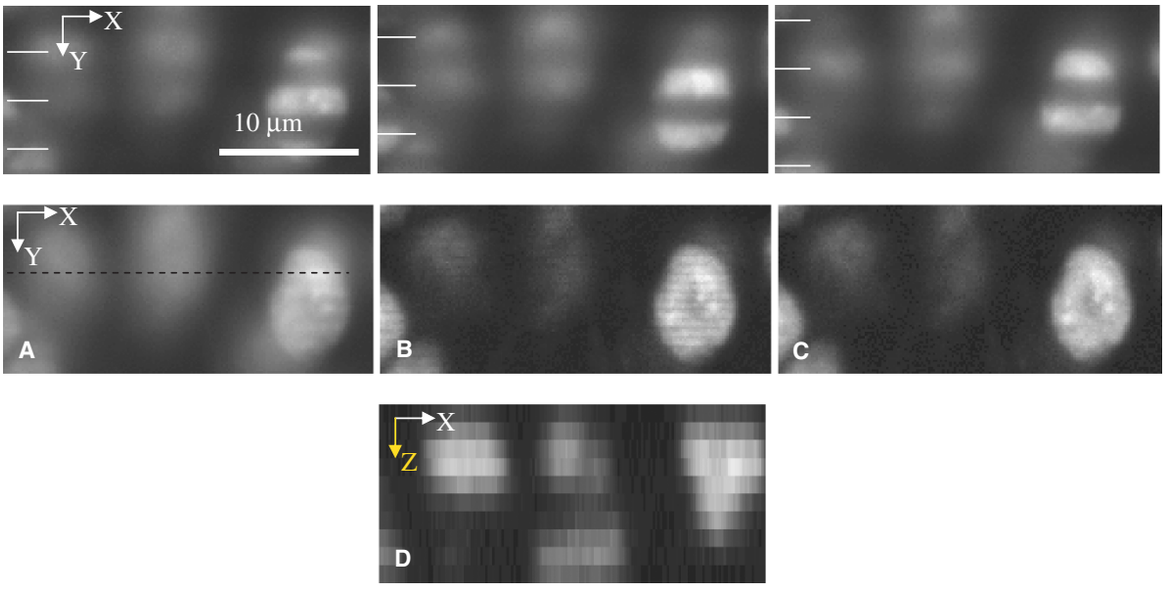


FIGURE 13.7. Reconstruction results obtained by different strategies. The top row shows the three individual raw data images taken at different illumination pattern positions (as indicated by the white lines at the left side of each image) with a Zeiss ApoTome setup (Axiovert, 40 × NA 1.3 objective, ~3.4 µm pattern pitch in the sample, Axiocam 6.7 µm pixel pitch). The middle row shows the results obtained by (A) The sum (B) max–min, Eq. 1, (C) quadrature method, Eq. 4. Panel (D) shows an *xz*-cut obtained from the ApoTome software at the approximate slicing position indicated by the dashed line in panel (A). The three-dimensional sectioning capability discriminating between layers of cells is seen nicely in (B), (C), and (D).

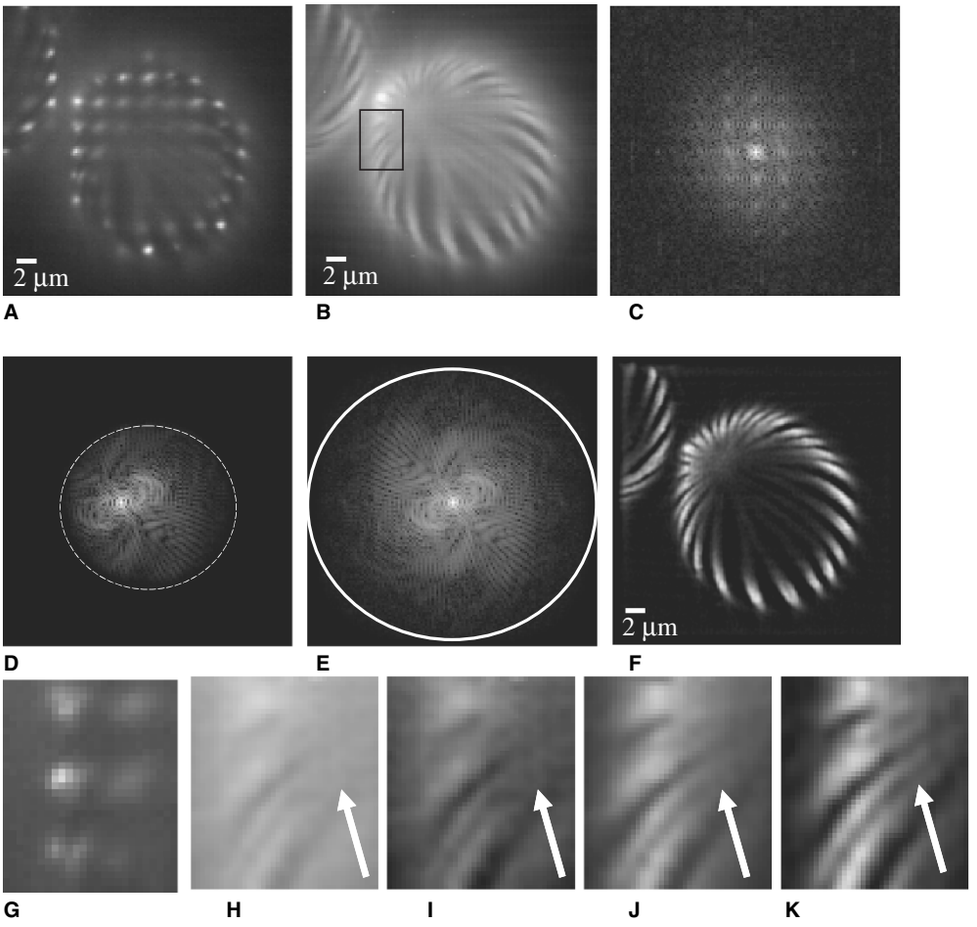


FIGURE 13.8. Various steps in the image reconstruction process. (A) An example raw data image. (B) The widefield image computed by summing over all partial images. The region of interest (ROI) used for images (G) to (K) is indicated as a black rectangle. (C) Magnitude of the Fourier transformation of (A), displaying the multiple overlapping components. (D) One ($k = 1.0$) object component separated from multiple measurements similar to (C) taken at varying illumination mask positions [one such position is shown in panel (A)]. The region of support in detection is indicated by the dotted white circle. (E) All components shifted, averaged, and apodized (border indicated by white circle). (F) Final reconstruction result in the linear case (total of 7 orders). (G) ROI extracted from raw data shown in panel (A). (H) ROI from widefield–like image as shown in (B). (I) Image (H) contrast-enhanced. (J) Contrast-enhanced ROI from confocal processing as shown in Figure 13.4(B). (K) Equivalent zoom of image (F). [The raw data for this figure was kindly provided by Pier Alberto Benedetti (for acquisition parameters see Figure 13.4).]

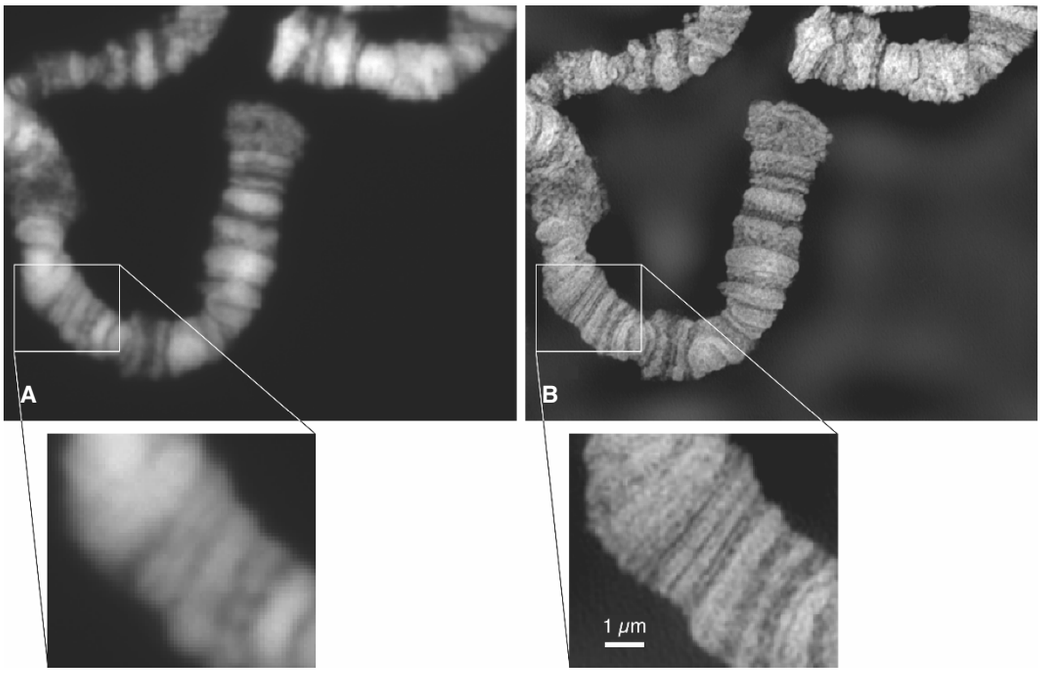


FIGURE 13.9. Demonstration of resolution extension by structured-illumination microscopy. The sample is a squash preparation of a polytene chromosome from a salivary gland of the fruitfly *Drosophila melanogaster*, stained for DNA with Oligreen to show the characteristic banding pattern. Many band features that are undetectable in the conventional microscope image (A) are clearly visible in the structured-illumination microscopy reconstruction (B). The structured illumination consisted of a one-directional pattern of parallel lines with a period of 0.20 μm, at a wavelength of 457 nm. This pattern frequency, about 80% of the resolution limit, is much higher that those used in the rest of this chapter. Nine raw data images were used: three images with a relative phase shift of $2\pi/3$, for each of three pattern orientations spaced 120° apart. The reconstruction used a Fourier-based algorithm that includes compensation for the detection OTF, as described in Gustafsson (2000). [These images were kindly provided by Mats Gustafsson (unpublished data) and the sample was prepared by Harry Saumweber.]

[Eq. 7(a); Gustafsson, 2000; Heintzmann, 2003; Fig. 13.8(E)]. The weights of this averaging in Fourier-space are adjusted as inverse variances of the noise such that the best quality reconstruction at each frequency is preferred over more noisy reconstructions. Finally, there is an inverse Fourier transformation back to real space [Figs. 13.8(F)]. The resolution improvement obtained can be seen in Figure 13.8(K) compared to what is obtained by just adding the widefield detected set of images [Fig. 13.8(H)] even after contrast enhancement [Fig. 13.8(I)] or by processing the same data to simulate confocal imaging [Fig. 13.8(J)]. In Figure 13.9 the resolution improvement is even more obvious. This figure was generated by illumination with a grating close to the highest transmittable spatial frequency, which leads to more prominent high-frequency components with less noise after their extraction (kindly provided by M. G. L. Gustafsson). In some of the figures [especially in Fig. 13.8(I)] a residual patterning can be observed. This can be attributed to having selected too few pattern positions (here $6 \times 6 = 36$) in the set.

It is interesting to note that the sampling of the raw data images need only satisfy the Nyquist limit of the widefield microscope even though the resolution finally achieved extends beyond this limit. During the relocation process of the object components in the reconstruction, the discrete frequency space can be "extended," essentially resampling the data onto a different grid. This reconstruction does not contradict information theory because many images, each with different high-frequency sample information (but downshifted into the detection pass-band) are used to construct a single image containing information outside the detection passband. Although negative intensities can in principle result during the process of image reconstruction, this does usually not pose a practical problem.

With this approach, the resolution of the microscope can theoretically be enhanced by a factor of about 2 in-plane (xy) as well as along the optic axis (z) compared to the standard epi-fluorescence widefield microscope. Although the fundamental pass-band limit obtained by this method is not larger than the pass-band of a confocal microscope, a substantial practical improvement over standard confocal microscopy is achieved. The high spatial frequencies of the object are detected much more efficiently because the moiré effect of the illumination grid shifts them into a region of the pass-band that is more efficiently detected.

Lucosz's formulation (Lucosz and Marchand, 1963; Lucosz, 1967) makes it possible to understand both the confocal microscope and multiple dot-scanning systems in the nomenclature of computational reconstruction. The moving detection mask of these systems, in combination with the integration of partial images on the detector, permits the required unmixing to be achieved automatically, the positions of the zero frequencies of the unmixed components to be correctly adjusted and integrated (which means essentially summed) in the detector with component-dependent weights. Thought of in this way, the shape and size of the detection pinhole defines the relative weights of individual object components.

As opposed to Lucosz' approach or scanning disk systems, in which the decoding is achieved by a detection mask, computational reconstruction is far more flexible. Assume as a gedanken experiment that we illuminate the specimen with an array of bright points and then scan these points over the field of view so that

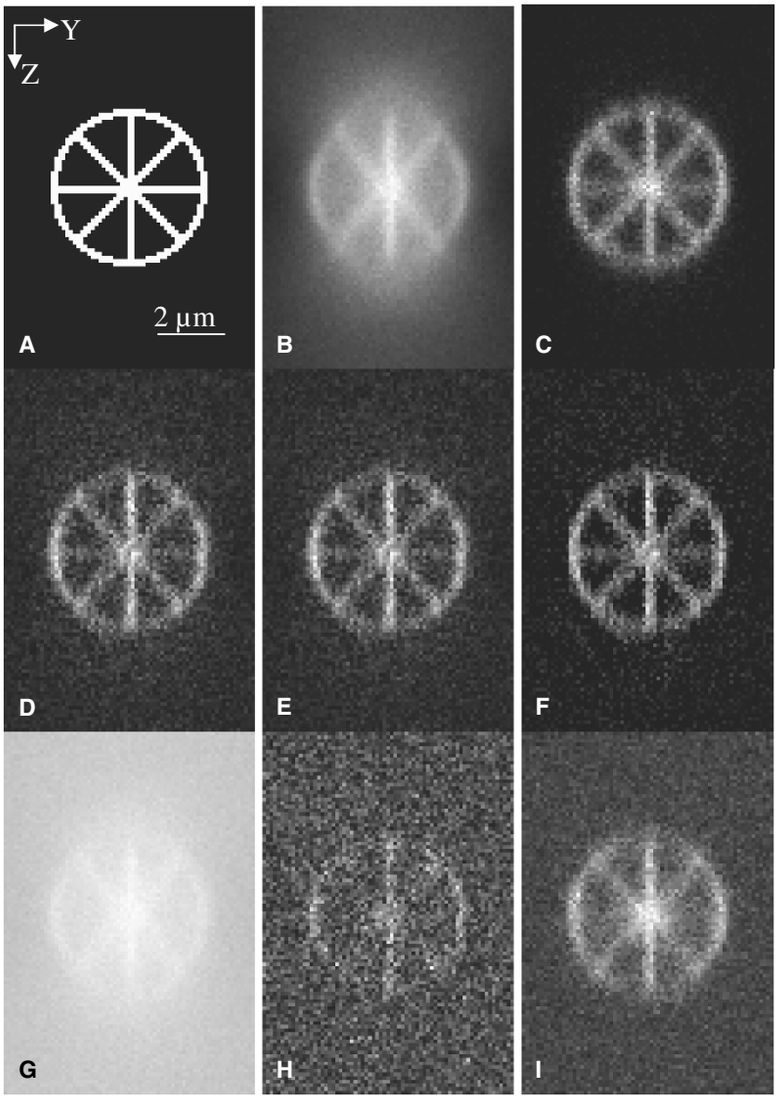


FIGURE 13.10. Performance simulation of dense structured illumination for thick samples. (A) Simulated object. (B) Widefield image (1000 expected photons in maximum). (C) Confocal image (pinhole size 0.5 Airy units, detector efficiency 20% that of panel B). (D) *yz*-Section computed using Eq. 1 from dense structured illumination, three phases. Further reconstructions were based on (E) Eq. 4, and (F) Eq. 6(b). (G) Widefield image with a background fluorescence added corresponding to approximately five layers of this object when densely packed. (H) Reconstruction (Eq. 4) of a structured-illumination dataset under similar sample conditions. (I) Reconstruction (Eq. 4) of data with the spacing between the illuminating bars increased 3-fold (total illumination dosage was kept constant for all simulations). Simulation parameters as described in the text.

eventually it is all covered. If we record a separate widefield image of the specimen for each location of the excitation array, we now have a stack of data that contains all the information we need to construct an optical section of the focus plane merely by summing the signal collected at virtual "pinholes" near the locations of the excitation points in each image of the stack (similar to the approach chosen for Fig. 13.4). Assuming the same illuminating power, the same scan time, and the same detector performance,[8] this optical section will be in every way identical to one made with a disk-scanning confocal microscope. However, this admittedly rather tedious approach has the added advantage that we could have used any of the seven methods (Eqs. 1–7) for computing optical sections discussed above and in addition we could compute results to reflect any detector pinhole size after the acquisition of the data.

Although this approaches pure confocal operation (by using very sparse structured illumination), it would be extremely time-consuming to take the many individual images. In addition, taking so many high-speed individual images will increase the readout noise with obvious consequences. Other problems would be caused by the massive amount of data (a full image acquired for each scan position, of which there could be a million). Thus, despite these theoretical advantages, practical limitations still render standard confocal microscopy more useful for imaging thick specimens (for a detailed example, see box "Imaging of Thick Specimens").

Approaches such as the programmable array microscope (Verveer *et al.*, 1998; Hanley *et al.*, 1999; Heintzmann *et al.*, 2001)

[8] Including pixels small enough to accurately delineate the image of each round pinhole in the image of the disk.

IMAGING OF THICK SPECIMENS

In Figure 13.10, a sample consisting of a *yz*-oriented star-shaped stack ("wagon-wheel pasta," see also Chapter 24, *this volume*) and its images were simulated [diameter of object: 4 µm, voxel size 100 × 100 × 100 nm, theoretical point spread function of 1.2 NA water immersion (n = 1.33) objective. Pattern spacing in sample: (B–H) 900 nm, (I) 2.7 µm, pattern width 300 nm.] The total dosage delivered to the sample for the acquisition of all of the raw data necessary for panels (B) to (I) was kept constant. This yielded a total of 1.2×10^6 detected photons for the central slice (B, D–F), 28×10^6 photons (G–I), and 36×10^3 photons for the confocal image (C).

The optical sectioning advantage of the confocal (C) over the widefield image (B) is clear even though the signal-to-noise ratio in the confocal image is lower due to rejection of light at the pinhole and lower detection quantum efficiency (QE). Note that in the widefield image only ~17% of the photons in the central slice stem from the in-focus region (3 voxels deep). Images obtained from processing the structured-illumination data (D–F) show only minor differences in quality and are comparable also to the confocal image. However, when additional background is added (as in G, H) stemming from a distant out-of-focus region in the form of five additional densely packed layers of overlying wagon-wheel pasta, the reconstructions from dense three-phase structured-illumination data are of poor quality (H), whereas the confocal image quality (C) would be unaffected. For this amount of background less than 5% of the collected photons stem from the in-focus area.

However, by adjusting the spacing between the illumination bars to yield a more sparse illumination (I), a better sectioning is achieved and the quality of the reconstruction becomes more acceptable. The price of this improvement is that data acquisition takes longer (if limited by the instrument) and the raw data file is larger. By going to even mores sparse illumination and a two-dimensional pattern, confocal quality will be reached, but the long acquisition times may be unacceptable. Note that each final reconstruction (including the widefield and confocal cases) assumed that the same total number of photons was emitted by the sample. The confocal detector (photomultiplier tube assumed) was assumed to have a quantum efficiency 20% as high as the detectors used in the widefield detection mode (a good quality CCD assumed). Read noise of the CCD was not accounted for because it would be of marginal influence in these bright images. For a further discussion on the effect of imaging thick specimens see the Appendix of this chapter.

that can rapidly change "pinhole patterns" using a digital mirror device for both illumination and detection, can make use of normally rejected light by sending it to a second detector (Heintzmann *et al.*, 2001) and have obvious advantages in speed and reduction of readout noise in comparison to acquiring all the individual images of a set. However, when integrating over a set of pinhole positions, these devices do not permit the widefield detection of each of the images of a set of structured-illumination data (e.g., changing the pinhole size retrospectively as in Fig. 13.4 is usually not possible).

Computational reconstruction of structured-illumination data is in some ways related to achieving resolution improvement by analysis of a series of intensity distributions at the pinhole plane based on a singular functional decomposition (Bertero *et al.*, 1989), the major difference being that aperture-modifying filters influence the light amplitude and not only the intensity as does reconstruction.

The minimum number of images required is defined by the number of object components that need to be separated [see Figs. 13.6(A) and 13.8(D)]. For a single optical slice, it ranges from three images when using a one-dimensional diffraction grid for improved sectioning (Neil *et al.*, 1997), a low number of images (typically 7–9) for in-plane resolution improvement with successive rotation of the illumination grid (Heintzmann and Cremer, 1999; Gustafsson, 2000) to many tens of images (Benedetti *et al.*, 1996) for use with relatively sparse two-dimensional patterns (pinhole distance ⩾PSF size).

However, looking at this issue from the perspective of information theory indicates that a reduction of this number should be possible (Cox and Sheppard, 1986). The weighted averaging in the reconstruction process also hints that much of the information has been acquired multiple times. The key to a major reduction in the minimum number of images required is to modify the reconstruction process so that both order separation and weighted averaging are combined into a single processing step (Heintzmann, 2003). When this idea is extended to three-dimensional data, another substantial reduction in the number of images per slice can be expected. For a *z*-sectioning image stack using dense grids, this could reduce the minimum to less than three images per slice on average.

When acquiring a focus series (a *z*-stack of image sets), the plane of focus for the illumination pattern usually coincides with the plane of focus of the detection path. In this situation, the theory of the imaging process becomes slightly more complex than outlined above. In the description above, the patterns were assumed as being "part of the object," that is, as its multiplicative modification. However, in *z*-direction, patterning has to be treated as being "part of the point spread function" because the illumination pattern usually stays aligned with the plane of best focus as it steps though the sample, and is not fixed to the object.

The standing-wavefield microscope (Bailey *et al.*, 1993; Lanni *et al.*, 1993; Krishnamurthi *et al.*, 1996; So *et al.*, 2001) and the incoherent illumination image interference imaging (I^5M) microscope (Gustafsson *et al.*, 1995, 1999) generate patterned illumination with either coherent laser light or an incoherent light source, respectively, and illuminate with alternating bright and dark *xy*-planes stacked along the optical axis. In I^5M, the maximum of the illumination pattern coincides with the plane of best focus in detection. The illumination pattern stays in a fixed spatial relation to the detection point spread function and can thus be treated as part of it. This simplifies the reconstruction, as no computational unmixing is required. However, standing-wavefield microscopy with illumination solely along both directions of the optic axis suffers from a large region of missing intermediate *z*-frequencies, essentially rendering three-dimensional reconstruction of large features impossible. (In real space this corresponds to the ambiguity problem between lobes along the *z*-axis of the PSF.)

In I^5M, the situation is much improved, such that it enables image reconstruction (Gustafsson *et al.*, 1999). The effect of noise on I^5M and 4Pi (which is essentially a point-scanning technique, described in Chapter 30, *this volume*) were compared by Nagorni and Hell (2001a, 2001b) indicating the superior performance of the 4Pi approach, especially along the axial direction. However, a combination of I^5M with additional patterning along the in-plane directions can be expected to yield an additional increase in resolution. This may also have the potential to overcome some of the signal-to-noise difficulties of I^5M in comparison to 4Pi microscopy.

All of the reconstruction techniques described above suffer to some extent from photobleaching of the fluorophores. Because bleaching is caused by structured illumination, patterns may be bleached into the sample and have to be compensated for during reconstruction. Efforts to compensate for patterned bleaching are treated in detail by Schaefer and colleagues (2004).

Although the three-dimensional imaging techniques described above have usually been developed for fluorescence, they have

also been applied to incoherent reflection (Neil *et al.*, 1997) and transmission (Dodt *et al.*, 2003). For the coherent case, approaches similar in spirit to the Fourier-techniques developed for synthetic aperture radar are used (Mermelstein, 1999; Schwarz *et al.*, 2003; Nellist *et al.*, 1995).

Nonlinear Structured Illumination

As described by Heintzmann and colleagues (2002), the methods of structured illumination can be extended to the nonlinear regime of the experiment in a straightforward way, and doing so yields another substantial resolution improvement over linear structured illumination. If any kind of nonlinearity exists between the illumination intensity and the emission intensity finally measured, further peaks in the Fourier-transformation of the effective excitation distribution will arise. In the absence of noise, this allows for any number of components to separate and thus, theoretically, for infinite resolution in the reconstruction. In practice, signal-to-noise issues and the type of nonlinearity limit the achievable resolution, even if grid quality, positioning accuracy, and detector linearity are perfect.

One of the nonlinear effects we have discussed (Heintzmann *et al.*, 2002) is fluorescence saturation (Sandison *et al.*, 1995). In this case, the sample is irradiated with structured illumination over the full field of view. The intensity required to achieve saturation is extremely high, but nevertheless possible by using pulse lasers and illuminating only a few nanoseconds. Recently, this approach has been practically demonstrated by Gustafsson (2005) who claimed an in-plane resolution of ~50 nm. This fluorescence saturation idea is related to the saturation of the stimulated emission employed in stimulated emission depletion (STED) microscopy (Klar *et al.*, 2000; see also Chapter 31, *this volume*).

It should be mentioned that multi-focal, two-photon microscopy yields inherent sectioning due to the two-photon effect and thus does not require a detection mask (see also Chapter 29, *this volume*; Andresen *et al.*, 2001). As these systems that illuminate with a pattern of light could allow the detection of the image at every pattern position, the reconstruction technique described above should also be applicable, with its potential for flexibility and resolution improvement. If one neglects the extra readout noise associated with recording all those images, a reconstruction based on such a set of structured-illumination images would increase the signal-to-noise ratio especially for high frequencies in comparison to just acquiring the summed images, as would be done in the standard system. However, because the excitation probability using the two-photon effect is proportional to the square of the incident intensity, analyzing the data as a case of structured illumination would contribute a factor of 2 increase in resolution from the excitation side of the scheme. This would compensate for the longer excitation wavelength used for two-photon excitation. Thus structured illumination based on the nonlinear two-photon effect leads to no major resolution increase compared to single-photon structured illumination. Other nonlinear effects, such as saturation phenomena, do have higher orders, which can also be utilized for substantial resolution improvements (such as in stimulated emission depletion microscopy).

As any type of nonlinearity can be used in combination with this concept, the nonlinearities considered in Hell and Kroug (1995) and Schönle and co-workers (1999) are also promising approaches for the concept described by Heintzmann and Cremer (1999b) and Heintzmann and colleagues (2002). Other extremely promising candidates are dyes (Corrie *et al.,* 2001; Giordano *et al.,* 2002) or proteins (Ando *et al.,* 2004) that can be converted between two (or multiple) states under wavelength selective illumination. These compounds constitute multi-level systems in which saturation characteristics can be utilized without requiring excessive illumination intensities (Hell, 2004).

SUMMARY

- Structured illumination in combination with widefield detection typically requires the acquisition of a large amount of data in comparison to standard confocal or Nipkow-type disk systems.
- One need not select a "pinhole size" during data acquisition. The data acquired can be processed in different ways to emphasize different contrast and resolution/noise trade-offs. Depending on the nature of the pattern employed, a practical resolution improvement of a factor slightly above 2 in each direction of space can be achieved compared to standard widefield microscopy. Using nonlinear approaches this factor can be made substantially bigger.
- Practical speed limits are imposed by the current camera and readout technology, but, more important, by the absence of bright light sources suitable for incoherent full-field illumination.

ACKNOWLEDGMENTS

Drs. James Pawley, Stefan Höppner, David Richards, Stefan Hell, Thomas Jovin, Anje Sporbert, Verena Hafner, and Keith Lidke are thanked for their help in improving this manuscript. I am very thankful to Dr. Pier Alberto Benedetti, who contributed experimental image data (Fig. 13.8) as did Drs. Bauch, Kempe, Schadwinkel, and Schaffer (Fig. 13.7) from Carl Zeiss, Göttingen, Germany. Furthermore, Drs. Thomas Jovin, Christoph Cremer, Mats Gustafsson, Stefan Hell, Jan Boese, and Quentin Hanley are thanked for many fruitful discussions regarding patterned illumination.

REFERENCES

Andresen, V., Egner, A., and Hell, S.W., 2001, Time-multiplexed multifocal multiphoton microscope, *Opt. Lett.* 26:75–77.

Ando, R., Mizuno, H., and Miyawaki, A., 2004, Regulated fast nucleocytoplasmic shuttling observed by reversible protein highlighting, *Science* 306:1370–1373.

Barth, M., and Stelzer, E.H.K., 1994, Boosting the optical transfer-function with a spatially resolving detector in a high numerical aperture confocal reflection microscope, *Optik* 96:53–58.

Bailey, B., Farkas, D.L., Taylor, D.L., and Lanni, F., 1993, Enhancement of axial resolution in fluorescence microscopy by standing wave excitation, *Nature* 366:44–48.

Ben-Levy, M., and Peleg, E., August 1995, WO 97/06509, US Patent 5,867,604.

Benedetti, P.A., Evangelista, V., Guidarini, D., and Vestri, S., 1996, US Patent 6,016,367.

Bertero, M., Boccacci, P., Defrise, M., De Mol, C., and Pike, E.R., 1989, Superresolution in confocal scanning microscopy: II. The incoherent case, *Inverse Problems* 5:441–461.

Bertero, M., De Mol, C., Pike, E.R, and Walzer, J.G., 1984, Resolution in diffraction-limited imaging, a singular value analysis. IV. The case of uncertain localization or non-uniform illumination of the object. *Opt. Acta* 31:923–946.

Bewersdorf, J., Pick, R., and Hell, S.W., 1998, Multifocal multiphoton microscopy, *Opt. Lett.* 23:655–657.

Corrie, J.E., Davis, C.T., and Eccleston, J.F., 2001, Chemistry of sulforhodamine-amine conjugates, *Bioconjug. Chem.* 12:186–194.

Cox, I.J., and Sheppard, C.J.R, 1986, Information capacity and resolution in an optical system, *J. Opt. Soc. Am. A* 3:1152–1158.

Dodt, H.-U., 1990, German Patent DE 40 23 650 A1.

Dodt, H.-U., and Becker, K., 2003, Confocal microscopy in transmitted light, *Proc. SPIE* 5139:79–87.

Dodt, H.-U., Becker, K., Eder, M., and Zieglgänsberger, W., 2001, Confocal microscopy of unstained neurons in brain slices, *Schloessmann Seminar 2001 Abstractbook*, Max-Planck Society, Schloss Elman, Oberbayern, DE, pp. 22–23.

Egner, A., Jakobs, S., and Hell, S.W., 2002, Fast 100-nm resolution 3D-microscope reveals structural plasticity of mitochondria in live yeast, *Proc. Natl. Acad. Sci. USA* 99:3370–3375.

Failla, A.V., Spoeri, U., Albrecht, B., Kroll, A., and Cremer, C., 2002, Nanosizing of fluorescent objects by spatially modulated illuminated microscopy, *Appl. Opt.* 41:7275–7283.

Frohn, J.T., Knapp, H.F., and Stemmer, A., 2000, True optical resolution beyond the Rayleigh limit achieved by standing wave illumination, *Proc. Natl. Acad. Sci. USA* 97:7232–7236.

Frohn, J.T., Knapp, H.F., and Stemmer, A., 2001, Three-dimensional resolution enhancement in fluorescence microscopy by harmonic excitation, *Opt. Lett.* 26:828–830.

Fukano, T., and Miyawaki, A., 2003, Whole-field fluorescence microscope with digital micromirror device: Imaging of biological samples, *Appl. Opt.* 42:4119–4124.

Giordano, L., Jovin, T.M., Irie, M., and Jares-Erijman, E.A., 2002, Diheteroarylethenes as thermally stable photoswitchable acceptors in photochromic fluorescence resonance energy transfer (pcFRET) *J. Am. Chem. Soc.* 124:7481–7489.

Gustafsson, M.G.L., 2000, Surpassing the lateral resolution limit by a factor of two using structured illumination microscopy, *J. Microsc.* 198:82–87.

Gustafsson, M.G.L., 2005, Non-linear structured-illumination microscopy: widefield fluorescence imaging with theoretically unlimited resolution, *Pro. Nat. Acad. Sci. USA* 102:13081–13086.

Gustafsson, M.G.L., Agard, D.A., and Sedat, J.W., 1999, I^5M: 3D widefield light microscopy with better than 100 nm axial resolution, *J. Microsc.* 195: 10–16.

Gustafsson, M.G.L., Agard, D.A., and Sedat, J.W., 2000, Doubling the lateral resolution of widefield fluorescence microscopy using structured illumination microscopy, *Proc. SPIE* 3919:141–150.

Gustafsson, M.G.L., Sedat, J.W., and Agard, D.A., US Patent 5,671,085.

Hanley, Q.S., Verveer, P.J., Gemkov, M.J., Arndt-Jovin, D., and Jovin, T.M., 1999, An optical sectioning programmable array microscope implemented with a digital micromirror device, *J. Microsc.* 196:317–331.

Heintzmann, R., 2003, Saturated patterned excitation microscopy with two-dimensional excitation patterns, *Micron* 34:283–291.

Heintzmann, R., and Cremer, C., 1999a, Laterally modulated excitation microscopy: improvement of resolution by using a diffraction grating, *Proc. SPIE* 3568:185–196.

Heintzmann, R., and Cremer, C., March 1999b, Patent WO 0052512.

Heintzmann, R., Jovin, T.M., and Cremer, C., 2002, Saturated patterned excitation microscopy — a concept for optical resolution improvement, *J. Opt. Soc. Am. A* 19:1599–1609.

Heintzmann, R., Hanley, Q.S., Arndt-Jovin, D., and Jovin, T.M., 2001, A dual path programmable array microscope (PAM): Simultaneous acquisition of conjugate and non-conjugate images, *J. Microsc.*, 204:119–137.

Hiraoka, Y., Sedat, J.W., and Agard, D.A., 1990, Determination of 3-dimensional imaging properties of a light-microscope system — partial confocal behaviour in epifluorescence microscopy, *Biophys. J.* 57:325–333.

Hell, S.W., 2004, Strategy for far-field optical imaging and writing without diffraction limit, *Phys. Lett. A* 326:140–145.

Hell, S.W., and Kroug, M., 1995, Ground-state depletion fluorescence microscopy, a concept for breaking the diffraction resolution limit, *Appl. Phys. B* 60:495–497.

Ichihara, A., Tanaami, T., Isozaki, K., Sugiyama, Y., Kosugi, Y., Mikuriya, K., Abe, M., and Uemura, I., 1996, High-speed confocal fluorescence microscopy using a Nipkow scanner with microlenses for 3-D imaging of single fluorescent molecules in real time, *Bioimages* 4:57–62.

Klar, T.A., Jakobs, S., Dyba, M., and Hell, S.W., 2000, Fluorescence microscopy with diffraction resolution barrier broken by stimulated emission, *Proc. Natl. Acad. Sci. USA* 97:8206–8210.

Krishnamurthi, V., Bailey, B., and Lanni, F., 1996, Image processing in 3D standing-wave fluorescence microscopy, *Proc. SPIE* 2655:18–25.

Lanni, F., Bailey, B., Farkas, D.L., and Taylor, D.L., 1993, Excitation field synthesis as a means for obtaining enhanced axial resolution in fluorescence microscopes, *Bioimaging* 1:187–196.

Lanni, F., Taylor, D.L., and Waggoner, A.S., 1986, US Patent 4,621,911.

Lukosz, W., 1967, Optical systems with resolving powers exceeding the classical limit. II, *J. Opt. Soc. Am.* 57:932–941.

Lukosz, W., and Marchand, M., 1963, Optischen Abbildung unter Überschreitung der beugungsbedingten Auflösungsgrenze [in German], *Opt. Acta* 10:241–255.

Majoul, I., Straub, M., Duden, R., Hell, S. W., and Söling, H. D., 2002, Fluorescence resonance energy transfer analysis of protein-protein interactions in single living cells by multifocal multiphoton microscopy, *Rev. Mol. Biotechnol.* 82:267–277.

Mermelstein, M.S., 1999, Synthetic aperture microscopy, Ph.D. thesis, Massachusetts Institute of Technology, Cambridge, MA, June 1999.

Nagorni, M., and Hell, S.W., 2001a, Coherent use of opposing lenses for axial resolution increase in fluorescence microscopy. I. Comparative study of concepts, *J. Opt. Soc. Am. A* 18:36–48.

Nagorni, M., and Hell, S.W., 2001b, Coherent use of opposing lenses for axial resolution increase. II. Power and limitation for nonlinear image restoration, *J. Opt. Soc. Am. A* 18:49–54.

Neil, M.A.A., Juskaitis, R., and Wilson, T., 1997, Method of obtaining optical sectioning by using structured light in a conventional microscope, *Opt. Lett.* 22:1905–1907.

Nellist, P.D., McCallum, B.C., and Rodenburg, J.M., 1995, Resolution beyond the "information limit" in transmission electron microscopy, *Nature* 374:630–632.

Pawley, J., Blouke, M., and Jenesick, J., 1996, The CCDiode: An optimal detector for laser confocal microscopes, *Proc. SPIE* 2655:125–129.

Petràň, M., Hadravsky, M., Egger, M.D., and Galambos, R., 1968, Tandem-scanning reflected-light microscope, *J. Opt. Soc. Am.* 58:661.

Sandison, D.R., Williams, R.M., Wells, K.S., Strickler, J., and Webb, W.W., 1995, Quantitative fluorescence confocal laser scanning microscopy (CLSM), In: *Handbook of Biological Confocal Microscopy*, 2nd ed. (J.B. Pawley, ed.), Plenum Press, New York, pp. 267–268.

Schaefer, L.H., Schuster, D., and Schaffer, J., 2004, Structured illumination microscopy: artefact analysis and reduction utilizing a parameter optimization approach, *J. Microsc.* 216:165–174.

Schönle, A., Hänninen, P.E., and Hell, S.W., 1999, Nonlinear fluorescence through intermolecular energy transfer and resolution increase in fluorescence microscopy, *Ann. Phys. (Leipzig)* 8:115–133.

Schwarz, C.J., Kuznetsova, Y., and Brueck, S.R.J., 2003, Imaging interferometric microscopy, *Opt. Lett.* 28:1424–1426.

Sheppard, C.J.R., and Cogswell, C.J., 1990, Confocal microscopy with detector arrays, *J. Modern Opt.* 37:267–279.

So, P.T.C., Kwon, H-S., and Dong, C.Y., 2001, Resolution enhancement in standing-wave total internal reflection microscopy: a point-spread-function engineering approach, *J. Opt. Soc. Am. A* 18:2833–2845.

Verveer, P.J., Hanley, Q.S., Verbeek, P.W., van Vliet, L.J., and Jovin, T.M., 1998, Theory of confocal fluorescence imaging in the programmable array microscope (PAM), *J. Microsc.* 189:192–198.

Wilson, T., Juskaitis, R., Neil, M.A.A., and Kozubek, M., 1996, Confocal microscopy by aperture correlation *Opt. Lett.* 21:1879–1881.

Yaroslavsky, L., 2003, Boundary effect free and adaptive discrete signal sinc-interpolation algorithms for signal and image resampling, *Appl. Opt.* 42:4166–4175.

APPENDIX: IMAGING THICK SPECIMEN WITH STRUCTURED ILLUMINATION

What illumination pattern do we choose for what specimen? If we neglect issues of resolution, it is apparent that a very thin sample (e.g., single molecules diffusing in a flat biomembrane) can be imaged with full-field illumination and widefield detection, whereas a very thick sample, containing a lot of fluorophores (e.g., a fish embryo expressing green fluorescent protein (GFP) throughout all the cells) requires confocal imaging. Widefield imaging has the advantage of being relatively fast and efficient in signal detection. Confocal imaging allows for the rejection of the "bad," that is, unemployable out-of-focus light that would dominate the signal in full-field illumination.

Structured illumination with a user-defined illumination pattern covers the entire range from full-field illumination through dense illumination patterns to sparse illumination, approximating single-spot confocal illumination conditions.

The crucial task is to obtain an estimate of the noise level that we should expect in the final data with different illumination patterns.

If we first assume full-field illumination with the fraction of the illumination area, the mark/area ratio $MAR = 1$, each horizontal plane will be illuminated with the same intensity, independent of its axial position. Depending on the structure of the sample, a defined thickness Z_{eq} will yield an equal amount of foreground signal and out-of-focus haze. Structured-illumination techniques and even widefield deconvolution aim at computationally removing this out-of-focus haze. However, although background removal (e.g., by subtraction) can be achieved, the noise contribution of the background to the signal will still be present. Thus, specimens considerably thicker than Z_{eq} (e.g., more than 10 times as thick) will run into signal-to-noise problems (see discussion below).

Consider now an illumination pattern of horizontal bars of a thickness of $d = 5\,\mu m$ with a pitch (distance between the beginning of one bar and the beginning of the next bar) of $D = 50\,\mu m$. The mark/area ratio is defined as $MAR = \frac{d}{D} = \frac{1}{10}$ which is related to the mark/space ratio by $MSR = \frac{d}{D-d} = \frac{1}{\frac{1}{MAR} - 1}$. If these bars are sufficiently wider than the diffraction limit, such that diffraction effects can be neglected, structured illumination allows the acquisition of the foreground in full brightness (knowing which parts of the in-focus slice are illuminated) while reducing the out-of-focus haze by the mark/area ratio.

When an in-focus structure of interest is not illuminated, which in this case happens in 90% of the images acquired in each set of frames, the background described above is still present. However, it can be assumed that the reconstruction algorithm can account for this foreground region not being illuminated because it knows the current illumination structure and uses this information merely for a precise estimate[9] of the amount of background. This estimate is then successively removed from the "foreground" data, acquired when the particle was illuminated (e.g., using Eqs. 6a and 6b).

[9] The quality of this estimate is better by a factor of $\sqrt{\frac{1}{MAR} - 1} = 3$ than the signal, thus exhibiting only 1/3 of the noise.

In the discussion above, it is assumed that out-of-focus light only influences the result as if it were detected as an additional, local uniform background (with its associated Poisson noise), and that a uniform illumination applies even to fluorophores situated directly behind or in front of the plane of focus. This is clearly NOT true for the patterned illumination geometry given in Figure 13.11(B). The parameters d and D define three illumination/detection regimes depending on whether the fluorescent structure is *in focus, close*, or *distant* from the focus plane. These regimes are characterized as follows:

- **In focus**: In this refined model, diffraction effects will blur the thin-line illumination, reducing its intensity. As a result, "background" contributions will arise from neighboring regions where illumination was not intended. These in-plane "spillover" effects are approximated in an *ad hoc* way by the following in-focus contrast reduction factor of the foreground:

  $$\text{contrast} = d_{rel}/(d_{rel} + \varepsilon),$$

  where $d_{rel} = d/d_{min}$ is the width of a bar compared to the smallest transmittable spatial wavelength of the objective at the emission wavelength $d_{min} = \lambda_{em}/(2NA)$.

  The number, $\varepsilon = 1.828$ was fitted from a simulation of the image of a bar with variable width at $NA = 1.4$.

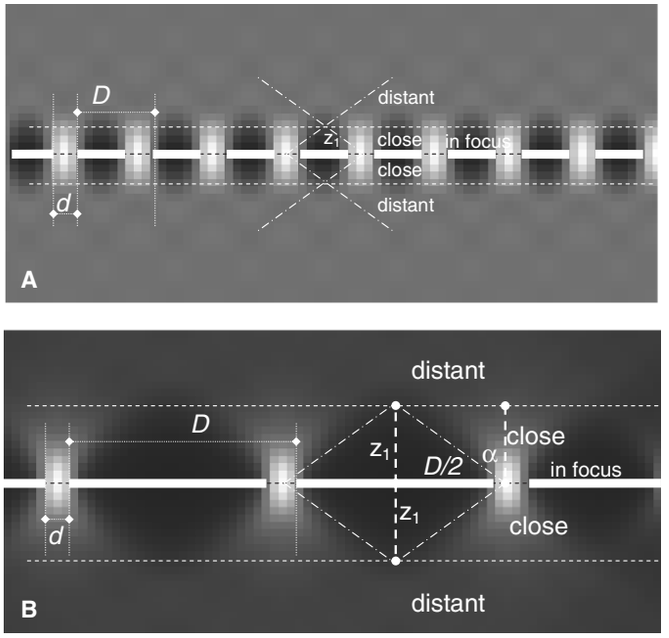


FIGURE 13.11. Background in thick samples. The sample is assumed to resemble a "sea" of fluorescence. The image depicts the illumination brightness distribution in the sample, viewed from the side. The fraction of emitted light from a specific plane falling on the illuminated grid-pattern geometric positions is also proportional to this distribution, which has to be integrated over a full unit-cell (here distance D). The region very close to the illuminating bars or squares should start with a widefield–like behavior. However, to keep the model simple the whole region from the bars to the *distant* region is denoted *close* in which a linear decay in the background stemming from an out-of-focus plane, detected at the nominally illuminated in-focus positions. Note the difference for dense (A) and sparse illumination (B) corresponding to the simulations shown in Figure 13.10.

- **Close** [$0 < z \le z_1 = D/(2 \tan\alpha)$]: Transition occurs between in-focus illumination and detection and dimmed-field scaling. This simplified model assumes a linear transition between the foreground in the *in-focus* slice and the background contributions in each plane of the *distant* region.
- **Distant** ($z_1 < z$): Dimmed-field scaling. Above the distance $z_1 = D/(2 \tan\alpha)$ from the plane of focus, all contributing background is assumed to be illuminated evenly as assumed in the discussion above. In contrast to the *in-focus* regime, features in this region receive illumination intensity dimmed by the mark/area ratio (MAR).

In Figure 13.12 the relative contribution of a planar fluorescent sheet at a defined distance from the plane of focus to the illuminated in-focus pixels is shown (simulation on a 400×400 pixel grid, pixel size 60 nm, at 520 nm, NA = 1.2 and water immersion $n = 1.33$). The simplified theory agrees reasonably well with the detailed simulation (with emission wavelength 520 nm, NA = 1.2, water immersion with refractive index $n = 1.33$). Here the *MAR* was kept constant as ¼ (e.g., as it could be in an ApoTome) and

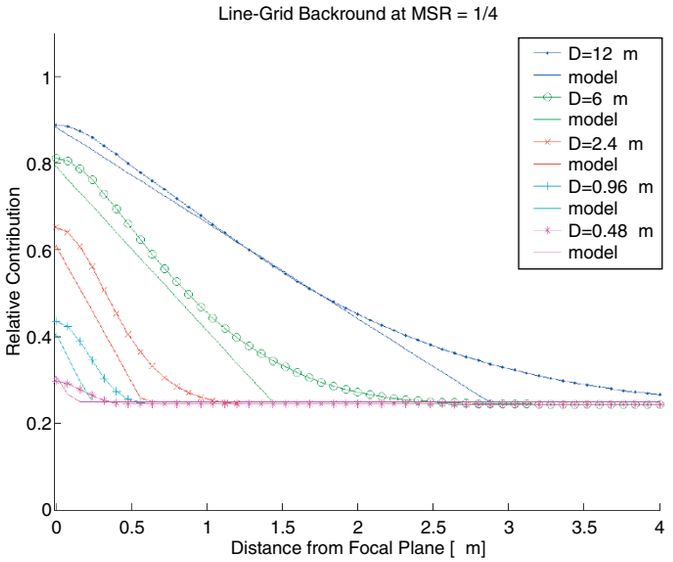


FIGURE 13.12. Comparison of rough model (from Fig. 13.11) with detailed calculations at *MAR* = 1/4. (A) Shown is the relative contribution each plane of focus makes to the signal detectable in the geometric position of the bars used for illumination. The "model" curves are calculated according to the approximations shown in Figure 13.11, the contribution of each plane to the background drops linearly (*close* regime) to reach a relative level of *MAR* = *d*/*D* at distances bigger than z_1 (*distant* regime).

the pitch and width of the bars were varied synchronously. As the width of the bars gets smaller, the foreground signal decreases. It is interesting to note that, for samples of relatively small depth, there is an optimal illumination pattern that provides the best signal-to-noise ratio. For thicker samples, the initial curve shape can be neglected as long as the width of the bars is well above the diffraction limit. The maximal achievable thickness then scales reciprocally with the chosen *MAR* as in the simplified initial model.

Similar simulations performed for two-dimensional patterns, revealed that the model can safely be extended in an *ad hoc* way by assuming the out-of-focus contributions to be described by a product of the results from the appropriate line grids (even though the problem is, strictly speaking, not separable).

Dependence of the Maximal Sample Thickness on the Number of Collected Photons

Let us assume that a total of 1000 photons/pixel are detected from a feature during the collection of as many images as are needed to illuminate the entire plane. In other words, if the dark space becomes larger, more exposures are needed to illuminate the entire plane but exposure must now involve fewer photons. Problems arise, if the foreground (1000 photons) cannot be distinguished from the noise of the total signal $s = fg + bg$ (sum of background bg and foreground fg). The noise scales with the square root of s. To achieve a defined signal-to-noise ratio (*S/N*) for the foreground-only signal (fg^{rec}) reconstructed by subtracting the background (here assumed to be estimated perfectly), we obtain:

$$\mathrm{S/N} = \frac{fg^{\mathrm{rec}}}{noise(fg^{\mathrm{rec}})} = \frac{fg}{\sqrt{fg + bg}}, \text{ thus } bg = \left(\frac{fg}{\mathrm{S/N}}\right)^2 - fg, \text{ which}$$

is the maximum acceptable background level given the specified foreground level (in photons) and the required signal-to-noise ratio. Assuming a signal-to-noise ratio of 10 gives reasonable image quality, and assuming essentially noise-free background estimation, the background level bg in the raw data can be as high as *9000 photons/pixel* (i.e., the background signal can be ~9 times higher than the foreground). However, if only 200 photons can be collected from the foreground object, the background cannot go above 200 photons without dropping the S/N below 10.

Therefore, two effects determine the maximum sample thickness. The structure of the illumination pattern will define the break-even distance Z_{eq} at which the out-of-focus haze equals the foreground. The number of collected photons from the structure of interest then finally determines the factor $\gamma = \frac{fg}{\mathrm{S/N}^2} - 1$ by which the sample thickness can exceed Z_{eq}, while still maintaining a signal-to-noise ratio above the given limit (S/N).

14

Visualization Systems for Multi-Dimensional Microscopy Images

N.S. White

INTRODUCTION

Rapid developments in biological microscopy have prompted many advances in multi-dimensional imaging. However, three-dimensional (3D) visualization techniques originated largely from applications involving computer-generated models of macroscopic objects. Subsequently, these methods have been adapted for biological visualization of mainly tomographic medical images and data from cut serial sections (e.g., Cookson *et al*., 1989 and review in Cookson, 1994). Most of these algorithms were not devised specifically for microscopy images, and only a few critical assessments have been made of suitable approaches for the most common 3D technique, laser-scanning microscopy (LSM) (Kriete and Pepping, 1992). Ultimately, we must rely on objective visualization of control, calibration, and test specimens in order to determine which visualization algorithms are appropriate for a particular analysis. Hardware developments and advances in software engineering tools have made available many 3D reconstruction systems that can be used to visualize multi-dimensional images. These are available from instrument manufacturers, third party vendors, research academics, and other microscopists. The author has attempted to collate important techniques used in these programs and to highlight particular packages that, not exclusively, illustrate various techniques described throughout the text. A representative collection of established commercial and non-commercial visualization programs available at the time of writing is listed in Table 14.1. For automatic image analysis and measurement, see Chapters 15 and 48, *this volume*.

The information presented in this chapter about the various programs is not the result of exhaustive tests or benchmarks but is merely an overall view of some key issues. The speed of changes and the rapid appearance (and loss) of particular programs and hardware from common use make it necessary to concentrate on important techniques and milestones rather than intricate details of each package.

Multi-dimensional microscopy data can also be obtained from instruments other than LSM configurations, such as non-laser confocal devices and widefield (conventional) systems combined with image restoration. Although the multi-dimensional data from different instruments may have different characteristics, the same basic visualization methods can be used to process the data.

Definitions

A consistent terminology is required to discuss components of any visualization system, maintaining a fundamental separation between (1) raw images and subsequent processed stages, (2) data values and the sampled space over which they extend, and (3) final results and the presentation form of those results. The author prefers the following terminology: Original intensities from the microscope comprise an **image**. Subsequent visualization steps produce a **view**. Intensities in an image or view represent the **data values**, and the sampling space over which they extend constitutes the **dimensions of the data**. Values presented on a screen, hard copy, etc., are **display views**. **Visualization** is the overall process by which a multi-dimensional display view is made from a biological specimen, although we will only be concerned with the software component of this in the present text. **Reconstruction** refers to the piecing together of optical sections into a representation of the specimen object. **Rendering** is a computer graphics term that describes the drawing of reconstructed objects into a display view.

What Is the Microscopist Trying to Achieve?

Human visual perception and cognition are highly adapted to interpret views of large-scale (macroscopic) objects. The human eye captures low numerical aperture (NA) views like photographic images. We get information from such views by calling (largely subconsciously) on *a priori* information about both the object and imaging system. High-NA microscope objectives produce images from which we generate views with properties that we are less equipped to interpret, for example, the apparent transparency of most biological samples. This arises from two main processes: (1) Samples are mostly thin, non-absorbing, and scatter only some of the illuminating light. Reduced out-of-focus blur, together with this real transparency enable the confocal and multi-photon LSMs to probe deep into intact specimens. (2) A high-NA microscope objective collects light from a large solid angle and can see around small opaque structures that would otherwise obscure or shadow details further into the sample. Such intrinsic properties in the resultant images must be sympathetically handled by an appropriate visualization system.

The goal of visualization is the formation of easily interpreted and, sometimes, realistic-looking display views. While pursuing these aims, several conflicts arise: (1) avoiding visualization artifacts from inappropriate *a priori* knowledge, (2) enhancing selected features of interest, and (3) retaining quantitative information. Maintaining these goals ensures that the final view can be used to help obtain unbiased measurements or to draw unambiguous conclusions. **The microscopist must be constantly vigilant to avoid unreasonably distorting the structural (and intensity) information in the original image data by over-zealous use of image processing.**

N.S. White • University of Oxford, Oxford OX1 3RE, United Kingdom

 Handbook of Biological Confocal Microscopy, Third Edition, edited by James B. Pawley, Springer Science+Business Media, LLC, New York, 2006.

Criteria for Choosing a Visualization System

Assessing any visualization system requires a judgment of (1) features, (2) usability or friendliness, (3) price/performance, (4) suitability of algorithms, (5) integration with existing systems, and (6) validation and documentation of methods or algorithms. The only way to determine ease of use is by testing the system with typical users and representative data. The best demonstration images saved at a facility should never be used to assess a visualization system for purchase! The host institution's user profile will help to formulate more specific questions: What is the purpose of the reconstructed views? What image information can be represented in the display views? How must the image data be organized? Are semi-automated or script-processing (programming) tools available for preprocessing and can the procedures be adequately tested and tracked?

WHY DO WE WANT TO VISUALIZE MULTI-DIMENSIONAL LASER-SCANNING MICROSCOPY DATA?

The principle uses of a visualization package are to generate subregion or composite reconstructions from multi-dimensional images (Fig. 14.1). To collect such views directly from the microscope is a time-consuming and inefficient process.

There are many advantages to interactively viewing multi-dimensional confocal images away from the microscope:

- Damage to the sample by the illumination is reduced.
- Sample throughput on a heavily used system is improved.
- Optimal equipment for data presentation and analysis can be employed. Serial two-dimensional (2D) orthogonal sections (e.g., *xy*, *xz*, *yz*, *xt*, etc.) must be extracted from a 3D/four-dimensional (4D) image interactively at speeds adequate for smooth animation. An animation of confocal sections corresponds to a digital focal series without contrast-degrading blur. Oblique sections overcome the serial section bias of all confocal instruments and their smooth, interactive animation is desirable.
- Reconstructed views are essential to conveniently display a 3D (Drebin *et al.*, 1988; Robb, 1990) or 4D image (Kriete and Pepping, 1992) on a 2D display device. The reconstructed volume may show features that are not discernible when animating sequential sections (Cookson *et al*., 1993; Foley *et al.*, 1990). Reconstructions further reduce the orientationally biased view obtained from serial sections alone.
- Multiple views are a useful way of extending the dimensional limitations of the 2D display device. Montages of views make more efficient use of the pixel display area. Animations make effective use of the display bandwidth. Intelligent use of color can further add to our understanding of the information in a display view (e.g., Boyde, 1992; Kriete and Pepping, 1992; Masters, 1992).
- For multiple-channel images, flexibility and interactive control are essential. Multiple channels may require complex color merging and processing in order to independently control the visualization of each component.

Data and Dimensional Reduction

Simplification of a complex multi-dimensional image to a 2D display view implies an important side effect — data and dimensional reduction. If the required information can be retained in a display view, substantial improvements in storage space and image transfer times are possible. This is increasingly important when presentation results must be disseminated via the Internet (now a routine option for medical imaging packages such as those from Cedara and Vital Images Inc.). Data reduction is most obvious in the case of a single (2D) view of a 3D volume or multiple-channel image but is actually more significant when 4D data can be distilled into a series of 2D views (Volocity, Imaris, and Amira, among other packages, can now seamlessly visualize multi-channel 4D images). Significant reduction can also be achieved when a single 3D volume of voxels can be represented by a smaller number of geometric objects. To combine data reduction with quantitative analyses, a precise description of the object extraction algorithm must be recorded along with the view; only then can the user determine the significance of extracted features.

Objective or Subjective Visualization?

The conflict between realistic display and objective reconstruction persists throughout the visualization process. All of the important information must be retained in a well-defined framework, defined by the chosen visualization model or algorithm. Recording of the parameters at every stage in the visualization is essential. This can be consistent with the production of convincing or realistic displays, provided enhancement parameters are clearly described and can be called upon during the interpretation phase. Multi-dimensional image editing must be faithfully logged in order to relate subregions, even those with expansion or zooming, back to their original context. Object extraction is a one-way operation that discards any original image data that falls outside the segmentation limits. To interpret a reconstruction based on graphically drawn surfaces we will need to refer back to the corresponding image voxels. To do this, we must either (1) superimpose the view on a reconstruction that shows the original voxels, using so-called embedded geometries (e.g., Analyze, Amira, Imaris VolVis and others), or (2) make references back to the original image. Voxel distribution statistics defining the degree to which a particular extracted object fits the image data would be a significant improvement.

Prefiltering

Low-pass or median filtering aids segmentation by reducing noise. Ideally, noise filters should operate over all image dimensions, and not just serially on 2D slices. Imaris, Voxblast, and FiRender/LaserVox, for example, have true 3D filters; the latter are particularly useful as they allow filtering of a subvolume for comparison within the original. Because Nyquist sampling will ideally have been adhered to in the image collection, the ideal preprocessing stage would include a suitable Gaussian filter or (even better) a point-spread function (PSF) deconvolution (Agard *et al.*, 1989). This step can effectively remove noise, that is, frequency components outside the contrast transfer function of the instrument.

Identifying Unknown Structures

The first thing to do with a newly acquired 3D image is a simple reconstruction (usually along the focus or *z*-axis). Even the simplest of visualization modules in 2D packages (such as Metamorph and the basic Scion Image) can rapidly project even modest size data sets. The aim is to get an unbiased impression of the significant structure(s). For the reasons discussed above, the method of

TABLE 14.1. A Representative Collection of Visualization Software Packages Available at the Time of Writing

System	Source	Supplier type	Platforms supported	Price Guide
Amira	TGS Inc. 5330 Carroll Canyon Road, Suite 201, San Diego CA 92121, USA www.amiravis.com	ind	Win, HP SGI, Sun Linux	(B)–(C)
Analyze	Analyze Direct 11425 Strang Line Road, Lenexa, KS 66215, USA www.analyzedirect.com	acad ind	Win Unix/Linux	(B)
3D for LSM & LSM Vis Art	Carl Zeiss Microscopy D07740 Jena, Germany www.zeiss.de/lsm	LSM, wf	Win	(A)–(B)
AutoMontage	Syncroscopy Ltd. Beacon House, Nuffield Road, Cambridge, CB4 1TF, UK www.syncroscopy.com	Ind wf	Win	(A)–(B)
AVS	Advanced Visual Systems Inc. 300 Fifth Avenue, Waltham, MA 02451, USA www.avs.com	ind	DEC, SGI, Sun, Linux	(A)–(B)
Cedara (formerly ISG)	Cedara Software Corp. 6509 Airport Road, Mississauga, Ontario, L4V 1S7, Canada www.cedara.com	med	Win	(B)–(C)
Deltavision & SoftWorx	Applied Precision, LLC 1040 12th Avenue Northwest, Issaquah, Washington 98027, USA www.api.com	wf	Win	(B)
FiRender	Fairfield Imaging Ltd. 1 Orchard Place, Nottingham Business Park, Nottingham, NE8 6PX, UK www.fairimag.co.uk	ind	Win	(B)
Image Pro Plus & 3D Constructor	Media Cybernetics, Inc. 8484 Georgia Avenue, Suite 200, Silver Spring, MD 20910–5611, USA www.mediacy.com	ind	Win	(B)
ImageJ	National Institutes of Health 9000 Rockville Pike, Bethesda, Maryland 20892, USA http://rsb.info.nih.gov/ij	acad	Win, Mac Linux, Unix	(A)–(B)
Imaris	Bitplane AG Badenerstrasse 682, CH-8048 Zurich, Switzerland www.bitplane.com	ind	Win	(A)–(C)
Lasersharp & LaserVox & LaserPix	Bio-Rad Microscience Ltd. Bio-Rad House, Maylands Avenue, Hemel Hempstead, HP2 7TD, UK www.cellscience.bio-rad.com	LSM	Win	(A)–(B)
LCS & LCS-3D	Leica Microsystems AG Ernst-Leitz-Strasse 17-37, Wetzlar, 35578, Germany www.leica-microsystems.com	LSM, wf	Win	(A)–(B)
Metamorph	Universal Imaging Corporation 402 Boot Road, Downingtown, PA 19335, USA www.image1.com	ind	Win	(A)–(B)
Northern Eclipse	Empix Imaging, Inc. 3075 Ridgeway Drive, Unit #13, Mississauga, ON, L5L 5M6, CANADA www.empix.com	ind	Win	(A)–(B)
Stereo Investigator	MicroBrightField, Inc. 185 Allen Brook Lane, Suite 201, Williston, VT 05495, USA www.microbrightfield.com	ind	Win	(A)–(B)
Scion Image	Scion Corp. 82 Worman's Mill Court, Suite H, Frederick, Maryland 21701, USA www.scioncorp.com	ind	Win Mac	(A)
Visilog/Kheops	Noesis 6–8, Rue de la Réunion, ZA Courtabœuf, 91540 Les Ulis Cedex, FR www.noesisvision.com	ind	Win Unix	(A)–(B)
Vitrea2 (formerly VoxelView)	ViTAL Images, Inc. 5850 Opus Parkway, Suite 300, Minnetonka, Minnesota 55343, USA www.vitalimages.com	med	Win SGI	(B)–(C)
Volocity & OpenLab	Improvision Inc 1 Cranberry Hill, Lexington, MA 02421, USA www.improvision.com	ind	Win Mac	(B)–(C)
VolumeJ (plug-in for ImageJ)	Michael Abramoff, MD, PhD University of Iowa Hospitals and Clinics, Iowa, USA http://bij.isi.uu.nl	acad	Win, Mac Linux, Unix	(A)–(B)
VolVis	Visualization Lab Stony Brook University, New York, USA www.cs.sunysb.edu/~vislab	ind	Unix source supplied	(A)

TABLE 14.1. (*Continued*)

System	Source	Supplier type	Platforms supported	Price Guide
VoxBlast	VayTek, Inc. 305 West Lowe Avenue, Suite 109, Fairfield, IA 52556, USA www.vaytek.com	ind	Win Mac SGI	(A)–(C)
Voxx	Indiana Center for Biological Microscopy Indiana University Medical Center www.nephrology.iupui.edu/imaging/voxx	acad	Win Mac Linux	(A)–(B)

Ind = independent supplier (not primarily a microscopy system supplier), acad = system developed in, and supported by, academic institution, LSM = LSM supplier, wf = widefield microscopy system supplier, med = medical imaging supplier. Win = Microsoft Windows, Mac = Apple Macintosh, SGI = Silicon Graphics workstation, HP = Hewlett Packard workstation. Price guide (very approximate, lowest price includes entry level hardware platform): (A) = < $5000, (B) = $5000–$15,000, (C) = > $15,000.

choice is voxel rendering, as it avoids potential artifacts of segmentation at this early stage. This catch-all algorithm could have interactive parameter entry in order to explore the new structure if the processing were fast enough. Contrast control and careful data thresholding (to remove background only) would normally be used with this quick-look approach. More specific voxel segmentation (removing data values outside a given brightness band, intensity gradient, or other parameter range) should be used with caution during the identification of a new structure. Artifactual boundaries (surfaces) or apparently connected structures (e.g., filaments) can always be found with the right segmentation and contrast settings.

In subsequent refinement stages, a case can usually be made for a more specific segmentation model. For example, maximum intensity segmentation can be used to visualize a topological reflection image of a surface. The prerequisites for such a choice can only be confirmed by inspection of the entire image data. Finally, visualization models involving more complex segmentation, absorption and lighting effects, whether artificial or based on *a priori* knowledge, must be introduced in stages after the basic distribution of image intensities has been established (Fig. 14.2).

Computer graphics research is beginning to offer techniques for automated or computer-assisted refinement of the visualization algorithm to automatically tune it for the particular supplied data (He *et al.*, 1996; Marks, 1997; Kindlmann and Durkin, 1998). Some useful user-interface tools, such the Visual Network Editor of AVS, assist in the design stages of more complex multi-step or interactive visualization procedures.

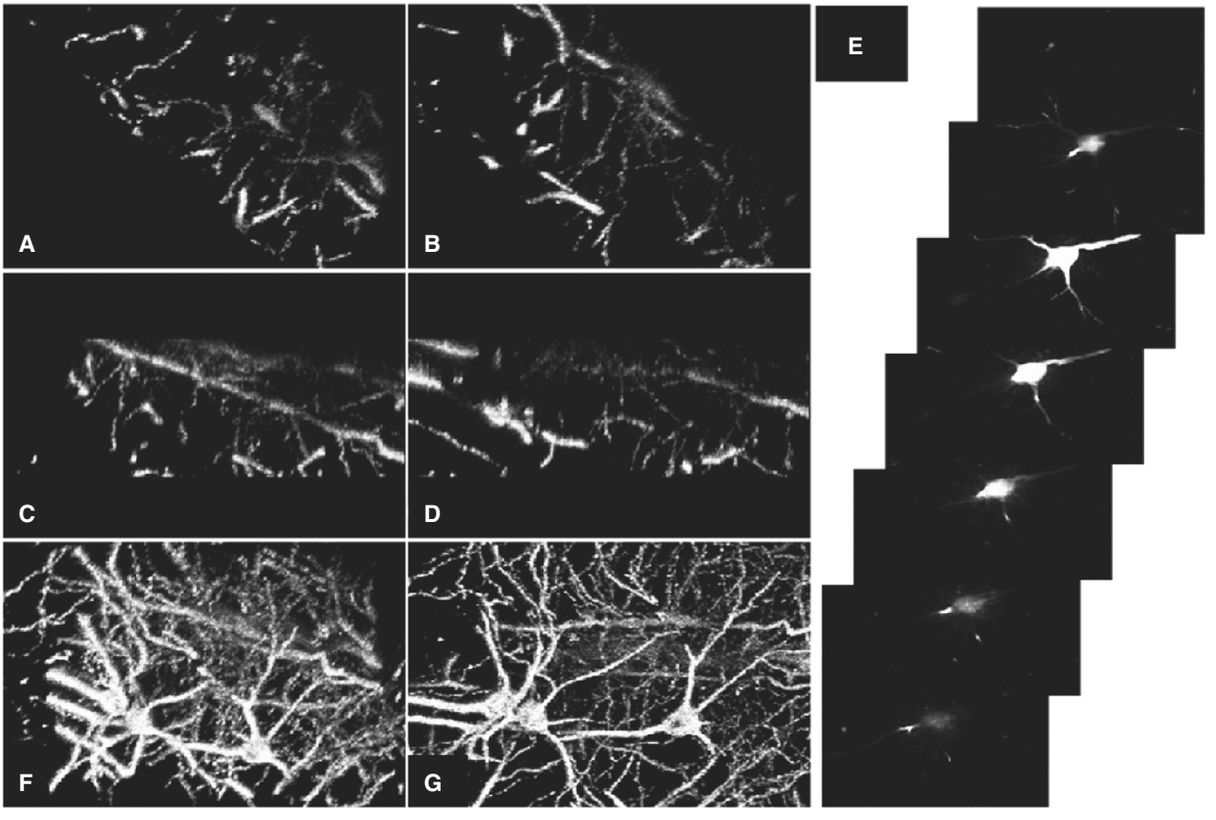


FIGURE 14.1. Viewing multidimensional LSM data. In order to make maximum use of imaging resources, multidimensional CLSM images are routinely viewed away from the microscope. "Thick" 2D oblique sections (A, B) can be extracted at moderate rates by many software packages. 2D orthogonal sections (C–E) can be viewed at video rate. Reconstructed 3D views (F, G) require more extensive processing, now common in all commercial systems. (A–D, F, G) are reflection images of Golgi-stained nerve cells. (E) Multiple *xy* views (e.g., from an animation) of fluorescently stained nerve cells.

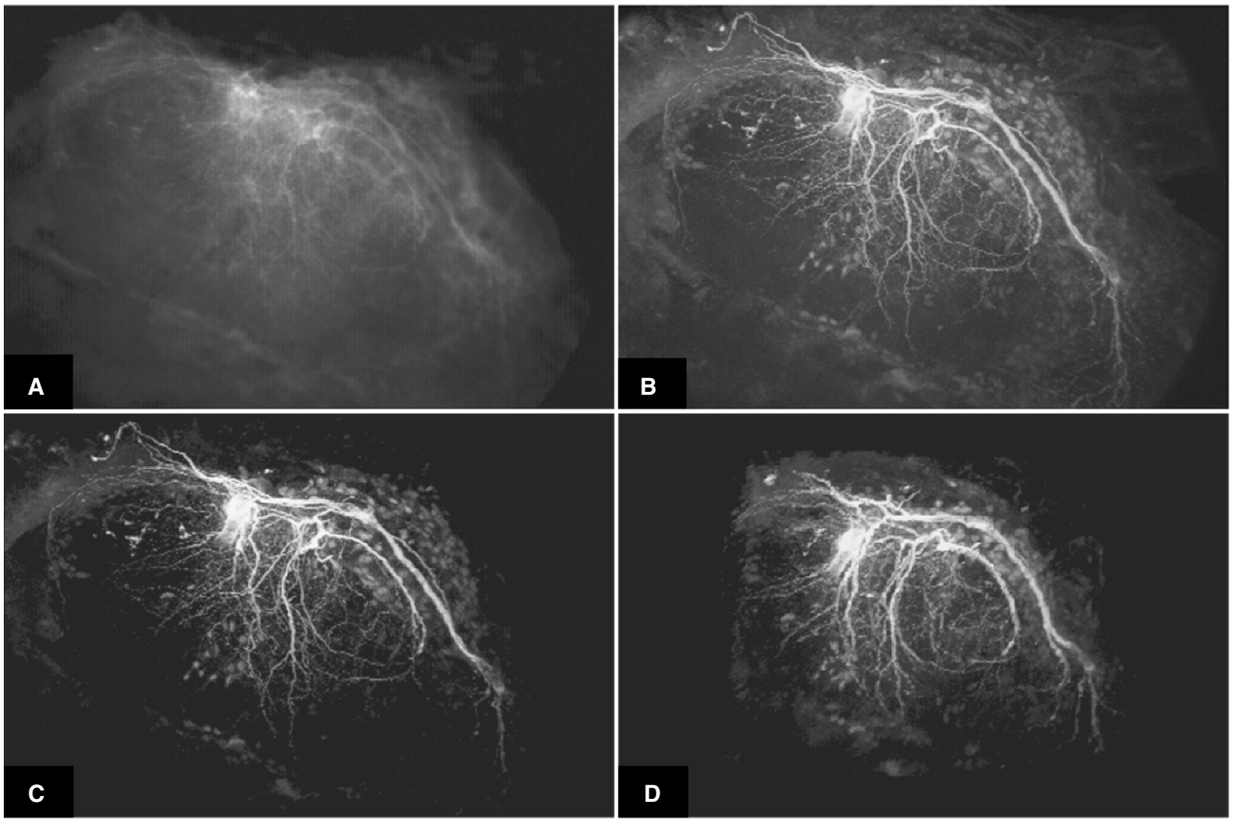


FIGURE 14.2. Identifying unknown structures. It is important to make as few assumptions as possible about the imaged structures during the exploratory phase of 3D visualization. Average (or summation) projection (A), though simple, often gives low-contrast views due to the low weight given to small structures. Maximum brightness (B) gives higher weight to small bright structures but when used in isolation provides no *z*-discrimination. (C) Background thresholding (setting to zero below a base line) is simple, easy to interpret and increases contrast in the view. (D) Re-orientating the 3D volume (even by a few degrees) can show details not seen in a "top down view," and coupled with animation (see text), this is a powerful exploratory visualization tool. (A–C) processed by simple *z*-axis projections, (D) "Maximum intensity" using the Lasersharp software. Lucifer Yellow stained nerve cell supplied by S. Roberts, Zoology Department, Oxford University.

Highlighting Previously Elucidated Structures

Having ascertained the importance of a particular feature, the next step is to enhance the appearance for presentation and measurement (Fig. 14.3). Connectivity between voxels in, for example, a filament or a positively stained volume, may be selectively enhanced (the extracted structures may even be modeled as graphical tubes or solid objects; see SoftWorx from API and Imaris packages for examples). A threshold segmentation band can be interactively set to remove intensities outside the particular structure. 3D fill routines, 3D gradient, dilation, and other rank filters are the basis for structural object segmentation. Opacity (reciprocal to transparency) is possibly the most used visualization parameter to highlight structures segmented by intensity bands. This parameter controls the extent to which an object in the foreground obscures features situated behind it. Consequently, it artificially opposes the intrinsic transparency of biological specimens. Artificial lighting is applied during the final stage. Artificial material properties (such as opacity, reflectivity, shininess, absorption, color, and fluorescence emission) are all used to simulate real or macroscopic objects with shadows, surface shading, and hidden features.

Visualization for Multi-Dimensional Measurements

Often, the final requirement of objective visualization is the ability to extract quantitative measurements. These can be made on the original image, using the reconstructed views as aids, or made directly on the display views. The success of either of these methods depends on the choice of reconstruction algorithm and the objective control of the rendering parameters.

Table 14.2 gives an overview of visualization tools that might be useful for objectively exploring the image data (see also Chapter 15, *this volume*).

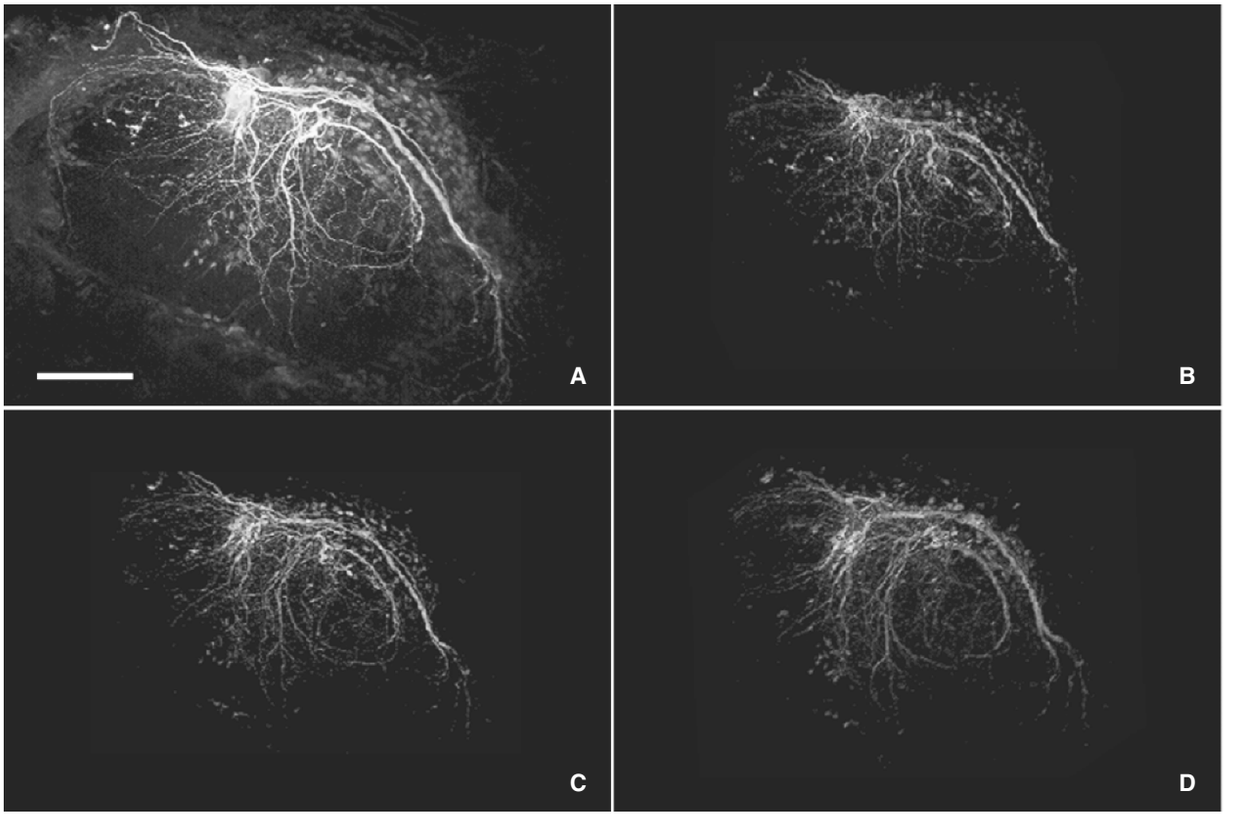


FIGURE 14.3. Enhancing and extracting objects. Having elucidated a particular structure within the volume, filtering and segmentation permit selective enhancement. (A) "Maximum intensity" view [as in Fig. 14.2(B)] after two cycles of alternate high-pass and noise-reduction filters on the original 2D *xy* sections (using 3×3 high-pass and low pass Gaussian filters). (B) More extreme threshold segmentation to extract the enhanced details during the projection. (C,D) two rotated and tilted views (Lasersharp software) using a "local average" (see text) to bring some "solidity" to the view. This example shows the principle danger of segmentation, that of losing fine details excluded from the intensity band.

TABLE 14.2. Overview of Visualization Parameters Desirable for Visualizing Multi-Dimensional Biological Microscopy Data

Processing step	Parameter	Minimum required	Desirable enhancements
[a]3D algorithms	General modes	*Xy*, *xz*, *yz* orthogonal slices	Arbitrary slices, Voxel α-blending
		Z-weighted "projections"	Surface rendering
	Quick modes	Fast *xy*, *xz* slices	Hardware acceleration, Sub-sampling data
		Maximum projection	
[b]Controlling the reconstruction process	Visualization parameters	Projection angles	Viewing angle, *z*-fill, Data threshold,
		z-stretch	Voxels/surfaces, Shading control, Lighting controls,
		Animation controls	Material properties, Opacity, SFP/"special" modes,
		Sequence (movie) mode	Perspective, Batch processing, Post-lighting
	Pre-processing tools	2D & 3D image edit	n-D image edit, n-D filters, image restoration *z*-correction,
		2D image rank filter	morphological filters, math operations
		threshold/background contrast	
[c]Interactive controls	Visualization parameters	Slice positions rotation angles	All render parameters, Data/view angles, View
		data threshold animation controls	Zoom & pan, "Real time" control
	Measurements on image	2D measures on slices	3D measures on slices, n-D measurements
	Measurements on views		3D measures on views, n-D measurements
	Simultaneous measures on image & views	Multiple measurements on screen	Measures auto, Tracked in both displays

[a]The range of 3D algorithms indicates diversity of modes for tackling various kinds of image data, while the quick-look modes include general sectioning and the fastest voxel algorithms. Simple projections and section movies are always faster than more sophisticated reconstruction modes. [b]Control of the visualization process suggests the range of parameters that the user can modify directly to influence the resulting views. More controls give more flexibility but also more complexity in use.
[c]A very rough idea of the level of interactive control (i.e., rapid changes of the result in response to mouse clicks, etc.) for visualization and for measurements on source image data and/or reconstructed views. n-D = any number of multiple dimensions.

WHAT CONFOCAL LASER SCANNING MICROSCOPY IMAGES CAN THE VISUALIZATION SYSTEM HANDLE?

Image Data: How Are Image Values Represented in the Program?

Storing the Image Values

All digital microscopes produce image data values from analog-to-digital (A/D) converters. These will be packed into one or more 8-bit byte values, each of which may have an uncalibrated intensity range of 0 to 255. Greater collection precision is possible by integration, averaging, or other high-dynamic-range filtering operations. However, improvements in electronics and detectors now make possible the direct acquisition of 12-bit, 16-bit, or even higher precision digital data. Single-byte storage is more efficient, and is adequate, for the majority of purposes, particularly for results from low photon-flux imaging of living cells. It is supported by all packages. Some instruments allow 16-bit storage (a range of 0 to 65,535). Intensity data digitized by 12-bit A/D converters (standard in most current LSMs) is usually packed and unpacked into 16-bit words by the loss-less conversion:

$$I_{16} = I_{12} \times 16 + 15$$

This slightly cumbersome conversion is necessary to correctly rescale values in the range 0 to $(2^n - 1)$ without any rounding errors. The 16- to 12-bit operation is rapidly achieved by bit-shifting the binary 12-bit values towards the high byte and filling the additional 4 bits with 1 s. This operation can be precisely reversed for any integer value in the range. Sixteen-bit processing of original 8-bit or 12-bit data may also be desirable for derived images such as those from some fluorescence ratio experiments. However, this is excessive for the majority of confocal fluorescence images, which seldom record more than a few hundred photons/pixel and therefore have 10% to 20% shot noise (see Chapter 2, *this volume*). Microscopy image pixel values and views are economically represented by integer values. Permanent floating-point storage is rarely supported. Floating-point calibrations of integer data are discussed in the following section.

A distinction should be made between storage and display precision. Historically, some digital microscopy systems have used the display memory as both a recording and a view buffer with a built-in image or signal processor. Current approaches use a virtual display in main computer memory, which is copied to the display view, allowing decoupling of data and display view and greater storage precision than video memory if required. This is necessary, for example, for storing and displaying intermediate results in image restoration programs.

Image processing systems developed for cross-platform compatibility (see Amira, Image/volumeJ, and AVS examples of packages running over four platforms) have always used virtual displays allowing arbitrary precision images and views to be manipulated with as little as 5- or 6-bits of display depth per primary color. The price of this flexibility used to be a significant reduction in interactive visualization and display speed, caused by the loss of direct processor access to the video memory. One solution is to isolate platform-specific accelerations and link them to core routines when porting to high-performance workstations with non-standard hardware. Although this approach allows the rapid introduction of new proprietary hardware, it has now been almost universally superseded by the use of agreed platform-independent hardware standards with a defined software interface. Of the several contenders for a universal graphics standard the clearly adopted winner is the OpenGL scheme [see http://www.OpenGL.org and Woo (1999) for details of the OpenGL software programming interface]. This evolving scheme adds definitions for the handling of new technologies as they are introduced into each newly released OpenGL compatible display card or system.

Calibrating the Image Data Values

Multi-dimensional microscopy instruments provide the means for obtaining accurate and repeatable quantitative measurements. All parameters including calibration must be linked to the corresponding image for inclusion in subsequent processing stages. A discussion of file formats follows the section on image dimensions. Software packages normally use their own internal calibration structures because most of the general or so-called standard image formats do not support all the parameters necessary to fully describe multi-dimensional microscopy data.

It might be thought desirable to store directly calibrated real number data values. A fixed-precision mantissa and exponent would certainly provide consistent relative accuracy, regardless of the magnitude of the data values. Constant precision could, however, be maintained by using a logarithmic digitization (or detector) response. This is consistent with the fact that the presence of shot noise means that, if gray levels are separated by one standard deviation they must become wider as the signal level increases. More bits would then be assigned to low intensities and less to brighter values. A fixed precision (log) calibration could then be attached to the 8- or 16-bit integer data values. The minimum requirement is a floating-point offset (the real value of a 0 pixel), an increment (the real increment/pixel value), and at least a text label or key for the linear parameter represented [e.g., log (intensity), concentration, pH, etc.]. Nonlinear changes require a look-up table (LUT) for calibrations. Multiple-channel images require separate calibrations for each component. Ion imaging data need at least a fixed precision calibration and often a sigmoidal scale (defined by R_{min}, R_{max}, and K; e.g., Bolsover *et al.*, 1995). Table 14.3 summarizes data value calibration, arithmetic, and measurement requirements for a multi-dimensional visualization system.

What Dimensions Can the Images and Views Have?

Programmable scanning capabilities of all LSM instruments, motorized focus and/or *xy*-stage control of any microscope, and spectral or time-lapse capabilities yield images with a number of spatial, temporal, and other dimensions. Point-scanning LSM instruments normally acquire a temporal (sequential) and spatial (line) scan in the *x*-axis, repeated at further time points and optionally at progressive *y*- and/or *z*-axis positions. Hence, spatial and temporal sampling dimensions are simultaneously generated. In this way, *xy*, *xt*, *xz*, etc., 2D sections and *xyz*, *zyt*, *xzy*, *xzt*, etc., 3D volume images are collected. Time-lapsed volumetric (e.g., *xyzt*, etc.) or multi-channel spectral (e.g., *xyzc*, *xyct*, etc.) are examples of 4D images. Once considered no more than a curiosity by biologists, new dimensions of data are becoming routine. The possible five-dimensional (5D) (*x*, *y*, *z*, *t*, *c*) imaging space can now be augmented with *xy*- (stage) position (δx, δy, δz), spatial rotation (θ, ϕ, ν), lifetime (τ), polarization angle (P), polarization anisotropy (r). This makes 3D to 6D data (from 12 or more possible dimensions available on a given system) a routine target for data management.

Visualization systems need to support multi-channel images (Tables 14.3, 14.4, 14.6). Although ultimately, each channel is processed separately and the results merged together for display,

TABLE 14.3. Overview of Image Data Handling Features for Visualizing Multidimensional Biological Microscopy Data

Data handling feature	Parameter	Minimum required	Desirable additional enhancements
[a]Data storage	Types	byte	Integer, fp, real
	Bits	8, 24 (3 × 8)	12/16, 24 (3 × 8), 36/48 (3 × 12/16), n × 8
	Channels	R,G,B, included, Merge function	Arbitrary no. of channels n-channel merge
[b]Calibration of intensities		Linear, Offset, Range	Non-linear, Log, Sigmoidal, arbitrary
Intensity measures (distribution of pixel values)		2D Point, 2D Line	3D point, 3D line, trace,
		2D Arbitrary area	3D area (surface),
		Summed area volume	Arbitrary 3D volume,
		2D histogram	Results histograms,
		ASCII file output	DDE to Excel
Math operations		+,–,/,* logical, Contrast/gamma mapping,	Trig functions, Log
		Manual *z*-weighting	Auto *z*-weighting

[a] All systems support 8-bit (byte) data types. A few allow higher precision. This is useful for high dynamic range images. The use of 8-bit indexed or 16-bit "hi-color" modes for multi-channel data is now less common than 24-bit RGB support. Most scientific CCD cameras and LSMs now support 12-bit data (usually packed into 16-bit words) but few packages support these data types for visualization.
[b] It is important to clearly distinguish calibration of the intensity data values from the image dimensions (Table 14.4). Calibrated intensities also allow real values of pH, Ca^{2+}, etc. and other concentrations to be visualized.

visualization packages must now manage these parallel operations seamlessly in order to show multi-channel changes interactively. This is particularly important where interaction between the values across channels is required by the chosen algorithm (e.g., the Imaris SFP algorithm allows transparency in one channel to alter the simulated light emission from another fluorochrome channel).

Image editing is required to extract (1) subregions of a large data set or (2) a structure from the complexity of surrounding features. Sub-region editing should be available through each of the many possible dimensions of the data. All these dimensions must be appropriately treated, for example, correctly calibrated, if the results are to have quantitative validity.

Image Size

Maximum image dimensions should support the full resolution of the instrument (see Table 14.4). In extreme cases, several adjacent sections or even volumes may be co-aligned (by correlation and warping) and tiled together to form a single giant data set (e.g., Oldmixon and Carlsson, 1993). Generally, total image size should be limited only by the available memory. Virtual memory management provides transparent swapping of programs and data between RAM and disk. This increases run-time significantly but can enable very large data sets to be processed. Many software developers prefer to implement a proprietary mechanism of image caching or data swapping between RAM and disk, even with the built-in capabilities of the Windows family of operating systems. The best way to minimize these overheads is by careful crafting of the visualization algorithm. The plummeting price of RAM makes the use of ever more memory irresistible by the programmer, and thus inevitable by the end user.

Anisotropic Sampling

Most multi-dimensional microscopes are operated with different sampling steps in two or more axes. Visualization software must produce views with correctly proportioned dimensions and preferably have the ability to expand or contract each individually (Table 14.4), for example, artificially expanding the *z*-dimension of an image through a thin preparation (such as a biofilm or a stratified tissue) to highlight the morphology in each layer. The most concise way of specifying this aspect ratio information is to apply a correction factor to the appropriate axis calibration. This should be done interactively so that some imaging distortions can be corrected (e.g., for a specimen such as skin with layers of different refractive index). This does not change the data values in any way and is preferable to resampling the entire data volume, which would tend to use up precious memory. When the data is subsequently processed or displayed, a floating-point *z*-stretch parameter (and equivalents for *x*, *y*, etc.) would correctly specify the spacing of each plane. An integer *z*-fill parameter represents the number of equally spaced sections to optionally add between each of the repositioned planes. These extra data values are derived by interpolation, by pixel replication or linear, cubic, or higher polynomial spline. An obvious question arises here: How real are the extra data points? *A priori* knowledge of the specimen and imaging system is required for an informed choice. On-the-fly data expansion during processing will conserve storage space but requires more computations. Pre-expansion, for example, during the image loading cycle, will optimize processing speed at the expense of memory. A good compromise is rapid expansion during the computation using precalculated linear geometric LUTs.

Calibrating the Image Space

To make measurements, image and view dimensions must have the correct calibrations (Table 14.4). These must be updated during any resampling, zooming, and image editing. Minimum requirements for each dimension are again floating-point values for offset and increment, and an axis label. Warping conveniently handles nonlinear dimensions by resampling onto a rectilinear grid. Correction of acquisition errors should ideally be incorporated into a single intensity and sampling interpolation. These errors include:

- Spherical aberration caused by mismatch between the refractive index of the immersion medium, the imbibing medium and the design of the objective.
- Axial chromatic aberration (a focus shift seen with all objectives).
- Lateral effects, such as chromatic magnification error.
- Photometric signal attenuation and correction of geometric distortions from refraction within the sample (e.g., Carlsson, 1991; Visser *et al.*, 1991, 1992; Fricker and White, 1992; Hell *et al.*, 1993) are desirable preprocessing tools.

TABLE 14.4. Overview of Desirable Image and View Dimension Parameters for Visualizing Multi-Dimensional Biological Microscopy Data

Feature	Parameter	Minimum required	Desirable additional enhancements
[a]Image dimensions	Single plane	Full un-edited image (from camera, LSM etc), Held in RAM	Unlimited Display independent Multiple images in RAM
	Total image size	Fully sampled 3D image, 3D image in RAM	Unlimited, Display independent, Multiple 3D images in RAM, n-D images in RAM, efficient caching
	[b]Supported dimensions	2D, 3D *x,y,z* time	n-D, View angles, Rotation angles, Stage position, Polarization/ anisotropy, Lifetime
Editing the dimensions (geometric operations)	Sub regions (ROI)	2D sub-area, 3D sub-volume, edit on slices	3D arbitrary sub volume, Edit in view, 3D cut-away, n-D ROI
	[c]Data corrections	Background normalization *z*-atttenuation	Non-linear corrections, Photobleaching, Flat field, n-D corrections, Optical corrections, Image restoration
Z-geometry	*z*-stretch	Integer value linear	Real value Non-linear (e.g., cubic, etc.)
	z-fill	Integer for large angles	Adaptive for chosen angles
View dimensions	Single view	3D diagonal of image View movie in RAM JPEG compression	Unlimited, Display independent Multiple views in RAM Efficient caching, Efficient compression
	Number of views	120 views (360 × 3 degs)	Unlimited, Display independent Multiple movies in RAM
	Channels in view	R.G.B	Arbitrary no. of channels
[d]Calibration of dimensions	Image	*X,y,z,t*	All dimensions
	View	*X,y,z,t*,angle	All dimensions
Dimension measures	On image	2D Point, 2D Line, 2D histogram, 2D Arbitrary area, ASCII file output, Summed area volume,	3D point, 3D line, trace, 3D area (surface), Arbitrary 3D volume, Results histograms, DDE to Excel
	On view		3D point, 3D line, Trace, 3D area (surface), Arbitrary 3D volume, Results histograms DDE to Excel

[a]In most cases the image data space is limited only by the amount of disk and/or memory available. The operating system and/or the application program may provide virtual memory management and disk caching.
[b]Most packages can handle time, spectral, etc., data as for a "*z*-stack" but few can directly interpret time or wavelength calibrations with any meaning.
[c]Complex corrections usually involve sample-specific data and some pre-processing.
[d]Calibration of dimensions should be clearly distinguished from those of the data intensity values (Table 14.3).
n-D = any number of multiple dimensions.

Standard File Formats for Calibration and Interpretation

While there are many standard formats, there is no universal standard currently adopted for microscope images. However, there are established imaging formats (e.g., DICOM, see http://medical.nema.org/) that are routinely used by visualization packages such as the Cedara, Vital Images, and Analyze software that fully describe multi-dimensional volume data from medical scanners. As LSM and other research microscopes become more routinely used as screening instruments and for clinical applications, it is hoped that such standards will become routine from these suppliers as well. A catch-all image input facility such as the RAW options offered by many programs allows any packed binary file with a fixed-size header to be read in. Microscope instrument manufacturers have taken one of two options: (1) developed a completely proprietary structure and made this available to other developers and users, or (2) taken an existing extendable format (such as the Tagged Image File Format [or TIFF]) and added system-specific components (e.g., for TIFF, licensed specific tags) to store the extra acquisition parameters. A problem with this second approach is the necessary proliferation of a number of variants or compliance classes of such formats. Any third-party reader program must recognize (and provide updates for) several different versions. A widely adopted alternative is to use a proprietary structure and to provide conversion tools to import/export data via standard formats. Unsupported parameters are transferred into the program by an *ad hoc* semi-manual process.

A flexible, industry-standard approach to image-related details is to use a conventional database to store preprogrammed fields of information (sometimes a third-party software product is used with the visualization tool — such as the ImageAccess database used by Imaris — which can manage all image and image-related files). Two types of information must be stored and linked with each image: (1) instrument-specific details describing the instrument settings used for the collection and (2) image-specific information describing the dimensions, calibration, and experimental details. The database can hold both sets of details, together with a pointer to the image data (or even the image data itself for small images). Alternatively, the database may hold just the system configurations used as stored settings or methods (e.g., the Bio-Rad Lasersharp program stores all the instrument and user settings in a Microsoft Access database). This latter approach requires a pointer to the relevant settings to be saved with the image data, separately from the database. Table 14.5 summarizes some important image and view data parameters.

Processing Image Data

Less obvious than the storage representation are the data type and precision used during computations. Floating-point representations

TABLE 14.5. Overview of Desirable File Format and Image Information Features for Visualizing Multi-Dimensional Biological Microscopy Data

Feature	Parameter	Minimum required	Desirable additional enhancements
[a]Image file format	Proprietary standard	Fully defined open source Multi-file TIFF, AVI (for series)	Fully defined open source, Full range of conversions, A Universal standard!
View file format	Proprietary standard	Fully defined open source Multi-file TIFF/BMP, JPEG, AVI	Fully defined open source, Full range of conversions, Efficient compression, A Universal standard!
[b]General params. stored	Size	All dimensions	All dimensions
	Calibration	*X,y,z,t* dimensions	All dimensions
	Annotation	ROIs	ROIs, Text, pointers
	Microscope	Data specific parameters Stored in image format, or ASCII file	All instrument parameters, Experimental parameters, Stored in image format and/or database
	Notes		User/exp notes, Informatics
Special view parameters stored	Source image		Image filename, Links in database etc., Visualization history/log
	Orientation etc.		Rotation angles, etc.
	Visualization parameters		Algorithm name, Algorithm parameters, Display options

[a]Proprietory file formats are used by most systems. "Standard formats" such as TIFF may also cause confusion as there are many different compliance classes of TIFF, so only a sub-set of the TIFF tags in a particular file may be recognized by a given reader.
[b]Some parameters may be stored with the image data in the same file, in a separate (e.g., ASCII) file or in a database. It is important to know the whereabouts of this information if the image is to be taken to another program with the associated data intact. ROI = region of interest.

reduce rounding errors during geometric transformation interpolations. Even this requirement for floating-point representation can be partly avoided by either (1) combining several interpolation steps into a single, composite geometric and photometric transformation, or (2) increasing the sampling by a factor of at least 2 for each subsequent interpolation. This second approach is somewhat extravagant in terms of storage and will not help if the sampling is already at the Nyquist limit. The processor architecture is an important factor in determining the processing speed. Fast multi-word and floating point arithmetic is now standard in microprocessors. Despite this, some instruments, notably the Zeiss range of LSMs, use specialized, programmable digital signal processors.

Processor Performance: How Fast Will My Computer Process Images?

Personal computer (PC) performance for image manipulation is constantly improving, making the specification of system performance in a text such as this somewhat pointless. However, the principal components of the computer system required can be described in terms of their relative importance to performance.

At the time of writing, the Pentium PC processors are the norm, running at around 4 GHz with bus speeds around 1 GHz. These are very approximately 30 times faster than 10 years ago, representing a doubling of speed every 2 years. Non-Intel processors with alternative combinations of price/performance through low power consumption, higher capacity of on-chip memory for data caching, and other enhancements appear from time to time with advantages in different applications. Alternative Intel processors, such as the Xeon, also compete in these areas and offer improved workstation and multi-processor performance. Provided the software is correctly designed, transfer bottlenecks can be reduced with a processor having at least 512 kB of level 2 memory cache. Apple Macintosh machines have undergone something of a renaissance in recent years; the current G5 is broadly equivalent to the latest Pentium devices, and still have competitive and equivalent components for efficient numerical performance and a highly optimized bus for image transfers. The current Macintosh OS X operating systems have been significantly updated and based on Unix technology in order to take advantage of the large software developer base. Unix workstations are still a costly alternative to ever-improving PC platforms. Improving processor performance alone is still reflected in the voxel rendering performance (in voxels/second or vps) for visualization of multi-dimensional microscopy data.

Improvements in other areas of the PC have been either necessary to keep pace with the processor speeds or provided enhanced capabilities directly. Hard disk drive data transfer speed can limit the speed of animations (movies) and 3D visualization when applied to large data sets. At the time of writing, so-called ultra-fast, ultra-wide SCSI interfaced devices, with capacities up to 250 Gb per disk still have higher performance than IDE devices and tend to be more robust and easier to upgrade, although plug-and-play technology makes this last issue less important in the latest PCs. The latest PCs and Macintosh computers can access 4 to 8 Gb of RAM. This is adequate for most multi-dimensional data sets but will inevitably still limit performance if many large data sets are opened simultaneously, especially if the software is designed to read in the entire data set and/or the system caching or swap file is inefficiently configured for the ratio of disk to RAM.

Computer video display subsystems have, over the last 10 years or so, taken on more and more graphics processing operations, allowing greater optimization and relinquishing the general purpose CPU for other tasks. The display system has become a dedicated graphics processing unit (GPU) and up to 256 Mb of dedicated display memory. Some entry-level PCs may still use portions of main memory, set aside for access by the display, but these are not recommended for multi-dimensional visualization. Many functions are carried out by dedicated hardware and/or firmware running on the GPU and associated devices. Depending on the sophistication of the chosen graphics system, supported operations may include:

- Rapid display of 2D views for animations, etc.
- Rendering of surfaces composed of triangle or other polygon primitives.

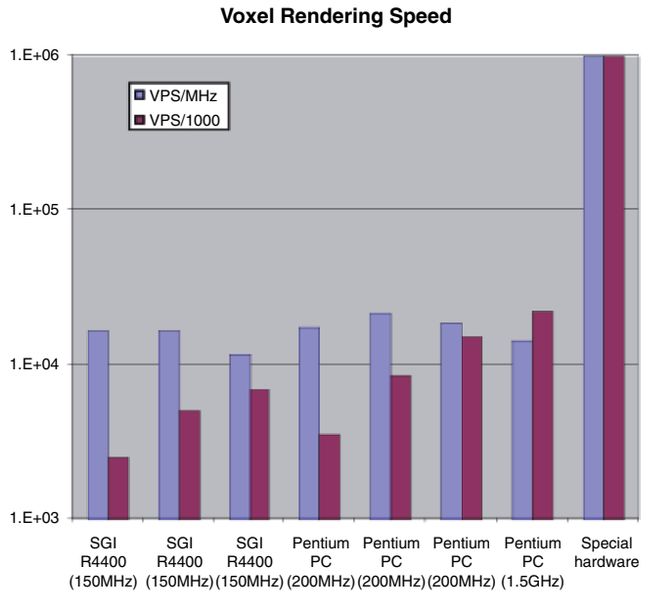


FIGURE 14.4. Voxel rendering speed: dependence on hardware performance. When assessing a visualization system, many factors need to be taken into account (see text). Parameters for individual performance figures should be assessed with care. On standard platforms, processor speed is still an important factor. From a simple ratio of voxels processed per second per MHz processor speed (with a basic algorithm) a figure of merit can be obtained. Running the same α-blended. voxel-rendering software (Voxblast) on multiple Pentium processors gives broadly the same figure of merit as single processors when normalized for the total processor speed. The same is found for multiprocessor graphics workstations. Running on special hardware (this example is the VolumePro board) sacrifices portability across platforms but (as has historically always been the case) gives vastly improved performance.

- Geometric manipulations (e.g., warping of data vectors).
- Rendering of voxel objects.
- Transparency/opacity of graphics and voxel objects.
- Artificial lighting and shading.
- Rapid manipulation of color or grayscale.
- Panning and zooming of the display.
- Texture mapping (used to rapidly render image layers onto a growing display view).

Figure 14.4 shows some approximate voxel rendering speeds that might be expected over a range of processing platforms (data corresponds to rendering speeds of Voxblast from Vaytek Inc.). Optimization of the GPU functions is controlled largely by the supplied driver software and contributes to the major differences between various hardware configurations. CPU operations are coded by the application programmer and this is also reflected in the performance of the software. The relative efficiency of these two aspects can have an important influence on the effectiveness of the package as a whole. An effective visualization algorithm for multi-dimensional data must include optimized numerical loops (particularly nested sequences) and use fast indexing into preprocessed parameter LUTs for frequently used values. The following section describes some of the optimizations that are responsible for the performance range seen between different programs.

HOW WILL THE SYSTEM GENERATE THE RECONSTRUCTED VIEWS?

Assessing the Four Basic Steps in the Generation of Reconstructed Views

(1) The image (or a subregion) is loaded into the data space (an area of computer memory). Preliminary image editing, preprocessing, and/or analysis is used to define calibrated image values with known dimensions. This constitutes the input to the visualization process. Packages such as Analyze have some useful preprocessing capabilities (Robb, 1990). Alternatively, a more general program such as Metamorph, ImageJ, and Image Pro, etc., can be run alongside the visualization package for image preprocessing (or the visualization component can be added to the 2D package).

(2) A view must be chosen (subject to the available reconstruction algorithms) that will produce the most flexible and appropriate representation of the image data. An intelligent choice of view can minimize the number of reprocessing cycles (see also He *et al.*, 1996; Marks, 1997; Kindlmann and Durkin, 1998, for attempts at computer-assisted choice of visualization algorithm). The visualization step consists of two transformations: First, a geometric orientational mapping of the image space into the reduced dimensions of the view, and, second, a photometric mapping (sometimes called a transfer function) whereby the image intensities are processed to determine the brightness of a pixel at each position within that view.

(3) The display step consists of a second geometric and photometric mapping that together constitute output or matching of the multi-dimensional view into the available physical display. In practice this may consist of scaling and copying or a more complex operation (e.g., animation or stereoscopic presentation). These presentation or output options, dictated by the display space capabilities, will determine the most efficient use of screen resolution, color, animation, etc. In turn, these will influence the choice of appropriate reconstruction algorithm.

(4) Dimensional loss during the visualization processing is partly restored by the display step and partly by *a priori* knowledge used to interpret the 2D display view (e.g., depth cues, animation, stereo, etc.). Inspection and analysis of the display view is the last step of the visualization process.

The next sections describe more details of these processes that are important for microscopy images using techniques found in the systems listed in Table 14.1.

Loading the Image Subregion

Any image processing program must first open the image file, read and interpret the file format information, and then load some or all of the data values. Interpretation of the file format largely determines the flexibility of subsequent manipulations. An on-screen view of (1) image sizes (in pixels and calibrated units), (2) intensity data calibrations, (3) associated notes and (4) a quick-look reconstruction will aid selecting the required image or subregion (Analyze and Imaris, e.g., show image volumes as thumbnail pictures with a grid showing the image dimensions, etc.). The file format information will determine whether the data needs resampling to produce correct image proportions, and interactive adjustment is essential for z-stretch/fill (see above). Interactive photometric rescaling or segmentation (in combination with a simple volume representation) are essential to remove (e.g., set to zero or ignore) background values that would unnecessarily

slow down computations. Multiple passes through the data will be time consuming for large images. A single composite geometric and photometric resampling (using fast LUTs) should be combined with loading the data from disk. Data expansion options (e.g., *z*-fill) may be temporarily restricted to speed up computations during the exploratory stages. Flexibility and control at this stage must be balanced against the efficiency of a single processing stage. Some image preparation options are detailed in Table 14.2.

Choosing a View: The 5D Image Display Space

As introduced above, the efficient use of all the available display space greatly increases the flexibility of visualization algorithms.

The 2D Pixel Display Space

Pixel resolution must accommodate a reconstructed view at least as big as the longest diagonal through the 3D volume. This means that, for example, to reconstruct a $768 \times 512 \times 16$ frame 3D image with *z*-stretch of 4 and arbitrary rotation, the display view that will be generated in memory could be up to 950 pixels square. For the same computation and display of 1024×1024 pixel frames, 1450 pixels square are required to avoid clipping. As it is advisable to display the views without resampling, these values represent the minimum display window in pixels. Processing time may dictate that only a subregion can be processed but, in general, display of a single full resolution frame should be considered a minimum. Although the display pixel range may be only 8 bits/channel, the ability to generate projected views with a higher intensity range (perhaps 16 bits) means that, for example, average projections of images with dimensions greater that 256 pixels can be made with no loss of detail. It is now standard practice to produce an output view that is independently rescaled according to the size of the display window as defined by the user. This is transparently handled by the software and display driver. However, rescaling can always give rise to unwanted aliasing effects so it is wise to restrict the display zoom to integral multiples of whole pixels. The application program, perhaps using features of the display driver, may allow an image of greater size than the physical display to be rapidly panned, giving access to display views of almost unlimited size. High-resolution non-interlaced displays are now standard for all computers. Although a single display may deliver resolutions up to 2650 pixels, it is now standard practice to provide multiple screen outputs from the best display systems. In this way, desktops of perhaps 2560×1024, 3200×1200 or more can be spread seamlessly across a pair of similar monitors placed together. The display drivers will automatically handle traversing of the mouse and program windows between the physical screens or even allow large images to straddle the entire display space. (A commonly recommended supplier of multi-view compatible OpenGL graphics cards for PCs is nVidia, http://www.nvia.com, while on Macintosh's they are built in.)

The Color Display Space

Color is a valuable resource for coding multi-dimensional information on a 2D device. It is important to ascertain the number of different colors that can be simultaneously displayed, as distinct from the number of possible colors present in the data or display view. The author prefers the generic term **palette** to represent the subset of simultaneously displayable colors and **color resolution** to indicate the full set of possible colors present in the data. Although many different graphics display resolutions have been used by imaging systems in the past, the plummeting cost of hardware have made the use of all 8-bit displays redundant. Useful display systems will be encountered that have either 16, 24, or 32 bits per pixel of display depth. It should be carefully noted that a display system may have additional memory associated with each pixel for storing other values important for controlling the display process, but here we are concerned only with the color and intensity information. A standard 24-bit display has 8 bits of memory storing 1 of 256 possible values each of red, green, and blue intensity. Additional display panes are available in 32 bit modes. With 2^{24} possible display colors (over 16 million), a 4000×4000 pixel image could display each pixel with a different and unique color. There is, therefore, significantly more contrast available in a color image than in a monochrome (e.g., grayscale) representation. However, it must always be remembered that the actual red, green, and blue colors corresponding to each component are fixed by the spectral characteristics of the physical screen material. These will, in general, never coincide with filter spectra of the microscope, or even with the nominal red, green, and blue characteristics of a color camera.

When more than 24 bits of data are stored for each pixel of the display view, such as for a 3-channel 16-bit color image (a 48-bit data set), the visualization software must resample this down to the available color space of the display system. An extreme example is the option in the Imaris program of having color-space computations carried out with 96-bit precision as opposed to 24-bit precision, improving accuracy at a 4-fold cost in extra memory. However, at present cathode-ray tube (CRT) and liquid-crystal displays (LCD) are capable of displaying little more than 8 or 9 bits of data in each color channel.

Pseudo Color

Pseudo or indexed color was used by older 8-bit displays. It is now only really important when a display system of very high resolution is implemented, for cost purposes, with 16 bits of high color pixel depth. Each of 65,536 entries (for a 16-bit mode) or 256 entries (for 8-bit modes) in a color look-up table (CO-LUT) is assigned a unique composite RGB value. This CO-LUT is an indexed palette and can be rapidly updated or modified to change the displayed colors without altering the view data values. It is the CO-LUT value pointed to by each data value that determines what RGB intensities appear on the monitor. Visual perception of color is far more acute than for intensity in bright VDU displays because cone density in the eye is highest in the fovea (Perry and Cowey, 1985). Pseudo color is, therefore, useful for presentation of calibrated 16-bit maps of image intensities, for example, from ion indicators. In general, it adds contrast to subtle changes in (1) brightness, (2) temporal, or (3) coordinate (typically *z*-relief) views.

True Color

True color means any display element can have independent values for each of its red, green, and blue components. The simplest way of representing these in a byte-structured format is a 24-bit (3×8 bit) RGB voxel. Other color-coding schemes are possible. Hue, saturation, and brightness (HSB) are useful for intensity-independent color transformations. Process color space (using cyan, magenta, yellow and black — CMYK) is the form used for hard copy and publication. RGB values map directly into a 24-bit display with no intermediate processing. Color manipulations can be carried out by modifying the component color data directly. Alternatively, each 8-bit channel may be driven by a monochrome (R, G, or B) 8-bit indexed CO-LUT (palette).

Multiple-Channel Color Display

Either color or brightness resolution (or both) can be traded for extra channels. A hue (preferably non-primary, i.e., magenta, cyan, yellow, orange, etc.) is defined by a unique RGB ratio for each channel. An intensity (brightness) scale in each hue then represents the indexed data values of that channel. All channels are combined into one true-color RGB view, adjusted to fit the display resolution, that is, each channel using a segment of the available palette. Figure 14.5 includes examples of the use of color for 3D multi-channel and stereo display.

Animations

As with pixels and color, the temporal display space can also be effectively used for visualization. The simplest temporal mapping is the sequential display of view sequences. Temporal range is determined by the number of frames that can be stored for rapid animation. Time resolution has two components: the frame rate (the time between successive views) and the refresh rate (how fast a single view is updated) (Table 14.6). The refresh rate contributes significantly to the perception of smooth animation. Retinal persistence results in a screen refresh rate of ≤1/18th of a second being perceived as virtually instantaneous. For through-focus sequences, fading between frames is advantageous. A long-persistence display phosphor (such as on older video-rate monitors) assists this fading process for low framing rates ≤4 Hz but contributes degrading blur at higher speeds. Perception of smooth motion requires high lateral resolution and visual acuity. Therefore, smooth rotation animations require (1) fine rotation steps, (2) a short persistence/high refresh rate display, and (3) an animation frame rate of above 10 Hz (with ≤0.05 s data refresh). Hardware and software compression/expansion (see Chapter 48, *this volume*) are built into some display systems, allowing suitable data to be animated at up to video rate with reduced storage requirements. Both RAM-based and hard-disk–based systems can now easily provide full-color video-rate animation. Screen update is improved by a double-buffered display comprised of both a visible and a

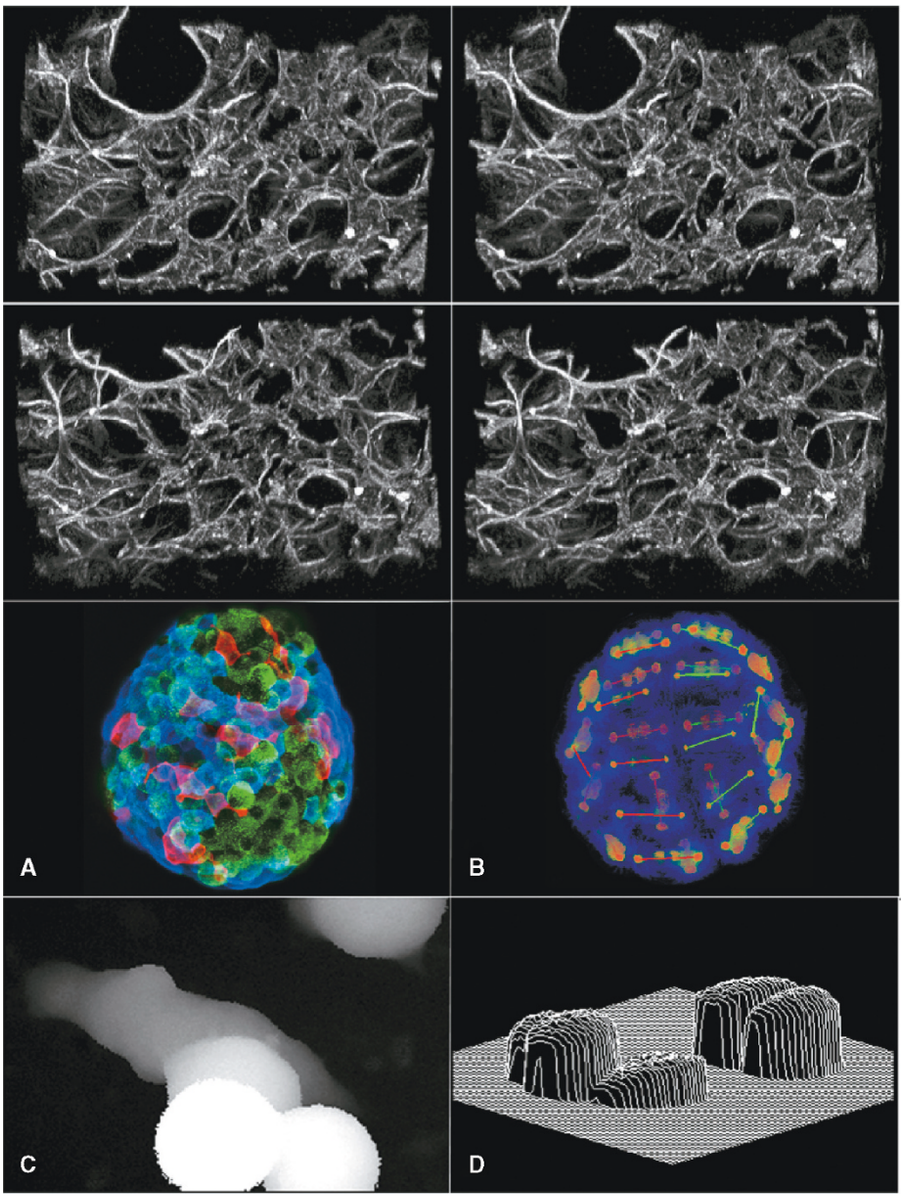


FIGURE 14.5. Efficient use of the 5D display space. The upper four images are two "maximum intensity" stereo-pairs (Lasersharp software). They were generated with ~8 deg of "rotation" around the *y* (vertical axis) giving binocular stereoscopy through the *x* display dimension and similar "tilts" around *x* to give motion parallax and temporal interpolation depth cues using the *y* display axis. In these static views, the top pair tilt forwards and the lower pair tilt backwards. With few exceptions, the most efficient use of the color space is for the display of multi-channel views. Data (courtesy of Bio-Rad Microscience) is from a large confocal series from lung tissue. (A) shows a triple-stained fluorescently labelled pancreatic islet, with each channel "maximum projected" and combined into a 24-bit Windows bit-map view (data collected by T.J. Brelje, University of Minnesota, Minneapolis, MN). (B) shows a dividing shrimp embryo stained with rhodamine-conjugated beta-tubulin antibody (27 five-micron optical sections) rendered using VoxelView/Ultra. Cell bodies and membranes (blue) are assigned low opacity so that microtubule structures (orange-red) can be viewed distinctly in their cellular context. Analytical geometric data (lines and surfaces) can also be inserted, not overlaid, using the VoxelView/Ultra Embedded Geometry tool. Embedded lines highlight the axes of division and centers of polarity of the dividing cells and help indicate directions of movement during mitosis. (Data courtesy of Dr. W. Clark, Jr., University of California, Bodega Marine Laboratory, CA). Intensity gray levels can also code for *z*-depth (see text). (C) shows a Lasersharp "height" view of a living fibroblast imaged by fluorescence optical sectioning of an excluded FITC-dextran-containing medium (see Shotton and White, 1989). (D) Binary (single-bit) line graphics make inefficient use of display space. However, this "YMOD" or height profile of BCECF-stained living chondrocytes from pig articular cartilage (data by R.J. Errington, Physiology Dept., Oxford University) does show relief more clearly than would an intensity view alone.

TABLE 14.6. Overview of Image and View Display Options Desirable Visualizing Multi-Dimensional Biological Microscopy Data

Feature	Parameter	Minimum Required	Desirable additional enhancements
[a]Display 2D pixel size		To show full image 1 : 1 without clipping (typically needs 1280 × 1024 or more)	As large as possible, Multiple-screens, Seamless desktop
Color	Display mode	24-bit RGB	24-bit of higher + overlays
	[b]Multiple-channels	Standard RGB	Arbitrary number of channels
Screen	Display refresh (Hz)	70 Hz	~100 Hz
	[c]Size (diagonal inches)	CRT: 19 Flat: 17	CRT: multi 21, Flat: multi 19, Wide-aspect & Specialist Mega-pixel screens
Movie	[d]FPS (Hz)	~10 at full image resolution Variable fps	Up to about 30 fps, Motion compression, Variable fps
	Recording	Store movies as digital file	Digital video store, Digital Compression, DVD recorder, DVD RAM
	Hardware assisted		z-buffer video system, Compression AV quality disk system
Stereoscopic	Modes	Manual stereo pairs Movie pairs Anaglyph display	Side-by-side, LCD viewers, Shuttered screen, Projection, Non-viewers (e.g., lenticular) Standard hardware (e.g., OpenGL)
	Animation	2 color anaglyph	Full color Auto stereo from 6 deg sequence

[a]Most operating systems and application programs decouple the image size from the display size. If the image must be sub-sampled by the system to display in the chosen window, aliasing may occur (some graphics systems have anti-aliasing devices built in). Usually, not all of the screen area is available for the image, so the screen needs to be bigger than the largest image. Some graphics systems allow an image larger than the screen to be "displayed" and the visible part is panned around with the mouse.
[b]With color-space mixing, it is possible to "merge" an arbitrary number of channels into a standard 3-color, RGB display.
[c]CRT sizes are usually given as the tube diagonal, not the visible screen size, flat panel displays indicate the actual viewing area.
[d]The animation software must be highly optimized to deliver the fastest, smoothest framing rates. This can be achieved in software at the expense of standardization and so the fastest systems may only work with a limited range of display hardware.
FPS = frames per second. LCD = liquid crystal display.

second (non-displayed) buffer. The second buffer is updated while the first is read out to the monitor and pointers to the two buffers are switched between successive frames. New graphics standards, especially OpenGL, now fully support double buffering on standard displays. Double buffering obviously needs twice the memory on the display card.

Stereoscopic Display

Depth perception by stereo parallax provides a third spatial display dimension. Some of the geometric *z*-information can be mapped into this stereo space. Like the color/intensity range compromise, the stereoscopic depth requires some reduction in bandwidth of another component. The two halves of a stereo-pair can be displayed using screen space components normally reserved for (1) 2D pixel area, (2) color, or (3) sequences (temporal space). Each of these methods requires an appropriate viewing aid to ensure that each view is presented only to the appropriate eye. The detailed implementation of stereo presentations are described in a later section. Table 14.6 shows some image and view display options for visualization systems.

Optimal Use of the 5D Display Space

Several conflicting factors must be balanced: (1) visual acuity in a particular display dimension, (2) efficient use of display resources, and (3) minimizing processing time. Because intensity variations are difficult to interpret in a low-contrast image, it is sometimes tempting to use *y*-mod geometric plots and other display tricks to represent, for example, a fluorescence ion concentration. Using the geometric space rather inefficiently in this way for a simple intensity display may allow us to view inherently planar information with greater accuracy. A contrasting example might be when a depth profile surface can be defined from a 3D object: (1) the geometric space in *x*, *y*, and *z* (e.g., stereo) could be used to show the object's surface relief, (2) color used for material properties (fluorescence, reflectivity, etc.), and (3) intensity (grayscale) employed to reinforce *z*-cues by depth weighting. Automontage is an interesting application (from Syncroscopy, Ltd.) where surfaces are extracted by ray-casting projections of widefield *z*-focus series. The resultant 3D data is then visualized using *z*-profile plots or stereoscopic views.

The best display space for a particular component will depend on the available resolution and the range of the data. In general, multi-channel images are best shown as different colors, in which case depth information must be coded using stereo or motion parallax or some lighting/shading mechanism. Binocular stereoscopy works for views rotated around the *y*-(vertical) axis when looking at the screen, that is, with parallax shifts in the horizontal *x*-direction (Frisby and Pollard, 1991; Poggio and Poggio, 1984) (for an upright observer!), while motion parallax is perceivable around any axis within the *xy*-plane. The perception of depth by so-called motion parallax is actually a subconscious interpolation of the images between each view to fill in the path of features presented at discrete loci along a simple trajectory (Nakayama, 1985; Fahle and de Luca, 1994). Therefore, a sequence of side-by-side stereo-pairs at increasing tilt angles only will give stereo depth in *x* and animation depth in *y* with minimum processing. Rotations are interpreted more readily by most observers than other temporal sequences, such as through focus *z*-series, largely because of our acute perception of parallax. Detailed assessment of particular presentation modes requires an in-depth knowledge of the physics and physiology of visual perception (e.g., Braddick and Sleigh, 1983; Murch, 1984; Landy and Movshom, 1991). Alternative temporal coding strategies, such as color-coded tixels (Kriete and Pepping, 1992) thus aid the presentation of non-rotated time series, partic-

ularly if interactive measurements are to be made. Figure 14.5 shows examples of the efficient use of display space for multi-dimensional display.

Mapping the Image Space into the Display Space

Having chosen both the image dimensions and display space, a suitable mapping of image space to the output view dimensions must be found. Choices for this geometry processing are intimately linked to the implementation of the transfer algorithm for combining the data intensities, however, it is more useful to consider these components separately in order to make the most of available resources; geometry and intensity processing software and hardware may reside in different subsystems of the visualization workstation.

For a general multi-dimensional image $I(x_i, y_i, z_i, t_i, c_i, \ldots)$ and view $V(x_v, y_v, z_v, t_v, c_v, \ldots)$ we can define an overall reconstruction function (R) such that

$$V(x_v, y_v, z_v, t_v, c_v \ldots) = R\ [I(x_i, y_i, z_i, t_i, c_i, \ldots)] \qquad \textbf{(1)}$$

where x, y, z are the spatial coordinates, t is time, c is color channels, etc.

R has two components: a geometric transform (G) converting image to view dimensions and a compositing (sometimes called transfer function) or projection operation (P) performed on intensities through the view space (Fig. 14.6). These components of R are thus related by

$$V = P(x_v, y_v, z_v, t_v, c_v, \ldots)$$
$$\text{where } x_v = G_x(x_i, y_i, z_i, t_i, c_i, \ldots), y_v = G_y(x_i, \ldots) \text{ etc.} \qquad \textbf{(2)}$$

The following sections describe various G functions used in visualization systems (listed in Table 14.7). Projections are described later (and listed in Table 14.8).

Simple Visualization: Reducing the Geometric Dimensions

This involves discarding all but two of the voxel coordinates and mapping the remaining dimensions to screen xy-positions. A non-rotated **orthoscopic** (non-perspective) view of a 3D (x_i, y_i, z_i) volume (viewed along the z_v-axis) is a simple geometric mapping of serial sections that can be projected (e.g., by summing, maximum intensity, etc.) onto a 2D orthogonal $(xy)_v$ display (Fig. 14.6). The G function is defined by

$$x_v = x_i,\ y_v = y_i,\ z_v = z_i, \text{ i.e., } V(x_v, y_v) = P(x_i, y_i, z_i) \qquad \textbf{(3)}$$

For a 3D time series (x_i, y_i, t_i) to be viewed edge-on, (x_i, t_i), the transformation is equally simple:

$$x_v = x_i,\ y_v = t_i,\ z_v = y_{\text{ii.e.}} \quad V(x_v, y_v) = P(x_i, t_i, y_i) \qquad \textbf{(4)}$$

These are the basis of the familiar three-pane orthogonal section views found in many visualization programs.

Rotations

A single, orthoscopic, x-axis rotation (θ) requires a geometric mapping given by

$$x_v = x_i, \quad y_v = y_i\cos\theta + z_i\sin\theta, \quad z_v = -y_i\sin\theta + z_i\cos\theta \qquad \textbf{(5)}$$

then $$V(x_v, y_v) = P(x_v, y_v, z_v)$$

The projection is then performed in the (re-oriented) view coordinates. Offset coordinates (i.e., $x_i - x_o$, etc.) are used for rotations around a point (x_o, y_o, z_o) other than the image center. Rotations are non-commutative, that is, the order of x-, y-, and z-axes matters. The observer's coordinate system (x_v, y_v, z_v) is static, and all orientations are given in this frame of reference. To generate a view of the image rotated simultaneously about the three image axes (i.e., a tumbling algorithm), three consecutive transformations are required. The first [e.g., a tilt around x_i, Eq. (5)] is obviously

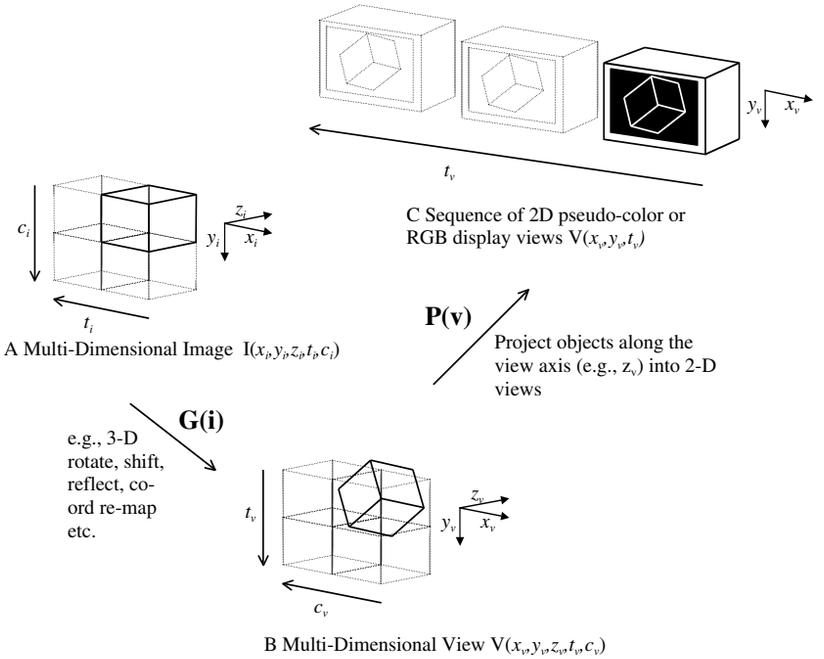


FIGURE 14.6. The visualization process. Voxel and object visualization algorithms proceed in three clear steps: (1) Multi-dimensional image space (A) is transformed by a geometric function (G) to the (re-orientated) view space (B). (2) Selected objects in the view space are combined using a projection operation (P) to produce a sequence of 2D views. (3) The 2D views are presented on the display device (C).

TABLE 14.7. Overview of Image-to-View Space (Geometric) Transformations for Visualizing Multi-Dimensional Biological Microscopy Data

Feature	Parameter	Minimum required	Desirable additional enhancements
[a]2D sections		Orthogonal	Arbitrary orientation, Section rotation,
		Sections with translation	Thick sections >1 pixel, Curved "surface" extraction
Projection geometries		[b]Isometric	Arbitrary orientation, Full matrix rotation,
		Pixel shift (limited angles)	Pan & zoom, Combinations (e.g., "fly-by"),
		Rotation or tilt	With cut-aways
Z-coding	"Focus" animation	Simple *z*-movie	Interactive arbitrary section movie
			On-the-fly section movie
	Motion parallax	Simple pre-calculated movie	Interactive pre-calculated movie, Motion compression,
			On-the-fly movie (with interaction)
	Stereo parallax	Manual stereo pairs	Automatic stereo, Stereo with perspective
	"Height" views	Maximum int *z*-coordinate	Threshold *z*-coordinate, *z*-coordinate of high gradient
	Perspective	Orthoscopic	[b]*z*-perspective
Time-coding		*t*-movie	*t*-coordinate
λ-coding		λ-movie	λ-coordinate, Arbitrary color channels
		3color channels	
Special geometry hardware			OpenGL with enhancement, *z*-buffer hardware "geometry engine"

[a]XY orthogonal sections are the basis of "thru-focus animations." Many systems now permit arbitrary (including "oblique") sections to be extracted from a 3D volume quickly enough to be considered interactive. Curved sections (rarely supported) are particularly useful for cellular structures. They can sometimes by produced by pre-processing using line-segments extracted serially from a 3D stack.
[b]Isometric and *z*-perspective mapping (G) functions increase the perception of depth in static views, and remove the ambiguity of depth seen in some rotating projections.

also around x_v. The following two transforms (around y_i and z_i) are then around oblique (i.e., general) axes in the view space. Our rotation is thus three separate twists around axes: $x_i = (a_x, b_x, c_x)$, followed by $y_i = (a_y, b_y, c_y)$ and then $z_i = (a_z, b_z, c_z)$. The G function, Eq. (2), for each twist is a formidable computation with three subcomponents

$$x_{twist} = x[a^2 + C(1 - a^2)] + y[ab(1 - C) + Sc] + z[ac(1 - C) - Sb] \quad \textbf{(6)}$$

$$y_{twist} = x[ab(1 - C) - Sc] + y[b^2 + C(1 - b^2)] + z[bc(1 - C) \text{ v } Sa]$$

$$z_{twist} = x[ac(1 - C) - Sb] + y[bc(1 - C) - Sa] + z[a^2 + C(1 - a^2)]$$

where S is the sin(twist angle), C is the cos(twist angle) around an axis (a, b, c), and a is the $\cos\Theta_{twist}$, b is the $\cos\Phi_{twist}$, $c = \cos\Psi_{twist}$, Θ, Φ, and Ψ are the view space polar coordinates of the twist axis (Fig. 14.7).

This whole transform must be repeated for each of the three re-orientation axes $(a, b, c)_x$, $(a, b, c)_y$, and $(a, b, c)_z$. A viewing transform should ideally be added to observe the rotated structure from different viewing positions. However, by fixing the view direction, this additional step is avoided. The efficiency (and ultimately, the speed) of the geometric algorithm is determined by the degree to which the general form (6) can be simplified. If all rotations are specified around the observer's axes (x_v, y_v, z_v) the direction cosines (a, b, c) become either zero or unity. It is also easier for the user to anticipate the final orientation when the rotation axes do not change between each component twist. For a fixed viewing axis along z_v, a tilt θ (around x_v) is obtained by a, b, c = 1, 0, 0 giving

$$x_\theta = x_i, y_\theta = y_i C + z_i S, \quad z_\theta = -y_i S + z_i C \quad \textbf{(7)}$$

where S is sinθ and C is cosθ. When combined with a subsequent φ rotate (around y_v) this becomes

$$x_\varphi = x_\theta C - z_\theta S, \quad y_\varphi = y_\theta, \quad z_\varphi = x_\theta S + z_\theta C \quad \textbf{(8)}$$

where S is sinθ, C is cosθ, and a final Ψ turn (around z_v) gives

$$x_\Psi = x_\varphi C - y_\varphi S, \; y_\Psi = x_\varphi S - z_\varphi C, \; z_\Psi = z_\varphi \quad \textbf{(9)}$$

where S is sinφ and C is cosΨ.

The projection will eventually be done in the reoriented view coordinates $V(x_v, y_v) = P(x_\Psi, y_\Psi, z_\Psi)$.

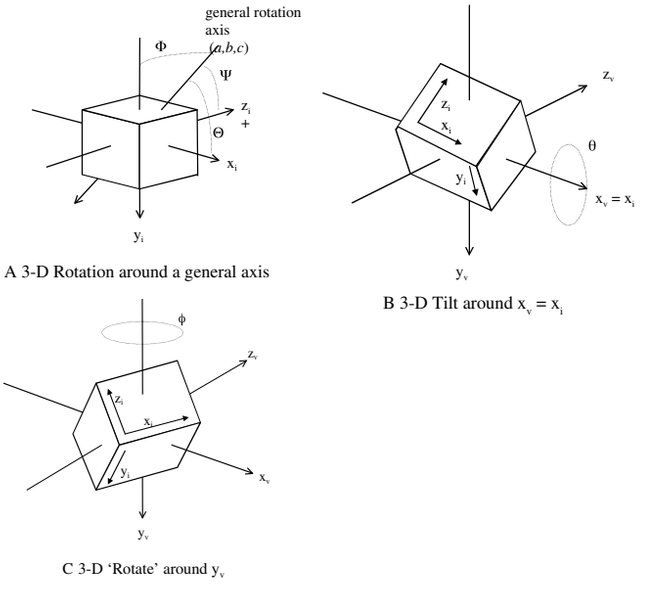


FIGURE 14.7. Rotation transformations. 3D rotations can be performed in the image-space around a general axis of rotation (A). General re-orientation requires rotation around three axes x_i, y_i and z_i. A simpler (and thus faster) scheme is to use a "tilt" (B) followed by a "rotate" (C) around x_v and y_v in the view-space. If viewing along z_v, no additional information is obtained by a z_v "turn."

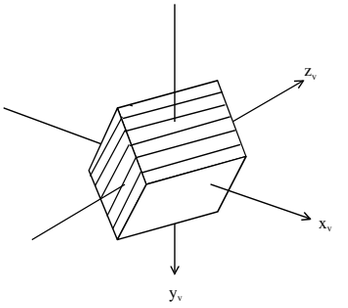
If the twists are "tilt first, followed by rotate" and the viewing axis is oriented along x_v, y_v, or z_v, the twist around that axis can (optionally) be omitted because no more structure will be revealed (Fig. 14.7). By thus omitting the turn (9) and projecting (and viewing) along z_v, the resultant (x_v, y_v, z_v) vectors only change as a function of x_v and z_v (i.e., $dy_v/dx_i = 0$) while traversing a row of image data. This can lead to extremely rapid projection algorithms. The above scheme is used for the 3D visualization routines in Lasersharp, which are executed entirely on the CPU without any involvement of the graphics hardware.

Other tricks can be used to optimize the rendering geometry.

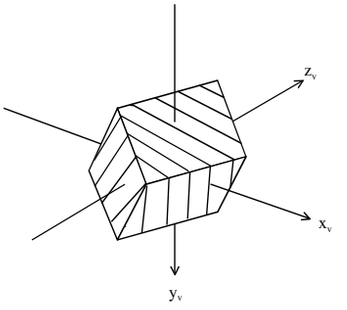
Working in Image or Space View

One implementation approach is to progress through the image space (I space) coordinates (in x_i, y_i, z_i), voxel by voxel, transforming each to view space (V space) coordinates (in x_v, y_v, z_v) before projecting each intensity into the final 2D view at (x_v, y_v). For an image of $nx_i \times ny_i \times nz_i$ voxels, the orthoscopic transformation proceeds via N serial planes or sections of data, normal to z_i in forward ($n = 1, nz_i$) or reverse ($n = nz_i, 1$) order. Alternatively the same G function can be implemented in V space. There are now N planes normal to z_v (and thus cut obliquely through the image volume). For each V(x_v, y_v, z_v) the contributing I(x_i, y_i, z_i) are found and the computation can again proceed in forward ($n = 1, nz_v$) or reverse ($n = nz_v, 1$) order. The V space implementation makes the G function more difficult but facilitates straightforward projections (P) (Fig. 14.8). The I space implementation is the reverse. The V space method has many more advantages for geometric polygon data than for rastered voxels. Hybrid implementations are also possible, combining both I and V space components. In a hardware-accelerated OpenGl implementation, a favorite approach is to take each image plane (i.e., to progress through I space) and warp it into its projected (rotated) aspect in view space. The warped frame is then mapped onto the view layer by layer. Sophisticated graphics cards have hardware for texture mapping that assists the painting of images onto objects using this technique by altering the view pixels according to the color of the image. This texture mapping hardware can be used to paint the warped frames into the growing view modifying the output by opacity values controlled by the voxel intensities. Hardware texture mapping is used extensively by Volocity and Amira packages.

In all these examples the reconstruction process has resulted in a loss of z_v dimensional information. Some of this may be automatically retained by the P function (discussed below), but an efficient G function can further optimize the dimensional content of the view.



A I-space projection via serial x_iy_i sections



B V-space projection via serial x_vy_v sections

FIGURE 14.8. V- and I-space projections. I-space voxel reconstructions (A) proceed via serial x_i,y_i sections that are oblique to the viewing axis. This is the most efficient way of processing voxels in "object order" and is used by most voxel renderers. V-space algorithms (B) process x_v,y_v sections that are normal to the viewing axis. This z_v-ordered reconstruction is more useful for constructing polygon objects than for voxels.

How Do 3D Visualizations Retain the *z*-Information?

True 3D visualization requires that z_v depth information is retained or at least partially restored when the image is mapped into a 2D view.

Stereoscopic Views

Some impressive methods of coding z_v information use stereoscopic techniques (Tables 14.6 and 14.7; Figs. 14.9 and 14.10). These require that an observer be simultaneously presented with a left-eye and right-eye view differing by a small φ rotation. The author has found the following geometry to give acceptable results: for views of width x, angular difference φ_s, viewed at a distance d with an interoccular spacing D

$$D = 0.05 - 0.07\,\text{m}, \quad d = 0.25 * x/D\ \text{m}, \quad \varphi_s = 2 * \arctan[(0.5 * D/d)] \qquad \textbf{(10)}$$

for example, if D = 0.06, x = 0.06, then d = 0.25 and $\varphi_s = 13.6°$.

A simpler alternative to the computationally intensive rotations is to shift each section horizontally (in x_v) by a constant factor of the z_v coordinate during a top-down compositing projection (3). This corresponds to a stereo pixel-shift G function

$$x_v = x_i + \delta x * z_v, \qquad y_v = y_i, \qquad z_v = z_i \qquad \textbf{(11)}$$

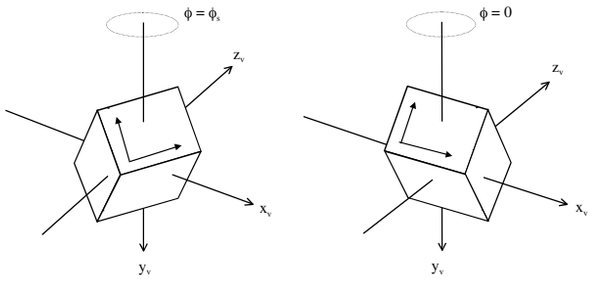
where $\delta x_{left} = \tan(0.5*\varphi_s)$ and $\delta x_{right} = -\delta x_{left}$.

From Eq. (11) and the viewing conditions of Eq. (10), δx is ± tan (7.8°) or about 0.14 times the z-spacing (Fig. 14.9). A slightly different equation is described by Cheng and colleagues (1992) and its derivation is attributed to Hudson and Makin (1970). It can be used to derive an optimal pixel-shift. Using a notation consistent with the above

$$\delta p = 2 * nz_{calib} * M * \sin(\arctan(\delta x * nz_i/nz_{calib}) \qquad \textbf{(12)}$$

where δp is the parallax shift between equivalent points in two views (ideally kept around 3–5 mm); nz_{calib} is the the calibrated z-size of the data (thickness of the original specimen), and M is the magnification.

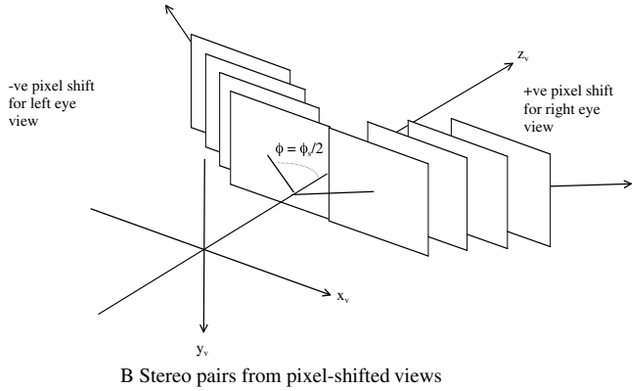
The pixel-shift method is only an approximation. In particular, the result is stretched out or warped in the x-direction by a small



(i) CCW (+ve) rotation around y_v for left eye view

(ii) Right eye view with 'Tilt' only (around x_v)

A Stereo pairs from rotated views



B Stereo pairs from pixel-shifted views

FIGURE 14.9. Pixel-shift and rotation stereo. Pairs of views differing by typically around ±7–8 deg (depending on pixel dimensions and inter-plane spacing) of y_v rotation ϕ_s (A) can be extracted from a sequence and displayed using anaglyph, switched-view or other stereo viewers (see text). The pixel-shift approximation to these rotations (B) results in only trivial distortion and is much faster to implement for small angles about the z_v axis. See Figures 14.5 and 14.10 for example images and the section on 3D depth information for details of stereo generation algorithms.

factor of $1/\cos(0.5 * \varphi_s)$, but for small angles this can be neglected. This shearing and warping algorithm is the basis for fast texture-mapped voxel projections (e.g., Cabral *et al.*, 1994; Lacroute and Levoy, 1994; Elisa *et al.*, 2000).

The two views, or stereo-pair, must be fused into a 3D representation by positioning each in the display space so as to occupy the entire field of view (or at least the central region) for each corresponding eye. The observer then perceives the combined information as a single 3D view located near the viewing distance d, depending on the origin of the z_i-coordinates used in the above equation. For z_i-coordinates centered in the middle of the image volume, the view depth is centered about d. A few high-contrast features must be present in the field in order to successfully fuse the reconstruction. This makes the choice of algorithm and associated parameters critical for successful stereo presentations. The stereo scene geometry is efficiently accomplished by placing the views in two halves of a display, bisected in x or y, and using a viewing aid. The viewer must make the two views appear to be coming from the center of the field while keeping the observer's ocular convergence/divergence near to parallel (i.e., relaxed as though viewing at a distance). By carefully editing a vertical subregion (e.g., 384 × 512 pixels) of interest, side-by-side pairs can be viewed in full color on a horizontal display format (e.g., 768 × 512, 1024 × 768, etc.) without subsampling. Side-by-side stereo-pairs are easily viewed with horizontal prismatic viewers. An alternative is to fix one's binocular convergence point at infinity and refocus each eye onto the respective view (using the lens and cornea only). The left and right views may also be swapped and the eyes crossed or converged to a point between the observer and screen. Some seasoned stereoscopists can fuse stereo-pairs using these methods without additional aids, although prolonged viewing can give rise to eye strain and headaches. Above-and-below pairs can be seen through vertical prismatic viewers, but this geometry cannot be so easily fused by the unaided observer!

Partitioning the color space into two distinct regions allows full size anaglyph stereo-pairs to be observed in monochrome (gray levels only). Both views occupy the entire pixel display area and are transmitted to the corresponding eyes by RG or RB spectacles. Due to the spectral characteristics of some monitor phosphors and the availability of low-cost filter materials, some bleed-through of signal between RG channels often occurs. Red/cyan viewers often have improved extinction. The optimal intensity balance between the component views must be individually determined. Anaglyph stereo-pairs can be fused by observers irrespective of their capacity to differentiate colors. Even rare red/green color blindness is no obstacle provided sufficient intensity levels can be differentiated, although it is usually found that around 10% of observers fail to perceive 3D effects from stereo cues alone (Richards, 1970). Because the anaglyph views occupy the same physical area, the eyes are drawn into a convergence naturally. The monitor should be as large as possible to increase the distance from the viewer and decrease eye strain, that is, so the convergence angle is as small as possible but each eye is focused at a distance. Health and safety recommendations usually specify at least 18″ comfortable viewing distance for VDUs (more for extended viewing) with alternative work breaks every hour.

In order to maximize simultaneously spatial and color resolution, the temporal display space can be partitioned to display the component stereo-pairs. This requires more sophisticated hardware than the previous methods at increased cost. The left and right component views are displayed alternately on the video monitor in rapid succession. Observers watch through a viewing device that synchronously blanks and unblanks the visual field of each eye while each corresponding view is displayed. These alternate (or switched) display stereo systems are characterized by differences in the format of the video signal, the switched viewing hardware, and the method of synchronization. Older video stereo systems display images in two alternate and interlaced **fields** of each video **frame**. This method gives half the temporal and y-axis resolution of a normal video signal, an obtrusive (25/30 Hz) display flicker, as well as the low intensity associated with interlaced displays. Computer displays are exclusively non-interlaced but alternative frames may be used to show stereo components rapidly in succession. An interlaced implementation will require the two component images to be interleaved line-by-line in the display memory. A more convenient organization is to have sequential buffers for the two fields which can be updated independently. Non-interlaced computer displays give a brighter view with a flicker-free refresh rate of 60 to 90 Hz. This would allow alternate frame non-interlaced stereo, but would still exhibit noticeable flickering around 30 to 45 Hz. A continuous stereo display requires at least 120 Hz and preferably a double-speed scan of 180 Hz.

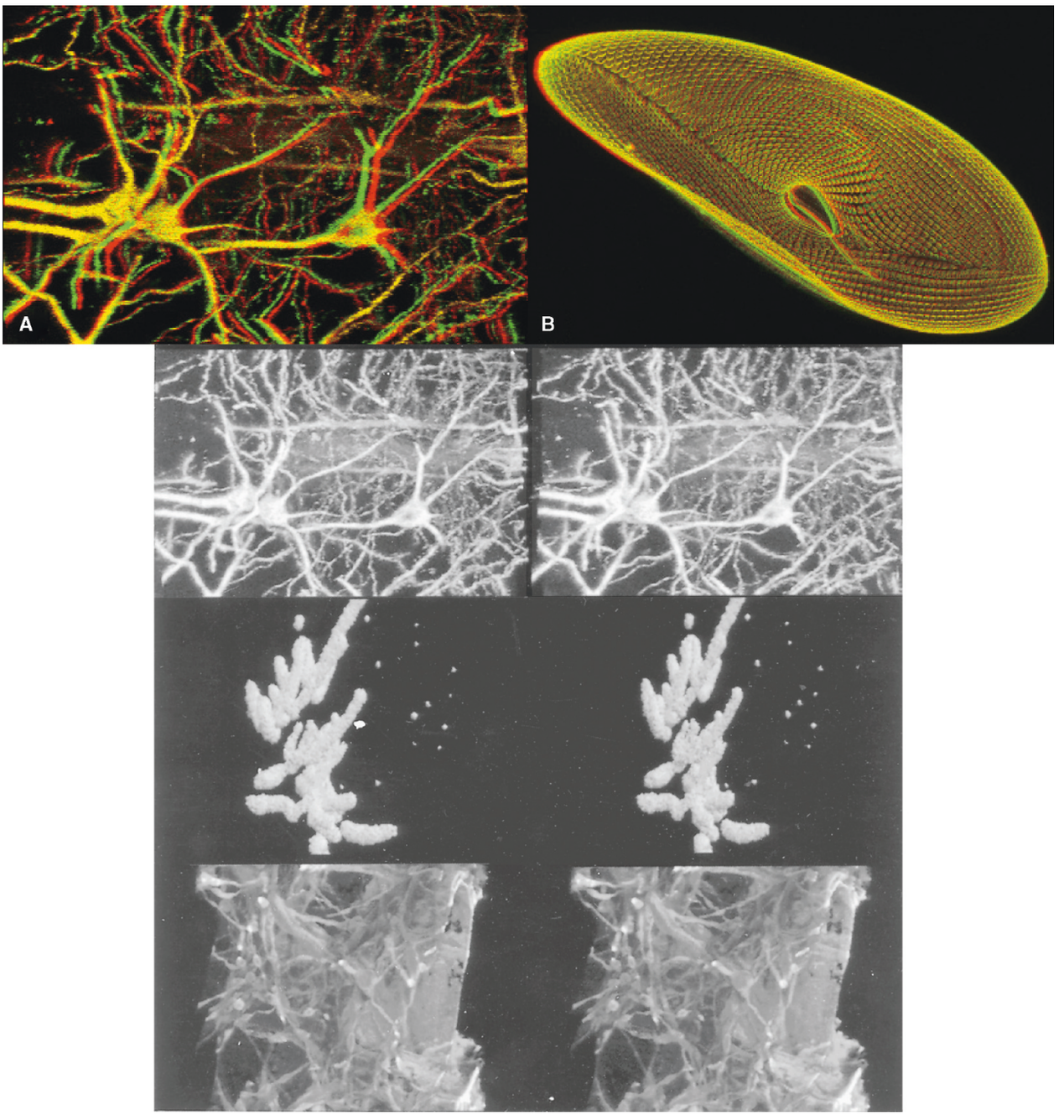


FIGURE 14.10. Example stereo images. (A) Anaglyph (two color, red/green) stereo-pair of Golgi-stained nerve cells, generated by the pixel-shift method (see text). The alternative method of extracting two images from a rotation series [shown immediately below (A) as a side-by-side pair] produces a virtually identical result to (A) for small angles about the *z*-axis. (B) Anaglyph stereo-pair of fluorescent Paramecium. [Data for (A) and (B) courtesy of Bio-Rad Microscience.] The third pair of panels shows a stereo-pair of voxel-rendered images representing Feulgen-stained chromosomes from the plant *Milium.* (Original data from Bennet *et al.,* 1990.) Voxel gradient lighting is used with a high-opacity α-blend algorithm to give an effect of "solid" structure. The final panels show a triple-stained thick section of skin showing extra cellular matrix proteins and vascular structures. Simple maximum projections of each channel *z*-series are combined into the 24-bit RGB view. While the anaglyph stereos can span the entire display window but require the color space for the stereo effect, these full color side-by-side stereo pairs (as for monochrome pairs) can span only half the available display resolution. These alternative stereo display methods illustrate the way that display resources can be "traded" for improved (*x*,*y*) resolution, *z*-depth or multi-channel (color) rendition. Side-by-side pairs in this figure should be viewed by divergent eyes or viewing aids (i.e., with eyes relaxed as when viewing distant objects but focused on the page). This is best achieved by focusing on a distant object and bringing the page into view while keeping the eyes relaxed but refocused on the page. If the eyes are crossed or a convergent viewing aid is used, the 3-D effect will appear "back-to-front." This can be problematic with some maximum projections (e.g., the Golgi-stained neurons above) where some brightest features are towards the "back" of the rotated object in some views. This is often found when there is attenuation with depth in the sample. Maximum intensity can incorrectly bring these features to the "front" of the view. Samples with more isotropic intensity distributions with depth (e.g., the skin images above) tend not to show these anomalies.

Some high-resolution stereo displays still use an interlaced storage mode (at half the *y*-resolution) for stereo presentation. All video display systems suffer to some extent from flicker arising from an interference with mains-powered room lights and should be run in reduced ambient lighting.

Synchronizing the display to the switched viewing system can be accomplished in a number of ways. A bright intensity marker in each video frame can identify the left and right views, and this has been used to trigger a photo switch placed over the corner of the video monitor. This switch controls synchronous LCD shuttered viewers. The synchronizing pulse can be generated directly from the field or frame synch of the display signal and passed to the viewers by cable or optical (infra-red) link. A more convenient alternative to switched viewers is the polarizing LCD shuttered screen. This is a large LCD shutter (often constructed from two parallel units for faster switching) that toggles between two polarization states. The left- and right-eye views are thus differently polarized and can be viewed through inexpensive glasses. Plane-polarized shutters (and glasses) give the best extinction, but clockwise and counterclockwise rotary polarization allows for more latitude in the orientation of the observer's head (important when a large group is viewing a single monitor!). Example stereo views are shown in Figure 14.10 (and also Figs. 14.5 and 14.24). The Imaris package has a number of selectable stereo modes depending on the type of viewers to be used (these include Raw Stereo — using the OpenGL functions, alternate image (interlaced modes), and three combinations of two-color anaglyphs). The 3D-constructor plug-in for ImagePro Plus (Media Cybernetics Inc.) also supports OpenGL stereo.

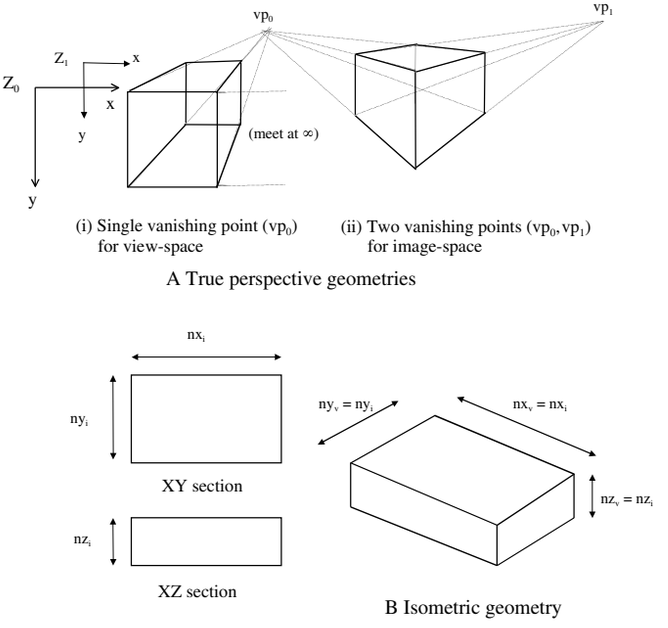


FIGURE 14.11. Non-orthosopic views. True perspective views (A) give the most "realistic" reconstruction geometries. A simple approximation can be implemented in the view-space (1) with one "vanishing point." x_v, y_v coordinates are reduced by a linear function of z_v between z_0 and z_1(see text). A general perspective G-function for image-space implementation (2) with rotation around y_v requires two vanishing points. Isometric reconstructions (B) retain the physical dimensions of the original image axes (rather than the trigonometrically projected axis lengths). 3D distance measurements can thus be made directly on the views.

Non-Orthoscopic Views

Visual perception of depth makes extensive use of non-stereoscopic cues, and these can be coded by appropriate algorithms into a corresponding part of the display space. A series of G functions exist that code depth information with unmodified intensities. These are the non-orthoscopic transformations and include both perspective and non-perspective geometries (Fig. 14.11). The most straightforward of these algorithms require that the corresponding view coordinates for each data voxel are modified by the image *z*-coordinates. The **isometric** G function involves a constant shift in screen x_v and/or y_v coordinates as the I space renderer traverses each dimension of the data

$$x_v = x_i + x_i\cos\Psi, \quad y_v = y_i + y_i\sin\Psi + z_i, \quad z_v = z_i \quad \text{and usually } \Psi = 60^\circ \qquad \textbf{(13)}$$

This geometry (as the name suggests) gives rotated x_v, y_v and z_v, axes in the same proportions as the original image axes (for rendered examples, see Wilson, 1990). Direct x_i, y_i, z_i measurements can be made from the 2D view screen.

True **perspective** views attempt to visualize the data as a large real-world or macroscopic object with x_v and y_v converging to a vanishing point at a large z_v distance. This point is on the horizon (usually in the center of the field). The perspective G function decreases the dimensions as a linear factor of the *z*-coordinate. So after the data have been rotated, the projection is accomplished through a new perspective space (x_p, y_p). True perspective can be approximated in the G function by

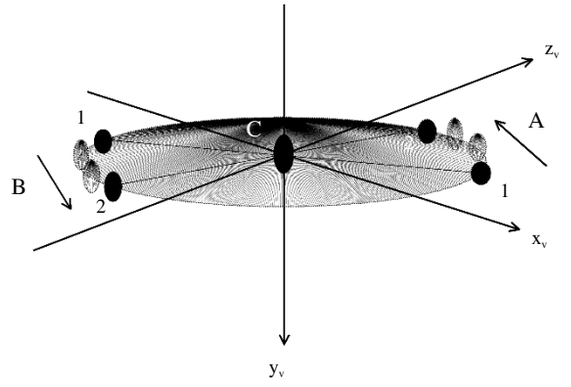
$$z_p = z_\Psi, \quad x_p = \mathbf{a}x_\Psi/z_\Psi, \quad y_p = \mathbf{a}y_\Psi/z_\Psi \qquad \textbf{(14)}$$

where **a** is a factor reflecting the object-to-observer distance.

Perspective views can be readily interpreted from objects with well-defined structures. This is because we assume such views arise from connected features such as real-world surfaces and edges. Popular optical illusions indicate this is not always true! Connectivity between neighboring voxels in a confocal laser scanning microscopy (CLSM) fluorescence image can rarely be assumed without substantial *a priori* knowledge and then only after careful control of noise. Non-orthoscopic depth coding is useful for removing ambiguity from stereoscopic views. Volocity and Imaris produce both orthoscopic and perspective 3D (and 4D) views.

Temporal Coding and *z* Depth

Time axes can often be treated in exactly the same manner as depth or *z*-coordinates. This is a useful observation because many visualization packages do not specifically recognize time points. Thus t-coordinates can be directly mapped by animation, coded in the intensity or color space, and even represented in non-orthoscopic or stereoscopic views. The importance of time points as a component sampling space in 4D imaging is encapsulated within the so-called 4D tixel object. Significant efforts have been invested in the efficient visualization of tixel images within the 5D display space (Kriete and Pepping, 1992). *z*-Position can be inferred from the display temporal space by animating serial sections as a through-focus sequence or by motion parallax (Fig. 14.12) from a rotation series (Wallen *et al.*, 1992). Since *xy*-acuity improves smooth motion perception, large rotated views require reduced angular increments as well as higher refresh and framing rates compared to those from smaller volumes.



Z-Depth perception by temporal interpolation and motion parallax

FIGURE 14.12. *Z*-depth by temporal interpolation and motion parallax. If a similar feature is seen in two sequential views of a rotation series viewed along z_v (e.g., the dark shape appearing at "1" in the first view and at "2" in the second), two processes contribute to the perception of its depth within the view. (1) The direction of motion, either left or right across the field of view will determine whether it is perceived to be behind (A), the center (C), or in front (B) of the screen. (2) provided the views are at small angles apart and shown in a "smooth" sequence (which may need up to 18 fps), the details are mentally interpolated in time (taking into account the perceived motion) to "fill in" the missing information (dotted features). For a fully transparent view with no other depth cues, front and back may be arbitrarily reversed by different observers.

Mapping the Data Values into the Display

As with the G function, data values must also be transformed to the display by a well-defined operation. This is the combination, compositing or projection function P, described in Figure 14.6 (examples in Table 14.8 and Fig. 14.14).

The Visualization Model

It is useful to consider even the simplest P function in terms of a lighting model. In a gross simplification, each image voxel is considered to have a brightness equivalent to the amount of light emanating from a corresponding point in the specimen and collected by the microscope objective. Digital processing to more closely realize this goal for CLSM imaging requires a knowledge of the microscope transfer function (e.g., Sheppard and Gu, 1992, 1993) and the use of digital restoration methods (e.g., Holmes and Liu, 1992; Shaw and Rawlins, 1991; see also Chapters 23 and 24, *this volume*). For now, the 3D image is considered as the physical or macroscsopic object, itself being imaged, as if by a lens or eye, to a 2D view. Light rays from each point voxel in the image would contribute to an equivalent (but not unique) point in that view. This mapping of object points × image voxels × display view pixels is the crude model. This is refined and made more elaborate by (1) segmenting the multi-dimensional image data into a set of objects, (2) considering other objects in the path of each simulated light ray, and (3) adding additional, artificial lighting and surface effects. These aims are met using physical or material properties attached to the objects.

Choosing the Data Objects

So far, we have considered the image as an array of voxel (3D) or tixel (4D *x*, *y*, *z*, t) objects with no implied connectivity. Computer-aided macroscopic imaging and display systems have fostered the growth of visualization models based on the grouping of voxel samples into geometric objects. The consequence is a growth in special hardware and software for efficient treatment of vectorized geometries. Microscope systems invariably produce rastered image arrays. The array dimensions (n*x*, n*y*, n*z*, etc.) imply the arrangement of rows, columns, sections, etc. Vector objects are non-ordered lists of geometric figures, each of which is defined by a very few parameters. Thus, a simple voxel might be five values (*x*, *y*, *z*, intensity, opacity, etc.) but a triangle comprising many tens or hundreds of voxels may be specified with only 10 to 15 parameters (three sets of coordinates plus some material properties). If the material properties vary across the polygon, values at each vertex only need be stored. Each vectoral component will need at least 16-bit integer precision and preferably floating-point. A compact form is to store all vertices in one list or table. Each geometric object is then a set of polygons, specified by indices pointing into the vertex table.

While early workstation programs stored voxels as vectors, the availability of optimized hardware and software for G functions and 3D rendering of rastered byte images has assisted the devel-

TABLE 14.8. Overview of Image-to-View Data Mapping (Projection) Options for Visualizing Multi-Dimensional Biological Microscopy Data

Feature	Parameter	Minimum required	Desirable additional enhancements
[a]Data objects	types	Voxels	n-D array of voxels, Object list, Surface (triangles), Surface (polygon net) Objects "embedded" within voxels
	storage	3D rastered array	n-D rastered array, object vector list
Selective enhancement of features		Basic filters, Volume cut-away Region of interest/edit, Intensity segment, Color channels	Gradient segmentation, Image masking, Opacity/transparency Material properties, Morphological filters, "Seed/flood fill" Object modelling
[b]Projection algorithms		Maximum Average	Front, *Z*-co-ordinate, α-blend, SFP, Iso-intensity surface, "Local" projection
[c]Special graphics resources		VGA graphics	OpenGL with acceleration, Texture mapping, Hardware shading/ lighting etc., α-buffer

[a]Data objects are usually voxels or lists of vertices defining geometric surfaces. Other surface descriptions are possible. AVS allows for a particularly large range of geometries, while in most object reconstructions, the options are usually restricted to triangulated surfaces — primarily to make use of efficient accelerations in the graphics system.

[b]Some geometric object renderers use Front or α-blend P-functions in the same way as for voxel objects. Specific "surface" algorithms may also be implemented that capitalize on the connectivity of the geometries. There is always a trade-off between the portability of a program across platforms (or over new versions of platforms) and the use of non-standard "special" hardware. The OpenGL standard largely avoids these problems by setting the interface requirements and providing standard support for new hardware. SFP = simulated fluorescence process.

opment of voxel visualization algorithms. The most efficient way to process rastered voxels is by whole-image operations. I space implementations effectively warp successive orthogonal (*xy*, *xz*, or $tz)_i$ sections, using a transformation geometry engine, to their projected shape in the final view. Rows and columns of data are traversed in forward or reverse order to preserve the forwards or backwards compositing direction. The only drawback of this method, as opposed to a *z*-ordered list of polygons, is the throughput to the display. Because the entire image data must be streamed into the display, bandwidth is critical. This requires highly efficient pipelined operations to achieve a display rate sufficient to service the output from an optimized geometry engine. The highest specification systems use multiple display devices (often video projectors) to simultaneously render multiple views for immersive reality installations. So-called multi-pipe versions of these visualization programs are used to massively increase the data throughput to the display. The vectoral representation is more efficient for triangles encompassing more than about 20 equivalent voxels, provided the segmentation algorithm is justified for the particular data. Computer models allow entire surfaces and bounded volumes to be described by single parametric equations using, for example, Bezier coefficients (see Watt, 1989). This type of simple object definition is generally not practical for confocal fluorescence data due to the low signal-to-noise and discontinuities in antibody or other stains. As a result, many vertices must be individually stored.

Vectored object lists can be traversed in I or V space in object order. Thus, complex figures can be rotated and projected individually. Refinements in geometric object technologies may appear to place voxel rendering at a disadvantage due to its ordered processing of many more data points. Choice of data objects is largely determined by the amount of information known about the specimen, the sophistication or realism required in each view and the availability of appropriate hardware and software on the chosen platform. It should now be apparent that there is no fundamental distinction between any of the data objects discussed. A trade-off between processing speed and transfer rate must be weighed against the problems or bias associated with segmentation of the image data into parametric structures. In any case, voxel rendering speeds are now equivalent to the speed at which vector graphics objects could be drawn just a few years ago. All of the compositing or P function rules described below can be applied to any data objects.

Sophisticated graphics systems are now relatively inexpensive and are supplied with even modest-specification PCs. Some include hardware accelerated geometry-processing engines, with standardized OpenGl interfaces, intimately linked with the GPU and display memory together with additional buffers, LUTs, etc. Thus many of the above operations are now readily available to any software developer writing for a standard hardware platform.

Segmenting the Data Objects

Segmentation is a process by which objects are extracted from the rastered voxel image data. Voxels are selected according to their brightness and/or by some property linking them to other voxels. A lower and/or upper threshold may be applied producing a segmented band containing all the voxels of a particular object. Most systems allow this intensity segmentation to remove background or to isolate a homogeneously stained structure. Threshold values are readily chosen by masking a histogram and observing this simultaneously with an interactive, color-banded screen display of the segmented voxels. Histogram peaks indicate subpopulations of background voxels, possible structural features, etc. This edited histogram produces a photometric look-up table (P-LUT) through which the image is rapidly mapped. Morphological segmentation requires a selection based on some connectivity rule such as the geometric surface objects extracted by the Marching Cubes (c.f. VoxBlast) or Delaunay Triangulation (c.f. Visilog) algorithms. Three-dimensional intensity gradient filters can also find or enhance boundaries between geometric objects. Cheng and coworkers describe the use of such a filter to extract a gradient image, which is then blended with the original to enhance edges. Using the earlier notation

$$I_{out}(x_i, y_i, z_i,) = I_{in}(x_i, y_i, z_i,) \; [k + (1 - k) \; \text{grad}(\arctan(I_{in}(x_i, y_i, z_i,))] \quad \textbf{(15)}$$

where the arctan is an (optional) approximation to a sigmoidal background suppressor and grad is the unsigned 3D gradient

$$\text{grad}(x_i, y_i, z_i) \grave{} = |[(dI/dx_i)^2 + (dI/dy_i)^2 + (dI/dz_i)^2]$$

This 3D gradient is simply the resultant of the unsigned component gradients along each axis. These individual components are conveniently approximated (for low noise data) by subtracting the values on each side of the voxel whose gradient is required, that is, grad = $(|((I(x_i + 1,y_i, z_i) - I(x_i - 1, y_i, z_i))^2 + (I(x_i, y_i + 1, z_i) - I(x_i, y_i - 1, z_i))^2 + (I(x_i, y_i, z_i + 1) - I(x_i, y_i, z_i - 1))^2))/2$.

Gradient filters are also extensively used to provide data for the realistic artificial lighting effects (discussed later). Other background filters are based on patch convolutions with kernel weights given by smoothing functions. Forsgren and colleagues (1990) use a 3D Gaussian filter where the mask weights are given by:

$$F(x, y, z) = 1/(\sigma^3 2\pi|(2\pi)) \exp(-(x^2 + y^2 + z^2)/\sigma^2) \quad \textbf{(16)}$$

different strengths are specified by the width term σ. This filter is separable and is readily implemented as a sequence of 1D filters, allowing for asymmetric sampling in the multi-dimensional image. A general approach is to use a 3D filter (or ideally a PSF deconvolution) with a cut-off at the Nyquist frequency (see also Chapters 4 and 25, *this volume*), followed by a threshold segmentation of the filtered output. The segmented output is then used in a logical test (or mask) to segment the original image. Segmentation (Fig. 14.13) may simply exclude background voxels or the included voxels can then be grouped into polygon objects. Voxel objects can use a material look-up table (M-LUT) for each property. It is possible to specify all material properties for any object types as indices in one or more material look-up tables (M-LUTs) and to use these to separate different materials within the volume. The Analyze package has a good example of a dedicated segmentation menu that brings together image edit, morphology operations, and object/surface extraction functions. The Surpass optional module in Imaris groups together the object segmentation capabilities of that package.

Scan Conversion

After geometric rotation, etc., the data objects are drawn into the final view. For polygons, surface nets, etc., this requires a scan conversion whereby the vectors are turned into rastered lines of pixels (Watt, 1989). A pixel view of each polygon patch is then composited into the final view as for rastered voxels. A simple approach is to draw a closed outline and to use a fast-fill algorithm, modified by any shading required. It is often more efficient to generate just the ends of each scan line through the polygon, filling the gaps by simple line drawing. For two vertices $S(x_s, y_s)$ and $E(x_e, y_e)$ defining the start and end of a polygon edge, there are $(y_e - y_s)$ intermediate scan lines. The view coordinates for the start of the *j*th scan line are

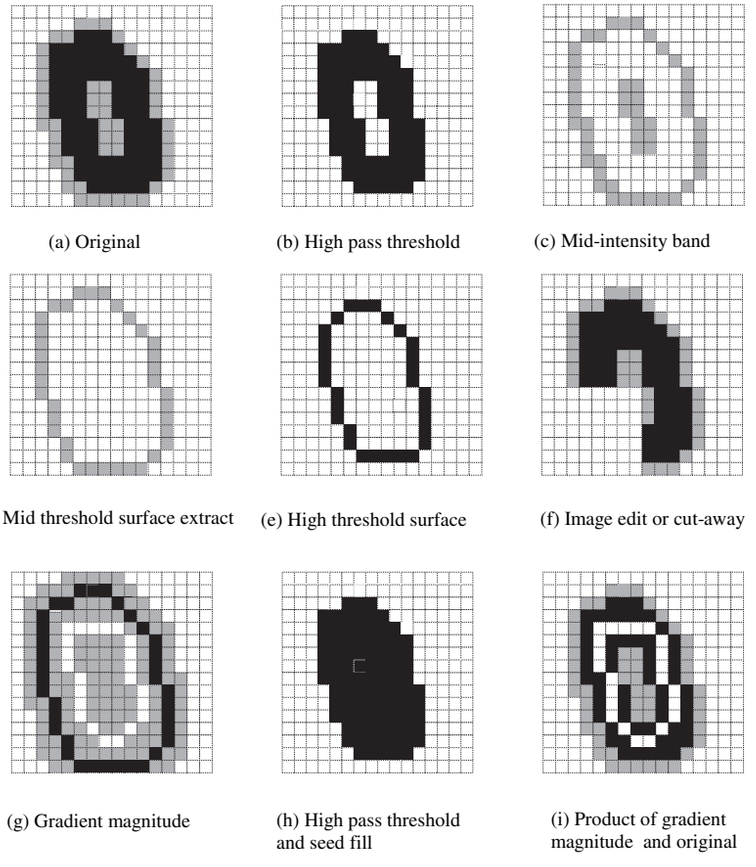


FIGURE 14.13. Object segmentation. Voxels may be segmented from the image volume only to remove background and unwanted features, or they may additionally be grouped into larger geometric objects. (A–I) show 2D slices from a small 3D volume before and after segmenting with various algorithms. High-pass (B) and mid-intensity band (C) are the simplest operations and are often used on their own, or in conjunction with other operators. Surface extractions (D,E) (e.g., Marching cubes, c.f. VoxBlast or Delaughney Triangulation, c.f. Visilog) produce bounded structures obscuring internal details. Manual or semi-automatic image editing or reconstruction cut-aways (F) reveal internal details without corrupting the data values. Gradient magnitude filters (G) highlight voxel boundaries and edges. Thresholded seed fill (H) (c.f. Visilog, ImageSpace) gives a solid object for simple volume estimates, etc. Complex modes such as the gradient magnitude blended with the image (I) (see text) can give reasonable enhancement of edges without artifactual "halos" (c.f. Prism II/DeltaVision).

$$x_v = (\text{int})(x_s + j\delta x), \quad y_v = y_s + j \tag{17}$$

where $\delta x = (x_e - x_s)/(y_e - y_s)$. The ends of each scan line are obtained by a similar calculation.

Scan conversion or rasterization is a well-defined component of the OpenGL graphics pipeline and this affords a convenient point in the reconstruction process to combine or embed graphical objects into a voxel or previously generated pixel view. This is a powerful technique used to good effect by the major rendering packages to show high contrast segmented objects within the context of a general volume view (Amira, for example, allows for an arbitrary number of datasets, image modalities and/or visualization modes within the same display view).

Projection Rules

As each geometric object or image plane is composited into the view, incoming data either replaces or is blended with the accumulating result. The algorithm used is usually a function of the z-coordinate, the intensity value, and the associated material properties (Table 14.8). This P function has two components: an arithmetic or compositing (C) function (which may be just a simple assignment) and an optional logical test (T). For the nth (of N) frames or objects composited into the view V, a general form is

$$\text{if } \{T\,[I(x_v, y_v, z_v)_n, V(x_v, y_v, z_v)_{n-1}]\} \text{ then } V(x_v, y_v)_n = C\,[V(x_v, y_v, z_v)_n, I(x_v, y_v, z_v)_n] \tag{18}$$

Simple compositing functions (Fig. 14.14) include:

- **Maximum Intensity**

$$\text{if } [I(x_v, y_v, z_v)_n \geq V(x_v, y_v, z_v)_{n-1}] \text{ then } V(x_v, y_v)_n = I(x_v, y_v, z_v)_n \tag{19}$$

Maximum intensity projection, or MIP (e.g., Sakas *et al.*, 1995), is now the most widely used quick visualization function (e.g., see Analyze, Cedara, Imaris, FIRender, Voxblast etc) and can be efficiently implemented as a stand-alone mode or in combination with other algorithms.

- **Average Intensity**

$$\text{(no test) } V(x_v, y_v)_n = V(x_v, y_v, z_v)_n + I(x_v, y_v, z_v)_n/N \tag{20}$$

Less common than MIP, mean intensity is found in the LSM programs and Analyze. It is useful when the data volume is very dense, which would tend to give a very saturated view with MIP. Because it effectively averages along the projected ray, this function reduces noise but produces lower contrast. This can be partly overcome with an appropriate display LUT.

- **First or Front Intensity ≥ t**

$$\text{if } \{[I(x_v, y_v, z_v)_n > t] \,\&\, [(z_{v,n-1}) < (z_{v,n})]\} \text{ then } V(x_v, y_v)_n = I(x_v, y_v, z_v)_n \tag{21}$$

This is a quick way of exploring a surface or boundary in a voxel representation, particularly as an aid to determining parameters for more complex modes (e.g., see Lasersharp projection modes).

- **Alpha Blend**

$$\text{(no test) } V(x_v, y_v)_n = (1 - \alpha)\, V(x_v, y_v, z_v)_{n-1} + (\alpha)\, I(x_v, y_v, z_v)_n \tag{22}$$

This is the standard mode used for object visualization and works particularly well for voxel objects and is implemented in virtually

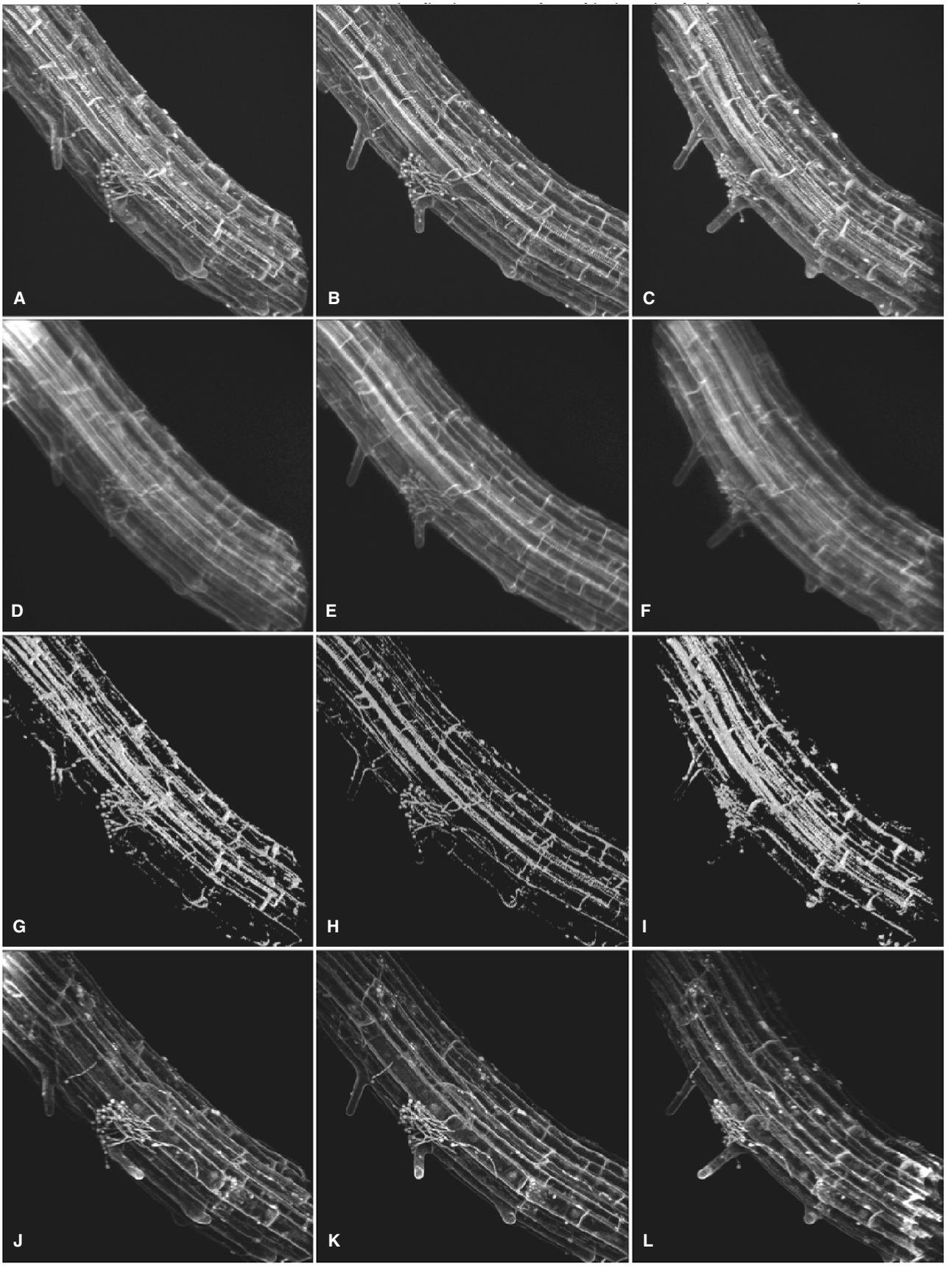


FIGURE 14.14. Projection combination or compositing rules. 3D visualizations of a stack of 130 confocal optical sections through a portion of *Arabidopsis* plant root using Lasersharp (A–C) and Imaris (J–L). Autofluorescence (and a little non-specific fluorescent thiol-staining) shows vascular tissue, cell walls and nuclei and lateral root buds. A small attached fungus is seen attacking the plant along the lower edge towards the center of this portion of root. (Maximum intensity projections as rotations at −30 deg (A), 0 deg (B) and +30 deg (C). Equivalent average projections (D–F) show the characteristic "fuzzy X-ray" character of images made with this algorithm. The first voxel (nearest the viewer) along each cast ray is recorded in (G–I) showing a more solid appearance while retaining original intensity values but at the expense of losing many details. α-rendering at the same angles (J–L) clearly represents the density of the structure as well as fine details but introduces some spurious high intensities where the structure is thin (e.g., at the end of the lateral root tips).

all of the packages in Table 14.1. Although the added complexity of having to set the α parameter sometimes makes it harder to use than MIP for LSM fluorescence data, this parameter is the basis for all opacity/transparency effects (see below).

The tests in Eqs. 19 and 21 may be reversed to obtain minimum and below-threshold versions. The alpha term is a general function that can partly define the physical properties of the rendered object. This blending factor can be dynamically modified as a function of z_v or n during the projection. A Kalman version of Eq. 20 may be implemented in this way; the number of composited frames N need not be known in advance, and the process can be stopped when the required result is reached.

- **Kalman Average**

$$V(x_v, y_v)_n = (1 - 1/n)\, V(x_v, y_v, z_v)_{n-1} + (1/n) I(x_v, y_v, z_v)_n \quad \textbf{(23)}$$

This is a dynamically modified $\alpha = 1/n$, and the projection may proceed in positive or negative z_v order. These define the front-to-back and back-to-front view space rendering geometries. It should be readily obvious that these two processes afford a simple means of modeling the lighting of voxels from front-to-back or the emission of light from voxels running from back-to-front with respect to the viewer. The latter rendering order also shows the view building up towards the viewer that can reveal internal details of an object during the visualization process, provided the screen is updated during the computation. A display equipped with α-plane hardware (with associated firmware or software) automatically blends the incoming data using factors stored and updated in an alpha memory plane. α-blending may also be implemented entirely in software. This is a standard OpenGL feature. The α value is an eighth parameter for vectors (after the coordinates and RGB intensity) or a fifth value for voxels (with implied coordinates) specifying blending properties for the intensities of that object. Visibility of an incoming voxel or data object can thus be made dependent on object opacity or transparency and therefore depth (z_v) in the rotated view (see below). Earlier we discussed ways in which the geometric transformation could be modified to encode additional z-information into the display geometry. In addition to z-related blending operations, the compositing algorithm can retain z-information within the displayed intensities using alternative algorithms.

How Can Intensities Be Used to Retain *z*-Information

z-Coordinate or Height Views

The **height**, **range**, **topological**, **relief** or (the author's preference) ***z*-coordinate** view (e.g., Boyde, 1987; Freire and Boyde, 1990; Forsgren *et al*., 1990; Odgaard *et al*., 1990) technique has been used for many years to directly record the z_v-depth in the intensity or color space (or both) of the display. The rule includes a test that selects a particular voxel along the observer's line of sight. The z_v-coordinate is then assigned [after an offset (z_o) and scaling (z_f)] to a value in the view. A range of z-coordinate tests, similar to the intensity tests (Eqs. 19, 20) above, are found (Fig. 14.15):

- **Coordinate of Maximum Intensity**

$$\text{if } [\, I(x_v, y_v, z_v)_n \geq V(x_v, y_v, z_v)_{n-1}] \text{ then } \quad V(x_v, y_v)_n = z_o + z_f z_{v,n} \quad \textbf{(24)}$$

- **Coordinate of First Intensity ≥ (t)** (i.e., **Maximum Height** or **Nearest**)

$$\text{if } \{[I(x_v, y_v, z_v)_{n-1} > t] \,\&\, [(z_{v,n-1}) < (z_{v,n})]\} \text{ then } V(x_v, y_v)_n = \text{etc.} \quad \textbf{(25)}$$

These z-coordinate modes are used by simple 3D topology programs (e.g., Automontage) as well as some renderers including Analyze, VolumeJ, Lasersharp. etc.

- **Iso-Intensity Surface**

$$\text{if } [I(x_v, y_v, z_v)_{n-1} = t)] \text{ then} \qquad \text{(etc.)} \quad \textbf{(26)}$$

Although related to the previous projections, the iso-surface routine is usually implemented by a recursive 3D algorithm such as the marching cubes (Lorensen and Cline, 1987) and is the basis of many surface object segmentation algorithms (e.g., Voxblast and Analyze).

Through-focus images from widefield microscopy have been processed using a maximum test applied to a prefiltered version of each frame. For example, the maximum local variance can produce an auto-focus intensity or coordinate view (c.f., Automontage). The depth discrimination of the confocal microscope allows a simpler auto-focus routine using just maximum brightness (for a single-surface object). This requires that the z-response for the particular specimen (point, plane, etc.) has no significant side lobes (the confocal PSF is investigated by Shaw and Rawlins, 1991). Instead of replacing the brightness with z_v, intensities can be modified (weighted) by their z-coordinate giving a so-called depth-weighted projection (Fig. 14.16). The simplest form is a linear weighting from 1 (nearest the observer) to 0 (furthest away).

- **Linear Depth-Weighted Projection**

$$V(x_v, y_v) = C[I(x_v, y_v, z_v)z] \quad \textbf{(27)}$$

where $z = (z_{back} - z_{v,n})/(z_{back} - z_{front})$, that is, a normalized z-coordinate. A more sophisticated form is

- **Exponential Depth Weighting**

$$V(x_v, y_v) = C[I(x_v, y_v, z_v) * f^z] \quad \textbf{(28)}$$

where f is a constant ≤1.

This algorithm (which can be implemented in any z-order) is often described as an attempt to model the absorption of light from a source directed along the z-axis of the data from behind (transmitted) or the attenuation of emitted fluorescence. Not surprisingly it turns out that this result is identical to that achieved by an ordered recursive algorithm traversing the data from front to back using a constant α-blending factor (≤1):

- **Recursive Exponential Weighting**

$$V(x_v, y_v) = C\{[(1 - f) * I(x_v, y_v, z_v)_n], [I(x_v, y_v, z_v)_{n+1} f]\} \quad \textbf{(29)}$$

The commonest form of Eqs. 27 to 29 is a linear average or summation, but any compositing function can, in principle, have a depth-weighted component. By making the factor equal to

$$f = z_{str}/(Nn), \quad \textbf{(30)}$$

where N is the number of serial planes in the projection, a non-linear projection of strength equal to z_{str} is obtained. If $z_{str} = N$, the result is identical to a Kalman average. For $z_{str} = 1$, the front or maximum height voxels completely dominate the view. Other values give intermediate results [Fig. 14.16(A–C)].

Hidden-Object Removal

Z-Buffering

z-Ordered compositing simplifies the implementation of z-algorithms. Front-to-back projections using the first-object test

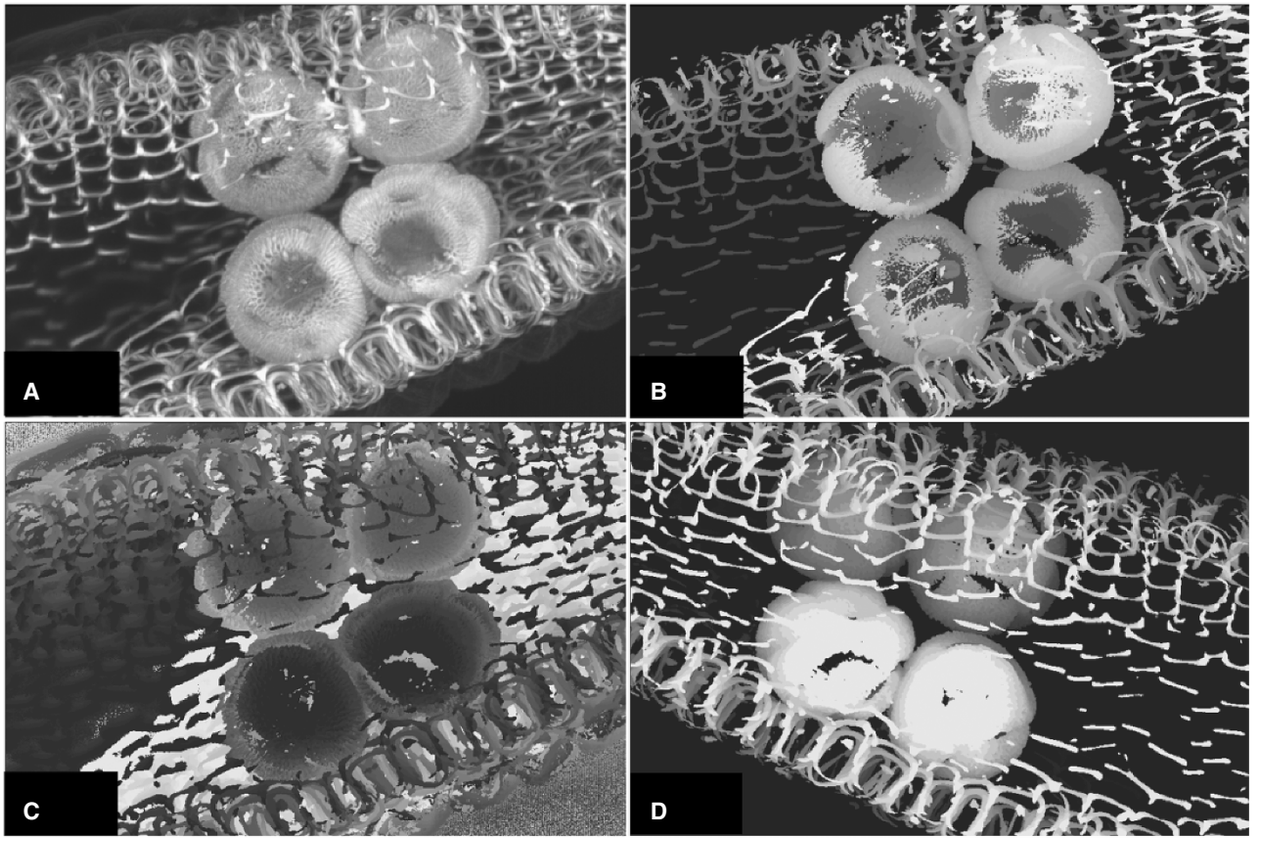


FIGURE 14.15. *Z*-coordinate views. (A) Maximum intensity projection of serial confocal optical sections through pollen grains in a partially dissected plant anther. Some sections are missing from the data stack (or perhaps the specimen is incomplete) but it cannot be elucidated whether the loss is from the top or bottom of the set from this projection, which carries no z-information. (B) shows a height or distance projection where the brightness is coded by axial distance from the viewer (dark is furthest away) recording the first voxel above a background threshold. It can now be seen that the lost sections are at the top of the stack which was projected top-to-bottom. (C) shows the height of each voxel chosen by maximum projection in (A), confirming the finding from (B). (D) shows the same algorithm as in (B) projecting bottom-to-top through the stack.

merely check if a non-zero intensity has been encountered. Hidden voxels are never processed. Conversely, if a back-to-front pass is used, the last voxel will be the one displayed and no test is required. The entire volume is now traversed and all voxels are processed. This can be very informative if the rendering process is visible on an interactive display. For non–z-ordered objects, a more intensive logical comparison of intensities and/or z-coordinates is needed, such as a front-object z-test; this is known as ***z*-buffering** and is a fundamentally important OpenGL-controlled process in modern graphics systems. Implementation can be at various stages of the rendering process. Voxel data is z-buffered efficiently as a whole section operation after warping. Polygon-ordered rendering uses standard pixel z-buffering but does not use information about adjacent vertices efficiently. Scan line z-buffering is more economical. It is intimately associated with the scan conversion of polygon edges to pixels line-by-line without needing a full 2D z-buffer. Spanning scan line z-buffering is highly optimized to extract visible object(s) from all structures that intersect the screen line that is currently being drawn. Modern graphics hardware can encompass intensity, z-buffer, and α-planes to program all of the computations described above into the display logic, releasing the processor for other computations.

Local Projections

The compositing functions described above can be used in combination for more control over the rendered objects. A conflict exists between hidden-object removal and significantly modifying the image intensities (by excessive use of α factors and lighting terms). A novel solution is implemented in the Lasersharp visualization program: the trick is to use coordinate or z-buffer algorithms to derive a segmentation reference (R_z) for projected pixels in the final view. R_z defines the z-coordinate of a surface [e.g., by maximum intensity (Eq. 24)] or boundary [e.g., by maximum height above threshold (Eq. 25)], etc. R_z (for each view pixel) can then become the center for a z-banded or **local projection**. This technique is another example of an intelligent z-buffer. The range of the local projection is defined by z_{front} and z_{back} given as z-offsets from the reference. Useful local projections include:

(1) **Reference Height Above Threshold + Local Maximum Intensity**, e.g., **Maximum Height ≥ t (Reference)**.

if $\{[I(x_v, y_v, z_v)_{n-1} > t] \;\&\; [(z_{n-1}) < (z_n)]\}$ then $R_z(x_v, y_v) = z_n$

followed by

Local maximum intensity

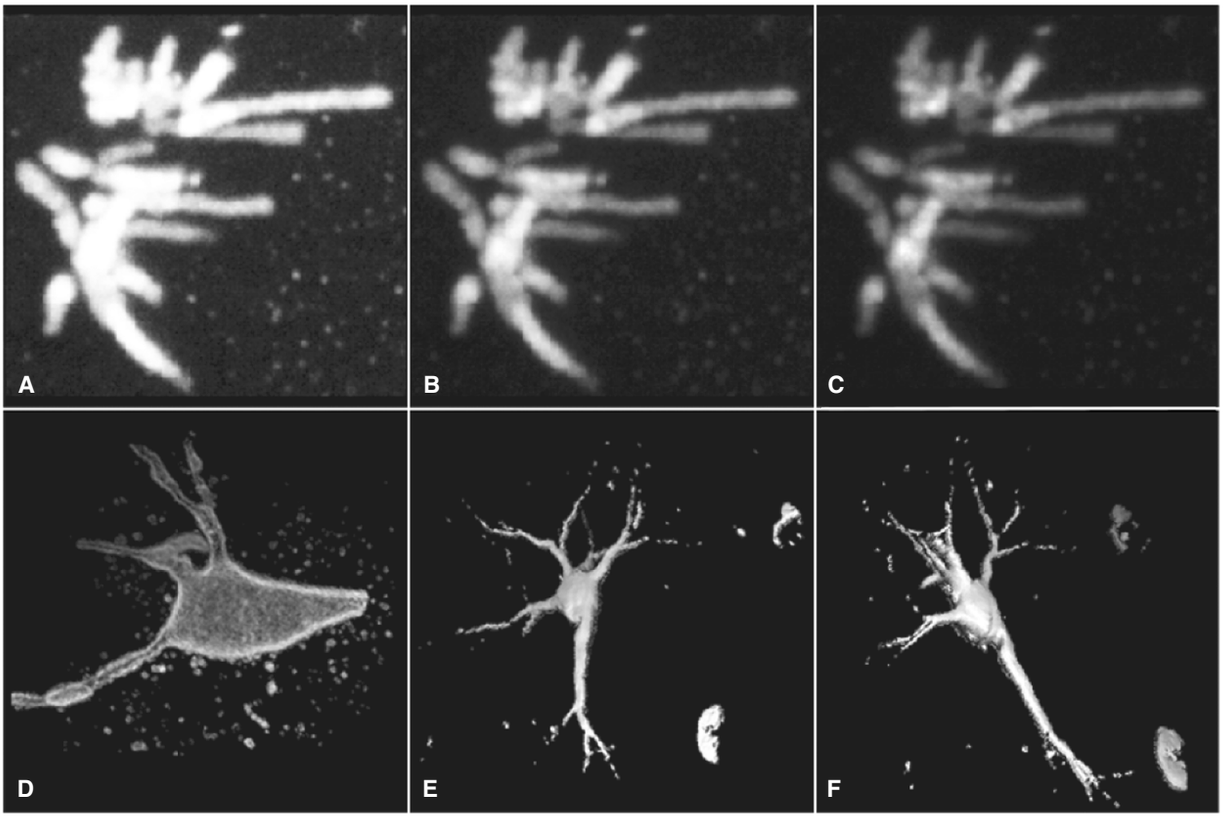


FIGURE 14.16. Depth weighting. (A–C) MPL "non-linear average" depth-weighted projections (see text) with "strengths" of 1 (A), 3 (B) and 9 (C) (number of sections = 50). MicroVoxel "depth-weighted" views (D) summation (average), (E,F) "first mode" renderings of nerve cells.

if $[I(x_v, y_v, z_r) \geq V(x_v, y_v, z_{r-1})]$ then $V(x_v, y_v) = I(x_v, y_v, z_r)$

where $[R_z(x_v, y_v) + z_{front}] \geq z_r \leq [R_z(x_v, y_v) + z_{back}]$, (i.e., the local range).

Similarly one might use

(2) **Height at Maximum Intensity + Local Kalman Average.**

(3) **Height at First Intensity $\geq t_1$ + Offset Local Height at Intensity $\geq t_2$**

e.g., with $z_{front} < z_{back} < R_z(x_v, y_v)$.

(4) **Height at Maximum Intensity + Offset Local Maximum Intensity**

e.g., with $z_{back} > z_{front} > R_z(x_v, y_v)$.

Local projections 3 and 4 use a range that is offset from, that is, does not span, R_z. This is an objective way to segment a second object or surface within a given range of a more dominant primary feature (which is used for the reference). Thus, a plant cell wall or animal cell membrane may be found by a reference segmentation, and then structures within z_{front} voxels outside or z_{back} voxels inside the cell can then be projected in isolation. Comparative results of some local projections from Lasersharp are shown in Figure 14.17.

Adding Realism to the View

The algorithms discussed so far use test and compositing rules to project multi-dimensional images into the view space. Views of macroscopic objects contain depth cues (similar to those described above) along with textural cues arising from the position and properties of light sources. These can be used to add realism to reconstructed views in microscopy by (1) mimicking artificial macroscopic lighting effects or (2) developing a more objective visualization model incorporating *a priori* knowledge concerning the optical properties of the sample. Advanced algorithm options are listed in Table 14.9 and described in Figures 14.18, 14.19, 14.21, and 14.22 with example results in Figures 14.17 and 14.20.

Artificial Lighting: Reflection Models

The ambient lighting of the model assumed above has no directional components. Artificial lights have intensity (photometric), directionality (geometric), and color (chromatic) properties. These characteristics interact with the material properties of data objects to modulate the rendering process. Local lights are near or within the data volume and infinity sources are parallel rays coming from infinity. Ambient lighting is a general level diffused by multiple reflections off all objects within the volume, as distinct from light coming direct from the source to a given object. Reflections from

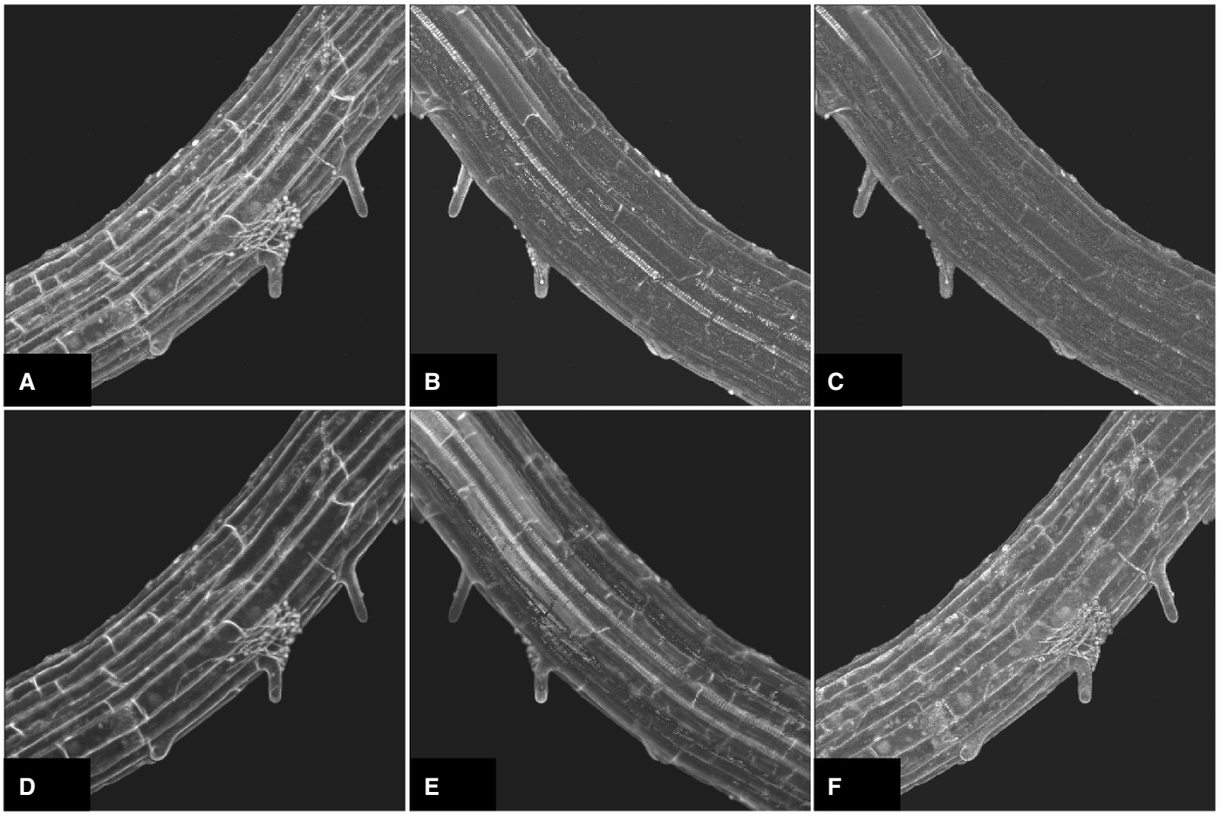


FIGURE 14.17. Local projections. These 3D views are made from the same data set shown in Figure 14.14. (A,B) show local projections where the maximum intensity is found through about one third of the depth of the sample above and below each voxel found by a previous application of the "above threshold" rule. (A) is from above and (B) below. (C,F) show the same operations applied through a depth of about one tenth of the sample thickness from the reference voxel. More structures towards the outer surface of the root are apparent compared to regular maximum projections, masking underlying features. (D,E) are local average projections corresponding to (A,B). Normalizing these intensities to fit the dynamic range of the display leads to lower contrast views than in (A,B) but shows some weak thiol-staining more clearly against the vascular autofluorescence. These views are more amenable to direct quantification than z or b.

an object (Fig. 14.18) can be approximated by a function (L) composed of (1) ambient reflections (L_a), (2) diffuse reflections (L_d), and (3) specular highlights (L_s) (strongest in the source direction).

$$L = L_a + (L_d + L_s)/(z_{obj} + \text{constant}) \quad \textbf{(31)}$$

where z_{obj} is the distance (in z_v of the object from the observer).

The denominator in Eq. 19 is an approximation to the z_v^2 denominator from the diffuse reflection law of Lambert (Born and Wolf, 1991, p. 183) for cases where z_{obs} is large compared to the object size. Each component L_m is the product of the light source intensity S_m, reflectivity R_m (a material property), and a direction term D_m (m = a, d, or s). The color of a voxel is determined by the

TABLE 14.9. Overview of "Realistic" Visualization Techniques for Multi-Dimensional Biological Microscopy Data

Feature	Parameter	Minimum Required	Desirable additional enhancements
[a]Visualization models		Voxel render	Shaded surface, Voxel gradient. Lighting models, SFP, Embedded objects
Material properties	color	RGB channels	Arbitrary colors/channels
	opacity		α-channel, channel dependent
	reflection		Diffuse, Specular ("shiny"), Interactive control
			Hardware texture mapping
	emission	Simulated fluor.	
	Hidden-objects	Software z-buffer	Hardware z-buffer
Surface shading models			Flat, Incremental, Gourard, Phong model
Artificial lighting	Color	RGB	Arbitrary colors & sources
	Lightable objects	Voxels	Voxels, Surface normal
	Lighting models	Ambient/diffuse (brightness)	Voxel gradient, Smoothed voxel "surface," Phong surface normal, Fast mode, Precision mode

[a]Realistic visualization modes are often used to promote particular packages, and **often with carefully chosen data!** Control of the object material properties and a clear understanding of each parameter are essential. The final reconstructed view should always be studied along with a record of all the steps and variables and preferably alongside the original image sections.
[b]Material properties and artificial lighting should be standardized for each view if intensity information is to be reliably compared between results (particularly for SFP and gradient-lit voxel modes). Hardware acceleration has made possible more interactive 3D views and "real-time" processing of modest data sets on desktop PCs.

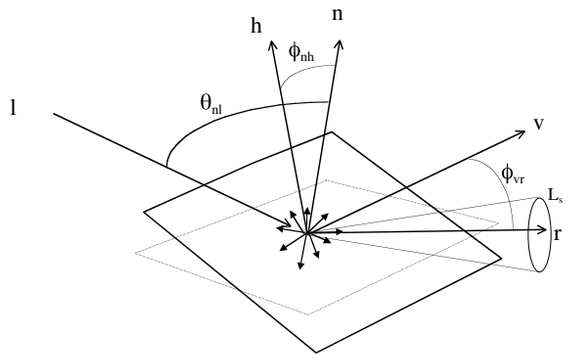


FIGURE 14.18. The artificial lighting model. Ambient lighting contributes only to the overall image brightness and has no directional components. An artificial light source is directed along l with parallel rays. Diffuse reflections from the object surface (solid panel) emanate in all directions (L_d). Some of L_d may be seen by the viewer along v. Specular reflections (L_s) occur in a narrow cone around the "reflection" direction r (θ_{nl} away from the surface normal n). These are observed along v if ϕ_{vr} is small enough. The width of the cone depends on the shininess term (see text). The Phong model describes this geometry in terms of ϕ_{vr} and θ_{nl}. Blinn showed that only ϕ_{nh} (between the surface normal and a theoretical plane, shaded, that would reflect all light from l to v) was needed for parallel lighting and a stationary observer.

light emanating from it. In general, colors are differentially reflected, absorbed, and fluorescently emitted (see below). The reflection components (Fig. 14.18) are

$$L_a = S_a\, R_a D_a \qquad \textbf{(32)}$$

where S_a is the ambient light level (constant), R_a is the diffuse reflectivity, and D_a equals 1.

$$L_d = S_d\, R_d D_d \qquad \textbf{(33)}$$

where S_d is the source intensity, R_d is the diffuse reflectivity, and D_d is $\cos\theta_{nl}$

$$L_s = S_s\, R_s D_s \qquad \textbf{(34)}$$

where S_s is the source intensity, R_s is the specular reflectivity, and D_s is $\cos^{sh}\varphi_{vr}$

where θ_{nl} is the angle between the local object surface normal and the light source direction; φ_{vr} is the angle between the reflection angle (center of the highlight) and the viewing angle; and sh is the shininess parameter, which for a perfect mirror is infinite.

This full form is the Phong model (Phong, 1975) and ignores secondary reflections (i.e., is a local approximation).

A global version requires multiple rays to be followed through many reflections. This is known as ray-tracing (as distinct from ray-casting often used for voxel projection methods) or photorealistic rendering (Kriete and Pepping, 1992) and is very computationally intensive. Ray-tracing applies reflection rules to rays from the source as they bounce from surface to surface within the volume. In practice, tracing is limited to rays seen by the viewer and the depth or number of surfaces considered is also restricted. The best implementations use an adaptive depth method varied according to local material properties (Watt, 1989). In the Phong model, as the shininess factor increases, the highlight sharpens and can be seen through a smaller angle (φ_{vr}) around the reflection angle ($2*\theta_{nl}$ away from the light source, i.e., on the other side of the surface normal). The Phong model is thus a simple, local approximation in terms of the light source direction, surface normal, material properties, and the viewing angle.

The computation can be simplified. For a light source at infinity, the viewing and lighting angles are constant over the volume. φ can then be expressed as the angle (φ_{nh}) between the surface normal (n) and the normal to a hypothetical surface (h) that would reflect all light to the viewer (Blinn, 1977). Then $\varphi_{nh} = \varphi_{vr}/2$ so larger values of sh are needed. These approximations mean that only the surface normal changes during rotations. A fast-lighting look-up table (L-LUT) can be used to precalculate the reflection terms and the surface normal used to index the L-LUT. Moving lights are also easy to implement because a static view has constant surface normals. Finally, the Phong model gives rise to (1) diffuse reflections that are the same color as the material, (2) specular highlights the same color as the light source, and (3) if the (z_{obj} + constant) term is ignored, flat surfaces (e.g., facets of a polygonal net) exhibit no shading variations. The RGB version of the Phong/Blinn model uses separate coefficients for each primary color

$$L\,(r,g,b) = S_a\, R_a\,(r,g,b) + S_d\,(R_d\,(r,g,b)\cos\theta_{nl} + R_s\cos^{sh}\varphi_{nh}) / (z_{obj} + \text{constant})_{optional} \qquad \textbf{(35)}$$

This is the usual tri-color space model. More subtle effects are obtained by using more than three channels. Imaris is a good example of a package with flexible lighting and materials properties options that include ambient, diffuse, and specular reflection colors and light emission characteristics (see also discussion of absorption and emission below).

Enhancing the Phong and Blinn Models

Criticisms of the basic reflection scheme include rather flat surfaces and an artifact at the polygon edges where the intensity changes rapidly. The eye overreacts because it is so well adapted to detect edges by the brightness second derivative. A thin bright Mach band is seen (Watt, 1989) and the rendered view has a synthetic appearance. Incremental surface shading is then required (Figs. 14.19, 14.20). Techniques are available to minimize these and similar artifacts, seen as stripes on many reconstructions (Amira uses surface smoothing and simplification, Cedara uses intelligent opacity to reduce Mach bands).

Gourard Shading

Incremental shading gives flat surfaces variable intensities by interpolation between the material properties at the vertices. Gourard shading (Gourard, 1971) applies bilinear in-plane interpolation between the (lit) vertex intensities. This gives a gradual change across each facet with a reduction, but not elimination, of Mach bands. Often only diffuse reflections are used because highlights not seen at the vertices cannot be reconstructed in the facet. Diffuse reflection is found in Eq. 33 for each vertex. The average surface normal for facets sharing each vertex is used to get θ_{nl}. Local vertex intensities are derived from Eq. 35. Line-by-line bilinear interpolation is then used (during the scan conversion) to vary intensity over the polygon. Gourard shading thus gives some smoothing, but with (1) residual Mach banding, (2) some artifactual loss of fine relief, and (3) discontinuities between animations of rotation sequences. Surface-shaded views are shown in Figure 14.20.

Phong Shading

Instead of using vertex intensities, Phong introduced the bilinear interpolation of vertex normals (Phong and Crow, 1975). Intensities are generated incrementally as before, but now include a spec-

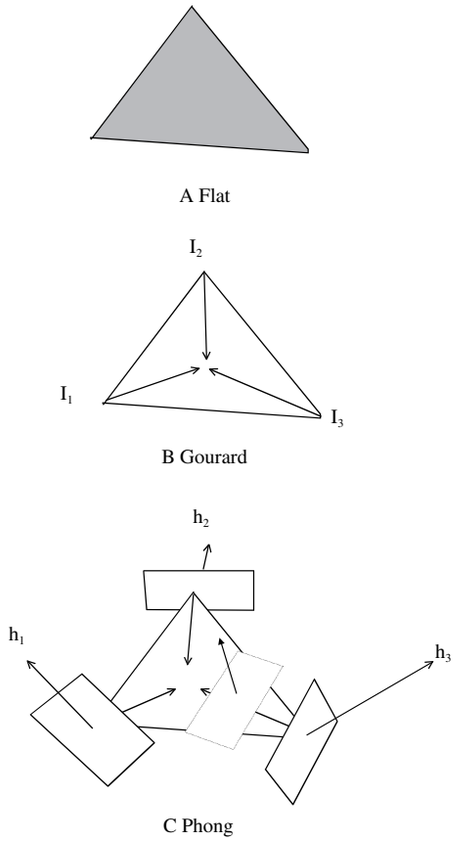


FIGURE 14.19. Incremental surface shading models. Once segmented from the voxel array, geometric objects (constructed from polygons) must be rendered to a "smooth" surface. Incremental shading is used to "fill in" the polygon areas. Flat shading (A) applies a single value (intensity, color, etc.) to the whole facet. This gives very matte views with Mach banding (see text) between facets. Gourard shading (B) interpolates the average intensity and color values (I_n) at the apices across the facet. This appears to "smooth" the surface, but still gives bands, disjointed rotations and inaccurate specular highlights. Phong shading (C) interpolates the surface normal (h_n) between the average values at each vertex across the facet. This can introduce highlights in the facet center as well as appearing to "round off" the abrupt edges and restoring the impression of a smoothly curved surface.

ular term at each point (instead of the optional Gourard single term for the whole facet). Thus, highlights within each face can now be generated, even if none was apparent at any vertex. Light sources are still at infinity so only the surface normal varies, but now within each facet. Thus, Phong interpolation tends to restore the curvature lost when a polygonal surface is approximated during segmentation or iso-surface coding. Phong interpolation can be speeded up with Gourard-type averaging in subregions of each face. A better efficiency return is to be gained by using the H-test (Watt, 1989) that decides which facets require a highlight and thus Phong shading. The rest are Gourard shaded with no quality loss. All packages that render graphical objects use surface shading with lighting and, perhaps, material properties. The user should carefully determine which modes are being used for any given rendering in order to correctly interpret the sophisticated views obtained.

Advanced Reflection Models

Although the Phong model attempts to mimic diffuse reflection by Lambert's law, the $\cos^{sh}\Phi$ specular terms are still empirically derived. Cook and Torrance (1982) modeled reflections, with advanced specular terms, using a physical model of incident light energy. The specular term is derived for micro facets within a locally averaged surface. Detailed surface models were also developed by Blinn (1977) and Torrance and Sparrow (1967). Cook and Torrance resolved the specular term into wavelength-dependent components using material refraction and the Fresnel equations (see Born and Wolf, 1991), thus modeling dispersion. Local and extended light sources have been simulated by Warn (1983) and others. Such advances produce smaller and smaller returns for the microscopist seeking to objectively render confocal images. The computational expense of even more sophisticated reflection models is rarely justified because the fine-tuning of relevant material properties cannot be reliably accomplished for biological specimens.

Gradient Lighting Models for Voxel Objects

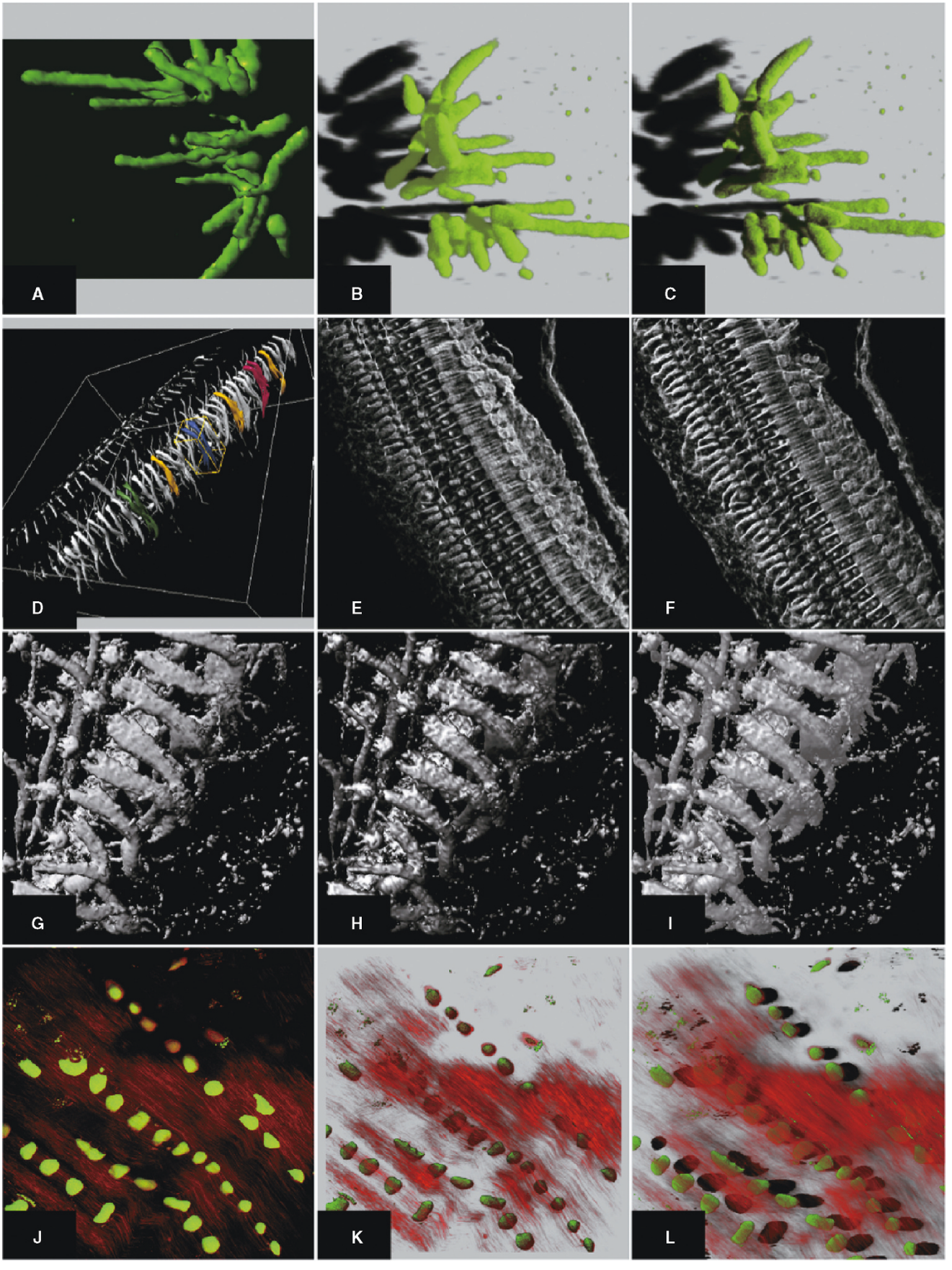
A surface normal is used for all reflective lighting models. Local topology must, therefore, be accurately determined. For rastered voxel data, the computations are greater in number and more prone to noise, etc. Fluorescence CLSM images suffer particularly from low signal-to-noise ratio (Sheppard *et al.*, 1992) and must therefore always be carefully filtered and/or PSF-deconvolved before gradient segmentation or lighting algorithms are applied. Gradient filters for edge and surface segmentation (Eq. 15) are often also used to highlight boundaries for voxel gradient lighting models (Fig. 14.20; see also Forsgren *et al.*, 1990; Odgaard, 1990). An alternative to these expensive 3D filters is to use a height or *zx*-coordinate view $z_{co}(x_v, y_v, z_v)$ (Eqs. 24–26). Surface normals can be derived from a local gradient in z_{co} in 2D V space (Gordon and Reynolds, 1985; Aslund *et al.*, 1988). This is the basis for post-lighting models (Fig. 14.21), which apply the lighting algorithm to a 2D *z*-buffer after the data projection stage (c.f., VoxBlast).

$$\text{grad}(x_v, y_v) = | \, [(dz_{co}/dx_v)^2 + (dz_{co}/dy_v)^2 + 1] = | \, \{[z_{co}(x_v + 1) - z_{co}(x_{v-} 1)]^2 + [z_{co}(y_v + 1) - z_{co}(y_{v-1})]^2 \} / 2 \quad \textbf{(36)}$$

The quantization of depth in z_{co} can give rise to artifactual edge effects, so at least 10- and preferably 16-bits of *z*-buffer are desirable. In both this and the 3D filters, steep gradients cannot be distinguished easily from discontinuities.

Artificial Lighting: Absorption and Transparency

Transparency can be modeled by an attenuation coefficient applied to each object. This can: (1) modify the light emanating towards the viewer (emission), (2) attenuate artificial light as it passes from the source through the data volume (illumination or excitation), and (3) modify the light emanating from an object that contributes to the lighting of another. Ray-tracing is required to properly implement (3). The first process (1) is the most often encountered in visualization programs. All objects are evenly lit by the ambient light, which does not include attenuation by nearby objects. Each object brightness is seen by the observer according to its opacity/transparency. This is achieved by α-blending (Eq. 22) with an α value derived by using the object intensity as an index into an opacity/transparency look-up table (OT-LUTs). By using the back-to-front projection, the combined opacity of all other objects through which the imaginary rays pass is taken into account.


A
B
C
D
E
F
G
H
I
J
K
L

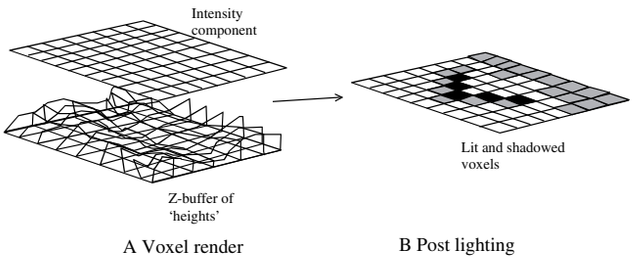


FIGURE 14.21. Post lighting is a rapid way of interactively applying lighting models to pre-rendered views. The z_v information is retained during the voxel intensity render in the z-buffer as a "height" view (A). If an iso-intensity surface is defined or a constant segmentation threshold used the intensity view may show little or no detail [upper part of (A)]. Local relief in the z-buffer is interrogated to produce a map of surface normals that are used as pointers into a fast lighting L-LUT (see text). These lighting terms are used to highlight and shadow the rendered voxels (B).

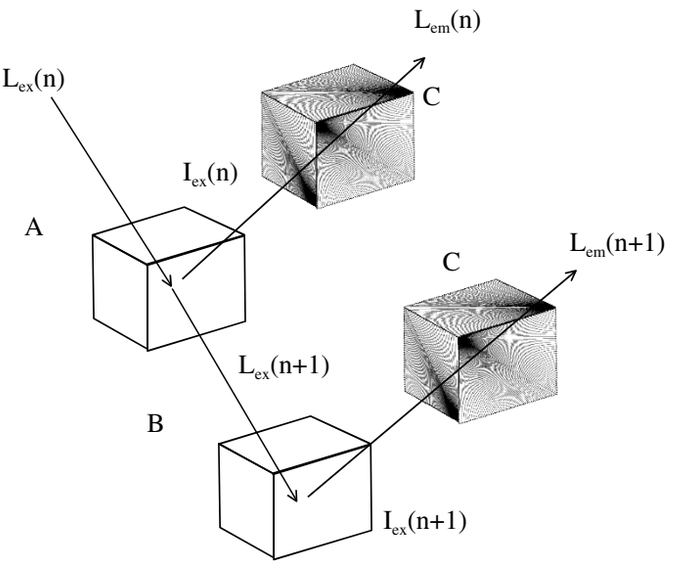


FIGURE 14.22. The simulated fluorescence process (SFP) algorithm (see also Fig. 14.20) attempts to simulate the excitation and emission from fluorescent features. Excitation light L_{ex} excites voxels in successive planes (n, n+1, etc.). Each illuminated voxel (I_{ex}) emits fluorescence (L_{em}) in all directions. Some of L_{em} is seen by the viewer. Excitation light not absorbed by the voxels in plane n (A) excites regions in plane n+1 (B), etc. Similarly, emitted light from each plane passes through other voxels (C) as it travels out of the volume. Absorption of L_{em} thus follows, but re-excitation by L_{em} is usually ignored. Separate absorption co-efficients for L_{ex} and L_{em} are used for selective control of transparency (see text).

Opaque objects at the front of the volume hide those at the back. The OT-LUT may have separate partitions for different structures within a single volume. Kay and Greenberg (1979) used the z_v component of the surface normal to attenuate rays traversing polygons. For voxel objects, the average opacity at each voxel is sufficient. This basic attenuation produces no lateral shading or shadowing.

The excitation part of the model (Eq. 2) is used to simulate the attenuation of illumination between a source at infinity and data objects. An excitation source is positioned at infinity with direction $L = (L_x, L_y, 1)$. This light illuminates the rotated image $I(x_v, y_v, z_v)$ by a plane wavefront normal to L passing through the volume. This wavefront intersects with the volume in serial (oblique) planes. Voxels cut by the nth plane during the excitation phase are given by

$$I(x_{ex}, y_{ex}, n) = I(x_v + L_x n, y_v + L_y n, n) \quad \textbf{(37)}$$

The components of the lighting vector can be made integers to speed up computations. As the excitation wave propagates through the volume, it is attenuated by preceding layers of objects according to an excitation extinction coefficient α_{ex}. Usually the object (or voxel, etc.) intensity is used to represent the amount of absorbing material at each position (α can be varied by an OT-LUT). The excitation wavefront at the nth plane is now

$$L_{ex}(x_{ex}, y_{ex}, n) = L_{ex}(x_{ex}, y_{ex}, n-1)(1 - \alpha_{ex})\, I(x_{ex}, y_{ex}, n) \quad \textbf{(38)}$$

A lit or excited image volume I_{ex} can then be constructed

$$I_{ex}(x_{ex}, y_{ex}, n) = I(x_{ex}, y_{ex}, n)\, L_{ex}(x_{ex}, y_{ex}, n) \quad \textbf{(39)}$$

This illuminated volume could be plugged directly into the reflection model. Alternatively, one can simulate the light emitted by each object as if it was self-luminous or fluorescent (Fig. 14.22). The simulated fluorescence process (SFP) has been refined by a number of workers (e.g., van der Voort *et al.*, 1989; Brakenhoff *et al.*, 1990; Hallgren and Buchholz, 1992; Messerli *et al.*, 1993). Excitation and emission phases are implemented as before. The

FIGURE 14.20. "Realistic" views by surface shading, gradient voxel and other lighting effects. (A) shows a Gourard-shaded geometric object surface rendering of one set of chromosomes from the plant *Milium* (Bennet *et al.*, 1990), using the Geometry render module of the AVS package. (See also Levoy 1988; Rigaut *et al.*, 1992, for Gourard-shaded reconstructions using the Visilog software). Since the segmented geometric polygons are very numerous but small, Mach band effects (see text) and the corruption of reflection highlights are not obvious, though the views have a certain "plastic" or "synthetic" look. (B–J, and L) are produced by the Imaris software. (B,C) show the same confocal data as (A) visualized using a simulated fluorescence process (SFP) voxel-based algorithm. Directional lighting (and resultant shadows) can be controlled independently from the ambient lighting (similar to a fluorescence emission property) to achieve stronger shadows (C) or a more "luminous" fluorescence (B). (D) shows the use of segmented objects and artificial colors to highlight individual or pairs of hair cells in this reconstruction of confocal data (courtesy of Bio-Rad Microscience) from a mouse inner ear preparation. (E, F) show voxel gradient lighting applied from the left and right respectively to a top-down reconstruction of the same data as (D). Combining object segmentation, surface shading and a Phong lighting model allows a material property defining reflectance to be attributed to structures. (G) shows a selected portion of the inner ear data surface rendered with a diffuse lighting model only. (H) shows a specular (highlight) lighting model and (J) combines the specular model with an ambient model rather like the SFP algorithms. (J) shows a two-channel fluorescence data set obtained by multi-photon LSM through rat intervertebral disk tissue (in consultation with Dr. R.J. Errington, Cardiff University, UK) and shows CMFDA-stained chondrocytes and autofluorescent extracellular matrix (mostly collagen) (Metamorph software). (K) shows the same data by a combination of surface-shaded object rendering (of the cells) and voxel-based rendering (of the ECM) with some directional lighting and careful application of transparency to render the tissue transparent. (L) shows the same data visualized by the SFP algorithm, exhibiting the characteristic shadows that are an optional feature of this method.

emitted light propagates to the viewer in a direction described by the vector (v) where

$$v = (v_x, v_y, 1) \quad \textbf{(40)}$$

The emitted light wavefront L_{em} is then found by:

$$L_{em}(x_v, y_v, n-1) = I_{em}(x_v, y_v, n-1) + L_{em}(x_v, y_v, n) [1 - \alpha_{em}) I(x_v, y_v, n-1)\} \quad \textbf{(41)}$$

where $I_{em}(x_v, y_v, n) = I_{ex}(x_v, y_v, n) A(x_v, y_v, n)$.

A is an empirical term encompassing the quantum efficiency and emissivity of the object. (This may be set to unity, i.e., determined solely by α_{ex}.) α_{em} is the opacity (or OT-LUT) for the emission wavelength. The emission computation is carried out in the reverse *n* order compared to excitation. A consequence of this absorption/emission model is the casting of shadows by the two waves as they pass densely absorbing structures. These shadows may fall onto the background or onto underlying structures. Coefficients should be implemented separately for each channel of a multichannel image. Opacity in one channel can then be used to modulate intensities in another, as in the Imaris and LCS (Leica) SFP mode. AVS uses a two-pass transparency operator to achieve a similar result.

HOW CAN I MAKE MEASUREMENTS USING THE RECONSTRUCTED VIEWS?

Direct measurements from image data can sometimes be automated (Cohen *et al.*, 1994; see also Chapter 15, *this volume*), but interactive 3D analysis often requires feedback from the volume reconstruction. Views are used in several ways during multi-dimensional measurements (a few examples are shown in Fig. 14.23).

(1) One or more sections may be displayed as a montage and their intersection with an interactive screen cursor used to pinpoint original image voxels in 3D. The image data can then be used to obtain a 3D intensity measurement. This gives the highest spatial and photometric reliability but cannot be used for complex structures that are not discernible from a few intersecting sections. The exception to this rule involves the use of stereological estimators to probe sections randomly oriented within the volume (e.g., see Analyze volume measuring tool). This is a particularly good method of estimating complex 3D measures such as surface area (e.g., Howard and Sandau, 1992) or orientation (Mattfeldt *et al.*, 1994). Other grid-sampling estimators (e.g., Gundersen *et al.*, 1988) have been implemented. The approach works best when an interactive cursor is tracked simultaneously in at least three different orthogonal cross-sections. Through-focus animations in all three directions are also useful aids in identifying structures passing through many planes. The orthogonal section display with cross-hair cursor is a standard element of most visualization programs. Some also allow oblique (arbitrary) sections to be displayed for measurements.

(2) A reconstructed view may be displayed to identify features to be measured (with animation, etc.) before interrogating the original image data for the precise values of each voxel. The problem remains of how to determine exactly which image data voxels are represented by a particular feature in the reconstruction. This stems from the fact that the third spatial (or temporal, etc.) dimension has been significantly reduced. The precise method of coding this reduced dimensional information determines how accurately original voxels may be retrieved. The method is most successful where high contrast objects have been efficiently segmented. An elegant solution is to embed a voxel section into a 3D rendered view so as to show both the reconstruction and the original data (see Amira, Analyze, Voxblast, Imaris, Volvis, and others for examples).

(3) A third method involves the direct measurement of reconstructed views. This is possible by improving the coding method used in (2). Parallax shifts are used effectively to measure depth in stereo views (Fig. 14.24). In practice, two cursors are moved in tandem through the left and right pairs of the stereoscopic space. Tandem movements of the two cursors sweep out x_v, y_v-coordinates. Z_v-distances are swept out by altering the separation of the two cursor components. An observer using the appropriate stereoscopic viewing aid will perceive the cursor to track in and out of the screen. This method is particularly useful for very transparent structures. Opaque objects are measured more easily by interrogating a *z*-coordinate or surface view. The *z*-value at each (x_v, y_v) pixel allows full 3D measurements to be made of the object's surface. Reconstructions from segmented objects defined by surfaces or *z*-coordinates almost always proceed via the generation of a *z*-buffer intermediate. This can be kept in memory while an intensity reconstruction is built up on the monitor. Visible features in the intensity view (which may be artificially lit, etc.), can return their *z*-position by interrogating the *z*-buffer (this technique is used efficiently by voxel renderers such as VoxBlast). Ten- to 16-bits of *z*-buffer are desirable. Line transects through the *z*-buffer return profile plots through a structure. Area measurements in the *z*-buffer return integrated heights that are equivalent to the volume under the surface. All these measures may be made alongside equivalent x_v, y_v and intensity plots (Fig. 14.23).

Geometric objects objectively segmented from the image volume for surface visualization can also report their total surface area (and also their included volume, e.g., Guilak, 1993). Because they are defined by polygons, many statistics of shape, asymmetry, etc., can be automatically recorded. Particle analysis software is now implemented in 3D (and 4D) to count segmented objects (most object-based systems) and even track them over time (e.g., Imaris, Volocity). A more extensive discussion of computerized measurements and multi-dimensional data can be found in the following chapter.

CONCLUSION

Visualization is not a precise science, but by understanding the functions of your display program, the user can derive useful objective information from views of multi-dimensional images. Image data collected from biological microscopes is necessarily complex and noisy, and it contains ill-defined structures with largely unknown photometric and geometric statistics. Step-by-step visualization algorithms of increasing sophistication must be applied in a controlled manner, with adequate parameter tracking and validation in order to have confidence that the final results portray real features. Quantitative measurement from multi-dimensional views adds additional constraints to the artificial properties that can be added to rendered views. Simple algorithms produce the fastest visualizations. Object-based reconstruction, though supported by a vast range of affordable, yet high specification graphics hardware, is critically dependent on the segmentation used to extract the vertex geometries from original 3D voxel data. Test samples and control data should always be processed in order to understand the significance of complex rendered views. Seeing should never be used as the sole criterion for believing.

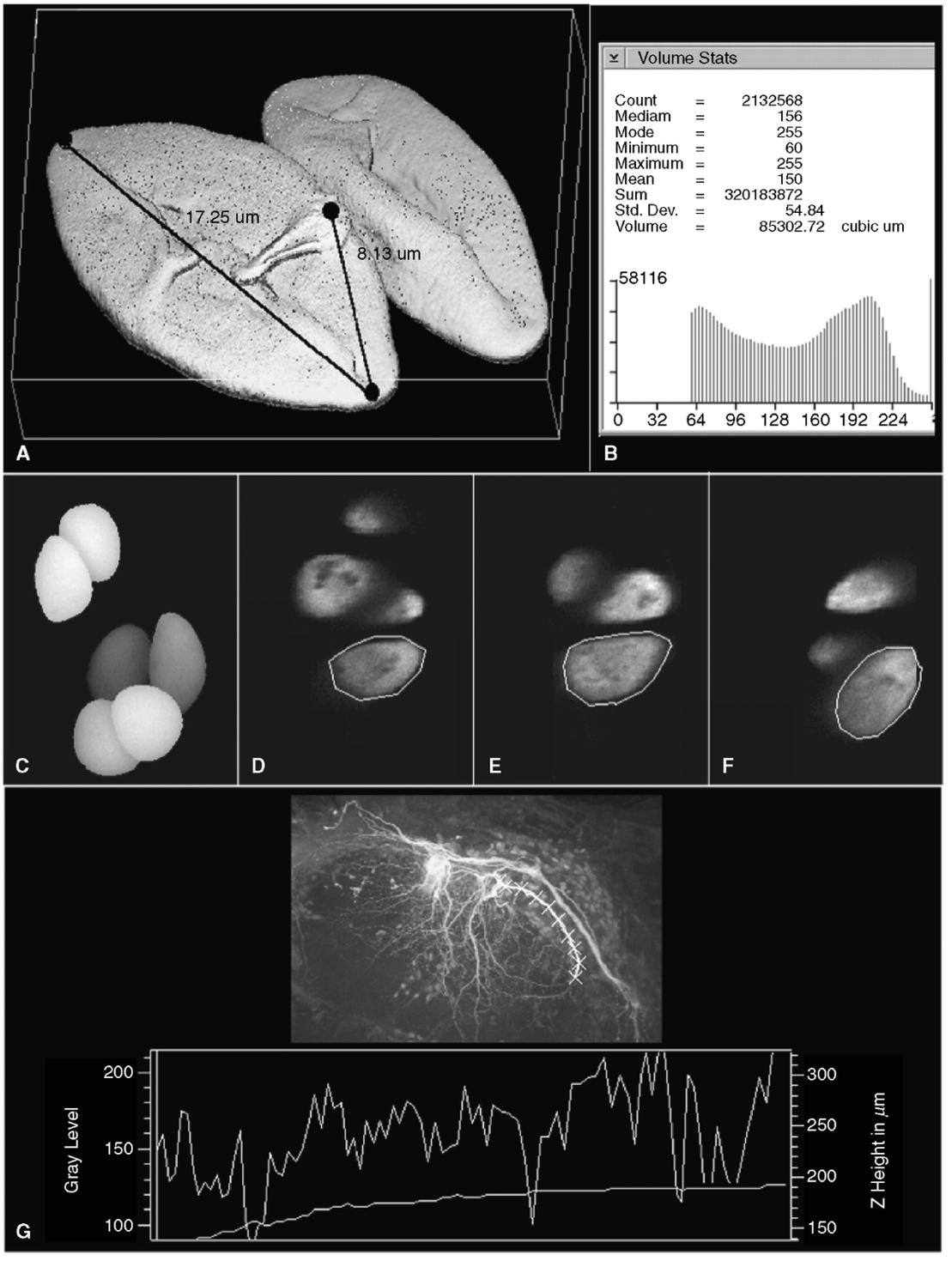


FIGURE 14.23. 3D Measurements on multiple sections and views. (A) shows the MicroVoxel "Caliper Tool" being used to make a distance measurement on a "First mode" rendered view of a pollen grain. (B) is a representative example of intensity statistics and 3D volume from a MicroVoxel volume measurement. (C–F) show ThruView PLUS views of living articular cartilage chondrocytes (data supplied by R.J. Errington, Physiology Dept., Oxford University) used for 3D measurements. (C) is a single time point from a 4D series of "height coded" views. Profiles and volumes of individual chondrocytes (here labeled with CMFDA) are derived directly from each reconstructed view. (D–F) show oblique sections through another data set with automatic serial "area" measurements being taken (using the MPL "area" verb in a macro program) of each segmented slice through a single cell. The corrected z-step applied to the integrated area sum gives a direct volume estimate. (G) shows the neurone of Figures 14.2 and 14.3, rendered using the MPL "maximum height" mode. MPL height modes automatically record both the z-coordinate (z-buffer) and the corresponding intensity view. Here the maximum intensity is shown in the inset gray-scale view with a cursor track along a prominent process. The corresponding intensity trace is shown in the upper plot and the z-depth in the lower trace.

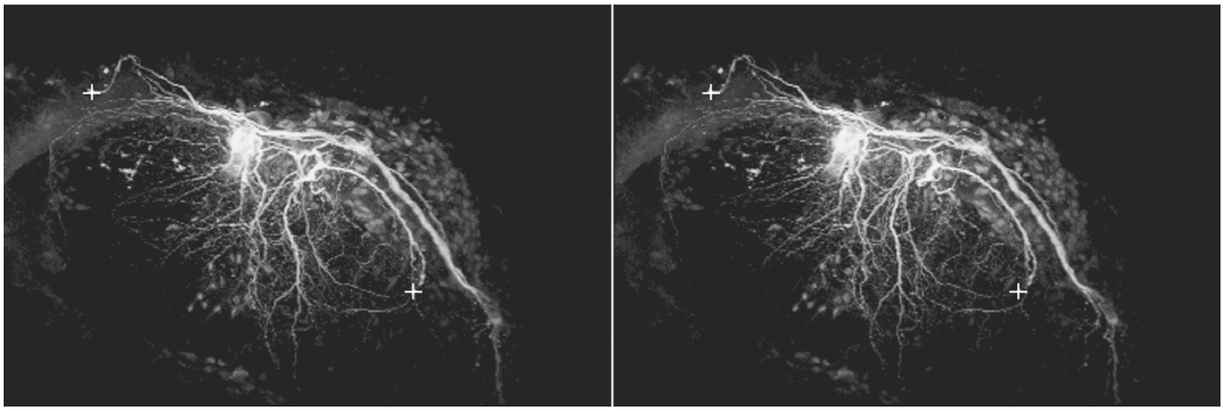


FIGURE 14.24. 3D Measurements using a stereoscopic cursor. Stereo pair of the Lucifer Yellow stained neuron also shown in Figures 14.2 and 14.3 showing the use of a pair of software-generated cursors with variable parallax shift between images to mark out *x*, *y* and *z* positions in the transparent reconstruction. These images were generated using MPL pixel-shifted maximum-intensity projections and the macro-programming language to generate the stereo cursors. On a fast '486 computer, these can be moved in and out along the *z*-direction interactively.

ACKNOWLEDGMENTS

I thank all contributors to the various sources of technical information (many of them Web accessible) for the packages listed in Table 14.1 and referred to throughout the text. Thanks also to all who provided images. The author would like to acknowledge the Wellcome Trust and the Sir William Dunn School of Pathology, University of Oxford, where he is Research Manager of the Bioimaging Service.

REFERENCES

Agard, D.A., Hiroaka, Y., Shaw, P., and Seadt, J.W., 1989, Microscopy in three dimensions, Methods Cell Biol., 30:353–377.

Aslund, N., Liljeborg, A. Forsgren, P.-O., and Wahlsten, S., 1988, 3D scanning reconstruction, *Laboratory Practice*, 37:58–61.

Bennet, S.T., Fricker, M.D., Bennet, M.D., and White, N.S., 1990, The 3D localisation of chromosomes using confocal microscopy, *Trans. Roy. Microscopic. Soc.* 1:441–444.

Blinn, J.F., 1977, Models of light reflection for computer synthesised pictures, *Computer Graphics* 11:192–198.

Bolsover, S., 1995, Using fluorescence to probe calcium signalling mechanisms. *Biochem. Soc. Trans.* 23(3):627–629. Review.

Born, M., and Wolf, E., 1991, *Principles of Optics*, Pergamon Press, Oxford.

Boyde, A., 1987, Colour coded stereo images from the tandem scanning reflected light microscope, *J. Microsc.* 146:137–145.

Boyde, A., 1992, Real time direct-view confocal light microscopy, In: *Electronic Light Microscopy* (D. Shotton, ed.), Wiley-Liss, New York, pp. 289–314.

Braddick, O.J., and Sleigh, A.C., 1983, *Physical and Biological Processing of Images*, Springer-Verlag, Berlin.

Brakenhoff, G.J., Van der Voort, H.T.M., and Oud, J.L., 1990, Three-dimensional representation in confocal microscopy, In: *Confocal Microscopy* (T. Wilson, ed.), Academic Press, London, pp. 185–197.

Carlsson, K., 1991, The influence of specimen refractive index, detector signal integration and non-uniform scan speed on the imaging properties in confocal microscopy, *J. Microsc.* 163:167–178.

Cabral, B., Cam, N., and Foran, J., 1994, Accelerated volume rendering and tomographic reconstruction using texture mapping hardware. In: *Symposium on Volume Visualization* (Kaufman and Krueger, eds.), ACM Press, New York, pp. 91–98.

Cheng, P.C., Acharya, R., Lin, T.H., Samarabandu, G., Shinozaki, D.D., Berezney, R., Meng, C., Tarng, W.H., Liou, W.S., Tan, T.C., Summers, R.G., Kuang, H., and Musial, C., 1992, 3D Image analysis and visualisation in light microscopy and X-ray micro-tomography, In: *Visualisation in Miomedical Microscopies* (A. Kriete, ed.), VCH, Weinhein, Germany.

Cohen, A.R., Roysam, B., and Turner, J.N., 1994, Automated tracing and volume measurements of neurons from 3D confocal fluorescence microscopy data, *J. Microsc.* 173:103–114.

Cook, R.L., and Torrance, K.E., 1982, A reflectance model for computer graphics, *Computer Graphics* 15:307–316.

Cookson, M.J., 1994, Three dimensional reconstruction in microscopy, *Proc. RMS* 29:3–10.

Cookson, M.J., Davies, C.J., Entwistle, A., and Whimster, W.F., 1993, The microanatomy of the alveolar duct of the human lung imaged by confocal microscopy and visualised with computer based 3D reconstruction, *Comput. Med. Imaging Graphics* 17:201–210.

Cookson, M.J., Dykes, E., Holman, J.G., and Gray, A., 1989, A microcomputer based system for generating realistic 3D shaded images reconstructed from serial section, *Eur. J. Cell Biol.* 48(Suppl 25):69–72.

Drebin, R.A., Carpenter, L., and Hanrahan, P., 1988, Volume rendering, *Computer Graphics* 22:65–74.

Elisa, A., Schmidt, F., Gattass, M., and Carvalho, P.C.P., 2000, Combined 3-D visualization of volume data and polygonal models using a shear-Warp algorithm, *Computer Graphics* 24:583–601.

Fahle, M., and de Luca, E., 1994, Spatio-temporal interpolation in depth, *Vision Res.* 34:343–348.

Forsgren, P.O., Franksson, O., and Liljeborg, A., 1990, Software and electronics for a digital 3D microscope, In: *Confocal Microscopy* (T. Wilson, ed.), Academic Press, London.

Freire, M., and Boyde, A., 1990, Study of Golgi-impregnated material using the confocal tandem scanning reflected light microscope, *J. Microsc.* 158:285–290.

Fricker, M.D., and White, N.S., 1992, Wavelength considerations in confocal microscopy of botanical specimens, *J. Microsc.* 166:29–42.

Frisby, J.P., and Pollard, S.B., 1991, Computational issues in solving the stereo correspondence problem, In: *Computational Models of Visual Processing* (M.S. Landy and J.A. Movshon, eds.), MIT Press, Cambridge, Massachusetts, pp. 331–358.

Foley, J.D., van Dam, A., Feiner, S.K., and Hughes, J.F., 1990, *Computer Graphics: Principles and Practice*, 2nd ed., Addison Wesley Publishing Co., Reading, Massachusetts.

Gordon, D., and Reynolds, A., 1995, Image shading of 3-dimensional objects, *Computer Vision Graph. Image Proc.* 29:361–376.

Gouraud, H., 1971, Continuous shading of curved surfaces, *IEEE Trans. Comput.* 20:623–629.

Guilak, F., 1993, Volume and surface area measurement of viable chondrocytes *in situ* using geometric modelling of serial confocal sections, *J. Microsc.* 173:245–256.

Gundersen, H.J.G., Bagger, P., Bendtsen, T.F., Evans, S.M., Korbo, L., Marcussen N., 1998, The new stereological tools: dissector, fractionator, nucleator, and point sampled intercepts and their use in pathological research and diagnosis. *Acta. Pathol. Microbiol. Scand.* 96:857–881.

Hallgren, R.C., and Buchholz, C., 1992, Improved solid surface rendering with the simulated fluorescence process (SFP) algorithm, *J. Microsc.* 166: rp3–rp4.

He, T.L., Hong, L., Kaufman, A., and Pfister, H., 1996, Generation of transfer functions with stochastic search techniques, *Proc. IEEE Visualization* 489:227–234.

Hell, S., Reiner, G., Cremer, C., and Stelzer, H.K., 1993, Aberrations in confocal fluorescence microscopy induced by mismatches in refractive index, *J. Microsc.* 169:391–405.

Holmes, T.J., and Liu, Y.-H., 1992, Image restoration for 2D and 3D fluorescence microscopy, In: *Visualization in Biomedical Microscopies* (A. Kriete, ed.), VCH, Weinheim, Germany, pp. 283–327.

Howard, C.V., and Sandau, K., 1992, Measuring the surface area of a cell by the method of spatial grid with a CLSM-a demonstration, *J. Microsc.* 165:183–188.

Hudson, B., and Makin, M.J., 1970, The optimum tilt angle for electron stereomicroscopy, *J. Sci. Instr. (J. Phys. Eng.)* 3:311.

Kay, D.S., and Greenberg, D., 1979, Transparency for computer synthesised objects, *Computer Graphics* 13:158–164.

Kindlmann, G., and Durkin, J., 1998, Semi automatic generation of transfer function for direct volume rendering, *Proc. IEEE* 170:78–86.

Kriete, A., and Pepping, T., 1992, Volumetric data representations in microscopy: Application to confocal and NMR-microimaging, In: *Visualization in Biomedical Microscopies* (A. Kriete, ed.), VCH, Weinheim, Germany, pp. 329–360.

Landy, M.S., and Movshom, J.A., 1991, *Computational Models of Visual Processing*, MIT Press, Cambridge, Massachusetts.

Lacroute, P., and Levoy, M., 1994, Fast volume rendering using a shear-warp factorization of the viewing, *SIGGRAPH* 1994:451–458.

Lorensen, W.E., and Cline, H.E., 1987, Marching cubes, a high resolution 3D surface construction algorithm. *Computer Graphics* 21:163–169.

Levoy, M., 1988, Display of surfaces from volume data, *IEEE Computer Graphics Appl.* 8:29–37.

Masters, B., 1992, Confocal ocular microscopy: a new paradigm for ocular visualisation, In: *Visualization in Biomedical Microscopies* (A. Kriete, ed.), VCH, Weinheim, Germany, pp. 183–203.

Mattfeldt, T., Clarke, A., and Archenhold, G., 1994, Estimation of the directional disribution of spatial fibre processes using stereology and confocal scanning laser microscopy, *J. Microsc.* 173:87–101.

Marks, J., 1997, Design galleries: A general approach to setting parameters for computer graphics and animation, *SIGGRAPH* 1997:389–400.

Messerli, J.M., van der Voort, H.T.M., Rungger-Brandle, and Perriard, J.-C., 1993, Three dimensional visualisation of multi-channel volume data: The smSFP algorithm, *Cytometry* 14:723–735.

Murch, G.M., 1984, Physiological principles for the effective use of colour, *IEEE Computer Graphics Appl.* 4:49–54.

Nakayama, 1985, Biological image motion processing: A review, *Vision Res.* 25:625–660.

Odgaard, A., Andersen, K., Melsen, F., and Gundersen, H.J., 1990, A direct method for fast three-dimensional serial reconstruction, *J. Microsc.* 159:335–342.

Oldmixon, E.H., and Carlsson, K., 1993, Methods for large data volumes from confocal scanning laser microscopy of lung, *J. Microsc.* 170:221–228.

Perry, V.H., and Cowey, A., 1985, The ganglion cell and cone distributions in the monkey's retina: Implications for central magnification factors, *Vision Res.* 25:1795–1810.

Phong, B.-T., 1975, Illumination for computer generated pictures, *Commun. ACM* 18:311–317.

Phong, B.-T., and Crow, F.C, 1975, Improved rendition of polygonal models of curved surfaces, In: *Proceedings of the 2nd USA-Japan Computer Conference*, ACM Press, New York, pp. 475–480.

Poggio, G., and Poggio, T., 1984, The analysis of stereopsis, *Ann. Rev. Neuro.* 7:379–412.

Richards, W., 1970, Stereopsis and stereoblindness, *Exp. Brain Res.* 10:380–388.

Rigaut, J.P., Carvajal-Gonzalez, S., and Vassy, J., 1992, 3D Image cytometry, In: *Visualization in Biomedical Microscopies* (A. Kriete, ed.), VCH, Weinheim, Germany, pp. 205–248.

Robb, R.A., 1990, A software system for interactive and quantitative analysis of biomedical images, In: *3D Imaging in Medicine*, NATO ASI Series, Vol. F (K.H. Hohne, H. Fuchs, and S.M. Pizer, eds.) 60:333–361.

Sakas, G., Grimm, M., and Savopoulos, A., 1995, An optimized maximum intensity projection (MIP), In: *Rendering Techniques '95* (P. Hanrahan and W. Purgathofer, eds.), Springer-Verlag, New York, pp. 51–63.

Shaw, P.J., and Rawlins, D.J., 1991, The point-spread function of a confocal microscope: Its measurement and use in deconvolution of 3-D data, *J. Microsc.* 163:151–165.

Sheppard, C.J.R., and Gu, M., 1992, The significance of 3-D transfer functions in confocal scanning microscopy, *J. Microsc.* 165:377–390.

Sheppard, C.J.R., and Gu, M., 1993, Modeling of three-dimensional fluorescence images of muscle fibres: An application of three-dimensional optical transfer function, *J. Microsc.* 169:339–345.

Sheppard, C.J.R., Gu, M., and Roy, M., 1992, Signal-to noise ratio in confocal microscopy systems, *J. Microsc.* 168:209–218.

Shotton, D.M., and White, N.S., 1989, Confocal scanning microscopy; 3-D biological imaging, *Trends Biochem. Sci.* 14:435–439.

Torrance, K.E., and Sparrow, E.M., 1967, Theory for off-specular reflection from roughened surfaces. *Opt. Soc. Am.* 57:1105–1114.

Van der Voort, H.T.M., Brakenhoff, G.J., and Baarslag, M.W., 1989, Three-dimensional visualization methods for confocal microscopy, *J. Microsc.* 153:123–132.

Van Zandt, W.L., and Argiro, V.J., 1989, A new inlook on life, *UNIX Rev.* 7:52–57.

Visser, T.D., Oud, J.L., and Brakenhoff, G.J., 1992, Refractive index and axial distance measurements in 3-D microscopy, *Optik* 90:17–19.

Visser, T.D., Groen, F.C.A., and Brakenhoff, G.J., 1991, Absorption and scaterring correction in fluorescence confocal microscopy, *J. Microsc.* 163:189–200.

Wallen, P., Carlsson, K., and Mossberg, K., 1992, Confocal laser scanning microscopy as a tool for studying the 3-D morphology of nerve cells, In: *Visualization in Biomedical Microscopies* (A. Kriete, ed.), VCH, Weinheim, Germany, pp. 109–143.

Warn, D.R., 1983, Lighting controls for synthetic images, *Computer Graphics* 17:13–24.

Watt, A., 1989, *Three Dimensional Computer Graphics*, Addison Wesley, Wokingham, England.

Wilson, T., 1990, Confocal microscopy, In: *Confocal Microscopy* (T. Wilson, ed.), Academic Press, London, pp. 1–64.

Woo, M. (1992). *OpenGL Programming Guide*, Addison Wesley, Wokingham, England.

15

Automated Three-Dimensional Image Analysis Methods for Confocal Microscopy

Badrinath Roysam, Gang Lin, Muhammad-Amri Abdul-Karim, Omar Al-Kofahi, Khalid Al-Kofahi, William Shain, Donald H. Szarowski, and James N. Turner

INTRODUCTION

Image analysis is the process of making **quantitative** structural and functional measurements from an image. With the widespread availability of three-dimensional (3D) microscopy, coupled with a growing trend towards quantitative studies, there is an increasing need for 3D image analysis. The goal of this chapter is to describe 3D image analysis techniques, with an emphasis on highly automated methods.

Figure 15.1 shows two examples of 3D image analysis. In the first (top row), confocal microscopy is used to image cell nuclei from the rat hippocampus using a DNA stain, and the transcription products (mRNA) of an immediate early gene (*Arc*) are labeled by fluorescence *in situ* hybridization (FISH) (Guzowski *et al*., 1999; Guzowski and Worley, 2001; Vazdarjanova *et al*., 2002). The table on the right is a partial display of the results of the 3D image analysis. It consists of a table listing all the nuclei, their morphometric features, and the amount of FISH signal associated with each nucleus. The second example (lower row) illustrates 3D analysis of a dye-injected neuron imaged by confocal microscopy (So *et al*., 2000; Brown *et al*., 2001; Al-Kofahi *et al*., 2002; Jain *et al*., 2002). Various windows in this screen view are from a software system (Neuroexplorer, Microbrightfield, Inc.) that indicates automatically generated traces, branch points, and morphological measurements.

The motivation for 3D image analysis is to achieve correct morphometry of biological structures without the errors associated with projecting onto a two-dimensional (2D) plane. For example, it is difficult to distinguish overlapping objects from 2D projections, whereas 3D imaging provides richer segmentation cues. Many structures, such as neurons and vasculature, are often thicker than the depth-of-field of the microscope, necessitating 3D imaging and analysis. Often, non-planar regions are of interest. For such cases, optical sectioning via confocal microscopy better preserves 3D spatial relationships compared to physical sectioning, and can therefore lead to more accurate morphometry, and correct topological analysis. Finally, 3D imaging can often result in faster and more convenient sampling of tissue for large-scale studies.

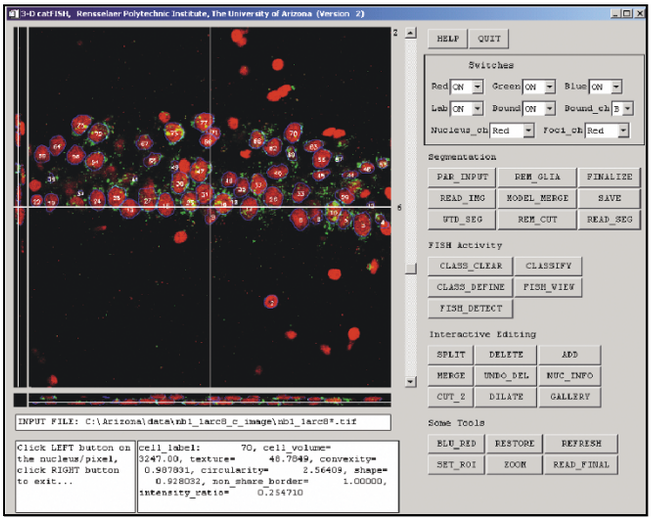
A particular emphasis of this chapter is *automated* 3D image analysis. This term is understood to imply that the amount of manual image analysis is minimal, typically in the 0% to 10% range. These methods are distinct from manual methods, whether or not computer assistance is involved. In other words, computer-assisted methods are not considered to be automated. For example, sophisticated software/hardware packages are available for tracing neuronal processes using a computer pointing device such as a tablet or mouse (Capowski, 1989; Glaser and Glaser, 1990). Often, these packages are enhanced with visualization tools such as stereo projections and devices such as the camera lucida (Glaser and Glaser, 1990; Marko and Leith, 1992). These are examples of computer-assisted, but not automated, image analysis. Computer-assisted methods are very appropriate when a small number of images need to be analyzed, or if the complexity of the scene is too high for successful automated analysis. On the other hand, there are software packages available that accept the 3D digital image file as input, and generate as output another computer file representing a tracing of the neuron (Al-Kofahi *et al*., 2002). This output may require modest amounts of oversight and/or editing. This latter type of software is appropriately termed automated and is needed when a large number of images must be analyzed.

Stereology is an important class of computer-assisted image analysis methods (Howard and Reed, 1998; Russ and DeHoff, 2000; Mouiton, 2002). In these methods, the manual observer performs a systematic subsampling of the image data using statistically motivated rules and assumptions. For example, it is assumed that the tissue of interest has certain uniformity properties. In contrast, the methods of interest in this chapter are designed to analyze *each and every* object in a given image, without assumptions.

Although manual image analysis methods are, in principle, far more powerful than automated methods, due to the inherent superiority of the human visual system over any algorithm, there are many reasons for seeking highly automated methods. While the human visual observer excels at pattern recognition/classification tasks, s/he is often poor at detailed scoring tasks. It is common for the human observer to miss objects, score objects twice, and produce unsteady traces (Jaeger, 2000; Al-Kofahi *et al*., 2002). Indeed, it is common for the same observer to produce different

Badrinath Roysam, Gang Lin, Muhammad-Amri Abdul-Karim, Omar Al-Kofahi, Khalid Al-Kofahi • Rensselaer Polytechnic Institute, Troy, New York 12180
William Shain, Donald H. Szarowski, James N. Turner • New York State Department of Health, Albany, New York 12201

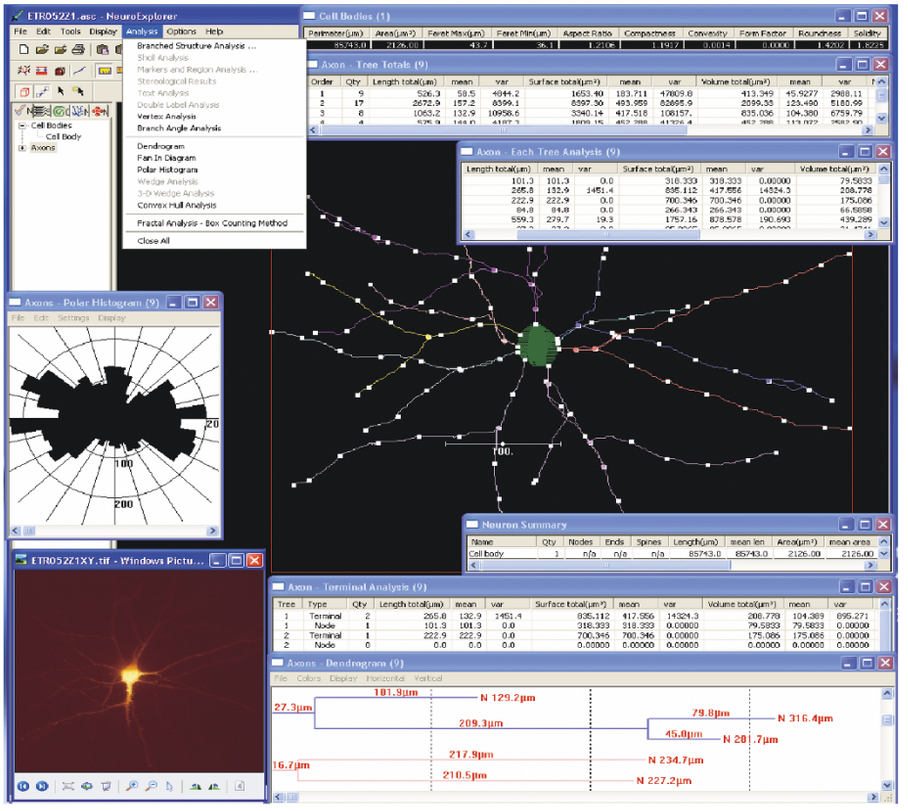
 Handbook of Biological Confocal Microscopy, Third Edition, edited by James B. Pawley, Springer Science+Business Media, LLC, New York, 2006.



A

Nuclei					Intra-nuclear FISH			Cytoplasmic FISH		
Label	Volume	Min_Z	Max_Z	Mean-Intensity	Spot #	Spot-Score	Max-score	Area	FISH-area	Distribution (%)
1	1472	2	7	110	0	0.00	0.00	40	17	6.41
2	2251	2	8	133	0	0.00	0.00	281	2	0.07
3	2768	1	7	110	0	0.00	0.00	98	1	0.38
4	2874	4	11	126	1	2.06	2.06	332	16	4.49
5	2447	1	6	105	1	1.41	1.41	65	15	5.83
6	3351	2	8	128	0	0.00	0.00	311	19	3.74
7	4011	4	14	131	1	4.13	4.13	282	6	1.31
8	2159	2	7	93	0	0.00	0.00	71	0	0.00
9	3592	3	12	135	0	0.00	0.00	99	4	0.65
10	3563	2	11	130	0	0.00	0.00	284	10	2.63
11	2672	2	9	138	1	0.47	0.47	74	3	0.46
12	3260	2	10	136	1	0.11	0.11	328	4	0.41
13	3370	7	14	138	1	20.86	20.88	304	6	1.35
14	3857	7	14	132	5	155.79, 0.75, 0.35, 0.29, 0.09	155.79	357	89	26.45
15	3300	2	8	129	1	102.08	102.08	16	20	5.18
16	3295	2	9	130	2	9.30, 1.22	9.30	304	11	3.06
17	871	9	15	104	1	29.28	29.28	163	2	0.68
18	2591	10	16	122	3	34.27, 0.70, 0.06	34.27	31	18	4.94
19	1271	9	15	134	0	0.00	0.00	11	6	0.64
20	3808	2	10	125	2	0.13, 0.10	0.13	296	34	10.51
21	726	9	15	90	0	0.00	0.00	38	4	2.79
22	3581	3	13	136	1	4.03	4.03	280	6	1.39
23	3264	2	9	130	2	23.18, 17.07	23.18	304	27	5.33
24	2936	2	10	131	0	0.00	0.00	299	10	2.45

B



C

FIGURE 15.1. Two illustrations of 3D image analysis. In the first example (top row), confocal microscopy is used to image cell nuclei from the rat hippocampus using a DNA stain, and fluorescence *in situ* hybridization (FISH) is used to image the transcription products (mRNA) of an immediate early gene (*Arc*). The cell nuclei are segmented, and FISH activity is measured relative to the segmentation, generating a wealth of measurements. The table on the right is a partial display of the results of 3D image analysis. In the second example (lower row), a dye-injected neuron is traced automatically, generating a wealth of topological and morphological measurements displayed in tables and dendrograms (image courtesy: Microbrightfield, Inc., USA).

markups for the same image at different times. Computer automation makes sense when a large number of images must be analyzed. It can eliminate the tedium and labor associated with manual methods. It is ruthlessly consistent compared to manual methods, eliminating the subjectivity inherent to manual analysis. Faster computers make automated methods faster, and they can work round the clock.

Automated methods are free from many limitations of manual analysis. For example, manual methods are limited in their ability to process 3D data because the manual observer is limited to visual observation of stereo pairs, which are merely a projection of the 3D reality of interest. Occasionally, some observers have visual handicaps, and most observers are susceptible to optical illusions. Finally, if a study needs to be redone, it is much easier to run modified software rather than ask manual scorers to repeat a tedious task. Overall, manual methods are limited to small numbers of images, are unavoidably subjective, and are limited in the handling of three-dimensionality.

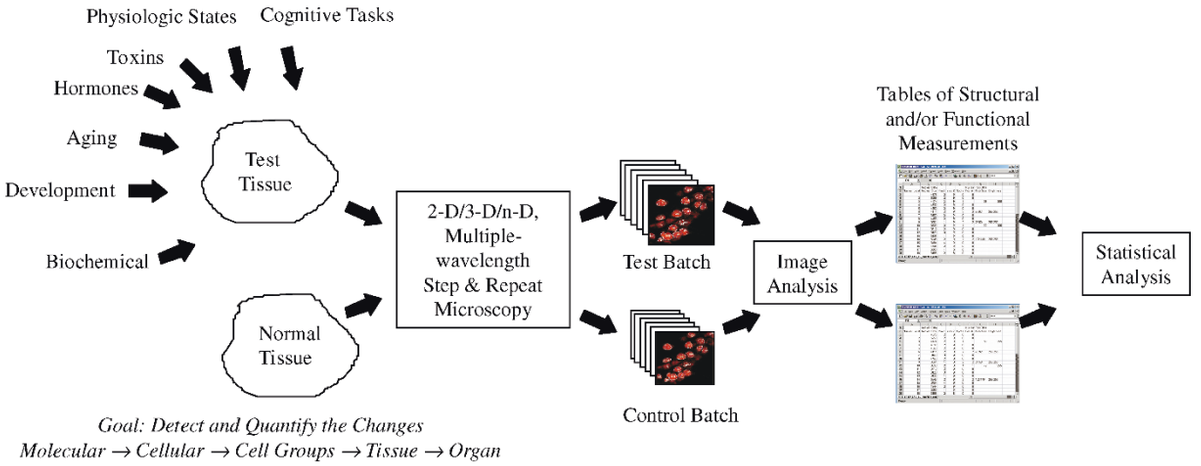


FIGURE 15.2. Illustrating the role of image analysis systems in hypothesis testing studies. Test and normal (control) tissue are imaged to generate batches of 3D images. Image analysis systems process this volumetric data to generate concise tables of measurements that are subjected to statistical analysis.

TYPES OF AUTOMATED IMAGE ANALYSIS STUDIES

Figure 15.2 illustrates the most common type of image analysis–based hypothesis testing study or assay. In this type of study, tissue samples are subjected to a condition of interest (e.g., exposed to a biochemical). As a reference, normal (untreated) tissue samples are also obtained, maintaining other conditions the same. Confocal microscopy is performed to generate batches of 3D images. Image analysis on these batches results in numerical tables representing cytometric and/or histometric data. Statistical hypothesis testing can be performed on these data. We are interested in discovery and quantification of all statistically significant differences between the treated and untreated samples. The result of hypothesis testing and an understanding of the nature of changes is a powerful source of biological insight.

Figure 15.3 illustrates a type of study that is now feasible, thanks to advances in methods and apparatus for live tissue imaging (*in vitro* or *in vivo*), as exemplified by the data in Figure 15.4. In this type of study, one collects a temporal series of images from the same region. In addition to statistical analysis of morphometric data as a function of time, it is possible to register the 3D time-series images, and identify the changes in a direct manner.

The types of changes that may be caused by the tested conditions can be diverse, and can occur at multiple levels. At the lowest level, molecular and subcellular effects can be detected by fluorescent tagging (Valeur, 2002). At the cellular level, changes can take the form of increasing/decreasing cell counts, and changes in morphometric features of cells. Finally, subtle high-level and/or long-range changes in tissue architecture can be analyzed by montaging the results of image analysis from a large number of overlapping windows across large specimens (Becker *et al*., 1996). The diversity and complexity of these changes define the breadth and scope of image analysis problems.

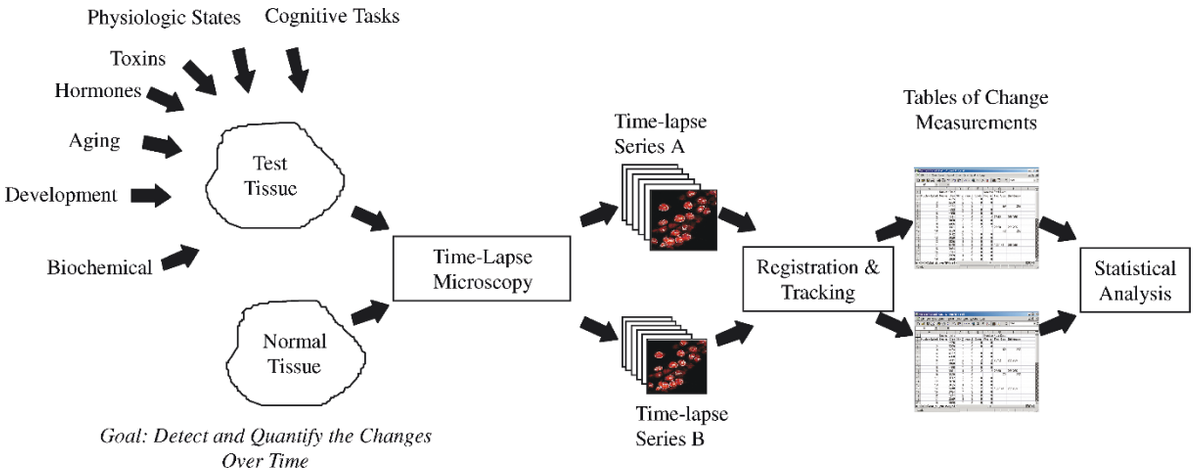


FIGURE 15.3. Illustrating the methodology for hypothesis testing with time-series data. In this case, successive images are registered (aligned) and compared. The registration algorithms usually, but not always, operate on the output of the image analysis results. Registered images (or summarized image analysis results) are compared to generate tables of change measurements that are analyzed statistically.

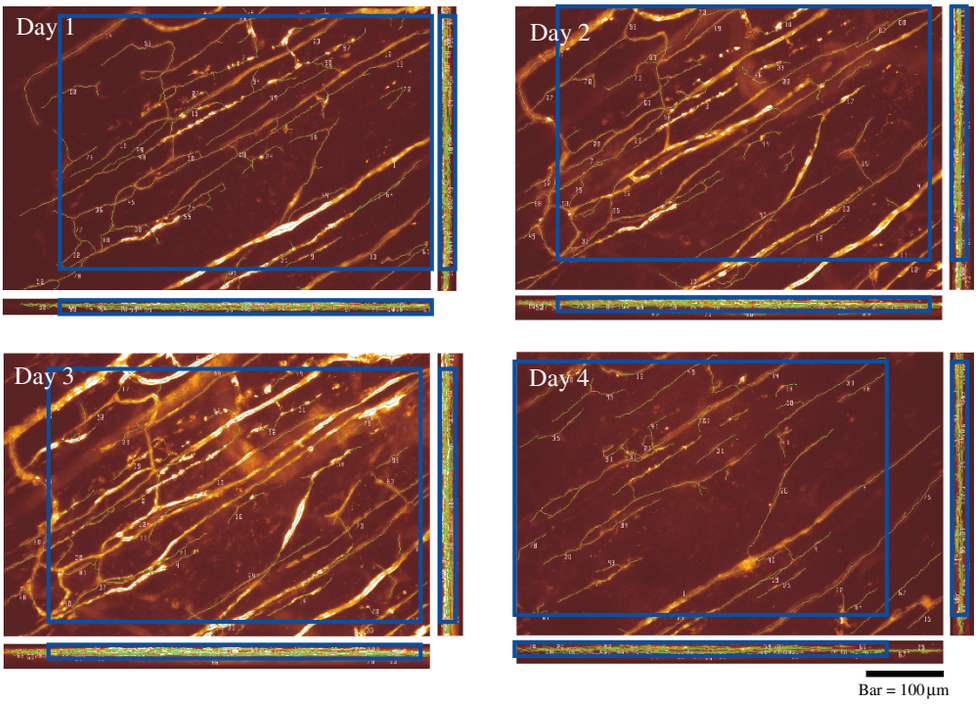


FIGURE 15.4. Time series *in vivo* images (each $768 \times 512 \times 32$, 8 bit/pixel) of fluorescently labeled skin vasculature altered by growth of a nearby tumor, shown in their maximum intensity projections (*x*-*y*, *y*-*z*, and *x*-*z*). Automated segmentation (tracing) results are overlaid in green. Volumes highlighted in blue are common overlapping regions across all images in this set of time series images, where measurements only from these common regions are used to analyze the changes in vasculature between time points. (image courtesy: Microvascular Research.)

COMMON TYPES OF BIOLOGICAL IMAGE OBJECTS

Notwithstanding the diversity of changes that may be of interest, it is advantageous to identify and study certain generic types of image objects, and common image analysis tasks associated with these object types. Practically speaking, an object is really a collection of voxels representing a biological structure imaged by the microscope. Three of the most common object types in the context of confocal microscopy are listed below.

1. **Blob-like objects**: The labeled cell nuclei in Figure 15.1(A) are examples of 3D blobs, and blobs are by far the most common type of object of interest in automated image analysis. Geometrically, they can be thought of as 3D ellipsoids that have been deformed irregularly. These apparently simple objects nevertheless provide a rich set of challenges from the standpoint of automated image analysis, due to preparation and imaging artifacts (Lin *et al*., 2003).

2. **Tube-like objects**: Vasculature and neurons [Fig. 15.1(C)] are examples of tube-like objects. Geometrically, they can be thought of as non-uniformly deformed 3D cylinders (Al-Kofahi *et al*., 2002; Abdul-Karim *et al*., 2003). Like blobs, these objects too provide a rich set of challenges for automated image analysis systems. Tube-like objects can be filled (i.e., solid) (Al-Kofahi *et al*., 2002; Abdul-Karim *et al*., 2003; He *et al*., 2003) or hollow (Weichert *et al*., 2003) in appearance.

3. **Irregular cloud-like distributions**: The diffuse FISH signals in Figure 15.1(A) are a good example of this class of object (Lin *et al*., 2003). The diversity and specificity of fluorophores, coupled with the ability of modern microscopes to image multiple fluorophores, makes this an important category of image analysis targets. Although these objects do not have distinctive geometries, they are amenable to quantitation by spatial association with biologically related blob-like or tube-like objects. For the example in Figure 15.1(A), segmentation of the nuclei provides spatial masks over which the intra-nuclear FISH signals are integrated. The extra-nuclear FISH signals are associated with the nearest nucleus by means of a Euclidean distance transformation (Lin *et al*., 2003).

SPECIMEN PREPARATION AND IMAGE PREPROCESSING METHODS

Data Collection Guidelines for Image Analysis Purposes

Specimen preparation and microscopy procedures for successful automated image analysis are stricter than for manual scoring. Unlike humans, computers are easily misled by confounding objects, artifacts, variability, and clutter. Therefore, it is important to make every effort during the specimen preparation and imaging procedures to ensure that the objects of interest are delineated with a high degree of contrast against the uninteresting structures in the tissue. It is helpful to experiment with specimen handling steps, reagents, fluorophores, and software tools such as those for spectral unmixing. Figure 15.5 illustrates structure-specific imaging using multiple fluorophores. The different highlighted structures (astrocytes, microglia, and vasculature) appear in separate image channels, eliminating the need for separating structures by image analysis. It is wise to make sure that the automated scoring software is well behaved when used on a small pilot set of images before embarking on large-scale data collection. It is important to maintain a high degree of uniformity in specimen handling, reagents, imaging protocols, and instrument settings across a batch.

Sampling conditions may be different for image analysis. For example, lossy image compression algorithms are best avoided. While image analysis algorithms are driven by the desire to maximize the accuracy of morphometry, the percentage impact of a single-voxel error depends heavily on the number of voxels representing the object. If the tissue is fairly uniform, it is often possible to sample across the tissue in a random manner, using standard stereological sampling principles (Howard and Reed,

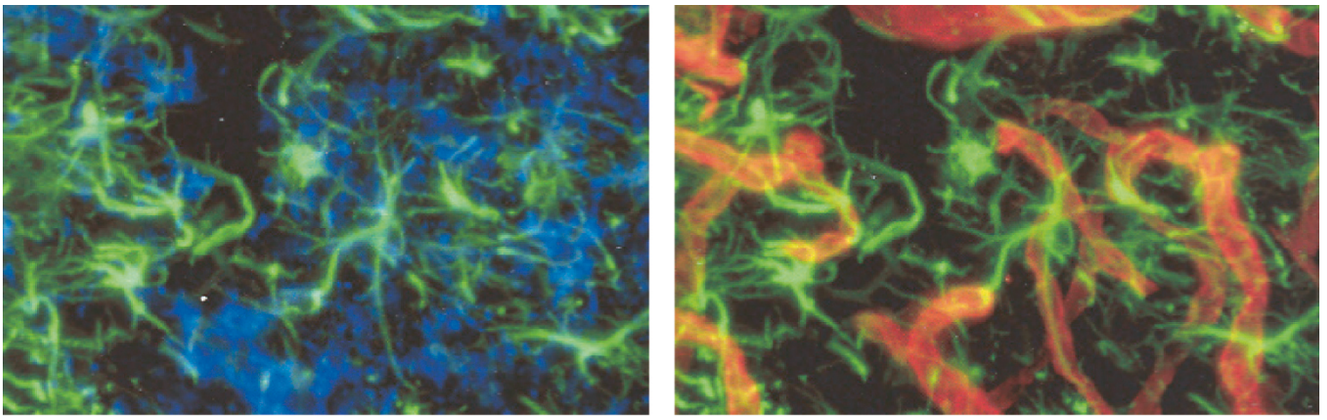


FIGURE 15.5. Neurobiology example illustrating the use of multiple fluorophores to simplify image analysis by performing selective imaging of specific structures in the same region of tissue. Maximum projections of rat cortices altered by the implantation of a model neuroprosthesis. In panel (A), the green regions represent astrocytes, the blue regions represent microglia. In panel (B), the red regions additionally represent vasculature. These different structures are available to the image analysis system as separate images. The images when compared to controls (not shown) demonstrate increased numbers of astrocytes, microglia and proliferator of vessels. (image courtesy: Dr. Beth Sipple at Wadsworth.)

1998; Russ and DeHoff, 2000; Mouton, 2002). If this assumption is not valid, it makes sense to resort to montaging. The border regions in 3D images and optical slices near the top and bottom of a stack often capture partial objects. These objects should be eliminated in a systematic manner using Howard's brick rule (Howard *et al*., 1985), which is easily implemented on the spreadsheet tables of measurements generated by the software.

If live tissue is being imaged in a time-lapse series, it is important to ensure that the same region of tissue is imaged every time (Brown *et al*., 2001). Additionally, automatic image registration tools can be used to refine the alignment (Al-Kofahi *et al*., 2003). Once registered, the changes can be quantified over the overlapping regions (Addul-Karim *et al*., 2003). Figure 15.4 shows a time series of *in vivo* images (each $768 \times 512 \times 32$, 8 bit/pixel) of fluorescently labeled vasculature of skin altered by growth of a nearby tumor.

Confocal microscopes are unavoidably anisotropic in terms of the spatial sampling density because the axial resolution of confocal microscopes is lower than the lateral resolution. Image resampling by techniques such as shape-based interpolation often simplifies 3D image analysis at the expense of generating a larger image data set (Raya and Udupa, 1990).

Finally, the image analyst must be aware that the brightness of a voxel in a confocal image is not necessarily only proportional to the fluorophore concentration (Pawley, 2000).

Image Preprocessing Methods

Common imaging artifacts include non-uniformity and the presence of uninteresting/nuisance objects. Their effects on the image analysis results can sometimes be reduced by preprocessing. Figure 15.6 shows several imaging artifacts in neuron and vasculature images.

Morphological filters (Serra and Soille, 1994; Bovik *et al*., 2001), background subtraction (Russ, 1994), and signal attenuation–correction (Adiga and Chaudhuri, 2001b; Can *et al*., 2003) are examples of common preprocessing methods for confocal images. Morphological filters, such as the median and top-hat filter, are typically utilized to reduce image noise, such as blobs of dye in the background, or to smooth out Poisson noise (Sarti *et al*., 2000) and non-uniformities of foreground intensity. However, the optimal method for removing Poisson noise is full 3D deconvolution (see Chapter 25, *this volume*). Background subtraction is performed to correct illumination non-uniformity across the entire image. Signal attenuation–correction is useful to rectify depth-

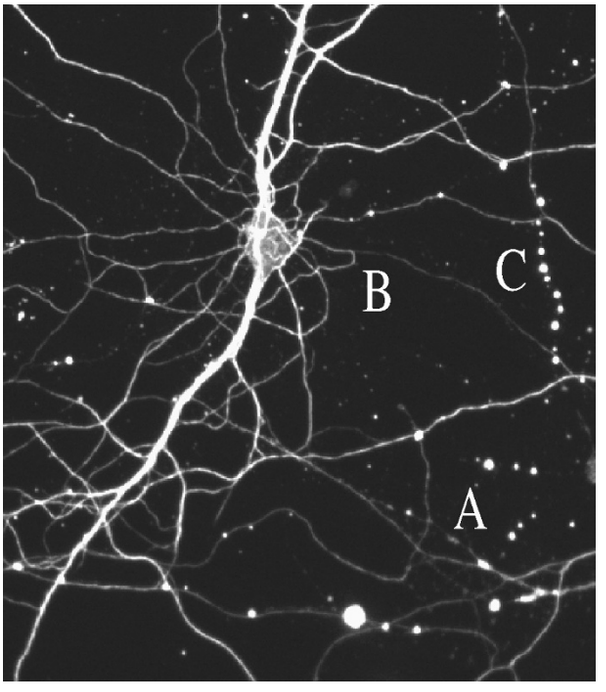


FIGURE 15.6. Examples of imaging artifacts in the context of neuron imaging. **(A)** Blobs of dye. **(B)** Neurites with relatively dim and discontinuous appearance. **(C)** Strip of noise, resembling neurites. (image courtesy: Natalie Dowell at the Wadsworth Center.)

dependent attenuation of signals (Can *et al*., 2003). In general, images are preprocessed globally, that is, without localizing the preprocessing operations to a subset of the image. This makes preprocessing computationally expensive. Furthermore, the preprocessor parameters usually need to be fine-tuned to ensure preservation of objects of interest while reducing unwanted artifacts.

Another rationale to preprocessing is to generate standardized images where one segmentation method is used for images coming from different sources. Yet another is to highlight particular structures, for example, images of neuronal processes and vasculature may be preprocessed to highlight the tube-like morphology of these biological objects (Sato *et al*., 1998).

GENERAL SEGMENTATION METHODS APPLICABLE TO CONFOCAL DATA

Segmentation is the process of labeling some or all of the voxels in the image as being part of specific objects of interest (the **foreground**) and not part of the **background**. This is the process of transitioning from a conceptually simple array of point measurements (voxels) to the more abstract and more informative notion of image objects, or parts thereof (Haralick and Shapiro, 1985). Following segmentation, it is straightforward to make morphological and functional measurements. The purpose of this section is to summarize the main segmentation approaches. The reader interested in more detailed descriptions is referred to other sources (Bhanu, 1982; Wilson and Spann, 1988; Bhanu and Lee, 1994; More and Solimini, 1995; Rezaee, 1998; Suri *et al*., 2002).

The difficulty of segmenting biological images is largely attributable to their sheer complexity and variability. Interestingly, it is simpler to segment 3D images, compared to 2D images because, in the former, some overlapping objects can be distinguished on the basis of 3D depth information (Ancin *et al*., 1996).

The prior literature on segmentation is vast (Zucker, 1977; Kanade, 1978; Sklansky, 1978; Rosenfeld and Davis, 1979; Ranade and Prewitt, 1980; Fu and Mui, 1981; di Zenzo, 1983; Haralick and Shapiro, 1985; Mitiche and Aggarwal, 1985; Nevatia, 1986; Cooper, 1998; Kerfoot and Bresler, 1999; Pham *et al*., 2000). Generally, techniques for image segmentation can be grouped into three categories: bottom-up methods, top-down methods, and hybrid methods. Regions and boundaries are two common concepts commonly used in segmentation. Intuitively, an **object** is outlined by its boundary and a **region** is contained by a boundary. In addition, segmentation may be performed either image wide, or in an exploratory manner. Non-exploratory methods visit each voxel and label them. Exploratory methods (Can *et al*., 1999; Al-Kofahi *et al*., 2002; Streekstra and van Pelt, 2002; Abdul-Karim *et al*., 2003) begin with voxels known or estimated to be on the object, such as a point on a vessel, and proceed to segment adjacent voxels of the same object.

Bottom-Up Segmentation Methods

Bottom-up methods start with an over-segmentation of the image and iteratively merge object fragments based on some measure of similarity. They can be described in terms of three steps: identifying the set of initial regions representing object fragments (Zucker, 1976; Besl and Jain, 1988; Adams and Bischof, 1994; Trucco and Fisher, 1995; Zhu and Yuille, 1996), identifying an appropriate region-similarity measure (Blake and Zisserman, 1987; Black and Rangarajan, 1996), and merging the voxels that share these features into objects (Guigues *et al*., 2003). Other related methods are graph based, for example, the work of Shi and colleagues (Beck *et al*., 2000) has presented a global criterion termed the "normalized cut" for segmenting the graph. Ying and Uberbacher (1997) proposed a 2D image segmentation using a minimum spanning tree partitioning approach. In the bottom-up category, there are four main approaches: intensity thresholding, region based, boundary based, and integrated techniques. These are detailed in the following paragraphs.

Intensity Threshold–Based Segmentation Methods

In this approach (Sahoo *et al*., 1988), all voxels whose values lie within a certain range belong to one class. *Global thresholding* (Shapiro and Stockman, 2001; Koh *et al*., 2002) uses a single threshold value for an entire image. When the threshold value changes for different regions of the image, it is called *adaptive thresholding* (Cohen *et al*., 1994; Kim *et al*., 2001; He *et al*., 2003). Thresholding may be sufficient for segmentation when the background intensity range does not overlap with the foreground intensity range. To overcome the limitations of thresholding, such as susceptibility to background noise and intensity non-uniformity, *connected components analysis* (Dillencourt *et al*., 1992; Ancin *et al*., 1996) is commonly used to link voxels belonging to an object of interest, and reject overly small clusters of pixels.

Region-Based Segmentation Methods

Region-based methods (Zucker, 1996; Hojjatoleslani and Kittler, 1998) rely on the assumption that neighboring voxels within one region of an object are homogeneous according to a specified measure. This leads to a class of algorithms known as split-and-merge (Horowitz and Pavlidis, 1974; Haralick and Shapiro, 1985; Chang and Li, 1994), seeded region growing (Adams and Bischof, 1994; Hojjatoleslami and Kittler, 1998), and partitional clustering (Mackin *et al*., 1993; Roysam *et al*., 1994). The general procedure is to compare each voxel to its neighbors. If the criterion of homogeneity is satisfied, the voxel is said to belong to the same class. Neighboring voxels are examined and added to the region if they are evaluated to have similar characteristics. This region growing process will eventually converge, yielding a delineation of the object. The growing volume should be constrained for maximum success. Multiple regions can be initialized in the image, and regions can be merged with each other. Obviously, the performance of this approach largely depends on the selected homogeneity criterion.

In the split-and-merge technique, the entire image is initially considered as one region. In each step, each heterogeneous region of the image is divided into four rectangular segments and the process is terminated when all regions are homogeneous. After the splitting, a merging process unifies the similar neighboring regions. Quadtree-structured split-and-merge (Pavlidis, 1977) is a popular approach because of its simplicity and computational efficiency. Seeded region growing techniques (Adams and Bischof, 1994; Hojjatoleslami and Kittler, 1998) select some initial image points, and then segments the image into regions, each originating with a single seed. Clustering-based methods (Mackin *et al*., 1993; Roysam *et al*., 1993, 1994) treat the segmentation problem as a partitional cluster analysis (Theodoridis and Koutroumbas, 1999) in a four-dimensional space $[(x, y, z), I(x, y, z)]$, combining the usual spatial coordinates with the image intensity. This approach is most valuable when the available geometric information about the objects is weak (Shain *et al*., 1999).

Boundary-Based Segmentation Methods

Boundary-based methods (Davis, 1975) detect image edges (Ballard and Brown, 1982), and link them into contours/surfaces representing object boundaries. The output of most existing edge detectors can only provide candidates for the region boundaries because the edges obtained are normally discontinuous or over-detected. However, the actual region boundaries should be closed curves. Therefore, some postprocessing, such as edge tracking, gap filling, smoothing, and thinning should be performed to obtain the closed region boundaries. Such postprocessing is often problematic, and this is an inherent limitation of boundary-based methods (Shapiro and Stockman, 2001).

Integrated Segmentation Methods

Integrated methods combine boundary and region criteria. In this class of methods, the morphological watershed algorithm is widely studied and used for efficient object separation (Beucher, 1991; Dougherty, 1993; Vincent, 1993; Serra and Soille, 1994; Shafarenko *et al*., 1997). Introduced by Digabel and Lantuejoul (1978), extended by Beucher (1982), analyzed theoretically by Maisonneuve (1982), and formally defined in terms of flooding simulations by Vincent and Soille (1991), the term "watershed" comes from a graphic analogy attributed to Vincent and Soille. In this analogy, the gray level image is treated as a topographic intensity surface. It is assumed that holes have been punched in each valley bottom. If this surface is "flooded" from these holes, the water will progressively flood the catchment basins (set of surface points whose steepest slope paths reach a given minimum) of the image. At the end of this flooding procedure, each minimum is completely surrounded by "dams," which delimit its associated "catchment basins." The set of dams obtained in this way corresponds to watersheds (called the watershed surface in 3D case) from a geophysical analogy, and provides a tessellation of the input image into its different catchment basins. Unlike the boundary-based methods above, the watershed is guaranteed to produce closed boundaries even if the transitions between regions are of variable strength or sharpness. Its popularity is also attributable to its computational efficiency and extendability to 3D spaces (Higgins and Ojard, 1993; Sijbers *et al*., 1997).

The second method in the class is variable-order surface fitting (Besl and Jain, 1988) that starts with a coarse segmentation of the image into several surface-curvature-sign primitives (e.g., pit, peak, ridge, etc.) which are refined by an iterative region-growing method based on variable-order surface fitting.

Another method in the class is to integrate region-growing and edge-detection (Pavlidis and Liow, 1990). This starts with a split-and-merge algorithm, and eliminates or modifies region boundaries based on some criterion using boundary smoothness and the variation of image gradients. Haddon and Boyce (1993) generate regions by partitioning the image co-occurrence matrix and then refining them by relaxation using edge information.

Top-Down Segmentation Methods

Unlike bottom-up algorithms, such as those described in the previous section, which are based on low-level image-based cues, such as coherence of brightness, color, texture or motion, top-down methods rely on prior models for the objects in the image to carry out the segmentation. Even sophisticated pre- and postprocessing techniques cannot overcome the inherent limitations of purely intensity-based methods. Actually, for automatic object segmentation, some kind of prior related knowledge can and must be incorporated into the algorithms. The mid- and high-level knowledge must be used to either confirm or modify the initial segmentation. This leads to the top-down approach, where the segmentation is guided by some known representation or prior knowledge of the objects under study. One method in this class is model-based segmentation, which optimizes the fit between a model and the image data. Different procedures, such as *deformable shape models* (Cootes *et al*., 1995; McInerney and Terzopoulos, 1996; Lorigo *et al*., 2001; Ghanei and Soltanian-Zadeh, 2002) and *statistical models* (Vemuri and Radisavljevic, 1994; Staib and Duncan, 1996), have been proposed. Deformable models, also known as "*snakes*" or "*active contours*," have been used as a way to incorporate application-specific *a priori* knowledge. For example, in order to segment a bone in a medical image or in order to visually track a person, models describing the possible contours of the objects of interest are used. The parameters of the models specify object properties such as the pose, size, and shape. Sunil Kumar and Desai (1999) presented a method of joint segmentation and image interpretation. Neumann (2003) proposed a knowledge-guided segmentation in 3D imagery. Statistical shape modeling methods depend upon the availability of parametric models to describe the objects. These parameters must be selected carefully in order to accurately characterize the objects, and discriminate outliers from real objects in an effective manner. The set of parameters must be rich enough to describe complex objects.

Although top-down methods are appealing because they seem similar to the human cognitive process, they have the disadvantage that they require a large amount of *a priori* knowledge (e.g., object models, number of regions) and this tends to limit the scope of applicability.

Hybrid Segmentation Methods Combining Bottom-Up and Top-Down Processing

Both top-down and bottom-up methods have their advantages and disadvantages. The latest segmentation methods often combine both low-level and high-level approaches (Roysam *et al*., 1992; Roysam and Miller, 1992; Bhattacharjya and Roysam, 1994). However, as these approaches tend to be computationally intensive and overly specialized, they are not described in further detail here. More pragmatic approaches do exist. One such is described in the following section.

EXAMPLE ILLUSTRATING BLOB SEGMENTATION

Accurate, reliable, and highly automated segmentation of fluorescently labeled cell nuclei from 3D confocal images is an essential first step for quantification by association of various genomic and proteomic products in nuclear or cytoplasmic compartments [Fig. 15.1(A)]. Tightly packed cell layers, which often result in the appearance of "touching objects" in image stacks, is a common segmentation problem. Precise segmentation of nuclei is an absolute requirement for correct assignment of gene transcription products to nuclear versus cytoplasmic locations for achieving optimal temporal resolution (Lin *et al*., 2003).

Lin and colleagues (2003, 2004) described an algorithm that uses a statistical model-based approach to combine the attractive

features of the 3D watershed algorithm, with algorithms that exploit available intensity-gradient–based cues, and the knowledge of the expected anatomic shape of the object. Whenever the cell shapes are well defined, the best-available methods for separating touching objects are based on the watershed algorithm (Ancin *et al*., 1996; Lin *et al*., 2003). When the cell shapes are poorly defined, partitional cluster-analysis algorithms work better (Roysam *et al*., 1994).

The watershed algorithm is widely studied and used for efficient object separation (Vincent and Soille, 1991; Ancin *et al*., 1996; Malpica *et al*., 1997; Solorzano and Rodriguez, 1999). Notwithstanding its popularity, watershed algorithm has several limitations arising from the fact that it relies on touching objects exhibiting a narrow "neck" in the region of contact. These necklines play a critical early role in estimating the number of objects in a given cluster, and is notoriously error prone. Considerable effort has been devoted to the design of algorithms for generating the correct set of "geometric markers" to guide the object segmentation. The problem of determining the correct number of such markers is inherently a difficult one, and is conceptually similar to the problem of automatically determining the number of groups in multi-dimensional statistical data. To overcome the above difficulties, Lin and colleagues (2003) proposed a "*gradient-weighted distance transform*," that combines object separation hints derived from geometric and intensity cues in the image data to improve watershed segmentation. Specifically, the geometric-distance transform **D** (Borgefors, 1986) and the gradient transform **G** (Lin *et al*., 2003) are combined into a single representation that captures the object separation cues available in the data, as given by the following formula.

$$\mathbf{D}' = \mathbf{D} \times \exp\left(1 - \frac{\mathbf{G} - G_{\min}}{G_{\max} - G_{\min}}\right),$$

where $G_{\min}$ and $G_{\max}$ are the minimum and maximum values of the gradient **G** needed for normalization. It is easy to observe that the modified distance value **D′**, has a high value at positions closer to the center of foreground objects, and for voxels with smaller gradient values. It has smaller values close to the boundary of the foreground objects, or where the gradient is relatively large. This expresses the object separation cue that the voxels with bigger gradient values tend to lie on the boundary of an object. In practice, the watershed algorithm requires the inverse of this distance transformation. This inverse is denoted **T**, and is computed as follows:

$$\mathbf{T} = S_g(\max(\mathbf{D}') - \mathbf{D}'),$$

where max(**D′**) is the global maximum within the distance images, and S_g represents a Gaussian smoothing operator (Castleman, 1996). The smoothing operation is needed because the transformed image may contain tiny noise-caused intensity peaks, usually due to uneven cell staining. Figure 15.7 illustrates the effectiveness of the combined measure. Panel (A) shows a sample image, with the nuclei indicated in blue, and the FISH signal displayed in red. Panel (B) is a surface plot of the geometric distance **D** for the region indicated by the white box in (A). Panel (C) is the result of combining the geometric and gradient measures **D** and **G** above. It is clear that the combined transformation in Panel (E) is effective in discriminating this touching nuclear cluster even though it does not have the characteristic bottleneck-shaped connection pattern.

Model-Based Object Merging

Although the gradient-weighted distance transform described above essentially eliminates under-segmentation, the problem of over-segmentation remains. To correct the over-segmentation, it is necessary to detect and break (eliminate) false watershed surfaces and thereby merge cell objects (Adiga amd Chaudhuri, 2001a; Lin

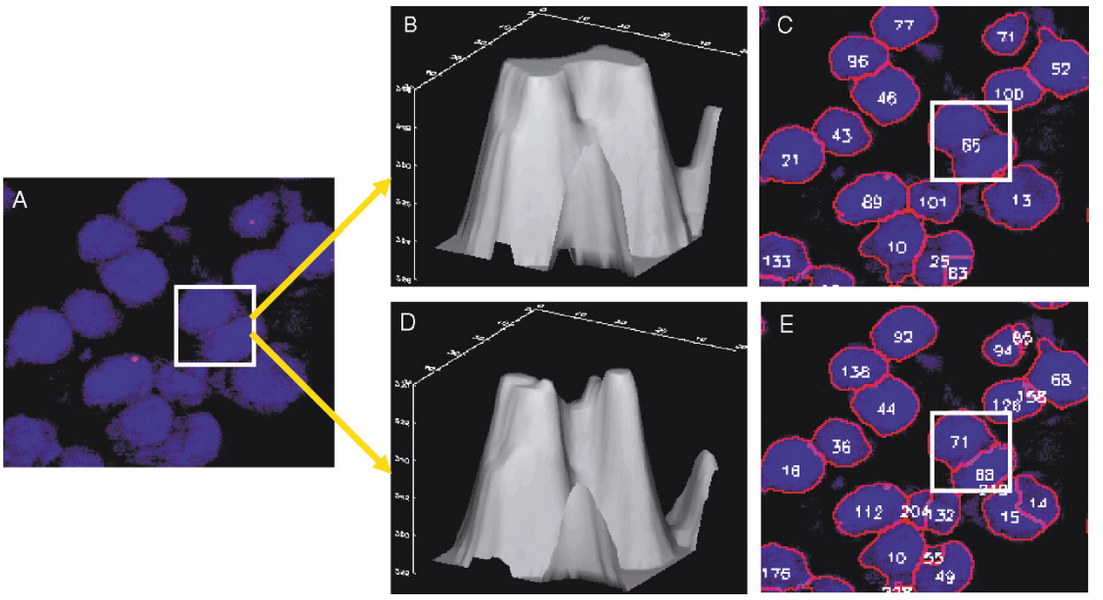


FIGURE 15.7. Illustrating the combined gradient-weighted distance transform as a cue of separating connected objects. (A) A small portion of a 3-D confocal image stack, showing nuclei in the *CA1* region of a rat brain. The white box in panel (A) indicates the region of interest, which includes two touching nuclei. Panel (B) shows a surface plot showing a standard geometric distance map ***D*** which is not adequate for nuclei separation. The combined gradient-weighted distance map in panel (D) results in the correct segmentation shown in panel (E). (Courtesy: Journal of Cytometry.)

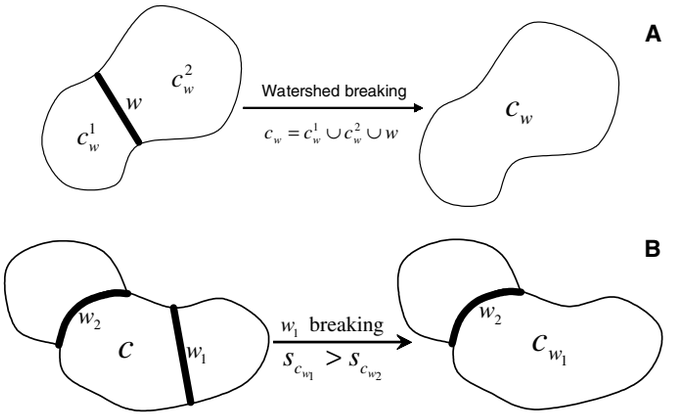


FIGURE 15.8. Illustrating two example cases encountered by the watershed surface-breaking algorithm for touching objects. Panel (A) shows a case that leads to merging of the two objects. Panel (B) shows the case that one object has multiple watershed surfaces (two in this example). In this case, there are two candidate watershed surfaces to choose from for breaking. The watershed surface w that has a greater merging score C_w is given the higher priority, indicating better fit to the object model, thus the higher confidence towards its breaking. (Courtesy: Journal of Cytometry.)

et al., 2003). Currently, the best methods rely on a quantitative score based on a mathematical model of the objects of interest (i.e., the nuclei). The object model is described by a vector of features that are denoted as X_c for object (cell nucleus) c. The features include measurements such as volume, texture, convexity, circularity, and shape. The merging score based on these features is given below assuming that they are Gaussian-distributed:

$$\mathbf{T} = S_g(\max(\mathbf{D}') - \mathbf{D}'),$$

where $\bar{X}$ and Σ_X are the mean and covariance matrix of the training feature set respectively, which are obtained from some example intact nuclei in the given image stack.

Intuitively, the merging decisions are based on the following two criteria: (i) the merging score S_{cw}, that is, the score of the combined object by nucleus c_w^1, c_w^2, and watershed surface w should be higher than the score of either nucleus S_{cw}^1 or S_{cw}^2 before merging. (ii) The gradient of watershed surface w should be relatively large compared with the gradient of the nucleus c_w^1 and c_w^2. It is assumed that intranuclear gradients are smaller than internuclear gradients. With these observations in mind, the following ratios are calculated:

$$R_{s_w} = \frac{2 \times S_{c_w}}{\left(S_{c_w^1} + S_{c_w^2}\right)};$$

$$R_{\gamma_w} = \frac{\left(\gamma_{c_w^1} + \gamma_{c_w^2}\right)}{2 \times \gamma_w}.$$

The final decision-making criterion is the combination of the above two ratios:

$$R_w = R_{s_w} \times R_{\gamma_w} \geq \beta,$$

where β is an empirically set decision threshold. Further details concerning the above algorithms are provided in Lin and colleagues (2003). Figure 15.8 illustrates two example cases encountered by the watershed surface-breaking algorithm for touching objects. The model-based watershed surface breaker effectively eliminates almost all of these over-segmented nuclei during the postprocessing. One example is shown in Figure 15.9, where the above algorithm achieves a 97% accuracy compared to a consensus of three expert observers.

EXAMPLE ILLUSTRATING SEGMENTATION OF TUBE-LIKE OBJECTS

Two broad types of algorithms exist for segmenting tube-like objects (neurons, vasculature): (i) skeletonization and (ii) vectorization. Skeletonization methods work by systematically eroding a binarized version (the results of adaptive thresholding) of the image until only the innermost voxels (i.e., the skeleton) remains. They are attractive for applications in which the objects are irregular, for example, spiny neurons (Koh *et al*., 2002). On the other hand, vectorization-based methods are valuable when the objects are much more regular in appearance, and can be modeled as generalized cylinders in 3D space (Al-Kofahi *et al*., 2002; Abdul-Karim *et al*., 2003, 2005). The latter method embeds more assumptions about the objects of interest, and is therefore better at rejecting image clutter than skeletonization-based methods. Figure 15.10 shows an example of skeletonization results (Koh *et al*., 2002; He *et al*., 2003) and Figure 15.11 exemplifies vectorization results (Al-Kofahi *et al*., 2002), both on dye-injected neurons imaged by a confocal microscope.

Skeletonization Methods

These methods work by performing adaptive segmentation (producing a binary image) followed by skeletonization and graph extraction (Koh *et al*., 2002; He *et al*., 2003). The 3D skeleton of an object is a connected set of lines (traces) that coincide with its medial axis, and which can be obtained by repeatedly performing erosion operations and connectivity analysis on the 3D binary volume, until only the medial skeleton of the object remains. During the thinning process, a voxel is considered deletable if its removal does not cause any other voxels to become disconnected. Clearly, improved detection of voxel connectivity allows more voxels to be deleted, and hence a more concise skeleton can be obtained. The traditional methods (Tsao and Fu, 1981; Gong and Bertrand, 1990) for 3D skeletonization are based on analyzing a $3 \times 3 \times 3$ window around each voxel to test for voxel deletability. One drawback of such methods is their inability to detect many cases when voxels are connected via more circuitous paths, especially in noisy data such as that from confocal microscopy. Specifically, these algorithms can magnify each of the however-small noise-caused surface irregularities into full skeletal appendages, resulting in an excessively complex skeleton. Cohen and colleagues (1994) developed a thinning algorithm based on performing voxel detability tests over windows much larger than $3 \times 3 \times 3$, and using long-range boundary detection criteria (He *et al*., 2003).

Vectorization Methods

In contrast, vectorization methods utilize a more rigid model that embeds tighter assumptions about the objects. For example, it often explicitly models tube-like objects geometrically, say using a generalized cylinder constrained by parallel boundaries (Al-Kofani *et al*., 2002) (Fig. 15.12). Figure 15.4 illustrates an example of tracing tumor microvasculature using a semi-rigid

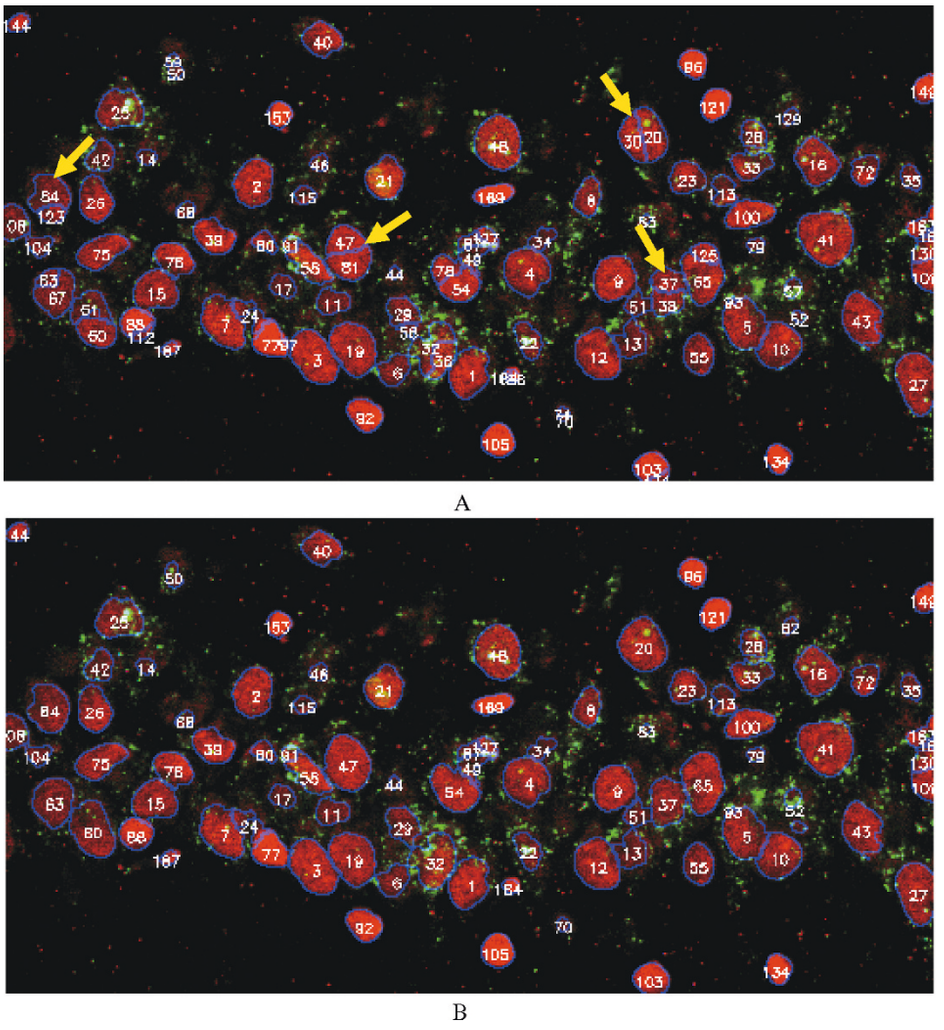


FIGURE 15.9. Segmentation result generated by the model-based merging procedure (i.e., the watershed surface breaker). There were 66 watershed surfaces broken, and most cases of over-segmentation were eliminated. An explicit mathematical model for the anatomic characteristics of cell nuclei, such as size, texture, convexity and shape measures, is incorporated during the post-merging procedure. Panel (A) shows the segmentation right after the enhanced watershed algorithm. As can be seen, clusters of nuclei are basically eliminated, and the over-segmentation is allowed, as indicated by yellow arrows. Panel (B) shows the final results after the model-based merging procedure. (Data courtesy: Carol Barnes Lab at the University of Arizona.)

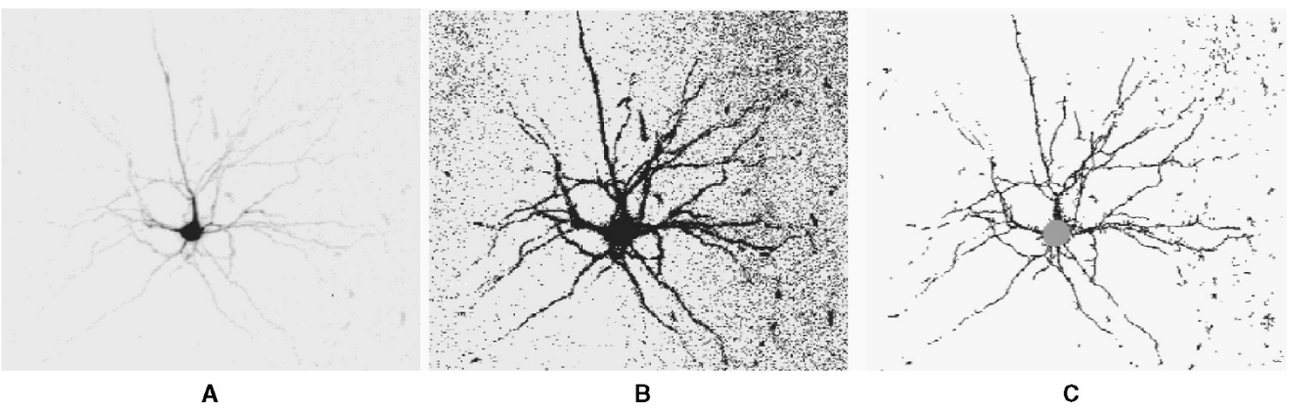


FIGURE 15.10. Illustrating neuron tracing by skeletonization. (A) 3-D image of a dye-injected neuron, shown in maximum-intensity projection (8-bit/voxel, $383 \times 328 \times 150$). (B) Segmented image by adaptive thresholding. (C) Skeletonized neuronal process shown with the detected soma. The skeletonization method is very general, so it can apply to spines, for example, but it is not nearly as fast and selective as the vectorization method. (image courtesy: Microscopy and Microanalysis.)

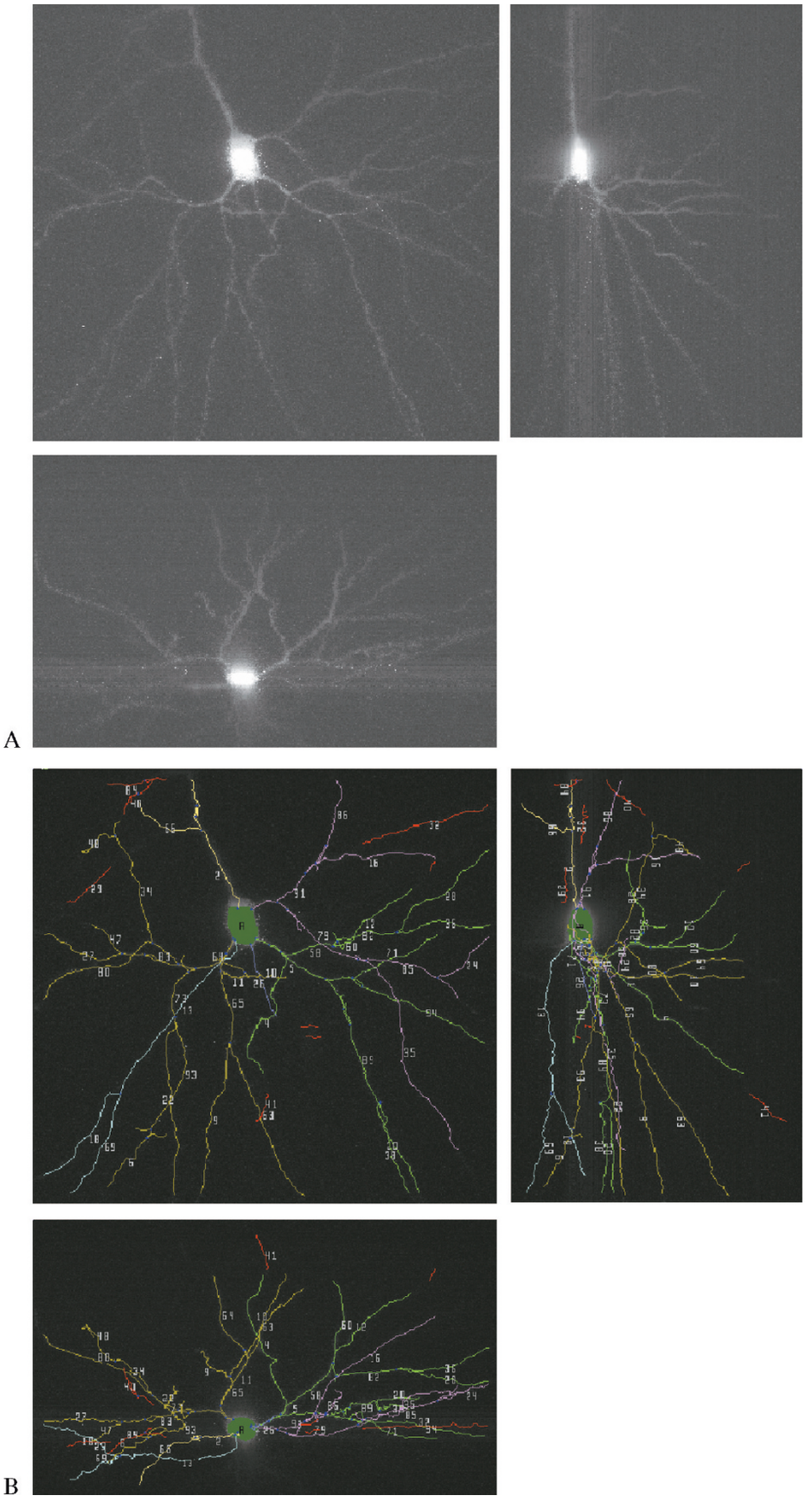


FIGURE 15.11. Illustrating neuron tracing using a generalized cylinder model and vectorization. (A) A 3-D, $512 \times 480 \times 301$ grayscale image of a dye-injected neuron shown by the *x-y*, *x-z*, and *y-z* maximum intensity projections. (B) The segmentation results using a rigid, generalized cylinder model. Notice that since the segmentation is guided using a spatio-physical model, no background voxels are misclassified since they do not fit the generalized cylinder model. This approach can be much more selective than the skeletonization method and substantially faster. However, it is not as effective at segmenting non-tube-like structures such as spines.

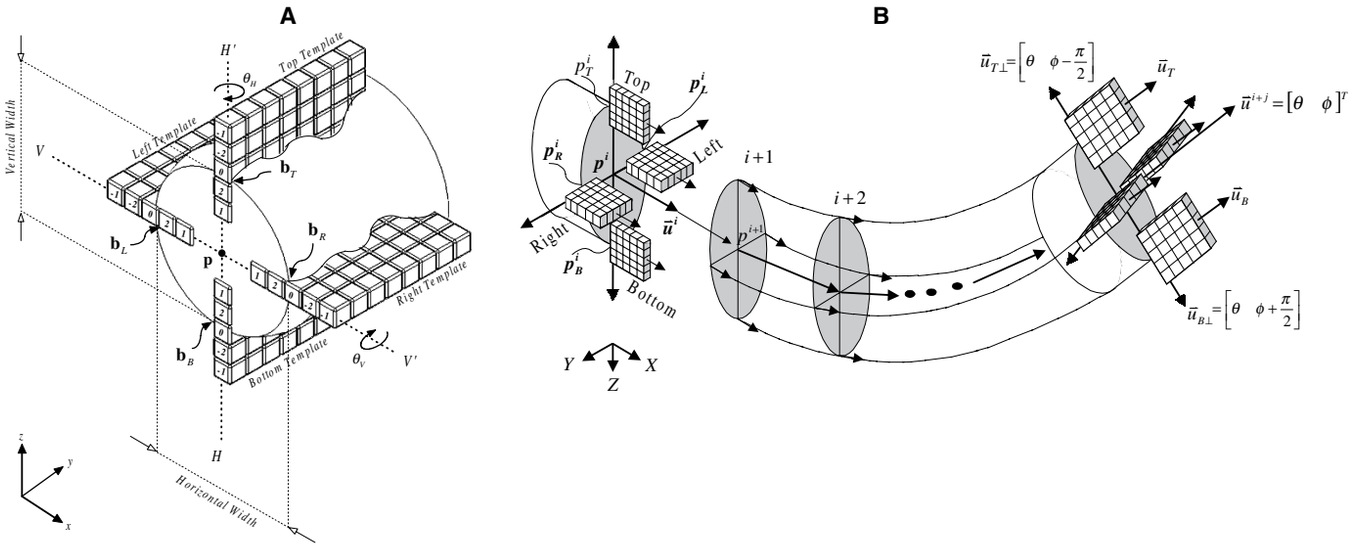


FIGURE 15.12. (A) Modeling a tube-like object using a generalized cylinder. Irregularities of the object boundary relative to the straight-boundary assumption are incorporated into the model. (B) Illustrates the recursive exploratory tracing (vectorization) of a tube-like structure, advancing with the information gathered from best-fit cylinder at each point. (pictures courtesy: Microvascular Research, IEEE Press.)

model. The following paragraphs describe the core ideas in further detail.

At the simplest level, tube-like structures can be modeled as piecewise-linear segments, where each segment is a generalized cylinder (Al-Kofahi *et al*., 2002). The key geometric property is the existence of anti-parallel edges located a small distance apart. Even this apparently simplistic modeling leads to a highly successful analysis exemplified by Figure 15.11. In practice, the strict cylinder model is relaxed to account for slight irregularities in the vasculature boundaries [Fig. 15.12(A)] by incorporating a tolerance to deviations from the strict cylinder model in the software implementation. Often, the structures of interest are much more irregular, as exemplified by the tumor microvasculature in Figure 15.4. This irregularity can be modeled by the use of robust statistics, which implies the use of a median instead of the arithmetic mean (Abdul-Karim *et al*., 2003). This method is described below, and illustrated diagrammatically in Figure 15.12(B).

At the core of this method is the estimation of boundary locations and direction. The estimation utilized directional edge detectors, called templates, comprised of linearly stacked one-dimensional (1D) edge detectors (Sun *et al*., 1995) of the form $[-1, -2, 0, 2, 1]^T$ along a direction. Along a particular direction, the edge strengths from each 1D edge detector are averaged [using mean (Al-Kofahi *et al*., 2002) or median (Abdul-Karim *et al*., 2003)] and the resulting value is associated with the corresponding template, referred to as a *template response*. This can be expressed mathematically as

$$(\mathbf{b}^i, \mathbf{u}^i, k^i) = \underset{\left\{(\mathbf{b},\mathbf{u},K)\,|\,\mathbf{b}=\mathbf{p}^i+m\mathbf{u}_\perp,\, m=1,\ldots,\frac{M}{2},\, \mathbf{u}\in\mathbf{U},\, k\in K\right\}}{\arg\max} [R(\mathbf{b}, \mathbf{u}, K)],$$

where $\mathbf{U}$ is the set of unit vectors along directions in the neighborhood of $\mathbf{u}^i$ and K is the set of all template lengths. The vector $\mathbf{u}$ is a unit vector along a particular 3D angle θ, while $\mathbf{u}_\perp$ is the unit vector perpendicular to $\mathbf{u}$. The parameter M is the user-defined diameter of the widest expected vasculature. Values $\mathbf{b}^i$, $\mathbf{u}^i$, k^i are the results of this exhaustive search at iteration i, each representing the $[x, y, z]$ location, orientation, and length, respectively, of the template that returns the maximum response R. This search is performed four times corresponding to the four templates that make up the generalized cylinder model [Fig. 15.12(A)]. The corresponding mean and median template response, respectively, are expressed as

$$R(\mathbf{b}, \mathbf{u}, K) = \underset{k\in K}{\arg\max} \{\underset{j=1..K}{median}(r(\mathbf{b}+j\mathbf{u}, \mathbf{u}_\perp))\},$$

and

$$R(\mathbf{b}, \mathbf{u}, K) = \underset{k\in K}{\arg\max} \left\{\frac{1}{k}\sum_{j=1}^{k}(r(\mathbf{b}+j\mathbf{u}, \mathbf{u}_\perp))\right\},$$

where $r(\mathbf{b},\mathbf{u}_\perp)$ is the response of a single 1D edge detector at $\mathbf{b}$ along the direction that is perpendicular to $\mathbf{u}$. Notice that a template of length k is comprised of k 1D edge detectors stacked together, hence, r is essentially a template of length 1. The simple switch from mean to median averaging deserves a closer inspection. By using the median, the response function is robust to at most 50% of outliers (Huber, 1981), loosely termed as *bad edges*. Figure 15.13 further demonstrates the difference between these two averaging methods.

Notice that by using this rigid model both the centerline and boundary are readily obtained while segmenting the image, yielding morphometrics such as length (cumulative distance between center points) and diameter (distance between boundary points) on the fly. In contrast, the skeletonization approach requires much more sophisticated postprocessing to extract these morphometrics. In either case, additional processing must be performed for branch analysis and to extract any other morphometrics from the segmented structure. Details of this method are described elsewhere (Al-Kofahi *et al*., 2002; Abdul-Karim *et al*., 2003).

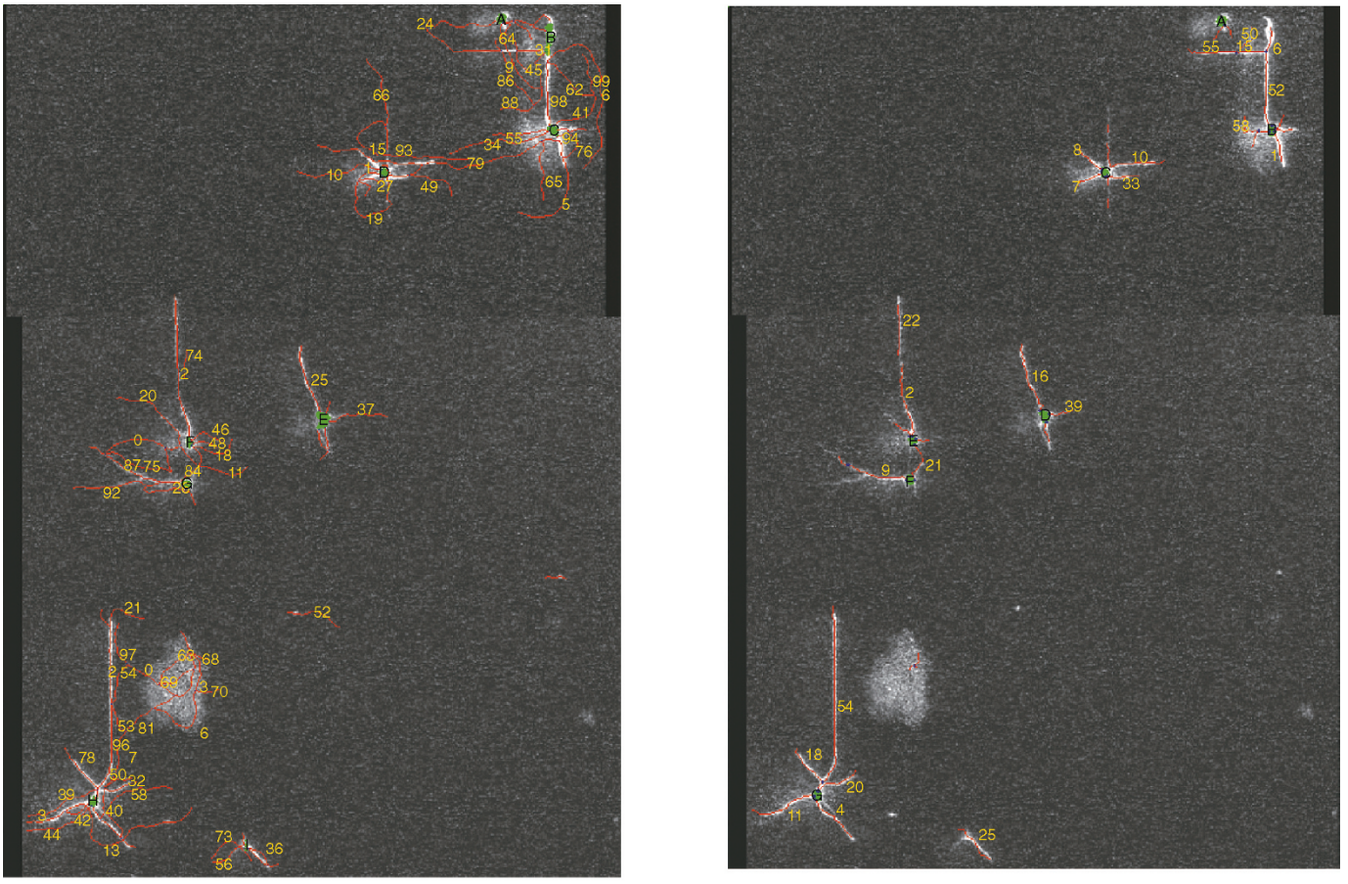


FIGURE 15.13. Illustrates the results of using mean template response (A), and the median template response (B) on noisy confocal images. Note the reduction in terms of erroneous false-positive traces when using the median template response. (image courtesy: IEEE Press.)

EXAMPLE COMBINING TUBE AND BLOB SEGMENTATION

One sometimes encounters images containing both blob-like and tube-like objects. From an image analysis standpoint, it is best to use distinctive fluorophores to highlight these two types of structures (e.g., Fig.15.5), and apply the appropriate analysis method to each image channel (Lin *et al.*, 2005). An example is shown in Figure 15.14(A), which shows an original image containing both blob-like objects (nuclei) in red and the tube-like cerebral vasculature in green. Figure 15.14(B) shows the resulting composite image after the separate segmentation of cell nuclei in the red channel and tracing of vasculature in the green channel. Figure 15.14(C) shows the original image containing blob-like objects (nuclei) in red and the cloud-like cytoskeleton in green. Figure 15.14(D) shows the resulting composite image after the segmentation of cell nuclei and cytoskeleton in the cytoplasm. After the initial image segmentation, a variety of postanalyses can be performed, such as morphometrics quantification, spatial analysis of different objects, object classification, and statistical analysis. Overall, these automated methods provide the useful tools for biologists replacing manual procedures that are tedious, subjective, and time consuming.

REGISTRATION AND MONTAGE SYNTHESIS METHODS

Registration is the process of spatially aligning two or more different images of the same region. When the object of interest is larger than the field-of-view of the microscope, two or more partially overlapping images must be acquired and then registered to provide an extended view of the specimen. Conversely, a sequence of images, taken at two different times, say before and after treatment, must then be registered to yield a common image subset to detect corresponding changes. Broadly, there are two approaches: landmark-based registration (Can *et al.*, 2002; Al-Kofahi *et al.*, 2003) and intensity-correlation based registration (Capek and Krekule, 1999; Beck *et al.*, 2000). Landmark-based registration relies on matching a set of distinctive points (landmarks) in pairs of the images in sequence, for example, spatially or temporally. Intensity-based registration methods work directly with the volumetric image data, utilizing all of the voxels. They compute a measure of correlation between the image pairs to estimate their relative spatial disposition. Finally, hybrid methods that combine ideas from landmark and intensity correlation methods are now emerging (Abu-Tarif, 2002). Most of these methods are well

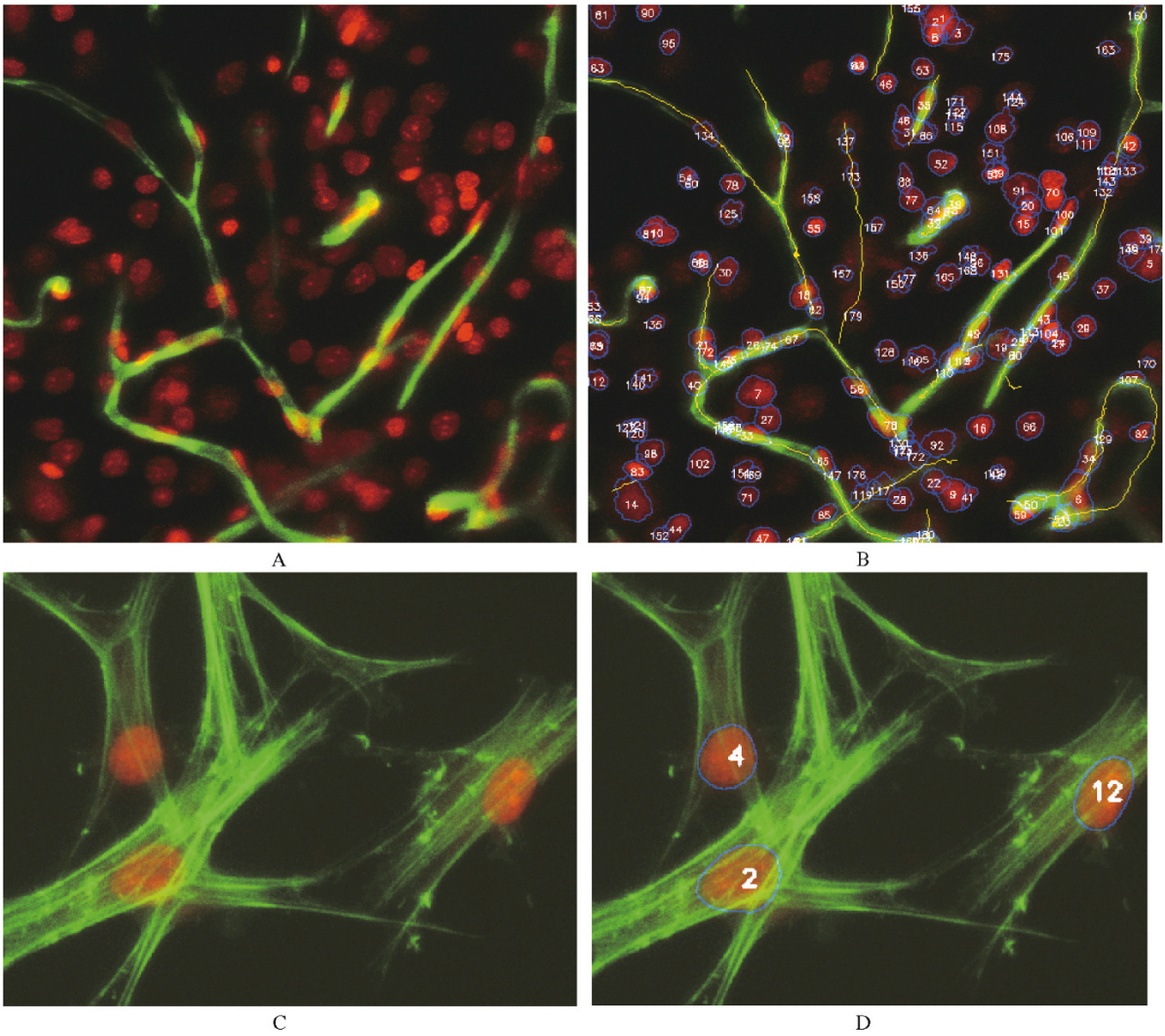


FIGURE 15.14. Image analysis examples illustrating (A) blob-like objects (nuclei) in red channel and tube-like objects (cerebral vasculature) in green channel; (C) blob-like objects (nuclei) in red channel and cloud-like objects (cytoskeleton) in the green channel. In both cases, image analysis is performed one spectral channel at a time, using separate methods for segmenting the blobs and tubes/clouds. Once this is done, it is possible to quantify the spatial relationships between the two kinds of objects. (data courtesy: Chris Bjornsson and Karen Smith at the Wadsworth Center, and Jan Stegemann Laboratory at Rensselaer.)

implemented in toolkit form, for example, the Insight toolkit from the National Library of Medicine (2001).

The transformation model used should have adequate degrees of freedom to account for motion and possible distortion between the two images (Hartley and Zisserman, 2000). For example, if only rigid body motion is considered between the two images, a rigid body transformation (rotation and translation) is adequate. However, if the anisotropic nature of the voxels and confocal system artifacts such as curvature of field and geometric distortions are present, a higher order transformation should be used. The affine model was proposed as a good compromise between model complexity and flexibility.

Landmark-based methods are generally fast and can scale up easily with higher-order transformation models, but their use is limited to the images where good landmarks can be extracted first. Centerline locations and branching points of tube-like objects (Al-Kofahi *et al*., 2003) and the centroids of blob-like objects (Becker *et al*., 1996) are examples of landmarks that can be used for registration. Although intensity-correlation–based methods do not require the landmark extraction step prior to registration, they are susceptible to imaging artifacts, such as non-uniform illumination, and do not exploit specific knowledge of the application context to simplify the problem. Furthermore, correlation-based algorithms are naturally far more computationally intensive than the landmark-based methods.

Montage synthesis, also known as mosaicing, is the process of stitching together a large number of partial local views ("windows") of the biological scene of interest to generate a more complete or extended field of view. This is especially valuable when the object/scene of interest is significantly larger than the

field of the microscope. The simplest type of montage synthesis consists of directly stitching together confocal images. Commonly, the microscope stage can be stepped in a series of overlapping two-dimensional (2D) or 3D windows that can then be merged into a single composite image that can be analyzed all at once. Alternatively, each of the windows can be subjected to automated image analysis, and the results stitched together to generate a synthetic montage-like representation. In addition to the common grayscale montage, it is possible to generate artificial representations such as segmentation label montages, and ball/stick diagrams, also known as object montages (Becker *et al*., 1996).

Another application for registration/montage synthesis is multi-view deconvolution (Cogswell *et al*., 1996; Heintzmann *et al*., 2000) and multi-view attenuation correction (Can *et al*., 2003). In the former, confocal images are blurred by the point spread function (PSF), which is asymmetric in the *x*-, *y*-, and *z*-dimensions. Multiple views can sometimes be used to account for the missing information and improve the axial resolution; ideally, we need tilted views separated by 90° angle. In the latter, the excitation/fluorescent light attenuates as a function of depth according to Beer's law (Weast, 1974) although spherical aberration is a more common cause of signal loss with depth. To correct for the attenuation, two views separated by 180° are used. In this scenario, the portions of one image with low signal-to-noise ratio (S/N) (far from the objective) are closer to the objective in the other image, with higher S/N, and vice versa (see also Chapter 37, *this volume*). These two images can be montaged to produce a more faithful representation of the entire specimen.

Figures 15.15 and 15.16 illustrate many of the issues described above. The neuron shown in Figure 15.15 was larger than the microscope field-of-view at the recording resolution. Also, the specimen was thick (more than 300 μm) which resulted in a significant signal loss for the deeper parts of the specimen. Montage synthesis was used to overcome these limitations; the specimen was mounted between two coverslips (Can *et al*., 2003) to allow imaging from both sides. The first image stack was captured in the conventional way, then the specimen was moved using the *x,y*-stage, and the second image stack was taken to capture the adjacent *x,y*-field. To correct for attenuation and to increase the imaging depth, the specimen was then flipped top-to-bottom, and two more sets of images were captured as before. Figure 15.16 shows the result of montaging the four image stacks with attenuation correction; the result is clearly a more faithful representation of the specimen. It captures the whole neuron, with high resolution and better S/N.

Finally, the microscopist is often faced with multi-channel data. Techniques for registering and montaging such data are

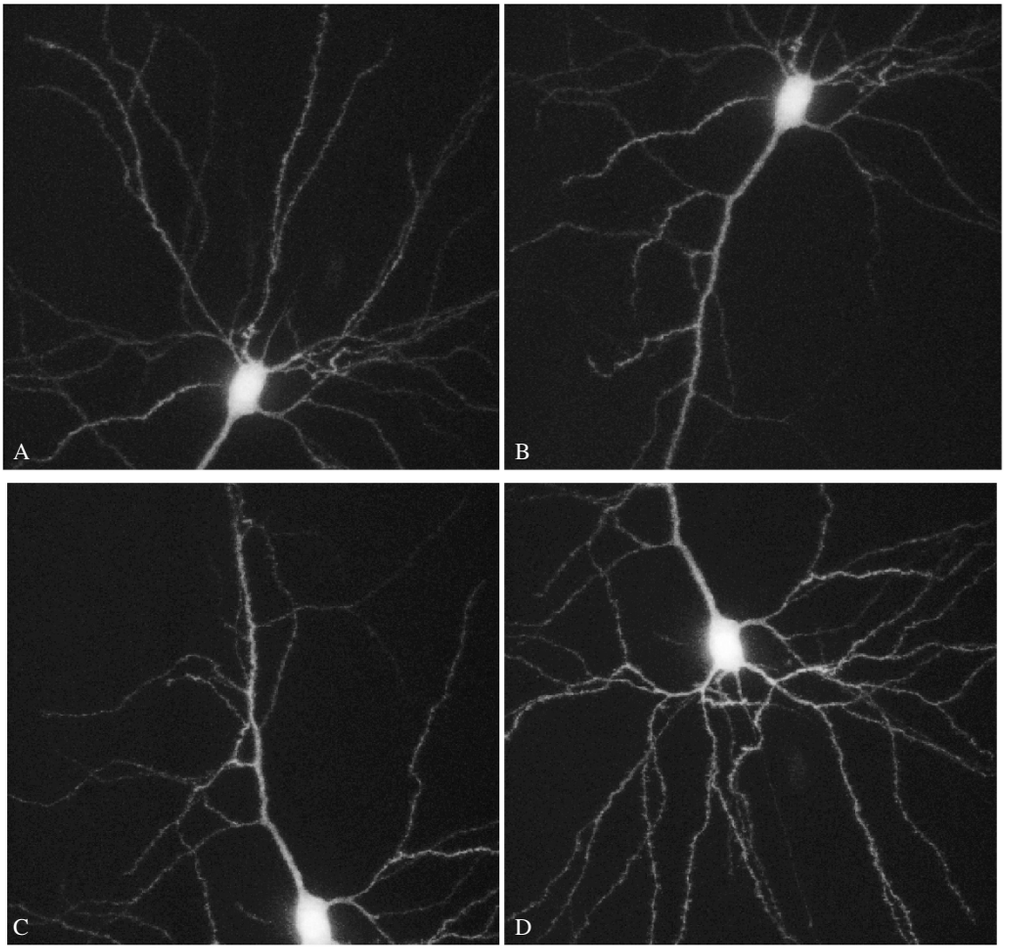


FIGURE 15.15. Sample views of an Alexa stained neuron from a rat brain. *X-y* maximum intensity projection. Top row, before flipping; the specimen was translated to capture the whole neuron between the positions in (A) and (B) respectively. Bottom row, after flipping; again, the specimen was translated to capture the whole neuron between the positions in (C) and (D) respectively. Each image is 512 × 480 × 261 voxels in size, except for the one in (C), 512 × 480 × 323 voxels. The neuron is larger than the microscope field of view, the four views cover the whole neuron maintaining high resolution. The sampling rates are 0.375 mm/voxel for x and y dimensions and 0.5 mm/voxel for the z dimension. (courtesy: Journal of Microscopy.)

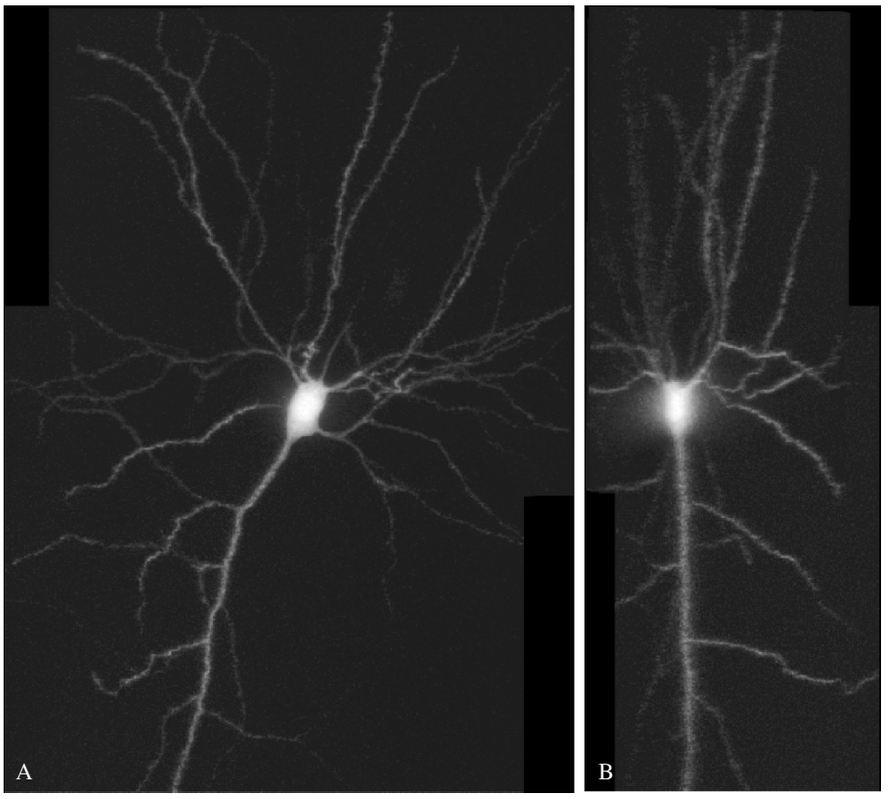


FIGURE 15.16. Mosaic image constructed from the four views in Figure 15.15 (A) top view (*x*-*y*), and (B) side view (*x*-*z*), maximum intensity projection. The result of the montaging is a high-resolution image for the whole neuron with increased effective imaging depth. (courtesy: Journal of Microscopy.)

analogous as long as corrections for chromatic aberration are performed. Figure 15.17(A) illustrates a two-channel mosaic representing one hemisphere of a rat brain section. The green regions are the nuclei and red color indicates the FISH signal. The full mosaic consists of 7911 × 6188 voxels (140 MB), and is synthesized from 70 imaging windows each of width 1024 × 1024 pixels. The inset is an enlarged view of a small portion of the montage at higher resolution. Figure 15.17(B) illustrates the montaging based on the traced vasculature structure.

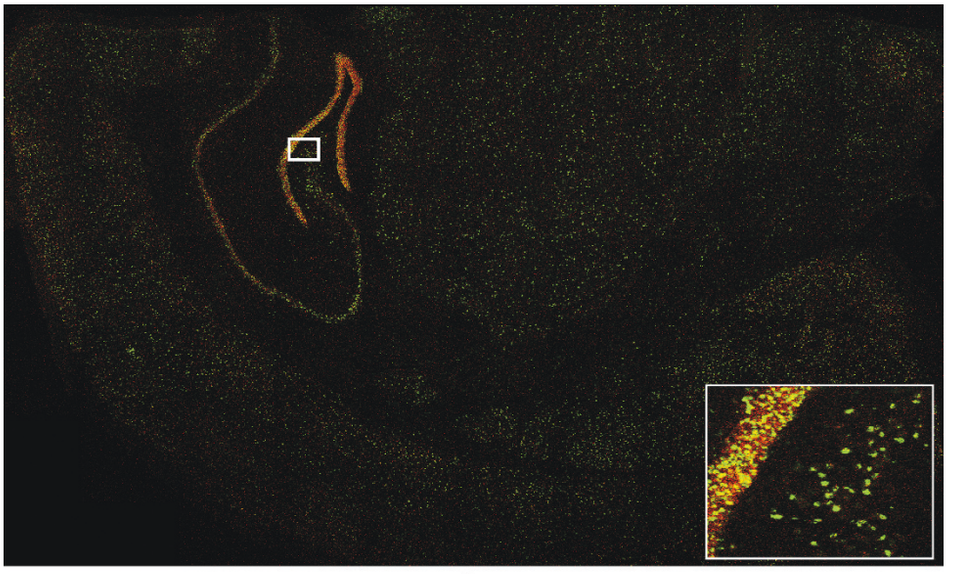
METHODS FOR QUANTITATIVE MORPHOMETRY

Morphometric data are either the end goal of image analysis or an intermediate step towards testing a hypothesis. Listed below are common types of object measurements for blob-like and/or tube-like objects. Interested readers are referred to other books (Theodoridis and Koutroumbas, 1999; Shapiro and Stockman, 2001) for details on the algorithms needed to calculate these measurements.

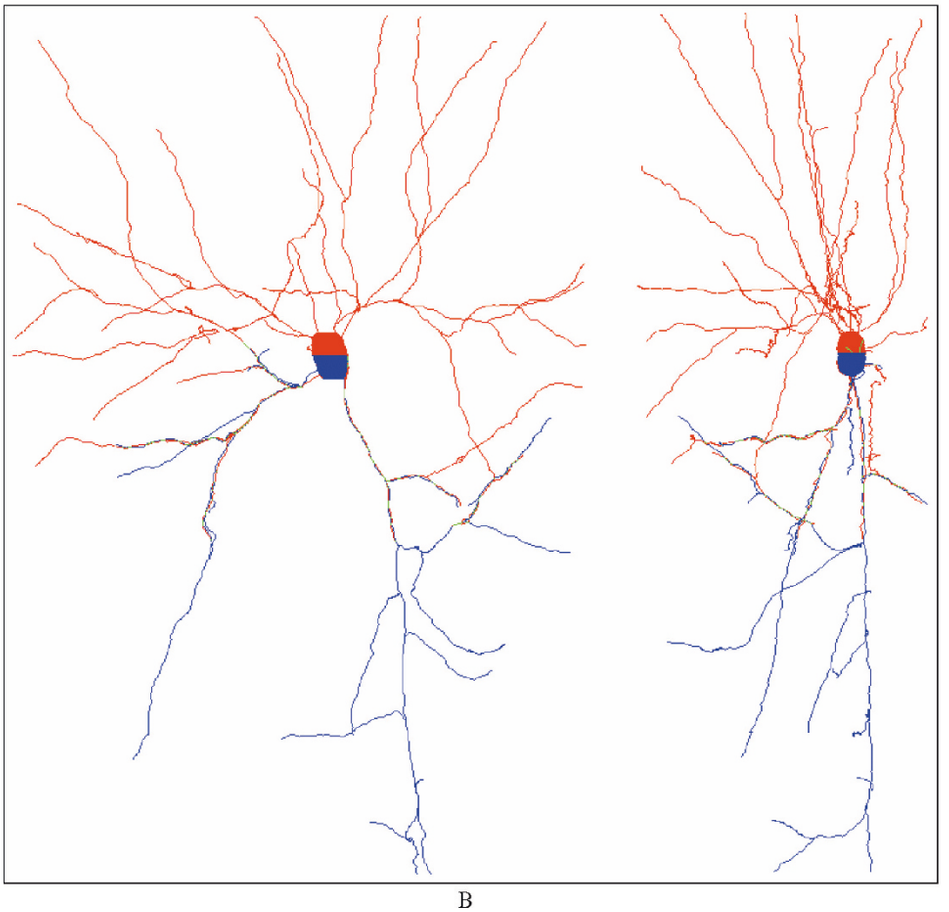
- **Size measures**: Diameter, volume, surface area, length, width.
- **Intensity and spectral measurements**: Integrated, mean, and median intensity of one or more spectral channels over an object.
- **Shape measures**: Eccentricity, elongatedness, compactness, convexity, thickness, shape complexity, tortuosity, area-perimeter ratio, bending energy.
- **Texture measures**: Intensity variance, clumping, homogeneity.
- **Location and pose**: Centroid, major and minor axes, angle of tilt.
- **Interest points**: Convex/concave corners, inflexion points, bifurcations.
- **Invariants**: Dimensionless ratios such as shape factors, affine invariant moments.
- **Topological measures**: Branching factors and angles.
- **Group properties**: Group size and shape, repetition length.

Morphometric data can be generated from the segmented objects during segmentation or by postprocessing the segmentation results (Koh *et al*., 2002; Williams *et al*., 2003). In some cases, the segmentation algorithms that produce just a segmented volume may need postprocessing steps such as skeletonization (Lee *et al*., 1994; Maddah *et al*., 2003) to obtain the measurements. In the analysis of cellular compartment temporal activity by fluorescence *in situ* hybridization (catFISH) example, a set of measurements are made for each segmented nucleus. The measurements include nuclear features such as volume, intensity, texture, shape, and FISH measurements such as FISH spot volume, *z*-depth and intensity value, intranuclear and cytoplasmic FISH measurement, etc. Figure 15.1(B) shows a part of a spreadsheet containing such data. This data is ready for the statistical analysis required for hypothesis testing. It can also be used for manual evaluation to verify the accuracy of the automated results.

In the vessel tracing example, a region of interest is defined for each image of a time series data set by the intersection of the image and all other images in the set. Morphometric data collected within these regions include total vasculature length, average vasculature segment length, average horizontal width, and average vertical width, all extracted by the tracing algorithm. Statistics and traces generated outside these regions are ignored. The generated statistics are entered into a spreadsheet and plotted to highlight the changes. Actual change measurements such as percentage reduction in the total number of vasculature segments or percentage increase in the total vasculature length can be obtained directly from the spreadsheet.



A



B

FIGURE 15.17. Illustrating the feature-based montaging of multi-spectral confocal microscope images. (A) Each individual image is first segmented, and a set of features (cell nuclei) are extracted from the segmented objects. These images are the basis of pairwise registration to montage the images. (B) Neurites are traced first, which become the basis of the montaging.

METHODS FOR VALIDATING THE SEGMENTATION AND MAKING CORRECTIONS

Validation can and should be performed at various stages of automatic image analysis. The main objective is to quantify the disagreement between automated results and the "ground truth," where a measurement of the disagreements is interpreted as the error. The ground truth is usually obtained manually. Being subjective, it is prone to inter- and intraobserver variability. This can be reduced by using multiple and independent manual segmentation results that are combined to approximate the ground truth. An effective method for combining the manual segmentations is to establish a consensus. For this, each disagreement between manual observers is resolved by careful discussion. Furthermore, the type of disagreement between the manual and automated results depends upon the type of objects.

For blobs, the types of errors include false detection (false positives), misses (false negatives), errors in separating connected objects, and errors in correctly delineating the boundaries of objects (Chawla *et al*., 2004). For tube-like objects, image analysis errors include falsely traced segments and branch points (false positives) and missed segments and branch points (false negatives), accuracy of the trace, accuracy of width measurements, and accuracy in locating branching/crossover points (Abu-Tarif *et al*., 2002; Al-Kofahi *et al*., 2003). When considering time-lapse series of live specimens (Abdul-Karim *et al*., 2003), it is also useful to quantify registration errors, and errors in detecting change.

As an example, the catFISH automated image analysis software was validated with respect to three criteria: (1) accuracy of nuclear segmentation, (2) accuracy in classifying intranuclear foci; and (3) accuracy in classifying cytoplasmic FISH signal. The manual image analysis was performed using MetaMorph software (Universal Imaging Corporation, West Chester, PA). Three separate experts manually rated each of the test image stacks for numbers of nuclei, nuclei that contained FISH signal, and cells that contained cytoplasmic FISH signal. Statistical analysis was done using a "consensus count" established by three experts.

Quantitative validation may also involve voxel-to-voxel comparisons of the segmented volume, or comparisons of any other entities derived from the segmented volume such as the vasculature centerline or the cell centroid. The comparison can be performed automatically to further reduce the subjectivity of validating the segmentation results (Al-Kofahi *et al*., 2002). In the case of tube-like objects, the centerline locations are extremely important because almost all morphometrics depend on them. Centerline locations are typically validated for the deviation from a "true" centerline (reflects the accuracy of the automated method), and the centerline coverage of the objects in the image (reflects how much manual editing the automated result needs). To obtain the accuracy metric, a distance map (Borgefors, 1986) can be used to calculate the average Euclidean distance between every voxel of manually segmented centerlines and every voxel of automatically segmented centerlines that are within a certain Euclidean distance.

Going further, validation of the extracted measurements from a segmented volume requires manual extraction of the measurements from the manually segmented volume. This is a prohibitively time-consuming procedure in 3D image analysis, and as the results will be subjective, it may not be useful. Instead, phantoms or artificial images are generated using ideal models (blobs, tubes, or clouds) of the biological objects with known morphometrics. Measurements are extracted automatically using the automated methods, and validated with the known values. Noise and other irregularities may be introduced to the phantoms to simulate actual images.

Manual editing is usually assisted by some software tools. Figure 15.2 shows the catFISH example of such software developed by this group. After manual validation obtained by consensus of several independent observers, automated segmentation results are further corrected using the convenient tools, such as buttons for add/delete, split/merge, and shrink/dilate in the catFISH system, as shown in Figure 15.18. Figure 15.19 illustrates the common editing to the tube-like object segmentation. Note that, by editing the automated results, the subjectivity factor of manual analysis is reduced down to the correspondence between manual and automated results.

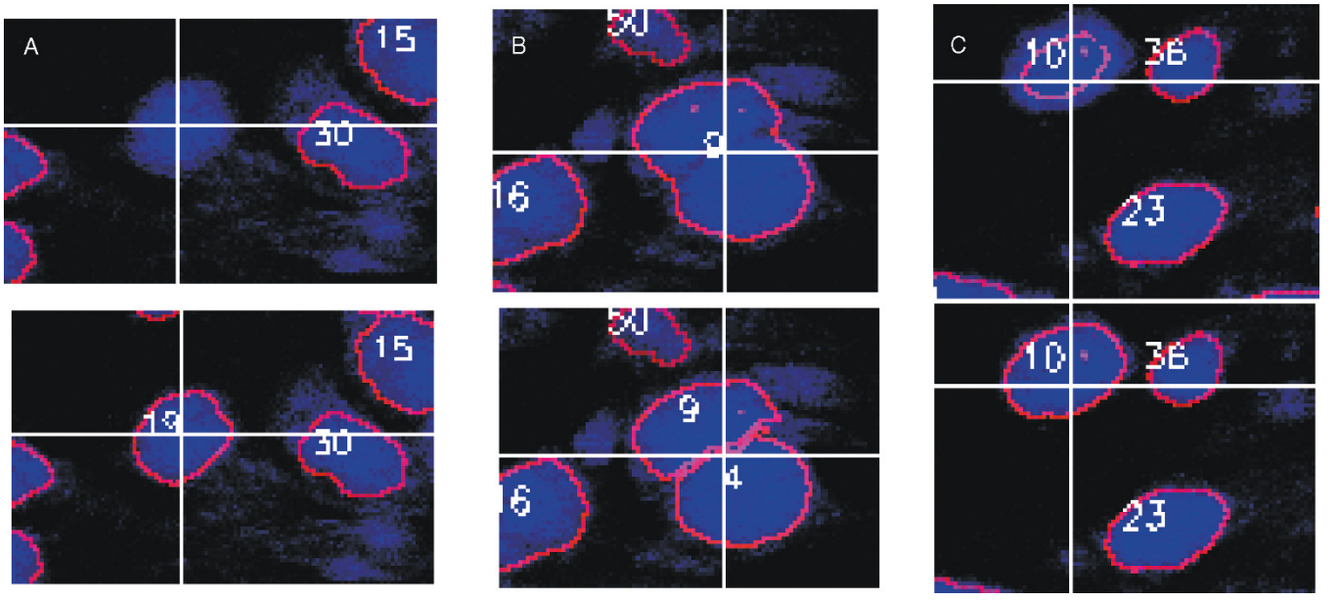


FIGURE 15.18. Illustrating common image analysis errors associated with blob segmentation, and manual editing tools to correct them: (A) Adding a missed object using a region growing tool; (B) Splitting connected objects; (C) Correcting a boundary location error.

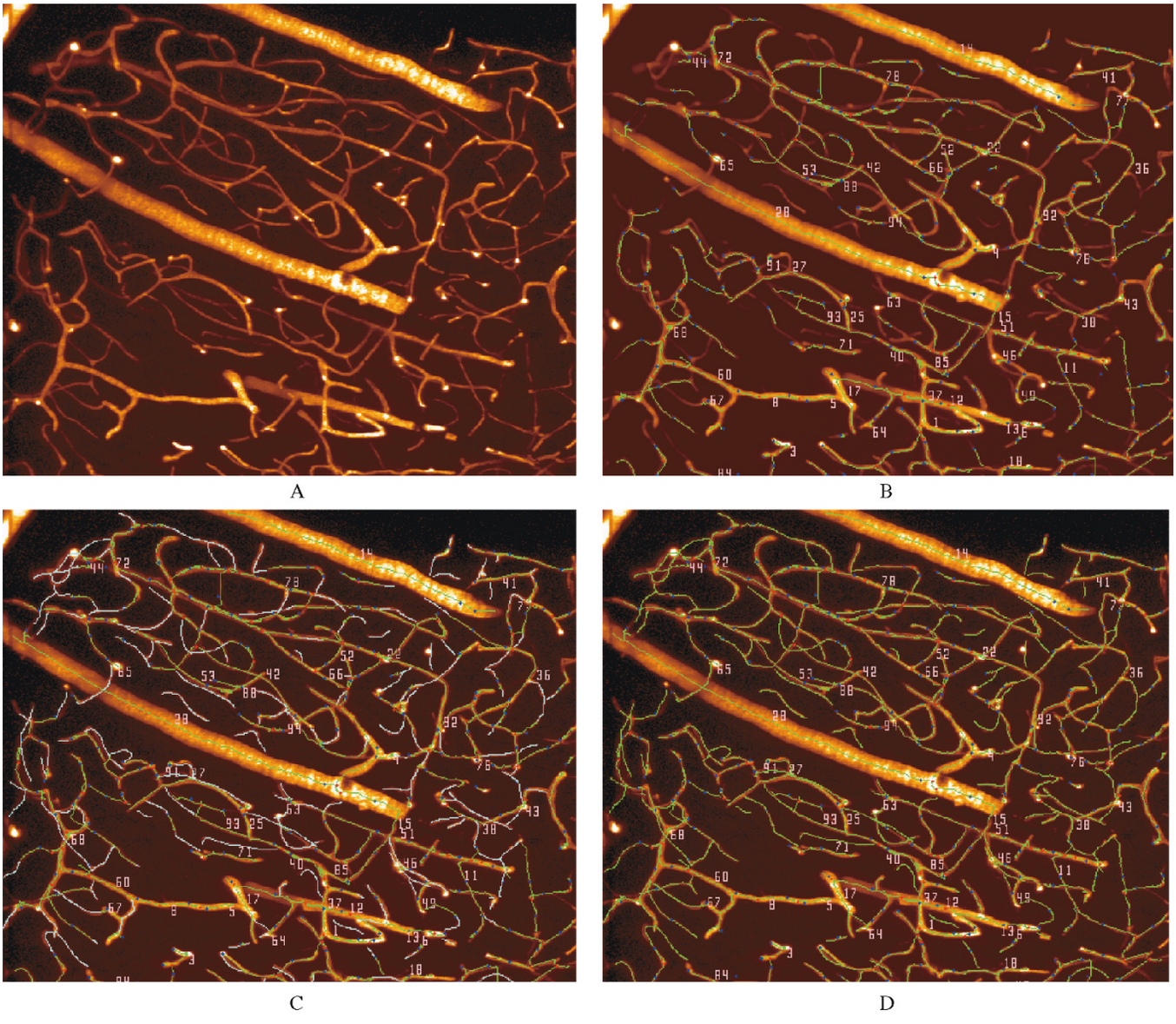


FIGURE 15.19. Illustrating the manual edits to the tube-like object segmentation. (A) Original image; (B) Automated tracing results; (C) Manually modified traces shown in light blue; (C) Final results.

ANALYSIS OF MORPHOMETRIC DATA

The statistical analysis of morphometric data is necessarily application-specific. The following paragraphs provide two examples illustrating the main ideas.

In the catFISH system, the important goal is to classify the nuclei in the image based on the presence of the intranuclear and cytoplasmic FISH signal. The measurements are integrated and associated spatially with the nuclear segmentation results to generate a detailed tabular/database representing the location and detailed morphometric parameters for each nucleus, and the associated FISH signals. Nucleus class information is defined by the user according to some criteria such as the color channels, presence or absence of signal, and location of the signal. The software uses this information to automatically classify each nucleus as negative or as containing intranuclear and/or cytoplasmic FISH signal based upon its morphometric and functional (FISH) measurements. The final result is output into a text file including total nuclear count and the number and percentage of nuclei in each class.

In the angiogenesis example, the primary intent is to quantitate temporal vessel changes in a set of time-series images. There are two broad methods for change analysis. One method is to compute morphometric data from images at each temporal sampling point, and to perform a statistical comparison of these data. A more ambitious approach is to register the images over time and extract detailed changes on a vessel-segment by vessel-segment basis. In this work, the less ambitious approach was adopted as a starting point. Vessel lengths, widths, and count can be readily obtained from the traces generated by the automatic tracing algorithm described. Naturally, only vasculature segments located in the volume common to all four images contributed to these statistics. An overall Change Index is calculated as the simple ratio of the current measurement over the previous measurement.

DISCUSSION, CONCLUSION, AND FUTURE DIRECTIONS

We have attempted to summarize techniques for automated 3D image analysis by organizing the methods into those suitable for a small number of categories of features (blobs, tubes, clouds, mixed). By recognizing image objects along these lines, the reader is better able to select from the available image analysis tools. It has also served as the basis for organizing image analysis packages such as the catFISH system.

The life-sciences researcher is often able to perform automated 2D image analysis using off-the-shelf software, for example, NIH Image, MetaMorph by Universal Imaging, and VoxelView by Vital Images (more examples discussed in Chapter 14, *this volume*). The sheer complexity and variability of biological imagery and the current state of evolution of automated 3D image analysis technology imply that the assistance of an image analysis specialist is often called for. It is hoped that the terminology and language presented here can bridge these disciplines. The organization of image analysis by type of objects also forms a good basis for facilitating productive discussion between life-sciences researchers and computer scientists.

Automated image analysis is a dynamic computer-intensive discipline. It has benefited tremendously from problems posed by life-science researchers. Much work remains to be done. For example, the algorithms are still not nearly as adaptive as the human visual system. Given a novel set of image data, the human observer can be trained much more quickly than new image analysis tools can be designed and tested. Nevertheless, development of new tools is worthwhile whenever large amounts of data must be processed, for instance, in the development of high-content screening assay as described in Chapter 46, *this volume*. This chapter has accordingly devoted attention to studies that require this type of sophisticated automation.

ACKNOWLEDGMENTS

The work described here was funded by a number of sponsors. Recent sponsorships include the National Science Foundation (award EEC-9986821 and various supplements), the National Institutes of Health (awards AG18230), MARA of Malaysia, and by MicroBrightfield Inc. This work was also partially supported by the Nanobiotechnology Center (NBTC), an STC Program of the National Science Foundation under Agreement No. ECS-9876771, and by grant NINDS 8R01EB-000359 from the National Institutes of Health.

The authors are grateful to a number of colleagues who have contributed data and insight leading to this book chapter. The catFISH example is drawn from collaborative work with Carol Barnes, John Guzowski, Kathy Olson, Monica Chawla, and Almira Vazarjanova at the University of Arizona, and Umesh Adiga at the Lawrence Berkeley Laboratory. The angiogenesis example is drawn from collaborative efforts with Rakesh K. Jain and Edward Brown at Massachusetts General Hospital. The neuron tracing examples are drawn from collaborations with Christopher Pace, Natalie Dowell, Chris Bjornsson, Danielle LeBlanc, and Karen Smith at the Wadsworth Center, and George Nagy at Rensselaer. The image registration examples are drawn from collaborative work with Ali Can and Hanu Singh at the Woods Hole Oceanographic Institute, and Charles Stewart at Rensselaer. The example in Figure 15.14 is drawn from collaborative projects with Jan Stegemann and Sung-Yun Lee at Rensselaer Polytechnic Institute.

REFERENCES

Abdul-Karim, M.-A., Al-Kofahi, K., Brown, E.B., Jain, R.K., and Roysam, B., 2003, Automated tracing and change analysis of angiogenic vasculature from in vivo multiphoton confocal image time series, *Microvasc. Res.* 66:113–125.

Abdul-Karim, M.-A., Roysam, N.M., Dowell-Mesfin, A., Jeromin, M., Yuksel, M., and Kalyanaraman, S., 2005, Automatic selection of parameters for vessel/neurite segmentation algorithms. *Image Processing, IEEE Trans.* 14(9):1338–1350.

Abu-Tarif, and Ahmad A., 2002, Volumetric registration based on intensity and geometry features, PhD Thesis, Rensselaer Polytechnic Institute, Troy, New York.

Adams, R., and Bischof, L., 1994, Seeded region growing, *IEEE Trans. Pattern Anal. Machine Intell.* 16:641–647.

Adiga, U., and Chaudhuri, B., 2001a, An efficient method based on watershed and rule-based merging for segmentation of 3D histo-pathological images, *Pattern Recognition* 34:1449–1458.

Adiga, U., and Chaudhuri, B., 2001b, Some efficient methods to correct confocal images for easy interpretation, *Micron* 32:363–370.

Al-Kofahi, K.A., Lasek, S., Szarowski, D.H., Pace, J., Nagy, G., Turner, J.N., and Roysam, B., 2002, Rapid automated three-dimensional tracing of neurons from confocal image stacks, *IEEE Trans. Inform. Technol. Biomed.* 6:171–187.

Al-Kofahi, O., Can, A., Lasek, S., Szarowski, D.H., Turner, J.N., and Roysam, B., 2003, Algorithms for accurate 3D registration of neuronal images acquired by confocal scanning laser microscopy, *J. Microsc.* 211:8–18.

Ancin, H., Roysam, B., Dufresne, T.E., Chestnut, M.M., Ridder, G.M., Szarowski, D.H., and Turner, J.N., 1996, Advances in automated 3-D image analyses of cell populations imaged by confocal microscopy, *Cytometry* 25:221–234.

Ballard, D.H., and Brown, C.M., 1982, *Computer Vision*, Prentice Hall, Englewood Cliffs, New Jersey.

Beck, J.C., Murray, J.A., Willows, A.O., and Cooper, M.S., 2000, Computer-assisted visualizations of neural networks: Expanding the field of view using seamless confocal montaging, *J. Neurosci. Methods* 98:155–163.

Becker, D.E., Ancin, H., Szarowski, D.H., Turner, J.N., and Roysam, B., 1996, Automated 3-D montage synthesis from laser-scanning confocal images: application to quantitative tissue-level cytological analysis, *Cytometry* 25:235–245.

Besl, P.J., and Jain, R.C., 1988, Segmentation through variable-order surface fitting, *IEEE Trans. Pattern Anal. Machine Intell.* 10:167–192.

Beucher, S., 1982, Watersheds of functions and picture segmentation, *IEEE International Conference on Acoustics, Speech, and Signal Processing*, pp. 1928–1931.

Beucher, S., 1991, The watershed transformation applied to image segmentation, *Conference on Signal and Image Processing in Microscopy and Microanalysis*, Cambridge, UK, pp. 299–314.

Bhanu, B., 1982, Shape matching and image segmentation using stochastic labeling, Los Angeles Image Processing Institute.

Bhanu, B., and Lee, S., 1994, *Genetic Learning for Adaptive Image Segmentation*, Kluwer Academic Publishers, Boston.

Bhattacharjya, A., and Roysam, B., 1994, Joint solution of low, intermediate and high-level vision tasks by evolutionary optimization: Application to computer vision at low SNR, *IEEE Trans. Neural Networks* 5:83–95.

Black, M., and Rangarajan, A., 1996, On the unification of line processes, outlier rejection, and robust statistics with applications in early vision, *Int. J. Comput. Vis.* 19(1).

Blake, A., and Zisserman, A., 1987, *Visual Reconstruction*, MIT Press, Cambridge, Massachusetts.

Borgefors, G., 1986, Distance transformations in digital images, *Comput. Vis. Graphics Im. Pract.* 34:344–371.

Bovik, A.C., Aggarwal, S.J., Merchant, F., Kim, N.H., and Diller, K.R., 2001, Automatic area and volume measurements from digital biomedical images. In: *Image Analysis: Methods and Applications* (D.-P. Häder, ed.), CRC Press, Boca Raton, Florida, pp. 23–64.

Brown, E.B., Campbell, R.B., Tsuzuki, Y., Xu, L., Carmeliet, P., Fukumura, D., and Jain, R.K., 2001, In vivo measurement of gene expression, angiogenesis and physiological function in tumors using multi-photon laser scanning microscopy, *Nat. Med.* 7:864–868.

Can, A., Al-Kofahi, O., Lasek, S., Szarowski, D.H., Turner, J.N., and Roysam, B., 2003, Attenuation correction in confocal laser microscopes: A novel two-view approach, *J. Microsc*. 211:67–79.

Can, A., Shen, H., Turner, J.N., Tanenbaum, H.L., and Raysam, B., 1999, Rapid automated tracing and feature extraction from retinal fundus images using direct exploratory algorithms, *IEEE Trans. Inform. Technol. Biomed*. 3:125–138.

Can, A., Stewart, C.V., Roysam, B., and Tanenbaum, H.L., 2002, A feature-based, robust, hierarchical algorithm for registering pairs of images of the curved human retina, *IEEE Trans. Pattern Anal. Machine Intell*. 24:347–364.

Capek, M., and Krekule, I., 1999, Alignment of adjacent picture frames captured by a CLSM, *IEEE Trans. Inform. Technol. Biomed.* 3:119–124.

Capowski, J.J., 1989, *Computer Techniques in Neuroanatomy*, Plenum Press, New York.

Castleman, K., 1996, *Digital Image Processing*, Prentice-Hall, Englewood Cliffs, New Jersey.

Chang, Y.-L., and Li, X., 1994, Adaptive image region-growing, *IEEE Trans. Image Processing* 3:868–872.

Chawla, M.K., Lin, G., Olson, K., Vazdarjanova, A., Burke, S.N., McNaughton, B.L., Worley, P.F., Guzowski, J.F., Roysam, B., and Barnes, C.A., 2004, 3D-catFISH: A system for automated quantitative three-dimensional compartmental analysis of temporal gene transcription activity imaged by fluorescence in situ hybridization, *J. Neurosci. Methods* 139:13–24.

Cogswell, C.J., Larkin, K.G., and Klemn H.U., 1996, Fluorescence microtomography: Multiangle image acquisition and 3D digital reconstruction. In: *Three-Dimensional Microscopy: Image Acquisition and Processing III*, SPIE, San Jose, California.

Cohen, A.R., Roysam, B., and Turner, J.N., 1994, Automated tracing and volume measurements of neurons from 3-D confocal fluorescence microscopy data, *J. Microsc*. 173:103–114.

Cooper, M., 1998, The tractability of segmentation and scene analysis, *Image and Vision Computing* 30(1):27–42.

Cootes, T.F., Taylor, C., Cooper, D., and Graham, J., 1995, Active shape models — Their training and application, *Comput. Vis. Image Understanding* 61:38–59.

Davis, L., 1975, A survey of edge detection techniques, *Comput. Graphics Image Process*. 4(3):248–270.

di Zenzo, S., 1983, Advances in image segmentation, *Image and Vision Computing* 1:196–210.

Digabel, H., and Lantuejoul, C., 1978, Iterative algorithms, *Pract. Methods* 8:85–99.

Dillencourt, M., Samet, H., and Tamminen, M., 1992, A general approach to connected-components labeling for arbitrary image representations, *J. ACM* 39:253–280.

Dougherty, E.R., 1993, Mathematical Morphology in Image Processing, Marcel Dekker, New York.

Fu, K., and Mui, J., 1981, A survey of image segmentation, *Pattern Recognition* 13:3–16.

Ghanei, A., and Soltanian-Zadeh, H., 2002, A discrete curvature-based deformable surface model with application to segmentation of volumetric images, *IEEE Trans. Inform. Technol. Biomed*. 6:285–295.

Glaser, J.R., and Glaser, E.M., 1990, Neuron imaging with Neurolucida — A PC-based system for image combining microscopy, *Comput. Med. Imaging Graphics* 14:307–317.

Gong, W., and Bertrand, G., 1990, A note on thinning of 3-D images using sage point thinning algorithm, *Pattern Recogn. Lett*. 11:499–500.

Guigues, L., Le Men, H., and Cocquerez, J.-P., 2003, The hierarchy of the cocoons of a graph and its application to image segmentation, *Pattern Recogn. Lett*. 24:1059–1066.

Guzowski, J., and Worley, P., 2001, *Cellular Compartment Analysis of Temporal Activity by Fluorescence In Situ Hybridization (catFISH)*, John Wiley and Sons, New York.

Guzowski, J.F., McNaughton, B.L., Barnes, C.A., and Worley, P.F., 1999, Environment-specific expression of the immediate-early gene Arc in hippocampal neuronal ensembles, *Nat. Neurosci*. 2:1120–1124.

Haddon, J.F., and Boyce, J.F., 1993, Co-occurrence matrices for image analysis, *Electron Commun. Eng.* J. 5:71–83.

Haralick, R., and Shapiro, L., 1985, Image segmentation techniques, *Computer Vision Graphics and Image Processing* 29:100–132.

Hartley, R., and Zisserman, A., 2000, Multiple View Geometry in Computer Vision, Cambridge University Press, New York.

He, W., Hamilton, T.A., Cohen, A.R., Holmes, T.J., Pace, C., Szarowski, D.H., Turner, J.N., and Roysam, B., 2003, Automated three-dimensional tracing of neurons in confocal and brightfield images, *Microsc. Microanal*. 9:296–310.

Heintzmann, R., Kreth, G., Cremer, C., 2000, Reconstruction of axial tomographic high resolution data from confocal fluorescence microscopy: A method for improving 3D FISH images, *Anal. Cell. Pathol*. 20:7–15.

Higgins, W., and Ojard, E., 1993, Interactive morphological watershed analysis for 3D medial images, *Comput. Med. Imaging Graphics* 17:387–395.

Hojjatoleslami, S.A., and Kittler, J., 1998, Region growing: A new approach, *IEEE Trans. Image Processing* 7:1079–1084.

Horowitz, S., and Pavlidis, T., 1974, Picture segmentation by a directed split and merge procedure. International Conference on Pattern Recognition, Copenhagen, Denmark, pp. 424–433.

Howard, V., and Reed, M.G., 1998, *Unbiased Stereology: Three-Dimensional Measurement in Microscopy*, Springer-Verlag, New York.

Howard, V., Reid, S., Baddeley, A., and Boyde, A., 1985, Unbiased estimation of particle density in the tandem scanning reflected light microscope, *J. Microsc*. 138:203–212.

Huber, P.J., 1981, *Robust Statistics*, John Wiley and Sons, New York.

ITK, 2001, *NLM Insight Segmentation and Registration Toolkit*, available at: http://www.itk.org.

Jaeger, D., 2000, Accurate reconstruction of neuronal morphology, In: *Computational Neuroscience: Realistic Modeling for Experimentalists* (E.D. Schutter, ed.), CRC Press, Boca Raton, Florida, pp. 159–178.

Jain, R.K., Munn, L.L., and Fukumura, D., 2002, Dissecting tumour pathophysiology using intravital microscopy, *Nat. Rev. Cancer* 2:266–276.

Kanade, T., 1978, Region segmentation: signal vs. semantics, International Conference on Pattern Recognition.

Kerfoot, I., and Bresler, Y., 1999, Theoretical analysis of multispectral image segmentation criteria, *IEEE Trans. Image Process*. 8(6):798.

Kim, B., Kim, D., and Park, D., 2001, Novel precision target detection with adaptive thresholding for dynamic image segmentation, *Machine Vis. Appl*. 12:259–270.

Koh, I.Y., Lindquist, W.B., Zito, K., Nimchinsky, E.A., and Svoboda, K., 2002, An image analysis algorithm for dendritic spines, *Neural Comput*. 14:128–1310.

Lee, T.C., Kashyap, R.L., and Chu C.N., 1994, Building skeleton models via 3-D medial surface axis thinning algorithms, *Graphic. Models Image Process*. 56:462–478.

Lin, G., Adiga, U., Olson, K., Guzowski, J., Barnes, C., and Roysam, B., 2003, A hybrid 3-D watershed algorithm incorporating gradient cues and object models for automatic segmentation of nuclei in confocal image stacks, *Cytometry* 56A:23–36.

Lin, G., Bjornsson C.S., Smith, K.L., Abdul-Karim, M.A., Turner, J.N., Shain, W., and Roysam, B., 2005, Automated image analysis methods for 3D quantification of the neurovascular unit from multi-channel confocal microscope images. *Cytometry* 66(1):9–23.

Lin, G., Chawla, M.K., Olson, K., Guzowski, J.F., Barnes, C.A., and Roysam, B., 2004, Hierarchial, model-based merging of multiple fragments for 3-D segmentation of nuclei, *Cytometry* DOI: 10.1002/cyto.a.20099.

Lorigo, L.M., Faugeras, O.D., Grimson, W.E., Keriven, R., Kikinis, A., Nabavi, A., and Westin, C.F., 2001, CURVES: Curve evolution for vessel segmentation, *Med. Image Anal*. 5:195–206.

Mackin, R., Roysam, B., Holmes, T., and Turner, J., 1993, Automated image analysis of thick cytological preparations using 3-D microscopy and 3-D image analysis: Applications of pap smears, *Anal. Quant. Cytol. Histol*. 15:405–417.

Maddah, M., Afzali-Kusha, A., and Soltanian-Zedeh, H., 2003, Efficient centerline extraction for quantification of vessels in confocal microscopy images, *Med. Phys*. 30:204–211.

Maisonneuve, F., 1982, Sue le partage des eaux, Technical report School of Mines.

Malpica, N., de Solorzano, C.O., Vaquero, J.J., Santos, A., Vallcorba, I., Garcia-Sagredo, J.M., and del Pozo, F., 1997, Applying watershed algorithms to the segmentation of clustered nuclei, *Cytometry* 28:289–297.

Marko, M., and Leith, A., 1992, Contour based 3-D surface reconstruction using stereoscopic contouring and digitized images, In: *Visualization in Biomedical Microscopics: 3-D Imaging and Computer Applications* (A. Kriete, ed.), VCH, Weinheim, Germany, pp. 45–74.

McInerney, T., and Terzopoulos, D., 1996, Deformable models in medical image analysis: A survey, *Med. Image Anal*. 1:91–108.

Mitiche, A., and Aggarwal, J., 1985, Image segmentation by conventional and information-integrating techniques: A synopsis, International Conference on Pattern Recognition 3:50–62.

Morel, J.-M., and Solimini, S., 1995, Variational Methods in Image Segmentation: With Seven Image Processing Experiments, Birkhèauser, Boston.

Mouton, P.R., 2002, *Principles and Practices of Unbiased Stereology: An Introduction for Bioscientists*, Johns Hopkins University Press, Baltimore.

Neumann, A., 2003, Graphical Gaussian shape models and their application to image segmentation, *IEEE Trans. Pattern Anal. Machine Intell*. 25:316–329.

Nevatia, R., 1986, Image segmentation, *Handbook of Pattern Recognition and Image Processing* 86.

Pavlidis, T., 1977, *Structural Pattern Recognition*, Springer-Verlag, Berlin, Germany.

Pavlidis, T., and Liow, Y.-T., 1990, Integrating region growing and edge detection, *IEEE Trans. Pattern Anal. Machine Intell*. 12:225–233.

Pawley, J., 2000, The 39 steps: A cautionary tale of quantitative 3-D fluorescence microscopy, *Bioimaging Biotechn*. 28:884–888.

Pham, D.L., Xu, C., and Prince, J.L., 2000, Current methods in medical image segmentation, Annu. Rev. Biomed. Eng. 2:315–337.

Ranade, S., and Prewitt, J., 1980, A comparison of some segmentation algorithms for cytology, *ICPR* 80.

Raya, S.P., and Udupa, J.K., 1990, Shape-based interpolation of multidimensional objects, *IEEE Trans. Med. Imaging* 9:32–42.

Rezaee, M.R., 1998, Application of fuzzy techniques in image segmentation, PhD thesis, University of Leiden, Leiden, The Netherlands.

Rosenfeld, A., and Davis, L., 1979, Image segmentation and image models, Proc. IEEE 67:764–772.

Roysam, B., Ancin, H., Bhattacharjya, A., Chisti, M., Seegal, R., and Turner, J., 1994, Algorithms for automated cell population analysis in thick specimens from 3-D confocal fluorescence microscopy data, *J. Microsc*. 173:115–126.

Roysam, B., Bhattacharjya, A., Srinivas, C., and Turner, J., 1993, Unsupervised noise removal algorithms for 3-D confocal fluorescence microscopy, *Micron Microscopica Acta* 23:447–461.

Roysam, B., and Miller, M., 1992, Combining stochastic and syntactic processing with analog computation methods, *Digital Signal Process*. 2:48–64.

Russ, J.C., 1994, *The Image Processing Handbook*, CRC Press, Boca Raton, Florida.

Russ, J.C., and DeHoff, R.T., 2000, *Practical Stereology*, Kluwer Academic/Plenum, New York.

Sahoo, P., Soltani, S., Wong, A., and Chen, Y., 1988, A survey of thresholding techniques, *Comput. Vis. Graphics Image Process*. 41:233–260.

Sarti, A., Ortiz de Solorzano, C., Lockett, S., and Malladi, R., 2000, A geometric model for 3-D confocal image analysis, *IEEE Trans. Biomed. Eng*. 47:1600–1609.

Sato, Y., Nakajima, S., Shiraga, N., Atsumi, H., Yoshida, S., Koller, T., Gerig, G., and Kikinis, R., 1998, Three-dimensional multi-scale line filter for segmentation and visualization of curvilinear structures in medical images, *Med. Image Anal*. 2:143–168.

Serra, J.P., and Soille, P., 1994, *Mathematical Morphology and Its Applications to Image Processing*, Kluwer Academic Publishers, Boston.

Shafarenko, L., Petrou, M., and Kittler, J., 1997, Automatic watershed segmentation of randomly textured color images, *IEEE Trans. Image Processing* 6:1530–1544.

Shain, W., Turner, J., Szarowski, D., Davis-Cox, M., Ancin, H., and Roysam, B., 1999, Application and quantitative validation of computer-automated 3-D counting of cell nuclei in brain tissue, *Microsc. Microanal*. 5:106–119.

Shapiro, L.G., and Stockman, G.C., 2001, *Computer Vision*, Prentice Hall, Upper Saddle River, New Jersey.

Sijbers, J., Scheunders, P., Verhoye, M., van der, L.A., van Dyck, D., and Raman, E., 1997, Watershed-based segmentation of 3D MR data for volume quantization, *Magn. Reson. Imaging* 15:679–688.

Sklansky, J., 1978, Image segmentation and feature extraction, *IEEE Transactions on Systems, Man, and Cybernetics* 8:237–247.

So, P.T., Dong, C.Y., Masters, B.R., and Berland, K.M., 2000, Two-photon excitation fluorescence microscopy, *Annu. Rev. Biomed. Eng*. 2:399–429.

Solorzano, C., and Rodriguez, E., 1999, Segmentation of confocal microscope images of cell nuclei in thick tissue sections, *J. Microsc*. 193:212–226.

Staib, L.H., and Duncan, J.S., 1996, Model-based deformable surface finding for medical images, *IEEE Trans. Medical Imaging* 15:720–731.

Streekstra, G.J., and van Pelt, J., 2002, Analysis of tubular structures in three-dimensional confocal images, *Network* 13:381–395.

Sun, Y., Lucariello, R.J., and Chiaramida, S.A., 1995, Directional low-pass filtering for improved accuracy and reproducibility of stenosis quantification in coronary arteriograms, *IEEE Trans. Medical Imaging*, 14:242–248.

Sunil Kumar, K., and Desai, U., 1999, Joint segmentation and image interpretation, *Pattern Recognition* 32:577–589.

Suri, J.S., Setarehdan, S.K., and Singh, S., 2002, Advanced algorithmic approaches to medical image segmentation: state-of-the-art applications in cardiology, neurology, mammography, and pathology, Springer-Verlag, New York.

Theodoridis, S., and Koutroumbas, K., 1999, *Pattern Recognition*, Academic Press, New York.

Trucco, E., and Fisher, R.B., 1995, Experiments in curvature-based segmentation of range data, *IEEE Trans. Pattern Anal. Machine Intell*. 17:177–182.

Tsao, Y., and Fu, K., 1981, A parallel thinning algorithm for 3-D pictures, *Comput. Graphics Image Process.* 17:315–331.

Valeur, B., 2002, *Molecular Fluorescence: Principles and Applications*, Wiley-VCH, Weinheim, Germany.

Vazdarjanova, A., McNaughton, B.L., Barnes, C.A., Worley, P.F., and Guzowski, J.F., 2002, Experience-dependent coincident expression of the effector immediate-early genes arc and Homer 1a in hippocampal and neocortical neuronal networks, *J. Neurosci*. 22:10067–10071.

Vemuri, B., and Radisavljevic, A., 1994, Multiresolution stochastic hybrid shape models with fractal priors, *ACM Trans. Graphics* 13:177–207.

Vincent, L., 1993, Morphological grayscale reconstruction in image analysis: Applications and efficient algorithms, *IEEE Trans. Image Processing* 2:176–201.

Vincent, L., and Soille, P., 1991, Watersheds in digital spaces: An efficient algorithm based on immersion simulations, *IEEE Trans. on Pattern Analysis and Machine Intelligence*, 13(6):583–598.

Weast, R.C., 1974, *Handbook of Chemistry and Physics; A Ready-Reference Book of Chemical and Physical Data*, Chemical Rubber Company, Cleveland, Ohio.

Weichert, F., Müller, H., Quast, U., Kraushaar, A., Spilles, P., Heintz, M., Wilke, C., van Birgelen, C., Erbel, R., and Wegener, D., 2003, Virtual 3D IVUS vessel model for intravascular brachytherapy planning. I. 3D segmentation, reconstruction, and visualization of coronary artery architecture and orientation, *Med. Phys*. 30:2530–2536.

Williams, J., Tek, H., Comaniciu, D., and Avants, B., 2003, Three-dimensional interactive vascular postprocessing techniques: Industrial perspective. In: *Angiography and Plaque Imaging: Advanced Segmentation Techniques* (J.S. Suri and S. Laxminarayan, eds.), CRC Press, Boca Raton, Florida, pp. 99–142.

Wilson, R., and Spann, M., 1988, *Image Segmentation and Uncertainty*, John Wiley and Sons, New York.

Ying, X., and Uberbacher, E.C., 1997, 2D image segmentation using minimum spanning trees, *Image Vis. Comput*. 15:47–57.

Zhu, S.C., and Yuille, A., 1996, Region competition: Unifying snakes, region growing, and Bayes/MDL for multiband image segmentation, *IEEE Trans. Pattern Anal. Machine Intell*. 18:884–900.

Zucker, S., 1977, Algorithms for image segmentation, Digital Image Processing and Analysis, 77:169–183.

Zucker, S.W., 1976, Region growing: Childhood and adolescence, *Comput. Vis. Graphics Image Process*. 5:382–399.

16

Fluorophores for Confocal Microscopy: Photophysics and Photochemistry

Roger Y. Tsien, Lauren Ernst, and Alan Waggoner

INTRODUCTION

Fluorescence is probably the most important optical readout mode in biological confocal microscopy because it can be much more sensitive and specific than absorbance or reflectance, and because it works well with epi-illumination, which greatly simplifies scanner design. These advantages of fluorescence are critically dependent on suitable fluorophores that can be tagged onto biological macromolecules to show their location, or whose optical properties are sensitive to the local environment. Despite the pivotal importance of good fluorophores, little is known about how rationally to design good ones. Whereas the concept of confocal microscopy is only a few decades old and nearly all the optical, electronic, and computer components to support it have been developed or redesigned in the last few years, the most popular fluorophores were developed more than a century ago (in the case of fluoresceins or rhodamines) or several billion years ago [in the case of phycobiliproteins and green fluorescent proteins (GFPs)]. Moreover, whereas competition between commercial makers of confocal microscopes stimulates ardent efforts to refine the instrumentation, relatively few companies or academic scientists are interested in improving fluorophores.

PHOTOPHYSICAL PROBLEMS RELATED TO HIGH INTENSITY EXCITATION

Singlet State Saturation

The properties of current fluorescent probes relevant to conventional fluorescence microscopy have been reviewed recently (e.g., Waggoner *et al.*, 1989; Tsien, 1989a,b; Chen and Scott, 1985; Sun *et al.*, 2004; Johnson, Chapter 17, *this volume*) and are listed in Table 16.1, see p. 344. Absorption spectra of several representative fluorescent probes in relation to the common laser line wavelengths available for confocal laser scanning microscopes are presented in Figure 16.1. Confocal microscopy using multiple apertures scanned across an image plane, that is, disk-scanning confocal microscopy, is essentially similar to conventional microscopy in its requirements on fluorophores. By contrast, continuous beam (not pulsed as in multi-photon excitation) laser-scanning microscopy subjects each fluorescent molecule to brief but extremely intense bursts of excitation as the focused laser beam sweeps past. If the laser-scanned image consists of n pixels (typically $n > 10^5$), any one pixel is illuminated for $1/n$ of the total time, or even somewhat less if some of the cycle time must be devoted to scan retrace; therefore, the peak instantaneous intensity must equal or exceed n times the long-term average excitation intensity.

Some idea of the quantitative magnitude may be gathered from the following example, analogous to that discussed by White and Stryer (1987). If just 1 mW of power at the popular 488 nm line of the argon-ion laser is focused to a Gaussian spot whose radius w at $1/e^2$ intensity is 0.25 µm, as is achieved by a microscope objective of 1.25 numerical aperture (Schneider and Webb, 1981), the peak excitation intensity I at the center will be $10^{-3}\,\mathrm{W}/[\mathrm{p} \cdot (0.25 \times 10^{-4}\,\mathrm{cm})^2] = 5.1 \times 10^5\,\mathrm{W/cm^2}$, or about 1.25×10^{24} photons/($\mathrm{cm^2} - \mathrm{s}$). Such intensities are well able to excite fluorophores so rapidly that few molecules are left in the ground state and the population is emitting photons nearly as fast as the limit set by the excited-state lifetime. For example, if fluorescein is the fluorophore, its decadic extinction coefficient ε at 488 nm is about $80{,}000\,\mathrm{L \cdot mole^{-1} cm^{-1}}$ at pH > 7. To convert this to the optical cross-section per molecule, one must multiply ε by $(1000\,\mathrm{cm^3/L}) \cdot (\ln 10)/(6.023 \times 10^{23}$ molecules/mole$) = 3.82 \times 10^{-21}\,\mathrm{cm^3 \cdot mole \cdot L^{-1} \cdot molecule^{-1}}$, giving a cross-section s of $3.06 \times 10^{-16}\,\mathrm{cm^2/molecule}$. In a beam of 1.25×10^{24} photons $\cdot\,\mathrm{cm^{-2} s^{-1}}$, each ground state molecule will be excited with a rate constant $k_a = \sigma I$, or $3.8 \times 10^8\,\mathrm{s^{-1}}$ in this example. The excited state lifetime τ_f of fluorescein in free aqueous solution is known to be about 4.5 ns (Bailey and Rollefson, 1953), which means that molecules in the excited state return to the ground state with a rate constant k_f of $2.2 \times 10^8\,\mathrm{s^{-1}}$. Note that k_f is defined here as the composite rate constant for all means of depopulating the singlet excited state, the sum of the rate constants for fluorescence emission, radiationless internal conversion, intersystem crossing to the triplet, etc.

Because of the Stokes shift between excitation and emission λs, k_f is not significantly enhanced by stimulated emission effects. If x is the fraction of molecules in the excited state and $(1 - x)$ is the fraction in the ground state, at steady-state $k_f x = k_a(1 - x)$. Solving for x yields the equation $x = k_a/(k_a + k_f)$, which shows that in this example 63% of the fluorescein molecules would be in the excited state and only 37% in the ground state. Obviously the emission is nearly saturated, and further increase in excitation intensity could hardly increase the output. The actual rate of photon output per molecule is $Q_e k_f x = Q_e k_f k_a/(k_a + k_f)$, where Q_e is the emission quantum efficiency, about 0.9 for free fluorescein dianion (but usually less for fluorescein bound to proteins, see below).

In this example each molecule would be emitting at an average rate of 1.3×10^8 photons/s, close to the absolute maximum of $Q_e k_f$ of about 2×10^8 photons/s. In current typical scanning confocal

Roger Y. Tsien • School of Medicine, University of California, San Diego, California 92093
Lauren Ernst and Alan Waggoner • Carnegie Mellon University, Pittsburgh, Pennsylvania 15213

 Handbook of Biological Confocal Microscopy, Third Edition, edited by James B. Pawley, Springer Science+Business Media, LLC, New York, 2006.

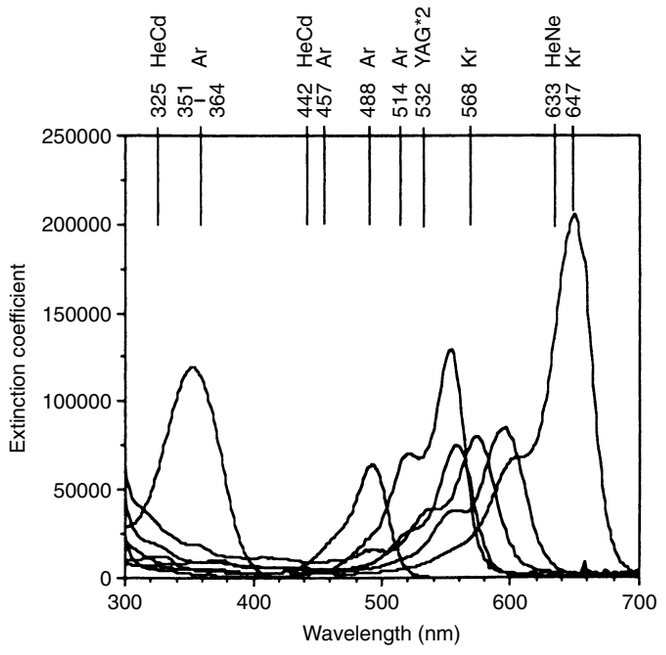


FIGURE 16.1. Absorption spectra from left to right of Hoechst 33342+DNA, and Fluorescein, CY3, TRITC, Lissamine Rhodamine B, Texas Red, and CY5 conjugated to antibodies. Extinction coefficients are given on a per-dye basis. Common laser emission λs are presented at the top of the figure. λs in bold are for the lower power, less expensive lasers, which provide sufficient excitation intensity for most fluorochromes imaged with laser-scanning microscopes with higher power objectives.

microscopes, the beam dwells on each pixel for 1 to 10 µs, so one would expect each molecule to produce several hundred photons. However, only a minority enter the microscope objective, only a fraction of these manage to pass all the way through the scanner optics, and only 10% to 20% of these create photoelectrons in the photomultiplier cathode, so that each molecule probably contributes on the order of only one photoelectron/pixel/sweep. Because of fluorescence saturation, increasing the laser power will not significantly increase the signal amplitude. In reality, it is difficult to accurately predict the laser power at which a fluorophore will saturate. Accurate knowledge of the extinction coefficient at the λ of excitation and the excited state lifetime of the fluorophore is essential but not always easy to obtain. Coumarins, for example (Table 16.1, see p. 344), have extinction coefficients approximately 2 to 5 times smaller than the fluoresceins, rhodamines, and cyanines, and would be expected on this basis alone to require a 2- to 5-fold increase in laser power before saturation. However, the emission lifetimes of coumarins are intrinsically longer than those of the fluoresceins, rhodamines, and cyanines, so that the factor of 2 to 5 is not realized in practice. To make calculations more difficult, the extinction coefficients and the excited state lifetimes of most probes depend on the environment of the fluorophore. For example, increasing the fluorochrome-to-protein ratio of a labeled antibody from 2 to 5 can reduce the average excited state lifetime of the bound fluorochromes several-fold. For these reasons, the power saturation values for the probes listed in Table 16.1 are not given. However, as a general rule, fluorochromes with extinction coefficients and quantum efficiencies similar to fluorescein will also saturate under similar conditions.

Triplet State Saturation

The above calculation considers only the ground state and lowest excited singlet state. Saturation of emission could occur at even lower excitation intensities if a significant population of fluorophores becomes trapped in a relatively long-lived triplet state. This would take place if a significant quantum yield exists for singlet-to-triplet conversion, or intersystem crossing. For example, if ground-state fluorescein molecules each absorb 3.8×10^8 photons $\cdot$ s^{-1}, have an excited singlet lifetime of 4.5 ns, cross to the triplet state with a quantum efficiency Q_{ISC} of 0.03 (Gandin *et al.*, 1983) and reside in the triplet state for a mean time τ_T of 10^{-6} s, the triplet state would contain 81% of the fluorophore population at steady state, which would be attained with a time constant of about $[\tau_T^{-1} + Q_{ISC}k_f k_a/(k_a + k_f)]^{-1}$ or about 190 ns in this case. Only 12% and 7% would be left in the first excited singlet and ground states, respectively, at steady state, so that the fluorescence emission would be weakened about 5-fold compared to its initial value just after the illumination began but before significant triplet occupancy had built up. Therefore, if the dwell time/pixel is comparable to or greater than the triplet lifetime, then a severe reduction in output intensity may be expected beyond that due simply to the finite rate of emission from the singlet state.

In the above calculation, the most uncertain figure is that for the triplet lifetime τ_T; in very thoroughly deoxygenated solution, τ_T for the fluorescein dianion is 20 ms (Lindqvist, 1960), but oxygen is expected to shorten τ_T down to the 0.1 to 1 µs range. The rate at which different fluorophore environments in a sample quench triplet states and reduce τ_T will of course affect the extent of triplet-state saturation and the apparent brightness of each pixel at these high illumination levels. When τ_T is long, triplet-state saturation is easily attained even without laser illumination (Lewis *et al.*, 1941).

Contaminating Background Signals

Rayleigh and Raman Scattering

Meanwhile, there may be unwanted signals, such as Rayleigh scattering, due either to excitation λs leaking through the dichroic mirror and barrier filter or to imperfect monochromaticity of the excitation source, for example, if the laser is being run in multi-line mode with only an interference filter to select one line. Even if all the λ filtering is perfect, Raman scattering will contribute a fluorescence-like signal, for example, at a λ of $[\lambda_{exc}^{-1} - 3380\,cm^{-1}]^{-1}$ due to the characteristic 3380 cm^{-1} Raman band of water. For an exciting λ_{exc} of 488 nm, the Raman peak would appear at 584 nm. At high concentrations of protein or embedding media, additional Raman bands closer to the excitation wavelength might appear. Both Rayleigh and Raman scattering are directly proportional to the laser power and will **not** saturate as the desired fluorescence does, so that excessive laser power diminishes the contrast between fluorescence and such scattering signals.

Autofluorescence from Endogenous Fluorophores

Another major source of unwanted background is autofluorescence from endogenous fluorophores. Flavins and flavoproteins absorb strongly at 488 nm and emit in the same spectral region as fluorescein. Reduced pyridine nucleotides (NADH, NADPH) and lipofuscin pigments absorb light from ultraviolet (UV) laser lines. These fluorophores usually have lower extinction coefficients or shorter fluorescence lifetimes than most exogenous fluorophores. For example, FMN (flavin mononucleotide) and FAD (flavin

adenine dinucleotide) have the extinction coefficients of 1.1 to 1.2 $\times 10^4\,M^{-1}\,cm^{-1}$ at 445 to 450 nm (Koziol, 1971) and fluorescence lifetimes of about 4.9 and 3.4/0.12 ns, respectively (Lakowicz, 1989), whereas NADH has an extinction coefficient of $6.2 \times 10^3\,M^{-1}\,cm^{-1}$ at its 340 nm peak (Kaplan, 1960) and a lifetime of about 0.4 ns (Lakowicz, 1983). Therefore autofluorescence from these molecules will be more difficult to saturate than the fluorescence from most of the common probes. See Chapter 27, *this volume*, for more on confocal lifetime.

What Is the Optimal Intensity?

The above discussion shows that if laser power is increased to nearly saturate the desired fluorophores, autofluorescence as well as Rayleigh and Raman scattering will increase background levels and decrease the overall signal-to-noise ratio (S/N). What is the optimal intensity? Assuming the system is limited by photon-counting statistics, the irreducible noise level N is proportional to the square root of the background signal level B. Both B and the absorption rate constant k_a of the desired probe are directly proportional to the illumination intensity I and to each other. Therefore N is directly proportional to $k_a^{1/2}$. If triplet state saturation can be ignored, for example, if the dwell time/pixel is short compared to the time for the triplet state to build up, then the desired signal is $Q_e k_f k_a/(k_a + k_f)$ as derived above, so that S/N is proportional to $k_a^{1/2}/(k_a + k_f)$. Regardless of the proportionality constant, this expression is maximal when $k_a = k_f$. This is a remarkably simple but important result, for which we are grateful to Prof. R. Mathies (University of California–Berkeley).

At the other extreme, once the ground state and excited singlet and triplet have all come to an equilibrium steady state, the desired signal is readily calculated to be

$$Q_e k_a/[1 + k_a\,(k_f^{-1} + Q_{ISC}\tau_T)]$$

so that the S/N is proportional to

$$Q_e k_a^{1/2}/[1 + k_a\,(k_f^3 + Q_{ISC}\tau_T)].$$

This reaches its maximum when $k_a(\tau_f + Q_{ISC}\tau_T) = 1$, where $\tau_f = k_f^{-1}$ is the lifetime of the excited singlet. In this approximation, appropriate for slow scans in which the dwell time/pixel is long compared to the time for triplet state equilibration, the laser power P in photons/s should be optimal at about $\pi w^2/[(3.82 \times 10^{-21}\,cm^3 \cdot M)\,\varepsilon\,(\tau_f + Q_{ISC}\tau_T)]$. For the present values of $w = 2.5 \times 10^{-5}$ cm, $\varepsilon = 8 \times 10^4\,M^{-1}\,cm^{-1}$, $\tau_f = 4.5 \times 10^{-9}$ sec, $Q_{ISC} = 0.03$, and $\tau_T = 10^{-6}$ s, this expression gives an optimal P of 1.86×10^{14} photons/s, or about 76 µW at 488 nm. If triplet formation could be neglected, the optimal P would be 590 µW, slightly less than the 1 mW initially postulated to be the input.

PHOTODESTRUCTION OF FLUOROPHORES AND BIOLOGICAL SPECIMENS

One obvious way to increase the total signal is to integrate for a longer time, either by slowing the scan, or by averaging for many scans. Given that image processors are now relatively cheap, the latter alternative is likely to be the easier to implement, and it has at least two major advantages: repetitive scans give time for triplet states to decay between each scan, and the user can watch the S/N gradually improve and choose when to stop accumulating. However, irreversible photochemical side effects such as bleaching of the fluorophore or damage to the specimen set limits on the useful duration of observation or total photon dose allowable. Photochemical damage is one of the most important yet least understood aspects of the use of fluorescence in biology; in this discussion we can do little more than define our ignorance.

At intensities of up to 3×10^{22} (Hirschfeld, 1976) or 4.4×10^{23} photons $\cdot\,cm^{-2} \cdot s^{-1}$ (Mathies and Stryer, 1986), fluorescein is known to bleach with a quantum efficiency Q_b of about 3×10^{-5}. If this value continues to hold at the somewhat higher intensity of the above example, the molecules would be bleaching with a rate constant of $Q_b k_f k_a/(k_a + k_f)$, or about $4.2 \times 10^3\,s^{-1}$. This would mean that 1/e or 37% of the molecules would be left after 240 µs of actual irradiation. The corresponding number of scans would be 240 µs divided by the dwell time that the beam actually spends on each pixel. The average number of photons emitted by a fluorophore before it bleaches is the ratio of emission quantum efficiency to bleaching quantum efficiency, or Q_e/Q_b; this is generally true regardless of whether the illumination is steady or pulsed. For fluorescein under ideal conditions, the above Q_e/Q_b works out to 30,000 to 40,000 photons ultimately emitted/dye molecule (Hirschfeld, 1976; Mathies and Stryer, 1986). The number of photons detected from each molecule will, of course, be considerably less.

Thus, in obtaining an image at a single plane by averaging say 16 scans, one would expect from 6% to 50% bleaching of a fluorescein signal (in the absence of antifade reagents), resulting from exp[–(16 sweeps) × (1–10 µs dwell time/sweep)/(240 µs lifetime)]. In an optical sectioning experiment, the cone of light illuminating the sample above and below each plane of data being acquired is causing photobleaching even though under confocal conditions no signal is being recorded from these regions. This means that if 16 optical sections are obtained with only one sweep each, the last image will have been bleached 10% to 50% by the preceding sweeps. If the signals are large, it may be possible for software to adjust the intensities of sequential images to compensate for bleaching. Of course, for quantitative fluorescence measurements it would be most desirable to use the most bleach-resistant fluorophores available.

Dependency on Intensity or Its Time Integral?

Theory

One major uncertainty is whether the bleaching quantum efficiency Q_b really does remain constant even at such high instantaneous excitation intensities. Theoretically, Q_b could rise at high intensities due to multi-photon absorptions. For example, the normal excited singlet or triplet state could itself absorb one or more additional photons to extra-high energy states, which will probably have picosecond lifetimes. If their main reaction pathway were back to the lowest excited state, then such higher-order states would be innocuous, but if bond dissociation competes with decay to the lowest excited state, then photodestruction will rise steeply as intensities reach levels that significantly deplete the ground state (as in the previous example).

One can also imagine the opposite dependency: bleaching mechanisms whose quantum efficiency might decrease when the excitation was bunched into brief intense pulses. For example, suppose the dye is bleached by a 1 : 1 reaction of its excited state with a molecule of oxygen, and that the overall dye concentration exceeds the oxygen concentration. Then within the zone of intense illumination, the first few excited dye molecules might react with all the locally available O_2, and the resulting anoxic environment would protect the rest of the excited molecules. Oxygen would be diffusing in from the surrounding non-illuminated environment, but the time required would be on the order of the spot radius squared

divided by the diffusion constant, that is, $(0.25 \times 10^{-4}\,\text{cm})^2/(3 \times 10^{-5}\,\text{cm}^2 \cdot \text{s}^{-1})$ or 20 µs, that is, considerably longer than the time for the beam to move to the next pixel. By contrast, with low-intensity illumination, no local anoxia would develop, and each fluorophore would take its chances with the full ambient oxygen concentration. Such a mechanism would be the photochemical equivalent of predator–prey interactions in ecology, where it is often advantageous for the prey to school together or breed in synchrony in order to minimize losses to predation (Wilson, 1975).

Experiment

Theory is all well and good, but empirically how does the photodestruction quantum yield depend on intensity? White and Stryer (1987) tested R-phycoerythrin in a flow system and found that the rate of photodestruction was indeed directly proportional to laser power so that the quantum yield was constant. Unfortunately, the range of intensities tested only went up to about 10^{20} photons $\cdot$ $\text{cm}^{-2}\cdot\text{s}^{-1}$, so that they were still 3 orders of magnitude below saturation of the phycoerythrin. Peck and colleagues (1989) examined B-phycoerythrin and found that photodestruction saturated with increasing input intensity in just the same way as fluorescence emission, so that the photodestruction quantum yield was roughly constant even when the phycobiliproteins were heavily driven into saturation. However, there was some indirect evidence that simpler fluorophores may undergo a nonlinear acceleration of bleaching under such conditions. White *et al.* (1987) reported that bleaching by their scanning confocal microscope seemed to be greatest at the plane of focus. Because the plane of focus receives about the same time-averaged photon flux but much higher peak intensities than out-of-focus planes do, preferential bleaching at the plane of focus would imply that a given number of photons are more injurious when they are bunched, that is, that the photodestruction quantum yield increases at high intensities. Obviously, further testing of this possibility and improvement in photon collection efficiency will be of great importance in confocal microscopy.

A number of workers have reported that damage to biological structures (as distinct from bleaching of the fluorophore) can sometimes be reduced if the given total number of photons is delivered with high intensities for short times rather than low intensities for long times. An early report of the advantage of pulsed illumination was by Sheetz and Koppel (1979) studying the crosslinkage of spectrin by illumination of fluoresceinated concanavalin A on erythrocyte membranes. Bloom and Webb (1984) found similar results for lysis of XRITC-labeled air-equilibrated erythrocytes, whereas well-deoxygenated cells were much more resistant but lysed after a constant total photon dose regardless of whether delivered quickly or slowly. Recently Vigers and colleagues (1988) showed that increasing the illumination intensity up to about $10^3\,\text{W/cm}^2$ decreased the time required for fluorescein-labeled microtubules to dissolve, as one might expect. Surprisingly, intensities above this threshold actually stabilized the microtubules against dissolution, so that the dissolution time became a linearly *increasing* function of intensity. This paradoxical stabilization at high intensities was attributed to local heating based on the assumption that diffusion of heat was negligible. Because this assumption needs to be checked (see Axelrod, 1977; Bloom and Webb, 1984) and because microtubule stabilization and dissolution are not well-defined molecular events, the local heating hypothesis should be viewed with caution. Bonhoeffer and Staiger (1988) have reported that photodynamic damage to rat hippocampal cells was reduced if the light is delivered at 100 exposures each 200 ms long separated by 30 s dark periods rather than continuously for 20 s. They speculated that intermittent illumination was better because it allowed repair mechanisms to operate during the dark intervals. It should be noted that in all the above biological examples, the illumination intensity was well below that expected to be necessary to reach saturation of excited state dye populations (see also Chapter 38, *this volume*).

STRATEGIES FOR SIGNAL OPTIMIZATION IN THE FACE OF PHOTOBLEACHING

Light Collection Efficiency

The above discussion has shown that to increase signal amplitude and S/N in laser-scanning confocal microscopy, increasing laser power helps only until the onset of saturation, and increasing observation time is limited by photodestruction. What other measures can be tried? Obviously any increase in light-collection efficiency (i.e., higher numerical aperture of the objective), transmission efficiency through the scanner and λ filters, and quantum efficiency of photodetection is extremely valuable. Despite the importance of these factors, newcomers to low-light-level microscopy often use low numerical aperture (NA) objectives, excessively narrow emission bandpass filters, inefficient optical couplings, and photomultipliers of less-than-optimal quantum efficiencies. Nearly all the fluorophores that fluoresce strongly in aqueous solution with visible λs of excitation are characterized by small Stokes shifts, or difference between absorption and emission peak λs. It may then be difficult to find or fabricate filters and dichroic mirrors that efficiently separate the two λ bands. In that case, it would usually be preferable to displace the excitation λ to shorter λs away from the peak of the excitation spectrum, so that the emission filters can accept as much of the entire output as possible. Although the excitation is less efficient, this can be made up by increased laser power as long as the photobleaching is reduced by the same factor. By contrast, if the excitation is at the peak λ and the emission acceptance band is pushed to longer λs that exclude much of the emission spectrum, then emitted photons are wasted, while excess scattered photons are collected. The S/N ratio is thus lowered. This is often a severe problem with rhodamine excited using the 514 nm line of the argon-ion laser.

Spatial Resolution

Another tactic to increase signal is to increase the effective size of the confocal apertures, that is, decrease the spatial resolution. If the illuminating and detecting aperture diameters are doubled, the pixel area quadruples and the volume sampled will increase 8-fold. Assuming the total laser power is increased to maintain the same intensity in photons $\cdot\,\text{cm}^{-1}\cdot\text{s}^{-1}$ and that the fluorophore concentration is uniform in the increased volume (as might be true for an ion indicator distributed in the cytosol), the signal should increase 8-fold, though at the price of degraded spatial resolution.

Protective Agents

As mentioned above, light-induced damage to both the fluorophore and to the biological specimen is often dependent on the presence of molecular oxygen, which reacts with the triplet excited states of many dyes to produce highly reactive singlet oxygen. Reduction of the partial pressure or concentration of oxygen often greatly increases the longevity of both the fluorophore and the specimen. In dead, fixed samples, it has become common to add antioxidants

such as propyl gallate (Giloh and Sedat, 1982), hydroquinone, *p*-phenylenediamine, etc., to the mounting medium. The preservative effects of these agents may go beyond removing oxygen because White and Stryer (1987) found propyl gallate to be more effective than thorough deoxygenation at protecting phycoerythrin *in vitro*. One might speculate that polyphenols like propyl gallate might quench dye triplet states and other free radicals, which could prevent forms of photodegradation other than singlet oxygen formation. Protection of GFP and fluorophores from photobleaching in fixed cells has been discussed recently by Bernas and colleagues (2004).

The problem of protecting living cells from oxygen-dependent photodynamic damage is more difficult. The above antioxidants would not be attractive because they would be expected to have strong pharmacological effects at the high concentrations generally employed on fixed tissue. If the tissue can tolerate hypoxia or anoxia, one would probably prefer to remove O_2 by bubbling the medium with N_2 or Ar rather than using chemical reductants. Biological oxygen-scavenging systems such as submitochondrial particles or glucose oxidase + glucose are often helpful (Bloom and Webb, 1984).

If one cannot reduce the O_2 concentration, the next best tactic may be to use singlet oxygen quenchers. The most attractive here are those already chosen by natural selection, namely carotenoids. Their effectiveness is shown by classic experiments in which carotenoid biosynthesis was blocked by mutation; the resulting mutants were rapidly killed by normal illumination levels at which the wild type thrived (Matthews and Sistrom, 1959). A water-soluble carotenoid would be easier to administer acutely than the usual extremely hydrophobic carotenoids such as carotene itself. The most accessible and promising candidate is crocetin, which is the chromophore that gives saffron its color, and which consists of seven conjugated C = C units with a carboxylate at each end. Crocetin quenches aqueous singlet oxygen with a bimolecular rate constant of $5.5 \times 10^9 M^{-1} \cdot s^{-1}$, which is almost diffusion controlled; of this rate, about 95% represents catalytic quenching and about 5% represents bleaching or consumption of the crocetin (Manitto *et al.*, 1987; somewhat more pessimistic rate constants are reported by Matheson and Rodgers, 1982). Longer-chain carotenoids are supposed to be even more efficient at destroying singlet oxygen without damage to themselves, but have not yet been tested in aqueous media. There is some evidence that 50 μM of either crocetin or etretinate (a synthetic aromatic retinoid) can protect cultured cells (L cells and WI-38 fibroblasts) from hematoporphyrin-induced photodynamic damage (Reyftmann *et al.*, 1986). Other water-soluble agents that might be considered as sacrificial reactants with reactive oxygen metabolites include ascorbate (e.g., Vigers *et al.*, 1988), imidazole, histidine, cysteamine, reduced glutathione (Sheetz and Koppel, 1979), uric acid, and Trolox, a vitamin E analog (Glazer, 1988); these would have the advantage over carotenoids of being colorless and non-fluorescent, but would have to be used in much higher concentrations (probably many millimolar) because their bimolecular reaction rates with oxygen metabolites are not as high and they are consumed by the reaction rather than being catalytic. It should also be remembered that thorough deoxygenation may increase the triplet state lifetime, τ_T and worsen the problem of excited-state saturation.

Fluorophore Concentration

Increasing the concentration of fluorophore molecules will only increase the signal as long as they do not get too close together. When multiple fluorophores are attached within a few nanometers of each other on a macromolecule, they usually begin to quench each other. For example, the relatively high quantum yield for free fluorescein in aqueous solution at pH 7 is reduced to near 0.25 when an average of 5 fluorophores are bound to each IgG antibody (Southwick *et al.*, 1990). Charge–transfer interactions with tryptophanes are yet another mechanism for quenching fluoresceins bound to a protein, for example, anti-fluorescein antibody (Watt and Voss, 1977). Most rhodamines and certain cyanines also show a striking reduction in average quantum yield on conjugation, which appears to arise from dye interactions on the protein surface. Absorption spectra of labeled antibodies clearly show evidence of dimers, and fluorescence excitation spectra demonstrate that these dimers are not fluorescent. The propensity of relatively nonpolar, planar rhodamines to interact with one another is not surprising. Even if the fluorophores do not form ground-state dimers, they can also rapidly transfer energy from one to another until a quencher such as O_2 is encountered. In other words, proximity-induced energy transfer between fluorophores multiplies the efficacy of quenchers. Perhaps fortunately it also shortens the excited-state lifetime, so that a higher intensity of laser excitation can be applied for a given degree of saturation (Hirschfeld, 1976). If such increased intensity is available, much of the emission intensity lost by fluorophore proximity can be regained, but at the cost of increased background signal from Rayleigh and Raman scattering and other non-saturated fluorophores.

Choice of Fluorophore

Perhaps the most drastic alteration is to change to a different fluorophore altogether. Unfortunately, there is not a wide selection of fluorescent physiological indicator probes that respond selectively to a cellular parameter and can be excited at appropriate λs. However, with fluorescent labeling reagents, it is sometimes possible to choose an optimal fluorophore within a defined λ range. A selection of fluorescent labels for confocal microscopy is described below.

FLUORESCENT LABELS FOR ANTIBODIES, OTHER PROTEINS, AND DNA PROBES

Fluorescent Organic Dyes

Certain fluorescent reagents carry reactive groups for covalent attachment to target biomolecules and show minimal spectral sensitivity to environmental changes (Table 16.1). These reagents are primarily used to quantify the presence and distribution of probes and targets. The most well-known dyes of this type are derivatives of fluorescein and rhodamine (e.g., tetramethyl rhodamine, lissamine rhodamine, and sulforhodamine 101). A variety of reactive groups have been incorporated into these dyes permitting coupling of the dyes to different functionalities. Isothiocyanates, succinimidyl esters, and pentafluorophenyl esters couple with amino groups of target molecules, while haloacetamides, maleimides, and vinyl sulfones react with sulfhydryl groups. Dichlorotriazinyl (DCT) groups can couple effectively with both amines and alcohols, depending upon reaction pH and temperature. Reactivity and selectivity of the conjugation reactions can be manipulated by the reactive groups chosen and the conditions of the coupling reaction (e.g., reaction pH, solvent polarity, and temperature).

The cyanine dyes (Mujumdar *et al.*, 1993), the borate–dipyrromethene (BODIPY) complexes (Wories *et al.*, 1985; Kang *et al.*, 1988), and the AlexaFluor dyes (Panchuk–Voloshina

et al., 1999) have been developed to complement the traditional fluorescein and rhodamine reagents. The sensitivity of detecting fluorescent conjugates is determined by the spectral properties of the fluorescent dye (its molar extinction coefficient and fluorescence quantum yield) and the quality of the dye–target conjugate (i.e., its tendency to precipitate and its degree of fluorescence quenching). The cyanine reagents, and later the AlexaFluor dyes, were engineered to have very high water solubility as well as excellent spectral properties. Galbraith and colleagues (1989) and Mujumdar and colleagues (1993) have shown that, at least in the case of cyanine dye labeling agents, appropriate placement of charged sulfonate groups on the fluorophore can reduce dye interactions and increase the brightness of relatively heavily labeled antibodies. Particularly useful in this regard are the indopentamethine–cyanines, CY5 dyes (excitation, 630–650 nm; emission 670 nm) and indotrimethine–cyanines, CY3 dyes (excitation, 530–550 nm; emission 575 nm). Antibodies labeled with these dyes have a brightness comparable to or brighter than fluorescein-labeled antibodies and have little tendency to precipitate from solution even when labeled with as many as 10 dye molecules/antibody (Wessendorf and Brelje, 1992). CY5 is somewhat more photostable than fluorescein, and CY3 is significantly more stable. CY5 can be optimally excited with a red He/Ne laser, whereas CY3 can be excited fairly efficiently with the 514 nm line and marginally well with the 488 nm line of the argon-ion laser. These fluorophores are useful for nucleic acid labeling and have found wide use in *in situ* hybridization and gene expression assays. Fluorescent reagents, structurally related to the cyanines, with a squaric acid group replacing part of the polymethine chain have been described (Oswald *et al.*, 1999). Also, novel polymethine dyes developed by Czerney's group were introduced recently as fluorescent reagents (Czerney *et al.*, 2001). These new fluorescent reagents in combination with fluorescein, the phycobiliproteins, or other fluorophores make it possible to do multi-color fluorescence imaging with laser-scanner microscopes equipped with an argon and a He/Ne laser or with the argon/krypton "white light" laser, which has lines at 488, 568, and 647 nm. Brelje and colleagues (1993) have described the use of the Ar/Kr laser to excite samples stained with fluorescein (488 excitation); Texas Red, Lissamine, or CY3 (568 nm); and CY5 (647). Fluorescent labeling reagents available commercially are described on the following Web sites: http://www.amershambiosciences.com; http://www.probes.com; http://www.dyomics.com; and http://www.mobitec.de.

Phycobiliproteins

Phycobiliproteins (Oi *et al.*, 1982) currently hold the record for the highest extinction coefficients and largest number of photons emitted before bleaching (Q_e/Q_b; Mathies and Stryer, 1986), partly because each macromolecule simply contains a large number of component fluorophores, partly because the proteins have been engineered by natural selection to protect the tetrapyrrole fluorophores from quenching processes (Glazer, 1989; Sun *et al.*, 2003). Suitable optimization of laser power, optics, flow rate, and detection permits the detection of fluorescence pulses from single phycobiliprotein molecules in flowing systems (Peck *et al.*, 1989; see also Nguyen *et al.*, 1987). Phycoerythrin (PE) in combination with fluorescein has been valuable for immunofluorescence determination of cell-surface markers by single laser (488 nm excitation) flow cytometry. This approach can also be useful in confocal microscopy, provided that the emission signal is split into a 530 nm (fluorescein) and a 575 nm component (PE) and two photomultipliers are used for detection. Detection of a third color is possible using another photosynthetic protein, PerCP (Rechtenwald, 1989), or the PE tandem conjugates formed by coupling energy acceptor fluorophores that emit at long λs to PE. PE conjugates with Texas Red or to CY5 (Waggoner *et al.*, 1993) have become popular for cell surface measurements with flow cytometers using a 488 nm laser. Phycobiliproteins have also been coupled with CY7 dyes providing additional choices of fluorescence colors (Gerstner *et al.*, 2002; Roederer *et al.*, 1996; Beavis and Pennline, 1996). The use of phycobiliproteins is likely to prove less useful for intracellular antigens because the size of a PE–antibody conjugate, around 410 kD, restricts penetration into denser regions of fixed cells and tissues. Efforts to develop low-molecular-weight analogs of PE that have similarly large Stokes shifts and excitation λs have not yet been successful, but work in this area continues. If fluorophores with large Stokes shifts could be found for both 488 nm and 633 nm excitation, a two-laser microscope could obtain four-color immunofluorescence images. Other probes are listed in Table 16.1.

DNA Probes

An application of fluorescent labels that has attracted a number of investigators is fluorescence *in situ* hybridization, or FISH (Trask, 1991). Initially, DNA to be used to probe genetic sequences in chromosomes and interphase nuclei was labeled by nick translation using biotin or digoxigenin-tagged deoxynucleotide triphosphates (dNTPs). Fluorescent secondary reagents were applied after hybridization to detect the binding of the DNA probe. The use of dNTPs attached by linker arms to fluorophores to form directly labeled fluorescent DNA probes is replacing methods involving fluorescent secondary reagents. Directly labeled DNA probes are simpler to use, often give less background and provide easier access to multi-color–multi-sequence detection (Ballard and Ward, 1993). However, for detection of short genetic sequences, use of multiple fluorescent secondary reagents may be required for sufficient sensitivity. Directly labeled oligonucleotides provide alternatives when there are numerous copies of the target sequence, as in the case of histone mRNA (Yu *et al.*, 1992). For non-specific, but stable labeling of DNA, the bis-intercalating reagents, TOTO, YOYO, DRAQ5, etc., provide an attractive solution, and the reagents are available in several fluorescent colors (Rye *et al.*, 1992). The anthraquinone derivative, DRAQ5, is membrane permeant, is highly selective for nuclear DNA, and can be used with two-photon excitation from 800 nm to beyond 1000 nm. Studies of living cells with DRAQ5 must be done with care because of its high cytotoxicity (Smith *et al.*, 2000; Errington *et al.*, 2005). Snyder (2003) suggests that some caution may be needed when combining DRAQ5 with other probes. There appears to be decreased uptake of bodipy-labelled compounds in the presence of the nuclear stain, DRAQ5.

Luminescent Nanocrystals

Fluorescent nanocrystals, or quantum dots, exhibit interesting properties for biological labeling reagents. These nanometer-sized inorganic crystalloid structures have broad absorption (and excitation) spectra with molar absorptivities of more than six million at 450 nm. The emission band, determined by particle composition and dimensions, can be very narrow (ca. 25 nm FWHM) with quantum yields approaching unity. Also, quantum dot luminescence is very resistant to photobleaching. Selection of uniformly sized quantum dots gives preparations with very sharp fluorescence bands. The challenge for biological applications is to provide biocompatible surfaces for the nanocrystals that maintain their fluorescence in

TABLE 16.1. Spectroscopic Properties of Selected Probes

Parameter	Probe[a]	Absorption Maximum[b]	Extinction Maximum[c]	Emission Maximum[b]	Quantum Yield	Measurement Conditions	References[d]
Covalent labeling reagents	Fluorescein-amines, sulfhydryl	490	67	520	0.71	pH 7, PBS	Haugland (1983), W, MP
	Tetramethylrhodamine-amines	554	85	573	0.28	pH 7, PBS	Haugland (1983), MP
	X-rhodamine-amines	582	79	601	0.26	pH 7, PBS	W
	Texas Red®-amines	596	85	620	0.51	pH 7, PBS	Titus *et al.* (1982), W, MP
	CY3	554	130	568	0.14[f]	pH 7, PBS	Mujumdar *et al.* (1993)
	CY5	652	200	672	0.18[f]	pH 7, PBS	Mujumdar *et al.* (1993)
	CY7	755	200	778	0.02[f]	pH 7, PBS	Mujumdar *et al.* (1993)
	BODIPY® FL	502	80	510		MeOH	MP
	BODIPY 581/591	581	136	591		MeOH	MP
	BODIPY 630/650	625	101	640		MeOH	MP
	Cascade Blue®	378, 399	26	423		Water	MP
	AlexaFluor® 430	430	15	545		pH 7	MP
	AlexaFluor 488	494	73	517		pH 7	MP
	AlexaFluor 532	530	81	555		pH 7	MP
	AlexaFluor 594	590	92	617		pH 7	MP
	NBD-amine	478	24.6	520–550	0.36/0.21	EtOH/MeOH	Kenner & Aboderin (1971), Allen & Lowe (1973), Bratcher (1979)
	NBD-S-CH2CH2OH	425	12.1	531	0.002	pH 7.5, 10% glycerol	
	Coumarin-phalloidin	387		470		Water	MP
	DY-555	555	100	580			MoBiTec GmbH (http://www.mobitec.com)
	DY-631	637	185	658			MoBiTec GmbH (http://www.mobitec.com)
	Phycoerythrin-R	480–565	1960	578	0.68	pH 7, PBS	Oi *et al.* (1982)
	Allophycocyanine	650	700	660	0.68	pH 7, PBS	Oi *et al.* (1982)
	PerCP	488		680		pH 7, PBS	Rechtenwald (1989)
Nanocrystals	*(quantum dots)*	365 & higher	~6000@400 nm	400–850+		PBS	
Lanthanide chelates	Europium chelate	340	Determined	615	See FN *i*	Water	Paul (2002)
	Terbium chelate	340	by ligand	545	See FN *j*		Paul (2002)
Expressible labels	EBFP	383	31	445	0.25	pH 7, PBS	Patterson *et al.* (2001)
	ECFP	434	26	477	0.40	pH 7, PBS	Patterson *et al.* (2001)
	EGFP	489	55	508	0.60	pH 7, PBS	Patterson *et al.* (2001)
	EYFP	514	84	527	0.61	pH 7, PBS	Patterson *et al.* (2001)
	DsRed	558	72.5	583	0.68	pH 7, PBS	Patterson *et al.* (2001)
DNA–RNA content[e]	Hoechst 33342	340	120	450	0.83	+DNA (excess)	W
	DAPI	350		470		+DNA (excess)	W
	DRAQ5	646	21	681		PBS	Smith, PJ *et al.* (2000)
	Ethidium Bromide	510	3.2	595		+DNA (excess)	Pohl *et al.* (1972)
	Propidium Iodide	536	6.4	623	0.09	+DNA (excess)	W
	Acridine Orange	480		520		+DNA	Kapuscinski *et al.* (1982), Shapiro (1985)
		440–470		650		+RNA	
	Pyronine Y	549–561	67–84	567–574	0.04–0.26	+ds DNA[f]	Darzynkiewicz *et al.* (1987), Kapuscinski & Darzynkriwicz (1987)
		560–562	70–90	565–574	0.05–0.21	+ds RNA[f]	
		497	42	563	Low	+ss RNA	
	Thiazole Orange	453	26	480	0.08	RNA	Lee *et al.* (1986)
	TOTO-1	514	112	533		MeOH	MP, Rye *et al.* (1992)
	YOYO-3	612	115	631		MeOH	MP, Rye *et al.* (1992)
Membrane potential	diO-Cn-(3)	485	149	505	0.05	MeOH	Sims *et al.* (1974), W
	diI-Cn-(5)	646	200	668	0.4	MeOH	Sims *et al.* (1974), W
	diBA-Isopr-(3)	493	130	517	0.03	MeOH	Sims *et al.* (1974), W
	diBA-C4-(5)	590	176	620		EtOH	W
	Rhodamine 123	511	85	534	0.9	EtOH	EK, Kubin & Fletcher (1983)

TABLE 16.1. (*Continued*)

Parameter	Probe[a]	Absorption Maximum[b]	Extinction Maximum[c]	Emission Maximum[b]	Quantum Yield	Measurement Conditions	References[d]
pH	BCECF	505		530		High pH	MP
		460				Low pH	MP
	SNARF-1 (pKa = 7.5)	518–548		587		pH 5.5	MP
		574		636		pH 10.0	MP
	DCDHB	340–360		500–580		High pH	Valet *et al*. (1981), MP
		340–360		420–440		Low pH	
Membrane location and fluidity	Diphenylhexatriene (DPH)	330, 351, 370	77 (351 nm)	430		Hexane	MP
	diI-C18-(3)	546	126	565	0.07	MeOH	W
	DiO	484	149	501		MeOH	MP
	DiA	491	52	613		MeOH	MP
	NBD phosphatidylethanolamine	450	24[g]	530		Lipid	Struck *et al*. (1981)
	Anthroyl stearate	361, 381	8.4, 7.5	446		MeOH	Waggoner & Stryer (1970)
	Pyrene-sulfonamidoalkyls	350	30	380–400			MP
Calcium[h]	Fura 2	335	33	512–518	0.23	Low calcium	Grynkiewicz *et al*. (1985)
		360	27	505–510	0.49	High calcium	
	Indo 1	330	34	390–410	0.56	High calcium	Grynkiewicz *et al*. (1985)
		350	34	482–485	0.38	Low calcium	
	Fluo-3	506	83	526	0.183	High calcium	Minata *et al*. (1989) & Mukkala *et al*. (1993), MP
		506	78	526	0.0051	Low calcium	
O_2 sensor	$Ru[dpp(SO_3Na)_2]_3$	365/450		590	$\tau = 3.7\,\mu s$	No oxygen	Castellano & Lakowicz (1981)
					$\tau = 0.93\,\mu s$	Air	
cAMP	FIERhR	490	70	520, 573	—	pH 7, cAMP	Adams *et al*. (1991)
Enzyme substrates	Rhodamine-di-arg-CBZ	495	—	532	0.09	Hepes pH 7.5	Leytus *et al*. (1983)
	Product of rxn. (rhodamine)	495	67	523	0.91	+15% EtOH	
	Coumarin-glucoside substr.	316	13	395		pH 5.5 + 1% Lubrol	W
	Rxn. product (hydroxy coumarin)	370	17	450		pH10 + 1% Lubrol	W
	Fluorescein digalactosidase product	490	67	520	0.71	pH 7, PBS	MP
	Resorufin galactosidase product	571	58	585		pH 9	MP
	ELF97 phosphatase product	345	Precipitate	530		pH 8	MP

[a] Abbreviations: NBD, 7-nitrobenz-2-oxa-1,3-diazole; DAPI, 4′,6-diamidino-2-phenylindole; DCDHB, dicyano-dihydroxybenzene.
[b] Measured in nanometers.
[c] Multiply value listed by 1000 to get liters/mol·cm.
[d] EK, Eastman Kodak Chemical Catalog; MP, Molecular Probes, Inc catalog; W, Waggoner laboratory determination.
[e] See Table III in Arndt-Jovin & Jovin (1989) for additional DNA content probes.
[f] Base-pair dependent.
[g] Value for NBD-ethanolamine in MeOH which has an abs.max at 470 nm and an emission max at 550 nm [Barak & Yocum (1981)].
[h] See Tsien (1989) for additional details and other ion indicators.
[i] See corporate Web sites: Quanturm Dot Corp. (www.qdots.com), Evident Technologies (www.evidenttech.com), BioCrystal, Ltd. (www.biocrystal.com) and Crystalplex Corp. (www.crystalplex.com).
[j] Time resolved detection. Extinction times quantum yield approx. 2100.

aqueous media. Promising results have been obtained using quantum dots (Jaiswal *et al.*, 2003; Hoshino *et al.*, 2004; Voura *et al.*, 2004). However, there is ample opportunity for significant improvements before these reagents can be used routinely for fluorescent labeling. Their relatively large size and high mass limit their use in applications requiring high diffusional mobility.

Fluorescent Lanthanide Chelates

Lanthanide chelates are another group of fluorescent reagents with special spectral properties. These reagents have microsecond fluorescence lifetimes that are readily distinguished from typical nanosecond autofluorescence background (Soini *et al.*, 1988; Seveus *et al.*, 1994; Vereb *et al.*, 1998). Temporal separation of probe fluorescence from background signal can give a very high S/N and highly sensitive probe detection even though the brightness of these reagents is only modest. The main advantage of these compounds is that, as their fluorescent properties are dependent on electron energy levels in an atom rather than those of a molecule, they are very resistant to photodamage (and perhaps also to phototoxicity). On the other hand, it is possible that the excitation light may break the bond with the chelator causing the "dye atom" to become a non-specific stain.

The current versions of these reagents require enhanced antennary ligands for more efficient lanthanide excitation and improved biological stability and compatibility. On the other hand, the long decay times give rise to problems when they are used in scanning microscopes. When the decay time is equal to the pixel dwell time,

each molecule can be excited no more than one time and signal levels are very low. As a result, these dyes will probably only be used with widefield imaging where the exposure time seen by each molecule is long compared to its fluorescent lifetime and discrimination from the fast decay of the autofluorescence is still useful.

FLUORESCENT INDICATORS FOR DYNAMIC INTRACELLULAR PARAMETERS

Membrane Potentials

The use of confocal microscopy to measure dynamic properties of living cells such as membrane potentials (Gross and Loew, 1989) or ion concentrations (Tsien, 1988, 1989a,b) deserves some special comment. Preliminary attempts to use fast-responding, non-redistributive voltage-sensitive dyes in neuronal tissues were unsuccessful (Fine *et al.*, 1988); the dye could be seen, but the S/N was inadequate to observe voltage-dependent changes, which would have been at most only a few percent of the resting intensity. Lasers are inherently noisy light sources; even with optical negative feedback, their fluctuations are greater than the stabilized tungsten filament lamps conventionally used to see the small changes in fluorescent output that characterize fast voltage-sensitive dyes (Cohen and Lesher, 1986). "Slow" redistributive dyes, which accumulate in cells according to the Nernst equilibrium (Ehrenberg *et al.*, 1988), would seem to be more suitable for present-day confocal microscopes because their signals are much bigger and the slowness of their response (seconds to minutes) is actually a better match to the rather slow scan times of the current instrumentation. Confocal optical sectioning should work well using such accumulative dyes because in principle one could directly compare the internal concentrations of dye accumulated without having to correct for the greater path length of a thicker cell or for extracellular dye above and below the plane of focus. Freely diffusing anionic oxonol dyes have been paired with dyes anchored at the cell surface permitting fast ratiometric detection of membrane potential changes in single cells by fluorescence resonance energy transfer (Gonzalez and Tsien, 1995, 1997; Gonzalez and Maher, 2002) (see also Figure 8.45, *this volume*).

Ion Concentrations

Wavelength Ratioing

Some indicators of ion concentrations respond not just with changes in fluorescence amplitude but also with λ shifts of the excitation or emission spectrum or both. Such shifts permit ratioing between signals obtained at two or more λs (Tsien, 1989a,b). Ratioing is highly valuable because it cancels out differences in dye concentration and path length as well as fluctuations in overall illumination intensity (Tsien and Poenie, 1986; Bright *et al.*, 1987). Emission ratioing is the most valuable because, with a single excitation λ, the emission can be passed through a dichroic mirror to split it into two bands that can be monitored absolutely simultaneously. Such ratioing would give the best possible cancellation of laser noise or specimen movement. Emission ratioing is particularly easy to do with a laser-scanning system, because one can simply add a dichroic mirror and an extra photodetector after the scanning system. Whereas geometrical registration of all the corresponding pixels in two separate low-light-level video cameras is quite difficult (Jericevic *et al.*, 1989), the registration problem is trivial in a laser-scanning system assuming that the deflection is achromatic, which it must be in order to get excitation and even one emission in register. Disk-scanning confocal microscopes use charge-coupled device (CCD) or electron multiplying CCD (EM-CCD) cameras as detectors and often lack this elegant compatibility with emission ratio scanning.

Excitation ratioing of images requires sequential illumination with the two excitation λs. Intensity fluctuations of the source and movement of the specimen are canceled out only if they are much slower than the rate of alternation. Excitation ratioing is most applicable to tandem-scanning systems where conventional systems for alternating two grating monochromators or interference filters could be used. Alternating between two laser lines is more convenient now that acousto-optical deflectors are common, but it is still less flexible in choice of λ pairs.

pH Indicators

A number of ratiometric pH indicators were reviewed by Tsien (1989b) and more recently by Yip and Kurtz (2002). The most popular excitation-ratioing indicator is probably the modified fluorescein, BCECF, whose pH-sensitive and insensitive λs are around 490 nm and 439 nm, respectively. Several emission-shifting probes, 3,6-dihydroxyphthalonitrile (also known as 2,3-dicyanohydroquinone; Kurtz and Balaban, 1985; Kurtz and Emmons, 1993), and various naphthofluorescein derivatives (SNAFs and SNARFs; Haugland, 1989) are also available.

Ca^{2+} Indicators

Three currently available Ca^{2+} indicators have different sets of advantages and disadvantages for confocal microscopy (Tsien, 1988, 1989a,b). Fura-2, the dye most used in conventional microscopic imaging, shows a good excitation shift with Ca^{2+}, typically ratioed between 340 to 350 nm and 380 to 385 nm, but hardly any emission shift, so it would be most effectively used with a UV-enhanced disk-scanning instrument. Considerable re-engineering would be necessary for those early designs of tandem-scanning confocal microscope designed mainly for reflectance rather than fluorescence. The beam-splitting pellicles used are inefficient because they are partially reflective but not dichroic; also, they are sometimes made from UV-blocking material in which the excitation has to pass through the pellicle whereas the emission would have to reflect off the pellicle. Even if the pellicle were replaced by a dichroic, this choice of beam geometry is unfortunate, as it is much easier to make good broadband dichroics in which the shorter λ reflects and the longer λ transmits than vice versa. Disk systems in which the same area of the disk is used for both source and detector may be more flexible (see Chapter 10, *this volume*).

Indo-1, the dye most used in laser flow cytometry for [Ca^{++}] determination, shows a fine emission shift from 485 to 405 nm with increasing Ca^{2+} and is preferred for ratiometric laser scanning. However, either a UV laser (e.g., a high-power argon-ion or krypton-ion system) or a titanium–sapphire two-photon system is required for excitation in the 350 to 365 nm region. Also, Indo-1 fluorescence has λs similar to those of reduced pyridine nucleotides, so autofluorescence could be a problem, and Indo-1 also bleaches much more quickly than Fura-2.

Fluo-3 and its less-tested rhodamine analogs are the only Ca^{2+} indicators currently available with visible λs suitable for low-power visible lasers (Minta *et al.*, 1989; Kao *et al.*, 1989). Therefore, it has been the first to be exploited in confocal microscopy (e.g., Hernandez-Cruz *et al.*, 1989), even though it lacks either an

excitation or emission shift and is restricted to simple intensity measurements that are relatively difficult to calibrate in terms of absolute $[Ca^{2+}]_i$ units.

Of course, the ideal would be an indicator excitable at 488 nm with a large emission shift, high quantum efficiency, and strong resistance to bleaching, but this goal is a difficult challenge in molecular engineering. In general, strong fluorescence in aqueous media is much easier to obtain using shorter excitation λs because fluorescence demands planarity and molecular rigidity, which is obviously easier to achieve in small molecules that absorb short λs than in the larger molecules with longer chromophores. Most of the known chromophores that combine large size, long λs, and rigidity are essentially insoluble in water. Even if solubilizing groups are added on the periphery, the huge expanse of hydrophobic surface still promotes the formation of non-fluorescent aggregates. Finally, the quantum mechanics of absorption and fluorescence predict that the intrinsic radiative lifetime of a chromophore is proportional to the cube of the λ if other factors remain constant (Strickler and Berg, 1962). Short radiative lifetimes mean that fluorescence emission competes more successfully with nonproductive forms of deactivation and, therefore, correlates with high quantum yields of fluorescence.

Oxygen Sensor

Much effort has been spent developing ruthenium chelates as luminescent reagents. Common ligands for the central ruthenium ion include substituted bipyridines and 1,10-phenanthrolines. Currently, the most promising applications for these complexes are for monitoring the oxygen tension of solutions (Li *et al.*, 1997; Castellano and Lakowicz, 1998; Ji *et al.*, 2002). As with the lanthanide complexes, the modest excitation efficiencies are dependent on energy transfer from the ligands to the metal ion. The emission spectra are relatively weak and broad. However, time-resolved detection of the long-lived ruthenium fluorescence yields excellent S/N even from these low intensities. The presence of oxygen, even at the levels found in air, decreases the fluorescence lifetimes of ruthenium chelates by a factor of 4, a factor that should make them suitable for fluorescence lifetime imaging (FLIM; see Chapter 27, *this volume*), now that the equipment is commercially available. Improved ligands with enhanced absorbance at visible wavelengths, more efficient energy transfer to the metal, and better biocompatibility are needed before these reagents find broader applications.

cAMP Indicators

The important intracellular messenger cAMP (cyclic adenosine 3,5-monophosphate) can now be imaged with a fluorescent indicator made from cAMP-dependent protein kinase labeled on its C and R subunits with fluorescein and tetramethylrhodamine respectively (Adams *et al.*, 1991). In the holoenzyme complex, the fluorescein and rhodamine are close enough for moderately efficient fluorescence resonance energy transfer, so that excitation of the fluorescein with blue-green light gives a significant amount of orange emission from the rhodamine. Binding of cAMP dissociates the subunits and eliminates energy transfer, increasing the emission of green light directly from the fluorescein and decreasing the amplitude in the rhodamine band. This change in emission ratio and the λs employed are ideal for dual-channel detection by confocal microscopy (Bacskai *et al.*, 1993). The strategy of labeling an important endogenous sensor protein gives both advantages and potential problems. Because careful derivatization of the kinase does not change its cAMP affinity and phosphorylating activity, the indicator is inherently tuned to the physiologically relevant concentration range (a few nanomoles to a few examoles), and molecules of cAMP that bind to the indicator can still have a biological effect. An indicator that was not a physiological effector molecule would have a greater tendency to competitively inhibit or buffer the pathway under study. Furthermore, after elevation of cAMP, the interesting trafficking of the R and C subunits can be separately observed by standard dual-label imaging (e.g. Harootunian *et al.*, 1993). However, scrambling of subunits with unlabeled endogenous kinase is a potential problem, so far rarely serious (for discussion of this point and a more extensive review of the entire technique, see Adams *et al.*, 1993).

Fatty Acid Indicator

Fatty acids are of considerable importance in nutrition, membrane structure, protein modification, eicosanoid formation, and modulation of cell signaling. Recently a group led by Alan Kleinfeld has developed an emission-ratioing fluorescent probe for free fatty acid levels (Richieri *et al.*, 1992) by labeling recombinant intestinal fatty-acid-binding protein with acrylodan, an environmentally sensitive fluorophore. The acrylodan reacts with surprising specificity for Lys27 of the protein and probably resides in the fatty-acid binding pocket. Binding of fatty acids shifts the emission peak from 432 nm to 505 nm, probably by displacing the acrylodan into an aqueous environment. The 505 nm/432 nm ratio thereby increases by up to 25-fold, which would be an ideal signal for confocal microscopy if the necessary excitation at 386 nm or 400 nm were available. The labeled protein (dubbed ADIFAB) binds all common long-chain fatty acids with approximately micromolar dissociation constants. In a cuvet, ADIFAB can detect free fatty acid concentrations as low as a few nanomolar. It has already proven highly useful in measuring the release of free fatty acids from stimulated rat basophilic leukemia (RBL) cells (Richieri *et al.*, 1992) and the binding constants of fatty acids to albumin (Richieri *et al.*, 1993) and to cells (Anel *et al.*, 1993).

Other Forms of Ratioing

Because ratioing is so desirable for quantitative measurements, but appropriate λ shifts are often unavailable, several alternatives to λ ratioing have been proposed. The easiest is simply to ratio poststimulus image intensities against a prestimulus image. An example is shown by Smith and Augustine (1988). This method has the advantage of minimal hardware requirements and high time resolution, though it only cancels out variations in dye loading and path length, not shape change or dye bleaching, and by itself cannot yield an absolute calibration of the analyte, for example, $[Ca^{2+}]_i$. Another approach would be to link the fluorescent indicator covalently to a separate reference fluorophore. This approach would ideally generate a composite molecule in which the ratio of the indicator fluorescence to the reference fluorescence would signal the analyte concentration. Potential disadvantages would be the requirement for significant skill in organic synthesis, the likelihood that the conjugate would be too large for loading by ester hydrolysis, and the possibility that the two fluorophores would bleach at different rates, so that the operation of ratioing would fail to correct for bleaching. Yet a third mode of ratioing could be based on temporal dissection of excited-state lifetimes, as first shown for quin-2 by Wages and colleagues (1987). If the free and bound forms of the indicator have sufficiently different fluorescence lifetimes, their relative contributions to the (ideally) biexponential decay might be separated by nanosecond or high frequency mod-

ulation techniques (see Chapter 27, *this volume*). However, even when the instrumentation challenge of combining lifetime kinetics with imaging has been solved, the problem remains that probes like fura-2 and Indo-1, which are fairly strongly fluorescent both when free and when bound to Ca^{2+}, have almost the same lifetimes in those two states. For example, fura-2 with and without Ca^{2+} has lifetimes of 1.8 ns and 1.3 ns, respectively, at 25°C; for Indo-1 the corresponding numbers are 1.7 ns and 1.3 ns at 20°C (Wages *et al.*, 1987). In order to have a significant difference in lifetimes between Ca^{2+}-bound and free indicator, as in quin-2 (10.1 ns and 1.3 ns, respectively, at 25°C), one of the species has to be much more dimly fluorescent than the other. As a result, the weaker and faster component will be hard to measure accurately and to distinguish from autofluorescence background.

Ratiometric measurements can also be applied to other parameters such as probe polarization and local viscosity (Tinoco *et al.*, 1987; Axelrod, 1989; Dix and Verkman, 1989), proximity between macromolecules by fluorescence energy transfer (Uster and Pagano, 1986; Herman, 1989), and even water permeability (Kuwahara and Verkman, 1988; Kuwahara *et al.*, 1988).

GENETICALLY EXPRESSED INTRACELLULAR FLUORESCENT INDICATORS

Green Fluorescent Protein

Fluorescent proteins from jellyfish and corals have revolutionized biological optical microscopy because they provide genetic encoding of strong visible fluorescence of a wide range of colors. Entire books (Chalfie and Kain, 1998; Sullivan and Kay, 1999; Hicks, 2002) have been devoted to many aspects of the prototypical fluorescent protein, the green fluorescent protein (GFP) from the jellyfish *Aequorea victoria*. A shorter, relatively self-contained introduction to GFP may be found in Tsien (1998). Other general reviews on applications of GFP and other members of the fluorescent protein superfamily include (Cubitt *et al.*, 1995, 1999; Hassler, 1995; Niswender *et al.*, 1995; Rizzuto *et al.*, 1995; Stearns, 1995; Kahana and Silver, 1996; Misteli and Spector, 1997; Patterson *et al.*, 1997; Tsien and Miyawaki, 1998; Ellenberg *et al.*, 1999; Heim, 1999; Lippincott-Schwartz *et al.*, 1999; Phillips, 1999; Piston *et al.*, 1999; Chamberlain and Hahn, 2000; Miyawaki and Tsien, 2000; Sacchetti *et al.*, 2000; Zaccolo and Pozzan, 2000; Zacharias *et al.*, 2000; Blab *et al.*, 2001; Chiesa *et al.*, 2001; Harms *et al.*, 2001; Lippincott-Schwartz *et al.*, 2001; Patterson *et al.*, 2001; Reits and Neefjes, 2001; Wahlfors *et al.*, 2001; Labas *et al.*, 2002; Matz *et al.*, 2002; Miyawaki, 2002; van Roessel and Brand, 2002; Zacharias, 2002; Zhang *et al.*, 2002; Zimmer, 2002; Choy *et al.*, 2003; Ehrhardt, 2003; Hadjantonakis *et al.*, 2003; Lippincott-Schwartz and Patterson, 2003; Lippincott-Schwartz *et al.*, 2003; March *et al.*, 2003; Meyer and Teruel, 2003; Miyawaki, 2003; Tsien, 2003; Viallet and Vo-Dinh, 2003; Weijer, 2003; Verkhusha and Lukyanov, 2004). Space does not permit listing the huge number of reviews and primary papers describing more specialized uses of fluorescent proteins.

Ligand-Binding Modules

Genetic manipulations have also been used to incorporate into cells expressible modules that bind fluorescent ligands. One type of module contains a tetracysteine motif, which binds biarsenical ligands (Griffin *et al.*, 1998; Adams *et al.*, 2002; Nakanishi *et al.*, 2004). These small, membrane-permeant ligands bind with high affinity and specificity to the four sulfhydryls arranged in an alpha helix domain. Biarsenical fluorescein (FlAsH), tetramethyl rhodamine (TrAsH), and a few additional dyes have been reported. In a different approach, cells transfected with the sequence encoding a single-chain antibody (scFv) expressed a module that tightly bound cell-permeant hapten–fluorophore conjugates (Farinas and Verkman, 1999). Incorporation of several scFvs would enable multiple ligands to be detected simultaneously. Like the expressible GFPs, these modules can be directed to specific intracellular compartments by including the appropriate localization sequences.

Ion Indicators

Mutants of GFP have been identified that show pH-dependent fluorescence properties (Kneen *et al.*, 1998; Llopis *et al.*, 1998). Reversible absorbance and fluorescence emission changes were observed with apparent pKa values ranging from 4.8 to 7.1. Combining the GFP sequences with specific targeting signals permitted the acidification of specific organelles to be followed noninvasively. Genetically encoded Ca^{2+} indicators, dubbed "chameleons," utilize fluorescence resonance energy transfer (FRET) between different emitting GFPs attached to calmodulin and a calmodulin-binding peptide, M13 (Miyawaki *et al.*, 1997, 1999). Binding of Ca^{2+} to calmodulin increases the interaction between the GFPs. Optimization of the relative orientation of the two GFPs in the chimeras has expanded the dynamic range of Ca^{2+} detection (Nagai *et al.*, 2001, 2004).

FUTURE DEVELOPMENTS

Speculation on future directions in fluorophore designs is difficult because the small number of laboratories working on fluorophore chemistry makes progress a much noisier function of time than advances in instrumentation or computers. One major advance seen since publication of the previous edition of this book is a recognition of the optimal characteristics for fluorescent reagents used in biology. A thought prompted by preparation of this review is that, for present purposes, the excited triplet state of the fluorophore is a major villain without any redeeming virtues. It is responsible for a pernicious form of output saturation, for singlet oxygen production, and for nearly all covalent photochemistry such as bleaching. Similar problems have been encountered in laser dyes; a proposed solution (Liphardt *et al.*, 1982, 1983; Schäfer, 1983) is to attach triplet-state quenchers to each fluorophore. Such a construction is reminiscent of the way that evolution has assembled photosynthetic complexes and may be an area where biology can repay its debt to synthetic chemistry. Little progress has been reported in this area during the two decades since these approaches were proposed, but the potential gains from triplet-state relaxation maintain this as an attractive area for study. The development of fluorescent inorganic nanocrystals and chelates may provide the needed photostable biological tagging reagents, however.

Another area ripe for development is signal amplification schemes for detecting low copy numbers of cell receptors and genetic sequences. Use of enzymes that produce fluorescent precipitates in a localized area offers promise (Haugland, 1989); again reported progress is limited.

Finally, there is always need for additional sensitivity. Time-resolved fluorescence detection, where the fluorescence signal is collected against a dark background after pulse excitation, offers a method to circumvent autofluorescence and Raman light scat-

tering that is becoming much more widely available (Lakowicz *et al.*, 1983; Marriott *et al.*, 1991; Chapters 27 and 31, *this volume*). This approach is now realized with sophisticated excitation/detection components and will work with any fluorophore with an excited state lifetime in the nanosecond time range. Quantum dots, with fluorescence lifetimes in the range of 20 ns, may prove particularly useful, but their early-stage development as biological labeling reagents has not provided sufficient incentives for the required detection system modifications. Another ingenious approach would involve excitation of an extended lifetime fluorophore with a scanning laser followed by detection of the signal with an array detector, such as a cooled EM-CCD camera, instead of a single photomultiplier tube. The signal could be integrated on the cleared pixels of the CCD chip, even milliseconds after the excitation beam has passed the corresponding region of the sample. The extended lifetime labels could be lanthanide complexes with millisecond lifetimes that have been developed as protein-labeling reagents by Hemmila and others (Soini *et al.*, 1988; Mukkala, 1993). In situations with heavy autofluorescence, the lanthanide complex labels have demonstrated sensitivity over fluorescein labels by factors of hundreds (Seveus *et al.*, 1994). Phosphor particles developed by Beverloo and colleagues (1992) could be used in a similar fashion. Surface chemistries used to improve the biocompatibility of quantum dots may also be effective in enhancing the fluorescence properties of these phosphors in biological applications. Chemistry will continue to play a major role in furthering the power of confocal microscopy.

ACKNOWLEDGMENTS

We thank Profs. Richard Mathies and Alex Glazer for helpful discussions and criticisms of the manuscript and permission to cite their unpublished data.

REFERENCES

Adams, S.R., Campbell, R.E., Gross, L.A., Martin, B.R., Walkup, G.K., Yao, Y., Llopis, J., and Tsien R.Y., 2002, New biarsenical ligands and tetracysteine motifs for protein labeling in vitro and in vivo: synthesis and biological applications, *J. Am. Chem. Soc*. 124:6063–6076.

Adams, S.R., Harootunian, A.T., Buechler, Y.J., Taylor, S.S., and Tsien, R.Y., 1991, Fluorescence ratio imaging of cyclic AMP in single cells, *Nature* 349:694–697.

Adams, S.R., and Tsien, R.Y., 1993, Controlling cell chemistry with caged compounds, *Annu. Rev. Physiol*. 55:755–784.

Anel, A., Richieri, G.V., and Kleinfeld, A.M., 1993, Membrane partition of fatty acids and inhibition of T cell function, *Biochemistry* 32:530–536.

Axelrod, D., 1977, Cell surface heating during fluorescence photobleaching recovery experiments, *Biophys. J*. 18:129–131.

Axelrod, D., 1989, Fluorescence polarization microscopy, *Methods Cell Biol*. 30:333–352.

Bacskai, B.J., Hochner, B., Mahaut-Smith, M., Adams, S.R., Kaang, B.-K., Kandel, E.R., and Tsien, R.Y., 1993, Spatially resolved dynamics of cAMP and protein kinase A subunits in Aplysia sensory neurons, *Science* 260:222–226.

Bailey, E.A. Jr., and Rollefson, G.K., 1953, The determination of the fluorescence lifetimes of dissolved substances by a phase shift method, *J. Chem. Phys*. 21:1315–1322.

Ballard, S.G., and Ward, D.C., 1993, Fluorescence in situ hybridization using digital imaging microscopy, *J. Histochem. Cytochem*. 12:1755–1759.

Beavis, A.J., and Pennline, K.J., 1996, Allo-7: a new fluorescent tandem dye for use in flow cytometry, *Cytometry* 24:390–395.

Bernas, T., Zarebski, M., Cook, R.R., and Dobrucki, J.W., 2004, Minimizing photobleaching during confocal microscopy of fluorescent probes bound to chromatin: Role of anoxia and photon flux, *J. Microsc*. 5:281–296.

Beverloo, H.B., van Schadewijk, A., Bonnet, J., van der Geest, R., Runia, R., Verwoerd, N.P., Vrolijk, J., Ploem, J.S., and Tanke, H.J., 1992, Preparation and microscopic visualization of multicolor luminescent immunophsphors, *Cytometry* 13:561070.

Blab, G.A., Lommerse, P.H.M., Cognet, L., Harms, G.S., and Schmidt, T., 2001, Two-photon excitation action cross-sections of the autofluorescent proteins, *Chem. Phys. Lett*. 350:71–77.

Bloom, J.A., and Webb, W.W., 1984, Photodamage to intact erythrocyte membranes at high laser intensities: methods of assay and suppression, *J. Histochem. Cytochem*. 32:608–616.

Bonhoeffer, T., and Staiger, V., 1988, Optical recording with single cell resolution from monolayered slice cultures of rat hippocampus, *Neurosci. Lett*. 92:259–264.

Brelje, T.C., Wessendorf, M.W., and Sorenson, R.L., 1993, Multicolor laser scanning confocal immunofluorescence microscopy: practical applications and limitations. In: *Methods in Cell Biology 38: Cell Biological Applications of Confocal Microscopy* (B. Matsumoto, ed.), Academic Press, San Diego, California.

Bright, G.R., Fisher, G.W., Rogowska, J., and Taylor, D.L., 1987, Fluorescence ratio imaging microscopy: Temporal and spatial measurements of cytoplasmic pH, *J. Cell Biol*. 104:1019–1033.

Castellano, F.N., and Lakowicz, J.R., 1998, A water-soluble luminescence oxygen sensor, *Photochem. Photobiol*. 67:179–183.

Chalfie, M., and Kain, S., 1998, *Green Fluorescent Protein: Properties, Applications, and Protocols*, Wiley-Liss, New York.

Chalfie, M., Tu, Y., Euskirchen, G., Ward, W.W., and Prasher, D.C., 1994, Green fluorescent protein as a marker for green expression, *Science* 263:802–805.

Chamberlain, C., and Hahn, K.M., 2000, Watching proteins in the wild: fluorescence methods to study protein dynamics in living cells, *Traffic* 1:755–762.

Chen, R.F., and Scott, C.H., 1985, Atlas of fluorescence spectra and lifetimes of dyes attached to protein, *Analyt. Lett*. 18:393–421.

Chiesa, A., Rapizzi, E., Tosello, V., Pinton, P., de Virgilio, M., Fogarty, K.E., and Rizzuto, R., 2001, Recombinant aequorin and green fluorescent protein as valuable tools in the study of cell signaling, *Biochem. J*. 355:1–12.

Choy, G., Choyke, P., and Libutti, S.K., 2003, Current advances in molecular imaging: noninvasive in vivo bioluminescent and fluorescent optical imaging in cancer research, *Mol. Imaging* 2:303–312.

Cohen, L.B., and Lesher, S., 1986, Optical monitoring of membrane potential: Methods of multisite optical measurement, In: *Optical Methods in Cell Physiology* (P. De Weer, B.M. Salzberg, eds.), John Wiley and Sons, New York, pp. 71–99.

Cubitt, A.B., Heim, R., Adams, S.R., Boyd, A.E., Gross, L.A., and Tsien, R.Y., 1995, Understanding, using and improving green fluorescent protein, *Trends Biochem. Sci*. 20:448–455.

Cubitt, A.B., Woollenweber, L.A., and Heim, R., 1999, Understanding structure-function relationships in the Aequorea victoria green fluorescent protein, *Methods Cell Biol*. 58:19–30.

Czerney, P., Lehmann, F., Wenzel, M., Buschmann, V., Dietrich, A., and Mohr, G.J., 2001, Tailor-made dyes for fluorescence correlation spectroscopy (FCS), *Biol. Chem*. 382:495–498.

Dix, J.A., and Verkman, A.S., 1989, Spatially resolved anisotropy images of fluorescent probes incorporated into living cells, *Biophys. J*. 55:189a.

Ehrenberg, B., Montana, V., Wei, M.D., Wuskell, J.P., and Loew, L.M., 1988, Membrane potentials can be determined in individual cells from the Nernstian distribution of cationic dyes, *Biophys. J*. 53:785–794.

Ehrhardt, D., 2003, GFP technology for live cell imaging, *Curr. Opin. Plant Biol*. 6:622–628.

Ellenberg, J., Lippincott-Schwartz, J., and Presley, J.F., 1999, Dual-colour imaging with GFP variants, *Trends Cell Biol*. 9:52–56.

Errington, R.J., Ameer-Beg, S.M., Vojnovic, B., Patterson, L.H., Zloh, M., Smith, P.J., 2005, Advanced microscopy solutions for monitoring the kinetics and dynamics of drug-DNA targeting in living cells, *Adv. Drug Deliv. Rev.* 57(1):153–167.

Farinas, J., and Verkman, A.S., 1999, Receptor-mediated targeting of fluorescent probes in living cells, *J Biol. Chem.* 274:7603–7606.

Fine, A., Amos, W.B., Durbin, R.M., and McNaughton, P.A., 1988, Confocal microscopy: Applications in neurobiology, *Trends Neurosci*. 11:346–351.

Galbraith, W., Ernst, L.A., Taylor, D.L., and Waggoner, A.S., 1989, Multiparameter fluorescence and the selection of optimal filter sets: Mathematics and computer program, *Proc. Soc. Photo. Opt. Instrum. Eng*. 1063:74–122.

Gandin, E., Lion, Y., and Van de Vorst, A., 1983, Quantum yields of singlet oxygen production by xanthene derivatives, *Photochem. Photobiol*. 37:271–278.

Gerstner, A.O., Lenz, D., Laffers, W., Hoffman, R.A., Steinbrecher, M., Bootz, F., and Tarnok, A., 2002, Near-infrared dyes for six-color immunophenotyping by laser scanning cytometry, *Cytometry* 48:115–123.

Giloh, H., and Sedat, J.W., 1982, Fluorescence microscopy: Reduced photobleaching of rhodamine and fluorescein protein conjugates by *n*-propyl gallate, *Science* 217:1252–1255.

Glazer, A.N., 1988, Fluorescence-based assay for reactive oxygen species: A protective role for creatinine, *FASEB J.* 2:2487–2491.

Glazer, A.N., 1989, Light guides. Directional energy transfer in a photosynthetic antenna, *J. Biol. Chem.* 264:1–4.

González, J.E., and Maher, M.P., 2002, Cellular fluorescent indicators and voltage/ion probe reader (VIPR$^{(tm)}$): Tools for ion channel and receptor drug discovery, *Receptors Channels* 8:283–295.

Gonzalez, J.E., and Tsien, R.Y., 1995, Voltage sensing by fluorescence resonance energy transfer in single cells, *Biophys. J*. 69:1272–1280.

Gonzalez, J.E., and Tsien, R.Y., 1997, Improved indicators of cell membrane potential that use fluorescence resonance energy transfer, *Chem. Biol*. 4:269–277.

Griffin, B.A., Adams, S.R., and Tsien, R.Y., 1998, Specific covalent labeling of recombinant protein molecules inside live cells, *Science* 281:269–272.

Gross, D., and Loew, L.M., 1989, Fluorescent indicators of membrane potential: Microspectrofluorometry and imaging, *Methods Cell Biol*. 30:193–218.

Hadjantonakis, A.K., Dickinson, M.E., Fraser, S.E., and Papaioannou, V.E., 2003, Technicolour transgenics: Imaging tools for functional genomics in the mouse, *Nat. Rev. Genet*. 4:613–625.

Harms, G.S., Cognet, L., Lommerse, P.H., Blab, G.A., and Schmidt, T., 2001, Autofluorescent proteins in single-molecule research: Applications to live cell imaging microscopy, *Biophys. J*. 80:2396–2408.

Harootunian, A.T., Adams, S.R., Wen, W., Meinkoth, J.L., Taylor, S.S., and Tsien, R.Y., 1993, Movement of the free catalytic subunit of cAMP dependent protein kinase into and out of the nucleus can be explained by diffusion, *Mol. Biol. Cell* 4:993–1002.

Hasan, M.T., Friedrich, R.W., Euler, T., Larkum, M.E., Giese, G., Both, M., Duebel, J., Waters, J., Bujard, H., Griesbeck, O., Tsien, R.Y., Nagai, T., Miyawaki, A., and Denk, W., 2004, Functional fluorescent Ca^{2+} indicator proteins in transgenic mice under TET control, *PLoS Biol*. 2:763–775.

Hassler, S., 1995, Green fluorescent protein — the next generation, *Bio/Technology* 13:103.

Haugland, R.P., 1989, *Molecular Probes: Handbook of Fluorescent Probes and Research Chemicals*, Molecular Probes Inc., Eugene, Oregon, pp. 86–94.

Heim, R., 1999, Green fluorescent protein forms for energy transfer, *Methods Enzymol*. 302:408–423.

Hernandez-Cruz, A., Sala, F., and Adams, P.R., 1989, Subcellular dynamics of $[Ca^{2+}]_i$ monitored with laser scanned confocal microscopy in a single voltage-clamped vertebrate neuron, *Biophys. J.* 55:216a.

Herman, B., 1989, Resonance energy transfer microscopy, *Methods Cell Biol*. 30:219–243.

Hicks, B.W., 2002, *Green Fluorescent Protein: Applications and Protocols*, Humana Press, Totowa, New Jersey.

Hirschfeld, T., 1976, Quantum efficiency independence of the time integrated emission from a fluorescent molecule, *Appl. Opt*. 15:3135–3139.

Hoshino, A., Hanaki, K., Suzuki, K., and Yamamoto, K., 2004, Applications of T-lymphoma labeled with fluorescent quantum dots to cell tracing markers in mouse body, *Biochem. Biophys. Res. Commun*. 314:46–53.

Jaiswal, J.K., Mattoussi, H., Mauro, J.M., and Simon, S.M., 2003, Long-term multiple color imaging of live cells using quantum dot bioconjugates, *Nat. Biotechnol*. 21:47–51.

Jericevic, Z., Wiese, B., Bryan, J., and Smith, L.C., 1989, Validation of an imaging system: Steps to evaluate and validate a microscope imaging system for quantitative studies, *Methods Cell Biol*. 30:47–83.

Ji, J., Rosenzweig, N., Jones, I., and Rosenzweig, Z., 2002, Novel fluorescent oxygen indicator for intracellular oxygen measurements, *J. Biomed. Opt.* 7:404–409.

Kahana, J., and Silver, P., 1996, Use of the A. victoria green fluorescent protein to study protein dynamics in vivo, In: *Current Protocols in Molecular Biology* (F.M. Ausabel, R. Brent, R.E. Kingston, D.D. Moore, J.G. Seidman, J.A. Smith, K. Struhl, eds.), John Wiley and Sons, New York, pp. 9.7.22–9.7.28.

Kang, H.C., Fisher, P.J., Prendergast, F.G., and Haugland, R.P., 1988, Bodipy: A novel fluorescein and NBD substitute, *J. Cell Biol.* 107:34a.

Kao, J.P.Y., Harootunian, A.T., and Tsien, R.Y., 1989, Photochemically generated cytosolic calcium pulses and their detection by fluo-3. *J. Biol. Chem*. 264:8179–8184.

Kaplan, N.O., 1960, The pyridine coenzymes, In: *The Enzymes*, 2nd ed. (P.D. Boyer, H. Lardy, K. Myrbäck, eds.), Academic Press, New York, pp. 105–169.

Kneen, M., Farinas, J., Li, Y., and Verkman, A.S., 1998, Green fluorescent protein as a noninvasive intracellular pH indicator, *Biophys. J*. 74:1591–1599.

Koziol, J., 1971, Fluorometric analyses of riboflavin and its coenzymes, *Methods Enzymol*. 18B:253–285.

Kurtz, I., and Balaban, R.S., 1985, Fluorescence emission spectroscopy of 1,4-dihydroxyphthalonitrile: A method for determining intracellular pH in cultured cells, *Biophys. J*. 48:499–508.

Kurtz, I., and Emmons, C., 1993, Measurement of intracellular pH with a laser scanning confocal microscope, In: *Methods in Cell Biology 38: Cell Biological Applications of Confocal Microscopy* (B. Matsumoto, ed.), Academic Press, San Diego, California.

Kuwahara, M., and Verkman, A.S., 1988, Direct fluorescence measurement of diffusional water permeability in the vasopressin-sensitive kidney collecting tubule, *Biophys. J.* 54:587–593.

Kuwahara, M., Berry, C.A., and Verkman, A.S., 1988, Rapid development of vasopressin-induced hydroosmosis in kidney collecting tubules measured by a new fluorescence technique, *Biophys. J.* 54:595–602.

Labas, Y.A., Gurskaya, N.G., Yanushevich, Y.G., Fradkov, A.F., Lukyanov, K.A., Lukyanov, S.A., and Matz, M.V., 2002, Diversity and evolution of the green fluorescent protein family, *Proc. Natl. Acad. Sci. USA* 99:4256–4261.

Lakowicz, J.R., 1983, Fluorescence lifetime imaging, *Anal. Biochem*. 202:316–330.

Lakowicz, J.R., 1989, *Principles of Fluorescence Spectroscopy*, 2nd ed., Kluwer Academic, Plenum Press, New York.

Lewis, G.N., Lipkin, D., and Magel, T.T., 1941, Reversible photochemical processes in rigid media. A study of the phosphorescent state, *J. Am. Chem. Soc*. 63:3005–3018.

Li, L., Szmacinski, H., and Lakowicz, J.R., 1997, Synthesis and luminescence spectral characterization of long-lifetime lipid metal-ligand probes, *Anal. Biochem*. 244:80–85.

Lindqvist, L., 1960, A flash photolysis study of fluorescein, *Arkiv. Kemi.* 16:79–138.

Liphardt, B., Liphardt, B., and Lüttke, W., 1982, Laserfarbstoffe mit intramolekularer Triplettlöschung, *Chemische Berichte* 115:2997–3010.

Liphardt, B., Liphardt, B., and Lüttke, W., 1983, Laser dyes III: Concepts to increase the photostability of laser dyes, *Opt. Commun*. 48:129–133.

Lippincott-Schwartz, J., and Patterson, G.H., 2003, Development and use of fluorescent protein markers in living cells, *Science* 300:87–91.

Lippincott-Schwartz, J., Altan-Bonnet, N., and Patterson, G.H., 2003, Photobleaching and photoactivation: following protein dynamics in living cells, *Nat. Cell Biol. Suppl*. S7–S14.

Lippincott-Schwartz, J., Presley, J.F., Zaal, K.J., Hirschberg, K., Miller, C.D., and Ellenberg, J., 1999, Monitoring the dynamics and mobility of membrane proteins tagged with green fluorescent protein, *Methods Cell Biol*. 58:261–281.

Lippincott-Schwartz, J., Snapp, E., and Kenworthy, A., 2001, Studying protein dynamics in living cells, *Nat. Rev. Mol. Cell Biol.* 2:444–456.

Llopis, J., McCaffery, J.M., Miyawaki, A., Farquhar, M.G., and Tsien, R.Y., 1998, Measurement of cytosolic, mitochondrial, and Golgi pH in single living cells with green fluorescent proteins, *Proc. Natl. Acad. Sci. USA* 95:6803–6808.

Loew, L.M., 1993, Confocal microscopy of potentiometric fluorescent dyes, In: *Methods in Cell Biology 38:Cell Biological Applications* (B. Matsumoto, ed.), Academic Press, San Diego, California, pp. 195–209.

Manitto, P., Speranza, G., Monti, D., and Gramatica, P., 1987, Singlet oxygen reactions in aqueous solution. Physical and chemical quenching rate constants of crocin and related carotenoids, *Tetrahedron Lett.* 28: 4221–4224.

March, J.C., Rao, G., and Bentley, W.E., 2003, Biotechnological applications of green fluorescent protein, *Appl. Microbiol. Biotechnol.* 62:303–315.

Marriott, G., Clegg, R.M., Arndt-Jovin, D.J., and Jovin, T.M., 1991, Time-resolved imaging studies. Phosphorescence and delayed fluorescence imaging, *Biophys. J.* 60:1374–1387.

Matheson, I.B.C., and Rodgers, M.A.J., 1982, Crocetin, a water soluble carotenoid monitor for singlet molecular oxygen, *Photochem. Photobiol.* 36:1–4.

Mathies, R.A., and Stryer, L., 1986, Single-molecule fluorescence detection: A feasibility study using phycoerythrin, In: *Applications of Fluorescence in the Biomedical Sciences* (D.L. Taylor, A.S. Waggoner, R.F. Murphy, F. Lanni, R.R. Birge, eds.), Alan R. Liss, New York, pp. 129–140.

Matthews, M.M., and Sistrom, W.R., 1959, Function of carotenoid pigments in nonphotosynthetic bacteria, *Nature (Lond.)* 184:1892–1893.

Matz, M.V., Lukyanov, K.A., and Lukyanov, S.A., 2002, Family of the green fluorescent protein: Journey to the end of the rainbow, *BioEssays* 24:953–959.

Meyer, T., and Teruel, M.N., 2003, Fluorescence imaging of signaling networks, *Trends Cell Biol.* 13:101–106.

Minta, A., Kao, J.P.Y., and Tsien, R.Y., 1989, Fluorescent indicators for cytosolic calcium based on rhodamine and fluorescein chromophores, *J. Biol. Chem.* 264:8171–8178.

Misteli, T., and Spector, D.L., 1997, Applications of the green fluorescent protein in cell biology and biotechnology, *Nat. Biotechnol.* 15:961–964.

Miyawaki, A., 2002, Green fluorescent protein-like proteins in reef Anthozoa animals, *Cell Struct. Funct.* 27:343–347.

Miyawaki, A., 2003, Fluorescence imaging of physiological activity in complex systems using GFP-based probes, *Curr. Opin. Neurobiol.* 13:591–596.

Miyawaki, A., and Tsien, R.Y., 2000, Monitoring protein conformations and interactions by fluorescence resonance energy transfer between mutants of green fluorescent protein, *Methods Enzymol.* 327:472–500.

Miyawaki, A., Griesbeck, O., Heim, R., and Tsien, R.Y., 1999, Dynamic and quantitative Ca2+ measurements using improved chameleons, *Proc. Natl. Acad. Sci. USA* 96:2135–2140.

Miyawaki, A., Llopis, J., Heim, R., *et al.*, 1997, Fluorescent indicators for Ca^{2+} based on green fluorescent proteins and calmodulin, *Nature* 388:882–887.

Miyawaki, A., Sawano, A., and Kogure, T., 2003, Lighting up cells: Labelling proteins with fluorophores. *Nat. Cell Biol.* 5(Suppl):S1–S7.

Mujumdar, R.B., Ernst, L.A., Mujumdar, S.R., Lewis, C.J., and Waggoner, A.S., 1993, Cyanine dye labeling reagents: Sulfoindocyanine succinimidyl esters, *Bioconjug. Chem.* 4:105–111.

Mukkala, V.M., 1993, Development of stable, photoluminescent Europium (III) and Terbium (III) chelates suitable as markers in bioaffinity assays: Their synthesis and luminescence properties, PhD thesis, University of Turku, Turku, Finland.

Nagai, T., Sawano, A., Park, E.S., and Miyawaki, A., 2001, Circularly permuted green fluorescent proteins engineered to sense Ca^{2+}, *Proc. Natl. Acad. Sci. USA* 98:3197–3202.

Nagai, T., Yamada, S., Tominaga, T., Ichikawa, M., and Miyawaki, A., 2004, Expanded dynamic range of fluorescent indicators for Ca(2+) by circularly permuted yellow fluorescent proteins, *Proc. Natl. Acad. Sci. USA* 101:10554–10559.

Nakanishi, J., Maeda, M., and Umezawa, Y., 2004, A new protein conformation indicator based on biarsenical fluorescein with an extended benzoic acid moiety, *Anal. Sci.* 20:273–278.

Nguyen, D.C., Keller, R.A., Jett, J.H., and Martin, J.C., 1987, Detection of single molecules of phycoerythrin in hydrodynamically focused flows by laser-induced fluorescence, *Anal. Chem.* 59:2158–2161.

Niswender, K.D., Blackman, S.M., Rohde, L., Magnuson, M.A., and Piston, D.W., 1995, Quantitative imaging of green fluorescent protein in cultured cells: Comparison of microscopic techniques, use in fusion proteins and detection limits, *J. Microsc.* 180:109–116.

Oi, V., Glazer, A.N., and Stryer, L., 1982, Fluorescent phycobiliprotein conjugates for analyses of cells and molecules, *J. Cell Biol.* 93:981–986.

Oswald, B., Duschl, J., Patsenker, L., Wolfbeis, O.S., and Terpetschnig, E., 1999, Synthesis, spectral properties, and detection limits of reactive squaraine dyes, a new class of diode laser compatible fluorescent protein labels, *Bioconjug. Chem.* 10:925–931.

Panchuk-Voloshina, N., Haugland, R.P., Bishop-Stewart, J., Bhalgat, M.K., Millard, P.J., Mao, F., Leung, W.-Y., and Haugland, R.P., 1999, Alexa dyes, a series of new fluorescent dyes that yield exceptionally bright, photostable conjugates, *J. Histochem. Cytochem.* 47:1179–1188.

Patterson, G., Day, R.N., and Piston, D., 2001, Fluorescent protein spectra, *J. Cell Sci.* 114:837–838.

Patterson, G.H., Knobel, S.M., Sharif, W.D., Kain, S.R., and Piston, D.W., 1997, Use of the green-fluorescent protein (GFP) and its mutants in quantitative fluorescence microscopy, *Biophys. J.* 73:2782–2790.

Peck, K., Stryer, L., Glazer, A.N., and Mathies, R.A., 1989, Single molecule fluorescence detection: Autocorrelation criterion and experimental realization with phycoerythrin, *Proc. Natl. Acad. Sci. USA*, 86:4087–4091.

Phillips, G.N., 1999, Structure and dynamics of green fluorescent protein, *Curr. Opin. Struc. Biol.* 7:821–827.

Piston, D.W., Patterson, G.H., and Knobel, S.M., 1999, Quantitative imaging of the green fluorescent protein (GFP), *Methods Cell Biol.* 58:31–47.

Prasher, D.C., Eckenrode, V.K., Ward, W.W., Prendergast, F.G., and Cormier, M.J., 1992, Primary structure of the Aequorea victoria green-fluorescent protein, *Gene* 111:229–233.

Rechtenwald, D.J., 1989, US Patent 4,876,190.

Reits, E.A., and Neefjes, J.J., 2001, From fixed to FRAP: Measuring protein mobility and activity in living cells, *Nat. Cell Biol.* 3:E145–E147.

Reyftmann, J.P., Kohen, E., Morliere, P., Santus, R., Kohen, C., Mangel, W.F., Dubertret, L., and Hirschberg, J.G., 1986, A microspectrofluorometric study of porphyrin-photosensitized single living cells — I. Membrane alterations, *Photochem. Photobiol.* 44:461–469.

Richieri, G.V., Ogata, R.T., and Kleinfeld, A.M., 1992, A fluorescently labeled intestinal fatty acid binding protein, *J. Biol. Chem.* 267:23495–23501.

Richieri, G.V., Anel, A., and Kleinfeld, A.M., 1993, Interactions of long-chain fatty acids and albumin: Determination of free fatty acid levels using the fluorescent probe ADIFAB, *Biochemistry* 32:7574–7580.

Rizzuto, R., Brini, M., Pizzo, P., Murgia, M., and Pozzan, T., 1995, Chimeric green fluorescent protein (GFP): A new tool for visualizing subcellular organelles in living cells, *Curr. Biol.* 5:635–642.

Roederer, M., Kantor, A.B., Parks, D.R., and Herzenberg, L.A., 1996, Cy7PE and Cy7APC: Bright new probes for immunofluorescence, *Cytometry* 24:191–197.

Rye, H.S., Yue, S., Wemmer, D.E., Quesada, M.A., Haugland, R.P., Mathies, R.A., and Glazer, R.N., 1992, Stable fluorescent complexes of double-stranded DNAs with bis-intercalating asymmetrical cyanine dyes: Properties and applications, *Nucleic Acids Res.* 20:2803–2812.

Sacchetti, A., Ciccocioppo, R., and Alberti, S., 2000, The molecular determinants of the efficiency of green fluorescent protein mutants, *Histol. Histopathol.* 15:101–107.

Schäfer, F.P., 1983, New developments in laser dyes, *Laser Chem.* 3:265–278.

Schneider, M.B., and Webb, W.W., 1981, Measurement of submicron laser beam radii, *Appl. Opt.* 20:1382–1388.

Seveus, L., Vaisala, M., Hemmlia, I., Kojola, H., Roomans, G.M., and Soini, E., 1994, Use of fluorescent Europium chelates as labels in microscopy allows glutaraldehyde fixation and permanent mounting and leads to reduced autofluorescence and good long-term stability, *Microsc. Res. Techn.* 28:149–154.

Sheetz, M.P., and Koppel, D.E., 1979, Membrane damage caused by irradiation of fluorescent concanavalin A, *Proc. Natl. Acad. Sci. USA* 76:3314–3317.

Smith, S.J., and Augustine, G.J., 1988, Calcium ions, active zones and synaptic transmitter release, *Trends Neurosci.* 11:458–464.

Smith, P.J., Blunt, N., Wiltshire, M., Hoy, T., Teesdale-Spittle, P., Craven, M.R., Watson, J.V., Amos, W.B., Errington, R.J., and Patterson, L.H., 2000, Characteristics of a novel deep red/infrared fluorescent cell-permeant DNA probe, DRAQ5, in intact human cells analyzed by flow cytometry, confocal and multiphoton microscopy, *Cytometry* 40(4):280–291.

Snyder, D.S., Garon, C.F., 2003, Decreased uptake of bodipy-labelled compounds in the presence of the nuclear stain, DRAQ5, *J. Microsc.* 211(Pt 3):208–211.

Soini, E.J., Pelliniemi, L.J., Hemmila, I.A., Mukkala, V.-M., Kankare, J.J., and Froidman, K., 1988, Lanthanide chelates as new fluorochrome labels for cytometry, *J. Histochem. Cytochem*. 36:1449–1451.

Southwick, P.L., Ernst, L.A., Tauriello, E.W., Parker, S.R., Mujumdar, R.B., Mujumdar, S.R., Clever, H.A., and Waggoner, A.S., 1990, Cyanine dye labeling reagents — Carboxymethylindocyanine succinimidyl esters, *Cytometry* 11:418–430.

Stearns, T., 1995, Green fluorescent protein — The green revolution, *Curr. Biol*. 5:262–264.

Strickler, S.J., and Berg, R.A., 1962, Relationship between absorption intensity and fluorescence lifetime of molecules, *J. Chem. Phys*. 37:814–822.

Sullivan, K.F., and Kay, S.A., 1999, *Green Fluorescent Proteins*, Academic Press, San Diego, California.

Sun, C., Yang, J., Li, L., Wu, X., Liu, Y., and Liu, S., 2004, Advances in the study of luminescence probes for proteins, *J. Chromat. B: Anal. Technol. Biomed. Life Sci*. 803:173–190.

Sun, L., Wang, S., Chen, L., and Gong, X., 2003, Promising fluorescent probes from phycobiliproteins, *IEEE J Select. Topics Quant. Electron*. 9:177–188.

Tinoco, I., Mickols, W., Maestre, M.F., and Bustamante, C., 1987, Absorption, scattering, and imaging of biomolecular structures with polarized light, *Annu. Rev. Biophys. Biophys. Chem*. 16:319–349.

Trask, B.J., 1991, DNA sequence localization in metaphase and interphase cells by fluorescence in situ hybridization, *Methods Cell Biol*. 35:1–35.

Tsien, R.Y., 1988, Fluorescence measurement and photochemical manipulation of cytosolic free calcium, *Trends Neurosci*. 11:419–424.

Tsien, R.Y., 1989a, Fluorescent probes of cell signaling, *Annu. Rev. Neurosci*. 12:227–253.

Tsien, R.Y., 1989b, Fluorescent indicators of ion concentrations, *Methods Cell Biol*. 30:127–156.

Tsien, R.Y., 1998, The green fluorescent protein, *Annu. Rev. Biochem*. 67:509–544.

Tsien, R.Y., 2003, Imagining imaging's future, *Nat. Rev. Mol. Cell Biol*. 4(Suppl):SS16–SS21.

Tsien, R.Y., and Miyawaki, A., 1998, Seeing the machinery of live cells, *Science* 280:1954–1955.

Tsien, R.Y., and Poenie, M., 1986, Fluorescence ratio imaging: A new window into intracellular ionic signaling, *Trends Biochem. Sci*. 11:450–455.

Uster, P.S., and Pagano, R.E., 1986, Resonance energy transfer microscopy: Observations of membrane-bound fluorescent probes in model membranes and in living cells, *J. Cell Biol*. 103:122–124.

van Roessel, P., and Brand, A.H., 2002, Imaging into the future: visualizing gene expression and protein interactions with fluorescent proteins, *Nat. Cell Biol*. 4:E15–E20.

Vereb, G., Jares-Erijman, E., Selvin, P.R., and Jovin, T.M., 1998, Temporally and spectrally resolved imaging microscopy of lanthanide chelates, *Biophys. J*. 74:2210–2222.

Verkhusha, V.V., and Lukyanov, K.A., 2004, The molecular properties and applications of Anthozoa fluorescent proteins and chromoproteins, *Nat. Biotechnol*. 22:289–296.

Viallet, P.M., and Vo-Dinh, T., 2003, Monitoring intracellular proteins using fluorescence techniques: From protein synthesis and localization to activity, *Curr. Protein Peptide Sci*. 4:375–388.

Vigers, G.P.A., Coue, M., and McIntosh, J.R., 1988, Fluorescent microtubules break up under illumination, *J. Cell Biol*. 107:1011–1024.

Voura, E.B., Jaiswal, J.K., Mattoussi, H., and Simon, S.M., 2004, Tracking metastatic tumor cell extravasation with quantum dot nanocrystals and fluorescence emission-scanning microscopy, *Nat. Med*. 10:993–998.

Wages, J., Packard, B., Edidin, M., and Brand, L., 1987, Time-resolved fluorescence of intracellular quin-2, *Biophys. J*. 51:284a.

Waggoner, A., DeBiasio, R., Conrad, P., Bright, G.R., Ernst, L., Ryan, K., Nederlof, M., and Taylor, D., 1989, Multiple spectral parameter imaging, *Methods Cell Biol*. 30:449–478.

Waggoner, A.S., Ernst, L.A., Chen, C.-H., and Rechtenwald, D.J., 1993, A new fluorescent antibody label for three-color flow cytometry with a single laser, *Ann. N.Y. Acad. Sci*. 677:185–193.

Wahlfors, J., Loimas, S., Pasanen, T., and Hakkarainen, T., 2001, Green fluorescent protein (GFP) fusion constructs in gene therapy research, *Histochem. Cell Biol*. 115:59–65.

Ward, W.W., Cody, C.W., and Hart, R.C., 1980, Spectrophotometric identity of the energy transfer chromophores in Renilla and Aequorea green-fluorescent proteins, *Photochem. Photobiol*. 31:611–615.

Watt, R.M., and Voss, E.W. Jr., 1977, Mechanism of quenching of fluorescein by anti-fluorescein IgG antibodies, *Immunochemistry* 14:533–541.

Weijer, C.J., 2003, Visualizing signals moving in cells, *Science 300*:96–100.

Wessendorf, M.W., and Brelje, T.C., 1992, Which fluorophore is brightest? A comparison of the staining obtained using fluorescein, tetramethylrhodamine, lissamine rhodamine, Texas Red, and cyanine 3.18, *Histochemistry* 98:81–85.

White, J.C., and Stryer, L., 1987, Photostability studies of phycobiliprotein fluorescent labels, *Anal. Biochem*. 161:442–452.

White, J.G., Amos, W.B., and Fordham, M., 1987, An evaluation of confocal versus conventional imaging of biological structures by fluorescence light microscopy, *J. Cell Biol*. 105:41–48.

Wilson, E.O., 1975, *Sociobiology*, Harvard University Press, Cambridge, Massachusetts, pp. 38–43.

Wories, H.J., Koek, J.H., Lodder, G., Lugtenburg, J., Fokkens, R., Driessen, O., and Mohn, G.R., 1985, A novel water-soluble fluorescent probe: synthesis, luminescence and biological properties of the sodium salt of the 4-sulfonato-3,3′,5,5′-tetramethyl-2,2′-pyrromethen-1,1′-BF_2 complex, *Recl. Trav. Chim. Pays-Bas* 104:288–291.

Yip, K.-P., and Kurtz, I., 2002, Confocal fluorescence microscopy measurements of pH and calcium in living cells, *Methods Cell Biol*. 70:417–427.

Yu, H., Ernst, L.A., Wagner, M., and Waggoner, A.S., 1992, Sensitive detection of RNAs in single cells by flow cytometry, *Nucleic Acids Res*. 20:83–88.

Zaccolo, M., and Pozzan, T., 2000, Imaging signal transduction in living cells with GFP-based probes. IUBMB, *Life* 49:375–379.

Zacharias, D.A., 2002, Sticky caveats in an otherwise glowing report: Oligomerizing fluorescent proteins and their use in cell biology, *Sci. STKE* 2002:E23.

Zacharias, D.A., Baird, G.S., and Tsien, R.Y., 2000, Recent advances in technology for measuring and manipulating cell signals, *Curr. Opin. Neurobiol*. 10:416–421.

Zhang, J., Campbell, R.E., Ting, A.Y., and Tsien, R.Y., 2002, Creating new fluorescent probes for cell biology, *Nat. Rev. Mol. Cell Biol*. 3:906–918.

Zimmer, M., 2002, Green fluorescent protein (GFP): Applications, structure, and related photophysical behavior, *Chem. Rev*. 102:759–781.

17

Practical Considerations in the Selection and Application of Fluorescent Probes

Iain D. Johnson

INTRODUCTION

Due to its sensitivity, multiplexing capacity, and applicability to live specimens, fluorescence is the dominant contrast mechanism used in three-dimensional (3D) biological microscopy. Use of fluorescence detection generally requires specimens to be labeled with extrinsic probes. This is because most biological molecules and structures of interest are not intrinsically fluorescent in spectral ranges that are useful for detection, and even those that are cannot usually be discriminated from each other on the basis of their intrinsic fluorescence. Extrinsic labeling circumvents these problems at the expense of introducing others. Extrinsic probes must be delivered to the region of interest and remain there for long enough to acquire the experimental data. Once *in situ*, the probe should ideally be a passive reporter that does not induce significant perturbations of the biological structure or function that we wish to study. Furthermore, the detection process itself may have deleterious side effects in the form of photobleaching and photoxicity, resulting from the interaction of excitation light with the probe and the specimen.

Based on the premise that understanding probe behavior is a key component in evaluating the information content of images obtained using fluorescence microscopy, this chapter reviews the practical considerations involved in probe selection and use. In Table 17.1, fourteen key characteristics of probes and specimens are listed in relation to their impact on labeling and detection processes. The ordering of topics in Table 17.1 reflects the sequence of discussion in subsequent sections of this chapter.

SELECTION CRITERIA FOR DYES AND PROBES

A fluorescent dye (or, synonymously, a fluorophore) is a fluorescent molecule that does not associate with any particular biological target. A fluorescent probe is a dye that has been modified in some way to detect specific biological targets (Fig. 17.1). Targets include specific groups of cells in a tissue, organelles, proteins, nucleic acids, ions (Ca^{2+}, Mg^{2+}, H^+, Na^+, etc.) and enzymes. From this perspective, fluorescein is a **dye** whereas fluorescein-labeled proteins and peptides are **probes**. Similarly, the green fluorescent protein (GFP) can be considered to be a "dye" and GFP fusion proteins are probes. In some cases, the structural characteristics of the dye itself are sufficient to confer biospecificity. For example, cationic dyes such as MitoTracker Red CMXRos, JC-1, and rhodamine 123 stain mitochondria driven by the internally negative membrane potential. Dyes and probes have both biochemical and spectroscopic properties. Biochemical properties determine the molecular association, transport, and metabolic fate of the probe. Examples include water solubility, membrane permeability, receptor binding affinity, and enzymatic conversion rates. Spectroscopic properties primarily determine the number and energy distribution of photons available for detection. They include excitation and emission spectra, molar absorptivity (extinction coefficient), fluorescence quantum yield, and photobleaching rate.

Organic Dyes

Fluorescein and its derivatives (Fig. 17.1) have been the most widely used class of organic dyes used as fluorescent probes. Their utility is derived in part from the fact that fluorescein is efficiently excited by the 488 nm argon-ion laser line. Coumarins and rhodamines have been the primary blue (~450 nm) and orange (~580 nm) emitting dyes used alongside fluorescein (green emission, ~520 nm) in two-color labeling applications. Each class has some significant disadvantages. Fluoresceins are pH sensitive and highly susceptible to photobleaching. Rhodamines have a tendency to aggregate in aqueous solutions resulting in self-quenching of fluorescence (see below). Coumarins have relatively low excitation efficiencies — ε_{max} ~ 20,000 $M^{-1}cm^{-1}$ compared to ε_{max} ~ 100,000 $M^{-1}cm^{-1}$ for fluoresceins and rhodamines. Coumarins also have other drawbacks associated with ultraviolet excitation, namely, phototoxicity and a requirement for expensive quartz optical components. These latter problems can be circumvented by use of two-photon excitation.

The deficiencies of fluorescein, rhodamine, and coumarin dyes have spurred the development of new dye classes that have been deliberately optimized for biomolecular detection applications. Three of these classes will be discussed here (in alphabetical order) — AlexaFluor dyes, BOPIDY dyes, and cyanine (Cy) dyes (Table 17.2). The AlexaFluor dye series has 19 members with excitation maxima matched to principal laser output lines between 350 and 750 nm (Fig. 17.2). The AlexaFluor dyes are more water-soluble than their fluorescein and rhodamine counterparts, resulting directly or indirectly in reduced levels of self-quenching upon coupling to proteins and improved photostability (Panchuk-Voloshina *et al.*,1999; Berlier *et al.*, 2003). The Cy dye series (Mujumdar *et al.*, 1993) has fewer excitation wavelength variants but contains similar design elements to the AlexaFluor dyes series — sulfonic acid substituents to increase aqueous solubility and the use of *N*-hydroxysuccinimidyl (NHS) ester reactive chemistry for cou-

Iain D. Johnson • Molecular Probes, Inc., Eugene, Oregon 97402

TABLE 17.1. Key Characteristics of Probes and Specimens

Property	Significance
1. Excitation spectrum	Should be wavelength-matched with instrument source output for optimum fluorescence excitation efficiency (see Fig. 17.2).
	Overlap with donor emission spectrum required for FRET.
2. Extinction coefficient (ε; units $M^{-1}cm^{-1}$)	Determining factor in fluorescence output per dye.
3. Emission spectrum	Ability to resolve probe signal from autofluorescence.
	Selection of probes for simultaneous imaging of multiple targets.[a]
	Overlap with acceptor excitation spectrum required for FRET.
4. Fluorescence quantum yield (QY)	Determining factor in fluorescence output per dye. Often environment dependent.
5. Environment sensitivity	Impacts the proportionality of dye fluorescence to concentration.
6. Probe size/permeability/solubility	Impacts choice of loading method.
7. Specimen type (single cell, cell population, tissue)	Impacts choice of loading method.
8. Target abundance	Determines total fluorescence output. May compel use of signal amplification techniques[b] or GFP overexpression.
9. Autofluorescence	Impacts selection of excitation/emission wavelength ranges and level of labeling required.
10. Probe localization	Localized accumulations are more readily detectable than the diffuse distributions.
11. Probe metabolism and retention	Determines stability of labeling.
12. Probe-mediated cytotoxicity	Impacts specimen viability.
	May require reduced loading concentration and/or selecting a different probe.
13. Photobleaching	May necessitate attenuation of excitation power.
	Determines ability to conduct time-lapse experiments.
14. Phototoxicity	Impacts specimen viability.

[a] Dyes with narrow emission bandwidths are preferred for minimizing spillover of the signal into adjacent detection channels (see Fig. 17.2).
Probes that exhibit environment-dependent spectral shifts, such as the JC-1 and BOPIDY FL ceramide are difficult to employ in these applications for this reason.
[b] See Wang and colleagues (1999) for example.

pling to free amine groups on proteins and other biomolecules [Fig. 17.3(A)]. In contrast to the AlexaFluor and Cy dye series, BOPIDY dyes are non-polar and relatively insoluble in water [Fig. 17.3(B)]. Instead of protein labeling, they are primarily utilized in fluorescent lipid analogs (Pagano *et al*., 2000; Farber *et al*., 2001) and analogs of receptor ligands such as nucleotides, steroids, alkaloids, and peptides (Daly and McGrath, 2003).

Environmental factors including pH, solvent polarity, binding to proteins, and dye–dye interactions can exert strong influences on dye fluorescence. Susceptibility to environment varies widely among dye classes. Dyes that are designed primarily for covalent labeling of proteins and nucleic acids such as AlexaFluor dyes and Cy dyes are highly fluorescent in water and retain similar levels of fluorescence after coupling. In histochemical and cytochemical

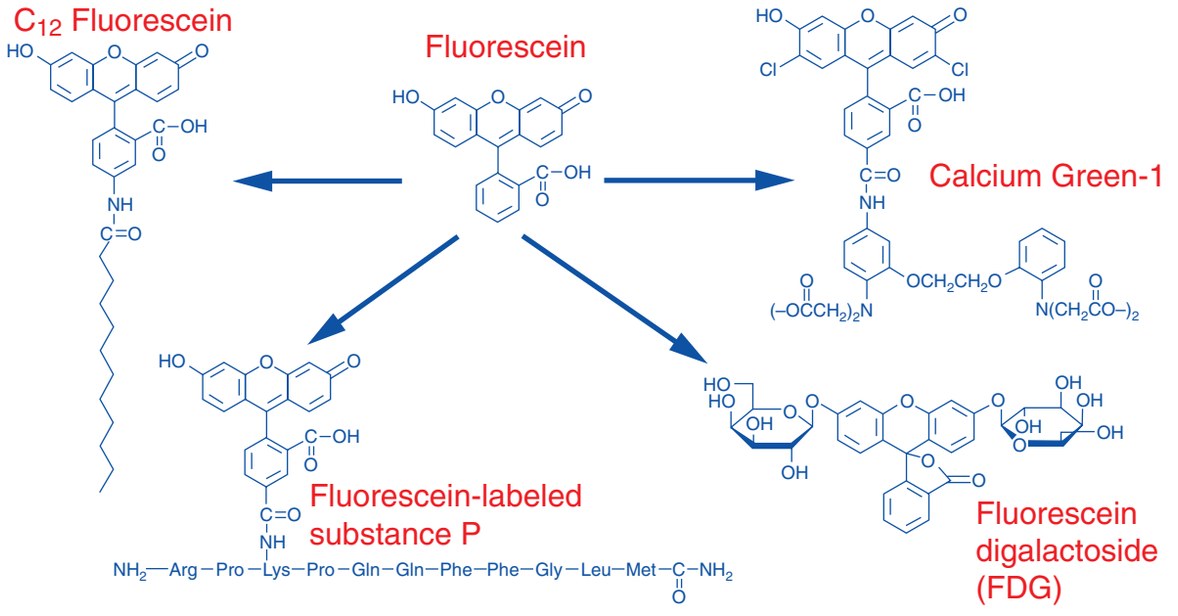


FIGURE 17.1. Derivatization of a fluorescent dye (fluorescein) to obtain target-specific response or localization characteristics. Clockwise from top left: The dodecanoyl (C_{12}) substituent of C_{12} fluorescein results in membrane localization. The intracellular Ca^{2+} indicator Calcium Green-1 consists of dichlorofluorescein coupled to the Ca^{2+}-selective chelator BAPTA. Fluorescein digalactoside (FDG) is a β-galactosidase activity sensor that generates an enzyme–dependent fluorescence intensity increase upon cleavage of the 3′- and 6′-galactose residues. Fluorescein-labeled substance P is a probe for neuropeptide receptors prepared by coupling 5-carboxyfluorescein, NHS-ester to the ε-amino group of lysine via the reaction chemistry outlined in Figure 17.3(D).

TABLE 17.2. Major Dye Classes

Dye Class	Examples	Brightness[a]	Environment Sensitivity[b]	Photostability	Biocompatability[c]	Two-Photon
Coumarin	AlexaFluor 350	+	++++	+	+++	+
Fluorescein	FITC, calcein AM, CFSE[d]	+++	++++	+	+++	++
BOPIDY	BOPIDY FL, BOPIDY TR	+++	+++	++	++++	++
Phycobiliproteins	R-phycoerythrin (R-PE)	++++	++	++	++	++++
AlexaFluor	AlexaFluor 488, AlexaFluor 568, AlexaFluor 594, AlexaFluor 647	++++	++	++++	++++	+++
Quantum dots	Qdot 605, Qdot 655	+++++	+	+++++	+	+++++
Cyanines	Cy3, Cy5, DiI ($DiIC_{18}(3)$), $DiOC_6(3)$	+++	++	++++	+++	+
Styryl dyes	FM 1-43, FM 4-64, Di-8-ANEPPS	++	+++++	++	+++	+++
Rhodamines	TRITC, TMRE[e], Rhodamine 123	+++	+++	++++	++	+++
Fluorescent proteins	ECFP, EGFP, EYFP, dsRed	++	++	++	+++++	++

[a] Approximate representation of the product of molar extinction coefficient and fluorescence quantum yield. In cellular imaging applications, this will be heavily weighted by concentration (target abundance, expression level) and localization factors that are discussed in the text but are not included in this consideration.
[b] Assessment of the extent to which brightness is modulated by factors such as pH, aqueous exposure, dye interactions etc.
[c] A compound assessment of factors such as cytotoxicity, ease of delivery, and extent to which the dye modifies the structure and behavior of molecules to which it is attached. GFP has the highest rating because it is the only dye class of entirely biosynthetic origin.
[d] CFSE, carboxyfluorescein diacetate, succinimidyl ester.
[e] TMRE, tetramethylrhodamine ethyl ester.

applications, the lack of environmental sensitivity of these dyes is advantageous, as fluorescence images of their distribution are not biased by environment-dependent factors. Other classes such as styryl dyes (e.g., FM 1-43, FM 4-64) and many non-covalent nucleic acid stains (e.g., DAPI, TO-PRO-3, propidium iodide) are essentially non-fluorescent in water and only fluoresce when bound to their respective targets (membrane surfaces and DNA). In this case, unbound dyes are undetectable and the need to perform wash steps to remove them prior to imaging is therefore eliminated.

Within the confines of a cell, dyes frequently come into close spatial proximity with each other, resulting in dye–dye interactions. Attachment of multiple copies of fluorescein or rhodamine dyes to a single protein molecule usually results in the formation of dimers or higher aggregates of the dye that absorb but do not fluoresce. The process is commonly referred to as self-quenching. Dye aggregation is signified by peaks or shoulders in the absorption spectrum of the labeled protein that are not replicated in the fluorescence excitation spectrum, and also by changes in the circular dichroism spectrum (Mercola *et al*., 1972). Self-quenching produces the counterintuitive but sometimes useful result of fluorescence output decreasing as dye concentration increases. This is clearly detrimental if one is attempting to increase the fluorescent brightness of a protein by labeling it more heavily. Therefore, AlexaFluor dyes and Cy dyes are designed to avoid self-quenching by incorporating negatively charged sulfonic acid substituent groups that produce mutual electrostatic repulsion and increased water solubility (Fig. 17.3). Self-quenching can be exploited to advantage for detection of proteolytic activity by preparation of protein conjugates that are deliberately over-labeled. Probes of this type allow *in situ* localization of enzymatic activity in tissues (Mook *et al*., 2003) and organisms (Farber *et al*.,

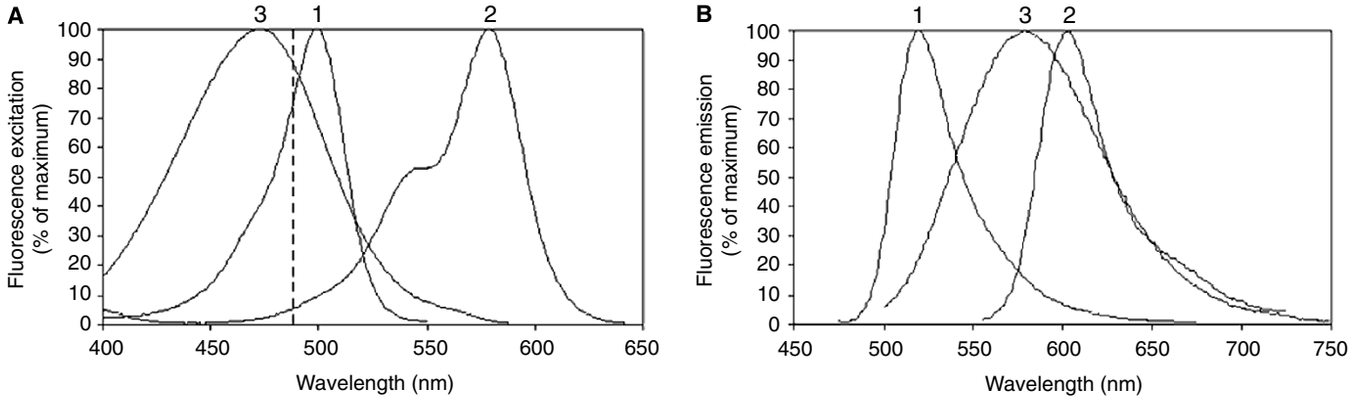


FIGURE 17.2. (A) Matching microscope excitation source outputs to dye spectra. Fluorescence excitation spectra of AlexaFluor 488 (1), AlexaFluor 568 (2), and FM 1-43 (3) dyes relative to the 488 nm argon-ion laser line (shown by the vertical dashed line). Due to the relatively inefficient excitation of the AlexaFluor 568 dye at 488 nm, it is not suitable for multiplex labeling in combination with FM 1-43 or AlexaFluor 488 nm dyes unless the microscope is also equipped with a 568 nm krypton-ion laser or 561 nm diode-pumped solid state laser. (B) Emission overspill considerations in multicolor detection. The wide emission spectral bandwidth of FM 1-43 (3) results in substantial overlap with both AlexaFluor 488 (1) and AlexaFluor 568 (2) dyes, making discrimination by means of wavelength filtering difficult to achieve. The AlexaFluor 488 and AlexaFluor 568 dyes are spectrally well resolved. Note, however, that the relative amplitudes of the spectra shown in the figure would only pertain in a real experimental situation if the dyes were excited with equal efficiency and were present at equal concentrations within the field of view.

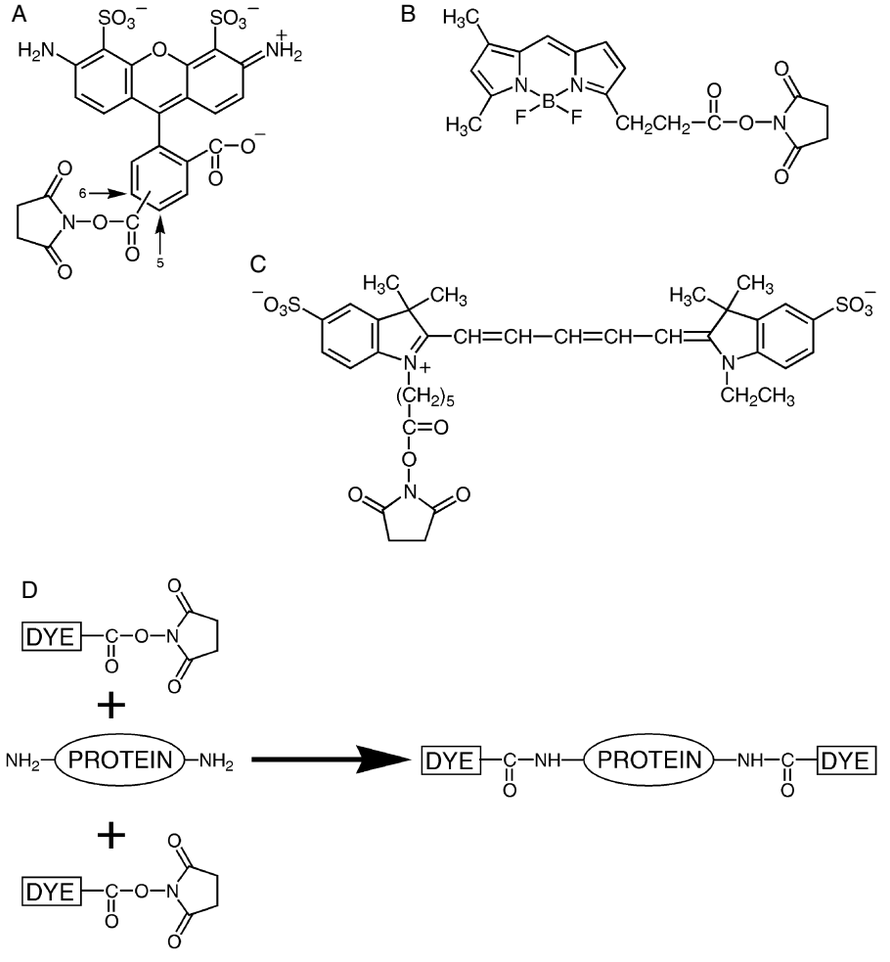


FIGURE 17.3. (A) Structures of amine-reactive dyes. (A) AlexaFluor 488, NHS ester; (B) BOPIDY FL, NHS ester; (C) Cy5, NHS ester (NHS = *N*-hydroxysuccinimidyl). (D) Reaction of a dye–NHS ester with protein amino groups yielding a stable carboxamide-linked conjugate.

2001). Fluorescent proteins and quantum dots have much less intrinsic environmental sensitivity than organic dyes because in both cases the fluorophore is encapsulated within one or more insulating layers. They are therefore more difficult to adapt for local environment sensing applications of the type described above. To do so, it is necessary to make use of fluorescence resonance energy transfer (FRET; Jales-Erijman and Jovin, 2003), a type of dye–dye interaction with a longer effective range than those responsible for self-quenching.

Stable coupling of organic dyes to proteins, nucleic acids, and other biomolecules can be accomplished using several well-characterized reaction chemistries. Currently, the most widely used method is the reaction of NHS ester dye derivatives with amines (e.g., ε–NH_2 of lysine) to form stable carboxamide linkages [Fig. 17.3(D)]. The principal alternative coupling method is reaction of iodoacetamide or maleimide derivatives of dyes with cysteine sulfhydryl groups to form thioether linkages. Textbook-level descriptions of these and other coupling chemistries may be consulted for further details (Hermanson, 1996; Haugland, 2002). Labeling protocols generally require some degree of protein-specific optimization with respect to the dye:protein ratio. This is merely a reflection of the fact that proteins vary widely in size and in the number and distribution of reactive targets. Typically, no more than about three to five dyes can be attached per protein without self-quenching of fluorescence and/or inactivating the protein. Note that degree-of-labeling values, as conventionally determined by absorption measurements, are sample averages. A preparation with an average of n dyes per protein will contain a range of labeling stoichiometries (. . . $n-2$, $n-1$, n, $n+1$, $n+2$ . . . etc.) that can be resolved by capillary electrophoresis or MALDI-TOF mass spectrometry (Lu and Zenobi, 2000). Furthermore, because the labeling reactions are indiscriminate with respect to the location of the target amino acid residue, labeling in a site that is critical for activity or binding may result in an inactive conjugate (Adamczyk *et al*., 1999). In these cases, activity can be preserved by performing the labeling reaction with the active site blocked by addition of its cognate substrate or ligand (Ramjeesingh *et al*., 1990).

Fluorescent Proteins: Green Fluorescent Protein and Phycobiliproteins

The cloning and heterologous expression of the *Aequoria victoria* green fluorescent protein in 1994 has had an immense impact on fluorescence microscopy of living cells in the past decade. There are many excellent review articles (Tsien, 1998; Zhang *et al*., 2002; Lippincott-Schwartz and Patterson, 2003) and entire books (Chalfie and Kain, 1998; Sullivan and Kay, 1999) devoted to the

properties and applications of GFP. Only selected points setting GFP in relation to other fluorescent labeling technologies will be considered here. The spectroscopic properties of GFP and its variants are unexceptional (ε_{max} ~ 53,000 $M^{-1}cm^{-1}$, QY ~ 0.6 for the most frequently used variant, EGFP (Patterson *et al*., 1997). However, the extraordinary utility of GFP resides in its biochemical properties — more specifically, in the ability to construct fusion proteins at the DNA level and express these in an almost unlimited range of cell types, tissues, and organisms. In principal, information on intracellular protein localization that has traditionally been obtained using dye-labeled antibodies in fixed cells can now be obtained in living cells, with the added dimension of following translocation processes in real time as opposed to observing only their end-points. Accurate localization of GFP fusion proteins relative to their native counterparts is clearly an essential prerequisite for these applications. GFP is a small protein (molecular weight ~27 kDa) consisting of 11 β-strands forming a hollow cylinder approximately 4.2 nm in length by 2.4 nm in diameter that encapsulate the *p*-hydroxybenzylideneimidazolidinone fluorophore. These dimensions are relatively large compared to organic dyes that typically have molecular weights <1000 and are represented by a flat disk of ~1 nm diameter. Intracellular GFP concentrations are determined by a combination of factors including levels of gene expression and rates of posttranslational folding and proteolysis. The spontaneous cyclization reaction responsible for formation of the fluorophore from residues 65 to 67 (Ser-Tyr-Gly in the wild-type *A. victoria* protein) requires molecular oxygen. Thus, only 16% of wild-type GFP synthesized *in vitro* under conditions of limited oxygen availability is fluorescent, compared to 88% in the presence of abundant oxygen (Nemetz *et al*., 2001). Therefore, GFP fluorescence in hypoxic cells and tissues such as tumors may not accurately reflect the level of gene expression (Coralli *et al*., 2001). Site-directed mutagenesis of *A. victoria* GFP has generated variants with shifted excitation and emission spectra. The cyan (CFP) and yellow (YFP) variants are particularly useful for co-localization of proteins via FRET imaging (Siegel *et al*., 2000). Spectral coverage has been extended to the red range by cloning and expression of a fluorescent protein known as DsRed from *Discosoma* coral (Matz *et al*., 1999). Major re-engineering of DsRed has been undertaken to eliminate some undesirable characteristics including slow maturation and obligate tetramerization (Campbell *et al*., 2002).

Phycobiliproteins are a family of photosynthetic accessory proteins from cyanobacteria and eukaryotic algae. The most commonly used phycobiliprotein for biomolecular labeling applications, R-phycoerythrin is a large cylindrical protein with a molecular weight of 240 kDa and dimensions of 6 nm in length by 12 nm in diameter. Each molecule contains 34 tetrapyrrole chromophores attached to the polypetide backbone via thioether linkages. To fulfill their biological role of transferring energy from absorbed light to chlorophyll in the photosynthetic reaction center, the positioning of the chromophores within the protein structure has evolved to maximize the efficiency of both absorption and fluorescence. Due to its exceptional light harvesting capacity, R-phycoerythrin can be efficiently excited at 488 nm ($\varepsilon_{488\,nm}$ ~ 1,100,000 $M^{-1}cm^{-1}$) even though this is far from its absorption maximum of 565 nm. It is therefore well suited for single excitation/dual emission detection in combination with fluorescein, AlexaFluor 488, GFP and other dyes with emission peaks around 520 nm. Due to their large size, phycobiliproteins are difficult to deliver to intracellular targets and are primarily of value for detection of low-abundance cell-surface antigens. Heterologous expression of C-phycocyanin has been accomplished in *E. coli* (Tooley *et al*., 2001). This is a much more technically demanding endeavor than GFP expression because it requires co-expression of enzymes required for the biosynthesis of the tetrapyrrole chromophores from heme.

Techniques for targeting dyes to specific binding motifs on intracellular proteins that combine elements of entirely intracellular expression of intrinsically fluorescent proteins and extracellular labeling of purified proteins by amine-reactive NHS chemistry are now emerging. These techniques include tetracysteine motif-binding biarsenical ligands (FlAsH; Adams *et al*., 2002) and engineered intracellular receptor proteins that recognize dyes or dye-coupled haptens (Beste *et al*.; 1999; Farinas and Verkman, 1999).

Quantum Dots

In complete contrast to fluorescent proteins, quantum dots have outstanding spectroscopic properties, whereas their biochemical properties of large size and inorganic composition represent a considerable challenge in biomolecular labeling applications. Quantum dots typically consist of a spherical core of the semiconductor cadmium selenide (CdSe) surrounded by a zinc sulfide (ZnS) shell which is in turn surrounded by a hydrophilic polymer surface coating (Bruchez *et al*., 1998; Chan and Nie, 1998). As well as stabilizing the electronic excited state of the semiconductor, the ZnS shell also prevents release of cytotoxic cadmium from the core (Derfus *et al*., 2004). The hydrophilic coating confers water solubility and incorporates functional groups for crosslinking to antibodies, streptavidin, and other targeting groups. Overall, the trilaminar particles are about 4 to 10 nm in diameter, comparable in size to the phycobiliproteins. The fluorescence output of a single quantum dot has been estimated to be approximately equivalent to 20 rhodamine dye molecules, similar to that of R-phycoerythrin (Chan and Nie, 1998). Due to their predominantly inorganic composition, quantum dots are largely invulnerable to the oxidative photobleaching reactions that affect organic dyes and fluorescent proteins. The diameter of the semiconductor core determines the fluorescence emission range of the particle (wavelength increases with increasing size). The excitation spectra of quantum dots are essentially continuous whereas the emission spectra are narrow and symmetrical (Fig. 17.4). Quantum dots exhibit exceptionally high molar absorptivity — for example, $\varepsilon_{600\,nm}$ = 650,000 $M^{-1}cm^{-1}$ and $\varepsilon_{400\,nm}$ = 3,500,000 $M^{-1}cm^{-1}$ (Watson *et al*., 2003). Furthermore, their two-photon excitation cross-sections exceed those of conventional organic dyes by factors of 100 to 1000 (Larson *et al*., 2003). Because quantum dots are extremely flexible with respect to excitation wavelength, they are well suited for simultaneous immunofluorescence detection of multiple targets (Wu *et al*., 2003). Careful optimization of staining conditions (buffer composition, etc.) is necessary to minimize non-specific labeling. The size and composition of quantum dots generally limits the range of accessible targets to cell-surface antigens and receptors and targets that can be accessed via endocytosis or injection (Jaiswal *et al*., 2003; Wu *et al*., 2003; Ballou *et al*., 2004). Development of intracellular delivery techniques using peptide vectors has recently been reported (Mattheakis *et al*., 2004).

Multi-Photon Excitation

The advent of two-photon excitation microsopy (Denk *et al*., 1990) has added a new spectral dimension to fluorescence microscopy, in addition to the benefits of increased imaging depth and reduced phototoxicity that derive from the transparency of tissues to infrared excitation light and confinement of excitation to the focal

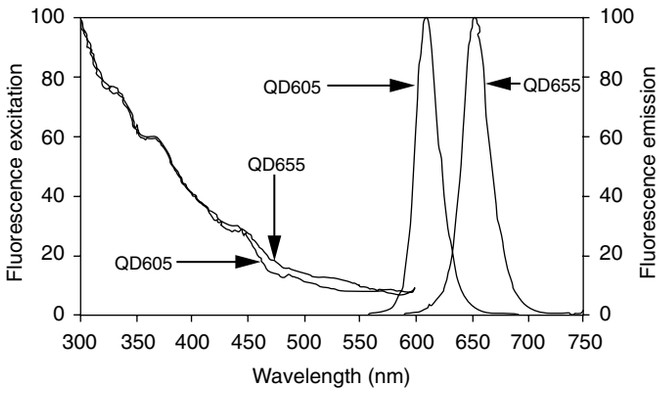


FIGURE 17.4. Fluorescence excitation and emission spectra of QD605–streptavidin and QD655–streptavidin (QD = quantum dot). The continuous and almost identical excitation spectra and the sharp, well-differentiated emission spectra contrast markedly with the corresponding characteristics of organic dyes [Fig. 17.2(A,B)].

plane (Zipfel *et al*., 2003a). Probes that were previously of limited utility in confocal microscopy due to their requirements for ultraviolet excitation, such as fura-2 (Ca^{2+}), SBFI (Na^{+}), monochlorobimane (glutathione), and DAPI (nuclear DNA), have acquired a new lease of life (Rose *et al*., 1999; Fricker and Meyer, 2001; Rubart *et al*., 2003). Furthermore, *in situ* imaging of small endogenous fluorophores such as serotonin and NADH, that are almost inaccessible to one-photon excitation, has now become practicable (Zipfel *et al*., 2003b; Rocheleau *et al*., 2004). With these exceptions, the collection of dyes and probes currently in use for two-photon excitation microscopy is largely the same as that employed in confocal and widefield fluorescence imaging. There are several published collections of two-photon excitation spectra and cross-sections that provide guidance on compatibility of dyes and probes with excitation sources (Xu and Webb, 1996; Xu *et al*., 1996; Bestvater *et al*., 2002; Dickinson *et al*., 2003). If two-photon spectral data is not available, the corresponding one-photon spectrum plotted on a doubled wavelength axis can be used as a first approximation. However two-photon excitation spectra differ from their one-photon counterparts to an extent that depends on the molecular orbital symmetry of the fluorophore (greater difference for higher symmetry fluorophores; Zipfel *et al*.,2003a). Consequently, most two-photon excitation spectra are blue shifted and broader compared to the corresponding one-photon spectra. Simply stated, a dye with a one-photon excitation peak at 500 nm will probably have a two-photon excitation maximum at <1000 nm (Ruthazer and Cline, 2002). In practice, most dyes with single-photon excitation maxima <600 nm can be effectively excited within the 700 nm to 1000 nm output range of the mode-locked titanium–sapphire laser sources used in the majority of two-photon excitation microscopes. In general, optimizing the excitation wavelength in relation to the peak of the dye excitation spectrum appears to be less critical than in the one-photon case.

INTRODUCING THE PROBE TO THE SPECIMEN

Loading Methods

After selecting a probe with appropriate biochemical and spectroscopic properties with regard to the experimental objectives and the microscope hardware to be used, the next task is to label the features of interest within the specimen. This is a relatively straightforward process in the fixed and permeabilized specimens used for immunofluorescence, for which there are well-established standard protocols (Brelje *et al*., 2002). The major practical concerns for immunolabeling of fixed specimens include antigen preservation and accessibility, non-specific binding and cross-reactivity of antibodies, and the potential for increased autofluorescence resulting from the chemical reactions used to achieve fixation (see also Chapter 18, *this volume*).

The permeability barriers and active metabolic processes of living cells and tissues present additional challenges for probe delivery and localization (Stephens and Pepperkok, 2001). Generally speaking, the severity of the intracellular delivery problem increases in proportion to the size of the probe and the complexity of the specimen (cell < tissue < whole organism). Ions are quite easy to deliver non-invasively via endogenous ion channels or using ionophores. Small organic dye-based probes are easy to moderately difficult, depending on their structural characteristics. For example, the rate of loading of the acetoxymethyl (AM) ester forms of intracellular Ca^{2+} indicators into intact frog muscle fibers decreases dramatically when their molecular weight exceeds about 850 (Zhao *et al*., 1997). In contrast, DAPI and lucifer yellow CH have similar molecular weights but can exhibit markedly different permeability through gap junctions due to their opposite electrostatic charges (Cao *et al*., 1998). Intracellular delivery of large probes such as phycobiliproteins, labeled antibodies, or quantum dots almost invariably requires invasive methods. An exception to the latter stipulation is GFP, which is synthesized and folded *in situ*, thereby eliminating the need for intracellular delivery except at the initial DNA transfection stage. Methods for transfection and expression of GFP will not be discussed here; detailed descriptions are available elsewhere (Sullivan and Kay, 1999; and in Chapter 45, *this volume*).

Several factors can be identified that influence loading method choices:

- Is the experimental specimen a pure or mixed cell culture or a tissue?
- If the specimen is multi-cellular, is disseminated (all cells) or selective (one cell or a subgroup of cells) loading desired?
- What is the size of the cells to be labeled?
- What is the size of the probe?
- Impact of loading on cell viability and function?
- Precision of amount delivered and location of delivery ("focal application")?

Before describing specific methods, a generally applicable guideline should be noted. Label the specimen to the minimum extent required to obtain the biological information that is sought. It is almost never desirable to increase fluorescence signals by increased dye loading or fluorescent protein expression. The following deleterious effects are all positively correlated with increased label concentration: phototoxicity, cytotoxicity, non-specific localization, and physiological or structural perturbation.

1. **Direct permeability:** This is the simplest of all techniques, involving nothing more than dispersing the probe in the extracellular medium and incubating for 5 to 60 minutes. It is generally applicable to neutral, monoanionic, and monocationic molecules with molecular weight <1000. Examples include JC-1, MitoTracker Red CMXRos, LysoTracker Red, BOPIDY FL ceramide, and $DiIC_{18}(3)$. Loading of lipophilic probes such as fluorescent lipid analogs (Tanhuanpaa and Somerharju, 1999) and acetoxymethyl (AM) esters (see item 3, below) is enhanced by the addition of

carriers and dispersing agents such as cyclodextrins, nonionic detergents (Pluronic F-127, Cremophor EL), and proteins such as bovine serum albumin (BSA). Also included in this general category are larger probe molecules that are taken up by endocytic processes such as dye-labeled transferrin conjugates.

2. **ATP-gated cation channels:** Provide a direct loading conduit for dyes with molecular weight <1000. Applicability restricted to cell types in which these channels are found (neurons and other sensory cells, dendritic cells, macrophages). Dyes to which this technique has been applied include FM 1-43 (Meyers *et al*., 2003), fura-2, and the pH indicator HPTS (pyranine; Gan *et al*., 1998).

3. **Membrane permeant esters:** An AM or acetate ester derivative of a polyanionic dye diffuses across the plasma membrane followed by intracellular release of free dye mediated by endogenous esterase activity (Fig. 17.5). The requirement for esterase activity imposes limitations on the cell types to which the technique can be applied, but provides a rapid and convenient method for uniform loading of adherent or suspended cells. Intracellular distribution of the dye can be manipulated to some extent by variations of temperature, dye structure, and incubation time (Lemasters *et al*., 1999), but cannot be precisely controlled (Fig. 17.5).

4. **Peptide-mediated uptake:** This relatively new technique is based on attachment of peptide vectors to molecular cargoes, which may be anything from small dyes to quantum dots (Mattheakis *et al*., 2004) or large (>100 kDa) proteins. The cellular uptake mechanism is not fully understood and remains under active investigation (Potocky *et al*., 2003). Efficacious peptide sequences (Fischer *et al*., 2001) consist of 8 to 30 amino acids with a preponderance of basic residues, and are largely derived from the proteins of infectious microorganisms. At present, this technique is far from being universally applicable and the attainable intracellular dye concentrations are rather low (10 to 100 n*M*; Waizenegger *et al*., 2002).

5. **Transient permeabilization:** Brief treatments of cells with low doses (≤0.1 mg/mL) of bacterial toxins (e.g., streptolysin O, staphylococcal α-toxin) or plant glycosides (β-escin, saponin) allows delivery of probes and other molecules. Although these treatments are easy to implement, the physiological integrity and viability of the cells is inevitably compromised to some extent. Walev and colleagues (2001) have provided a detailed analysis of the efficacy and collateral effects of streptolysin-O permeabilization of adherent and non-adherent cell types. The molecular weight cutoff for loading was found to be ~100,000 with intracellular concentrations of 10^5 to 10^6 molecules per cell.

6. **Osmotic permeabilization:** Similar to bacterial toxin permeabilization in applicability (non-selective loading of cell populations) and potential for compromising cellular integrity. Applicable to large proteins such as antibodies (Chakrabati *et al*., 1989).

7. **Electroporation:** Perhaps the most versatile technique currently available. Applicable to single cells (Haas *et al*., 2001), bulk loading of cell populations (Hashimoto *et al*., 1989), and focal

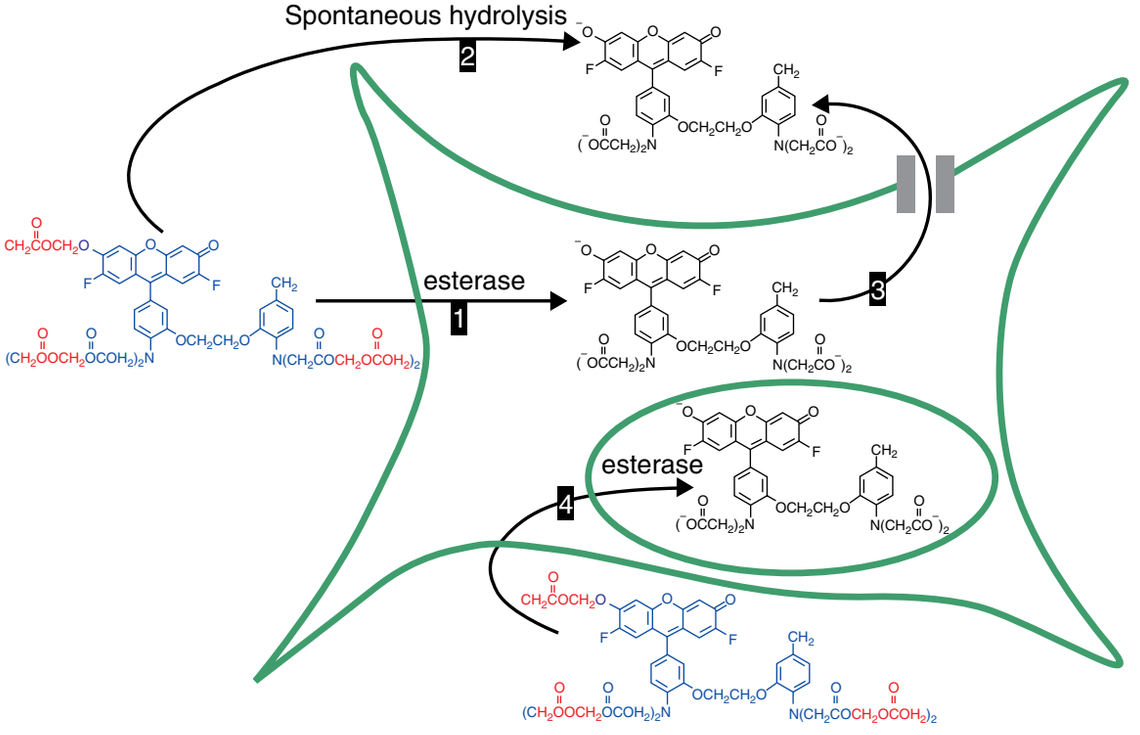


FIGURE 17.5. Cell loading with acetoxymethyl (AM) esters. The example shown represents the calcium indicator fluo-4. The intended objective of most measurements using fluo-4 is imaging of cytosolic Ca^{2+} dynamics. Loading of the dye via process (1), consisting of spontaneous permeation of the AM ester derivative of fluo-4 (shown in red and blue) across the plasma membrane followed by cleavage of the acetoxymethyl groups (red) by intracellular esterases is therefore the desired outcome. However, other dye transport processes may occur simultaneously. These include extracellular hydrolysis of the AM ester (2), extrusion of intracellular fluo-4 via organic anion transporters (3), and compartmentalization in membrane-enclosed organelles and vesicles (4). Processes (2–4) all result in fluorescence signals that are not responsive to cytosolic Ca^{2+} (see Fig. 17.6). The actual cellular labeling pattern obtained is determined by the relative rates of the permeation, transport, enzymatic, and chemical hydrolysis that contribute to pathways 1–4. These in turn are dependent on experimental variables such as cell type, cell viability, incubation medium composition, and temperature.

(spatially localized) delivery within tissues and organisms (Yasuda *et al*., 2000). Applicable to molecules large and small, from dyes and peptides up to antibodies (Marrero *et al*., 1995).

8. **Ballistic microprojectile (gene gun) delivery:** Primarily useful for labeling groups of cells deep (up to 300 μm) inside tissues. Widely used for transfection of GFP vectors in brain slices (O'Brien *et al*., 2001). Applications for loading neuronal tracers and intracellular calcium indicators have also been reported (Grutzendler *et al*., 2003).

9. **Microinjection:** Invasive, sequential (one cell at a time) but extremely precise. Provides exquisite control over the amount of probe delivered and in the selection of individual cells for labeling. Microinjection is quite demanding in terms of technical skill and instrumentation, and is difficult to apply to small cells (e.g., hepatocytes). Either pneumatic pressure or electrical current (iontophoresis) may be used as the driving force for injection. These two methods may produce significantly different cellular labeling results, even when they are applied to the same dye (Gerhardt and Palmer, 1987; Storms *et al*., 1998). Iontophoretic microinjection is restricted to electrostatically charged dyes such as lucifer yellow CH and AlexaFluor 594 hydrazide and is difficult to apply to large molecules (molecular weight >1000).

10. **Whole-cell patch pipette delivery:** Similar to microinjection in applicability with the additional capacity for simultaneous imaging and electrophysiological measurements (Eilers and Konnerth, 2000). Inward diffusion of solutes from the patch pipette allows precise control of the intracellular environment but outward diffusion of cytoplasmic contents may be deleterious.

A selection of probes with proven utility for general characterization of living specimens using simple and rapid labeling protocols is listed in Table 17.3.

Tissues

Scientific imperatives allied to technical developments such as two-photon excitation and confocal endoscopy (Helmchen, 2002) mean that fluorescence microscopy is increasingly being applied to tissues and entire organisms. Most of the techniques described above can be adapted for application to tissue specimens, while GFP expression can be confined to specific cell types by coupling to tissue-specific promoters (Hara *et al*., 2003). Water-soluble dyes such as FM 1-43 and lucifer yellow CH generally show deeper penetration into tissues than non-polar molecules such as AM esters, which tend to accumulate in the superficial cell layers (Takahashi *et al*., 2002). A modification of the AM ester technique, referred to as multi-cell bolus loading (MCBL), utilizes localized ejection of small volumes (~0.4 nL) of dye loading solution from a micropipette to label populations of neurons in brain tissue (Stosiek *et al*., 2003). For imaging tissues *in situ*, probe delivery is typically accomplished via the internal pathways of the digestive (Farber *et al*., 2001), respiratory (Lombry *et al*., 2002), circulatory (Ballou *et al*., 2004), or nervous (Grutzendler *et al*., 2003) systems.

Target Abundance and Autofluorescence Considerations

We have considered spectroscopic properties relating to the fluorescence output of labels such as excitation wavelength, exctinction coefficent, photobleaching, and fluorescence quantum yield. However, factors such as the abundance and spatial distribution of the target and the levels of background autofluorescence often have more impact on the contrast and resolution of the final image. The abundance and degree of localization of the target within the specimen are critical determinants in probe selection. For example, it is much easier to image DNA localized in the nucleus than receptors distributed on the plasma membrane surface. The DNA content of a typical mammalian cell is about 7 pg, corresponding to about 6×10^9 base pairs. This amount of DNA can accommodate the binding of up to 1.2×10^9 intercalating dyes (1 dye: 5 base pairs). Consequently, nuclear stains such as propidium iodide (PI) are easily detectable despite the fact that the fluorescence intensity per dye is relatively modest ($\varepsilon_{max} \sim 5000\,M^{-1}cm^{-1}$ and QY ~ 0.1). In contrast, detection of cell-surface EGF receptors, present at ~10,000 copies/cell, by confocal microscopy may require the use of fluorophores such as R-phycoerythrin ($\varepsilon_{max} \sim 1{,}960{,}000\,M^{-1}cm^{-1}$ and QY ~ 0.82) to generate sufficient signal (Good *et al*., 1992). Similar considerations apply when simultaneously imaging two targets using a single excitation wavelength. Typically it is quite difficult to find two dyes that can be excited with equal efficiency at the selected wavelength and also have

TABLE 17.3. Dyes for Rapid Assessment of Living Cells by Fluorescence Microscopy

	Labeling Target	Incubation Concentration[a]	Ex/Em[b]	Laser Lines[c]	GFP Compatible[d]
Hoechst 33342	Nucleus	1 μM*	350/460	351–364 nm or 405 nm	Y
Calcein AM	Cytosol[e]	2 μM*	494/515	488 nm	N
FM 4-64	Plasma membrane, endosomes	5 μM*	506/750[f]	488 nm, 514 nm, or 568 nm	Y
Propidium iodide	Nucleus (dead cells)[g]	5 μM*	535/620	488 nm or 514 nm	Y
LysoTracker Red DND-99	Lysosomes	50 nM	575/590	568 nm	Y
MitoTracker Red CMXRos	Mitochondria	50 nM	578/600	568 nm	Y
AlexaFluor 594 hydrazide	Water (fluid phase tracer)	10 mM[h]	588/615	568 nm	Y

[a] These dyes can generally be used to stain live eukaryotic cells by incubation for 15 to 30 min at the indicated concentration. Dyes marked with an asterisk (*) can be imaged directly in the dye incubation medium, without a subsequent wash step.
[b] Fluorescence excitation/emission maxima in nanometers.
[c] Laser lines suitable for excitation.
[d] Y, fluorescence emission is spectrally well resolved from that of GFP.
[e] Fluorescence is dependent on cytosolic esterase activity and is therefore positively correlated with cell viability.
[f] The fluorescence emission of FM 4-64 has a wide spectral bandwidth and can be detected anywhere from 625 to 800 nm.
[g] Propidium iodide is impermeant to live cells; fluorescence is therefore inversely correlated with cell viability.
[h] Used to fill cells (typically neurons) via microinjection of a 10 mM aqueous solution. Lucifer yellow CH excited at 405 nm is a widely used alternative but is not spectrally well resolved from GFP.

emission spectra that are sufficiently well separated to be discriminated without resorting to spectral unmixing (Fig. 17.2) or the use of quantum dot labels. In this situation, the less efficiently excited dye should be used to detect the more abundant target, thereby equalizing the two emission signals.

Bulk loading procedures, such as AM ester loading, generate intracellular concentrations of up to 100 μ*M*, corresponding to about 1×10^8 molecules in the cytoplasm of a typical mammalian culture cell with a total volume of 4000 μm^3 (of which about 50% is occupied by organelles). Perhaps of more immediate concern to the experimentalist is the cell-to-cell concentration uniformity. A confocal imaging study of neuroblastoma cells loaded with fura-2, AM by Fink and colleagues (1998) found a mean intracellular dye concentration of 38 μ*M* in 123 cells, with individual cell values ranging from 10 to 90 μ*M*. Self-referencing, ratiometric measurements are often used to correct for variability of dye concentration when making cell-to-cell comparisons of fluorescence intensity. Similar intracellular concentrations are achieved in typical microinjection protocols in which 10 m*M* dye solution equivalent to about 1% of cell volume is injected. Much higher concentrations can be attained in situations where probes are sequestered in subcellular compartments. For example, potential-driven uptake of cationic dyes in mitochondria can result in concentrations that are up to 1000-fold higher than in the cytosol (Nicholls and Ward, 2000). These probes should therefore be applied at very low external concentrations (<10 n*M*) to avoid fluorescence self-quenching and respiratory inhibition effects (Rottenberg and Wu, 1998).

The minimum concentration of cytoplasmic EGFP required to be detectable above autofluorescence is about 0.2 μ*M* (Patterson *et al*., 1997), equivalent to about 200,000 copies per cell. This is considerably above the native expression levels of many cellular proteins (range, ~50 – 10^7 copies per cell), making it necessary to overexpress GFP fusion proteins to obtain detectable fluorescence levels. Much lower copy numbers can be detected in restricted volumes. For example, viral particles (~100 nm diameter) containing 120 GFP fusion proteins each are detectable both in isolation and after uptake into cells (Charpilienne *et al*., 2001). Because the number of GFP molecules in these particles is genetically prescribed, they provide useful standards for quantitation of intracellular GFP expression levels (Dundr *et al*., 2002).

Autofluorescence is often the limiting factor that determines how many probe molecules must be introduced into a cell in order to be detectable above background. The autofluorescence of a single 3T3 fibroblast cell has been estimated to be equivalent to about 34,000 fluorescein molecules (Roederer and Murphy, 1986). Surveys of spectral data (Billinton and Knight, 2001; DaCosta *et al*., 2003) show that autofluorescence originates from a wide variety of molecular sources and generally decreases at longer wavelengths. Autofluorescence levels also depend on cell or tissue type and physiological status (Croce *et al*., 1999). For example, lipofuscin, a heterogeneous complex of lipids and proteins found in brain tissues, increases in prevalence with age and the extent of oxidative metabolism (Haralampus-Grynaviski *et al*., 2003). The fluorescence excitation (400–550 nm) and emission (550–750 nm) spectra of lipofuscin are broad, overlapping with many common probes including GFP (Doyle *et al*., 2003). Other significant sources of autofluorescence are NADH/NADPH, flavins, and flavoproteins in mammalian cells, chlorophylls and flavonoids in plants, and collagen and elastin in connective tissues.

Components of culture media such as riboflavin (excitation, 450–490 nm; emission, 500–560 nm) are also significant sources of autofluorescence. The use of minimal media such as Hank's balanced salt solution (HBSS) or media with low riboflavin content such as Ham's F12 is often preferable for live-cell fluorescence imaging. Phenol Red, included as a pH indicator in common culture media, sometimes causes significant quenching of fluorescence. Phenol Red-free media are available from most commercial suppliers of culture media. To provide pH monitoring for cells cultured in Phenol Red-free medium, it is useful to prepare parallel control cultures in conventional Phenol Red-containing medium. A significant technical advance in dealing with autofluorescence problems is the advent of microscopes with spectral analysis and linear unmixing capabilities, which allow probe and autofluorescence background signals to be resolved based on their different spectral fingerprints (Dickinson *et al*., 2001). Likewise, fluorescence lifetime analysis (FLIM) can also sometimes be of use for this purpose. Multi-photon excitation can produce an additional type of background signal in the form of scattered second and third harmonic generation signals (SHG, THG; see Chapter 40, *this volume*). SHG and THG signals are in the visible range at exactly 1/2 or 1/3 of the excitation wavelength. Their production does not depend on the absorption and re-emission of photons but purely on structural features: usually ordered structures such as collagen and cellulose for SHG and surface features for THG. Although the emission of SHG and THG is very strongly oriented in the direction of the beam, in scattering specimens some photons can still be deflected towards the detector.

INTERACTIONS OF PROBES AND SPECIMENS

Once labeling of the specimen is complete, it is imperative that the probe should display appropriate localization for the duration of the planned imaging experiments. Furthermore, the presence of the probe should perturb the normal physiology and structure of the cell or tissue as little as possible.

Localization and Metabolism

As previously discussed, the association between a probe and its target is critical to the accurate representation of the biological properties of the specimen in a fluorescence image. This association is obtained by a variety of mechanisms, some more target-specific than others. The majority of fluorescent probes are labeled analogs of proteins, peptides, lipids, nucleotides, and other biomolecules. In these cases, there is the potential for perturbations to native distribution and activity induced by the attachment of the fluorescent label. However, despite the fact that fluorescent dyes and proteins are not insignificantly small relative to the molecules to which they are attached, their presence is usually tolerated surprisingly well. For example, there are very few examples reported in the literature of aberrant localization of GFP fusion proteins (Katz *et al*., 1998; Unkila *et al*., 2001; Lim *et al*., 2002).

Many dye-based probes, such as nucleic acid stains, ion indicators, and mitochondrial markers are not direct biomolecular analogs. The behavior of these probes is better represented in terms of molecular pharmacology than cell biology. Like therapeutic drugs, their distribution is determined by a combination of several factors including the applied external concentration and rates of transmembrane transport and intracellular metabolism (Fig. 17.5). The staining pattern obtained is usually quite time-dependent and sensitive to factors such as temperature and removal of extracellular dye by washing (Lemasters *et al*., 1999). This can lead to situations such as that depicted in Figure 17.6, where most of the fluorescent labeling is insensitive to the physiological process that it was intended to detect. Another example is provided by non-fluorescent dihydrorhodamine 123, which is oxidized intracellu-

larly by reactive oxygen species (ROS) such as superoxide, hydrogen peroxide, and hydroxyl radicals. The product of this reaction is the cationic fluorescent dye rhodamine 123. It could be concluded from the resulting mitochondrially localized fluorescence that mitochondrially localized ROS generation is being detected when in fact that localization reflects the redistribution of rhodamine 123 from the cytosol to mitochondria (Diaz *et al*., 2003). Many dyes are susceptible to extrusion by active transporters such as the ATP binding cassette (ABC) protein superfamily. Transport rates are governed by transporter substrate specificity and are therefore quite dependent on the molecular structure of the dye (Passamonti and Sottocasa, 1988; Wadkins and Houghton, 1995; Loetchutinat *et al*., 2003). Inhibitors such as sulfinpyrazone, probenecid, MK571, and verapamil can be used to stabilize intracellular dye retention (Di Virgilio *et al*., 1990). Dye extrusion can be advantageously exploited to monitor transporter activity and distribution (weak cellular staining corresponds to high transporter activity) (Hollo *et al*., 1994; Martin *et al*., 2003; Breen *et al*., 2004). In contrast, experiments designed to track the distribution of cell populations in tissues and organisms during processes such as embryological development demand stable and innocuous incorporation of dyes. Dyes useful in these applications are irreversibly coupled to proteins [e.g., carboxyfluoresceindiacetate, succinimidyl ester (CFSE); Parish, 1999] embryological or inert dextran carriers, or are incorporated into membrane lipids (e.g., DiI).

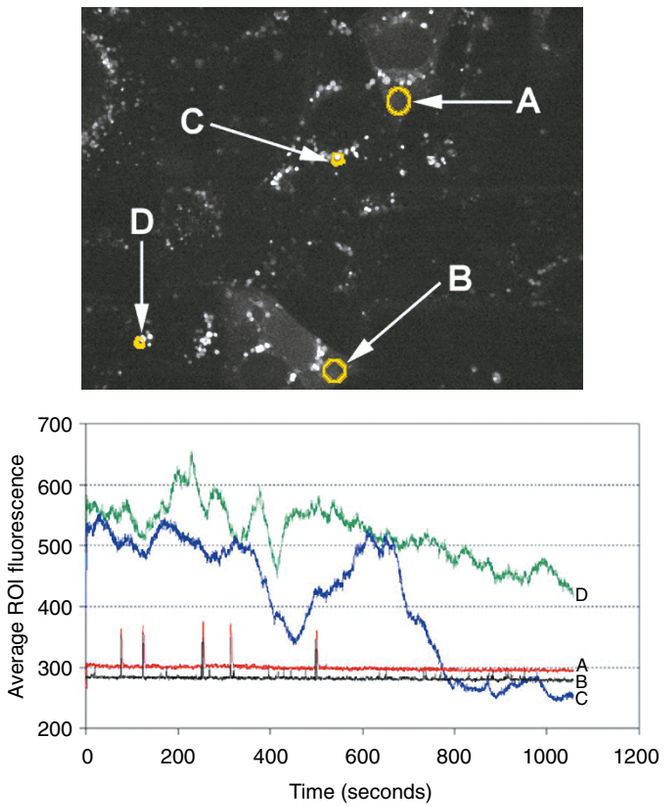


FIGURE 17.6. (Top panel) HL-1 cardiomyocytes (White *et al*., 2004) loaded by incubation with the fluo-4, AM as represented schematically in Figure 17.5. The bright, punctate labeling is due to compartmentalized dye. Cytosolic labeling is faint, diffuse, and only marginally visible in this image. The image was acquired using a PerkinElmer UltraView laser-scanning confocal microscope with a 60×, 1.2 NA, water immersion objective (pixel size = 0.4 µm). (Bottom panel) Photometric traces representing the average fluorescence intensities in the regions of interest A–D (A) as a function of time. The cytosolic regions of two different cells (A and B) exhibit synchronized Ca^{2+} spikes associated with the spontaneous contractile activity of the cells. No systematic variation of Ca^{2+} is detected by the compartmentalized dye (C and D).

Perturbation and Cytotoxicity

Compared to electron microscopy, specimen preparation for fluorescence microscopy is relatively non-invasive. Nevertheless, the concentrations of extrinsic probes required for practical applications are not insignificant in relation to physiological concentrations. Consequently, control experiments to verify that observations are independent of the applied probe concentration are always worthwhile. Severe dye-induced structural and physiological perturbations result in cytotoxicity and cell death. As one might intuitively expect, the most pronounced cytotoxic and perturbative effects tend to be exerted by dyes that accumulate in the organelles most essential to respiration and replication — the mitochondrion and the nucleus. Concentrations of cyanine dyes such as $DiOC_6(3)$ as low as 10 n*M* cause significant inhibition of mitochondrial respiration (Rottenberg and Wu, 1998; Scorrano *et al*., 1999). Subtoxic doses (1–10 µ*M*) of the DNA-binding dye Hoechst 33342 cause increased luciferase gene expression in transfected myocytes (Zhang and Kiechle, 2003). Conversely, probes that are diffusely distributed in the cytosol or the plasma membrane are relatively non-cytotoxic. Cells labeled with CFSE continue to divide and the ensuing bipartition of cellular fluorescence intensity provides a direct indication of proliferation (Parish, 1999). The utility of calcein AM labeling for monitoring cell adhesion and migration derives from its benign effects on these functional properties (De Clerck *et al*., 1994).

A significant concern in the application of GFP chimeras is the need, in some cases, to overexpress a fusion protein in order to achieve detectability over the autofluorescence background. Although overexpression is not usually cytotoxic, it may induce abnormal growth or physiology (Gunjan *et al*., 1999; Wendland and Bumann, 2002). In some cases, cytotoxicty of GFP has been found to be due to products of adjacent expression vector sequences (Endemann *et al*., 2003). Despite their disruptive potential, cytotoxic and perturbative effects of probes are almost always manageable. Even notoriously cytotoxic probes such as dye-labeled phallotoxins can still be used effectively in living cells if the applied concentration is sufficiently low (Pu *et al*., 2000).

UNDER THE MICROSCOPE

Photobleaching

Photobleaching and phototoxicity are two aspects of the same underlying process — generation of reactive oxygen species (ROS) in the specimen as a by-product of fluorescence excitation. Both are of particular concern in prolonged imaging experiments such as long time-lapse sequences. Although photobleaching is usually problematic, resulting in an effective time-dependent decrease in fluorophore concentration, it can be turned to advantage in some cases. Examples include the use of FRAP (fluorescence recovery after photobleaching) to measure diffusion rates and acceptor photobleaching to establish no-transfer reference points in FRET microscopy (Jales-Erijman and Jovin, 2003). With single-photon excitation, the rate of photobleaching and the rate of fluorescence emission are usually both linear functions of excitation intensity. The primary causative mechanism appears to be photosensitization of singlet oxygen ($^1O_2$) generation by the dye triplet excited state (Gandin *et al*., 1983; Song *et al*., 1996;

Eggeling *et al*., 1999; Stracke *et al*.,1999; Gaigalas *et al*., 2002). Singlet oxygen is a highly reactive transient species with a lifetime of about 4 μs in water. In cells, the lifetime of $^1O_2$ is reduced to <0.5 μs due to the increased number of reactive targets presented by proteins and nucleic acids. Therefore, the radius of action of $^1O_2$ is limited to <50 nm from its point of origin. The short range of this effect may be important when "acceptor photobleaching" is used as a rough measure of FRET (see also Chapter 45, *this volume*), because $^1O_2$ produced by excitation of the acceptor is just as likely to bleach any nearby donor. Reaction of $^1O_2$ with dyes generally results in irreversible severance of the conjugated π-electron system responsible for fluorescence.

The extent of photobleaching can be lessened by adjusting any of the three participants in the reaction — excitation light, dye, and oxygen. Decreasing excitation light levels, in both intensity and duration, offers the most direct and consistently effective approach. The intrinsic photostability of organic dyes varies widely depending on their molecular structure (Eggeling *et al*., 1999; Kanofsky and Sima, 2000). The photobleaching quantum yield (the number of photobleaching events per photon absorbed) provides a quantitative expression of propensity for photobleaching. The ratio of the fluorescence quantum yield to the photobleaching quantum yield represents the average number of fluorescence photons generated by a dye before it is photobleached. For fluorescein, this ratio is about 30,000 whereas for rhodamine dyes it is >100,000. Although tabulations of photobleaching quantum yields (Eggeling *et al*., 1999) provide useful guidance, photobleaching rates are also dependent on environmental factors. For example, dye–dye interactions, such as those induced by attaching multiple dyes to a protein, result in increased rates of photobleaching relative to the free monomeric dye (Byers *et al*., 1976; Song *et al*., 1995, 1997). This may account at least partly for the photostability of protein conjugates labeled with AlexaFluor dyes, which are designed to minimize dye–dye interactions via electrostatic repulsion. The availability of reactive oxygen species (primarily $^1O_2$) contributing to photobleaching can be reduced by addition of scavengers, commonly referred to as antifade reagents, to the specimen. Several effective antifade formulations are commercially available; unfortunately these are only applicable to fixed specimens (Berrios *et al*., 1999). Furthermore, antifade reagents may cause fluorescence quenching in addition to attenuation of photobleaching, yielding only a small net increase in the number of photons available for detection (Eggeling *et al*., 1999; see also Chapter 39, *this volume*). Some live cell-compatible antifade reagents have been reported in the literature including Trolox (an analog of vitamin E), ascorbic acid and enzymatic deoxygenation systems (e.g., Oxyrase; Oxyrase Inc., Mansfield, OH; Adler, 1990). However their usage appears to be rather sporadic, suggesting that they are not consistently effective.

Photobleaching in two-photon microscopy is fundamentally a rather different problem than in the one-photon excitation case. The extraordinarily high spatial and temporal confinement of excitation photons required to achieve two-photon excitation (Zipfel *et al*., 2003a) potentially opens photobleaching reaction pathways that are not accessible through one-photon excitation. Whereas the rate of two-photon excited fluorescence emission increases as the square of excitation intensity (I^2), photobleaching rates show higher order ($I^{>2}$) increases (Patterson and Piston, 2000; Dittrich and Schwille, 2001). Analysis by fluorescence correlation spectroscopy (FCS) indicates that the reaction pathways are distinct from photobleaching arising from one-photon excitation in that they do not involve dye triplet excited states (Dittrich and Schwille, 2001).

Phototoxicity

To a large extent, phototoxicity and photobleaching go hand-in-hand. Phototoxicity results from damage exerted by photogenerated reactive oxygen species on proteins, nucleic acids, and other cellular components. Photodamage is usually restricted to the near vicinity of the sensitizer due to the limited diffusional range of $^1O_2$ (Greenbaum *et al*., 2000). Effects farther afield can occur through the action of secondary ROS initially generated from $^1O_2$ (Ouedraogo and Redmond, 2003). Cell death is only the most extreme manifestation of phototoxicity. Other effects may be much more subtle, such as photoinduction of intracellular Ca^{2+} release (Knight *et al*., 2003) or failure to divide.

Although phototoxicity has many determining factors (Table 17.4), controlling light exposure is the most effective limitation

TABLE 17.4. Factors Influencing Phototoxic Effects

Factor[a]	Trend	References
Excitation wavelength	Longer wavelength produce less photodamage.	Bloom & Webb (1984) Manders *et al*. (1999)
Excitation intensity and duration	Higher power and longer exposure result in more photodamage.[b]	Vigers *et al*. (1988) Oh *et al*. (1999) Schafer & Buettner (1999) Manders *et al*. (1999)
Cell type/status	Larger cells can sustain a higher phototoxic burden. Mitotic cells are particularly susceptible to photodamage.	Schafer & Buettner (1999) Manders *et al*., (1999)
Culture medium	Riboflavin and tryptophan induce phototoxicity.	Stoien & Wang (1974) Grzelak *et al*., (2001)
Dye concentration	Higher concentrations produce more photodamage.	Vigers *et al*. (1988) Oh *et al*. (1999)
Dye type	Cyanines and halogenated xanthenes are particularly phototoxic.	Bunting (1992) Gandin *et al*. (1983) Lee *et al*. (1995)
Dye localization	Calcein and GFP phototoxicity is decreased upon compartmentalization in mitochondria and endoplasmic reticulum, respectively.	Beghetto *et al*. (2000) Haseloff *et al*. (1997)
Antioxidant additives	Ascorbic acid and enzymatic deoxygenation systems reduce photoxicity.	Bloom & Webb (1984) Vigers *et al*. (1988).

[a] Note that some factors are strongly interdependent, for example, dye localization and dye concentration. [b] These dependences may by highly nonlinear.

strategy (Manders *et al*., 2004). Reduced photodamage and concomitantly increased specimen viability is one of the principal benefits of two-photon excitation. However, as in the case of photobleaching, although the overall phototoxic burden is vastly reduced compared to one-photon excitation, the severity of photodamage in the focal volume is substantially higher (Koester *et al*., 1999; Tirlapur *et al*., 2001; see also Chapter 38, *this volume*).

SUMMARY

An extensive range of dyes and probes, and techniques for incorporating them into living and fixed specimens, has been developed over the past 30 years. This development, allied to complementary advances in optical engineering and image processing, has propelled fluorescence to become the dominant contrast mechanism used in biological microscopy. Fluorescent labeling technology is a much less exact science than physical optics. This situation is a reflection of the fact that labeling technology must interface directly with the morphological and physiological diversity of biological specimens, rather than any intrinsic shortcomings in the technology itself. Nevertheless, understanding the design and implementation of labeling techniques is an essential element in the ultimate objective of deriving biological information from image data. This chapter has therefore endeavored to assemble a fraction of the extensive and diverse knowledge base on fluorescent probe techniques in one place, with the aim of facilitating critical evaluations of labeling strategies by experimenters.

ACKNOWLEDGMENTS

My thanks to Henry Haeberle (UCSF) and John Jordan (PerkinElmer Life and Analytical Sciences) for their collaboration in the experiments shown in Figure 17.6, which were carried out at the 2004 International 3D Microscopy of Living Cells course (University of British Colombia).

REFERENCES

Adamczyk, M., Mattingly, P.G., Shreder, K., and Yu, Z., 1999, Surface plasmon resonance (SPR) as a tool for antibody conjugate analysis, *Bioconjug. Chem.* 10:1032–1037.

Adams, S.R., Campbell, R.E., Gross, L.A., Martin, B.R., Walkup, G.K., Yao, Y., Llopis, J., and Tsien, R.Y., 2002, New biarsenical ligands and tetracysteine motifs for protein labeling in vitro and in vivo: synthesis and biological applications, *J. Am. Chem. Soc.* 124:6063–6076.

Adler, H.I., 1990, The use of microbial membranes to achieve anaerobiosis, *Crit. Rev. Biotechnol.* 10:119–127.

Ballou, B., Lagerholm, B.C., Ernst, L.A., Bruchez, M.P., and Waggoner, A.S., 2004, Noninvasive imaging of quantum dots in mice, *Bioconjug. Chem.* 15:79–86.

Beghetto, C., Renken, C., Eriksson, O., Jori, G., Bernardi, P., and Ricchelli, F., 2000, Implications of the generation of reactive oxygen species by photoactivated calcein for mitochondrial studies, *Eur. J. Biochem.* 267:5585–5592.

Berlier, J.E., Rothe, A., Buller, G., Bradford, J., Gray, D.R., Filanowski, B.J., Telford, W.G., Yue, S., Liu, J., Cheung, C.Y., Chang, W., Hirsch, J.D., Beechem, J.M., Haugland, R.P., and Haugland, R.P., 2003, Quantitative comparison of long-wavelength AlexaFluor dyes to Cy dyes: Fluorescence of the dyes and their conjugates, *J. Histochem. Cytochem.* 51:1699–1712.

Berrios, M., Conlon, K.A., and Colflesh, D.E., 1999, Antifading agents for confocal fluorescence microscopy, *Methods Enzymol.* 307:55–79.

Beste, G., Schmidt, F.S., Stibora, T., and Skerra, A., 1999, Small antibody-like proteins with prescribed ligand specificities derived from the lipocalin fold, *Proc. Natl. Acad. Sci. USA* 96: 1898–1903.

Bestvater, F., Spiess, E., Stobrawa, G., Hacker, M., Feurer, T., Porwol, T., Berchner-Pfannschmidt, U., Wotzlaw, C., and Acker, H., 2002, Two-photon fluorescence absorption and emission spectra of dyes relevant for cell imaging, *J. Microsc.* 208:108–115.

Billinton, N., and Knight, A.W., 2001, Seeing the wood through the trees: a review of techniques for distinguishing green fluorescent protein from endogenous autofluorescence, *Anal. Biochem.* 291:175–197.

Bloom, J.A., and Webb, W.W., 1984, Photodamage to intact erythrocyte membranes at high laser intensities: methods of assay and suppression, *J. Histochem. Cytochem*. 32:608–616.

Breen, C.M., Sykes, D.B., Baehr, C., Fricker, G., and Miller, D.S., 2004, Fluorescein-methotrexate transport in rat choroid plexus analyzed using confocal microscopy, *Am. J. Physiol.* 287:F562–F569.

Brelje, T.C., Wessendorf, M.W., and Sorenson, R.L., 2002, Multicolor laser scanning confocal immunofluorescence microscopy: Practical application and limitations, *Methods Cell Biol.* 70:165–244.

Bruchez, M. Jr, Moronne, M., Gin, P., Weiss, S., and Alivisatos, A.P., 1998, Semiconductor nanocrystals as fluorescent biological labels, *Science* 281:2013–2016.

Bunting, J.R., 1992, A test of the singlet oxygen mechanism of cationic dye photosensitization of mitochondrial damage, *Photochem. Photobiol.* 55: 81–87.

Byers, G.W., Gross, S., and Henrichs, P.M., 1976, Direct and sensitized photooxidation of cyanine dyes, *Photochem. Photobiol.* 23:37–43.

Campbell, R.E., Tour, O., Palmer, A.E., Steinbach, P.A., Baird, G.S., Zacharias, D.A., and Tsien, R.Y., 2002, A monomeric red fluorescent protein, *Proc. Natl. Acad. Sci. USA* 99:7877–7882.

Cao, F., Eckert, R., Elfgang, C., Nitsche, J.M., Snyder, S.A., Hulser, D.F., Willecke, K., and Nicholson, B.J., 1998, A quantitative analysis of connexin-specific permeability differences of gap junctions expressed in HeLa transfectants and Xenopus oocytes, *J. Cell Sci.* 111:31–43.

Chakrabarti, R., Pfeiffer, N.E., Wylie, D.E., and Schuster, S.M., 1989, Incorporation of monoclonal antibodies into cells by osmotic permeabilization: effect on cellular metabolism, *J. Biol. Chem.* 264:8214–8221.

Chalfie, M., and Kain, S., eds., 1998, *Green Fluorescent Protein: Properties, Applications and Protocols*, Wiley-Liss, New York.

Chan, W.C., and Nie, S., 1998, Quantum dot bioconjugates for ultrasensitive nonisotopic detection, *Science* 281:2016–2018.

Charpilienne, A., Nejmeddine, M., Berois, M., Parez, N., Neumann, E., Hewat, E., Trugnan, G., and Cohen, J., 2001, Individual rotavirus-like particles containing 120 molecules of fluorescent protein are visible in living cells, *J. Biol. Chem.* 276:29361–29367.

Coralli, C., Cemazar, M., Kanthou, C., Tozer, G.M., and Dachs, G.U., 2001, Limitations of the reporter green fluorescent protein under simulated tumor conditions, *Cancer Res* 61:4784–4790.

Croce, A.C., Spano, A., Locatelli, D., Barni, S., Sciola, L., and Bottiroli, G., 1999, Dependence of fibroblast autofluorescence properties on normal and transformed conditions. Role of the metabolic activity, *Photochem. Photobiol.* 69:364–374.

DaCosta, R.S., Andersson, H., and Wilson, B.C., 2003, Molecular fluorescence excitation-emission matrices relevant to tissue spectroscopy, *Photochem. Photobiol.* 78:384–392.

Daly, C., and McGrath, J.C., 2003, Fluorescent ligands, antibodies and preoteins for the study of receptors, *Pharmacol. Ther.* 100:101–118.

De Clerck, L.S., Bridts, C.H., Mertens, A.M., Moens, M.M., and Stevens, W.J., 1994, Use of fluorescent dyes in the determination of adherence of human leucocytes to endothelial cells and the effect of fluorochromes on cellular function, *J. Immunol. Methods* 172:115–124.

Denk, W., Strickler, J.H., and Webb, W.W., 1990, Two-photon laser scanning fluorescence microscopy, *Science* 248:73–76.

Derfus, A.M., Chan, W.C.W., and Bhatia, S.N., 2004, Probing the cytotoxicity of semiconductor quantum dots, *Nano. Lett*. 4:11–18.

Diaz, G., Liu, S., Isola, R., Diana, A., and Falchi, A.M., 2003, Mitochondrial localization of reactive oxygen species by dihydrofluorescein probes, *Histochem. Cell Biol.* 120:319–325.

Dickinson, M.E., Bearman, G., Tille, S., Lansford, R., and Fraser, S.E., 2001, Multi-spectral imaging and linear unmixing add a whole new dimension to laser scanning fluorescence microscopy, *Biotechniques* 31:1272–1278.

Dickinson, M.E., Simbuerger, E., Zimmermann, B., Waters, C.W., and Fraser, S.E., 2003, Multiphoton excitation spectra in biological samples, *J. Biomed. Opt.* 8:329–338.

Dittrich, P.S., and Schwille, P., 2001, Photobleaching and stabilization of fluorophores used for single molecule analysis with one- and two-photon excitation, *Appl. Phys. B* 73:829–837.

Di Virgilio, F., Steinberg T.H., and Silverstein, S.C., 1990, Inhibition of fura-2 sequestration and secretion with organic anion transport blockers, *Cell Calcium* 11:57–62.

Doyle, K.P., Simon, R.P., Snyder, A., and Stenzel-Poore, M.P., 2003, Working with GFP in the brain. *BioTechniques* 34:492–494.

Dundr, M., McNally, J.G., Cohen, J., and Mistelli, T., 2002, Quantitation of GFP-fusion proteins in single living cells, *J. Struct. Biol.* 140:92–99.

Eggeling, C., Widengren, J., Rigler, R., and Seidel C.A.M., 1999, In: *Applied Fluorescence in Chemistry, Biology and Medicine* (W. Rettig, B. Strehmel, S. Schrader, and H. Seifert, eds.), Springer-Verlag, Berlin, pp. 193–240.

Eilers, J., and Konnerth, A., 2000, Dye loading with patch pipets, In: *Imaging Neurons. A Laboratory Manual* (R. Yuste, F. Lanni, and A. Konnerth, eds.), Cold Spring Harbor Laboratory Press, Cold Spring Harbor, New York, pp. 35.1–35.10.

Endemann, G., Schechtman, D., and Mochly-Rosen, D., 2003, Cytotoxicity of pEGFP vector is due to residues encoded by multiple cloning site, *Anal. Biochem.* 313:345–347.

Farber, S.A., Pack, M., Ho, S.Y., Johnson, I.D., Wagner, D.S., Dosch, R., Mullins, M.C., Hendrickson, H.S., Hendrickson, E.K., and Halpern, M.E., 2001, Genetic analysis of digestive physiology using fluorescent phospholipid reporters, *Science* 292:1385–1388.

Farinas, J., and Verkman, A.S., 1999, Receptor-mediated targeting of fluorescent probes in living cells, *J. Biol. Chem.* 274:7603–7606.

Fink, C., Morgan, F., and Loew, L.M., 1998, Intracellular fluorescent probe concentrations by confocal microscopy, *Biophys. J.* 75:1648–1658.

Fischer, P.M., Krausz, E., and Lane, D.P., 2001, Cellular delivery of impermeable effector molecules in the form of conjugates with peptides capable of mediating membrane translocation, *Bioconj. Chem.* 12:825–841.

Fricker, M.D., and Meyer, A.J., 2001, Confocal imaging of metabolism in vivo: Pitfalls and possibilities, *J. Exp. Bot.* 52:631–640.

Gaigalas, A.K., Wang, L., and Vogt, R.F., 2002, Frequency-domain measurement of the photodegradation process of fluorescein, *Photochem. Photobiol.* 76:22–28.

Gan, B.S., Krump, E., Shrode, L.D., and Grinstein, S., 1998, Loading pyranine via purinergic recepetors or hypotonic stress for measurement of cytosolic pH by imaging, *Am. J. Physiol.* 275: C1158–C1166.

Gandin, E., Lion, Y., and Van de Vorst, A., 1983, Quantum yield of singlet oxygen production by xanthene derivatives, *Photochem. Photobiol.* 37:271–278.

Gerhardt, G.A., and Palmer, M.R., 1987, Characterization of the techniques of pressure ejection and microiontophoresis using in vivo electrochemistry, *J. Neurosci. Methods* 22:147–159.

Good, M.J., Hage, W.J., Mummery, C.L., De Laat, S.W., and Boonstra, J., 1992, Localization and quantification of epidermal growth factor receptors on single cells by confocal laser scanning microscopy, *J. Histochem. Cytochem.* 40:1353–1361.

Greenbaum, L., Rothmann, C., Lavie, R., and Malik Z., 2000, Green fluorescent protein photobleaching: A model for protein damage by endogenous and exogenous singlet oxygen, *Biol. Chem.* 381:1251–1258.

Grzelak, A., Rychlik, B., and Bartosz, G., 2001, Light-dependent generation of reactive oxygen species in cell culture media, *Free Radic. Biol. Med.* 30:1418–1425.

Grutzendler, J., Tsai, J., and Gan, W.G., 2003, Rapid labeling of neuronal populations by ballistic delivery of fluorescent dyes, *Methods* 30:79–85.

Gunjan, A., Alexander, B.T., Sittman, D.B., and Brown, D.T., 1999, Effects of H1 histone variant overexpression on chromatin structure, *J. Biol. Chem.* 274:37950–37956.

Haas, K., Sin, W.-C., Javaherian, A., Li, Z., and Cline, H.T., 2001, Single-cell electroporation for gene transfer in vivo, *Neuron* 29:583–591.

Hara, M., Wang, X., Kawamura, T., Bindokas, V.P., Dizon, R.F, Alcoser, S.Y., Magnuson, M.A., and Bell, G.I., 2003, Transgenic mice with green fluorescent protein–labeled pancreatic β-cells, *Am. J. Physiol.* 284:E1177–E1183.

Haralampus-Grynaviski, N.M., Lamb, L.E., Clancy, C.M., Skumatz, C., Burke, J.M., Sarna, T., and Simon, J.D., 2003, Spectroscopic and morphological studies of human retinal lipofuscin granules, *Proc. Natl. Acad. Sci. USA* 100:3179–3184.

Haseloff, J., Siemering, K.R., Prasher, D.C., and Hodge, S., 1997, Removal of a cryptic intron and subcellular localization of green fluorescent protein are required to mark transgenic Arabidopsis plants brightly, *Proc. Natl. Acad. Sci. USA* 94:2122–2127.

Hashimoto, K., Tatsumi, N., and Okada, K., 1989, Introduction of phalloidin labelled with fluorescein isothiocyanate into living polymorphonuclear leukocytes by electroporation, *J. Biochem. Biophys. Methods* 19:143–154.

Haugland, R.P., 2002, *Handbook of Fluorescent Probes and Research Products, Ninth Edition,* Molecular Probes, Inc., Eugene, Oregon.

Helmchen, F., 2002, Miniaturization of fluorescence microscopes using fibre optics, *Exp. Physiol.* 87:737–745.

Hermanson, G.P., 1996, *Bioconjugate Techniques,* Academic Press, San Diego, California.

Hollo, Z., Homolya, L., Davis, C.W., and Sarkadi, B., 1994, Calcein accumulation as a fluorometric functional assay of the multidrug transporter, *Biochim. Biophys. Acta* 1191:384–388.

Jaiswal, J.K., Mattoussi, H., Mauro, J.M., and Simon, S.M., 2003, Long-term multiple color imaging of live cells using quantum dot bioconjugates, *Nat. Biotechnol.* 21:47–52.

Jales-Erijman, E.A., and Jovin, T.M., 2003, FRET imaging, *Nat. Biotechnol.* 21:1387–1395.

Kanofsky, J.R., and Sima P.D., 2000, Structural and environmental requirements for quenching of singlet oxygen by cyanine dyes, *Photochem. Photobiol.* 71:361–368.

Katz, B.Z., Krylov, D., Aota, S.I., Olive, M., Vinson, C., and Yamada, K.M., 1998, Green fluorescent protein labeling of cytoskeletal structures — Novel targeting approach based on leucine zippers, *BioTechniques* 25: 298–304.

Knight, M.M., Roberts, S.R., Lee, D.A., and Bader, D.L., 2003, Live cell imaging using confocal microscopy induces intracellular calcium transients and cell death, *Am. J. Physiol.* 284:C1083–C1089.

Koester, H.J., Baur, D., Uhl, R., and Hell, S.W., 1999, Ca^{2+} fluorescence imaging with pico- and femtosecond two-photon excitation: signal and photodamage, *Biophys. J.* 77:2226–2236.

Larson, D.R., Zipfel, W.R., Williams, R.M., Clark, S.W., Bruchez, M.P., Wise, F.W., and Webb, W.W., 2003, Water soluble quantum dots for multiphoton fluorescence imaging *in vivo*, *Science* 300:1434–1436.

Lee, C., Wu, S.S., and Chen, L.B., 1995, Photosensitization by 3,3′-dihexyloxacarbocyanine iodide: Specific disruption of microtubules and inactivation of organelle motility, *Cancer Res.* 55:2063–2069.

Lemasters, J.J., Trollinger, D.R., Qian, T., Cascio, W.E., and Ohata, H., 1999, Confocal imaging of Ca^{2+}, pH, electrical potential and membrane permeability in single living cells, *Methods Enzymol.* 302:341–358.

Lim, M.L., Lum, M.G., Hansen, T.M., Roucou, X., and Nagley, P., 2002, On the release of cytochrome c from mitochondria during cell death signaling, *J. Biomed. Sci.* 9:488–506.

Lippincott-Schwartz, J., and Patterson, G.H., 2003, Development and use of fluorescent protein markers in living cells, *Science* 300:87–91.

Loetchutinat, C., Saengkhae, C., Marbeuf-Gueye, C., and Garnier-Suillerot, A., 2003, New insights into the P-glycoprotein-mediated effluxes of rhodamines, *Eur. J. Biochem.* 270:476–485.

Lombry, C., Bosquillon, C., Preat, V., and Vanbever, R., 2002, Confocal imaging of rat lungs following intratracheal delivery of dry powders or solutions of fluorescent probes, *J. Controlled Release* 83:331–341.

Lu, J., and Zenobi, R., 2000, *In-situ* monitoring of protein labeling reactions by matrix-assisted laser desorption/ionization mass spectrometry, *Fresnius J. Anal. Chem.* 366:3–9.

Manders, E.M., Kimura, H., and Cook, P.R., 1999, Direct imaging of DNA in living cells reveals the dynamics of chromosome formation, *J. Cell Biol.* 144:813–821.

Manders, E., Van Oven, C., and Hoebe, R., 2004, Phototoxicity in live-cell imaging and an effective way to reduce it: Controlled light exposure microscopy (CLEM), In: *Abstracts of Focus on Microscopy 2004 Meeting*.

Marrero, M.B., Schieffer, B., Paxton, W.G., Schieffer, E., and Bernstein, K.E., 1995, Electroporation of pp60*c-src* antibodies inhibits the angiotensin II activation of phospholipase C-γ1 in rat aortic smooth muscle cells, *J. Biol. Chem*. 270:15734–15738.

Martin, C., Walker, J., Rothnie, A., and Callaghan, R., 2003, The expression of P-glycoprotein does influence the distribution of novel fluorescent compounds in solid tumour models, *Br. J. Cancer* 89:1581–1589.

Mattheakis, L.C., Dias, J.M., Choi, Y.J., Gong, J., Bruchez, M.P., Liu, J., and Wang, E., 2004, Optical coding of mammalian cells using semiconductor quantum dots, *Anal. Biochem.* 327:200–208.

Matz M.V., Fradkov, A.F., Labas, Y.A., Savitsky, A.P., Zaraisky, A.G., Markelov, M.L., and Lukyanov, S.A., 1999, Fluorescent proteins from nonbioluminescent Anthozoa species, *Nat. Biotechnol.* 17:969–973.

Mercola, D.A., Morris, J.W.S., and Arquilla, E.R., 1972, Use of resonance interaction in the study of the chain folding of insulin in solution, *Biochemistry* 11:3860–3874.

Meyers, J.R., MacDonald, R.B., Duggan, A., Lenzi, D., Standaert, D.G., Corwin, J.T., and Corey, D.P., 2003, Lighting up the senses: FM1-43 loading of sensory cells through nonselective ion channels, *J. Neurosci.* 23:4054–4065.

Mook, O.R., Van Overbeek C., Ackema, E.G., Van Maldegem, F., and Frederiks, W.M., 2003, In situ localization of gelatinolytic activity in the extracellular matrix of metastases of colon cancer in rat liver using quenched fluorogenic DQ-gelatin, *J. Histochem. Cytochem.* 51:821–829.

Mujumdar, R.B., Ernst, L.A., Mujumdar, S.R., Lewis, C.J., and Waggoner, A.S., 1993, Cyanine dye labeling reagents: Sulfoindocyanine succinimidyl esters, *Bioconjug. Chem.* 4:105–111.

Nemetz, C., Reichhuber, R., Schweizer, R., Hloch, P., and Watzele, M., 2001, Reliable quantification of in vitro synthesized green fluorescent protein: Comparison of fluorescence activity and total protein levels, *Electrophoresis* 22:966–969.

Nicholls, D.G., and Ward, M.W., 2000, Mitochondrial membrane potential and neuronal glutamate excitotoxicity: mortality and millivolts, *Trends Neurosci.* 23:166–174.

O'Brien, J.A, Holt, M., Whiteside, G., Lummis, S.C., and Hastings, M.H., 2001, Improvements to the hand-held Gene Gun: Improvements for in vitro biolistic transfection of organotypic neuronal tissue, *J. Neurosci. Methods* 112:57–64.

Oh, D.J., Lee, G.M., Francis, K., and Palsson, B.O., 1999, Phototoxicity of the fluorescent membrane dyes PKH2 and PKH26 on the human hematopoietic KG1a progenitor cell line, *Cytometry* 36:312–318.

Ouedraogo, G.D., and Redmond, R.W., 2003, Secondary reactive oxygen species extend the range of photosensitization effects in cells: DNA damage produced via initial membrane photosensitization, *Photochem. Photobiol.* 77:192–203.

Pagano, R.E., Watanabe, R., Wheatley, C., and Dominguez, M., 2000, Applications of BOPIDY-sphingolipid analogs to study lipid traffic and metabolism in cells, *Methods Enzymol.* 312:523–534.

Panchuk-Voloshina, N., Haugland, R.P., Bishop-Stewart, J., Bhalgat, M.K., Millard, P.J., Mao, F., Leung, W.-Y., and Haugland, R.P., 1999, Alexa dyes, a series of new fluorescent dyes that yield exceptionally bright, photostable conjugates, *J. Histochem. Cytochem.* 47:1179–1188.

Parish, C.R., 1999, Fluorescent dyes for lymphocyte migration and proliferation studies, *Immunol. Cell Biol.* 77:499–508.

Passamonti, S., and Sottocasa, G., 1988, The quinoid structure is the molecular requirement for recognition of phthaleins by the organic anion carrier at the sinusoidal plasma membrane level in the liver, *Biochim. Biophys. Acta* 943:119–125.

Patterson, G.H., Knobel, S.M., Sharif, W.D., Kain, S.R., and Piston, D.W., 1997, Use of the green fluorescent protein and its mutants in quantitative fluorescence microscopy, *Biophys. J.* 73:2782–2790.

Patterson, G.H., and Piston, D.W., 2000, Photobleaching in two-photon excitation microscopy, *Biophys. J.* 78:2159–2162.

Potocky, T.B., Menon, A.K., and Gellman, S.H., 2003, Cytoplasmic and nuclear delivery of a TAT-derived peptide and a β-peptide after endocytic uptake into HeLa cells, *J. Biol. Chem.* 278:50188–50194.

Pu, R., Wozniak, M., and Robinson, K.R., 2000, Cortical actin filaments form rapidly during photopolarization and are required for the development of calcium gradients in Pelvetia compressa zygotes, *Dev. Biol.* 222:440–449.

Ramjeesingh, M., Zywulko, M., Rothstein, A., Whyte, R., and Shami, E.Y., 1990, Antigen protection of monoclonal antibodies undergoing labeling, *J. Immunol. Methods* 133:159–167.

Rocheleau, J.V., Head, W.S., and Piston, D.W., 2004, Quantitative NAD(P)H/flavoprotein autofluorescence imaging reveals metabolic mechanisms of pancreatic islet pyruvate response, *J. Biol. Chem.* 279: 31780–31787

Roederer, M., and Murphy, R.F., 1986, Cell-by-cell autofluorescence correction for low signal-to-noise systems: Application to epidermal growth factor endocytosis by 3T3 fibroblasts, *Cytometry* 7:558–565.

Rose, C.R., Kovalchuk, Y., Eilers, J., and Konnerth, A., 1999, Two-photon Na^+ imaging in spines and fine dendrites of central neurons, *Pflügers Arch.* 439:201–207.

Rottenberg, H., and Wu, S., 1998, Quantitative assay by flow cytometry of the mitochondrial membrane potential in intact cells, *Biochim. Biophys. Acta* 1404:393–404.

Rubart, M., Wang, E., Dunn, K.W., and Field, L.J., 2003, Two-photon molecular excitation imaging of Ca^{2+} transients in Langendorff-perfused mouse hearts, *Am. J. Physiol. Cell Physiol.* 284:C1654–C1668.

Ruthazer, E.S., and Cline, H.T., 2002, Multiphoton imaging of neurons in living tissue: Acquisition and analysis of time-lapse morphological data, *Real-Time Imaging* 8:175–188.

Schafer, F.Q., and Buettner, G.R., 1999, Singlet oxygen toxicity is cell line-dependent: a study of lipid peroxidation in nine leukemia cell lines, *Photochem. Photobiol.* 70:858–867.

Scorrano, L., Petronilli, V., Colonna, R., Di Lisa, F., and Bernardi, P., 1999, Chloromethyltetramethylrosamine (Mitotracker Orange) induces the mitochondrial permeability transition and inhibits respiratory complex I, *J. Biol. Chem.* 274:24657–24663.

Siegel, R.M., Chan, F.K., Zacharias, D.A., Swofford, R., Holmes, K.L., Tsien, R.Y., and Lenardo, M.J., 2000, Measurement of molecular interactions in living cells by fluorescence resonance energy transfer between variants of the green fluorescent protein, *Science Signal Transduction Knowledge Environment,* available at http://stke.sciencemag.org/cgi/content/full/OC_sigtrans;2000/38/pl1.

Song, L., Hennink, E.J., Young, I.T., and Tanke, H.J., 1995, Photobleaching kinetics of fluorescein in quantitative fluorescence microscopy, *Biophys. J.* 68:2588–2600.

Song, L., Varma, C.A., Verhoeven, J.W., and Tanke, H.J., 1996, Influence of the triplet excited state on the photobleaching kinetics of fluorescein in microscopy, *Biophys. J.* 70:2959–2968.

Song, L., van Gijlswijk, R.P., Young, I.T., and Tanke, H.J., 1997, Influence of fluorochrome labeling density on the photobleaching kinetics of fluorescein in microscopy, *Cytometry* 27:213–223.

Stephens, D.G., and Pepperkok, R., 2001, The many ways to cross the plasma membrane, *Proc. Natl. Acad. Sci. USA* 98:4295–4298.

Stoien, J.D., and Wang, R.J., 1974, Effect of near-ultraviolet and visible light on mammalian cells in culture II. Formation of toxic photoproducts in tissue culture medium by blacklight, *Proc. Natl. Acad. Sci. USA* 71:3961–3965.

Storms, M.M.H., Van der Schoot, C., Prins, M., Kormelink, R., Van Lent, J.W.M., and Goldbach, R.W., 1998, A comparison of two methods of microinjection for assessing altered plasmodesmal gating in tissues expressing viral movement proteins, *Plant J.* 13:131–140.

Stosiek, C., Garaschuk, O., Holthoff, K., and Konnerth, A., 2003, *In vivo* two-photon calcium imaging of neuronal networks, *Proc. Natl. Acad. Sci. USA* 100:7319–7324.

Stracke, F., Heupel, M., and Thiel, E., 1999, Singlet molecular oxygen photosensitized by rhodamine dyes: Correlation with photophysical properties of the sensitizers, *J. Photochem. Photobiol. A* 126:51–58.

Sullivan, K.F., and Kay, S.A., eds., 1999, *Green Fluorescent Proteins,* Academic Press, San Diego, California.

Takahashi, N., Nemoto, T., Kimura, R., Tachikawa, A., Miwa, A., Okado, H., Miyashita, Y., Iino, M., Kadowaki, T., and Kasai, H., 2002, Two-photon excitation imaging of pancreatic islets with various fluorescent probes, *Diabetes* 51:S25–S28.

Tanhuanpaa, K., and Somerharju, P., 1999, Gamma-cyclodextrins greatly enhance translocation of hydrophobic fluorescent phospholipids from vesicles to cells in culture. Importance of molecular hydrophobicity in phospholipid trafficking studies, *J. Biol. Chem.* 274:35359–35366.

Tirlapur, U.K., Konig, K., Peuckert, C., Krieg, R., and Halbhuber, K.J., 2001, Femtosecond near-infrared laser pulses elicit generation of reactive oxygen species in mammalian cells leading to apoptosis-like death, *Exp. Cell Res.* 263:88–97.

Tooley, A.J., Cai, Y.A., and Glazer, A.N., 2001, Biosynthesis of a fluorescent cyanobacterial C-phycocyanin holo-alpha subunit in a heterologous host, *Proc. Natl. Acad. Sci. USA* 98:10560–10565.

Tsien, R.Y., 1998, The green fluorescent protein, *Ann. Rev. Biochem.* 67:509–544.

Unkila, M., McColl, K.S., Thomenius, M.J., Heiskanen, K., and Distelhorst, C.W., 2001, Unreliability of the cytochrome c-enhanced green fluorescent fusion protein as a marker of cytochrome c release in cells that overexpress Bcl-2, *J. Biol. Chem.* 276:39132–39137.

Vigers, G.P., Coue, M., and McIntosh, J.R., 1988, Fluorescent microtubules break up under illumination, *J. Cell Biol.* 107:1011–1024.

Wadkins, R.M., and Houghton, P.J., 1995, Kinetics of transport of dialkyloxacarbocyanines in multidrug-resistant cell lines overexpressing P-glycoprotein: Interrelationship of dye alkyl chain length, cellular flux, and drug resistance, *Biochemistry* 34:3858–3872.

Waizenegger, T., Fischer, R., and Brock, R., 2002, Intracellular concentration measurement in adherent cells: A comparison of import efficiencies of cell-permeable peptides, *Biol. Chem.* 383:291–299.

Walev, I., Bhakdi, S.C., Hofmann, F., Djonder, N., Valeva, A., Aktories, K., and Bhakdi, S., 2001, Delivery of proteins into living cells by reversible membrane permeabilization with streptolysin O, *Proc. Natl. Acad. Sci. USA* 98:3185–3190.

Wang, G., Achim, C.L., Hamilton, R.L., Wiley, C.A., and Soontornniyomkij, V., 1999, Tyramide signal amplification method in multiple-label immunofluorescence confocal microscopy, *Methods* 18:459–464.

Watson, A., Wu, X., and Bruchez, M., 2003, Lighting up cells with quantum dots, *BioTechniques* 34:296–303.

Wendland, M., and Bumann, D., 2002, Optimization of GFP levels for analyzing Salmonella gene expression during an infection, *FEBS Lett.* 521:105–108.

White, S.M, Constantin, P.E., and Claycomb, W.C., 2004, Cardiac physiology at the cellular level: use of cultured HL-1 cardiomyocytes for studies of cardiac muscle cell structure and function, *Am. J. Physiol.* 286:H823–H829.

Wu, X., Liu, H., Liu, J., Haley, K.N., Treadway, J.A., Larson, J.P., Ge, N., Peale, F., and Bruchez, M.P., 2003, Immunofluorescent labeling of cancer marker Her2 and other cellular targets with semiconductor quantum dots, *Nat. Biotechnol.* 21:41–46.

Xu, C., and Webb, W.W., 1996, Measurement of two-photon excitation cross sections of molecular fluorophores with data from 690 to 1050 nm, *J. Opt. Soc. Am. B* 13:481–491.

Xu, C., Zipfel, W., Shear, J.B., Williams, R.M., and Webb, W.W., 1996, Multiphoton fluorescence excitation: new spectral windows for biological nonlinear microscopy, *Proc. Natl. Acad. Sci. USA* 93:10763–10768.

Yasuda, K., Momose, T., and Takahashi, Y., 2000, Applications of microelectroporation for studies of chick embryogenesis, *Dev. Growth Differ.* 42:203–206.

Zipfel, W., Williams, R.M., and Webb, W.W., 2003a, Nonlinear magic: Multiphoton microscopy in the biosciences, *Nat. Biotechol.* 21:1369–1377.

Zipfel, W.R., Williams, R.M., Christie, R., Nikitin, A.Y., Hyman, B.T., and Webb, W.W., 2003b, Live tissue intrinsic emission microscopy using multiphoton-excited native fluorescence and second harmonic generation, *Proc. Natl. Acad. Sci. USA* 100:7075–7080.

Zhang, J., Campbell, R.E., Ting, A.Y., and Tsien, R.Y., 2002, Creating new fluorescent probes for cell biology, *Nat. Rev. Mol. Cell Biol.* 3:906–918.

Zhang, X., and Kiechle, F.L., 2003, Hoechst 33342 alters luciferase gene expression in transfected BC3H-1 myocytes, *Arch. Pathol. Lab. Med.* 127:1124–1132.

Zhao, M., Hollingworth, S., and Baylor, S.M., 1997, AM-loading of fluorescent Ca^{2+} indicators into intact fibers of frog muscle, *Biophys. J.* 72:2736–2747.

18

Guiding Principles of Specimen Preservation for Confocal Fluorescence Microscopy

Robert Bacallao, Sadaf Sohrab, and Carrie Phillips

INTRODUCTION

Traditionally, biologists have been confined to transmission electron microscopy (TEM) and light microscopy (LM) in order to correlate biochemical and molecular data with morphology. Electron microscopy (EM) provides fine ultrastructural detail but is limited to the study of cellular structures that react with electron dense stains deposited in fixed specimens. Immunogold labeling permits the study of non–electron-dense material, but EM sections must still be very thin to avoid problems with the penetration of the labeled antibodies and to reduce scattering of the electron beam.

The electron microscopist faces the same problem in reconstructing three-dimensional (3D) cellular structures from two-dimensional (2D) projections. In practice, the better the ultramicrotome, the more accurate the 3D reconstruction. In any event, reconstruction from serial EM sections is a laborious process.

The use of traditional LM methods, such as Nomarski optics and phase-contrast microscopy, confines one to specimens observable by transmitted light, such as *in vitro* studies involving cytoskeletal elements (Abbott, 1884; Ito, 1962; Scheetz and Spudich, 1983; Inoué, 1986; Dabora and Sheetz, 1988; Lee and Chen, 1988). The use of vital dyes and fluorescent labeling has allowed researchers to correlate functional biochemical data with structural data. The introduction of the confocal microscope has finally allowed the present generation of structural biologists to escape from Flatland. However, this instrument requires not only an imaging system, but also an object worth viewing.

Although it would probably be ideal if all biological confocal studies could be carried out on living specimens (Chapter 19, *this volume*), this is not always possible. Apart from the problem of cell movement and the nuisance of keeping cells physiologically "happy" on the microscope stage, there are additional complications in exposing such cells to antibody labeling or embedding them in antibleaching agents. As a result, the vast majority of confocal images are made from material that has been fixed, stained, and in most cases, dehydrated. However, because most LM specimen preparation techniques were developed to produce only pleasing 2D images, they are often inadequate to the task of producing specimens that retain their 3D structure.

Indeed, because of the difficulty in obtaining high contrast images from non-planar objects using conventional microscopic techniques, immunofluorescence-staining protocols that tended to flatten the specimens under study have often gained acceptance specifically because they tend to reduce the effect of out-of-focus light on the final image. This tendency has pushed the biologist to study either thin cells or cells grown under conditions that are not optimal for the expression of the full phenotype of the cell.

Confocal fluorescence microscopy extends the value of these fluorescence-labeling techniques because its ability to exclude out-of-focus information from the image data permits the acquisition of 3D intensity data sets that can be viewed as 3D images. The purpose of this chapter is to discuss methods for ensuring that the specimens from which such data are acquired maintain the 3D structure they had *in vivo*.

We have studied the Madin–Darby canine kidney (MDCK) cell line grown on Costar polycarbonate membrane filter supports. The filter supports have the disadvantage of being opaque, but they do allow the cells to be supplied with nutrients in a more physiological way. Under these growth conditions, the basal membrane has access to nutrients at all times, somewhat reproducing growth conditions *in vivo*. MDCK cells form a more completely polarized monolayer when grown on the membrane filters (Bomsel *et al.*, 1989).

These studies have asked specific questions about cellular organization both *in vitro* and *in vivo* during the formation of an epithelial monolayer. This chapter reflects the lessons learned while attempting to study these cells under growth conditions that are not very amenable to study by immunofluorescence methods.

We will begin with a description of fixatives and fixation methods. This will be followed by a section that explains how to prepare and use the two fixatives that we have found most useful (glutaraldehyde and pH shift/formaldehyde) and that also describes mounting and staining procedures. We will then describe how these procedures were evaluated and conclude with some general comments on the subject.

This chapter will discuss many of these methods and address some of the potential pitfalls of specimen preparation.

CHARACTERISTICS OF FIXATIVES

The first problem about fixatives is their name, as it may give the impression that treatment with fixatives really does "fix" or render immovable the macromolecular components of the cell. In fact, most fixation protocols are really just chemical or physical processes that cause metabolism to stop and that preserve microstructures down to some size level by destroying other structures, such as enzymes, which have sizes below that level. The best fixation for a given experiment is that which does the best job of preserving structure down to the level required.

Robert Bacallao and Sadaf Sohrab • Division of Nephrology, Department of Medicine, Indiana University School of Medicine, Indianapolis, Indiana, 46202
Carrie Phillips • Division of Nephrology and Department of Pathology, Indiana University School of Medicine, Indianapolis, Indiana, 46202

 Handbook of Biological Confocal Microscopy, Third Edition, edited by James B. Pawley, Springer Science+Business Media, LLC, New York, 2006.

No fixation protocol is perfect, but its imperfection is often masked by the fact that the specimen dimensions in the plane of the image are maintained by the adherence of the specimen to the glass substrate. As a result, shrinkage in the *z*-direction is often pronounced. Such shrinkage is particularly serious when it occurs on specimens to be viewed in the confocal microscope, which allows one to obtain information in the *z*-direction.

There are three general types of fixation protocol available for biological specimen preparation. **Chemical fixatives** fix tissue either by **coagulating** proteins or by chemically **crosslinking them**. The other two methods of fixation, **freeze substitution** (Steinbrecht and Zierold, 1987) and **microwave fixation** (Jackson, 1991) will not be considered here.

The *coagulating* fixatives, such as ethanol, methanol, or acetone, fix the specimen by rapidly changing the hydration state of the cellular component. Proteins either coagulate or are extracted during this process. Coagulating fixatives are popular, as they are easy to apply reproducibly and tend to preserve the antigen recognition sites for immunolabeling very well. The major problem with the use of coagulating fixatives in confocal microscopy is the profound shrinkage of the specimen that these fixatives produce. We have found that methanol will shrink cell height by 50% during the fixation. This artifact renders the spatial information obtained by confocal microscopy inaccurate and should not be depended on, especially when the data sets are to be used for 3D reconstruction. It is also important to note that commercial preparations of formaldehyde often contain significant amounts of methanol as a stabilizing agent, and this can induce the same shrinkage artifact.

Commonly used **crosslinking** fixatives include glutaraldehyde, formaldehyde, and ethylene glycol-*bis*-succinimidyl succinate (EGS). These fixation chemicals form covalent crosslinks that are determined by the active groups in each compound.

The ideal fixative should penetrate tissues quickly, act rapidly, and preserve the cellular structure before the cell can react to produce structural artifacts. Unfortunately, no single agent has emerged as the ideal fixative and a pragmatic approach to the use of a particular fixative is determined by the experimental requirements. Although tissue fixation is incompletely understood, an understanding of the characteristics of chemical fixatives can provide a rational approach to their use.

Glutaraldehyde

Since its introduction in 1962, glutaraldehyde has been used extensively for EM specimen preparation (Sabatini *et al.*, 1962). This diadehyde is composed of five carbons with a molecular weight of 100.12. Extensive evaluation of the preservation properties of glutaraldehyde by EM has shown that it preserves subcellular structures well (Sabatini *et al.*, 1963, 1964; Barrnett *et al.*, 1964). Glutaraldehyde has been less popular as a fixative for fluorescence microscopy because it renders tissue autofluorescent and destroys antibody-binding sites. Fortunately, the autofluorescence can usually be adequately attenuated by post-treating samples with $NaBH_4$ (Tagliaferro *et al.*, 1997). Recent work utilizes ethanol extraction to remove autofluorescent chemicals or Sudan black to quench autofluorescent signals (Baschong *et al.*, 2001).

The chemistry of glutaraldehyde fixation is complex and not fully understood. Glutaraldehyde forms a Schiff's base with amino groups on proteins and polymerizes via Schiff's base catalyzed reactions (Johnson, 1985; Tashima *et al.*, 1987). The ability to polymerize allows glutaraldehyde to form extended crosslinks (Meek and Chapman, 1985). Glutaraldehyde reacts with the ε-amino group of lysine and will react with the α-amino group amino acids. It will also react with tyrosine, tryptophan, histidine, phenylalanine, and cysteine (Hayat, 1989). While glutaraldehyde fixes proteins rapidly, its main disadvantage is its relatively slow rate of penetration into the cell compared to formaldehyde. Other problems associated with glutaraldehyde fixation are the propensity of many cells to form membrane blebs as they die (as is common to all the aldehyde fixatives) and its inability to crosslink neutral lipids, DNA, or RNA (Hopwood, 1975). Not all proteins are inactivated by glutaraldehyde, and some proteins can still be extracted from fixed tissue (Blanchette-Mackie and Scow, 1981; Hayat, 1989).

Glutaraldehyde is supplied commercially as a 25% or 8% solution. Commercial preparations of glutaraldehyde may contain significant amounts of impurities, which can affect the reproducibility of the fixation method or induce fixation artifacts. In our experience, it is important to use only those commercial preparations that list the impurities. We have tended to use the glutaraldehyde solutions supplied by Polysciences (Warrington, PA) and have noted satisfactory reproducibility between commercial lots.

As the glutaraldehyde solution ages, it polymerizes and turns yellow. Because this changes the reproducibility of the fixation and can produce artifacts, it is important to identify old solutions and to store the fixative so as to inhibit polymerization (Hayat, 1989). As the polymerization rate increases with temperature and at high pH, it can be minimized by storing both unbuffered glutaraldehyde and working solutions at −20°C. These solutions should be thawed only once and used the same day.

One useful way to monitor the quality of glutaraldehyde is to measure the absorbance of a 0.5% solution at 235 nm and 280 nm. Pure glutaraldehyde has an A235/A280 ratio of less than 0.2. Artifacts tend to occur with ratios of >2.0 (Bowers and Maser, 1988).

A variety of buffers and co-fixatives can be used with glutaraldehyde. The advantages and changes in fixation chemistry that occur when it is used in combination with other fixatives have been reviewed elsewhere (Hayat, 1981; Hayat, 1986).

Formaldehyde

As mentioned above, commercial solutions of formaldehyde contain significant amounts of methanol. Formaldehyde fixation for confocal microscopy should be prepared fresh from paraformaldehyde dissolved in water (see protocol described below). Formaldehyde (MW 30.0) crosslinks proteins by forming methylene bridges between reactive groups. The rate-limiting step is a deprotonation of amino groups, hence the pH dependence of the crosslinking reaction. Other functional groups that are reactive with formaldehyde include amido, guanidine, thiol, phenol, imidazolyl, and indolyl groups (Hayat, 1989). When lysine is added to the fixation buffer, it can participate in the crosslinking reaction, and this is the basis for its inclusion in the paraformaldehyde–lysine–periodate fixation first described by McLean and Nakane (1974).

One advantage of formaldehyde as a fixative is its ability to crosslink nucleic acids. This makes it the preferred fixative for *in situ* hybridization. This aldehyde does not crosslink lipids and, in some cell types, it produces extensive vesiculation of the plasma membrane. In some cases, small amounts of $CaCl_2$ in the fixation buffer have been shown to stabilize the plasma membrane during fixation. However, labile structures such as microtubules are not well preserved by formaldehyde at physiologic pH (Sato *et al.*, 1976; Wild *et al.*, 1987). Observation of the nucleus by phase-contract microscopy during formaldehyde fixation reveals marked changes in the size and shape during fixation (J. DeMey, personal

communication). During the fixation process, the nucleus oscillates, alternating between swelling and shrinking. It is not clear what happens to the nuclear contents during this time.

The rate of protein crosslinking is slower with formaldehyde than with glutaraldehyde, however, formaldehyde penetrates cells 10 times faster (Hopwood, 1967). Attempts have been made to try to optimize fixation by mixing glutaraldehyde with formaldehyde. The idea is to take advantage of the rapid penetration of formaldehyde into the tissue and the high speed of glutaraldehyde crosslinking (Karnovsky, 1965). Although what happens to the fixation chemistry when these mixtures are employed is not clearly understood, in our experience Karnovsky's fixative has been useful for some preparations and appears to preserve the 3D structure well.

EGS is another bifunctional crosslinking agent that reacts with primary amino groups and with the ε-amino groups on lysine. A major advantage of this fixative is its reversibility. The crosslinks are cleavable at pH 8.5, an attractive feature because reversible crosslinking may be used to restore antigen binding sites (Abdella *et al.*, 1979). This fixative is useful for membrane-bound proteins, but its limited solubility in water makes its performance highly variable. Sulfated forms of this crosslinking agent [ethylene glycobis (sulfo-succimidylsuccinate)] (Pierce Co., Pierce, IL) are available and are water soluble (Abdella *et al.*, 1979). We have not tried this particular crosslinking agent as yet but it is also cleavable.

FIXATION STAINING AND MOUNTING METHODS

The fixation methods described below have been optimized for the confocal fluorescence microscope in studies in which MDCK cells have been grown on opaque filter supports (Bacallao and Stelzer, 1989). The cells grow to a uniform height of 18 µm and form a dense monolayer under the growth conditions we used. These fixation and staining protocols have been tested using the criteria described in the next section.

Glutaraldehyde Fixation

Stock Solutions

- 8% glutaraldehyde EM grade (Polysciences, Warrington, PA).
- 80 m*M* Kpipes, pH 6.8, 5 m*M* EGTA, 2 m*M* $MgCl_2$, both with and without 0.1% Triton X-100 depending on the target antigen; use Triton if you intend to stain cytoskeletal proteins.
- Phosphate-buffered saline without $Ca^{2+}MG^{+}$ (PBS–).
- Phosphate-buffered saline without $Ca^{2+}MG^{+}$, pH 8.0.

Preparation of the Stock Solutions

EM grade glutaraldehyde was obtained from Polysciences. It is supplied as an 8% aqueous solution. When a new vial is opened, the glutaraldehyde is diluted to 0.3% in a solution of 80 m*M* Kpipes, pH 6.8, 5 m*M* EGTA, 2 m*M* $MgCl_2$, 0.1% Triton X-100. The aliquots are stored at –20°C. Prior to each experiment, a fresh aliquot is used soon after thawing. These aliquots are never frozen again or reused because this causes a loss of efficacy. Bring up the pH of the PBS by adding a few drops of 6 *N* NaOH to PBS.

Fixation Protocol

1. Warm 100 mL of 80 m*M* Kpipes, pH 6.8, 5 m*M* EGTA, 2 m*M* $MgCl_2$ without Triton X-100 to 37°C in a beaker.
2. Pour off the media in the apical well of the Costar filter. Dip the entire filter plus filter holder into this modified 80 m*M* Kpipes buffer for 5 s.
3. Transfer the filter to the 6-well plate supplied with the polycarbonate filters to permit convenient fixation and washing steps.
4. Fix the cells for 10 min with 0.3% glutaraldehyde +0.1% Triton X-100 at room temperature. The glutaraldehyde fixative is added to both the apical (2 mL) and basal (3 mL) portions of the filter. During all the incubation steps and washes, the 6-well plate is agitated on a rotary shaker.
5. During the fixation period, weigh out 3- to 10-mg aliquots of fresh $NaBH_4$. The $NaBH_4$ powder is then stored in 50 mL sterilized conical tubes with screw caps. The $NaBH_4$ should be kept in an anhydrous state, preferably under dry nitrogen gas because it is a very strong reducing agent and, when combined with water, hydrogen gas is released. **Explosions in the laboratory setting have been reported so this agent should be used with care.**
6. Aspirate the fixative, and dip the entire filter successively in three separate 100 mL beakers containing PBS–.
7. Add PBS–, pH 8.0 to the $NaBH_4$ to make a final concentration of 1 mg/mL. Add 3 mL of this solution to the apical portion of the cell and 4 mL to the basal chamber. Incubate 15 min at room temperature. You should see gas bubbles in the solution during this step. Repeat this step two more times using freshly dissolved $NaBH_4$. The adjustment of the pH to 8.0 increases the half-life of $NaBH_4$ in solution. This step is essential to decrease the autofluorescence of the glutaraldehyde-fixed cells.
8. Wash the cells with PBS– by dipping the preparation in three beakers containing PBS–. Return the filters to the 6-well plate with PBS– bathing the apical and basal side. The filter is now ready for immunofluorescence staining.

pH Shift/Formaldehyde Fixation

The pH shift/formaldehyde method was first used for fixing rat brain, in which it showed excellent preservation of neuronal cells and intracellular compartments (Berod *et al.*, 1981). This technique applies the formaldehyde to the tissue twice: once at near physiological pH to halt metabolism, and then again at high pH, where the crosslinking action of the fixative is more effective.

Stock Solutions

- 40% formaldehyde (Merck) in H_2O.
- 80 m*M* Kpipes, pH 6.8, 5 m*M* EGTA, 2 m*M* $MgCl_2$.
- 100 m*M* NaB_4O_7 pH 11.0.
- Phosphate-buffered saline without Ca^{2+}/Mg^{2+} (PBS–) pH 8.0.
- Phosphate-buffered saline without Ca^{2+}/Mg^{2+} (PBS–) and both with and without 0.1 % Triton X-100.
- Premeasured 10-mg aliquots of dry $NaBH_4$.

Preparation of the Stock Solutions

Preparation of the formaldehyde stock solution is based on the description by Robertson and colleagues (1963). Forty grams of paraformaldehyde $(CH_2O)_n$; MW 30.3 is added to 100 mL of H_2O. While continuously stirring, the mixture is heated above to 70°C. A few drops of 6 *N* NaOH are added to dissolve the formaldehyde, but do not allow the solution to boil. The stock solution is divided into aliquots and stored at –20°C. Prior to use, aliquots are thawed by warming in a water bath. The formaldehyde is diluted to 2% to 4% in both the Kpipes and sodium borate buffers. For our purposes, a 3% solution of formaldehyde was adequate for preserv-

ing both the structure and antigenic determinants on a wide variety of cell organelles. The pH of the Kpipes buffer is brought to 6.5 with 1 *N* HCl after the formaldehyde has been added.

PBS–, pH 8.0 is made by adding a few drops of 6 *N* NaOH to normal PBS, made without calcium or magnesium; 100 m*M* NaB_4O_7 is titrated to pH 11.0 by adding 6 *N* NaOH to the buffer.

Fixation Protocol

1. Pour off the media in the apical well of the filter.
2. Dip the filters in 80 m*M* Kpipes solution pre-warmed to 37°C.
3. Add 3 mL of 3.0% formaldehyde in the 80 m*M* Kpipes solution to the basal chamber of the 6-well dish, and add 2 mL of this solution to the apical surface of the cells. Incubate the cells with agitation on a rotary table for 5 min at room temperature.
4. Aspirate the formaldehyde/Kpipes solution; then add 3 mL of 3% formaldehyde in 100 m*M* NaB_4O_7, pH 11.0, to the basal side and 2 mL to the apical side of each filter. Incubate with agitation on a rotary table for 10 min at room temperature.
5. Weigh out two 10-mg aliquots of $NaBH_4$ for each filter and store in a conical tube with a screw cap.
6. Aspirate the fixation solution. Wash the filters by successively dipping the filters in three beakers containing 100 mL of PBS–.
7. Dissolve each aliquot of $NaBH_4$ in 10 mL PBS–, pH 8.0 (final concentration of $NaBH_4$ should be 1 mg/mL). Vortex the solution briefly, and add it to the apical (2 mL) and basal (3 mL) portions of the filters. Incubate 15 min while shaking the filters on a rotary table. Repeat this step one more time using a fresh solution of $NaBH_4$ in PBS–, pH 8.0.
8. Wash the filters by successively dipping the filters in three beakers containing 100 mL of PBS–. The filters can be stored overnight at 4°C with PBS–/0.1% NaN_3.
9. The sample is permeabilized by washing with PBS (–) + 0.1% Triton X-100.

Immunofluorescence Staining

1. Cut the filter from its plastic holder. Be sure to note which side of the filter has the cells layered on it! Cut the filter into four squares using a sharp scalpel while keeping it wet with PBS. To ensure that the cell side of the filter can be readily identified, we routinely cut a slit in the upper right corner of the filter. The filter is cut into squares because this tends to give a flat field of cells after the filter has been mounted. Dividing a filter into quadrants with one rounded edge causes the filter to ripple during mounting.
2. Wash the filter squares in PBS– containing 0.2% fish skin gelatin (FSG), which is used as a carrier protein instead of albumin in this protocol (Sigma, St. Louis, MO) and the appropriate percentage of detergent. The amount of detergent must be determined empirically. Usually 0.1% to 0.3% Triton X-100 will suffice. Wash the filter squares in a 6-well plate. All washes are done in 4 mL of solution, at room temperature, with agitation. Unless otherwise stated, the filters are washed for 15 min after every change of washing buffer.
3. Place a 50 µL drop of the first antibody diluted in PBS– containing 0.2% FSG on a piece of parafilm on the bottom of a petri dish.
4. Place a filter square, cell-side down, on the antibody solution. Place a piece of wet Whatman filter paper in the petri dish, well away from the antibody solution and then cover to form a small, humidified chamber.
5. Incubate at 37°C for 1 h (for specimens that are <10 µm thick, 35 min is an adequate incubation time).
6. Wash the filter twice with PBS– containing 0.2% FSG. Follow this with three successive washes with PBS–.
7. Wash the filter once more with PBS– containing 0.2% FSG.
8. Add the second antibody as described for the first antibody.
9. Incubate at 37°C for 1 h.
10. Wash the filters in PBS– containing 0.2% FSG twice.
11. Wash three times in PBS–.
12. Incubate once in PBS containing 0.2% Triton X-100 for 5 min.
13. Wash twice in PBS– for 5 min each time.

The filter squares are ready for mounting.

Mounting the Specimen

Place four drops of clear acrylic nail polish on a microscope slide to make corner supports for a coverslip. Each drop should be at a point corresponding to the corner of a coverslip. We use 22 × 22 mm 1.5 coverslips. Place the filter square in the center of the area demarcated by the nail polish. Take care to ensure that the cells are facing up. Put a drop of 50% glycerol / 50%PBS / 0.1%NaN_3 / 100 mg/mL DABCO (1,4-diazabicyclo [2.2.2.] octane; Sigma) on the filter. Carefully place the coverslip over the filter. Avoid trapping air bubbles in the specimen mount and make sure that the corners lie on the drops of polish. Aspirate the excess glycerol medium. Put four drops of nail polish on the four corners of the coverslip to stabilize the mount. Alternatively, shards of broken coverslips can be used as coverslip supports. Once the nail polish on the corners has dried, the entire mount can be sealed with nail polish. The specimen should be viewed within 24 h because these are not permanent mounts.

Semi-permanent samples can be made by post-fixing the filter in 4% formaldehyde dissolved in 100 m*M* Na cacodylate, pH 7.5, for 30 min at room temperature followed by quenching with 50 m*M* NH_4Cl in PBS for 15 min. Post-fixed samples can maintain excellent labeling characteristics for over 6 months when stored at 4°C or at –20°C. Figure 18.4 shows the unfortunate result of an improper mounting method. In this case, the coverslip was not adequately supported because the acrylic nail polish posts were set too far apart: clearly, attention to the details can determine the success or failure of specimen preparation.

CRITICAL EVALUATION OF LIGHT MICROSCOPY FIXATION AND MOUNTING METHODS

Immunofluorescence labeling methods have been widely employed in cell biology (Osborn *et al.*, 1980; Osborn and Weber, 1982). The major concerns when using these methods to study cell morphology have been to preserve the antigenic and structural integrity of the specimen. In general, the goal is to immobilize the antigen quickly, while preserving the cell's organization. All too frequently, the best preservation methods destroy the epitopes required for antibody binding. Because this is a particular problem with glutaraldehyde (Nakane, 1975; Cande *et al.*, 1977; Weber *et al.*, 1978), formaldehyde is often used as a fixative despite its poorer preservation.

Our initial attempts to use the "classical" fixation and mounting methods for normal epi-fluorescence microscopy yielded images that were markedly deformed in the third dimension. It became apparent that these methods had been specifically designed to shrink the cells flat to the coverslip in order to reduce the out-of-focus light in standard epi-fluorescence images. To avoid this, it became necessary to meld some of the fixation methods devel-

oped for EM with the techniques of classic immunofluorescence. This meant that, in addition to the requirements for structural and antigenic preservation, the 3D spatial preservation had to be considered as well. This matter has also been a concern for workers using scanning EM and those doing stereographic analysis of TEM images. Because samples being prepared for immunofluorescence microscopy do not have to be dried, the major concern we had was shrinkage induced by fixation or dehydration. This problem has been examined by several workers (Tooze, 1964; Boyde and Maconnachie, 1979, 1981; Lee *et al.*, 1979, 1982; Wangensteen *et al.*, 1981; Lee, 1984). Glutaraldehyde fixation has been found to induce cell shrinkage when hypertonic buffers are used. Additionally, Lee has shown that the total osmolarity of the fixative and the type of buffer used determine the extent of gross specimen shrinkage (Lee *et al.*, 1982; Lee, 1984). These findings have important implications for the preparation of tissue samples for two-photon microscopy where thicker tissue sections can be imaged.

Other fixation procedures can also affect the degree of cell shrinkage. For example, osmium tetroxide fixation causes a variable degree of volume shrinkage in erythrocytes. It has been suggested that the amount of shrinkage induced by this fixative depends on the interplay between the electrostatic interactions between charged protein particles and osmotic forces (Tooze, 1964). A recent review and study on the effect of formaldehyde fixation on cell volume found that rat liver strips shrank in length by only 3% when fixed at room temperature. The liver strips were immersed in fixative and observed by video microscopy, but the assessment of shrinkage was only measured in the length dimension. Raising the temperature to 39°C diminished the amount of shrinkage observed (Fox *et al.*, 1985). It was also noted that, in general, increasing the concentration of formaldehyde paradoxically seemed to cause swelling of the sample. This effect has not been satisfactorily explained but has been noted by other investigators (Bradbury and Meek, 1960). The shrinkage is due to the extremely high total osmolality of fixative solutions containing formaldehyde. It should be noted that a 3% solution of paraformaldehyde has a far higher osmolality (approximately 1000 mOsm) than that of a 3% solution of glutaraldehyde (300 mOsm) because of the large difference in their molecular weights (Fox *et al.*, 1985). The buffer should be optimized to be isotonic with the specimen when paraformaldehyde is used.

Our overall approach to resolve these conflicting requirements reflected a bias toward immunofluorescence studies. We started with fixation methods that still preserved the epitope binding sites for our antibody label and then tried modifications designed to be freely transferred from one system to another. An example of this occurred when the paraformaldehyde/pH shift fixation protocol was adopted to study microtubule/kinetochore interactions during mitosis in newt lung epithelial cells. While the microtubules were well preserved, it was found by differential interference contrast (DIC)–video microscopy that the chromosomes continued to move during the low-pH incubation step (A. Merdes, unpublished observations). This indicated that the cells were not immediately immobilized by the first step of the fixation and, as a result, this method was not useful for these cells in this particular study. This example points out the advantage of observing the specimen under phase contrast or DIC during fixation to detect potential artifacts.

Use of the Cell Height to Evaluate the Fixation Method

In order to generate 3D images that accurately reflect *in vivo* cellular architecture, it was necessary to employ fixation methods that minimize cell shrinkage or distortion. To study this issue, we took advantage of the ability of the fluorescent lipid analog C6-NBD-ceramide to label the plasma membrane *in vivo* (Lipsky and Pagano, 1985). The plasma membrane of MDCK cells, grown to confluence on filter supports, was labeled as described by van Meer and colleagues (1987). The height of the living cells was determined from randomly selected vertical sections using confocal *xz*-images (Fig. 18.1). The samples were then fixed and stained with probes that recognized either actin filaments or microtubules, using procedures described previously. Actin staining and microtubule staining were used as markers for the cell height in the fixed cells because these networks lie close to the plasma membrane. Furthermore, the preservation of the cytoskeletal network is particularly sensitive to fixation methodology. The mean height of the fixed cells was then determined again at randomly selected sites and the results from the two groups (fixed vs. *in vivo* cells) were analyzed by Student's *t* test. Figure 18.1(A) shows the plasma membrane labeling observed in cells labeled *in vivo* with C6-NDB-ceramide and Figure 18.1(B) shows immunofluorescence labeling of another part of the same sample after glutaraldehyde fixation. Both samples were mounted in PBS. The height and shape of both samples are quite similar. We observed that the shape of the apical dome was very sensitive to fixation artifacts and that glutaraldehyde fixation, with or without Triton X-100 in the buffer, preserved

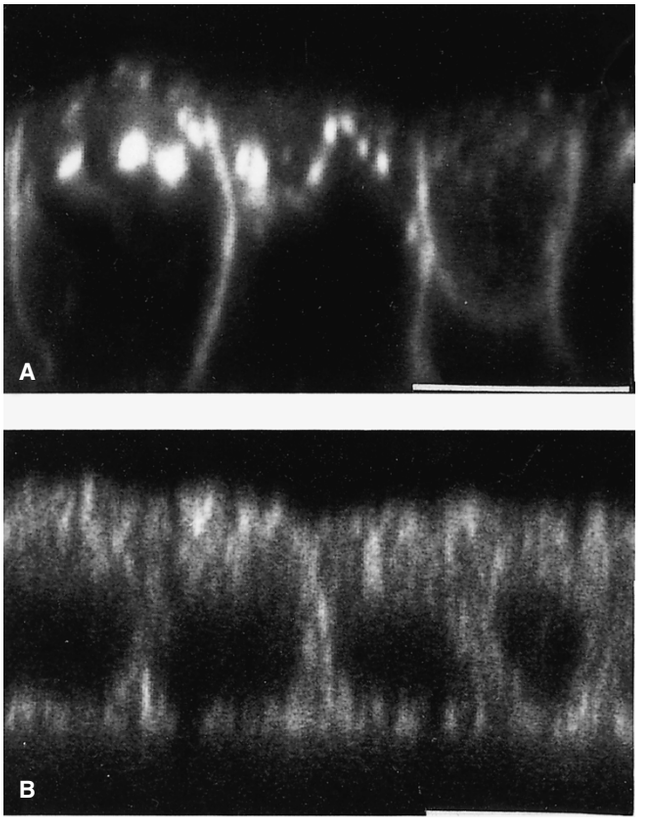


FIGURE 18.1. Vertical optical sections of MDCK cells. MDCK cells were plated on polycarbonate filters and grown for 5 days in culture. The cells have formed a columnar epithelium of fairly uniform height. (A) C6-NBD-ceramide labeling of the plasma membrane. Note the curved appearance of the apical plasma membrane. (B) Microtubule staining in glutaraldehyde-fixed cells. Note that the cell height and apical membrane curvature are roughly comparable. Bar = 10 μm.

the cell height most accurately with very little shrinkage detected as long as the buffer was isotonic.

Less than 5% increase in the cell height was caused by pH shift/formaldehyde fixation. We consider this degree of distortion acceptable in some well-defined situations. However, fixation with paraformaldehyde alone had a paradoxical effect on cell size noted above when the pH shift method was not used. Higher concentrations of paraformaldehyde (4%) dissolved in low-ionic-strength buffers were less likely to cause cell swelling. Lower concentrations of paraformaldehyde in hyperosmotic buffers either showed no change in cell size or caused shrinkage. It became apparent that no single buffer yielded optimal fixation when paraformaldehyde was used as a fixative.

Figure 18.2 shows stereo images of isolated cells fixed with methanol and then the formaldehyde/pH shift method. The methanol has caused a flattening of the area overlying the nucleus and a 10% to 20% decrease in cell height. Whenever methanol was used on confluent cells as either a fixative or as a permeabilization agent, it caused a 20% to 50% decrease in cell height. We consider it inappropriate to use this agent on samples prepared for 3D examination in a confocal fluorescence microscope.

Use of Cell Height to Evaluate Mounting Media

Shrinkage is often associated with removing biological structures from the aqueous environment and placing them in less polar solvents having a lower dielectric constant (Boyde and Maconnachie, 1979, 1981). Confocal *xz*-images were also employed to evaluate the effects of different mounting methods and mounting media. However, as all such media have different indices of refraction (η) and as the apparent specimen height measured in this way is only accurate if the specimen is immersed in a medium having the η for which the objective is corrected (see Chapter 20, *this volume*; Hell *et al.*, 1993), these measurements should be considered more comparative than quantitative.

Gross distortion is produced if the coverslip touches the specimen (Fig. 18.4). To avoid this, we suspended the coverslip using four posts of nail polish as mentioned above.

The best mounting media was found to be 50% glycerol in PBS, which showed no detectable shrinkage in fixed specimens compared to *in vivo* labeled cells. Mowoil and Gelvatol caused a 10% decrease in cell height in glutaraldehyde-fixed cells. This amount of shrinkage was considered to be significant because the apical domes, seen *in vivo*, in polarized MDCK cells were completely flattened by these mounting agents. The mounting media appeared to have an even greater effect on the shape of formaldehyde-fixed cells, probably due to the lower degree of crosslinking in formaldehyde-fixed specimens.

Well-Defined Structures Can Be Used to Evaluate Fixation Methods

A second method used to evaluate fixation was to examine structures that have a well-defined morphology. Because we had an interest in microtubule organization in epithelial cells, we examined the preservation of mitotic spindles in our sample preparations. Changes in the natural symmetry of the mitotic spindle, due

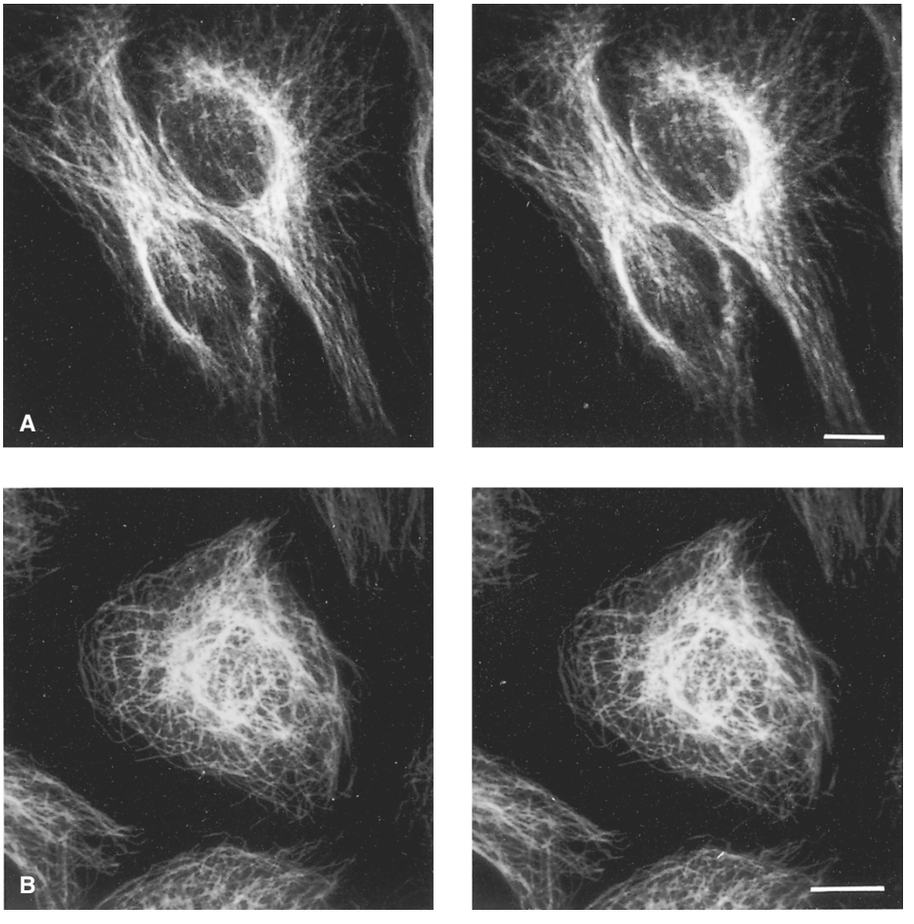


FIGURE 18.2. Stereo image of isolated MDCK cells. MDCK cells were plated at a low density, one day prior to fixation and staining. This image was reconstructed from a series of optical sections taken in the *x-y* plane from consecutive "*z*"-positions, 0.4 µm apart. No other image processing was performed. Each field is made up of 512 × 512 pixels. The image is the average of four scans per line. (A) Microtubule staining in methanol-fixed cells. Note the flattening over the nuclear region. The distance from the top of the cell to bottom is 4.1 µm. (B) Microtubule staining in cells fixed with the formaldehyde/pH-shift method. No flattening is noted and the microtubules are well preserved. The distance from the top of the cell to the bottom is 4.5 µm. Bar = 10 µm.

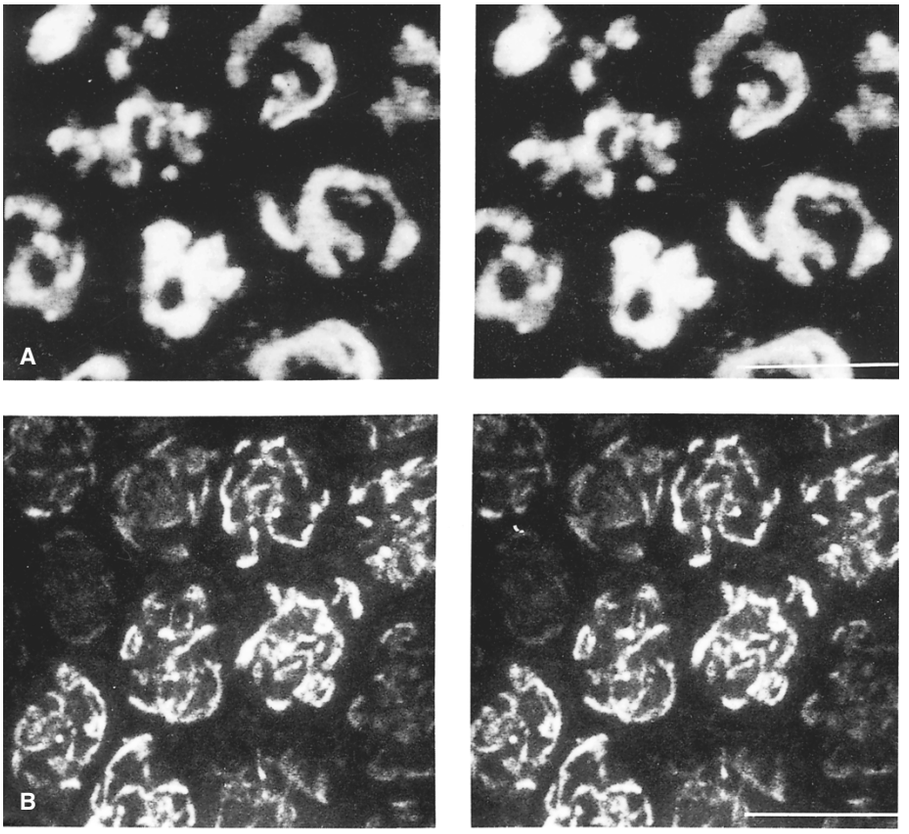


FIGURE 18.3. (A) Stereo images of the Golgi apparatus in confluent MDCK cells labeled *in vivo* with C6-NBD-ceramide made under the same conditions as Figure 18.2. Note the convoluted morphology. The distance from the top of the Golgi to the bottom is 6.4 μm. (B) Stereo images of the Golgi apparatus in confluent MDCK cells labeled by a monoclonal antibody. Cells were fixed by the formaldehyde/pH-shift method described in this chapter. Note that the overall morphology is similar to the ceramide labeled morphology. The image was generated as described above. Bar = 10 μm.

to fixation or mounting artifacts, were easily detected. Breaks in the microtubules or shortening of those within the spindle could be seen readily, and such changes were used to disqualify some fixation methods.

In general, formaldehyde fixation yielded poorly preserved microtubules, however, the formaldehyde/pH shift fixation method gave acceptable microtubule preservation of the mitotic spindles. When compared directly with glutaraldehyde fixed cells, the formaldehyde/pH shift method was not so good, but it was an acceptable compromise. In direct comparisons, the staining of formaldehyde/pH shift–fixed specimens was slightly lower in intensity than that in specimens fixed with formaldehyde alone. However, we found it was useful for double-immunofluorescence labeling with antigenic epitopes that were destroyed by glutaraldehyde fixation. The periodate–lysine–formaldehyde fixation described by McLean and Nakane (1974) did not preserve mitotic spindles well.

Comparison of *In Vivo* Labeled Cell Organelles with Immunolabeled Cell Organelles

Sometimes membrane structures can be distorted even though the fixation method does not affect cell height. As noted above, light microscopic observation of cell nuclei during fixation with formaldehyde revealed marked changes in nuclear size and shape during the pH 6.5 step of the fixation that showed it was unsuitable for the examination of nuclear membrane antigens, at least at this tonicity.

The use of vital fluorescent dyes such as rhodamine 123,3,3′-dihexyloxacarbo-cyanine (DiOC6) and C6-NBD-ceramide permits comparison of the effects of subsequent fixation on the morphology of the mitochondria, rough endoplasmic reticulum (RER), and Golgi apparatus, respectively (Walsh *et al.*, 1979; Terasaki *et al.*, 1984; Lipsky and Pagano, 1985; see Chapter 19, *this volume*).

MDCK cells undergo striking changes in the morphology of their Golgi apparatus during the formation of a polarized epithelium (Bacallao *et al.*, 1989). The morphology in the final polarized state was examined *in vivo* using the fluorescent lipid analog, C6-NBD-ceramide. The morphology seen *in vivo* was very similar to that in samples fixed and stained using a Golgi-specific monoclonal antibody generously supplied by Dr. M. Bornens (Fig. 18.3) and to that seen in non-ciliated epithelial cells, as determined by an analysis of thick sections viewed at low magnification in the high-voltage electron microscope (HVEM) (Rambourg *et al.*, 1989). Both glutaraldehyde fixation, and the pH shift/formaldehyde fixation protocol, preserved the morphology of the Golgi apparatus well.

GENERAL NOTES

The repeated use of borohydride in these fixation protocols was found to decrease endogenous cellular fluorescence significantly. Other quenching agents, such as ammonium chloride and lysine, were also tried, but borohydride worked best. This was a crucial obstacle to overcome in our work because our specimens had high cell densities when the MDCK cells grew to confluence on mem-

brane filter supports. Initially, high endogenous background fluorescence caused our images to have poor contrast, obscuring important details.

These fixation methods also work well with thinner cells grown on coverslips, but some shortening of the fixation time is necessary. Typically, a 4-min fixation in the pH 6.5 buffer and an 8-min fixation in the pH 11.0 buffer worked well with glass-grown cells. Although in some tissues there is a tendency for formaldehyde to induce vesiculation of cell membranes, this artifact was not observed in all tissues.

Both saponin and Triton X-100 have been used as permeabilization agents in the formaldehyde fixation method. Triton X-100 has been most effective when used after the fixation was complete, while saponin worked best when included with the borate buffer. NP-40 worked very well for specimens in which the microtubules were stained with monoclonal antibodies to α and β tubulin.

We have used DABCO at a concentration of 100 mg/mL as an antibleaching agent (Langanger *et al.*, 1983). Yellowing of the specimen occurs 1 month after mounting when DABCO is included with the mounting media, but this does not seem to produce a significant change in the images produced from such samples. A recent paper suggested that 5 *M* NaN_3 is a better antibleaching agent than DABCO (Bock *et al.*, 1985), however, in our experience, we found the reverse (Merdes *et al.*, 1991). *n*-Propylgallate has been tried as an antibleaching agent but in our hands it caused a dimming of the fluorescent signal. We did not use *p*-phenylenediamine as an antibleaching agent because this agent destroys the sample over time (Langanger *et al.*, 1983). Some investigators have tried to make mixtures of antibleaching agents such as 5% *n*-propylgallate-0.0025% *p*-phenylenediamine dissolved in glycerol. Another mixture suggested by Peter Hahn (Thomas Jefferson University, Philadelphia, PA) is a 0.25% *p*-phenylenediamine, 0.0025% DABCO, 5% *n*-propylgallate dissolved in glycerol with a pH value of approximately 7.6. These investigators did note some increase in background signal, however (see also Chapter 39, *this volume*).

The pH of the mounting media can be an important parameter to consider, especially when fluorescein is used as a fluorophore. The fluorescent emission of fluorescein conjugates increases up to pH 10. For additional insights on the effect of pH on fluorescent compounds, the readers are referred elsewhere (Hiramoto *et al.*, 1964; Klugerman, 1965).

Labeling Samples with Two or More Probes

One of the unique aspects of 3D imaging is that it gives one the power to determine spatial relationships. However, this can also pose problems if one can see only the stained structure. For example, in our early work using C6-NBD-ceramide to study the Golgi morphology, we found ourselves dissatisfied with the images. One frequently wanted to know where the Golgi apparatus was located with reference to other cellular structures (see Fig. 18.3). Sometimes a reference image can be provided by detecting and displaying the light scattered back by optical inhomogeneities in the specimen. This signal can be obtained without interfering with the collection of the fluorescence signal (Pawley *et al.*, 1993; Chapter 2, *this volume*) but, as doing so requires equipment that is only now becoming generally available, it has been more common to image other cellular structures using a second fluorescent dye.

Our early attempts to label these structures simultaneously led to unforeseen difficulties. The first major pitfall was the finding that fluoroscein isothiocyanate (FITC) and rhodamine could not be used simultaneously in combination with the filter sets then available to us. Although the cutoff filters were supposed to eliminate signals above 530 nm, we were unable to separate cleanly the FITC image from the rhodamine image. This was due in part to the fact that the confocal microscope we used had an argon-ion laser with lines at 528.7 and 476.5 nm, so even when the 528.7 line is used, FITC is still slightly excited and the cutoff filters cannot completely eliminate the FITC signal. At the shorter wavelength, we experienced problems with fluorescence energy transfer because the light emitted from the FITC was exciting the rhodamine. This problem was partially overcome by combining FITC with Texas Red for double-labeling experiments. Each of the two laser wavelengths was used to excite a single fluorophore, but using 528.7 nm excitation, a higher cutoff filter (580 nm) could then be used to block out the FITC signal. There were no detectable problems with fluorescence energy transfer with this combination; however, it did present another difficulty. Although the laser we used has lines available at 528.7 and 476.5 nm, the power at these wavelengths varies markedly with time and temperature, and, in addition, if a double dichroic is not used (Chapter 9, *this volume*), changing the filters to select a different wavelength can produce mis-registration between the two images. Both of these situations can produce sets of images that are not matched in intensity, and the detector gain must be adjusted to "normalize" them.

Another useful combination was Lucifer Yellow and Texas Red, which were used to study the endocytic compartments in filter-grown MDCK cells *in vivo*.

Using a krypton–argon laser, which has lines at 488 nm and 567 nm, has reduced difficulties with bleed-through. The 567 nm line is closer to the excitation maximum of Texas Red and, with the proper configuration of cutoff filters, allows the user to label specimens with FITC and Texas Red (see Chapters 16 and 36, *this volume*).

We have successfully double-labeled specimens with FITC and rhodamine/Texas Red using a helium–argon (He-Ar) laser. One of the cellular components is labeled with two secondary antibodies having the same antigenic specificity. The secondary antibody mixture contains a 1 : 4 molar ratio of rhodamine/Texas Red conjugated antibodies. We found that there was no bleed-through when the FITC signal was imaged. However, using the 514 nm line gave an excellent signal from the rhodamine/Texas Red mixture (Bacallao and Garfinkel, 1994).

Some consideration must be given prior to the experiment as to what structures will be labeled with which fluorophore. In our experience, perhaps because of the higher quantum efficiency of the detector or the lower diffraction limit, FITC appears to give images with better contrast than does Texas Red, so structures with fine detail (e.g., microtubules) tend to yield a better image when stained with FITC (Fig. 18.4). In samples that have been labeled with both FITC and Texas Red, the FITC image must be obtained first, followed by the Texas Red image, because FITC bleaches rapidly even with antibleaching agents present. Most microscopes now permit the simultaneous acquisition of images produced by these fluorophores (Chapters 2 and 9, *this volume*).

Triple Labeling

One promising method for triple labeling involves the use of immunogold, silver-enhancement labeling techniques (Lackie *et al.*, 1985; Scopsi and Larsson, 1985; Bastholm *et al.*, 1986; Birrell and Hedbert, 1987; Danscher *et al.*, 1987). This labeling method has been used successfully to stain cell adhesion plaques (Paddock, 1989, 2002).

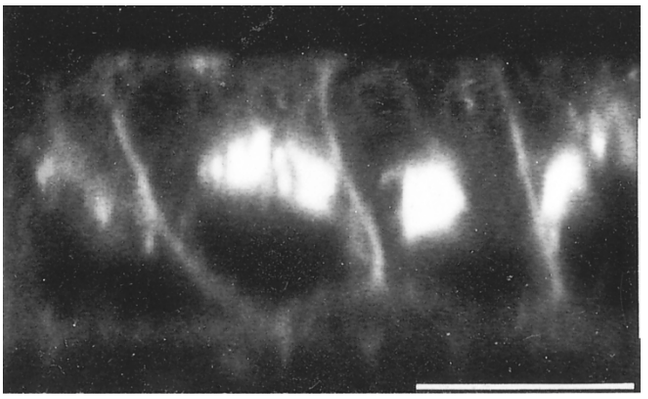


FIGURE 18.4. Deformation of a sample due to improper mounting. A confluent monolayer of MDCK cells was labeled *in vivo* with C6-NBD-ceramide. The coverslip was placed on the acrylic spacing mounts incorrectly. The apical surface has been completely flattened. The basolateral membranes are no longer vertical probably due to shearing. Bar = 10 µm.

A third label can be added to a double-labeled fluorescent sample using gold-conjugated antibodies, which can be imaged in the backscattered light mode (Pawley *et al.*, 1993; Linares-Cruz *et al.*, 1994). Image-processing techniques should allow one to overlay all three images. Once again, the cellular structures to be studied should be matched with the particular labeling method employed. In our initial attempts to study mitotic spindles using immunogold labels, the gold was so dense that it acted as a mirror, preventing us from obtaining an image below the upper half of the spindle.

We have routinely used three or more fluorescent probes on single samples to image various intracellular compartments using the Zeiss 510 confocal microscope equipped with an Enterprise laser (Spectra Physics, Mountain View, CA), two helium–neon (He-Ne) lasers and a Kr-Ar laser. Laser lines at 353 nm, 383 nm, 488 nm, 512 nm, 563 nm, and 650 nm are available for imaging. Appropriate emission filter sets are available on this system that make four-color fluorescence imaging routine. We have found it to be particularly useful to routinely label nuclear compartments with DAPI or Hoescht 3314. Computer programs designed to measure the extent of co-localization between two or more labeled marker proteins give correlations greater than 0.5 for any two markers, even if there is no visual evidence for co-localization. This is because the nucleus comprises approximately 50% of total cell volume, so any cytoplasmic protein excluded from the nucleus is automatically constrained to the other 50% of the total volume. By routinely labeling the nuclear compartment, we can make masks that remove the nucleus from the analyzed volumes to obtain realistic correlation coefficients. A computer program that give percentage of co-localization and correlation coefficients is under development and is called CORR3D (Christopher Constantine, manuscript in preparation). It will be available as shareware at http://www.nephrology.iupui.edu.

Preparation of Tissue Specimens

Preparation of tissues for examination by confocal microscopy is complicated by problems of fixative penetration, the heterogeneous cellular composition of tissues, and the presence of the extracellular matrix. Tissue slices are fixed by two general approaches: immersion and perfusion. With immersion fixation, the tissue is dissected, cut into small pieces, and immersed in the fixation solution. The dissection must be performed carefully in order to avoid damaging the specimen. Penetration of the fixative is dependent on the thickness of the specimen and the type of fixative (formaldehyde penetrates faster). During immersion fixation, cells are exposed to anaerobic conditions; a gradient of fixative concentration means that deeper regions are often fixed less well than superficial regions.

Fixation of tissues by perfusion is preferable in most examples because the fixative reaches all of the tissue more rapidly (Ericsson and Biberfeld, 1967; Fahimi, 1967; Petersen, 1977; Nowell and Pawley, 1980), and the cells are less likely to develop anoxic damage (Rostgaard *et al.*, 1993). The perfusion pressure must be carefully controlled because otherwise this can be a source of tissue damage. A recommended list of organ-specific perfusion pressures has been reported by Hayat (1989). We have used either diluted Karnovsky's fixative or paraformaldehyde fixative with a perfusion pump to fix kidneys with satisfactory morphological preservation. The osmolality of the paraformaldehyde fixation buffer must be optimized depending on the region of the renal tubule one wishes to study (Hayat, 1989).

Preparing tissue for confocal microscopy brings separate concerns. Because excitation wavelengths are shifted toward infrared, it is possible to image deeper into tissue (Brakenhoff *et al.*, 1996; Soeller and Cannell, 1996). We routinely image 100 µm thick vibratome sections labeled with a variety of antibodies and fluorescent-tagged lectins. The preparation method for labeling thick sections is provided here.

Labeling Thick Sections

1. **Perfuse-fix** anesthesized mice with 4% paraformaldehyde (PFA) (made in 1× PBS). Flush ice cold 1× PBS through vasculature via left ventricle before PFA perfusion.
2. **Cut** vibratome sections of kidneys (50–200 µm thickness).
3. **Wash** sections at room temperature, 2 to 4 h, in 1× PBS (vigorously on orbital shaker/rocker). We use 14 mL in a 15 mL Falcon tube (air bubble helps with agitation). Carefully transfer wet sections with soft bristle brush or one tip of forceps — don't squeeze tissue!
4. **Block**: incubate tissue sections in ~200 µL blocking buffer — sections should be in small PCR tubes (blocking buffer is 0.1% to 1% Triton X-100*, 1% to 2% BSA, 1× PBS, make fresh). Put back on rotator/shaker for 1 to 2 h.
5. Add **primary antibody** diluted in blocking buffer (we use 200 µL total volume in small PCR tubes) — place labeled tubes in dry 50 mL Falcon tube and rotate overnight on rotator/rocker 4°C (or 4+h at room temperature, depending on thickness of sections).
6. Next morning repeat **wash** (see step 3).
7. Incubate in fluorescent-labeled** **secondary antibody** diluted in blocking buffer (same conditions as step 5 above). Also good time to add fluorescent-labeled lectins (e.g., from Vector labs, usually around 1 : 200 dilution), DAPI*** or phalloidin. Put PCR tubes in dry, foil-wrapped 50 mL Falcon tube (protect from light), place on rocker in 4°C refrigerator, overnight. Lectins that work well in mouse tissues:
   A. peanut agglutinin-rhodamine (PNA) proximal tubules and collecting ducts
   B. lotus tetragonolobus-fluorescein (LTG) proximal tubules
   C. dolichos biflorus-rhodamine (DBA) collecting ducts
   D. lens culinaris agglutin (LCA) GBM, mesangial matrix
8. Next morning **wash** sections in 1× PBS (in 15 mL blue cap tubes), 2 to 4 hours or overnight.

9. Transfer to round base of clean coverslip dishes in preparation for imaging (pre-measure coverslip thickness with micrometer). Keep wet in PBS. To prevent tissue from floating around, you may need to stabilize (not squish! with a cap of cooled agarose or a second coverslip (square or round). Avoid air bubbles!
10. Adjust microscope objective collar to match coverslip thickness.
11. Capture *z*-stacks at 0.4 µm intervals with 60× water-immersion objective.
12. Render 3D image with Voxx or other 3D reconstruction software packages.

Important Points

- *1% is better than 0.1% Triton X-100.
- **Better depth of imaging is achieved with Rhodamine as the label for the fluorescent probe than fluorescein.
- ***DAPI can be added 5 min before imaging (must be washed).

Refractive Index Mismatch

Unfortunately, the imaging of thick sections is often hampered by η mismatch, which can lead to a significant loss of both resolution and signal intensity. The problem becomes serious when one sections more than 10 µm into an aqueous specimen while using a high numerical aperture (NA) oil objective (Hell *et al.*, 1993). The problem can be solved by using objective lenses designed for water immersion together with coverslips with lower η such as CYTOP, which has η = 1.34 (compared to η = 1.33 for water) and 95% transmittance in the range of visible light (developed by Asahi Glass, Yokohama, Japan). Water-immersion objectives that are designed to work without glass coverslips can take advantage of this new material.

Another solution to the RI problem is to mount the specimen in a media that matches both the refractive index of immersion oil and that of a standard coverslip. Mounting media with η = 1.518 can be made from mixtures of glycerol, borate, and potassium iodide (W. McCrone, personal communication). Mounting media with a range of refractive indexes can be bought from R.P. Cargille Labs (NJ) or McCrone Accessories and Components (Westmont, IL).

Table 18.1 lists values of η measured with a Bausch and Lomb, Abbe 3-L refractometer by Dr. M. Wessendorf (University of Minnesota, St. Paul, MN) and Dr. Y. Prakesh (Mayo Clinic, Rochester, MN) for a number of commercially available mounting media. Table 18.2 lists the refractive index of commonly imaged tissues (Biswas and Gupta, 2002).

TABLE 18.1. Refractive Index of Common Mounting Media

Mounting Media	Refractive Index[a]
Gel/mount (Biomeda)	1.3641
Methyl salicylate (Sigma)	1.5409
Dimethyl sulfoxide (Sigma)	1.4836
VectaShield (Vector Labs)	1.4577
DPX (Fluka)	1.5251
50% glycerol/PBS/DABCO	1.4159
Water	1.3381
Cargille index of refraction liquids	1.460–1.700[b]
5% *n*-propyl gallate/0.0025% *p*-phenylene gallate (PPD) dissolved in glycerol	1.4739
0.25% PPD, 0.0025% DABCO, 5% n-propyl gallate dissolved in glycerol	1.4732

[a] Corrected to 20°C.
[b] Can be ordered as a set of liquids with refractive index intervals between each samples as low as 0.002.

TABLE 18.2. Refractive Index of Different Tissue and Organs

Organ/Tissue	Refractive Index
Spleen	1.443 + 0.002
Liver	1.448 + 0.002
Kidney	
Cortex	1.444 + 0.002
Medulla	1.438 + 0.002
Pancreas	1.435 + 0.002
Intestinal wall	1.436 + 0.002
Fat	1.472 + 0.002
Bone	1.556 + 0.002
Cartilage	1.492 + 0.002
Muscle	1.431 + 0.002
Lung	1.342 + 0.002
Gall bladder wall	1.350 + 0.002
Blood (uncoagulated)	
Serum	1.330
Formed elements	1.432 + 0.003
Coagulated blood	1.465 + 0.003
Gray matter	1.395 + 0.002
White matter	1.467 + 0.002
Cerebellum	1.470 + 0.002

From Biswas and Gaupta (2002).

Screening Antibodies on Glutaraldehyde-Fixed Specimens

In our experience, glutaraldehyde fixation best preserves the structural and spatial integrity of the cell. The main difficulty with glutaraldehyde fixation is the frequent loss of epitope antigenicity. However, there may be an alternative to formaldehyde fixation to avoid this problem. It is possible to screen monoclonal antibodies against antigens that had been fixed in glutaraldehyde. Frequently, clones are screened against samples fixed with methanol or formaldehyde, but then they are actually used on glutaraldehyde-fixed specimens. Clearly, this process may produce disappointing results. Better results should be obtained if only those monoclonal antibodies that bind to glutaraldehyde-fixed proteins are used for detailed structural studies.

Microwave Fixation

Microwave heating with and without chemical fixatives has been used for specimen preparation (Thoolen, 1990; Benhamou *et al.*, 1991; Jackson, 1991). The intense heat generated by microwave radiation directly coagulates the proteins and also accelerates chemical fixation. It is not clear what artifacts are created by this fixation method, but some denaturation of protein is to be expected, and there may be problems with reproducibility related to the precise location of the specimen in the chamber, etc. (Giberson and Demaree, 1995). Some investigators have combined chemical fixation with microwave treatment to accelerate the rate of chemical fixation with satisfactory tissue preservation (Jamur *et al.*, 1995; Sawitzky *et al.*, 1996). Clearly, further development of this fixation method might be productive.

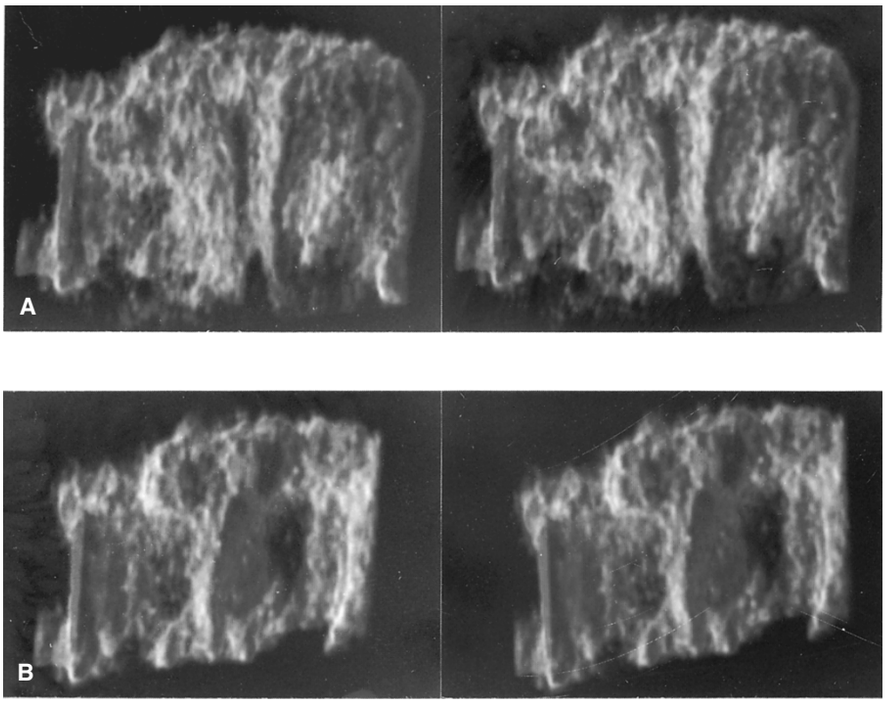


FIGURE 18.5. Stereo image of the actin cytoskeleton in MDCK cells. The cells were labeled with rhodamine phalloidin after fixation with glutaraldehyde. The image was reconstructed using Advanced Visualization Software (Stardent, CA) on a Kubota Pacific workstation. (Photo courtesy of A. Garfinkel and S. Monke.)

A review of the literature shows that the confocal microscope is often used only to produce 2D images and that its ability to generate data sets suitable for 3D reconstruction has been underused. Advances in image-processing and image-analysis techniques now provide the biologist with an array of quantitative 3D measurement tools (Chapters 14 and 15, *this volume*). Figure 18.5 shows such a reconstruction of the actin cytoskeleton of some MDCK cells grown on filter supports in which the images are cut-away views generated by the Advanced Visualization Software program (Stardent, CA) supported by a Kubota Pacific workstation (generously provided by A. Garfinkel and S. Monke, UCLA, Los Angeles, CA). By applying this computer analysis system to this type of data, one can determine the relative intensity values for every voxel in the image, calculate the volume of the actin network in the cell, and determine the volume that demonstrates more than some threshold level of staining as well as displaying a stereo image showing its 3D spatial distribution.

Two-photon microscopy is being used to study tissue morphology due to its ability to penetrate deep into tissue at infrared wavelengths. In our experience we routinely image up to 100 microns into tissue. For our preparations this has been the limit that an image can be acquired. However, we have not performed a rigorous assessment of fixation conditions versus imaging depth. It is possible that optimizing fixation conditions and matching the refractive index of the mounting media may increase the maximal depth of image acquisition. The optimal fluorophores have yet to be determined for imaging deep into tissues and it may be possible to obtain clearer images by measuring the point spread functions at various tissue depths to deconvolved confocal images obtained at greater depths.

It is important to remember that the accuracy of any three-dimensional reconstruction depends on the extent to which the specimen examined in the microscope retained the structural features it had *in vivo*.

CONCLUSION

In molecular cell biology, the microarchitecture of organisms is rapidly becoming a major subject for analysis. For example, the temporal sequence of morphogenetic changes readily observable in embryos makes an excellent system to test the effect of gene deletions, protein overproduction, and changes in transcriptional control on the development of an organism. The ability of the confocal microscope to render accurate, 3D images using immunofluorescence techniques means that it will be a major tool in the analysis of morphogenesis. To ensure that these 3D images carry real 3D information, it is important that whenever possible, structural morphology obtained by various preservation methods should be compared to that observed *in vivo*. In some cases, a compromise will have to be made with respect to fixation methods in order to preserve the antigenicity of a particular protein. These compromises should only be made if the *in vivo* data suggest that the compromise does not affect the relevance of the data. Only vigorous attention to the details of specimen preparation, and in particular, constant comparison between living and prepared specimens, can ensure that an accurate understanding of the 3D structure of the living cell is achieved.

REFERENCES

Abbott, E., 1884, *Flatland: A Romance of Many Dimensions*. London, Dover.

Abdella, P.M., Smith, P.K., and Royer, G.P., 1979, "A new cleavable reagent for crosslinking and reversible immobilization of proteins." *Biochem. Biophys. Res. Comm.* 87:734–42.

Bacallao, R., Dotti, C., Antony, C., Stelzer, E.H.K., Karsenti, E., and Simons, K., 1989, "Subcellular organization of MDCK cells during the formation of a polarized epithelium." *J. Cell Biol.* 109:2817–2832.

Bacallao, R., and Garfinkel, A., 1994, Volume reconstruction of confocal microscopic images: Practical considerations. *Three-Dimensional Confo-*

cal Microscopy: Volume Investigation of Biological Systems. J.K. Stevens, L.R. Mills and J.E. Trogadis. San Diego, Academic Press: 169–180.

Bacallao, R., and Stelzer, E.H.K., 1989, "Preservations of biological specimens for observation in a confocal fluorescence microscopy, operational principles of confocal fluorescence microscopy." *Methods Cell Biol.* 31:437–452.

Barrnett, R.J., Perney, D.P., and Hagstrom, P.E., 1964, "Additional new aldehyde fixatives for histochemistry and electron microscopy." *J. Histochem.* 12:36.

Baschong, W., Suetterlin, R., and Laeng, R.H., 2001, "Control of autofluorescence of archival formaldehyde-fixed, paraffin-embedded tissue in confocal laser scanning microscopy (CLSM)." *Journal of Histochemistry & Cytochemistry.* 49(12):1565–1572.

Bastholm, L., Scopsi, L., and Nielsen, M.H., 1986, "Silver-enhanced immunogold staining of semithin and ultrathin cryosections." *J. Electron Microsc. Technique* 4:175–176.

Benhamou, N., Noel, S., Greniere, J., and Asselin, A., 1991, "Microwave energy fixation of plant tissue: An alternative approach that provides excellent preservation of ultrastructure and antigenicity." *J. Electron Microsc. Technique* 17:81–94.

Berod A., Hartman, B.K., and Pujol, J.E., 1981, Importance of fixation in immunohistochemistry. *J. Histochem. Cytochem.* 29:844–850.

Birrell, G.B., and Hedbert, K.K., 1987, "Immunogold labeling with small gold particles: Silver enhancement provides increased detectablility at low magnifications." *J. Electron Microsc. Technique* 5:219–220.

Biswas, T.K., and Gupta, A.K., 2002, "Retrieval of True Color of the Internal Organ of CT Images and Attempt to Tissue Characterization by Refractive Index: Initial Experience." *Ind. J. Radiol. Imag.* 12:169–178.

Blanchette-Mackie, E.J., and Scow, R.O., 1981, "Lipolysis and lamellar structures in white adipose tissue of young rats: Lipid movement in membranes." *J. Ultrastuct. Res.* 77:295–318.

Bock, G., Hilchenbach, M., Schauenstein, K., and Wick, G., 1985, "Photometric analysis of anti-fading reagents for immunofluorescence with laser and conventional illumination sources." *J. Histochem. Cytochem.* 33:699–705.

Bomsel, M., Prydz, K., Parton, R.G., Gruenberg, J., and Simons, K., 1989, "Functional and topological organization of apical and basolateral endocytic pathways in MDCK cells." *J. Cell Biol.* 109:3243–3258.

Bowers, B., and Maser, M., 1988, Artifacts in fixation for transmission electronmicrosocopy. *Artifacts in Biological Electron Microscopy*. R.F.E. Crang and K.L. Klomparns. New York, Plenum Press: 13–41.

Boyde, A., and Maconnachie, E., 1979, "Volume changes during preparation of mouse embryonic tissue for scanning electron microscopy." *Scanning* 2:149–163.

Boyde, A., and Maconnachie, E., 1981, "Morphological correlations with dimensional change during SEM specimen preparation." *Scanning Electron Microsc.* 4:278–34.

Bradbury, S., and Meek, G.A., 1960, "A study of potassium permanganate 'fixation' for electron microscopy." *Q. J. Microsc. Sci.* 101:241–150.

Brakenhoff, G.J., Squier, J., Norris, T., Bliton, A.C., Wade, M.H., and Athey, B., 1996, "Real-time two-photon confocal microscopy using a femtosecond, amplified Ti:sapphire system." *Journal of Microscopy.* 181(Pt 3): 253–259.

Cande, W.Z., Lazarides, E., and McIntosh, J.R., 1977, "Composition and distribution of actin and tubulin in mammalian mitotic spindle as seen by indirect immunofluorescence." *J. Cell Biol.* 72:552–567.

Clendenon, J.L., Phillips, C.L., Sandoval, R.M., Fang, S., and Dunn, K.W., 2002, "Voxx: a PC-based, near real-time volume rendering system for biological microscopy." *Am. J. Physiol. Cell Physiol.* 282:C213–C218.

Dabora, S.L., and Sheetz, M.P., 1988, "The microtubule-dependent formation of tubulovesicular network with characteristics of the endoplasmic-reticulum from cultured cell extracts." *Cell* 54:27–35.

Danscher, G., Rytter Nergaard, J.O., and Baatrup, E., 1987, "Autometallography-tissue metals demonstrated by a silver enhancement kit." *Histochemistry* 71:1–16.

Ericsson, J.L.E., and Biberfeld, P., 1967, "Studies on aldehyde fixation. Fixation rates and their relation to fine structure and some histochemical reactions in the liver." *Lab. Invest.* 17:281–298.

Fahimi, H.D., 1967, "Perfusion and immersion fixation of rat liver with glutaraldehyde." *Lab. Invest.* 16:736–750.

Fox, C.H., Johnson, F.B., Whiting, J., and Roller, P.P., 1985, "Formaldehyde fixation." *J. Histochem. Cytochem.* 33:845–853.

Giberson, R.T., and Demaree, R.S. Jr., 1995, "Microwave fixation: understanding the variables to achieve rapid reproducible results." *Microscopy Research & Technique* 32(3):246–54.

Hayat, M.A., 1981, *Fixation for Electron Microscopy*. San Diego, Academic Press.

Hayat, M.A., 1986, "Glutaraldehyde: Role in electron microscopy." *Micron Microsc. Acta* 17:115.

Hayat, M.A., 1989, Chemical Fixation. *Principles and Techniques of Electron Miroscopy: Biological Applications.* Boca Raton, CRC Press: 1–74.

Hell, S., Reiner, G., Cremer, C., and Stelzer, E.H.K., 1993, "Aberrations in confocal fluorescence microscopy introduced by mismatches in refractive index." *J. Microsc.* 169:391–405.

Hiramoto, R., Berneck, J., Jurand, J., and Hamlin, M., 1964, "The effect of hydrogen ion concentration on fluorescent labelled antibodies." *J. Histochem. Cytochem.* 12:271–274.

Hopwood, D., 1967, "Some aspects of fixation with glutaraldehyde. A biochemical and histochemical comparision of the effects of formaldehyde and glutaraldehyde fixation on various enzymes and glycogen, with a note on penetration of glutaraldehyde into the liver." *J. Anat.* 101:83–92.

Hopwood, D., 1975, "The reactions of glutaraldehyde with nucleic acids." *Histochem. J.* 7:267–276.

Inoué, S., 1986, *Video Microscopy*. New York, Plenum Press.

Ito, S., 1962, Light and electron microscopic study of membranous cytoplasmic organelles. *The Interpretation of Ultrastructure*. R.J.C. Harris. San Diego, Academic Press: 129–148.

Jackson, P., 1991, "Microwave fixation in molecular biology." *Eur. J. Morphol.* 29:57–59.

Jamur, M.C., Faraco, C.D., Lunardi, L.O., Siraganian, R.P., and Oliver, C., 1995, "Microwave fixation improves antigenicity of glutaraldehyde-sensitive antigens while preserving ultrastructural detail." *Journal of Histochemistry & Cytochemistry.* 43(3):307–311.

Johnson, T.J.A., 1985, Glutaraldehyde fixation chemistry. *The Science of Biological Specimen Preparation for Microscopy and Microanalysis.* M. Muller, R.P. Becker, A. Boyde and J.J. Wolosewick. Chicago, Scanning Electron Microscopy: 51–62.

Karnovsky, M.J., 1965, "A formaldehyde-glutaraldehyde fixative of high osmolarity for use in electron microscopy." *J. Cell Biol.* 27:137.

Klugerman, M.R., 1965, "Chemical and physical variables affecting the properties of fluorescein isothiocyanate and its protein conjugates." *J. Immunol.* 95:1165–1173.

Lackie, P.M., Hennessy, R.J., Hacker, G.W., and Pollak, J.M., 1985, "Investigation of immunogold-silver staining by electron microscopy." *Histochemistry* 83:545–530.

Langanger, G., De Mey, J., and Adam, H., 1983, "1,4 Diazobizyklo-[2.2.2]oktan (DABCO) verzogest das Ausbleichen von immunofluoreszenzpraparaten." *Mikroskopie* 40:237–241.

Lee, C., and Chen, L.B., 1988, "Dynamic behavior of endoplasmic-reticulum in living cells." *Cell* 54:37–46.

Lee, R.M.K., 1984, A critical appraisal of the effects of fixation, dehydration and embedding on cell volume. *The Science of Biological Specimen Preservation for Microscopy and Microanalysis*. J.-P. Revel, T. Barnard, G.H. Haggis and S.A. Bhatt. AMF O'Hare, Chicago, Scanning Electron Microscopy: 61–70.

Lee, R.M.K., Garfield, R.E., Forrest, J.B., and Daniel, E.E., 1979, "The effects of fixation, dehydration and critical point drying on the size of cultured smooth-muscle cells." *Scanning Electron Microsc.* 3:439–448.

Lee, R.M.K., McKenzie, R., Kobayashi, K., Garfield, R.E., Forrest, J.B., and Daniel, E.E., 1982, "Effects of glutaraldehyde fixative osmolalities on smooth-muscle cell-volume and osmotic reactivity of the cells after fixation." *J. Microsc.* 125:77–88.

Linares-Cruz, G., Rigault, J.P., Vassy, J., De Oliveira, T.C., De Cremoux, P., Olofsson, B., and Calvo, F., 1994, "Reflectance in situ hybridization (RISH): Detection, by confocal reflectance laser microscopy, of gold-labeled riboprobes in breast cancer cell lines and histological specimens." *J. Microsc.* 173:27–38.

Lipsky, N., and Pagano, R.E., 1985, "A vital stain for the Golgi apparatus." *J. Cell Biol.* 100:27–34.

McLean, I.W., and Nakane, P.K., 1974, "Periodate-lysine-formaldehyde fixation — a new fixative for immunoelectron microscopy." *J. Histochem. Cytochem.* 22:1077–1083.

Meek, K.M., and Chapman, J.A., 1985, Demonstrable fixative interactions. *The Science of Biological Specimen Preparation for Microscopy and Microanalysis*. M. Muller, R.P. Becker, A. Boyde and J.J. Wolosewick. AMF O'Hare, Chicago, Scanning Electron Microscopy: 63–72.

Merdes, A., Stelzer, E.H.K., and De Mey, J., 1991, "Three dimensional architecture of the mitotic spindle analyzed by confocal fluorescence and electron microscopy." *J. Electron Microsc. Technique* 18:61–73.

Nakane, P., 1975, "Recent progress in peroxidase-labeled antibody method." *Ann. N.Y. Acad. Sci. USA* 254:203–210.

Nowell, J.A., and Pawley, J.B., 1980, "Preparation of experimental animal tissue for SEM." *Scanning Electron Microsc.* 11:1–20.

Osborn, M., Franke, W., and Weber, K., 1980, "Direct demonstration of the presence of two immunologically distinct intermediate-sized filament systems with the same cell by double immunofluorescence microscopy. Vimentin and cytokeratin fibers in cultured epithelial cells." *Exp. Cell Res.* 125:37–46.

Osborn, M., and Weber, K., 1982, "Immunofluorescence and immunocytochemical procedures with affinity purified antibodies: Tubulin-containing structures." *Methods Cell Biol.* 24:97–132.

Paddock, S., 2002, "Confocal reflection microscopy: the 'other' confocal mode." *Biotechniques.* 32(2):274, 276–278.

Paddock, S.W., 1989, "Tandem scanning reflected light microscopy of cell substratum adhesions and stress fibers in Swiss 3T3 cells." *J. Cell Sci.* 93:143–146.

Pawley, J.B., Amos, W.B., Dixon, A., and Brelje, T.C., 1993, *Simultaneous, non-interfering collection of optimal fluorescent and backscattered light signals on the MRC 500/600.* Fifty-first Annual Meeting of the Microscopy Society of America, San Francisco, San Francisco Press.

Petersen, P., 1977, "Glutaraldehyde fixation for electron microscopy of needle biopsies of human livers." *Acta. Pathol. Microbiol. Scand.* 85: 373–383.

Rambourg, A., Clermont, Y., Hermo, L., and Segretain, D., 1989, "Tridimensional structure of the Golgi apparatus of non-ciliated epithelial cells of the ductuli efferentes in rat." *Biol. Cell* 60:103–116.

Robertson, J.D., Bodenheimer, T.S., and Stage, D.E., 1963, "Ultrastructure of Mauthner cell synapses and nodes in goldfish brains." *J. Cell Biol.* 19:159–199.

Rostgaard, J., Qvortrup, K., and Poulsen, S.S., 1993, "Improvements in the technique of vascular perfusion-fixation employing a fluorocarbon-containing perfusate and a peristaltic pump controlled by pressure feedback." *Journal of Microscopy*. 172(Pt 2):137–151.

Sabatini, D.D., Bensch, K., and Barrnett, R.J., 1962, "New means of fixation for electron microscopy and histochemistry." *Anat. Rec.* 142:274.

Sabatini, D.D., Bensch, K., and Barrnett, R.J., 1963, "Cytochemistry and electron microscopy. The preservation of cellular structure and enzymatic activity by aldehyde fixation." *J. Cell Biol.* 17:19.

Sabatini, D.D., Bensch, K., and Barrnett, R.J., 1964, "Aldehyde fixation for morphological and enzyme histochemical studies with the electron microscope." *J. Histochem. Cytochem.* 12:57.

Sato, H., Ohnuki, Y., and Fujiwara, K., 1976, Immunofluorescent anti-tubulin staining of spindle microtubules and critique for the technique. *Cell Motility*. R. Goldman, T. Pollard and J. Rosenbaum. Cold Spring Harbor, Cold Spring Harbor Laboratory Press: 419–433.

Sawitzky, H., Willingale-Theune, J., and Menzel, D., 1996, "Improved visualization of F-actin in the green alga Acetabularia by microwave-accelerated fixation and simultaneous FITC-Phalloidin staining." *Histochemical Journal.* 28(5):353–360.

Scheetz, M.P., and Spudich, J.A., 1983, "Movement of myosin-coated fluorescent beads on actin cables *in vitro*." *Nature* 303:31–35.

Scopsi, L., and Larsson, L.-I., 1985, "Increased sensitivity in immunocytochemistry effects of double amplification of antibodies and of silver intensification on immunogold and peroxidase-antiperoxidase staining techniques." *Histochemistry* 82:321–329.

Soeller, C., and Cannell, M.B., 1996, "Construction of a two-photon microscope and optimisation of illumination pulse duration." *Pflugers Archiv — European Journal of Physiology.* 432(3):555–561.

Steinbrecht, R.A., and Zierold, K., 1987, *Cryotechniques in Biological Electron Microscopy*. Berlin, Springer-Verlag.

Tagliaferro, P., Tandler, C.J., Ramos, A.J., Pecci Saavedra, J., and Brusco, A., 1997, "Immunofluorescence and glutaraldehyde fixation. A new procedure based on the Schiff-quenching method. [erratum appears in J Neurosci Methods 1998 Aug 1;82(2):235–236]." *Journal of Neuroscience Methods.* 77(2):191–197.

Tashima, T., Kawakami, U., Harada, M., Sakata, T., Satoh, N., Nakagawa, T., and Tanaka, H., 1987, "Isolation and identification of new oligomers in aqueous solution of glutaraldehyde." *Chem. Pharm. Bull* 35:4169.

Terasaki, M., Song, J., Wong, J.R., Weiss, M.J., and Chen, L.B., 1984, "Localization of endoplasmic-reticulum in living and glutaraldehyde-fixed cells with fluorescent dyes." *Cell* 38:101–108.

Thoolen, B., 1990, "BrdUrd labeling of S-phase cells in testes and small intestine of mice; using microwave irradiation for immunogold-silver staining: An immunocytochemical study." *J. Histochem. Cytochem.* 38:267–273.

Tooze, J., 1964, "Measurements of some cellular changes during fixation of amphibian erythrocytes with osmium tetroxide solutions." *J. Cell Biol.* 22:551–563.

van Meer, G., Stelzer, E.H.K., Wijnaendts van Resandt, R.W., and Simons, K., 1987, "Sorting of glycolipids in epithelial (Madin-Darby canine kidney) cells." *J. Cell Biol.* 105:1623–1635.

Walsh, M.L., Jen, J., and Chen, L.B., 1979, "Transport of serum components into structures similar to mitochondria." *Cold Spring Harbor Conf. Cell Prolif.* 6:513–520.

Wangensteen, D., Bachofen, H., and Weibel, E.R., 1981, "Effects of glutaraldehyde or osmium tetroxide fixation on the osmotic properties of lung cells." *J. Microsc.* 124:189–196.

Weber, K., Rathke, P.C., and Osborn, M., 1978, "Cytoplasmic microtubular images in glutaraldehyde-fixed tissue culture cells by electron microscopy and by immunofluorescence microscopy." *Proc. Natl. Acad. Sci. USA* 75:1820–1824.

Wild, P., Bertoni, G., Schraner, E.M., and Beglinger, R., 1987, "Influence of calcium and magnesium containing fixatives of the ultrastructure of parathyroids." *Micron Microsc. Acta* 18:259.

19

Confocal Microscopy of Living Cells

Michael E. Dailey, Erik Manders, David R. Soll, and Mark Terasaki

INTRODUCTION

If a picture is worth a thousand words, then a movie may be worth a million words. Microcinematography and, later, video microscopy have provided great insight into biological phenomena. One limitation, however, has been the difficulty of imaging in three dimensions. In many cases, observations have been made on cultured cells that are thin to start with or tissue preparations that have been sectioned.

The development of the first beam-scanning confocal microscope was motivated by the goal of making observations in the tissues of living organisms (Petran *et al.*, 1986). The optical sectioning capability of the confocal or multi-photon (MP) microscope allows one to make thin-slice views in intact cells or even intact animals. Confocal microscopes are now fairly common, and because they employ non-ionizing radiation, they are increasingly being used to study living cells and tissue preparations.

What are the specific challenges of applying confocal imaging to studies of living cells? First, the experimenter must do no harm. Arguably, the main obstacle in living cells microscopy is not "getting an image" but doing so without upsetting the cell. To be useful, the study must be carried out on a biological system that retains normal function and can be subjected to controlled conditions while on the stage of the microscope. Often, environmental variables such as temperature, CO_2, or pH must be regulated and/or an efficient directional perfusion system must be used. Unfortunately, the difficulty of keeping cells alive and functioning on the microscope discourages many researchers. This chapter is designed to help them succeed well enough to become convinced of the importance and utility of this approach.

Other difficulties are more specific to confocal fluorescence microscopy. All studies with fluorescence benefit from collecting as much of the emitted fluorescent light as is possible, but this is particularly important for studies of living cells because photodynamic damage and consequent alteration in normal cell behavior is a very real possibility (see Chapters 16 and 38, *this volume*). Therefore, optimizing microscope photon collection efficiency is crucial for successful confocal microscopy of living cells.

Another difference between living and fixed cell studies is the element of time. All living processes have an inherent time course, and the imaging system must produce images at the appropriate rate to show the changes involved. The amount of light necessary to obtain the data must be apportioned over time so that enough images can be obtained to describe the process under investigation without damaging the cells. Although early confocal microscopes had a relatively slow scan speed, newer technology now permits very rapid image collection to explore spatially and temporally dynamic biological processes (see Chapter 10, *this volume*). In single-beam scanning systems, the field of view often is reduced to achieve higher imaging speeds.

The fluorescent probes used in studies of living cells must not impair normal cell function. Immunofluorescence, which has been used so successfully to localize molecules in fixed cells, has not been practical in living cells. However, there are now many commercially available fluorescent probes for structural and physiological studies of cells and tissues (see Chapters 16 and 17, *this volume*). Of even more importance, the "green revolution" based on the green fluorescent protein (GFP) has changed the landscape and is ushering in an exciting period of biological imaging of proteins in living cells, and of various cell types in living, intact tissue preparations (Chalfie *et al.*, 1994; Bastieans and Pepperkok, 2000).

Although confocal microscopy of living cells is difficult, its usefulness was demonstrated over 15 years ago in two pioneering studies. Cornell-Bell and colleagues (1990) used confocal microscopy to make a major discovery: the existence of glutamate-stimulated, transcellular Ca^{2+} waves in astroglia. In the same year, confocal microscopy was used to characterize developmental changes in an intact animal by imaging neuronal axons and their growth cones in the developing brain of a tadpole (O'Rourke and Fraser, 1990). Ever since these pioneering studies, there has been an increasing use of confocal microscopy to study dynamic processes in an array of diverse biological preparations. When the second edition of this volume appeared in 1995, about 80 papers using confocal microscopy on living cells were found. Today (early 2005), there are over 500 published studies using live-cell confocal imaging.

While live-cell applications of confocal imaging have expanded significantly over the past decade, multi-photon imaging (see Chapters 21 and 28, *this volume*) is poised to make a similar impact on live-cell and tissue studies in the next decade. There are trade-offs, however. MP imaging can be useful especially for very deep penetration in tissues (>100 µm) where non-descanned detection increases signal substantially, but on thinner specimens, the actual damage/excitation may be greater for MP than for single-photon confocal imaging (Tauer, 2002; see also Chapter 38, *this volume*). Moreover, the cost differential is such that one could have two to three graduate students working away on disk scanners or simpler beam-scanning confocal units for every one on a MP unit. At any rate, most of the topics covered in this chapter are relevant for both single-photon confocal and MP excitation.

Michael E. Dailey • University of Iowa, Iowa City, Iowa 52242
Erik Manders • Swammerdam Institute for Life Sciences, University of Amsterdam, Amsterdam, The Netherlands
David R. Soll • University of Iowa, Iowa City, Iowa 52242
Mark Terasaki • University of Connecticut Health Center, Farmington, Connecticut 06032

Handbook of Biological Confocal Microscopy, Third Edition, edited by James B. Pawley, Springer Science+Business Media, LLC, New York, 2006.

OVERVIEW OF LIVING-CELL CONFOCAL IMAGING TECHNIQUES

Although live-cell imaging often involves time-lapse microscopy to monitor cell movements, modern approaches are extending these observations well beyond simply making movies of cell structure. Increasingly, time-lapse imaging is being integrated with specialized techniques for monitoring, measuring, and perturbing dynamic activities of cells and subcellular structures. Below we summarize some major techniques available for studying the dynamic organization of molecules and cells in live biological specimen. These techniques are summarized in Table 19.1.

Time-Lapse Fluorescence Imaging

Time-lapse fluorescence imaging involves repeated imaging of a labeled specimen at defined time points, thereby permitting studies on the dynamic distribution of fluorescently labeled components in living systems. Imaging can be performed in one, two, or three spatial dimensions: one-dimensional (1D) imaging involves rapid and repeated imaging of single scan lines; two-dimensional (2D) imaging involves repeated imaging of single focal planes; and three-dimensional (3D) imaging involves repeated imaging of multiple focal planes in a thick specimen. The time intervals for sequential image collection can range from sub-second to days or even months (e.g., Gan *et al.*, 2003).

Many small molecule, vital fluorescent probes that give highly specific cellular or subcellular patterns of labeling are now available (see below and Chapters 16 and 17, *this volume*). In addition, GFP or GFP-related proteins are now routinely fused to other proteins of interest, and the inherent brightness and photostability of many of these fluorescent proteins make them well suited for the repeated imaging needed for time-lapse studies. Together, these fluorescent probes are affording a seemingly limitless array of possibilities for imaging molecular components in live cells.

Multi-Channel Time-Lapse Fluorescence Imaging

The plethora of excellent vital fluorescent labels with varying spectral characteristics (including spectral variants of GFP) allows multi-label experiments to visualize the relative distribution of several different cell or tissue components simultaneously. Advances in imaging technology have facilitated automated collection of more than one fluorescent channel (either sequentially or simultaneously) with improved ability to maximize signal collection and to separate partially overlapping signals.

In addition to studies using multiple fluorescent tags, multi-channel data collection permits ratiometric imaging of single probes whose spectral properties (absorption or emission) change depending on ionic conditions, such as the Ca^{2+} sensitive physiological indicator, indo-1 (see Chapter 42, *this volume*).

Spectral Imaging and Linear Unmixing

Increasingly, experiments are incorporating multiple fluorescent probes within single cells or tissues to define the differential distribution of more than one labeled structure or molecular species. Such multi-color or multi-spectral imaging experiments require adequate separation of the fluorescent emissions, and this is especially problematic when the spectra are substantially overlapping. Spectral imaging utilizes hardware to separate the emitted light into its spectral components. Linear unmixing is a computational process related to deconvolution that uses the spectra of each dye as though it were a point-spread function at a fixed location to "unmix" the component signals (Tsurui *et al.*, 2000; Lansford *et al.*, 2001; Hiraoka *et al.*, 2002). Although together these analytical tools can be used to discriminate distinct fluorophores with highly overlapping spectra (Zimmermann *et al.*, 2003), they do so at the cost of requiring that significantly more photons be detected from each pixel.

Fluorescence Recovery After Photobleaching

Fluorescence recovery after photobleaching (FRAP), also known as fluorescence photobleaching recovery (FPR), is a technique for defining the diffusion properties of a population of fluorescently labeled molecules (Axelrod *et al.*, 1976; Koppel *et al.*, 1976; for review, see Lippincott-Schwarz *et al.*, 2003). Typically, a spot or line of intense illumination is used to bleach a portion of a fluorescent cell, and the recovery of fluorescent signal back into the bleached area from adjacent areas is monitored over time (usually seconds to minutes). Although this technique can yield quantitative information on the diffusion coefficient, mobile fraction, and binding/dissociation of a protein, care has to be taken not to use so much power in the bleach beam that the cellular structure is disrupted (Bloom and Webb, 1984; Flock *et al.*, 1998; see also Figures 49.10 through 49.14, *this volume*). Quantitative assessments of FRAP data, which can be confounded by uncertainties in the experimental and biological parameters in living cells, may benefit from computer simulations (Weiss, 2004).

Fluorescence Loss in Photobleaching

This technique utilizes repeated photobleaching in an attempt to bleach all fluorophores within a given cellular compartment (Lippincott-Schwarz *et al.*, 2001). Thus, fluorescence loss in photobleaching (FLIP) can be used to assess the continuity of membrane bounded compartments (e.g., endoplasmic reticulum [ER] or Golgi apparatus) and to define the diffusional properties of components within, or on the surface of, these compartments.

Fluorescence Resonance Energy Transfer

Fluorescence resonance energy transfer (FRET) is a technique for defining interactions between two molecular species tagged with different fluorophores (Stryer, 1978; Sekar and Periasamy, 2003). It takes advantage of the fact that the emission energy of a fluorescent "donor" can be absorbed by (i.e., transferred to) an "acceptor" fluorophore when these fluorophores are in nanometer proximity and have overlapping spectra (see Chapters 16, 27, and 45, *this volume*).

Fluorescence Lifetime Imaging

This technique measures the lifetime of the excited state of a fluorophore (Lakowicz *et al.*, 1992 and Chapter 27, *this volume*). Each fluorescent dye has a characteristic "lifetime" in the excited state (usually 1–20 ns), and detection of this lifetime can be used to distinguish different dyes in samples labeled with multiple dyes. Fluorescence lifetime imaging (FLIM) can be utilized in conjunction with FRET analysis because the lifetime of the donor fluorophore is shortened by FRET. In fact, FLIM can improve the measurement during FRET analysis because the fluorescence lifetime is independent of the fluorophore concentration and excitation energy (Bastiaens and Squire, 1999; Elangovan *et al.*, 2002;

Chen *et al.*, 2003; Chapter 27, *this volume*). However, the lifetime can be modulated by environmental considerations (e.g., pH, ion concentration), and this change can be used to measure changes in the concentration of certain ions (Lin *et al.*, 2003).

Fluorescence Correlation Spectroscopy

Fluorescence correlation spectroscopy (FCS) measures spontaneous fluorescence intensity fluctuations in a stationary microscopic detection volume (about 1 fL) (Magde *et al.*, 1974). Such intensity fluctuations represent changes in the number or quantum yield of fluorescent molecules in the detection volume. By analyzing these fluctuations statistically, FCS can provide information on equilibrium concentrations, reaction kinetics, and diffusion rates of fluorescently tagged molecules (Elson, 2001). An advantage of this approach is the ability to measure the mobility of molecules down to the single molecule level and to do so using a light dose orders of magnitude lower than used for FRAP.

Fluorescence Speckle Microscopy

The dynamic growth and movement of fluorescently labeled structures can be difficult to analyze when these structures are densely packed and overlapping within living cells. Fluorescent speckle microscopy (FSM) is a technique compatible with widefield or confocal microscopy (Adams *et al.*, 2003) that uses a very low concentration of fluorescently labeled subunits to reduce out-of-focus fluorescence and improve visibility of labeled structures and their dynamics in thick regions of living cells (Waterman-Storer *et al.*, 1998). This is accomplished by labeling only a fraction of the entire structure of interest. In that sense, it is akin to performing FCS over an entire field of view, albeit with more focus on spatial patterns than on quantitative temporal analysis. FSM has been especially useful for defining the movement and polymerization/depolymerization of polymeric cytoskeletal elements, such as actin and microtubules, in motile cells (Salmon *et al.*, 2002).

Photo-Uncaging/Photoactivation

Photo-uncaging is a light-induced process of releasing a "caged" molecule from a caging group to produce an active molecule (Politz, 1999; Dorman and Prestwich, 2000). A variety of caged molecules have been synthesized and used experimentally, but in some examples cages have been used to mask a fluorophore, inducing a non-fluorescent state. Excitation light of ~350 nm is used to break photolabile bonds between the caging group and fluorophore, thereby uncaging the fluorophore and yielding a fluorescent molecule.

A related technique utilizes genetically encoded, photoactivatable fluorescent proteins, of which there are currently about a dozen (for review, see Patterson and Lippincott-Schwartz, 2004). Two examples include a photoactivatable (PA) form of GFP, called PA-GFP (ex/em: 504/517), which shows a 100-fold increase in fluorescence following irradiation at 413 nm (Patterson and Lippincott-Schwartz, 2002), and Kaede (ex/em: 572/582), which shows a 2000-fold increase following irradiation at 405 nm (Ando *et al.*, 2002; see also Figure 8.37, *this volume*).

An extension of the photoactivation approach, termed reversible protein highlighting, has been developed (Ando *et al.*, 2004). This involves reversible, light-induced conversion of a coral protein, Dronpa, between fluorescent and non-fluorescent states. One study used this approach to monitor fast protein dynamics in and out of cell nuclei (Ando *et al.*, 2004). Thus, photo-uncaging and photoactivation are complementary to FRAP and can be used in conjunction with time-lapse imaging to mark and follow a population of molecules in order to study their kinetic properties within living cells.

Optical Tweezers/Laser Trapping

Optical tweezers, or single beam laser traps, use the "radiation pressure" of a stream of photons emitted from an infrared laser to "trap" small objects (often a protein-coated bead) and to move them around (Sheetz, 1998; Kuo, 2001; Chapters 5 and 9, *this volume*). This technique has been especially useful for quantifying forces generated by motor protein movement (Ashkin *et al.*, 1990; Block *et al.*, 1990; Kuo and Sheetz, 1993) or the strength of adhesions mediated by cell adhesion molecules (e.g., Schmidt *et al.*, 1993; Baumgartner *et al.*, 2003). Although "laser tweezers" often are used in widefield imaging systems, they also have been incorporated into confocal (Visscher and Brakenhoff, 1991) and MP (Goksor *et al.*, 2004) imaging systems.

Physiological Fluorescence Imaging

The availability of fluorescent physiological indicators extends live-cell confocal and MP imaging studies beyond structural aspects to study cell and tissue physiology (Niggli and Egger, 2004; Rubart, 2004; Wang *et al.*, 2004). Calcium indicators have been the most commonly used physiological probes because calcium is a central signal transduction molecule and in many cell preparations the calcium-sensitive probes give robust signals. These signals often are temporally resolvable in full field scans as calcium transients that persist for several seconds. Fast scanning systems, or line-scanning mode in laser scanning systems, have been used to resolve more rapid calcium events (e.g., Fan *et al.*, 1999; Wang *et al.*, 2004). Although non-ratiometric, visible wavelength calcium indicators (e.g., fluo-3, calcium green) have been more widely used in confocal applications, some studies have employed ultraviolet (UV) excited ratiometric calcium indicators, such as indo-1 (e.g., Pasti *et al.*, 2001).

In addition to calcium indicators, other fluorescent physiological probes are useful for reporting various ions including sodium, magnesium, potassium, and chloride, pH, heavy metals such as zinc, and membrane potential, to name a few (see Chapter 42, *this volume*). Although many of these probes are small molecules, genetic (GFP-based) probes have been developed (see Miyawaki, 2003) and are being incorporated into transgenic animals (e.g., Hasan *et al.*, 2004). In combination with state-of-the-art confocal and MP imaging systems, these probes will increasingly permit detailed spatio-temporal analyses of physiological processes in intact tissues and organisms (Ashworth, 2004).

Combining Fluorescence and Other Imaging Modalities

Although advancements in fluorescence imaging technology coupled with the availability of a multitude of vital fluorescent probes have combined to make fluorescence the method of choice for most high resolution studies of living cells, it is sometimes advantageous to combine fluorescence imaging with other imaging modalities. For example, differential interference contrast (DIC) microscopy can be used in conjunction with laser-scanning confocal microscopy to simultaneously monitor the whole cell in DIC mode while imaging the phagocytic uptake of fluorescent microspheres (Hook and Odeyvale, 1989) or the distribution of fluores-

TABLE 19.1. Overview of Live Cell Fluorescence Confocal Imaging Techniques

Technique	Description	Review Article(s)	Selected Examples/References
1 Time-lapse fluorescence imaging.	Repeated imaging of a field of view (single optical section) in live specimen over time.	• Cooper *et al.*, 1999	• Imaged dynamic changes in fluorescently labeled Golgi membranes (Cooper *et al.*, 1990)
2 Multi-channel or ratiometric time-lapse fluorescence imaging.	Simultaneous or sequential imaging in two or more fluorescent channels over time.	• Stricker, 2004 • Ellenberg *et al.*, 1999	• Monitored sorting of CFP- and YFP-tagged proteins through the Golgi Apparatus (Keller *et al.*, 2001)
3 Three-dimensional time-lapse (4D) imaging.	Repeated collection of *z*-series stacks of images over time.	• Gerlich & Ellenberg, 2003 • Bement *et al.*, 2003 • Hammond & Glick, 2000 • Thomas & White, 1998	• Imaged neuronal dendritic spines in brain slice cultures (Marrs *et al.*, 2001) • Imaged mitosis and migration of developing cortical neurons (Noctor *et al.*, 2004)
4 Three-dimensional multi-channel (5D) time-lapse fluorescence imaging.	Repeated collection of *z*-stacks in two or more fluorescent channels over time.	• Andrews *et al.*, 2002 • Gerlich *et al.*, 2001	• Imaged T-cell–dendritic cell interactions in lymph nodes (Stoll *et al.*, 2002) • Microglial phagocytosis in brain slices (Petersen & Dailey, 2004)
5 Spectral imaging and linear unmixing.	Method for discriminating distinct fluorophores with strongly overlapping emission spectra.	• Berg, 2004 • Zimmermann *et al.*, 2003 • Seyfried *et al.*, 2003 • Hiraoka *et al.*, 2002 • Dickenson *et al.*, 2001	• Unmix spectrally similar fluorophores in plant cells (Berg, 2004) • Resolve multiple fluorescent proteins in vertebrate cells by multiphoton imaging spectroscopy (Lansford *et al.*, 2001)
6 Fluorescence recovery after photobleaching (FRAP).	Measures recovery of fluorescence after bleaching of a portion of the specimen. Recovery may be due to protein diffusion, binding/dissociation or transport processes.	• Lippincott-Schwarz *et al.*, 2003 • Meyvis *et al.*, 1999	• Used FRAP to study integrin turnover at focal adhesions (Ballestrem *et al.*, 2001)
7 Fluorescence loss in photobleaching (FLIP).	Repeated photobleaching used to determine continuity of cell compartments and mobility of fluorescent proteins within these compartments.	• Lippincott-Schwartz *et al.*, 2001	• Dynamics and retention of correctly folded and misfolded proteins were compared in native ER membranes (Nehls *et al.*, 2000)
8 Fluorescence localization after photobleaching (FLAP).	Method for localized photo-labeling and subsequent tracking of specific molecules bearing two different fluorophores within living cells.	• Dunn *et al.*, 2002	• Used FLAP to show that actin is rapidly delivered to the leading edge of protruding cells (Zicha *et al.*, 2003)
9 Fluorescence resonance energy transfer (FRET).	Non-radiative energy transfer from a donor to an acceptor fluorophore with overlapping emission and excitation spectra. Useful for measuring interactions between two fluorescently tagged proteins.	• Sekar and Periasamy, 2003 • Wouters *et al.*, 2001	• FRET used to study activation of small G proteins during phagocytosis (Hoppe and Swanson, 2004) • FRET analysis shows that GTP-Rac coupling to effectors is locally enhanced in lamellipodia (Del Pozo *et al.*, 2002)

10	Fluorescence lifetime imaging (FLIM).	Method to investigate molecular interactions, metabolic reactions, and energy transfer in cells and subcellular structures.	• Peter and Ameer-Beg, 2004 • Periasamy *et al.*, 2002 • Bastiaens and Squire, 1999 • Pepperkok *et al.*, 1999	• Used FLIM to study interaction between CD44 and ezrin (Legg *et al.*, 2002) • Quantified dimerization of transcription factor CAATT/enhancer binding protein alpha in living pituitary cells (Elangovan *et al.*, 2002)
11	Fluorescence correlation spectroscopy (FCS).	Measures spontaneous fluorescence intensity fluctuations in a microscopic detection volume. Provides information on equilibrium concentrations, reaction kinetics, and diffusion rates of molecules.	• Bacia & Schwille, 2003 • Hess *et al.*, 2002 • Elson, 2001	• Compared mobility and molecular interactions between CaM and CaMKII in solution and in living cells (Kim *et al.*, 2004)
12	Fluorescence speckle microscopy.	Uses very low concentration of fluorescent subunits to reduce out-of-focus fluorescence and improve visibility of fluorescently labeled structures and their dynamics in thick regions of living cells.	• Adams *et al.*, 2003 • Waterman-Storer *et al.*, 1998	• Studied coupling of microtubule and actin movements in migrating cells (Salmon *et al.*, 2002)
13	Photo-uncaging/ Photoactivation.	Photo-induced activation of an inert molecule to an active state (e.g., release of a caging group from a "caged" compound), or activation of a photoactivatable fluorescent protein (e.g., PA-GFP, Kaede).	• Patterson & Lippincott-Schwartz, 2004 • Park *et al.*, 2002 • Dorman and Prestwich, 2000 • Politz, 1999	• Photo-release of caged Ca^{2+} in brain astrocytes regulates vascular constriction (Mulligan and MacVicar, 2004) • Used a reversible photoactivatable fluorescent protein to study nuclear import and export of ERK1 and importin (Ando *et al.*, 2004)
14	Optical tweezers/laser trapping.	Uses the "radiation pressure" of a stream of photons emitted from an infrared laser to "trap" small objects and molecules.	• Kuo, 2001 • Schwarzbauer, 1997	• Studied strength of cadherin adhesions in endothelial cells (Baumgartner *et al.*, 2003)
15	Fast physiological imaging • Full field • Line-scanning	Rapid, repeated collection of single scan lines or 2D images of specimen labeled with physiological indicators.	• Rubart, 2004 • Wang *et al.*, 2004 • Ashworth, 2004 • Niggli & Egger, 2004 • Miyawaki, 2003	• Imaged Ca^{2+} sparks in muscle fibers (Hollingworth *et al.*, 2000; Brum *et al.*, 2000) • Ca^{2+} imaging in neuronal dendritic spines (Pologruto *et al.*, 2004)
16	Combined fluorescence and transmitted light imaging.	Repeated simultaneous collection of one or more fluorescent channels and a transmitted light channel (e.g., DIC).	• Cogswell & Sheppard, 1991, 1992	• Imaged chromatin dynamics during the formation of the interphase nucleus (Manders *et al.*, 2003) • Imaged E-cadherin-GFP accumulation at cell adhesions in epithelial cells (Adams *et al.*, 1998).

cently tagged proteins and molecules (e.g., Adams *et al.*, 1998) within these cells. Although it is difficult to perform DIC and epi-fluorescence imaging both simultaneously and optimally in widefield microscopy, it is somewhat easier to ensure that the fluorescence signal is not subjected to the light loss that occurs in the analyzer used as part of the DIC system if one uses a single-beam confocal. Thus, the DIC image can be collected from a fluorescently labeled specimen using transmitted light that would otherwise be wasted. Recently, differential phase contrast (DPC) has been implemented in a scanning laser microscope system (Amos *et al.*, 2003), and this may offer additional capabilities where DIC optics are unsuitable. Notably for live-cell imaging, DPC reportedly needs 20 times less laser power at the specimen than DIC.

GENERAL CONSIDERATIONS FOR CONFOCAL MICROSCOPY OF LIVING CELLS

What factors must be considered when performing a live-cell confocal imaging experiment or observation? The major factors are to (1) label the preparation in order to clearly visualize the biological component of interest, (2) maintain the preparation in a condition that will support normal cell or tissue health, and (3) image the specimen with sufficient spatial and temporal resolution in a way that does not perturb or compromise it. Table 19.2 outlines several of the most important experimental considerations for live-cell imaging, including the most common problems and some potential solutions.

TABLE 19.2. Experimental Considerations for Live Cell Imaging

Consideration	Problem	Potential solution(s)
1 Temperature	Many biological phenomena are temperature sensitive.	• Use stage heaters; inline perfusion heaters; objective lens heaters; environmental boxes. • Take precautions against stage drift: — increase thermal mass, — use open-loop controls
2 Oxygenation	Most live biological specimens require O_2 (and removal of CO_2) to remain healthy. Oxygen may become depleted in closed chambers.	• Use a perfusion chamber. • Exchange used chamber media with oxygenated media intermittently or continuously. • Increase volume of chamber to promote health.
3 pH	Metabolism of live biological tissues can induce severe pH changes in chamber media over time.	• Monitor chamber pH. • Use HEPES (10–25 mM)-buffered media. • Exchange chamber media intermittently or continuously (perfusion). • Use media without phenol red pH indicator.
4 Humidity	Stage heating (especially with forced air) may cause evaporation from an open chamber, leading to dramatic changes in salinity and pH.	• Use closed chamber configuration (perfusion chamber). • Use humidified environmental box. • Use auto-fill system for open chambers.
5 Fluorescence signal strength	Weakly fluorescent probes or low concentration of probes can yield weak signals that produce images with low signal-to-noise ratio.	• Increase pixel dwell time. • Open confocal pinhole aperture (e.g., to >2 Airy disks). • Maximize throughput of emission pathway (e.g., in spectral imaging systems with variable spectral filters). • Use line or frame averaging to improve signal-to-noise ratio. • Adjust illumination (filling) of back aperture of objective lens.
6 Channel bleed-through or cross-talk	In biological specimens labeled with multiple fluorescent probes, signals from one channel may be detected in other channels.	• Image separate fluorescence channels sequentially (either line-by-line or frame-by-frame in scanning systems). • Use spectral imaging and linear unmixing algorithms. • Use modern, hard-coated interference filters and dichroics.
7 Photobleaching	Fluorescent probes bleach with repeated illumination. Some fluorescent probes bleach quickly.	• Reduce incident illumination. Then reduce it again! • Use fade resistant dyes. • Open confocal pinhole aperture. • Maximize throughput of emission pathway (e.g., in spectral imaging systems with variable spectral filters). • Reduce pixel dwell time (in scanning systems). • Reduce frequency of image capture. • Blank laser beam during flyback (in scanning systems). • Only scan specimen when actually collecting data. • To improve S/N, always deconvolve 3D data before viewing.
8 Spatial resolution	Some observations require very high spatial resolution in *x*-*y* or *z*.	• Use high NA objectives. • Reduce size of confocal pinhole aperture (to ~1 Airy disk). • Increase spatial sampling frequency (guided by Nyquist theorem). • Increase electronic zoom (but avoid empty magnification). • Decrease step size in *z*-stacks. • Use water-immersion objective lenses to reduce spherical aberration. • Deconvolve the images.
9 Temporal resolution	Some biological phenomena are rapid relative to the rate of image collection (especially problematic with laser scanning confocal systems).	• Reduce field of view (e.g., collect fewer horizontal lines). • Reduce pixel dwell time (e.g., increase scan speed). • Reduce spatial sampling frequency (e.g., reduce pixel array from 1024 to 512).
10 Focus drift	Live biological specimens on heated microscope stages, or features within live specimens (e.g., mitotic cells), can move relative to a fixed focal plane.	• Collect a *z*-stack of images, and reconstruct these images following the observation. • Manual focus adjustments may be required periodically. • Auto-focus methodology may be employed in some cases.

Maintenance of Living Cells and Tissue Preparations

In Vitro Preparations

Specimen maintenance is a very important part of any live imaging study and usually requires both mechanical ingenuity and insight into the biology of the cell or tissue under study. The specimen chamber must keep the cells or tissues healthy and functioning normally for the duration of the experiment while allowing access to the microscope objective. This can be particularly difficult when high-numerical-aperture (NA) oil- or water-immersion lenses are used. In many cases, there must also be a controlled and efficient way to introduce a reagent to perturb a particular cellular process. Other important factors are simplicity, reliability, and low cost. It is advisable to monitor the conditions within the imaging chamber carefully. It may be helpful to use microprobes that can detect pH, O_2, and CO_2 (e.g., Lazar Research Laboratories, Inc., Los Angeles, CA).

The early closed perfusion chambers designed by Dvorak and Stotler (1971) and later by Vesely and colleagues (1982) were inexpensive and permitted high-resolution transmitted light observation. They relied on an external heater that warmed the entire stage area for temperature control.

Setups for different cells vary widely. Mammalian cells probably pose the greatest problems. McKenna and Wang's article (1986) is a general introduction to the problems associated with keeping such cells alive and functioning on the microscope stage. This article discusses culture chamber design as well as strategies for controlling pH, osmolarity, and temperature. The authors describe their own chamber, in which temperature is controlled by heating the air in a box surrounding the stage area, and mention earlier designs such as the resistively heated Lieden Culture System first described by Ince and colleagues (1983) and later improved by Forsythe (1991).

Strange and Spring (1986) describe their setup for imaging renal tubule cells where temperature, pH, and CO_2 are controlled. They provide a detailed account of the problems of establishing laminar flow perfusion systems, temperature regulation, and maintenance of pH by CO_2 buffering. Somewhat later, Delbridge and colleagues (1990) describe a sophisticated, open-chamber superfusion system permitting programmed changes of media, precision control of media surface height, and temperature regulation between 4°C and 70°C using a Peltier device to control the perfusate temperature. Myrdal and Foster (1994) used a temperature-stabilized liquid passing through a small coil suspended in media filling a plastic Nunc chamber to provide temperature control for confocal observations of the penetration of fluorescent antibodies into solid tumor spheroids. An automatic system maintained fluid level and bathed the area in CO_2 but special precautions were required to prevent drift of the confocal focus plane during long time-lapse sequences. Methods for observing microglial cell movements in mammalian brain slices are described in detail in a later section of this chapter.

Chambers have even been built for the microscopic observation of cells as they are being either frozen or thawed in the presence of media that could be changed during the process (e.g., Walcerz and Diller, 1991). In this case, computer-controlled pumps deliver temperature-controlled nitrogen gas at between −120°C and 100°C to special ports connected to a temperature cell (−55°C to 60°C) that forms the upper boundary of the perfusion chamber. Other ports carry either the perfusate or a separate nucleating agent to the cell chamber itself.

More recently, a specialized *in vitro* cell culture system has been developed to maintain mammalian neuronal cells for over a year (Potter and DeMarse, 2001)!

There are several companies that provide ready-made microscope stage chambers, temperature-control units, automated perfusion systems, and a variety of related accessories. These are summarized in Table 19.3.

In Vivo Preparations

The ultimate goal of many research programs is to understand the normal (or abnormal) structure and function of molecules, cells, and tissues *in vivo*, that is, in the living organism functioning within its native environment (Frosting, 2002; Megason and Fraser, 2003). There has been some remarkable progress recently on extending high resolution confocal and MP imaging in this direction, especially in preparations that are essentially translucent. Several model organisms, including zebrafish (Cooper *et al.*, 1999), frog (Fraser and O'Rourke, 1990; Robb and Wylie, 1999), fruit fly (Paddock, 2002), leech (Baker *et al.*, 2003), and worm (Crittenden and Kimble, 1999), have emerged as excellent preparations for cellular and molecular imaging studies spanning a variety of biological questions. As an example, studies in the zebrafish have been carried out on the structural development of vasculature (Lawson and Weinstein, 2002; Isogai *et al.*, 2003), cell division (Gong *et al.*, 2004; Das *et al.*, 2003), neuronal migration (Koster and Fraser, 2001), axonal pathfinding (Dynes and Ngai, 1998), synapse formation (Jontes *et al.*, 2000; Niell *et al.*, 2004), and synaptic plasticity (Gleason *et al.*, 2003), to name a few. Physiological studies in zebrafish have included, for example, imaging intracellular calcium during gastrulation (Gilland *et al.*, 1999), in the intact spinal cord (O'Malley *et al.*, 1996; Gahtan *et al.*, 2002), and in brain (Brustein *et al.*, 2003). Other examples related to studies of embryos are covered in Chapter 43. Each of these biological preparations embodies its own unique set of specimen mounting and maintenance challenges. Indeed, it is sometimes necessary to anesthetize the preparation to prevent it from crawling or swimming away during the imaging session!

Perhaps the most difficult conditions involve imaging in a living mammal, an undertaking for which the confocal or MP microscope enjoys the twin advantages of epi-illumination and optical sectioning that make it possible to view solid tissues without mechanical disruption. Confocal microscopy has long been an important tool for *in vivo* imaging of eye tissues non-invasively (Petran *et al.*, 1986; Jester *et al.*, 1991, 1992; Masters, 1992; Petroll *et al.*, 1992, 1993; Poole *et al.*, 1993). In terms of imaging interior tissues, early studies described methods for examining microcirculation of the brain cortex in anesthetized rats (Dirnagl *et al.*, 1992) or changes in kidney tubules during ischemia (Andrews *et al.*, 1991). Confocal microscopy also has been used to image leukocyte–endothelium interactions during infections through closed cranial windows (Lorenzl *et al.*, 1993). More recently, MP has been used to image live mammalian brain tissues *in vivo*, either through a cranial window (Svoboda *et al.*, 1997; Trachtenberg *et al.*, 2002), fiber-optic coupled devices (Mehta *et al.*, 2004), or directly through the intact but thinned skull (Yoder and Kleinfeld, 2002; Zhang *et al.*, 2005). Dual-channel MP imaging also has been used to image other tissues *in vivo*, including lymphoid organs (e.g., Miller *et al.*, 2002). It is generally accepted that MP imaging is superior to single-photon confocal for these *in vivo* imaging studies (Cahalan *et al.*, 2002).

Fluorescent Probes

Except in those cases where an adequate image can be derived from either the backscattered-light signal or from autofluorescence, confocal microscopy of living cells is dependent on the properties and availability of suitable fluorescent probes. In addition to binding specifically to what one is interested in studying,

TABLE 19.3. Commercially Available Chambers for Live Cell Imaging

Source	Description/Features	Contact Info
20/20 Technology, Inc. Bldg. 2, Unit A 311 Judges Road Wilmington, NC 28405 USA	Heating, cooling, atmosphere control instrumentation for microscopy.	TEL: 1-910-791-9226 WEB: http://20-20tech.com/
ALA Scientific Instruments Inc. 1100 Shames Dr. Westbury, NY 11590 USA	Microincubators and temperature control; Peltier heating & cooling pre-stage; recording chambers; inline perfusion heating tube.	TEL: 516-997-5780 WEB: www.alascience.com EMAIL: sales@alascience.com
ASI / Applied Scientific Instrumentation Inc. 29391 W. Enid Rd. Eugene, OR 97402 USA	Supplier for Solent and Bioptechs incubation chambers.	TEL: 541-461-8181 WEB: http://www.asiimaging.com/ EMAIL: info@ASIimaging.com
AutoMate Scientific, Inc. 336 Baden Street San Francisco, California 94131 USA	Programmable controlled perfusion systems, temperature control, valves and fittings, oocyte perfusion chamber, Petri dish perfusion chamber, sub-millisecond switching, submerged and interface tissue and brain slice chambers.	TEL: 415-239-6080 WEB: http://www.autom8.com/ EMAIL: info@autom8.com
Bellco Glass, Inc. 340 Edrudo Road, Vineland, NJ 08360 USA	Sykes-Moore culture chambers; used with stationary culture when medium is changed intermittently.	TEL: 1-800-257-7043 WEB: http://www.bellcoglass.com/ EMAIL: cservice@bellcoglass.com
BioCrystal Ltd OptiCell 575 McCorkle Blvd. Westerville, OH 43082 USA	OptiCell is a sterile, sealed cell culture environment between two optically clear gas-permeable growth surfaces in a standard microtiter plate-sized plastic frame with ports for access to the contents.	TEL: 614-818-0019 WEB: http://www.opticell.com EMAIL: sales@opticell.com
Bioptechs, Inc. 3560 Beck Road Butler, PA 16002 USA	Live cell microscopy environmental control systems. Thermal regulation of specimen and objective, electronic control and integration of temperature and perfusion.	TEL: 724-282-7145 WEB: http://www.bioptechs.com/ EMAIL: info@bioptechs.com
Bioscience Tools — CB Consulting Inc., 4527 52nd Street, San Diego, CA 92115 USA	Glass bottom Petri dishes; ultra-thin imaging chambers; temperature control; perfusion systems; small volume delivery systems; ultra-fast temperature/solution switch.	TEL: 1-877-853-9755 WEB: http://biosciencetools.com/ EMAIL: info@biosciencetools.com
C&L Instruments, Inc. 314 Scout Lane Hummelstown, PA 17036 USA	Fluorometers and fluorometer components for steady-state fluorescence measurements; complete fluorescence systems for photometry and fluorescence imaging.	TEL: 1-717-564-9491 WEB: http://www.fluorescence.com/ EMAIL: support@fluorescence.com
CellBiology Trading Hinsbeker Berg 28a Hamburg, 22399 Germany	Microinjection and incubation; EMBL live cell observation chamber.	TEL: 49-0-40-53889432 WEB: http://cellbiology-trading.com/ EMAIL: info@cellbiology-trading.com
Dagan Corporation 2855 Park Avenue, Minneapolis, Minnesota 55407 USA	Microscope stage temperature controller; perfusion controller.	TEL: 612-827-5959 WEB: http://www.dagan.com/ EMAIL: support@dagan.com
Digitimer Ltd 37 Hydeway Welwyn Garden City Hertfordshire, AL7 3BE, England	AutoMate Scientific, Medical Systems and Scientific Systems Design incubators, chambers, and perfusion systems.	TEL: +44 (0) 1707 328347 WEB: http://www.digitimer.com/ EMAIL: sales@digitimer.com
Grace Bio-Labs, Inc. P.O. Box 228 Bend, OR 97709 USA	Manufactures 3-D microporous coatings on microscope slides, and a variety of "press to seal" enclosures for microarrays, cell culture, and high throughput cytochemistry, hybridization, cytogenetics, and fluorescent imaging applications.	TEL: 1-800-813-7339 WEB: http://www.gracebio.com/ EMAIL: custservice@gracebio.com
Harvard Apparatus Inc. 84 October Hill Rd. Holliston, MA 01746 USA	Variety of valve controlled perfusion systems.	TEL: 508-893-8999 WEB: http://www.harvardapparatus.com EMAIL: bioscience@harvardapparatus.com
Integrated BioDiagnostics Schellingstrasse 4 80799 München, Germany	The µ-slide family of live cell imaging flow chambers; suited for optical studies of hydrodynamic shear stress on biofilms or adhesion studies on cell layers.	TEL: +49 (0)89 / 2180 64 19 WEB: http://www.ibidi.de/ EMAIL: info@ibidi.de
Intracel, Ltd. Unit 4 Station Road Shepreth, Royston Herts, SG8 6PZ England	WillCo glass bottomed dishes; Bioptechs micro-environmental control systems.	TEL: 01763 262680 WEB: http://www.intracel.co.uk/ EMAIL: intracel@intracel.co.uk
In Vitro Systems & Services GmbH Rudolf-Wissell-Str. 28 37079 Göttingen, Germany	Gas-permeable plastic foil (bioFOLIE 25); sterile tissue culture dish (petriPERM); Petri dish with gas-permeable base; two-compartment system.	TEL: ++49 551 500 97-0 WEB: http://www.ivss.de/ EMAIL: info@ivss.de
Life Imaging Services Kaegenstrasse 17 CH-4153 Reinach, Switzerland	Ludin imaging chamber; microscope temperature control system	TEL: ++41 (0)61 7116461 WEB: http://www.lis.ch/ EMAIL: info@lis.ch
MatTek Corporation 200 Homer Avenue Ashland, MA 01721 USA	Glass bottom culture dishes	TEL: 1-800-634-9018 WEB: http://www.glass-bottom-dishes.com/ EMAIL: DishInfo@mattek.com
Molecular Probes, Inc. 29851 Willow Creek Road Eugene, OR 97402 USA	Attofluor cell chamber designed for viewing live-cell specimens on upright or inverted microscopes. Chamber gaskets for imaging, perfusion, and incubation.	TEL: 1-541-465-8300 WEB: http://www.probes.com/ EMAIL: tech@probes.com

TABLE 19.3. (*Continued*)

Source	Description/Features	Contact Info
PeCon GmbH Ziegeleistraße 50 89155 Erbach Germany	Live cell imaging solutions including stage heating and cooling, CO_2 and O_2 regulation, and evaporation reduction.	TEL: 0049 (0) 7305 95666-0 WEB: http://www.pe-con.de/pecon/index.htm EMAIL: info@pecon.biz
Physitemp Instruments, Inc. 154 Huron Avenue Clifton, New Jersey 07013 USA	Heating & cooling stages (Peltier) for microscopes (–20° to +100°C); custom thermal stages.	TEL: 1-973-779-5577 WEB: http://www.physitemp.com/ EMAIL: physitemp@aol.com
SDR Clinical Technology 213 Eastern Valley Way Middle Cove, NSW 2068 Australia	Physiological recording chambers & accessories for use on the microscope stage; bath perfusion; temperature control.	TEL: +61-2-9958-2688 WEB: http://www.sdr.com.au/ EMAIL: sdr@sdr.com.au
Solent Scientific Limited 14 Matrix Park, Talbot Road, Segensworth PO15 5AP, UK	Manufacturers of full enclosure incubation chambers for research inverted microscopes, confocal microscopes and multi-photon microscopes.	TEL: +44 (0)870 774 7140 WEB: http://www.solentsci.com/ EMAIL: sales@solentsci.com
Stratech Scientific, Ltd. Unit 4 Northfield Business Park, Northfield Road, Soham, Cambridgshire CB7 5UE UK	CoverWell imaging chambers are designed to stabilize and support thick and free-floating specimens for confocal microscopy and imaging applications.	TEL: +44 (0)1353 722500 WEB: http://www.stratech.co.uk/
Warner Instruments, Inc. 1125 Dixwell Avenue, Hamden, CT 06514, USA	Full range of recording, imaging, and perfusion chambers; perfusion and valve control.	TEL: 1-800-599-4203 WEB: http://www.warneronline.com/ EMAIL: support@warneronline.com
WillCo Wells BV WG Plein 287 1054 SE Amsterdam, The Netherlands	WillCo-dish glass bottom dishes.	TEL: ++31(0)20 685 0171 WEB: http://www.willcowells.com EMAIL: info@willcowells.com
World Precision Instruments, Inc. 175 Sarasota Center Boulevard Sarasota, Florida 34240 USA	FluoroDish glass-bottom culture dish; Air-Therm ATX Air Heater Controller; programmable automated multi-channel perfusion system.	TEL: 941-371-1003 WEB: http://www.wpiinc.com/

the fluorescent probe should produce a strong signal and be both slow to bleach and non-toxic. Chapters 16 and 17 discuss fluorescent dyes that have been used in published work with confocal microscopy in detail.

Many dyes are useful when introduced to the medium surrounding cells to be labeled. Some of the classic and most commonly used cell stains include DiI for labeling the plasma membrane (Honig and Hume, 1986; Baker and Reese, 1993), $DiOC_6(3)$ for labeling internal membranes (Terasaki *et al.*, 1984), NBD–ceramide and bodipy–ceramide which label the Golgi apparatus (Pagano *et al.*, 1991), rhodamine 123 which labels mitochondria (Johnson *et al.*, 1980), potential sensitive dyes such as $DISBAC_2(3)$ (see Fig. 8.65, *this volume*) (Loew, 1993), and FM 1-43 (Betz *et al.*, 1992) which is used to follow plasma membrane turnover and vesicular release. Fluorescent ion indicators such as Fluo-3 (Minta *et al.*, 1989) can either be microinjected or added to the media in a cell-permeant acetoxymethylester form that becomes trapped inside the cell after being cleaved by intracellular esterases (see Chapter 42, *this volume*).

Minimizing Photodynamic Damage

Once the cells are labeled and on the microscope, one is faced with the challenge of collecting data without compromising the cell or bleaching the label. In practice, the major problem is light-induced damage. Fluorescent molecules in their excited state react with molecular oxygen to produce free radicals that can then damage cellular components and compromise cell health (Dixit and Cyr, 2003; see also Chapters 38 and 39, *this volume*).

In addition, several studies suggest that components of standard culture media might also contribute to adverse light-induced effects on cultured cells (see Siegel and Pritchett, 2000). Some early studies (Spierenburg *et al.*, 1984; Zigler *et al.*, 1985, 1991; Lepe-Zuniga *et al.*, 1987) indicated a phototoxic effect of *N*-2-hydroxyethylpiperazine-*N*′-2-ethanesulfonic acid (HEPES) containing media on cells under some circumstances. It seems possible that this effect might be more directly related to inadequate levels of bicarbonate (Cechin *et al.*, 2002). Other studies suggest that riboflavin/vitamin B2 (Zigler *et al.*, 1985; Lucius *et al.*, 1998) and the essential amino acid tryptophan (Griffin *et al.*, 1981; Silva *et al.*, 1991; Silva and Godoy, 1994; Edwards *et al.*, 1994) may mediate phototoxic effects. Whether these effects occur under typical confocal imaging conditions is unknown, but many of the photoeffects are reduced by antioxidants, so it seems advisable to maintain antioxidants (and some bicarbonate, as well) in the specimen chamber (see below) and to use photons with great efficiency.

Improving Photon Efficiency

There are several strategies to minimize the amount of excitation light required to collect data (see Chapters 2 and 9, *this volume*, for more details). Briefly, higher-NA objective lenses collect more of the fluorescent emission. For a given lens, there is also a theoretical optimal setting of the zoom magnification that best matches the resolution required to the allowable dose (see Chapter 4, *this volume*). When the focus plane is more than 5 µm from the coverslip, water-immersion lenses should be used to avoid the signal loss caused by spherical aberration when using an oil lens (see Chapters 7 and 20, *this volume*).

Another way to reduce light damage is to minimize the duration of the light exposure during the experimental setup. For example, one should try to focus as rapidly as possible and turn off the light source as soon as the focus range has been chosen. In addition, in single-beam scanning systems, make sure that your scanner is set up to blank the laser beam during scan retrace. Otherwise, areas on both sides of the imaged area will receive a very high light exposure as the beam slows down to change direction.

Finally, photon efficiency can be maximized by using the best mirrors, the correct pinhole size for the resolution required (in *x*,

y, and *z*), and photodetectors that yield the highest quantum efficiency at the wavelength of the signal.

Antioxidants

As noted above, one can also reduce photodynamic damage by adding antioxidants to the medium. Oxyrase (Oxyrase Inc., http://www.oxyrase.com) is an enzyme additive used to deplete oxygen in order to grow anaerobic bacteria. It has been used at 0.3 unit/mL to reduce photodynamic damage during observations of mitosis (Waterman-Storer *et al.*, 1993). Another approach is to include ascorbic acid in the medium. This reducing agent is typically used at 0.1 to 1.0 mg/mL but has been used at up to 3 mg/mL. A recent confocal study of calcium transients in isolated chondrocytes reported a relationship between laser intensity and the frequency of Ca^{2+} oscillations and cell viability: Ca^{2+} events were more frequent and cell viability was decreased with higher laser intensity (Knight *et al.*, 2003). Treatment with ascorbic acid reduced the Ca^{2+} events and improved cell viability (see also Chapters 16 and 17, *this volume*).

THE ONLINE CONFOCAL COMMUNITY

Confocal microscopy of living cells is an area of active research where individuals are constantly developing new techniques and approaches. One way to keep up with current practice is to join about 1600 others who subscribe to the Confocal e-mail listserver. This can be done by registering at the listserver Web site, located at http://listserv.buffalo.edu/archives/confocal.html. You will then begin to receive messages from other microscopists. Recent topics have included discussions on such diverse issues as autofluorescence problems, glass-bottomed culture chambers, damage to live cells during FRAP experiments, and announcements of confocal workshops. The listserver also has an extensive, searchable archive dating back to 1991, and this is freely accessible.

A CONVENIENT TEST SPECIMEN

Knebel *et al.* (1990) showed that onion epithelium (*Allium cepa*) is a simple preparation that can be used as a convenient test specimen for confocal microscopy of living cells. Figure 19.1 shows how to prepare onion epithelium. First, a small square of a layer is cut out using a razor blade. A forceps is used to peel off the thin epithelium on the inner surface of the onion layer. The epithelium is then put onto a microscope slide, covered with a drop or two of staining solution containing $DiOC_6(3)$, a marker of mitochondria and endoplasmic reticulum, and coverslipped. The stock solution of $DiOC_6(3)$ (0.5 mg/mL in ethanol) can be kept indefinitely if protected from light in a scintillation vial. The staining solution is a 1 : 1000 dilution in water on the day of the experiment. The center of these cells is usually occupied by a large vacuole, and the ER and mitochondria are located in a thin cytoplasmic region near the plasma membrane. Motion of the ER is relatively quick and easily detected in consecutive 1-s scans.

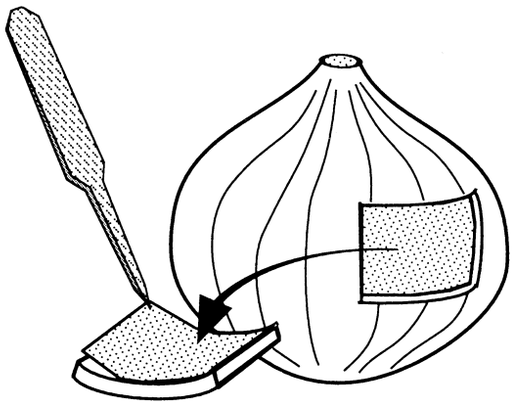


FIGURE 19.1. A convenient test specimen for confocal microscopy of cells in a living tissue: onion epithelium. This drawing shows how to obtain onion epithelium. As described in the text, the epithelium is stained with $DiOC_6(3)$, and the ER and mitochondria within the cells provide a bright and motile specimen.

SPECIFIC EXAMPLE I: VISUALIZING CHROMATIN DYNAMICS USING VERY LOW LIGHT LEVELS

It is clear from the discussion above that microscopy of living cells has become a technique of major importance in cell biology: it can be used to tell us *where* molecules are located, *when* they become localized, *how fast* they are moving, with which molecules they are *interacting*, and how long they stay *attached* to these molecules. All these properties can be observed in the natural environment of the living cell. The major limiting factor in live-cell imaging is phototoxic effect of light used for the observation of the cell. Here we will address some practical issues of phototoxicity based on our experience in imaging chromatin dynamics in living cells (Manders *et al.*, 1996; 1999; 2003; Verschure *et al.*, 1999; Moné *et al.*, 2004).

Phototoxicity

A large number of photochemical reactions are responsible for the phototoxic effect of light. Light can be absorbed by cellular components and induce chemical alterations in their molecular structure. For example, UV light is absorbed by DNA (absorption peak at 280 nm), directly inducing DNA damage. Here we assume that, working with visible light, the direct photodamage is negligible. In fluorescently labeled cells, the main source of photodamage is the production of reactive oxygen species (ROS) including singlet oxygen ($^1O_2$), superoxide ($\cdot O_2^-$), hydroxyl radical (HO·), and various peroxides. These activated oxygen species react with a large variety of easily oxidizable cellular components, such as proteins, nucleic acids, and membrane lipids. Singlet oxygen is responsible for much of the physiological damage caused by reactive oxygen species. For the production of singlet oxygen, the fluorescent label acts as a photosynthesizer in a photochemical reaction where dioxygen ($^3O_2$) converts into singlet oxygen ($^1O_2$). Singlet oxygen mainly modifies nucleic acid through the selective oxidation of deoxyguanosine into 8-oxo-7,8-dihydro-2′-deoxyguanonine. Proteins and lipids also will be damaged by ROS. Phototoxicity likely depends on several variables:

- **The photochemical properties of the fluorescent molecule.** Some molecules induce more phototoxicity than others, depending on the lifetime of their triplet state. For photodynamic therapy (PDT), dedicated molecules called photosensitizers have been designed in order to induce a maximum damage in tissue for the treatment of cancer (e.g., halogenated fluorescein is much more toxic than fluorescein). Another property that influences the phototoxicity of a molecule is the

local environment of the molecule. The active fluorophore of a GFP molecule is positioned on the inside of the protein, within the barrel structure (the "β-can"). Probably this hydrophobic protein environment contributes to the relatively low phototoxicity of GFP compared with naked fluorophores such as fluorescein or rhodamine.

- **The subcellular location of the fluorescent molecule.** When fluorescent molecules are situated close to DNA, the damaging effect of singlet oxygen is more pronounced. Despite several DNA-repair mechanisms, the cell will not continue its cell cycle (arrest) and may even die if there is too much DNA damage. Therefore, fluorophores in the cytoplasm seem to induce less phototoxicity than fluorophores in the nucleus.
- **The concentration of fluorophore.** It is clear that there is a relationship between the local concentration of fluorophore and the level of phototoxicity. We assume a linear relationship between fluorophore concentration and toxicity, although this has not been assessed directly and is complicated by the fact that if there is more dye, one need use less excitation.
- **The excitation intensity.** Fluorescent cells in a dark incubator are quite happy for weeks as long they are maintained in the dark. As the word *phototoxicity* implies, photons are needed to induce toxicity in a fluorescently labeled specimen. We usually assume a linear relationship between excitation light dose and toxicity, although the temporal regimen of the excitation may be important to how cells handle the accumulation of phototoxic biproducts. Phototoxicity is dependent on the wavelength of light in the sense that the wavelength of the toxic excitation light matches the excitation curve of the fluorophore. In other words, it is the excited fluorophore that is toxic. Koenig also found that, with two-photon excitation, the damage is proportional to the number of molecular excitations (see Chapter 38, *this volume*).

There is no clear evidence for differences in phototoxicity between green, red, or far-red fluorophores. In principle, excited Cy5 can be as toxic as excited FITC. However, the wavelength of excitation light can be a factor when imaging in thick specimen because stronger incident illumination is needed for comparable excitation of shorter wavelength fluorophores due to increased tissue scatter at shorter wavelengths.

Reduction of Phototoxicity

For many researchers, phototoxicity is a serious (and annoying!) limitation of their observations of living cells. When you do not look at a cell it is alive, but the moment you start to observe how it lives, it is killed by the light used to observe it. In experiments so far, we have succeeded in obtaining acceptable time series of living cells by carefully optimizing all steps in the imaging process in an effort to achieve (i) maximal signal-to-noise ratio (S/N), (ii) maximal spatial and temporal resolution, and (iii) minimal phototoxic effects. Specifically, phototoxicity has been minimized by (i) using radical scavengers (e.g., trolox) in the culture medium and (ii) using culture medium without phenol-red. Most important of all, however, is minimizing the total excitation light dose. The excitation light dose is the product of the light intensity and the exposure time. Decreasing either the excitation intensity or the excitation dose implies a loss of fluorescent signal. It is inevitable that a reduction of light dose puts a limitation on the S/N and the spatial and temporal resolution. The art of successful live-cell microscopy is finding the balance between image quality and cell vitality.

Improving Image Quality in Low-Dose Microscopy

Figure 19.2(A) shows a single time frame projection from a 3D time-series of a HeLa cell expressing the fluorescent histone fusion protein, H2B-GFP. In the time series shown in Figure 19.2(B), the cell is in late telophase at the start of the imaging and proceeds into interphase during the movie. This movie shows data from a study on the dynamics of chromatin during decondensation (Manders *et al.*, 2003).[1] In these experiments, the excitation light intensity was kept below 150 nW and the total exposure time[2] of a cell that was 3D imaged for 3 h was not more than 70 s. Under these conditions the total light dose was approximately $10\,J\,cm^{-2}$. In experiments where we used a higher dose of light we observed phototoxic effects, such as cell cycle arrest and cell death.

Reducing the total light dose during an experiment requires that the number of 3D images in the sequence (temporal sampling rate) be low. Because of this limited sampling rate, live-cell movies are usually under-sampled in time according to the Nyquist criterion. As a result, such movies often show cells that nervously move from one place to another and sometimes suddenly rotate. We have applied an image processing procedure to correct for all the movements (translation and rotation) of the cell. For each 3D image of the time sequence, a translation and rotation transform vector was calculated in order to obtain a best fit with the previous image in the sequence. After a series of such transformations, a new movie was produced showing a stable cell that does not move or rotate. Only internal movements are visible. After this correction procedure, we applied a simple Gaussian spatial filter to reduce noise in the image [Fig. 19.2(C,D)]. We also applied a temporal filter by adding to each voxel of the 3D image at each time-point the value for that voxel in the previous and subsequent image multiplied by an intensity factor of 0.5. Our experience is that temporal filtering makes the movie easier to interpret.

Low-Dose Imaging Conclusion

The success of live-cell microscopy is very much dependent on minimizing or avoiding any toxic effect of light on the biological system under observation. A certain dose of light may induce serious DNA damage that may arrest the cell cycle, whereas the diffusion coefficient of a certain protein is not influenced at all at the same dose. In the experimental example shown here [Fig. 19.2(B)], we used only 150 nW of incident beam power. This dose was found to be phototoxic in other experiments using fluorescein instead of GFP, and it was found necessary to drop the laser power to 50 nW [Fig. 19.2(E)]. These power levels are far lower than (i.e., <1% of) those commonly used in confocal microscopy, a circumstance facilitated at least in part by the fact that the chromosomes are quite heavily stained.

Our collective experiences indicate that the effect of phototoxicity depends on the cell type, the stage of the cell cycle, the fluorophore, the observed biological process, and many other experimental conditions. We conclude that there is no general guideline for the maximum allowable laser power: it must be assessed empirically for each experimental condition. As a general

[1] Both movies are on the Springer Web site associated with this book.
[2] Power levels were measured using a photometer sensor that was oil-coupled to the specimen side of an oil-coupled coverslip.

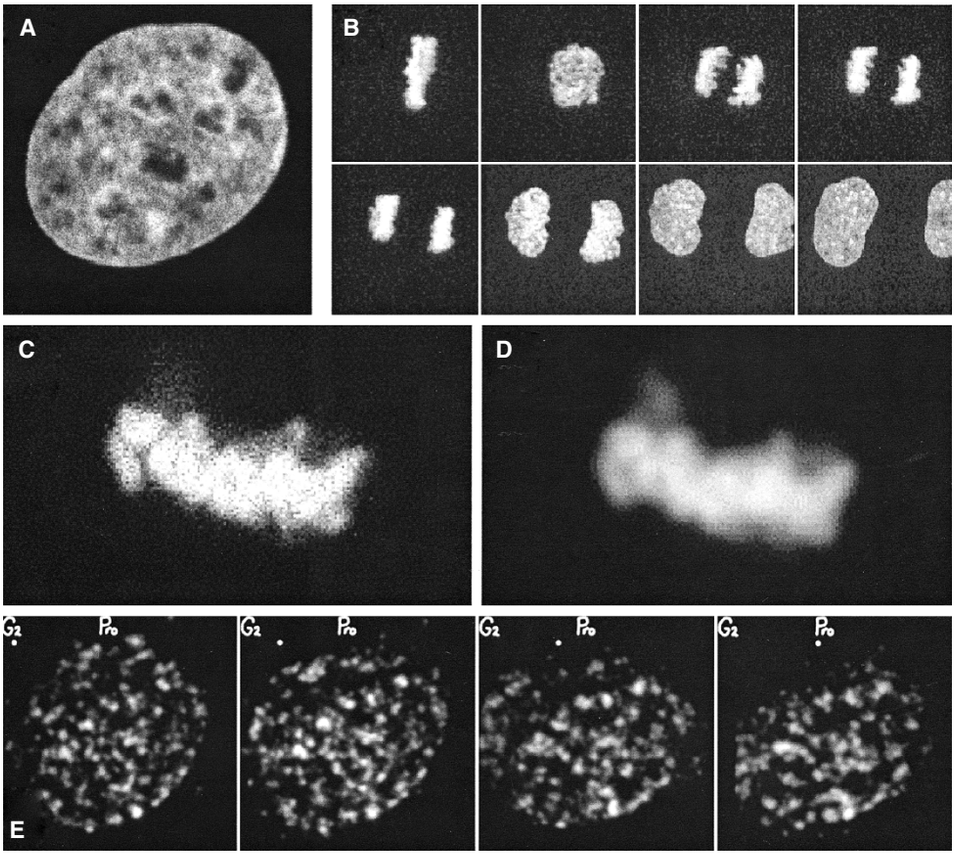


FIGURE 19.2. (A) A single time frame from a time-series of a HeLa cell expressing the fluorescent histone fusion protein, H2B-GFP. The cell is in late telophase. (B) A time-series of another cell shows how it proceeds into interphase during chromatin decondensation. In this experiment, the excitation light intensity was kept below 150 nW. Higher laser power induced cell cycle arrest. (C, D) Application of a simple Gaussian spatial filter reduces noise in the raw image (C) and improves image quality (D). (E) Time-series showing chromatin structure in a cell proceeding from G2 (*left*) to prophase (*right*). Note that the images were captured with a very low power dose (50 nW). See the supplemental video movie at http://www.springer.com/0-387-25921-X. For details, see Manders and colleagues (2003).

rule, however, images of living cells are almost always more noisy than images of fixed preparations because the incident illumination intensity needs to be kept to a minimum to maintain cell viability. A noisy image in which one can see what is absolutely essential is of more use than a "better" image of a damaged cell. Keep in mind that not all types of damage are equally easy to detect. Damage may disturb (or create!) a monitored process, it may interfere with cell division, or it may cause the cell to bleb and pop! We recommend that the experimentalist BEGIN by assuming that "to observe is to disturb." Measure the power level coming out of the objective. Try your experiment again using twice the power, and again using half the power. Make sure that you can explain any "behavioral" differences between these runs.

We show here that some simple image processing (deconvolution) can help facilitate the analysis of live-cell imaging data by reducing noise and improving the point-to-point coherence when viewing a time-series of images. Note the reduction in noise level between Figure 19.2(C) and 19.2(D).

SPECIFIC EXAMPLE II: MULTI-DIMENSIONAL IMAGING OF MICROGLIAL CELL BEHAVIORS IN LIVE RODENT BRAIN SLICES

The example above serves to illustrate that confocal microscopy is an important tool for studying dynamic subcellular processes in live, isolated cells. Many biologists are also interested in understanding dynamic structural and functional aspects of cells within the context of a natural tissue environment. As noted above, confocal and multi-photon imaging have been applied to intact, normally functioning systems such as the eye, skin, or kidney. Some recent studies have even extended these observations beyond superficial tissues to deep tissues of the brain (e.g., Mizrahi *et al.*, 2004).

However, some tissues are much less accessible, or it may be of interest to be able to experimentally perturb or control the system under study. For these purposes, the *in vitro* tissue slice has been an important experimental preparation (e.g., Gähwiler *et al.*, 1997). Smith and colleagues (1990) were among the first to show the feasibility of imaging the structure and physiology of living mammalian brain tissue slices at high resolution using fluorescence confocal microscopy. Since then many confocal studies of both the structural and the physiological dynamics of cells in tissue slices have appeared, and it seems that interest in imaging *in vitro* tissues is continuing to grow. We will address here some of the most common problems, challenges, and limitations inherent in confocal studies of live tissue slices. These points will be illustrated by drawing from our own time-lapse studies in live tissue slices of developing mammalian central nervous system (CNS) (Dailey and Smith, 1993, 1994, 1996; Dailey *et al.*, 1994; Dailey and Waite, 1999; Marrs *et al.*, 2001; Stence *et al.*, 2001; Grossmann *et al.*, 2002; Petersen and Dailey, 2004; Benediktsson *et al.*, 2005).

Some of the major problems encountered when imaging fluorescently labeled cells in live tissue slices are:

- **Attaining a suitable level and specificity of staining.**
- **Maintaining cell/tissue health**: pH, temperature, oxygen, etc.

- **Keeping cells in focus**: Can be an immense problem when following cells over long periods of time:
  - Movement of the microscope stage, especially when stage heaters are used.
  - Movement of the tissue: apparent movement that is really caused by movement of the focal plane within the specimen; natural movement of whole organisms or those caused by heartbeat, etc.
  - Movement of cells within the tissue, for example, cell migration, extension/retraction of cell processes.
  - Movement related to experimental procedures, for example, stimulus-induced osmotic changes.
- **Attaining a useful image with a high S/N of cells deep within tissue:**
  - Imaging away from damaged tissue surfaces.
  - Light scatter by the tissue.
  - The problem of spherical aberration.
- **Handling data**: viewing, storing, retrieving, and analyzing four-dimensional (4D) data sets:
  - Short term: monitoring experiments on the fly; adjusting focus.
  - Long term: accessibility and security of archived data.

We have been exploring the dynamic behavior of a type of brain cell, termed microglia, following brain tissue injury. These cells undergo a dramatic transformation ("activation") from a resting, ramified form to an amoeboid-like form within a few hours after traumatic tissue injury. Activation of microglia is triggered by signals from injured cells (including neurons), and this mobilizes microglia to engage neighboring dead and dying cells. Naturally, these events are best studied in the context of a complex tissue environment containing the native arrangement of tissue components; thus time-lapse confocal microscopy is well suited to examine these events. The general approach we have taken is to label the cell surface of microglia with fluorescent probes and, subsequently, to follow the dynamic movements of these cells, as well as their interactions with other labeled cells, within live tissue slices continuously over periods of time up to 28 h (Dailey and Waite, 1999; Stence *et al.*, 2001; Grossmann *et al.*, 2002; Petersen and Dailey, 2004).

Preparation of Central Nervous System Tissue Slices

A useful method of preparing and maintaining live brain tissue slices for microscopy is based on the organotypic (roller-tube) culture technique of Gähwiler (1984) or the static filter culture technique of Stoppini and colleagues (1991). Briefly, these techniques involve rapidly removing the tissue of interest (in this case, neonatal rat or mouse hippocampus), then slicing the tissue with a manual tissue chopper (Stoelting, Chicago, IL) at a thickness of 300 to 400 μm. Others have used a vibratome or custom-built instruments akin to an egg slicer. In the case of the roller tube technique, the tissue slices are secured to an alcohol-cleaned coverslip (11 × 22 mm) with a mixture of chicken plasma (10 μL; Cocalico) and bovine thrombin (10 μL; Sigma). Collagen gels (Vitrogen; CellTrix; O'Rourke *et al.*, 1992) and Cell-Tak (BioPolymers Inc.; Barber *et al.*, 1993) have also been used successfully to attach slices. In the case of the plasma clot, the slices are adherent within about 10 min, at which point the coverslips are placed in a test tube with 1 mL of HEPES-buffered culture media containing 25% serum. The tubes are kept in a warm box (37°C) and rotated at 12 rph in a roller drum tilted at 5° to the horizontal. In the case of the static filter cultures, brain slices are placed on porous cell culture inserts in 6-well plates containing ~1 mL of bicarbonate-buffered culture media per well. The filter cultures are maintained at 36°C in a 5% CO_2 incubator. In either case, these "organotypic" culture methods provide a means for maintaining tissue slices *in vitro* for up to several weeks (Gähwiler *et al.*, 1997).

Fluorescent Staining

Microglia

Often it is most useful to label only a small percentage of the total number of cells within a tissue volume, and in certain cases it is desirable to label only an identified subset of cells. Vital fluorescent probes must be non-toxic and resistant to photobleaching. In the case of microglia, there are several commercially available fluorescent conjugates (FITC, Alexa Fluor–488, –568, or –647) of a highly selective, non-toxic lectin (IB_4) derived from *Griffonia simplicifolia* seeds (Sigma; Molecular Probes). This lectin (IB_4) has an exclusive affinity for α-D-galactosyl sugar residues on glycoproteins and glycolipids (Wood *et al.*, 1979). In mammalian brain tissues, IB_4 labels only microglia and endothelial cells lining blood vessels and capillaries (Streit and Kreutzberg, 1987). The simultaneous labeling of microglial cell populations and blood vessels has revealed novel, dynamic interactions between these structures (Grossmann *et al.*, 2002). Incubation of brain slices or slice cultures for 1 h in IB_4-containing medium (5 μg/mL) is sufficient for robust labeling of microglia up to ~50 μm deep within tissues (Kurpius and Dailey, 2005).

Nuclei of Live or Dead Cells

One of a variety of fluorescent DNA-binding dyes is used to label live or dead cell nuclei in brain tissue slices (Dailey and Waite, 1999; Petersen and Dailey, 2004). To visualize the nuclei of live cells, we use one of the membrane-permeant dyes that have spectra in the far-red, SYTO59 (abs/em: 622/645 nm) or SYTO61 (620/647 nm). For labeling the nuclei of dead cells, we use one of the membrane impermeant dyes, Sytox Green (504/523 nm), Sytox Orange (547/570 nm), or To-Pro-3 (642/661 nm) (all from Molecular Probes). All DNA-binding dyes are applied for 10 to 20 min (1 : 10,000). These dyes are used in combination with fluorescently tagged IB_4 to image microglial behaviors in relation to other cells.

Maintaining Tissue Health on the Microscope Stage

Image data obtained from compromised tissue is useless at best, and deceiving at worst. For example, CNS slice physiologists have long known that oxygen deprivation can have severe effects on synaptic activity, although CNS tissues from developing animals seem to have a fairly high resistance to hypoxia (Dunwiddie, 1981).

It is not always easy to assess the health of living tissue on the microscope stage, but in the case of dynamic processes such as cell division or cell migration, one would at least expect that the cells perform these activities at rates near that expected based on other methods of determination. Also, one should become suspicious if the rate of activity consistently increases or decreases over the imaging session. For example, exposure of fluorescently labeled axons to high light levels can reduce the rate of extension or cause retraction. In contrast, high light levels can produce a long-lasting increase in the frequency of Ca^{2+} spikes in Fluo-3-labeled astrocytes in cultured brain slices. In many cases, there will not be a useful benchmark for determining phototoxic effects, but consis-

tent changes during imaging will serve to warn the concerned microscopist. It may be worth sacrificing a few well-labeled preps to determine if different imaging protocols, such as lower light levels or longer time intervals between images, significantly alter the biological activity under study.

Requirements for maintaining healthy tissue during imaging dictate specimen chamber design. A closed specimen chamber has the advantage of preventing evaporation during long experiments and stabilizing temperature fluctuations caused by this evaporation. We found that microglia in tissue slices maintained in a closed chamber (volume ~1 mL) with HEPES-buffered culture medium remain viable and vigorous for about 6 h, after which point the chamber medium acidifies and cell motility declines. However, when the old chamber medium is exchanged with fresh medium, the cells jump back to life again. This crude method of periodic medium exchange has supported continuous observation of DiI-labeled migrating cells in tissue slices on the microscope stage for as long as 45 h (O'Rourke *et al.*, 1992). However, when using this approach, one runs the risk of mechanically disturbing the chamber or inducing a temperature change and thereby causing a jump in focus.

A more elegant method for medium exchange and introduction of reagents involves continuous superfusion. A variety of perfusion chambers with either open or closed configurations are available (see Table 19.3). Sometimes it is necessary to design and construct very sophisticated temperature and fluid-level control systems (e.g., Delbridge *et al.*, 1990; or Walcerz and Diller, 1991). Such chambers permit very rapid exchange of medium (seconds rather than minutes), which is necessary for physiological experiments requiring high time resolution. There are also now commercially available, programmable, automated perfusion systems that permit rapid switching between one of several perfusion channels (see Table 19.3). Some experimental conditions require only relatively simple, low-cost chambers and perfusion systems, such as the one depicted in Figure 19.3 (see also Dailey *et al.*, 2005). We have used such a design to continuously superfuse tissue slices on the microscope stage for many hours. The tissues seem to remain healthy for at least 20 h when perfused (10–20 mL/h) with either the culture medium (see Dailey *et al.*, 1994) or normal saline, both of which are buffered with 25 m*M* HEPES.

Specimen heating is essential for many experiments, but this can induce an agonizing battle with focus stability (see below) as the chamber and stage components heat up. Because there is always a time lag between when the sensor of the temperature control detects that the temperature is too high (or low) and the time that the heater is able to warm the whole stage, the actual temperature of most stage heaters is always slowly oscillating, a fact that causes the focus plane to shift in a periodic manner. A sufficient period of preheating can sometimes reduce this problem. Another approach is to use a modified hair dryer to blow warm air onto both the chamber and the stage (see Dailey *et al.*, 2005) or an egg-incubator heater to heat all the air in an insulated box surrounding the entire microscope (Potter, 2004).

It is also important to monitor the temperature of the perfusing medium very near to the specimen. A low-cost microprocessor temperature controller that reduces fluctuations in the heating/cooling cycle can be obtained from Omega Engineering (Stamford, CT).

Imaging Methods

It should by now be evident that a primary concern when imaging living cells is photon collection efficiency. This is especially true when imaging dynamic processes, such as cell migration, over long periods of time. Higher collection efficiency will afford effectively lower excitation light levels, thus permitting more frequent sampling or observations of longer duration.

We have been using commercially available laser scanning confocal systems (Leica TCS NT and Leica SP2 AOBS). For illumination, the microscopes are equipped with multiple lasers. Both systems offer simultaneous excitation and detection in more than one epi-fluorescent channel. In addition, the SP2 acousto-optic

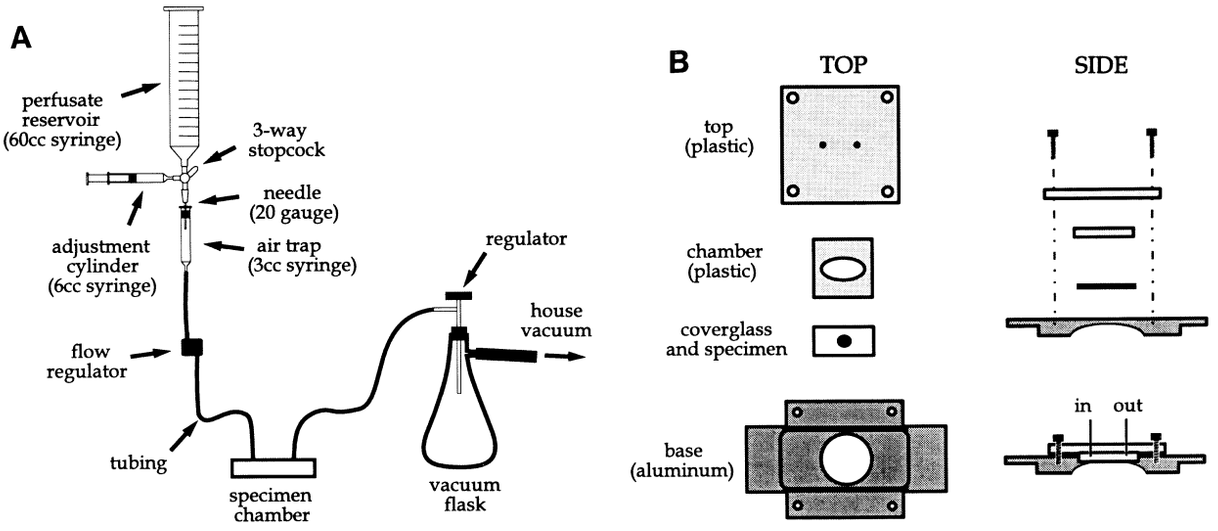


FIGURE 19.3. Schematic diagram of a simple perfusion system for maintaining tissue slices on the microscope stage. The gravity perfusion system is constructed using readily available syringes, three-way stopcocks, and tubing. The perfusion rate is adjusted using a simple thumb-wheel regulator. Perfusate is removed through a vacuum line and flask.

beam splitter (AOBS) system offers increased flexibility by providing continuously variable wavelength selection in the excitation pathway. This permits customizing the spectral detection to maximize throughput in separate channels. The Leica objectives that we find most useful are a dry 20×/0.75 PlanApo lens, and a 63×/1.2 water-immersion PlanApo objective lens.

Imaging Deep Within Tissue

Often the goal of studies in tissue slices is to examine biological processes within a cellular environment that approximates that found *in situ*. In the case of tissue slices, it is usually desirable to image as far from cut tissue surfaces as possible to avoid artifacts associated with tissue damage. However, the cut surfaces of developing CNS tissue slice cultures contain a plethora of astrocytes, activated microglia, and a mat of growing neuronal processes. Time-lapse imaging of these regions provides striking footage of glial cell movements, proliferation, and phagocytosis (Stence *et al.*, 2001; Petersen and Dailey, 2004).

If high-NA (1.3, 1.4) oil-immersion lenses are used to focus more than 5–10 μm into most living specimens, spherical aberration will severely reduce resolution and consequently diminish signal levels (see also Chapters 1, 7 and 20, *this volume*). Instead one should use water-immersion lenses, or on tissue having a refractive index (RI) around 1.48, an objective designed for glycerin immersion. Table 18.2 in the preceding Chapter lists RI values for a number of tissues. Efforts to image more than 50μm into tissue is also complicated by a number of other factors:

- Weak staining of cells due to poor dye penetration.
- Light scatter by the overlying tissue components.
- Spherical aberration.

The first problem can be overcome if the dye can be injected into the tissue with a minimum of disruption, or if tissues can be harvested from transgenic animals expressing fluorescent proteins in subsets of cells (e.g., Zuo *et al.*, 2004). Light scatter by the tissue can be minimized by using longer-wavelength dyes (see Chapters 28 and 37, *this volume*). Indeed, we find that a long-wavelength (Alexa Fluor-647; Molecular Probes) conjugate of IB_4 noticeably improves visibility of labeled cells in deeper portions of the tissue slice. Imaging at longer wavelengths may also reduce phototoxic effects because the light is of lower energy. Finally, the problem of spherical aberration can be improved by using water-immersion objective lenses or the recently introduced automatic spherical aberration corrector (Intelligent Imaging Innovations, Denver, CO; and also Chapters 1, 7, and 20, *this volume*).

Keeping Cells in Focus

The optical sectioning capability of the confocal microscope can be simultaneously a blessing and a curse. On the one hand, thin optical sections reduce out-of-focus flare and improve resolution. However, with such a shallow depth of focus, even very small changes in the position of the objective lens relative to the object of interest within the specimen can ruin an otherwise perfect experiment. This is a particular problem when imaging thin, tortuous structures such as axons or dendritic spines within neural tissue. A moving focal plane can, for example, give one the erroneous impression of dendritic spine extension or retraction. This problem is compounded when imaging cells and cell processes that are in fact actively moving within the tissue.

One obvious approach is to image the cells in four dimensions (3D × time). This can absorb some changes in tissue and stage movement as well as help track cells that move from one focal plane to another. In addition, our strategy has been to image with the detector pinhole aperture substantially open, corresponding to a pinhole size roughly 4 Airy units in size. Although this reduces the axial resolution slightly, it has the dual advantage of achieving a higher S/N at a given illumination intensity, as well as thickening the optical section. On our microscope systems, the open pinhole configuration gives an apparent optical section thickness of about 3 μm when using a 20× NA 0.7 objective. Thus, for each time point, we collect about 15 images at axial step intervals of ~2 μm. The guiding principle here is to space the image planes in the axial dimension so as to maximize the volume of tissue imaged but not lose continuity between individual optical-section images.

When these image stacks are collected at ~5-min intervals at power levels of ~50 to 75 μW (back aperture of objective), IB_4-labeled cells do not appear to suffer phototoxic effects and can be imaged continuously for over 20 h. Image stacks can be recombined later using a maximum brightness operation. Unfortunately, even when *z*-axis stacks of images are collected, tissue movements can be so severe as to necessitate a continuous "tweaking" of the focus. Thus, it is helpful to monitor image features on the screen (by making fiduciary marks on an acetate sheet taped to the monitor screen), or to store the data in such a way that they are quickly accessible and can be reviewed on the fly to make corrective focus adjustments.

Ideally, one would like an automated means of maintaining the desired plane of focus, especially for long imaging sessions. Although there are several autofocus methods that work for simple specimens (e.g., Firestone *et al.*, 1991), imaging structures in 3D tissue presents a significant challenge because there is no single image plane on which to calculate focus.

Handling the Data

Imaging tissue in 3D over time solves some problems but generates others. In particular, how does one deal with the gigabytes of image data that are often obtained in a single experiment? Fortunately, improvements in desktop computer performance and storage capacity, coupled with lower cost, make this much less of a problem than it used to be. Desktop workstations now contain hard drives with very large storage capacities (hundreds of gigabytes), and archiving methods and media are readily accessible and inexpensive. We typically store newly acquired data on a network server for image processing (such as spatial filtering or deconvolution) and analysis, then archive the data onto compact disks (CDs) or digital video disks (DVDs). This is a technology that is sure to continue rapid advancement, making it easier to store and access image data. At the end of the time-lapse experiment, the *z*-axis image stacks are combined in a variety of ways for viewing. For time-lapse studies, it is generally most useful to produce a set of "extended focus" images for viewing time-points in rapid succession. Depending on the file format, these image series can be viewed in one of a number of image viewers, including Scion Image or ImageJ (freely available from Scion Corp.). To create the projection images, we use a maximum brightness operation running in a custom-written Pascal macro to construct a 2D representation of each 3D data set (Stence *et al.*, 2001). When the axial step interval is appropriate (see above), portions of single cells that pass through the various focal planes appear contiguous. Alternatively, the image stacks can be reassembled into a set of

red–green 3D stereo images. Such images, when played in rapid succession, provide 3D depth information as well as time information in thick tissue samples. If more than one fluorescent channel is used, they can be combined to create multicolor images.

Results

The ability to collect 3D image data sets over long periods of time and at relatively short time intervals has revealed new information on the dynamics of microglial cell activation, migration, and cell–cell interactions in live mammalian brain tissues. Here we offer some examples of the kinds of data that can be obtained, along with some possible modes of data analysis.

In Figure 19.4, we show an example of a one-channel, single focal plane confocal time-lapse observation. Several IB_4-labeled microglial cells in a live, "roller tube" slice culture were repeatedly imaged at intervals of a few minutes to reveal movements of microglial cells over time. These movements can be quantified using automated edge detection [Fig. 19.4(A)]. Computer analysis using 2D Dynamic Image Analysis Software (DIAS; Soll, 1995) shows differences in motile behavior of three cells, as determined by tracing the cell perimeter [Fig. 19.4(B)]. Cell motility movements can be displayed as regions of protrusion (green) or retraction (red) by comparing cell shape over successive time-points [Fig. 19.4(C)]. Many parameters of cell shape and movement can be quantified easily using DIAS (Soll, 1995, 1999; Heid *et al.*, 2002).

Dual-channel, time-lapse confocal imaging of a specimen labeled with more than one fluorophore can provide information on the dynamic relationship between cell components or diverse cell types. In Figure 19.5, we show a two-channel time-lapse series of IB_4-labeled microglia and cell nuclei. Images from each channel (green and red) were collected simultaneously using a two-detector system. The nuclear marker (SYTO 61) labels all cells, including microglia. Time-lapse imaging shows the location of nuclei within migrating cells [Fig. 19.5(A)], and DIAS analysis can be used to plot and analyze the movements of nuclei [Fig. 19.5(B)].

Dual-channel, 3D time-lapse confocal imaging can yield information on the relative movement and location of structures labeled with two or more fluorophores within a thick tissue specimen. In the example shown in Figure 19.6, the movements of IB_4-labeled microglia are observed in the context of dead cell nuclei labeled with To-Pro-3, a membrane-impermeant DNA binding dye. The stereo images reveal the movements of microglia on the surface of the tissue slice as well as deep within the tissue. Such information is being used to study differences in the behaviors and cell–cell interactions of microglia in a brain tissue environment. Note, for example, the rapid microglial movement and phagocytosis of a dead cell nucleus in the time-lapse series [Fig. 19.6(D)].

In summary, the 4D and five-dimensional (5D) imaging methods outlined here capture more of the events occurring within the tissue and also provide the researcher with assurance that apparent changes in the length of even the smallest branches and fine filopodia are not due to the structures moving in and out of the focal plane. They also provide a means for exploring the dynamic interactions between different molecules, cells, and cell types within thick biological specimen.

Conclusion

Imaging of living specimens at a high S/N can be achieved with very low levels of incident illumination.

Imaging with a fairly large pinhole strikes a balance between image quality and focus problems during long-term observation of live tissue.

Four-dimensional time-lapse imaging is useful for following moving cells and fine cellular processes within complex tissues. Under optimal conditions, 3D data can be collected over long periods of time (>20 h) at relatively short time intervals (~5 min).

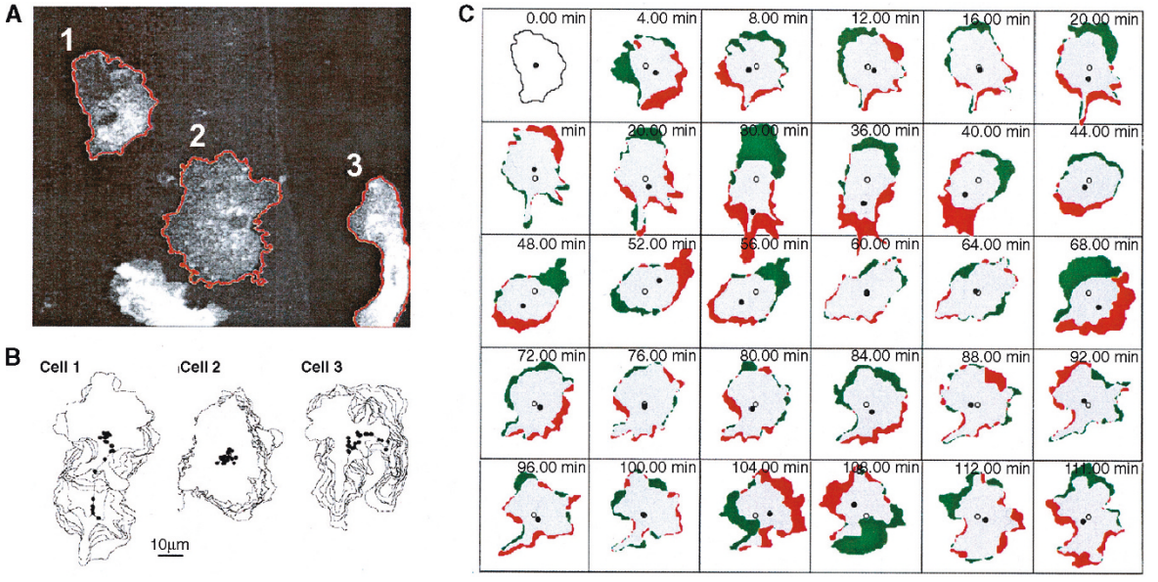


FIGURE 19.4. Use of a Dynamic Image Analysis System (DIAS; Soll, 1995, 1999) to characterize microglial motility behaviors in time-lapse imaging experiments. (A) Boundaries (*red lines*) of three FITC–IB_4-labeled microglial cells were defined by automated, computer-assisted edge detection. (B) Tracings of the three cells show motility behaviors over a 2 h period. The cell centroid (*black dots*) were computed and plotted for each time-point. Note that all three cells are motile, but cell 2 does not locomote. (C) Areas of new protrusion (*green*) and resorption (*red*) are shown for cell 1 at 4 min intervals. The new centroid (*open dot*) is shown in relation to the former centroid (*filled dot*).

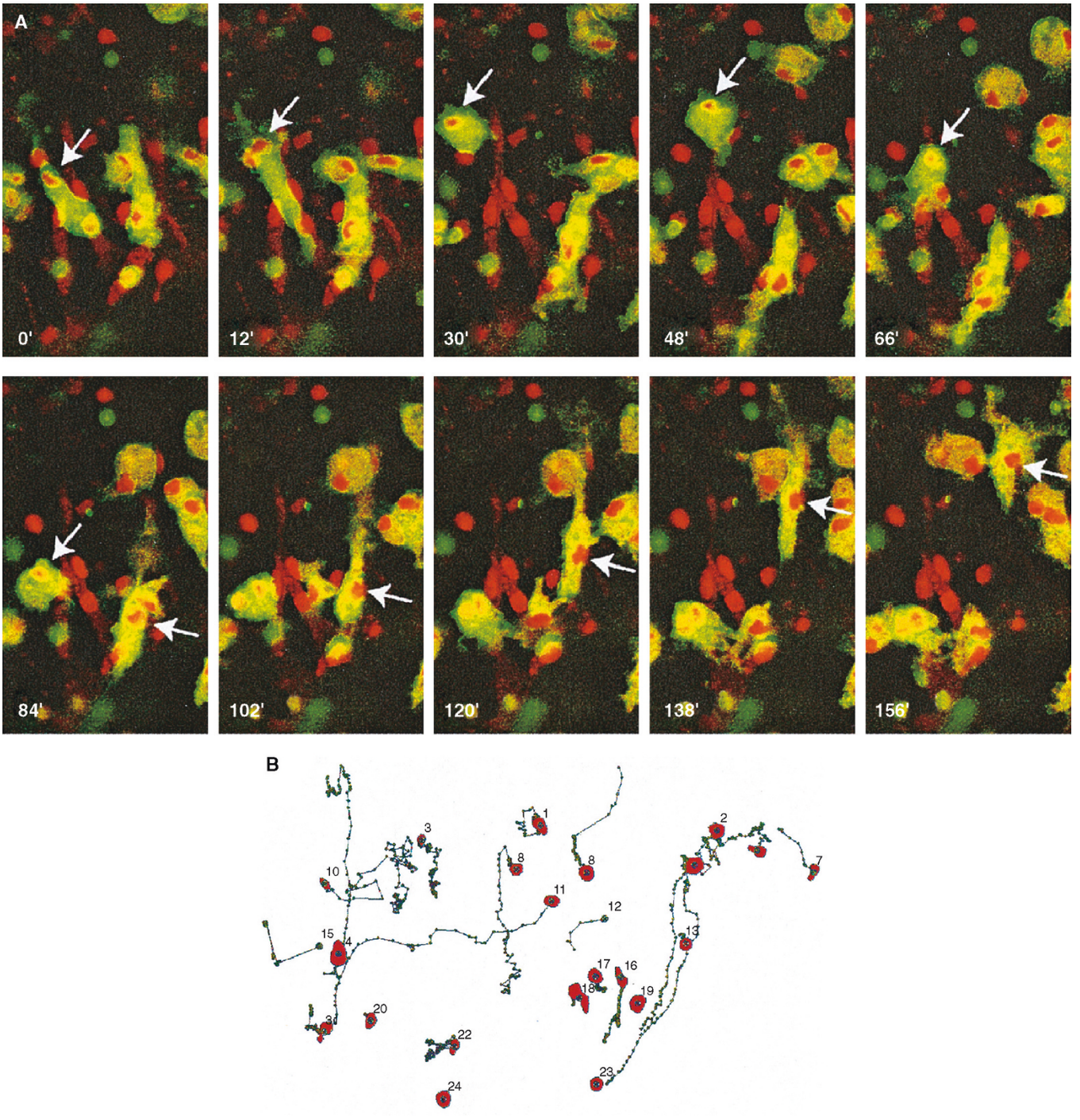


FIGURE 19.5. Two-channel time-lapse imaging of microglia (*green*) and cell nuclei (*red*). (A) Time lapse sequence shows capability of simultaneously imaging IB_4-labeled microglia and nuclei of cells using a cell membrane permeant DNA binding dye (Syto61). Note the nuclei (*arrows*) in two different migrating microglial cells. The sequence spans 156 min. Only a small portion of the original field of view is shown. (B) Automated tracing of the movement of cell nuclei shows paths taken by nuclei of cells in the experiment show in (A). Nuclei were detected by DIAS software (Soll, 1995). Only a select subset of nuclei are shown. Note differences in the movement among different cells.

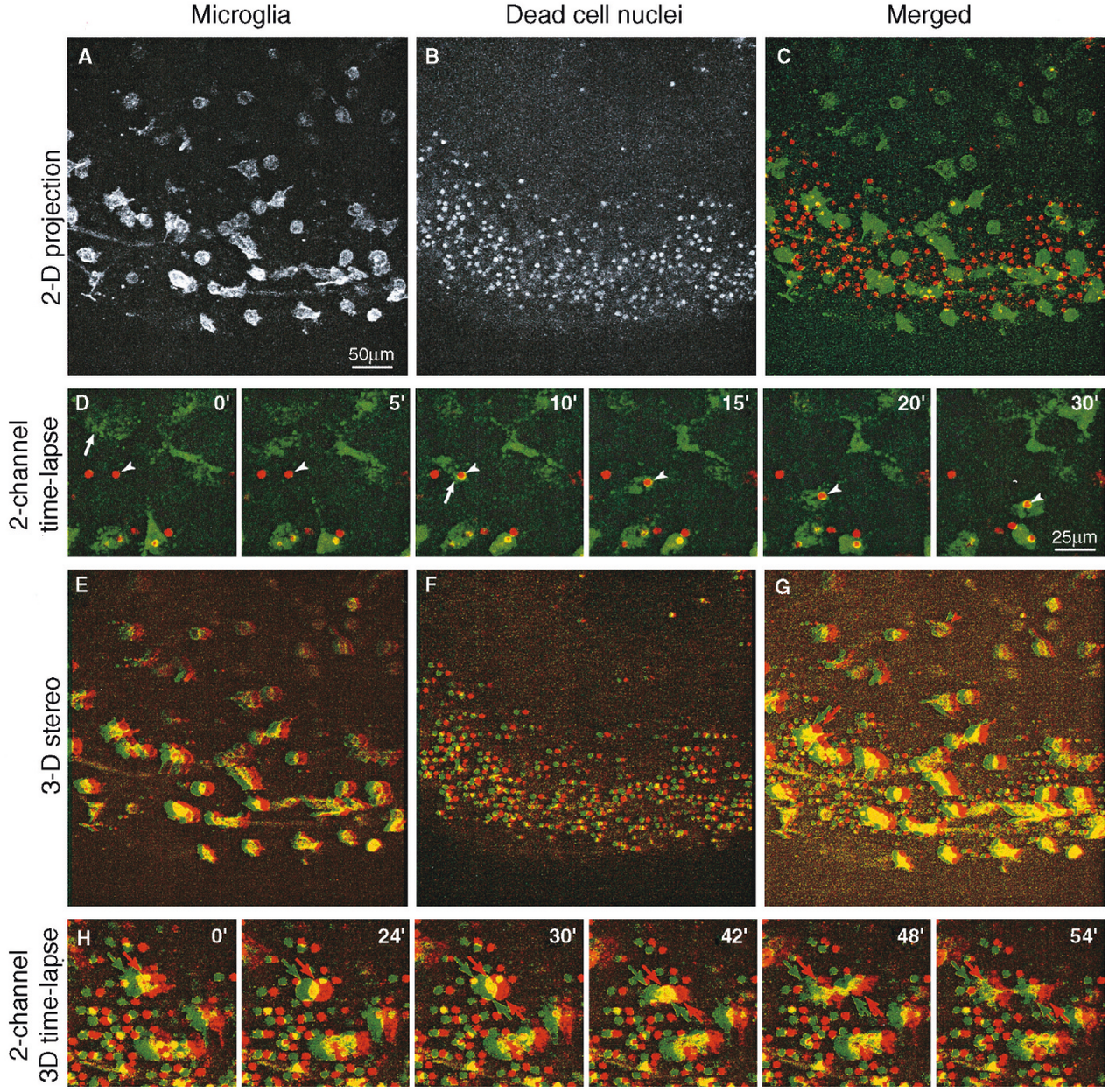


FIGURE 19.6. Two- and three-dimensional, two-channel time-lapse imaging of microglial movements and phagocytosis of dead cell nuclei in live rat brain tissue slice cultures (P6+2DIV). (A) Microglia are stained with a fluorescent lectin, FITC-IB_4. (B) Dead cell nuclei are stained with To-Pro-3. (C) Merged image of (A) and (B). The image represents a projection of nine optical sections spanning 40 μm in *z*-depth. Images were captured using a 20×/0.7 dry objective. (D) Time-lapse sequence of a portion of the field of view above showing phagocytic clearance of a dead cell nucleus (*arrowhead*) by a locomotory microglial cell (*arrow*). Note that the microglial cell maintains a rapid rate of locomotion as it sweeps over and picks up the dead cell nucleus. (E–G) 3D stereo projections of images in A through C above. Use red–green glasses (red over left eye) to view depth. (H) 3D stereo time-lapse sequence showing mitosis of a microglial cell (*arrow*) near the surface of the brain slice culture. The small, round objects represent the condensed nuclei of dead cells. Time is shown in minutes. See the supplemental video movies at http://www.springer.com/0-387-25921-X (Adapted from Petersen and Dailey, 2004.)

Multi-channel (5D) imaging can provide information on the dynamic relationship of different cell or tissue components. Future developments should address constraints on high-resolution imaging deep (>50 μm) within tissue. Improvements will likely be achieved by using water-immersion lenses and external automatic spherical aberration correctors (see Chapter 20, *this volume*) and by employing longer wavelength dyes to reduce light scatter by the tissue and to minimize phototoxic effects.

FUTURE DIRECTIONS

For confocal microscopy of living cells, the most important characteristic of the instrument is its efficiency in collecting and detecting the fluorescence emission light from the specimen (Chapter 2, *this volume*). Any improvement in this efficiency reduces the amount of light damage and allows the gathering of more data. The increased data can either be in the form of more images, images

with less statistical noise, or images obtained with greater spatial or temporal resolution. Newer models of existing commercial confocal microscopes have substantially improved photon efficiency. In addition, there have been technological improvements in the ability to separate the excitation and fluorescence emission of fluorophores, providing greater flexibility for multi-channel imaging and quantitative image analysis in live cells and tissues. Finally, the advantages of either Gaussian-filtering 2D data or deconvolving 3D data to reduce the effects of Poisson noise are now widely appreciated. Routine application of this approach can reduce the light load to the specimen by a factor of from 10 to 100 while still producing images with the same apparent resolution and signal-to-noise ratio.

Technological and conceptual advancements are also likely to push the spatial and temporal resolution and other modes of fluorescence microscopy (e.g., Gustafsson, 1999; Hell *et al.*, 2004; Chapters 13, 30, and 31, *this volume*). Some of these approaches (e.g., 4Pi-microscopy) look promising for live cells (Gugel *et al.*, 2004), but their potential for widespread use in biological applications has yet to be established, and there are limitations on the sample thickness (Gustafsson, 1999 and Chapter 21, *this volume*). In addition, higher resolution implies smaller pixels and therefore more photons/square micrometer and more bleaching and toxicity. Undoubtedly, there will be more improvements and wider applications along these lines in the future.

Although it is difficult to predict the future of confocal microscopy of living cells, as confocal microscopy (and its richer cousin, multi-photon microscopy) are in all probability the optimal methods for studying the 3D structure of living cells, the future seems sure to be bright!

ACKNOWLEDGMENTS

The authors thank Glen MacDonald for helpful information on autofluorescence and light sensitivity of culture media, and for bringing relevant literature to our attention. MED thanks the staff of the W.M. Keck Motion Analysis Facility in the Department of Biological Sciences, University of Iowa, for their assistance in obtaining the data shown in Figures 19.4 and 19.5. Data for Figures 19.4 and 19.5 were kindly provided by Marc Waite. Data for Figure 19.6 were kindly provided by Mark Petersen.

REFERENCES

Adams, C.L., Chen, Y.T., Smith, S.J., and Nelson, W.J., 1998, Mechanisms of epithelial cell-cell adhesion and cell compaction revealed by high-resolution tracking of E-cadherin-green fluorescent protein, *J. Cell Biol.* 142:1105–1119.

Adams, M.C., Salmon, W.C., Gupton, S.L., Cohan, C.S., Wittmann, T., Prigozhina, N., and Waterman-Storer, C.M., 2003, A high-speed multispectral spinning-disk confocal microscope system for fluorescent speckle microscopy of living cells, *Methods* 29:29–41.

Amos, W.B., Reichelt, S., Cattermole, D.M., and Laufer, J., 2003, Re-evaluation of differential phase contrast (DPC) in a scanning laser microscope using a split detector as an alternative to differential interference contrast (DIC) optics, *J. Microsc.* 210:166–175.

Ando, R., Hama, H., Yamamoto-Hino, M., Mizuno, H., and Miyawaki, A., 2002, An optical marker based on the UV-induced green-to-red photoconversion of a fluorescent protein, *Proc. Natl. Acad. Sci. USA* 99:12651–12656.

Ando, R., Mizuno, H., and Miyawaki, A., 2004, Regulated fast nucleocytoplasmic shuttling observed by reversible protein highlighting, *Science* 306:1370–1373.

Andrews, P.M., Petroll, W.M., Cavanagh, H.D., and Jester, J.V., 1991, Tandem scanning confocal microscopy (TSCM) of normal and ischemic living kidneys, *Am. J. Anat.* 191:95–102.

Andrews, P.D., Harper, I.S., and Swedlow, J.R., 2002, To 5D and beyond: Quantitative fluorescence microscopy in the postgenomic era, *Traffic* 3:29–36.

Ashkin, A., Schutze, K., Dziedzic, J.M., Euteneuer, U., and Schliwa, M., 1990, Force generation of organelle transport measured *in vivo* by an infrared laser trap, *Nature* 348:346–348.

Ashworth, R., 2004, Approaches to measuring calcium in zebrafish: Focus on neuronal development, *Cell Calcium* 35:393–402.

Axelrod, D., Koppel, D.E., Schlessinger, J., Elson, E., and Webb, W.W., 1976, Mobility measurement by analysis of fluorescence photobleaching recovery kinetics, *Biophys. J.* 16:1055–1069.

Bacia, K., and Schwille, P., 2003, A dynamic view of cellular processes by in vivo fluorescence auto- and cross-correlation spectroscopy, *Methods* 29:74–85.

Baker, G.E., and Reese, B.E., 1993, Using confocal laser scanning microscopy to investigate the organization and development of neuronal projections labeled with DiI, *Methods Cell Biol.* 38:325–344.

Baker, M.W., Kauffman B., Macagno, E.R., and Zipser, B., 2003, *In vivo* dynamics of CNS sensory arbor formation: a time-lapse study in the embryonic leech, *J. Neurobiol.* 56:41–53.

Ballestrem, C., Hinz, B., Imhof, B.A., Wehrle-Haller, B., 2001, Marching at the front and dragging behind: differential alphaVbeta3-integrin turnover regulates focal adhesion behavior, *J. Cell Biol.* 155(7):1319–1332.

Barber, R.P., Phelps, P.E., and Vaughn, J.E., 1993, Preganglionic autonomic motor neurons display normal translocation patterns in slice cultures of embryonic rat spinal cord, *J. Neurosci.* 13:4898–4907.

Bastiaens, P.I., and Pepperkok, R., 2000, Observing proteins in their natural habitat: The living cell, *Trends Biochem. Sci.* 25:631–637.

Bastiaens, P.I., and Squire, A. 1999, Fluorescence lifetime imaging microscopy: Spatial resolution of biochemical processes in the cell, *Trends Cell Biol.* 9:48–52.

Baumgartner, W., Schutz, G.J., Wiegand, J., Golenhofen, N., and Drenckhahn, D., 2003, Cadherin function probed by laser tweezer and single molecule fluorescence in vascular endothelial cells, *J. Cell Sci.* 116:1001–1011.

Bement, W.M., Sokac, A.M., and Mandato, C.A., 2003, Four-dimensional imaging of cytoskeletal dynamics in *Xenopus* oocytes and eggs, *Differentiation* 71:518–527.

Benediktsson, A.M., Schachtele, S.J., Green, S.H., and Dailey, M.E., 2005, Ballistic labeling and dynamic imaging of astrocytes in organotypic hippocampal slice cultures, *J. Neurosci. Methods* 141:41–53.

Berg, R.H., 2004, Evaluation of spectral imaging for plant cell analysis, *J. Microsc.* 214(Pt 2):174–181.

Betz, W.J., Mao, F., and Bewick, G.S., 1992, Activity-dependent fluorescent staining and destaining of living vertebrate motor nerve terminals, *J. Neurosci.* 12:363–375.

Block, S.M., Goldstein, L.S., and Schnapp, B.J., 1990, Bead movement by single kinesin molecules studied with optical tweezers, *Nature* 348:348–352.

Bloom, J.A., and Webb, W.W., 1984, Photodamage to intact erythrocyte membranes at high laser intensities: methods of assay and suppression, *J. Histochem. Cytochem.* 32:608–616.

Brum, G., Gonzalez, A., Rengifo, J., Shirokova, N., and Rios, E., 2000, Fast imaging in two dimensions resolves extensive sources of Ca^{2+} sparks in frog skeletal muscle, *J. Physiol.* 528:419–433.

Brustein, E., Marandi, N., Kovalchuk, Y., Drapeau, P., and Konnerth, A., 2003, "In vivo" monitoring of neuronal network activity in zebrafish by two-photon Ca(2+) imaging, *Pflugers Arch.* 446(6):766–773.

Cahalan, M.D., Parker, I., Wei, S.H., and Miller, M.J., 2002, Two-photon tissue imaging: Seeing the immune system in a fresh light, *Nat. Rev. Immunol.* 2:872–880.

Chalfie, M., Tu, Y., Euskirchen, G., Ward, W.W., and Prasher, D.C., 1994, Green fluorescent protein as a marker for gene expression, *Science* 263:802–805.

Chen, Y., Mills, J.D., and Periasamy, A., 2003, Protein localization in living cells and tissues using FRET and FLIM, *Differentiation* 71:528–541.

Cechin, S.R., Gottfried, C., Prestes, C.C., Andrighetti, L., Wofchuk, S.T., and Rodnight, R., 2002, Astrocyte stellation in saline media lacking bicarbon-

ate: possible relation to intracellular pH and tyrosine phosphorylation, *Brain Res*. 946:12–23.

Cleemann, L., Wang, W., and Morad, M., 1998, Two-dimensional confocal images of organization, density and gating of focal Ca^{2+} release sites in rat cardiac myocytes, *Proc. Natl. Acad. Sci. USA* 95:10984–10989.

Cogswell, C.J., and Sheppard, C.J.R., 1991, Visualization of 3-D phase structure in confocal and conventional microscopy, *Proc. SPIE*. 1450:323–328.

Cogswell, C.J., and Sheppard, C.J.R., 1992, Confocal differential interference contrast (DIC) microscopy: Including a theoretical analysis of conventional and confocal DIC imaging, *J. Microsc*. 165:81–101.

Cooper, M.S., Cornell-Bell, A.H., Chernjavsky, A., Dani, J.W., and Smith, S.J., 1990, Tubulovesicular processes emerge from trans-Golgi cisternae, extend along microtubules, and interlink adjacent trans-Golgi elements into a reticulum, *Cell* 61:135–145.

Cooper, M.S., D'Amico, L.A., and Henry, C.A., 1999, Confocal microscopic analysis of morphogenetic movements, *Methods Cell Biol*. 59:179–204.

Cornell-Bell, A.H., Finkbeiner, S.M., Cooper, M.S., and Smith, S.J., 1990, Glutamate induces calcium waves in cultured astrocytes: Long-range glial signaling, *Science* 247:470–473.

Crittenden, S.L., and Kimble J., 1999, Confocal methods for *Caenorhabditis elegans*, *Methods Mol Biol*. 122:141–151.

Dailey, M.E., and Smith, S.J., 1993, Confocal imaging of mossy fiber growth in live hippocampal slices, *Jpn. J. Physiol*. 43:S183–S192.

Dailey, M.E., and Smith, S.J., 1994, Spontaneous Ca^{2+} transients in developing hippocampal pyramidal cells, *J. Neurobiol*. 25:243–251.

Dailey, M.E., and Smith, S.J., 1996, The dynamics of dendritic structure in developing hippocampal slices, *J. Neurosci*. 16:2983–2994.

Dailey, M.E., Buchanan, J., Bergles, D.E., and Smith, S.J., 1994, Mossy fiber growth and synaptogenesis in rat hippocampal slices *in vitro*, *J. Neurosci*. 14:1060–1078.

Dailey, M.E., and Waite, M., 1999, Confocal imaging of microglial cell dynamics in hippocampal slice cultures, *Methods* 18:222–230.

Dailey, M.E., Marrs, G.S., and Kurpius, D., 2005, Maintaining live cells and tissue slices in the imaging setup, In: *Imaging in Neuroscience and Development* (R. Yuste and A. Konnerth, eds.), Cold Spring Harbor Laboratory Press, Cold Spring Harbor, New York.

Das, T., Payer, B., Cayouette, M., and Harris, W.A., 2003, *In vivo* time-lapse imaging of cell divisions during neurogenesis in the developing zebrafish retina, *Neuron* 37:597–609.

Delbridge, L.M., Harris, P.J., Pringle, J.T., Dally, L.J., and Morgan, T.O., 1990, A superfusion bath for single-cell recording with high-precision optical depth control, temperature regulation, and rapid solution switching, *Pfluegers Arch*. 416:94–97.

Del Pozo, M.A., Kiosses, W.B., Alderson, N.B., Meller, N., Hahn, K.M., Schwartz, M.A., 2002, Integrins regulate GTP-Rac localized effector interactions through dissociation of Rho-GDI, *Nat. Cell Biol.* 4(3):232–239.

Dickinson, M.E., Bearman, G., Tille, S., Lansford, R., Fraser, S.E., 2001, Multispectral imaging and linear unmixing add a whole new dimension to laser scanning fluorescence microscopy, *Biotechniques* 31(6):1272, 1274–1276, 1278.

Dirnagl, U., Villringer, A., and Einhaupi, K.M., 1992, *In vivo* confocal scanning laser microscopy of the cerebral microcirculation, *J. Microsc*. 165:147–157.

Dixit, R., and Cyr, R., 2003, Cell damage and reactive oxygen species production induced by fluorescence microscopy: Effect on mitosis and guidelines for non-invasive fluorescence microscopy, *Plant J*. 36:280–290.

Dorman, G., and Prestwich, G.D., 2000, Using photolabile ligands in drug discovery and development, *Trends Biotechnol*. 18:64–77.

Dunn, G.A., Dobbie, I.M., Monypenny, J., Holt, M.R., and Zicha, D., 2002, Fluorescence localization after photobleaching (FLAP): A new method for studying protein dynamics in living cells, *J. Microsc*. 205:109–112.

Dunwiddie, T.V., 1981, Age-related differences in the *in vitro* rat hippocampus: Development of inhibition and the effects of hypoxia, *Dev. Neurosci*. 4:165–175.

Dvorak, J.A., and Stotler, W.F., 1971, A controlled-environment culture system for high resolution light microscopy, *Exp. Cell Res*. 68:269–275.

Dynes, J.L., and Ngai, J., 1998, Pathfinding of olfactory neuron axons to stereotyped glomerular targets revealed by dynamic imaging in living zebrafish embryos, *Neuron* 20:1081–1091.

Edwards, A.M., Silva, E., Jofre, B., Becker, M.I., and De Ioannes, A.E., 1994, Visible light effects on tumoral cells in a culture medium enriched with tryptophan and riboflavin, *J. Photochem. Photobiol*. B 24:179–186.

Elangovan, M., Day, R.N., and Periasamy, A., 2002, Nanosecond fluorescence resonance energy transfer-fluorescence lifetime imaging microscopy to localize the protein interactions in a single living cell, *J. Microsc*. 205:3–14.

Ellenberg, J., Lippincott-Schwartz, J., and Presley, J.F., 1999, Dual-colour imaging with GFP variants, *Trends Cell Biol*. 9:52–56.

Elson, E.L., 2001, Fluorescence correlation spectroscopy measures molecular transport in cells, *Traffic* 2:789–796.

Fan, G.Y., Fujisaki, H., Miyawaki, A., Tsay, R.K., Tsien, R.Y., and Ellisman, M.H., 1999, Video-rate scanning two-photon excitation fluorescence microscopy and ratio imaging with chameleons, *Biophys. J*. 76:2412–2120.

Firestone, L., Cook, K., Culp, K., Talsania, N., and Preston, K. Jr., 1991, Comparison of autofocus methods for automated microscopy, *Cytometry* 12:195–206.

Flock, A., Flock, B., and Scarfone, E., 1998, Laser scanning confocal microscopy of the hearing organ: fluorochrome-dependent cellular damage is seen after overexposure, *J. Neurocytol*. 27:507–516.

Forsythe, I.W., 1991, Microincubator for regulating temperature and superfusion of tissue-cultured neurons during electrophysiological or optical studies, *Methods Neurosci*. 4:301–318.

Fraser, S.E., and O'Rourke, N.A., 1990, *In situ* analysis of neuronal dynamics and positional cues in the patterning of nerve connections, *J. Exp. Biol*. 153:61–70.

Frostig, R., ed., 2002, In Vivo *Optical Imaging of Brain Function*, CRC Press, Boca Raton, Florida.

Gahtan, E., Sankrithi, N., Campos, J.B., and O'Malley, D.M., 2002, Evidence for a widespread brain stem escape network in larval zebrafish, *J. Neurophysiol.* 87(1):608–614.

Gähwiler, B.H., 1984, Development of the hippocampus *in vitro*: Cell types, synapses, and receptors, *Neuroscience* 11:751–760.

Gähwiler B.H., Capogna M., Debanne D., McKinney R.A., and Thompson S.M., 1997, Organotypic slice cultures: A technique has come of age, *Trends Neurosci*. 20:471–477.

Gan, W.B., Kwon, E., Feng, G., Sanes, J.R., and Lichtman, J.W., 2003, Synaptic dynamism measured over minutes to months: Age-dependent decline in an autonomic ganglion, *Nat. Neurosci*. 6:956–960.

Gerlich, D., and Ellenberg, J., 2003, 4D imaging to assay complex dynamics in live specimens, *Nat. Cell Biol*. 5:S14–S19.

Gerlich, D., Beaudouin, J., Gebhard, M., Ellenberg, J., and Eils, R., 2001, Four-dimensional imaging and quantitative reconstruction to analyse complex spatiotemporal processes in live cells, *Nat. Cell Biol*. 3:852.

Gilland, E., Miller, A.L., Karplus, E., Baker. R., and Webb, S.E., 1999, Imaging of multicellular large-scale rhythmic calcium waves during zebrafish gastrulation, *Proc. Natl. Acad. Sci. USA* 96:157–161.

Gleason, M.R., Higashijima, S., Dallman, J., Liu, K., Mandel, G., and Fetcho, J.R., 2003, Translocation of CaM kinase II to synaptic sites *in vivo, Nat. Neurosci*. 6:217–218.

Goksor, M., Enger, J., and Hanstorp, D., 2004, Optical manipulation in combination with multiphoton microscopy for single-cell studies, *Appl. Opt*. 43:4831–4837.

Gong, Y., Mo, C., and Fraser, S.E., 2004, Planar cell polarity signalling controls cell division orientation during zebrafish gastrulation, *Nature* 430:689–693.

Griffin, F.M., Ashland, G., and Capizzi, R.L., 1981, Kinetics of phototoxicity of Fischer's medium for L5178Y leukemic cells, *Cancer Res*. 41:2241–2248.

Grossmann, R., Stence, N., Carr, J., Fuller, L., Waite, M., and Dailey, M.E., 2002, Juxtavascular microglia migrate along brain capillaries following activation during early postnatal development, *Glia* 37:229–240.

Gugel, H., Bewersdorf, J., Jakobs, S., Engelhardt, J., Storz, R., and Hell, S.W., 2004, Combining 4Pi excitation and detection delivers seven-fold sharper sections in confocal imaging of live cells, *Biophys. J*. 87(6):4146–4152.

Gustafsson, M., 1999, Extended resolution fluorescence microscopy, *Curr. Opin. Struct. Biol*. 9:627–634.

Hammond, A.T., and Glick, B.S., 2000, Raising the speed limits for 4D fluorescence microscopy, *Traffic* 1:935–40.

Hasan, M.T., Friedrich, R.W., Euler, T., Larkum, M.E., Giese, G., Both, M., Duebel, J., Waters, J., Bujard, H., Griesbeck, O., Tsien, R.Y., Nagai, T., Miyawaki, A., and Denk, W., 2004, Functional fluorescent Ca^{2+} indicator proteins in transgenic mice under TET control, *PLoS Biol*. 2:e163. Epub 2004 Jun 15.

Heid, P.J., Voss, E., and Soll, D.R., 2002, 3D-DIASemb: A computer-assisted system for reconstructing and motion analyzing in 4D every cell and nucleus in a developing embryo, *Dev. Biol*. 245:329–347.

Hell, S.W., Dyba, M., and Jakobs, S., 2004, Concepts for nanoscale resolution in fluorescence microscopy, *Curr. Opin. Neurobiol*. 14:599–609.

Hess, S.T., Huang, S., Heikal, A.A., and Webb, W.W., 2002, Biological and chemical applications of fluorescence correlation spectroscopy: A review, *Biochemistry* 41:697–705.

Hiraoka, Y., Shimi, T., and Haraguchi, T., 2002, Multispectral imaging fluorescence microscopy for living cells, *Cell Struct. Funct*, 27:367–374.

Hollingworth, S., Soeller, C., Baylor, S.M., and Cannell, M.B., 2000, Sarcomeric Ca^{2+} gradients during activation of frog skeletal muscle fibres imaged with confocal and two-photon microscopy, *J. Physiol*. 526:551–560.

Honig, M.G., and Hume, R.I., 1986, Fluorescent carbocyanine dyes allow living neurons of identified origin to be studied in long-term cultures, *J. Cell Biol*. 103:171–187.

Hook, G.R., and Odeyale, C.O., 1989, Confocal scanning fluorescence microscopy: A new method for phagocytosis research, *J. Leukoc. Biol*. 45:277–282.

Hoppe, A.D., Swanson, J.A., 2004, Cdc42, Rac1, and Rac2 display distinct patterns of activation during phagocytosis, *Mol. Biol. Cell* 15(8):3509–3519.

Ince, C., Ypey, D.L., Diesselhoff-Den Dulk, M.M., Visser, J.A., De Vos, A., and Van Furth, R., 1983, Micro-CO_2-incubator for use on a microscope, *J. Immun. Methods* 60:269–275.

Isogai, S., Lawson, N.D., Torrealday, S., Horiguchi, M., and Weinstein, B.M., 2003, Angiogenic network formation in the developing vertebrate trunk, *Development* 130:5281–5290.

Jester, J.V., Andrews, P.M., Petroll, W.M., Lemp, M.A., and Cavanagh, H.D., 1991, *In vivo*, real-time confocal imaging, *J. Electron Microsc. Tech*. 18:50–60.

Jester, J.V., Petroll, W.M., Garana, R.M.R., Lemp, M.A., and Cavanagh, H.D., 1992, Comparison of *in vivo* and *ex vivo* cellular structure in rabbit eyes by tandem scanning microscopy, *J. Microsc*. 165:169–181.

Johnson, L.V., Walsh, M.L., and Chen, L.B., 1980, Localization of mitochondria in living cells with rhodamine 123, *Proc. Natl. Acad. Sci. USA* 77:990–994.

Jontes, J.D., Buchanan, J., and Smith, S.J., 2000, Growth cone and dendrite dynamics in zebrafish embryos: early events in synaptogenesis imaged *in vivo, Nat. Neurosci*. 3:231–237.

Kim, S.A., Heinze, K.G., Waxham, M.N., and Schwille, P., 2004, Intracellular calmodulin availability accessed with two-photon cross-correlation, *Proc. Natl. Acad. Sci. USA* 101:105–110.

Keller, P., Toomre, D., Díaz, E., White, J., and Simons, K., 2001, Multicolour imaging of post-Golgi sorting and trafficking in live cells, *Nat. Cell Biol*. 3:140–149.

Knebel, W., Quader, H., and Schnepf, E., 1990, Mobile and immobile endoplasmic reticulum in onion bulb epidermis cells: short- and long-term observations with a confocal laser scanning microscope, *Eur. J. Cell Biol*. 52:328–340.

Knight, M.M., Roberts, S.R., Lee, D.A., and Bader, D.L., 2003, Live-cell imaging using confocal microscopy induces intracellular calcium transients and cell death, *Am. J. Physiol. Cell Physiol*. 284:C1083–C10839.

Koppel, D.E., Axelrod, D., Schlessinger, J., Elson, E.L., and Webb, W.W., 1976, Dynamics of fluorescence marker concentration as a probe of mobility, *Biophys. J*. 16:1315–1329.

Koster, R.W., and Fraser, S.E., 2001, Direct imaging of *in vivo* neuronal migration in the developing cerebellum, *Curr. Biol*. 11:1858–1863.

Kuo, S.C., 2001, Review: Using optics to measure biological forces and mechanics, *Traffic* 2:757–763.

Kuo, S.C., and Sheetz, M.P., 1993, Force of single kinesin molecules measured with optical tweezers, *Science* 260:232–234.

Kurpius, D., and Dailey, M.E., 2005, Imaging microglia in live brain slices and slice cultures, In: *Imaging in Neuroscience and Development* (R. Yuste and A. Konnerth, eds.), Cold Spring Harbor Laboratory Press, Cold Spring Harbor, New York.

Lakowicz, J.R., Szmacinski, H., Nowaczyk, K., Berndt, K.W., and Johnson, M., 1992, Fluorescence lifetime imaging, *Anal. Biochem*. 202:316–330.

Lansford, R., Bearman, G., and Fraser, S.E., 2001, Resolution of multiple green fluorescent protein color variants and dyes using two-photon microscopy and imaging spectroscopy, *J. Biomed. Opt*. 6:311–318.

Lawson, N.D., and Weinstein, B.M., 2002, *In vivo* imaging of embryonic vascular development using transgenic zebrafish, *Dev. Biol*. 248:307–318.

Legg, J.W., Lewis, C.A., Parsons, M., Ng, T., Isacke, C.M., 2002, A novel PKC-regulated mechanism controls CD44 ezrin association and directional cell motility, *Nat. Cell Biol.* 4(6):399–407.

Lepe-Zuniga, J.L., Zigler, J.S. Jr., and Gery, I., 1987, Toxicity of light-exposed Hepes media, *J. Immunol. Methods* 103:145.

Lin, H.J., Herman, P., and Lakowicz, J.R., 2003, Fluorescence lifetime-resolved pH imaging of living cells, *Cytometry* 52A:77–89.

Lippincott-Schwartz, J., Snapp, E., and Kenworthy, A., 2001, Studying protein dynamics in living cells, *Nat. Rev. Mol. Cell. Biol*. 2:444–456.

Lippincott-Schwartz, J., Altan-Bonnet, N., and Patterson, G.H., 2003, Review: Photobleaching and photoactivation: Following protein dynamics in living cells, *Nat. Cell Biol*. 5:S7–S14.

Loew, L.M., 1993, Confocal microscopy of potentiometric fluorescent dyes, *Methods Cell Biol*. 38:195–209.

Lorenzl, S., Koedel, U., Dirnagl, U., Ruckdeschel, G., and Pfister, H.W., 1993, Imaging of leukocyte-endothelium interaction using *in vivo* confocal laser scanning microscopy during the early phase of experimental pneumococcal meningitis, *J. Infect. Dis*. 168:927–933.

Lucius, R., Mentlein, R., and Sievers, J., 1998, Riboflavin-mediated axonal degeneration of postnatal retinal ganglion cells *in vitro* is related to the formation of free radicals, *Free Radic. Biol. Med*. 24:798–808.

Magde, D., Elson, E.L., and Webb, W.W., 1974, Fluorescence correlation spectroscopy. II. An experimental realization, *Biopolymers* 13:29–61.

Manders, E.M.M., Stap, J., Strackee, J., Van Driel, R., and Aten, J.A., 1996, Dynamic behavior of DNA replication domains, *Exp. Cell Res*. 226:328–335.

Manders, E.M.M., Kimura, H., and Cook, P.R., 1999, Direct imaging of DNA in living cells reveals the dynamics of chromosome formation, *J. Cell Biol*. 144:813–821.

Manders, E.M.M., Visser, A.E., Koppen, A., de Leeuw, W.C., van Liere, R., Brakenhoff, G.J., and van Driel, R., 2003, Four-dimensional imaging of chromatin dynamics during the assembly of the interphase nucleus, *Chromosome Res*. 11:537–547.

Marrs, G.S., Green, S.H., and Dailey, M.E., 2001, Rapid formation and remodeling of postsynaptic densities in developing dendrites, *Nat. Neurosci*. 4:1006–1013.

Masters, B.R., 1992, Confocal microscopy of the in-situ crystalline lens, *J. Microsc*. 165:159–167.

McKenna, N., and Wang, Y.L., 1986, Culturing cells on the microscope stage, *Methods Cell Biol*. 29:195–205.

Megason, S.G., and Fraser, S.E., 2003, Digitizing life at the level of the cell: High-performance laser-scanning microscopy and image analysis for in toto imaging of development, *Mechan. Dev*. 120:1407–1420.

Mehta, A.D., Jung, J.C., Blusberg, B.A., and Schnitzer, M.J., 2004, Fiber-optic *in vivo* imaging in the mammalian nervous system, *Curr. Opin. Neurobiol*. 14:617–628.

Meyvis, T.K., De Smedt, S.C., Van Oostveldt, P., and Demeester, J., 1999, Fluorescence recovery after photobleaching: A versatile tool for mobility and interaction measurements in pharmaceutical research, *Pharm. Res*. 16: 1153–1162.

Miller, M.J., Wei, S.H., Parker, I., and Cahalan, M.D., 2002, Two-photon imaging of lymphocyte motility and antigen response in intact lymph node, *Science* 296:1869–1973.

Miller, M.J., Safrina, O., Parker, I., and Cahalan, M.D., 2004, Imaging the single cell dynamics of CD4+ T cell activation by dendritic cells in lymph nodes, *J. Exp. Med*. 200:847–856.

Minta, A., Kao, J., and Tsien, R., 1989, Fluorescent indicators for cytosolic calcium based on rhodamine and fluorescein chromophores, *J. Biol Chem*. 264:8171–8178.

Miyawaki, A., 2003, Fluorescence imaging of physiological activity in complex systems using GFP-based probes, *Curr. Opin. Neurobiol*. 13:591–596.

Mizrahi, A., Crowley, J.C., Shtoyerman, E., and Katz, L.C., 2004, High-resolution *in vivo* imaging of hippocampal dendrites and spines, *J. Neurosci*. 24:3147–3151.

Moné, M.J., Bernas, T., Dinant, C., Goedvree, F.A., Manders, E.M.M., Volker, M., Houtsmuller, A.B., Hoeijmakers, J.H.J., Vermeulen, W., and van Driel, R., 2004, *In vivo* dynamics of chromatin-associated complex formation in mammalian nucleotide excision repair, *Proc. Natl. Acad. Sci. USA* 101:15933–15937.

Montoya, M.C., Sancho, D., Bonello, G., Collette, P., Langlet, C., He, H.T., Aparicio, P., Alcover, A., Olive, D., and Sanchez-Madrid, F., 2002, Role of ICAM-3 in the initial interaction of T lymphocytes and APCs, *Nat. Immunol*. 3:159–168.

Mulligan, S.J., MacVicar, B.A., 2004, Calcium transients in astrocyte endfeet cause cerebrovascular constrictions, *Nature* 431(7005):195–199.

Myrdal, S., and Foster, M., 1994, Time-resolved confocal analysis of antibody penetration into living, solid tumor spheroids, *Scanning* 16:155–167.

Nehls, S., Snapp, E.L., Cole, N.B., Zaal, K.J., Kenworthy, A.K., Robert, T.H., Ellenberg, J., Presley, J.F., Siggia, E., and Lippincott-Schwartz, J., 2000, Dynamics and retention of misfolded proteins in native ER membranes, *Nat. Cell Biol*. 2:288–295.

Niell, C.M., Meyer, M.P., and Smith, S.J., 2004, *In vivo* imaging of synapse formation on a growing dendritic arbor, *Nat. Neurosci*. 7:254–260.

Niggli, E., and Egger, M., 2004, Applications of multi-photon microscopy in cell physiology, *Front Biosci*. 9:1598–1610.

Noctor, S.C., Martinez-Cerdeno, V., Ivic, L., and Kriegstein, A.R., 2004, Cortical neurons arise in symmetric and asymmetric division zones and migrate through specific phases, *Nat. Neurosci*. 7:136–144.

O'Malley, D.M., Kao, Y.H., and Fetcho, J.R., 1996, Imaging the functional organization of zebrafish hindbrain segments during escape behaviors, *Neuron* 17:1145–1155.

O'Rourke, N.A., and Fraser, S.E., 1990, Dynamic changes in optic fiber terminal arbors lead to retinotopic map formation: An *in vivo* confocal microscopic study, *Neuron* 5:159–171.

O'Rourke, N.A., Dailey, M.E., Smith, S.J., and McConnell, S.K., 1992, Diverse migratory pathways in the developing cerebral cortex, *Science* 258:299–302.

Paddock, S.W., 2002, Confocal imaging of *Drosophila* embryos, *Methods Cell Biol*. 70:361–378.

Pagano, R.E., Martin, O.C., Kang, H.C., and Haugland, R.P., 1991, A novel fluorescent ceramide analogue for studying membrane traffic in animal cells: Accumulation at the Golgi apparatus results in altered spectral properties of the sphingoid precursor, *J. Cell Biol*. 11:1267–1279.

Park, M.K., Tepikin, A.V., and Petersen, O.H., 2002, What can we learn about cell signalling by combining optical imaging and patch clamp techniques? *Pflugers Arch*. 444:305–316.

Pasti, L., Zonta, M., Pozzan, T., Vicini, S., and Carmignoto, G., 2001, Cytosolic calcium oscillations in astrocytes may regulate exocytotic release of glutamate, *J. Neurosci*. 21:477–484.

Patterson, G.H., and Lippincott-Schwartz, J., 2002, A photoactivatable GFP for selective photolabeling of proteins and cells, *Science* 297:1873–1877.

Patterson, G.H., and Lippincott-Schwartz, J., 2004, Selective photolabeling of proteins using photoactivatable GFP, *Methods* 32:445–450.

Pepperkok, R., Squire, A., Geley, S., and Bastiaens, P.I., 1999, Simultaneous detection of multiple green fluorescent proteins in live cells by fluorescence lifetime imaging microscopy, *Curr. Biol*. 9:269–272.

Periasamy, A., and Day, R.N., 1999, Visualizing protein interactions in living cells using digitized GFP imaging and FRET microscopy, *Methods Cell Biol*. 58:293–314.

Periasamy, A., Elangovan, M., Elliott, E., and Brautigan, D.L., 2002, Fluorescence lifetime imaging (FLIM) of green fluorescent fusion proteins in living cells, *Methods Mol. Biol*. 183:89–100.

Peter, M., Ameer-Beg, S.M., 2004, Imaging molecular interactions by multiphoton FLIM, *Biol. Cell.* 96(3):231–236.

Petersen, M., and Dailey, M.E., 2004, Diverse microglial motility behaviors during clearance of dead cells in hippocampal slices, *Glia* 46:195–206.

Petran, M., Hadravsky, M., Benes, J., and Boyde, A., 1986, *In vivo* microscopy using the tandem scanning microscope, *Ann. N.Y. Acad. Sci*. 483:440–447.

Petroll, W.M., Cavanagh, H.D., Lemp, M.A., Andrews, P.M., and Jester, J.V., 1992, Digital image acquisition in *in vivo* confocal microscopy, *J. Microsc*. 165:61–69.

Petroll, W.M., Cavanagh, H.D., and Jester, J.V., 1993, Three-dimensional imaging of corneal cells using *in vivo* confocal microscopy, *J. Microsc*. 170:213–219.

Politz, J.C., 1999, Use of caged fluorochromes to track macromolecular movement in living cells, *Trends Cell Biol*. 9:284–287.

Pologruto, T.A., Yasuda, R., and Svoboda, K., 2004, Monitoring neural activity and [Ca^{2+}] with genetically encoded Ca^{2+} indicators, *J. Neurosci*. 24:9572–9579.

Poole, C.A., Brookes, N.H., and Clover, G.M., 1993, Keratocyte networks visualized in the living cornea using vital dyes, *J. Cell Sci*. 106:685–692.

Potter, S. M., 2004. Two-photon microscopy for 4D imaging of living neurons, In: *Imaging in Neuroscience and Development: A Laboratory Manual*, 2nd ed., (R. Yuste and A. Konnerth, eds.), Cold Spring Harbor Laboratory Press, Cold Spring Harbor, New York, pp. 8.1–8.12.

Potter, S.M., and DeMarse, T.B., 2001, A new approach to neural cell culture for long-term studies, *J. Neurosci. Methods* 110:17–24.

Reits, E.A., and Neefjes, J.J., 2001, From fixed to FRAP: measuring protein mobility and activity in living cells. *Nat. Cell Biol*. 3(6):E145–E147.

Rios, E., Shirokova, N., Kirsch, W.G., Pizarro, G., Stern, M.D., Cheng, H., and Gonzalez, A., 2001, A preferred amplitude of calcium sparks in skeletal muscle, *Biophys. J*. 80:169–183.

Robb, D.L., and Wylie, C., 1999, Confocal microscopy on *Xenopus laevis* oocytes and embryos, *Methods Mol. Biol*. 122:173–183.

Rubart, M., 2004, Two-photon microscopy of cells and tissue, *Circ. Res*. 95:1154–1166.

Salmon, W.C., Adams, M.C., and Waterman-Storer, C.M., 2002, Dual-wavelength fluorescent speckle microscopy reveals coupling of microtubule and actin movements in migrating cells, *J. Cell Biol*. 158:31–37.

Schmidt, C.E., Horwitz, A.F., Lauffenburger, D.A., and Sheetz, M.P., 1993, Integrin-cytoskeletal interactions in migrating fibroblasts are dynamic, asymmetric, and regulated, *J. Cell Biol*. 123:977–991.

Schwarzbauer, J.E., 1997, Cell migration: may the force be with you, *Curr. Biol.* 7(5):R292–R294.

Sekar, R.B., and Periasamy, A., 2003, Fluorescence resonance energy transfer (FRET) microscopy imaging of live-cell protein localizations, *J. Cell Biol*. 160:629–633.

Seyfried, V., Birk, H., Storz, R., and Ulrich, H., 2003, Advances in multispectral confocal imaging, *Progress in Biomedical Optics and Imaging* 5139:146–157.

Sheetz, M.P., ed., 1998, *Laser Tweezers in Cell Biology*, Academic Press, San Diego, California.

Siegel, W.H., and Pritchett, T., 2000, Tutorial: Examining the relationship between media and light, *Biopharmaceuticals* 13:65–66.

Silva, E., Salim-Hanna, M., Edwards, A.M., Becker, M.I., and De Ioannes, A.E., 1991, A light-induced tryptophan-riboflavin binding: biological implications, *Adv. Exp. Med. Biol*. 289:33–48.

Silva, E., and Godoy, J., 1994, Riboflavin sensitized photooxidation of tyrosine, *Int. J. Vitam. Nutr. Res*. 64:253–256.

Smith, S.J., Cooper, M., and Waxman, A., 1990, Laser microscopy of subcellular structure in living neocortex: Can one see dendritic spines twitch? In: *XYIII Symposia Medica Hoechst, Biology of Memory* (L. Squire and E. Lindenlaub, eds.), Schattauer, Stuttgart, Germany, pp. 49–71.

Soll, D., 1995, The use of computers in understanding how animal cells crawl, *Int. Rev. Cytol*. 163:43–104.

Soll, D.R., 1999, Computer-assisted three-dimensional reconstruction and motion analysis of living, crawling cells, *Comput. Med. Imaging Graphics* 23:3–14.

Spierenburg, G.T., Oerlemans, F.T., van Laarhoven, J.P., and de Bruyn, C.H., 1984, Phototoxicity of N-2-hydroxyethylpiperazine-N′-2-ethanesulfonic acid-buffered culture media for human leukemic cell lines, *Cancer Res*. 44:2253–2254.

Stence, N., Waite, M., and Dailey, M.E., 2001, Dynamics of microglial activation: A confocal time-lapse analysis in hippocampal slices, *Glia* 33:256–266.

Stoll, S., Delon, J., Brotz, T.M., and Germain, R.N., 2002, Dynamic imaging of T cell-dendritic cell interactions in lymph nodes, *Science* 296:1873–1876.

Stoppini, L., Buchs, P.A., and Muller, D., 1991, A simple method for organotypic cultures of nervous tissue, *J. Neurosci. Methods* 37:173–182.

Strange, K., and Spring, K.R., 1986, Methods for imaging renal tubule cells, *Kidney Int*. 30:192–200.

Streit, W.J., and Kreutzberg, G.W., 1987, Lectin binding by resting and reactive microglia, *J. Neurocytol*. 16:249–260.

Stricker, S.A., 2004, Dual-channel confocal ratioing of calcium dynamics in living eggs and oocytes, *Methods Mol. Biol*. 254:137–148.

Stryer, L., 1978, Fluorescence energy transfer as a spectroscopic ruler, *Annu. Rev. Biochem*. 47:819–846.

Sullivan, W., Daily, D.R., Fogarty, P., Yook, K.J., and Pimpinelli, S., 1993, Delays in anaphase initiation occur in individual nuclei of the syncytial *Drosophila* embryo, *Mol. Biol. Cell* 4:885–896.

Svoboda, K., Denk, W., Kleinfeld, D., and Tank, D., 1997, *In vivo* dendritic calcium dynamics in neocortical pyramidal neurons, *Nature* 385:161–165.

Tauer, U., 2002, Advantages and risks of multiphoton microscopy in physiology, *Exp. Physiol*. 87:709–714.

Terasaki, M., Song, J., Wong, J.R., Weiss, M.J., and Chen, L.B., 1984, Localization of endoplasmic reticulum in living and glutaraldehyde fixed cells with fluorescent dyes, *Cell* 8:101–108.

Thomas, C.F., and White, J.G., 1998, Four-dimensional imaging: The exploration of space and time, *Trends Biotechnol*. 16:175–182.

Thompson, N.L., 1991, Fluorescence correlation spectroscopy, In: *Topics in Fluorescence Spectroscopy*, Vol. 1 (J. R. Lakowicz, ed.), Plenum Press, New York, pp. 337–378.

Trachtenberg, J.T., Chen, B.E., Knott, G.W., Feng, G., Sanes, J.R., Welker, E., and Svoboda, K., 2002, Long-term *in vivo* imaging of experience-dependent synaptic plasticity in adult cortex, *Nature* 420:788–794.

Tsurui, H., Nishimura, H., Hattori, S., Hirose, S., Okumura, K., and Shirai, T., 2000, Seven-color fluorescence imaging of tissue samples based on Fourier spectroscopy and singular value decomposition, *J. Histochem. Cytochem*. 48:653–662.

Verschure, P.J., van der Kraan, I., Manders, E.M., and van Driel, R., 1999, Spatial relationship between transcription sites and chromosome territories, *J. Cell Biol*. 147:13–24.

Vesely, P., Maly, J., Cumpelik, J., Pluta, M., and Tuma V., 1982, Improved spatial and temporal resolution in an apparatus for time-lapse, phase contrast cine light micrography of cells *in vitro*, *J. Microsc*. 125:67–76.

Visscher, K., and Brakenhoff, G.J., 1991, Single beam optical trapping integrated in a confocal microscope for biological applications, *Cytometry* 12:486–491.

Walcerz, D.B., and Diller, K.R., 1991, Quantitative light microscopy of combined perfusion and freezing processes, *J. Microsc*. 161:297–311, and US Patent 5,257,128.

Wang, S.Q., Wei, C., Zhao, G., Brochet, D.X., Shen, J., Song, L.S., Wang, W., Yang, D., and Cheng, H., 2004, Imaging microdomain Ca^{2+} in muscle cells, *Circ. Res*. 94:1011–1022.

Waterman-Storer, C.M., Sanger, J.W., and Sanger, J.M., 1993, Dynamics of organelles in the mitotic spindles of living cells: Membrane and microtubule interactions, *Cell Motil. Cytosketelon* 26:19–39.

Waterman-Storer, C.M., Desai, A., Bulinski, J.C., and Salmon, E.D., 1998, Fluorescent speckle microscopy, a method to visualize the dynamics of protein assemblies in living cells, *Curr. Biol*. 8:1227–1230.

Weiss, M., 2004, Challenges and artifacts in quantitative photobleaching experiments, *Traffic* 5:662–671.

Wiseman, P.W., and Petersen, N.O., 1999, Image correlation spectroscopy. II. Optimization for ultrasensitive detection of preexisting platelet-derived growth factor-beta receptor oligomers on intact cells, *Biophys. J*. 76:963–977.

Wiseman, P.W., Squier, J.A., Ellisman, M.H., and Wilson, K.R., 2000, Two-photon image correlation spectroscopy and image cross-correlation spectroscopy, *J. Microsc*. 200:14–25.

Wood, C., Kabat, E.A., Murphy, L.A., and Goldstein, I.J., 1979, Immunochemical studies of the combining sites of the two isolectins, A4 and B4, isolated from Bandeiraea simplicifolia, *Arch. Biochem. Biophys*. 198:1–11.

Wouters, F.S., Verveer, P.J., and Bastiaens, P.I.H., 2001, Imaging biochemistry inside cells, *Trends Cell Biol.* 11:203–211.

Yoder, E.J., and Kleinfeld, D., 2002, Cortical imaging through the intact mouse skull using two-photon excitation laser scanning microscopy, *Microsc. Res. Techn*. 56:304–305.

Zhang, S., Boyd, J., Delaney, K., Murphy, T.H., 2005, Rapid reversible changes in dendritic spine structure in vivo gated by the degree of ischemia, *J. Neurosci.* 25(22):5333–5338.

Zicha, D., Dobbie, I.M., Holt, M.R., Monypenny, J., Soong, D.Y., Gray, C., and Dunn, G.A., 2003, Rapid actin transport during cell protrusion, *Science* 300:142–145.

Zieger, M.A., Glofcheski, D.J., Lepock, J.R., and Kruuv, J., 1991, Factors influencing survival of mammalian cells exposed to hypothermia. V. Effects of hepes, free radicals, and H_2O_2 under light and dark conditions, *Cryobiology* 28:8–17.

Zigler, J.S. Jr., Lepe-Zuniga, J.L., Vistica, B., and Gery, I., 1985, Analysis of the cytotoxic effects of light-exposed HEPES-containing culture medium, In Vitro *Cell Dev. Biol*. 21:282–287.

Zimmermann, T., Rietdorf, J., Girod, A., Georget, V., and Pepperkok, R., 2002, Spectral imaging and linear un-mixing enables improved FRET efficiency with a novel GFP2-YFP FRET pair, *FEBS Lett*. 531:245–249.

Zimmermann, T., Rietdorf, J., and Pepperkok, R., 2003, Spectral imaging and its applications in live-cell microscopy, *FEBS Lett*. 546:87–92.

Zuo, Y., Lubischer, J.L., Kang, H., Tian, L., Mikesh, M., Marks, A., Scofield, V.L., Maika, S., Newman, C., Krieg, P., and Thompson, W.J., 2004. Fluorescent proteins expressed in mouse transgenic lines mark subsets of glia, neurons, macrophages, and dendritic cells for vital examination, *J. Neurosci*. 24:10999–11009.

20

Aberrations in Confocal and Multi-Photon Fluorescence Microscopy Induced by Refractive Index Mismatch

Alexander Egner and Stefan W. Hell

INTRODUCTION

Modern optical microscopes are so good that many scientists forget that these instruments only provide their optimal performance if they are used under certain operating conditions. Typical users may be unaware of the very existence of such limitations either because they may unwittingly work within the limits or because they fail to recognize their effects. It is probably also correct to assume that the manufacturer does not intend to discourage purchase by emphasizing the pitfalls that unavoidably arise from the physics of imaging. However, advanced microscopists tend to use their instruments at the limits of their performance. They wish to use lasers from the ultraviolet (UV) to the infrared (IR), special emission lines from very large arc-lamps, charge-coupled device (CCD) cameras with a dynamic range of up to 16 bits, photon-counting avalanche photodiodes with unmatched sensitivity, and several fast photomultiplier tubes. They want to observe two or more dyes simultaneously. They expect the stage to remain in a stable position for several hours, possibly while going through heating and cooling cycles, and sometimes they want to record low-level fluorescence emissions from rather thick specimens mounted in an aqueous medium with high numerical aperture (NA) oil-immersion lenses. Is this possible? Can one expect an off-the-shelf product to perform well under all these circumstances? The answer is: Within certain limits, yes, you can. The issue is to specify and recognize these limits.

This chapter describes the problems that occur when observing specimens that are mounted in a medium whose refractive index is different from that of the immersion liquid. Classic examples are live cells kept in a physiological buffer solution or even fixed cells kept in a glycerol-based mountant that are imaged by an oil-immersion lens of large numerical aperture. This chapter first outlines the physics of the situation, both for confocal and multi-photon microscopy, then presents the results of a theoretical investigation, compares them with a series of experiments, and finally draws conclusions that are particularly relevant to the quantitative observation of (living) biological specimens.

THE SITUATION

Figure 20.1 describes a common situation encountered in microscopy. The sample is mounted between a coverslip and a glass slide, which in fact can be another coverslip, and is immersed in a special mounting medium, such as an aqueous buffer or a more viscous solution based on glycerol. Coverslip glass has a refractive index (RI) $n = 1.518$. The immersion oil between the coverslip and the objective lens is assumed to have the same n. The n of the mounting medium around the sample will usually be different from that of the glass and of the immersion oil. Water has an index of $n = 1.33$ and glycerol has $n = 1.47$. The sample itself will have an n that is not much different from that of the mounting medium and slightly higher than that of water (see Chapter 18, *this volume*, for the RIs of common mounting media).

A light ray emerging from an oil-immersion objective lens that is coupled to the coverslip with the appropriate oil will not be refracted until it passes the interface from the coverslip into the mounting medium. The light ray is usually only slightly affected by the sample itself and is assumed to carry on straight towards the focal region once it has passed the interface between the mounting medium and the coverslip. The discussion can therefore be restricted to the effects caused by the change in n at the glass–medium boundary and to the distance from this interface to the focus point somewhere inside the sample. What effects can be expected?

- A light ray is refracted at the glass–medium interface. The angle of the ray is changed; therefore, the different rays focus at different positions along the z-axis than they would in a perfectly matched optical system. In microscopy, n_1 is usually larger than n_2, and the focus is, therefore, closer to the coverslip than under ideal conditions. The position of an object will then appear to be further away from the coverslip. If n_1 were smaller than n_2, the focus would be further from the coverslip than it should be and the object would then appear to be closer to the coverslip.
- Whenever light is refracted, some light is also reflected (Born and Wolf, 2002). As refraction occurs only when the angle of incidence is lower than the angle of total internal reflection, the NA of the immersion system is effectively reduced.
- Perfect imaging is only possible if the wavefront remains spherical. Any deviation from sphericity results in a larger spread of the focus and hence in a reduction in both spatial resolution and peak intensity.
- This spreading of the focus means that the image of the focal spot focused back towards the confocal pinhole is also spread. This second defocus effect means that less light penetrates the pinhole, and the observed intensity decreases still more.

THEORY

The calculations are performed in a vectorial theory following Hell and colleagues (1992). The sample object is a layer of fluorophore immersed in the mounting medium. The immersion oil and the

Alexander Egner and Stefan W. Hell • Department of NanoBiophotonics; Max Planck-Institute for Biophysical Chemistry, Am Fassberg 11; D-37077 Goettingen, Germany

 Handbook of Biological Confocal Microscopy, Third Edition, edited by James B. Pawley, Springer Science+Business Media, LLC, New York, 2006.

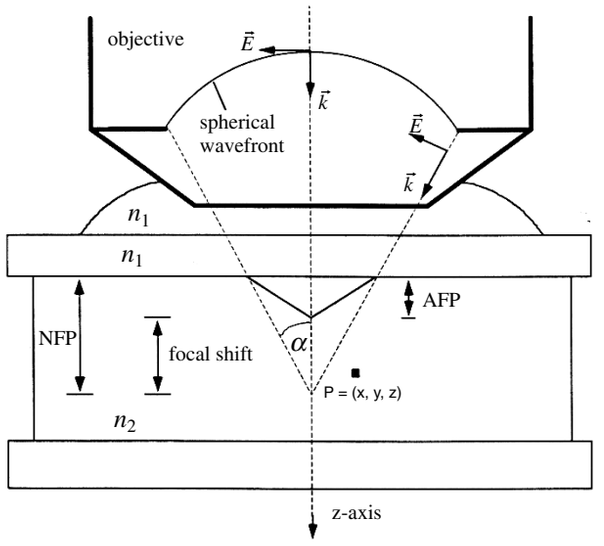


FIGURE 20.1. Terminology used for the calculation of point spread functions in optically mismatched systems. A spherical wavefront emerges from the objective lens. The wavefront is described by its electric field strength $\vec{E}$ and its direction $\vec{k}$, while the objective lens is described by its focal length and its numerical aperture $(NA) = n_1 \sin(\alpha)$. The sample consists of two coverslips, each with a refractive index of n_1 and the mounting medium with a homogeneous refractive index of n_2. The immersion medium between the upper coverslip and the objective lens has the same n as the coverslip. In a perfectly matched system, n_1 is equal to n_2 and the geometrical focus is a distance NFP (nominal focal position) away from the glass/mounting medium interface. In a mismatched system, n_1 is not equal to n_2. The focus suffers from a focal shift and is found at AFP (actual focal position). The theory describes the calculation of the electric field strength $\vec{E}$ in a point $P(x,y,z)$ close to both AFP and NFP.

coverslip have $n = n_1$ and the mounting medium $n = n_2$. Focusing into the sample is achieved by mechanically varying the distance between the objective lens and the bottom of the coverslip. The distance between this surface and the geometrical focus in a perfectly matched system is referred to as the nominal focal position (NFP).[1] The difference between the NFP and the actual focal position (AFP) is referred to as the focal shift in the optically mismatched system. We wish to calculate the AFP and the intensity at a point $P(x,y,z)$ in the vicinity of the AFP. The optical system is described by the wavelength of the incident light ray (λ), the NA of the objective lens, and the diameter of the aperture in the lens. In a modern optically perfectly matched microscope, the so-called infinity-corrected lens is assumed to accept a perfectly planar incoming-wavefront and produce a perfectly spherical outgoing wavefront that produces an aberration free point spread function (PSF) at the focal point. We note that our considerations apply to any point within the field of view specified for the lens.

In a confocal microscope, a point source is used to define the extent and the position of illumination, whereas a point detector discriminates against any light emitted outside a certain region. In physical terms, the effective PSF (Hell *et al.*, 1992) of the confocal fluorescence microscope is given by the product of the illumination intensity and detection PSF:

$$h_{cf} = \left|\vec{h}_{ill}\right|^2 \times \left|\vec{h}_{\mathrm{det}}\right|^2 \approx \left|\vec{h}_{ill}\right|^4 \qquad \textbf{(1)}$$

where $\vec{h}_{ill}$ denotes the amplitude of the illumination light in the focal region and $\vec{h}_{\mathrm{det}}$ is the amplitude distribution for the detection, which is similar to $\vec{h}_{ill}$, but is calculated for the wavelength of fluorescence emission. So, while $\vec{h}_{ill}$ is proportional to the light field used for illumination, and $|\vec{h}_{ill}|^2$ to its intensity, the effective confocal PSF h_{cf} is proportional to the probability that a given focal coordinate contributes to the signal at the confocal detector. If the excitation and emission wavelengths are rather similar, it follows that $|\vec{h}_{ill}|^2 \approx |\vec{h}_{\mathrm{det}}|^2$. In this case, h_{cf} is proportional to the fourth power of the illumination amplitude and hence to the square of the illumination intensity (Wilson and Sheppard, 1984), as indicated on the right-hand side of Eq. 1. This quasi-quadratic signal dependence of the recorded intensity on the illumination intensity causes a drop of the detected fluorescence from points away from the geometrical focus and is the actual physical reason why a confocal setup defines a confined recording volume in three-dimensional (3D) space.

The z-response $I(z)$ to infinitely thin fluorescent planes and the response $I_{\mathrm{edge}}(z)$ to half-volumes in the z-direction are of practical importance as well because they quantify the ability of a microscope to distinguish planes that are stacked in the z-direction:

$$I(z) = \int_{-\infty}^{\infty}\int_{-\infty}^{\infty} h_{cf}(\vec{r})dx\,dy \text{ and } I_{edge}(z) = \int_{-\infty}^{z} I(z')dz' \qquad \textbf{(2)}$$

A volume confinement can also be achieved by multi-photon excitation of the fluorophores (Denk *et al.*, 1990; Sheppard and Gu, 1992a, 1992b) (Chapters 28 and 37, *this volume*). The probability of two photons being simultaneously absorbed by the same molecule is proportional to the square of the local intensity (Kaiser and Garret, 1961). Therefore, the effective PSF of a microscope based on two-photon absorption is described by the square of the illumination PSF, that is, the fourth power of the field amplitude for illumination:

$$h_{2h\nu} = \left|\vec{h}_{ill}\right|^4 \qquad \textbf{(3)}$$

The similarity to Eq. 1 indicates that the illumination process defines a volume in a manner similar to the combined illumination and detection processes in a confocal single-photon excitation fluorescence microscope (Hell and Stelzer, 1992; Sheppard and Gu, 1992b; Stelzer *et al.*, 1994). This means that all the problems discussed for single-photon confocal microscopy are also encountered in two-photon fluorescence microscopes. The only real difference is that the latter requires wavelength doubling. Additional confocalization of the system means that the effective PSF is given by $h_{cf\,2h\nu} = |\vec{h}_{ill}|^4 \times |\vec{h}_{\mathrm{det}}|^2$ and for an n-photon confocalized system we obviously have

$$h_{cf\,2h\nu} = \left|\vec{h}_{ill}\right|^{2n} \times \left|\vec{h}_{\mathrm{det}}\right|^2. \qquad \textbf{(4)}$$

In an aberration-free system, the calculation of the fields $\vec{h}_{ill}$ and $\vec{h}_{\mathrm{det}}$ is rather straightforward because these functions solely depend on the wavelength and the NA. By contrast, when focusing through RI interfaces, the evaluation of $\vec{h}_{ill}$ and $\vec{h}_{\mathrm{det}}$ is complicated by the fact that, loosely speaking, it has to be calculated once for medium n_1 and then for medium n_2 (Hell *et al.*, 1993). The latter publication treated the problem with specific regard to confocal microscopy and quantitatively predicted all the effects

[1] It should be noticed that the NFP is the actual distance of a feature in the object from the surface of the coverslip.

encountered with refractive index mismatched samples. Therefore, in this chapter we will follow the argument presented in that publication. In the meantime, significant advancements in the formulation of this theory have been made. These are considered later in this chapter (Török *et al.*, 1995; Egner and Hell, 1999).

Starting from simple terms, the calculation basically requires the solution of a variational problem in optics, that is, the application of Fermat's principle from a point of the converging spherical wavefront to the point of the focal region in question [Fig. 20.2(A)]. According to the Huygens–Fresnel construction, each point on the spherical wavefront is a source of secondary spherical wavelets (Hopkins, 1943; Li and Wolf, 1981). In a matched medium, we have

$$\vec{h}(\vec{r}) = c\int_F\int \vec{A}(F)\frac{1}{s}K(\chi)\exp(iks)dF \tag{5}$$

where $\vec{A}(F)$ denotes the wavefront amplitude over the surface F of the spherical wavefront and dF is the surface element (see Fig. 20.2); s is the distance between the origin of the wavelet q and the point P, and χ is the angle of inclination between the normal at q and the direction from q to P.

$$K(\chi) = -\frac{1}{2\lambda}(1+\cos(\chi)) \tag{6}$$

In an aplanatic objective lens, the wavefront $\vec{A}(F)$ is given for in the x-direction polarized light of Amplitude A_i by Richards and Wolf (1959):

$$\vec{A}(F) = A_i\sqrt{\cos(\theta)}\begin{pmatrix}\cos(\theta)+(1-\cos(\theta))\sin^2(\varphi)\\(1-\cos(\theta))\cos(\varphi)\sin(\varphi)\\\sin(\theta)\sin(\varphi)\end{pmatrix} \tag{7}$$

For the numerical calculation of $\vec{h}(\vec{r})$, the term $K(\chi)$ can be neglected because it varies by only a small amount. Because the calculation is restricted to the volume close to the geometrical focus, $1/s$ remains a constant and can therefore also be neglected. The function $\vec{h}(\vec{r})$ can be simplified to

$$\vec{h}(\vec{r}) = c\int_0^a\int_0^{2\pi}\sqrt{\cos(\theta)}\begin{pmatrix}\cos(\theta)+(1-\cos(\theta))\sin^2(\varphi)\\(1-\cos(\theta))\cos(\varphi)\sin(\varphi)\\\sin(\theta)\sin(\varphi)\end{pmatrix}\exp(iks)\sin(\theta)d\varphi\, d\theta \tag{8}$$

The final problem is the determination of s, which, as is pointed out above, is a variational problem and a careful analysis of the light transition at the interface between n_1 and n_2, to which one solution has been provided (Hell *et al.*, 1993).

If the NFP is small compared to the focal length of the objective lens, an assumption which is well met in confocal microscopy, the variational problem can be solved analytically for the region near the NFP (Egner and Hell, 1999). Török and colleagues derived an identical solution (Török *et al.*, 1995) using a plane wave expansion of the light field, that is, the Debye approximation instead of the Huygens–Fresnel construction. In both cases the solution for $\vec{h}(\vec{r})$ is given by:

$$\vec{h}(\vec{r}) = c\begin{pmatrix}i(I_0(\vec{r})+I_2(\vec{r})\cos(2\varphi))\\I_2(\vec{r})\sin(2\varphi)\\i\,2I_1(\vec{r})\cos(\varphi)\end{pmatrix} \tag{9}$$

Where the diffraction integrals I_n are defined by:

$$\begin{aligned}
I_0 &:= \int_0^a \sqrt{\cos(\theta_1)}\sin(\theta_1)\left(\tau_s+\tau_p\cos(\theta_2)\right)J_0\left(kn_1\sqrt{x^2+y^2}\sin(\theta_1)\right)\\
&\quad \exp(ik(\Phi(NFP)+n_2z\cos(\theta_2)))d\theta_1\\
I_1 &:= \int_0^a \sqrt{\cos(\theta_1)}\sin(\theta_1)\left(\tau_p\sin(\theta_2)\right)J_1\left(kn_1\sqrt{x^2+y^2}\sin(\theta_1)\right)\\
&\quad \exp(ik(\Phi(NFP)+n_2z\cos(\theta_2)))d\theta_1\\
I_2 &:= \int_0^a \sqrt{\cos(\theta_1)}\sin(\theta_1)\left(\tau_s-\tau_p\cos(\theta_2)\right)J_2\left(kn_1\sqrt{x^2+y^2}\sin(\theta_1)\right)\\
&\quad \exp(ik(\Phi(NFP)+n_2z\cos(\theta_2)))d\theta_1
\end{aligned} \tag{10}$$

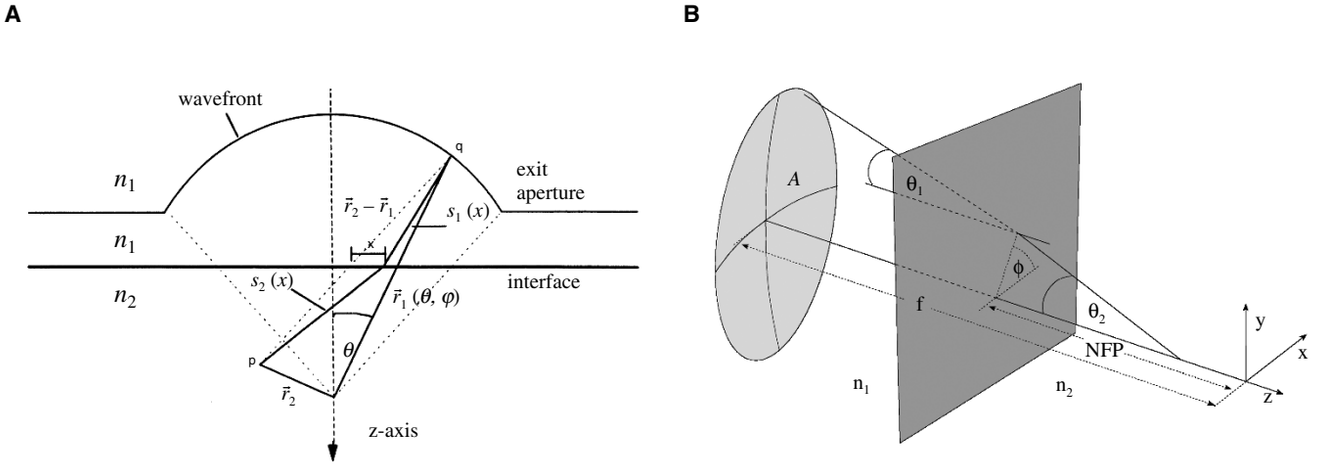


FIGURE 20.2. (A) The variational approach to the calculation of the electric field strength $\vec{E}$ at a point $P(x,y,z)$ close to both the AFP and the NFP. The geometry is basically the same as described in Figure 20.1. The problem is to minimize the distance $s_1(x) + s_2(x)$. It can be shown that this sum depends on the angle and on the origin of the beam in the primary spherical wavefront. The calculation, therefore, has to search for those beams that contribute to the field at position P according to Fermat's principle. For each point P(x,y,z) in the object, the contribution is found by integrating the complex electric field across the whole exit aperture. This makes the calculations somewhat tedious. (B) If the NFP is small compared to the focal length of the objective lens, which is always the case in microscopy, the calculation becomes much easier as only the transmission and refraction for a beam incident upon the boundary with an angle θ_1 has to be known.

J_n are Bessel functions of the first kind and nth order and $\tau_{p,s}$ are Fresnel transmission coefficients for s- and p-polarized light (Born and Wolf, 2002). The aberration function

$$\Phi(NFP) = -NFP(n_1 \cos(\theta_1) - n_2 \cos(\theta_2)) \quad \textbf{(11)}$$

depends on the nominal focusing position, the azimuth angle θ and therefore on the aperture angle α and the difference of the refractive indices n_1 and n_2. The differences between the calculations of the illumination and the detection PSFs are the wavelength and the term $\sqrt{\cos(\theta)}$ which is omitted.

RESULTS OF THEORETICAL CALCULATIONS

The theory described above does not result in an analytical description of the PSF. The PSFs have to be calculated numerically as a function of the NA, excitation and emission wavelengths, NFP, n_1, and n_2. In order to illustrate how focusing into a mismatched medium affects the PSF, Figure 20.3 shows xz-images of calculated PSFs (logarithmic scale) and the corresponding experimental through-focus series (linear scale) for focusing with a water-immersion lens either 10 µm deep into water [Fig. 20.3(A,B)] or into immersion oil [Fig. 20.3(C,D)]. In the mismatched case, the main maximum is shifted, becomes relatively broader, and drops in peak intensity (Fig. 20.4). In addition, the PSF loses its axial symmetry with respect to the main maximum whereby focusing above the AFP leads to a different image from focusing below the AFP [Fig. 20.3(D)], an effect that is not present in the matched case [Fig. 20.3(B)].

The results of several calculations are summarized in Figures 20.4, 20.6, 20.7, 20.8, 20.9, and 20.10 and in Tables 20.1 and 20.2 for water and for glycerol mounting media. Figure 20.4 shows the integrated intensity for various NFPs using water as the mounting medium. The first image indicates the ideal situation encountered with a fluorophore mounted in immersion oil. The following images show again that the integrated intensity is smeared along the optical axis, and an additional peak appears below the main maximum. The main maximum itself is shifted, drops in peak intensity, and becomes relatively broader. These values can be evaluated to obtain the focal shift [(NFP) – (AFP)], the drop in peak intensity, and the full-width half-maximum (FWHM) of the main peak. While, because of its convoluted shape (Fig. 20.5), it is difficult to specify a simple metric that quantifies the sharpness of a spherically aberrated focal spot, the FWHM of the main peak is relatively simple to measure and hence has become the most common measure of the xy or axial resolution.

Calculations for some numbers encountered in real situations have been combined with the experimental results in Figures 20.6, 20.7, and 20.8. Figure 20.9 shows the focal shift of the excitation PSF of a 0.6 oil-immersion objective lens directly as a function of NFP for various refractive indices. Figure 20.10 also plots the focal shift but for an NA 1.4 oil-immersion objective lens. The AFP is regarded as the position of the global maximum of the PSF along the optical axis rather than the center of gravity or some other measure of this complex shape.

An important result of these calculations is that the effects of spherical aberration increase rapidly with $(n_1 - n_2)$, NA, and distance of the object from the coverslip (NFP). As long as the

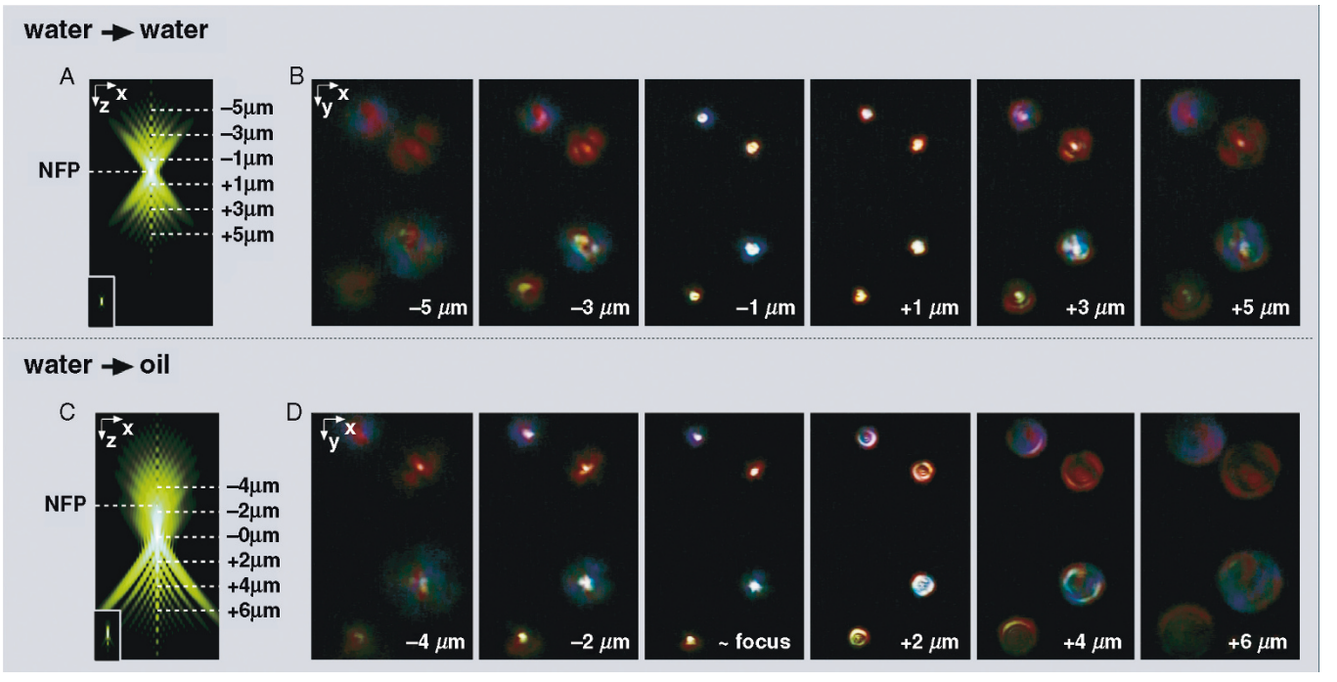


FIGURE 20.3. Influence of a mismatched medium on the PSF. (A) and (C) show xz-images of calculated PSFs in logarithmic scale for focusing with a water-immersion lens (n = 1.334) 10 µm deep into water and immersion oil (n = 1.518), respectively. The inlets in the lower left corners show the central part of the PSFs in linear scale. (B) and (D) show corresponding experimental through-focus series in a linear scale. These series represent exactly what one would see when focusing through a point-like object. Focusing into a mismatched medium causes a shift and a broadening of the main maximum. The aberrated PSF can be clearly identified in the through-focus series as focusing above the AFP leads to a different image from focusing below the AFP. The image series was made of a mirror specimen by J. Pawley using a Zeiss Axioskpp 50, with a 40×/NA1.2 C-Apo objective, and recorded with a Sony TRV-900 camcorder using the zoom lens to provide the high magnification.

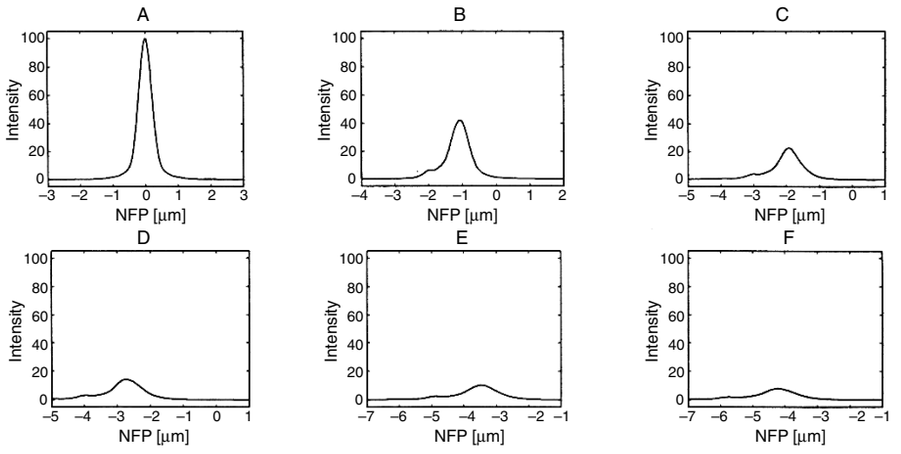


FIGURE 20.4. Integrated z-responses for various penetration depths (NFP) in water for an NA = 1.3 oil-immersion objective lens. The excitation and emission wavelengths were 514 nm and 590 nm, respectively. (A) Ideal situation in oil, penetration depths of (B) 5 μm, (C) 10 μm, (D) 15 μm, (E) 20 μm, and (F) 25 μm. All curves are normalized to the ideal situation encountered with immersion oil as the mounting medium. The point spread function is obviously not confined to the minimal volume but instead continues to spread the larger NFP becomes. This causes a decrease of the maximal intensity, an increase of the full-width half-maximum, and a focal shift. The intensity is distributed among several axial peaks of which at least two are clearly visible. Please note that the NFP axis has been offset.

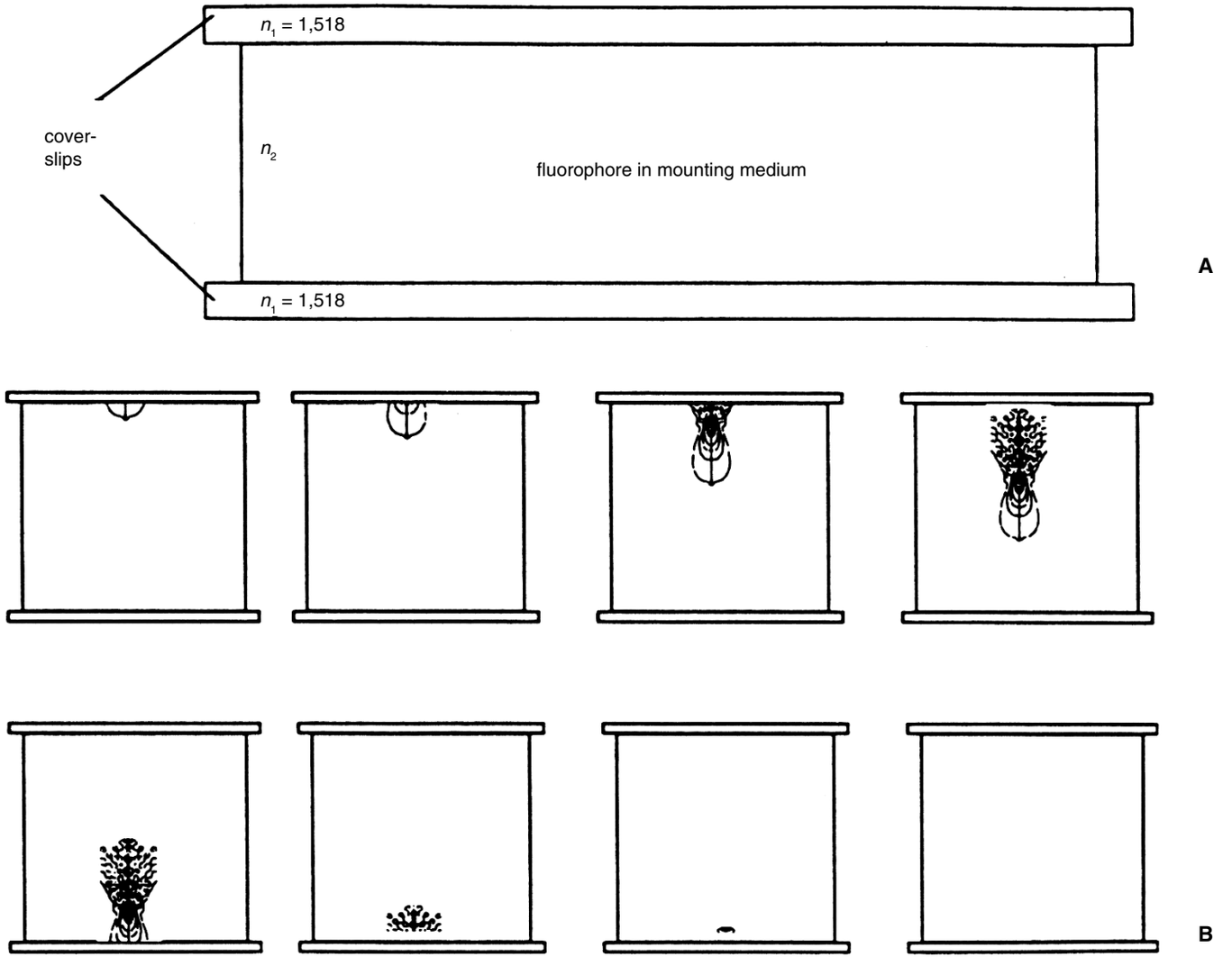


FIGURE 20.5. Sample used for measuring the edge response in a confocal laser-scanning microscope. (A) The sample consists of two coverslips or a coverslip and a glass slide with a fluorophore dissolved in the mounting medium (water, glycerol, immersion oil) in between. The sample thickness (upper/lower interface distance) is at most 100 μm. In this sample, the concentration of the fluorophore is zero inside the glass and abruptly reaches a high concentration when moving the probe along the optical axis. (B) During the experiment, the point spread function penetrates the mounting medium through a coverslip. The measured fluorescence intensity signal depends on the penetration depth. The fluorescence emission is maximal when the point spread function is completely inside the sample. Because the point spread function has a finite size, it has a response curve with a finite steepness. The slopes close to the interfaces can, therefore, be used to determine the extent of the point spread function along the optical axis, and this is the axial resolution of the instrument.

TABLE 20.1. Result of Calculations for Glycerol[a,b]

NFP (μm)	Focal Shift (μm)	Normalized Intensity	Axial Edge FWHM (μm)	Axial PSF FWHM (μm)	Lateral PSF FWHM (μm)
0	0	100	0.53	0.47	0.16
5	–0.28	95	0.53	0.47	0.16
10	–0.55	91	0.53	0.47	0.16
15	–0.83	78	0.555	0.47	0.16
20	–1.10	62	0.65	0.50	0.18
25	–1.33	50	0.81	0.57	0.18
30	–1.54	40	0.97	0.77	0.20
50	–2.30	31	1.00	0.72	0.20

[a] For various nominal focal positions (NFP), the focal shift, the normalized intensity, the axial edge response, the axial width of the PSF, and the lateral width of the PSF have been calculated for an NA = 1.3 oil-immersion objective lens and excitation and emission wavelengths of 514 nm and 590 nm, respectively.
[b] The values for an NFP = 0 are the ideal values if immersion oil is used as the mounting medium.

TABLE 20.2. Result of Calculations for Water[a]

NFP (μm)	Focal Shift (μm)	Normalized Intensity	Axial Edge FWHM (μm)	Axial PSF FWHM (μm)	Lateral PSF FWHM (μm)
0	0	100	0.53	0.47	0.16
5	–1.0	60	0.68	0.58	0.20
10	–1.83	39	0.90	0.70	0.20
15	–2.57	28.50	1.08	0.88	0.23
20	–3.30	23	1.22	0.93	0.24
25	–4.02	19	1.37	1.00	0.24
30	–4.72	16.60	1.45	1.11	0.24
50	–7.57	11	1.79	1.37	0.24

[a] For various nominal focal positions (NFP), the focal shift, normalized intensity, axial edge response, axial width of the PSF, and lateral width of the PSF have been calculated for an NA = 1.3 oil-immersion objective lens and excitation and emission wavelengths of 514 nm and 590 nm, respectively. The values for an NFP = 0 are the ideal values if immersion oil is used as the mounting medium.

spherical aberrations are below a certain threshold, the focal shift depends linearly on the NFP which can be used to correct the apparent thickness of a sample. If the spherical aberrations exceed the threshold, the relation between the NFP and the focal shift becomes nonlinear which leads to image distortions along the *z*-axis and a rapid drop in intensity as the excitation and emission PSF will be substantially displaced. This effect is most prominent with high NAs and very low for oil-immersion lenses having an NA of <0.85.

EXPERIMENTS

To verify these calculations, Rhodamine 6G was dissolved in water, glycerol, and immersion oil to form ~10^{-5} *M* solutions. The solutions were mounted between a glass slide and a coverslip using droplets of dried nail polish as spacers. The samples were placed either onto a home-built confocal microscope (Stelzer *et al.*, 1991) [Figs. 20.6, 20.7(A), 20.8] or a commercial confocal microscope (TCS SP2, Leica Microsystems Heidelberg, Mannheim, Germany) (Martini *et al.*, 2002) [Fig. 20.7(B)]. The dye was excited at a wavelength of 488 nm and observed either above 530 nm [Figs. 20.6, 20.7(A), 20.8] or between 495 nm and 530 nm [Fig. 20.7(B)]. For the data presented in the Figures 20.6, 20.7(A) and 20.8, a Zeiss Apochromat 100× oil objective with an adjustable aperture (NA 0.8–1.4) was used, whereas the data of Figure 20.7(B) was recorded with a 100× adjustable aperture Leica oil-immersion lens (HCX PL APO 1.4–0.7) and a 100×, 1.35 NA Leica glycerol-immersion lens (HCX PL APO, GLYC CORR). The instruments were used to record *xz*-images, that is, images in a plane parallel to the optical axis (Fig. 20.5). These images started with the focus in the coverslip and ended with the focus in the glass slide. The

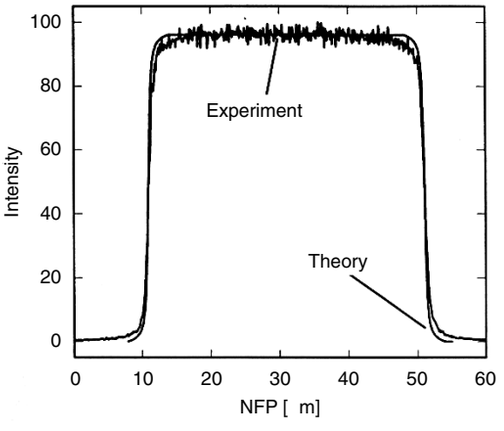


FIGURE 20.6. The experimental and the theoretical edge-response curves for immersion oil. The theoretical curve was fitted to the experimental data set to comply with the apparent sample thickness and the maximum intensity in the sample. The theoretical calculations assume a perfect match of the refractive indices of the immersion oil, the glass, and the mounting medium. As shown, this condition is almost, but not perfectly, fulfilled under real conditions. The theory predicts a slightly steeper slope.

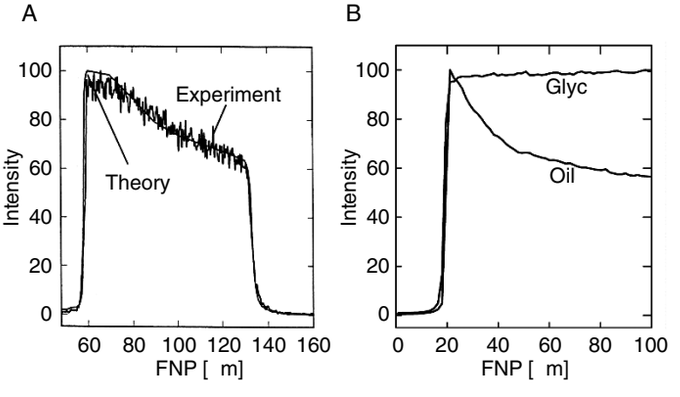


FIGURE 20.7. The experimental and the theoretical edge-response curves for glycerol. Focusing with an oil-immersion lens into glycerol leads to a significant drop in image brightness (A). The theoretical curve was fitted to the experimental data set to comply with the apparent sample thickness and the maximum intensity in the sample. The intensity decrease is perfectly reproduced. (B) By using a glycerol-immersion lens the drop in image brightness can be prevented.

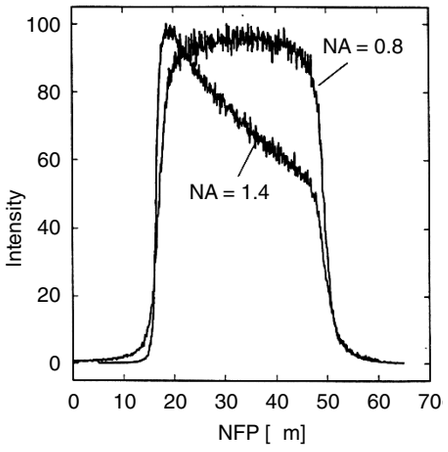


FIGURE 20.8. Two edge-response curves in a water sample. The graph shows the intensities as a function of NFP for NA 1.4 and 0.8. Both curves were recorded with the same sample in the same position. This is possible because the objective lens (Zeiss Plan-Apochromat 100×, NA 1.4) has an adjustable NA. The figure demonstrates that the loss in resolution and the loss in intensity are due to the effects of high NA and not to quenching or bleaching.

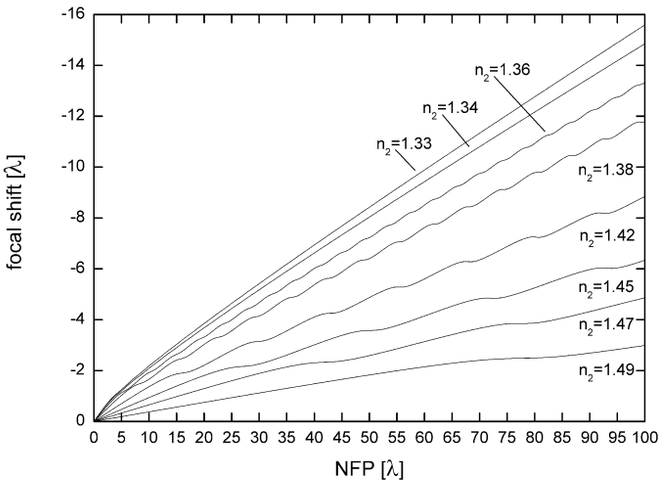


FIGURE 20.10. Dependence of the focal shift for an NA = 1.4 oil-immersion objective lens on the nominal focal position for various refractive indices between 1.33 and 1.49. For such a high NA objective lens, the variation is only linear up to a certain maximum NFP, which strongly depends on the difference in the refractive index and the aperture angle. After that, the focal shift starts to show some kind of oscillation. In the linear regime the curves can be used to correct the apparent thickness of a sample in a mounting medium with a known refractive index by multiplying it by an appropriate factor.

64 central columns were then averaged to generate the edge-response curves (see Eq. 6) shown in Figures 20.6 through 20.8. These graphs resemble intensity signals as a function of the NFP. Of interest is the edge steepness on both sides and the variation in peak intensity with depth. The results are summarized in Table 20.3. Because it was not possible to systematically vary the thickness of the dye layer (usually between 50 µm and 100 µm), the focal shift was not measured directly.

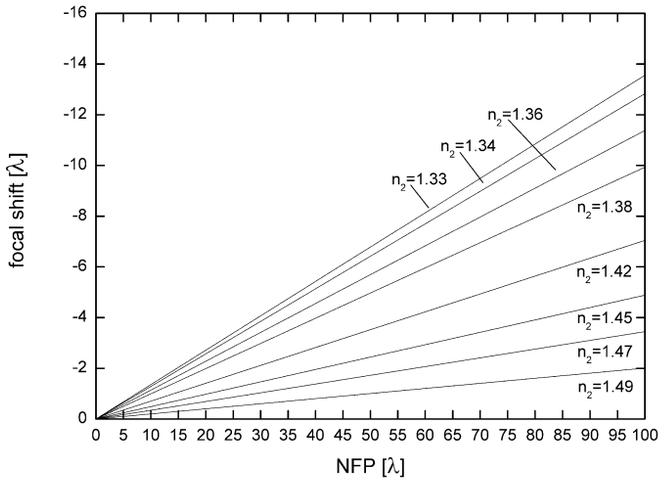


FIGURE 20.9. Dependence of the focal shift for an NA = 0.6 oil-immersion objective lens on the nominal focal position for various refractive indices between 1.33 and 1.49. For such a low NA objective lens, the variation is linear for the whole range. The curves can be used to correct the apparent thickness of a sample in a mounting medium with a known refractive index by multiplying it by an appropriate factor.

OTHER CONSIDERATIONS

Dry Objectives

The use of dry, high-NA lenses for the observation of wet specimens, or even those sealed behind glass coverslips, causes aberrations that are much worse than for any of the situations described above.

First, the difference between the refractive indices of the immersion and embedding media is larger than for any other type of objective. Therefore, focusing even a few micrometers into the sample will result in a severe drop of intensity and resolution. Of course, this can be avoided by adjusting the correction collar. Most high-NA dry objectives are equipped with such a collar but the correct adjustment only works for a single plane. Every change of the NFP will result in serious degradation of the PSF. For the same reason, dry objectives are very sensitive to the coverslip thickness.

Second, due to total internal reflection, the maximum angle transmitted as the emerging light moves from glass to air is 41° and 49° as it moves from water to air. The PSF is therefore dominated by the illumination PSF. The situation is much relaxed when using lenses having an NA of 0.6 or less because the angle inside the water layer is then 26° and relatively uncritical. On the other

TABLE 20.3. Result of the Experiments with Water and Glycerol

	Water (NA = 0.8)	Water (NA = 1.3)	Glycerol (NA = 1.3)
Upper edge (µm)	1.5	1.0	1.0
Lower edge (µm)	2.0	5.7	2.3
Ratio upper/lower	1.3	5.7	2.3

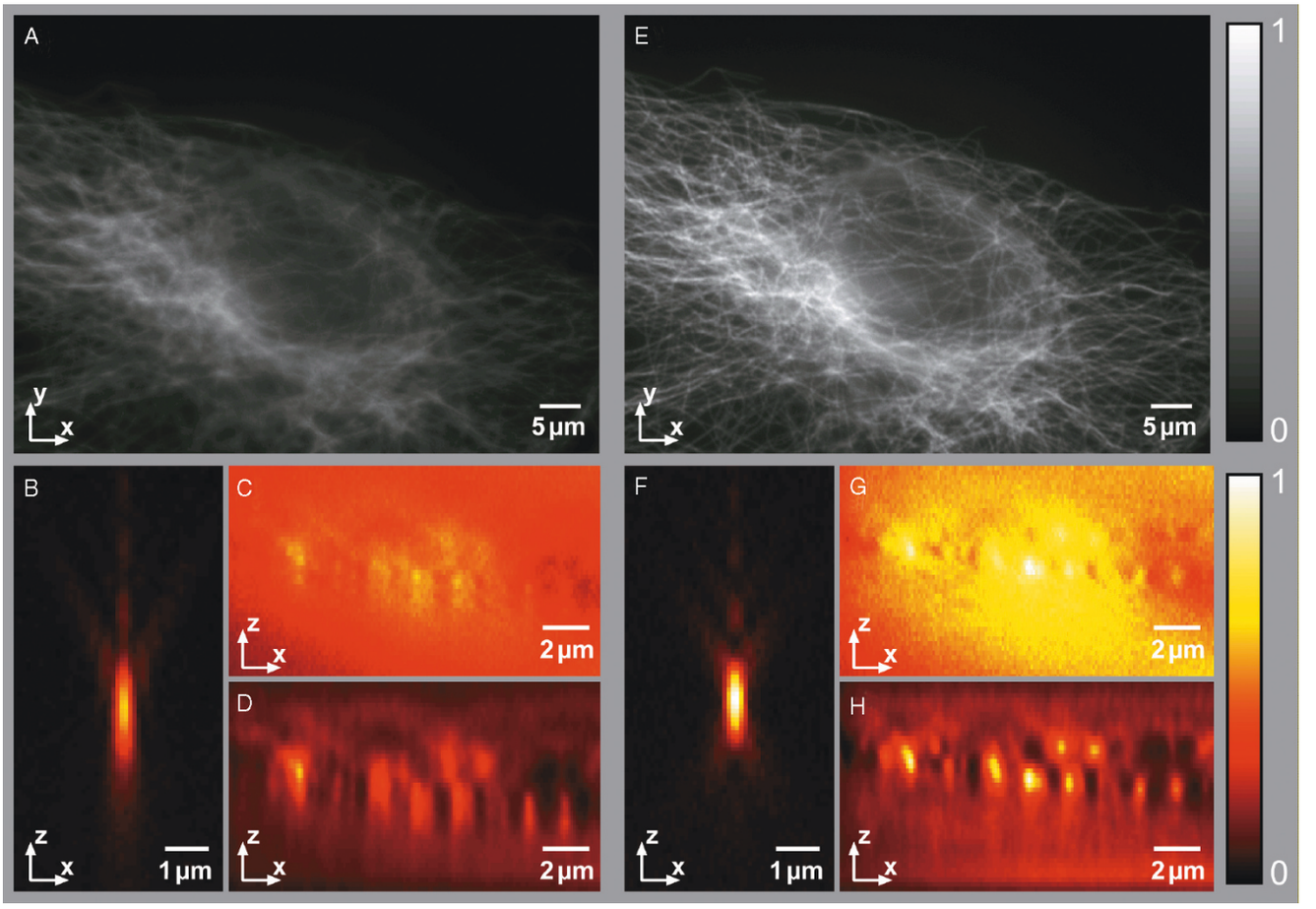


FIGURE 20.11. Optical spherical aberration correction. Images of aqueous PTK2 cells stained with Oregon green anti-tubulin and made using an NA 1.4 oil objective. Replacing microns of glass by water introduces distinct spherical aberrations [(A) *xy* image; (B) *xz* PSF; (C) raw *xz* image; (D) deconvolved *xz* image] that are not present in the corrected images [(E) *xy* image; (F) *xz* PSF; (G) raw *xz* image; (H) deconvolved *xz* image]. The loss in peak intensity and contrast is clearly visible in the images of the same *xy* plane (A,E). The *zx* images of the fluorescent microsphere show the asymmetry in the *z* direction and the loss in axial resolution (B,F). As a result, after deconvolution, tubulin fibers lying on top of each other can be clearly distinguished only in the unaberrated case.

hand, the axial resolution improvement produced by confocal microscopy under these conditions is so low that it is fair to ask if it makes sense to use such a microscope under these circumstances.

Refractive Index, Wavelength, and Temperature

The refractive index is not a constant but depends on the wavelength (a phenomenon referred to as dispersion) and on the temperature of the medium (especially with liquids). Standard immersion oil has a refractive index of 1.518 at the n_e line of the Hg spectrum (486 nm) and a temperature of 23°C, but performance away from these standard conditions may vary depending on the manufacturer of the oil. Perfect imaging is, therefore, not straightforward to achieve. Special immersion oils and gels with many different RI and varying temperature behavior are available through Cargille Laboratories (Cedar Grove, NJ).

Spherical Aberration Correction

The loss in intensity and resolution caused by RI mismatch induced spherical aberrations can highly degrade the imaging process. Therefore, it is advisable to reduce the RI mismatch as much as possible (see section Consequences). Unfortunately, this is not always possible in a specific experimental setting. For example, when using dipping water-immersion objective lenses together with a coverslip, the spherical aberrations caused by the water–glass–water transitions induce spherical aberrations that are much stronger than those shown in the preceding examples. Fortunately, it is possible to cancel out aberrations emerging at one point in the imaging process by introducing negative aberrations at another point. For example, in water-immersion objective lenses, this is done inside the lens and the spherical aberration can be adjusted using a correction collar. Of course this balancing can also be performed anywhere else in the optical path by either using a deformable mirror (Booth *et al.*, 2002), or a spatial light modulator or altering the effective tube length (Sheppard and Gu, 1992b). While the first two approaches can also correct for non-spherical aberrations, the latter can only be used for balancing spherical aberrations. Figure 20.11 shows an example for aberration correction by altering the effective tube length through a commercially available system (SAC, Intelligent Imaging Innovations Inc., Denver, CO).

Replacing micrometers of glass by water results in pronounced spherical aberration. One can recognize the severe loss in intensity and contrast in Figure 20.11(A,E), an *xy* image of tubulin in PTK2 cells stained with Oregon green. The axial resolution is also

strongly reduced [Fig. 20.11(B,F)], an effect that be compensated for by deconvolution only approximately (see Chapter 24, *this volume*). While in the aberrated case, it is difficult to distinguish individual fibers lying near each other [Fig. 20.11(C,D)], they are well separated in the aberration-free images [Fig. 20.11(G,H)].

It is important to point out that much of the charm of correcting spherical aberration by moving optical components that are not mounted in the objective lens comes from the fact that the motion of such a correcting element can now be driven by a motor.[2] As all optical devices that change the spherical correction of an optical system by tube length alteration also change its focal length, changing the correction implies creating a shift in the focal plane. However, if the motion of the corrector is driven by a computer, this same computer can also adjust the focus control in a compensatory direction to maintain the focus plane. The SAC is the first device to do this automatically. One hopes that such devices may soon be incorporated into microscope stands as a standard attachment, similar to a magnification shifter or a Bertrand lens.

CONCLUSION

The effects mentioned in this chapter are so important that most practicing microscopists will have already encountered them. The effects are mainly visible when using lenses with a high NA or, more correctly, when using lenses whose cone angle is larger than 40°. Some of the older confocal microscopes did not fill the back-focal plane completely (see Chapter 2, *this volume*) and the higher angles were basically not present, especially when using high-NA objectives of relatively low magnification (–40×), as such lenses have very large entrance pupils. Therefore, it can be assumed that these problems will become more obvious as the quality of the instruments improves and more scientists work with aqueous specimens.

Consequences

The qualitative relevance of these experiments for the observation of thick specimens mounted in an aqueous medium with a high-NA, oil-immersion objective in a confocal microscope is as follows:

- There is a serious loss of intensity when recording optical sections in focal planes away from the coverslip and this loss becomes greater as the distance from the coverslip increases.
- The PSF suffers from a serious axial smearing; consequently, the axial resolution is lower.
- The *xy*-resolution is also lower because the high-NA rays no longer reach the focal spot.
- Less fluorescence intensity is detected behind the confocal pinhole.
- The distances measured along the optical axis are smaller than the geometrical distances in the object. The benchmark to remember is that in water, the focal shift is 13λ at a penetration depth of 100λ.
- In a mismatched system, the only part of the specimen that can be observed without the severe effects described above is that immediately next to the coverslip.
- The problem is encountered in every single-photon confocal and two-photon scanning microscope.

The physical relevance of these experiments is that, in the case of a noticeably mismatched sample, a single PSF, or a single optical transfer function (OTF) is not valid throughout the sample. As the PSF or OTF can be defined only locally, a global deconvolution to remove the effect of spherical aberration using the system response is unlikely to be successful.

This chapter also shows that an aberrated PSF can be accurately calculated from an initial unaberrated PSF. The deviations follow an approximately linear relationship, and a simple linear expansion is likely to be able to describe the PSF in different locations of the object fairly well. However, this does not mean that the effect can be easily corrected. If not counteracted optically, the loss in signal level and resolution cannot be recalled.

Practical Strategies to Reduce Refractive Index Mismatch

The biologist can avoid these problems by adhering to the following guidelines:

- Always use the appropriate objective lens. High resolving objective lenses like NA 1.4 oil-immersion lenses are usually designed to be used for thin specimens mounted behind a coverslip. For other experimental settings, like imaging through the bottom of a petri dish, there are other more appropriate lenses available, particularly those that incorporate a correction collar for spherical aberration minimization. These should always be properly adjusted.
- Thick specimens should only be observed in matched systems. This means the RI of the mounting medium and the immersion medium should be identical at all wavelengths of interest. Therefore, water-immersion and glycerol-immersion lenses should be used for water- and glycerol-embedded specimens, respectively.
- Avoid situations in which the sample is thin but far away from the coverslip. This often happens when the object is either attached permanently to the glass microscope slide or when viewing cells grown on filters but separated from the protective coverslip by an unknown amount of aqueous medium.
- If you cannot match the RI of the mounting medium to that of the immersion, try to get its refractive index as similar as possible. This can be accomplished by preparing mixtures of glycerol and water or by adding large amounts of dextrose to the mounting medium. This will at least reduce the amount of spherical aberrations incident at a certain focusing depth.
- For unmatched systems, increase the size of the detection pinhole as a function of the penetration depth. This will not improve the PSF, but it will increase the detectable signal without any further losses in resolution, and at least the brightness will not decrease so much as the image series extends farther from the coverslip surface.
- If you have to image deeper into unmatched samples and no appropriate lens is available, use a lower NA immersion objective. As demonstrated in Figure 20.8, for small mismatches, the loss in intensity is much less below NA 0.85. However, the lower NA has its own disadvantages: lower light collection and lower resolution. As shown in Table 20.3, looking through

[2] Other methods proposed for the automatic correction of spherical aberrations include deformable mirrors and spatial light modulators. Like the SAC, these devices would be introduced after the objective, where their operation could be computer controlled and any adjustments could be coupled with any changes in stage position that might be required.

50 µm of aqueous specimen with an NA 1.4 oil lens decreases the axial resolution by a factor of 6 and the intensity becomes as low as 11%. If you use instead a NA 0.8 lens, the axial resolution at the surface will be $(0.8/1.4)^2 = 3$ times worse and only 36% of the fluorescence photons of the oil lens will be collected due to the smaller aperture angle. At an imaging depth of 50 µm things will have changed: The peak light intensity will drop to only about 33%, which is about the same signal as we would get with the oil lens (36% * 33% = 12%) and the resolution will be 6 / (3 * 1.3) = 1.5 times that of the oil lens. Clearly, this is an improvement, and the advantage becomes even more prominent as the sample becomes thicker. On the other hand, imaging through a 20 µm layer of water gives about the same image with either lens, and any features closer to the coverslip will be imaged better by the larger NA lens. Of course, one must keep in mind that imaging through ~10 µm of water with an oil immersion lens leads to a seriously aberrated PSF.

- Spherical aberration (and *not* absorption) is the major source of the reduction in fluorescence signal with focus depth commonly noted by most practicing confocal microscopists.
- Optimal observation of thick living specimens occurs when the sample is observed using water-immersion objectives and no coverslip. Upright microscopes are best suited for this purpose because the water is then less likely to leak into the objective. However, the absence of a coverslip may cause the specimen to move as the focus plane changes to record 3D data. Under these conditions, one may be able to use either water-immersion lenses corrected for use with a coverslip (see Chapter 7, *this volume*) or CYTOP plastic coverslips, which have $n = 1.34$, and as a result can be used with normal water-immersion lenses.
- If the experimental setting does not allow for spherical aberration minimization, think about aberration balancing inside the optical light path by introducing a spherical aberration correction device.

ACKNOWLEDGMENTS

This chapter is in part based on Chapter 20 of the previous edition. We acknowledge earlier suggestions and contributions by Gernot Reiner and Ernst Stelzer. We thank Julia König and Nicole Zobiack from Intelligent Imaging Innovations for granting us access to the spherical aberration corrector, Scientific Volume Imaging for providing us with their Huygens deconvolution software, Andreas Schönle for providing us with his image acquisition and analysis software Imspector, Jaydev Jethwa for carefully proofreading the manuscript, and all the members of the Department of NanoBiophotonics and James Pawley for valuable discussions.

REFERENCES

Booth, M.J., Neil, M.A.A., Juskaitis, R., and Wilson, T., 2002, Adaptive aberration correction in a confocal microscope, *Proc. Natl. Acad. Sci. USA* 99:5788–5792.

Born, M., and Wolf, E., 2002, *Principles of Optics*, Cambridge University Press, Cambridge, New York.

Denk, W., Strickler, J.H., and Webb, W.W., 1990, Two-photon laser scanning fluorescence microscopy, *Science* 248:73–76.

Egner, A., and Hell, S.W., 1999, Equivalence of the Huygens-Fresnel and Debye approach for the calculation of high aperture point-spread-functions in the presence of refractive index mismatch, *J. Microsc*. 193:244–249.

Hell, S.W., and Stelzer, E.H.K., 1992, Fundamental improvement of resolution with a 4Pi-confocal fluorescence microscope using two-photon excitation, *Opt. Commun*. 93:277–282.

Hell, S.W., Lehtonen, E., and Stelzer, E.H.K., 1992, Confocal fluorescence microscopy: Wave optics considerations and applications to cell biology, In: *Visualization in Biomedical Microscopies: 3-D Imaging and Computer Applications* (A. Kriete, ed.), VCH, Weinheim, Germany, pp. 145–160.

Hell, S.W., Reiner, G., Cremer, C., and Stelzer, E.H.K., 1993, Aberrations in confocal fluorescence microscopy induced by mismatches in refractive index, *J. Microsc*. 169:391–405.

Hopkins, H.H., 1943, The Airy disc formula for systems of high relative aperture, *Proc. Phys. Soc*. 55:116.

Kaiser, W., and Garret, C.B., 1961, Two-photon excitation in CaF2:Eu2+, *Phys. Rev. Lett*. 7:229–231.

Li, Y.W., and Wolf, E., 1981, Focal shifts in diffracted converging spherical waves, *Opt. Commun*. 39:221–215.

Martini, N., Bewersdorf, J., and Hell, S.W., 2002, A new high-aperture glycerol immersion objective lens and its application to 3D-fluorescence microscopy, *J. Microsc*. 206:146–151.

Richards, B., and Wolf, E., 1959, Electromagnetic diffraction in optical systems II. Structure of the image field in an aplanatic system, *Proc. R. Soc. Lond. A* 253:358–379.

Sheppard, C.J.R., and Gu, M., 1992a, Axial imaging through an aberrating layer of water in confocal microscopy, *Opt. Commun*. 88:180–190.

Sheppard, C.J.R., and Gu, M., 1992b, Image formation in two-photon fluorescence microscopy, *Optik* 86:104–106.

Stelzer, E.H.K., Hell, S., Lindek, S., Pick, R., Storz, C., Stricker, R., Ritter, G., and Salmon, N., 1994, Nonlinear absorption extends confocal fluorescence microscopy into the ultra-violet regime and confines the illumination volume, *Opt. Commun*. 104:223–228.

Stelzer, E.H.K., Wacker, I., and De Mey, J.R., 1991, Confocal fluorescence microscopy in modern cell biology, *Semin. Cell. Biol*. 2:145–152.

Török, P., Varga, P., Laczik, Z., and Booker, G.R., 1995, Electromagnetic diffraction of light focused through a planar interface between materials of mismatched refraction indices: An integral representation, *J. Opt. Soc. Am. A* 12:325–332.

Wilson, T., and Sheppard, C.J.R., 1984, *Theory and Practice of Scanning Optical Microscopy*, Academic Press, New York.

21

Interaction of Light with Botanical Specimens

Ping-Chin Cheng

INTRODUCTION

In recent years, plant biotechnology has become an important sector, with the agricultural and pharmaceutical industries promoting research activities in plant sciences. This has placed increased demands on sophisticated optical microscopy to assist plant research. While most of the discussion of confocal and multiphoton fluorescence microscopy concentrates on the imaging of animal tissues and cells, very little attention has been paid to the imaging of botanical specimens. As a result, plant researchers frequently have to rely on the imaging technology developed primarily from animal work. While there is nothing wrong with using suitable technology developed for other systems, in this case allowance must be made for the optical characteristics of botanical specimens. Unlike animal cells, plant cells are designed to interact with light, either to harvest energy or to protect sensitive organelles. As a result, plant cells are generally more optically active and heterogeneous and contain significantly more absorbing, scattering, and fluorescent structures. In addition, many botanical specimens exhibit birefringence and are also capable of generating strong second and third harmonic signals.

The specimen is an integral part of any microscope system and its optical characteristics directly affect the performance of the microscope. To image botanical specimens effectively, one must first understand their optical properties. Plant tissues are generally bulkier than their animal counterparts and their cells are usually larger. As most plant cells contain a significant number of fluorescent molecules tightly coupled to the photosynthetic system, they interact with the illumination very differently from animal cells.

Optical microscopy is likely to cause significant disturbances to the physiology of plant cells. For example, the autofluorescence intensity and spectra varies with the duration and intensity of the illumination (Cheng *et al*., 2000a; 2001). This chapter discusses the various optical and fluorescence properties that affect the optical microscopy of plant specimens. A number of plant tissues, both photosynthetic and non-photosynthetic, will be used to illustrate the imaging characteristics of botanical specimens, including their ability to produce useful and informative contrast using second and third harmonic generation signals (SHG and THG). In addition, the methods suitable for imaging various plant organs and tissues are discussed.

LIGHT ATTENUATION IN PLANT TISSUE

The **transmission** of light incident on plant tissue is mainly determined by the amount of absorption and scattering in the specimen. Because it is technically difficult to separate these two factors, we will refer to their joint effects as attenuation. In this article, we estimate attenuation using a detector equal to the size of a parallel illumination beam and placed behind a specimen with a detecting solid angle no larger than 5°. The measured transmission intensity (I_{tran}) is approximated as

$$I_{tran} = I_0 - I_{abs} - I_s$$

where I_0 is the incident intensity, I_{abs} is the intensity lost due to absorption, and I_s is the decrease of transmitted intensity due to light scattering out of the beam.

Linear Absorption

As water is the most abundant material in living systems, light absorption of water determines the usable spectral range of optical microscopy of living material. Figure 21.1 shows the absorption spectrum of water from 200 to 1400 nm. Note that water is transparent at the shorter wavelengths, with two minor absorption peaks at approximately 1000 and 1200 nm, but becomes opaque at wavelengths longer than 1300 nm. Besides water, botanical tissue consists of organic molecules similar to those found in animal tissue, plus cellulose, chlorophylls, anthocyanins, flavonols, lignin, sporopollenin, polyesters (cuticle), starch, inorganic deposits, and other light absorbing pigments. The pigments can play havoc with labeling studies while cellulose structures scatter and refract the light. Fortunately, the latter problem is really a cloud with a "silver lining" because such structures are also very efficient at producing SHG and THG signals.

Figure 21.1 shows the attenuation spectra of plant tissue (rice leaf, *Oryza sativa*) and animal tissue (chicken dermis). Compared to animal tissue, plant tissue, particularly photosynthetic tissue, has significantly higher absorbance in the visible spectrum but similar attenuation in the near infrared (NIR) range. It is evident that the most transparent region of both animal and plant tissue is around 1300 nm. Figure 21.2 shows the attenuation spectra of a number of other plant tissues including maize leaf (green), etiolated maize leaf (yellow), carrot (orange), and rose petal (red).

Ping-Chin Cheng • State University of New York, Buffalo, New York 14260 and Department of Biological Sciences, National University of Singapore, Singapore

 Handbook of Biological Confocal Microscopy, Third Edition, edited by James B. Pawley, Springer Science+Business Media, LLC, New York, 2006.

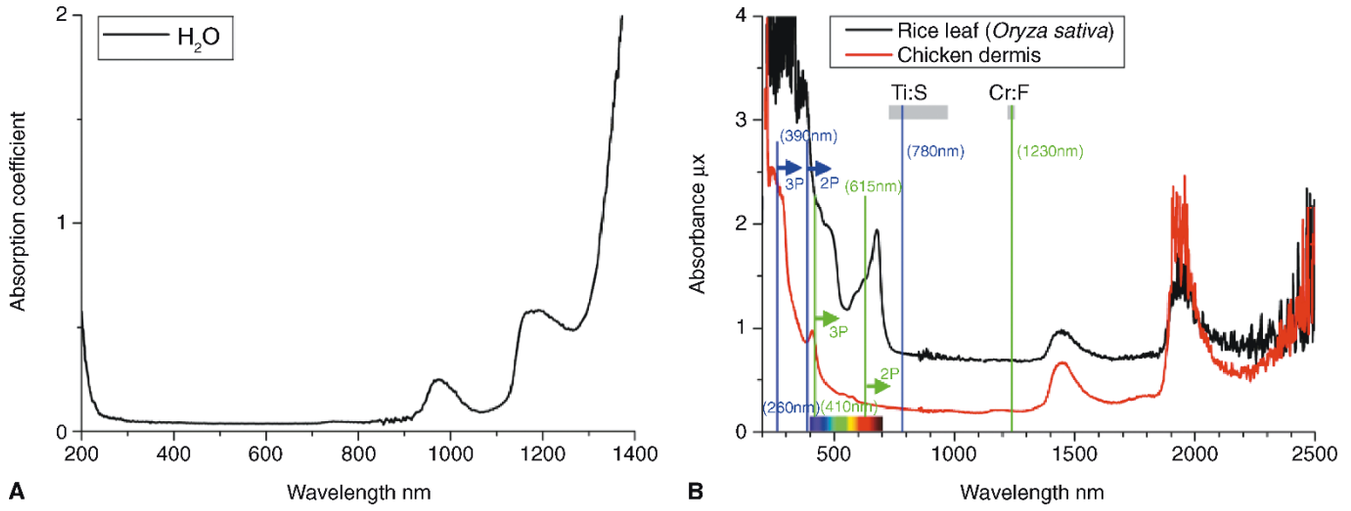


FIGURE 21.1. Absorption spectrum of water (A) and attenuation spectra of living rice leaf (*Oryza sativa* L.) and chicken dermis (B). The low absorption ($\mu < 0.5$) window of water between 200 to 1300 nm determines the useful range of optical microscopy for living biological specimens. Water becomes opaque for wavelengths longer than 1300 nm. Note that, while the photosynthetic pigments in plant tissue produce additional absorption peaks in the blue and red region not found in animal tissue, both types of specimen show little attenuation in the NIR. The blue and green lines show the typical operating wavelengths of Ti:sapphire and Cr:forsterite lasers, respectively. The *colored arrows* indicate the upper limit of two- and three-photon excitation. The gray bars indicate the tuning range of the respective lasers.

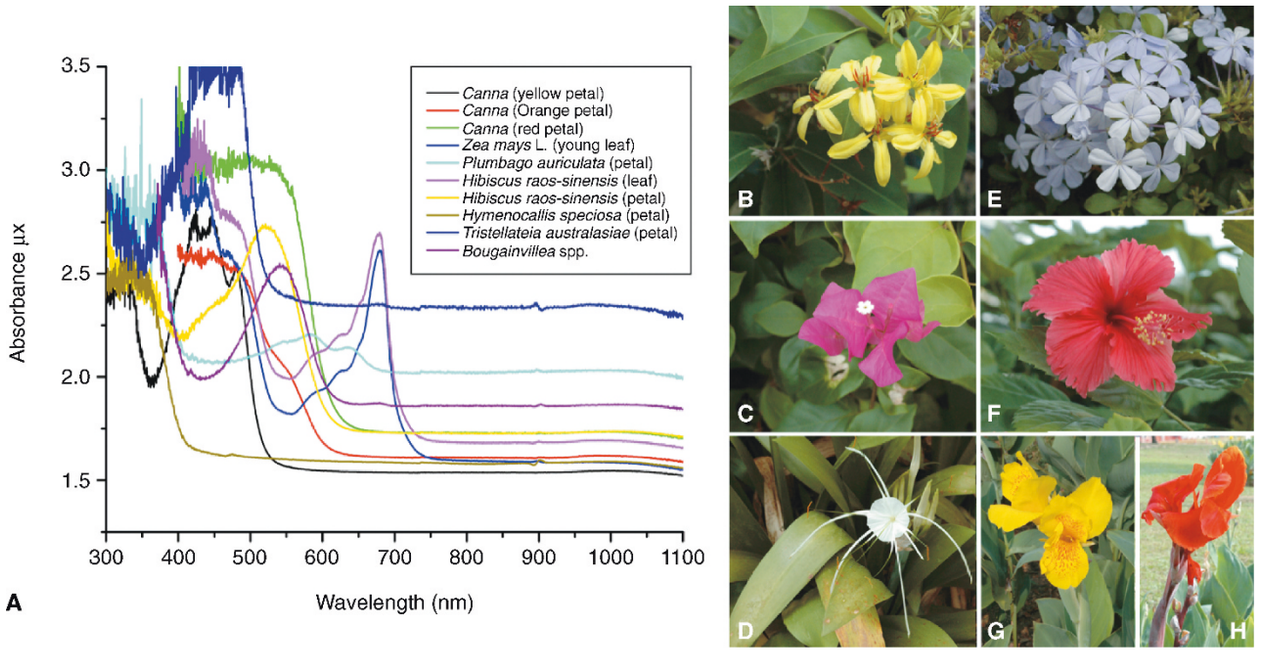


FIGURE 21.2. Attenuation spectra of various plant petals and leaves.

Using *Arabidopsis thaliana* leaf as an example, Figure 21.3(A) is an attenuation spectrum showing a general increase in optical density towards the shorter wavelengths. Two prominent absorption peaks are contributed by leaf pigmentation, mainly the chlorophylls. The attenuation spectrum of an acetone-extracted, pigment-free leaf shows the removal of both peaks and lower overall attenuation [Fig. 21.3(B)]. Figure 21.3(C) shows the attenuation of protoplasts in culture medium (ca. 2×10^4 cells/mL). Because the light-scattering cell wall is now absent, the attenuation at 400 nm is very similar to that at 1000 nm. However, in the more fibrous *Marsilea quadrifolia* leaf, where scattering is significant, removal of the pigments does little to lower the light attenuation (Fig. 21.4). It is worth noting that, over the spectral range of 520 to 850 nm, the light attenuation is very similar in the leaves of both species. These spectra show that using NIR (700–900 nm) illumination for multi-photon microscopy offers only a limited penetration advantage over the shorter wavelength light used in single-photon excitation. Although a significant increase in penetration depth can be gained by using wavelengths in the 1200 nm range (Fricker *et al.*, 1992; White *et al.*, 1996; Lin *et al.*, 2000c, 2001; Chu *et al.*, 2003a), resolution will be lower because of the longer wavelength and because most objectives are corrected only for visible light. On the other hand, if the refractive index (RI) of a sample does not match that of the medium in which it is immersed, the use of a longer wavelength often reduces the aberrations caused by this mismatch (because all RIs drop with wavelength and the differences between the RIs of the different components become smaller), and this factor compensates somewhat for the loss of resolution.

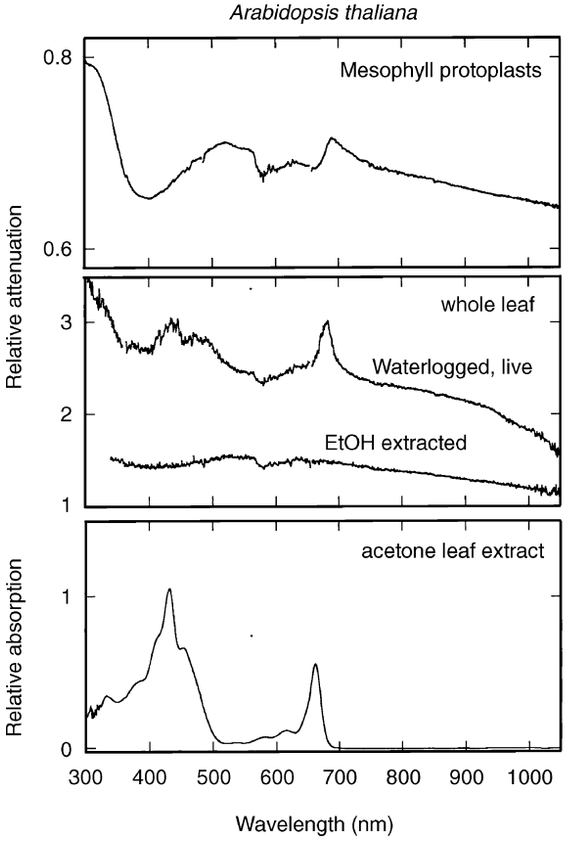


FIGURE 21.3. Attenuation spectra of (A) *Arabidopsis thaliana* protoplast, (B) water-logged whole leaf and EtOH-extracted leaf, and (C) acetone-extracted leaf.

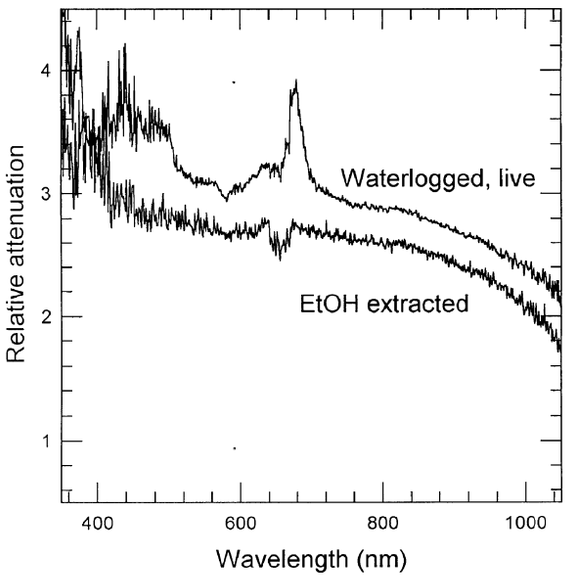


FIGURE 21.4. Attenuation spectra of a living leaf of *Marsilea quadrifolia* and after ethyl alcohol extraction.

In addition to the 700 to 1300 nm region, green plant tissue shows a secondary low attenuation window around 550 nm. Selecting a flurophore with an emission peak within this region improves the detectable fluorescence signal as long as there is no overlapping autofluorescence. In addition, the 550 nm region is suitable for backscattered light (BSL) imaging within the visible spectrum. Fluorochromes with their fluorescence emission longer than 650 nm, such as Alexa Fluor 680, Alexa Fluor 750, Cy5.5, and Cy7 (Molecular Probes Inc.), can be very useful for botanical specimens. In this spectral region, the absorption of plant material is low, relatively little autofluorescence is produced, and the signal is still suitable for high quantum efficiency (QE), Si-based photodetectors.

Nonlinear Absorption

In nonlinear optics, the nonlinear optical response can be described by the power series

$$\begin{aligned}\tilde{P}(t) &= \varepsilon_0\chi^{(1)}\tilde{E}(t) + \varepsilon_0\chi^{(2)}\tilde{E}(t)^2 + \varepsilon_0\chi^{(3)}\tilde{E}(t)^3 + \ldots \\ &\equiv \tilde{P}^{(1)}(t) + \tilde{P}^{(2)}(t) + \tilde{P}^{(3)}(t) + \ldots\end{aligned}$$

where $\chi^{(2)}$ is the the second-order nonlinear susceptibility and $\chi^{(3)}$ is the third-order nonlinear susceptibility.

Although the nonlinear optical response of man-made materials has been extensively studied, the nonlinear absorption properties of plant specimens are poorly understood. Figure 21.5 shows a transmission versus incident intensity curve of a flurophore (APSS; Cheng *et al.*, 1998) at 780 nm. Although the absorption increases as the incident power increases, one should note that a specimen showing little absorbance in the NIR may exhibit significant nonlinear (two-photon) absorption at high peak illumination intensity, and significant energy can thus be absorbed by the specimen. This is the case for the chloroplast. Even though the APSS fluorophore shows low absorbance in the NIR region, significant two-photon absorption is evident. The shaded bar in Figure

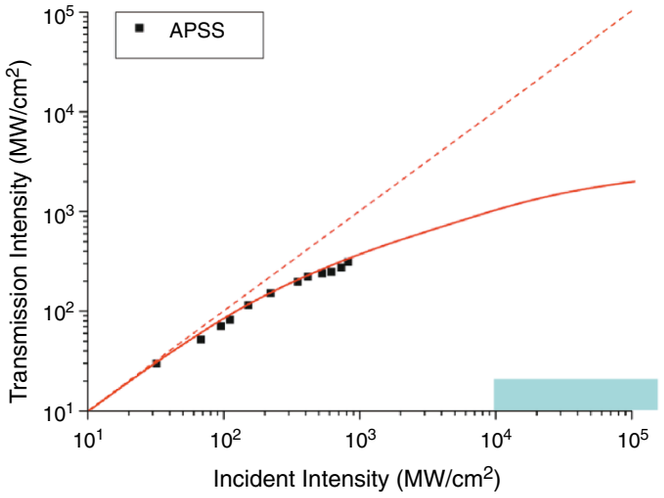


FIGURE 21.5. Nonlinear absorption of APSS fluorophore solution. The *light blue bar* represents the range of power densities used in a typical multi-photon fluorescence microscopy setup, In general, higher power density occurs when a high-NA objective is used because the focal spot is smaller.

21.5 represents the power density used in a typical multi-photon fluorescence microscope. Under high power density IR illumination, significant cellular damage can result (Konig *et al.*, 1995, 1996a,b, 1997; Oehring *et al.*, 2000; Chapter 38, *this volume*; and see paragraph below on light–specimen interactions).

Scattering

Both Rayleigh and Mie scattering occur in botanical specimens. Rayleigh scattering is produced by small particles (less than a tenth of the wavelength) and is more effective at shorter wavelengths; the intensity of the Rayleigh-scattered light I is

$$I = I_0 \frac{8\pi^4 N\alpha^2}{\lambda^4 R^2}(1+\cos^2\theta)$$

where N is the number of scatters, α is the polarizability, and R is the distance from the scatterer.

Clearly, Rayleigh scattering is highly wavelength dependent:

$$I \propto \frac{1}{\lambda^4}$$

Therefore, the wavelength-dependent attenuation observed in the spectrum (Fig. 21.6) is mainly due to Rayleigh scattering.

In contrast, Mie scattering predominates for particles that are larger than a wavelength. This scattering produces a pattern similar to an antenna lobe, with a sharper and more intense forward lobe for larger particles. Mie scattering is generated mainly by the organelles in the cell and, while not strongly wavelength dependent, the scattering intensity is proportional to the square of the ratio of the RI of the feature to the RI of the media (see Fig. 8.2, *this volume*). Figure 21.6 shows the contribution of scattering to the light attenuation in hydrated and methyl salicylate–cleared parenchyma cells in a maize stem (Cheng *et al.*, 2001a). By index-matching many of these small particles, the clearing process greatly reduces scattering within a specimen. This allows one to image significantly deeper into the tissue.

In a simulation of biological specimens, Gu and colleagues (2000) have demonstrated that Mie scattering is the dominant scattering event in milk and that, as long as spherical aberration is not a problem, scattering is the determining factor for the depth limit in multi-photon microscopy. Figure 21.7 shows a high-intensity NIR beam incident on a 1 mm cuvet containing diluted (20% dilution) 2% homogenized milk; note the two-photon excited fluorescence in the second cuvet and the scattered NIR in the milk-containing cuvet.

Between the outer layers of epidermal cells, leaves consist mainly of mesophyll tissue, each cell being rich in photosynthetic pigments confined within light-scattering cell walls. The outer surface of epidermal cells is generally covered with a layer of cuticle that has a refractive index significantly different from that of water. As a result, the cuticle surface reflects incident light particularly that impinging at low angles, preventing some of it from entering the leaf and effectively reducing the NA of the objective. The cuticle surface may be covered with a complex surface pattern (Cheng *et al.*, 1979a, 1981, 1986; Cutler *et al.*, 1982), which further increases scattering and lowers the intensity of the illumination penetrating the tissue.

Specialized cells on the leaf surface, such as heavily walled guard cells and silica cells (frequently found in grasses; Jones and Handreck, 1967), provide additional scattering centers that can also significantly attenuate the illumination. Finally, a significant volume of the leaf is occupied by an air space that becomes the major reflection and scattering center within the tissue.

One method commonly used to combat these problems in freshly excised tissue is to soak the leaf in air-deficient culture medium/water (Cheng *et al.*, 2001a) or to place the leaf in water but under a partial vacuum to remove the air trapped in the mesophyll. Air-deficient water is prepared by filling a bottle with boiling water, recapping the bottle when the water is hot and without any trapped air bubbles, and then letting the water cool down. The bubbling and high temperature removes dissolved air. Soaking leaves in this air-deficient water can quickly and efficiently dissolve away air bubbles trapped in tissue without the damage caused when the air trapped in the leaf expands under vacuum. Figure 21.8 shows

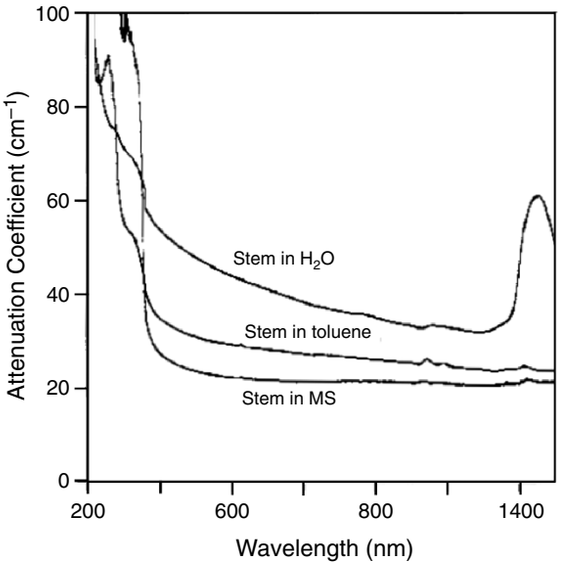


FIGURE 21.6. Attenuation spectra of maize stem (pith) in water, xylene, and methyl salicylate (after dehydration with EtOH). All spectra were obtained from the same spot on the sample.

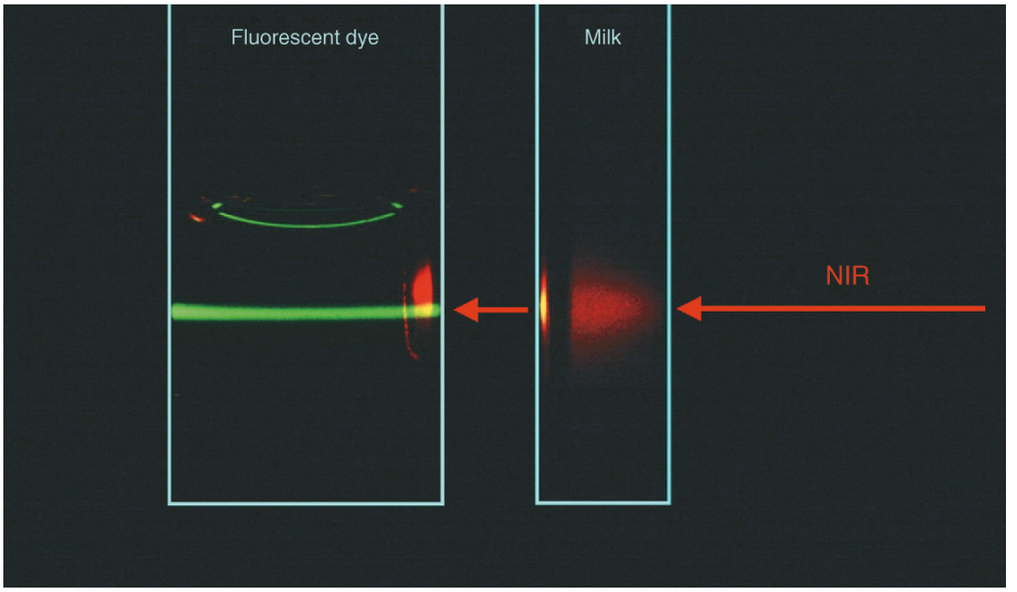


FIGURE 21.7. Demonstration of high penetration of NIR beam in turbid medium. High intensity IR beam incident on a cuvet filled with diluted milk. The ballistic photons leaving the milk are intense enough to excite 2P fluorescence in the dye solution in the second cuvet.

significantly less scattering from waterlogged leaves and this allows an increase in imaging depth.

If living tissue observation is not required, the high scattering of botanical specimens can be minimized by fixation, dehydration, and clearing procedures commonly used in traditional microtechniques. Figure 21.6 demonstrates the effect of such a clearing procedure on the scattering properties of the parenchyma cells of maize stem (pith). Untreated, these cells have no pigmentation and appear white to the naked eye (mainly due to Mie scattering). However, after clearing, the tissue becomes nearly transparent. The absence of the absorption peak at 1450 nm is due to the absence of water.

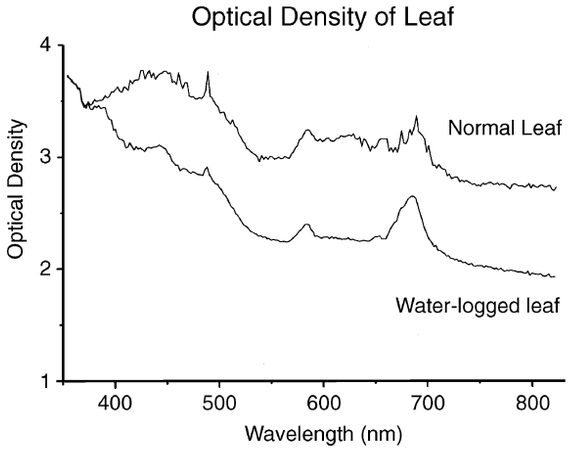


FIGURE 21.8. Attenuation spectra of a live maize leaf before and after being waterlogged. Note the significant decrease in attenuation [nearly 1 optical density (OD) unit in the red] due to the elimination of the air spaces in mesophyll tissue. This significantly improves the penetration of the excitation light in single-photon excitation and also greatly increases the returning fluorescence signal.

REFRACTIVE INDEX HETEROGENEITY

Any optical heterogeneity within the specimen or deviation in the refractive index from the design specification of the objective can produce spherical aberration (Chapter 20, *this volume*). Structures having different refractive indexes can also affect the flatness of an optical section. Recently, spherical aberration introduced by a living specimen has focused attention on the need to process specimens properly to minimize refractive index mismatches within them (Cheng and Cheng, 2001; Cheng *et al*., 2002; Pawley, 2002).

Examples of optical heterogeneity in plant specimens can be demonstrated by laying maize tissue sections on the surface of a slide made of fluorescent plastic (Cheng *et al.*, 2002). Figure 21.9 shows an *xz* image of such a specimen. Refractive index heterogeneity within the tissue slice causes the image of the surface of the fluorescent slide not to be flat as it should be (marked by horizontal line). Figure 21.10 shows *xy*, *xz*, and *yz* views of a submerged leaf of *Marsilea quadrifolia* using two-photon fluorescence microscopy. Note the smearing of the image in the deeper part of the tissue (*xz* and *yz*) as the result of specimen-introduced spherical aberration. Apparently, the depth limit is around 50 to 60 µm in this case. Inspection of the *xz* and *yz* sections reveals that the lower left portions of the *xy* image were obtained near the surface of the specimen while the upper right portion of the image was obtained through 30 µm of tissue. Significant differences in image resolution and signal level are evident.

Historically, this heterogeneity is overcome by dehydration and by clearing and mounting the tissue sections between a slide and coverslip in proper mounting medium. This procedure matches the optical properties of the specimen to the design conditions of the objective lens, and should not be overlooked in modern wide-field, confocal, and multi-photon microscopy. When imaging fixed tissues and cells, always use a clearing agent to reduce scattering and aberrations.

A number of clearing methods are used in optical microscopy, most of them involving the use of organic solvents such as methyl

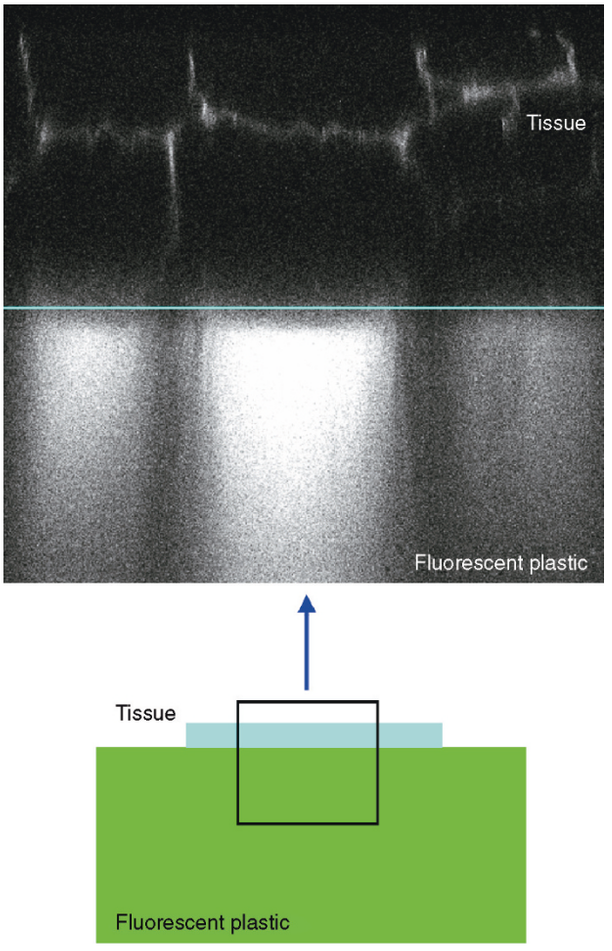


FIGURE 21.9. Optical *xz* section of a piece of maize stem (pith) mounted on a fluorescent plastic slide (Chroma Technology, Inc., and AMIL Technology) showing how the optical heterogeneity of the tissue section dramatically affects the image of the homogeneous fluorescent plastic slide. The horizontal line demarcates the slide surface. Note that the image of the surface of the plastic slide is not flat because RI variations in the overlying section cause the focal length of the relatively low-NA objective to vary.

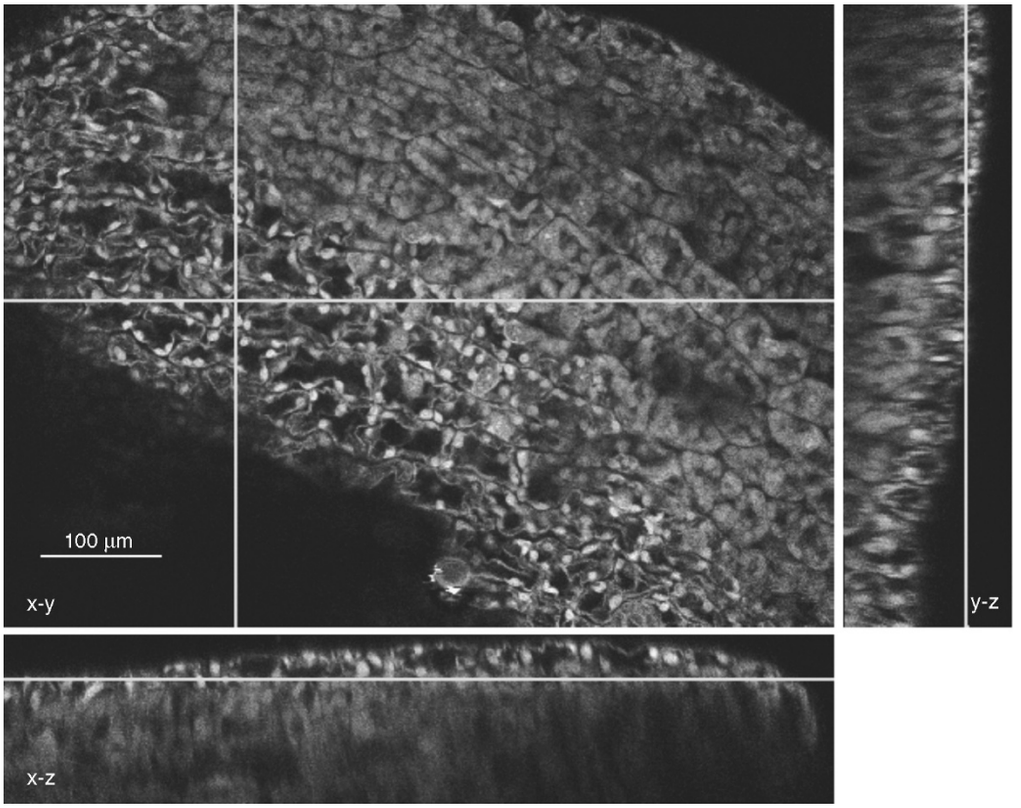


FIGURE 21.10. Two-photon *xy*, *xz*, and *yz* sections of young leaf (the submerged form) of *M. quadrifolia*. The reduction of signal strength and image quality as a function of depth is evident. The *white lines* on the *xy* section indicate the positions where the *xz* and *yz* sections were obtained; similarly, the white lines on the *xz* and *yz* images indicate the corresponding position of the *xy* image. The image was obtained by two-photon fluorescence microscopy of a water-mounted spe-cimen using 800 nm excitation with a water-immersion objective on Olympus Fluroview FV300 confocal microscope.

salicylate (η = 1.52), xylene (η = 1.5055), or toludine (η = 1.4961) (Stelly *et al*., 1984; Cheng *et al.*, 1993). Examples using methyl salicylate include the study of ovules of *Zephyranthaceae* (Crane and Carman, 1987), grass ovules (Young *et al.,* 1979), and maize apical meristem (Bommineni *et al*., 1990, 1993, 1995). For hydrated tissue, aqueous based glycerol–Ppda, glycerol (η = 1.4746) and recently FocusClear (η = 1.43) and MountClear (η = 1.43; Pacgen, BC, Canada) can be used in conjunction with Immersion Solution-M (η = 1.43). All these methods work well with botanical specimens.

In addition to the agents mentioned above, several clearing techniques have been developed for the study of whole-mount plant tissue in the past three decades. These include the BB-4 1/2 clearing fluid (Herr, 1971), the improved BB-4 1/2 (Herr, 1974), and the mixture of benzyl benzoate and dibutyl phthalate (2 : 1, v/v, Crane and Carman, 1987). Examples of the applications of these clearing agents have appeared in many botanical publications, such as the use of Herr's BB-4 1/2 for the study of ovules, pollen, and pollen tubes (Fredrikson, 1992), and the use of benzyl benzoate and dibutyl phthalate mixture in the study of apomixis in *Elymus* (Crane and Carman, 1987). Both Herr's BB-4 1/2 and BB-4 1/2 fluids turn dark brown after 2 to 4 weeks in the light at room temperature because the clove oil photo-oxidizes (Herr, 1992). Because the browning results in a significant increase in light absorbance, it is important to keep the clearing agents in dark bottles and in the refrigerator. Substituting the clove oil with dibutyl phthalate produces a superb photostable clearing agent (Herr's BB-DP-4 1/2; Herr, 1992).

BIREFRINGENT STRUCTURES IN PLANT CELLS

In crystalline materials, it is well known that different refraction indices may be associated with different crystallographic orientations. Mineral crystals frequently show two distinct indices of refraction, and are referred to as birefringent materials. If the *y*- and *z*-directions are equivalent in terms of the crystalline forces, then the *x*-axis is unique and is called the optic axis of the material. The propagation of light along the optic axis is independent of its polarization: its electric field is everywhere perpendicular to the optic axis and is called the ordinary- or o-wave. The light wave with its E-field parallel to the optic axis is called the extraordinary- or e-wave.

Birefringence has to do with anisotropy in the binding forces between the atoms forming the crystal. It can be visualized as the atoms having stronger "springs" holding them together in some crystalline directions than in others. A number of structures in plant tissue exhibit birefringence. These include microtubules, spindles, secondary cell wall, cuticle, surface wax, starch granules, and SiO_2 deposits (bio-opals). For example, paracrystalline cellulose in the cell walls of trichomes of *Arabidopis thaliana* shows birefringence (Brininstool, 2003). Figure 21.11 shows the birefringent properties of maize starch granules as observed under a conventional polarization microscope.

Placing a birefringent material between a pair of crossed polarizers gives rise to interference colors. When light passes through a polarizer to produce linearly polarized light and that light then passes through a piece of birefringent material, the light is broken up into two components. Because the index of refraction for one of them is larger than for the other, that component will lag in phase (retardance) and these components will emerge from the specimen out of phase with each other. Then if the light is passed through a crossed polarizer (the analyzer), only the part of each component that is in the transmission plane of the analyzer will emerge. This emerging ray consists of two co-planar components that differ in phase. If the refraction indices of the material also change with wavelength, then for a given thickness of birefringent material, some wavelengths will undergo destructive interference and some constructive, giving an interference pattern of changing colors similar in appearance to the interference colors of a thin film of oil floating on water. If monochromatic light is used, interfer-

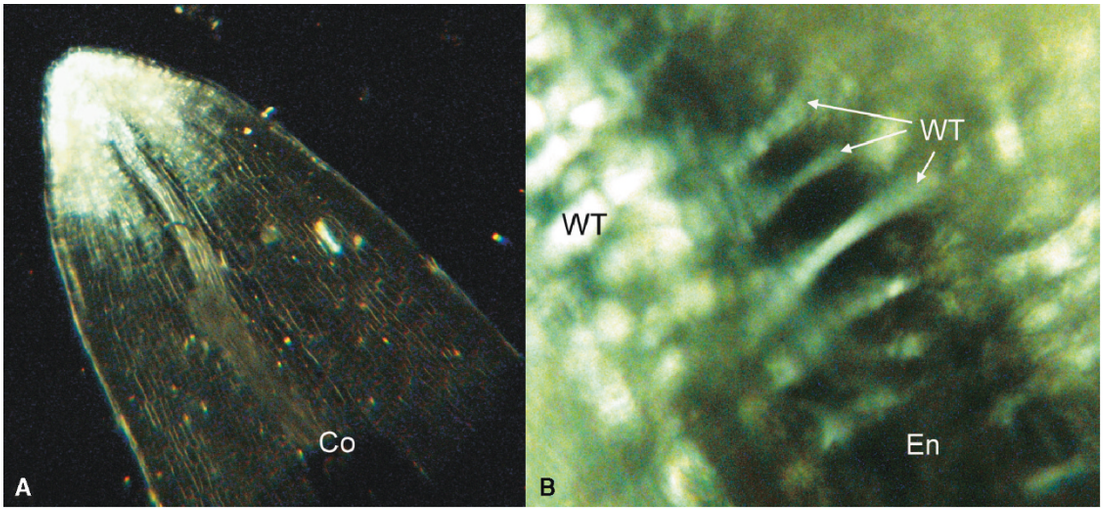


FIGURE 21.11. Birefringent properties in the secondary wall thickenings in the endothelium cells of maize anther.

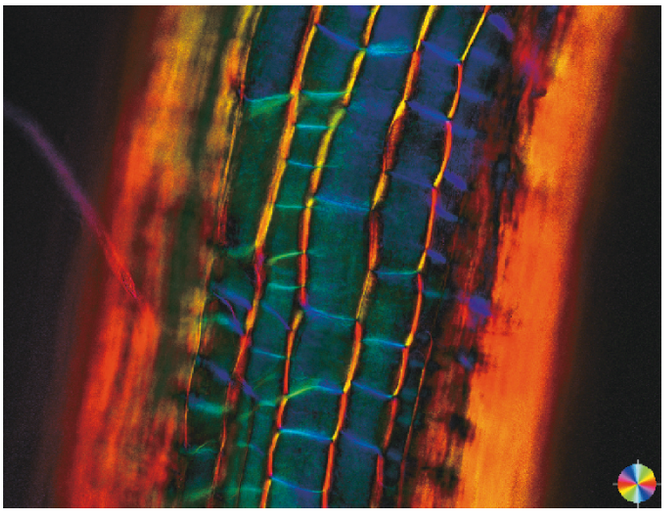


FIGURE 21.12. Dynamic polarization microscopy showing the cell wall orientation (color-coded wheel shows *s*-axis) in the root of *A. thaliana*. The images were obtained by using Polscope. (Images courtesy of Cambridge Research Instruments, Woburn, MA.)

ence fringes are produced. These interference color/fringes can be used to study the thickness and internal stress of plant cuticles (i.e., photoelasticity).

The use of either a conventional or a dynamic, tunable polarization microscope (Polscope, Cambridge Instrument Inc.) can provide image contrast specific to birefringent structures such as the microtubules in the mitotic spindle during cell division. Because of the nature of transmission polarization microscopy, only low intensity light is required, which minimizes phototoxicity. However, as the retardance of many botanical structures, such as cell walls and starch granules, are relatively large, contrast produced by low retardance structures such as microtubules (MT) (typical retardance for a single MT is 0.07 nm) often becomes lost in the high background retardance contributed from the cell wall. Figure 21.12 shows the orientation of cellulose microfibrils in the root cell wall of *A. thaliana*. The cellulose microfibril shows excellent birefringence contrast. The color indicates the orientation of the microfibril molecules.

FLUORESCENCE PROPERTIES OF PLANTS

Plant tissue generally contains a large number of light-absorbing pigments, including those responsible for photosynthesis. Many of these pigments produce autofluorescence (Figs. 21.13, 21.14, and 21.15). Figure 21.13 shows a collection of fluorescence spectra excited at different wavelengths from various plant specimens. Note the spectral variation as the excitation wavelength changes. Figure 21.14 shows the fluorescence spectrum of maize leaf grown in either normal lighting or dark (etiolated) conditions, while Figure 21.15 demonstrates the fluorescence spectra of a methanol extract of etiolated maize leaf at various excitation wavelengths. Because plant tissue consists of a mixture of many fluorescent compounds, each with different absorption spectrum and quantum yield (QY), the resulting fluorescence spectra can vary greatly when subject to different excitation wavelengths. As these endogenous fluorophores produce high intensity background autofluorescence throughout the entire visible spectrum, it is very difficult to separate their output from that emitted by introduced fluorescent probes.

Even worse, the emitted autofluorescence is often so intense that it can, in turn, excite nearby fluorescent tags at a wavelength different from the applied illumination. Therefore, the apparent spectral fingerprint of a fluorescent dye may vary depending on the presence or absence and the location of nearby autofluorescing structures. An example might be the vacuole found in many flower petals. Vacuoles can contain large amounts of anthocyanins and flavonols that produce intense autofluorescence, the emission spectra of which varies according to local pH and ionic conditions. Any fluorescently labeled organelle near the vacuole may be excited by this autofluorescence. Figure 21.16 shows an *xz* section of the petal of tree peony (*Paeonia suffruticosa*), the green channel is the BSL image and the red channel is the autofluorescence image.

Changes in Emission Spectra Depending on One- Versus Two-Photon Excitation

When subjected to excitation illumination at 380 nm, the living, freshly excised leaves of *A. thaliana* emit both strong red fluorescence peaks at 684 nm and 714 nm and blue-green fluorescence in the range of <550 nm [Fig. 21.17(A)]. In contrast, high intensity excitation by 760 nm NIR illumination produces a significantly different upconverting fluorescence spectrum, as shown in Figure 21.17(B). The green and red fluorescence now peaks at 500 nm and 688 nm, respectively. Under 380 nm excitation, the mesophyll protoplasts of *A. thaliana*, exhibit strong red fluorescence, peaking at 680 nm, and very low broadband emission in the 450 to 550 nm range [Fig. 21.17(C)]. The two-photon–excited fluorescence spectrum of these protoplasts is similar to that obtained from the whole leaf but with the 688 nm peak blue-shifted to approximately 660 nm [Fig. 21.17(D)]. It is important to note that the fluorescence emission spectra generated by the excitation with single-photon excitation is not identical to that produced by two-photon excitation at double the wavelength. Kennedy and Lytle (1986) have also reported a difference between the excitation spectra obtained from single-photon and two-photon excitation. Therefore, two-photon images may well be different from those obtained from single-photon excitation with half of the wavelength.

Microspectroscopy

Because of the complexity of plant autofluorescence, it is frequently advisable to obtain fluorescence spectra from the organelles of interest to confirm their fluorescence signature. This can be achieved using either single-photon or two-photon microspectroscopy (Cheng and Cheng, 2000; Kao *et al.*, 2000a,b; Chu *et al.*, 2001). The latter has the advantage of providing excellent three-dimensional spatial resolution of the location from which the fluorescence spectra can be obtained.

This technique can also be used to separate SHG and THG signals from background fluorescence (Sun *et al.*, 2001). Figure 21.18 shows the setup of a home-built microspectroscopy system [Fig. 21.18(A)] and a fluorescence spectrum of a parenchyma cell in maize stem [Fig. 21.18(B)]; the spectrum was obtained by two-photon excitation (λ_{ex} = 800 nm) from the fluorescent spot indicated by the arrow in Figure 21.18(C). The setup consists of a linear charge-coupled device (CCD)-equipped (Roper Scientific) Acton 2300i spectrometer connected to the photo port of an Olympus IX70 inverted microscope via a fiber bundle. A

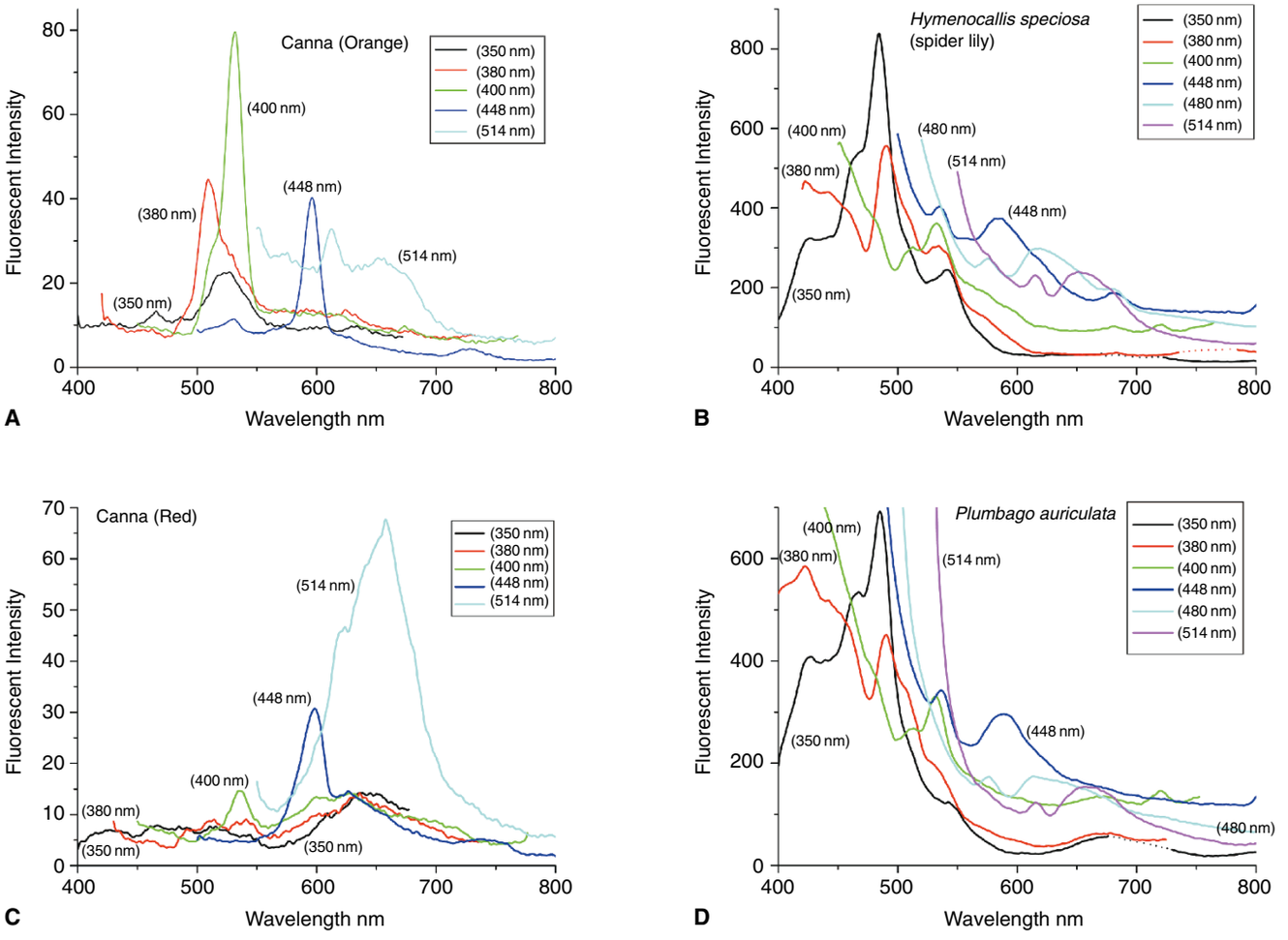


FIGURE 21.13. (A–D) Comparative fluorescence spectra of various plant materials [the petal of yellow, orange, and red varieties of *Canna* L., spider lily (*Hymenocallis speciosa*) and forget-me-not (*Plumbago auriculata*)]. The interruption in the spectra (*dashed line*) is the estimated spectrum as the data were contaminated by scattered excitation illumination leaving the spectrometer grating as a 2nd order diffraction peak.

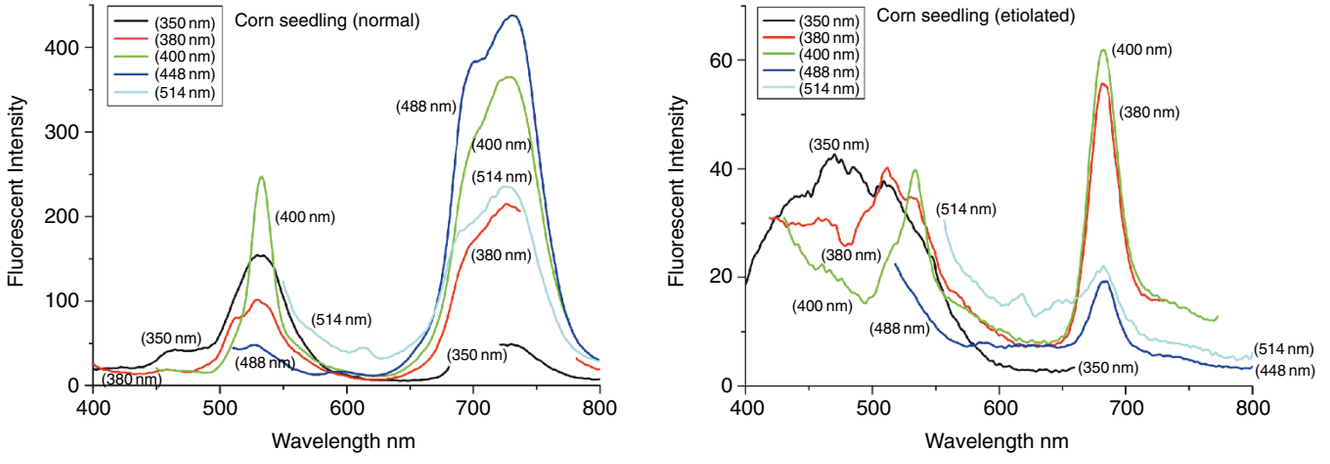


FIGURE 21.14. Autofluorescence spectra of normal and etiolated maize seedling (*Zea mays* L., var. Golden Beauty) excited by light at different wavelengths.

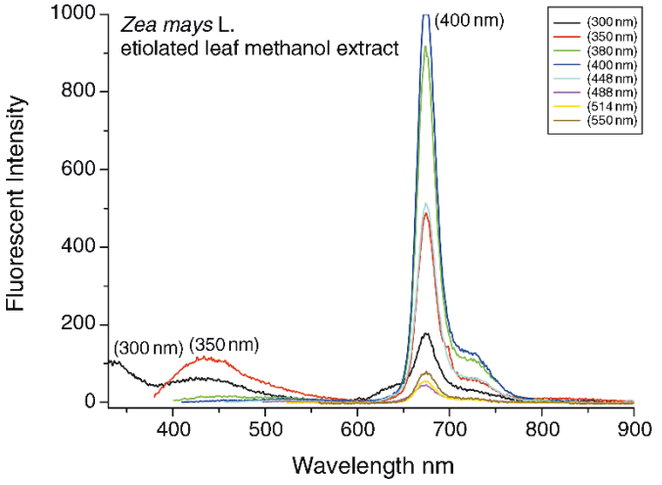


FIGURE 21.15. Fluorescence spectra of the leaf methanol extract obtained from etiolated maize seedlings (*Zea mays* L., var. Golden Beauty) shows significant change in fluorescence spectra when excited by different excitation wavelengths.

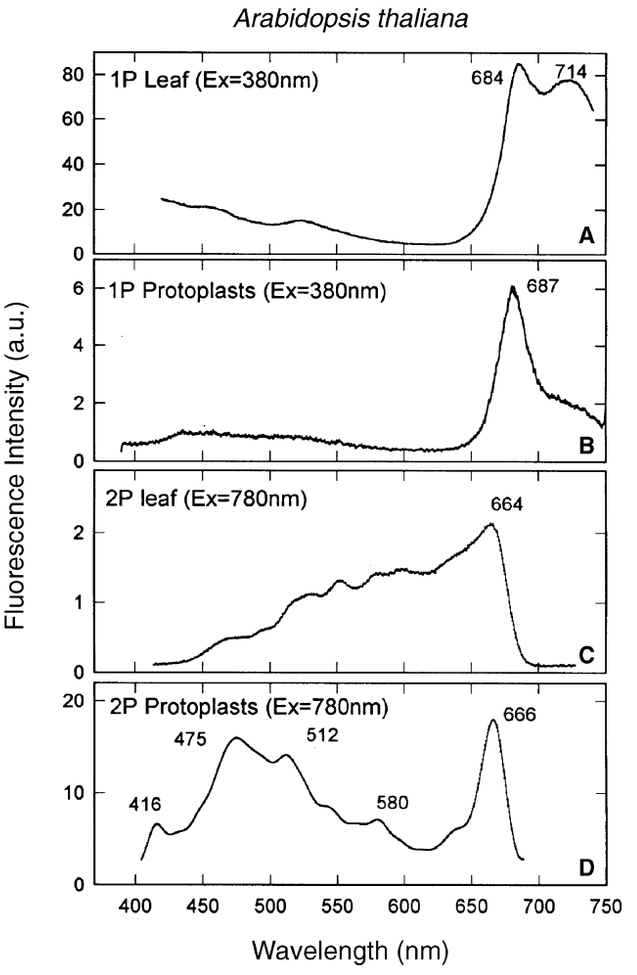


FIGURE 21.17. Comparison of fluorescence spectra obtained with single-photon and two-photon excitation in a leaf preparation of *A. thaliana*. (A) Single-photon excited fluorescence spectrum of fresh, untreated leaf, excited at 380 nm, (B) fluorescence spectrum of mesophyll protoplasts excited with 380 nm, (C) two-photon fluorescence spectrum of leaf excited at 780 nm, (D) two-photon fluorescence spectrum of protoplast excited at 780 nm. (Ti:Sa mode-lock laser operated at 82 MHz, 100 fs pulse at an average power of 600 mW, beam diameter approximately 0.8 mm in diameter.)

mode-lock ultra-fast titanium–sapphire laser was used as the light source for two-photon fluorescence excitation.

A number of modern confocal microscopes are capable of recording fluorescence spectra and these should be used to understand the fluorescence signature and photobleaching dynamics of the specimen under study. Figure 21.19 shows an example of spectra of a living maize chloroplast as a function of light exposure. The three dimensional (3D) spectra (intensity vs. wavelength vs. time) demonstrates the evolution of chloroplast fluorescence when it is subjected to light at high enough intensity to cause significant radiation damage (Konig *et al*., 1995, 1996a, 1997; Cheng *et al*., 2000a, 2001; Kao *et al*., 2000b; Lin *et al*., 2000a,b; Chen *et al*., 2002).

Fluorescence spectra obtained from botanical specimens are generally contributed by the emission of many fluorophores, frequently with overlapping emission peaks. There are a number of methods to separate/minimize the overlapping spectra, such as sequentially exciting the specimen with various excitation wavelengths or using spectral unmixing techniques.

The term *spectral unmixing* refers to a series of computer algorithms that are used to separate a spectral signal recorded from a single pixel or a defined area containing a number of fluorophores into separate intensity signals for each one of them. The algorithms vary depending on the hardware used to initially record the spectral data but all of them have a close similarity to the programs used to deconvolve 3D widefield data or data from energy-dispersive X-ray spectrometers (EDS) in electron microscopy. In spectral unmixing, the spectrum of each individual dye serves as if it were one of a series of "point-spread functions" and it is the function of the unmixing algorithm to make the best fit between the recorded data and a weighted sum of the emission spectra of the dyes (i.e., each one acting like a "PSF" with a shape and a position) thought to be present. This is based on the assumption that the spectra of the individual dyes are not changed by their being combined in the pixel or area of interest (i.e., that micro-environmental differences are either absent or inconsequential). On the other hand, it is common to use signal from a nearby pixel(s) that is felt to be producing only background autofluorescence, as the reference to unmix the pixel of interest and obtain a background-free spectrum. This assumes that the reference background also represents the background present in the measured pixel(s).

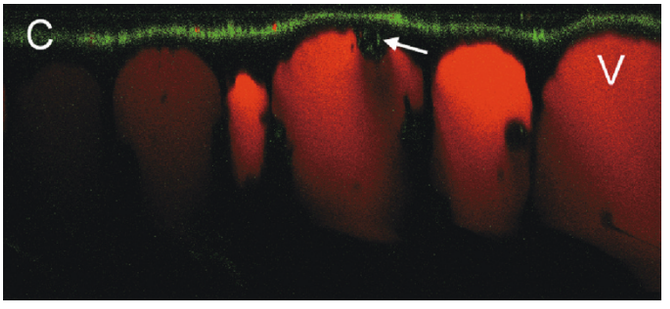


FIGURE 21.16. Two channel (backscattered light and autofluorescence) confocal *xz* section of a tree peony *(Paeonia suffruticosa)* petal.

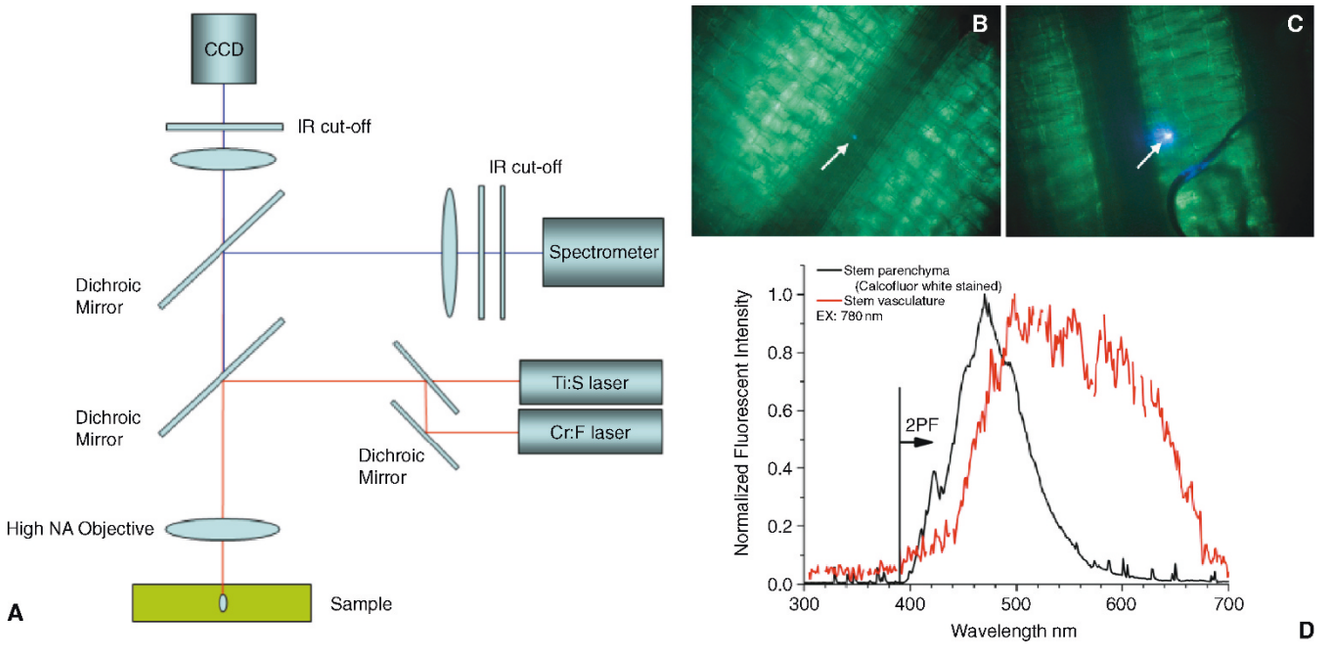


FIGURE 21.18. (A) A multi-photon microspectrometer setup, (B) two-photon excited fluorescent spot (*arrow*) in a maize stem, (C) two-photon excited fluorescent spot (*arrow*) in a maize stem stained with Calcofluor white, and (D) the recorded fluorescence spectra.

For example, it is difficult to detect green fluorescent protein (GFP) expression in chloroplasts because the chloroplast contains not only strongly fluorescing chlorophylls, but also the many highly fluorescent associate pigments of the photosynthetic apparatus, some of which emit in the green region. Exciting each fluorophore sequentially with the appropriate excitation wavelengths may also be helpful in reducing the problem of crosstalk between detection channels. Unfortunately, multi-photon excitation generally causes all fluorophores to fluoresce, creating broadband fluorescence emission for which the only really effective antidote is unmixing (Figs. 21.13 and 21.14).

Figure 21.20 demonstrates the use of spectral unmixing in conventional transmitted and epi-fluorescence microscopy of the rhizome of lily of the valley (*Convalaria majalis*) to separate the

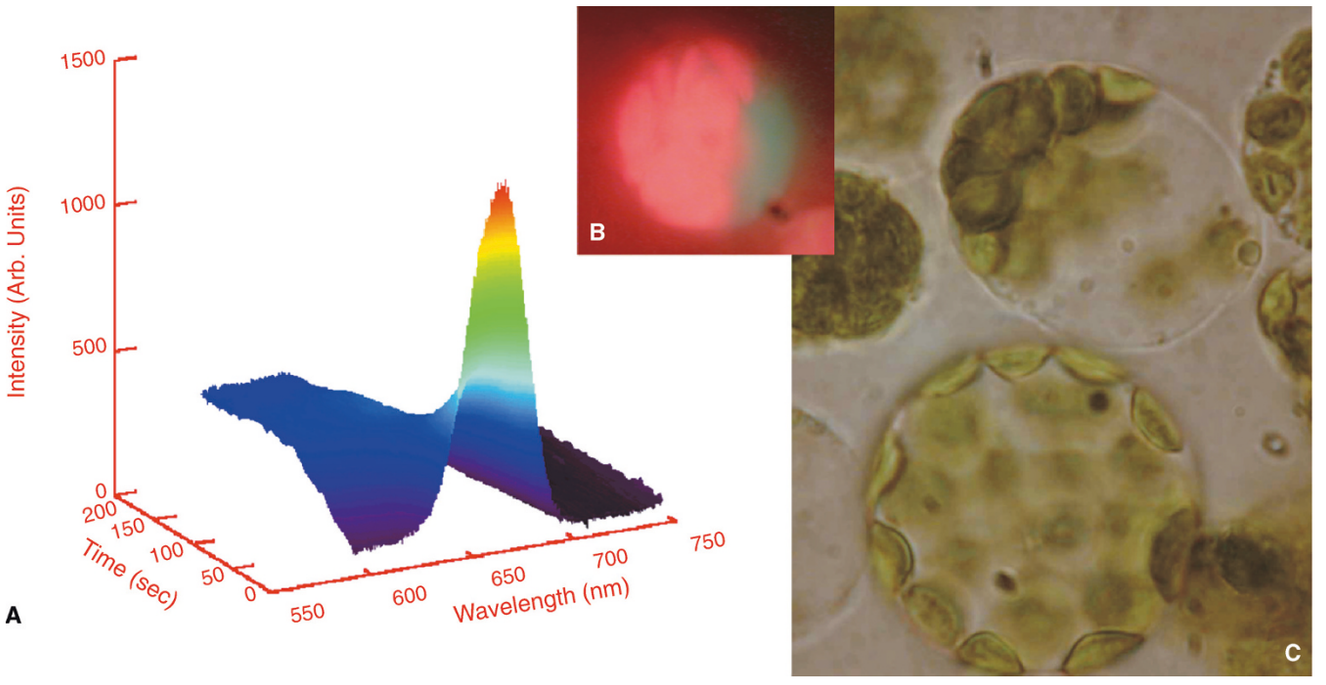


FIGURE 21.19. (A) Two-photon excited, time-lapse, microspectroscopy of maize (*Zea mays* L., Ohio 43) chloroplast in mesophyll protoplast, (B) conventional fluorescence micrograph of a maize protoplast, (C) conventional transmission micrograph of a maize protoplast.

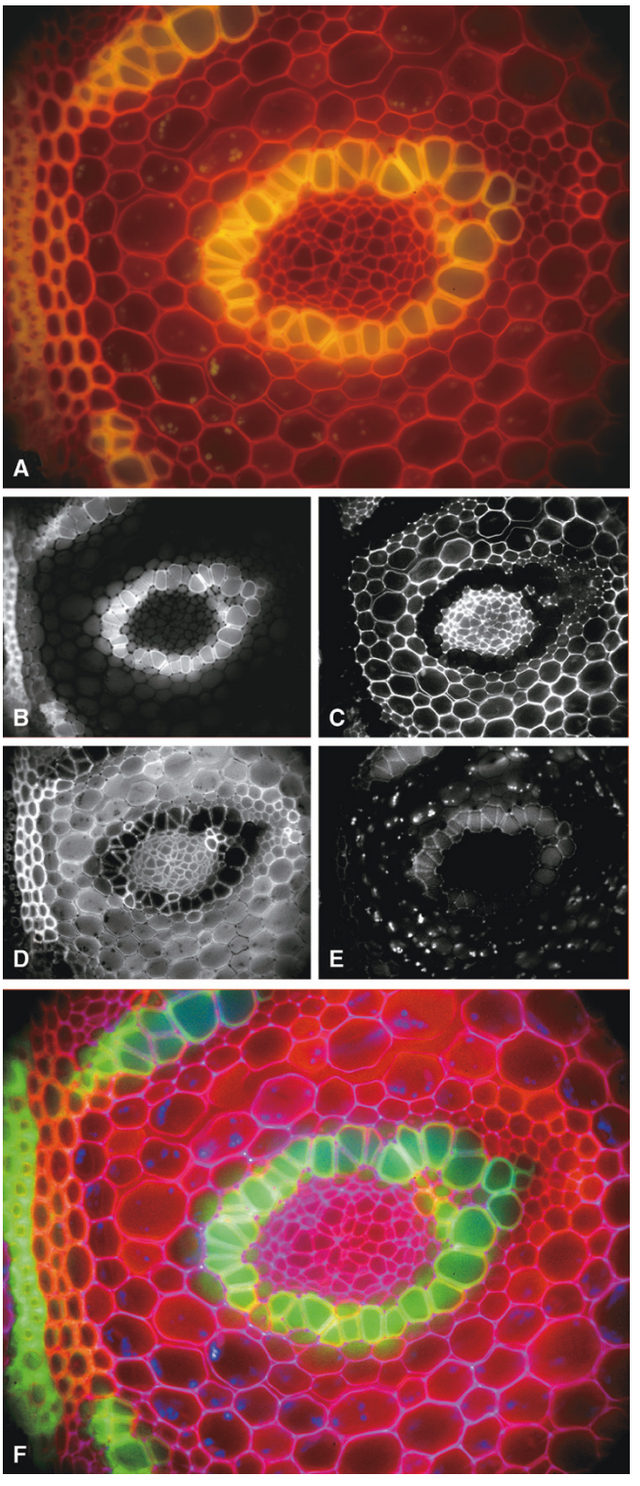


FIGURE 21.20. (A) Conventional fluorescence microscopy of the rhizome of lily-of-the-valley (*Convalaria majalis*). Classification of tissue structures based on their autofluorescence spectra, produced four images (B–E). (F) False color image of the combination of (B–E). Image obtained by using the Nuance Spectral Imaging System. (Images courtesy of Cambridge Research Instrument, Woburn, MA.)

overlapping autofluorescence. The *xy*-λ image was obtained by using a tunable, liquid-crystal (LC)–based, bandpass filter at 20 nm bandwidth and 30 nm steps. Different autofluorescence was chosen in various regions of the image, and spectral unmixing was performed on the image to remove the mixed autofluorescence. The technique clearly separates the fluorescence from parachyma cells from the Casparian band (Nuance Imaging System, Cambridge Research Instruments, Woburn, MA).

Light–Specimen Interaction (Fluorescence Emission)

Photoinduced damage can be characterized by a typical fluorescent intensity versus dose curve. Although usually the fluorescent intensity decreases as a function of exposure, this frequently does not apply to specimens of botanical origin. As plant cells generally, and particularly those capable of photosynthesis, are designed to capture and utilize light energy, light–specimen interactions often involve a series of pigment systems, and are much more complex than those observed in animal cells. On the other hand, as it is highly possible that fluorescence resonance energy transfer (FRET) occurs naturally in the photosynthetic system, introducing an exogenous donor–acceptor pair for a FRET study may be complicated by FRET from endogenous fluorophores in the plant cells. For example, one often notices an increase in chloroplast fluorescent intensity and a blue shift in autofluorescent spectrum upon illumination. Figure 21.21 shows the two-photon–excited fluorescence spectra of a protoplast culture versus exposure time. Note the initial increase in fluorescent intensity in the 630 nm chlorophyll peak.

Time-lapse, two-photon fluorescence microscopy (*xyt*) of the mesophyll protoplasts of *A. thaliana* yielded interesting results concerning cell viability under the high illumination intensity commonly used in multi-photon fluorescence microscopy. Upon NIR (760 nm) irradiation, the protoplasts emit blue-shifted fluorescence as shown in the two-channel, false-color image [combination of green (~500 nm) and red (~660 nm) channels]. In time-lapse studies, it was observed that the red fluorescence diminishes much more rapidly than the green fluorescence. This results in a blue shift of the fluorescence as a function of irradiation dose. Because

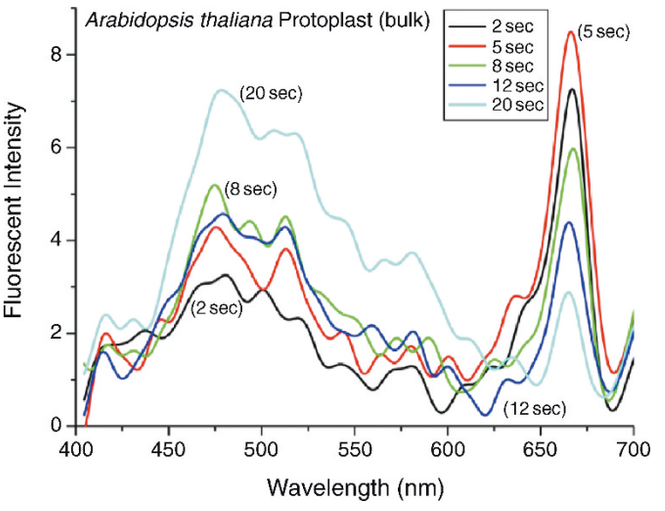


FIGURE 21.21. Two-photon fluorescence spectra of *Arabidopsis thaliana* protoplasts (in culture medium) versus exposure time. Note the red fluorescence intensity first increases before decreasing. Excitation, 760 nm.

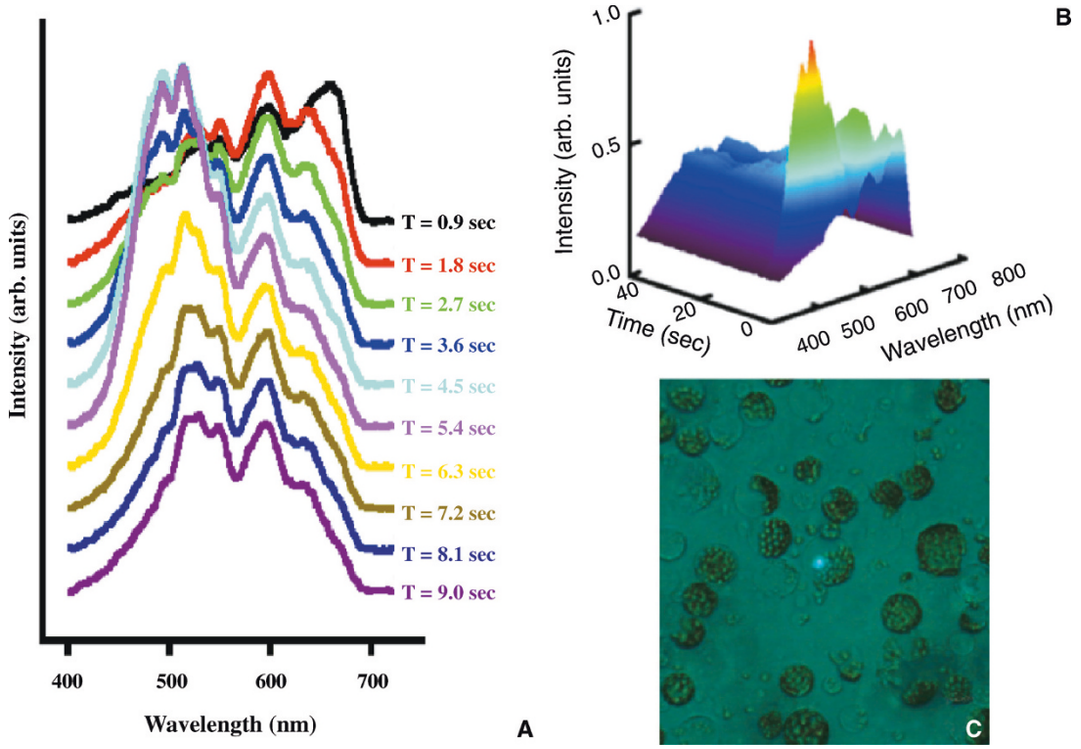


FIGURE 21.22. Two-photon time-lapse microspectroscopy of a single chloroplast (from *A. thaliana* mesophyll protoplast) showing complex spectral changes as a function of increasing exposure dose.

this rapid decrease in red fluorescence is accompanied by cellular uptake of neutral red/propidium iodide or the rapid loss of cytoplasmic-loaded Calcien dye (both of which indicate cellular damage), it might be possible to use the red-to-green fluorescence intensity ratio as an indicator of cell vitality (Cheng *et al.*, 2000a, 2001). This fluorescence study of protoplasts was confirmed by microspectroscopy of a single chloroplast, as shown in Figure 21.22. Figure 21.23 shows an area that received a single 3.3 s/frame scan (8.4 µs dwell time/pixel) at 768 × 512 pixels. As the total irradiated area is 180 µm × 120 µm and the average power was measured as 6.4 mW, the average energy striking each pixel is approximately 54 nJ (i.e., 8.4 µs at 6.4 mW). On the other hand, considering that the laser was operating at 82 MHz with 100 fs pulse with a numerical aperture (NA) 1.2 objective lens, the average and peak power densities at the focal point are approximately 3×10^6 W/cm^2 and 3.9×10^{11} W/cm^2, respectively. A significant reduction in red fluorescence is evident after such scans. Detailed analysis revealed that the red fluorescence, from chlorophyll-a and -b, initially increases slightly before decreasing. This initial increase is in agreement with the study of protoplast fluorescence in culture (Fig. 21.21), and is believed to be a physiological response to adjust the photosynthetic system to the high light intensity, perhaps involving the xenthophyll cycle.

As pointed out above, under high intensity illumination, cell survival can be monitored by the cytoplasmic retention of Calcein dye (loaded with Calcein-AM form; Molecular Probe Inc.) or by the entrance of neutral red/propidium iodide (cell death). It has been reported that multiple scans during image acquisition causes neutral red to enter the cells and/or Calcein dye to escape from them. These changes are then followed by visible structural damage such as shriveling or bursting of the cell. Figure 21.24 is a series of images obtained in sequence demonstrating cell damage under high intensity NIR illumination. Note the cell most heavily loaded with Calcein dye was damaged first (arrow). The high concentration of Calcein dye in the cell significantly increases the nonlinear absorption of NIR, causing more rapid damage.

It has been reported that, for a comparable red fluorescence signal level, single-photon excitation using 488 nm allows significantly more imaging scans before the cell begins to show photodamage (Cheng *et al.*, 2001a). Typical one-photon illumination power is in the order of 0.1 ~ 0.5 mW at the focal point (power density at 5×10^4 W/cm^2 ~ 2.5×10^5 W/cm^2), more than 6 orders of magnitude lower in power density than the peak power used in the two-photon imaging mode (3.9×10^{11} W/cm^2). Although two-photon fluorescence microscopy limits the photon-induced damage to the vicinity of the focal point, while in single-photon excitation damage is spread over the entire illuminated volume, many studies now show that, for the same signal level, high intensity, pulsed NIR illumination produces far greater damage to many living plant cells. This may be due to the fact that in a multi-photon excitation scheme, broadband absorption/excitation involving all the absorbers is possible, while in single-photon excitation, compounds only absorb energy if they have an absorption peak(s) at the excitation wavelength. It is important to point out that photo-induced damage occurs not only via the absorption/excitation of fluorescent molecules, but also because of absorption by any of the vast majority of non-fluorescing molecules.

When Schilders and Gu (2000) investigated the effect of multiple scattering in a turbid medium in single-photon and two-photon fluorescence microscopy, they demonstrated that

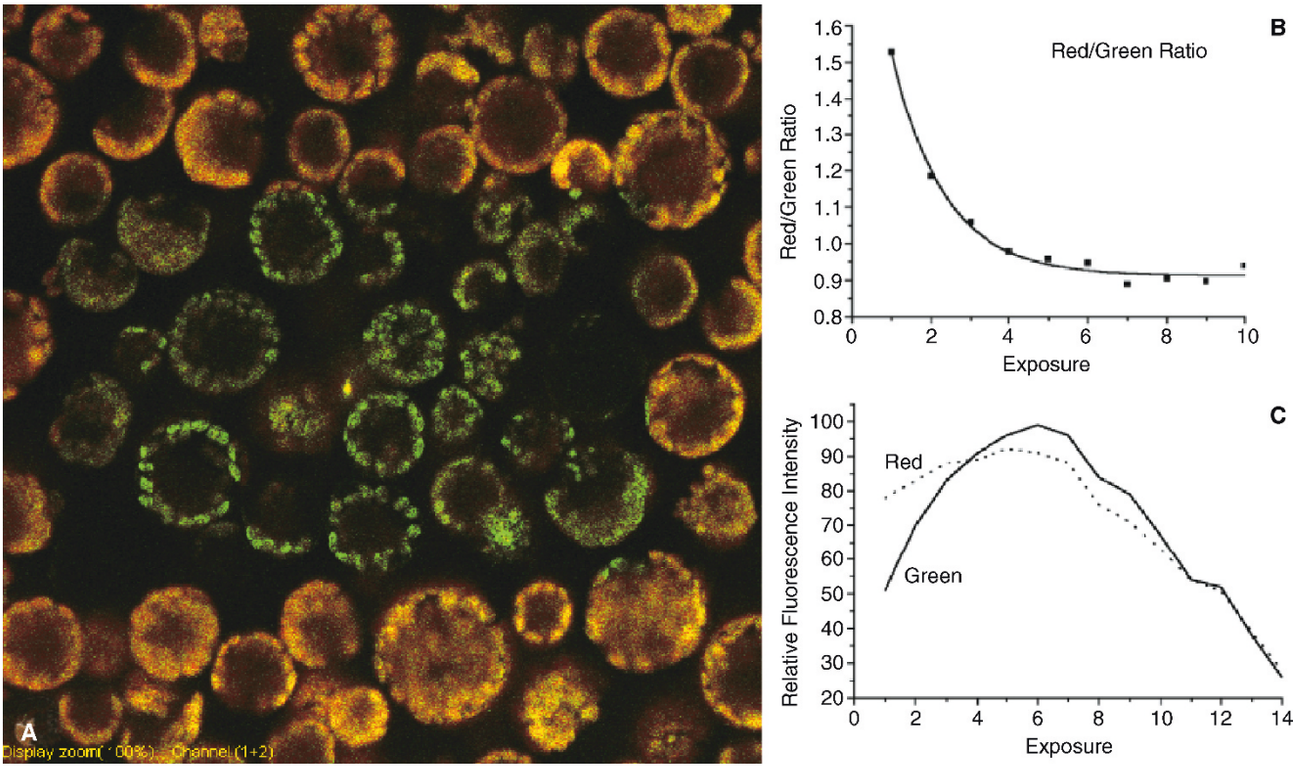


FIGURE 21.23. Two-photon fluorescence image of *A. thaliana* protoplasts. (A) The image was obtained by first scanning the central portion of the field (rectangular area) followed by a second scan to record a larger view. Note the single scan causes significant intensity and spectral changes in the autofluorescence (760 nm NIR excitation). (B) The ratio of the green and red channel intensity; (C) intensity variation plot of the green and red channels showing the initial increase in intensity.

two-photon excitation provides significant improvement in penetration depth in terms of resolution because the longer wavelength is scattered less. However, the two-photon image signal-to-noise (S/N) was appreciably degraded if a large fraction of the so-called ballistic photons in the excitation beam scattered. In addition, it was noted that the effective absorbance of a biological specimen in NIR (i.e., 800 nm) can be significantly higher at high illumination intensities because the nonlinear absorption coefficient increases with power level. Thus, the nonlinear absorption cross-section increases as the beam intensity increases towards the focal point and the effective opacity of the specimen can be much higher than the linear absorption measured at lower intensity (Fig. 21.5).

In two-photon fluorescence imaging, the achievable image quality is more often limited by low signal strength than by the optical resolution per se. In the case of the highly scattering *M. quadrifolia* leaf (Fig. 21.10), the optical sectioning depth is limited to approximately 40 to 50 µm. The two-photon image was obtained by using an Olympus Fluroview 300 confocal scanner and the flu-

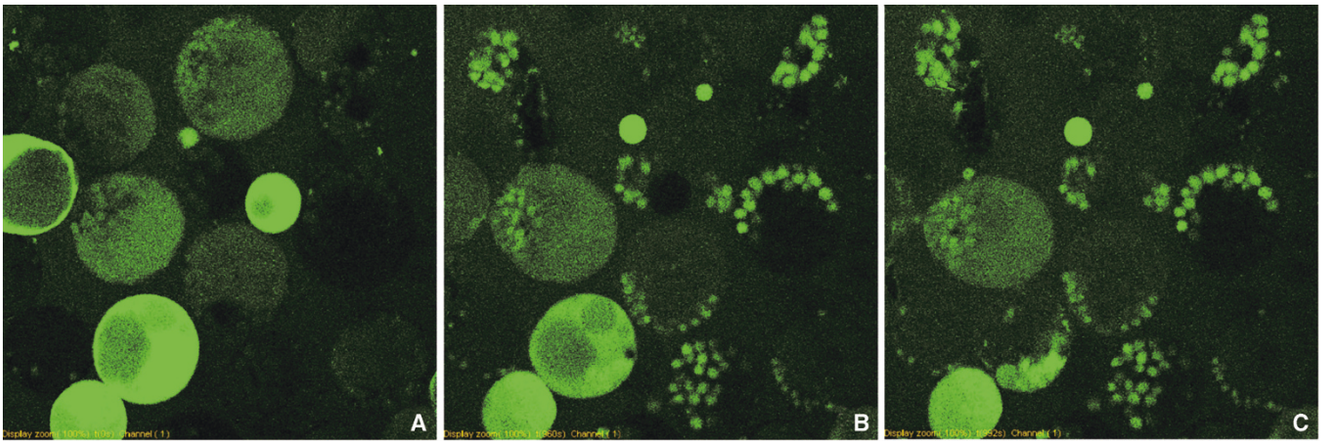


FIGURE 21.24. Series of two-photon fluorescence micrographs showing the photodamage of Calcein-loaded protoplast of *A. thaliana*. Note the cell most heavily loaded with dye is the first to be damaged (excitation, 760 nm; emission, 550 nm + 20 nm band; peak power density at focus is approximately 3.9×10^{11} W/cm^2 at 8.4 µs dwell time/pixel).

orescence signal was descanned and detected with the built-in photomultiplier tube (PMT) but no detector aperture was used. The fact that the two-photon excited fluorescence peaks are located near the attenuation maximum of this specimen further limits the detectable fluorescence. For comparison, the same specimen imaged in single-photon mode gave a usable depth of approximately 30 µm.

HARMONIC GENERATION PROPERTIES

A number of plant structures are capable of efficiently generating second harmonic signals. These include stacked membrane structures such as grana, starch granules, secondary cell wall, cuticle and cuticular waxes, and silica deposits (bio-opals). Starch granules exhibit high conversion efficiency in SHG, in fact, a piece of potato tuber placed in an unfocused, ultra-fast laser beam can efficiently generate a bright SHG beam in the forward direction (Fig. 40.10, *this volume*). Due to the radial symmetry of the molecular structure of a starch grain, starch granules exhibit birefringence, and it is believed that this molecular arrangement is also responsible for the SGH property. The efficiency varies with potato variety, presumably because of differences in the structure and size of the starch granules.

Cellulose is a linear molecule without branching. Neighboring cellulose chains may form hydrogen bonds leading to the formation of microfibrils (20 to 30 nm) with partially crystalline parts called micelles. This highly organized structure may be responsible for the strong SHG properties of cell walls. The term *biophotonic crystal* is used to describe biological structures having the physical properties required to generate harmonic signals (Sun *et al.*, 2001; Cheng *et al.*, 2003).

The SHG signal depends strongly on the polarization of the illumination beam. Figure 40.9 shows the rotation of SHG signal in maize silica cell as the polarization of the illumination changes. Because removing the organic matrix, using a $ZnCl_2$–HCl solution, destroys the SHG signal, it seems likely that it is the arrangement of the amorphous silica in the organic matrix that is important for SHG.

As the third harmonic signal is generated at optical interfaces, and as plant tissues are frequently highly heterogeneous in terms of refractive index, it is not surprising that many plant tissues generate strong THG. The surfaces of organelles, such as mitochondria and chloroplasts, lipid droplets, storage bodies (e.g., starch granules and protein bodies in seeds) and cell–wall interfaces are all capable of generating strong THG signals. Figure 21.25 shows a set of chloroplast images [THG (a), SHG (b), 2P-fluorescence (c), and combined image (e)] of mesophyll cells of *Commelina communis* L. obtained using 150 fs, 1230 nm illumination.

THE EFFECT OF FIXATION ON THE OPTICAL PROPERTIES OF PLANTS

When live-cell imaging is impractical or unnecessary, fixation by means of chemicals provides a way to avoid/minimize the problems with "uncleared" botanical specimens that are cataloged above.

While the primary purpose of the fixation process is to preserve the structure of interest, it may also be desirable to remove any constituents that might interfere with the observation. For example, alcohol-based fixatives (e.g., 1:3 EtOH/acetic acid; methanol, etc.) usually extract significant amounts of pigments from plant tissue, greatly reducing the autofluorescence background (Figs. 21.13, 21.14, and 21.15). These alcohol-based fixatives are commonly used to preserve protein structures. The use of a simple aldehyde fixative, such as formaldehyde, acroline, or 1:1:3 EtOH/formaldehyde/acetic acid mixtures, is also recommended.

As aldehyde fixation causes condensation reactions with tissue proteins that can result in ring formation and autofluorescence, it is normally avoided to prevent high background autofluorescence. However, Fredrickson used autofluorescence enhanced in this way, combined with excitation from the 488 nm Ar line to study the development of the female gametophyte in *Epipactis* (Fredrikson, 1992). Because glutaraldehyde, a di-aldehyde, can greatly increase background autofluorescence by forming excess crosslinkage of proteins, its usage should generally be avoided (for exception, see Chapter 18, *this volume*). The use of a fixative containing 1% freshly prepared para-formaldehyde and 1.5% acroline in 0.05 *M* phosphate buffer (pH 7.0) is recommended for its high penetration and excellent ultrastructural preservation (Cheng *et al.*, 1979b; use without the glutaraldehyde component). This fixative offers relatively low fixative-induced, autofluorescence and offers the possibility of both SEM and TEM studies after optical observations (see Chapter 49, *this volume*). The brownish coloration of plant tissue caused by natural tannins or the oxidized products of fixation can be removed by the treatment in Stockwell's solution for 10 to 20 h (Johansen, 1940; Herr, 1985, 1992; Palser *et al.*, 1989).

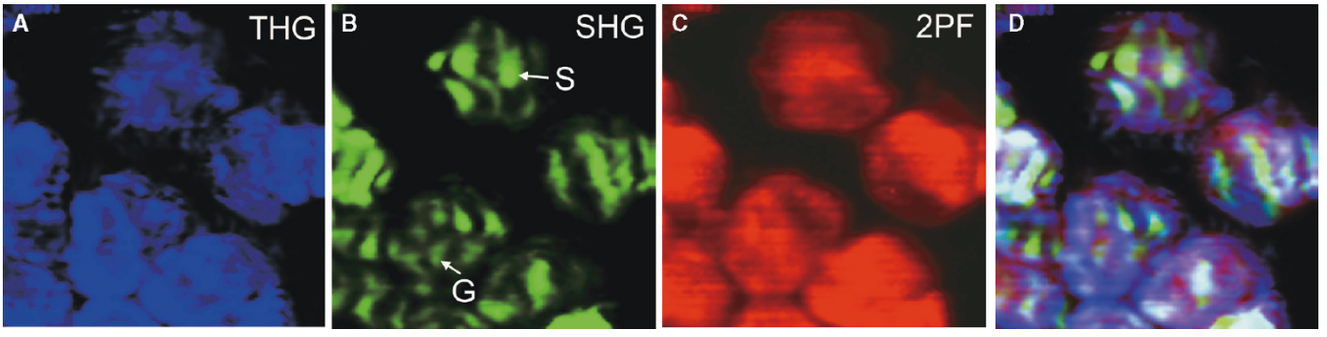


FIGURE 21.25. SHG, THG, and two-photon fluorescence image of chloroplast. (A) The THG signal is generated at the interfaces of refractive index while the SHG signal (B) is generated by the stacked membranes in the grana (G) and by the starch granules (S). The 2P-fluorescence (2PF) signal is the result of chloroplast autofluorescence. Panel (D) combines images of (A), (B), and (C).

LIVING PLANT CELLS

As it is not possible to modify the optical properties of a living plant cell, one can only optimize the imaging method to achieve best attainable images. These methods include the selection of the proper excitation wavelength(s), a suitable detecting wavelength (if possible), a suitable water-immersion or dipping objective and the choice of single- or multi-photon excitation. In addition, imaging modalities such as BSL imaging or SHG should be considered as these methods do not deposit any energy in the specimen. Spectral imaging may help to separate the emission from the fluorescent tag(s) from that caused by autofluorescence.

Unlike many common cultured animal cells, neither suspension-cultured plant cells nor free-living algae attach to culture dishes or to any other substrates. As a result, immobilizing suspending cells can become a challenge. Most of the discussion so far in this chapter has been focused on the photosynthetic tissues. The following sections will discuss the technical issues specific to imaging particular organs and tissues.

Callus, Suspension Culture Cells and Protoplasts

Parenchymal tissues can be cultured in suitable artificial media. The cells remain in an undifferentiated state and form aggregates called callus. The callus remains colorless when kept in the dark, but generally turns green under light. Therefore, depending on the type of callus, one may encounter different levels of autofluorescence background. Imaging GFP, yellow fluorescent protein (YFP), and DsRed is relatively easy in a colorless callus, but spectral overlap will occur in green callus. In order to improve the optical properties of the specimen, it is important to mount the callus under a coverslip and in a suitable culture medium, so that there is no air interface between the water-immersion objective lens and the callus.

Suspension-Cultured Cells

Suspension-cultured cells are relatively easy to image because most of them develop only the primary cell wall. However, immobilizing suspension cells requires some effort. Methyl-cellulose, agrose (0.5%–1%) and polyvinyl alcohol gel (such as K-Y Jelly) can be used to immobilize such cells in a chambered slide [Fig. 21.26(A)]. Cells can also be held in a specially designed chamber

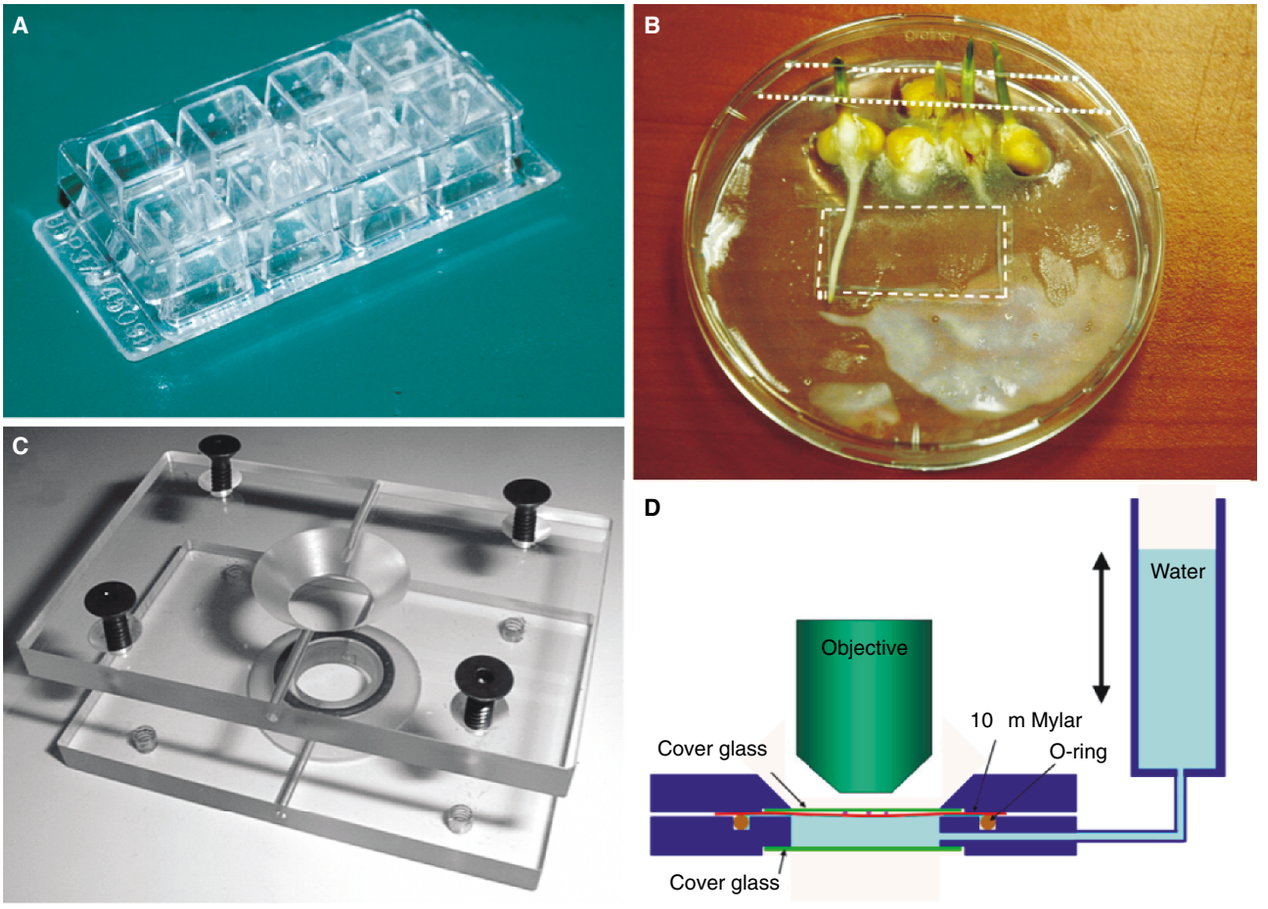


FIGURE 21.26. (A) Chamber slides commonly used in handling cultured plant cells. (B) A homemade, larger version of the chambered slide, filled with agrose gel, can be used to observe the roots of small plants — note the opening in the upper lid to allow plants to grow and the bottom of the Petri dish (*dotted rectangular area*) has a window made of a coverslip having the proper thickness. (C) A specimen chamber designed to handle loose tissue or cultured cells; (D) diagrammatic representation of the chamber shown in (C). The chamber is made of an upper and a lower cover glass window (green) with a 10 µm Mylar film (red) located just below the upper coverslip. Cells or loose tissues are held between the upper coverslip and a Mylar film. The lower chamber is filled with water and connected to a water reservoir via a flexible tube. The amount of "holding" pressure exerted on the specimen by the Mylar film can be adjusted by the height of the water head (Cheng *et al*., 1999a). (Other chambers are discussed in Chapter 19, *this volume*)

such as that shown in Figure 21.26(B) (Cheng *et al.*, 1999a). Figure 21.27 shows GFP-expressing tobacco cells held in a chamber slide with 0.5% agrose gel. Through-focus series of fluorescence images were obtained at video rate using the widefield, epi-fluorescence mode and subsequent deconvolved (AutoDeburr, AutoQuant Inc., Troy, NY) to obtain optical sections. Success in this technique requires that the specimen be immobile during the entire data collection process.

Protoplasts are plant cells that have had their cell walls removed by enzymatic digestion. When suspended in liquid medium, they are generally spherical in shape and can be imaged using the same methods as for suspension cells. If the protoplast is derived from a mesophyll cell, it may contain large numbers of chloroplasts as shown in Figure 21.28. The image shows the red autofluorescing chloroplasts and green fluorescing mitochondria in a mesophyll protoplast of *A. thaliana*. The cell was labelled with Mitotracker (Molecular Probes Inc.) in culture medium (Huang and Chen, 1988).

Calcein AM dye (Molecular Probes Inc.) provides a good measure of plant cell and protoplast viability. The AM–ester salt can be loaded into the protoplast. After incubation, wash with fresh medium and mount in a chamber slide. Lower concentrations of dye may be necessary as excess dye loading can greatly increase the linear and nonlinear opacity of the cell. This results in a significant increase in energy deposition by the illumination and can pose a serious problem in confocal or multi-photon fluorescence microscopy. Figure 21.24 shows a series of images taken from Calcein AM-loaded protoplasts (leaf of *Zea mays* L.). Note the rapid cellular damage in the cells most heavily loaded with dye.

Meristem

The apical meristem is the site of the tip growth that is one of the most striking features of plant growth. Although meristems potentially have an unlimited ability to divide, division is controlled and regulated resulting in the proper initiation of leaves and suppression of the development of lateral buds (apical dominance). Confocal microscopy and multi-photon fluorescence microscopy is well suited for the study of leaf and floral initiation in the meristem. Backscattered light mode can be used to perform time-lapse imaging on the transformation of vegetative to reproductive growth in the apical meristem. On the other hand, multi-photon fluorescence microscopy can be used to image cell organization and division orientation in an initiating leaf primordium (Bommineni *et al.*, 1990, 1993, 1995). Figure 21.29 is a BSL image of a maize apical meristem.

Stem and Root

In the stem and root, vasculature is the most frequently studied tissue. The vascular bundle consists of the elements of water conduction, the xylem, and those of assimilate conduction, the phloem. The phloem is the principal food-conducting tissue in vascular plants. Mature phloem elements are called sieve tubes. At regular intervals callose is deposited to form sieve plates between sieve-tube members and these can be detected with Resorcin blue. Decolorized aniline blue (pH 10) can be used for staining both fresh sieve tubes and those fixed in EtOH–acetic acid (3 : 1). The amount of callose increases as the cell ages, and this continuously reduces the diameter of the pores. Because increased callose formation

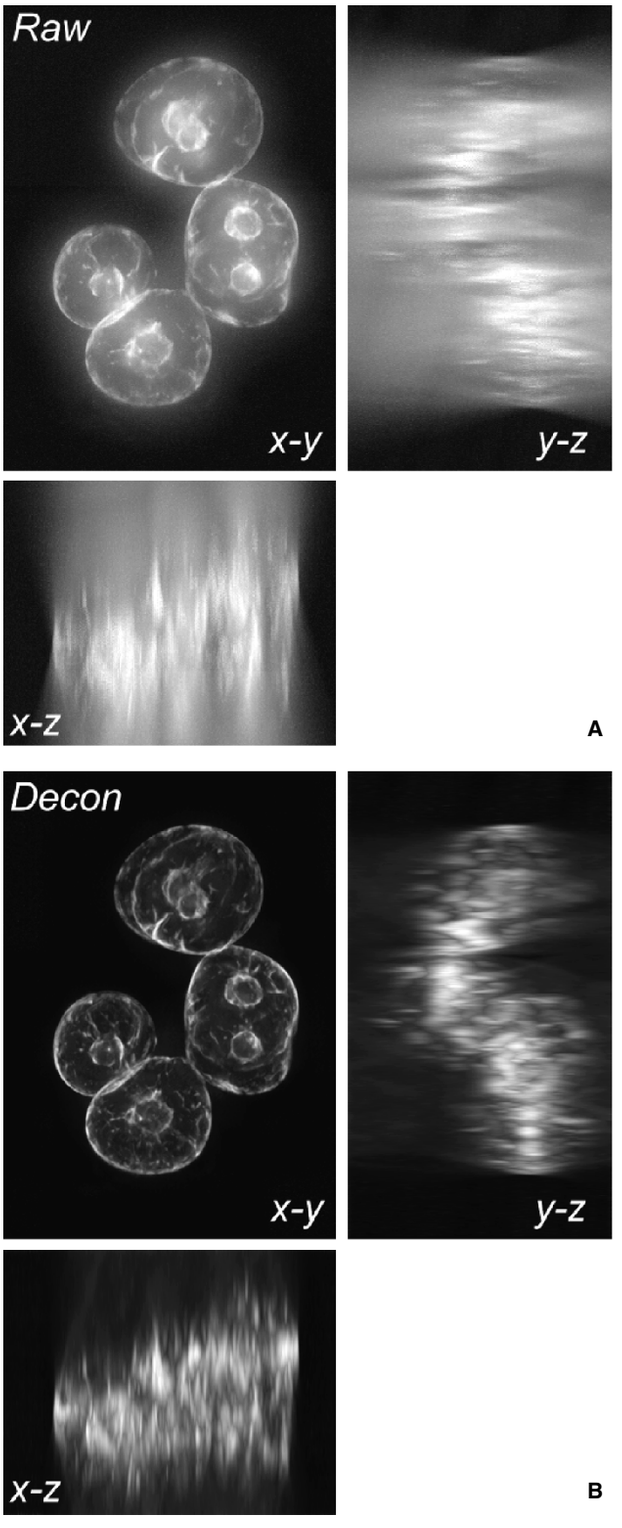


FIGURE 21.27. Widefield fluorescence microscopy of suspension-cultured GFP-tobacco cells. (A) Projection of a series of widefield, epi-fluorescence, through-focus images (*xy*, *xz*, and *yz* views). (B) Projection of a deconvolved image stack from (A). Fluorescence images were obtained with blue excitation and recorded as 550 nm emission. Image was recorded with a low cost video-rate CCD camera using ImageAcquire acquisition software (Ming-mei Technology Inc., Taipei). Deconvolution was performed using AutoDeblur v.9.3 (AutoQuant Inc.). (Image obtained at the 2002 International Course on Live Cell Imaging held at the University of British Columbia, Vancouver, Canada.)

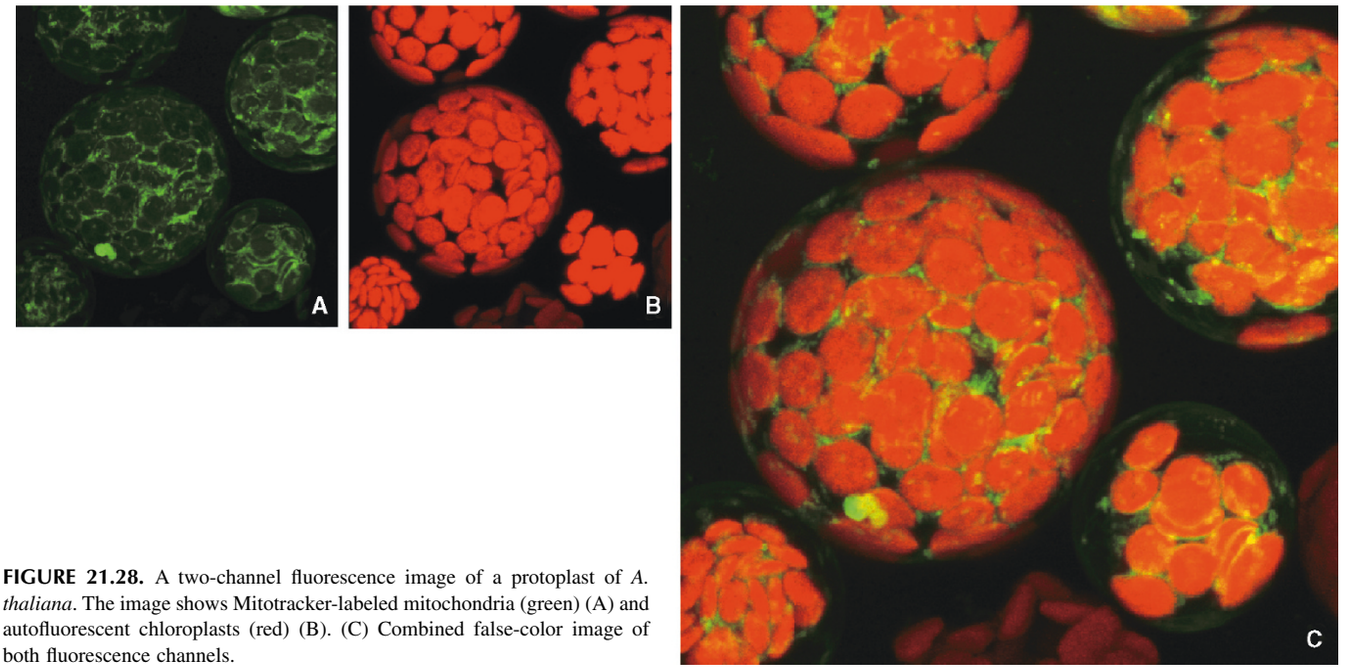


FIGURE 21.28. A two-channel fluorescence image of a protoplast of *A. thaliana*. The image shows Mitotracker-labeled mitochondria (green) (A) and autofluorescent chloroplasts (red) (B). (C) Combined false-color image of both fluorescence channels.

occurs in response to injury or infection, this staining method can also be used in pathological studies of plant tissue. In addition, callose can also be stained by the use of Cellufluor. The Casparian band in root can be stained by berberin hemisulphate/aniline-blue (Brundrett *et al.*, 1990; Hose *et al.*, 2001).

One of the common features of vascular plants is their ability to synthesize lignin. This substance is deposited in the cell walls of lignified tissue, particularly the xylem, to provide rigidity to the otherwise elastic polysaccharide cell walls. Lignin is a high-molecular-weight polymer of substituted cinnamyl alcohols that contributes about 20% to 30% of the dry weight in woody stems. It gives strong autofluorescence when excited by ultraviolet (UV)/blue light or by multi-photon NIR. These autofluorescence properties can be used to study vascular bundles or secondary wall thickenings. Woody root tissues that contain so much of lignin and alkaloids produce such intense autofluorescence that it is generally difficult to image exogenous dyes in them, although the fluorescence emission can sometimes be separated using spectral unmixing (Fig. 21.20).

Synchronous mitosis can be achieved in plant tissue by the use of colchicine or hydroxyurea (Carvalho *et al.*, 2002). This technique is commonly used in the treatment of root tips to obtain a high number of mitotic figures. Polarization microscopy can be used in the study of the dynamics of mitotic spindles consisting of birefringent microtubules.

Mounting Roots for Imaging

The glass-bottomed Petri dish shown in Figure 21.26(B) can be used in the study of root tips and root hairs. A rectangular hole was cut at the bottom of the Petri dish and a coverslip was glued over it with SilGaurd. Then, 0.5% to 2% agrose gel was pipetted into the dish and allowed to set. Seeds can be set on the surface or embedded in agrose in one side of the dish so that the seed can germinate while the dish is placed horizontally. As soon as the young roots reach the bottom of the dish, place the petri dish at a 45° to 60° angle on a stand, to force the root to grow downwards along the surface of the cover glass. This method minimizes the distance of root tissue from the coverslip, creating good optical conditions for microscopy. The root portion of the dish should be kept in the dark and an opening in the cover may be needed to allow the seedlings to emerge. Smaller plants, such as *Arabidopsis*, can be seeded in a small-chambered glass [Lab-Tek; Fig. 21.26(A)]. An inoculation of a fungal plant pathogen can be applied to the agrose after germination and pathogen–root interactions can be studied through the coverslip window at the bottom of the Petri dish. Figure 21.30 is a fluorescence confocal image of the root tip of maize.

Microspores and Pollen Grains

Microsporogenesis can be imaged either by isolating the microspore from an anther or by studying a whole-mount specimen. Isolated pollen mother cells or microspores can be handled the same way as suspension-cultured cells. However, it is frequently desirable to image the microspores *in situ* (Pace *et al.*, 1987) through the anther wall. Multi-photon fluorescence microscopy is the choice for this application. Because high resolution is generally needed to study this type of specimen (i.e., chromosomes, microtubules, etc.), special care should be taken to ensure that the optical properties are matched as closely as possible to the design criteria of the objective lens. If the tissue can be fixed, stained, and cleared in methyl-salicylate, it can produce exceptional images (Cheng *et al.*, 1999b; Fig. 21.31). In addition, it can be helpful to apply adaptive deconvolution [i.e., "blind" deconvolution, capable of finding the best-fit PSF for 3D multi-photon or confocal data stacks (see Chapter 24, *this volume*)]. The three-dimensional chromosomal arrangement can also be obtained by using widefield epi-fluorescence microscopy and deconvolution (Agard and Sedat, 1983; Agard *et al.*, 1989; Dawe *et al.*, 1992); the technique is particularly attractive when DAPI (Vergne *et al.*, 1987) is used for staining of the chromosomes because UV excitation is readily available in conventional epi-fluorescence.

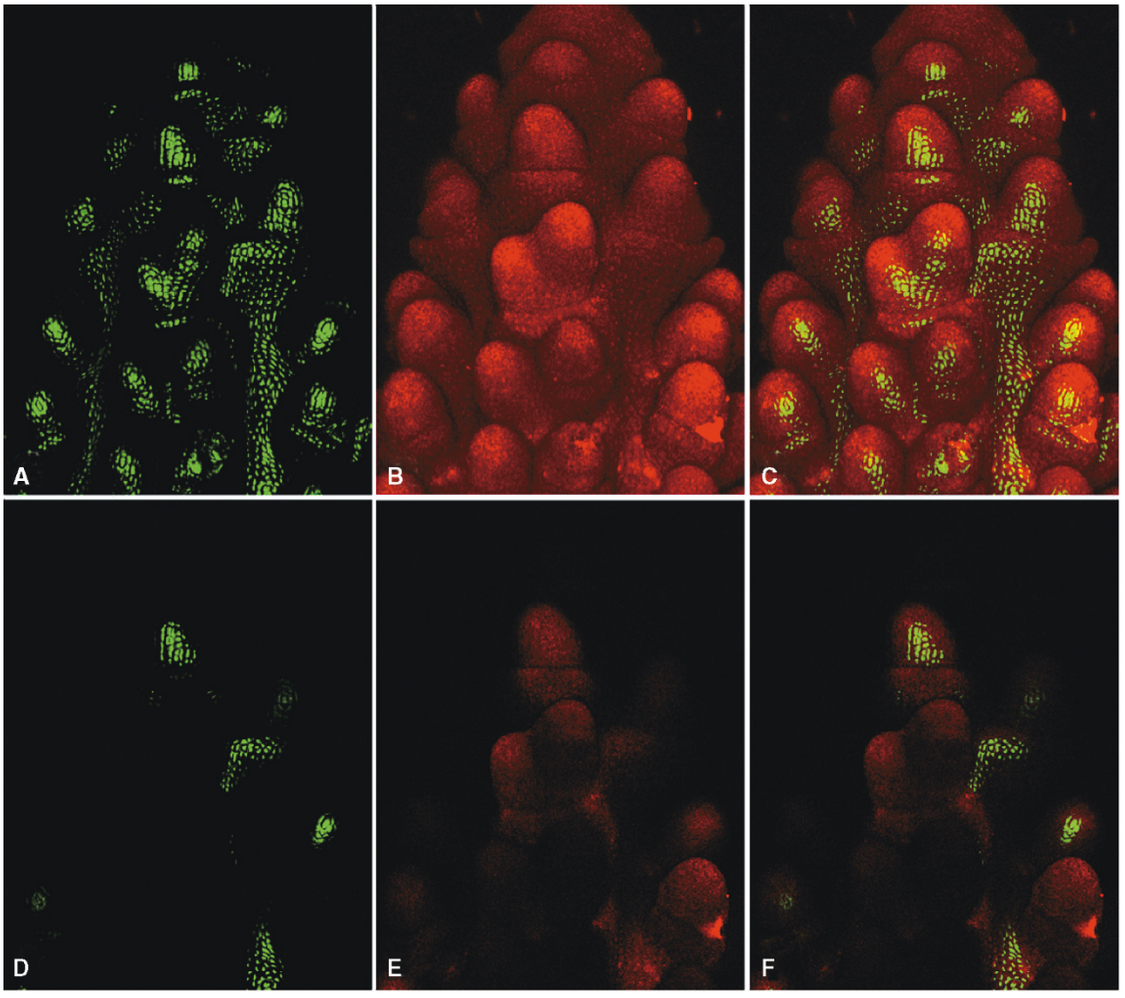


FIGURE 21.29. Confocal image of the apical meristem of maize.

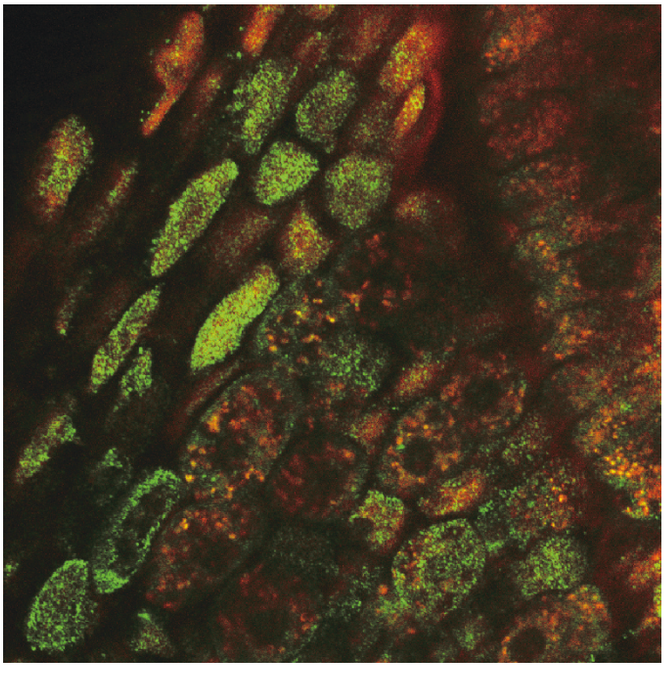


FIGURE 21.30. Two-channel confocal image of root apex of maize.

Because microtubules are birefringent structures, the spindle in the dividing cells can also be imaged by dynamic polarization microscopy (e.g., Spindleview from Cambridge Research Instruments, Woburn, MA). However, as the anther wall can also be highly birefringent, it may be better to image isolated pollen mother cells.

Pollen Grains

Pollen grains are difficult specimens to image as they are frequently both highly scattering and pigmented. The surface of the pollen grain is covered with a sporopollenin exine and a cellulose intine (Heslop-Harrison and Dickinson, 1969). The exine consists of complex fine structures that make the pollen grain not only a highly absorbing but also a highly scattering specimen. Because pollen grains also frequently contain a large number of starch granules and a relatively dense cytoplasm, significant self-shadowing can occur when imaging them. Figure 21.32(A) shows the autofluorescence spectra of maize pollen. As it is clear that this autofluorescence background is high for almost the entire visible spectrum, when studying pollen grains, consider fluorescent dyes that emit in the NIR. The autofluorescent signal can be excited by UV, blue light or multi-photon of NIR. Figure 21.32(B,C) shows a pollen tube (PT) penetrating the hair (hr) of silk (S). Note the high autofluorescence of the pollen grain (P). Other pollen images can be found in Figures 8.49 and 8.60.

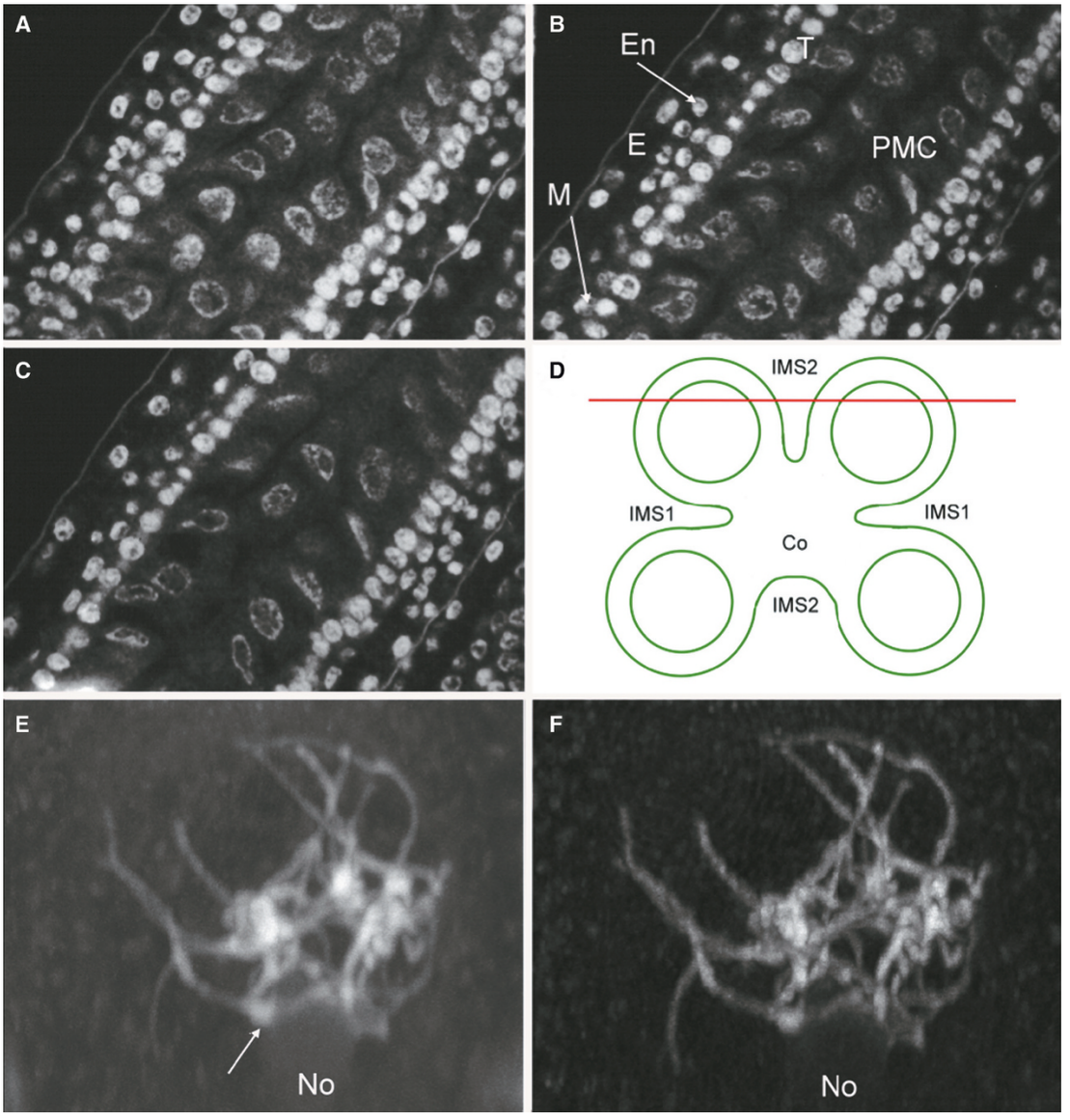


FIGURE 21.31. (A) Meiosis of maize pollen mother cell. (A, B, C) Representative images from an optical section stack of maize anther. (D) Approximate position where the optical sections were obtained from the maize anther. (E) Pachytene chromosomes in the pollen mother cell (PMC); this image was obtained directly through the four-layer anther wall using a confocal microscope (excitation, 514 nm; emission, 600 nm). (D) Deconvolved image of (E). Specimen was stained with Feulgen reaction and cleared in methyl salicylate. IMS1 and IMS2 are intermicrosporangial stripe 1 and 2, respectively. Co, anther connective; E, epidermal cell; En, endothecium; M, middle layer; T, tapetum; No, nucleolus.

Tapetum

The tapetum film and the orbicule [Ubish body, Fig. 21.32(D)] are also made of sporopollenin (a polyester of several monomers of which beta-carotene and zeaxanthin are the most common) and have the same autofluorescence properties as pollen exine (Echlin and Godwin, 1968; Dickinson and Bell, 1972; Cheng *et al.*, 2004) that produces intense autofluorescence [Fig. 21.32(E)]. Therefore, because studying tapetum development after the young microspore stage (onset of sporopollenin deposition) may suffer from high background autofluorescence, it may help to use fluorescent probes excited in deep red or even NIR.

Starch Granules

As stated above, starch granules are efficient SHG producers. Therefore, when imaging pollen with a multi-photon fluorescence microscope, it is highly possible that the scattered SHG signal can significantly contaminate the recorded fluorescence signal. In this case, it is wise to check the fluorescence spectrum to ensure that SHG signal is not present. Alternatively, one can place a long-pass barrier filter to remove the SHG signal from the fluorescence-detecting path. This SHG light can also excite additional autofluorescence.

Pollen Germination

Although it is common to image pollen germination on the surface of an agrose gel, imaging the penetration of a pollen tube into a style can be more challenging. In order to optically match the design criteria of a "non-dipping" water-immersion objective lens, it is essential that a coverslip with proper thickness be added on top of the agrose gel. A small spacer may be needed in between

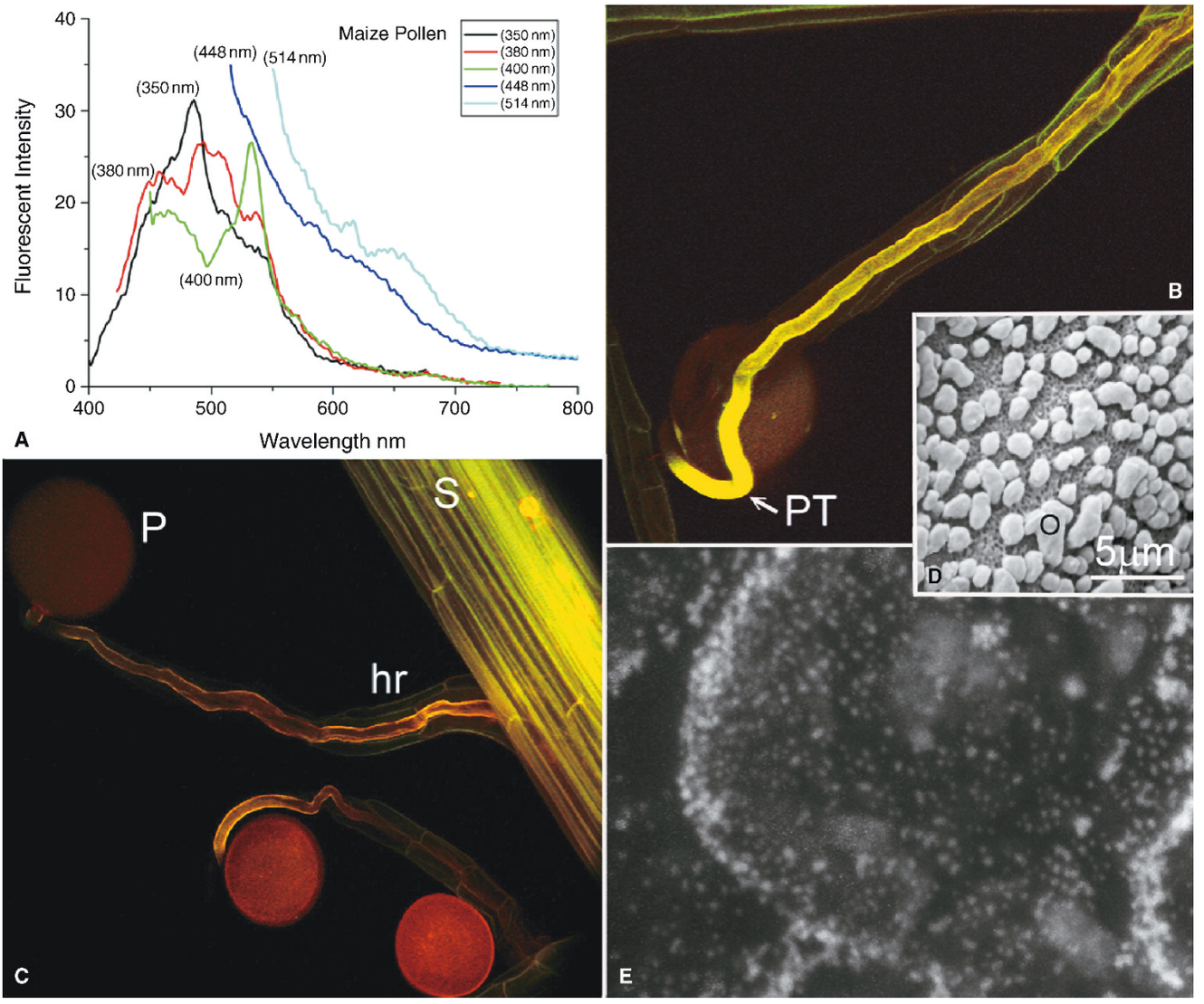


FIGURE 21.32. (A) Single-photon–excited fluorescence spectra of maize pollen grains (*Zea mays* L., var. KYS). The spectra were obtained by exciting pollen grains with 350 nm, 380 nm, 400 nm, 448 nm, and 514 nm. Note the strong autofluorescence in the blue and green regions when excited with UV and deep blue light (350, 380, and 400 nm), and significant red fluorescence when excited with blue and green light (448 and 514 nm). (B and C) Single-photon, two-channel fluorescence image of germinating pollen grain (P) on the hair (hr) of the silk (S). Note the penetrating pollen tube (PT). (D) SEM image of isolated tapetum film with orbicules (O). (E): (Style) autofluorescence image of orbicules in maize (excitation, 488 nm; emission, 610 nm).

the agrose gel and the coverslip to prevent it crashing into the germinating pollen grain. Decolorized aniline blue (pH 10) can be used for staining both EtOH–acetic acid (3 : 1) fixed and fresh callosic inner wall of the pollen tube (Pareddy *et al.*, 1989).

Rapid cytoplasmic streaming within the pollen tube usually requires high-speed imaging devices such as the disk-scanning confocal microscope (for more about fast confocal imaging see Chapter 10, *this volume*). High-speed, ratiometric imaging also allows the study of Ca^{++} gradients at the tip of the pollen tube using Ca^{++} sensitive dyes (see Chapter 42, *this volume*). Figure 21.33 shows a Ca^{++} ratiometric image of the tip of lily pollen tube, imaged by a confocal microscopy using the Fluo-3/Fura Red scheme.

Cuticles, Hairs, and Waxes

The outer surfaces of terrestrial plants are generally covered with an inert polymer of cutin and waxes (Cheng *et al.*, 1981, 1986; Cutler *et al.*, 1982; Juniper and Jeffree, 1983; Cheng and Walden, 2005). The most common constituents of the cuticle are 9,10,18-trihydroxyoctadecanoic acid and 19,16-dihydroxyhexadecanoic acid (Holloway, 1982). The reactive groups of these molecules link and crosslink into a high-molecular-weight, three-dimensional network. There is usually an excess of free hydroxyl (–OH) and carboxyl (–COOH) groups that can be stained with basic dyes. In some cases, such as that of tomato fruit, the cuticle is pigmented with carotinoids and shows strong autofluorescence. Cuticle can also be stained by the fluorescent dye berberin sulphate. The reverse (or "negative") fluorescence method can also be used to study the surface topography of a cuticle layer, such as the ridged cuticle found on the anther surface of maize (Cheng *et al.*, 1986).

Terrestrial plants frequently have additional wax covering the surface of the cuticle. These waxes can be laid down in complex structures (plates, needles, etc.) and can be highly birefringent. Plant surface waxes are complex chemical mixtures composed

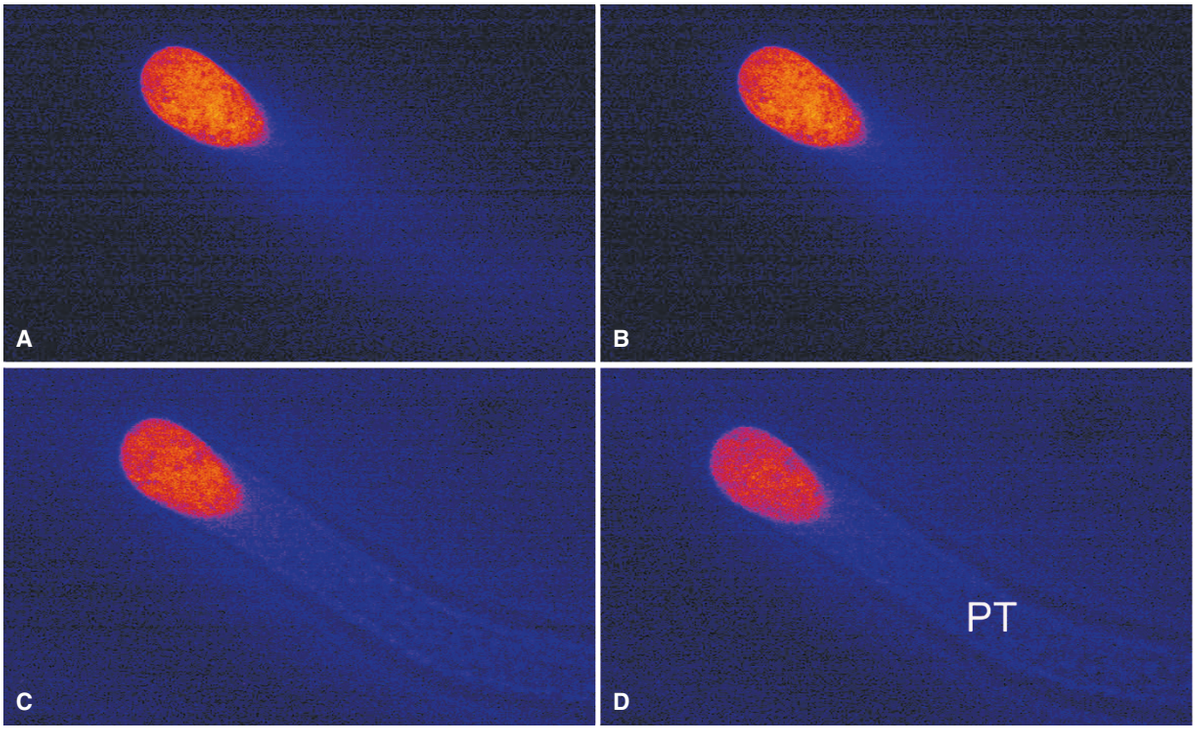


FIGURE 21.33. Ca^{++} ratiometric image (serial optical sections) of the tip of lily pollen tube (PT). (Image obtained at the 2002 International Course on Live Cell Imaging held at the University of British Columbia, Vancouver, Canada.)

mainly of long-chain aliphatic hydrocarbons with chain lengths ranging from C_{20} to C_{35} (Bianchi and Salamini, 1975; Bianchi *et al.*, 1977, 1978; Tulloch, 1981; Baker, 1982; Blaker 1989; Cheng *et al.*, 1986). These waxes can form complex surface structures and are difficult to study morphologically because of their sensitivity to electron beam irradiation in a scanning electron microscope. The waxy surface structures can be studied by using a confocal microscope with either BSL imaging or reverse contrast fluorescence in which the surface is wetted by the fluorescent solution.[1]

The air–cuticle–water interfaces are optical interfaces between RI = 1/1.4/1.3. This difference is high enough to effectively lower the solid-angle of high-NA objectives. The air–cuticle–water interfaces can also generate THG signal when illuminated at high intensity. Trichomes and hairs are additional strongly-scattering structures on the surfaces of many plants. To reduce the deleterious optical effects of these structures, it is wise to mount such plant tissues in water or, if possible, in RI-matching glycerol/water solution. This measure reduces the RI difference between the medium and the epidermal surface (wax and cuticle) from 1.0/1.4 (air/cuticle) to 1.3/1.4 (water/cuticle). However, if one is trying to image the organ surface (i.e., the surface of the leaf), an air/tissue interface is desirable as it can easily be imaged using BSL. This imaging modality allows researchers to monitor the development of an organ or tissue over a long period of time using low light intensity and without adding fluorescent dyes. Cuticle can also be separated from the cell wall and studied in this way (Holloway and Baker, 1968). Figure 21.34 shows extended-focus images of the surface of the leaf by BSL mode (green) and underlying cells in fluorescence mode (red).

Storage Structures

Starch granules, protein bodies, and lipid granules are commonly found in plant cells. In most cases, if the density of these granules is relatively low, no significant influence on the signal strength will be detected. However, in tissues where a large number of storage granules is present (endosperm cells, pollen grains, and other storage cells), significant deterioration both in image quality and signal strength should be expected. This is particularly serious when the granules are stained with dyes that have strong absorption characteristics in the excitation and/or emission wavelengths.

Oils found in plant cells commonly have refractive indices higher than that of water. For example, most of the commercially used plant oils have refractive indices in the range of 1.4 (Lide, 1991). Therefore, these substances can generally be imaged in the BSL mode as well as by using fluorescent dyes such as Neutral Red (Kirk, 1970) or Nile Red. The fluorescence excitation and emission maxima of these dyes may vary, depending on the hydrophobicity of the environment. Nile Red can be used at a concentration of 100 ng/mL, and can be excited with the 488 nm/514 nm Ar-ion lines, with emission detected using a 530 nm/590 nm longpass. Figure 21.35 shows the lipid and protein storage granules of maize endosperm imaged by two-channel fluorescence confocal microscopy. Note the dense tissue resulting in very shallow penetration.

[1] To ensure low staining of the waxy structures, it is important to use dyes that have a low partition coefficient in waxes.

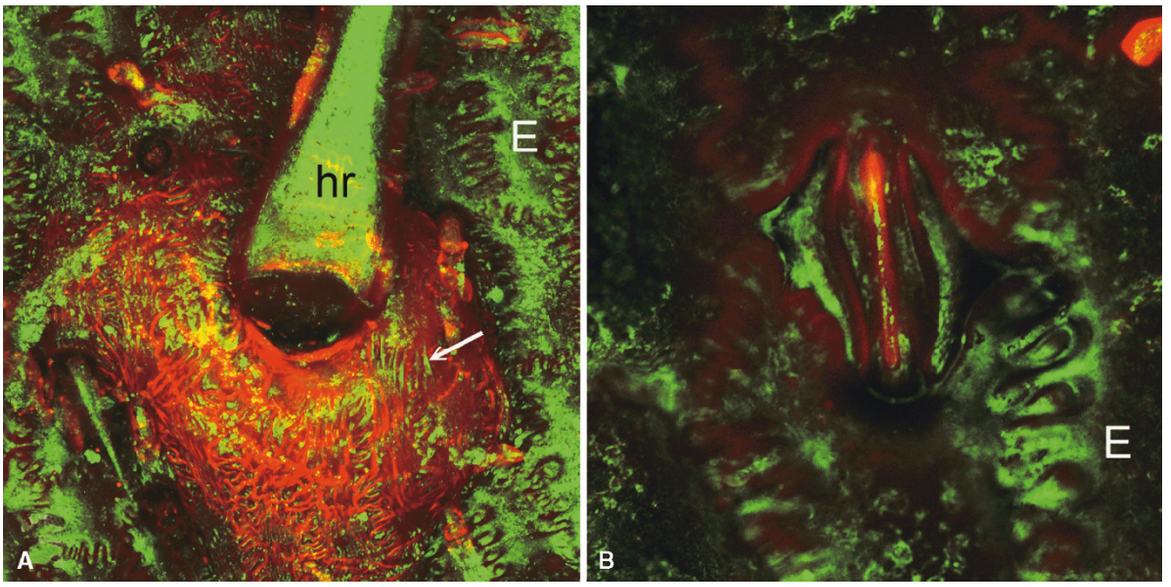


FIGURE 21.34. Extended-focus image of the leaf surface of maize. (A) Ridged cuticle (*arrow*) can be found at the base of a hair (hr); the surface of the interlocking epidermal cells (E) is clearly visible. (B) Stomata and interlocking epidermal cells. Note that the secondary wall of the guard cells produces intense autofluorescence. Green, backscattered light signal; red, autofluorescence signal.

Mineral Deposits

Mineral deposits are frequently found in and around cells in plants. For example, SiO_2 deposits are common in specialized cells and in the cell wall of the epidermal cells of grasses (Dayanandan *et al.*, 1983; Hodson and Sangster, 1988; Cheng *et al.*, 1990; Kim *et al.*, 1990) and *Equisetum*. The SiO_2 deposition is amorphous in nature and commonly referred to as biological opal. Bio-opals have an RI of around 1.42. As this is significantly different from that of the surrounding aqueous medium, it produces a strong BSL signal. The surface of these deposits can be rough (on the hundreds of nanometer scale) and they often have many internal lacunae from a remnant of cytoplasmic strands. Figure 21.36(A) shows a confocal image of silica cells in maize (*Zea mays* L.). Silica cells also exhibit strong birefringence [Fig. 21.36(B)] (Sun *et al.*, 2001; Cheng *et al.*, 2003a; Chu *et al.*, 2003a) (Fig. 21.37).

Diatom frustules are also made of silica and can exhibit strong birefringent, scattering, and SHG properties (Fig. 21.38). In addition, calcium oxalate (Jauregui-Zuniga *et al.*, 2003), and calcium carbonate (in the form of calcite and argonite) and other mineral deposits (Homer and Wagner, 1992) are present in plant tissues and generally can be imaged by either BSL or by negative staining (filling the surrounding medium with fluorescent dye to "highlight" the non-fluorescing crystals) (Cheng and Kriete, 1995).

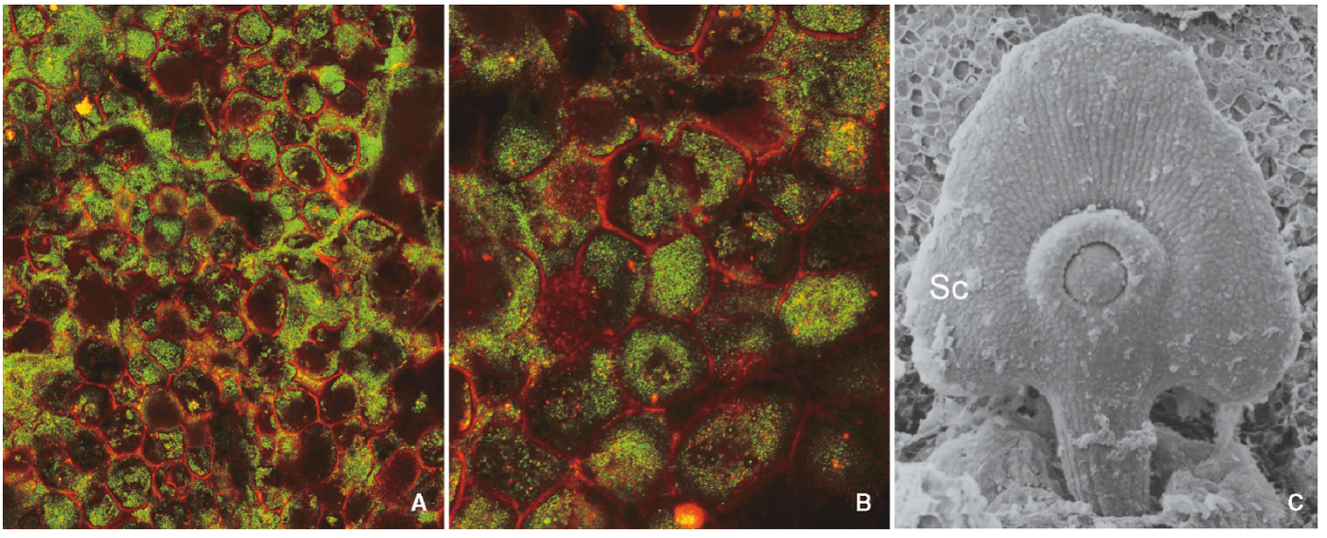


FIGURE 21.35. Two-channel confocal fluorescence image of maize scutellum showing the lipid and protein storage granules: (A) near surface, (B) 5 µm farther into the surface, (C) scanning electron microscope image of the same type of structure. Note the signal degrades rapidly in the tissue because of the high density of fluorescent features in the specimen.

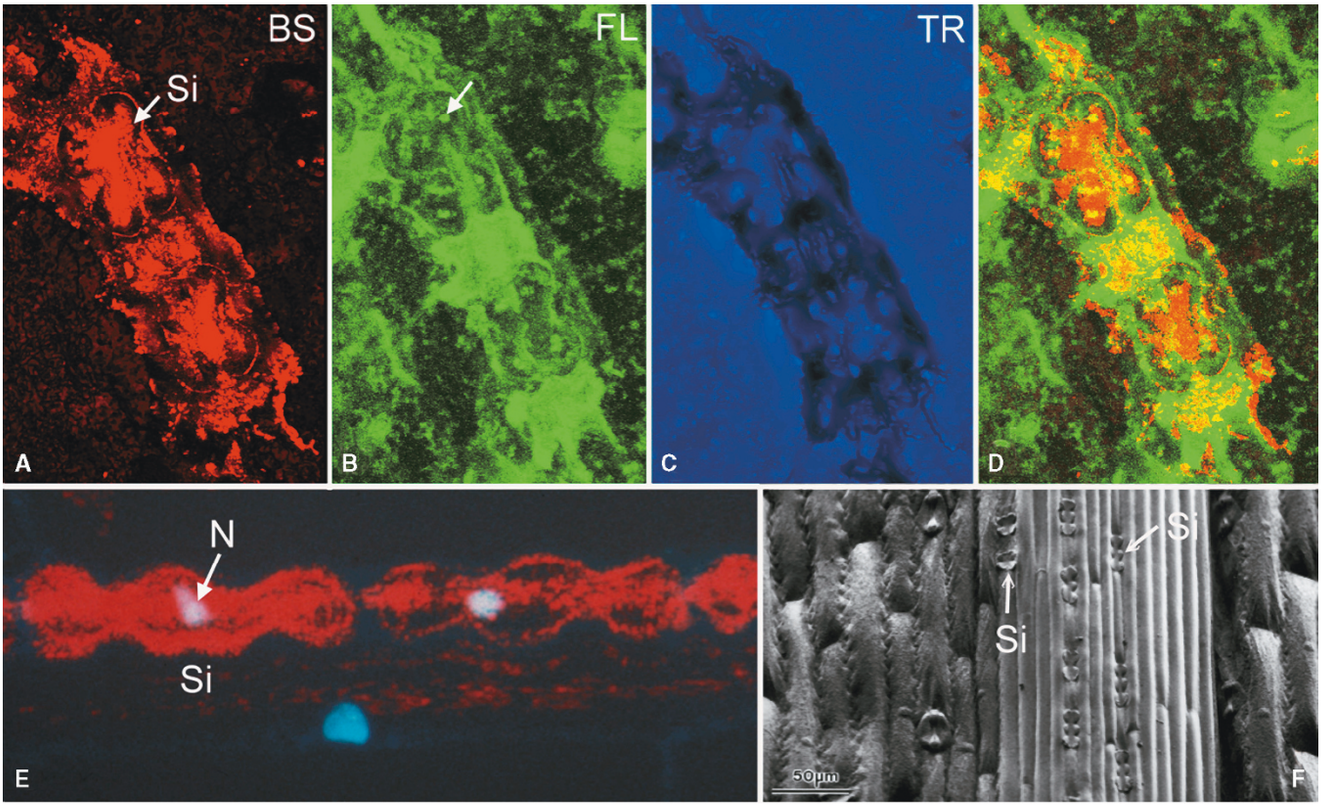


FIGURE 21.36. Silica cells in maize leaf. (A–D) $ZnCl_2$–HCl isolated cuticle with attached silica deposition imaged in (A) confocal backscattered light mode, (B) confocal autofluorescence mode (FL), and (C) conventional transmission image (TR). (D) False color combination of (A) and (B). The *arrow* in (B) indicates the center of the silica deposit and becomes visible in the isolated specimen. The isolated cuticle was mounted in water on a microscope slide. The significant difference in RI between silica and water provides the contrast in the conventional transmission image. (E) Silica cell stained in Feulgen showing the cell nuclei (N) in fluorescence mode (blue) and silica deposits in backscattered light mode (red). (F) SEM surface view (low-loss electron mode, LLE) of leaf surface showing the location of the silica cells (Si) (Wells and Cheng, 1992).

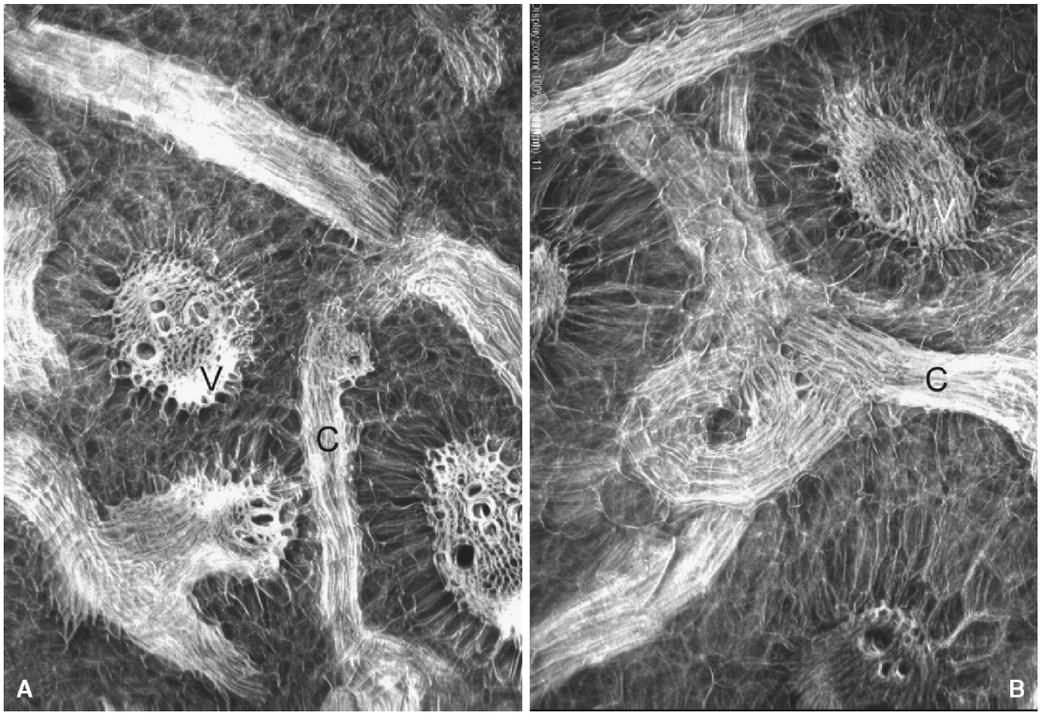


FIGURE 21.37. Two-photon, extended focus, fluorescence image of abnormal vasculature in a dwarf mutant, *na1/na1*, of maize (*Zea mays* L.) stained with analine blue. The secondary wall of the vascular bundles produce intense autofluorecence when excited with 780 nm NIR. V, vertically oriented vascular bundle; C, connecting bundle.

Primary and Secondary Cell Walls

Most plant cells are covered with an extracellular wall composed mainly of cellulose with additional lignins and sometimes, mineral deposits. Cellufluor (Polysciences) and other similar brighteners can be used in the study of cell walls in both UV confocal and multi-photon fluorescence microscopy. These dyes are frequently used for assaying cell wall regeneration of plant protoplasts and studying the development of tracheary elements (Taylor and Peterson, 2001). Cellufluor binds non-specifically to beta-linked polysaccharides such as chitin and cellulose. In addition, cellulose, carboxylated polysaccharides, beta-l, 3-glucans, pectin, callose, and certain other polysaccharides in the extracellular mucilages of root caps can be stained with Calcofluor White M2R [disodium salt of 4,4-bis-(4-anilino-bis-diethylamino-S-triazinyl-2-aminol)-2,2-stilbene-disulfonic acid; Hughes and McCully, 1975]. This fluorochrome stains most types of cell walls but usually not cell contents. Therefore, it is a useful dye for demarcating cellular boundaries and may also bind to lignin and some regions of starch grains. It has been reported that Calcofluor White M2R exhibits fluorescence dichroism: Two distinct colors are seen, depending on the relationship between the orientation of the structural elements in the wall and the polarization direction of the illumination (Hughes and McCully, 1975). If the plane of polarization of the illumination beam is known, one can study the orientation of the cell wall. Because at low concentration Calcofluor has no detectable effect on the root growth, it may also be used as a vital dye. A typical staining protocol follows.

Calcofluor Staining Procedure for Fixed and Fresh Tissue (Clark, 1981)

1. Fresh or 3% glutaraldehyde-fixed tissue can be used.
2. Stain the tissue in 0.01% Calcofluor solution for 20 to 60 s.
3. Destain in water for 1 min.
4. Mount in water for microscopy.

In contrast to the primary cell wall, the secondary wall contains less pectin and hemicellulose, but lignin and other components are still present. Lignin consists of polymerized phenylpropane units and acts as a structural component. The other non-structural components found in the secondary wall are tannins, oligosaccharides, and glycoproteins. Figure 21.37 shows a projection of the vasculature of a dwarf mutant of maize (*Zea mays* L., na1/na1 homozygous, Cheng *et al*., 2001b). Two-photon fluorescence imaging was used to achieve deep-tissue imaging at low magnification. In certain cells, such as the pollen mother cell at the Central Callose stage (Cheng *et al.*, 1979a), callosic wall is present. Callose is a helical molecule made of glucose units linked via 1,3 glycosidic linkages (callose contains also 1,4 and 1,6 linkages). Aniline blue binds to the helix, and the resulting complex produces yellow fluorescence.

Cell walls can exhibit strong birefringence and have been reported to have strong SHG properties (Cheng *et al.*, 2002b; Chu *et al.*, 2003a,b). The cell wall and the surrounding water are sufficiently different in RI to be capable of generating THG signals.

The structural components of the cell walls of algae consist of mannanes, xylanes, alginic acid, sulfonated polysaccharides, silicon, sporopollenin, and calcium carbonate (in the form of calcite and argonite). For those species with a high degree of mineralization, BSL mode is ideal for imaging the surface of the algae while fluorescence mode is used for cellular organelles. Figure 21.38 shows a diatom imaged in backscattered (silica surface) and fluorescence mode (chloroplast). Note that the particle (arrow) casts a shadow on the diatom below.

Fungi

Although fungi are not plants, and are usually classified as a separate kingdom, it is necessary to discuss the imaging of these important organisms here as many fungi are plant pathogens. Yeast and many other fungi have a highly reflective chitin surface and

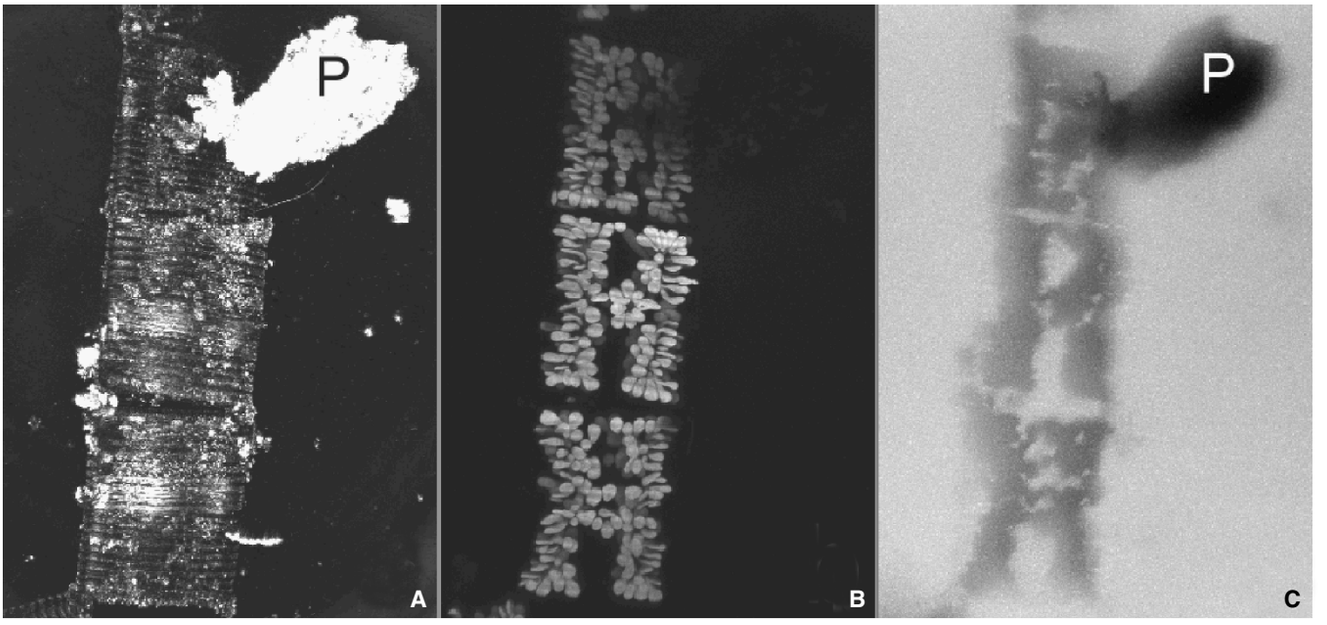


FIGURE 21.38. Fluorescence and backscattered light images of diatoms. (A) The silica wall produces an excellent backscattered light signal and (B) the chloroplasts emit strong autofluorescence. (C) Transmission image showing a soil particle (P) which casts a shadow in the fluorescence image (B) and produces strong scattering signal in the BSL image (A).

are frequently difficult to image. Imaging the penetration of fungal hyphae into plant tissue can also be challenging as hyphae often have a RI higher than the surrounding medium.

Chitin is a polymer that consists of glucose derivatives, *N*-acetyl glucosamine units connected by 1,4 linkages. Although occasionally found in algae, chitin is the main structural component in the cell wall of most fungi. Because Cellufluor binds non-specifically to beta-linked polysaccharides such as chitin and cellulose, high purity Cellufluor in deionized water (0.05% solution), with potassium hydroxide added as a clearing agent, can be used for the identification of various fungi. This dye is commercially available as Fungi-Fluor kit from Polysciences (Warrington, PA). Müller and Sengbusch (1983) have shown that Calcufluor white reveals the rhizoid system of the fungus *Blastocladiella anabaenae* on *Anabaena flosaquae* (a filamentous cyanobacteria).

CONCLUSION

Because plant cells contain light-scattering cell walls and a high concentration of pigments, they pose a challenge to both single-photon confocal and multi-photon fluorescence microscopy. In plant tissues free of pigmentation, two-photon fluorescence microscopy outperforms conventional single-photon confocal microscopy because of its increased depth penetration (Bhawalkar *et al.*, 1996; Cheng *et al.*, 1998). However, when the two-photon light is strongly absorbed, it can cause even more damage than single-photon excitation.

On the other hand, even heavily pigmented plant specimens do show significantly lower attenuation at wavelengths longer than 1000 nm, and therefore, long-wavelength two- and three-photon excitation can be considered. Results indicate that significant differences exist in fluorescence emission spectra between single-photon and two-photon excitation. Therefore, one should generally NOT select two-photon excitation wavelengths by simply doubling the wavelength of the linear absorption maximum of the fluorophore.

Mesophyll protoplast viability tests indicate that heavily pigmented (or heavily dye-loaded) plant cells can experience extensive photodamage under high-intensity NIR illumination. Even though photodamage is limited to the immediate vicinity of the focal point in two-photon fluorescence microscopy, overall cell viability is often lower than with single-photon confocal microscopy, assuming that the criterion is to obtain the same fluorescence signal level. Therefore, the choice of using single-photon confocal microscopy versus multi-photon fluorescence microscopy for plant material comes down to a careful analysis of attenuation and excitation spectra to determine which imaging modality is most likely to allow one to obtain the required information.

ACKNOWLEDGMENTS

Images presented in this chapter were obtained mostly from the author's laboratory at the State University of New York and at the National University of Singapore (NUS), where he is an adjunct professor of the Department of Biological Sciences (DBS). Most of the absorption and fluorescence spectra were prepared exclusively for this chapter using equipment at DBS-NUS. The author is grateful for the wonderful support and friendship from Professor Hew Choy Leong, Head of DBS-NUS and Professor Hanry Yu (Department of Physiology, NUS) during his 2003–2004 stay. The SHG work is a collaborative work with Professor Chi-kuang Sun of the Department of Electrical Engineering, National Taiwan University, Taipei, Republic of China. Some of the images used in this chapter were obtained by the author in demonstration experiments at the International 3D Microscopy of Living Cells Course (organized by Professor J. Pawley) held annually at the University of British Columbia, Canada. Special thanks to Dr. T. Holmes at AutoQuant for providing the Auto-Deblur deconvolution software and to Cambridge Research Instruments (Woburn, MA) for Figures 21.12 and 21.20. Thanks are also due to Nick White, Sir William Dunn School of Pathology, University of Oxford for his help editing the proofs.

REFERENCES

Agard, D.A., and Sedat, J.W., 1983, Three-dimensional architecture of a polytene nucleus, *Nature* 302:676–681.

Agard, D.A., Hiraoka, Y., Shaw, P., and Sedat, J.W., 1989, Fluorescence microscopy in three dimensions, *Meth. Cell Viol.* 30:353–377.

Bhawalkar, J.D., Shih, A., Pan, S.J., Liou, W.S., Swiatkiewicz, J., Reinhard, B.A., and Cheng, P.C., 1996, Two-photon laser scanning fluorescent microscopy – from a fluorophore and specimen perspective, *Bioimaging* 4:168–178.

Baker, E.A., 1982, Chemistry and morphology of plant epicuticular waxes, In: *The Plant Cuticle* (D.P. Cutler, K.L. Alvin, and C.E. Price, eds.), Academic Press, London, pp. 139–165.

Bianchi, G.P., and Salamini, F., 1975, Glossy mutants of maize, IV. Chemical composition of normal epicuticular waxes, *Maydica* 20:1–3.

Bianchi, G.P., Avato, P., and Salamini, F., 1977, Glossy mutant of maize. VII. Chemistry of glossy 7 epicuticular waxes, *Maydica* 22:9–17.

Bianchi, G.P., Avato, P., and Salamini, F., 1978, Glossy mutant of maize. IX. Chemistry of *glossy 4*, *glossy 8*, *glossy 15* and *glossy 18* surface waxes, *Heredity* 42:391–395.

Blaker, T.W., Greyson, R.I., and Walden, D.B., 1989, Variation among inbred lines of maize for leaf surface wax composition, *Crop Sci.* 29:28–32.

Bommineni, V.R., and Cheng, P.C., 1990, The use of confocal microscopy to study the developmental morphology of shoot apical meristems: A procedure to prepare the specimen. *Maize Genetic Cooperation Newsletter* 64:34.

Bommineni, V.R., Cheng, P.C., and Walden, D.B., 1995, Re-organization of cells in the maize apical dome within six days of culture after microsurgery, *Maydica* 40:289–298.

Bommineni, V.R., Cheng, P.C., Samarabandu, J.K., Lin, T.H., and Walden, D.B., 1993, Estimation of cell number in the maize apical meristematic dome and a three dimensional view of the reconstructed apical meristem by confocal microscopy and multidimensional image analysis, *Scanning* 15(Suppl. Ill):21–22.

Brininstool, G., 2003, A role for constitutive pathogen resistance in promoting cell expansion in *Arabidopis thaliana*, PhD thesis, Louisiana State University and Agricultural and Mechanical College, Baton Rouge, LA.

Brundrett, M.C., Murase, G., and Kendrick, B., 1990, Comparative anatomy of roots and mycorrhizae of common Ontario trees, *Can. J. Botany* 68: 551–578.

Carvalho, C.R., Saraiva, L.S., and Otoni, W.C., 2002, Maize root tip cell cycle synchronization, *Maize Genetic Cooperation Newsletter* 76:69.

Chen, I.-H., Chu, S.-W., Sun, C.-K., Lin, B.-L., and Cheng, P.C., 2002, Wavelength dependent damage in biological multi-photon confocal microscopy: A micro-spectroscopic comparison between femtosecond Ti:sapphire and Cr:forsterite laser sources, *Opt. Quantum. Electron*. 34:1251–1266.

Cheng, P.C., and Cheng, W.Y., 2001a, Artifacts in confocal and multi-photon microscopy, *Microsc. Microanal*. 7(Suppl. 2):1018–1019.

Cheng, P.C., and Kriete, A., 1995, Image contrast in confocal light microscopy, In: *Handbook of Biological Confocal Microscopy* (J.B. Pawley, ed.), Plenum Press, New York, pp. 267–281.

Cheng, P.C., and Walden, B., 2005, The cuticle of maize anther, *Microsc. Microanal.* Suppl. 2.

Cheng, P.C., Cheng, Y.K., and Huang, C.S., 1981, The structure of anther cuticle in rice *Oryza sativa* L., var. Taichung 65, *Natl. Sci. Council Monthly* 9:983–994.

Cheng, P.C., Greyson, R.I., and Walden, D.B., 1979a, Comparison of anther development in genic male-sterile (ms10) and in male-fertile corn (Zea mays) from light microscopy and scanning electron microscopy, *Can. J. Botany* 57:578–596.

Cheng, P.C., Greyson, R.I., and Walden, D.B., 1986, Anther cuticle of *Zea mays, Can. J. Botany* 64:2088–2079.

Cheng, P.C., Hibbs, A.R., Yu, H., Lin, P.C., and Cheng, W.Y., 2002, An estimate of the contribution of spherical aberration and self-shadowing in confocal and multi-photon fluorescent microscopy, *Microsc. Microanal.* 8(Suppl. 2):1068–1069.

Cheng, P.C., Lin, B.L., Kao, F.J., and Sun, C.K., 2000a, Multi-photon microscopy – Behavior of biological specimen under high intensity illumination, *SPIE Proc.* 4082:134–138.

Cheng, P.C., Lin, B.L., Kao, F.J., Sun, C.-K., and Johnson, I., 2000b, Multiphoton fluorescence spectroscopy of common nucleic acid probes, *Microsc. Microanal.* 6:820–821.

Cheng, P.C., Lin, B.L., Kao, F.J., Gu, M., Xu, M.-G., Gan, X., Huang, M.-K., and Wang, Y.-S., 2001, Multi-photon fluorescence microscopy – The response of plant cells to high intensity illumination, *Micron* 32:661–669.

Cheng, P.C., Newberry, S.P., Kim, H.G., Wittman, M.D., and Hwang, I.-S., 1990, X-ray contact microradiography and shadow projection microscopy, In: *Modern Microscopy* (P. Duke and A. Michette, eds.), Plenum Press, New York, pp. 87–117.

Cheng, P.C., Pareddy, D., Lin, T.H., Samarabandu, J.K., Acharya, R., Wang, and Liou, W.S., 1993, Confocal microscopy of botanical specimens, In: *Multi-Dimensional microscopy* (P.C. Cheng, T.H. Lin, W.L. Wu, and J.L. Wu, eds.), Springer-Verlag, New York, pp. 339–380.

Cheng, P.C., Pan, S.I., Shih, A., Kim, K.S., Liou, W.S., and Park, M.S., 1998, High efficient upconverters for multi-photon fluorescence microscopy, *J. Microsc.* 189:199–212.

Cheng, P.C., Sun, C.K., Cheng, P.C., and Walden, D.B., 2003*,* Nonlinear biophotonic crystal effect of opaline silica deposits in maize, *J. Scanning Microsc.* 235:80–81.

Cheng, P.C., Sun, C.K., Lin, B.L., and Chu, S.W., 2002, Bio-photonic crystal: SHG imaging, *Maize Genetics Cooperation Newsletter* 76:8–9.

Cheng, P.C., Walden, D.B., and Greyson, R.I., 1979b, Improved plant microtechnique for TEM, SEM and LM specimen preparation, *Natl. Sci. Council Monthly* 7:1000–1007.

Cheng, W.Y., Cheng, P.C., Gu, M., Gan, X.-S., and Walden, D.B., 2001b, The stem vasculature of *na1/na1* and *na2/na2* in *Zea mays, Scanning* 23:136–137.

Cheng, W.Y., Cheng, V.C., Cheng, P.C., and Walden, D.B., 2004, The orbicule in the anther of maize (*Zea mays* L.), *Scanning* 26:150–151.

Cheng, W.Y., Lee, T.C., and Cheng, P.C., 1999a, A loose-cell holder for confocal and multi-photon fluorescence microscopy, *Scanning* 21:61.

Cheng, W.Y., Lee, T.C., Walden, D.B., and Cheng, P.C., 1999b, Three-dimensional visualization of meiotic chromosomes in maize trisomy 6, *Microsc. Microanal.* 5(Suppl. 2):1262–1263.

Chu, S.W., Chen, I.S., Liu, T.M., Lin, B.L., Cheng, P.C., and Sun, C.K., 2001, Multi-modality nonlinear spectral microscopy based on a femtosecond Cr:Forsterite laser, *Opt. Lett.* 26:1909–1911.

Chu, S.W., Chen, I.S., Liu, T.-M., Sun, C.-K., Lin, B.L., Lee, S.P., Cheng, P.C., Liu, H.-L., Kuo, M-X., and Lin, D.-J., 2003, Nonlinear bio-photonic crystal effects revealed with multi-modal nonlinear microscopy, *J. Microsc.* 208:190–200.

Chu, S.W., Liu, T.M., Sun, C.K., Lin, C.Y., and Tsai, H.J., 2003, Real-time second-harmonic-generation microscopy based on a 2-GHz repetition rate Ti:sapphire laser, *Opt. Express* 11:933–938.

Clark, G., ed., 1981, *Staining Procedures*, Williams & Wilkins, Baltimore.

Crane, C.P., and Carman, J.G., 1987, Mechanisms of apomixis in *Elymus rectisetus* from eastern Australia and New Zealand, *Am. J. Botany* 72:477–496.

Cutler, D.P., Alvin, K.L., and Price, C.E., 1982, *The Plant Cuticle,* Academic Press, New York.

Dayanandan, P., Kaufman, P.B., and Franklin, C.I., 1983, Detection of silica in plants, *Am. J. Botany* 70:1079–1084.

Dawe, R.K., Agard, D.A., Sedat, J.W., and Cande, W.Z., 1992, Pachytene DAPI map, *Maize Genetics Cooperative Newsletter* 66:23–25.

Dickinson, H.G., and Bell, P.R., 1972, The role of the tapetum in the formation of sporopollenin-containing structures during microsporogenesis in *Pinus banksiana, Planta* (*Berl*.) 107:205–215.

Echlin, P., and Godwin, G., 1968, The ultras tructure and ontogeny of pollen in *Heleborus foetidus* L., I. The development of the tapetum and Ubisch body, *J. Cell Biol.* 3:161–174.

Federikson, M., 1992, The development of the female gametophyte of *Epipactis* (Orchidaceae) and its inference for reproductive ecology, *Am. J. Botany* 79:63–68.

Fricker, M.D., and White, N.S., 1992, Wavelength considerations in confocal microscopy of botanical specimens, *J. Microsc.* 166:29–42.

Greenspan, P., Mayer, E.P., and Fowler, S.D., 1985, Nile red: A selective fluorescent stain for intracellularlipid droplets, *J. Cell Biol.* 100:965–973.

Gu, M., Schilder, S., and Gan, X., 2000, Two-photon fluorescence image of microspheres embedded in turbid media, *J. Mod. Opt.* 47:959–965.

Herr, J.M. Jr., 1971, A new clearing squash technique for the study of ovule development in anger-sperms, *Am. J. Botany* 58:785–790.

Herr, J.M. Jr., 1974, A clearing-squash technique for the study of ovule and megagametophyte development in angiosperms, In: *Vascular Plant Systematics* (A.E. Radford, W.C. Dickison, J.R., Massey, and C.R. Bell, eds.), Harper & Row, New York.

Herr, J.M. Jr., 1985, The removal of phlobaphenes for improved clearing of sections and whole structures, *Am. J. Botany* 72:817.

Herr, J.M. Jr., 1992, Recent advances in clearing techniques for study of ovule and female gametophyte development, In: *Angersperm Pollen and Ovules* (E. Ottaviano, W.L. Mulcahy, M. SariGorIa, and G.B. Mulcahy, eds.), Springer-Verlag, New York, pp. 149–154.

Heslop-Harrison, J., and Dickinson, H.G., 1969, Time relationship of sporopollenin synthesis associated with tapetum and microspores in *Lilium, Planta* (*Berl*.) 84:199–214.

Hodson, M.J., and Sangster, A.G., 1988, Silica deposition in the inflorescence bracts of wheat *(Triticum aestivum)*, I. Scanning electron microscopy and light microscopy, *Can. J. Botany* 66:829–838.

Holloway, P.J., 1982, The chemical constitution of plant cutins, In: *The Plant Cuticle* (D. P. Cutler, K.L. Alvin, and C.E. Price, eds.), Academic Press, London, pp. 45–85.

Holloway, P.J., and Baker, E.A., 1968, Isolation of plant cuticles with zinc chloride-hydrochloric acid solution, *Plant Physiol.* 43:1878–1879.

Homer, H.T., and Wagner, B.L., 1992, Association of four different calcium crystals in the anther connective tissue and hypodermal stomium of *Capsicum annuum* (Sola-naceae) during microsporogenesis, *Am. J. Botany* 79:531–541.

Hose, E., Clarkson, D.T., Steudle, E., Schreiber, L., and Hartung, W., 2001, The exodermis: A variable apoplastic barrier, *J. Exp. Botany* 52:2245–2264.

Hughes, J., and McCully, M.E., 1975, The use of an optical brightener in the study of plant structure. *Stain Technol.* 50:319–329.

Huang, H.-C., and Chen, C.C., 1988, Genome multiplication in cultured protoplasts of two *Nicotiana* species, *J. Heredity* 79:28–32.

Johansen, D.A., 1940, *Plant Microtechnique*, McGraw-Hill, New York.

Jauregui-Zuniga, D., Eyes-Grajeda, J.P., Sepulveda-Sanchez, J.D., Whitaker, J.R., and Moreno, A., 2003, Crystallochemical characterization of calcium oxalate crystals, *J. Plant Physiol*. 160:239–245.

Jones, L.H.P., and Handreck, K.A., 1967, Silica in soils, plants and animals, *Adv. Agron.* 19:107–149.

Juniper, B.E., and Jeffree, C.E., 1983, *Plant Surfaces*, Edward Arnold, London.

Kao, F.J., Lin, B.L., and Cheng, P.C., 2000a, Multi-photon fluorescence microspectroscopy *SPIE Proc.* 3919:2–8.

Kao, F.J., Wang, Y.S., Huang, W.W., Huang, S.L., and Cheng, P.C., 2000b, Second-harmonic generation microscopy of tooth, *SPIE Proc.* 4082:119–124.

Kao, F.J., Cheng, P.C., Sun, C.-K., Lin, B.L., Wang, Y.-M., Chen, J.-C., Wang, Y.-S., Liu, T.-M., and Huang, M.-K., 2000c, Multi-photon spectroscopy of plant tissues, *Scanning* 22:193–195.

Kennedy, S.M., and Lytle, F.E., 1986, P-Bis(o-methylstytyl)benzene as a power squared tensor for two-photon absorption measurement between 537 and 694 nm, *Anal. Chem*. 58:2643–2647.

Kim, H.G., Cheng, P.C., Wittman, M.D., and Kong, H.J., 1990, Pulsed X-ray contact microscopy and its applications to structural and developmental botany, In: *X-Ray Microscopy in Biology and Medicine* (K. Shinohara, ed.), Springer-Verlag, New York, pp. 233–242.

Kirk, P.Kl. Jr., 1970, Neutral red as a lipid fluorochrome, *Stain Technol.* 45: 1–4.

Konig, K.H., Liang, H., Berns, M.W., and Tromberg, B.J., 1995, Cell damage by near-IR microbeams, *Nature* 377:20–21.

Konig, K., Liang, H., Berns, M.W., and Tromberg, B.J., 1996a, Cell damage in near-infrared multimode optical traps as a result of multi-photon absorption, *Opt. Lett*. 21:1090–1092.

Konig, K., So, P.T.C., Mantulin, W.W., and Gratton, E., 1997, Cellular response to near-infrared femtosecond laser in two-photon microscopes, *Opt. Lett.* 22:135–136.

Konig, K., So, P.T.C., Mantulin, W.W., Tromberg, B.J., and Gratton, E., 1996b, Two-photon excitation lifetime imaging of autofluorescence in cell during UVA and NIR photostress, *J. Microsc.* 183:197–204.

Lide, D.R., ed., 1991, *Handbook of Chemistry and Physics*, CRC Press, Boca Raton, Florida, pp. 7–29.

Lin, B.L., Cheng, P.C., and Sun, C.-K., 2001, Optical density of leaf, *Maize Genetics Cooperation Newsletter* 75:61–62.

Lin, B.L., Kao, F.J., Cheng, P.C., and Cheng, W., 2000a, The response of maize protoplasts to high intensity illumination in multi-photon fluorescence microscopy, *Microsc. Microanal.* 6(Suppl. 2):806–807.

Lin, B.L., Kao, F.J., Cheng, P.C., Chen, R.W., Huang, M.K., Wang, Y.S., Chen, J.C., Wang, Y.S., and Cheng, W.Y., 2000b, The response of maize protoplast in multi-photon fluorescent microscopy, *Scanning* 22:196–197.

Lin, B.L., Kao, F.J., Sun, K.-C., and Cheng, P.C., 2000c, Absorption and multi-photon excited fluorescence properties of maize tissue, *Maize Genetics Cooperation Newsletter* 74:63–64.

Müller, U., and Sengbusch, P.v., 1983, Interactions of species in an *Anabaena flosaque* association from the Plußsee (East-Holstein, Federal Republic of Germany). Studies by use of fluorescent markers, *Oecologia* 58: 215.

Oehring, H., Riemann, I., Fischer, P., Halbhuber, K.-J., and König, K., 2000, Ultrastructure and reproduction behaviour of single CHO-K1 cells exposed to near infrared femtosecond laser pulses, *Scanning* 22:263.

Pace, G.M., Reed, J.N., Ho, L.C., and Fahey, J.W., 1987, Anther culture of maize and the visualization of embryogenic microspores by fluorescent microscopy, *Theor. Appl. Genet*. 73:863–869.

Palser, B.F., Rouse, J.L., and Williams, E.G., 1989, Coordinated timetables for mega-gametophyte development and pollen tube growth in *Rhododendron nuttalli* from anthesis to early post-fertilization, *Am. J. Botany* 76:1167–1202.

Pareddy, D.R., Greyson, R.I., and Walden, D.B., 1989, Production of normal, germinable and viable pollen from *in vitro* cultured maize tassels, *Theor. Appl. Genet.* 77:521–526.

Pawley, J.B., 2002, Limitations on optical sectioning in live-cell confocal microscopy, *Scanning* 24:241.

Schilders, S.P., and Gu, M., 2000, Limiting factors on image quality in imaging through turbid media under single-photon and two-photon excitation, *Microsc. Microanal*. 6:156–160.

Stelly, D.M., Peloquin, S.J., Palmer, R.G., and Crane, C.F., 1984, Mayor's hemalum-methyl salicylate: a stain-clearing technique for observations within whole ovules. *Stain Technol.* 59:155–161.

Sun, C.K, Chu, S.W., Liu, T.M., and Cheng, P.C., 2001, High intensity scanning microscopy with a femtosecond Cr:Forsterite laser, *Scanning* 22:95–96.

Taylor, J.H., and Peterson, C.A., 2001, Maturation of the tracheary elements in the roots of *Pinus banksiana* and *Eucalyptus grandis*, *Can. J. Botany* 79:844–849.

Tulloch, A.P., 1981, Composition of epicuticular waxes from 28 genera of Gramineas: Differences between subfamilies, *Can. J. Botany* 59:1213–1221.

Vergne, P., Delvallee, I., and Dumas, C., 1987, Rapid assessment of microspore and pollen development stages in wheat and maize using DAPI and membrane permeabilization, *Stain Technol.* 62:299–304.

Young, B.A., Sherwood, R.T., and Bashaw, E.C., 1979, Cleared-pistil and thick-sectioning techniques for detecting aposporous apomixis in grasses, *Can. J. Botany* 57:1668–1672.

Wells, O.C., and Cheng, P.C., 1992, High-resolution backscattered electron images in the scanning electron microscope, *Proc. EMSA* 50:1608–1609.

White, N.S., Errington, R.J., Wood, J.L. and Fricker, M.D., 1996, Quantitative measurements in multidimensional, botanical fluorescence images, *J. Microsc.* 181(2):99–116.

22

Signal-to-Noise Ratio in Confocal Microscopes

Colin J.R. Sheppard, Xiaosong Gan, Min Gu, and Maitreyee Roy

INTRODUCTION

Strictly, to obtain true confocal imaging the detector pinhole must be infinitesimally small, which would of course result in a vanishingly weak image signal. On the other hand, a very large pinhole degrades the confocal imaging effect. So in practice it is necessary to adopt some optimum diameter for the pinhole, which will depend on the design of the microscope, how it is operated, and the type of specimen. The resultant imaging performance then also depends on these various factors. In this way we can compare the performance of different designs of confocal microscope, and also compare them with widefield (WF) microscopes that have electronic image capture coupled with digital three-dimensional (3D) image restoration. In addition, we can understand how best to use the microscope in order to achieve optimum imaging performance.

In many biological applications of confocal microscopy the signal level is weak. In fluorescence microscopy, the fluorophore **bleaches** after exposure to light, thus limiting the total exposure and hence the number of photons that can be detected. This results in shot noise in the final image, degrading the image and limiting the number of gray levels that can be perceived. The overall image quality can be determined by considering the signal-to-noise ratio (S/N) of the image. If the only source of noise were the shot noise on the detected signal, then S/N would increase as the pinhole diameter was increased. However, there will always be some unwanted background that also contributes to the noise. In general, the background originating from non-specific staining or autofluorescence, from either the specimen or optical elements, increases as the pinhole diameter is increased so that for very large pinhole diameters S/N actually decreases. Thus, there is an optimum pinhole size that is large enough to allow the signal to be detected with adequate S/N, but small enough to reject the noise from the background.

For a given imaging frame time, it is tempting to increase the signal level by increasing the incident laser power. However, too high a laser power results in **saturation** of the fluorophore. As well as limiting the signal that can be detected, this also has the effect of giving a nonlinear relationship between fluorophore concentration and detected signal so that quantitative interpretation of the image is difficult. These effects are particularly noticeable in the fast-scanning systems that are often needed for live-cell studies. The result is that if the signal is limited by saturation rather than bleaching, the relative performance of the various systems with regard to S/N is very different, as will be discussed later.

Similar conclusions hold in backscattered light (BSL) imaging rather than fluorescence imaging (Cogswell and Sheppard, 1990; Sheppard and Cogswell, 1990; Dunn *et al*., 1996). BSL imaging is growing in importance for clinical diagnostic and biopsy applications (Lucid VivaScope). The confocal principle is also of importance in optical coherence tomography (OCT) (Huang *et al*., 1991). The BSL signal from biological samples, produced by variations in specimen refractive index, stains, or immuno-gold labeling can all be very weak (10^{-4}–10^{-6} relative to the incident power). In addition, the allowable incident laser power is limited by specimen damage. The main difference (advantage) in BSL imaging is that there is no bleaching of the signal, so that if the specimen is unchanging in time there is in principle no limit to the signal that can be obtained over a long period of time, and hence S/N can be increased to any desired level.

SOURCES OF NOISE

Shot Noise and Quantum Efficiency

As described in the previous section, the most important source of noise is shot noise. The importance of shot noise is that it is the fundamental limit of S/N. [We mention here that an active area of present fundamental research is in reducing noise below the classic limit as a result of quantum-mechanical effects (Slusher *et al*., 1985).] Light consists of particles called photons, each of which has an energy hv, where h ($= 6.626 \times 10^{-34} Js$) is Planck's constant and v is the frequency. As the frequency is related to the wavelength by

$$c = v\lambda \tag{1}$$

c being the velocity of light ($= 2.998 \times 10^{8}\,\mathrm{ms}^{-1}$), a beam of light of power p incident for a time t contains n_p photons, where

$$n_p = \frac{Pt\lambda}{hc} \tag{2}$$

Shot noise results from the statistical variation in the number of detected photons, which obeys a Poisson distribution. The Poisson distribution is a skewed distribution for small numbers of photons, but tends to the symmetrical normal distribution for large numbers. The Poisson distribution has the property that its mean is equal to its variance, and as the noise is given by the square root of the variance the shot noise on a signal of $n_p$is $\sqrt{n_p}$, so that

Colin J.R. Sheppard • National University of Singapore, Singapore
Xiaosong Gan and Min Gu • Swinburne University, Australia
Maitreyee Roy • University of Sydney, Australia

 Handbook of Biological Confocal Microscopy, Third Edition, edited by James B. Pawley, Springer Science+Business Media, LLC, New York, 2006.

$$S/N = \frac{n_p}{\sqrt{n_p}} = \sqrt{n_p}. \quad (3)$$

Suppose now the light is detected (Sheppard *et al.*, 1992) by a photodetector of quantum efficiency Q_P, which is simply the fraction of photons which are detected by the detector. If the detector also contributes a sensor noise of n_n electrons then *S/N* is given by

$$S/N = \frac{Q_E n_p}{\sqrt{Q_E n_p + n_n^2}}. \quad (4)$$

The overall behavior of the detector for a given number of incident photons depends on both the quantum efficiency and the sensor noise: for a large number of photons, S/N is proportional to $\sqrt{Q_E}$, whereas, for a very small number of photons, it is proportional to the ratio Q_E/n_n.

We can consider the information content, b, in the image, in bits, given by Shannon (1949)

$$b = \log_2(1 + S/N). \quad (5)$$

In terms of the number of discernible gray levels g, we can write

$$b = \log_2(g), \quad (6)$$

so that the number of gray levels is simply

$$g = 1 + S/N = 1 + \frac{Q_E n_p}{\sqrt{Q_E n_p + n_n^2}}. \quad (7)$$

Thus, if *S/N* is zero, we can only perceive a single gray level, that is, the image is featureless. For *S/N* = 1, we see two gray levels, corresponding to a binary (black and white) image. For large values of *S/N*, the number of gray levels increases linearly with *S/N*. Note that this derivation of the number of gray levels is based on the information content in the image, which is an objective property. Although it does require that the specimen be capable of producing the measured signal levels (i.e., having a certain voxel staining ratio), it does not rely on the subjective perception of an observer, as do some investigations of the number of discernible gray levels. The disadvantage of the latter approach is that the number of perceived gray levels is altered by changing the properties of the display (e.g., by altering the lookup table), so that the results are no longer a property of the image data alone.

In Figure 22.1, the gray-level behavior of a photomultiplier tube (PMT, S20 photocathode, $Q_E = 13\%$ and $n_n \approx 0$), predicted by Eq. 7, is compared with that of a cooled frame-transfer charge-coupled device (CCD) detector ($Q_E = 70\%$, $n_n = 9$ RMS electrons/pixel). The sensor noise of the PMT has been neglected because of its very high gain.[1] The behavior of an ideal detector ($Q_E = 100\%$, $n_n = 0$) is also shown for comparison. For all detectors the number of gray levels increases from unity with the number of photons incident on each pixel. The behavior of the PMT is limited by the poor quantum efficiency. It is clear that for greater than about 25 photons incident per pixel the CCD exhibits superior performance, whereas for a smaller number of photons the photomultiplier tube is better. In the region where the photomultiplier is superior, the number of gray levels is less than $1 + \sqrt{13\% \times 25}$, or about three, so that the image is of poor quality.

[1] Actually, the PMT has considerable multiplicative noise but, in this discussion, this noise has been accounted for by assuming a fairly low QE.

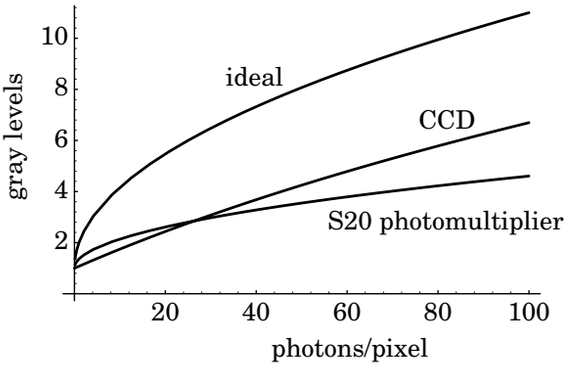


FIGURE 22.1. The number of gray levels discernible in an image formed using various detectors under different illumination conditions.

Background Noise

Next, we can incorporate noise emanating from the background (stray light) in the measured signal. A number of different models for stray light have been considered. Here we consider two different models. In the first, which we shall term N1, the stray light is assumed constant in intensity over the detector plane. In fluorescence this would be an appropriate model for noise that originates from autofluorescence in the cements and coatings of the optical elements of the microscope system, particularly the objective lens, as in single molecule fluorescence studies. It is also a good model for BSL imaging into a scattering medium. This background $n_p B_{N1}$ can be assumed to be distributed uniformly over the detector pinhole, so that the intensity that passes through the pinhole is proportional to its area and can be written

$$B_{N1} = a v_d^2/4, \quad (8)$$

where a is a constant, discussed later, and v_d is the radius of the detector in normalized coordinates

$$v_d = (2\pi r_d/\lambda)\sin\alpha_d, \quad (9)$$

where r_d is the true radius of the pinhole and $\sin\alpha_d$ is the numerical aperture (NA) of the system in detector space (= $n\sin\alpha/M$, where $n\sin\alpha$ is the NA of the objective in object space, and M is the lateral magnification from object plane to detector). A value of $v_d = 3.83$ corresponds to the first zero of the Airy disk, that is, to 1 Airy unit. For simplicity, the λ of the fluorescent radiation is assumed equal to that of the incident radiation throughout this chapter, that is, there is no Stokes shift. As the increase in λ for common dyes, such as fluoroscein isothiocyanate fluorescein, rhodamine, Texas Red, or allophycocyanine, is usually in the range 3% to 8%, its effect of the behavior of the system is unlikely to be very significant.

Model N1 has been found useful (Sheppard, 1991) for describing the behavior of confocal BSL microscopy, in which case the background can come from specular reflection from the optical elements and light scattered from within the microscope body. Of course, in fluorescence microscopy, both these contributions are substantially removed by the barrier filters. Wells and colleagues (1990) showed in their experiments on fluorescence microscopy that N1 was not a good model. This may be an indication that autofluorescence was the primary cause of the background. Webb and colleagues (1990, pp. 73–108) have considered a further model in which the signal was considered to originate from within the resolution element while detected light not from this source is considered as background. This model has the disadvantages that the

boundary between signal and background is arbitrary and that the size of the resolution element varies with the parameters of the microscope. It also assumes an infinite field together with a finite object thickness (infinite field with an infinite object thickness gives infinite background for a WF microscope). We choose to assume a finite field and an infinite object thickness in order to stress the fact that reduction of the field size is an important factor in improving noise performance. Our second model (N2) assumes that the background originates uniformly from everywhere within an infinitely large fluorescent object. This model would be appropriate for the case of observing fluorescence labeling in the presence of background object autofluorescence. In this case, the intensity that passes through the pinhole $n_p B_{N2}(v)$ is a function of the pinhole size, as will be described in the next section. Both these background contributions are detected by the photodetector and the statistical variations of this value give rise to noise in the image. Thus, the overall S/N is given by

$$S/N = \frac{Q_E n_p F(v_d)}{\sqrt{Q_E n_p [F(v_d) + a v_d^2/4 + B_{N2}(v_d)] + n_n^2}}, \qquad (10)$$

where $F(v_d)$ is the fraction of signal light incident on the pinhole that passes through to the detector.

SIGNAL LEVEL IN CONFOCAL MICROSCOPES

Consider a single point object situated at the focal point of the microscope. For a confocal system with a point source, the intensity in the detector plane is an Airy disk

$$I = \frac{1}{4\pi}\left(\frac{2J_1(v)}{v}\right)^2, \qquad (11)$$

where $J_n(v)$ is a Bessel function of order n and the factor $1/4\pi$ normalizes the total intensity in the detector plane to unity. The normalized signal for a circular detector radius v_d is (Cox and Sheppard, 1986)

$$F_1(v_d) = \frac{1}{4\pi}\int_0^{v_d}\left(\frac{2J_1(v)}{v}\right)^2 2\pi v\,dv \qquad (12)$$
$$= 1 - J_0^2(v_d) - J_1^2(v_d).$$

For small pinhole radii, we have

$$F_1(v_d) \approx v_d^2/4. \qquad (13)$$

For a slit detector, width $2v_d$, placed in front of the detector (i.e., an incoherent slit detector) and a point source, the normalized signal we denote $F_2(v_d)$. Then $F_2(v_d)$ is

$$F_2(v_d) = \frac{2}{\pi}\int_0^{v_d}\frac{\mathbf{H}_1(2v)}{v^2}dv \qquad (14)$$

where $\mathbf{H}_1$ is a Struve function. For long slits, the signal from a point object is independent of the length of the slit. For small v_d the normalized signal is (Sheppard and Mao, 1988)

$$F_2(v_d) \approx 16v_d/3\pi^2, \qquad (15)$$

so that the signal is proportional to the width of the slit.

For a square detector, side $2v_d$, as is the case for a single CCD element, the signal can be evaluated by integrating over the Airy disk. As the signal for a small detector is proportional to the area of the detector, for small detectors we have

$$F_3(v_d) \approx v_d^2/\pi. \qquad (16)$$

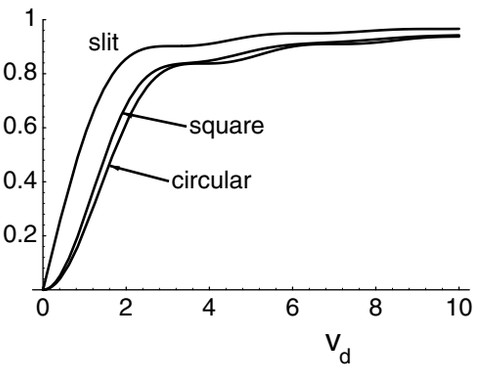


FIGURE 22.2. The signal level from a point object as a function of detector aperture shape and size.

These functions are illustrated in Figure 22.2. It is seen that in each case the normalized signal rises from zero until it approaches unity for large pinhole diameters. For a circular pinhole the normalized signal reaches about 85% at $v_d = 4$, and thereafter there is little increase in signal level. In practice, if the pinhole diameter is increased further the signal collected from a thick object increases as the optical sectioning effect is weaker. However, this increased signal is not useful as it represents light collected from out-of-focus regions of the specimen. As is apparent from Figure 22.2, slit apertures can give increased signal strength, but this is associated with poorer optical sectioning performance compared with that from a circular aperture. Figure 22.3 shows the effect of pinhole or slit width on various imaging properties of a confocal fluorescence microscope. The transverse resolution is measured as the reciprocal of the full-width at half-maximum (FWHM) of the image of a point object, normalized by that for a point detector. There is a small improvement in transverse resolution for small

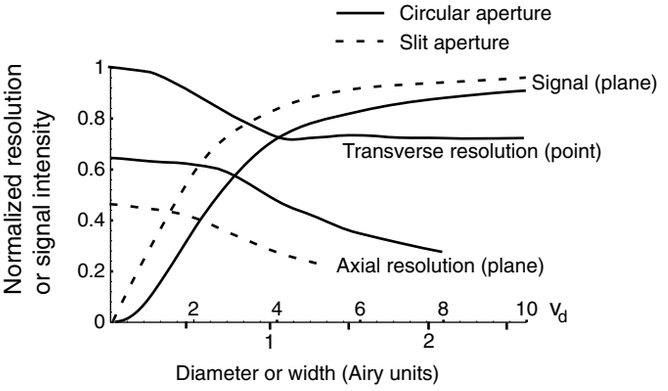


FIGURE 22.3. The effect of pinhole or slit size on various imaging properties of a confocal fluorescence microscope. The transverse resolution for a pinhole aperture is defined as the reciprocal of the full-width at half-maximum (FWHM) of the image of a point object, normalized by that for a point detector. The axial resolution, for pinhole or slit apertures, is defined as the reciprocal of the FWHM of the image of a thin fluorescent planar object, normalized by the FWHM of a planar object in a confocal BSL microscope with point detector. The signal level from a planar fluorescent object is also shown.

pinhole sizes, but the pinhole radius, v_d has to be very small ($v_d < 2$) for this to be appreciable. The behavior is identical for fluorescence or BSL systems. The axial resolution is measured as the reciprocal of the FWHM of the image of a thin fluorescent planar object, normalized by the FWHM of a planar object in a confocal BSL microscope with point detector. The axial resolution steadily degrades as the pinhole diameter is increased, until there is no z-resolution for a large detector, equivalent to a WF microscope. Even for a point detector, the axial resolution is poorer than for a confocal BSL microscope. The signal level from a planar fluorescent object is also shown. The behavior is qualitatively similar to that for a point object, as shown in Figure 22.2. As the pinhole radius is increased, the signal level increases, but the resolution also decreases, so that there is an optimum behavior for some intermediate pinhole radius. Turning now to the slit aperture, although the signal level is greater than for a circular pinhole of the same width, the z-resolution is worse. Overall, there is little to be gained from using a slit aperture from the point of view of image quality.

Experimental results (Sheppard *et al.*, 1991) have confirmed that the theoretically predicted behavior is observed in practice for pinhole radii up to a value v_d of about 100. For very large pinholes, optical behavior will eventually be limited by other apertures present in the optical system.

SIGNAL-TO-NOISE RATIO FOR CONFOCAL MICROSCOPES

Q_E, N1, and Stain Level

Signal-to-noise ratios for a confocal microscope can be calculated from Eq. 10. In the following we shall assume for simplicity that the sensor noise n_n is zero so that

$$S/N = \sqrt{Q_E n_p}\,\frac{F(v_d)}{\sqrt{F(v_d) + a v_d^2/4 + B_{N2}(v_d)}}. \qquad \textbf{(17)}$$

In the rest of this chapter S/N is normalized by the constant factor $\sqrt{Q_E n_p}$.

Let us consider first the case of noise model N1 so that B_{N2} is taken as zero, and after normalization (Sheppard *et al.*, 1991)

$$S/N = \frac{F(v_d)}{\sqrt{F(v_d) + a v_d^2/\sqrt{4}}}. \qquad \textbf{(18)}$$

For a circular pinhole and small values of v_d, using Eq. 13 we have

$$S/N = \frac{v_d}{2\sqrt{1+a}}, \qquad \textbf{(19)}$$

so that a represents the magnitude of the background from noise model N1 relative to the signal for a small circular pinhole. Thus, a is smaller for stronger staining. The behavior of S/N with pinhole radius for different strengths of background is shown in Figure 22.4. For a particular value of a, S/N increases as the pinhole radius increases, reaches a maximum value for an optimum pinhole size, and then decreases as $1/v_d$ as the pinhole is made larger. For a wide range of values of a, the optimum pinhole radius corresponds to values of v_d between about 2 and 3. Simply, a larger pinhole lets in more background but does not produce a significantly stronger signal. Interestingly, as the strength of the signal relative to the background decreases (i.e., a increases), the optimum pinhole radius decreases so that, contrary to expected behavior, the pinhole should actually be closed down for very weak signals. For a value of a of unity, for example, the optimum pinhole radius has decreased to $v_d = 2.3$. For S/N to be better than

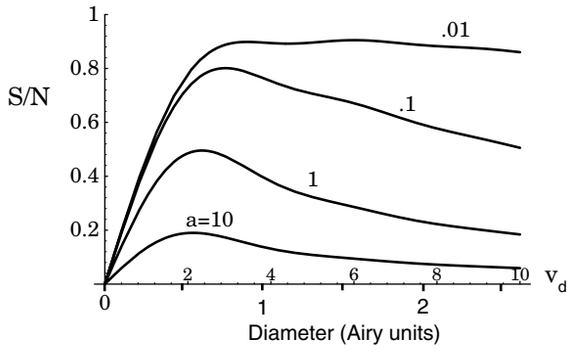


FIGURE 22.4. Variation in S/N with pinhole size for different strengths of background (noise model N1: background from autofluorescence from optical components).

50% of that achieved at the optimum pinhole radius, v_d must be kept in the range between 0.8 and 5.6. Using a larger pinhole radius further decreases S/N. Thus, using a pinhole radius that is too large, as well as not giving an increase in useful signal, actually results in a decrease in S/N from weakly fluorescent objects.

On the other hand, it should be noted that for small values of a the maximum in S/N is broad, so that choice of an appropriate pinhole diameter is not critical from the point of view of S/N.

Thus, if the background is weak, the pinhole can be opened up to increase the number of detected photons, and hence S/N. Although one would expect this to reduce the z-resolution, it is very common for the z-resolution to be limited more stringently by low signal level (and the resulting inability to measure pixel brightness accurately) than by purely optical considerations. In this case, the extra signal may enable one to make a better estimate of the true structure of the dye in the specimen in spite of the large PSF.

For instance, if we are imaging a small, bright, spherical object say 20 voxels in diameter, surrounded by a low intensity background (~1% of the peak), the signal obtained from a voxel in the center of this object will be substantially greater and the uncertainty of the measurement will be less if the pinhole is opened from 1 to perhaps 2 or 3 Airy units. Then the difference between this signal and that from a nearby background voxel located above the object will be greater but the absolute value of this background measurement will also be more because the reduced z-resolution means that the sensed volume is larger and contains more dye. Although one can retrieve some of this lost resolution if one deconvolves the data recorded, using a PSF measured at the same pinhole size, this will be decreasingly effective as the pinhole gets bigger. Specifically, the S/N of the imaging system will begin to decrease as the size of the detection PSF exceeds the size of the object.

From this discussion, one can see that the optimal pinhole size becomes highly dependent on the details of the 3D stain distribution in the specimen (both signal and background), and that deconvolving the recorded data will always help. However, even though one can calculate the S/N for some limiting conditions (as is done below) in the end, one must often determine the optimal pinhole size for a given type of specimen experimentally.

For large values of a, corresponding to weak signals, S/N tends to a behavior independent of the value of a. In this case, again renormalizing S/N, we obtain for a circular pinhole, a slit detector, and a square detector

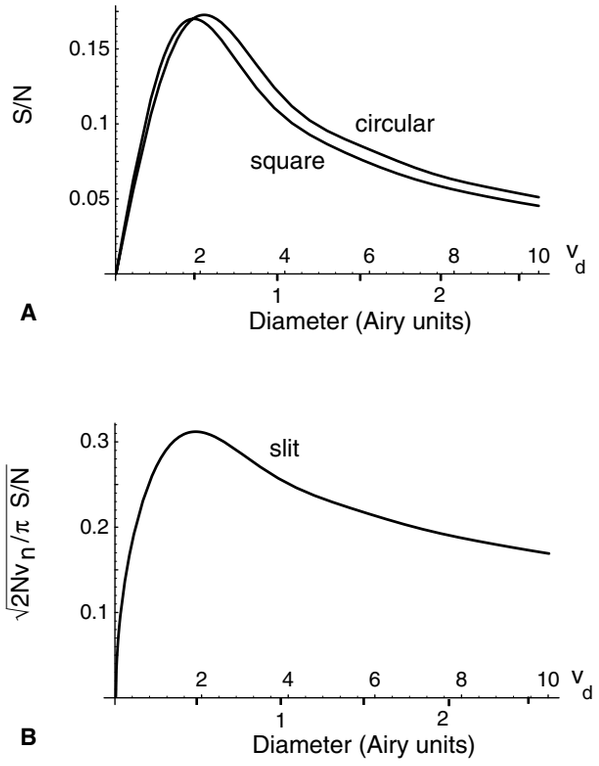


FIGURE 22.5. Variation in S/N with aperture shape and size for weak signal (noise model N1): (A) circular or square detector; (B) slit detector with length $2v_s = 2nv_d$.

$$S/N = \frac{F_1(v_d)}{\sqrt{\pi}v_d}, \frac{F_2(v_d)}{2\sqrt{v_d v_s}}, \frac{F_3(v_d)}{2v_d}, \tag{20}$$

respectively, where $2v_s$ is the length of the slit. These are shown in Figure 22.5. The peak value for *S/N* is slightly higher for a circular, rather than a square, aperture. For the circular pinhole the peak *S/N* occurs at about 0.52 Airy units ($v_d \approx 2$). For the slit aperture the optimum *S/N* occurs at 0.48 Airy units ($v_d = 1.84$). The S/N is decreased relative to the confocal case with a circular detector by a factor of about $\sqrt{n}/2$, where $n = v_s/v_d$.

N2 and Detectability

Turning now to the second noise model, N2, the background B_{N2} resulting from a featureless volume can also be calculated for these various systems (Gu and Sheppard, 1991).

The intensity in the detector region produced by a volume object is given by the convolution of the intensity point spread function of the illumination lens with that of the collection lens. Assuming these are identical, this is conveniently calculated as the 3D Fourier transform of the square of the optical transfer function (OTF). Then the normalized intensity in the plane of the detector aperture is

$$I(v) = \frac{1}{12}\int_0^2 (2-l)^2(4+l)J_0(vl)dl. \tag{21}$$

This is illustrated in Figure 22.6. The intensity decays monotonically with distance from the axis, for large distances decaying as $1/v^3$. The background detected can then be calculated by integrating over the detector aperture. For a circular pinhole radius v_d we obtain

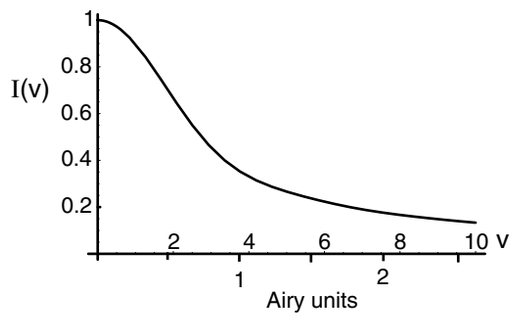


FIGURE 22.6. The variation in the intensity of the fluorescence arriving at the plane of the detector when a thick featureless volume is illuminated by an axial focused laser beam. The horizontal axis is calibrated in Airy units, with zero being the optical axis.

$$B_{N2}(v_d) = \frac{1}{24}\int_0^2 (2-l)^2(4+l)\frac{J_1(v_d l)}{l}dl. \tag{22}$$

Figure 22.7 shows the variation in background with pinhole radius for a circular pinhole. For small pinhole sizes the background is $v_d^2/4$ (as in Eq. 13), that is, proportional to the area of the pinhole, but for large pinholes it is proportional to v_d. This is because for large v_d the thickness of the optical section is proportional to v_d. This is an idealized model: the situation is more complex when the background is not featureless but contains structures in out-of-focus planes.

We have for the normalized S/N for weak signals

$$S/N = \frac{F(v_d)}{\sqrt{B_{N2}(v_d)}}. \tag{23}$$

We have termed this property the detectability (Gan and Sheppard, 1993) of the system: it describes the ability with which a weakly fluorescent point object can be detected in a background of a uniformly fluorescent background. Actually, other forms of detectability have also been defined (Gan and Sheppard, 1993). These describe the ease with which a point object can be detected within a background uniform over a plane [the two-dimensional (2D) detectability], and the ease with which a planar object can be detected within a background volume (the axial detectability). Here we shall only discuss the 3D detectability, appropriate for detecting a point in a background volume.

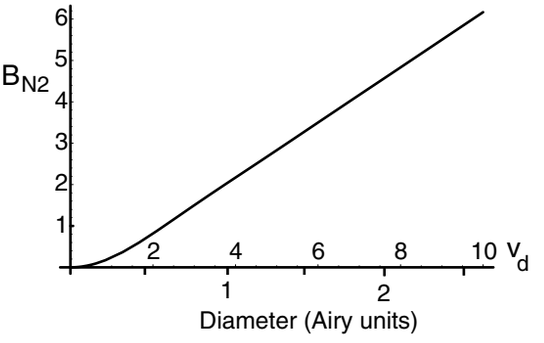


FIGURE 22.7. The background from a thick featureless volume as a function of pinhole radius.

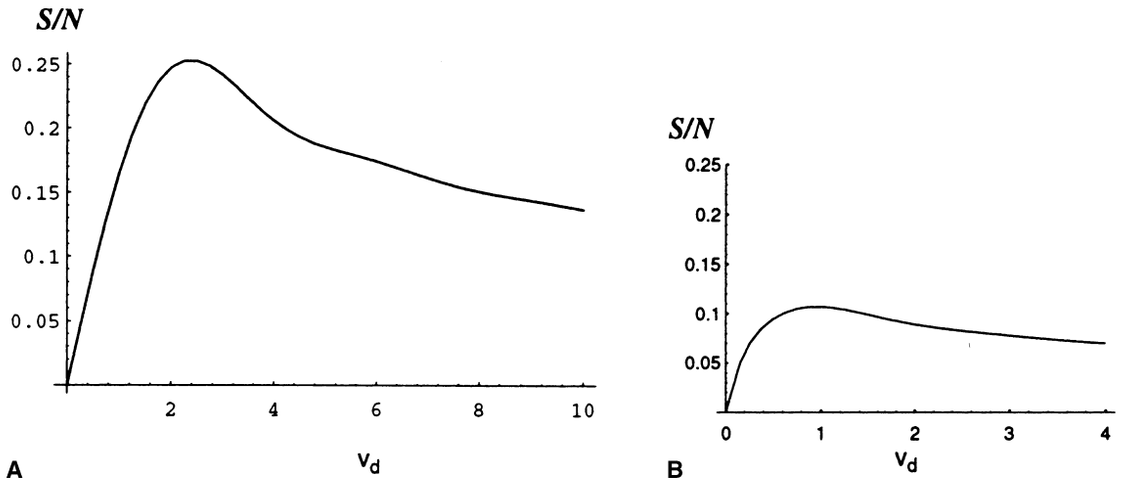


FIGURE 22.8. Variation in S/N with aperture size for (A) circular and (B) slit apertures, for weak signal (noise model N2: background from autofluorescence from specimen bulk).

The S/N for N2 for a confocal microscope with a circular or slit detector is shown in Figure 22.8. The behavior is broadly the same as for the case of N1 in that S/N reaches a maximum value for an optimum aperture dimension, which is $v_d \approx 2.4$ for the circular pinhole, and $v_d \approx 1$ for the slit aperture. For the case of noise model N2, for large circular pinholes S/N decays as $1/\sqrt{v_d}$.

Multi-Photon Fluorescence Microscopy

The S/N can be calculated in a similar way for multi-photon fluorescence microscopy (Gauderon and Sheppard, 1999). The S/N for model N2 for a multi-photon microscope with a circular detector is shown in Figure 22.9. In this case, for large pinholes the S/N does not tend to zero as in the single-photon fluorescence microscope, so the S/N can be normalized to unity for large pinhole diameters (i.e., non-descanned detection). It is found that the S/N exhibits an optimum value for a pinhole radius of 0.63 Airy units ($v_d = 2.42$) for two-photon fluorescence, and 0.64 Airy units ($v_d = 2.44$) for three-photon fluorescence. The value of S/N is then a factor of 1.6 or 1.9 better than for a system with a large pinhole, for two-photon and three-photon fluorescence, respectively. These results are quantitatively in agreement with experimental observations (Wang and Fraser, 1997).

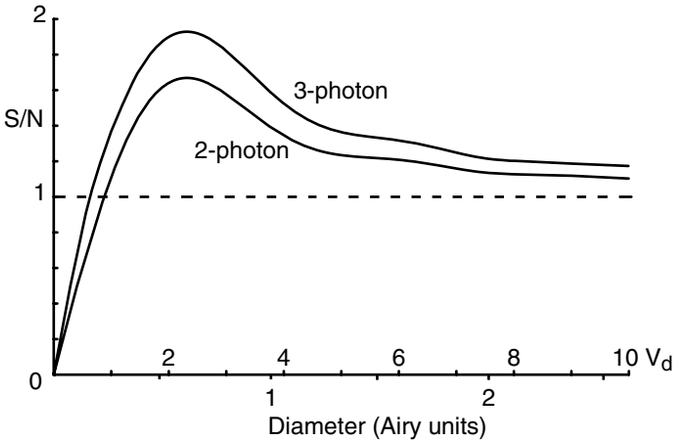


FIGURE 22.9. Signal-to-noise ratio for two-photon and three-photon fluorescence microscopes (noise model N2: background from autofluorescence from specimen bulk).

DESIGNS OF CONFOCAL MICROSCOPES

The basic form of the confocal microscope uses illumination from a point source, coupled with a photodetector spatially limited by a pinhole. Scanning can be achieved by either moving the specimen stage relative to a stationary light spot, or by scanning the beam. The most common method of beam scanning uses galvomirrors, which, as is also the case for stage scanning, is limited to comparatively slow scan rates, up to a few frames per second. Resonant scanners can achieve faster scan rates, and acousto-optic deflection is even faster but results have other problems for fluorescence imaging, notably the fact that the fluorescent signal cannot be descanned in a simple manner because of the Stokes shift. A solution to this problem is to use a slit-shaped detector aperture and to descan only in one direction (Draaijer and Houpt, 1988).

An alternative approach for increasing scan speed is to scan simultaneously with an array of points. The earliest example of this method is the tandem-scanning microscope, in which a rotating disk with an array of holes is used (Petráň *et al.*, 1968). It is also possible to use an array of holes, a slit, or an array of slits. In the line-illumination microscope, such as the Zeiss 5 Live, a line of the specimen is illuminated (Koester, 1980; Sheppard and Mao, 1988; Benedetti *et al.*, 1992; Brakenhoff and Visscher, 1992) and the image of the whole line can be recorded using a linear CCD array.

Figure 22.10 shows schematic diagrams for three different systems using line-illumination and/or linear CCD detectors. In Figure 22.10(A) a scanning spot is deflected over the specimen and partially descanned onto a CCD detector. In Figure 22.10(B) the scanning spot is again partially descanned, but on to a single point detector with a slit aperture. In Figure 22.10(C), the object is illuminated by a line of light, and the image along the line recorded by a CCD detector. By including a coupled display *y*-scan, the 2D image can be observed directly or recorded using a 2D CCD detector. These various systems have been compared by Awamura and Ode (1992), in which they claim that arrangement (A) is superior

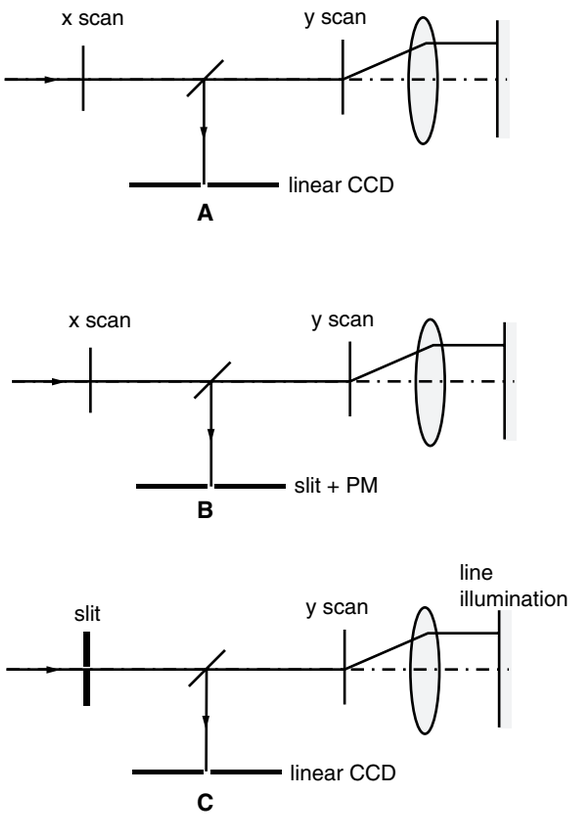


FIGURE 22.10. Schematic diagrams of various optical arrangements using line-illumination and/or linear CCD detectors.

in resolution to either (B) or (C). Arrangement (A) also has the major advantage for metrological work that geometrical distortion is absent. In (C), speckle noise can be a problem in BSL imaging unless the spatial coherence of the illumination is destroyed. However, (C) has the major advantage for fluorescence imaging that a complete line of information can be recorded simultaneously with the result that data can be acquired rapidly and with less danger of fluorescence saturation.

SAMPLING

For WF fluorescence imaging, the Nyquist sampling spacing is $v_N = \pi/2$. As the first zero of the Airy disk occurs at $v = 3.83$, corresponding to 1 Airy unit (AU), the Nyquist sampling spacing is $v_N = \pi/(2 \times 3.83) = 0.41\,\text{AU} = 1\,\text{AU}/2.44$. If the image is sampled at the Nyquist spacing, or more closely, in the absence of noise, the exact image profile can be recovered. When sampling further apart than the Nyquist spacing, aliasing occurs. Note that for fluorescence imaging with sampling at the Nyquist spacing, the image can be recovered, but for bright-field imaging sampling must be closer than, rather than equal to, the Nyquist spacing.

For a detector array with elements each of length $2v_d$, to achieve Nyquist sampling we have $v_d = \pi/4$ (in optical units). With line illumination and a linear detector array, imaging along the array has the same spatial frequency cut-off as for WF imaging so that sampling at the Nyquist rate is appropriate. If there are n samples in a one-dimensional (1D) image, the field of view is

$$2v_s = n\pi/2. \qquad \textbf{(24)}$$

If the number stored as the intensity value for a given pixel is proportional to the total number of photons striking a specific area of the CCD, then the resolution of the image data is degraded somewhat compared with that produced by digitizing a continuous, bandwidth-limited signal at equally spaced time points (i.e., integral vs. point sampling). The resultant point spread function is the one without sampling, convolved with the detector sensitivity distribution for a single picture element. In the absence of noise, the more frequent the sampling, the closer the behavior tends to the ideal response.

COMPARATIVE PERFORMANCE OF FLUORESCENCE MICROSCOPES

Bleaching-Limited Performance

The comparative performance with regard to S/N of various designs of the fluorescence microscope can be considered by calculating the appropriate signal and background levels. In this section we consider the case when S/N is limited by bleaching of the fluorophore. Thus, a finite number of fluorescent photons can be emitted before the fluorophore bleaches. (This assumes that photobleaching rate is independent of illumination intensity.) We term this regime R1.

We have considered a wide range of different configurations including confocal microscopes with circular, square, or slit detector apertures, and point source or finite-sized source; line illumination with coherent or incoherent lines having vanishingly small width, or finite width; disk-scanning systems with arrays of apertures of various geometries; and WF microscopy with a finite source and a detector array.

Figure 22.11 shows five different configurations of microscope that we designate as follows:

C1. Confocal microscope with a point source and a finite-sized detector radius v_d.
C2. Line illumination with a coherent line source length $2v_s$ and a linear array of square detector elements, each with dimensions $2v_d$.
C3. Confocal microscope with a point source and a slit detector length $2v_s$ and breadth $2v_d$.
C4. Disk-scanning microscope with a square array of incoherent sources, separation v_h, radius v_d and a similar array of detectors.
C5. WF microscope with a square source, sides $2v_s$, and a 2D array of square incoherent detectors dimensions $2v_d$.

In order to model these different configurations of microscope we need to know the relative values of signal in the various systems.

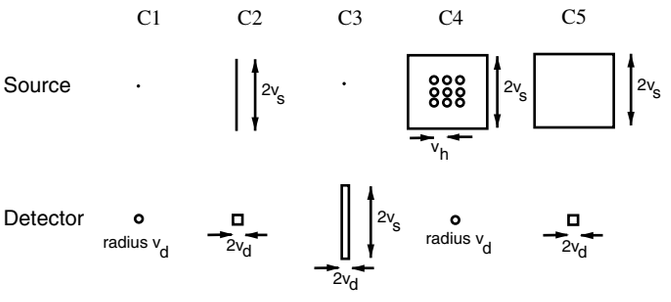


FIGURE 22.11. Five different configurations of microscope.

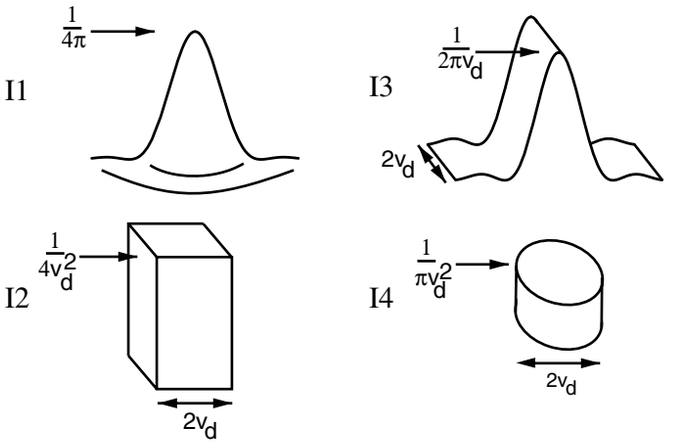


FIGURE 22.12. Four different illumination models.

We consider the illumination models shown in Figure 22.12. Great care must be taken in obtaining the correct normalization for the various different microscope configurations. The appropriate assumption is that the total power incident on the specimen in forming a complete 2D image is kept constant:

I1. A point source. Normalizing the total power in the focal plane to unity, the image of a point source in the object plane is an Airy disk

$$I = \frac{1}{4\pi}\left(\frac{2J_1(v)}{v}\right)^2 \tag{25}$$

so that the intensity at the focal point is $1/4\pi$.

I2. The pixel is illuminated uniformly with intensity $1/4v_d^2$. This normalization is taken so that the total exposure in recording a complete section is the same as for I1, as a conventional microscope images the whole section simultaneously.

I3. The image of a long line source gives in the focal plane.

$$I = \frac{1}{2\pi v_d}\left(\frac{\sin v}{v}\right)^2. \tag{26}$$

The line illumination microscope images a whole line at a time.

I4. The image of a circular source radius v_d, for v_d large enough that diffraction effects can be neglected. This will be approximately true for v_d larger than about 3.

For the alternative illumination schemes, the signal is scaled by the appropriate intensity at the focal point. In particular, for I2 and a square detector (C5), for I3 and a square detector (C2), and for I4 and a circular detector (C4)

$$S = (\pi/v_d^2)F_3(v_d),(2/v_d)F_3(v_d),(4/v_d^2)F_1(v_d), \tag{27}$$

respectively.

The comparative behavior has been investigated for background originating either from the optical components (noise model N1), or from the 3D bulk of the specimen (noise model N2). We take as the worst case a weak signal compared with the background ($a > 1$), so that the noise from the signal fluctuations is negligible compared with that of the background.

When using noise model N1, the background is proportional to the area of the detector aperture. For the confocal system, the relative background is thus πv_d^2: $4v_dv_s$: $4v_d^2$ for circular, slit, and square detectors, respectively. The total energy that illuminates the sample in forming a complete image in a confocal microscope of a section is proportional to n^2.

For the line-scanning microscope, a whole line of the specimen is illuminated at a time. Thus, the background is increased by a factor n. Thus for I3 and a square detector (C2), instead of Eq. 8,

$$B_{N1} = \pi n v_d^2. \tag{28}$$

Similarly, for a conventional microscope a whole field is illuminated at one time and the background is increased by a factor n^2. For I2 and a square detector (C5)

$$B = 4n^2 v_d^2. \tag{29}$$

For the disk-scanning microscope, the distance between the samples is taken as v_h. If n_s is the number of samples needed to form a line image $n_s = v_h/2v_d$. We also introduce the number of points in a line illuminated simultaneously $n_h = 2v_s/v_h$ so that $n = n_s n_h$. Again the total energy incident in forming an image of a section is n^2. The background for the disk-scanning microscope is

$$B = \pi n_h^2 v_d^2. \tag{30}$$

For line illumination, C2, we have

$$S/N = \frac{F_3(v_d)}{v_d^2\sqrt{n}} \tag{31}$$

In Figure 22.13, the dashed line is a plot of this value against v_d for $N = 512$. Unlike the confocal microscope with a slit detector (C3) as shown in Figure 22.5, the S/N decreases monotonically for increasing detector element size. This is because the length of the detector array is proportional to v_d if the detector elements are square. For $v_d = \pi/4$, satisfying the Nyquist criterion the S/N is 0.012.

For the disk-scanning microscope, C4, the S/N for large v_d, using I4, is

$$S/N = \frac{4F_1(v_d)}{\sqrt{\pi}v_d^2 n_h} \tag{32}$$

On the other hand, for illumination by an array of points, which is a good approximation for small values of v_d,

$$S/N = \frac{F_1(v_d)}{\sqrt{\pi}v_d n_h} \tag{33}$$

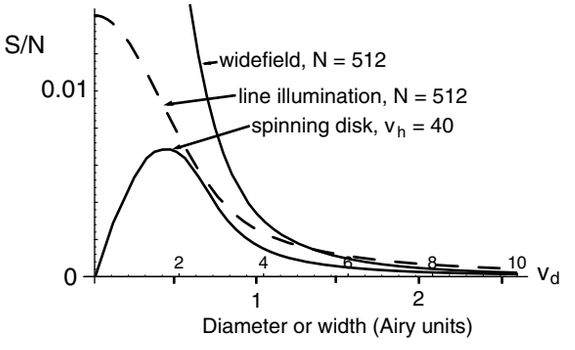


FIGURE 22.13. Signal-to-noise ratio for line illumination C2, noise model N1 (*dotted*), the disk scanning microscope C4, noise model N1 (lower), and the conventional microscope C5, noise model N1 (upper).

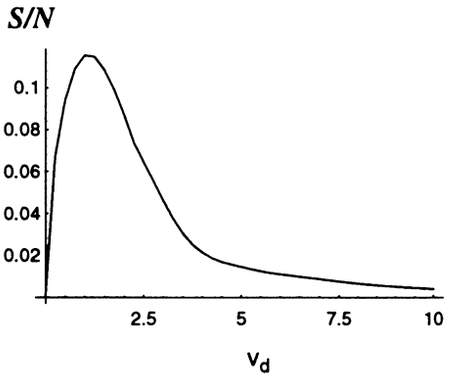


FIGURE 22.14. The variation with detector element size in S/N for incoherent line illumination (noise model N2, width of line equal to detector element, 512 samples).

Let us assume that v_h, the hole spacing, is 40, corresponding to $N_h = 20.1$ for $N = 512$ and sampling at the Nyquist rate. Then the variation in S/N is shown as the lower line in Figure 22.13. The optimum S/N of ~0.006 occurs at about 0.52 Airy units ($v_d \sim 2$). The S/N decays quickly with increasing hole diameter as the source hole illuminates a larger region of the object as well as the detector hole collecting more background.

For the WF microscope, C5,

$$S/N = \frac{\pi F_3(v_d)}{2v_d^3 n} \tag{34}$$

which is plotted as the upper line in Figure 22.13. Again, the S/N decays quickly with v_d as the area of illumination, that is, the field of view, increases as the area of a detector element is made larger. At the Nyquist sampling rate the signal to noise ratio is ~0.001.

The thickness of the object is assumed infinite, so that for noise model N2, finite dimensions for the length of line illumination, for the finite source in WF microscopy, or for the array in the disk-scanning microscope are assumed. These are assumed to be just large enough for Nyquist sampling of an $n \times n$ image (Eq. 23).

As an example of S/N for noise model N2 for a line-illumination system, with an incoherent line source of width $2v_d$ and of length $2nv_d$ and a detector element that is square with sides $2v_d$, is shown in Figure 22.14 for $n = 512$. The S/N reaches an optimum value at about 0.29 Airy units ($v_d \approx 1.1$). For a very narrow line illumination the optimum width of detector element is slightly larger and S/N falls off more slowly with v_d. The value for the optimum S/N is much the same in either case.

Table 22.1 summarizes results for S/N according to noise models N1 and N2 for the various forms of microscope. Roughly, compared with a confocal microscope with optimum pinhole diameter, line-illumination or slit-detection systems are a factor of 2 worse for noise model N2, while conventional microscopes are about an order of magnitude worse.

Saturation-Limited Performance

If the behavior of the various systems is limited by saturation, rather than bleaching, their relative merits are very different. In this case, which we call regime R2, the limit to the number of photons detected per pixel is set not by the total energy incident per pixel, but by the illumination intensity. For a given illumination power striking the specimen, the line-illumination, disk-scanning, or WF systems have the advantage that numerous pixels are imaged simultaneously. For line illumination n pixels are imaged in parallel, so that for a given illumination power the background in forming a complete image is reduced by a factor n, so that S/N is increased by a factor $\sqrt{n}$ compared with a point source. Similarly, for a WF microscope, n^2 pixels are imaged in parallel, and S/N is multiplied by n. The relative S/N, assuming all are operated at the onset of saturation, are shown in Table 22.1. Under these conditions, the line-illumination microscope's behavior is superior to the confocal microscope with a circular pinhole.

Effects of Scanning Speed

If our specimen is unchanging with time, we can in principle take as much time as we like in forming an image. Thus, we can always scan slowly enough that saturation effects are insignificant. The S/N behavior is then limited by bleaching (regime R1), and the confocal microscope with a point source and a circular pinhole of optimum diameter is clearly the best performer. If we choose to speed up the scan so that a complete 2D image is recorded in some particular finite time, then the confocal microscope with a point source will reach saturation of the fluorophore before the other systems because the dwell time on each pixel must be shorter. We can define a characteristic time T_c as the time per pixel needed to generate a 2D image while just avoiding saturation. The characteristic time T_c is a property of the particular fluorophore that depends critically on its environment. It is thus the energy per pixel that can be incident on the pixel before photobleaching of the fluorophore (saturation to the $1/e$ point) divided by the maximum power that can be incident on the pixel without significant saturation (the power needed to give an output fluorescent intensity that is half its saturated value). The frame scan time for onset of saturation is reduced by a factor $\sqrt{N}$ for a line-scanning system and by N for a WF microscope. In the regime R2, where behavior is limited by saturation, S/N is proportional to the square root of the imaging time. The S/N behavior is thus as shown in Figure 22.15.

Let us consider a particular example. Suppose the fluorophore is such that an incident power of 1 mW is just enough to cause saturation, and that bleaching occurs after 10 frames when scanning at 3 s/frame in a confocal microscope with point source. Then the best S/N is achieved if all 10 frames are averaged to collect the maximum possible number of photons. The dwell time/pixel/frame is about 10 µs, so that the total dwell time (per pixel) for 10 frames is 100 µs. In this case, the characteristic time T_c for the fluorophore in the confocal microscope is also 100 µs. For collection of 10 frames at 3 s/frame (dwell time 100 µs), the point-source confocal microscope is clearly the best performer.

TABLE 22.1. Signal-to-Noise Ratio

	Noise model	
	N1	N2
Regime R1		
Confocal	1.0	1.0
Line illumination	0.07	0.5
Slit detector	0.07	0.4
WF	0.006	0.08
Regime R2		
Confocal	1.0	1.0
Line illumination	1.6	11.0
Slit detector	0.07	0.4
WF	3.0	40.0

WF, widefield.

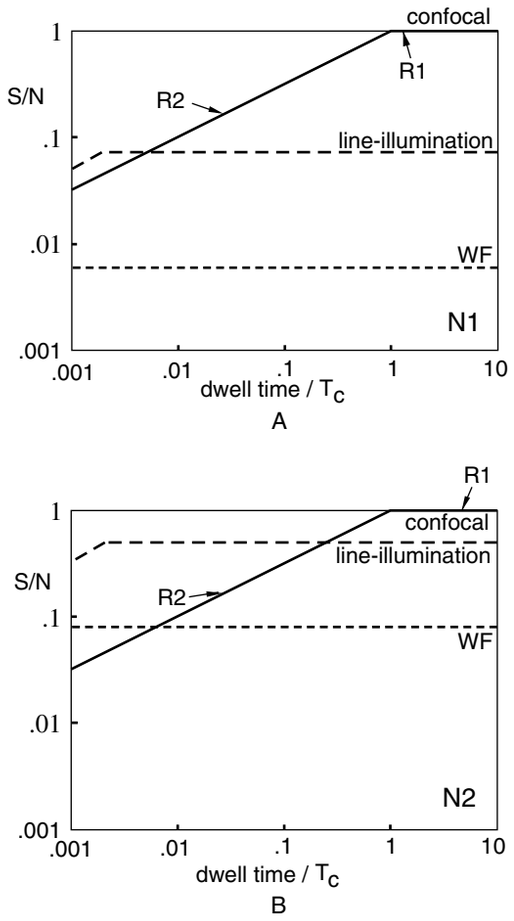


FIGURE 22.15. Effect of pixel dwell time on S/N: (A) Noise model N1; (B) noise model N2.

As discussed in a later section, these 10 frames can be 10 different axial sections, and the noise still tends to average out when forming a projection as the total number of photons per display pixel is increased. When forming a single image at 3 s/frame, the line-illumination system achieves slightly better S/N according to noise model N2 [Fig. 22.10(B)], whereas the WF microscope still exhibits inferior S/N. For ten frames at television rates, the line-illumination performs best with respect to S/N, while for a single television-rate frame both the line-illumination and the WF microscope have better S/N than for the point source confocal microscope. (Note that it is not possible to read out the cooled-CCD detector we have assumed for the WF case at video rates without degrading its performance.) However, for noise model N1, where the background comes from autofluorescence of the optical components, the confocal microscope maintains its superior S/N performance even for high scan speeds.

3D IMAGING

Once a 3D data set, representing the intensity variations in the image, is stored in the computer imaging system, in many cases it is necessary to generate a projection through the 3D object rather than a single section. There are a number of ways of doing this, but the most usual are the mean-projection algorithm (Wilson and Hamilton, 1982; Sheppard *et al.*, 1983), and the peak-projection algorithm (Cox and Sheppard, 1983). These two methods result in substantially similar images, with the mean-projection method giving lower apparent noise levels, but lower levels of contrast as well, which makes it particularly sensitive to the correct setting of the zero signal level. Generation of two projections in different directions gives a stereo-pair. The process of generating a projection improves its noise performance compared with a single section (Roy and Sheppard, 1993). This is the case for both mean and peak projections, although the mean-projection method is more effective at reducing noise. The mean-projection method increases S/N as the square root of the number of sections processed that have significant signal: only four such sections are required to increase S/N by a factor of 2.[2]

The S/N behavior of the peak-projection method depends on the statistical properties of the signal and the display lookup table. For large numbers of photons per pixel, the noise level is reduced by a factor of 2 by processing 24 sections, while for just two photons per pixel, thousands of sections are required to double the S/N.

In general, in order to produce a projection with a given S/N, it is not necessary for each section to have that S/N. The mean-projection algorithm reduces noise as a direct result of the averaging inherent in the method, no averaging of the individual sections being necessary. There will still then be noise on the depth information in a stereo-pair presentation, but this is a second-order effect and is expected to be much less important perceptually.

SUMMARY

- Care is necessary in selecting the various system parameters, such as pinhole diameter, type of detector, pixel size, illumination intensity, and scan rate, in order to optimize the performance of the microscope system.
- Optimum operation will also depend on the shape of the stain in the object, how the image is to be processed, and what information is eventually required from the image.
- Usually a relatively small setting for pinhole diameter results in improved S/N, and a circular confocal aperture of about 0.63 times the diameter of the first dark ring of the Airy disk is a good benchmark for optimum performance.
- Even if a single frame looks noisy, the noise may be reduced by the generation of projections, especially using the mean-projection algorithm and an even greater improvement can be gained by deconvolving the dataset in 3D.
- The S/N performance of a point-source confocal microscope is most noticeably better than other forms in the presence of background from autofluorescence from the cements and coatings of the optical elements.
- Point-source confocal microscopes are preferable for generation of high-quality 3D data sets when there is no limit on the time available for a single frame.
- Line-scanning systems, or even WF microscopes with cooled-CCD detector arrays, can give superior S/N performance for fast scanning, particularly in the presence of background consisting of autofluorescence from around the stained object.
- In both these cases, the illumination field should be reduced so that it is not much larger than the observed region to increase S/N.

[2] As the process of calculating the mean value at each pixel reduces the brightness, the resulting image may be hard to see unless the contrast is expanded using a simple lookup table. Doing so does not decrease the S/N.

REFERENCES

Awamura, D., and Ode, T., 1992, *Optical Properties of Type1 — Type 2 Microscopes*, New Trends in Scanning Optical Microscopy, Okinawa, Japan.

Benedetti, D.A., Evangelista, V., et al., 1992, Confocal line microscopy, *J. Microsc.* 165:119–129.

Brakenhoff, G.J., and Visscher, K., 1992, Confocal imaging with bilateral scanning and array detectors, *J. Microsc*. 165:139–146.

Cogswell, C.J., and Sheppard, C.J.R., 1990, Confocal brightfield imaging techniques using an on-axis scanning optical microscope, In: *Confocal Microscopy* (T. Wilson, ed.), Academic Press, London, pp. 213–243.

Cox, I.J., and Sheppard, C.J.R., 1983, Digital image processing of confocal images, *Image Vis. Comput.* 1:52–56.

Draaijer, A., and Houpt, P.M., 1988, A standard video-rate confocal laser-scanning reflection and fluorescence microscope, *Scanning* 10:139–145.

Dunn, A.K., Smithpeter, C., et al., 1996, Sources of contrast in confocal reflectance imaging, *Appl. Opt*. 35:3441–3446.

Gan, X.S., and Sheppard, C.J.R., 1993, Detectability: A new criterion for evaluation of the confocal microscope, *Scanning* 15:187–192.

Gu, M., and Sheppard, C.J.R., 1991, Effects of finite-sized detector on the OTF of confocal fluorescent microscopy, *Optik* 89:65–69.

Huang, D., Swanson, E.A., et al., 1991, Optical coherence tomography, *Science* 254:1178–1181.

Koester, C.J., 1980, A scanning mirror microscope with optical sectioning characteristics: Applications in ophthalmology, *Appl. Opt*. 19:1749–1757.

Petráň, M., Hadravsky, M., et al., 1968, Tandem scanning reflected light microscope, *J. Opt. Soc. Am.* 58:661–664.

Roy, M., and Sheppard, C.J.R., 1993, Effect of image processing on the noise properties of confocal imaging, *Micron* 24:623–635.

Shannon, C.E., 1949, Communications in the presence of noise, *Proc. Inst. Radio Eng.* 37:10–21.

Sheppard, C.J.R., 1991, Stray light and noise in confocal microscopy, *Micron Microsc. Acta* 22:239–243.

Sheppard, C.J.R., and Cogswell, C.J., 1990, Three-dimensional imaging in confocal microscopy, In: *Confocal Microscopy* (T. Wilson, ed.), Academic Press, London, pp. 143–169.

Sheppard, C.J.R., Cogswell, C.J., et al., 1991, Signal strength and noise in confocal microscopy: Factors influencing selection of an optimum detector aperture, *Scanning* 13:233–240.

Sheppard, C.J.R., Gu, M., et al., 1992, Signal to noise ratio in confocal microscope systems, *J. Microsc.* 168:209–218.

Sheppard, C.J.R., Hamilton, D.K., et al., 1983, Optical microscopy with extended depth of field, *Proc. Roy. Soc. Lond. A* 387:171–186.

Sheppard, C.J.R., and Mao, X., 1988, Confocal microscopes with slit apertures, *J. Mod. Opt*. 35:1169–1185.

Slusher, R.E., Hollberg, L.W., et al., 1985, Observation of squeezed states generated by four-wave mixing in an optical cavity, *Phys. Rev. Lett.* 55:2409–2412.

Webb, W.W., Wells, K.S., et al., 1990, *Optical Microscopy for Biology*, Wiley-Liss, New York.

Wells, K.S., Sandison, D.R., et al., 1990, Quantitative confocal fluorescence with laser scanning confocal microscopy, In: *Handbook of Biological Confocal Microscopy* (J. B. Pawley, ed.), Plenum Press, New York, pp. 23–35.

Wilson, T., and Hamilton, D.K., 1982, Dynamic focussing in the confocal microscope, *J. Microsc*. 128:139–148.

23

Comparison of Widefield/Deconvolution and Confocal Microscopy for Three-Dimensional Imaging

Peter J. Shaw

INTRODUCTION

The biggest limitation inherent in optical microscopy is its lateral spatial resolution, which is determined by the wavelength of the light used and the numerical aperture (NA) of the objective lens. Another important limitation is the resolution in the direction of the optical axis, conventionally called z, which is related to the depth of field. The presence of a finite aperture gives rise to undesirable and rather complicated characteristics in the image. In essence, the depth of field depends on the size of structure or spatial frequency being imaged. Fine image detail, which is generally of most interest, has a small depth of field, and only features within a small distance of the focal plane contribute to the image. On the other hand, large structures — low spatial frequency components — have a relatively large depth of field, and contribute to the detected image seen at distant focal planes. This is very noticeable in dark-field imaging modes, such as epi-fluorescence, and means that the fine image detail may be swamped by low resolution "out-of-focus" light and thus either lost, or visualized with very much reduced contrast.

The principal advantage of confocal microscopy for biological imaging is that the optical arrangement has the effect of eliminating much of the out-of-focus light from detection, therefore improving the fidelity of focal sectioning (and hence the three-dimensional imaging properties), and increasing the contrast of the fine image detail. But the rejection of the out-of-focus light necessarily means that a proportion of the light emitted by the specimen is intentionally excluded from measurement. All illumination of the specimen has deleterious effects — bleaching of the fluorochrome or phototoxicity to living cells. These specimen-dependent factors are the ultimate limitation to the quality of the image, and inevitably confocal imaging does not detect much of the emitted light.

An alternative way of removing the out-of-focus light involves recording images at a series of focal planes using a conventional microscope, often called widefield (WF) to distinguish it from confocal imaging, and then using a detailed knowledge of the imaging process to correct for it by computer image processing. This procedure is called deconvolution, and its application to biological problems actually preceded the widespread introduction of biological confocal microscopes (Castleman, 1979; Agard and Sedat, 1983; Agard *et al.*, 1989). In contrast to confocal imaging, up to 30% of the total fluorescent light emitted by the specimen can be recorded (i.e., all the light that can be collected by a single, high-NA objective). This chapter examines the question: Is it better to record all the light emitted and process the WF images to redistribute the out-of-focus light to produce a more accurate three-dimensional (3D) image, or to exclude the out-of-focus light from measurement in the first place by confocal optics and then deconvolve the confocal data?

THE POINT SPREAD FUNCTION: IMAGING AS A CONVOLUTION

In order to derive a soundly based description of the degradation introduced by an optical microscope, especially if any attempt is to be made to reverse this degradation, it is necessary to be able to describe the relation between the specimen and its optical image in mathematical terms. We shall give here a very condensed explanation — the interested reader is referred elsewhere for more rigorous mathematical derivations (Agard *et al.*, 1989; Shaw, 1993; Young, 1989; and Chapters 20, 21, 22, 24, and 25, *this volume*). Within some quite general limitations, the object (specimen) and image are related by an operation known as convolution. In a convolution, each point of the object is replaced by a blurred image of the point having a relative brightness proportional to that of the object point. The final image is the sum of all these blurred point images. The way each individual point is blurred is described by the point spread function (PSF), which is simply the image of a single point. This is illustrated diagrammatically in Figure 23.1.

The conditions that must be met for an imaging process to be described as a convolution are that it should be linear and shift invariant (Young, 1989). Imagine cutting the specimen into two parts and imaging each part separately with the microscope. If adding these two subimages together produces the same result as imaging the whole specimen, and does this irrespective of how the specimen is cut up, then the imaging is said to be linear. If the imaging is indeed linear, then the specimen can be imagined cut up into smaller and smaller pieces, until the size of each piece is well below the resolution limit, and can be considered to be simply a point. The image is then the sum of the images of each of the points, each multiplied by a function corresponding to the amount of light coming from that point. The multiplication and summing is represented mathematically by an operation called convolution. Shift invariance simply means that the imaging characteristics and thus the PSF are the same over the whole field of view, and knowing one PSF is enough to characterize the imaging properties of the microscope (Agard *et al.*, 1989; Shaw and Rawlins, 1991a).

Although imaging modes such as phase contrast and differential interference contrast (DIC) are not linear, because their contrast depends on differences of refractive index within the object,

Peter J. Shaw • John Innes Centre, Colney, Norwich NR4 7UH, United Kingdom

Handbook of Biological Confocal Microscopy, Third Edition, edited by James B. Pawley, Springer Science+Business Media, LLC, New York, 2006.

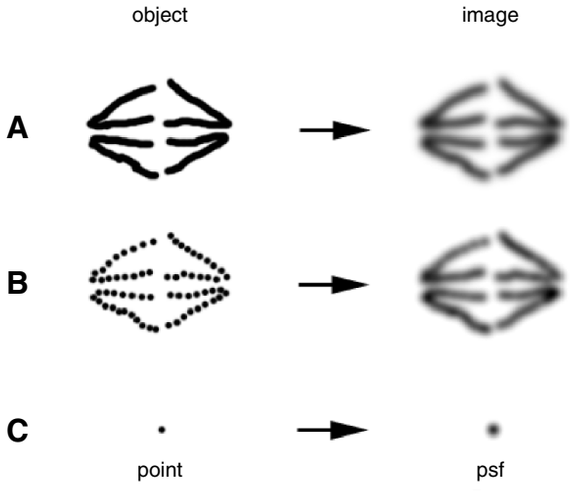


FIGURE 23.1. Diagram showing how a single point is imaged as the PSF by a microscope, and thus that the image of an extended object is the convolution of the object with the PSF.

both WF and confocal epi-fluorescence microscopy are linear and shift invariant processes to a good approximation (Young, 1989; Wilson, 1993).

Restating the foregoing discussion mathematically, we will denote the object as a function of position $f(\mathbf{r})$ and the resulting image as $g(\mathbf{r})$, and represent the imaging operation by I:

$$\mathbf{I}[f(\mathbf{r})] = g(\mathbf{r}) \tag{1}$$

Mathematically, linearity means that a linear combination of objects produces the same linear combination of images:

$$\begin{aligned}\mathbf{I}[k_1 f_1(\mathbf{r}) + k_2 f_2(\mathbf{r}) + \ldots] &= k_1 \mathbf{I}[f_1(\mathbf{r})] + k_2 \mathbf{I}[f_2(\mathbf{r})] + \ldots \\ &= k_1 g_1(\mathbf{r}) + k_2 g_2(\mathbf{r}) + \ldots\end{aligned} \tag{2}$$

where k_1 and k_2 are constants, that is, the imaging operation is applied individually to each component in the sum.

If linearity and shift invariance hold, the image of an object may be described as the sum of the images of its parts. We may approximate the object as closely as we like as the sum of points of suitably weighted intensity. We denote a set of regularly spaced sampling points by the "comb" function $\delta(\mathbf{r} - \mathbf{s}_i)$ — a set of spikes at the points $\mathbf{s}_i$, spaced at $\Delta\mathbf{s}$. Then the object can be represented by the sum:

$$f'(\mathbf{r}) = \sum_{-\infty}^{+\infty} f(\mathbf{s}_i)\delta(\mathbf{r} - \mathbf{s}_i)\Delta\mathbf{s} \tag{3}$$

or, in the limit:

$$f'(\mathbf{r}) = \int_{-\infty}^{+\infty} f(\mathbf{s})\delta(\mathbf{r} - \mathbf{s})d\mathbf{s} \tag{4}$$

The image of each point $\delta(\mathbf{r})$ is simply the point spread function — we shall call it $o(\mathbf{r})$: That is,

$$\mathrm{I}[\delta(\mathbf{r})] = o(\mathbf{r})$$

$$\text{then,} \quad \mathbf{I}[\delta(\mathbf{r} - \mathbf{s})] = o(\mathbf{r} - \mathbf{s}) \tag{5}$$

and

$$\begin{aligned}\mathbf{I}[f'(\mathbf{r})] &= I\left[\int_{-\infty}^{+\infty} f(\mathbf{s})\delta(\mathbf{r} - \mathbf{s})d\mathbf{s}\right] \\ &= \int_{-\infty}^{+\infty} f(\mathbf{s})[\delta(\mathbf{r} - \mathbf{s})]d\mathbf{s} \\ &= \int_{-\infty}^{+\infty} f(\mathbf{s})o(\mathbf{r} - \mathbf{s})d\mathbf{s} \\ &= g(\mathbf{r})\end{aligned} \tag{6}$$

because I can be taken inside the integral from Eq. 2, and substituting from Eq. 5. Thus, the image is the convolution ($\otimes$) of the object with the point spread function. More concisely:

$$g(\mathbf{r}) = f(\mathbf{r}) \otimes o(\mathbf{r}) \tag{7}$$

Convolutions are often more easily handled as Fourier transforms (FT). The convolution theorem shows that the FT of a convolution of two functions is simply the product of the individual transforms of the functions. Thus, the FT of the image is given by the multiplication of the FT of the object by the FT of the PSF (usually called the optical transfer function or OTF),

$$G(\mathbf{S}) = F(\mathbf{S})O(\mathbf{S}) \tag{8}$$

where $F(\mathbf{S})$, $G(\mathbf{S})$, and $O(\mathbf{S})$ are the Fourier transforms of $f(\mathbf{r})$, $g(\mathbf{r})$, and $o(\mathbf{r})$, respectively. Thus the FT of the image is the transform of the object multiplied point-by-point by a weighting function. An image processing operation of this type is often termed a filter.

The difference in the images produced by WF and confocal imaging can be regarded simply as a difference in their respective PSFs. In the WF case, both theory (Stokseth, 1969; Castleman, 1979) and measurement using subresolution fluorescent beads (Hiraoka *et al.*, 1988), show that the PSF has the form of concentric cones diverging from either side of the focal plane; they intersect the focal plane to give the Airy pattern of concentric rings. Figures 23.2(A) and 23.3(A) show an example of the widefield PSF for a high numerical aperture objective (Leitz plan apochromat, 63×, NA 1.4), determined from optical sections of subresolution fluorescent beads. Figure 23.2(A) shows some of the original WF optical sections through a single fluorescent bead. The Airy disk can be seen expanding into a series of concentric rings. In Figure 23.3(A), the raw data have been cylindrically averaged and smoothed by fitting 3D spline functions to it. A central section through the 3D PSF parallel to the optical axis is shown. The rings constitute a diverging series of cones, which can be seen in section as subsidiary maxima diverging away from the central focal plane. In fact, the out-of-focus rings can often be detected extending many micrometers on either side of the central maximum if the data are sufficiently accurate (see Hiraoka *et al.*, 1988, 1990).

In the ideal case, the total integrated intensity at each out-of-focus plane is the same as that at the focal plane, but in practice the intensity level of a typical point object such as a small fluorescent bead drops below the noise level of a charge-coupled device (CCD) camera a few micrometers away from the focus plane. In the absence of aberrations, the PSF has rotational symmetry about the optical axis, and reflection symmetry about the plane of focus. The PSF shown here is clearly far from being symmetrical in the axial direction. This is due to spherical aberration and is very common when imaging typical biological fluorescence specimens. Microscope objective lenses are designed to image optimally a specimen immediately beneath a coverslip of the correct thickness. Typical specimens used in 3D biological microscopy are rather thick, and so there is an additional optical path length through a layer of water, glycerol, or other mounting medium that leads to

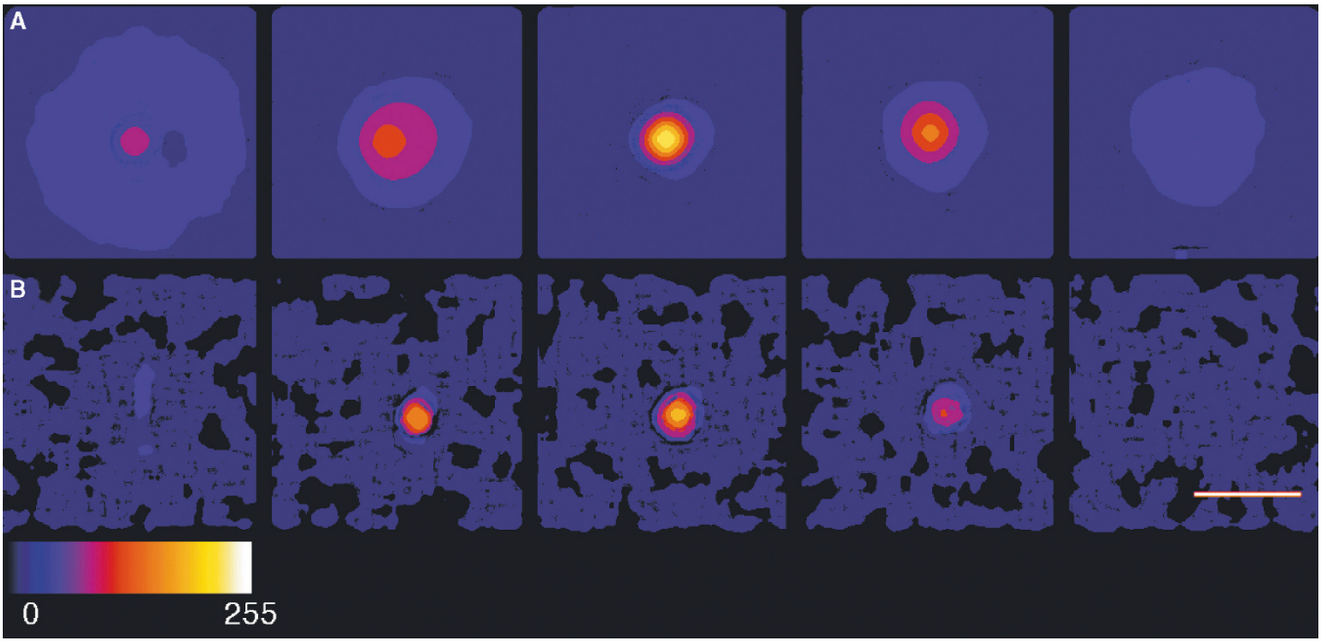


FIGURE 23.2. Sections through measured WF (A) and confocal (B) PSFs. The objective lens was a planapochromat 63×, NA 1.4 (Leitz). Confocal detector aperture size was 0.7 Airy units. In order to emphasize the fainter components, the square root of the intensity is shown. Spacing between sections (z) is 0.4 µm. Bar = 1 µm.

increased spherical aberration (Chapters 7 and 20, *this volume*). Hiraoka and colleagues (1990) have shown that this can be compensated for, to some extent, by modifying the refractive index of the immersion oil, and computer-controlled "add-on" optical systems are now available for the correction of this error.

Departures from rotational symmetry have also been noted (Hiraoka *et al.*, 1988), due either to misalignment of the illumination system with the microscope optical axis or to misalignment of the optical surfaces within the objective itself. (See Chapters 11 and 20, *this volume*, for a more complete discussion of the effect of various aberrations on confocal imaging.)

The usual way to measure a WF image is by means of conventional epi-fluorescence optics. The entire specimen is illuminated, ideally by filling the back aperture of the objective with light emanating from an extended, perfectly uniform light source. The importance of the light source has received much less attention in epi-fluorescence imaging than in transmitted light imaging such as DIC (Inoué, 1986), but it is equally important to obtain a uniform PSF (see Chapter 6, *this volume*). The resulting image is projected by suitable relay optics onto an image detector. Currently, scientific-grade, cooled CCD-array cameras are the best image acquisition devices for this type of microscopy (Hiraoka *et al.*, 1988; Aikens *et al.*, 1989). It has also been shown that a type I scanning microscope, in which only a single aperture is used, is equivalent to the WF arrangement (Sheppard and Choudhury, 1977). In theory, opening the detector aperture of a confocal laser scanning

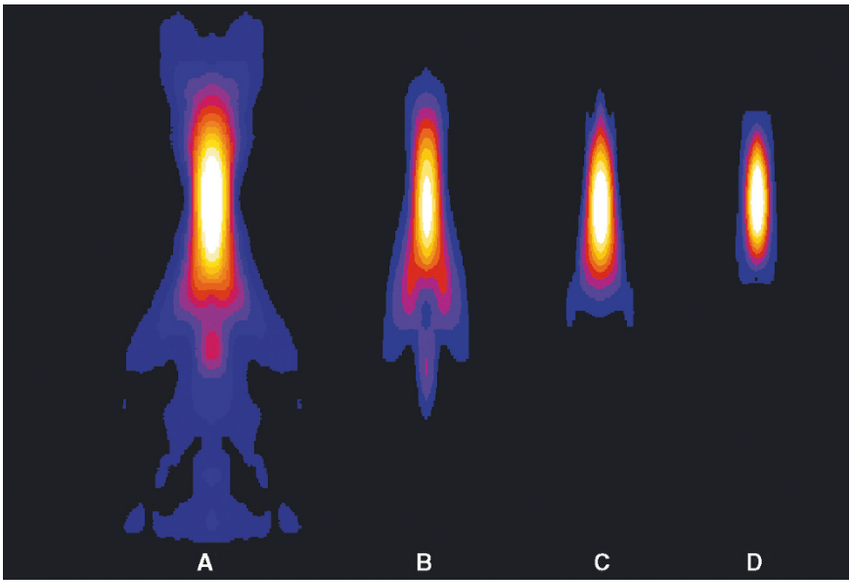


FIGURE 23.3. The PSFs shown in Figure 23.2 have been fitted by 3D cubic splines and cylindrically averaged. In each case a central x,z section is shown. The square root of the intensity is shown, and false gray level contouring has been used. The direction of the optical axis is vertical. The divergent cones are clearly seen in the WF data, but much reduced in the confocal data. (A) widefield PSF, (B–D) confocal PSFs with different detector apertures; (B) 4.3 Airy units, (C) 2.5 Airy units, (D) 0.7 Airy units. The optical axis is vertical, the radial axis is horizontal.

microscope (CLSM) infinitely wide should produce the same imaging as WF optics. In practice, it is not possible to have a large enough effective detector aperture to obtain WF behavior; if this were possible, the comparison between WF and confocal imaging for a given instrument would be much easier. Currently, only the non-descanned detectors, commonly found on single-beam multiphoton excitation fluorescent microscopes, closely mimic the optics of an infinite detector diameter.

The form of the widefield PSF, in particular, the diverging cones of subsidiary maxima on either side of the focal plane, shows why the out-of-focus components of the image extend a long way either side of the focal plane; each point in the specimen is replaced in the image by a suitably weighted copy of the PSF.

The degradation of the image can also be understood by considering the OTF, which is the FT of the PSF. The spatial frequency components of the specimen, that is, the specimen Fourier transform components, are multiplied by the OTF to give the spatial frequencies transferred to the image. For example, where the OTF is small at high spatial frequencies, the components of the specimen that correspond to these frequencies are greatly attenuated in the image. The widefield OTF has the form of a torus with a "missing cone," which corresponds to the attenuation of low spatial frequencies along the direction of the optical axis, and represents the lack of resolution in this direction, that is, closely spaced, horizontal, planar features in this direction are not resolved.

Figure 23.4(A) shows a central section through the OTF derived from the widefield PSF shown in Figures 23.2(A) and 23.3(A). The optical axis is vertical, and the full 3D OTF is the torus produced by rotating the function shown about this axis. Deconvolution seeks to reverse this attenuation and to restore as far as possible the image spatial frequency components to their true values. This has the effect of removing the out-of-focus contamination of the focal plane, giving truer focal sections, and also restoring the in-plane high frequency attenuation suggested by the form of the OTF. In addition, deconvolution strongly suppresses any details that have spatial frequencies outside the OTF and that may have arisen because of the effects of Poisson noise on the intensity measurements in individual pixels.

In an ideal confocal microscope, light from a small illuminated aperture is focused to a diffraction-limited spot in the specimen, in effect producing a light distribution equivalent to the widefield PSF. However, it should be noted that the focused spot from a laser beam is not identical to the focused spot from a conventional light source because of the Gaussian intensity profile of the laser source (Self, 1983; Chapter 5, *this volume*). The light emerging from the specimen is then spatially filtered through a second aperture — the detector aperture or pinhole — that is also in a plane conjugate to the focal plane and to the illuminating aperture. The effect of this is to apply the PSF twice; thus the combined, confocal PSF is the square of the widefield PSF. This reduces the intensity of the subsidiary maxima very considerably, particularly away from the plane of focus. Therefore, the out-of-focus flare is substantially reduced, and the images are much cleaner optical sections. Figure 23.2(B) shows confocal bead data and Figure 23.3(B–D) shows confocal PSFs for the same objective as Figures 23.2(A) and 23.3(A), measured using three different settings of the detector aperture (4.3, 2.5 and 0.7 Airy units respectively; see Shaw and Rawlins, 1991b). The rejection of the light from the out-of-focus rings is seen clearly by comparison with the widefield PSF [but note that the confocal data in Fig. 23.2(B) is noisier than the WF data, complicating the comparison]. The difference is also clearly seen in the OTFs (Fig. 23.4). The "missing cone" is largely filled in, although in-plane high frequency attenuation is still apparent,

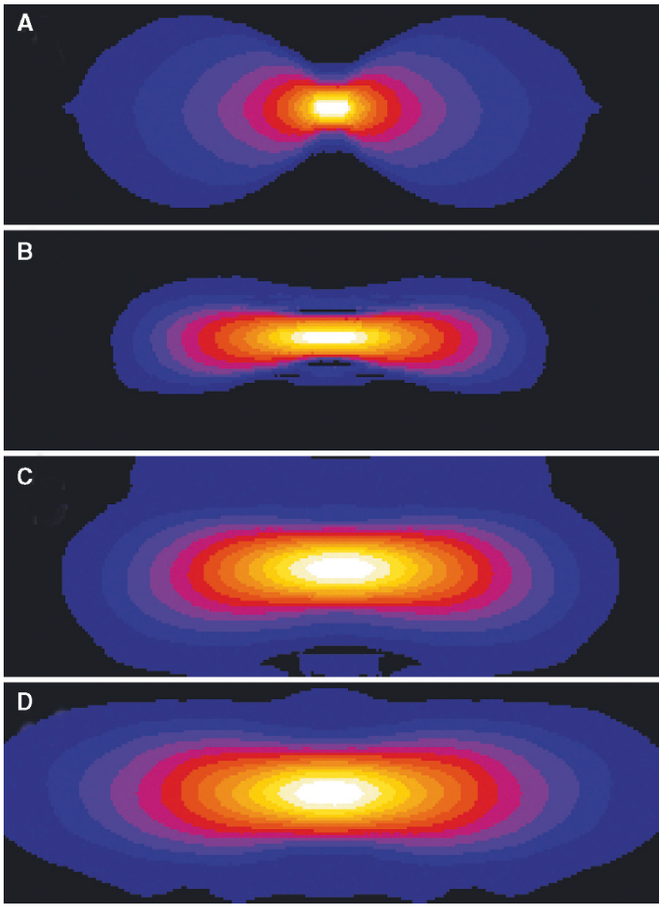


FIGURE 23.4. Central sections through the WF (A) and confocal (B–D) OTFs derived from the PSFs shown in Figure 23.3. The optical axis is vertical, the radial axis horizontal. The 3D OTFs are the solids of revolution about the optical axis. In the WF case this gives a torus; in the confocal case, an approximate ellipsoid, the size of which varies inversely with pinhole diameter.

and the resolution in the direction of the optical axis (vertical in Fig. 23.4) is 3 to 4 times worse than the in-plane resolution even with the smallest pinhole setting.

In principle, the ideal confocal PSF shows a narrower peak in the focal plane, and so should give slightly better in-plane resolution. However, the increase in in-plane resolution requires a very small detector aperture and the consequent loss of light makes it difficult to obtain good images from even the brightest fluorescent biological specimens. In practical biological confocal microscopes, the detector aperture is generally adjustable. The larger it is made, the more light is detected, but the more the imaging tends towards WF optics. On the other hand, opening the aperture a little way greatly increases the detected light and reduces the in-plane resolution virtually to the WF case but still maintains much-improved optical sectioning. For given assumptions about the thickness and fluorochrome distribution in a sample, it is possible to show that there is an optimum size that maximizes the signal-to-noise ratio (S/N) obtained. (See Sandison *et al.*, 1993; and Chapters 2 and 22, *this volume.*) The resolution implied by a PSF may be quantified by measuring the peak width at half-maximum peak height (FWHM), either in-plane (d_{xy}) or along the optical axis (d_z). For the confocal PSF shown in Figure 23.4(D), $d_{xy} = 0.23\,\mu m$, and $d_z = 0.8\,\mu m$. These values agree reasonably well with theory and other measurements.

Limits to Linearity and Shift Invariance

We need to bear in mind that deconvolution procedures are critically dependent on the assumptions of linearity and shift invariance. It is difficult to measure the extent to which linearity is obeyed in a real imaging experiment. The most obvious reason that might cause deviation from linearity in fluorescence microscopy would be strong absorption effects; the image seen for a given point might then depend on the way the incident beam interacted with other parts of the specimen. Departures from shift invariance are much easier to assess. They may arise across a field of view in a microscope because of lack of flatness of field, or other image plane aberrations. An example of a large field of view in a confocal microscope showing different bead images at different x,y positions (i.e., different PSFs at different positions) is shown in Figure 23.5. The PSF also often changes with depth within a biological specimen. High NA objectives are usually designed to image specimens through exactly the correct thickness of cover glass, as mentioned above. However, in many 3D biological specimens there is an additional layer of mounting medium between the cover glass and the specimen, and this introduces some spherical aberration. The deeper into the specimen the image plane is, the thicker the intervening layer, and the more the spherical aberration.

Departures from linearity would be difficult to deal with computationally, but departures from shift invariance are not so hard. One simple approach, which has been used, is to divide the original 3D image into small blocks within which the PSF does not vary appreciably, and then deconvolve each subimage with the appropriate PSF, finally recombining the subimages. A more elegant solution would be to determine the PSF as a function of x,y and z, and use this function to determine the degraded image in a restoration algorithm. However, as the degraded image would no longer be a simple convolution, and it could not be calculated by the efficient Fourier transform methods, the computational cost would be very high.

DECONVOLUTION

Convolution of the object with the PSF is a simple mathematical transformation that is reversible in principle — a procedure called deconvolution. This is particularly clear in the formulation in terms

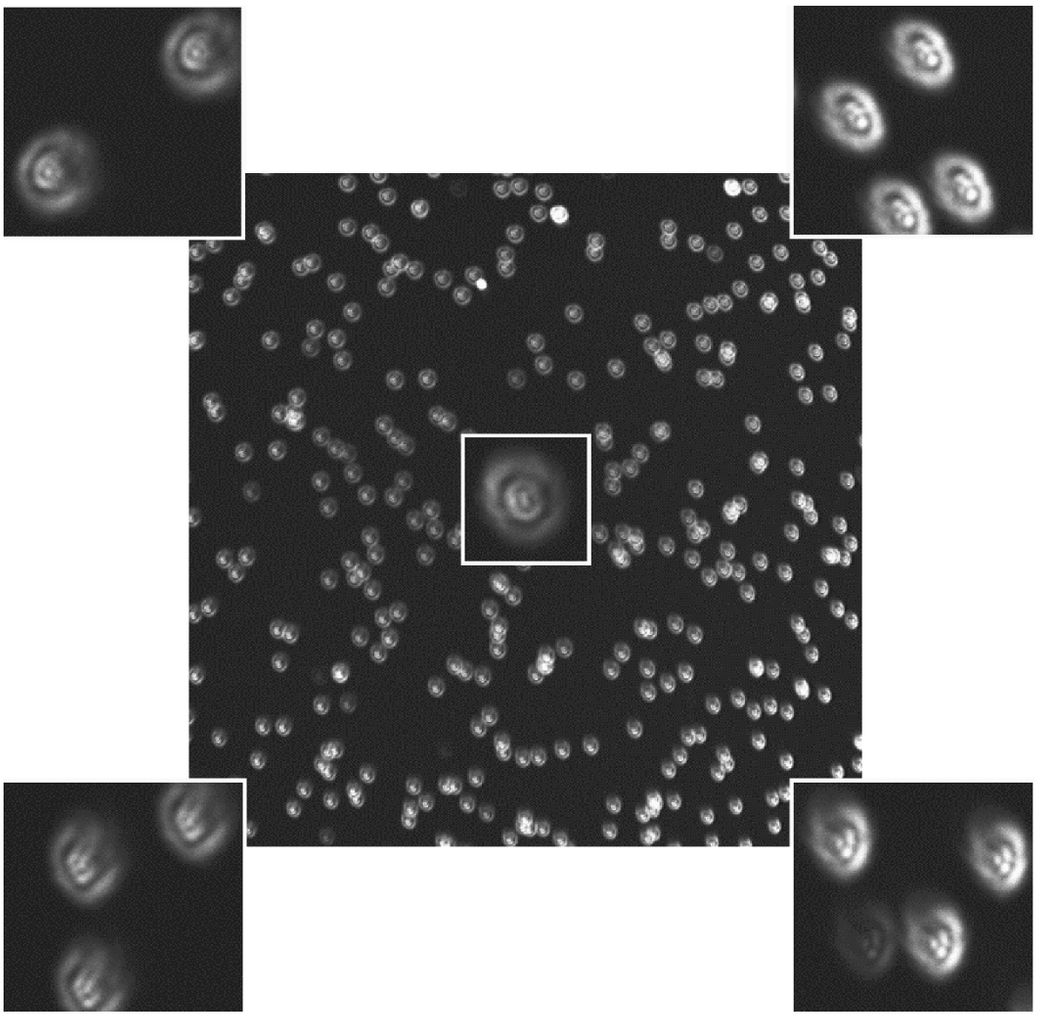


FIGURE 23.5. Confocal image of a field of beads. The focal plane has been set away from the central, in-focus, section to show some of the out-of-focus parts of the PSF. The lack of shift invariance is evident in this image, as the defocused bead structure is different in different parts of the field of view. The insets show enlargements from different parts of the field. The image is also dimmer in the cental area due to field curvature. (Objective used was Leitz Planapo, NA 1.4, oil immersion.)

of FTs (Eq. 8). Because the image transform is simply the object transform multiplied by the OTF, it should be possible to recover the desired object transform by dividing the image transform point-by-point by the OTF.

$$G(\mathbf{S}) = F(\mathbf{S})O(\mathbf{S}) \Rightarrow F(\mathbf{S}) = G(\mathbf{S})/O(\mathbf{S}) \quad \textbf{(9)}$$

The undegraded object would then be obtained by an inverse FT of the result. Unfortunately, this simple approach is made impossible by the inevitable presence of noise in any real image. There are regions where the OTF becomes very small or zero (see Fig. 23.4); however these regions of the image transforms still have a noise component. Thus, dividing by the very small OTF values will boost the noise component of the data to a level where it dominates the final reconstruction, rendering it meaningless.

The problem of restoring noisy data is one common to many fields in spectroscopic, optical, and medical imaging. The most powerful methods of solution apply "constraints" to the solution, typically requiring the result to be positive and smooth — both physically reasonable requirements. A simple way to visualize this is to consider fitting a curve to some noisy data points. If the fitted curve is allowed to have many parameters, it can pass right through all the points but may well contain wild and meaningless oscillations in regions away from the points. If we put some constraints on the curve, such as preventing physically meaningless values or ensuring a certain degree of smoothness, the curve may not pass exactly through any point, but will be near them all, and therefore a more reasonable and "believable" solution. This is the basis of constrained deconvolution methods. They are invariably more complex and time consuming to compute than the simpler methods, and usually require multiple rounds of iterative approximation to the reconstructed image. However, their power and the rapidly increasing speed and decreasing cost of computers make them the most attractive option for 3D digital image deconvolution. There are many different methods for this type of restoration, differing in their degrees of rigor and their computing requirements. The various deconvolution methods are discussed in more detail in Chapters 24 and 25. The examples shown here are all calculated by the constrained, iterative method developed by Jansson and others (Jansson *et al.*, 1970; Agard and Sedat, 1983; Agard *et al.*, 1989; Shaw, 1993). We believe that the Jansson method represents a good compromise between rigor and computational efficiency.

PRACTICAL DIFFERENCES

A few practical differences relating to the implementation of WF or confocal imaging should be mentioned.

Temporal Resolution

With a single-beam confocal microscope, each focal section generally requires image averaging to obtain an acceptable S/N, and this may take several seconds. Some confocal microscopes are capable of scanning at video rates or faster, but the image quality is then limited by the amount of light measured during each scan. If the specimens are very bright, good time resolution is possible, but in many (perhaps most) biological applications, the faster scan rate will simply mean that more frames must be accumulated and averaged. Higher speed is possible in disk-scanning confocals in which the maximum possible data rate is increased by the use of hundreds of beams striking the specimen simultaneously, as discussed below.

However, even the slower scan-rate CLSMs are capable of very good time resolution in some respects; the scanning beam only passes over each pixel for a very short time and therefore takes a frozen snapshot of that pixel. It is possible to scan a very small area or a single line, and to obtain very good temporal resolution from the restricted set of pixels. A single CCD image from a typical biological specimen may require only a fraction of a second to record and a little longer for image readout, but deconvolution is much more time consuming on current computers, and may take seconds or even hours depending on the data-set size. CCD imaging thus has reasonably good time-resolution for recording images, but it takes much longer to produce deconvolved focal sections. In either case specimen motion during data collection will produce artifacts. As WF deconvolution can only obtain optical section data by first collecting and then processing a complete 3D data stack, confocal clearly is faster when information about only a single optical section is needed.

Combination of Charged-Coupled Device and Confocal Imaging

A fundamental difference between CCD capture of WF images and imaging by a conventional spot-scanning confocal microscope is that the image is scanned one pixel at a time by the confocal microscope, whereas all the pixels for the whole WF image are recorded simultaneously by the CCD detector. The CLSM could be regarded as a serial device, whereas the CCD-WF microscope is a parallel device. If, for the sake of argument, the image contains 10^6 pixels, then to excite the specimen with the same number of photons in the CLSM will require each pixel to be illuminated with 10^6 higher light intensity, although for 10^{-6} as long, compared to the continuous illumination in WF. This may be impossible in practice, because the excited state of the fluorochrome molecules present in the focused laser spot may become saturated. Even at lower light levels, the photodamage related to producing a fixed number of excitations using the high instantaneous intensity of laser light may be more than that produced by the much lower, sustained illumination of the WF microscope (see Chapter 39, *this volume*). The only solution with a single-beam CLSM may be to reduce the illuminating intensity, and either scan for correspondingly longer times, or accept a noisier image.

A solution that combines parallel image detection with confocal imaging is to scan the specimen with an array of light spots, instead of the single spot used in most CLSMs (see Chapter 10, *this volume*). One of the first confocal microscopes, designed by Petran and colleagues (1968) used this principle. The excitation light passed through a Nipkow disk, which contained thousands of pinholes in a spiral pattern, and the emitted light was passed back through the same disk to produce confocal optics. The disk was spun so that the spiral pinholes scanned the entire specimen. In its original design, this microscope had extremely low sensitivity because the pinholes occupied only a very small proportion of the area of the disk, and so most of the excitation light was lost. Yokogawa introduced a radical improvement in the design by adding a microlens above each pinhole, increasing the illumination efficiency by more than an order of magnitude. The Yokogawa spinning disk can be combined with image detection using a CCD camera to produce a very sensitive confocal microscope, and instruments of this design are now made by a number of companies. Initial results suggest that this type of instrument may be much better than single-beam CLSMs for low light level and live-cell imaging, even though the confocal optics is not quite so good, and the image contains somewhat more out-of-focus light. When

coupled with one of the new electron-multiplier CCDs (EM-CCDs) having quantum efficiency (QE) and noise specifications very like those of the PMT, this combination can collect 10-plane 3D images fast enough for use in high content screening applications (see Chapter 46, *this volume*).

Integration of Fluorescence Intensity

It is sometimes important to obtain values for the total fluorescence intensity from all or part of a specimen. For example, one may wish to obtain a value for the DNA content of a cell by integrating the fluorescence emission from a DNA-binding stain. In the WF case, this can be obtained from any single optical section because the total integrated fluorescence is almost the same in each optical section (as long as the NA is not too high). The partial confocality of the WF mode (Hiraoka *et al.*, 1990) means that if a small field aperture is used, the focus plane of the optical section should be reasonably close to the center of the object of interest (a few microns). In the confocal case, it is necessary to sum the contributions from each section of a focal series, and the section spacing has to be comparable to or less than the confocal depth of field (≤1 µm with a 2 Airy pinhole). This means that WF imaging is much more efficient for such measurements, providing that the objects to be quantified do not overlap significantly, even when out of focus.

RESOLUTION, SENSITIVITY, AND NOISE

Leaving aside the practical differences mentioned above, given a fluorescent specimen, what is the optimal method to excite the fluorescence, and then to extract the maximum amount of useful structural information from the resulting fluorescent light?

Fluorescence Excitation

Laser-scanning confocal and WF microscopy differ markedly in the way the fluorochrome molecules in the specimen are excited (see Table 23.1). In WF microscopy, each and every plane of the specimen is evenly illuminated while its image is recorded. In a scanning confocal microscope, the illuminating beam rapidly traverses the specimen, giving very high light intensity at the center of the focal spot and rapidly decreasing intensity over a broad region above and below this spot. The instantaneous light distribution in the CLSM is given approximately by the form of the widefield PSF (although the focused laser beam has a somewhat different detailed distribution). As discussed above, at excitation levels above ~1 mW the light intensity can easily saturate the fluorochromes at the center of the focal spot, and the need to avoid this in turn limits the usable excitation intensity. When the laser light intensity is reduced enough to avoid saturation, the amount of emitted light recorded is very small: 10 to 20 photons/pixel/1 s scan in the stained areas of most fluorescent biological specimens. Therefore, it is necessary to sum the light from many scans. Thus, each part of the specimen is illuminated by a succession of high-intensity pulses of light. The difference in behavior between multiple short exposures of high-intensity light and continuous exposure to much lower light levels may yield important differences in the lifetime of fluorochrome before fading or phototoxicity in living cells. To date, experiences vary with very sensitive specimens such as living cells loaded with fluorescent labels. Some investigators have used confocal imaging successfully on such specimens (Zhang *et al.*, 1990); others have found that the only feasible method is low light level recording with WF optics (Hiraoka *et al.*, 1989), and others have used two-photon excitation (Chapter 28, *this volume*). It is probable that the behavior of different types of cells and of different fluorochromes varies (see Chapters 38 and 39, *this volume*).

Fluorescent Light Detection

The overall performance of any 3D light microscope depends strongly on the capabilities of the photodetectors used. We consider here the relative photon detection efficiency and associated measurement noise for the most usual detectors in WF microscopy (and in the spinning disk CLSM) and in the single-beam CLSM. See Chapter 12 for a more detailed discussion of image detection, and Pawley (1994) for a detailed assessment of the sources of noise. The best area/image detector for most epi-fluorescence microscopy is a scientific grade, cooled CCD camera. This has excellent geometrical and photometric linearity, a wide dynamic range, and good photon detection efficiency. Possibly most important, the image can be accumulated on the chip for an arbitrarily long time, which means that, as long as they do not move, specimens can be imaged with very low photon emission fluxes (Aikens *et al.*, 1989).

Rather than repeating a more general discussion well covered in Chapter 12, we shall illustrate this by taking the CCD camera in use in our laboratory as an example. This is a Photometrics camera electrically cooled to about −40°C. The detective QE (in effect, the proportion of photons reaching the faceplate of the CCD camera that are converted to electrons in the charge wells) ranges between 20% in the ultraviolet (UV) to 50% at 650 nm. The charge is converted by a 12-bit A-D converter, giving a maximum value of 4096, which, according to the manufacturer's specifications for the maximum amplifier gain setting, corresponds to about 6700 electrons in the CCD pixel or 13,400 photons reaching the CCD faceplate, assuming the wavelength for maximum QE. The relay optics are arranged to give a pixel spacing without binning of about

TABLE 23.1. Summary of Pros and Cons of 3D Microscopy Methods

	Widefield Deconvolution	Single Spot Confocal	Scanning-Disk Confocal	Two-Photon
Effective detector QE.	60%–80% (CCD)	3%–12% (PMT)	60%–80% (CCD)	3%–12% (PMT)
Detector noise (rms e/pixel)	4–12	<1	4–12 (<1 for EM-CCD)	<1
Peak signal (photons/pixel)	>30,000	20–100	~5000	20–100
Acquisition time (s/frame)	Depends on CCD readout (>0.05)	0.2–10	Depends on CCD readout (>0.05)	0.2–10
Peak excitation intensity/µm^2	10 nW	1 mW	1 µW	10 W
Excitation wavelengths	Hg arc 350–650 nm	Available laser lines	Available laser lines	Ti:Sa 700–900 nm

0.07 μm at the specimen, which is somewhat better than required by the Nyquist criterion, assuming ~0.2 μm data. If specimen fading or phototoxicity is not a problem, it is usual to collect for a time that nearly fills the wells at the brightest points. Typically for a bright specimen that is easily visible to the eye through the microscope, this takes an exposure of a fraction of a second. Thus, in CCD imaging, it is quite common to collect images with about 10,000 photons at the brightest pixels and many times this number from the several pixels that cover the image of a point object.

However, this can be reduced substantially. The limit to sensitivity is determined by the system measurement noise and the intrinsic photon (Poisson) shot noise. The sources of system noise are primarily dark current and readout noise. The dark current in our CCD is 0.33 electrons/min/pixel, which is negligible. The readout noise is much larger — ±13 electrons root mean squared (RMS). This means the Poisson noise, given by the square root of the number of electrons, will be less than the readout noise in any pixel having an image intensity of less than 169 electrons. The QE cannot be improved much — a factor of 2 at most — but the readout noise can be much lower. In many CCD cameras ±6 electrons (RMS) is typical, and slow-readout cameras optimized for low-noise operation can have values down to ±3 electrons (RMS) readout noise. This is comparable with the Poisson noise at a signal level of about 9 electrons.

In the case of single-beam CLSM, the image detector is generally a photomultiplier (PMT; see Chapters 2 and 12, *this volume*). It is much harder to estimate the light levels being measured (photons/μm^2), but they are probably substantially lower than in CCD imaging. [This should not be confused with the photon fluxes (photons/μm^2/s), which are much higher, but each pixel only emits the photons for a very short time.] It is common for the brightest pixel intensity in a single scan of a CLSM to represent only 10 detected photons (Pawley and Smallcomb, 1992; Pawley, 1994). One might integrate 30 scans for an image plane in a weak specimen, giving perhaps 300 detected photons and an associated Poisson noise of about 17 photons. This is much larger than the typical measurement noise in a PMT, which can be reduced to extremely low levels, especially by photon counting (see Chapter 12, *this volume*). However, the QE for a PMT is worse than for a cooled CCD; perhaps only 15% of the photons reaching the detector faceplate produce signal. In this case, the 300 detected photons would represent 2000 photons going through the confocal pinhole.

Another way of comparing the two detection methods is to consider the number of gray levels into which the recorded data can be reliably placed. The conventional way to do this is to space the gray levels by one standard deviation. Where the only source of noise is Poisson noise, this gives $N/\sqrt{N}$ or $\sqrt{N}$ levels for N detected photons (see Chapter 4, *this volume*). Where other sources of noise are present, the situation is more complicated. (See Pawley, 1994, for a full discussion.) We can get an estimate by assuming the additional noise is purely additive, random, and signal independent (e.g., readout noise in the CCD). If we want an image with 10 statistically significant gray levels, the brightest pixel would require 100 electrons in the absence of readout noise. This would require 200 photons reaching the camera faceplate at 50% QE. For our CCD camera with 13 electrons/pixel readout noise, 10 gray levels would require $(10 + 13)^2 = 529$ electrons/pixel, or 1058 photons. If the CCD camera was equal to the best available with 3 electrons/pixel readout noise, 10 gray levels would require $(10 + 3)^2 = 169$ electrons, or 338 photons. If we had an optimally sensitive camera with 80% QE, then 211 photons would be enough for 10 gray levels. In the confocal case, the PMT noise is less than 1 count, so 10 gray levels would require $(10 + 1)^2 = 121$ counts. However, because the QE of the PMT is only about 15%, this would require 806 photons. The PMT multiplicative noise can be reduced to extremely low levels by photon counting. Perhaps then 100 counts would be enough to define 10 gray levels, but with 15% efficiency, this would still require 666 photons.

Clearly, as long as we assume that we still need 10 gray levels, low QE is a limitation in current single-beam confocal systems. However, in the confocal approach, only in-focus photons are counted and they represent the final data, while in the WF approach, more gray levels need to be recorded because some may be lost when the data is processed to remove out-of-focus light, and thus it could be argued that a statistically less well-defined confocal image would be sufficient for direct interpretation than would be required for reliable WF deconvolution. Ultimately, there will probably not be a great deal of difference in the effective QE possible with the two detection technologies. The noise in the PMT is considerably more complicated than this brief discussion would imply but ultimately it can be reduced below that attainable in conventional CCD cameras. However, even if the detection can be made optimally efficient in both cases, for specimens where fluorochrome fading is not a problem, it will be easier to record images with very low statistical noise with the CCD because, as a parallel device, it can accumulate data more rapidly than a single-beam CLSM. For this reason, the combination of multiple-spot scanning, such as the spinning disk, with CCD detection, currently probably has the best mix of sensitivity and overall speed for confocal imaging.

Gain Register Charge-Coupled Devices

As discussed above, CCD cameras suffer from relatively high readout noise, compared with PMTs. Even with the slowest readout rates, it becomes very difficult to reduce the readout noise below about 3 electrons/pixel. This limits their usefulness at low photon levels. A recent development in CCD technology significantly improves CCD detector performance at low light levels. The new CCD chips, called gain register CCDs or EM-CCDs (for electron multiplier), incorporate an on-chip amplification register, which amplifies the electrons in the charge wells by a small amount every time the charge is moved from one well to the next during the readout phase. By repeating this amplification hundreds of times the accumulated charge packet can be amplified by very large overall factors before digitization. In effect this means that the charge can be increased to the extent that the readout noise becomes negligible, and this makes the CCDs usable at extremely low photon levels, and even in a photon-counting mode. The penalty is that the effective QE is reduced by a factor of 2 by the amplification noise. Dark current is also amplified, and so needs to be reduced to very low levels by cooling. At high photon fluxes, the gain can be reduced to 1, and the chips behave as conventional CCD chips.

Cameras incorporating these new chips will probably be most useful in applications where intensified CCDs or photon-counting cameras have been used in the past because the EM-CCD overcomes many of the problems of these cameras. The EM-CCDs probably do not have any advantages for most CCD WF imaging when the image intensity is greater than ~100 photons/pixel. However, they may well be ideal for spinning-disk confocal CCD applications, where a single camera could cover the range from photon-counting levels up to many thousands of photons/pixel. The new CCD chips are at present manufactured by E2V (Enfield, UK) and Texas Instruments (Houston, TX). All the major CCD manufacturers now offer cameras using EM-CCD technology.

Measuring the sensitivity of light detection systems is not straightforward and requires specialized equipment not generally available in a biological laboratory. Even with a CCD camera, where the observed counts should be simply related to the incident photons, we must rely on data supplied by the manufacturer to make the conversion, and assume that the electronics is working optimally. There are also sources of variability in the PMT and associated electronics. It would be a great help to have standard intensity specimens, in addition to resolution specimens, which could be checked on a regular basis in any imaging laboratory (see Chapters 2, and 36, *this volume*, for more discussion). It would then be easy to determine whether the noise in the image of such a specimen was at a level consistent with the quoted measurement noise and Poisson statistics.

Out-of-Focus Light

The main effect of the confocal pinhole is to exclude most of the out-of-focus light from measurement, and thus to produce cleaner optical sections. Clearly, if the out-of-focus component is regarded purely as unwanted noise, then it is better not to measure it; the total number of photons measured, and thus the Poisson noise, are increased without increasing the in-focus "signal." Conversely, to the extent that the out-of-focus light carries useful information, it should be measured and computational deconvolution should be used to process the information and obtain accurate focal sections. The relative merits of the two approaches must depend on how much useful information the out-of-focus light carries and the characteristics of the noise associated with this light. The amount of useful information contained in the out-of-focus light depends on the specimen in question.

The respective OTFs for confocal and WF imaging provide an alternative way to look at this problem (see Fig. 23.4). The toroidal form of the WF-OTF means that image components at low spatial frequencies away from the *x*,*y*-plane are highly attenuated — the region of the "missing cone" — whereas the confocal OTF has an appreciable value in these regions. Thus, it is the spatial frequencies that define the depth of field for large-scale structure that are much better determined by the CLSM. There is much less difference between WF and confocal images in the higher spatial frequencies away from the focus plane. The difference in imaging therefore depends on the importance in particular objects of the contrast components in the missing cone region, and on how the noise is distributed between the different spatial frequencies. The noise, in turn, determines the ultimate accuracy to which the missing and attenuated components can be restored.

Model Specimens

It is possible to devise specimens, real or imagined, which are far better imaged by confocal optics. For example, a uniform, infinite, flat layer of fluorescent dye has spatial frequency components only in the *z*-direction. Because the integrated intensity at each plane of the ideal widefield PSF is the same, this specimen would give exactly the same light level no matter where the plane of focus was and would therefore be completely unresolved by a WF microscope, while a confocal microscope would genuinely resolve this specimen in *z*. It should be noted, however, that an actual WF microscope would resolve such a specimen to a limited extent, giving a very broad maximum to the light intensity at the relevant focal plane. This is because the effective field aperture in the WF optical system is not infinite, and so there is always some degree of "confocality." Hiraoka and colleagues (1990) have measured this effect experimentally and discussed it in some detail. This is one reason why it is a good idea, in WF microscopy, to use the field diaphragm of the epi-illumination system to limit the field of illumination to the area of interest in the specimen and to collect the PSF data using this same illumination.

On the other hand, the ability to image an "infinite plane" specimen is of little practical importance. A more interesting case is a very thin specimen (comparable to or less than the depth of field) containing structure of interest within the plane. In this case, the WF image focused on the appropriate plane should be a true representation of the light emitted because there is no out-of-focus structure to contaminate it. The confocal image should be identical, except that some of the light is excluded by the detector aperture, and the overall image resolution should be slightly increased. Now consider collecting a through-focal series of this specimen by WF microscopy. Several of the images will presumably contain out-of-focus information well above the noise level, although the high spatial frequencies will be attenuated according to the OTF. Thus, to some extent, this set of images must be equivalent to multiple measurements of the specimen plane, and a reconstruction scheme should be capable of using them to improve the statistical reliability of the in-focus image.

Figure 23.6 shows some images from a real biological specimen (immunofluorescent labeling of a very thin plant cytoskeleton "footprint") that attempts to model this situation. Three confocal images taken from a through-focal series starting with the in-focus image and spaced by 2 μm are shown in Figure 23.6(A). An equivalent WF series of images of another footprint on the same slide is shown in Figure 23.6(B). Given the specimen thickness (probably well under 1 μm), there should be no out-of-focus light to contaminate the WF image. The in-focus WF image should be little different from the confocal image. (A 63×, NA 1.4 objective was used, and the pinhole was set at approximately 3 Airy disk diameters.) There is surprisingly little difference between these two focal series. This implies that relatively little of the out-of-focus data is eliminated with a detector aperture of this size in a specimen such as this, because it consists of thin fibers arranged in a plane and produces large components at high, in-plane spatial frequencies.

The Best Solution: Deconvolving Confocal Data

The main effect of the confocal optics should be to remove the very low spatial frequency out-of-focus components. Conversely, this means that with a detector aperture in this size range, there is still residual degradation by the out-of-focus high frequency components from nearby planes in just the same way as for WF optics. Unless a very small detector aperture can be used, confocal optics do not provide a complete solution to this "high frequency out-of-focus problem." Because it is almost invariably impossible to use such very small detector apertures, deconvolution offers a practicable way to improve the fidelity of the high spatial frequencies in both WF and confocal 3D images. These considerations as well as the practical examples given below suggest that it will often be helpful, or even necessary, to apply deconvolution to confocal data to obtain the best resolution of 3D structures. Furthermore, in images where the pixel spacing is smaller than the Nyquist frequency, any spatial frequencies present in the image beyond the Nyquist frequency should be removed before the image is displayed. This is because any such high spatial frequencies cannot contain meaningful information, and may confuse interpretation of the image.

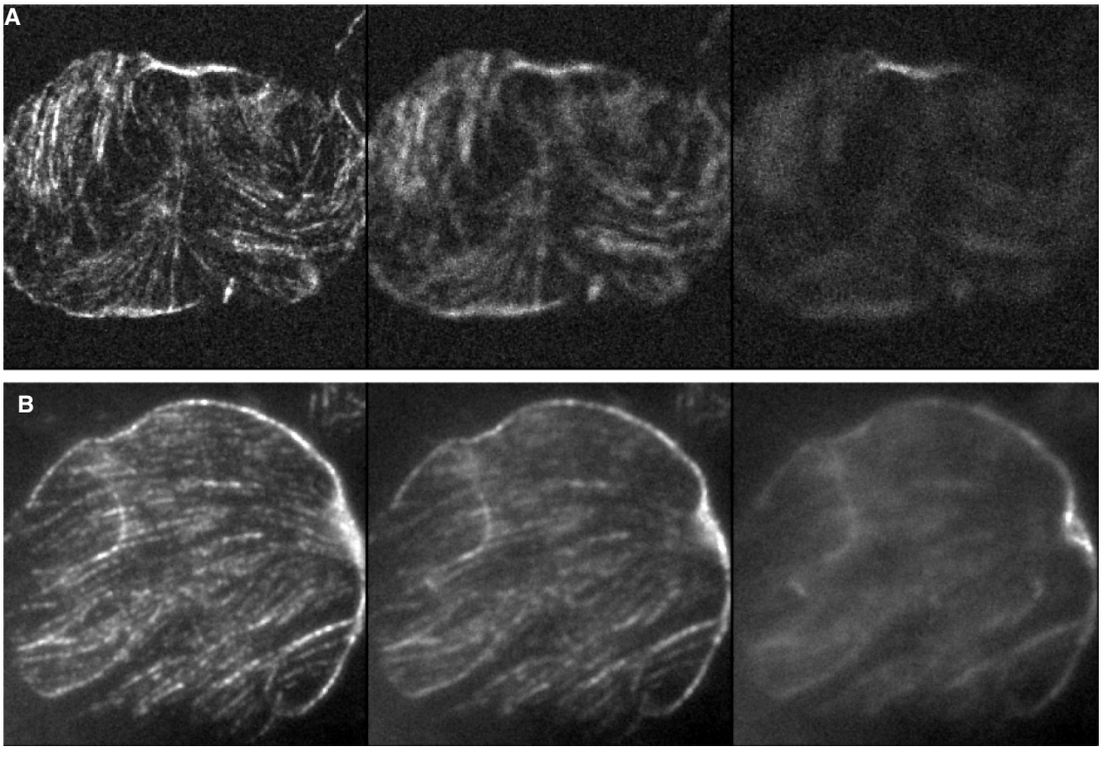


FIGURE 23.6. A series of confocal (A) and WF (B) optical sections of a plant cytoskeleton "footprint" fluorescently labeled with anti-tubulin. The specimen thickness is less than 1 µm. The confocal detector aperture size was approximately 3 Airy units. The spacing between the optical sections was 2 µm. Field width, 37 µm. (Specimen courtesy of Dr. Clive Lloyd.)

As another way of looking at this aspect of the comparison between WF and confocal imaging, consider again the respective PSFs and OTFs (see Figs. 23.2–23.4). The confocal PSF has much reduced subsidiary maxima (see Figs. 23.2 and 23.3), largely eliminating the low spatial frequency out-of-focus light. This corresponds to the missing cone region of the WF-OTF being "filled in" in the confocal OTF. This reduction of the out-of-focus contribution is one effect of deconvolution on the WF data. However, in addition to this, both WF and confocal OTFs imply an attenuation of higher spatial frequencies both in-plane and more markedly in the z-direction. Deconvolution has the effect of compensating for this attenuation, in effect sharpening the image.

For most specimens, it seems unlikely that the low spatial frequency out-of-focus light can be regarded as carrying much if any useful information (i.e., any useful information that is present for a given focal section is likely to be restricted to focal sections very close in z: 1–2 µm). The net result of the light that is more out of focus being present in WF images must be to increase at least the Poisson noise associated with the measurement of a given in-focus signal.

Although the previous example may seem somewhat atypical, it has features in common with many real specimens. For example, a specimen may consist of isolated regions of bright labeling that are thin compared to the depth of field and that occur at significantly different depths. We might describe such a specimen as "punctate" and an example might be fluorescent, *in situ* hybridized chromosomes, which typically contain only a few bright spots at or near the resolution limit and at various focal planes. Unless there is a substantial real background originating from other focal planes, widefield CCD imaging is likely to be better than confocal imaging for this type of specimen with currently available equipment. There is relatively little out-of-focus light at low spatial frequencies, so in these circumstances, the QE of the CCD camera would probably override the disadvantage that it detects low-frequency out-of-focus light. Similar considerations would apply to punctate labeling at the membrane of a cell or organelle.

If, in addition to the thin plane of interest, the specimen had uniform background intensity, B, throughout the rest of its volume, the WF result would become worse as the specimen becomes thicker, and confocal imaging would become better than WF imaging. This is because the intensity from each additional slice of the background is added in its entirety to all of the WF images. Thus, the S/N decreases linearly with specimen thickness in the WF case, whereas the background is excluded from the confocal image, and the S/B is largely independent of specimen thickness. Sandison and colleagues (1993) have calculated the effect on S/N and signal contrast of the confocal out-of-focus light exclusion. Sandison and colleagues (1993) and Inoué (1986) define contrast as the S/B. Ignoring other sources of noise, the Poisson noise for N counts is $\sqrt{N}$ and the S/N = $\sqrt{N}$. In the presence of background, N = S + B and S/N = S/$\sqrt{(S+B)}$. As B is increased for a given signal, both the contrast, S/B, and the S/N decrease. There comes a point when the in-focus signal, S, becomes lost in the Poisson shot noise [$\sqrt{(S+B)}$] produced by both in-focus and out-of-focus light. According to this argument, in the WF case the background, B, is increased, while the in-focus "signal" S remains the same.

Sandison and colleagues have calculated for model specimens how S, $\sqrt{(S+B)}$, and B are affected by the size of the detector aperture, how confocal imaging compares with WF imaging, and how to determine the detector aperture size which maximizes detected S/N. This is also covered in Chapter 22.

The results of this type of analysis clearly depend on the assumptions made about the distribution of fluorescent material in the specimen; similar analyses need to be made for various different specimen geometries. Furthermore, the detector aperture size that maximizes S/N will not in general give the maximum resolution; deconvolution can be used to improve this situation.

PRACTICAL COMPARISONS

We have undertaken some comparisons of CLSM and CCD imaging of some of the specimens we are using in our work — fluorescent *in situ* labeling of plant root tip tissue slices ~50 µm in thickness (Shaw and Rawlins, 1991b; Highett *et al.*, 1993a,b). Deconvolution can be equally well applied to confocal data, using the confocal OTF, to reverse as far as possible the attenuation implied by these PSF measurements and to substantially reduce Poisson noise. Figure 23.7 shows the confocal bead data used to derive the confocal OTF both before [Fig. 23.7(A,C)] and after [Fig. 23.7(B,D)] deconvolution.

In both data sets, deconvolution clearly sharpens the bead image, particularly in z, and gives some confidence in applying the procedure to 3D confocal data sets. In Figure 23.8(A–C), the same portion of a specimen was imaged with three different settings of the detector aperture (0.7, 2.5, and 4 Airy units; Shaw and Rawlins, 1991b). In each case, a 3D focal section stack of about 30 sections separated by 0.2 µm was collected. A single equivalent section from these data sets is shown in Figure 23.8. The increase in aperture size clearly degrades the resolution. This must be attributed primarily to contamination of the optical sections with out-of-focus light from nearby parts of the specimen that were too near for the detector aperture to eliminate. In each case, the data was deconvolved by the iterative Jansson method, using the appropriate PSF measured with the relevant aperture settings. The equivalent sections are shown after deconvolution in Figure 23.8(D–F). The deconvolution has restored each image to an equivalent result. Provided the image data has been measured with sufficient accuracy, deconvolution can restore the different degrees of image degradation given by different sizes of detector aperture. Figure 23.8(G–L) shows enlargements of the small area boxed in Figure 23.8(A). These enlargements show the effect of the deconvolution algorithm in reducing the noise in the images.

Whatever the relative merits of confocal and WF imaging, it is clear that deconvolution can make good confocal data look even better. Figure 23.9 shows another example of this from our work (Beven *et al.*, 1996). In this image deconvolution clearly resolves the labeling of transcription sites within a plant nucleolus to show that they are composed of many closely packed foci.

Figure 23.10 shows a specimen imaged by both WF [Fig. 23.10(A)] and confocal [Fig. 23.10(C)] microscopy. The agreement between the deconvolved WF data [Fig. 23.10(B)] and the raw confocal data [Fig. 23.10(C)] is remarkably good, and gives confidence that either method will give satisfactory results. The deconvolved WF data seems somewhat better than the confocal data in both x,y and x,z sections. However, the deconvolution applied to the confocal data gives the clearest image of all [Fig. 23.10(D)].

In Figure 23.11, the same data sets are resectioned parallel to the optical axis (x,z) and lead to very similar conclusions. It should be noted that diverging cones from very bright features are still visible after deconvolution of the WF data. This is because the PSF used in deconvolution is not exactly right for the conditions under which the data set was collected. There is clearly considerable spherical aberration, producing an asymmetrical PSF, possibly because the cell was deep within a tissue slice. Obtaining accurate PSFs for a given specimen is often a substantial problem. The ideal solution would be to determine the PSF from the data set itself before deconvolution or perhaps to use "blind" deconvolution as described in Chapter 24.

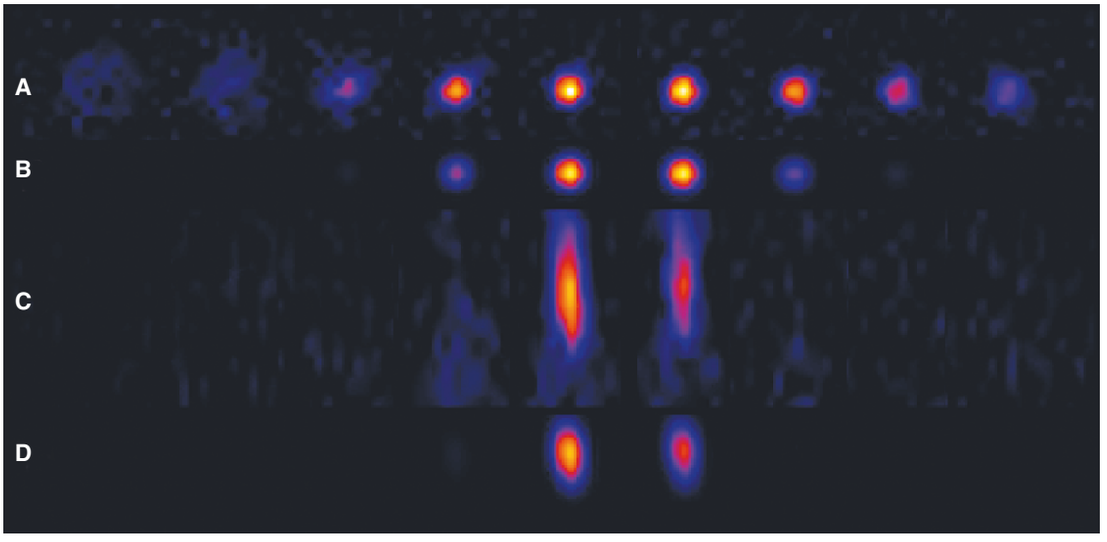


FIGURE 23.7. Deconvolution of confocal bead data. (A) x,y sections before deconvolution. (B) x,y sections after deconvolution. (C) x,z sections before deconvolution. (D) x,z sections after deconvolution. (Reproduced from Shaw and Rawlins, 1991b, *J. Microsc.* 163:151–165.)

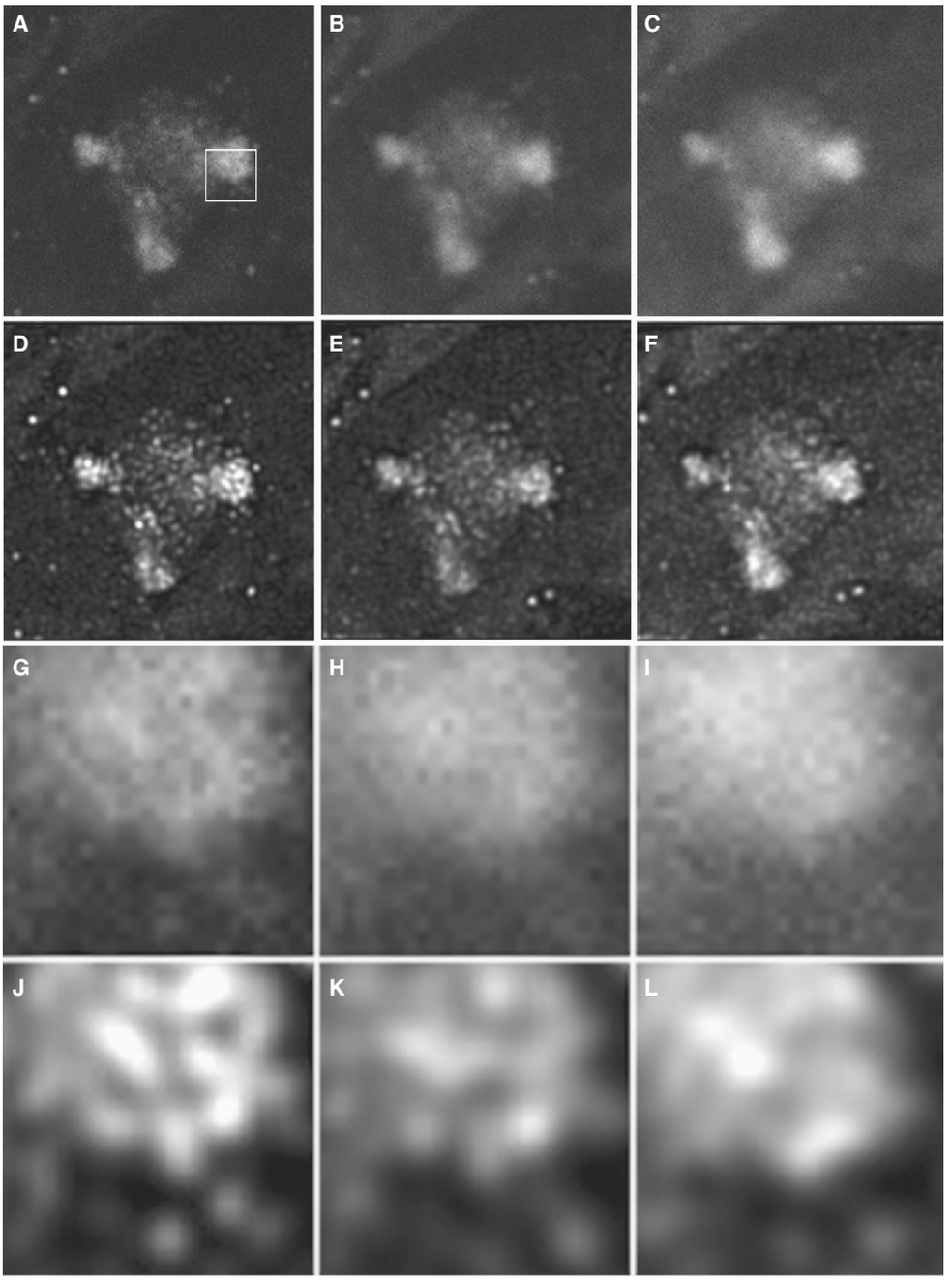
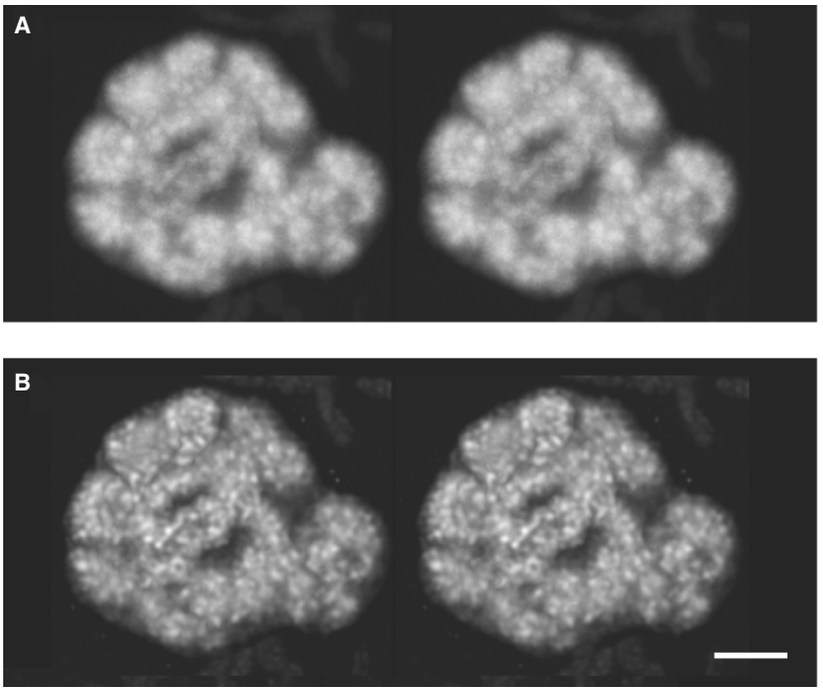


FIGURE 23.8. Single equivalent sections from confocal data sets collected with different detector aperture settings before and after deconvolution with the appropriate OTF. (The specimen was a pea root tissue slice labeled by fluorescence *in situ* hybridization with a probe to the rDNA.) (A–C) Unprocessed confocal data. (A) Detector aperture, 0.7 Airy units. (B) Detector aperture, 2.5 Airy units. (C) Detector aperture, 4.3 Airy units. (D–F) Equivalent sections to (A–E) after deconvolution. Although the image degradation due to increasing the detector aperture is clear, the reconstructed results are all very similar to each other. (G–L) Enlargements of the equivalent areas from (A–F) to the boxed area in (A), showing the effect of deconvolution on the noise in the image. Field width, 12.3 µm. (Reproduced from Shaw and Rawlins, 1991b, *J. Microsc.* 163:151–165.)

FIGURE 23.9. Stereo projections of a confocal data set before (A) and after (B) deconvolution. The data is from a pea root slice labeled by fluorescence *in situ* hybridization with a probe to the external transcribed spacer of the ribosomal RNA transcript, which marks the transcription sites within the nucleolus. Deconvolution clearly shows these sites as closely packed foci within a subregion of the nucleolus, each of which corresponds to an active gene copy. Bar = 2 µm.



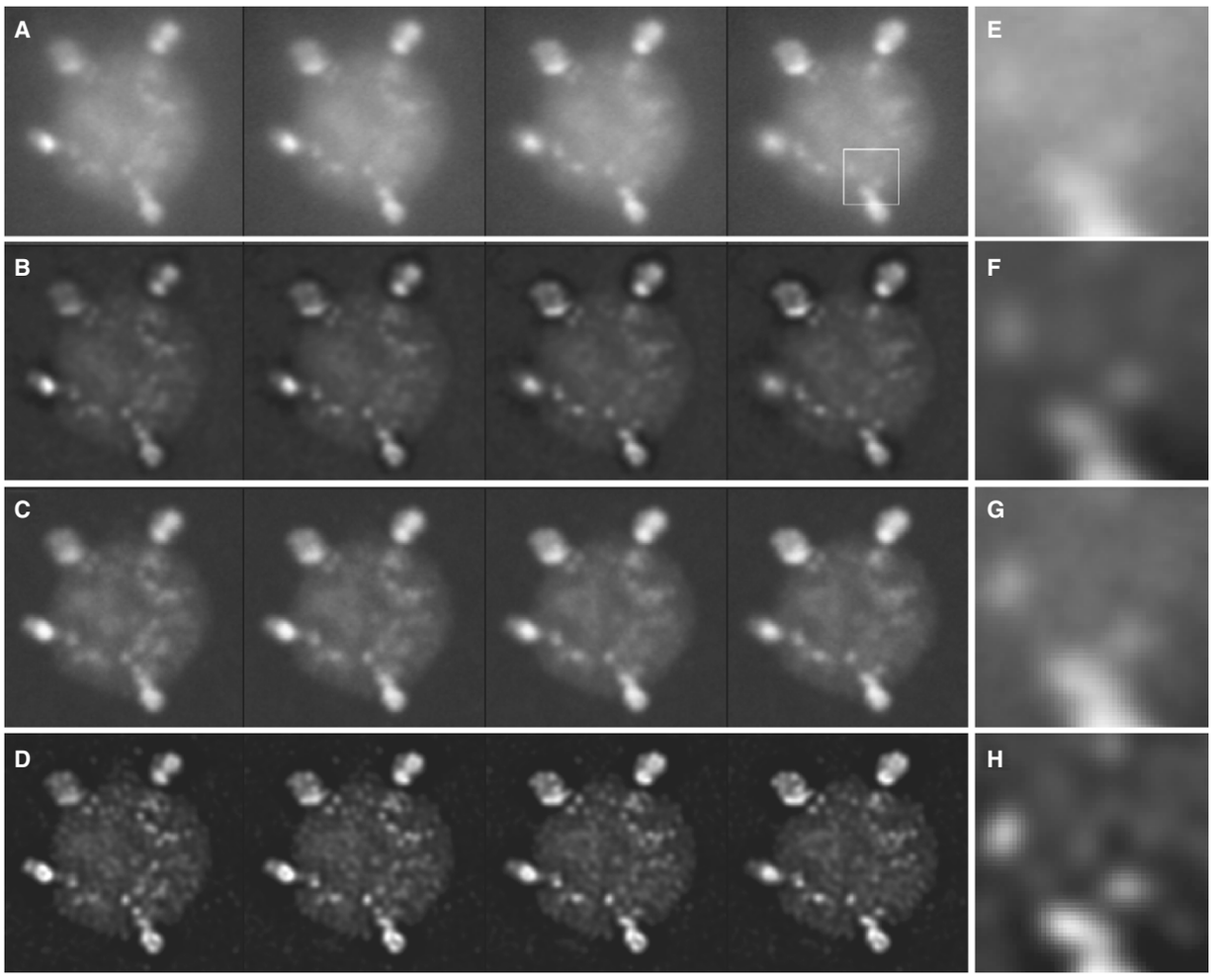


FIGURE 23.10. Comparison of WF and confocal images from the same specimen (a nucleolus from a pea root tissue slice labeled by fluorescence *in situ* hybridization with probe to the rDNA). (A) Four consecutive optical sections from a 3D data set imaged by WF microscopy. Data collected on a cooled CCD camera, using Leitz 63×, 1.4 NA objective. (B) Equivalent sections from the same data set as in (A) after deconvolution. The background flare is eliminated and the contrast of the fine image detail is greatly improved. (C) Equivalent confocal sections from the same specimen. The same objective was used and the confocal detector aperture was set to 2.5 Airy units. The images are remarkably similar to the deconvolved WF ones, although the contrast of the fine detail is perhaps a little worse. (D) Equivalent sections from the same data set as (C) after deconvolution. The clarity of the fine detail is clearly best in this data. (E–H) Enlargements of the equivalent areas to the area boxed in (A). Spacing between sections is 0.25 µm. Field width, 8 µm.

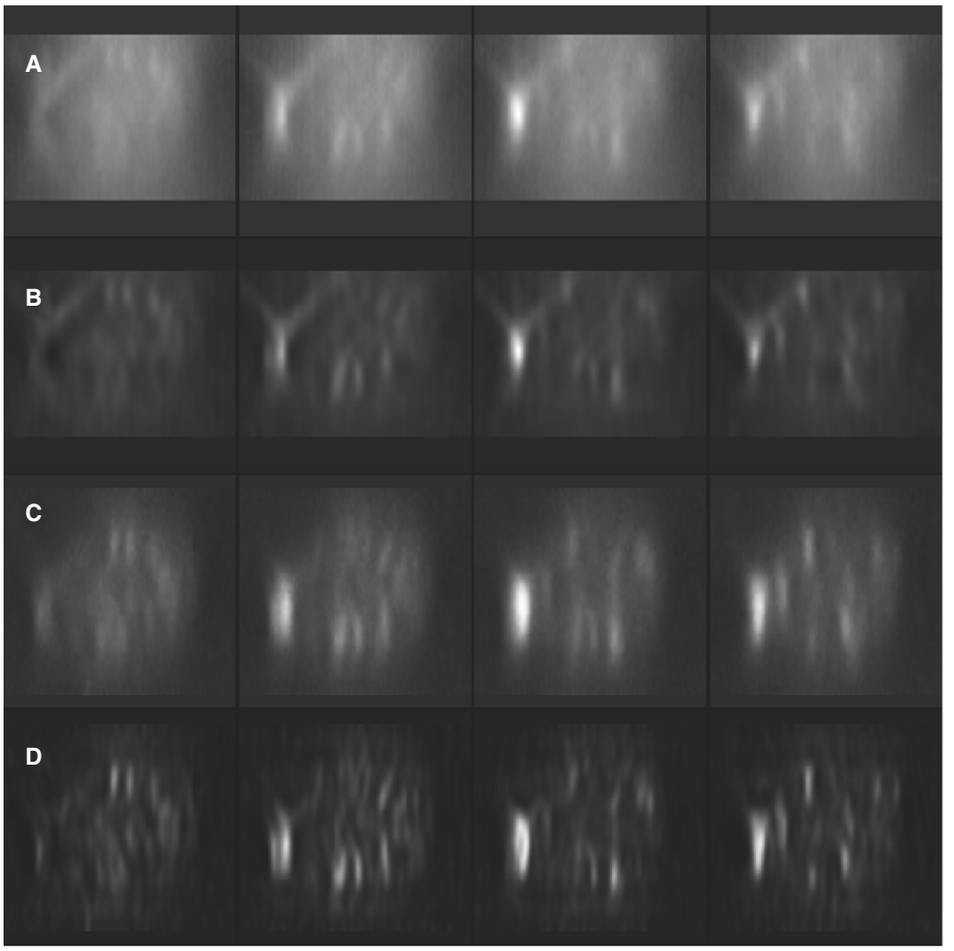


FIGURE 23.11. The same data as in Figure 23.8 in the same order, resectioned to show *x*,*z* sections. Although the poor *z*-resolution compared to the in-plane resolution is very apparent, the comparison between the four data sets leads to the same conclusions as Figure 23.8; the deconvolved WF and unprocessed confocal data are fairly similar, whereas deconvolution of the confocal data gives the best result. Note also the residual out-of-focus cone around the bright feature remaining after deconvolution of the WF data. This is due to a mismatch between the actual PSF and the PSF used for the deconvolution, probably because the data was recorded deep inside a tissue slice, and spherical aberration caused the PSF to be asymmetric at this depth. Spacing between sections is 0.25 µm. Field width, 8 µm.

CONCLUSION

Speed, convenience, and ease of use have until recently favored confocal microscopy over WF/deconvolution approaches. However, widefield CCD microscopes and associated operation and deconvolution software are now much more user friendly, and limitations in computer power for deconvolution much less of a problem. This has led to much more widespread use of widefield CCD/deconvolution imaging. Aside from these considerations, various factors are important in assessing the relative image quality achievable by the two methods.

- Effective QE is currently better with a cooled CCD camera than with either the PMTs used in most single-beam CLSMs or the EM-CCDs likely be used with disk scanners.
- Low spatial frequency, out-of-focus light or flare, corresponding to the missing cone region in the widefield OTF is largely eliminated with confocal microscopy using even a relatively large detector aperture. Other things being equal, it should always be preferable to eliminate this light because it can almost never be considered to contain useful information and its inclusion will increase Poisson noise, decreasing the signal contrast and hence the S/N of the data. In some cases, particularly with thick specimens, the low frequency out-of-focus light can completely swamp the in-focus signal, and confocal microscopy then has an overwhelming advantage. However, deconvolution of WF data does a good job of removing moderate levels of out-of-focus flare.
- Attenuation of higher spatial frequencies is approximately the same with either WF or confocal imaging unless a very small confocal detector aperture can be used. This is almost invariably impossible with the signal levels encountered in biological microscopy. This high frequency attenuation can be corrected by deconvolution of WF data and means that deconvolved WF data may often show higher effective resolution than unprocessed confocal data.
- However, a genuine comparison should also include deconvolution of the confocal data, and in the cases we have shown, deconvolved confocal data shows even better resolution than deconvolved WF data.
- Spinning-disk confocal microscopy combined with CCD image detection in many ways gives the best of both

approaches. The confocal optics eliminates much of the out-of-focus light, and its associated noise, and the CCD camera provides sensitive and accurate image detection. Parallel imaging at correspondingly lower peak light levels seems to have definite advantages, particularly for live cells and photosensitive specimens. Subsequent deconvolution should have the effect of increasing the clarity of the image, as it does with data from a single-beam instrument. This situation can be expected to improve with the widespread use of EM-CCDs.

SUMMARY

- The relative merits of confocal and WF microscopy depend on the amount and spatial frequency spectrum of the out-of-focus light.
- The amount of out-of-focus light depends on the specimen, the depth distribution of the significant fluorescent intensity, the level of generally distributed non-specific background, and the thickness of the specimen.
- For very thin specimens, or specimens with high fluorescent intensities restricted to thin shells within thick specimens of low background intensity, there is little out-of-focus light to be excluded. In these cases, the CCD cameras in use in WF imaging give better QE and therefore statistically better-defined images for a given dose of illuminating photons.
- Image deconvolution should be applied to confocal images as well as to WF images if the highest resolution is needed and to remove image noise.

ACKNOWLEDGMENTS

This work was supported by the Biotechnology and Biological Sciences Research Council of the United Kingdom. I thank Jim Pawley and Jason Swedlow for stimulating discussions and correspondence. I thank Richard Lee for the data shown in Figures 23.2, 23.3, and 23.4.

REFERENCES

Agard, D.A., and Sedat, J.W., 1983, Three-dimensional architecture of a polytene nucleus, *Nature* 302:676–681.

Agard, D.A., Hiraoka, Y., Shaw, P.J., and Sedat, J.W., 1989, Fluorescence microscopy in three dimensions, *Methods Cell Biol.* 30:353–378.

Aikens, R.S., Agard, D.A., and Sedat, J.W., 1989, Solid state imagers for microscopy, *Methods Cell Biol.* 29:291–313.

Beven, A.F., Lee, R., Razaz, M., Leader, D.J., Brown, J.W., and Shaw, P.J., 1996, The organization of ribosomal RNA processing correlates with the distribution of nucleolar snRNAs, *J. Cell Sci.* 109:1241–1251.

Castleman, K.R., 1979, *Digital Image Processing*, Prentice-Hall, Englewood Cliffs, New Jersey.

Highett, M.I., Rawlins, D.J., and Shaw, P.J., 1993a, Different patterns of rDNA distribution in *Pisum sativum* nucleoli correlate with different levels of nucleolar activity, *J. Cell Sci.* 104:843–852.

Highett, M.I., Beven, A.F., and Shaw, P.J., 1993b, Localization of 5S genes and transcripts in *Pisum sativum* nuclei, *J. Cell Sci.* 105:1151–1158.

Hiraoka Y., Minden, J.S., Swedlow, J.R., Sedat, J.W., and Agard, D.A., 1989, Focal points for chromosome condensation and decondensation from three-dimensional *in vivo* time-lapse microscopy, *Nature* 342:293–296.

Hiraoka, Y., Sedat, J.W., and Agard, D.A., 1988, The use of a charge-coupled device for quantitative optical microscopy of biological structures, *Science* 238:36–41.

Hiraoka, Y., Sedat, J.W., and Agard, D.A., 1990, Determination of three-dimensional imaging properties of a light microscope system: Partial confocal behavior in epifluorescence microscopy, *Biophys. J.* 57:325–333.

Inoué, S., 1986, *Video Microscopy*, Plenum Press, New York.

Jansson, P.A., Hunt, R.M., and Plyler, E.K., 1970, Resolution enhancement of spectra, *J. Opt. Soc. Am.* 60:596–599.

Pawley, J.B., 1994, The sources of noise in three-dimensional microscopical data sets, In: *Three-Dimensional Confocal Microscopy: Volume Investigation of Biological Specimens* (J.K. Stevens, L.R. Mills, and J.E. Trogadis, eds.), Academic Press, New York, pp. 48–94.

Pawley, J.B., and Smallcomb, A., 1992, An introduction to practical confocal microscopy: The ultimate form of biological light microscopy? *Acta Microsc.* 1:58–73.

Petran, M., Hadravsky, M., Egger, M.D., and Galambos, R., 1968, Tandem-scanning reflected light microscope, *J. Opt. Soc. Am.* 58:661–664.

Sandison, D.R., Piston, D.W., and Webb, W.W., 1993, Background rejection and optimization of signal-to-noise in confocal microscopy, In: *Three-Dimensional Confocal Microscopy: Volume Investigation of Biological Specimens* (J.K. Stevens, L.R. Mills, and J.E. Trogadis, eds.), Academic Press, New York, pp. 211–230.

Self, S.A., 1983, Focusing of spherical Gaussian beams, *Appl. Opt.* 22:658–661.

Shaw, P.J., 1993, Computer reconstruction in three-dimensional fluorescence microscopy, In: *Electronic Light Microscopy* (D. Shotton, ed.), Wiley-Liss, New York, pp. 211–230.

Shaw, P.J., and Rawlins, D.J., 1991a, Three-dimensional fluorescence microscopy, *Prog. Biophys. Molec. Biol.* 56:187–213.

Shaw, P.J., and Rawlins, D.J., 1991b, The point spread function of a confocal microscope: Its measurement and use in deconvolution of 3D data, *J. Microsc.* 163:151–165.

Sheppard, C.J.R., and Choudhury, A., 1977, Image formation in the scanning microscope, *Opt. Acta.* 24:1051–1073.

Stokseth, P.A., 1969, Properties of a defocused optical system, *J. Opt. Soc. Am.* 59:1314–1321.

Wilson, T., 1993, Image formation in confocal microscopy, In: *Electronic Light Microscopy* (D.M. Shotton, ed.), Wiley-Liss, New York.

Young, I.T., 1989, Image fidelity: Characterizing the imaging transfer function, *Methods Cell Biol.* 30:2–47.

Zhang, D.H., Wadsworth, P., and Hepler, P.K., 1990, Microtubule dynamics in living dividing plant cells: Confocal imaging of microinjected fluorescent brain tubulin, *Proc. Natl. Acad. Sci. U S A* 87:8820–8824.

24

Blind Deconvolution

Timothy J. Holmes, David Biggs, and Asad Abu-Tarif

INTRODUCTION

Purpose of Deconvolution

Deconvolution[1] is a process most often applied to three-dimensional (3D) data sets from widefield fluorescence (WFF) microscopy. Additionally, it can be applied to 3D data for transmitted light bright-field (TLB) and other widefield modalities. It improves resolving power and signal-to-noise ratio in data from confocal laser-scanning microscopes (CLSM) and confocal spinning-disk microscopes, and it provides a transformation to data from differential interference contrast (DIC) images to effectively extract a 3D image of refractive index distribution.

With WF microscopes, 3D data are collected by optical sectioning (Castleman, 1979; Agard, 1984, 1989). As illustrated in Figures 24.1 and 24.2, an automatic focus controller and digital camera record a sequence of images of a thick specimen. The focus controller drives either a stepper motor focus or a piezo crystal embedded within a customized objective lens mount. When a microscope having a narrow depth of field (DOF) is focused on a plane, the image contains both sharp, in-focus features originating from the plane of focus and blurred features originating from planes above and below. After storing an image, the microscope is focused to an adjacent plane, which is about one DOF away, and another image is recorded. This process is repeated until the entire specimen is scanned. The result is a 3D data set that contains the out-of-focus blur. Deconvolution eliminates the blur to restore clarity of the image. An example is shown in Figure 24.3. After deconvolution, the image may be rendered for 3D viewing and quantitation by methods discussed in Chapters 14 and 15.

When using confocal microscopes, including both the CLSM and the spinning-disk microscopes (such as the Yokogawa CSU22, PerkinElmer Life Sciences, Boston, MA; the CARV–2 from Atto Biosciences, Rockville, MD; or the DSU from Olympus), images of adjacent planes are optically sectioned in a similar way, except that each frame is collected using either a single, scanned light spot and a photodetector or a structured array of scanned pinholes that serve as both light spots and point detectors. Each confocal image is, by itself, already partially deconvolved because the optics reject most of the out-of-focus light. Most of the features recorded in a 3D confocal data set are in focus. However, the CLSM has its own limitations. While it rejects most of the out-of-focus light, it does not reject all of it. Some haze remains. In addition, the 3D data set has axial smearing. Point objects look like American footballs oriented along z. As fewer photons are detected compared to WFF, the raw data contains much quantum or Poisson noise. This noise not only obscures real structures in the image, as explained in Chapter 4, it can actually create impossible features. As Poisson noise affects the intensity recorded in each pixel separately, random positive excursions can give the appearance of small bright features that are only one pixel big. Such a feature is impossible because, assuming that the data was recorded using Nyquist sampling, no real feature should be smaller than 4 to 5 pixels across. Because deconvolution suppresses data corresponding to features smaller than the point-spread function (PSF), it eliminates such noise features from the data and thereby meets the Nyquist reconstruction criterion. Simply put, properly sampled, noisy 3D data sets are almost always improved by deconvolution. Deconvolution reduces or eliminates all four of these problems and thereby improves the confocal image. An example is shown in Figure 24.4.

To a first approximation, DIC contrast is produced by a set of polarizers and Wollaston prisms that form an image that is the differential in the direction of shear of the refractive index of the specimen at the focus plane. The image contains information about the 3D refractive index distribution, although this information is convolved and non-linearly distorted by the objective lens, polarizers, and differential interference optics. Deconvolution can be used to invert this process and to produce an image whose intensity is proportional to the 3D refractive index distribution. An example is shown in Figure 24.5.

Advantages and Limitations

Early deconvolution methods used a calculated or measured PSF (Hiraoka *et al.*, 1990; see also Chapter 25, *this volume*). The PSF was measured by collecting a 3D image of a subresolution fluorescent microsphere. The accuracy of this process is limited by the fact that the biological sample itself is part of the optics of the system. It has its own heterogeneous refractive index, and this changes the PSF. In principle, the only way to measure the correct PSF is to measure it within the biological sample itself, by placing microspheres in the sample at the depth being imaged. The depth is important because the blurring caused by spherical aberration is the most prominent factor that changes in the PSF, and spherical aberration changes with depth (Gibson, 1991; Visser, 1992; see also Chapter 20, *this volume*). Although people have succeeded at

[1] Deconvolution is a mathematical process that is the opposite to convolution. Convolution is described in the Appendix at the end of this chapter. Convolution is useful because it can mimic the blurring effects of diffraction and geometrical optics. Deconvolution is important because, to the extent that the blurring effect can be described mathematically, it can reverse this blurring effect.

Timothy J. Holmes • AutoQuant Imaging, Inc., Troy, New York 12180 and Rensselaer Polytechnic Institute, Troy, New York 12180
David Biggs and Asad Abu-Tarif • AutoQuant Imaging, Inc., Troy, New York 12180

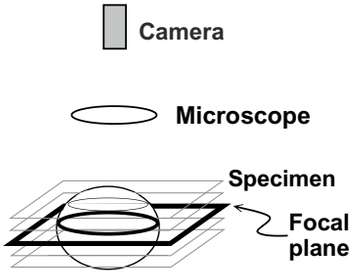


FIGURE 24.1. Optical sectioning schematic. This setup is used with the wide-field modalities, including WFF, TLB, DIC, and polarized light.

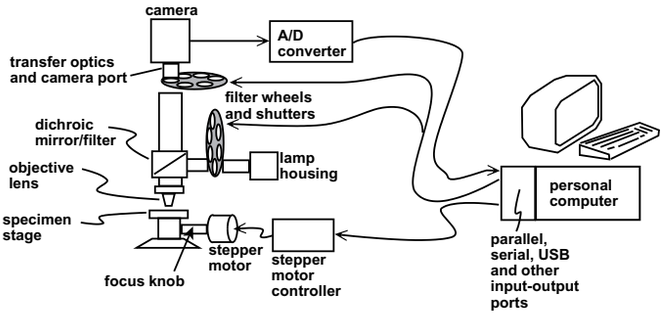


FIGURE 24.2. Hardware components needed for optical sectioning.

inserting microspheres into some samples, it is impractical to do so routinely.

The approach highlighted in this chapter does not use a calculated or measured PSF and is therefore called *blind deconvolution* (Ayers and Dainty, 1988; Bhattacharyya *et al*., 1996; Holmes, 1992; Krishnamurthi *et al*., 1995). The actual PSF is degraded by any heterogeneity in the refractive index of the specimen (Gibson and Lanni, 1991). These complications are compounded in CLSM fluorescence, where light levels are very low and the effect of refractive index variations are even more severe (Visser *et al*., 1992; Chapter 20, *this volume*).

Blind deconvolution uses an iterative process to produce both a reconstructed estimate of the PSF as well as the deconvolved data. Realistic mathematical constraints on the PSF are used. Figures 24.6 and 24.7 demonstrate a blind deconvolution of a data set with severe spherical aberration, including the PSFs at the beginning and end of the reconstruction. Figures 24.6(A) and 24.7(A) show *xz* views that have a non-symmetrical flare along *z*

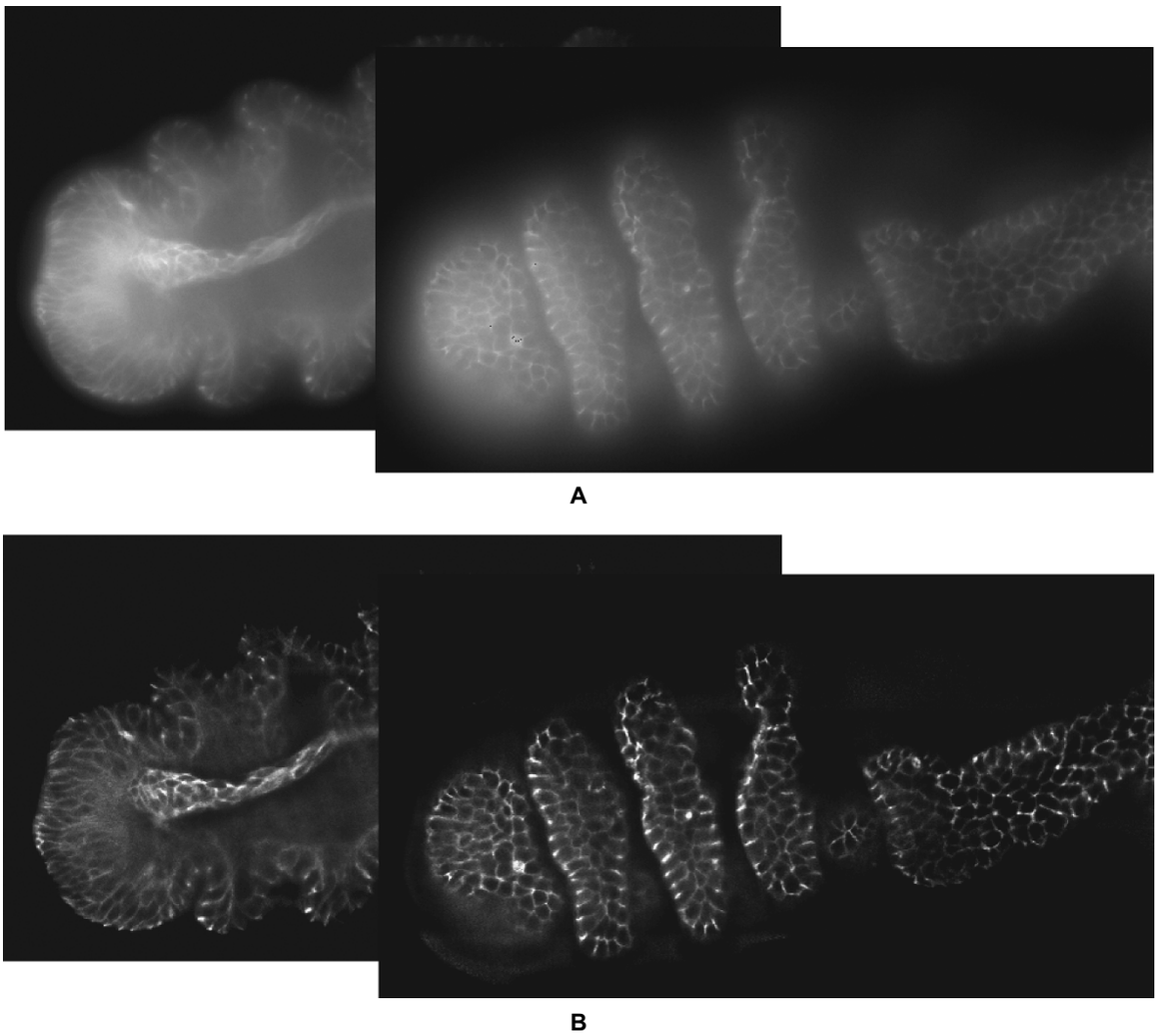


FIGURE 24.3. (A) Two slices from an unprocessed WFF stack. (B) Deconvolved slices from the blind deconvolution. (Image courtesy of M. Schechter, Leica Microsystems.)

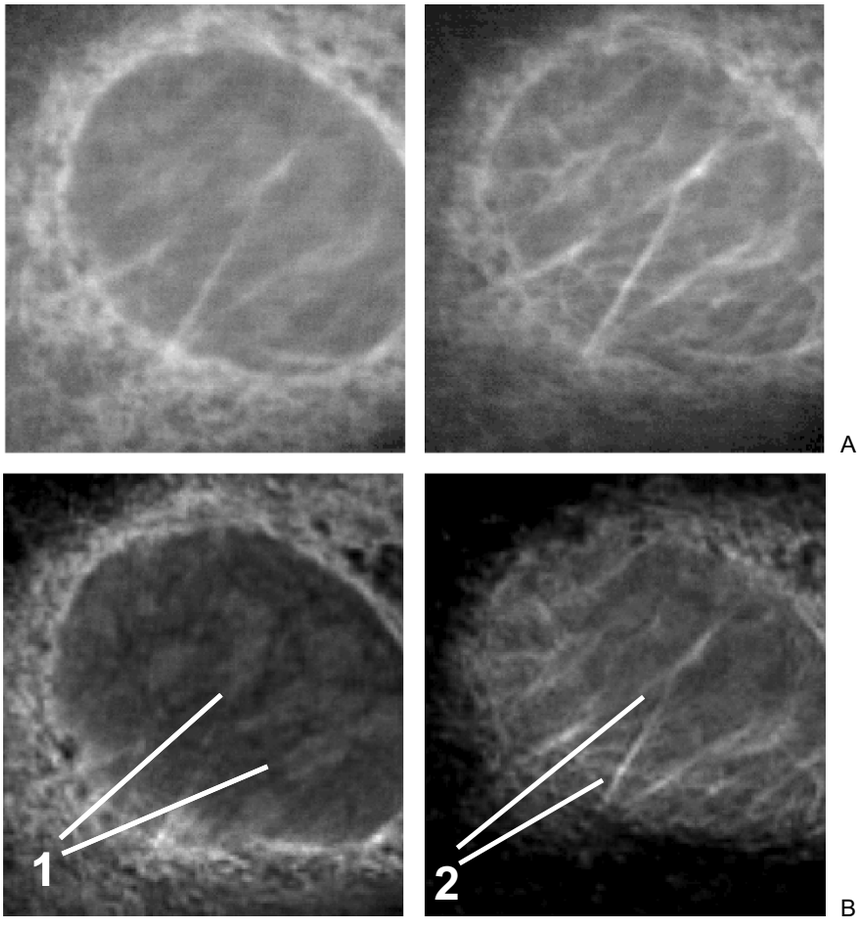


FIGURE 24.4. (A) Two sections from a confocal stack. (B) After deconvolution. Resolving power along *z*, signal-to-noise ratio and contrast are improved. Chromosomes are now apparent (1) and vimentin fibers are seen above and below the nucleus (2), as they should be, but are not seen within the nucleus [left frame of (B)]. (Image courtesy of M. Hoppe, Leica Microsystems.)

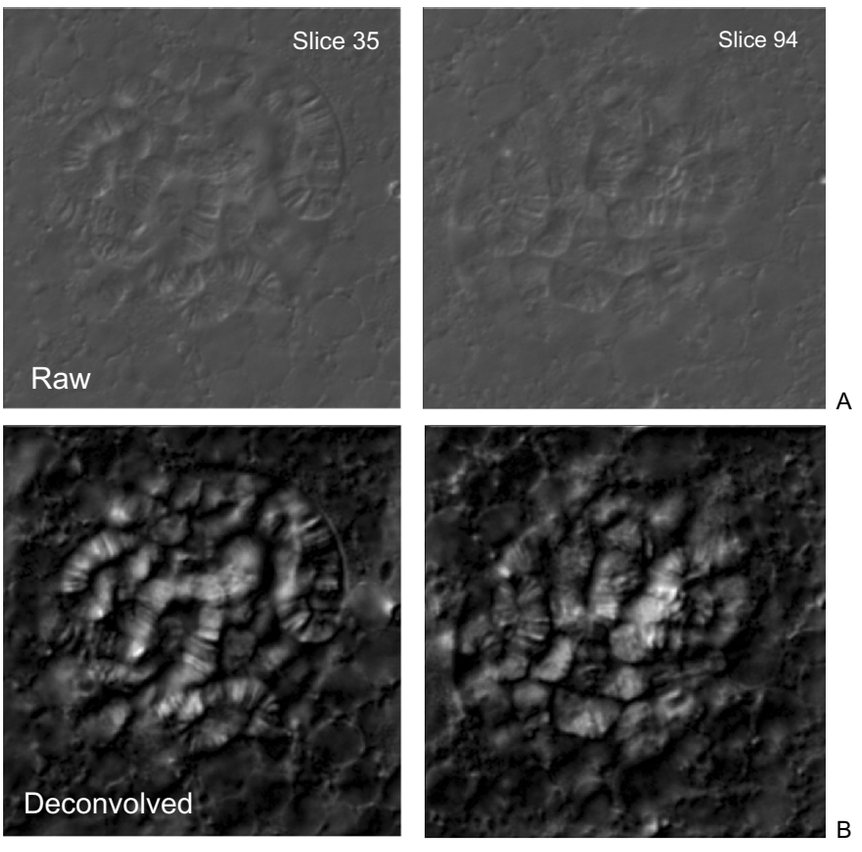


FIGURE 24.5. (A) Two optical sections from a DIC stack. (B) After deconvolution. The deconvolved images appear like CLSM fluorescent samples. No stain is used, but the brightness is proportional to the refractive index of the sample, resulting in a virtual refractive index map.

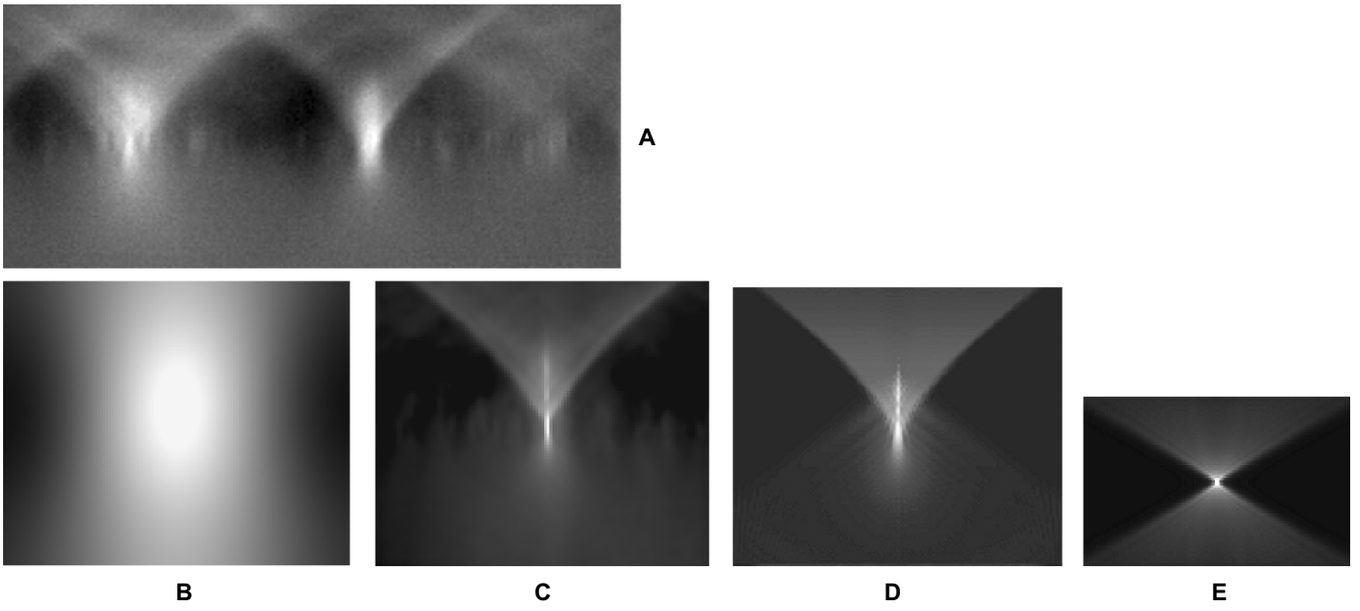


FIGURE 24.6. (A) *xz* slice through a 3D WF fluorescent data set collected with a water-immersion lens, showing spherical aberration. (Image courtesy of D. Kube, Case Western Reserve University.) (B) *xz* sum projection of the first guess of the PSF used to seed the first iteration of the blind deconvolution. (C) *xz* sum projection of the PSF produced by the blind deconvolution procedure. (D) Theoretically calculated PSF with a spherical aberration coefficient chosen to match the flare seen in Figure 24.6(A). (E) Theoretically calculated PSF without spherical aberration, for comparison.

that is characteristic of spherical aberration. This condition is especially evident with water-immersion lenses, when the collar on the objective has not been properly adjusted for the coverslip thickness. The PSF reconstruction is shown in Figure 24.6(B,C) and is discussed later in the section entitled "More Examples — Blind Deconvolution and Spherical Aberration."

A *non-blind* version of this algorithm (Holmes and Liu, 1991) is available for cases where the PSF can be accurately measured (Hiraoka *et al*., 1990) or calculated (Gibson and Lanni, 1991).

The approach highlighted in this chapter uses a mathematical tool called maximum likelihood estimation (MLE). As this approach includes quantum photons as an underlying assumption, it results in a reduction in the noise that is caused by Poisson noise. Because of diffraction, any microscope represents a bandlimited system. As explained later, this means that any "good" signal lies inside the bandlimit. Much of the undesirable noise energy (i.e., noise signal) lies outside the bandlimit. The algorithm recognizes this and subsequently rejects the out-of-band noise automatically.

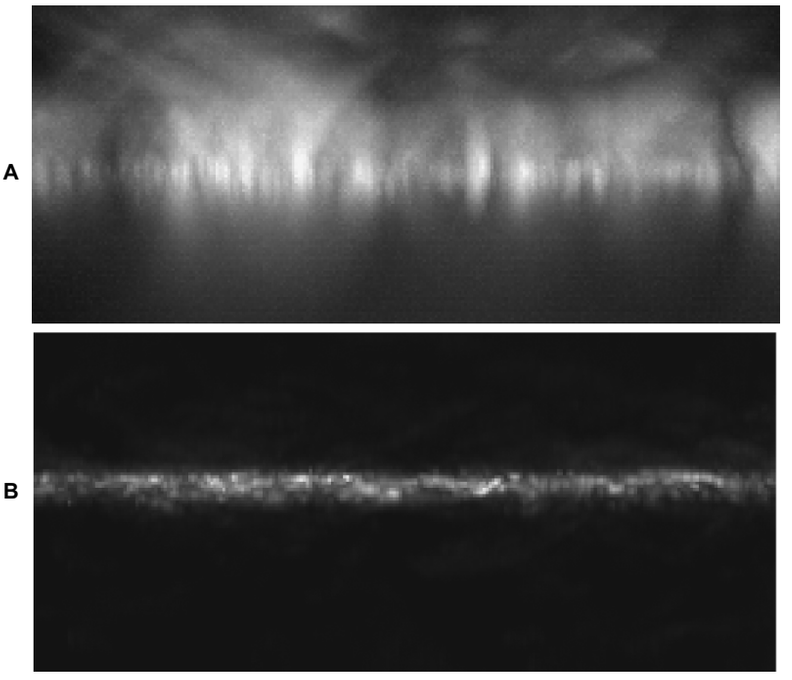


FIGURE 24.7. (A) *xz* maximum projection of the data set shown in Figure 24.6(A). Spherical aberration is apparent by the asymmetry in the amount of flare above and below the sample. (B) Blind deconvolution result, showing the elimination of spherical aberration. The PSF shown in Figure 24.6(B) was used as the PSF first guess, and the PSF shown in Figure 24.6(C) was produced by the blind deconvolution procedure.

It also constrains the deconvolved image to have only non-negative values, a process that cannot be implemented with a simple bandlimiting filter. Best results are achieved when the pixel or optical section spacing is finer than required by Nyquist sampling (Chapters 2 and 4, *this volume*).

PRINCIPLES

Data Collection Model

The data collection is modeled (Holmes, 1989, 1992; Holmes and Liu, 1989, 1991; Holmes *et al*., 1991) according to the following equations:

$$\mu(x, y, z) = f(x, y, z) \; *h(x, y, z), \tag{1}$$

$$\mu_b(x, y, z) = \mu(x, y, z) + b(x, y, z), \tag{2}$$

and

$$\mu_n(x, y, z) = \mu_b(x, y, z) + N(x, y, z), \tag{3}$$

where x and y are the in-plane coordinates, z is the axial coordinate, $\mu()$ is the data collected under ideal conditions where there is no background level or noise, $f()$ is the fluorescent dye concentration as a function of position, * represents the convolution operation, $h()$ is the PSF, $\mu_b()$ is the ideal measured intensity with background and without noise, $b()$ is a background level mainly due to non-specific staining and the dark current in the image sensor (Janesick *et al*., 1987; Snyder et al., 1993), $\mu_n()$ is the collected image data that contains noise, and $N()$ is noise, primarily due to quantum variations in the number of photons recorded.

Deconvolution produces an estimate, or restoration, of $f()$. The background level $b()$ is calibrated as discussed later and is addressed by precorrecting the raw data (Chapters 3 and 13, *this volume*).

MAXIMUM LIKELIHOOD ESTIMATION

Maximum likelihood estimation is a mathematical optimization strategy (Van Trees, 1968) used for producing best estimates of quantities from data corrupted by random noise. Because of the randomness of quantum photon emissions, the collected image represents data having a certain likelihood of having been produced among a host of other data that might have been recorded. MLE produces the estimate of $f()$ that has the highest likelihood of having given rise to the specific data collected.

In mathematical terms, we are formulating a *log-likelihood function* that represents a measure of the likelihood that one would collect the specific noisy data that were actually collected. This function is actually a functional (i.e., a function of a function) of $f()$, $h()$, and $\mu_n()$. Its formulation is based on the random nature of the quantum photon noise. This functional is solved iteratively to produce its maximum value. In blind deconvolution, specific quantities of $f()$ and $h()$ are solved using an iterative search (Dempster *et al*., 1977). The specific quantities of $f()$ and $h()$ that produce this maximum become the reconstructed image and the reconstructed PSF. With non-blind deconvolution, $h()$ is known from a prior measurement and the deconvolution algorithm solves only for $f()$.

Algorithms

WFF and CLSM Fluorescence

The flowchart for the blind deconvolution is shown in Figure 24.8. In Step 1, first guesses of $f^{(0)}()$ and $h^{(0)}()$ are made. Step 2 is designed from the expectation-maximization (EM) algorithm (Dempster *et al*., 1977; Holmes, 1989, 1992; Holmes and Liu, 1989, 1991; Holmes *et al*., 1991). Step 3 enforces the constraints placed on the solution of the PSF. The details of Step 3 are outlined in Figure 24.9.

The system may use a quantitative criterion for stopping the iterations. Several quantitative stopping criteria have been studied for applications in nuclear medicine (Veklerov and Llacer, 1987; Llacer and Veklerov, 1989). We prefer methods that monitor the progress in the likelihood value and then stop the iterations when the improvement in this functional between the last two iterations drops below a selected threshold.

The design of the flowchart in Figure 24.9 is modeled after the Gerchberg–Saxton approach (Gerchberg and Saxton, 1974). Step 1 enforces a unit summation constraint. Step 2 constrains the energy of the PSF to lie within an hourglass region b_h that is illustrated in Figure 24.10. This constraint prevents portions of the background intensity $b()$ from being mistakenly assigned to the PSF. Step 3 forces the 3D optical transfer function [OTF, the Fourier transform (FT) of the PSF] to be bandlimited. The 3D OTF has a frequency band (BW_{xy}) wherein it may be non-zero, with a missing cone region illustrated in Figure 24.11. Step 4 ensures non-negativity. This step is needed because Step 3 would otherwise cause negative numbers to appear in the result, but light intensity is never negative (these negative pixel values are set to zero). In the two-dimensional (2D) diffraction-limited case, the OTF frequency band is described by the interior of a circle having a radius of BW_{xy}, following the same formula as in the caption of Figure 24.11.

The CLSM fluorescence algorithm is similar to the WFF algorithm. The hourglass region of Figure 24.10 is replaced by a cylinder of radius r, and the bandlimit region of Figure 24.11 is replaced by a cylinder with twice the bandwidth along x,y and z and with no missing cone region. The bandwidths are doubled because the confocal PSF, when theoretically determined according to Fourier optics (Conchello *et al*., 1994), is approximated by a multiplication of two widefield PSFs. By the convolution theorem, when any two functions are multiplied their bandwidths are added. In real life, however, the truly confocal condition is only met if the detector pinhole is infinitely small, and the signal level is so high that Poisson noise can be ignored. Clearly this can never happen and a smaller diameter of BW_{xy} is appropriate.

Transmitted Light, Bright-field (TLB)

The deconvolution of TLB images of absorbing stains are produced using a variation on the WFF algorithm (Holmes *et al*., 1995; Holmes and O'Connor, 2000). The main requirement is that the condenser aperture must be larger than the objective lens aperture. This variation of the algorithms depends on the approximation that the raw TLB data $\mu()$ [(with noise $N()$ and background $b()$ ignored] follows a simple linear-systems model according to:

$$\mu(x, y, z) = B - h(x, y, z)*f(x, y, z), \tag{4}$$

where B is the bright background intensity, and $f()$ is the absorption coefficient. This approximation follows from Macias-Garza and colleagues (1989) when geometrical optics are considered, from Streibl (1984; Eq. 28) and when the phase contribution to the intensity in the image is ignored (i.e., the refractive index of the

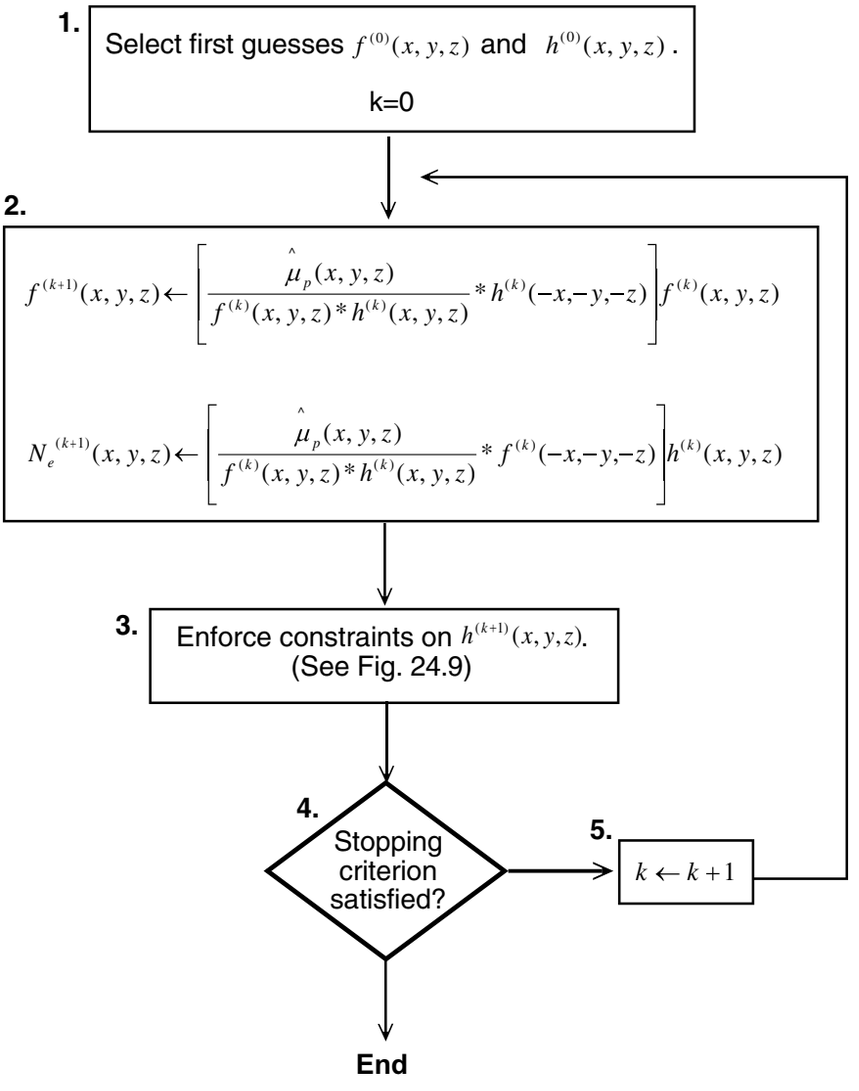


FIGURE 24.8. Flowchart of the MLE blind deconvolution algorithm: $f^{(k)}(x, y, z)$ is the reconstructed dye concentration of the kth iteration, $h^{(k)}(x, y, z)$ is the reconstructed PSF of the kth iteration, $\hat{\mu}_p$ is the optically sectioned image data, after being corrected for nonuniform sensitivity and shutter-speed instability, $N_e^{(k)}(x, y, z)$ is the temporary data array that stores an unconstrained form of the PSF estimate. Figure 24.9 shows details of the constraints in Step 3.

specimen is the same as that of the mounting medium), from Erhardt and colleagues (1985) when light emanating from the specimen is approximated as being fully incoherent, and from Sheppard and Gu (1994) when the specimen is considered to be a weakly scattering object (i.e., structures not stained enough to make them opaque). We noticed that by preprocessing this noise-free raw data according to:

$$\mu_p(x, y, z) = B - \mu(x, y, z) \quad \textbf{(5)}$$

we have a model expressed according to:

$$\mu_p(x, y, z) = f(x, y, z) * h(x, y, z), \quad \textbf{(6)}$$

which is identical to Eq. 1.

The deconvolution is carried out as follows: First, the raw data are precorrected for background, flat-field non-uniformities and shutter-speed fluctuations (Cooper *et al.*, 1993; to arrive at $\hat{\mu}(x, y, z)$, which is an estimate of the $\mu(x, y, z)$ shown in Eq. 4. Then, $\hat{\mu}(x, y, z)$ is preprocessed according to Eq. 5 to produce an estimate of $\mu_p(x, y, z)$, which is denoted in Figure 24.8 as $\hat{\mu}_p(x, y, z)$. Finally, the flowchart of Figure 24.8 is executed on $\hat{\mu}_p(x, y, z)$.

Figure 24.12 shows stereo-pairs both before and after a TLB deconvolution of bright-field data.

Differential Interference Contrast (DIC)

The objective of DIC deconvolution is to produce a 3D image of the refractive index distribution. The DIC image formation model is nonlinear and uses Fourier optics principles (Holmes and Levy, 1987; Hansen and Conchello, 1988; Preza *et al.*, 1998). A rough conceptual schematic of the components in a DIC microscope is shown in Figure 24.13. Two orthogonally polarized beams are produced by Wollaston prisms and pass through the specimen as separate ray bundles slightly displaced from each other in the shear direction. The image represents a coherent-light interference pattern that is formed at the image sensor when the two beams are combined. Image contrast is produced by inhomogeneity of the sample's refractive index (RI) distribution near the plane of focus.

The observed image g is modeled by a linearized approximation according to the following equation:

$$g = s(K \cdot f * h_1 * h_2) + n \quad \textbf{(7)}$$

where f is the original refractive index distribution, h_1 is the theoretical DIC PSF that reduces to two delta functions (van Munster *et al.*, 1997), h_2 is the PSF that accounts for the resolution limit of the optics, n is Gaussian noise, and * is the convolution operator. K is a constant that converts the change in RI to a phase differ-

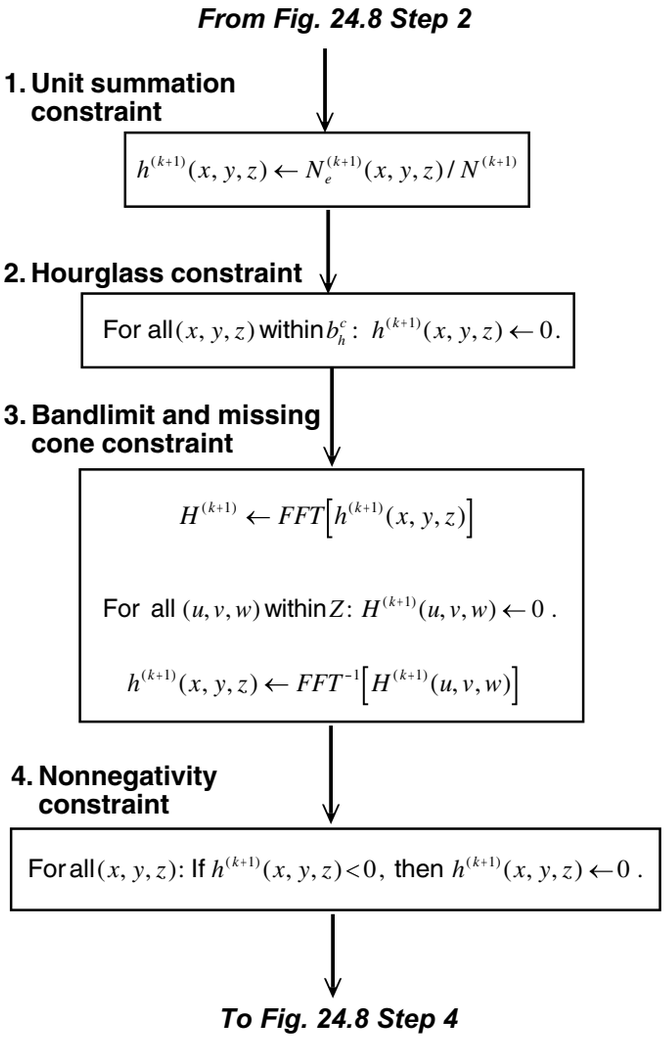


FIGURE 24.9. Flowchart of constraints applied in WFF and TLB. These blocks make up Step 3 in Figure 24.8. The term b_h^c is the complement of b_h (see Fig. 24.10) and is the region wherein $h()$ is near zero. $H^{(k+1)}$(u, v, w) is the Fourier transform of $h^{(k+1)}()$. Z is the region of $H()$ which is zero. FFT and FFT^{-1} indicate the forward and inverse fast Fourier transforms, respectively. These constraints are carried out iteratively.

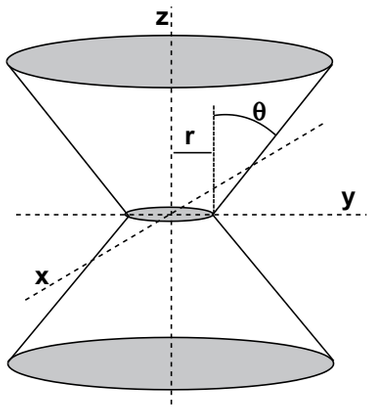


FIGURE 24.10. Hourglass region used in constraining the widefield PSF. The terms b_h and b_h^c denote the regions inside and outside the hourglass, respectively. The radius r is set to be a number of Airy disk widths according to $r = 0.61\,c\lambda/\mathrm{NA}$, where λ and NA are the wavelength and numerical aperture, respectively. We use $c = 1$. The acceptance angle θ is found from $\theta = \sin^{-1}(\mathrm{NA}/\eta)$, where η is the refractive index.

ence. The function $s()$ represents the transformation of the phase differences to intensity values that occurs when the two waves are combined at the image sensor.

The deconvolution process uses an iterative optimization algorithm that is complicated by several factors. First, DIC produces contrast only from changes in RI that occur in the shear direction. As a result the differential PSF has a significant null spectral component in the direction perpendicular to the shear, and this must be accounted for. Otherwise, streaking artifacts will appear parallel to the orientation in which the beams are separated (Kam, 1998). Second, one cannot assume nonnegativity in the RI change, relative to the background. Instead, negative values are only penalized. This approach provides a soft constraint where the negative values are, in a sense, minimized but not prevented altogether. This is a reasonable assumption because, typically, biological structures have a higher RI than the aqueous embedding medium. In cases where the specimen refractive index is less than the embedding medium, the data are processed using a penalty on positive values. Finally, for proper reconstruction, the intensity data should be converted to phase data by reversing the effect of the nonlinear function $s()$.

The result of the reconstruction is a map of RI, or optical path length, from a DIC image, which is similar in nature to that produced by a transmitted light interference microscope (Inoué and Spring, 1997, p. 86; Dunn, 1988). The technique also requires only one image per focal plane, compared to the several images per focal plane that are required by the rotational diversity technique (Preza *et al*., 1998). While reconstructed DIC data bear a superficial resemblance to darkfield (DF) images, it's important to remember that it is impossible to know if a bright feature in a DF image represents a structure having an RI that is higher or lower than its surroundings.

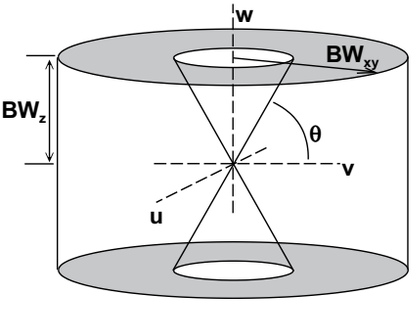


FIGURE 24.11. Illustration of the region wherein the widefield 3D OTF may be non-zero. The 3D coordinates u, v, and w are the frequencies with respect to x, y, and z, respectively. The radial bandlimit follows the formula: $BW_{xy} = 2\,\mathrm{NA}/\lambda$. The axial bandlimit follows the formula $BW_z = (\mathrm{NA})^2/(2\eta\lambda)$. θ follows the same formula as shown in the caption of Figure 24.10. The biconic region is the "missing cone." The region of the OTF where it is known to have all zero values, Z, is the union of this missing cone with the region outside of the cylinder.

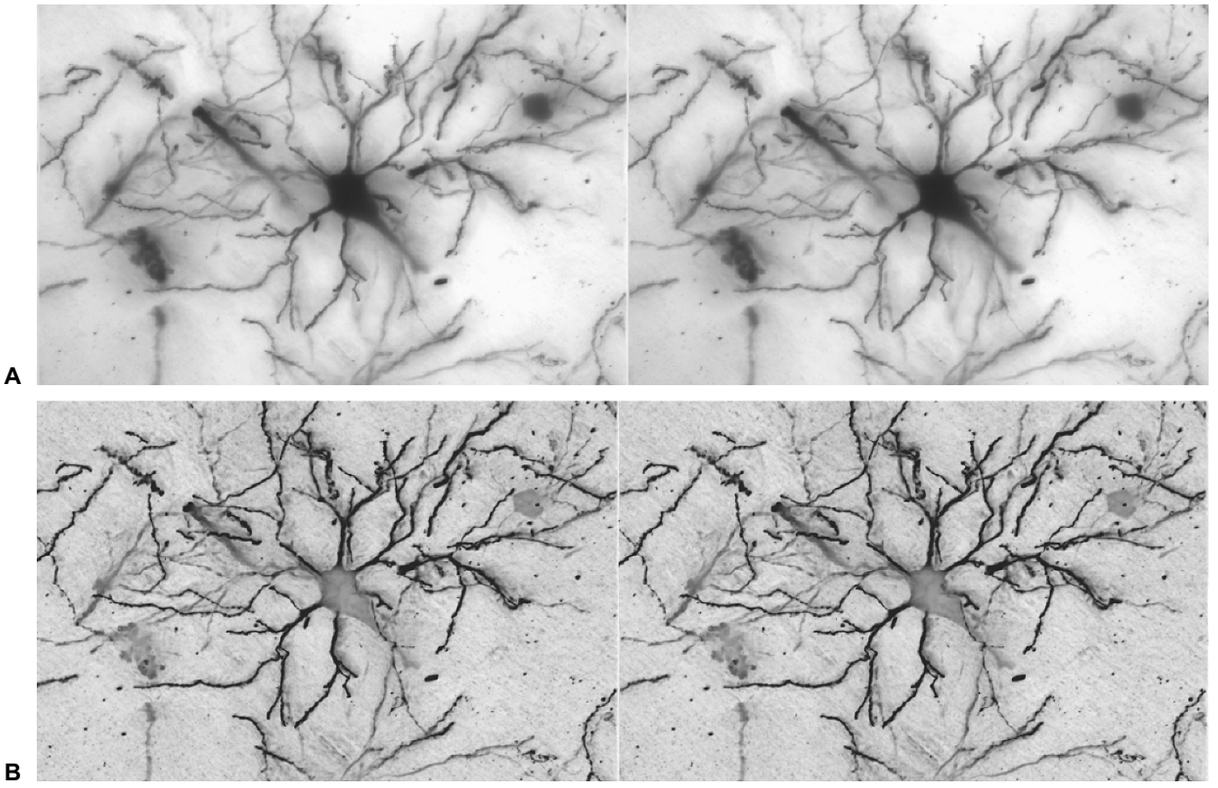


FIGURE 24.12. (A) Stereo-pair of a TLB stack. (B) After deconvolution.

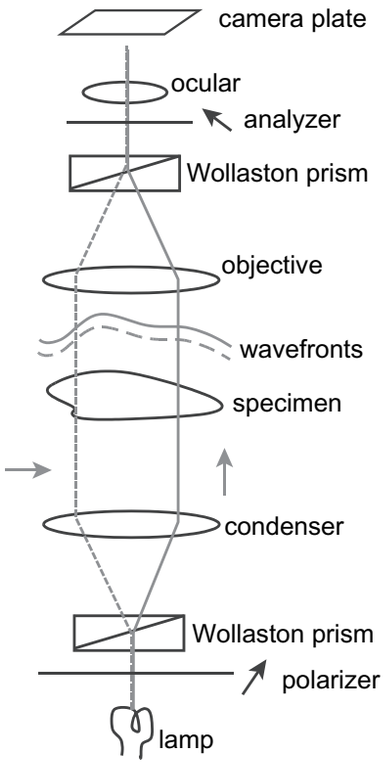


FIGURE 24.13. Rough schematic of the DIC microscope.

DIFFERENT APPROACHES

3D

The MLE algorithms, both *blind* and *non-blind*, are in a category of algorithms known as the *iterative constrained* algorithms (Wallace *et al*., 2002). They are called *iterative* because they repeat the same steps to update $f^{(k)}()$, as shown in Figure 24.8. They are called *constrained* because the bandwidth is limited and the values of $f^{(k)}()$ are allowed only to be nonnegative. Among other approaches, described below, these iterative constrained approaches are considered to be the most quantitatively accurate; that is, the summation of the intensity in all the pixels of the image is preserved. The total number of photons in the final reconstruction is the same as was collected from all the charged-coupled device (CCD) images. As, in some sense, this is a normalization, one might expect that any deconvolution approach can yield a similar result, simply by following the deconvolution with a normalization operation. However, what is different here is that the normalization is inherent within the deconvolution operation itself. It is an intrinsic fallout of the MLE process and not something that must be done afterwards.

One reason these iterative constrained algorithms are more accurate is that they are capable of recovering Fourier transform information, such as the missing cone information, which was removed by the optics. Details about the missing Fourier components and how they are recovered may be found in Holmes and Liu (1989). The inverse filter and nearest neighbor approaches

Table 24.1. Processing Times and Memory Requirements for Implementation on a Windows 2000/NT/XP 3 GHz Computer

Image Size	10 Iterations, Blind Deconvolution	Inverse Filter
256 × 256 × 10	13 s	1.3 s
1024 × 1024 × 50	20 min	2 min

Requirements for other data-set sizes can be approximated. Processing time will be proportional to *M log M* (*M* = number of voxels) which is the proportionality of an FFT (Oppenheim and Schafer, 1975). Most of the processing time is taken by calculating the FFTs. Extra memory is not needed for large image sizes because the image may be decomposed into subregions that are deconvolved separately. For future computers with faster chip sets, processing speed is roughly proportional to the Pentium computer chip speed (e.g., 3 GHz).

described below do not recover this information. Other iterative constrained approaches include the *Jansson–van Cittert* algorithm (Holmes and Liu, 1992b) and *least squares* (Carrington, 1990) algorithms. Iterative-constrained algorithms are generally much slower to compute than the *inverse filter* or *nearest-neighbor* algorithms. However, as computer speed has increased, this issue has been mitigated significantly in recent years (Table 24.1). Today, typical iterative deconvolutions require only a few seconds to a few minutes on a personal computer (PC).

A variant on *Gold's* ratio method (Agard *et al*., 1989) is another iterative-constrained algorithm. It is similar to the algorithm shown in Figure 24.8, except that the convolution of $h(-x, -y, -z)$ is removed. It has been developed by Sibarita and colleagues (2002) to provide high-throughput of hundreds of volumes in a short time. The advantage of this approach is that of speed, while some noise reduction is sacrificed.

The *nearest-neighbor* algorithm is the fastest algorithm. It is a 2D algorithm that works by sharpening each image in the stack one at a time. Mathematical details are in Holmes (1992) and Agard and colleagues (1989). The two adjacent images in the stack (above and below) are reblurred by convolving them with an approximation to the PSF. These two reblurred images are then multiplied by a coefficient (<1) and subtracted from the image being sharpened. This operation is known generically as unsharp masking (Russ, 1995). This algorithm is not quantitative. Image intensities are not preserved. A summation of the processed image is just a fraction of the summation of the original image. This algorithm is really an *image enhancement* method, although it is sometimes controversially called a deconvolution. A more generally accepted term is *deblurring* algorithm (Wallace *et al*., 2002). Its main advantage is that it runs in a fraction of a second on a PC. Figure 24.14 shows a nearest-neighbor processed image of the optical section shown in Figure 24.3.

The inverse filter is another fast approach. The Fourier transform of Eq. 1 is expressed as:

$$M_p(u, v, w) = F(u, v, w)H(u, v, w) \quad \textbf{(8)}$$

where $F()$ and $H()$ are the Fourier transforms of $f()$ and $h()$, respectively. Ideally, $f()$ ought to be recoverable from $M_p()$ by taking the inverse Fourier transform of the following operation:

$$\Lambda(u, v, w) = M_p(u, v, w)H_r(u, v, w), \quad \textbf{(9)}$$

where

$$H_r(u,v,w) = \frac{1}{H(u,v,w)}. \quad \textbf{(10)}$$

In reality, $H(u, v, w)$ contains zeros, so Eq. 10 is mathematically unstable and this approach does not work. Instead, a regularized variant of $H_r(u, v, w)$ is used, according to the expression:

$$H_r(u,v,w) = \frac{H^*(u,v,w)}{|H(u,v,w)|^2 + k}, \quad \textbf{(11)}$$

where the * superscript denotes complex conjugate and the term k is a very small number that is empirically chosen. Equation 11 is a regularized approximation to Eq. 10 that is based on the principles of the Wiener filter (Castleman, 1979). It approximately equates to Eq. 10, except where $H(u, v, w)$ is near zero.

The inverse filter is fast to execute (Table 24.1), yet preserves reasonable quantitative accuracy. Figure 24.15 shows the optical slice shown in Figure 24.3 after application of an inverse filter.

The inverse filter works well with phase objects imaged under a TLB microscope with a small condenser aperture. Iterative constrained methods will not work well to deconvolve such an image because it does not follow the mathematical model where $\mu_p()$ must be nonnegative and constructive interference causes areas in the specimen to be brighter than the background. An inverse filter works because it does not rely on $\mu_p()$ being nonnegative. Figure 24.16 shows summed intensity projections of an unprocessed stack and a processed stack.

2D Image Filtering

The nearest-neighbor algorithm has a variant, called the no-neighbors algorithm, which operates only on a single 2D plane of

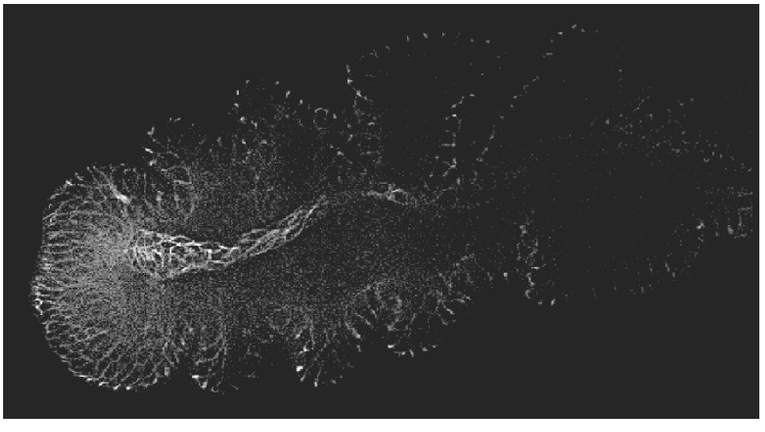


FIGURE 24.14. Optical section shown in Figure 24.3(A) after the nearest-neighbor algorithm.

the image being sharpened. Instead of reblurring adjacent images, the image being sharpened is reblurred, multiplied by the coefficient, and subtracted from itself. Because this no-neighbors variant operates on 2D data alone, it does not require 3D data, so it is a much simpler technique to use and requires inexpensive equipment. The complete system shown in Figure 24.2 is no longer needed to take advantage of 2D deblurring. Any microscope with a digital camera will benefit.

There is also a purely 2D variant of the MLE blind deconvolution algorithm (Biggs, 1998) which shares some of these 2D advantages. As with the no-neighbors algorithm, any microscope with a digital camera will benefit. This 2D MLE algorithm works well when the sample is inherently 2D, as with flat samples that fit within the depth of field, with objectives having a large depth of field or with total internal reflection (TIRF) microscopy. It works surprisingly well even in many cases where the sample is inherently 3D, as long as high-NA optics are used to reduce depth of field. However, in these inherently 3D cases, it is more accurate to think of this algorithm as a nonlinear sharpening filter than as a deconvolution because the algorithm assumes that the imaging process is 2D and this is an inaccurate assumption.

DATA CORRECTIONS

Images recorded using common intensified and standard CCD digital cameras can be deconvolved. Peltier-cooled sensors (−70° or lower) are preferred because they have the lowest noise level, the best linearity, the highest dynamic range (16 bits), and the lowest background levels. Image data collected from any cooled-CCD camera must be calibrated for the background level $b(x, y, z)$, non-uniform pixel sensitivity, $\beta(x, y)$, and the camera exposure-time instability $T(z)$ such that the raw collected data $\mu_r(x, y, z)$ are composed of:

$$\hat{\mu}_r(x, y, z) = \beta(x, y, z)T(z)\mu(x, y, z) + b(x, y, z). \qquad (12)$$

The exposure time $T(z)$ varies with z as the shutter may fluctuate by several milliseconds between frames. When non-mechanical shutters are used, the exposure time does not vary, but the illumination varies because arc lamps wander and power variations affect incandescent lamps. The $T(z)$ term accommodates these variations. The correction method is outlined in Cooper and colleagues (1993).

The corrected data set $\hat{\mu}()$ is an estimate of $\hat{\mu}()$. For TLB, this estimate is further processed by Eq. 5, and for WFF it is substituted directly for $\mu_p()$ in Figure 24.8.

In CLSM fluorescent data, $\beta()$ and $T(z)$ are irrelevant, and only $b()$ must be determined. To estimate b, a background region of interest is chosen and the average background level is calculated from this data. Alternatively, a histogram of intensity levels is calculated on the image, and the background level is detected automatically by identifying the peak in the histogram that is close to zero.

LIGHT SOURCE AND OPTICS ALIGNMENT

Deconvolution is forgiving about microscope misalignment, but only to a limit. Misalignment causes degradation in the PSF. When the optics are misaligned, the PSF is less symmetric, and deviates from ideal theory in other ways. The non-blind algorithms and the inverse filter algorithm that use a PSF measurement, adapt to this assymetry, to a degree, because the assymetry occurs in both the measured and actual PSF. The blind deconvolution will adapt to misalignments too, much in the way that it adapts to spherical aberration as shown in Figure 24.6(C).

On the other hand, deconvolution follows the proverbial "garbage-in garbage-out" principle. Circular averaging is often performed to reduce the noisiness of the measured PSF and this causes the calibrated PSF to deviate from the true, assymetric PSF. The best images are obtained with proper Köhler alignment (see Chapter 36, *this volume*). For non-blind deconvolution, this limit is partly because the PSF measured with a fluorescent bead is not the same PSF that exists in the biological sample. As the sample itself is a heterogeneous refracting medium that is part of the optics, when the sample changes, the PSF changes. Although blind deconvolution adapts to PSF changes, the closer the true PSF is to the theoretical PSF, the better the results.

Another consideration in obtaining a well-behaving PSF, which works well for immersion lenses, is to adjust the refractive index of the medium that is between the objective lens and the coverslip. The technique described in Hiraoka and colleagues (1990) uses finely adjusted immersion media to minimize the spherical aberration (see Chapter 20, *this volume*). Oils having a different RI are placed onto and removed from the coverslip, one-by-one, with RI differences of 0.002. The refractive index that provides the most symmetrical PSF along the z axis is chosen. It is straightforward to see the symmetry by focusing up and down on a bead and noticing if the out-of-focus bead seen while focusing up looks the same as the out-of-focus bead seen while focusing down (see also Fig. 20.3, *this volume*). It is necessary to match the oil in this same way with the specimen. A fine structure needs to be identi-

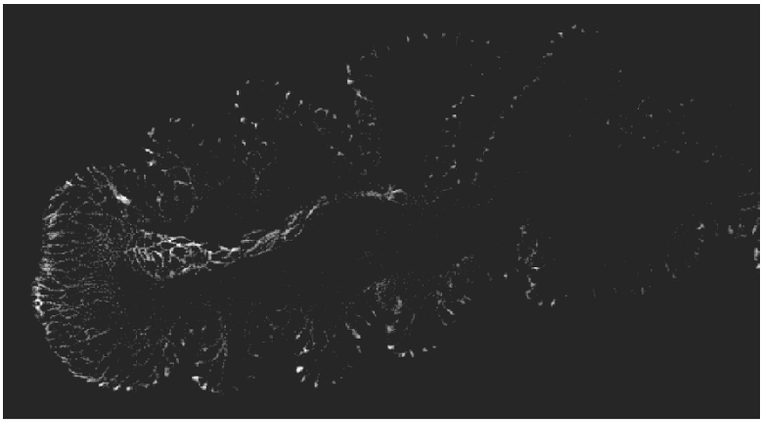


FIGURE 24.15. Optical section shown in Figure 24.3(A) after the inverse filter.

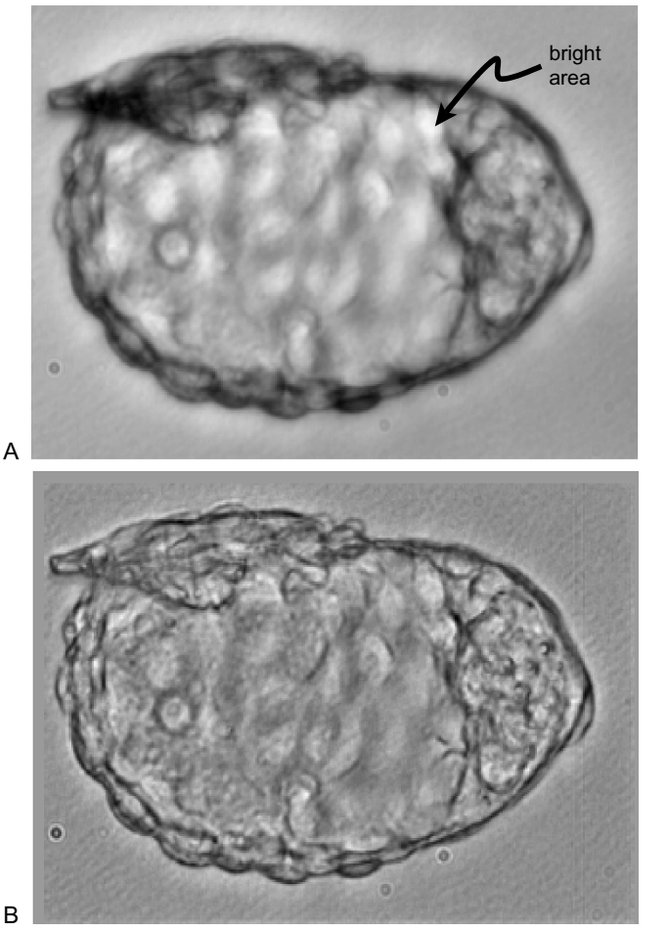


FIGURE 24.16. Summed projections of a phase object obtained by TLB. (A) Unprocessed; (B) deconvolved. (Image courtesy of G. Eddlestone, Empire Imaging Systems.)

fied in the sample, such as a microtubule, or anything that is small, and then focusing up and down while noticing if the out-of-focus object looks the same while focusing up compared to focusing down. This procedure minimizes the spherical aberration, which is the most severe aberration. Alternatively, the microscope manufacturers produce special lenses with adjustable "correction collars" that affect a correction for spherical aberration.

In polarizing and TLB imaging, non-uniformity in the light source can also cause problems (see Chapter 6, *this volume*). The theoretical PSF is cylindrically symmetric because it is formulated under the assumption that light enters the sample with equal intensity at every angle within the numerical aperture. In fact, light enters the sample at different intensities depending upon the angle because the lamp is not uniform. A point in the plane of the lamp corresponds to an angle of parallel light rays in the specimen. The intensity at the center of the lamp is proportional to the intensity of parallel rays passing through the sample at zero angle. The intensity at a distance from the center of the lamp enters the sample at an angle that is proportional to this distance. A mercury-arc lamp is brightest within its arc of light, so angles that correspond to points in this arc have the brightest intensity impinging on the sample. As a result the PSF is not circularly symmetric. Although deconvolution is forgiving of an asymmetric PSF, it still works best with a symmetric one. Ellis designed an illuminator using a vibrating fiber-optic that provides a uniform light source and thereby provides a symmetic PSF (Ellis, 1979; Inoué and Spring, 1997, p. 160). These non-uniform lamp effects do not exist with the WFF microscope. In this case, the symmetric PSF relies on having spatially uniform excitation light, which is guaranteed by Köhler illumination, and on having well-aligned emission optics. The WFF PSF does not rely on having uniform intensity with respect to the angle of illumination.

The partial confocal effect also causes PSF assymetry (Hiraoka *et al*., 1990). The field diaphragm behaves like a confocal detector aperture of sorts because it is conjugate to the specimen plane. As it is stopped down, it causes the WFF PSF to look ever more confocal-like and the intensity of the PSF along the optic axis decays more quickly than WFF theory predicts. Furthermore, this decay is assymetric and makes it more difficult to match the measured PSF (with the bead present) to the true PSF (with the specimen present). This effect makes it more difficult to match the assumptions that are used in blind deconvolution. Therefore, it is best, for deconvolution, to keep the field aperture wide open. The partial confocal effect still exists, but it is minimal.

NEWEST DEVELOPMENTS

Subpixel

Images may be deconvolved to produce results that have a pixel resolution different from the original data (Carrington *et al*., 1995; Conchello and McNally, 1997; Wang, 2002). The idea is illustrated in Figure 24.17. Unobserved pixels are inserted into the mathematical model of the image. They are recovered by treating them as "unknown data" regions as outlined in Holmes (1989).

Figure 24.18(A) shows an image slice from a data stack (Wang, 2002). This is an image of a centrosome labeled with green fluorescent protein (GFP)–gamma-tubulin. The length of the centrosome, along its long axis, is ~1 µm. Figure 24.18(B) shows a deconvolved result made by increasing the pixel resolution by a factor of 3 along x and y. A verification of the structure is shown in Figure 24.18(C). This figure shows a TEM image of the same sample taken afterwards and verifies the recovered structure.

Khodjakov and colleagues (2002) discovered that these centrosomes are sometimes formed *de novo*, without association with a pre-existing organelle. Deconvolution was used to observe changes in the shape of the pericentriolar material cloud in living samples. Only TEM can record such shapes directly, but not in living cells.

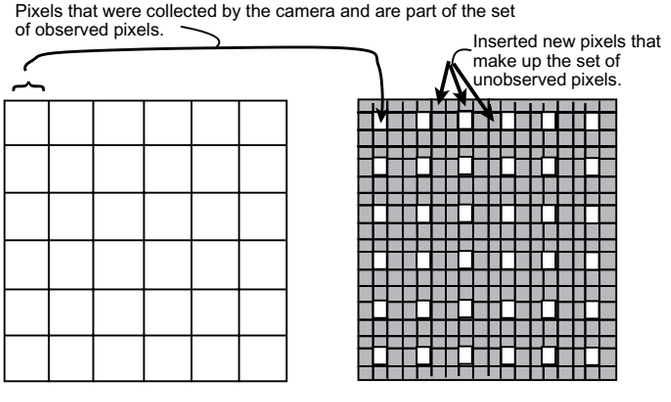


FIGURE 24.17. Schematic of subpixel deconvolution.

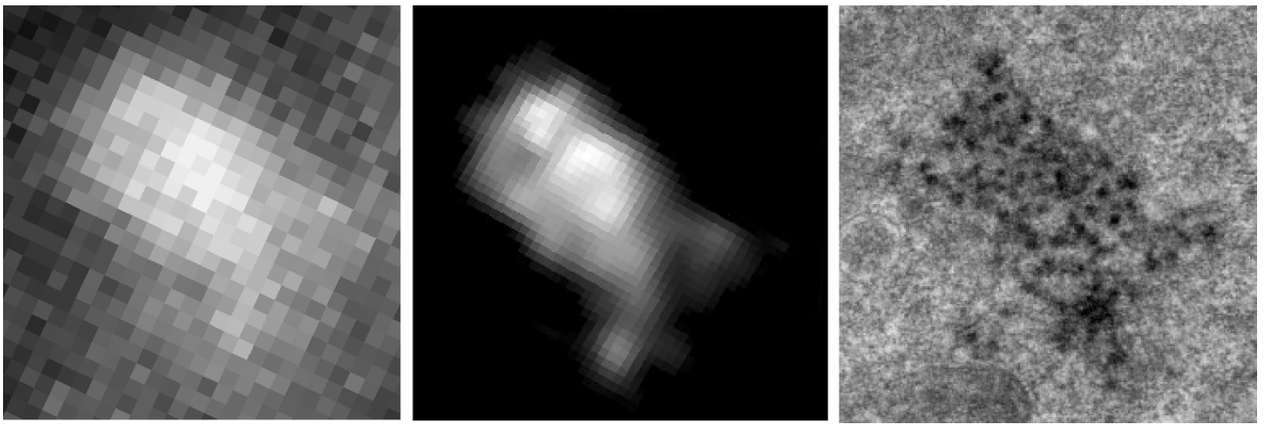


FIGURE 24.18. A subpixel deconvolution. (A) Optical section taken from a stack. The sample is a centrosome labeled with GFP–gamma-tubulin. It is just over 1 µm long. (B) Subpixel deconvolution. The pixel size was reduced by 3 in both directions. (C) EM micrograph of the same sample, verifying the structure shown in (B). (Image courtesy of A. Khodjakov, Wadsworth Laboratories.)

Polarized Light

It is possible to deconvolve 3D optical section data of birefringent samples made using a polarized light microscope. Strictly speaking, the image formation model for a polarized-light microscope is nonlinear (Hansen and Conchello, 1988), so from a pure standpoint, a PSF model such as the one used for WFF ought not to apply. However, from a practical standpoint, it is common engineering practice (Close and Frederick, 1993) to introduce a linear approximation to make any nonlinear model tractable. From this perspective, Eqs. 1 to 3 may apply, and can be considered to be a linearized approximation for the polarized-light microscope. Furthermore, optically sectioned images of birefringent samples sometimes appear similar to WFF samples as is the case shown in Figure 24.19(A), which shows a maximum-value projection stereo-pair of the raw data. Figure 24.19(B) shows the stereo-pair after deconvolution. This deconvolution should work as well with the Pol-Scope developed by Oldenbourg and Mei (1995), which is

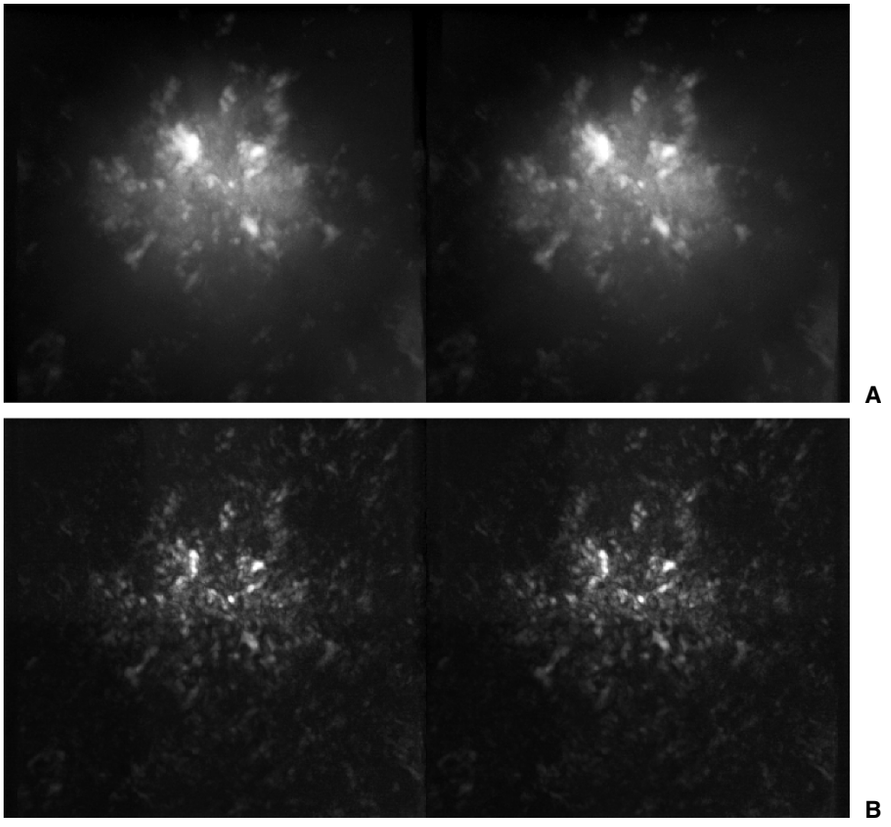


FIGURE 24.19. (A) Stereo-pair of a polarized light stack. This stack was acquired from an ice-cream sample as part of a study of food production quality. The object is a fat crystal. (B) After blind deconvolution. (Image courtesy of K. Baker, University of Guelph.)

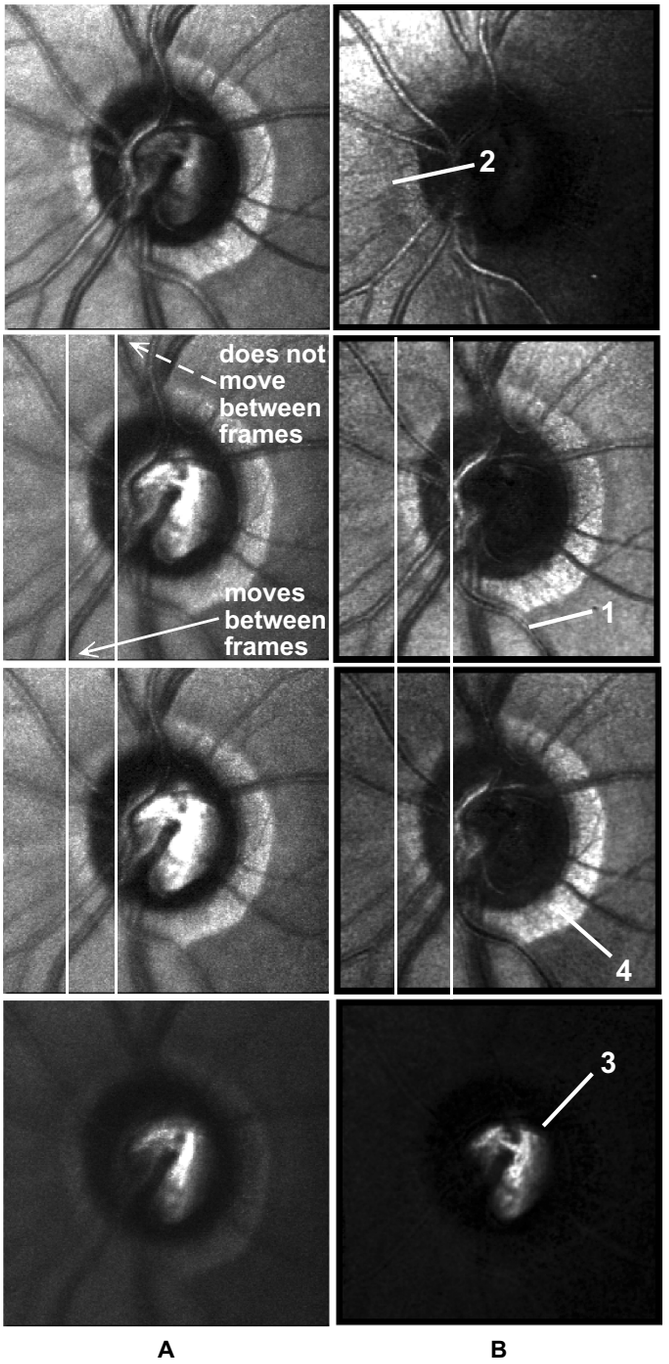


FIGURE 24.20. Sections from an SLO in the reflected light mode. The optic nerve region is shown with large vasculature (1), capillaries (2), the lamina cibrosa (3), and the scleral ring (4). These structures are clearer after deconvolution. Structures are isolated better to their proper location along z, as seen by the improved discrimination between the slices. Before deconvolution, the scleral ring and *lamina cibrosa* appear in most slices. After deconvolution, they are properly isolated to their appropriate locations. (Data collected using the Heidelberg Retinal Tomograph (HRT), Heidelberg Engineering, Heidelberg, Germany. Image courtesy of D. Garway-Heath, Moorfields Eye Hospital.)

a special type of polarized light microscope designed for sensitivity and quantitative accuracy. It yields an image in which the intensity is, to a first approximation, proportional to the magnitude of the birefringence. Strictly speaking, there will be a positive, nonlinear dependence on the scalar birefringence.

Live Imaging

Two important issues arise with live imaging: (1) when tissue is monitored over time, many deconvolutions (sometimes hundreds) must be performed. Such applications benefit from processing times on the order of seconds. (2) The sample moves during the image acquisition. The first issue is addressed in "Future Directions."

An example of the second issue is shown in Figure 24.20, which shows confocal sections from a scanning laser ophthalmoscope (SLO; Bartsch and Freeman, 1994; shown schematically in Fig. 24.21). Reflected light confocal sections were acquired during an outpatient procedure. Although the motion of the eye is mitigated by having the patient fixate on a blinking light, the eye still moves between frames and during the 1/20th of a second that each frame is acquired. There is an x,y translation and a rotation as well as geometric distortion between frames (O'Connor *et al.*, 1998). The two lines overlaid on Figure 24.20(A) show that there is motion of the blood vessel shown by the solid arrow and, as a result, there is geometric distortion between frames.

The alignment, rotation, and geometric distortion are corrected by preprocessing the optical sections with a software motion-detection algorithm that is based on a mathematical cross-correlation. Figure 24.20(B) shows the deconvolved optical sections. The algorithm described in the section "Algorithms — WFF and CLSM Fluorescence" was used. The geometric distortion is removed. Improved optical sections and better discrimination between slices are produced. The scleral ring, and other known anatomical structures are better isolated to a slice, while blood vessels and capillaries are clearer. Figure 24.22 shows a stereo-pair of the deconvolved stack.

MORE EXAMPLES

Blind Deconvolution and Spherical Aberration

An example of a blind deconvolution was presented earlier in the section entitled "Advantages and Limitations." The first guess of the PSF [Fig. 24.6(B)], used to seed the first iteration of the blind deconvolution of Step 2 in Figure 24.8, was calculated as the autocorrelation of the raw data. The autocorrelation operation may be found in the book by Gaskill (1978). It is, in essence (although not precisely), the convolution (see the Appendix for this chapter) of the PSF with itself. More precisely, it is expressed according to

$$h^{(0)}(x, y, z) = N(x, y, z) * N(-x, -y, -z), \qquad \textbf{(13)}$$

where $h^{(0)}()$ is the first guess of the PSF.

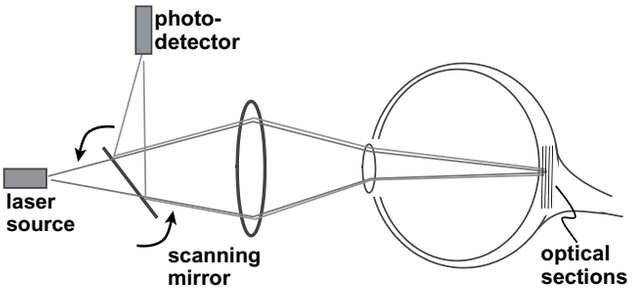


FIGURE 24.21. Schematic of the SLO.

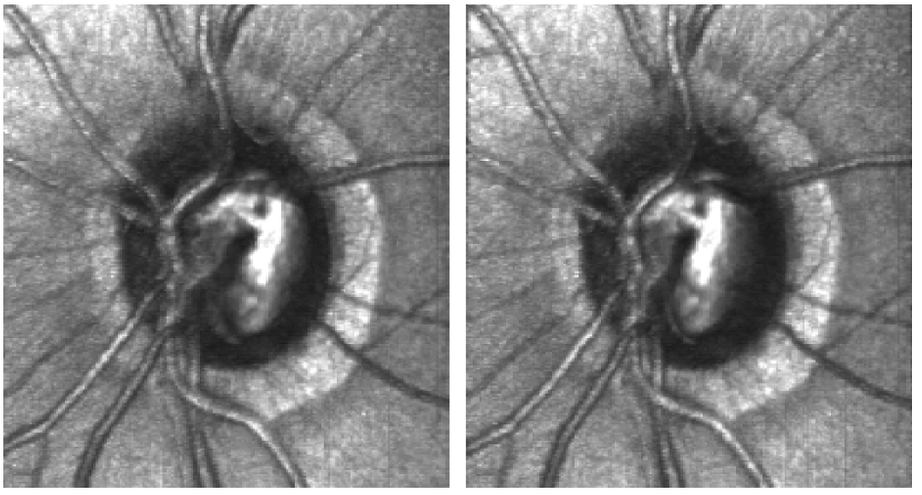


FIGURE 24.22. Stereo-pair of the optic nerve data set shown in Figure 24.20.

The PSF that resulted after running the blind deconvolution starting from this first guess is shown in Figure 24.6(C). Note that it contains the same flare seen in the raw data of Figure 24.6(A). For comparison, Figure 24.6(D) shows a theoretically calculated PSF with spherical aberration that matches the flare seen in Figure 24.6(A). Figure 24.6(E) shows a theoretically calculated PSF without spherical aberration. From these comparisons it is obvious that the predominant flare character seen in raw data of Figure 24.6(A) and in the recovered PSF of Figure 24.6(C) is due to spherical aberration.

Widefield Fluorescence Simulation

Simulated deconvolutions have been carried out to guide development of deconvolution programs. Though not exhaustive, these simulations are instructive because, unlike a biological specimen, the original "test object" is known. Simulations provide insight into the advantages and limitations of different deconvolution approaches. Figures 24.23 and 24.24 show a WFF simulation.

A computer program created the object shown in Figures 24.23 and 24.24(A). The theoretical widefield PSF, like the one shown in Figure 24.6(E), was created by a computer program that used the diffraction theory as explained by Streibl (1984). This 3D PSF was convolved with the 3D object using Fourier transforms (Gaskill, 1978), and the Fast-Fourier-Transform algorithm (Oppenheim and Schafer, 1975). Once the diffraction-limited 3D data set was created in this way, quantum-photon noise was simulated by software written to create random numbers that follow Poisson statistics (Mortensen, 1987).

Figure 24.23 shows a schematic of the simulated test object (Markham and Conchello, 1998). It has the shape of wagon wheel pasta. When the out-of-focus haze is removed by the deconvolution, the spokes on the wagon wheel and the surface of the wheel are restored, except for those parts that are horizontally planar. The inability of deconvolution to restore horizontal planes is a well-known limitation of widefield deconvolution and is caused by the missing cone region (Holmes, 1992; Holmes *et al*., 1995; Streibl, 1984) (Fig. 24.11) which removes all of the information necessary to restore a horizontal plane. Fortunately, very few biological structures have perfectly horizontal planar components labeled by the dye. Those that do are better imaged with a confocal microscope. Note that the same horizontal spokes that are not restored in Figure 24.24(C) are restored in Figure 24.24(D), where the horizontal parts are at the edge of the cylinder, so they are not planar. Here, the necessary Fourier components needed to restore the horizontal parts reside outside of the missing cone, and therefore the deconvolution algorithm has sufficient information to recover them.

Spinning-Disk Confocal

Figure 24.25 shows a deconvolved data set from a spinning-disk confocal microscope. An advantage of the blind deconvolution is that it is capable of adapting to many modalities because the PSF does not need to be known perfectly.

Two Photon

Figure 24.26 shows optical sections made with a two-photon microscope, before and after deconvolution. The algorithm used is identical to that used with the confocal microscope, because the PSF of the two-photon microscope is similar to that of the confocal microscope. The signal-to-noise level and optical sectioning discrimination are improved by the deconvolution. Although not clear from this example, the in-plane resolving power may also be improved (see also Chapter 25, *this volume*).

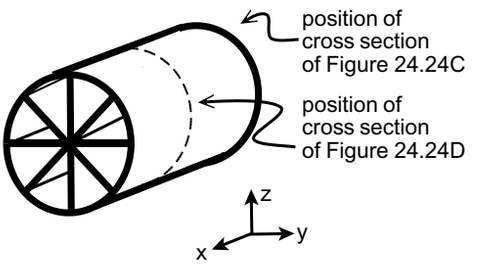


FIGURE 24.23. Schematic of the simulated test object.

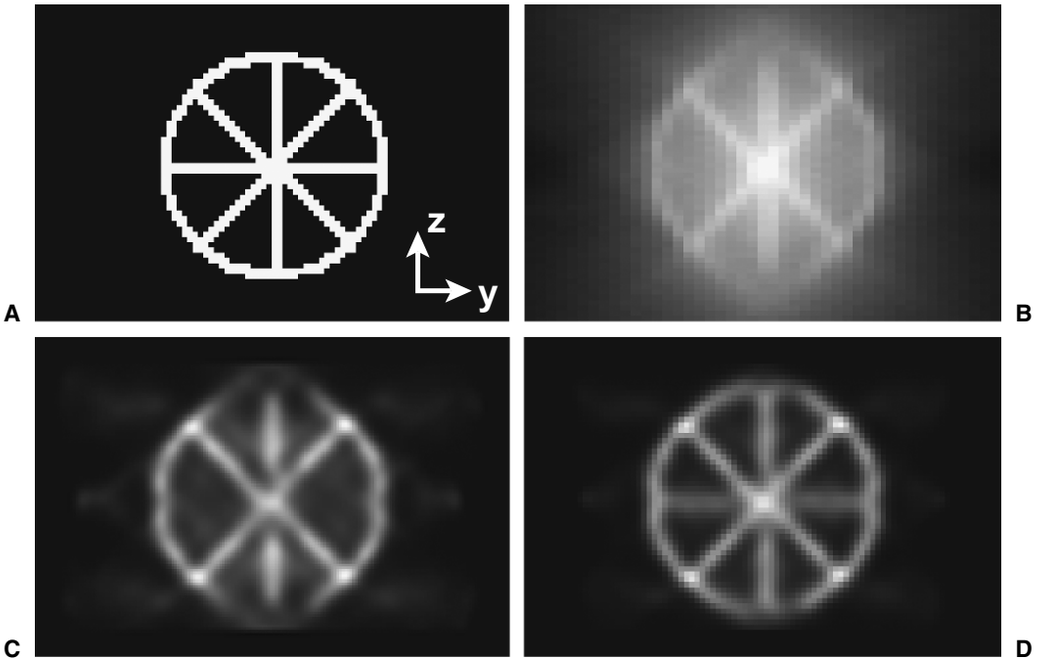


FIGURE 24.24. (A) *yz* slice of the test object (Fig. 24.23). (B) *yz* slice of the simulated WFF data. (C) Deconvolution of the central cross-section. (D) Deconvolution of the cross-section taken at the end of the cylinder.

SPEED

Prior speed limitations (Holmes *et al*., 1995) are now less of a problem. Twelve years ago deconvolutions were performed on a mainframe supercomputer and now they are performed on a PC. Numbers of iterations used to be in the 100s and now they are on the order of 10. Deconvolutions are performed in seconds rather than hours. Even so, there will always be demand for higher speed. The operator needs fast visual feedback during four-dimensional (4D) live imaging, especially now that the electron multiplier CCD (EM-CCD) makes it possible to see faint signals at high frame rates with little readout noise. Current deconvolution speeds are listed in Table 24.1, see p. 476.

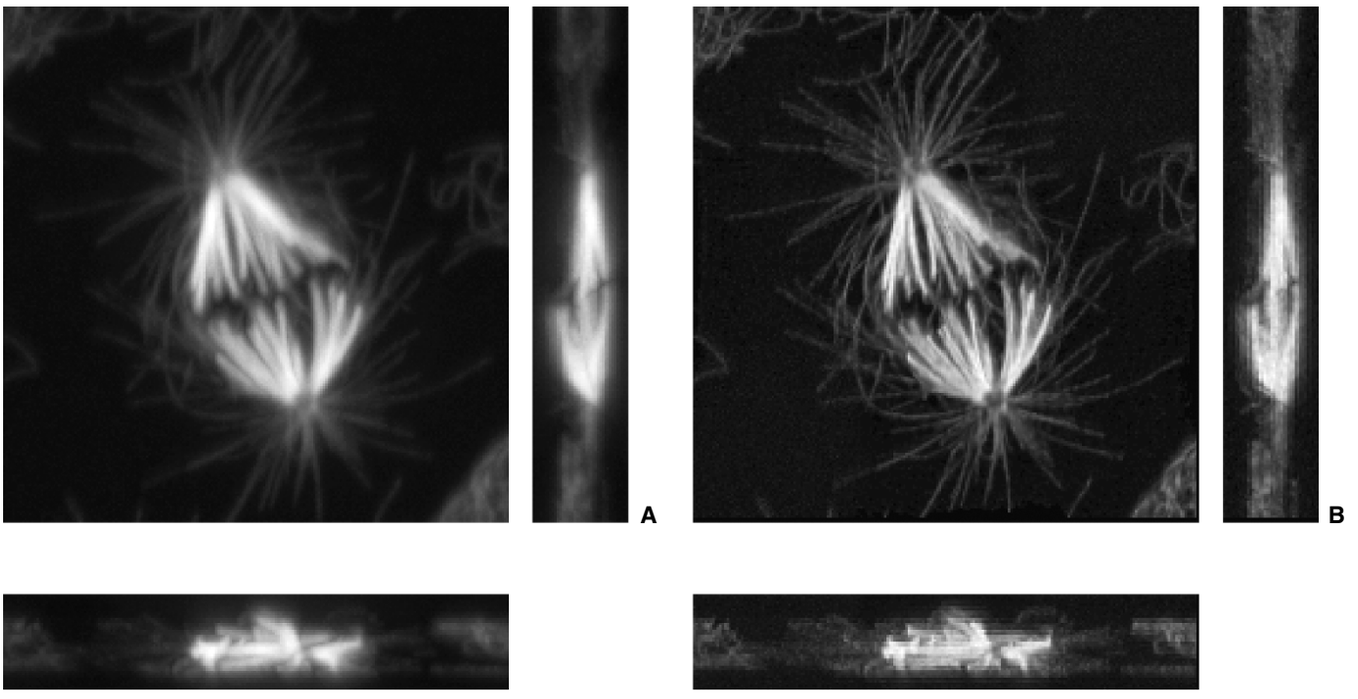


FIGURE 24.25. (A) Orthogonal maximum projections of a fluorescent sample taken from a Yokogawa spinning-disk microscope (Ichihara *et al.*, 1996). (Image courtesy of Baggi Somusundaram, PerkinElmer Life Sciences.) (B) Deconvolved result.

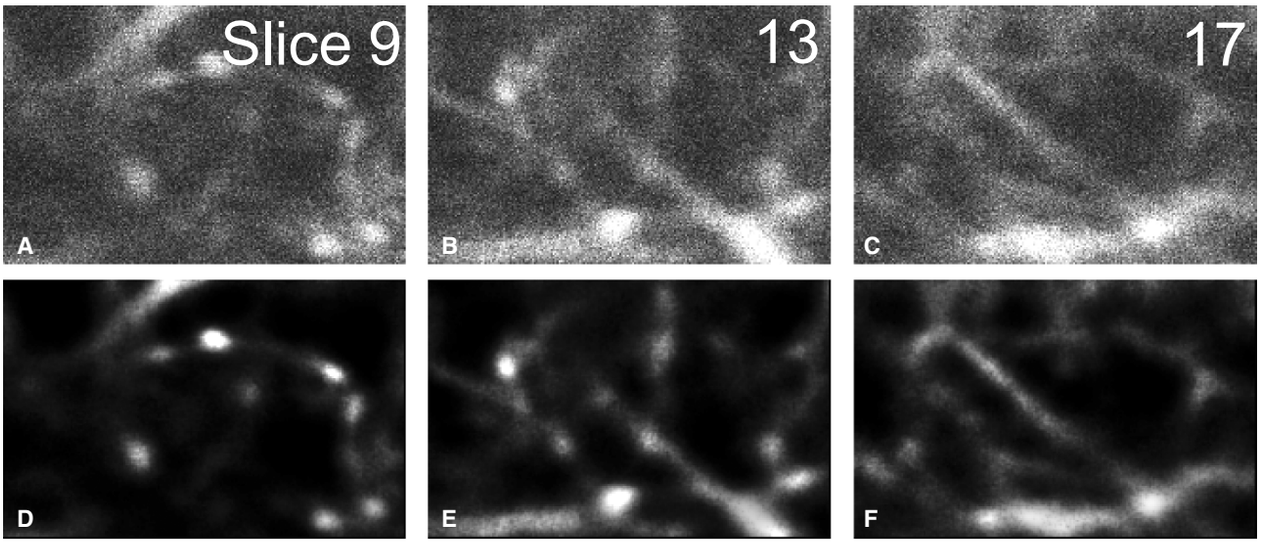


FIGURE 24.26. Sections of a two-photon data set. (A–C) Unprocessed. (D–F) Deconvolved. (Image courtesy of M. Ellisman, University of California, San Diego.)

FUTURE DIRECTIONS

Parametric modeling of more aberrations for the calculation of the PSF during the blind deconvolution by Markham and Conchello, (1999) will make the deconvolution more robust against aberrations. These aberrations include astigmatism, coma, and various types of chromatic aberration.

The blind deconvolution approach provides many efficient ways to utilize the reconstructed PSF obtained from one deconvolution to help make the next deconvolution converge more rapidly. One way is to use the PSF arrived at from a given data set as the first-guess PSF when processing other data collected under similar conditions. Another way is to use the PSF that was arrived at from a given subfield (or sub-volume) in a data set as a first guess when deconvolving a neighboring subfield. The actual PSF varies across a large field because the wavefront aberrations are dependent upon the *x*-, *y*-, and *z*-locations (see Fig. 23.5, *this volume*). Presently, blind deconvolution adapts to these positional changes by breaking up the data set into smaller sub-volumes and reconstructing an independent/adaptive PSF for each sub-volume.

Although, in a strict sense, every pixel ought to have its own PSF, the amount of computation necessary makes doing this extremely impractical. Having subfields with constant PSFs within each field is a compromise that works because, even though the PSF varies, it varies slowly across the field.

Because camera sizes and the number of channels will increase, and live, time-series imaging will become ever more common, processing speed improvements will always be a requirement of advancing work. Now that we can achieve deconvolutions in seconds instead of minutes, we would like to have them done in milliseconds. High-throughput pharmeceutical screening requires deconvolving large 3D data sets in real time (see Chapter 46, *this volume*). To measure ion concentrations in 3D and in real time requires millisecond deconvolutions.

There are two main approaches to meet these speed demands. The algorithmic approach involves refining the mathematical models and designing trade-offs so that the algorithm converges mathematically at a faster rate. A second approach is to utilize distributed processing and distributed computing. Distributed processing is a term used to describe the decomposition of computations into independent modules and sending each of these modules to a different CPU within the same computer. The Windows platform uses a programming technique called multithreading, which provides the tools that allow programmers to carry out distributed processing in the Windows environment. Many of the Apple and Unix-based computers also provide distributed processing capabilities. In distributed computing, which is different from distributed processing, these self-contained parts are sent over the local network to different computers (rather than to different CPUs on the same computer) and then returned to the host computer after the tasks are completed. Deconvolution procedures can easily be decomposed by breaking up the data set into subvolumes (Bhattacharyya *et al*., 1996).

SUMMARY OF MAIN POINTS

- The MLE blind deconvolution approach to deconvolution has a number of important advantages — no measurement of PSF is needed and inherent noise suppression.
- There are many other types of deconvolution, each one having different speed and performance advantages. Generally, speed is traded for image quality (resolution and/or noise).
- Deconvolution algorithms exist for many microscopic contrast modes: WFF, CLSM fluorescence, SLO, spinning-disk confocal, TLB, DIC, polarized light, two-photon.
- Although past limitations in speed have been surpassed, the need to process data from larger cameras more rapidly means that the processor is still a limit. Distributed processing and algorithm improvements will meet this increasing demand.

ACKNOWLEDGMENTS

Research carried out at AutoQuant Imaging has been funded in part by the National Institutes of Health under Small Business Innovation Research (SBIR) grants from the National Eye Institute and the National Institutes of Mental Health and General Medical

Science. We are grateful to many collaborators for their contributions to this research: Alexey Khodjakov (Wadsworth Laboratories), Shinya Inoué (Marine Biological Laboratory), Dirk-Uwe Bartsch (UCSD), D. Garway-Heath (Moorfields Eye Hospital), J. Flanagan (University of Waterloo), N. Hutchings (University of Waterloo), Gerhard Zinser (Heidelberg Engineering), and Zhou Wang (formerly with AutoQuant and now with New York University).

REFERENCES

Agard, D.A., 1984, Optical sectioning microscopy: Cellular architecture in three dimensions, *Annu. Rev. Biophys. Bioeng.* 13:191–219.

Agard, D.A., Hiraoka, Y., and Sedat, J.W., 1989, Three-dimensional microscopy: Image processing for high resolution subcellular imaging, *SPIE* 1161:24–30.

Ayers, G.R., and Dainty, J.C., 1988, Iterative blind deconvolution method and its applications, *Opt. Lett*. 13:547–549.

Bartsch, D., and Freeman, W.R., 1994, Axial instensity distribution of the human retina with a confocal scanning laser tomograph, *Exp. Eye Res*. 58:161–173.

Bhattacharyya, S., Szarowski, D.H., Turner, J.N., O'Connor, N.J., and Holmes, T.J., 1996, The ML blind deconvolution algorithm: Recent developments, *SPIE* 2655:175–186.

Biggs, D.S.C., 1998, Accelerated iterative blind deconvolution, PhD thesis, University of Auckland, New Zealand.

Carrington, W.A., 1990, Image restoration in 3D microscopy with limited data, bioimaging and two-dimensional spectroscopy, *SPIE* 1205:72–83.

Carrington, W.A., Lynch, R.M., Moore, E., Isenberg, G., Fogarty, K.E., and Fay, F.S., 1995, Superresolution three-dimensional images of fluorescence in cells with minimal light exposure, *Science* 268:1483–1487.

Castleman, K.R., 1979, *Digital Image Processing*, Prentice-Hall, Englewood Cliffs, New Jersey.

Close, C.M., and Frederick, D.K., 1993, Modeling and Analysis of Dynamic Systems, 2nd ed., Houghton Mifflin, Boston.

Conchello, J.A., and McNally, J.G., 1997, Subpixel resolution in maximum likelihood image restoration, *SPIE* 2984:158–168.

Conchello, J., Kim, J., and Hansen, E.W., 1994, Enhanced three-dimensional reconstruction from confocal scanning microscope images. II. Depth discrimination versus signal-to-noise ratio in partially confocal images, *Appl. Opt*. 33:3740–3750.

Cooper, J.A., Bhattacharyya, S., Turner, J.N., and Holmes, T.J., 1993, Three-dimensional transmitted light brightfield imaging: Pragmatic data collection and preprocessing considerations, *MSA Annu*. 51:276–277.

Dempster, A.P., Laird, N.M., and Rubin, D.B., 1977, Maximum likelihood from incomplete data via the EM algorithm, *J. Roy. Statistic. Soc. B*. 39:1–37.

Dunn, G.A., 1988, Transmitted-light interference microscopy: A technique born before its time, *Proc. Roy. Microsc. Soc*. 33:189–196.

Ellis, G.W., 1979, A fiber-optic phase randomizer for microscope illumination by laser, *J. Cell. Biol.* 83:303a.

Erhardt, A., Zinser, G., Komitowski, D., and Bille, J., 1985, Reconstructing 3-D light-microscopic images by digital image processing, *Appl. Opt*. 24:194–200.

Gaskill, J.D., 1978, *Linear Systems, Fourier Transforms and Optics*, John Wiley and Sons, New York.

Gerchberg, R.W., and Saxton, W.O., 1974, Super-resolution through error energy reduction, *Opt. Acta* 21:709–720.

Gibson, S.F., and Lanni, F., 1991, Experimental test of an analytical model of aberration in an oil-immersion objective lens used in three-dimensional light microscopy, *J. Opt. Soc. Am. A* 8:1601–1613.

Hansen, E., and Conchello, J., 1988, Restoring image quality in the polarizing microscope: Analysis of the Allen video-enhanced contrast method, *J. Opt. Soc. Am. A* 5:1836–1847.

Hiraoka, Y., Sedat, J.W., and Agard, D.A., 1990, Determination of three-dimensional imaging properties of a light microscope system: Partial confocal behavior in epifluorescence microscopy, *Biophys. J.* 57:325–333.

Holmes, T.J., 1989, Expectation-maximization restoration of band-limited, truncated point-process intensities with application in microscopy, *J. Opt. Soc. Am. A* 6:1006–1014.

Holmes, T.J., 1992, Blind deconvolution of quantum-limited incoherent imagery, *J. Opt. Soc. Am. A* 9:1052–1061.

Holmes, T.J., and Levy, W.J., 1987, Signal-processing characteristics of differential-interference-contrast microscopy, *Appl. Opt.* 26:3929–3939.

Holmes, T.J., and Liu, Y., 1989, Richardson-Lucy/maximum likelihood image restoration algorithm for fluorescence microscopy: Further testing, *Appl. Opt*. 28:4930–4938.

Holmes, T.J., and Liu, Y.H., 1991, Acceleration of maximum-likelihood image-restoration for fluorescence microscopy and other noncoherent imagery, *J. Opt. Soc. Am. A* 8:893–907.

Holmes, T.J., and Liu, Y., 1992, Image restoration for 2-D and 3-D fluorescence microscopy, In: *Visualization in Biomedical Microscopies: 3-D Imaging and Computer Applications*, (A. Kriete, ed.), VCH, Weinheim, Germany, pp. 282–327.

Holmes, T.J., and O'Connor, N.J., 2000, Blind deconvolution of 3D transmitted light brightfield micrographs, *J. Microsc.* 200:114–127.

Holmes, T.J., Bhattacharyya, S., Cooper, J.A., Hanzel, D., Krishnamurthi, V., Lin, W., Roysam, B., Szarowski, D.H., and Turner, J.N., 1995, Light microscopic images reconstructed by maximum likelihood deconvolution, In: *Handbook of Biological Confocal Microscopy* (J.B. Pawley, ed.), 2nd ed., Plenum Press, New York, pp. 389–402.

Holmes, T.J., Liu, Y.H., Khosla, D., and Agard, D.A., 1991, Increased depth-of-field and stereo pairs of fluorescence micrographs via inverse filtering and maximum likelihood estimation, *J. Microsc*. 164:217–237.

Ichihara, A., Tanaami, T., Isozaki, K., Sugiyama, Y., Kosugi, Y., Mikuriya, Abe, M., and Uemura, I., 1996, high-speed confocal fluorescence microscopy using a Nipkow scanner with microlenses for 3-D imaging of single fluorescent molecule in real time, *BioImage* 4:57–62.

Inoué, S., and Spring, K.R., 1997, *Video Microscopy*, 2nd ed., Plenum Press, New York.

Janesick, J.R., Elliott, T., and Collins, S., 1987, Scientific charge-coupled devices, *Opt. Eng*. 26:692–714.

Kam, Z., 1998, Microscopic differential interference contrast image processing by line integration (LID) and deconvolution, *Bioimaging* 6: 166–176.

Khodjakov, A., Rieder, C.L., Cassels, G., Sibon, O., and Wang, C.-L., 2002, De novo formation of centrosomes in culture cells arrested during s phase. *J. Cell Biol*. 158:1171–1181.

Krishnamurthi, V., Turner, J.N., Liu, Y., and Holmes, T.J., 1995, Blind deconvolution of fluorescence microscographs by maximum likelihood estimation, *Appl. Opt*. 34:6633–6647.

Llacer, J., and Veklerov, E., 1989, Feasible images and practical stopping rules for iterative algorithms in emission tomography [errata published in *IEEE Trans. Med. Imaging* 1990;9:112], *IEEE Trans. Med. Imaging* 8:186–193.

Macias-Garza, F., Diller, K.R., Bovik, A.C., Aggarwal, S.J., and Aggarwal, J.K., 1989, Improvement in the resolution of three-dimensional data sets collected using optical serial sectioning, *J. Microsc*. 153:205–221.

Markham, J., and Conchello, J.A., 1998. Parametric blind deconvolution of microscopic images: Further results, *SPIE Proc*. 3261:38–49.

Markham, J., and Conchello, J.A., 1999. Parametric blind deconvolution: A robust method for the simultaneous estimation of image and blur, *J. Opt. Soc. Am. A* 16:2377–2391.

Mortensen, R.E., 1987. *Random Signals and Systems*, John Wiley and Sons, New York.

O'Connor, N.J., Bartsch, D., Freeman, W.J., Mueller, A.J., and Holmes, T.J., 1998, Fluorescent infrared scanning-laser ophthalmoscope for three-dimensional visualization: Automatic random-eye motion correction and deconvolution, *Appl. Opt*. 37:2021–2033.

Oldenbourg, R., and Mei, G., 1995, New polarized light microscope with precision universal compensator, *J. Microsc*. 180:140–147.

Oppenheim, A.V., and Schafer, R.W., 1975, *Digital Signal Processing*, Prentice-Hall, Englewood Cliffs, New Jersey.

Preza, C., van Munster, E.B., Aten, J.A., Snyder, D.L., and Rosenberger, F.U., 1998, Determination of direction-independent optical path-length distribution of cells using rotational diversity transmitted-light differential interference contrast (DIC) images, *SPIE Proc*. 3261:60–70.

Russ, J.C., 1995, *The Image Processing Handbook*, 2nd ed., CRC Press, Boca Raton, Florida.

Sheppard, C.J.R., and Gu, M., 1994, Three-dimensional transfer functions for high-aperture systems, *J. Opt. Soc. Am. A.* 11(2):593–598.

Sibarita, J.-B., Magnin, H., and De Mey, J.R., 2002, Ultra-fast 4D microscopy and high throughput distributed deconvolution, *Proc. 2002 Int. Symp. Biomed. Imaging* 2002:769–772.

Snyder, D.L., Hammoud, A.M., and White, R.L., 1993, Image recovery from data acquired with a charge-coupled-device camera, *J. Opt. Soc. Am. A* 10:1014–1023.

Streibl, N., 1984, Depth transfer by an imaging system, *Opt. Acta.* 31:1233–1241.

van Munster, E.B., van Vliet, L.J., and Aten, J.A., 1997, Reconstruction of optical pathlength distributions from images obtained by a widefield differential interference contrast microscope, *J. Microsc.* 188:149–157.

Van Trees, H.L., 1968, *Detection, Estimation, and Modulation Theory*, John Wiley and Sons, New York.

Veklerov, E., and Llacer, J., 1987, Stopping rule for the MLE algorithm based on statistical hypothesis testing, *IEEE Trans. Biomed. Imaging* 6: 313–319.

Visser, T.D., Oud, J.L., and Brakenhoff, G.J., 1992, Refractive index and axial distance measurements in 3-D microscopy, *Optik* 90:17–19.

Wallace, W., Schaefer, L.H., and Swedlow, J.R., 2002, A workingperson's guide to deconvolution in light microscopy, *Biotechniques* 31:1–16.

Wang, C., 2002, Three-dimensional blind deconvolution for light microscopy: Fundamental studies and practical implementations, PhD thesis, Rensselaer Polytechnic Institute, Troy, New York.

APPENDIX

Convolution: An Introduction For Those Who Don't Remember Second-Year Calculus

James B. Pawley and Timothy J. Holmes

The word "deconvolution" has achieved a mantra-like status among many light microscopists. It is often translated as the magic process that starts with blurry, hazy 3D data and produces sharp, contrasty 3D structures. While this is a powerful capability, and, as is stated throughout this volume, 3D data sets are almost always improved by being deconvolved, it is important to recognize that deconvolution is just the reverse of a mathematical operation called convolution. In the context of 3D light microscopy, convolution can be thought of as a function that mimics the effect of the blurring caused by diffraction and the addition of out-of-focus light.

The purpose of this Appendix is to demystify deconvolution by explaining (albeit in a simplified, heuristic way) the essential features of the mathematical process called convolution.

Let us start with the mathematical process of multiplication. We all understand multiplication: You take one number (a constant) and add it to itself as many times as the values of some second number. Integration is similar, except that one of the things you are "multiplying" is a variable, usually called the function and plotted in the *y*-direction. The integral of a function is the area under the plot of the function between some upper and lower "limits" along the *x* axis. So if you imagine dividing this space up into vertical strips, all of the same width (the constant), but of variable length (where the length is the value of the function for this value of *x*), then the total area can be thought of as multiplying a constant by a variable.

Convolution takes this process a step further. It is a special type of integration in which one multiplies one function (or variable) by another function (or variable), and to make things even more fun, the function can be a variable in more than one dimension (i.e., in *x*, *y*, and *z*, rather than just *x* as above).

I can hear your eyes glazing over!

Before you panic about functions, you don't have to think about equations here. Any set of paired numbers will do. For example, the pairing of a set of intensity numbers with locations in an *xy* raster is a function. In other words, a digital image is a function of *x* and *y*.

Perhaps some pictures can help show how this works, at least for a 2D function (i.e., a sort of image) as shown in Figure 24.A1.

We will start with two very simple 2D functions:

- A point object (shown in green): all the pixels equal 0 except the one in the middle, which equals 1.
- A simple blurring function (shown in red): a 2D blob about the shape of the central peak of an Airy disk, sampled with Nyquist-sized pixels.

To convolve the red function with the green one, first imagine setting the center pixel of the red function over the pixel at the top-left corner of the green one and then multiplying the value in each red pixel by the value in the green pixel that it overlaps. Then add up all these products and enter the sum in the top left pixel of a new "result" raster (in black). As initially all the multiplications involve a zero, all the products are zero and so is their sum, so you enter a zero in the top-left pixel (long arrow). Now step the red mask one step to the right and repeat. Another zero (short arrow). Eventually, however, as you proceed to step the red mask across and down, a time will come when the non-zero pixel in the green mask will coincide with a non-zero pixel in the red mask and a non-zero sum of products will be entered in the black raster (long, pink arrow, Fig. 24.A2).

It now becomes obvious that this slow, boring process will make the result look just like the red function. In fact, we have just mimicked the process of making a blurry image of a point object and our black result is, therefore, the infamous point-spread function, or PSF. To see that this process is a little more useful than just copying the red function, suppose now that the object is composed of two point objects, separated by five "zero pixels," as

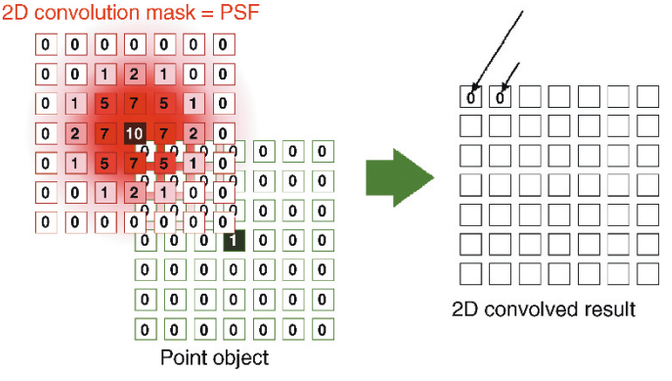


FIGURE 24.A1. First two steps of convolution operation between a point and a mask.

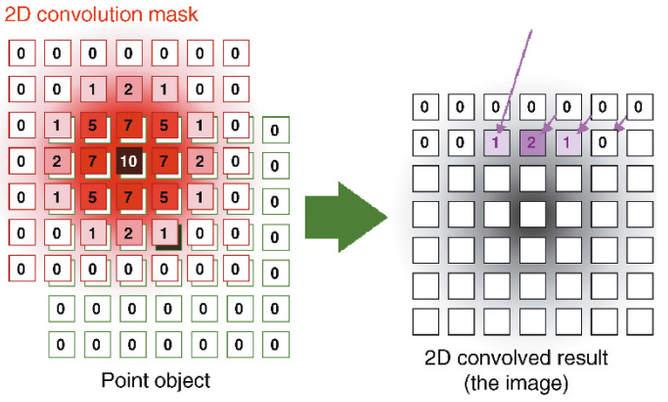


FIGURE 24.A2. Convolution of a point with a mask, continued.

shown in the green raster of Figure 24.A3. When this object is convolved with the mask, the result (black raster) resembles a blurred image of two points.

To the extent that the mask mimics a 2D, diffraction-limited, point-spread function, the result in the black raster will look like a diffraction-limited image of an object composed of two dark points on a white background. As we have chosen a pixel size close to half of the Rayleigh resolution, two points separated by six pixels will be represented by two discernible features in the black raster. You may be more convinced of this if you look at Figure 24.A3 from the other side of the room.

The discussion so far has implied that convolution is a process that occurs in just two dimensions. Of course, in the case of microscopy, this is not true. Because the Airy figure is a 3D structure, the blurring it causes occurs in three dimensions. The 3D blurring in the near-focus region is difficult to diagram in 2D. However, as one moves away from this plane, it is a fair approximation to assume that the light passing through the objective appears as a circle. This circle is the cross-section of a cone centered at the plane of the object. The point object defines the apex of the cone and the objective NA defines its angle (Fig. 24.A4).

Three-dimensional convolution requires considering the out-of-focus light in the vertical direction as well as blurred light from the in-focus plane. The problem becomes more complex when two points are located at different heights in the specimen (see Fig. 24.A5).

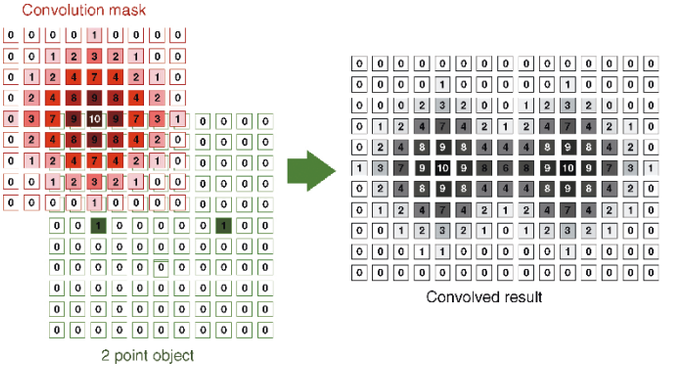


FIGURE 24.A3. Convolution of a mask and a two-point object.

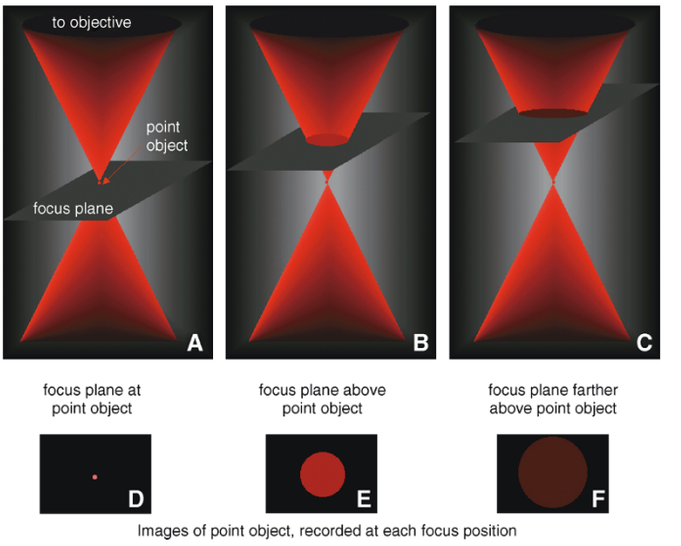


FIGURE 24.A4. Three-dimensional blurring function applied to a point object in widefield fluorescence.

It is important to remember that the total number of photons leaving the point and passing through the objective remains virtually constant no matter where the objective is focused. Therefore, the image of an in-focus point appears very intense, while the image of an out-of-focus point is much dimmer because now the same number of photons are being spread over a larger, blurred circle. It can be instructive to see just how important this effect can be.

About Out-of-Focus Light

Suppose that under given widefield illumination conditions, a CCD with Nyquist-sized pixels (0.1 µm referred to the sample) records a total of 10,000 photons from a particular point object in each image in the stack. When the point object is located at the focus plane, as illustrated in Figure 24.A6, about 80% of the 10,000 photons are distributed between the 12 bright pixels centered on the object or about 650 photons/pixel. Assuming a high-NA lens

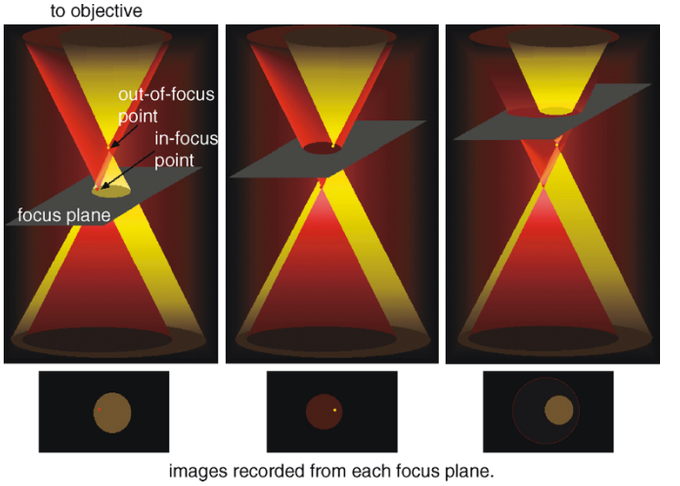


FIGURE 24.A5. Three-dimensional blurring function applied to two point objects in different planes in widefield fluorescence.

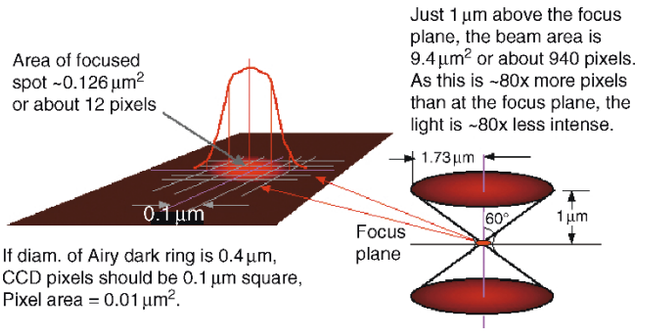


FIGURE 24.A6. Geometrical optics used to calculate the rapidity with which the signal from a point object diminishes with distance from the focus plane in widefield microscopy.

($\alpha = 60°$) and simple geometrical optics,[2] by the time the feature is only 1 μm out of focus, these photons will be spread over a circle having an area of 9.4 μm² or 940 pixels. If the intensity is spread evenly over this circle, then the detected signal level from the now out-of-focus feature drops to <7 photons/pixel. As this is only slightly more than the RMS noise level of a good, slow-scan CCD, it is hard to see how the detection of this out-of-focus light can provide much useful structural information.

The result is that, when the NA is high, the signal intensity recorded per pixel from a point source drops off very fast as the point goes out of focus, even in widefield fluorescence microscopy. As noted in Chapter 23, signals emanating from small features located much more than 2 μm from the focus plane are more likely to add Poisson noise than to add useful structural information.

Convolution, Fourier Transforms, and the FFT

The tedious process of overlapping, multiplying, adding, and replacing would not be of much use were it not for the fact that the process can be greatly simplified if we first apply a mathematical operation called the Fourier transform (FT) to the 3D data sets representing the PSF and the object. The FT of an object looks a lot like its diffraction pattern. Like the "real-space" object, the "Fourier-space object" is a 3D distribution of values but, whereas the real object has only a single value at each 3D location (the intensity), the FT of the object has both an intensity and a phase angle. The phase angle information is used by the inverse FT process to convert the FT data back into a real-space object. To perform the process of convolution using FTs, we must:

1. Calculate the 3D FT of the object, creating a 3D array of intensity and phase values.
2. Calculate the 3D FT of the PSF, creating a second 3D array of intensity and phase values.
3. Simply **multiply** these two arrays, point by point, creating a new 3D intensity/phase array.
4. Calculate the inverse Fourier transform of this product array.

This may all sound very obscure, but fortunately there is a very fast and helpful computer algorithm called the fast Fourier transform that can rapidly perform both the 3D transform and its inverse!

Coincidentally, calculating the FT of an object exactly duplicates the effect that a perfect lens has on light that diffracts at its focus plane and then proceeds to its back-focal plane (BFP). That is, given a perfect lens, the phase and intensity pattern of the light passing through the BFP *is*[3] the 2D FT of the object at the focus plane. Unfortunately, we cannot just record the image of the BPF and then apply the inverse FT to reconstruct the 2D object because we can only record the intensity, not the phase, of this pattern.

X-ray diffraction studies confront the same problem but in this case, the ordered, crystalline nature of the specimen makes it possible to make shrewd guesses about the phases. As a result, success in discerning molecular structure depends on first measuring the intensity of the diffraction pattern and then on guessing and iterating ever-more-accurate estimates of the phases.

[2] An admitted oversimplification that works better as the distance from the focus plane increases.

[3] Strictly speaking, it is the **magnitude** and the phase of E-field in the BFP that is the FT of the E-field and phase in the object plane. The light **intensity** in each plane, is the square of these magnitudes. But, this is getting us into technical details that require their own chapter.

25

Image Enhancement by Deconvolution

Mark B. Cannell, Angus McMorland, and Christian Soeller

INTRODUCTION

In this chapter we will try to provide a more intuitive (and less mathematical) insight into image formation and practical image restoration by deconvolution methods. The mathematics of image formation and deconvolution microscopy have been described in greater detail elsewhere (see Chapters 11, 22, 23, and 24), so we will limit our discussion to fundamental issues and gloss over most of the mathematics of image restoration. We will also focus on practical ways of assessing microscope performance and getting the best possible data before applying more sophisticated image processing methods than are usually seen in the literature. Before we lose the interest of the confocalist, we would point out there is no such thing as a real widefield microscope because real microscopes have limited field of view and other apertures within the optical train. These apertures introduce a limited degree of confocality *even into widefield microscopes* that, as we will see, improves the behavior of the microscope in a way that makes quantitative image restoration both possible and very worthwhile. The methods (and software) that improve images from conventional widefield (WF) microscopes will also significantly improve confocal images and our practical experience shows that the output of both confocal and multi-photon microscope systems benefit from application of image restoration methods. For those who wish to know the conclusion of this chapter without further reading, it is simply: deconvolve *all* data (if you can). To stress this point, we suggest that even a properly adjusted confocal microscope will not give the best possible confocal image and the application of appropriate deconvolution methods will increase contrast, reduce noise, and even improve resolution. That such worthwhile effects are made possible by computation resides in the fact that during deconvolution the information content of the image can be increased by the addition of information about the imaging process itself as well as that about the statistics of photon capture. Thus, in our opinion, the application of deconvolution methods can always increase image quality, regardless of the source of the image.

BACKGROUND

The resolution of a measurement instrument is always limited so that the recorded *image* of the sample is completely dependent on the properties of the measurement device. Microscopy is simply a measurement process used to quantify information about small objects, and the limits to resolution in microscopy are manifest as blurring in the acquired images. Blurring arises from the intensity of signal at any point in the image being some weighted sum of intensities from all points in the object space. With detailed understanding of the weighting function, we can develop ways of correcting the image for the limiting behavior of the microscope. In addition, almost all microscopic samples are inherently three-dimensional while the detectors [such as the eye, charge-coupled device (CCD) camera, or photographic film] are two-dimensional. Because it is well known that two-dimensional representations of three-dimensional objects lead to artifacts and ambiguity, one should expect fundamental imaging problems in microscopy.

A number of phenomena contribute to the blurring process in light microscopy. First, the wave nature of light dictates that as it passes through apertures (e.g., the optical components making up the microscope), diffraction occurs, which results in spreading and merging of light rays in the image (Abbe, 1873; see Chapter 22). Second, samples can scatter light thereby removing the correspondence between the source of a light ray and its final location in the image plane. This problem makes high-quality imaging in turbid, thick samples (such as brain slices) highly problematic. We should also note that this scattering also prevents certain light rays from passing through the optical train and thereby prevents some information from the object reaching the image. Similarly, a dense object can obscure an (in-focus) object behind it and prevent information from it reaching the image. Finally, refractive index mismatches in the light path (e.g., between the immersion medium and sample) and imperfections in the optical components (and their alignment) can add to aberrations that will also cause light rays to be misdirected.

The conventional WF microscope is designed to correctly image a sample at the focal plane of the objective; however any light source within the conical volume of light collected by the objective lens can contribute light to the image plane. While this is not blurring, it will introduce a loss of contrast for in-plane objects and contribute to the perception of a blurred image. Objects outside the plane of sharp focus are also seen in the image plane as blurred images that also reduce contrast for in-focus objects. (It is the reduction of this effect by confocal microscopes that makes them so useful.) Finally, the limited aperture of the microscope system (i.e., its limited light and information gathering ability) and the limited wavelength of light itself lead to blurring of objects. With so many limiting factors, it is not surprising that real microscope imaging always represents a trade-off between various problems. For example, increasing the numerical aperture of the system may decrease blurring and increase signal from in-focus objects but can also lead to a loss of image contrast due to the acceptance of more scattered light from thick samples. In addition, high

Mark B. Cannell, Angus McMorland, and Christian Soeller • Department of Physiology, University of Auckland, 85 Park Road, Grafton, Auckland, New Zealand

 Handbook of Biological Confocal Microscopy, Third Edition, edited by James B. Pawley, Springer Science+Business Media, LLC, New York, 2006.

numerical aperture objectives have limited working distances that may limit their ability for deep sectioning.

Image Formation

The transformation of information from a real object to blurred image can be expressed mathematically using an operation called convolution. Deconvolution is the reverse operation, whose purpose in microscopy is to remove the contribution of out-of-focus objects from the image plane as well as (partially) reverse aberrations arising from imperfections in the optical train. It should be intuitive that, by using information about the imaging process, deconvolution techniques should be able to improve the quality of the image above that which could be achieved by any other method which does not provide extra information (beyond that contained in the image plane itself). The transformation carried out by the microscope on data from the object can be defined by a mathematical function called the point spread function (PSF). The PSF is the multi-dimensional image of a point in space and it can be practically measured by imaging very small objects (which must be less than the wavelength of light in size) or computed from the physical and optical properties of the imaging system (see Fig. 25.1). Given imperfections in the imaging system (or put another way, limited knowledge of the real optical system) the latter approach is inherently limited, but assumptions about the properties of the PSF can help some blind deconvolution methods.

Put simply:

$$i(x, y, z, t) = o(x, y, z, t) \otimes psf(x, y, z, t) \quad \textbf{(1)}$$

where x, y, z, t are the dimensions of space and time and i is the recorded image, o the actual underlying object. The $\otimes$ operator is convolution (see below and Fig. 25.2). If we take the Fourier transform ($F\{\}$) of this equation, the $\otimes$ is replaced by multiplication:

$$F\{i(x, y, z, t)\} = F\{o(x, y, z, t)\} \times F\{psf(x, y, z, t)\} \quad \textbf{(2)}$$

This simple equation shows that image restoration should be possible and might be achievable by dividing the Fourier transform of the image by the Fourier transform of the PSF and then taking the inverse Fourier transform. Before exploring this idea further, it should be noted that these equations remind us of the importance of correct data sampling (image and PSF) and the behavior of the PSF over time and space. For example, although we generally assume that the microscopes do not change properties as we focus through the sample and from day to day, is this really so? When objectives are damaged by lack of care (such as from a collision with slide/stage or accumulation of dirt), the gradual loss of imaging performance may go undetected. This is particularly a problem for confocal microscopes whose pinhole can effectively hide a poor or deteriorating PSF at the expense of signal strength. Also note that coverslips (which are an integral part of the optical system) vary in thickness from batch to batch and therefore introduce variable amounts of spherical aberration.

From here on, we assume that everything is time invariant. (This is not a trivial assumption as, in reality, samples are *never* time invariant, they move — especially if alive, they bleach, the microscope focus drifts with temperature, etc.) So, from Eq. 2, if one can measure or compute the PSF with sufficient accuracy, why can images not be restored to the point where any desired resolution is achieved? The major problem resides in the noise that is always present in a physical measurement. The convolution or blurring of the object by the PSF is spatial frequency–dependent and attenuates high-frequency components (provided by small features and edges) more than low frequency (large, smooth) objects. Hence, deconvolution must boost high spatial frequency components more than low spatial frequency components. Because noise

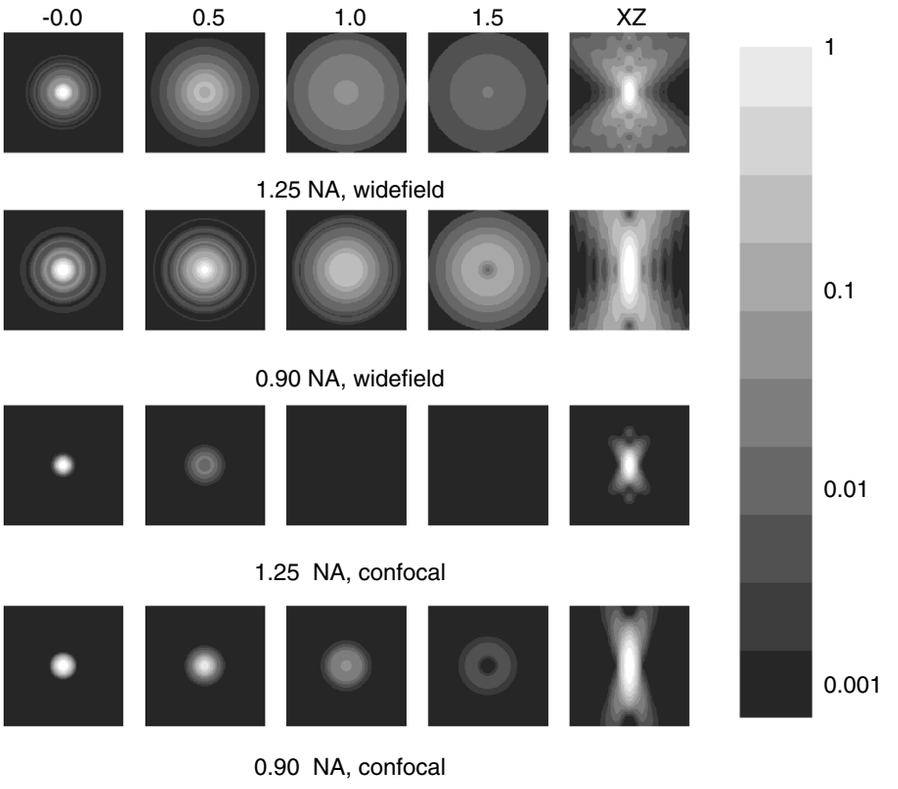


FIGURE 25.1. Theoretical PSFs calculated using widefield equations. On the left, sections at 0.5 µm z-intervals from the plane of sharp focus are shown while xz sections are shown on the right. Panel (A) shows PSFs for two typical lenses. Note the effect of reducing NA on the axial extent of the PSF. Panel (B) shows equivalent PSFs for the above lenses in a confocal configuration. Note that the confocal PSF looks very similar to the widefield PSF with the outlying wings removed. Again, the improved axial response of the higher NA lens is quite clear in these images. The gray scale is shown on the right and is logarithmic.

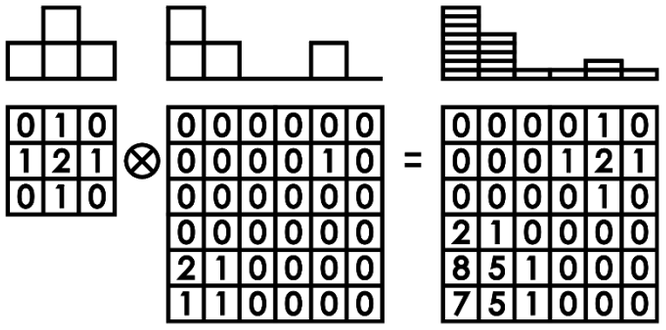


FIGURE 25.2. Schematic diagram demonstrating the convolution (⊗) operation with a 6 × 6 pixel object and a 3 × 3 pixel blurring kernel. The profiles above show the maximum projection of the two-dimensional grids as would be seen looking across the planes from above. Note how the contrast of the peaks in the image is reduced and smeared across the image.

is present at all frequencies in the image right up to the spatial sampling frequency which is 1/(pixel size), noise components are boosted at all frequencies during deconvolution. At more than half the sampling frequency of the image, there is no real object data retained (from the Nyquist sampling theorem) but the ever-present noise receives an even larger boost during deconvolution.

Put another way, because noise does not come directly from the object, but is introduced during the imaging process, and because noise is rich in high-frequency components, deconvolution (which seeks to boost high-frequency content) can amplify noise to the point where it masks, and renders useless, any information in the resulting deconvolved image. The addition of noise also generates ambiguity in the image restoration (deconvolution) process so that more than one optimal restoration solution exists with no *a priori* method of determining which solution best represents the real object. Current deconvolution algorithms work around some of these limitations, often by making a number of reasonable assumptions about the object (such as smoothness and nonnegativity) and include extra information about the noise process itself.

Having introduced image restoration by deconvolution, we will now describe the convolution and deconvolution processes in more detail and give a guide to some of the practical issues regarding image deconvolution. We will also discuss how some popular deconvolution algorithms vary, and assess the utility of image restoration. We will show that deconvolution can substantially improve WF microscopy, to the point where it can be used as a viable and practical alternative to confocal laser scanning microscopy (CLSM) and can also be used to good effect to improve the quality of confocal and multi-photon microscope images.

FORWARDS: CONVOLUTION AND THE IMAGING SYSTEM

Before it is possible to develop an algorithm for reversing the defects induced during the imaging process, it is necessary to develop a basis for image formation. This section will give a shortened version of that formalization and more detailed descriptions can be found in Agard and colleagues (1989) and Young (1989). The notation used generally follows the conventions of Press and colleagues (1992).

The starting point for this formulation requires two assumptions regarding the imaging process: linearity and shift invariance. The principle of linearity is met if the sum of the images of two separate objects is the same as the image of the combined objects. The assumption of linearity is generally safe in fluorescence microscopy provided that detectors are linear and we avoid self-quenching and self-absorption by the fluorophores (Chapters 16 and 17, *this volume*). Shift invariance implies that the image of an object will be the same regardless of where in the field of view that object lies. (While no real imaging system meets the requirement of shift invariance, it is a reasonable assumption for a high-quality research microscope, subject to our being aware of the potential complication introduced by changing aberrations across the field and with focus.) Now, because any object can be represented by a superposition of many delta functions (point light sources) whose individual images are simply shifted copies of the PSF, it follows from the principles of linearity and shift invariance that the whole image is made from the superposition (sum) of appropriately scaled and shifted instances of the PSF. For clarity, we can express this in one dimension as an equation:

$$i(x) = \int_{-\infty}^{+\infty} o(x - x')psf(x')dx' \qquad \textbf{(3)}$$

which is, in fact, mathematically the same as the convolution of the object with the PSF. In symbolic form:

$$i(x) = o(x) \otimes psf(x) \qquad \textbf{(4)}$$

which gives a basis for the first general equation given above. As noted above, convolution in the spatial domain is equivalent to multiplication in the frequency domain so we can write (for three-dimensional objects):

$$F\{i(x, y, z)\} = F\{o(x, y, z)\} \times OTF(\varsigma, \psi, \zeta) \qquad \textbf{(5)}$$

where OTF() is the optical transfer function and is the Fourier transform of the PSF (see Figs. 25.3 and 25.4), ξ, ψ, and ζ are the spatial frequency coordinates of the OTF in Fourier space, derived from the PSF sampled in x, y, and z, respectively. The OTF is introduced here because convolutions are most quickly computed in the frequency domain by using the fast Fourier transform (FFT). Because the PSF is assumed to be shift invariant, only a single Fourier-transformed PSF is used for computations and the values of the PSF in the spatial domain *per se* have no practical value for deconvolution. Thus, it is more convenient to describe the PSF of a microscope in terms of its OTF rather than its PSF. The OTF directly describes how blurring affects the various frequency components making up an object and immediately gives insight into the resolving power of the microscope. Although we usually measure the PSF in the image plane (rather than at the rear aperture of the objective where the OTF exists) and most researchers are more familiar with an ideal PSF and can identify microscope defects by inspecting it (see below), the OTF is actually more useful. Put another way, because the performance of the entire microscope is the result of the combination of the OTFs of each optical lens and aperture, it is easier to immediately determine the effect of an aperture or lens in a microscope from its OTF. As an example, because a circular aperture reduces the amplitude of the OTF with increasing spatial frequency, it is immediately clear that the ultimate determinant of resolution must be the most limiting aperture in the system [usually the numerical aperture (NA) of the objective lens].

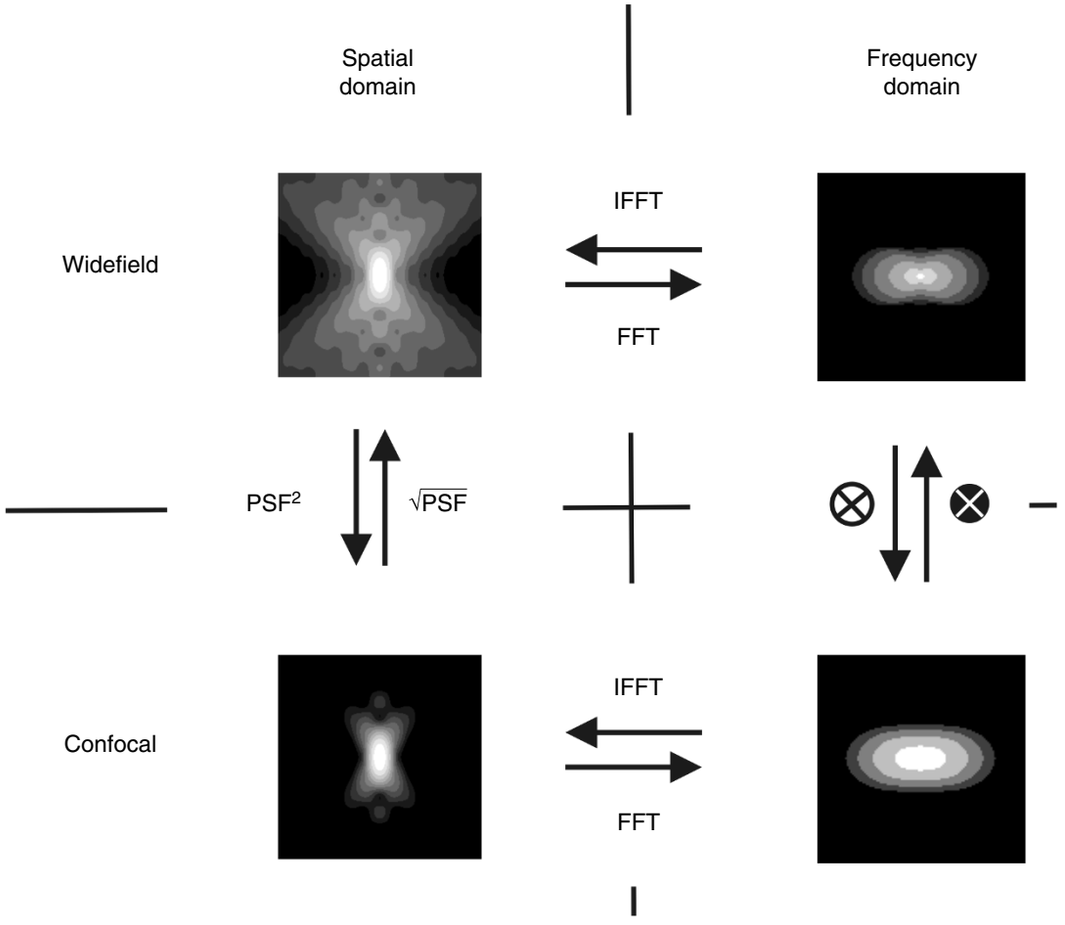


FIGURE 25.3. The relationship between the PSF and OTF in confocal and widefield modes of a microscope. For simplicity, we assume that the pinhole function leads to a simple squaring of the PSF, a reasonable approximation for an optimal pinhole with similar excitation and emission wavelengths. The convolution of the widefield OTF with itself in the frequency (Fourier) domain is the equivalent of squaring in the spatial domain. Note that the inversion of the convolution (inverted convolution symbol) is difficult in the frequency domain and is more easily accomplished in the spatial domain (by taking the square root). This illustrates that some operations are more simply carried out by operating in the appropriate domain; convolution is easier in the frequency domain while multiplication is simpler in the spatial domain. Such interchangeability between spatial and frequency domains is central to deconvolution methods.

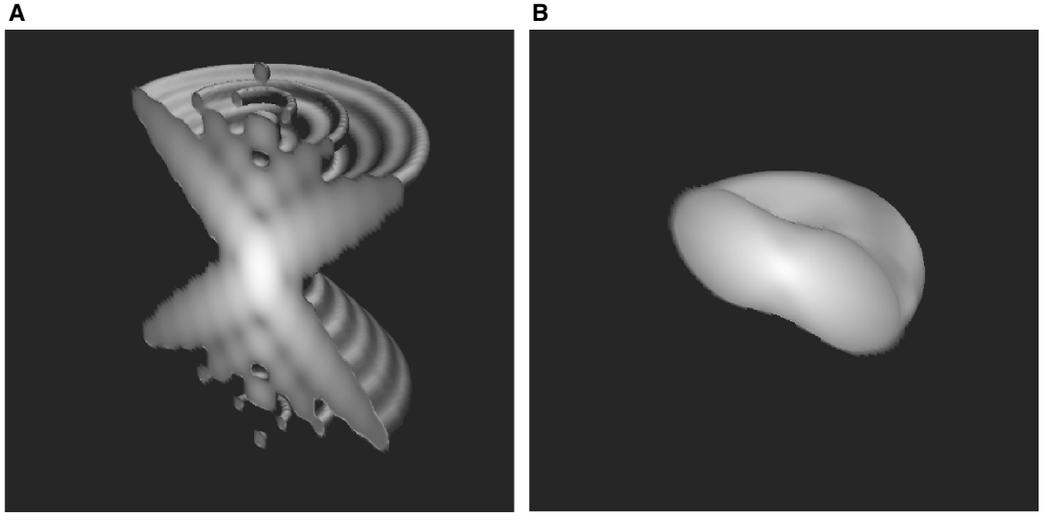


FIGURE 25.4. Volume rendered illustrations of the widefield PSF (A) and OTF (B). The PSF extends to infinity as a cone with ripples in the intensity in all directions. The OTF appears smaller being closer to a toroidal shape except that the center values are non-zero. This leads to a cone of low values in the center of the toroid. The toroid width in both directions is limited by diffraction. The gray scale shading is proportional to the logarithm of the intensity.

PROPERTIES OF THE POINT SPREAD FUNCTION

Because the PSF of a microscope determines how it creates images of an object, the shape of the PSF determines the way in which images of objects blur into each other in the final image. At the focal plane of a WF microscope, the PSF [see Fig. 25.1(A)] exists as a central Airy disk, surrounded by dimmer concentric rings that are the result of diffraction occurring as light passes through the circular apertures of the microscope. Away from the plane-of-focus, the PSF spreads outwards, forming two apex-opposed cones with diffraction ripples within them [Fig. 25.4(A)]. This pattern reflects the fact that WF microscopes form images from cones of light gathered by an objective lens, with the angle of the cone and thus the shape of the PSF being determined primarily by the NA of the objective lens (Chapters 11, 22, 23, and 24, *this volume*). The axial extent of the concentric cones of the widefield PSF at z-levels well removed from the focal plane show how significant the out-of-focus contribution is to a WF image. This is not the case for the CLSM PSF whose PSF approaches background levels with distance [Fig. 25.1(B)], a point which will be revisited later.

It is important to note that, unlike theoretically derived widefield PSFs, measured widefield PSFs are rarely symmetric around the focal plane, nor radially symmetrical about the optical axis. Asymmetry along the optical axis (z-axis) is commonly due to spherical aberration, which may result from refractive index mismatches between the objective, immersion medium, and sample or tube length/coverslip thickness errors. Radial asymmetries in the PSF are commonly the result of misalignment of optical components about the z-axis, either as tilt or decentration (see Cagnet *et al*., 1962; Keller, 1995) (see Fig. 25.5).

The extent of the PSF determines the resolution of the microscope. PSF size is often expressed in terms of the width at which it is half the maximum intensity (full-width half-maximum, or FWHM). A typical FWHM for the widefield PSF of a high power immersion objective lens might be <0.4 µm in the focal plane. The axial extent of a true widefield PSF should be infinite with constant energy at all planes, but real microscopes lose signal energy with distance because additional apertures (beyond the entrance pupil) in the system lead to the more-distant wings of the widefield PSF being clipped (or vignetted). Nevertheless, the extended axial response of the WF microscope results in a massive loss of in-plane contrast for extended specimens which are either fluorescent or scattering.

QUANTIFYING THE POINT SPREAD FUNCTION

Most deconvolution methods (i.e., not blind ones) require knowledge of the PSF relevant to the particular imaging conditions encountered. PSFs can be estimated either mathematically or from direct measurement. In blind deconvolution methods an estimate of the PSF is also produced by the deconvolution algorithm. (Note that if the object and image are known, the OTF is given by the Fourier transform of the image divided by the Fourier transform of the object; see Eq. 5.) While it is relatively easy to quantify the PSF of a microscope under controlled conditions (see Fig. 25.5), matching the conditions encountered during an experimental imaging situation is often impractical, and commonly some approximation to the likely real PSF is used.

Most methods for calculating theoretical PSFs are based on equations in the definitive work of Born and Wolf (1980). A good description of the calculations for a confocal PSF is given by van der Voort and Brakenhoff (1990), in which the PSF is calculated

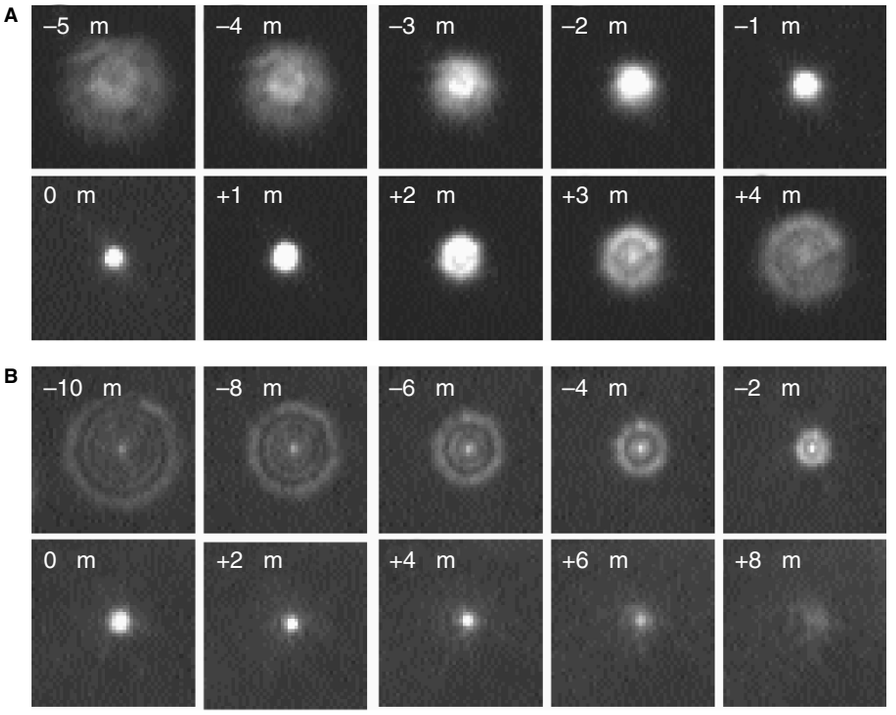


FIGURE 25.5. Measuring the widefield PSF. (A) shows the appearance of a 0.2 µm bead with varying degrees of defocus. Note that although the most focused image is reasonably circular, with defocus extra structure appears in the Airy disk. These uncontrolled aberrations need to be measured for correct deconvolution. Note also that the aberrations are not symmetrical about the point of sharp focus so that enforcement of symmetry in blind deconvolution would be problematic. (B) shows a through-focus series with spherical aberration. Asymmetry above and below best focus is evident.

from the NA of the objective, the illuminating and emitted wavelengths, and the refractive index of the immersion medium in either (simpler) paraxial forms or with WF integrals (see Fig. 25.6). Numerically derived expressions for the PSF give an indication of the best possible resolution for a given objective but these limits are not achievable. The real world limitations in alignment of the optical path and lens aberrations inevitably lead to a real PSF that is larger and has more asymmetric structure than predicted by mathematical approaches. Particular attention should be paid to whether a paraxial approximation is appropriate because there are considerable differences between the results of paraxial and WF calculations for the high-NA objectives which are often used in experiments (Fig. 25.6). The problem is confounded by software packages that do not reveal what method is used to calculate the PSF. In our experience, real PSFs are typically >20% bigger than calculated versions (based on the stated NA) and their shapes are rarely perfectly symmetrical about the optical axis and focal plane, even when we have tried to control refractive index mismatches. It should be intuitively obvious (from the preceding discussion) that the accuracy of the deconvolved image can be no better than that of the PSF that was used for the deconvolution. Errors in the PSF can produce bizarre artifacts in the image (such as hollow cones or slanting tails around bright objects) as well as the algorithm not properly converging to minimum noise (see Fig. 25.7).

The PSF of a microscope can be measured by taking images of commercially available fluorescent beads of <0.2 μm diameter. These, being smaller than the diffraction limit of visible light, act like point light sources, and their imaged size and shape therefore represent the microscope PSF. It is a common misconception that even smaller beads give better estimates of the PSF. This is not the case as the imaging process is a convolution and the convolution is dominated by the larger of the two objects being convolved. In addition, the beads become much less bright as smaller beads are used (note that the signal intensity will fall with the cube of the diameter) so precise measurement of the entire PSF becomes very difficult, especially as the PSF is recorded away from the focal plane. For those who feel uncomfortable using 0.2 μm spheres, it is possible to use deconvolution of the PSF image using a 0.2 μm sphere (the actual object) to yield the precise PSF (from Eq. 5), but in practice it is rarely necessary to go to such lengths. In our experience, the difference in the final results of deconvolution using bead images and PSFs derived by deconvolution of bead images with spherical sources is negligible.

When imaging beads for the purposes of PSF measurement, the image data should be obtained at as high a resolution as possible. In this case, Nyquist's criterion of using twice the desired resolution is insufficient, and pixel resolutions 0.05 μm (or even better) are desirable. This has some advantages: (1) The fine data spacing facilitates data resampling to enable the PSF resolution to match that of the recorded image. It is often the case, especially when confocal variable zoom controls are used, that the final image resolution may be different from that used to acquire the PSF. (2) Generous over-sampling also allows a greater dynamic range to be recorded as the received photons are recorded in more voxels. Even if the detector is only 8 bit, over-sampling by a factor of 2 in all three dimensions raises the effective bit resolution to 11 bits. This increase in effective dynamic range is very useful as it enables both the bright center of the PSF as well as more dim distant features to be recorded. For deconvolution, low noise PSFs are required and this can be achieved by averaging a number of individual bead images, possibly from different beads (because the principle of shift invariance requires that the bead image — the PSF — is not affected by the position of the bead). This approach requires an algorithm for aligning the centers of the image of each bead so that the averaging operation can combine data points in each bead image. The coordinates of the center of the 3D bead image can be derived by calculating the center of signal mass of an image that has been subjected to a thresholding procedure to completely remove any background signal. The most distal parts of the image should also be removed by the chosen threshold to prevent the estimate of the bead centroid depending on the position of the bead within the sampled data volume.

Perhaps the most problematic aspect of measuring PSFs using fluorescent beads is matching the experimental imaging conditions to which the PSF is to be applied. First, to account for the effect of any chromatic aberrations (as well as the direct effect of wavelength on resolution), PSFs should be measured from beads that emit light of a similar wavelength to the experimental fluorophore being imaged. (Beads are available with a range of emission wavelengths from 415 to 680 nm.) Errors in refractive index, either between the objective and immersion medium or between immersion and bathing/mounting media, need to be consistent for correct replication of the aberrated PSF. Because experimental samples are often less well controlled than calibration bead samples, we often add a few beads to critical experimental samples to provide a check of the actual PSF in the biological sample. These beads are readily recognized in images as they usually stick to the outside of cells (in live-cell imaging) and do not bleach as rapidly as the experimental sample. Although it is possible to remove the bead from the experimental image digitally, we have never had to do this in practice as it is usually possible to find a suitable field of view free of beads.

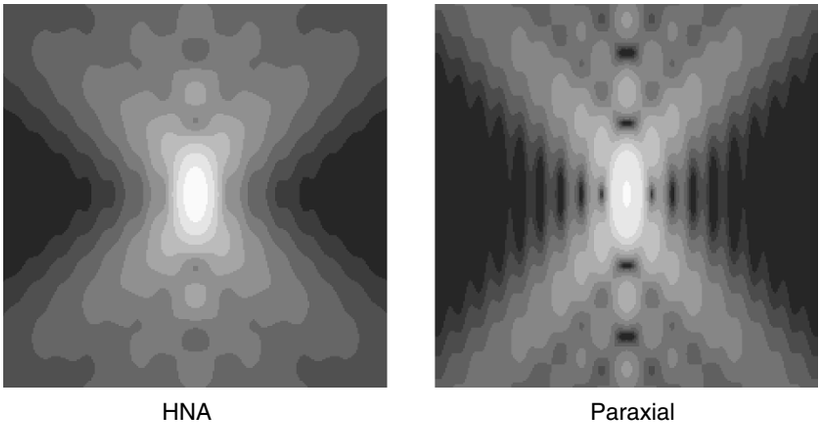


FIGURE 25.6. Comparison of widefield and paraxial computations of the PSF. The left panel shows the computed PSF for a 1.25 NA objective using the integrated field equations (van der Voort and Brakenhoff, 1990). The right panel shows the equivalent results for the paraxial equations which combines the electric vectors using the assumption that $\sin(\theta) = \theta$. The paraxial assumption leads to greater ringing in the response but a narrower Airy disk.

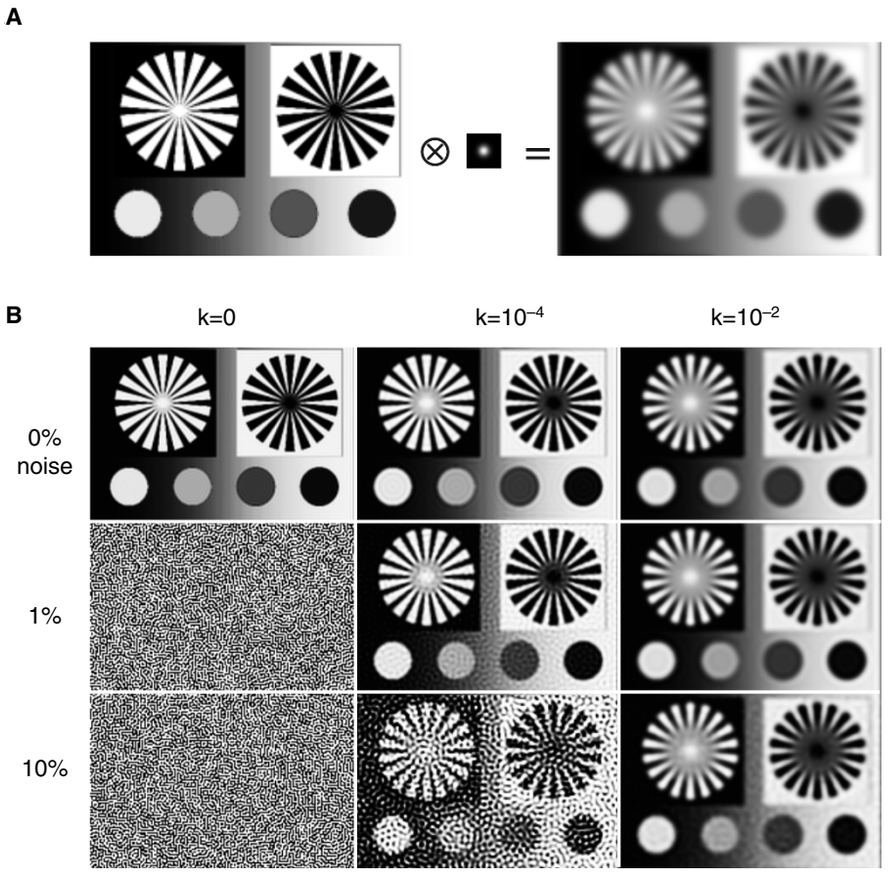


FIGURE 25.7. Image restoration by Wiener filtering. Panel (A) shows the original test image and the PSF used to blur it. The resulting blurred image has lost contrast for all small features. Panel (B) shows the results of image restoration with variable amounts of noise added to the blurred image for various values of k (see Eq. 10). On the left side, without noise the inverse operation perfectly restores the data. However, even with 1% noise ($N = 0.01$) inverse filtering yields fewer data than even the original blurred image. When $k = 10^{-4}$, the effect of noise is reduced but at the expense of high frequency performance. The loss of high frequency components leads to ringing near sharp edges and can be seen in the small colored circles. When $k = 5 \cdot 10^{-2}$, noise is even better controlled but the loss of high frequency information is more severe. This can be clearly seen by comparing the centers of the spoked targets. Note that the image where $k = 10^{-4}$ and $N = 0.01$ is comparable in appearance to the image $k = 5 \cdot 10^{-2}$ and $N = 0.1$. Thus increasing k controls increasing noise at the expense of reduced spatial resolution.

THE MISSING CONE PROBLEM

As noted above, while the PSF provides information about the spatial throughput of a microscope, its Fourier transform (the OTF) gives information about the frequency response of a microscope directly. While the NA of the microscope limits the highest spatial frequency that can be recorded, extended sources (i.e., lower spatial frequency objects) lose signal strength with defocus because source light rays must originate in the finite field of view of the microscope. Thus, the OTF of the WF microscope looks like a toroid [Fig. 25.3 and 25.4(B)] with so-called missing cones above and below the focal plane. These missing cones of reduced signal reflect the cone of light acceptance of the objective (assuming it is the limiting aperture in the microscope). The width of the torus in all planes is limited by the numerical aperture of the objective giving rise to a bandlimit equal to $2NA/\lambda$ (as required from Nyquist sampling of the object using the spatial frequency of light in the immersion medium). The axial band limit is $NA^2/2\eta\lambda$ while the angle of the missing cone is $\arcsin(NA/\eta)$, where η is the limiting refractive index of the mounting media between objective and specimen.

In a CLSM, the pinhole aperture restricts the ability of light from out-of-focus objects to reach the detector. This means the light-focusing pattern of the objective is used to determine both the illumination and emission light paths, and so the PSF of a CLSM is approximately the square of the widefield PSF (assuming that the ratio of excitation to emission wavelength is close to 1). The PSF of a two-photon microscope is similarly related to the power of the widefield PSF because the probability of near simultaneous multiple photon absorptions is proportional to the illuminating intensity raised to the nth power, where n is the nearest integer ratio of illumination to excitation wavelengths (Denk *et al.*, 1990). As a result, the PSFs [Fig. 25.2(A–C)] are ovoids with the long axis corresponding to the optical axis of the microscope. The corresponding OTF does not have missing cones and is closer to an ovoid (Fig. 25.3). This can be explained by the fact that the confocal PSF is the product of the illumination and detection PSFs (Wilson, 1990) and in Fourier space, multiplication becomes convolution. Convolution of one toroid by another tends to fill in the center void.

As pointed out earlier, deconvolution can be thought of as the division of the Fourier transform of the image by the OTF of the microscope. The low values of the OTF in the neighborhood of the missing cone and near the bandlimit greatly amplify any noise in the image and this severely limits the ability of deconvolution methods to restore images. This problem is partly ameliorated by the apertures in the optical train that limit the ability of the microscope to capture light from distant objects (whose in-plane components would have low OTF values); their attenuation prevents the massive amount of signal (and noise) in the integrated far field from completely swamping in-focus data. Put another way, blurring of data from nearby objects is the biggest problem, while signal from more distant objects is attenuated because real microscopes are not true WF instruments. This problem is reduced in the CLSM because the missing cone does not exist, however, the loss of photons due to the pinhole reduces the signal-

to-noise ratio in the image and, during deconvolution, all noise is amplified.

NOISE

Photon noise is always present. The quantal nature of light means that a given illumination intensity is associated with statistical variation in the time at which photons are detected. The number of photons observed over any period behaves as a Poisson process whose variance is equal to the mean. In fluorescence microscopy, the number of photons that can be collected is limited by photodamage (bleaching) and the signal-to-noise ratios are quite low. In addition, although the PSF and object are generally considered to be three-dimensional, the bleaching processes, fluctuations in illumination intensity, and even movement of the object make real objects four-dimensional. To remove this fourth dimension we need to take a three-dimensional snapshot to freeze time-dependent changes. This implies limited exposure periods must be used, which of course further limits light collection.

Photons need to be converted to electrical signals for quantification and this process also introduces noise. Even in the absence of photons, all detectors give spurious signals (dark current) while undetected photons lead to a reduced signal-to-noise ratio. Over a range of wavelengths, average detector efficiencies are generally below 50% and this figure is further degraded by significant losses in the optical components in front of the detector (such as barrier filters and mirrors). It is not unusual to see overall detection efficiencies well below 5% in real microscope systems at some wavelengths and in the face of such signal losses the photon (shot) noise in the system can be severe. In addition, the detector may add electrical noise to the signal before digitization.

A third source of noise resides in the digitization of the signal. In most systems, the detector provides an analog signal that is digitized into discrete levels, and 8- to 12-bit detectors are most common. There is, of course, a one-half–bit uncertainty in the digitization of any such signal and this typically leads to between 0.2% to 0.01% noise. Although this may seem small (compared to photon noise), this noise is also amplified during data processing. (To appreciate the potential contribution of this component we should recall that the original in-focus data may represent <5% of the total signal.) The digitization noise does not apply to all digital photon-counting systems. Despite the concerns, photon noise generally remains the dominant noise source (Mullikin *et al*., 1994; Pawley, 1995; van Kempen *et al*., 1997) in microscopic fluorescence images, at least when using PMTs. When using CCD detectors, other sources of noise are added. For a very good CCD with a readout noise of ±10 photoelectrons, readout noise will dominate until 100 photons are detected (at which point these noise sources are equivalent). For cameras, another source of noise is added due to pixel-to-pixel variation in gain (and/or sensitivity). This flat-field noise is age and temperature sensitive, it increases in direct proportion to signal strength, and it might be equivalent to photon noise at a signal strength of ~5000 photons. At high light levels this noise source dominates but can often be partially controlled by correcting the image for the gain/sensitivity variation (by normalizing the image to a reference image of a white field).

Finally, the thousands of computations required during deconvolution may lead to computational errors due to truncation. Fortunately, modern computers have quite long word lengths so this problem is largely disappearing, but errors in programming such as inappropriate typecasting can lead to truncation errors propagating. Computational errors are often hard to diagnose as they usually appear as general noise in the image.

DECONVOLUTION ALGORITHMS

In the previous discussion we have shown that in fluorescence microscopy (in all its modes including widefield, confocal, and multi-photon) the imaging process can be mathematically described by a convolution. Convolution consists of replacing each point in the original object with its blurred image (the PSF) in all three dimensions and summing together overlapping contributions from adjacent points to generate the resulting three-dimensional image. As pointed out above, the inverse operation or deconvolution can be performed (at least in principle) by dividing the Fourier transform of the recorded image by the Fourier transform of the PSF (this argument followed from Eq. 6). Although mathematically correct, this inverse filter algorithm does not work well in practice because the inevitable noise in the recorded data can be so strongly amplified as to render the deconvolved data useless. It is this problem that more sophisticated deconvolution algorithms have been developed to overcome and more robust methods are well established. In this section we will describe the ideas behind these improved methods without too much mathematics. Note that when using the term image here, we mean the full three-dimensional data set, often called an image stack. If desired, the reader can consult one of the *Numerical Recipes in X* texts (where *X* may be Fortran, C or C++; see also http://www.nr.com for online access) for more detailed discussion of some of the fundamental mathematical concepts involved (i.e., maximum likelihood, minimization of functions, etc.).

Nearest-Neighbor Deconvolution

Deconvolution algorithms vary greatly with respect to computational intensity, that is, how long it actually takes to compute the deconvolved image. Among the simplest algorithms that are of practical use are the nearest-neighbor approaches. Such algorithms are based on the simplifying assumption that the loss of contrast in any given plane is only due to signal arising from objects in planes immediately above and below it. To restore the data with this assumption, we can subtract appropriately blurred versions of the object planes above and below the current focal plane from the recorded image data. The blurring of the adjacent planes is, of course, determined by the PSF. For example, the signal contribution from object structures in the plane immediately above can be obtained by a two-dimensional convolution:

$$o_{j+1} \otimes psf_{j+1} \qquad \textbf{(6)}$$

where, assuming that image planes are recorded a spacing Δz apart, psf_{j+1} denotes the values of the PSF in the next image plane, Δz from the focus. To calculate this contribution we would need to know o_{j+1} (in addition to the three-dimensional PSF), but we only have image data at this point. We therefore make a second approximation (which is no worse than the first) that $o_{j+1} = i_{j+1}$. Thus, a fraction of this blurred nearest-neighbor data is then subtracted from the data recorded in the current image plane, or, as an equation:

$$o_j = [i_j - c(i_{j-1} \otimes psf_{j-1} + i_{j+1} \otimes psf_{j+1})] \qquad \textbf{(7)}$$

where the index j identifies the current plane, $j - 1$ and $j + 1$ the planes immediately below and above, o and i are the deconvolved object and recorded image, respectively, and c is a constant <1.

This algorithm increases in-plane contrast and blurring in the focal plane can also be reduced by applying a 2D inverse filter of the in-focus PSF (psf_j^{-1}). For further details see Agard and colleagues (1989):

$$o_j = [i_j - c(i_{j-1} \otimes psf_{j-1} + i_{j+1} \otimes psf_{j+1})] \otimes psf_j^{-1} \quad \textbf{(8)}$$

Note that all the convolutions are two-dimensional, making this method suitable for real-time implementation with FFTs. On the other hand, one should not be surprised that the enhancement obtained with this method is only moderate and (most important) not quantitative. These limitations reside in the subtractive nature of the process which will add noise and alter signal amplitudes. Nevertheless, where qualitative imaging at high speed is required, useful increases in in-plane contrast can be achieved with this method. For better results one needs to resort to fully three-dimensional algorithms.

An even faster implementation can be made by assuming that the data in adjacent planes is the same as that in the image plane, that is, $i_{j\pm1} = i_j$. In this no-neighbors method, the PSF is used to subtract a blurred contribution of the image plane from itself. Strictly speaking, this is not a deconvolution method at all but is formally equivalent to an unsharp-mask high-pass filter. Clearly, the gross assumption underlying this approach limits its applicability to very sparse three-dimensional objects and any intensity quantitation would be out of the question.

Wiener Filtering

Turning now to full three-dimensional approaches, as noted above the object can be deconvolved by inverse filtering, that is, direct division of the Fourier transform of the data by the OTF:

$$F\{o\} = \frac{F\{i\}}{OTF} \quad \textbf{(9)}$$

In this equation, the low values of the OTF in the region of the missing cone will increase noise in the restored image. Put another way, the data which is lost in the missing cone cannot be replaced unless we supply some other information that acts as a constraint on the restoration. Nevertheless, while the amplification of noise makes direct inversion nearly useless (at least for microscopic images), it can be improved by a simple modification (Shaw and Rawlins, 1991):

$$F\{o\} = F\{i\} \times \frac{OTF}{OTF^2 + K} \quad \textbf{(10)}$$

where K is an additive correction factor (see Figure 25.7). By adding K, noise amplification will be limited where the OTF is small. It can be seen that if $K = 0$, the equation reduces to the original inverse filter (Eq. 9). The impact of K can be reduced in the low frequency domain (where noise is less of a problem) by making it depend on the spectral characteristics of noise and object data. In this case, K can be mathematically optimized and this optimal filter is called the Wiener filter. Unfortunately, Wiener filters do not generally provide optimal image quality because: (1) suppression of any part of OTF during restoration affects the entire image, (2) where the OTF is small, noise will be amplified, possibly to an unacceptable degree, and (3) small errors or uncertainties in the OTF will lead to large errors in the reconstruction. Generally, for microscopic imaging purposes, Wiener and similar linear filters have been superseded by nonlinear iterative deconvolution algorithms that have become more applicable with increasing computer power.

Nonlinear Constrained Iterative Deconvolution Algorithms

Why use nonlinear methods? The problem resides in the fact that linear methods cannot guarantee that the deconvolved object is positive. Rather, in the presence of noisy image data, some pixels in the deconvolved object will assume negative values, a result which is obviously incorrect. For fluorescent images all photon fluxes must be positive so nonlinear algorithms that ensure no negative data values in the reconstructed object are clearly preferable. Such positivity constraints can be easily enforced within iterative algorithms. In iterative algorithms, the deconvolved object is not computed in a single pass (as is the case in nearest-neighbor or Wiener filtering) but the object is calculated in a series of steps that are then repeated. Each step results in a new estimate of the object that should be somewhat closer to the actual object. During this process, positivity can be enforced by explicitly setting negative values in the current estimate to zero. The small error that is introduced by this clipping procedure should be corrected in the next iteration and, with a well-behaved algorithm, the estimate converges to a nonnegative solution that closely approximates the true object. After a certain number of steps, the process is terminated by the user to yield the deconvolved data.

All iterative algorithms start from an initial estimate and we will discuss reasonable starting choices briefly later. The algorithm then enters the iterative loop in which a new estimate is calculated from the current estimate and the recorded image data. The positivity constraint is then enforced by setting all negative pixels in the new estimate to zero. New estimates are calculated repeatedly using this scheme until the user (or the software implementation that he uses) decides to terminate the computation and accept the last calculated estimate as the deconvolved object.

Expressed as a piece of pseudo code:

1. Pick a starting estimate o^0
   a. Calculate OTF (if blind)
2. Compute an initial new estimate (o^{k+1}) from previous estimate o^k, recorded image data i and OTF
3. Set all negative pixels in o^{k+1} to zero to give the current best estimate and apply any other constraints
   a. If blind, estimate a new OTF from F{i}/F{o^{k+1}} applying any constraints such as NA, symmetry and nonnegativity.
4. Go to step 2 unless a stop criterion is reached

Differences between iterative algorithms primarily arise from the way in which the new estimate is calculated (step 2).

To calculate a better estimate of the object, we must have some way to find out if our current object guess (o^k) is good (or not). Ideally, the estimate blurred by the PSF would be the same as our recorded image i except for some small difference due to the noise in the image data. Following this idea, we can calculate an error signal as the difference between our blurred guess and the actual image data. So to update the estimate we can take a fraction of error signal and add it to the current estimate (a Newton iterative approach). This approach underlies the Jansson–van Cittert algorithm (Jansson *et al.*, 1976). As an equation:

$$o^{k+1} = o^k + \gamma(i - (o^k \otimes psf)) \quad \textbf{(11)}$$

and with a good choice for γ (which can vary across the image) this scheme should lead to successively better estimates. However, in early implementations the choice of γ was rather *ad hoc* (Jannson, 1970; Agard *et al.*, 1989) and noise leads to uncertainty as to whether the algorithm actually achieves the optimal solution.

In more recent iterative algorithms, the updating scheme is derived from more stringent mathematical reasoning. One class of algorithms that work well in practice are called maximum likelihood algorithms. The idea behind this approach is based on the notion of the likelihood of a certain object o to underlie our recorded data i. In this context, we can view the deconvolution problem as a multi-dimensional fitting problem. In this view we anticipate that for the correct choice of fitting parameters (actually the pixels values in o), there should be a finite probability that our data should have been observed. Thus, we have to try to find the object o which *maximizes* the likelihood that our data would have occurred given a specific noise model (which is required to mathematically calculate these probabilities). Put simply, the idea is to fit a function (the blurred object guess) to the data with appropriate weighting for noise (which should be a concept familiar to all experiment scientists); see also the discussion in Press and colleagues (1992, section 15.1).

To deal with noisy fluorescence data, we can therefore calculate the probability that our data would have occurred, assuming the noise follows a Poisson (or some other noise model) distribution. Having found an explicit mathematical expression for this probability we then proceed to find the object o that maximizes this probability. Instead of trying to find this maximum directly we can make life a bit easier by looking for the maximum of the logarithm of the probability. Due to the properties of logarithms, this log-likelihood is maximal at the same location that the likelihood itself is maximal, however, the mathematical expressions generally become easier to handle after taking the logarithm. To actually find the maximum, mathematicians use the observation that at a maximum the derivative of the log-likelihood will be zero. Cutting through the mathematical derivation, one finally arrives at an expression for the updating step in the presence of Poisson noise:

$$o^{k+1} = o^k \times IF\left\{F\left\{\frac{i}{o^k \otimes psf}\right\} \times OTF'\right\} \qquad \textbf{(12)}$$

where $IF\{\}$ is the inverse Fourier transform and OTF' is the complex conjugate of the OTF. (The Fourier transform yields real and imaginary parts so the OTF is complex.) By definition, the complex conjugate of a complex number $x + iy$ is $x - iy$. Multiplication by the complex conjugate in Fourier space is known as correlation. Note that in this algorithm we do not use the additive error $I - o^k \otimes psf$ but rather the relative difference $i/(o^k \otimes psf)$. This algorithm is also known as the Richardson–Lucy algorithm after the authors who first derived this scheme for astronomical applications (Richardson, 1972; Lucy, 1974). For an example of the image enhancement possible with this algorithm see Figures 25.8 and 25.9. Assuming Gaussian noise in the data (for large photon fluxes, the Poisson noise model approaches Gaussian noise) we arrive at an alternative updating step that uses the additive error signal:

$$o^{k+1} = o^k + IF\{F\{i - o^k \otimes psf\} \times OTF'\} \qquad \textbf{(13)}$$

With both types of maximum likelihood algorithms, we should stop after a certain number of iterations for best results as, eventually, the error and/or noise starts to increase again.

This brings us back to the start and stopping choices that must be made with iterative deconvolution algorithms. Reasonable choices for the first estimate are (a) the recorded image itself, (b) a constant estimate with every value set to the mean of the recorded image, and (c) a smoothed version of the recorded image. Using the Richardson–Lucy maximum-likelihood algorithm (Eqs. 12, 13) choices (b) or (c) are recommended. A more detailed discussion can be found in van Kempen and van Vliet (2000). We also need a criterion of when to stop the iterative procedure and accept the current estimate as the deconvolved object. A reasonable approach involves monitoring the relative change between estimates as the iteration proceeds. As the relative difference

$$\frac{o_{k+1} - o_k}{o_k} \qquad \textbf{(14)}$$

between subsequent estimates falls below a chosen threshold (that generally depends on the amount of noise in the images) the iterations should be stopped. For example, with some of the data shown in this chapter, thresholds of $\sim 10^{-4}$ were used.

There are other issues that should be considered in a serious implementation of constrained-iterative deconvolution methods, for example, background estimation (van Kempen and van Vliet, 2000) and prefiltering of data and PSF (van Kempen *et al*., 1997). The other approach to iterative deconvolution is to use a regularization term, often the Tikhonov functional, as set out by Tikhonov and Arsenin (1977), which aims to limit the generation of large intensity oscillations in the deconvolved image (which will grow as the loss of high frequency information in the OTF becomes limiting). A number of similar methods based on this approach exist, and these vary primarily in the approach taken to find the solution to the regularization term which minimizes the signal oscillations or roughness in the deconvolved image. One such solution is the iterative constrained Tikhonov–Miller (ICTM) algorithm, which uses a minimization strategy based on conjugate gradients to minimize the Tikhonov functional. Tikhonov-regularized forms of the Richardson–Lucy algorithm also exist, representing a consolidation of these two classes of solution.

Comparisons of a number of deconvolution algorithms (van Kempen *et al.*, 1997; van Kempen, 1999) show that there is relatively little difference between their various deconvolved results. The regularized algorithms tend to be less sensitive to noise than Richardson–Lucy-based methods, and reach an appropriate stopping point sooner. However the RL algorithm provides slightly better deconvolution results, as quantified by the mean square error between the image and the PSF-blurred estimate of the deconvolved object. A useful improvement in the Richardson–Lucy method can be achieved by prefiltering the image and PSF with a Gaussian smoothing filter which reduces high frequency noise contributions without affecting the deconvolution of lower frequency image components.

One other variant of the general deconvolution algorithm is blind deconvolution (Holmes and O'Connor, 2000 and Chapter 24, *this volume*), where the deconvolution is performed in the absence of an independently measured (or calculated) PSF. Instead, the PSF is iteratively estimated along with the experimental data during the deconvolution process simultaneously. Proponents of blind deconvolution suggest this method is superior to using PSF-dependent calculations with a PSF rendered incorrect by sample-induced aberrations and scattering. On the other hand, one can argue that by supplying less information to the reconstruction, the final result must be inferior, if the PSF was known to sufficient precision. In addition, if the blind method makes use of symmetry in the PSF and/or the NA of the objective, artifacts will be produced if lens aberrations are present and/or the assumed NA is modified by, for example, improper illumination of the rear aperture of the lens.

Comparison of Methods

A common question is: What method works best? Unfortunately, there is no single answer because all imaging methods represent a

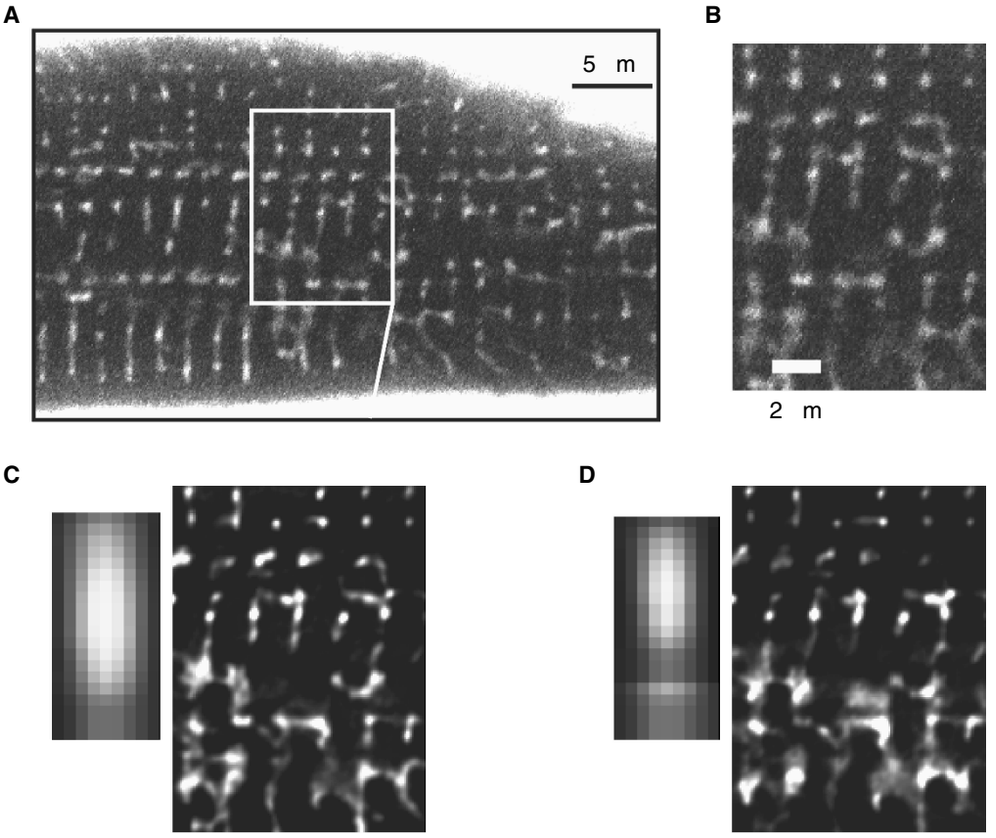


FIGURE 25.8. Maximum likelihood deconvolution of the cardiac *t*-system. (A) shows a two-photon image of a single, rat cardiac cell in dextran-linked fluorescein. The fluorescein has filled the *t*-tubules which are <~300 nm in diameter. (B) shows an enlarged view from a part of (A). Note the relatively low signal-to-noise present in this image although tubules can be clearly seen. (C) shows the restored image. Note the improvement in signal-to-noise ratio as well as the increased contrast. There has also been a useful but moderate increase in spatial resolution. The fine structure of the *t*-system can now be appreciated. (D) shows the effect of deconvolving the image with an incorrect PSF. At first sight, the results appear reasonable, but closer inspection reveals the presence of artifactual data when compared to (C). In view of the general problem of controlling spherical aberration, without good controls such artifact could easily lead to erroneous conclusions.

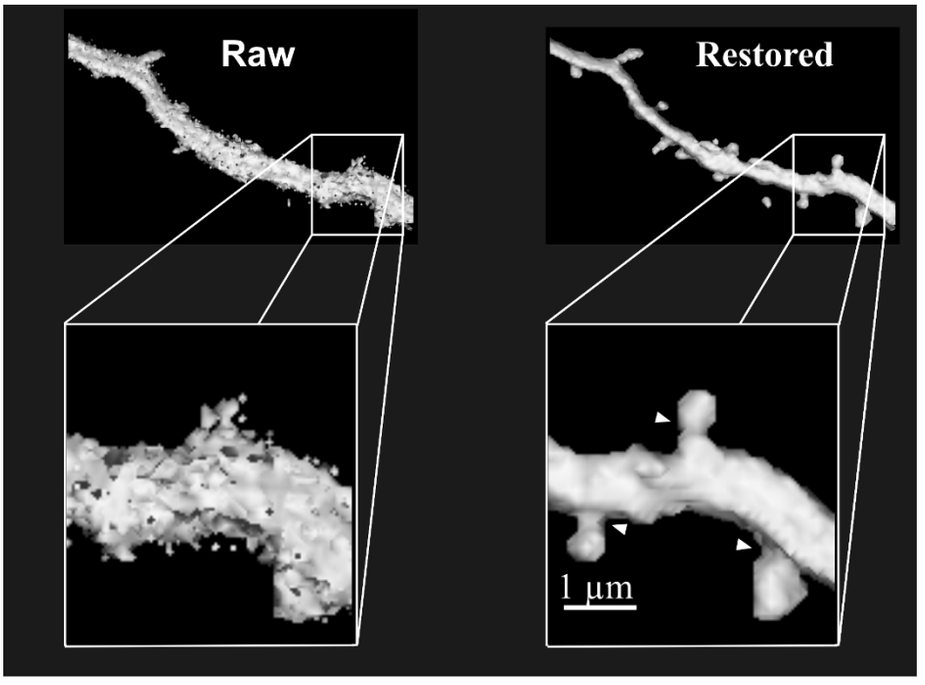


FIGURE 25.9. Enhancement of two-photon images by deconvolution. The panel at the left shows a neuronal dendrite in a living brain slice. The limited photon yield leads to little fine structure being visible in the volume-rendered image. After maximum likelihood deconvolution, synaptic spines are clearly visible and even appear to have necks (*arrows*). In this case, deconvolution has been much more useful to control noise rather than increase optical resolution.

trade-off between the three fundamental limits in information transfer processes: resolution versus speed versus noise. Thus, improvements in one area will usually compromise another and it is up to the experimenter to consider what is actually desired of the imaging method. This principle is generally limiting even within a chosen restoration method, because once resolution has been increased to a certain point, further gains can only be made by compromising noise and/or speed. As a guide, we suggest that deconvolved confocal/multi-photon images provide the ultimate image in terms of resolution (see Figs. 25.8 and 25.9). In some cases, deconvolved WF images with iterative methods can achieve comparable resolution to confocal/multi-photon methods. Nearest-neighbor methods provide a lower level of image improvement that can help control loss of contrast in WF images but suffer from their non-quantitative nature (i.e., one should not compare brightness between different parts of the image). Deconvolution of WF images may provide a resolution approaching that of confocal methods but would be problematic in scattering specimens or in the face of spherical aberration.

In terms of speed, nearest-neighbor methods are fastest with execution times for interative-constrained methods being comparable regardless of whether the source images are WF or confocal/multi-photon. This pecking order also seems to apply in terms of signal-to-noise ratio (including errors in absolute signal levels) with nearest-neighbor methods being worst and iterative constrained methods being best. In terms of noise, WF methods are initially superior until resolution starts to become limiting, at which point differences between methods largely disappear.

Finally, because even after deconvolution, image quality is critically dependent on the quality of the input data, we suggest 20 tips for better imaging:

1. Store unused objectives lens down, clean, and dry in the manufacturer's case.
2. Before using an objective, inspect it with a microscope eyepiece for cleanliness and damage — note any scratches across the metal front of the lens — possibly resulting from collisions with stage or specimens. If spring-loaded, check the objective front is not locked down.
3. Check the coverslips for thickness (check the coverslip requirement on the microscope barrel, usually 0.17 mm) and that they are suitable for the chosen objective. If the objective has a correction collar, use it!
4. Get a supply of subresolution fluorescent beads in a wide range of excitation and emission wavelengths to measure the PSF and test microscope performance. Mount them in standard slides (avoid mountants with harsh solvents); you can also purchase slides already made up.
5. Oversample the PSF and subsequently resample to image resolution by applying a Gaussian filter (to reduce noise) followed by a cubic-spline interpolation. If appropriate, apply a circular-symmetry constraint on the PSF to further reduce noise.
6. Add a small quantity of beads to samples before sealing the coverslip to enable visual inspection of the PSF in widefield.
7. Always seal wet-mounted specimens to prevent them drying out.
8. Minimize spherical aberration by appropriate selection of objective lenses/mounting media. If the objective has a correction collar, adjust it to make the observed PSF as symmetrical as possible. This can be achieved by watching the bead image as the microscope is slightly defocused. The Airy disk should grow symmetrically in both directions with defocus (see Fig. 20.3, *this volume*).
9. If a high-power oil lens must be used with a water-based specimen, try raising the refractive index of the specimen with sucrose, mannitol, or salt if osmotic pressure is not a problem, but be careful not to allow crystal formation. It should be noted that an 84% weight/volume sucrose solution has the same refractive index as glass (~1.5). Alternatively, use immersion oil having a refractive index >1.52.
10. In confocal applications, always open the pinhole slightly to increase light flux while maintaining a reasonable degree of confocality to achieve the desired axial resolution.
11. Use the highest voxel resolution possible in *xy* and *z*, but try to avoid bleaching problems.
12. Minimize bleaching problems with antifade mountants and latest-generation fluorochromes.
13. If imaging multiple wavelengths sequentially, image the longest wavelength fluorochromes first.
14. Ascertain the minimum and maximum extents of the specimen at the lowest possible illumination intensity (with the pinhole quite open in confocal applications). The idea is not to produce a nice image at this point but simply detect where the fluorescent specimen resides.
15. Keep a copy of the lens PSF with the image data and record voxel dimensions, objective, mounting media (some imaging software allows comments to be placed in the image header).
16. Image stacks will usually fit within a single CD-ROM (do not use any data compression unless you are sure it is lossless) so make a CD-ROM copy of the data before leaving the laboratory.
17. Avoid mechanical artifacts during imaging by keeping acoustic noise down, the door closed, and avoiding touching any part of the microscope system. Vibration isolation systems may be essential in laboratories with suspended floors. Air-cooled laser system fans should be mechanically decoupled from the microscope with a duct to a separate exhaust fan.
18. Use dimmable incandescent lighting in the laboratory and dim the lights while collecting data. On inverted microscopes, cover the specimen with a black cup.
19. Use a lookup table that makes it easy to spot over- and underflows in the data. Make sure the black level of the imaging system is set to >0; this is even more important than having a few pixels saturated.
20. Always have sample slides containing beads on hand and always check the microscope image quality with them before starting imaging, every day.
21. Deconvolve everything!

REFERENCES

Abbe, E., 1873, Beitrage zur theorie des microscopes und der mikroskopischen wahrnehmung, *Schultzes Arch f. Mikr. Anat*. 9:413:468.

Agard, D.A., Hiraoka, Y., Shaw, P., and Sedat, J.W., 1989, Fluorescence microscopy in three dimensions, *Methods Cell Biol*. 30:353–377.

Born, M., and Wolf, E., 1980, *Principles of Optics: Electromagnetic Theory of Propagation, Interference and Diffraction of Light*, Pergamon Press, Oxford, England.

Cagnet, M., Francon, M., and Thrierr, J.C., 1962, *An Atlas of Optical Phenomena*, Springer-Verlag, Berlin.

Denk, W., Strickler, J.H., and Webb, W.W., 1990, Two-photon laser scanning fluorescence microscopy, *Science* 248:73–76.

Holmes, T.J., and O'Connor, N.J., 2000, Blind deconvolution of 3D transmitted light brightfield micrographs, *J. Microsc*. 200:114–127.

Jansson, P.A., Hunt, R.H., and Plyler, E.K., 1970, Resolution enhancement of spectra, *J. Opt. Soc. Am*. 60:596–599.

Keller, H.E., 1995, Objective lenses for confocal microscopy, In: *Handbook of Biological Confocal Microscopy* (J.B. Pawley, ed.), Plenum Press, New York, pp. 111–126 or Chapter 7, *this volume*.

Lucy, L.B., 1974, An iterative technique for the rectification of observed distributions, *Astronomy J*. 79:745–765.

Mullikin, J.C., Van Vliet, L.J., Netten, H., Boddeke, F.R., van der Feltz, G.W., and Young, I.T., 1994, Methods for CCD camera characterization. *Proc. SPIE* 2173:73–84.

Pawley, J.B., 1995, *Handbook of Biological Confocal Microscopy*, 2nd ed., Plenum Press, New York.

Press, W.H., Teukolsky, S.A., Vetterling, W.T., and Flannery, B.P., 2002, Numerical recipes in C: The art of scientific computing. Cambridge University Press, Cambridge, UK, 1–970; available free, on-line at www.library.cornell.edu.

Richardson, W.H., 1972, Bayesian-based iterative method of image restoration, *J. Opt. Soc. Am*. 62:55–59.

Shaw, P.J., and Rawlins, D.J., 1991, Three-dimensional fluorescence microscopy, *Prog. Biophys. Mol. Biol.* 56:187–213.

Tikhonov, A.N., and Arsenin, V.I., 1977, *Solutions of Ill-Posed Problems*, V.H. Winston, Washington, DC.

van der Voort, H.T.M., and Brakenhoff, G.J., 1990, 3-D image formation in high-aperture fluorescence confocal microscopy: A numerical analysis, *J. Microsc*. 158:43–54.

van Kempen, G.M., 1999, Image restoration in fluorescence microscopy, In: *Advanced School for Computing and Imaging*, Delft University of Technology, Delft, The Netherlands, p. 161.

van Kempen, G.M.P., and van Vliet, L.J., 2000, Background estimation in nonlinear image restoration; *J. Opt. Soc. Am. A-Opt. and Im. Sci.* 17(3): 425–433.

van Kempen, G.M., van Vliet, L., Verveer, P., and van der Voort, H., 1997, A quantitative comparison of image restoration methods for confocal microscopy, *J. Microsc*. 185:354–365.

Wilson, T., 1990, Confocal microscopy, In: *Confocal Miscrocopy* (T. Wilson, ed), Academic Press, London, pp. 1–64.

Young, I.T., 1989, Image fidelity: Characterizing the imaging transfer function, *Methods Cell Biol*. 30:1–45.

26

Fiber-Optics in Scanning Optical Microscopy

Peter Delaney and Martin Harris

INTRODUCTION

Fifteen years ago, exploitation of fiber-optics in scanning confocal optical microscopy was minimal. Most practical applications relied upon technology derived quite directly from telecommunications applications (particularly the types of fibers themselves and the methods by which they were produced, packaged, and interfaced).

Since that time, there has been increasing acceptance of fiber components as illumination and detection elements in commercial scanning microscopes, and a marked increase in development of basic fiber technologies for scanning microscopy applications. Substantial progress has also been made in developing entirely new classes of highly miniaturized scanning confocal microscopes made possible only by fiber technologies.

Invention and production of more specialized optical fibers and fiber-optic devices has not only increased the practical opportunity to replace many of the conventional optical components with their more flexible fiber-optic counterparts, but in many cases has yielded completely novel and unique fiber components. Beyond the use of fiber-optic elements as efficient, flexible light conduits, fibers are now available that can act as spectral, spatial, and polarization filters, beam-splitters, lasers, and nonlinear devices for delivering light from pulsed lasers.

This chapter will introduce some of the relevant theoretical and practical parameters of fiber-optics, discuss these in the context of the role of fibers performing key functions within scanning microscopes, then move to a system-focused level that reviews the types of instruments that use fiber components and their capabilities and performance.

KEY FIBER TECHNOLOGIES RELEVANT TO SCANNING MICROSCOPY

Optical fibers with properties relevant to confocal microscopy range in complexity from slight variants of standard, telecommunications fiber through to novel fibers exploiting complex microstructures. An understanding of fiber design and function is pivotal to understanding their exploitation in scanning microscopes. We now overview the particular aspects of various fiber technologies that define their roles in various implementations of confocal microscopy.

Glass Made from Gas and Its Transmission Properties

Fiber technology is largely founded on production of ultra-pure glasses. This is achieved by creating glass from gas by bubbling hydrogen, oxygen, and helium through containers of volatile silicon tetrachloride, germanium tetrachloride, and, often, phosphorus and boron halide compounds. The vapor is burned to form a chalky, white deposit and further heating collapses this to produce an ultra-clear glass rod known as a preform. During this process, the composition of the vapor is varied to produce a specific cross-sectional refractive index profile. The preform is then melted and drawn down into fiber, jacketed for protection, and wound onto drums. Importantly, the drawing process preserves the cross-sectional profile of composition and associated refractive index (RI), and these are captured into the glass preform during its fabrication. Thus, simple or complex RI profiles can be made in the macroscopic domain (over many millimeters) of the preform, and subsequently become microscopic during the drawing process.

For the glass compositions most commonly used in optical fibers, the purity ensures that there is virtually no absorption of light during transmission for almost the entire wavelength range from 350 nm to 1600 nm (the transmission curve for silica glass is shown in Fig. 26.1). The predominant loss mechanism through this wavelength range is Raleigh scattering.

This transmission efficiency can be difficult to appreciate when working with the relatively short lengths of fiber used for microscopy applications. Although at wavelengths commonly used in scanning microscopy, losses in silica glass are orders of magnitude higher than at the wavelengths for which telecommunications fiber is commonly designed, telecommunications requires transmission over the 50 to 80 km distances between repeater stations. Thus, even for blue light over distances of several meters, losses are a fraction of a percentage. Inefficiencies in the optics used to launch the input (so-called insertion losses) or project the fiber output (e.g., excluding part of the Gaussian beam profile) are much more significant. If improperly managed, these losses can lead to the perception that fiber propagation is lossy.

Step Index and Gradient Index Optical Fibers

Some of the simplest optical fiber designs are comprised of a core of glass surrounded by a cladding of a different glass having a

Peter Delaney and Martin Harris • Optiscan Pty Ltd, Victoria 3149, Australia

Handbook of Biological Confocal Microscopy, Third Edition, edited by James B. Pawley, Springer Science+Business Media, LLC, New York, 2006.

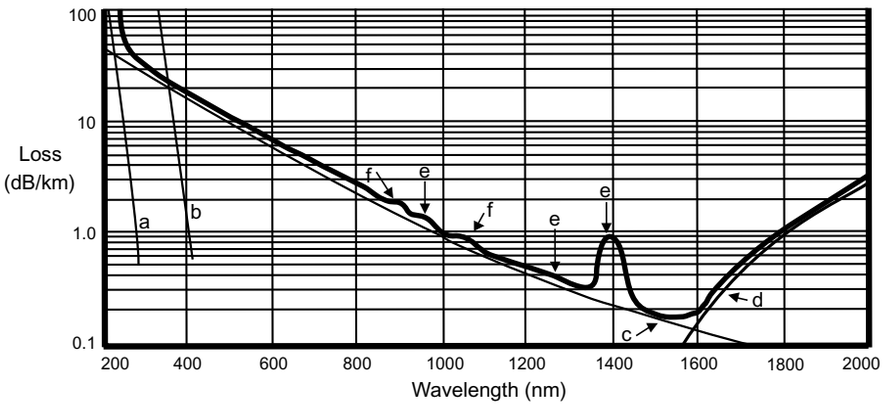


FIGURE 26.1. Transmission losses in silica glass optical fiber versus wavelength: (A) material bandgap absorption of silica; (B) material bandgap absorption of germania; (C) Raleigh scattering contributes loss mechanisms, which form bounding asymptotes to the overall shape of this spectrum; (D) infrared (IR) photon interactions; (E) absorption by residual water (OH bonds) in the glass superimpose several peaks in the spectrum; and (F) transition metal absorption bands.

lower refractive index (a so-called step index optical fiber). This forms a closed, cylindrical refractive index boundary that serves to entrap and propagate light by total internal reflection.

One of the properties of step index optical fibers is that the light that converges onto the input surface at higher angles must traverse a greater effective path length before it reaches the exit surface than light incident at lower angles. Hence, any pulse of light will be temporally dispersed. To overcome this limitation, gradient index optical fibers were developed (Wilson and Hawkes, 1989a). Gradient index fibers, as their name suggests, possess a gradient of RI from highest (at the center of the core) to that of the cladding [as depicted in Fig. 26.3(B)]. Rather than being reflected at an abrupt core/cladding boundary, the wavefront of light is steered continuously as it traverses the RI gradient. Light travels faster through the outer, lower RI medium, and hence tends to keep up with light propagating in the inner regions of the core, resulting in less temporal dispersion of the wavefronts of light propagated.

Modes in Optical Fibers

A propagating wavefront can interfere constructively or destructively with totally internally reflected regions of the same wavefront traveling across the fiber at a slightly different angle. Where this interference is constructive, the light propagates efficiently along the fiber. Hence, propagation of wavefronts at a particular wavelength is only supported for specific paths or angles within the fiber. These are called modes.

The modes that a given fiber will support are a function of the diameter of the fiber core d, the wavelength of light λ, and the RIs of the core and cladding, as well as the RI profile itself (in the case of gradient index fiber). An important parameter incorporating all these factors is called the V-number. The larger the V-number, the more modes a fiber will support, down to a cutoff value of V = 2.405, at which only a single, fundamental mode can be propagated by the fiber (Wilson and Hawkes, 1989b). This mode can be launched by focusing a train of converging concentric wavefronts to an appropriate diffraction-limited spot on the end of the core, and the light will then essentially propagate as a train of parallel wavefronts, as depicted in Figure 26.2. The light emergent at the output of such a fiber will also form a coherent virtual point source, radiating a train of diverging, concentric wavefronts analogous to laser light diverging from the waist region to which it has been focused, but with the numerical aperture (NA) of the fiber determining the angle of divergence. As will be discussed later, this ability of single-mode fibers to maintain coherence has many important properties relevant to their use in confocal microscopy. Importantly, when the V-number falls below the single-mode cutoff, the fiber still guides the fundamental mode. Note that V-number is related to wavelength in such a way that a fiber is single mode for all wavelengths longer than the wavelength associated with the single-mode cutoff. Thus, a fiber can be single mode across a range of wavelengths.

Modes can be visualized by viewing the far field projection of light emerging from a fiber (i.e., the appearance of the light output falling onto a piece of paper). For example, a large-cored step index fiber [such as depicted in Fig. 26.2] will be heavily multimode and may support hundreds or thousands of modes, which will appear as very fine spots that move rapidly with any disturbance to the fiber. Smaller-cored gradient-index fiber may support just a few modes and these will appear as characteristic lobes. The output of single-mode fiber appears as essentially a radially symmetric Gaussian-distributed disk.

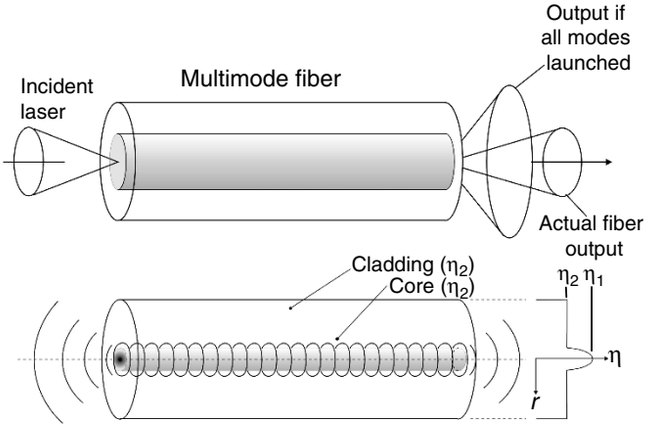


FIGURE 26.2. Diagrammatic representation of key differences between light propagation in step index multi-mode fiber and gradient index single-moded fiber. In a large core step index multi-moded fiber, the superset of all mode fields are confined to a cone which defines the NA of the fiber. The various modes allow propagation of light involving low through high angles of total internal reflection. It is possible to couple laser light into subsets of these modes. In the example depicted here, launching of laser light at lower than the maximum NA launches lower order modes, resulting in fiber output that is likewise lower in NA than that defined by the full set of modes supported by the fiber.

Evanescent Wave and Polarization Effects in Optical Fibers

When light is guided by total internal reflection from an RI gradient, a portion of the electromagnetic wave, called the evanescent wave, travels on the "far side" of the boundary (i.e., in the cladding) relative to where the mode is traveling. Correspondingly, an appreciable amount of the optical energy carried by a fiber is transmitted by the evanescent wave in the cladding surrounding the core, even for a step-index core.

The phase shift and lateral displacement that takes place when light is guided by the refractive index gradient is different for the two orthogonal polarization planes of the light. The distance that the evanescent wave penetrates into the cladding depends on the angle of incidence and the polarization state.

Light from lasers is usually linearly polarized. Conventional optical fiber has radial symmetry and if this symmetry were perfect and the fiber was held straight, then the polarization plane would not be changed during transmission. In practice, neither of these two conditions holds, so that the polarization plane of the emerging light may be rotated or it may be converted into a left- or right-handed circular or elliptically polarized beam. This is essentially uncontrolled in circular cross-section fiber.

Polarization-Maintaining Fibers

There are several designs of optical fiber that allow polarization to be maintained. It is either possible to make a fiber with an elliptical core cross-section or one with a circular core that is stressed by structures within the fiber but outside of the light-carrying core. These are made of a different glass type, which contracts more and produces stress in the core as the molten fiber cools. This stress produces a birefringence causing the speed of light traveling in the fiber in one polarization plane to differ from the speed in the other direction (by about 1 wavelength every millimeter of travel). This distance, called the beat length, is equivalent to a retardation in crystals and wave plates of one full wavelength. The phase between the two orthogonal polarization propagation modes thus changes back and forth and the coupling of energy from one polarization mode that occurs in one half beat length is reversed in the next half beat (hence little net change results). These so-called high birefringence (Hi-Bi) fibers can be bent without altering the polarization state of the output light. Two common designs of stressed fiber are called, descriptively, Panda and Bow Tie fibers (see diagrams in Fig. 26.3). The Panda fiber is made by drilling holes in the preform on either side of the core and inserting rods of glass having a higher thermal expansion coefficient before the fiber is drawn. The Bow Tie and elliptical core structures are made as the preform is deposited from the gas. When using polarization-maintaining fibers in some applications, it is critically important to ensure that the laser launch polarization is aligned with either the fast or the slow axis of the fiber. Rotating the fiber exit tip will rotate the polarization plane by exactly the same angle and this can be employed to align polarization when setting up experiments. It also should be pointed out that each of the modes in a multimode fiber can have its own separate linear polarization state. Failure to perform alignment correctly can cause large variations (commonly from 30% to 80%, but up to 100%) in the delivery of the desired polarization mode into the microscope. In some cases, this can be monitored by direct power measurements at the objective, or, more generally, by evaluating the images of a stable test specimen such as a mirror. Note that swings in polarization mode might not be measurable directly at the fiber output, as the light may still be coupled into a non-desired polarization mode, and the polarization change may only become evident as an intensity change after the light interacts with microscope or detection components that are polarization dependent. Any significant swings in these observations (more than a few percentage points) should flag the possible need to realign the fiber launch and/or alignment of the fiber output to the microscope.

Fused Biconical Taper Couplers: Fiber-Optic Beam-Splitters

If two sections of optical fiber are fused together and then stretched while still viscous, the cores are tapered, thinned out, and brought very close together. Each core overlaps significantly with the evanescent wave associated with light guided by the other. This allows light energy to be transferred from one core to the other, forming a type of beam-splitter. Such devices are called fused biconical taper couplers (FBTCs) [Fig. 26.4(A)], and may fit into a capsule the size of a match. They have been manufactured with net optical power losses of less than 0.01%. The theory covering the division of the light is not intuitive and is covered in Snyder and Love (1983). These couplers can produce a 50 : 50 division of the the light or any other desired ratio.

Although the split ratio of any FBTC varies with λ, couplers can be fabricated to be relatively λ-independent or highly λ-dependent. In the latter case, they can be used as dichroic beam-splitters [Figure 26.4(B)]. They can also be made to split the incoming light from one fiber so that light with orthogonal polarization modes emerges from the two output legs of the coupler. Alternatively, they can split light in a ratio that is independent of the polarization plane (Wilson and Hawkes, 1989c).

FBTCs can be used to combine the light from separate laser sources and they can also function as beam-splitters in confocal microscopy, where they offer additional modularity by providing separate fiber arms for laser launch, fiber output, and signal detection. They have also been a key component in making optical

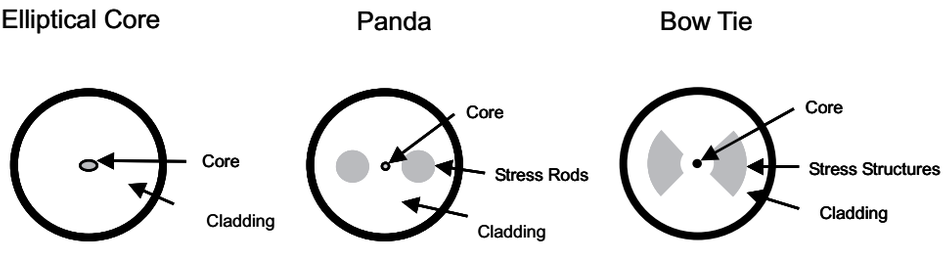


FIGURE 26.3. Polarization maintaining fiber core patterns. Various means are pictured whereby specific core profiles and stress structures are fabricated into a fiber preform prior to drawing. This results in an orthogonally biased pair of modes, each favoring one linear polarization plane.

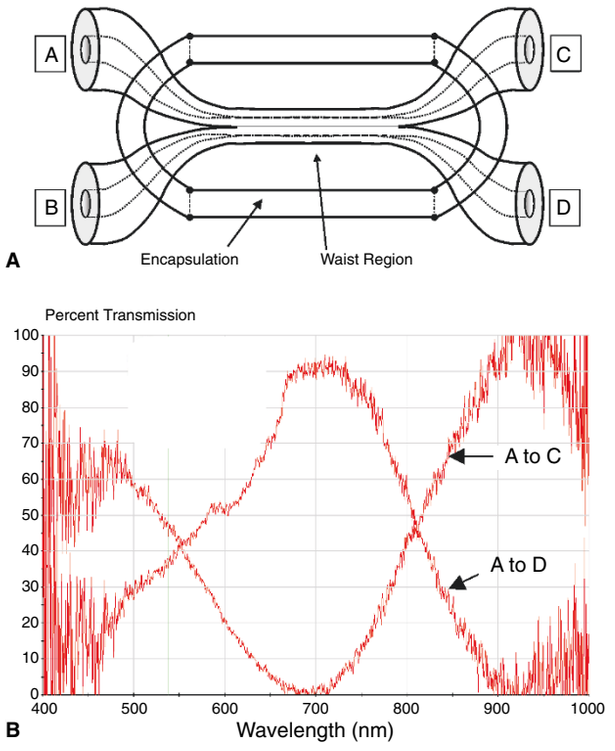


FIGURE 26.4. Fused biconical taper couplers. The general configuration is shown in (A), whereby two fibers are melted together and drawn, forming a waist region in which the mode fields guided by the cores overlap and exchange energy. Laser light coupled into any arm of the coupler will be apportioned in the two opposing arms in a ratio that is dependent upon the wavelength characteristics of the coupler, which can be varied by design. An example is given in (B) for a coupler with strong wavelength dependence that could be used, for example, to provide a 50 : 50 split for laser illumination at 488 nm, while favoring the transmission of confocal green fluorescence emission on one particular arm. Thus, the coupler could be used as for laser illumination, pinhole detection, and a dichroic beam-splitter in a fiber-based confocal microscope.

coherence tomography a useful *in vivo* imaging technique, where they provide the beam-splitting and recombination paths for the requisite interferometer (OCT; see also Chapter 34, *this volume*). One of the advantages in these applications is that fiber-based interferometers are not troubled by dust, as are conventional interferometers.

Microstructure Fibers

New designs of fibers, collectively called microstructure-core fibers (but also referred to as photonic crystals, air-clad fibers, or endlessly single-mode fibers, etc.) have recently been introduced. The cross-sectional views of several such designs are presented in Figure 26.5. Rather than exploiting a simple radially symmetric refractive index profile to guide light, these fibers consist of complex patterns of air holes and glass fins.

These structures give rise to unique optical properties, in particular nonlinear propagation effects that are not handled well by the conventional descriptors of linear modes in cylindrical fibers. Some of these fibers [see Fig. 26.5(A,E)] suspend what is effectively a large fiber core in a web of glass supports. Others [Fig. 26.5(B–F)] have a series of thin tubes around a hollow core. Although this pattern appears to defy the theory of conducting light by total internal reflection (TIR) in a high-RI core, they can be understood as Bragg-grating mirrors/photonic bandgap structures, surrounding and guiding the wave energy. The light is trapped between mirror structures in the cladding formed by the surfaces of the regular array of holes. Common examples of intrinsically colorless, transparent, multi-layer structures that act as mirrors include the reflective skin cells of fish, gel holograms, and the iridescent scales on butterfly wings. Applications of these fibers will be discussed in the context of optical fiber illumination.

Fiber Image Transfer Bundles

Coherent image transfer bundles are one of the earliest applications of optical fibers. Tens or hundreds of thousands of fibers are

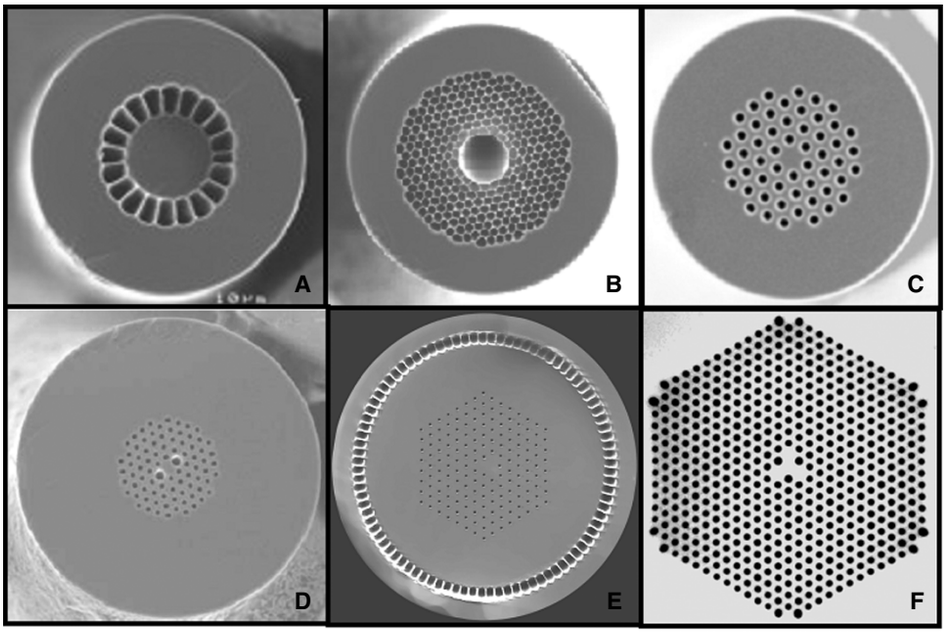


FIGURE 26.5. Images of the profiles of various microstructured optical fiber. Air cored fibers (B–E) exhibit low or negligible chromatic dispersion, whereas air cladding structures (A), and in a hybrid with an air core (E and F) can be pre-reverse chirped to excite nonlinear modes of propagation of ultra-short, high peak power pulses. The two larger air cores in (D) give this fiber polarization-preserving properties.

combined in a bundle, each fiber transferring one spot of light from a focused image at one end of the bundle to an identical configuration of fiber tips at the opposite end. This process reconstitutes the image. Invented by Logie-Baird in 1927, fiber-optical bundles were widely used for internal endoscopy after the 1950s, but now have largely been replaced by miniature solid-state video cameras. These devices present particular issues in terms of the way that they sample the image plane to be transferred. Because the fiber cores are separated by the cladding regions (unavoidable if the cores are to guide light), the image plane is sampled only at discrete locations. This complicates the interpretation of their performance and will be discussed below in more detail in the context of the microscope configurations that exploit them.

Two processes are commonly used to make coherent image transfer bundles. Fibers or preform rods with high RI centers can be packed together in a hexagonal pattern and then fused and drawn out. The hexagonal array and RI pattern are maintained in miniature form during the drawing. This process may be repeated if a smaller core is required. Alternatively, coherent bundles can be formed by winding very thin fibers on a mandrel, gluing together all the fibers in one section, and then cutting through and polishing both ends of that section. Bundles of fiber made by the latter method are as flexible as a hank of silk. Fused bundles are generally stiffer.

KEY FUNCTIONS OF FIBERS IN OPTICAL MICROSCOPES

Fiber technologies are presently exploited in various instruments including confocal microscopes, OCT scanners, and laser scanning nonlinear microscopy systems. Most of these applications involve the use of fibers, either for remote laser delivery and/or as a detection aperture and some use fibers that serve both these functions simultaneously. The major factors important in such systems are (1) the efficient launch of laser light into the optical fiber; (2) proper handling of the fiber output as a light source; (3) efficient projection of the returning signal light onto a fiber that is acting as a detector aperture; and (4) transmission of short pulses suitable for nonlinear microscopy. Note that these functions are not necessarily independent.

Optical Fiber for Delivering Light

The use of optical fibers as flexible laser delivery systems has been established for many years, proving particularly useful in medical laser delivery [e.g., in "laser knife" surgery or laser ablation of skin blemishes (Katzir, 1993)]. Among the major advantages to be gained by fiber-optic light delivery are the isolation of bulky laser equipment (including vibration isolation) and the flexibility provided by being able to actually handle and manipulate the laser output (e.g., in hand-held laser cutting devices). The properties of the output depends both on key fiber parameters (e.g., RI gradient, V-number) and those of the coupled laser (modes, wavelength, etc.).

The most common application of optical fibers in confocal microscopy is the use of a single-mode laser beam coupled to an optical fiber that is single-mode at the laser wavelength(s).

Factors important to efficient coupling of laser light into an optical fiber include: the beam profile and polarization of the laser, the mode profile of the fiber, its NA and, in the case of a pol-preserving fiber, its orientation, and the relative position of the lens system used to project the laser output into the fiber core. The key requirement is to focus the beam onto the fiber in a manner that achieves maximum overlap between the distribution of energy in the focused spot and the modal field that exists near the fiber tip, that is, there must be a complete overlap between the focused beam and the acceptance cone of the fiber. In practical terms, this means that the beam to be launched into the fiber must itself be everywhere coincident with the light that would emerge from the fiber had it been launched from the opposite end. Indeed, actually back launching a small amount of light in this manner serves as a very useful tool in the alignment of a laser/fiber coupling apparatus.

Many devices for launching laser light into optical fibers consist of a lens holder that can be aligned to the laser beam and a means of positioning an optical fiber at the focused spot, including an adjustment of its tilt. Orienting the fiber to maximize light throughput will in general correspond with translational alignment of the spot onto the fiber core (Figure 26.6). However, Figure 26.6 also shows that this will not necessarily be sufficient to ensure maximum coupling efficiency as this also requires both perfect axial (tilt) alignment and matching of the NA of the fiber with that of the incident, converging wavefront (Fig. 26.6).

Although the Gaussian beam profile of single-mode transverse electromagnetic mode (TEM_{00}) lasers is typically well matched (but not perfectly) to the modal field of single-mode optical fiber (Snyder and Love, 1983), the output from a solid-state laser is typically asymmetric and astigmatic unless corrected with dedicated anamorphic lenses. If the lens system is very well corrected for the application and meticulously aligned, coupling efficiency of approximately 90% is possible; however, with commonly available components (dedicated lens systems that are commercially available for common laser and fiber types) 60% to 70% should be routinely expected.

Instabilities in the output power can be caused by instability in any of the parameters mentioned above as being important to efficient launch.

Consideration should also be given to the light that is not propagated in the core of the fiber. For an air-to-fiber launch, approximately 4% will be lost at the air–glass interface by Fresnel reflection (assuming the fiber end has no anti-reflection coatings). Light that enters the fiber but is not propagated in modes will travel short distances in the cladding (centimeters to tens of centimeters)

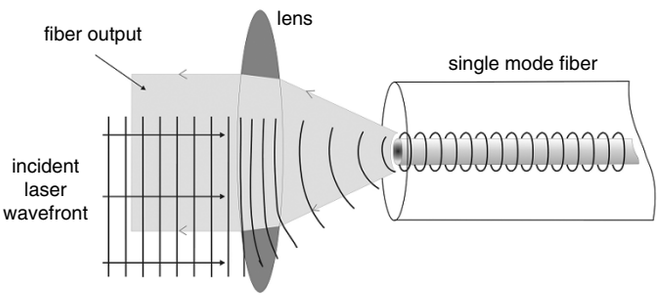


FIGURE 26.6. Single-mode fiber launch. Efficient coupling of a TEM_{00} laser beam into a single-mode fiber requires optimization of multiple degrees of freedom. First, the beam must be focused onto the core region. Second, the beam NA must be matched to the fiber NA and the axis of the convergent cone of light must be aligned with the mode field of the fiber. The incident beam in the diagram that is not overlapping with the mode field of the fiber will not be coupled into the fundamental mode, and will be radiated away over a short distance of fiber.

before being entirely radiated away, and will generally have a negligible impact on the output of fibers having lengths typical of those used for microscope illumination. However, the unguided light can excite fluorescence in fiber jacketing materials, a very small proportion of which may be propagated and contribute to background in the optical path of the microscope. Careful selection of non-fluorescent materials for fiber jacketing (particularly near the launch end) can eliminate this problem.

As discussed previously, the emergent light will be a series of concentric, diverging wavefronts, as though from a focused point of laser light. These spherical waves can then be re-collimated to provide a beam having the characteristics of a pure, fundamental-mode laser beam. Note that although collimation may only be required for certain applications, the preservation of this coherent laser wavefront is a critical optical property that affects all subsequent handling and propagation of the beam. When the output is projected into an optical system such as a confocal microscope, the output of the single-mode optical fiber is best considered to be equivalent to a TEM_{00} laser beam diverging from the point at which it is focused.

In contrast, if a multimode fiber is used for laser delivery, the different modes will act as a series of light sources or pinholes, each of which will image to a separate spot within the specimen. Note, however, that in a practical situation, the number of possible modes that actually propagate light is very sensitive to the launch conditions (it is often possible to launch only the fundamental mode or a limited subset of modes in a multimode fiber by careful launch alignment). Coupling efficiency for launching laser light into the fundamental mode of a few-mode fiber is comparable to that for single-mode fiber. The treatment of single-mode optical fiber output as a coherent point source cannot be accurately generalized to the case of a multimode fiber. Although each of the different individual modes will still maintain coherence, the overall output will be the sum of all modes propagated. The most important difference will generally be that the output can neither be restored to a single, parallel wavefront, nor focused to a diffraction-limited spot.

Optical Fiber as a Detection Aperture

The use of optical fiber as a detection aperture offers the potential for transmitting the signal light returning from the specimen to an external detector. The detectors themselves may include specialized devices such as spectrometers as well as the more common photomultiplier tube. The intrinsic properties of the single-mode fiber allow it to provide imaging characteristics similar to those of a conventional pinhole detector. The core size is related to the NA of the beam entering it in the same manner but it is defined in terms of the soft edges of a Gaussian mode field, instead of the abrupt edges of a physical pinhole in an opaque material (i.e., the edges of the "virtual" pinhole are fuzzy).

Single-mode, few-mode, and multi-mode fibers can also act as coherent detectors. This has been demonstrated for the case of a two-mode optical fiber, for which differential measurement of the modes permits phase-contrast imaging of surfaces with very accurate height determination (Kimura and Wilson, 1991; Wilson *et al*., 1992).

The spatial distribution of modes within a multimode detection fiber may also carry information regarding the source of the signal. For example, spatial filtering of light from the near field or the far field projection of the fiber can mimic the role of a variable detection aperture. A rather elegant example uses the difference in RI coefficients between silica glass and the silicone elastomer jacket to form a temperature-tuned variable pinhole with no moving parts. (Harris and Delaney, patent). The variation in pinhole function achievable by this approach is dependent upon the number of modes supported by the fiber, and the extent to which the coupling optics distribute light into these modes. It is possible to control the effective pinhole size continuously from that of a single-mode fiber up to a large-core multimode fiber, or a change of several times in effective pinhole diameter. This approach is applicable to single fibers only and not to fiber bundles.

Same Fiber for Both Source and Confocal Detection

The use of a single fiber as both the source and detection aperture best exploits the potential for fibers to offer stability and robustness in alignment, as well as to enable miniaturization of the imaging head. This made it possible to construct compact scanning heads to mount on microscopes as well as highly miniaturized imaging heads (both in single-fiber and fiber bundle configurations, see below).

One technical difficulty in implementing any approach whereby light is detected from the illuminating fiber (as in a single-optical-fiber confocal microscope; Delaney *et al*., 1994a) relates to the fact that both ends of the fiber are in image planes of the microscope. As a result reflections of the excitation light that are generated at the fiber tip must be suppressed. Fresnel reflection of the incident laser at optical surfaces can direct a significant amount of light into the detection path. As a result, careful management of launch conditions becomes critical for reasons other than efficiency, as it represents a source of background noise or artifacts. Both the launch efficiency itself and the control of light scattering at both fiber ends assume paramount importance.

Standard methods commonly used to manage insertion losses in telecommunications fibers can be applied directly to these situations:

- Angle polishing of fiber tips so that the reflected portion of the launched laser is reflected along a separate path than the mode field of the fiber (i.e., the path that light emerging from the fiber will follow). Any light to be measured back through this fiber can thus be spatially separated from the reflected light. Angle polishing can also be used to suppress return loss from the distal endface because the light reflecting back from the angled surface will not be aligned with that in the propagated mode.
- Index matching of fiber or bundle terminations (e.g., by filling the space between the launch optics and the fiber tip with an immersion medium). This minimizes or eliminates reflections that occur at an air–glass refractive index boundary, or deflects them away from the detection path.
- Anti-reflection coating the fiber tips.

Other sources of background include Raman generation in the fiber core and fluorescence from the polymers used in the fiber coating and connectors. Careful selection of fiber jacketing and the materials used in connectors (including glues) is essential if one is to minimize sources of stray light. If handled carefully, background levels 5 to 6 orders of magnitude below the incident laser power are achievable.

Note that, as polarization sensitivity of modes may confound efficient detection of the randomly polarized fluorescence signal (e.g., from unbound fluorescent probes), systems based on this design tend to use optical fibers that are not polarization-preserving.

Fiber Delivery for Nonlinear Microscopy with Femtosecond Lasers

Two-photon, three-photon, and allied nonlinear microscopy requires ultra-short (femtosecond domain) pulses delivered at very high peak optical powers to generate second- and third-order effects. Although titanium–sapphire femtosecond lasers are widely employed for this purpose with direct beam delivery, the use of fibers to transmit the pulses would provide greater convenience if a number of difficult technical challenges can be overcome. Short pulses necessarily contain a small range of wavelengths (10 nm at 100 fs, white light at 1 fs). Once the pulse is in the fiber, chromatic dispersion (due to different wavelengths propagating at different speeds) causes the shorter wavelength components to lag those with longer wavelength. This makes the pulse last longer. For example, a 50 fs pulse [which has a spectral spread of around 20 nm full-width half-maximum (FWHM)] can spread to several picoseconds in the process of traversing a meter of fiber. Some investigators have attempted to overcome this problem by using a device known as a pre-reverse chirper to progressively delay the longer wavelengths relative to the shorter wavelengths. Thus, the slower-traveling blue components gain a head start on the faster-traveling red components. If tuned correctly, the faster red components catch up to the slower blue just as they reach the end of the fiber, reconstituting the original short pulse at their target destination in the sample.

Although elegant, this approach has two limitations. First, it does not deal with a secondary spectrum, which is not so easily corrected. Second, even if the chromatic dispersion is perfectly corrected, the presence of high peak powers concentrated into a tiny fiber core can alter its function of, or even destroy it (Fork *et al*., 1984).

Although pre-reverse chirping can result in fiber delivery of pulses short enough to excite two-photon fluorescence, the limitations of pulse restoration and peak power have prevented such systems from imaging specimens to a greater depth than single-photon confocal microscopy, thus negating the benefit of nonlinear excitation. However, various microstructure fibers now hold much promise for bringing practical fiber-optic illumination to nonlinear optical microscopy.

Some classes of air-core optical fiber have been shown to have virtually zero chromatic dispersion and are also capable of transmitting high power levels (Knight *et al.*, 1998; Bjarklev *et al.*, 2003). Other fibers that suspend a large central core by a fine structure of spokes have been shown to be capable of transmitting 140 fs pulses at high peak power (Ouzounov *et al.*, 2002).

Some of these nonlinear effects are caused by the fact that the pulse intensity is so high that it locally changes the RI of the glass and allows the trailing part of the wave to catch up in a process called self-phase modulation. This can generate ultra-short isolated wave sets called optical solitons, which are able to travel in such fibers over considerable distances without spreading. The process is analogous to that which produces tidal bores in some estuaries.

Not surprisingly, microstructured fibers demonstrate different properties for the linear propagation of continuous light energy than for the nonlinear propagation of pulsed energy. In particular, some feature very large core diameters that are massively multimode in the linear domain. Thus, they may function as a large area detection pinhole. This may be appealing in many nonlinear microscopy applications because nonlinear illumination can be combined with non-confocal linear detection using the same fiber.

Large Core Fibers as Source or Detection Apertures

In addition to their function as a point source or a detection aperture, optical fibers can also provide diffuse illumination and large area detection.

For example, very large fluid-core fibers can scramble the spatial or temporal structure of arc or filament light sources with the result that the endface of the core serves as a uniform, diffuse source (Ellis, 1985) (as described in Chapter 6, *this volume*).

Likewise, large-core fibers can be used to carry the signal light passing through a physical pinhole aperture in the scan head to a remotely mounted photodetector. When used in this fashion, it is important to remember that, no matter how sophisticated the optics used to magnify or demagnify the semi-coherent light coming through the pinhole, one cannot demagnify the original source of the signal without losing photons. Therefore, the distal end of the fiber must always be at least as large as the source of light in the specimen and, were such a fiber to be used as a collector for non-descanned detection in nonlinear microscopy, its input surface should be larger than the area of the **raster** scanned in the specimen.

BENCHTOP SCANNING MICROSCOPES EXPLOITING FIBER COMPONENTS

Single-mode fiber-optic laser delivery is almost standard on modern commercial laser scanning confocal microscopes. Over several design generations, this has enabled the design of more compact scanning heads, eliminated laser vibration from the microscope stand, and increased the flexibility in laser delivery, although fused biconical taper couplers are not yet commonly used for mixing the outputs from multiple lasers.

Most systems require control of the polarization state of the laser illumination for multiple reasons. First, the quarter-wave-plate antiflex systems for suppressing specular reflections from lens surfaces are polarization dependent (see Chapter 7, *this volume*). Second, as the split ratio of the 45° reflecting surface in beam-splitter cubes exhibits strong polarization dependence, any change in beam polarization can produce significant changes in the excitation power delivered to the specimen. Third, differential interference contrast (DIC) and other contrast techniques require a fixed, linear polarization state. Consequently, most laser-scanning confocal microscopes deliver the laser light with polarization-maintaining fibers. Due to their specialized core profiles (Fig. 26.3), polarization-maintaining fibers can support each of two polarization-dependant modes and act as a single-mode fiber for each of them. Hence, when properly coupled to a linearly polarized laser source, they act as a single-mode fiber.

At different times, several systems have also been produced that utilize fiber-optics on the detection path, enabling modularization of the detection scheme.

The use of one fiber for illumination and another for detection offers a high degree of modularity and flexibility (e.g., as exploited in the Nikon C1 system). This has been employed in a system for confocal micro-Raman imaging (Sharonov *et al*., 1992), offering great flexibility in laser sources and detection components.

Incorporation of fiber delivery in multi-photon microscopes has remained a niche field for many of the reasons described above. Although there have been numerous attempts to modify commercial laser-scanning microscopes to accept fiber-delivered pulsed light sources using reverse pre-chirping and a standard

cylindrical fiber, these have remained limited to applications requiring longer pulse lengths and lower peak powers. Such systems have not provided the deep tissue imaging and flexibility in multi-photon excitation cross-section common from conventional systems.

Now, however, microstructure fiber is rapidly being applied to this area and early data suggests exciting progress. With these advances, fiber delivery will be increasingly adopted for nonlinear microscopy in experimental and commercial systems. This will allow novel configurations and the development of miniaturized scanning systems, such as those already available in confocal microscopy.

MINIATURIZED SCANNING CONFOCAL MICROSCOPE IMAGING HEADS

The most basic properties of confocal microscopy suggest numerous applications involving microscopic imaging of living tissue *in vivo*. In particular, the transition of biomedical research from bench to bedside faces numerous obstacles in understanding biological and morphological events in complex living systems on a microscopic scale. Until now, relatively few applications have been realized due in no small part to the cumbersome nature of bench-based microscope configurations. The development of miniaturized, scanning-probe devices suitable for practical *in vivo* confocal microscopy has long been a goal. The requirements of a miniature confocal imaging head for *in vivo* microscopy are small diameter (one to several millimeters), short rigid length (millimeters to several centimeters), and flexible umbilical connection to the rest of the instrument. In some applications (particularly in clinical medicine), there are further requirements for compatibility with conventional endoscope components and for disinfection or sterilization.

Fiber-optic technologies have played an enabling role in these developments, some of which have led to practical products and medical devices that employ various optical schema, as depicted in Figure 26.7 and described below.

Miniature Confocal Imaging Heads Based on Coherent Imaging Bundles

Coherent imaging fiber bundles present an intriguing range of trade-offs between the need for image quality versus simplicity of miniaturization and implementation.

A coherent fiber-optic imaging bundle can be used to transfer the scanned image plane from an open location to one with spatial constraints [i.e., one mounted on an endoscope; Gmitro and Aziz, 1993; Fig. 26.6(A)]. The focused laser beam is scanned across the proximal surface of the bundle injecting light sequentially into each of the fibers. Each fiber can then act as a confocal pinhole, returning light from the field on which its projection is focused in the sample.

Such a microscope can operate in a contact mode in which the polished end of the fiber bundle defines the image-isolation plane by directly touching the tissue. Alternatively, an appropriate lens can be mounted distal to the exit surface of the bundle to allow the projected image of the scanned spot or line to be refocused onto the specimen to obtain confocal images. In this case, any individual fiber in the bundle functions in a manner equivalent to the single fiber in Figure 42.6B as described in the next section. Contact imaging provides the smallest practicable endomicroscope but the resolution is effectively limited by the physical spacing of the fibers (~5 μm). The second method can have a higher resolution if the projected image of the fiber bundle is de-magnified by the lens system (Fig. 42.7, insert).

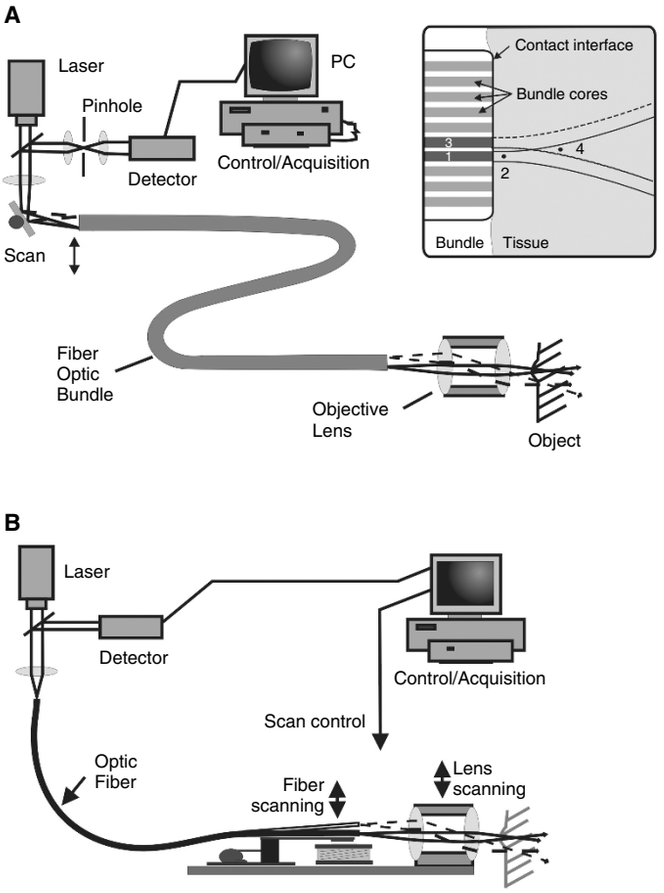


FIGURE 26.7. Optical schema for miniaturized confocal microscopy systems and heads. (A) Scanning the proximal end of a coherent fiber bundle transfers the illumination sequentially to the fibers in the bundle. The light emerging from one or more fibers is coupled to the tissue either by a lens system (main diagram) or by direct tissue contact (inset). In the former case (main diagram), the design of the lens system dictates the resolution achieved for imaging the specimen, and in particular how the discontinuous nature of the bundle impacts the optical sampling of the tissue (see main text). In the latter case, light emergent from a given core in the bundle (e.g., core 1, inset) will illuminate its mode field in the tissue. A near field point (2, inset) in the mode field will return light to core 1, but not to adjacent cores. Slightly further from the end of the bundle, points illuminated by core 1 (point 4, inset) can return light both to the illuminating core 1 and to adjacent core 4. Thus, the sampling of the tissue is governed by the NA of the fibers, scattering in the tissue, and the geometry of the bundle. (B) A single fiber is used as the illumination source and confocal detection path aperture, coupled to the focus in the tissue by a miniature lens system. Scanning can then be achieved by a variety of means. The fiber can be physically scanned relative to a laterally fixed lens, or the fiber can be fixed and the lens itself laterally scanned. Alternatively, the fiber and lens can be fixed and scanning performed by micromirror devices, or microlenses fitted to the tip of the fiber itself, which are scanned together (not shown).

Although sampling artifacts can occur when the hexagonal pattern of the fibers is imaged onto the CCD, to reveal the black cladding around each core, this can be overcome by software processing to reconstitute the signals from the individual fibers, producing an image that appears continuous [as it does, for instance, in the Mauna Kea Technologies system (Paris, France) (see Fig. 42.9].

However, such correction does not address the potential undersampling in the objective imaging-plane, where the output of each fiber (and its corresponding detected field) is discrete from that interrogated by neighboring fibers.

A successful optical-sampling system would not waste any light, and would both illuminate the focus plane in the object uniformly and project the image of an in-focus point object so that it is at least 4 core-spacings wide when it strikes the distal end of the fiber bundle (see Chapter 4 about sampling, *this volume*).

Several interacting operational variables affect this sampling problem and its impact on photon efficiency: packing the fibers more closely at the bundle output requires the use of high-RI glass cores and this results in the fiber having a higher NA and therefore emitting light into a larger spot at the BFP of the objective. If the NA of the fiber is larger than the back-NA of the objective [$NA_{back} = NA_{front}$]/M, where M is the (de)magnification], then much of the excitation light emerging from the fiber core will miss the objective. This reduces the photon efficiency in proportion to the square of the ratio of the respective NAs.

The objective lens system itself has both a magnification and an NA. As long as the BFP is filled, a larger NA implies smaller spots in the focus plane,[1] and consequently makes it more likely that the focused spots will not overlap. Higher demagnification not only implies a lower NA_{back}, but also ensures, that for a given fiber spacing, the spots at the focus plane in the specimen will be closer together.

The optimization depends heavily on the properties of the bundle. The most suitable bundles are densely packed, and consist of cores of approximately 4 µm diameter with a center-to-center fiber spacing of approximately 6 µm (i.e., the cladding between is ~2 µm). This yields a high-density 30,000 element bundle that is about 2 mm in diameter, including the jacket. If the cores get much smaller, they begin to act as single-mode fibers, especially at longer wavelengths, slightly reducing their throughput of incoherent fluorescent light. If the cladding gets much thinner, light begins to leak to adjacent fibers. To reduce this effect, the-core-to-cladding RI difference must be made as high as possible, resulting in a high fiber NA (0.3–0.4, versus NA 0.1–0.15 for communication fiber). As the NA of the objective varies between 0.4 and 0.5, operation at a magnification as low as 5× will still reduce the back NA to ~0.1, meaning that only 1/16 of the light emitted by a 0.4 NA fiber will strike it: 10× operation would be 4× worse.

A 0.5 NA objective demagnifying 488 nm light emerging from a bundle with 5 µm spacing by 10 : 1 will produce spots of that are ~0.75 µm at FWHM on a 0.5 µm spacing in the focus plane. These spots should overlap fairly well, and when the scanning system scans the laser beam over the proximal surface of the bundle, sequentially illuminating the cores on the distal surface, the entire focus plane will eventually be excited. However, any fluorescent or scattered light from an in-focus point object that returns through the objective, will form an image with a FWHM of only 5 µm in diameter at the fiber bundle surface. This is two times smaller than it should be to be sampled by at least 2 measurements (i.e., 2 cores across the FWHM, 4 cores across its entire diameter) as is required by Nyquist.

As with any form of undersampling, it can be overcome by increasing the sampling frequency (i.e., increasing the optical magnification or decreasing the core spacing) to meet the Nyquist criterion. Alternatively, one can "spoil the optical resolution," perhaps by introducing aberrations into the optics. As a result, energy from each fiber will be spread over a larger area in the specimen and the returning confocal signal will again be further defocused on its way back to the bundle. This results in some light striking adjacent fibers, achieving a similar result to increasing the sampling rate. It was employed by the authors in the prototype constructed to obtain Figures 42.8E and 42.8F.

Because any method used to overcome this problem necessarily involves mismatching the NAs of the fiber and the optical system, substantial reductions (i.e., from 90–99%) in photon efficiency cannot be avoided. The optimization and compromises depend heavily on the properties of the bundle.

Resolution and Optical Efficiency of Bundles

It can be seen from the above that the resolution achievable with a bundle system cannot be directly derived from the number and spacing of the fibers in the bundle and the objective lens magnification and NA. For a properly sampled objective space, several fibers are required per objective resel. A properly matched laser system can achieve a 70% launch efficiency into a single core, but measurements show that the light throughput drops to ~20% when the spot is defocused to cover several fibers at the polished end of a bundle. From geometrical arguments, it follows that if Nyquist-sampled resolution is required, then a considerable amount of excitation light (>75%) will be lost due to overfilling and around 70% of the confocal return is lost at the cladding interface.

As with any fiber-based confocal system involving illumination and detection via the same fiber, end-face reflections and fluorescence from the fibers or associated packaging may give rise to artifactual background signal. As with single-fiber confocal systems, these reflections may be minimized using the same techniques as those exploited in telecommunications (i.e., refractive index matching). Images from the Mauna Kea bundle system show effective removal of the fiber bundle autofluorescence pattern. This may be achieved by first using a high degree of over-sampling to properly capture the fine structure of the pattern, and then subtracting the fluorescence pattern from the bundle from the raw tissue data sets.

Bundle Imagers for *In Vivo* Studies in Animals

Despite the above compromises, the imaging probes that have been produced using bundles have produced the smallest confocal microscopes. Probes range from approximately 0.3 to several millimeters in diameter, and produce images with several thousand to several tens of thousands of resels per image. Bundle probes are thus well suited to *in vivo* microscopy in small animal models, and potentially in clinical applications that require access to very small orifices. For example, these devices enable colonoscopy in mouse models of early colorectal cancer formation, permitting longitudinal studies of individual tumors (Cavé *et al.*, 2005). A range of examples of animal tissues examined using miniature fiber-bundle confocal microscopes is presented in Figure 26.9.

[1] This illustrative calculation assumes that the light emerging from each core is fully coherent (i.e., that the fiber supports only a single mode). Because the fibers are actually multimode, the size of spots in the focus plane is not directly proportional to the NA and they are actually somewhat larger than stated. However, on the return journey, correct fiber spacing, not fiber size, is the parameter required to properly sample the magnified image of an in-focus point object.

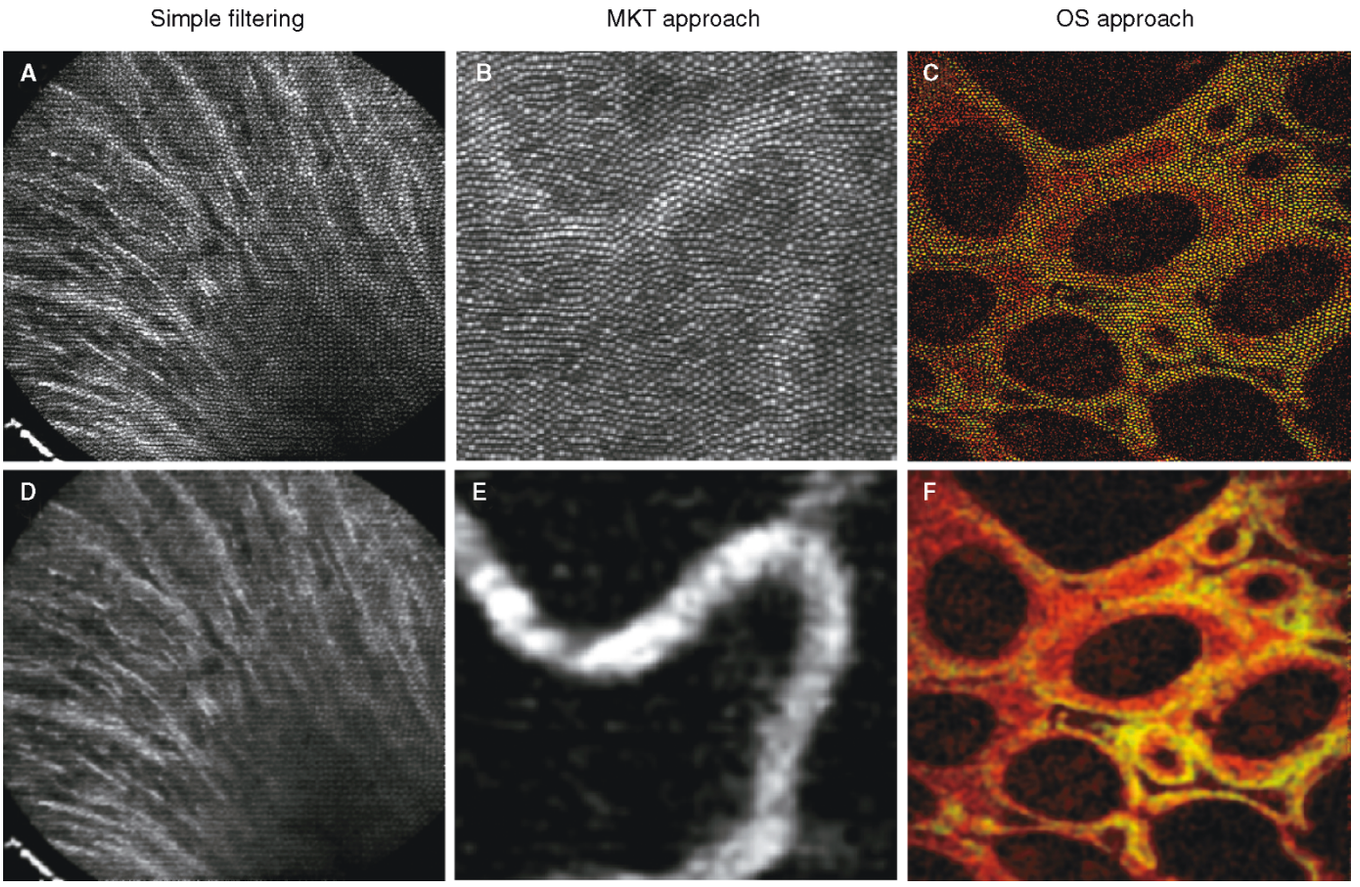


FIGURE 26.8. Software compensation of bundle artifacts. The pattern formed by the structure of the fiber bundle can be reduced using various software approaches. Simple spatial filtering can soften the bundle artifact, but significantly degrades resolution and contrast: (A) raw image, (D) image filtered with four passes of a 5×5 pixel Gaussian blur. A better approach involves collecting a reference image of the bundle pattern to subtract artifacts such as bundle autofluorescence (C) raw image, (E) processed image. A combination of background subtraction, pixel dilation, and filtering was used to process image (C) and to produce image (E). Potential artifacts of each of these approaches must be considered in the context of how the distal optical sampling is represented by the raw data obtained by scanning the proximal end of the fiber bundle (particularly when this is optimized for maximum laser launch efficiency, which results in clear resolution of the bundle elements). [Images (B) and (E) courtesy of Mauna Kea Technologies, Paris, France. Images (A), (C), (D), and (F) courtesy of Optiscan, Melbourne, Australia.]

Scan Heads Based on Single Fibers with Miniature Scanning Mechanisms

The use of a single fiber acting as both the source and detection aperture offers contiguous sampling of the imaging plane comparable to that offered by conventional scanning mirrors. However, the requirement to miniaturize a scanning mechanism for incorporation into the probe tip presents substantial technical challenges. Several approaches have been taken and practical devices have been realized, some of which are diagrammed in Figure 26.7. Scanning mechanisms include electromagnetic or piezoelectric scanning of the fiber itself, scanning of micro-mirrors, and scanning of a miniature lens.

Vibrating the Fiber Tip

In Figure 26.6(B) (Delaney *et al.*, 1993a), the output of a single-mode fiber is projected by a lens to form a collimated beam. This beam is focused by a second lens into an image plane in the specimen. These components form the confocal illumination path and the same fiber acts as the detection aperture for the return light. Scanning is implemented by moving the fiber tip, and being contiuous, this system suffers from none of the sampling problems that complicate the design of the fiber-bundle confocals.

All systems in which mechanical scanning is carried out at the tip require a counter-vibrating mass if small size and fast scan are desired. For example, the Optiscan system carries the fiber along one tine of a tuning fork to produce a resonant sinusoidal scan. The second tine moves in opposition balancing the reaction forces, which would otherwise move the case and result in visco-elastic damping by interaction with the tissue (Harris, patent). This approach has been used for a scanner that is 5 mm in diameter (see Fig. 26.10 inset) and forms the basis of a commercial clinical endomicroscope for human imaging (see Fig. 26.13).

Vibrating the Lens and Fiber

An alternative to scanning the fiber tip in front of static projection optics is from an endoscope image by mounting a very small lens on the tip of the fiber, so that the fiber output is focused to a point

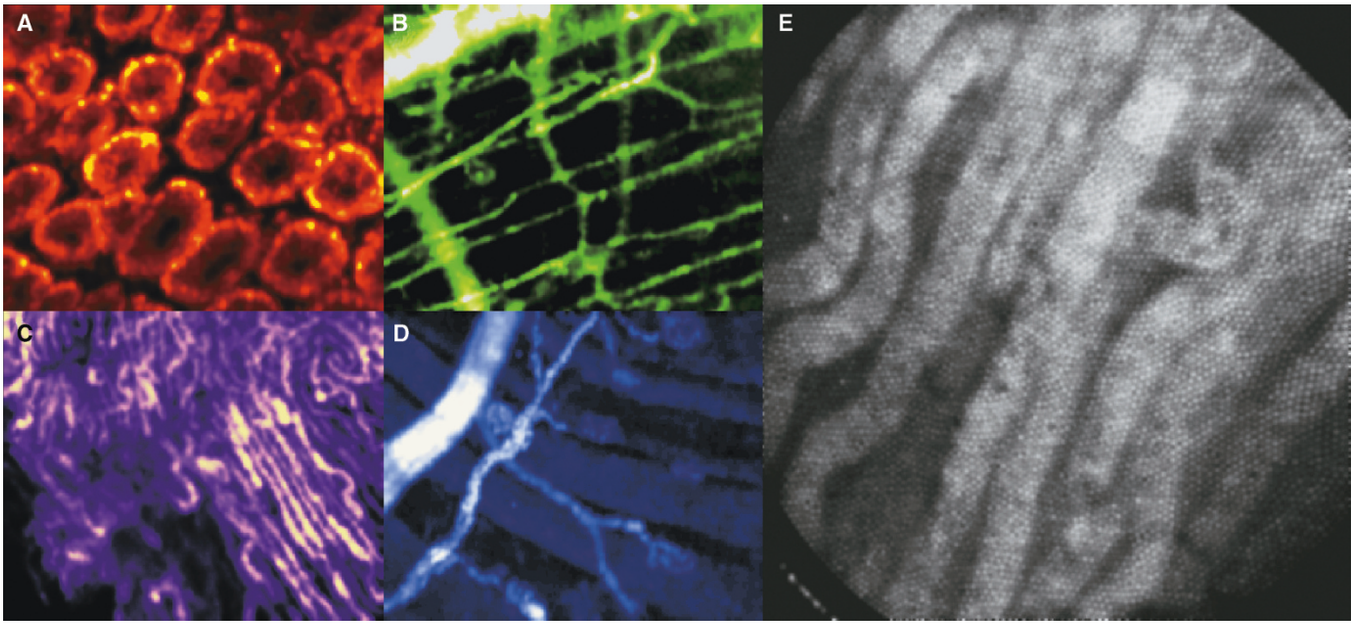


FIGURE 26.9. Imaging of animal tissue using miniature bundle systems. (A) Colonic crypts of a mouse mucosa after vital application of cresyl violet marking the cytoplasm and Syto13 marking the nuclei. Imaged endoscopically using the Cell~vizio, with a ProFlex S-1500, FOV: 400 × 280 µm. (B) Distal axon and motor endplates of a neuromuscular junction of a transgenically marked nervous system (Thy1-YFP mouse) with skeletal muscle fibers marked by topical application of Syto13. Imaged with the Cell~vizio and the direct contact of a ProFlex S-0650. (C) Proximal end of a cut sciatic nerve in a transgenic Thy1-YFP mouse, demonstrating the single-axon resolution. Imaged using a hand-held ProFlex S-0650. FOV: 400 × 280 µm. (D) Mouse cremaster microvasculature stained with FITC-albumin, injected intravenously. Imaged by the Cell~vizio and a hand-held ProFlex S-1500. FOV: 400 × 280 µm. (E) Rat kidney imaged with a prototype bundle contact tip, scanned using a desktop confocal microscope (Optiscan f900e). Field width, 400 µm. [Images (A), (B), and (C) courtesy of Igor Charvet and Paolo Meda CMU, Geneva, Switzerland, using equipment provided by Mauna Kea Technologies, Paris, France; (D) courtesy of Elisabeth Laemmel and Eric Vicaut, LEM, Paris, France; and (E) courtesy of Vladimir Dubaj and Andrew Wood, Swinburne University, Melbourne, Australia, utilizing equipment provided by Optiscan, Melbourne, Australia.]

near the fiber tip (Giniunas *et al*., 1991). Fused-fiber microlenses, gradient index lenses, and polymer lenses formed by the light leaving the fiber tip have all been tried. While offering appealing dimensions in both diameter and length, such systems are generally impractical due to their short working distance and/or narrow beam diameter.

Scanning with Micromirrors

Dickinsheets and Kino (1996) have demonstrated a system using two mirrors micro-machined from crystalline silicon. An optical design by Olympus using a single mirror held in a gimbal arrangement with torsion strips to provide resonance has also been demon-

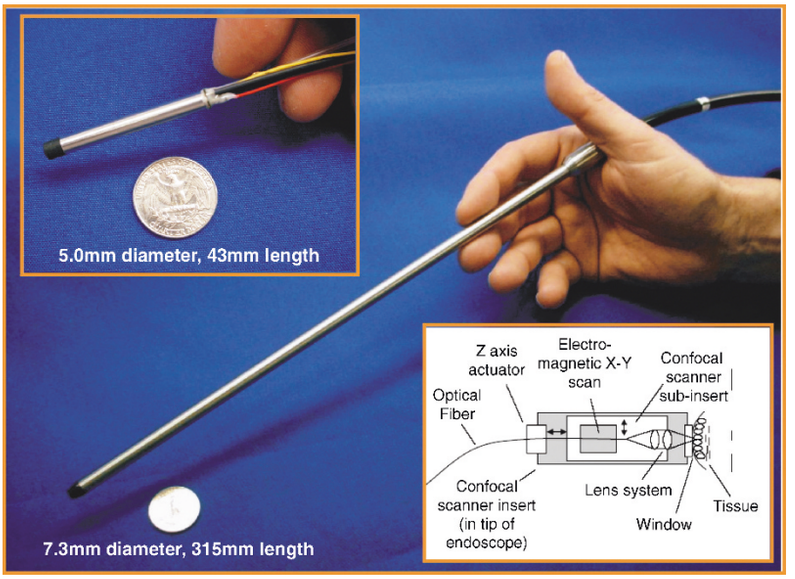


FIGURE 26.10. Miniature scanning-fiber confocal microscope scanner and rigid endoscope. The scanner (pictured inset top left) contains integrated raster scanning, a *z*-axis actuator, and projection objective optics encapsulated behind a fixed external window. The scanner produces 1024 × 1024 images at 1 frame per second. The objective NA is 0.55, providing lateral resolution of 0.7 µm and axial resolution of 7 µm. The external window is placed into contact with the sample and the *z*-axis actuator shifts the imaging depth from 0 to 250 µm relative to the contact surface. For *in vivo* microscopy, the scanner is packaged for the requirements of the application, in this case as a rigid arthroscope for minimally invasive surgical access to internal organs, or in the flexible endomicroscope shown in Figure 26.13. Images show a prototype made by Optiscan Pty Ltd, Melbourne, Australia. A schematic representation of the configuration of key components in the scanner is shown inset at lower right.

strated. The fiber emits light through a hole in the center of a primary catadioptic scanning mirror. The beam path is then folded by a secondary mirror on the surface of the first lens element (Murakami *et al*., 2005).

Scanning Fiber Confocal Microscopes for *In Vivo* Imaging in Animals

The scanning fiber approach, described above and diagrammed in Figure 26.7, has been implemented in a 5 mm diameter scanner and packaged either as a hand-held probe or as a rigid endoscope, as shown in Figure 26.10. The devices also include an active *z*-axis actuator that moves the entire scanning mechanism and lens system relative to an imaging window incorporated into the end of the device. The window at the tip of the device is thus placed directly against the animal tissue of interest, rather than the tissue being placed onto a stage. Mechanical contact provides a high degree of stability, and the images are obtained interactively, with hand-held controls to adjust the imaging plane depth relative to the window surface. Sample images are presented in Figure 26.11, demonstrating practical imaging of microvascular, cellular, and subcellular structures *in vivo*.

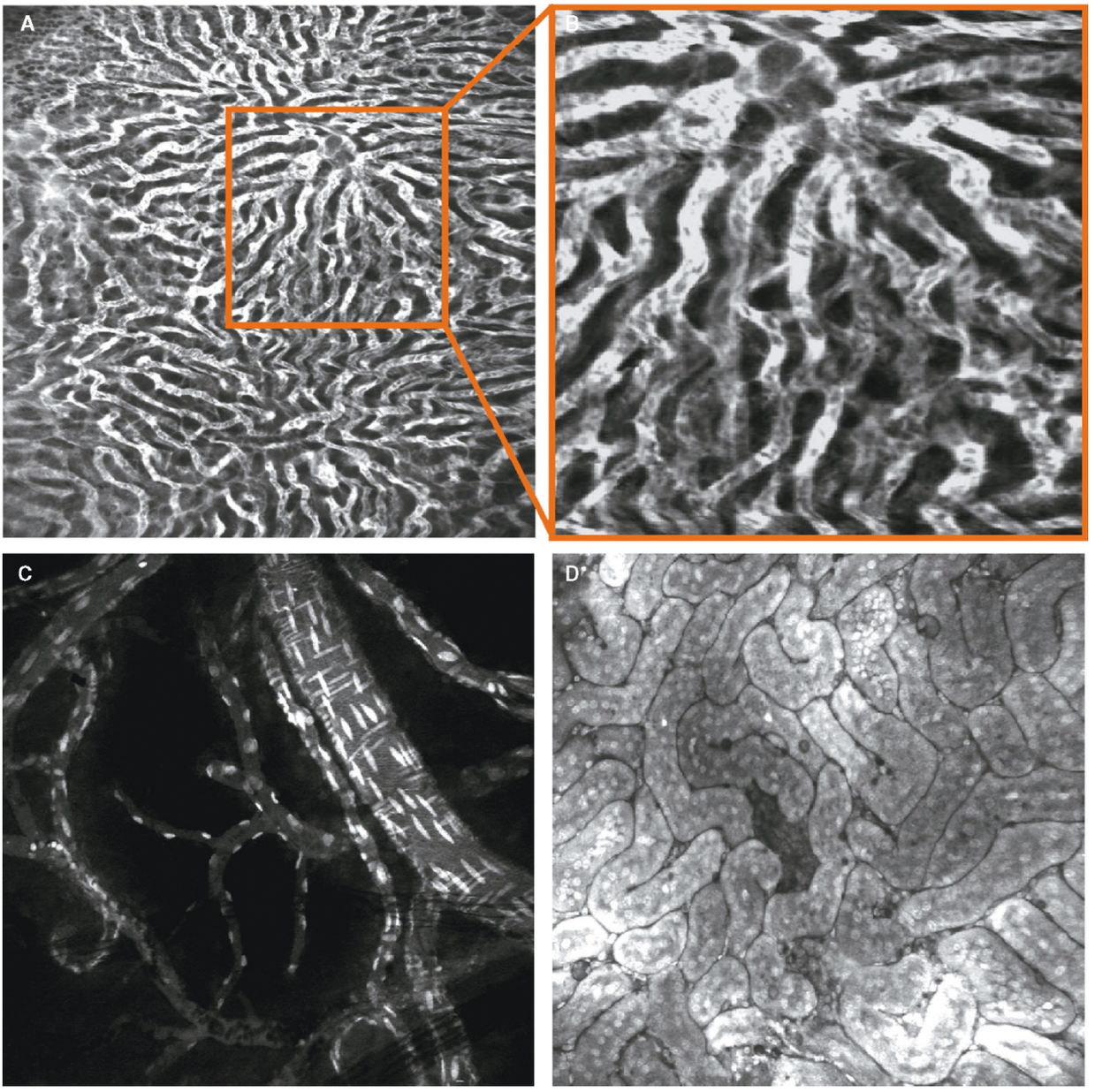


FIGURE 26.11. *In vivo* microscopy using the scanning fiber confocal microscope shown in Figure 26.10. (A) Mouse liver imaged following intravenous administration of FITC-dextran. (B) A region of this image zoomed in software to reveal the high information content and stability achievable *in vivo*. (C) Image of mouse brain following intravenous administration of Acriflavine, highlighting the longitudinal orientation of the nuclei of vascular epithelial cells versus the circumferential orientation of nuclei in vascular smooth muscle and muscle. All images are single 1 s scans at 1024 × 1024 pixel resolution, ex = 488 nm, det = 505–585 nm, and are courtesy of Dr. Ralf Kiesslich and Dr. Martin Goetz, Mainz University Hospital, Mainz, Germany.

IMPLEMENTATIONS FOR CLINICAL ENDOMICROSCOPY

Trends in medical diagnostics and therapeutics are towards point-of-care diagnostics and ever more rapid delivery of diagnostic information for guiding timely medical interventions. There has thus been growing interest in, and research into, various techniques for achieving non-invasive histologic imaging using miniaturized devices suitable for *in vivo* microscopy. In the past few years, numerous clinical applications have arisen, accelerated by the relatively recent development of prototypes and commercial systems certified for clinical investigation.

Three areas have involved substantial research and development effort and have been applied clinically:

Skin: Both non–fiber-optic and scanning fiber (Gonzalez and Tannous, 2002; Swindle *et al.*, 2003).

Cervix: Both fiber bundle and scanning fiber (Liang *et al.*, 2001; McLaren *et al.*, 2003; Fig. 26.12).

Gastrointestinal tract: The scanning fiber approach has resulted in a certified commercial gastrointestinal endomicroscope by Pentax, Japan (Delaney *et al.*, 1994b; Kiesslich *et al.*, 2004; see Fig. 26.14).

Clinical studies in all three areas have achieved diagnostic significance, suggesting a likely role for these technologies in clinical practice.

SUMMARY

Although to date relatively few developments have resulted in practical systems for clinical investigation, numerous ongoing efforts are aimed at achieving clinical confocal microscopy, and

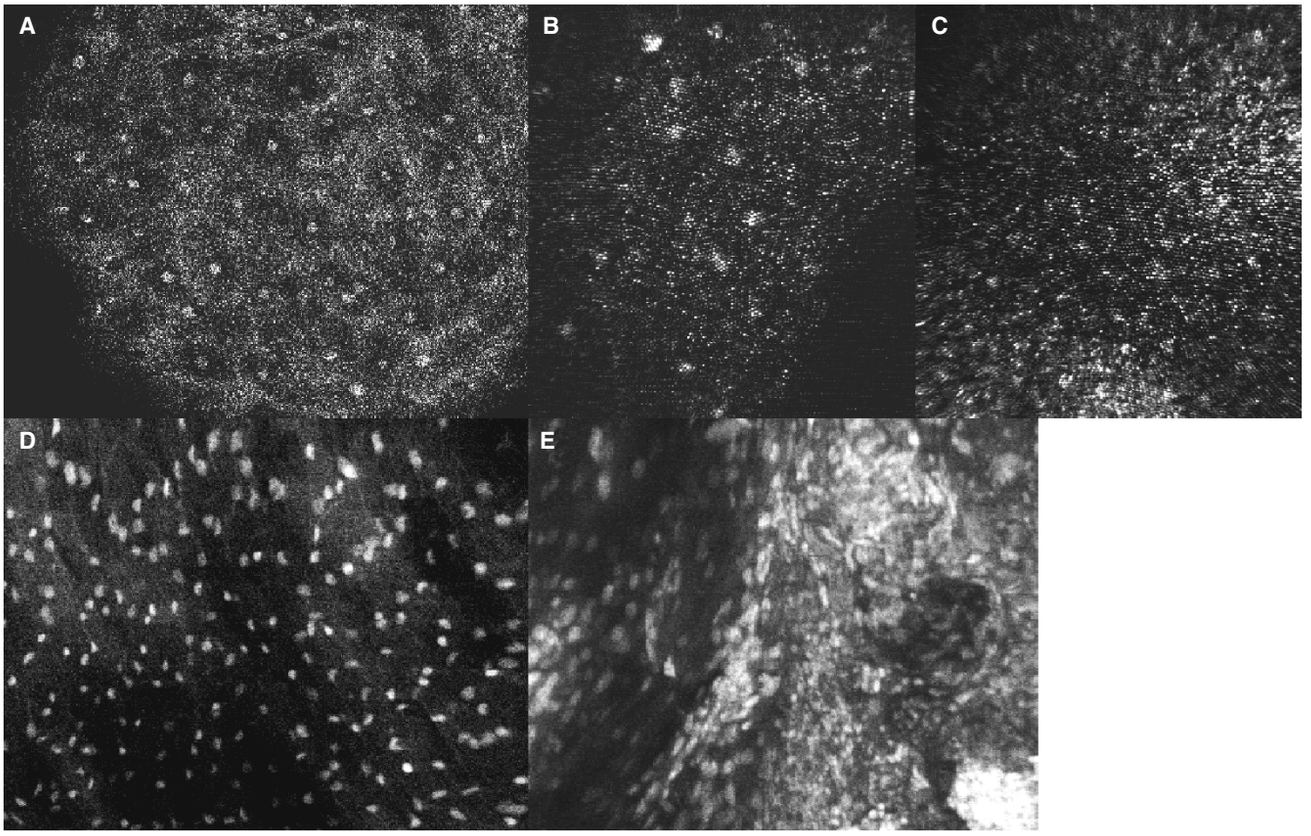


FIGURE 26.12. Imaging of the human cervix using miniature confocal microscope heads. (A) The *in vitro* images of cervical epithelium obtained with a reflectance confocal microscope demonstrates the ability to resolve cellular and nuclear structures in whole tissues. This epi-illumination confocal microscope consists of an 810 nm continuous-wave diode laser, a pair of galvanometer scanning mirrors, a scan lens, and a 25 × 0.8 NA water-immersion objective lens. The measured lateral and axial resolution of this system are 0.8 and 2 to 3 µm, respectively. The focus plane is 50 µm below the surface, the field width ~460. (B, C) *In vivo* fiber-optic confocal microscope backscattered light images of cervical epithelium classified as (A) normal and (B) abnormal, CIN II/III at histologic examination. FOV ~200 × 200 µm. The prototype constructed for this study scans 1064 nm continuous illumination from a Nd : YAG laser focused into a 30,000-fiber coherent imaging bundle (average core diameter 4 µm, average pitch 7 µm, fiber NA 0.3). A miniature objective lens at the distal tip has a back NA of 0.3 and an objective NA of 1.0. Specular reflection from the fiber surfaces is reduced by a polarizing beam-splitter, index-matching oil at both fiber bundle surfaces, and a 7° angle polish on the distal fiber bundle surface. The measured lateral and axial resolution for this fiber-optic confocal microscope are 2.1 and 3 to 6 µm, respectively. Images are obtained at 15 frames per second. Hydraulic suction is used to axially scan tissue through the fixed focal plane. The water is also used to reduce specular reflection from the surface of the tissue. (Images courtesy of Rebecca Richards-Kortum.) (D, E) Clinical *in vivo* imaging of human cervix using a fiber-scanning confocal microscope prototype similar to that pictured in Figure 26.10. Fluorescence images (excitation 488 nm, detection above 505 nm) following topical applications of 0.05% Acriflavine (FOV: 500 × 350 µm). Nuclei are well resolved, showing regular nuclear size, shape, and distribution in normal cervix (D) versus crowded distribution and irregular size and shape of nuclei (E) in squamous cell carcinoma (diagnoses provided by conventional histopathological assessment of biopsies). (Images courtesy of Dr. Jeffrey Tan, Royal Women's Hospital, Melbourne, Australia.)

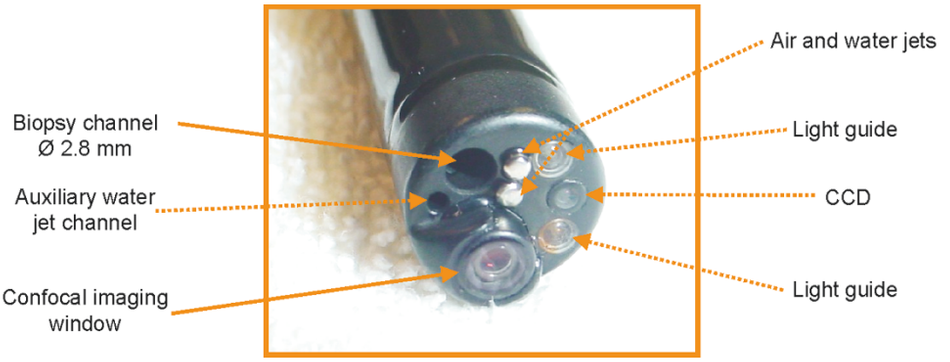


FIGURE 26.13. Clinical endomicroscope distal tip. The single-fiber scanner shown in Figure 26.10 has been incorporated into a clinical endomicroscopy system by Pentax Corporation, Medical Division (Tokyo, Japan). The distal tip is 12.8 mm in diameter, and accommodates the conventional endoscope components and functions (labeled) for macroscopic imaging, illumination, biopsy suction, spraying, and articulation. The confocal scanner protrudes by several millimeters, and appears within the corner of the conventional charge-coupled device (CCD) view, thus allowing the endoscopist to target it to specific locations on the tissue. (Image courtesy of Pentax Corporation.)

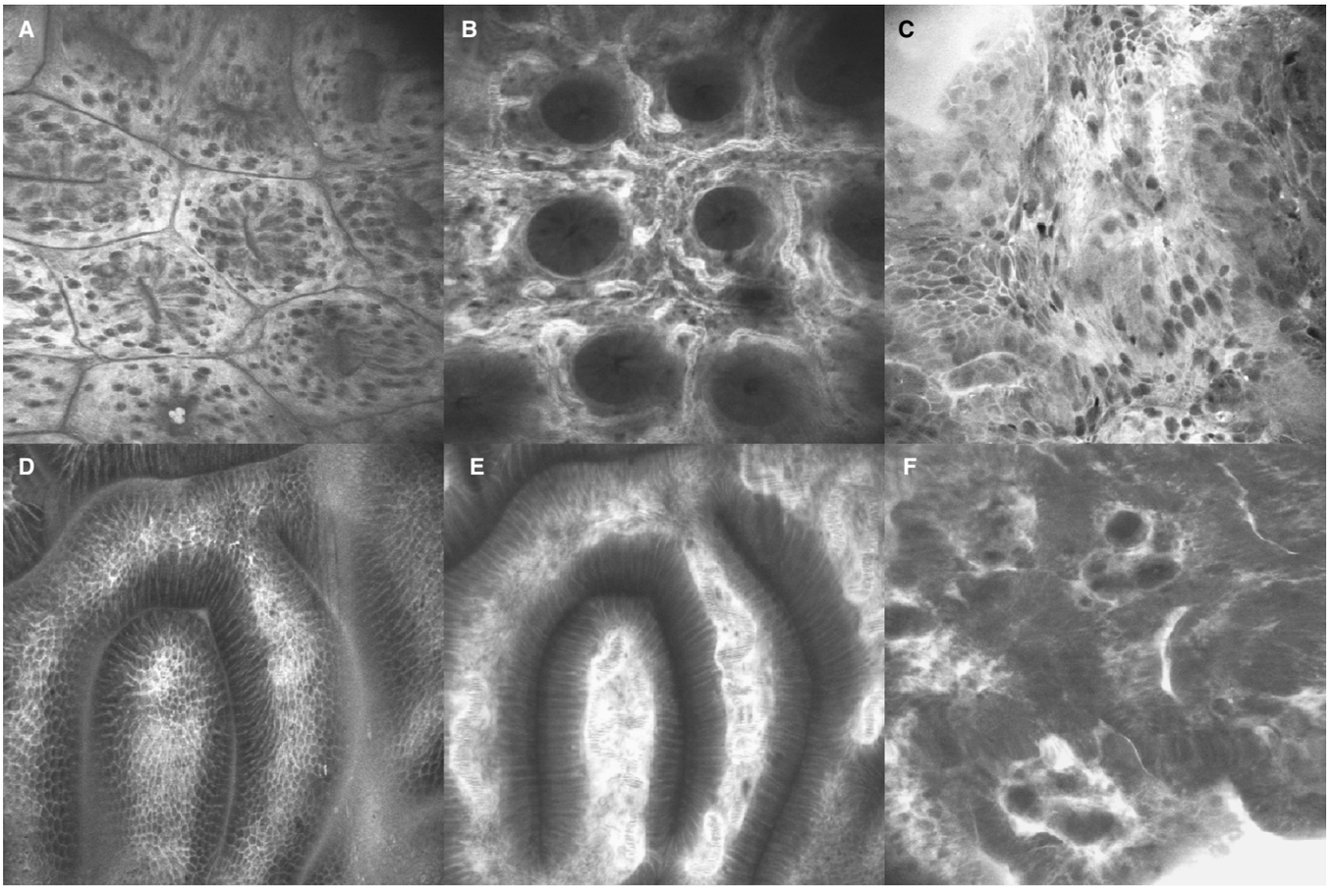


FIGURE 26.14. Confocal imaging of the human gastrointestinal tract in patients undergoing clinical endoscopy. (A–C) Colonic mucosa. (A) Crypt architecture, goblet cells, and epithelial cells in the plane of the superficial epithlelium. (B) Subsurface microvasculature surrounded by the collagen matrix of the *lamina propria*, 50 µm beneath the tissue surface, presenting the radial alignment of epithelial (including goblet) cells lining the crypt lumen. (C) Imaging of a rectal adenocarcinoma showing complete loss of crypt architecture, marked cellular pleomorphism, and patchy distribution of goblet cells throughout the image plane. (D–F) Human upper gastrointestinal images. (D) Surface epithelium and (E) hyper-vascularization of the *lamina propria* in a 66-year-old male with portal hypertension. (F) In a 62-year-old patient with Barrett's esophagus, a small region of neoplasia is imaged with the endomicroscope. [Images (A,B) courtesy of Prof. Adrian Polglase, Cabrini Monash University Department of Surgery, Melbourne, Australia. Images (C–F) courtesy of Dr. Ralf Kiesslich, Mainz University Hospital, Mainz, Germany.]

even the miniaturization of multi-photon microscopes suitable for *in vivo* microscopy. Thus, it is reasonable to expect that many other approaches will soon become practical tools for clinical and laboratory *in vivo* scanning optical microscopy.

ACKNOWLEDGMENTS

We are grateful to Mauna Kea Technologies (Paris, France) for Figure 26.8(A,B,D,E), to Igor Charvet and Paolo Meda (CMU, Geneva, Switzerland) for Figure 26.9(A,B,C), to Vladimir Dubaj and Andrew Wood (Swinburne University, Melbourne, Australia) for Figure 26.9(E), to Elisabeth Laemmel and Eric Vicaut (LEM, Paris, France) for Figure 26.9(D), to Dr. Ralf Kiesslich and Dr. Martin Goetz (Mainz University Hospital, Mainz, Germany) for Figure 26.11, to Rebecca Richards-Kortum (Rice University, Houston, TX) for Figure 26.12(A–C), to Dr. Jeffrey Tan (Royal Women's Hospital, Melbourne, Australia) for Figure 26.12(D,E), and to the Pentax Conporation (Tokyo, Japan) for Figures 26.13 and 26.14. Dr. Wendy McLaren provided invaluable assistance with the figures.

REFERENCES

Bjarklev, A., Broeng, J., and Bjarklev, A.S., 2003, *Photonic Crystal Fibers*, Kluwer Academic Publications, New York, pp. 1–298.

Cavé, C., Fourmeaux du Sartel, M., and Abrat, B., 2005, Fibered confocal fluorescence microscopy: A new tool to perform colonoscopy in mice, *Gastroenterology* 128(Suppl 2):A–249.

Delaney, P., Harris, M., and King, R., 1993a, Novel microscopy using fiber-optic confocal imaging and its suitability for subsurface blood vessel imaging *in vivo*, *Clin. Exp. Pharmacol. Physiol.* 20:197–198.

Delaney, P., Harris, M., and King, R., 1993b, Remote interrogation of objective lenses using a novel fiber-optic confocal microscope reduces movement artifacts, In: *The 1993 International Conference on Confocal Microscopy and 3D Image Processing Proceedings*, Sydney, Australia, p. 66.

Delaney, P., Harris, M., and King, R.G., 1994a, Fiber-optic laser scanning confocal microscope suitable for fluorescence imaging, *Appl. Opt.* 33:573–577.

Delaney, P., King, R., Lambert, J., and Harris, M., 1994b, Fiber-optic confocal imaging (FOCI) for subsurface imaging of the colon *in vivo*. *J. Anat.* 184:157–160.

Dickensheets, D.L., and Kino, 1996, A micromachine scanning confocal optical microscope, *Opt. Lett.* 21:764–766.

Ellis, G.W., 1985, Microscope illuminator with fiber-optic source integrator, *J. Cell. Biol.* 101:832a.

Fork, R., Martinez, O.E., and Gordon, J., 1984, Negative dispersion using pairs of prisms, *Opt. Lett*. 9:150.

Gmitro, A., and Aziz, D., 1993, Confocal microscopy through a fiber-optic imaging bundle, *Opt. Lett.* 18:565–567.

Giniunas, L., Juskaitis, R., and Shatalin,V., 1991, Scanning fiber-optic microscope, *Electron Lett.* 27:724–726.

Gonzalez, S., and Tannous, Z., 2002, Real-time, in vivo confocal reflectance microscopy of basal cell carcinoma, *J. Am. Acad. Dermatol*. 47:869–874.

Harris, M.R., UK Patent, GB 2,340,332. Granted 16-02-2000.

Harris, M., and Delaney P.M., US Patent, 5,926,592. Granted 20-07-1999.

Harris, M., and Delaney, P., US Patent no. 5,926,592.

Katzir, A., 1993, Applications of lasers in therapy and diagnosis, In: *Lasers and Optical Fibers in Medicine*, Academic Press, San Diego, California.

Kiesslich, R., Burg, J., Veith, M., Burg, J.,Vieth, M., Gnaendiger, J., Enders, M., Delaney, P., Polglase, A., McLaren, W., Janell, D., Thomas, S., Nafe, B., Galle, P., and Neurath, M., 2004, Confocal laser endoscopy for diagnosing intraepithelial neoplasias and colorectal cancer *in vivo*, *Gastroenterology* 127:706–713.

Kiesslich, R., et al., 2005, Diagnosing *Helicobacter pylori in vivo* by confocal laser endoscopy, *Gastroenterology*. Forthcoming.

Kimura, S., and Wilson, T., 1991, Confocal scanning optical microscope using single mode fiber for signal detection, *Appl. Opt.* 30:2143–2150.

Kino and Dickinsheets, D.L., US Patent no. 6,172,789.

Knight, J., Broeng, J., Birks, T., and Russel, P., 1998, Photonic bandgap guidance in optic fibers, *Science* 282:1476

Liang, C., Sung, K., Richards-Kortum, R., and Descour, M., 2001, Fiber confocal reflectance microscope (FCRM) for in-vivo imaging, *Opt. Express* 9:821–830.

McLaren, W., Tan, J., and Quinn, M., 2003, Detection of cervical neoplasia using non-invasive fibreoptic confocal microscopy, In: *Eurogin 2003* (J. Monsonego, ed.), Monduzzi Editore, Bologna, Italy, pp. 213–217.

Murakami, M., 2005, A miniature confocal optical scanning microscope for endoscopy, in MOEMS display and imaging systems III, (H. Urey and D.L. Dickensheets, eds.), *Proc SPIE.* 5721:119–131.

Ouzounov, D., Moll, K., Forster, M., Zipfel, W., Webb, W., and Gaeta, A., 2002, Delivery of nanojoule femtosecond pulses through large-core microsure fibers, *Opt. Lett.* 27:1513–1515.

Sharonov, S., Morjani, H., and Manfait, M., Confocal spectral imaging analysis: A new concept to study the drug distribution in a single living cancer cell, *Anticancer Res.* 12:1804.

Snyder, A., and Love, J., *Optical Waveguide Theory*, Chapman and Hall, London 1983.

Sung, K., Liang, C., Descour, M., Collier, T., Follen, M., and Richards-Kortum, R., 2002, Fiber-optic confocal reflectance microscope with miniature objective for *in vivo* imaging of human tissues, *IEEE Trans. Biomed. Eng*. 49:1168–1172.

Swindle, L., Thomas, S., Freeman, M., and Delaney, P., 2003, View of normal human skin in vivo as observed using fluorescent fiber-optic confocal microscopic imaging, J. *Invest. Dermatol*. 121:706–712.

Wilson, J., and Hawkes, J., *Optoelectronics. An Introduction*, 2nd ed., Prentice-Hall, Hemel Hempstead, UK Sects. 8.3.3, 8.3.4, and 8.5.2.

Wilson, T., Juskaitis, R., and Rimvydas, 1992, Confocal and differential microscopy using optical fiber detection. In: *Proceedings of SPIE-International Society for Optical Engineering*. Vol. 1660 pt 2.

27

Fluorescence Lifetime Imaging in Scanning Microscopy

H.C. Gerritsen, A. Draaijer, D.J. van den Heuvel, and A.V. Agronskaia

INTRODUCTION

Fluorescence, Lifetime, and Quantum Efficiency

It was not until the 1930s that measurement of the fluorescence lifetime (τ_f) and the confirmation of theory on this phenomenon became possible (Pringsheim, 1961). Before that time only phosphorescence lifetimes had been measured, evidently because this phenomenon is one or more orders of magnitude slower. The distinction between fluorescence and phosphorescence was first made by the observation of the afterglow. Emission having a noticeable afterglow was called phosphorescence. All other processes that did not have a noticeable afterglow were called fluorescence. Later, the distinction between the two was based on quantum mechanics. In phosphorescence a triplet to ground state transition is involved. Quantum mechanically such a transition is spin forbidden and therefore has a low probability. Consequently, the rate at which such a process occurs is low and the lifetime is long. The fluorescence phenomenon only involves singlet states with transition probabilities that are much higher, making the process faster. In its simplest form, the fluorescence or phosphorescence intensity decay after the excitation source is shut off follows an exponential curve described by:

$$I(t) = I_0 e^{-t/\tau} \quad \textbf{(1)}$$

where $I(t)$ is the fluorescence intensity at time t, I_0 is the the fluorescence intensity at time zero, and τ_f is the time when the fluorescence has dropped to I_0/e.

The fluorescence quantum efficiency Φ_f (Straughan and Walker, 1976) is defined as the ratio of the number of photons absorbed to the number of photons emitted as fluorescence by the molecule. It is dependent on the relative magnitudes of the rate constants involved in fluorescence and other competing decay processes. The processes involved in the decay of a molecule with singlet ground state, S_0, excited singlet state, S_1, and excited triplet state, T_1 are diagrammed in Figure 27.1 (Jablonski diagram) and listed in Table 27.1.

It can be shown that $\Phi_f = k_f/\Sigma k_{Processes}$ and $\tau_f = 1/\Sigma k_{Processes} = \Phi_f/k_f$ where Φ_f is the fluorescence quantum efficiency, k_f is the fluorescence decay rate constant, k_{ISC} is the rate constant of intersystem crossing, k_{IC} is the rate constant of internal conversion, and k_{Re} is the rate constant for reaction product.

In the case of, for example, different microenvironments or different conformations of the fluorescent molecules, the decay curve may become multi-exponential.

Fluorescence Lifetime Spectroscopy

Early measurements of nanosecond lifetimes on bulk specimens were performed by means of Pockel or Kerr cells (Pringsheim, 1961). Such devices contain an optically transparent, nonlinear crystalline solid (Pockel cell) or an optically transparent, nonlinear liquid (Kerr cell). The polarization direction of light passing through these cells is rotated by putting a voltage across them.

Because detectors and amplifier electronics were not yet fast enough for direct measurements, τ_f could only be measured by applying a time difference between the excitation and emission cells. This was accomplished by changing the distance between the two cells and measuring the average intensity as a function of the time difference between the two cells. Light travels 30 cm in 1ns.

The popularity of fluorescence lifetime spectroscopy has grown considerably in recent decades because of the availability of fast electronics, detectors, and light sources.

A number of techniques are available to measure the decay curves of fluorescence processes. In general, τ_f measurements are either made in the time domain or in the frequency domain. In the frequency domain, one measures the phase shift of the fluorescent light with respect to the phase of a modulated excitation source. Measurements in the time domain are generally performed by measuring the time dependency of the fluorescence intensity with respect to a short excitation pulse. It falls beyond the scope of this chapter to give a detailed overview of all the numerous implementations and applications of fluorescence lifetime spectroscopy. The reader is referred to the existing literature (Lakowicz, 1983; O'Connor and Phillips, 1984; Clark and Hester, 1989). Many applications of fluorescence lifetime spectroscopy can be found in the fields of protein studies, membranes and cells, and energy transfer and ion concentration measurements. We will restrict our consideration to microscopic applications.

Fluorescence Lifetime Imaging Applications

Apart from measurements on bulk specimens, fluorescence lifetime spectroscopy equipment can be modified for microspectroscopy and microscopy. This makes it possible to measure τ_f of small volumes in a specimen. Starting in the last decade of the 20th century, fluorescence lifetime measurements were extended into the field of widefield imaging (Morgan *et al.*, 1990, 1992; Lakowicz and Berndt, 1991; Ni and Melton, 1991; Wang *et al.*, 1991; Gadella *et al.*, 1993; Lakowicz and Szmacinski, 1993; Webb *et al.*, 2002), confocal imaging (Bugiel *et al.*, 1989; Buurman *et al.*, 1992; Sanders *et al.*, 1994), and multi-photon excitation

H.C. Gerritsen, D.J. van den Heuvel, and A.V. Agronskaia • Utrecht University, Utrecht, The Netherlands
A. Draaijer • TNO-Voeding, Utrecht, The Netherlands

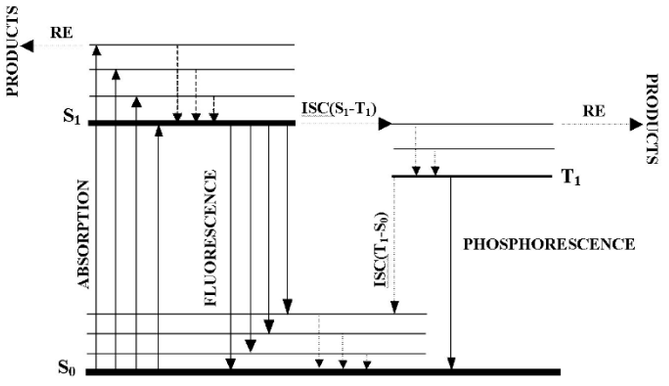


FIGURE 27.1. Jablonski diagram showing the processes involved in the decay of a molecule with singlet ground state S_0, excited singlet state S_1, and excited triplet state T_1.

imaging (Piston *et al.*, 1992; So *et al.*, 1996; French *et al.*, 1998; Sytsma *et al.*, 1998). Fluorescence lifetime imaging (FLIM) can be used, for example, in multi-labeling experiments, for measuring ion concentration or cell chemistry, and for measuring fluorescence resonance energy transfer (FRET) efficiencies. These uses are discussed below.

Multi-Labeling with Dyes

In general, probes that have the same emission wavelength usually do not have the same τ_f, so they can be distinguished based on their lifetime differences provided the microscope has sufficient lifetime resolution. The number of probes that can be imaged simultaneously depends on the lifetime range of the FLIM system. In the spectral domain, the emission bands are broad and in conventional fluorescence microscopes not more than two or three probes can be imaged simultaneously, with each probe necessarily having its own detection channel. However, given a typical τ_f resolution in the sub-nanosecond range and a dynamic range of tens of nanoseconds, it should be possible to simultaneously image 10 to 20 probes.[1] Recording probes with differing τ_f can be achieved with only a single detector and one excitation wavelength, and it does not require the use of spectral selection on the emission side. Because no bandpass filters are needed, the complete spectral band is detected and detector sensitivity is increased.

Discrimination of the signals from specific probes based on their τ_f alone can be done using simple image processing. In combination with spectral selection, the number of distinct probes that can be imaged becomes even larger.

With some *a priori* knowledge of the τ_f of the probes used, signals from mixtures of probes are easily deconvolved and the relative abundances calculated (Verveer *et al.*, 2000). Some probes have even been designed specifically for τ_f imaging (Sauer *et al.*, 1993).

Concentration Imaging (pH, Ca^{2+}, K^+, Na^+, O_2, etc.)

For many existing fluorescent ion indicators, the τ_f of the free form differs from that of the ion-bound form. In principle this property can be used for the quantitative imaging of ions (pH, Ca^{2+}, K^+, Na^+) (Lakowicz and Szmacinski, 1993; Lakowicz *et al.*, 1994; Sanders *et al.*, 1994, 1995). Oxygen and other quenching agents reduce τ_f (Gerritsen *et al.*, 1997). This effect can also be used for imaging purposes, making it possible to image important biological parameters.

Fluorescence lifetime imaging has tremendous advantages compared to other methods that are either invasive (microelectrodes) or require a calibration on the specimen (ratio imaging). Using τ_f as a parameter for measuring dye concentrations makes the measurements independent of intensity effects such as shading in the image, changes in laser intensity, or absorption in the specimen, and calibration is often easier than calibration of λ-ratio images. For several fluorescent ion indicators it was shown that no *in vivo* calibration procedure is required (Sanders *et al.*, 1995; Herman *et al.*, 1997).

Chemical Environment

The τ_f of a given probe is often sensitive to local differences in chemical environment. This can be exploited to obtain information about micro-environments in general. For example, one could image hydrophobicity, viscosity (molecular friction effects), mobility, or membrane potential.

Quantitative Fluorescence Intensity Measurements

Most users of a fluorescence microscope measure the concentration of a fluorescent probe to get information about, for example, the extent of DNA damage or the structure of an object. However, the intensity signal is only a good measure of the dye concentration if the quantum efficiency stays constant and the environment often affects the quantum efficiency. A calibration procedure is required to correlate the fluorescence intensity to the probe concentration and this procedure may be suspect because the calibration environment is different from the specimen environment. Fortunately, τ_f is closely related to the quantum efficiency and so a measurement of τ_f can be used to check the validity of the calibration procedure. If the τ_f measured during calibration is equal to that in the specimen, this indicates that the quantum efficiency is the same in both cases and thus the intensity can be correlated to the concentration. If factors that do not effect τ_f, such as photobleaching, occur, making the τ_f measurement increases the reliability of the intensity measurement. In some cases it has been possible to correct for changes in the quantum efficiency by using τ_f information (Morgan *et al.*, 1990).

Fluorescence Resonance Energy Transfer

One of the more recent applications of fluorescence microscopy is the imaging of colocalization on a nanometer scale by means of Förster resonance energy transfer (Förster, 1946; Lakowicz, 1983; Clegg, 1996). This technique is also often referred to as fluorescence resonance energy transfer (FRET). More details on FRET can be found in Chapter 45. In conventional fluorescence microscopy colocalization can be studied by using two differently labeled molecules that emit in two distinct emission bands. As soon as signals from both detection channels occur in the same pixel the two molecules colocalize within the resolution limit of the microscope. Because the resolution of the microscope is much larger than the size of the molecules, colocalization measured in this way does not prove that the two molecules interact. FRET can be employed to study colocalization on a scale of a few nanometers and therefore this method does yield information about molecular interactions. In FRET an excited

[1] As long as they do not all occur in the same location.

TABLE 27.1. Processes Involved in the Decay of an Excited Molecule

Molecule $S_0 + h\nu$	$\longrightarrow$	Molecule S_1	Excitation
Molecule S_1	$\xrightarrow{K_F}$	Molecule $S_0 + h\nu$	Fluorescence (F)
Molecule S_1	$\xrightarrow{K_{ISC}}$	Molecule T_1	Intersystem crossing (ISC); non-destructive quenching effect (triplet state build-up) where molecule will become available again only after returning to the ground state (phosphorescence)
Molecule S_1	$\xrightarrow{K_{IC}}$	Molecule S_0	Internal conversion (IC); non-destructive quenching effect (molecule stays available)
Molecule S_1	$\xrightarrow{K_{Re}}$	Products	Reaction (Re); Destructive quenching effect (molecule is lost for fluorescence)
Molecule S_1	$\xrightarrow{K_{NR}}$	Molecule S_0	Non-radiative decay (NR); molecule returns to the ground state without fluorescing

fluorescent donor molecule directly transfers its excited state energy to an acceptor molecule. This is a resonant process that occurs through a dipole–dipole interaction between the donor and acceptor. A prerequisite for FRET to occur is that the emission band of the donor overlaps with the absorption band of the acceptor and in addition the two molecules should be within a few nanometers of each other. The presence of the acceptor results in the introduction of an additional decay channel for the excited donor molecules and therefore the total decay rate of the donor molecule is increased. Consequently, FRET results in a reduction of both the donor fluorescence intensity and the fluorescence lifetime ($\tau_f = 1/\Sigma k_{Processes}$). FRET can be conveniently quantified in terms of the energy transfer efficiency E. E can be expressed in the relative donor intensity reduction $E = 1 - I_{DA}/I_D$, and in the relative donor lifetime reduction $E = 1 - \tau_{DA}/\tau_D$. Here, I_{DA} and I_D are the intensities of the donor in the presence and absence of the acceptor respectively. τ_{DA} and τ_D are the lifetimes of the donor in the presence and absence of the acceptor, respectively.

FRET imaging experiments can be carried out by means of fluorescence intensity measurements. However, this approach requires the use of emission filters and quantification of E is complicated by, for example, filter bleedthrough and direct excitation of the acceptor. In order to correct for these effects multiple reference images need to be recorded.

FRET imaging can also be accomplished by means of FLIM (Wouters and Bastiaens, 1999). Now, the energy transfer efficiency E can be directly derived from a single measurement of the donor lifetime, provided that the donor lifetime of dye in the absence of the acceptor is homogeneous throughout the specimen. This approach is straightforward and at present FLIM-based FRET imaging seems to be the preferred method to carry out quantitative FRET experiments on interactions between molecules.

From the applications listed above it is obvious that fluorescence lifetime contrast is a versatile and powerful tool in microscopy. In the next section we discuss the basics of frequency- and time-domain methods for implementing FLIM and a number of applications of this technique will then be described.

FLUORESCENCE LIFETIME IMAGING METHODS

Introduction

FLIM can be implemented in widefield microscopes (WF), confocal laser-scanning microscopes (CLSMs), and multi-photon excitation microscopes (MPEMs). The use of the point scanning geometry in FLIM is advantageous. If a diffraction-limited volume element in a specimen with a lifetime τ_1 is embedded in a homogeneous background with lifetime τ_2 and imaged in a WF microscope, the measured τ_f will be averaged over the entire excited volume. This will contribute a large τ_2 background fluorescence component to the measured decay. In the confocal setup, however, only the small volume element near the focal plane is sampled, and therefore much less of the τ_2 background component is observed.

At present, several techniques are being employed for the measurement of τ_f on bulk specimens. Basically the techniques can be subdivided in frequency-domain–based methods such as phase fluorometry (Gratton and Limkeman, 1983; Jameson and Gratton, 1983; Lakowicz, 1983) and time-domain–based methods such as time-correlated single-photon counting (O'Connor and Phillips, 1984) and methods based on time-gated detection. In either method, both the light source and the detection system have to be modified.

A major difference between fluorescence lifetime measurements on bulk specimens and fluorescence lifetime imaging is the number of fluorophores available in the detection volume. In conventional non-imaging spectroscopy experiments, a large number of fluorescent molecules is present in the detection volume and the accuracy of the experiments is, in general, not limited by the strength of the fluorescence signal. In a typical confocal or multi-photon imaging experiment, only a small volume is imaged and in general a low number of fluorescent molecules is present in this volume. On assuming typical dye concentrations of tens of micromolar, we find that on the order of 100 to 200 dye molecules are present in the focus of the microscope objective. Furthermore, photobleaching constrains the maximum number of photons that can be emitted per fluorescent molecules to values between 10^3 to 10^5 photons before photobleaching takes place.

For conventional confocal and multi-photon fluorescence intensity imaging, images of reasonable quality can be acquired with as few as 20 to 30 detected photons per pixel. FLIM requires much more signal per pixel to produce acceptable images. In general, at least one order of magnitude more signal is required to obtain images of reasonable quality. Therefore, the efficiency of the microscope, the detector, and the lifetime acquisition method are of crucial importance. For this reason we will discuss the factors that determine the sensitivity of the different lifetime imaging methods in detail.

Lifetime Sensing in the Frequency Domain

The Phase Fluorometry Method

Phase fluorometry is one of the oldest methods used for the determination of τ_f. The essence of the method is phase-sensitive detection in combination with intensity-modulated excitation of the specimen. Either a pulsed or a sinusoidally modulated light source is used in this technique. In the case of sinusoidally modulated

excitation, the time-dependent excitation intensity, $E(t)$ (see Fig. 27.2) is given by:

$$E(t) = E_0(1 + M_E \sin(\omega t)) \quad \textbf{(2)}$$

with ω the modulation frequency, E_0 the average excitation intensity, and M_E the modulation depth of the excitation, defined as the ratio between the AC amplitude and the DC component of the excitation signal. The delay between the absorption of an excitation photon and the emission of the fluorescence introduces a phase-shift ϕ and demodulation of the emission $F(t)$ with respect to the excitation light (see Fig. 27.2).

$F(t)$ can be written as:

$$F(t) = F_0[1 + M_F \sin(\omega t + \phi)] \quad \textbf{(3)}$$

with M_F the modulation depth of the emission. For a simple mono-exponentially decaying fluorescence signal, the following relation can be derived relating τ_f, ω and ϕ:

$$\tau_f = \frac{1}{\omega}\tan(\phi) \quad \textbf{(4)}$$

The τ_f of a specimen can be accurately determined by measuring the phase difference between the excitation signal and the fluorescence signal. Assuming a strong signal, ϕ can usually be determined to an accuracy of $\pm 0.2°$. The phase measurements are usually done at a number of different frequencies ranging from several hundred kilohertz up to many hundred megahertz. Using this approach, fluorescence decays containing more than one decay component can be examined. The value of each τ_f as well as its relative contribution to the total fluorescence signal can be determined (Gratton *et al.*, 1984).

As the ratio M_F/M_E is affected by τ_f, this ratio can be also employed to obtain quantitative lifetime information. The relation between the relative modulation (M_F/M_E) and τ_f is:

$$\tau_f = \frac{1}{\omega}\left[\frac{1}{\left[\frac{M_\Phi}{M_E}\right]^2} - 1\right]^{1/2} \quad \textbf{(5)}$$

Intensity modulation of the exciting light can easily be accomplished by using electro-optical modulators (EOM) or acousto-optical modulators (AOM) (see Chapter 3, *this volume*). These devices allow modulation over a wide range of modulation frequencies, up to about 1 GHz, and can be used in combination with comparatively cheap CW lasers.

Alternatively a pico- or femtosecond pulsed laser source can be used as a modulated light source. In this case one can use the harmonic content of the excitation signal to produce a range of modulation frequencies. Depending on the pulse-width of the laser, the frequency content can extend up to 200 GHz, far higher than the best available detectors.

On the detection side, a phase-sensitive detector is required. This is often realized by using a gain-modulated photomultiplier tube (PMT) or a micro-channel-plate detector, modulated at exactly the same frequency (homodyning) or slightly different frequency (heterodyning) as the excitation light source. In practice the detector system will limit the maximum useful excitation frequency. Cross-modulation is normally used to transform the high frequency signal to a lower frequency domain because this improves noise immunity. All the noise picked up at high frequencies is simply filtered out. In the case of a fast PMT, the modulation frequencies will be limited to <1.4 GHz while microchannel plates (MCP) can be used up to 20 GHz.

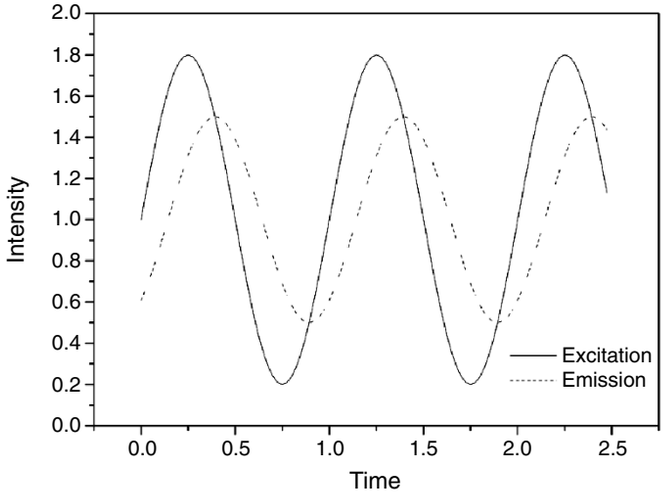


FIGURE 27.2. The excitation and emission signals in phase fluorometry. The emission is delayed and demodulated with respect to the excitation signal.

Fluorescence Lifetime Imaging Using Phase Fluorometry

Widefield, Slit-Scanning, and Spinning-Disk Implementations

In several laboratories a phase-fluorometry–based detection scheme has been incorporated in a WF microscope (see, e.g., Morgan *et al.*, 1990, 1992; Lakowicz and Berndt, 1991; Marriott *et al.*, 1991a; Gadella *et al.*, 1993). In order to combine the phase fluorometry method with WF microscopy, a detector sensitive to phase and position is required. One possibility is a gain-modulated image intensifier in combination with a charge-coupled device (CCD) detector. The intensifier is modulated at the same frequency as the excitation source, with a fixed phase angle difference with respect to the phase of the excitation source. Although the gain of the intensifier is modulated at very high frequencies, its output signal does not show high frequency components because it is time averaged by the slow response of its output phosphor (about 1 ms). Consequently, the CCD detector records a time-averaged (low-pass filtered) intensity image where the intensities depend on the phase difference between the modulated excitation source and the modulated detector gain. The time-averaged fluorescence intensity recorded in one CCD pixel is determined by the detector gain modulation depth, M_D, the modulation depth of the fluorescence emission, M_F, and the phase difference between the gain modulation signal and the emission modulation signal $\phi_D - \phi_F$.

$$I \sim 1 + 0.5\, M_D\, M_F \cos(\phi_F - \phi_D) \quad \textbf{(6)}$$

By recording a number of images at different $\phi_D - \phi_F$ phase angles, the phase angle and modulation depth of each pixel can be established. This set of detector-phase–dependent images can then be converted into a τ_f map of the specimen. Because of the constant DC background excitation on which the modulated fluorescence signal is superimposed, a minimum of two images must be recorded in order to obtain τ_f information.

Several modes of operation have been suggested for this type of setup (Lakowicz and Berndt, 1991). One possible mode of operation is to record one image at a specific phase angle ϕ_x and another one with no detector modulation. After subtracting the unmodu-

lated image (I_{off}) from the modulated image (I_{on}), the value in one specific pixel will be:

$$I_{on} - I_{off} = A\ 0.5\ M_D\ M_F \cos(\phi_F - \phi_x) \quad \textbf{(7)}$$

From this equation it can be seen that for $\phi_F = \pi/2 + \phi_x$, $I_{on} - I_{off}$ equals zero. Effectively this means that the signal arising from fluorescence with a lifetime $\tau_x = \tan(\pi/2 + \phi_x)/\omega$ is zero and thus is in a sense suppressed. Phase angles $\phi_F > \pi/2 + \phi_x$ ($\tau < \tau_x$) or smaller than $\pi/2 + \phi_x$ ($\tau > \tau_x$) will give rise to negative and positive values of $I_{on} - I_{off}$, respectively. This scheme, however, is less suitable for absolute τ_f determinations because $I_{on} - I_{off}$ still contains constants related to the quantum efficiency, the concentration of the fluorescent material, and various instrumental parameters.

This limitation can be overcome by recording three images: one with a detector modulation phase ϕ_x, one at $\phi_x + \pi/2$, and one with no detector modulation. After subtracting the unmodulated image from each of the modulated images, the values at one pixel for the two detector modulation phases will be

$$I(\phi_x) - I_{off} = 0.5\ A\ M_D\ M_F \cos(\phi_F - \phi_x) \quad \textbf{(8)}$$

and

$$I(\phi_x + \pi/2) - I_{off} = 0.5\ A\ M_D\ M_F \cos(\phi_F - \phi_x - \pi/2) \quad \textbf{(9)}$$

respectively. After taking the ratio of Eqs. 8 and 9 we obtain

$$I = \frac{\cos(\phi_F - \phi_x)}{\cos(\phi_F - \phi_x - \pi/2)} = \tan(\phi_F - \phi_x) = \omega\tau_{F,x} \quad \textbf{(10)}$$

For $\phi_x = 0$, Eq. 10 only depends on ϕ_F and the known modulation frequency ω. Therefore, this mode of operation does provide fully quantitative τ_f imaging. However, in the case of multi-exponential decay of the fluorescence, the measured τ_f will be concentration- and quantum-efficiency–weighted average lifetime over all the decay components. Consequently, a mixture of a number of fluorescent species with different lifetimes will yield only a single value, and truly selective imaging of one particular species is difficult.

Alternatively, a large number of images recorded at different detector phase angles and modulation frequencies can be recorded. After a full analysis of each pixel, using a nonlinear, least-squares fitting procedure, the τ_f and relative contribution of each individual fluorescence decay can be resolved (Jameson and Gratton, 1983; Gratton *et al.*, 1984) and the relative abundance of each species can be determined directly. However, because point-scanning confocal data acquisition times are on the order of 1 to 10 s/frame, the total data acquisition time may become long, and as the images are recorded sequentially, this method is sensitive to photobleaching. The effects of bleaching may be reduced by averaging a number of interleaved data sets, each one recorded using a different phase sequence.

A significant amount of computational power is required for the analyses of complete images, and one must also consider the non-uniform response of the image intensifier. At high modulation frequencies, a difference in the modulation depth and the phase shift is observed between the center and the edge of intensifiers (Lakowicz and Berndt, 1991). This can be compensated for by a calibration method using a uniform reference specimen for which τ_f is known. Another way to reduce this effect is to use small diameter intensifiers.

Disk-Scanning Implementations

Implementation of τ_f imaging based on phase fluorometry is straightforward when the method is combined with a spinning-disk type of confocal microscope. Here, the light source can easily be modulated using EOMs or AOMs or by using a pulsed-laser system and any of the phase-sensitive detection schemes described above can be used.

Point-Scanning Implementations

The phase-fluorometry–based method of τ_f sensing can be easily implemented in a point-scanning microscope. An example of a phase-fluorometry–based detection method in a scanning two-photon excitation microscope is given below. This work concerns one of the first lifetime imaging scanning microscopes (Piston *et al.*, 1992).

Here, a mode-locked dye laser producing femtosecond pulses at a repetition frequency of 75.6 MHz was used as a light source and a simple modulated PMT detector was employed, but the detection scheme was somewhat different from that discussed above. The detector was modulated at a frequency slightly higher than the excitation frequency and as a result the fluorescence is detected at Δf, the difference frequency between the excitation and detection modulation frequencies. This cross-correlation detection scheme (heterodyning) transforms the signal to the low-frequency domain and assures high noise immunity. In order to obtain τ_f images, three images are acquired, each one with an additional 120° phase shift.

Test measurements on rat basophilic leukemia cells, stained with the DNA indicator Hoechst 33342, were recorded with a total pixel dwell time of 18 µs (3 × 6 µs/pixel). In the original paper describing this work, only fluorescence lifetime line profiles are shown. Based on the noise level in the lifetime traces, the accuracy in the lifetime is estimated to be 10%. Higher pixel dwell times will result in more accurate lifetime images.

In Figure 27.3 the original lifetime images from which the line profiles were extracted are shown (image courtesy Dr. Dave Piston). Areas outside the nuclei yield low signal and therefore have lifetimes assigned as zero. A clear difference is visible between the lifetime calculated from the demodulation and that of the phase shift. This difference in lifetime is indicative of a multi-exponential decay of the fluorescence.

Another example of frequency-domain fluorescence lifetime imaging can be found in So and colleagues (1996). This implementation is also based on a multi-photon microscope. However, these approaches could easily also be implemented on a conventional CLSM.

Fluorescence Lifetime Sensing in the Time Domain

Time-Domain–Based Methods

Streak Camera Implementations

In time-domain methods, the fluorescence intensity decay as a function of time is recorded after excitation with a pulsed light source. A good example of this is the combination of a picosecond pulsed laser for the excitation of the specimen coupled with a streak camera (O'Connor and Phillips, 1984). Here, the streak camera records the whole fluorescence decay curve after the specimen has been excited with a laser pulse.

Time Correlated Single-Photon Counting Implementations

A more common way to record τ_f is time-correlated single-photon counting (TCSPC) (Lakowicz, 1983; O'Connor and Phillips, 1984). Here, the fluorescent molecules are excited using a brief

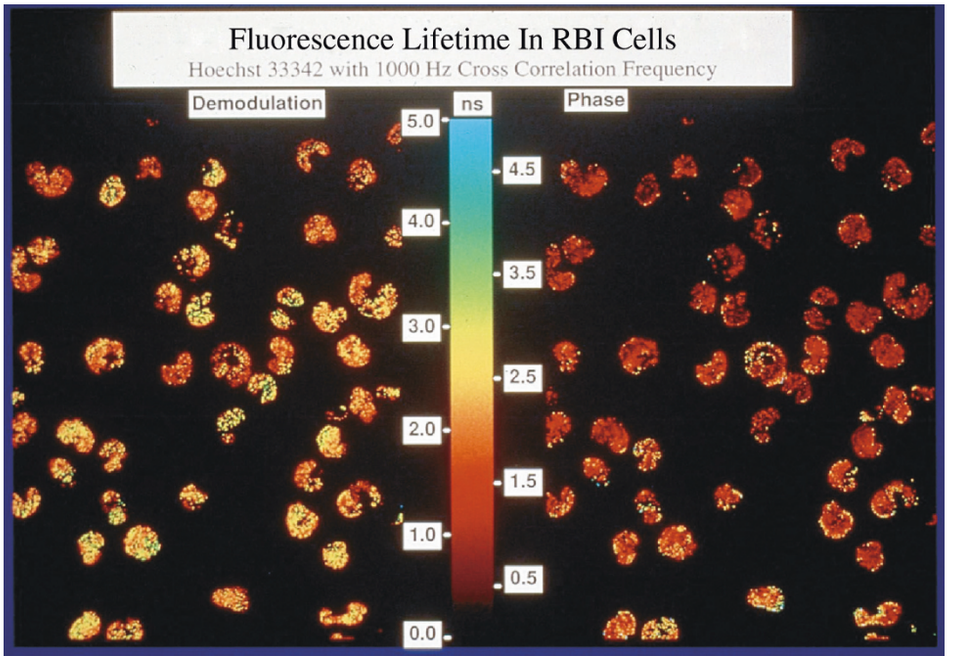


FIGURE 27.3. Multi-photon phase-fluorometry–based FLIM image of rat basophilic leukemia cells, stained with Hoechst 33342.

light pulse after which the timing of single-photon emission is recorded. Using this approach the probability distribution for the emission of a single photon, and thus the fluorescence decay curve, is recorded. The high time resolution, 25 to 250 ps, and wide dynamic range of τ_f of this technique have made it popular for spectroscopic applications. A typical experimental geometry is depicted in Figure 27.4. The specimen is excited by the pulsed light source. A trigger pulse synchronized with the excitation light pulse is used to start a time-to-amplitude converter (TAC). The fluorescence emitted by the specimen is detected by a PMT, sent through a discriminator (DISC), and then used to stop the TAC. The output from the TAC will be proportional to the time difference between the start and stop pulses. The TAC output is now converted to a digital word by means of an analog-to-digital converter (ADC). This digital word is used as a pointer to an address in a histogramming memory. Finally, the value at this specific address is incremented. After repeating this process numerous times, a histogram of the fluorescence decay curve is recorded in the memory. The dead-time of the TAC electronics is comparatively long, typically 300 to 1000 ns. Therefore, care must be taken that the count rate of the experiment is sufficiently low to prevent pulse pile-up. The TAC usually operates in the reversed start–stop geometry. Here, the TAC is started by the fluorescence signal and stopped by the laser trigger. In this way the TAC is only triggered by usable events, and not by laser trigger pulses that do not result in a detected fluorescence photon. Therefore, this mode of operation suffers less from dead-time effects. In the reversed start–stop geometry, pile-up is minimized by reducing the excitation intensity to about 1 to 5 detected photons per 100 excitation pulses. Furthermore, in spectroscopy applications excitation frequencies not exceeding 10 MHz are employed to ensure that the fluorescence decay signal from one excitation pulse is not affected by that of other excitation pulses. Therefore, the maximum count rate in conventional TCSPC is less than 100 kHz. The time required to transfer the decay curve from the histogramming memory to the computer system can be substantial. Instead of the TAC, time-to-digital converters (TDCs) can be used. Here, the timing of events is determined by means of solid-state delay lines and directly translated into a digital word. In practice TDCs have very similar properties as TACs.

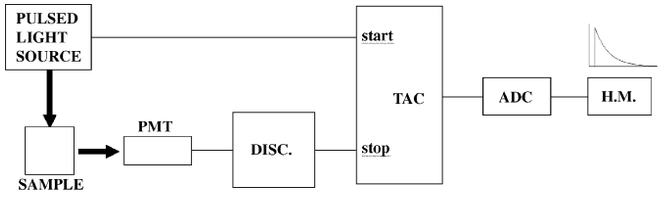


FIGURE 27.4. A schematic diagram of a TCSPC setup.

In general, the decay curves recorded by TCSPC are fitted to a (multi) exponential decay. Here, usually the time response of the instrument is taken into account by employing an iterative deconvolution technique.

In general, the use of conventional TCSPC equipment for imaging results in very long acquisition times. Conventional TCSPC equipment, however, has been employed in CLSM for fluorescence spectroscopy on discrete microscopic volumes (Ghiggino *et al.*, 1992; Vanderoord *et al.*, 1995) and for fluorescence lifetime imaging at a low acquisition speed (Bugiel *et al.*, 1989). Operating the TCSPC detection system at too high detection rates, above 5% of the excitation frequency, results in distortion of the recorded decay curve (Lakowicz, 1999).

More recently, TCSPC plug-in cards for PCs have been developed that are optimized for imaging applications. These cards have a much lower dead time than the conventional TCSPC electronics intended for use in spectroscopy (Becker *et al.*, 2003; Kwak and Vanden Bout, 2003).

Time-Gating Implementations

Another approach to fluorescence lifetime imaging is based on combining pulsed excitation with time-gated detection. In time-gated detection, use is made of one or more time channels, each with a different time offset with respect to the excitation pulse. Time gating can be implemented using both single-photon counting and analog detection methods. Here, we will restrict ourselves to implementations based on single-photon counting. In time-gated photon counting, the dead time of the detection electronics can be very low (sub-nanoseconds) and consequently such a detection system can be operated at very high count rates. In principle, multiple fluorescence photons can be detected for each excitation pulse. By sampling the fluorescence decay at different offsets with respect to the excitation pulse, information about the fluorescence lifetime can be obtained. In the early days of lifetime imaging often only two time-gated detection channels were used (see Fig. 27.5), each with a different delay time with respect to the excitation pulse. For a mono-exponential fluorescence decay, τ_f can be calculated from the ratio I_A/I_B of the intensities recorded in the two time windows A and B.

$$\tau = \frac{\Delta t}{\log(I_A/I_B)} \qquad \textbf{(11)}$$

with Δt the time difference between the start of the two time windows. This equation is only valid for windows of equal width and provided the excitation pulse is short compared to τ_f. It must be noted here that, although the fluorescence signal is convolved with the excitation pulse, the intrinsic fluorescence decay is observed after the excitation pulse has died out. The optimum gate width Δt for a particular τ_f amounts to 2.5 τ_f (Ballew and Demas, 1989).

In two-channel, time-gated detection, only one decay time can be determined, and a multi-exponential fluorescence decay yields only a single effective τ_f. This limitation can be overcome in principle by using more detection windows. The time gates can be acquired in one single pass or in multiple passes. In the case of a multiple-pass implementation, all photons arriving at the detector when it is gated off are lost. As a result, sensing more channels reduces the efficiency of the system. If the time gates are all activated sequentially after each and every excitation pulse, a much better photon economy can be realized even when a large number of gates are employed.

Time-Domain Fluorescence Lifetime Imaging

Widefield, Slit-Scanning, and Spinning-Disk Microscopy Implementations

Several groups have been working on WF imaging systems that employ time-gated detection (see, e.g., Ni and Melton, 1991; Wang *et al.*, 1991; Schneckenburger and Konig, 1992; Periasamy *et al.*, 1996). Often, gated, image intensifiers are used with minimum gate times of several nanoseconds. This limits the use of these imaging systems to measuring fluorescence lifetimes greater than 1 ns. After the acquisition of two images, Eq. 11 can be used to transform the two intensity images into a τ_f image. Because the images are acquired sequentially, this approach is sensitive to photobleaching effects. Much faster gated, image intensifiers that allow sub-nanosecond time gating are also available (Scully *et al.*, 1997). Using this type of system, complete decays can be sampled by recording sequences of images at different gate offsets. The efficiency of such systems goes down inversely with the number of time gates. Again, averaging schemes can be employed to compensate somewhat for the effect of photobleaching on the measurement of τ_f.

A streak-camera–based lifetime imaging system was employed by, for example, Minami and Hirayama (1990). More recently, Krishann and colleagues (2003) employed a two-dimensional (2D) streak camera in combination with a slit-scanning multi-photon excitation microscope. Time traces were recorded for all the points imaged onto the entrance slit. The system can be employed for lifetime imaging with picosecond time resolution.

Point Scanning Implementations

Most of the present implementations of FLIM in point-scanning microscopes are based on photon-counting techniques. Several commercial suppliers exist for both TCSPC PC plug-in cards and for fast time-gated photon counting detection systems (Van der Oord *et al.*, 2001; Becker *et al.*, 2003; Kwak and Vanden Bout, 2003).

TCSPC FLIM

TCSPC PC plug-in cards have been optimized for high throughput data collection. Some of the cards have comparatively large onboard memory banks that remove the memory transfer bottleneck. Here, the maximum frame size is restricted by the amount of on-board memory. In other plug-in cards, the memory of the

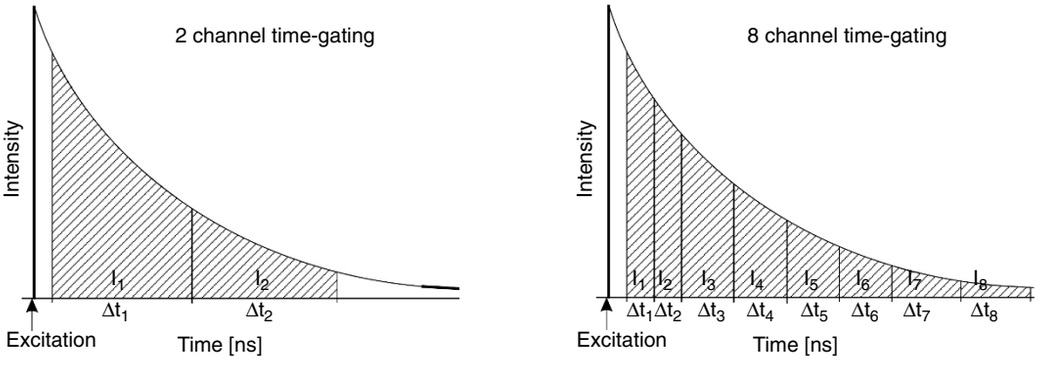


FIGURE 27.5. Time gating.

host computer is used and the timing histogram is built up in the computer memory. Furthermore, the dead time of the electronics has been reduced to 150 to 300 ns. Therefore, these TCSPC cards are considerably faster than conventional TCSPC electronics designed for spectroscopy applications (Becker *et al.*, 2003; Kwak and Vanden Bout, 2003).

The dead time of the TCSPC detection electronics is dominated by that of the TAC or TDC. FLIM systems based on this type of acquisition electronics typically employ a large number of time channels (typically 64–4096) that are comparatively narrow (25–200 ps). In principle, these FLIM systems are still based on the concepts used in the conventional spectroscopic TCSPC electronics. Therefore, they can in principle provide spectroscopic information as long as sufficient fluorescence signal is present.

It should be stressed though that a large number of detected photons is required in order to realize spectroscopic accuracy. In spectroscopy experiments whole decay curves are recorded with as many as one million counts in the decay. This is far more than is available in fluorescence imaging experiments. Furthermore, care must be taken to not operate the TCSPC electronics at too high count rates. Operation of detection systems at a rate of one over the dead time at the input will result in a loss of 50% of the detection efficiency due to pile-up. Moreover, operation of TCSPC at too high count rates will result in distortion of the decays. True spectroscopic accuracy can only be realized when the detection count rate is below 5% of the excitation rate (O'Connor and Phillips, 1984; Lakowicz, 1999).

Time-Gated FLIM

Our group has implemented time-gated detection in several point-scanning microscopes. Originally we employed a system based on two time gates (Buurman *et al.*, 1992; Draaijer and Houpt, 1988). Here, the detection channel of an existing CLSM was modified to accommodate the time-gated detection technique in combination with single-photon counting detection. A fast (0.8 ns rise time) red-sensitive PMT was followed by a fast discriminator with a 3 ns pulse pair resolution. The output signal from the discriminator was fed to two time-gated counter circuits that were both synchronized with the excitation source. All the time-critical electronics were built using emitter coupled logic (ECL) electronics. This detection circuit could be used at count rates of up to about 10^7 cps without serious pile-up effects visible in the lifetime. The minimum gate width of this system was approximately 2 ns and using this setup lifetimes of less than 1 ns could be imaged. An important advantage of using two time-gated detection channels, which are opened sequentially after every laser pulse, is the relative insensitivity to photobleaching. Furthermore, at the optimum gate width of 2.5 τ_f, the total acquisition time per excitation pulse amounts to 5 τ_f and approximately 99.3% of the total decay is captured within this period.

More recently we investigated the performance of time-gating systems with 4 and 8 channels, respectively (Van der Oord *et al.*, 2001; de Grauw and Gerritsen, 2001). Here, the same design philosophy was used. Again all the gates open sequentially after each and every excitation pulse. This approach ensures both high photon efficiency and a high maximum count rate capability. The dead time of the electronics is below 1 ns and therefore doesn't limit the maximum count rate of the lifetime acquisition system. In practice the performance of such a lifetime imaging systems is dominated by the properties of the detector.

Comparison of Confocal Fluorescence Lifetime Imaging Methods

Three detection methods have been used so far for recording fluorescence lifetime images in point-scanning microscopes: time gating, TCSPC, and phase fluorometry. In this section we will attempt to compare these approaches. Aspects that we take into consideration are the shortest observable lifetimes, the possibility of recording multiple lifetimes per pixel (multi-exponential decays), the sensitivity for bleaching, the photon economy, and the acquisition time. It must be stressed, though, that the limitations of all methods are to a large extent determined by the present state-of-the-art of the technology. The properties of the detector have a profound influence on the performance of the different lifetime imaging methods. Therefore, a separate section is included to summarize detector properties.

Shortest Lifetime

The shortest lifetime that can be imaged using phase fluorometry is limited by the speed of the detector and the modulation frequency or pulse repetition frequency of the light source. Based on the experience in non-imaging experiments using the fastest detectors, lifetime imaging down to 0.2 ns should be feasible (Ven, personal communication).

In the case of time-gated detection, the minimum lifetime is determined by the minimum gate width, the width of the excitation pulse, and the speed of the detector. Gate widths of less than 1 ns can be realized by the use of fast electronics. In combination with the fastest PMTs, the minimum observable lifetime is again estimated to be about 0.2 ns.

The TCSPC systems can be operated with channel widths down to 10 to 40 ps. Therefore, the minimum observable lifetime in this type of system will be only limited by the timing properties of the detector and the laser pulse width rather than the performance of the detection electronics. In practice the fastest available detectors (MCP-PMT) exhibit a timing jitter (transit time spread, TTS) of about 25 ps (Hamamatsu, 1997). Accurate determination of lifetimes close to or shorter than the TTS is difficult. Therefore, the limiting lifetime for TCSPC–based systems will be in practice on the order of 50 to 100 ps when a fast detector is employed.

Experience with conventional (TCSPC, phase fluorometry) fluorescence lifetime spectroscopy has shown that measuring short lifetimes (<0.5 ns) is not straightforward and prone to errors. Measurements carried out using different setups often produce different results; differences of 0.1 ns or larger are not unusual. Moreover, short lifetimes are often the result of quenching processes such as collisional quenching and FRET that not only reduce the lifetime but also the quantum efficiency of the fluorescent molecules. Therefore, short lifetimes are often accompanied by low intensities that make lifetime imaging of very short lifetimes far from trivial.

Multi-Exponential Lifetimes

The first frequency-domain FLIM systems were only capable of the recording one average lifetime per pixel. Multiple lifetimes per pixel from multi-exponential decays can in principle be recorded by acquiring sets of images at different excitation modulation frequencies. This increases both the data acquisition time and the dose of light to the specimen by an amount proportional to the number of modulation frequencies.

For example, Squire and colleagues (2000) recently demonstrated that multi-exponential lifetime imaging is in principle possible using frequency-domain FLIM. Here, use was being made of a WF microscope equipped with a laser modulated at a set of harmonic frequencies. Homodyne detection at each of these frequencies was carried out simultaneously by mixing with matching harmonics present in the gain characteristics of a MCP-based image intensifier. In principle, this approach should also be usable in scanning microscopes.

The time-gated detection scheme based on two time gates yields only an average lifetime. Multiple lifetimes per pixel can be obtained by extending the number of gates. This was demonstrated by, for example, Scully and colleagues (1997) in WF microscopy and by de Grauw and Gerritsen (2001) in a time-gated system equipped with eight gates. In principle, this should also be possible by using a system equipped with only four time gates. For the TCSPC–based FLIM systems, obtaining of multiple lifetimes is straightforward.

All of the above FLIM methods are in principle capable of resolving multiple lifetimes. However, at present only very few examples are available of multi-exponential analyses of FLIM images of biological specimens at the single-pixel level. The main problem with the multi-exponential analyses of FLIM images is the limited amount of signal available in imaging experiments. In spectroscopy-based experiments usually about 10^6 counts are accumulated in the decay and, in general, up to three decay components can be resolved. In exceptional cases, in particular when the decay components are far apart, more decay components can be separated.

An estimate of the total amount of signal available from one detected volume element in the specimen shows that it is difficult to realize high signal levels in a scanning microscope. In practice a few thousand detected photons per pixel can be obtained from a strongly fluorescing specimen. However, photobleaching effects often limit the amount of signal to (much) lower signal levels. By spatially binning the amount of signal per pixel can be increased at the price of a loss of spatial resolution.

A thorough statistical analysis by Kollner and Wolfrum (1992) showed that about two orders of magnitude more fluorescence signal is required for the resolving of two lifetimes differing by a factor of 2, than acquiring a single lifetime with the same accuracy.

Bleaching

One of the attractive properties of FLIM is that the fluorescence lifetime is not affected by fading due to photobleaching. The ability to take advantage of this property depends on the practical implementation of the method.

In the phase-fluorometry–based methods, at least two but preferably three measurements need to be recorded at different detection phase angles in order to obtain the lifetime information. Because these measurements are recorded sequentially, bleaching occurs between each acquisition, leading to a distortion of the observed lifetime. To some extent this can be compensated for by averaging over all the possible recording sequences at the different detector phase angles. However, this requires a highly stable excitation source, which may be a limiting factor for both the time resolution and the accuracy in the obtained lifetime.

In the time-gated method, the sensitivity to photobleaching depends on the implementation. If the signal is acquired in each of the time-gated detection channels after every excitation pulse, the method is not sensitive to fading due to photobleaching effects. The TCSPC–based FLIM method is also not affected by fading due to photobleaching.

It should be stressed that photobleaching may be accompanied by other photodegradation processes, including the production of fluorescing photoproducts. These photoproducts may introduce new decay components and affect the quality of the data.

Photon Economy

Unfortunately, no experimental information is available which can be used to make a quantitative comparison of the photon economy of different FLIM methods. However, some theoretical work has been carried out on the statistics of time-domain–based lifetime acquisition (Ballew and Demas, 1989; Kollner and Wolfrum, 1992). In addition, computer simulations have been carried out to compare different methods (Gerritsen *et al.*, 1996, 2002; Periasamy *et al.*, 1999).

In order to compare the different methods, a figure of merit is required. Here, we employ a figure of merit, F, which compares the accuracy of the lifetime acquisition method with that of a simple intensity measurement with the same number of detected photons, $F = (\Delta\tau/\tau)/(\Delta I/I)$, with τ the lifetime, $\Delta\tau$ the standard deviation of the lifetime determination, I the number of detected photons in the intensity measurement, and ΔI the standard deviation of the intensity determination. On assuming Poisson statistics, $\Delta I/I$ is proportional to $1/\sqrt{I}$ and the expression for F can be rewritten as:

$$F = \frac{\Delta\tau}{\tau} \cdot \sqrt{I} \qquad \textbf{(12)}$$

Now, F is a measure for the sensitivity of the lifetime acquisition method that is independent of the number of counts in the decay, provided that $\Delta\tau/\tau$ is also governed by Poisson statistics. F is always larger than 1 and a low value of F indicates a high sensitivity. The calculations and simulations presented here concern ideal photon-counting systems. Effects related to noise and timing jitter of the electronics and detectors are not included. The parameters in the simulations were chosen to yield the optimum sensitivity at a lifetime of 2 to 3 ns. Using Eq. 12, the F values can be converted into the number of counts (in the total decay) required to realize a specific accuracy, $I = [F/(\Delta\tau/\tau)]^2$. Sensitivities of two configurations can be compared by taking the square of the ratio of their figures of merit, $(F_1/F_2)^2$.

The figure of merit of phase-fluorometry–based FLIM methods used were investigated by simulating three time-dependent fluorescence signals, each with the same limited number of counts. Here, 1000 counts were used for each of the three simulated signals. Next, the fluorescence signals were multiplied by the detector response at detector phase angles 0 and $\pi/2$ and with the detector modulation switched off ($M_D = 0$), respectively. The fluorescence lifetime can be calculated from the three simulated detector images using Eq. 10. After repeating this procedure 1000 times, the relative standard deviation from the real τ_f was calculated.

The phase fluorometry simulations were performed for pulsed (delta pulse) as well as sinusoidally modulated excitation sources. In the case of pulsed excitation, a mono-exponential decay curve was simulated (Eq. 1), while in the case of sinusoidal modulation, a signal distribution proportional to Eq. 3 was simulated. In both cases, M_D and M_E were set to 1 (best case) while the optimum value of ω_f for τ_f was used.

The results of the computer simulations are summarized in Figure 27.6(A). In the case of sinusoidal modulation of the excitation source, the values of F are large (minimum value about 6), indicating a low sensitivity. In the case of pulsed excitation, a much lower value of F is found of about 1.5. This comparison shows

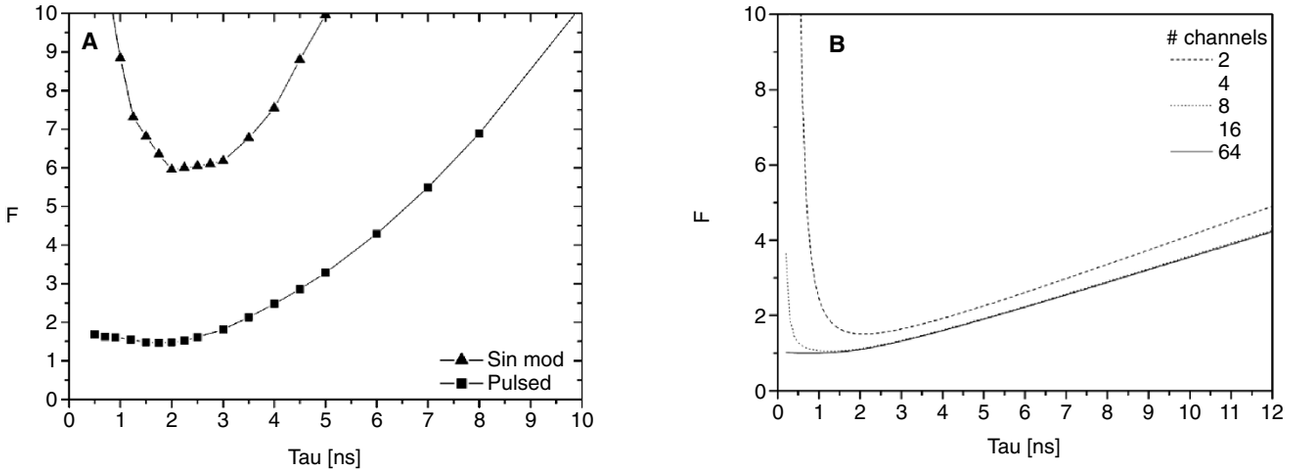


FIGURE 27.6. Figure of merit F for frequency-domain–based lifetime detection (A) and time-domain–based lifetime detection with a variable number of equal time channels (B). Low values of F indicate high sensitivity.

that phase fluorometry using pulsed excitation requires at least $(6/1.5)^2 = 16$ times fewer photons to reach the same accuracy in τ_f sensing compared with sinusoidal modulation. In practice the difference may even be more dramatic because $M_D < 1$ when sinusoidal excitation is being used.

The performance of systems with gates of equal width can be calculated analytically (Ballew and Demas, 1989; Kollner and Wolfrum, 1992). Here, we present analytical calculations on systems with equal gate widths based on the work by Kollner, but now expressed in terms of the figure of merit, F, defined earlier. For gates of non-equal width, such calculations are difficult or even impossible. However, previous work by our group on systems with four and eight gates of non-equal width shows great similarities with the results presented here (de Grauw and Gerritsen, 2001).

Here, we restrict ourselves to systems with 2, 4, 8, 16, and 64 time channels of equal width and a total collection time per laser pulse of 10 ns. A 10 to 12 ns collection time per laser pulse is typical for FLIM systems equipped with high-repetition-rate lasers such as titanium:sapphire lasers. The results of the figure of merit calculations are summarized in Figure 27.6(B). At all lifetimes the figure of merit of the two gate systems is significantly larger than that of the systems with four or more gates. In particular, at lifetimes below 2 ns the difference grows rapidly. At a lifetime of 2 ns the difference in sensitivity $[(F_1/F_2)^2]$ is about 70%.

Interestingly, above 2 ns no significant differences in F are found for systems with four or more gates. The differences between systems with four and more gates only show up below 1.5 ns and they all seem to be very well usable down to lifetimes as short as 0.5 ns or even shorter. The system with 64 gates has a very low figure of merit down to the shortest lifetimes. In practice the theoretical figures of merit cannot be realized for lifetimes of the order of, or shorter than, the time response of the detection system. Usually the time response is on the order of several hundred picoseconds. Therefore, for short lifetimes the sensitivity of real FLIM systems will be lower than the theoretical calculations indicate.

At long lifetime the sensitivity of all configurations in Figure 27.6 go down. Now, the total collection time is short compared with the lifetime and counts in the tail of the decay are not detected. Consequently the sensitivity goes down. The performance for longer lifetimes can be improved by increasing the total gate width. However, this will reduce the duty cycle of the system and the acquisition time will go up.

The figure of merit of the time-domain–based systems is somewhat lower than of the phase-fluorometry–based systems. However, the phase-fluorometry–based systems equipped with pulsed excitation perform well at short lifetimes. At longer lifetimes, however, the figure of merit rises more rapidly than in the case of the time-domain–based methods.

In the above comparison, only the effect of Poisson noise on the accuracy in τ_f was taken into account. In practice, other factors such as detector noise and dead time effects will affect the photon economy as well. Nevertheless, it is clear from the calculations that time-gated detection, TCSPC, and phase fluorometry using pulsed excitation are in principle all suitable for lifetime imaging.

Acquisition Time

The data acquisition time is governed by the photon economy as well as by other factors such as the duty cycle and the maximum signal strength with which the detection electronics and detector can cope. For FLIM methods employing pulsed excitation, the duty cycle will be determined by τ_f as well as the period T between two laser pulses. In this case, the ratio τ_f/T is a good measure of the duty cycle of the experiment.

When a high-repetition laser such as, for example, a titanium: sapphire laser, is being used, the maximum repetition frequency of the light source is about 80 MHz, and $\tau_f/T = 0.24$ for $\tau_f = 3$ ns. For longer lifetimes the duty cycle goes up, however, the figure of merit in general also goes up. In practice it will be difficult to measure long lifetimes with high repetition rate light sources. Such lifetimes require lower repetition rates of the light source and therefore the acquisition time will go up.

For the phase fluorometry method, using pulsed excitation, τ_f/T has a similar value at optimum ω_f. The duty cycle in a phase fluorometry experiment using sinusoidal excitation is about 50%, which somewhat compensates for the poor photon economy.

Because both the photon economy and the duty cycle of the methods using pulsed excitation are about the same, in theory similar acquisition times are expected. In our experience, the acquisition time in time-gated lifetime imaging can be as short as 10 µs/pixel for strongly fluorescing specimen. Here, the maximum count rate of the photon-counting detector of 5 to 10 MHz is the

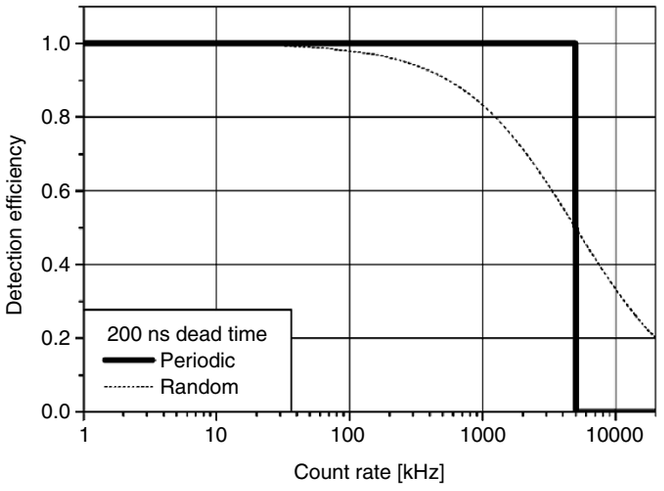


FIGURE 27.7. The effect of pile-up on the detection efficiency as a function of the incident count rate and a dead time of 200 ns (*dashed curve*).

limiting factor. The dead time of the detection electronics of 1 ns is not a limiting factor.

In TCSPC-based FLIM, however, the acquisition times are, in general, much longer. Here, the bottleneck is not the photon economy but the maximum count rate of the detection electronics. The dead time of the TCSPC electronics is comparatively large, on the order of 200 to 300 ns. The fraction of detected photons, f, amounts to:

$$f = \frac{1}{1 + t_d \cdot C_i} \tag{13}$$

with t_d the dead time of the system and C_i the incident count rate. This equation only accounts for the number of counts lost due to pile-up. Compared to a detector without a dead time, a 200 ns dead time would result in a 50% loss of detected photons at 1/200 ns = 5 MHz (see Fig. 27.7). At a count rate of 1 MHz, about 17% of the signal is lost due to pile-up. Importantly, besides the loss of sensitivity due to pile-up the decay curve may be distorted when the TCSPC system is operated at too high a count rate (Demas, 1983). In practice one should ensure that the most strongly fluorescing areas in the specimen do not show serious pile-up effects. For these reasons TCSPC-based FLIM should be operated at low average count rates of the order of several 100 kHz. Consequently, the acquisition times are comparatively long.

The phase fluorometry methods that employ pulsed excitation are usually equipped with PMTs operating as analog (non-photon counting) detectors. In this mode of operation, much stronger signals can be detected than in the photon-counting mode. Therefore, it is expected that the phase-fluorometry method using pulsed excitation can be operated at higher acquisition rates than the photon-counting–based methods. This is supported by some recent work carried out by Gratton's group (Gratton *et al.*, 2003). In this work it is demonstrated that the (analog) phase fluorometry method can handle significantly larger signal intensities than the TCSPC methods. Here, however, the shortest pixel dwell time amounts to 50 µs. The phase fluorometry method will also be better able to deal with large signals than other photon-counting–based methods.

In the case of the phase fluorometry method using a sinusoidally modulated light source and phase sensitive detection, comparatively long acquisition times are expected due to the low sensitivity.

Costs

The costs of the phase fluorometry method using sinusoidal excitation are mainly determined by the comparatively low costs of the EOM or AOM and that of the CW laser, if it is not already available. The detection system for either method is a modulated PMT. The costs of the methods requiring pulsed-excitation sources have always been dominated by the price of pulsed lasers. However, comparatively cheap pulsed diode lasers have recently become available (Pico Quant Gmbh). The lasers provide picosecond pulses, repetition rates as high as 40 MHz, and 1 to 2 mW of average power. At present lasers with wavelengths in the range 375 to 445 nm and 635 to 1550 nm are available. Other wavelengths close to 480 nm are expected to become available soon. The average power of the lasers does not allow high acquisition rate FLIM, but suffices for the acquisition of good quality FLIM data at moderate-to-slow speed.

Table 27.2 summarizes the (estimated) features of time-gating, TCSPC and phase fluorometry.

Detectors for Fluorescence Lifetime Imaging

The performance of fluorescence lifetime imaging systems critically depends on the detector properties. Here, we will restrict ourselves to detectors operating in photon-counting mode. However, most of the discussion below also applies to the non–photon-counting mode of operation.

The properties considered here are detector timing behavior, maximum count rate, and quantum efficiency. Side-on PMTs are often used in scanning microscopes because of their high quantum efficiency of up to about 35%. However, the side-on tubes

TABLE 27.2. Comparison of Different Lifetime Imaging Methods

			Phase Fluorometry	
	Time Gating	TCSPC	Pulsed	Sinusoidal
Shortest τ_f	0.2–0.5 ns	0.1 ns	0.2–0.5 ns	0.2–0.5 ns
Sensitive to bleaching	No	No	Yes	Yes
Photon economy	Good	Good	Good	Poor
Duty cycle	<0.1	<0.1	<0.1	50%
Acquisition time per pixel	$>10^{-5}$ s	$>10^{-4}$ s	$>10^{-5}$ s	$>10^{-4}$ s
Costs	Moderate/high	Moderate/high	Moderate/high	Low

employed in scanning microscopes usually show very poor timing properties and transit-time spreads (TTS) of several nanoseconds are not uncommon. Therefore, such detectors are not usable for FLIM. Fast, head-on PMTs exhibit a TTS as low as several hundred picoseconds and are in general much better for timing-critical applications. Usually their quantum efficiency does not exceed 10% and they can operate at maximum count rates of 5 to 10 MHz. At higher count rates, pulse pile-up degrades their performance and they may even be damaged when the maximum anode current is exceeded.

The shortest lifetimes that can be measured with a lifetime imaging system depend on both the timing properties of the detector and of the detection electronics. PMTs optimized for fast timing applications have a TTS as low as 200 to 400 ps. This limits the shortest lifetimes that can be measured with this type of tube to similar values. In order to measure shorter lifetimes microchannel plate PMTs (MCP-PMTs) (McLoskey *et al.*, 1996) can be employed. These detectors have a quantum efficiency of about 10% and a TTS as low as 25 ps. At present the MCP-PMTs have the best timing performance for the measurement of fast decays. However, the MCP-PMTs are expensive and vulnerable and their maximum count rate is limited. For example, the popular Hamamatsu R3809U-50 MCP-PMT has a maximum average anode output current of 100 nA, corresponding to a maximum count rate of 100 to 300 kHz. However, Hamamatsu advises operating this device at less than a maximum count rate of 20 kHz (Hamamatsu, 1997). In general, all detectors exhibit a wavelength-dependent time response that complicates the accurate determination of short decay times (Lakowicz, 1999).

Both PMTs and MCP-PMTs show a rather poor quantum efficiency of about 10%. Alternatively, single-photon counting avalanche photo diodes (SPADs) or PMTs with a GaAs photo cathode can be used. The SPADs have high quantum efficiencies, about 70% at 650 nm, and can be used for single-photon counting applications at count rates of up to 1 to 2 MHz. Their typical timing jitter is specified by PerkinElmer to be about 350 picoseconds and no maximum value is specified. In practice we found that values on the order of 700 ps are more common. Moreover, the timing properties of these devices are count-rate dependent. These properties make the SPADs less suitable for lifetime imaging. The GaAs photocathodes, also have comparatively high quantum efficiencies of about 40% in the red part of the spectrum. Their maximum count rate is limited to about 1 to 3 MHz and their timing resolution is about 350 ps.

The above figures can be used to make an estimate of the maximum frame rate for a specific type of detector. Assuming a 256×256 pixel image and an average number of counts per pixel of 250, we find frame acquisition times of 3.2 to 1.6 s, 500 to 160 s, 16 to 8 s, and 16 to 5 s for the PMT, MCP-PMT, SPAD, and GaAs PMT, respectively. Very short lifetimes of about 25 ps can only be measured with a MCP-PMT at the price of long acquisition times. Fast acquisition speeds, in combination with a lower lifetime limit of a few hundred picoseconds, can be realized with fast PMTs. Interestingly, the GaAs PMT combines a lifetime limit comparable with that of fast PMTs, with high quantum efficiency. This makes this detector an interesting alternative for low light level FLIM.

The acquisition time performance not only depends on the properties of the detector but also on the properties of the acquisition electronics. The dead time of the acquisition electronics is particularly important; large dead times will result in the loss of counts at high count rates.

In lifetime imaging, the probability of a photon arriving at the detector usually follows a (multi) exponential distribution. Therefore, the probability of pile-up is non-uniform in time and peaks at time equals zero of the exponential function. Consequently, when pile-up takes place the recorded fluorescence decay is distorted and the fitted lifetimes show a count-rate dependency. In our experience, a pile-up of 5% to 10% does not significantly affect the recorded fluorescence lifetimes. For a detection system with a dead time of 10 ns, this corresponds to a maximum count rate of 5 to 10 MHz. This goes down to 250 to 500 kHz for a detection system with a dead time of 200 ns.

APPLICATIONS

Multi-Labeling and Segmentation

Fluorescence lifetime imaging is able to discriminate between a large number of probes based on lifetime differences alone. In Figure 27.8, an example of fluorescence-lifetime–based discrimination of fluorescent probes is shown. Here, a mixture of seven different fluorescent probes (Yellow Green beads, NYO beads, FITC

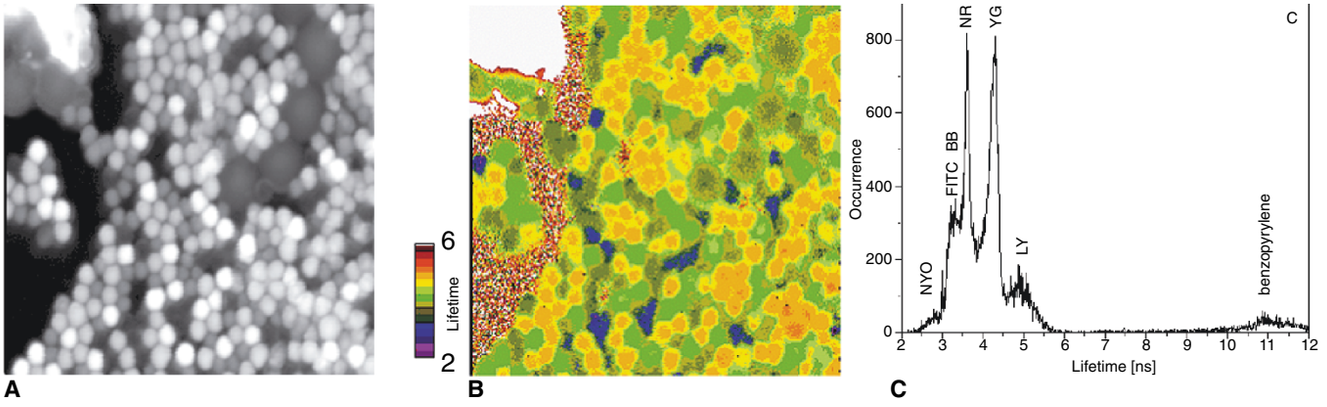


FIGURE 27.8. (A) Intensity image of a specimen containing a number of different fluorescent beads and crystals. (B) Corresponding fluorescence lifetime image. (C) The histogram of fluorescence lifetimes.

beads, Bright Blue beads, Nile Red beads, Lucifer Yellow solution, and benzopyrylene crystals) was imaged with a homemade two-photon fluorescence lifetime microscope equipped with an 8-channel time-gated detector (Sytsma *et al.*, 1998). In the lifetime image and in the lifetime histogram, six different lifetimes are clearly visible. The areas with the highest intensities yield the narrowest lifetime distributions. The fluorescence lifetimes of the beads were determined by means of TCSPC. The yellow-green beads and the Lucifer Yellow solution showed mono-exponential decays with decay times of 4.27 ns and 4.95 ns, respectively. The other beads and the crystal showed multi-exponential decays. The average lifetimes of these decays were 2.8 ns for NYO beads, 3.1 ns for FITC beads, 3.2 ns for Bright Blue beads, 3.6 ns for Nile Red beads, and 10.8 ns for the benzopyrylene. The lifetimes of FITC and Bright Blue beads are separated by only 0.1 ns and show up as one broadened peak in the histogram. The widths of peaks in the histogram are determined by statistics alone. Here, the minimum and maximum intensity per pixel amounted to 70 counts and 140,000 counts for the Lucifer Yellow solution and benzopyrylene, respectively. A higher signal per pixel improves the signal-to-noise ratio and, therefore, reduces the widths of the lifetime peaks in the histogram. Here, the time between two excitation pulses amounts to 12.2 ns (82 MHz Ti:Sa laser). Consequently, the lifetime sensitivity for the long lifetime benzopyrylene (10.8 ns) is poor.

In Figure 27.9, confocal fluorescence intensity and fluorescence lifetime images from the alga *Gymnodinium nagasakience* are shown. The images were recorded with a confocal microscope equipped with a simple time-gated detection system with two, 2 ns-wide gates (Buurman *et al.*, 1992). The alga was stained with an antibody–FITC conjugate against its outer membrane. The fluorescence intensity image in Figure 27.9(A) shows signal from both the antibody–FITC and the autofluorescence of the chlorophyll contained in the chloroplasts because no spectral discrimination was used to separate the fluorescence of these two substances. Figure 27.9(B) shows a fluorescence lifetime image of the alga; the gray value is a measure for τ_f. Chloroplasts show up as dark spots because for chlorophyll $\tau_f \approx 0.7$ ns, while the areas around the membrane are lighter because of the FITC $\tau_f \approx 1.1$ ns.

The lifetime image can be segmented and used as a mask to obtain two separate images: one with fluorescence intensity representing chlorophyll [Fig. 27.10(A)] and the other with fluorescence intensity representing FITC [Fig. 27.10(B)]. For comparison, two images obtained by filtering the emission in the conventional way are also shown. Figure 27.10(C) shows the chlorophyll signal recorded through a long-pass 580 filter and Figure 27.10(D) shows the FITC signal detected through a bandpass filter. There is a high degree of correlation between the FLIM and spectral images. However, a subtle detail coming from a dimple in the center of the alga shell shows up in both members of the spectrally resolved image pair showing that this filter combination is not good enough to discriminate between chlorophyll and FITC. This detail is not visible in the lifetime image.

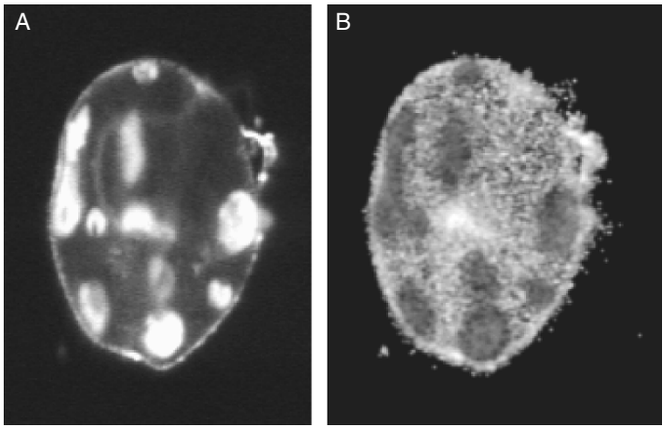


FIGURE 27.9. Confocal fluorescence intensity (A) and fluorescence lifetime images (B) from the alga *Gymnodinium nagasakience* stained with antibody–FITC conjugate against its outer membrane ($\tau_f \approx 1.1$ ns). In addition, autofluorescence of chlorophyll is visible ($\tau_f \approx 0.7$ ns).

Ion-Concentration Determination

Ion concentrations in biological systems, such as pH, Ca^{2+}, and Na^+, are widely studied with fluorescent probes. The probes have a high selectivity for specific ions and exhibit marked changes in their photophysical properties upon binding. Often the probes exist in two states, bound to the ion and free, that have distinct fluorescence lifetimes. The average fluorescence lifetime is a good measure for the ion concentration and can be used for the quantitative imaging. Some of the examples obtained in our lab are discussed below. Others can be seen in Chapter 42, *this volume*.

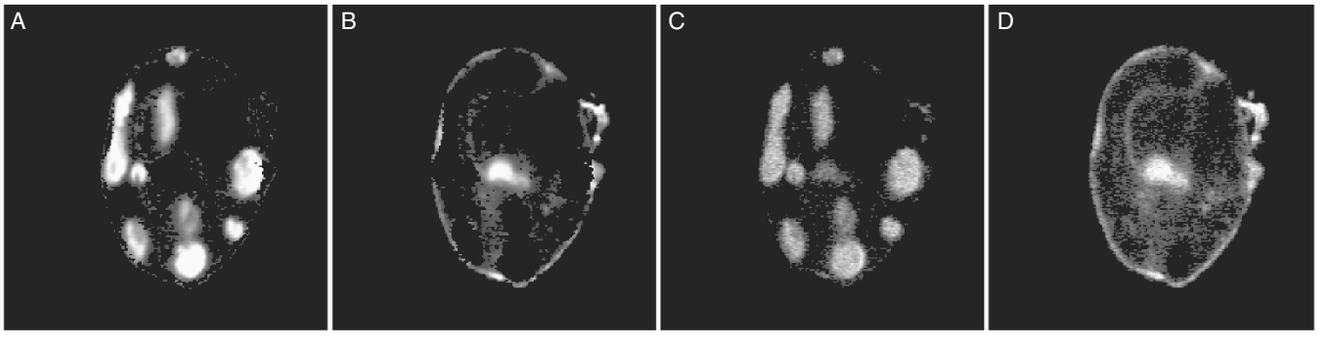


FIGURE 27.10. The chlorophyll (A,C) and FITC (B,D) signals after fluorescence lifetime–based segmentation (A,B) and segmentation based on differences in emission spectra (C,D).

Calcium Imaging

Calcium plays a central role as a second messenger in plant and animal cells and is involved in controlling numerous biological processes. Fluorescent probes are widely used in macroscopic and microscopic studies of $[Ca^{2+}]$. These probes have a high selectivity for free Ca^{2+} over other ions and the probes undergo a significant change in fluorescence properties upon binding to Ca^{2+}. Current fluorescent calcium probes can be divided in two groups: ratio or dual-wavelength probes and non-ratio or single-wavelength probes. Due to calibration problems, single-wavelength probes produce very ambiguous results. The fluorescence intensity increases as a result of an increase in $[Ca^{2+}]$. However, the fluorescence intensity not only depends on the $[Ca^{2+}]$ but also on the dye concentration, which can vary as a result of unequal cytosol thickness, inhomogeneous dye distribution within or between cells, and leakage and/or photobleaching during an experiment.

Quantification of $[Ca^{2+}]$ can be more accurate when ratio probes are used. These probes show a marked shift in either excitation or emission spectra upon binding to Ca^{2+} and are referred to as dual-excitation or dual-emission probes. This feature allows these probes to be used for ratio analysis (Rink *et al.*, 1982; Grynkiewicz *et al.*, 1985; Tsien and Poenie, 1986). The ratioing method is independent of dye distribution inhomogeneities within or between cells, and leakage and/or photobleaching during an experiment. Unfortunately, a laborious *in situ* calibration procedure is required when ratio probes are being used in fluorescence microscopy.

Most of the commercially available ratio probes such as Fura-2 and Indo-1 have to be excited in the ultraviolet (UV). UV wavelengths can potentially injure cells and tend to excite autofluorescence; therefore, it is preferable to use probes that have their excitation wavelength in the visible.

FLIM is an interesting alternative for the imaging of free Ca^{2+}. The binding of Ca^{2+} to the single-wavelength probes results in a large increase of the quantum efficiency of the probe. This is in general accompanied by a substantial increase of the fluorescence lifetime of the probe. Depending on the free calcium concentration and the K_d of the probe, different amounts of bound and free probe will be present in the specimen, $K_d = ([\text{free probe}]\cdot[Ca^{2+}])/[\text{bound probe}]$. In general the fluorescence decay will be (at least) bi-exponential. The amplitudes of the different lifetime components depend on the calcium concentration and it turns out that the average lifetime is a good measure of the calcium concentration (Sanders *et al.*, 1994).

Interestingly, in principle FLIM allows quantitative imaging of Ca^{2+} using single wavelength probes that are excited with visible light. There are several indications that this approach is more reliable than the approaches based on ratio imaging (Sanders *et al.*, 1995; Herman *et al.*, 1997).

In general, the free probe has both a short lifetime and low quantum efficiency. The ion-bound probe, on the other hand, has both a long lifetime and high quantum efficiency. Therefore, the ion-bound form dominates the fluorescence decay and the usable ion concentration range of the probe is shifted to lower ion concentrations.

Early work on the quantitative FLIM of calcium required comparatively long acquisition times. Recently, we carried out fast-time-gating-based FLIM measurements of Indo-1 stained rat myocytes (see Fig. 27.11) (Gerritsen *et al.*, 2002). The rat myocytes spontaneously beat at rates of 0.5 to 2 Hz at 37°C and the beating is accompanied by large Ca^{2+} fluxes (Berlin and Konishi, 1993). The images were recorded in a homemade two-photon excitation microscope (Sytsma *et al.*, 1998) equipped with an 8-channel time-gated detector and a femtosecond titanium:sapphire laser operating at 82 MHz and an excitation wavelength of 700 nm. Indo-1 exhibits a 1.4 ns lifetime for the free probe and a 1.66 ns lifetime for the ion-bound probe (Lakowicz and Szmacinski, 1993). Despite the small lifetime difference between the free and bound forms of the probe, lifetime images (256×256 pixels) could be recorded at a rate of 1 frame per second. Here, a Hamamatsu R1894 PMT was used at an average count rate close to 10 MHz. Both the intensity [Fig. 27.11(A)] and the lifetime image [Fig. 27.11(B)] were median-filtered. The edges of the lifetime image are somewhat sharpened due to the thresholding, lifetimes were only calculated for pixels with 50 or more counts. Pixels with fewer counts were set to zero. The calibration bar below the lifetime image gives an indication of the lifetimes. No attempt was made to convert the lifetimes into calcium concentrations. The beating of the myocyte during image acquisition shows up as a band in both the FLIM and the intensity image. Here, the myocyte beat about twice during the image acquisition.

pH Imaging

Dental biofilm can be several hundred micrometers thick and exhibits an intricate three-dimensional (3D) structure (see also Chapter 51, *this volume*). This type of specimen is strongly scattering and two-photon excitation (TPE) microscopy is therefore the preferred imaging method to study it. pH is one of the key

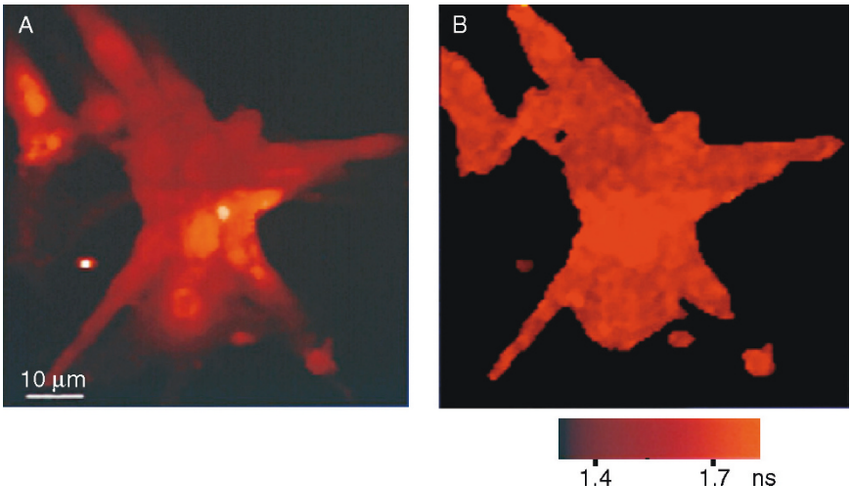


FIGURE 27.11. Intensity image (A) and fluorescence lifetime image (B) of an Indo-1 stained beating rat myocyte. The beating, approximately 2 Hz, results in the bands in the image. The 256×256 pixel image was recorded in 1 s using a two-photon excitation microscope equipped with a time-gated detection system.

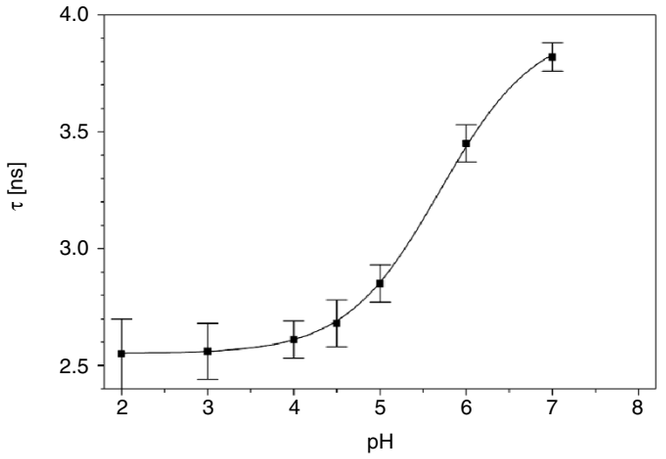


FIGURE 27.12. The pH calibration (carboxy–fluorescein) of the two-photon FLIM system.

parameters in biofilm research. The pH in the biofilm is in the acidic range and quantitative imaging of the pH in this range is usually accomplished by means of excitation-ratio imaging. Implementation of excitation ratio-imaging in TPE imaging is hampered by the requirement of two measurements at different excitation wavelengths. Fluorescence lifetime imaging is an excellent alternative for the quantitative imaging of pH in the acidic range.

Here, we employed TPE in combination with FLIM to study the pH in a biofilm (Bradshaw *et al.*, 1998; Vroom *et al.*, 1999). Carboxy–fluorescein was used as a fluorescent pH indicator. The carboxy form of the probe is cell impermeable, so it senses only the extracellular pH, the pH of interest in the biofilms. TCSPC measurements on a series of carboxy–fluorescein buffers of different pH revealed a clear pH-dependent average fluorescence lifetime of 4.0 ns at high pH (pH > 7) and 3.0 ns at low pH (pH < 3). In addition to the fluorescence lifetime effect, the quantum yield of carboxy–fluorescein went down to 5% at pH 3, relative to that at pH 7.

At an excitation wavelength of 800 nm, the biofilms show some autofluorescence with an average fluorescence lifetime of less than 1 ns. The difference in fluorescence lifetime between the autofluorescence and the carboxy–fluorescein was exploited to suppress the autofluorescence in the pH measurements. This was achieved by opening the first gate 1 ns after the excitation pulse. This suppresses 80% of the autofluorescence and only 20% of the carboxy–fluorescein signal. In addition, a comparatively high probe concentration of 50 to 100 μ*M* was used in the pH imaging experiments. The autofluorescence was less than 1% of the total fluorescence intensity in all the measurements, even at low pH.

In Figure 27.12, the pH calibration of the microscope is shown. Intensity and pH *xy*-images ($30 \times 30\,\mu m^2$, $z = 60\,\mu m$) of carboxy–fluorescein stained biofilm are shown in Figure 27.13. The intensity image [Fig. 27.13(A)] shows individual bacteria, while the fluorescence lifetime image [Fig. 27.13(B)] shows an almost homogeneous pH of pH 6.2 ± 0.3. At a constant pH the quantum efficiency of the carboxy–fluorescein is constant. Therefore, the heterogeneous fluorescence intensity distribution can be attributed to a non-homogeneous probe distribution. Binding of some of the probe to the bacteria may cause this.

A pH gradient was induced by overlaying the specimen with a 14 m*M* sucrose solution. The fermentation of sucrose lowers the pH outside the bacteria. In Figure 27.14, the intensity [Fig. 27.14(A)] and fluorescence lifetime [Fig. 27.14(B)] images 94 min after the addition of the sucrose are shown. These images were recorded at the same position as that of Figure 27.13.

The fluorescence intensity image shows some brightly fluorescing areas. At the same position in the fluorescence lifetime image, a pH is found of less than 3. This observation is somewhat unexpected because the quantum efficiency of the probe goes down with pH. It suggests that a high local probe concentration is present at the bright spots. This effect may be caused by probe precipitation and makes the measurements at these locations less reliable. Therefore, the bright spots were excluded from the pH analysis. The average pH of this image is 5.2 ± 0.4, one pH unit lower than the average pH of the reference image.

Probes for Fluorescence Lifetime Microscopy

A literature study and some measurements on probes in our own laboratory revealed a large list of probes which can potentially be used for fluorescence lifetime imaging, this list is summarized in Table 27.3.

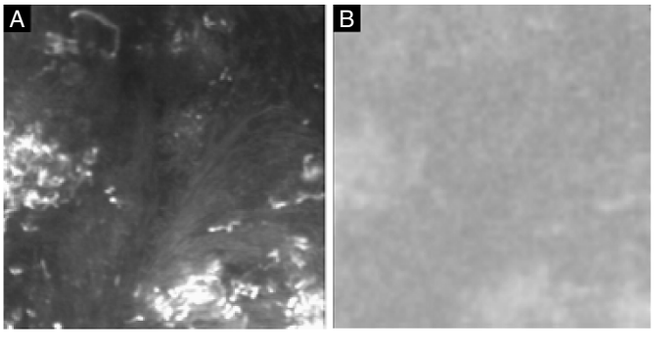


FIGURE 27.13. Intensity image of biofilm (A) with individual bacteria visible. Fluorescence lifetime image (B) shows a homogeneous pH of 6.2 ± 0.3.

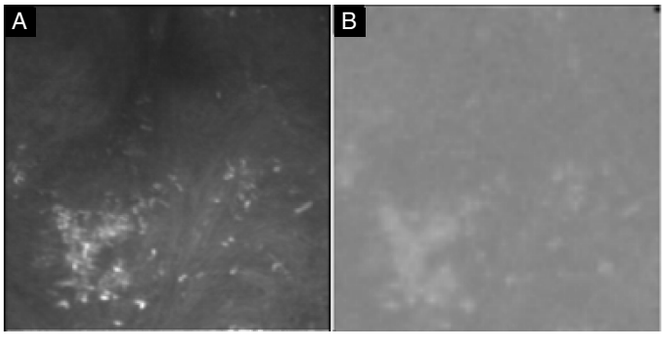


FIGURE 27.14. Intensity (A) and lifetime (B) images after overlaying the biofilm specimen with a 14 m*M* sucrose solution. The average pH is 5.2 ± 0.4.

TABLE 27.3. Ion Sensitive Probes

PH Probes				
Probe	$\lambda_{exc}/\lambda_{em}$ (nm)	τ_{acid}[a] (ns)	τ_{base}[a] (ns)	Reference
SNAFL-1	295[a]/500[b]	3.58	1.14	Whitaker *et al.* (1991)
Carboxy-SNAFL-1	295[a]/500[b]	3.44	0.95	Whitaker *et al.* (1991)
Carboxy SNAFL-2	295[a]/500[b]	4.19	0.87	Whitaker *et al.* (1991)
Carboxy SNAFL-3	295[a]/500[b]	3.63	1.16	Whitaker *et al.* (1991)
Carboxy SNARF-5	295[a]/500[b]	4.21	0.73	Whitaker *et al.* (1991)
SNARF-6				Whitaker *et al.* (1991)
Carboxy SNARF-6	295[a]/500[b]	4.50	1.04	Whitaker *et al.* (1991)
SNARF-1	295[a]/500[b]	0.46	1.54	Whitaker *et al.* (1991)
SNARF-2	295[a]/500[b]	0.30	1.75	Whitaker *et al.* (1991)
Carboxy SNARF-1	295[a]/500[b]	0.60	1.32	Whitaker *et al.* (1991)
Carboxy SNARF-1	295[a]/500[b]	0.60	1.32	Whitaker *et al.* (1991)
Carboxy SNARF-2	295[a]/500[b]	0.27	1.67	Whitaker *et al.* (1991)
2-Naphtol	313/360	0.80 (0.35) 7.30 (1.91)	4.82	Laws and Brand (1979)
Acridine	348/560	9.6	31.1	Gafni and Brand (1978)
Virginiamycin S[c]	330/420	0.48	1.9	Clays *et al.* (1991)
BCECF	490/520	3.0	3.8	This laboratory
DM-NERF	490/520	2.3	4.0	This laboratory
Carboxy-fluorescein[d]	490/520	3.0	4.0	This laboratory
Cl-NERF	490/520	1.3	4.0	This laboratory
Acridine Orange	490/520	1.8	5.3	This laboratory

Ca^{2+} Probes				
Probe	$\lambda_{exc}/\lambda_{em}$ (nm)	$\tau_{no\ Ca++}$[a] (ns)	τ_{Ca++}[a] (ns)	Reference
Fura-2	340/420 380/420	0.77(0.49) 1.5(0.51)	1.77	Keating *et al.* (1989)
Quin-2				Lakowicz *et al.* (1994)
Calcium green Bapta 1	488/520	1.6	3.5	This laboratory
Calcium green Bapta 2	488/520	2.1	3.6	This laboratory
Calcium green Bapta 5N	488/520	0.5	3.4	This laboratory
Oregon Green Bapta 1,2	488/520	1.5	3.7	This laboratory
Oregon Green Bapta 5N	488/520	0.5	2.8	This laboratory
BTC		0.7	1.2	This laboratory
Indo 1	340/400–475	1.4	1.7	Lakowicz and Szmacinski (1993)
Indo 5F	340/400–475	1.4	1.4	This laboratory

Cl Probes				
Probe	$\lambda_{exc}/\lambda_{em}$ (nm)	τ_{noCl}[a] (ns)	τ_{Cl}[a] (ns)	Reference
SPQ/Cl–	—/—	26.0	2.0	Dix and Verkman (1990)

DNA or RNA Selective Probes				
Lifetime Differences with Free Probe and Probe Bound to DNA				
Probe	$\lambda_{exc}/\lambda_{em}$ (nm)	λ_{free}[a] (ns)	τ_{bound}[a]	Reference
Proflavine, acriflavine, acridine yellow (208C)	—/—	4.5	4 (0.7) 7 (0.3)	Duportail *et al.* (1977)
9-Aminoacridine	—/—	15	10.5 (0.7) 31 (0.3)	Duportail *et al.* (1977)
Rivanol	—/—	6.5	5.5 (0.7) 13 (0.3)	Duportail *et al.* (1977)
Quinacrine	—/—	4	3.5 (0.7) 19 (0.3)	Duportail *et al.* (1977)
Ethidium bromide	532/—	1.7	24.2	Atherton and Beaumont (1984)
Acridine orange, DNA	488/520	—	1.7–1.9	Marriott *et al.* (1991b)
RNA	488/520	—	1.7–1.9	Marriott *et al.* (1991b)
RNA	488/>630	—	5–20	Marriott *et al.* (1991b)

continued

TABLE 27.3. Ion Sensitive Probes (*Continued*)

Lifetime Differences with Different Amounts of A + T				
Probe	$\lambda_{exc}/\lambda_{em}$ (nm)	τ_{much} AT[a] (ns)	τ_{little} AT[a] (ns)	Reference
Rivanol	—/—	5.5 (0.8)[e]	11	Duportail *et al*. (1977)
		13 (0.2)		
Quinacrine	—/—	2.2 (0.9)	16	Duportail *et al*. (1977)
		15 (0.1)		
Quinacrine	435/516	2.6 (0.35)[f]	1.1 (0.06)	Arndt-Jovin *et al*. (1979)
		11 (0.39)	7.90 (0.33)	Arndt-Jovin *et al*. (1979)
		27 (0.26)	26 (0.60)	Arndt-Jovin *et al*. (1979)
Probes Which Are Sensitive to Other Factors as Ions or DNA or RNA				
Probe	$\lambda_{exc}/\lambda_{em}$ (nm)	τ_{free}[a] (ns)	τ_{bound}[a] (ns)	Reference
SR33557	H_2O/EtOH [50/50]	336/400	4	Chatelain *et al*. (1992)
Calcium—	EtOH	336/403	8.5	Chatelain *et al*. (1992)
entry blocker	Erythrocytes	—/—	13.3 (0.91)	Chatelain *et al*. (1992)
			2.9 (0.09)	
	Egg PC vesicle	—/—	13.6 (0.81)	Chatelain *et al*. (1992)
			5.0 (0.19)	
Fluoranthene	In N2 gas	355/—	51	Ni *et al*. (1991)
	In air	32	51	
	In O2 gas	14	51	
FITC	pH 7.2	490/520	3.9	This laboratory
FITC-	pH 7.4	490/520	1.5 (0.38)	This laboratory
transferin			3.6 (0.62)	
FITC-KE2	pH 7.4	485/—	1.32 (0.28)	Matko *et al.* (1992)
	Fab complex		4.11 (0.72)	

λ_{exc} (nm), excitation wavelength; λ_{em} (nm), emission wavelength; τ_f, fluorescence lifetime, a is the amplitude of the respective components in case of multi-exponential decay.
[a] Absorption maxima between 480 and 580 nm.
[b] 500 nm long-pass filter.
[c] Virginiamycin S has three different pKs and thus four different protolytic forms.
[d] Affected by other effects such as binding.
[e] 28% A + T.
[f] 55% A + T.

SUMMARY

Fluorescence lifetime imaging is a powerful tool that can be used for a large number of different applications. Since its introduction around 1990, it has significantly matured and at present several companies supply complete FLIM detection systems. The advantages and disadvantages of FLIM and the different implementations are summarized below.

- Fluorescence lifetime imaging is insensitive to intensity effects such as shading, photobleaching, absorption, and light source noise. This can be an important advantage, especially in confocal and multi-photon studies of thick specimens. Here, absorption effects and photobleaching are important limitations.
- Fluorescence lifetime imaging is a powerful tool in the field of ion-concentration imaging. The comparison between emission-ratio imaging and lifetime-imaging suggests that lifetime-imaging can yield quantitative results without a cumbersome *in vivo* calibration procedure.
- In theory, lifetime imaging is able to separate the signals from a large number of different probes in parallel using a single detector. Image-processing can be simplified by using fluorescence lifetime data as the basis of segmentation.
- In recent years it has been demonstrated that FLIM is an excellent and straightforward method to carry out FRET experiments. The simple calibration of FLIM/FRET experiments is particularly appealing (Fig. 27.15).
- The image acquisition times of lifetime-imaging microscopes strongly differ. Potentially, the phase-fluorometry–based technique combined with pulsed excitation has the shortest acquisition times due to its ability to cope with large signal intensities. The phase technique employing sinusoidally modulated excitation, however, will require very long acquisition times when combined with scanning microscopy. The acquisition time of the time-gated or phase techniques in combination with pulsed lasers will be at least one order of magnitude shorter than in TCSPC.
- In principle the photon economy of all methods employing pulsed excitation is excellent. The photon economy of phase of fluorometry with sinuoidal excitation, however, is poor. Furthermore, the photon economy may vary per implementation. For example, systems with a long electronics dead time (TCSPC) or slow detectors will show a reduction of the photon economy (detection efficiency) above a certain count rate.
- At present the systems equipped with TCSPC are best suited for the imaging of very short lifetimes, provided that they are equipped with a fast detector (MCP-PMT). This type of detector should, however, be operated at very low count rates (50–200 kHz).

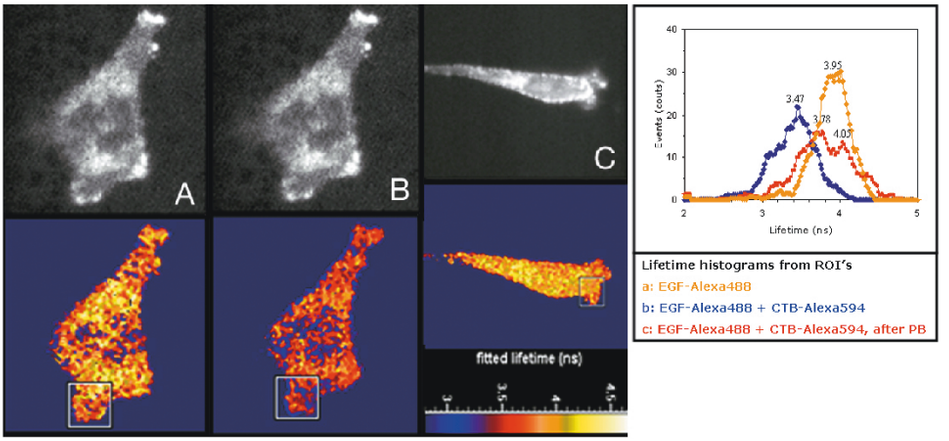


Figure 27.15. A FRET-FLIM experiment involving living HER14 cells was designed to determine if the EGF receptor (labeled with EGF-Alexa-488) co-localized with the lipid raft marker CTB (labeled with Alexa-594). The top row shows donor fluorescence intensity images and the bottom row donor lifetime images (256 × 256 pixel). The graph on the right plots a histogram of the τ_f values derived from pixels in the regions of interest (gray boxes) under the conditions noted. (A) The donor-only lifetime image (lower) yields an average lifetime of 4.0 ns (yellow curve). (B) In the presence of the acceptor, FRET reduces the donor lifetime to about 3.5 ns (lower image and blue curve). (C) After photobleaching the acceptor, the donor lifetime (lower image and red curve) returns almost completely to the donor-only lifetime (experiment on a different cell).

REFERENCES

Atherton, S.J., and Beaumont, P.C., 1984, Ethidium bromide as a fluorescent probe of the accessibility of water to the interior of DNA, *Photobiochem Photobiophys* 8:103–113.

Ballew, R.M., and Demas, J.N., 1989, An error analysis of the rapid lifetime determination method for the evaluation of single exponential decays, *Anal. Chem.* 61:30–33.

Becker, W., Bergmann, A., Biskup, C., Kelbauskas, L., Zimmer, T., Klöcker, N., and Benndorf, K., 2003, High resolution TCSPC lifetime imaging, *Proc. SPIE* 4963:175–184.

Berlin, J., and Konishi, M., 1993, Ca^{2+} transients in cardiac myocytes measured with high and low affinity Ca^{2+} indicators, *Biophys. J.* 65:1632–1647.

Bradshaw, D.J., Marsh, P.D., Gerritsen, H., Vroom, J., Watson, G.K., and Allison, C., 1998, Detection of pH gradients in biofilms using 2-photon excitation microscopy, *J. Dent. Res.* 77:2854.

Bugiel, I., König, K., and Wabnitz, H., 1989, Investigation of cells by fluorescence laser scanning microscopy with subnanosecond time resolution, *Laser Life Sci.* 3:1–7.

Buurman, E.P., Sanders, R., Draaijer, A., Gerritsen, H.C., Van Veen, J.J.F., Houpt, P.M., and Levine, Y.K., 1992, Fluorescence lifetime imaging using a confocal laser scanning microscope, *Scanning* 14:155–159.

Clark, R.J.H., and Hester, R.E., 1989, *Time Resolved Spectroscopy*, John Wiley and Sons, Chichester, United Kingdom.

Clays, K., Giambattista, M.D., Persoons, A., and Engelborghs, Y., 1991, A fluorescence lifetime study of virginiamycin S using multifrequency phase fluorometry, *Biochemistry* 30:7271–7276.

Clegg, R.M., 1996, Fluorescence resonance energy transfer, In: *Fluorescence Imaging Spectroscopy and Microscopy* (X.F. Wang and B. Herman, eds.), John Wiley and Sons, New York, pp. 179–236.

de Grauw, C.J., and Gerritsen, H.C., 2001, Multiple time-gate module for fluorescence lifetime imaging, *Appl. Spectrosc.* 55:670–678.

Demas, J.N., 1983, *Excited State Lifetime Measurements*, Academic Press, New York.

Dix, J.A., and Verkman, A.S., 1990, Mapping of fluorescence anisotropy in living cells by ratio imaging. Application to cytoplasmic viscosity, *Biophys. J.* 57:231–240.

Draaijer, A., and Houpt, P.M., 1988, A standard video-rate confocal laser scanning reflection and fluorescence microscope, *Scanning* 10:139–145.

Duportail, G., Mauss, Y., and Chambron, J., 1977, Quantum yields and fluorescence lifetimes of acridine derivatives interacting with DNA, *Biopolymers* 16:1397–1413.

Förster, T., 1946, Energiewanderung und Fluoreszenz, *Naturwissenschaften* 6:166–175.

French, T., So, P.T.C., Dong, C.Y., Berland, K.M., and Gratton, E., 1998, Fluorescence lifetime imaging techniques for microscopy, *Methods Cell Biol.* 56:277–304.

Gadella, T.W., Jovin, T.M., and Clegg, R.M., 1993, Fluorescence lifetime imaging microscopy (FLIM) — spatial resolutions of microstructures on the nanosecond time scale, *Biophys. Chem.* 48:221–239.

Gafni, A., and Brand, L., 1978, Excited state proton transfer reactions of acridine studied by nanosecond fluorometry, *Chem. Phys. Lett.* 58:346.

Gerritsen, H.C., Asselbergs, M.A.H., Agronskaia, A.V., and Van Sark, W., 2002, Fluorescence lifetime imaging in scanning microscopes: Acquisition speed, photon economy and lifetime resolution, *J. Microsc.* 206:218–224.

Gerritsen, H.C., Sanders, R., Draaijer, A., and Levine, Y.K., 1996, The photon economy of fluorescence lifetime imaging, *Scanning* 18:55–56.

Gerritsen, H.C., Sanders, R., Draaijer, A., and Levine, Y.K., 1997, Fluorescence lifetime imaging of oxygen in living cells, *J. Fluoresc.* 7:11–16.

Ghiggino, K.P., Harris, M.R., and Spizzirri, P.G., 1992, Fluorescence lifetime measurements using a novel fiberoptic laser scanning confocal microscope, *Rev. Sci. Instrum.* 63:2999–3002.

Gratton, E., and Limkeman, M., 1983, A continuously variable frequency cross-correlation phase fluorometer with picosecond resolution, *Biophys. J.* 44:315–324.

Gratton, E., Breusegem, S., Sutin, J., Ruan, Q., and Barry, N., 2003, Fluorescence lifetime imaging for the two photon microscope: Time-domain and frequency-domain methods, *J. Biomed. Opt.* 8:381–390.

Gratton, E., Jameson, D.M., and Hall, R.D., 1984, Multifrequency phase and modulation fluorometry, *Ann. Rev. Biophys. Bioeng.* 13:105–124.

Grynkiewicz, G., Poenie, M., and Tsien, R.Y., 1985, A new generation of Ca^{2+} indicators with greatly improved fluorescence properties, *J. Biol. Chem.* 260:3440–3450.

Hamamatsu, 1997. Data sheet MCP-PMT R3809U-50 Series.

Herman, B., Wodnicki, P., Kwon, S., Periasamy, A., Gordon, G.W., Mahajan, N., and Wang, X.F., 1997, Recent developments in monitoring calcium and protein interactions in cells using fluorescence lifetime microscopy, *J. Fluoresc.* 7:85–92.

Jameson, D.M., and Gratton, E., 1983, Analysis of heterogeneous emissions by multifrequency phase and modulation fluorometry, In: *New Directions in Molecular Luminescence* (D. Eastwood and L. Cline-Love, eds.), American Society for Testing and Materials, Philadelphia, pp. 67–81.

Keating, S.M., Wensell, T.G., Meyer, T., and Stryer, L., 1989, Nanosecond fluorescence and emission anisotropy kinetics of fura-2 in single cells, *Biophys. J.* 55:518a.

Kollner, M., and Wolfrum, J., 1992, How many photons are necessary for fluorescence-lifetime measurements? *Chem. Phys. Lett*. 200:199–204.

Krishnan, R.V., Saitoh, H., Terada, H., Centonze, V.E., and Herman, B., 2003, Development of a multiphoton fluorescence lifetime imaging microscopy system using a streak camera, *Rev. Sci. Instrum*. 74:2714–2721.

Kwak, E.-S., and Vanden Bout, D.A., 2003, Fully time-resolved near-field scanning optical microscopy fluorescence imaging, *Anal. Chim. Acta*. 496:259–266.

Lakowicz, J.R., 1983, *Principles of Fluorescence Spectroscopy*, Plenum Press, New York.

Lakowicz, J.R., 1999, *Principles of Fluorescence Spectroscopy*, Plenum Press, New York.

Lakowicz, J.R., and Berndt, K.W., 1991, Lifetime-selective fluorescence imaging using an Rf phase-sensitive camera, *Rev. Sci. Instrum*. 62: 1727–1734.

Lakowicz, J.R., and Szmacinski, H., 1993, Fluorescence lifetime-based sensing of Ph, Ca-2(+), K+ and glucose. *Sens. Actuator B Chem*. 11:133–143.

Lakowicz, J.R., Szmacinski, H., Lederer, W.J., Kirby, M.S., Johnson, M.L., and Nowaczyk, K., 1994, Fluorescence lifetime imaging of intracellular calcium in Cos cells using Quin-2, *Cell Calcium* 15:7–27.

Laws, W.R., and Brand, L., 1979, Analysis of two-state excited-state reactions. The fluorescence decay of 2-naphtol, *J. Phys. Chem*. 83:795–802.

Marriott, G., Clegg, R.M., Arndtjovin, D.J., and Jovin, T.M., 1991a, Time resolved imaging microscopy — phosphorescence and delayed fluorescence imaging, *Biophys. J*. 60:1374–1387.

Marriott, G., Clegg, R.M., Arndt-Jovin, D.J., and Jovin, T.M., 1991b, Time resolved imaging microscopy. Phosphorescence and delayed fluorescence imaging, *Biophys. J*. 60:1374–1387.

McLoskey, D., Birch, D.J.S., Sanderson, A., Suhling, K., Welch, E., and Hicks, P.J., 1996, Multiplexed single-photon counting. 1. A time-correlated fluorescence lifetime camera, *Rev. Sci. Instrum*. 67:2228–2237.

Minami, T., and Hirayama, S., 1990, High-quality fluorescence decay curves and lifetime imaging using an elliptic scan streak camera, *J. Photochem. Photobiol. A Chem*. 53:11–21.

Morgan, C.G., Mitchel, A.C., and Murray, J.G., 1992, Prospects for confocal imaging based on nanosecond fluorescence decay time, *J. Microsc*. 165:49–60.

Morgan, C.G., Mitchell, A.C., and Murray, J.G., 1990, Nano-second time-resolved fluorescence microscopy: principles and practice, *Trans. R. Microsc. Soc*. 1:463–466.

Ni, T.Q., and Melton, L.A., 1991, Fluorescence lifetime imaging — an approach for fuel equivalence ratio imaging, *Appl. Spectrosc*. 45:938–943.

O'Connor, D.V., and Phillips, D., 1984, *Time-Correlated Single Photon Counting*, Academic Press, London.

Periasamy, A., Sharman, K.K., and Demas, J.N., 1999, Fluorescence lifetime imaging microscopy using rapid lifetime determination method: Theory and applications, *Biophys. J*. 76:A10.

Periasamy, A., Wodnicki, P., Wang, X.F., Kwon, S., Gordon, G.W., and Herman, B., 1996, Time-resolved fluorescence lifetime imaging microscopy using a picosecond pulsed tunable dye laser system, *Rev. Sci. Instrum*. 67:3722–3731.

Piston, D.W., Sandison, D.R., and Webb, W.W., 1992, Time-resolved fluorescence imaging and background rejection by two-photon excitation in laser scanning microscopy, *SPIE* 1640:379–387.

Pringsheim, P., 1961, *Fluorescence and Phosphorescence*, Interscience Publishers, New York.

Rink, T.J., Tsien, R.Y., and Pozzan, T., 1982, Cytoplasmic pH and free Mg2+ in lymphocytes, *J. Cell Biol*. 95:189–196.

Sanders, R., Draaijer, A., Gerritsen, H.C., Houpt, P.M., and Levine, Y.K., 1995, Quantitative Ph imaging in cells using confocal fluorescence lifetime imaging microscopy, *Anal. Biochem*. 227:302–308.

Sanders, R., Gerritsen, H., Draaijer, A., Houpt, P., and Levine, Y.K., 1994, Fluorescence lifetime imaging of free calcium in single cells, *Bioimaging* 2:131–138.

Sauer, M., Schulz, A., Seeger, S., and Wolfrum, J., 1993, Design of multiplex dyes*, Phys. Chem.* 1734–1737.

Schneckenburger, H., and Konig, K., 1992, Fluorescence decay kinetics and imaging of Nad(P)H and flavins as metabolic indicators, *Opt. Eng*. 31:1447–1451.

Scully, A.D., Ostler, R.B., Phillips, D., O'Neill, P.O., Townsend, K.M., Parker, A.W., and MacRobert, A.J., 1997, Application of fluorescence lifetime imaging microscopy to the investigation of intracellular PDT mechanisms, *Bioimaging* 5:9–18.

So, P.T.C., French, T., Yu, W.M., Berland, K.M., Dong, C.Y., and Gratton, E., 1996, Two photon microscopy: Time-resolved and intensity imaging, In: *Fluorescence Imaging Spectroscopy and Microscopy* (X.F. Wang and B. Herman, eds.), John Wiley and Sons, New York, pp. 351–371.

Squire, A., Verveer, P.J., and Bastiaens, P.I.H., 2000, Multiple frequency fluorescence lifetime imaging microscopy, *J. Microsc*. 197:136–149.

Straughan, B.P., and Walker, S., 1976, *Spectroscopy*, Chapman and Hall, London.

Sytsma, J., Vroom, J.M., De Grauw, C.J., and Gerritsen, H.C., 1998, Time-gated fluorescence lifetime imaging and microvolume spectroscopy using two-photon excitation, *J. Microsc*. 191:39–51.

Tsien, R.Y., and Poenie, M., 1986, Fluorescence ratio imaging: A new window into intracellular ionic signaling, *Trends Biochem. Sci*. 11:450–455.

Van der Oord, C.J., De Grauw, C.J., and Gerritsen, H.C., 2001, Fluorescence lifetime imaging module LIMO for CLSM, *Proc. SPIE* 4252:119–123.

Vanderoord, C.J.R., Gerritsen, H.C., Rommerts, F.F.G., Shaw, D.A., Munro, I.H., and Levine, Y.K., 1995, Microvolume time-resolved fluorescence spectroscopy using a confocal synchrotron-radiation microscope, *Appl. Spectrosc*. 49:1469–1473.

Verveer, P.J., Squire, A., and Bastiaens, P.I.H., 2000, Global analysis of fluorescence lifetime imaging microscopy data, *Biophys. J*. 78:2127–2137.

Vroom, J.M., De Grauw, K.J., Gerritsen, H.C., Bradshaw, D.J., Marsh, P.D., Watson, G.K., Birmingham, J.J., and Allison, C., 1999, Depth penetration and detection of pH gradients in biofilms by two-photon excitation microscopy, *Appl. Environ. Microbiol*. 65:3502–3511.

Wang, X.F., Uchida, T., Coleman, D.M., and Minami, S., 1991, A 2-dimensional fluorescence lifetime imaging-system using a gated image intensifier, *Appl. Spectrosc*. 45:360–366.

Webb, S.E.D., Gu, Y., Leveque-Fort, S., Siegel, J., Cole, M.J., Dowling, K., Jones, R., French, P.M.W., Neil, M.A.A., Juskaitis, R., Sucharov, L.O.D., Wilson, T., and Lever, M.J., 2002, A widefield time-domain fluorescence lifetime imaging microscope with optical sectioning, *Rev. Sci. Instrum.* 73:1898–1907.

Whitaker, J.E., Haugland, R.P., and Prendergast, F.G., 1991, Spectral and photophysical studies of benzo[c]xanthene dyes: Dual emission pH sensors, *Anal. Biochem*. 194:330–344.

Wouters, F.S., and Bastiaens, P.I.H., 1999, Fluorescence lifetime imaging of receptor tyrosine kinase activity in cells, *Curr. Biol*. 9:1127–1130.

28

Multi-Photon Molecular Excitation in Laser-Scanning Microscopy

Winfried Denk, David W. Piston, and Watt W. Webb

INTRODUCTION

Multi-photon microscopy (MPM), which is based on molecular excitation by multi-photon absorption (MPA) and is usually combined with laser-scanning microscopy (LSM), has fulfilled its early promise (Denk *et al.*, 1990), as evidenced by continued growth of its application to vital imaging of biological systems (for a recent collection of reprints, see Masters, 2003). Conventional fluorescence microscopy can provide submicron spatial resolution of chemical dynamics within living cells, but is frequently limited in sensitivity and spatial resolution by background due to out-of-focus and scattered fluorescence. The superlinear character of multi-photon excitation (MPE) avoids background because the excitation is almost entirely confined to the high-intensity region near the focal point. As excitation of the out-of-focus background fluorescence is avoided, no confocal spatial filter is required; we retain all of the advantages of a (single-photon) confocal microscope and gain the absence of out-of-focus photobleaching and photodamage.

Multi-photon molecular excitation during a single quantum event was first predicted more than 75 years ago (Goeppert-Mayer, 1931) and consists of the simultaneous absorption of multiple photons that combine their energies to cause the transition to the excited state of the chromophore. For example, simultaneous absorption of two photons of red or infrared light can excite a fluorophore that normally absorbs ultraviolet (UV) or blue/green light. The fluorophore then emits fluorescence with a wavelength that usually is *shorter* than the exciting laser wavelength. Because multi-photon absorption requires at least two photons for each excitation, its rate depends on a higher algebraic power of the instantaneous intensity, just as the rate of a chemical reaction, $n\mathrm{A} + \mathrm{B} \rightarrow \mathrm{C}$, varies with the nth power of the concentration of A. Because of the large intensities required, the first experimental observation of two-photon excitation (2PE) (Kaiser and Garrett, 1961) and three-photon excitation (3PE) (Singh and Bradley, 1964) had to wait for the invention of the laser (Maiman, 1960), more than 30 years after Maria Goeppert-Mayer's prediction. In the decades following Kaiser and Garrett's work, a fair number of spectroscopic studies using 2PE were performed (reviewed, e.g., by Friedrich and McClain, 1980; Birge 1986), mainly to exploit the different quantum-mechanical selection rules that govern 2PE.

Nonlinear optical effects were first used in microscopy to produce images of second harmonic generation in crystals (Hellwarth and Christiansen 1974; Sheppard and Kompfner 1978). The first MPM images (using 2PE) were reported in 1990 (Denk *et al.*, 1990), with the expectation from its inception to develop nonlinear laser microscopy as a new tool for biophysical research.

Technological advances in two different areas have made nonlinear laser microscopy, in general, and MPM, in particular, practical: first, the development of LSM (Davidovits and Egger, 1969; Wilson and Sheppard, 1984) and, second, the development of mode-locked lasers that are capable of generating ultrashort pulses (≈100 fs) of red or infrared light at high repetition rates (≈100 MHz). (For a selection of reprints on this subject, see Gosnell and Taylor, 1991.)

Early applications of two-photon microscopy (2PM) to the study of dynamic biochemical processes in living cells demonstrated some of the advantages for quantitative three-dimensional (3D) and four-dimensional (4D) (space and time) resolved fluorescence microscopy (see below). Much progress has since been made in recognizing the important fundamental parameters. Solutions have been found for technological problems such as efficient detection in scattering samples and effective commercial instrumentation has been created. This has resulted in many important biomedical research problems being successfully attacked using MPM (see below), in particular those requiring visualization of dynamic cellular processes. One of the main areas of application has been high-resolution imaging inside highly scattering brain tissue *in vitro* and *in vivo*.

The goal of this chapter is to elaborate on the physical principles of MPM, and to point out their relevance to actual instrument design, including the selection of the appropriate laser light source. We also discuss the challenges related to chromophore selection and characterization and then list some of the applications where MPM has made a difference.

PHYSICAL PRINCIPLES OF MULTI-PHOTON EXCITATION AND THEIR IMPLICATIONS FOR IMAGE FORMATION

Physics of Multi-Photon Excitation

How and why is MPE different from 1PE and how does this lead to the unique properties of MPM? Because most aspects become clear when considering 2PE, we will discuss mostly 2PM and point to differences with higher orders where necessary. We will especially explore the complications involved in determining reliable numbers for multi-photon absorption cross-sections and why and how the temporal structure of the excitation light can affect imaging performance.

Winfried Denk • Max-Planck Institute for Medical Research, Heidelberg, Germany
David W. Piston • Molecular Physiology Biophysics, Vanderblt University, Nashville, Tennessee 37323
Watt W. Webb • School of Applied and Engineering Physics, Cornell University, 212 Clark Hall, Ithaca, New York 14853

Handbook of Biological Confocal Microscopy, Third Edition, edited by James B. Pawley, Springer Science+Business Media, LLC, New York, 2006.

2PE as used here refers to the *simultaneous* absorption of two photons of longer, not necessarily identical, wavelengths, λ_1 and λ_2, that combine their energies to cause a molecular excitation that would otherwise require a single photon with a shorter wavelength $(\lambda_1^{-1} + \lambda_2^{-1})^{-1}$. This situation is distinct from *sequential* two-photon absorption (2PA), not considered here, where the molecule is excited into an intermediate (metastable) state by the first photon, and from there into the final state by the second photon.

The transition probability for simultaneous 2PA depends (as mentioned above) on the square of the instantaneous light intensity. The use of brief but intense pulses, therefore, increases the average two-photon absorption probability for a given average incident power. It is desirable to minimize the average excitation power to minimize undesirable 1PA, which can occur all along the excitation beam and is usually responsible for most heating (see below) and may also cause photodamage directly. The multiphoton "advantage" (defined below) for *n*-photon excitation is proportional to the inverse excitation duty cycle to the n^{-1} power. For example, using 100 fs (1 fs = 10^{-15} s) duration pulses at a 100 MHz repetition rate leads to 100,000-fold and 10^{10}-fold improvements over CW illumination for 2PA and 3PA, respectively. The use of such short pulses and small duty cycles is, in fact, essential to permit image acquisition within a reasonable time while using biologically tolerable power levels. What constitutes a tolerable power level is, however, hard to define and depends on sample properties, as well as imaging parameters such as magnification and scan speed. With high numerical-aperture (*NA*) diffraction-limited illumination, tolerable average power levels are generally around a few milliwatts at the focal spot. Due to losses in instrument optics and sample, source laser powers of over 1 W may still be needed for deep imaging in scattering tissue (Denk, 1996).

The probability p_a that a fluorophore at the center of the focus absorbs a photon pair during a single pulse is, using the paraxial approximation, given by Denk and colleagues (1990):

$$p_a = \delta \langle P \rangle^2 F_p^{-1} \left(\frac{\pi NA^2}{2\pi \hbar c \lambda} \right)^2 \xi, \qquad \textbf{(1)}$$

which depends linearly on the two-photon cross-section δ, quadratically on the average power $\langle P \rangle$, on the fourth power of the *ANA*, and inversely on the repetition frequency F_P; λ, c, $\hbar$ are the wavelength, the speed of light in vacuum, and the Planck quantum of action, respectively; the two-photon "advantage" factor ξ, is calculated as follows:

$$\xi = \frac{\langle P^2 \rangle}{\langle P \rangle^2} = \frac{(t_1 - t_2) \int_{t_1}^{t_2} P^2(t) dt}{\left(\int_{t_1}^{t_2} P^2(t) dt \right)^2}, \qquad \textbf{(2)}$$

with $(t_1 - t_2) = F_p^{-1}$. For a pulse that is Gaussian in time (see below) with a width τ_p (time between the half-power points) one finds $\xi \approx (F_p \tau_p)^{-1} 0.664$, and for a pulse with a hyperbolic-secant shape the quite similar value of $\xi \approx (F_p \tau_p)^{-1} 0.558$.

A curious property of 2PE (but not of >2 PE) is that, in spite of the strong *NA* dependence of the peak excitation rate, the *total* amount of 2PE arising from a focused laser beam in a homogeneous distribution of fluorophores is independent of *NA*. This can be understood intuitively by realizing that the decline of the peak 2PA probability by reducing *NA* is exactly compensated by an increase in the focal volume, and thus an increase in the number of fluorophores in the excitation region. The total absorbed power can be calculated using a slightly modified form of Eq. 4 of Birge (1986):

$$p_{abs} = \frac{\delta C \langle P \rangle^2 \eta \xi}{2\pi \hbar c} \qquad \textbf{(3)}$$

where C is the chromophore concentration and η is the refractive index.

The quantum-mechanical selection rules for 2PA differ from those for 1PA (Birge, 1979, 1986; Friedrich and McClain, 1980; Loudon, 1983). In fact, for isolated atoms a transition allowed for 1PA would be strictly forbidden for 2PA and vice versa. However, due to their reduced symmetry and the effect of molecular vibrations, strict parity selection rules do not usually hold for complex dye molecules (McClain, 1971).

A number of heuristic rules for the expected two-photon spectra can nevertheless be formulated when the single-photon spectrum is known: (1) Some 2PE usually occurs at a particular λ whenever 1PE occurs at $\lambda/2$. (2) Additional features appear, if at all, on the short wavelength side of the spectrum. (3) Two-photon spectra are generally broader than single-photon spectra. (4) Good (strongly absorbing) single-photon fluorophores are often *very* good two-photon fluorophores, whereas bad single-photon absorbers tend to be *very* bad two-photon absorbers. The absence of additional long-λ features is simply due to the fact that, toward longer wavelengths, the combined energy of the photons is no longer sufficient to reach the excited state. Both rules 2 and 3 arise because single-photon inaccessible states with higher energy that have no direct wave-function overlap with the ground state can often be reached with two-photon excitation through intermediate (virtual) states that do overlap with both the initial and the final state (Mortensen and Svendsen, 1981; Loudon, 1983; Birge, 1986). Rule 4 arises because, as the two-photon excitation process uses the typical transition matrix element twice, its size affects the two-photon cross-section quadratically.

Equation 1 is only correct as long as the probability P_a for each fluorophore to be excited during a single pulse is much smaller than one. The reason for this is that during the pulse (given a pulse length of about 100 fs and a typical excited-state lifetime τ_f in the nanosecond range), the molecule has insufficient time to relax to the ground state, which is a prerequisite of being able to absorb another photon pair. Therefore, whenever P_a approaches unity, saturation effects begin to occur. In a strongly focused beam with pulse lengths and repetition rates as mentioned above, average power levels of several tens of milliwatts were estimated to cause saturation (Denk *et al.*, 1990). However, the use of recently developed fluorophores and, particularly, of quantum nanoparticles with large two-photon cross-sections can lead to saturation at much lower power levels. Because saturation depends on the location within the focal spot, the point spread function is altered in a way that reduces the resolution. For comparison, the power levels leading to ground-state depletion in single-photon excitation are on the order of 1 mW (see Chapter 2, *this volume*). Often (but not always) the desirable time between pulses is around τ_f because slower repetition rates leave the fluorophore idle between pulses, thus lowering the saturation limit on fluorescence output, and faster repetition rates erode the two-photon advantage ξ, raising the required average power to achieve a particular fluorescence level. Repetition rates of around 100 MHz (one pulse every 10 ns), which are common in commercially available mode-locked lasers, are thus in the desirable range even though somewhat higher repetition rates can reduce saturation and nonlinear bleaching effects

when high fluorescence rates are needed and average power is not limiting.

Saturation due to ground state depletion limits the amount of two-photon excitation power that can be usefully directed into a single, diffraction-limited spot and thus limits the maximally available fluorescence power and hence the signal acquisition rate. Given sufficient laser power, simultaneous illumination of multiple focal volumes (e.g., with line or microlens-array illumination (Chapters 10 and 29, *this volume*) (Brakenhoff *et al.*, 1996; Straub and Hell, 1998; Egner and Hell, 2000; Andresen *et al.*, 2001) can evade this image-rate limitation by a factor given by the number of simultaneously illuminated focal volumes (n_s). It is, however, necessary to use either n_s descanned detectors (see below), or an imaging detector. This, in turn, precludes the use of multi-spot excitation in strongly scattering specimens (see below).

Optical Pulse Length

It might appear that in order to increase the two-photon advantage the excitation pulses should be as short as possible. This is not so mainly for two reasons: first, and of greater practical importance, is the fact that during propagation through optical materials and reflection off multi-layer dielectric coatings, pulses are spread in time due to group velocity dispersion (GVD). This effect, illustrated in Figure 28.1, is due to the fact that the light in ultrashort pulses consists of quite a range of optical frequencies, and thus wavelengths. A 70 fs pulse centered at 800 nm, for example, is spread over 13 nm in wavelength. For a Gaussian pulse (intensity as a function of time t: $n(t) \propto \exp\lfloor -4\ln(2)(t-t_0)^2\tau_p^{-2}\rfloor$ with a pulse width τ_s (between the points of half maximum intensity) the so-called "transform-limited" bandwidth ($\Delta\lambda$), where the phases of all wavelength components are arranged to yield the shortest pulse possible, is related to the spread in optical frequencies (Δf) by: $\tau_p = 2\ln(2)\pi^{-1}\Delta f^{-1} = 0.441271/\Delta f$, where $\Delta f = c\Delta\lambda/(\lambda_c^2)$, with λ_c the center wavelength. GVD arises in optical materials as wave packets of different wavelength travel with different speeds, determined by their *group* velocities $c_g = \partial\omega/\partial k = \partial(ck/\eta)/k = c/\eta - ck(\partial\eta/\partial k)/\eta^2$ (not to be confused with the *phase* velocity $\omega/k = f\lambda = c/\eta$) where ω is the angular frequency, k and λ, are, respectively, the wave number and the wavelength *inside* the material, and c is the speed of light in vacuum, and η is the refractive index. For a given optical path, the accumulated GVD then gives rise to a certain amount of group delay dispersion (GDD), i.e., light from the red end of the spectrum arrives at a different, usually earlier, time than light from the blue end. This leads to a chirped (frequency swept) pulse that is longer than the original pulse but still contains (at unchanged spectral density) the same optical frequencies and hence wavelengths. Because the pulse's total energy content is unchanged by GDD, chirping always reduces the peak intensity and hence the average squared intensity, which, in turn, determines the two-photon excitation probability. The difference in the arrival times increases with increasing $\Delta\lambda$, and because shorter pulses have a broader spectrum (see above), they are, for a given amount of GDD, stretched more than longer pulses. This effect is compounded by the fact that the same amount of stretching lengthens a shorter pulse by a larger fraction of its original length τ_p^0. Therefore, the two-photon advantage ξ, which depends on τ_p, is degraded by a pulse-broadening factor depending on the inverse square of τ_p^0. For a Gaussian pulse we find for the spread pulse

$$\tau_p = \tau_p^0\sqrt{1+\left[4\ln(2)l\varsigma/\tau_p^2\right]^2}, \qquad \textbf{(4)}$$

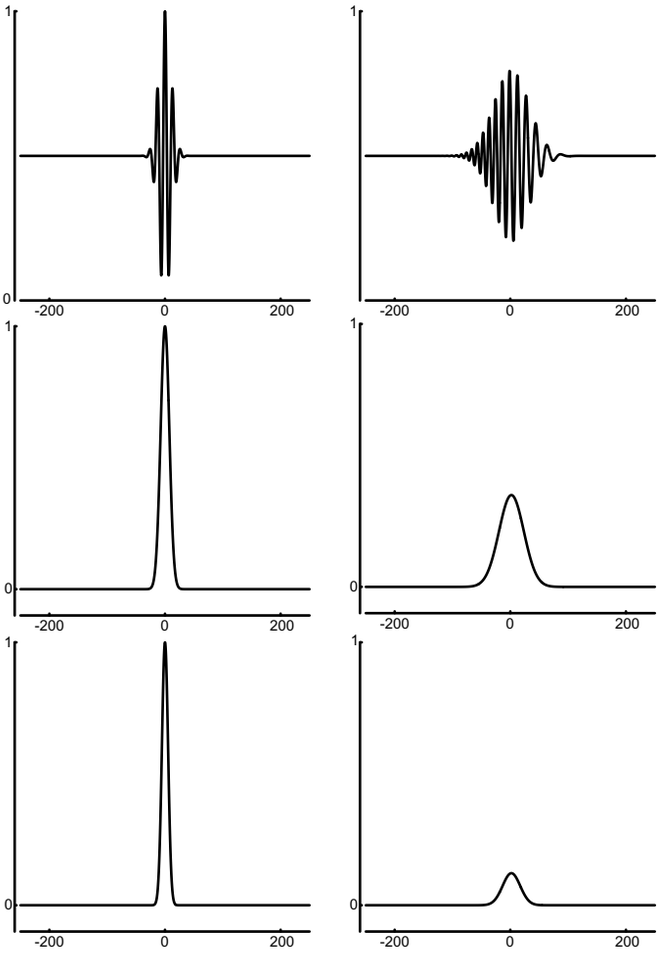


FIGURE 28.1. Simulating the effect of group velocity dispersion (GVD) on the pulse shape of an ultrashort pulse. The pulse has initially a FWHM width of 40 fs and is then dispersed by about 1250 fs² of GDD (corresponding to about 35 mm of fused silica or less than 5 mm of SF59 glass). For comparison the electric field (top row of panels), the intensity (middle row), and the squared intensity (bottom row; corresponding to the two-photon excitation efficiency) are shown both without (left column) and with dispersion (right column). An unrealistically long center λ (4000 nm) was chosen in order to emphasize the chirping effect. In reality (for 900 nm light), a 30 fs pulse would be 10 full cycles long rather than about 2 cycles as shown here.

where l is the length of the light path inside the material and $\varsigma = c^{-1}\,\partial^2(\eta\omega)/\partial\omega^2$ the GVD parameter. Therefore, for a given amount of GDD ($l\zeta$) there is an optimal τ_p^0 that leads to the shortest τ_p after passing the group-velocity-dispersing elements. For example, for 1 cm of fused silica, with $\varsigma = 362\,\text{fs}^2/\text{cm}$ at $\lambda = 800$ nm, the shortest τ_p (≈45 fs) is obtained for $\tau_p^0 = 30$ fs. Highly corrected lenses often use optical glasses that have considerably larger GVDs, and in most microscopes, light passes through considerably more than 1 cm of glass. For example, GVD values at 800 nm are 338, 453, 447, 870, 1187, 1193, 1896, 2236, and 2936 fs²/cm for the Schott glasses FK51, BK7, BKI, LFS, SF2, TiF6, SF11, SF57, and SF59, respectively (calculated from refractive index data in the Schott glass catalog; Schott Glass Technologies, Duryea, PA). The GDDs of microscope objectives and whole laser-scanning microscopes have been explored experimentally and theoretically (Guild *et al.*, 1997; Muller *et al.*, 1998; Wolleschensky *et al.*, 1998). The effects of GDD in MPM are discussed again below.

In theory, broadening that is due to the GDD can be compensated by prechirping the pulse (giving the blue wavelengths a head start), using a prism or grating arrangement (Fork *et al.*, 1984) in such a way that different wavelengths arrive at the sample almost simultaneously after passing the microscope optics. However, in view of the added alignment complexity and possible power losses in the compensation optics as well as the need for readjustment to a different GDD value for each objective lens and excitation wavelength, it has to be carefully weighed whether prechirping is worth the effort, as it might well be if single-photon absorption or lack of laser power are an issue. It is worth noting (Eq. 4) that for large amount of GDD the pulse length roughly increases linearly with the amount of GDD, but small amounts affect the pulse length disproportionately less.

Even if pulse broadening by GDD is completely compensated, there is a second factor putting a lower bound on the optimal τ_p^0. As the λ spectrum broadens with the shortening of the pulses, it will eventually become wider than the absorption spectrum of the chromophore. This limit is, however, not pressing because most chromophores used in fluorescence microscopy have spectra between 20 and 50 nm wide (full-width half-maximum, FWHM), for which pulses with a length of 23 and 9 fs, respectively, have a matched (doubled) spectral width at 700 nm. A very interesting development in this context is the use of coherent control techniques that apply complex phase relationships between the different λ components to select particular excitation pathways (see, e.g., Walowicz *et al.*, 2002; Lozovoy *et al.*, 2003).

Excitation Localization

Most of the properties that make MPM so useful for fluorescence microscopy derive from the quadratic or stronger dependence of the excitation probability on the excitation light intensity. In a strongly focused excitation beam, the excitation probability outside the focal region falls off with z^{-2n}, where z is the distance from the focal plane and n is the number of photons absorbed per quantum event. In a thick sample with a spatially homogeneous distribution of chromophores and for a Gaussian beam, about 80% of the two-photon absorption, and therefore 80% of the total fluorescence, occurs in a volume bounded by the e^{-2} iso-intensity surface, which for an objective lens with an $NA = 1.4$ is contained within an ellipsoid (0.3 µm in diameter and 1 µm long for $\lambda = 700$ nm) or approximately 0.1 femtoliter (µm^3) in volume (Sandison and Webb, 1994). This means that MP (unlike 1P) excitation is truly localized and as a consequence provides excellent depth discrimination, which is similar (for the 2P case nearly identical) to that of an ideal 1P confocal microscope. Because, in contrast to the 1P case, 3D resolution is due to the confinement of excitation to the focal volume, out-of-focus photobleaching and photodamage and the attenuation of the excitation beam by out-of-focus absorption do not occur, and because no spatial filter (detection pinhole) is required, none needs to be aligned. Figure 28.2 shows a comparison between an *xz*-section through a bleaching pattern that was generated by repeated 2P scanning of a rectangular area in a single *xy*-plane in a thick, rhodamine-stained Formvar layer and an *xz*-section through a bleaching pattern caused by 1P scanning. In the 1P case bleaching occurs throughout the depth of the sample.

Detection

The fact that resolution and discrimination are defined by the excitation process alone leaves substantially more freedom when choosing the detection strategy: (1) The emitted light does not have to pass through the microscope objective at all, allowing the use of emission wavelengths that are not transmitted by the objective lens but could instead be detected by a photodetector placed, for example, on the far side of the sample. (2) The emitted light does not have to be focused. Therefore, scattering of emitted light can be tolerated without any loss of detection efficiency or resolution (Denk *et al.*, 1994; Denk and Svoboda, 1997). This is especially useful in strongly scattering samples, such as brain tissue (Denk *et al.*, 1994; Yuste and Denk, 1995; Svoboda *et al.*, 1997). Furthermore, due to reduced scattering at longer wavelength, the 2P excitation wavelength (λ_{2ex}) can be focused to an adequately defined focus (which might be impossible for the corresponding λ_{1ex}). Only a vanishing fraction of the short wavelength (λ_{em}) and hence strongly scattered emission light emerges unscattered (ballistic) and could be used for confocal detection, virtually precluding the use of 1P confocal microscopy in such samples.

(3) Non-optical signals such as photo-chemically induced current signals in biological cells (Denk, 1994; Furuta *et al.*, 1999; Matsuzaki *et al.*, 2001) or photo-induced currents from semiconductor circuits (Xu and Denk, 1997, 1999) can be used to generate optically sectioned images.

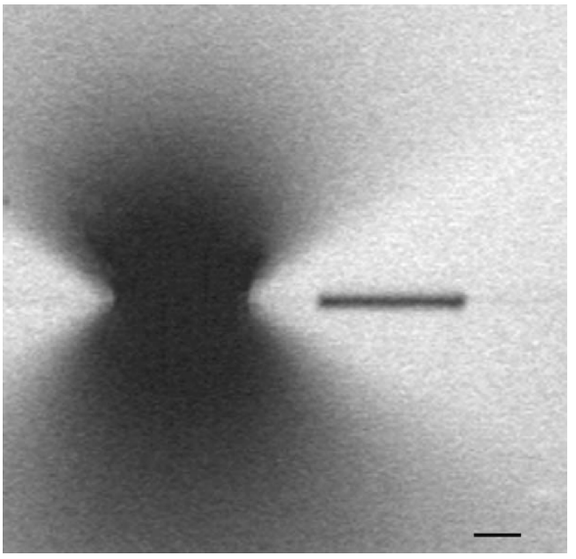


FIGURE 28.2. Confinement of photodynamic effects, such as bleaching, to the focal slice. *xz*-profiles of the bleach patterns formed by repeatedly scanning the laser focus over a single *xy* optical section in a thick film of rhodamine-doped Formvar until the fluorescence from the focal plane was largely bleached. The scanned area extends through about half the image width shown. Single-photon excitation was used on the left and two-photon excitation on the right. 1P bleaching extends throughout the sample thickness while 2P bleaching is confined to a thin region around the focal plane. The widening of the bleached region seen above and below the focal plan for 1P bleaching is due to the high NA illumination cone.

Wavelengths

The range of 350 nm < λ_{1ex} < 500 nm (700 nm < λ_{2ex} < 1000 nm) is most widely used to excite fluorescence indicators and photoactivatable compounds. The ability of MPM to reach short UV excitation energies beyond those reachable with 1PE (λ_{1ex} < 300 nm) has so far only rarely been used for imaging applications (Wokosin *et al.*, 1996b; Xu *et al.*, 1996; Maiti *et al.*, 1997; Williams *et al.*, 1999). One reason is that photodamage can occur due to MPE

by intrinsic chromophores (Rehms and Callis, 1993) in proteins and DNA (Williams and Callis, 1990). While photodamage has been insufficiently studied (there are many anecdotal reports on tissue and cell photodamage, but few non-controversial facts) it appears that longer excitation wavelengths are better tolerated by living cells and tissues, especially at high excitation intensities.

Resolution

Another important question is the resolution of 1PCM versus MPM. This was first quantitatively discussed by Sheppard and Gu (1990) and Nakamura (1993). The answer depends strongly on whether the fluorophore or the excitation energy is held fixed. Using the same excitation wavelengths, the 2PM, even without a detector spatial filter (pinhole), has a slightly improved resolution due to the lack of a Stokes-shift effect and a very small equivalent pinhole size (Sheppard and Gu, 1994). When using, more appropriately, the same fluorophore, $\lambda_{2ex} \approx 2 \times \lambda_{1ex}$, the resolution of the 2PM is degraded by a factor of almost 2 (somewhat less if the fluorophore has a large Stokes shift) compared to the ideal (zero-pinhole size) confocal microscope. However, for a realistic pinhole size (Gauderon and Sheppard, 1999), the performance of the 1PCM deteriorates, so that in practice the resolution in 1PCM and MPM is about the same. A significant resolution enhancement in multi-photon microscopy, albeit at the expense of collection efficiency (see below), can be achieved by using a detection spatial filter in conjunction with a relatively short excitation wavelength (Stelzer *et al.*, 1994). The resolution can be substantially improved in both 1PM and MPM along the axial direction by using illumination from almost all directions as with the 4-Pi microscope (Hell and Stelzer, 1992) (see also Chapter 30, *this volume*).

In conclusion, 2PE does not normally lead to resolution improvements over confocal microscopy. In fact, if resolution is of paramount importance and scattering is moderate, 1PE confocal microcopy is usually better. Recently it has been shown that stimulated emission depletion (STED) microscopy, a very different type of nonlinear optical microscopy, can overcome the far-field diffraction limit (Dyba and Hell, 2002) (see also Chapter 31, *this volume*).

Photodamage: Heating and Bleaching

Photodamage to cells and tissue can result from 1PA or MPA, depending on illumination wavelength, on type and concentration of chromophores present, and on the power level. In particular, when infrared λs are used (>900 nm), we have to consider heating due to increased absorption by liquid water, which is not a problem at visible and near-UV λs where water is very transparent (e.g., see Fig. 3 in Svoboda and Block, 1994 or Fig. 23.3, *this volume*).

For 1PE, an upper-bound estimate of the temperature rise can be made using a 2D approximation because absorption occurs all along the beam path. The calculation sketched here is the same as was used to analyze thermal lens effects (Whinnery, 1974; Kliger, 1983, and references therein). For the temperature rise T at the center of the beam ($r = 0$) as a function of the time t after switching on the beam one obtains

$$T_{2D}(t, r=0) = \frac{\alpha P}{4\pi k_T} \ln\left(\frac{2t}{\tau_c} + 1\right) \qquad \textbf{(5)}$$

where a is the absorption coefficient, P the laser power, k_T the thermal conductivity, and $\tau_c = \omega_0^2/(4\kappa)$ the thermal time constant, which is a measure of how fast steady-state conditions are approached and which depends on ω_0, the Gaussian beam parameter and is equivalent to the beam radius ($1/e^2$ intensity) in the focal plane, and on the thermal diffusivity $\kappa = k_T/\rho$ where ρ is the volume heat capacity. For a diffraction-limited beam at high-NA ($w_o = 200$ nm), $\tau_c \approx 70\,ns$ in water (using $k_w = 0.6\,WK^{-1}m^{-1}$, $\kappa_w = 1.44 \times 10^{-7}$ m^2s^{-1}) and for absorption by pure water, the pre-factor in Eq. 4 is 0.013, 0.21, and 0.66 K at λs of 700, 1000, and 1300 nm, using the absorption coefficients for water of 0.02, 0.32, and 1.0 cm^{-1}, respectively; the laser power was assumed to be 50 mW (approximately the saturating intensity; Denk *et al.*, 1990). Slightly lower values, still logarithmically diverging with time, are found if axial heat transport is taken into account (Schönle and Hell, 1998). Due to the small beam diameter, τ_c is rather short (≈70 ns) for high-NA objectives. For video-rate scanning microscopes (Goldstein *et al.*, 1992; Fan *et al.*, 1999; see Chapter 29, *this volume*) this results in a temperature rise of only 1.55 times the pre-factor but at 10 μs dwell-time (typical for non-resonant mirror-scanned instruments), the temperature rise is 5 times the prefactor. For an infinite sample no steady-state value for the temperature would ever be reached. In practice, the temperature rise will eventually be limited, by the finite sample size and by convection or bath perfusion, which remove heat at a rate much faster than heat conduction alone. For stationary applications or when continuously scanning a small area, rather large logarithmic factors can occur, however. Therefore, water absorption may have to be taken seriously, particularly at high illumination powers and long wavelengths or when attempting multi-photon excitation with CW lasers (Hanninen *et al.*, 1994, 1996; Booth and Hell, 1998; Hell *et al.*, 1998). Fast scan rates, rapid bath perfusion, thin sample cells, and, of course, maximizing the two-photon advantage using the shortest pulses possible are remedies to reduce high peak temperatures. To assess the 1P effects of infrared (IR) beams on biological specimens, we can also exploit the experience gained with optical tweezers, which are routinely used on living cells at comparable or higher power densities (Ashkin *et al.*, 1987; Svoboda and Block, 1994) and for which damage has been assessed for most of the wavelength regime used in 2PM (Neuman *et al.*, 1999).

Heating due to 2PA is restricted to the focal region. A 3D model is, therefore, appropriate. Because we are interested in the case of high-NA, we can use the approximation that the release of heat occurs uniformly within a sphere with radius ω_0 centered at the focus. The relationship one gets for the temperature rise is:

$$T_{3D} = \frac{P_{abs}}{\omega_0 4\pi k_T}\left[1 - \sqrt{\frac{2\tau_c}{2\tau_c + 3t}}\right] \qquad \textbf{(6)}$$

where P_{abs} is the total absorbed power (see below). For large t, when the square root goes to zero, T_{3D}, unlike T_{2D}, approaches an asymptotic value, given by the factor in front of the square brackets.

For high energy (mJ) pulses at low repetition rate, the local temperature rise during a single pulse can easily be large enough to cause damage, but we know little about how damage might be exacerbated for the case of pulsed light at high repetition rates ($f_R \approx 100\,MHz$) compared to the CW case with the same average power. Because τ_c is longer than the interpulse interval ($1/f_R$), the incremental temperature rise during a single pulse is smaller than the steady-state temperature rise T_{3D} ($t = \infty$) roughly by a factor of $\tau_c F_r$.

We conclude that heating during high-repetition-rate pulsed illumination can largely be treated like CW illumination and is often negligible at practical 2PM parameters. Attention has to be paid to situations where high local concentrations of chromophore

occur, as, for example, for DNA stains, which can bind at a concentration of one per base pair or where equilibration of the molecular temperature with its environment cannot be automatically assumed (Akaaboune *et al.*, 2002).

Because of the localization of excitation to the focal volume, total photobleaching in MPM is generally much reduced compared to 1PE microscopy. However, it has been shown that an increased photobleaching rate from within the focal volume can occur by a mechanism where the fluorophore is initially excited by simultaneous 2PA, and then one or more photons interact with the excited molecule, possibly via higher-order resonance absorption (Patterson and Piston, 2000). This effect can be quite pronounced for readily photobleachable dyes, such as fluorescein, where the difference between one- and two-photon photobleaching rates can be a factor of 10 at the power levels that are typically used in biological imaging (100 µW CW for single-photon excitation, and 3 mW 150 fs pulses for MPM). However, for more stable dyes, such as the green fluorescent proteins (GFPs), carbocyanines, and AlexaFluors, the photobleaching rate is in our experience often too small for the difference to be measurable at the usual imaging intensities. While in some cases direct higher-order absorption (three or more photons) may be relevant, several studies (Koester *et al.*, 1999; Konig *et al.*, 1999) have found that longer pulses (which reduce higher-order absorption) do *not* reduce the damage done per excitation event.

INSTRUMENTATION

Setup (Fig. 28.3) and operation of a MPM system are very similar to those of a 1P laser-scanning microscope. The main differences lie in the type of excitation lasers and in the increased number of options for detection. In this section we will discuss laser sources suitable for MPE, the advantages and drawbacks of the various methods of detecting fluorescence and other contrast signals, and specific problems that occur with non-mechanical (e.g., acousto-optical) beam power control and deflection. We assume that the reader of this chapter is familiar with the principles of 1PCM (other chapters, *this volume*). Short shrift will, therefore, be given to those aspects such as mechanical beam scanning, data collection, storage, and display that are largely identical for 1PCM and MPM instruments. The potential user should also be aware that MPMs are relatively easy to set up and are now available as integrated systems from several manufacturers. MPM systems are still expensive with the price of the laser system (>$150,000) being between one third to one half of the total system cost. With a mode-locked laser, one has, however, also acquired the light source necessary to do time-resolved fluorescence measurements (Piston *et al.*, 1992; Zhang *et al.*, 2002; and Chapter 27, *this volume*).

Lasers and the Choice of Excitation Wavelengths

CPM Laser

The first 2P images (Denk *et al.*, 1990) and 2P photochemical microcopy images (Denk, 1994) were recorded using colliding-pulse mode-locked (CPM) lasers (Valdmanis and Fork, 1986) at 615 nm excitation wavelength. Today this laser type is of only historical interest.

Hybrid Mode-Locked Dye Laser

Another early type of ultrashort pulse dye laser system is the hybrid mode-locked dye laser. These systems use an actively mode-locked argon-ion or a frequency-doubled neodymium: YAG

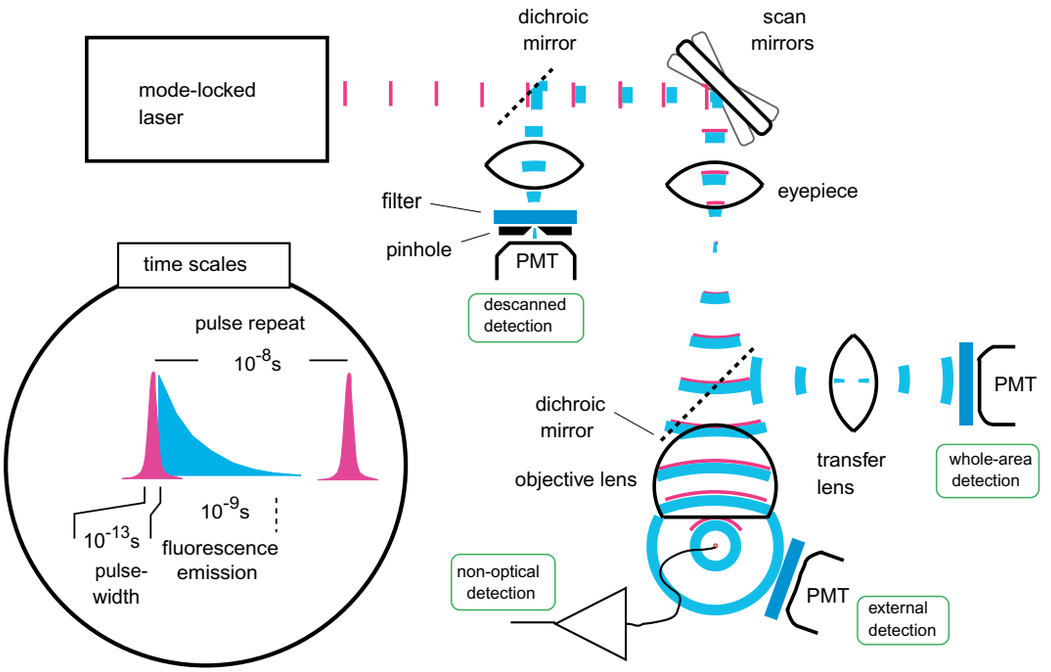


FIGURE 28.3. Schematic diagram of a two-photon laser-scanning microscope illustrating various detection possibilities. The stream of incoming laser light pulses is raster scanned (*xy* scanner, only one axis is shown here) in a way that is identical to the single-photon LSM. For fluorescence microscopy, several detection possibilities are indicated: (1) ***external***: fluorescence light bypasses objective lens; (2) ***whole-area***: fluorescence light passes objective lens and is then deflected by a dichroic mirror to be focused onto the detector by a transfer lens; (3) ***descanned***: as in the 1PLSM, the fluorescence light is reflected off the scanning mirrors, allowing confocal detection (see text). Not shown, but possible and occasionally used, is ***focal-array*** detection, where, after deflection by a dichroic mirror, fluorescence light is detected by an array detector located in an image plane. Yet another possibility is ***non-optical*** detection using, for example, an electrically recorded signal from the sample. Time scales are indicated in the left inset.

laser to pump a dye laser that also contains an intracavity saturable absorber jet. Such systems are rather expensive and difficult to operate and are therefore rarely used for multi-photon imaging. The remaining advantage over the titanium : sapphire laser (see below) is the access to the range 550 nm < λ < 700 nm, which is desirable for some uncaging experiments but has been virtually abandoned for imaging due to photodamage problems (Kiskin *et al.*, 2002).

Titanium : Sapphire Laser

For most applications, the light source of choice for MPM currently is the self-mode–locked titanium : sapphire (Ti : Sa) laser (Spence *et al.*, 1991), nowadays pumped by a frequency-doubled diode-pumped Nd : Vanadate laser rather than a power- and cooling-water hungry argon-ion laser. The Ti : Sa laser provides a large tuning range (from slightly below 700 nm to slightly above 1050 nm) with pulse lengths shorter than 100 fs and sufficient power (2 W average at the peak of the tuning curve, down to a few hundreds of milliwatts at the edges when pumped with 10 W) to permit saturating excitation (see Physical Principles) of most fluorophores with a high-NA objective over much of the laser's tuning range. The tuning range of Ti : Sa is now covered by a single set of cavity mirrors, with optics changes only required to reach wavelength above 1000 nm or below 700 nm. Currently, several manufacturers offer turnkey laser systems that contain the pump source and Ti : Sa laser inside a single housing, are computer controlled, and no longer require any mechanical adjustments by the operator.

Other Light Sources

If losses in the excitation path are too large, it is sometimes not possible to achieve the desired excitation rates with the multi-photon advantage factors available for a laser oscillator alone. A reduction in repetition rate while maintaining average power can then increase the excitation efficiency substantially (Beaurepaire *et al.*, 2001). This can be achieved by increasing the cavity length, cavity dumping, or regenerative amplification. The last approach has recently been shown to allow imaging down to the surface-generated-background limit (Theer *et al.*, 2003). Direct use or frequency doubling of femtosecond pulses from optical parametric oscillators (OPO) (Cheung and Liu, 1991; Fu *et al.*, 1992; Powers *et al.*, 1994; Keller, 1996) may provide an almost universal, if expensive, solution to cover almost all of the desired wavelength range.

One factor limiting multi-photon microscopy is the cost of the laser source, which, in spite of early hopes, has not come down significantly with the introduction of diode pumping (for a review, see Keller, 1994). One reason is that gain materials that can be directly diode-pumped (Keller, 1996) have insufficient tuning ranges and/or unfavorable thermal characteristics.

In niche applications, other sources (Wokosin *et al.*, 1996a) have been used, partly within, for example, the Cr : LiSaF laser (Svoboda *et al.*, 1996a) or outside, for example the Cr : Forsterite laser (Liu *et al.*, 2001), the Ti : Sa tuning range.

Excitation Wavelengths

One reason for the success of the Ti : Sa laser for MPM is that the range 700 nm < λ_{2ex} < 1050 nm (corresponding to 350 nm < λ_{1ex} < 525 nm) covers the range of excited state energies for many commonly used fluorophores (see below). Much shorter wavelengths, in particular λ_{2ex} < 640 nm, are likely to cause photodamage due to intrinsic absorption, for example, by tryptophan rich proteins (Rehms and Callis, 1993). To minimize scattering one might lengthen the excitation wavelengths and take advantage of a dip in the absorption spectrum of water around 1040 nm, which is well known from optical trapping experiments (Svoboda and Block, 1994). Fortunately, a large selection of microscope lenses has become available with excellent transmission and optical correction in the near IR (Chapter 7, *this volume*). The use of older lenses that were not designed for the infrared can be problematic, particularly in the case of highly corrected lenses (Neuman *et al.*, 1999), where non-optimal performance of the antireflective multi-layer coatings on each of the numerous internal surfaces can reduce overall transmission catastrophically.

Beam Delivery and Power Requirements

In general, the laser is mounted on the same vibration isolation platform as the microscope because delivery of ultrashort pulses through standard, single-mode fibers, which is possible in principle (Wolleschensky *et al.*, 1998) (see also Chapter 26, *this volume*), requires substantial technical efforts to prevent unacceptable pulse broadening at the laser powers routinely required. Development of special optical fibers, such as photonic band gap fibers or large cross-section single-mode fibers (Helmchen *et al.*, 2002; Ouzounov *et al.*, 2002), may facilitate MPM applications where fiber delivery is essential (Helmchen *et al.*, 2001). In non-absorbing, non-scattering samples saturating pulse energies (corresponding to several tens of milliwatts of average power) can easily be reached over most of the Ti : Sa tuning range even with 5 W of green pump power. However, one rarely has more than the desirable power in scattering samples such as in brain slices or the intact brain. Power availability may also be limiting when attempting to optimize resolution by overfilling the objective back aperture.

Detection

As discussed above, excellent 3D localization is accomplished in MPM by excitation alone. This allows more flexibility in the optical design and, as a consequence, considerable improvements of fluorescence collection efficiency are possible compared to the 1PCM. Figure 28.3 depicts the various options. The positions of non-imaging detectors are designated PMT because photomultiplier tubes are usually the detectors of choice for MPM. In general, considerations as to which detector type to use in MPM are quite similar to those for 1PCM, and the reader is referred to Chapter 12 of this book. Among non-imaging schemes (one or a few detector elements), the main distinction is whether the emitted light passes back through the scanning mirrors (*descanned* detection) or whether the detector is sensitive to emitted light from the whole image area at all times (*whole-area* detection). A variant of the latter is *external* detection, where detected light does not pass through the objective lens.

Whole-Area and External Detection

Whole-area detection (WAD) (Piston *et al.*, 1992, 1994) is now the detection mode of choice in the majority of MPM applications. The WAD pathway uses a dichroic mirror somewhere between the scanner and the objective to separate excitation and fluorescence (alternatively the excitation light can be coupled in by reflection from a dichroic), preferably after a minimum number of optical surfaces to maximize detection efficiency. The signal is then passed through the collection optics, which needs to avoid vignetting. If the back aperture of the objective is conjugate to the photocathode of the PMT the effect of spatial heterogeneities in the photocathode sensitivity is reduced. One of the main advantages of WAD is the ability to efficiently collect fluorescence from

specimens that scatter light at λ_{em} so strongly that only a very small fraction can be refocused for confocal detection (Denk *et al.*, 1994; Denk and Svoboda, 1997; Beaurepaire and Mertz, 2002).

WAD is as vulnerable to contamination from ambient room light as is widefield imaging with highly sensitive cameras. One thus loses a convenient but rarely essential advantage of confocal imaging. While WAD through the excitation lens is usually the most convenient and efficient mode, external detection, where the detected light bypasses the objective lens, can be necessary when light needs to be detected that cannot (e.g., because it is of too short a wavelength) or did not (e.g., because it went off in the wrong direction) pass the objective. Combining through-the-lens collecting with collecting the light passing through the condenser has been used successfully to increase the signal-to-noise ratio in embryo (Denk *et al.*, 1997) and in brain slice imaging (Koester and Sakmann, 1998; Mainen *et al.*, 1999a, 1999b).

Another disadvantage of WAD is that detectors with a large "phase-space volume" (given by the product of detector area and acceptance angle) are needed thus ruling out the use of small-area photon-counting avalanche photodiodes (Tan *et al.*, 1999) or of spectrometers (Lansford *et al.*, 2001).

Descanned Detection

When converting a confocal microscope to multi-photon operation (Denk *et al.*, 1990) descanned detection naturally results. While this mode is less efficient than WAD, even for clear specimens, descanned detection does allow the use of detectors with small apertures such as avalanche photodiodes or spectrometers. A pinhole that is several times larger than the optimal confocal size can be useful for excluding room light contamination from the detected signal while still being near optimal for signal collection.

The use of a confocal pinhole as a tight spatial filter in addition to multi-photon excitation (Stelzer et al., 1994) is rarely used because it is fraught with several drawbacks: (1) A pinhole small enough to produce any substantial increase in resolution causes a large drop in detection efficiency due to the fact that the diffraction-limited volume at the λ_{em} is smaller than the excitation volume determined by the λ_{2ex} because $\lambda_{em} < \lambda_{2ex}$. Such a loss of detection efficiency is particularly serious because fluorescence imaging of living specimens is often limited by photobleaching and photodamage. A technically complex yet feasible solution to this problem might be to use a small array of detectors together with the appropriate deconvolution algorithms (Sheppard and Cogswell, 1990).

Chromatic aberration, already a problem in 1PCM, is exacerbated in the confocal operation of MPM because the typical shift between λ_{2ex} and λ_{em} is much larger ($50\,\text{nm} < \lambda_{em} - \lambda_{1ex} < 200$ for 1PE, $200\,\text{nm} < \lambda_{2ex} - \lambda_{em} < 500$ in 2PE, and further increasing with >2 PE).

Non-Optical Detection

A number of non-optical detection schemes have become very promising owing to the high degree of spatial localization achieved during excitation alone. Two-photon scanning photochemical microscopy (Denk, 1994; Furuta *et al.*, 1999; Matsuzaki *et al.*, 2001) generates images of receptor distributions by locally releasing agonists such as neurotransmitters from "caged" precursors and detecting the agonist-induced ionic current in voltage-clamped cells. In fact this concept was one of the motivating factors for the initial development of MPM. Opto-acoustic detection, which has been used to measure two-photon absorption coefficients (Patel and Tam, 1981; Bindhu *et al.*, 1998) could be used to measure spatially resolved absorption that is not accompanied by fluorescence or induced current, but has to date not been tried as a contrast mechanism in MPM.

Focal-Plane Array Detection

A rather different strategy, which does not rely on scan-synchronized detection to build up the image, is the use of an imaging detector. As in conventional fluorescence microscopy, the fluorescence is refocused to an image plane, and the image is generated by spatially sorting the fluorescence photons into the pixels of an array detector such as a charge-coupled device (CCD). The lateral resolution is then determined solely by λ_{em}, which is considerably shorter than λ_{2ex}. The optical sectioning effect due to two-photon excitation is, however, retained and provides discrimination and resolution in z-direction. This method is the equivalent of widefield fluorescence microscopy with only a thin focal slice rather than the whole thickness of the sample excited. Focal array detection is particularly useful in connection with multi-point illumination, where it allows the acceleration of image acquisition (Straub and Hell, 1998; Egner and Hell, 2000; Andresen *et al.*, 2001; Fittinghoff *et al.*, 2001; Hell and Andresen, 2001; Nielsen *et al.*, 2001; Egner *et al.*, 2002). The main disadvantage of focal array detection is that, different from the case of single-point scanning, with whole-area detection, scattering of fluorescence light leads to an immediate degradation of image contrast and resolution.

Optical Aberrations

Aberrations inherent in the microscope and spherical aberration introduced by focusing through refractile layers such as the coverslip, immersion oil, and sample (Sheppard and Cogswell, 1991; Hell *et al.*, 1993) broaden the focus, shift the apparent focal point (Visser *et al.*, 1991), and reduce the peak excitation intensity. Due to the mathematical equivalence between the optical transfer function of the non-confocal 2PM and that of the confocal 1PM (Sheppard and Gu, 1990; for a minor modification, see Visser *et al.*, 1991), the effects of monochromatic aberrations, such as spherical aberration and astigmatism, on the amplitude and resolution of the detected signal are the same in both cases. In the two-photon case, however, the number of molecular excitations is actually reduced due to the smeared-out focus spot and the intensity-squared dependence of the excitation probability (see above). When photobleaching or photodamage are the limiting factors, this can provide a significant advantage of MPM over the 1PCM case, where the same number of excitations occur, but the fraction of the emitted light that reaches the detector is reduced. Nonetheless, one must take the same precautions with MPM as with 1PCM when interpreting absolute light levels as a function of focusing depth. Note also, that most aberrations become rapidly less severe as *NA* is reduced. The best way to avoid spherical aberration in aqueous specimens, even at high-NA, is the use of water-immersion objective lenses, which are now widely available corrected even for the IR range (Chapter 7, *this volume*).

A significant motivation for the development of 2PM was the circumvention of the poor chromatic correction then found for most microscope lenses in the UV. Chromatic aberration problems play a role in (non-confocal) 2PM only in connection with the broad λ spectrum of ultrashort pulses (see above). However, this spread is generally smaller than a typical Stokes shift and chromatic correction is easier in the IR where glass dispersion flattens out.

Pulse Spreading Due to Group Delay Dispersion

As discussed above, the optical materials comprising the microscope optics cause the excitation pulses to spread in time and thus become less efficient in exciting multi-photon transitions. The group delay dispersion (GDD) has been measured for some objectives (Guild *et al.*, 1997; Squier *et al.*, 1998). As mentioned above, the optical effort needed to generate the prechirping necessary to compensate for the GDD has to be weighed against the improvements expected. As a general rule, GDD compensation will be helpful or even essential when laser power is limiting, such as for deep tissue imaging, or when single-photon absorption contributes to damage. If coherent control techniques are used, complete dispersion control is, of course, essential but then the optics used to tailor phases can be employed for dispersion control as well.

Control of Laser Power

For slow control of the laser power, mechanically actuated devices such as filter wheels, graded neutral density filters, or rotating half-wave-plate/polarizer combinations (Denk, 2001) can be used. Faster shuttering (e.g., in order to blank the beam during retrace) or modulation requires non-mechanical devices such as acousto-optical (AO) or electro-optical (EO) modulators (i.e., Pockels cells), which can respond on the microsecond and even nanosecond timescale (Chapter 3, *this volume*). EOMs achieve high throughput but often incomplete extinction, while AOMs are lossy, and due to limited diffraction efficiency, their extinction is excellent.

A few problems arise specifically when ultrashort pulses are used together with such devices: (1) In AOM, AOD, or acousto-optic tuning filter (AOTF) devices, an acoustic wave diffracts the incoming beam by an angle that is dependent on λ_{ex}. For ultrashort pulses, which are spectrally broad, the focus, therefore, becomes distorted and diffraction efficiency is reduced. (2) Both EOMs and AOMs use dispersive materials, which spread the laser pulse temporally (see above).

While the temporal spread can be easily compensated (in a few cases multi-photon microscopy setups already contain GDD compensators), it is much more difficult but not impossible to compensate for the angular spread in an AOM (Lechleiter *et al.*, 2002). Limited extinction from the EOMs is often not a serious problem because the quadratic intensity dependence of two-photon excitation allows even a moderate power reduction ratio to translate into almost complete elimination of unwanted excitation.

Resonance and Non-Mechanical Scanning

The time resolution of closed loop galvanometer scanners is sufficient for most applications, in particular if a limited number of measurement points can be selected. However, because the time per line cannot be reduced significantly below the about 1 ms with closed-loop scanners, scan times for large areas can become too long for the time resolution desired. One solution to this problem is the use of resonant galvanometer scanner (Fan *et al.*, 1999; see also Chapters 3 and 29, *this volume*) which provide a fixed line rate about 10 times faster, albeit at some loss of flexibility. Acousto-optical scanning (Art and Goodman, 1993) requires correction of the diffractive spread of the wavelengths comprising short-pulse light (Lechleiter *et al.*, 2002), but has the advantage of more rapid access (still limited by the acoustic transit time across the diffraction medium) and allows both scanning and intensity control.

CHROMOPHORES (FLUOROPHORES AND CAGED COMPOUNDS)

The criteria for choosing, or designing, fluorophores for MPM are essentially the same as for any other fluorescence microscopy technique: large absorption cross-section at convenient λ_{ex}s, high quantum yield, low rate of photobleaching, and minimal chemical or photochemical toxicity to living cells. In the early days of MPM, a heuristic approach prevailed and fluorophores were selected that had proven useful in widefield fluorescence microscopy or 1PCM. In most cases, two-photon excitation was found whenever there is single-photon absorption at a λ corresponding to twice the energy of the excitation photons. Most MPM imaging still uses conventional fluorophores, and we now have two-photon spectra for many of these (Xu and Webb, 1996; Xu *et al.*, 1996; Zipfel *et al.*, 2003). On the other hand, there is a considerable effort to generate chromophores tailored to MP excitation using a donor–acceptor–donor or acceptor–donor–acceptor strategy. These molecules maximize the electrical dipole transition by electron transfer over relatively long distances from donor to acceptor. By this approach, molecules can be created with two-photon excitation cross-sections about 10-fold greater than conventional fluorophores (Albota *et al.*, 1998b; Ventelon *et al.*, 1999). Nanoparticles, also called quantum dots (Bruchez *et al.*, 1998; Han *et al.*, 2001), which offer broad excitation spectra, but very narrow emission spectra, have the largest measured two-photon cross-sections seen to date. This allows their detection at very low concentrations, even *in vivo* (Larson *et al.*, 2003).

Another notable development is the movement to longer wavelengths. While in the early days of MPM the emphasis was on UV-excited dyes that were 2P-excited by red lasers, the emphasis now is on fluorophores normally excited by visible light and 2P-excited by IR light. This trend is mainly driven by the desire for lower background fluorescence and deeper penetration into scattering tissue.

Two-Photon Absorption Cross-Sections

Differences between one- and the two-photon excitation spectra have been exploited in molecular spectroscopy because they provide additional information about the structure of excited states. These differences can be quite significant, see, for example, the case of Bis-MSB (Kennedy and Lytle, 1986) or the aromatic amino acids tyrosine and phenylalanine (Rehms and Callis, 1993), but note the spectral similarities for tryptophan. As a rule of thumb, in symmetrical molecules one expects $\lambda_{2ex} < 2\lambda_{ex}$.

Calculations of two-photon cross-sections are difficult to perform for complex molecules. Direct experimental measurements of multi-photon absorption are equally difficult because even under optimal conditions, the fraction of the incident power that is absorbed is rather small (using Eq. 4 we find, e.g., $p_{abs}/p = 3 \times 10^{-5}$ for a chromophore with a cross-section of 10^{-50} m^{4}s photon^{-1}, at a concentration of 10 mM and a laser power of 100 mW with a two-photon advantage of 10^5). While thermal lensing or acousto-optical techniques have been used to measure two-photon absorption (Kliger, 1983), these techniques are much more complicated than single-photon spectrophotometry.

For fluorescent molecules, the shape of the two-photon excitation spectrum can be determined by detecting the intensity of fluorescence emission as a function of excitation wavelength. In order to determine the action spectrum, the incident average laser power (P_i), the probability of detecting fluorescence photons, and the two-

photon advantage ξ (Eq. 2) need to be known (Xu *et al.*, 1995). The absolute value of the two-photon *absorption* cross-section can then be calculated using the fluorescence quantum yield. Quite a number of measured spectra are now available in the literature (Xu *et al.*, 1996; Albota *et al.*, 1998b also includes URL.)

While precise calculations of two-photon absorption cross-sections are difficult, several new fluorophores with particularly large two-photon absorption cross-sections have been designed using theoretical considerations (He *et al.*, 1995, 1997; Marder *et al.*, 1997; Albota *et al.*, 1998a; Ventelon *et al.*, 1999, 2002; Adronov *et al.*, 2000; Kim *et al.*, 2000; Zojer *et al.*, 2002). Before such fluorophores can come into common use, however, problems with water solubility, derivatization, etc., will have to be solved.

For the fluorophores studied so far, the spectra of the emitted fluorescence were found to be essentially independent of whether excitation occurs via single- or two-photon excitation (Curley *et al.*, 1992). This is not surprising because the molecular relaxation process (on the picosecond scale) almost always occurs to the same state (the lowest excited singlet state) prior to the emission (on the nanosecond scale) and therefore erases the memory of the excitation pathway and energy.

Caged Compounds

Two-photon absorption spectra for caged compounds are more difficult to measure than those for fluorophores because the amount of uncaged material generated is too small to be easily measured with most analytical techniques. In some cases, uncaging can be detected when fluorescence assays for the released agonist exist, such as for caged ATP (Denk *et al.*, 1990), when the product itself is fluorescent, as it is with caged fluorescein (Svoboda *et al.*, 1996b), or when biological effects can be detected, such as the opening of ion channels by the two-photon–induced release of caged neurotransmitters (Denk, 1994; Matsuzaki *et al.*, 2001; Kasai *et al.*, 2002). Photochemical reactions are often much slower than fluorescence emission and their speed can strongly depend on the chemical environment such as pH and ionic strength (Milburn *et al.*, 1989; Corrie and Trentham, 1993; Kao and Adams, 1993). The speed of release is important for at least two reasons: (1) The pixel dwell-time must be at least as long as the duration of the signal used to generate image contrast, which at best is as fast as the photochemical reaction rate; (2) diffusion of the released agonist tends to blur the image and thus prevents high-resolution mapping. A delay of 10 ms, for example, allows the released agonist, typically a small organic molecule with a diffusion constant of $5 \times 10^{-9}\,m^2\,s^{-1}$, to diffuse a distance of about 3 µm (Kiskin *et al.*, 2002).

CELL VIABILITY DURING IMAGING

The survival of the biological sample while it is being imaged is one of the most important constraints on the usefulness of any vital microscopy technique. While one of the reasons for pursuing MPM as a new technique was the expectation of greatly reduced photodamage (Denk *et al.*, 1990), it has to be kept in mind that *in the focal plane*, for a given excitation rate the damage is expected to be at least as large for 2P as it is for 1P excitation. This is because any effect due to reactions initiated from the excited state of the chromophore are independent of the mode of excitation. Furthermore, it cannot be ruled out that some endogenous biological molecules have unusually large two-photon cross-sections (such as bacteriorhodopsin; Birge and Zhang, 1990) and are, therefore, particularly susceptible to damage. Another concern is the possibility of excited state absorption, particularly at excitation rates near saturation.

Considerable work has been performed in this area since the first edition of this book. Two-photon excitation, particularly when using wavelengths below 800 nm (Konig *et al.*, 1996; Oehring *et al.*, 2000) (see Chapter 38, *this volume*) can, not surprisingly, generate reactive oxygen species, which are implicated frequently in photodamage (Tirlapur *et al.*, 2001). On the other hand, when using longer wavelengths (1064 nm), generation of reactive oxygen species by flavin-containing proteins seems to be greatly reduced compared to single-photon excitation (Hockberger *et al.*, 1999).

At higher excitation levels, a steeper than quadratic power dependence is often found both for cellular photodamage (Koester *et al.*, 1999; Oehring *et al.*, 2000; Hopt and Neher, 2001) and for photobleaching (Eggeling *et al.*, 1998; Patterson and Piston, 2000). It appears, however, that the damage nonlinearity is not instantaneous (i.e., three- or four-photon excitation) because for the same mean two-photon excitation rate no change in the damage is seen with pulse width (Koester *et al.*, 1999; Konig *et al.*, 1999).

There is virtually no experimental indication that heating by water absorption (discussed in Physical Principles) is a limiting factor in multi-photon microscopy. Heating may yet become an issue as substantially longer wavelengths are beginning to be used for the excitation of long wavelength fluorophores. A number of explicit examples show an actual and significant reduction of photodamage when using two-photon rather than single-photon imaging in biological specimens such as cultured cells (Hockberger *et al.*, 1999), cardiac myocytes (Niggli *et al.*, 1994b; Piston *et al.*, 1994), and mammalian (Squirrell *et al.*, 1999) and invertebrate embryos (Summers *et al.*, 1993).

The experience of many a microscopist is that live-cell imaging can often be performed by reducing the excitation light intensity to the lowest possible level, using efficient optics and sensitive detectors (Chapters 17, 19, and 29, *this volume*). The experience in 2PM is similar, but the range of imageable specimens is larger. For example, in both the sea urchin (Piston *et al.*, 1993) and hamster embryos (Squirrell *et al.*, 1999), two-photon excitation allows extended observation of embryonic development, under conditions where single-photon excitation is unsuccessful. In another case, as part of a direct comparison of scanned laser UV and two-photon excitation (Niggli *et al.*, 1994a; Piston *et al.*, 1994), it was found that two-photon excitation allowed imaging of the calcium indicator dye Indo-1 continuously for 5 min without compromising cell viability. Equivalent single-photon scanning with UV light resulted in considerable photobleaching, and over 80% cell death (Piston *et al.*, 1994).

Those studies indicate that, even though damage is less than with conventional UV illumination, cultured-animal-cell viability can be compromised by two-photon excitation. Particularly worrying, and as yet unresolved, is the observation that at high illumination levels the two-photon photobleaching rate can increase much faster than the excitation rate (Patterson and Piston, 2000), even though it is not known whether there is a corresponding increase in phototoxicity and whether these highly nonlinear bleaching phenomena are limited to certain narrow classes of dyes, such as the xanthene dyes.

A question that often arises is how to determine the mechanism of damage. Important information is provided by its power dependence (Neuman *et al.*, 1999; Hopt and Neher, 2001). For example, two-photon photochemical damage should be proportional to the square of the incident power. While a linear power dependence all but rules out two-photon effects, a superlinear dependence on the average excitation power could result from single-photon absorp-

tion coupled with a nonlinear mediator for damage. Thermally induced damage can have a rather sharp temperature threshold due to cooperative phenomena such as protein denaturation. A definitive distinction between single- and multi-photon absorption is their dependence on pulse length; if the pulse length is varied by introducing a variable degree of GDD (see above), the spectrum, and hence the amount of linear (single-photon) absorption, remains completely unchanged while 2PA drops.

Knowing the mechanism of damage is, of course, crucial for choosing the optimal excitation strategy. For example, to reduce single-photon, dose-rate–independent damage, a reduction of F_p might seem appropriate in order to increase the two-photon advantage but the peak temperature during each pulse increases as F_p^{-1}, and can become larger than the thermal time constant. Unpleasant surprises could also arise from additional absorption by molecules already in the excited state (something that is more likely to occur when operating closer to saturation) or from proximity effects mediated by free radicals (Konig *et al.*, 1996; Hockberger *et al.*, 1999; Koester *et al.*, 1999; Konig *et al.*, 1999; Oehring *et al.*, 2000; Hopt and Neher, 2001; Tirlapur *et al.*, 2001).

APPLICATIONS

MPM has been used to address questions in quite a few areas of biology. Particularly the imaging of intact tissue has benefited from the properties of the multi-photon (predominantly two-photon) microscope.

Calcium Imaging

Intracellular messenger dynamics, such as calcium ion concentration has been measured in single cells (Piston *et al.*, 1994), but the particular advantages of MPM over single-photon techniques come to bear most in scattering tissue such as brain slices (Denk *et al.*, 1995, 1996; Yuste and Denk, 1995; Mainen *et al.*, 1999b; Sabatini and Svoboda, 2000; Wang *et al.*, 2000; Oertner *et al.*, 2002), the stomatogastric ganglion (Kloppenburg *et al.*, 2000), and *in vivo* (Svoboda *et al.*, 1997, 1999; Debarbieux *et al.*, 2003). In isolated retina 2PM allowed the recording of dendritic calcium signals during visual stimulation (Denk and Detwiler, 1999; Euler *et al.*, 2002).

Uncaging and Photobleaching

Multi-photon photochemistry has been used to map receptor sensitivities in single cells (Denk, 1994) and inside neural tissue (Matsuzaki *et al.*, 2001; Kasai *et al.*, 2002).

Autofluorescence

Because MPM easily reaches into UV transition energies, it has increasingly been used to study biological autofluorescence such as from NADH (Piston *et al.*, 1995; Piston and Knobel, 1999), serotonin in living cells (Maiti *et al.*, 1997), skin (Masters *et al.*, 1997), muscle cells (Schilders and Gu, 1999), glutathione in arabidopsis (Meyer and Fricker, 2000), mast cell secretion using 3P excitation of serotonin (Williams *et al.*, 1999), arctic fungus (Arcangeli *et al.*, 2000), collagen (Agarwal *et al.*, 2001), biofilm (Neu *et al.*, 2002), tryptophan in proteins (Lippitz *et al.*, 2002), and flavoproteins (Huang *et al.*, 2002). Recently, the sources of autofluorescence from living tissue have been analyzed in more detail (Zipfel *et al.*, 2003) (see also Chapter 21, *this volume*).

Developmental Biology

Because of the superior depth penetration and the localized excitation associated with MPM, this approach has proven useful in many developmental biological applications. Lineage tracing has been performed using two-photon photorelease of caged fluorophores in sea urchin embryos (Summers *et al.*, 1996; Piston *et al.*, 1998). Cellular and subcellular dynamics have been imaged and measured using MPM during development of sea urchin embryos (Summers *et al.*, 1993, 1996), cell fusion in *C. elegans* (Mohler *et al.*, 1998; Periasamy *et al.*, 1999), mammalian embryos (Squirrell *et al.*, 1999), zebrafish (Huang *et al.*, 2001), and birds (Dickinson *et al.*, 2002).

In Vivo (Intact Animal) Imaging

In intact animals, the need for tissue penetration is maximal. High resolution optical imaging inside living whole animals has therefore become the almost exclusive domain of two-photon microscopy not only for functional calcium imaging (Svoboda *et al.*, 1997, 1999), but also to image blood flow in the fine capillaries (Kleinfeld *et al.*, 1998; Chaigneau *et al.*, 2003), gene expression and angiogenesis (Brown *et al.*, 2001), and even the dynamics of Alzheimer's disease pathologies (Christie *et al.*, 1998, 1999, 2001; Backskai *et al.*, 2001) and, having previously been applied to observe changes in dendrite structure in brain slices (Engert and Bonhoeffer, 1999; Maletic-Savatic *et al.*, 1999), two-photon microscopy has most recently been used to study the long-term dynamics of neuronal fine structure (Grutzendler *et al.*, 2002; Trachtenberg *et al.*, 2002) in living animals.

OUTLOOK

Multi-photon excitation microscopy has extended the range of laser scanning fluorescence microscopy especially where dynamic imaging in living specimens is needed. Much progress has been made in solving many of the technical impediments that existed in the early days of MPM. Still, only a few of the many potential contrast mechanisms established for nonlinear optical spectroscopy have been used for imaging purposes. This is mainly due to the fact that often only a small number of photons can be collected from each volume element in the small amount of time that the beam dwells on each location. Increasing use is being made, however, of second harmonic generation (Moreaux *et al.*, 2001) and Raman scattering (Zumbusch *et al.*, 1999; Potma *et al.*, 2002; Volkmer *et al.*, 2002) (see also Chapter 33, *this volume*.)

Phototoxicity in cells is still not well understood in general and for ultrashort pulse illumination in particular. But the main limitation to even more widespread use of multi-photon excitation is not due to fundamental physical, chemical, or biological problems, but to the price and complexity of the instrumentation.

ACKNOWLEDGMENTS

The authors' research underlying this chapter was sponsored by the Developmental Resource for Biophysical Imaging and Optoelectronics at Cornell University (NIH-9 P41 EB001976 and NSF-DIR-8800278), the Material Science Center Computing Facility (NSF-DMR-9121564), other grants from NIH (DK53434, CA86283) and NSF (BIR-98-71063), Lucent Technologies, Bell Labs, and the Max-Planck Society.

REFERENCES

Adronov, A., Frechet, J.M.J., He, G.S., Kim, K.S., Chung, S.J., Swiatkiewicz, J., and Prasad, P.N., 2000, Novel two-photon absorbing dendritic structures, *Chem. Mater.* 12:2838–2841.

Agarwal, A., Coleno, M.L., Wallace, V.P., Wu, W.Y., Sun, C.H., Tromberg, B.J., and George, S.C., 2001, Two-photon laser scanning microscopy of epithelial cell-modulated collagen density in engineered human lung tissue, *Tissue Eng*. 7:191–202.

Akaaboune, M., Grady, R.M., Turney, S., Sanes, J.R., and Lichtman, J.W., 2002, Neurotransmitter receptor dynamics studied *in vivo* by reversible photo-unbinding of fluorescent ligands, *Neuron* 34:865–876.

Albota, M., Beljonne, D., Bredas, J.L., Ehrlich, J.E., Fu, J.Y., Heikal, A.A., Hess, S.E., Kogej, T., Levin, M.D., Marder, S.R., McCord-Maughon, D., Perry, J.W., Rockel, H., Rumi, M., Subramaniam, C., Webb, W.W., Wu, X.L., and Xu, C., 1998a, Design of organic molecules with large two-photon absorption cross sections, *Science* 281:1653–1656.

Albota, M.A., Xu, C., and Webb, W.W., 1998b, Two-photon fluorescence excitation cross sections of biomolecular probes from 690 to 960 nm, *Appl. Opt*. 37:7352–7356. http://www.drbio.cornell.edu/Infrastructure/FluorescentProbes_WWW/CommerciallyAvailable.htm; http://www.drbio.cornell.edu/Infrastructure/NonlinearMicroscopies_WWW/vit.htm; http://www.drbio.cornell.edu/Infrastructure/NonlinearMicroscopies_WWW/3P/3PE.htm).

Andresen, V., Egner, A., and Hell, S.W., 2001, Time-multiplexed multifocal multiphoton microscope, *Opt. Lett*. 26:75–77.

Arcangeli, C., Yu, W., Cannistraro, S., and Gratton, E., 2000, Two-photon autofluorescence microscopy and spectroscopy of antarctic fungus: New approach for studying effects of UV-B irradiation, *Biopolymers* 57: 218–225.

Art, J.J., and Goodman, M.B., 1993, Rapid-scanning confocal microscopy, *Methods Cell Biol*. 38:47–77.

Ashkin, A., Dziedzic, J.M., and Yamane, T., 1987, Optical trapping and manipulation of single cells using infrared laser beams, *Nature* 330:769–771.

Backskai, B.J., Kajdasz, S.T., Christie, R.H., Carter, C., Games, D., Seubert, P., Schenk, D., and Hyman, B.T., 2001, Imaging of amyloid-beta deposits in brains of living mice permits direct observation of clearance of plaques with immunotherapy, *Nat. Med*. 7:369–372.

Beaurepaire, E., and Mertz, J., 2002, Epifluorescence collection in two-photon microscopy, *Appl. Opt*. 41:5376–5382.

Beaurepaire, E., Oheim, M., and Mertz, J., 2001, Ultra-deep two-photon fluorescence excitation in turbid media, *Opt. Commun*. 188:25–29.

Bindhu, C.V., Harilal, S.S., Kurian, A., Nampoori, V.P.N., and Vallabhan, C.P.G., 1998, Two and three photon absorption in rhodamine 6G methanol solutions using pulsed thermal lens technique, *J. Nonlinear Opt. Phys. Mater*. 7:531–538.

Birge, R.R., 1979, A theoretical analysis of the two-photon properties of linear polyenes and the visual chromophores, *J. Chem. Phys*. 70:165–177.

Birge, R.R., 1986, Two-photon spectroscopy of protein-bound chromophores, *Acc. Chem. Res*. 19:138–146.

Birge, R.R., and Zhang, C.-F., 1990, Two-photon double resonance spectroscopy of bacteriorhodopsin. Assignment of the electronic and dipolar properties of the low-lying $^1A^{*+}_g$-like and $^1B^{*+}_u$like π,π^* states, *J. Chem. Phys*. 92:7178–7195.

Booth, M.J., and Hell, S.W., 1998, Continuous wave excitation two-photon fluorescence microscopy exemplified with the 647-nm ArKr laser line, *J. Microsc*. 190:298–304.

Brakenhoff, G.J., Squier, J., Norris, T., Bliton, A.C., Wade, M.H., and Athey, B., 1996, Real-time two-photon confocal microscopy using a femtosecond, amplified Ti : sapphire system, *J. Microsc*. 181:253–259.

Brown, E.B., Campbell, R.B., Tsuzuki, Y., Xu, L., Carmeliet, P., Fukumura, D., and Jain, R.K., 2001, *In vivo* measurement of gene expression, angiogenesis and physiological function in tumors using multiphoton laser scanning microscopy, *Nat. Med*. 7:866–870.

Bruchez, M. Jr., Moronne, M., Gin, P., Weiss, S., and Alivisatos, A.P., 1998, Semiconductor nanocrystals as fluorescent biological labels, *Science* 281:2013–2016.

Chaigneau, E., Oheim, M., Audinat, E., and Charpak, S., 2003, Two-photon imaging of capillary blood flow in olfactory bulb glomeruli, *Proc. Natl. Acad. Sci. USA* 100:13081–13086.

Cheung, E.C., and Liu, J.M., 1991, Efficient generation of ultrashort, wavelenght-tunable infrared pulses, *J. Opt. Soc. Am. B* 8:1491–1506.

Christie, R.H., Bacskai, B.J., Zipfel, W.R., Williams, R.M., Kajdasz, S.T., Webb, W.W., and Hyman, B.T., 2001, Growth arrest of individual senile plaques in a model of Alzheimer's disease observed by *in vivo* multiphoton microscopy, *J. Neurosci*. 21:858–864.

Christie, R.H., Zipfel, W.R., Williams, R.M., Webb, W.W., and Hyman, B.T., 1998, Multiphoton imaging of Alzheimer's disease neuropathology, *J. Neuropathol. Exp. Neurol*. 57:145.

Christie, R.H., Zipfel, W.R., Williams, R.M., Webb, W.W., and Hyman, B.T., 1999, *In vivo* multiphoton imaging of amyloid deposition in transgenic mice, *J. Neuropathol. Exp. Neurol*. 58:204.

Corrie, J.E.T., and Trentham, D.R., 1993, Caged nucleotides and neurotransmitters, *Bioorgan. Photochem*. 2:243–305.

Curley, P.F., Ferguson, A.I., White, J.G., and Amos, W.B., 1992, Application of a femtosecond self-sustaining mode-locked Ti-sapphire laser to the field of laser scanning confocal microscopy, *Opt. Quantum Electron*. 24:851–859.

Davidovits, P., and Egger, M.D., 1969, Scanning laser microscope, *Nature* 233:831.

Debarbieux, F., Audinat, E., and Charpak, S., 2003, Action potential propagation in dendrites of rat mitral cells *in vivo*, *J. Neurosci*. 23:5553–5560.

Denk, W., 1994, Two-photon scanning photochemical microscopy — Mapping ligand-gated ion-channel distributions, *Proc. Natl. Acad. Sci. USA* 91:6629–6633.

Denk, W., 1996, Two-photon excitation in functional biological imaging, *J. Biomed. Opt*. 1:296–304.

Denk, W., 2001, Optical beam power controller using a tiltable birefringent plate, US Patent no. 6249379.

Denk, W., and Detwiler, P.B., 1999, Optical recording of light-evoked calcium signals in the functionally intact retina, *Proc. Natl. Acad. Sci. USA* 96:7035–7040.

Denk, W., and Svoboda, K., 1997, Photon upmanship: Why multiphoton imaging is more than a gimmick, *Neuron* 18:351–357.

Denk, W., Aksay, E., Baker, R., and Tank, D.W., 1997, Long term imaging of [Ca++] in zebrafish embryos using two-photon microscopy, *Soc. Neurosci. Abstr*. 646.

Denk, W., Delaney, K.R., Gelperin, A., Kleinfeld, D., Strowbridge, B.W., Tank, D.W., and Yuste, R., 1994, Anatomical and functional imaging of neurons using two-photon laser scanning microscopy, *J. Neurosci. Methods* 54: 151–162.

Denk, W., Strickler, J.H., and Webb, W.W., 1990, Two-photon laser scanning fluorescence microscopy, *Science* 248:73–76.

Denk, W., Sugimori, M., and Llinas, R., 1995, Two types of calcium response limited to single spines in cerebellar Purkinje cells, *Proc. Natl. Acad. Sci. USA* 92:8279–8282.

Denk, W., Yuste, R., Svoboda, K., and Tank, D.W., 1996, Imaging calcium dynamics in dendritic spines, *Curr. Opin. Neurobiol*. 6:372–378.

Dickinson, M.E., Murray, B.A., Haynes, S.M., Waters, C.W., and Longmuir, K.J., 2002, Using electroporation and lipid-mediated transfection of GFP-expressing plasmids to label embryonic avian cells for vital confocal and two-photon microscopy, *Differentiation* 70:172–180.

Dyba, M., and Hell, S.W., 2002, Focal spots of size lambda/23 open up far-field fluorescence microscopy at 33 nm axial resolution, *Phys. Rev. Lett.* 88:163901.

Eggeling, C., Widengren, J., Rigler, R., and Seidel, C.A.M., 1998, Photobleaching of fluorescent dyes under conditions used for single-molecule detection: Evidence of two-step photolysis, *Anal. Chem.* 70:2651–2659.

Egner, A., and Hell, S.W., 2000, Time multiplexing and parallelization in multifocal multiphoton microscopy, *J. Opt. Soc. A* 17:1192–1201.

Egner, A., Jakobs, S., and Hell, S.W., 2002, Fast 100-nm resolution three-dimensional microscope reveals structural plasticity of mitochondria in live yeast, *Proc. Natl. Acad. Sci. USA* 99:3370–3375.

Engert, F., and Bonhoeffer, T., 1999, Dendritic spine changes associated with hippocampal long-term synaptic plasticity, *Nature* 399:66–70.

Euler, T., Detwiler, P.B., and Denk, W., 2002, Directionally selective calcium signals in dendrites of starburst amacrine cells, *Nature* 418:845–852.

Fan, G.Y., Fujisaki, H., Miyawaki, A., Tsay, R.K., Tsien, R.Y., and Ellisman, M.H., 1999, Video-rate scanning two-photon excitation fluorescence microscopy and ratio imaging with cameleons, *Biophys. J*. 76:2412–2420.

Fittinghoff, D.N., Schaffer, C.B., Mazur, E., and Squier, J.A., 2001, Time-decorrelated multifocal micromachining and trapping, *IEEE J. Select Topics Quantum Electron*. 7:559–566.

Fork, R.L., Martinez, O.E., and Gordon, J.P., 1984, Negative dispersion using pairs of prisms, *Opt. Lett*. 9:150–152.

Friedrich, D.M., and McClain, W.M., 1980, Two-photon molecular spectroscopy, *Ann. Rev. Phys. Chem*. 31:559–577.

Fu, Q., Mak, G., and van Driel, H.M., 1992, High-power, 62fs infrared optical parametric oscillator synchronously pumped by a 76-MHz Ti:sapphire laser, *Opt. Lett*. 17:1006–1010.

Furuta, T., Wang, S.S.H., Dantzker, J.L., Dore, T.M., Bybee, W.J., Callaway, E.M., Denk, W., and Tsien, R.Y., 1999, Brominated 7-hydroxycoumarin-4-ylmethyls: Photolabile protecting groups with biologically useful cross-sections for two photon photolysis, *Proc. Natl. Acad. Sci. USA* 96: 1193–1200.

Gauderon, R., and Sheppard, C.J.R., 1999, Effect of a finite-size pinhole on noise performance in single-, two-, and three-photon confocal fluorescence microscopy, *Appl. Opt*. 38:3562–3565.

Goeppert-Mayer, M., 1931, Ueber Elementarakte mit zwei Quantenspruengen, *Ann. Phys*. 9:273.

Goldstein, S.R., Hubin, T., and Smith, T.G., 1992, An improved no-moving-parts video-rate confocal microscope, *Microsc. Microanal*. 23:437–446.

Gosnell, T.R., and Taylor, A.J., eds., 1991, *Selected Papers on Ultrafast Laser Technology*, SPIE, Bellingham.

Grutzendler, J., Kasthuri, N., and Gan, W.B., 2002, Long-term dendritic spine stability in the adult cortex, *Nature* 420:812–816.

Guild, J.B., Xu, C., and Webb, W.W., 1997, Measurement of group delay dispersion of high numerical aperture objective lenses using two-photon excited fluorescence, *Appl. Opt*. 36:397–401.

Han, M.Y., Gao, X.H., Su, J.Z., and Nie, S., 2001, Quantum-dot-tagged microbeads for multiplexed optical coding of biomolecules, *Nat. Biotechnol*. 19:631–635.

Hanninen, P.E., Lehtela, L., and Hell, S.W., 1996, Two- and multiphoton excitation of conjugate-dyes using a continuous wave laser, *Opt. Commun*. 130:29–33.

Hanninen, P.E., Soini, E., and Hell, S.W., 1994, Continuous-wave excitation two-photon fluorescence microscopy, *J. Microsc*. 176:222–225.

He, G.S., Xu, G.C., Prasad, P.N., Reinhardt, B.A., Bhatt, J.C., and Dillard, A.G., 1995, Two-photon absorption and optical-limiting properties of novel organic-compounds, *Opt. Lett*. 20:435–437.

He, G.S., Yuan, L.X., Cheng, N., Bhawalkar, J.D., Prasad, P.N., Brott, L.L., Clarson, S.J., and Reinhardt, B.A., 1997, Nonlinear optical properties of a new chromophore, *J. Opt. Soc. Am. B* 14:1079–1087.

Hell, S., and Stelzer, E.K.H., 1992, Fundamental improvement of resolution with a 4pi-confocal fluorescence microscope using two-photon excitation, *Opt. Commun*. 93:277–282.

Hell, S., Reiner, G., Cremer, C., and Stelzer, E.K.H., 1993, Aberrations in confocal fluorescence microscopy induced by mismatches in refractive index, *J. Microsc*. 169:391–405.

Hell, S.W., and Andresen, V., 2001, Space-multiplexed multifocal nonlinear microscopy, *J. Microsc*. 202:457–463.

Hell, S.W., Booth, M., Wilms, S., Schnetter, C.M., Kirsch, A.K., Arndt-Jovin, D.J., and Jovin, T.M., 1998, Two-photon near- and far-field fluorescence microscopy with continuous-wave excitation, *Opt. Lett*. 23:1238–1240.

Hellwarth, R., and Christiansen, P., 1974, Nonlinear optical microscopy examination of structure in polycrystalline ZnSe, *Opt. Commun*. 12:318–322.

Helmchen, F., Fee, M.S., Tank, D.W., and Denk, W., 2001, A miniature head-mounted two-photon microscope. High-resolution brain imaging in freely moving animals, *Neuron* 31:903–912.

Helmchen, F., Tank, D.W., and Denk, W., 2002, Enhanced two-photon excitation through optical fiber by single-mode propagation in a large core, *Appl. Opt*. 41:2930–2934.

Hockberger, P.E., Skimina, T.A., Centonze, V.E., Lavin, C., Chu, S., Dadras, S., Reddy, J.K., and White, J.G., 1999, Activation of flavin-containing oxidases underlies light-induced production of H_2O_2 in mammalian cells, *Proc. Natl. Acad. Sci. USA* 96:6255–6260.

Hopt, A., and Neher, E., 2001, Highly nonlinear photodamage in two-photon fluorescence microscopy, *Biophys. J*. 80:2029–2036.

Huang, H., Vogel, S.S., Liu, N., Melton, D.A., and Lin, S., 2001, Analysis of pancreatic development in living transgenic zebrafish embryos, *Mol. Cell Endocrinol*. 177:117–124.

Huang, S.H., Heikal, A.A., and Webb, W.W., 2002, Two-photon fluorescence spectroscopy and microscopy of NAD(P)H and flavoprotein, *Biophys. J*. 82:2811–2825.

Kaiser, W., and Garrett, C.B.G., 1961, Two-photon excitation in $CaF_2:Eu^{2+}$, *Phys. Rev. Lett*. 7:229–231.

Kao, J.P.K., and Adams, S.R., 1993, Photosensitive caged compounds, In: *Optical Microscopy, Emerging Methods and Applications* (B. Herman and J.J. Lemasters, eds.), Academic Press, San Diego, California, pp. 27–85.

Kasai, H., Matsuzaki, M., and Ellis-Davies, G.C.R., 2002, Two-photon mapping of functional glutamate receptors in dendritic spines of hippocampal CA1 pyramidal neurons, *Jpn. J. Pharmacol*. 88:S22.

Keller, U., 1994, Ultrafast all-solid-state laser technology, *Appl. Phys. B Lasers Opt*. 58:347–363.

Keller, U., 1996, Materials and new approaches for ultrashort pulse lasers, *Curr. Opin. Solid State Mater. Sci*. 1:218–224.

Kennedy, S.M., and Lytle, F.E., 1986, *p*-Bis(*i*-methylstyryl)benzene as a power-squared sensor for two-photon absorption measurements between 537 and 694 nm, *Anal. Chem*. 58:2643–2647.

Kim, O.K., Lee, K.S., Woo, H.Y., Kim, K.S., He, G.S., Swiatkiewicz, J., and Prasad, P.N., 2000, New class of two-photon-absorbing chromophores based on dithienothiophene, *Chem. Mater*. 12:284.

Kiskin, N.I., Chillingworth, R., McCray, J.A., Piston, D., and Ogden, D., 2002, The efficiency of two-photon photolysis of a "caged" fluorophore, o-1-(2-nitrophenyl)ethylpyranine, in relation to photodamage of synaptic terminals, *Eur. Biophys. J. Biophys. Lett*. 30:588–604.

Kleinfeld, D., Mitra, P.P., Helmchen, F., and Denk, W., 1998, Fluctuations and stimulus-induced changes in blood flow observed in individual capillaries in layers 2 through 4 of rat neocortex, *Proc. Natl. Acad. Sci. USA* 95:15741–15746.

Kliger, D.S.E., 1983, *Ultrasensitive Laser Spectroscopy*, Academic Press, New York.

Kloppenburg, P., Zipfel, W.R., Webb, W.W., and Harris-Warrick, R.M., 2000, Highly localized Ca2+ accumulation revealed by multiphoton microscopy in an identified motoneuron and its modulation by dopamine, *J. Neurosci*. 20:2523–2533.

Koester, H.J., and Sakmann, B., 1998, Calcium dynamics in single spines during coincident pre- and postsynaptic activity depend on relative timing of back-propagating action potentials and subthreshold excitatory postsynaptic potentials, *Proc. Natl. Acad. Sci. USA* 95:9596–9601.

Koester, H.J., Baur, D., Uhl, R., and Hell, S.W., 1999, Ca2+ fluorescence imaging with pico- and femtosecond two-photon excitation: Signal and photodamage, *Biophys. J*. 77:2226–2236.

Konig, K., Becker, T.W., Fischer, P., Riemann, I., and Halbhuber, K.J., 1999, Pulse-length dependence of cellular response to intense near-infrared laser pulses in multiphoton microscopes, *Opt. Lett*. 24:113–115.

Konig, K., Kimel, S., and Berns, M.W., 1996, Photodynamic effects on human and chicken erythrocytes studied with microirradiation and confocal laser scanning microscopy, *Lasers Surg. Med*. 19:284–298.

Lansford, R., Bearman, G., and Fraser, S.E., 2001, Resolution of multiple green fluorescent protein color variants and dyes using two-photon microscopy and imaging spectroscopy, *J. Biomed. Opt*. 6:311–318.

Larson, D.R., Zipfel, W.R., Williams, R.M., Clark, S.W., Bruchez, M.P., Wise, F.W., and Webb, W.W., 2003, Water-soluble quantum dots for multiphoton fluorescence imaging *in vivo*, *Science* 300:1434–1436.

Lechleiter, J.D., Lin, D.T., and Sieneart, I., 2002, Multi-photon laser scanning microscopy using an acoustic optical deflector, *Biophys. J*. 83:2292–2299.

Lippitz, M., Erker, W., Decker, H., van Holde, K.E., and Basche, T., 2002, Two-photon excitation microscopy of tryptophan-containing proteins, *Proc. Natl. Acad. Sci. USA* 99:2772–2777.

Liu, T.M., Chu, S.W., Sun, C.K., Lin, B.L., Cheng, P.C., and Johnson, I., 2001, Multiphoton confocal microscopy using a femtosecond Cr:forsterite laser, *Scanning* 23:249–254.

Loudon, R., 1983, *The Quantum Theory of Light*, Oxford University Press, New York.

Lozovoy, V.V., Pastirk, I., Walowicz, K.A., and Dantus, M., 2003, Multiphoton intrapulse interference. II. Control of two- and three-photon laser induced fluorescence with shaped pulses, *J. Chem. Phys*. 118:3187–3196.

Maiman, T.H., 1960, Stimulated optical radiation in ruby, *Nature* 187:493–494.

Mainen, Z.F., Maletic-Savatic, M., Shi, S.H., Hayashi, Y., Malinow, R., and Svoboda, K., 1999a, Two-photon imaging in living brain slices, *Methods* 18:231–239.

Mainen, Z.F., Malinow, R., and Svoboda, K., 1999b, Synaptic calcium transients in single spines indicate that NMDA receptors are not saturated, *Nature* 399:151–155.

Maiti, S., Shear, J.B., Williams, R.M., Zipfel, W.R., and Webb, W.W., 1997, Measuring serotonin distribution in live cells with three-photon excitation, *Science* 275:530–532.

Maletic-Savatic, M., Malinow, R., and Svoboda, K., 1999, Rapid dendritic morphogenesis in CA1 hippocampal dendrites induced by synaptic activity, *Science* 283:1923–1927.

Marder, S.R., Torruellas, W.E., BlanchardDesce, M., Ricci, V., Stegeman, G.I., Gilmour, S., Bredas, J.L., Li, J., Bublitz, G.U., and Boxer, S.G., 1997, Large molecular third-order optical nonlinearities in polarized carotenoids, *Science* 276:1233–1236.

Masters, B.R., ed., 2003, *Selected Papers on Multi-Photon Excitation Microscopy*, SPIE, Bellingham.

Masters, B.R., So, P.T.C., and Gratton, E., 1997, Multiphoton excitation fluorescence microscopy and spectroscopy of *in vivo* human skin, *Biophys. J*. 72:2405–2412.

Matsuzaki, M., Ellis-Davies, G.C.R., Nemoto, T., Miyashita, Y., Iino, M., and Kasai, H., 2001, Dendritic spine geometry is critical for AMPA receptor expression in hippocampal CA1 pyramidal neurons, *Nat. Neurosci*. 4: 1086–1092.

McClain, W.M., 1971, Excited state symmetry assignment through polarized two-photon absorption studies of fluids, *J. Chem. Phys*. 55:2789–2796.

Meyer, A.J., and Fricker, M.D., 2000, Direct measurement of glutathione in epidermal cells of intact Arabidopsis roots by two-photon laser scanning microscopy, *J. Microsc*. 198:174–181.

Milburn, T., Matsubara, N., Billington, A.P., Udgaonkar, J.B., Walker, J.W., Carpenter, B.K., Webb, W.W., Marque, J., Denk, W., McCray, J.A., and Hess, G.P., 1989, Synthesis, photochemistry, and biological-activity of a caged photolabile acetylcholine-receptor ligand, *Biochemistry* 28:49–55.

Mohler, W.A., Simske, J.S., Williams-Masson, E.M., Hardin, J.D., and White, J.G., 1998, Dynamics and ultrastructure of developmental cell fusions in the *Caenorhabditis elegans* hypodermis, *Curr. Biol*. 8:1087–1090.

Moreaux, L., Sandre, O., Charpak, S., Blanchard-Desce, M., and Mertz, J., 2001, Coherent scattering in multi-harmonic light microscopy, *Biophys. J*. 80:1568–1574.

Mortensen, O.S., and Svendsen, E.N., 1981, Initial and final molecular states as "virtual" states in two-photon processes, *J. Chem. Phys*. 74:3185–3189.

Muller, M., Squier, J., Wolleschensky, R., Simon, U., and Brakenhoff, G.J., 1998, Dispersion pre-compensation of 15 femtosecond optical pulses for high-numerical-aperture objectives, *J. Microsc*. 191:141–150.

Nakamura, O., 1993, Three-dimensional imaging characteristics of laser scan fluorescence microscopy — two-photon excitation vs single-photon excitation, *Optik* 93:39–42.

Neu, T.R., Kuhlicke, U., and Lawrence, J.R., 2002, Assessment of fluorochromes for two-photon laser scanning microscopy of biofilms, *Appl. Environ. Microbiol*. 68:901–909.

Neuman, K.C., Chadd, E., Liou, G.F., Brau, A., Bergman, K., and Block, S.M., 1999, Characterization of photodamage induced by optical traps, *Biophys. J*. 76:A96.

Nielsen, T., Frick, M., Hellweg., D., and Andresen, P., 2001, High efficiency beam splitter for multifocal multiphoton microscopy, *J. Microsc*. 201:368–376.

Niggli, E., Piston, D.W., Kirby, M.S., Cheng, H., Sandison, D.R., Webb, W.W., and Lederer, W.J., 1994, A confocal laser scanning microscope designed for indicators with ultraviolet excitation wavelengths, *Am. J. Physiol*. 266:C303–C310.

Oehring, H., Riemann, I., Fischer, P., Halbhuber, K.J., and Konig, K., 2000, Ultrastructure and reproduction behaviour of single CHO-K1 cells exposed to near-infrared femtosecond laser pulses, *Scanning* 22:263–270.

Oertner, T.G., Sabatini, B.L., Nimchinsky, E.A., and Svoboda, K., 2002, Facilitation at single synapses probed with optical quantal analysis, *Nat. Neurosci*. 10:10.

Ouzounov, D.G., Moll, K.D., Foster, M.A., Zipfel, W.R., Webb, W.W., and Gaeta, A.L., 2002, Delivery of nanojoule femtosecond pulses through large-core microstructured fibers, *Opt. Lett*. 27:1513–1515.

Patel, C.K.N., and Tam, A.C., 1981, Pulsed optoacoustic spectroscopy of condensed matter, *Rev. Mod. Phys*. 53:517–550.

Patterson, G.H., and Piston, D.W., 2000, Photobleaching in two-photon excitation microscopy, *Biophys. J*. 78:2159–2162.

Periasamy, A., Skoglund, P., Noakes, C., and Keller, R., 1999, An evaluation of two-photon excitation versus confocal and digital deconvolution fluorescence microscopy imaging in *Xenopus* morphogenesis, *Microsc. Res. Technol*. 47:172–181.

Piston, D.W., and Knobel, S.M., 1999, Real-time analysis of glucose metabolism by microscopy, *Trends Endocrinol. Metab*. 10:413–417.

Piston, D.W., Kirby, M.S., Cheng, H.P., Lederer, W.J., and Webb, W.W., 1994, Two-photon-excitation fluorescence imaging of 3-dimensional calcium-ion activity, *Appl. Opt.* 33:662–669.

Piston, D.W., Masters, B.R., and Webb, W.W., 1995, 3-dimensionally resolved Nad(P)H cellular metabolic redox imaging of the *in-situ* cornea with two-photon excitation laser-scanning microscopy, *J. Microsc*. 178:20–27.

Piston, D.W., Sandison, D.R., and Webb, W.W., 1992, Time-resolved fluorescence imaging and background rejection by two-photon excitation in laser scanning microscopy, *Proc. SPIE*. 1640:379–389.

Piston, D.W., Summers, R.G., and Webb, W.W., 1993, Observation of nuclear division in living sea urchin embryos by two-photon fluorescence microscopy, *Biophys. J*. 63:A110.

Piston, D.W., Summers, R.G., Knobel, S.M., and Morrill, J.B., 1998, Characterization of involution during sea urchin gastrulation using two-photon excited photorelease and confocal microscopy, *Microsc. Microanal*. 4:404–414.

Potma, E.O., Jones, D.J., Cheng, J.X., Xie, X.S., and Ye, J., 2002, High-sensitivity coherent anti-Stokes Raman scattering microscopy with two tightly synchronized picosecond laser, *Opt. Lett*. 27:1168–1170.

Powers, P.E., Tang, C.L., and Cheng, L.K., 1994, High-repetition-rate femtosecond optical parametric oscillator based on Cstioaso4, *Opt. Lett*. 19: 37–39.

Rehms, A.A., and Callis, P.R., 1993, Two-photon fluorescence excitation-spectra of aromatic-amino-acids, *Chem. Phys. Lett*. 208:276–282.

Sabatini, B.L., and Svoboda, K., 2000, Analysis of calcium channels in single spines using optical fluctuation analysis, *Nature* 408:589–593.

Sandison, D.R., and Webb, W.W., 1994, Background rejection and signal-to-noise optimization in confocal and alternative fluorescence microscopes, *Appl. Opt*. 33:603–615.

Schilders, S.P., and Gu, M., 1999, Three-dimensional autofluorescence spectroscopy of rat skeletal muscle tissue under two-photon excitation, *Appl. Opt*. 38:720–723.

Schönle, A., and Hell, S.W., 1998, Heating by absorption in the focus of an objective lens, *Opt. Lett*. 23:325–327.

Sheppard, C.J.R., and Cogswell, C.J., 1990, Confocal microscopy with detector arrays, *J. Mod. Opt*. 37:267–279.

Sheppard, C.J.R., and Cogswell, C.J., 1991, Effects of aberrating layers and tube length on confocal imaging properties, *Optik* 87:34–38.

Sheppard, C.J.R., and Gu, M., 1990, Image-formation in two-photon fluorescence microscopy, *Optik* 86:104–106.

Sheppard, C.J.R., and Gu, M., 1994, Imaging performance of confocal fluorescence microscopes with finite-sized source, *J. Mod. Opt*. 41:1521–1530.

Sheppard, C.J.R., and Kompfner, R., 1978, Resonant scanning optical microscope, *Appl. Opt*. 17:2879–2882.

Singh, S., and Bradley, L.T., 1964, Three-photon absorption in napthalene crystals by laser excitation, *Phys. Rev. Lett*. 12:612.

Spence, D.E., Kean, P.N., and Sibbett, W., 1991, 60-fsec pulse generation from a self-mode-locked Ti:sapphire laser, *Opt. Lett*. 16:42–44.

Squier, J.A., Fittinghoff, D.N., Barty, C.P.J., Wilson, K.R, Muller, M., and Brakenhoff, C.J., 1998, Characterization of femtosecond pulses focused with high numerical aperture optics using interferometric surface-third-harmonic generation, *Opt. Commun*. 147:153–156.

Squirrell, J.M., Wokosin, D.L., White, J.G., and Bavister, B.D., 1999, Long-term two-photon fluorescence imaging of mammalian embryos without compromising viability, *Nat. Biotechnol*. 17:763–767.

Stelzer, E.H.K., Hell, S., and Lindek, S., 1994, Nonlinear absorption extends confocal fluorescence microscopy into the ultra-violet regime and confines the illumination volume, *Opt. Commun*. 104:223–228.

Straub, M., and Hell, S.W., 1998, Multifocal multiphoton microscopy: A fast and efficient tool for 3-D fluorescence imaging, *Bioimaging* 6:177–185.

Summers, R.G., Morrill, J.B., Leith, A., Marko, M., Piston, D.W., and Stonebraker, A.T., 1993, A stereometric analysis of karyokinesis, cytokinesis and cell arrangements during and following 4th cleavage period in the sea-urchin, *Lytechinus variegatus*, *Dev. Growth Diff*. 35:41–57.

Summers, R.G., Piston, D.W., Harris, K.M., and Morrill, J.B., 1996, The orientation of first cleavage in the sea urchin embryo, *Lytechinus variegatus*, does not specify the axes of bilateral symmetry, *Dev. Biol*. 175:177–183.

Svoboda, K., and Block, S.M., 1994, Biological applications of optical forces, *Ann. Rev. Biophys. Biomol. Struct*. 23:247–285.

Svoboda, K., Denk, W., Kleinfeld, D., and Tank, D.W., 1997, *In vivo* dendritic calcium dynamics in neocortical pyramidal neurons, *Nature* 385:161–165.

Svoboda, K., Denk, W., Knox, W., and Tsuda, S., 1996a, Two-photon laser scanning fluorescence microscopy of living neurons using a diode-pumped Cr : LiSrAlFl laser mode-locked with a saturable Bragg reflector, *Opt. Lett*. 21:1411–1413.

Svoboda, K., Helmchen, F., Denk, W., and Tank, D.W., 1999, Spread of dendritic excitation in layer 2/3 pyramidal neurons in rat barrel cortex *in vivo*, *Nat. Neurosci*. 2:65–73.

Svoboda, K., Tank, D.W., and Denk, W., 1996b, Direct measurement of coupling between dendritic spines and shafts, *Science* 272:716–719.

Tan, Y.P., Llano, I., Hopt, A., Wurriehausen, F., and Neher, E., 1999, Fast scanning and efficient photodetection in a simple two-photon microscope, *J. Neurosci. Methods* 92:123–135.

Theer, P., Hasan, M.T., and Denk, W., 2003, Two-photon imaging to a depth of 1000 µm in living brains by use of a $Ti:Al_2O_3$ regenerative amplifier, *Opt. Lett*. 28:1022–1024.

Tirlapur, U.K., Konig, K., Peuckert, C., Krieg, R., and Halbhuber, K.J., 2001, Femtosecond near-infrared laser pulses elicit generation of reactive oxygen species in mammalian cells leading to apoptosis-like death, *Exp. Cell Res*. 263:88–97.

Trachtenberg, J.T., Chen, B.E., Knott, G.W., Feng, G., Sanes, J.R., Welker, E., and Svoboda, K., 2002, Long-term *in vivo* imaging of experience-dependent synaptic plasticity in adult cortex, *Nature* 420:788–794.

Valdmanis, J.A., and Fork, R.L., 1986, Design considerations for a femtosecond pulse laser balancing self phase modulation, group-velocity dispersion, saturable absorption, and saturable gain, *IEEE J. Quant. Electron*. 22:112–118.

Ventelon, L., Moreaux, L., Mertz, J., and Blanchard-Desce, M., 1999, New quadrupolar fluorophores with high two-photon excited fluorescence, *Chem. Commun*. 20:2055–2056.

Ventelon, L., Moreaux, L., Mertz, J., and Blanchard-Desce, M., 2002, Optimization of quadrupolar chromophores for molecular two-photon absorption, *Synth. Met*. 127:17–21.

Visser, T.D., Brakenhoff, G.J., and Groen, F.C.A., 1991, The one-point fluorescence response in confocal microscopy, *Optik* 87:39–40.

Volkmer, A., Book, L.D., and Xie, X.S., 2002, Time-resolved coherent anti-Stokes Raman scattering microscopy: Imaging based on Raman free induction decay, *Appl. Phys. Lett*. 80:1505–1507.

Walowicz, K.A., Pastirk, I., Lozovoy, V.V., and Dantus, M., 2002, Multiphoton intrapulse interference. 1. Control of multiphoton processes in condensed phases, *J. Phys. Chem. A* 106:9369–9373.

Wang, S.S.H., Denk, W., and Hausser, M., 2000, Coincidence detection in single dendritic spines mediated by calcium release, *Nat. Neurosci*. 3:1266–1273.

Whinnery, J.R., 1974, Laser measurement of optical absorption in liquids, *Acc. Chem. Res*. 7:225–231.

Williams, R.M., Shear, J.B., Zipfel, W.R., Maiti, S., and Webb, WW., 1999, Mucosal mast cell secretion processes imaged using three-photon microscopy of 5-hydroxytryptamine autofluorescence, *Biophys. J*. 76:1835–1846.

Williams, S.A., and Callis, P.R., 1990, Two-photon electronic spectra of nucleotides, *Proc. SPIE* 1204:332–343.

Wilson, T., and Sheppard, C., 1984, *Theory and Practice of Scanning Optical Microscopy*, Academic Press, New York.

Wokosin, D.L., Centonze, V., White, J.G., Armstrong, D., Robertson, G., and Ferguson, A.I., 1996a, All-solid-state ultrafast lasers facilitate multiphoton excitation fluorescence imaging, *IEEE J. Quant. Electron*. 2:1051–1065.

Wokosin, D.L., Centonze, V.E., Crittenden, S., and White, J., 1996b, Three-photon excitation fluorescence imaging of biological specimens using an all-solid-state laser, *Bioimaging* 4:1–7.

Wolleschensky, R., Feurer, T., Sauerbrey, R., and Simon, I., 1998, Characterization and optimization of a laser-scanning microscope in the femtosecond regime, *Appl. Phys. B Lasers Opt*. 67:87–94.

Xu, C., and Denk, W., 1997, Two-photon optical beam induced current imaging through the backside of integrated circuits, *Appl. Phys. Lett*. 71: 2578–2580.

Xu, C., and Denk, W., 1999, Comparison of one- and two-photon optical beam-induced current imaging, *J. Appl. Phys*. 86:2226–2231.

Xu, C., and Webb, W.W., 1996, Measurement of two-photon excitation cross sections of molecular fluorophores with data from 690 to 1050 nm, *J. Opt. Soc. Am. B* 13:481–491.

Xu, C., Guild, J., Webb, W.W., and Denk, W., 1995, Determination of absolute two-photon excitation cross-sections by *in-situ* 2nd-order autocorrelation, *Opt. Lett*. 20:2372–2374.

Xu, C., Zipfel, W., Shear, J., Williams, R., and Webb, W., 1996, Multiphoton fluorescence excitation: New spectral windows for biological nonlinear microscopy, *Proc. Natl. Acad. Sci. USA* 93:10763–10768.

Yuste, R., and Denk, W., 1995, Dendritic spines as basic functional units of neuronal integration, *Nature* 375:682–684.

Zhang, Q., Piston, D.W., and Goodman, R.H., 2002, Regulation of corepressor function by nuclear NADH, *Science* 295:1895–1897.

Zipfel, W.R., Williams, R.M., Christie, R., Nikitin, A.Y., Hyman, B.T., and Webb, W.W., 2003, Live tissue intrinsic emission microscopy using multiphoton-excited native fluorescence and second harmonic generation, *Proc. Natl. Acad. Sci. USA* 100:7075–7080.

Zojer, E., Beljonne, D., Kogej, T., Vogel, H., Marder, S.R., Perry, J.W., and Bredas, J.L., 2002, Tuning the two-photon absorption response of quadrupolar organic molecules, *J. Chem. Phys*. 116:3646–3658.

Zumbusch, A., Holtom, G.R., and Xie, X.S., 1999, Three-dimensional vibrational imaging by coherent anti-Stokes Raman scattering, *Phys. Rev. Lett*. 82:4142–4145.

29

Multifocal Multi-Photon Microscopy

Jörg Bewersdorf, Alexander Egner, and Stefan W. Hell

INTRODUCTION

Multi-photon processes relying on the cooperative action of two or more photons can broadly be divided into two families that are distinguished by the fact that the photons are either absorbed or scattered (Shen, 1984). Whereas the scattering events relevant to microscopy are second and third harmonic generation (SHG, THG), as well as coherent anti-Stokes Raman scattering (CARS), the useful multi-photon absorption events are two- and three-photon excitation (2PE, 3PE). The first multi-photon phenomenon that entered microscopy was SHG (Hellwarth and Christensen, 1974; Gannaway, 1978), followed by CARS (Duncan *et al.*, 1982), 2PE (Denk *et al.*, 1990; Curley *et al.*, 1992), 3PE (Hell *et al.*, 1996; Maiti *et al.*, 1997), and THG (Barad *et al.*, 1997; Müller *et al.*, 1998). Timed with the advent of more accessible pulsed lasers, the seminal work by Denk and colleagues (1990) on 2PE microscopy opened a new epoch of research and application with multi-photon processes in microscopy (Guo *et al.*, 1997; Gauderon *et al.*, 1998; Zumbusch *et al.*, 1999; Campagnola *et al.*, 2002; Cheng *et al.*, 2002; Müller and Schins, 2002; Yelin *et al.*, 2002; Theer *et al.*, 2003; Zipfel *et al.*, 2003).

The use of multi-photon phenomena provides several advantages over their single-photon counterparts. The most prominent is the confinement of signal generation to the focal region where the simultaneous occurrence of multiple photons is highest. Another important advantage is the capability to penetrate deeper into strongly scattering specimens (Denk and Svoboda, 1997; Centonze and White, 1998). Moreover, SHG, THG, and CARS (Zoumi *et al.*, 2002; Cox *et al.*, 2003) generate signals that are not accessible through single-photon interactions, thus complementing fluorescence imaging in a unique way.

Unfortunately, multi-photon events have a low probability of occurrence, that is, they have a small cross-section. Small cross-sections can be compensated by large excitation intensities. In microscopy, the strong focusing provided by the objective lens readily yields large intensities, in particular in conjunction with pulsed illumination. The only issue is that the applicable intensity is limited by photodamage, which also has a major nonlinear component (see Chapter 38, *this volume*). In some cases, multi-photon absorption may also reach (singlet-state) saturation. With the exception of the important application of imaging into strongly scattering tissue, the power of presently available lasers usually greatly exceeds the power required at a given point. Therefore, the use of several parallel foci may be regarded as an obvious solution to this problem. In multi-photon microscopy, this solution is particularly attractive because the optical sectioning is provided by the multi-photon interaction alone. No back-imaging onto an array of pinholes is needed, which otherwise would require delicate alignment and the compensation of chromatic aberrations. In this chapter, we give an overview of parallelized multi-photon imaging methods, which are commonly referred to as multi-focal multi-photon microscopy (MMM).

Background

Owing to their wavelength tunability, short pulse length, and high repetition rate, mode-locked titanium : sapphire (Ti : Sa) lasers have become the light sources of choice for multi-photon microscopes. Mode-locked Ti : Sa and similar laser systems typically provide 1 to 2 W of average power at a repetition rate of ~80 MHz at pulse lengths of ~200 fs or 1 to 2 ps. This is ample light for a single scanning beam since nonlinear damaging effects normally limit the usable intensity to about 200 GW/cm^2 at 200 fs and 70 GW/cm^2 at 1 to 2 ps in the focus (Hänninen *et al.*, 1995; König *et al.*, 1996, 1999; Hopt and Neher, 2001). At typical repetition rates and focal spot sizes, this maximum focal intensity amounts to 3 to 10 mW at 200 fs and 10 to 30 mW in the picosecond range average power. An important exception is the imaging of layers inside strongly scattering specimens, such as skin and brain at >250 µm depth, where most of the laser light is needed and femtosecond operation is preferable. Therefore, in regular, single-spot multi-photon microscopy, more than 90% of the laser power is discarded because applying more power would be detrimental. This holds both for the multi-photon absorption and the multi-photon scattering microscopy modes. By splitting up the beam of a mode-locked Ti : Sa laser into several beamlets and applying multiple, well-separated foci simultaneously, MMM exploits a much larger fraction of the available laser power, and at the same time it parallelizes the imaging process without significant trade-offs in the resolution (Bewersdorf *et al.*, 1998; Buist *et al.*, 1998).

Determination of the Optimum Degree of Parallelization

If photodamage, photobleaching, or saturation of an excited state of the chromophore can be neglected, the signal S from a single focus n-photon excitation microscope, per time unit, is proportional to $\sigma_S P_{avg}^n/\tau^{n-1} f^{n-1}$, with P_{avg} being the average laser power in the focus, τ and f being the pulse length in the sample and the repetition rate, respectively. σ_S is the multi-photon cross-section. In MMM, the laser beam is split up into N beamlets with an average power of $P_{avg,MMM}/N$ each. The signal of the N independent foci adds up to an overall signal $S \propto \sigma_S P_{avg,MMM}^n/(\tau f N)^{n-1}$. Within the framework of sheer signal generation, the parameters τf and N are of equal

Jörg Bewersdorf, Alexander Egner, and Stefan W. Hell • Max Planck Institute for Biophysical Chemistry, 37070 Göttingen, Germany

importance and therefore the change of one parameter can be compensated by adjusting one of the others. This can be illustrated by looking at the laser pulse train at a certain spot in the sample. The number of pulses arriving per second is proportional to f times N. Whether the repetition rate f is halved and N is doubled or vice versa is of no importance. A doubled pulse length τ can similarly be interpreted as two subsequent pulses. While τ and f are given by the laser system, the degree of parallelization N introduces a new degree of freedom to optimize the performance of a multi-photon microscope. It has to be noted though that N strongly influences the microscope design and thus can be changed only in a certain range without major technical modifications.

The choice of the parameters for MMM depends on the limiting factors: saturation, photodamage, and the available laser power. Saturation obviously does not play a role for the scattering modes because in this case no long-lived state of the sample is involved. The overall damage per time unit can be written as a polynomial series $D \propto \sum_{i=1}^{\infty} \delta_i P_{avg,MMM}^i \big/ (\tau f N)^{i-1}$, with δ_i expressing the relative weight (including the damaging cross-sections) of the damaging mechanisms of the different orders of non-linearity. For a certain range of laser and imaging parameters P_{avg}, τ, f and N, D can be approximated by $D \propto \sigma_D P_{avg,MMM}^d / (\tau f N)^{d-1}$, where d is the effective order of non-linearity that typically is not an integer. d is close to the order of non-linearity of the dominating damaging mechanism which can change, for example, with the applied laser power P_{avg}. Similarly, σ_D is the effective damaging cross-section in this parameter range.

As a result, the performance ratio β of the signal S to the damage D is proportional to $\sigma_S/\sigma_D (P_{avg,MMM}/\tau f N)^{n-d} = \sigma_S/\sigma_D P_{peak}^{n-d}$. The goal obviously is to maximize the performance β. For this purpose, one has to distinguish between two different situations:

- ***n > d* (the excitation process is of higher order of non-linearity than the dominating damaging process)**: Maximizing the peak power P_{peak} yields the highest value for β. Short pulses and low repetition rates are therefore favorable. Parallelization only decreases β. However, an increase of P_{peak} is only reasonable up to a value where damaging processes of higher order become significant.
- ***n < d* (the excitation process is of lower order of non-linearity than the dominating damaging process)**: P_{peak} must be minimized to optimize β. Apart from applying long pulses and high repetition rates, parallelization is the best alternative. Moreover, by increasing the overall average power $P_{avg,MMM}$ and N simultaneously, β can be kept constant while at the same time the recorded signal per unit time S increases by a factor of N. This allows an acceleration of the imaging speed by this factor without increasing the damage. The maximum N is limited by the available laser power only as long as no low order damaging processes (such as heating) become dominant.

In the case of $n = d$, β does not depend on the peak power. Therefore, parallelization or a change in τ or f has no real influence. We note that the distance between the focal spots and the size of the scanning field additionally influence the relative weights δ_i of the damaging processes. Heating may be a problem if all of the average power is concentrated on a rather small scanning area of a few micrometers.

With regard to the damage, parallelization is only reasonable in the case of a higher degree of non-linearity d of the dominant damage process as compared to that of the excitation process ($n > d$). Another reason for the parallelization is enhanced scanning speed where parallelization is important even if $n > d$.

For the multi-photon excitation processes, the (rather rare case of) saturation is in the same way a highly nonlinear phenomenon. In this situation, a maximum acceptable saturation level can be defined with a corresponding focal average power P_{sat}. The ratio between the totally available average power $P_{avg,MMM}$ and P_{sat} gives the optimum degree of parallelization N_{opt}.

Investigations of photodamage with pulsed NIR illumination in living cells showed prevalent cell-damage mechanisms of the order of $2 < d < 2.5$ (König *et al.*, 1999; Hopt and Neher, 2001). *In vitro* photobleaching measurements have shown a power-dependence of $d \geq 3$ (Patterson and Piston, 2000). These findings make parallelization advisable especially for two-photon processes ($n = 2$) such as SHG, CARS, and 2PE. Whether parallelization is beneficial for higher-order multi-photon processes, such as THG and 3PE, depends on the dominating damage mechanism.

In the case of 2PE and a given laser system, the optimum degree of parallelization N_{opt} is estimated by considering the optimal focal laser power $P_{opt}(\tau,f)$ for given laser parameters and samples. N_{opt} is just given by $N_{opt} = P_{avg}/P_{opt}(\tau,f)$. This number is also the optimum increase in the recording speed of MMM compared to standard single-beam multi-photon microscopy. For a mode-locked femtosecond laser, the repeatedly confirmed power limit in the focus is reached at $P_{opt}(\tau \approx 200\,\text{fsec}, f \approx 80\,\text{MHz}) = 1$ to 10 mW (Hänninen *et al.*, 1995; König *et al.*, 1996, 1999; Hopt and Neher, 2001). If we assume that because of over-filling and reflection losses on average only 10% of the laser power can be transferred into the sample in a nearly diffraction-limited manner, this results in an optimum beamlet number $N_{opt} = 20$ to 100 with $P_{avg,MMM} \sim 100$ to 200 mW in the sample. The fraction of power transferred can of course be increased by slightly compromising the axial resolution of the system, in which case N_{opt} can be further enlarged significantly.

EXPERIMENTAL REALIZATION

A Multi-Focal Multi-Photon Microscopy Setup Using a Nipkow-Type Microlens Array

We now discuss a typical implementation of a MMM setup that was originally designed for 2PE fluorescence (Bewersdorf *et al.*, 1998) using a Nipkow-type arranged focal pattern for scanning the object. Adapting this type of microscope to other types of multi-photon microscopes is straightforward as a recently published setup for SHG multi-focal microscopy (Kobayashi *et al.*, 2002) shows. In the setup displayed in Figure 29.1(A), the expanded and collimated laser beam of a mode-locked Ti : Sa laser illuminates an array of microlenses (460 µm diameter, 6–12 mm focal length) etched on a fused-silica disk. The lenses are arranged in a hexagonal pattern such that the illuminating beam is split into small beams, referred to as beamlets, and focused into an array of approximately 5×5 foci of ~6 µm beam waist at the prefocusing plane (PFP). After the intermediate optics, the beamlets are directed into a conventional fluorescence microscope. The role of the intermediate optics is to ensure that the array of foci is imaged into the focal plane of the lens and that each beamlet is parallel at, and over-illuminates, the objective entrance pupil. The objective lens then produces a pattern of high-resolution foci at the sample. Figure 29.1(B) shows a recording of the 2PE fluorescence created by focusing into a dye solution. The typical number of 25 foci can be easily varied by changing the intermediate optics. The

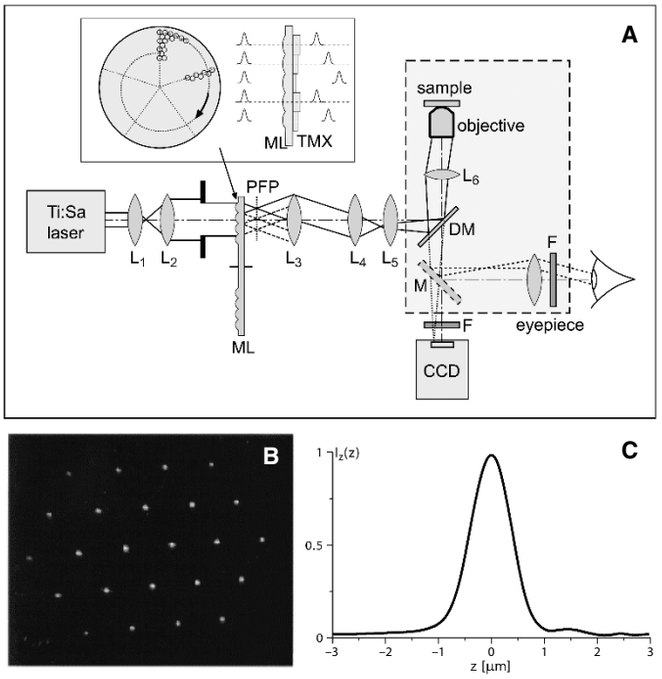


FIGURE 29.1. (A) Schematic of the first implementation of multi-focal multi-photon microscopy (MMM), including time-multiplexing (TMX). The laser beam is expanded by the lenses L_1 and L_2 and illuminates the microlens disk (ML; also shown in the inset). The microlenses focus the laser beam in the pre-focal plane (PFP), which is imaged into the sample by the lenses L_3 to L_6 and the objective lens; L_6 is the tube lens. The two-photon-excited fluorescence passes the dichroic mirror (DM) and is focused onto the CCD camera. A short-pass filter F eliminates the remaining laser light. Alternatively, by placing a mirror M into the optical detection path, the fluorescence from the focal plane in the sample can be viewed by eye. The dashed bordered box marks the parts of the conventional inverted microscope used (Leica DM-IRB). (B) The excitation pattern of the foci, recorded with the microlens disk stopped and a fluorescent solution. The experimental axial resolution of the microscope with a 1.2 NA water-immersion lens (Leica 63 × 1.2 NA water) is shown by the z-response in (C) featuring a FWHM of 890 ± 20 nm.

microlenses are arranged with a constant helical pitch [see the inset in Fig. 29.1(A)], forming spirals with typically 10 rows in a Nipkow fashion. Moreover, the layout and, in particular, the spiral pitch of the lenses are designed in such a way that the disk contains several (typically 5–12) equivalent segments. The layout of the microlenses is chosen such that upon rotation, each segment produces a complete scan of the focal area. Upon rotation of the disk, each microlens scans one line in the sample. The distance between the lines of two subsequent microlens foci in the sample remains well below the lateral resolution assuring homogeneous scanning of the sample. In the setup described the distance between the lines is 60 nm for a 100× lens. With ~500 lines per segment this results in a field of view of 35 µm diameter.[1]

In our example, the center diameter of the helix is 80 mm. The round microlenses are hexagonally closed-packed. A perfect hexagonally closed-packed plane possesses a fill factor of 90.6%. However, because of the spiral arrangement of the microlenses, the pattern is locally skewed, leading to a smaller fill factor of slightly more than 80%. The precise value slightly varies with the position on the disk. To minimize the NIR light that may pass straight to the sample causing residual out-of-focus excitation, the area between the lenses is masked. Tube lenses with different magnifications are mounted on a revolver to vary the distances between the foci in the sample and the over-illumination of the objective entrance pupil. In this way, the imaging parameters can be adapted to the specimen.

Rotating the disk by 360° renders as many complete lateral scans as segments on the disk, typically 5 to 12. The disk can be rotated at more than 100 Hz resulting in scanning rates of more than 1000 frames/s. Unlike galvanometer-based scanners, this scanning mechanism does not involve any dead time. The image rate is ultimately determined by the camera frame rate, depending on the readout rate and the number of pixels. It may range well above 30 images/s. The signal is readily separated from the NIR excitation light by a dichroic mirror and imaged directly onto a charge-coupled device (CCD) camera mounted at the microscope. With faster and more sensitive cameras, the actual limit is solely determined by the number of multi-photon–induced signal photons (fluorescence or alternatively SHG, THG, CARS, etc.) that are produced in the focal plane. Blocking the near-infrared (NIR) excitation light in the eyepieces with an absorption filter allows real-time observation of multi-photon generated images by eye. Because the excitation is restricted to the focal plane, features inside bulky objects are easily revealed.

Resolution

Because the image acquisition time is usually much slower than the scan speed, the focal plane is scanned several times during image acquisition. Mathematically, the nonlinear excitation point-spread function (PSF) $H_{exc,MMM}(x,y,z)$ of the focal pattern is integrated over the focal plane, smearing out the PSF laterally. Thus, the excitation efficiency is proportional to the z-response (Egner and Hell, 2000):

$$I_{z,exc}(z) = \int_{-\infty}^{\infty}\int_{-\infty}^{\infty} H_{exc,MMM}(x',\ y',\ z)dx'dy'. \qquad \textbf{(1)}$$

The focal plane is then imaged onto the CCD camera. This process is described by the detection PSF $H_{\mathrm{det}}(x,y,z)$, resulting in the effective PSF

$$H_{eff,MMM}(x,y,z) \propto I_{z,exc}(z)H_{\mathrm{det}}(x,y,z). \qquad \textbf{(2)}$$

This equation holds only for multi-photon absorption phenomena such as 2PE or 3PE. For scattering events, because of their coherent nature and the concomitant conservation of the phase, complex amplitude rather than intensity PSFs have to be combined in the derivation of the effective PSF. This complicates the calculation massively.

According to Eq. 2, the lateral resolution of the MMM is determined by the detection PSF in the visible wavelength range, thus, in a non-scattering specimen, it is superior to the resolution in standard non-descanned 2PE microscopy. The axial resolution, characterized by the z-response, is given by $I_{z,exc}(z)$ only, because the integral of $H_{\mathrm{det}}(x,y,z)$ across the lateral plane is of constant value. Hence we have $I_z(z) = I_{z,exc}(z)$.

The response to a homogeneously excitable half space, the so-called sea response, is a good measure for the axial imaging of an axially extended object:

[1] With a center diameter of the helical structure on the disk of ~80 mm and a microlens diameter of 460 µm, the simultaneous usage of 5 × 5 foci results in ~2500 lines scanning across the sample per revolution of the disk. For five equivalent segments, this results in ~500 lines per complete scan of the field.

$$I_{sea}(z) = \int_{-z}^{\infty} I_z(z')dz' = \int_{-z}^{\infty}\int_{-\infty}^{\infty}\int_{-\infty}^{\infty} H_{exc,MMM}(x',\ y',\ z')dx'dy'dz'. \quad \textbf{(3)}$$

Averaging a three dimensional (3D) image stack of a 2PE fluorescent solution behind a coverslip recorded with a 100× /1.4 numerical aperture (NA) oil-immersion lens, across an area several micrometers in diameter yields the sea response $I_{sea}(z)$. Figure 29.1(C) shows the experimental z-response $I_z(z)$ obtained from the derivative of the experimental $I_{sea}(z)$.

Time Multiplexing as a Solution to Interfocal Crosstalk

As with all parallelized 3D microscopes, standard MMM needs to compromise between the degree of parallelization and the crosstalk between the multiple beams. For absorption processes of the order of n, the excitation PSF of the MMM describing the distribution of the excitation efficiency in the sample at a particular instant (i.e., scanning movement neglected) is given by

$$H_{exc,MMM}(x,\ y,\ z) \propto [\tilde{h}_{ill}(x,\ y,\ z) \otimes g(x,\ y,\ z)]^{2n} \quad \textbf{(4)}$$

$\tilde{h}_{ill}$ describes the (single-focus) amplitude PSF of the illumination and the grating function g is the sum of several δ functions in the focal plane, one for each focus (Egner and Hell, 2000).

Reducing the distance between the lens foci increases the interference between the focal fields especially in the planes away from the focal plane. Because of the periodic arrangement of the lenses, the focal fields add up constructively in the so-called Talbot and fractional Talbot planes. In these out-of-focus planes, the field of different foci reinforce each other by constructive interference, yielding periodic patterns of excitation light, which results in increased out-of-focus excitation (Egner and Hell, 2000). Conventional detection with a CCD camera through a high aperture lens, images these out-of-focus-planes onto the camera where they appear mostly as a featureless background. Hence, the z-response of an MMM may differ from that of a single-beam system by an axially expanded shoulder of low amplitude [see Fig. 29.1(C) or Fig. 29.2(C)]. Problems arise if small or dim structures need to be imaged that are located in front of or behind bright voluminous objects. In this case, the shoulder may lead to a significant background signal. For a thorough discussion of this subject, including the influence of the number of foci and the distance between neighboring foci onto the z-response (Eq. 1) and the sea response (Eq. 3), we refer to Egner and Hell (2000).

Introducing a temporal delay between the beamlets solves this problem by ensuring that light pulses of neighboring foci pass the focal region at different time points (Buist *et al.*, 1998; Egner and Hell, 2000). Interference will not occur because the pulses simply do not meet each other. Hence, the excitation PSF is

$$H^{(TMX)}_{exc,MMM}(x,y,z) \propto \tilde{h}^{2n}_{ill}(x,y,z) \otimes g(x,y,z), \quad \textbf{(5)}$$

preventing the formation of Talbot planes. Apart from a constant factor denoting the number of foci, the z-response of this function does not differ from that of a single-focus multi-photon excitation PSF. Extensive calculations of different possible realizations of this time-multiplexed MMM (TMX-MMM) as well as its practical implementation have been reported (Egner and Hell, 2000; Andresen *et al.*, 2001). Using typical operation parameters (distance between foci ~4 µm, 37 foci), the use of three delay subclasses decreases the background excitation by a factor of ~3.5, whereas four subclasses decreases background excitation by a factor of ~4.5. The subclasses are chosen such that each microlens is surrounded by microlenses of the other two delay subclasses, in alternating order. For a random distribution of three subclasses, the creation of distinct Talbot planes is precluded, but the average background remains unchanged (Egner and Hell, 2000).

A realization of TMX in MMM is sketched in the inset of Figure 29.1(A). Two 300 µm thick disks with holes at the position of every third microlens (first disk) or at two of three microlenses (second disk) were glued onto the original microlens disk. The holes have the same diameter as the microlenses (460 µm) so that the microlens beamlets are divided into three subclasses: beamlets unaffected by the additional disks, beamlets delayed by ~500 fs due to one additional layer of 300 µm glass, and beamlets delayed by ~1 ps. Because of the low microlens NA (typically ~0.02), the axial focal shift induced by the additional glass is negligible. Figure 29.2 shows the comparison between the TMX-MMM and a typical Nipkow disk microscope with single-photon excitation when imaging a challenging but realistic specimen. In Figure 29.2(C), the z-profile through a 3D-image series of a fluorescent solution between two coverslips demonstrates the superior suppression of the crosstalk between the excitation foci with the TMX-MMM. This results in a much clearer representation of small details above or below bulky objects; see Figures 29.2(A,B). Although TMX has been demonstrated for 2PE only, the idea can

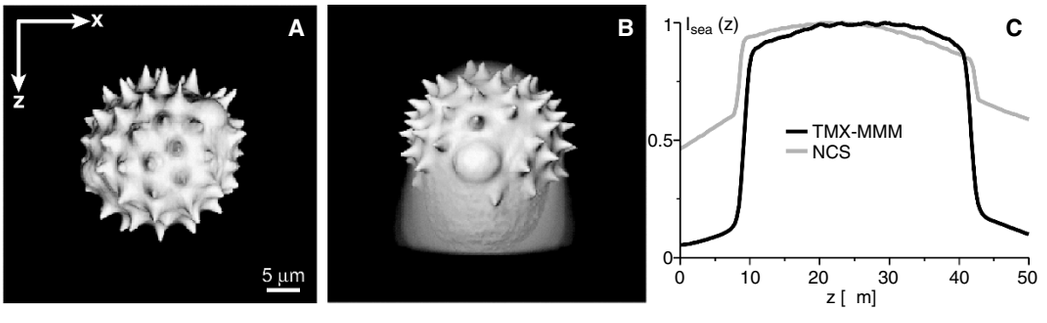


FIGURE 29.2. (A) and (B) show surfaces 3D-rendered using AMIRA Voltex of 2 grains of similar diameter (~25 µm) recorded with a 100× 1.4 NA oil-immersion lens with the TMX-MMM and a typical Nipkow confocal scanner (NCS), respectively. For a fair comparison, the parameters were selected to take the higher background of the NCS into account. Due to specimen-induced aberrations, the background behind the pollen grain in the NCS data is increased. For details see Egner and colleagues (2002). (C) The experimental sea response of a Rhodamine 6G solution of ~30 µm thickness. Note the higher background of the NCS. For example, at a distance of 5 µm away from the focal point, the background of the TMX-MMM is about seven times lower than that of the NCS.

be exploited in all multi-focal microscopy modes using pulsed or short-coherence-length illumination. It should be noted however, that for linear and multi-photon scattering events the conservation of the phase upon scattering plays a crucial role in the formation of the effective PSF.

Alternative Realizations

Besides the Nipkow-type scanning scheme, other scanning mechanisms can also be implemented. For example Buist *et al.*, (1998), use a rectangular microlens arrangement. Scanning is accomplished by rapidly moving the foci in a Lissajous pattern with an *xy* galvanometric mirror. Proper adjustment of the frequency and the amplitude of the scanning movement allows nearly uniform illumination conditions at video rate, with ~25% efficiency of light usage. MMM was also implemented in 4Pi-microscopy (Egner *et al.*, 2002b) in which case a square array of microlenses was selected. This realization was chosen because of its greater flexibility in combination with an array of detection pinholes in the focal plane of the microlenses, allowing an easy change of the pinhole size, of the focal lengths of the microlenses, as well as of the distance between the foci.

All of these setups use microlenses illuminated by an expanded and collimated laser beam to create the beamlets. To avoid wasting of the laser light, a large area of the Gaussian beam profile is used for illumination. The microlenses are much smaller than the expanded beam profile so that each individual lens is illuminated virtually uniformly. However, the microlenses in the periphery of the Gaussian profile are illuminated by less intense light than those in the center of the laser beam. This difference is carried forward to the field of view, resulting in a decrease of the intensity of the foci towards the rim. Unfortunately, the nonlinear dependence of the multi-photon process on the illumination intensity enhances this effect. If no measures are taken to homogenize this beam profile, the efficient use of the available laser power and the inhomogeneity across the field of view has to be balanced.

Masking the expanded laser beam with a rectangular aperture that blocks 70% of the laser power of a Gaussian beam, results in a ~50% decrease of the excitation efficiency at the edge of the field of view in a 2PE setup. A more constant light distribution with a better exploitation of the available laser power can be achieved by homogenizing the illumination of the microlens array. To avoid wasting large amounts of the laser light, sophisticated Gaussian-to-flat-top converters may prove useful. These use either a combination of aspheric lenses or an afocal spherical lens arrangement to redistribute the intensity to produce a homogeneous beam that also has a flat wavefront (Shafer, 1982).

Instead of dividing the expanded laser beam across its profile, the beam intensity can also be portioned by an etalon (Fittinghoff and Squier, 2000) or a cascade of beam-splitters (Fittinghoff *et al.*, 2000; Nielsen *et al.*, 2001). In this case, the beam profile is maintained for each beamlet and not relayed to the focal plane. In order to achieve the best possible resolution, the objective entrance pupil still needs to be uniformly illuminated. Dividing the beam into virtually equally intense beamlets is imperative because each beamlet illuminates a different subfield. If the ratio between the reflected and the transmitted light is not carefully chosen, discontinuous steps are obtained at the edges of the subfields in the image (e.g., a chessboard pattern). As the non-linearity n of the excitation process increases, the borders between two subfields become more noticeable. By using a high reflectivity etalon, this problem can be avoided, but a large fraction of the laser light is wasted to attain equal beamlet intensities (Fittinghoff and Squier, 2000). In addition, the tilting of the beam-splitters must be handled with particular care in order to obtain equidistant foci with each beamlet centered on the objective entrance pupil (Nielsen *et al.*, 2001).

These intensity-dividing approaches have several advantages: They are flexible, they provide a homogeneously illuminated field of view, and inherent to the beam splitting is the time multiplexing which minimizes crosstalk. Unfortunately, none of them is compatible with the spinning disk scanner. They are restricted to galvanometer or stage scanning and thus are limited in scanning speed. In addition, they involve scanning dead times.

Combining multi-focal excitation with a sample scanning setup ensures that the fluorescent light emerging from the foci is always imaged onto the same pixels of the CCD (Nielsen *et al.*, 2001). In this case, one can use the spatially resolved detection on the CCD image to remove crosstalk in the detection path between the signal emitted from adjacent foci; this may be regarded as a confocal pinhole mask by software. The approach works as long as the lateral crosstalk is limited to a region smaller than the distance between two neighboring foci.

Significant crosstalk reduction is achieved by using a pinhole array in combination with microlenses in a beam-scanning setup (Fujita *et al.*, 2000). Re-scanning of the signal across the CCD camera behind the pinholes (Egner *et al.*, 2002b) solves the problems with image acquisition encountered by Nielsen and colleagues. Detecting through pinholes slightly increases the resolution at the expense of some signal loss. For sectioning, the use of a confocal pinhole array (Fujita *et al.*, 2000) is of course not needed. However, an undeniable benefit is that the undesired scattered (fluorescence) light in multi-focal microscopy is even more suppressed.[2]

Confocalization certainly increases the contrast in the image. Unfortunately, if chromatic aberrations are not compensated, the use of pinholes always results in a significant signal loss.

The combination of MMM with a regenerative amplifier featuring a repetition rate of 1 kHz (800 nm wavelength, 110 fs pulse length) has also been demonstrated (Fujita *et al.*, 1999). To avoid severe photodamage and saturation due to the high peak powers, the setup had to be parallelized approximately 1000-fold as in a typical single-photon Nipkow confocal system (Petran *et al.*, 1968, 1985). The interfocal distance is about the same as in the systems described above. Thus, the observation of structures smaller than ~20 µm does not profit from this high degree of parallelization. Rather, the low duty cycle for each focus makes the rapid recording of small structures nearly impossible.

A commercially available version of MMM (LaVision BioTec, Bielefeld, Germany) based on an improved version of the system of Nielsen and colleagues (Nielsen *et al.*, 2001) produces a line of up to 64 foci, scanned in two dimensions by a set of galvanometer mirrors. The beam-splitter operates over the whole spectral range of the Ti : Sa laser generating foci of nearly the same intensity (difference in fluorescence ≤5%). The distance between the foci (typically 600 nm for a 60× lens) can be changed by the intermediate optics implemented. Setting the focal separation to approximately the lateral full width at half maximum (FWHM) of the PSF produces a homogeneous line of 18 µm length with high resolution. Fast scanning perpendicular to this line (up to 3.5 kHz) allows the recording of 18 µm wide rectangles of variable length, in principle, in about 0.3 ms. The recording time is currently

[2] Because in single-beam multi-photon microscopes there is no crosstalk, pinholes are reasonable only in MMM.

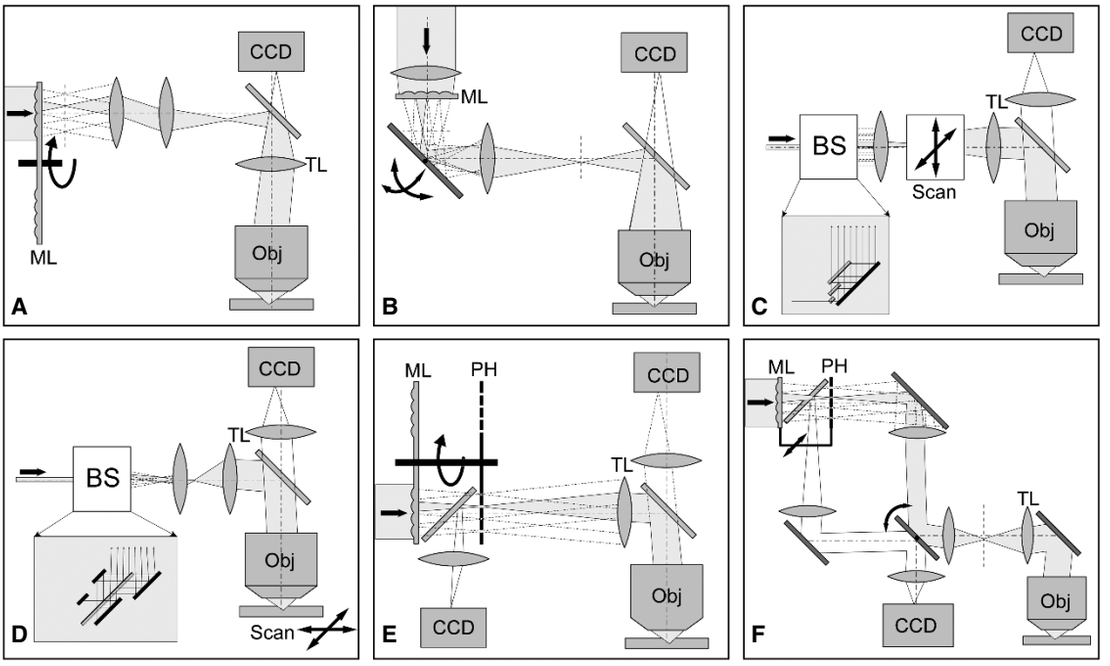


FIGURE 29.3. Different realizations of MMM. The images show sketches drawn after the original publications named, but are here simplified and rotated to ease comparison: (A) Bewersdorf and colleagues (1998), (B) Buist and colleagues (1998), (C) Fittinghoff and Squier (2000), (d) Nielsen and colleagues (2001), (E) Fujita and colleagues (2000), (F) Egner and colleagues (2002b). BS denotes the beam-splitting units of Fittinghoff, as well as of Nielsen and co-workers. Details are shown in the insets. TL, tube lens; ML, microlenses; PH, pinhole disk; Obj, objective lens.

limited by the readout speed of the camera used and the available signal. By moving the beam-splitter, the degree of parallelization can be decreased by a factor of 2. In this setup, neighboring foci are polarized perpendicular to each other allowing polarization-sensitive measurements. Figure 29.3 compares the different schemes of realizing MMM.

ADVANCED VARIANTS OF MULTI-FOCAL MULTI-PHOTON MICROSCOPY

Space Multiplexing

An option which permits improved exploitation of the total laser power and facilitates the changing of intensity levels in selected regions without attenuating the total laser power is space multiplexing (SMX) MMM (Hell and Andresen, 2001). The basic idea of SMX MMM is to modulate the intensity across the sample by the spatially modulated interference resulting from overlapping arrays of slightly offset focal fields. For a given degree of parallelization and power, SMX increases the two- and three-photon excited signal of parallelized multi-photon microscopy by a factor of up to 1.5 and 2.5, respectively. To some extent, sensitive regions may be spared, whereas in regions with weaker nonlinear susceptibilities the excitation intensity can be increased.

SMX was implemented in the MMM by splitting the collimated laser beam, combining it again with a wedge mirror and then illuminating the microlens disk. The optical path difference between the two recombined beams was changed with a piezo-driven mirror. By carefully adjusting the angle between the two beams, the interference pattern can be modified. Because the interference pattern is generated in front of the microlenses, it modulates mainly the illumination of the individual microlenses, and the influence of specimen-induced aberrations does not differ from standard MMM. As with TMX, the SMX is relevant to all modes of multi-photon microscopy, including parallelized SHG and THG imaging, CARS, and widefield multi-photon excitation.

Fluorescence Lifetime Imaging

Lifetime imaging of the fluorescent state is an important development in fluorescence microscopy. Fluorescence lifetimes are sensitive to the fluorophore environment and can be used to distinguish fluorophores with overlapping emission spectra where spectral separation is difficult. The advent of gated, intensified CCD cameras with a gate width of 200 ps and gating repetition rates of up to 100 MHz provides the opportunity of combining multifocality with lifetime imaging. Using gated cameras, lifetime images of fluorescent samples can be easily recorded with MMM (Straub and Hell, 1998a). The necessary modification includes the exchange of the standard MMM camera with a gated, intensified-CCD camera (Picostar HR, La Vision, Göttingen, Germany) and additional electronics to trigger the intensifier gate a fixed time after the excitation laser pulses. A programmable delay unit enables the recording of the fluorescence decay curves in 100 ps steps. The gate width of 200 ps and a time gap of 12.5 ns between the laser pulses, allow for the measurement of fluorophore decay times in the 0.5 to 10 ns range. Figure 29.4 shows an example of a lifetime measurement for two types of beads taken with the MMM. By using a series of time gates after each photomultiplier in a PMT array to detect all time windows instead of using a gated camera that collects signal in only a single window, the acquisition speed could be enhanced by a factor greater than 2 (see Chapter 27, *this volume*).

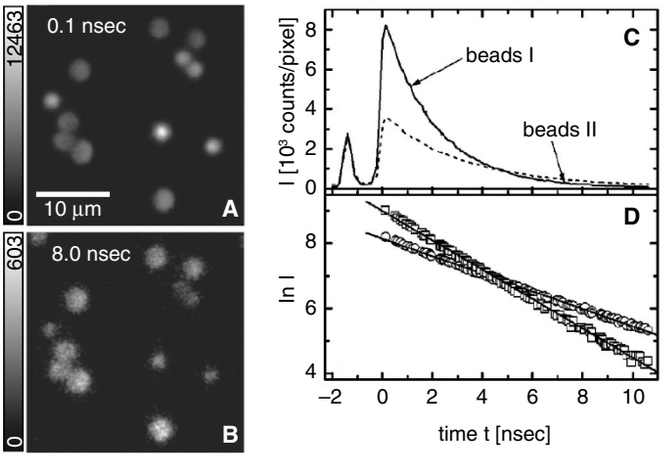


FIGURE 29.4. Fluorescence lifetime imaging with MMM. Panels (A) and (B) show images of randomly dispersed fluorescent polystyrene beads (Polysciences Inc., beads I) and larger latex beads (Molecular Probes Inc., beads II) recorded directly after the onset of fluorescence and after 8.0 ns with a gate width of 200 ps. The analysis of the decay of the fluorescence intensity *I* displayed in (C) and on a logarithmic scale in (D) yields the lifetimes of the fluorophores (2.2 and 3.7 ns for beads I and II, respectively).

Second Harmonic Generation Multi-Focal Multi-Photon Microscopy

Because SHG light is mainly forwardly scattered, the microscope is preferably used in a transmission arrangement (Kobayashi *et al.*, 2002). By modifying the MMM design, Kobayashi and co-workers imaged the focal plane with an intensified CCD camera on the far side of the sample. The sample was illuminated with a 1.2 NA water-immersion lens by applying ~100 foci with an average intensity of less than 2 mW each. By placing appropriate filters in the detection beam, the laser light ($\lambda = 896$ nm, 82 MHz repetition rate, 80 fs pulse length at the laser output) as well as light above $\lambda = 500$ nm from 2PE fluorescence was filtered out. Thereby it was possible to record multi-focal SHG images at $\lambda = 448$ nm with a typical overall exposure time between 33 ms and ~500 ms. By exchanging the detection filters, 2PE fluorescence images of the same sample can also be recorded. Kobayashi and colleagues (2002) recorded the contraction of rat cardiac myocytes with this multi-focal SHG microscope at video rate.

Multi-Focal Multi-Photon Microscopy-4Pi Microscopy

The application of MMM to 4Pi-confocal microscopy demonstrates that multiple beamlets of high optical quality can be produced. The recording times of living specimens with 4Pi-confocal microscopy can be decreased to a fraction of the rate of former setups (Egner *et al.*, 2002b, 2004).

IMAGING APPLICATIONS

MMM can be advantageously applied to the 3D imaging of biological specimens, including living cells, whenever rapid multi-photon imaging of not too-strongly-scattering specimens is needed. Pollen grains and the stem of *Prionium* stained with safranin-fast green are relatively thick, scattering test objects that have been imaged using oil-immersion lenses. Living PC12 cells stained with acridine orange, and neurons in the temporal cortex, that have been ionophoretically injected with Lucifer Yellow (Straub and Hell, 1998b) were recorded using water-immersion lenses. Nielsen and co-workers recorded 3D stacks of a CHO cell, doubly stained with ethidium bromide and fluorescein (Nielsen *et al.*, 2001). Fujita and colleagues imaged rat heart cells stained with eosin (Fujita *et al.*, 1999) as well as sections of a root of *convallaria* (Fujita *et al.*, 2000). In another study, bovine chromafin cells and NGF-differentiated PC12 cells, stained with the dyes acridin orange, FM1-43 and DiA as well as by transfection of the cells with green fluorescent protein (GFP), have been examined (Straub *et al.*, 2000). Moreover, the sectioning capability of MMM has been demonstrated in combination with 4Pi-confocal microscopy (for details see Chapter 30, *this volume*; Egner *et al.*, 2002b, 2004).

Examples of fast imaging of dynamic processes include the production of time sequences of sections through living boar sperm cells (Bewersdorf *et al.*, 1998) (Fig. 29.5), the imaging of Ca^{2+} dynamics (Fujita *et al.*, 2000), as well as a video-rate movie of the contraction of the motile microorganism *Euglena*, showing chlorophyll autofluorescence (Fittinghoff *et al.*, 2000). Using SHG-MMM, Kobayashi and colleagues recorded the contraction of rat cardiac myocytes at video rate (Kobayashi *et al.*, 2002). A study of particular biological relevance mapped Förster resonance energy transfer (FRET) using MMM to reveal important aspects of protein interaction in the Golgi apparatus in living cells (Majoul *et al.*, 2001, 2002) (see also Chapter 45, *this volume*).

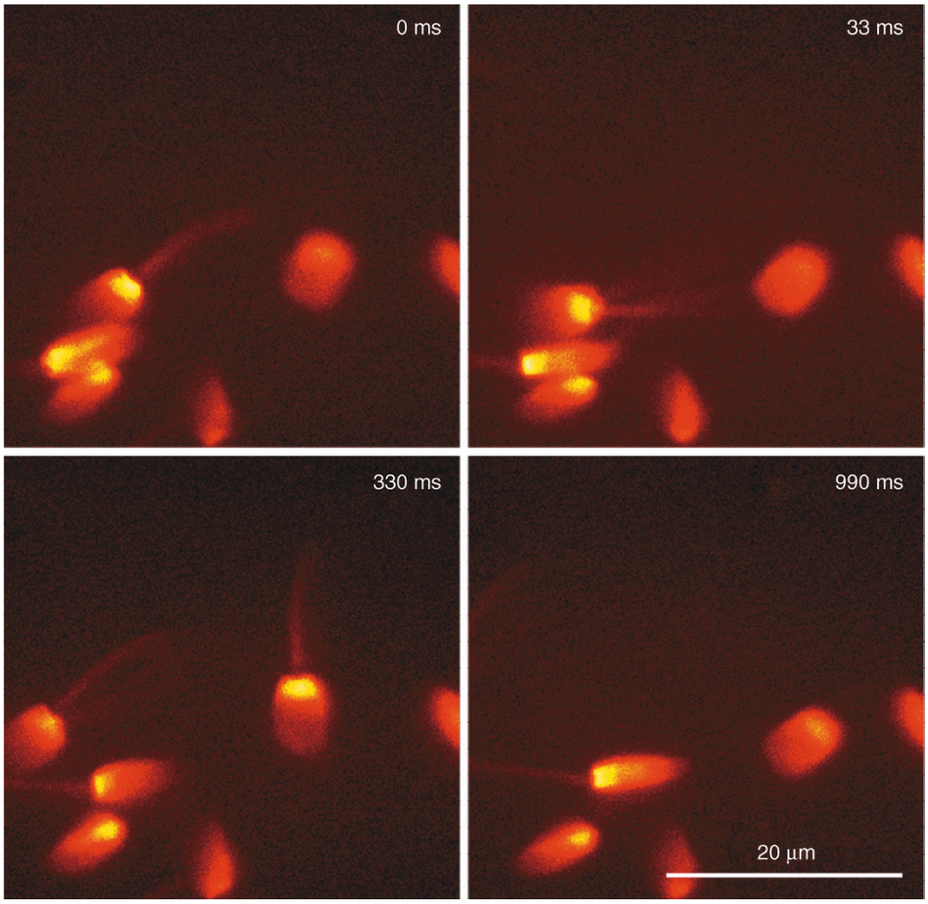
An interesting application of MMM in neurobiology involved the measurement of rapid changes in free Ca^{2+} concentration over a large field of view (Cossart *et al.*, 2003). By measuring the time traces of the 2PE fluorescence of the Ca^{2+}-sensitive dye FURA2-AM simultaneously in a few hundred cell bodies in hippocampal brain slices of mice, Cossart and colleagues localized microcircuits in the neuronal network. In the example shown in Figure 29.6, they recorded time series of a single *xy*-section (443 µm × 335 µm, ~100 µm deep inside the tissue) at a rate of 150 ms/frame over 5 min with the LaVision BioTec version of the MMM and identified the cell bodies from the averaged frames [Fig. 29.6(A,B)] (Cossart *et al.*, 2005). With this information, the fluorescence time traces [Fig. 29.6(C)] corresponding to the Ca^{2+} concentration in the individual cells can be analyzed. Every dip in a time trace is interpreted as the result of an action potential. By searching for correlations in the event patterns of all the recorded cell bodies [Fig. 29.6(D)], neural microcircuits were identified [marked red in Fig. 29.6(B)]. These studies allow simultaneous measurements of the dynamic and global characterization of neuronal network activity for the first time and permit one to determine the single-cell properties of the unitary microcircuits involved in this activity.

LIMITATIONS

While it does reduce higher order photodamage effects through parallelization, MMM has its own constraints. Though normally negligible in single-beam systems (Schönle and Hell, 1998), heating of the sample may become a problem if the overall average laser power supplied to the sample is relatively large. This holds in particular for small scanning areas or if the sample contains strong single-photon absorbers.

Multifocality also leads to crosstalk arising from the reinforced overlap of the focal fields of the multiple foci. Fortunately, with the mandatory pulsed illumination, the crosstalk of the illumination light can be almost entirely eliminated by time-multiplexing every beam. The only relevant crosstalk remaining then is that

FIGURE 29.5. *xy* images of living boar-sperm cells taken with the MMM within 33 ms (30 images/s). Four typical images from a movie of 191 images are displayed. Note the movement of the sperm tail within the first 33 ms.



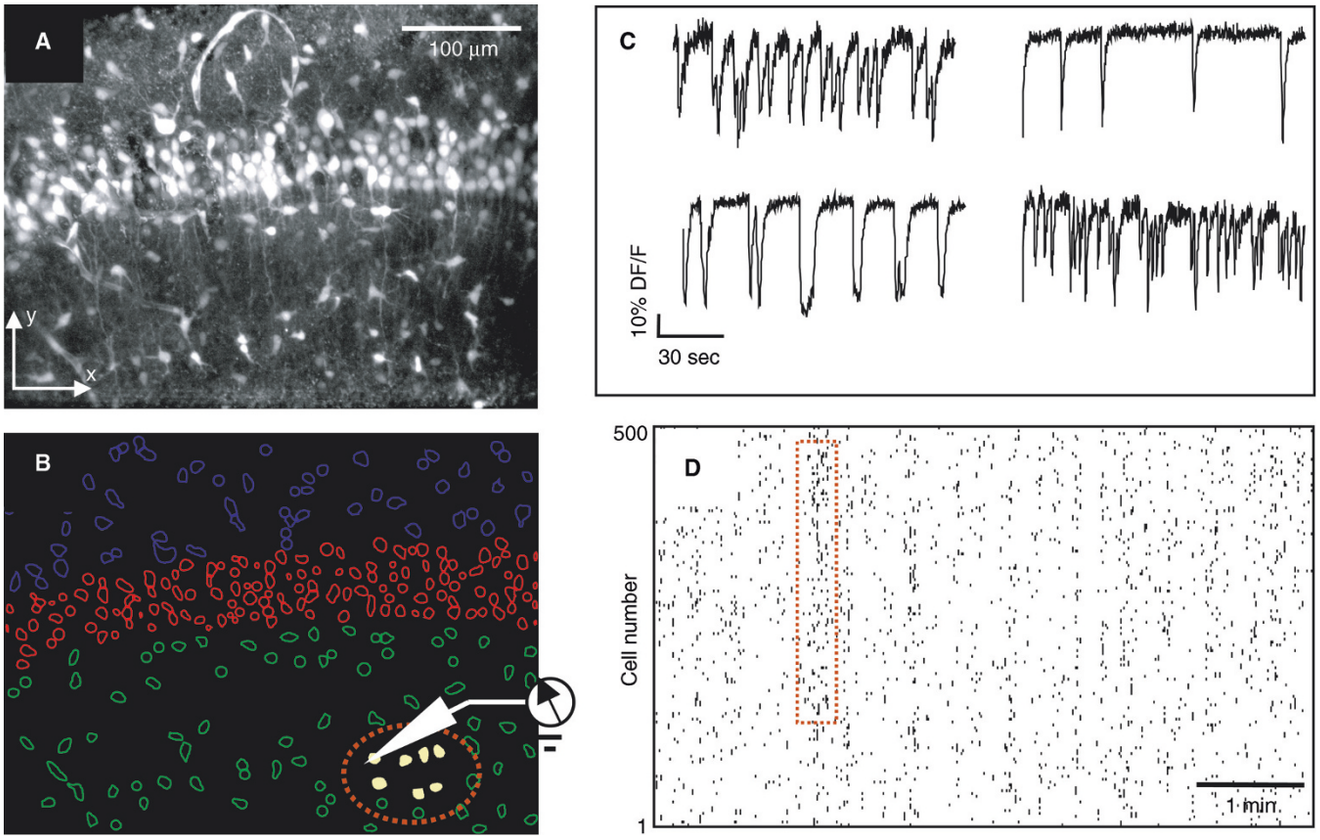


FIGURE 29.6. Identification of microcircuits in hippocampal brain slices with MMM. (A) Average of a time series of 500 consecutive frames showing the fluorescence of the Ca^{2+}-sensitive dye FURA2-AM (Olympus 20 × 0.95 NA water immersion, 150 ms/frame recording time). (B) Contours of the cell bodies automatically identified from (A). (C) Typical time traces of the fluorescence for single cell bodies taken from the time series. Each dip corresponds to an action potential causing the release of Ca^{2+} and is marked as an event in (D). (D) Rasterplot: Each horizontal line represents the time trace of a single cell. Networks are identified by correlated events (*red box*) in the rasterplot and can be visualized in the slice [*filled yellow contours* in (B)]. (Cossart *et al.*, 2005.)

which occurs because of scattering during the backimaging of the signal onto the plane of detection. However, this can be reduced by imaging the signal through an array of confocal pinholes. It also is less severe than in a conventional or in single-photon parallelized microscope, because the multi-photon–induced signal originates only at the focal plane. Figure 29.2 illustrates that the larger focal distance, the smaller number of foci, the implementation of TMX, as well as the nonlinear signal dependence in MMM leads to a crosstalk much smaller than in parallelized, single-photon confocal (Nipkow disk) microscopy (Egner *et al.*, 2002a). However, TMX could also be applied to the latter if lasers with short coherence lengths are used.

The crosstalk in the detection path and the attenuation of the intensity with deeper penetration depth may hamper the imaging of planes lying deep in strongly scattering specimens. For example, MMM is not advantageous for imaging hundreds of micrometers inside of brain tissue. Nevertheless, the success of this concept very much depends on the adaptation of the system layout to the detailed optical properties of the object. For example, one could still imagine an array of a comparatively small number of distinct foci, say 2×2, coupled to a matched array of detectors. Even without this, imaging approximately 50 µm inside of a scattering pollen grain or 100 µm inside of brain tissue is possible without major drawbacks in resolution or signal (see Figs. 29.2 and 29.6).

CURRENT DEVELOPMENTS

Of the known multi-photon imaging modes in microscopy, 2PE and SHG have already been implemented in the MMM fashion. The extension to 3PE (or even 4PE) is technically straightforward. Furthermore, the application of other multi-photon techniques to multi-focal microscopy should be uncomplicated if the microscope parameters are adjusted to the physical and biological limits of interaction cross-section and photodamage.

With the current progress in laser technology, the efficiency of MMM is expected to improve. The parallelization in MMM is not fundamentally limited by photophysical processes such as highly nonlinear damaging or bleaching or by the scanning speed. The enhancement of the efficiency in signal generation by parallelization scales directly with the increase in laser power. Thus, MMM profits directly from the new developments in laser technology. Even with the presently available lasers, a doubling of the efficiency can be achieved by combining the beams from two synchronized lasers with a polarizing beam-splitter to a single beam. Apart from a pure increase in laser power, the parameters of pulse length and repetition rate can be adapted to MMM for a more efficient operation. An increase in the repetition rate creates a better match than that between the typical 12.5 ns pulse interval of a 80 MHz laser and the 2 ns characteristic of most fluorophore decay constants, allowing a more time-efficient excitation (Bewersdorf and Hell, 1998). For samples particularly susceptible to highly nonlinear photodamage, the pulse length can be increased to reduce the peak intensity (Bewersdorf and Hell, 1998). In the opposite case, or to exploit excitation mechanisms having a higher degree of non-linearity, shorter pulse lengths can be advantageous.

A new generation of CCD cameras with on-chip amplification records with virtually no readout noise. Even though the amplification process increases the effective shot noise typically by a factor of $\sqrt{2}$ (Basden *et al.*, 2003), this allows faster imaging with frame rates at which the signal had been dominated by readout noise in the past. Alternatively, by using stage-scanning (Nielsen *et al.*, 2001), or even better, by descanning in the detection path, the CCD can also be replaced by an array of photomultipliers or avalanche photodiodes. A setup can, for example, be realized by exchanging the CCD camera in Figure 29.3(F) with a detector array and modifying the detection path so that the fluorescence light is not scanned. This alternative makes sense when imaging samples that exhibit significant scattering. By separating the foci and the concomitant detectors by a distance that is larger than the average radius of the "scattering bulb" induced by the sample, one can reduce crosstalk in the detection, while still detecting most of the fluorescence.

The design of the spinning microlens disk could easily be changed to a system that scans a line rather than a two-dimensional field. Scan rates of several thousand hertz are also in the range of resonant galvanometer scanners. However, with the spinning disk, dead times can be avoided (as long as the CCD can be read out fast enough). These features may be advantageous in physiological applications. The modification of the MMM concept to accommodate several lines at a defined distance, to a single broader line, or to other custom-defined illumination areas is also possible. Implementing microlenses with different focal lengths on the same spinning disk may be used to vary the scan plane within small dimensions as long as these are compatible with the aplanatic correction of the lens. A very interesting and promising realization of MMM implies a reduction of the lateral distance between the foci down to the size of the spot. With such an implementation scanning becomes obsolete. The result is a scanning microscope without any moving parts that, apart from the sample's linear-damage susceptibility, is limited in speed only by the pulse-repetition rate, the power of the laser, the stability of the specimen, and the readout speed of the detector (Egner and Hell, 2000; Andresen *et al.*, 2001). The realization of such a system has been demonstrated recently (Fricke and Nielsen, 2005).

For physiological applications, in which the signal of a confined illuminated region must be recorded with high temporal resolution, the MMM design can be modified so that the detection

TABLE 29.1. Advantages and Disadvantages of the Two Different Approaches of Subdividing the Beam

	Wavefront Division (Microlenses) [e.g., Fig. 29.3(A,B,E,F)]	Amplitude Division (Beam-Splitter, Etalon) [e.g., Fig. 29.3(C,D)]
Beam profile	+ Beamlet profiles close to uniform	– Each beamlet profile is a replica of the entire original laser beam profile
Homogeneity of the field of view	– Laser beam profile is transferred to field of view, resulting in lower amplitudes for outer beamlets	+ Same amplitude for all beamlets is achievable, but differences result in chessboard pattern effects
Scan speed	+ Possible use of spinning disk design allows extremely fast scan speeds >1000 frames/s	– Limited by galvanometer scanners
Handling	+ Spinning disk easy to adjust + Robust	– Adjustment more difficult + Flexible

provides no spatial resolution, for example, by using a photomultiplier tube that collects light from the illuminated area of the sample. While such a device would not provide spatial information, it would allow very fast readout of sequential data. The intrinsic 3D spatial confinement of the multi-photon–induced signal alone defines the observed volume. The illuminated region could be chosen so that signal generation is confined to a functional compartment allowing the accumulation of the signal of a larger area, increasing the sensitivity of the system. In contrast to single-beam microscopes, the shape of the illuminated region can be chosen more freely.

SUMMARY

Multi-photon microscopy complements conventional microscopy in numerous ways. However, the underlying low interaction cross-sections severely limit the resulting imaging speed and sensitivity. The use of multiple foci as practiced in MMM is an attractive solution to this problem that increases the data rate by the factor of the parallelization and avoids limitations arising from highly nonlinear damage effects or saturation. Several MMM setups have been realized, all demonstrating the various technical possibilities to parallelize multi-photon microscopy. They can broadly be divided into two groups that differ by the way they subdivide the laser beam into beamlets. Either it is the wavefront across the beam that is split into several adjacent fragments, or it is the amplitude of the laser beam that is divided into several consecutive beamlets that are eventually spread out in angle and then in space. Table 29.1 compares the advantages and disadvantages of the two approaches.

For regular imaging applications, MMM features an axial resolution that is largely uncompromised with respect to that of a single-beam scanning system. The interbeam crosstalk results in an elevated background but, in the illumination path, this can be largely avoided by time multiplexing. Due to the conservation of the phase in (nonlinear) scattering, time multiplexing is even more important for CARS, SHG, THG, etc., than for fluorescence imaging as it simply precludes non-linearly scattered light from interfering in the detection plane.

The spatial blur resulting from the transverse propagation of the non-linearly generated photons needs to be considered, but owing to the confinement of signal generation to the focal plane, this effect is significantly less pronounced than in widefield microscopy. Scattering can degrade the image quality and thus limit the maximum imaging depth. Most of the other advantages of multi-photon imaging, such as making ultraviolet (UV) illumination unnecessary for UV dyes, as well as the additional information gained from imaging modes that use nonlinear scattering, are retained.

Progress in the development of detectors and light sources will contribute to the enhancement and enlargement of the MMM family of microscopes. Additionally, new scanner and parallelization designs will further improve the performance of MMM, leading, among other things, to a fast scanning multi-photon microscopy without any moving parts.

ACKNOWLEDGMENTS

We thank R. Cossart, D. Aronov, and V. Crepel for the contribution of data about their experiments.

REFERENCES

Andresen, V., Egner, A., and Hell, S.W., 2001, Time-multiplexed multifocal multi-photon microscope, *Opt. Lett.* 26:75–77.

Barad, Y., Eisenberg, H., Horowitz, M., and Silberberg, Y., 1997, Nonlinear scanning laser microscopy by third harmonic generation, *Appl. Phys. Lett.* 70:922–924.

Basden, A.G., Haniff, C.A., and Mackay, C.D., 2003, Photon counting strategies with low-light-level CCDs, *Monthly Notices RAS* 345:985–991.

Bewersdorf, J., and Hell, S.W., 1998, Picosecond pulsed two-photon imaging with repetition rates of 200 and 400 MHz., *J. Microsc.* 191:28–38.

Bewersdorf, J., Pick, R., and Hell, S.W., 1998, Multifocal multi-photon microscopy, *Opt. Lett.* 23:655–657.

Buist, A.H., Müller, M., Squier, J., and Brakenhoff, G.J., 1998, Real time two-photon absorption microscopy using multipoint excitation, *J. Microsc.* 192:217–226.

Campagnola, P.J., Millard, A.C., Terasaki, M., Hoppe, P.E., Malone, C.J., and Mohler, W.A., 2002, Three-dimensional high-resolution second-harmonic generation imaging of endogenous structural proteins in biological tissues, *Biophys. J.* 81:493–508.

Centonze, V.E., and White, J.G., 1998, Multi-photon excitation provides optical sections from deeper within scattering specimens than confocal imaging, *Biophys. J.* 75:2015–2024.

Cheng, J.X., Jia, Y.K., Zheng, G., and Xie, X.S., 2002, Laser-scanning coherent anti-Stokes Raman scattering microscopy and applications to cell biology, *Biophys. J.* 83:502–509.

Cossart, R., Aronov, D., and Yuste, R., 2003, Attractor dynamics of network UP states in the neocortex, *Nature* 423:283–288.

Cossart, R., Ikegaya, Y., and Yuste, R., 2005, Calcuim imaging of cortical network dynamics, *Cell* 37:451–457.

Cox, G., Kable, E., Jones, A., Fraser, I., Manconi, F., and Gorrell, M.D., 2003, Three-dimensional imaging of collagen using second harmonic generation, *J. Struct. Biol.* 141:53–62.

Curley, P.F., Ferguson, A.I., White, J.G., and Amos, W.B., 1992, Applications of a femtosecond self-sustained mode-locked Ti : sapphire laser to the field of laser scanning confocal microscopy, *Opt. Quantum Electron.* 24:851–859.

Denk, W., and Svoboda, K., 1997, Photon upmanship: Why multi-photon imaging is more than a gimmick, *Neuron* 18:351–357.

Denk, W., Strickler, J.H., and Webb, W.W., 1990, Two-photon laser scanning fluorescence microscopy, *Science* 248:73–76.

Duncan, M.D., Reintjes, J., and Manuccia, T.J., 1982, Scanning coherent anti-Stokes Raman microscope, *Optics Lett.* 7:350–352.

Egner, A., and Hell, S.W., 2000, Time multiplexing and parallelization in multifocal multi-photon microscopy, *J. Opt. Soc. Am. A.* 17:1192–1201.

Egner, A., Andresen, V., and Hell, S.W., 2002a, Comparison of the axial resolution of practical Nipkow-disk confocal fluorescence microscopy with that of multifocal multi-photon microscopy: Theory and experiment, *J. Microsc.* 206:24–32.

Egner, A., Jakobs, S., and Hell, S.W., 2002b, Fast 100-nm resolution 3D-microscope reveals structural plasticity of mitochondria in live yeast, *Proc. Natl. Acad. Sci. USA* 99:3370–3375.

Egner, A., Verrier, S., Goroshkov, A., Söling, H.-D., and Hell, S.W., 2004, 4Pi-microscopy of the Golgi apparatus in live mammalian cells, *J. Struct. Biol.* 147:70–76.

Fittinghoff, D.N., and Squier, J.A., 2000, Time-decorrelated multifocal array for multi-photon microscopy and micromachining, *Opt. Lett.* 25:1213–1215.

Fittinghoff, D.N., Wiseman, P.W., and Squier, J.A., 2000, Widefield multiphoton and temporally decorrelated multifocal multi-photon microscopy, *Opt. Express* 7:273–279.

Fricke, M., and Nielsen, T., 2005, Two-dimensional imaging without scanning by multifocal multiphoton microscopy, *Appl. Opt.* 45(15):2984–2988.

Fujita, K., Nakamura, O., Kaneko, T., Kawata, S., Oyamada, M., and Takamatsu, T., 1999, Real-time imaging of two-photon-induced fluorescence with a microlens-array scanner and a regenerative amplifier, *J. Microsc.* 194:528–531.

Fujita, K., Nakamura, O., Kaneko, T., Oyamada, M., Takamatsu, T., and Kawata, S., 2000, Confocal multipoint multi-photon excitation microscope with microlens and pinhole arrays, *Opt. Commun.* 174:7–12.

Gannaway, J.N., 1978, Second-harmonic imaging in the scanning optical microscope, *Opt. Quant. Electr.* 10:435–439.

Gauderon, R., Lukins, P.B., and Sheppard, C.J.R., 1998, Three-dimensional second-harmonic generation imaging with femtosecond laser pulses, *Opt. Lett.* 23:1209–1211.

Guo, Y., Ho, P.P., Savage, H., Harris, D., Sacks, P., Schantz, S., Liu, F., Zhadin, N., and Alfano, R.R., 1997, Second-harmonic tomography of tissues, *Opt. Lett.* 22:1323–1325.

Hänninen, P.E., Schrader, M., Soini, E., and Hell, S.W., 1995, Two-photon excitation fluorescence microscopy using a semiconductor laser, *Bioimaging* 3:70–75.

Hell, S.W., and Andresen, V., 2001, Space-multiplexed multifocal nonlinear microscopy, *J. Microsc.* 202:457–463.

Hell, S.W., Bahlmann, K., Schrader, M., Soini, A., Malak, H., Gryczynski, I., and Lakowicz, J.R., 1996, Three-photon excitation in fluorescence microscopy, *J. Biomed. Opt.* 1:71–73.

Hellwarth, R., and Christensen, P., 1974, Nonlinear optical microscopic examination of structures in polycrystalline ZnSe, *Opt. Commun.* 12:318–322.

Hopt, A., and Neher, E., 2001, Highly nonlinear photodamage in two-photon fluorescence microscopy, *Biophys. J.* 2029–2036.

Kobayashi, M., Fujita, K., Kaneko, T., Takamatsu, T., Nakamura, O., and Kawata, S., 2002, Second-harmonic-generation microscope with a microlens array scanner, *Opt. Lett.* 27:1324.

König, K., Becker, T.W., Fischer, P., Riemann, I., and Halbhuber, K.-J., 1999, Pulse-length dependence of cellular response to intense near-infrared laser pulses in multi-photon microscopes, *Opt. Lett.* 24:113–115.

König, K., So, P.T.C., Mantulin, W.W., Tromberg, B.J., and Gratton, E., 1996, Two-photon excited lifetime imaging of autofluorescence in cells during UVA and NIR photostress, *J. Microsc.* 183:197–204.

Maiti, S., Shear, J.B., Williams, R.M., Zipfel, W.R., and Webb, W.W., 1997, Measuring serotonin distribution in live cells with three-photon excitation, *Science* 275:530–532.

Majoul, I., Straub, M., Duden, R., Hell, S.W., and Söling, H.D., 2002, Fluorescence resonance energy transfer analysis of protein–protein interactions in single living cells by multifocal multi-photon microscopy, *Rev. Mol. Biotechnol.* 82:267–277.

Majoul, I., Straub, M., Hell, S.W., Duden, R., and Söling, H.-D., 2001, KDEL-cargo regulates interactions between proteins involved in COPI vesicle traffic: Measurements in living cells using FRET, *Dev. Cell* 1:139–153.

Müller, M., and Schins, J.M., 2002, Imaging the thermodynamic state of lipid membranes with multiplex CARS microscopy, *J. Phys. Chem. B* 106: 3715–3723.

Müller, M., Squier, J., Wilson, K.R., and Brakenhoff, G.J., 1998, 3D microscopy of transparent objects using third-harmonic generation, *J. Microsc.* 191:266–274.

Nielsen, T., Fricke, M., Hellwig, D., and Andersen, P., 2001, High efficiency beam splitter for multifocal multi-photon microscopy, *J. Microsc.* 201:368–376.

Patterson, G.H., and Piston, D.W., 2000, Photobleaching in two-photon excitation microscopy, *Biophys. J.* 78:2159–2162.

Petran, M., Hadravsky, M., and Boyde, A., 1985, The tandem scanning reflected light microscope, *Scanning* 7:97–108.

Petran, M., Hadravsky, M., Egger, M.D., and Galambos, R., 1968, Tandem-scanning reflected-light microscope, *J. Opt. Soc. Am.* 58:661–664.

Schönle, A., and Hell, S.W., 1998, Heating by absorption in the focus of an objective lens, *Opt. Lett.* 23:325–327.

Shafer, D., 1982, Gaussian to flat-top intensity distribution lens, *Opt. Laser Technol.* 14:159–160.

Shen, Y.R., 1984, *The Principles of Nonlinear Optics*, John Wiley and Sons, New York.

Straub, M., and Hell, S.W., 1998a, Fluorescence lifetime three-dimensional microscopy with picosecond precision using a multifocal multi-photon microscope, *Appl. Phys. Lett.* 73:1769–1771.

Straub, M., and Hell, S.W., 1998b, Multifocal multi-photon microscopy: A fast and efficient tool for 3-D fluorescence imaging, *Bioimaging* 6:177–185.

Straub, M., Lodemann, P., Holroyd, P., Jahn, R., and Hell, S.W., 2000, Live cell imaging by multifocal multi-photon microscopy, *Eur. J. Cell Biol.* 79:726–734.

Theer, P., Mazahir, H.T., and Denk, W., 2003, Two-photon imaging to a depth of 1000 μm in living brains by use of a Ti:Al_2O_3 regenerative amplifier, *Opt. Lett.* 28:1022–1024.

Yelin, D., Oron, D., Korkotian, E., Segal, M., and Silberberg, Y., 2002, Third-harmonic microscopy with a titanium–sapphire laser, *Appl. Phys. B* 74(Suppl):S97–S101.

Zipfel, W.R., Williams, R.E., and Webb, W.W., 2003, Nonlinear magic: Multi-photon microscopy in the biosciences, *Nat. Biotechnol.* 21:1369–1377.

Zoumi, A., Yeh, A., and Tromberg, B.J., 2002, Imaging cells and extracellular matrix *in vivo* by using second-harmonic generation and two-photon excited fluorescence, *Proc. Natl. Acad. Sci. USA* 99:11014–11019.

Zumbusch, A., Holtom, G.R., and Xie, X.S., 1999, Three-dimensional vibrational imaging by coherent anti-Stokes Raman scattering, *Phys. Rev. Lett.* 82:4142–4145.

30

4Pi Microscopy

Jörg Bewersdorf, Alexander Egner, and Stefan W. Hell

INTRODUCTION

The axial (z-) resolution of any fluorescence microscope using a single lens is limited by diffraction to >500 nm. While a modest improvement by up to a factor of 2 may be achieved by mathematical deconvolution, a substantial improvement of the axial resolution requires a radical change of the physics of imaging. Since the 1990s, two families of methods have evolved that accomplished substantially improved axial resolution in three-dimensional (3D) imaging. The first family, comprising 4Pi microscopy and I^{5}M, coherently combines the aperture of two opposing lenses (Hell and Stelzer, 1992a, 1992b; Gustafsson *et al.*, 1995, 1999; Egner and Hell, 2005). The second family, of which stimulated emission depletion (STED) microscopy (Hell and Wichmann, 1994; see also Chapter 31, *this volume*) is the most established member, exploits photophysical or photochemical properties of the dye to break the diffraction barrier. Using two lenses for STED, the axial resolution was improved down to 30 to 50 nm (Dyba and Hell, 2002; Dyba *et al.*, 2003). However, as STED is still in its infancy and, unlike I^{5}M and 4Pi microscopy, relies on the specific properties of the dye, it is not surprising that the majority of recent 3D-imaging applications showing axial super-resolution in (live) cells have been carried out with the 4Pi microscope (Egner *et al.*, 2002b, 2004; Gugel *et al.*, 2004).

4Pi microscopy coherently illuminates the sample through two opposing lenses. Constructive interference of the counterpropagating spherical wavefronts narrows the main focal maximum of the excitation light in the z-direction, and this forms the basis for a 3- to 7-fold improved axial resolution. Unfortunately, the interference of spherical wavefronts also produces so-called sidelobes[1] that are located at about half a wavelength above and below the focal plane. Moreover, these primary lobes are accompanied by weaker periodic lobes that increase in height with decreasing semi-aperture angle α. The lobes produce ghost images that have to be removed by mathematically postprocessing the 3D data. The accuracy with which these ghost images can be removed depends on the relative height of the sidelobes compared to the main peak. As a rule of thumb, the primary lobe height should never exceed ~50% of the main focal spot. Unfortunately, available immersion lenses all feature $\alpha < 68°$ so that the primary lobe height ranges from 60% to 70% of the main peak. Additional optical techniques for lobe suppression thus have to be implemented, of which the most effective are:

- **Confocal detection**: Fluorescence emitted from out-of-focus planes is detected less efficiently, thus suppressing fluorescence detection from the sidelobes.
- **Two-photon excitation (2PE)**: The quadratic dependence of the excitation efficiency on the illumination intensity lowers the excitation sidelobe height relative to the central peak. Additionally, due to the longer wavelength of the near-infrared light used (Denk *et al.*, 1990), the sidelobes are shifted away from the focal plane and are better suppressed by the pinhole.[2]
- **Combined interference of the excitation and the detection wavefront pairs**: The wavelength disparity leads to different axial positions of the excitation and the detection sidelobes. As a result, fluorescence originating from the excitation sidelobes is weakened by incomplete detection. 2PE entails a pronounced and very useful wavelength disparity (Hell and Stelzer, 1992a, 1992b; Gugel *et al.*, 2004).

The potential of these three lobe-suppression techniques was already recognized in the early stages of 4Pi microscopy (Hell and Stelzer, 1992a, 1992b). In fact, the use of 2PE together with confocal detection has been the method of choice ever since. The third technique is more difficult to realize. The optical setup must be designed such that not only the excitation light interferes at the sample (Type A 4Pi), but also the detection light interferes at the point of detection (Type C 4Pi). Initially, Type C 4Pi-microscopy could be demonstrated only for scattered light, where excitation and detection wavelengths are the same and the implementation is much simpler (Hell *et al.*, 1994). A feasible realization for fluorescence that exploits the suppression potential of this technique is shown in a recent publication (Gugel *et al.*, 2004). The 2PE Type C mode combines all three mechanisms and thus features the lowest achievable sidelobes. This attribute greatly simplifies the image restoration process. Additionally, Type C 4Pi microscopy obtains a ~30% better resolution than its Type A counterpart.

In contrast to 4Pi microscopy, I^{5}M uses planar standing waves for fluorescence excitation; in fluorescence detection, the coherent addition of spherical waves is performed just as in a 4Pi Type C microscope. In I^{5}M, the joint action of illumination and detection interference is mandatory because other mechanisms of lobe suppression are absent here. This results in relatively high sidelobes making image restoration more difficult (Bewersdorf *et al.*, 2005; see Appendix, *this chapter*).

[1] Actually they are located above and below, rather than to either side.

[2] On the other hand, 2-photon 4Pi can only be implemented optimally if the total optical lengths of each side of the interferometer are equal, ±10 µm.

Jörg Bewersdorf, Alexander Egner, and Stefan W. Hell • Max Planck Institute for Biophysical Chemistry, 37070 Göttingen, Germany

Apart from the sidelobe reduction, 4Pi microscopy has also undergone significant progress in terms of increasing the recording speed. Due to the smaller focal volume of excitation, less total fluorescence is excited at a given time point. Additionally, the axially narrower focal spot requires finer sampling. The deconvolution required for the lobe removal also sets a limit to the acceptable minimum signal-to-noise ratio (S/N). Thus, to achieve an adequate S/N, the recording time may easily take longer by the factor by which the volume resolution is reduced typically by a factor of two. Lengthened recording times may be counteracted by investigating smaller regions. Another powerful approach is to parallelize the recording process by using many 4Pi foci in parallel, as in a multifocal multi-photon microscope (MMM, see Chapter 29, *this volume*) (Bewersdorf *et al.*, 1998). In fact, the combination of MMM with 4Pi microscopy has resulted in a fast axially super-resolving microscope (Egner *et al.*, 2002b, 2004). In this chapter we give an overview of modern beam-scanning 4Pi microscopy based on the two most recent realizations: the MMM-4Pi as described by Egner and colleagues and the Leica TCS 4PI, which is a compact Type C 4Pi microscope that has recently become commercially available.

THEORETICAL BACKGROUND

The Point Spread Function

The imaging capabilities of a microscope, such as the resolution, are quantified by the effective PSF $h(\vec{x})$, that is, the response of the microscope to a fluorescent point. The effective PSF can be calculated as the product of the excitation PSF and the detection PSF, $h_{exc}(\vec{x})\, h_{det}(\vec{x})$. The excitation PSF $h_{exc}(\vec{x})$ is proportional to the illumination intensity squared in the focal region and, apart from a constant factor, can be written as

$$h_{exc}(\vec{x}) = |\vec{E}_{ill}(\vec{x}) + \hat{M} \cdot \vec{E}_{ill}\,(\hat{M} \cdot \vec{x})|^4$$

with

$$\hat{M} := \begin{pmatrix} 1 & 0 & 0 \\ 0 & 1 & 0 \\ 0 & 0 & -1 \end{pmatrix}$$

where $\vec{E}_{ill}(\vec{x})$ denotes the focal light field of the illumination by a single lens and $\hat{M}$ is a transformation matrix accounting for the counterpropagation of the fields in the 4Pi microscope. 2PE is incorporated by the forth power of the illumination light field (instead of the quadratic power for single-photon excitation).

For the detection PSF $h_{det}(\vec{x})$ that expresses the spatial distribution of the detection efficiency, the finite pinhole size has to be taken into account. $h_{det}(\vec{x})$ also depends on the 4Pi mode:

$$h_{det,4Pi-A}(\vec{x}) = |\vec{E}_{det}(\vec{x})|^2 \otimes p(\vec{x}) \quad \text{for Type A}$$

$$h_{det,4Pi-C}(\vec{x}) = |\vec{E}_{det}(\vec{x}) + \hat{M} \cdot \vec{E}_{det}(\hat{M} \cdot \vec{x})|^2 \otimes p(\vec{x}) \quad \text{for Type C}$$

In analogy to the illumination light field and due to reasons of symmetry, $\vec{E}_{det}(\vec{x})$ represents the normalized amplitude of the detection of the fluorescence light field emanating from the focal region. To consider the role of the pinhole, $\vec{h}_{det}(\vec{x})$ is convolved with $p(\vec{x})$, denoting the pinhole function is effective in the focal region. Using a vectorial focusing theory (Richards and Wolf, 1959) $\vec{E}_{ill}(\vec{x})$ and $\vec{E}_{det}(\vec{x})$ can be calculated thoroughly. Theoretical PSFs for Type A and C 4Pi microscopy are displayed in Figure 30.1. Comparing the extent of the central maxima of the 4Pi PSFs with that of the

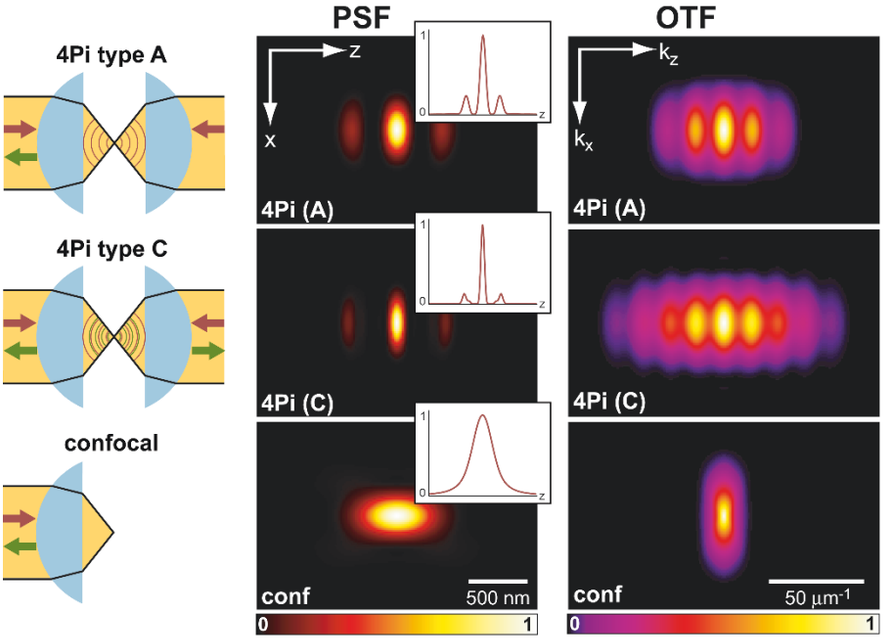


FIGURE 30.1. The PSFs and OTFs of two-photon excitation 4Pi microscopy. In Type A 4Pi microscopy, the sample placed between two coverslips is coherently illuminated by two opposing objective lenses focusing a pulsed infrared laser beam into the same spot. The 2PE fluorescence is collected from a single side and focused onto a (variable) confocal pinhole. While the excitation mode is the same, in Type C 4Pi microscopy, the fluorescence is collected by both lenses and coherently combined at the detector. As can be seen from the calculated PSFs and the z-responses shown as insets, the 4Pi microscope (water-immersion lens 1.20 NA, $\lambda_{0,exc} = 870\,\text{nm}$, $\lambda_{0,det} = 510\,\text{nm}$, pinhole diameter of 1 Airy disk) features a four- to sevenfold enhanced axial FWHM compared to confocal microscopy ($\lambda_{0,exc} = 488\,\text{nm}$, $\lambda_{0,det} = 510\,\text{nm}$, pinhole diameter of 1 Airy disk). Due to the combination of the interference in excitation and detection, the Type C mode exhibits lower sidelobes and by a ~30% increased axial resolution compared to Type A. The superior resolution of 4Pi microscopy also becomes evident in the much larger support of the 4Pi-OTFs as compared to the confocal OTF. Due to the low sidelobes in the PSF, the 4Pi-OTF is not only free of missing frequencies but also of weak amplitudes within the region of support.

standard confocal PSF makes the resolution increase evident. The sidelobes located ~$\lambda_{0,exc}/2$ away are also visible.

In the case of the MMM-4Pi, the PSF has to be modified in order to take into account the multiple foci and the charge-coupled device (CCD) camera detection. However, the differences between the PSFs of a single focus Type A 4Pi microscope and the actual MMM-4Pi instrument are almost negligible (Egner *et al.*, 2002b).

The *z*-Response and the Axial Resolution

4Pi microscopy improves the resolution only along the optic axis. The lateral resolution remains, strictly speaking, the same. However, one has to realize that the fundamental reduction in the thickness of the optical sections also yields a significantly improved perception of details in the focal plane, almost as a beneficial side effect. This is because details that are only slightly (35–75 nm) away from the focal plane are suppressed significantly better than in a confocal microscope, in which a similar reduction requires a displacement of >250 nm.

The z-response of an infinitely thin fluorescent layer, $I_z(z) = \int\int h(\vec{x})dxdy$, is a good benchmark for the axial resolution. The insets in Figure 30.1 show the z-responses for Type A and Type C 4Pi microscopes compared with that of the standard confocal system. For typical imaging conditions, the height of the sidelobes in 2PE Type A 4Pi microscopy remains well below 50%; for the Type C it is lowest. Importantly, the sidelobes increase dramatically in height for decreasing aperture angles. Typically, one uses immersion lenses of a numerical aperture (NA) of 1.4 (oil), 1.35 (glycerol), and 1.2 (water), featuring semi-aperture angles of $\alpha = 67°$, 68° and 64°, respectively. In 4Pi microscopy, the aperture angle has only a marginal impact on the axial width of the central spot. Because it is an interference phenomenon of the two counterpropagating waves, the z-width of the central spot scales predominantly with the wavelength in the embedding medium. For $\lambda_{0,exc} = 870$ nm, $\lambda_{0,det} = 510$ nm, $n = 1.334$ (water immersion) and an angle α of ~65°, axial resolutions of ~150 nm (Type A 4Pi) and ~105 nm (Type C 4Pi) are reliably obtained.

The Optical Transfer Function

Representing the Fourier transform of the PSF, the OTF indicates which spatial frequencies of the sample are transmitted by the microscope to form the image. A poorly transmitted spatial frequency means that two objects separated by the corresponding distance (the reciprocal value of the frequency) are blurred into each other in the image. The periodic pattern of the sidelobes of the 4Pi microscope represents such a correlation in space. The more pronounced the sidelobes in the PSF are, the lower the OTF amplitude at the matching spatial frequency is. The removal of the ghost images in the image data by deconvolution methods is in fact an amplification of the weakly transmitted frequencies so that the final OTF becomes smooth and contiguous. The more these amplitudes are masked by noise the more difficult is their reconstruction. Therefore, by analyzing the frequency content of the OTF and the concomitant noise level presented by an object, one learns whether a microscope and the imaging of a particular object are vulnerable to artifacts. The theoretical OTFs for Type A and Type C 4Pi together with their confocal counterpart are shown in Figure 30.1. The 4Pi-OTFs are contiguous; there are no missing gaps or strongly suppressed regions. Compared to the standard confocal OTF, the 4Pi-OTF features a 4- to 7-fold expanded region of support.

MULTI-FOCAL MULTI-PHOTON MICROSCOPY-4Pi MICROSCOPY

The MMM-4Pi microscope (Egner *et al.*, 2002a) has been designed to increase the recording speed compared to a single-beam 4Pi microscope. It consists of the two subunits sketched in Figure 30.2. The head of the MMM-4Pi includes the beam-splitter and the objective lenses that are illuminated through balanced interferometric arms. Axial scanning is performed by moving the sample along the optic axis (z) as in standard confocal microscopes. The multi-focal beam scanning arrangement is shown in the lower part of Figure 30.2. The beam of a mode-locked titanium:sapphire (Ti:Sa) laser is split by an array of microlenses, producing an $n \times m$ array of beamlets that, after passing through a dichroic mirror, are focused onto an array of pinholes. The pinholes act as point sources for creating the 4Pi illumination spots in the sample. After passing the pinholes, each beamlet is collimated by an achromatic lens and directed towards a rapidly oscillating galvanometric mirror. The following lenses ensure that the galvanometric mirror is imaged into the entrance pupils of the objective lenses. The rapid tilt of the mirror results in lateral scanning of the illumination 4Pi foci in the x-direction; this is the standard scanning procedure found in state-of-the-art confocal beam scanners. Scanning of the beamlets in the y-direction is accomplished by translating the combined

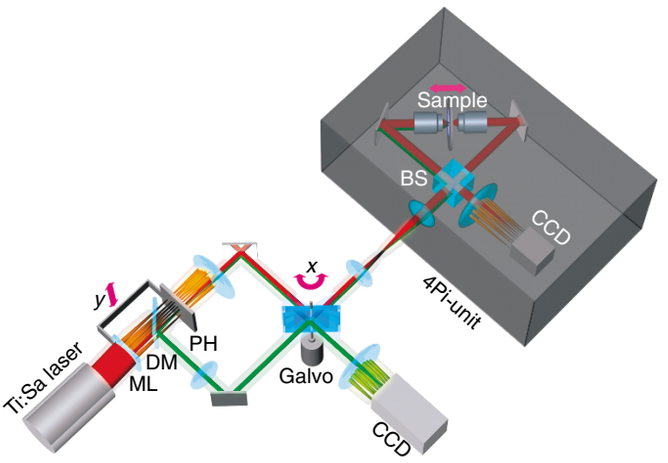


FIGURE 30.2. Scheme of the MMM-4Pi. An array of microlenses (ML) divides the laser beam of a Ti:Sa laser into an array of beamlets. Focused onto a pinhole array (PH), the emerging cleaned beamlets act as point sources for the 4Pi illumination. The beamlets are deflected by the scan mirror (Galvo) and directed towards the 4Pi unit. The beam-splitter (BS) splits up the beams and the beamlets are focused into the sample by both objective lenses. The small CCD detector in the 4Pi unit that detects laser light transmitted through both objective lenses serves as an alignment tool. The fluorescence light is collected by the left objective lens and imaged back onto the pinholes. A dichroic mirror (DM) separates the fluorescence light from the laser light and directs the fluorescence towards the CCD camera. Axial scanning is performed by moving the sample stage along the optic axis. The lateral scan is performed by a rapid tilt of the galvanometric mirror in conjunction with a slower, coordinated movement of the microlens–pinhole array unit. By reflecting the detection light at the backside of the galvanometric mirror, the fluorescence foci are scanned across the CCD camera.

microlens and pinhole array. The fluorescence is collected by the objective lens on the left-hand side and deflected by the galvanometric mirror in order to be back-imaged onto the pinhole array. The diameter of the pinholes corresponds to 1.25 times the diameter of the back-projected Airy disk (i.e., the diameter of the first dark ring). This slight confocalization allows the suppression of the axial sidelobes and also reduces the residual aberrations stemming from the microlenses. After the filtering by the pinholes, the fluorescence light is reflected by the long-pass dichroic mirror towards the reflective backside of the galvanometric mirror. The tilt movement of the latter scans the array of fluorescence beamlets across a CCD camera. Scanning the fluorescence beamlets with the backside of the galvanometric mirrors locks the scan of the excitation foci with that of fluorescence (Brakenhoff and Visscher, 1992). n and m range between 4 and 8, so that a total of $N = n \times m = 16$ to 64 parallel 4Pi foci is typical. Each of them usually performs $\sim 4 \times 4\,\mu m^2$ scans resulting in a field of view of up to $\sim 32 \times 32\,\mu m^2$.

The speed of the MMM-4Pi depends on the degree of parallelization N. The parallelization in turn depends on the available laser power. The average power of 1 to 2 mW in each 4Pi spot leads to a focal peak intensity of $\sim 80\,GW/cm^2$, which is lower than the $\sim 200\,GW/cm^2$ considered as an upper limit with ~200 fs pulses (König *et al.*, 1999). As a mode-locked Ti:Sa laser emits 1 to 2 W of average power, a parallelization by 1000 foci rather than by $N = 16$ to 64 appears to be possible. At present, such a degree of parallelization is precluded by the losses connected with the "cleaning" of the laser output and clipping of the beamlet profile by the pinhole array.

A fundamental problem of any parallelized 3D microscope is the potential crosstalk between neighboring illumination and detection foci. If present, crosstalk deteriorates the axial resolution of the system by re-enforcing specific planes above and beneath the focal plane (Egner and Hell, 2000; Egner *et al.*, 2002a). It was found that in an MMM-4Pi featuring a quadratic grid arrangement, the 4Pi-foci can be brought as close as $3.5\,\lambda_{exc} \approx 2.8\,\mu m$ without inducing significant crosstalk. Therefore, parallelization does not compromise the resolution of a properly designed MMM-4Pi setup (see also Chapter 29, *this volume*).

Space Invariance of the Point Spread Function

To assure accurate image deconvolution, the PSF must be the same throughout the recorded volume. In 4Pi microscopy, this issue is particularly relevant because the phase difference between the two interfering wavefronts has to be kept constant. A (random) change in phase would mean that the PSF varies greatly in the sample. While the envelope of the 4Pi-PSF usually does not significantly change for thin cell layers, a change in phase difference radically alters the interference of the two beams and hence the structure of the 4Pi spot. The following issues are relevant:

- The MMM-4Pi and the Leica TCS 4PI are beam-scanning systems. To ensure the invariance of the PSF over the whole field of view, the two interferometric arms of the 4Pi microscope are constructed symmetrically. Proper adjustment ensures that the phase is constant over a field >30 μm, as can be seen in Figure 30.3(A–C) (Egner *et al.*, 2002a).
- Slight differences in the refractive index of immersion and mounting medium lead to a z-dependent phase. For the refractive index mismatches typically encountered in the sample, it has been shown that this relationship is linear over a large distance (Egner *et al.*, 1998). If the magnitude of this distortion is known, a linear change in the length of one of the 4Pi arms with changing z-position of the sample can correct for this phase shift during scanning.
- Irregular changes of the refractive index within the specimen also influence the phase difference between the interfering wavefronts.

To explore whether these conditions can be fulfilled, 3D stacks of (mammalian) *Vero* cells were recorded with water immersion lenses (Egner *et al.*, 2004). The cells were grown on a coverslip coated with Oregon Green and then covered with a similar coverslip so that they were essentially sandwiched between two ultrathin fluorescent layers. To correct for the difference in the refractive indices of the aqueous mounting medium (1.34) and water (1.33) used as immersion medium, the phase had to be adjusted linearly with the z-position. Figure 30.3(D) shows an xz-section of a typical 3D data stack containing a part of the nucleus. The xz-section through the layers on the coverslips and the resulting z-profile disclose the quality of the interference between the two wavefronts. Profiles are extracted from three different sites in the nuclear region, in which the local variations in refractive index are strongly pronounced: completely outside the nucleus, at the nuclear periphery, and straight through the nucleus [Fig. 30.3(E)]. Although slight changes become apparent, the phase does not notably change with the axial translation. This can be inferred from the comparison between the profiles in the same line, pertinent to the different coverslips. Comparison of the profiles from the same coverslip reveals that the presence of the nucleus introduces aberrations leading to elevated sidelobes, but again the changes in refractive index are not pronounced enough to distort the PSF of the 4Pi microscope. In the perinuclear region, the sidelobe height is lower than the critical value of 50% of the central peak, but if the nucleus is directly involved, the lobes are slightly elevated. The upper profile of Figure 30.3(E) also shows that the refractive index challenges are relaxed when largely omitting the nucleus–cytosol interface.

Live Mammalian Cell 4Pi Imaging

In order to further substantiate the applicability of 4Pi microscopy to living mammalian cells, the distribution of two Golgi marker enzymes labeled by EGPF inside living *Vero* cells have been imaged at 32°C with the MMM-4Pi microscope. The marker enzymes were UDP-galactosyl:glycoprotein,1,4-β-galactosyl transferase (GalT), which is highly enriched in the middle and trans Golgi membranes and 3′-phosphoadenylyl-sulfate:uronyl-2-O-sulfotransferase (2-OST) which is a *cis* Golgi marker.

The analysis of series of subsequent 3D recordings of the GalT-EGFP distribution in a live *Vero* cell at 32°C with the MMM-4Pi showed that the movement of the living Golgi apparatus does not pose particular challenges. The slight morphological changes observed between two subsequent recordings occur on a much larger time scale than the scanning of the 4Pi-PSF across each position in the cell. Thus, they did not compromise the space invariance of the PSF and the slight changes did not preclude the proper deconvolution of the data to achieve a 3D resolution of ~100 nm. In addition, the repeated recording of the Golgi apparatus did not show a significant reduction in image brightness. Therefore, photobleaching of EGFP was not an issue in these samples. The cells remained viable even after prolonged mounting in the custom-built chamber for several days. The comparatively large space of 175 μm between the two coverslips and the addition of a suitable air/CO_2 mix is adequate to maintain division and propagation without apparent degradation.

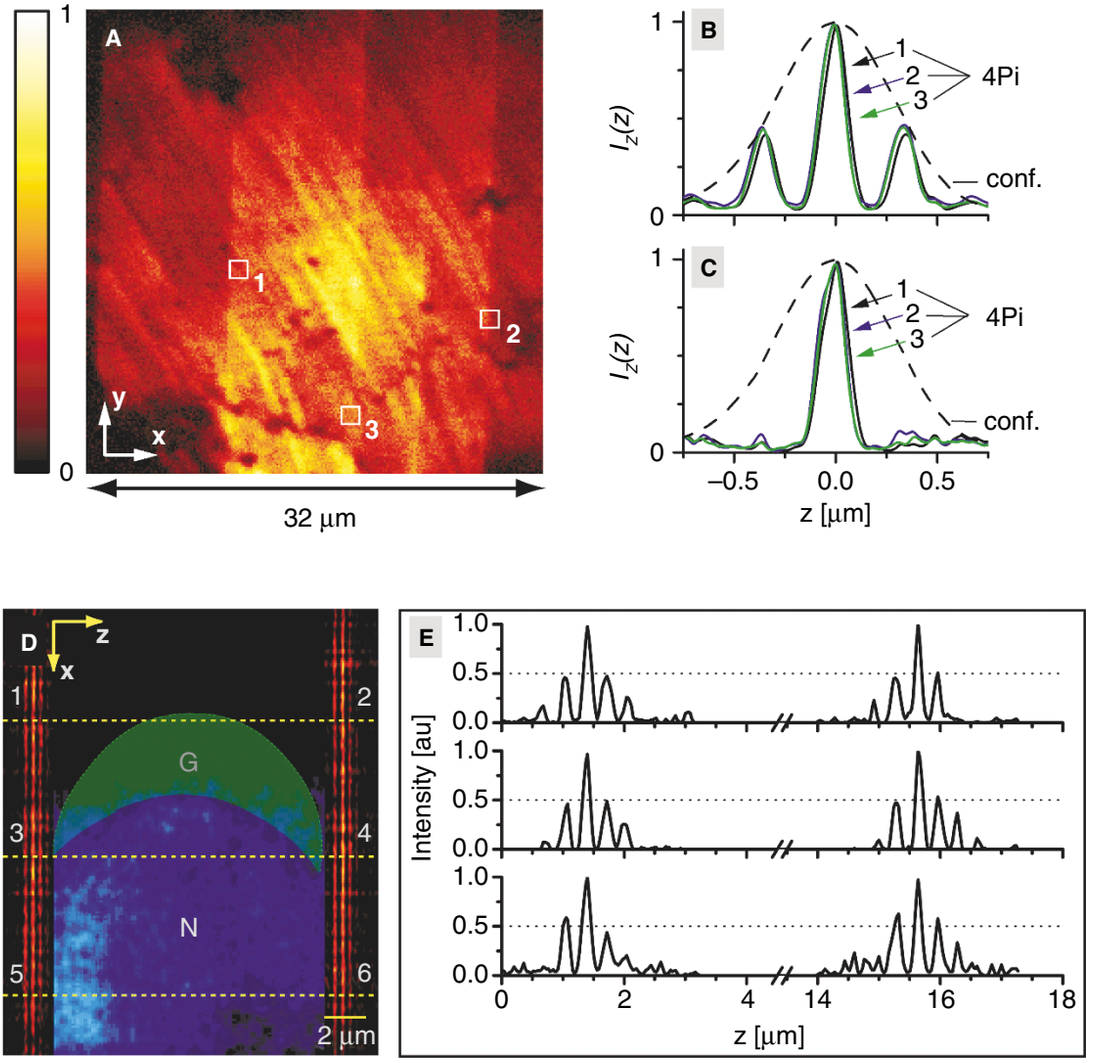


FIGURE 30.3. Basics of MMM-4Pi imaging. (A) *xy* image of a fluorescent polydiacetylene monolayer taken from a 3D stack. The chessboard appearance is due to the different intensities in the neighboring 4Pi foci; the tilted stripes are inherent to the polydiacetylene monolayer. (B) Axial intensity profiles, $I_z(z)$, through the 3D stack exhibiting a sharp maximum and two lobes, recorded at three different coordinates (x,y). The spatial invariance of the three profiles indicates that the 4Pi-PSF is constant over the whole field of view, irrespective of the microlens used. Fast linear one-step deconvolution can be applied throughout the field of view to remove the sidelobes (C). (D) *xz*-section recorded at the periphery of the nucleus of living *Vero* cell sandwiched between two coverslips each thinly coated with a fluorescence layer. The nucleus (N) is highlighted by Hoechst counterstaining and outlined; the region where the Golgi resides (G) is briefly sketched. The cell is significantly larger than the whole *xz*-section. The three vertical lines on either side (orange) are due to the interference between the counterpropagating focused fields, representing the main maximum of the 4Pi-PSF and the two axially offset sidelobes. (E) Enlarged intensity profiles of the axial responses of the microscope to the thin fluorescent layers, revealing the height of the lobes and the relative phase in greater detail. Outside and at the edge of the nucleus, the primary lobes are <50%. Focusing through the nucleus slightly increases the lobes and induces a noticeable but comparatively small phase shift. The parallelism of the orange lines in the displayed *xz*-section indicates that the cell does not gravely distort the interference between the wavefronts.

The inset in the upper left-hand corner of Figure 30.4(A) displays a conventional overview *xy*-image of the GalT-EGFP–labeled Golgi apparatus located close to the nucleus counterstained with the fluorophore Hoechst. The central panel of Figure 30.4(A) displays the corresponding 3D surface-rendered image at 100 nm resolution. The 3D image clearly reveals ribbons, fractioned stacks, as well as smaller tubular and vesicular subcompartments. Furthermore, protrusions and invaginations in the 200 nm range can be discerned. Figure 30.4(B) shows a typical distribution of 2-OST-EGFP in interphase cells. This image also displays a convoluted structure of the Golgi apparatus, similar to that observed for GalT. We think that in the near future, the discrimination of intra-Golgi localization of 2-OST and GalT will be possible by applying two-color 4Pi microscopy.

TYPE C 4Pi MICROSCOPY WITH THE LEICA TCS 4PI

The Leica TCS 4PI (Gugel *et al.*, 2004) consists of a commercially available confocal microscope (Leica Microsystems Heidelberg, Mannheim, Germany) combined with a 4Pi unit. The 4Pi unit is tightly mounted to the microscope turret to maintain all the capabilities of the scanning confocal unit in the microscope body (Fig.

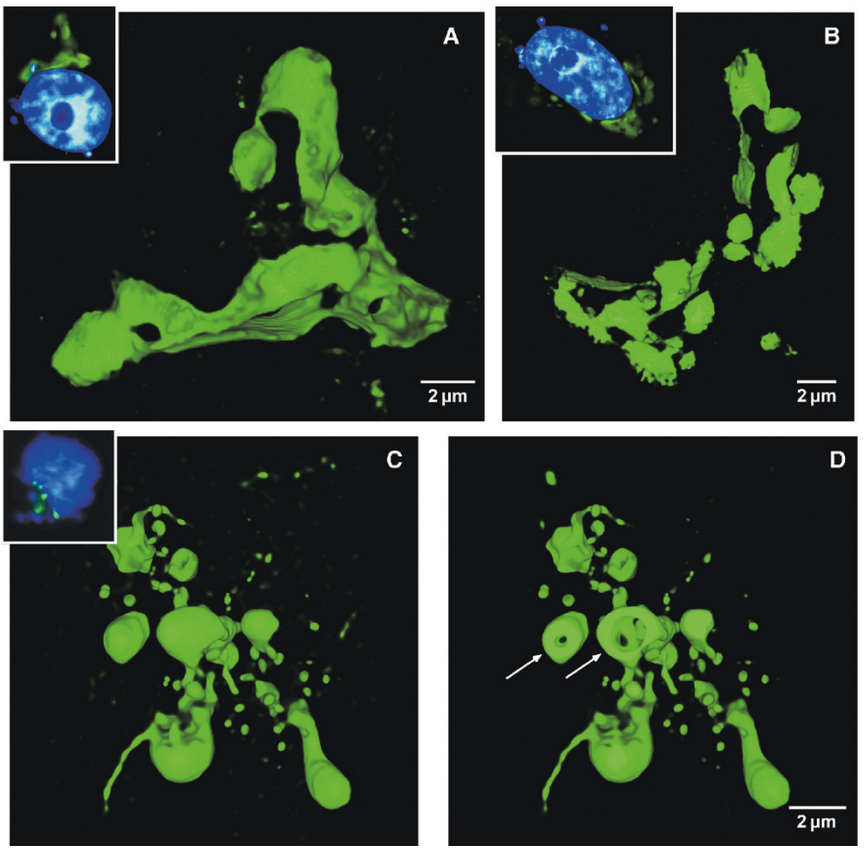


FIGURE 30.4. Golgi apparatus as obtained through 4Pi confocal imaging of GalT-EGFP (A) and 2-OST-EGFP (B) in living *Vero* cells at ~100 nm axial resolution. The insets show epi-fluorescence images to correlate the Golgi with the nucleus. The Hoechst staining of the nucleus indicates that the cells were in interphase. This was not the case for the GalT-EGFP transfected cell in (C). Though this cell is apoptotic, the data clearly pinpoint the ability of the 4Pi microscope to resolve small structures like the cavities, which become apparent when the upper caps of the balloon-like structures are removed (D).

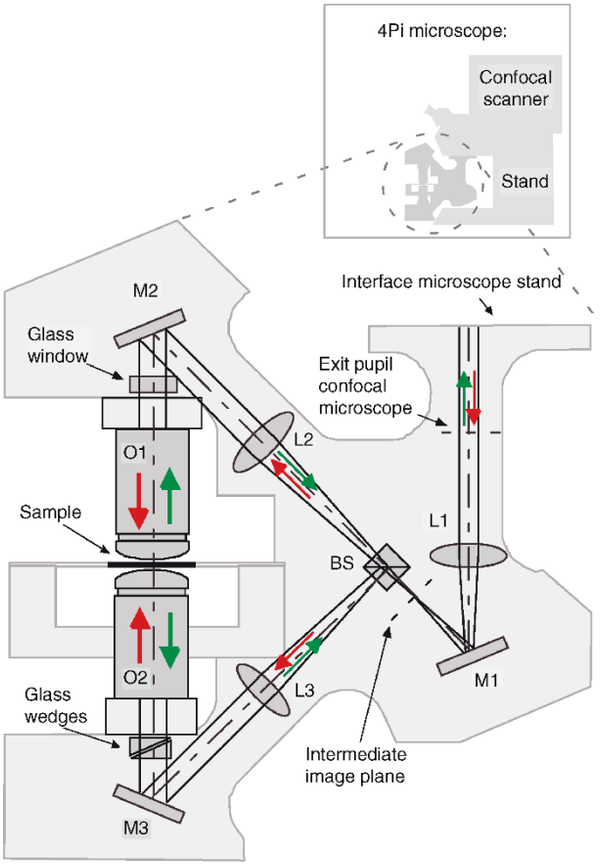


FIGURE 30.5. Sketch of the Leica TCS 4PI. Excitation light originating from the microscope stand is divided by the beam-splitter (BS) and focused onto the same spot by the opposing objective lenses O1 and O2. The lenses L1, L2, L3 and the mirrors M1, M2, M3 form the intermediate optical system, ensuring that the two scanning pivotal points coincide with the entrance pupils of the two objective lenses. Fluorescence is collected by both lenses, recombined at BS and directed towards the microscope stand. Dispersion compensation over a large wavelength range is ensured by movable optical wedges in the lower interferometric arm whose thickness is compensated by a glass window in the upper arm. Scanning is performed by a standard confocal microscope unit.

30.5). For 2PE, the beam of a mode-locked Ti:Sa laser is coupled into the confocal microscope and directed towards the 4Pi unit, where it is split into two beams of equal intensity by the beam-splitter BS and focused into the sample by the objective lenses O1 and O2. To maintain the beam-scanning capabilities of the confocal microscope, the former exit pupil of the confocal microscope is imaged into the entrance pupils of the objective lenses by the telescope optics L1, L2, and L3.

In order to minimize the effects of thermal fluctuations, the 4Pi unit is designed symmetrically. The objective lenses are mounted on a mechanical translation stage and a piezo-mechanical translation stage, respectively. This allows the alignment of the two objective lenses along a common optic axis and the concurrence of their foci. The excitation beams can be aligned parallel to the optic axis of the objective lenses, as well as centric to the entrance pupil of the lenses, by adjusting the mirrors M1, M2, M3, and the beam-splitter. The mirrors M2, mounted on a mechanical translation stage, and M3, on a piezo-translation stage, also allow the adjustment and control of the balance of the interferometric arms.

Lateral scanning is performed by the usual fast tilting of the beam in the pupil of the lenses. Axial scanning is accomplished by translating the sample along the optic axis with a piezo scanning stage. The optical design of the 4Pi unit ensures invariance of the 4Pi-PSF across a field of 50 µm diameter. The sample stage is horizontally oriented, as in the case of standard confocal microscopes. In fact, the typical scanning conditions of a standard confocal scanner are retained.

The fluorescence is collected with both objective lenses, merged at the beam-splitter and partially reflected backwards to the confocal microscope, producing a Type C, 4Pi microscope. In contrast to the Type A mode, the beam-splitter divides the fluorescence light into a constructively interfering part that is directed towards the detection pinhole (corresponding to a detection PSF consisting of a central peak and symmetrically arranged sidelobes) and a destructive part (featuring a central minimum) emitted at the fourth side of the beam-splitter cube. The light emerging from a homogeneously fluorescing sample is in this way divided into two beams of half the available brightness. This loss is offset by the doubled detection efficiency achieved by the use of two objective lenses. However, the combination of constructive 4Pi excitation and constructive detection sharpens the central peak of the effective PSF and lowers the sidelobes.

Even though the same optical components are used in both interferometric arms of the 4Pi unit, the relevant thickness of the glass components is not exactly the same. In a Type A 4Pi microscopy, the resulting optical path difference can be adjusted by moving one of the mirrors along the optic axis, thereby changing the length of the air spacing. This is not possible in Type C 4Pi microscopy. Due to the different dispersion in the glasses and in air, dispersion compensation is necessary to balance the arms for multiple wavelengths. This is implemented by a pair of adjustable glass wedges in one of the interferometric arms. The mean thickness of the wedge-pair is precompensated in the other arm by a glass window of the average thickness of the wedges. The effective dispersion can be tuned by displacing the wedges against each other.

Resolution

The experimentally achievable resolution and sidelobe heights of 4Pi microscopy are shown in Figure 30.6 by measured z-responses of the Leica TCS 4PI for water-immersion lenses (PL APO 63×/1.20 W CORR, Leica Microsystems, Wetzlar, Germany) and glycerol-immersion lenses (HCX PL APO 100×/1.35 GLYC CORR, Leica Microsystems, Wetzlar, Germany). For both measurements, a detection pinhole diameter corresponding to the size of the backprojected Airy disk of the fluorescent light was chosen. A comparison of the measured axial responses with the theoretical ones (Fig. 30.6) shows remarkable agreement. The full-width at half-maximum (FWHM) of the z-response was measured as 105 nm and 112 nm for the glycerol- and water-immersion lens, respectively. In Type C 4Pi microscopy, the height and shape of the sidelobes are determined by the ratio of the excitation and the detection wavelength. The z-response of the glycerol lens features lower sidelobes in this experiment because of the slightly more suitable wavelength ratio, but also because the glycerol-immersion lenses feature an aperture angle that is larger by 4° than the water-immersion counterparts.

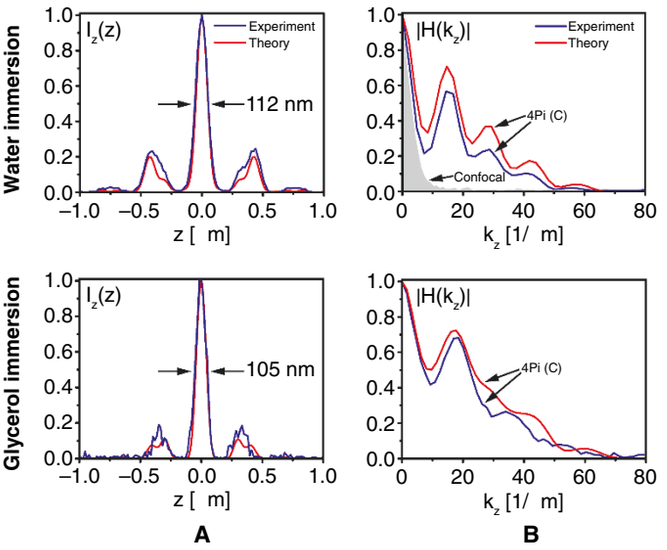


FIGURE 30.6. Experimental z-responses for water and glycerol-immersion lenses (PL APO 63×/1.20 W CORR and HCX PL APO 100×/1.35 GLYC CORR, Leica Microsystems, Wetzlar, Germany). The measurement for the water-immersion lenses was carried out with a fluorescent layer consisting of Oregon green dye molecules excited with laser light at a wavelength of 880 nm. The z-response of the glycerol-immersion lenses was obtained with a polydiacetylene layer excited at a wavelength of 840 nm. The central wavelength of the emission light is 565 nm in the case of the polydiacetylene layer, while it is 526 nm for the Oregon green layer. The pinhole diameter was set to the size of the backprojected Airy disk at the detection wavelengths used. The z-response of the water-immersion lens was recorded with an avalanche photodiode (APD), which results in a higher signal-to-noise ratio compared to the measured z-response of the glycerol-immersion lens recorded with a photomultiplier. For comparison, theoretical calculations are shown. To account for apodization at the periphery of the aperture, theoretical NAs of 1.15 and 1.30 were taken for the water- and the glycerol-immersion lens, respectively. The first minima in the OTF measured with the glycerol-immersion lens exhibits a value of 0.4. As a result of the higher sidelobes of the z-response, the value of the OTF measured with the water-immersion lens decreases to 0.22 at the first minima.

The OTF of the Type C 4Pi microscope along the reciprocal optic axis was calculated from the theoretical and experimental z-responses by Fourier transformation. It is completely contiguous with low intraband modulation. In fact, Type C 4Pi shows the best-filled OTF support reported with these types of microscopes (Nagorni and Hell, 2001). This well-filled OTF makes it suitable for routine operation. The largest transmitted object frequencies range between 45 μm^{-1} and 50 μm^{-1}. This corresponds to a 7-fold enlargement of the OTF compared to the confocal microscope (7 μm^{-1}).

Type C 4Pi Imaging in Living Cells

The suitability of Type C 4Pi microscopy in living cells was demonstrated by recording 3D images of the mitochondrial compartment in yeast cells (Gugel *et al.*, 2004). The mitochondrial matrix of *Saccharomyces cerevisiae* was labeled with green fluorescent protein (GFP). The cells were embedded in PBS with 1% low melting agarose and mounted between two coverslips. Apart from immobilizing the yeast cells, the agarose slightly increases the refractive index of the aqueous medium from 1.33 to 1.34. This reduces the effect of refractive index changes in the sample. The slight index mismatch between the medium and the immersion liquid induces a linear phase shift, which was actively compensated. The phase of the PSF in the stack was monitored with a fluorescent layer placed on one of the coverslips. The phase variation of the PSF throughout the whole stack was found to be less than $\pi/6$. Therefore, aberrations introduced by the biological sample were negligible in this case. The measurements were performed in a bidirectional scanning mode with a line frequency of 400 Hz. Due to the fast beam-scanning system, imaging speed is only determined by the sensitivity of the scanner. A typical mitochondrial stack of $6.25 \times 6.25 \times 4.5\,\mu m^3$ ($x \times y \times z$) in size was recorded in 1.5 min. During this time span, the mitochondria did not change significantly. The wavelength of the excitation light was 880 nm.

The recorded data stacks were deconvolved with theoretical PSFs calculated according to the parameters used in the experiment, that is, a detection pinhole diameter corresponding to the size of the backprojected Airy disk of the light and an emission wavelength of 510 nm. The sidelobes obtained by recording the yeast mitochondria are of the same height as the sidelobes measured for the fluorescent layer, that is, below 30% of the main peak intensity. Figure 30.7 shows a typical surface-rendered reconstruction of a recorded stack. The data set was restored with nonlinear image processing using the Richardson–Lucy algorithm [Fig. 30.7(A)] as was applied for Type A 4Pi images in other publications (Nagorni and Hell, 2001). The good agreement of the measured axial response with the theory and the low sidelobes of the Type C 4Pi PSF enabled the recorded data stack to be linearly deconvolved. The linear filtering with a Wiener filter and an adapted theoretical OTF not only removed the sidelobes but also increased the axial resolution to slightly better than 80 nm. Figure 30.7(B) illustrates the surface-rendered data set of the same mitochondrial compartment, but this time attained through linear image restoration. The similarity of the results obtained with linear filtering and nonlinear deconvolution demonstrates the applicability of linear filtering in Type C 4Pi microscopy.

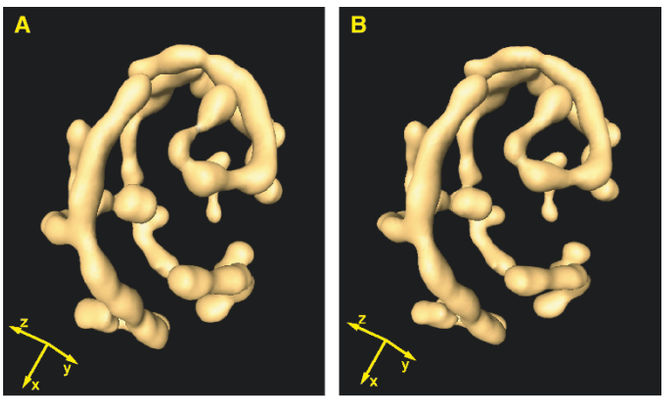


FIGURE 30.7. Mitochondrial network of a living yeast cell recorded with the Leica TCS 4PI. The 3D image displayed was obtained after nonlinear (A) and linear (B) deconvolution and subsequent surface rendering of the raw 3D data. Note the good agreement of the two images indicating the efficiency of the mathematically simpler and arguably more reliable linear deconvolution. The mitochondrial matrix was labeled with EGFP. The diameter of the mitochondrial network shown is ~5 µm.

SUMMARY AND OUTLOOK

With the latest instruments, MMM-4Pi and Leica TCS 4PI, 4Pi microscopy has evolved from a laboratory imaging setup to an instrument for super-resolved 3D imaging of cells. Multiple images of the Golgi apparatus in living *Vero* cells (Egner *et al.*, 2004) as well as extensive studies of the topology of the mitochondrial network in live yeast cells (Egner *et al.*, 2002b) have exhibited reliable everyday operation. 4Pi microscopy has been shown to work with oil-immersion as well as with water- and glycerol-immersion lenses and can thus be applied under many biological imaging conditions for individual cells. However, at the present state of development, the allowable sample thickness is limited by two factors. First, the free working distance of the high NA lenses used sets an upper limit to the maximum distance between the two coverslips (typically ~80–200 µm). Second, thick strongly scattering specimens cause wavefront aberrations compromising the 4Pi interference. While for single cell layers 4Pi microscopy has been shown to work reliably, the applicability of 4Pi microscopy to somewhat thicker samples is left to be solved in the future. The usage of adaptive optics (Booth *et al.*, 2002) may be very helpful in that regard.

It is not absolutely necessary to mount the specimen between two coverslips: the upper lens can be a dipping lens. Combined with a standard water-immersion lens of the same NA and magnification in the lower arm, the Leica TCS 4PI can be used with only one coverslip. This facilitates chemical, thermal, and also limited mechanical stimulation of the cells. Chambers have been developed allowing the buffered medium to be exchanged (Egner *et al.*, 2004), thus enabling the investigation of time-dependent changes as well as the effect of certain stimuli over many hours.

In conclusion, with the current 4Pi microscopes it is possible to record 3D data stacks from living cells in typically 1 to 20 min with an axial resolution of better than 100 nm. Strictly speaking, the lateral resolution does not change, but the significantly improved optical sectioning leads to an enhanced clarity of the details located in the focal plane. The MMM version of 4Pi microscopy has the potential of imaging a whole cell in less than a minute. By combining coherent excitation and detection, the Type C mode in the Leica TCS 4PI allows imaging with a state-of-the-art confocal scanner featuring a confocal sectioning capability of ~80 nm.

A further increase in resolution can be achieved by merging 4Pi microscopy with other independent, resolution-enhancing techniques. Taking into account that the axial resolution is now slightly better than its transverse counterpart, rotating the sample (Bradl *et al.*, 1992; Heintzmann and Cremer, 2002) may allow a tomographic version of 4Pi microscopy which would further increase the 3D resolution optically. The combination of 4Pi and STED microscopy has already been demonstrated (Dyba and Hell, 2002; Dyba *et al.*, 2003) to attain an axial resolution of 33 nm. Being based on a reversible saturable transition (RESOLFT) (Hell, 2004; Hell *et al.*, 2004), STED has no inherent conceptual resolution limit. The limits are rather given by the limited performance

of the fluorophores in terms of emission cycles, quantum efficiency, and photobleaching. For living cells, this demand will be increased due to rapid movements of proteins and organelles within the sample. If these issues can be satisfactorily addressed in the future, the synergistic combination of STED or another RESOLFT mechanism is likely to provide true optical resolution of <10 nm along the optic axis. At the same time, an increase in image acquisition speed through more sensitive and parallelized detection is expected.

ACKNOWLEDGMENTS

We thank Hilmar Gugel (Leica Microsystems Heidelberg GmbH) for contributing to the recent developments, as well as Alexander Goroshkov and Sophie Verrier for participating in the living mammalian cell studies.

REFERENCES

Bewersdorf, J., Pick, R., and Hell, S.W., 1998, Multifocal multiphoton microscopy, *Opt. Lett.* 23:655–657.

Bewersdorf, J., Schmidt, R., and Hell, S.W., 2005, Comparison of 4Pi-confocal microscopy and I5M, *submitted.*

Booth, M.J., Neil, M.A.A., Juskaitis, R., and Wilson, T., 2002, Adaptive aberration correction in a confocal microscope, *Proc. Natl. Acad. Sci. USA* 99:5788–5792.

Bornfleth, H., Satzler, K., Eils, R., and Cremer, C., 1998, High-precision distance measurements and volume-conserving segmentation of objects near and below the resolution limit in three-dimensional confocal fluorescence microscopy, *J. Microsc.* 189:118–136.

Bradl, J., Hausmann, M., Ehemann, V., Komitowski, D., and Cremer, C., 1992, A tilting device for 3-dimensional microscopy — Application to in situ imaging of interphase cell-nuclei, *J. Microsc.* 168:47–57.

Brakenhoff, G.J., and Visscher, K., 1992, Confocal imaging with bilateral scanning and array detectors, *J. Microsc.* 165:139–146.

Denk, W., Strickler, J.H., and Webb, W.W., 1990, Two-photon laser scanning fluorescence microscopy, *Science* 248:73–76.

Dyba, M., and Hell, S.W., 2002, Focal spots of size l/23 open up far-field fluorescence microscopy at 33 nm axial resolution, *Phys. Rev. Lett.* 88:163901.

Dyba, M., Jakobs, S., and Hell, S.W., 2003, Immunofluorescence stimulated emission depletion microscopy, *Nat. Biotechnol.* 21:1303–1304.

Egner, A., and Hell, S.W., 2000, Time multiplexing and parallelization in multifocal multiphoton microscopy, *J. Opt. Soc. Am. A.* 17:1192–1201.

Egner, A., Andresen, V., and Hell, S.W., 2002a, Comparison of the axial resolution of practical Nipkow-disk confocal fluorescence microscopy with that of multifocal multiphoton microscopy: Theory and experiment, *J. Microsc.* 206:24–32.

Egner, A., Jakobs, S., and Hell, S.W., 2002b, Fast 100-nm resolution 3D-microscope reveals structural plasticity of mitochondria in live yeast, *Proc. Natl. Acad. Sci. USA* 99:3370–3375.

Egner, A., Schrader, M., and Hell, S.W., 1998, Refractive index mismatch induced intensity and phase variations in fluorescence confocal, multiphoton and 4Pi-microscopy, *Opt. Commun.* 153:211–217.

Egner, A., Verrier, S., Goroshkov, A., Söling, H.-D., and Hell, S.W., 2004, 4Pi-microscopy of the Golgi apparatus in live mammalian cells, *J. Struct. Biol.* 147:70–76.

Egner, A., and Hell, S.W., 2005, Fluorescence microscopy with super-resolved optical section, *Trends Cell Biol.* 15:207–215.

Gelles, J., Schnapp, B.J., and Sheetz, M.P., 1988, Tracking kinesin-driven movements with nanometre-scale precision, *Nature* 331:450–453.

Gugel, H., Bewersdorf, J., Jakobs, S., Engelhardt, J., Storz, R., and Hell, S.W., 2004, Combining 4Pi excitation and detection delivers seven-fold sharper sections in confocal imaging of live cells, *Biophys. J.* 87:4146–4152.

Gustafsson, M.G.L., Agard, D.A., and Sedat, J.W., 1995, Sevenfold improvement of axial resolution in 3D widefield microscopy using two objective lenses, *Proc. SPIE* 2412:147–156.

Gustafsson, M.G.L., Agard, D.A., and Sedat, J.W., 1999, I5M: 3D widefield light microscopy with better than 100 nm axial resolution, *J. Microsc.* 195:10–16.

Heintzmann, R., and Cremer, C., 2002, Axial tomographic confocal fluorescence microscopy, *J. Microsc.* 206:7–23.

Hell, S.W., 1990, Double-confocal microscrope, European Patent 0491289.

Hell, S., and Stelzer, E.H.K., 1992a, Properties of a 4Pi-confocal fluorescence microscope, *J. Opt. Soc. Am. A* 9:2159–2166.

Hell, S.W., 2004, Strategy for far-field optical imaging and writing without diffraction limit, *Phys. Lett. A* 326:140–145.

Hell, S.W., and Stelzer, E.H.K., 1992b, Fundamental improvement of resolution with a 4Pi-confocal fluorescence microscope using two-photon excitation, *Opt. Commun.* 93:277–282.

Hell, S.W., and Wichmann, J., 1994, Breaking the diffraction resolution limit by stimulated emission: stimulated emission depletion microscopy, *Opt. Lett.* 19:780–782.

Hell, S.W., Dyba, M., and Jakobs, S., 2004, Concepts for nanoscale resolution in fluorescence microscopy, *Curr. Opin. Neurobio.* 14:599–609.

Hell, S.W., Lindek, S., Cremer, C., and Stelzer, E.H.K., 1994, Measurement of the 4Pi-confocal point spread function proves 75 nm resolution, *Appl. Phys. Lett.* 64:1335–1338.

Khurich, D., Nouvain, R., Pujol, R., Dieck, S., Egner, A., Gundelfinger, E., and Moser, T., 2005, Hair cell synaptic ribbons are essential for synchronous auditory signalling, *Nature* 434:889–894.

König, K., Becker, T.W., Fischer, P., Riemann, I., and Halbhuber, K.-J. 1999, Pulse-length dependence of cellular response to intense near-infrared laser pulses in multiphoton microscopes, *Opt. Lett.* 24:113–115.

Lacoste, T.D., Michalet, X., Pinaud, F., Chemla, D.S., Alivisatos, A.P., and Weiss, S., 2000, Ultrahigh-resolution multicolor colocalization of single fluorescent probes, *Proc. Natl. Acad. Sci. USA* 97:9461–9466.

Nagorni, M., and Hell, S.W., 2001a, Coherent use of opposing lenses for axial resolution increase in fluorescence microscopy. I. Comparative study of concepts, *J. Opt. Soc. Am. A* 18:36–48.

Nagorni, M., and Hell, S.W., 2001b, Coherent use of opposing lenses for axial resolution increase in fluorescence microscopy. II. Power and limitation of nonlinear image restoration, *J. Opt. Soc. Am. A* 18:49–54.

Richards, B., and Wolf, E., 1959, Electromagnetic diffraction in optical systems II. Structure of the image field in an aplanatic system, *Proc. R. Soc. Lond. A* 253:358–379.

Schmidt, M., Nagorni, M., and Hell, S.W., 2000, Subresolution axial distance measurements in far-field fluorescence microscopy with precision of 1 nanometer, *Rev. Sci. Instrum.* 71:2742–2745.

Thompson, R.E., Larson, D.R., and Webb, W.W., 2002, Precise nanometer localization analysis for individual fluorescent probes, *Biophys. J.* 82:2775–2783.

APPENDIX

I^{5}M-OTF

Utilizing Köhler illumination with a lamp, I^{5}M applies single-photon, plane standing-wave excitation. However, the fluorescence detection is as in a Type C 4Pi microscope: the spherical wavefronts of fluorescent light emerging at the sample are combined by interference at the detector which is a CCD camera. The OTF of the I^{5}M is much more structured than that of the 2PE Type A and Type C 4Pi microscopes (see Fig. 30.A1) and therefore I^{5}M transfers data at some of these extended spatial frequencies only weakly. To visualize these components in the I^{5}M-OTF, the inset of Figure 30.A1 displays the same OTF after normalization to 10% of its maximum value (Bewersdorf *et al.*, 2005). If the weakly transferred frequencies (at or even below the noise level) fall

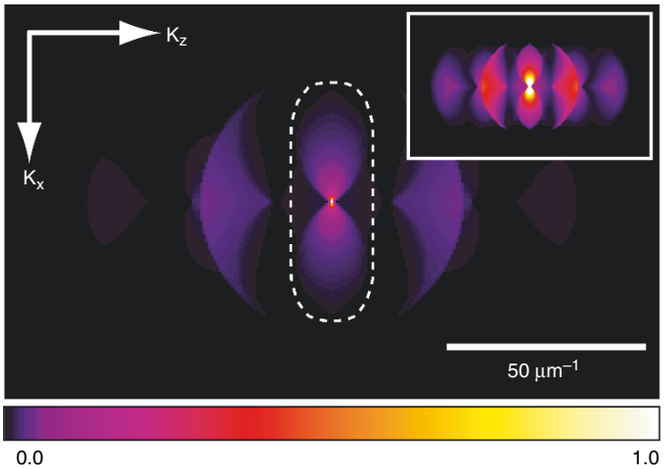


FIGURE 30.A1. OTF of the I^{5}M. The inset shows the same OTF normalized to 10% of the maximum to highlight the weak regions of the OTF. The white *dashed line* shows the support of a standard confocal fluorescence microscope.

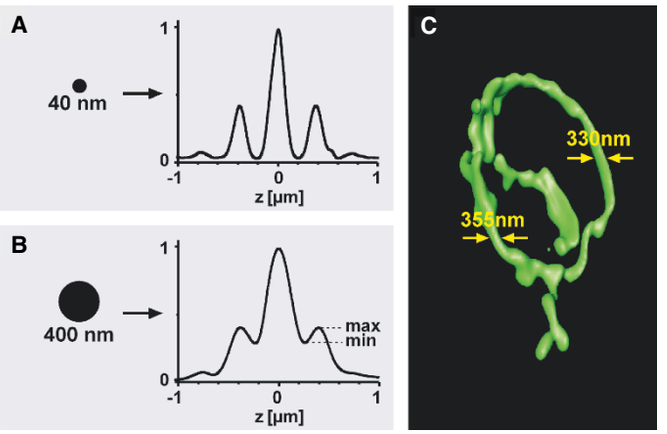


FIGURE 30.A2. Measuring diameters in the subresolution range with 4Pi microscopy. (A) and (B) show the intensity profiles through a laterally oriented rod with a diameter of 40 and 400 nm, respectively. The depth of the minima of the profiles is correlated to the thickness of the rod. By measuring the depth of the minima, the thickness of rod-like objects such as the yeast mitochondria can be derived (C).

within the region of support of the OTF, periodic artifacts arise in the image. The white dashed line in Figure 30.A1 displays the support of the OTF of a normal confocal microscope. For the I^{5}M-OTF calculations, a fluorescence wavelength of 510 nm, a single-photon excitation wavelength at 480 nm, and a 1.20 NA water-immersion lens were assumed. The height of the singularity in the center corresponds to an imaging size of ~10 µm cubed.

Additional Information from the 4Pi-PSF

The sharper spot of the 4Pi microscope can be used to increase the localization accuracy of point-like objects in tracking experiments, or to enhance the measurement of distances between two known objects. Likewise, knowledge about the symmetry of the feature of interest can be used to determine its center of mass and, therefore, its position. The precision of the position measurement is not challenged by diffraction and may far exceed the resolution (Gelles *et al.*, 1988; Bornfleth *et al.*, 1998; Lacoste *et al.*, 2000; Thompson *et al.*, 2002). The precision of this method scales, however, with the resolution and thus benefits from the narrow 4Pi focus. In fact, localization accuracies below 1 nm have been demonstrated with 4Pi microscopy (Schmidt *et al.*, 2000). Additionally, the 4Pi-PSF allows one to measure object thicknesses down to 60 nm. Figure 30.A2 illustrates the determination of the diameter of mitochondria in a yeast cell. In this example, it was possible to measure the average diameter with an accuracy of ~5 nm (Egner *et al.*, 2002b).

31

Nanoscale Resolution with Focused Light: Stimulated Emission Depletion and Other Reversible Saturable Optical Fluorescence Transitions Microscopy Concepts

Stefan W. Hell, Katrin I. Willig, Marcus Dyba, Stefan Jakobs, Lars Kastrup, and Volker Westphal

THE RESOLUTION ISSUE

Although most specifically labeled cellular constituents can readily be detected in a conventional fluorescence light microscope, their submicron-scale structure cannot be perceived. For example, despite the fact that many proteins of the inner mitochondrial membrane can be labeled by tagging with the green fluorescent protein (GFP), the cristae are too small to be represented in an image recorded with light.

Resolution is the minimal distance at which a microscope may discriminate two or more features of the same kind (Abbe, 1873). Therefore, resolution must not be confused with localization precision. While it may easily be possible to localize the center of the fluorescence patch generated by a membrane-labeled synaptic vesicle with nanometer precision in a microscope, its visualization as a 30 to 50 nm hollow sphere fails because the latter requires nanometer scale *resolution*. In fact, conventional epi-fluorescence microscopy may not even resolve two synaptic vesicles touching each other. Similarly, it may be possible to track the trajectory of a single virus particle with nanometer precision but still its inner structure remains elusive to light microscopy.

The resolution limitation is ultimately rooted in the phenomenon of diffraction (Abbe, 1873). Loosely speaking, focusing of light always results in a blurred spot (Born and Wolf, 2002) whose size determines the resolution. According to Abbe, the transverse (i.e., focal plane) full-width at half-maximum (FWHM) of the focal spot is given by

$$\Delta x, \Delta y = \frac{\lambda}{2n\sin\alpha} \qquad (1)$$

with λ, n, and α denoting the wavelength, the refractive index, and the semi-aperture angle of the objective lens, respectively. Along the direction of light propagation (i.e., the optic axis), the spot size is about $\Delta z = 2\lambda/(n\sin^2\alpha)$ (Born and Wolf, 2002).

In the visible optical range, the most sophisticated immersion lenses feature a maximum angle of $\alpha = 73°$; the shortest live cell compatible wavelength is around 400 nm which is almost in the near ultraviolet (UV) (König *et al.*, 1996). Thus, it seemed obvious that if visible light and regular lenses were to be used, the resolution in the focal plane Δx,Δy would always be poorer than 150 nm (Pohl and Courjon, 1993). In the axial direction the resolution is even worse (Δz > 500 nm). In recent years significant improvements of axial resolution have been achieved through the coherent use of two opposing lenses as is realized, for example, in 4Pi microscopy (see Chapter 30, *this volume*). However, these systems are still limited by diffraction. In this chapter, we report on concepts for radically overcoming the diffraction barrier and attaining a resolution of few nanometers: a figure that has been considered impossible with focused light for more than a century.

BREAKING THE DIFFRACTION BARRIER: THE CONCEPT OF REVERSIBLE SATURABLE OPTICAL FLUORESCENCE TRANSITIONS

Since the inception of nonlinear optics (Shen, 1984), it has been speculated that a nonlinear relationship between the applied intensity and the measured (fluorescence) signal could — at least in principle — expand the resolution capabilities of a focusing (far-field) optical system. However, these notions remained vague and without consequence because a concrete physical recipe could not be given. In fact, the multi-photon processes that had initially been considered for significantly improving the spatial resolution turned out to be unsuitable. Therefore, it was not until the early 1990s that concrete physical concepts appeared for breaking the diffraction resolution barrier with focused light (Hell and Wichmann, 1994; Hell and Kroug, 1995; Hell, 1997). In fact these concepts can be viewed as a family of concepts that utilize *re*versible *s*aturable *o*ptica*l* (*f*luorescence) *t*ransitions, which we now name reversible saturable optical fluorescence transitions (RESOLFT). They can be described in a common formalism (Hell, 2003).

Let us assume a fluorescent molecule with two distinct states A and B, whereby the transition from $A \rightarrow B$ can be optically induced at a rate $k_{AB} = \sigma I$ [Fig. 31.1(A)]. The variables σ and I denote the transition cross-section and the light intensity, respectively. The rate for the reverse transition $B \rightarrow A$ is denoted with k_{BA}. It may be driven by light, by a chemical reaction, by heat, or any other means, or simply be spontaneous. The kinetics of the molecular states is described by $dN_A/dt = -dN_B/dt = k_{BA}N_B - k_{AB}N_A$, with $N_{A,B}$ denoting the normalized population probability of each state. After a time period $t >> (k_{AB} + k_{BA})^{-1}$, the populations have reached a dynamical equilibrium at $N_A^\infty = k_{BA}/(k_{AB} + k_{BA})$. The molecule's probability to be in A or B basically depends on k_{AB} and hence on I. At the saturation intensity $I_{sat} = k_{BA}/\sigma$, we have equal probability $N_A^\infty = 1/2$. Increasing $I >> I_{sat}$ renders $k_{AB} >> k_{BA}$, so that the molecule is virtually shifted to B: $N_A^\infty \rightarrow 0$.

Figure 31.1(B) illustrates how this behavior can be exploited for creating arbitrarily sharp regions of state A molecules. The scheme in Figure 31.1(B) is one-dimensional (x), but can be

Stefan W. Hell, Katrin I. Willig, Marcus Dyba, Stefan Jakobs, Lars Kastrup, and Volker Westphal • Max Planck Institute for Biophysical Chemistry, 37070 Göttingen, Germany

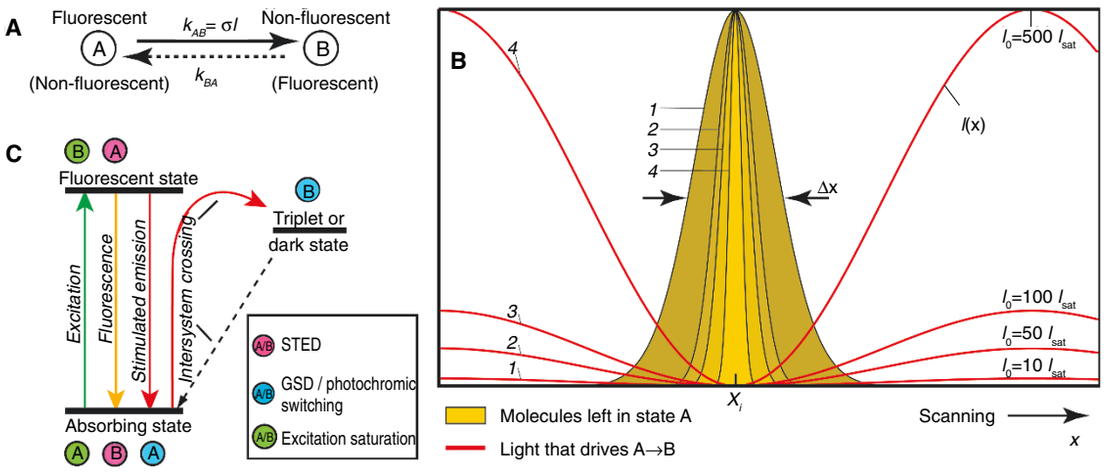


FIGURE 31.1. Breaking the diffraction barrier by reversible saturable optical transitions (RESOLFT) requires (A) two states *A* and *B* of a label that are distinct in their optical properties. The optical transition $A \rightarrow B$ takes place at a rate $k_{AB} = \sigma I$ that is proportional to the light intensity *I* applied. The reverse transition $B \rightarrow A$ of rate k_{BA} brings the label back to its initial state. (B) The profiles 1 to 4 show the spatial region in which the label is allowed to be in state *A*, if the region is subject to a standing wave of light with peak intensities I_0 = 10, 50, 100, and 500 times I_{sat} and with a zero at x_i. Increasing I_0 ensures that the region in which the label may reside in *A* is squeezed down, in principle, indefinitely. If *A* is the fluorescent state of the label, this ultrasharp region functions as the effective fluorescent spot of the microscope and Δx is its FWHM. The creation of a fluorescence image requires scanning that is moving the zero along the *x*-axis with subsequent storage of the recorded fluorescence. If *B* is the fluorescent state, then the ultrasharp regions of state *A* are dark. In this case, a sort of negative image is recorded. Nevertheless, with suitable mathematical postprocessing, similar optical resolution can be obtained. In any case, the resolution is no longer limited by diffraction, but only determined by the value of I_0/I_{sat}. (C) The simplified energy diagram of a fluorophore depicts possible schemes for implementing saturable optical transitions.

readily extended to three dimensions. For this purpose we require the spatial intensity distribution $I = I(x)$ to be zero at a point x_i in space: $I(x_i) = 0$. Whereas in two dimensions or three dimensions, the light intensity distribution would be a two-dimensional (2D) or three-dimensional (3D) doughnut mode, in one dimension the zero is best produced by a standing wave $I(x) = I_0 \cos^2(2\pi n x/\lambda)$. If we now apply $I(x)$ to a spatial distribution of molecules (in *x*) that are first in state *A*, then for $I_0 >> I_{sat}$, virtually all the molecules will be transferred to *B*, except for those that are very close to x_i. The larger the ratio $I/I_{sat} >> 1$, the sharper is the region where state *A* persists [note the increase in curve steepness with increasing saturation level I/I_{sat} in Fig. 31.1(B)]. The FWHM of the resulting spot of state *A* is readily calculated as:

$$\Delta x \approx \frac{\lambda}{\pi n \sqrt{I/I_{sat}}} \qquad (2)$$

In microscopy, the spatial distribution $I(x)$ may be produced by the objective lens itself. If it is produced through the finite aperture of the objective lens, the smallest spot that can be obtained is

$$\Delta x \approx \frac{\lambda}{\pi n \sin\alpha \sqrt{I/I_{sat}}} \qquad (3)$$

which may be regarded as an extension of Abbe's equation (Hell, 2003, 2004). In fact, one can easily show that if the zero is produced by focusing the light through the lens, the equation becomes:

$$\Delta x \approx \frac{\lambda}{2\pi n \sin\alpha \sqrt{1 + I/I_{sat}}} \qquad (4)$$

For $I/I_{sat} = 100$, the theoretical resolution improvement over Abbe is by about 10. Despite the dependence of Δx on $\lambda/\sin\alpha$ and in contrast to Eq. 1, the new Eqs. 2, 3 and 4 allow diffraction-unlimited spatial resolution.

For a 3D doughnut, we obtain a confined spatial volume of molecules in state *A* whose dimensions scale inversely with $\sqrt{I_i/I_{sat}}$, $i = x, y, z$, with I_i denoting the peak intensities along the respective axes. Hence, the reduction in volume scales with $\sqrt{I_x I_y I_z / I_{sat}^3}$. In RESOLFT microscopy while the resolution still scales with the wavelength λ, its limit only depends on the applicable light intensity *I* at a given I_{sat}.

If we now assume that state *A* but not state *B* is a fluorescent state, the relevance to imaging becomes obvious: our scheme allows us to create arbitrarily small fluorescence spots (Hell and Wichmann, 1994; Hell, 2003, 2004; Hell *et al.*, 2003). Moreover, by scanning the zero x_i across (or through) the specimen, we can record the fluorophore distribution point by point, and thus assemble a fluorescence 3D image with arbitrary resolution. Identical fluorescent objects can be imaged as separate in space irrespective of their proximity and size because the fluorescence spot (state *A*) can be made so small that only one of the objects fluoresces.

The concept of RESOLFT inevitably requires scanning (with a zero), but not necessarily with a single beam or a point-like zero. Multiple zeros or dark lines produced by the interference of counter-propagating waves (Cragg and So, 2000; Heintzmann *et al.*, 2002) in conjunction with conventional charge-coupled device (CCD) camera detection can also be used, provided the zeros or the dark lines are farther apart than about the distance required by the diffraction resolution limit of conventional CCD camera imaging (Cragg and So, 2000; Hell, 2003). Dark lines increase the resolution in a single direction only, but stepwise rotation of the pattern plus interleaved scanning of the minima (e.g., by shifting the phase in the interference pattern) and subsequent computational reassignment (Heintzmann and Cremer, 1998; Heintzmann *et al.*, 2002) may provide, under some conditions, similar transverse resolution as with points and do so at higher recording speed. The obligation for scanning remains. The need for scanning is also

the reason why the saturable optical transition $A \rightarrow B$ has to be *reversible*. The molecule in state B must be able to return to the state A at the latest when the zero comes across its site.

DIFFERENT APPROACHES OF REVERSIBLE SATURABLE OPTICAL FLUORESCENCE TRANSITIONS MICROSCOPY

The RESOLFT scheme and the subsequent breaking of the diffraction barrier is the actual idea behind stimulated emission depletion (STED) microscopy (Hell and Wichmann, 1994; Hell, 1997; Klar *et al.*, 2000). In STED microscopy, many of the molecules that have just been excited to the fluorescent state S_1 (A) are immediately transferred by a further light intensity I to the molecular ground state S_0 (B), so that fluorescence emission is prevented [Fig. 31.1(B,C) and Fig. 31.2(A)]. The physical effect responsible for this transfer is stimulated emission, a basic single-photon phenomenon that has about the same cross-section as single-photon absorption ($\sigma \approx 10^{-16}$–$10^{-18}\,cm^2$). Because STED competes with the spontaneous fluorescence decay of $k_{fl} \approx (1\,ns)^{-1}$ of the S_1, the saturation intensity I_{sat} can be approximated as k_{fl}/σ or about 10^{25} to 10^{27} photons per square centimeter and second, that is, several tens to a hundred megawatts per square centimeter [Fig. 31.2(B)]. Saturated depletion of the excited state with a focal spot containing a zero squeezes the extent of the fluorescent spot to a subdiffraction size that is not any longer limited by the wavelength, but only by the applied intensity. The potential and details of STED microscopy will be discussed later.

Other variants of RESOLFT microscopy employing different physical realizations of states A and B have also been suggested [Fig. 31.1(C)] (Hell *et al.*, 2003). For example, in ground state depletion (GSD) microscopy (Hell and Kroug, 1995; Hell, 1997), the ground state S_0 has the role of state A, while state B is a metastable triplet state; more precisely, A and B are the singlet and triplet systems of the dye, respectively. For a number of dyes, intersystem crossing ($A \rightarrow B$) occurs as a byproduct of the regular dye excitation because during each excitation cycle, the molecule crosses to the triplet state with a probability $p \approx 0.05$ to 0.2. Because of its metastability, the triplet state is relatively easily filled up by repeated regular excitation. For saturation, the triplet buildup rate $k_{AB} = p\sigma I$ must be larger than the decay to the S_0, $k_{BA} \approx (10^{-6}$ to $10^{-2}\,s)^{-1}$, which is comparatively slow. Thus, typical I_{sat} is several tens of kilowatts per square centimeter, which is by 2 to 4 orders of magnitude lower than with STED. Low I_{sat} is invaluable with regard to the attainable resolution (see Eq. 2), and with regard to sample compatibility. However, the experimental realization of this member of the RESOLFT family will be complicated by the fact that the triplet state is involved in the photobleaching pathway (Schäfer, 1973).

Perhaps the simplest way of realizing a saturated optical transition is through an intense excitation (Heintzmann *et al.*, 2002). In this case, the ground state S_0 (A) is depleted and expected to reside in the fluorescent state S_1 (B). The same RESOLFT for-

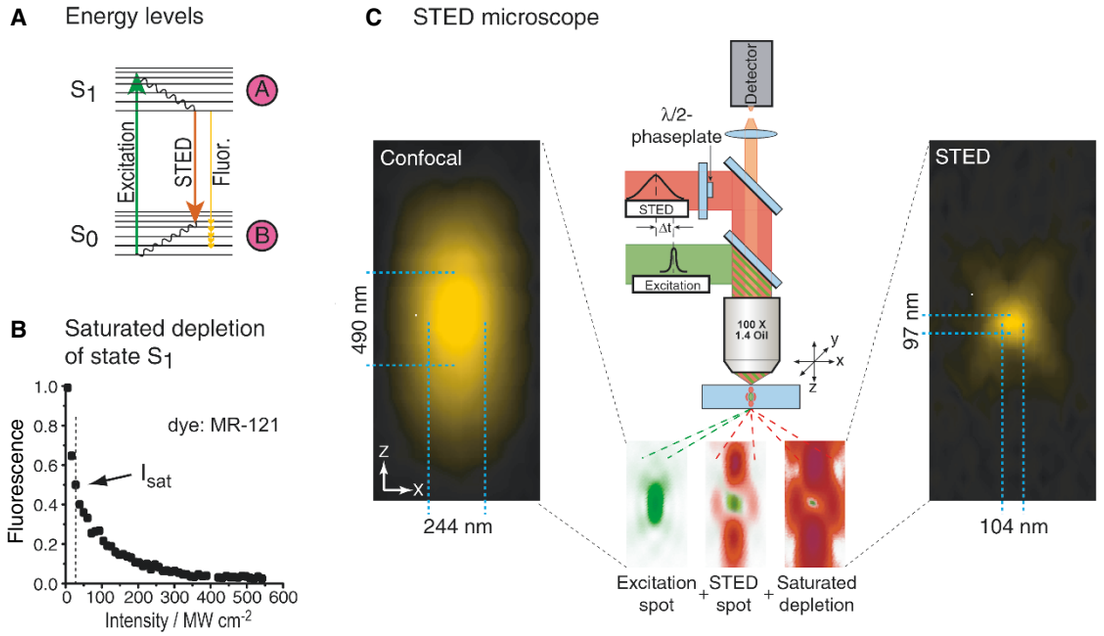


FIGURE 31.2. STED microscopy. (A) Molecules in the fluorescent state S_1 (state A) return to the ground state S_0 (state B) by spontaneous fluorescence emission. Return to S_0 may also be optically enforced through stimulated emission. To prevail over the spontaneous emission, stimulated emission depletion of the S_1 requires relatively intense light pulses with durations of a fraction of the S_1 lifetime. (B) Saturated depletion of the S_1 with increasing peak intensity of STED pulses of ~100 ps duration, as measured by the remaining fluorescence of a monomolecular layer of the dye MR-121. For the higher intensity levels, the S_1 is optically depleted. The saturation intensity is defined as the intensity value at which the S_1 is depleted by half. (C) *Center*: Sketch of a point-scanning STED microscope. Excitation and STED are accomplished with synchronized laser pulses focused by a lens into the sample, sketched as green and red beams, respectively. Fluorescence is registered by a detector. *Bottom*: Intensity distributions in the focus. The diffraction-limited excitation spot is overlapped with the doughnut-shaped STED spot featuring a central zero. Saturated depletion by the STED beam confines the region of excited molecules to the zero, leaving a fluorescent spot of subdiffraction dimensions. *Outer left and right insets*: the confocal and the subdiffraction-sized spot left by STED, respectively. Note the doubled lateral and 5-fold improved axial resolution over confocal microscopy. The reduction in dimensions (x, y, z) yields an ultrasmall volume of subdiffraction dimensions, here 0.67 attoliter, corresponding to an 18-fold reduction compared to its confocal counterpart. In spite of using diffraction-limited beams, the concept of STED fluorescence microscopy may, under very favorable conditions, reach spatial resolution at the molecular scale.

malism applies, except that it is state B that is now fluorescent. State A is depleted such that ultrasharp dark regions are created that are surrounded by bright fluorescent regions. In a sense, this approach records negative images, which are subsequently made positive by mathematical postprocessing. The dark regions can be lines produced by interference patterns, but also 3D doughnuts. In the latter case, one would produce dark 3D volumes that are confined by walls of intense fluorescence. The challenges with this otherwise very appealing approach are that the mandatory computations require an excellent signal-to-noise ratio. As with STED, excitation saturation competes with fluorescence emission, so that I_{sat} is also given by k_{fl}/σ which is of the order of 10^{25} photons per cm^2 - second, several tens of megawatts per square centimeter (Hell, 2003). Compared to STED, the intensity needed for saturated optical transitions should actually be up to 10 times lower because the dye can be excited at the maximum of the emission spectrum where cross-sections are largest. Still, intense excitation increases photobleaching. Relief could possibly be brought by using non-blinking semiconductor quantum dots as labels (Alivisatos, 1996; Bruchez *et al.*, 1998; Peng *et al.*, 2000).

Hence, while the family of RESOLFT concepts is not subject to Abbe's diffraction barrier anymore, the dependence of the resolution gain on $\sqrt{I/I_{sat}}$ entails another soft barrier which is the maximum intensity I that the sample can tolerate. Fortunately, the remedy is the use of transitions with low values of I_{sat}, that is, optical transitions that are easy to saturate.

An example is the optical switching of bistable compounds from a fluorescent state (A) into a non-fluorescent state (B), or vice versa. Optical bistability can be realized by photo-induced *cis-trans* isomerization (Dyba and Hell, 2002; Hell *et al.*, 2003). If both states A and B are (meta)stable, the optical transition $A \rightarrow B$ or $B \rightarrow A$ can be completed at very long, if not arbitrary, time scales. Thus, the light energy needed for these transitions can be spread in time (Hell *et al.*, 2003), reducing I_{sat} to values that are lower by many orders of magnitude compared to those of STED or the other RESOLFT family members. These processes would also readily lend themselves for parallelization through large area widefield imaging. However, the principal advantage is the insight that nanoscale resolution does not necessarily require extreme intensities of light (Hell, 2003, 2004; Hell *et al.*, 2003).

Suitable candidates for this concept are the optically switchable fluorescent proteins. For example, the protein asFP595 can be switched on by green light ($B \rightarrow A$) and also switched off ($A \rightarrow B$) by blue light recurrently (Lukyanov *et al.*, 2000; Chudakov *et al.*, 2003). Although known proteins such as asF595 may have major limitations, such as a low quantum efficiency and a strong tendency to form oligomers, these problems could possibly be solved by strategic mutagenesis. Alternatively, new switchable proteins could be found by targeted exploration. A RESOLFT concept based on genetically encoded optically switchable tags is extremely appealing, because it would allow highly specific imaging in live cells with unprecedented optical resolution. We expect that further variants of RESOLFT will emerge in the future.

STIMULATED EMISSION DEPLETION MICROSCOPY

So far, STED microscopy is the only member of the RESOLFT schemes that has been realized (Klar *et al.*, 2000, 2001). In its initial demonstration, STED microscopy has been realized as a point-scanning system, whereby excitation and STED is performed with two synchronized ultrashort pulses [Fig. 31.2(C)]. The first pulse excites the molecule into the fluorescent state S_1 at a suitable wavelength. The red-shifted second pulse that follows a few picoseconds later transfers the molecules away from the zero back to the ground state S_0. Although I_{sat} is several tens of megawatts per square centimeter, it scales inversely with the pulse duration of 10 to 300 ps. Because the breaking of the diffraction barrier calls for $I >> I_{sat}$, focal intensities of 100 to 500 MW/cm^2 are required (Hell and Wichmann, 1994). For comparison, live-cell multi-photon microscopy typically uses 10^3 to 10^4 times shorter pulses of 10^3 to 10^4 greater intensity: 200 GW/cm^2. As most sample damage mechanisms depend nonlinearly on the intensity, the typical values used for STED so far have been live-cell compatible (Klar *et al.*, 2000).

Figure 31.2(C) shows a typical experimental focal intensity distribution of the excitation spot (green), overlapping with a STED spot (red) featuring a central hole. Saturated depletion inhibits fluorescence everywhere except for the very center of the focal region (Klar *et al.*, 2000). For the $I/I_{sat} \approx 100$ applied for the measurement in Figure 31.2, the net 3D spot becomes almost spherical with a diameter of ~100 nm, which amounts to an almost 6-fold and 2.3-fold increase in axial and lateral resolution, respectively. Although theory permits much higher resolution (in principle, molecular scale), in this experiment the production of a smaller spot was challenged by experimental imperfections (Klar *et al.*, 2000), such as a finite depth of the central zero, and increased photobleaching with increasing I/I_{sat}.

The fact that the spot is squeezed more in the z-direction than in the focal plane is due to the higher local intensity of this particular quenching spot along the optic axis. Using a STED beam of different shape, an improvement of more than 5-fold in the focal plane resolution, compared to Abbe's barrier, has recently been demonstrated with single molecules dispersed on a surface (see Fig. 31.3 and Westphal *et al.*, 2003). Furthermore, Figure 31.3(B) proves that objects separated by much less than the diffraction limit can clearly be distinguished. Recent experiments also indicate that, in accordance with Equations 2 and 3, even higher lateral resolution is possible with STED, provided that photobleaching can be avoided. In fact, it has been shown that a focal spot width of 16 nm, corresponding to little more than 2% of the wavelength used can be obtained [see Fig. 31.7(A)] (Westphal and Hell, 2005). Because the diffraction barrier is broken, STED microscopy does not have a firm resolution limit. The ultimate resolution solely depends on how well the operational conditions can be realized.

In frequency space, the sample structure is described in terms of spatial frequencies. Therefore, microscope performance is defined by the OTF (optical transfer function), describing the strength with which these frequencies are transferred to the image. Thus, the resolution limit is given by the highest frequency that produces a signal above the noise level. Point spread function (PSF) and OTF are intertwined by Fourier mathematics: the sharper the PSF, the broader the OTF. The OTF extension of STED is very smooth [see Fig. 31.3(C)], without any gaps, simplifying the deconvolution techniques needed to produce the best final results.

At present, the fact that relatively few fast, pulsed, tunable, visible lasers are available places some practical limits on the dyes that can be used for STED microscopy. The STED laser system must be able to produce two short laser pulses that follow one another in the picosecond time domain. The first pulse must be at a wavelength capable of exciting the dye, and the second, more powerful pulse must be at a wavelength capable of quenching it. Although early STED studies were confined to red-emitting dyes by the availability of appropriate lasers, this is no longer the case.

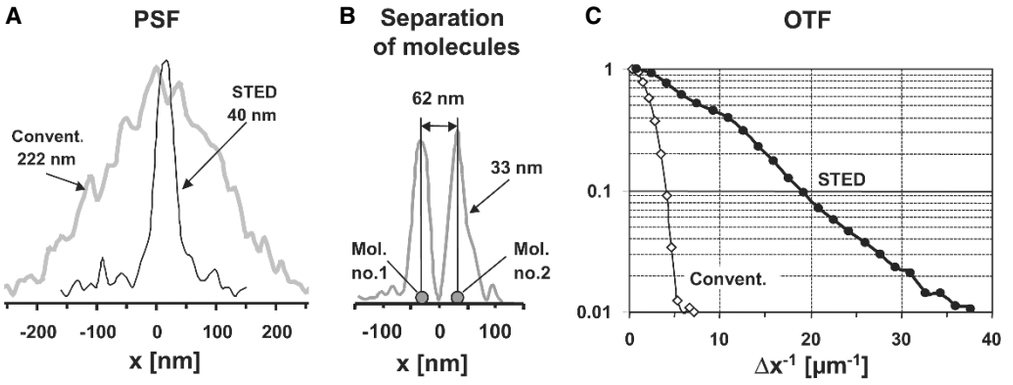


FIGURE 31.3. Quantifying lateral resolution in STED microscopy through imaging of point-like objects. (A) The effective point spread function (PSF) of a conventional microscope and a (laser-diode) STED microscope, determined on single dye molecules (JA 26). (B) Molecules spaced apart far below the diffraction limit could be clearly separated in STED microscopy (slightly augmented by deconvolution). (C) For STED microscopy the gain in transmitted bandwidth of the optical transfer function (OTF) is more than 5-fold, compared with conventional microscopy. Objective lens, NA = 1.4 (oil); wavelengths λ, 635 nm (excitation), 650 to 720 nm (fluorescence detection), 781 nm (STED).

A list of the dyes used so far, is found in Table 31.1. This list is likely to be expanded as the number of pulsed-laser diodes increases and lasers become available that are capable of doing STED on blue, green, and yellow fluorophores, as well as fluorescent proteins. Studies aimed at identifying suitable laser/dye pairs are ongoing.

Recently, a very compact STED microscope was demonstrated using a laser diode for the blue excitation and a second diode laser for STED at around 780 nm (Westphal *et al.*, 2003). As the set of available wavelengths expands over the next decade, it should in the future become possible to realize STED microscopy at lower cost and on most dyes.

Although shorter wavelengths will lead to higher spatial resolution, a further increase in intensity may be barred in aqueous media by intolerable photobleaching. Saturation factors of >200 might not be readily attainable.

STED microscopy is still in its infancy. So far, most of the applications have been aimed at exploring its principles. Tackling cell biology questions will be a task for the years to come. Strong fluorescence suppression (reduction by 90%) is conceptually not mandatory, but practically important to attain subdiffraction resolution. Among the first biological stains described that allows this level of suppression to be reached were lipophilic dyes such as Styryl 6, 7, and 8, 9M, LDS 751, Pyridine 1, 2, 4 and RH 414, or Oxazine 170 and Nile Red. Because STED was first realized with a titanium : sapphire (Ti : Sa) laser emitting in the far-red (750–800 nm), the emission maximum of these dyes is located around 650 to 700 nm (Klar *et al.*, 2000).

Pyridine 4 was used to label the membranes of live *Escherichia coli.* A simultaneous doubling of both the axial and lateral resolution was observed using a 3D doughnut and STED pulses of ~30 ps duration. This initial improvement is likely to be augmented by further optimization of the wavelengths, of the doughnut, and of the pulse duration. Indeed, recent studies revealed that STED-related photobleaching dramatically decreases with the duration of the STED pulse, which indicates a strongly nonlinear dependence of bleaching on the STED-pulse intensity (Dyba and Hell, 2003). Although bleaching is substantially reduced with pulses >120 ps duration, more studies are required to address this critical issue.

In budding yeast, the dye RH 414 is taken up by bulk membrane internalization and subsequently transported to the vacuolar membrane. The structural integrity of vacuolar membranes is sensitive to many stress factors. Therefore, the subdiffraction resolution imaging of vacuoles in living yeast by STED microscopy confirmed that STED microscopy is amenable to imaging living cells (Klar *et al.*, 2000).

Recent progress in laser technology has enabled STED microscopy employing dyes that fluoresce in the visible range. These dyes offer several significant advantages: The shorter wavelengths involved inherently improve the Abbe resolution, while a better quantum efficiency [compared with near-infrared (NIR) dyes] leads to brighter images. Furthermore, the fact that they are visible by eye simplifies sample inspection and image region selection. As a first example, a dramatic enhancement of the resolution in the focal plane is demonstrated on yellow-green fluorescent microspheres (FluoSpheres 505/515, Molecular Probes, OR) in Figure 31.4.

Although the principle of STED applies to any fluorophore, new fluorescent markers require prior investigation. Sometimes the narrow spectral window for efficient STED depends on the chemical environment and has to be established through meticu-

TABLE 31.1. Listing of Example Dyes That Have Been Used Successfully for STED

Category	Name	Emission nm	STED nm	Manufacturer	Notes
Green dye*	Atto532	540–570	615	Atto-tec GmbH, Siegen, DE	Used for single-molecule studies
Yellow dye*	DY-510XL	560–630	625	Dyomics GmbH, Jena, DE	Immunofluorescence label
Red dye*	Atto647N	650–720	760	Atto-tec GmbH, Siegen, DE	Used for single-molecule studies
Far red dye	Pyridine 2	680–750	750–780	SigmaAldrich, St. Louis, MO	Membrane label
Infrared dye	Pyridine 4	710–800	780–800	SigmaAldrich, St. Louis, MO	Membrane label

* These dyes have functional groups and can be coupled to proteins making simultaneous, 3-color, immuno-fluorescence STED imaging possible.

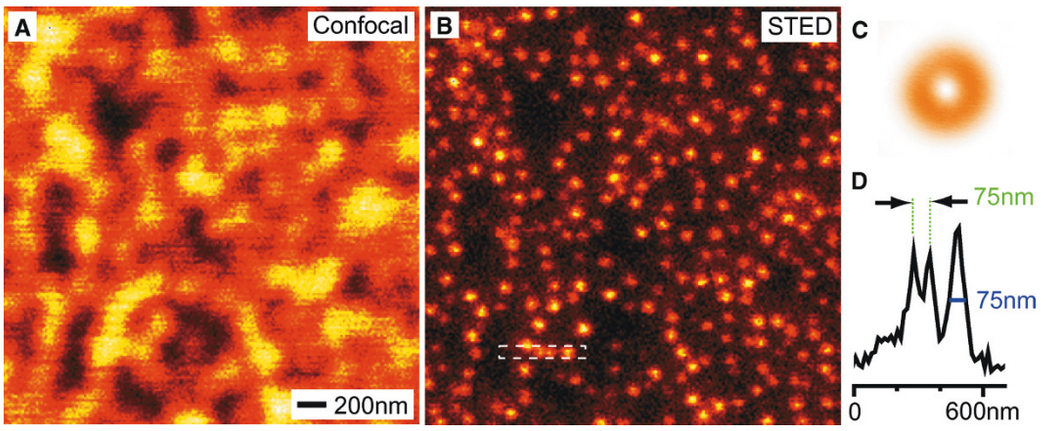


FIGURE 31.4. Beyond the diffraction barrier: STED versus confocal fluorescence microscopy on 40 nm fluorescent microspheres (emission maximum at 515 nm) spread out on a coverslip. The comparison of the confocal (A) and the STED (B) image demonstrates the superior resolution of STED microscopy; neighboring beads are clearly separated. (C) STED intensity distribution employed for depletion, featuring a prominent zero in the center. Drawn to scale with the images. (D) Vertical sum of marked region in (B) illustrates both the clear separation capabilities and subdiffraction resolution of STED microscopy. Objective lens, NA = 1.4 (oil); wavelengths λ, 469 nm (excitation), 500 to 550 nm (fluorescence detection), 585 nm (STED).

lous screening. Ongoing investigations on fluorescent proteins will establish the operational conditions for STED and its potential with these important labels.

Recently, the resolving power of STED has been synergistically combined with that of 4Pi microscopy to achieve nanoscale axial resolution (Dyba and Hell, 2002). Destructive interference of the counterpropagating spherical wavefronts of the STED pulse at the focal point produces a narrow focal *minimum* for STED with an axial FWHM of $\sim\lambda/(4n) \approx 100$ to 120 nm. Overlap with the regular excitation spot of a single lens has so far rendered focal spots down to $\Delta z = 40$ to 50 nm. Linear deconvolution of the data removes the effect of the weak (<30%) sidelobes that accompany the narrow focal spot. Moreover, it further increases the axial resolution up to 30 to 40 nm. This is exemplified in Figure 31.5(C,D),

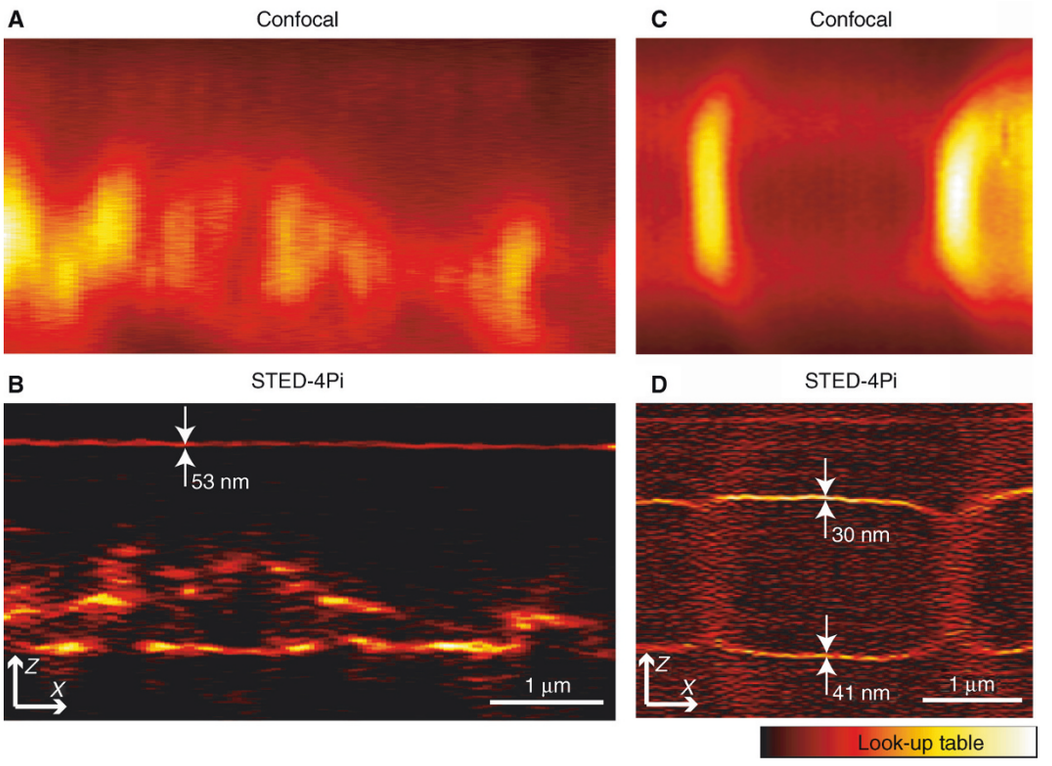


FIGURE 31.5. Axial resolution increase provided by STED–4Pi (B, D) over confocal microscopy (A,C). *xz*-images from the immunolabeled microtubular network of a HEK cell as recorded with a (A) confocal and (B) STED–4Pi microscope. Both images have been recorded at the same site in the cell. The microtubules were labeled using a primary anti–β-tubulin antibody and a secondary antibody coupled to MR-121. The STED–4Pi images were linearly deconvolved to remove the effect of the 4Pi sidelobes. Note the straight horizontal line which stems from an MR-121 layer on the coverslip. At this layer, the resolution of the STED–4Pi microscope is determined as 53 nm after linear deconvolution. The HEK cell was mounted in aqueous buffer and recorded with water-immersion lenses. In another experiment the membranes of a live bacterium (*Bacillus megaterium*) were stained with the RH 414. Next it was simultaneously imaged in the confocal (C) and in the STED–4Pi microscopy mode (D). Note that the axial resolution of this focusing microscope is of the order of 30 to 40 nm.

which shows *xz*-images of the membrane-labeled *Bacillus megaterium* (Dyba and Hell, 2002).

The STED–4Pi setup realized so far improves the resolution along the *z*-axis only, thus rendering a disk-shaped focal spot whose effect is also noticeable in Figure 31.5(B,D). The spot could be sculpted down to a spherical shape by applying a second, STED, pulse whose spatial form is designed to squeeze the spot laterally.

STED–4Pi microscopy has also been applied to the imaging of the microtubular cytoskeleton of human embryonic kidney (HEK) cells (Dyba *et al.*, 2003). The HEK cells were decorated with an anti–β-tubulin antibody and a secondary antibody coupled to the red-emitting dye MR-121. The latter displays high STED efficiency (>90%) at a STED wavelength of ~780 to 795 nm. Contrary to the confocal *xz*-sections, in the linearly deconvolved STED–4Pi counterpart, most of the microtubules appear as distinct objects [Fig. 31.5(A,B)].

The axial resolution attained can be inferred from the FWHM of a fluorescent mono layer that has been deposited on the coverslip; it is ~50 nm, corresponding to 1/16 of the irradiation wavelength of 793 nm. It is interesting to note that in the STED–4Pi image, the brightness of the monomolecular layer is of the same order as that of the microtubules. By contrast, in the confocal image, signal from the layer is overwhelmed by the total signal from the larger focal volume of the confocal microscope.

An important task for the near future is to define the optimal parameters for specific imaging applications. The results obtained with STED and STED–4Pi microscopy demonstrate that the basic physical Abbe limit has been broken and we are now moving towards attaining a 3D resolution of the order of a few tens of nanometers.

CHALLENGES AND OUTLOOK

Given the limits on the rate of excitation and fluorescence emission, high temporal and high spatial resolution may be mutually exclusive in many cases, simply because of the poor statistics of the collected photon signal. High spatial resolution also requires small pixels, which is not favorable for fast imaging of large areas. Downsizing the region of interest will be inevitable. A remedy is to parallelize the scanning system, either by applying many foci or by utilizing sophisticated structured illumination schemes. Likewise, the limited number of emission cycles that characterizes many fluorophores, caps the signal that is available from a sample, and, thus, the signal per sample volume. For a number of staining protocols and applications, the available signal might not match up with the number of photons that must be detected in order to benefit from the increase in spatial resolution. Therefore, potential improvements in fluorescent labels as well as strategies for avoiding photobleaching will play a vital role in firmly establishing nanoscale resolution in light microscopy.

Still, even under poor signal conditions, a RESOLFT method creating ultrasmall focal volumes, such as STED, may be extremely helpful for techniques that exploit fluorescence statistics. For example, fluorescence correlation spectroscopy (Magde *et al.*, 1972) depends on small focal volumes to detect rare molecular species or rare molecular interactions in concentrated solutions (Eigen and Rigler, 1994; Levene *et al.*, 2003). STED may be the key to interrogating nanosized volumes in intact cells. In fact, it is so far the only method reported to squeeze a fluorescence volume to the zeptoliter scale without mechanical confinement. Published results imply the possibility of sampling spherical focal volumes of only 30 nm diameter (Kastrup *et al.*, 2005).

The past decade has witnessed the emergence of a family of physical concepts for attaining diffraction-unlimited spatial resolution in focusing fluorescence microscopy. Relying on reversible saturable optical (fluorescence) transitions (RESOLFT), the spatial resolution of these concepts is eventually determined by the saturation level that can be realized. Saturation brings about an essential nonlinear relationship between the signal and the applied intensity that allows one to overcome diffraction fundamentally.

The nonlinearity brought about by saturation is radically different from that of the well-known multi-photon events. In the latter cases, the nonlinearity stems from the contemporaneous action of more than one photon, which inevitably demands high focal intensities. In contrast, the nonlinearity brought about by saturated depletion stems from the population kinetics of the states involved (Hell, 2003). This opened the door to attaining marked nonlinearities even with linear optical transitions such as single-photon excitation and stimulated emission. Semistable molecular states enable saturable optical transitions at even lower light intensities. Bistable fluorophore constructs and switchable fluorescent proteins should allow very high levels of saturation at the low light intensities essential for live-cell imaging. This insight may be critical to opening up the cellular nanoscale with visible light and regular lenses (Hell, 2003; Hell *et al.*, 2003).

In fact, it is interesting that the demand for high intensities is the reason why the typical nonlinear optical processes of multi-photon fluorescence excitation and multi-photon scattering [second and third harmonic generation (SHG, THG), coherent anti-Stokes Raman scattering (CARS), etc.] could not substantially improve the spatial resolution. It is also clear that as *n*-photon excitation of the fluorescent state (i.e., the S_1) eventually requires the subdivision of the excitation energy into *n* photons, it leads to an *n* times larger wavelength. As an *n* times larger wavelength leads to *n* times larger focal spots, multi-photon excitation processes are counterproductive when it comes to sharpening the focal spot size in the focal plane. Exceptions have been given (Hänninen *et al.*, 1996; Schönle and Hell, 1999; Schönle *et al.*, 1999) but they currently appear less promising than the concept of RESOLFT.

The principles of the concept of RESOLFT have been validated through STED microscopy, whose ability to break the diffraction resolution barrier has been experimentally demonstrated. It is worth mentioning that the strategy of utilizing reversible saturable optical transitions also has the potential to break the diffraction barrier in nanoscale writing and data storage (Hell, 2004). The coming years will show whether STED and its RESOLFT cousins are going to establish themselves as part of the microscopic toolbox to elucidate dynamics and structure of cellular networks. The chances are better than ever.

A taste of what is to come can be seen in Figure 31.6, which shows small patches of cell membrane, immuno-stained against the SNARE protein SNAP25, and viewed both by confocal and STED microscopy using the exact same optics. The improvement is even more obvious in Figure 31.7.

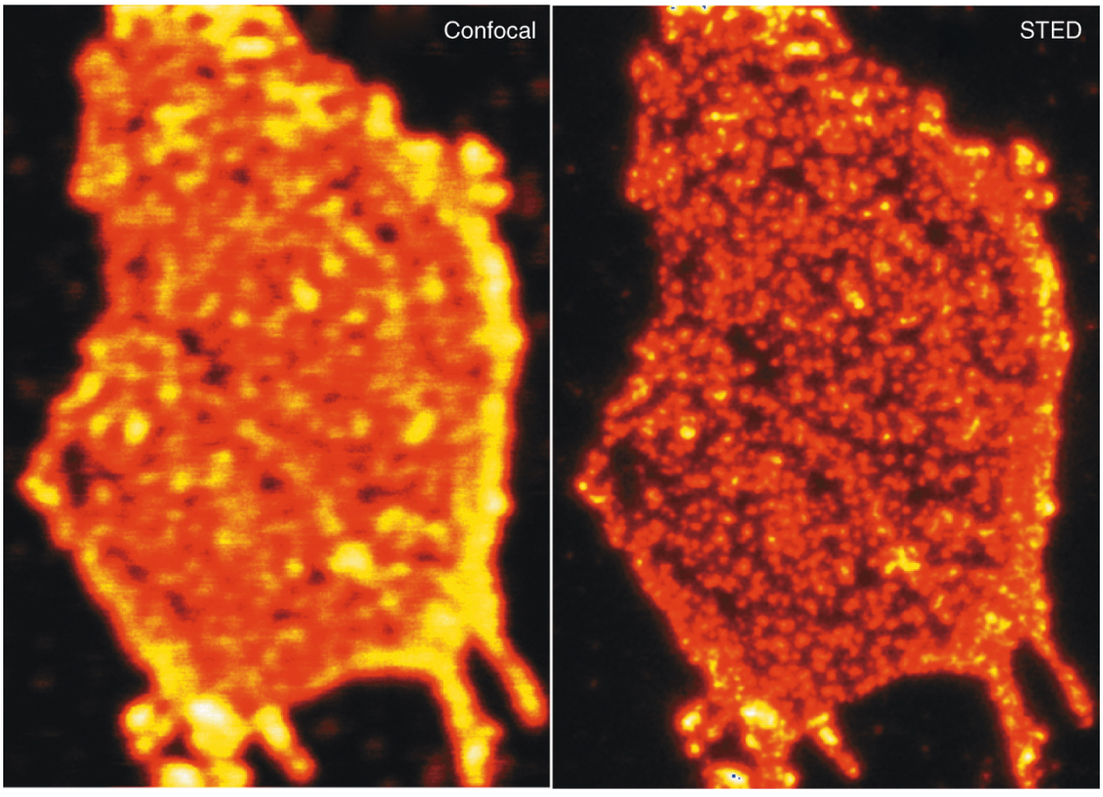


FIGURE 31.6. Resolution comparison of confocal versus STED-microscopy; plasma membrane patches immuno-stained against the SNARE protein SNAP25; secondary antibody labeled with Atto 532-NHS; Emission 540–570 nm, STED at 615 nm. The confocal image was recorded by simply turning off the STED beam with no other changes.

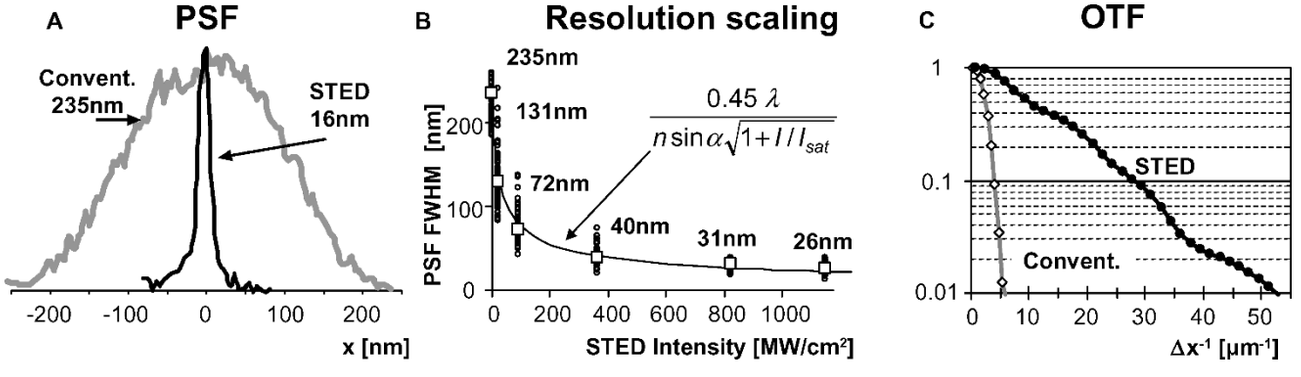


FIGURE 31.7. STED-microscopy hits the nanoscale. (A) Comparison of the PSF (x-axis) of a conventional and a STED microscope probed with a single dye molecule whose orientation is parallel to the polarization of the STED-beam; for details see (Westphal and Hell, 2005). The up-to 15-fold reduction in lateral width underscores the potential of STED-microscopy to attain true nanoscale resolution. (B) The resolution of a STED microscope scales with the square root of the intensity used in the STED beam, with no firm limit, as predicted by equation (4). The gain in resolution also entails an increase of the OTF bandwidth over the diffraction barrier. (C) Shows an example where the usable bandwidth (magnitude >1%) of the OTF is broader by about an order of magnitude than in a conventional microscope. All measurements were performed with the red emitting dye JA26 and with a STED-wavelength of ~780 nm. Being a far-field optical microscope, the resolution of STED-microscopy increases inversely with the wavelength. Therefore, in (A) reducing the wavelength for STED to 500 nm would decrease the FWHM down to ~10 nm.

REFERENCES

Abbe, E., 1873, Beiträge zur Theorie des Mikroskops und der mikroskopischen Wahrnehmung, *Arch. f. Mikroskop. Anat.* 9:413–420.

Alivisatos, A.P., 1996, Semiconductor clusters, nanocrystals, and quantum dots, *Science* 271:933–937.

Bruchez, M. Jr., Moronne, M., Gin, P., Weiss, S., and Alivisatos, A.P., 1998, Semiconductor nanocrystals as fluorescent biological labels, *Science* 281:2013–2015.

Chudakov, D.M., Belousov, V.V., Zaraisky, A.G., Novoselov, V.V., Staroverov, D.B., Zorov, D.B., Lukyanov, S., and Lukyanov, K.A., 2003, Kindling fluorescent proteins for precise *in vivo* photolabeling, *Nat. Biotechnol.* 21:191–194.

Cragg, G.E., and So, P.T.C., 2000, Lateral resolution enhancement with standing wave evanescent waves, *Opt. Lett.* 25:46–48.

Dyba, M., and Hell, S.W., 2002, Focal spots of size l/23 open up far-field fluorescence microscopy at 33 nm axial resolution, *Phys. Rev. Lett.* 88:163901.

Dyba, M., and Hell, S.W., 2003, Photostability of a fluorescent marker under pulsed excited-state depletion through stimulated emission, *Appl. Opt.* 42:5123–5129.

Dyba, M., Jakobs, S., and Hell, S.W., 2003, Immunofluorescence stimulated emission depletion microscopy, *Nat. Biotechnol.* 21:1303–1304.

Eigen, M., and Rigler, R., 1994, Sorting single molecules: applications to diagnostics and evolutionary biotechnology, *Proc. Natl. Acad. Sci. USA* 91:5740–5747.

Hänninen, P.E., Lehtelä, L., and Hell, S.W., 1996, Two- and multiphoton excitation of conjugate dyes with continuous wave lasers, *Opt. Commun.* 130:29–33.

Heintzmann, R., and Cremer, C., 1998, Laterally modulated excitation microscopy: Improvement of resolution by using a diffraction grating, *SPIE Proc.* 3568:185–195.

Heintzmann, R., Jovin, T.M., and Cremer, C., 2002, Saturated patterned excitation microscopy – A concept for optical resolution improvement, *J. Opt. Soc. Am. A* 19:1599–1609.

Hell, S.W., 1997, Increasing the resolution of far-field fluorescence light microscopy by point-spread-function engineering, In: *Topics in Fluorescence Spectroscopy* (J.R. Lakowicz, ed.), Vol. 5, Plenum Press, New York, pp. 361–422.

Hell, S.W., 2003, Toward fluorescence nanoscopy, *Nat. Biotechnol.* 21: 1347–1355.

Hell, S.W., 2004, Strategy for far-field optical imaging and writing without diffraction limit, *Phys. Lett. A* 326:140–145.

Hell, S.W., and Kroug, M., 1995, Ground-state depletion fluorescence microscopy, a concept for breaking the diffraction resolution limit, *Appl. Phys. B* 60:495–497.

Hell, S.W., and Wichmann, J., 1994, Breaking the diffraction resolution limit by stimulated emission: Stimulated emission depletion microscopy, *Opt. Lett.* 19:780–782.

Hell, S.W., Jakobs, S., and Kastrup, L., 2003, Imaging and writing at the nanoscale with focused visible light through saturable optical transitions, *Appl. Phys. A* 77:859–860.

Kastrup, L., Blom, H., Eggeling, C., and Hell, S.W., 2005, Fluorescence fluctuation spectroscopy in subdiffraction focal volumes, *Phys. Rev. Lett.* 94:178104.

Klar, T.A., Engel, E., and Hell, S.W., 2001, Breaking Abbe's diffraction resolution limit in fluorescence microscopy with stimulated emission depletion beams of various shapes, *Phys. Rev. E* 64:1–9.

Klar, T.A., Jakobs, S., Dyba, M., Egner, A., and Hell, S.W., 2000, Fluorescence microscopy with diffraction resolution limit broken by stimulated emission, *Proc. Natl. Acad. Sci. USA* 97:8206–8210.

König, K., Tadir, Y., Patrizio, P., Berns, M.W., and Tromberg, B.J., 1996, Effects of ultraviolet exposure and near-infrared laser tweezers on human spermatozoa, *Hum. Reprod.* 11:2162–2164.

Levene, M.J., Korlach, J., Turner, S.W., Foquet, M., Craighead, H.G., and Webb, W.W., 2003, Zero-mode waveguides for single-molecule analysis at high concentrations, *Science* 299:682–686.

Lukyanov, K.A., Fradkov, A.F., Gurskaya, N.G., Matz, M.V., Labas, Y.A., Savitsky, A.P., Markelov, M.L., Zaraisky, A.G., Zhao, X., Fang, Y., Tan, W., and Lukyanov, S.A., 2000, Natural animal coloration can be determined by a nonfluorescent green fluorescent protein homolog, *J. Biol. Chem.* 275:25879–25882.

Magde, D., Elson, E.L., and Webb, W.W., 1972, Thermodynamic fluctuations in a reacting system – measurements by fluorescence correlation spectroscopy, *Phys. Rev. Lett.* 29:705–708.

Peng, X., Manna, L., Yang, W., Wickham, J., Scher, E., Kadavanich, A., and Alivisatos, A.P., 2000, Shape control of CdSe nanocrystals, *Nature* 404:59–61.

Schönle, A., Hänninen, P.E., and Hell, S.W., 1999, Nonlinear fluorescence through intermolecular energy transfer and resolution increase in fluorescence microscopy, *Ann. Phys. (Leipzig)* 8:115–133.

Schönle, A., and Hell, S.W., 1999, Far-field fluorescence microscopy with repetitive excitation, *Eur. Phys. J. D* 6:283–290.

Westphal, V., and Hell, S.W., 2005, Nanoscale resolution in the focal plane of an optical microscope, *Phys. Rev. Lett.* 94:143903.

Westphal, V., Blanca, C.M., Dyba, M., Kastrup, L., and Hell, S.W., 2003, Laser-diode-stimulated emission depletion microscopy, *Appl. Phys. Lett.* 82:3125–3127.

Westphal, V., Kastrup, L., and Hell, S.W., 2003, Lateral resolution of 28 nm (lambda/25) in far-field fluorescence microscopy, *Appl. Phys. B* 77:377–380.

32

Mass Storage, Display, and Hard Copy

Guy Cox

INTRODUCTION

Confocal microscopes commonly generate their images not as real or virtual patterns of light, but as pixel values in the memory of a computer (Cox, 1993). This gives the image a measure of permanence — unlike a visual image, once acquired it will not fade — but it will be lost if the computer is turned off, or if that area of memory is overwritten. To store that image with all its information intact we must write it in digital form — a copy on paper or film, however good, cannot contain all the information of the original. However, a copy on disk or tape is not directly accessible to human senses. For publication or presentation of the image, or even just to access it, we must have a display or a hard copy, a picture which can be viewed by the human eye.

This chapter reviews the range of possible solutions to these two problems. Because this is a rapidly moving area, new alternatives will doubtless become available almost as soon as this is printed. A measure of the rate at which this happens is that many of the technologies reviewed in the previous edition are now obsolete, leaving users with the task of copying images to new media if they are to retain access to their data. As well as assessing currently available technologies, therefore, I will try to provide enough background information to enable users to assess the latest high technology advances in a rational way. It is always worth considering the scale of the adoption of a technique as well as its technical efficiency because most of us will still want to be able to use our data in 10 or even 20 years' time, and only mass-market solutions are likely to survive on that timescale.

MASS STORAGE

The major problem in storing confocal images is their sheer size. The smallest image we are likely to acquire would be 512 × 512 pixels, at one plane only and containing only one detector channel. Assuming that we store only 1 byte per pixel (that is, each point in the image can have one of 256 possible gray levels) this will require one quarter of a megabyte (MB) to store. We will require a little more space to store basic information about how the picture was acquired, either in a header at the start of the file, or at the end, or even in a separate file. Most confocal microscopes will capture larger images than this, and most will capture more than one channel. A three-channel, 2048 × 2048 pixel image (routine on any current system) will require 12 MB to store one plane. A three-dimensional (3D) image data set could easily contain 100 or more planes, thus requiring 1200 MB (1.2 gigabytes, GB) or more to store. At the time of this writing, current personal computers typically have 80 to 200 GB hard disks, a 200-fold increase on the norm when the last edition of this chapter was written, but still not enough to be regarded as a permanent store. To provide archival storage, we must have some form of removable storage media.

Data Compression

Before considering the contending bulk storage devices, is there any way we can reduce the size of the problem? Can we compress the image data to make it smaller? Lossless data compression systems, which preserve the integrity of our original image data, generally work on some variation or combination of three well-known algorithms. Run-length encoding (RLE) looks for sequences of identical values and replaces them with one copy of the value and a multiplier. It works very well with binary (black/white) images or simple graphics using a few bold colors, and is used, for example, for all the splash screens in Microsoft Windows.

Lempel–Ziv–Welch (LZW) and Huffman encoding look for repeated sequences, assign each a token, then replace each occurrence by its token. Neither of these works well with real images (though they do an excellent job with computer-generated graphics). Thus, if you save a confocal image as a GIF (graphics interchange format) file, or as a compressed TIFF (tagged image file format) file, both of which use LZW compression, you will be lucky to get even a 10% to 20% decrease in size, and sometimes your file size will actually get larger. You will not do much better with the popular archiving systems PKzip, gzip, or WinZip, which (to avoid patent problems) use LZ77, an earlier Lempel–Ziv algorithm, and Huffman encoding (Deutsch, 1996), though these systems do at least recognize if compression is not working and insert the uncompressed data instead, so your file should not get larger.

There are a couple of exceptions to this generalization. First, some confocal microscopes store 12 bits of data at each pixel (4096 gray levels), but they store this as 16-bit numerical values. Clearly these images have redundant space — a quarter of the file contains no information — and they will therefore at least compress to 75% of the original size. The file will nevertheless become even smaller, often with little or no real loss, if it is converted to 8-bit data. Second, even though it may not immediately be obvious, a three-channel image of moderate size, saved as a 24-bit RGB file, must always have redundant information. Twenty-four bits of data can specify 16.7 million colors, but a 512 × 512 image with only a quarter of a million pixels can contain at most a quarter of a million colors. Efficient algorithms will automatically find this redundancy and yield effective compression (how this is done is explained in the description of the PNG format, below).

Guy Cox • University of Sydney, New South Wales 2006, Australia

PNG, which stands for portable network graphic, but is pronounced "ping," is a lossless compression system (Roelofs, 2003). It will usually offer the highest lossless compression currently attainable for confocal images. The formal compression system is identical to that of the "zip" systems; the deflate algorithm (Deutsch, 1996) a combination of Huffman and Lempel–Ziv algorithms that in essence looks for repeated patterns. The secret of PNG's improved performance lies in its prefiltering of the image to establish the best way to represent the data. In a real-world image of any kind, the difference between adjacent pixels will rarely be extreme so often the data can be reduced substantially by storing only the difference. The different filters vary essentially in the pixels used for comparison (no filtering, pixel before, or before and after, or before and above, etc). Any implementation contains all filters and so will decode any image, but the better implementations will offer improved compression by careful choice of which filter to apply. (The standard allows different filters to be used on each line of the image if required.) So if lossless compression is important it may be worth experimenting with different vendors' implementations of PNG (see below). It tends to be much slower than LZW to compress, partly because it is a two-pass process but mainly because, to get the best results, the program should test which algorithm will give best results. Decompression is fast (see Table 32.1).

The demands of computer multi-media have led to the development of compression techniques specifically aimed at real-world images, both still and moving. Unlike the compression techniques mentioned above, which are completely reversible, these approaches discard information from the image. The picture created after compression and decompression will not be the same as the original. However, very large file compressions can often be achieved with losses which are barely detectable to the eye, though they may affect numerical properties of the image.

TABLE 32.1. Time to Compress and Read Back an Image Using Different Techniques

Compression	Save Time (s)	Read Time (s)	File Size (KB)
Uncompressed TIFF	5	3	9220
LZW TIFF	7	5	6014
PNG	40	5	2861
Wavelet (lossless)	9	12	1934
Wavelet (high-quality)[a]	16	10	841
Wavelet (high-quality)[b]	8	10	821
Wavelet (low-quality)[a]	15	6	9
Wavelet (low-quality)[b]	6	6	10
Lossless JPEG	8	7	3877
DCT JPEG (high-quality)	4	4	840
DCT JPEG (low-quality)	4	4	164

[a] Specifying required quality.
[b] Specifying required file size.
The image used was that seen in Figure 32.1, but scaled up (using bicubic interpolation) 6-fold to 3072×3072 pixels in order to make the times measurable. All conversions were done using Paint Shop Pro version 8 (Jasc Software); the results should only be taken as relative and will vary greatly with processor speed. Scaling the image means that it contains substantial redundancy and therefore the compression levels achieved are unrealistic; the file sizes are given mainly to illustrate the trade-off between processing time and disk access. PNG was by far the slowest in compressing the image, but was rapid to read back. The processing requirements of DCT JPEG compression were more than compensated for by the reduction in disk access, so that it was very fast, but lossless JPEG was slower and its compression did not match lossless wavelet or PNG. Wavelet compression (JPEG 2000) showed the curious result that selecting a "compression quality" gave much longer save times than selecting the "desired output file size." At equivalent final sizes, the resulting images seemed similar. This is probably a quirk of the implementation of what is, at the time of this writing, a very new standard. Wavelet images were the slowest to read back, particularly at high image qualities.

The most common still image format is the Joint Photographic Experts' Group (JPEG) compression protocol (Redfern, 1989; Anson, 1993; Pennebaker and Mitchell, 1993), which is supported by many paint and image manipulation programs. This breaks the image into blocks of 8×8 pixels, each of which is then processed through a discrete cosine transform (DCT). This is similar to a Fourier transform, but much faster to implement, and gives an 8×8 array in frequency space. The frequency components with the lowest information content are then eliminated, after which high-frequency information (fine detail) will be selectively discarded to give the desired degree of compression. The remaining components are stored (using Huffman encoding) in the compressed image. The amount to be discarded in frequency space can be specified, which gives the user control over the trade-off between image quality and degree of compression. Typically, monochrome images can be compressed down to one fifth or less of their original size with no visible loss of quality (Avinash, 1993). Compression and decompression are similar operations, and require similar amounts of computer time. Ten years ago, when the standard was first published (Pennebaker and Mitchell, 1993), the time required was quite noticeable but with a modern processor the reduced amount of disk access will more than compensate for the processing time (Table 32.1).

Color images can be compressed further than monochrome because luminance (brightness) and chrominance (color) are treated separately. The eye can tolerate a greater loss of information in the chrominance signal, so this is normally handled at half the resolution. (The standard allows many different options here but specific implementations usually do not make these evident to the user.) This has certain consequences in confocal microscopy because a three-channel confocal image is *not* a real-color, real-world image but three images which are largely independent of each other. A three-channel confocal image compressed as a color image will look quite adequate but should not be used reliably for numerical analysis; for example, the lower resolution of the color information would make many pixels show colocalization when in fact there is none.

The JPEG standard itself specifies a compression technique, not a file format. As such it is used in many different situations (including one of the compression options in the TIFF standard and in programs such as Microsoft PowerPoint). However, it is most familiar to the end user in the form of files conforming to the JFIF (JPEG file interchange format) standard, which typically use the suffix .jpg. JPEG compression is designed for photographic images so that it only manipulates gray-scale or true color (RGB) images. Adding a false-color palette to a gray-scale image will make it less suitable for JPEG compression because the JPEG algorithm would convert it to a full color image, tripling its size, before compression. Lossless JPEG compression also exists; there have been two distinct lossless compression modes specified in the JPEG standard over the years, but these do *not* use DCT to compress the image and typically do not perform very well, so they have not become popular. The current version, JPEG-LS, uses a predictive algorithm formerly called LoCo, and is designed to be both fast and easy to implement.

Other specific image compression techniques show considerable potential but have yet to achieve the popularity of JPEG (DCT). Fractal compression, a proprietary technique developed by Iterative Systems Inc. (Anson, 1993; Barnsley and Hurd, 1993), creates mathematical expressions which, when iterated, recreate the original image. It can give spectacular levels of compression. Unlike JPEG compression, creating the compressed image is a very time-consuming process but decompression is very quick.

This has made it most useful for such items as CD-ROM encyclopedias but its initial promise has not led to widespread adoption.

Wavelet compression is currently the hot topic in image compression and will undoubtedly be in common use throughout the lifetime of the current edition of this book, though at the time of this writing it is only just appearing in the latest releases of mainstream implementations. It is, in a sense, mathematically comparable to JPEG in that it separates the frequency components in an image, but it works in real space rather than reciprocal space. The basic idea of separating an image into components of different resolution and discarding the lowest information content and highest frequencies first is similar, but it is achieved by passing a series of filters over the image at a range of different scales. The filters — wavelet filters — are the key to this, and are designed to be reversible. The claim is that wavelets can offer useful compression without loss, and much greater compression with losses that are not obvious to the eye. Other advantages include the ability to rapidly generate a low-resolution image (using the coarsest wavelets) and fill in the detail afterwards.

Wavelet compression can treat an image as a whole or break it down into blocks which are compressed individually. The JPEG has introduced wavelet compression into a new version of the JPEG standard (JPEG 2000), and it is in this format that most mainstream applications will offer wavelet compression. In the interests of speed and portability (wavelet compression is intrinsically slower than DCT), the JPEG 2000 implementation uses only two wavelet filters, one for lossless compression and one for lossy compression. Even so, the time required is quite noticeable even on a fast computer (Table 32.1). While a wider range could offer better performance by finding the best wavelet for each image, the practical difficulties involved were deemed to make it not worthwhile. Also, in the JPEG implementation the image is broken into blocks before compression. A major criticism of the DCT JPEG standard was that the 8×8 blocks could often become visible at high levels of compression and JPEG 2000 therefore offers variable sized blocks within a single image, so that one compression level can be applied to featureless regions (such as sky, or the background in a confocal image) and another to regions containing fine detail.

In practice, however, wavelet compression does not seem to offer superior performance over DCT for confocal images, as Figure 32.1 shows. Figure 32.1(A) shows a cultured He-La cell labeled with fluoroscein isothiocyanate (FITC) tagged to an antibody against β-tubulin. It is an average projection from 16 confocal optical sections — a 512×512 pixel 8-bit image. Using an average projection rather than a maximum brightness projection improves the signal-to-noise ratio, but it also reduces the total intensity (because so much of the image is dark) and this therefore reduces the number of gray values present (there are only 120 values in this image). Both factors make the image a better candidate for compression. To preserve the visual quality the contrast has been scaled and the gamma changed (see below); these operations simply change the values assigned to each of the 120 tones, they do not change the number of tones and should not affect how it will compress. Figure 32.1(B) is one of the original slice images with no modifications to gray values. It shows more noise than the projection, but contains 248 gray levels, showing that the gain and black level controls had been used optimally to make use of the full dynamic range without overflow or underflow.

The raw image size in each case is 256 KB, and tif and bmp files are 257 KB. An LZW-compressed tif file of Figure 32.1(A) offered a reasonably useful reduction to 170 KB, while a PNG file created with the well-known program Paint Shop Pro (JASC Software) did rather better at 143 KB. The PNG optimizing program Pngcrush (freeware; see Roelofs, 2003) made an insignificant improvement to 142 KB. This is 55% of the original file size and shows that with a restricted gray range and dark noise-free background reasonable compression can be achieved without loss. Lossless wavelet compression (JPEG 2000) was less effective, giving a file size of 168 KB, scarcely better than LZW-compressed tiff but taking very much longer to compress and decompress. Lossless JPEG was comparable, at 169 KB.

As predicted, the original single-slice image [Fig. 32.1(B)] did not compress nearly so well; the LZW version, at 256 KB, was hardly changed from the original size. PNG did better, at 195 KB (204 KB before optimization). But at 76% of the original size it hardly seems worth the effort. It does, though, reinforce the point that PNG is the only format worth considering for lossless compression of confocal images.

DCT (JPEG) compression of the projection [Fig. 32.1(A)] to two different levels is seen in Figure 32.1(C,D). Figure 32.1(C) shows the image compressed to 26.4 KB, around 10% of its original size. While some loss of quality is evident, the image remains perfectly usable and the compression is very substantial. In Figure 32.1(D), compression has been increased to the point where the image is visibly degraded but still recognizable and even informative, though the file size is only 7.7KB, a mere 3% of the original! Figure 32.1(E,F) shows the same levels of compression but using wavelet compression with JPEG 2000. Both are substantially worse than equivalent DCT images. A specialist wavelet compression program (not using JPEG 2000) was also tried, and gave worse results at equivalent compression levels. It seems probable that the relative failure of wavelets to compete with DCT lies in the rather limited range of resolution levels which contain substantial information in these confocal images. The interest lies primarily in the microtubules, all of which are the same size. In reciprocal space, regions with no information will automatically compress to nothing, whereas the wavelet function may perhaps be chosen to treat all frequencies more or less equally because this may be the best strategy for conventional photographic images. There may therefore be scope for a wavelet implementation dedicated particularly to confocal images.

Figure 32.2 shows the histograms of the images in Figure 32.1. In Figure 32.2(A) the missing gray values are obvious, whereas the single optical section [Fig. 32.2(B)] shows a continuous spectrum. At 10% compression the DCT image [Fig. 32.2(C)] shows a similar spectrum, but smoothed and with the gaps in the gray levels now filled. The wavelet version [Fig. 32.2(E)] also preserves the same shape, but is rather more smoothed at the same compression. At 3% of the original size the DCT histogram [Fig. 32.2(D)] is very much changed, while the wavelet one [Fig. 32.2(F)] shows little change from the 10% compression. In each case, the mean value remains unchanged. These figures show that photometric parameters are surprisingly well conserved even at levels of compression that would seldom be used in practice. While wavelet compression affects the histogram more than DCT at 10% compression, it is more accurate than DCT at 3% compression so that even though the image looks worse, its photometric parameters remain closer to the original.

In practice these compression levels would only be used for such purposes as Internet transmission of images. Compression to between 25% and 50% of the original size would give images of more general usefulness, with little visible change from the original. Even essential photometric parameters are preserved. In spite of the current interest in wavelet compression, DCT still seems a

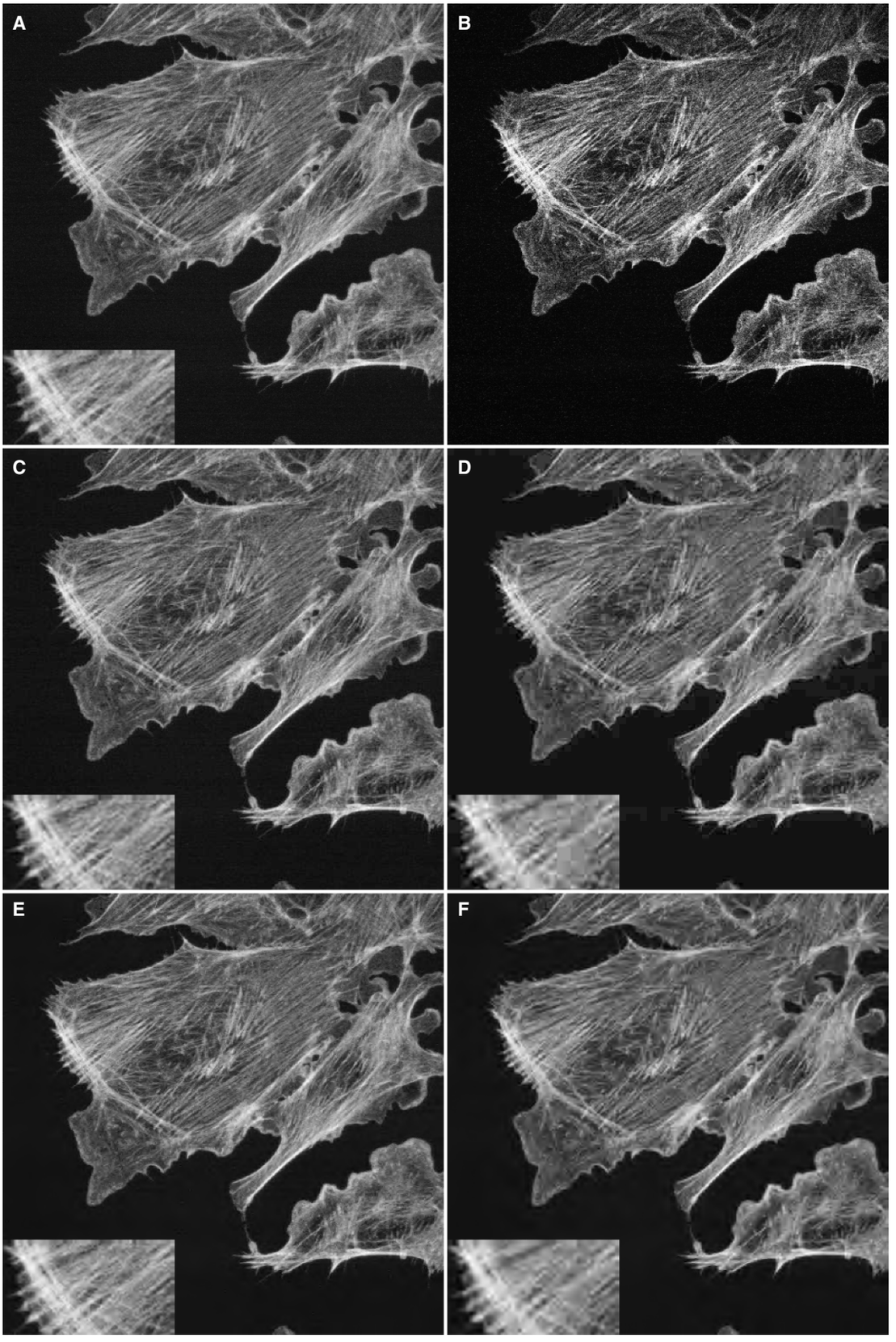


FIGURE 32.1. Effects of image compression on a confocal fluorescence image of a cultured He-La cell immunostained with FITC against β-tubulin. (A) Average projection of the original dataset of 16 optical sections, with contrast scaled and gamma subsequently corrected; original uncompressed image. (B) One optical section from the stack, with no subsequent processing. (C) JPEG compressed (DCT) to ~10% of the original size. (D) JPEG compressed (DCT) to ~3% of the original size. (E) Wavelet compressed (JPEG 2000) to ~10% of the original size. (F) Wavelet compressed (JPEG 2000) to ~3% of the original size. Insets in (A, C–F) are part of the image at 2× magnification to show the losses in compression more clearly.

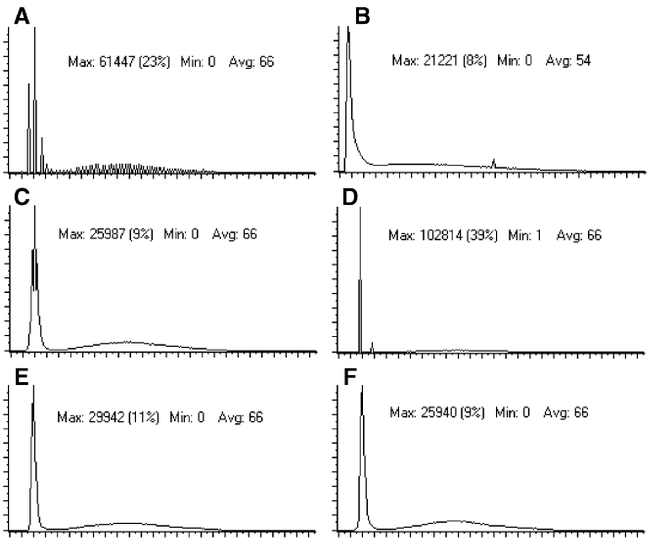


FIGURE 32.2. (A–F) Histograms of pixel intensities in Figure 32.1(A–F), respectively.

better choice for confocal images in cell biology. Not only is it more effective, it is much faster then wavelet compression (Table 32.1). Lossless compression only gives useful results on images with large amounts of uniform background and low noise but in these cases it can be effective. The most likely use would be for storing the output of 3D reconstructions, as in Figure 32.1(A). Although generating a complex 3D movie sequence can take as long as acquiring the original confocal data, and the output files can be just as large, we typically do not have the same concerns about preserving data integrity. It is therefore sensible to use JPEG compression for storing the output.

Some confocal datasets contain only very sparse information. Figure 32.3(A) provides an example, a frame (pre-calcium wave) from a time series of calcium transients induced by testosterone. There were 193 images in the series and without compression this dataset occupies close to 50 MB. However, as only 12% of the pixels lie above the background noise level, the dataset even in its original form compresses without loss to below 100 kB per frame — 40% of the original — with LZW or PNG. If we remove background by setting pixels with a gray value of 14 or below to zero [Fig. 32.3(B)], we have a virtually unchanged image which is now highly compressible without further loss. PNG compression gave a file size of only 49.3 KB, less than 20% of the original. Our original 50 MB dataset will now only be 10 MB. Lossy JPEG compression makes no sense with such a dataset — using a typical setting for reasonable image quality the resultant file size was actually larger (59.3 KB) than the lossless one. What is more, the compression process brought background back into the dark areas. So the message is either use a lossy compression on the original data or compress it by background subtraction and then save it without further loss — do not do both.

Other image manipulations will also affect the compressibility of images. Smoothing, to remove noise, will reduce the high-frequency content and therefore make images more compressible. Deconvolution, on the other hand, aims to restore high-frequency content. This will make images less compressible, or will mean that more is lost in lossy compression. Figure 32.4 illustrates this

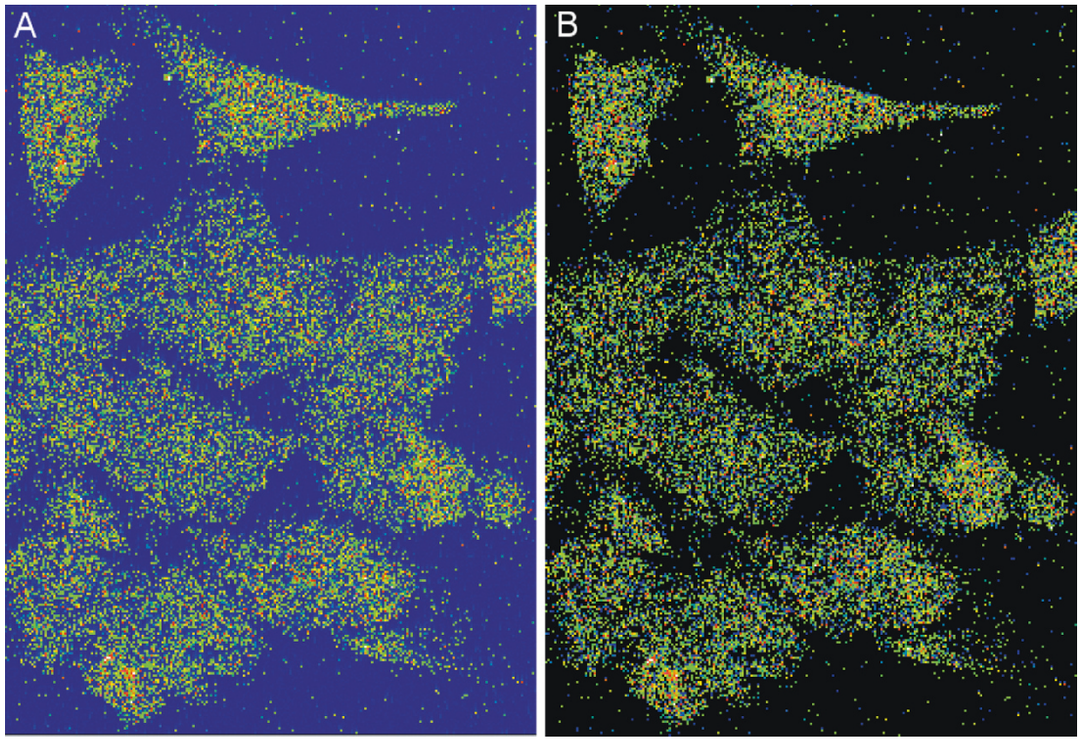


FIGURE 32.3. Calcium imaging (non-ratiometric) of transients induced by testosterone in cultured cells. Pre-stimulation, time point 42 from 193 images taken at 1-second intervals. (A) original image (B) background removed by setting all pixels below a value of 15 to zero, a process that permits no-loss compression to reduce file size of (B) by a factor of two compared to (A). A false-color palette has been added to show how the background has been set to black but none of the "data" pixels have changed. Taken using a 63x/NA 1.2 water-immersion lens. Image width as shown (only part of the original image) is 154μm. Image courtesy Dr. Alison Death.

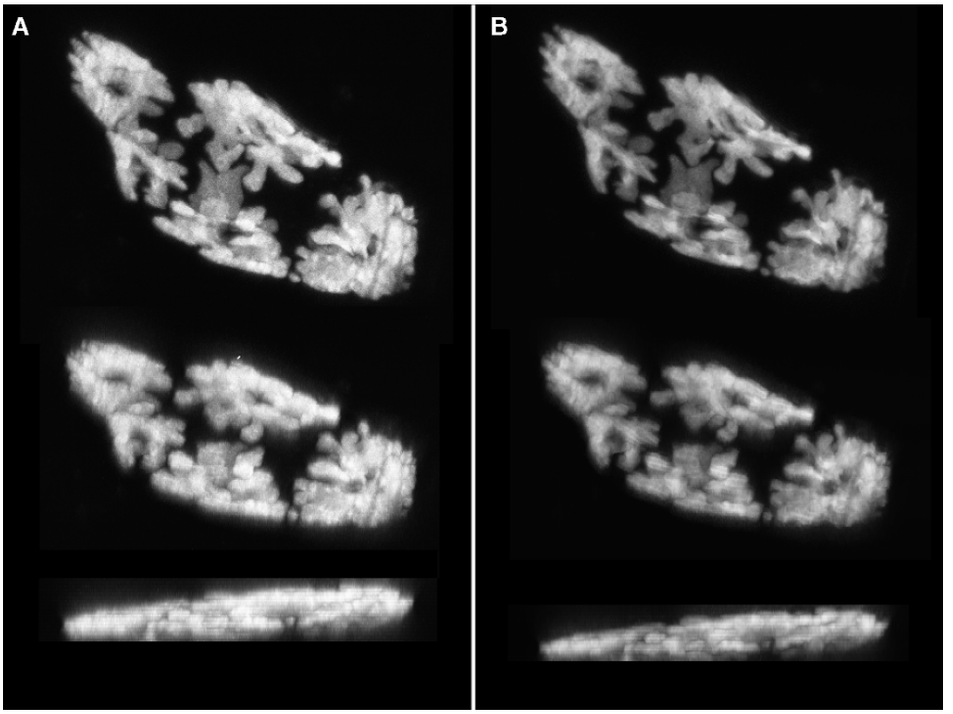


FIGURE 32.4. Three different angle projections (0°, 45°, and 90°) from a 3D dataset of the dinoflagellate alga *Dinophysis*. (A) Maximum intensity projection from the original dataset. (B) Maximum intensity projection after smoothing (3D median filter) and one-dimensional deconvolution.

point. This is a 3D dataset of the dinoflagellate alga *Dinophysis*, which was collected at 3 pixels per resel and therefore is slightly oversampled. This provides the opportunity to smooth the data down to the Nyquist limit and thereby reduce noise without adversely affecting resolution. Figure 32.4(A) shows maximum intensity projections, at three angles, from the original dataset. This type of projection leaves noise unchanged so the view shows an accurate impression of the noise content of the original set. Compressed with LZ77 the original 4.5 MB dataset reduces to 1.9 MB, a useful saving, reflecting the large proportion of background in the set. When the entire dataset is smoothed with a median filter, acting in three dimensions (Cox and Sheppard, 1999), it becomes more compressible, now reducing to 1.38 MB. If we deconvolve this dataset we can restore some of the resolution lost in the *z*-(depth) direction by the transfer function of the microscope (Cox and Sheppard, 1993, 1999). As expected, it is now rather less compressible, at 1.47 MB, but this is still a useful saving on the original. The smoothed, deconvolved dataset is shown in the same projections in Figure 32.4(B).

In any image compression strategy, it is important to bear in mind that confocal images can become virtually meaningless if the information about the acquisition is lost. Some confocal systems (e.g., Bio-Rad) store this data in a header within the same, single file as a series of optical sections. Even if the slice images are exported by the Bio-Rad software, the acquisition data is not exported and the images cannot be re-imported for subsequent processing. Other systems (e.g., Leica, Zeiss) store a database of information about the images — exported images generated within the acquisition software will still retain some of this information but typically 3D reconstructions can only be done from the original images. In either case it is important to ensure that the all-important image acquisition data are preserved, and if possible that the images can be restored to their original file name and type.

A final point: the most common waste of disk space consists of storing completely featureless areas! If your sample is rectangular, select a rectangular window to image it rather than collecting a strip of nothing on each optical section. And do not collect three channels if you have only two labels! Modern systems make it all too easy to accept the default method, or configuration; it will save a lot of time in the long run if you spend a minute or two changing settings to collect only what you want.

Removable Storage Media

Storage media can be divided into those which are sequential (records are written and read from one end only) and those which are random access (it is possible to move directly to any record, whenever it was written).

Sequential Devices

Sequential devices are tapes of various formats and sizes storing up to 200 GB on a single cassette. Tape is still the largest-capacity bulk storage medium available, but is no longer competitive in cost with optical storage. As an image storage system, it also suffers from the time taken to locate and recover any one file. A single file cannot be erased and replaced by another; one must erase either the whole tape or a large group of files, depending upon the recording system. Also, although it is rewritable it will not stand an infinite number of uses. The tape surface has a much harder life than the surface of a disk — it comes into direct contact with the recording heads and capstans, and is coiled and uncoiled each time. Even reading files repeatedly wears the tape, and its long-term archival potential is dubious. Once tape drives were regularly used for data storage and transfer but now their use is almost exclusively for backup purposes — making a copy of a complete file system or subsystem which will typically be read only once, in the event of a hard disk failure.

Modern tape systems are very specifically designed for this task; their purchase cost is high but cost per megabyte stored can be low compared to other rewritable media. This gives them some attraction for long-term archival storage of images that will not need to be accessed regularly, and for very large collections of images. Dumping a 40 or 100 GB hard disk full of images on to a single tape will be much quicker and simpler than writing to

dozens of compact disks (CDs) or digital video disks (DVDs). However, most tape systems now rely on specific software to handle them and both this software and suitable hardware will need to be available for the tape to be read in the future — past experience suggests that this will limit effective use to 5 years or so, and this is probably the realistic limit for tape life also.

Transfer rates up to 24 MB s^{-1} are available on expensive high-end systems, although systems designed for small computer use will offer no better than 3 MB s^{-1}. At 24 MB s^{-1} writing one CD worth of data will take only 30 s, but it will take a quarter of an hour to copy a 20 GB hard disk. At 3 MB s^{-1} that same disk will take almost 2 h to copy.

Manufacturers typically quote compressed capacities for their tape drives, based on a notional 2-fold compression ratio that they expect to achieve with their archiving software. This is unrealistic when dealing with image files, and when evaluating competing systems, it is important to compare actual, uncompressed, storage capacities; this is much closer to the figure achievable with microscope images.

Random-Access Devices

Random-access devices comprise a range of disk media, either magnetic or optical, and solid-state devices.

Magnetic Disks

The oldest and simplest of removable media, rewritable, random-access systems is the humble floppy diskette. These are now virtually obsolete, limited by their small capacity — 1.4 MB in the only (marginally) surviving 3.5″ version. As many will have found out, finding a drive to read the once ubiquitous 5.25″ disks is already difficult. In any case, they are too small to be relevant for confocal images.

Various types of super-floppy have had a vogue in the past, but the only current survivor seems to be the Iomega Zip disk, which originally held 100 MB but now comes in capacities up to 750 MB. These are robust and durable but seem unlikely to be current for very much longer, driven out by far cheaper optical technology. They are also too limited in space to meet most modern needs for confocal image storage. Cost per gigabyte is around US$20–100.

Other removable platter magnetic devices have been current, and suffer from the same limitation that in the course of time there may no longer be hardware available to read them. One of the most successful at the time of writing is the Orb drive, available in capacities from 2 to 5 GB. Like many other portable devices they connect to the host computer by the USB (universal serial bus) port, or the parallel printer port. Parallel port connection is relatively slow and USB is by far the preferable option. Cost per gigabyte is of the order of US$10 to US$20, so it is a reasonably affordable option.

There remains the option of just using conventional hard disks. Mounting kits are available to fit a conventional disk in a pull-out mount; disks are also available in cases for connecting to USB, Fire Wire, or SCSI (small computer systems interface) ports, and there are microsized ones which fit the PC card (PCMCIA) slot in notebook computers. The recent fall in price and increase in capacity of hard disks has made this a surprisingly affordable option (below US$1.00 per gigabyte for IDE disks, more for SCSI). Data transfer is as fast as the disk — certainly faster than most other options — and rewriting capacity is effectively unlimited. The long-term potential is less certain because the durability of the system depends not only on the longevity of the magnetic medium, but also on the lifespan of the motor and heads.

Optical Disks

In the previous edition, devices such as WORM (write once, read many) and MO (magneto-optical) disks were discussed. These, like so many technologies, are not only dead but virtually forgotten except by those laboratories which have a huge stock of the disks! However, optical technology is certainly the current preferred option because there is good reason to have faith in the archival durability of the media. Furthermore, mass-market devices now have sufficient capacity to meet many users' demands so that one can have some confidence in the longevity of the technology.

Compact Disks

Compact disks (CDs) have already been with us for over 20 years, and writable CDs for 10. The cost, high when the previous edition was written, is now very low both in first cost and media (around US$0.70 per gigabyte). Speed, though it has increased about 12-fold since then, is still the major problem. The rate of data transfer for an audio CD is a rather pedestrian 150 KB s^{-1}, and this is referred to as single speed. Read and write speeds up to 52× this base value are now available. A complete 700 MB CD can thus be written in 5 min or so, and modern software will adjust the writing speed on the fly so that the need to maintain a constant data stream is less of an issue. This means that CDs can now even be written across a network, though this will inevitably carry a speed penalty. It may still be preferable to carry the additional overhead of first copying files to the writing computer.

Rewritable CDs are also widely available at a cost only a little higher than conventional single-use CDs. Erasing data for re-use is, however, a relatively slow process. They may be useful when images are to be stored for a short time only, but for long-term archival use it would seem wiser to use single-use disks. Many manufacturers have conducted accelerated-aging tests on their single-use CDs and their security as archival storage seems to be the best of all mass-market computer media. It seems inevitable that rewritable disks could not offer equal security, and the risk of accidental deletion is always present with any rewritable medium. In fact, the time spent trying to decide which files can be overwritten is usually worth much more than the disk space saved.

Various formatting options now allow multiple use, either by writing multiple sessions (which does carry an overhead of about 15 MB per session) or by using the packet CD format, which allows a CD to be treated almost exactly like a conventional mounted drive. Multi-session CDs can be read on most systems but the packet CD format cannot. Because it reduces compatibility with other systems and has little point when the content of a CD is relatively small compared to a modern hard disk, packet CD has not become widely popular.

One of the limitations of the CD format is its handling of file names. The standard laid down by the International Standards Organization (ISO) requires file names to fit an 8 + 3 character format similar (but not identical) to that of MS-DOS. ISO-compatible CDs are readable on Apple, PC, and Unix computers, which is very convenient for data exchange. Unfortunately, most confocal microscopes give files and directories (folders) much longer names. Extensions to the standard allow for longer files names in both Macintosh and Windows computers, but these are unfortunately not cross-platform compatible. Because most confocal microscopes use Windows it is important to use the Joliet extension which caters for these file names, otherwise the disk will contain a useless collection of truncated names, particularly with microscopes such as current Leica models, which save each plane and channel as a separate file, and rely on a database program to

identify these images. On an ISO disk, it will be impossible to identify which plane and channel are which, and the data becomes completely useless.

Because CDs are likely to be a major archival medium, in the medium term at least, the question obviously arises as to how permanent they are. Pressed CDs have a polycarbonate blank into which the pits are pressed to carry the information. This surface is then coated with an evaporated metal layer, and then a coat of varnish and the printed label (Fig. 32.5, upper). The CD is read through the thickness of the blank. If the clear side of the blank gets scratched, it will hinder reading but it can often be repolished. The label side is more vulnerable because only a layer of varnish and the printed label lie between the data and the outside world. Recordable CDs have a dye layer between the polycarbonate blank and the metal film and it is this which is modified by the writing laser beam (Fig. 32.5, lower).

In terms of pressed CDs, excluding physical damage, the key issues are the aluminum reflective coating (which can get oxidized, particularly if there are any flaws in the varnish) and the polycarbonate blank. So far, no plastic seems to last forever and I doubt if polycarbonate will stay clear and flexible indefinitely. However, as polycarbonate is vulnerable to almost all organic solvents, excluding light and solvent fumes will doubtless help.

Archival quality recordable CDs usually use something better than aluminum. Several manufacturers offer silver, silver + gold, or pure gold. Obviously pure gold should be highly stable, but it is less reflective, which increases the risk of read errors. Whatever metal is used, archival life still depends on the dye layer in front of it remaining stable. The claims made by the manufacturer for their different dyes (typically cyanine, phthalocyanine, or azo) are difficult to evaluate. The cyanine dyes used in the earliest recordable CDs were rather vulnerable to bright ambient light. Some manufacturers have chosen to concentrate on extending the durability of these dyes, whereas others have turned to alternative dyes such as azo or phthalocyanine. All archival tests depend on accelerated aging (typically at higher temperature) and, while this is valid up to a point, it is unwise to trust it too implicitly (Nugent, 1989; Stinson *et al.*, 1995).

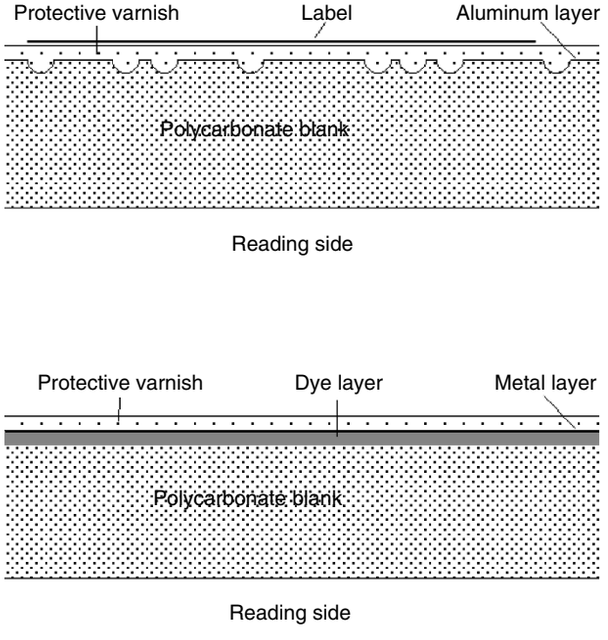


FIGURE 32.5. Structure of a pressed (above) and recordable (below) CDs (not to scale).

The speed at which drives will write CDs has increased enormously over the years, with 52× now routine. This has placed pressure on manufacturers to increase the response time of the dye layer but it would seem logical that a dye which can be bleached at 50 times the original speed is unlikely to be as archivally stable as the older disks. Often the layer is made much thinner to enable the high-speed writing. Of course, dye technology is also evolving but, if an archival-quality disk will not support the latest writing speeds, there may be a good reason.

Because one is likely to write or put a label on the back, the varnish is important. Most makers object to labels even though labeling kits are widely sold. The varnish is typically water based because the polycarbonate of the disks is very vulnerable to solvents. This leaves one in a cleft stick as to how to label it because water-based inks may loosen the varnish but solvent ones may attack the disk! Different manufacturers vary in their recommendations and the safest approach is to follow the recommendation for each particular brand. Quality disks will have an extra writable protective layer over the base varnish giving you a bit of extra security, and this is well worth having.

Kodak recommends that CDs not be stacked adjacent to each other or to any other surface. They should therefore be stored in "jewel cases" or in a custom storage box which separates the disks, and not kept in envelopes or stacked on a spindle.

Blank CDs are now so cheap that the cost of storage is below US$1 per gigabyte, depending on the brand and quality of the media. Common sense suggests that, however reasonable it may be to choose cheap disks when just sending data through the post or taking it from laboratory to laboratory, saving a few cents by choosing unknown brands is a false economy if the intention is archival storage. Writers are very cheap and quite fast (48 speed corresponds to 7 MB/s, comparable with modern tape systems). Best of all, every computer can read the disk without extra hardware. The huge range of commercial CD-ROMs ensures that readers will remain available for many years, so that archival material will be accessible as well as secure.

Digital Video Disk (DVD)

DVD (digital video disks) represent the next stage of optical disk technology. Using similar technology, but shorter wavelength lasers so that resolution is better, 4.7 GB can be stored on one side of a disk with the same size as a CD. Because the optics that read the disk are confocal, a DVD can carry two separate layers of information, thus storing over 9 GB, but recordable two-layer disks are only just coming on to the market at the time of this writing.

DVD-R write-once DVD disks — are now reasonable in price, at around US$1.00 per disk from the cheapest sources, and the writers are now reasonable at US$200 to US$300 (a mere 1% of their price 4 years ago!). Two standards (DVD+R and DVD-R) exist for these disks. This has hindered their general acceptance, but newer players will handle both (Nathans, 2003). At 4.7 GB, it is clear that DVD is now both cheaper and more convenient than CD-R for storage of confocal images, though the question of the long-term stability and longevity of the format is still not so well known as that of the CD format. Nevertheless, DVD players are now common domestic appliances, so it seems likely that the standard will be durable.

Rewritable DVD disks also suffer from incompatible standards and because they are of lower reflectivity are sometimes difficult to read in DVD players. The older standards (DVD-ROM and

DVD-RAM) were also lower capacity than 4.7 GB. As with CD-RW, they are probably not the best alternative for archival storage, but could have their place for data transfer. Current drives mostly handle RW and R disks in both + and − options. As with CDs, rewritable disks are always slower to write.

It is only in the past couple of years that the DVD market has really showed signs of maturity. Because most computer drives will read and write the CD format as well, it would seem to be the logical choice when purchasing a new system, and DVD writers are now routine on new confocal microscopes.

Solid State Devices

A development which was not foreseen in the last edition of this chapter has been the proliferation of ultra-compact solid state memory devices which retain data even without a source of power. While small in capacity compared to a hard disk, these range up to more than the capacity of a CD in a tiny fraction of the space. Much of this development has been driven by the explosive growth of the digital camera market.

Compact flash cards (Compact Flash Association, 2003) are used by many such cameras, making the computer accessories to read them an essential. Typically these use either the PC-card (PCMCIA) slots in notebook computers or else the USB or Fire Wire ports found on both desktop and notebook systems. A key feature is that both are designed to appear as hard disks to the computer without the need to install any drivers. As the card is the size of a postage stamp, and about 3 mm thick, it represents a highly portable data store, and many people use them for convenient portable storage or transfer between computers without reference to digital cameras. Flash drives currently can hold up to 2 GB. Data transfer rates of the compact flash (confocal) chips are currently 5 to 7 MB/s, but the latest revision of the interface is designed to cope with rates of up to 16 MB/s to allow for advances in chip technology in the future. Practical test speeds achieved in computers (Digital Photography Review, 2003) are around 3 to 4 MB/s with writing being slower than reading; performance in digital cameras will always be much slower. The cost is still around US$100 a gigabyte so it will not compete with CDs for archival storage, but as a fast, rewritable method of transporting relatively large files — whether images, documents, or digital presentations — compact flash has an important place.

Memory Stick (Sony) and Smart Media (Samsung) are similar, more proprietary flash memory devices which fulfill similar functions, but so far offer a smaller range of useful options than the more open standard Compact Flash. They tend to be more popular in the portable music player market, showing again how several once-different technologies are converging. The Sony Micro Vault is a dedicated USB-only version that comes in capacities from 32 MB to 256 MB, and requires no further accessories; it even has a cover for the plug when removed from the computer. Similar "keychain" memory devices are available from other manufacturers.

These flash memory devices have established a quite different market niche from other removable storage devices, but as photography becomes increasingly a digital process, this convergence seems likely to continue.

DISPLAY

Before looking in detail at how the image is displayed and printed, we should consider the nature of the confocal image (see Chapter 4, *this volume*). The image in a conventional optical microscope has an infinite gradation of tones within it, whereas the confocal image typically has just 256, if it is monochrome or false color. Merged two- or three-channel images may have up to 256^3 colors, but often have considerably fewer. Confocal images have a finite number of pixels, whereas photographic images have limited resolution, but a smooth transition from point to point. In more general terms, a confocal image is quantized in both spatial (x, y, z) and intensity dimensions (see Chapter 4, *this volume*).

What the microscopist actually sees is not the image itself, but a display on a monitor. Both the monitor and the way it is driven will have a major effect on the appearance of the image. This in turn is interpreted by the human eye when we see it directly, or by a camera if we record the image photographically. As a preliminary, we should therefore look at how monitors display confocal images.

Monitors

Monochrome cathode ray tube (CRT) monitors simply have a layer of phosphor coated on the inside of the glass, so that an illuminated spot will be produced wherever the electron beam hits. The resolution of the monitor, therefore, depends solely on how small the electron beam hitting the screen can be. Color monitors, on the other hand, have red, green, and blue phosphors arranged either in dots (shadow-mask tube) or stripes (Trinitron tube). The image on a color monitor will always be made up of a mosaic of the three primary colors; the finer this mosaic, the better the image will be. This is specified by the dot pitch of the tube in millimeters — 0.28 mm would be a typical value for a good quality modern PC monitor, though pitches as small as 0.18 mm are available, and cheaper or older monitors will have pitches up to 0.4 mm. These are absolute values, so a larger monitor will have more dots in the total width of the image.

The number of pixels that may be displayed on the monitor is a function of the speed at which the electron beam can respond to a changing signal, and is not related to the actual dot pitch of the CRT. Thus, a confocal image displayed on a color monitor will have each pixel subdivided into a pattern of red, green, and blue dots. If the pixel spacing of the data comes close to the dot pitch on the screen, *aliasing* (below) may occur, creating undesirable effects. Many color monitors can be set up to display more pixels than there are dot triplets available, so the full resolution of the image cannot actually be shown. Thus, a large monitor is essential on a confocal microscope if we are to be able to see the detail in a high-resolution image.

A CRT-based monitor is intrinsically capable of displaying an almost infinite number of colors.[1] However, the video board inside the computer imposes its own restrictions. Display boards suitable for a confocal microscope will permit 256 gradations in each primary color, so that a 24-bit (three 8-bit channels) confocal image can be displayed without compromising the intensity range. (12-bit or 16-bit images will, however, need to be reduced to 8-bit for display.)

The other factor determining the appearance of the image is the frequency with which the display is scanned. The more rapidly the screen is refreshed, the less the image will flicker, and a suitable monitor should redraw the entire image at least 70 times per second. Low cost boards will often compromise one or other of these attributes at their highest resolution and are therefore inher-

[1] Limited only by Poisson noise as it affects the charge deposited by the electron beam during the pixel dwell time and the number of phosphor grains in each dot, etc.).

ently unsuitable for confocal use, but because high-end display boards are now very cheap compared to confocal microscopes, this is not likely to be a problem so long as it is understood that just any computer will not do.

Displaying large numbers of pixels on low-priced monitors can reduce the refresh rate to 60 per second, which is about the lowest tolerable value. Interlaced scanning is a strategy used to reduce flicker when it is not possible to scan the entire image at a sufficient rate. First, the odd lines of the image are drawn, then the next scan draws the even lines. This technique is primarily used for broadcast video signals to enable the signal to fit into the available bandwidth, but it has in the past also been used to obtain higher resolution on low-cost computer monitors.

International television standards use 625 scan lines per frame, with each interlace drawn 50 times a second (and thus a full-frame rate of 25/s). The system used in the Americas and Japan uses only 525 lines, but a faster refresh rate of 60 interlaces per second. (Not all scan lines are available for display; standard video can display only 512 pixels vertically, US video only 483.) Video displays once played a significant part in confocal microscopy (they were standard, e.g., on the widely popular Bio-Rad MRC 500 and 600) but they are not used now. Apart from the low resolution and refresh rate, the problem of displaying multi-channel images adequately led to their demise. In broadcast television, the color signal is encoded as a chrominance signal at much lower resolution than the monochrome luminance signal, and this does not give adequate quality for a multi-channel confocal image. The alternative is to generate a three-channel video signal that will give a much higher quality display (on the same monitor so long as the appropriate inputs are provided). However, this signal cannot now be recorded on a standard video cassette recorder (VCR) or printed on a low-cost video printer. The utility of video in microscopy is primarily in recording fast-moving items and it may still have a part to play with direct-vision confocal systems (Nipkow disk or slit scanners), but it is no longer relevant to point-scan systems.

In a confocal image, pixel intensity values are linearly related to the numbers of photons captured from the specimen. However, this linearity may not be preserved when the image is displayed. In the simplest case, if the value of the pixel is converted directly to the voltage at the control grid of the CRT, the actual brightness of the pixel on the screen will be proportional to the three-halves power of the pixel value. This may not be all bad because the human eye responds logarithmically, not linearly, to light (Mortimer and Sowerby, 1941). However, confocal images often look excessively contrasty on an uncorrected display, and fine detail in the mid-tones will be lost.

This relationship may be modified by more sophisticated display electronics, and high-quality display cards typically come with software to allow the user to set up the display optimally. These are all too often ignored by researchers who "don't have time" (and then waste much more time struggling with pictures which fail to show details which "were there when they took the picture"). Failing such an option, image manipulation programs such as Photoshop, Paint Shop Pro, and Corel PhotoPaint place the display gamma under user control; but there again the user must make the effort to use that control (for more discussion, see Chapter 4, *this volume*).

Liquid Crystal Displays

Flat screen (liquid crystal) monitors are inherently different from CRTs. They use liquid crystal devices between crossed polarizers to display the image, and as each pixel is addressed independently, the question of display resolution not matching the pixel resolution does not arise. Typically different resolutions are not available on LCD monitors; in the rare cases that they are, the pixels are remapped in software (see below and Fig. 32.6). Therefore, LCD monitors will often give a crisper display than CRTs, though on the other hand the pixels may be more visible simply because their edges are more clearly defined. Some older displays (typically used on lower cost notebook computers) used passive supertwisted nematic (STN) displays instead of active thin-film transistor (TFT) technology. These are both cheaper and far less demanding of power. However, they may not offer full 24-bit color, and the image may be less bright and have a smaller viewing angle. Large freestanding monitors are always TFT.

Large LCD monitors have many advantages in the confocal laboratory. Because the display is not continually redrawn as in a



FIGURE 32.6. Halftoning (A) versus dithering (B). Highly enlarged view of part of an image of an integrated circuit chip; above printed by halftoning using a 4×4 matrix of laser dots, below printed by dithering using a 3×3 matrix.

CRT, flicker is not an issue. Consequently, neither is refresh rate (it can become an issue with video images). The screen is flat and compact, and as confocal systems often include two monitors and three lasers in a small room, minimizing heat is worthwhile. However, LCDs are costly, and the cheaper models often sacrifice color quality, viewing angle, or both. These are sacrifices which are not worth making. Good saturation, wide control over contrast and gamma, and a wide viewing angle are all essential. If you can afford it, buy a pair of top-quality LCD monitors (and don't just take price as a criterion of excellence, check them out carefully yourself). If cost is a major issue, buy high-quality CRT monitors rather than low-quality LCDs.

Data Projectors

Data projectors are now a very common display format for confocal images, and naturally they often represent the occasion when high-quality display is most important. However, they typically have lower resolution and often a poorer gray-scale rendition than computer monitors. In terms of resolution, 800 × 600 pixels (SVGA) is common on projectors intended for the home market and 1024 × 768 (XGA) on ones intended for academic and teaching use, though higher resolutions are available at correspondingly higher prices.

Two different technologies are used in these projectors. A very good description is given by Powell (2004). LCD projectors use liquid crystal screens, as in flat panel monitors, except these do not have a color mosaic. Instead, three panels are used, one for each of the primary colors. Digital light processor (DLP) projectors use a micromirror array, where the pixels are tiny mirrors and these are tilted to send more or less light to the image. Very expensive projectors use three DLP chips, one for each primary color, but these are rare. The projectors one is likely to encounter in a lecture room or conference have one DLP chip, with a rapidly spinning filter wheel in front of it. The colors are therefore generated sequentially and merged by persistence of vision.

The two types have their own strong and weak points, and typically DLP projectors are favored for home theatre use and LCD for data projection. As a comparison, for this review the signal from a notebook computer was sent simultaneously to two moderately high-end projectors, projecting on to adjacent screens. One was a DLP projector, the other an LCD, and price and luminous output were comparable. Contrast, brightness, and other display parameters were set to midpoint values on both projectors.

The native resolution of both projectors was 1024 × 768, and the computer was set to the same value. Both projectors were able to handle higher resolutions and scale them down, but the quality suffered very markedly when this was done. The first lesson, therefore, is to set your screen display to the resolution of the projector, if possible. Even at the native projector resolution there may still be some pixel re-mapping taking place because projectors correct for keystone distortion caused by a non-horizontal projection angle. This means that either the top or bottom of the image cannot use all the displayable pixels.

The LCD projector gave a much sharper image, which was obviously preferable for fine text. However, its color rendition, particularly on real-world photographic images, was inferior, having a slight color cast and excessive saturation. The DLP projector gave images with a very accurate color rendition, free of any cast and natural in appearance. The two projectors differed markedly in gamma. The DLP projector had a gamma of 1 (measured with the gamma test function of an imaging package), while the LCD projector was around 1.6 (slightly higher in blue and red than in the green). This means that the LCD projector was very comparable to both the screen of the laptop and to a CRT monitor, both of which checked out with similar values, but the DLP is more accurate for confocal images in which pixel value is typically linear with number of photons.

To test the displayable gray scales, a test image with intensity scaling from 0 (black) on one side to 255 (white) on the other was used. All 256 values were present, and on both CRT and notebook monitors the change seemed totally smooth. On the LCD projector it also seemed smooth, though with some minor streaks, which may have been aliasing rather than posterizing (see Digital Printers, below). However, there were noticeable bands with the DLP projector. This implies it was incapable of reproducing a full 8 bits in each color, and in fact posterizing was noticeable in large pale areas of scanned pictures. Also relevant in this context is the contrast range of the projector: the difference between its whitest white and darkest black. This is an important figure of merit for a digital projector and is always quoted by manufacturers. The number of tones which can be reproduced has little relevance if they are squeezed into such a small range that the eye cannot distinguish them. In the past this has been a major concern when projecting confocal images, with detail disappearing in both highlights and shadows. This is an area in which digital projectors (of either technology) have made huge strides in recent years. DLP is normally regarded as leading in contrast ratio but in this test both projectors seemed comparable, with good rich blacks.

Both projectors seemed evenly balanced in response time, with rapid mouse movements appearing equally (and acceptably) jerky in both (at 60 Hz refresh rate). At very close quarters some misalignment of the different color images was visible with the LCD projector. This was invisible at normal viewing distance and may be inevitable in a projector with three different LCD arrays (especially one which is regularly transported). This would not be expected in a DLP projector because there is only one display element, but in fact some color fringing could still be seen at the edges of the screen, though not in the center.

The verdict on this test was that the LCD projector was way ahead for text, diagrams, and other computer-generated graphics, but the DLP had the edge for micrographs and other real-world images. This is in line with the commonly accepted merits of the two technologies. The question of different gamma is likely to be significant when projecting confocal images, and in the rare case where one knows in advance which type of projector will be used, the images in a presentation could be adjusted to suit. But the most useful point to remember when giving a presentation at a conference is still to set your screen resolution to the native resolution of the projector.

HARD COPY

When it comes to recording images, the confocal microscopist has to make a choice between two fundamentally different technologies. One option, **photography**, was in the past familiar ground to most microscopists. The other option, computer **printers** of one sort or another, are more likely to be relevant in the 21st century.

Photographic Systems

In the 10 years since the previous edition of this book, photography has almost completely disappeared from the cell biology laboratory. So far as confocal images are concerned, this is all to the good because there is a fundamental mismatch between film and the

digital image. A photograph can reproduce far more tones than the 256 that an 8-bit image possesses, but the interposition of lenses and film means that pixel positions are not reproduced sharply and with complete accuracy. Blurring below the level of microscope resolution will not be noticeable in a conventional micrograph, but if pixels are not rendered clearly in a confocal image it will look soft — especially if there is any text superimposed on the image. At one time, screen-shooting devices were standard equipment with confocal microscopes but now they are no more than historical curiosities.

Digital Printers

Printers typically work by putting dots on a page of paper. As printer technology has evolved, the size and resolution of these dots has become smaller and more precise, but in general the dots are still either present or absent, which limits the ability of a printer to represent images with a range of tones. However, these pixels are placed with extreme accuracy, so providing the data is handled properly (below), it is possible for each pixel in a confocal image to be printed sharply and in its correct place. There are two ways in which we can break up a gray-scale image into a pattern of black dots for printing: *halftoning* or *dithering*.

Halftoning is the way images are reproduced in printed books and newspapers. The image is broken into a series of black dots of varying size, darker grays being represented by larger dots. Halftoning is unarguably the method of choice if the resolution of the output medium is sufficient. However, it will be clear that to produce halftone dots of varying sizes, each dot must be a multiple of the basic dot pattern of the printer. If the halftone dots are to be small, the printer's basic dots must be *very* small. The halftone screen in a printed book is typically 133 or 150 dots per inch (Cox, 1987). A 1200 dpi printer can give is 8×8 dots — 65 gray shades — within that resolution. To get 256 gray shades at 150 dpi, we need a 2400 dpi printer.

Dithering uses a probabilistic method to decide whether a printer dot should be present or not. If the pixel is dark, there is a high probability that a black dot will be printed; if it is light that probability is low. The effect is of a grainy image without any regularly repeating pattern. When using a low-resolution output device, dithering is the only option; halftoning would result in an impossibly coarse screen. Figure 32.6 shows a magnified view of a confocal image of an integrated circuit, (IC) device, printed by halftoning and dithering. In the dithered image each pixel of the original micrograph is represented nine times, by a 3×3 matrix of laser dots, the probabilistic dithering calculation being applied independently each time. Thus, on average, a 50% gray would have either four or five dots black, the others being white, but which of the nine dots were black would vary each time.

The eye can perceive about 64 shades of gray reflected from a solid surface. If fewer shades than this are used to reproduce an image, areas that should show a smooth transition in tone will reproduce as a series of bands. Because the human visual system is extremely sensitive to edges, this can be extremely distracting. This effect is termed *posterizing*. In printing it occurs when the printer is unable to reproduce at least 64 shades of gray. Figure 32.7 shows an example of this. In Figure 32.7(A), using 16 gray tones (roughly what an old 300 dpi laser printer can give) the smoothly-graded gray appears as a series of discrete bands. To some extent, the problem can be reduced by combining dithering with halftoning — values which bridge the boundaries between the levels the printer can produce are randomized to decide which value they should have [Fig. 32.7(B)]. Ultimately, though, good reproduction of a confocal image will require at least 64 gray levels to be reproduced on paper [Fig. 32.7(C)].

Proper reproduction of a confocal image by a printer will generally require the image to be reproduced either pixel for pixel, or with an integer multiple (or fraction) of printer pixels or half-tone dots to each dot of the confocal image. If this is not the case, aliasing (Chapter 4, *this volume*) will generate artifactual patterning in the image. This is shown in Figure 32.8; scaling the original 465-pixel wide image [Fig. 32.8(A)] to fit the common 512-pixel size has given the diagonal lines and the circle a very jagged appearance [Fig. 32.8(B)]. This introduces a considerable constraint on printing confocal images; photography can reproduce them with equal accuracy at any size, but printing works best with integer multiples or fractions of the image pixels. The only ways out of this are either to use such a high-resolution print device that it

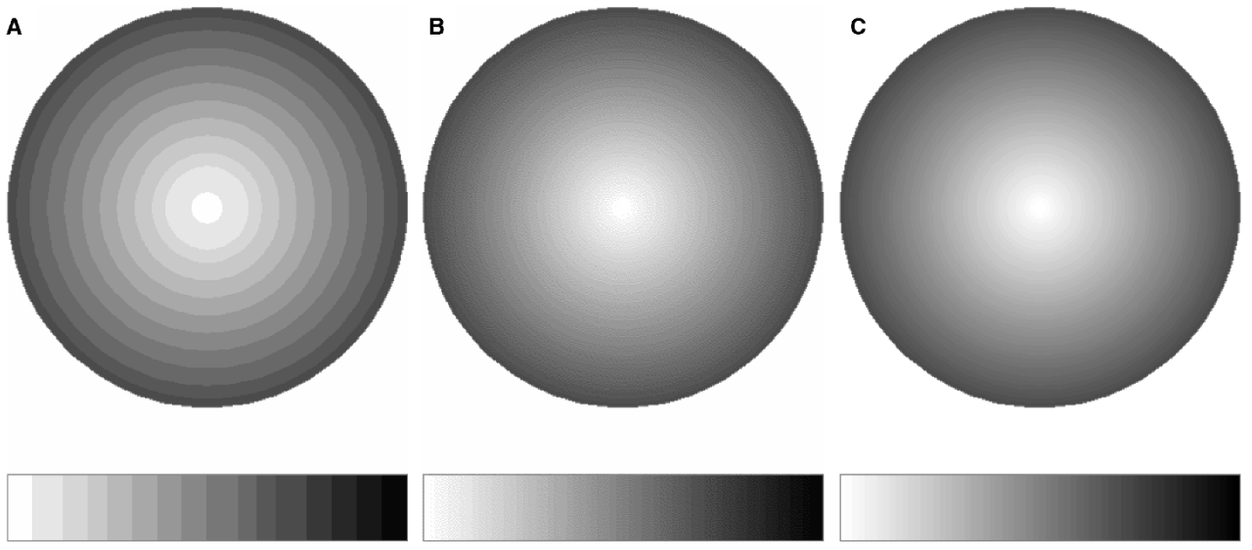


FIGURE 32.7. Posterizing. The smooth ramp of shade in the original shows banding when reproduced with only 16 gray levels (A). This can be partly disguised by dithering, still only using 16 levels (B), but using 80 gray levels is enough to give a smooth-looking result (C).

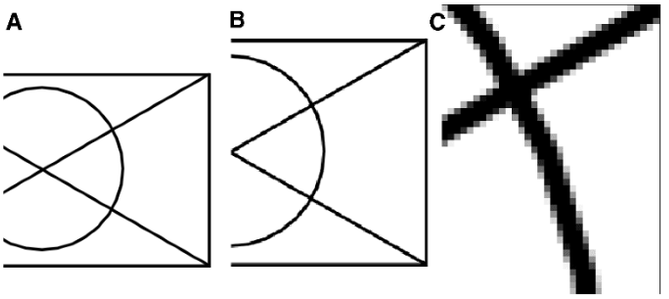


FIGURE 32.8. Aliasing. The circle and the diagonal lines appear as smooth as the horizontal and vertical ones in the original image (A), but when it is scaled up slightly they become jagged (B). In the original image the curved and slanting lines are actually made up of black and various shades of gray, shown much enlarged in (C).

exceeds the Nyquist criterion at the output resolution or else to remap the image with sophisticated software (several algorithms are in general use, and bilinear or bicubic resampling are probably the commonest) to the output resolution. The first option is becoming more common as printer resolution improves but cannot yet be guaranteed. Figure 32.9 shows the effect of different remapping algorithms. The image (shown in the inset) is a tiny part of Figure 32.1(A), enlarged by the odd amount of 467%. Direct pixel scaling [Fig. 32.9(A)] gives, as expected, very poor results, and bilinear resampling [Fig. 32.9(B)] is very little better. Bicubic resampling [Fig. 32.9(C)] is hugely better and obviously the only useful choice in this case.

Aliasing can also appear if the printer's gray levels do not match the intensity levels of the image. When a black diagonal, or curved, line is reproduced in a pixelated image it will appear as a mixture of gray and black pixels [Fig. 32.8(C)]. Pixels which lie wholly within the line are black; those which were partially intersected by the line are gray. So long as they are reproduced at their original intensity the line will retain the illusion of smoothness, but as soon as they are made lighter or darker the line will appear jagged.

Color images present all the above problems, as well as some of their own. Most laser-scanning confocal microscopes (CLSM) do not produce color images in the sense that a conventional optical microscope does. Color images produced on a CLSM are either pseudo-color images in which a false-color palette is applied to a gray-scale image, or multi-channel images in which two or three different signals are each assigned to a different primary color. An image with a fluorescein signal in the green channel and a rhodamine image in the red channel might look very similar to a real color photomicrograph of the same slide, but the way the image is made up is very different.

A further problem arises because multi-channel images, and some false-color palettes, tend to use fully saturated colors. These almost never occur in nature. On a monitor, which emits light, these can look very effective, not least because confocal microscopes commonly operate in dimly lit rooms. They can also make good slides. However, when printed on paper, where the image is created by light reflected from the paper through the ink, the image will look very dark. This problem is exacerbated by the different color models used to form the image.

A computer image is usually stored, and always displayed, using an RGB (red/green/blue) or additive color model. Adjacent points on the monitor screen emit light of the three primary colors,

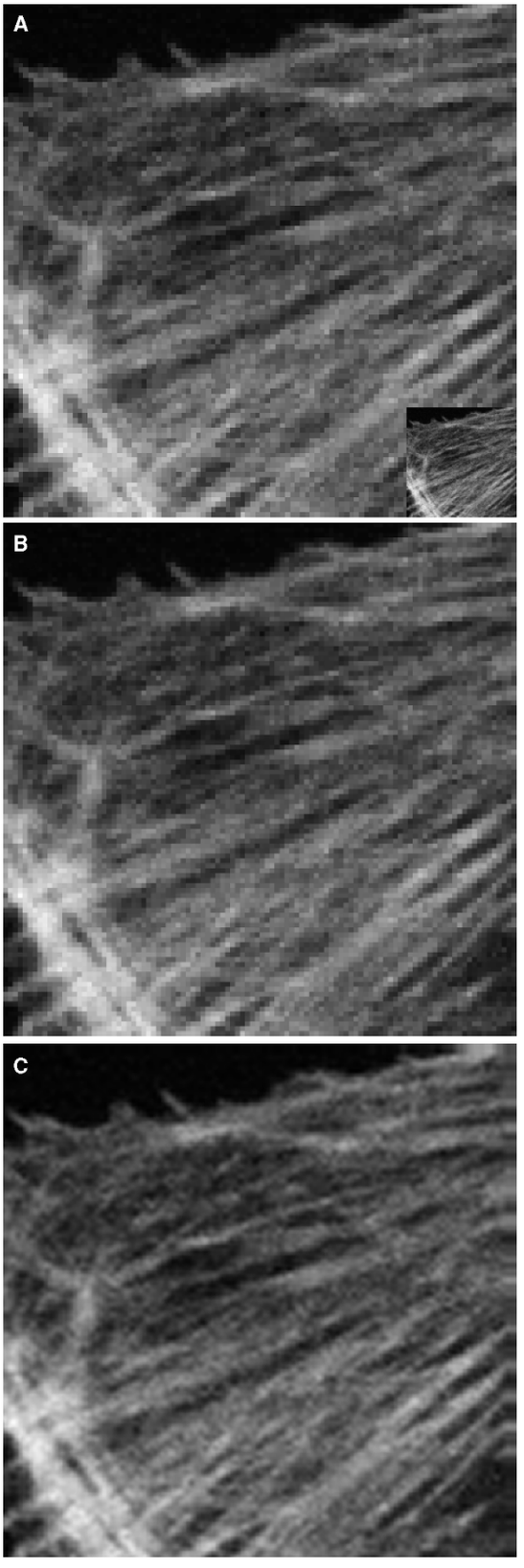


FIGURE 32.9. Scaling techniques. A small part of the image shown in Figure 32.1(A) enlarged by the odd amount of 467%, which cannot be achieved by simple scaling of pixel size. (A) Pixel enlargement, as well as looking blocky, severe aliasing is obvious. (Inset) The original image. (B) Bilinear resampling: aliasing is much reduced but the image is still blocky. Little use is made of the extra pixels now available. (C) Bicubic resampling gives a hugely better result; it cannot produce more resolution than the original data contains, but it does the optimum job of mapping it to the output resolution.

and the different colors are created by adding these together. A printed page uses the CMY (cyan/magenta/yellow) or subtractive model. A red point is created by putting on the paper both magenta (which subtracts green from the reflected light) and yellow (which subtracts blue) so that only red will be reflected. [Commercial printing, and many computer printers, also add a black ink to compensate for the fact that the three color inks may not add up to a perfect black. This is then a CMYK (cyan/magenta/yellow/black) color model.]

Thus, reproducing each of the primary colors that look so brilliant when formed by a single phosphor on a monitor requires the light to pass through two separate color dyes before being reflected by the paper. To put back brilliance into such an image, it is necessary to unsaturate the colors — to add some "white" into them. Many computer image-manipulation programs provide this facility. Often, some experimentation is required before a good screen image can be turned into a good print and it can be very useful to have a program that permits one to print an array of small test images, each made using slightly different settings.

Laser Printers

Laser printers are the workhorse of the modern office. Their crisp black type and graphics are unrivaled for most computer output. For reproduction of confocal (or other) images their abilities are more limited, though they can produce quite reasonable proof prints. Laser printers use a low power laser to write dots directly onto the charged drum of a photocopier.

The limitation of a laser printer is that it is difficult to get the pattern of dots fine enough to reproduce a full range of tones by halftoning (above). However, laser printers with 1200 dpi resolution are now common, and many also have the capability of modulating the size of the spot to some extent. Output from such a printer is adequate for many purposes, and the cost is far lower than either photography or higher-class printing. Their weakest point is that large expanses of black are still not rendered as uniformly as in a photograph.

Color laser printers have only recently started to make a significant impact on the marketplace. This is partly because of a huge decrease in price, and partly because of improvements in resolution (600 dpi is common) and in the tricks used by the built-in firmware, which at last make near-photographic quality routinely attainable. The quality does not yet match that offered by inkjet and dye sublimation printers, but on a cost-versus-quality basis it hugely exceeds it, so that a color laser printer is ideal for such purposes as printing preprints of journal articles in quantity.

Ink Jet Printers

These have long ago taken over from dot matrix as the everyday printer for home and single-user office use. They operate by squirting small jets of ink on the paper (for best results, a slightly absorbent paper). They typically offer three- or four-color printing at much finer resolution than any other printers. Some use seven inks (high and low intensities of the three subtractive primaries) to give more realistic results. Though the tendency of the ink to spread limits their ultimate performance, it also helps improve the perceived realism of the image by making individual pixels less visible. Printing to photographic quality requires special paper and also uses large amounts of the expensive ink, so it is not cheap, but the results bear comparison with those from expensive dye sublimation printers. Because (unlike other printer technologies) there is no inherent limitation on the size of the paper, A3 and larger printers are readily available for such tasks as printing conference posters. Unlike dye sublimation printers there is always the option with an inkjet of printing at lower quality and hugely lower cost for proofing and layout purposes.

Dye Sublimation Printers

These printers have changed little since they the previous edition of this book. They are still an excellent output medium for routine production of photographic quality output, and although still not cheap, the price has not increased in line with inflation so they are not much more expensive per page than the inkjet for photo-quality output, though the purchase price is much greater. They use a full-page sheet of ink for each color they print, but in this case the ink sublimes when heated and is absorbed by a specially coated sheet of paper. The vaporized ink will tend to diffuse laterally to a limited extent, making pixelation less obvious. More or less ink can be transferred, depending upon the amount of heat applied, so that true gray scales can be produced. The output from the best dye sublimation printers can be comparable to photography, but the cost is also similar — up to US$5.00 for an A4 size color print. The cost per page is fixed, unlike a laser or inkjet printer, where the cost per page depends upon the degree of coverage.

CONCLUSION

The big change since the previous edition of this book 10 years ago is that now mass-market media are effectively equal to the demands of the confocal user. It is a truism that for several years now developments in the personal computer market have been driven not by business or scientific usage, but by the domestic market. The requirements of games, music, digital photography, and video have been the driving factors for processor speed, interfaces, display quality, print output, and data storage. We no longer need specialist image manipulation hardware, custom video cards, non-standard monitors, dedicated data buses, or expensive storage devices. Computers are fast enough for the necessary image manipulation, everyday video cards handle 24-bit images at high resolutions and fast refresh rates, as well as providing hard-wired image manipulation functions. Monitors offer megapixel displays at high bit depths and refresh rates. Fire Wire and USB-2 will carry data faster than any point-scanning confocal can scan, and domestic video disks are big enough to handle huge data sets. Just about every home has a printer giving photographic quality output — and these are printing higher resolution images than most microscope users generate.

The major computer magazines generally run annual surveys of color printers and it is always worth seeking out the latest of these before making a purchase. A final word of warning: If you are evaluating a hard copy system, of whatever sort, insist on testing it on real confocal images from your own work. Every manufacturer has a gallery of images which reproduce superbly on his own hardware, and if you try to judge a system on the basis of such pictures you will be disappointed once you start using it yourself.

SUMMARY

Bulk Storage

Image compression has made huge strides but still, as always, needs to be used with care. The new wavelet compression system seems to offer little to the confocal user but the PNG format has at last given us a lossless technique that works. Recordable CDs

are currently the most common and most reliable choice for mass storage, though recordable DVDs seem likely to take over during the lifetime of this edition. For archival purposes, there seems little merit in selecting the rewritable version of either of these media. Tiny solid-state FLASH memory devices have become a very effective way to carry presentations from place to place.

Display

Monitors are no longer a problem; 24-bit displays of adequate size and refresh rate, as well as the display boards to drive them, are now the norm rather than expensive exceptions. Flat-screen LCD displays are still expensive, but worth the cost for their extra sharpness and for the complete elimination of flicker.

Hard Copy

Inkjet printers have now essentially replaced dye sublimation printers for optimal photographic output. They have much lower purchase cost but the cost per glossy print is still high. Color laser printers are now more than adequate for proofing and preprints. Finally, if you are evaluating a hard copy system, insist on testing it on real confocal images from your own work.

ACKNOWLEDGMENTS

I am very grateful to Mike Speak and Dennis Dwarte, who have been generous with their time and effort in helping me prepare this chapter. I also owe a debt of gratitude to Todd Brelje, who wrote the original outline but who was unable to proceed with the chapter due to other commitments. In spite of this, he gave much assistance in producing the original edition, for which Martin Wessendorf, Nick White, Andrew Dixon, and Jim Pawley also provided a tremendous amount of information and help. The revision for the 3rd edition was carried out while I was at the Instituto Gulbenkian de Ciência, Oeiras, Portugal, and I thank them for their hospitality; Nuno Moreno and José Feíjo provided much help and assistance, and critical reading of the manuscript.

REFERENCES

Anson, L.F., 1993, Fractal image compression, *Byte* 19(11):195–202.

Avinash, G.B., 1993, Image compression and data integrity in confocal microscopy, *Proc. Microsc. Soc. Am.*, Jones and Begell, New York, 51: 206–207.

Barnsley, M.F., and Hurd, L.P., 1993, *Fractal Image Compression*, A.K. Peters, Wellsley, Massachusetts.

Compact Flash Association, 2003, *The Compact Flash Standard*, available from: http://www.compactflash.org/.

Cox, G.C., 1987, What went wrong with my micrograph? *Aust. EM Newslett.* 16:12–13.

Cox, G.C., 1993, Trends in confocal microscopy, *Micron* 24:237–247.

Cox, G.C., and Sheppard, C., 1993, Effects of image deconvolution on optical sectioning in conventional and confocal microscopes, *Bioimaging* 1:82–95.

Cox, C.G., and Sheppard, C., 1999, Appropriate image processing for confocal microscopy, In: *Focus on Multidimensional Microscopy* (P.C. Cheng, P.P. Hwang, J.L. Wu, G. Wang, and H, Kim, eds.), World Scientific Publishing, Singapore, pp. 42–54.

Deutsch, P.L., 1996, *DEFLATE Compressed Data Format Specification version 1.3*, available from: ftp://ftp.uu.net/graphics/png/documents/zlib/zdoc-index.html.

Digital Photography Review, 2003, *Digital Film Comparison*, available from: http://www.dpreview.com/articles/mediacompare/.

Mortimer, F.J., and Sowerby, A.L.M., 1941, *Wall's Dictionary of Photography, Sixteenth Edition*, Iliffe & Sons, Ltd., London.

Nathans, S.F., ed., 2003, *Writable DVD Drives*, available from: http://www.emedialive.com/r18/.

Nugent, W.R., 1989, *Estimating the Permanence of Optical Disks by Accelerated Aging and Arrhenius Extrapolation*, ANSI X3B11/89–101.

Pennebaker, W.B., and Mitchell, J., 1993, *JPEG Still Image Compression Standard*, Van Nostrand Rheinhold, New York.

Powell, E., 2004, *The Great Technology War: LCD vs. DLP*, available from: http://www.projectorcentral.com/lcd_dlp_update.htm.

Redfern, A., 1989, A discrete transformation, *Australian Personal Computer* 10(12):144–154.

Roelofs, G., 2003, *Portable Network Graphics*, available from: http://www.libpng.org/pub/png/.

Stinson, D, Ameli, F., and Zaino, N., 1995, *Lifetime of KODAK Writable CD and Photo CD Media*, available from: http://www.cd-info.com/CDIC/Technology/CD-R/Media/Kodak.html.

33

Coherent Anti-Stokes Raman Scattering Microscopy

X. Sunney Xie, Ji-Xin Cheng, and Eric Potma

INTRODUCTION

Advances in biological sciences are often facilitated by new tools in microscopy. Confocal and nonlinear or multi-photon fluorescence microscopy (Chapters 21 and 28) have become powerful techniques for three-dimensional (3D) imaging of living cells. This coincides with developments of various natural and artificial fluorescent probes for cellular constituents (Chapters 16 and 17). For biochemical species or cellular components that neither fluoresce nor tolerate labeling, other contrast mechanisms with molecular specificity are needed. Vibrational microscopy based on infrared absorption and spontaneous Raman scattering has been used for chemically selective imaging. Although infrared microscopy is a powerful tool, it is limited to low spatial resolution because of the long wavelength of light used (Humecki, 1995; Jamin *et al.*, 1998). Furthermore, the absorption of water in the infrared region makes it difficult to image through living cells. In contrast, Raman microscopy can overcome these limitations, as the wavelength of the excitation light is much shorter and there is essentially no absorption of water at these wavelengths. Raman spectroscopy has been applied extensively to biological molecules and cellular constituents (Turrell and Corset, 1996; Puppels, 1999; Shafer-Peltier *et al.*, 2002). Confocal Raman microscopy of biological samples has resulted in high-resolution images of living cells. However, the intrinsically weak Raman signal necessitates high laser power (typically >100 mW) and long integration times, and the signal is often overwhelmed by the fluorescence background of the sample, limiting its application in biology. In this chapter, we present coherent anti-Stokes Raman scattering (CARS) microscopy, a nonlinear vibrational imaging technique that overcomes the limitations of the linear techniques mentioned above.

Coherent anti-Stokes Raman scattering as a nonlinear optical process was first reported in 1965 by Maker and Terhune at Ford Motor Company (Maker and Terhune, 1965), and later named CARS by Begley and colleagues (1974). Since then, CARS spectroscopy has been used widely as a spectroscopic tool for chemical analyses in the condensed and gas phases and has become the most extensively used nonlinear Raman technique (Clark and Hester, 1988; Tolles *et al.*, 1977). In CARS spectroscopy, a pump laser and a Stokes laser, with center frequencies of ω_p and ω_s, respectively, stimulate a sample through a wave-mixing process. The pump field $E_p(\omega_p)$ and the Stokes field $E_s(\omega_s)$ interact with the sample and generate an anti-Stokes field E_{as} at the frequency $\omega_{as} = 2\omega_p - \omega_s$. The energy diagrams of CARS are shown in Figure 33.1.

The induced nonlinear polarization at the anti-Stokes frequency is given by $P^{(3)} = \chi^{(3)}E_p^2E_s^*$. Where $\chi^{(3)}$ is the third-order susceptibility,

$$\chi^{(3)} = \frac{A_R}{\Omega - (\omega_p - \omega_s) - i\Gamma_R} + \chi_{nr}^{(3)} \qquad (1)$$

where Ω is the vibrational frequency and Γ_R is the half width at half maximum of the Raman line. A_R is a constant representing the Raman scattering cross-section. The first term in Equation 1 is a vibrationally resonant contribution, which is maximized when the Raman shift $\omega_p - \omega_s$ coincides with the frequency of a molecular vibration of the sample. The second term includes contributions to the third-order susceptibility that are off the vibrational resonance and are independent of the Raman shift. Figure 33.1(B) shows the energy diagram of one of the non-resonant contributions. The CARS signal intensity is proportional to the square modulus of $P^{(3)}$ and has a quadratic dependence on the pump field intensity and a linear dependence on the Stokes field intensity:

$$I_{as} \approx |\chi^{(3)}|^2 I_p^2 I_s \left[\frac{\sin(\Delta k \cdot L/2)}{\Delta k/2}\right]^2 \qquad (2)$$

The last factor in Equation 2 is maximized when the wave vectors of the pump, Stokes, and CARS fields, $\mathbf{k}_p$, $\mathbf{k}_s$, and $\mathbf{k}_{as}$, respectively, satisfy the phase-matching condition:

$$|\Delta\mathbf{k}| \cdot L = |\mathbf{k}_{as} - (2\mathbf{k}_p - \mathbf{k}_s)| \cdot L < \pi, \qquad (3)$$

where L is the sample interaction length (Shen, 1984; Clark and Hester, 1988; Levenson and Kano, 1988; Mukamel, 1995).

The physical picture is that CARS, unlike fluorescence, is a coherent process in which the induced dipoles ($P^{(3)}$) within the sample have a well-defined phase relationship. Consequently, the CARS signal is normally only generated in a specific direction, shown in Figure 33.1(C), at which constructive interference of the anti-Stokes field occurs.

Like other nonlinear optical processes, high peak powers are necessary for the efficient generation of a CARS signal. These are readily available using picosecond or femtosecond light pulses. CARS detection exhibits higher sensitivity than spontaneous Raman. For spontaneous Raman, the molecular oscillators within the sample are random in phase. For CARS, however, the molecular oscillators are stimulated to vibrate in phase when the beating frequency of the pump and Stokes laser beams, $\omega_p - \omega_s$, matches their Raman-active vibrational frequency. The constructive interference of the coherent radiation results in a stronger signal than attained in spontaneous Raman. The CARS signal

Part of this chapter is a condensation of a feature article by J.-X. Cheng and X.S. Xie in the *Journal of Physical Chemistry*.

X. Sunney Xie, Ji-Xin Cheng, and Eric Potma • Harvard University, Cambridge, Massachusetts 02138

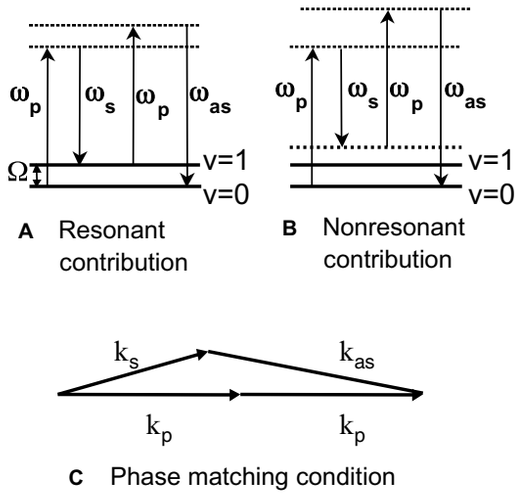


FIGURE 33.1. Energy diagram of CARS. (A) Resonant CARS characterized by $A_R/[\Omega - (\omega_p - \omega_s) - i\Gamma_R]$. (B) Non-resonant CARS from an electronic contribution to $\chi^{(3)}_{nr}$, where the dotted lines indicate virtual states. (C) The phase-matching condition.

intensity is proportional to n^2 (or $|\chi^{(3)}|^2$), with n being the number of oscillators.

Unlike spontaneous Raman, CARS is not background free. The non-resonant background, the second terms in Equation 1, limits the vibrational contrast and spectral selectivity. Fortunately, as shown below, methods for suppressing non-resonant background can overcome this difficulty.

The Reintjes group at the Naval Research Laboratory reported the first CARS microscope in 1982. Using two picosecond dye lasers with a non-collinear beam geometry, they detected the signal in the phase-matching direction with a two-dimensional detector. However, the non-collinear beam geometry used in their work had many limitations, and the use of visible excitation created an overwhelming non-resonant background (high $\chi^{(3)}_{nr}$, thus low contrast) because of its two-photon electronic (rather than vibrational) resonance at the excitation frequencies.

Due to these technical difficulties, there were limited further developments until the Xie group at Pacific Northwest National Laboratory revived CARS microscopy in 1999. In this work, Zumbusch and colleagues used near-infrared laser pulses that led to a significant reduction of the two-photon enhanced non-resonant background (Zumbusch *et al*., 1999). More importantly, they used highly-focused, collinear-propagating pump and Stokes beams that relaxed the phase-matching condition. This implies that the large cone angle of the **k** vectors and the small sample interaction length (L) guarantee that the phase-matching condition Equation 3 is still satisfied under the tight focusing condition. CARS images were acquired by raster scanning the sample with respect to the small laser focal volume, resulting in high 3D resolution and sectioning capability based on the nonlinear intensity dependence.

To sum up, CARS microscopy offers the following advantages:

1. CARS microscopy provides a contrast mechanism based on molecular vibrations that are intrinsic to the sample. It does not require natural or artificial fluorescent probes. This avoids the toxicity and artifacts associated with staining, and avoids photobleaching of fluorophores.
2. CARS microscopy is orders of magnitude more sensitive than spontaneous Raman microscopy. Therefore, CARS microscopy permits fast vibrational imaging at moderate average excitation powers (i.e., up to ~10 mW) that are tolerated by most biological samples.
3. Because the nonlinear CARS signal is only generated at the focus where the laser intensities are the highest, CARS microscopy has a 3D sectioning capability and is useful for imaging thick tissues or cellular structures.
4. The anti-Stokes signal is blue-shifted from the two excitation frequencies, and can thus be easily detected in the presence of one-photon fluorescence background.
5. With the near-infrared excitation wavelengths used, CARS microscopy has a large penetration depth of more than 0.3 mm into a sample, allowing imaging through thick tissues.
6. Under typical conditions, there is little linear or nonlinear absorption of the two excitation beams. This reduces photodamage to biological specimens.

In addition to CARS, other nonlinear coherent processes, including second harmonic generation (SHG) (Gannaway and Sheppard, 1978; Campagnola *et al*., 1999; Moreaux *et al*., 2000) and third harmonic generation (THG) (Barad *et al*., 1997; Müller *et al*., 1998; Yelin and Silberberg, 1999; Cheng and Xie, 2002; Yelin *et al*., 2002), have also been incorporated with scanning microscopy, and are discussed in Chapter 40. Like CARS, the coherent radiation of these multi-photon processes is intrinsically different from the incoherent emission of multi-photon fluorescence. SHG and THG arise from electronic contributions to the second and third order susceptibility, respectively, and have essentially no spectroscopic specificity. CARS microscopy, however, is more informative than SHG and THG microscopy in that it contains rich spectroscopic information about specific molecular species.

The advances made in 1999 immediately triggered the research of several groups and brought about a rapid growth of the CARS microscopy literature. CARS microscopy has now matured into a powerful method for biological imaging. In this chapter, we summarize recent progress in this area.

UNIQUE FEATURES OF COHERENT ANTI-STOKES RAMAN SCATTERING UNDER THE TIGHT-FOCUSING CONDITION

CARS microscopy is distinguished from CARS spectroscopy in that the laser beams are tightly focused with a high numerical-aperture (NA) objective lens. In CARS spectroscopy, non-collinear beam geometries such as the BOXCARS geometry (Shirley *et al*., 1980) were conventionally used to minimize the wave vector mismatch and thus maximize the interaction length. Although these geometries have also been used for CARS microscopy (Müller *et al*., 2000), it became clear that the non-collinear geometry is difficult to implement and results in poor lateral resolution. The collinear geometry (Zumbusch *et al*., 1999) has become the method of choice because of its ease of use and high spatial resolution, and has been widely implemented (Zumbusch *et al*., 1999; Hashimoto *et al*., 2000; Potma *et al*., 2000; Cheng *et al*., 2001a,b; Volkmer *et al*., 2001, 2002; Cheng *et al*., 2002a).

It is important to emphasize some of the differences between coherent and incoherent imaging. For incoherent imaging methods such as fluorescence and spontaneous Raman microscopy, the image profile is the convolution of the object profile with the diffraction-limited point spread function of the excitation intensity. In CARS, however, the image intensity is a squared modulus of

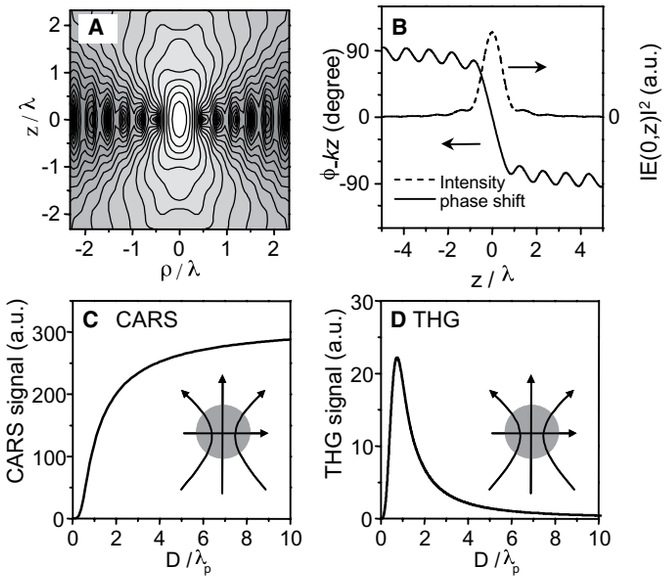


FIGURE 33.2. (A) Intensity distribution on a log scale and (B) axial intensity and phase shift in the focal region of a fundamental Gaussian beam focused by an objective lens of NA = 1.4. $\rho = \sqrt{x^2 + y^2}$. (C) Forward-detected CARS and (D) forward-detected THG signals calculated as a function of the diameter of a spherical sample centered at the focus.

the coherently-superimposed radiation fields from different parts of the sample in the focal volume. Consequently, standard deconvolution methods cannot be used. Cheng and colleagues have investigated signal generation in CARS and THG microscopy by using the Green's function method, in which the CARS signal is calculated as a coherent addition of the radiation fields from the induced dipoles in the focal region (Cheng and Xie, 2002; Cheng *et al*., 2002d). This model makes it possible to calculate nonlinear optical signals from a 3D sample of arbitrary size and shape under the assumption that the scatterer and the surrounding medium are index-matched.

Tightly-focused excitation fields were described by Richards and Wolf using diffraction theory (Richards and Wolf, 1959). The intensity distribution in the focal region of a Gaussian beam at wavelength λ focused by a NA = 1.4 objective lens is depicted in Figure 33.2(A). The FWHM (full-width at half-maximum) of the lateral profile at $z = 0$ and of the axial profile is 0.4λ and 1.0λ, respectively. A negative phase shift (~180° in addition to kz) along the axial direction, shown in Figure 33.2(B), is known as the Gouy phase shift (Siegman, 1986).

For tightly-focused laser beams, the Gouy phase shift gives rise to a π phase delay of the excitation fields within the depth of focus, which is on the order of the optical wavelength. The total Gouy phase shift of the excitation fields is the sum of the phase shift $\delta\phi_i$ of each participating field E_i. For CARS, the total Gouy phase shift in the excitation fields is $\delta\phi_{CARS} = 2\delta\phi_p - \delta\phi_S \approx \pi$. To understand the buildup of coherent signal in the focal volume, this rapid phase change needs to be taken into consideration. Such a Gouy phase shift is not only important in CARS microscopy but also in other forms of nonlinear coherent microscopy, such as SHG and THG. The Gouy phase shift is a critical factor that determines the imaging properties of the microscope. In THG, for instance, the total Gouy phase shift is $\delta\phi_{THG} = 3\delta\phi_p \approx 3\pi$.

It is interesting to compare the CARS and THG signals as a function of the diameter of a spherical sample centered at the laser focus, as displayed in Figure 33.2(C,D), respectively. Although both CARS and THG are four-wave mixing processes, the effect of the Gouy phase shift on the CARS field, $E_{as} = \chi^{(3)}E_p^2E_s^*$, is partially cancelled through the interaction of the pump field (E_p) and the conjugate Stokes field (E_s^*). On the other hand, the effect of the Gouy phase shift on the third harmonic field, $E_{3\omega} = \chi^{(3)}E_\omega^3$, is much larger. The large Gouy phase shift in the THG process results in a substantial phase mismatch under tight-focusing conditions (Boyd, 1992). Consequently, THG signal from an isotropic bulk that fills the focal volume is extremely low because of destructive interference. On the other hand, the phase mismatch in CARS is much smaller. This results in constructive interference across the entire focal volume, giving rise to a strong signal. Details about the effect of the Gouy phase shift on SHG, CARS, and THG microscopy can be found elsewhere (Moreaux *et al*., 2000; Cheng and Xie, 2002; Cheng *et al*., 2002d).

FORWARD AND BACKWARD DETECTED COHERENT ANTI-STOKES RAMAN SCATTERING

The conventional wisdom is that the CARS signal travels in the forward direction, the phase-matched direction, which is the same direction as the collinearly-propagating pump and Stokes beams. Contrary to this, Volkmer and colleagues (2001) also observed a backward-going CARS signal using an epi-detection microscope. The presence of an epi-detected CARS (E-CARS) signal can be rationalized as follows: When the size of the scatterer is much smaller than the pump wavelength, the CARS radiation goes forward and backward symmetrically [Fig. 33.3(A)], similar to radiation from an induced Hertzian dipole in the plane normal to the light propagation. Coherent addition of induced dipoles in this plane results in CARS radiation propagating in both the forward and the backward direction but confined to a smaller cone angle [Fig. 33.3(B)]. In contrast, coherent addition of the induced dipoles along the axial direction results in the constructive interference in the forward direction and destructive interference in the backward direction [Fig. 33.3(C)], which is the basis for the phase-matching condition. However, this is only true when the sample interaction length is larger than the wavelength, as was the case for most of the experiments prior to the CARS microscopy work. It is important to realize that the phase-matching condition is relaxed when the size of the object is comparable or smaller than the wavelengths of the excitation beams. Hence, when the backward-going wave has a large $|\Delta k|$, the phase mismatch $|\Delta k| \cdot L$ is compensated by the short interaction length L of the object and the phase-mismatch condition of Equation 3 is still satisfied.

Figure 33.3(D) displays the calculated F-CARS and E-CARS signals of a spherical scatterer with $\chi^{(3)}_{sca}$ centered in the focus as a function of the object's diameter (Cheng *et al*., 2002d). The epi-detected signal is only significant when the diameter of the object is small. The first maximum is reached when the diameter D equals $0.3\lambda_p$. The intensity oscillation as a function of the diameter is due to the interference effect. At $D = 8.0\lambda_p$, the epi-detected signal is 10^5 times smaller than the forward-detected signal. For a scatterer with $\chi^{(3)}_{sca}$ embedded in a solvent with $\chi^{(3)}_{sca}$, the epi-detected signal exhibits the same behavior but with a modified sample susceptibility of $\chi^{(3)}_{sca} - \chi^{(3)}_{sol}$. Interestingly, the result is independent of the sign of $\chi^{(3)}_{sca} - \chi^{(3)}_{sol}$ (Cheng *et al*., 2002d). The distribution of CARS radiation is also dependent on the shape of the object. When shaped like a long rod along the axial (z) direction, the signal predominantly goes forward [Fig. 33.3(C)]. When shaped like a

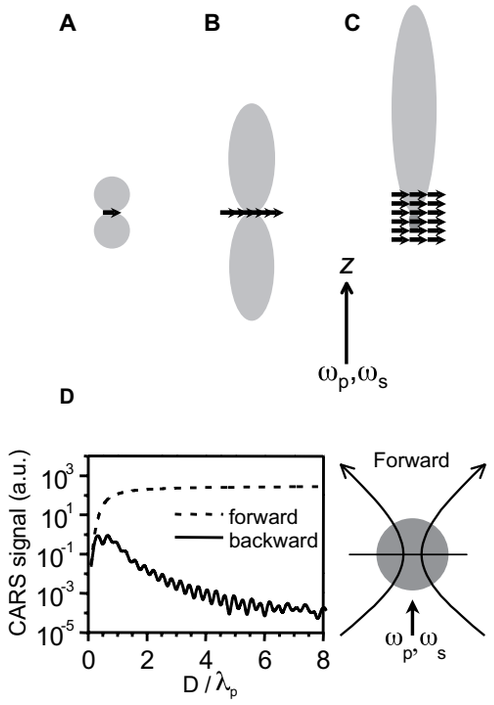


FIGURE 33.3. (A) Sketches of the Hertzian dipole radiation pattern; (B) Hertzian dipoles are coherently added up in the sample plane. (C) Addition of multiple Hertzian dipoles leads to constructive interference in the forward direction and destructive interference in the backward direction. (D) Forward- and backward-detected CARS signals as a function of the diameter D of a spherical sample centered at the focus.

thin disk, the signal goes in both forward and backward directions [Fig. 33.3(B)] (Cheng *et al.*, 2002d).

The forward and backward CARS signals provide complementary information about a sample. Forward-detected CARS (F-CARS) microscopy is suitable for imaging objects of a size comparable to or larger than the excitation wavelength. For smaller objects, the F-CARS contrast can be overwhelmed by the large non-resonant background from the solvent. The main purpose of E-CARS microscopy is to provide a sensitive means of imaging objects with an axial length smaller than the excitation wavelength, circumventing the large background from the solvent (Cheng *et al.*, 2001b, 2002d; Volkmer *et al.*, 2001).

As a demonstration, Figure 33.4 shows the simultaneous F-CARS and E-CARS images of an epithelial cell with the Raman shift tuned to the CH-stretching vibration frequency at 2847 cm^{-1}. The resonant CARS signal arises from lipids that are rich in C-H vibration. Although the F-CARS image has large signal amplitudes, it has a constant non-resonant background from the surroundings. A better contrast for small objects is seen in the E-CARS image with minimal non-resonant background from the surroundings.

Figure 33.5 shows the experimental configuration of the CARS microscope. The collinearly-overlapped pump and Stokes laser beams are tightly focused into a sample by a high-NA objective in an inverted microscope. A condenser lens (or objective lens) is used to collect the forward CARS signal. The forward propagating signal has a relatively small cone angle and an air condenser generally suffices for efficient signal collection (Cheng *et al.*, 2002a). The large working distance of the air condenser increases the accessibility to the sample and thus facilitates imaging of living cells.

The CARS signal is conveniently separated from the excitation beams using bandpass filters. The backward CARS signal is

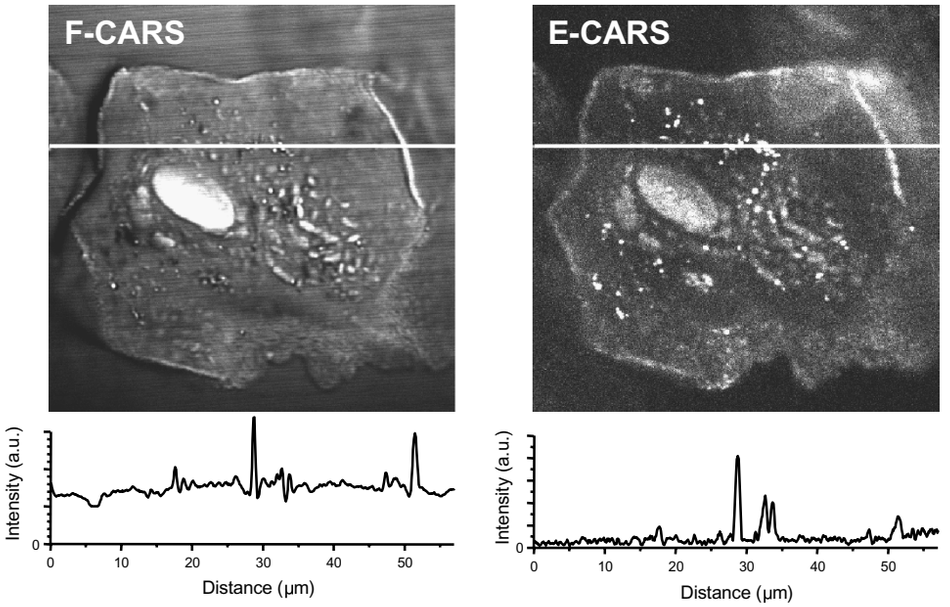


FIGURE 33.4. Forward-detected (F-CARS) and epi-detected (E-CARS) images of an epithelial cell with the Raman shift tuned to the C-H stretching vibration at 2850 cm^{-1}. The intensity profiles of the two white lines are shown in the lower panels. Note the offset in the F-CARS image due to the non-resonant background of the solvent. The background-free E-CARS image shows better contrast for small features.

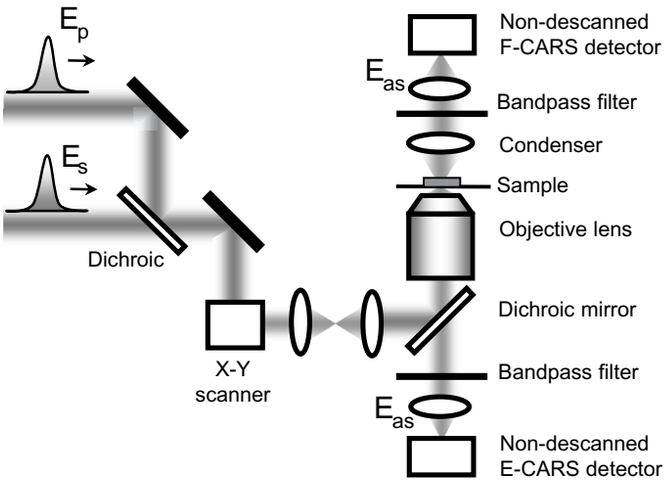


FIGURE 33.5. Schematic of a CARS microscope with both forward and backward detection. The synchronized pump and Stokes picosecond pulse trains are collinearly combined on a dichroic mirror and are directed to a beam-scanning microscope. A high-NA objective focuses the beams to a diffraction-limited spot in the sample. CARS signal is detected simultaneously in the forward and backward direction. Non-descanned photomultipliers (PMT) are typically used as detectors.

collected with the same objective used for focusing the laser beams, passing through the dichroic beam-splitter that is used to reflect the incoming excitation beams. F- and E-CARS images are simultaneously recorded by raster scanning the two laser beams with a pair of galvanometer mirrors. With a laser-scanning CARS microscope using two near-infrared (IR) laser beams of high repetition rate (Cheng *et al*., 2002a), forward- and epi-detected images (512×512 pixels) from the same sample can be taken simultaneously in less than 1 s.

The imaging properties of F-CARS and E-CARS have been characterized by using laser-scanning CARS images of polymer beads embedded in agarose gel (Cheng *et al*., 2002a). The typical FWHMs of the lateral and axial intensity profiles for a 0.2 μm bead are 0.28 μm and 0.75 μm, respectively. Using a NA = 1.2 water-immersion objective lens, the lateral FWHM for 0.1 μm beads is 0.23 μm. These FWHM should be used with caution as simple deconvolution methods cannot be applied to CARS images.

It should be noted that, besides the mechanism associated with small scatterers, there are two additional mechanisms responsible for backward CARS. One occurs at the interface of two homogeneous media with different $\chi^{(3)}$ (Cheng *et al*., 2002d), while the other results from the back reflection or backscattering of the forward CARS in a heterogeneous sample. Such animal tissue (Evans *et al.*, 2005).

OPTIMAL LASER SOURCES FOR COHERENT ANTI-STOKES RAMAN SCATTERING MICROSCOPY

It is known that the non-resonant electronic contribution to the signal can be enhanced by two-photon electronic resonance (Maeda *et al*., 1988). This is evidenced by the fact that CARS images of liposomes taken with visible dye lasers are dominated by the non-resonant background (Duncan, 1984). The use of near-IR laser beams reduced the two-photon enhancement of $\chi^{(3)}_{nr}$ and accordingly improved the image contrast (Zumbusch *et al*., 1999; Cheng *et al*., 2001b). On the other hand, CARS spectroscopy with visible laser beams can take advantage of one-photon electronic resonance (Hudson *et al*., 1976; Carreira *et al*., 1977; Dutta and Spiro, 1978; Dutta *et al*., 1980; Andrews *et al*., 1981; Igarashi *et al*., 1981; Schneider *et al*., 1988; Ujj *et al*., 1994; Voroshilov *et al*., 1995) for chemical species with absorption in the visible wavelength range, such as cytochrome c (Dutta *et al*., 1980; Andrews *et al*., 1981), β-carotene (Carreira *et al*., 1977; Dutta *et al*., 1980), bateriorhodopsin (Ujj *et al*., 1994), and hemoglobin (Voroshilov *et al*., 1995). Electronically-resonant CARS provides a way to suppress the non-resonant solvent background by enhancing the signal from the scatterer. The signal enhancement and the photodamage associated with one-photon electronic resonance has yet to be explored in CARS microscopy.

The 1999 work used femtosecond lasers that have a high peak power and are widely used in multi-photon fluorescence microscopy. However, it turns out that femtosecond pulses are not optimal for vibrational imaging. Whereas a few molecules such as water have broad Raman spectra, the typical Raman line width at room temperature is around 10 cm^{-1} in the condensed phase. The spectral width of a 100 femtosecond pulse is 333 cm^{-1}, much wider than the Raman line width. Therefore, most of the pulse energy ends up being used to generate the non-resonant background. On the other hand, the spectral width of a picosecond pulse is comparable to the Raman line width, so that the excitation energy is fully utilized to maximize the vibrationally resonant CARS signal. It has been shown theoretically that the optimal signal-to-background ratio occurs with spectral pulse widths of 1~2 ps for a typical Raman band at room temperature (Cheng and Xie, 2003). A pulse width of a few picosecond provides a good compromise between the spectral resolution and the peak power, and improved the signal-to-background ratio. In 2001, Cheng and colleagues constructed a new CARS microscope with two synchronized picosecond titanium : sapphire (Ti : Sa) lasers, and experimentally demonstrated improved spectral resolution and high signal-to-background ratio (Cheng *et al*., 2001b).

In general, the timing jitter between the pump and the Stokes pulses introduces a fluctuation to the CARS intensity and this limits the image acquisition rate. This is particularly important when two independent, passively mode-locked lasers are used. Recently, tight synchronization between the pulse trains with jitters of 20 to 100 fs has been realized (Jones *et al*., 2002; Potma *et al*., 2002). This has allowed acquisition of high-quality CARS images using 2 ps pulse trains (Potma and Xie, 2003).

Picosecond pulses from a Ti : Sa oscillator typically have an energy ~6 nJ at an average power level of about 500 mW and a repetition rate of around 80 MHz. Such laser pulses have been successfully applied for high-speed CARS imaging (Cheng *et al*., 2002a). The integrated CARS signal intensity can be enhanced by a factor of m^2 ($= m^3/m$) if the pump and Stokes pulse energies are increased by a factor of m and the repetition rate is lowered by the same factor. On the other hand, high peak power can be hazardous to the sample and a high repetition rate is beneficial for fast image acquisition. A repetition rate of 100 kHz to 1 MHz is a good compromise.

Recently, Ye and co-workers have shown that enhancement of pulse energy can be realized through coherent storage of radiation in a high finesse cavity without a gain medium (Jones and Ye, 2002). Using a high finesse cavity equipped with a cavity dumper, Potma and colleagues demonstrated amplification of mode-locked picosecond pulses that is greater than a factor of 30 at a repetition

rate of 253 kHz (Potma *et al*., 2003). These novel sources provide new possibilities for improving the speed and sensitivity of CARS imaging.

The timing jitter between the pump and probe pulses can be avoided if one uses synchronously pumped optical parametric oscillator (OPO) systems. When a commercial, near-IR picosecond OPO based on periodically-poled nonlinear crystals, pumped by a mode-locked laser with semiconductor saturable absorber mirrors (SESAMs) becomes available, it can serve as an ideal laser source for CARS imaging.

SUPPRESSION OF THE NON-RESONANT BACKGROUND

The suppression of both the non-resonant background from the solvent and that from the scatterers is key to improving the detection sensitivity and spectral selectivity of CARS microscopy. Several schemes for background suppression have been developed and are summarized as follows.

Use of Picosecond Instead of Femtosecond Pulses

A straightforward way to minimize the non-resonant background is not to generate it in the first place. As outlined above, compared to the broadband pulses of fs lasers, the spectral bandwidth of 1 to 2 ps pulses matches the linewidth of the Raman bands and minimizes generation of non-resonant spectral components. A picosecond laser system thus represents a better light source for CARS imaging in terms of the signal–to–non-resonant background ratio.

Epi-Detection

As already discussed, this method introduces a large wave vector mismatch, which acts as a size-selective filter that rejects the background signal (resonant or non-resonant) from the bulk solvent and allows high-sensitivity imaging of small objects (Volkmer *et al*., 2001; Cheng *et al*., 2001b). Because E-CARS rejects signal contributions based on size and not on vibrational properties, the non-resonant signal from the small objects themselves still contributes to the image. Hence, for weak resonant signals (e.g., from the protein amide I band), the vibrational sensitivity of E-CARS can be limited due to the non-resonant background from the small objects themselves.

Polarization-Sensitive Detection

This method is based on the different polarization properties of the electronic ($P^{(3)NR}$) and resonant ($P^{(3)R}$) portions of the third order polarization (Akhmanov *et al*., 1977; Oudar *et al*., 1979; Brakel and Schneider, 1988). The polarization direction of the emitted CARS field is determined by the polarization of the incident pump and Stokes fields and the Raman depolarization ratio ρ of the material. The depolarization ratio of the resonant signal ρ_R depends on the molecular vibrational mode and usually differs from the constant depolarization ratio of the isotropic non-resonant background ρ_{NR} (Kleinman, 1962). With linearly-polarized pump and Stokes beams, a difference between ρ_R and ρ_{NR} leads to non-parallel, linearly-polarized resonant and non-resonant anti-Stokes fields. In polarization-sensitive CARS, a polarization analyzer in front of the detector blocks the non-resonant signal, whereas a portion of the differently polarized resonant signal leaks through the analyzer. The detected resonant signal is optimized when the polarization difference between $P^{(3)R}$ and $P^{(3)NR}$ is maximized. This is achieved by introducing a polarization difference of 71.6° between the pump and the Stokes beams (Brakel and Schneider, 1988).

The efficient background rejection of the P-CARS microscope permits vibrational imaging of intracellular proteins (Cheng *et al*., 2001a). Figure 33.6(A) shows the P-CARS spectrum of *N*-methylacetamide, a model compound containing the characteristic amide I vibration at 1652 cm^{-1}, which is a signature band for peptides and proteins. As the P-CARS band positions coincide with the corresponding Raman band positions, one can assign the P-CARS bands based on the Raman literature. The difference in the relative intensity of the bands in the two spectra arises from the quadratic dependence on the number of vibrational oscillators and the Raman depolarization ratios of the bands. Figure 33.6(B,C) shows the background-free P-CARS images of an unstained epithelial cell with $\omega_p - \omega_s$ tuned to the amide I band [Fig. 33.7(B)]. Tuning $\omega_p - \omega_s$ away from the amide I band to 1745 cm^{-1} resulted in a faint contrast [Fig. 33.7(C)], proving that the image contrast was due to proteins, the distribution of which is heterogeneous in the cell (Cheng *et al*., 2001a).

Time-Resolved Coherent Anti-Stokes Raman Scattering Detection

The vibrationally-resonant signal can be separated from the non-resonant electronic contribution by use of pulse-sequenced detection with femtosecond pulse excitation (Laubereau and Kaiser, 1978; Kamga and Sceats, 1980). In time-resolved CARS detection, a signal-generating probe pulse is time delayed with respect to a temporally-overlapped pump/Stokes pulse-pair. Because of the instantaneous dephasing time of the non-resonant signal, the non-resonant CARS signal only exists when the pump/Stokes pulse-pair overlaps with the probe pulse. On the other hand, the vibrationally-resonant CARS signal decays with the finite dephasing time of the vibrational mode. The dephasing time is related to the spectral width of the corresponding Raman band and is typically several hundred femtoseconds for a mode in the condensed phase (Fickenscher *et al*., 1992). The non-resonant background in the CARS images can thus be eliminated by introducing a suitable delay between the femtosecond pump/Stokes and the probe pulses. Time-resolved CARS imaging has been demonstrated by Volkmer and colleagues with a three-color excitation scheme (Volkmer *et al*., 2002). The disadvantages of this approach are the photodamage induced by the femtosecond pulses and the necessity of adding a third laser beam of a different color.

Phase Control of Excitation Pulses

With femtosecond lasers, another way to reduce the electronic contribution is phase-shaping of the pulses. Phase-shaping of femtosecond pump and Stokes pulses suppresses the non-resonant signal by introducing a phase mismatch in the coherent addition of non-resonant spectral components, whereas the resonant contribution still adds up in phase (Oron *et al*., 2002). This method has been applied to CARS spectroscopy and microscopy with single, femtosecond pulses (Dudovich *et al*., 2002). Recently, Oron and colleagues reported a combination of phase and polarization shaping for background-free single-pulse CARS spectroscopy (Oron *et al*., 2003).

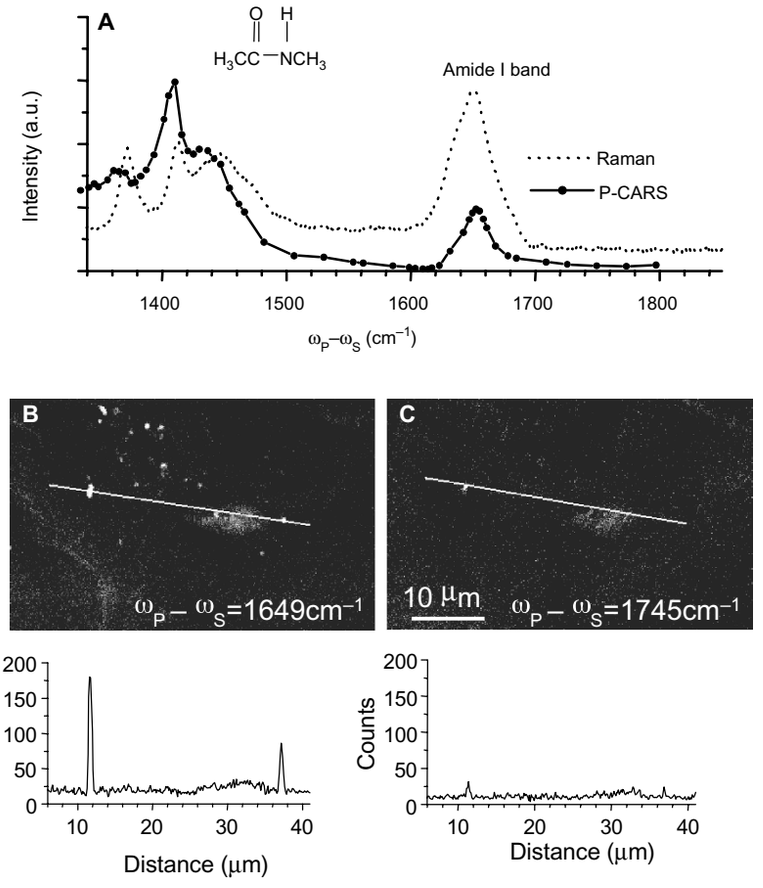


FIGURE 33.6. (A) P-CARS and spontaneous Raman spectra of pure *N*-methylacetamide liquid recorded at room temperature. (B, C) Polarization CARS images of an unstained epithelial cell with $\omega_p - \omega_s$ tuned to 1650 cm^{-1} and 1745 cm^{-1}, respectively. Each image was acquired by raster scanning the sample with an acquisition time of 8 min. The pump and Stokes power were 1.8 and 1.0 mW, respectively, at a repetition rate of 400 kHz.

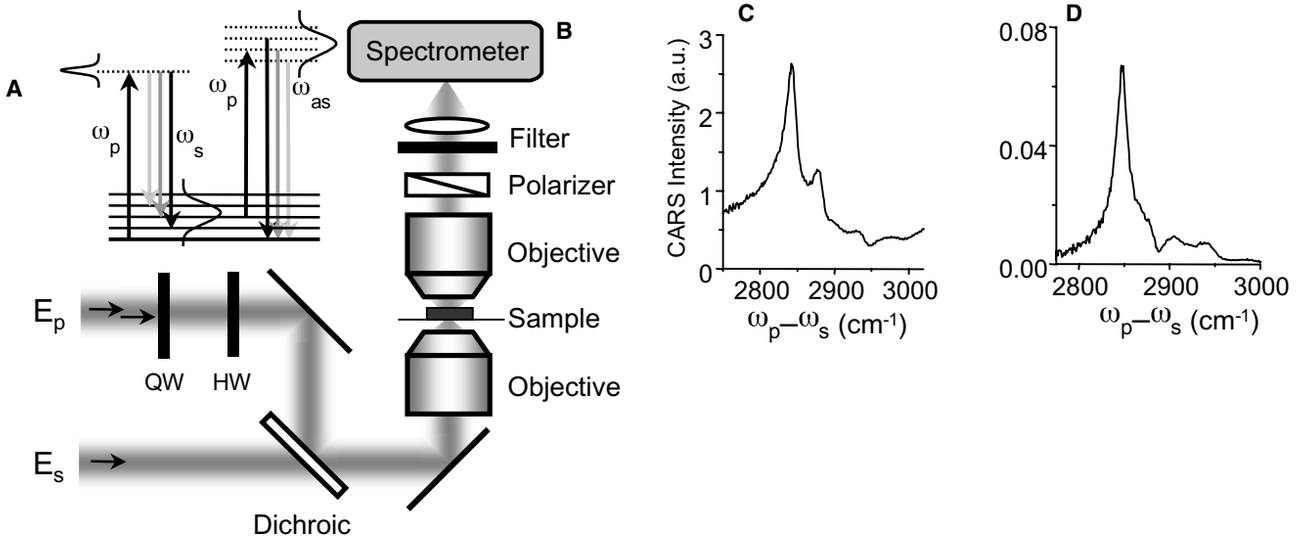


FIGURE 33.7. (A) Energy diagram for multiplex CARS microspectroscopy using a picosecond pump beam and a femtosecond Stokes beam. (B) Schematic of the setup for multiplex CARS microspectroscopy. (C) Multiplex CARS spectrum of a DSPC (1,2-distearoyl-*sn*-glycero-3-phosphocholine) liposome. The pump and Stokes beam were centered at 713 nm and 900 nm, with average powers of 0.6 mW and 0.3 mW at a repetition rate of 400 kHz. The integration time was 2 s. (D) Polarization-sensitive multiplex CARS spectrum of the same liposome sample. The average power of the pump and the Stokes beams was 1.2 mW and 0.6 mW, respectively. The other parameters are the same as in (C).

MULTIPLEX COHERENT ANTI-STOKES RAMAN SCATTERING MICROSPECTROSCOPY

While CARS microscopy allows high-sensitivity vibrational imaging of particular molecules, CARS microspectroscopy can provide molecular structure information about samples with 3D spatial resolution. Picosecond excitation enables high-sensitivity CARS imaging based on a particular band; however, it is time consuming to record a CARS spectrum by tuning the Stokes frequency point by point (Hashimoto *et al*., 2000; Cheng *et al*., 2001a,b). Multiplex CARS (M-CARS) spectroscopy first demonstrated by Akhmanov and colleagues permits fast spectral data acquisition (Akhmanov *et al*., 1977). In previous work, a narrowband and a broadband dye laser were used for the pump and the Stokes beams, respectively (Toleutaev *et al*., 1994; Ujj *et al*., 1994; Voroshilov *et al*., 1996). Recently, M-CARS microspectroscopy has been developed for fast spectral characterization of microscopic samples (Müller and Schins, 2002; Cheng *et al*., 2002c; Kee and Cicerone, 2004; Otto *et al*., 2001).

Figure 33.7(A) shows the energy diagram and the schematic of an M-CARS microscope using a picosecond and a femtosecond pulse train. In a theoretical investigation by Cheng and colleagues (Cheng *et al*., 2002c), it was shown that the frequency chirp in the femtosecond Stokes pulse induces little distortion to the CARS spectrum of a sample. The chirped pulses are desirable because of reduced sample damage. Polarization-sensitive detection has been incorporated into an M-CARS microscope to suppress the nonresonant background (Cheng *et al*., 2002c). Figure 33.7(B,C) shows the M-CARS spectra of the C-H stretching vibrational bands in a DSPC liposome recorded with parallel-polarized beams and with polarization-sensitive detection, respectively. The P-CARS spectrum is free from the complication of the non-resonant background and spectral distortion. The symmetric CH_2 stretching vibration at 2845 cm^{-1} exhibits a high signal-to-background ratio and has been used for imaging lipids as shown in the images of Figures 33.4, 33.8, and 33.11.

M-CARS microspectroscopy has been applied to distinguish the gel and the liquid crystal phases in liposomes. Müller and colleagues have shown that it is possible to distinguish the two different phases by using the CARS spectra of the C-C stretching vibration (Müller and Schins, 2002). Cheng and colleagues have shown that the different lipid phases are also reflected in the spectral differences in the C-H stretching vibration region (Cheng *et al*., 2002c).

COHERENT ANTI-STOKES RAMAN SCATTERING CORRELATION SPECTROSCOPY

Fast dynamical processes can be probed by optical intensity correlation spectroscopy. Fluorescence correlation spectroscopy (FCS) measures the concentration fluctuation of specific fluorescent molecules (Magde *et al*., 1972; Elson and Magde, 1974). FCS has found wide application with the development of confocal detection (Eigen and Rigler, 1994; Maiti *et al*., 1997). For probing diffusion processes with vibrational selectivity, CARS correlation spectroscopy (CARS-CS) has been developed recently (Cheng *et al*., 2002b; Hellerer *et al*., 2002). This technique measures the fluctuation of the CARS signal from a subfemtoliter excitation volume. CARS-CS has been carried out with epi-detection and/or polarization-sensitive detection. Figure 33.8 shows the epi-detected CARS intensity fluctuations and autocorrelation curves that characterize the diffusion of 0.175 µm polystyrene beads in

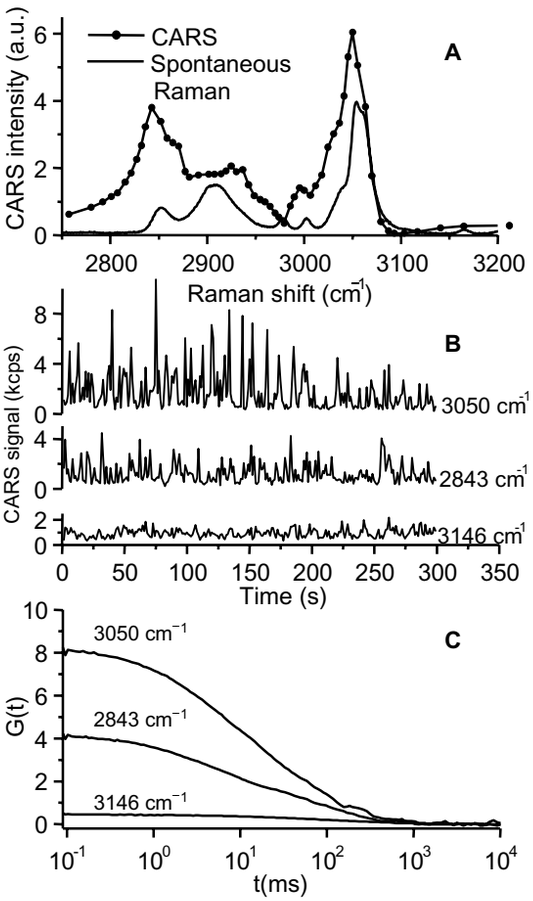


FIGURE 33.8. (A) CARS and spontaneous Raman spectra of a polystyrene film coated on a coverslip. The CARS spectrum was recorded with parallel-polarized pump and Stokes beams. The pump frequency was fixed at 14,047 cm^{-1} whereas the Stokes frequency was scanned. (B) Epi-detected CARS signal traces of a diluted aqueous suspension of 0.175 µm polystyrene spheres ($\langle N \rangle \approx 0.04$). The average pump and Stokes power measured after the beam combiner were 1.3 and 0.6 mW, respectively. (C) Epi-detected CARS intensity autocorrelation curves corresponding to the signal traces in (B).

water. The spectral selectivity is illustrated by the CARS spectrum of polystyrene, in which the aromatic C-H (3052 cm^{-1}), the symmetric aliphatic C-H (2852 cm^{-1}), and the asymmetric aliphatic C-H (2907 cm^{-1}) stretching bands display a high signal-to-background ratio. With $\omega_p - \omega_s$ tuned to the aromatic C-H band at 3050 cm^{-1} and the aliphatic C-H band at 2843 cm^{-1}, the intensity autocorrelation revealed a diffusion time of 27.3 ± 0.7 ms and 28.6 ± 1.0 ms, respectively, fitted with a CARS-CS model (Cheng *et al*., 2002b). Tuning $\omega_p - \omega_s$ to 3146 cm^{-1}, away from any Raman resonance, resulted in an autocorrelation curve that is smaller by 16 times in amplitude than the curve at 3050 cm^{-1}. The residual intensity autocorrelation with a diffusion time of 160 (±6) ms was attributed to the water signal back-reflected by the diffusing beads. It has been demonstrated that CARS-CS can provide quantitative information about the diffusion coefficient, particle concentration, and viscosity of a medium in a chemically selective and noninvasive manner (Cheng *et al*., 2002b).

The intensity autocorrelation function of CARS-CS bears much similarity to the FCS autocorrelation function at low scatterer concentration. However, a careful analysis, in which the phase of the CARS field is included, shows that the E-CARS cor-

relation function is different from the FCS correlation function. Whereas the autocorrelation amplitude in FCS is inversely proportional to the average number of particles $\langle N \rangle$ in the excitation volume and vanishes at high concentration, the E-CARS correlation function contains a term that is independent of $\langle N \rangle$. This implies that the E-CARS autocorrelation amplitude does not vanish for higher $\langle N \rangle$. This concentration-independent term has been confirmed experimentally and provides a way of probing the diffusion of objects at high concentrations (Cheng *et al.*, 2002b).

COHERENT ANTI-STOKES RAMAN SCATTERING IMAGING OF BIOLOGICAL SAMPLES

The capability of CARS microscopy to generate chemically-selective images with a high 3D spatial resolution offers an attractive method for cellular imaging. In Figure 33.9, a 3D reconstruction made from CARS recordings of three epithelial cells is depicted. Similar to multi-photon fluorescence microscopy, the intrinsic sectioning capability of CARS ensures that the cells are resolved in three dimensions. The Raman shift was tuned to the symmetric CH_2 stretch vibration of the lipid's aliphatic chains at 2845 cm^{-1}, a vibrational mode that is abundant in lipids. The contrast observed in the image is therefore largely due to the phospholipid membranes, such as the plasma membrane, and intracellular lipid droplets mainly composed of triglyceride. The CARS signal from the aliphatic CH_2 vibrational band has been used in imaging studies of various cell types (Zumbusch *et al.*, 1999; Holtom *et al.*, 2001; Cheng *et al.*, 2002a).

The CARS sensitivity to lipids is so high that single phospolipid bilayers can be visualized (Potma and Xie, 2003). Figure 33.10(A) depicts an image of the natural membrane of an erythrocyte ghost, taken at the symmetric CH_2 stretch vibration frequency of lipids. This image was recorded in the forward direction with the bilayer parallel to the propagation direction of the beams. The higher signal intensities at the top and bottom of the cell image relative to the left and right of the cell image are a result of the relative orientation of the acyl chains in the membrane. The stronger signals were generated when the CH_2 stretching normal modes are aligned with the polarization direction of the pump and Stokes beams. This feature can be used to determine molecular orientation with CARS microscopy (Wurpel *et al.*, 2005; Cheng *et al.* 2003). When the membrane surface is perpendicular to the optical axis, as in Figure 33.10(B), the bilayer is conveniently visualized in the epi-direction, demonstrating the high sensitivity of CARS microscopy.

The ability of visualizing single bilayers enables the study of lipid phase segregation in membranes. Phase-segregated domains, also known as lipid rafts, form when lipids of different thermodynamic phase are mixed. Lipid rafts are thought to play crucial roles in such processes as protein sorting and signaling on cell membranes. With CARS, micrometer-sized lipid domains can be directly detected without the introduction of fluorescent membrane labels (Potma and Xie, 2005). In Figure 33.10(C), a clear phase separation is observed between the phospholipids DOPC (1,2-dioleoyl-*sn*-glycero-3-phosphocholine) and deuterated DSPC (1,2-distearoyl-*sn*-glycero-3-phosphocholine) by tuning into the C-D stretching frequency of the latter. This underlines the potential for CARS microscopy to detect lipid rafts in cells non-invasively.

Lipid droplets are typically found in adipocytes and hepatocytes as energy reservoirs and are thought of as playing important roles in cellular processes (Murphy, 2001). Because lipid droplets

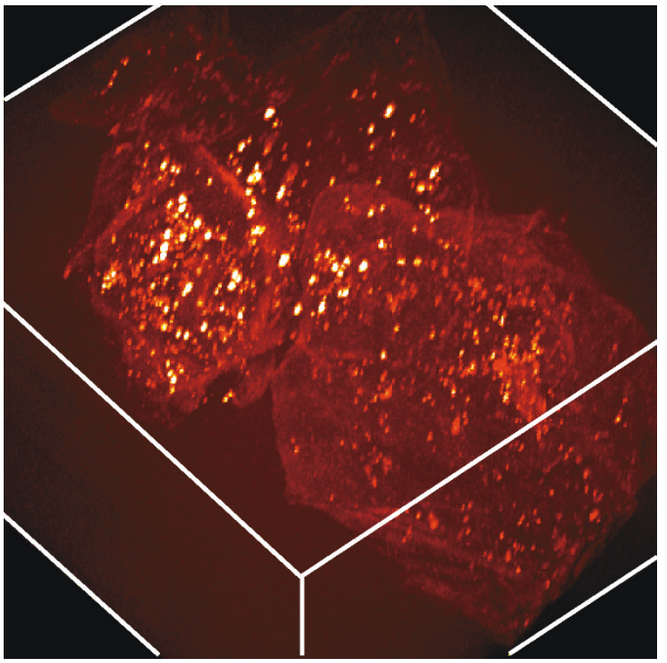


FIGURE 33.9. Three-dimensional reconstruction of three epithelial cells. The Raman shift is tuned to the C-H stretch vibration at 2845 cm^{-1}. The 3D image is composed of 71 planes of 512 × 512 pixels each. Pump beam power was 15 mW and Stokes beam power was 10 mW at a repetition rate of 76 MHz. Each plane was recorded in 2 s. The total dimension is 92 × 92 × 50 µm.

are aggregates of neutral lipids, they are rich in CH_2 bonds and yield very strong CARS signals. Traditionally, lipid droplets can be labeled with Oil Red O in fixed cells and imaged with fluorescence microscopy. In a recent study, Nan and colleagues applied CARS microscopy to monitor the growth of triglyceride droplets during the differentiation process of 3T3-L1 cells (Nan *et al.*, 2003). In addition to the traditional picture of lipid accumulation in the differentiation process, the P-CARS images shown in Figure 33.11 indicate an intermediate stage, that is, the removal of cytoplasmic lipid droplets after the addition of the induction medium. This reduction of lipid droplets was attributed to an increased activity of hormone-sensitive lipase, the enzyme responsible for hydrolyzing intracellular triglyceride and sterol esters (Kawamura *et al.*, 1981).

So far, we have discussed imaging of aggregates of lipids (membranes and droplets) and proteins in cells using the C-H stretching band and the amide I band, respectively. In order to follow the distribution and diffusion of specific molecules in living cells, isotopic substitution provides a good strategy to enhance molecular selectivity. For example, the Raman shift of the aliphatic and the aromatic C-D vibration bands lies in the region of 2100 to 2300 cm^{-1}, isolated from the Raman bands of endogenous molecules. In earlier work using picosecond dye lasers, Duncan and colleagues showed that CARS microscopy could distinguish deuterated liposomes from non-deuterated ones (Duncan, 1984). The deuteration method has been applied to living cells by Holtom and colleagues, who demonstrated selective mapping of deuterated lipid vesicles in a macrophage cell (Holtom *et al.*, 2001).

The high signal level in CARS microscopy permits high-speed imaging of intracellular dynamics. Potma and colleagues used the resonant CARS signal from the O-H stretching vibration of water to visualize intracellular hydrodynamics (Potma *et al.*, 2001). By line-scanning the laser beams, they measured the intracellular

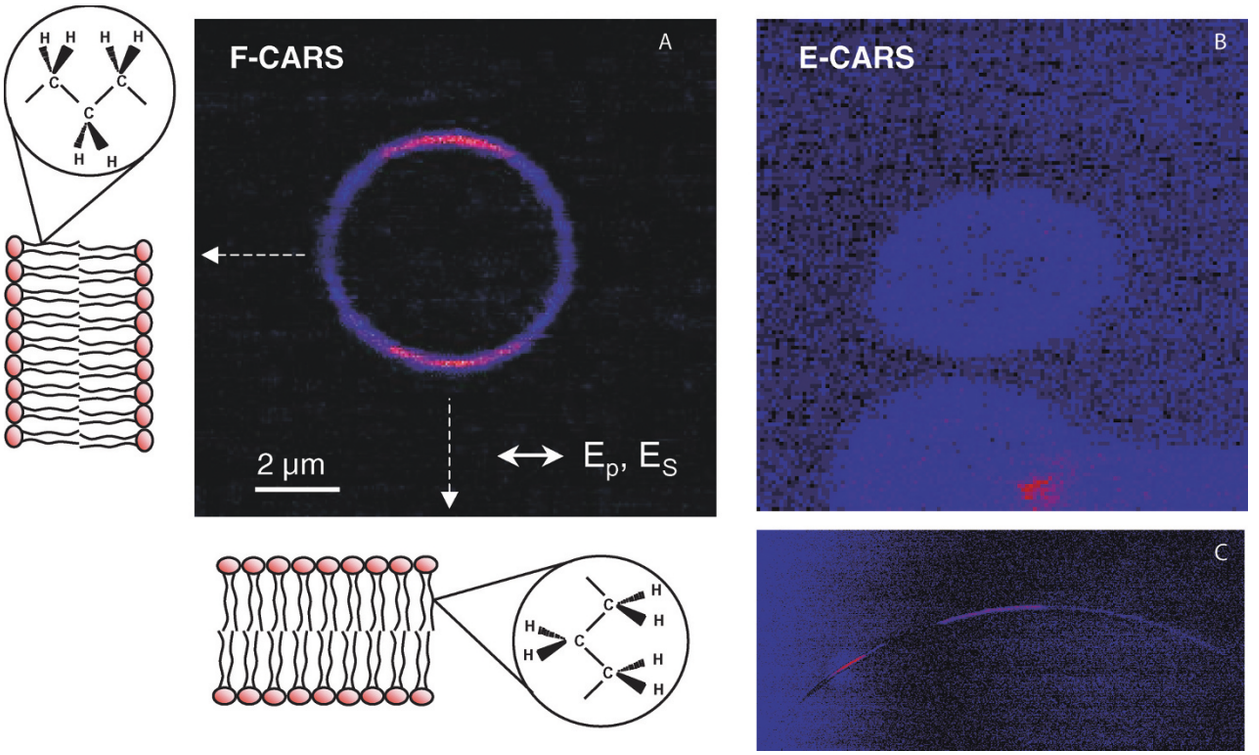


FIGURE 33.10. CARS images of erythrocyte ghosts recorded at C-H stretching vibration of 2845 cm^{-1}. (A) F-CARS image in the equatorial plane of the cell. Note the orientation-dependent signal of the C-H bonds in the bilayer. (B) E-CARS image of the bottom of the cells close to the coverslip. Pump beam power was 0.3 mW and Stokes beam power was 0.1 mW at a repetition rate of 250 kHz. Images are 256 × 256 pixels and the pixel dwell time was 1 ms. (C) Part of a giant unilamellar vesicle composed of an equimolar ratio of the phospholipids DOPC and DSPC, showing a clear phase separation of the lipids. To enhance contrast, deuterated DSPC was used and the image was taken at the C-D stretch vibrational band at 2090 cm^{-1}, giving rise to bright signals from the DSPC-enriched domains.

water diffusion coefficient and the membrane permeability. Using laser-scanning CARS microscopy, Cheng and co-workers characterized apoptosis induced by L-asparaginase in unstained NIH3T3 fibroblasts (Cheng *et al.*, 2002a). They tuned $\omega_p - \omega_s$ to the aliphatic C-H vibrational frequency and were able to identify different stages in the apoptotic process, such as the compaction of cytoplasmic organelles and the rounding of the cells.

CONCLUSIONS AND PERSPECTIVES

CARS microscopy is a new approach for chemical and biological imaging of unstained samples with vibrational selectivity and 3D spatial resolution. On the method-development side, various schemes including picosecond excitation, epi-detection, and polarization-sensitive detection have significantly improved the

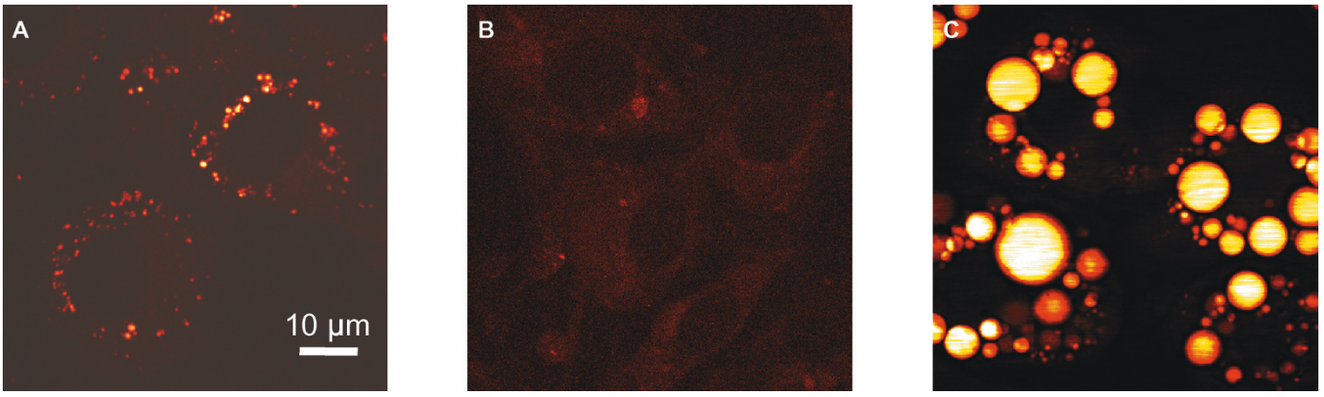


FIGURE 33.11. P-CARS images 3T3-L1 preadipocytes differentiating into adipocyte cells at different stages, recorded at the C-H stretching vibration of 2845 cm^{-1}. Differentiation is induced with insulin, isobutylmethylxanthine, and dexamethasone 2 days postconfluence (A). The dots seen in (A) are lipid droplets. Note the clearance of lipid droplets from the cytoplasm 48 h after initiation (B). After that cells accumulate lipid droplets again as differentiation went on. In fully differentiated cells (C), the cytoplasm are full of large droplets (Nan *et al.*, 2003). Pump beam power was 15 mW and Stokes beam power was 7.5 mW at a repetition rate of 80 MHz. Image acquisition time was 2.7 s.

ratio of the resonant signal to the non-resonant background. High imaging speed (video rate) has been achieved with a laser-scanning microscope. New developments in laser technologies are boosting the imaging sensitivity to higher levels. Meanwhile, a rigorous theoretical model based on the Green's function method has led to a better understanding of the contrast mechanisms of CARS microscopy and nonlinear coherent microscopy in general. Multiplex CARS microspectroscopy for localized structure characterization and CARS correlation spectroscopy for probing fast diffusion dynamics have also been developed.

On the application side, CARS microscopy has been used for mapping the distribution, orientation, and diffusion of specific compounds, for imaging lipids, proteins, and chromosomes in unstained living cells, and for monitoring cellular processes such as apoptosis and lipogenesis. Looking into the future, CARS microscopy provides exciting possibilities for tackling a broad range of chemical and biological problems. It is expected to have potential applications in such fields as membrane biology, neurobiology, and pathology. In the meantime, there are many opportunities to push the fundamental limits of CARS microscopy to the next level.

ACKNOWLEDGMENT

We are indebted to previous and current group members, A. Zumbusch, G. R. Holtom, A. Volkmer, L. Book, X. Nan, L. Kaufman, C. Evans, and W. Yang for their contributions to CARS microscopy. It is our pleasure to acknowledge our collaborators, J. Ye, D. Jones, J. Jones, Y. Pang, B. Burfeindt, and K. Jia, for fruitful collaborations. This work was supported by a National Institutes of Health grant (GM62536–01) and a National Science Foundation Grant (DB1–0138028).

REFERENCES

Akhmanov, S.A., Bunkin, A.F., Ivanov, S.G., and Koroteev, N.I., 1977, Coherent ellipsometry of Raman scattering of light, *JETP Lett.* 25:416–420.

Andrews, J.R., Hochstrasser, R.M., and Trommsdorff, H.P., 1981, Vibrational transitions in excited states of molecules using coherent Stokes Raman spectroscopy: Application to ferrocytochrome-C, *Chem. Phys.* 62:87–101.

Barad, Y., Eisenberg, H., Horowitz, M., and Silberberg, Y., 1997, Nonlinear scanning laser microscopy by third-harmonic generation, *Appl. Phys. Lett.* 70:922–924.

Begley, R.F., Harvey, A.B., and Byer, R.L., 1974, Coherent anti-Stokes Raman scattering, *Appl. Phys. Lett.* 25:387–390.

Boyd, R.W., 1992, *Nonlinear Optics*, Academic Press, Boston.

Brakel, R., and Schneider, F.W., 1988, Polarization CARS spectroscopy, *In: Advances in NonLinear Spectroscopy* (R.J.H. Clark and R.E. Hester, eds.), John Wiley and Sons, New York, p. 149.

Campagnola, P.J., Wei, M.-D., Lewis, A., and Loew, L.M., 1999, High-resolution nonlinear optical imaging of live cells by second harmonic generation, *Biophys. J.* 77:3341–3349.

Carreira, L.A., Goss, L.P., and Malloy, J.T.B., 1977, Comparison of the coherent anti-Stokes and coherent Stokes Raman line shapes of the n_1 line of b-carotene near a one-photon resonance, *J. Chem. Phys.* 69:855–862.

Cheng, J.X., and Xie, X.S., 2002, Green's function formulation for third-harmonic generation microscopy, *J. Op. Soc. Am. B* 19:1604–1610.

Cheng, J.X., and Xie, X.S., 2003, Coherent anti-Stokes Raman scattering microscopy: Instrumentation, theory, and applications. *J. Phys. Chem. B.*

Cheng, J.X., Book, L.D., and Xie, X.S., 2001a, Polarization coherent anti-Stokes Raman scattering microscopy, *Opt. Lett.* 26:1341–1343.

Cheng, J.X., Jia, Y.K., Zheng, G., and Xie, X.S., 2002a, Laser-scanning coherent anti-Stokes Raman scattering microscopy and applications to cell biology, *Biophys. J.* 83:502–509.

Cheng, J.X., Pautot, S., Weitz, D.A., and Xie, X.S., 2003, Ordering of water molecules between phospholipid bilayers visualized by coherent anti-Stokes Raman scattering microscopy, *Proc. Natl. Acad. Sci.* USA 100:9826–9830.

Cheng, J.X., Potma, E.O., and Xie, X.S., 2002b, Coherent anti-Stokes Raman scattering correlation spectroscopy: Probing dynamical processes with chemical selectivity, *J. Phys. Chem. A* 106:8561–8568.

Cheng, J.X., Volkmer, A., Book, L.D., and Xie, X.S., 2001b, An epi-detected coherent anti-Stokes Raman scattering (E-CARS) microscope with high spectral resolution and high sensitivity, *J. Phys. Chem. B* 105: 1277–1280.

Cheng, J.X., Volkmer, A., Book, L.D., and Xie, X.S., 2002c, Multiplex coherent anti-Stokes Raman scattering microspectroscopy and study of lipid vesicles, *J. Phys. Chem.* 106:8493–8498.

Cheng, J.X., Volkmer, A., and Xie, X.S., 2002d, Theoretical and experimental characterization of coherent anti-Stokes Raman scattering microscopy, *J. Opt. Soc. Am. B* 19:1363–1375.

Cheng, J.X., and Xie, X.S., 2004, Coherent anti-Stokes Raman scattering microscopy: Instrumentation, theory and applications, *J. Phys. Chem. B.* 108:827–840.

Clark, R.J.H., and Hester, R.E., 1988, *Advances in NonLinear Spectroscopy*, John Wiley and Sons, New York.

Dudovich, N., Oron, D., and Silberberg, Y., 2002, Single-pulse coherently controlled nonlinear Raman spectroscopy and microscopy, *Nature* 418:512–514.

Duncan, M.D., 1984, Molecular discrimination and contrast enhancement using a scanning coherent anti-Stokes Raman microscope, *Opt. Commun.* 50:307–312.

Dutta, P.K., and Spiro, T.G., 1978, Resonance CARS line shapes: Excited state parameters for flavin adenine dinucleotide, *J. Chem. Phys.* 69:3119–3123.

Dutta, P.K., Dallinger, R., and Spiro, T.G., 1980, Resonance CARS (coherent anti-Stokes Raman scattering) line shapes via Frank-Condon scattering: Cytochrome c and b-carotene, *J. Chem. Phys.* 73:3580–3585.

Eigen, M., and Rigler, R., 1994, Sorting single molecules: Application to diagnostic and evolutionary biotechnology, *Proc. Natl. Acad. Sci. USA* 91:5740–5747.

Elson, E.L., and Magde, D., 1974, Fluorescence correlation spectroscopy I. Conceptual basis and theory, *Biopolymers* 13:1–27.

Evans, C.L., Potma, E.O., Pourgish'haag, M., Cote, D., Lin, C.P., Xie, X.S., 2005, Chemical imaging of tissue in vivo with video-rate coherent anti-Stokes Raman scattering (CARS) microscopy, *Proc. Nat. Acad. Sci.* 102: 16807–16812.

Fickenscher, M., Purucker, H.-G., and Laubereau, A., 1992, Resonant vibrational dephasing investigated by high-precision femtosecond CARS, *Chem. Phys. Lett.* 191:182–188.

Gannaway, J.N., and Sheppard, C.J.R., 1978, Second-harmonic imaging in the optical microscope, *Opt. Quantum Electron.* 10:435–439.

Hashimoto, M., Araki, T., and Kawata, S., 2000, Molecular vibration imaging in the fingerprint region by use of coherent anti-Stokes Raman scattering microscopy with a collinear configuration, *Opt. Lett.* 25:1768–1770.

Hellerer, T., Schiller, A., Jung, G., and Zumbusch, A., 2002, Coherent anti-Stokes Raman scattering (CARS) correlation spectroscopy, *Chemphyschem* 7:630–633.

Holtom, G.R., Thrall, B.D., Chin, B.-Y., Wiley, H.S., and Colson, S.D., 2001, Achieving molecular selectivity in imaging using multiphoton Raman spectroscopy techniques, *Traffic* 2:781–788.

Hudson, B., Hetherington, W., Cramer, S., Chabay, I., and Klauminzer, G.K., 1976, Resonance enhanced coherent anti-Stokes Raman scattering, *Proc. Natl. Acad. Sci. USA* 73:3798–3802.

Humecki, H.J., 1995, Practical guide to infrared microspectroscopy, *In*: *Practical Spectroscopy* (J.E.G. Brame, ed.), Marcel Dekker, New York.

Igarashi, R., Iida, F., Hirose, C., and Fujiyama, T., 1981, The application of polarization coherent anti-Stokes Raman spectroscopy to the line-shape analysis of liquid sample, *Bull. Chem. Soc. Jpn.* 54:3691–3695.

Jamin, N., Dumas, P., Moncuit, J., Fridman, W.H., Teilland, J.L., Carr, G.L., and Williams, G.P., 1998, Highly resolved chemical imaging of living cells by using synchrotron infrared microspectrometry, *Proc. Natl. Acad. Sci. USA* 95:4837–4840.

Jones, D.J., Potma, E.O., Cheng, J.X., Burfeindt, B., Pang, Y., Ye, J., and Xie, X.S., 2002, Synchronization of two passively mode-locked, ps lasers within 20 fs for coherent anti-Stokes Raman scattering microscopy, *Rev. Sci. Instr.* 73:2843–2848.

Jones, R.J., and Ye, J., 2002, Femtosecond pulse amplification by coherent addition in a passive optical cavity, *Opt. Lett.* 27:1848–1850.

Kamga, F.M., and Sceats, M.J., 1980, Pulse-sequenced coherent anti-Stokes Raman scattering spectroscopy: A method for suppression of the non-resonant background, *Opt. Lett.* 5:126–128.

Kawamura, M., Jennis, D.F., Wancewicz, E.V., Joy, L.L., Khoo, J.C., and Steinberg, D., 1981, Hormone-senitive lipase in differentiated 3T3-L1 cells and its activation by cyclic AMP-dependent protein kinase, *Proc. Natl. Acad. Sci. USA* 78:732–736.

Kee, T.W., and Cicerone, M.T., 2004, Simple approach to one-laser, broadband coherent anti-Stokes Raman scattering microscopy, *Opt. Lett.* 29:2701–2703.

Kleinman, D.A., 1962, Nonlinear dielectric polarization in optical media, *Phys. Rev.* 126:1977–1979.

Laubereau, A., and Kaiser, W., 1978, Vibrational dynamics of solids and liquids investigated by picosecond light pulses, *Rev. Mod. Phys.* 50:607–665.

Levenson, M.D., and Kano, S.S., 1988, *Introduction to Nonlinear Laser Spectroscopy*, Academic Press, San Diego, California.

Maeda, S., Kamisuki, T., and Adachi, Y., 1988, Condensed phase CARS, *In*: *Advances in NonLinear Spectroscopy* (R.J.H. Clark and R.E. Hester, eds.), John Wiley and Sons, New York, p. 253.

Magde, D., Elson, E., and Webb, W.W., 1972, Thermodynamic fluctuations in a reacting system — Measurement by fluorescence correlation spectroscopy, *Phys. Rev. Lett.* 29:705–708.

Maiti, S., Hapts, U., and Webb, W.W., 1997, Fluorescence correlation spectroscopy: Diagnostics for sparse molecules, *Proc. Natl. Acad. Sci. USA* 94:11753–11757.

Maker, P.D., and Terhune, R.W., 1965, Study of optical effects due to an induced polarization third order in the electric field strength, *Phys. Rev.* 137:A801–A818.

Moreaux, L., Sandre, O., and Mertz, J., 2000, Membrane imaging by second-harmonic generation microscopy, *J. Opt. Soc. Am. B* 17:1685–1694.

Mukamel, S., 1995, *Principles of Nonlinear Optical Spectroscopy*, Oxford University Press, New York.

Müller, M., and Schins, J.M., 2002, Imaging the thermodynamics state of lipid membranes with multiplex CARS microscopy, *J. Phys. Chem. B* 106: 3715–3723.

Müller, M., Squier, J., Lange, C.A.D., and Brakenhoff, G.J., 2000, CARS microscopy with folded BOXCARS phasematching, *J. Microsc.* 197:150–158.

Müller, M., Squier, J., Wilson, K.R., and Brakenhoff, G.J., 1998, 3D-microscopy of transparent objects using third-harmonic generation, *J. Microsc.* 191:266–274.

Murphy, D.J., 2001, The biogenesis and functions of lipid bodies in animals, plants and microorganisms, *Prog. Lipid Res.* 40:325–438.

Nan, X.L., Cheng, J.X., and Xie, X.S., 2003, Vibrational imaging of lipid droplets in live fibroblast cells with coherent anti-Stokes Raman scattering microscopy, *J. Lipid Res.* 44:2202–2208.

Oron, D., Dudovich, N., and Silberberg, Y., 2003, Femtosecond phase-and-polarization control for background-free coherent anti-Stokes Raman spectroscopy, *Phys. Rev. Lett.* 90:213902–1.

Oron, D., Dudovich, N., Yelin, D., and Silberberg, Y., 2002, Quantum control of coherent anti-Stokes Raman process, *Phys. Rev. A.* 65:0434081–0434084.

Otto, C., Voroshilov, A., Kruglik, S.G., and Greve, J., 2001, Vibrational bands of luminescent zinc(II)-octaethyl-porphyrin using a polarization-sensitive "microscopic" multiplex CARS technique, *J. Raman Spectrosc.* 32:495–501.

Oudar, J.-L., Smith, R.W., and Shen, Y.R., 1979, Polarization-sensitive coherent anti-Stokes Raman spectroscopy, *Appl. Phys. Lett.* 34:758–760.

Potma, E.O., and Xie, X.S., 2003, Detection of single lipid bilayers in coherent anti-Stokes Raman scattering (CARS) microscopy, *J. Raman Spectrosc.* 34:642–650.

Potma, E.O., and Xie, X.S., 2004, CARS microscopy for biology and medicine, *Opt. Photonic News* 15:40–45.

Potma, E.O., and Xie, X.S., 2005, Direct visualization of lipid phase segregation in single lipid bilayers with coherent anti-Stokes Raman scattering (CARS) microscopy, *Chemphyschem* 6:1–3.

Potma, E.O., de Boeji, W.P., and Wiersma, D.A., 2000, Nonlinear coherent four-wave mixing in optical microscopy, *J. Opt. Soc. Am. B* 17:1678–1684.

Potma, E.O., de Boeji, W.P., Haastert, P.J., and Wiersma, D.A., 2001, Real-time visualization of intracellular hydrodynamics in single living cells, *Proc. Natl. Acad. Sci. USA* 98:1577–1582.

Potma, E.O., Evans, C., Xie, X.S., Jones, R.J., and Ye, J., 2003, Picosecond pulse amplification with an external passive optical cavity, *Opt. Lett.* 28:1835–1837.

Potma, E.O., Jones, D.J., Cheng, J.X., Xie, X.S., and Ye, J., 2002, High-sensitivity coherent anti-Stokes Raman microscopy with two tightly synchronized picosecond lasers, *Opt. Lett.* 27:1168–1170.

Puppels, G.J., 1999, Confocal Raman microscopy, *In*: *Fluorescent and Luminescent Probes for Biological Activity* (W.T. Mason, ed.), Academic Press, New York, p. 377.

Richards, B., and Wolf, E., 1959, Electromagnetic diffraction in optical systems II. Structure of the image field in an aplanatic system, *Proc. Roy. Soc. A* 253:358–379.

Schneider, S., Baumann, F., Klüter, U., and Gege, P., 1988, Resonance-enhanced CARS spectroscopy of biliproteins, *Croat. Chem. Acta* 61:505–527.

Shafer-Peltier, K.E., Haka, A.S., Fitzmaurice, M., Crowe, J., Myles, J., Dasari, R.R., and Feld, M.S., 2002, Raman microspectroscopic model of human breast tissue: implications for breast cancer diagnosis *in vivo*, *J. Raman Spectrosc.* 33:2002.

Shen, Y.R., 1984, *The Principles of Nonlinear Optics*, John Wiley and Sons, New York.

Shirley, J.A., Hall, R.J., and Eckbreth, A.C., 1980, Folded BOXCARS for rotational Raman studies, *Opt. Lett.* 5:380–382.

Siegman, A.E., 1986, *Lasers*, University Science Books, Mill Valley, California.

Toleutaev, B.N., Tahara, T., and Hamaguchi, H., 1994, Broadband ($1000\,cm^{-1}$ multiplex CARS spectroscopy: Application to polarization sensitive and time-resolved measurements, *Appl. Phys. B* 59:369–375.

Tolles, W.M., Nibler, J.W., McDonald, J.R., Harvey, A.B., 1977, A review of the theory and application of coherent anti-Stokes Raman spectroscopy (CARS), *Appl. Spectrosc.* 31:253–272.

Turrell, G., and Corset, J., 1996, *Raman Microscopy: Development and Applications*, Academic Press, San Diego, California.

Ujj, L., Volodin, B.L., Popp, A., Delaney, J.K., and Atkinson, G.H., 1994, Picosecond resonance coherent anti-Stokes Raman spectroscopy of bacteriorhodopsin: Spectra and quantitative third-order susceptibility analysis of the light-adapted BR-570, *Chem. Phys.* 182:291–311.

Volkmer, A., Book, L.D., and Xie, X.S., 2002, Time-resolved coherent anti-Stokes Raman scattering microscopy: Imaging based on Raman free induction decay, *Appl. Phys. Lett.* 80:1505–1507.

Volkmer, A., Cheng, J.X., and Xie, X.S., 2001, Vibrational imaging with high sensitivity via epi-detected coherent anti-Stokes Raman scattering microscopy, *Phys. Rev. Lett.* 87:023901.

Voroshilov, A., Lucassen, G.W., Otto, C., and Greve, J., 1995, Polarization-sensitive resonance CSRS of deoxy- and oxyhaemoglobin, *J. Raman Spectrosc.* 26:443–450.

Voroshilov, A., Otto, C., and Greve, J., 1996, Secondary structure of bovine albumin as studied by polarization-sensitive multiplex CARS spectroscopy, *Appl. Spectrosc.* 50:78–85.

Wurpel, G.W.H., Rinia, H.A., and Müller, M., 2005, Imaging orientational order and lipid density in multilamellar vesicles with multiplex CARS microscopy, *J. Microsc.* 218:37–45.

Yelin, D., and Silberberg, Y., 1999, Laser scanning third-harmonic-generation microscopy in biology, *Opt. Express* 5:169–175.

Yelin, D., Oron, D., Korkotian, E., Segal, M., and Silberberg, Y., 2002, Third-harmonic microscopy with a titanium-sapphire laser, *Appl. Phys. B.* 74:S97–S101.

Zumbusch, A., Holtom, G.R., and Xie, X.S., 1999, Three-dimensional vibrational imaging by coherent anti-Stokes Raman scattering, *Phys. Rev. Lett.* 82:4142–4145.

34

Related Methods for Three-Dimensional Imaging

J. Michael Tyszka, Seth W. Ruffins, Jamey P. Weichert, Michael J. Paulus, and Scott E. Fraser

INTRODUCTION

The ability of confocal laser-scanning microscopy to collect stacks of optical sections has made three-dimensional (volumetric) imaging a standard analytical tool in experimental cell and developmental biology. Parallel developments in deconvolution techniques, especially as computational power increased and costs decreased, offered tools to make three-dimensional (3D) imaging from widefield as well as confocal microscopes possible. Despite the high spatial resolution provided by these 3D methods, they all suffer from a common limitation: light scattering in the specimen limits them to operating in the outer few hundred micrometers of the specimen. Even the greater depth of penetration and reduced photobleaching provided by two-photon laser-scanning microscopy falls short for larger specimens such as embryos. To perform volumetric imaging on larger specimens, alternative approaches are needed. This chapter examines four light-optical methods: surface imaging microscopy (SIM), optical coherence tomography (OCT), optical projection tomography (OPT), and the recently developed selective plane illumination microscope (SPIM), as well as microscopic magnetic resonance imaging (μMRI) and microscopic computed tomography (CT) as potential solutions to the challenges of collecting high-quality 3D image data.

Each of these volumetric imaging methodologies has particular strengths and limitations; no single method addresses all 3D imaging requirements. SIM (also referred to as episcopic fluorescence image capture (EFIC) takes a brute force approach, physically sectioning the specimen and obtaining a series of two-dimensional images that can later be assembled into a volumetric reconstruction. Both OPT and OCT employ different tomographic approaches to obtain data from the depth of the specimen, building up a 3D model from a series of 2D data sets. OPT transilluminates the specimen, and collects a large number of 2D images from different orientations; OCT uses depth encoding of reflected light and is conceptually similar to ultrasound imaging. SPIM represents a hybrid between these approaches, using transverse, sheet-like illumination to generate series of 2D image stacks from different orientations that can be assembled with computational tools. Finally, μMRI and micro-computerized tomography (micro-CT) are non-optical. The former derives image contrast from the water contained in the specimen. This permits the entire volume of an opaque object to be imaged. The latter is merely a micro version of the CAT scanner used in hospitals. We will describe each of these techniques and suggest how each might be used.

SURFACE IMAGING MICROSCOPY AND EPISCOPIC FLUORESCENCE IMAGE CAPTURE

Surface imaging microscopy is a form of physical serial sectioning where one images the cut face of the embedded specimen instead of the ribbon of removed sections.

A SIM/EFIC device is essentially a widefield microscope mounted on a precision microtome. Dry objectives ranging from 2× to 40× magnification are used to image the face of the embedding block to an in-plane resolution of 8.8 to 0.4 μm, respectively. As each section is cut, the face of the remaining block is recorded with a charge-coupled device (CCD) camera (Ewald *et al*., 2002, 2004; Weninger and Mohun, 2002) (Fig. 34.1). The stack of images is then reconstructed into a high-resolution image volume.

Imaging the block face rather than the ribbon has significant advantages. The mass of embedding medium supports the specimen and minimizes sectioning artifacts such as compression, folding, and tearing. Perfectly-registered data volumes are easily reconstructed as the block face is photographed at the same position in the microtome's sectioning cycle.

SIM/EFIC is a fluorescence imaging modality that relies on endogenous autofluorescence or exogenous dye labeling of the specimen. To prevent out-of-focus fluorescence from compromising image quality, specimens are embedded in highly light absorbent black paraffin or dark embedding resins; the opacity of the embedding medium can be adjusted to match the in-plane resolution of the objective being used and the section thickness, producing isotropic image volumes (Fig. 34.2). SIM can produce stunning 3D image volumes with isotropic voxel resolutions of ~0.5 μm.

At such high resolution, individual cell morphology can be examined within the context of tissues and entire organisms. SIM has been used in morphogentic studies to reveal the relationship between cell morphology and overall tissue shape and to follow the changes that occur during embryonic development (Ewald *et al*., 2002). SIM has also been used in the materials sciences to understand how microscopic structure relates to the strength, feel, texture, and other properties of textiles and papers.

SIM, however, is a destructive imaging modality that allows no other data collection from a given specimen. In combination with the non-destructive methods discussed below, SIM can be used to add a content-rich description of a single specimen.

J. Michael Tyszka, Seth W. Ruffins, and Scott E. Fraser • California Institute of Technology, Pasadena, California 91125
Jamey P. Weichert • University of Wisconsin, Madison, Wisconsin 53706
Michael J. Paulus • ORNL and CTI-Concorde Microsystems, Knoxville, Tennessee 37932

Handbook of Biological Confocal Microscopy, Third Edition, edited by James B. Pawley, Springer Science+Business Media, LLC, New York, 2006.

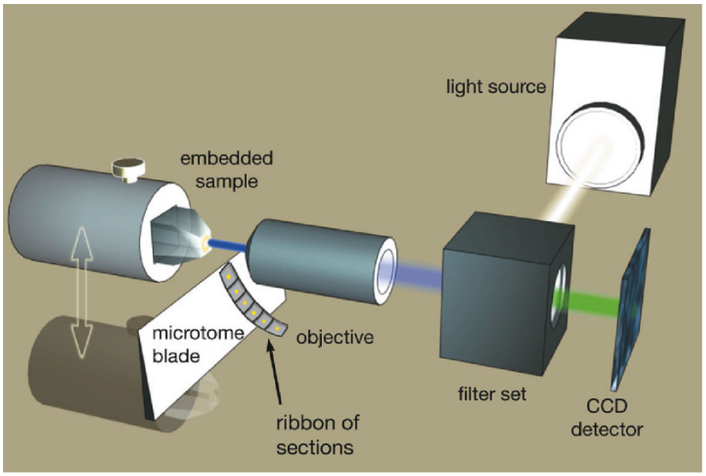


FIGURE 34.1. Surface imaging microscopy/episcopic fluorescence image capture setup. SIM/EFIC is a block-face imaging modality. Essentially, a microtome is outfitted with a microscope imaging system. A sample is embedded in an opaque medium and sectioned using a diamond knife. A horizontally-mounted microscope captures an image of the block face as the chuck returns to a specific position after each section is cut. The resulting image series is reconstructed into a perfectly-registered image volume with high resolution.

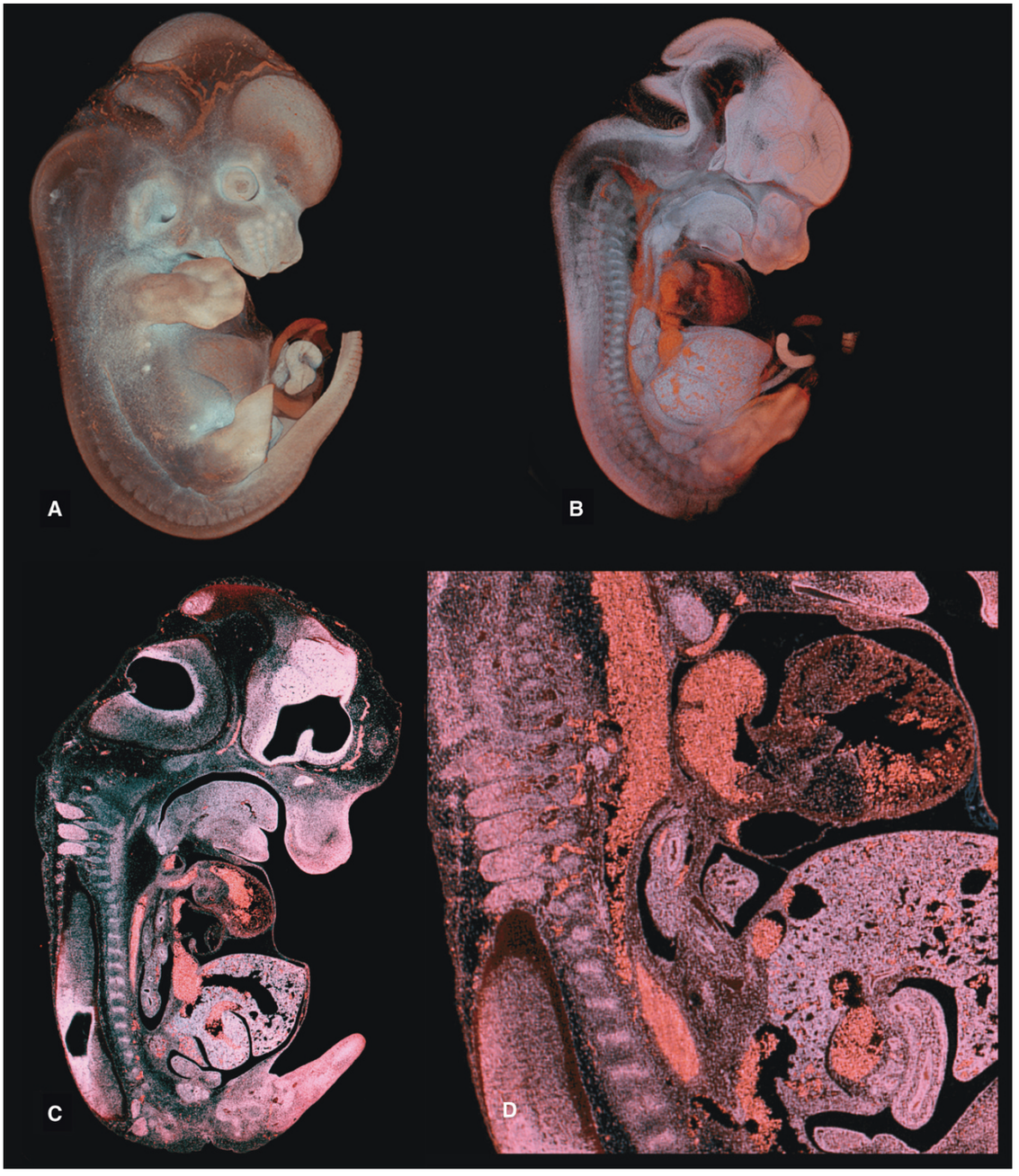


FIGURE 34.2. SIM of 12.5 dpc mouse embryo stained with fluorescent analog of H&E staining. The image volume was collected with a 2× objective and provides approximately 8 µm/pixel resolution. This data volume is 1517 × 1016 × 664 pixels. (A) Whole embryo view shows external structures with high fidelity. (B) A slab section ~1700 µm thick. (C) A single section through the embryo, and (D) the high magnification view. SIM provides a global view of the specimen at near cellular resolution.

OPTICAL COHERENCE TOMOGRAPHY

Optical coherence tomography (Huang *et al*., 1991; Tearney *et al*., 1997; Masters, 1999) is well suited to examining tissue geometry and organization, even in living, unstained tissues (Boppart *et al*., 1996, 1997, 1998; Yazdanfar *et al*., 1997; Rollins *et al*., 1998). OCT is based upon the reflection/backscattering of light and is not unlike sonar, detecting the amount of light reflected from different depths (up to a few millimeters) in the specimen to build up a voxel-by-voxel image. The challenge of OCT is to optically section the huge amount of backscattered light to create an image of a single plane at depths several-fold greater than the mean free path of light in the specimen. To meet this challenge, OCT uses interference between the light reflected by the specimen and the light reflected by a reference mirror to isolate individual optical sections.

Although its ability to image deep in a specimen far outperforms confocal microscopy, an OCT shares many features with the optics of a reflected light confocal microscope. An OCT microscope images the output of an optical fiber through an objective lens, and re-images the backscattered signal from specimen into the same fiber, creating a confocal aperture; the difference is that an OCT uses a short coherence length light source and an interferometer to add a "coherence gate" that suppresses the signal from out-of-focus planes by 6 orders of magnitude (Rollins and Izatt, 1999). The Michelson interferometer of a typical OCT is created from optical fibers; the beam-splitter is created by fusing the two optical fibers into a 2×2 coupler. The reference arm fiber is terminated with a collimating lens and retro-reflector; the specimen arm is terminated by a collimating lens, beam-steering galvonometers, and an imaging lens such as a microscope objective. Both the length of the two arms and the materials must be closely matched to avoid unequal group velocity dispersion in the specimen and reference arms. The creation of interference fringes involves modulating the length of the arms by means ranging from stretching the optical fibers with piezoelectric devices to a grating-based phase-delay retro-reflector.

In an OCT, the signal is derived from interference fringes, as light back-reflected from the reference mirror and the specimen interferes coherently. Fringes will only result if the optical path lengths of the reference and specimen arms are equal to within half of the coherence length of the light source (the "coherence gate"). Signal from multiply-scattered photons are rejected by the concerted action of the confocal aperture and the coherence gate. The frequency of the interference fringes is set by the motion of the reference reflector (or interferometer arms), giving the detection electronics a defined lock-in frequency to detect, and thereby rejecting the signal from light that is backscattered (but not interfering) from above and below the focal plane. Thus, resolution of an OCT microscope is set by two factors: the coherence length of the light source (for depth) and the size of the illuminated spot (for lateral resolution).

A typical OCT generates a scan perpendicular to the surface, much like the *xz*-scans generated in confocal microscopy, creating a slice through the depth of the specimen (Fig. 34.3). A galvonometer mirror translates the beam in one axis; at each spot along this line, a rapid change in the length of the reference arm (changing the length or the retro-reflector position) scans the coherence volume by millimeters. Such a rapid depth scan with a slower lateral scan creates an image reminiscent of that created by ultrasonography. Volumetric (3D) images can be assembled by collecting a series of neighboring depth scans. OCT scans can be generated quickly, with depth discrimination set by the coherence length of the light source; however, the lateral resolution of the images is typically compromised because the coherence volume must move very rapidly in depth, much more rapidly than it is possible to refocus the light in the specimen. As a result, the lens focusing the light into the specimen must employ a relatively shallow convergence angle so that the spot size does not change too dramatically over the ±2 mm motion of the coherence volume in depth. Thus, B-mode instruments often achieve resolutions of less than 10 μm in depth, but greater than 10 μm in lateral extent (see Izatt *et al*., 1996). Given the laminar organization of many

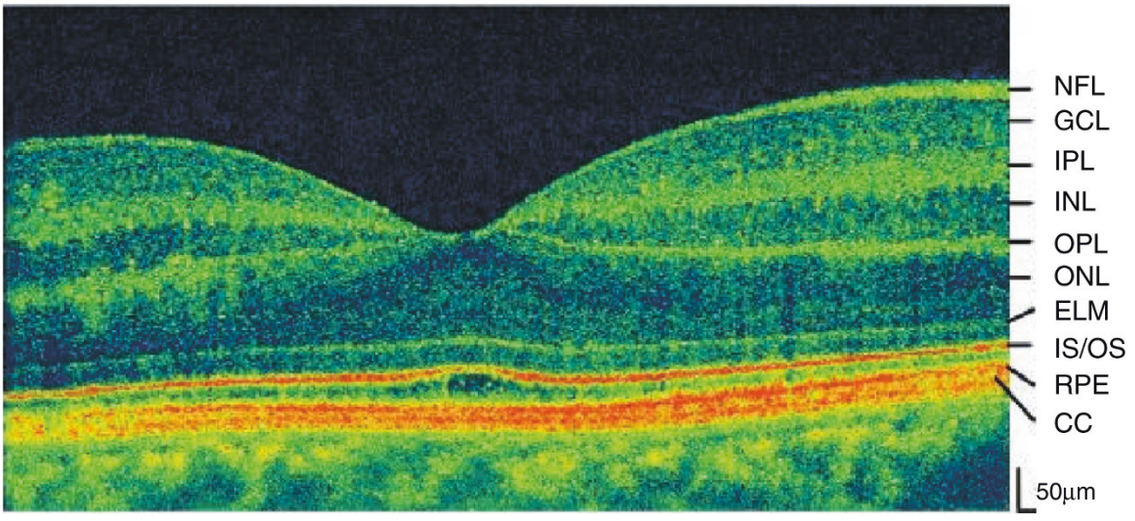


FIGURE 34.3. *In vivo* ultrahigh resolution OCT B mode (*xz*) section through a human retina, viewed through the cornea. A depth resolution of less than 5 microns was achieved using a very broad bandwidth light source. Transverse resolution was limited by the numerical aperture of the lens in the human eye and by imperfections in its optical characteristics. Abbreviations: NFL = Nerve Fiber Layer, GCL = Ganglion Cell Layer, IPL = Inner Plexiform Layer, INL = Inner Nuclear Layer, OPL = Outer Plexiform Layer, ONL = Outer Nuclear Layer, ELM = External Limiting Membrane, IS/OS = Photoreceptor Inner/Outer Segment Junction, RPE = Retinal Pigment Epithelium, CC = *Choriocapillaris*. (Reproduced with permission from Wojtkowski, 2004 © Optical Society of America.)

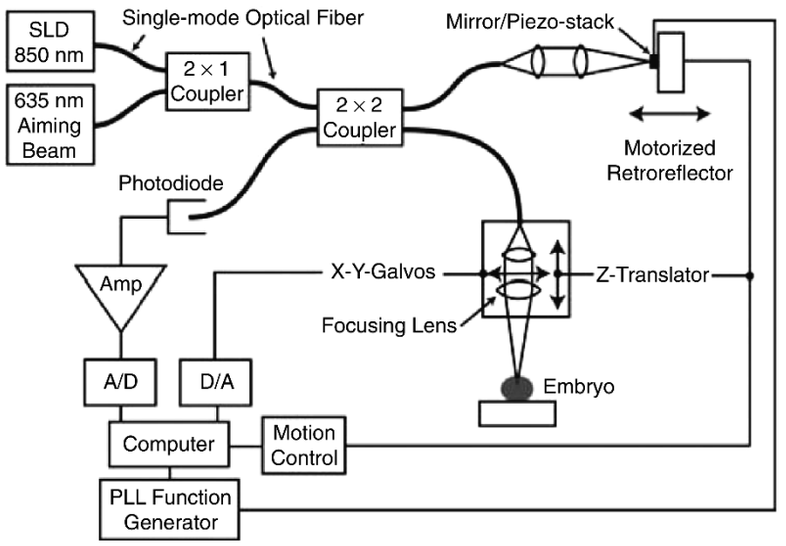


FIGURE 34.4. Schematic of an *en face* OCT system. The superluminescent diode (SLD), which provides the broad bandwidth light for OCT imaging, is combined with an alignment laser diode at 635 nm using a 2 × 1 coupler. The 2 × 2 coupler splits the light between the sample arm with the focusing lens and the reference arm with the motorized retro-reflector. The reflected light from both arms interferes and is measured by the photodiode at the output of the 2 × 2 coupler. Electronic demodulation of the photodiode signal produces an OCT signal for a given depth position in the sample. Transverse scanning and subsequent depth scanning produce a 2D *en face* image and a 3D image, respectively. (Reproduced with permission from Haskell *et al*., 2004 © IEEE.)

specimens, such as the layered organization of the retina, striking images can result.

En face OCT is an alternative approach for OCT imaging that can optimize lateral resolution by using a higher numerical-aperture (NA) imaging lens (Hoeling *et al*., 2000, 2001). A smaller spot size, more similar to that used in confocal microscopy is created, and galvomometer mirrors are used to scan the beam through a complete optical section (Fig. 34.4). The focal depth and coherence depth must be aligned to the same optical section by the positioning of the retro-reflector. Interference fringes are generated by changing the length of the reference arm, typically by oscillating a small mirror or by using an acousto-optical device, by an amount far less than the coherence length. Thus, the depth resolution is set at roughly half the coherence length of the light source. Volumetric images are built up from collecting a series of 2D (*en face*) scans, adjusting the focus (and coherence depth) after each scan to build up a *z*-series of images (Fig. 34.5). Given the performance of inexpensive wide-bandwidth light sources, and the index of refraction of tissue (>1.3), *en face* OCT microscopy can generate images with isotropic resolution of ~5 µm.

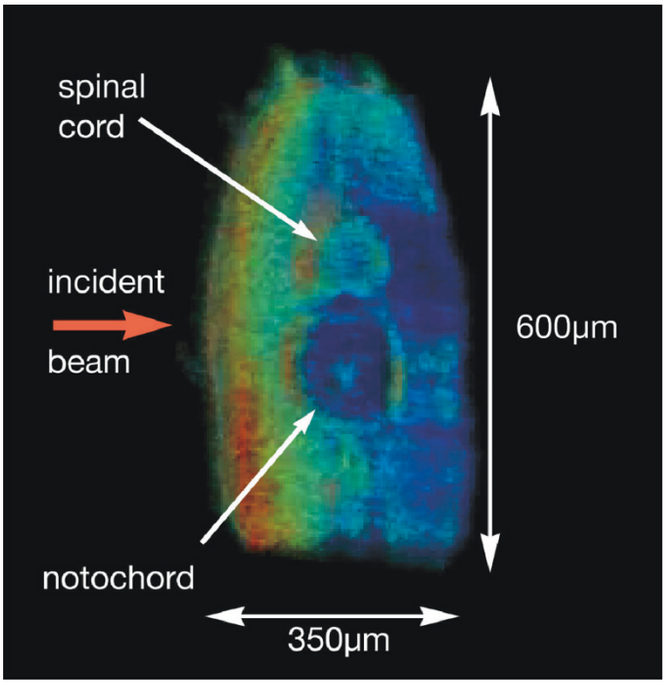


FIGURE 34.5. OCT section of a paraformaldehyde-fixed stage 41 *Xenopus laevis* embryo viewed along the spinal cord from the tail towards the head with dorsal at the top of the figure. The beam is incident from the left side of the embryo and the colorscale encodes backscatter intensity from blue (low) to red (high). (Reproduced with permission from Hoeling *et al*., 2000. © Optical Society of America.)

OPTICAL PROJECTION TOMOGRAPHY

Optical projection tomography is a projection tomographic method akin to X-ray computed axial tomography (commonly called CT or CAT, see micro-CT below) and electron microscopy tomography (EMT). Like other projection tomogram methods, OPT uses 2D projections of 3D objects to reconstruct the volume of an object using a Radon-backplane reconstruction algorithm (for review, see Herman, 1980). Each point in the projected image is the result of the cumulative absorption or emission of light rays propagating through an object. OPT operates in both bright-field (transmission) and fluorescence (emission) modes and is proving useful in capturing patterns of gene expression and antibody staining *in situ*. Image volumes reconstructed from projection tomogram data differs from the optical and physical sectioning methods described above in that the location of features within an object are not explicitly sampled. Instead, the location of features is computed from a series of 2D projections collected from many axial positions around the object.

An OPT instrument is a relatively simple device consisting of a sample chamber with a rotating sample platform, imaging optics for capturing projections, and a diffuse light source for bright-field mode (Fig. 34.6). In fluorescence mode, the imaging optics are used for widefield illumination of the specimen. OPT requires that the specimen be transparent and indexed-matched with the surrounding media to permit light to pass through the object with minimal refraction. Currently this is achieved by clearing and imaging specimens in a mixture of benzyl alcohol and benzyl benzoate (BABB). Typically, a sample is suspended in agarose and

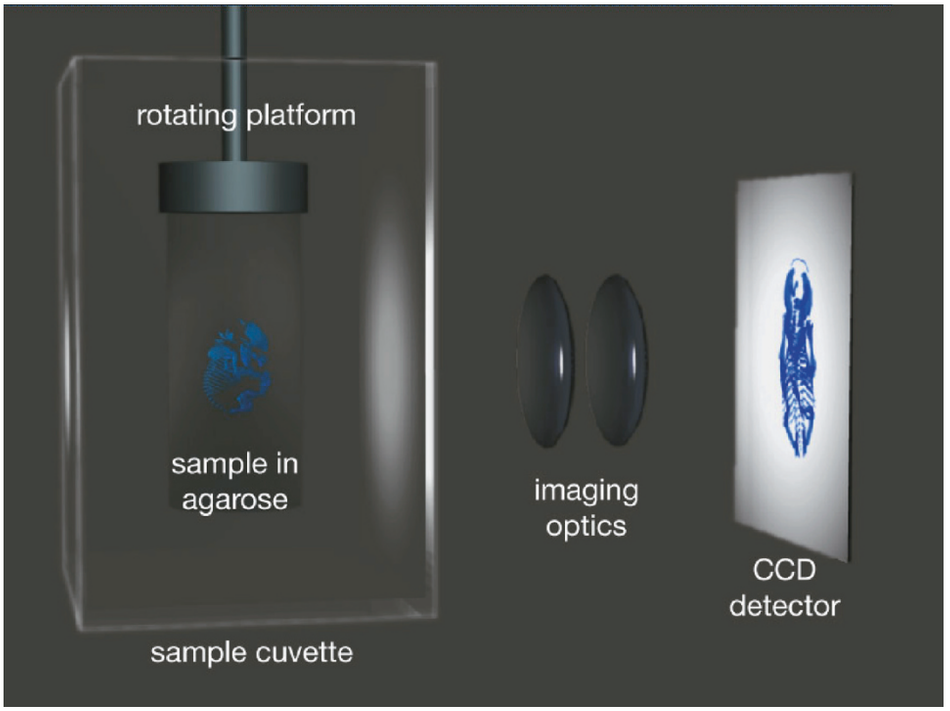


FIGURE 34.6. Optical projection tomography setup (bright-field mode). (A) Cleared specimen is suspended in agarose gel, mounted to a rotating platform, and placed in chamber containing indexed-matched media. Imaging optics (B) are used to focus the projected image and reject light scattered by the specimen. The projected image (C) is collected with a CCD camera. Multiple projections are used to reconstruct an image volume.

serially dehydrated in methanol and then cleared in BABB. The sample in the agarose block is placed onto the rotating stage in a sample chamber containing BABB (Sharpe *et al*., 2002).

X-ray computed axial tomography (CAT or CT) and electron microscopy tomography (EMT) assume that the specimen is transparent to the probing rays and that refraction is non-existent. The paths of the projected rays are straight and produce a perfect "shadow projection." Because, in fact, the probing light rays are susceptible to scatter and some degree of diffraction and refraction as they pass through the specimen, the resulting projection is "confused" and blurred as it is composed of rays that have followed the predicted path through the subject as well as stray rays. The imaging optics focus the projection and collimate the rays that are projected along an approximately straight path through the sample (Fig. 34.7).

The limited depth of focus inherent in all optical microscope systems requires that modifications be made to the collection and projection reconstruction (Sharpe, 2004). Projections captured by OPT represent only the volume residing within the region of the depth of focus. During imaging, the center of focus is set to a plane approximately half the distance between the axis of rotation and the near side of the specimen. Because each projection only represents about half the specimen volume, a complete projection set requires the specimen be rotated through 360° at 0.9° intervals. Volume reconstruction is performed using a modified back-plane projection algorithm to compensate for the limited projected volume.

For small objects (on the order of 5 mm diameter) light scatter is not severe and internal details can be readily resolved. The

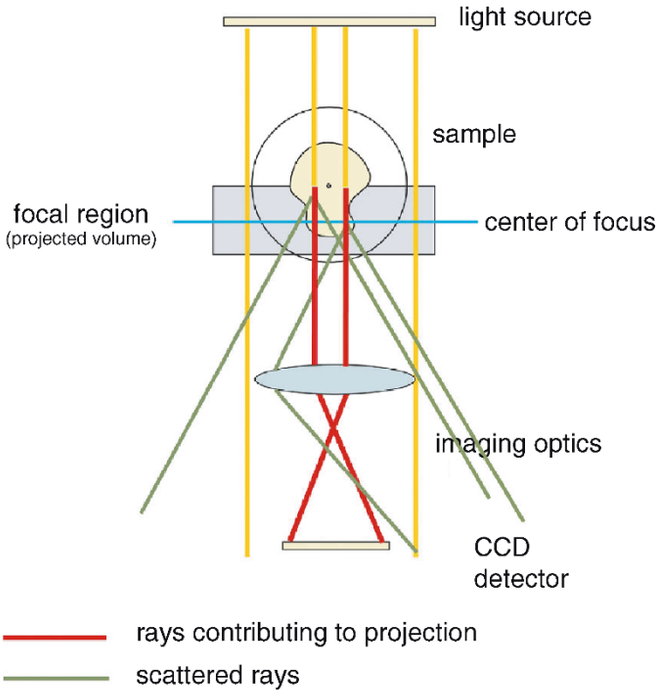


FIGURE 34.7. Due to the limited focal depth of the imaging optics, the focus is set to the region between the axis of rotation and the imaging optics. Each projection represents only half the specimen volume requiring that the subject be rotated through 360° to collect a full projection set.

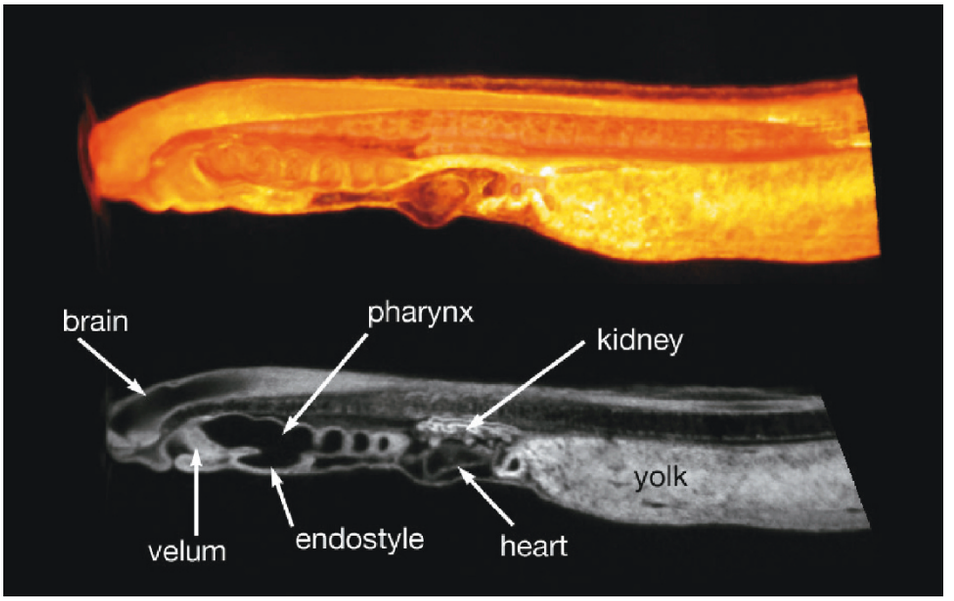


FIGURE 34.8. Autofluorescent OPT reconstruction of 17-day lamprey larva. The larva was imaged using a Texas Red filter set and mounted with the anterior–posterior axis (long axis) along the axis of rotation. The light path is between 1.5 to 3 mm (left–right, dorsal–ventral axis, respectively). The larva is virtually opaque in visible light yet internal structures are easily identifiable using near IR autofluorescence.

quality of the projections diminishes as the objects imaged become larger because of the increased light scattering. The result is that fewer internal details are resolved, and opaque regions, such as highly pigmented tissues, similarly degrade the projections (Fig. 34.5).

The time required to collect a complete projection set (400 images) ranges between 3 (for bright-field and strong fluorescent signals) and 15 min, depending on signal strength. Current reconstruction performance is about 6 min for a 512^3 voxel image volume on a standard 4 GHz Pentium 4 class workstation.

OPT has only recently become a practical device for routine 3D imaging, but it is proving to be useful as an analytical tool for developmental biology as it is capable of imaging anatomy, gene expression patterns and the distribution of specific cell populations, extracellular matrix components, etc., as revealed by antibody labeling. One of its first uses was to collect anatomical data of early human and mouse development for the creation of volumetric atlases for the analysis of aberrant embryogenesis (Sharpe, 2003; Kerwin *et al*., 2004; Robson *et al*., 2004).

The anatomy of unlabeled embryos can be collected in either bright-field and/or fluorescent modes. Each modality reveals different features depending on the wavelength of the probing light. In the bright-field mode, tissue transparency increases as the illumination moves into the near-infrared (IR), allowing deeper imaging of larger embryos. Structures that are opaque in visible light, such as the pigmented retina, can be imaged using transmitted light at these longer wavelengths. In the fluorescence mode, the vasculature is revealed as blood fluoresces brightly when Texas Red filter sets are used (562 nm excitation to 624 nm emission). The autofluorescence of the lamprey larva has been used to reveal internal structures without physical sectioning (Fig. 34.8). However, the information content within an embryo is not limited to its intrinsic optical properties. Cell- and tissue-specific chemical composition can be made visible using labeled antibodies and classic histological stains while RNA hybridization and green fluorescent protein (GFP) reporter constructs show gene activity. Many of these protocols are compatible with OPT imaging.

Bright-field OPT has successfully been used to image the intricate spatial arrangement of the developing skeleton using the common histological stain Alcian Blue (Fig. 34.9). *In situ* RNA



FIGURE 34.9. Bright-field OPT reconstruction of Alcian Blue stained 12.5 dpc mouse embryo. Non-ossified skeletal elements stained with Alcian Blue reveal the intricate and delicate structure of the fetal mouse. Note that dermal bone has not yet formed.

hybridization reveals the global pattern of specific gene activity using a color precipitate indicator. Standard whole-mount photography reveals regions of gene activity but sections are needed to define the precise location of expressing tissues and cells. Once sectioned, the 3D context is lost. Additionally, weak signals may not be detected in thin sections. OPT is a powerful tool in that a single imaging experiment places local and specific activity in the context of the entire embryo. Potentially, OPT may be able to capture weak signals as projections that are cumulative through the sample volume (up to 2 mm compared with 10–15 µm for histological sections).

OPT requires that the light rays be able to pass through the object with minimal scatter. This limits OPT use to transparent specimens with a homogeneous refractive index (RI). Thus far, OPT has primarily been used for fixed specimens but there is a potential for imaging live specimens, such as tissue explants and early embryogenesis of aquatic organisms. This method could be used for time-lapse studies with the shortest interval being the time required to acquire a full set of projections. Currently, the minimum time interval for collecting 400 projections is about 3 min but as there is a trade-off between spatial resolution and number of projections, one can acquire a smaller set of images more rapidly if one is willing to settle for less resolution.

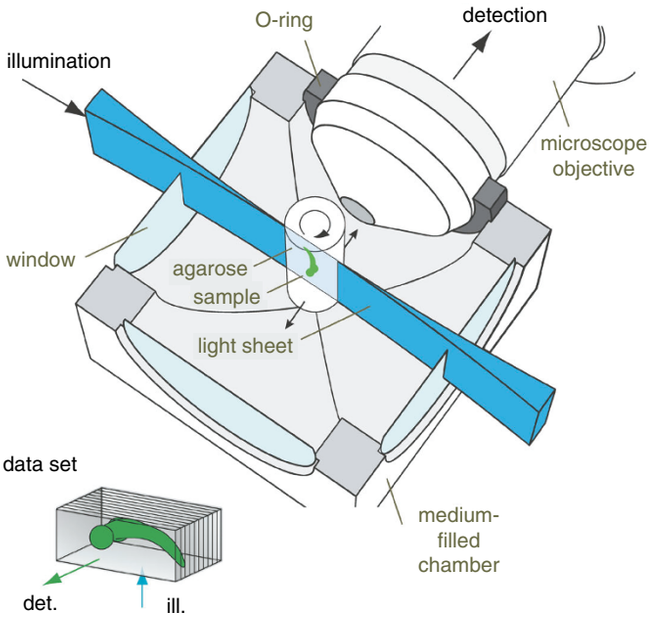


FIGURE 34.10. Selective plane illumination microscope (SPIM) setup. The specimen is suspended in agarose in a medium-filled sample chamber. The SPIM device optically sections the sample as it is illuminated by a "light sheet" perpendicular to the imaging axis and coincident with the focus plane of the imaging optics. The sample can be rotated to collect multiple views for the reconstruction of subjects that cannot be imaged through their entire volume.

LIGHT SHEET MICROSCOPY

"Light sheet" fluorescence microscopy, originally developed by Voie (1995, 2002), is an optical-sectioning technique whereby only the plane being imaged is illuminated. The concept is not unlike that of multi-photon microscopy in that only the fluorophores in the focus plane are excited, thus minimizing photodamage. Rather than using the imaging optics to illuminate the specimen, as in epi-fluorescence microscopes, light-sheet microscopy uses separate illumination optics to produce an illuminated layer perpendicular to the imaging axis. Optical sectioning is achieved by moving the light sheet through the specimen coincident with the focus plane of the imaging optics (also see Chapter 37, *this volume*).

Optical Setup

Selective plane illumination microscopy (SPIM) is the name given to an updated version of light-sheet microscopy developed by the Stelzer group at the EMBL/Heidelberg. In this system, the microscope optics are arranged horizontally to accommodate a cylindrical sample immersed in a fluid-filled sample chamber and capable of being rotated around its vertical axis. This arrangement provides an ideal environment for imaging living specimens as it permits the media to be replaced and additional agents, such as nutrients, growth factors, gases, etc., to be introduced during imaging. Samples are typically suspended in soft agarose and placed into the sample chamber containing liquid medium. The sample is imaged using a water dipping lens inserted through one wall of the sample chamber. Windows on the lateral walls (perpendicular to the imaging axis) allow the light sheet to illuminate the specimen. The light sheet is formed by passing collimated laser light through a cylindrical lens and controls are provided to adjust the thickness and convergence of this sheet (Huisken *et al*., 2004) (Fig. 34.10).

The lateral (*xy*) resolution of SPIM is limited by the light scattering and absorption properties of the specimen being imaged while the axial (*z*) resolution is dependent on the thickness of the light sheet. The lateral penetration and scatter of the light sheet will affect the thickness and intensity of the illuminated layer across the field of view.

SPIM is an excellent imaging modality for transparent specimens such as Medaka and zebrafish embryos. Developing larval Medaka fish have been imaged to a depth of 500 µm with an axial resolution of 6 µm. The imaging depth, however, is not great enough to encompass the entire embryo and images of deeper structures are of a lower quality than those of features near the surface. A solution to this problem has been to collect multiple image stacks from different views of the specimen. Each view produces a set of data that includes information not available in other views. Combining the multiple views into a single image volume produces a reconstruction of the entire specimen. Entire volumes nearly 2 mm thick can be reconstructed at a voxel size of ~5 µm.

SPIM is also useful as a tool for capturing dynamic events on time scales ranging from fractions of a second to days. The use of a narrow light sheet plane allows widefield optics to be used, maximizing the emitted light collection without compromising axial resolution. Maximizing light collection minimizes the excitation time required for each image. Short exposure times minimize photodamage and permit long-term imaging experiments. The use of high-speed cameras allows SPIM to be used for observing dynamic events such as the beating heart of a Medaka embryo (Fig. 34.11).

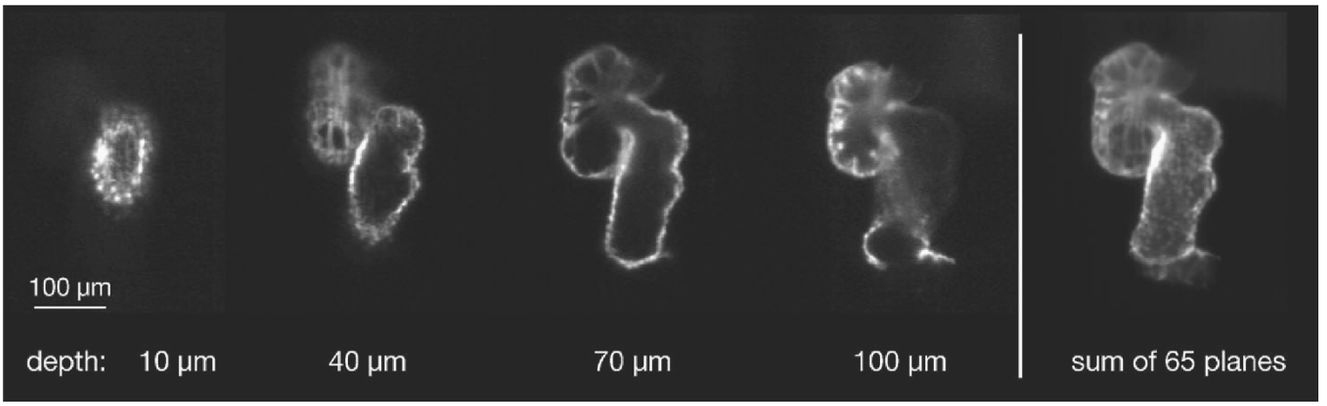


FIGURE 34.11. GFP expression in the developing heart of Medaka imaged by SPIM. Optical sectioning of Medaka heart tube can be performed because fluorescent signal is only emitted from the plane illuminated by of the light sheet. This series of images demonstrates the axial resolving capabilities of SPIM. Each image is separated by 30 µm along the imaging axis. The three-dimensional reconstruction is very good with no out-of-focus data confounding the image.

MICRO-COMPUTERIZED TOMOGRAPHY IMAGING

The recent introduction of commercial ultra-high-resolution laboratory micro-computerized tomography (micro-CT) scanners has revolutionized our ability to non-invasively examine tissues and organs in living experimental animal models, including mice, at spatial resolutions of less than 20 microns. In a 3D sense, this makes it possible to image a 1 µL volume *in vivo*. Several excellent reviews have recently appeared that discuss in detail the physical differences as well as the advantages and limitations associated with each type of small animal imaging system, including micro-CT (Paulus *et al.*, 2000, 2001; Holdsworth *et al.*, 2002).

Operating Principle

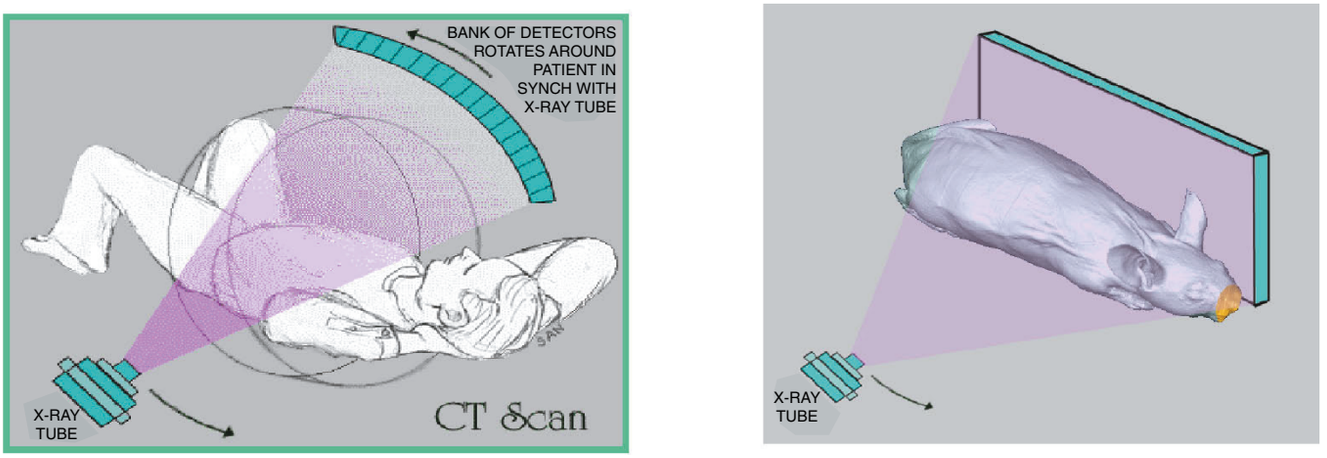
The general principles of micro-CT are similar to those used in clinical CT scanners. Most clinical systems consist of a high-power X-ray point source, between 1 and 64 rows of detector elements, and a mechanical gantry that rotates around the patient over a period of minutes [Fig. 34.12(A)]. X rays emitted by the source are collimated into a fan-shaped beam, oriented perpendicular to the rotation axis passing through the patient. Most of the X rays not absorbed by the patient are detected by the detector rows.

Contrast and Dose

The relationship between the X-ray flux emitted by the source, φ_0 and the detected flux, φ, is given by the expression

$$\phi = \phi_o \exp\left(-\int_l \mu_x dx \right)$$

where μ_x is the spatially-varying X-ray attenuation coefficient of the tissue and l is the path of the X rays. This expression may be solved to determine the line integral of the attenuation coefficient to yield



A B

FIGURE 34.12. (A) Layout of a CT scanner showing orientation of body, X-ray source, and detector for a hospital scanner (A) that collimates the X rays into a fan-shaped beam with the long axis parallel to the rotation axis and (B) a micro-CT that uses a cone-shaped X-ray beam and a large 2D X-ray detector that is slightly larger than the mouse and has an effective pixel size of 25 to 40 µm. The detector counts about 50% of the X-ray photons striking it (depending on kilovolts) and X rays passing through the body of the mouse are usually digitized to 10-bit accuracy (12- to 14-bits overall). The distance from the source to the rotation axis is variable from about 5 to 30 cm; shorter spacing gives shorter exposure times but lower MTF and more complex computations.

$$\int_l \mu_x dx = \ln\left(\frac{\phi_o}{\phi}\right)$$

Tomographic image reconstruction is the process of using a number of these integral expressions to calculate values for *m* in a 2D slice or 3D volume. The calculated values for the attenuation produced by each voxel are typically normalized to the attenuation coefficient of water and scaled following the expression

$$CT\ Number = \frac{\mu - \mu_{H_2O}}{\mu_{H_2O}} \times 1000.$$

Although the scaled attenuation coefficient is actually unitless, the reported values are typically cited in pseudo-units of *CT Numbers* or *Hounsfield Units*. Of course, like any other imaging system that relies on the detection of photons, micro-CT is limited by the Poisson noise associated with actually detecting the signal. However, simple calculations relating visibility to contrast and detected signal levels (such as those in Chapters 4 and 8, *this volume*) are complicated by the fact that the imaging algorithms extract 3D information from an entire series of between 90 and 360 2D projection images.

Micro-CT systems typically have poorer contrast resolution than clinical systems. The combination of small detector elements and low X-ray flux leads to signal-to-noise ratios in micro-CT systems that are typically an order of magnitude lower than those of their clinical counterparts. Signal-to-noise ratios can be improved by either increasing the detector element size (at the expense of resolution) or by increasing the number of X rays collected (at the expense of scan time and the dose to the animal).

As in other imaging modalities, the ability to discern structure depends on the contrast of the structure. Generally speaking, contrast in the raw data from the 2D X-ray detector goes down as the overall thickness of the object increases, and goes up as the attenuation of a feature varies from that of its surroundings (as measured in Hounsfield units). In the micro-CT, the kilovolts applied to the X-ray source changes both the peak and the average energy of the X rays emitted: higher energy X rays are more likely to penetrate through the mouse but usually show less differential attenuation (i.e., raw contrast). In theory, information about features with low contrast (soft tissue), will be maximized if about 60% of the X rays are absorbed in the mouse and the remaining 40% detected by the detector. In practice, much mouse work is done with the X ray source operating at ~80 kV (range, 40–100 kV), with the beam filtered through about 0.5 mm of Al to remove very low energy photons that can't penetrate the mouse but can cause damage.

In general, micro-CT scanners only have sufficient contrast resolution to differentiate between different soft tissue types after radio-opaque contrast agents have been added. Figure 34.13 illustrates the use of these compounds in micro-CT animal studies.

Computed Tomography Scanning Systems

Even the largest multi-detector row (multi-slice) clinical X-ray CT systems image only a slice of tissue a few centimeters thick in a single rotation. To image a larger volume, the X-ray source and detector rotate through multiple orbits as the patient bed moves linearly through the gantry. This process of acquiring volumetric image data by translating the patient through the imaging path of a continuously rotating X-ray source and detector is called spiral CT, and is now the dominant clinical method for acquiring volumetric CT data.

In contrast, most preclinical micro-CT systems [Fig. 34.12(B)] employ a large area detector, sized to detect X-rays illuminating much of the test subject in a single exposure. The X-ray source is uncollimated, generating a cone beam rather than a fan beam as in a clinical system. X-ray data is typically collected as a series of 90 to 720 discrete exposures (i.e., step-and-shoot acquisition), and the entire image volume is often acquired in a single orbit acquisition rather than in a multi-orbit spiral acquisition. The bed does not move during the acquisition.

The motivation for using a cone beam configuration for high-resolution micro-CT studies stems from the requirement for a very

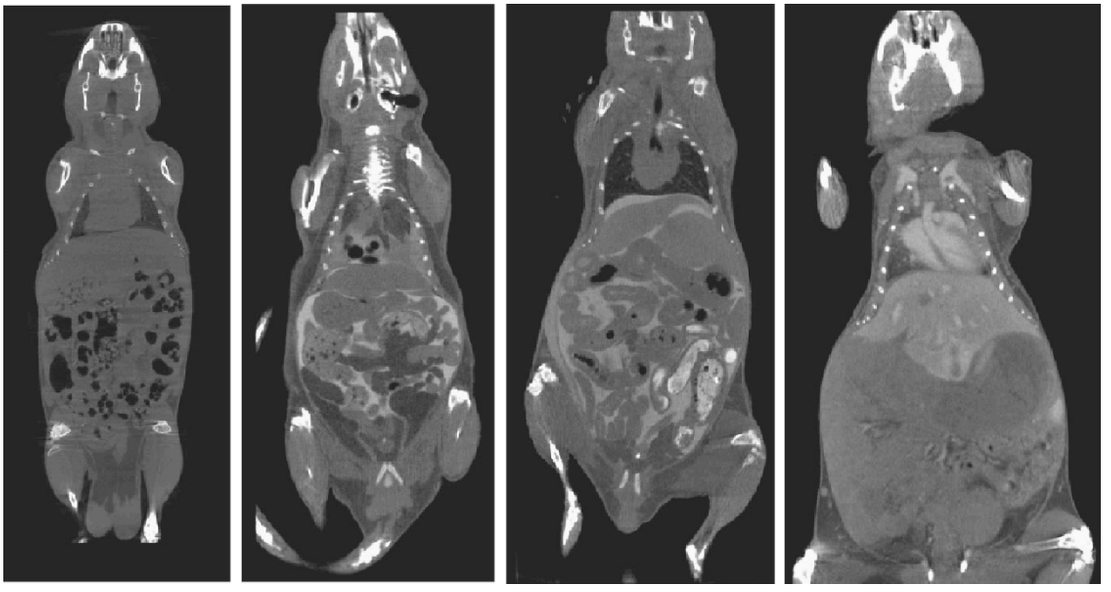


FIGURE 34.13. Micro-CT images of mice with (A) no contrast media, (B) intraperitoneally injected water-soluble contrast medium, (C) intraperitoneally injected water-soluble and oral contrast medium, and (D) blood pool and hepatophillic contrast media. (Images courtesy of CTI/Concorde Microsystems, LLC, Knoxville, TN.)

small (10–15 µm focal spot) microfocus X-ray source. The small focal spot is required to achieve the <50 µm resolution required for most laboratory animal imaging studies. Microfocus X-ray sources operate at very low power, typically less than 100 W, and consequently generate several orders of magnitude lower X-ray flux intensities than their clinical counterparts. In order to make efficient use of the available X rays, the clinical fan beam is expanded into a cone beam, leading to the scanner geometry described above.

The 2D micro-CT detector is typically a large format CCD camera which collects images appearing on a high-resolution phosphor screen. The phosphor screen images are transferred to the CCD by either a conventional lens or a fiber-optic array.

Micro-CT scanners are intrinsically high-resolution devices. Available X-ray sources can have a focal spot size of <10 µm and detector pixel sizes range from 10 to 40 µm. With these components, volumetric image resolutions on the order of 10 µm are readily achievable but only at the cost of either being restricted to imaging high-contrast structures, such as bone, or exposing the mouse to dangerous levels of X-ray radiation. A typical high-resolution micro-CT image of a mouse femur is shown in Figure 34.14.

When seeking to enhance micro-CT contrast/resolution, X-ray dose is an important consideration. A typical micro-CT study with ~100 µm spatial resolution and sufficient contrast resolution to differentiate between bone, soft tissue, and fat exposes a mouse to approximately 5 to 10 cGy. This is below the dose expected to produce chronic or acute physiological responses in mice (~20 cGy). As the spatial and contrast resolution are increased, some physiological effects may be expected and in the limit, the typical LD 50/30 of 7 Gy may be approached. Figure 34.15 shows the approximate dose/resolution trade-off for studies designed to image only bones (2500 HU contrast resolution); to separate bones, soft tissue, and fat (100 HU contrast resolution); and for studies designed to differentiate between soft tissues (5 HU contrast resolution). Based on this chart, if one sets an exposure limit to 10 cGy, it is possible to image bone at a resolution of 20 µm; separate bone, soft tissue, and fat at a resolution of 100 µm and to differentiate between soft tissue organs at a resolution of 400 µm without causing harm to the animal.

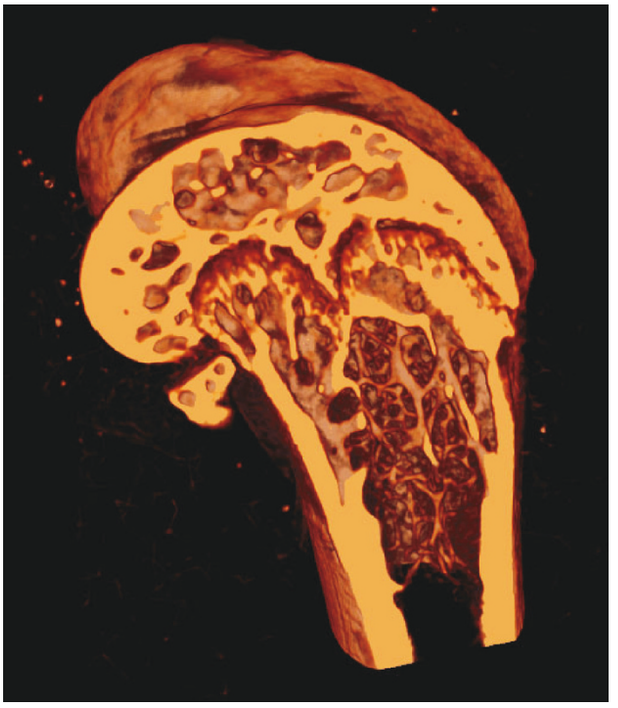


FIGURE 34.14. High resolution micro-CT image of a mouse femur. Field width, 4 mm. (Image courtesy of CTI/Concorde Microsystems, LLC, Knoxville, TN.)

In the recent past, the resolution, image quality, and scan times of micro-CT have increased substantially, chiefly because of

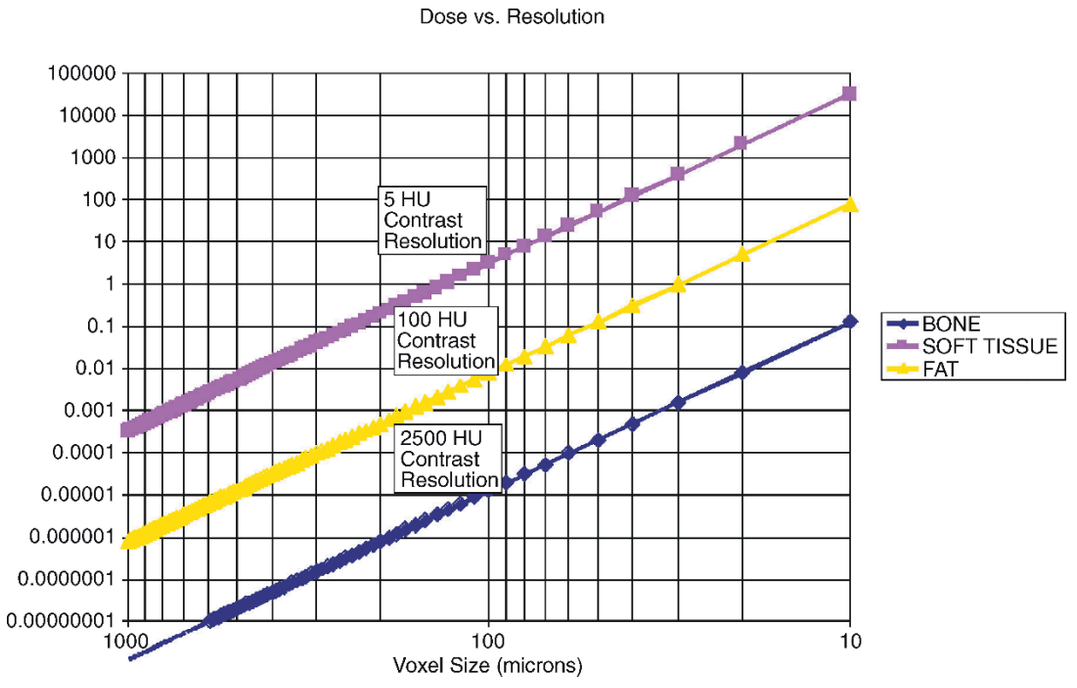


FIGURE 34.15. Approximate relationship between resolution and dose for micro-CT studies as a function of required contrast resolution. (Chart courtesy of CTI/Concorde Microsystems, LLC, Knoxville, TN.)

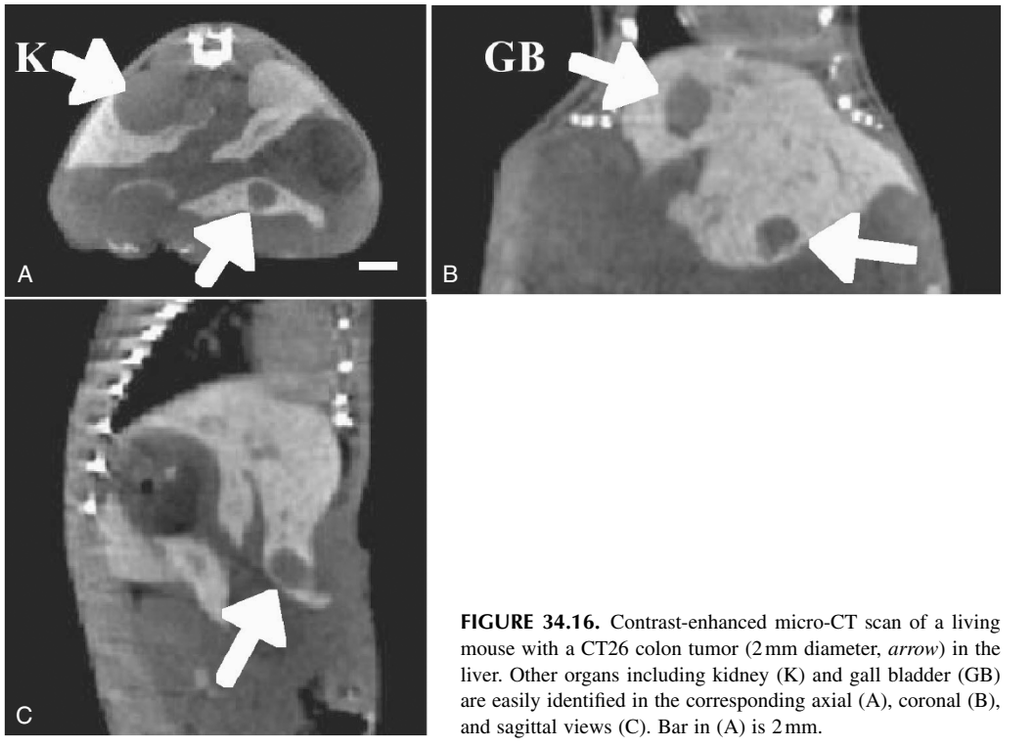


FIGURE 34.16. Contrast-enhanced micro-CT scan of a living mouse with a CT26 colon tumor (2 mm diameter, *arrow*) in the liver. Other organs including kidney (K) and gall bladder (GB) are easily identified in the corresponding axial (A), coronal (B), and sagittal views (C). Bar in (A) is 2 mm.

improvements in 2D CCD X-ray detectors and the algorithms used to reconstruct the image data. The main areas in which additional improvements can be expected include the development of new iterative reconstruction algorithms and higher power microfocus X-ray sources. Should both these succeed, whole animal scan times of a few seconds may be achieved and high-resolution, high-contrast images may be generated at significantly reduced doses.

Although micro-CT scanning of bones and skeletal features produces outstanding images due to the inherently high density of these tissues, success in imaging native soft-tissue structures has thus far been modest at best. As mentioned above, soft tissue contrast can be enhanced in clinical CT with the use of non-targeted, water-soluble radiographic contrast agents such as iohexol. These agents are non-specific in that they are not designed to target any particular tissue. The contrast agents used on clinical CT scanners are not suitable for use with research micro-CT scanners because they rapidly undergo renal elimination and localize in the urinary bladder within a few minutes of injection. This pharmacodynamic mismatch between the agent lifetime and the relatively long data acquisition times associated with micro-CT precludes their use. Recently however, tissue-specific agents suitable for use in micro-CT have significantly extended the usefulness of this non-invasive imaging technique, allowing exquisite vascular and soft tissue images to be made in living mice (Figs. 34.16 and 34.17; Weichert, 2004). Moreover, it is now possible to non-invasively perform virtual serial colonoscopy in mouse colon cancer models (Pickhardt *et al.*, 2005). This finding is paramount in drug development because it is now possible to non-invasively monitor the effectiveness of anticancer agents over time in living mouse tumor models. Finally, although *in vitro* systems are currently capable of sub-10 µm spatial resolution, these systems are typically only used for imaging non-living tissue specimens due to the long acquisition time requirements and associated radiation dose. While *in vivo* scanners are certainly capable of obtaining sub-20 µm spatial

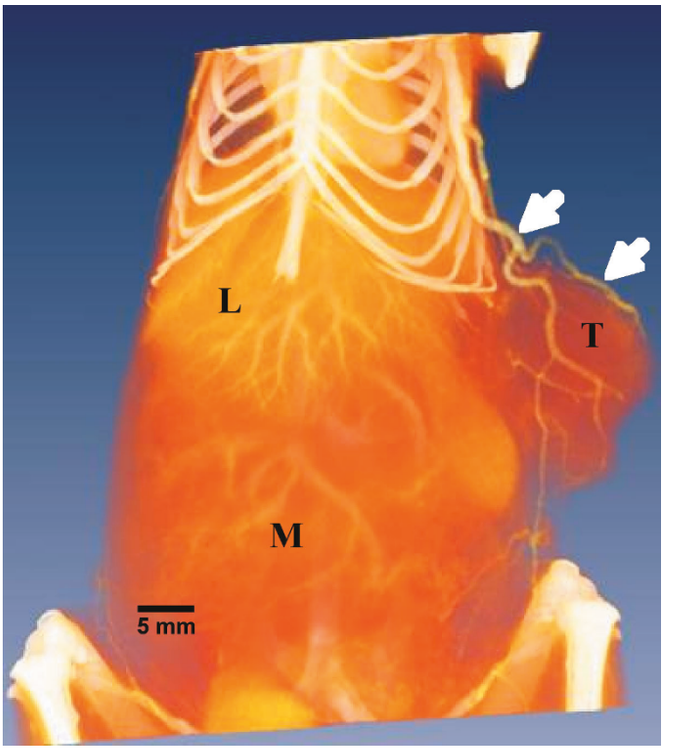


FIGURE 34.17. Three-dimensional volume-rendered micro-CT image of a Colon-51 tumor-bearing live mouse, showing tumor vasculature contrast enhanced using a blood pool agent developed by Weichert and now being marketed as Fenestra VC (Alerion Biomedical, San Diego, CA). Tumor (T) feeder vessels are easily visible (*arrows*) with the aid of this contrast agent. The heart is visible within the rib cage and exquisite vascular details are also visible in the liver (L) and mesentary (M).

resolution, absorbed radiation dose becomes a concern due to increased scan times. Using appropriate long-acting contrast agents, exquisite micro-CT images can be obtained from soft tissues and tumors in live mice at 90 to 100 µm without harming the animal. In our hands, we have performed serial imaging studies at this resolution in the same mice over several weeks with no apparent harm to the animals.

Technological enhancements have truly revolutionized small animal imaging capabilities within the past several years alone. It is now possible to generate spectacular anatomic images at ultra-high resolution in living animals by micro-CT. Although this affords anatomic information, the recent introduction of hybrid microscanners, including a micro-CT/micro-SPECT hybrid, will significantly extend our capabilities to non-invasively garner both anatomic and biochemical information simultaneously with the use of molecular imaging agents.

MAGNETIC RESONANCE MICROSCOPY

Magnetic resonance imaging (MRI) is very well established as a non-invasive diagnostic technique in human medicine with particular strength in visualizing soft tissue. In comparison to a typical clinical MRI with spatial resolution on the order of 1 mm, magnetic resonance microscopy (MRM) can be broadly defined as MRI with a spatial resolution less than 100 microns.

MRM applications are dominated by *in vivo* and *ex vivo* structural biological imaging, concentrated almost exclusively on mapping water and mobile lipid distributions in soft tissues. MRM is unfettered by the optical opacity of a material, and is particularly suited to absolute measurements of mass transport and flow that cannot be obtained by optical methods. However, MRM is hindered by a low intrinsic sensitivity, which ultimately limits spatial and temporal resolution to significantly more modest values than can be achieved with optical techniques.

Basic Principles of Nuclear Magnetic Resonance

MRM relies on nuclear magnetic resonance (NMR) as a source of spatially resolvable signal. NMR is a phenomenon observed when nuclei possessing a non-zero nuclear spin, and therefore a magnetic moment, are placed in a strong magnetic field and excited away from equilibrium with radiofrequency energy [Fig. 34.18(B)]. The most common biologically-abundant nuclei targeted by NMR and MRI include ^{1}H, ^{13}C, ^{23}Na, and ^{31}P. ^{19}F is also used as an NMR/MRI label due to its low natural biological abundance. The magnetic field polarizes the population of nuclear dipoles according to quantum mechanical rules, generating a bulk nuclear paramagnetism within a sample [Fig. 34.8(A)].

At equilibrium, the bulk magnetization is aligned parallel to the polarizing magnetic field and is undetectable. The magnetization becomes detectable following excitation by a radiofrequency pulse at a specific frequency, f, determined by the Larmor equation

$$f = \frac{\gamma}{2\pi} B \qquad (1)$$

where B is magnetic flux density in Tesla, and γ is the gyromagnetic ratio for a given nucleus in rad/s/T. For example, $\gamma/2\pi$ for the ^{1}H nucleus is approximately 42 MHz/T, so for a magnetic field strength of 7.0 T, the Larmor or resonance frequency is close to 300 MHz. The excited bulk magnetization has a component per-

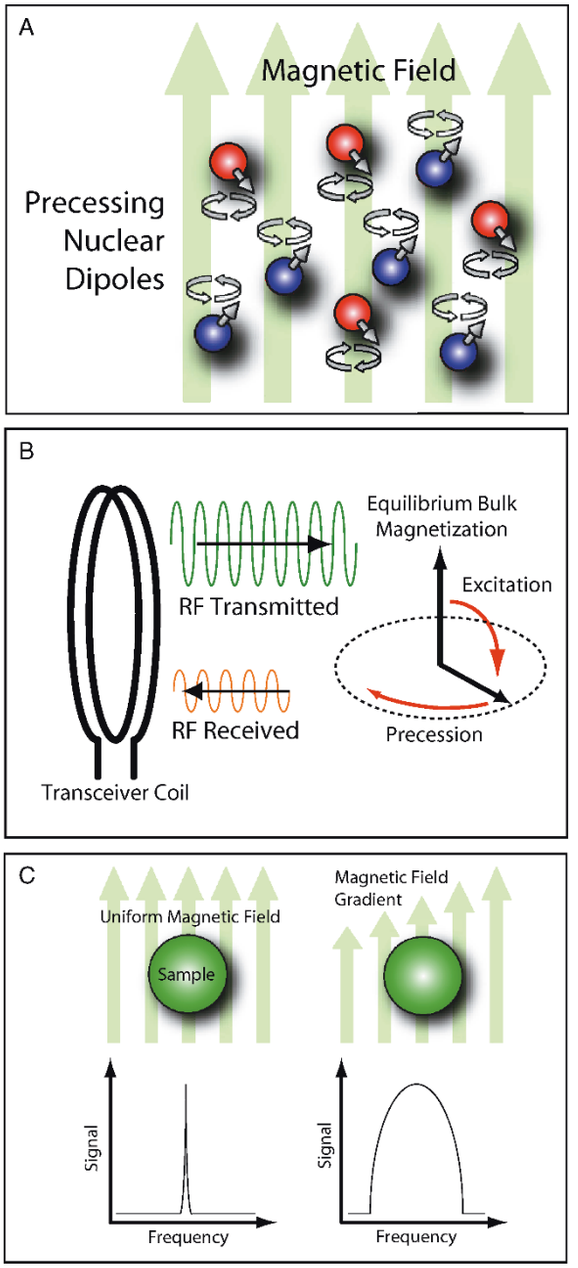


FIGURE 34.18. Basic principles of magnetic resonance microscopy. (A) A strong magnetic field polarizes the population of nuclear dipoles within a material. In this case a spin-1/2 nucleus is shown, which can adopt only one of two energy states (red and blue nuclei) in the magnetic field. The dipoles precess around the applied field at the Larmor frequency (see text). The slight excess of dipoles aligned with the field in the low energy state (typically 10–100 ppm) leads to a bulk nuclear paramagnetism. (B) A radiofrequency pulse at the Larmor frequency excites the bulk nuclear magnetization away from equilibrium. Once excited, the bulk magnetization precesses at the Larmor frequency and induces a small voltage in the transceiver coil which decays as the nuclear spin system returns to equilibrium. (C) In a uniform magnetic field (above left) there is no spatial variation in resonance frequency as seen in the spectrum for a water sample (below left). Application of a magnetic field gradient (above right) encodes spatial position in the precessional frequency of the spin system. Fourier analysis of the frequency and phase of the detected signal allows the spatial distribution of spins in the gradient direction to be reconstructed as a 1D projection of the sample (below right). Additional pulsed gradients in orthogonal directions allow 2D and 3D image formation (not shown).

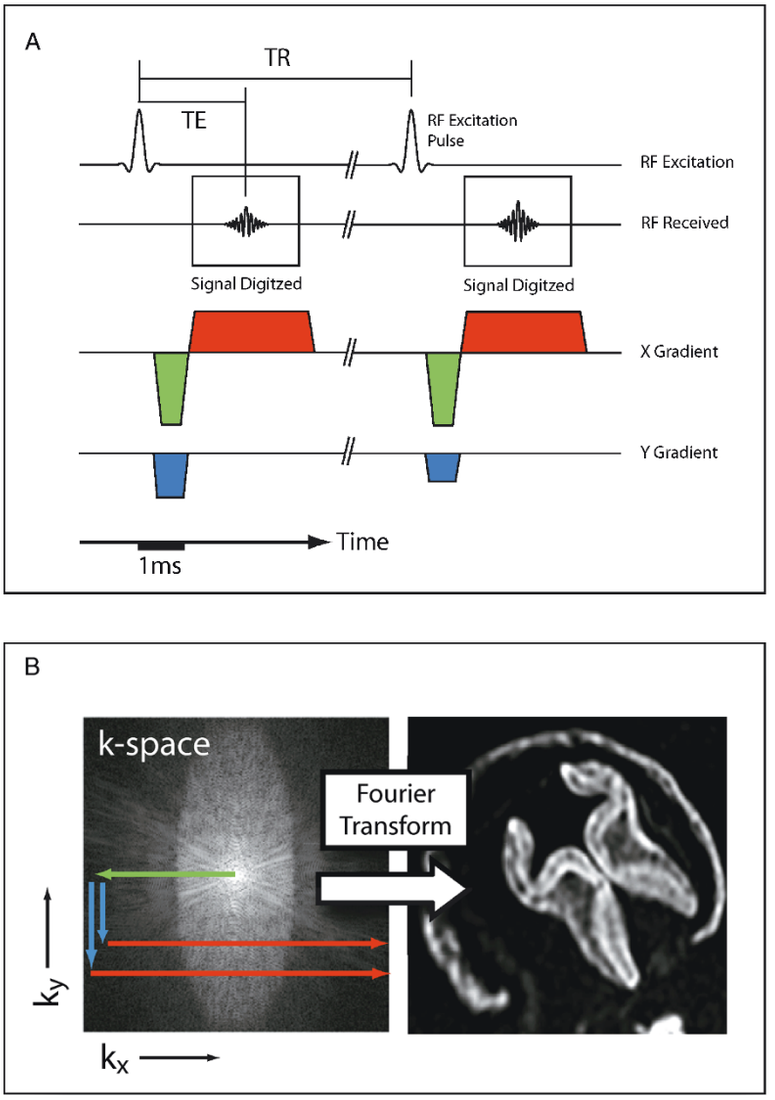


FIGURE 34.19. (A) Simplified schematic of a magnetic resonance imaging pulse sequence with the gradient pulses associated with slice selection omitted for clarity. Two excitation pulses are shown separated by a repetition time (TR) in the range 10 ms to 10 s. The time between the excitation pulse and the signal echo (TE) is in the 1 ms to 50 ms range for high-field microscopy. The 1 ms time bar is a representative reference only. (B) Following the RF excitation pulse, all ^{1}H nuclear spins are at the center of *k*-space: (k_x, k_y) = (0, 0). The negative *x*-gradient (*green*) and *y*-gradient (*blue*) pulses are played out simultaneously and move the spin system in *k*-space as shown. The positive *x*-gradient pulse (*red*) is then played out and the spin-system moves in the k_x direction at a fixed k_y coordinate (*lower red line*). During this gradient pulse, the received signal from the sample is digitized and saved to a 2D data array. This process is then repeated as the amplitude of the blue pulse is changed to sweep data acquisition across *k*-space (*upper red line*). The final spatial resolution of the real-space image is determined by the maximum *k* coordinate reached in each dimension. Conversely, the field of view of the final image is determined by the digitized sampling interval in *k*-space. Following a complete traverse of the required region of *k*-space, the final real-space image is reconstructed using a 2D Fourier transform. In practice, phase-sensitive quadrature detection of the received signal is equated to the real and imaginary parts of *k*-space required for the Fourier transform. The complex image resulting from Fourier transformation is then converted to a magnitude image for display purposes.

pendicular to the polarizing field (the transverse component) and precesses around the field direction at the Larmor frequency, a process that induces a detectable voltage in an appropriately-placed receiver coil [Fig. 34.19(B)].

Following excitation, the precessing transverse component decays or relaxes exponentially with a time constant, T_2. Simultaneously, the magnetization component parallel to the main field relaxes back to its equilibrium value with a time constant, T_1. Typical relaxation times for liquid water in tissues range from milliseconds to seconds with T_1 always greater than T_2. Consequently, the natural resonance line-widths in NMR fall in the 1 Hz to 1 kHz range and are therefore extremely narrow when compared with the Larmor resonance frequency.

Magnetic Resonance Image Formation

Unlike most other imaging modalities, MRM does not physically "scan" real space because the wavelength of the radiofrequency radiation involved is typically much larger than the length-scale of the sample (extreme near field). It turns out instead, that the Larmor Eq. (1) can be exploited to spatially resolve the NMR signal. If we arrange for the magnetic field to vary linearly across a sample, then the resonance frequency becomes proportional to distance along the gradient direction (frequency encoding). In the following description of MR image formation, we will assume that the sample contains only water (singlet resonance) and that other parameters such as relaxation, diffusion, motion, etc., can be ignored. At this point it is worth looking at how the phase of the NMR signal varies with time in a field gradient that may also vary with time. In one dimension, with the gradient along the *x*-axis, we have

$$\begin{aligned}\phi(x,t) &= \int_0^t dt'\omega(x,t') \\ &= \int_0^t dt'\gamma B(x,t') \\ &= \int_0^t dt'\gamma G_x(t')x \end{aligned} \quad \textbf{(2)}$$

where $G_x(t)$ is a time-varying magnetic field gradient (in *T/m*) and x is the position of a water molecule (spin) in the gradient direction, ignoring diffusion and bulk motion. We can define a new variable, $k_x(t)$, the significance of which will become apparent, as

$$k_x(t) = \int_0^t dt'\gamma G_x(t') \quad \textbf{(3)}$$

The time-varying signal arising from water at a given position in the gradient can be expressed, using Eqs. 2 and 3, as

$$S(x,t) = \rho(x)e^{i\phi(x,t)} = \rho(x)e^{ik_x(t)x} \quad \textbf{(4)}$$

where $\rho(x)$ is the so-called proton density which is proportional to ^{1}H nucleus concentration. Additional terms describing the effects of relaxation, motion, and RF-pulse-sequence timing are omitted here for simplicity. This expression in turn leads to the total signal detected from a sample as a function of k_x

$$S_{tot}(k_x) = \int_{-\infty}^{\infty} dx \rho(x) e^{ik_x x} \quad \textbf{(5)}$$

which is the inverse Fourier transform of the proton density in x. k_x can be thought of as a spatial frequency of the proton signal, with units of m^{-1} (as opposed to s^{-1} for temporal frequency) and is the coordinate for the one-dimensional (1D) Fourier inverse-space of x. This expression is easily extended to three dimensions

$$S_{tot}(k_x, k_y, k_z) = \int_{-\infty}^{\infty} dx \int_{-\infty}^{\infty} dy \int_{-\infty}^{\infty} dz\, \rho(x, y, z) e^{i(k_x x + k_y y + k_z z)}$$

with $\rho(x,y,z)$ being the sought-for image. All positions in real space only occupy one position in k-space at a given time, so an MR image must be acquired by scanning k-space, then Fourier transforming the resulting inverse-space image to reconstruct the real-space image (Fig. 34.19). From Eq. 3 we can see that the sample can be moved in k-space by applying appropriate sequences of time-varying field gradients to traverse k-space in one or more dimensions. An example k-space trajectory for the gradient echo imaging sequence is detailed in Figure 34.19. Digital signal acquisition can take place continuously or discontinuously during only specific parts of the k-space trajectory. The most common k-space scanning trajectory involves acquiring one line of data in k_x (with k_y and k_z fixed) per radiofrequency (RF) excitation pulse. Rapid scanning can be achieved by scanning larger regions of k-space per excitation pulse, as is the case for the echo-planar imaging (EPI) sequence 1. Finally, the real-space image, $\rho(x,y,z)$, is reconstructed by Fourier transformation of the scanned k-space data.

The deviation in the Larmor frequency brought about by the field gradient creates a frequency difference across a sample of between 10 kHz and 1 MHz in conventional liquid-state MRM. A single line of k-space is acquired in milliseconds, with a whole plane of k-space traversed in anything from tens of milliseconds to minutes depending on the pulse sequence employed. Signal averaging is achieved by simple repetition of a trajectory segment. The RF excitation pulse resets the k-space.

The complement of frequency-encoded signal detection is frequency selective excitation. Here a magnetic field gradient is applied in conjunction with an amplitude-modulated (and in some cases) phase-modulated RF pulse (Fig. 34.20). The modulation of

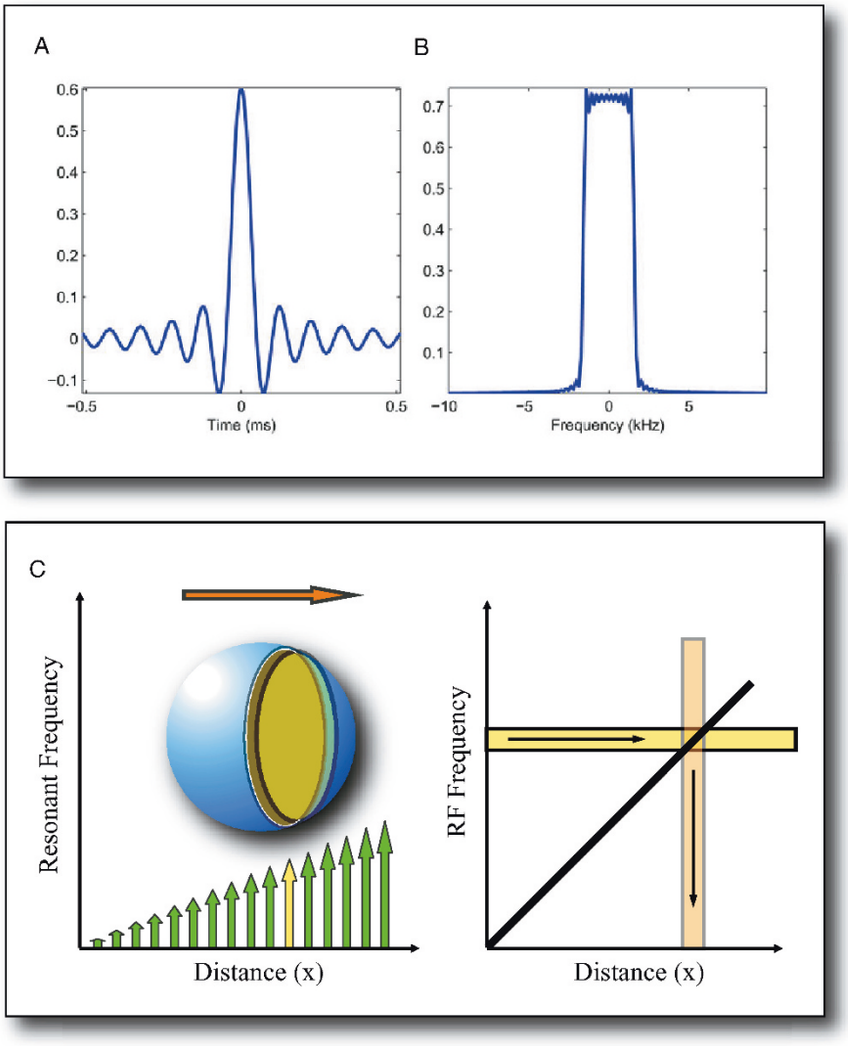


FIGURE 34.20. An amplitude modulation waveform for the RF carrier at the Larmor frequency (A) produces a band-limited excitation of the nuclear spins (B). If such an RF waveform is used in combination with a linear magnetic field gradient, then only a limited slice or slab will be excited perpendicular to the gradient direction. Three such slice-selective pulses could be combined to limit excitation to a cubic sub-volume within a sample.

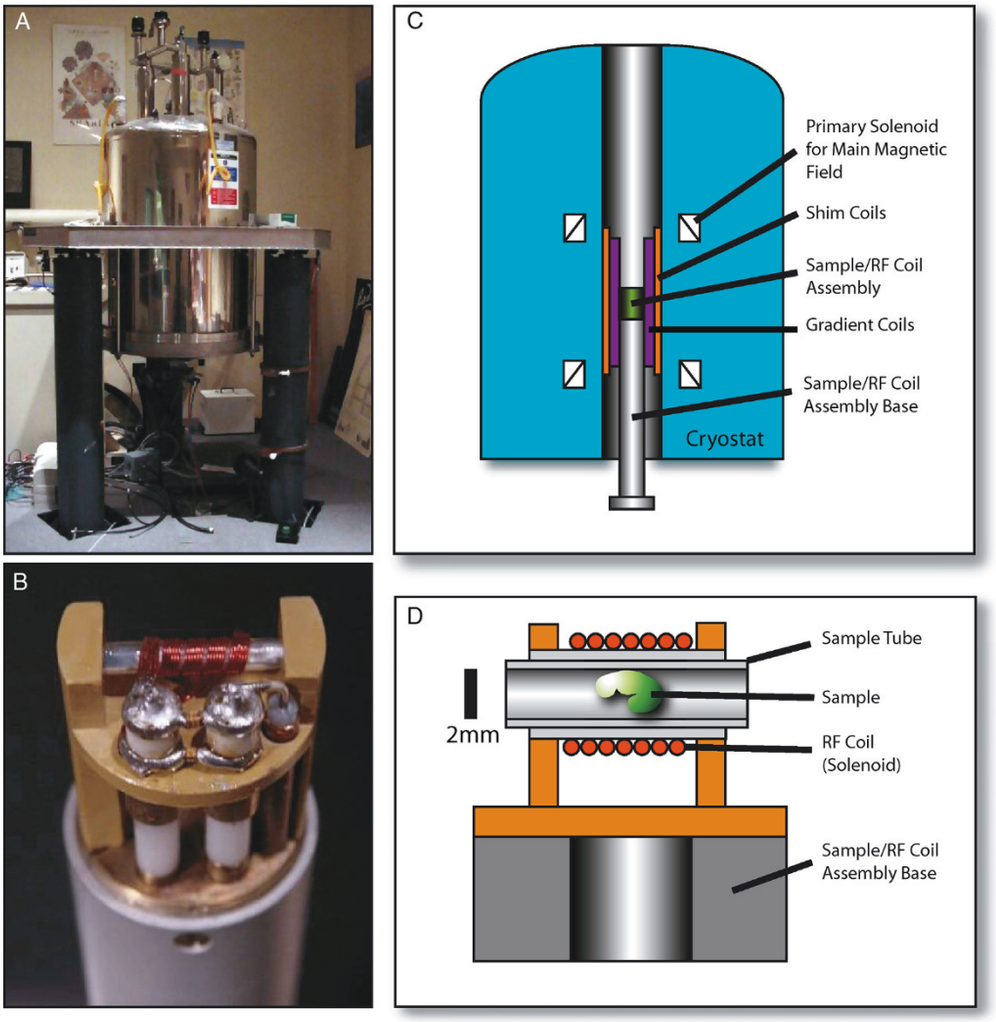


FIGURE 34.21. A typical MRM hardware configuration: (A) an 11.7 Tesla vertical bore superconducting magnet. This hardware is identical to that used for high-resolution NMR spectroscopy. (B) Three millimeter transverse RF solenoid (copper winding at upper center) and tuning circuitry for excitation and detection of the MR signal. (C) Simplified schematic cross-section of a vertical bore MRM setup. The gradient and shim coils are secured within the magnet bore and the RF coil/sample assembly introduced for each experiment. (D) Enlargement of a transverse configuration for the solenoidal RF coil and sample tube. The sample is often surrounded by a suitable fluid, such as buffered saline or culture medium. For fixed samples where background signal needs to be eliminated, the sample can be surrounded by ^{1}H-free, fluorinated fluids. Environmental control can be provided by thermostatically controlled airflow through the bore of the coil/sample assembly base.

the carrier frequency of the excitation pulse limits the frequency content, so that the excitation becomes spatially limited in the presence of a field gradient. For example, a 1 ms shaped pulse might have a bandwidth of 4 kHz that, in the presence of a 10 mT/m field gradient would limit NMR excitation to a region approximately 1 cm wide in the gradient direction, but would be unlimited perpendicular to the gradient direction. This process is termed slice or slab selection and can be extended to line and volume selections by using multiple, selective RF pulse/gradient combinations. Slice selection is often used for *in vivo* imaging where interleaved acquisition of multiple 2D k_{xy}-spaces separated in z is more time-efficient than scanning the complete 3D k_{xyz}-space.

In a typical MRM experiment, a sample, such as an anesthetized mouse or a fixed embryo, is secured within an appropriate holder and placed within the RF coil. Additional physiological monitoring, anesthesia lines, and environmental control are often integrated into the RF coils/sample assembly. The gradient and shim coils are normally secured more permanently within the main magnet bore (Fig. 34.21) requiring only the RF coil and sample to be introduced for each experiment. The RF coil/sample assembly is then placed at the center of the main field and gradient coils for imaging. The shim coil currents are adjusted to minimize magnetic inhomogeneities in the sample, the synthesizer frequency set to the Larmor frequency determined from the received signal and the strength of the RF excitation pulses calibrated. The duration of an image acquisition may vary from less than a second to more than a day and is largely determined by the required spatial resolution and signal-to-noise ratio. The RF power deposition in the sample varies widely with pulse sequence design and has the potential to cause significant heating. Changes to the pulse sequence timing and RF pulse waveform specifications can minimize peak and average power deposition. Heating effects increase rapidly with the Larmor frequency (increasing field strength) and power deposition can be estimated, monitored and controlled for *in vivo* imaging studies.

Magnetic Resonance Microscopy Hardware

The hardware for MRM consists of three major components and their associated electronics: (1) a permanent or electromagnet that generates the main polarizing field, (2) one or more radiofrequency coils for excitation and signal detection, and (3) a three-axis set of magnetic-field-gradient coils. The sample is placed within the RF coil which in turn is placed within the gradient and the main solenoid. The main, polarizing field is typically generated by a cryogenically-cooled, superconducting electromagnet, although permanent magnets and even resistive electromagnets are in use. The uniformity or homogeneity of the polarizing field plays a critical role in successful high-quality MRM. Additional room-temperature field correction or shim coils are routinely used to improve the fundamental homogeneity of the magnetic field within the imaging volume. RF coils for MRM are most commonly simple loops, solenoidal resonators, or a volume resonator design called a birdcage. A single coil may be used for both transmission/excitation and reception, or a larger transmitting volume coil with good RF field homogeneity can be used with a high-sensitivity receiver loop coil (surface coil).

The RF power absorbed by a sample during imaging varies widely with the type of pulse sequence employed. Some sequences involve rapid RF pulsing at relatively high power which ultimately will lead to tissue heating. Power deposition also increases rapidly with field strength for a given pulse sequence.

The signal received from the RF coil is amplified by a low noise preamplifier prior to demodulation from the Larmor frequency (see sidebar) and digitized at rates from about 100 kS/s to 2 MS/s. Raw *k*-space data is reconstructed and displayed by the operating-console computer.

The coils generating magnetic field gradients (gradient coils) are usually wound on a cylindrical former within the main magnet bore. The coil windings are designed to produce independent, linear field gradients over the imaging volume in each of the three cardinal directions (x, y, z). The maximum gradient strengths required for MRM typically exceed 500 mT/m and may rise to more than 5 T/m in high-performance hardware. Even at these strengths, the maximum field perturbation from the gradient coils rarely exceeds 1% of the main magnetic field.

A functional MRM system requires a high-stability, high-accuracy frequency synthesizer that provides the reference oscillation for both RF transmission and reception. Amplifiers for the RF and gradient coils are controlled by a pulse sequencer that in turn is coordinated by the operating-console computer.

Strengths and Limitations of Magnetic Resonance Microscopy

Whereas magnetic resonance imaging of humans is very well established as a medical diagnostic tool, microscopy has developed at a slower rate. MRM cannot compete with optical microscopy in terms of spatial resolution and sensitivity, but has several unique strengths that benefit certain applications. Specifically, MRM is not limited by the opacity of an object to light, because it employs radiofrequency radiation with wavelengths much larger than the typical sample size.

Optimizing MRM is a complex trade-off between acceptable signal-to-noise ratio, temporal resolution, and spatial resolution. The NMR experiment has an intrinsically low sensitivity, so requirements for minimum SNR tend to place lower bounds on spatial and temporal resolution. Consequently, acquiring high spatial resolution MRM with voxel sizes in the 10 to 100 micron range typically requires tens of minutes to hours to achieve an acceptable SNR.

Various estimates place the ultimate limit for MRM spatial resolution in the neighborhood of 1 μm for liquid water at room or physiological temperatures.[1] These estimates consider the effects of molecular diffusion, T_2 relaxation, microscopic field inhomogeneity, and sensitivity (Callaghan, 1991). Other factors, including hardware design and sample size, lead to practical MRM isotropic resolution limits greater than 10 μm. The achievable spatial resolution is limited by sensitivity factors, specifically the signal-to-noise ratio achievable in a given acquisition time.

As a general rule, high-resolution MRM with spatial resolutions less than 100 μm benefits from the use of polarizing magnetic fields greater than 3 Tesla, sometimes as high as 17.5 Tesla. Although this leads to a greater nuclear paramagnetic polarization, other factors such as increasing T_1 relaxation times, decreasing T_2 relaxation times, and increased susceptibility-based field inhomogeneities tend to diminish the expected gains in sensitivity and signal-to-noise ratio efficiency.

High-performance gradient hardware, with higher maximum amplitudes (*T/m*) and faster slew rates (*T/m/s*) are almost always an advantage in MRM. Microscopy gradients capable of 10 *T/m* allow high spatial and temporal resolution imaging of small samples.

Another approach to increasing the sensitivity of MRM is through RF coil design. Various groups have developed microcoils with dimensions smaller than 1mm to boost sensitivity in very small samples. Some of the highest resolution MRM images obtained have employed such designs (Grant *et al*., 2001; Lee *et al*., 2001; Ciobanu and Pennington, 2004).

Image Contrast in Magnetic Resonance Microscopy

Signal differences between tissues in ^{1}H MRM of biological samples largely arise from differences in the microscopic environment of intracellular and interstitial water. Chemical differences between molecules containing ^{1}H nuclei also contribute to image contrast, for example, between water and lipid-rich tissues. Parameters influencing MRM image contrast include T_1 and T_2 relaxation times, NMR nucleus concentration, temperature, diffusion coefficient, fluid velocity, magnetic susceptibility, and magnetization transfer coefficients of a material. The influence that each of these parameters has on image contrast can be accentuated or suppressed by careful design of the sequence of radiofrequency and field gradient pulses played out prior to signal acquisition. For example, specific pulse sequence designs allow the time delay between excitation and signal acquisition to be increased, accentuating differences in the T_2 relaxation time of materials. Reducing the time delay between excitation pulses accentuates short T_1 materials that appear brighter in such images.

Motion of water and other fluids can be encoded in the phase or amplitude of MRM images using gradient pulse combinations. Both coherent motion (flow) and incoherent motion (diffusion) can be quantified by MRM over a 2D plane or 3D volume of an optically opaque material. MRM measurements of water diffusion within organized tissues have been particularly well developed and are capable of quantifying subresolution ensemble molecular interactions with restrictive or hindering boundaries (Tuch, 2003). For example, diffusion tensor imaging (DTI) maps diffusion

[1] About 3 to 4 μm has been obtained on very small specimens (9 Tesla; Ciobanu and Pennington, 2004).

anisotropy within tissues using a simplified model of molecule-boundary interactions (Pierpaoli *et al*., 1996). Diffusion tensor MRM has been applied to brain development in mice (Zhang *et al*., 2003), dysmyelination models (Song *et al*., 2002), and myocardial fiber structure (Jiang *et al*., 2004).

In addition to endogenous image contrasts, such as relaxation time and molecular diffusion, it is possible to introduce exogenous MRM contrast agents that target specific tissues or physiology within a living system. Gadolinium chelates are widely used, both individually and bound to larger molecules, to reduce the T_1 relaxation time of surrounding water (Weinmann *et al*., 1984, 2003). Ionic manganese is a calcium analog and T_1 contrast agent that, at low concentrations, has been used as an *in vivo* trans-synaptic axonal transport tracer (Pautler and Koretsky, 2002; Pautler *et al*., 2003; Aoki *et al*., 2004). Tracking of progenitor, stem, or immune cells using MRM is a recent growth area (Hinds *et al*., 2003; Shapiro *et al*., 2004) typically employing variants of superparamagnetic iron oxide (SPIO) particles as intracellular T_2* contrast agents (Foster-Gareau *et al*., 2003). The development of molecular imaging for MRM, targeting both gene expression and metabolism within a living organism is likely to be the next significant field of investigation (Louie, 2000; Allen, 2004) and holds great promise for future non-invasive biomedical research.

Magnetic Resonance Microscopy Applications

Phenotyping

MRM is widely used for phenotyping genetically manipulated organisms such as transgenic mice (Johnson *et al*., 2002a, 2002b; Lo *et al*., 2003) leading to the development of high throughput techniques for imaging more than one animal simultaneously (Bock *et al*., 2003). MRM brain atlases of adult inbred mouse strains are being constructed by several groups (Kovacevic *et al*., 2005; Segars *et al*., 2004).

Histology

Ex vivo MR histology exploits the lack of physiological motion and extended data acquisition times to generate high-resolution structural images of various organisms (Figs. 34.22 and 34.23) (Johnson *et al*., 1993; Johnson *et al*., 2002a). MRM lacks the spatial resolution and staining flexibility of optical histology, but preserves the 3D structure of tissues and eliminates the need for dehydration, embedding, and physical sectioning and their associated artifacts. As a non-invasive technique, MRM can even precede conventional histology, providing a valuable structural reference for subsequent histological sections.

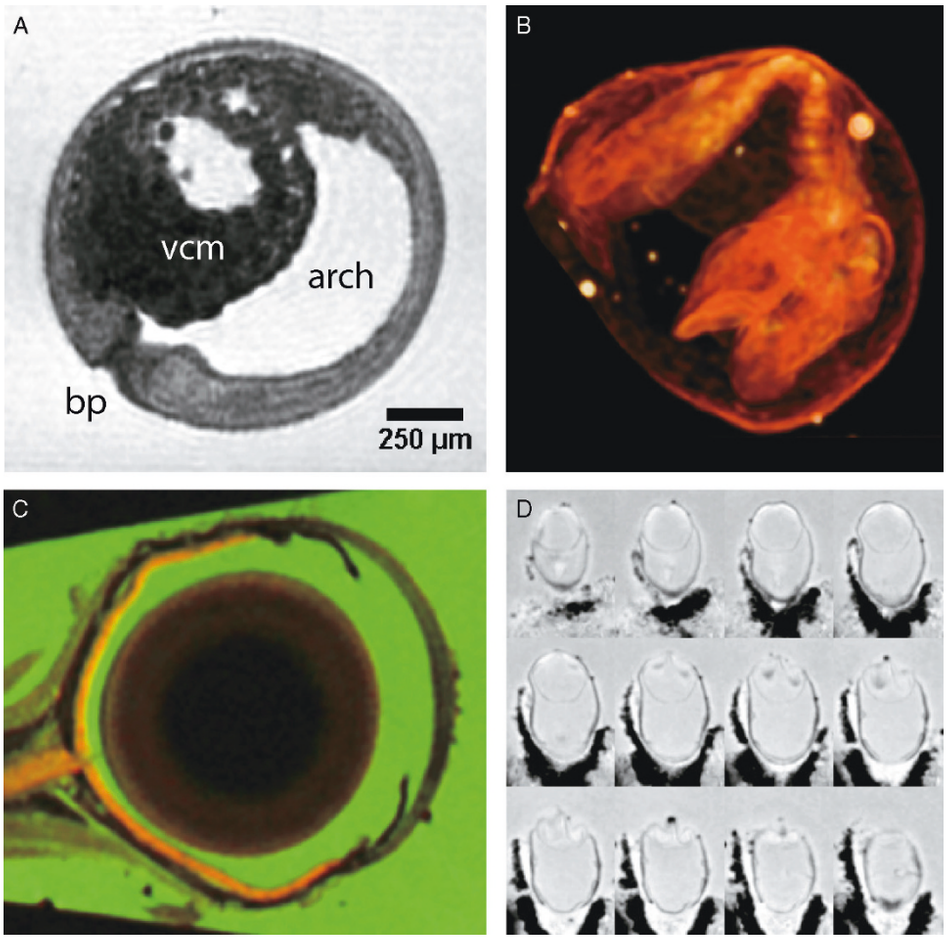


FIGURE 34.22. Examples of MRM histology of biological samples. (A) High-resolution 3D MRM of a fixed late gastrula stage *Xenopus laevis* embryo with a nominal isotropic spatial resolution of 16 microns. The vegetal cell mass (vcm), blastopore (bp), and archenteron (arch) are clearly visualized in this section. (B) Volume texture rendering of a 3D MRM image of a fixed 8.5 dpc mouse embryo within its yolk sac. (C) Central section through a composite MRM image of a fixed mouse eye. The red channel encodes the isotropic-diffusion-weighted image, highlighting regions of restricted diffusion within the chorioretina (*orange*). The green channel encodes the T_2-weighted image in which free-fluid appears bright. The low intensity circular feature within the globe of the eye is the crystalline lens. (D) Montage of sections from a 3D MRM image of a fixed 7 dpc mouse embryo with nominal 20 micron isotropic spatial resolution.

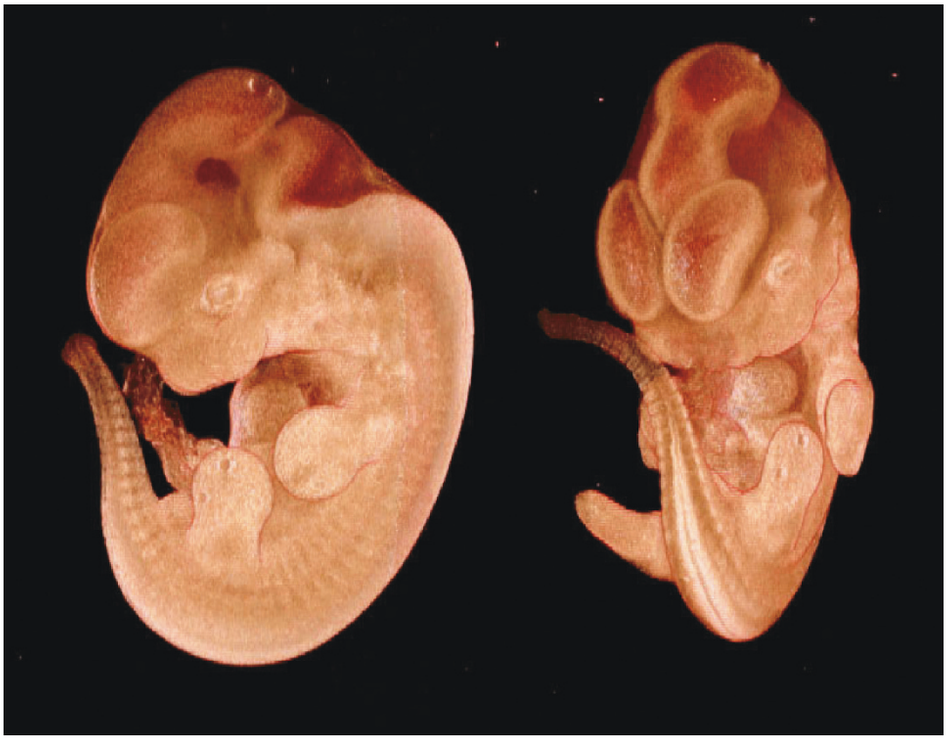


FIGURE 34.23. Volumetric rendering of an 11-day postcoital mouse embryo. Because the sample has not been dehydrated, the global geometric preservation of the embryo is excellent.

Developmental Biology

MRM has been applied to structural imaging of mouse (Jacobs, 1999; Chapon, 2002) and quail embryos and to serial *in vivo* imaging of the *Xenopus laevis* embryo (Papan *et al*., 2001; Jacobs *et al*., 2003). MRM leverages its ability to image optically opaque specimens to generate 3D data which would be difficult or impossible to obtain by other methods. MRM is particularly suited to studies of dynamic developmental processes such as morphogenesis. As for phenotyping, MRM is proving valuable in the construction of reference developmental atlases for mouse, quail, and other embryos that are too large or opaque at later stages for optical imaging (Dhenain *et al*., 2001; Matsuda *et al*., 2003).

Other Applications

MRM is in many ways underexploited outside the realm of vertebrate imaging. MRM is an excellent resource for botanical imaging, exploiting minimal physiological motion to generate high spatial resolution images (Edzes, 1998; Kockenberger, 2001, 2004) and is especially suited to imaging flow and water distribution within plant samples (Kuchenbrod *et al*., 1998). MRM has also seen applications in opaque bioreactors and biofilms, studying local flow and structure beyond the capabilities of optical microscopy (As and Lens, 2001; Paterson-Beedle *et al*., 2001; Manz *et al*., 2003; Seymour *et al*., 2004).

Future Development of Magnetic Resonance Microscopy

The future of MRM is likely to include incremental improvements in spatial resolution and sensitivity as hardware design and fabrication methods are refined. Ironically, clinical MRI has led the way in technical advances, driven by the needs and resources of medical diagnosis and therapy. Some of these technologies, including phased-array RF coils and advanced pulse sequence designs, will be reapplied to MRM applications. However, it is in the development of new molecular imaging agents in model organisms that we will most likely see the greatest advances in MRM in the near future.

CONCLUSION

The imaging modalities discussed in this chapter are emerging tools directed at meeting the growing need for volumetric microscopy of challenging specimens. They join confocal laser-scanning and two-photon laser-scanning microscopy in the suite of microscopic imaging techniques that enable entire, whole-mounted specimens to be studied. Each of these volumetric imaging tools plays an important role in the imaging toolkit, as none answers all needs. SIM/EFIC is a high-resolution method that is capable of capturing the entire volume of large specimens; however, it is inherently destructive as biological samples must be fixed, dehydrated, and embedded, and then must be sectioned. Although imaging the block face avoids the distortions resulting from the sectioning process, the specimen is still subject to any fixation and dehydration artifacts. As presently employed, OPT requires extensive clearing of a specimen to render it translucent, and so is subject to the same fixation and shrinkage artifacts as SIM/EFIC. A major strength of OPT on fixed specimens is its ability to capture the distribution of molecular markers such as antibody staining and gene expression *in situ* using common molecular biological and histological techniques. Of course, on living specimens that are small and transparent, OPT can be performed without processing, and at the time of writing, live OPT imaging experiments are being performed.

A subset of the volumetric imaging tools are designed to image living specimens: OCT, SPIM, and MRM. OCT, a reflected light

modality, requires no extrinsic labels and is ideal for optical imaging deep within specimens, and for following motions such as blood flow. SPIM offers an important tool at the confluence of imaging and molecular biology technologies, as it is a fluorescent optical sectioning technique, ideal for capturing the expression of GFP reporter genes in living specimens. The use of transgenic GFP reporter constructs allows for the direct *in vivo* visualization of gene transcription during development within the context of the living embryo: the SPIM sample chamber is designed for maintaining physiological conditions and the use of the light sheet minimizes sample bleaching and reduces blur from structures not in the focus plane. Using SPIM, dynamic events ranging from fractions of a second to days can be recorded at voxel sizes of ~0.5 µm.

MRM is not an optical modality and therefore is not limited by the optical properties of the subject. MRM is non-invasive and allows long-term observation of living biological specimens as no ionizing radiation is employed. Although MRM is slower, more expensive, and offers lower resolution than most optical methods, it offers direct observation of morphogenic movements in opaque embryos. Previously, these movements could only be inferred from static sections. Clinically, MRI has a proven diagnostic history but is only in its infancy as a microscopic technique. Tools proven in the clinic are being modified for microscopic use, promising a growing set of techniques for following tissue fine structure and blood flow.

As with any review of finite length, there are a great many modalities and modifications to existing techniques that have not been treated here. Adapting non-conventional elements to conventional devices pushes microscopy development forward. The field of view of confocal microscopy has been greatly increased (20 mm^2 at 2 µm resolution) with the use of a high-NA f-theta telecentric objective (Dixon, 1995). Microscopic versions of clinical imaging tools are emerging and improving at an alarming rate. These include positron emission tomography (micro-PET), and ultrasonography (micro-US). Typing in any of these key terms in a Web- or library-based search will find a rapidly growing set of offerings. The resolution of these techniques has improved dramatically. The omission of these powerful approaches is in no way intended to diminish their potential role for volumetric imaging, but instead a statement of how rapidly these fields are advancing. The future will see the toolkit for volumetric imaging grow at an increasing rate.

ACKNOWLEDGMENTS

The authors thank Jeff Fingler for additional expert OCT content.

REFERENCES

Allen, M.J., and Meade, T.J., 2004, Magnetic resonance contrast agents for medical and molecular imaging. *Met. Ions. Biol. Syst.* 42:1–38.

Aoki, I., Wu, Y.J., Silva, A.C., Lynch, R.M., and Koretsky, A.P., 2004, *In vivo* detection of neuroarchitecture in the rodent brain using manganese-enhanced MRI, *Neuroimage* 22:1046–1059.

As, H.V., and Lens, P., 2001, Use of 1H NMR to study transport processes in porous biosystems, *J. Ind. Microbiol. Biotechnol*. 26:43–52.

Bock, N.A., Konyer, N.B., and Henkelman, R.M., 2003, Multiple-mouse MRI, *Magn. Reson. Med*. 49:158–167.

Boppart, S.A., Bouma, B.E., Pitris, C., Southern, J.F., Brezinski, M.E., and Fujimoto, J.G., 1998, *In vivo* cellular optical coherence tomography imaging, *Nat. Med*. 4:861–865.

Boppart, S.A., Brezinski, M.E., Bouma, B.E., Tearney, G.J., and Fujimoto, J.G., 1996, Investigation of developing embryonic morphology using optical coherence tomography, *Dev. Biol*. 177:54–63.

Boppart, S.A., Tearney, G.J., Bouma, B.E., Southern, J.F., Brezinski, M.E., and Fujimoto, J.G., 1997, Noninvasive assessment of the developing *Xenopus* cardiovascular system using optical coherence tomography, *Proc. Natl. Acad. Sci. USA* 94:4256–4261.

Callaghan, P.T., 1991, *Principles of Nuclear Magnetic Resonance Microscopy*, Oxford University Press, Oxford, United Kingdom.

Chapon, C., Franconi, F., Roux, J., Marescaux, L., Le Jeune, J.J., and Lemaire, L., 2002, In utero time-course assessment of mouse embryo development using high resolution magnetic resonance imaging, *Anat. Embryol.* 206(1–2):131–137.

Ciobanu, L., and Pennington, C.H., 2004, 3D micron-scale MRI of single biological cells, *Solid State Nucl. Magn. Reson*. 25:138–141.

Dhenain, M., Ruffins, S.W., and Jacobs, R.E., 2001, Three-dimensional digital mouse atlas using high-resolution MRI, *Dev. Biol*. 232:458–470.

Dixon, A.E., Damaskinos, S., Ribes, A., and Beesley, K.M., 1995, A new confocal scanning beam laser macroscope using a telecentric, f-theta laser scan lens, *J. Microsc*. 178:261–266.

Edzes, H.T., van Dusschoten, D., and Van As, H., 1998, Quantitative T2 imaging of plant tissues by means of multi-echo MRI microscopy, *Magn. Reson. Imaging* 16(2):185–96.

Ewald, A.J., McBride, H., Reddington, M., Fraser, S.E., and Kerschmann, R., 2002, Surface imaging microscopy, an automated method for visualizing whole embryo samples in three dimensions at high resolution, *Dev. Dyn*. 225:369–375.

Ewald, A.J., Peyrot, S.M., Tyszka, J.M., Fraser, S.E., and Wallingford, J.B., 2004, Regional requirements for Dishevelled signaling during *Xenopus* gastrulation: Separable effects on blastopore closure, mesendoderm internalization and archenteron formation, *Development* 131:6195–6209.

Fercher, A.F., 1996, Optical coherence tomography, *J. Biomed. Opt*. 1:157–173.

Foster-Gareau, P., Heyn, C., Alejski, A., and Rutt, B.K., 2003, Imaging single mammalian cells with a 1.5 T clinical MRI scanner, *Magn. Reson. Med*. 49:968–971.

Grant, S.C., Buckley, D.L., Gibbs, S., Webb, A.G., and Blackband, S.J., 2001, MR microscopy of multicomponent diffusion in single neurons, *Magn. Reson. Med*. 46:1107–1112.

Haskell, R.C., Williams, M.E., Petersen, D.C., *et al*., 2004, Visualizing early frog development with motion-sensitive 3-D optical coherence microscopy, In: *Proceedings of the 26th Annual International Conference of the IEEE EMBS*, IEEE, San Francisco, CA, USA.

Herman, G.T., 1980, *Image Reconstruction from Projections: The Fundamentals of Computerized Tomography*, Academic Press, San Francisco.

Hinds, K.A., Hill, J.M., Shapiro, E.M., *et al*., 2003, Highly efficient endosomal labeling of progenitor and stem cells with large magnetic particles allows magnetic resonance imaging of single cells, *Blood* 102:867–872.

Hoeling, B.M., Fernandez, A.D., Haskell, R.C., and Petersen, D.C., 2001, Phase modulation at 125 kHz in a Michelson interferometer using an inexpensive piezoelectric stack driven at resonance, *Rev. Sci. Instrum.* 72:1630–1633.

Hoeling, B.M., Fernandez, A.D., Haskell, R.C., Huang, E., Meyers, W.R., Petersen, D.C., Ungersma, S.E., Wang, R., and Williams, M.E., 2000, An optical coherence microscope for 3-dimensional imaging in developmental biology, *Opt. Express* 6:136–146.

Holdsworth, D.W., and Thornton, M.M., 2002, MicroCT in small animal and specimen imaging, *Trends Biotechnol*. 20(Suppl.):S34–S39.

Huang, D., Swanson, E.A., Lin, C.P., Schuman, J.S., Stinson, W.G., Chang, W., Hee, M.R., Flotte, T., Gregory, K., Puliafito, C.A., Fujimoto, J.G., 1991, Opt. Coherence Tomogr. *Sci.* 254:1178–1181.

Huisken, J., Swoger, J., Del Bene, F., Wittbrodt, J., and Stelzer, E.H.K., 2004, Optical sectioning deep inside live embryos by selective plane illumination microscopy, *Science* 305:1007–1009.

Izatt, J.A., Kulkarni, M.D., Wang, H.-W., Kobayashi, K., and Sivak, M.V. Jr., 1996, Optical coherence tomography and microscopy in gastrointestinal tissues, *IEEE J. Sel. Topics Quant. Electron.* 2:1017–1028.

Jacobs, R.E., Ahrens, E.T., Dickinson, M.E., and Laidlaw, D., 1999, Towards a microMRI atlas of mouse development, *Comput. Med. Imaging Graph.* 23(1):15–24.

Jacobs, R.E., Papan, C., Ruffins, S., Tyszka, J.M., and Fraser, S.E., 2003, MRI: Volumetric imaging for vital imaging and atlas construction, *Nat. Cell Biol*. Ss10–Ss16.

Jiang, Y., Pandya, K., Smithies, O., and Hsu, E.W., 2004, Three-dimensional diffusion tensor microscopy of fixed mouse hearts, *Magn. Reson. Med*. 52:453–460.

Johnson, G.A., Benveniste, H., Black, R.D., Hedlund, L.W., Maronpot, R.R., and Smith, B.R., 1993, Histology by magnetic resonance microscopy, *Magn. Reson. Q* 9:1–30.

Johnson, G.A., Cofer, G.P., Fubara, B., Gewalt, S.L., Hedlund, L.W., and Maronpot, R.R., 2002a, Magnetic resonance histology for morphologic phenotyping, *J. Magn. Reson. Imaging* 16:423–429.

Johnson, G.A., Cofer, G.P., Gewalt, S.L., and Hedlund, L.W., 2002b, Morphologic phenotyping with MR microscopy: The visible mouse, *Radiology* 222:789–793.

Keng, W.T., Sharpe, J., *et al*., 2002, Optical projection tomographic examination of miscarried human embryos, *J. Med. Genet*. 39:S23–S23.

Kerwin, J., Scott, M., Sharpe, J., *et al*., 2004, 3 dimensional modelling of early human brain development using optical projection tomography, *BMC Neurosci*. 5:27–27.

Kockenberger, W., 2001, Nuclear magnetic resonance micro-imaging in the investigation of plant cell metabolism, *J. Exp. Bot.* 52(356):641–652.

Kockenberger, W., De Panfilis, C., Santoro, D., Dahiya, P., and Rawsthorne, S., 2004, High resolution NMR microscopy of plants and fungi, *J. Micros.* 214(Pt2):182–189.

Kovacevic, N., Henderson, J.T., Chan, E., *et al.*, 2005, A three-dimensional MRI atlas of the mouse brain with estimates of the average and variability, *Cereb. Cortex.* 15(5):639–645.

Kuchenbrod, E., Kahler, E., Thurmer, F., Deichmann, R., Zimmermann, U., and Haase, A., 1998, Functional magnetic resonance imaging in intact plants–quantitative observation of flow in plant vessels, *Magn. Reson. Imaging* 16:331–338.

Lee, S.C., Kim, K., and Kim, J., 2001, One micrometer resolution NMR microscopy, *J. Magn. Reson*. 150:207–213.

Lo, C., Nabel, E., and Balahan, R., 2003, Meeting report: NHLBI symposium on phenotyping: Mouse cardiovascular function and development, *Physiol. Genomics* 13(3):185–186.

Louie, A.Y., Huber, M.M., Ahrens, E.T., *et al.*, 2000, In vivo visualization of gene expression using magnetic resonance imaging. *Nat. Biotechnol.* 18(3):321–325.

Mansfield, P., 1977, Multi-planar image formation using NMR spin echoes, *J. Phys. C* 10:L55–L58.

Manz, B., Volke, F., Goll, D., and Horn, H., 2003, Measuring local flow velocities and biofilm structure in biofilm systems with magnetic resonance imaging (MRI), *Biotechnol. Bioeng*. 84:424–432.

Masters, B.R., 1999, Early development of optical low-coherence reflectometry and some recent biomedical applications, *J. Biomed. Opt*. 4:236–247.

Matsuda, Y., Utsuzawa, S., Kurimoto, T., 2003, Super-parallel MR microscope, *Magn. Reson. Med*. 50:183–189.

Papan, C., Velan, S.S., Fraser, S.E., and Jacobs, R.E., 2001, 3D time-lapse analysis of *Xenopus* gastrulation movements using mu MRI, *Dev. Biol*. 235:189.

Paterson-Beedle, M., Nott, K.P., Macaskie, L.E., and Hall, L.D., 2001, Study of biofilm within a packed-bed reactor by three-dimensional magnetic resonance imaging, *Methods Enzymol*. 337:285–305.

Paulus M.J., Gleason, S.S., Easterly, M.E., and Foltz, C.J., 2001, A review of high resolution X-ray computed tomography and other imaging modalities for small animal research, *Lab. Animal* 30(3):36–45.

Paulus, M.J., Gleason, S.S., Kennel, S.J., Hunsicker, P.R., and Johnson, D.K., 2000, High-resolution x-ray computed tomography: An emerging tool for small animal cancer research, *Neoplasia* 2:62–70.

Pautler, R.G., and Koretsky, A.P., 2002, Tracing odor-induced activation in the olfactory bulbs of mice using manganese-enhanced magnetic resonance imaging, *Neuroimage* 16:441–448.

Pautler, R.G., Mongeau, R., and Jacobs, R.E., 2003, *In vivo* trans-synaptic tract tracing from the murine striatum and amygdala utilizing manganese enhanced MRI (MEMRI), *Magn. Reson. Med*. 50:33–39.

Pickhardt, P.J., Halberg, R.B., Taylor, A.J., Durkee, B.Y., Fine, J., Lee, Jr., F.T., and Weichert, J.P., 2005, Microcomputed tomography colonography for polyp detection in an *in vivo* mouse tumor model. *PNAS* 102:3419–3422.

Pierpaoli, C., Jezzard, P., Basser, P.J., Barnett, A., and DiChiro, G., 1996, Diffusion tensor MR imaging of the human brain, *Radiology* 201:637–648.

Robson, S.C., Woods, H.M., *et al*., 2004, 3-dimensional modelling of human development using optical projection tomography, *J. Soc. Gynecol. Invest*. 11:296A.

Rollins, A.M., and Izatt, J.A., 1999, Optimal interferometer designs for optical coherence tomography, *Opt. Lett*. 24:1484–1486.

Rollins, A.M., Kulkarni, M.D., Yazdanfar, S., Ung-arunyawee, R., and Izatt, J.A., 1998, *In vivo* video rate optical coherence tomography, *Opt. Express* 3:219–229.

Segars, W.P., Tsui, B.M., Frey, E.C., Johnson, G.A., and Berr, S.S., 2004, Development of a 4-D digital mouse phantom for molecular imaging research, *Mol. Imaging Biol*. 6:149–159.

Seymour, J.D., Codd, S.L., Gjersing, E.L., and Stewart, P.S., 2004, Magnetic resonance microscopy of biofilm structure and impact on transport in a capillary bioreactor, *J. Magn. Reson*. 167:322–327.

Shapiro, E.M., Skrtic, S., Sharer, K., Hill, J.M., Dunbar, C.E., and Koretsky, A.P., 2004, MRI detection of single particles for cellular imaging, *Proc. Natl. Acad. Sci. USA* 101:10901–10906.

Sharpe, J., 2003, Optical projection tomography as a new tool for studying embryo anatomy, *J. Anat.* 202:175–181.

Sharpe, J., 2004, Optical projection tomography, *Annu. Rev. Biomed. Eng*. 6:209–228.

Sharpe, J., Ahlgren, U., Perry, P., *et al.*, 2002, Optical projection tomography as a tool for 3D microscopy and gene expression studies, *Science* 296:541–545.

Song, S.K., Sun, S.W., Ramsbottom, M.J., Chang, C. Russell, J., and Cross, A.H., 2002, Dysmyelination revealed through MRI as increased radial (but unchanged axial) diffusion of water, *Neuroimage* 17:1429–1436.

Tearney, G.J., Bouma, B.E., Boppart, S.A., Golubovic, B., Swanson, E.A., and Fujimoto, J.G., 1996, Rapid acquisition of *in vivo* biological images by use of optical coherence tomography, *Opt. Lett.* 21:1408–1410.

Tearney, G.J., Brezinski, M.E., Bouma, B.E., Boppart, S.A., Pitris, C., Southern, J.F., and Fujimoto, J.G., 1997, *In vivo* endoscopic optical biopsy with optical coherence tomography, *Science* 276:2037–2039.

Tuch, D.S., Reese, T.G., Wiegell, M.R., and Wedeen, V.J., 2003, Diffusion MRI of complex neural architecture, *Neuron* 40:885–895.

Weichert, J.P., 2004, Micro-computed tomography of mouse cancer models, *In: Mouse Models of Human Cancer* (E.C. Holland, ed.), John Wiley and Sons, New York, pp. 339–348.

Weinmann, H.J., Brasch, R.C., Press, W.R., and Wesbey, G.E., 1984, Characteristics of gadolinium-DTPA complex: A potential NMR contrast agent, *AJR Am J Roentgenol* 142:619–624.

Weinmann, H.J., Ebert, W., Misselwitz, B., and Schmitt-Willich H., 2003, Tissue-specific MR contrast agents, *Eur. J. Radiol*. 46:33–44.

Weninger, W., and Mohun, T., 2002, Cardiac phenotyping of transgenic embryos: A rapid 3D-screening method based on episcopic fluorescence imaging capturing (EFIC), *Clin. Exp. Pharmacol. Physiol.* 29:A70–A71.

Wojtkowski, M., Srinivasan, V.J., Ko, T.H., Fujimoto, J.G., Kowalczyk, A., and Duker, J.S., 2004, Ultrahigh-resolution, high-speed, Fourier domain optical coherence tomography and methods for dispersion compensation, *Optics. Express* 12(11):2404–2422.

Yazdanfar, S., Kulkarni, M.D., and Izatt, J.A., High resolution imaging of *in vivo* cardiac dynamics using color Doppler optical coherence tomography, *Opt. Express* 1:424–431.

Zhang, J., Richards, L.J., Yarowsky, P., Huang, H., van Zijl, P.C., and Mori, S., 2003, Three-dimensional anatomical characterization of the developing mouse brain by diffusion tensor microimaging, *Neuroimage* 20: 1639–1648.

35

Tutorial on Practical Confocal Microscopy and Use of the Confocal Test Specimen

Victoria Centonze and James B. Pawley

INTRODUCTION

The other chapters in this book give the reader an in-depth description of every important aspect of biological confocal microscopy that we could think of. This chapter is to provide the novice user of this instrument with a basic understanding of the practical information needed to use it effectively. Because the computer interfaces of the various commercial instruments vary greatly, this chapter will stress the important features of microscopical optics and the basics of sampling that are common to all instruments. The underlying agenda of these suggestions is based on two principles:

- Don't waste photons.
- Get all of the optical performance that you have paid for.

Getting Started

In order to be able to operate a confocal microscope properly, one must first be thoroughly familiar with the basic principles of nonconfocal microscopy. The user must understand the concept of conjugate image planes, Köhler illumination, and how to set up a microscope to produce it [i.e., the field diaphragm must be in focus in the image plane and the condenser aperture set so that the illumination almost fills the back-focal plane (BFP) of the objective lens. See the Appendix to this chapter or Chapter 6, *this volume*, for a refresher]. The user must also understand how the phenomenon of diffraction acts to place **the** fundamental limitation on the resolution that any optical system can attain (see Chapters 1, 8, and 11, *this volume*, or an introductory text such as Bradbury, 1984, Inoué 1986, Pawley and Centonze, 1997).

The next step is to get an image of some specimen that you understand. Without going into the details of the many available commercial confocal systems, we note that most confocal microscopes permit the user to set up the microscope for normal, nonconfocal use, and then switch over to confocal operation by changing the position of a single control. The user should follow the instructions from the manufacturer to produce such a confocal image using a live mode (i.e., producing an image that is continuous and not frame-averaged or Kalman filtered).

In most cases, the fluorescent specimen chosen for this first attempt at using the confocal microscope should be similar or identical to one that has just been viewed with success on a conventional instrument. Almost invariably, new users will close the detection pinhole in order to get the highest resolution and increase the zoom magnification to increase the size of the image on the display. They will then try to adjust the focus, but after a few seconds, the image will begin to fade and become indistinct. Reducing the zoom magnification will reveal the terrible truth: the observations so far have severely bleached the dye in the rectangular area that was being scanned at the higher zoom magnification. This is the moment at which would-be users either decide right then and there that the confocal microscope clearly produces far more bleaching than they are used to and leave the room, never to return, or they decide that there may be a bit more to operating this instrument than they had bargained for and set out to do better. This chapter is written for those who fall into the latter category.

Bleaching — The Only Thing That Really Matters

There are three reasons that the bleaching rate of a confocal microscope often **seems** to be much higher than that of a conventional epi-fluorescent microscope:

1. The instrument **can** be used in such a way that the **supposition is correct**! A laser is a far more intense light source than a Hg arc. Although the total power striking the entire specimen may be less with the laser, the area of the specimen over which it is absorbed can be reduced arbitrarily by increasing the setting of the zoom magnification control, thus increasing the power/unit area. The crucial difference between the two microscopical methods is that in normal epi-fluorescence, the power/area on the specimen is fixed by the type of arc and the illumination optics, while in confocal microscopy, the power/area increases with the square of the zoom magnification. In normal epi-fluorescence, one does not expect to see an image that is **both large enough** to see the finest details and **bright enough** to view by eye because it is not possible. In the confocal microscope, the extreme intensity of the laser does make it possible, though only for the moment until bleaching occurs!
2. If one is accustomed to viewing a widefield (WF) image in which fluorescence from a large number of focal planes is added together into a single image, a confocal image may look somewhat anemic because, ideally, it records only the fluorescence features present in a single optical section. When presented with an image of the few features that happen to be in the focus plane, one may be tempted to use a much longer exposure than is necessary in a vain attempt to record features that are not really there.
3. A final factor contributing to the perception that confocal bleaches faster is that, in normal epi-fluorescence, one expects to make one exposure that may require 30 to 60 s, while in the confocal microscope one often wants an image that is bright enough to look at after collecting for only 1 to 2 s and then sets out to

Victoria Centonze • University of Texas Health Science Center, San Antonio, Texas 78229
James B. Pawley • University of Wisconsin, Madison, Wisconsin 53706

Handbook of Biological Confocal Microscopy, Third Edition, edited by James B. Pawley, Springer Science+Business Media, LLC, New York, 2006.

record 20 to 30 similar images of the adjacent planes to form a three-dimensional (3D) stack. Each of these 20 to 30 images will cause additional bleaching.

In actual fact, what one should be interested in is not so much the bleaching rate but some sort of efficiency ratio of information recorded to illuminating dose. This ratio is set by the numerical aperture (NA) and transmission (T) of the optics and the quantum efficiency (QE) of the photodetector. Therefore, assuming equal optics, the confocal microscope is 10× to 100× more efficient than photography, because at these low light levels, the photomultiplier tube (PMT) photodetector that it uses is 10× to 100× more efficient than film (Chapter 12, *this volume*). The only photodetector more efficient than the PMT is the cooled charge-coupled device (CCD), and this detector can be used in disk-scanning confocal microscopes (Chapters 10, 12, 21, 25, and Appendix 3, *this volume*).

While on the subject of bleaching, there are a few additional items that should be mentioned. It is generally assumed (1) that bleaching is proportional to the total dose of light where dose is the illumination level (in photons/μm^{2s}) × time, and (2) that, as absorption is usually low, the total number of photons passing through any horizontal plane is a constant. From these facts, some jump to the conclusion that bleaching occurs at the same rate in the focus plane as it does outside this plane. While this may be true for short distances above and below the focus plane and when using lenses of low NA, it is not true once the height of a stack of images becomes comparable with the width of the scanned area. Figure 28.3(B) in Chapter 28 shows an *xz*-image through such a bleach pattern made with an NA 1.4 in a specimen of fluorescent plastic. It confirms that there is a pyramid of bleached dye expanding above and below the plane of focus. As the illumination intensity at any level is proportional to the cross-sectional area of the light cone at that level, one can see that, with a large NA lens, the illumination level and, therefore, the bleach rate drops off quite quickly with distance away from the focus plane. The illumination level at these planes is not constant within the cone but is less strong near the edges.

Figure 35.1 is a diagram to help visualize this process. We assume that the BFP of the objective is uniformly illuminated and, therefore, light is focused into the focused spot from all angles equally. As a result, the total number of photons passing through any particular level within the cone of the beam is a constant. The intensity itself decreases roughly with the square of the distance away from the focus plane but, as the beam scans over the raster, this effect is counterbalanced by the fact that most points in non-focus planes will be illuminated for a longer time. Although points that are only illuminated by the outer rays of the cone when the beam is scanning near the edge of the raster will only be illuminated once per scan, those near the center of the raster will be illuminated for a time that is longer in direct proportion to the reduction in the illumination intensity at any instant. All of the points for which this is true for a particular focus position will lie inside a bleaching octahedron having the scanned area as its base and a defining angle equal to the acceptance half-angle of the objective (α). Inside this octahedron the bleach rate is constant, while outside it the bleach rate decreases slowly until it becomes zero in the region where even the outer rays of a beam scanning the edge of the raster never reach.

As the focus plane moves up or down in the specimen during a *z*-series, the total bleaching will be proportional to the superposition of the octahedra of the individual planes. The result is that points inside the octahedron associated with the central focus plane will receive a maximum dose while those farther from the center will receive less. The reason for mentioning these simple consequences of geometrical optics here is to emphasize the difficulty of devising a computer program to correct for bleaching artifacts even if the bleach rate is assumed to be directly proportional to the energy deposited and the dye stays in one place. The best plan is to be careful not to waste photons and thereby minimize the amount of bleaching that occurs.

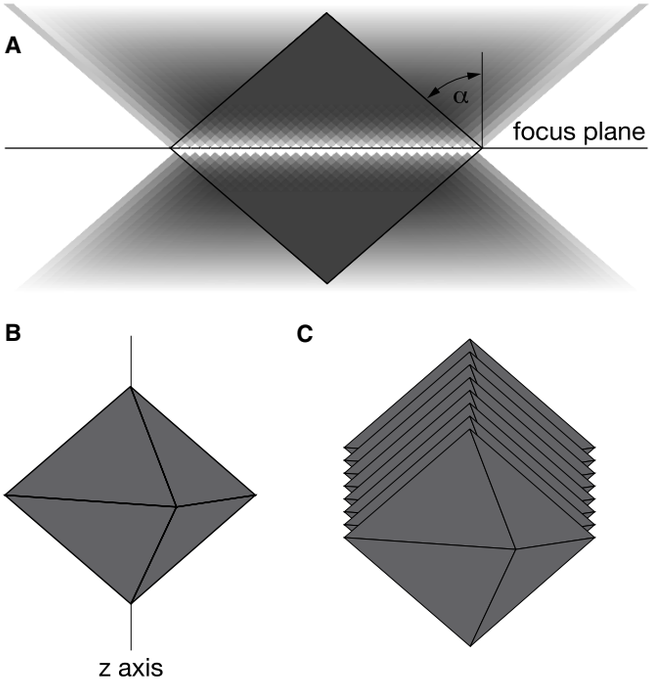


FIGURE 35.1. Pattern of bleaching in the confocal microscope. A stationary, focused light beam will bleach a conical volume in a uniform fluorescent specimen. The severity of the bleaching at any one level in the cone is inversely proportional to the area of the cone at that level and is most severe at the focus plane. However, as the beam is scanned over the focus plane, points in this plane are only illuminated a few times while points in adjacent planes will be illuminated for a longer time. As the beam is scanned over a line in the focus plane, the convergence angle of the beam (α) defines a triangle inside which reside points at which the lower intensity of the flux associated with not being in the focus plane is exactly compensated for by the increased amount of time they are illuminated [*black diamond* (A)]. As this line scans to create a 2D image, the triangle of equal total illumination becomes an octahedron (B). As the 2D focus plane is scanned in *z* to create a 3D image, the octahedrons add up to produce more damage near the center of the raster, where the planar constant bleach pattern is thickest (C). It should be noted that, because of the rather slow response of the mechanical scanning mirrors, a considerably higher level (10×–20×) of bleaching will occur to either side of the imaged area of the focus plane where the horizontal motion of the mirrors slows down and reverses. In some confocal instruments, the beam is blanked during this retrace period.

Although the bleaching problem may be no worse in confocal microscopy than in normal fluorescence microscopy, it is still a very serious problem. In fact, it is not unlikely that, particularly when viewing living cells, one's success at using either method will depend on how successful one is at collecting and recording as great a fraction as possible of the fluorescent photons produced and at recording only the information that one really needs while using no more than the minimum necessary exposure. We explain how to do this in the sections that follow.

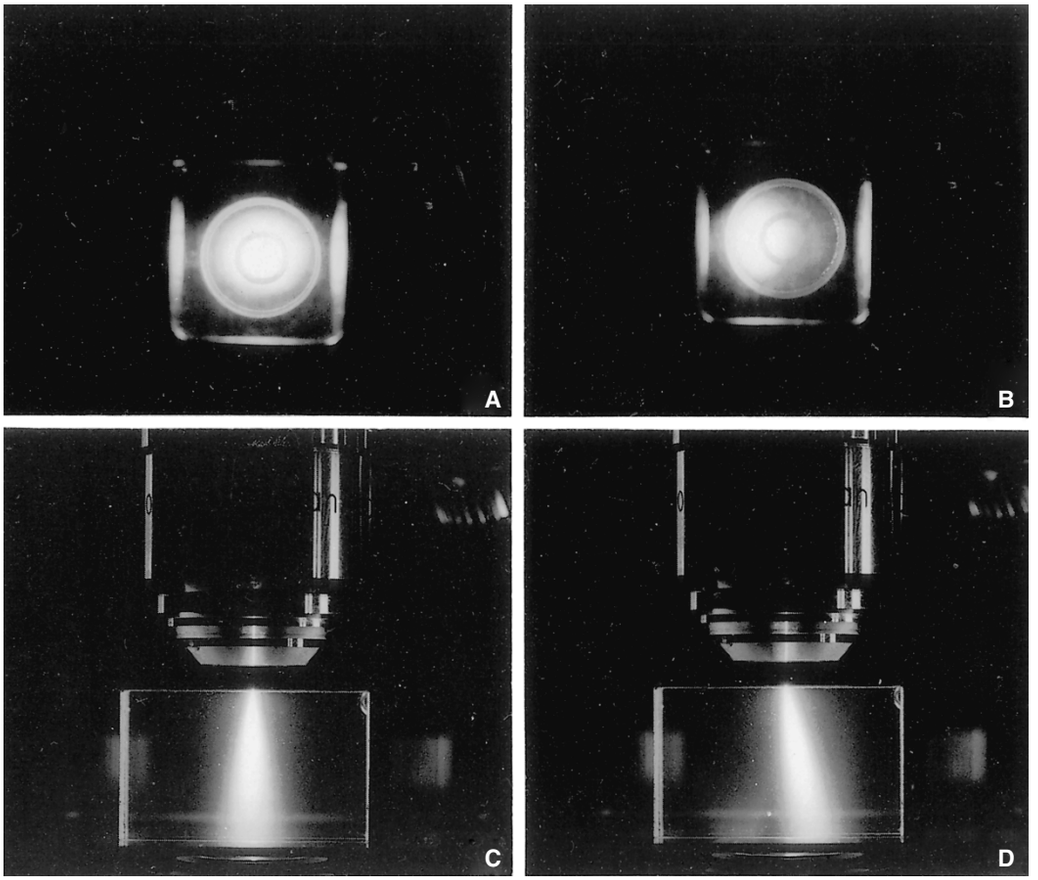


FIGURE 35.2. Alignment of the laser in the back-focal plane (BFP) of the objective as seen using a 45° prism that allows one to view a circular target situated in the BFP. (A) Properly centered, (C) misaligned. The two lower images show the bundle of light rays projected into the specimen under each alignment condition. These images were made by photographing the fluorescent light emanating from a cube of uranium-doped glass placed in the specimen plane of a 10×/0.45 objective. The angles involved are somewhat smaller than expected because the glass has a very high index of refraction.

GETTING A GOOD CONFOCAL IMAGE

To obtain an optimal confocal image, a fluorescent specimen must first be in focus under the right type of objective: that is, one that is designed to focus into a medium having the refractive index of your specimen, thereby avoiding problems with spherical and chromatic aberration (see Chapters 7 and 20, *this volume*). Because of the optical sectioning property on the confocal microscope, specimens that are far out of focus will produce **no signal**! If you are having trouble finding the specimen, open the pinhole all the way, focus on the specimen, then close it down again.

Next, the scanhead must be properly aligned. When the beam scans over the center of the raster pattern, the light from the laser should be both on axis and fill the BFP of the objective, and the light passing up from the focused spot to the PMTs must be aligned to pass through the pinhole. Once alignment has been achieved, the pinhole size should be set for the best compromise between signal strength and *xy*- and *z*-resolution, (for details see Chapter 22, *this volume*) the PMTs should be adjusted to produce an appropriate signal level and the monitors should be adjusted so that the full range of signal can be viewed.

Proper alignment[1] of the scanhead first requires adjustment of the mirror(s) that direct(s) the laser light down the optical path of the microscope. A 45° angle prism (or even just a small piece of lens-cleaning tissue) can be positioned in place of an objective so that the laser light path can be viewed with respect to the BFP (Fig. 35.2). Although the **angle** at which it passes the BFP is proportional to the instantaneous position of the beam in the imaged plane, the laser beam should **always** pass through the center of the BFP and then be focused by the objective to form a symmetrical spot at the specimen plane [Fig. 35.2(A,B)]. Misalignment at the BFP may mean that the light does not fill the pupil of the objective, reducing its effective resolution and causing it to pass through the specimen at an angle [Fig. 35.2(C,D)].

Next, a standard fluorescent or reflective test specimen must be used to align the scanhead so that the central maximum of the

[1] Many newer confocal microscopes come pre-aligned and there are no user controls for adjusting the alignment as described in this section. However, some of the tests used to check performance can still be used to see if you need a service visit.

diffraction-limited spot (Airy disk) in the specimen is focused through the pinhole where it can be detected by the PMT. When aligning for peak signal, it may be helpful to change the display to have a colorized lookup table (LUT). A colorized LUT emphasizes small changes in signal intensity because the eye is more sensitive to absolute hue than to absolute gray level. While scanning, adjust the scanhead mirrors or pinhole location to maximize the signal received by the PMT. For the time being, you need only be concerned with obtaining the brightest image, not one of maximum quality. It is advisable to make the mirror adjustments using the objective you plan to use for your final high-quality image. Because wedge errors in the dichroic beam-splitter can displace the apparent position of the pinhole (Chapter 9, *this volume*), older instruments will require re-alignment of the scanhead whenever the dichroic is changed.

Once one has a reasonable image, it is probably worthwhile to make a note of the settings of all the user controls. These can later be used to monitor instrument (and operator!) performance and to serve as starting conditions after one has implemented major service or development changes.

With basic alignment complete, you may find it interesting to view the Airy disk in the pinhole plane. On older scopes this can be accomplished by placing a small CCD camera in the intermediate image plane, but if your instrument uses a larger, iris-diaphragm aperture rather than a real pinhole, you may be able to see the light directly by viewing it scattered by a piece of paper placed in front of the pinhole. Figure 35.3 shows the sort of image you can expect to see if you do this by placing a piece of paper in the second filter well of a Bio-Rad MRC series scope that has been set up to measure BSL from a plane mirror surface that is either in focus [Fig. 35.3(A)] or just out of focus [Fig. 35.3(B)]. The in-focus image shows some astigmatism, probably caused by imperfections in the beam-splitter. It is informative to see how the image of the Airy disk degrades if one reduces the zoom magnification, a process that reveals the deleterious effect of off-axis aberrations such as astigmatism, curvature of field, and coma (see also Chapter 11, *this volume*). One can also use this setup to view the asymmetrical increase in Airy disk size (and decrease in resolution) caused by misaligning the illumination in the objective BFP (as in Fig. 35.2).

Actually, viewing the Airy disk helps to make clear the idea that each objective has an optimum pinhole size because it becomes evident that the light at the pinhole plane is simply a magnified view of the light in the image plane and that, therefore, at a fixed NA, the size of the image of the spot will be proportional to the magnification of the objective. A pinhole aperture equal to the diameter of the first minimum in the Airy disk (i.e., 1 Airy unit) will pass about 80% of the in-focus signal and still have a bit better *xy*-resolution than a widefield microscope. Once this benchmark detector aperture is known for a given optical setup (wavelength, NA, magnification), it is possible to make informed choices about the most appropriate aperture for any other objective.

Specimen preparation, objective lens, pinhole size and alignment, and focus plane all affect the amount of light collected from the specimen. Adjustment of the display monitor and the PMT affect the image viewed. The black level of the PMT amplifier must be set so the full range of signal can be detected. This can be done by scanning while light is blocked from entering the PMT and adjusting the black level until the rastered area becomes **just visible** compared to the unscanned part of the monitor screen.[2]

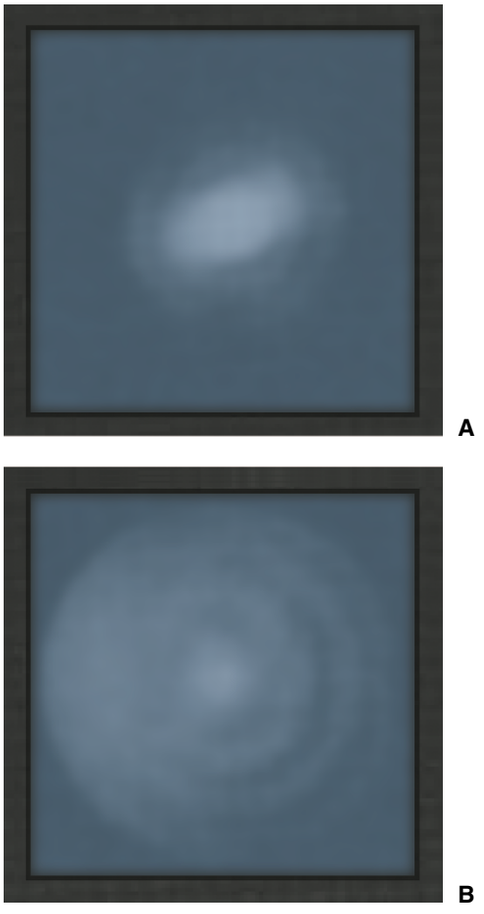


FIGURE 35.3. The Airy disk reflected back from a mirror test specimen can be viewed directly at the pinhole plane of a Bio-Rad MRC confocal microscope by removing the second filter block and placing a piece of paper into the bottom of the well. (Turn the PMT all the way down before doing this!) (A) In focus, but showing slight astigmatism, probably because of distortion by the dichroic; (B) slightly out of focus. Random points of light well away from the optical axis defined by the Airy disk represent stray light. This is less evident in (A) because of the higher relative brightness of the central spot and because the beam dump in first filter block had been improved by the addition of a piece of black velvet.

Note that if the black level is set too high, some intensity values may fall below the voltage corresponding to the zero value of the analog-to-digital converter (ADC) and so not be recorded. If, after setting the black level in this way, the image on the display has insufficient brightness, this can usually be best adjusted by modifying the display LUT in the computer.

The gain of the detector circuitry (i.e., how much it amplifies) is changed by adjusting the accelerating voltage of the PMT. In round figures, a 50 V increase in the accelerating voltage doubles the gain. Practically speaking, the gain controls both the brightness and the contrast of the image. When it is properly adjusted, the pixels in the brightest areas of the image should be bright white in order to utilize the full gray-scale range of the data handling system. However, one must also be careful not to **saturate** the ADC and this may be more difficult to avoid than expected because, in fluorescence confocal microscopy, the brightest signal may represent only <16 counts/pixel. Because of statistical factors discussed later in this chapter, an average value of 16 counts/pixel really implies 16 ± 4 counts/pixel. Therefore, if one is to avoid

[2] When the black-level control is set correctly, black areas will register as 2 to 3 ADU levels out of 255.

truncating data representing such small numbers of quantum events, one must be careful that the highest value of the ADC output (usually 255) represents **not the average** value of the brightest pixel but rather an unusually high measurement of this bright value (at least 16 + 4 = 20 in this example). In other words, if the gain is set properly, the value of the brightest pixel of a fluorescent image resulting from the average of several frames[3] should probably be no more than 200 to 220 and not 255. One can check the gain setting by plotting a histogram of pixel intensities or by using a colorized LUT to verify that the brightest pixels in a live (not averaged) image are below the saturation level of the digitizer.

It should now be possible to obtain a reasonably good image of the specimen. If, however, the images are not satisfactory, one should check the following parameters:

No Signal

- Can you see laser light of the appropriate color **emerging** from the objective? Is a shutter or a prism obscuring the beam?
- Is the specimen near the focus plane?
- Is the computer system adjusted to display the signal from the PMT that is actually receiving the light signal?
- **Never panic** and turn up the PMT all the way in a vain search for a signal that does not exist only to find that you have damaged the PMT by overloading it when you finally reset the control that had been obscuring the signal!

Low Signal

- Do **small** adjustments of the alignment knobs **reduce** the signal level as they should if the beam is properly aligned?
- Is the laser power sufficient? Are neutral density filters attenuating the light too much? Does the laser cavity need retuning? Are the optics used to launch the laser light into the fiber correctly aligned?
- Is the laser line appropriate for exciting your dye and are the correct filters in place?
- Is the specimen stained properly and has an anti-fade agent been included in the mounting media? Check by viewing the same specimen in the non-confocal fluorescence mode if available.
- Is the sample too opaque for the laser light to reach the focus plane and for the emitted light to exit the specimen without excessive scattering losses?
- Are the settings of pinhole size, PMT gain, and computer display system correct?

Simultaneous Detection of Backscattered Light and Fluorescence

The exercises that will be described in the following sections are easier to perform if one can arrange the system so that it can detect both backscattered light (BSL or reflected light) and fluorescent light simultaneously (Pawley *et al.*, 1993). Such a system is diagrammed in Figure 2.7 and provides the optimal removal of specular reflection artifacts from optical surfaces above the objective. A 1/2-wave plate in front of the laser is used to rotate the polarization plane of the beam so that a suitable fraction of it (0.8%–5.0%) is reflected down the microscope axis by an uncoated, clear glass beam-splitter in the first filter block. The light then passes through a 1/4-wave plate between the ocular and the objective before reaching the specimen. Light either reflected and/or emitted from the specimen returns via this same pathway, through the 1/4-wave plate and the dichroic beam-splitter to the second filter set. This system is constructed to pass the fluorescence signal to PMT 1 and the reflectance signal to PMT 2 via a rotatable 1/4-wave plate, analyzer, and laser-line filter. During setup, the rotatable elements of the second filter block are adjusted to eliminate axial specular reflections and the lower 1/4-wave plate is rotated to obtain a maximum signal from a biological specimen (Fig. 35.12 shows a stereo, BSL image obtained with this system). The operation of a similar system is described in more detail in Chapter 17. Because this system uses a different beam-splitter, the mirrors of the scanhead will need to be re-adjusted as described above.

NEW CONTROLS

Getting the best out of a confocal fluorescence microscope requires consideration of several matters that do not affect normal light microscopy. In order to extract as much information as possible from every photon emitted by the specimen, the user must set two unfamiliar parameters properly: pinhole size and zoom magnification.

Photon Efficiency

If either the pinhole size or the zoom setting are set incorrectly, the specimen may be subjected to much greater levels of exciting light than should be necessary to produce an image of a given quality. This will increase bleaching unnecessarily.

This is particularly important when examining living specimens containing fluorescent substances because, in this case, the exciting illumination inevitably produces both bleaching and cytotoxicity (MacIntosh *et al.*, 1990; Chapter 39, *this volume*). The bleaching itself will be more severe than with fixed specimens because on living specimens, one generally cannot use anti-fade agents (except, perhaps, oxygen deprivation or Trolox). In general, the **biological reliability** of the data is likely to be inversely proportional to the laser power used. In other words, even though using more light may make the **image appear more distinct**, it may also damage the object that the image is supposed to represent so seriously that the data is merely a better image of a worse specimen (see Chapters 38 and 39, *this volume*).

Pinhole Size

The advantage of the confocal method of image formation is that light emitted or scattered into the objective from planes other than the focus plane will be out of focus when it reaches the pinhole plane [Fig. 35.4(A)]. As a result, most of it will **not** pass through the pinhole and, to the extent that this happens, any image produced from the detected signal will be characteristic of only a single plane. For this reason, the confocal microscope is said to make optical sections.

The diameter of the aperture in front of the photodetector is usually adjustable so that it can be matched to the size of the image of the Airy disk (r_{Airy}) that the objective lens projects from the excited spot in the specimen to the pinhole plane [Fig. 35.4(B)]. The diameter of this disk is directly proportional to the total magnification between the object and the pinhole plane (see Chapter 2, *this volume*) and through the Abbe equation,

[3] Averaging several frames reduces statistical noise and means that the number recorded is closer to the real intensity value for each pixel.

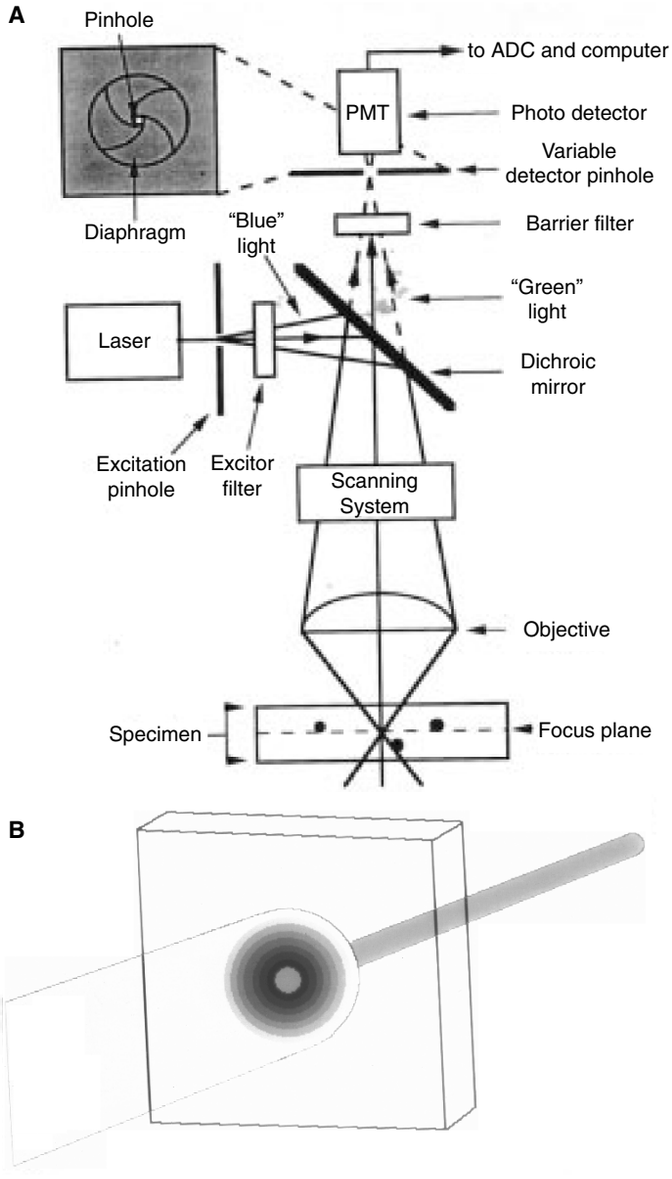


FIGURE 35.4. Confocal schematic. (A) Block diagram of the optical components of a fluorescent, laser-scanning confocal microscope: Short wavelength blue light from the laser passes through an exciter pinhole and filter and is then reflected by the dichroic mirror into the objective lens. The lens focuses it at a spot within the specimen. Some of the green fluorescent light from the specimen returns through the objective. Because of its longer wavelength, it can pass through the dichroic and barrier filters, and it comes to a focus at the plane of the detector pinhole. That fluorescent light which originated from the plane-of-focus passes through the pinhole to the detector while that from other planes is out-of-focus at the pinhole plane and so is selectively excluded from the detector. (B) The relationship between the hole in the pinhole and the Airy disk focused at this plane.

$$r_{\text{Abbe}} = 0.61\lambda/NA \quad \textbf{(1)}$$

it is proportional to the wavelength λ and inversely proportional to the NA of the objective. The **area** of the central spot of the Airy disk at the pinhole plane increases by a factor of over 12 if, for example, a 10× NA 0.5 lens is replaced by a 100× NA 1.3 lens (assuming that both are used in such a way that their BFPs are fully illuminated). Because the signal that passes through the aperture from a non-planar specimen is generally proportional to the pinhole area, an incorrect adjustment of the pinhole size can significantly reduce the effective sensitivity of the microscope.

However, there is a second constraint on the choice of pinhole size. Because almost all of the light originating from the plane of focus will pass through a properly-aligned pinhole, 1 Airy unit in size, one might expect that there could be no reason for ever wanting to use any other aperture size. This might be the case if the diameter of the pinhole did not also affect the spatial resolution of the microscope in both the *xy*-plane and, to a lesser extent, in *z*. If the pinhole is made very small (<0.1 Airy units), the *xy*-resolution of the instrument is improved by ~40% over that set by the Abbe limit, but only at the cost of reducing the signal level by 95%. As the pinhole is made larger, it begins to accept more light while the *xy*-resolution is reduced. When it equals 1 Airy unit, 80% of the light originating from the focus plane is accepted, while a 10% resolution gain is still being realized. On the other hand, when the pinhole is opened still more, any extra light that it accepts **must** be that originating from either above or below the focus plane, and this reduces the optical sectioning effect as well as providing more photons.

Therefore, depending on the particulars of the experiment, it may be preferable to either close the pinhole down to improve *xy* spatial resolution or open it up in order to collect more signal at somewhat reduced *z*-resolution. The latter is particularly true when viewing sensitive living specimens because, as these will usually not tolerate the multiple exposures needed to record many, closely-spaced optical sections in any case, the *z*-resolution is bound to be compromised by inadequate sampling (see below) **unless** the optical section is broadened. In this case, lower *z*-resolution will actually **improve** the image.

For most specimens protected by anti-fade agents (Chapters 18 and 39, *this volume*), the best compromise between sensitivity and spatial resolution is found by setting the aperture to be equal to 0.5 Airy units, the diameter at which the Airy disk reaches 50% of its peak intensity. At this setting, about 60% of the light from the plane of focus will reach the detector, and the *xy*-resolution will still be a bit better than that produced by the same optics when used in a non-confocal manner.

It should be emphasized that, as the presence of epi-fluorescence and DIC attachments on an older non-infinity microscope may increase the effective magnification of the objective lens, these figures should only be used as a guide.

Stray Light

Stray light can reach the pinhole plane in many ways but, when imaging in BSL mode, the most common is **laser light** reflected back by the beam dump and then up the optical axis by the upper surface of the beam-splitter or scattered in all directions by dust on optical and mirror surfaces. Most of the diffuse off-axis scattering visible in Figure 35.3 is from this source, but one must also be wary of **room light** entering through the objective or through holes in the light-tight box surrounding the detection optics. Stray light can sometimes be reduced by improving the efficiency of the beam dump (see Appendix 1, *this volume*) but, in general, one can only control for it by measuring the PMT output for different pinhole sizes **without** a reflective specimen in the focus plane and then subtracting these values from the corresponding readings made with the reflecting surface in focus.

Is the Back-Focal Plane Filled?

Some early confocal microscopes applied the laser output directly to the BFP without first expanding it (Chapter 9, *this volume*). Though the exact size of the beam depends on the details of the design of the laser, it is usually ~1 mm. While this is a fairly good match to a 100× NA 0.8 objective, it is too small by a factor of 10 for a 10× NA 0.45 objective. If such a beam is used with such a lens, the effective NA on the illumination side will be only 10% of that marked on the lens, and the *xy*-resolution will be 10× larger. On air lenses, one can check the filling of the BFP by turning on the microscope with no specimen present and either parking the beam on axis or going to the highest possible zoom and then observing the pattern that the light leaving the objective makes when it falls on a screen (a piece of lens tissue will do) held a few centimeters away from the front of the lens. If the BFP is overfilled, the boundary of the bright ring of light will have a sharp edge to it. (For a listing of the dimensions of the BFP for representative objectives see Table 9.2, *this volume*.)

Pinhole Summary

- Make the pinhole a little smaller than the first dark ring of the Airy disk (~0.8 Airy unit).
- On **a non-planar (bulk) specimen**, the signal level is generally proportional to the area of the detector pinhole.
- At a fixed NA, the optimal pinhole diameter is proportional to the magnification of the objective, that is, the diameter appropriate for 40× NA 1.3 is only 40% as large as that proper for 100×, NA 1.3.
- Not adjusting for this fact can reduce signal 6.25×.

Circumstances may often require deviations from the benchmark settings of the pinhole size given above, but this should only be done after considering the potential cost in terms of biological reliability (smaller pinholes give better *z*-resolution but less signal, meaning the specimen must endure more excitation light).

Statistical Considerations in Confocal Microscopy

The visibility of small objects viewed in a confocal microscope depends not only on the optics of the beam-forming system but also on detecting a sufficient number of photons to permit the signal from the feature to be statistically discriminated from that of the background. The matter of visibility is complicated by the fact that the images of small features are transmitted through the optical system with less contrast than are the images of large features. In other words, one must detect and record an image with more statistically-defined gray levels if one expects to make small features visible.

A confocal image is recorded by detecting the light signal from each point in the scanned raster and storing a number proportional to this light intensity in a computer. The image can be seen by displaying these numbers as distinct gray levels at the appropriate location on a monitor (see Chapter 4, *this volume*).

The PMT detector used in most laser confocal microscopes is extremely sensitive. It is capable of producing one recordable event (a photoelectron, PE) for every 5 to 10 photons striking it, and as long as it does not get too warm and is shielded from all sources of extraneous light, it has almost no dark current. Using the fast photon-counting mode found on some instruments, useful images can be recorded in which the brightest pixel may represent only 10 PE (~100 photons) while the dimmest pixel may average only 0.1 PE (1 photon).[4]

Even though this performance is impressive, it is important to remember that the visibility of features in any image is limited by a relationship between three factors: the contrast intrinsic to the signal from the feature, the transfer of this contrast by the optics to the detector, and the statistical uncertainty associated with the number of photons detected from it.

When one records an image photographically, the number of photons involved is so much greater and the chance of detecting an individual photon is so much less, that the topic of photon statistics is seldom explicitly considered. In the discussion that follows, contrast refers to a measure of the variation of the signal intensity within the image.

The term "photon statistics" recognizes the fact that a beam of light is actually composed of photons, which, as elementary particles, are governed only by statistical laws. If, after many measurements, the mean brightness of a given pixel is found to be 25 PE, random statistical variations ensure that the actual number counted on any given measurement will be somewhere in the range of ±1 standard deviation (SD) from this mean value only 67% of the time. As photons obey Poisson statistics, the standard deviation is simply the square root of the mean, so 67% of the measurements will be in the range of 20 to 30 counts/pixel, and 33% of the measurements will be outside this range!

As a practical matter, a feature that is one pixel in size will only be recognizable or visible above the statistical noise present in the surrounding pixels if it differs from the mean of the background by 5 SD (Rose, 1948). In the case noted above, the 25-count single-pixel feature would only be visible if the average background signal level was about 1 count/pixel. In other words, in order to produce a visible feature in the image, the staining of an isolated bright pixel must be sufficiently intense that, even after its contrast has been reduced by the optical system, it can still produce a detectable signal that is ~25× larger than that of its surroundings. The effects of this statistical limitation can be seen in Figure 35.5, in which part of the test specimen has been imaged with an average of 2, 4, 8, and 16 counts/pixel in the bright features. We must emphasis that the improved visibility *per se* of the bars in the middle two patches is not caused by improved optical resolution, but merely by counting enough particles so that the features of smaller size can be recognized.

[4] Novice confocal users, having made an intensity histogram of one of their images and having found that at least a few pixels have every one of the 256 intensities possible in an 8-bit image, may jump to the conclusion that the stored number is equal to the number of detected photons. Although not quite impossible, this situation is extremely unlikely to be true. The misunderstanding is related to the role of the multiplicative noise that characterizes the performance of all PMTs. Once a photon is absorbed and a free photoelectron (PE) produced, the PE is attracted to the first dynode where it collides producing, say, four secondary electrons (SE), which then proceed to the second dynode. As Poisson statistics controls this process, on many repetitions, 4 ± 2 SE will be produced. Because a PE that produces 6 SE that strike the next dynode is likely to produce a larger final pulse at the far end of the dynode chain than one that produces only 2 SE, it becomes clear that all PE are not amplified equally. As a result, given suitable signal levels and contrast settings, even an image that actually consists of only two signal intensities (0 and 1 ± 1) **can** yield an image histogram showing all possible stored values from 1 to 255. Multiplicative noise masks the fact that fluorescent confocal images usually represent the detection of very few photons/pixel. If it did not, and if the system gain was scaled so that 1 PE = 1 unit in the memory, the posterized nature of the image would warn the viewer against having great confidence in the values actually recorded.

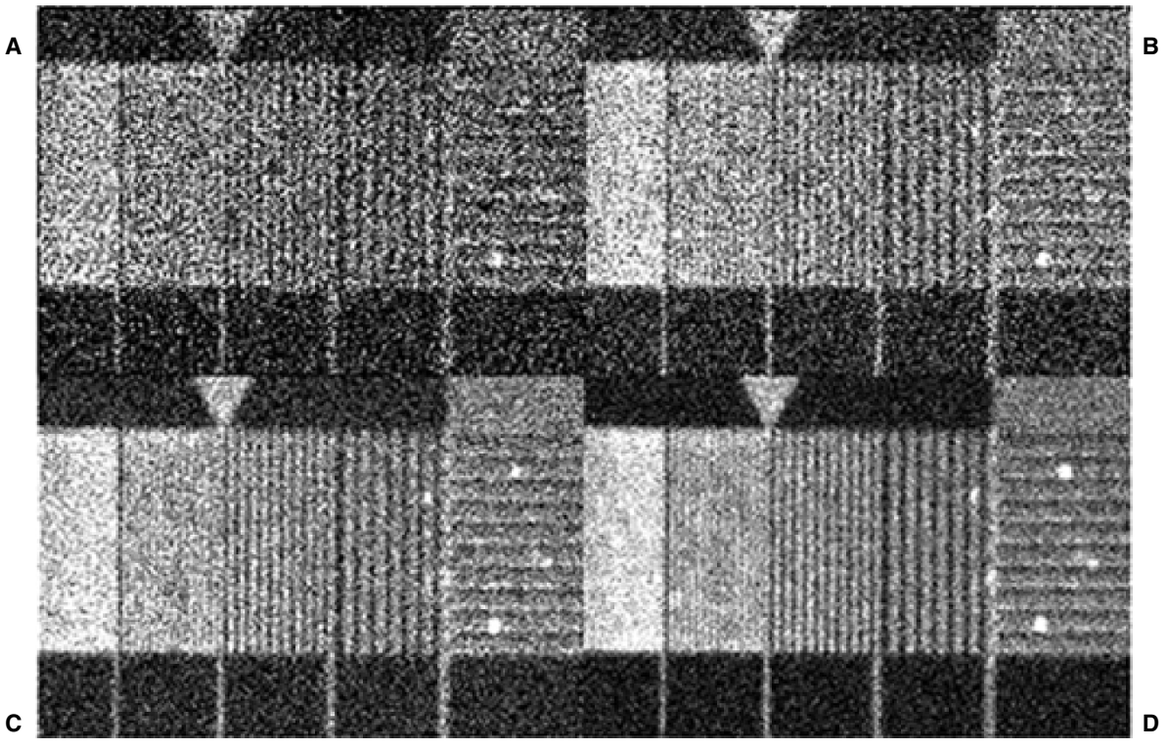


FIGURE 35.5. Confocal images made with few photons. Part of the test specimen has been imaged with an average of (A) 2, (B) 4, (C) 8, and (D) 16 counts/pixel. The improved visibility of the bars in the smaller patches is not caused by improved optical resolution but merely by counting enough particles so that these low-contrast features can be recognized.

Fortunately, as is shown in Chapter 4, with Nyquist sampling (see also next section) all real features cover at least 16 to 25 pixels in a two-dimensional (2D) image. Under these circumstances, it is the total number of counts recorded for the whole feature that is relevant to its visibility. Images containing six gray levels (corresponding to 0, 1, 4, 9, 16, and 25 events) can be usefully recorded with ~25 counts in the brightest pixel. The number of photons needed to see the bars in Figure 35.5 is less than the 25 PE used in the example above because the features are much more than one pixel in size.

The limitations imposed by counting statistics on feature visibility are immutable and are not affected by linear image processing (i.e., contrast and brightness settings). Therefore, when imaging specimens that have a stain contrast that is lower than 25 : 1, it is often necessary to average a number of scans to produce a useful image. This process does not literally "remove the noise," it merely permits more photons to be utilized, and this reduces the statistical variations in each of the thousands of the intensity measurements that make up the image. Because this process obeys Poisson statistics and the ratio of signal-to-noise (S/N), $S/N = n/\sqrt{n} = \sqrt{n}$, and counting 4× as many photons, will double the S/N making it possible to detect features in the image having only half as much contrast.

The Importance of Pixel Size

A pixel is that part of a digital image whose intensity can be accurately represented by a single number. Normally, each horizontal line of the rectangular scanning raster is divided into either 512, 768, or 1024 subdivisions, and each one of these subunits represents one pixel. The area of the specimen that can be properly represented by a single pixel varies with the magnification and NA of the objective and on the adjustment of the zoom magnification. The zoom setting controls the magnitude of the current waveforms supplied to the scanning mirrors and hence the size of the raster scanned on the specimen. Smaller currents make the light beam scan over smaller areas of the specimen, producing a higher magnification in the final image as displayed on the computer screen; larger scan currents produce lower magnification as the raster scanned on the object is larger in area.

Although the ability to arbitrarily change the magnification in this way is usually seen as a great convenience in terms of being able to fit the scanned area to the size of the object of interest, there can be hidden dangers associated with the incautious use of this control. As there is usually a fixed ratio between the size of the raster and the size of an individual pixel, adjusting the zoom control changes the area of the specimen represented by a single intensity value. However, all possible pixel sizes are not equally suitable for recording a set of digital data that retains all of the spatial information present in the original analog image.

The Nyquist Sampling Theorem states that, when a continuous, analog image is digitized, the information content of the signal will be retained only if the diameter of the area represented by each pixel (referred to the specimen) is at least 2.3× smaller in linear dimension than the resolution limit of the optical system (in x, y, and z!).[5]

[5] In various chapters in this book, the optimal number of samples/resolution-element varies between 2.3 and 4.0. Although reasonable arguments can be made for all these numbers, it seems safe to say that the larger ones are appropriate when the noise level in the image is low and when viewing small periodic objects. The smaller numbers are suitable for most confocal fluorescence images, because in these images, the high noise level prevents one from seeing small, low-contrast features. Consequently, the actual resolution may be considerably less than that predicted by the Abbe equation.

The optical resolution limit in the *xy*-plane is set by the Abbe equation (Eq. 1). This implies that, for each λ and objective lens used, there is an optimal setting for the zoom control. In the same way, the interplane sampling interval in a 3D data set should ideally be a bit less than half the *z*-resolution. Taking 200 nm as a typical value for r_{Abbe} for a high-resolution, NA 1.4 objective, a pixel width of 200/2.3 = 80 nm is needed to properly sample the data in the *xy*-plane, while the interplane spacing for the same optical conditions should be about 3× larger, or 240 nm. This means that the blob in the image that represents a point object will always be at least 5 pixels wide and 5 planes in height. It also means that the diameter of the probing beam is ~5 times larger than the interline spacing.

Measuring Pixel Size

Increasingly, the control software of the confocal microscope calculates and displays the pixel size currently in effect. If this is not so on your instrument, it is easy to calculate the pixel size as long as you know the dimensions of your raster. Just image a stage micrometer (available from major microscope manufacturers — a hemacytometer makes an inexpensive substitute for magnification calibrations), determine the actual width of the field of view in micrometers by matching it to the calibrated lines on the test specimen, and divide this number by the number of pixels in a line.

Alternatively, assuming that the service engineer calibrated the *x*- and *y*-magnification when the instrument was installed and that you have entered into the computer the NA and magnification of the objective in use, you can display a scale bar, and by measuring both it and the entire screen with a ruler, you can again find the field width and make the same calculation.

Finally, if your system allows you to measure the length of the scale bar in pixels, you can use this information to calculate the dimensions of the pixel. To meet the requirements set by the Nyquist criterion for a NA 1.4 objective, a 5 µm bar should be 5 µm/0.08 µm = 62 pixels long.

Adjust the zoom setting until this criterion is met. Note that **pixel size**, referred to the object, is **inversely proportional to zoom** magnification.

It should be noted that, contrary to much legend, satisfying the sampling criterion often requires a **higher zoom** setting for **low magnification** objectives than for those with high magnification. The reason for this is that although a 100× NA 1.2 lens has three times the resolution of a 10× NA 0.4 lens, the latter produces an image in which all features are 10× smaller, so the smallest visible feature (an Airy disk) will be 3.3× smaller in any image plane when using the 10× lens.

The exact mirror movements that produce a given pixel size will vary somewhat with the field of view that characterizes the microscope being used, with the way the instrument has been adjusted, and (on older instruments) with the presence of accessories, such as epi-fluorescence or differential interference contrast (DIC) attachments, that increase the effective magnification of the objective lens. As a result, the scanning system must be re-calibrated if it is moved from one type of microscope to another.

Over-Sampling and Under-Sampling

Now that we have determined the correct zoom setting needed to record the full resolution in your image from the sampling point of view, we should point out that there may be circumstances where other settings may be more appropriate.

Under-sampling

Using a lower zoom setting has the advantage of reducing the bleach rate and increasing the field of view: bleaching rate = $k(\text{zoom factor})^2$. On living specimens, therefore, one may wish to work at a lower zoom setting to preserve the specimen. Under these circumstances, you will lose little more in terms of image resolution if you also open the detector aperture somewhat. This will make the *z*-resolution somewhat worse, but as you will probably also have decided to image fewer optical sections, the lower *z*-resolution will actually assist in coming closer to the Nyquist criterion for sampling in *z*. It will also permit more signal to be recorded at each pixel. As a result of this under-sampling, you can get sufficient image quality using less laser power (i.e., use a darker neutral density (ND) filter).

Over-sampling

Using a zoom setting higher than that needed to satisfy the Nyquist criterion leads to over-sampling. Although over-sampling implies a smaller field of view and causes more bleaching in fluorescent specimens, it provides a larger image that may be easier to view and it will provide data that are marginally more suitable for image deconvolution, a digital image processing technique that can be used to increase image contrast and reduce noise (see next section). Over-sampling is also needed when imaging a periodic specimen having features near the resolution limit.

Nyquist Reconstruction and Deconvolution

It is often forgotten that Nyquist digital sampling has two parts: first digitizing and recording the digital data and then reconstructing the analog output from this data. The latter process imposes important limits on digital microscopy. Because the Abbe equation places an absolute limit on the resolution of microscopical image data, it is relatively easy to calculate the proper size of a pixel if you know λ and NA. However, Nyquist reconstruction requires that these same resolution bandwidth limits also be applied when the digital data is turned back into an image. Of course, it is easy to assume that, because no information regarding features smaller than the resolution limit of the optical system can emerge from the microscope, such information cannot possibly be present in the data and therefore, that it need not be removed. Sadly, this is not so. Because pixel-to-pixel intensity variations associated with measurement and Poisson noise are added to the signal before it is digitized and because these are often big enough to produce contrast comparable to that produced by variations in dye concentration in the specimen, Nyquist-sampled confocal data sets always include single-pixel noise that appears to represent features 4× to 5× smaller than the optical system could possibly have imaged.

This spurious data can only be eliminated by deconvolving the raw digital data using any reasonable point spread function (PSF). Although deconvolution is usually thought of primarily as a means of removing out-of-focus blur from 3D widefield data sets, the process has many other useful functions. In the present context, the chief among these is that deconvolution effectively suppresses spatial frequencies above the bandwidth of the microscope optics.

This idea is important enough to be repeated: Poisson noise can introduce features into the data that appear to be ~1 pixel in size when the smallest Nyquist-sampled feature should be >5 pixels across. These noise features can and should be eliminated by deconvolving the data, preferably in 3D.

As an aside, because the confocal PSF can be approximated as a 3D Gaussian blob, 3D Gaussian filtering has almost the same

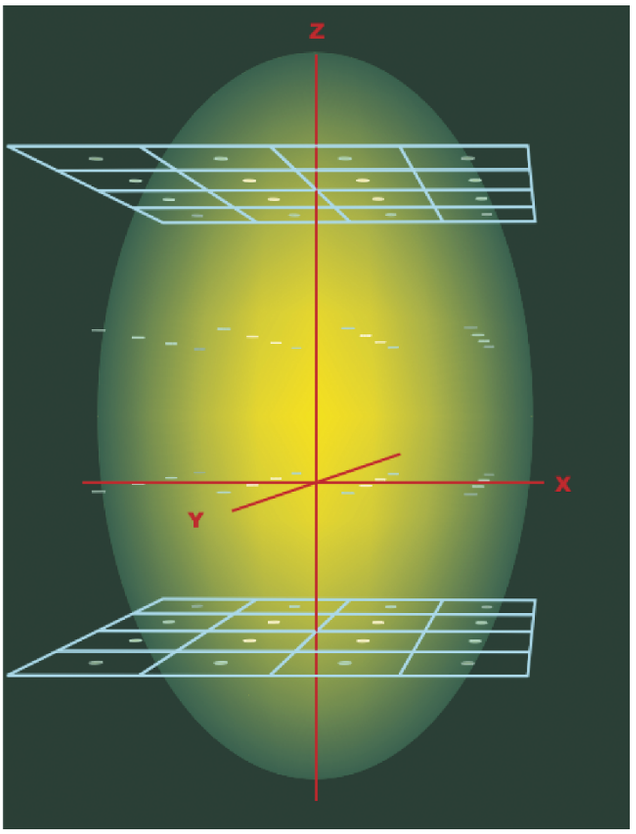


FIGURE 35.6. The relationship between resolution and the number of voxels needed to Nyquyist-sample the point-spread function. According to standard light microscopy theory, the Abbe resolution, δ, is defined as the radius of the first dark ring of the Airy disk. In confocal microscopy, this defines a blob with a diameter of 2δ. If we assume that a pixel is δ/2, then the 2D image of a point object will put signal into at least 12 to 16 bright pixels in the focus plane. The 3D image of a point requires collecting signal from at least four planes, separated by a distance equal to one half of the *z*-resolution. As a consequence of these factors, the 3D image of a point object requires measuring signal in 50 to 100 voxels. Averaging signal over these voxels (e.g., by deconvolution) does not reduce spatial resolution but does greatly improve the S/N of the resulting data. (See Chapter 25, this volume.)

effect as a full-scale 3D deconvolution, as least in terms of suppressing noise features.

Filtering the data in this way has another benefit: it effectively averages the voxel intensity data over the number of voxels containing significant counts in the Gaussian blob that represents the PSF. If we estimate that the blob is ~5 pixels wide in *x*, *y*, and *z* (see Fig. 35.6), then it will have significant counts in $5 \times 5 \times 5 = 125$ voxels. Therefore, 3D deconvolution will effectively average out Poisson noise over ~125 voxels: a significant factor (Chapters 19 and 25, *this volume*)!

Pixel Size Summary

To preserve all of the information in your data, you must use a pixel (or, in three dimensions, a voxel) size at least 2.3× smaller than the Abbe resolution limit of your optical system in (*x*, *y*, and *z*!!). This means that, for each objective, there is an optimal setting for both the zoom control and the interplane spacing of 3D data sets.

- The amount of light passing through the specimen is not affected by the zoom setting.
- At high zoom settings, the confocal microscope can easily illuminate the specimen with an intensity (and a bleaching rate!) that is 100× greater than in a normal fluorescence microscope using a Hg arc source.
- Fortunately, because the PMT detector is more sensitive than film, less illumination is actually required to record a usable confocal image.
- Set the zoom to produce a pixel size satisfying the sampling criterion for the lens in use.
- Don't forget to deconvolve (or 3D Gaussian filter) your data before viewing it.

USING A TEST SPECIMEN

Why Use a Test Specimen?

The tendency to use tried-and-true specimens when testing or learning how to operate the confocal microscope is so marked that it would be fruitless to recommend against it. However, it does have some disadvantages, and the chief of these is that one probably really does not know what a good confocal image of such a specimen would look like. This is because any stained biological specimen is probably too complex to understand so well that one can predict what a 3D image of it should look like and then adjust the instrument until this result is attained. Although we may have prepared hundreds of similar specimens and may recognize some as successes and others as failures, we seldom really know in a quantitative way either the exact size of any of the specific features that they contain, how much they have been stained, or how much this stain may have faded or bleached (Chapters 16 and 39, *this volume*). We may believe that such a specimen possesses a particular 3D structure when, if fact, this structure has been lost when it was inadvertently flattened during specimen preparation (Chapter 18, *this volume*). In short, such a specimen is not a test specimen, and one cannot really use it to measure either your own skill or the performance of the microscope.

Description of the Test Specimen

Microscope manufacturers have long produced a variety of test specimens for measuring the performance of their instruments. The most common of these is the stage micrometer, which usually consists of a graticle etched into a metal film on the lower side of a coverslip. Such patterns can be very useful for checking magnification but, because they are made using light optics, the finest spacings that can be produced on them are ~1 to 2 µm, and this is not fine enough to really test the ultimate **resolution** of a good optical microscope. To fill this void, we followed the lead of Oldenbourg and Inoué (Chapter 1, *this volume*) and designed a test specimen that we then fabricated at the National Nanofabrication Facility at Cornell University using electron-beam lithography (Pawley *et al.*, 1993).[6] The patterns were etched into a 50 nm Al film on the lower side of a 1 × 1 cm piece of #1.5 coverslip and

[6] Similar test specimens may soon be available again from Louie Kerr, at the Marine Biological Laboratory, Woods Hole, MA. Other test specimens are discussed in Chapter 36.

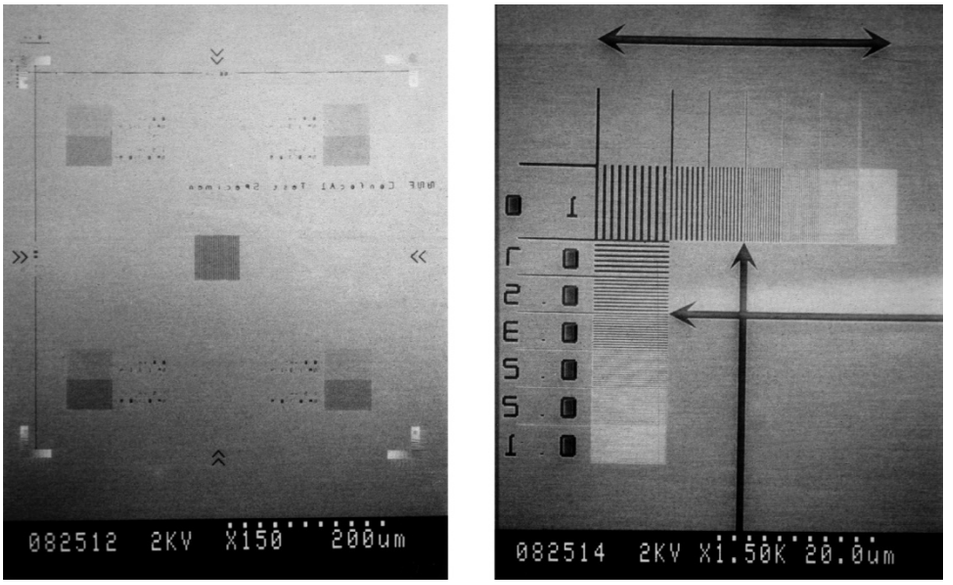


FIGURE 35.7. Scanning electron micrographs of a confocal test specimen fabricated at the National Nanofabrication Facility at Cornell University using electron-beam lithography. The pattern is etched into a 50 nm Al film on the lower side of a 1 × 1 cm piece of #1.5 coverslip and laid out as a square about 500 µm on a side (left). There is an L-shaped, resolution test pattern, 40 µm along each arm, at each corner with one 10 × 10 µm square of 1 µm period at the corner and six 5 × 10 µm rectangles of 0.7, 0.5, 0.35, 0.25, 0.20 and 0.17 µm period along each arm (right).

were laid out as a square about 500 µm on a side [Fig. 35.7(A)]. There is an L-shaped resolution test pattern, 40 µm along each arm, at each corner with one 10 × 10 µm square of 1 µm period at the corner and six 5 × 10 µm rectangles of 0.7, 0.5, 0.35, 0.25, 0.20, and 0.17 µm period along each arm [Fig. 35.7(B)]. The periods of the spacings are listed next to the pattern in the top right corner when the coverslip is mounted, Al-side down, so that the writing is legible. The procedure for measuring the optical transfer function of your microscope from images of such patterns is explained at the end of Chapter 1.

Such a test specimen can be used to record images using transmitted light, reflected light, or fluorescence. For the latter, the coverslip is mounted over a well into which dye-laced immersion oil has been introduced. As the test pattern is predominantly opaque, light can only reach the dye through the clear areas of the pattern [Fig. 35.8(A,B)]. Although the dye itself is essentially infinite in thickness, as long as the NA is reasonably high, most of the excitation is confined to a thin triangular region just under a clear space in the pattern and next to the coverslip [Fig. 35.8(C)]. Although some excitation light does reach the dye through adjacent clear lines in the pattern, this is only a minor effect as can be seen in the *xy*- and *xz*-images of such a specimen, shown in the upper half of Figure 35.8(A,B). Because the dye is a liquid, any bleaching that may occur is masked by the diffusion of new dye into the imaged area.

Using the Test Specimen

To image the test specimen in **reflected** light, treat it as you would any other. However, you may find it difficult to adjust the plane of focus to exactly coincide with the metal film. This is because, as is mentioned in Chapters 14 and 15, the **position** of maximum signal can be determined to a small fraction of the ***z*-resolution**, and in the case of reflected light, the stage-motion control on your instrument may not have sufficient precision to allow you to focus exactly on the metal surface.

Because you are attempting to view a periodic object, the zoom setting should be set about 2× higher than that normally required by the Nyquist criterion (i.e., 4 to 6 samples/resolution element). This is because the Nyquist analysis is based on information theory and, according to information theory, a periodic object contains only two items of information: the frequency and the phase. Although these can be determined from data sampled at the Nyquist rate, the image can look very poor. Figure 35.9 shows how,

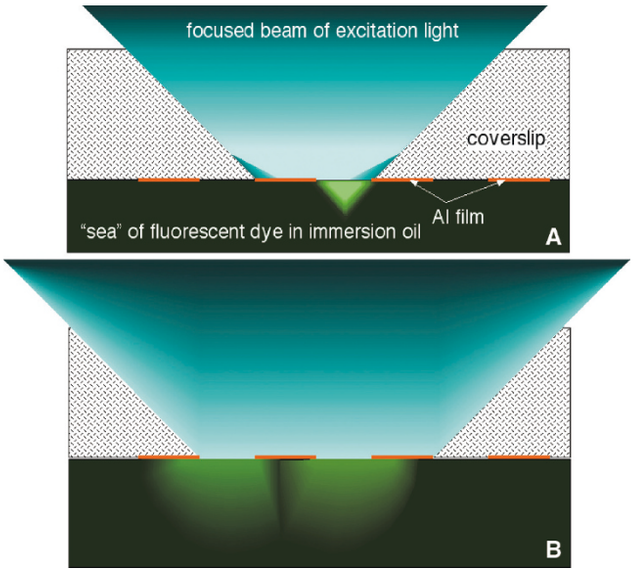


FIGURE 35.8. (A) Diagram of the fluorescent test object. Because it is difficult to fabricate a planar fluorescent test object that does not bleach, this device works by placing a pool of fluorescent immersion oil just below the etched metal pattern on the bottom of the coverslip. As long as the BFP of the objective is filled uniformly, much of the illumination will approach the specimen at relatively large angles, selectively exciting a triangular prism of dye beneath each etched line. (B) As the focus plane moves into the dye, some of the dye deeper in the specimen is excited by rays that pass through adjacent etched lines. However, this is only a minor effect that makes the *z*-response somewhat asymmetrical.

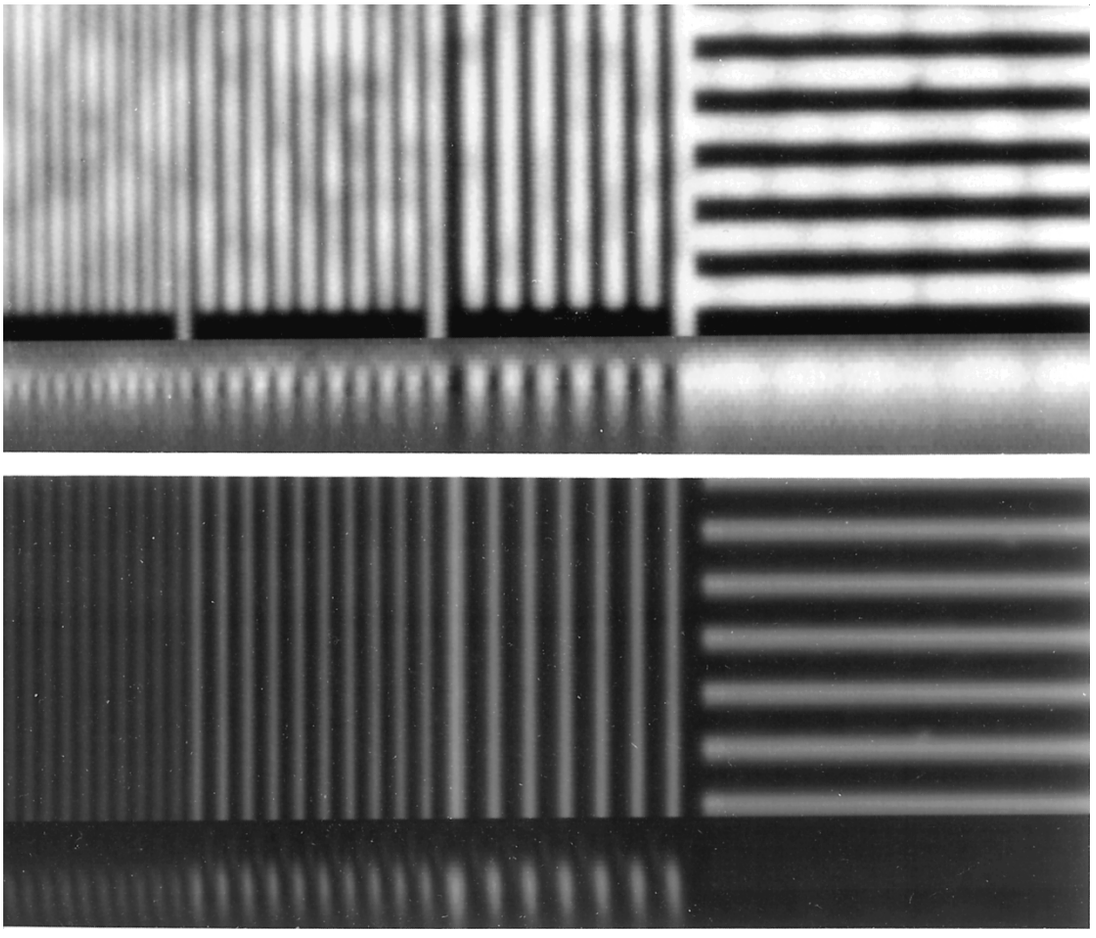


FIGURE 35.9. Images of the test specimen made using fluorescence (upper pair) or backscattered/reflected light (lower pair). The images were collected simultaneously and show mirror symmetry because the fluorescent light emerges from those areas not covered with the metal film that provides the reflected signal. The upper member of each pair shows an *xy*-image and the lower member shows an *xz*-image that makes more evident the asymmetry of the fluorescent signal. Nikon 60×/1.4 on a Bio-Rad 600/Optiphot. The vertical spacings have the following spacings left to right: 0.35, 0.5, and 0.7 µm (vertical) and 1.0 µm (horizontal).

when sampling at twice the frequency of the analog data but doing so just as the signal crosses zero, it is possible to miss the variations in a periodic signal entirely. As a result, one should choose 0.05 µm pixels or about 35 µm field width for a 768 pixel line for use with an NA 1.3 to 1.4 objective.

If you have done things correctly, the picture that you see should look like that in Figure 35.10(A). In these images, it can be seen that the edges of the vertical lines have a high-frequency wiggle (period about 4–5 raster lines = 16.6–20 ms), indicating the presence of mains-frequency electronic, magnetic, or mechanical interference. In Figure 35.10(B), the sets of horizontal lines above and below the axis of the computer-calculated Fourier transform (FT) below each image clearly demonstrate the presence of some other periodic instability present in these single-scan images. As the vertical spacings of the two finer periods are near the cut-off frequency of the contrast-transfer function, only a single spot is shown along the horizontal axis on either side of the vertical axis, but the spacing of all the first-order spots can be seen to be inversely related to the actual spacing of the features in each segment of the image. The horizontal bars in the FTs to the left of Figure 35.10(C,D) show the effect of Kalman averaging. Not only do the spots corresponding to the fine serrations of the edge get averaged out, but the S/N of the FT is markedly higher. The FT in the lower right of Figure 35.10(E) was made from a larger patch of the specimen having a 0.8 µm spacing. Three harmonics can be seen easily, but the fourth, representing 0.8/4 = 0.2 µm data, is barely visible.

If you have the equipment for simultaneous fluorescent/BSL imaging, the specimen can be imaged in **fluorescence** light simply by switching to the other channel. Otherwise the microscope must first be reconfigured for fluorescent light imaging. The image that you see should look like that in Figure 35.11.

The Diatom: A Natural 3D Test Specimen

The test specimens discussed have the disadvantage of being planar. Making a test specimen having precise structural features in the third dimension is more difficult.

The best solution so far is to immerse diatom frustules (North Carolina Biological) in fluorescent oil and view them as negative objects, as suggested by Roger Tsien (University of California, San Diego). Figure 35.12 shows a stereo view of such a preparation, imaged with BSL using the system mentioned above. Although careful attention to the exact species of diatom can result in highly reproducible spacings, this specimen is not without its problems.

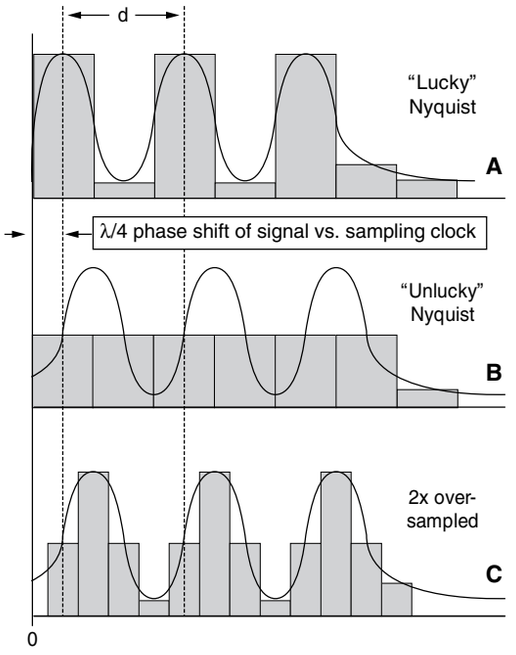


FIGURE 35.10. Data sampling of periodic objects. Although the Nyquist criterion states that only ~2 samples are required for each period of the highest spatial frequency in the data, this does not always work for periodic objects. Although a fortuitous phase relationship between the sampling instant and the positive and negative peaks of the highest frequency can lead to an accurate digitization (A), a phase relationship that sampled the signal only at the instant that the signal crossed the axis would not record this contrast at all (B). For this reason, it is safer to digitize images of periodic objects with at least four samples/period (C).

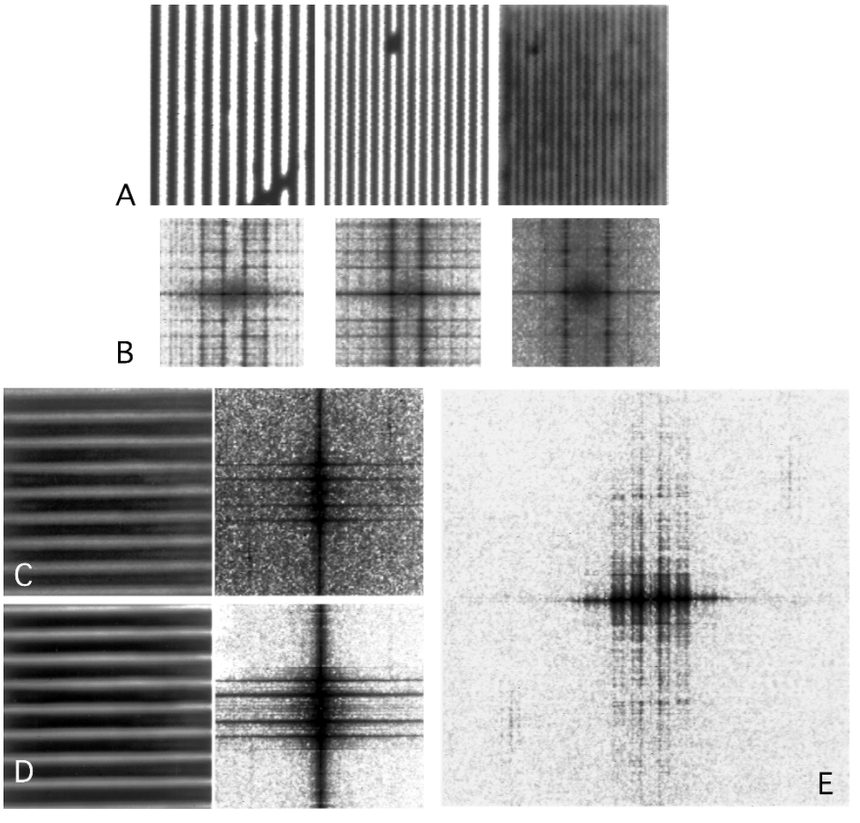


FIGURE 35.11. (A) High resolution reflected light image of test specimen recorded using a Nikon 60×/1.4 lens on a Bio-Rad 600/Optiphot. Spacing, left to right: 0.5, 0.35, and 0.25 µm. In (B), the sets of horizontal lines above and below the axis of the computer-calculated FT below each image clearly demonstrate the presence of a periodic instability in these single-scan images. As the two finer spacings are near the cut-off frequency of the contrast–transfer function, only a single spot is shown along the horizontal axis on either side of the vertical axis, but the spacing of all the first-order spots can be seen to be inversely related to the actual spacing of the features in each segment of the image. Panels (C, D) are reflected light images of 0.7 µm horizontal spacings made either live (C) or after averaging 20 scans (D). The horizontal bars in the FT plots to the left of each image show the effect of averaging. Not only do the spots corresponding to the fine serrations of the edge get averaged out, but the S/N of the lower FT is markedly higher. The FT in the lower right (E) was made from an image of a larger patch of the specimen having an 0.8 µm spacing. Three harmonics can be seen easily, but the fourth, representing 0.8/4 = 0.2 µm data, is barely visible.

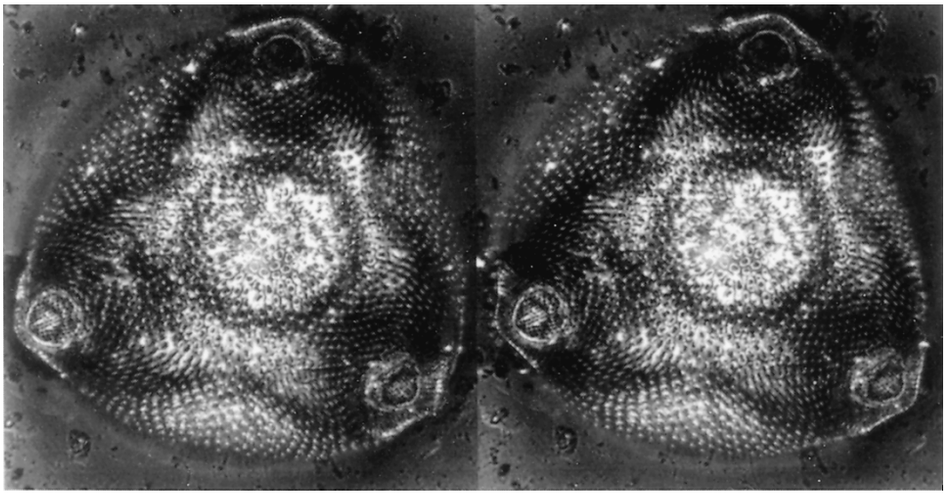


FIGURE 35.12. Stereo image of part of a diatom immersed in immersion oil made with BSL using a Nikon 60×/1.4 lens on a Bio-Rad 600/Optiphot equipped with the optimized BSL system described in the text and diagrammed in Figure 2.3. The diatom is resting on a microscope slide and is viewed from the top through the coverslip and two layers of immersion oil. The signal reflected from the slide surface can be seen around the edge of the image but the presence of the diatom distorts the focus plane away from the surface in the center of the field of view. (Specimen kindly provided by Nelson Navaro, C.U.P.R., Puerto Rico.)

Because the amorphous silica out of which the frustule is made has an index of refraction different from that of either water or immersion oil, it refracts and also scatters considerable light. While this is convenient for BSL imaging, it produces aberrations whenever the focus plane penetrates too far. This effect can be seen in Figure 35.12 where, around the edge of the image, one can see the signal reflected back from the flat surface of the glass slide on which the diatom is resting. However, in the center of the field the beam must pass the through the frustule to reach the surface and its presence distorts the focus plane away from the surface of the glass making it appear dark.

REASONS FOR POOR PERFORMANCE

Sampling Problems

As mentioned above, when imaging periodic objects, it is necessary to sample the image data at higher than the Nyquist rate. Failure to do so will result in the aliasing artifacts shown in Figure 35.13.

Optical Problems

Aberrations

As is mentioned above and covered in Chapters 1, 7, 8, and 20, one can only obtain diffraction-limited resolution if all optical aberrations are absent. The major aberrations are spherical aberration and chromatic aberration. In a high NA objective, spherical aberration is usually corrected for a number of wavelengths but **only** for one immersion medium. To get the recommended performance, you must use the immersion liquid for which the lens was designed or use a lens having a correction collar to adjust for different media.

As the focal length of any objective changes slightly with wavelength, its magnification also changes with wavelength, only in the opposite sense. As a result, when operating in fluorescence, an off-axis ray at the excitation wavelength will cross the intermediate image plane at a different point from the longer wavelength emission ray coming from the same point on the specimen. As a result, the emission ray may partially or totally miss the pinhole, resulting in loss of signal (Fig. 35.14)! Two other points are worth mentioning in regard to this second point:

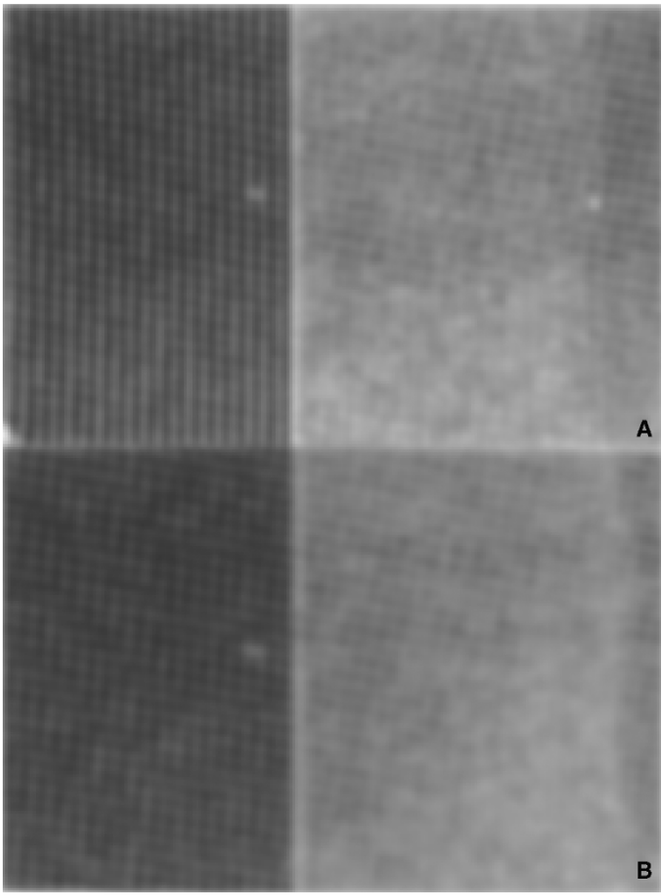


FIGURE 35.13. The effect of under-sampling on a periodic image. The upper image was recorded using reflected light with a Nikon 60×/1.4 lens on a Bio-Rad 600/Optiphot with 0.04 µm/pixel (twice the Nyquist rate for 0.2 µm structures) and then printed on a dye sublimation printer having pixels the equivalent of 0.018 µm in size. In it, both the 0.25 µm (left) and 0.2 µm (right) spacings are clearly seen. The lower image was made with identical optical conditions but the pixel size was 0.08 µm (exactly the Nyquist limit) and the image was recorded photographically from a video monitor having a screen pitch equivalent to 0.05 µm/elements. To some extent, the reduced contrast in the 0.25 µm spacing may be due to the bandwidth limitations of the monitor or the vagaries of the photographic process, but the virtual absence of the 0.2 µm spacings is probably due to sampling problems, as is evidenced by the presence of a faint aliasing pattern at about twice the period of the actual features in the image.

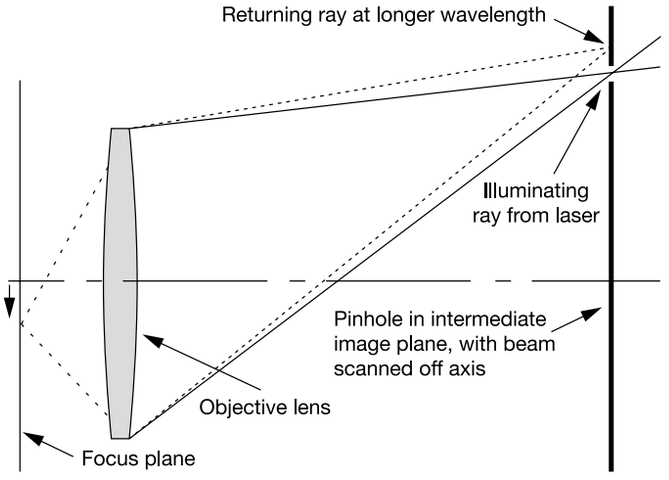


FIGURE 35.14. Lateral chromatic aberration. The effect of chromatic magnification error on signal level in the confocal microscope. The focal length and, hence, the magnification of any optical system varies with wavelength. Consequently, an off-axis ray of short wavelength light will not follow the same path as that of a ray of longer wavelength light originating from the same point. In the laser-scanning confocal microscope, the scanning mirrors are supposed to deflect both the source and the detector pinhole off-axis by the same amount. However, this will not happen if the optical system has high chromatic aberration and the system is used for fluorescence, because the exciting and emitting wavelengths are magnified by different amounts. As a result, the signal light will miss the pinhole and the image will become darker away from the axis. The problem can be reduced only by using optical systems that are highly corrected for chromatic aberration and by placing the field-of-view as near to the optical axis as possible.

- In many older microscopes, it was common to correct chromatic aberration in the eyepiece. Objectives from such microscopes will demonstrate totally unacceptable levels of chromatic aberration if they are not used in conjunction with the appropriate correcting eyepieces. Generally one should use only modern, highly-corrected objectives for fluorescence confocal microscopy and use them only with other components that are properly matched.
- The magnitude of the displacement caused by the chromatic magnification error is generally proportional to the distance that the point in the image is away from the optical axis. Therefore, the effect will be less severe if imaging is restricted to an area near the optical axis.

Curvature of Field

Unless concrete steps are taken to prevent it, simple lenses will focus a plane surface onto a segment of a sphere. Objectives designated "plan" are supposed to have flatter fields of view than most, but this feature is usually incorporated at the cost of additional elements and often lower light transmission. Figure 35.15 shows two images of a plane mirror, one made with a non-plan lens (upper) and one with a planapo-correction (lower). The images have been posterized to emphasize the variation in signal caused by field curvature. The variation in signal strength across the field is shown with greater precision in the *x*-profile plots at the bottom. We should emphasize that these plots show variation in the measured intensity of reflected light passing the confocal pinhole, not the actual geometrical curvature of the field! Although the upper image displays a variation in focus that could degrade the image of a flat test object such as that mentioned above, one

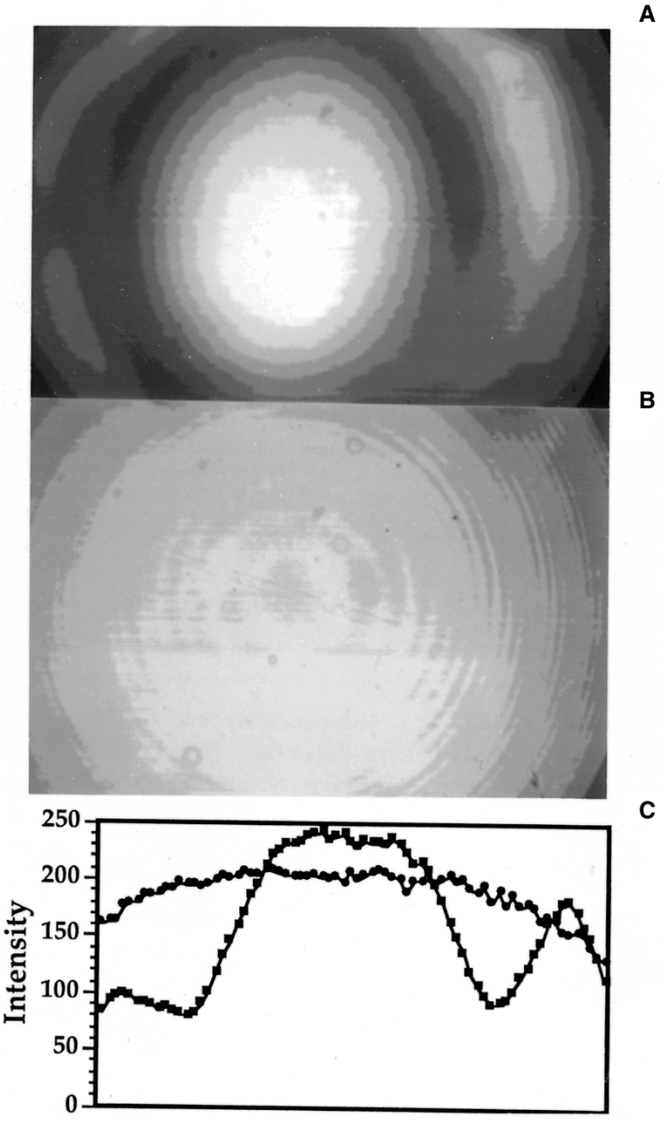


FIGURE 35.15. Curvature of field. In general, lenses focus a plane surface onto a spherical one. In objectives not specifically corrected for plan operation, the curvature of field has the effect that an image of a plane surface loses intensity off-axis. This figure shows two images of a plane mirror, one made with an uncorrected lens (A) and one with a planapo correction (B). The variation in signal strength across the field is shown with greater precision in the two *x*-profile plots (C). (We should emphasize that these plots show variation in the measured **intensity** of reflected light passing the confocal pinhole, and are not a measure of the actual geometrical curvature of the field!) Although field curvature can be a serious problem when viewing planar specimens, it is often less serious when making 3D fluorescent images of biological specimens because in the latter case there is no signal loss but simply a slight dish-shaped distortion in the final 3D data. However, if this distortion is to be kept symmetrical, it is important not to pan the scanned area away from the center of the field of view when using such a lens.

should remember that, with a *z*-resolution of ~0.6 µm, even an intensity drop of 90% between the center and the edge of the field would only indicate a field curvature of <1 µm. However, this image does show the penalty of panning the zoomed area away from the optical axis (e.g., to avoid reflection artifacts in BSL imaging) when using a non-plan lens.

Not Filling the Objective Pupil

We have mentioned above that one can only expect an optical system to reach its diffraction-limited performance if it is operated at its full NA. Check that the size of the laser beam at the BFP (upper part of Fig. 35.2) is equal to the diameter of the hole in the rear of the objective that you are using. If you are in doubt, compare its *x-y* resolution performance with an objective of the same NA but a higher magnification, as this will have a smaller BFP. If the performance is better with the higher magnification objective, the lower magnification one was probably being under-filled.

Dirty Objective

Common blemishes found on optical elements, such as dust, smudges, or old immersion oil, significantly reduce their optical performance and contribute to stray light. In fact, any smudge or smear that shifts the phase of the light passing through it by as little as $^1/_4\ \lambda$ will prevent those rays from contributing to a diffraction-limited image (see Chapter 11, *this volume*).

Especially disturbing are blemishes at or near the conjugate image planes or on the front surface of the objective. Specks of dust or fibers can be carefully removed by lightly sweeping the surface with a soft camel-hair brush or by blowing them off with a puffer made of a large rubber bulb fitted with a **plastic** micropipette tip. Canned-air blowers should be used with caution as these sometimes deposit oil or condensed impurities from the propellant onto optical surfaces.

Material that is more adherent may require wiping with a cleaning solution or solvent. The type of cleaning solution required depends on the specific material involved. Water, glycerol, and salt crystals can easily be removed using double-distilled water, while immersion oil and some mounting media respond well to the household glass cleaner Sparkle (A.J. Funk and Company, Elgin, IL), which, despite its humble origin, is recommended by several optical manufacturers. This cleaner is effective at removing oil, evaporates fairly quickly, and does not contain harsh solvents that might attack the cement holding the lens elements together. Because it is non-flammable and non-toxic, it can be stored right beside the microscope.

One should not resort to harsher solvents such as ether, benzene, xylene, or acetone until the more benign ones have proved ineffective. Although these solvents can damage some lens cements, the bigger danger is that they may infiltrate the lens to wet the interior glass/air surface, where they will then deposit impurities when they dry. When using such solvents, clean the surfaces quickly so that the solvent evaporates before it has a chance to leak inside the lens. **Never soak an objective in anything!** If organic solvents must be used, take proper safety precautions, such as working in a fume hood. Whenever wiping is necessary, one must use clean lens tissue (i.e., one that has not been exposed to dust deposit from the air), free from finger oils, and never use the same area of the lens tissue twice.

With hard surfaces such as oculars and camera lenses, it may be sufficient to fog the lens with your breath and gently wipe the surface with clean lens tissue. Either use the folded edge of the tissue or, if needed, apply slight finger pressure. Be sure to use several thicknesses of tissue so that finger oils do not penetrate to the glass.

To clean more delicate lens surfaces, a non-contact method is preferred. Apply a drop of the cleaning solution of choice at the near-edge of a piece of lens tissue held horizontally (be sure this area was not previously touched by your fingers). Lower the drop of cleaning solution to the surface of the lens standing upright on the tabletop and gently draw the lens tissue over its surface (Fig. 35.16). There is no need to apply pressure. Repeat this procedure three or four times. As the tissue is drawn across the surface, most of the cleaning solution and the oil and dirt are drawn off by capillary action, and the remaining solution evaporates.

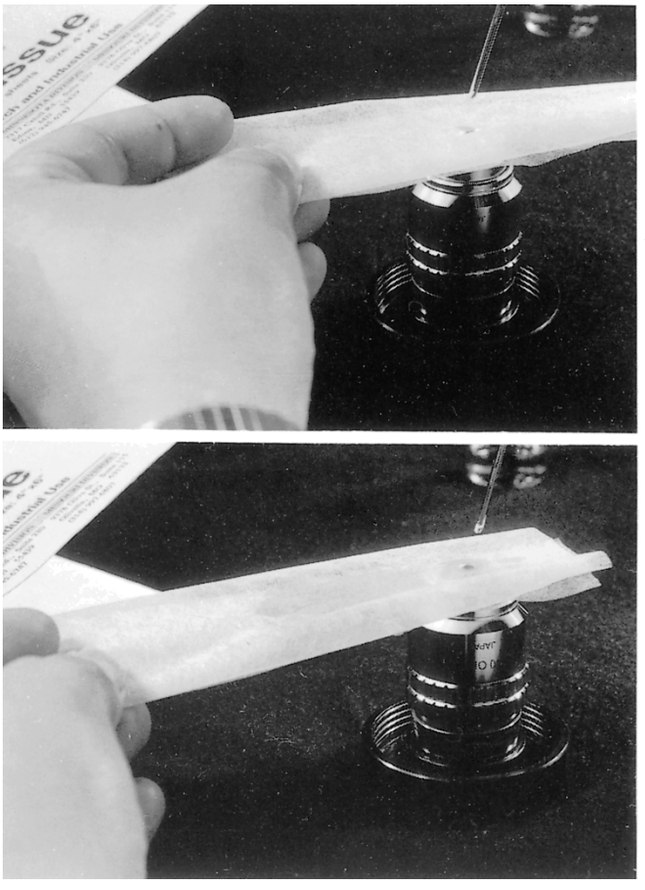


FIGURE 35.16. How to clean objectives. (A) Apply a drop of the cleaning solution of choice at the near-edge of a piece of lens tissue held horizontally (be sure this area was not previously touched by your fingers). (B) Lower the drop of cleaning solution to the surface of the lens and gently draw the lens tissue over the surface as shown. There is no need to apply pressure. Repeat this procedure as necessary.

Use an inverted ocular as a magnifier to check that the oil or dirt has been removed and that there are no streaks on the outer surface of the objective. Surface films are most easily seen if you orient the objective so that you are viewing an overhead light reflecting directly off the surface of interest. When a film of solvent dries onto a surface, any impurities in it will be deposited onto the surface. Use very clean solvents!

This cleaning method works well for all types of objective lenses, even those with recessed surfaces. To clean oculars, CCD camera sensors, or the back surface of the objective, you must make a swab of lens tissue. Wrap the end of a wooden applicator stick with lens paper or carefully washed cotton batting. Do not use a commercial cotton swab, even if wrapped with lens tissue, because it may contaminate the lens with the glue used to secure the cotton fibers. Wet the end of the applicator with cleaning solution and, starting from the center of the lens, gently sweep from

the center to the edge of the surface in a continuous spiral while twirling the applicator. Using a new lens tissue swab each time, repeat this procedure until the lens surface has been cleaned.

If one is using an inverted microscope with an oil- or water-immersion lens, there is the potential for oil or water to seep down the barrel and into the body of the lens. This can be an annoying problem and objectives can be expensive to clean (US$1,000–US$2,000). Some simple devices can prevent this problem. Placing a rubber O-ring around the upper part of the lens will act as an oil dam. As long as there are no cracks in the O-ring and excess oil is blotted away periodically, this remedy works exceptionally well. Some people replace the O-ring with a "scrunchie," an elasticated device normally used to confine hanks of human hair! Other remedies to the problem can compromise the spring shock absorber that is a feature of most short-working-distance lenses. One can also wrap the inner barrel of the lens with Teflon tape to seal the point where the oil enters the inside of the lens or place a rubber sleeve over the entire lens. Such a sleeve can be made by cutting one of the digits from a rubber surgical glove and making a small hole at the tip. The sleeve is stretched over the entire objective so that only the front element pokes through the small hole.

Air Bubbles

An air bubble in the immersion oil will act as a small, yet extremely powerful lens, which can have a pronounced and deleterious effect on the optical performance of the microscope. Fortunately, such bubbles can be detected by imaging the oil layer directly. It is possible to focus on a plane within the oil by adjusting either an internal Bertrand lens (also called a phase lens as it is used to observe the process of centering the phase-contrast rings) or an external phase-telescope fitted in place of one of the oculars.

The best plan is to try to avoid the formation of the air bubbles in the first place by making sure that any bubbles have a chance to float up, away from the tip of the dispenser before you express a drop or, perhaps even better, dip a drop of oil out of the oil container using a glass rod.

Imaging Depth

An important aspect of any microscope used for making 3D images is how far below the surface of the specimen it can obtain useful data. The most obvious limitation is the mechanical one imposed by the finite working distance of the objective (Chapter 7, Table 7.3, *this volume*). Once the objective touches the specimen surface, it clearly cannot be focused to yet deeper planes.

Unfortunately, the opacity and optical inhomogeneity of the specimen usually impose more stringent limits (for more details, see Chapters 17 and 20, *this volume*). To the extent that the illuminating beam is either scattered or absorbed as it passes through the upper layers of the specimen, it will fail to reach any plane of focus located farther into the specimen. Likewise, signal light that is scattered or absorbed between the focus plane and the detector cannot be measured (except when non-descanned detection is used with two-photon excitation). Finally, any optical inhomogeneity in the specimen between the focus plane and the objective will tend to defocus both the beam of incident illumination and the returning signal. This will increase the effective size of the focused spot that is returned to the pinhole, so that much of the light that should pass through it does not do so (Pawley, 2000; Chapter 21, *this volume*).

All three of these effects reduce the fraction of the signal that is detected as the focus plane is pushed progressively farther into the specimen. In addition, the last mechanism also reduces the spatial resolution. Together, these three factors usually place a practical limit on the effective penetration depth of the confocal light microscope, and all of them depend on the optical properties of the specimen.

When using an oil-immersion objective on a biological specimen that is only lightly stained and has been cleared by replacing the water with an imbibing medium having an index of refraction close to both that of the solid components of the cell and that of immersion oil, then the useful penetration depth can be several hundred micrometers, but on less ideal specimens it is usually much less. On the other hand, even deeper penetration is sometimes possible if the microscope is used at lower magnification with an immersion objective having an NA of <0.8, because the defocusing effects of the specimen are usually less serious under these circumstances (Chapter 20, *this volume*).

Singlet-State Saturation

The intensity of the light at the focus of a high-NA objective lens is so high that, if the beam power is more than ~1 mW, a large fraction of the fluorescent molecules within the focal region are in the excited state at any given time. As excited molecules are unlikely to absorb a second photon, they represent a reduction in the effective stain concentration.

Saturation can be avoided by using less input power. However, as the rate at which data is produced from the specimen is proportional to the excitation intensity, dye saturation places an absolute limit on the **rate** at which fluorescence information can be obtained. This limit is most severe when the instrument is operating at high spatial resolution because this implies a smaller focused spot and, therefore, a higher light flux density. Fortunately, many fluorescent specimens produce adequate images using as little as a few microwatts (Pawley and Centonze, 1997) or even nanowatts (Fig. 19.2, *this volume*) of laser power. At these levels it is often possible to make thousands of images before the specimen bleaches.

Because of fluorescence saturation, one cannot expect to scan a single beam rapidly [e.g., at television (TV) scan rate] and also produce a statistically well-defined, high-resolution, fluorescent, confocal image unless one also reduces the number of pixels and, therefore, the raster size of each image.

- Because the degree of saturation is directly proportional to the fluorescent lifetime, operating at or near saturation means that signal intensity may reflect environmental conditions that affect this parameter as well as reflecting the active concentration of the dye.
- As saturation is a function of the dye molecule, rather than, for example, the detector, it affects all parts of the image equally. As a result, areas with more dye will still appear brighter than areas with less, and the image does not look saturated in the same way as an over-exposed photograph does.
- As most photodamage processes do not saturate, operating near saturation produces relatively more photodamage for the amount of data that is obtained.
- As the degree of saturation depends on the intensity of the incident light flux, saturation losses are highest near the focus plane where the light beam is narrowest. As a result, an image recorded from a dye that is saturated tends to record relatively more signal representing light from planes that are out of focus. This reduces the z-resolution.
- The saturation problem decreases with the square of the resolution of the optical system.

WHICH 3D METHOD IS BEST?

Elsewhere in this book, you will find chapters describing all the major methods of 3D light microscopy: widefield/deconvolution, confocal, and two-photon (the latter two, in both single-beam and multi-beam versions). You will also find chapters pointing out the advantages of combining deconvolution with the other two methods and comparing their performance from a theoretical point of view. However, because each of these chapters is written by skilled practitioners of the particular method described, there is little discussion of some of the fundamental differences between them. This section sets out to fill this gap.

As making comparisons of any type is always invidious, we must start by explaining what we will not do. We will not recommend one method over another nor will we provide more than a rudimentary description of the operating principles. What we will do is point to the features of each one that makes it particularly suitable for certain studies, particularly studies of living specimens. Our discussions will cover differences in the shape of the bleach pattern, the power density of the excitation, the differences in the quantum efficiency and noise level of the detector, and how these affect resolution and S/N of the final image.

Because widefield techniques collect data in parallel and use CCDs with high effective quantum efficiency (QE), while single-beam scanning techniques are serial devices and use photomultiplier tubes with 5× to 10× lower QE, one can both elicit and detect many more photons/second with widefield techniques. Figure 35.17 shows the excitation aspect of this difference. Assuming a 1024 × 1024 pixels CCD, widefield will be exciting and recording data from 10^6 pixels, while the single beam of the confocal will be highly exciting about 12 Nyquist pixels and collecting data from most of these.[7]

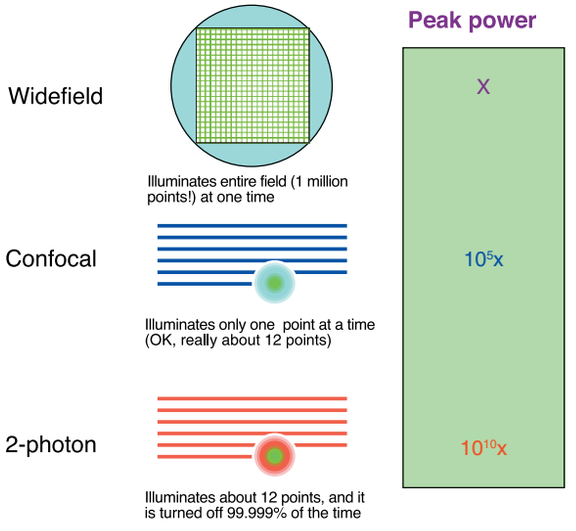


FIGURE 35.17. Variation in peak brightness of the excitation light in the three common forms of 3D fluorescence microscopy. Assuming that one needs to excite a fixed number of photons from the focus plane in the specimen in order to record a 1000 × 1000 image of a given quality, the level of excitation at the focus plane, in photons/square micrometer, must be much higher in a scanning microscope, where only about 12 pixels are excited at any one time, than with a widefield microscope in which 10^6 pixels are illuminated simultaneously. The low duty-cycle of femtosecond two-photon excitation produces a peak power that is about 10^5 to 10^6 times higher again. It is now clear that many dyes bleach more rapidly at these extremely high excitation levels (see Chapters 38 and 39, *this volume*).

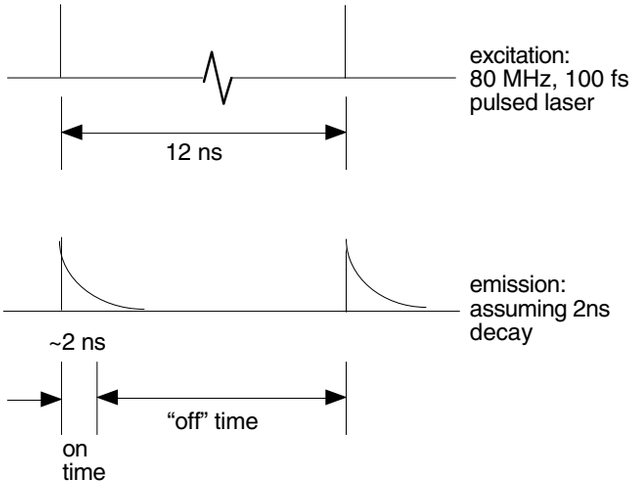


FIGURE 35.18. Excitation duty cycle for 80 MHz, pulsed illumination. Because the time between the excitation pulses of an 80 MHz pulsed laser is long (12 ns) compared to the decay time of most fluorescent dyes, such dyes are driven into singlet-state saturation at a signal level about 10× lower than they can produce with continuous illumination.

To collect an image in the same time period, the total flux of detected photons/s must be the same in both cases and this can only occur if the laser is 10^5× more intense (in photons/μm^2 at the focus plane) than the Hg illumination used in widefield microscopy.[8] When one moves to two-photon microscopy, there is another major increase in the peak flux required and this is provided by the fact that the duty cycle of a 100 fs pulsed laser operating at 100 MHz is a 10^{-5} and this means that the peak intensity is $10^{5\times}$ higher than confocal, for the same average beam power. In fact, two-photon systems are commonly operated with an average power about 10× to 50× higher than that used for confocal, but it is also true that, with a wavelength that is 2× longer, the area of the two-photon spot is 4× larger in area and the intensity is consequently 4× lower. Because excitation is proportional to the square of the intensity, the **area** from which the fluorescent light emerges is about 1.4× larger in diameter and 2× larger in area than would be the case with single-photon excitation.

A second factor relates to the fact that using a 100 MHz laser excites organic dyes inefficiently. Figure 35.18 shows that even if each pulse excites essentially all the dye in the focal volume, because the decay time of most common dyes is short compared to the time between pulses, the system is essentially turned off for about 90% of the time.

[7] Assuming that the pinhole is set to 1 to 2 Airy units, some of the photons emitted from all these 12 pixels on the specimen will be stored as the value for a single pixel in the computer (see Fig. 24.A6 in the appendix to Chapter 24, *this volume*, for more on this).

[8] Strictly speaking, to account for the lower detector QE, it might require 10^6× more brightness. However, because better image data is needed if one must later remove the out-of-focus light by deconvolution, things get complex and we will leave this argument to other chapters.

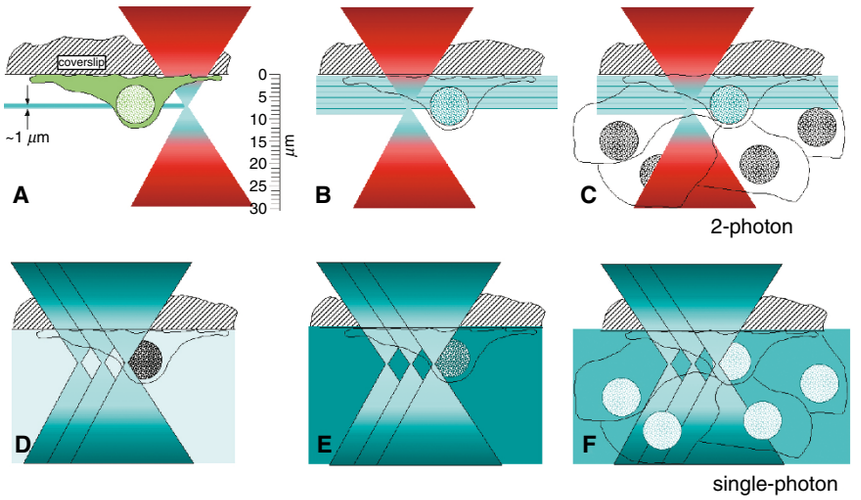


FIGURE 35.19. Dependence of total photodamage on damage/emitted-photon and specimen thickness in single- and two-photon excitation fluorescence imaging. One of the signature advantages of two-photon excitation is that excitation/damage is normally confined to the focus plane (A, D). However, if as seems likely, in many cases, the damage/excitation produced by two-photon excitation is greater than with single-photon excitation by a factor γ, then two-photon excitation will only be advantageous when the specimen is so thick that the number of single-photon excitations produced as the beam passes through the entire specimen exceeds the two-photon excitations produced in the focus plane by a factor of >γ (C, F).

It would be surprising indeed if excitation of the dye was entirely unaffected by these very marked differences in photon flux. At the very least, one can see that one must operate ~10^5 × closer to singlet-state saturation with single-beam confocal than with widefield and at least another factor of 10× closer with two-photon microscopy. The two simplest responses to this problem are: (1) to take more time to collect data from a single plane in confocal and two-photon microscopy, and (2) to settle for detecting 100× to 1000× fewer photons/pixel than is common in widefield/deconvolution.[9]

Numerous studies now connect phototoxicity to excitation of the dye. By themselves either the dye or the light are relatively innocuous. Together, energy is deposited and some of this energy produces damaging compounds. Although it is often said that both widefield and confocal systems do the same amount of bleaching above and below the plane of focus, this is not, strictly speaking, true. Figure 35.1(B) shows the situation for confocal in which the worst bleaching is confined to two pyramids, above and below the central focus plane. On the other hand, if widefield microscopy is performed using a light source that does fill the objective BFP and with the field diaphragm set to confine the illumination to a circle just large enough to contain the area imaged by the CCD,[10] then the excitation away from the focus plane depends only on defocus. Damage is not peaked towards the center of the out-of-focus planes. On the other hand, probably the best known feature of two-photon imaging is that excitation is confined close to the focus plane. What complicates the choice is that, for many dyes, the damage/excitation produced by two-photon excitation is higher than when the same dye is excited by a single photon (see Chapters 38 and 39, *this volume*). This differing dye-damage sensitivity is almost undoubtedly related to the marked differences in peak excitation intensity noted above.

Although the magnitude of the nonlinear damage effect is poorly understood, let us consider the implications if the damage/excitation is 10× higher for two-photon than it is for single-photon microscopy. Figure 35.19(A,B) diagrams the two-photon excitation of a tissue-culture cell on a coverslip. The damage at the plane of focus is worse locally but no damage occurs away from it. Figure 35.19(D,E) shows the situation for single-photon excitation: damage is less at any point but extends throughout the cell. Clearly, if the cell is less than 10× thicker than the two-photon excitation plane, the total amount of photodamage from a single scan will be more with two-photon excitation. Assuming a damage plane thickness of about 1 μm, single-photon excitation would have the advantage for most common tissue culture cell preparations.

However, given our assumptions, if the stained volume of the preparation is more than 10× thicker than the two-photon damage plane, there will be less damage with two-photon excitation [Figs. 35.19(C,F)].

If the damage/excitation discrepancy is less than 10×, the advantage will switch to two-photon excitation at a specimen thickness that is somewhat less than 10 μm.

Finally, there is the matter of how much power is needed for two-photon microscopy. In Chapter 38, Karsten Koenig points out that about 5 mW of femtosecond pulsed laser light is sufficient to prevent cells from dividing **if it is focused into a small spot by a high-NA objective** [Fig. 35.20(A)]. On the other hand, the popular titanium : sapphire (Ti : Sa) lasers only work properly if they are producing about a watt of optical output. Although some users have taken advantage of this surplus power to make many-beam two-photon excitation systems, it has also been utilized to overcome the losses imposed by imaging thick, scattering specimens where hundreds of milliwatts must be used to get sufficient intensity to produce two-photon effects in an aberrated spot located some hundreds of micrometers from the surface of the specimen. This topic is worth talking about here because a number of new femtosecond mode-locked lasers are now in development that couple great operating convenience with potentially much lower cost but that produce comparatively modest amounts of power (10–20 mW). It seems likely that these systems will find applications in which operation on specimens 50 to 100 μm thick is routine.

[9] These estimates are just that. Different users viewing specimens with widely different staining levels may find that they can produce acceptable results with recorded signals that vary over a range at least this large. The numbers used are meant to be illustrative, not definitive. It is also important to remember that, because of the difference in detector QE, this may only amount to a 10× to 100× difference in the number signal photons detected from near the plane of focus.

[10] This setup is recommended both to reduce damage to those parts of the preparation not being imaged and also to reduce stray and scattered light to a minimum.

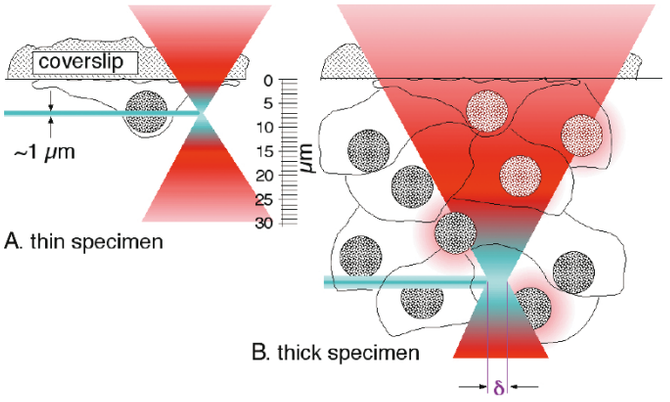


FIGURE 35.20. Total beam power required varies with specimen thickness in two-photon excitation. (A) When focused near the coverslip, scattering and aberrations are low and most of the laser light passing through the objective is focused into a small, high-intensity spot. (B) As the focus plane moves farther into the specimen, more light is scattered out of the beam and aberrations increase beam diameter (δ), further reducing peak intensity. Maintaining signal level under these circumstances can require 10× to 100× more beam power.

Optimal 3D Light Microscopy Summary

After all these words, important questions remain:

- How important are "dose-rate effects"?
  - — Are dye molecules that have been excited to the singlet state more likely to absorb a second, damaging photon in laser confocal microscopy? In two-photon microscopy? Why does this problem seem worse with some dyes than others?
  - — How fast does the risk of bleaching/emitted photon increase as the excitation gets more intense?
  - — Does crossing to the triplet state significantly reduce the effective dye concentration in laser confocal microscopy? In two-photon microscopy?
  - — If so, how does this depend on the type of dye and the local environment?
- When does staining geometry and density become a serious problem for widefield/deconvolution?
- Are there aspects of dye performance under two-photon excitation that may limit the use of certain dyes?
  - — Absorption spectra
  - — Absorption cross-sections
  - — Quantum efficiency
  - — Bleaching/phototoxicity
  - — New dye molecules developed for two-photon excitation
- Do confocal and two-photon excitation bleach dyes by different mechanisms? (Probably!)

Things to Remember About Deconvolution

- Deconvolution effectively averages signal over data stored in >64 voxels, reducing Poisson noise.
- Deconvolution separates in-focus from out-of-focus light by imposing PSF, non-negativity, and other constraints.
- Deconvolution has more problems if there is too much out-of-focus light.
- Deconvolution should be applied to both confocal and widefield data.
- Blind deconvolution techniques can be subject to bootstrap errors. (If you start with a "bad" first estimate, or iterate too long, you may "create" structure.)
- Deconvolution requires very high positioning accuracy and a relatively constant, known PSF. Remember, the widefield PSF varies with wavelength, NA, field and aperture diaphragm diameters, alignment of the arc (or use of ground glass), and the immersion medium.

Decision Time

Premise: **All** 3D microscopical data should be deconvolved before viewing and that the object is to get the best 2D (optical section) or 3D data possible from a fixed number of excitations in the specimen.

MULTI-PHOTON VERSUS SINGLE-PHOTON EXCITATION

The advantages of multi-photon excitation include:

- Only the focus plane subjected to short wavelength damage:
  - — Less damage as long as specimen is thick.
  - — Less absorption of the excitation beam by heavily-stained specimens.
- Optical sectioning without use of a pinhole:
  - — On thick, scattering specimens, non-descanned detection of scattered signal can be up to 300% more efficient than normal semi-confocal detection.
- Longer wavelengths are scattered less by the specimen: better penetration of excitation.
- Can excite ultraviolet (UV) dyes without needing UV lasers or UV optics.
- System acts as if the pinhole is infinitely small, and perfectly aligned.
- Huge Stokes shift means that dichroic beam-splitters and filters can be more efficient.
- Laser often tunable to optimal excitation wavelength.

The disadvantages of MP include:

- Longer wavelength, somewhat lower resolution: not 2× worse, more like 20% to 40%.
- Excitation duty cycle only ~10% forces one to work closer to singlet-state saturation.
- Hard to arrange >1 distinct excitation wavelengths.
- Requires expensive, pulsed laser: compare the productivity of one two-photon versus two confocals.
- Higher average beam power destroys cells that absorb infrared (IR) light.
- Many dyes emit >10× fewer photons/molecule before being destroyed.
- Hard to use with fiber-optics and acousto-optical deflectors.
- Laser-tweezer effects may displace some small particles.

- Nonlinear dependence of both signal and damage on laser power makes it crucially important to set this parameter accurately.

Widefield Versus Beam Scanning

Advantages of widefield scanning include:

- Well-optimized systems available.
- High detector QE and optical simplicity means more fluorescent photons are detected.

Disadvantages of widefield scanning include:

- Cannot view optical section directly (must collect several planes, then deconvolve).
- Image noise from out-of-focus fluorescence eventually swamps the advantage of higher detector QE.
- Rapid 2D imaging difficult.
- CCD read noise rises with square-root of the readout speed.

The question between widefield/deconvolution and confocal is: Assuming that you have set up both instruments in an optimal manner, to what extent does the statistical noise produced by out-of-focus light from your WF specimen offset the increased QE of the CCD detector used in widefield scanning?

- Thin, sparsely-stained specimens are good for widefield/deconvolution.
- Confocal is good if you only need to see one plane.

The questions between confocal and two-photon excitation are:

- Do you need to look more than 20 µm into your specimen?
- Are you content to excite at only one wavelength at a time?
- Will you get more successful live-cell experiments done on one two-photon setup than on two confocals?
- Are your specimens free from important structures that absorb in the near IR or that might be damaged by three-photon excitation at the wavelengths you plan to use?
- Do you have enough room for a two-photon system?
- Can you get along without video-rate imaging or rapid wavelength switching?
- Do you have the technical support needed to keep the pulsed laser happy or can you live with one of the automated femtosecond lasers with a reduced wavelength range? (See Chapters 21 and 40, *this volume*, for a discussion of the advantages of using wavelengths >1000 nm for multi-photon excitation.)

If YES to all of these, then the greater signal collection efficiency and reduced bleaching volume should make two-photon your best bet. These characteristics are summarized in Table 35.1

SUMMARY

As with any type of sophisticated instrument, the best results can only be obtained if the operator uses a confocal microscope correctly. Many aspects of proper practice are either similar or identical to those that govern the operation of the conventional light microscope. However, there are two controls, one contrast effect and one optical effect, that are unique to the confocal microscope. The limitations imposed on confocal imaging by these four factors — pixel size, pinhole size, fluorescence saturation, and chromatic magnification error — must be understood if one is to make best use of this highly productive instrument. In addition, an appreciation of the effects of photon statistics will enable users to get the most possible information from their specimens.

Remember that when using a confocal microscope, the resolution visible in the final image can be limited by three considerations in addition to the optics defining the volume of the specimen that is sampled by both the laser beam and the confocal pinhole. These three considerations are:

1. The choice of pixel size (referred to the specimen): Pixel size is a function of the zoom setting and the NA and magnification of the objective lens.
2. Deconvolving, or at least filtering, the 3D data before displaying or measuring suppresses artifactual single-pixel noise features and improves S/N by averaging the photon signal over many voxels.
3. The S/N of the intensity signal recorded can be optimized by maximizing dye contrast and counting as many of the photons produced by the specimen as possible.

TABLE 35.1. Three-Dimensional Microscopy Methods: Summary

	Widefield/Deconvolution	Confocal Single-Beam	Confocal Disk Scanner	Two-Photon
Effective detector QE	60%–80% (CCD)	3%–12% (PMT)	30%–40% (EM-CCD)	3%–12% (PMT)
Detector noise (RMS electrons pixel)	±4	<0.01	0.01	<0.01
Peak signal[a]	>20,000	20–100	1–3000	20–100 photons/pixel
Acquistition time (s/frame)	Depends on CCD readout	0.33–3	0.002–10	0.33–10
Excitation intensity power/µm^2	10 nW	0.1 mW	1–10 µW	10 W
Excitation wavelengths	350–650 nm (Hg arc)	Laser lines (fiber-coupled)	2–3 laser lines (dichroic hard to change)	700–900 nm Ti : Sa
Major limitation	Poisson noise from out-of-focus light	Singlet saturation limits data rate Scattering samples defocus signal Galvo limits scan speed	Less sectioning than single-beam Scattering samples defocus signal	Singlet saturation Hard to excite only one member of FRET pair Damage/excitation greater for many dyes

[a]These figures assume data collected from same volume of the specimen in same time period. Ideally, the raw data from all methods should be deconvolved (see Chapter 25, *this volume*).

Determine and use the optimal pixel and pinhole sizes for each objective and, if the confocal bleaching rate seems higher than that you have come to expect from normal, photographic epi-fluorescent microscopy, **you are probably doing something wrong!**

While the points that we have tried to emphasize in this chapter were chosen because they seemed to us to be those most often misunderstood by novice users of the confocal microscope, they certainly do not cover all of the possible problem situations that can occur in this field. A better understanding of more complex problems of a general and theoretical nature can be obtained by reading the other 50 chapters in this book while specific problems that apply to a certain type of instrument or dye are best forwarded either to the appropriate supplier or to discussion on the Confocal (LISTSERVER) E-mail Network. This network supports active, informal, and informative discussions of current topics in confocal microscopy by over two thousand scientists having a wide variety of experience. Anyone on the Internet can subscribe to this service by sending the message: "subscribe confocal <your name>" to the address "LISTSERV@UBVM.CC.BUFFALO.EDU". You will then receive a message describing the rules and purpose of the group as well as future postings to it.

ACKNOWLEDGMENTS

Thanks are due to Peter Shaw (Norwich, UK) for his cooperation in providing the 2D FTs of test pattern images, to Nelson Navarro (C.U.P.R., Puerto Rico) who provided the diatom preparation used for Figure 35.12, to Richard Tiberio of the National Nanofabrication Facility (Cornell) who made it possible to fabricate the confocal test specimens, and to Bill Feeney, the artist in the Zoology Department, University of Wisconsin, Madison, who made the line drawings. This work was supported by grant DIR-90-17534 from the US National Science Foundation (JP) and grant DRR-570 from the US National Institutes of Health to the Integrated Microscopy Laboratory, Madison, Wisconsin (VC).

REFERENCES

Bradbury, S., 1984, *An Introduction to the Optical Microscope*, Oxford University Press, New York.

Inoué, S., 1986, *Video Microscopy*, Plenum Press, New York.

Pawley, J.B., 2000, The 39 steps: A cautionary tale about "quantitative" 3D Fluorescence Microscopy, *BioTechiques*, 28:884–886.

Pawley, J.B., Amos, W.B., Dixon, A., and Brelje, T.C., 1993, Simultaneous, non-interfering, collection of optimal fluorescent and backscattered light signals on the MRC-500/600, *Proc. Microsc. Soc. Am.* 51:156–157.

Pawley, J.B., and Centonze, V., 1997, Practical laser-scanning confocal light microscopy: Obtaining optimal performance from your instrument, In: *Cell Biology: A Laboratory Handbook* (J.E. Celis, ed.), Academic Press, New York, pp. 44–64.

Rose, A., 1948, Television pickup tubes and the problem of noise, *Adv. Electron.* 1:131.

APPENDIX

Normal Köhler Illumination

Proper alignment of a light microscope begins with the microscopist setting up the optical components for Köhler illumination (see also Figs. 6.3 and 6.7, *this volume*). This mode of illumination establishes two important sets of conjugate image planes. Conjugate planes are sets planes perpendicular to the optical path that focus onto each other, that is, the same features will be visible in each plane of a set of conjugate planes, although the size may vary. There are an infinite number of such sets of conjugate planes in any optical system but only two of these sets are of particular interest in microscopy: aperture planes and image planes. In Köhler illumination, the aperture planes are at the light source, the iris diaphragm of the condenser, the BFP of the objective, and the eyepoint (i.e., where you are supposed to place your cornea). The image planes are the field diaphragm, the focus plane in the specimen, the field stop in the eyepiece (located 1 cm inside the tube holding the occular), and the retina of the eye or the camera film plane. These two sets of planes are reciprocally related to one another in the following way: light passing through any **location** (point) in any **image plane** will be found to have passed at a specific **angle** through any **aperture plane** and vice versa.

To produce maximum resolution, light must leave (or approach) the specimen from as many angles as permitted by the size (or NA) of the objective. This means that, for full performance, all aperture planes must be filled to the full NA of the system. In addition, the optical components for phase and DIC contrast enhancement need to be placed in aperture planes.

Setting up for Köhler illumination ensures that these conditions are met. If all specimens had exactly the same thickness (±1 µm) and refractive index, it would be possible to preset the microscope for Köhler illumination. As they do not, one must set it up manually every time a new specimen is mounted.

To achieve Köhler illumination for transmitted light microscopy, one must first center and focus the illuminator (this step is usually not required in modern microscopes in which the illuminator is built into the microscope base). Remove all filters from the lamp housing, close down the field diaphragm, and focus the collector lens to obtain a sharp image of the filament on a target placed at a distance of ~25 cm away. The lamp centering screws should then be adjusted to insure that the collector lens and the source are aligned and the image of the filament is centered. [Note: If using a Hg-arc source it is better to align the source while viewing an aperture plane in the microscope (and using a lot of neutral density filters!) in order to avoid exposure to UV light.]

Next, the condenser must be aligned. Using a low-power objective, focus on a specimen on the microscope stage, close down the field diaphragm (the field diaphragm is usually in the base of the microscope while the condenser aperture, described below, is actually incorporated into the condenser that is mounted under the stage), and adjust the height of the condenser until you obtain a sharp image of the edge of the field diaphragm superimposed on the focus plane in the specimen. Move the condenser adjustment screws to center the opening of the field diaphragm in the field of view. If the condenser is badly misaligned, you may not see any light if you initially close the field diaphragm down all the way. In this case, do it a little bit at a time, focusing and centering at each step.

The field diaphragm should then be opened to the edges of the field of view or at least until it surrounds the area of interest. Opening it more than necessary will let more light into the system than you need, and the extra light will cause reflections that produce flare and hot spots that reduce image contrast.

The working NA of an objective used in transmission is set by the aperture diaphragm. Closing the condenser iris reduces the angle of the illumination striking the specimen, lowering the effective NA of the system. Opening the condenser increases the working NA, increasing the resolution but usually reducing the depth of field, the contrast and sometimes introducing flare. Consequently, final adjustments to the condenser iris are a compromise between resolution and image contrast.

Because the condenser is often fixed to the stage, the objective and condenser usually do not maintain their spacing as the focus is adjusted or as additional optical components such as filters are introduced. Therefore, one must readjust for Köhler and reset the field diaphragm and the condenser iris to obtain the best image possible each time the optical system is changed (e.g., by changing objectives). When the microscope is properly adjusted for Köhler illumination, the result is maximum lateral and axial resolution, optimum contrast, a uniform level of illumination across the field, and a minimum amount of flare from internal reflections.

Strictly speaking, conventional, transmitted light, Köhler illumination is not necessary for epi-fluorescent confocal microscopy because both excited and emitted light travel through the same objective. However, one must set up the epi-illumination system for Köhler in order to ensure even illumination and to use the epi-field diaphragm to restrict the excitation to just the area being imaged, a habit that greatly reduces non-specific flare.

Transmitted Köhler is also necessary if one needs an optimal phase contrast or bright-field image to locate the most interesting part of one's specimen before beginning confocal work. In addition, the non-confocal transmitted-light detectors provided with many instruments will only work correctly if the condenser has been properly adjusted for Köhler illumination.

36

Practical Confocal Microscopy

Alan R. Hibbs, Glen MacDonald, and Karl Garsha

THE ART OF IMAGING BY CONFOCAL MICROSCOPY

This chapter is aimed at giving a practical overview of using confocal microscopes and monitoring their performance. Confocal microscopy is a multi-skilled endeavor that requires a considerable level of competence in sample preparation, knowledge of potential sources of artifact and appropriate controls samples, instrumentation evaluation and operation, computational post-processing, as well as knowledge of a multitude of fluorescent probes (Hibbs, 2004).

Do not overlook the specimen itself as a component of the imaging process. As living cells are often particularly optically active, it is important to understand the mechanisms of intentional as well as unintentional contrast generation in confocal microscopy. Appropriate controls are crucial to the production of reliable multi-dimensional image data.

Balancing Multiple Parameters

The goal of instrument adjustment during image collection on a confocal microscope is to balance a number of potentially conflicting parameters on the instrument. The main paradox involves achieving adequate spatial resolution while keeping cells alive and healthy or at least unbleached. Recording dynamic cellular processes with minimal light exposure may require a significant compromise in the degree of resolution that can be obtained.

Every image should be acquired using parameters that maximize its information content within the limitations of the selected mode of microscopy. Post-acquisition processing, such as deconvolution or three-dimensional (3D) Gaussian filtering, histogram stretching, or projections of multiple planes, can be employed to reveal the important details under photon-limited conditions (see Chapters 32 and 48, *this volume*).

MONITORING INSTRUMENT PERFORMANCE

The ability to determine relative dye concentrations, colocalization, Förster resonance energy transfer (FRET), shifts in emission spectra, and identity of ambiguous fluorescent signals is highly dependent on the accuracy and precision of a multitude of instrument functions. To ensure consistent peak performance, one must monitor performance at regular intervals and keep good documentation. Benchmarks of functionality can be organized around four major subsystems common to scanning microscopes: (1) illumination source, (2) signal detection subsystem, (3) scan raster mechanisms, and (4) lenses and other optical elements. In order for accurate and precise data to be recorded, not only must each subsystem perform well on its own merits, but they must also be carefully orchestrated to work together in synergy.

Illumination Source

Power Measurement

Obtaining consistent results from a confocal microscope requires knowledge of the actual laser power level at the specimen and its temporal stability. A well-equipped microscopy facility needs a reliable, accurate power meter (a photometer) suitable for making measurements at the specimen plane. Otherwise, low signal level can be wrongly attributed to poor specimen preparation or problems in the detection channel when the actual fault is low excitation power. Such devices may be acquired from optics companies such as Newport (Irvine, CA), Melles Griot (Carlsbad, CA), and Linos Photonics (Milford, MA), among others. Adjustments such as the re-alignment of the fiber to the laser output may occasionally be needed. Changes in the illumination stability often reflect the gradual deterioration of lasers and arc bulbs over the long term. As a laser cavity nears the end of its lifetime, it may also display a reduced output level that may be abrupt and very obvious. In lasers with multiple lines, it is common for one line to lose power before the others.

Tracking long-term changes in power output requires the use of standardized settings.[1] The appropriate dichroic mirror should be used for each laser line. Because objectives vary in terms of their transmission and pupil diameter, it is important to use the same objective for standard laser power measurements. To measure laser power, use the beam-parking or point-bleaching features to place a diffraction-limited point near the center of the field of view, and turn on the beam for an exposure of ~30 s. As the laser

[1] On instruments where the beam expander is under software control, the control should be disabled or it should be removed from the optical path.

Alan R. Hibbs • BIOCON, Melbourne, Australia
Glen MacDonald • Core for Communication Research, Virginia Merrill Bloedel Hearing Research Center, University of Washington, Seattle, WA, USA
Karl Garsha • Imaging Technology Group, Beckman Institute for Advanced Science and Technology, University of Illinois at Urbana-Champaign, IL 61801, USA

power is not modulated during beam-parking it is ideal for power measurement. On older scanners that do not have acousto-optic tuning filter (AOTF) beam blanking during retrace, use the maximum zoom setting.

The AOTF settings (or neutral density filters) should be configured to provide maximum power, and if there is a coarse adjustment for the laser power, this should be maximized as well. The power meter sensor should be carefully positioned over the field of view near the focal plane of a dry objective and perpendicular to the optical axis. Because most sensors are not equally sensitive across the entire surface, use a stable sensor mounting system so as to use the same area of the sensor surface. Be sure the laser power meter is set to the appropriate detection wavelength.[2]

To measure the power, start the point bleach sequence for a single laser line and record the meter readout. Repeat for each laser line in turn. For accurate readings the room should be dark, the lasers adequately warmed up, and several measurements should be taken to check data precision.

Similar readings taken in the standard scanning mode will be lower than this value if the laser beam is blanked by the AOTF during the flyback and during the interval between consecutive frames.

Laser Stability

Although laser stability on the order of seconds can be measured with a photometer, rapid oscillations of laser output are beyond the temporal resolution of the power meter. To measure high frequency stability, image a bright standardized, stable fluorescent sample such as a coverslipped piece of fluorescent plastic (Chroma Technologies Inc., Rockingham, VT; Applied Precision, Issaquah, WA), or a high concentration of fluorescent dye in oil (fluorescent seas; see Chapters 2 and 35, *this volume*; also Model and Burkhardt, 2001). To reduce photobleaching, use a freshly prepared, standardized dilution of fluorochrome in an index-matched solvent.[3]

On inverted microscopes, use chambered coverslips with multiple wells (Nalge Nunc International, Rochester, NY) to hold the fluorescent liquid. Carefully prepared concavity slides (Electron Microscopy Sciences, Hatfield, PA) can be used as an alternative on upright microscopes. It is a good idea to centrifuge the test solution in order to remove particulates prior to use. Focus the microscope into the bulk fluorescent standard near (but not at) the dye–coverslip interface.

Set up a two-dimensional (2D) time series with an appropriate acquisition interval and overall duration. The scan area can be reduced to only a few lines in order to reduce the acquisition interval for greater temporal resolution. Settings should be configured such that the laser power is standardized to a value high enough to provide a reasonably noise-free image, yet low enough that bleaching is not a problem, and the detectors adjusted such that the measured mean pixel intensity is within the linear response range (see Chapter 2, *this volume*). Analyze the acquired dataset by eye for obvious indications of instability, such as some lines being brighter than others, etc., or by graphing the mean intensity of each time point. Small, periodic variations will be made more obvious in a Fourier transform of the data.

Scan Raster and Focus Positioning

Spatial measurements and accurate morphometric classification rely on the accuracy and precision of the mechanisms used to move the focal volume through the specimen in the *x*-, *y*-, and *z*-dimensions. **From a practical standpoint, measures of the lateral and axial resolution on a laser-scanning instrument are meaningless unless the accuracy and precision of pixel-to-pixel spacing in the *x*, *y*, and *z* can be verified.** A non-uniform scan speed will also result in differential exposure of localized areas within the field of view (Carlsson, 1991). This confounds accurate photometry and can result in increased phototoxicity when living specimens are being imaged (Fig. 36.1).

x and *y* Galvanometers

Standards for verifying lateral scan accuracy are easily purchased or fashioned from readily available components. Because the response of the galvanometer to a change in either zoom or scan speed frequently departs from an ideal linear relationship, it is not adequate to confirm scan calibrations at a single magnification and horizontal scan frequency, and, thus, one needs a standard specimen that can be used at high as well as low zoom settings. A grid standard provides an efficient means of evaluating both *x*- and *y*-scan rasters simultaneously. Suitable standards include a 2000-mesh transmission electron microscope (TEM) grid mounted in appropriate media (Electron Microscopy Sciences, Hatfield, PA), an etched silicon 10 µm grid standard for reflected light microscopy (Electron Microscopy Sciences), a carbon replica of a diffraction

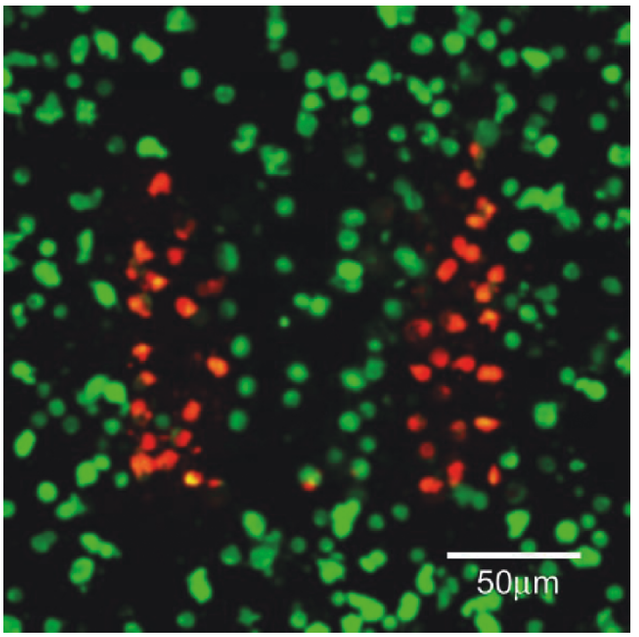


FIGURE 36.1. Differential phototoxicity as a result of uneven scan speed across the field of view. In this image, metabolically-active cells are stained with fluorescein diacetate (green); the onset of propidium iodide (red) indicates compromise of the plasma membrane associated with cell death. The speed of the scan raster was slower at the edges than in the center of the field of view in this case.

[2] Most meters actually measure the number of photons/second. As red photons carry less energy than blue ones, the meter needs to know the wavelength in order to calculate the energy/second or power.

[3] Bleaching can be removed as a variable by using a coverslipped, first-surface mirror as the test specimen. When viewed using reflected light, such a specimen produces a very high signal level (and consequently a very low level of Poisson noise), although system vibrations are more likely to account for any variations that you see due to the surface going in and out of focus, than by laser instability. This vibration sensitivity can be reduced by using an objective with low NA.

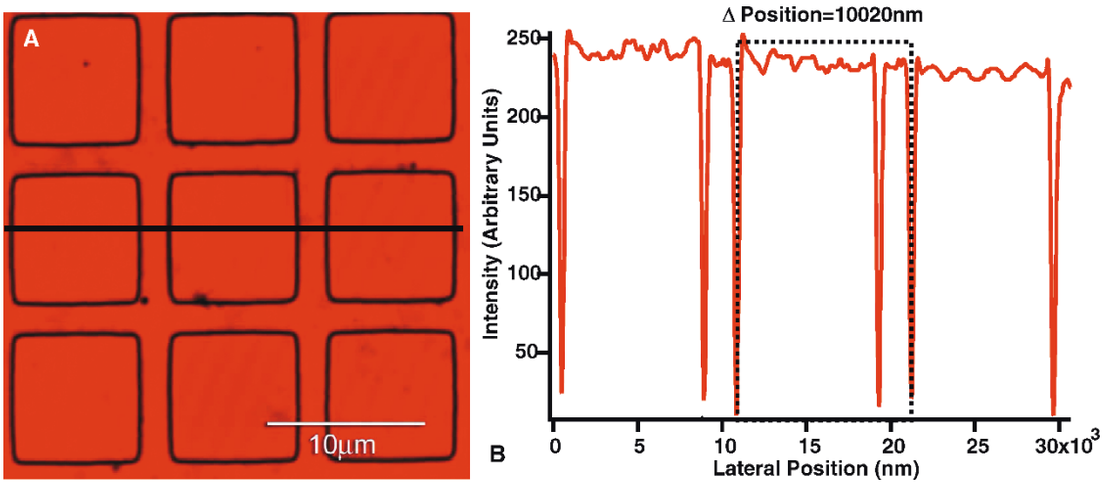


FIGURE 36.2. A well-calibrated system. (A) The standard in this case is a reflective etched silicon standard designed for reflected light microscopy. Each square is 10 microns per side; (B) a graph of intensity as a function of position on the black line in (A). Quantitative measurements confirm the accuracy and precision of the *x*- and *y*-galvanometers in this example.

grating or MBL-NNF Test Slide[4] (see Chapter 35, *this volume*), and related products such as the Microscopic Image Analysis Micrometer (Edmunds Optics, Barrington, NJ) and the Richardson test slide (Electron Microscopy Sciences). If a TEM grid (or other uncharacterized standard) is used, the accuracy and precision of center-to-center spacing between grid bars can be accurately determined using a properly calibrated widefield system.

Measurements of the center-to-center (side of one grid bar to the same side of the next) distance at different points within the field of view should be conducted for both *x*- and *y*-axes in conventional *xyz*-imaging mode. It is important to realize the effect that under-sampling can have on such measurements; sampling intervals for the scan resolution should satisfy the Nyquist criteria (see Chapters 2, 4, and 35, *this volume*). A well-calibrated instrument will have accuracy within 1% of the known value and less than 1% variability between measurements. This should hold at both high and low zoom values, and across all scan speeds. Results from an instrument that is well calibrated can be seen in Figure 36.2, and the opposite is shown in Figure 36.3.

z-Drive Mechanism

The performance of the *z*-stepping or *z*-scanning system can be evaluated using large diameter beads, for example, 10.2 µm (see Table 36.1), carefully mounted in an **index-matched** [i.e., refractive index (RI) = 1.515; see Chapters 8 and 20, *this volume*] semi-solid or high-viscosity mountant. High axial resolution requires proper refractive index with a high numerical aperture (NA) oil-immersion objective (designed for RI of 1.51; polystyrene beads have RI between 1.55 and 1.59). Do not use a dry objective (Carlsson, 1991).

Commercially prepared fluorescent bead calibration slides can be purchased from Spherotech and Molecular Probes (Table 36.1). *z*-Calibration measurements should be performed at both high and low magnification by making *xz*-images across the center of a bead. The height of several beads from several levels within the *z*-plane should be measured. The diameter of the bead with respect to *z* is taken as the distance between half-maximum intensity values on the steep-sloped rising and falling intensity gradients that indicate the top and bottom of the bead. The accuracy and precision of the values obtained are then compared to the stated tolerances of the calibration beads. Unless the calibration beads have been severely compressed, the mean value and standard deviation taken from a sample should be the same in the *xz*-image as in the *xy*-image [Fig. 36.4(A,B)]. A large systematic departure from the values as measured with respect to the *xy*-plane likely represents poor performance of the *z*-movement mechanism, miscalibration of the control mechanisms, or the use of a mounting or immersion liquid having the wrong RI for the lens in use.

z-Positioning Stability

In both volumetric imaging and 2D time-lapse imaging, it is important that the relationship between the position of the sample and the optics is stable. As noted in the earlier footnote, this can be assayed using a mirror standard viewed in reflected light (described below under tests for axial resolution) over a time course. Motion of structures in an *xy*-image of the mirror surface shows vibration, while collecting a time-lapse series of 3D images through the reflective interface will reveal stage or focus drift. Rapid *xz*-scanning over time can assist in resolving high frequency drift. After acquisition, the position of the reflection intensity maximum with respect to *z* can be found at each time point and plotted as a function of time.

Vibration can be reduced by using a vibration-isolation table and making sure that all the wires or hoses connecting the table to the outside world are bent to reduce their ability to transmit mechanical forces. The most likely cause of drift is temperature change, often caused by the air conditioning going on and off, or in actual use, by components involved in heating the specimen and the objective for living-cell studies. The solution is to insulate your setup from changes in room air and run stage-heater controllers in the open-loop mode or place the entire microscope in a heated enclosure (see Chapter 19, *this volume*).

Optical Performance and Objective Lenses

Because the performance of the objective is crucial to the overall performance of an imaging system (see Chapter 11, *this volume*),

[4] Louie Kerr (Marine Biological Laboratory, Woods Hole, MA) has fabricated suitable test slides in the past using electron beam lithography at the National Nanofabrication Facility (NNF) at Cornell University. He expects to do so in the future.

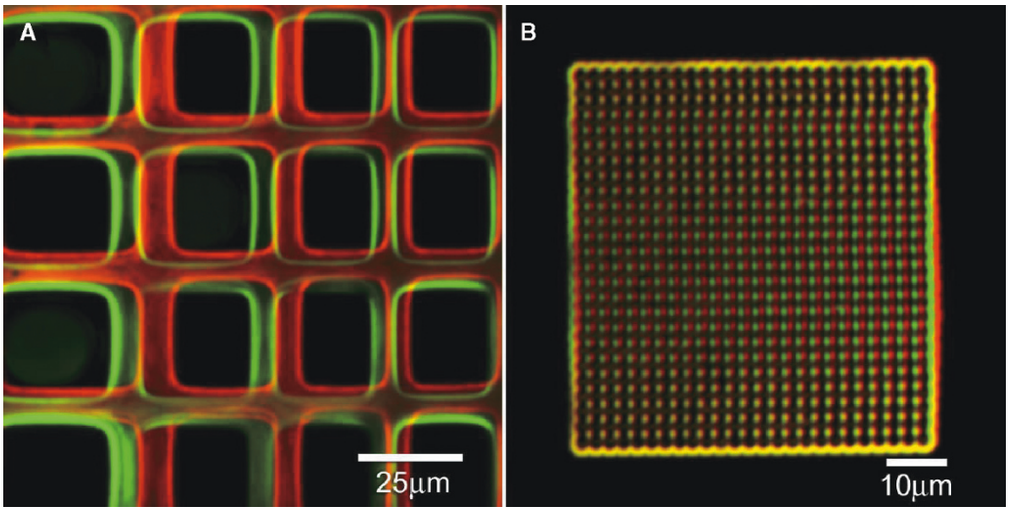


FIGURE 36.3. A malfunctioning system. (A) Observation at low magnification indicates problems with both accuracy and precision between scans. Two scans taken in sequence are indicated by the red and green channels of the image. (B) A scan taken at higher magnification on the same instrument. The standard in this case is milled into a coverslip surface with a focused ion beam (kind gift of Dr. Carlos Martinez, NIST, Gaithersburg, MD). Again, red and green components of the image reflect the lack of precision. Wavering in the scan raster appears as distortion in the grid standard. The square pattern appears rectangular (narrower in the *x*-direction) because of poor calibration of the *x*-scan galvanometer.

TABLE 36.1. Sources of Fluorescent Beads

Manufacturer	Address	Telephone	Web site/E-Mail
Bangs Laboratories, Inc.	9025 Technology Drive Fishers, IN 46038–2886 USA	Phone: +1 317-570-7020 USA: +1 800-387-0672 Fax: +1 317-570-7034	www.bangslabs.com info@bangslabs.com
Brookhaven Instruments, Ltd.	Chapel House, Stock Wood Redditch, Worcestershire B96 6ST, UK	Phone: +44 (0) 1386-792727 Fax: +44 (0) 1386-792720	www.brookhaven.co.uk enquiries@brookhaven.co.uk
Duke Scientific Corporation	2463 Faber Place Palo Alto, CA 94303 USA	Phone: +1 650-424-1177 USA: +1 800-334-3883 Fax: +1 650-424-1158	www.dukescientific.com info@dukescientific.com
G.Kisker GbR Produkte f.d.Biotechnologie	Postfach 1329 48543 Steinfurt Germany	Phone: +49 2551-864310 Fax: +49 2551-864312	www.kisker-biotech.com contact@kisker-biotech.com
Molecular Probes, Inc.	29851 Willow Creek Road Eugene, OR 97402 USA	Phone: +1 541-465-8300 Fax: +1 541-335-0504 Order: + 1 800-438-2209	www.probes.invitrogen.com order@probes.com
Polysciences, Inc.	400 Valley Road Warrington, PA 18976 USA	Phone: +1 215-343-6484 USA: +1 800-523-2575 Fax: +1 800-343-3291	www.polysciences.com info@polysciences.com
Sigma-Aldrich Corp.	3050 Spruce Street St. Louis, MO 63103 USA	Phone: +1 314-771-5765 USA: +1 800-325-3010 Fax: +1 314-771-5757	www.sigmaaldrich.com OC_DOM_HC@sial.com
Spherotech, Inc.	1840 Industrial Dr. Suite 270 Libertyville, IL 60048-9467 USA	Phone: +1 847-680-8922 USA: +1 800-368-0822 Fax: +1 847-680-8927	service@spherotec.com jwsphero@aol.com

These vendors offer beads down to subresolution sizes in single and multiple wavelengths. Many offer larger beads in a variety of configurations. Larger beads may be solidly fluorescent, contain surface rings, overlapping concentric rings, concentric rings that do not overlap, and combinations of solid and ring labels. Some vendors in this list also offer silica, glass, or melamine beads that possess different physical properties compared to the commonly used polystyrene or latex.
This list does not include vendors of fluorescent beads where the bead preparations are specifically designed for flow cytometry.

all objectives should be tested for performance. Objectives do vary within brand and type and should be carefully compared before purchase and then regularly monitored (see Chapter 11, *this volume*, for more details). The most common tests of imaging optics, those for lateral and axial resolution and chromatic aberration, should be performed periodically as objective lens performance may deteriorate over time.

Spherical aberration created by the specimen is a serious constraint in the creation of high-quality images, particularly when imaging living biological material. As described in detail in Chapters 2, 7, and 20, when using an oil-immersion lens to image living biological material there will be a serious mismatch in RI between the design parameters of the objective and the aqueous sample. Even using an oil-immersion objective with a sample mounted in a media with a relatively high RI, such as glycerol (RI = 1.47), there is still be a significant level of spherical aberration present.

The best plan is to use objective lenses designed for the imaging conditions under which they are being used. Some objectives are equipped with a collar to correct for routine variations in coverslip thickness, as noted in Table 36.2. However, RI mismatches can also be partially corrected by coverslip-thickness correction collars or using the automated spherical-aberration corrector (SAC) now offered by Intelligent Imaging (Denver, CO). This will greatly diminish spherical aberration, and result in improved resolution and signal level, particularly when imaging deep into the sample. The effect of spherical aberration on signal intensity is readily demonstrated by collecting an *xz*-image into a dilute fluorescent solution such as 0.01% coumarin in water (Fig. 36.5). In Figure 36.5(A,B), a 40× NA 0.60 non-immersion dry objective lens has been used to image into a dilute coumarin solution contained in a sealed imaging chamber. The base of the chamber is a 0.17 mm thick coverslip, with the correction collar on the objective set for 0.17 mm [Fig. 36.5(A)] or 0.5 mm [Fig. 36.5(B)]. Even when the spherical aberration collar is correctly matched to the thickness of the coverslip, the intensity profile diminishes significantly as the focus plane moves away from the coverslip [Fig. 36.5(A)]. This drop-off in intensity is due to the RI mismatch between the immersion media (in this case, air) and the sample (water). If the spherical aberration correction collar is adjusted to 0.50 mm, while retaining a coverslip thickness of 0.17 mm, then the zone of maximum intensity in the image is moved farther into the sample [Fig. 36.5(A)]. This simple adjustment can be used to collect good images over a limited range of depths within living tissue samples using a non-immersion air lens.

Figure 36.5(C) shows the performance of a 40× NA 1.20 water-immersion lens (with 0.17 mm coverslip correction). Because the objective is used with water on both sides of the coverslip, the total thickness of water and glass between the front of the objective and the focus plane does not change with focus position and therefore, intensity of the signal in this *xz*-image does not diminish throughout the full depth of the scan (200 µm).

TABLE 36.2. Coverslip Thickness and Refractive Index

Designated Size	Tolerance (mm)
#00	0.06–0.08
#0	0.08–0.12
#1	0.13–0.16
#1.5	0.16–0.19
#2	0.19–0.23
#3	0.28–0.30
#4	0.38–0.42
#5	0.50–0.60
Refractive Index at 20°C for Commonly Used Glass	
Desag D-263	(546 nm) = 1.5255
	(588 nm) = 1.5230
Corning 0211	(589 nm) = 1.5230

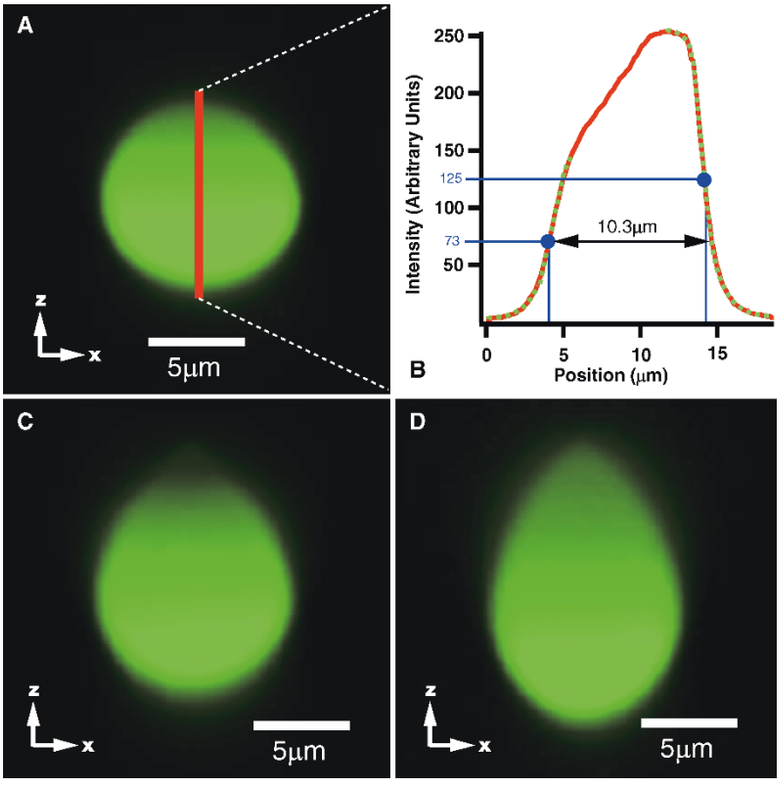


FIGURE 36.4. Checking *z*-positioning calibration using fluorescent beads. (A) 10.2 µm polystyrene spheres in immersion oil. The data maintain the correct aspect ratio, and accurate measurements in the *z*-axis are possible with an oil-immersion lens. (B) Measurement of calibration beads in the *z*-axis under properly index-matched conditions permits evaluation of the *z*-drive calibration. The midpoint on each of the steep-sloped lines depicting the edge response of the top and bottom limits of the bead are found (*green/red dotted lines*). The distance between these points on the *x*-axis of the intensity plot is the height of the bead. Note that the intensity of the bead is not constant through the diameter of the bead due to absorption of excitation light by the bead. For this reason, the halfway points of the bottom and top edge response are located at different intensity levels. In this case the *z*-drive (a *z*-galvanometer stage) is performing well, and measurement of the axial dimensions of the calibration beads are both accurate and precise. (C) The same beads in a classic 9 : 1 glycerol/PBS buffer mountant of RI = 1.43 viewed with an oil-immersion lens. Significant distortion in the *z*-axis is evident due to spherical aberration as well as self-lensing. Accurate measurements with respect to *z* are not possible under these conditions. (D) 10.2 micron polystyrene spheres in water (RI = 1.32) viewed with an oil-immersion lens. Distortion in the *z*-axis is exacerbated in accordance with Snell's law.

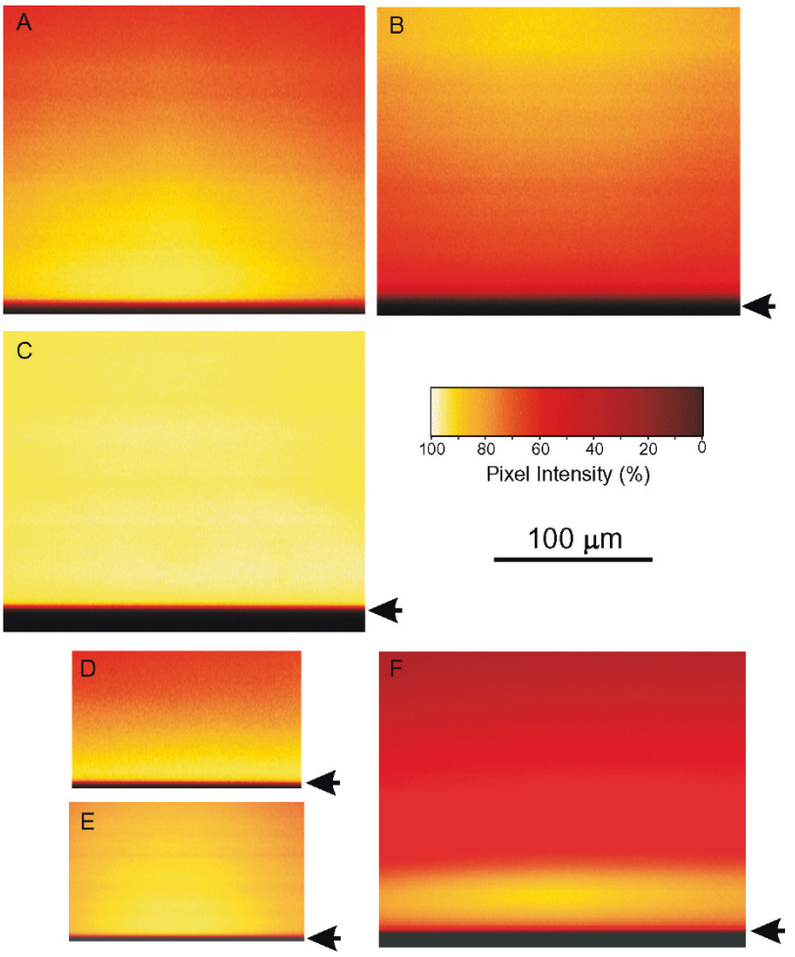


FIGURE 36.5. Correcting for spherical aberration. *xz*-images were collected on a Zeiss 510 META confocal microscope while imaging into (1) a dilute aqueous fluorescent coumarin solution (approximately 0.1 m*M*) and (2) green fluorescent plastic. The 488 nm blue laser line from an argon-ion laser was used for excitation, and the fluorescent light between 510 and 520 nm was collected into a single detection channel. Each image represents a single line collected at increasing depth (1 µm deeper per scan) within the solution or plastic. The position of the coverslip is marked with an arrow (←). All images were obtained using a 0.17 mm thick coverslip, with various adjustments of coverslip correction collars as described below. All images were collected using a pinhole size of 1 Airy disk. (1) Imaging into fluorescent aqueous media: a Zeiss LD-Achroplan 40× 0.60 NA dry lens was used to collect images into the fluorescent aqueous media with the coverslip thickness correction collar set to (A) 0.17 mm and (B) 0.50 mm. A Zeiss C-Apochromat 40 × 1.2 NA water-immersion lens with coverslip-correction collar set to 0.17 mm (C), and a Zeiss Plan-Apochromat 63 × 1.4 NA oil-immersion lens with 0.17 mm coverslip correction (D) were used to collect *xz*-images in the fluorescent coumarin solution. (2) Imaging into fluorescent plastic: a 0.17 mm thick coverslip was placed on the surface of a small sheet of green fluorescent plastic using a small amount of immersion oil between the coverslip and the plastic. *xz*-images were collected using a Zeiss Plan-Apochromat 63 × 1.4 NA oil-immersion lens with 0.17 mm coverslip correction (E) and a Zeiss C-Apochromat 40 × 1.2 NA water-immersion lens with the coverslip thickness correction collar set to 0.17 mm (F).

In Figure 36.5(D), a 63× NA 1.40 oil-immersion lens (corrected for 0.17 mm thick coverslip) has been used to image into the dilute coumarin solution. The severe RI mismatch between the immersion media (oil) and the sample (aqueous solution of coumarin) results in a significant reduction in the intensity of the fluorescent signal with increased imaging depth. The *z*-position of maximum signal detection is nearly always located close to the coverslip when using an oil lens to image into samples mounted in aqueous media. Oil-immersion lenses do not have spherical aberration correction collars.

Lateral Resolution

The lateral resolution of a digital microscope is usually measured with either a subresolution point source standard or a special test slide (see Chapter 35, *this volume*; Stark *et al.*, 2003).

Subresolution Beads

The 3D diffraction pattern characteristic of a microscopic imaging system is known as a point spread function (PSF; see Fig. 36.6; Chapters 7, 11, and 20, *this volume*; also Hiraoka *et al.*, 1990; Shaw and Rawlins, 1991; Wilson and Juškaitis, 1995; Scalettar *et al.*, 1996; Booth and Wilson, 2001; Wallace *et al.*, 2001; Cox and Sheppard, 2004). The PSF defines the spatial resolution of a particular optical train. Where deconvolution software is employed, one should record a library of PSF images for each objective lens and wavelength (see Chapter 11, *this volume*).

Fluorescent polystyrene beads measuring less than 200 nm (or even less than 100 nm) can be purchased prelabeled with dyes suitable for measuring resolution at different wavelengths (see Table 36.1 for a list of suppliers). They are conveniently prepared for imaging by allowing a few microliters of a bead suspension to spread over, and dry onto, the surface of a coverslip.[5] This ensures that all the beads are in the same focal plane and also eliminates Brownian motion. Most aqueous mounting agents used for fluorescent samples can be used with beads, but take care when using solvent-based mountants or immersion oil as the dyes may leach out or the beads may even dissolve.

The PSF is acquired by collecting a *z*-series extending about 6 to 8 µm axially above and below the bead. The pixel size and focus interval should be appropriate for the objective (i.e., 0.08 µm pixels and 0.3 µm focus step for NA 1.4, and 0.16 µm pixels and 1.2 µm focus step for NA 0.7).

Select single beads that are well separated from others and near the center of the field. Because Poisson noise imparts a great degree of ambiguity to such images, either select a slow scan speed or Kalman average at least three scans during image collection. Most deconvolution software packages capable of utilizing a measured PSF also have a provision for averaging several individual PSF volumes together to reduce from the effects of noise, drift, focusing errors, and intensity fluctuations in the illumination.

[5] The coverslip should be first cleaned by soaking in 1% HCl in 70% ethanol for 5 min, then rinsing thoroughly with H_2O and air drying. Application of the beads in 70% ethanol will aid in dispersion, although prolonged exposure may extract the dye.

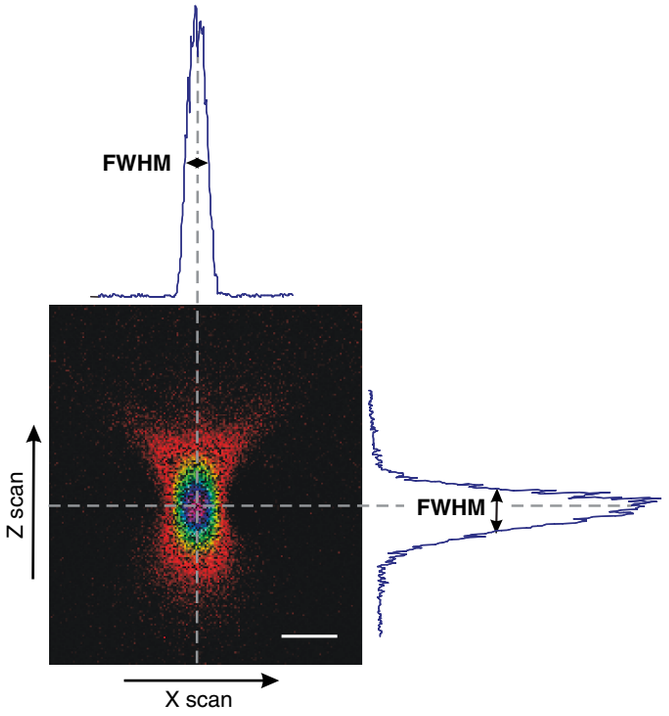


FIGURE 36.6. Determining *xy*- and *z*-resolution using fluorescent beads. The *x*-, *y*-, and *z*-resolution of a confocal microscope can be determined by imaging latex beads or quantum dots that are smaller than the resolution limit of the instrument. The beads will need to be immobilized by attaching them to the glass coverslip (e.g., by coating the coverslip with poly-L-lysine). The image shown here is a single *xz* optical slice taken through a small subresolution fluorescent latex bead (0.03 µm diameter) attached to a coverslip using poly-L-lysine and mounted in aqueous media. The image was collected on a Leica SP2 laser-scanning confocal microscope using a Leica 60 × 1.20 NA water-immersion objective. The FWHM, derived from the plot of the intensity profile in the *x*- and *z*-directions can be used to determine the resolution limit of the instrument. The scale bar represents 300 nm.

The lateral resolution of a PSF is taken as full width at half maximum (FWHM, the width of the intensity peak at 50% of its maximum intensity; see Fig. 36.6). The FWHM is measured by first finding half the maximum peak height of the intensity profile above background ($I_{\text{half max}}$, Eq. 1) and then determining the width of the intensity profile at $I_{\text{half max}}$ (denoted by the double ended arrow in Fig. 36.6).

$$I_{\text{half}} = \frac{I_{\text{max}} - I_{\text{background}}}{2} + I_{\text{background}} \qquad \textbf{(1)}$$

A projection along the *z*-axis and through the center of a volumetric dataset of a point source will ensure that the centroid of the intensity distribution is measured.

Some drawbacks to using fluorescent polystyrene spheres include the fact that they may bleach under high zoom or high laser intensity conditions and, after a time the dye may leach into organic mountants such as immersion oil.

Resolution Test Slides

As an alternative to point source standards, lateral resolution can be tested using specially designed microscopy standard slides such as the Richardson Test Slide Gen III (Richardson Technologies Inc., Toronto, Canada), the Microscopic Image Analysis Micrometer (Edmund Optics, Barrington, NJ), and the MBL-NNF Test Slide (Marine Biological Laboratory, Woods Hole, MA). The aforementioned slides have periodic line gratings of various spatial frequencies that are usually imaged in the reflected light mode, although some varieties are printed using fluorescent phosphors. The spatial frequency at which the image contrast disappears is taken as the resolution limit. This test emphasizes the relationship between contrast and resolution. This relationship is described by the **contrast transfer function** (CTF; see Chapters 1, 2, 4, and 8, *this volume*; also van der Voort *et al*., 1988; Pawley, 1994; van den Doel *et al*., 1998; Young, 2000).

Axial Resolution

Because *z*-resolution is affected by the setting of the adjustable pinhole (or pinholes as the case may be), as well as by the NA and wavelength, it is prudent to take measurements over the full range of pinhole settings (Fig. 36.7). Doing so will also reveal anomalies in the pinhole alignment. Misaligned pinholes will yield poor results for axial resolution and the expected relationship between pinhole diameter, signal intensity, and axial resolution will be disturbed (see Chapters 2, 3, 8, 11, and 22, *this volume*; also Cox and Sheppard, 2004).

Two methods are frequently employed to judge *z*-resolution. The first is the use of subresolution fluorescent particles to generate a PSF as above (Ho and Shao, 1991; Shaw and Rawlins, 1991). The second approach involves making an *xz* reflected light image of the surface of a mirror slide as described below (Ho and Shao, 1991; Visser *et al*., 1991; Cox, 1999; Zucker and Price, 2001a).

Axial Resolution Using a Mirror

A front-face mirror slide can be purchased (Electron Microscopy Sciences; Spherotech, Libertyville, IL) or made from a high-quality coverslip onto which a reflective metal surface has been deposited on one side using either sputter coating or vacuum depo-

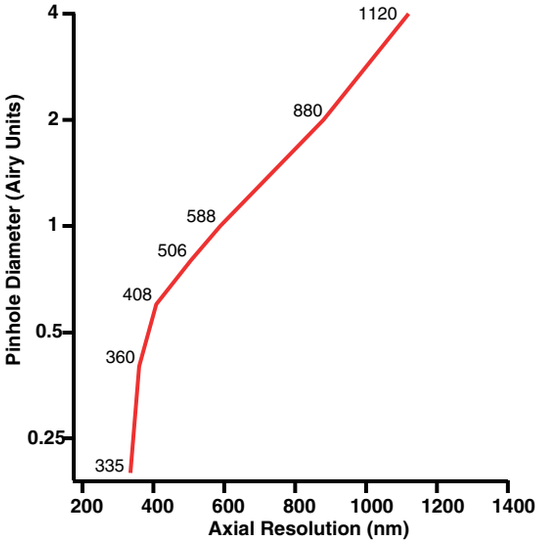


FIGURE 36.7. Axial resolution as a function of pinhole diameter. Measurements were conducted using a mirror standard with a 63× oil-immersion objective with NA 1.32.

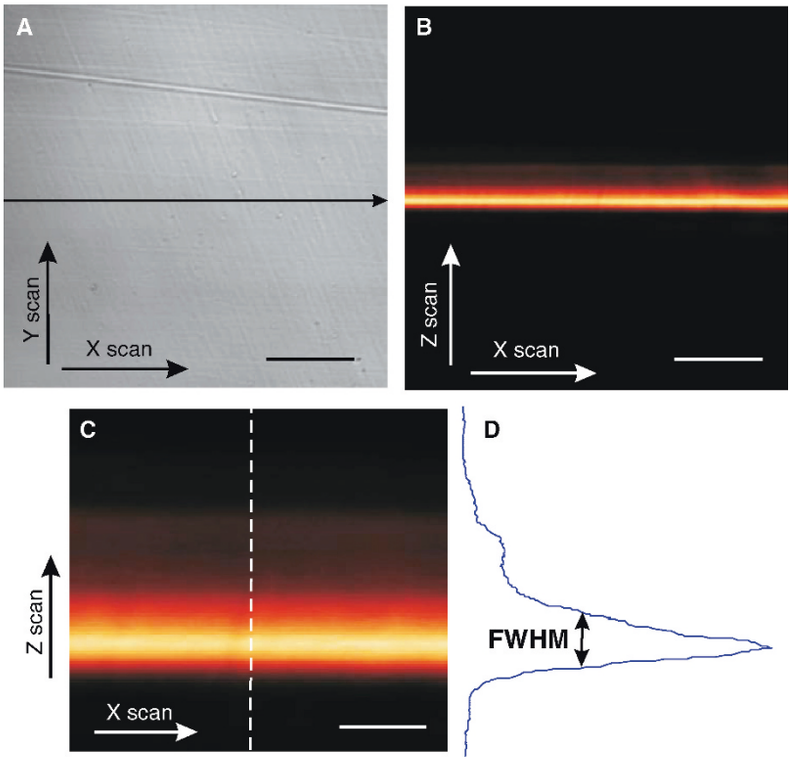


FIGURE 36.8. Determining *z*-resolution using a mirror. Backscatter images of a front surface silvered mirror using a Nikon 100× 1.40 NA oil-immersion lens on a Bio-Rad MRC-1024 confocal microscope with the 488 nm blue line from an argon-ion laser and a pinhole size of 1 Airy disk. The front-surfaced mirror was imaged by placing a small drop of immersion oil directly on the mirror surface and then placing a coverslip onto the oil. Immersion oil was then placed on top of the coverslip to create a continuum with the objective lens. (A) Backscatter image of the mirror surface (*xy*-image), (b) backscatter image through the mirror surface (*xz*-image), and (C) confocal zoom of a small section of the *xz*-image in (B) showing an intensity profile graph (D) at the position of the dotted line in image (C). The full-width at half-maximum (FWHM) of the intensity profile shown in (D) (measured in microns) is a measure of the *z*-resolution of the instrument. The slight asymmetry of the profile is due to a small amount of spherical aberration of the optical system. To establish whether this is due to an imperfection in the objective lens you would need to rigorously establish that the preparation of the sample has not introduced minor optical aberrations. The asymmetry of the plot shows the presence of spherical aberration. The scale bar in (A) and (B) represents 1.6 µm and in (C) represents 0.4 µm.

sition (Fig. 36.8). The coverslip should be mounted on the slide with the metallic side away from the objective. Purchased mirrors must be coverslipped (immersion oil makes a good mountant).

When determining axial resolution using a reflective surface, use a neutral density filter or the AOTF to reduce laser power to as low as possible (less than 100 µW should be adequate) and choose dichroic and filter settings that allow the wavelength of the laser line to reach the detector. Adjust the focus until you begin to detect a signal with the pinhole fully open. Then reduce the pinhole size as the reflection signal increases. At the focus position producing the highest reflected signal, adjust the PMT gain to create a bright image that does not quite saturate any pixels [Fig. 36.8(A)].

The mirror should then be moved to an area lacking major defects and an *xz*-image (vertical section) through the surface of the mirror is collected [Fig. 36.8(B)]. The upper and lower focus limits should be set sufficiently far apart to collect all the diffraction maxima. The *z*-step should be chosen to allow for more than Nyquist sampling through the profile of the mirror [Fig. 36.8(C)]. An *xz*-intensity profile through the mirror can also be obtained by collecting a stack of *xy*-images, and then extracting the *xz*-image using suitable software. The field curvature from any lens can be tested using either a mirror or a thin fluorescent film by collecting *xy*-scans or a *z*-series. Collect a 3D data stack that includes the full depth of the reflection image over the entire field at zoom = 1. An *xz*- or *yz*-profile through this stack will reveal the degree of curvature [Fig. 36.8(C); also see Chapter 11, *this volume*].

Asymmetry in the *xz*-profile through the mirror is usually indicative of spherical aberration. In the example shown in Figure 36.8, a slight asymmetry is evident. The use of incorrect immersion media or incorrect settings on the spherical aberration correction collar (often marked as a coverslip thickness or immersion media correction collar) will induce spherical aberration.

Chromatic Registration

For multi-channel laser scanning microscopy, it is important that the spatial registration of all channels can be confirmed. This is particularly true where experiments involve colocalization and/or ratiometric measurements. Probable sources of lateral chromatic registration error are found in situations where lasers delivered through separate fibers (or direct couplings) are used together, and/or when different optics such as dichroic beam-splitters or beam expanders are used for separate channels in an automated sequential-scanning strategy. Lens aberrations or mismatched optics can also be a source of lateral chromatic aberration (see Chapter 7, *this volume*). Although the laser launch into the scanhead is aligned when the instrument is installed, measurements should be conducted immediately following installation or just before the end of any service call. Widefield systems also suffer from alignment problems when filter cubes and dichroic mirrors are moved. In addition, the relay lenses in some camera couplers impart chromatic aberration.

Lateral Chromatic Registration

This aberration can cause points in the image to be shifted radially in a wavelength-dependent manner that becomes progressively larger towards the periphery of the field (see Chapter 7, *this volume*). The relatively large (4–15 µm in diameter) multi-labeled Focal Check beads marketed by Molecular Probes (Eugene, OR) are useful for evaluating the lateral registration of multiple channels. These beads are made of a series of fluorescent shells, each of which is excitable at a different wavelength. A multi-channel image through the lateral central plane of these spheres shows a different colored ring for each channel. An overlay of all channels should depict colocalized signals (Fig. 36.9).

Alternatively, one can use a mixture of subresolution beads (Zucker and Price, 2001a) that fluoresce over a wide range of wavelengths providing that individual channels are excited

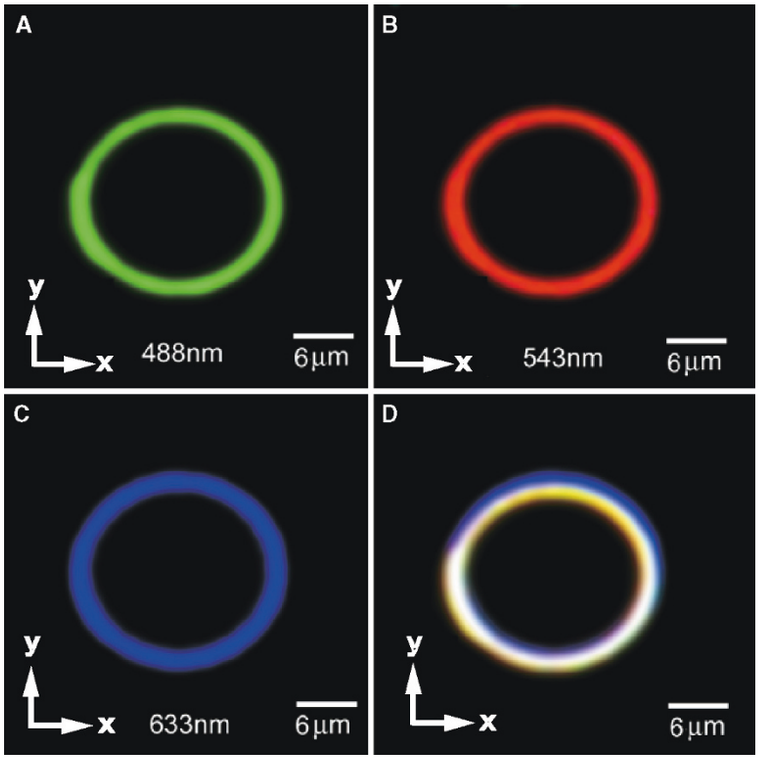


FIGURE 36.9. Lateral view of Focal Check beads in three channels. In this case, the lateral registration of channels excited by 488 nm, 543 nm, and 633 nm laser wavelengths is in agreement. All wavelengths are delivered through the same fiber-optic to the scanhead and a triple dichroic beam-splitter was used, thereby eliminating two of the primary causes of problems with lateral registration.

sequentially. When testing laser lines that are delivered to the scanning optics through separate couplings, it is advantageous to use a multi-wavelength dichroic beam-splitter to reduce the potential for ambiguity regarding the source of any displacement (e.g., dichroic vs. laser coupling alignment). By the same token, when one suspects misalignment in the beam-splitter or the dichroics, laser lines should be delivered through the same fiber or use beads that offer multi-channel emissions from a single excitation line.

Evaluation of multi-channel registration is most easily facilitated when the intensity levels are closely matched for each channel. Use an intensity profile plot through the image to determine the degree of misalignment, rather than relying on the multicolored image shown on the screen.

Axial Chromatic Registration

This type of aberration, in which the image channels shift in the *z*-axis, is described in Chapter 7. It is as important for 2D images as for 3D images. The large beads described above are not the best solution for evaluating chromatic aberration in the *z*-dimension. Due to a refractive index mismatch between the core of the bead and the fluorescent shell, the beads act as ball lenses and produce impressive (not to mention alarming) artifacts in the *z*-dimension (Fig. 36.10; also see Pawley, 2002). Axial chromatic aberration is best evaluated utilizing the same front-face mirror test used to determine axial resolution, except in this case the data from multiple laser lines are collected in separate channels. This test is very sensitive to chromatic aberration in the optical system, and even very small axial displacements of the focal plane between laser wavelengths can be quantified (see Chapter 15, *this volume*; also Akinyemi *et al.*, 1992; Browne *et al.*, 1992; Maly and Boyde, 1994).[6] Axial chromatic aberration is evaluated by plotting intensity as a function of *z*-position for multiple channels simultaneously (Fig. 36.11). A mismatch between the refractive index of the lens immersion media and the specimen can exacerbate longitudinal chromatic aberration because the spherical aberration produced by the mismatch has a chromatic component. Such discrepancies can be a major concern in resolution-sensitive multi-channel experiments.

Field Illumination

One cannot assume a correlation between signal intensity and fluorochrome concentration unless the illumination pattern is uniform across the field of view. This can be checked using a fluorescent sea (see above), fluorescent plastic slides (van den Doel *et al.*, 1998; Zucker and Price, 1999) or using reflected light from a mirror standard. At a sequence of increasing zoom levels, record the fluorescence intensity near to the coverslip interface over the field of view (FOV). Adjust the mean pixel intensity to fall within the linear response range of the digitizer.

To evaluate the data, draw a diagonal region of interest (ROI) from one corner to the opposite corner and graph the intensity values as a function of position along this line (Fig. 36.12). At low zoom, the distribution of pixel intensities should be *symmetrical*, and the hot spot should be located at the center of the field of view. At higher zoom levels, the intensity distribution should flatten out such that the values of the sampled pixels approach the mean pixel intensity integrated over the entire FOV. When this is not the case, it is likely that there is an alignment problem in the optical train (van den Doel *et al.*, 1998).[7]

[6] However, although this measurement gives some measure of lens performance, one should note that it does not measure lens performance at wavelengths between the laser lines where the fluorescent signal is actually recorded.

[7] Recently, thin-film (150 to 200 nm) fluorescent, specimens have been developed by Brakenhoff to measure the performance of optical-sectioning imaging systems (Zwier, *et al.*, 2004). These films permit standardized evaluation of illumination and signal-collection uniformity, axial resolution; spherical aberration, and off-axis chromatic aberrations in the form of sectioned imaging property (SIP) charts (Brakenhoff, *et al.*, 2005).

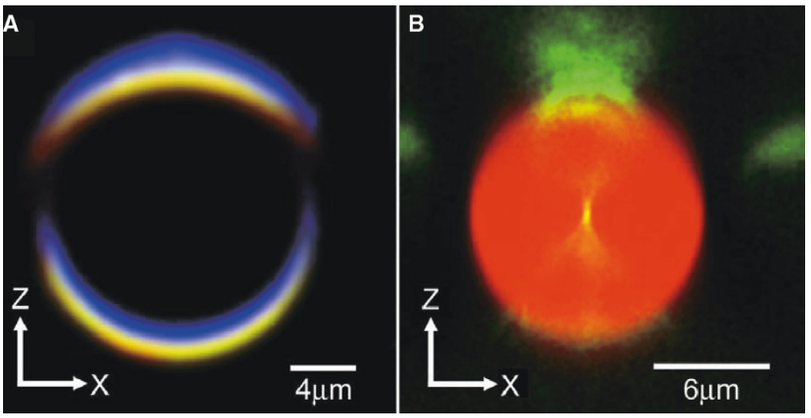


FIGURE 36.10. Self-lensing artifacts. (A) Axial view through center of Focal Check bead. Lensing by the fluorescent bead shell causes the artifact illustrated in this example. (B) Axial view through a 10 µm polystyrene sphere in both backscatter (green) and fluorescence (red) channels. Despite reasonable refractive index matching, enough of a difference exists to cause the bead to act as a ball lens. Concentrated patches of scattered light (green) are evident as a result of self-focusing.

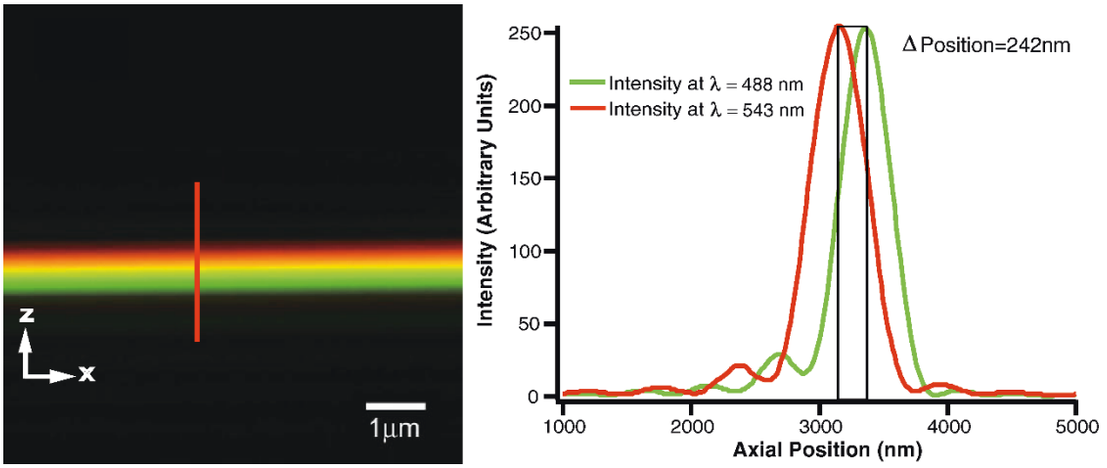


FIGURE 36.11. Chromatic aberration. In this example, a mirror standard is imaged simultaneously in two channels; the peak-to-peak distance between the first-order intensity maximum for each respective channel is 242 nm (about half the axial resolution of the lens). The wavelengths for this image were 488 and 543 nm, and a 63× NA 1.32 plan-apochromatic (oil-immersion) lens was used.

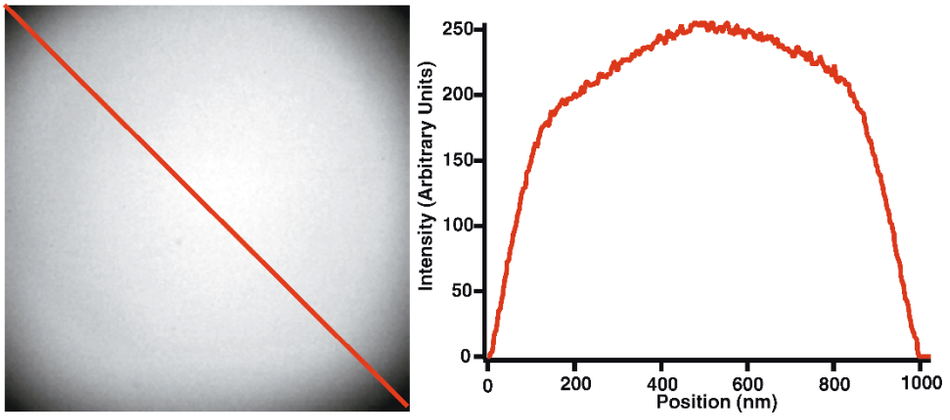


FIGURE 36.12. Flatness of field. Flatness of field is evaluated by plotting intensity as a function of position on a line drawn diagonally across the field of view (in this case the same 63× objective used above, at zoom = 1). The intensity values have been normalized for purposes of illustration in this case.

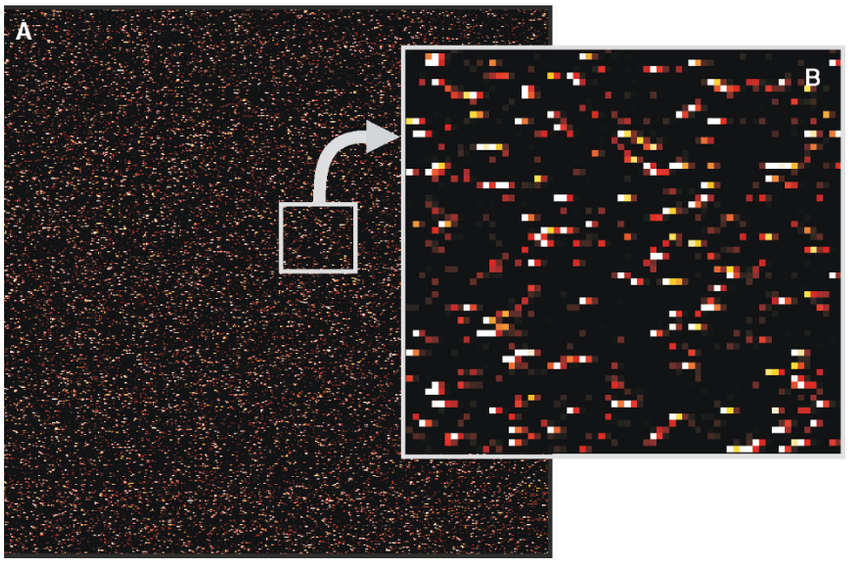


FIGURE 36.13. Instrument noise. Instrument noise may result in a speckled appearance within an image collected on a confocal microscope, although this will normally only become apparent if the instrument is used at near maximum gain or PMT voltage settings. In this example, an image was collected on a Zeiss 510 META confocal microscope with no laser light and no fluorophore present, while the PMT voltage was set to maximum (1250 V) and the amplifier gain set to 1 (the lowest setting). Panel (A) shows a 512×512 pixel image collected in a single pass, and panel (B) shows a digitally enlarged view of a small region of the image shown in panel (A). Minimal room lighting and a dark enclosure over the objective lens were used during image acquisition to eliminate the possibility of stray light entering the scanhead of the instrument. Note the relatively few high intensity pixels adjacent to a large number of very low intensity pixels. In some cases the noise is only detected in a single pixel, but in others the noise is distributed across 2 or even 3 pixels in the horizontal direction (the direction of scanning).

Signal Detection

The Signal-to-Noise Ratio and Coefficient of Variation

The sensitivity in an imaging system depends on the ratio of the signal generated by the stain and registered by the detector to the sum of all the noise signals (i.e., detector noise, stray light, nonspecific staining, etc.), as recorded under imaging conditions (see Chapters 2, 4, 22, and 35, *this volume*; also Pawley, 1994; Tran, 2005). This is referred to as *the* signal-to-noise ratio (S/N). The S/N capability of a microscope is reflected in the intensity distribution of pixels corresponding to a constant signal level. Thus, for routine evaluation, the S/N can be conveniently gauged from image data in terms of a percentage known as the **coefficient of variation** or CV (Eq. 2) measured from a known and homogeneous specimen using a fixed amount of excitation. (Zucker and Price, 2001b):

$$CV = \frac{(\sigma)}{I_{av}} 100\% \qquad \textbf{(2)}$$

where I_{av} is the mean pixel intensity and σ is the standard deviation of the pixel intensities in the measured region.

Many factors influence the signal measured by the detector on a laser-scanning confocal microscope. In order to attribute any variation *between* measurements to the detection subsystem, all of these other factors must be held constant (Pawley, 2000). Furthermore, the noise level in a confocal microscope has two fundamentally different components, the noise level of the instrumentation itself (dark noise) and photon (shot or Poisson) noise. PMTs vary in their quantum efficiency (QE), gain response, and dark-count rate, even within the same model and manufacturing lot. More to the point, some tubes break down when used with a high gain voltage and this increases their noise output substantially.[8] Strategies for evaluating and documenting the relative contributions of dark noise and shot noise under standardized conditions are described below.

Instrument Dark Noise

To determine the level of dark noise first turn on the confocal microscope and associated equipment and allow it to reach the normal operating temperature. Prevent stray light from entering the detectors by turning off room lights and shielding the objective from any light from computer monitors and other sources of ambient lighting [the laser(s) may also need to be turned off as there can be some light leakage through an AOTF filter even when set to 0% transmission]. Using standardized settings for PMT gain and offset, collect a single-scan image (Fig. 36.13). If the microscope is working properly, the small image features will actually be PMT dark noise counts. PMT noise will be displayed as a single high-intensity pixel (or sometimes 2 or 3 bright pixels, always oriented in the direction of the scan line) scattered randomly throughout the image. Changing the confocal zoom setting will usually not alter the presence or size of these high-intensity noise pixels.

When using standardized settings for scan speed and sampling resolution (pixel size), it may be wise to record the PMT dark counts for a series of increasing PMT gain voltages so that a baseline relationship between PMT gain and dark noise is characterized. The mean pixel value and standard deviation of pixel values from images of dark noise counts can be used to calculate the CV associated with standard PMT gain settings. Dark noise should be re-evaluated whenever one suspects problems with the imaging electronics.

Photon (Shot) Noise

One might expect that imaging a solution of a small molecular weight fluorophore would show a perfectly even intensity image (no variation between pixels). However, when imaging a fluorescent specimen of low quantum yield, a great deal of speckle is evident within the image (Fig. 36.14). Assuming that the PMT gain is set below the level at which electrical breakdown occurs, this non-uniformity mainly reflects the statistical uncertainty inherent in the detection of any photon signal. This uncertainty is called photon noise (shot noise; see above and Chapters 2, 4, 22, and 35, *this volume*).

[8] Because the rule of thumb states that PMT gain increases by a factor of 2 for every 40 to 50 volts of acceleration, one expects noise pulses to become bigger and more visible as the PMT voltage is increased. Breakdown is different in that it is characterized by the relatively sudden onset of greatly increased noise: not only bigger pulses, but many more of them.

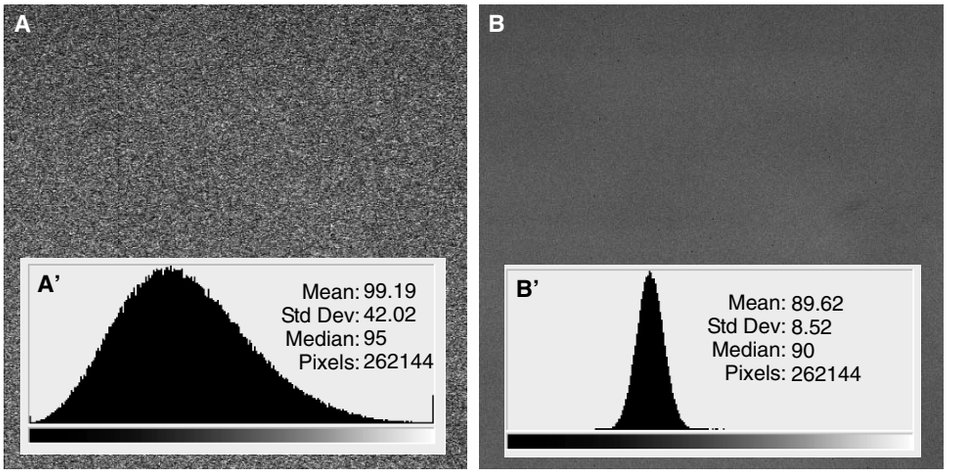


FIGURE 36.14. Demonstrating noise in images. Photon or shot noise can be seen in images collected on a confocal microscope as speckle within that part of the image where fluorescent light is being emitted. To demonstrate the effect of averaging on the level of shot noise a dilute solution of coumarin (in a sealed imaging chamber) was imaged on a Zeiss 510 Meta confocal microscope using a 60× 1.20 NA water-immersion objective. Image (A) shows a single 1 s scan with an image collection box size of 512 × 512 pixels. The whole-image intensity histogram (A′) demonstrates the wide spread of the signal (large standard deviation) due both to statistical variation in the arrival of photons at the detector and multiplicative noise in the PMT (see also Chapter 2, *this volume*). Image (B) was averaged by 16 line scans taken at the same scan speed as that shown in image (A). The whole image intensity histogram (B′) now has a much smaller standard deviation (narrower histogram profile), indicative of less variation between individual pixels within the image.

The histogram of the intensity levels within the image (Fig. 36.14) provides an intuitive way to visually assess this noise level (a broader spread in intensities results in a broad histogram). As long as the signal source is uniform,[9] the FWHM of this intensity histogram is a measure of the noise in the image. The width of the distribution can be expressed quantitatively by calculating the CV for the image.

A metric that tests the detection efficiency of imaging instrumentation is valuable for determining whether problems with image quality are due to poor specimen preparation, or to less than optimal instrument performance. With this in mind, it is useful to measure and record CV values over a range of signal intensities (Fig. 36.15) as a reference of relative detector performance at a particular point in time. Special calibration slides covered with microspheres having discrete intensity levels are available (log and linear scales; Rainbow Particle Slide, Spherotech, Libertyville, IL). Fresh dilutions of fluorochrome are a convenient alternative. Such standards could be used to record CV over a range of intensity values using a fixed laser power.

An analogous test uses a sample having a standardized quantum yield and monitors CV as a function of the laser power (Zucker and Price, 2001b). Fluorescent plastic slides are useful in this context. Most plastics behave as a highly viscous solution of fluorescent dye, which has the advantage that any photobleached areas will no longer be distinguishable from the surrounding plastic after several hours of storage. However, the fact that it is difficult to confirm that the quantum yield of fluorescent plastics is stable over long-term use introduces uncertainty into quantitative comparisons of instrument performance over time. In addition, as the RI of the plastic is not one for which objective lenses are normally corrected, spherical aberration will reduce the recorded signal significantly as one focuses further into it.

[9] That is, not only no visible features but not even any shading such as might be caused by signal loss at the edges of the field of view. This condition is more easily met by using a medium zoom.

PMT Linearity

To establish that the relationship between the signal digitized from the PMT responds linearly with the fluorescence signal produced by the specimen, first prepare a fresh standardized dilution of flu-

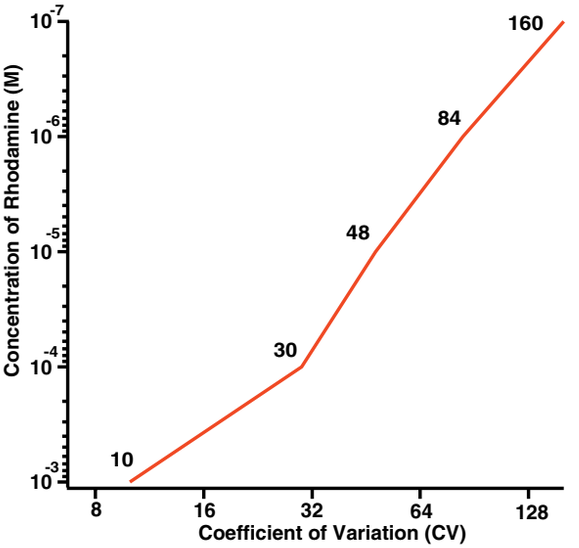


FIGURE 36.15. Detector response to decreased signal. Coefficient of variation as a function of fluorochrome concentration. CV values were taken from the spectral image that corresponds to the peak emission range (568–573 nm) at minimal bandwidth (5 nm) using a spectral detection system. The series is a 10-fold dilution of Rhodamine 6G; the laser power was held constant and the PMT gain was increased at each reduction in concentration to maintain a mean signal of 130 A.U. (scale 0–255). The PMT gain was maximized (1000 V) at a 10^{-6} dilution. At the lowest concentration (10^{-7}), the system is unable to produce a mean signal above 50 A.U. As the PMT gain is already maximized at a dilution of 10^{-6}, the decreased signal is responsible for the increase in apparent noise at the lowest concentration.

orochrome in the appropriate refractive index solvent. Then adjust the PMT gain setting to give a signal within the linear response range and finally record the mean signal as a function of the illumination intensity. The mean brightness should be proportional to laser power until the laser becomes so bright that the molecules in the focused spot are driven into singlet-state saturation (i.e., so many of the molecules are in the excited state that there is no dye left to excite;[10] see Chapters 2, 16, and 35, *this volume*). Approaching saturation will produce a less than proportional increase in signal for an increase in excitation. Although the effect of saturation can be reduced by going to a lens with lower NA because this makes the spot bigger and the light less intense, you then have a dry lens and all the SA problems associated thereto. One should validate the performance of the detector subsystem periodically as the instrument gets older.

Spectral Systems

An exciting development in laser-scanning microscopy is the increasing availability of signal detection systems capable of recording crude emission spectra at each pixel in an image. Evidence of the ability of such systems to solve problems, such as distinguishing the identity of overlapping emission profiles, has been established (Dickinson *et al.*, 2001; Lansford, *et al.*, 2001; LaMorte *et al.*, 2003; Huth *et al.*, 2004; Hutter, 2004). The accuracy of such extrapolations is dependent on the accuracy and reliability of the underlying system (Garini *et al.*, 1999; Neher and Neher, 2004; Zucker and Lerner, 2004).

Spectral detection devices can be made in several ways. The advantages of a particular system will depend on the scope of applications an instrument is expected to handle. As all such systems are complex (and expensive!) compared to traditional filter-based systems, finding a convenient strategy to evaluate their performance is of prime importance.

Three major aspects of the spectral imaging subsystem should be periodically evaluated: (1) calibration accuracy of the system (wavelength accuracy), (2) resolution in terms of the minimum resolvable bandwidth, and (3) variation of sensor efficiency with wavelength.

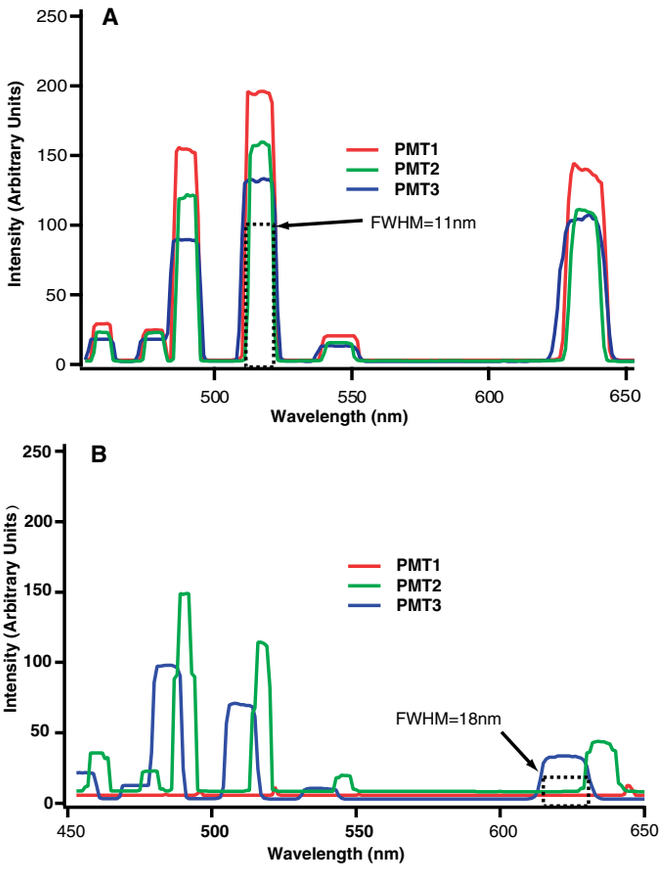


FIGURE 36.16. Spectral scan over laser lines using reflected light. (A) A typical plot for a spectral imaging instrument working correctly. The signature for the laser lines are centered about the appropriate wavelength and the spectral resolution (FWHM) is close to 10 nm. (B) A malfunctioning system. The wavelength selection mechanism for PMT 1 is inoperable, hence the low signal for that channel. The spectral reading for each channel is centered about a different wavelength and the spectral resolution approaches 18 nm in places.

Spectral Accuracy

The best way to test accuracy is to image a standard that displays narrow peaks in known locations. When doing these tests, all sources of extraneous light (overhead lamps and computer monitors) that might contaminate the spectrum of the illumination source should be masked (often a black velvet shroud or a black box can be carefully placed over the imaging area). Using the reflected light from a mirror test slide and a high zoom to avoid off-axis aberrations, the lasers installed on the system can be used as a convenient source of monochromatic light. In order to check the accuracy of spectral registration, it is advantageous to use as many laser lines as possible. PMT gain voltage should be adjusted such that the magnitude of the intensity peak reflected from the strongest laser line is within the linear response range of the PMT/digitizer. Acquire a high-resolution spectral scan over the visible spectrum, and observe the location of the spectral features corresponding to the laser wavelengths. This can often be recorded as a plot of intensity versus wavelength [Fig. 36.16(A)]. If the peaks are not where they are expected [Fig. 36.16(B)], either the detector is miscalibrated or one or more of the system components has failed.

Alternatively, if the laser lines available don't properly cover the full wavelength range, one can use an NIST-certified multi-ion discharge calibration lamp (MIDL, LightForm Inc., Hillsborough, NJ) in the manner described by Zucker and Lerner (2004). In this approach, a lamp with very well-characterized peaks in its spectral output is placed directly above the objective being used for measurement, and a spectral reading is taken using the acquisition subsystem of the microscope. The NIST calibration lamp has numerous spectral features that form a sophisticated spectral fingerprint. In theory, all instruments should reproduce the characteristic set of relative heights of peaks and valleys provided by the standard. The effect of under-sampling in the wavelength dimension on the accuracy and precision of the recorded spectra is easily demonstrated using this standard (see Chapter 4, *this volume*; also Zucker and Price, 2001b).

Spectral Resolution

The resolution is indicated by the FWHM of peaks in spectra derived from subresolution spectral features (such as monochromatic laser output). Presently, most systems are designed for 2 nm

[10] Because the degree of saturation varies throughout the PSF, this saturation is not a "hard" effect in the sense that an absolute limit is reached and no further increase is possible. Rather the signal increases asymptotically as the degree of saturation increases at ever greater distances from the center of the PSF.

to 10 nm bandwidth resolution, with the value for each particular system available from the manufacturer. When spectral resolution values are less than expected [Fig. 36.16(B)], the boundaries of virtual filter bandpass settings may be offset to some degree unknown to the operator (in the case of the Leica, the moveable mirrors may be miscalibrated or stuck in one position). Such errors produce much higher background than expected because, under imaging conditions, scattered light from the laser can reach the detector. Data collected with poor or shifted spectral resolution can also produce anomalous fluorochrome localization results when treated using spectral deconvolution algorithms.

Wavelength Response

The reflected laser light test paradigm outlined above can be used to provide an expedient measure of sensor response in different wavelength regimes; anomalous sensor response with respect to frequency will seriously affect the accuracy of spectral un-mixing schemes. Fingerprints or other contamination on certain mirrors within the detection system can easily cause diminished response in part of the spectrum. In this test, the relative laser powers for all the individual lines used are known. First, the laser lines are individually adjusted to some standard value (e.g., 15 µW, emerging from the same dry objective) then the PMT gain and offset are configured so that the entire intensity range is within the linear response range of the PMT(s). A spectral scan is taken across the part of the spectrum containing the laser lines. On the resultant plot of intensity versus wavelength, the intensity values measured for the laser lines should be of roughly the same magnitude,[11] and the mean value of the noise level should remain constant in the domains between laser lines. On systems with multiple spectral detectors, each detector should be checked in turn. A method for performing the equivalent test using the NIST standard lamp is discussed in Zucker and Lerner (2004).

The uniformity of the response of a spectral detector can be assayed by collecting a spectrum from the light transmitted through a microscope slide from the transmitted light source. Assuming that this source uses a tungsten/halogen bulb, apply the correct voltage to heat the filament to 3400 K, and set the condenser for Köhler illumination. If you now collect a spectrum with the laser turned off, it should slope from higher in the red to lower in the blue. When recorded on the Zeiss, META, valleys in this spectrum probably correspond to individual micro-PMTs that have lower than average gain or QE. Although this is to be expected, it is the reason why it is better to collect reference spectra using the specific setup that will be used for the experiment, rather than relying on stored spectra that were obtained at the factory. This same transmitted light setup can be use with a Hg-arc source that provides additional calibration lines (see Chapter 4, *this volume*).

OPTIMIZING MULTI-LABELING APPLICATIONS

Confocal microscopy is ideally suited to multi-labeling applications due to the ease and flexibility with which multiple fluorophores can be viewed and recorded as separate images. This includes the more traditional spectral separation of fluorescence from different dyes as well as the ability to separate highly-overlapping fluorophores using spectral unmixing.

Control Samples Establish the Limits

The relationship between the fluorescence intensity data content of an image and the distribution of the fluorophore of interest in the sample can only be verified by collecting reference images from the correct controls. Controls are also essential for establishing the detection limits.

Establishing the Level of Autofluorescence

Fluorescence emission from a sample to which you have not yet added a fluorophore is termed autofluorescence (for further discussion, see Chapters 8, 21, 44, *this volume*). Many naturally occurring compounds in plant and animal tissues will fluoresce, and various cellular treatments, including the media in which they are grown and the physical manipulation (including the method of fixation), may influence the intensity and wavelengths of emission.

An unlabeled control is essential for establishing the level of autofluorescence in the sample. Additional images of the unlabeled control collected with increased detector gain, pinhole size, or excitation power can be used to establish the upper limit of detection of your fluorophore. However, even a high level of autofluorescence is not necessarily a problem, as long as the intensity, location, or the spectral characteristics of the probe can be distinguished from autofluorescence.

Is Reflected Light Contributing to Your Fluorescence Image?

The level of signal intensity from an unlabeled control is also essential for establishing the level of backscattered or reflected light that is contributing to the image (Pawley, 2002). Any excitation light that is reflected or backscattered back toward the detector will be registered as a signal unless the barrier filter stops it. Even the very best barrier filters are not 100% efficient; and because the intensity of illumination is several orders of magnitude higher than that of the fluorescence signal even very small percentages of reflected light passing through a barrier filter may be of similar intensity to that of a fluorescent signal. Small refractile features that produce much backscattered light may also appear to show specifically labeled subcellular detail. A useful test for distinguishing contributions from backscattered illumination compared to autofluorescence is whether or not one detects a uniform background signal level as the focus plane coincides with the surface between the coverslip and the aqueous media. While such a signal can be a handy marker for the location of the glass surface, it is also an indication that some of the signal recorded in this channel stems from backscattered light.

How Much Is Bleed-Through Contributing to the Image?

Bleed-through is the appearance of fluorescence from one fluorophore in the detection channel set up to detect another fluorophore. The amount of bleed-through is determined by imaging control slides in which only one dye is present while using the dual-channel settings you plan to use for your dual-labeled samples. Images collected at various gain, pinhole, and laser intensity levels may be useful for establishing the amount of bleed-through at various settings. This information should be used to set limits for the various settings that will result in an acceptably low bleed-through level.

[11] There are two offsetting factors at work here. If the photometer is calibrated for the measured wavelength, then 15 µW will correspond to more red photons than blue photons. As the output of the PMT is proportional to the number of electrons produced at the photocathode, one might expect that the PMT would produce more signal from the red beam because it has more photons. However, this tendency is usually more than cancelled out by the fact that the QE of the PMT drops at longer wavelengths.

How Much Is the Secondary Conjugate in Immunolabeling Contributing to the Signal?

Secondary conjugates (including avidin/biotin systems as well as secondary antibodies) often contribute to background signal in immunolabeling procedures. Application of fluorescently-labeled secondary conjugate, in the absence of its target primary antibody, is an essential control in all immunolabeling experiments. The contribution of the secondary conjugate to the fluorescent signal is determined by imaging a sample labeled using the secondary conjugate alone under the same conditions as employed for the experimental sample. In addition, as discussed above for autofluorescence, images collected at increased detector gain, pinhole size, and laser power, will be useful for establishing the limits to detection for the binding of your primary antibody.

A Positively Labeled Sample

It is a great asset to have a cell or tissue sample, or an environmental/metabolic condition that you know will produce a positive response for your target molecule. This can assist in establishing the probe concentrations, imaging conditions, and the instrument settings that can be used on your experimental sample. A positive control closely related to your test sample (e.g., the same cell line, but stimulated to produce a known positive response) is an ideal model of the labeling and imaging conditions used for the experimental sample. A known positive is particularly important when troubleshooting problems with an immunolabeling protocol.

Separation of Fluorescence into Spectral Regions

Traditionally, one images multiple fluorophores by using interference filters to separate the fluorescent light into different spectral regions. Although the use of dichroic mirrors and optical filters has the advantage of being a robust and relatively simple technology, the regions of the spectrum directed to individual channels is constrained by the availability of suitable mirrors and filters.

Another way to separate the fluorescent light into different spectral regions is to use a prism or diffraction grating to separate the light spatially and to then use either a mirror/slit mechanism or photomultiplier tube array to select the region of the spectrum that will be digitized in each channel. This type of spectral separation has the advantage that the operator has full control of the region of the light spectrum directed to each channel, without being constrained by the available optical filters. A variety of light separation approaches are used by different confocal microscope manufacturers, sometimes more than one approach being incorporated into a single instrument.

Spectral unmixing, described in detail below, is a method of separating the signals from various fluorophores based on their spectral profile, rather than by their presence or absence in a specified spectral window. Spectral unmixing has the important advantage that fluorophores with highly overlapping spectral emission profiles can be separated into individual channels.

Sequential Channel Collection to Minimize Bleed-Through

Bleed-through occurs predominantly when multiple fluorophores are excited simultaneously and portions of their emission spectra overlap with the spectral region accepted by more than one channel. Simply exciting and collecting each channel sequentially, sometimes called multi-tracking, is a very practical means of substantially reducing bleed-through. Although this can be done on older confocal systems that use slow, motor-driven filter wheels to switch laser lines, newer systems using acoustic-optical devices (AOD) are far more flexible and allow nearly instantaneous laser line selection. This allows sequential channel acquisition to become practical for routine use. Some instruments are capable of line-by-line multi-tracking, where one wavelength is used to excite the sample as the beam travels in one direction and the second marker is excited by a different wavelength on the return scan. Although faster, one must adjust the instrument (sometimes called phase control) to ensure that the digitizer stays in synch with the position of the galvanometer mirror. Otherwise the two sets of data can be displaced horizontally from each other.

Spectral Unmixing

Spectral unmixing is a computational method of separating the signals from various fluorophores based on their spectral profile rather than by their presence or absence in a specified spectral window. Spectral unmixing has the important advantage that the fluorescence from fluorophores with highly overlapping spectral emission profiles can be reliably separated.

In spectral unmixing, the emission spectrum of each fluorophore is characterized in the form of a plot of its fluorescence emission intensity as a function of wavelength. Because the shape of this emission profile is assumed to be fairly stable,[12] one may infer the magnitude of signal that would be detected on-peak using a portion of the emission signal that was measured using a spectral window located on the tail of the spectrum. Multiple samples of the signal intensity taken over the entire the emission profile may provide an even more accurate estimate of the peak signal.

It is then possible to use a deconvolution operation to separate overlapped spectra in a manner analogous to the way in which spatial deconvolution is used to separate overlapped structural features. The process starts with the collection of a reference spectrum from each positive control sample.[13] Next, spectral data is collected at each voxel in a 2D or 3D image. To unmix the data, the computer fits the measured data to a weighted sum of the reference spectra. Spectral unmixing can be performed on as few as two spectral windows of the emission spectra at each pixel, but using data from multiple spectral windows at each pixel greatly improves the degree of separation that can be achieved.

Spectral Unmixing to Separate Overlapping Fluorophores

In Figure 36.17, live cells labeled with acridine orange have been imaged using two conventional channels on a Zeiss Meta confocal microscope. The green fluorescent light (500–530 nm) has been directed to one channel [Fig. 36.17(A)] and the red fluorescent light (565–615 nm) has been directed to a second channel [Fig. 36.17(B)]. Although the two channels do show some differences, the high degree of overlap is evident by the yellowish color that

[12] There are lots of counterexamples, such as carboxyfluorescein, that changes its output spectrum in response to the environment, such as changes in pH.

[13] Although the manufacturer often provides such spectra for common dyes, these will only be accurate to the extent that (1) the QE/wavelength curves of the detectors used in the factory are the same as those on your machine; (2) the dye spectra has not been modified by the local environment; and (3) your system remains aligned.

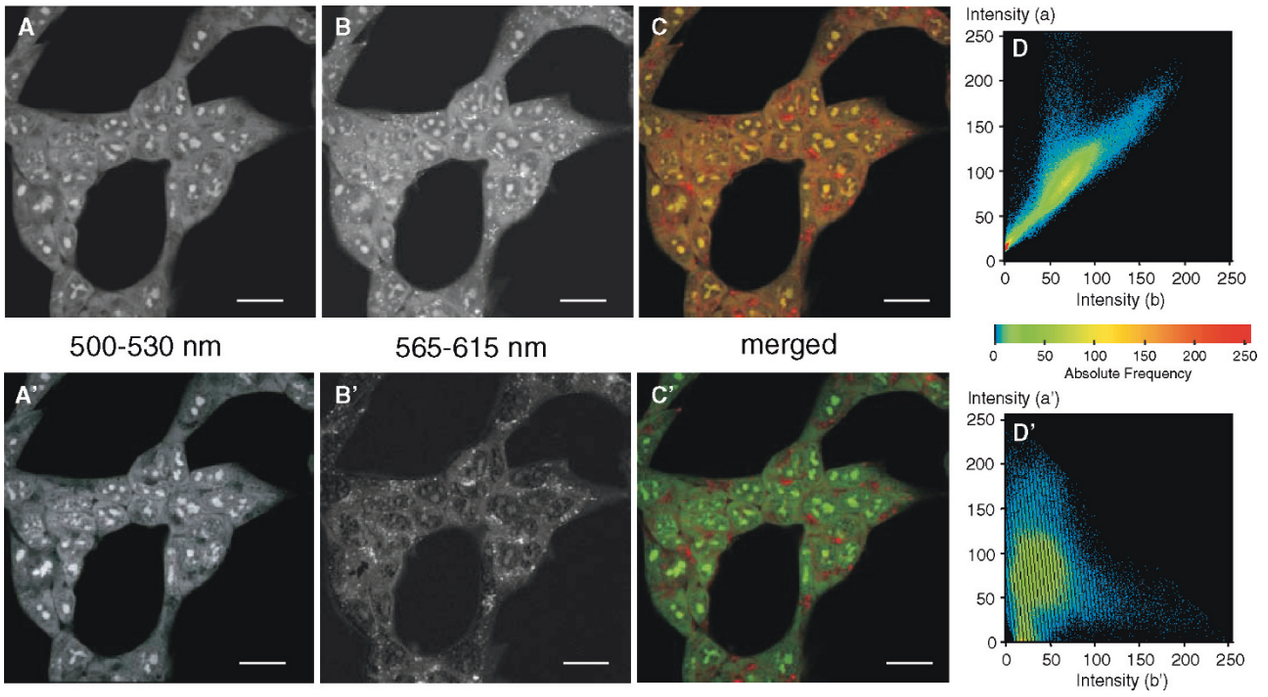


FIGURE 36.17. Spectral separation using two spectral images. The process of linear unmixing can be used with as few as two spectral images to improve the separation between the two channels. In this example HEK496 cells have been labeled with Acridine Orange (final concentration 0.5 µg/mL) for 1 h at room temperature and images were collected on a Zeiss 510 Meta confocal microscope using two "conventional" optical filter separation channels. Images were collected from (A) the green (500–530 nm) region of the light spectrum and (B) the red region of the spectrum (565–615 nm). A merged two-color image of the green and the red channel is shown in (C). In (D) a fluorogram of the two channels is shown. The corresponding images after spectral reassignment are shown in (A′) green (500–530 nm), (B′) red (565–615) nm. and both channels merged (C′). (D′) A fluorogram of the reassigned merged image is shown in (C′). There is considerable overlap between these two original imaging channels, which is shown graphically in the scattergram shown in (D). Applying the process of linear unmixing (using the Zeiss LSM 510 Meta software) the separation between these two channels has improved [(A) and (B)], which is shown by comparing the fluorogram before (D) and after linear unmixing (D′). The scale bar represents 20 µm.

predominates in the merged image [Fig. 36.17(C)]. This overlap is also shown by the tight central location of the dots in the whole-image intensity histogram [Fig. 36.17(D)]. However, after linear unmixing of these two images, the difference between the two images becomes more distinct [Fig. 36.17(A′,B′)]. A merged two-color image of the two reassigned channels [Fig. 36.17(C′)] clearly shows that a population of vesicles has now been separated from the bulk of the staining. Spectral reassignment has resulted in a significant movement of red and green pixels towards their respective single label axes [see the greater spread of the pixel intensity histogram in Fig. 36.17(D′) compared with Fig. 36.17(D)]. However, the separation is by no means complete as the majority of structures are still being detected in both channels.

Figure 36.18 demonstrates that multiple spectral images permit an even more refined separation of subcellular structures. In this experiment, 10 individual spectral images (each with a spectral window of 21.4 nm) [Fig. 36.18(A)] were collected using two sequential scans on a Zeiss 510 Meta confocal microscope (up to eight spectrally distinct images can be collected simultaneously). These 10 images are then analyzed as a "spectral stack" [Fig. 36.18(B)], and four separate regions of the image stack are highlighted with a numbered cross. The spectral information from each of these regions is shown graphically in Figure 36.18(C). Using this graphical display of the four different spectra found within the sample, two spectral regions, green (504–569 nm), which predominantly covers the spectral emission of ROI 2 to 4, and red (591–719 nm), covering ROI 1 have been chosen for the extraction of two channels [Fig. 36.18(D)]. The population of small vesicles with a spectral emission consisting predominantly of red fluorescence can be clearly distinguished from the structures emitting in the green region of the spectrum. However, the separation of the red vesicles from the rest of the cell is not complete; the majority of the red vesicles also contain green pixels [seen as yellow/orange pixels in the merged image of Fig. 36.18(D)].

The spectral information shown graphically in Figure 36.18(C) can be used to locate and extract other regions of the specimen having a similar spectral fingerprint using linear unmixing. In this case, the software has separated the stack into four separate channels [Fig. 36.18(E)] plus a residual channel (regions of the stack that cannot be assigned using spectral information from the selected areas). The merged two-color image of channels 1 and 3 [Fig. 36.18(E)] shows two distinct populations of vesicles clearly separated from any background fluorescence. The vesicles that were partially separated from the other cellular labeling using conventional optics [Fig. 36.17(A,B)] or channel extraction from the spectral stack [Fig. 36.18(D)], as described above, have now been separated into two distinct subpopulations that are also separated from other subcellular structures. This example shows that spectral imaging can be used both to separate the fluorescence from different overlapping signals into separate channels, and also to

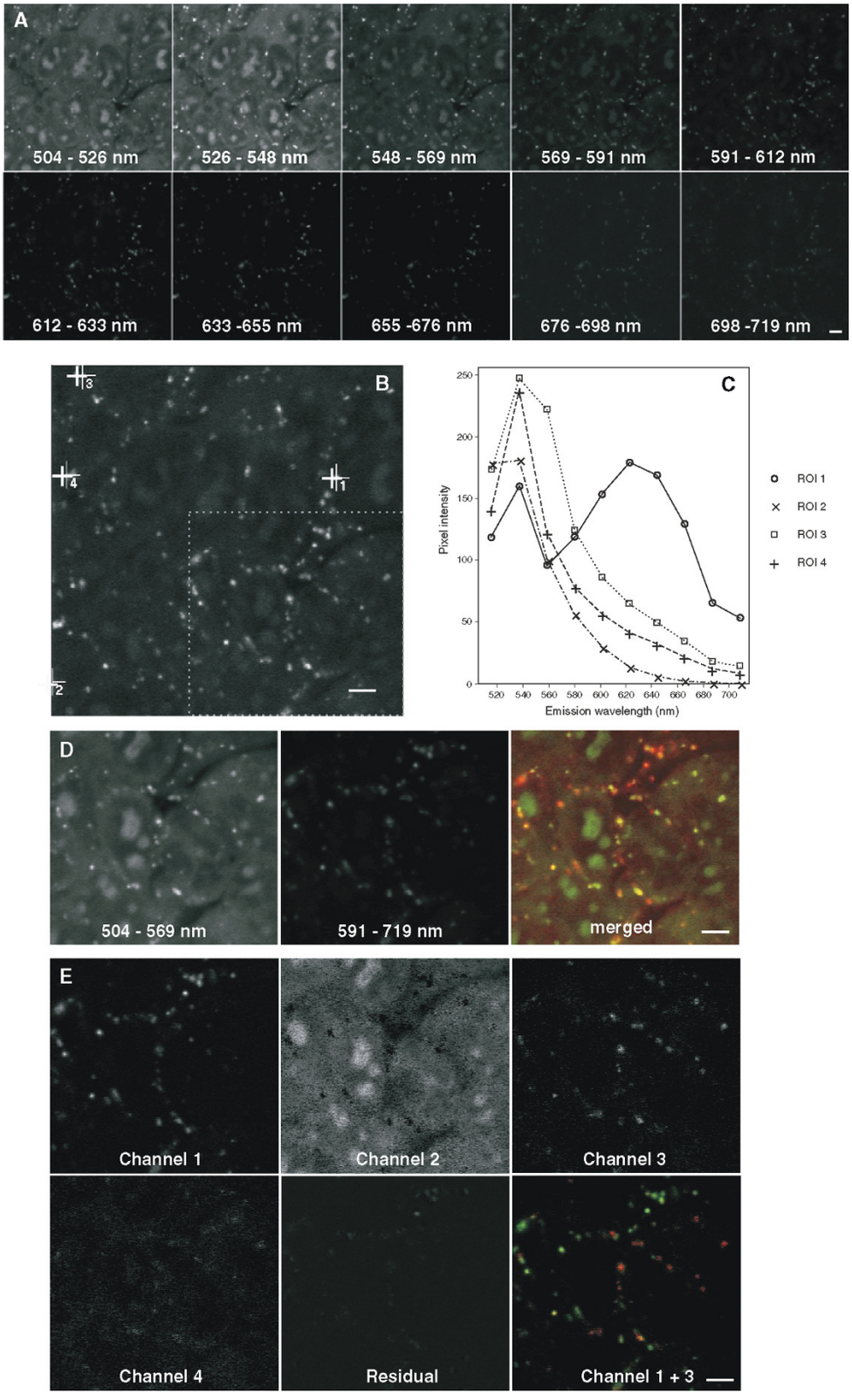


FIGURE 36.18. Spectral separation using multiple spectral images. Linear unmixing using multiple spectral images results in better separation of fluorophores with overlapping emission spectra. HEK496 cells were labeled with Acridine Orange (final concentration 0.5 µg/mL) for 1 h at room temperature and multiple spectral images were collected (A) from 21.4 nm wide regions of the light spectrum using the Meta channel on a Zeiss 510 Meta confocal microscope. The 10 spectral images were analyzed as a spectral stack (B) and the spectra extracted from four specified single-pixel regions of interest (ROI, marked with + in the spectral stack) are shown in (C). Two defined spectral regions (504–569 and 591–719 nm) were selected and the spectral information extracted into separate channels (D). Four spectrally-reassigned channels plus a residual channel after linear unmixing are shown in (E). The scale bar represents 5 µm.

collect and recognize the spectral fingerprint of specific structures within the sample.

Removing Autofluorescence Using Spectral Unmixing

Two different approaches to separating autofluorescence from the signal produced by an added label can be employed. The first approach is to treat the autofluorescence as an endogenous fluorophore that will be placed in a separate channel after linear unmixing. This approach works well when the autofluorescence is dominated by a single endogenous fluorophore. Unfortunately, this is rarely an accurate assumption. Another approach to unmixing autofluorescence from specific labels is to use spectral profiles from the fluorophore positive controls for spectral unmixing, and to assign any measured fluorescence emission that does not fit these reference spectra to a "residual channel" [Fig. 36.18(E)]. In this way complex spectral emission due to autofluorescence can often be separated from the more specific emission associated with the particular probes added. However, caution is needed to prevent "seeing what one wants to see," especially when the level of Poisson noise is high.

Limitations to Spectral Unmixing

Even though spectral unmixing has a remarkable ability to separate similar fluorescence emission spectra, there are disadvantages that should not be overlooked. Spatial deconvolution (see Chapters 25, *this volume*) can help improve the integrity of results from spectral unmixing. The procedure would be to spatially deconvolve or at least Gaussian filter[14] the data from each wavelength segment prior to unmixing.

Poisson uncertainty (see Chapters 2, 4, and 35, *this volume*) places severe restraints on the accuracy with which spectral unmixing can be carried out. Supposing that a particular dye produces 100 ± 10 detected photons/voxel, if these are then shared among only four channels of a spectral detector, the signal drops to 25 ± 5 or 20% noise. It is also notable that the *effective* QE of the mini-PMT arrays used in some systems is lower than that found on many standard PMT tubes used in confocal microscopes. Furthermore, the layout of the very small electron multipliers that they contain precludes taking actions that would reduce multiplicative noise. Thus, contributions from both Poisson noise and multiplicative noise to the uncertainty of spectral unmixing may be exacerbated by detector design.

The collection of spectral information frequently necessitates the collection of several images in series, which may subject the specimen to damaging doses of light.

Another potential problem is that the composite spectrum may be distorted because any segment of the spectrum that overlaps a dichroic mirror blocking range will exhibit a prominent dip in the signal intensity. In addition, if the spectra being collected overlaps with an active laser line, excessive backscattered light may contaminate the signal.

Environmentally caused variation in the spectral characteristics of a fluorophore may lead to the inappropriate signal separation. Many fluorophores, such as Acridine Orange, as used in the example above (see also Chapter 39, *this volume*), can respond differentially to environmental influences.

[14] Because the data is so noisy and the PSF of a confocal or multi-photon microscope is so simple, 3D Gaussian filtering and deconvolution have much the same effect. Gaussian filtering can also be applied to 2D data, a point that is important because much unmixing work is carried out on 2D data.

COLOCALIZATION

Colocalization is a tool for quantifying the degree of association or codistribution of labeled structures between any two channels in an image. Although colocalization is a very powerful tool for determining subcellular associations, even under ideal imaging conditions the resolution limit of light microscopy severely constrains the validity of any colocalization analysis.

Image Collection for Colocalization

Colocalization by counting overlapping signals is very sensitive to intensity imbalances between each channel, as are methods utilizing channel subtraction and cross-correlation analysis (for discussion see Manders *et al.,* 1993; Costes *et al.*, 2004). As the initial assessment of the degree of colocalization often relies on a quick visual inspection of a merged two-channel image, it is advisable to always collect relatively balanced signal intensities for each channel. Signal balance is also important so that spread of the signal outwards from the highest intensity areas does not bias the results. This phenomenon is particularly noticeable in small structures with one or more dimensions close to the resolution limit of the microscope.

Fluorophore selection is an important part of any colocalization study, and is discussed in detail by Smallcombe (2001). Suitable pairs of fluorophores should have a wide separation between their emissions or bleed-through between collection channels will be registered as colocalization, no matter which method of analysis is used. Filter selection (see Chapter 3, *this volume*) and proper controls (discussed above) are crucial for the validity of any colocalization analysis. Single image planes from any volume should be examined carefully before any attempt at quantification. Noise and all sources of background (e.g., blur, autofluorescence, nonspecific labeling, reflections, and bleed-through) have a major impact on the quantification of colocalization (Manders *et al.*, 1993). Optical misalignment of the instrument will also have a big impact on the apparent degree of colocalization. As a general rule, problems of image quality should be addressed at the time of data collection, rather than by postprocessing. Providing the guidelines for Nyquist-pixel sampling have been observed and the raw data has been 3D spatially deconvolved or 2D filtered to remove "single-pixel noise" (see below and Chapter 4, *this volume*), the validity of colocalization analysis is constrained by the resolution limit of light microscopy.

Complex images should be examined carefully, and specific regions or structures within the image analyzed in detail before attempting to quantify the degree of colocalization. Information on the biology of the sample will be of great value in determining the approaches taken to quantifying the degree of colocalization. Projection images from optical volumes cannot be utilized for colocalization because pixels mapped to the projection image may have originated in planes displaced axially by several microns.

Temporal resolution should not be overlooked when using sequential imaging on living cells. This is particularly important when sequential frame scanning, but even when sequential line scanning, or using a CCD camera on high-speed Nipkow disk systems, a delay of as little as 100 ms between channels can allow a structure to change position in resting cells, this includes the normal movement of vesicles, organelles, filopodia, or neuronal growth cones. The temporal sampling rate becomes more critical when attempting colocalization of more dynamic processes. The result, of course, is that instead of observing a possible colocal-

ization event, one observes the structure as single-labeled and spatially separated in two separate channels.

Quantifying Colocalization

The 2D histogram, sometimes called a fluorogram, is a powerful tool for exploring the relationship of the intensities between two channels in an image (or within a defined region of the image). The 2D histogram is a scatter plot with the intensities of all the pixels in one image channel plotted along the *x*-axis versus the intensities of the same pixels in the other channel plotted along the *y*-axis (Demandolx and Davoust, 1995, 1997). For example, in Figure 36.20, the green channel is plotted along the *y*-axis and the red channel is plotted along the *x*-axis, with 0 at the origin. Given equal background levels in the channels, pixels possessing nearly equal intensities in both channels would plot along a 45° line passing through the origin, similar to the distribution in the fluorogram in Figure 36.17(D). Custom color tables can be useful to highlight potential colocalizations when working with rare events or imbalances in channel intensities (Demandolx and Davoust, 1997; Agnati *et al.*, 2005).

The most commonly employed algorithms for quantifying colocalization measurement are derived from Pearson's correlation coefficient, first applied for this purpose by Manders and colleagues (1992). The Pearson's coefficient, *R*, describes the correlation between the intensity distribution, or pattern overlap, in two channels in terms of a least-squares fit (Eq. 3). This value can be between −1 and 1, where $R = -1$ indicates complete exclusion and $R = 1$ indicates complete correlation between the two channels. Values between 0 and 1 indicate a proportional degree of overlap between the two channels. Values between −1 and 0 are ambiguous, indicating some form of inverse relationship between the channels, as may occur when one channel is very dim and the other is bright, or even when non-overlapping.

$$R = \frac{\sum_i \left(S1_i - S1_{avg}\right) \times \left(S2_i - S2_{avg}\right)}{\sqrt{\sum_i \left(S1_i - S1_{avg}\right)^2 \times \sum_i \left(S2_i - S2_{avg}\right)^2}} \quad \textbf{(3)}$$

where $S1_i$ is the intensity of the *i*th pixel in channel 1; $S1_{avg}$ is the average intensity of all pixels in channel 1; $S2_i$ is the intensity of the *i*th pixel in channel 2; and $S2_{avg}$ is the average intensity of all pixels in channel 2.

Other coefficients have been subsequently derived to provide additional information regarding the nature of the colocalization, as well as providing less sensitivity to channel imbalances (Manders *et al.*, 1993). The overlap coefficient, *r*, describes the degree of overlap between the signals on a range of 0 to 1 (Eq. 4)

$$r = \frac{\sum_i (S1_i \times S2_i)}{\sqrt{\sum_i (S1_i)^2 \times \sum_i (S2_i)^2}} \quad \textbf{(4)}$$

This coefficient provides a significant result only when the number of colocalizing objects in both channels is greater than zero. The advantage of this coefficient is that, unlike *R*, it is not as affected by differences in intensities between the channels, reducing the impact of channel imbalance. Although the overlap coefficient has these advantages, the Pearson's coefficient is less sensitive to image background levels. Both of these coefficients, *R* and *r*, are affected by the relative number of labeled objects (or voxels) in each channel of the image.

The colocalization coefficients *M*1 (Eq. 5) and *M*2 (Eq. 6) are often the most biologically useful, representing the proportion of pixels from each channel that contribute to the colocalized area. They can be determined regardless of the balance between the number of pixels colocalizing in each channel or between the average intensities of the two channels. The only limitation is that there must be some colocalization present.

$$M1 = \frac{\sum_i S1_{i,coloc}}{\sum_i S1_i} \quad \textbf{(5)}$$

where $S1_{i,coloc} = S1_i$ *if* $S2_i > 0$ and $S1_{i,coloc} = 0$ *if* $S2_i = 0$

$$M2 = \frac{\sum_i S2_{i,coloc}}{\sum_i S2_i} \quad \textbf{(6)}$$

where $S2_{i,coloc} = S1_i$ *if* $S1_i > 0$ and $S2_{i,coloc} = 0$ *if* $S1_i = 0$.

Each numerator represents colocalized pixels — the sum of intensities from pixels within one channel that also contain some intensity component from the other channel. The denominators constitute the summed intensities of all pixels, above threshold, in the channel. Some software applications use upper- and lowercase to distinguish colocalization coefficients calculated from the global image from those calculated from a thresholded image or a region selected from the fluorogram.

Setting Thresholds

Quantitation in colocalization studies is usually dependent upon the subjective application of thresholds. Establishing the threshold to eliminate noise or background is sometimes carried out by subtracting the threshold from the image, or by setting limits in the 2D histogram, which many find to be more intuitive. One may have to test multiple thresholds before finding the levels that are supported by correlative methods and the controls. When software recommends threshold settings (or setting background levels), it is important to know how those settings are being calculated. A background derived from the darkest pixels within the image more correctly represents the noise floor of the image rather than the amount of background from bleed-through, autofluorescence, or non-specific labeling. A new approach has been developed that estimates thresholds for both channels simultaneously over a range of decreasing thresholds until the probability of correlation equals zero (Costes *et al.*, 2004). This approach promises to be less subjective, but can be still skewed by an imbalance in average channel intensities.

Spatial Deconvolution in Colocalization Studies

Noise and background in colocalization can be reduced by employing restorative deconvolution (Van Steensel *et al.*, 1996; Landemann, 2002; Landmann and Marbet, 2004). Even analysis intended for 2D images can benefit from deconvolution if the data is collected as a shallow *z*-series and the single 2D image selected following deconvolution of the *z*-series. Alternatively, 2D confocal images can be Gaussian filtered if sampled adequately.

In the example shown in Figure 36.19, a field of peripheral nerves in rat tooth pulp is shown as a single optical slice from a *z*-stack collected at low resolution [Fig. 36.19(A)], with a small region of the sample [small box in panel (A)] shown at higher optical resolution [Fig. 36.19(B)]. The arrowhead points to the same fiber in both panels. Panel (B) indicates that there are actually two populations of closely intertwining nerve fibers, larger fibers predominantly labeled red (arrowhead), and the smaller, somewhat beaded fibers labeled green (arrows). Closer examina-

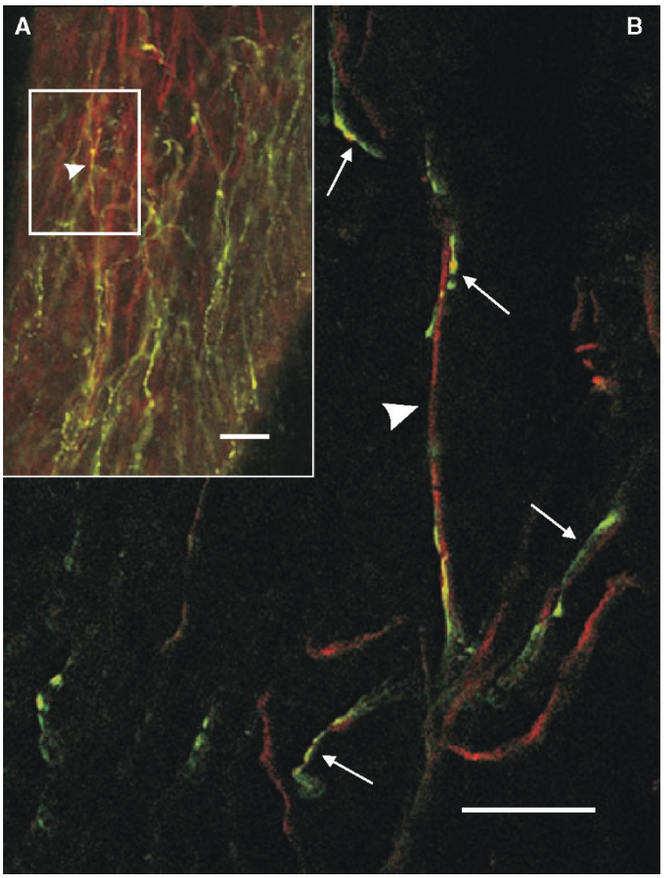


FIGURE 36.19. Colocalization. Nerve fibers labeled for peripherin (red) and CGRP (green) in tooth pulp from rats 3 weeks of age. Initial observations with a 20 × 0.75 NA Fluor lens (Nikon) (A) suggest a population of nerves co-immunostained for both proteins, appearing yellow. A 60 × 1.4 NA PlanApo lens (Nikon) with zoom = 2 (B) reveals two distinct populations of fibers: a thicker population labeled with peripherin (*arrowhead*), and smaller, beaded fibers, labeled with CGRP (*small arrows*). Both images are single planes from *z*-stacks. High magnification images were undersampled 60% laterally (150 nm vs. 83 nm) for this sample. Image (B) has been deconvolved by a maximum likelihood estimate algorithm (MLE). Scale bars represent 25 µm (A) and 10 µm (B).

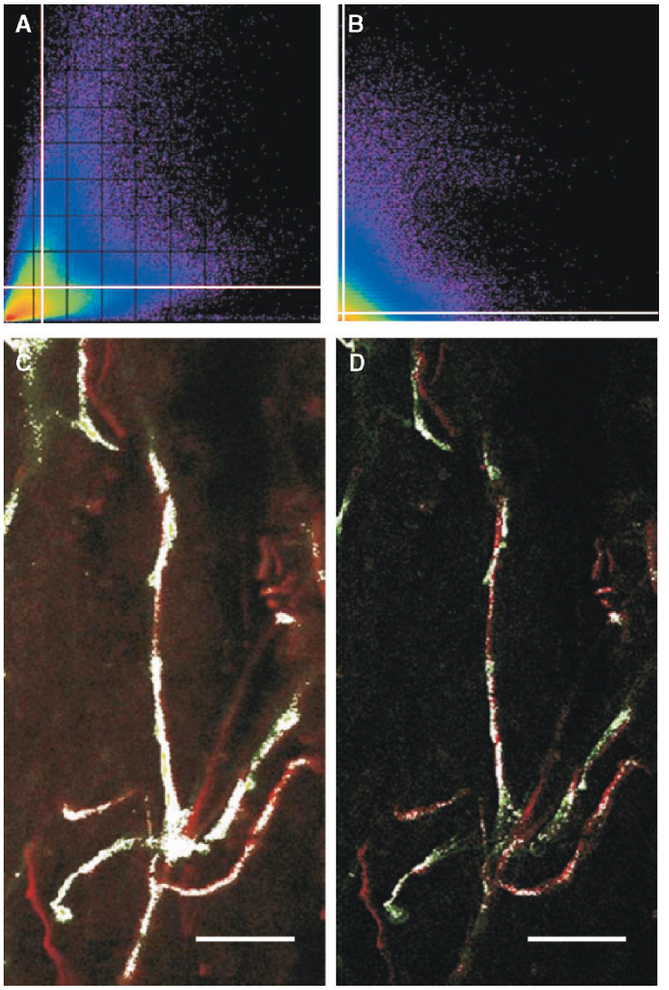


FIGURE 36.20. Fluorogram analysis of colocalization. 2D histograms of the volumes shown in Figure 36.19. Green intensities are plotted on the *y*-axis (0–255), and red intensities are plotted on the *x*-axis (0–255). The fluorogram before deconvolution (A) shows low intensity background in the green channel indicated by a layer of points lying above the *x*-axis and two correlations of unequal intensity possibly existing between the two channels. After restorative deconvolution the 2D histogram (B) has less background and shows the effect of background removal on putative colocalization. While (A) suggests a possible weak correlation in a bimodal distribution, (B) suggests a lack of colocalization. The white lines in both plots represent threshold levels applied to both channels for subsequent analysis on the volume (Table 36.3), and shown by white masks in panel (C) and (D). Panel (C) is the same field as that shown in Figure 36.19(B), but taken from the volume before deconvolution, and panel (D) is the same field after deconvolution. The scale bar represents 10 µm.

tion shows that the two labels may be co-existing (as noted by yellow) only where the fibers cross, or in some of the thickened regions along the small green fibers. Given that the *z*-resolution of the confocal microscope is significantly less than the *xy*-resolution, such overlaps may simply be due to the diminished *z*-resolution.

The 2D histograms in Figure 36.20 are derived from the high-resolution volume shown in Figure 36.19(B), and graphically demonstrate the impact on colocalization of background removal through deconvolution. The 2D histogram of the original (non-deconvolved) volume [Fig. 36.20(A)] displays two putative correlations, suggesting that each fiber is predominantly labeled for one protein, but containing the other protein in reduced amount. Pixels plotting close to the *x*-axis represent low intensity green label, such as the line of pixels very close to the *x*-axis (below the threshold line) indicating low-intensity background fluorescence in the green channel that associates with all levels of red fluorescence. Pixels plotting near the *y*-axis represent low intensity red label.

The 2D histogram changes dramatically after restorative deconvolution by maximum likelihood estimation (MLE, using Huygens, Scientific Volume Imaging) of the *z*-stack [Fig. 36.20(B)]. The low-intensity background from the green channel has been removed and the two regions of correlation observed in Figure 36.20(A) have been sharply reduced, suggesting that they were due to blur, as does the fact that most pixels are now shifted towards the *x*- or *y*-axis.

The impact of MLE on the correlation coefficients is shown in Table 36.3. The red and green labels show very high correlations in the original, undeconvolved low resolution volume [Fig. 36.19(A)], with values of 0.817 and 0.896 for *R* and *r*, respectively, in Table 36.3, Line 1. The colocalization coefficients *M*1 and *M*2 indicate that all voxels are colocalized because 100% of voxels in each channel are contributing to the colocalization. The higher

TABLE 36.3. Effect of MLE and Threshold on Colocalization

	Sample	MLE	Threshold	*R*	*r*	*M*1	*M*2
1	Fig. 36.19(A)	No	No	0.817	0.896	1.00	1.00
2	Fig. 36.19(B)	No	No	0.624	0.803	1.00	1.00
3	Fig. 36.19(B)	No	37/37	0.457	0.461	0.496	0.789
4	Fig. 36.19(B)	Yes	No	0.345	0.475	0.807	0.833
5	Fig. 36.19(B)	Yes	20/20	0.298	0.303	0.254	0.556

resolution volume [Fig. 36.19(B)] displays some reduction in both Pearson's coefficient and overlap coefficient (Table 36.3, Line 2) as the two populations of fibers are now resolved into separate objects. However, the colocalization coefficients for both channels are still at unity suggesting either perfect correlation or, more likely, significant levels of background.

MLE processing also changes the colocalization values, as shown in Table 36.3, Line 4. The amount of correlation from Pearson's coefficient drops to 34.5% and the overlap coefficient is reduced to 47.5%. The proportion of contribution to colocalization by the two channels (*M*1 and *M*2) are reduced to 80.7% for the red channel (*M*1) and 83.3% for the green channel (*M*2).

The threshold is important for determining the level of fluorescence that is to be considered significant. Thresholds were set for both channels by measurements of presumed background from the darker regions between the labeled fibers. These thresholds are represented by the white lines in Figure 36.20(A), at a threshold of 37 for the original image stack and at a threshold of 20 in Figure 36.20(B), the fluorogram of the volume after MLE. Table 36.3 provides the corresponding coefficients for the volumes following application of thresholds. The field in Figure 36.20(C) is the same field as in Figure 36.19(B), but taken from the high resolution volume before deconvolution. The white mask represents the pixels above threshold, as applied to this image plane. Figure 36.19(D) is the same field as Figure 36.19(B), taken from the volume after deconvolution. Pixels above the threshold applied to this image after deconvolution are represented by the white mask. The differences between Figure 36.20(C) and Figure 36.20(D) not only include the difference in number of colocalized pixels, but extend to the apparent thicknesses of the nerve fibers and background around the fibers.

Clearly, the apparent colocalization in the low magnification image and the high-resolution image was due to blending of the two channels by blur, noise and bleed-through. Restorative deconvolution reduced these contributions in a far more meaningful manner than was possible with simple thresholding. The remaining colocalization in this example is likely due to bleed-through, blur at the intersections of fibers, as well as blur from fibers in adjacent volume planes (not shown).

Using deconvolution, direct inspection of the image, and the 2D histogram in conjunction with the quantitative analysis tools available for colocalization can provide far greater insight into the relationships between the two labels in a volume than can any single tool alone. While we may be left with questions regarding the exact nature and extent of colocalization in this example, these tools can be used together to indicate directions that might be taken to determine the relationship between these two proteins more closely. Careful use of adequate controls to establish acquisition parameters that avoid bleed-through, noise, blur and autofluorescence, as described in detail by Costes *et al.* 2004, is essential for obtaining sound datasets for colocalization.

DISCUSSION

Recent advances spanning only the past 20 to 30 years have fueled extremely rapid development and popular adoption of laser-scanning microscopy as a practical and uniquely powerful tool for scientific discovery. The capabilities of these instruments have two faces — on one hand, they can gather light with unprecedented sensitivity, lack of noise, and resolution so that we can work at the limits of physics on biological questions that were unapproachable in an earlier era. On the other hand, they can also generate exquisitely stunning images of artifact or elevate the most mundane source of background into signals that overwhelm all meaningful information from the sample. Adequate controls are an absolute requirement to understand the interplay of the instrument controls and your samples. The regular application of standard confidence tests applied to both the instrument and the biological samples serve to demonstrate the outstanding capabilities of a well-maintained imaging system as well as providing meaningful information on the limitations of such equipment.

To ensure maximum productivity, it is advantageous to monitor the progress of declining performance so that the system may be restored to peak performance before the potential for grievous artifact or frank system failure becomes a reality. Murphy's Law dictates that there is a disproportionate chance such problems will be discovered at the onset of an important experiment or when results are needed in the face of looming deadlines. Quantitative measures of performance may serve to aid remote diagnosis by a field engineer and expedite subsequent ordering of the necessary parts. It is hoped that the tests outlined in this chapter will aid you in realizing the goals of data integrity, peak performance, and high instrument reliability when using laser-scanning confocal microscopes in a variety of environments.

ACKNOWLEDGMENTS

The images used to illustrate colocalization (Fig. 36.19 and Fig. 36.20) were generously provided by Dr. Orapin Veerayutthwilai (DDS, MS), Department of Oral Biology, and Dr. Margie Byers (PhD), Department of Anesthesiology, University of Washington, Seattle, WA. The image of a subresolution fluorescent bead in Figure 36.6 was kindly provided by Michael Weiss, Pacific Agri-Food Research Centre, Summerland, BC, Canada.

REFERENCES

Agnati, L.F., Fuxe, K., Torvinen, M., Genedani, S., Franco, R., Watson, S., Nussdorfer, G.G., Leo, G., Guidolin, D., 2005, New methods to evaluate colocalization of fluorophores in immunocytochemical preparations as exemplified by a study on A_{2A} and D_2 receptors in Chinese hamster ovary cells, *J. Histochem. Cytochem.* 53:941–953.

Akinyemi, O., Boyde, A., Browne, M.A., Hadravsky, M., and Petran, M., 1992, Chromatism and confocality in confocal microscopes, *Scanning* 14:136–143.

Booth, M.J., and Wilson, T., 2001, Refractive-index-mismatch induced aberrations in single-photon and two-photon microscopy and the use of aberration correction, *J. Biomed. Opt.* 6:266–272.

Brakenhoff, G.J. Wurpel, G.W.H., Jalink, K., Oomen, L., Brocks, L., and Zwier, J.M., 2005, Characterization of sectioning fluorescence microscopy with thin uniform fluorescent layers: Sectioned imaging property or SIPcharts. *J. Microsc.* 219:122–132.

Browne, M.A., Akinyemi, O., and Boyde, A., 1992, Confocal surface profiling utilizing chromatic aberration, *Scanning* 14:145–153.

Carlsson, K., 1991, The influence of specimen refractive index, detector signal integration, and non-uniform scan speed on the imaging properties in confocal microscopy, *J. Microsc.* 163:167–178.

Costes, S.V., Daelemans, D., Cho, E.H., Dobbin, Z., and Pavlakis, G., 2004, Automatic and quantitative measurement of protein-protein colocalization in live cells, *Biophys. J.* 86:3993–4003.

Cox, G., 1999, Measurement in the confocal microscope, *Methods Mol. Biol.* 122:357–371.

Cox, G., and Sheppard, C.J.R., 2004, Practical limits of resolution in confocal and nonlinear microscopy, *Microsc. Res. Tech.* 63:18–22.

Demandolx, D., and Davoust, J., 1995, Multicolor analysis in confocal immunofluorescence microscopy, *J. Trace Microprobe Tech.* 13:217–225.

Demandolx, D., and Davoust, J., 1997, Multicolour analysis and local image correlation in confocal microscopy, *J. Microsc.* 185:21–36.

Dickinson, M.E., Bearman, G., Tille, S., Lansford, R., and Fraser, S.E., 2001, Multi-spectral imaging and linear unmixing add a whole new dimension to laser scanning fluorescence microscopy, *Biotechniques* 31:1272–1278.

Garini, Y., Gil, A., Bar-Am, I., Cabib, D., and Katzir, N., 1999, Signal to noise analysis of multiple color fluorescence imaging microscopy, *Cytometry* 35:214–226.

Hibbs, A.R., 2004, *Confocal Microscopy for Biologists*, Kluwer Academic/Plenum Publishers, New York.

Hiraoka, Y., Sedat, J.W., and Agard, D.A., 1990, Determination of three-dimensional imaging properties of a light microscope system, *Biophys. J.* 57:325–333.

Ho, R., and Shao, Z., 1991, Axial resolution of confocal microscopes revisited. *Optik* 88:147–154.

Huth, U., Wieschollck., A, Garini, Y., Schubert, R., and Peschka-Süss, R., 2004, Fourier transformed spectral bio-imaging for studying the intracellular fate of liposomes, *Cytometry* 57A:10–21.

Hutter, H., 2004, Five-colour in vivo imaging of neurons in *Caenorhabditis elegans*, *J. Microsc*. 215:213–218.

LaMorte, V.J., Zoumi, A., and Tromberg, B.J., 2003, Spectroscopic approach for monitoring two-photon excited fluorescence resonance energy transfer from homodimers at the subcellular level, *J. Biomed. Opt.* 8:357–361.

Landmann, L., Deconvolution improves colocalization analysis of multiple fluorochromes in 3D data sets more than filtering techniques, 2002, *J. Microsc.* 208:134–147.

Landmann, L., and Marbet, P., 2004, Colocalization analysis yields superior results after image restoration, *Microsc. Res. Tech.* 64:103–112.

Lansford, R., Bearman, G., and Fraser, S.E., 2001, Resolution of multiple green fluorescent protein color variants and dyes using two-photon microscopy and imaging spectroscopy, *J. Biomed. Opt*. 6:311–318.

Maly, M., and Boyde, A., 1994, Real-time stereoscopic confocal reflection confocal microscopy using objective lenses with linear longitudinal chromatic dispersion, *Scanning* 16:187–193.

Manders, E.M.M., Stap, J., Brakenhoff, G.J., van Driel, R., and Aten, J.A., 1992, Dynamics of three-dimensional replication patterns during the S-phase, analysed by double labeling of DNA and confocal microscopy, *J. Cell Sci*. 103:857–862.

Manders, E.M.M., Verbeek, F.J., and Aten, J.A., 1993, Measurement of co-localization of objects in dual-colour confocal images, *J. Microsc*. 169:375–382.

Model, M., and Burkhardt, J., 2001, A standard for calibration and shading correction of a fluorescence microscope, *Cytometry* 44:309–316.

Neher, R., and Neher, E., 2004, Optimizing imaging parameters for the separation of multiple labels in a fluorescence image, *J. Microsc*. 213: 46–62.

Pawley, J.B., 1994, Sources of noise in three-dimensional microscopical data sets, In: *Three-Dimensional Confocal Microscopy: Volume Investigation of Biological Specimens* (J.K. Stevens, L.R. Mills, and J.E. Trogadis, eds.), Academic Press, London, pp. 47–93.

Pawley, J.B., 2000, The 39 steps: A cautionary tale of quantitative 3-D fluorescence microscopy, *Biotechniques* 28:884–886, 888.

Pawley, J.B., 2002, Limitations on optical sectioning in live-cell confocal microscopy, *Scanning* 24:241–246.

Scalettar, B.A., Swedlow, J.R., Sedat, J.W., and Agard, D.A., 1996, Dispersion, aberration and deconvolution in multi-wavelength fluorescence images, *J. Microsc*. 182:50–60.

Shaw, P.J., and Rawlins, D.J., 1991, The point-spread function of a confocal microscope: Its measurement and use in deconvolution of 3-D data, *J. Microsc.* 163:151–165.

Smallcombe, A., 2001, Multicolor imaging: The important question of co-localization, *Biotechniques* 30:1240–1246.

Stark, P.R.H., Rinko, L.J., and Larson, D.N., 2003, Fluorescent resolution target for super-resolution microscopy, *J. Microsc*. 212:307–310.

Tran, P., 2005, CCD cameras for fluorescence imaging of living cells, In: *Live Cell Imaging: A Laboratory Manual* (R.D. Goldman and D.L. Spector, eds.), Cold Spring Harbor Laboratory Press, Cold Spring Harbor, New York, pp. 87–100.

van den Doel, L.R., Klein, A.D., Ellenberger, S.L., Netten, H., Boddeke, F.R., van Vliet, L.J., and Young, I.T., 1998, Quantititative evaluation of light microscopes based on image processing techniques, *Bioimaging* 6:138–149.

van der Voort, H.T.M, Brakenhoff, G.J., and Janssen, G.C.A.M., 1988, Determination of the 3-dimensional optical properties of a confocal scanning laser microscope, *Optik* 78:48–53.

Van Steensel, B., van Binnendijk, E.P., Hornsby, C.D., van der Voort, H.T.M., Krozowski, Z.S., de Kloet, E.R., and van Driel, R., 1996, Partial colocalization of glucocorticoid and mineralocorticoid receptors in discrete compartments in nuclei of rat hippocampus neurons, *J. Cell Sci.* 109: 787–792.

Visser, T.D., Brakenhoff, G.J., and Groen, F.C.A., 1991, The one-point fluorescence response in confocal microscopy, *Optik* 87:39–40.

Wallace, W., Schaefer, L.H., and Swedlow, J.R., 2001, A workingperson's guide to deconvolution in light microscopy, *Biotechniques* 31:1076–1097.

Wilson, T., and Juskaitis, R., 1995, The axial response of confocal microscopes with high numerical aperture objective lenses, *Bioimaging* 3:35–38.

Young, M., 2000, Impulse response and transfer function, In: *Optics and Lasers* (M. Young, ed.), Springer-Verlag, New York, pp. 181–192.

Zucker, R.M., and Lerner, J.M., 2004, Calibration and validation of confocal spectral imaging systems, *Cytometry* 62A:8–34.

Zucker, R.M., and Price, O.T., 1999, Practical confocal microscopy and the evaluation of system performance, *Methods* 18:447–458.

Zucker, R.M., and Price, O.T., 2001a, Evaluation of confocal microscopy system performance, *Cytometry* 44:273–294.

Zucker, R.M., and Price, O.T., 2001b, Statistical evaluation of confocal microscopy images, *Cytometry* 44:295–308.

Zwier, J.M., Van Rooij, G.J., Hofstraat, J.W., and Brakenhoff, G.J., 2004, Image calibration in fluorescence microscopy, *J. Microsc.* 216:15–24.

37

Selective Plane Illumination Microscopy

Jan Huisken, Jim Swoger, Steffen Lindek, and Ernst H.K. Stelzer

INTRODUCTION

In this chapter we present an alternative way of optically sectioning the sample in fluorescence microscopy. By illuminating the sample from the side with a sheet of light, and viewing the light emitted or scattered by this layer with a widefield microscope oriented on an axis perpendicular to the sheet, a sectioning effect that is similar to that in confocal microscopy can be produced. Such an approach has several advantages over confocal scanning microscopy and these make the technology especially well suited for relatively large samples such as embryos. However, the principle is universal and can also be applied to micrometer-sized samples.

This chapter introduces light-sheet microcopy by providing an overview of microscopy techniques for large samples and the history of techniques employing plane illumination. The light-sheet microscope that we have developed at the EMBL is illustrated and explained, its characteristics are described and evaluated in the context of confocal microscopy and its performance demonstrated by a few applications.

The stereo microscope is the most commonly used microscope in developmental biology. It provides a stereoscopic image of the sample while keeping it under ideal conditions for sorting and selecting embryos (e.g., in a Petri dish filled with an appropriate medium). A camera can be used to record images or even movies of the developing embryo for later reference. However, no volumetric quantification can be made because the stereo microscope offers little depth discrimination and no optical sectioning. The same holds true for conventional widefield microscopes, which in addition often suffer from short working distances that are inadequate for imaging large samples.

Quantitative analysis of three-dimensional (3D) structures requires sectioning (optical or otherwise). Out-of-focus light is rejected in confocal microscopy by coupling point excitation with a laser beam to point detection through a pinhole, so that in general only in-focus light is detected. This principle works well in relatively thin samples (up to ca. 100 µm); however, in large and scattering objects, the signal is lost since most of the fluorescent light is scattered and therefore rejected by the pinhole. The confocal microscope, therefore, suffers from a limited penetration depth, and cannot be applied for *in toto* studies of most embryos. In such samples, the best resolution is obtained by physically sectioning the sample (Weninger, 2002), which is slow, laborious, destroys the sample irretrievably, and is not applicable for studies of living preparations.

The many methods that have recently been developed to enhance the resolution, e.g., 4Pi-confocal (Hell, 1992), confocal theta microscopy (Stelzer, 1994), I^5M microscopy (Gustafsson, 1999), and Stimulated Emission Depletion (STED) microscopy (Klar, 2000) do not address the challenges encountered in large and scattering samples such as embryos. Their improved resolution is easily degraded by sample-induced wavefront distortions, and in addition, they generally require quite complex instrumentation. Chapter 34 presents an overview of imaging techniques for large samples, such as Optical Projection Tomography (OPT; Sharpe, 2002) and Micro Magnetic Resonance Imaging (µMRI; Louie, 2000), which to some extent attempt to overcome these challenges.

COMBINING LIGHT SHEET ILLUMINATION AND ORTHOGONAL DETECTION

"Light-sheet" microscopy now provides an alternative approach for imaging large samples at high resolution. Like confocal microscopy, techniques based on sheet illumination have been "invented" a number of times and all owe much to the "Ultramikroskop," an orthogonal, darkfield illuminator invented by Siedentopf and Zsigmondy in 1903, to visualize gold particles much smaller than the resolution limit by detecting light scattered perpendicular to the illumination.

The light-sheet concept has been used in several other microscopes since then. For decades the slit-lamp was used for viewing the human eye (Campbell *et al*., 1974) and similar techniques were reviewed by Webb in Chapter 34 of the second edition of this Handbook. More recently, Voie used the high coherence of laser light to develop orthogonal-plane fluorescence sectioning (OPFOS) and applied it to the cochlea (Voie, 1993, Voie *et al*., 1995).[1] Although initially operating at a fixed magnification and a resolution set by the close-focus camera lens used to convey the image to the CCD camera, more recent implementations (Voie, 2002) used a 4× optical system and a rotating specimen immersed in index-matching medium to record details about 10 µm in size.

In 2002, Fuchs described the Thin Laser Light Sheet Microscope (TLLSM) (Fuchs, 2002) to detect, discriminate and document microbes passing through the light sheet. Although it has the same optical arrangement as Siedentopf and Zsigmondy, TLLSM uses fluorescence, which was not practical 100 years ago. Because in this system, the stage is stationary relative to the light sheet, only the slice of the sample that happens to intercept the sheet is imaged, making the system unsuitable for generating three-dimensional images.

Another technique with orthogonal illumination and detection is 3D Light Scanning Macrography (Huber, 2001), which is used for generating macroscopic reconstructions of samples using scat-

[1] More information on this system can be obtained at www.spencertechnologies.com

Jan Huisken, Jim Swoger, Steffen Lindek, and Ernst H.K. Stelzer • European Molecular Biology Laboratory (EMBL), 69012 Heidelberg, Germany

tered light. The orthogonal arrangement of illumination and detection was also used in theta microscopy (Stelzer, 1994), although no light sheet is formed in this variant of the single-point confocal scanning microscope.

Our current implementation of the technique is the latest of three versions of the selective plane illumination microscope (SPIM). It is embodied in a compact, stable, and economical system based on three operating principles: illumination of the sample with a light sheet, observation of light coming from the sample in a direction perpendicular to the illumination axis, and, optionally, rotation of the sample about an axis parallel to gravity. A 3D image is recorded by scanning the sample through the stationary light sheet and recording the fluorescence or scattered light with a CCD camera. The sample, which can be as small as a few micrometers or as large as several millimeters depending on the working distance of the objective lenses, can be embedded in a gel, immersed in a liquid or held in air. As it is mounted on a stage that can be rotated as well as translated, one can record 3D images from multiple directions, and these data sets can be combined into a single 3D data set with a spatial resolution dominated by the lateral resolution of the detection system.

SELECTIVE PLANE ILLUMINATION MICROSCOPY SETUP

Figure 37.1 shows the main components of SPIM. A series of lasers [several helium–neon (He–Ne) and a multi-line argon (Ar)-ion laser] provide a range of excitation wavelengths, which can be focused by a cylindrical lens to form a thin light sheet. The sample is mounted in a transparent cylinder, typically made of agarose prepared using an aqueous solution suitable for the sample (e.g., phosphate-buffered saline, PBS). The agarose cylinder is then immersed in a bath of this solution, virtually eliminating refractive index artifacts at the surface. The cylinder is held from above by a micropositioning device with four degrees of freedom (three translational, one rotational), which allows positioning the sample such that the excitation light illuminates any plane of interest. An objective lens placed perpendicular to the illumination plane, a detection filter, and a tube lens are used to image fluorescent light excited by the light sheet onto a CCD camera. A variety of objective lenses can be used (preferably those designed for imaging in water without a coverslip), with magnifications ranging from 2.5×

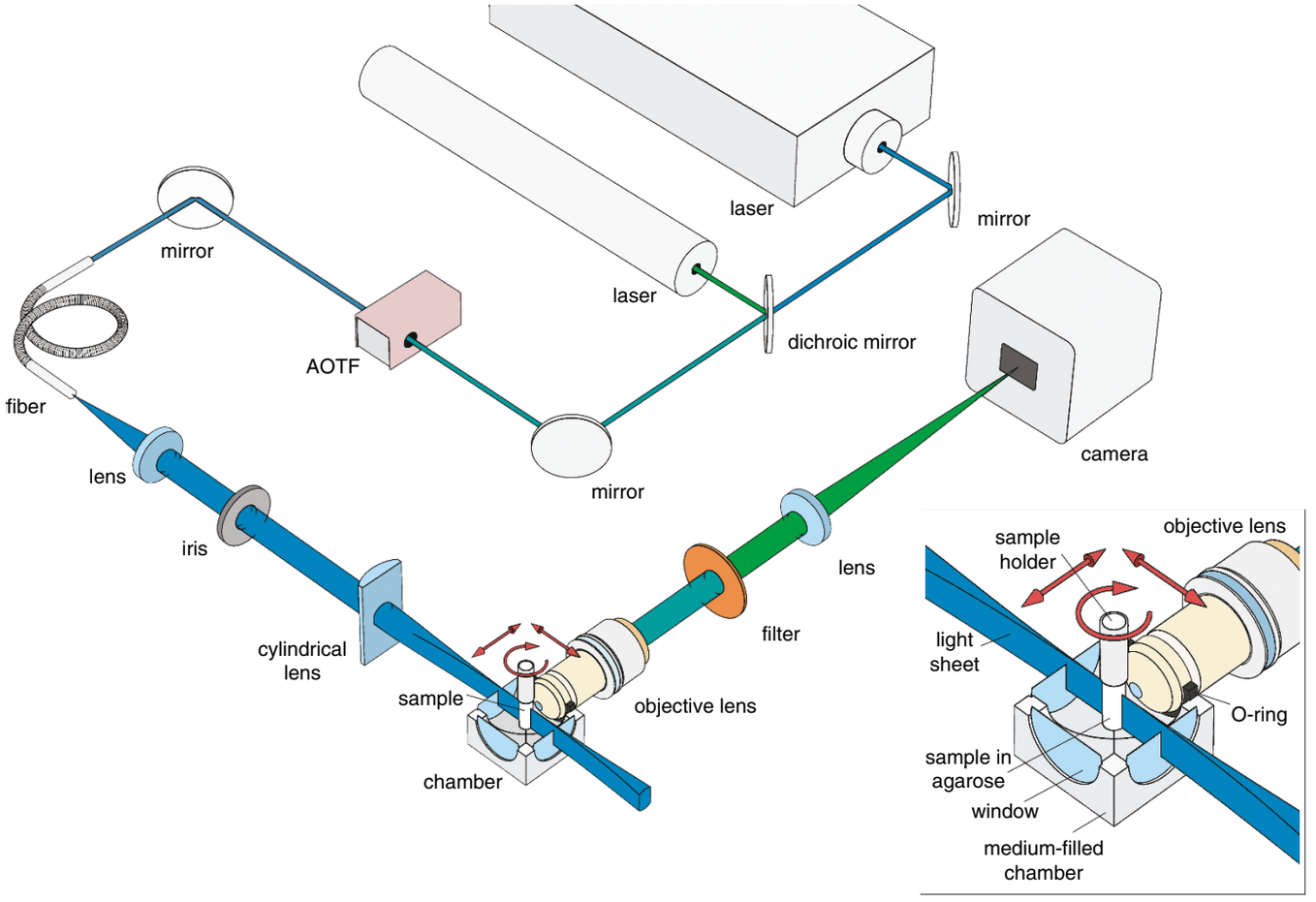


FIGURE 37.1. Schematic setup of a selective plane illumination microscope. The light sources (back), illumination path (front, left), and detection path (front, right) are shown. The beams of two lasers are superimposed and the acousto-optical tunable filter (AOTF) is used to select and to attenuate the desired laser line. (The use of the optical fiber to deliver the laser light to the microscope helps to reduce mechanical vibrations, but is actually optional.) The laser light is focused by the cylindrical lens to form a light sheet that traverses the chamber. The sample is placed into the chamber in the path of the light sheet. Widefield detection is performed with the objective lens, filter, tube lens, and CCD camera. (Inset) Detailed view of the chamber with sample, illumination beam, and detection lens. The light sheet enters the aqueous medium-filled chamber (shown cut open) through a thin glass window. The sample is embedded in a cylinder of agarose, which is supported from above and can be moved by a translating and rotating stage. The objective lens is sealed into the chamber with a rubber O-ring, and can be moved axially to focus on the plane of fluorescence excited by the light sheet. The sample is then moved through the light sheet to acquire a 3D data set.

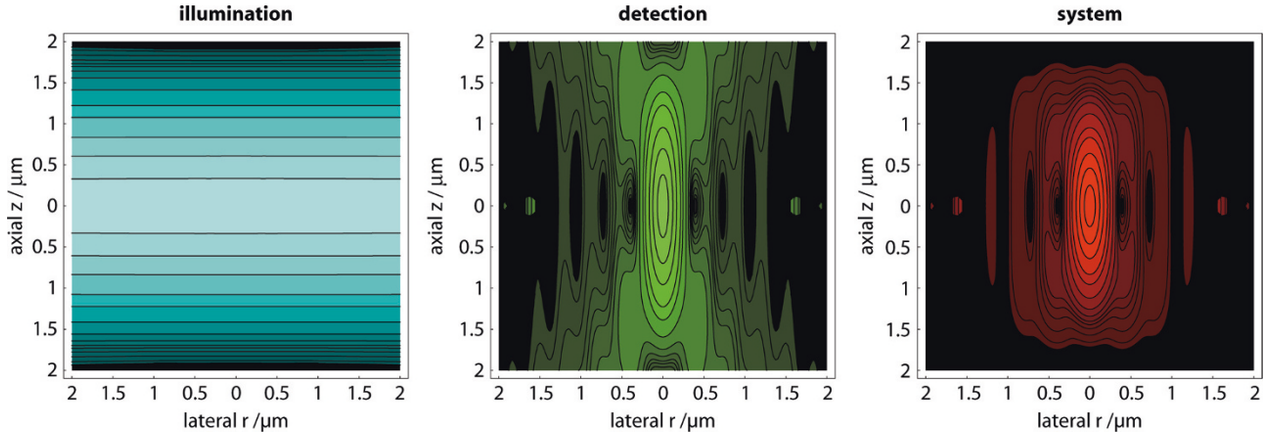


FIGURE 37.2. Theoretical intensity point spread functions (PSF) in the SPIM. The system PSF (right) is obtained by multiplying the illumination (left) and detection PSFs (center). $\lambda_{ill} = 488\,nm$, $\lambda_{det} = 520\,nm$, $NA_{ill} = 0.15$, $NA_{det} = 0.8$, $n = 1.33$. Contour lines are plotted for intensities of 0.9, 0.7, 0.5, 0.3, 0.2, 0.1, 0.05, 0.03, 0.02, 0.015, 0.01, 0.005, 0.002, and 0.001. The intensities are shown with a lookup table (LUT) of $\gamma = 0.25$, in blue for excitation, in green for detection, and in red for the system.

to 100×, numerical apertures (NAs) from 0.16 to 1.0, and working distances of 1 to 12 mm.

LATERAL RESOLUTION

The lateral resolution of SPIM is determined by the NA of the detection lens, as is generally the case in widefield microscopy. However, if the images are under-sampled by the CCD, the lateral resolution of the detection lens is not fully exploited, and the pixel size of the camera determines the lateral resolution. This is a general problem in digital microscopy using currently available objective lenses and cameras, and is not unique to SPIM. Figure 37.2 shows the point spread functions (PSF) of illumination and detection in SPIM, as well as the product of the two, that is, the system PSF, for typical NAs. The light sheet illumination does not affect the lateral resolution.

LIGHT SHEET THICKNESS AND AXIAL RESOLUTION

There are two distinct yet related effects of the light sheet dimensions that are relevant to SPIM. First, selective illumination by the light sheet provides optical sectioning in SPIM, and the extent of this capability depends on the thickness of the light sheet. Second, the light sheet improves the axial resolution of the SPIM *if* it is thinner than the axial extent of the detection PSF (Fig. 37.2). For both of these reasons the optimal light sheet for SPIM is made as thin as possible, while maintaining its properties approximately uniform across the field of view. The relations between the light sheet dimensions and the detection field of view are schematically illustrated in Figure 37.3.

The minimum thickness of the light sheet is inversely proportional to the NA of the cylindrical illumination lens, while the width of this thin waist (i.e., its extent along the illumination axis) is inversely proportional to its NA^2. While the importance of the thickness of the light sheet is obvious (for the reasons given above), that of its width is perhaps less so. However, when one considers that it is desirable to have the extent of the optical sectioning uniform across the field of view, it becomes clear that it is necessary to have the light sheet width at least as large as the detection field of view (see Fig. 37.3). Thus, the optimal SPIM design involves a compromise between strong optical sectioning (requiring a large illumination NA) and a large field of view (requiring a small illumination NA).

The simplest means of balancing these two parameters is to change the focal length of the cylindrical lens or the size of its aperture. As an example of a configuration suitable for relatively large samples, with a 10×/0.30 detection objective lens the SPIM has a field of view of 660 µm. A Gaussian light sheet can be formed with a thickness that varies between 6 µm and 9 µm across this distance by using a cylindrical lens of focal length 100 mm and aperture 6 mm. In addition to providing optical sectioning, this considerably improves the axial resolution of the system, which would be ~14 µm with conventional illumination.

If SPIM is to be used for higher-resolution imaging of smaller samples, a 100×/1.0 with an axial PSF width of 1.08 µm and a field

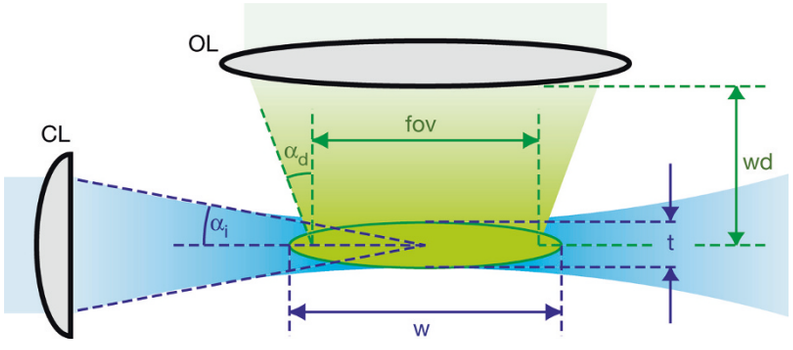


FIGURE 37.3. Light sheet illumination (blue) and widefield detection (green) in the SPIM. Illumination: CL, cylindrical lens; $NA_{ill} = n \sin \alpha_i$; t, light sheet thickness; w, light sheet width. Detection: OL, objective lens; $NA_{det} = n \sin \alpha_d$; fov, field of view; wd, working distance.

of view of 66 µm is more appropriate. For this detection lens, a light sheet thickness of 2 µm yields a reasonably uniform illumination across the field of view (thickness variation <70%). In this case, although the light sheet does not significantly decrease the axial extent of the widefield PSF [as defined by its full-width at half-maximum (FWHM)], it can still contribute to the image quality in a thick fluorescent sample by providing optical sectioning, and thereby increasing image contrast (Stelzer, 1998). When imaging a 200 µm thick sample in the SPIM with a 2 µm wide light sheet, the contrast of features in the focus plane will be improved by a factor of up to 100× compared to imaging with uniform illumination.

In addition to the use of light sheet illumination, the resolution in SPIM can be significantly improved by multi-view reconstruction (see section below on Processing SPIM Images/Multi-View Reconstruction; Shaw, 1989; Swoger *et al*., 2003; Huisken *et al*., 2004). When this is done, the lateral resolution of the individual views determines the overall resolution in the fused dataset, that is, the axial resolution becomes as good as the lateral.

APPLICATIONS

SPIM technology can be readily applied to a wide range of specimens, from living, fully intact organisms to single cells. Because the method of embedding the sample in a low concentration (0.5%) agarose cylinder is non-disruptive, SPIM is well suited for high-resolution visualization of spatiotemporal patterns of gene and protein expression. To demonstrate this, we imaged the transgenic Medaka line Arnie, which expresses green fluorescent protein (GFP) in somatic and smooth muscles. A 4-day-old fixed Arnie embryo is shown in Figure 37.4. SPIM was capable of resolving the internal structures of the organism with high resolution (better than 6 µm) as deep as 500 µm inside the fish, a penetration depth that cannot be reached using confocal laser-scanning microscopy. Figure 37.4 also includes a comparison of widefield and SPIM illumination. The optical sectioning capability of SPIM is apparent.

Figure 37.5 shows the summary of an experiment in which a relatively opaque *Drosophila* embryo was observed over a period of 17 h. Even after being illuminated to generate 11,480 two-dimensional (2D) images, the embryo completed embryogenesis normally. SPIM is ideally suited for tracking the development of intact embryos: internal structures are clearly identifiable and traceable and even subcellular resolution can be obtained in living samples kept in a biologically relevant environment within the organism or in culture.

PROCESSING SELECTIVE PLANE ILLUMINATION MICROSCOPY IMAGES/MULTI-VIEW RECONSTRUCTION

One of the advantages of SPIM is that it is possible to generate improved sample reconstructions by taking multiple 3D views of the sample. As discussed above, multiple 3D images of the sample are generated from varying directions. These different views can contain information about different aspects of the sample: they can cover different regions of the sample, either in physical space (in a semi-opaque sample where only part of it can be imaged from a given direction) or in Fourier space (because of the anisotropy of the system resolution). The goal of the multi-view reconstruction is to combine the best components of each view into a single 3D representation of the sample.

The data processing steps used for the fusion of multi-view SPIM images are similar to those described by Shaw (1989), and outlined below:

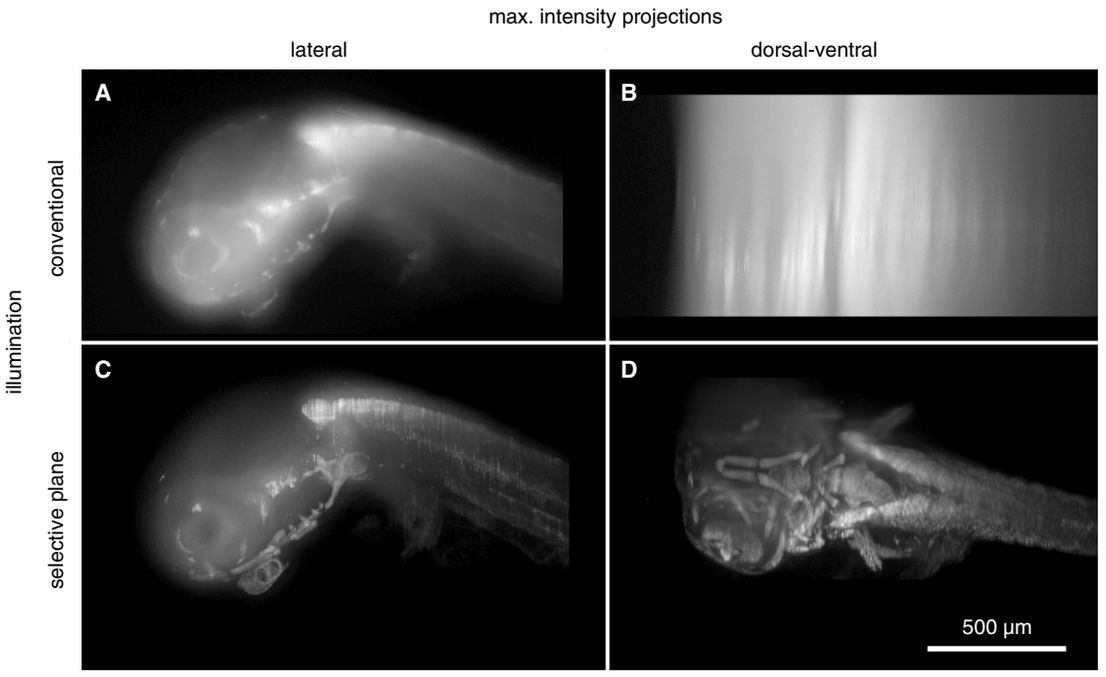


FIGURE 37.4. A Medaka embryo imaged with SPIM by two different modes of illumination. Lateral (A, C) and dorsal–ventral (B, D) maximum projections are shown. In (A) and (B), the sample was illuminated uniformly, that is, without the cylindrical lens, as in a conventional widefield microscope. There is no optical sectioning; the elongation of fluorescent features along the detection axis is clearly visible in (B). In contrast, selective plane illumination (C, D) provided optical sectioning. Both image stacks were taken with a 5×, 0.25 objective lens. The embryo shows GFP expression in the eyes and muscles (sample provided by J. Wittbrodt).

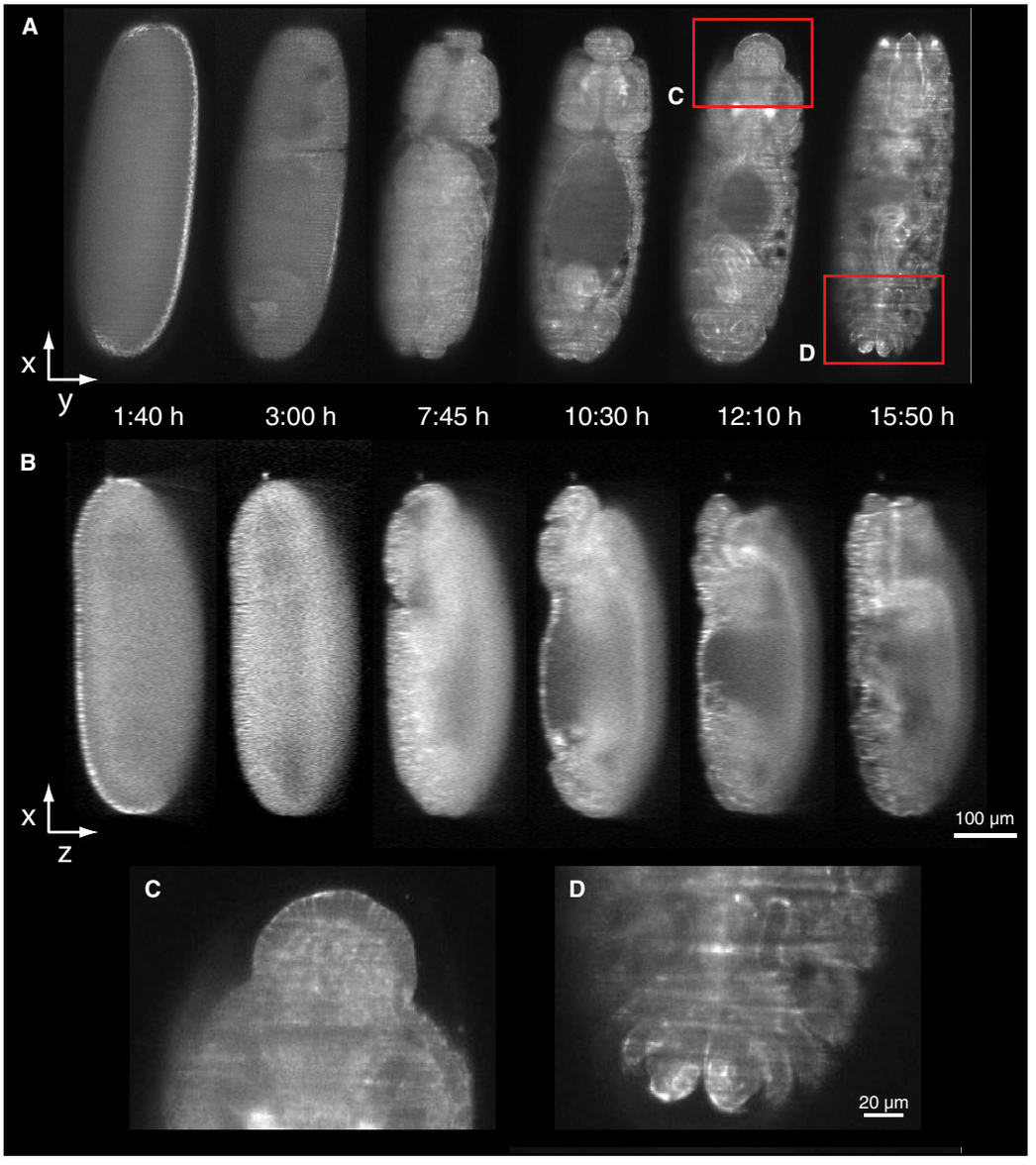


FIGURE 37.5. Time-lapse imaging of *Drosophila melanogaster* embryogenesis: 56 planes were recorded at 205 time points, creating a four-dimensional (4D) dataset 30 GB in size. (A) A single plane at six selected time points. (B) A corresponding central vertical plane, that is, one parallel to the detection axis *z*, showing the deep penetration of SPIM. Despite the optically dense structure of the *Drosophila* embryo, features are well resolved in the sample (see insets) and the overall morphogenetic movements during embryonic development can be followed (a 4D movie is available on this volume's Web site). The images were normalized to exhibit the same overall intensity, thus compensating for the continuous production of GFP-moesin. 10×, 0.30 W objective lens (sample provided by F. Jankovics).

1. **Preprocessing** includes cropping of the region of interest in all three dimensions, rescaling along the detection axis (to make the lateral and axial voxel dimensions equal), and rotating the images to a common orientation.
2. **Registration** is the process of aligning the different views so that features visible in more than one view overlap. The stacks are high-pass filtered to reduce background-induced registration artifacts[2] and cross-correlated. The position of the resulting correlation peak determines the translation that is applied to register the preprocessed (but otherwise raw, unfiltered) images.
3. Image **fusion** is the final stage, in which a single, optimal image is produced. The high-resolution features are extracted from each view and combined to form a single data set. The data sets are fused by:
   a. Fourier transforming the individual views to generate (complex-valued) spatial frequency representations.
   b. For each spatial frequency (i.e., each voxel in Fourier space), one selects the (complex) value from the view with the largest magnitude, and inserts it into the new, fused dataset. This effectively combines the images by selecting the component with the highest information content at each spatial frequency.

[2] Note that the high-pass, 3D, Fourier tranform–Gaussian filtering (with the standard deviation set to one half of the maximum spatial frequency possible for this pixel size) is only applied for the purposes of creating the cross-correlations: the subsequent processing is done with the non-filtered data sets.

c. Inverse Fourier transforming this selected, fused Fourier transform of the data to obtain the final, fused image.

4. In addition, if the single-view PSFs are known, the fused image can also benefit from the effects of deconvolution. In such cases we use a multi-view deconvolution algorithm similar to that described in Bertero and Boccacci (2000), adapted to allow processing of 3D microscopy datasets.

If the datasets overlap sufficiently in the multi-view reconstruction, the lateral resolution dominates and the multi-view reconstruction compensates the poor axial resolution in any single view with information from others, providing a nearly isotropic resolution as demonstrated with subresolution bead data in Swoger and colleagues (2003).

We performed a multi-view reconstruction with four views of a Medaka embryo (see Fig. 37.6). Combining these stacks yielded a complete view of the sample, and the decrease in image quality with penetration depth is corrected by the fusion process. In such a sample, image fusion compensates for *spatially varying* image quality caused by aberrations and scattering. As long as

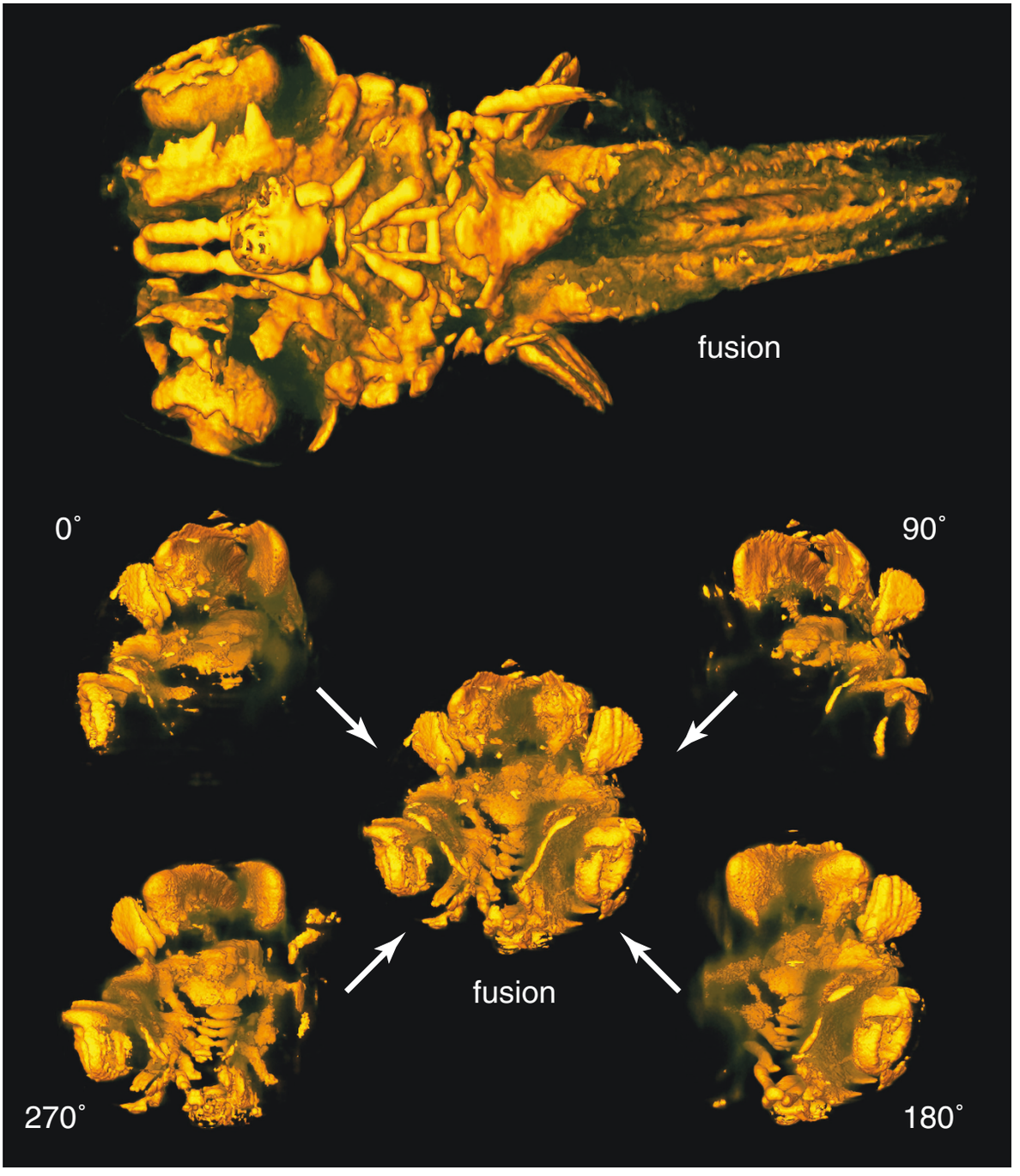


FIGURE 37.6. Volume renderings representing the result of fusing four datasets taken with 0°, 90°, 180°, and 270° orientations of the sample (same sample as in Fig. 37.4). (Top) Ventral view of the fused data. (Bottom) Anterior view of the single views and fusion. The multi-view reconstruction combines information from the single views while preserving the high-resolution parts.

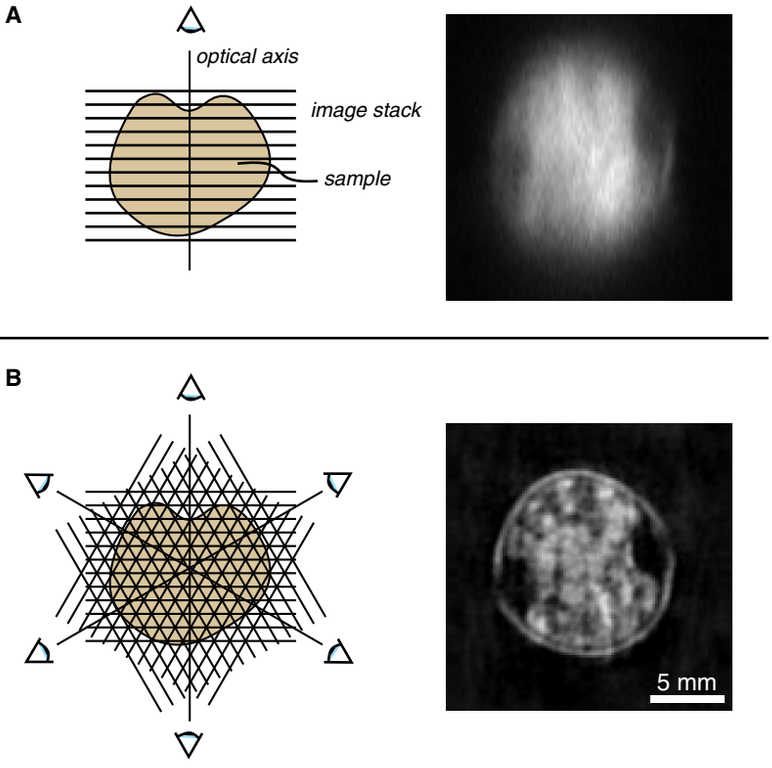


FIGURE 37.7. For an almost transparent sample, a multi-view reconstruction provides isotropic resolution because imaging from multiple directions provides overlapping datasets. (A) A single dataset of the autofluorescence from a grain of paper mulberry pollen suffers from poor axial resolution. (Seventeen similar datasets were taken with 10° angular shifts, not shown.) (B) The multi-view reconstruction incorporates all of the high-resolution information available in the individual views. Single slices parallel to the detection axis are shown. Objective lens, 63×; NA, 0.9 W.

high-resolution information is available in at least one view of a given region of the sample, the reconstruction algorithm will favor this information over the low-resolution information of the same area found in other views. The outcome is high-resolution data over a much larger volume than in a single unprocessed stack. Using this approach, the whole sample can be viewed at high resolution as long as the penetration depth is at least half its thickness.

When used to image transparent samples (i.e., those in which scattering/absorption are negligible), multi-view SPIM can provide isotropic resolution. This is demonstrated in Figure 37.7, which shows single-view and multi-view processed (optical) slices through a pollen grain. Unlike in the Medaka embryo shown in Figure 37.6, in the individual pollen views (only one is shown in Fig. 37.7) the issue is not *spatially varying* resolution, but rather *anisotropic* resolution. However, the algorithm presented here for fusion of multiple SPIM views is seen to compensate for both of these artifacts.

While multi-view data can be processed to yield a further increase in image quality and axial resolution compared to a single stack, in many cases a single, unprocessed, 3D SPIM stack alone provides sufficient information. This can be particularly important in live imaging of transient phenomena, where data acquisition speed can be of primary importance.

SUMMARY

If one is solely interested in near-surface features, a confocal laser-scanning microscope (CLSM) can be ideal because of its optical sectioning and compatibility with high-NA objective lenses. However, this absolutely precludes imaging the entirety of many thick samples, because currently available high-NA lenses do not have sufficient working distance. In addition, the severe drop in signal intensity caused by aberrations and scattering with increasing depth in heterogeneous specimens is more pronounced when working with a high NA lens. Because it uses planar illumination, SPIM does not suffer from scattering as much as the confocal microscope does: scattering of the illumination *within* the plane of the light sheet does not deteriorate the image at all, although scattering *out of* the plane will widen the thickness of the light sheet.

In a CLSM, fluorescence light is collected by a photomultiplier during the short time the focal spot rests at each pixel (0.1–10 µs). In contrast, the 1344 × 1024 pixel Hamamatsu ORCA ER CCD camera used in SPIM allows integration times of 0.1 to 1 s, which has the result that the local illumination intensity can be decreased, reducing the likelihood of fluorophore saturation. To reduce the dose to the sample even further, we have also used an EM-CCD and a result made using this camera is shown in Figures 10.12, 10.15 and 43.5 in other Chapters, *this volume*).

Like multi-photon microscopy, SPIM illumination provides intrinsic optical sectioning because no out-of-focus light is generated. This is in contrast to CLSM, where out-of-focus light is generated but rejected by the detection pinhole. In CLSM, the entire volume of the sample is illuminated, even if only a single plane is being imaged generating a 3D image with a confocal fluorescence microscope can therefore result in excessive photobleaching. Because of these two factors, imaging a 3D sample in SPIM requires a much smaller total number of fluorophore excitations than does any widefield or confocal microscope. This is a particular advantage when imaging thick specimens.

Samples mounted in agarose gel for SPIM enjoy conditions that are certainly much closer to physiological relevance than samples flattened on coverslips. The environment is more appropriate for embryos, 3D cell cultures, stem cell research, and many other areas of biological research. Fragile objects can be carefully

immersed in the liquid agarose gel[3] and remain in their natural form when the gel sets.

SPIM is a 3D optical technique capable of imaging deep inside both fixed and living organisms. Selective illumination of a single plane provides efficient optical sectioning and reduces photodamage in samples large or small. The method of sample mounting allows positioning and rotation to orient the sample for optimal imaging conditions. Image fusion can combine data from different SPIM views to produce an optimal 3D representation of the sample. Because the system is also inexpensive, compact, fast, optically stable, and easy to use, it is clear that there are many applications that are ideally suited to be investigated with SPIM techniques.

REFERENCES

Bertero, M., and Boccacci, P., 2000, Image restoration methods for the Large Binocular Telescope (LBT), *Astron. Astrophys. Suppl. Ser.* 147:323–333.

Campbell, C.J., Koester, C.J., Rittler, M.C., and Tackberry, R.B., 1974, *Physiological Optics*, Harper & Row, Hagerstown, MD, p. 179.

Fuchs, E., Jaffe, J.S., Long, R.A., and Azam, F., 2002, Thin laser light sheet microscope for microbial oceanography, *Opt. Express* 10:145–154.

Gustafsson, M.G.L., Agard, D.A., and Sedat, J.W., 1999, I^{5}M: 3D widefield light microscopy with better than 100 nm axial resolution, *J. Microsc.* 195:10–16.

Hecksher-Sorensen, J., and Sharpe, J., 2001, 3D confocal reconstruction of gene expression in mouse, *Mech. Dev.* 100:59–63.

Hell, S., and Stelzer, E.H.K., 1992, Properties of a 4Pi confocal fluorescence microscope, *J. Opt. Soc. Am. A* 9:2159–2166.

Huber, D., Keller, M., and Robert, D., 2001, 3D light scanning macrography, *J. Microsc.* 203:208–213.

[3] A 1% concentration of low-melting agarose is typically used. This provides sufficient mechanical stability to support the sample and does not require subjecting it to temperatures above 30°C.

Huisken, J., Swoger, J., Del Bene, F., Wittbrodt, J., and Stelzer, E.H.K., 2004, Optical sectioning deep inside live embryos by selective plane illumination microscopy, *Science* 305:1007–1009.

Klar, T.A., Jakobs, S., Dyba, M., Egner, A., and Hell, S.W., 2000, Fluorescence microscopy with diffraction resolution limit broken by stimulated emission, *Proc. Natl. Acad. Sci. USA* 97: 8206–8210.

Louie, A.Y., *et al*., 2000, *In vivo* visualization of gene expression using magnetic resonance imaging, *Nat. Biotechnol.* 18:321–325.

Sharpe, J., Ahlgren, U., Perry, P., Hill, B., Ross, A., Hecksher-Sørensen, J., Baldock, R., and Davidson, D., 2002, Optical projection tomography as a tool for 3D microscopy and gene expression studies, *Science* 296:541–545.

Shaw, P., 1989, Tilted view reconstruction in optical microscopy, *Biophys. J.* 55:101–110.

Siedentopf, H., and Zsigmondy, R., 1903, Über Sichtbarmachung und Grössenbestimmung ultramikroskopischer Teilchen, *Ann. Phys.* 10:1.

Stelzer, E.H.K., 1998, Contrast, resolution and the signal to noise ratio in fluorescence microscopy, *J. Microsc.* 189:15–24.

Stelzer, E.H.K., and Lindek, S., 1994, Fundamental reduction of the observation volume in far-field light microscopy by detection orthogonal to the illumination axis: Confocal theta microscopy, *Opt. Commun.* 111:536–547.

Swoger, J., Huisken, J., and Stelzer, E.H.K., 2003, Multiple imaging axis microscopy improves resolution for thick-sample applications, *Opt. Lett.* 28:1654–1656.

Voie, A.H., 2002, Imaging the intact guinea pig tympanic bulla by orthogonal-plane fluorescence optical sectioning microscopy, *Hearing Research*, 171(2):119–128.

Voie, A.H., Burns, D.H., and Spelman, F.A., 1993, Orthogonal-plane fluorescence optical sectioning: three-dimensional imaging of macroscopic biological specimens, *J Microsc.* 170:229–236.

Voie, A.H., and Spelman, F.A., 1995, Three-dimensional reconstruction of the cochlea from two-dimensional images of optical sections, *Comput. Med. Imaging Graphics*, 19(5):377–384.

Weninger, W.J., and Mohun, T., 2002, Phenotyping transgenic embryos: A rapid 3-D screening method based on episcopic fluorescence image capturing, *Nat. Genet.* 30:59–65.

38

Cell Damage During Multi-Photon Microscopy

Karsten König

INTRODUCTION

Conventional fluorescence microscopes are based on the excitation of exogenous and endogenous fluorophores by ultraviolet (UV) and visible (VIS) radiation. The fluorescence excitation radiation in non-laser microscopes is provided by high-pressure 50 W/100 W mercury lamps with typical emission lines at 365 nm, 505 nm, 436 nm, etc., and broadband 75 W xenon lamps. Most laser-scanning microscopes possess the argon (Ar)-ion laser at 364 nm, 488 nm, and 515 nm emission, the frequency-doubled and -tripled Nd:YAG laser at 532 nm and 355 nm, and the helium–neon (He-Ne) laser at 543 nm and 633 nm.

Typically, the radiation power of these microscopes is on the order of 10 to 100 µW. This corresponds to light intensities in the range of kilowatts per square centimeter when focused to diffraction-limited spots by objectives with a numerical aperture (NA) larger than 1. These light intensities are not sufficient to induce multi-photon effects.

In spite of the low radiation power, photodestructive effects occur. In particular, UVA radiation, including 365 nm lamp radiation, 364 nm argon laser radiation, and 337 nm laser radiation of a nitrogen laser has a relatively high damage potential compared to VIS radiation. Although not directly absorbed by DNA, UVA radiation may also induce DNA strand breaks (König *et al*., 1996a).

In contrast to one-photon fluorescence microscopes, multi-photon microscopes are based on the application of low energy photons in the near infrared (NIR) between 700 nm and 1200 nm. This spectral range is also called the "optical window of cells and tissues" where the one-photon absorption and scattering coefficients of unstained cells and tissues are relatively low and where the light penetration depth is high (Fig. 38.1). In the view of one-photon processes, most cells appear transparent and do not experience destructive effects due to the lack of efficient absorption. Exceptions are pigmented cells (e.g., cells containing melanin, hemoglobin, or chlorophyll) where linear absorption is likely to occur.

In the case of non-resonant two-photon absorption, NIR radiation may induce UVA effects — including photodamage — in particular when using wavelengths below 800 nm. However, the destructive UV effect is, in principle, confined to the tiny focal volume where the nonlinear absorption occurs and does not affect the out-of-focus regions.

When four photons or more are involved in the nonlinear process, ionization of the target combined with the formation of free or quasi-free electrons may occur. This can lead to optical breakdown and plasma formation. These multi-photon processes result in immediate photodamage.

Nonlinear effects such as non-resonant multi-photon absorption require high light intensities in the range from megawatts per square centimeter up to terawatts per square centimeter. In order to obtain such intensities, higher light powers than are used in one-photon microscopy are required. When using continuous wave (CW) NIR radiation, powers of at least 100 mW are necessary (Hänninen *et al*., 1994; König *et al*., 1995, 1996b). That means about 3 orders of magnitude higher power levels or more have to be applied in multi-photon microscopy.

Power levels in the range of 100 mW of NIR light have been used for optical micromanipulation of living cells using laser tweezers. In the case of multi-photon scanning microscopy for fluorescence imaging, such trapping effects may disturb the specimen.

In order to avoid trapping effects and to reduce the mean power, ultrashort laser pulses with kilowatts of peak power but a mean power in the microwatt and milliwatt range are commonly used in multi-photon microscopy.

Almost all multi-photon laser-scanning microscopes are based on the application of ultrashort laser pulses at high repetition rate. Because the multi-photon efficiency of an n-photon process depends on the peak power P according to a P^n relation, the use of pulsed laser beams enables efficient fluorophore excitation at a fast scanning rate.

The major application of multi-photon microscopes in life sciences involves the excitation of a variety of intracellular fluorescent probes that lack one-photon absorption bands in the NIR by the simultaneous absorption of two or three NIR photons (Denk *et al*., 1990). Typical two-photon and three-photon absorption cross-sections of these fluorophores are about 10^{-48} to 10^{-50} cm^4 s/photon and 10^{-75} to 10^{-84} cm^6 (s/photon)^2 (Xu *et al*., 1995; Maiti *et al*., 1997).

In a first approximation, the probability of two-photon absorption decreases with the distance d from the focal plane according to a d^{-4} relation. When using high-NA objectives and appropriate power levels, two-photon effects can be limited to a minute sub-femtoliter volume. By contrast, microscopy with UV or VIS lamp/laser light implies possible destructive effects by one-photon absorption in out-of-focus illuminated regions. This problem is often encountered in conventional confocal laser-scanning microscopy as well as in conventional intracellular laser surgery performed with pulsed UV and VIS laser beams (Berns, 1998; Greulich, 1999).

In particular, when studying thick 3D objects such as large cells, multi-cell aggregates, embryos, and tissues by optical sectioning, multi-photon microscopy with its tiny excitation volume can be the superior method compared to one-photon confocal scanning microscopy with its large excitation cones (Fig. 38.2).

Karsten König • Fraunhofer Institute of Biomedical Technology (IBMT), D-66386 St. Ingbert, Germany and University of the Saarland, Faculty of Mechatronics and Physics, D-66123 Saarbrücken, Germany

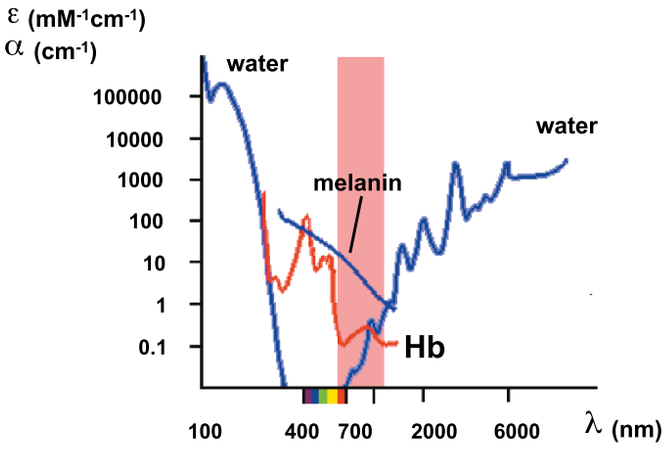


FIGURE 38.1. Absorption spectra of the cellular absorbers water, melanin, and hemoglobin. The range of low absorption and low scattering is from about 600 nm up to 1200 nm (optical window). At higher NIR wavelength, linear absorption of water increases and may induce destructive linear heating effects.

Multi-photon microscopy on living specimens can be performed without phototoxic effects under certain conditions. This has been demonstrated by long-term scanning experiments on (i) single hamster ovarian cells with a peak intensity of about 200 GW/cm^2, where laser exposure even for hours had no impact on cellular reproduction and vitality (König, 2000) as well as (ii) on living hamster embryos. The embryos were exposed for 24 h with NIR femtosecond laser pulses of a multi-photon fluorescence microscope without impact on embryo development in contrast to control studies performed with a conventional one-photon VIS laser scanning microscope (Squirrel *et al.*, 1999).

Nevertheless, NIR multi-photon microscopes can potentially induce undesirable destructive multi-photon effects by the high light intensity within the focal volume (König *et al.*, 2000; Diaspro and Robello, 1999). Indeed, an additional optical window exists for the safe, non-destructive observations of the specimens of interest. It is mainly defined by light intensity thresholds but also has a dependence on NIR wavelength. Outside this window, cells may undergo either (i) a photothermal damage in the case of pigmented cells, (ii) a slow destructive effect related to multi-photon

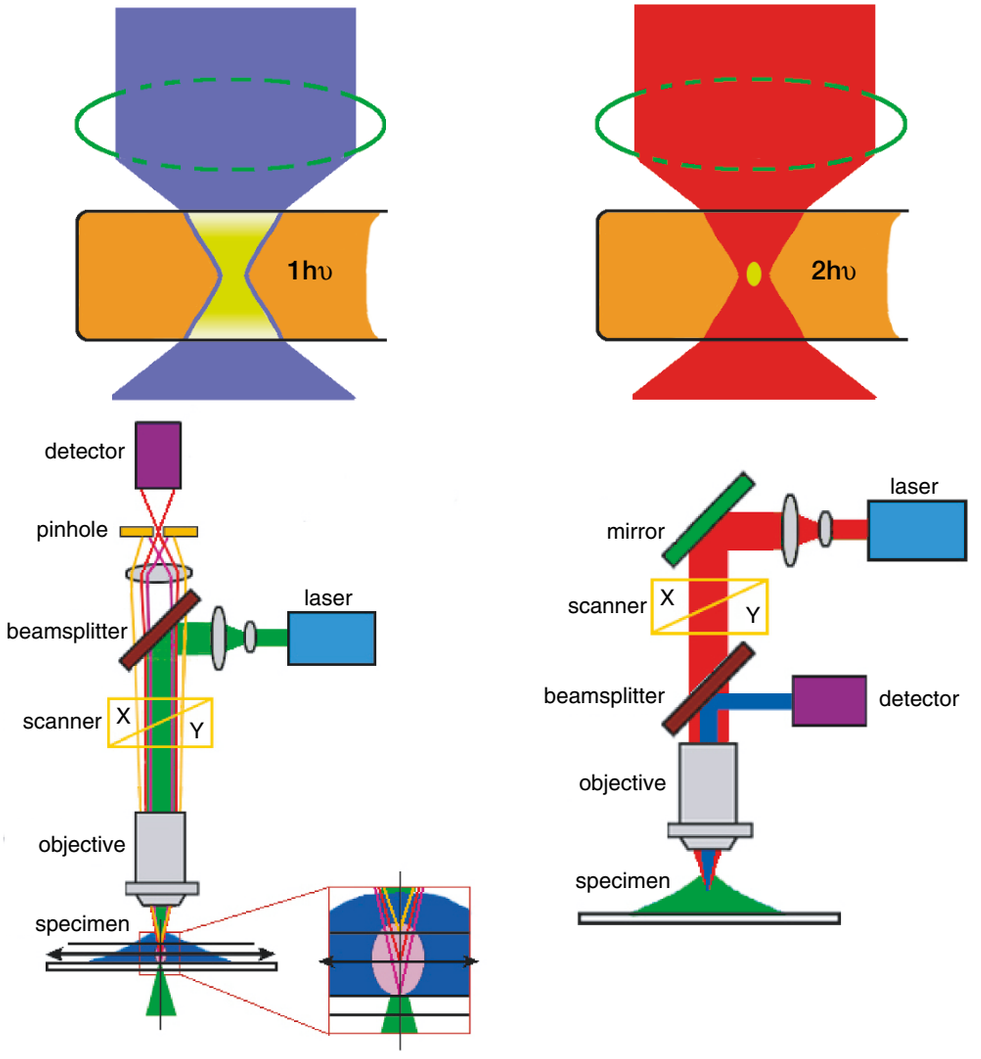


FIGURE 38.2. Scheme of one-photon excitation versus multi-photon excitation and corresponding scanning microscopes. Optical sectioning based on multi-photon excitation of fluorophores does not require spatial pinholes and can avoid out-of-focus photodamage/bleaching.

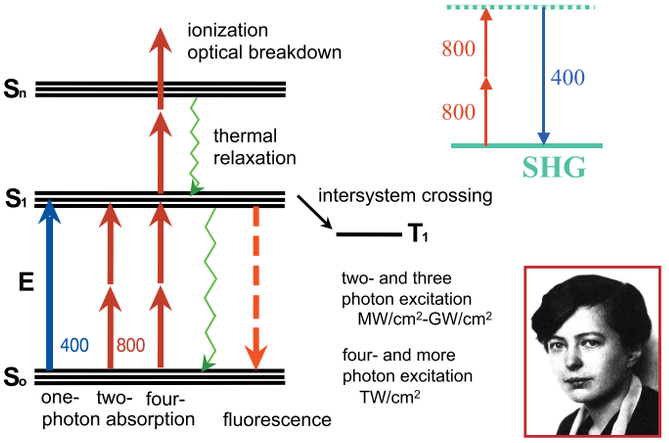


FIGURE 38.3. Two-photon effects with intense near-infrared radiation can induce visible fluorescence, second harmonic generation, and photochemical reactions. Photochemical reactions such as photo-oxidation processes may lead to slow photodestructive effects. When using laser intensities in the range of terawatts/cm^2, multi-photon ionization and plasma formation may occur that can result in immediate cell damage. Maria Göppert-Mayer predicted two-photon effects in her 1930 Ph.D. thesis.

excitation of cellular absorbers and subsequent cytotoxic photochemical reactions, or (iii) an instantaneous destructive opto-mechanical effect by optical breakdown phenomena and plasma formation due to multi-photon–mediated ionization of molecules (Fig. 38.3).

Interestingly, the highly localized destructive multi-photon effects can be used to realize precise, 3D nanoprocessing of biological structures such as cell membranes, intracellular organelles, and human chromosomes, as well as corneal and brain tissues. Therefore, multi-photon microscopes can also be used to knock out single mitochondria, to realize efficient targeted transfection (Tirlapur and König, 2002), and chromosome dissection as well as to perform intrastromal nanosurgery in eyes. Multi-photon–induced minimum cut sizes of 85 nm full-width at half-maximum (FWHM) have been realized in the human chromosome 1 using 80 MHz NIR nanojoule femtosecond laser pulses.

This chapter provides a review (i) of potential photo-induced effects that may cause cellular damage and (ii) the use of destructive multi-photon effects with nanojoule and sub-nanojoule femtosecond laser pulses for nanosurgery and gene technology.

PHOTOCHEMICAL DAMAGE IN MULTI-PHOTON MICROSCOPES

Absorbers and Targets in Biological Specimens

Photochemical damage can be induced by the nonlinear excitation of endogenous and exogenous absorbers followed by phototoxic reactions. These reactions include the formation of reactive oxygen species (ROS), which result in oxidative stress. A wide variety of endogenous cellular absorbers can be excited with multi-photon microscopes. Some of them are fluorescent and can be imaged by autofluorescence detection. Table 38.1 represents important naturally occurring endogenous absorbers in cells and tissues which can be excited with NIR radiation via two- or three-photon excitation processes.

For example, amino acids with a one-photon absorption maximum below 300 nm can be excited via a three-photon process with NIR photons. The reduced coenzymes NAD(P)H absorb intense NIR radiation in the 700 nm to 800 nm range by two-photon excitation. It is known from one-photon studies that excitation of amino acids as well as of NAD(P)H can induce irreversible DNA damage (Cunningham *et al.*, 1985; Tyrell and Keyse, 1990; Bertling *et al.*, 1996). Excitation of flavins, which can also be excited by a two-photon process, may also cause cell damage by the photo-induced production of H_2O_2 and its metabolites, which are hydroxyl radicals (Hockberger *et al.*, 1999).

In addition, the excitation of cellular porphyrins leads to the formation of ROS. Singlet oxygen is produced by a type II photo-oxidation process (photodynamic reaction). Metal-free porphyrins, such as coproporphyrin and protoporphyrin, are such efficient ROS producers that they are termed photosensitizers. As known from photodynamic porphyrin therapy, ROS formation in mitochondria often leads to apoptosis, whereas ROS formation in lysosomes or other organelles may induce either necrosis or apoptosis (Doiron and Gomer, 1985; Moor, 2000). Photodynamic reactions are also the major source of phototoxic response when using fluorescent markers or other exogenous absorbers.

Laser Exposure Parameters

In most experiments we have used compact solid-state 80 MHz titanium : sapphire lasers (Vitesse, Coherent; MaiTai, Spectra Physics) as turn-key laser sources; however, a tunable Ar-ion laser-pumped Mira system (Coherent) was employed for some of this work. The laser was coupled to an adapter module (JenLab GmbH, Jena, Germany) which consisted of a 1 : 5 beam expander, a step-motor driven beam attenuator, a fast photodiode for power measurements, a trigger pulse supply, a laser control unit, and a shutter. The expanded beam at tunable power was introduced into a modified laser-scanning microscope (LSM 410, Carl Zeiss Jena GmbH, Jena, Germany) with baseport detector (König, 2000) as well as into a compact scanning microscope where the galvoscanners were attached to the side port of an inverted Zeiss Axiovert microscope (TauMap, JenLab GmbH) (Ulrich *et al.*, 2004). The beam was focused to a diffraction-limited spot by conventional high-NA objectives. The typical NIR transmission of the objective was found to be 50%, whereas the overall transmission was typically

TABLE 38.1. Spectral Characteristics (One-Photon Maxima) of Important Endogenous Absorbers

Absorber	Absorption Maximum (nm)	Fluorescence Maximum (nm)
Water	1500, 1900, 2900	—
Hemoglobin	410, 540, 580, 760	—
Tryptophan	220, 280–290	320–350
NAD(P)H	340	450–470
Flavins	370, 450	530
Melanin	<300	575
PP IX	405, 505, 540, 575, 630	635

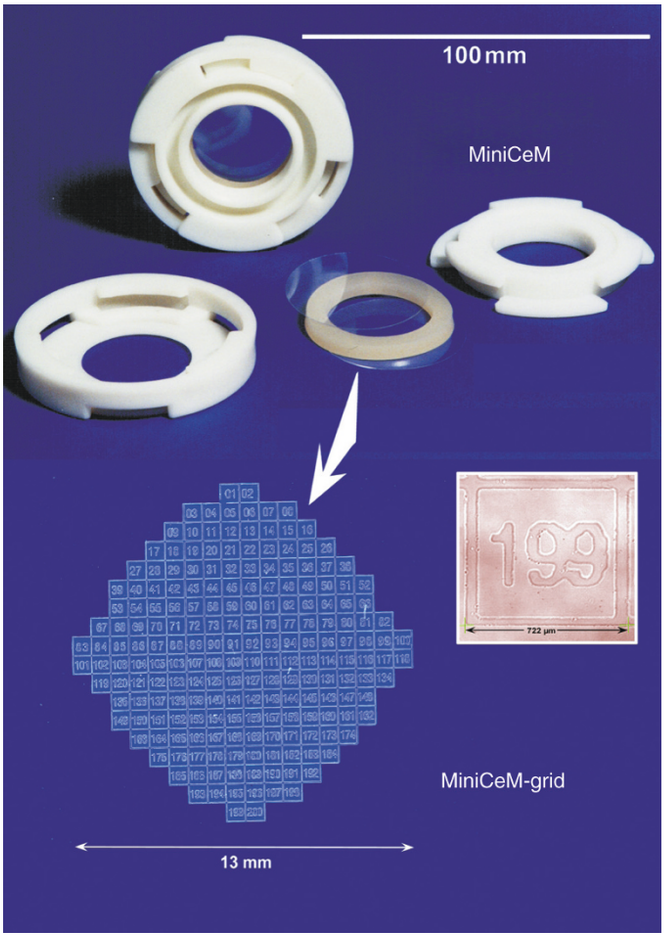


FIGURE 38.4. Cell chamber for high-resolution microscopy with two thin 170 µm thick glass windows with grid. Cells can grow as monolayers on the windows. Media and dyes can be added by injection through the gas-permeable silicone gasket.

in the range of 30%. When studying living cells, a closed microchamber made of two 170 µm thick glass windows (one with an etched grid) was used (MiniCeM-grid, JenLab GmbH) (Fig. 38.4).

We used three illumination modes: (i) scanning a 512 × 512 pixel area, (ii) scanning a defined region of interest (ROI), or (iii) single point exposure, where the beam is parked at pixels of interest within the living cell.

The high sensitivity of the baseport photomultiplier enabled the detection of two-photon excited intracellular fluorophores with high fluorescence quantum yield (e.g., DAPI and Hoechst) using a low mean power at the sample of from 25 µW to 1 mW at a frame rate of 1 Hz (512 × 512 pixels). More importantly, detection of endogenous fluorophores, such as fluorescent coenzymes, was possible with a mean excitation power of less than 2 mW at the specimen at appropriate NIR wavelengths.

The laser power after transmission through the whole microscope was measured in air using a Fieldmaster power meter with the two detector heads LM-2 and LM-3. In order to correct for the true photon flux through oil and the chamber window into the medium as well as for the limited detection angle of the power detector heads, correction values of 1.1 and 2.0 had been determined using a sandwich system (Fig. 38.5; König *et al.*, 1997a).

Optical dispersion results in pulse broadening during transmission through microscope optics. Typically, the pulse width at the sample was about 150 fs to 250 fs (König, 2000). At 10 mW mean power, the peak power and the peak intensities were 0.8 kW and 1.2×10^{12} W/cm^2 (1.2 TW/cm^2), respectively, assuming a FWHM beam size of $\lambda/2$ NA ≈ 310 nm. A typical beam dwell time (time of exposure per pixel) during one scan was about 30 µs, which resulted in a frame rate of 8 s/frame. At zoom setting 2, 512 × 512 pixels covered an area of 160 µm × 160 µm. For cell damage studies, typically one or more cells of interest were scanned 10 times in the same focal plane.

Evidence for Near Infrared-Induced Reactive Oxygen Species Formation

In order to know if multi-photon NIR laser-scanning microscopy with 80 MHz laser radiation above certain intensity levels is able to induce ROS formation and DNA breaks in living cells, we have performed extensive photodamage studies on PTK2 cells.

Using 170 fs laser pulses at 800 nm, we found that a mean power of ≥7 mW was sufficient to evoke ROS in PTK2 cells within a scanned region of interest. By contrast, no ROS formation was detected in the non-irradiated adjacent cells. As a ROS indicator, we used the fluorescent probe *Jenchrom px blue* (JenLab GmbH). The punctate fluorescence of the *Jenchrom* reaction product was found to be exclusively confined to the irradiated cells (Tirlapur *et al.*, 2001).

In addition, we have used the membrane-permeable dye dihydrofluorescein (DHF) for *in situ* detection of ROS (Hockberger *et al.*, 1999) in PTK2 cells. We exposed one half of the DHF-loaded PTK2 cells to 170 fs pulses at 800 nm using a mean power of 2, 5, 7, 10, 12, or 15 mW. There was virtually no DHF fluorescence in cells exposed to mean laser power of ≤5 mW. However, diffuse DHF fluorescence was exclusively present in cells exposed to a

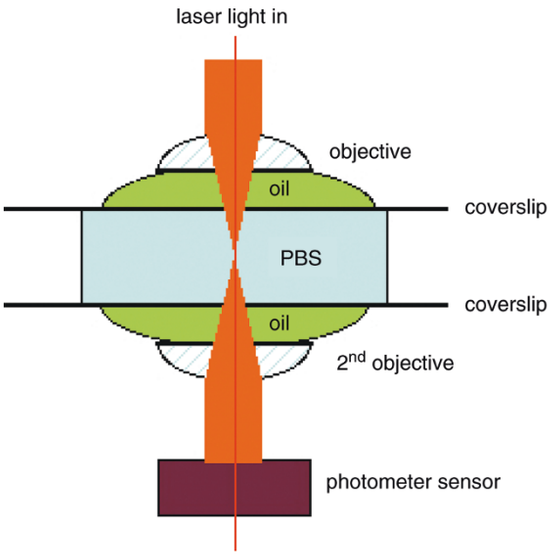


FIGURE 38.5. Diagram of the system used to measure the beam power actually reaching the specimen.

higher mean laser powers and was very intense in cells exposed to a mean laser power of 15 mW.

Evidence for Near Infrared-Induced DNA Strand Breaks

Shafirovich and colleagues (1999) have demonstrated *in vitro* that excitation of pBR322 supercoiled plasmid DNA with intense 810 nm NIR femtosecond laser pulses having a pulse width of 140 fs, a pulse repetition rate of 76 MHz and an average intensity of 1.2 mW/cm^2 (GW/cm^2 peak intensities) resulted in single strand breaks as a result of a simultaneous multi-photon absorption process.

Using the well-established TdT-mediated dUTP-nick end labeling (TUNEL) assay (Gavrieli *et al*., 1992; Negri *et al*., 1997), we have undertaken a more detailed *in situ* analysis of the effect of 800 nm NIR femtosecond laser pulses at different mean laser powers on DNA in unlabelled PTK2 cells. Cells were irradiated with the 800 nm (170 fs pulse duration) NIR scanning beam 10 times with a beam dwell time of ~60 or ~120 µs per pixel that corresponded to 16 or 32 s per frame of 512 × 512 pixels (at zoom setting 2) using mean powers of 2, 5, 10, and 20 mW.

Neither control PTK2 cells (not exposed to the 800 nm laser beam) nor those exposed to 2 to 3 mW mean power showed any TUNEL-positive green fluorescence in their nuclei. This indicates that lower mean laser powers do not induce any DNA strand breaks *in situ* and hence are not deleterious.

However, most of the PTK2 cells exposed to a mean power of 5 mW demonstrated TUNEL-positive green fluorescence, mostly in the nuclear area. When the mean laser power was increased to 10 or 15 mW, almost all of the cells had TUNEL-positive nuclei. When cells were exposed to 20 mW, green fluorescence was seen in all nuclei (Fig. 38.6).

The pattern of this green fluorescence, indicative of DNA strand breaks in cells exposed to high power NIR, is strikingly similar to that reported for apoptosis in other mammalian cells (Negri *et al*., 1997).

Our *in vivo* findings of NIR laser-induced DNA fragmentation is consistent and corroborates those of Shafirovich and colleagues (1999). Nuclear events during programmed cell death (apoptosis) are known to begin with the changes in the chromatin in the nuclear periphery (Tirlapur *et al*., 2000). Because the structural changes and DNA breaks in the nuclei of NIR-exposed cells seem quite similar to those occurring during apoptosis in different cell types (Negri *et al*., 1997; Bedner *et al*., 2000), it is therefore conceivable that NIR laser irradiation of PTK2 cells may under certain exposure conditions lead to apoptosis-like cell death.

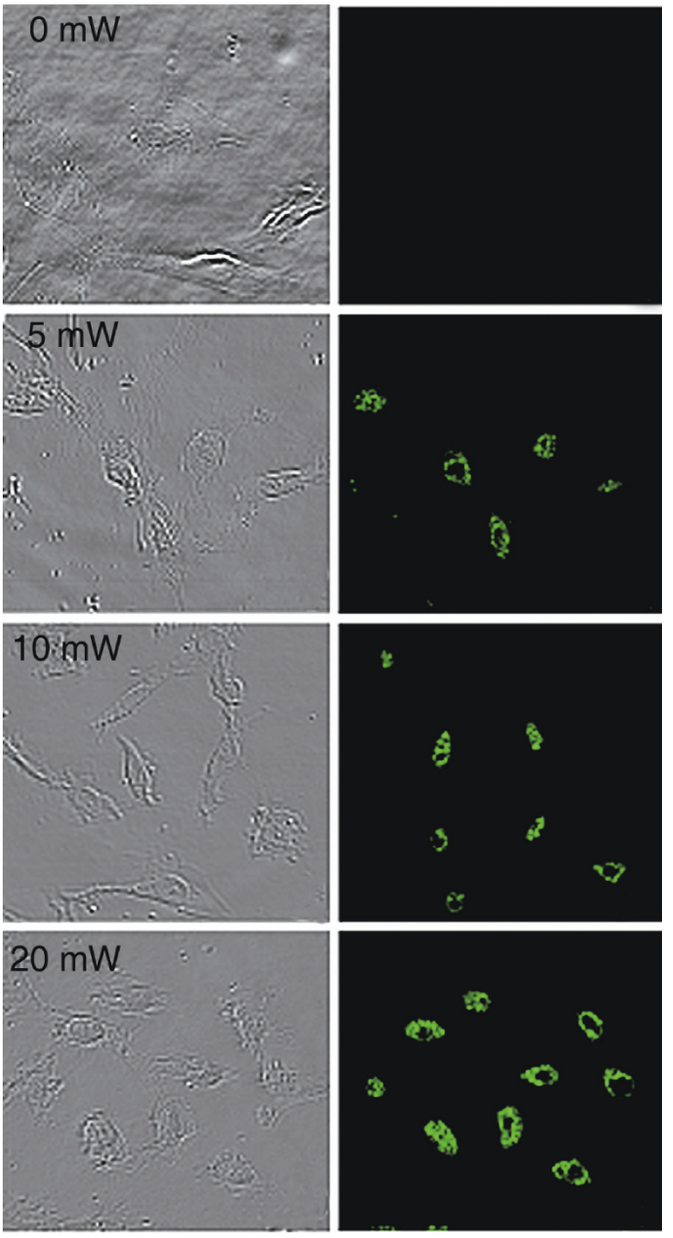


FIGURE 38.6. Evidence of DNA damage in PTK2 cells exposed to intense NIR femtosecond laser radiation. The green-colored fluorescein fluorescence images indicate TUNEL-positive and TUNEL-negative nuclei in dependence on mean laser power.

Photodynamic-Induced Effects

We studied the effect of two-photon excitation of porphyrins and their subsequent interaction with molecular oxygen. Light-excited porphyrin photosensitizers react with oxygen by a type II photo-oxidation process where energy transfer occurs from the metastable triplet state to molecular oxygen. This results in the formation of reactive singlet oxygen which induces cytotoxic effects.

In particular, we studied the effect of 780 nm-excited protoporphyrin IX that was synthesized in the mitochondria of Chinese hamster ovary (CHO) cells after external administration of the porphyrin precursor aminolevulinic acid (ALA, 1.5 mg/mL). Four hours after incubation, cells were exposed to 170 fs pulses at a mean power of 2 mW and a frame rate of 0.0625 s^{-1} (16 s/frame). This corresponds to a typical exposure time of ≈400 ms per scan on a single cell. Live/dead assays revealed lethal effects and fading of the red PP IX fluorescence in most of the cells after 100 scans in the same focal plane. Control cells without ALA could be scanned more than 700 times (up to 3 h) without affecting vitality (König *et al*., 1999b) (Fig. 38.7).

Nonlinear excitation of porphyrins can be used to induce desired photodynamic reactions in tumor tissue. The major advantages of NIR porphyrin photodynamic treatment are the excitation of higher order singlet states (Soret band excitation) and the high light penetration depth. Two-photon excitation can also be used to evoke type I photo-oxidation processes (charge transfer) (Fisher *et al*., 1997).

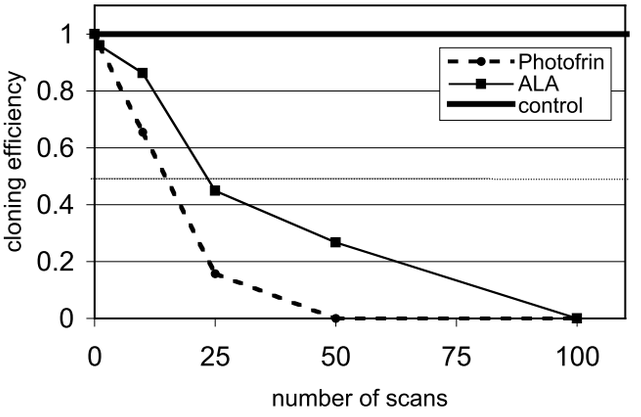


FIGURE 38.7. Impact of exogenous absorbers on reproduction of laser-exposed CHO cells. Two-photon induced photodynamic reactions lead to cell damage.

PHOTOTHERMAL DAMAGE

As we lack detailed knowledge of either the precise intracellular concentration, location, or NIR-absorption of the one-photon or multi-photon endogenous absorbers found in cells, we had to assume that water, with a typical absorption coefficient of less than $0.1\,cm^{-1}$, is the most important absorber in the optical window of non-pigmented cells and tissues. However, our studies using CHO cells exposed to femtosecond and CW lasers showed that the cell damage at 920 nm was less pronounced than that caused by 780 nm radiation even though water absorbs less at 780 nm. It therefore seems likely that the photodamage caused by intense femtosecond laser radiation is not based on linear water heating.

We measured a warming of only 1°K/100 mW in CHO cells exposed to CW 1064 nm microbeams at mW/cm^2 intensity and GJ/cm^2 fluence (Liu *et al*., 1995). The temperature measurements were performed by microspectrofluorometry. CHO cells were labeled with the thermosensitive, fluorescent membrane stain Laurdan, which manifests a red shift of the fluorescence maximum with increasing temperature. Calibration enabled the determination of a mean intracellular temperature with an accuracy of about 0.1°K. This is in line with temperature calculations for non-pigmented cells exposed to femtosecond and picosecond pulses, which predict only a slight, non-toxic increase in temperature (0.1°K/100 mW at 850 nm) (Schönle and Hell, 1998).

Nevertheless, pigmented cells such as erythrocytes and those containing melanin may undergo photothermal destruction. In the optical window of cells and tissues, the one-photon absorption coefficients of these pigments are much higher than that of water. Whereas the absorption of melanin decreases with increasing wavelength, the pigment hemoglobin has an absorption maximum in this spectral region. Reduced hemoglobin possess a 760 nm absorption band with a one-photon molecular absorption coefficient of about $1\,mM^{-1}cm^{-1}$. Our studies have shown that human erythrocytes ($\alpha \approx 30\,cm^{-1}$) exposed to 780 nm CW microirradiation at room temperature undergo hemolysis within 120 s when the power exceeds the value of 60 mW. A heating rate of about 60 °K/100 mW can be estimated from these experimental data. The heating rate decreased at wavelengths longer than 760 nm.

Interestingly, the photoinduced hemolysis studies revealed that femtosecond laser pulses at high repetition rate cannot simply be considered as quasi-CW beams. Damage may occur at a much lower mean power of pulsed radiation at high repetition frequency compared to power values of CW radiation. Using 130 fs pulses (76 MHz) at the same wavelength, a mean power of less than 10 mW was found to be sufficient to induce hemolysis (König *et al*., 1996c).

DAMAGE BY OPTICAL BREAKDOWN

The high transient powers, in particular in the kilowatt range, combined with submicron exposure spots result in enormous light intensities in the terawatt per square centimeter range. These can cause optical breakdown phenomena resulting in plasma formation and destructive thermomechanical effects. Optical breakdown induces immediate cell damage.

The threshold for optical breakdown decreases with the pulse width. In water, the threshold for 100 fs pulses was found to be 2 orders lower than for 6 ns pulses (Vogel *et al*., 1999). The primary cause for optical breakdown in the case of femtosecond pulses is efficient multi-photon absorption. Inverse Bremsstrahlung and collision processes are not dominant.

The onset of optical breakdown depends on the material. For some materials, femtosecond laser pulses at light intensities of about $0.1\,TW/cm^2$ are sufficient to induce optical breakdown. Optical breakdown and plasma formation is often accompanied by the occurrence of a nearly white luminescence and a complex subnanosecond emission decay (König *et al*., 1996d).

We have observed instantaneous white light luminescence and immediate damage of intracellular structures in CHO cells during scanning with 76 MHz, 170 fs pulses at mean powers higher than 10 mW. Interestingly, the optical breakdown occurred preferentially in the mitochondrial region and did not start in either the extracellular medium or the nucleus. Evaluation with the fluorescent live/dead fluorophore kit (calcein and ethidium homodimer from Molecular Probes, Inc., Eugene, OR) confirmed immediate death in scanned cells with extended plasma formation. However, when the phenomenon of optical breakdown was highly confined to a tiny perinuclear region, the cell often appeared to survive. At even higher laser powers, shockwave-induced morphological damage was manifested by total cell fragmentation (König *et al*., 1996d).

MODIFICATIONS OF ULTRASTRUCTURE

Our ultrastructural studies on CHO cells reveal that mitochondria are the major targets of NIR irradiation. Femtosecond laser exposure induced swollen mitochondria accompanied by loss of christae and the formation of electron dense bodies in the mitochondrial matrix (Oehring *et al*., 2000). In addition, the lumen of the endoplasmatic reticulum was enlarged. For a mean laser power of more than 12 mW at 800 nm, the complete destruction of mitochondria and their transformation to electron dense structures was observed (Fig. 38.8). At higher power levels, the outer membranes ruptured.

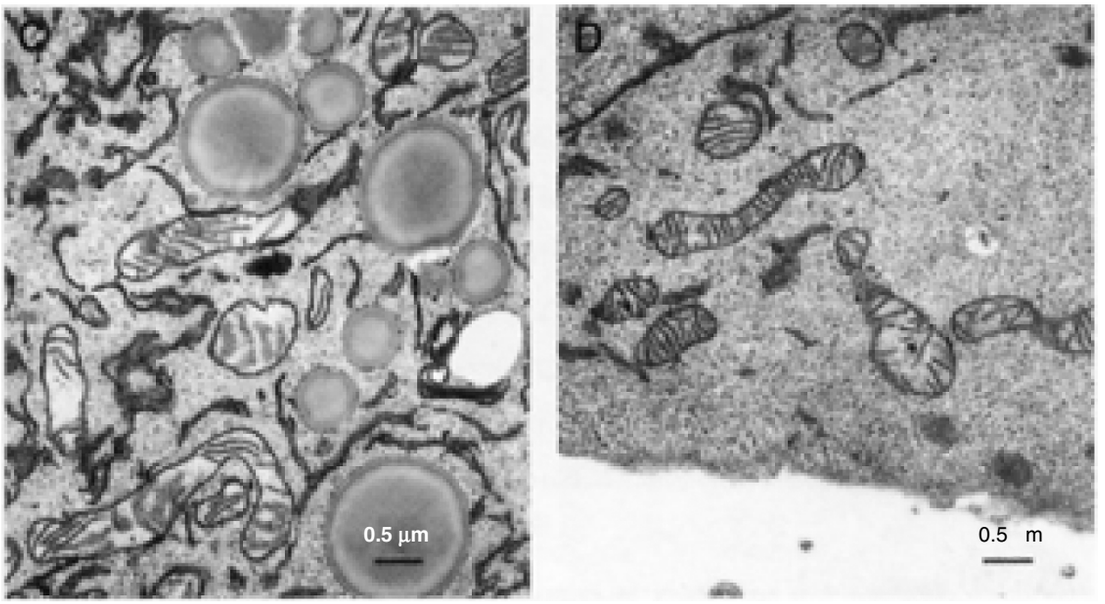


FIGURE 38.8. Electron microscopy reveals significant damage to mitochondria (left) as the major target of multi-photon microscopy. (Right) Control image of non-exposed cell.

INFLUENCE OF ULTRASHORT NEAR INFRARED PULSES ON REPRODUCTIVE BEHAVIOR

Squirrel and colleagues (1999) intermittently exposed Chinese hamster embryos for 24 h with femtosecond 1047 nm laser pulses of gigawatt per square centimeter peak intensity without impact on embryo development, in contrast to visible light exposure which the embryos did not survive. We have studied the influence of intense NIR exposure on the reproductive behavior of more than 3000 CHO cells. For that purpose, adherent CHO cells were maintained in a sterile cell chamber and exposed through the glass window. Following laser scanning, the cell division of the exposed cell as well as of its daughter cells was monitored up to 3 days. If the cell was not affected by the NIR light, division occurred every 12 h and the cell produced a clone of up to 64 cells within 3 days.

We found that CHO cells can be scanned with an 800 nm 80 MHz femtosecond laser beam at 2 mW mean power for hours without damage to the exposed cells and their derivatives. In particular we irradiated single CHO cells for a time period of 700 scans and 3 h, respectively (16 s/frame). However, at higher mean powers and intensities, a significant decrease in cloning efficiency occurred. In order to study the dependence on power, wavelength, and pulse width we used tunable laser beams which passed pulse stretching units based on prisms pairs and grating pairs. Typically, single CHO cells were scanned at microsecond pixel dwell times, 10 times in the same focal plane (König *et al*., 1997b, 1999a).

We found less damage at wavelengths in the 800 nm to 900 nm range compared to the 700 nm to 800 nm range. Interestingly, at the same average excitation power photodamage was found to be more pronounced in the case of femtosecond laser pulses compared to picosecond laser pulses (1–5 ps, same energy per pulse). At 780 nm, impaired cell division was found for 50% of the cells at 11 mW mean power (P_{50}) in the case of 2 ps pulses and at 3 mW for 240 fs pulses. CW scanning beams did not impair cellular reproduction up to 35 mW power. Using mean laser powers of <2 mW, CHO cells could be scanned with picosecond and femtosecond pulses for hours without impact on reproduction. This implies that below certain power (intensity) thresholds, "safe" multi-photon microscopy is possible.

When the P_{50} value is plotted against the square root of the pulse broadening, a nearly linear function is obtained (König *et al*., 1999a). This indicates that the photodamage process is likely based on a two-photon excitation process rather than on one-photon or three-photon events. This relationship was confirmed by Koester and colleagues (1999) based on calcium measurements in neocortical neurons in rat brain slices.

In order to compare photodamage in NIR multi-photon microscopes versus UV one-photon microscopes, the same cloning assay was performed on CHO cells using a 364 nm beam from a conventional Ar^+ laser scanning microscope. The 50% cloning efficiency was obtained at the low power of 4 µW. Therefore, UV-induced damage occurs at about 3 orders of magnitude lower power (4 µW) compared to the mean values of NIR femtosecond laser pulses (2–8 mW, 750 nm–800 nm).

NANOSURGERY

As pointed out in the section on photodamage by optical breakdown phenomena, the cell can survive if the damage induced by the high-intensity beam is confined to a minute subcellular volume. Exposure of a small region of interest including single spot exposure may therefore be useful for intracellular processing of biological material.

We increased the mean power in femtosecond laser microscopes with high numerical aperture objectives to values of 30 mW to 50 mW and light intensities of terawatts per square centimeter, respectively, to knockout intracellular material, to perform nanodissections (König *et al*., 1999c; König, 2000), and to "drill" holes.

By fine-tuning the laser power, only the central part of the beam spot provided sufficient intensity for material removal. Therefore, we were able to drill holes and to cut structures with a precision below the diffraction limit, that is, the cut size was below the size of the submicron beam spot.

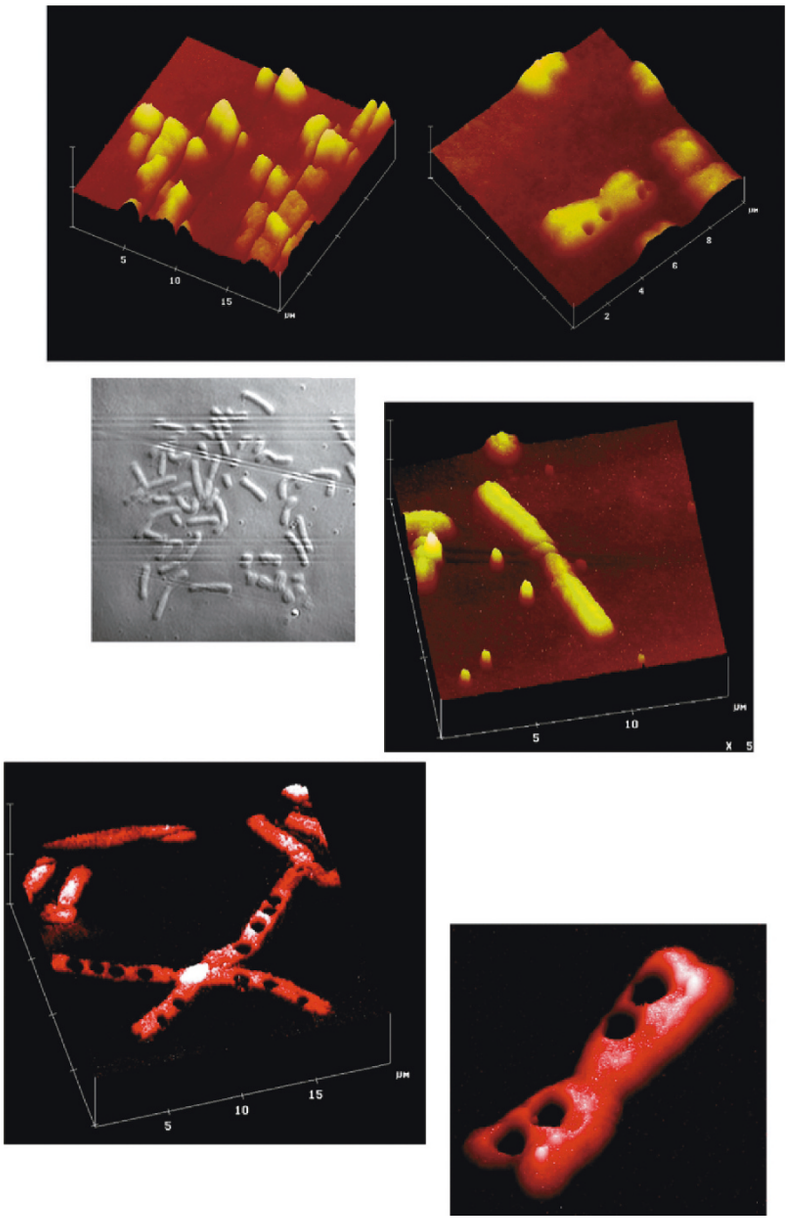


FIGURE 38.9. Nanoprocessing of human chromosomes with 80 MHz NIR femtosecond laser pulses at 800 nm.

For example, we used the multi-photon–induced ablation process to cut human chromosomes. Measurements with the atomic force scanning microscope reveal chromosome dissection with a FWHM cut size below 200 nm under conditions where the calculated Abbe diameter of the beam was ~600 nm. In addition, partial removal (incisions) of chromosome material with a precision of 110 nm and a FWHM of 85 nm was observed, which is likely the smallest laser cut ever performed in biological material. Figure 38.9 demonstrates examples of hole drilling and line cutting in human chromosomes.

Multi-photon laser microscopes can therefore be used as a noncontact nanoscalpel for surgery inside the cell, inside the cell nucleus, or even inside an organelle without affecting other cellular compartments. Indeed, we were able to cut chromosomes within a living PTK cell without loss of vitality. The cells finished cell division after laser surgery (Fig. 38.10) (König *et al*., 2005).

CONCLUSION

Multi-photon microscopes can be used in live-cell fluorescence microscopy at moderate laser powers apparently without damaging the target. Repeated scanning of the biological object of investigation over extended time periods is possible without affecting reproductive behavior or producing lethal effects.

Above certain intensity thresholds, which depend on laser wavelength and pulse width, apoptosis-like gradual cell damage by two-photon photochemistry may occur. When studying pigmented cells and tissues, such as erythrocytes or skin with a high amount of melanin, photothermal damage has to be considered. Immediate damage occurs at high light intensities in the range of a terawatt per square centimeter by optical breakdown phenomena. Plasma-induced ablation can be used for intracellular nanosurgery. Femtosecond lasers at high repetition rate and low

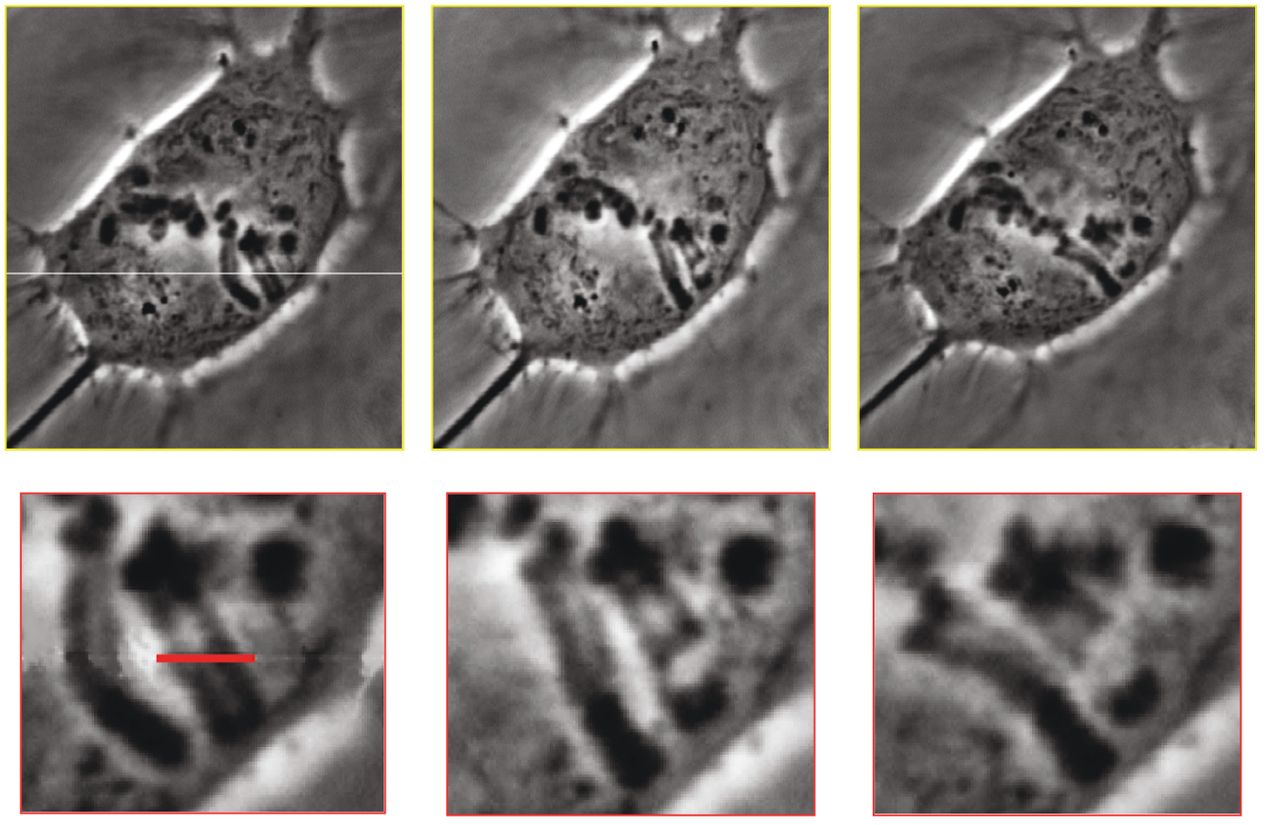


FIGURE 38.10. Intracellular chromosome dissection within a living PTK cell.

pulse energies of 0.1–10 nJ provide novel tools for laser nanomedicine (König *et al.*, 2005).

Meanwhile, the first femtosecond clinical laser imaging device, DermaInspect (JenLab GmbH) is in clinical use. The system is based on a tunable 80/90 MHz Ti:sapphire laser and operates in the safe optical window with low <10 mW laser power on the human skin for cancer diagnosis and *in situ* screening of pharmaceutical and cosmetic compounds (König and Riemann, 2003; König *et al.*, 2006).

ACKNOWLEDGMENTS

We thank I. Riemann (Fraunhofer IBMT, St. Ingbert) for her support in multi-photon microscopy, H. Oehring (Jena University) for his assistance with electron microscopy, and U. K. Tirlapur for the common studies on DNA damage. The authors are grateful to Peter So (MIT) and E. Gratton (University of Illinois) in whose laboratories the first damage studies by femtosecond laser pulses were performed. The work was in part supported by grants from the German Science Foundation (DFG), the Federal Ministry of Education, Science, Research and Technology (BMBF), the Ministry of Science, Research, and Culture of the state of Thuringia, Zeiss Jena, Coherent, and JenLab GmbH.

REFERENCES

Bedner, E., Smolewski, P., Amstad, P., and Darzynkiewicz, Z., 2000, Activation of caspases measured *in situ* by binding of fluorochrome-labeled inhibitors of caspases (FLICA): Correlation with DNA fragmentation, *Exp. Cell Res*. 259:308–313.

Berns, M.W., 1998, Laser scissors and tweezers, *Sci. Am*. 278:62–67.

Bertling, C.J., Lin, F., and Girotti, A.W., 1996, Role of hydrogen peroxide in the cytotoxic effects of UVA/B radiation on mammalian cells, *Photochem. Photobiol.* 64:137–142.

Cunningham, M.L., Johnson, J.S., Giovanazzi, S.M., and Peak, M.J., 1985, Photosensitised production of superoxide anion by monochromatic (290–405 nm) ultraviolet irradiation of NADH and NADPH coenzymes, *Photochem. Photobiol*. 42:125–128.

Denk, W., Strickler, J.H., and Webb, W.W., 1990, Two-photon laser scanning microscope, *Science* 248:73–76.

Diaspro, A., and Robello, M., 1999, Two-photon excitation of fluorescence in three-dimensional microscopy, *Eur. J. Histochem*. 43:169–178.

Doiron, D.R., and Gomer, C.J., 1984, *Porphyrin Localisation and Treatment of Tumours*, Alan R. Liss, New York.

Fisher, W.G., Partridge, W.P., Dees, C., and Wachter, E.A., 1997, Simultaneous two-photon activation of type I photodynamic therapy agents, *Photochem. Photobiol*. 66:141–155.

Gavrieli, Y., Sherman, Y., and Ben-Sasson, S.A., 1992, Identification of programmed cell death *in situ* via specific labelling of nuclear DNA fragmentation, *J. Cell Biol*. 119:493–501.

Greulich, K.O., 1999, *Micromanipulation by Light in Biology and Medicine*, Birkhäuser, Basel, Switzerland.

Hänninen, P.E., Soini, E., and Hell, S.W., 1994, Continuous wave excitation two-photon fluorescence microscopy, *J. Microsc*. 176:222–225.

Hockberger, P.E., Skimina, T.A., Centonze, V.E., Lavin, C., Chu, S., Dadras, S., Reddy, J.K., and White, J.G., 1999, Activation of flavin-containing oxidases underlies light-induced production of H_2O_2 in mammalian cells, *Proc. Natl. Acad. Sci. USA* 96:6255–6260.

König, K., 2000, Invited review: Multiphoton microscopy in life sciences, *J. Microsc*. 200:83–104.

König, K., and Riemann, I., 2003, High resolution multiphoton tomography of human skin with subcellular spatial resolution and picosecond time resolution. *J. Biomedical Optics.* 8:432–439.

König, K., Becker, T.W., Fischer, P., Riemann, I., and Halbhuber, K.J., 1999a, Pulse-length dependence of cellular response to intense near-infrared laser pulses in multiphoton microscopes, *Opt. Lett*. 24:113–115.

König, K., Krasieva, T., Bauer, E., Fiedler, U., Berns, M.W., Tromberg, B.J., and Greulich, K.O., 1996a, Cell damage by UVA radiation of a mercury microscopy lamp probed by autofluorescence modifications, cloning assay, and comet assay, *J. Biomed. Opt*. 1:217–222.

König, K., Liang, H., Berns, M.W., and Tromberg, B.J., 1995, Cell damage by near-IR microbeams, *Nature* 377:20–21.

König, K., Liang, H., Berns, M.W., and Tromberg, B.J., 1996b, Cell damage in near-infrared multimode optical traps as a result of multiphoton absorption, *Opt. Lett*. 21:1090–1092.

König, K., Liang, H., Kimel, S., Svaasand, L.O., Tromberg, B.J., Krasieva, T., Berns, M.W., Halbhuber, K.J., So, P.T.C., Mantulin, W.W., and Gratton, E., 1997a, Cell damage in UVA and cw/femtosecond NIR microscopes, *SPIE Proc*. 2983:37–44.

König, K., Riemann, I., and Fischer, P., 1999b, Photodynamic therapy by non-resonant two-photon excitation, *SPIE Proc*. 3592.

König, K., Riemann, I., Fischer, P., and Halbhuber, K.J., 1999c, Intracellular nanosurgery with near-infrared femtosecond laser pulses, *Cell Mol. Biol*. 45:195–201.

König, K., Simon, U., and Halbhuber, K.J., 1996c, 3D resolved two-photon fluorescence microscopy of living cells using a modified confocal laser scanning microscope, *Cell Mol. Biol*. 42:1181–1194.

König, K., So, P., Mantulin, W.W., Tromberg, B.J., and Gratton, E., 1997b, Cellular response to near-infrared femtosecond laser pulses in two-photon microscopes, *Opt. Lett*. 22:135.

König, K., So, P.T.C., Mantulin, W.W., Tromberg, B.J., and Gratton, E., 1996d, Two-photon excited lifetime imaging of autofluorescence in cells during UVA and NIR photostress, *J. Microsc*. 183:197–204.

König, K., Riemann, I., Stracke, F., and LeHarzic, R., 2005, Nanoprocessing with nanojoule femtosecond laser pulses, *Med. Laser Appl.* 10:1016.

Koester, H.J., Baur, D., Uhl, R., and Hell, S.W., 1999, Ca2+ fluorescence imaging with pico- and femtosecond two-photon excitation: Signal and photodamage, *Biophys. J.* 77:2226–2236.

Liu, Y., Cheng, D., Sonek, G.J., Berns, M.W., Chapman, C.F., and Tromberg, B.J., 1995, Evidence for localised cell heating induced by near-infrared optical tweezers, *Biophys. J*. 68:2137–2144.

Maiti, S., Shear, J.B., Williams, R.M., Zipfel, W.R., and Webb, W.W., 1997, Measuring serotonin distribution in live cells with three-photon excitation, *Science* 275:530–532.

Moor, A.C.E., 2000, Signaling pathways in cell death and survival after photodynamic therapy, *J. Photochem. Photobiol*. 57:1–13.

Negri, C., Donzelli, M., Bernardi, R., Rossi, L., Bürkle, A., and Scovassi, I.A., 1997, Multiparametric staining to identify apoptotic human cells, *Exp. Cell Res*. 234:174–177.

Oehring, H., Riemann, I., Fischer, P., Halbhuber, K.J., and König, K., 2000, Ultrastructure and reproduction behaviour of single CHO-K1 cells exposed to near-infrared femtosecond laser pulses, *Scanning* 22:263–270.

Schönle, A., and Hell, S., 1998, Heating by absorption in the focus of an objective lens, *Opt. Lett*. 23:325–327.

Shafirovich, V., Dourandin, A., Luneva, N.P., Singh, C., Kirigin, F., and Geacintov, N.E., 1999, Multiphoton near-infrared femtosecond laser pulse-induce DNA damage with and without the photosensitizer proflavine, *Photochem. Photobiol*. 68:265–274.

Squirrel, J.M., Wokosin, D.L., White, J.G., and Bavister, B.D., 1999, Long-term two-photon fluorescence imaging of mammalian embryos without compromising viability, *Nat. Biotechnol.* 17:763–767.

Tirlapur, U.K., and König, K., 2002, Targeted transfection by femtosecond laser, *Nature* 418:290–291.

Tirlapur, U.K., König, K., Peuckert, C., Krieg, R., and Halbhuber, K.J., 2001, Femtosecond near-infrared laser pulses elicit generation of reactive oxygen species in mammalian cells leading to apoptosis-like death, *Exp. Cell Res*. 263:88–97.

Tyrell, R.M., and Keyse, S.M., 1990, The interaction of UVA radiation with cultured cells, *J. Photochem. Photobiol*. 4:349–361.

Ulrich, V., Fischer, P., Riemann, I., and König, K., 2004, Compact multi-photon/single photon laser scanning microscope for spectral imaging and fluorescence lifetime imaging, *Scanning*. 26:217–225.

Vogel, A., Nahen, K., Theisen, D., Birngruber, R., Thomas, R.J., and Rockwell, B.A., 1999, *Appl. Phys. B* 68:271.

Xu, C., Guild, J., Webb, W.W., and Denk, W., 1995, Determination of absolute two-photon excitation cross sections by in situ second-order autocorrelation, *Opt. Lett*. 20:2372–2374.

39

Photobleaching

Alberto Diaspro, Giuseppe Chirico, Cesare Usai, Paola Ramoino, and Jurek Dobrucki

INTRODUCTION

Thanks to the wide variety of applications, fluorescence microscopy is now one of the most popular imaging techniques in biology (Weber, 1960; Lakowicz, 1999; Periasamy, 2001; Michalet *et al.*, 2003; Tsien, 2003; Bastiens and Hell, 2004; Taroni and Valentini, 2004; Diaspro *et al.*, 2005). Fluorescence microscopy utilizes fluorescently labeled probes of high biochemical affinity to image the molecular composition and dynamics of biological structures. Moreover, the use of probes that change their fluorescence properties in response to specific physiological parameters enables one to analyze the physiological state of cells or tissues (Birks, 1970; Emptage, 2001; Zhang *et al.*, 2002; Lippincott-Schwartz and Patterson, 2003; Stephens and Allan, 2003). Fluorescence is highly specific either as an exogenous label (e.g., 4′,6-diamidino-2-phenylindole (DAPI) bound to DNA) or an endogenous tracker [(e.g., autofluorescence of NADH, or visible fluorescent proteins such as green fluorescent protein (GFP)] providing spatial and functional information through precise photophysical properties such as absorption, emission, lifetime, and anisotropy. Furthermore, sample preparation is relatively simple, allowing non-invasive imaging and three-dimensional (3D) mapping within cells and tissues to be achieved by means of computational optical sectioning, confocal laser-scanning microscopy (CLSM), and two-photon excitation microscopy (TPEM) (Periasamy, 2001). In particular, CLSM and TPEM are two comparatively recent fluorescence microscopy techniques that have improved the quality of biological images (Wilson and Sheppard, 1984; Denk *et al.*, 1990; Pawley, 1995a; Diaspro, 2002, 2004; Matsumoto, 2002; Amos and White, 2003).

The main value of both CLSM and TPEM is their ability to produce optical section images through very thick biological specimens, such as embryos or tissue slices. As these images exclude optical information from out-of-focus planes, they can be combined to make a 3D reconstruction of the specimen (Kriete, 1992; Bonetto *et al.*, 2004). The ability of fluorescence microscopy to detect specific molecules at very low concentrations depends strictly on the performance of fluorophores used. Fluorescent dyes featuring high extinction coefficients, high quantum yields, and large Stokes shift are now widely available. However, one must remember that their photostability is another attribute of crucial importance. In CLSM, where the fluorescence signal is collected from only a thin layer of the sample, the laser beam must be intense enough to obtain an adequate signal to form an image with a good signal-to-noise ratio in a reasonable scan time. Under these imaging conditions, the fluorescence emitted is often observed to decrease substantially with time, a phenomenon referred to as photobleaching. This shows that in CLSM the photostability problem can have a severe impact on the image formation process. Even in TPEM, despite the tight confinement of the excitation volume and the use of infrared light, the high peak power of the laser pulses may cause photodamage of the fluorescent probes being used (Brakenhoff *et al.*, 1996; Mertz, 1998; Patterson and Piston, 2000; Dittrich and Schwille, 2001; Konig and Tirlapur, 2002). In general, the loss of fluorescence that comes along with photobleaching has the undesirable effect of reducing the signal-to-noise ratio and the quality of the collected images and data (Pawley, 1995b).

On the other hand, it is worth noting that photobleaching has been exploited since the mid-1970s (Peters *et al.*, 1974; Poo and Cone, 1974; Edidin *et al.*, 1976; Axelrod *et al.*, 1976) for producing valuable information about biological system dynamics and the advent of GFPs (Tsien, 1998) has led to renewed interest in photobleaching experiments including the utilization of selective photobleaching for information encoding (Cole *et al.*, 1996; White and Stelzer, 1999; Reits and Neefjes, 2001; Davis and Bardeen, 2002; Braeckmans *et al.*, 2003; Braga *et al.*, 2004; Delon *et al.*, 2004; Stavreva and McNally, 2004; Straub, 2003). Fluorescence recovery after photobleaching (FRAP) and fluorescence loss in photobleaching (FLIP) are the most popular photobleaching-based techniques (McNally and Smith, 2002) and are technically based on the ability of the confocal and multi-photon microscopes to confine photobleaching to an arbitrary pattern or region of interest. Unfortunately, the mechanism of photobleaching during confocal or multi-photon imaging is not fully understood and some aspects still remain obscure, even in the case of very popular molecules such as fluorescein in solution (Song *et al.*, 1995).

As lack of signal limits the precision of most fluorescent techniques and as bleaching and phototoxicity limit the available signal, we feel that photobleaching is one of the most important factors restraining future developments in all these fields. Although we are not yet in the position of being able to develop dyes that do not bleach, any attempt to do so must start with an effort to assemble what we know so far. This chapter attempts to do just that. We will attack this topic using both microscopic imaging and single-molecule studies under confocal and multi-photon excitation conditions.

Alberto Diaspro • LAMBS-IFOM/MICROSCOPIO, Department of Physics, University of Genoa, Genoa, Italy, and The National Institute for the Physics of Matter, Italy
Giuseppe Chirico • University of Milano Bicocca, Milan, Italy, and The National Institute for the Physics of Matter, Italy
Cesare Usai • National Research Council (CNR), Genoa, Italy
Paola Ramoino • University of Genoa, Genoa, Italy
Jurek Dobrucki • Cell Biophysics Division, Jagiellonian University, Gronostajowa 7, 30-387 Krakow, Poland

 Handbook of Biological Confocal Microscopy, Third Edition, edited by James B. Pawley, Springer Science+Business Media, LLC, New York, 2006.

PHOTOBLEACHING

Fluorescence emitted by almost all fluorescent dyes fades during observation. This phenomenon is called photobleaching or dye photolysis[1] and involves a photochemical modification of the dye resulting in the irreversible loss of its ability to fluoresce. Even though, in some cases, a fluorescent molecule can be switched on again after an apparent loss of emission ability or from a natural initial dark state (photocycling) or is able to switch on and off by itself (blinking) within a short timescale, we refer to photobleaching as an irreversible phenomenon.[2] This point is particularly relevant in FRAP and FLIP because these techniques are rigorously based on the idea that fluorescence recovers only because fluorescent molecules diffuse into the bleached sample volume. In this case, it is even more important to be clear that the photobleached state cannot be reversed.

Apart from this warning, we focus now on how photobleaching affects the image formation process. Indeed, fluorescent dyes in the excited state may undergo chemical or biochemical reactions that lead to their rapid degradation and destruction and consequent loss of image quality during measurement. In a certain sense, fluorophores are consumed by being observed. When fluorescent molecules are illuminated at a wavelength for which they exhibit a "good" cross-section (Weber and Teale, 1958; Chen and Scott, 1985; Tsien and Waggoner, 1995; Harper, 2001; Xu, 2002), possibly close to the cross-section maximum, there is a shift from the ground energy level (S) to the singlet-excited energy level (S*). Such a temporary excess of energy can be dissipated by the emission of fluorescence, or in radiationless processes such as internal conversion and intersystem crossing to the excited triplet state (T*). The decay times from S* and T* to S are different according to the selection rules, and are of the order of 1 to 10 ns and 10^{-3} to 10^{-6} s, respectively.

However, a molecule in the excited singlet or triplet state can also undergo a permanent structural change that often annihilates its ability to fluoresce, thereby becoming a photobleached molecule. Many factors, such as the molecular environment and the intensity of excitation light, may affect the mechanism, and thus the reaction order and the rates of photobleaching (Bernas *et al.*, 2004). In fact, spatial variability in the photobleaching process has been demonstrated within individual cells (Benson *et al.*, 1985). Figure 39.1 demonstrates an example, where Acridine Orange bound to DNA and RNA (green fluorescence and red luminescence,[3] respectively) of the same cell bleaches at different rates. This dye binds to double-stranded nucleic acids by intercalation, while stacks are formed on single-stranded nucleic acids. Apparently these two forms of the same dye exhibit different photostability under the same illumination conditions.

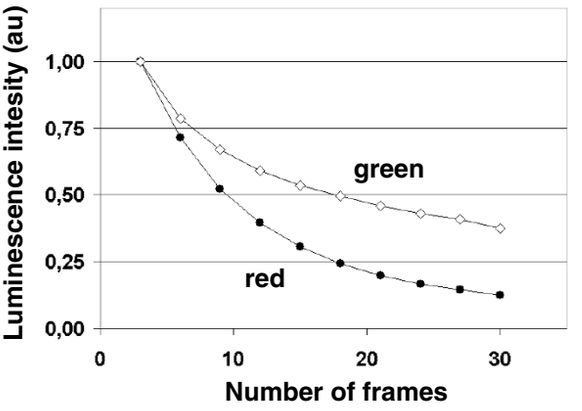


FIGURE 39.1. Loss of luminescence intensity of Acridine Orange bound to DNA in the nucleus and RNA in the cytoplasm of a fixed human fibroblast during acquisition of subsequent confocal frames. The initial intensities of luminescence in two areas of nucleus and cytoplasm were normalized. Images collected on Bio-Rad MRC1024, simultaneous excitation 488 nm, 0.5 mW at the specimen, dichroics 527DRLP, 565DRLP, emission filters 540/30nm and RG630, lens 60× NA 1.4 PlanApo (Zarebski and Dobrucki, unpublished; see also Dobrucki and Darzynkiewicz, 2001; Bernas *et al.*, 2004, 2005, for further information on the kinetics of this process and the way to minimize the differential photobleaching).

Figure 39.2 shows a similar effect obtained using two-photon excitation in the picosecond regime. Even if the sample is relatively thin, significant photobleaching occurs under two-photon excitation after delivering a larger dose of light.

Photobleaching Mechanisms

Many phenomena, such as self-quenching or fluorescence (or Förster) resonance energy transfer (FRET), are known to affect the amount of light emitted by an excited fluorescent molecule. The manner in which these processes reduce the fluorescence intensity is relatively well understood. In contrast, photodestruction is still a poorly understood phenomenon and few data are available on the bleaching properties of most common fluorophores. Dye photolysis is a very complex process.

Several theories have been proposed to explain photobleaching. The main causes seem to involve photodynamic interactions between excited fluorophores and molecular oxygen (O_2) in its triplet ground state and dissolved in the sample media. If the dye has a relatively high quantum yield for intersystem crossing, a significant number of dye molecules may cross from a singlet excited state S* to the long-lived triplet excited state T*, a process that permits these molecules to interact with their environment for a much longer time (milliseconds instead of nanoseconds). Interactions between O_2 and dye triplets may generate singlet oxygen according to $T^* + {}^3O_2 \rightarrow S + {}^1O_2$. Singlet oxygen has a longer lifetime than the excited triplet states of the dyes. Moreover, several types of damaging oxygen free radicals can be created when it decays. A fluorophore in the excited triplet state is also highly reactive and may undergo irreversible chemical reactions involving other intracellular organic molecules. All these chemical reactions depend both on the intracellular singlet oxygen concentration and on the distance between the dye and intracellular components such as proteins, lipids, etc. Therefore, the number of photons emitted before a dye molecule is destroyed depends both on the nature of the dye molecule itself and on its environment.

[1] Photobleaching is the process whereby a molecule is rendered non-fluorescent. This may be caused by photolysis (lysis, breaking open) or other mechanisms such as bonding of excited fluorophores to nearby molecules. Photo-oxidation describes the first stage of many such processes.

[2] We should also note here another confusing parameter. If a macromolecular target is over-labeled in the sense of being bound to more than the optimal number of dye molecules, then they may tend to quench each other and so reduce the total emission. Under these conditions, bleaching some dye molecules may actually increase total light output from the preparation because the bleached molecules no longer quench.

[3] Because the red component of Acridine Orange (AO) emission has a long time component, it is more properly called luminescence. In a single-beam confocal, only the fast component is seen because the signal can only reach the PMT for a few microseconds.

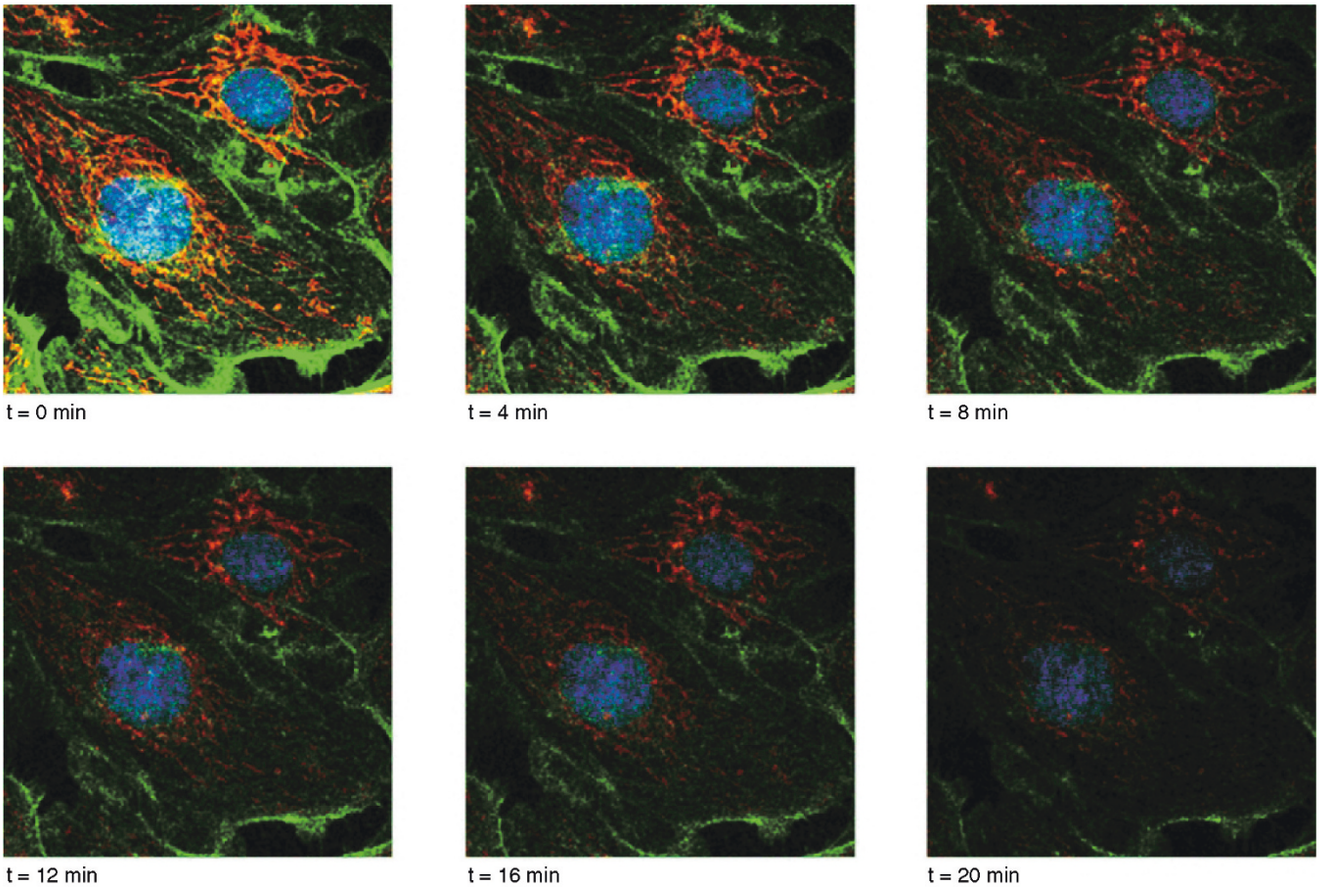


FIGURE 39.2. Loss of fluorescence intensity of three probes, bound to DNA (DAPI, blue), mitochondria (MitoTracker Red CMXRos, red), and actin filaments (BODIPY-FL phallacidin, green) in fixed bovine pulmonary artery endothelial (BPAE) cells. Two-photon excitation was provided by a Leica TCS SP2 AOBS confocal microscope coupled to a Chameleon-XR (Coherent, Santa Clara, CA) ultrafast tunable titanium–sapphire laser through the IR port. Pulse width was increased to picoseconds from 140 fs, 760 nm wavelength, 20 mW average power at the entrance of the scanning head. Temporal series was acquired at a rate of 729 ms per image every 6 s. Image dimensions are 512 × 512 pixels over a 79.76 × 79.76 μm^2. (Images collected by Paolo Bianchini, LAMBS-MicroScoBio, University of Genoa, http://www.lambs.it.)

Some fluorophores have a very short useful lifetime, fading after the emission of only a few hundred photons, whereas other molecules in other surroundings can emit a very large number of photons (tens of millions) before being bleached. If a dye is protected from reaction with environmental molecular oxygen, the observed rate of photobleaching is lower (Bernas *et al.*, 2004). This occurs naturally in GFP (Tsien, 1998), where the intrinsic chromophore is positioned in the core of a β-barrel structure (Ormo *et al.*, 1996).

In addition, either multi-photon events or the absorption of a second photon by a molecule already in an excited state may also be involved in the photobleaching of some dyes. Because of the low absorption cross-section and its quadratic dependence on the incident power, multi-photon excitation requires an excitation intensity several orders of magnitude higher than that needed for one-photon excitation. Unfortunately, this increases photobleaching because of the high probability of photochemical degradation in the long-lived triplet state and the interplay of multi-photon ionization processes (Dittrich and Schwille, 2001; Michalet *et al.*, 2003).

On the other hand, as excitation only takes place in a tightly confined volume of the sample, bleaching away from the plane of focus is essentially eliminated and the overall photobleaching and photodamage within the whole sample is usually less (Bianco and Diaspro, 1989; Denk *et al.*, 1990; Diaspro, 2004). Moreover, the tightly controlled excitation volume can allow very precise control of intentional photodamage that might be used for uncaging or even microsurgery when needed (Diaspro *et al.*, 2003; Chapter 38, *this volume*).

Until now, the photochemical reactions responsible for the photobleaching have been investigated in greatest detail for the dye fluorescein. Bleaching can be described in terms of a photobleaching quantum efficiency Q_b, defined as the ratio between the number of molecules that have been bleached and the total number of photons absorbed during the exposure period. The average number of photons emitted before a dye molecule bleaches is the ratio between the fluorescence quantum yield Q_f of the dye and Q_b. At excitation intensities of 10^{23} to 10^{24} photons $cm^{-2} s^{-1}$, approximately corresponding to 1 mW of power incident on a spot of 0.25 μm radius at 488 nm wavelength (Schneider and Webb, 1981), fluorescein bleaches with a $Q_b \approx 3 \times 10^{-5}$. Therefore, during its useful lifetime the average fluorescein molecule dissolved in water emits 30,000 to 40,000 photons before being permanently bleached (Hirschfeld, 1976; Mathies and Stryer, 1986; Tsien and Waggoner, 1995).

Both the experiments and the mathematical models used to investigate the behavior of free and bound fluorescein have demonstrated that, in fluorescence microscopy, its photobleaching cannot be described by a single-exponential process. However, the single-exponential process is appropriate for the special case when the photobleaching reaction is primarily between the triplet state of the dye and molecular oxygen (Hirschfeld, 1976; Song *et al.*, 1995).

Although quenching of the triplet excited state (that forms a semi-oxidized radical form of the dye) by mercaptoethylamine restores fluorescein molecules to their singlet ground state, and reduces photobleaching (Song *et al.*, 1996), there is no general agreement on the energy states involved in photobleaching. In single-molecule detection conditions, evidence of a two-step photolysis has been reported for several coumarin and rhodamine derivatives (Eggeling *et al.*, 1998). These authors suggest that excited triplet states T_n, higher in energy than T*, can occur when two, distinct, successive photon absorptions occur at high irradiance. Excitation at low irradiance yields longer survival times because, at any instant, fewer molecules are in the T* state to be excited to T_n (Eggeling *et al.*, 1998; Deschenes and van den Bout, 2002).

Fluorescence correlation spectroscopy has been used to measure and characterize the photobleaching of rhodamine 6G and FITC in different solutions (Widengren and Rigler, 1996; Delon *et al.*, 2004).

The high photon flux used in two-photon excitation microscopy seems to lead to higher-order photon interactions. The dependence of fluorescence intensity and photobleaching rate on excitation power have been studied for Indo-1, NADH, and aminocoumarin under one- and two-photon excitation (Patterson and Piston, 2000). The results of these studies suggest that higher-order photobleaching is common in two-photon excitation microscopy. Therefore, the advantage of reduced photobleaching associated with the limited excitation volume, characteristic of TPEM in thick samples, is offset by greater in-focus damage, making the technique less suitable for studying thin specimens. A comparison of photobleaching effects under single- and multi-photon excitation has been performed in plant cells (Kao *et al.*, 2002). At the laser intensities used to study chloroplasts in the protoplasts from *Arabidopsis thaliana*, the photobleaching cross-section under two-photon excitation is low, requiring the high peak power levels common in TPEM. This generates greater localized photobleaching effects than using conventional excitation (Kao *et al.*, 2002). However, reducing specimen exposure allows one to obtain significantly more signal by multi-photon than by one-photon excitation in high-resolution optical sectioning of thick samples (Drummond *et al.*, 2002). In addition, the use of phase-optimized, shaped pulses in two-photon excitation microscopy has been demonstrated to attenuate the photobleaching of a GFP variant by a factor of 4 (Kawano *et al.*, 2003).

Intrinsically fluorescent proteins such as the phycobiliproteins (PBP) generate reactive oxygen species (ROS) in living cells. Photoactivation of R-phycoerytrin, C-phycocyanin, and allophycocyanin by visible light results in the generation of both singlet oxygen and superoxide. This contributes to both the photobleaching and the phototoxicity of PBPs *in vivo* (He *et al.*, 1997). In addition, flavins and flavoproteins excited to a triplet state by violet-blue light can be reduced by endogenous cellular reducing agents, resulting in the production of H_2O_2 in cultured mouse, monkey, and human cells (Hockberger *et al.*, 1999). However, imaging the same cells by TPEM at 1047 nm did not induce measurable production of H_2O_2 (Hockberger *et al.*, 1999). Although the molecular oxygen present in the surrounding environment does not interact directly with the chromophore of GFP, photoactivation is thought to generate endogenous singlet oxygen, which induces damage to this chromophore, as demonstrated in transfected COS7 kidney cells and *E. coli* bacteria (Greenbaum *et al.*, 2000). In BY-2 tobacco cells loaded with oxidation-sensitive dyes, excitation light induces the production of ROS. The amount of ROS increases if the cells express an intrinsically fluorescent protein that absorbs the excitation light (Dixit and Cyr, 2003). This process results in an increase in mitotic arrests and shows a nonlinear relationship to the excitation light intensity (Dixit and Cyr, 2003). The role of molecular oxygen in phototoxicity exerted by extracellular fluors has been demonstrated in animal and plant cells (Dobrucki, 2001). The involvement of oxygen in photobleaching processes is supported by data, which demonstrate that anoxia significantly reduces photobleaching rates of propidium and chromomycin A_3 bound to DNA (Bernas *et al.*, 2004).

Apart from fluorescent proteins, nonlinear multi-photon excitation in the near-infrared of a variety of endogenous absorbers, such as water and NAD(P)H, can induce the formation of ROS resulting in oxidative stress (Konig and Tirlapur, 2002).

Reducing Photobleaching

The prevention of the fading of fluorescence emission intensity is very important not only for quantitative microscopy but also for obtaining high-quality images. Unfortunately, reducing photobleaching by decreasing the excitation time or by lowering the excitation intensity leads to a reduction of the fluorescence signal. As lower signal increases the effect of Poisson noise and obscures low-contrast features, deciding on the optimal excitation level is always a trade-off in which ideally one reduces the light dose until one can no longer see the details one needs to understand. Optimizing the excitation intensity can be beneficial in 3D imaging (Bernas *et al.*, 2004).

A good strategy starts with the selection of a fluorophore with the high photostability. Figure 39.3 (A,B) shows a comparison of the results of photobleaching of four fluorescent probes associated with chromatin in different preparations of fixed HeLa cells. The probes differ in molecular structures and mechanisms of binding to chromatin. The same dose of light delivered at similar photon fluxes resulted in dramatically different loss of fluorescence signal [Fig. 39.3(A)] and a different number of total photons recorded (Fig. 39.3(B)]. The choice of the best fluorophore is not trivial, however. In this example, one might draw the conclusion that propidium, a DNA intercalator, is the best choice for imaging chromatin. In fact, eGFP fused with histone H2B gave the best results in this experiment because eGFP yielded reasonable images even at an excitation photon flux of 0.17 W/cm^2, where photobleaching was negligible. Thus, the total number of photons emitted by GFP before bleaching was the greatest. The other probes tested required higher intensities of excitation light, bleached at greater rates and provided less total photons (Bernas *et al.*, 2004).

As molecular oxygen is one of the main actors in photobleaching, deoxygenating the specimen often improves the survival period of both the dye and the cell. In living cells or tissues that tolerate anoxia, or even hypoxia, oxygen may be removed by bubbling N_2 through the media or by using biological oxygen scavengers (Bloom and Webb, 1984; Dobrucki, 2001). Chemicals capable of quenching singlet oxygen can also be employed to reduce the effects of photobleaching. Carotenoids such as as crocetin and etretinate are good singlet oxygen quenchers in cell cultures (Kohen *et al.*, 1986; Reyftmann *et al.*, 1986; Manitto

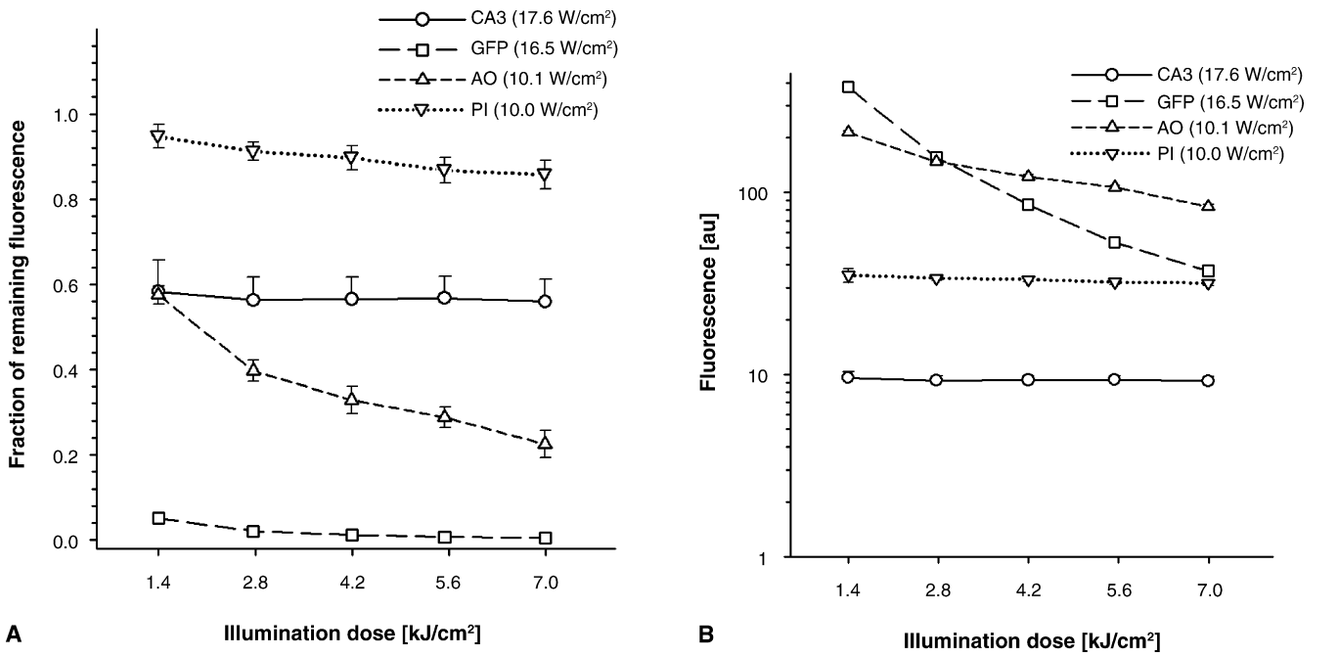


FIGURE 39.3. Loss of signal of four fluorescent probes bound to chromatin due to photobleaching by exciting light. Fraction of fluorescence remaining (A) and the total number of photons detected per one pixel (dwell time 13.3 µs; B) after delivering increasing doses of excitation light is shown for propidium (PI), Acridine Orange (AO, green fluorescence of intercalated monomers), chromomycin A_3 (CA3), and eGFP fused to histone H2B. The conditions of the experiment are described elsewhere (Bernas *et al.*, 2004, 2005).

et al., 1987). Other oxygen-reactive protective molecules include vitamin E analogues, vitamin C, reduced glutathione, imidazole, cysteamine, and the amino acid histidine (Tsien and Waggoner, 1985).[4]

Figure 39.4 compares the photobleaching kinetics of propidium bound to the DNA of fixed human fibroblasts, equilibrated with air or argon, as a function of the excitation dose in the range from 0 to 50 kJ/cm^2 and it shows that argon lessens signal loss resulting from photobleaching. Figure 39.5 shows the fraction of fluorescence that remains unbleached after the same type of cells have received the same total dose of light at different photon fluxes in the range from 1 to 111 W/cm^2, respectively. It demonstrates how a given dose of illumination causes less bleaching when delivered at a low photon flux, or under argon (Bernas *et al.*, 2004). Figure 39.6 shows the potential of anoxic imaging in protecting fluorescence and facilitating collection of full 3D datasets (after Bernas *et al.*, 2004).

Other common antifade reagents are diazabicyclo-2,2,2-octane (DABCO), *n*-propyl gallate and *p*-phenylenediamine. 2-mercaptoethylamine is used mainly when observing chromosome and DNA specimens stained with propidium iodide, Acridine Orange, or chromomycin A_3.

Although the anti-fade agents, whose effects are diagrammed in Figure 39.7, are highly efficient in retarding photobleaching, each has side effects. One of the most effective antifade reagents, *p*-phenylenediamine (PPD), suffers from thermosensitivity, autofluorescence, and cell toxicity, making it unsuitable for *in vivo* studies (Bock *et al.*, 1985; Krenik *et al.*, 1989). *N*-propyl gallate (NPG) is both photo- and thermostable. While not as effective as PPD, it can be used for *in vivo* studies. However, although NPG is very effective in retarding bleaching in FITC-stained Reh6 cells, it reduces the initial value of fluorescence intensity both in conventional epi-fluorescence and in confocal microscopy (Souchier *et al.*, 1993). Comparing NPG with other anti-fading agents, these authors conclude that the choice of an anti-fading medium depends on the desired results: a slower decay of fluorescence combined with initial quenching versus a faster photobleaching rate but starting at a higher initial emission intensity.

An extensive comparison among different homemade and commercial anti-fading media has been performed by CLSM in NIH 3T3 cells stained with FITC-phalloidin (Ono *et al.*, 2001). These authors use the equation $EM_t = (EM_0 - B)e^{-t/A} + B$, where EM_t is the emission intensity at time t, B the background intensity, and A the anti-fading factor, that is, the time spent until fluorescence intensity decays to $1/e$ of EM_0. As a general rule, for the media examined (SlowFade and ProLong, Molecular Probes, Inc., Eugene, OR; PermaFluor, Lipshaw/Immunon, Pittsburgh, PA; FluoroGuard, Bio-Rad Labs, Hercules, CA), and in agreement with Souchier and colleagues, they found that high initial emission intensities are accompanied by faster decreases of fluorescence. With bright and photostable molecules, such as the Alexa dyes (Landon, 1997), media that include an anti-fading agent are a good choice, even if they have a lower initial fluorescence intensity.

Very recently, a new family of synthetic nanoparticle fluorophores has been introduced. They mainly consist of a core of cadmium selenide coated with zinc sulfide. These nanocrystals, named Quantum Dots (Quantum Dot Corporation, Hayward, CA) have a large Stokes shift and are very bright and photostable (Hines

[4] To be effective as radical scavengers, these agents must be used at concentrations high enough to be incompatible with live-cell studies. Even cells that do seem to not die in terms of popular viability assays often suffer other types of damage that may affect their physiology sufficiently to preclude acquisition of relevant information. See also Chapter 38, *this volume*.

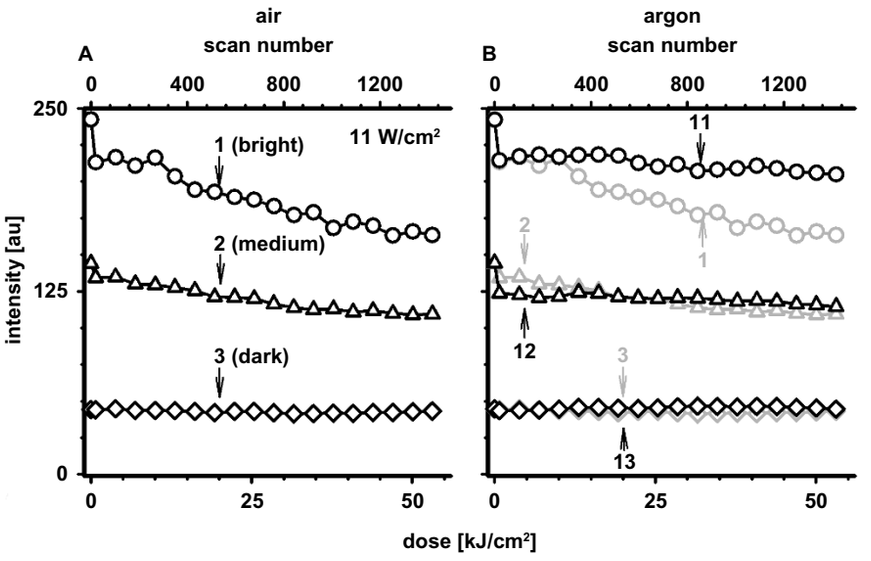


FIGURE 39.4. Kinetics of photobleaching of propidium bound to DNA, in air or argon. Intensity (0–250 a.u.) versus dose (0–50 kJ/cm^2). Fixed cells were stained with propidium, and equatorial sections scanned with the laser in a confocal microscope under air (A) or argon (B). Twenty scans were accumulated to form one image, and the average intensity (arbitrary units; a.u.) of pixels of different initial brightness in images is plotted relative to the accumulated dose of light. The flux of the incident light is indicated. (A) Bright pixels (curve 1) are bleached more rapidly than darker ones (curves 2, 3). Curves for only three of the 25 brightness classes are shown for clarity. The results are the means of five experiments. (B) Argon lessens photobleaching. Curves 1 to 3 from (A) are included for comparison with their counterparts (i.e., 11–13) in argon (after Bernas *et al.*, 2004).

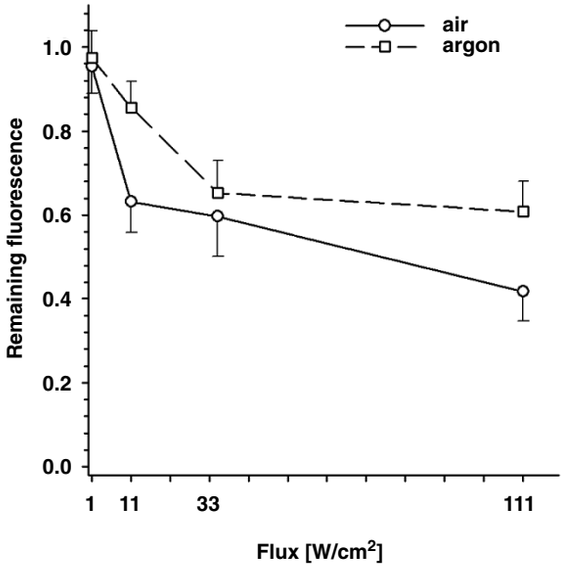


FIGURE 39.5. Analysis of photobleaching of propidium bound to DNA in air and argon. The fraction of fluorescence remaining after exposure to the same total dose of exciting light, but delivered by laser beams of different photon fluxes. Laser intensity was adjusted using neutral density filters and the total time of illumination was adjusted to deliver the same total light dose to each sample. Error bars: 95% confidence intervals (after Bernas *et al.*, 2004).

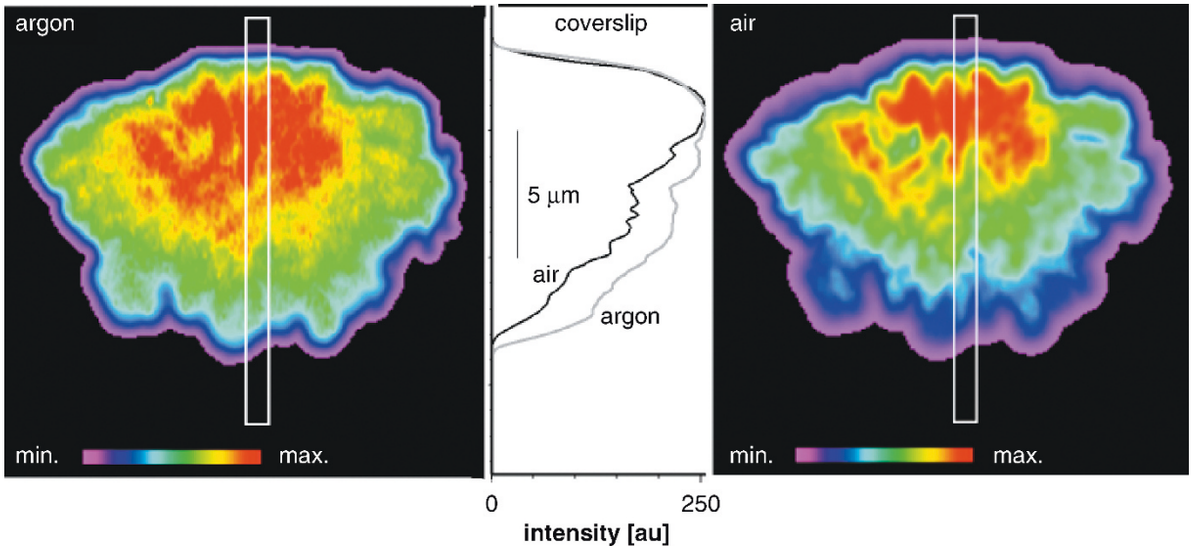


FIGURE 39.6. An *xz*-projection from 3D images collected in argon (left) or in air (right) of chromatin in a cell in mitosis, with condensed chromosomes stained with propidium. Sixty-nine consecutive images were collected at a 330 nm *z*-spacing using an average excitation flux of 11 W cm^{-2} in the focal plane and starting near the coverslip. Maximum intensity projections (right and left) and fluorescence (center) measured along the white vertical bar. The intensity drops off more rapidly as one moves away from the coverslip under air because of increased photobleaching (after Bernas *et al.*, 2004).

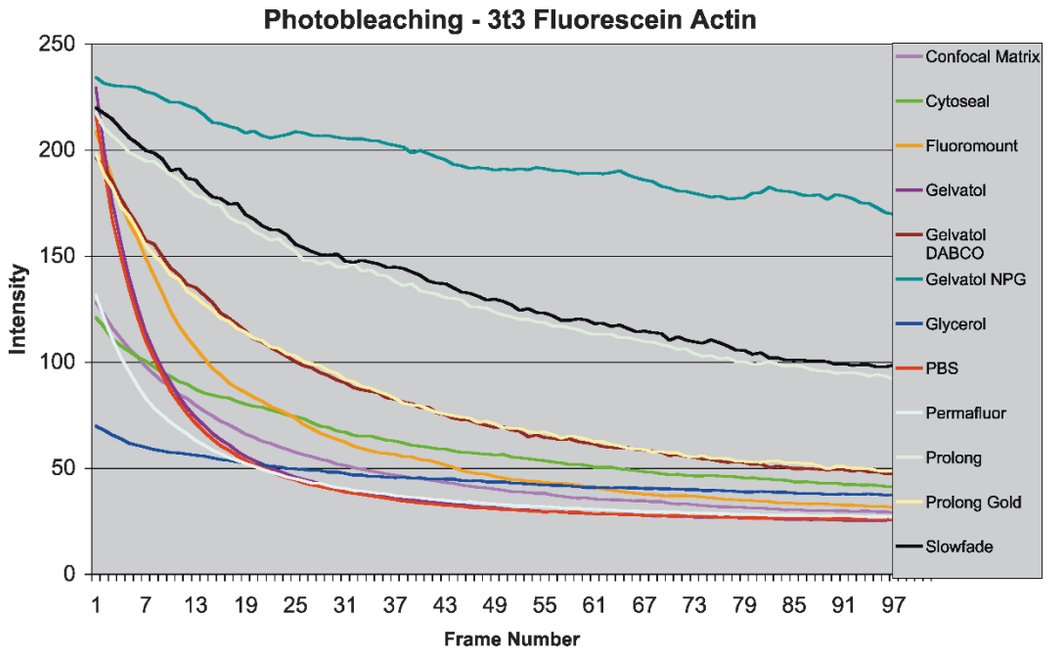


FIGURE 39.7. Loss of fluorescence intensity due to photobleaching in similar samples submerged in physiological saline or in mounting media supplemented with various commercial anti-fade agents. The efficiency of countering photobleaching and a loss of the initial signal varied widely among different formulations. Samples: fixed FoLu lung fibroblasts, actin stress fibers stained with phalloidin-fluorescein. (Data kindly provided by M.W. Davidson.)

and Guyot-Sionnest, 1996; Mattoussi *et al.*, 2000; Watson *et al.*, 2003; Jaiswal and Simon, 2004). A surface polymer layer enables conjugation of Quantum Dots to antibodies and other biomolecules (Wu *et al.*, 2003), allowing the development of new immunofluorescence protocols that take advantage of their fluorescent properties (Ness *et al.*, 2003). Quantum Dots allow multicolor imaging in demanding biological environments such as in living animals or organs and within cellular cytoplasm (Sokolov *et al.*, 2003; Larson *et al.*, 2003; Jaiswal and Simon, 2004). These fluorescent probes exhibit two-photon cross-sections of the order of thousands of Goeppert-Meyer units (GM), (1 GM = 10^{-50} cm^{4}s/photon) and a wide range of emission wavelengths (Diaspro *et al.*, 2005). They should be good candidates for deep, multi-color imaging in biological and medical applications (Sokolov *et al.*, 2003; Voura *et al.*, 2004). On the other hand, some problems in using Quantum Dots relate to their relatively large size and mass, their intermittent fluorescent behavior, their high propensity for aggregation, and the fact that their high cross-section and relatively long singlet-state lifetime, cause them to reach singlet-state saturation at relatively low power levels in scanned-beam microscopy.

PHOTOBLEACHING AT THE SINGLE-MOLECULE LEVEL

Any single-molecule spectroscopy experiment stops when the probe molecule photobleaches. This limitation becomes crucial when the time scale of the biological process under examination is comparable to the survival time for the molecule itself (Deschenes and van den Bout, 2002). In certain matrices and at low temperature, photobleaching can be delayed almost indefinitely (Basché, 1998). However, under usual laboratory conditions (room temperature, in atmosphere) each molecule can emit a finite, though sometimes very large (Deschenes and van den Bout, 2002), number of photons.

Single-molecule photobleaching can be defined as a permanent transition to a dark electronic state that occurs typically after N ~ 10^6 to 10^8 photon absorption events. This implies a few seconds of observation at an average emission of 10^6 fluorescence photons/second, and leads to significant signal-to-noise challenges for single-molecule spectroscopists.

In fluorescence laser scanning microscopy, excitation volumes range from 0.1 to 1 μm^3. For molecular concentrations of about 100 n*M* to 1 μ*M* (i.e., similar to that of most of the protein systems in cells), the number of fluorescent emitters in the excitation volume varies from 10 to 1000. This number lies between the single-molecule and the bulk level. Fading of images of cells and tissues under repeated imaging in fluorescence CLSM or TPEM, can be ascribed to: (1) a change in the number of fluorophores present (single-molecule bleaching), (2) a variation of the fluorescence quantum yield, and (3) a change in the fluorescence emission dynamics (single-molecule blinking).

The first mechanism leads to photobleaching when viewed at the bulk level. The second mechanism can be due to chemical reactions (e.g., photo-induced protonation/deprotonation) or to photo-induced transitions to other electronic states. At the bulk level, an overall decrease in the fluorescence quantum yield can also be due to an increase in the rate of reversible transitions between a bright and a dark state of the individual molecules, a phenomenon known as blinking. All these situations may lead to a decrease in overall fluorescence emission under imaging conditions.

In general, blinking characteristic times usually occur on a time scale of 1 to 100 ms, but they can also extend to much longer intervals. Fluorescence emission can sometimes recover after minutes to hours making it difficult to discriminate between permanent bleaching and blinking.

Photobleaching of Single Molecules

Not much data and few systematic studies are available on single-molecule photobleaching, a process that is usually characterized, at the time resolution of CLSM or TPEM, by a steep drop of the fluorescence emission to the background level. The observation of such a sharp transition is indeed used as a fingerprint of the single-molecule emission and has been used to discriminate single-molecule spots in fluorescence images from those representing aggregates (Chirico *et al.*, 2001, 2002; Diaspro *et al.*, 2001; Maher *et al.*, 2002; Cannone *et al.*, 2003). Photobleaching also affects other single-molecule spectroscopic approaches such as surface-enhanced resonant Raman spectroscopy, a process recently highlighted by Maher and colleagues (2002).

The photophysical origin of single-molecule photobleaching has been investigated on several dyes used for microscopy. One of the first attempts at a systematic study dealt with a series of four dyes, pyrene, rhodamine 6G fluorescein and indo-1, spread by spin-coating on a chemically etched glass (see details in Chirico *et al.*, 2001, 2003).[5] For the two-photon excitation used in the study, the authors found a power law dependence of the bleaching rate on the excitation power with an exponent ≈2.5. This finding proved that increasing the excitation power does not imply a gain in the total fluorescence photon flux. Because the fluorescence emission depends on the second power of the excitation intensity, the dependence of the total number of photons emitted versus the excitation intensity, for TPE, scales as $\sim I^{-0.5}$, where I is the excitation intensity. Moreover the bleaching rate depends on the duty cycle of the excitation. If continuous excitation is replaced by pulsed excitation without increasing the peak brightness, the bleaching rate diminishes linearly with the excitation duty cycle (the ratio of the time the molecules are irradiated to that when they are not irradiated). A marked dependence of the bleaching rate on the substrate temperature was also reported.

Recently, Deschenes and van den Bout (2002) reported a detailed single-molecule study of rhodamine 6G molecules embedded in a film of poly(methylacrylate) (PMA) under vacuum and using very low excitation intensities, between 2 W/cm^2 and 10,000 W/cm^2. The authors reported a remarkable decrease of the photobleaching rate at low excitation intensities and an increase in the total number of photons emitted up to $\sim 10^9$ photons per molecule before bleaching. They propose a four-state model, sketched in Figure 39.8, that accounts for the observed nonlinear intensity dependence of the photobleaching rate. This model seems to fit most of the single-molecule photobleaching studies published up to now.

Photobleaching causes the fluorescent output from a group of dye molecules to decay in a manner described by either a single- or a multi-exponential function of the total accumulated exposure (Xie and Trautman, 1998; Widengren and Riegler, 1996; Eggeling *et al.*, 1997, 1998; Wennmalm and Riegler, 1999; Ko, 2004).

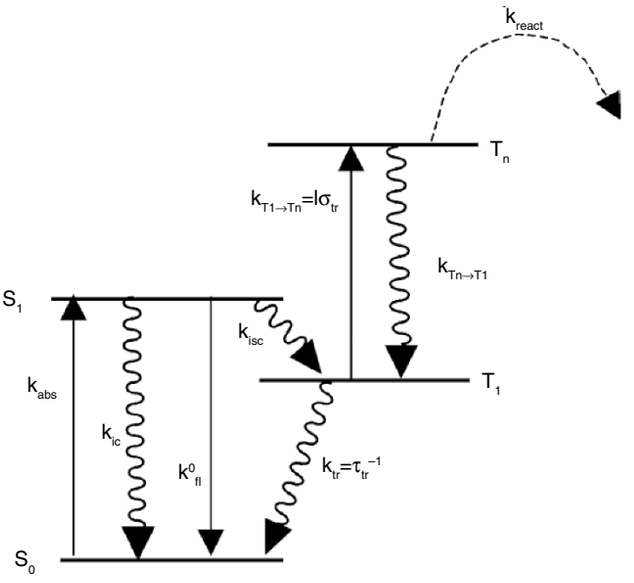


FIGURE 39.8. Perrin–Jablonski diagram of the relevant states for rhodamine 6G photobleaching. Absorption (k_{abs}) from S_0 to S_1 may lead to non-radiative internal conversion (k_{ic}), fluorescence (k_{fl}^0), or intersystem crossing (k_{isc}) to T_1. From T_1, the molecule may relax back to S_0 (k_{tr}), or absorb a second 532 nm photon ($k_{T1\rightarrow Tn}$) and go to T_n. From there, the molecule may either relax back to T_1 ($k_{Tn\rightarrow T1}$) or react (k_{react}), leading to irreversible photobleaching. (Derived from Deschennes and van den Bout, 2002.)

Multi-exponential distributions are typically found for ensemble measurements while single-exponential bleaching times are measured on a series of single, entrapped molecules.

The multi-exponential distribution of photobleaching times has been interpreted either as being caused by intrinsic heterogeneity of the biological sample (Xie and Trautman, 1998), or as an artifact caused by the use of non-uniform excitation profiles in the beams used to produce the bleach. Molski (2001), who calculated bleaching kinetics in single-molecule fluorescence spectroscopy using renewal theory, suggested that non-single-exponential distributions of bleaching times could be due to true heterogeneity in the sample (in-homogeneous broadening). He suggested a five-state model where bleaching occurs from the excited triplet states, and found an exact formalism to calculate distributions of the number of photon counts and the time before photobleaching. He found exponential distributions for the average bleaching number and the average bleaching time and related these two quantities to the transition rate constants. Berglund (2004) has extended these results by considering theoretical models of the decay, via photobleaching, of surface-immobilized fluorescent molecules excited by a spatially varying laser intensity profile. He shows that the fluorescence decay measured in a non-uniform excitation profile is always non-exponential because molecules near the edge of the spot, where the light is dimmer, bleach more slowly.

These results suggest that the observation of multiple exponentials in the distributions of single-molecule photobleaching times could arise at least partially as an artifact of a spatially varying laser profile rather than indicating any heterogeneity in the bleaching process. Experimental support of this study appeared in an article by Ko (2004), who showed that, for rhodamine 6G in agarose gel, the bulk bleaching decays are described by a three-exponential decay while the single-molecule bleaching times are

[5] Solutions of various dyes were prepared as follows: (1) 100 m*M* rhodamine 6G in dimethylsulfoxide; (2) 100 m*M* fluorescein in TRIS buffer; (3) 100 m*M* pyrene powder in DMSO; (4) 100 m*M* Indo-1 powder in MilliQ water. The rhodamine and fluoroscein solutions were later diluted to 70 to 300 n*M* in ethanol before use. The glass slides were cleaned by being soaked in a 1% sodium dodecyl-sulfate for 24 h, then in a saturated NaOH-methanol solution for 2 h. The NaOH is removed by soaking the slides in 0.1% HCl for 2 h and then in diluted chromic solution (K_2CrO_4 in concentrated phosphoric acid) for 2 h. The slides were then stored in ethanol and finally rinsed thoroughly with MilliQ water and dried with nitrogen flow just before use. A drop of one of these work solutions was placed on a glass slide and spin-coated at 1000 rpm in a hood.

distributed according to a single-exponential function. It is encouraging that the average bleaching time they observed in bulk agrees very well with the mean of the single-molecule distribution. Rhodamine 6G entrapped in poly(vinyl alcohol) has been the object of another recent study of photobleaching at the single-molecule level (Zondervan *et al.*, 2004). These authors have investigated photobleaching as a function of illumination time, excitation intensity, the presence of oxygen, and temperature. They observed non-exponential kinetics related to primary photobleaching through two dark states — the triplet state and a radical anion — and to secondary photobleaching after the optical excitation of those dark states. The important claim of this study is that the presence of metastable states other than the triplet can drastically affect the photobleaching rate.

Photobleaching and Photocycling of Single Fluorescent Proteins

Among fluorescent biomolecules, single-molecule photobleaching studies have been reported on several variants of the GFP, and more generally, of the so-called visible fluorescent proteins (VFPs). Blue mutants, used in combination with yellow GFP were well known to cellular microscopists as a good donor–acceptor pair for measuring intracellular interactions via FRET. However, as blue GFP variants are generally dim (Rizzuto *et al.*, 1996; Cubitt *et al.*, 1997) and tend to photobleach readily (Ellenberg *et al.*, 1998), alternative multicolor pairs were developed. Of these, the most popular currently is cyan fluorescent protein (CFP) (Heim *et al.*, 1994) and the red-shifted yellow fluorescent protein (YFP) (Ormö *et al.*, 1996). CFP is brighter than BFP and is more photostable under imaging (Ellenberg *et al.*, 1998; see Chapter 45, this volume).

Spontaneous fluorescence recovery of YFP molecules from seemingly irreversible photobleaching using 405 nm excitation was reported very early in the GFP literature (Dickson *et al.*, 1997). The authors have called this effect optically induced switching. In fact, the chromophores of GFP occur in at least three protonation states. Two of them correspond to the cases in which the oxydril of the tyrosine 66 is protonated (neutral state) or de-protonated (anionic state). A third state corresponds to a zwitterionic case (Zimmer, 2002). Most of the observations on the recovery of GFP mutants after bleaching hint at the possibility that some of the presumably photobleached proteins were actually residing in a dark state caused by a neutral chromophore. The switching effect has an important impact on the suitability of GFP mutants for both cellular imaging and single molecule experiments. However, investigations on the widely used EGFP mutant showed no optical switching behavior under a variety of experimental conditions (Cinelli *et al.*, 2000).

It is possible to detect single-molecule signals with sub-millisecond time resolution using an avalanche photodiode, provided that a sufficiently high fluorescence photon flux can be established. Early confocal microscopy experiments on single molecules of the GFP mutant E222 by Jung and colleagues (1998) increased the time resolution to a minimum integration time of 10 ms, a limit more recently reduced to 800 µs (Garcia-Parajo *et al.*, 2000). These experiments showed that spontaneous recovery of fluorescence emission from single GFP molecules can be observed as long as 180 min after an apparent photobleaching event and that photoinduced blinking was also present. The blinking on-times measured for this mutant were dependent on the excitation power with values comparable to those previously reported (Dickson *et al.*, 1997; Moerner *et al.*, 1999; Peterman *et al.*, 1999). At moderate illumination intensities of 1.5 kW/cm^2, half of the molecules reside in a dark state (Garcia-Parajo *et al.*, 2000). It is worth noting that this high proportion is not caused by the comparatively small transition yield of $5 \cdot 10^{-6}$ into the dark state so much, as by the long lifetime of this state $t_{off} = 1.6$ s.

An enhanced YFP mutant, termed E^{2}GFP, has been obtained that might be used as a single-biomolecule optical switch (Cinelli *et al.*, 2001). As with most GFP molecules, prolonged or intense excitation results in photobleaching (at 476 nm in the case of E^{2}GFP). However, E^{2}GFP is the only known mutant in which irradiation of the dark photobleached state (at 350 nm) produces an excited state that photoconverts to an anionic B form, which is also fluorescent.

Recently, a TPE investigation (Chirico *et al.*, 2004) at the single-molecule level showed that single-molecule photobleaching increases with a power law of 2.4 and that the fluorescence recovery after bleaching can be induced also by near-infrared light at 720 nm (Fig. 39.9). Several characteristics of this infrared (IR)-induced recovery makes this mutant promising both for prolonged cellular imaging and for opto-electronic data storage applications. Recovery spectra are very narrow and their widths do not change appreciably with the excitation power, as shown in Figure 39.10. Maximum recovery efficiency occurs at 720 nm. This corresponds to twice the peak wavelength of the spectrum of the dark state obtained in single-photon experiments (Nifosì *et al.*, 2003). The fourth-power dependence of the recovery shown in Figure 39.10(B) indicates that two two-photon transitions are required to overcome the energy barrier from a dark state to the optically active form coupled to it. The second transition is likely to bring the system from the excited dark state (or its relaxed form) to a higher excited level. Detuning between the two transitions may cause the observed sharp recovery spectrum. Vibrational–electronic couplings could also contribute to reduce the width of the recovery spectrum.

Bleaching and Autofluorescence

A main concern about photobleaching at the single-molecule level stems from the effort to follow a single-protein system *in vivo*. The ability to do this would allow one to study in detail basic processes such as cellular internalization and cell trafficking by exploiting all the known photophysical properties of the probes being used. Although, within the nucleus, autofluorescence is only slightly above the level encountered in common gel samples, investigations in the cytoplasm are hampered by a significant level of background signal. It is therefore necessary to optimize the experimental conditions, including the choice of a fluorophore with minimal photobleaching, before single-molecule detection in living cells becomes conceivable. As an important step to this end, Kubitschek and co-workers have again employed YFP proteins. The authors investigated the diffusion of the S65G/S72A/T203F mutant in glycerol/water mixtures (Kubitschek *et al.*, 2000). They were able to track single YFP molecules with a time resolution of 10 ms, a signal of 8 ± 3 counts/pixel above background, and a signal-to-noise ratio of 4. Photobleaching was still a limiting factor, yielding, on average, a maximum of only 10^5 emitted photons and an observation time of 100 ms.

Other Fluorescent Proteins

Besides GFPs, the light harvesting protein systems of photosynthetic organisms have been investigated in terms of their single-molecule photodynamics. These systems consist of protein assemblies in which various chromophores are electronically coupled so that the summed absorption covers a wide spectral

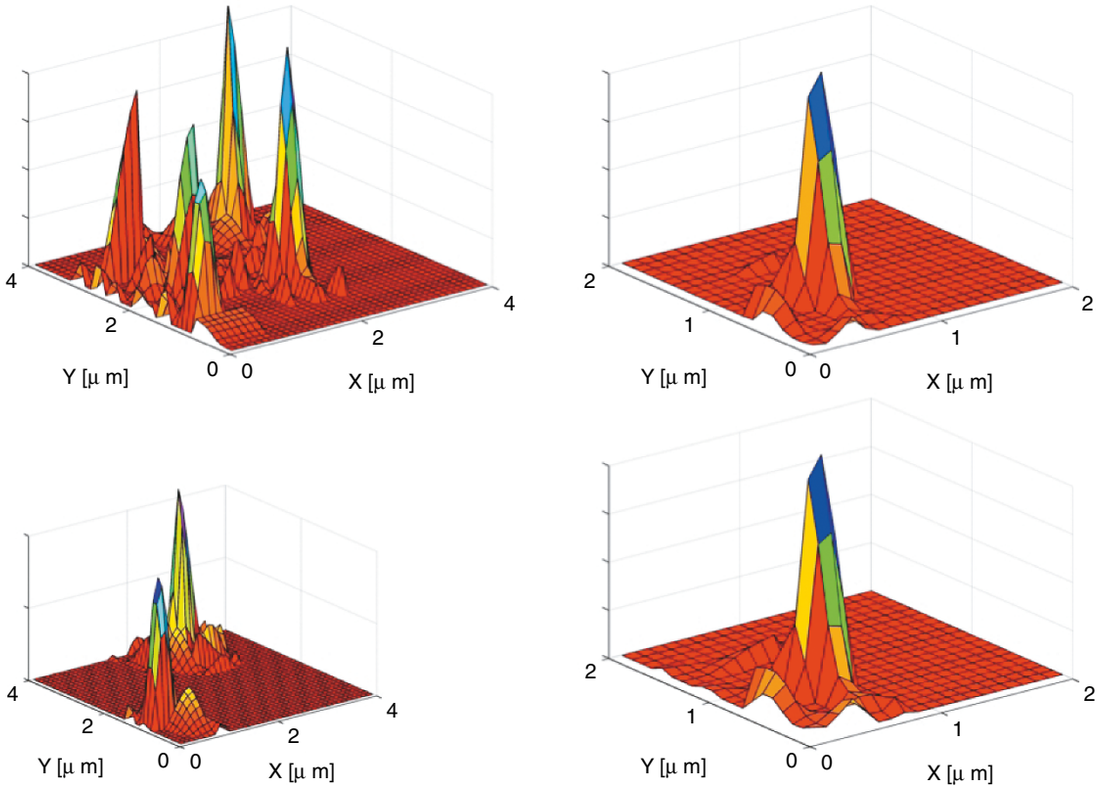


FIGURE 39.9. Fluorescence image of single proteins excited in the A band (excitation at 780 nm, emission at 440 nm) (upper left). (Right) Same field of view but on the B channel (excitation at 880 nm emission at 535 nm). (Lower panel, left) Fluorescent image in the A channel after irradiation at 710 nm (2 mW and 50 ms). (Lower panel, right) Same field of view but on the B channel and after irradiation at 720 nm (2 mW and 50 ms). Color levels of left panels are five times those in right panels. (After Chirico *et al.*, 2004.)

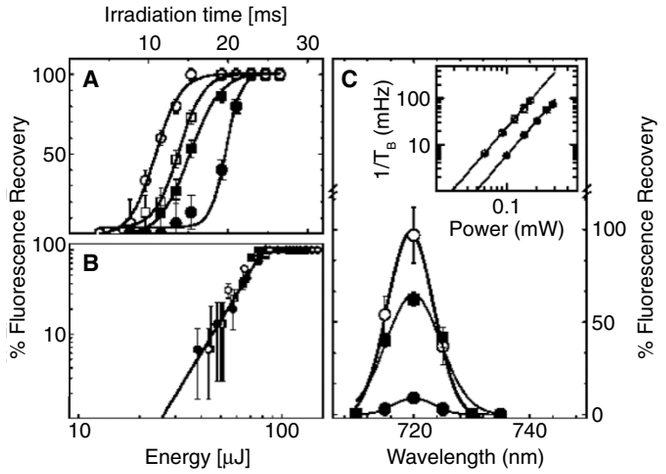


FIGURE 39.10. (A) Percentage of single-protein fluorescence recovery versus the illumination time at 720 nm for different excitation powers: 3.34 mW (*solid circles*), 4.34 mW (*solid squares*), 5 mW (*open squares*), and 5.7 mW (*open circles*). The solid lines are best-fit to a sigmoidal function. (B) Recovery efficiency with laser excitation at 720 nm versus the product of the illumination time with excitation power: 3.34 mW (*solid circles*), 4.34 mW (*solid squares*), 5 mW (*open squares*), and 5.7 mW (*open circles*). The solid line is the best-fit power law with an exponent of 3.8 ± 0.2. (C) Recovery efficiency at a fixed illumination time of 16.5 ms versus the excitation wavelength at 5.7 mW (*open circles*), 4.34 mW (*filled squares*), and 3.34 mW (*filled circles*). The error bars are the 95% statistical errors due to the number of events observed. The inset shows the photobleaching rate $1/T_b$ versus excitation power for the two states (A, *open squares*; B, *filled squares*). (After Chirico *et al.*, 2004.)

range. A subtle interplay between different electronic coupling mechanisms is responsible for an efficient transfer of the absorbed energy to the reaction center. Recently, a study of photobleaching and energy transfer in single phycoerythrocyanin (PEC) monomer has been presented by Zehetmayer and colleagues (2002). The PEC monomer contains two different chromophores, phycoviolobilin (PVB) and phycocyanobilin (PCB) (Zhao and Scheer, 1995). Zehetmayer and co-workers (2002) recorded single-molecule images of phycoerythrocyanin monomers. Their photobleaching behavior was studied by simultaneously exciting at two wavelengths according to a method earlier applied on the E222Q GFP mutant by the same group (Jung *et al.*, 2001). The PVB chromophore was found to be responsible for the photobleaching of PEC. On the other hand, it was possible to ascertain that the 15E form of PVB corresponds to one of the short-lived dark states of PEC. This form does not induce real photobleaching but simply reduces the average fluorescence emission, as is the case in most of the GFP mutants. The difficulty in discriminating between nonreversible photobleaching and long-term blinking therefore seems to be ubiquitous in single-protein photophysics.

CONCLUSION

It is not easy to indicate conclusions that define an optimal strategy for either reducing or exploiting the photobleaching process. We hope that the facts reported in this chapter could be useful to design new experiments or to revise old ones with the aim of a better understanding of the delicate, intricate, and complex structure–function

relationship that is the basis of our job as microscopists or, more generally, as biophysicists. We decided to attack photobleaching by considering both its imaging and its single-molecule aspects because we think that feedback between these related aspects of the problem can greatly improve our knowledge of photobleaching.

ACKNOWLEDGMENTS

We are greatly indebted to Michael W. Davidson of Florida State University (Tallahassee, FL) for providing Figure 39.7. We also acknowledge the work of collaborators in our laboratories by mentioning, in random order, Davide Mazza, Maddalena Collini, Valentina Caorsi, Michele Caccia, Paolo Bianchini, Fabio Cannone, Laura D'Alfonso, Giuseppe Vicidomini, Tytus Bernas, Marc Schneider, Silke Krol, Raffaella Magrassi, Miroslaw Zarebski, Ilaria Testa, Federica Morotti, Mattia Pesce, and Francesca Cella. Alberto Diaspro thanks Teresa and Claudia for accepting long weekends and nights writing and revising. Last, but not least, the authors are very grateful to Jim Pawley for his patience and constructive criticism. This work was supported by MIUR, INFM, IFOM, compagnia di San Paolo (AD), and The Wellcome Trust (JD) grants.

REFERENCES

Agard, D.A., Hiraoka, Y., Shaw, P.J., and Sedat, J.W., 1989, Fluorescence microscopy in three-dimensions, *Methods Cell Biol*. 30:353–378.

Amos, W.B., and White, J.G., 2003, How the confocal laser scanning microscope entered biological research, *Biol. Cell* 95:335–342.

Arndt-Jovin, D.J., Nicoud, R.M., Kaufmann, J., and Jovin, T.M., 1985, Fluorescence digital-imaging microscopy in cell biology, *Science* 230:13330–13335.

Axelrod, D., Koppel, D.E., Schlessinger, J., Elson, E., and Webb, W.W., 1976, Mobility measurement by analysis of fluorescence photobleaching recovery kinetics, *Biophys. J*. 16:1055–1069.

Basche, T., 1998, Fluorescence intensity fluctuations of single atoms, molecules and nanoparticles, *J. Lumin.* 76–7:263–269.

Bastiaens, P.I., and Hell, S.W., 2004, Recent advances in light microscopy, *J. Struct. Biol*. 147:1–89.

Benson, D.M., Bryan, J., Plant, A.L., Gotto, A.M. Jr., and Smith, L.C., 1985, Digital image fluorescence microscopy: Spatial heterogeneity of photobleaching rate constants in individual cells, *J. Cell Biol*. 100:1309–1323.

Berglund, A.J., 2004, Nonexponential statistics of fluorescence photobleaching, *J. Chem. Phys*. 121:2899–2903.

Bernas, T., Cook, P.R., and Dobrucki, J.W., 2005, Confocal fluorescence imaging of photosensitised DNA denaturation in cell nuclei, *Photochem. Photobiol*. 81(4):960–969.

Bernas, T., Zarębski, M., Cook, P.R., and Dobrucki, J.W., 2004, Minimizing photobleaching during confocal microscopy of fluorescent probes bound to chromatin: role of anoxia and photon flux, *J. Microsc*. 215:281–296.

Bianco, B., and Diaspro, A., 1989, Analysis of the three dimensional cell imaging obtained with optical microscopy techniques based on defocusing, *Cell Biophys*. 15:189–200.

Birks, J.B., 1970, *Photophysics of Aromatic Molecules*, Wiley Interscience, London.

Bloom, J.A., and Webb, W.W., 1984, Photodamage to intact erythrocyte membranes at high laser intensities: Methods of assay and suppression, *J. Histochem. Cytochem*. 32:608–616.

Bock, G., Hilchenbach, M., Schauenstein, K., and Wick, G., 1985, Photometric analysis of antifading reagents for immunofluorescence with laser and conventional illumination sources, *J. Histochem. Cytochem*. 33:699–705.

Bonetto, P., Boccacci, P., Scarito, M., Davolio, M., Epifani, M., Vicidomini, G., Tacchetti, C., Ramoino, P., Usai, C., and Diaspro, A., 2004, Three-dimensional microscopy migrates to the Web with PowerUp Your Microscope, *Microsc. Res. Tech*. 64:196–203.

Braeckmans, K., De Smedt, S.C., Roelant, C., Leblans, M., Pauwels, R., and Demeester, J., 2003, Encoding microcarriers by spatial selective photobleaching, *Nat. Mater*. 2:169–173.

Braga, J., Desterro, J.M.P., and Carmo-Fonseca, M., 2004, Intracellular macromolecular mobility measured by fluorescence recovery after photobleaching with confocal laser scanning microscopes, *Mol. Biol. Cell* 15:4749–4760.

Brakenhoff, G.J., Muller, M., and Ghauharali, R.I., 1996, Analysis of efficiency of two-photon versus single-photon absorption of fluorescence generation in biological objects, *J. Microsc*. 183:140–144.

Cannone, F., Chirico, G., and Diaspro, A., 2003, Two-photon interactions at single fluorescent molecule level, *J. Biomed. Opt*. 8:391–395.

Chen, R.F., and Scott, C.H., 1985, Atlas of fluorescence spectra and lifetimes of dyes attached to protein, *Anal. Lett*. 18:393–421.

Chirico, G., Cannone, F., Baldini, G., and Diaspro, A., 2003, Two-photon thermal bleaching of single fluorescent molecules, *Biophys. J*. 84:588–598.

Chirico, G., Cannone, F., Beretta, S., and Diaspro, A., 2001, Single molecule studies by means of the two-photon fluorescence distribution, *Microsc. Res. Tech*. 55:359–364.

Chirico, G., Cannone, F., Beretta, S., Diaspro, A., Campanini, B., Bettati, S., Ruotolo, R., and Mozzarelli, A., 2002, Dynamics of green fluorescent protein mutant2 in solution, on spin-coated glasses, and encapsulated in wet silica gels, *Protein Sci*. 11:1152–1161.

Chirico, G., Cannone, F., Diaspro, A., Bologna, S., Pellegrini, V., Nifosi, R., and Beltram, F., 2004, Multiphoton switching dynamics of single green fluorescent proteins, *Phys. Rev. E Stat. Nonlin. Soft. Matter Phys.* 70:030901(R).

Cinelli, R.A.G., Ferrari, A., Pellegrini, V., Tyagi, M., Giacca, M., and Beltram, F., 2000, The enhanced green fluorescent protein as a tool for the analysis of protein dynamics and localization: Local fluorescence study at the single-molecule level. *Photochem. Photobiol*. 71:771–776.

Cinelli, R.A.G., Pellegrini, V., Ferrari, A., Faraci, P., Nifosi, R., Tyagi, M., Giacca, M., and Beltram, F., 2001, Green fluorescent proteins as optically controllable elements in bioelectronics, *Appl. Phys. Lett*. 79:3353–3355.

Cole, N.B., Smith, C.L., Sciaky, N., Terasaki, M., Edidin, M., and Lippincott-Schwartz, J., 1996, Diffusional mobility of Golgi proteins in membranes of living cells, *Science* 273:797–801.

Cubitt, A.B., Woollenweber, L.A., and Heim, R., 1997, Understanding structure-function relationship in the Aequoria Victoria Green Fluorescent Protein, In: *Green Fluorescent Proteins* (K.F. Sullivan and S.A. Kay, eds.), Academic Press, San Diego, California, p. 19.

Davis, S.K., and Bardeen, C.J., 2002, Using two-photon standing waves and patterned photobleaching to measure diffusion from nanometers to microns in biological systems, *Rev. Sci. Instrum*. 73:2128–2135.

Delon, A., Usson, Y., Derouard, J., Biben, T., and Souchier, C., 2004, Photobleaching, mobility and compartmentalisation: inferences in fluorescence correlation spectroscopy, *J. Fluoresc*. 14:255–267.

Denk, W., Strickler, J.H., and Webb, W.W., 1990, Two-photon laser scanning fluorescence microscopy, *Science* 248:73–76.

Deschenes, L.A., and van den Bout, D.A., 2002, Single molecule photobleaching: increasing photon yield and survival time through suppression of two step photolysis, *Chem. Phys. Lett*. 365:387–395.

Diaspro, A., 2002, *Confocal and Two-Photon Microscopy: Foundations, Applications, and Advances*, Wiley-Liss, New York.

Diaspro, A., 2004, Confocal and multiphoton microscopy, In: *Lasers and Current Optical Techniques in Biology* (G. Palumbo and R. Pratesi, eds.), RSC-Royal Society of Chemistry, Cambridge, United Kingdom, pp. 429–478.

Diaspro, A., and Robello, M., 2000, Two-photon excitation of fluorescence for three-dimensional optical imaging of biological structures, *J. Photochem. Photobiol. B* 55:1–8.

Diaspro, A., Chirico, G., and Collini, M., 2005, Two-photon fluorescence excitation in biological microscopy and related techniques, *Quart. Rev. Biophys*. In press.

Diaspro, A., Chirico, G., Federici, F., Cannone, F., Beretta, S., and Robello, M., 2001, Two-photon microscopy and spectroscopy based on a compact confocal scanning head, J. *Biomed. Opt*. 6:300–310.

Diaspro, A., Federici, F., Viappiani, C., Krol, S., Pisciotta, M., Chirico, G., Cannone, F., and Gliozzi, A., 2003, Two-photon photolysis of 2-nitrobenzaldehyde monitored by fluorescent-labeled nanocapsules, *J. Phys. Chem. B* 107:11008–11012.

Dickson, R.M., Cubitt, A.B., Tsien, R.Y., and Moerner, W.E., 1997, On/off blinking and switching behaviour of single molecules of green fluorescent protein, *Nature* 388:355–358.

Dittrich, P.S., and Schwille, P., 2001, Photobleaching and stabilization of fluorophores used for single molecule analysis with one- and two-photon excitation, *Appl. Phys. B* 73:829–837.

Dixit, R., and Cyr, R., 2003, Cell damage and reactive oxygen species production induced by fluorescence microscopy: Effect on mitosis and guidelines for non-invasive fluorescence microscopy, *Plant J*. 36: 280–290.

Dobrucki, J.W., 2001, Interaction of oxygen-sensitive luminescent probes $Ru(phen)_3^{2+}$ and $Ru(bipy)_3^{2+}$ with animal and plant cells *in vitro*. Mechanisms of phototoxicity and conditions for non-invasive oxygen measurements. *J. Photochem. Photobiol. B*. 65:136–144.

Dobrucki, J.W., and Darzynkiewicz, Z., 2001, Chromatin condensation and sensitivity of DNA in situ to denaturation during cell cycle and apoptosis — a confocal microscopy study, *Micron*. 32:645–652.

Drummond, D.R., Carter, N., and Cross, R.A., 2002, Multiphoton versus confocal high-resolution z-sectioning of enhanced green fluorescent microtubules: Increased multiphoton photobleaching within the focal plane can be compensated using a Pockels cell and dual widefield detectors, *J. Microsc*. 206:161–169.

Edidin, M., Zagyansky, Y., and Lardner, T.J., 1976, Measurement of membrane protein lateral diffusion in single cells, *Science*. 191:466–468.

Eggeling, C., Brand, L., and Seidel, C.A.M., 1997, Laser-induced fluorescence of coumarin derivatives in aqueous solution: Photochemical aspects for single molecule detection, *Bioimaging*. 5:105–115.

Eggeling, C., Widengren, J., Rigler, R., and Seidel, C.A.M., 1998, Photobleaching of fluorescent dyes under conditions used for single molecule detection: Evidence of two step photolysis, *Anal. Chem*. 70:2651–2659.

Ellenberg, J., Lippincott-Schwartz, J., and Presley, J.F., 1998, Two-color green fluorescent protein time-lapse imaging, *Biotechniques*. 25:838–842, 844–846.

Emptage, N.J., 2001, Fluorescent imaging in living systems, *Curr. Opin. Pharmacol*. 1:521–525.

Garcia-Parajo, M.F., Segers-Nolten, G.M.J., Veerman, J.-A., Greve, J., and van Hulst, N.F., 2000, Real-time light-driven dynamics of the fluorescence emission in single green fluorescent protein molecules, *Proc. Nat. Acad. Sci. USA* 97:7237–7242.

Greenbaum, L., Rothmann, C., Lavie, R., and Malik, Z., 2000, Green fluorescent protein photobleaching: a model for protein damage by endogenous and exogenous singlet oxygen, *Biol. Chem*. 381:1251–1258.

Harper, I.S., 2001, Fluorophores and their labeling procedures for monitoring various biological signals, In: *Methods in Cellular Imaging* (A. Periasamy, ed.), Oxford University Press, New York, pp. 20–39.

He, J.A., Hu, Y.Z., and Jiang, L.J., 1997, Photodynamic action of phycobiliproteins: *In situ* generation of reactive oxygen species, *Biochim. Biophys. Acta* 1320:165–174.

Heim, R., Prasher, D.C., and Tsien, R.Y., 1994, Wavelength mutations and post-translational autoxidation of green fluorescent protein, *Proc. Natl. Acad. Sci. USA* 91:12501–12504.

Hines, M.A., and Guyot-Sionnest, P., 1996, Synthesis and characterization of strongly luminescing ZnS-Capped CdSe nanocrystals, *J. Phys. Chem*. 100:468–471.

Hirschfeld, T., 1976, Quantum efficiency independence of the time integrated emission from a fluorescent molecule, *Appl. Opt*. 15:3135–3139.

Hockberger, P.E., Skimina, T.A., Centonze, V.E., Lavin, C., Chu, S., Dadras, S., Reddy, J.K., and White, J.G., 1999, Activation of flavin-containing oxidases underlies light-induced production of H_2O_2 in mammalian cells, *Proc. Nat. Acad. Sci. USA* 96:6255–6260.

Jaiswal, J.K., and Simon, S., 2004, Potentials and pitfalls of fluorescent quantum dots for biological imaging, *Trends Cell Biol*. 14:497–504.

Jung, G., Wiehler, J., Göhde, W., Tittel, J., Basché, Th., Steipe, B., and Bräuchle, C., 1998, Confocal microscopy of single molecules of the green fluorescent protein, *Bioimaging* 6:54–61.

Kao, F.J., Wang, Y.M., Chen, J.C., Cheng, P.C., Chen, R.W., and Lin, B.L., 2002, Photobleaching under single photon and multi-photon excitation: Chloroplasts in protoplasts from *Arabidopsis thaliana, Opt. Commun*. 201:85–91.

Kawano, H., Nabekawa, Y., Suda, A., Oishi, Y., Mizuno, H., Mijawaki, A., and Midorikawa, K., 2003, Attenuation of photobleaching in two-photon excitation fluorescence from green fluorescent protein with shaped excitation pulses, *Biochem. Biophys. Res. Commun*. 311:592–596.

Ko, D.S., 2004, Photobleaching time distribution of a single tetramethylrhodamine molecule in agarose gel, *J. Chem. Phys*. 120:2530–2531.

Kohen, E., Reyftmann, J.P., Morliere, P., Santus, R., Kohen, C., Mangel, W.F., Dubertret, L., and Hirschberg, J.G., 1986, A microspectrofluorometric study of porphyrin-photosensitized single living cells. II. Metabolic alterations, *Photochem. Photobiol*. 44:471–475.

König, K., and Tirlapur, U.K., 2002, Cellular and subcellular perturbations during multiphoton microscopy, In: *Confocal and Two-Photon Microscopy: Foundations, Applications and Advances* (A. Diaspro, ed.), Wiley-Liss, New York, pp. 191–205.

Krenik, K.D., Kephart, G.M., Offord, K.P., Dunnette, S.L., and Gleich, G.J., 1989, Comparison of antifading agents used in immunofluorescence, *J. Immunol. Methods* 117:91–97.

Kriete, A., 1992, *Visualization in Biomedical Microscopies*, VCH, Weinheim, Germany.

Kubitschek, U., Kückmann, O., Kues, T., and Peters, R., 2000, Imaging and tracking of single GFP molecules in solution, *Biophys. J*. 78: 2170–2179.

Lakowicz, J.R., 1999, *Principles of Fluorescence Microscopy*, Plenum Press, New York.

Landon, T.M., 1997, Alexa dyes, tracers and conjugates, *Bioprobes* 26:1–6.

Larson, D.R., Zipfel, W.R., Williams, R.M., Clark, S.W., Bruchez, M.P., Wise, F.W., and Webb, W.W., 2003, Water-soluble quantum dots for multiphoton fluorescence imaging *in vivo*, *Science* 300:1434–1436.

Lippincott-Schwartz, J., and Patterson, G.H., 2003, Development and use of fluorescent protein markers in living cells, *Science* 300:87–91.

Maher, R.C., Cohen, L.F., and Etchegoin, P., 2002, Single molecule photobleaching observed by surface enhanced resonant Raman scattering (SERRS), *Chem. Phys. Lett*. 352:378–384.

Manitto, P., Speranza, G., Monti, D., and Gramatica, P., 1987, Singlet oxygen reactions in aqueous solution. Physical and chemical quenching rate constants of crocin and related carotenoids, *Tetrahedron Lett*. 28: 4221–4224.

Mathies, R.A., and Stryer, L., 1986, Single-molecule fluorescence detection: A feasibility study using phycoerythrin, In: *Applications of Fluorescence in the Biomedical Sciences* (D.L. Taylor, A.S. Waggoner, R.F. Murphy, F. Lanni, and R.R. Birge, eds.), Alan R. Liss, New York, pp. 129–140.

Matsumoto, B., 2002, *Cell Biological Applications of Confocal Microscopy*, 2nd ed., Academic Press, San Diego, California.

Mattoussi, H., Mauro, J.M., Goldman, E.R., Anderson, G.P., Sundar, V.C., Mikulec, F.V., and Bawendi, M.G., 2000, Self-assembly of CdSe-ZnS quantum dot bioconjugates using an engineered recombinant protein, *J. Am. Chem. Soc*. 122:12142–12150.

McNally, J.G., and Smith, C.L., 2002, Photobleaching by confocal microscopy. In: *Confocal and Two-Photon Microscopy: Foundations, Applications, and Advances* (A. Diaspro, ed.), Wiley-Liss, Inc., New York, pp. 525–538.

Mertz, J., 1998, Molecular photodynamics involved in multi-photon excitation fluorescence, *Eur. Phys. J*. D3:53–66.

Michalet, X., Kapanidis, A.N., Laurence, T., Pinaud, F., Doose, S., Pflughoefft, M., and Weiss, S., 2003, The power and prospects of fluorescence microscopies and spectroscopies, *Annu. Rev. Biophys. Biomol. Struct*. 32:161–182.

Moerner, W.E., Peterman, E.J.G., Brasselet, S., Kummer, S., and Dickson, R.M., 1999, Optical methods for exploring dynamics of single copies of green fluorescent protein, *Cytometry* 36:232–238.

Molski, A., 2001, Statistics of the bleaching number and the bleaching time in single-molecule fluorescence spectroscopy, *J. Chem. Phys*. 114: 1142–1147.

Ness, J.M., Akhtar, R.S., Latham, C.B., and Roth, K.A., 2003, Combined tyramide signal amplification and quantum dots for sensitive and photostable immunofluorescence detection, *J. Histochem. Cytochem.* 5:981–987.

Nifosì, R., Ferrari, A., Arcangeli, C., Tozzini, V., Pellegrini, V., and Beltram, F., 2003, Photoreversible dark state in a tristable green fluorescent protein variant, *J. Chem. Phys. B* 107:1679–1684.

Ono, M., Murakami, T., Kudo, A., Isshiki, M., Sawada, H., and Segawa, A., 2001, Quantitative comparison of anti-fading mounting media for confocal laser scanning microscopy, *J. Histochem. Cytochem*. 49:305–311.

Ormo, M., Cubitt, A.B., Kallio, K., Gross, L.A., Tsien, R.Y., and Remington, S.J., 1996, Crystal structure of the *Aequorea victoria* green fluorescent protein, *Science* 273:1392–1395.

Patterson, G.H., and Piston, D.W., 2000, Photobleaching in two-photon excitation microscopy, *Biophys. J.* 78:2159–2162.

Pawley, J.B., 1995a, *Handbook of Biological Confocal Microscopy*, Plenum Press, New York.

Pawley, J.B., 1995b, Fundamental limits in confocal microscopy, In: *Handbook of Biological Confocal Microscopy* (J.B. Pawley, ed.), Plenum Press, New York, pp. 19–37.

Periasamy, A., 2001, *Methods in Cellular Imaging*, Oxford University Press, New York.

Peterman, E.J.G., Brasselet, S., and Moerner, W.E., 1999, Optical methods for exploring dynamics of single copies of green fluorescent protein, *J. Phys. Chem. A* 103:10553–10560.

Peters, R., Peters, J., Tews, K.H., and Bahr, W., 1974, A microfluorimetric study of translational diffusion in erythrocyte membranes, *Biochem. Biophys. Acta* 367:282–294.

Poo, M., and Cone, R.A., 1974, Lateral diffusion of rhodopsin in the photoreceptor membrane, *Nature* 247:438–441.

Reits, E.A., and Neefjes, J.J., 2001, From fixed to FRAP: measuring protein mobility and activity in living cells, *Nat. Cell Biol*. 3:E145–E147.

Reyftmann, J.P., Kohen, E., Morliere, P., Santus, R., Kohen, C., Mangel, W.F., Dubertret, L., and Hirschberg, J.G., 1986, A microspectrofluorometric study of porphyrin-photosensitized single living cells. I. Membrane alterations, *Photochem. Photobiol*. 44:461–469.

Rizzuto, R., Brini, M., DeGiorgi, F., Rossi, R., Heim, R., Tsien, R.Y., and Pozzan, T., 1996, Double labelling of subcellular structures with organelle-targeted GFP mutants *in vivo*, *Curr. Biol*. 6:183–188.

Schneider, M.B., and Webb, W.W., 1981, Measurements of submicron laser beam radii, *Appl. Opt.* 20:1382–1388.

Sokolov, K., Aaron, J., Hsu, B., Nida, D., Gillenwater, A., Follen, M., MacAulay, C., Adler-Storthz, K., Korgel, B., Descour, M., Pasqualini, R., Arap, W., Lam, W., and Richards-Kortum, R., 2003, Optical systems for in vivo molecular imaging of cancer, *Technol. Cancer Res. Treat*. 2:491–504.

Song, L., Hennink, E.J., Young, I.T., and Tanke, H.J., 1995, Photobleaching kinetics of fluorescein in quantitative fluorescence microscopy, *Biophys. J.* 68:2588–2600.

Song, L., Varma, C.A., Verhoeven, J.W., and Tanke, H.J., 1996, Influence of the triplet excited state on the photobleaching kinetics of fluorescein in microscopy, *Biophys. J*. 70:2959–2968.

Souchier, L.A., Ffrench, M., and Bryon, P.A., 1993, Comparison of anti-fading agents used in fluorescence microscopy: image analysis and laser confocal microscopy study, *J. Histochem. Cytochem*. 41:1833–1840.

Stavreva, D.A., and McNally, J.G., 2004, Fluorescence recovery after photobleaching (FRAP) methods for visualizing protein dynamics in living mammalian cell nuclei, *Methods Enzymol*. 375:443–455.

Stelzer, E.H.K., 1998, Contrast, resolution, pixelation, dynamic range and signal to noise ratio: fundamental to its resolution in fluorescence light microscopy, *J. Microsc*. 189:15–24.

Stephens, D.J., and Allan, V.J., 2003, Light microscopy techniques for live cell imaging, *Science* 300:82–86.

Straub, T., 2003, Heterochromatin dynamics, *PLoS Biol*. 1:E14.

Taroni, P., and Valentini, G., 2004, Fluorescence spectroscopy and imaging (non microscopic). Part I: Basic principles and techniques, In: *Lasers and Current Optical Techniques in Biology* (G. Palumbo and R. Pratesi, eds.), RSC-Royal Society of Chemistry, Cambridge, United Kingdom, pp. 259–290.

Tsien, R.Y., 1998, The green fluorescent protein, *Annu. Rev. Biochem*. 67:509–544.

Tsien, R.Y., 2003, Imagining imaging's future, *Nat. Rev. Mol. Cell Biol*. 4:SS16–SS21.

Tsien, R.Y., and Waggoner, A.S., 1995, Fluorophores for confocal microscopy. Photophysics and photochemistry, In: *Handbook of Biological Confocal Microscopy* (J.B. Pawley, ed.), Plenum Press, New York, pp. 267–279.

Voura, E.B., Jaiswal, J.K., Mattoussi, H., and Simon, S.M., 2004, Tracking metastatic tumor cell extravasation with quantum dot nanocrystals and fluorescence emission-scanning microscopy, *Nat. Med*. 10:993–998.

Watson, A., Wu, X., and Bruchez, M., 2003, Lighting up cells with quantum dots, *Biotechnology* 34:296–303.

Weber, G., 1960, Enumeration of components in complex systems by fluorescence spectrophotometry, *Nature* 190:27–29.

Weber, G., and Teale, F.W.J., 1958, Fluorescence excitation spectrum of organic compounds in solution, *Trans. Faraday Soc*. 54:640–648.

Wennmalm, S., and Rigler, R., 1999, On death numbers and survival times of single dye molecules, *J. Phys. Chem. B* 103:2516–2519.

White, J., and Stelzer, E., 1999, Photobleaching GFP reveals protein dynamics inside live cells, *Trends Cell Biol*. 9:61–65.

Widengren, J., and Rigler, R., 1996, Mechanisms of photobleaching investigated by fluorescence correlation spectroscopy, *Bioimaging* 4:149–157.

Wilson, T., and Sheppard, C.J.R., 1984, *Theory and Practice of Scanning Optical Microscopy*, Academic Press, London.

Wu, X., Liu, H., Liu, J., Haley, K.N., Treadway, J.A., Larson, J.P., Ge, N., Peale, F., and Bruchez, M.P., 2003, Immunofluorescent labeling of cancer marker Her2 and other cellular targets with semiconductor quantum dots, *Nat. Biotechnol*. 21:41–46.

Xie, X.S., and Trautman, J.K., 1998. Optical studies of single molecules at room temperature, *Annu. Rev. Phys. Chem*. 49:441.

Xu, C., 2002, Cross-section of fluorescent molecules in multiphoton microscopy, In: *Confocal and Two-Photon Microscopy: Foundations, Applications, and Advances* (A. Diaspro, ed.), Wiley-Liss, New York, pp. 75–99.

Zehetmayer, P., Hellerer, Th., Parbel, A., Scheer, H., and Zumbusch, A., 2002, Spectroscopy of single phycoerythrocyanin monomers: dark state identification and observation of energy transfer heterogeneities, *Biophys. J.* 83:407–415.

Zhang, J., Campbell, R.E., Ting, A.Y., and Tsien, R.Y., 2002, Creating new fluorescent probes for cell biology, *Nat. Rev. Mol. Cell Biol*. 3:906–918.

Zhao, K.H., and Scheer, H., 1995, Type I and type II reversible photochemistry of phycoerythrocyanin α-subunit from *Mastigocladus laminosus* both involve *Z*, *E* isomerization of phycoviolobilin chromophore and are controlled by sulfhydryls in apoprotein, *Biochem. Biophys. Acta* 1228:244–253.

Zimmer, M., 2002, Green fluorescent protein (GFP): Applications, structure, and related photophysical behavior, *Chem. Rev*. 102:759–781.

Zondervan, R., Kulzer, F., Kol'chenko, M.A., and Orrit, M., 2004, Photobleaching of rhodamine 6G in poly(vinyl alcohol) at the ensemble and single-molecule levels, *J. Phys. Chem. A* 108:1657–1665.

40

Nonlinear (Harmonic Generation) Optical Microscopy

Ping-Chin Cheng and C.K. Sun

INTRODUCTION

In recent years, light microscopy, particularly fluorescence microscopy, has been extensively useful in the study of living cells and tissues. Although it has become an important tool in biological research, both single- (Sheppard and Shotton, 1997) or two-photon (Denk *et al.*, 1990; Cheng *et al.*, 1998, 2001) excitation schemes require that the specimen contain either intrinsic or extrinsic fluorescent probes. These probes include fluorescent dyes, fluorescent proteins, and quantum dots and common problems include probe penetration, probe toxicity, and photobleaching/damage (Konig, 1995; Cheng *et al.*, 2001a). To be useful, the fluorescent probes must usually be bound to specific biostructures or molecules, either by partition of the dye into various compartments, antigen–antibody reactions, affinity or site-specific binding of dye(s), or the transgenic expression of fluorescent and luminescent proteins. In addition, the probe may interact with the ionic environment to give a specific fluorescence signature. In all these cases, the fluorescence signals are related to the chemistry of the dye and the chemistry of the interaction between the dye and the cell or tissue or the genetic expression of the probe. Therefore, the term "chemical" and "biochemical" contrast is frequently used to describe the fluorescence imaging modality.

On the other hand, nonlinear imaging modalities exist that create contrast based on the organization and orientation of nanostructures in the specimen, and these can often provide an alternative tool for studying the dynamics of cellular structures and functions. These nonlinear imaging modalities include second and third harmonic generation (SHG and THG), in which specific structural features of the optical configuration of the native specimen generate prompt signals. In this case, signal is generated by nonlinearity in the physical properties of the specimen (such as short-period modulations or discontinuities in its refractive index, RI) particularly those that occur at very high excitation intensity, such as that present at the focus point of an objective lens illuminated with high-intensity, femtosecond pulsed laser. Unlike fluorescence, these harmonic signals are generated with no time delay at all and emerge at wavelenghts that are exact integer submultiples of the excitation wavelength and traveling in the same direction (forward).

Recent studies on man-made nanoperiodic structures (e.g., super-lattices) indicate a strong enhancement in SHG when high-intensity light is incident on non–centri-symmetric structures (Zhao *et al.*, 1999; Kao *et al.*, 2000; Sun *et al.*, 2000). SHG occurs because the structure violates the condition of optical centro-symmetry. This sort of breakdown occurs in the inorganic crystals used for doubling the frequency of laser light (see Chapter 5, *this volume*). A typical application is the frequency doubling of 1064 nm emission from a semiconductor laser to produce the 532 nm light in the green-laser pointer. More generally, SHG occurs in many other structured samples, some of which are biological.

A super-lattice structure is basically a one-dimensional nonlinear $\chi^{(2)}$ photonic crystal (where $\chi^{(2)}$ is the second-order nonlinear susceptibility), which is defined as a material with a periodicity in its second-order nonlinear dielectric properties (Berger, 1998). Strong SHG-enhancement has also been reported in one-dimensional and two-dimensional nonlinear photonic crystals (Broderick *et al.*, 2000; Dumeige *et al.*, 2001). The mechanism is similar to the bandgap-resonant enhancement that occurs in common SHG-conversion crystals and, although SHG conversion efficiency is always highest near the nonlinear photonic bandgap, it does not vanish even when the illumination (pump) wavelength is far away from the spatial modulation period (the bandgap). Quasi–phase-matching is an example of this, as the operating wavelength of the excitation is much shorter than the spatial modulation period of the nonlinear coefficient $\chi^{(2)}$. Recently, strong SHG has been reported in several types of biological material, mainly in orderly packed biomolecules or macromolecular structures (Chu *et al.*, 2001; Cheng *et al.*, 2002; Sun *et al.*, 2003). In contrast, no SHG occurs in amorphous materials, such as the almost randomly arranged macromolecules and other nanostructures that make up a cell.

The enhancement of SHG by the nanophotonic crystals of the membrane protein bacteriorhodopsin (bR), has recently been demonstrated using hyper-Rayleigh scattering (Clays *et al.*, 2001). The bR protein forms a two-dimensional (2D) crystal in the purple membrane of *Halobacterium salinarium* (Birge *et al.*, 1990). This structure has an alternating change in second-order nonlinearity with a ~5 nm period, causing it to act as a nonlinear photonic crystal (Berger, 1998). A number of other highly organized biological nanostructures have been reported that appear to break optical centro-symmetry and behave as SHG-active nonlinear photonic crystals. Such structures include stacked membranes such as those found in the myelin sheath, the endoplasmic reticulum (ER), the Golgi apparatus, and the grana in the chloroplast, microtubules, cellulosic microfibrils, collagen fibers, enamel prisms, bone matrix, starch granules, and mineral deposits in plants (Chu *et al.*, 2001; Cheng *et al.*, 2002; Sun *et al.*, 2003, 2004). Similar to the backward SHG and THG detected in a waveguide, Gu and colleagues (1999) and Sun and co-workers (2005) reported strong backward SHG from microtubules, a fact that allows imaging the cytoskeleton and the mitotic spindle in living tissue.

Collagen, the major protein of the extracellular matrix, is one of the best-known SHG structures in biology. The collagen mole-

Ping-Chin Cheng • State University of New York, Buffalo, New York 14260, and National University of Singapore, Singapore
C.K. Sun • National Taiwan University, Taipei, Taiwan, Republic of China

cule is a long, stiff, triple-stranded helical structure, in which three collagen polypeptide chains, called α-chains, are wound around one another in a ropelike superhelix. After being secreted into the extracellular space, these collagen molecules assemble into high-order polymers called collagen fibrils that are 10 to 300 nm in diameter and many hundreds of micrometers long. Collagen fibrils often aggregate into larger, cable-like bundles, several micrometers in diameter, which can be seen in the light microscope as collagen fibers. Under electron microscopy, collagen fibrils have characteristic cross-striations every 67 nm, reflecting the regularly staggered packing of the individual collagen molecules in the fibril. This regularly staggered packing order provides the needed structural condition for efficient SHG (Williams *et al.*, 2005; Sun *et al.*, 2004).

The SHG signal is created in proportion to the square of the instantaneous local intensity (Gannaway and Sheppard, 1978). As a result, like two-photon fluorescence (2PF) microscopy (Denk *et al.*, 1990; Cheng *et al.*, 1998), SHG provides intrinsic axial resolution. SHG microscopy was first demonstrated in studies of SHG photonic crystals (Gannaway and Sheppard, 1978), surfaces/interfaces (Shen, 1989), electric field distribution in semiconductors (Sun *et al.*, 2001), and was also shown to be present in studies of tissue polarity (Freund *et al.*, 1986; Guo *et al.*, 1997) and of membrane potentials in cells (Campagnola *et al.*, 1999; Peleg *et al.*, 1999; Moreaux *et al.*, 2000b).

Because most biological structures are not highly ordered, they are optically isotropic and do not produce any SHG signal. Only those few biological structures that are ordered or that involve some spatial organization that breaks the optical centro-symmetry can produce harmonic signals. In contrast to fluorescence processes that involve the excitation of the fluorescent molecule to an excited state having a finite lifetime, harmonically generated signals involve only virtual states that involve no time delay. The marked advantage of this virtual transition is the lack of energy deposition in the specimen. As a result, SHG produces no photodamage or bleaching, and like backscattered light, can be regarded as a truly "non-invasive" imaging modality. However, it is important to remember that the very high instantaneous power levels required to produce the effect may cause other novel and damaging nonlinear damage mechanisms to occur (see Chapter 38, *this volume*). As both harmonic generation and nonlinear absorption processes can occur simultaneously, it is also possible to produce photodamage due to absorption processes if absorbers are present. In fact, as some small amount of nonlinear absorption always occurs in biological specimens, the main advantages of SHG are not just that the signal generation process involves no energy deposition, but that it provides specific structural information. In contrast to the chemical specificity that characterizes fluorescence imaging, harmonic generation (SHG and THG) provides an imaging modality specific for structural configuration.

Discontinuities in RI or the optical dispersion properties of biological tissues can generate third harmonic generation (THG) signals (Barad *et al.*, 1997; Muller *et al.*, 1998; Moreaux *et al.*, 2000a,b; Sun *et al.*, 2001) and the intensity of these signals is proportional to the third power of the illumination intensity. Using the same illumination wavelength, THG provides even better optical-sectioning resolution than SHG or 2PF, but is also more sensitive to changes in the intensity of the light in the focused spot, such as those caused by laser instability or by scattering or defocusing of the illumination. The THG can be used to study optical interfaces in the cell such as those at cell membranes or organelle surfaces. For example, the surface of the erythrocyte can generate significant THG (Sun *et al.*, 2004).

HARMONIC GENERATION

Shortly after the first demonstration of the laser by Maiman in 1960, the next year Franken and co-workers discovered the process of SHG in man-made materials. This work is often taken as the beginning of the field of nonlinear optics. Nonlinear optical phenomena are "nonlinear" in the sense that they occur when the response of a specimen depends upon the strength of the optical electric field in a nonlinear manner. For example, SHG occurs as a result of that part of the atomic response to the oscillating field of the light that depends quadratically on the strength of this optical field. Consequently, the intensity of the signal generated by the SHG mechanism increases as the square of the intensity of the incident light. By the same token, THG signals vary with the cube of the intensity of the incident light.

An image is a two-dimensional recording of the interaction between light and a specimen, and therefore is a representation of the optical properties of the specimen. In conventional optical imaging, contrast mechanisms include interactions such as absorption, reflection, scattering, and fluorescence, and the response recorded is linearly dependent on the intensity of the incident light. In the nonlinear optical domain, high-intensity light causes a variety of "anomalous" optical responses, and therefore the image contrast mechanism represents not only the differences in optical properties of the specimen, but also the result of the modification of those optical properties that depend on the intensity of the light in a nonlinear manner. In the case of conventional (linear) optics, a linear relationship exists between the electric field strength of the light and the induced polarization of the object. At relatively low incident intensity, the optical response can be approximated to be the first-order response as:

$$\tilde{P}(t) = \varepsilon_0 \chi^{(1)} \tilde{E}(t) \qquad \textbf{(1)}$$

where $\chi^{(1)}$ is the linear susceptibility, $\tilde{P}(t)$ is the dipole moment per unit volume, or polarization of a material system, $\tilde{E}(t)$ is the strength of an applied optical field, and ω is the frequency.

Second Harmonic Generation

In contrast, at high incident intensity, the nonlinear optical response can be described by:

$$\begin{aligned}\tilde{P}(t) &= \varepsilon_0 \chi^{(1)} \tilde{E}(t) + \varepsilon_0 \chi^{(2)} \tilde{E}(t)^2 + \varepsilon_0 \chi^{(3)} \tilde{E}(t)^3 + \ldots \\ &\equiv \tilde{P}^{(1)}(t) + \tilde{P}^{(2)}(t) + \tilde{P}^{(3)}(t) + \ldots \end{aligned} \qquad \textbf{(2)}$$

where $\chi^{(2)}$ is the second-order nonlinear susceptibility and $\chi^{(3)}$ is the third-order nonlinear susceptibility.

In the above equation, because the fields are vectors, the nonlinear susceptibilities are tensors. As each atom acts as an oscillating dipole that radiates in a dipole radiation pattern, the radiation phase among the enormous number of atoms must be matched to induce constructive interference and thus nonlinear generation is allowed under phase-matching conditions (i.e., when the scattered light **is** in phase). This leads to the generation of radiation at the second harmonic frequency (half the wavelength of the illumination). However, this situation does not lead to the generation of electromagnetic radiation because its second time derivative vanishes and a static electric field is created within the nonlinear crystal.

Second harmonic generation can also be considered as an interaction involving the exchange of photons between the various frequency components of the field. In SHG, two photons of frequency ω are destroyed and one photon of frequency 2ω is simultaneously created in a single quantum-mechanical process. The

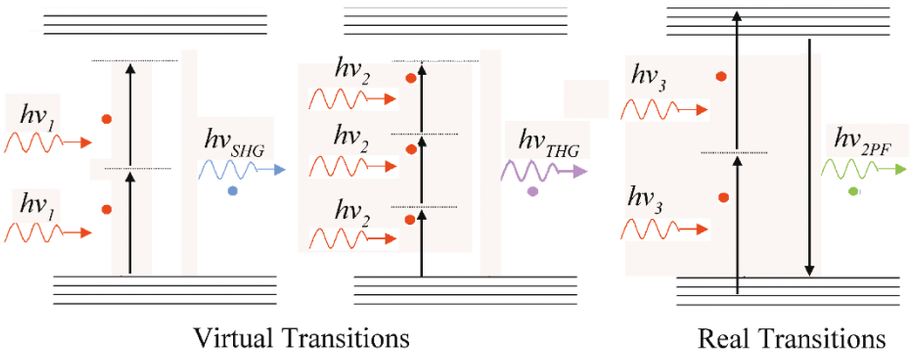


FIGURE 40.1. Energy state diagram. Both SHG and THG involve virtual transitions in which no energy is absorbed by the specimen. In contrast, two-photon fluorescence (2PF) involves the absorption of energy (real transitions) and excitation of molecules. The wavelength of SHG is half and THG is one third that of the incident wavelength, while 2PF has an emission wavelength more than half of the incident wavelength.

solid lines in Figure 40.1 represent the atomic ground states, and the dashed lines represent virtual levels. These levels are not energy eigenlevels of the free atom, but rather represent the combined energy of one of the energy eigenstates of the atom and of one or more photons of the radiation field.

The fact that SHG vanishes in any material system that possesses centro-symmetry (i.e., one that has a center of inversion) can be explained by changing the sign of the applied electric field in Eq. 2. In a medium possessing inversion symmetry, the sign of the induced polarization must also change. Hence, relation 2 is replaced by

$$-\tilde{p}^{(2)}(t) = \varepsilon_0\chi^{(2)}[-\tilde{E}(t)]^2 = \varepsilon_0\chi^{(2)}\tilde{E}(t)^2 \qquad \textbf{(3)}$$

By comparing Eq. 3 with Eq. 2, $\tilde{P}(t)$ must equal $-\tilde{P}(t)$, and this can occur only if $\tilde{P}(t)$ vanishes identically. So $\chi^{(2)}$ is equal to zero for centro-symmetric media and no SHG signal is expected. Because the molecules making up most biological materials are oriented more or less "at random" (compared to a crystal, for example), they generate no SHG signals. The phase-matching condition in SHG is that the wave vector difference between input excitation light and output harmonic light is zero. Therefore, phase-matching is seriously affected by polarization, and SHG is sensitive to the angle between the polarization of the incident light and the symmetry condition of the material. Pol-dependent SHG can provide information about crystal orientation and imperfection, macromolecular structure and orientation, and regions where the centro-symmetry either breaks down, such as at surfaces and optical interfaces or where it is induced by organized, submicron structures. It can also be created by large localized residual electric fields, such as those across electrically polarized cell membranes.

Third Harmonic Generation

Third harmonic generation involves a process whereby three photons of frequency ω are destroyed and one photon of frequency 3ω is created. A nonlinear contribution to the polarization of the medium at the frequency of the incident field leads to a nonlinear contribution to the refractive index experienced by a wave at frequency ω.

Normally, the tightly focused condition in a microscope setup inhibits the production of third harmonic signals (Barad *et al.*, 1997; Berger, 1998), and a positive wave vector ($\Delta k = 3k_\omega - k_{3\omega} > 0$) mismatch between the fundamental and harmonic beam is required to achieve phase-matching. Under tight focusing conditions, third harmonic production is allowed if an optical interface is present within the focal volume, no mismatch is required, and the resulting breakdown in focal volume symmetry enables efficient THG generation for $\Delta k < 0$ (normal dispersion).

When one calculates the third harmonic power as a function of the interface uniformity, there is a change in either the refractive index or in the third-order nonlinear susceptibility, and this has the result that the third harmonic power does not vanish. Barad and colleagues (1997) demonstrated that, as a result of this interface effect, imaging with the third harmonic is possible and is especially suitable for transparent phase specimens with low intrinsic contrast such as the cell boundary. The THG signal strength is sensitive to changes in the nonlinear optical properties of the specimen.

Multi-Photon Absorption and Fluorescence

Because in 2PF, the absorbed power is proportional to the square of the incident light intensity (i.e., as if it depended on the square of the photon concentration), this process is called two-photon absorption. The absorbed two-photon energy can excite a molecule to its excited state or even to ionization (two-photon ionization). In the process of two-photon fluorescence, an atom/molecule makes a transition from its ground state (S_0) to a real excited state (S_2) by the simultaneous absorption of two laser photons and quickly transits to a metastable state (S_1) and then emits one photon with higher frequency (ν_{em} but less than $2\nu_{ex}$) while returning to the ground state ($S_1 \rightarrow S_0$). The transition between the first excited state and the metastable state can produce chemical events that lead to photobleaching, a process that removes the fluorescent species from the fluorescing pool (see Chapter 39, *this volume*). Moreover, the excess absorbed energy that is lost as vibrational energy during the transition, can result in photodamage, and this process may become even worse as the energy difference between these two states increases.

LIGHT SOURCES AND DETECTORS FOR SECOND HARMONIC GENERATION AND THIRD HARMONIC GENERATION IMAGING

Because SHG and THG signal strength is quadratically or third-power dependent on the intensity of the illumination, high illumination intensity is required for the efficient generation of these signals. As continuous illumination (CW) at such high intensity would result in unacceptably high energy deposition, one instead uses the high instantaneous power density that can be achieved using a mode-locked, ultra-fast pulsed laser. Four such laser systems (Table 40.1) are currently available for use in nonlinear microscopy: the titanium:sapphire (Ti:Sa) (various suppliers), the Cr:forsterite laser (Avista Project, Russia; Ming-mei Technology, Taiwan, Republic of China), the Nd:glass laser (Time-Bandwidth Products, Switzerland), and the femtosecond ytterbium laser (Amplitude System, Talence, France).

The Ti:Sa has a tuning range of about 700 to 980 nm [near-infrared (NIR)] and is currently used extensively in two-photon fluorescence microscopy. The SHG wavelength excited by a Ti:Sa femtosecond laser operating at 810 nm will be in the deep blue at 405 nm, while 2PF will be in the visible region (>405 nm). However, the THG signal generated by a 810 nm primary beam will fall at 270 nm, in the deep ultraviolet (UV) region, while three-photon fluorescence (3PF) will be found at >270 nm. Consequently, the THG and 3PF signals will suffer from the high UV absorption of most biological specimens (Fig. 40.2; Cheng *et al.*, 2001a; Lin *et al.*, 2001), making signal detection difficult. In addition, one would need special (and expensive!) UV objectives, mirrors and photomultiplier tubes (PMT) in the detecting path.

In contrast, the Cr:forsterite laser operates in the range of 1230 to 1270 nm in the IR spectrum, making it an excellent light source for multi-modality microscopy (Bouma *et al.*, 1996; Chu *et al.*, 2002). For example, operating a Cr:forsterite laser at 1230 nm allows SHG (615 nm), THG (410 nm), 2PF (>615 nm), and 3PF (>410 nm), all to fall within the visible spectrum. In addition, the lowest light attenuation in biological material is generally found in the 1000 to 1300 nm range (Fig. 40.2). By moving the excitation wavelength to 1230 nm, not only the visible but also the NIR spectrum is open for signal recording. This could be important in imaging botanical specimens that have a high autofluorescence output over nearly the entire visible spectrum (see Fig. 20.2, *this volume*). The fact that autofluorescence diminishes at wavelengths longer than the fluorescence emission of chlorophylls makes NIR fluorescent probes, such as AlexaFluor 750, Cy5.5 and Cy7 (Molecular Probes Inc., Eugene, OR), very attractive. Development of endogenous fluorophore mutants (i.e., long-wavelength fluorescent proteins) having emission wavelengths longer than DsRed will be helpful for the study of botanical specimens. Liu and colleagues (2001) and Cheng and co-workers (2001) have demonstrated that a number of commonly used fluorescent probes can be efficiently excited at 1230 nm by 2PF and 3PF.

On the other hand, mode-locked femtosecond Nd:glass and diode-pumped ytterbium lasers provide an alternative choice. A typical femtosecond Nd:glass system offers a tuning range of 1053 to 1064 nm, with a repetition rate of 70 to 150 MHz and a 150fs pulse width (Time-Bandwidth Products, Zurich). This laser will produce SHG signal at 526 to 532 nm, which is at the second attenuation minimum of green botanical specimens (Fig. 40.2). The

TABLE 40.1. Pulsed Lasers Suitable for Generating SHG and THG Signals

Laser System	Wavelength Range (nm)	Pulse Width (fs)	Repetition Rate (Hz)
Ti:Sa	700–980	100	76–100 MHz 2 GHz, Chu *et al.*, 2003b
Nd:glass	1053–1064	150	70–150 MHz
Cr:forsterite	1230–1270	65	76–120 MHz
Diode-pumped ytterbium	1030	200	50 MHz

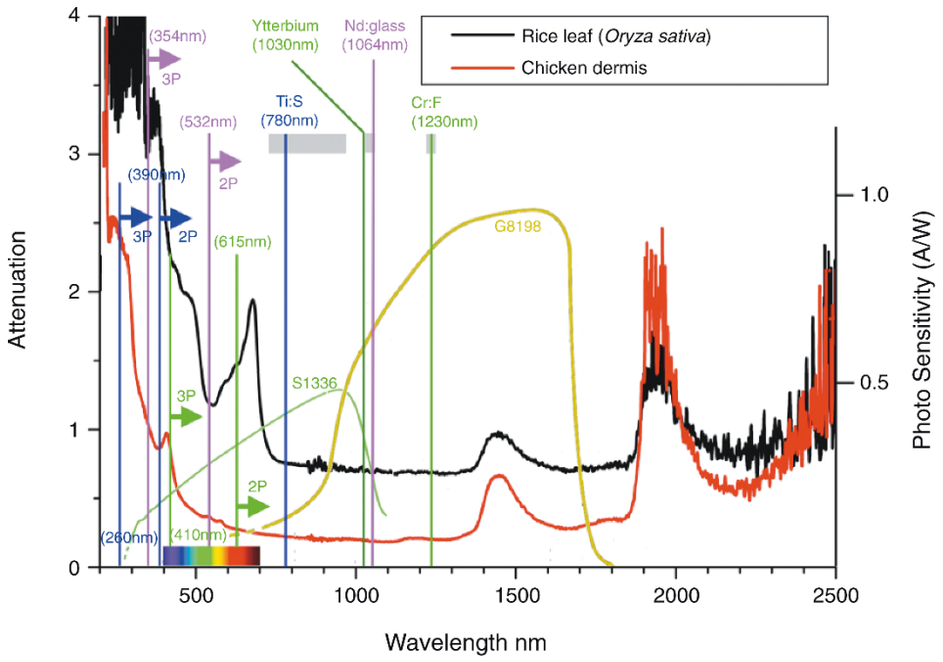


FIGURE 40.2. Light attenuation spectra (absorption and scattering) in rice leaf (*Oryza sativa*) and chicken dermis. Note the operating ranges of Ti:Sa, ytterbium, Nd:glass, and Cr:Forsterite lasers. The light green lines indicate a typical emission wavelength of Cr:Forsterite (1230 nm) and its corresponding SHG (615 nm) and THG (410 nm). The blue lines represent a typical Ti:Sa emission wavelength (780 nm) and the corresponding SHG (390 nm) and THG (260 nm) wavelengths. The purple lines indicate the emission line of Nd:glass and corresponding SHG (532 nm) and THG (352 nm) lines. The dark green line indicates the emission line of ytterbium laser (1030 nm). The curves labeled S1336 and G8198 represent the sensitivity of typical visible and NIR photodiode detectors.

THG is situated at 351 to 354 nm. Because both the excitation and emission wavelength are optimized at an attenuation minimum, using Nd:glass greatly increases the imaging depth in tissue, particularly green plant tissue. Using this laser system, one can obtain useful 3PF, 2PF, and SHG simultaneously and it has the added advantage that many commercially available IR objectives have reasonable transmittance at the 1064 nm wavelength. On the other hand, the diode-pumped ytterbium laser operates at 1030 nm, with SHG and THG at 515 nm and 343 nm, respectively.

Figure 40.2 summarizes the operating wavelengths and the SHG and THG signals of the four mode-locked ultra-fast lasers in reference to the attenuation spectra of biological specimens and detector sensitivity. In the near UV wavelength region, attenuation is dominated by the strong absorption of common tissue constituents such as proteins and carbohydrates. For IR wavelengths longer than 1400 nm, however, the molecular resonance absorption of water starts to dominate the attenuation. As a result, biological specimens have a relatively transparent window between 350 to 1300 nm.

Although the Ti:Sa laser, operating at around 720–950 nm, has been widely adopted as the preferred light source for multi-photon microscopy, one can easily see that the attenuation minimum is around 1000 to 1300 nm, not in the Ti:Sa range. In fact, this should not be surprising because scattering cross-sections become smaller as the wavelength increases. This plot is also in good agreement with previous measurements of the attenuation coefficients of biological materials such as human skin (Anderson and Parrish, 1981), maize stem (Cheng *et al.*, 1998), and leaves (Lin *et al.*, 2001).

The advantage of the Ti:Sa laser is its large tuning range compared to the Cr:forsterite and Nd:glass lasers. In addition, while most objective lenses work well in the NIR spectrum (up to 900 nm) and some IR objectives have reasonable transmission up to ~1100 nm, obtaining reasonable transmission and optical correction in the 1230 nm range requires special objective lenses and other optical components (see Chapter 7, *this volume*).

How do the signals produced by these four lasers match the performance of the available detectors? Because the Ti:Sa wavelengths are well within in the sensitivity range of both high quantum efficiency (QE) silicon-based detectors and most PMT photocathodes, any scattered excitation illumination will be detected by these detectors and recorded as background. Although this reduces the signal-to-noise (S/N) ratio of fluorescence signals, it also affords the benefit of being able to detect the backscattered light (BSL) signal as an additional, non-damaging imaging modality.

On the other hand, because the emission wavelengths of Nd:glass and Cr:forsterite lasers are beyond the sensitivity of most of the commonly used PMT and silicon detectors (Table 40.2), detector insensitivity guarantees a low background level from scattered light but sacrifices availability of BSL modality unless a special NIR detector (e.g., InGaAs photodiode, Edmund Scientific) is installed. Table 40.2 lists the sensitivity, the sensitivity range, and the wavelength of maximum sensitivity for each of the photodetectors commonly used in microscopy (see also Chapter 12, *this volume*). Because the peak intensity of the ultra-fast laser is so high, a dichroic beam-splitter and a barrier filter may not be sufficient to exclude the background signal caused by light leakage. This is a particular problem when collecting SHG and THG signals in the transmission mode where the excitation striking the emission filter may be $10^7\times$ brighter than the SHG/THG signal. In this case, using detectors insensitive to the illumination wavelength can further limit the background signal level, improving the S/N of the image.

Using a Cr:forsterite or Nd:glass laser at 1230 nm/1064 nm for nonlinear microscopy allows one to fully utilize the transparent window in most biological specimens. At 1230 nm, Chu and colleagues found that the SHG and 2PF signal dropped by only 1 order of magnitude, when generated at a depth of 360 μm in a maize stem fixed in 70% ethanol (Chu *et al.*, 2001). This is in good agreement with previous light attenuation measurements of maize stems (Cheng *et al.*, 1998). Comparing the attenuation spectra of

TABLE 40.2. Characteristics of Photodetectors Used for SHG and THG Microscopy

Type	Photocathode Composition	Photoemission Threshold (nm)	Wavelength at Maximum Sensitivity (nm)	Radiant Sensitivity at λ_{max} (mA/W)	Quantum Efficiency at λ_{max} (%)
S1	AgOCs	1100	800	2.3	0.4
S4	$SbCs_3$	680	400	50	16
S11	$SbCs_3$	700	440	80	22
S13					
S20	$SbNa_2KCs$	850	420	70	20
S20 (extended-red multi-alkal)	$SbNa_2KCs$	900	550	35	8
Bialkali	SbKCs	630	400	90	28
Bialkali (green extended)	SbKCs	700	440	100	28
Solar blind	CsTe	340	235	20	10
		Spectral range		Photo sensitivity (A/W)	
Silicon photodiode		320 (190)–1100 nm	960 nm	0.33 (λ = 633 nm)	
InGaAs photo-diode		900–1700 nm	1550 nm	0.9 (λ = 1300 nm) 0.95 (λ = 1550 nm)	

The short wavelength limit of the PMT is determined by the window material (lime glass, 300 nm; borosilicate glass, 250 nm; fused silica, 180 nm. The short wavelength sensitivity cut-off of photodiode is also limited by the package window material; number in parentheses represents fused silica window. (Data adopted from Photonics, Brive, France and Hamamatsu Inc., Japan. QE data refer to the photocathode response only.)

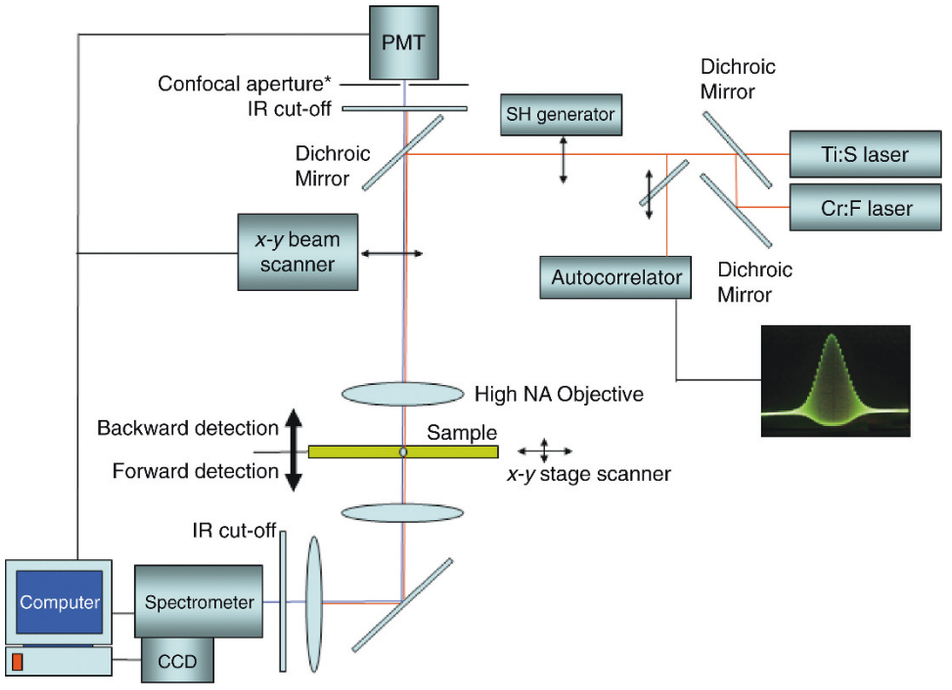


FIGURE 40.3. (A) Diagrammatic representation of a nonlinear laser-scanning microscope. The *xy*-beam scanner can be removed (by parking the *xy*-mirror at the center position) from the system to allow stage-scanning operation. An autocorrelator can be introduced into the beam to monitor the pulse width. A second harmonic generating crystal can also be introduced into the beam to allow the illumination to operate at λ/2. The spectrometer can also be connected to the epi-illumination path to detect the backward SHG signal. CCD, charge-coupled device; *, optional.

plant tissue with that of a chicken skin (Fig. 40.1), over the emission range of the Ti:Sa laser, one can expect significantly better depth penetration performance from Cr:forsterite/Nd:glass/ytterbium laser sources in brain-slice research. This superior depth performance agrees well with previous studies comparing the penetration depth of optical coherence tomography (OCT) between 800 nm and 1300 nm light (see Chapter 34, *this volume*; Bouma *et al.*, 1996).

Moreover, a significant reduction in photo-induced damage was observed in plant materials when 2PF microscopy was conducted using a femtosecond Cr:forsterite laser rather than a femtosecond Ti:Sa laser, under similar illumination intensity and exposure conditions (Chen *et al.*, 2002).

NONLINEAR OPTICAL MICROSCOPY SETUP

Figure 40.3 shows a diagrammatic representation of a typical imaging system for multi-modal, nonlinear microscope using either Cr:forsterite, Nd:glass, ytterbium, or Ti:Sa lasers (Cheng *et al.*, 2001b). In our setup, the laser beam profile is first shaped with a spatial filter and collimated by a beam expander to fill the back aperture of the objective lens. The collimated beam was coupled into an Olympus IX71 microscope through the confocal scanning unit with a 45° dichroic beam-splitter (Chroma 970dcspxr) to reflect the IR and transmit visible light. The original aluminum coating on the *xy*-scanning mirrors was replaced with a silver coating to enhance IR reflectivity. A second beam path was constructed to bypass the scan mirrors for fixed-beam, stage-scanning operation. The excitation IR light is focused onto the biological sample with a spot size close to diffraction limit using high-NA objectives [such as Olympus ULWD MIR 80×/0.75; or UPlanApo water-immersion 60×/1.20] and the excited photoemission spectrum was collected using an opposing high-NA objective (of the same type as the illuminating objective). The fundamental IR beam was removed with an infrared-blocking filter in conjunction with a dichroic beam-splitter (Chroma 970dcspxr). The collected light (visible and NIR) was then directed into a spectrometer (SpectraPro-2300i, Roper Scientific) and recorded by a Peltier-cooled charge-coupled device (CCD) detector (DV42-0E, Andor Technology). Transmission detection is used because most SHG and THG is emitted in the forward direction (i.e., in the same direction as the pump beam; Cheng and Lin, 1990).[1] In addition, a mechanical scanning stage is included to permit stable raster scanning so that *xyz*λ-images can be obtained. Is these images, a detailed nonlinear spectrum is recorded at each pixel (*xy*-plane is defined as the plane perpendicular to the laser propagation direction). The signal spectrum is obtained using a scanning spectrometer equipped with an InGaAs photodiode (Edmund Scientific). When beam scanning, a flat mirror is placed in the back-focal plane of the collector objective to send the SHG/THG signal back up the optical path so that it can be de-scanned and detected by the PMTs (the same setup as the transmission confocal microscope method discussed in Chapter 8, *this volume*). To obtain an image with a set signal wavelength, we used a simple scanning-monochrometer method, adopted from astronomy. The actual system is shown in Figure 40.4.

Although it is possible to select harmonic signals using narrow bandpass interference filters, it is important to take special precautions if the bandpass filter is used to isolate the SHG signal from multi-photon-excited fluorescence. In certain types of specimen, where the fluorescence emission wavelength generated by

[1] Recent results have shown that, in certain biological structures, backward SHG signals can be even stronger than forward SHG signals (Sun *et al.*, 2005).

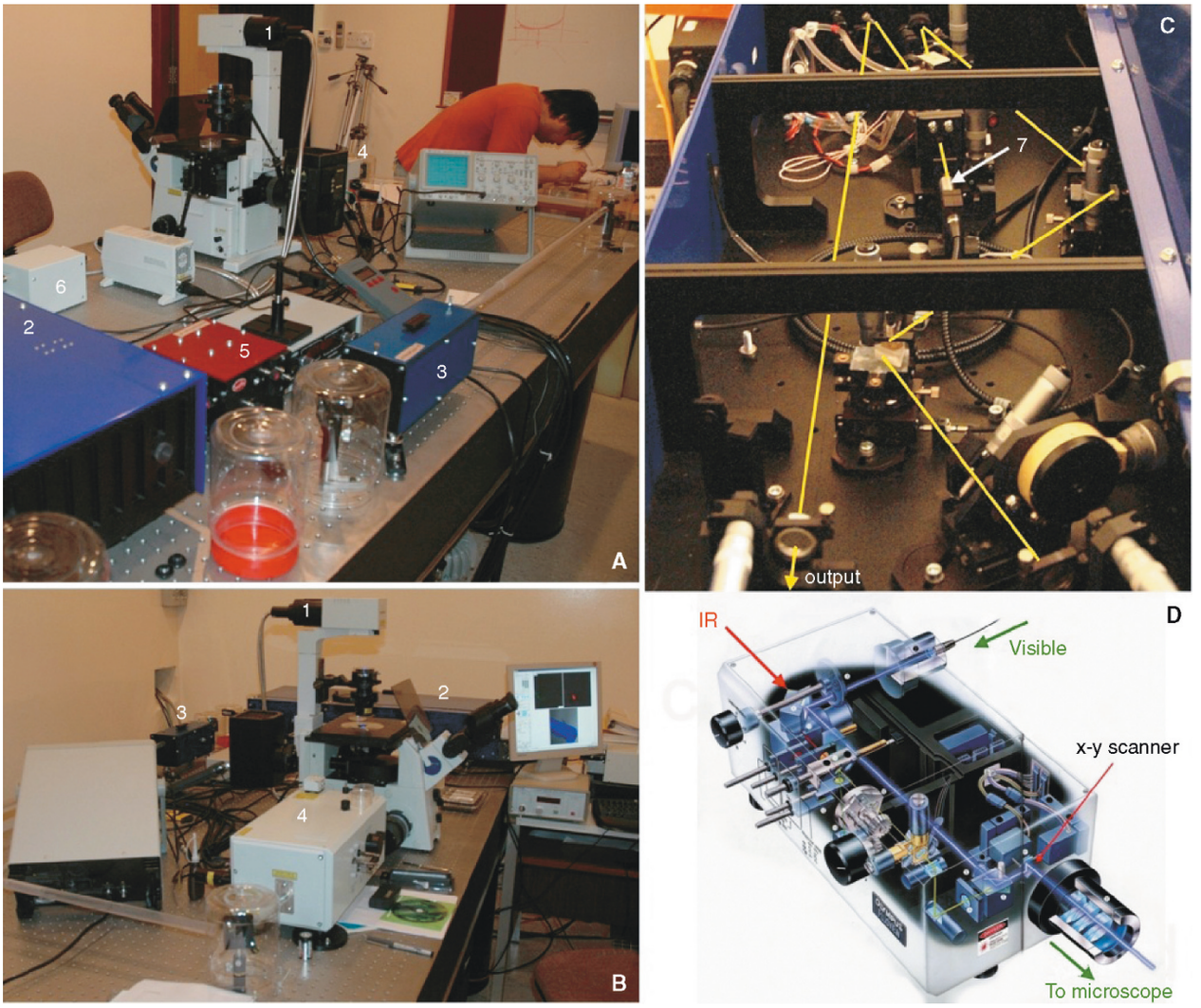


FIGURE 40.4. The nonlinear microscope setup in the laboratory of one of the authors (PCC) at the Department of Biological Sciences, National University of Singapore (A, B). The system is based on a mode-locked, ultra-fast Cr:forsterite laser (65 fs; 120 MHz; tuning range, 1230–1270 nm) (C) and an Olympus Fluroview FV300 confocal scanning unit (D). 1, transmission detector fiber connection; 2, Cr:forsterite laser; 3, SH generator; 4, beam scanner; 5, autocorrelator; 6, transmission detector; 7, pump input for Cr:forsterite laser.

three-photon excitation coincides with the SHG wavelength, spectral contamination can be serious even when a narrow-bandpass SHG isolating filter is used. Figure 40.5(A) shows a fluorescence spectrum when LysoTracker Red (Molecular Probes, Inc., L7528) is excited by Cr:forsterite laser at 1240 nm. If a biological specimen is stained with the dye and imaged simultaneously in SHG and fluorescence mode, the expected SHG signal is at 620 nm and THG at 413 nm, but the multi-photon-excited fluorescence (both 2PF and 3PF) of LysoTracker Red extends from ~580 nm to 720 nm. Therefore, even a very narrow bandpass filter centered at 620 nm will allow significant fluorescence contamination in the SHG signals, particularly if the SHG is relatively weak.

The best way to obtain a "pure" SHG signal is to use a monochrometer. Figure 40.5(B) shows the emission spectrum of the red leaf of *Euphorbia pulcherrima* (poinsettia) excited by 1234 nm IR, and the fluorescence emission consisting of 2PF and 3PF. Note the position of the SHG at 617 nm. No trace of SHG can be recognized in this spectrum because, in this case, the SHG is in the forward direction with respect to the illumination beam, while this spectrum was recorded from the same side as the incident illumination.

Figure 40.5(C) shows the emission spectrum of the leaf of *Zea mays* (corn). The fluorescence emission is in the red region and a small peak at 617 nm is the SHG signal scattered back from the leaf tissue. Because the SHG signal propagates in the same direction as the illumination beam, placing detector on the far side of the specimen will ensure better signal strength. Figure 40.6 shows nonlinear absorption by a methanol extract from the yellow petals of *Canna*. Readers are also referred to the nonlinear absorption spectrum of the highly efficient APSS fluorophore [(Fig. 8.5(A)]. Sun and colleagues (2003) have reported that using a longer

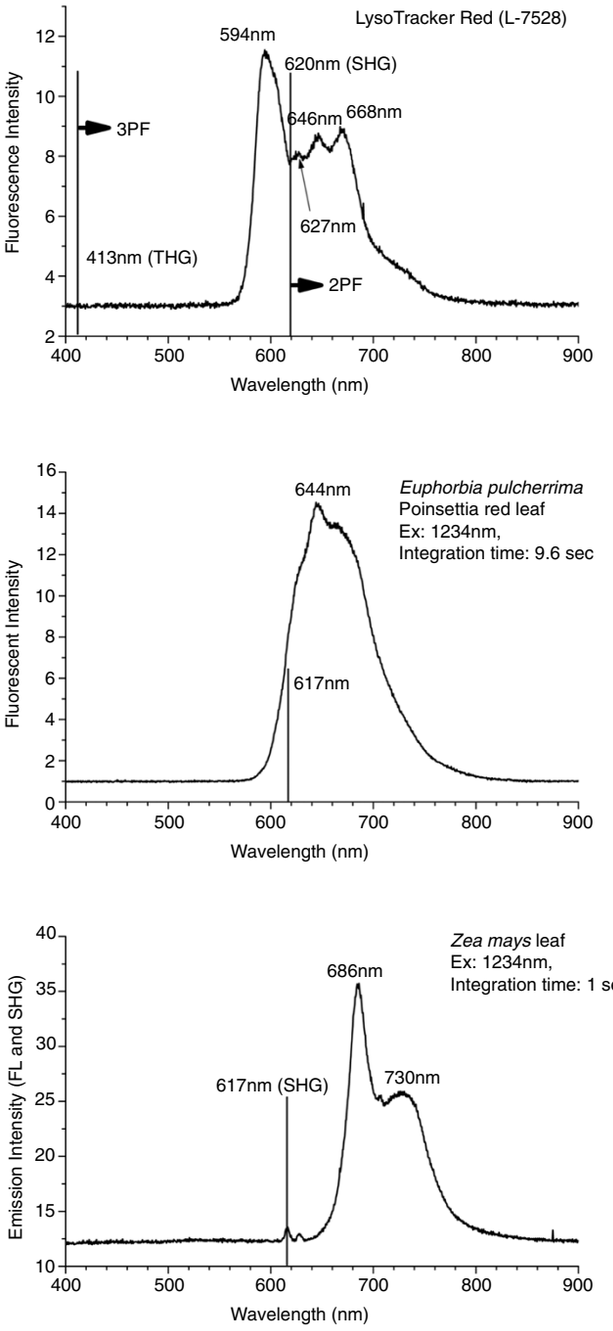


FIGURE 40.5. Two-photon fluorescence spectra of three different samples. (Top) LysoTracker Red (L-752, Molecular Probes), excitation at 1240 nm; (middle) red leaf of *Euphorbia pulcherrima* (excitation, 1234 nm); and (Bottom) leaf of *Zea mays* (excitation, 1234 nm), note the small SHG peak at 617 nm. The top two spectra show overlap between the 2PF emission and that from SHG.

wavelength excitation (1230 nm vs. 800 nm) can minimize the two-photon autofluorescence signal, hence improve the S/N in harmonic generation images. However, it is not clear if this reduction in autofluorescence intensity corresponds to a lower nonlinear absorbance of the specimen or a reduction in the quantum yield of the fluorophore.

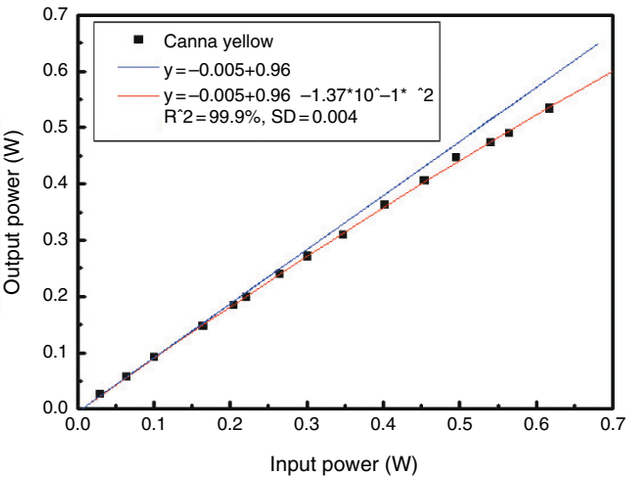


FIGURE 40.6. Nonlinear absorption of the methanol extract of the yellow petal of *Canna*. (Measurement was performed by Ms. Mei-Hsin Chen, Graduate Institute of Electro-Optical Engineering and Department of Electrical Engineering, National Taiwan University, Taipei, Taiwan.)

OPTICALLY ACTIVE BIOLOGICAL STRUCTURES

Optically Active Structures in Plants

The cell wall of higher plants consists of macrofibrils, which are orderly bundles of cellulose microfibrils each with a diameter about 10 nm. Within the microfibrils are micelles, representing another degree of highly ordered crystalline structure (Peter *et al.*, 1992). These photonic-crystal–like structures produce the optical anisotropy that gives rise to SHG. Figure 40.7(A) shows the nonlinear emission spectra measured from the cell wall of a parenchyma cell in maize stem (*Zea mays* L.). Symmetric THG and SHG emission peaks are visible, centered at 410 nm and 615 nm, with an intensity similar to or stronger than the two-photon autofluorescence centered at 680 nm. The strong THG signal is induced by the optical inhomogeneity within, and surrounding, the cell wall, while the SHG signal reflects the highly organized crystalline structures in the wall that break three-dimensional (3D) optical centro-symmetry. Figure 40.7(B–D) shows the THG, SHG, and 2PF images made by detecting wavelengths corresponding to the peaks in the spectrum shown in Figure 40.7(A). The source of SHG is further confirmed by the strong SHG signal obtained from the stone cell of pear (*Pyrus serotina* R.) (Fig. 40.8). The extensive secondary wall development of the sclerenchyma cell generates significant SHG signals.

The starch granule, a highly birefringent structure, consists of crystalline amylopectin lamellae organized into effectively spherical blocklets and large concentric growth rings (Gallant *et al.*, 1997) (Fig. 40.9). The crystalline lamellae in starch granules are believed to consist of the ordered, double-helical amylopectin side chains and are interleaved with more amorphous lamellae consisting of the amylopectin branching regions. The amylopectin side-chain clusters within the crystalline lamellae have varying sizes but, on average, are around 10 nm wide by 9 to 10 nm long (the length represents the thickness of the lamellae). These orderly nanolayers form the biophotonic structure, breaking the centro-symmetry and producing strong SHG. On the other hand, starch granules contain other, larger structures made up of crystalline hard shells and semi-crystalline soft shells having dimensions of hundreds of nanometers. These alternating crystalline and semi-

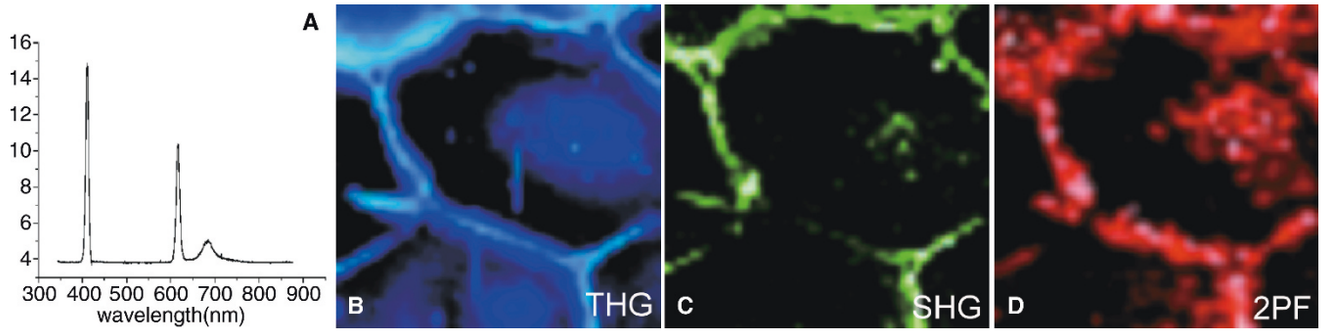


FIGURE 40.7. Nonlinear emission spectra measured from the cell wall of a parenchyma cell in maize stem (*Zea mays*). (A) The spectrum present a point in the image of (B); (B) THG image; (C) SHG; and (D) 2PF images.

crystalline rings have spatially-modulated nonlinear properties that could behave as 3D nonlinear photonic bandgap crystals (Berger, 1998) and may be responsible for the strong SHG observed. For example, the SHG signal from a potato (*Solanum tuberosum* L.) starch granule is so strong that is visible to the naked eye, even under ambient room light (Fig. 40.10). This unexpectedly strong SHG activity may be the result not only of the superhelical amylopectin nanostructure but also suggests that the specimen may be acting as a collection of 3D photonic bandgap crystals, the reciprocal lattice basis vectors of which would be capable of producing SHG by meeting the non-collinear phase-matching condition. Depending on the illumination wavelength and the materials of which the specimen is composed, the spatial frequencies present in high-order structures from 200 nm to 10 μm in size, can provide the non-collinear phase-matching base vector needed to produce SHG. The potato specimen is acting as an array of nonlinear, biophotonic bandgap crystals.

Figure 40.11(A–C) shows THG, SHG, and 2PF images, respectively. of a mesophyll cell of *Commelina communis* L.; Figure 40.11(D) is the corresponding three-channel, false-color image. The THG image shows the interface signal between the chloroplast and the surrounding cytoplasm while the SHG reveals starch granules and possibly grana and thylakoid membranes in the chloroplasts and the 2PF results from chlorophyll autofluorescence. Enlarged images of individual chloroplasts are shown in Figure 40.11(E–H).

The distribution of chlorophyll inside the chloroplasts is shown by the 2PF signals while THG signal provides information on various sub-organelle interfaces. SHG signal, on the other hand, indicates the presence of nano-organized biophotonic structures in the chloroplast. By matching the SHG image with transmission electron microscope (TEM) images of similar specimens, it has been possible to conclude that the SHG signals are produced by stacked thylakoid membranes present in the grana (crescent shaped) and by highly birefringent starch granules (oval or round shaped) in the chloroplasts (Gunning and Steer, 1996). The stacked thylakoid membranes of the grana and the orderly deposits of amylopectin in the starch granules provide the structural requirement for efficient SHG, again resembling the behavior of photonic crystals.

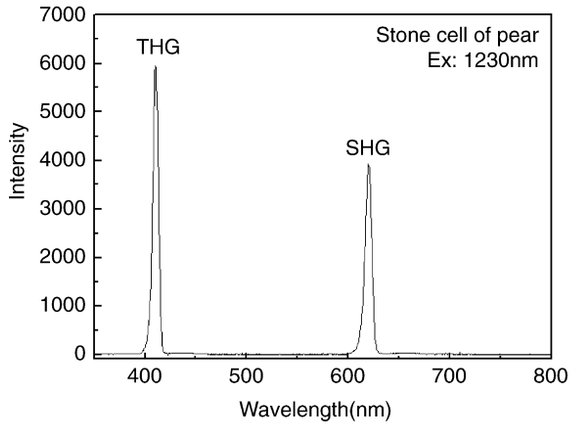


FIGURE 40.8. Spectrum of the stone cell of a pear fruit (*Pyrus serotina* R.) recorded with 0.1-s integration time.

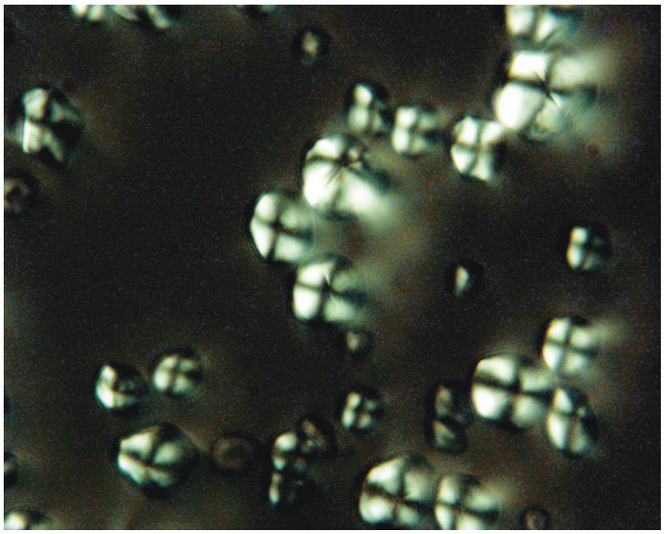


FIGURE 40.9. Conventional polarization microscopy of maize starch granules. The image was taken with an oblique-illuminated microscope equipped with cross-polarizer. Note the strong birefringence of the starch granules.

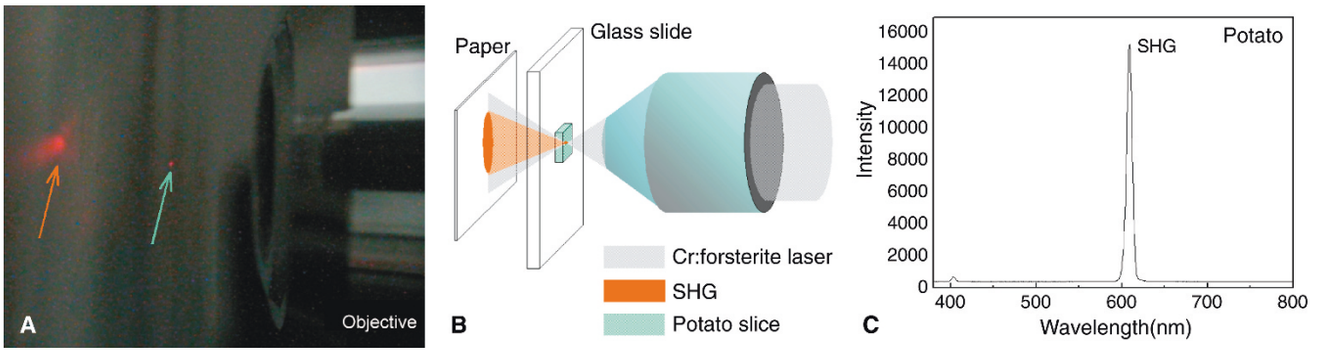


FIGURE 40.10. Photograph showing the red SHG signal generated from a thin slice of potato tuber (*blue arrow*) by a focused laser beam at a wavelength of 1230 nm and projected onto a white paper (*orange arrow*) (A). As this photograph was taken with a conventional camera, which is insensitive to 1230 nm light, the small red spot on the potato slice is the scattered SHG signal. The corresponding setup is schematically shown in (B). The emission spectrum is shown in (C).

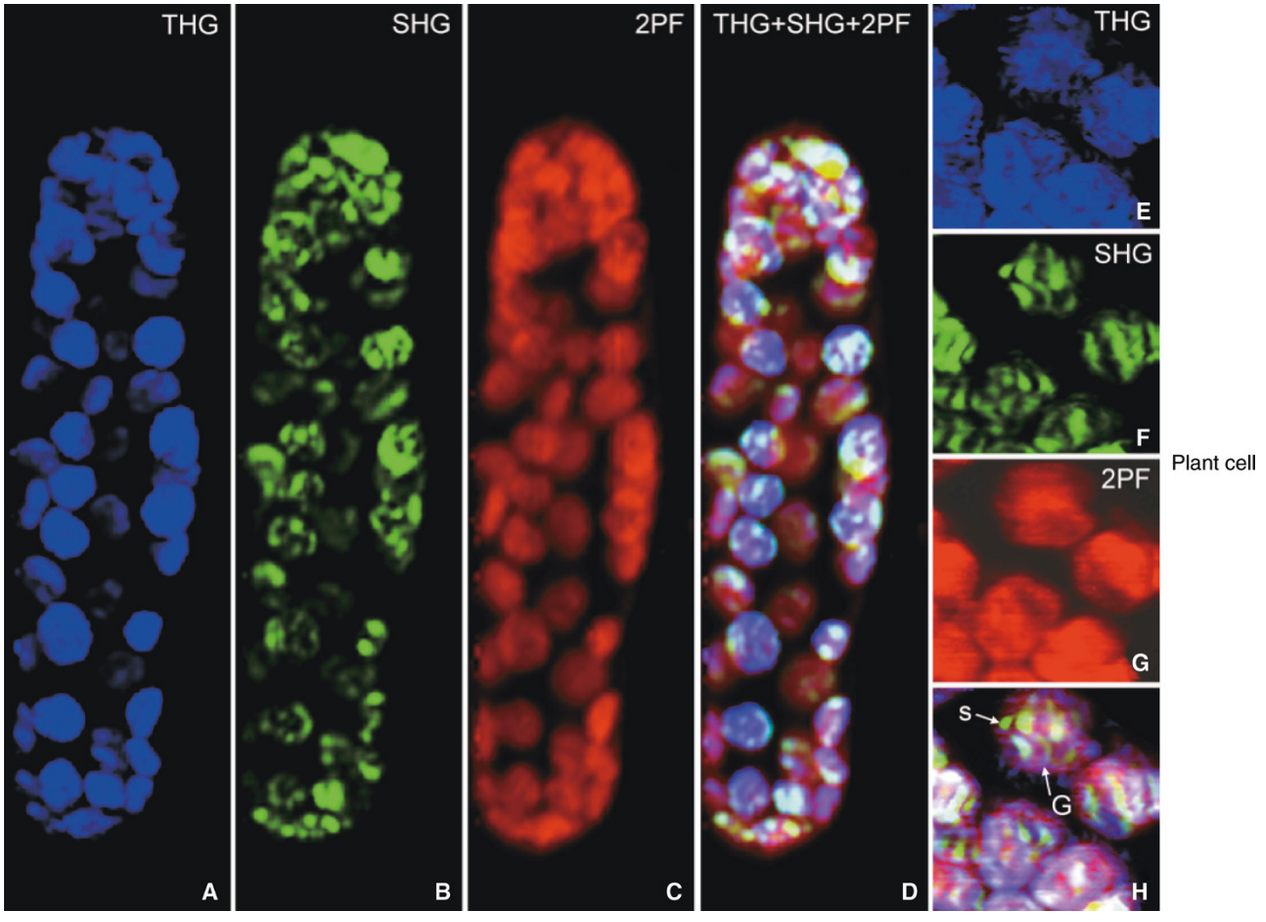


FIGURE 40.11. Harmonic and fluorescence images of a mesophyll cell of *Commelina communis* L. (A) THG image; (B) SHG image; (C) 2PF image; (D) false-color image of the combination of THG-SHG and 2PF. (E–H) High magnification images of chloroplasts showing strong SHG generation from starch granules (s) and possible grana (G). Ex, 1230 nm.

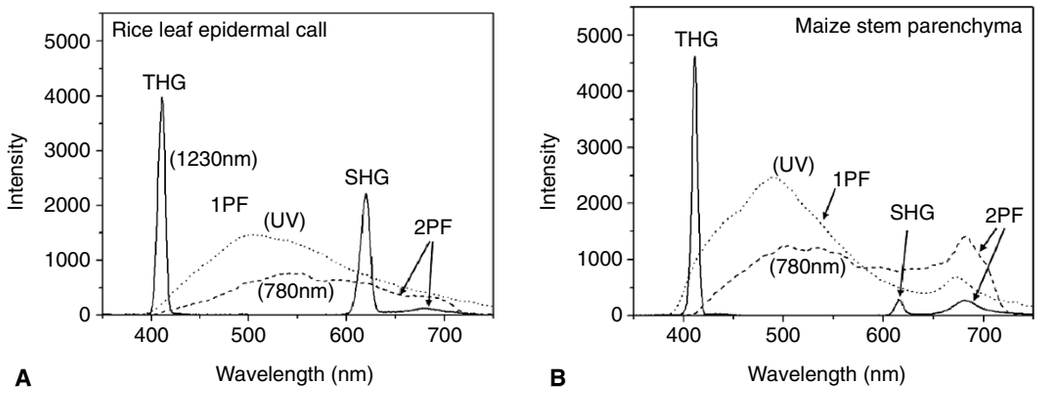


FIGURE 40.12. Nonlinear emission spectra from the cell wall of (A) an epidermal cell in rice leaf and (B) parenchyma cells in maize stem with three different sources: UV light (dotted *line*), 780 nm pulsed signal (*dashed line*), and 1230 nm pulsed laser (*solid line*). The suppression of background 2PF and the symmetric peaks of THG and SHG in 1230 nm excitata spectra are evident.

The tumbling movement of chloroplasts in cytoplasm results in changes in the apparent periodicity of the thylakoid membrane stacks along the direction of the illuminating beam. This tumbling therefore changes the SHG efficiency, a fact that can be used to study chloroplast tumbling, a phenomenon that is difficult to study by other means.

Compared with the emission spectra excited by a femtosecond Ti:Sa laser in these plant specimens, the intrinsic 2PF signals are generally reduced by using a longer wavelength as the pumping source (Chu *et al.*, 2001). As an example, Figure 40.12 shows a quantitative comparison between the emission spectra excited by a 150 mW 1230 nm Cr:forsterite femtosecond laser (120 fs pulse width, solid line), a 50 mW 780 nm Ti:Sa femtosecond laser (120 fs pulse width, dashed line), and a 0.45 mW 365 nm UV light source from a frequency-doubled Ti:Sa laser (dotted line). The emission spectra from the cell wall of rice leaf (*Oryza sativa*) epidermis and of the parenchyma cells in a maize stem are shown in Figure 40.12(A,B), respectively. Broad autofluorescence covering the whole visible and NIR region is evident with both UV (single-photon fluorescence) and 780 nm excitation (2PF); whereas with 1230 nm excitation, only weak residual 2PF and efficient harmonic generation were observed. With background autofluorescence suppressed by using a longer excitation wavelength, the whole visible and NIR region is available for detecting signals from specially designed, multi-photon excited fluorescence dyes that can be used to label different functional molecules (Cheng *et al.*, 1998). Furthermore, as there is no energy deposition at all during harmonic generation processes, no photodamage effect is expected with SHG and THG. Thus, with efficient SHG and THG signals, along with the reduced but still-measurable intrinsic 2PF signals, the longer wavelength light source appears to be a better choice for intrinsic harmonic generation imaging because it leaves a wider spectrum available for extrinsic multi-photon dye labeling. Figure 40.13 compares the emission spectra of maize leaf and stem (epidermal cells) when excited by 1230 nm, 780 nm, and 400 nm.

Figure 40.14 shows the specific *xyλ*-images corresponding to THG, SHG, and 2PF in the parenchyma cells of a maize stem, taken at a depth of 110 µm from the sample surface. The total sample thickness was around 500 µm. With an average power of 100 mW before entering the sample and a focused spot diameter of ~1.3 µm, the intensity at focus ranges from 9 to 50×10^{10} W/cm,[2] depending on the focal depth inside the sample. As expected, strong SHG and THG can be observed in the cell wall. THG shows the longitudinal cell walls in the center of the image as well as the transverse cell walls of several adjacent cells [Fig. 40.14(A)], This demonstrates the ability of THG to pick up the outline of the whole cell. SHG may show the relative position of the secondary walls (arrows). In regions with extensive secondary wall growth, the separation of the secondary wall can be clearly observed in Figure 40.14(B) and the 2PF signal indicates the distribution of fluorescent molecules [Fig. 40.14(C)]. By comparing different images made using different modalities, one can image the relation-

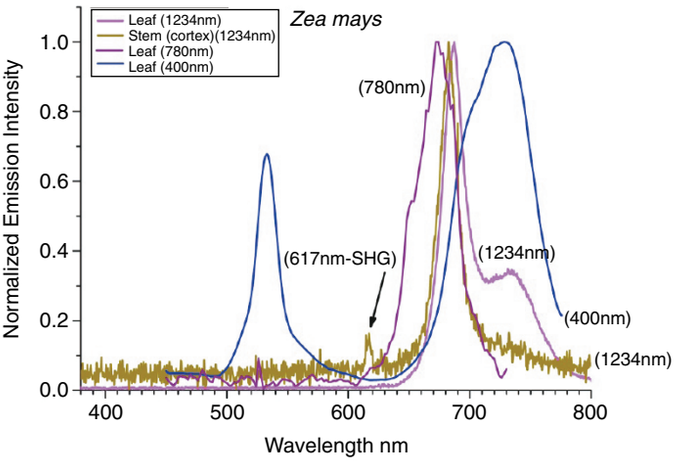


FIGURE 40.13. Normalized emission spectra of maize tissue under different types of excitation. 1PF at 400 nm (blue). Two-photon excited spectra generated at 1234 nm from a leaf (green) lacks the hump due to fluorescence of the cell wall found in stems (magenta). It also lacks the SHG peak at 617 nm, probably generated by the secondary cell walls in the stem sample. Two-photon excitation at 780 nm produces fluorescence (maroon) that peaks at a shorter wavelength than the fluorescence excited by the other modes.

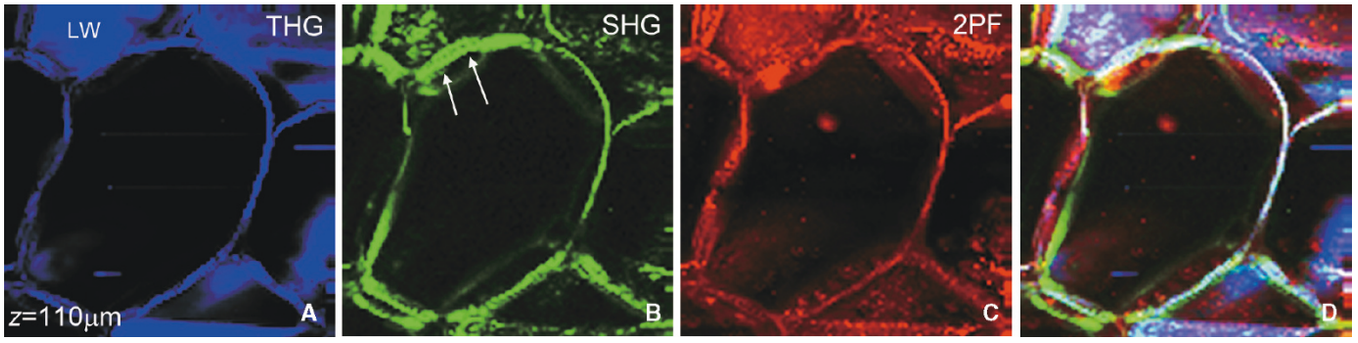


FIGURE 40.14. Optical section obtained near the longitudinal wall (LW) of a parenchyma cell in maize stem. Note the strong THG from the radial wall (RW) (A), the SHG (B), 2PF (C), and combination of THG-SHG-2PF (D). *Arrows*: possible secondary wall material. The image was obtained 110 μm below the surface of the specimen.

ships between structural (harmonic generations) and chemical information (two- and multi-photon fluorescence) in biological tissues. A penetration depth of more than 500 μm has been achieved in the maize stem sample with 1230 nm excitation (Chu *et al.*, 2001).

Figure 40.15 shows paradermal optical sections of the adaxial surface of rice (*Oryza sativa* L.) leaf. THG provides structural interfaces, such as the papillae from the cuticular layer and the cell wall of bulliform cells [Fig. 40.15(B)]. As expected, SHG reflects biophotonic structures including the cuticular papillae and longitudinal cell walls [Fig. 40.15(B)], due to the orderly arrangement of cutin, waxes, and cellulose microfibrils, respectively. 2PF, on the other hand, picks up the fluorescent chromophores [Fig. 40.15(C)]. Figure 40.16 shows a through-focus series (5 μm step) of an area on the surface of rice leaf where silica cells can be found (Hodson and Sangster, 1989; Cheng 1987, Cheng *et al.*, 1990). Note the outline of the silica cell in the THG images and the high SHG signals from the silica deposits. A strong SHG signal can also be obtained from the silica wall of a diatom.

Optically Active Structures in Animal Tissues

There are many structures in animal tissue that are also good candidates to produce a strong biophotonic effect (Table 40.3). For example, the sarcomeres in skeletal muscles are composed of crystalline myosin and actin nanofilaments, with periods of 40 and 20 nm, respectively, that fall into the spatial range required for strong SHG activity. Figure 40.17 shows longitudinally sectioned *xy*-images obtained from the somites of a zebrafish embryo. The cardiac muscle fiber produces intense SHG signal [green, Fig.40.17(A–D)] and the surfaces of the red blood cells (RBC) produce intense THG signal [blue, Fig. 40.17(C,D)].

Figure 40.18 shows a two-channel harmonic image of somites in a zebrafish embryo. At low magnification, the somites are seen to be separated by clefts [Cl, Fig. 40.18(A)]. At higher magnification [Fig. 40.18(B,C)], the green SHG image of the sarcomeres (s: between the two arrows) indicate that the strong blue THG signal in Figure 40.18(A) is probably generated by the optical discontinuity occurring between the somites. The SHG intensity difference in individual sarcomeres [Fig 40.18(C), between arrows] reflects differences in the spatial packing of F-actin and myosin in dark bands and light bands. The strong SHG activity from the actin/myosin complex can make harmonic imaging a useful tool for the study of muscle cell dynamics as the arrangement changes during muscle contraction and relaxation.

Microtubule bundles are birefringent structures that can be studied in living cells using polarization microscopy. Recent

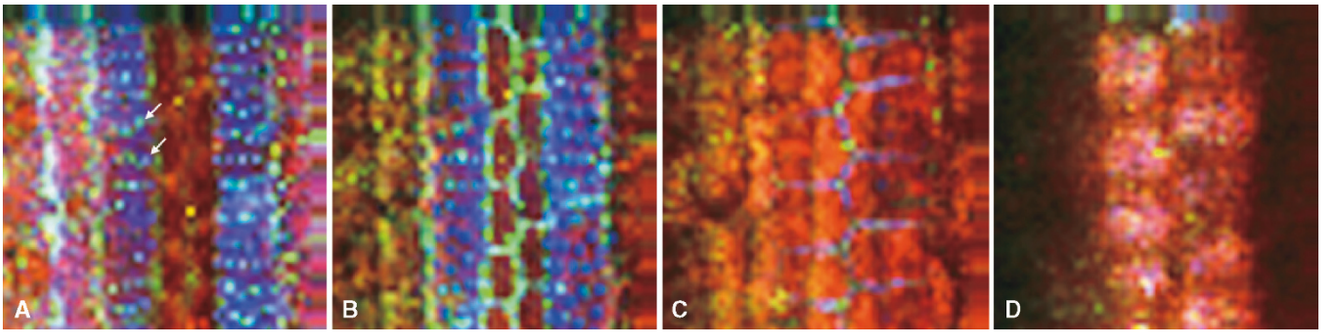


FIGURE 40.15. Through-focus, three-channel harmonic fluorescence images of the adaxial surface of rice leaf. (A) Near surface, (B) epidermal cells, (C) epidermal–mesophyll interface, (D) mesophyll cells. Note the strong 2PF emission from the chlorophyll of the mesophyll cells. *White arrows*: cuticular papillae.

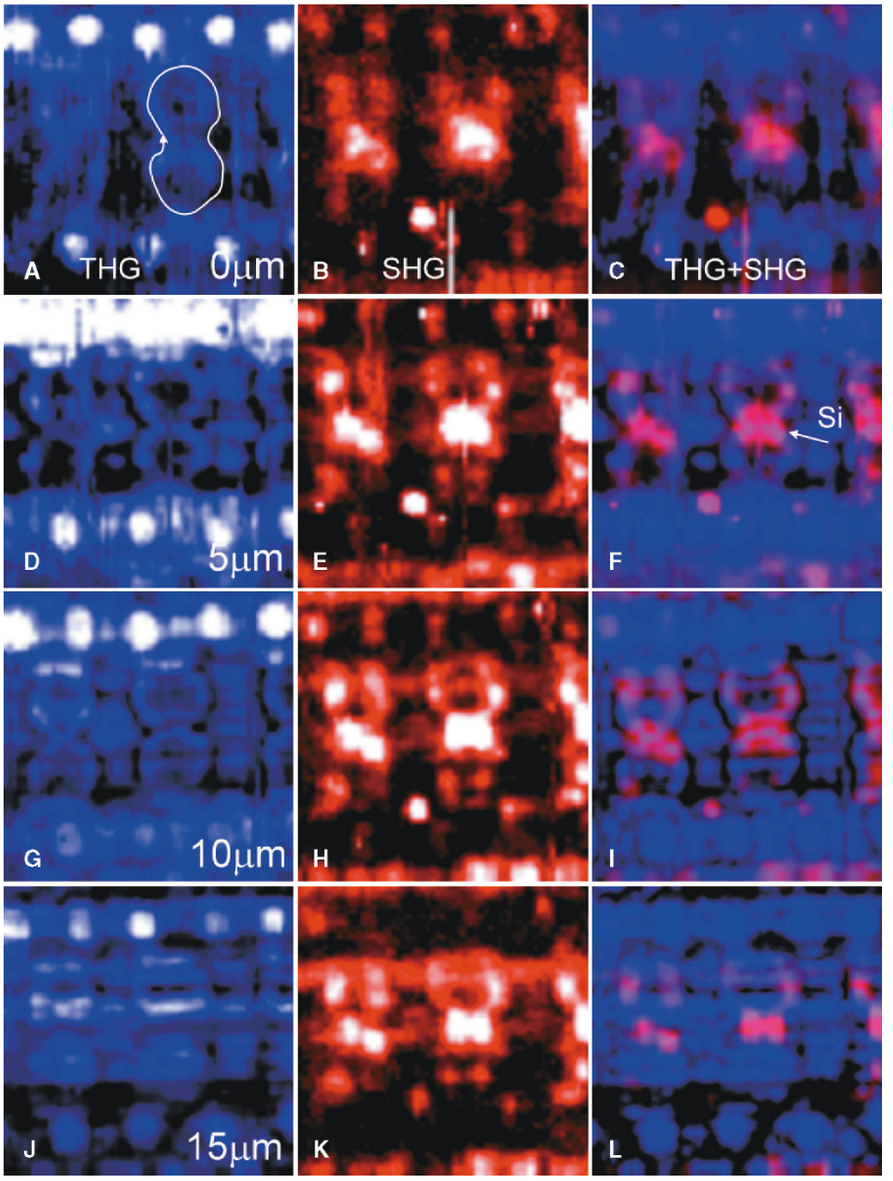


FIGURE 40.16. Through-focus, two-channel images of the surface of rice leaf, showing a silica cell. As it can be seen in the focal series (A–D), the SHG signal is generated by the bulk of the phytolith (Si), not by the surface of the silica deposit.

advances in dynamic polarization microscopy utilizing tunable liquid–crystal polarizers now allow one to study cytoskeleton dynamics and spindle behavior. The technique not only provides information on the retardance of the birefringent structure, but can also provide data of the molecular orientation of the structures (*s*-axis) (Oldenbourg and Mei, 1995).

Figure 40.19 shows a typical example in which polarization microscopy has been used to determine the orientation of the collagen fiber scaffold in an engineered tissue. Polarization microscopy can also allow one to directly visualize the spindle during cell division under low light conditions. Figure 40.20 shows the spindle of a fertilized oocyte during a cloning operation. Microtubules have also been shown to produce strong SHG signal in both the forward and the backward configurations (Sun *et al.*, 2005). Figure 40.21 demonstrates the specificity of the SHG signal from the spindle apparatus of a developing zebrafish embryo. The interface between the cell membrane and the surrounding aqueous medium produces a strong THG signal (blue) that provides the

TABLE 40.3. Biological Structures that Produce Harmonic Signals

Structures	Birefringence	SHG
Microtubules	+	+
Microfilaments	+	+
Spindle	+	+
Collagen fiber	+	+
Elastic fiber	+	+
Cuticle	+	?
Cuticular wax	+	?
Sarcomere	+	+
Grana and thylakoid	?	+
SiO2 deposit	+	+
Starch granules	+	+
Cell wall	+	+
Bone matrix	+	+
Dentine	+	+
Enamel	+	+

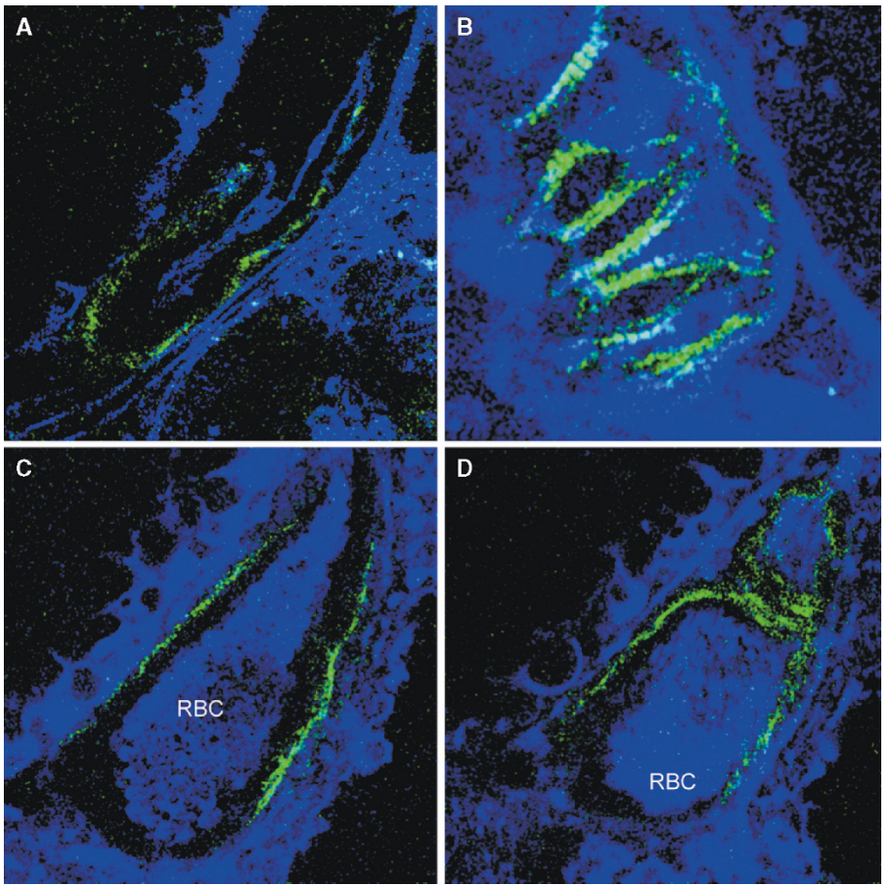


FIGURE 40.17. Two-channel, harmonic images of developing heart in a zebrafish embryo. The cardiac muscle fiber produces intense SHG signal (green, A–D). The red blood cells (RBC) produce intense THG signal (blue, C and D).

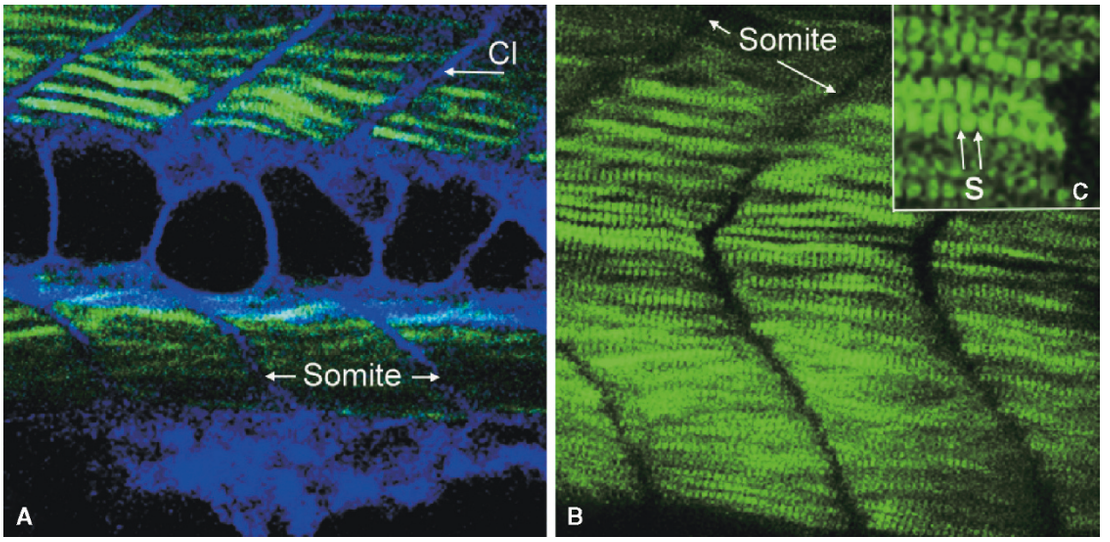


FIGURE 40.18. Two-channel harmonic image of somites in a zebrafish embryo. (A) Low magnification view of the somites separated by clefts (Cl); SHG, green; THG, blue. (B) SHG image showing developing myofibrils. Note: individual sarcomeres are clearly visible. (C) Higher magnification, SHG image of the sarcomere (s: between the two arrows) indicating that the strong SHG signal is likely generated from the dark band of sarcomere.

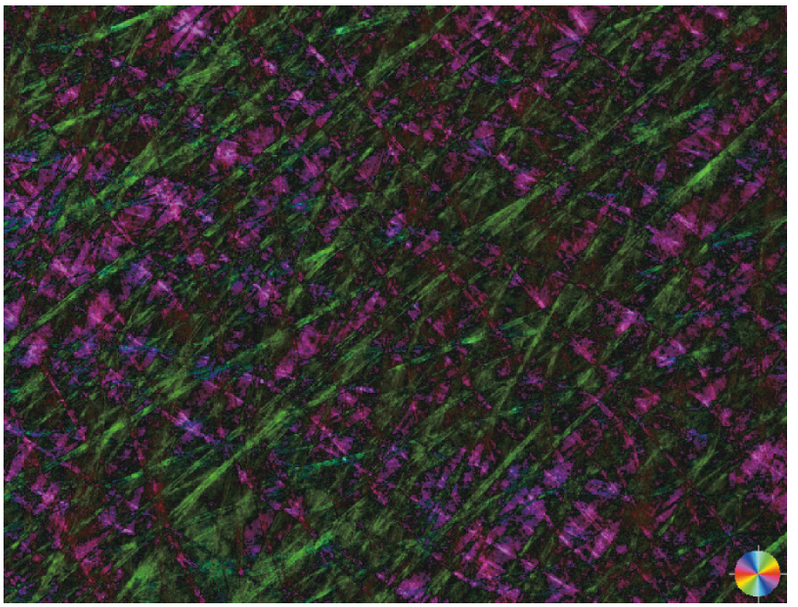


FIGURE 40.19. Polarization microscopy of man-made collagen fiber. The image demonstrates the orientation of the collagen fiber imaged by using a Polscope. The color wheel indicates the orientation of the *s*-axis of the collagen fiber. (Image courtesy of Prof. Hanry Yu, Department of Physiology, National University of Singapore.)

general outline of the embryo. Figure 40.20 is a set of high magnification, polarization microscope images showing a cell in various stages of cell division.

As multi-harmonic imaging (SHG and THG) allows deep-tissue imaging of biological specimens, it is suitable in developmental biology where larger specimens are commonly encountered. The use of a high-repetition-rate Ti:Sa laser offers the possibility of real-time, harmonic imaging of biological specimens (Chu *et al.*, 2003a; Sun *et al.*, 2002).

Collagen fibers are abundant in animal tissue, and are both birefringent and capable of producing SHG signals. SHG is now often used to visualize the orientation-dependent properties of connective tissue and the extracellular matrix (Roth and Freund, 1979, 1981; Freund *et al.*, 1986; Guo *et al.*, 1997; Stoller *et al.*, 2002a,b; Zipfel *et al.*, 2003; Williams *et al.*, 2005).

Polarization Dependence of Second Harmonic Generation

SHG signal strength from biophotonic structures varies according to the relative orientation between the beam and the organized structure. This allows one to study the orientation of a structure using SHG with controlled illumination polarization. For example, the dumbbell-shaped silica deposits on rice and maize leaves produce intense SHG signals. By varying the incident light polarization (Fig. 40.23), the concentrically deposited silica layers in the lumen of silica cells (Hodson and Sangster, 1989) produces SHG images that depend on the orientation of the illumination polarization. The polarization direction of the excitation is marked in the LR corner of the left-hand image in each row. The white outlines in Figure 40.23(A) demarcate the locations of two dumbbell-shaped silica cells. In contrast, no polarization dependency is evident in THG images. It is possible to isolate the epidermal cuticle with the attached phytolith (silica deposits) by $ZnCl_2$—HCl treatment. The fact that images of these isolated, silica deposits reveal little polarization dependency in the SHG signal (Fig. 40.24) suggests that the organic matrix on which the silica is deposited is the source of the photonic activity in the phytolith. Polarization-dependent contrast can also be used to study the orientation of collagen fibers in tissue engineering research (Freund *et al.*, 1986; Stroller *et al.*, 2002a,b; Chu *et al.*, 2004).

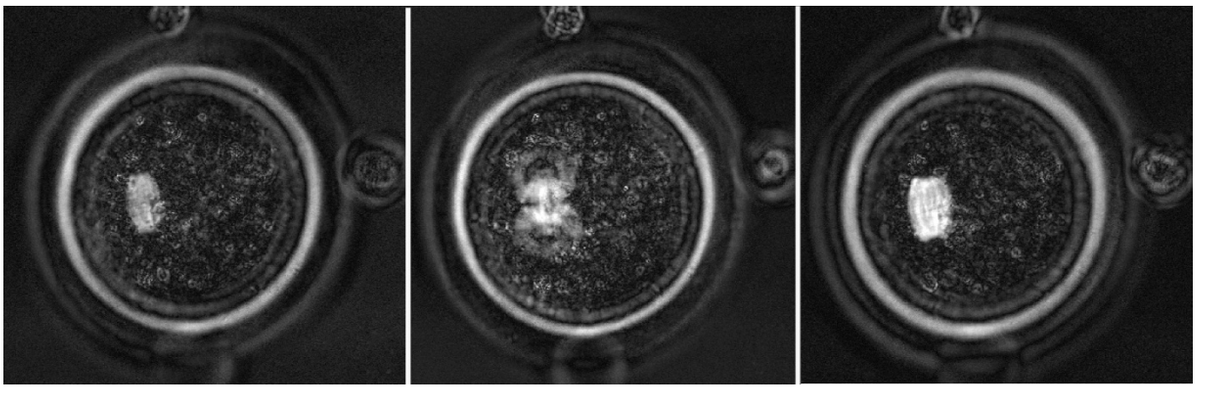


FIGURE 40.20. The spindle apparatus in the first division of a mouse zygote imaged by polarization microscopy. [The image was obtained by Ms. Gina Chen of Ming-mei Technology, Taipei, using a Spindleview dynamic polarization microscope (Cambridge Research Instrument, Cambridge, MA).]

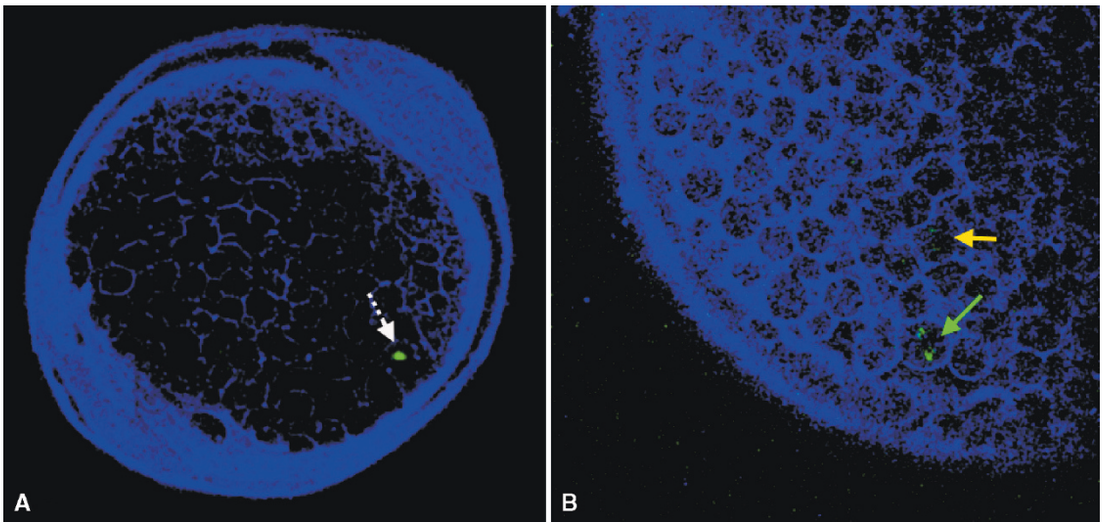


FIGURE 40.21. Dual-channel, harmonic image of a zebrafish embryo showing the cells and the embryo outlined by THG (blue) and a mitotic spindle (green, *arrows*) in SHG. (A) Overall view of the embryo; (B) part of the embryo showing cells in telophase (*yellow arrow*) and anaphase (*green arrow*).

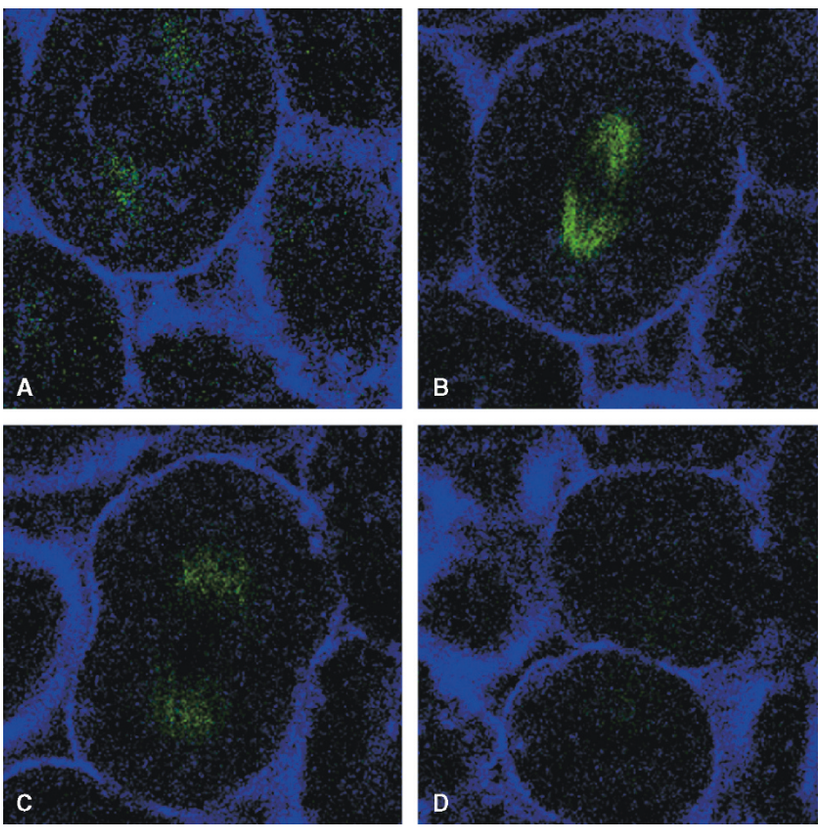


FIGURE 40.22. High magnification views of various stages in the formation of the spindle in a zebrafish embryo. (A) Telophase, (B) anaphase, (C) late anaphase, and (D) after cytokinesis, viewed in SHG (green) and THG (blue).

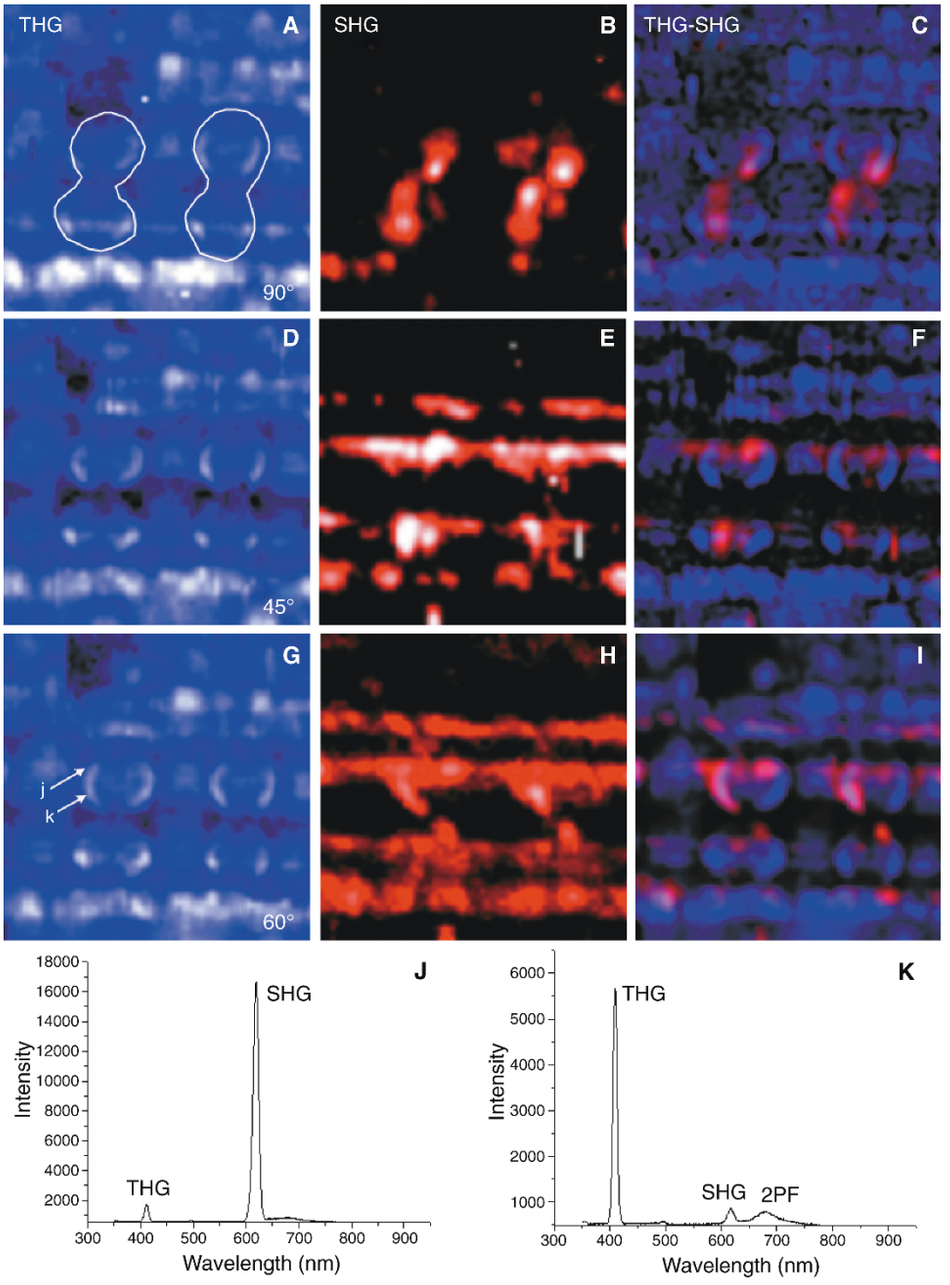


FIGURE 40.23. Polarization dependence of the SHG signal. (A–C) Ninety-degree polarization; (D–F) 45° polarization; and (G–I) 60° polarization. Note that the change of illumination polarization has little effect to the THG image, but the SHG signal does show polarization dependence. The spectra at the bottom of this figure (J, K) were obtained at the points labeled in (G).

SUMMARY

Highly organized nanoperiodic structures in biological samples exhibit strong SHG activity resembling that of nonlinear photonic crystals and thus they can be treated as nonlinear biophotonic crystals. Many biological structures, such as microfibrils in cell walls, alternating crystalline lamellae in starch granules, cuticular papillae on the leaf surface, crystalline myosin and actin nanofilaments in the myofibrils of skeletal and cardiac muscle, thylakoid membranes and grana in chloroplasts, and microtubules in both the cytoskeleton and the mitotic apparatus, all exhibit strong biophotonic effects. Many of the birefringent structures found in biological specimens also exhibit SHG properties (Table 40.3). The relative locations and orientation of these biophotonic structures can be examined using SHG microscopy, while optical interfaces and the functional molecules can be separately located by THG and 2PF contrast. In contrast to single- and multi-photon absorption, harmonic generation involves only virtual states and does not involve energy deposition. The harmonic signals allow 3D structural visualization with minimal or no additional preparation of the sample. Meanwhile, 2PF imaging modes can be added to monitor multiple molecular probes in living cells and tissues, such as those

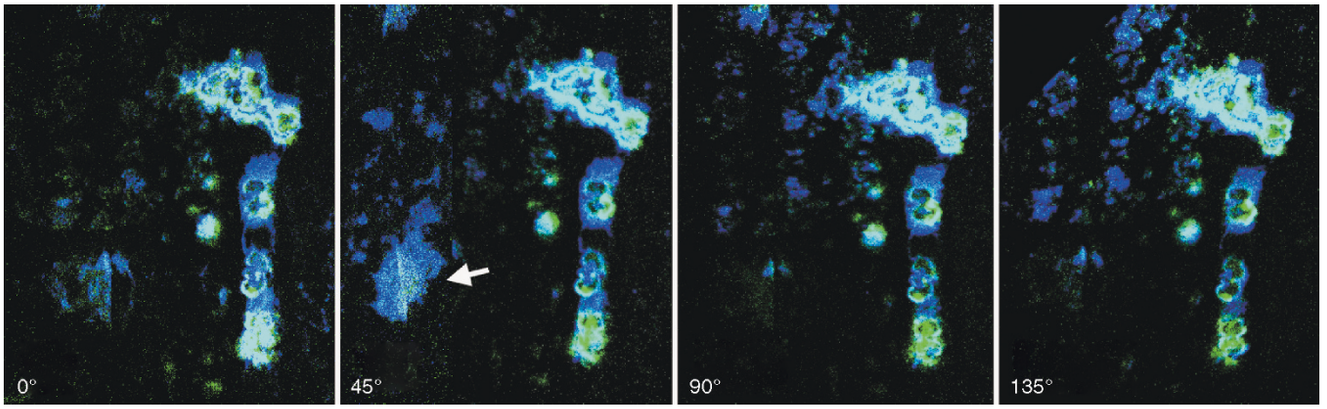


FIGURE 40.24. Isolated phytoliths, illuminated using different polarization directions. Note that the SHG (green) and THG (blue) signals vary little with different illumination conditions. The THG patch (*arrow*) in the 45° image may be the result of focal drift bringing the underlying cuticular surface into focus.

composed of transformed cells or taken from transgenic organisms. Multi-modal microscopy can provide a powerful tool for investigating the dynamics of structure–function relationships at the molecular and subcellular levels.

ACKNOWLEDGMENTS

Most of the images presented in this chapter come from research performed at the Graduate Institute of Electro-Optical Engineering and Department of Electrical Engineering, National Taiwan University, Taipei, Taiwan, by a number of researchers: I. H. Chen, T.-M. Liu, Mei-Hsin Chen, Szu-Yu Chen, and Shi-Wei Chu. Most of the biological work was done by Huai-Jen Tsai and Chung-Yung Lin of the Graduate Institute of Molecular and Cell Biology, National Taiwan University, and B.-L. Lin, S.-P. Lee of Molecular and Cell Biology Division, Development Center for Biotechnology, Taipei. The transmission spectroscopy was done by M.-X. Kuo, D.-J. Lin, and H.-L. Liu. Thanks are also due to Nick White, Sir William Dunn School of Pathology, University of Oxford for his help editing the proofs.

REFERENCES

Anderson, R.R., and Parrish, J.A., 1981, The optics of human skin, *J. Invest. Dermatol.* 77:13–19.

Barad, Y., Eisenberg, E., Horowitz, M., and Silberberg, Y., 1997, Nonlinear scanning laser microscopy by third harmonic generation, *Appl. Phys. Lett.* 70:922–924.

Berger, V., 1998, Nonlinear photonic crystals, *Phys. Rev. Lett.* 81:4136–4139.

Birge, R.R., Fleitz, P.A., Lawrence, A.F., Masthay, M.A., and Zhang, C.F., 1990, Nonlinear optical properties of bacteriorhodopsin: Assignment of second order hyperpolarizabilities of randomly oriented systems using two-photon spectroscopy, *Mol. Cryst. Liq. Cryst.* 189:107–122.

Bouma, B.E., Tearney, G.J., Bilinsky, I.P., Golubovic, B., and Fujimoto, J.G., 1996, Self-phase-modulated Kerr-lens mode-locked Cr:Forsterite laser source for optical coherence tomography, *Opt. Lett.* 21:1839.

Broderick, N.G.R., Ross, G.W., Offerhaus, H.L., Richardson, D.J., and Hanna, D.C., 2000, Hexagonally poled lithium niobate: A two-dimensional nonlinear photonic crystal, *Phys. Rev. Lett.* 84:4345–4348.

Campagnola, P.J., Wei, M.-D., Lewis, A., and Loew, L.M., 1999, High resolution nonlinear optical imaging of live cells by second harmonc generation, *Biophys. J.* 77:3341–3349.

Chen, I.-H., Chu, S.-W., Sun, C.-K., Cheng, P.C., and Lin, B.L., 2002, Wavelength dependent cell damages in multi-photon confocal microscopy, *Opt. Quantum Electron*. 34:1251–1266.

Cheng, P.C., 1987, Sample preparation for X-ray imaging and examples of biological X-ray images, In: *X-Ray Microscopy-Instrumentation and Biological Applications* (P.C. Cheng and G.J. Jan, eds.), Springer-Verlag, Berlin, pp. 289–310.

Cheng, P.C., and Lin, T.H., 1990, The use of computer-controlled substage folding optics to enhance signal strength in fluorescent confocal microscopy, *Trans. Royal Microscop. Soc.* 1:459–462.

Cheng, P.C., Lin, B.L., Kao, F.J., Gu, M., Xu, M.-G., Gan, X., Huang, M.-K., and Wang, Y.-S., 2001a, Multi-photon fluorescence microscopy — The response of plant cells to high intensity illumination, *Micron* 32:661–669.

Cheng, P.C., Newberry, S.P., Kim, H.G., Wittman, M.D., and Hwang, I.-S., 1990, X-ray contact microradiography and shadow projection microscopy, In: *Modern Microscopy* (P. Duke and A. Michette, eds.), Plenum Press, New York, pp. 87–117.

Cheng, P.C., Pan, S.J., Shih, A., Kim, K.S., Liou, W.S., and Park, M.S., 1998, Highly efficient upconverters for multiphoton fluorescence microscopy, *J. Microsc.* 189:199–212.

Cheng, P.C., Sun, C.-K., Kao, F.-J., Lin, B.-L., and Chu, S.-W., 2001b, Nonlinear multi-modality spectro-microscopy: Multiphoton fluorescence, SHG and THG of biological specimen, *SPIE Proc.* 4262:98–103.

Cheng, P.C., Sun, C.K., Lin, B.L., and Chu, S.W., 2002, Bio-photonic crystal: SHG imaging. *Maize Genetics Cooperation Newsletter* 76:8–9.

Chu, S.W., Chen, I.S., Li, T.M., Lin, B.L., Cheng, P.C., and Sun, C.K., 2001, Multi-modality nonlinear spectral microscopy based on a femtosecond Cr:Forsterite laser, *Opt. Lett.* 26:1909–1911.

Chu, S.-W., Chen, I.-S., Liu, T.-M., Sun, C.-K., Lee, S.-P., Lin, B.-L., Cheng, P.-C., Kuo, M.-X., Lin, D.-J., and Liu, H.-L., 2002, Nonlinear bio-photonic crystal effects revealed with multi-modal nonlinear microscopy, *J. Microsc.* 208:190–200.

Chu, S.-W., Chen, S.-Y., Tsai, T.-H., Liu, T.-M., Lin, C.-Y., Tsai, H.J., and Sun, C.-K., 2003a, *In vivo* developmental biology study using noninvasive multi-harmonic generation microscopy, *Opt. Express* 11:3093–3099.

Chu, S.W., Liu, T.M., Sun, C.K., Lin, C.Y., and Tsai, H.J., 2003b, Real-time second-harmonic-generation microscopy on a 2-GHz repetition rate Ti:Sapphire laser, *Opt. Express* 8:933–938.

Chu, S.-W., Chen, S.-Y., Chern, G.-W., Tsai, T.-H., Chen, Y.-C., Lin, B.-L., and Sun, C.-K., 2004, Studies of (2)/(3) tensors in submicron-scaled biotissues by polarization harmonics optical microscopy, *Biophys. J.* 86:3914–3922.

Clays, K., Elshocht, S.V., Chi, M., Lepoudre, E., and Persoons, A., 2001, Bacteriorhodopsin: A natural, efficient (nonlinear) photonic crystal, *J. Opt. Soc. Am. B* 18:1474–1482.

Denk, W., Strickler, J.H., and Webb, W.W., 1990, Two-photon laser scanning fluorescence microscopy, *Science* 248:73–76.

Dumeige, Y., Vidakovic, P., Sauvage, S., Levenson, J.A., Sibilla, C., Centini, M., D'Aguanno, G., and Scalora, M., 2001, Enhancement of second-harmonic generation in a one-dimensional semiconductor photonic band gap, *Appl. Phys. Lett.* 78:3021–3023.

Freund, I., Deutsch, M., and Sprecher, A., 1986, Connective tissue polarity: Optical second-harmonic microscopy, crossed-beam summation, and small-angle scattering in rat-tail tendon, *Biophys. J.* 50:693–712.

Gallant, D.J., Bouchet, B., and Baldwin, P.M., 1997, Microscopy of starch: Evidence of a new level of granule organization, *Carbohydrate Polym.* 32:177–191.

Gannaway, J.N., and Sheppard, C.J.R., 1978, Second-harmonic imaging in the scanning optical microscope, *Opt. Quantum Electron.* 10:435–439.

Gunning, B., and Steer, M., 1996, *Plant Cell Biology: Structure and Function*, Jones and Bartlett Publishers, Sudbury, Massachusetts, p. 21.

Gu, X., Makarov, M., Ding, Y.J., Khurgin, J.B., and Risk, W.P., 1999, Backward second-harmonic and third-harmonic generation in a periodically poled potassium titanyl phosphate waveguide, *Opt. Lett*. 24:127.

Guo, Y., Ho, P.P., Tirksliunas, A., Liu, F., and Alfano, R.R., 1997, Optical harmonic generation from animal tissues by the use of picosecond and femtosecond laser pulses, *Opt. Lett*. 22:1323–1325.

Hodson, M.J., and Sangster, A.G., 1989, Silica deposition in the inflorescence bracts of wheat (Triticum aestivum). II X-ray microanalysis and backscattered electron imaging, *Can. J. Botany* 67:281–287.

Kao, F.J., Huang, M.K., Wang, Y.S., Hung, S.L., Lee, M.K., Sun, C.K., and Cheng, P.C., 2000, Two-photon optical-beam-induced current microscopy of indium gallium nitride light emitting diodes, *SPIE Proc.* 4082:92–98.

Konig, K.H., Liang, M., Berns, W., and Tromberg, B.J., 1995, Cell damage by near-IR microbeams, *Nature* 377:20–21.

Lin, B.-L., Cheng, P.C., and Sun, C.-K., 2001, Optical density of leaf, *Maize Genetics Cooperation Newsletter,* 75:61–62.

Liu, T.M., Chu, S.W., Sun, C.K., Lin, B.L., Cheng, P.C., and Johnson, I., 2001, Multiphoton confocal microscopy using a femtosecond Cr:Forsterite laser, *Scanning* 23:249–254.

Moreaux, E., Sandre, O., and Mertz, J., 2000a, Membrane imaging by second-harmonic generation microscopy, *J. Opt. Soc. Am. B*. 17:1685–1694.

Moreaux, L., Sandre, O., Blanchard-Desce, M., and Mertz, J., 2000b, Membrane imaging by simultaneous second-harmonic generation and two-photon microscopy, *Opt. Lett.* 25:320–322.

Muller, M., Squier, J., Wilson, K.R., and Brakenhoff, G.J., 1998, 3D microscopy of transparent objects using third-harmonic generation, *J. Microsc*. 191:266–274.

Oldenbourg, R., and Mei, G., 1995, A new polarized light microscope with precision universal compensator, *J. Microsc.* 180:140–147.

Peleg, G., Lewis, A., Linial, M., and Loew, L.M., 1999, Nonlinear optical measurement of membrane potential around single molecules at selected cellular sites, *Proc. Natl. Acad. Sci. USA* 96:6700–6704.

Peter, H.R., Ray, F.E., and Susan, E.E., 1992, *Biology of Plants*, Worth Publishers, New York, p. 36.

Roth, S., and Freund, I., 1979, Second harmonic-generation in collagen, *J. Chem. Phys.* 70:1637–1643.

Roth, S., and Freund, I., 1981, Optical second-harmonic scattering in rat-tail tendon, *Biopolymers* 20:1271–1290.

Shen, Y.R., 1989, Surface properties probed by 2nd harmonic and sum frequency generation, *Nature* 337:519–525.

Sheppard, C.J.R., and Shotton, D.M., 1997, *Confocal Laser Scanning Microscopy,* BIOS Scientific Publisher, Oxford, United Kingdom.

Stoller, P., Kim, B.M., Rubenchik, A.M., Reiser, K.M., and Da Silva, L.B., 2002a, Polarization-dependent optical second-harmonic imaging of a rat-tail tendon, *J. Biomed. Opt*. 7:205–214.

Stoller, P., Reiser, K.M., Celliers, P.M., and Rubenchik, A.M., 2002b, Polarization-modulated second harmonic generation in collagen, *Biophys. J*. 82:3330–3342.

Sun, C.K., 2005, Higher Harmonic generation biopsy, *Focus on Microscopy 2005*, Jena, Germany.

Sun, C.-K., Chen, C.-C., Chu, S.-W., Tsai, T.-H., Chen, Y.-C., and Lin, B.-L., 2003, Multiharmonic generation biopsy of skin, *Opt. Lett*. 28:2488–2490.

Sun, C.-K., Chu, S.-W., and Liu, T.-M., 2002, High frame-rate second-harmonic generation micoscopy based on a 2 GHz Ti: sapphire laser, *Proc. OSA* paper TuH4.

Sun, C.-K., Chu, S.-W., Chen, S.-Y., Tsai, T.-H., Liu, T.-M., Lin, C.-Y., and Tsai, H.-J., 2004, Higher harmonic generation microscopy for developmental biology, *J. Struct. Biol*. 147:19–30.

Sun C.-K., Chu, S.-W., Tai, S.P., Keller, S., Abare, A., Mishira, U.K., and DenBaars, S.P., 2001, Mapping piezoelectric-field distribution in gallium nitride with scanning second-harmonic generation microscopy, *Scanning* 23:182–192.

Sun, C.-K., Chu, S.-W., Tai, S.-P., Keller, S., Mishra, U.K., and DenBaars, S.P., 2000, Scanning second-harmonic-generation and third-harmonic-generation microscopy of GaN, *Appl. Phys. Lett.* 77:2331–2333.

Williams, R.M., Zipfel, W.R., and Webb, W.W., 2005, Interpreting second-harmonic generation images of collagen I fibrils, *Biophys. J.* 88:1377–1386.

Zhao, T., Chen, Z.-H., Chen, F., Shi, W.-S., Lu, H.-B., and Yang, G.-Z., 1999, Enhancement of second-harmonic generation in $BaTiO_3/SrTiO_3$ superlattices, *Phys. Rev. B* 60:1697–1700.

Zipfel, W.R., Williams, R.M., Christie, R., Nikitin, A.Y., Hyman, B.T., and Webb, W.W., 2003, Live tissue intrinsic emission microscopy using multiphoton excited intrinsic fluorescence and second harmonic generation, *Proc. Natl. Acad. Sci. USA* 100:7075–7080.

41

Imaging Brain Slices

Ayumu Tashiro, Gloster Aaron, Dmitriy Aronov, Rosa Cossart, Daniella Dumitriu, Vivian Fenstermaker, Jesse Goldberg, Farid Hamzei-Sichani, Yuji Ikegaya, Sila Konur, Jason MacLean, Boaz Nemet, Volodymyr Nikolenko, Carlos Portera-Cailliau, and Rafael Yuste

INTRODUCTION

Brain slices are convenient preparations to study synapses, neurons, and neural circuits because, while they are easily accessed by experimental manipulations such as drug applications, intracellular recordings, and optical imaging, they preserve many of the essential functional properties of these circuits. In this chapter, we describe techniques of live brain-slice imaging used in our laboratory. We cover in detail experimental protocols and know-how acquired over the years about preparing neocortical and hippocampal slices and slice cultures, loading neurons with dyes or using biolistic transfection techniques, two-photon and second harmonic imaging, morphological reconstructions, and image processing and analysis. These techniques are used to study the functional or morphological dynamics of synaptic structures, including dendritic spines and axon terminals, and to characterize circuit connectivity and dynamics.

The importance of developing methods is underestimated in modern biology. The education of biomedical researchers and the federal granting agencies are dominated by the ideology that good research is question-driven, whereas technique-driven research is of lesser quality. We disagree with this exclusive view because it seems to us that the specific technique used is as important as the question addressed. As Sydney Brenner put it: "Progress in science depends on new techniques, new discoveries, and new ideas, probably in that order." (Brenner, 2002). As an example, we would argue that the invention of high-affinity, selective calcium indicators have revolutionized many fields of biology (Grynkiewicz *et al*., 1985; Tsien, 1989).

We feel that methods are essential, not only for performing and validating experiments, but as exploratory tools that generate new ideas, leading into new fields. Moreover, in our experience, the difference between a difficult experiment working or not often depends on minute technical details. These details are normally acquired with great effort by the investigator, yet generally they must be left out of publications. To help compensate for this, we present in this chapter a detailed account of current methods used in our laboratory to image living brain slices. The general goal of our work is to use brain tissue specimens thin enough so that they can be successfully imaged optically. As explained in detail below, we use different types of brain slices and keep them in submerged chambers, where we seek to preserve ideal conditions of temperature, ionic composition, and nutrients to enable the slices to survive as long as possible. Slices are imaged normally in upright microscopes, in order to enable electrical, as well as optical, access to the surface of the slice. In this respect, fixed stage microscopes are ideal because they enable the stable positioning of micromanipulators and mechanical independence of the focusing of the objective. Although inverted microscopes enable better optics, they are very difficult to use for electrophysiological experiments with slices because the electrical approach to the preparation comes from the opposite side of the slice than the optical approach.

In this chapter we will discuss a combination of methods to image brain slices that are used in our laboratory. We will first cover in detail the preparation of different types of brain slices, discuss how to label cells in slices with optical probes, and then specifically discuss different types of imaging approaches to slices. We finish with an additional section of useful methods to morphologically reconstruct neurons from slices for histological or ultrastructural work and a brief discussion of different image processing strategies that we use. We hope that other investigators will profit and learn from our experience and that this will enable more research teams to enter the exciting territory of imaging slices.

MAKING BRAIN SLICES

Acute Slices

Acute live slices prepared from the brain have become a standard preparation commonly used to study electrophysiological properties of neurons in circuits (Alger *et al*., 1984) and, more recently, imaging (Yuste, 2000b). Most of our work is carried out with slices from mouse primary visual cortex (Fig. 41.1). The relatively high degree of preservation of neuronal organization after slicing and the availability of a variety of easy experimental manipulations make acute slices an attractive experimental preparation. Generally, acute slices can be maintained in good condition for up to 12 h. At the same time, we find a lot of variability in the quality of slices from day to day and even from slice to slice. The large number of variables that are likely to be important in the preservation of the health of the slice make obtaining good slices somewhat of an art form. Unfortunately, systematic studies to determine

Ayumu Tashiro, Gloster Aaron, Dmitriy Aronov, Rosa Cossart, Daniella Dumitriu, Vivian Fenstermaker, Jesse Goldberg, Farid Hamzei-Sichani, Yuji Ikegaya, Sıla Konur, Jason MacLean, Boaz Nemet, Volodymyr Nikolenko, Carlos Portera-Cailliau, and Rafael Yuste • HHMI, Columbia University, New York, New York 10027

 Handbook of Biological Confocal Microscopy, Third Edition, edited by James B. Pawley, Springer Science+Business Media, LLC, New York, 2006.

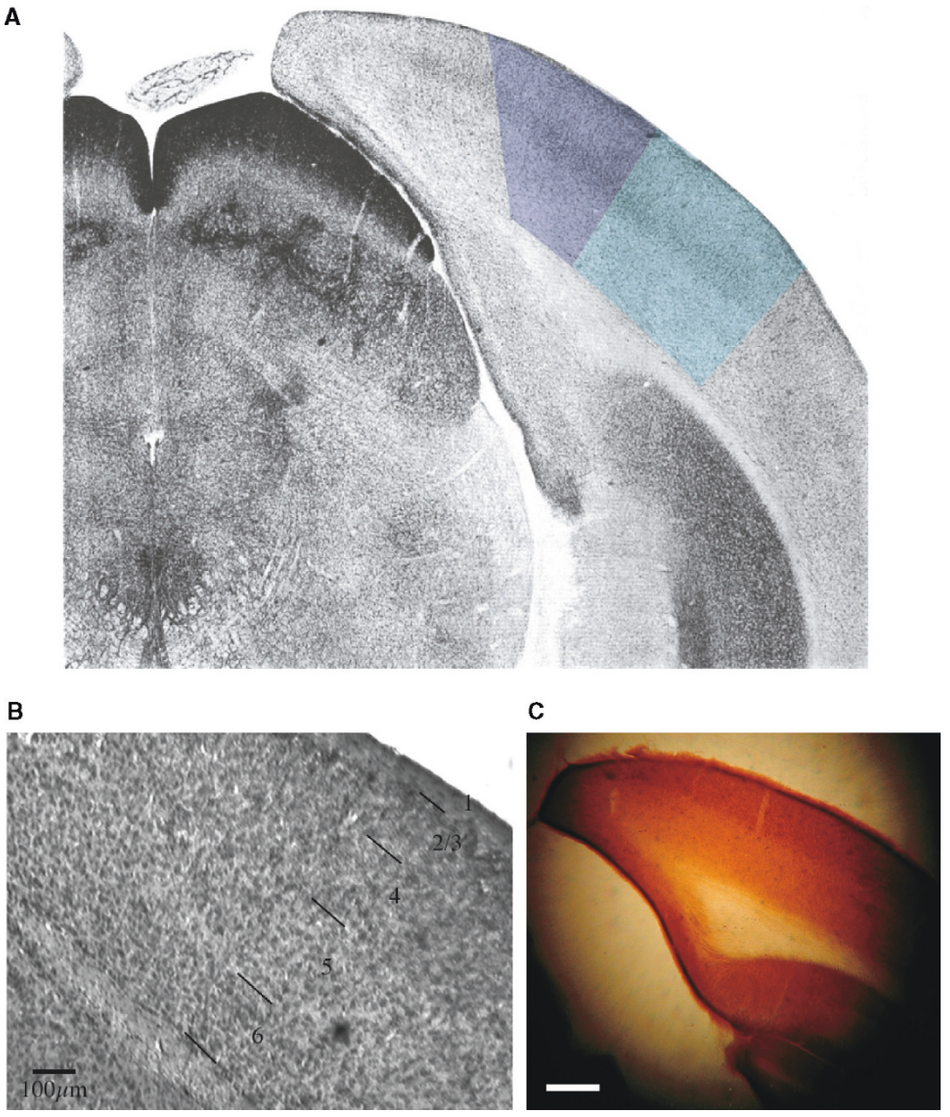


FIGURE 41.1. Brain slices of mouse visual cortex. Representative coronal slices from mouse primary visual cortex. Sections cut through the posterior pole of the cerebral hemisphere. (A) Photomicrograph of an acetylcholinesterase-labeled coronal section taken from the Franklin and Paxinos (1997) atlas. Note the more intense staining in layer 4 due to the high density of small granule cells. Violet and blue shaded areas indicate the monocular and binocular regions of the mouse primary visual cortex, respectively. (B) Nissl stain of a mouse visual cortex slice from a P18 animal. Note the prominent layer 4. (C) Cytochrome oxidase staining of a similar section. Note the intense staining near layer 4, which is an indication of the primary visual cortex. Scale bar = 500 μm. (Courtesy of Z. Peterlin and A. Tsiola.)

which variables are important to make healthy brain slices have not yet been done.

Protocol for Acute Neocortical Slices

Mice are anesthetized with 120 mg/kg ketamine and 10 mg/kg xylazine (intraperitoneally) and decapitated with scissors. Some investigators in our laboratory prefer to perfuse the mouse with a gravity-fed cold saline solution prior to decapitation. The skin covering the skull is severed with a fresh razor blade above the midsaggital line of the skull. The skull is then cut along this line and forceps are slid under the skull posteriorly, such that an air bubble forms anterior to the forceps tips. This air bubble provides a perfect pocket for the forceps to slide anteriorly, with care taken not to touch cortical tissue with the forceps. Each half of the skull may then be retracted laterally. The brain is then exposed and should be immediately placed into ice-cold sucrose artificial cerebrospinal fluid (sucrose-ACSF; 222 m*M* sucrose, 2.6 m*M* KCl, 27 m*M* $NaHCO_3$, 1.5 m*M* NaH_2PO_4, 2 m*M* $CaCl_2$, 2 m*M* $MgSO_4$, bubbled with 95% O_2, 5% CO_2). After approximately 3 min in ice-cold sucrose ACSF, the brain is removed and situated on the cutting block such that the cortex faces the approaching blade. Slices 300 to 400 μm thick are cut with a vibratome (Leica VT1000S; Leica, Nussloch, Germany; high vibration and slow speed setting) and incubated at 37°C for 30 min in a submerged slice chamber. Slices are then incubated at room temperature for up to 12 h, until used for experiments.

Identification of Primary Visual Cortex

The primary visual cortex, or area 17, of the mouse is located in the occipital region of the brain. In the adult animals it extends 1.3 mm anteriorly from the posterior end of the cortex (interaural line). In coronal sections it extends between 1 to 2 mm laterally from the medial line at its anterior border and between 2 to 3 mm in the most posterior (Franklin and Paxinos, 1997). The primary visual cortex of the mouse is divided into two regions: the monocular region, which receives input from the contralateral retina and is located in the medial part, and the binocular region, which receives input from both retinas and is placed laterally (Zilles and Wree, 1985). The primary visual cortex can be identified in coronal sections by the densely arranged granule cells of layer 4 (Fig. 41.1).

Thalamocortical Slice Protocol

Thalamocortical slices are an ideal preparation to investigate the effect of thalamic inputs onto cortical neurons or circuits because it preserves both structures and connections between the ventrobasal nucleus of the thalamus and the somatosensory cortex. Preparation of the thalamocortical slice is slightly modified from Agmon and Connors (1991), as previously described (Beierlein *et al*., 2002). Briefly, C57BL/6 mice postnatal (P) 10 to 18 are anesthetized with 120 mg/kg ketamine and 10 mg/kg xylazine and decapitated. The brain is quickly removed and placed into cold artificial CSF (ASCF) containing the following (in millimolars): 126 NaCl, 3 KCl, 1.25 NaH_2PO_4, 26 $NaHCO_3$, 10 dextrose, 1.3 $MgSO_4$, and 2.5 $CaCl_2$ (saturated with 95% O_2 and 5% CO_2). The brain is midsagittally sectioned into the left and right hemispheres. Each hemisphere is glued (standard cyanacrylate "super" glue) to a plastic block, midline down, anterior end pointing toward the floor and ventral surfaces facing in, toward one another. The hemispheres are rotated 10° from center line of the block. The plastic block is actually a right triangle with the hypotenuse 55° from the level (floor). Slices, 400 µm thick, are cut with a vibratome (VT1000S) and then incubated at 32°C for 45 min. Usually two or three viable thalamocortical slices can be made from each hemisphere.

Cultured Slices

Because acute slices cannot be maintained in good condition for more than 12 h, long-term culture is required for manipulations involving long-term experiments, such as those requiring the expression of genes. Below, we describe the protocol for mouse hippocampal slice cultures, which we have used extensively to image the morphology of single neurons transfected with the green fluorescent protein (GFP) (Dunaevsky *et al*., 1999; Tashiro *et al*., 2000).

Protocol for Hippocampal Cultured Slices

Neonatal mice (P0–P3) are cryoanesthetized on ice for 1 min and decapitated with scissors. In a tissue culture hood, skin and skull are cut with scissors and separated with forceps. The brain is then gently removed and placed into a 35 mm tissue culture dish filled with cold sucrose-ACSF (see above). Under a dissecting microscope, the two hemispheres are separated with a surgical blade and oriented such that the medial surface faces down. The cerebellum and the mesencephalon are carefully dissected away and discarded. Then, after the hemisphere is rotated such that its medial side faces up, the diencephalon is removed with a surgical blade and a flat-ended spatula. The remaining piece of tissue, representing the cortex and the hippocampus, is trimmed into a rectangular block along the anterior edge of the hippocampus parallel to the septotemporal axis. The tissue is transferred onto a tissue chopper (TC-2 Tissue Sectioner; Smith & Farquhar) with two spatulas. The rectangular block of tissue is positioned such that the chopping orientation is perpendicular to the septotemporal axis of the hippocampus. Slices 300 µm thick are obtained. With two flat-ended spatulas, the slices are transferred to a fresh culture dish containing cold sucrose-ACSF. The slices are separated from each other with a surgical blade and a flat-ended spatula as soon as possible.

Slices are cultured in culture medium, 100 mL of which contains 50 mL Basal Medium Eagle (catalog #21010-046, Invitrogen), 25 mL Hank's Balanced Salt Solution (catalog #24020-117, Invitrogen), 25 mL heat-inactivated horse serum (Hyclone), 0.65 g dextrose, 0.5 mL L-glutamine (catalog #25030-149, Invitrogen), 1.0 mL HEPES (catalog #15630-106, Invitrogen), and 1.0 mL 100X Pen-strep (catalog #15140-148, Invitrogen). Approximately 1 mL of medium is poured onto and under the culture inserts (catalog #PICM 030 50 or PICM ORG 50, Millipore) in the sterile hood, so that the membrane of the inserts is completely submerged in culture medium. We find that the use of serum from Hyclone (Logan, UT) is a particularly important variable because cultures made with serum from other sources were not successful. Individual slices are then transferred onto the membrane with a flat-ended spatula. Three to six slices are cultivated on single inserts. Most of the medium (but not all) is removed from the inserts with a pipette, and the slices are positioned with the spatula at the center of the insert, but separated from each other by at least 2 to 3 mm. Then, all remaining medium in the inserts is aspirated. The inserts are transferred into 6-well culture plates, in which each well contains 1 mL of culture medium. The culture plates are kept in the incubator (5% CO_2, 37°C). Every other day, 0.6 mL of culture medium is changed with fresh medium. During the first few days in culture, slices spread slightly and become flattened to a 150 to 250 µm thickness.

LABELING CELLS

Biolistic Transfection

To image neuronal morphology, we transfect GFP using biolistics ("gene gun") (Arnold *et al*., 1994; Lo *et al*., 1994). The principle of this method is that metal particles coated with DNA are transferred physically into nucleus by pressured gas. Transferred GFP genes are expressed and the whole neuronal cytoplasm, including their axons and dendrites, can be visualized (Fig. 41.2).

Biolistic Protocol

We use the Helios Gene Gun System (Bio-Rad), and the following protocol is modified from the procedure described in the manual for the system. Plasmids are purified on a Qiagen Maxiprep kit. Weigh 12.5 mg gold (1 µm diameter) in a 1.5 mL tube and add 100 µL of 0.05 *M* Spermidine. Sonicate the tube for 5 s to dissociate aggregated gold particles (FS30, Fisher Scientific; 40 kHz, 130 W). Add solution containing desired amount of plasmid [for eGFP-C1 plasmid (Clontech), 100 µg] and precipitate plasmid onto gold particles with 100 µL of 1 m*M* $CaCl_2$. In 10 min, gold particles precipitate to the bottom of the tube. Then, remove supernatant solution without disturbing the particles and wash particles three times with 100% EtOH. The particles are then suspended in 100% EtOH and transferred into a new 15 mL tube to a final volume of 3 mL. Transfer particles in EtOH into Tefzel tube (Bio-Rad). In approximately 90 s, gold particles precipitate to

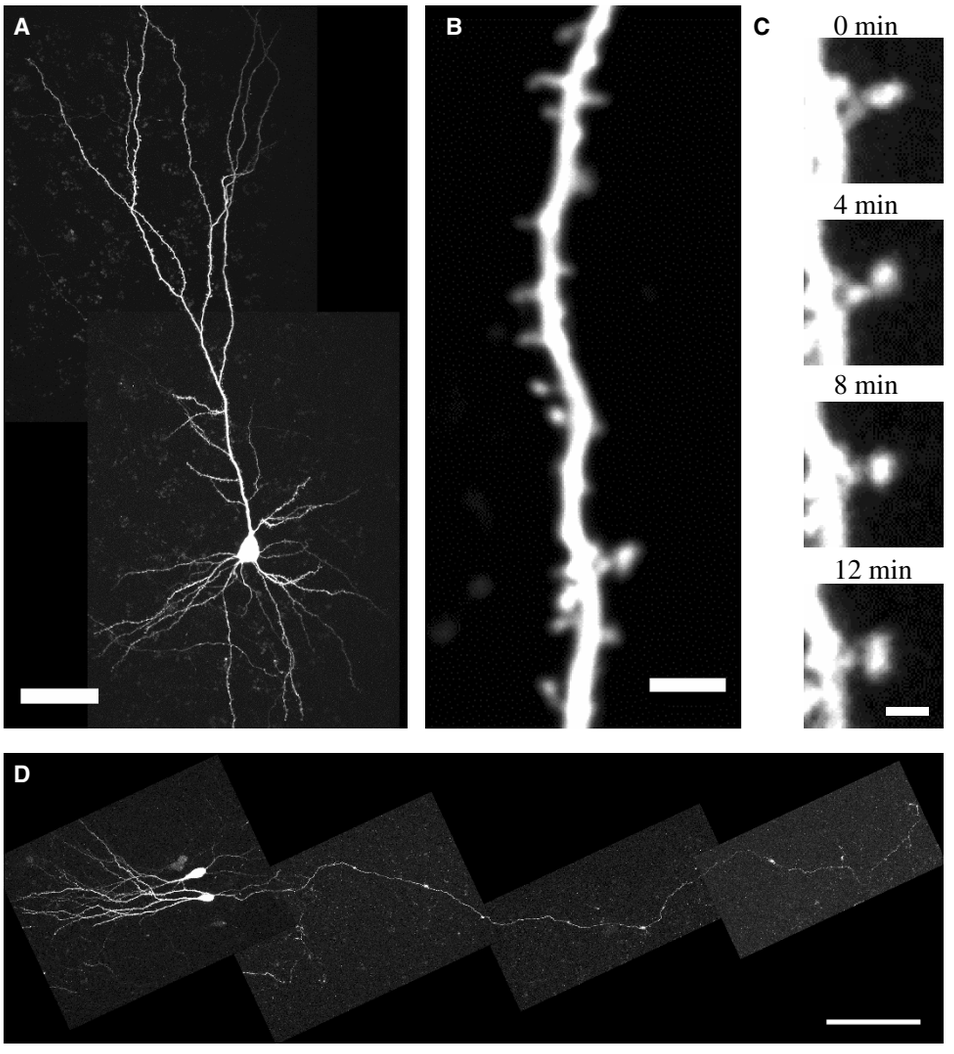


FIGURE 41.2. Two-photon imaging of living neurons in slices. Two-photon micrographs of GFP-transfected neurons in hippocampal brain slice cultures. (A) A CA3 pyramidal neuron at 14 days *in vitro*. (B) Apical dendrite of a CA3 pyramidal neuron at 11 days *in vitro*. (C) Time-lapse sequence of a dendritic spine in (B). Note the morphological rearrangements occurring in a few minutes. (D) Dentate granule cells at 14 days *in vitro*. Note that the entire dendritic and axonal processes are visualized. Scale bar: (A) 50 μm, (B) 2.5 μm, (C) 1 μm. (D) 150 μm.

the bottom of the tube. Then, EtOH is removed from the tube slowly without disturbing the particles. Tube is dried with nitrogen gas until the inside surface of the tube becomes completely dry. With tubing cutter (Bio-Rad), the tube is cut into small pieces, which are used for single shots. Tubing sets can be stored with desiccant at 4°C for up to a month and at −80°C for longer storage.

To drive gold particles into neuronal nuclei, we use high-pressure helium flow. We adjust the helium pressure to 100 to 150 psi for transfection of slice cultures and acute slices. Two to three "preshots" are fired with an empty cartridge holder to clean the helium pathway and make sure that pressure is stable after each shot. In order to reduce the damage to slices caused by high-pressure flow, the tips of barrel liners are covered by a nylon mesh (ϕ90 μm, Small Parts, Inc). For cultured slices, the cover of the culture plate is removed, and the gun is fired perpendicular to the plate with a distance of 10 mm between the tip of the barrel liner and the insert. The culture plates are immediately put back into the incubator. Slices are incubated for 2 to 5 days before imaging.

Genetic Manipulation with Dominant-Negative and Constitutively Active Mutants

One of the advantages of biolistics over other transfection methods is that cotransfection of multiple genes is quite easy. If the two genes are in separate mammalian vectors, they can be cotransfected with high cotransfection efficiency (>90% in our hands) by simultaneously coating gold particles with these two vectors. With cotransfection of GFP and dominant-negative or constitutively active mutant genes, the roles of specific molecular signaling cascades in the regulation of neuronal morphology can be examined. For example, we have been studying the roles of Rho GTPases in

regulating morphology and motility of dendritic spines (Tashiro *et al*., 2000; Tashiro and Yuste, 2004).

Diolistics and Calistics

Conventionally, lipophilic dyes, such as DiO and DiI, are used to label axonal projections between different regions of the brain by placing a crystal of these dyes in a defined region (Honig and Hume, 1989). However, this method is not suitable for imaging the morphology of single neurons because the region near the crystal is stained too densely to visualize single neurons. To label single neurons, Gan and colleagues developed diolistics, a variant of particle-mediated gene transfer, which transfers metal particles coated by fluorescent dyes onto cells (Gan *et al*., 2000). Our group has extensively used this method to visualize neurons in fixed tissue and classified cortical pyramidal neurons in mouse V1 into different morphological categories (Tsiola and Yuste, 2003).

Calistic, another variant of biolistics, serves to inject Ca^{2+} indicators such as calcium green-1 and fura-2 into neuronal cytoplasm (Kettunen *et al*., 2002). With this method, an apparently higher concentration of calcium indicators can be injected into neurons than using acetoxymethyl ester (AM) loading, and a large number of neurons can be visualized. Calistic also allows the simultaneous measurement of morphological and calcium dynamics of single neurons (Lohmann *et al*., 2002).

Dye Injection with Whole-Cell Patch Clamp

Whole-cell patch clamp is commonly used to study electrophysiological properties of neurons in brain slices (Edwards *et al*., 1989). Using electrodes filled with fluorescent dyes, the whole-cell configuration of patch clamp injects the dyes into neurons by diffusion through the pipette tip into the neuron. This technique has the advantages that the labeling procedure is rapid and that any neuron in the slice can be targeted and therefore visualized. When electrophysiological measurements are combined with imaging, a lower concentration of dyes is used and the whole-cell patch clamp is maintained during an experiment (Yuste and Denk, 1995). However, an extended period of patch clamp may interfere with cellular functions such as spine motility (Majewska *et al*., 2000a), possibly because the biochemistry in the neuron is perturbed by the perfusion of intracellular solution or the diffusion of cytoplasm into the patch electrode. Because of this problem, we routinely fill the electrode with higher concentration of fluorescent dyes and pull out the electrode a few minutes after whole cell recording is established (bolus technique, see below; Helmchen *et al*., 1996; Majewska *et al*., 2000a).

Bolus Injection Protocol

Neurons of interest are identified using differential interference contrast (DIC) optics, and then patched and recorded using the whole-cell patch clamp technique in current-clamp configuration to ensure the neurons are healthy. Electrodes are filled with a solution containing (in millimolars): 5 NaCl, 10 KCl, 10 HEPES, 135 $KMeSO_4$, 2.5 to 4 Mg-ATP, 0.3 Na-GTP, and 100 to 500 µ*M* fluorescent dye such as Calcium Green-1 or Alexa-488 (Molecular Probes, Inc., Eugene, OR). Electrodes are then pulled out 1 to 3 min after patching to prevent dialysis of cytoplasm. The resistance of patch electrodes is typically 7 to 14 MΩ. Diffusion of dyes is so rapid that the whole dendritic tree is visualized in a few minutes.

Slice Loading and "Painting" with Acetoxymethyl Ester Indicators

In our past work we have pioneered the use of calcium imaging to characterize the activity of neuronal populations (Yuste and Katz, 1989, 1991; Smetters *et al*., 1999; Peterlin *et al*., 2000). The bulk loading method for double incubation of cortical slices with fura-2 AM or indo-1 AM (Molecular Probes) calcium indicators has been previously described (Yuste and Katz, 1989; Yuste, 2000a). Briefly, cortical slices are initially incubated with 2 to 5 µL of a 1 m*M* fura-2 AM or indo-1 AM in 100% DMSO solution for 2 min, followed by a second incubation in 3 mL of 10 µ*M* fura-2 AM in ACSF for 60 min. However, the use of the thalamocortical slice preparation (Beierlein *et al*., 2002) necessitated the development of a modified bulk-loading procedure because the long-projecting thalamocortical (TC) axons are particularly sensitive to the double incubation methodology, even though local connections within the cortex remain intact (Kozloski *et al*., 2001).

We have been able to circumvent this problem by applying the fura-2 AM or indo-1 AM solution directly to the region of interest in the cortical slice with a pipette, tip diameter approximately 30 µm, filled with fura-2 AM. The region of interest of the slice can be "painted" with fura-2 AM or indo-1 AM. In this way one is able to achieve good loading while preserving TC connections up to postnatal day 18 in mouse barrel cortex (Fig. 41.3). The maintenance of intact TC projections was confirmed using thalamic stimulation that elicits a calcium response in barrel cortex indicative of intact thalamocortical axons (Beierlein *et al*., 2002).

Protocol for Slice AM Painting

1. Deposit TC slice carefully onto the bottom of a small Petri dish (35 × 10 mm) filled with 2 mL of ACSF aspirated with 95% O_2 and 5% CO_2 and place onto microscope stage.
2. Fill a fire-polished pipette (tip diameter ~30 µm) with fura-2 AM from a previously prepared aliquot of 50 µg of fura-2 AM

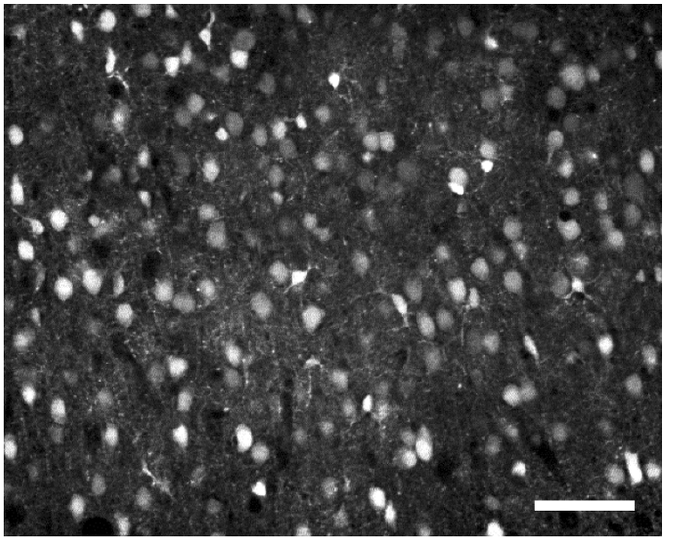


FIGURE 41.3. Two-photon imaging of neuronal ensembles. Two-photon micrograph of an acute cortical brain slice, loaded with indo-1 AM. A number of neurons are loaded with the calcium-sensitive indicator, indo-1. Note that dendritic processes are also visualized in many neurons. 60 pixels correspond to 20 µm. Scale bar: 50 µm.

dissolved in 10 µL of DMSO and 2 µL of pluronic acid (F127, Molecular Probes).
3. Insert the filled pipette into a standard patch clamp electrode holder, with tubing attached, and using a micromanipulator, place pipette tip 100 to 200 µm above the surface of the slice. Apply 5 to 10 psi positive pressure to the pipette. Slowly move the pipette across the surface of the slice using the manipulator, covering the area of interest with the dissolved fura-2 AM.
4. Incubate the slices at 32°C for 24 to 28 min depending on the age of the animal from which the slices were taken (younger animals require shorter incubation times), aspirated with 95% O_2 and 5% CO_2 throughout.
5. Finally transfer the slices to oxygenated ACSF at room temperature at least 15 min before use for the experiment.

Green Fluorescent Protein Transgenic Mice

Recently, a number of different types of GFP transgenic mice have become available commercially or from independent investigators. If these mice express GFP in neurons of interest at the right age, the labeling procedures described above are circumvented. For example, we have used the GFP-M line of GFP transgenic mice developed by Feng and colleagues (Feng *et al*., 2000). At the second postnatal week, this line of mice expresses GFP weakly in V1, but strongly in pyramidal neurons in pyriform cortex. In addition, too many pyramidal neurons in the hippocampal CA1 region are labeled by GFP, so background fluorescence makes it difficult to visualize single neurons.

IMAGING SLICES

Two-Photon Imaging of Slices

For imaging brain slices we almost exclusively use upright microscopes (Olympus BX50WI) because they can provide easy combination of electrophysiological techniques (whole-cell patch clamp and extracellular stimulation) with simultaneous imaging of patched and/or stimulated cells. As explained, with inverted microscopes it is difficult to position the patch/stimulating electrode from one side of the slice and image from the same side. This requirement is satisfied in the case of upright microscope and dipping-type water-immersion objectives with a working distance large enough to enable bringing the electrode in the field of view from the same side.

Two-photon imaging is carried out with a custom-built two-photon laser-scanning microscope (Majewska *et al*., 2000b). A more recent description of our system can be found at www.twophoton.com or at http://www.columbia.edu/cu/biology/faculty/yuste/index.html. The microscope consists of a modified Fluoview (Olympus, Melville, NY) confocal microscope with a titanium : sapphire (Ti : Sa) laser providing ~130 fs pulses at 76 MHz at wavelengths of 700 to 900 nm (Mira, Coherent, Santa Clara, CA) pumped by a solid-state source (Verdi, Coherent). We detect the fluorescence with a non-descanned detector (see below).

Imaging is done at low excitation intensities (3–10 mW at sample). Under these conditions no significant photobleaching or photodamage is observed, allowing us to image for long periods of time. For fast time resolution we can record continuous movies (1000 frames per movie, 0.2–1.6 s/frame), acquiring individual calcium fluorescence signals from hundreds of neurons simultaneously. Alternatively, in a time-lapse mode (1 frame/15 s), we can image the same region for up to 6 h without appreciable photodamage. The major limitation of the use of two-photon imaging to monitor the activity of large neuronal populations is the slow time resolution associated with laser-scanning methods. It is therefore best suited for the study of slow events rather than to detect single spike correlations. By performing online analysis, we can identify prominent features of spontaneous activity, target key elements of the network, perform whole-cell recordings while continuing to image the slice, and characterize electrophysiologically the neurons that participate in these events.

Slice Chamber Protocol

Acute and cultured slices are continuously perfused with standard ACSF containing (in m*M*): 126 NaCl, 3 KCl, 2 $CaCl_2$, 1 $MgSO_4$, 1.1 NaH_3PO_4, 26 $NaHCO_3$, and 10 dextrose and saturated with 95%O_2 and 5%CO_2. To hold the slices on the microscope, we use a temperature-controlled chamber (Series 20 imaging chamber, Warner Instrument). Flow is gravity-driven by raising a container (60 ml syringe, for example) above the chamber and controlled by a flow regulator. ACSF is sucked from the chamber by a vacuum pump. Sometimes it is necessity to use an additional flow regulator in the vacuum line to stabilize the level of liquid in the recording chamber, especially when a powerful vacuum pump ("Air Admiral"; ColeParmer) is used. Medium flow in the chamber can cause movement of the whole slice, which is a serious problem in time-lapse imaging, especially with small structure such as presynaptic and postsynaptic structures. To minimize movement artifacts, medium flow is reduced to 1 ml/min and the slices are stabilized with a slice anchor (Warner Instrument). As an alternative to using a weight that can damage the slice, we also use the direct adherence of the slice to the chamber. To do so, we position the slice on the bottom glass of the chamber and drain all the ACSF. After a few seconds, we reperfuse the chamber carefully so as not to lift the slice. In most cases, the slice has adhered to the chamber and will not move for the rest of the experiment.

ACSF is heated before flowing into the chamber by an in-line heater (SH-27B, Warner Instrument), and the base of the chamber is also heated by a platform heater (Series 20 platform, Warner Instrument). These heaters are controlled by a dual channel heater Controller (TC-344B, Warner Instrument). The temperature of the in-line heater is set at ~39°C and the platform heater is kept at ~39°C, in order to keep the liquid in the chamber at ~36–37C. As an independent control of the liquid temperature, we use an additional thermosensor (Warner) or a thermocouple-based handheld digital thermometer (TES 1300). If ACSF is saturated with O_2 and CO_2 at room temperature, these gases come out of solution in the heated imaging chamber and produce a number of small bubbles. These bubbles degrade image quality and can damage the slices. To prevent this, we keep the ACSF container in a hot bath and saturate the ACSF with the gases at 37°C.

Choice of Objectives

We use 40× (0.8NA) or 60× (0.9NA) dipping-type water immersion objectives (Olympus), although we have recently started to use the new 20× 0.95 NA objective (Olympus) to image a larger number of cortical neurons. With this low-magnification, high-numerical aperture (NA) objective, we can simultaneously monitor the activity of large neuronal populations (average 650 neurons, range 184–1396) in a thin optical section of the slice. The area

viewed covers up to 5 different layers of the primary visual cortex (~400 × 700 μm). The improved depth penetration and the high sensitivity of two-photon imaging allows us to image at depths of >100 μm from the slice surface, where connectivity is less affected by the slicing procedure. High-NA objectives further increase the fluorescence collection and thus allow deeper fluorescence measurements with good resolution than conventional objectives. Even at low magnification, we can resolve individual neurons and some of their dendritic processes. However, a major difficulty associated with the use of the 20× objective for patching, stems from its large dimensions, which restricts access for electrodes.

In general, it is also necessary to minimize the working depth in the tissue. Deeper imaging leads to loss of excitation light and fluorescence signal because of light scattering by the tissue. Also deeper imaging leads to lower contrast in bright-field and makes patching extremely difficult. That is why one of the major requirements for objectives is a long working distance. The Olympus 20×, 40× and 60× water-immersion objectives satisfy this requirement, with working distances of at least 2 mm. On the other hand it is possible to use objectives with shorter working distances for studies which do not require simultaneous imaging and electrophysiological recording (morphological studies of cells labeled genetically or by bolus injection).

The efficiency of signal collection in the case of two-photon laser scanning microscopy using the whole-area detection mode directly depends on the NA of the objective lens used. Also, a higher NA decreases the diffraction-limited size of the excitation spot, which gives better spatial resolution and provides higher local intensity of the excitation light, thus increasing the efficiency of nonlinear optical effects (multi-photon absorption or second-harmonic generation). In this respect, the Olympus 20× 0.95 NA water-immersion objective was crucial and allows 2P Ca^{2+} imaging of large neuronal populations with excellent signal to noise ratio (Fig. 41.3A).

Choosing the right magnification for the objective lens is another practical issue. Lower magnification is good for imaging larger structures; although low-magnification objectives are not convenient for simultaneous electrophysiological recordings, if cells have to be patched while visualizing them through the eyepieces. In some cases, increasing magnification with a separate system of lenses solves this problem. As an example, we have a "U-CA" adaptor from Olympus for the BX 50WI microscope, which works as a magnifying telescope and is inserted into the optical pathway of the microscope in the region where the light is collimated. On the other hand it is not ideal to use magnifying adaptors for imaging, because they lead to a loss of fluorescence signal in collection pathway. Hence this adaptor should be used only for convenience when observing with low-magnification objectives (20×) through the eyepieces.

High magnification lenses (40×, 60×, 100×) with higher numerical apertures provide images with higher spatial resolution in 3D. Using the "digital zoom" option available in majority systems for laser scanning microscopy, allows one to set the pixel size according to Nyquist. This kind of spatial sampling is not always necessary. For example, when imaging neuronal populations, we are interested mostly in the integrated signal from individual cells. Nyquist sampling, or even oversampling, is important if we ask questions about sub-resolution movements of small structures (i.e., quantitative analysis of spine movement). In this case, one should not consider a laser scanning microscope as an imaging device with resolution limit defined by diffraction, but more as a position-measuring instrument that measures the centroid of the distribution of fluorescent molecules and the dynamics of the position of this centroid.

For two-photon laser scanning microscopy, it is important to make sure that all the components of the excitation pathway have good transmission in the near IR. Users should use objective lenses corrected for optical distortions and made to be transparent in the NIR. In many cases, additional changes are needed in the installed optics to make them IR-transparent (pupil-transfer lens in our case; (Majewska *et al*., 2000b).

Objective lenses used for multi-photon imaging should be free of geometrical (spherical) aberrations. The requirement for the absence of chromatic aberrations is not so important — excitation light is practically monochromatic (the spectrum widening caused by the finite length of pulse from mode-locked lasers is negligible). Also, the absence of a confocal aperture in front of the detector and the general architecture of the collection system, emphasizes collecting the maximum fraction of the emitted light, and allows one the freedom of using collecting optics (objectives in case of 2P-fluorescence and condenser lens in the case of SHG) not well-corrected for chromatic aberration.

Beam Collimation and Pulse Broadening

The majority of modern microscopes are designed for infinity-corrected objective lenses, so it is important to provide collimated laser light to the back-aperture of the objective (Tsai and Kleinfield, 2002). Even if initially the microscope system and scanning head are designed to provide collimated light at the back-aperture of objectives, custom modifications of the optical pathway and the switch to NIR excitation can distort this collimation. This indeed happened in our custom-made 2P-microscope and we solved the problem by introducing additional optics into the excitation pathway (Nikolenko *et al.*, 2003). Specifically, we use a simple system of 2 lenses in order to collimate the light to the objective lens.

Our system also works as a "beam expander" — it modifies the laser beam in such a way that the excitation beam at the back aperture of objective is not only collimated, but also is large enough to slightly overfill the objective pupil. One of the major requirements for laser scanning microscopes is that the back aperture should be overfilled by the excitation light (Tsai and Kleinfield, 2002). This minimizes variation of excitation power across the field of view and guarantees that the full numerical aperture of the objective lens is used. The level of overfilling should be minimal to maximize the amount of excitation power deliveried to the sample.

Another important factor in 2P microscopy is the problem of pulse broadening. Nonlinear microscopy requires using pulsed laser light. Mode-locked lasers generate a train of pulses of finite length at certain repetition rate. Even though each pulse represents monochromatic light, the finite length of each pulse leads to a spectrum with certain width in Fourier-space. Linear dispersion of this light in the intermediate optical elements disturbs the phase relations between the different spectral components of the pulse, which in practice leads to the pulse being broadened in time. This decreases the peak excitation intensity, and hence decreases the efficiency of nonlinear excitation. In order to avoid this, the optical system should use the minimum number of lenses between the laser and the specimen. Alternatively, one can add additional optics with negative dispersion in order to compensate for the positive dispersion of the rest of the optics (Lechleiter *et al*., 2002).

Image Production, Resolution, and *z*-Sectioning

In our two-photon microscope, fluorescence is detected with photomultiplier tubes (PMTs; HC125-02, Hamamatsu, Japan) used in an external, whole-area detection mode, and images are acquired using Fluoview software (Olympus). Images are sometimes taken at the highest digital zoom, resulting in a nominal spatial resolution of 20–30 pixels per μm with the 40×. This spatial resolution is suitable for imaging very small structures including dendritic spines, the size of which is typically on the order of μm.

Since brain slices are three-dimensional, we collect a series of images (*z*-stack) from different focal planes to cover the whole neuronal structure of interest. In principle, three-dimensional structures can be reconstructed from the *z*-stack. However, this is not practical when the same structure is imaged repeatedly, particularly in time-lapse imaging, for the following reasons: (1) perfusion causes small movements of the slice so the reconstructed structures are not accurate and (2) to achieve pixelation in the *z*-direction at a similar level to the *x*- and *y*-direction, many focal planes have to be scanned. This is impractical because it compromises fast time-lapse imaging and increases the possibility of photodamage.

To circumvent these problems, we scan the images with a 1 μm difference between focal planes (up to 9 planes), and then project the *z*-stack into a single, two-dimensional image. Since the point spread function of the 60× objective lens in our microscope measures approximately 0.4 × 0.4 × 1.3 μm (Majewska *et al*., 2000b), the images with 1 μm focal distance have enough overlap to produce a good projection.

A major problem associated with time-lapse imaging of brain slices is slice movement in the *x*, *y* and *z*-directions. To minimize movement in *z*, we routinely scan extra focal planes at the top and the bottom of the *z*-stack. If movement in the structure of interest is evident in these extra focal planes, we move the whole *z*-stack 1 μm up or down. Thus, structures of interest are not lost from the *z*-stack. Structures of interest can also move out of the images by moving in the *x* or *y* directions. To minimize this, we try to make the slice adhere to the bottom glass of the chamber. In addition, we avoid placing the structures of interest near the edge of the image, and if the structures move near the edge, we reposition the specimen so that the structures move toward the center of the imaged area. Although this prevents the loss of structures of interest from the *z*-stack, *xy* movement results in the drift of the whole image in the time-lapse movies. In these movies, it is extremely difficult to observe and analyze changes in morphology and fluorescence intensity. Therefore, in the analysis we compensate the *xy* movement as described below.

Choice of Indicators for Two-Photon Imaging of Calcium

Two-photon excitation of calcium indicators loaded via whole-cell recording is ideal for imaging calcium during action potential generation or during synaptic excitation (Yuste and Denk, 1995). We have used both calcium green-1 and fluo-4 successfully and find that both indicators are excited well by a mode-locked laser at 800 nm. However, we find that each indicator is suited for different conditions. Because calcium green-1 is brighter at low calcium concentrations, it is ideally suited for visualizing fine structures such as dendritic spines. However, in part due to its high fluorescence at rest, its increase in intensity on binding calcium is compromised (F_{ca}/F_{free} = ~14), such that it is imperfect for detecting small or heavily buffered signals. On the other hand, although fluo-4 is dim at rest and therefore demands higher excitation laser power, it undergoes a large change in fluorescence on binding calcium (F_{max}/F_{min} = ~100). Thus, fluo-4 is ideal for imaging small or heavily buffered signals, such as in cortical interneurons, which have high endogenous buffering capacities. We have used calcium green-1 over the concentration range of 50 to 200 μ*M*, and fluo-4 from 100 to 400 μ*M*. Because increased indicator concentrations cause larger distortions of the true calcium signals, the smaller the concentrations yield more physiologically-relevant data; however, if higher laser intensities are necessary to observe signals in environments with low concentration, photodamage may be accelerated.

In our hands, indo-1 is the best choice when shorter wavelengths (<750 nm for two-photon excitation) are needed to combine calcium imaging with uncaging techniques. The two-photon sensitivity of calcium indicators is available from http://cellscience.bio-rad.com/products/multiphoton/Radiance2100MP/mpspectra.htm.

Photodamage

The Achilles' heel of all live imaging is phototoxicity. Using our two-photon microscope, we experience two types of photodamage, when imaging neurons with too-high laser power (>20 mW at the sample). First, unstained cells that show strong autofluorescence suddenly collapse, emitting high-intensity light, like an explosion. This often masks the structure of interest. We recommend not including any structures with high autofluorescence in the imaging area. Second, stable structures in labeled neurons can show abnormal morphological rearrangements, particularly beading. This type of photodamage is nonlinear and, in some cases, can start to occur even minutes after the illumination has stopped. Moreover, even though previous scans can be normal, the same intensity of excitation can suddenly cause photodamage, particularly if the imaged structures are near the surface of the slice and if the concentration of dye is high. As is the norm in all microscopy, we recommend imaging with as low an excitation intensity as possible and adjusting this intensity for each sample depending on the brightness of the image.

In some experiments where photodamage becomes a persistent problem, we use the antioxidant Trolox (Sigma, 10–100 μ*M*), added to the ACSF (Sheenen *et al*., 1996). We have not noticed any effect of Trolox on the physiology of the neurons, although it has been suggested that high concentrations of it can block NMDAR (A. Konnerth, personal communication).

Second Harmonic Imaging

Second harmonic generation (SHG) is a nonlinear optical effect in which the incident light is coherently scattered by the specimen at twice the optical frequency and at certain angles (Lewis *et al*., 1999; see Chapter 40, *this volume*). The signal can be produced by endogenous structures or from inserted chromophores. Unlike fluorescence, in which emitted photons are best detected in the epi configuration, SHG photons are best detected in the transmission path of the microscope. The SHG photons, generated at the focal spot of the laser in the sample, are collected by a condenser lens which has to have the same NA as the objective lens in order to collect the whole cone of light. This is important because the SHG radiation in the forward direction is restricted to certain off-axis angles. It is best to have a spatially filtered laser beam for SHG because it is a coherent process — the spatial filter acts as a point source and restores the Gaussian wavefront and phase. Spatial filtering can be achieved by a telescopic system of two positive lenses and a pinhole placed between them such that the pinhole-

to-lens distance equals the focal length, respectively. In front of the photomultiplier tube (PMT), which is placed in the transmission path, is a narrow band (~20 nm) filter centered at half the wavelength of the laser. The amplification of the signal is done by standard methods as in fluorescence detection. Specific instructions to adapt a two-photon microscope for SHG imaging can be found in Nikolenko and colleagues (2003).

Silicon-Intensified Target Camera Imaging

While two-photon imaging results in a high spatial resolution imaging with the least photobleaching and most depth penetration, there is a cost, as with any laser-scanning microscopy, in terms of temporal resolution when many neurons are simultaneously imaged because the laser beam must be systematically moved over a large area. While future scanning modifications may alleviate this problem, at present single-photon fluorescence imaging has proved a useful technique for measuring the fluorescence changes in several neurons simultaneously (Peterlin *et al*., 2000; Kozloski *et al*., 2001).

For example, using calcium imaging with fura-2, the typical detectable change in fluorescence that can be measured in a neuron from a single action potential has a fast onset (<100 ms rise time) and slow decay (>2 s; Smetters *et al*., 1999). This allows one to detect the time of occurrence of action potentials in identifiable neurons with 100 ms temporal resolution, provided that frames are acquired at a rate of 50 ms or less. We have achieved this using a SIT camera (Dage), BX50WI microscope (Olympus), 40× 0.8 NA water-immersion lens, an LG-3 frame grabber (Scion Corp.) in a Power Macintosh 7600, and NIH image software. With this equipment, we can view an area of cortex of 320 × 240 µm with a spatial resolution of 640 × 480 pixels, and we can capture frames at a rate of 30 frames/s. Using fura-2 AM loaded slices (see above for loading technique), we can image dozens of neuronal somata using a mercury source (Olympus), a 380 nm excitation filter and 510 nm emission filter. The gating of the light source is accomplished via a triggered shutter (Uniblitz), which fully opens in less than 30 ms after the triggering TTL pulse. The acquisition of a frame or a set of frames (a "movie") can also be initiated from an external trigger. The delay from triggering the movie to acquisition of fully illuminated frames is from 100 to 150 ms to compensate for the 100 to 150 ms lag of the camera. Each captured frame uses 307.3 kB of memory. Homemade macros have been written using NIH image, controlling the shutter through the modem port of the computer. These macros enable the acquisition of movies time-locked to either depolarizing current pulses in current-clamped neurons (as in Kozloski *et al*., 2001) or to a large PSC recorded in a voltage-clamped neuron via a window discriminator (WPI).

MORPHOLOGICAL PROCESSING AND ANALYSIS

As our most reliable method for morphological reconstructions, we use biocytin fills and processing to recover the morphologies of the neurons imaged (Fig. 41.4).

Biocytin Protocol

Following electrophysiological recordings, the slices are immediately placed in 4% paraformaldehyde in 0.12 *M* phosphate buffer (PB) and kept at 4°C overnight. Slices are then cryoprotected in 20% sucrose in 0.12 *M* PB for 2 to 8 h and frozen on dry ice in tissue freezing medium (catalog #H-TFM, Triangle Biomedical Sciences). Upon defrosting, slices are rinsed in 0.12 *M* PB three times and pretreated with 1% hydrogen peroxide in 0.12 *M* PB for 30 min under agitation at room temperature. The tissue is then rinsed in 0.02 *M* potassium phosphate saline (KPBS) and incubated in Avidin-Biotin-Peroxidase Complex (catalog #PK-6100, Vector Laboratories, Inc.) overnight under agitation at room temperature (10 µL solution A and 10 µL solution B per 1 mL of 0.02 *M* KPBS and 0.3% Triton-X). Slices are rinsed in 0.02 *M* KPBS three times and incubated in 0.7 mg/mL 3,3′-diaminobenzidine, 0.2 mg/mL urea hydrogen peroxide, 0.06 *M* Tris buffer (catalog #D-4293, Sigma-Aldrich) in 0.02 *M* KPBS for 5 to 15 min. Upon completed DAB reaction, the slices are rinsed in 0.02 *M* KPBS and mounted in Vectashield mounting medium (catalog #H-1000, Vector Laboratories, Inc.).

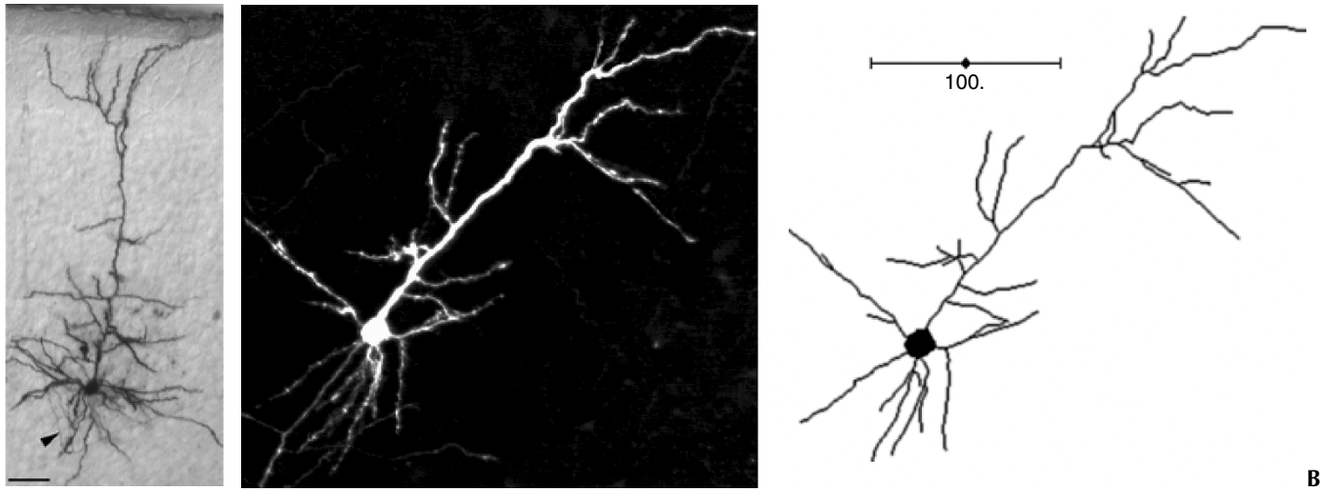


FIGURE 41.4. Histological reconstruction of neurons using biocytin and Neurolucida. (A) Biocytin staining. A pyramidal cell in a coronal section from mouse visual cortex was filled intracellularly with biocytin and then processed for visualization. Intracellular biocytin staining enables a large signal/noise and allows a fairly accurate reconstruction of the dendritic arbor of the neuron. Structures as small as spines (~1 µm in diameter) can be visualized. Arrowhead indicates the axon. Scale bar = 50 µm. (Courtesy of Z. Peterlin and A. Tsiola.) (B) Neurolucida reconstruction. (Left panel) Confocal image of a pyramidal neuron from a P7 mouse slice, cultured for 6 days. The cells were transfected with EGFP using a gene gun. (Right panel) Reconstruction of the neuron using Neurolucida.

Anatomy with a Two-Photon/Neurolucida System

We have experimented with direct two-photon reconstructions of the cells in the brain slices. This procedure enables the investigator to quickly reconstruct the morphology of the imaged cell. Images of neurons from both live and fixed tissue can be taken by the two-photon microscope and the stacks of images can be imported into a computerized reconstruction and measuring program, such as Neurolucida (Microbrightfield, Brattleboro, VT).

Two-Photon/Neurolucida Protocol

When examining dendritic morphology alone, *z*-stacks of the neuron of interest can be captured using a 20× or 40× objective. When spines and filopodia are also of interest, a 60× objective with a 2.5× digital zoom yields good images. For detailed reconstructions of the protrusions from the entire neuron, small overlapping sections of the neuron are imaged using the 60× objective and 2.5× digital zoom. After capturing the *z*-stack of images, they should be saved as a Fluoview Multi-Tiff (*.tiff) and transferred to a computer running the Neurolucida software. The images can either be burned onto a recordable CD, or can be transferred to the computer over a local area network.

The neurons can then be reconstructed using Neurolucida software. The stack can be opened using the Image Stack Open command under the File icon on the menu bar. Once the image is opened, the brightness and contrast of the image can be adjusted by selecting Image Effects under the Video icon. Once the picture is in clear focus, the neuron is ready to be reconstructed. The image must be calibrated and a reference point chosen. The PgUp and PgDn keys on the keyboard will allow for scrolling through the stack of images. The mouse is used to trace the neuron and the type of tracing can be set by right clicking on the image. We find that rubber line tracing is very effective. The thickness of the line can be determined by the scroll feature on the mouse (the wheel or center button). In the tool bar we are able to select the section of the neuron we are drawing, for example, apical dendrite or cell body. Nodes and branches are added by right clicking on the image during tracing. After the contour is completed, it can be saved and opened in the Neuroexplorer program. This program will allow for easy analysis of the reconstruction.

Correlated Electron Microscopy

Although we can image neuronal structures in live brain slices at quite high resolution with two-photon microscopy, for some questions, such as confirming the existence of a synapse, we find it necessary to use electron microscopy. We have pioneered the combination of two-photon live imaging with serial thin-section electron microscopy to enable us to examine the ultrastructure of dendritic spines and axonal filopodia (Dunaevsky *et al.*, 2001; Tashiro *et al.*, 2003).

Protocol for Two-Photon/Electron Microscopy Imaging of GFP-Labeled Cells

Neurons are transfected with eGFP using biolistics. Slices imaged with two-photon microscopy are fixed with 5% glutaraldehyde in PB for 1 h. The slices are then embedded in 3% agar and resectioned at 75 μm with a vibratome (Technical Products International, St. Louis). After locating the imaged neuronal structure in the sections using a fluorescence microscope, the sections are immunostained with anti-GFP antibody (Roche Diagnostics Corp.) overnight at 4°C, and then with peroxidase-conjugated goal anti-rabbit IgG antibody (Roche Diagnostics) for 1 h at room temperature. After developing with DAB, the sections are postfixed in 1% osmium tetroxide in PB, dehydrated, and then infiltrated with Epox 812 resin (Fullam), placed flat in resin between two plastic slides, and polymerized in the oven at 60°C. After polymerization, the plastic slides are separated and the imaged areas of interest were cut out, mounted on a blank block, and sectioned to 10 μm for examination under phase contrast. The 10 μm sections with the imaged areas of interest were then remounted on a blank block, thin sectioned, and examined in the electron microscope (JEM 1200EX). Imaged mossy terminals with filopodia are reconstructed from serial sections (see also Chapter 49, *this volume*).

Protocol for Two-Photon/EM Imaging of Biocytin Labeled Cells

Neurons are bolus injected with electrode containing 0.4% biocytin and 1 m*M* Alexa-488 as described before. Immediately after imaging, brain slices are immersion fixed with 4% paraformaldehyde and 0.5% glutaraldehyde in 0.1 *M* PB overnight at 4°C. They are washed three times 10 min on shaker at room temperature with 0.1 *M* PB. Then, slices are incubated in 1% hydrogen peroxide, 50% ethanol, and 0.05 *M* PB for 30 min at room temperature on shaker for eliminating internal peroxidase activity. After washing again, they are incubated with ABC (Vectastain) overnight at 4°C and 1 h at room temperature. After washing again, they are DAB reacted using fast DAB‰ from Sigma for about 3 min. Then, pictures are taken from the imaged region to facilitate its EM reconstruction. At this point, slices can be postfixed with glutaraldehyde. Finally, slices are osmicated by 1% osmium tetroxide together with 7% glucose and 0.005% $CaCl_2$. If there is a problem of revealing the imaged region with biocytin, slices can be resectioned after fixation. For this, slices are embedded in 3% agarose and resectioned using a vibratome. Freeze–thawing is another method to increase the penetration of reactants like ABC. For this, slices are kept in 30% sucrose until the slices sink to the bottom, and then dipped (in the plastic container with sucrose) into liquid nitrogen.

As a variant on this protocol, for fixing slices for EM, prepare a fix solution of 4% paraformaldehyde, 0.05% glutaraldehyde, and 15 mL of saturated picric acid in 100 mL of 0.1 *M* PB. Slice should be kept in this solution for approximately 3 h. Thereafter, slices may be stored in a solution of 0.05 *M* sodium azide in 0.1 *M* PB. Then follow the protocol above.

Morphological Classification of Neurons Using Cluster Analysis

One of the problems in classifying cortical neurons is their heterogeneity and the vast number of parameters that can be used for this purpose. These parameters usually encompass a massive array of physiological, morphological, and, most recently, gene expression data. A rigorous approach to classifying cortical neurons must involve a thorough analysis of the structure of the data before one attempts to assign neurons to certain clusters. Principal component analysis (PCA) and cluster analysis (CA) are valuable multivariate data analysis methods that can be used jointly with CA to address these issues (Kozloski *et al.*, 2001).

Protocol for PCA/CA

As a first step, we perform a PCA analysis using Statistica on the variables automatically measured by the Neurolucida program. In a second step, we perform cluster analysis (Wards's methods), also using Statistica.

Let $\boldsymbol{X}$ denote an $m \times n$ matrix of m cells (cortical neurons) with n measured or computed parameters. The elements of this matrix denoted by x_{ij} represent the value of the jth parameter for the ith neuron. For values of $n \leqslant 3$, visualization of data is impossible and thus the overall distribution of cells in their n-dimensional parameter space is not accessible. In the case of cortical neurons the number of dimensions can easily exceed tens or even hundreds with the inclusion of gene expression data. The major advantage of PCA methods is to help reconstruct a new parameter space with (optimally) three dimensions in such a way that it still faithfully represents the data with the minimum loss of information during the process of space transformation. This transformation involves computating eigenvalues (Σ) and eigenvectors (u) of the $n \times n$ correlation matrix ($\boldsymbol{R}$) of the original data matrix $\boldsymbol{X}$. The goal is to map the n-dimensional vector describing the parameters of each neuron to a vector with, for example, three dimensions, so that each neuron can be plotted in a three-dimensional (3D) graph. The desired new dimensions, also called principal factors or components, are extracted from the original space through the eigenvalue decomposition of the correlation matrix. This decomposition will provide the eigenvectors (principal components) and its related eigenvalue (total variance accounted for by each component). Principal component scores computed for each principal component give the coordinates of neurons in the reduced space. PCA methods also provide a matrix of factor or principal component loadings that show the correlation value of each original parameter with the newly computed components. These loading values show which parameters contribute significantly (highly positive or negative correlations) to the derived dimensions. It can be seen that, while some original parameters contribute significantly to some components, they contribute very little to others. Meanwhile, some original variables only contribute to principal components that carry a relatively low proportion of the total variance (low relative eigenvalue). These latter parameters are thus found to be less important in the characterization of the data structure.

The final stage of classification involves application of CA to the new coordinate values (principal component scores) of the neurons in the reduced space. Appropriate linkage rules for CA can be chosen based on the apparent shape of the clusters as seen in the scatter plot of neurons in the principal component space. Application of PCA before CA allows a rational choice of linkage rules which would lead to a better segregation of clusters.

IMAGE PROCESSING

Compensation for the Drift and the Vibration of the Slices

As described above, one of our problems is the movement of slices that produces the drift of images during long (>10 min) time-lapse movies. This drift of structures of interest makes it particularly difficult to observe and analyze changes in morphology and fluorescence intensity. Indeed, spine motility was only discovered in our laboratory after the alignment of time-lapse movies was performed (Dunaevsky *et al*., 1999). Therefore, we always compensate for the movement of slices.

Although manual alignment of time-lapse movies using the structures which are always stable as references works well, this is time consuming. Instead, we have been using three automatic methods of alignment. Two of them are custom-made programs based on the overlap between the images and the center of mass, respectively. These programs are written in NIH image and ImageJ software, respectively. The other is commercially available software from AutoQuant Imaging, Inc.

Alignment Based on the Overlap Between Images

This alignment program is written as an NIH image macro. The principle of this macro is quite simple. Take two images, project these two images, and compare the average pixel values of the projected image and the original image. The more similar the two original images are and the more overlap they have, the closer the two average pixel values will be.

Protocol for Overlap Alignment

Before performing automatic alignment, images are thresholded to highlight neuronal structures. Ideally, the original images should work as well. However, because optical noise changes during time-lapse sequences, in practice, thresholded images work better. The macro selects two images and performs multiple iterations of an alignment procedure using the above principle. Each iteration comprises shifting the second original image by 1 to a certain number of pixels in four directions (up, down, left, right), comparing the average pixel values of the projected images and the first image, determining the optimal shift, where the average pixel values of the projected image and the original image are closest, and moving the second image by this optimal shift. From the second iteration on, images are only shifted in three directions because one of four directions is toward a starting point to the previous iteration. To avoid including the blank peripheral area which arises from the shift of the second image, only the area where the first original image and the shifted second image overlap are used to calculate the average pixel values of the projected image and the first original image. These iterations are repeated until an iteration finds that the original position of the second image in the iteration is optimal, or, in other words, the average pixel values of the projected image and the original image are closest in the ending position of the iteration.

This alignment macro works very well for most time-lapse sequences of projected images when the images have more area with stable structures than with unstable ones. For example, in the case of the time-lapse imaging of dendritic spine motility, the morphological changes in spines are quite small compared to the stability of the much larger dendritic shafts. Thus, in most cases, the alignment macro works reasonably well. When, in rare cases, alignment does not work completely, we align the movies manually using NIH image software.

We use this alignment for z-stacks where the structure of interest shifts between focal planes because of slice movement. Images in z-stacks are not aligned as well as time-lapse movies consisting of projected images since each image in a z-stack is different from the next image (with small overlapping). Although not ideal, the same macro helps to align z-stacks. We check all aligned stacks and correct them manually if the alignment is not good.

Alignment Based on the Center of Mass

We have created a different alignment program as a plug-in for ImageJ software using Java programming language. This program is based on the calculating relative positions of the center of mass of the drifting objects.

Protocol for Center of Mass Alignment

The coordinates of center of mass are calculated by using the pixel value as a mass. For meaningful calculations, a cut-off value is used in order to prevent including background pixels in the calculation. Our program calculates the center of the first frame in the image stack and uses these coordinates as the reference point for aligning the rest of the image stack (i.e., It considers the first frame as not drifted).

The program then calculates coordinates of the center of mass of the each image in the stack. The program then shifts each image in order to align images in such a way that centers of mass of all frames have the same coordinates (they overlap each other).

If a region of interest (ROI) is chosen, the program aligns to the center of mass of the ROI. The ROI can be any shape and allows aligning by using center of mass of a selected object, not whole image.

This algorithm is quite simple, fast, and works well if the center of mass is always calculated from the same structure. However, drift of the slices can make a new structure appear or a part of a structure disappear from the edge of the image. Because this edge effect can make the center of mass move to completely different positions in different images, purely automatic alignment is sometimes unsuccessful. On the other hand, choosing a stable structure as the ROI for alignment can prevent this artifact.

The next logical step in the development of this type of algorithm could be using spatial moments of higher order (center mass coordinates are spatial moments of the first order; and the total mass is spatial moment of zero order). For example, including in the alignment algorithm, spatial moments of the second order and third order will allow compensating not only for drift, but also for image rotation and squeezing.

Online Cell Detection of Neurons

Using AM loading, we can simultaneously image over 3000 neurons (Fig. 41.3). To analyze fluorescence changes, such as those indicating Ca^{2+} concentration, of a large number of individual cells, we need to identify and select all the neurons. As manual selection of this many cells is quite tedious and cannot be performed online, automatic cell detection algorithms were developed in ImageJ (NIH, Bethesda, MD) and Matlab (MathWorks, Natick, MA) [Fig. 41.5(A)].

Protocol for Center of Mass Alignment

First, time-lapse movies are collapsed in time, creating a single projected image by averaging the fluorescence of each pixel throughout the recording. This effectively reduces the amount of spatial noise in the image and reveals smaller elements, such as dendrites. Due to the slightly unequal loading of different regions

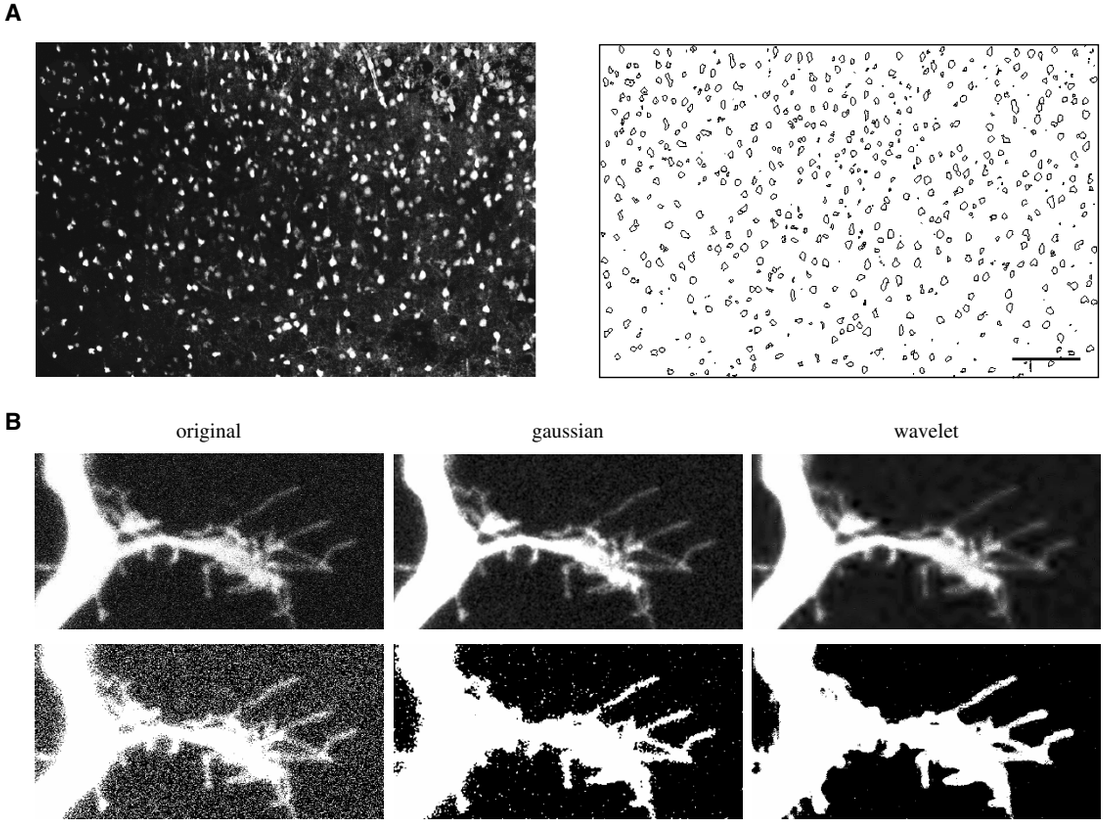


FIGURE 41.5. Image processing algorithms. (A) Cell detection algorithm. (Left) An original image of a fura-2 loaded acute slice. Note how the staining is not even throughout the image. (Right) An image with outlines of all detected cells. The contours of the cells are drawn. (B) De-noising algorithms. (Upper panels) Images of a dendritic growth cone from a cortical pyramidal neuron. All three images are shown with the same brightness and contrast. (Lower panels) Binarized images. All three images are thresholded with the same pixel value. (Left) Original images. (Center) Gaussian-filtered images. (Right) Images de-noised with wavelet transformation.

of the slice, the average fluorescence level of cells in the same slice often vary, making automatic detection problematic. To account for these spatial fluorescence variations, the value of each pixel is normalized, dividing it by the average fluorescence of a 25 × 25 µm square centered at that pixel. In the resulting image, the fluorescence level is almost constant for all cells and is typically between 1.2 and 1.5. Contours can be plotted at a manually chosen value in this range using the Matlab contour drawing algorithm. Every closed contour corresponds to the accurately detected boundary of a fluorescent entity in the imaged field. This method identifies practically all cells, as well as a large number of smaller non-cellular elements in the slice [Fig. 41.3(A)]. By measuring the average fluorescence value of the pixels inside each contour as a function of time, we can quickly reconstruct fluorescence changes of large populations with single-cell resolution. In total, this allows us to measure calcium fluorescence signals from roughly 400 to 1400 entities per slice.

Image De-Noising Using Wavelets

The external PMT in our two-photon system produces uncorrelated dark noise, primarily of thermal origin. This type of noise has a strong dependence on applied bias voltage (Majewska *et al*., 2000b; www.twophoton.com). It is therefore important to correctly choose the bias voltage in order to balance the resulting gain of the PMT versus noise.

This type of noise is intrinsically random and does not have specific spectral components. Therefore, it cannot be distinguished from the real signal by classic methods of linear filtration. For example, the widely used mean and Gaussian windows filters are not efficient in terms of removing this type of noise (Fig. 41.5). Indeed, background noise removal is very important for quantitative analysis of thresholded images, and linear filtration of noisy images usually gives artifacts [Fig. 41.5(B)].

As an alternative approach, we use wavelet transformation for the purpose of image de-noising (Lio, 2003). Wavelet transformation is widely used for signal compression and de-noising and represents further development of classic methods of analysis such as Fourier, Gabor, and short-time Fourier transformation. The wavelet transformation gives full representation of the signal [for one-dimensional (1D) time signals, a correct representation in time and frequency domains; for two-dimensional (2D) images, a representation of spatial frequencies and coordinates]. Whereas Fourier transformation presumes the infinite dimensions of the image space, wavelet transformation is inherently local and gives a better representation of naturally occurring finite-size objects in image.

Protocol for Wavelet De-Noising

The general de-noising procedure consists of the following steps:

In case of image de-noising, an individual image is represented as 2D array of numbers (pixel values). The wavelet transformation decomposes this 2D signal into wavelet space by using a specified wavelet family. In case of discrete wavelet transformations, it computes the detail coefficient of the signal up to the certain predefined level. For the purpose of signal de-noising, the detail coefficients at all levels of decomposition have to be thresholded. The numerical value of the threshold can be chosen based on the noise model used.

There are several methods of thresholding. The practical choice of the method depends on the nature of the signal and the chosen model. Reverse wavelet reconstruction is then performed using the modified detail coefficients, and the filtered image is regenerated from thresholded detail coefficients by using the inverse wavelet transformation.

The latest release of the Wavelet Toolbox (version 2.2) for Matlab (The MathWorks Inc., Natick, MA) provides a variety of ready-to-use tools for wavelet transformation and signal de-noising. There is an interactive graphical user interface in Wavelet Toolbox, which simplifies the task of choosing the parameters for signal de-noising and compression. In the simplest case, practical de-noising can be done based on the visual perception of the de-noising quality, but also using different recovery criteria (e.g., based on entropy estimation).

For large-scale image processing, we created a custom code in Matlab, which performs simple image de-noising based on the chosen model. As a model, we use wavelet decomposition to level 4 with symlet-6 wavelets, and soft thresholding (see more theory of de-noising procedure in Wavelet Toolbox documentation). The script processes raw images in a multi-TIFF format, gives acceptable de-noising, and does not change the quantitative values of intensity in the principal image details [see Fig. 41.3(B)]. Our algorithm processes each frame individually, therefore processing time depends linearly on the size of the image stack. The algorithm is not memory demanding and turned out to be relatively fast — it takes approximately 5 s to process a 800 × 600 pixel, 16-bit image on a 1.9 GHz Pentium 4 PC.

SUMMARY

- Brain slices are convenient preparations because they permit the easy manipulation of their environment, access for imaging or electrophysiological equipment, and preservation of three-dimensional organization of the brain region studied.
- We describe the techniques of live-slice imaging we use in our laboratory, including slice preparation (acute and cultured slices), cell labeling (biolistics, diolistic, calistics, injection with patch electrodes, and AM loading), morphological processing and analysis, imaging procedures (two-photon, second harmonic, and camera imaging), and image processing.
- Although *in vivo* imaging techniques have recently developed in many species, brain-slice imaging has advantages for studying many questions and will be increasingly important for cortical research.

ACKNOWLEDGMENTS

We thank the National Eye Institute (EY11787 and EY13237), the NINDS (NS40726), the New York STAR Center for High Resolution Imaging of Functional Neural Circuits, the HFSP, and the John Merck Fund for their support.

REFERENCES

Agmon, A., and Connors, B.W., 1991, Thalamocortical responses of mouse somatosensory (barrel) cortex *in vitro*, *Neuroscience* 41:365–379.

Alger, B.E., Dhanjal, S.S., Dingledine, R., Garthwaite, J., Henderson, G., King, G.L., Lipton, P., North, A., Schwartzkroin, P.A., Sears, T.A., Segal, M., Whittingham, T.S., and Williams, J., 1984, Brain slice methods, In: *Brain Slices* (R. Dingledine, ed.), Plenum Press, New York, pp. 381–437.

Arnold, D., Feng, L., Kim, J., and Heintz, N., 1994, A strategy for the analysis of gene expression during neural development, *Proc. Natl. Acad. Sci. USA* 91:9970–9974.

Beierlein, M., Fall, C.P., Rinzel, J., and Yuste, R., 2002, Thalamocortical bursts trigger recurrent activity in neocortical networks: Layer 4 as a frequency-dependent gate, *J. Neurosci.* 22:9885–9894.

Brenner, S., 2002, Life sciences: Detective rummages, investigates, *The Scientist*, 16(6):15–16.

Dunaevsky, A., Blazeski, R., Yuste, R., and Mason, C., 2001, Spine motility with synaptic contact, *Nat. Neurosci*. 4:685–686.

Dunaevsky, A., Tashiro, A., Majewska, A., Mason, C.A., and Yuste, R., 1999, Developmental regulation of spine motility in mammalian CNS, *Proc. Natl. Acad. Sci. USA* 96:13438–13443.

Edwards, F.A., Konnerth, A., Sakmann, B., and Takahashi, T., 1989, A thin slice preparation for patch recordings from neurones of mamalian central nervous system, *Pflugers Arch*. 414:600–612.

Feng, G., Mellor, R.H., Bernstein, M., Keller-Peck, C., Nguyen, Q.T., Wallace, M., Nerbonne, J.M., Lichtman, J.W., and Sanes, J.R., 2000, Imaging neuronal subsets in transgenic mice expressing multiple spectral variants of GFP, *Neuron* 28:41–51.

Franklin, K.B.J., and Paxinos, G., 1997, *The mouse brain in stereotaxic coordinates*, Academic Press, San Diego, California.

Gan, W.B., Grutzendler, J., Wong, W.T., Wong, R.O., and Lichtman, J.W., 2000, Multicolor "DiOlistic" labeling of the nervous system using lipophilic dye combinations, *Neuron* 27:219–225.

Grynkiewicz, G., Poenie, M., and Tsien, R.Y., 1985, A new generation of Ca^{2+} indicators with greatly improved fluorescence properties, *J. Biol. Chem*. 260:3440–3450.

Helmchen, F., Imoto, K., and Sakmann, B., 1996, Ca2+ buffering and action potential-evoked Ca2+ signalling in dendrites of pyramidal neurons, *Biophys. J.* 70:1069–1081.

Honig, M.G., and Hume, R.I., 1989, DiI and DiO: Versatile fluorescent dyes for neuronal labelling and pathway tracing, *Trends Neurosci*. 334:333–340.

Kettunen, P., Demas, J., Lohmann, C., Kasthuri, N., Gong, Y., Wong, R.O., and Gan, W.B., 2002, Imaging calcium dynamics in the nervous system by means of ballistic delivery of indicators, *J. Neurosci. Methods* 119:37–43.

Kozloski, J., Hamzei-Sichani, F., and Yuste, R., 2001, Stereotyped position of local synaptic targets in neocortex, *Science* 293:868–872.

Lechleiter, J.D., Lin, D.T., and Sieneart, I., 2002, Multi-photon laser scanning microscopy using an acoustic optical deflector, *Biophys. J*. 83:2292–2299.

Lewis, A., Khatchatouriants, A., Treinin, M., Chen, Z., Peleg, G., Friedman, N., Bouevitch, O., Rothman, Z., Loew, L., and Sheves, M., 1999, Second harmonic generation of biological interfaces: Probing membrane proteins and imaging membrane potential around GFP molecules at specific sites in neuronal cells of *C. elegans*, *Chem. Phys*. 245:133–144.

Lio, P., 2003, Wavelets in bioinformatics and computational biology: state of art and perspectives, *Bioinformatics* 19:2–9.

Lo, D.C., McAllister, A.K., and Katz, L.C., 1994, Neuronal transfection in brain slices using particle-mediated gene transfer, *Neuron* 13:1263–1268.

Lohmann, C., Myhr, K.L., and Wong, R.O., 2002, Transmitter-evoked local calcium release stabilizes developing dendrites, *Nature* 418:177–181.

Majewska, A., Tashiro, A., and Yuste, R., 2000a, Regulation of spine calcium compartmentalization by rapid spine motility, *J. Neurosci*. 20:8262–8268.

Majewska, A., Yiu, G., and Yuste, R., 2000b, A custom-made two-photon microscope and deconvolution system, *Eur. J. Physiol*. 441:398–409.

Nikolenko, V., Nemet, B., and Yuste, R., 2003, A custom two-photon and second harmonic microscope, *Methods*. 30(1):3–15.

Peterlin, Z.A., Kozloski, J., Mao, B., Tsiola, A., and Yuste, R., 2000, Optical probing of neuronal circuits with calcium indicators, *Proc. Natl. Acad. Sci. USA* 97:3619–3624.

Sheenen, W.J.J.M., Makings, L.R., Gross, L.R., Pozzan, T., and Tsien, R.Y., 1996, Photodegration of indo-1 and its effect on apparent Ca concentrations, *Chem. Biol*. 3:765–774.

Smetters, D.K., Majewska, A., and Yuste, R., 1999, Detecting action potentials in neuronal populations with calcium imaging, *Methods* 18:215–221.

Tashiro, A., and Yuste, R., 2004, Regulation of dendritic spine motility and stability by Rac1 and Rho kinase: evidence for two forms of spine motility, *Mol. Cell Neurosci.* 26(3):429–440.

Tashiro, A., Dunaersky, A., Blazeski, R., Mason, C.A., and Yuste, R., 2003, Bidirectional regulation of hippocampal mossy fiber filopodial motility in kainate receptors: a two-step model of synaptogenesis, *Neuron*, 38(5):773–784.

Tashiro, A., Minden, A., and Yuste, R., 2000, Regulation of dendritic spine morphology by the Rho family of small GTPases: Antagonistic roles of Rac and Rho, *Cerebral Cortex* 10:927–938.

Tsai, P.S., Nishimura, N., Yoder, E.J., White, A., Doluick, E., and Kleinfeld, D., 2002, Principles, design and construction of a two-photon scanning microscope for *in vitro* and *in vivo* studies, in Methods for *in vivo* Optical Imaging (R. Frostig, ed.), CRC Press, pp. 113–171.

Tsien, R.Y., 1989, Fluorescent probes of cell signaling, *Ann. Rev. Neurosci*. 12:227–253.

Tsiola, A., and Yuste, R., 2003, Classification of neurons in the mouse primary visual cortex, *J. Comp. Neurol*. 461(4):415–428.

Yuste, R., 2000a, Loading populations neurons in slices with AM calcium indicators, In: *Imaging Neurons: A Laboratory Manual* (R. Yuste, F. Lanni, A. Konnerth, eds.), Cold Spring Harbor Press, Cold Spring Harbor, New York, pp. 34.31–34.39.

Yuste, R., 2000b, *Imaging Neurons: A Laboratory Manual*, Cold Spring Harbor Press, Cold Spring Harbor, New York.

Yuste, R., and Denk, W., 1995, Dendritic spines as basic units of synaptic integration, *Nature* 375:682–684.

Yuste, R., and Katz, L.C., 1989, Transmitter-induced changes in intracellular free calcium in brain slice of developing neocortex, *Soc. Neurosci. Abstr*. 4.5:2.

Yuste, R., and Katz, L.C., 1991, Control of postsynaptic Ca2+ influx in developing neocortex by excitatory and inhibitory neurotransmitters, *Neuron* 6:333–344.

Zilles, K., and Wree, A., 1985, Cortex: A real and laminar structure, In: *The Rat Nervous System* (G. Paxinos, ed.), Academic Press, Sydney, pp. 375–415.

42

Fluorescent Ion Measurement

Mark B. Cannell and Stephen H. Cody

INTRODUCTION

It is likely that cell behavior is regulated by the summation of subcellular transduction events and these are generally linked, non-linearly, to subsequent stages of signal transduction. Hence, a full understanding of signal transduction can only arise from the analysis of subcellular behavior and this is one reason why microscopic imaging has become so important. To carry this idea further, since the cell is a three-dimensional (3D) structure, methods that provide 3D imaging (as in confocal and multi-photon methods) are likely to provide better insight than even widefield/deconvolution imaging which is, itself, an improvement on either widefield or simple photometric methods.

To analyze cell behavior, we need to measure *something*, and then after a period of time, we need to measure it again. This often implies the use of probes that can report the behavior of interest. In the case of intracellular ions, because calcium has been found to be a ubiquitous second messenger system, it is not surprising that many methods for measuring it have been developed, each with unique advantages and disadvantages. Here, we will tend to focus on calcium and pH measurements in living cells, but the ideas and problems that will be discussed are generally applicable to all methods that employ optical probes of function;[1] the differences between approaches and techniques reside in the degree of applicability rather than the presence or absence of any single problem.

The continuing effort to improve signal-to-noise ratio, specificity, and resolution (spatial and temporal) of these techniques has brought wonderful new insight into our understanding of cell function. Each major new advance seems to have taken approximately a decade to achieve and each decade has improved spatio-temporal resolution by something like 2 orders of magnitude (for constant signal-to-noise). Thus, from the development and application of aequorin to giant nerve and muscle cells in the 1960s (which supplanted tissue-level chemical methods), we are now measuring subcellular events on the scale of microns with fluorescent probes. Resolution in both space and intensity is currently limited by the quantal nature of light itself. Further major advances in resolution may be confounded by the problems of excessive buffering (or perturbation) of responses by the probe and by cell damage caused by the excitation light. This pessimism is tempered by the fact that a little more than two decades ago, it was thought unlikely that it would ever be possible to resolve the microscopic gradients of calcium that exist inside the muscle sarcomere during activation [which at that time were only predicted on the basis of computer modeling (Cannell and Allen, 1984)]. However, the early 1990s saw the potential of the laser-scanning confocal microscope (LSCM) applied to Roger Tsien's dyes (e.g., for reviews see special edition of *Cell Calcium* 11 (2–3), Williams (1993). The discovery of calcium sparks (Cheng *et al.*, 1993; Cannell *et al.*, 1994; see Fig. 42.1) while one of the authors (MBC) was developing methods needed to look for some spatial non-unformity in the cardiac Ca^{++} transient (during a sabbatical in Dr. Lederer's laboratory) was completely unexpected and would probably not have occurred without the LSCM. Imagine the excitement at seeing these events rise out of the background noise displayed on a dimmed computer screen in a blacked-out laboratory.

There is something compelling about imaging responses under carefully-optimized experimental conditions, perhaps related to the immediacy and tangibility of the results. Seeing *is* believing and imaging, in its many modalities, allows us to see otherwise invisible and unexpected cell signaling events as they occur. Provided artifacts are recognized and rejected, new insights develop as we try to understand the cellular basis of what has been observed. Therein lies a caveat: Poor science inevitably results from not appreciating the limitations of the method. Having a new instrument or method does not remove the possibility that artifactual results may be obtained from excessive perturbation of the experimental system and measuring something about a system inevitably involves some sort of perturbation. Both light and probes can easily damage cells or modify their responses. As we seek to resolve ever smaller and faster events, the perturbation of natural responses becomes larger.

In general, experimental problems arise from:

1. The quantal nature of light (it is not possible to *directly* measure a response that is associated with a change of signal of less than a single photon/pixel).
2. Buffering the cell response (any probe must interfere with the cell processes by its interaction with the chemical process of interest).
3. Limited time resolution (all chemical reactions take time before the products become available for analysis).
4. Damage to the cell either by the toxicity of the probe or damage by the light irradiating the system.
5. Limited spatial resolution associated with the wavelength of light itself.

In this chapter, we will discuss how these problems relate to the measurement of calcium levels inside living cells, although the discussion applies to all other optical measurements as well.

The Limiting Case

If we confine our discussion to optical resolution, the smallest cell volume that can be observed in practical light microscopy is about

[1] Functional probes also exist for cAMP, Na, K, Mg, and many other ions (see Chapters 16 and 17, *this volume*).

Mark B. Cannell • University of Auckland, Auckland, New Zealand
Stephen H. Cody • Ludwig Institute for Cancer Research, Royal Melbourne Hospital, Parkville Victoria, Australia

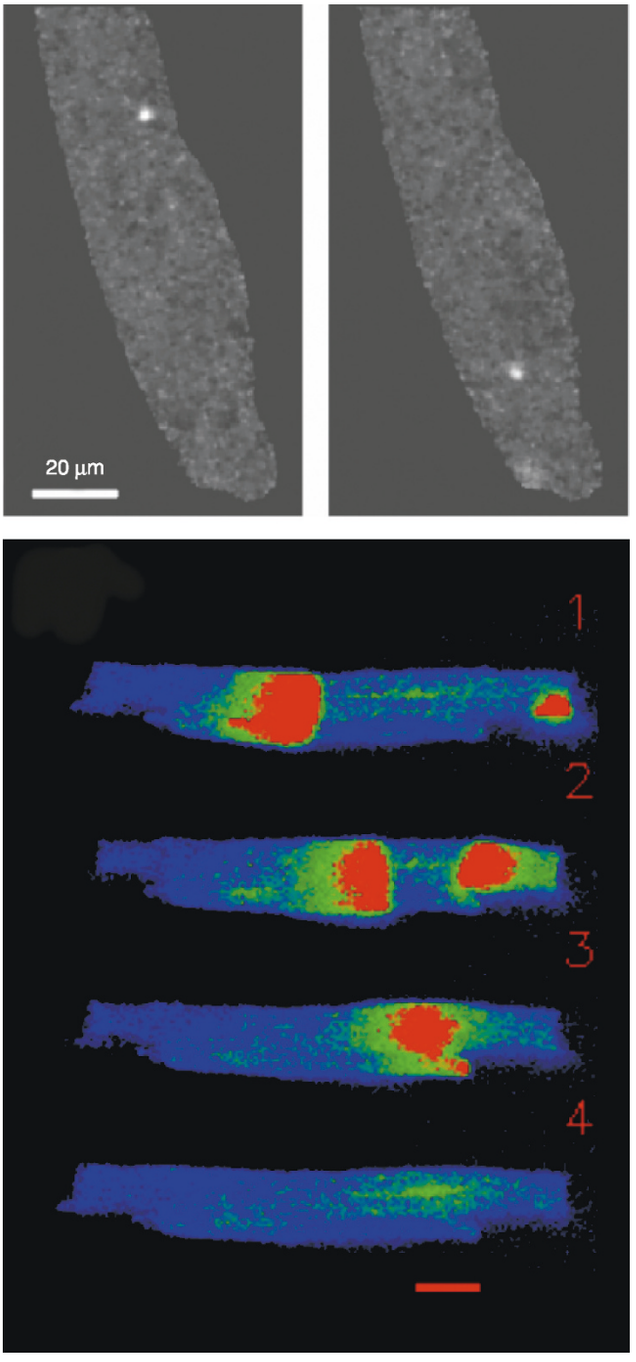


FIGURE 42.1. Two consecutive confocal images of a fluo-3 loaded cardiac myocyte. The areas of increased fluorescence are spontaneous Ca^{++} sparks. Note the scale of this image. The lower panel shows sequential confocal images of spontaneous Ca^{++} waves propagating and colliding within a cardiac cell. Scale bar 20 µm. Frame scan time, 0.7 s.

0.06 fl (i.e., 0.25 × 0.25 × 0.5 µm). If a single ion resides in this volume (high) the concentration is about 1 µ*M*/L. In the case of calcium, this is a high physiological level. However, we cannot directly measure an ion in solution inside a cell: it must be bound to a probe whose physical properties are altered by that binding. If the ion is always bound to the probe then we must detect a single probe molecule in that volume (note that we have also reduced the level of free calcium to zero at the same time — a serious problem that will be discussed later). It is unlikely that we could detect the bound probe by a change in absorbance because this would be akin to directly imaging a single molecule in transmission light microscopy and Beers Law shows the futility of such an approach.

Instead, we could use a change in probe fluorescence and current fluorochromes have a fluorescence lifetime of 1 to 10 ns. This implies that, with the maximum possible excitation rate, we might expect to generate 10^8 photons/s/molecule. This large number rapidly declines when we consider the detection efficiency of the instrument. A good water-immersion dipping objective lens may collect about 10% of the emitted light (as limited by the numerical aperture of the lens and bathing solution refractive index) and after accessory optics to separate the excitation light from the emitted light, focus the light on a confocal pinhole and detector, typically <5% of the light collected by the objective will be recorded by the instrument. This implies a maximum potential signal rate of ~5×10^5 events/s. If the probe is free to diffuse, it will remain in our measurement volume for ~0.1 ms so that we might hope to detect 50 photons/s residence. If the probe movement is detected by scanning, then the dwell time per pixel becomes limiting and for a scanning rate of 1 ms/512 pixel line, the pixel dwell time approaches 2 µs. In this case, the average signal is 1 event/pixel. However, it is unusual to excite probes at such a high rate as photodamage becomes a serious problem. These rough calculations show why trying to perform Ca^{++} imaging at the limits of optical resolution generally produces very noisy results. To improve the signal-to-noise ratio we must either increase (1) the concentration of the probe (assuming there are enough ions to bind to it); (2) the measurement volume and sacrifice spatial resolution; or (3) the measurement period and sacrifice temporal resolution.

Put another way, in every case improvements in spatial resolution, temporal resolution, or signal-to-noise ratio implies a reduction in one of the other two parameters, a problem that arises from the quantal nature of both light and molecules.

As noted above, optical probes of ions work by binding to the ion, a process that changes the characteristics of the probe. In the case of aequorin and other protein-based bioluminescent probes, ion binding triggers a conformational change in the protein that allows it to oxidize a chromophore which emits light. The quantum efficiency of this process is about 0.3 and after a single oxidation no further photons are emitted. Thus, while the specificity of the reaction for calcium is quite good, the photon yield is extremely low and does not usually provide sufficient light flux for imaging — except in large cells or for lower time resolution studies (Blinks *et al.*, 1976).

Because aequorin emits light spontaneously rather than in response to exciting radiation, confocal imaging of aequorin signals is impossible. Only a widefield detector such as an intensified charge-coupled device (CCD) or electron-multiplier CCD (EM-CCD) has any chance of detecting such light, and even then, the fact that each aequorin molecule emits, on average, less than a single photon places stringent limits on the statistical accuracy of signals. As this book emphasizes microscopic 3D techniques, we therefore do not consider aequorin as a viable technique for live-cell 3D (confocal) imaging.

CHOICE OF INDICATOR

In many cases, several different indicators may be available for the ion of interest. Fluorescent indicators are the best choice for confocal microscopy as they are generally bright, while biolumines-

cent probes and absorbance probes produce very small signals in single cells. Choice should be guided by the following factors:

1. Are suitable excitation wavelengths available (note that multiphoton methods can make some ultraviolet (UV)-excited indicators work well and avoid chromatic aberration problems)?
2. Is an absolute signal calibration important? If so, ratiometric indictors are the best choice.
3. Can the cell be loaded with the indicator? All dyes can be injected but chemical loading methods do not work well in all cells/tissues (see below).
4. Does the indicator produce large signal changes for ion levels in the range of interest?
5. Does the indicator respond fast enough?
6. How well does the cell tolerate the indicator and the illumination during imaging?
7. Is the indicator compartmentalized within the cell or expelled from it?
8. Is the perturbation of the normal response by the indicator acceptable?

INTRODUCING THE INDICATORS INTO CELLS

The most reliable method of indicator loading is by direct injection through a microelectrode or patch pipette (e.g., Cannell *et al.*, 1987), but this method is limited by the increased complexity of cell injection. Once introduced into cells, most fluorescent indicators generally remain there for a reasonable period (typically a few hours), allowing stable recordings to be made. Even if there is some loss of indicator over time (either by cell extrusion/compartmentation or dye bleaching), the effects can sometimes be compensated for by ratiometric measurement methods (see below).

However, there are cases in which loss of indicator is a problem, and this effect can be reduced by injecting the indicator in a dextran-linked form. Linkage of the indicators to the dextran polymer does not in general seem to affect their properties significantly but does inhibit cellular transport of the indicator [see the Molecular Probes, Inc. (Eugene, OR) catalogue for further information and for availability of these forms]. An alternative method is to use a drug to inhibit the cell transport of the dye. Because most dyes are organic acids, inhibitors such as probenecid may be useful. For acute experiments, these drugs do not produce obvious changes in cell behavior but for longer experiments they may be a problem. Finally, lowering the temperature can also reduce the rate of loss of dye (along with having a number of other effects!).

Many indicators can be introduced into cells by the ester-loading technique (Tsien, 1981). This technique has extended fluorescence Ca^{++} measurements into the realm of very small cell fragments such as blood platelets, that cannot be microinjected. Because most fluorescent ion indicators are multiply charged at neutral pH with many of the charges being on carboxyl groups, they are not very lipid soluble. By esterifying these carboxyl groups, an uncharged derivative of the indicator can be produced. While this derivative is not an active indicator, it is sufficiently lipophilic to permeate biological membranes and thereby enter cells. Inside cells, the derivative is converted to the active indicator by the action of intrinsic esterase enzymes (see Fig. 42.2). Because the active indicator is relatively membrane impermeant, it is now trapped inside the cell and accumulates under the continued action of the esterase(s). Incubation conditions need to be adjusted carefully in order to achieve satisfactory loading of the cells.

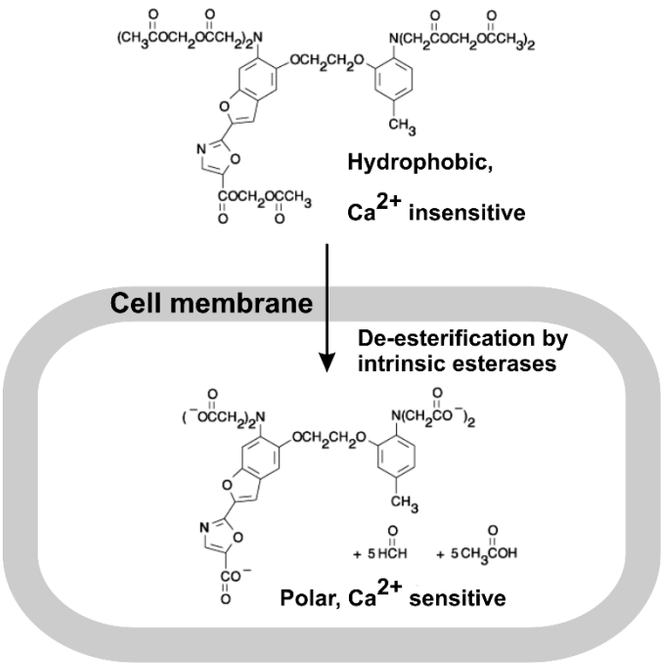


FIGURE 42.2. Illustration of the method for trapping an indicator inside the cell with acetoxymethyl derivatization. The highly polar carboxyl groups (which form the Ca^{++} binding region of the BAPTA region) are modified as shown. This polar molecule then enters the cell and is modified to release the active indicator. Clearly, the extent of trapping is esterase dependent and partial de-esterification is also a possibility.

It must also be noted that de-esterification of acetoxymethyl esters liberates formaldehyde as a hydrolysis product. Although serious toxicity has not been reported, one should always remember that formaldehyde may be affecting your results.

The major problem with the ester (or AM) loading technique is that the experimenter has little direct control over where the indicator ends up in the cell. As the ester will enter all intracellular compartments, the active indicator concentration in each compartment will depend on the relative esterase activity. Thus, the endoplasmic reticulum and mitochondria will also contain an indicator that may confound interpretation of cytoplasmic signals. An additional problem is that de-esterification may be incomplete, creating a fluorescent intermediate that is **not** ion sensitive (e.g., Highsmith *et al.*, 1986). The magnitude of these effects can only be ascertained with careful control experiments. At the very least, the images need to be critically examined during imaging to ascertain where the fluorescent signals are actually coming from.

A related problem is that some types of cells seem to be very good at clearing the indicator from their cytoplasm. In endothelial cells, for example, after about an hour the cell fluorescence appears punctate and mitochondria are clearly visible (unpublished observations). Whether this represents simply the removal of cytoplasmic indicator or accumulation of indicator in the punctate regions is unclear. In any case, considerable caution should be applied to the interpretation of signals from the cells loaded with the AM ester form of the indicator. It appears that cells labeled with fluorescent probes give a smaller fluorescence change when the AM indicator is used compared to direct injection (unpublished observation). In summary, good results can be obtained with the ester loading technique, provided adequate control experiments are performed

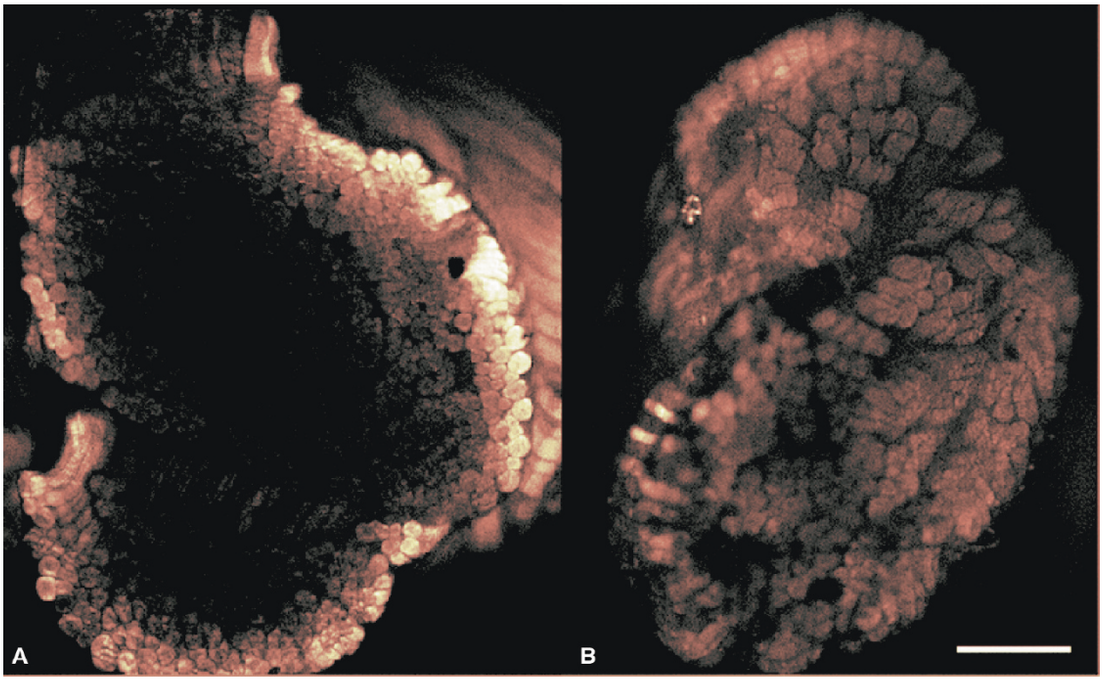


FIGURE 42.3. A comparison of different incubation temperatures used to stain rat interossi muscles with SNARF-1. Cross-sections through the two muscles after staining reveals that: (A) when stained at room temperature (22°C for 30 min, 30°C for 20 mins) nearly all the SNARF-1 is immobilized in the outermost fibers. (B) Cold loading of the muscle (5°C for 60 min, 30°C for 20 mins) allowed SNARF-1 to diffuse evenly throughout the fibers. Bar = 250 µm. (Bowser *et al.*, 1999.)

and it may be the only route to take if cells cannot be loaded by patch pipette.

An additional problem for tissues is that as cells efficiently cleave the dye into its non-membrane permeant, fluorescent form, it can become trapped in outer cell layers (See Fig. 42.3A). This can be ameliorated by using cold loading techniques (Cody *et al.*, 1993; Williams *et al.*, 1993, Bowser *et al.*, 1999), to slow down the activity of the intrinsic cellular esterases. For example, incubation of mammalian skeletal muscle for 1 hour at 5°C to allow the pH indicator SNARF-1 to penetrate the deeper fibers and an incubation for a further 20 mins at 30°C to facilitate dye cleavage, results in more uniform dye distribution throughout the preparation (Fig. 42.3B). Figure 42.4 shows dual-channel images of SNARF-1 fluorescence were collected before the fatigue stimulation (Fig. 42.4A and 42.4B). The relative uniformity of dye loading is apparent and as ratio images show, immediately after fatigue (Fig. 42.4C) and after a fifteen minute rest period (Fig. 42.4D) there were almost no changes in pH with fatigue in either the EDL or the soleus muscles (Cody *et al.*, 1993).

An alternative strategy is to use protein expression of a genetically engineered variant of a fluorescent protein [most often green fluorescent protein (GFP)] that includes an ion-binding region in its structure. While this method requires time for the expressed protein to be produced, it offers great promise as the indicator protein can be targeted to organelles [(as was first demonstrated with recombinant aequorin (Rizzuto *et al.*, 1983)] or other cell locations. At the present time, these methods are still being developed and further work is needed to make the probes faster, show larger signal changes, and be more specific in their response. Nevertheless, in principle the method could be used to make a probe for almost any compound and many probes of this type have already been produced. Refer to Zhang *et al.* (2002) for an excellent review.

CARE OF FLUORESCENT PROBES

A few words on the handling of the indicators may be in order. The fluorescent indicators are all subject to oxidation during storage and will lose activity in a few days if exposed to light and air at room temperature. It is best to make up the acetoxymethyl esters in dry dimethylsulfoxide (DMSO) (solubility may require the addition of a non-ionic detergent as well such as Pluronic [Molecular Probes]) as a stock solution that will be diluted more than 100× when used. This stock should then be split into a number of ampoules, each of which contains enough indicator for a single experiment. The ampoules can then be frozen (at −80°C) and this will avoid repeated freeze/thawing cycles. A similar procedure should be used for the free-acid form of the indicator except that one should use a suitable buffer solution (e.g., 140 m*M* KCl) instead of DMSO.

The free-acid form of the indicator should not be exposed to metal (such as stainless-steel syringe needles). Prior to microinjection on the day of the experiment, the aliquot of indicator should be dissolved in about 1 mL of intracellular solution and placed in a 1 mL polyethylene tuberculin syringe, the end of which has been drawn over a flame into a fine capillary (to allow it to pass down inside the electrode barrel). The syringe is used to place ~50 µL at the shoulder of the electrode, allowing a reasonable number of electrodes and cells to be filled before the syringe needs to be refilled. Finally, positive pressure must be maintained on the back of the electrode at all times before forming a giga-seal or else the experimenter will find that the indicator will be seriously diluted at the tip of the electrode (quite apart from the problem of contamination of the intracellular solution by bathing solution!). After breaking into the cell, dialysis of the cell may take 5 to 20 min, but the speed of dialysis can be markedly improved by applying brief pulses of positive pressure to the back of the electrode to inject the indicator

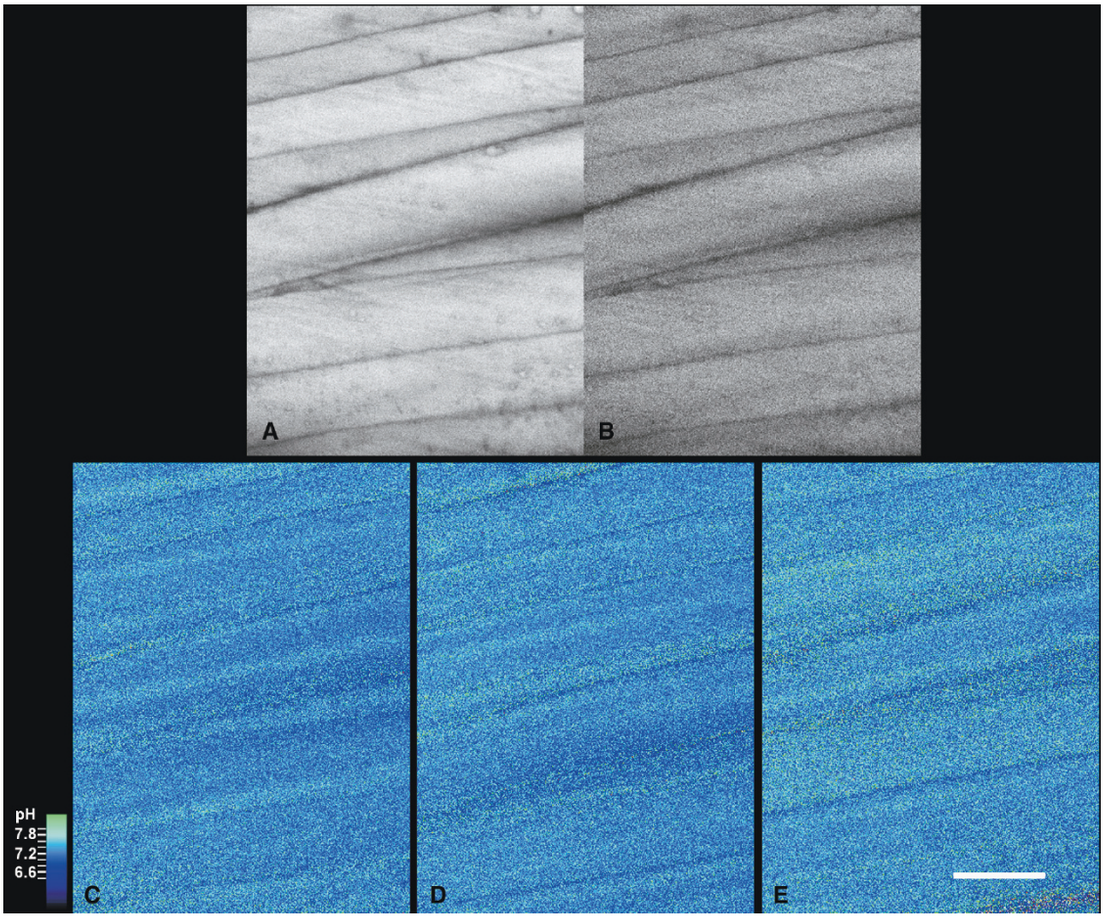


FIGURE 42.4. A rat EDL muscle, stained with SNARF-1. Ratio images are quantitatively calibrated in units of pH. No physiologically relevant change in pH was detected. (A) Dual-emission image. (B) Control. (C) Immediately after fatigue stimulation. (D) After a 15 minute recovery period. Bar = 100 µm. (Cody *et al.*, previously unpublished.)

(considerable care and experience is needed for this technique!). The extent of dialysis can be determined from the magnitude of the resting fluorescence signal, and experienced patch clamp electrophysiologists may be amazed at how slow dialysis can be.

INTERPRETATION OF MEASUREMENTS

Although fluorescent indicators have proved to be extremely powerful, it is important to bear in mind that they share (as with all other recording techniques) the possibility of giving inaccurate measurements and/or of influencing whatever is being measured. In particular, it should be appreciated that the indicators work by reversibly binding to the target, so by definition they have a buffering action. The extent of the buffering will depend on the concentration of the indicator relative to the free concentration of the target ion as well as the affinity of the indicator, so it will be most significant for those ions whose free concentrations are relatively low, that is, Ca^{++} and protons. Although, the natural cell buffering capacity for these ions reduces the effect of indicator buffering, the amplitudes and time courses of ion changes may still be significantly altered by the increased buffering. To gauge this, one really needs to carry out experiments over a range of indicator concentrations to demonstrate that the results are reasonably independent of the indicator concentration. The binding equation is:

$$F = [X]/(K_d + [X])$$

where F is the fraction bound, and K_d the dissociation constant. As an example, consider an experiment using a calcium ion indicator with a K_d of 300 nM and a resting Ca^{++} level of 100 nM, the fraction bound = 0.4. If the concentration of the indicator is 0.1 mM (a typical value), 40 µM Ca^{++} is bound to the dye. Thus, the buffering power (B) = bound/free = 400. This value can be compared to the endogenous Ca^{++} buffering powers of 75 for immobile buffers and 20 for mobile buffers (Neher and Augustine, 1992). From this, it is clear that high-affinity indicators can dominate the intrinsic buffers which will result in a significant reduction in the amplitude of physiological Ca^{++} transients, as well as a slowing in their time course. For a constant signal-to-noise ratio, this problem cannot be circumvented by using a lower affinity indicator, as the signal depends on detecting the bound form whose reduction in concentration (due to a reduction in affinity) must be offset by an equivalent increase in overall indicator concentration. However, using a lower affinity indicator does improve the response speed. Thus the speed of response may be increased if very high concentrations of a low affinity dye are used so that most of the released ions become bound to the dye (Pape *et al.*, 1993). Of course, this means that other physiological responses are blocked, but the speed of response can be increased several-hundred-fold. To produce such high dye concentrations, some injection method is needed as the

esterase technique produces dye concentrations of typically <1 m*M* (unpublished observations).

Finally, buffering of ions by the indicator is likely to alter free diffusion of the ion. If the indicator is relatively immobile, free diffusion may be hindered by a fraction equal to the fraction bound. On the other hand, if the buffer is mobile, diffusion may be enhanced as the buffer can act as a carrier that limits intrinsic binding by cell constituents which serve to reduce the diffusion coefficient.

KINETICS

With most ion probes, the kinetics of the fluorescence change does not reflect the kinetics of the underlying ion transient. This disparity arises from (1) saturation effects in the indicator response and (2) the kinetics of dye-ion binding. While the first problem can be circumvented by converting the dye signal to ion concentrations (but see below), workers often assume that, because the dye : ion stoichiometry is 1 : 1, the dye is a linear indicator of ion concentration and that the time course of fluorescence change should reflect the time course of calcium change. However, this is not the case. From the equation

$$dF/dt = (d[X]/dt)\ (dF/dX)$$

where $dF/d[X]$ is the slope of the relationship between F and $[X]$, it is clear that we must consider the properties of the relationship between F and $[X]$. Even if the dye kinetics are so fast that the dye reaction is at equilibrium at all times (see below) and the binding is 1:1 with no buffering, the time constant of the dye response is quite different from the underlying time constant of ion change. This is illustrated in Figure 42.5(A), which shows the relationship between F and $dF/d[X]$ as a function of $[X]/K_d$ (the ligand concentration divided by the affinity of the indicator for the ligand). It is clear that $dF/d[X]$ is considerably less than unity at $[X] > 0.1\,K_d$. As this is the range within which most indicators are used, the dye response is generally quite nonlinear. Put another way, if the observed signal changes with a time constant of Y, the underlying ion change occurred with a faster time constant equal to YdF/dX. The simplest way around this problem is to convert F (or the ratio measurement) to $[X]$ with a calibration curve, if one is available for the experimental conditions.

However, $dF/d[X]$ is also a function of time as the kinetics of the dye are limited. For the bimolecular reaction $D + X = DX$ with a forward rate of k_{on} and a back rate of k_{off}, if the ion concentration undergoes a step change to $[X]$, the indicator signal will change exponentially to a new level with a rate constant of $(k_{on}[X] + k_{off})$. For most ion indicators, the forward rate is generally diffusion-limited at ~$2.10^8/M$/s so different affinities are mostly due to changes in k_{off}. In this case, we can examine the likely kinetics of response from the dye K_d and the ion concentration range. Figure 42.5(B) shows the time constant of response for a range of hypothetical Ca^{++} dyes with K_d in the range 100 to 1000 nm for a jump in [Ca] from 50 to 5000 n*M*. From this double logarithmic plot, it is clear that the response is in the range of 2 to 40 ms and highly dependent on the ion level. High dye concentrations can alter the kinetics of the response, albeit at the expense of buffering effects (see above).

It is worth noting that, as most LSCM scan lines at about 2 ms/line, typical dye kinetic changes may be faithfully recorded in line-scanning modes but not when full frame imaging is used. This problem may be reduced with disk-scanning or slit-scanning instruments (see Chapter 10, *this volume*). In terms of microscopic

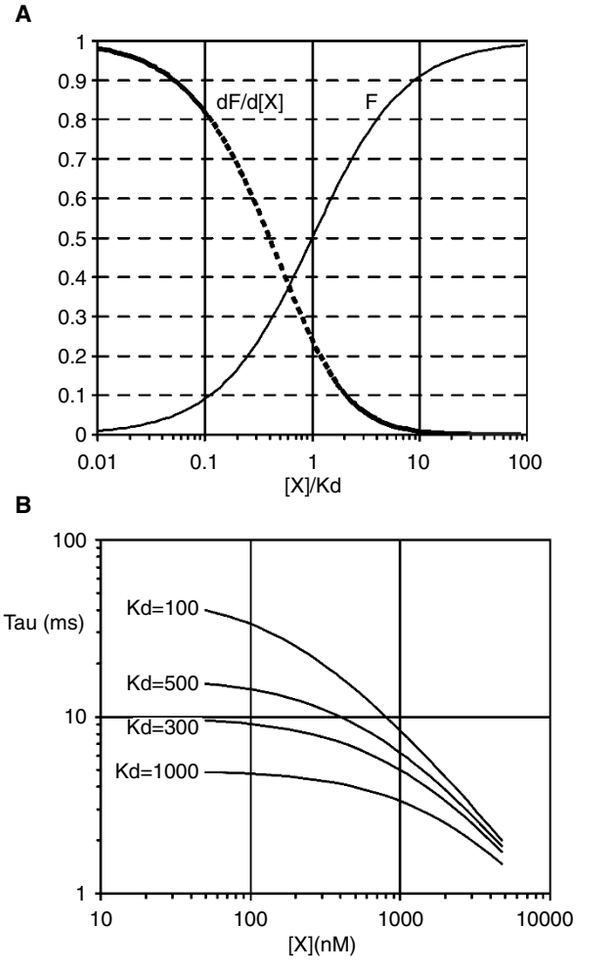


FIGURE 42.5. The relationship between fluorescence and ion level for a 1 : 1 stoichiometry. The ion concentration is expressed in units of K_d. The rate of change of fluorescence with ion levels is also shown and this is considerably less than unity for ion levels $>0.1\,K_d$. The lower panel shows the rate of dye response (assuming a diffusion limited on rate) for different K_d and ion levels.

subcellular signals, these times correspond to the time of diffusion over a few micrometers so that it is possible that attempts to image the evolution of small spatial changes will be contaminated by the kinetics of dye response.

To put this analysis in more concrete terms, the kinetics of the fura-2 reactions with calcium have been investigated in stopped-flow experiments (Jackson *et al.*, 1987). The rate of calcium binding by fura-2 is 2.5 to 6.5 $10^8/M$/s and the rate of dissociation is 84/s at 20°C. Thus, at a level of 200 n*M* free calcium, the fura-2 reaction will proceed at ~180/s. While this response speed is clearly superior to that of a calcium-selective microelectrode and at least as fast as aequorin, it is not so fast that possible kinetic distortion of the calcium signal can be ignored. It is notable that Baylor and Hollingworth (1988) reported that the fura-2 kinetics appeared to be considerably slower in single, frog muscle fibers than measurements of Jackson and colleagues (1987) would suggest. Baylor and Hollingworth (1988) compared the antipyrylazo absorbance signal to the fura-2 signal and suggested that the fura-2 signal might be explained if the fura-2 off-rate were about 25 s^{-1}, a value three to four times lower than that expected from *in vitro* experiments. The importance of this observation is underscored by the fact that the exact effect of the intracellular envi-

ronment on the properties of most dyes remains largely unknown. It is notable that Williams and colleagues (1985) and Weir and co-workers (1987) found that the maximum fluorescence ratio obtained from the intracellular dye appeared to be slightly less than that obtained in calibrating solutions. This suggests that the intracellular milieu alters the properties of the dye. Baylor and Hollingworth also observed a reduced diffusion coefficient for fura-2 (1988), an effect also found by Timmerman and Ashley (1986) in barnacle muscle.

Fluorescence anisotropy measurements suggest that some dye is immobilized (Baylor and Hollingworth, 1988). These results may all be due to the dye binding to some intracellular constituent, but whether such binding seriously alters the calcium sensitivity of the dye remains unclear. On the other hand, both Williams and colleagues (1985) and Baylor and Hollingworth (1988) reported that the fluorescence spectrum of fura-2 inside single smooth muscle cells was very similar to the spectrum obtained in a cuvette and this lends confidence regarding the reliability of these dyes in general. Without more detailed research into quantifying these problems, it is clear that caution should be applied to quantitative interpretation of signals from cells. Fortunately, we are usually more interested in relative changes in $[Ca^{++}]$ than in its absolute value.

Another potential difficulty concerns the fact that any indicator will report concentration accurately only over a fairly narrow ion concentration range. As a result, attempts to use one indicator to cover all experimental situations are likely to give inaccurate results. For example, the early fluorescent indicators for Ca^{++} ions (Grynkiewicz *et al.*, 1985) were devised primarily to measure resting ion concentrations in small cells. Because the indicator fluorescence will be midway between its values at the concentration extremes, the greatest accuracy for such measurements is obtained when the dissociation constant of the Ca–indicator complex is similar to the free Ca^{++} concentration. Unfortunately, this is not the best situation for measuring transient changes in concentration where buffering and kinetic responses will be far from optimal (see above). In addition, as the Ca^{++} diffuses away from the release sites, the **total fluorescence signal** will increase, even though the average Ca^{++} concentration may remain the same, because the reduction in fluorescence in the areas near the release sites is less than the increase in fluorescence in the areas further away, a problem not entirely removed at the limit of resolution of the light microscope.

In summary, for accurate transient measurements, one should try to use an indicator with a dissociation constant that is no lower than the highest concentration transient expected, even though this may lead to poor signals at resting ion levels.

CALIBRATION

Although ion concentrations can be estimated from fluorescence recordings by reference to *in vitro* calibration solutions, ideally, such methods should be supplemented by measurements in which known ion concentrations are measured. For example, a known Ca^{++} concentration, near to the resting level of Ca^{++} can be imposed by using an appropriate buffer solution outside the cell, and then permeabilizing the membrane with a Ca^{++} ionophore such as ionomycin. For fluorescence measurements made at a single wavelength, the free-ion concentration $[X]$ is related to the fluorescence F by

$$[X] = K_d(F - F_{min})/(F_{max} - F)$$

where F_{min} and F_{max} are respectively the fluorescence levels at zero and saturating ion concentrations, and K_d is the dissociation of the ion–indicator complex.

For ratiometric indicators (where the response to ions is different at each of two wavelengths (F_1,F_2), a ratio $R = F_1/F_2$ is obtained leading to

$$[X] = K_d(R - R_{min})/(R_{max} - R)(SF_2/SB_2)$$

where R_{min} is the ratio of fluorescence at zero $[X]$, R_{max} is the ratio at saturating $[X]$, and SF_2/SB_2 the fluorescence at zero $[X]$ divided by the fluorescence at saturating $[X]$ at F_2. This method removes the concentration dependence of the absolute fluorescence level and should result in a signal that depends only on the ion concentration (see Fig. 42.6). SF_2/SB_2 effectively scales the K_d and alters the midpoint of the response, but it does not affect the amount bound to the indicator as this is determined by $[X]$ and the K_d. To alter the ion levels inside the cell, one can use an ionophore such as ionomycin (for Ca^{++}), gramicidin (for Na^{++}), nigericin (for H^+ and K^+) or valinomycin (for K^+). The external ion levels can then be manipulated to allow one to measure F_{min} and F_{max} at all important wavelengths.

In an attempt to avoid having to measure both F_{min} and F_{max} to calibrate signals from non-ratiometric indicators, Cannell and colleagues (1994) suggested that if one used a Ca^{++} indicator with a negligible F_{min} (such as fluo-3) in cells whose resting ion level was relatively constant (see Wier *et al.*, 1987), F_{max} could then be estimated from the signal at the resting level of Ca^{++}. In this case, $F_{max} = F_{rest}(K_d/[Ca^{++}]_{rest} + 1)$. Because, in the confocal microscope, the volume sampled is more or less constant, if an experimental image is divided by one taken when the cell was at rest, a pseudo-ratio (R) in which $[Ca^{++}] = K_d \cdot R[(K_d/[Ca^{++}]_{rest} + 1) - R]$. This method allows comparisons to be carried between different experiments and, if the resting level of Ca^{++} is known to reasonable accuracy, estimates of $[Ca^{++}]$ recorded in the experimental images will be equally accurate.

Using this method, we found that the amplitude of the evoked Ca^{++} transient agreed well with that obtained by ratiometric indicators and allowed estimation of the level of Ca^{++} produced by Ca^{++} sparks and the spark Ca^{++} release flux (Cheng *et al.*, 1993; Cannell *et al.*, 1994). Nevertheless, it is important not to lose sight of the assumptions underlying this method.

Cell autofluorescence must also be measured and subtracted from all measurements, and if it is not practical to do this before indicator loading, the fluorescence of the indicator may be quenched with Mn^{2+} at the end of the experiment (see Fig. 42.7). These measurements can then be referred to an *in vitro* calibration curve and, if all is well, R_{min} and R_{max} should agree with this curve.

For confocal microscopes, it is more convenient to use a ratio-dye that shows an emission shift (such as indo-1 for Ca^{++} and SNARF-1 for pH) rather than a shift in excitation wavelength, because most microscopes have multiple detector channels but few are able to rapidly modulate the laser excitation wavelength (especially in the UV!). The spectral properties of Indo-1 and SNARF-1 allow 2-channel, truly simultaneous acquisition of ratiometric images on a standard confocal microscope by splitting the emitted light to two detector channels. SNARF-1, (5-(and-6)-carboxy seminaphthorhodafluor) was developed by Molecular Probes (Whitaker *et al.*, 1991) and is widely used in micro-spectrofluorimetry (e.g., Buckler & Vaughan-Jones, 1990; Bassnett, 1990; Opitz *et al.*, 1994). When this dye is combined with the optical-sectioning capability of the confocal microscope (Cody *et al.*, 1993), it is possible to map intracellular pH in three dimensions with a very high spatial resolution (Fig. 42.8). Furthermore,

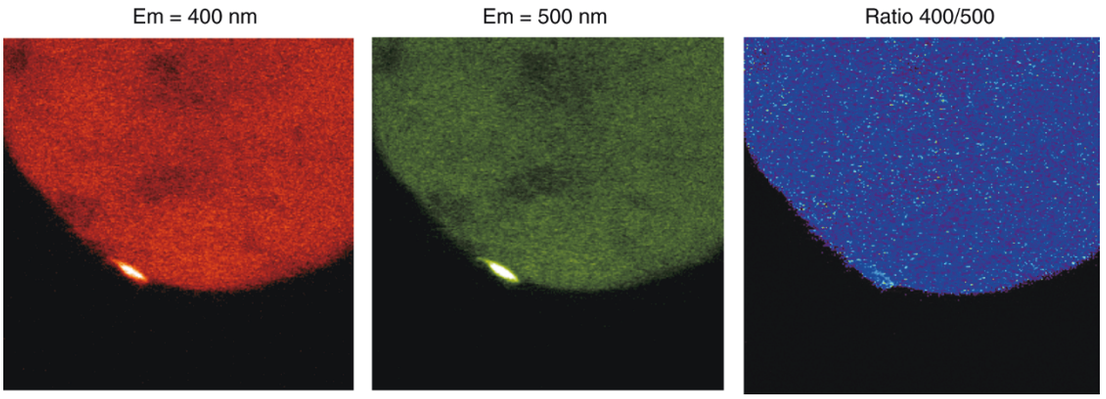


FIGURE 42.6. Use of a ratiometric indicator in mouse egg cells. Indo-1 fluorescence at 400 and 400 nm was produced by two-photon excitation at 690 nm. Note the difference in Ca^{++} signals from the sperm and egg are removed in their ratio so the overall image becomes flat. From this we can conclude that level of Ca^{++} shortly after sperm fusion matches that of the egg and that the egg cytoplasm is quite uniform (Jones *et al.*, 1998).

SNARF-1 has such excellent cellular retention that the manufacturer also promotes it as a long-term, cell-tracing dye — (Haugland, 2005). Similarly, Indo-1 can be used for confocal or 2-photon ratiometric Ca^{++} measurements (e.g., Jones *et al.*, 1998), although there are significant cell retention and bleaching problems associated with this probe.

No matter how much care is taken in performing these measurements, the values calculated using the calibration equations listed above must still be treated with some caution. Apart from the obvious risk that K_d may be somewhat different in the cell from in the calibration solution, there is also the possibility that the fluorescence properties of the indicator may be different in the cell, and such effects have been observed for several indicators (see above).

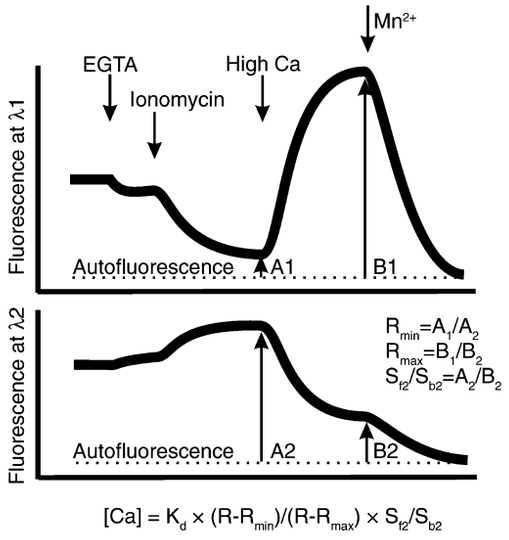


FIGURE 42.7. Illustration of the method for calibrating an intracellular Ca^{++} indicator by imposing known ion levels and quenching fluorescence. After external Ca^{++} is removed (by adding EGTA), ionomycin (a Ca ionophore) is added to the bathing solution to give F_{min} (after subtraction of autofluorescence). Subsequent addition of a saturating Ca solution (>100 μ*M*) allows determination of F_{max}. Adding Mn^{++} quenches the dye fluorescence, allowing a determination of cell autofluorescence. It is assumed that the latter was not affected by Mn^{++} and separate experiments should be carried out to show whether this is the case.

The possible errors caused by not using a ratiometric approach are illustrated in Figure 42.9 where a proximal tubule has been labeled with pH indicator BCECF and imaged at a single wavelength. The low intensity fluorescence evident in the brush border, could be caused by one of three factors: a lower pH in the brush border, a lower concentration of dye in this region, or the fact that there is more unstained, extracellular space in the brush border (path-length error). However, when a similar preparation is labeled with the ratiometric SNARF-1 (Fig. 42.10), the ratio image shows the true pH distribution map and it becomes evident that apparent pH differences are simply dye-concentration artifacts. Similar artifacts were also observed in a single wavelength study that used Fura-2 in heart cell nuclei (Wier *et al.*, 1987).

Application of the calibration equations also assumes that the indicator is sufficiently selective not to form complexes with other ions to any significant extent. Although this may be a questionable assumption, the fluorescent indicators generally perform quite well in this respect. This is particularly true for Ca^{++} indicators based on the BAPTA molecule, for example, fura-2 and indo-1 (Grynkiewicz *et al.*, 1985), which are more selective against Mg^{++} and protons than are (say) any of the metallochromic Ca^{++} indicators, where competing effects from such ions pose a major calibration problem (Thomas, 1991). In the case of pH indicators, selectivity is quite good so intracellular pH may be simply manipulated by adding nigericin and a CO_2 — bicarbonate-based buffer system. For example, in the experiments shown in Figure 42.4 a high potassium solution was used (to zero the membrane potential) and the pH of the superfusate measured with a pH electrode. By using three, premixed gasses (100% O_2, 5%CO_2/95% O_2 and 100% CO_2) to bubble the superperfusate (which included 18.5 m*M* $NaHCO_3$), the intracellular pH changes could be calibrated without needing multiple solution changes. This increased the reproducibility of the intracellular calibrations as the specimen did not need to be manipulated unnecessarily (Fig. 42.11). A disadvantage with this method is that Ca^{++} must be removed if alkaline pH calibrations are needed, otherwise the Ca^{++} in the perfusate will precipitate with the bicarbonate.

When the interference effects from other ions are significant, the simplest approach is to calibrate the indicator in a solution that contains appropriate concentrations of those ions. Of course, such calibrations only apply so long as the concentrations of the inter-

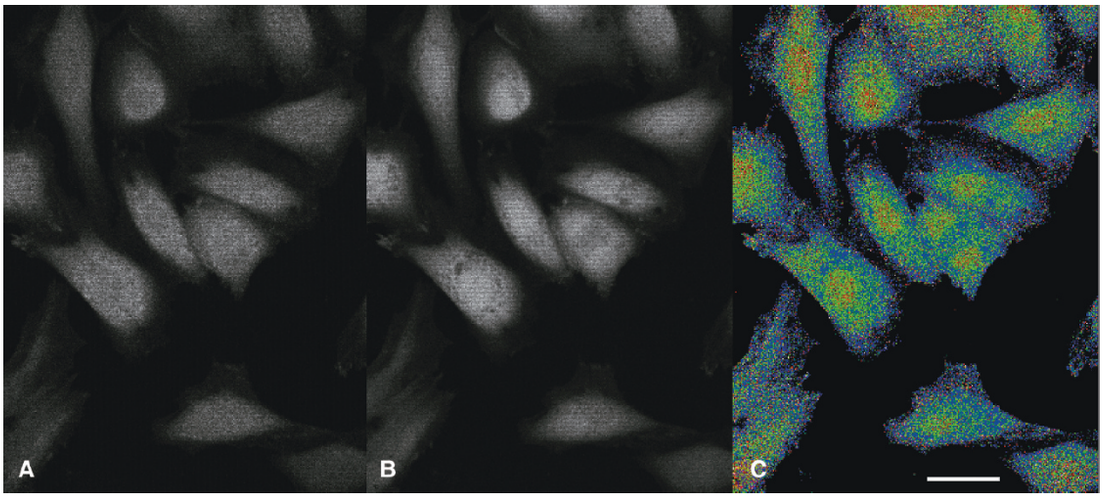


FIGURE 42.8. Cultured monolayer of rabbit proximal tubule cells stained with the acetoxymethyl ester of SNARF-1. (A) Wavelengths greater than 595 nm. (B) Wavelengths lower than 595 nm. C: A ratio image of A divided by B (>595 nm/<595 nm) creates an intracellular pH distribution map that shows the nuclei have a higher pH (up to 0.5 pH units higher) that the cytosol. Bar = 25 µm. (Dubbin *et al.*, 1993.)

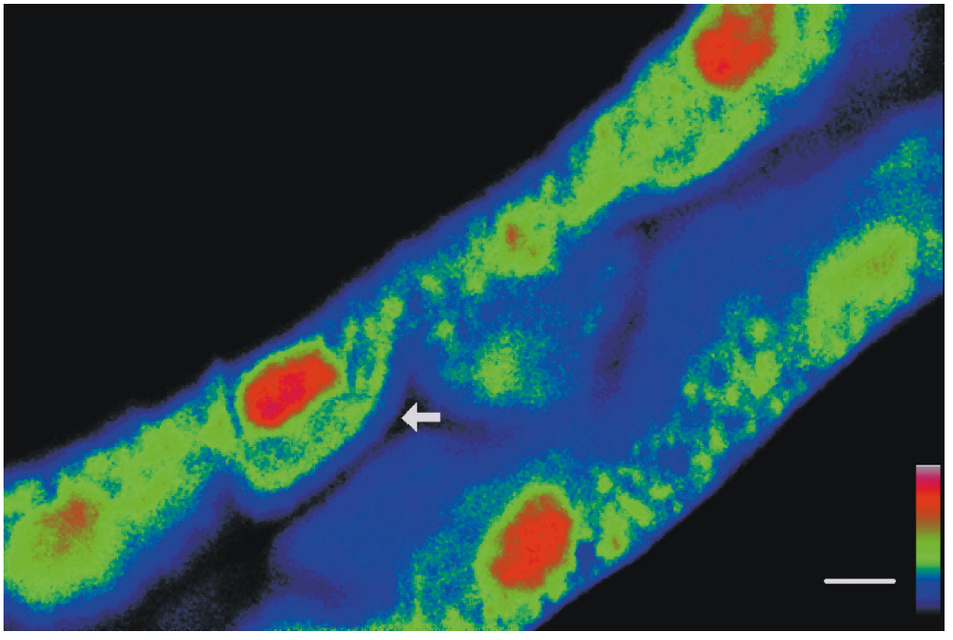


FIGURE 42.9. Rabbit kidney proximal tubule stained with the pH-sensitive dye BCECF: single excitation (ex. 488 nm) image where intensity is a function not only of pH but also dye concentration. Arrow indicates the brush border. Bar = 5 µm. (Cody and Williams, 1999.)

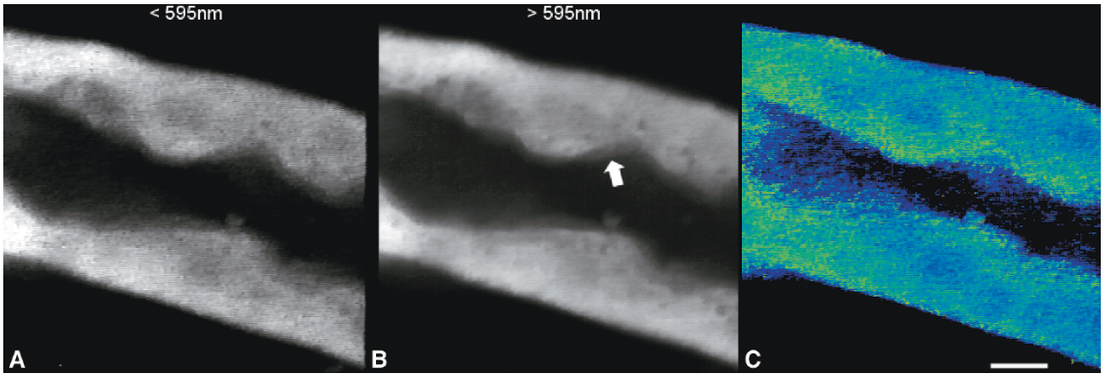


FIGURE 42.10. Rabbit kidney proximal tubule stained with SNARF-1. (A) Emission wavelengths less than 595 nm. (B) Wavelengths greater than 595 nm. Arrow indicates the brush border, with lower intensity fluorescence. (C) Ratio image (<595 nm/>595 nm) provides a pH distribution map that is independent to photobleaching, dye distribution and path length artifacts. Bar = 5 µm. (Cody and Williams 1999.)

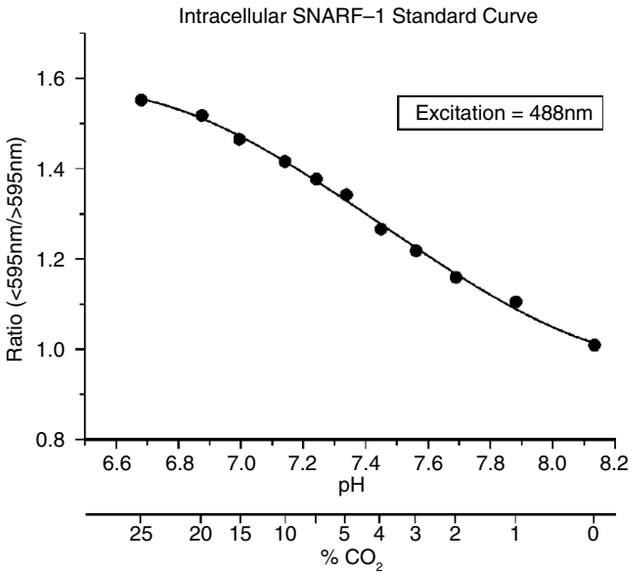


FIGURE 42.11. A typical intracellular calibration curve of SNARF-1. Muscles stained with SNARF-1 and treated with the hydrogen ion ionophore nigericin (50 μM). The pH of the modified Kreb's solution was altered by bubbling with different concentrations of CO_2. The extracellular pH was monitored with a pH electrode, and dual channel ratiometric images of intracellular SNARF-1 fluorescence were recorded. (Cody *et al.*, previously unpublished.)

fering ions in the cell do not change significantly during the experimental procedures and autofluorescence remains constant. As accurate calibration remains problematic and time consuming to do properly with appropriate controls, it may be better to design experiments where one need only determine the direction of change rather than measure the absolute ion levels.

CONCLUSION

The new fluorescent probes coupled with the LSCM allow unprecedented sensitivity and resolution for the detection of ion levels in four dimensions within living cells. The current range of dyes and the equipment available has enabled resolution of microscopic signaling on the scale of <1 µm and 1 ms for quite long periods. At this level, we are measuring such small numbers of ions and molecules that the system can become severely photon limited. To increase resolution much further, a very different approach will be needed, perhaps one where we no longer look at the second messenger *per se* but force the cell to report its response by generating fluorescent signals from engineered target proteins. Whatever method is used, we should not lose sight of the fact that measurement of responses *will* perturb the cell response we are studying.

ACKNOWLEDGMENTS

Financial support of MBC has been provided by the NIH, Wellcome Trust, American Heart Association, HRC (NZ), Marsden Fund (NZ), and NZHF. He would also like to thank all his coworkers who have helped him carry out these imaging experiments over the years and to whom he owes a debt of knowledge. The pH-mapping projects were conducted by SHC in the Department of Physiology, University of Melbourne under the mentorship of Prof. David A. Williams and with a major contribution from Mr. Philip N. Dubbin. Major contributors to the muscle fatigue project were made by Dr. Gordon S. Lynch and Dr. Noel D. Duncan. Kidney tubule preparations kindly supplied by Prof. Peter Harris, University of Melbourne.

REFERENCES

Baylor, S.M., and Hollingworth, S., 1988, Fura-2 calcium transients in frog skeletal muscle fibers. *J. Physiol*. 403:151–192.

Blinks, J.R., Prendegast, F.G., and Allen, D.G., 1976, Photoproteins as biological calcium indicators, *Pharm. Rev*. 28:1–28.

Cannell, M.B., and Allen, D.G., 1984, A model of calcium movements during activation in the sarcomere of frog skeletal muscle. *Biophys. J*. 45:913–925.

Cannell, M.B., Berlin, J.R., and Lederer, W.J., 1987, Effect of membrane potential changes on the calcium transient in single rat cardiac muscle cells, *Science* 238:1419–1423.

Cannell, M.B., Cheng, H., and Lederer, W.J., 1994, Spatial non-uniformities in $[Ca^{2+}]_i$ during excitation-contraction coupling in cardiac myocytes, *Biophys. J*. 67:1942–1956.

Cheng, H., Lederer, W.J., and Cannell, M.B., 1993, Calcium sparks: Elementary events underlying excitation-contraction coupling in heart muscle, *Science* 262:740–744.

Grynkiewicz, G., Poenie, M., and Tsien, R.Y., 1985, A new generation of Ca^{2+} indicators with greatly improved fluorescence properties, *J. Biol. Chem*. 260:3440–3450.

Highsmith, S., Bloebaum, P., and Snowdowne, K.W., 1986, Sarcoplasmic reticulum interacts with the Ca(2+) indicator precursor fura-2-am, *Biochem. Biophys. Res. Commun*. 138:1153–1162.

Jackson, A.P., Timmerman, M.P., Bagshaw, C.R., and Ashley, C.C., 1987, The kinetics of calcium binding to fura-2, *FEBS Lett*. 216:35–39.

Jones, K.T., Soeller, C., and Cannell, M.B., 1998, The passage of Ca^{2+} and fluorescent markers between the sperm and egg after fusion in the mouse. *Development* 125:4627–4635.

Molecular Probes, 2003, *Handbook of Fluorescent Probes and Research Chemicals*, Molecular Probes, Inc., Eugene, Oregon.

Neher, E., and Augustine, G.J., 1992, Calcium gradients and buffers in bovine chromaffin cells, *J. Physiol*. 450:273–301.

Pape, P.C., Jong, D.S., Chandler, W.K., and Baylor, S.M., 1993, Effect of fura-2 on action potential-stimulated calcium release in cut twitch fibers from frog muscle, *J. Gen. Physiol*. 102:295–332.

Rizzuto, R., Simpson, A.W.M., Brini, M., and Pozzan, T., 1983, Rapid changes in mitochondrial Ca2+ revealed by specifically targeted recombinant aequorin, *Nature* 358:325–327.

Thomas, M.V., 1991, Metallochromic indicators, In: *Cellular Calcium: A Practical Approach* (J.G. McCormack and P.H. Cobbold, eds.), IRL Press, Oxford, United Kingdom.

Timmerman, M.P., and Ashley, C.C., 1986, Fura-2 diffusion and its use as an indicator of transient free calcium changes in single striated muscle cells, *FEBS Lett*. 209:1–8.

Tsien, R.Y., 1981, A non-disruptive technique for loading calcium buffers and indicators into cells, *Nature* 290:527–528.

Wier, W.G., Cannell, M.B., Berlin, J.R., Marban, E., and Lederer, W.J., 1987, Fura-2 fluorescence imaging reveals cellular and sub-cellular heterogeneity of [Ca2+]i in single heart cells, *Science* 235:325–328.

Williams, D.A., 1993, Mechanisms of calcium release and propagation in cardiac cells. Do studies with confocal microscopy add to our understanding? *Cell Calcium* 14:724–735.

Williams, D.A., Fogerty, K.E., Tsien, R.Y., and Fay, F.S., 1985, Calicium gradients in single smooth muscle cells revealed by the digital imaging microscope using Fura-2, *Nature* 318:558–561.

Zhang, J., Campbell, R.E., Ting, A.Y., and Tsien, R.Y, 2002, Creating new fluorescent probes for cell biology, *Nat. Rev. Mol. Cell Biol*. 2002;3:906–918.

43

Confocal and Multi-Photon Imaging of Living Embryos

Jeff Hardin

INTRODUCTION

By its very nature, developmental biology requires thinking in four dimensions. Not only do embryos change dramatically over time, as the seemingly featureless single-celled zygote is transformed into an embryo with recognizable body axes and organ systems, but this remarkable transformation occurs in three spatial dimensions. The coordinated changes that occur within the developing embryo include carefully orchestrated signaling events, changes in gene expression, and morphogenetic movements, that is, regulated cell divisions and cell movements that sculpt the basic body plan as a recognizable organism emerges.

Non-confocal imaging modalities, such as Nomarski microscopy and widefield epifluorescence, have played a key role in the analysis of whole, living embryos in several important model systems, such as *Caenorhabditis elegans* (Thomas *et al*., 1996; Thomas and White, 2000) and zebrafish and other teleosts (Concha and Adams, 1998). In less transparent embryos, including amphibians such as *Xenopus* (Wilson and Keller, 1991) and avian embryos (Chapman *et al*., 2001; Czirok *et al*., 2002), important work has been done to analyze overall changes in shape of embryos or in microsurgically explanted tissues. However, it is no exaggeration to say that confocal microcopy has been a revolutionary technology in the resurgence of microscopy as a key analytical tool of the developmental biologist. Beginning in the late 1980s and continuing throughout the decade of the 1990s to the present, the development of devices that could capture four-dimensional (4D) datasets of fluorescent molecules within embryos with increasing temporal and spatial resolution has allowed processes progressively deeper within embryos to be studied for the first time. As laser, photomultiplier, and charge-coupled device (CCD) technologies have improved, so has our ability to image large embryos *in situ*, including opaque embryos, such as *Xenopus* and the chick. The impact of confocal microscopy has not been restricted to the specialist; the striking images obtained using confocal microscopy have also transformed how data are presented in the teaching laboratory and classroom.

Despite these successes, challenges remain. Some of these challenges are specific to particular types of embryos, but others are faced by all developmental biologists, no matter which model system they choose. This chapter sets out several of these common challenges, and how developmental biologists are overcoming them as they attempt to bring modern confocal and multi-photon microscopy to bear on key developmental events.

INTO THE DEPTHS: EMBRYOS ARE THICK, REFRACTILE, AND SUSCEPTIBLE TO PHOTODAMAGE

Imaging Embryos Often Requires "4D" Imaging

One of the vicissitudes of imaging living embryos is that they are thick, and their structure is constantly changing. As a result, embryos must often be imaged throughout their thickness and over time. Such 4D imaging entails the collection of a stack of images made at different focal depths along the imaging axis at specified time intervals. Once each three-dimensional (3D) image stack has been collected, the objective is repositioned at the starting position in preparation for the next time point, at which time this cycle is repeated. For typical long-term acquisition experiments involving fluorescent probes detected in living embryos, exposure of embryos to the excitation beam is prevented between time points by a shuttering system, thereby minimizing photodamage to the embryo.[1] Although the details differ, modern commercial confocal, multi-photon, and widefield/deconvolution microscopes all offer acquisition packages that allow for the collection of such 4D datasets.

Four-dimensional datasets of fluorescent specimens acquired using confocal, multi-photon, or widefield deconvolution techniques have several advantages over 4D datasets acquired using transmitted light optics, such as Nomarski microscopy (Thomas *et al*., 1996; Thomas and White, 2000). First, confocal acquisition permits much more refined optical sectioning of the specimen with little contribution by out-of-focus information. For large, thick embryos, this means that events at significant distances from the coverslip can be imaged crisply without contaminating signal from other regions of the embryo. Second, but of equal importance, it is much easier to understand the distribution of the fluorescent

[1] In this chapter, as elsewhere in this book, we assume, that, to a first approximation, photodamage is proportional to the total number of fluorescent signal photons actually excited and that one scan at a power level of 100 μW will do the same damage as 10 scans at 10 μW. This means that one must use much lower levels of excitation in a study requiring many planes per *z*-stack and many time points in the time series. This proportionality may break down at higher power levels that approach singlet-state saturation of the fluorophore where the chance increases that each excitation will produce damage.

Jeff Hardin • University of Wisconsin, Madison, Wisconsin 53706

signal from a sample on the basis of a 3D voxel rendering than to derive any sort of "real" data from a 3D stack of differential interference contrast (DIC) images (for an attempt at the latter, see Heid *et al*., 2002 and Chapter 24, *this volume*).

The Quest for Better Resolution: Aberration and the Challenge of Imaging Thick Embryos

It is common for beginning students of developmental biology to become preoccupied by the dazzling sophistication of modern computer visualization techniques. While they certainly have visual appeal, it is sometime less obvious to students and researchers that optimizing the optical system to get better data can often be more important for imaging embryos than the subsequent use of software to display the raw image data.

Although it may seem obvious to anyone who has tried to image events during embryogenesis, it is worth considering the crucial optical challenge developmental biologists face as they try to capture and analyze dynamic processes during embryogenesis: *embryos are rarely flat.* Indeed, often they are extremely thick along the axis of the light path. For example, *Xenopus* embryos are roughly 1 mm in diameter, and chick embryos are larger still at late stages in development. These distances mean that even in the absence of significant light scattering by the specimen, spherical aberration can be an important constraint on obtaining quality images deep within a specimen (see Chapters 2, 7, and 20, *this volume*, for further details on the effects of spherical aberration). For thick specimens, aberration introduced due to refractive index mismatch between oil-immersion objectives and the aqueous medium is significant. For thin specimens imaged within 5 µm of the coverslip (such as *C. elegans* embryos, in cases where surface features are of interest, or when an explant technique has been used to effectively flatten the specimen), a high numerical aperture (NA) lens (NA = 1.4) is typically the best choice.

The spatial effects of these aberrations have been determined for both confocal and two-photon microscopes, and they can be profound. Mismatch artifacts can affect axial resolution, introduce focal shifts of the image plane, and result in dramatic decreases in image intensity (Hell *et al*., 1993; DeGrauw *et al*., 2002). Such problems may be solved in part by using water-immersion lenses for specimens more than ~10 µm in thickness, although many developmental biologists assume that maximizing numerical aperture by using oil-immersion lenses is the *sine qua non* of high-resolution imaging. For aqueous specimens thicker than ~10 µm, a water-immersion lens with a lower NA outperforms a high-NA oil-immersion lens.

Embryos Are Highly Scattering and Refractile Specimens

Light scattering is often fairly acute, even in the case of relatively small embryos, such as *C. elegans* and *Drosophila* (~25 µm and 200 µm along their short axes, respectively). Within the cells of such embryos particles that are significantly smaller than the excitation and emission wavelengths contribute to Rayleigh scattering (see Chapter 21, *this volume*), which depends inversely on the fourth power of the wavelength. Consequently, such scattering can be lessened by using longer excitation wavelengths; for strongly scattering specimens, two- or multi-photon imaging can further reduce scattering of excitation photons (see below). Unfortunately, there are other major sources of scattering in embryos. The cells of early embryos typically have yolk platelets or other highly refractile granules within the cytoplasm that deflect both excited and emitted light. Moreover, most embryos are spherical; the curvature of their outer surface is also a major source of refraction.

Imaging Embryos Involves Inherent Trade-Offs

Imaging thick embryos typically means a trade-off between lateral and axial resolution and signal strength on the one hand, and working distance and field diameter on the other. Typical epifluorescence objectives effectively act as both condenser for incident light passing through the excitation filter and off the dichroic mirrors, as well as serving as the objective lens that collects and focuses the photons emitted from the specimen. As magnification increases, signal/area in the image decreases, but this is counterbalanced by the higher NA of the objective. For high-resolution imaging, developmental biologists typically seek to maximize numerical aperture while keeping the magnification low enough to permit them to see the whole embryo or at least the part of it of most interest.

Although the discussion of contrast is complex, it is clear that for fluorescent specimens, contrast and effective resolution of structures labeled with fluorophores are linked (for further discussion of the issues relating the contrast transfer function, CTF, see Chapters 2, 4, 8, and 35, *this volume*). At a simple level, contrast is determined by the ratio of local intensity differences in the specimen to the local average intensity in the image, $\Delta I/I$. To a first approximation, the local emission intensity difference for typical applications in embryos is proportional to the local concentration of fluorophores above background. Moreover, as the emitted signal is proportional to the local fluorophore concentration, developmental biologists usually seek to increase the local signal as much as possible by increasing staining intensity or the concentration of green fluorescent protein (GFP)-tagged molecules per unit volume. Here again, however, there are often trade-offs because excessive labeling achieved by over-expression of a fluorescent protein can interfere with cellular function.

Although increasing the illumination intensity increases the fluorescent signal, dynamic imaging of fluorophores within living embryos requires multiple exposures to the excitation light, so developmental biologists can rarely afford to use high illumination intensity. Indeed, they are acutely aware that this simple solution typically results in dead embryos! Therefore, a balance must be sought between the intensity of the illumination and a host of other factors important to achieving quality images. Because embryos are so thick and their cells are moving in four dimensions, multiple focal planes must be acquired at each successive time point. While such 4D information is powerful, it requires exposing the region of interest to more laser light than that required for viewing flat cells in culture. Thus, minimizing exposure to the excitation wavelength is a key factor in maintaining the viability of embryos during 4D experiments.

The photobleaching that accompanies repeated observation in 4D experiments also complicates image quantification. If photobleaching is not too severe, it is sometimes possible to normalize the signal from bleached specimens using a reference fluorescent signal, but this only works if the specimen and the reference bleach at the same rate. In general, the best solution to this problem is reducing the power of the excitation beam as much as possible. Although multi-photon microscopy has the advantage that fluorophore is excited only within a small volume near the focal plane of the objective, this advantage must be balanced against the fact that some dyes bleach more rapidly per photon emitted with two-photon than with single-photon excitation. Clearly, multi-photon

excitation is the imaging modality of choice if bleaching is a serious concern and the stained thickness of the specimen is high.

Common Themes in Living Embryo Imaging Have System-Specific Solutions

Although developmental biologists have developed several ways to address challenges common to imaging all living embryos, given the dramatic differences in the basic cell biology between the most common model organisms, solutions are typically specific to a particular model system. Rather than reviewing the virtues and drawbacks of each model system and describing highly detailed techniques for solving particular imaging issues in each one, the remainder of this chapter will focus on examples of ways in which developmental biologists are meeting the challenges of long-term imaging of fluorescent molecules deep within living embryos.

Before reviewing such examples, several generalizations about the apparatus and dyes useful in imaging living embryos are in order. First, there is a necessary element of empiricism in determining which type of microscope is necessary for a particular fluorophore in a particular embryonic context. Currently, standard laser-scanning confocal systems still dominate over other types of imaging equipment, and thus a significant amount of live embryo imaging is being attempted — and successfully performed — on such equipment. While it is true that there are advantages to multi-photon microscopy in terms of depth of penetration into a specimen and, in some cases, viability, laser scanning suffices for a wide variety of imaging situations. Depending on the density of fluorophore labeling and the nature of the tagged moiety, the majority of experiments have been performed using rather unremarkable equipment, such as a Bio-Rad 1024 or similar laser-scanning confocal apparatus.[2] Although such experiments sometimes suffer from limited image acquisition speed, live imaging of embryos using laser-scanning confocal microscopy has been extremely successful.

A second general consideration is that the way in which a fluorophore affects viability is crucially dependent on the macromolecule to which it is attached. For example, in our laboratory, transcriptional reporters that drive the expression of GFP in the cytosol can withstand irradiation at 10% to 30% power of the 488 line on a conventional Bio-Rad 1024 microscope with a krypton/argon (Kr/Ar) laser for many minutes to hours, whereas imaging embryos expressing a GFP-tagged protein found at epithelial junctions under the same imaging conditions either kills the cells or renders them unable to develop properly (J. Hardin, unpublished observations).

Third, even if the problems of working with thick, refractile embryos can be at least partially solved by using confocal or multi-photon microscopy, developmental biologists still need ways to specifically label interesting features in living embryos. In some cases, they wish to highlight multiple structures simultaneously within the same specimen, and this requires delivering multiple fluorophores to specific sites within embryos. Although not specific to confocal and multi-photon microscopy, specific labeling strategies are nevertheless a key adjunct to these imaging technologies. In essence, this is a continuation of the microscopist's quest to increase specimen contrast, no matter what imaging modality is being used.

[2] Interested readers are urged to consult reviews describing methods of confocal and multi-photon imaging in specific model systems. These include methods for imaging *Xenopus* (Bement *et al*., 2003), zebrafish (Cooper *et al*., 1999), *Drosophila* (Wood and Jacinto, 2004), and *C. elegans* (Mohler, 1999) embryos.

DEALING WITH DEPTH: STRATEGIES FOR IMAGING THICK SPECIMENS

Avoiding the Thickness Dilemma: Going Small

Model systems in developmental biology are often chosen to avoid the thickness dilemma. For example, *C. elegans* embryos are only ~25 µm thick along their dorsoventral axis, commonly used echinoderm embryos are only 80 to 120 µm in diameter, and *Drosophila* embryos are ~200 µm along their dorsoventral axis. Zebrafish are at the limits of penetration via multi-photon microscopy (~600 µm in diameter), but because most relevant events occur near the surface, they too are effectively fairly flat. As a result, there are many examples in which embryos from these model systems are imaged in 4D using confocal and multi-photon techniques. These include the imaging of GFP-tagged proteins in *Drosophila* embryos during dorsal closure and germ band extension, processes that take several hours (Wood and Jacinto, 2004), cell migration in the epidermis during morphogenesis of *C. elegans* embryos (Mohler *et al*., 1998; Heid *et al*., 2001), events during fertilization and subsequent early development of echinoderm embryos (Terasaki, 1998), and 4D analysis of morphogenesis in zebrafish embryos (Cooper *et al*., 1999).

Grazing the Surface: Superficial Optical Sections Are Often Sufficient

While many model systems are small in size, some are at the limits of standard confocal microscopy. For example, *Xenopus* embryos are a full 1 mm in diameter. Moreover, because their dense yolk platelets scatter light, imaging deep into the interior of amphibian embryos is an acute technical challenge. One simple strategy is to concede that imaging events deep within the embryo is not possible, and to focus on what can be seen near the surface of the oocyte, fertilized egg, or early zygote. Such events can be imaged extremely well using a single-beam confocal microscope and a variety of labeling techniques, including fluorescent dextrans, lipophilic dyes, fluorescently labeled proteins or antibodies introduced via microinjection, or by expressing GFP-tagged proteins following injection of mRNA (Bement *et al*., 2003). A montage from a representative dataset from a *Xenopus* oocyte is shown in Figure 43.1(A), which shows the redistribution of active Rho and actin during the closure of a wound in a *Xenopus* oocyte. Such imaging experiments often involve 4D imaging, although because of the high speed of the movements involved, only a few optical sections (<10) can typically be recorded at each time point (Bement *et al*., 2003). To image events deeper within the embryo, however, additional techniques must be employed.

Up from the Deep: Explants Can Reduce the Thickness of Specimens Dramatically

In some cases, imaging the surface of thick embryos is simply not sufficient. For example, during gastrulation, cells move large distances within the interior of the embryo. In the case of the relatively opaque *Xenopus* embryo, it is simply not feasible to image such tissues directly, because they may be several hundred

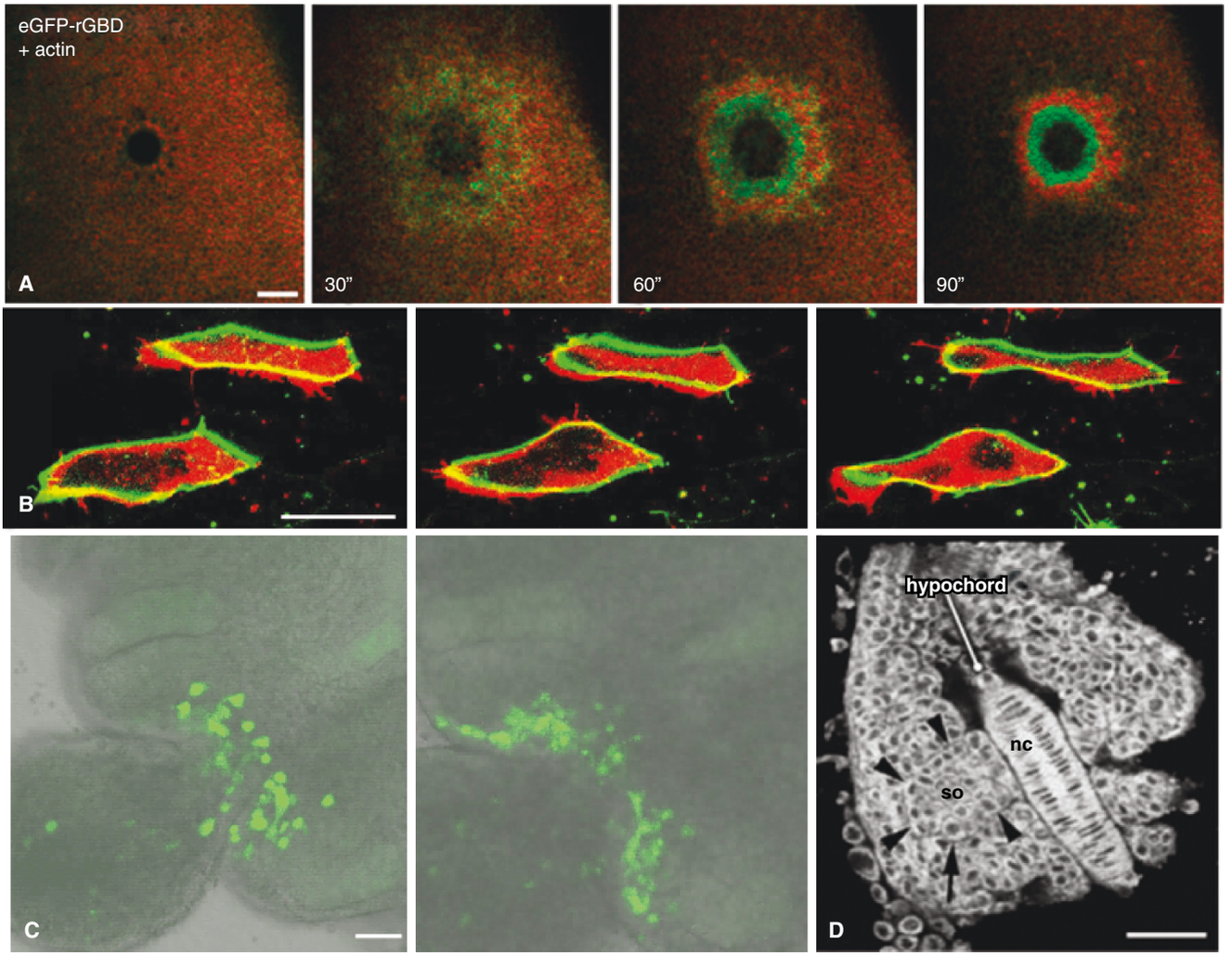


FIGURE 43.1. Strategies for imaging very thick embryos. (A) A 4D study of events on the surface of a *Xenopus* oocyte. Shows wound closure in a *Xenopus* oocyte expressing a protein that binds active Rho fused to eGFP (eGFP-rGBD; green) and Alexa-568 labeled actin (red) imaged using a Bio-Rad 1024 CLSM. Bar = 15 µm. Times indicated are in seconds. (B–D) Imaging events in an explant. (B) Frames from a fluorescence confocal movie in which intercalating *Xenopus* mesodermal cells are visualized at two levels: the surface of the explant (red channel) and 5 µm deep in the tissue (green channel). Cell membranes are labeled with GAP-43::GFP. Bar = 50 µm. (C) Frames from a confocal time-lapse sequence showing migration of primordial germ cells (PGCs) in a slice from a stage E9.5 embryo expressing Oct4ΔPE::GFP, imaged at 7 min intervals using a Zeiss LSM-510 CLSM. PGCs migrate into the genital ridges. Data taken 455 min later. Bar = 50 µm. (D) Ventral view of an explanted zebrafish tail rudiment (14-somite stage) mounted ventral side down using plasma clot immobilization vitally stained with Bodipy 505/515 imaged using a Bio-Rad MRC600 CLSM. The notochord and a neighboring somite (so, *arrowheads*) are visible. An individual somitic mesodermal cell (*arrow*) is in mitotic prophase. Scale bars = 50 µm. [(A) is from Benink and Bement (2005); (B) is from Keller (2002); (C) is from Molyneaux and colleagues (2003); (D) is from Langenberg and colleagues (2003), used by permission.]

micrometers from the surface, and light scattering is severe at that depth. In this case, a better approach is to isolate the tissue of interest using microsurgery. By isolating a sheet of tissue that is relatively thin along the imaging axis, the embryo has in effect been flattened. Such an embryo, expressing a membrane-localized GFP, is shown in Figure 43.1(B). Although 4D datasets must still be acquired to capture the relevant aspects of cell motility in this specimen, the explant is sufficiently transparent that one can acquire *z*-stacks that encompass its entire thickness (Keller, 2002). Other similar techniques have been used to render tissues in other large embryos amenable to 4D analysis. These include analysis of primordial germ cell migration in mouse embryos (Molyneaux *et al.*, 2003) [Fig. 43.1(C)] and the microsurgical removal of the yolk cells from post-gastrula stage zebrafish embryos (Langenberg *et al.*, 2003) [Fig. 43.1(D)].

Multi-Photon Microscopy Can Penetrate More Deeply into Specimens

Multi-photon laser-scanning microscopy (MPLSM) has gained wide acceptance as an alternative to standard laser-scanning confocal microcopy because it has several potential advantages over CLSM for live imaging of embryos. MPLSM excites fluorescence using a series of short, high-energy pulses of near-infrared (NIR) photons from a mode-locked laser. At the very high photon densities that result, two or more photons can be absorbed simultaneously to excite a single fluorophore, which then returns to the unexcited ground state by a standard fluorescence emission event. In the case of two-photon excitation, the excitation wavelength is set to roughly twice that used for single-photon (i.e., normal) excitation of the same fluorophore (see Chapter 28, *this volume*, for a

detailed description of multi-photon microscopy). Although theoretical calculations and measurements of actual point spread functions indicate that the axial resolution in MPLSM is about 40% lower than in CLSM (Jonkman and Stelzer, 2002), MPLSM has two key advantages for live embryo imaging experiments.

As the two-photon excitation probability is proportional to the square of the local beam intensity (see Chapter 28, *this volume*), given the conical shape of the standard excitation beam, the probability of excitation varies as the inverse fourth power of the distance from the focal plane. The result is that photons are absorbed only in a very small volume centered on the plane of focus. As long as no regions of the specimen cause single-photon absorption of light at this wavelength, it is essentially transparent to the incident laser light. This eliminates photobleaching and photodamage caused by excitation of fluorophores above and below the plane of focus.

The resulting improvements in viability can be quite dramatic. For example, hamster embryos imaged with CLSM using the mitochondrial marker Mitotracker Rosamine did not develop to the blastocyst stage, whereas similarly labeled embryos imaged using MPLSM at 1047 nm were capable of late fetal development and even birth (Squirrel *et al*., 1999). In our own laboratory, *C. elegans* embryos expressing a GFP-tagged junctional protein survive for 30 to 90 min when imaged using a Bio-Rad 1024 CLSM at low power (10%; J. Hardin, unpublished observations) but the same embryos can be imaged for many hours using MPLSM.

Second, the longer wavelength of the MPLSM excitation beam scatters less and is not absorbed by fluorophores located above the focus plane. These characteristics permit it to excite fluorophores deep inside the specimen (Fig. 43.2), in some transparent embryos such as zebrafish, up to ~500 µm from the surface (Megason and Fraser, 2003). In addition, because multi-photon excitation generates significant signal only at the plane of focus, no pinhole is required to detect an image resolved in three dimensions. One must simply detect light that was emitted at a specific time. As a result, one can used non-descanned detection, a process in which even fluorescent light that had suffered multiple scattering events can still contribute to the image as long as it reaches a photodetector. For thick specimens, this can increase signal level by a factor of up to 3× (Centonze and White, 1998).

Although MPLSM can be superior to CLSM for many applications, there are several issues that can make MPLSM less than optimal. First, the typical MPLSM device is expensive, placing it out of reach of most individual laboratories. In contrast, individual labs can often afford disk-scanning confocal microscopes, a factor that is particularly important for live embryo studies, which often monopolize microscope time. Second, for certain fluorophores, for example, those that emit in the red portion of the visible spectrum, the wavelengths needed to generate a two-photon event are longer than those produced by the titanium : sapphire (Ti : Sa) lasers commonly used in commercial MPLSM devices. For such dyes, Nd : YLF lasers, which emit at 1047 nm, are very effective (Mohler *et al*., 1998; Squirrell *et al*., 1999; see also Fig. 43.9), but may not be readily available. Third, some pigments, such as those found in living *Xenopus* embryos, absorb the NIR light used to excite GFP and other green-emitting fluorophores by two-photon events. Such absorption usually causes severe damage (see Chapter 38, *this volume*).

Although MPLSM is clearly a tremendous tool in the arsenal of the developmental biologist, in light of these caveats, it is

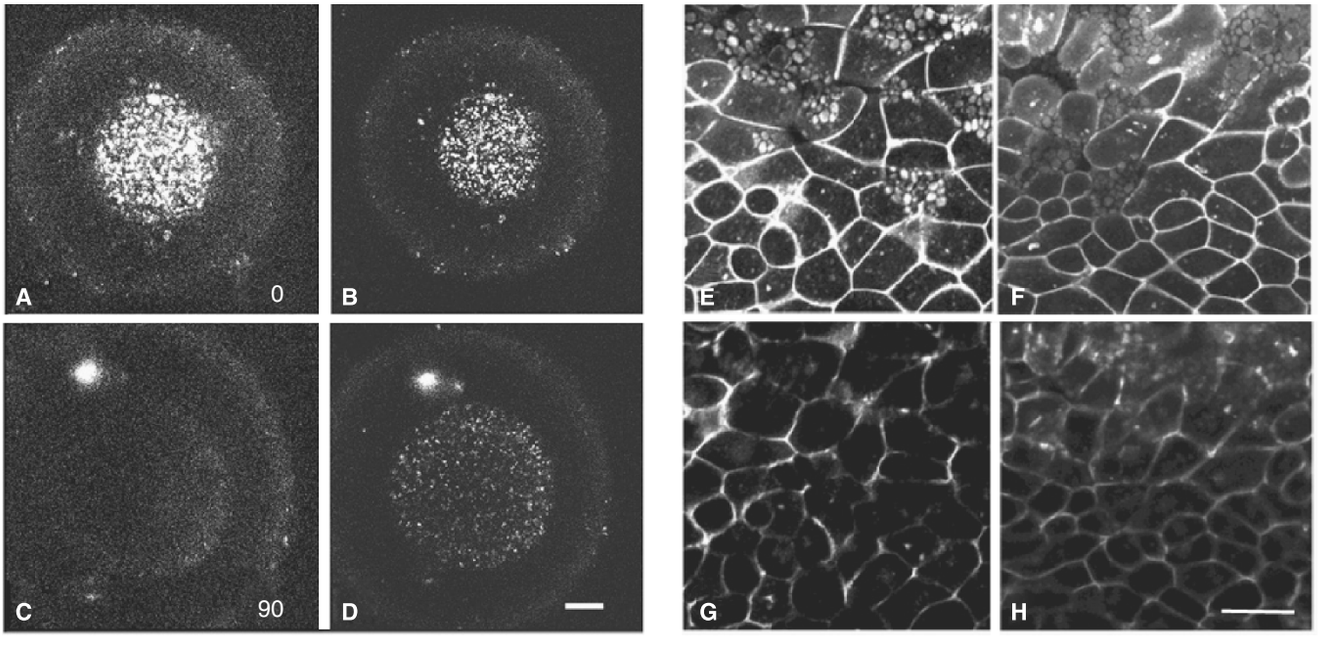


FIGURE 43.2. Multi-photon microscopy is useful for penetrating more deeply into embryos. (A) A bovine embryo stained with Mitotracker rosamine to detect mitochondria, imaged via confocal microscopy (left; 3.5 W of 532 nm light) and by multi-photon microscopy (right; YLF laser, direct detection, 10 mW of 1047 nm light), using a Kalman three-collection average. Mitochondria are roughly uniformly distributed in such embryos. Mitochondria cannot be visualized using the CLSM, but are clearly visible using the MPLSM. Bar = 20 µm. (B) Comparison of multi-photon and confocal microscopy for imaging morphogenesis in the *Xenopus* embryo. Images of GAP-43 :: GFP fusion protein in developing *Xenopus* embryos were acquired with the same objective lens using CLSM (Nikon PCM 2000) and TPLSM systems (Bio-Rad MRC 600 scan head, with Ti : Sa laser at 870 nm). Less detail is evident deeper in the specimen with CLSM. Bar = 50 µm. [(A) is from Centonze and White (1998); (B) is adapted from Periasamy and colleagues (1999), used by permission.]

usually wise to try standard confocal imaging first before assuming that MPLSM is necessary for a particular specimen. Our own laboratory has found, for example, that GFP-tagged proteins can usually be imaged in living *C. elegans* embryos with disk-scanning or standard CLSM; on the rare occasions that the image series must proceed for many hours and many focal planes must be acquired, MPLSM remains the method of choice.

Selective Plane Illumination Can Provide Optical Sectioning in Very Thick Specimens

Originally developed by Voie *et al.* (1993) and more recently improved by Stelzer and colleagues (Huisken *et al*., 2004), selective plane illumination microscopy (SPIM; Fig. 43.3), involves a strategy akin to that achieved in nonlinear (two- and multi-photon) microscopy, that is, fluorescence is only excited in a narrow plane perpendicular to the imaging axis (see Chapter 37, *this volume*). A cylindrical lens is used to focus laser light into a light sheet that illuminates only a thin slice of material. In the current configuration, a specimen is embedded in an agarose capsule, and the entire specimen is moved within a bath of liquid. Because only the focal plane being observed is illuminated, the SPIM has similar advantages to MPLSM: far fewer excitations are produced during the acquisition of a 3D dataset. Unlike MPLSM, however, the signal is recorded on a high quantum efficiency CCD camera. These features make SPIM well suited to imaging specimens up to a millimeter in size (see also Chapter 37, *this volume*).

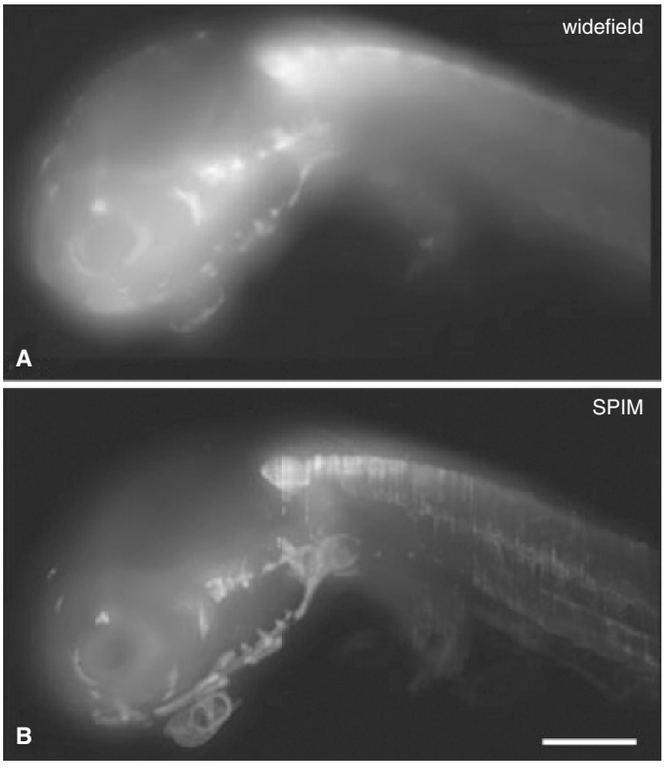


FIGURE 43.3. Selective-plane illumination (SPIM) can optically section huge embryos. A lateral view of a medaka embryo imaged with SPIM by two different modes of illumination. (A) The sample was illuminated uniformly, that is, without the cylindrical lens, as in a conventional wide-field microscope. (B) In contrast, selective plane illumination results in optical sectioning. Bar = 500 μm. [From Huisken and colleagues (2004), used by permission.]

In analogy to the pinhole setting on a standard laser-scanning confocal microscope, the axial resolution in SPIM depends on the thickness of the light sheet, which depends in turn on the working aperture of the cylindrical lens and ranges from 1 μm to 6 μm. This performance can be improved by obtaining additional 3D stacks after rotating the specimen, a process that can provide isotropic resolution down to about 1 μm.

Despite these impressive results, SPIM is still an emerging technology. The current device relies on embedding specimens in low-melting-point agarose, which does not appear to affect the development of fish and *Drosophila* embryos (Huisken *et al*., 2004). Our laboratory has shown that *C. elegans* and sea urchin embryos embedded in agarose also develop surprisingly well (J. Hardin, unpublished observations), suggesting that such embedment may not be a serious limitation. However, as agarose embedding imposes a mechanical impediment to the normal development of those embryos whose overall shape changes dramatically during the period of observation, other specimen stages may have to be developed to accommodate these specimens. In addition, SPIM cannot currently achieve spatial resolution comparable to confocal or multi-photon imaging. Nevertheless, the fact that SPIM has the resolution to identify individual cells in the context of embryos up to 1 mm thick makes it likely that it will become a useful addition to the arsenal of imaging techniques at the disposal of the development biologist.

Deconvolution and Other Post-Acquisition Processing

Widefield deconvolution has typically not been as widely used for imaging whole embryos as have confocal and multi-photon techniques. However, widefield acquisition, followed by post-acquisition deconvolution, can yield images comparable in quality to confocal or multi-photon datasets (Paddy *et al*., 1996) [Fig. 43.4(A,B)]. In deconvolution microscopy, a conventional epi-fluorescence microscope with attached CCD camera, shuttering system, and focus motor is used to capture a 4D dataset. The dataset is subsequently processed to remove out-of-focus contributions to the image at each focal plane (see Chapters 23, 24, and 25, *this volume*, for a detailed discussion of the merits of various deconvolution algorithms that is beyond the scope of this chapter).

Deconvolution has been used less frequently for imaging living embryos for several reasons. First, because the computations involved are extensive, there is no immediate visual feedback regarding the deconvolved image. This immediacy often has a significant psychological effect on the developmental biologist and may help her to guide the experimental procedure. Second, the success of deconvolution is limited by the noise level in the recorded image data. This noise is primarily Poisson noise, and the Poisson noise associated with the measurement of light away from the focus plane is particularly troublesome. Consequently, deconvolution works best when the fluorescent structures are confined to a relatively thin layer of the specimen. Finally, in studies that concentrate on imaging only a single plane over time, confocal and multi-photon imaging are both faster and less damaging to the specimen.

Despite these caveats, widefield/deconvolution microscopy has several advantages for imaging embryos. First, excitation wavelengths are not limited by available laser lines; deconvolution microscopes use standard fluorescence filter sets, and so they can easily visualize many common fluorophores, such as the cyan and yellow variants of GFP.

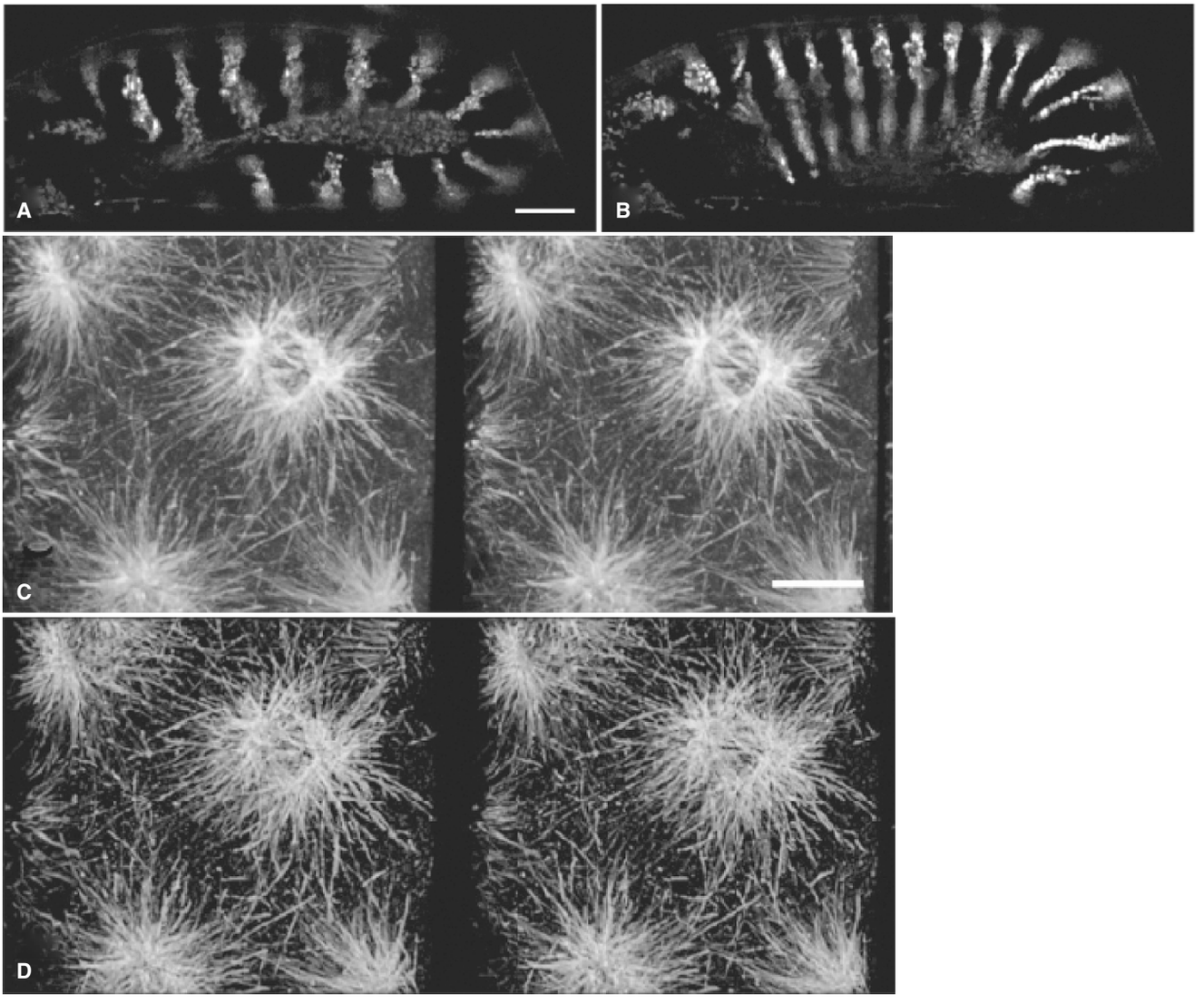


FIGURE 43.4. Deconvolution microscopy can improve optical sectioning of embryos. (A, B) Frames from a time-lapse movie of germ band retraction in a *Drosophila* embryo expressing an *Engrailed:: GFP* reporter, which localizes to nuclei in specific subdomains within each of 14 segments in the embryo, obtained using a DeltaVision deconvolution system. Fine details of the expression pattern are well defined. Bar = 50 µm. (C, D) Stereo-pair images of immunostaining to reveal microtubule distribution in a syncytial stage *Drosophila* embryo imaged using a Bio-Rad MRC-600 LSCM (C), and the same dataset after multiple rounds of deconvolution (D). Fine details within the mitotic spindle regions are visible after deconvolution that were poorly defined prior to deconvolution. Bar = 10 µm. [(A, B) Courtesy of I. Davis, University of Edinburgh. (C, D) Courtesy of G. Odell, University of Washington.]

Another purported advantage of deconvolution microscopy is its claim to cause less photodamage than confocal microscopy when producing an image of a given quality. If true, this difference can probably be traced to the fact that the arc lamps used in widefield epifluorescence produce lower intensity excitation light, and to a lesser extent, because all of the emitted light returned through the optical path reaches the camera (Hammond and Glick, 2000) (see also Chapter 39, *this volume*).

As with most other important parameters for live embryo imaging, the best approach is probably an empirical one. Performing a "test drive" of an expensive imaging system can save time and significant financial resources. Sometimes, the best way to take such a test drive in which living specimens are viewed on a variety of microscopes over a relatively prolonged period is to attend one of the many short courses offered on the topic.

Deconvolution has another important use: it can almost always improve the appearance and accuracy of 4D datasets acquired using confocal or multi-photon imaging [Fig. 43.4(C,D)]. Several studies have shown that postprocessing of confocal and multi-photon stacks using deconvolution can significantly improve their *z*-resolution (Periasamy *et al*., 1999), which is at least 4× lower than their *xy*-resolution, even when using a high-NA lens (Jonkman and Stelzer, 2002).[3] Of more importance for studying living embryos is the fact, that because Nyquist sampling spreads the signal from a single point over about 100 voxels, 3D deconvolution has the effect of averaging the data over about 100 voxels. This greatly reduces the effects of Poisson noise, thereby allowing one to use much lower excitation intensity (see Chapter 19, *this volume*, for 3D data collected using only 50 nW of laser power, and Chapter 25, *this volume*, for more on deconvolving confocal and multi-photon data).

[3] Three times worse for oil, NA 1.4 and 4× for water, NA 1.2. *z*-resolution is proportional to $1/(NA)^2$.

Deconvolution can be especially useful for confocal datasets of living embryos as these are often collected with the pinhole opened somewhat to increase signal. While this compromise increases the total signal and reduces Poisson noise, it also reduces the resolution in the *z*-dimension significantly, and so postprocessing may provide a significant improvement in *z*-resolution as well as signal-to-noise ratio (see Chapter 22, *this volume*). Likewise, 3D datasets from disk-scanning confocal microscopes, which have inherently less resolution along the imaging axis than CLSM, can typically benefit from deconvolution. Here again, however, whether such gains are worth the cost in computation time and effort can only be determined empirically.

STRIVING FOR SPEED: STRATEGIES FOR REDUCING SPECIMEN EXPOSURE

Simple Solutions: Reducing Image Dimensions, Increasing Slice Spacing, and Scan Speed

Two concerns motivate the need for increasing the acquisition speed when imaging embryos. First, rapid cellular events, such as cortical granule release, transport of cellular components along microtubules, and responses to wounding, occur so fast that there simply is not time to acquire finely spaced *z*-stacks of full-field images at maximal resolution. Second, and perhaps more importantly, as exposure to the scanning beam is proportional to the number of images acquired, acquiring more images/second means that the specimen is damaged more rapidly. As a result, the speed with which images can and should be collected must be tailored to each new situation empirically.

From the technical point of view, the speed at which one can acquire images is limited by the rate at which photons are emitted by the specimen: if more frames must be imaged, more photons are needed. The rate at which photons are produced is proportional to the concentration of fluorophore in the focal volume and the intensity of the light striking this volume. Although each of these parameters can be increased, neither can be increased arbitrarily. More laser power will produce additional signal (and additional photodamage!) only until one approaches the power level that produces singlet-state saturation.[4] This saturation limit can only be avoided by using a disk- or line-scanning confocal in which the excitation light is distributed either among an array of many individual points or among a similar number of points arranged to form a line (see Chapter 10, *this volume*).

Of course, the signal must not only be produced, it must also be detected. For this reason, high-speed imaging is also constrained by the quantum efficiency and read noise of the photodetector (a factor that will be discussed below in the context of the development of a new photodetector, the electron-multiplier CCD, or EM-CCD).

Another instrumental constraint is the speed of the scanning system. Single-beam systems that rely on galvanometers to scan the beam are limited to at most 8 k/line/s or about 16 frames/second if the raster size is 512 × 512, while those employing acousto-optical scanners move about 5× faster. On the other hand, the maximum scan rate of disk scanners, which have over a thousand beams in the field of view at any one time, is thousands of frames/second, and is limited chiefly by the vibration produced by the rotating disk. Of course, to collect 3D data one must also scan in the *z*-direction, and whether this is accomplished by moving the specimen or the objective, maximum *z*-scan rates are often limited by the deflection of the specimen slide or coverslip by the forces transmitted through the immersion medium.

The final limit imposed by the acquisition hardware is the rate at which the signal from each pixel can be read out and digitized. On systems utilizing detectors based on advanced CCDs, this is currently about 35 megapixel/s, but if these devices do not employ EM-CCD techniques, the read noise becomes substantial (~±50 electrons/pixel). Although it is possible to digitize the output of a photomultiplier tube at even higher clock speeds, as noted above, this is of little assistance if the dye in the voxel being interrogated is in singlet-state saturation.

A final limitation to consider is the size of the embryo in the *x*- and *y*-dimensions. For some embryos, such as later-stage chick embryos, the region of the embryo that must be imaged constrains acquisition speed. If the linear dimensions of the embryo in the *xy*-plane are large (in the case of a chick embryo, e.g., these dimensions can easily exceed 1 mm), then it may be necessary to image multiple *xy*-sectors. These sectors would then have to be joined into a seamless montage. While semi-automated methods (Beck *et al*., 2000) and fully automated (Czirok *et al*., 2002) methods are becoming available for such montage construction, the initial acquisition of multiple sectors is clearly an additional possible constraint on speed of acquisition and, hence, specimen exposure.

Within the constraints of the limitations listed above, a variety of other parameters can be reduced to optimize data acquisition. These include (1) the number of focal planes acquired at each time point; (2) the number of lines imaged; (3) the time required to build up an acceptable image of the specified *xy*-area in each focal plane; and (4) the interval between the acquisition of each *z*-series. The time required for an "acceptable" image will depend on the type of apparatus. In the case of laser-scanning confocal microscopes, the time required per focal plane will depend on the scanning speed and the number of scans integrated to build up the final signal. Here again, the intensity and contrast of the signal in the specimen will dictate the number of focal planes and the sampling interval and the investigator may have to change several parameters to achieve a satisfactory result. For example, when imaging *C. elegans* embryos in typical 4D experiments in our laboratory using a Bio-Rad 1024 CLSM or a Bio-Rad 1024 scan head for descanned multi-photon imaging, we often use a 1024 × 1024 *xy* pixel box size using the "slow" scan setting, with 30 focal planes 0.5 µm apart collected over a period of ~180 s. This is possible because stacks need only be acquired at 3 to 5 min intervals. In contrast, to image actin coat assembly around exocytosed cortical granules in *Xenopus* oocytes, 15 focal planes must be acquired, and sampling intervals need to be 5 to 10 s. This necessitates a much smaller box size (256 × 256 or 128 × 128 pixels) and higher scan speeds (Bement *et al*., 2003).

When speed is at a premium, single fast scans can often yield acceptable results, especially if a Gaussian filter is applied to the resulting 2D images. Acquiring single fast scans and deconvolving the resulting 3D images will also enhance the signal-to-noise ratio substantially (Jeff Hardin, unpublished observations). In the case of widefield deconvolution or disk-scanning confocal microscopy, the time needed to acquire an image typically represents the time required to integrate sufficient signal on the CCD camera.

[4] In the small spot produced by a high NA oil lens, this occurs for most dyes at about 1 mW. Because a 10× NA 0.5 objective will produce a spot ~3× larger in diameter and 10× larger in area, the same dye would now saturate at 10 mW. In addition to issues regarding saturation itself, there is reason to believe that the bleaching rate/emitted photon increases as one operates closer to saturation (see Chapters 38 and 39, *this volume*).

A final constraint on the speed of acquisition of a *z*-stack involves the eventual display of the collected data in 3D. The process of calculating and displaying renderings of 3D microscopical datasets is complicated by the fact that the resolution in the *z*-direction is always substantially less than that in the *x*- and *y*-directions. The interplane spacing is usually 3× to 4× larger than the *xy*-pixel dimension, and this causes a problem for 3D voxel-rendering algorithms that assume that voxel dimensions are the same in all three dimensions.

There are three solutions to this problem: duplication of slices, interpolation of slices, and collection of more data. The simplest solution involves duplicating the raw data three or four times to fill in the missing planes. This process is fast and restores the proper proportions; however, it makes the resulting images look like a stack of coins and, if the image stack is retained in memory, requires significantly more RAM. The second solution is to derive the missing planes from the measured planes by 2D or 3D interpolation. This process makes the rendering less blocky, but suffers from similar RAM constraints, and also requires significant computer processing time. Finally, one can simply collect data from more planes in the first place, perhaps collecting single-scan images at four focus positions where, to satisfy Nyquist sampling, one would be justified in collecting the Kalman average of four scans over a single plane. Because it avoids additional processing steps, this last solution is the one we most often employ, even thought it entails increased exposure of the embryo to the excitation beam.

Disk-Scanning Confocal Microscopy Allows High-Speed Acquisition

As mentioned above, multi-point confocal microscopes that employ Nipkow disk-scanning technology are another option for increasing data acquisition speed. Because the Yokagawa scan head combines laser excitation with an array of microlenses to force more light through each pinhole in the disk, a high rate of signal production is possible. Because the intensity in each spot is far from singlet saturation and because the effective quantum efficiency of the CCD is higher than that of the photomultiplier tube, disk scanners seem to produce little photobleaching while recording sufficient signal to perform high-quality 4D experiments.

The literature is replete with examples of the use of Yokagawa-based systems for imaging embryos of *C. elegans* (Oegema *et al*., 2001; Cockell *et al*., 2004) and *Drosophila* (Bloor and Kiehart, 2002; Grevengoed *et al*., 2001) in particular. Such microscopes also offer the advantage that the confocal image can be viewed directly, by eye, in real time (see Chapter 10, *this volume*, for an extensive discussion of Yokagawa-based systems and other related technologies).

For the developmental biologist, such systems are an inexpensive alternative to CLSM, and provide many of the benefits of more elaborate technologies, such as multi-photon microscopy. Because disk-scanning systems use an off-the-shelf focus motor, CCD, filter wheel, and shutter components, commercial imaging packages can be used to drive data acquisition. For some laboratories, this may be an advantage compared to the proprietary software that ships with some of these units, especially if they are already using such a software package for other imaging tasks. Although on thick specimens, disk-scanning systems are significantly inferior to CLSM in their optical sectioning capabilities, post-acquisition deconvolution can be an extremely useful adjunct for improving such 4D datasets. In our laboratory, disk-scanning technology has largely replaced both CLSM and multi-photon microscopy for routine 4D data acquisition [Fig. 43.5(A–C)].

As an alternative to laser-based disk-scanning systems, other systems, such as the Atto CARV, use an arc lamp illumination source. When such systems are paired with sensitive EM-CCD cameras, they can often detect sufficient signal for studies on living embryos because, in this case, the fact that they send less excitation light to the specimen than the laser/micro-lens systems can be seen as an advantage [Fig. 43.5(D–F)].

Additional Hardware Improvements Can Increase Acquisition Speed

Additional improvements in the imaging system may also improve acquisition speed. An often-overlooked area in which significant gains have been made in recent years is in optical coatings and objective lens technology. Recent lenses from the major manufacturers have greatly improved transmission, and this has resulted in corresponding improvements in the ability to imaging very thin, small, dim structures in the light microscope.

A second potential improvement involves the use of piezoelectric focus controls, such as those on the PerkinElmer UltraView RS, which can move the objective lens rapidly and with little hysteresis in a step-wise fashion. Similar focus controls have been employed to move the objective continuously in the *z*-direction during a scan. Although this produces optical sections that are slightly tilted relative to the focal plane, one avoids the vibration and specimen movement that occurs when an immersion objective moves rapidly in a stepped manner (Hammond and Glick, 2000).

Finally, significant advances in camera technology allow for unprecedented speed of data collection. Back-thinned CCD cameras, such as those produced by Roper Scientific and Hamamatsu Corporation, and EM-CCD cameras, such as those produced by Andor Corporation (Chong *et al*., 2004), are having a profound influence on low-light microscopy. These cameras provide extremely fast readout with very low read noise and effective quantum efficiency, 2× to 3× higher than the best PMTs. EM-CCD technology in particular yields dramatic improvements in signal-to-noise ratio under ultra low-light conditions and high-speed operation. These cameras make it possible to capture low-read-noise images much more quickly for use in either deconvolution or disk-scanning confocal microscopy.

In the latter case, however, because the current generation EM-CCD cameras rely on frame transfer rather than interline transfer, the integrated charge pattern sweeps across the image field as it is being read out (i.e., the "electronic shutter" does not work so well, especially for short exposures). This creates a new source of artifact: if the position of the scanning disk is not synchronized with the CCD camera exposure and the vertical transfer axis of the CCD is not oriented properly with respect to the motion of the scanning disk, Moiré-type banding patterns are superimposed onto the image [Fig. 43.5(G–J)], particularly when one uses short exposure times. Although the time scale over which events in embryos occur is relatively long compared to the CCD exposure, this interference can nevertheless be a significant problem when attempting to minimize CCD exposure time during 4D acquisition.

Such "banding" can be greatly reduced or eliminated by carefully matching CCD frame transfer rates to the speed of Nipkow disk rotation. The newer CSU22 Yokagawa units permit variable speed disk rotation, which makes such matching easier (Chong *et al*., 2004). With some effort one can also match the fixed scan speed of the older CSU10 scan head, with the exposure times of at least some cameras, such as the iXon (Andor Corp., Belfast, UK). As this moiré problem is unrelated to the operation of the

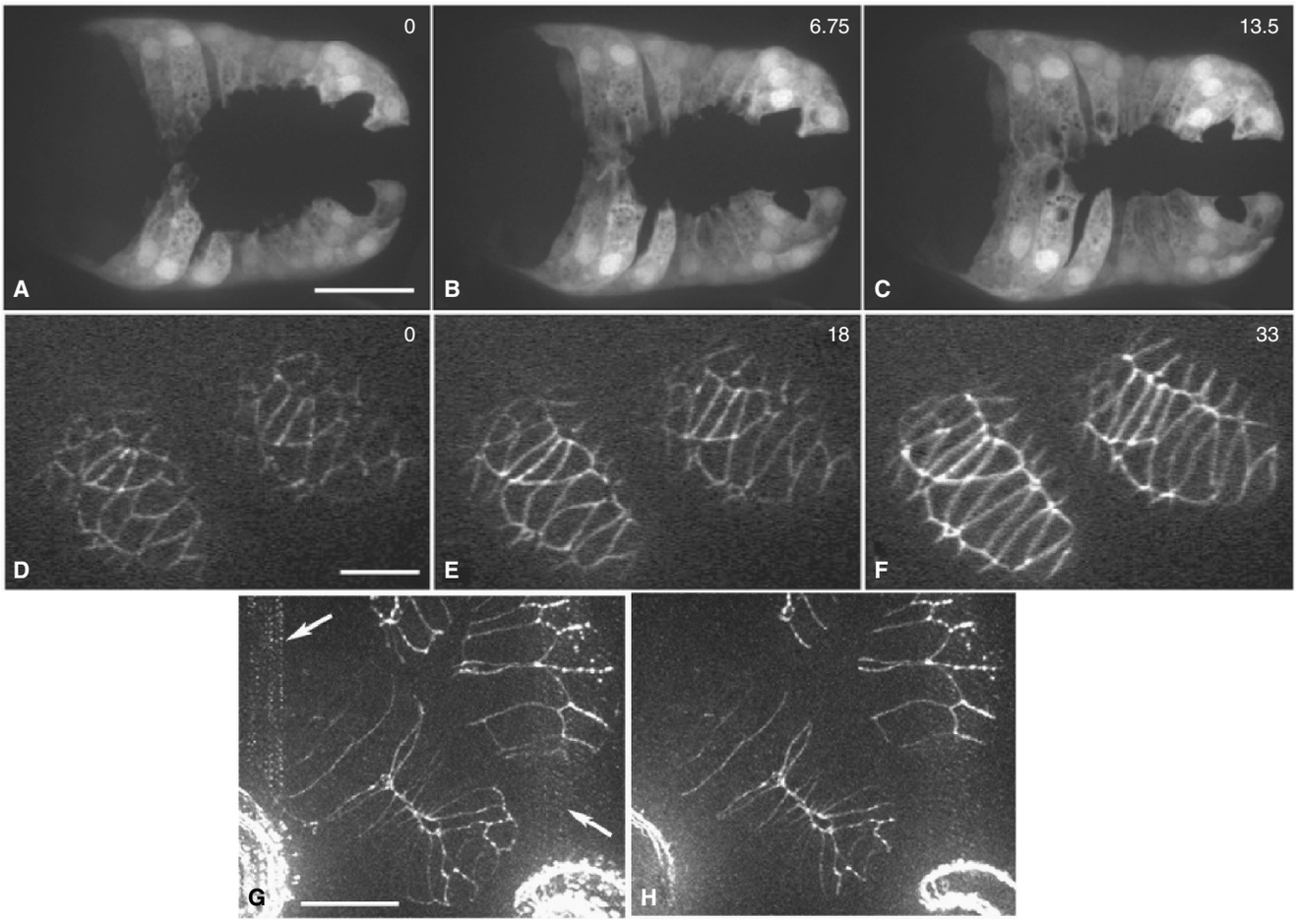


FIGURE 43.5. Disk-scanning microscopes can acquire 4D data quickly. (A–C) Frames from a 4D movie of ventral enclosure in a *C. elegans* embryo expressing a *dlg-1p : gfp* reporter acquired using a PerkinElmer UltraView LCI system equipped with a Hamamatsu Orca II ER CCD camera. Elapsed time in minutes is shown. *z*-stacks were acquired at 50 s intervals, 20 focal planes/stack; acquisition time/image, 300 ms. Fine details of protrusions are visible against a dark background using this particular transcriptional reporter. (D–F) Frames from a 4D movie of dorsal intercalation in a *C. elegans* embryo expressing AJM-1 : GFP, which localizes to epithelial junctions, acquired using an ATTO Carv system and a Roper Cascade B camera. *z*-stacks were acquired at 3 min intervals, 20 focal planes/stack; acquisition time/image, 700 ms. (G, H) A 30-focal-plane *z*-stack of images acquired using the system in (A), but imaged using an Andor iXon EM-CCD camera. Acquisition time/image 15 ms. Despite >30× shorter exposure time, junctional details are clearly visible. During acquisition, stop frame motion of maturing larvae was achieved for individual focal planes, despite their rapid muscle contractions (J. Hardin, data not shown). In (G), all 50 frames of the stack were projected using a maximum intensity procedure. Moiré banding is clearly visible (*arrow*). In (H), the top 30 frames were projected. No banding is visible, because the moiré pattern only became pronounced as the bottom half of the embryo was imaged. Bars = 10 µm.

electron multiplier, it will cease to exist when interline-transfer CCDs with EM readouts are introduced.

LOCALIZING LABEL: STRATEGIES FOR INCREASING EFFECTIVE CONTRAST IN THICK SPECIMENS

Methods for introducing fluorescent probes into living embryos vary from one model system to another. With the exception of fluorescent lipid dyes, fluorescent probes, including dyes and mRNA encoding various fluorescent proteins, are usually introduced into echinoderm, *Xenopus*, and zebrafish oocytes and embryos by microinjection. In other cases, fluorescent protein probes are introduced as transgenes, which are then expressed by the embryo as fluorescently tagged proteins. No matter what the method of introduction, there are several issues that must be addressed by developmental biologists as they use such probes. First, any probe can be susceptible to dominant-negative effects when used at high concentrations; fluorescent protein–tagged mRNAs or transgenes are no exception. Thus, developmental biologists must often balance the need for higher fluorophore concentration with such dominant-negative effects. Second, such effects appear to be system specific. Probes that work well in one system may be unacceptably toxic in another. As one of many examples, the lipid dye FM1-43, which has been used in several studies to label intracellular vesicles in living embryos (see below), causes toxicity to *Xenopus* oocytes, which are ordinarily fairly robust (Bement *et al*., 2003). Thus, as with most imaging experiments in living embryos, trial and error will be unavoidable. Third, in multi-channel experiments, the amounts of each labeled protein may need to be adjusted to avoid additive toxicity or artifactual effects. This issue is particularly important when the two proteins physically interact. Overexpression of such interactors can lead to large, artifactual aggregates within the cells expressing them (J. Hardin and C. Lockwood, unpublished observations).

Addition of Labeled Proteins to Embryos

Direct labeling of proteins or other probes is a tried and true method for introducing fluorescently labeled proteins into living embryos. This approach has worked particularly well for studying very early embryos or oocytes in amphibians (Bement *et al*., 2003) and echinoderms (Jaffe and Terasaki, 2004; Strickland *et al*., 2004). Although falling out of favor in deference to mRNA expression for production of transgenic embryos, direct labeling has the advantage that, unlike injection of mRNA or expression of fluorescently tagged transgenic constructs, there is no lag before expression is evident, and there are no complications involving efficient maternal expression of constructs. This virtue can also be a liability for studying events late in development: turnover of the labeled proteins may attenuate the concentration of labeled protein so severely by the stage of interest that it can be difficult to detect. However, this approach has worked well in some cases, including the study of embryonic neurons in amphibian embryos (Gomez and Spitzer, 1999). On the other hand, production and purification of fluorescently labeled proteins is typically much more difficult than injecting mRNA or making transgenics (at least in some organisms, such as *C. elegans* or *Drosophila*). Moreover, directly conjugated fluorescent proteins must typically be centrifuged at high speed to remove unconjugated label (e.g., 100,000 g). Several companies make prelabeled proteins for study of the cytoskeleton that ameliorate these difficulties, including fluorescently labeled phalloidin and taxol for labeling F-actin, as well as cytoskeletal monomers labeled with fluorophores (Bement *et al*., 2003).

Expressing Green Fluorescent Protein and mRFP Constructs in Embryos Allows Dynamic Analysis of Embryos at Multiple Wavelengths

The discovery and widespread use of GFP as a tag for visualizing gene expression and protein localization within living organisms has revolutionized live embryo imaging (Chalfie *et al*., 1994). GFP (especially the widely used multiply-mutated version known as EGFP) is bright, generally non-toxic, and resistant to photobleaching. The advent of numerous color shifted spectral variants of GFP (Miyawaki *et al*., 2003), including enhanced cyan and yellow fluorescent proteins (ECFP and EYFP, respectively) has allowed multiple fluorescent proteins to be detected simultaneously in living embryos (Hadjantonakis *et al*., 2003), and has made possible techniques such as *in vivo* FRET (see below). Recent identification of a red fluorescent protein from coral (DsRed) allows the fluorescent-protein approach to be extended deep into the red portion of the visible spectrum. Although earlier versions of DsRed were multimeric and hence slow to assemble into a functional fluorophore, multiple mutations have now resulted in a monomeric form of the protein, mRFP1 (Campbell *et al*., 2002), that folds much more rapidly and hence serves as a suitable FP for dynamic events in early embryos. The recent advent of color-shifted variants of DsRed (Shaner *et al*., 2004) will make this family of fluorophores even more useful. We (see Fig. 43.7) and others (Benink and Bement, 2005) have begun using mRFP1 along with EGFP to perform dual-channel imaging of fluorescence, indicating that fluorescent proteins will continue to be the method of choice in genetic systems in which fluorescent-protein-tagged transgenes can be introduced. Ways of introducing fluorescent-protein-tagged constructs into embryos involve system-specific techniques beyond the scope of this chapter; here we make several generalizations about the uses of various strategies for imaging embryos expressing fluorescent-protein-tagged constructs.

Transcriptional Reporters Allow Analysis of Dynamic Processes in Embryos

To developmental biologists, fusing the coding region of EGFP to the regulatory DNA associated with a gene of interest (i.e., GFP reporter constructs) is often used to assess the tissue-specific and temporal patterns of the transcriptional activation of a gene. Such data provides valuable information about how the expression of a gene is regulated. However, such transcriptional reporters can also be invaluable for live embryo imaging for several reasons. First, such reporter constructs result in the expression of GFP in the cytosol; because GFP is fairly small, these reporters are capable of percolating into small volumes within the cytoplasm, including the fine protrusions extended by cells as they migrate (Fig. 43.6). Second, the highly specific expression pattern of some genes allows either many or a very small number of cells to be visualized against a dark background, dramatically improving the effective contrast of the specimen being imaged. In some cases, such effective contrast enhancement can be aided by dual labeling with more general fluorescent counterstains (see below). Third, imaging cytosolic GFP reporters typically does not cause as much photodamage as with GFP translational fusions. Thus, in some cases where a membrane-localized GFP or similar translational fusion construct might be desirable, a cytosolic GFP may be sufficient for tracking cell trajectories or monitoring protrusive activity.

Translational Fusions Allow Analysis of the Subcellular Distribution of Specific Proteins

Using molecular techniques to fuse fluorescent proteins to a peptide or protein sequence has transformed cell and developmental biology by allowing the *in vivo* analysis of intracellular protein dynamics (Lippincott-Schwartz and Patterson, 2003). In addition, however, fluorescent-protein-labeled proteins can serve the developmental biologist by allowing the analysis of cell and tissue movement in 4D. For live embryo work, several such translational fusions are generally useful. Fluorescent-protein-tagged nuclear proteins, such as histone H2B (Megason and Fraser, 2003) can be an effective means by which to track cell positions, in addition to their obvious use in studying nuclear dynamics in embryos. As an indirect readout of cell position without the complexities of fluorescent cell borders, tracking of nuclei can be a useful tool for charting overall cell movements. Cell membrane localized fusions, such as fusions to the GAP-43 membrane-localization signal or the Lck membrane-localization signal to drive membrane localization (Megason and Fraser, 2003) can be used to outline cell membranes. For studying morphogenetic movements in embryos, junction-localized fluorescent proteins are extremely useful. Our laboratory has used junction-localized fluorescent proteins to study epithelial sheet movement in *C. elegans* (Mohler *et al*., 1998; Köppen *et al*., 2001). Others have used moesin :: GFP to analyze *Drosophila* morphogenesis in a similar manner (Edwards *et al*., 1997). Three examples of dual labeling with EGFP and mRFP1 fusions are shown in Figure 43.7.

Translational fusions can, of course, be coupled to highly tissue-specific promoters to yield probes that are both subcellularly localized and expressed in a restricted group of cells. As one example among many, this approach has been used to visualize actin-based protrusions in leading edge cells during dorsal closure in *Drosophila* by driving expression of constructs using the engrailed promoter, which yields well-defined stripes of expression (Jacinto *et al*., 2000).

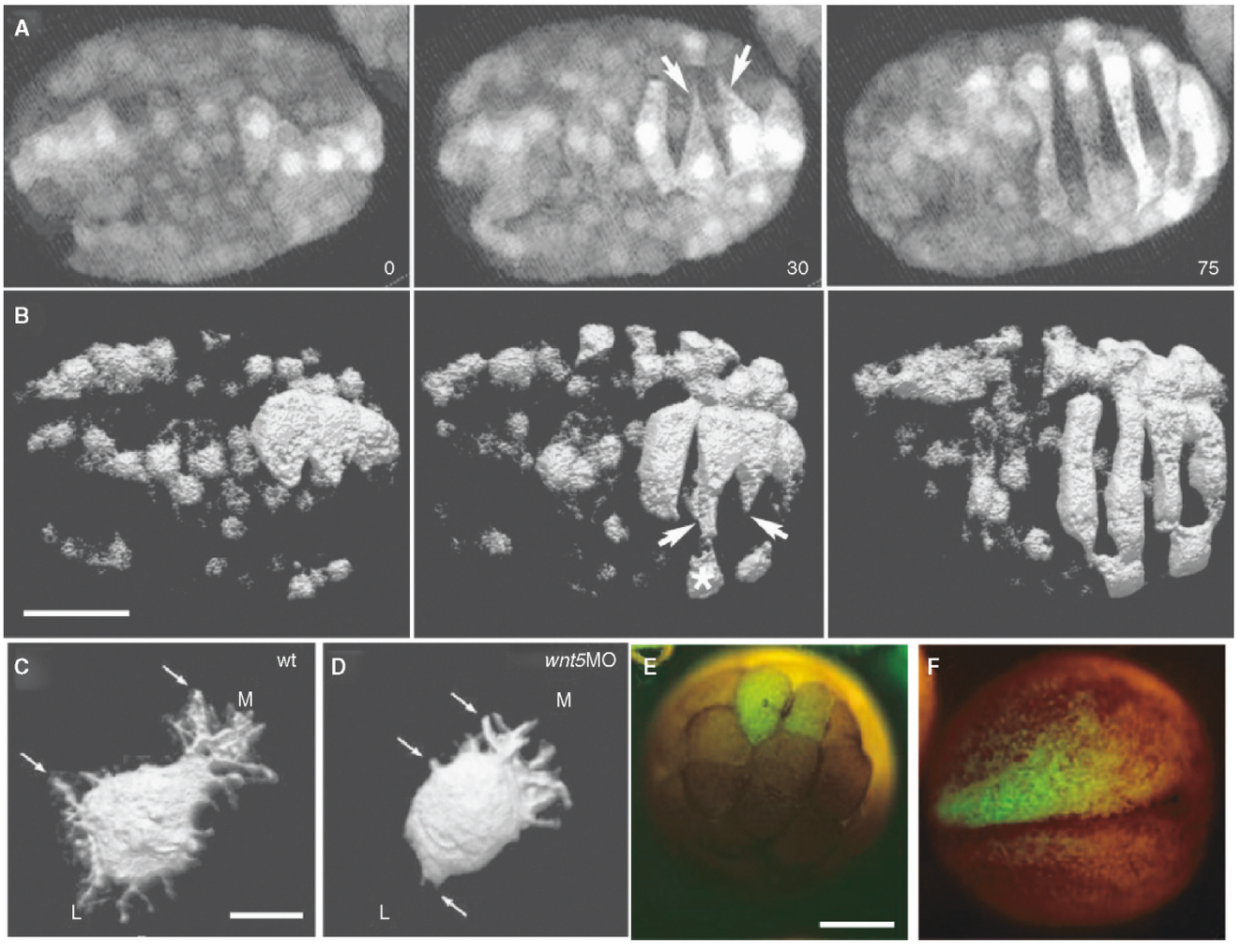


FIGURE 43.6. Cytosolic markers allow imaging of cell motility and cell movement in embryos. (A, B) Frames from 4D movies of dorsal intercalation in *C. elegans* embryos expressing *lbp-1p::gfp*, which is expressed in a subset of dorsal epidermal cells. (A) An embryo imaged using MPLSM (Heid *et al*., 2001) using a Ti:Sa laser and descanning through a Bio-Rad 1024 scanhead. *z*-stacks were subsequently 3D projected using a maximum brightness procedure. (B) A similar embryo imaged using the disk-scanning apparatus described in Figure 43.5(A). The dataset in (B) was subsequently subjected to surface rendering using Volocity software. Fine protrusions are visible in both cases. In (B), it is clear that the protrusions are wedge-shaped in the *z*-dimension, and that the non-dorsal cell (*asterisk*) also produces fine protrusions. Bar = 10 µm. (C, D) Protrusive activity of zebrafish mesodermal cells imaged in wild-type (C) and Wnt5a morpholino injected embryos (D) expressing a combination of cell surface (GAP43::GFP) and cytosolic GFP. Images were acquired using a Bio-Rad Radiance 2000 MPLSM equipped with a Ti:Sa laser; three successive stacks of 120 focal planes each were acquired, one of which is shown here. The resulting images were surface rendered using Volocity software. These cells display oriented protrusive activity. The cell from the morpholino injected embryo displays impaired motility. Bar = 10 µm. (E, F) Quantum dot (QD) labeling of cells in an early *Xenopus* embryo. QD micelles were injected into an individual blastomere during very early cleavage stages. Between 1.5 and 3 nL of a 2.3 µ*M* suspension of QDs were injected, corresponding to 2.1 to 4.2×10^9 injected particles per cell. (E) Injection of one cell in an eight-cell-stage embryo resulted in labeling of individual blastomeres. (F) The daughter cells of the injected blastomere are labeled at the neurula stage. Embryos were imaged with Chroma filter set 41015 (wild-type GFP longpass emission with a 50 nm wide bandpass excitation centered at 450 nm) mounted on a Zeiss fluorescence microscope. Bar = 500 µm. [(A) is from Heid and colleagues (2001); (B) is courtesy R. King and T. Walston, University of Wisconsin; (C, D) are from Kilian and colleagues (2003); (E, F) are from Dubertret and colleagues (2002), used by permission.]

Using Selective Labeling to Reduce the Number of Labeled Structures

Dextran Labeling

Injecting fluorescent dextrans into the blastomeres of early embryos has a long history in developmental biology (e.g., Gimlich, 1991). Focal injections allow the progeny of injected cells to be visualized against an unlabeled background during later development, a process that permits one to develop fate maps. Live 4D imaging using confocal or multi-photon microscopes allows the progeny of such injected cells to be followed with remarkable clarity. For example, the cells shown in Figure 43.10(D–F) are the progeny of blastomeres of a zebrafish embryo injected early in development, and have been imaged at high resolution and followed in 4D space.

Quantum Dots

Fluorescent semiconductor nanocrystals, or quantum dots (QDs), have the potential to be useful for long-term observations via confocal and (especially) multi-photon microscopy as an alternative

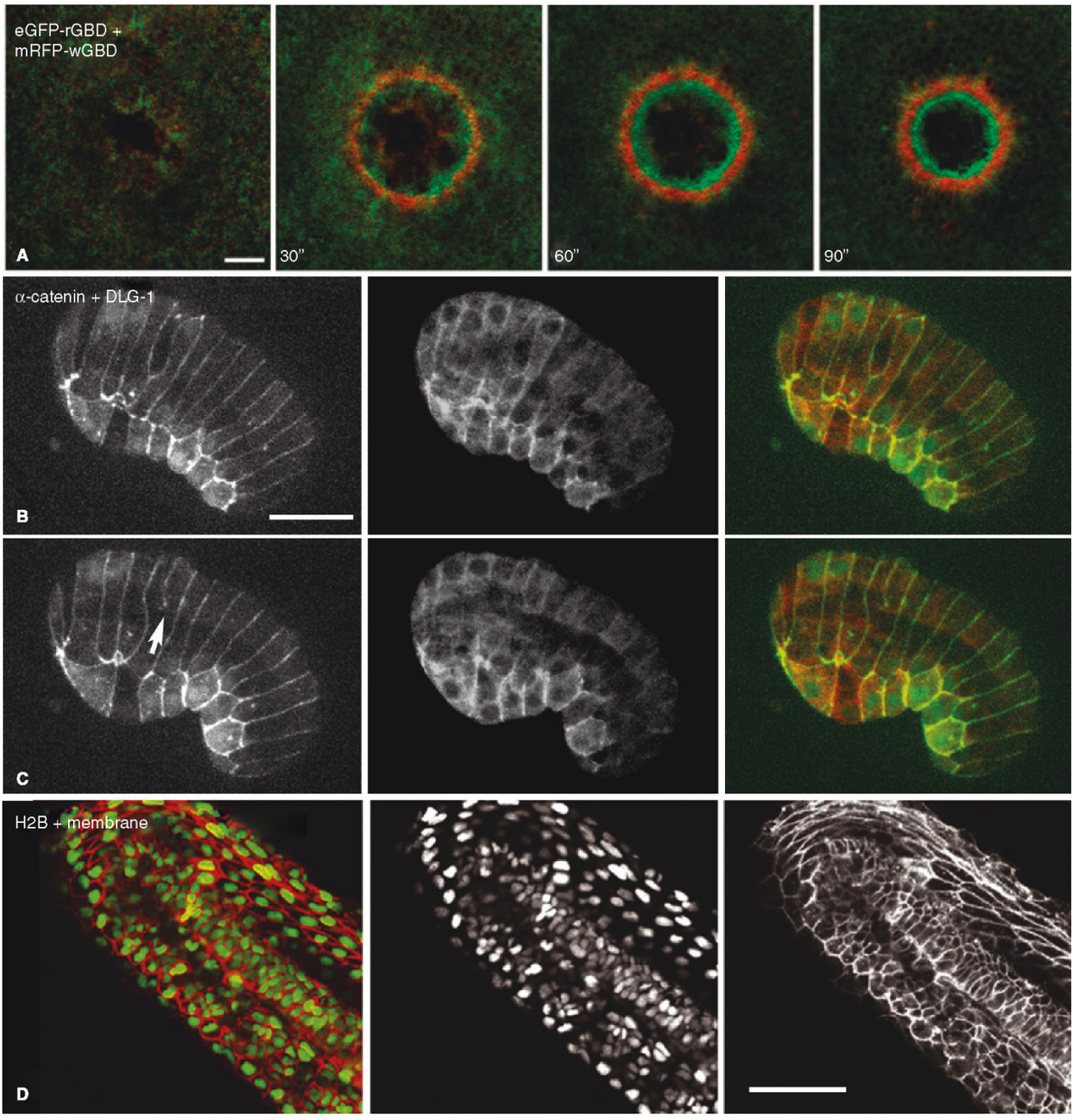


FIGURE 43.7. Simultaneous imaging of GFP- and mRFP-tagged proteins in living oocytes and embryos. Three different examples of using dual-channel imaging to detect GFP- and mRFP translational fusions. (A) Frames from a movie showing that RhoA (detected using eGFP-rGBD; green) and Cdc42 (detected using a fusion between mRFP and a protein fragment that binds active Cdc42; red) segregate into discrete zones during wound healing in a *Xenopus* oocyte (time in seconds). Imaging was performed as in Figure 43.1(A). Bar = 10 µm. (B, C) Frames from a movie of elongation of a *C. elegans* embryo expressing DLG-1 :: mRFP and HMP-1/α-catenin :: GFP (left) DLG-1 :: mRFP; (middle) HMP-1 :: GFP (right, overlay). Loss of junctional material occurs at sites where epidermal cells are fusing (*arrow*). (B, C) are 75 min apart. Imaging was performed as in Figure 43.6(A). Bar = 10 µm. (D) Dorsal–lateral view of the tail of 24 h living zebrafish embryo injected with RNA for Histone H2B–EGFP and membrane-localized mRFP1. (Left) Both channels together. (Center) Histone H2B–EGFP channel. (Right) Membrane mRFP1 channel. The nuclei can be discerned even in areas where they are closely packed such as the spinal cord (running along middle of the tail). Bar = 100 µm. [(A) is from Benink and Bement (2005); (B, C) are courtesy C. Lockwood, University of Wisconsin; (D) is from Megason and Fraser (2003), used by permission.]

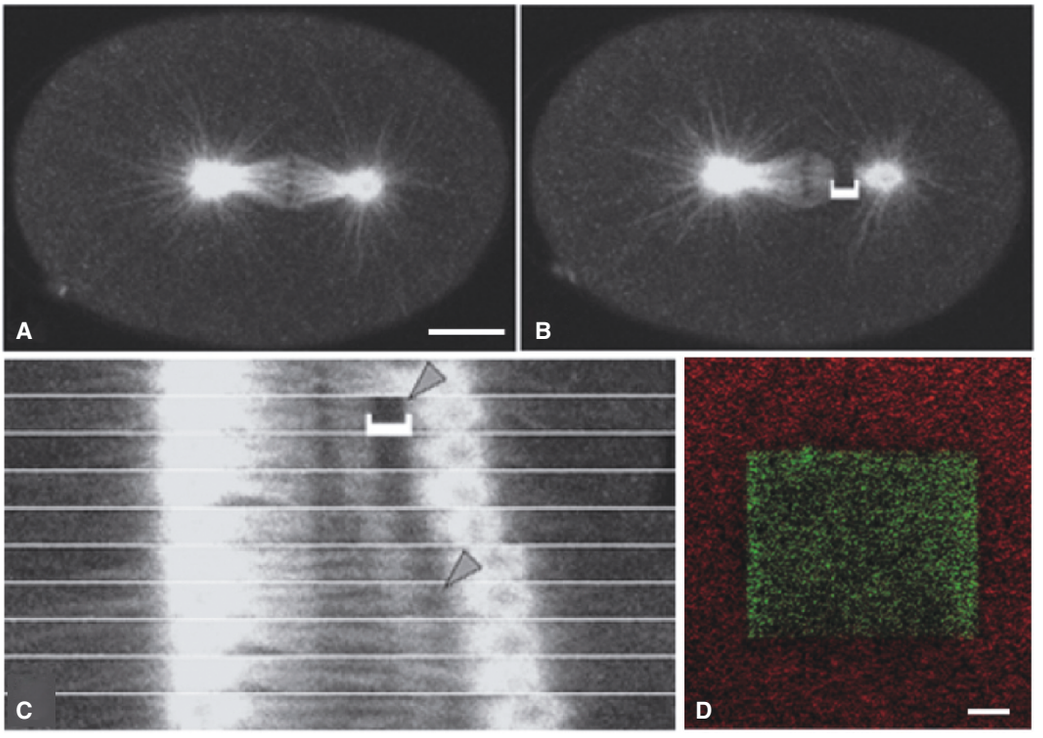


FIGURE 43.8. Using fluorescence recovery after photobleaching (FRAP) and photoactivatiable GFP in embryos. (A–C) FRAP of GFP-tagged microtubules in a living *C. elegans* zygote. Time-lapse images of embryo expressing β-tubulin::GFP (A) in which a short region of the posterior spindle microtubules was photobleached during anaphase onset (B, *bracket*). The kymograph below (C) follows the movement of the photobleached region (indicated by *gray arrowheads*). Frames were acquired at 7 s intervals using a Zeiss LSM 510 LCSM. For photobleaching, a selected region of interest was photobleached using 50 to 150 1s scans of 100% 488 nm laser power. Bar = 10 µm. (D) Photoactivation of PA-GFP at the surface of a *Xenopus* oocyte using a LCSM. A *Xenopus* oocyte injected with mRNA encoding mRFP- (red) and PA-GFP tagged forms of a synthetic F-actin binding peptide was scanned repeatedly with the 488 nm line from a Bio-Rad 1024 LCSM to photoactivate PA-GFP. Bar = 10 µm. [(A–C) are from Labbe and colleagues (2004); (D) is courtesy of B. Burkel and W. Bement, University of Wisconsin.]

to fluorescent dextrans for lineage tracing. Compared with organic dyes and fluorescent proteins, QDs offer several advantages (Gao *et al*., 2005; Michalet *et al*., 2005). First, the manufacturing process yields QDs with highly specific composition- and size-dependent emission characteristics that are tunable throughout essentially the entire visible and NIR spectrum, all excitable by a single wavelength. Second, QDs have a very high absorption cross-section. As a result, a very small number of QDs are necessary to achieve a detectable signal; in some cases it has been possible to detect the fluorescence of single or small numbers of QDs. Third, QDs have a large Stokes shift, which may be an advantage in situations where autofluorescence of the tissue would mask the emission signal of fluorescent dyes. Finally, the high electron density of QDs allows them to be viewed via TEM, making them useful for correlative studies (see Chapter 49, *this volume*).

Although QDs have been used without derivatization, typically they are encapsulated in a polymer shell. Dubertret and colleagues encapsulated QDs within PEG-derivatized phospholipid micelles, and injected them into early blastomeres in *Xenopus* embryos (Dubertret *et al*., 2002). They found that the QDs were extremely stable, and when injected at sufficiently low concentrations caused no toxicity [Fig. 43.6(E,F)]. Although this technology is still emerging, QDs have tremendous promise in the future for use in living embryos under prolonged observation.

Photobleaching

GFP can be used very successfully in studies involving fluorescence recovery after photobleaching (FRAP) and related technologies (Lippincott-Schwartz *et al*., 2003), which is easily done via repeated scanning of a selected area in the LSCM. Although in some cases, it is likely that photobleaching will result in unacceptable photodamage (see Chapter 49, *this volume*), it has been used successfully in several experiments with live embryos (e.g., Benink *et al*., 2000; Labbe *et al*., 2004) [Fig. 43.8(A–C)].

Photo-Activatable Dyes and Photo-Activable GFP

Another technique for marking small groups of cells involves the use of photo-activatable, or caged, fluorophores. Such fluorophores only fluoresce after the caging group is removed by photocleavage at the appropriate wavelength, typically in the violet or near ultraviolet (UV). Caged fluorescein dextran has been used for fate mapping in both *Drosophila* (Girdham and O'Farrell, 1994) and zebrafish (Kozlowski *et al*., 1997). Although widefield imaging was used to track the resulting fluorescein fluorescence, confocal and multi-photon imaging are also well-suited to this approach.

More recently, a photoactivatable variant of GFP (PA-GFP) was described (Patterson and Lippincott-Schwartz, 2002). PA-GFP

only fluoresces after photo-activation via intense irradiation with 413 nm laser light, or by exposure to a standard mercury arc. The fluorescence of PA-GFP has been reported to increase at least 60× after activation *in vivo*. Once activated, it appears to be as stable as other GFP variants (Patterson and Lippincott-Schwartz, 2002). Recently, PA-GFP was used to follow local movements of, and recruitment of actin in, wounded *Xenopus* oocytes [Fig. 43.8(D)]; in this case, PA-GFP was photoactivated by a brief pulse of laser light from the standard 488 nm line of a Bio-Rad 1024 CLSM, indicating that all steps, from photo-activation to imaging, can be performed using 4D CLSM (B. Burkel and W. Bement, personal communication). The use of PA-GFP in the live imaging of embryos will undoubtedly become more widespread in the immediate future.

An alternative to PA-GFP is the use of kindling proteins (Chudakov *et al*., 2003). This approach relies on a chromoprotein, asCP, isolated from the sea anemone *Anemonia sulcata*. asCP is not fluorescent until it is irradiated , or kindled, using intense green light; kindled asCP then emits at 595 nm. A mutant form of asCP (KFP1) has been produced that undergoes irreversible kindling when irradiated with intense green light (e.g., brief irradiation at 30% power using a 543 nm laser on a Zeiss LSM 510 CLSM), but can be reversibly kindled when irradiated at lower power (e.g., 5% power on the same apparatus). Reversibly kindled KFP1 can be quenched by irradiation with blue light (using the 458 nm line of the same device at 1% power). Like original forms of DsRed, KFP1 currently requires multimerization for function. If a monomeric form of KFP1 can be produced, it may have properties which will be more generally useful for imaging living embryos beyond current applications, which only involve fate mapping (Chudakov *et al*., 2003).

Directly Conjugated Antibodies for Visualizing the Extracellular Matrix

Although extracellular matrix (ECM) components have been successfully visualized by making GFP-tagged translational fusions, another approach for localized labeling of the ECM is the injection of antibodies specific for particular components directly conjugated to fluorophore. This approach has been used successfully to visualize fibrillin in the chick embryo (Czirok *et al*., 2004), and fibronectin in *Xenopus* embryos (L. Davidson, R. Keller, and D. Desimone, personal communication). Using this approach, labeled fibrils can be imaged for long periods of time to track their movement during morphogenesis (Czirok *et al*., 2004).

Bulk Vital Labeling Can Enhance Contrast

While the use of GFP, mRFP1, and their spectral variants has led to huge advances in our ability to image embryos, these approaches have some limitations. First, producing DNA constructs for expressing GFP-tagged versions of proteins within embryos requires multiple cloning steps, some of which can be arduous, especially for large genes. Second, when introduced as mRNA or as transgenes, these proteins are often over-expressed, and care must be taken so that over-expression artifacts do not compromise the final results. Third, it is often difficult to target GFP- or mRFP-tagged constructs to a broad spectrum of subcellular compartments, although there are several recent examples in which GFP has been targeted to membranous organelles (Poteryaev *et al*., 2005). Finally, in organisms such as *C. elegans*, it is difficult to introduce mRNAs by direct injection. This can make it hard to achieve high levels of expression in the germline, with the result that exogenous promoters must sometimes be used to generate enough expression to visualize the protein of interest in the early embryo (Strome *et al*., 2001).

One solution to these problems is to use fluorescent vital dyes. Such dyes have the virtue that they can label many cells in the embryo simultaneously, partitioning preferentially into specific cellular structures based on their chemical properties. Several dyes have proven useful for this purpose:

1. **Unconjugated BODIPY and BODIPY-ceramide dyes**: "BODIPY" is a trade name for a class of photostable, neutrally charged, boron-containing diazaindacene fluorophores that span much of the visible spectrum (Molecular Probes, 2004). Several unconjugated BODIPY fluorophores, such as BODIPY 505/515, have been used as vital fluorescent stains for zebrafish embryos, where they localize to intracellular yolk platelets and in intercellular spaces. BODIPY-ceramide has been used to label the plasma membrane and endomembranes [Fig. 43.9(A–C)]. Embryos can be bathed in these dyes, allowing most cells in the embryo to be stained rapidly (Cooper *et al*., 1999).

2. **FM4-64, FM1-43, and other lipophilic membrane dyes**: FM4-64 is a red fluorescent membrane dye that is useful for outlining plasma membranes. Such lipophilic dyes work well for bulk labeling of plasma membranes in a variety of species. Like DiI, multi-photon imaging of FM4-64 requires the use of a Nd:YLF laser. Using such technology, dynamic membrane-associated events have been followed during *C. elegans* development using 4D imaging (Mohler *et al*., 1998) [Fig. 43.9(D)]. An alternative is FM1-43, a water-soluble, styrylpyridinium dye that more generally labels membranous structures, likely by inserting into the outer leaflet of the plasma membrane, where it becomes highly fluorescent. FM1-43 has been used to study exocytosis during echinoderm fertilization (Terasaki and Jaffe, 2004) and to study vesicular trafficking in early *C. elegans* embryos (Skop *et al*., 2001) [Fig. 43.9(E)].

3. **DiI derivatives**: The lipophilic carbocyanines DiI [DiIC18(3)], DiO [DiOC18(3)], DiD [DiIC18(5)], and DiR [DiIC18(7)], are weakly fluorescent in water but highly fluorescent and very photostable when incorporated into membranes. DiI, DiO, DiD, and DiR exhibit distinct orange, green, red, and infrared fluorescence, respectively, thus facilitating multi-color imaging (Molecular Probes, 2004). By varying the number of carbons attached to the fluorophore, the hydrophobicity of the dye can be varied. The slightly less lipophilic DiIC12(3), DiIC16(3), and DiOC16(3) are sometimes easier to dissolve and load into membranes than their C18 homologs (Molecular Probes, 2004), but can also yield more non-specific labeling than their longer-chain counterparts (J. Hardin, unpublished observations). Longer carbon chains result in poor solubility, even in the presence of a carrier such as DMSO. The result is that, in saline media or seawater, the dye forms tiny crystals. Cellular structures are only labeled when a crystal physically touches a membranous structure. In the case of sea urchin embryos, for example, incubation of embryos with DiC_{16} for 5 min results in a salt-and-pepper pattern of cell labeling that allows individual cells to be followed against a dark background. Multi-photon imaging of labeled cells is possible using a Nd:YLF laser operating at 1047 nm [Fig. 43.9(F,G)].

4. **BODIPY TR, methyl ester dye**: BODIPY TR, methyl ester dye, readily crosses cell membranes and localizes to membrane-bound organelles. Because the dye does not localize strongly to the plasma membrane, BODIPY TR, methyl ester is useful for determining the position of the nucleus and the shapes of cells, and for outlining whole tissues. The emission maximum

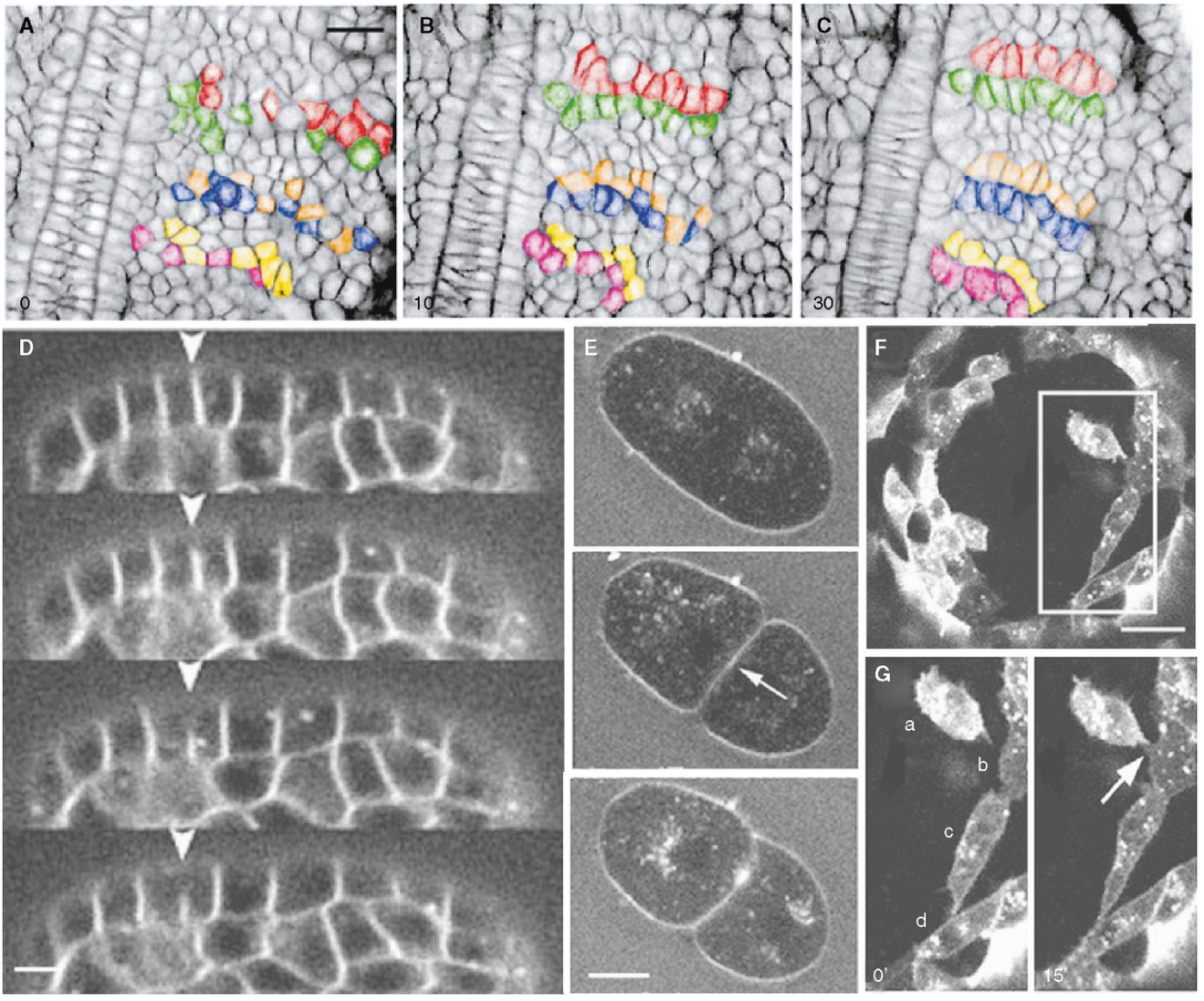


FIGURE 43.9. Bulk labeling with dyes in living embryos. Four different examples of the use of bulk-dye labeling in living embryos. (A–C) Time-lapse sequence showing somitogenesis in a one-somite stage zebrafish embryo (dorsal view, anterior at top). Embryos were vitally stained with the fluorescent lipid Bodipy-C5 ceramide and observed using a Bio-Rad MRC-600 CLSM. The elapsed time (min) is indicated in each panel. Individual somitic cells are colorized for clarity. As somites form, intercalation of cells forces colorized and non-colorized cells to rearrange, changing the overall shape of the tissue. Bar = 20 µm. (D) Live MPLSM imaging of epidermal cell fusions in the *C. elegans* embryo. Frames are 5.5 min apart. Disappearance of lateral membranes (*arrowhead*) in an optical cross-section of an embryo labeled with FM4-64 indicates cell–cell fusion is occurring. Images were acquired using a 1047 nm Nd : YLF laser and a Bio-Rad MRC-600 scan head with no pinhole inserted in the optical path. Bar = 5 µm. (E) Plasma membrane dynamics in the early *C. elegans* embryo studied using FM1-43. MPLSM time course of a single focal plane taken from an embryo labeled with FM1-43 during cytokinesis. Elapsed time is shown in minutes. Cytokinetic furrow formation completed at 3.0 min. Membrane accumulates at a specific focal spot (*arrow*, 4 min), and continues to accumulate in successive time points. Bar = 10 µm. (F–G) Cell rearrangement at the blastopore of a sea urchin embryo visualized using $DiIC_{16}$. (F) Blastopore view of a $DiIC_{16}$ normal late-gastrula embryo. The dark area in the center is the blastopore surrounded by $DiIC_{16}$-labeled cells at the blastopore lip; the inset is enlarged in (G, H). (G, H) Frames acquired 15 min apart showing movements of cells. Cell **a** has produced a protrusion (*arrow*) and made contact with cell **b**, while cells **c** and **d** have shifted positions. Bar = 10 µm. [(A–C) are from Henry and colleagues (2000); (D) is from Mohler and colleagues (1998), used by permission.]

of BODIPY TR, methyl ester is at ~625 nm, making it an excellent counterstain for eGFP (emission maximum ~508 nm; Cooper *et al*., 2005), one that produces little spectral bleed-through of GFP fluorescence into the BODIPY TR channel. The excitation curves of the two fluorophores are well separated as well, making them suitable for dual-channel confocal imaging [Fig. 43.10(A–C)].

5. **Scatter labeling using lineage tracers**: When injected into blastomeres that generate a large sector of the embryo, lineage tracers, such as fluorescent dextrans, can serve as an effective counterstain. This technique has been used effectively in zebrafish embryos [Fig. 43.10(D–G)].

SEEING IN SPACE: STRATEGIES FOR 4D VISUALIZATION

To one accustomed to normal, 2D, widefield fluorescent microscopy, the images presented by any of the 3D microscopy methods mentioned above can seem such an improvement that many are tempted simply to page through the planar images, feeling perhaps that the time spent to make a proper 3D or 4D rendering would be better spent obtaining more data. However, this temptation should be avoided, because 3D reconstructions provide wonderful new perceptual insights into embryogenesis.

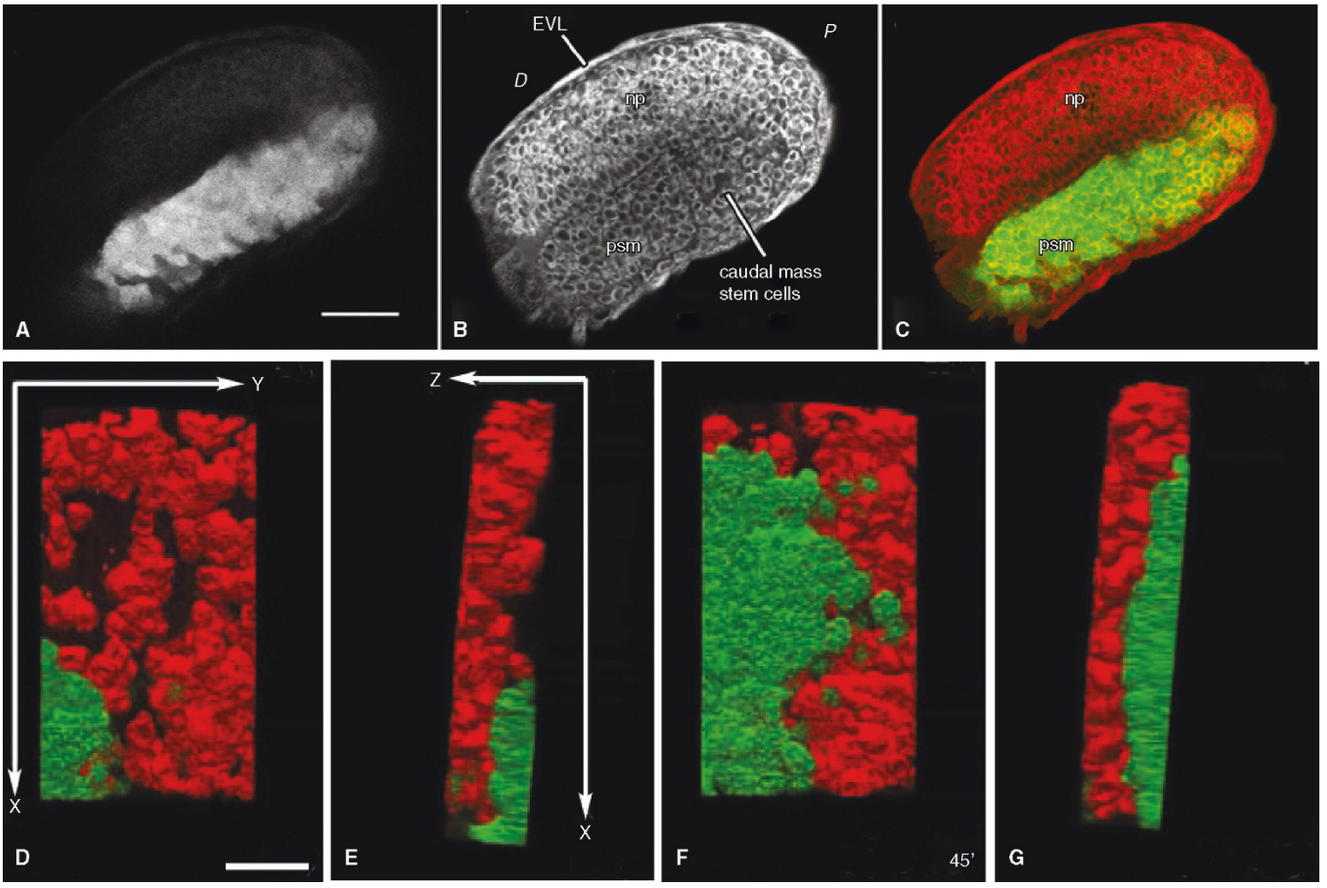


FIGURE 43.10. Counterstains can improve visualization of GFP-expressing cells in embryos. (A–C) BODIPY TR methyl ester counterstaining in a living zebrafish embryo, imaged using a Bio-Rad MRC-600 CLSM. (A) Tail rudiment of a tbx6-GFP transgenic, 19-somite embryo (lateral view). GFP is expressed in the caudal mass stem cells. D, dorsal; P, posterior. (B) BODIPY TR methyl ester dye fluorescence. Loosely organized mesenchymal stem cells join cells in the posterior limit of the presomitic mesoderm (psm). Np, neural plate. (C) Merge. Scale bar = 100 µm. (D–G) Counterstaining using fluorescent dextran. Zebrafish embryos expressing GFP (green) under the control of the goosecoid (gsc) promoter in prechordal plate precursor cells were scatter-labeled with rhodamine (red) in epiblast cells overlying the presumptive prechordal plate and followed in 3D over time by dual-channel confocal microscopy using a Bio-Rad Radiance 2000 CLSM. Surface renderings were performed using Volocity software. gscGFP embryos at shield stage (D, E; E is a rotated view of D) and 45 min later (F, G). In all pictures, anterior is to the top and posterior to the bottom. Bar = 50 µm. [A–C are from Cooper *et al.* (2005); D–G are from Ulrich *et al.* (2003). Used by permission.]

One of the challenges of 4D live imaging of embryos is visualizing the resulting datasets in meaningful ways. Although these challenges are not unique to embryos, the widespread use of 4D imaging in developmental biology requires efficient ways to navigate through 4D datasets, to project or render them as 2D + time or 3D + time datasets, and to provide compiled datasets to other researchers in a portable, compact format.[5] As an example, consider the embryo in Figure 43.11, which expresses a GFP-tagged protein that localizes to epithelial junctions, and has been imaged using two-photon microscopy (Köppen *et al.*, 2001). Images acquired at different focal depths provide simultaneous information about structures throughout the thickness of the embryo [Fig. 43.11(A,B)], but without any sort of projection or reconstruction, it is difficult for the typical student or researcher to mentally manipulate information from each of the focal planes simultaneously.

Depicting Embryos in Time and Space: 2D + Time Versus 3D + Time

While 4D confocal datasets can yield powerful views of single focal planes in embryos over time, examination of such datasets immediately presents a challenge: single optical planes contain a limited amount of spatial information along the imaging axis. Thus, a key challenge in 4D confocal imaging of embryos is navigating through the raw 4D dataset quickly and easily (i.e., up and down within a single time point, and a single plane across time points). The challenge extends beyond navigation through the raw

[5] Older, platform-specific software solutions for compiling and browsing 4D datasets have been described (Mohler, 1999). More recently, several platform-independent solutions have emerged; several make use of the extensible plug-in architecture of ImageJ (http://rsb.info.nih.gov/ij/). These include the HyperVolume Browser plug-in by P. Pirrotte and J. Mutterer (http://rsb.info.nih.gov/ij/plugins/hypervolume-browser.html), which allows a folder of images collected as a 4D dataset to be played back within RAM. A solution that is much less RAM-intensive is to compile 4D datasets into QuickTime movies; such movies have the tremendous advantage that they are portable, and can be played back on rather unremarkable computer hardware. I have written a Java-based software suite that fulfills this purpose within ImageJ, including a browser to preview 4D datasets before compression (Browse4D), a compressor (QT4D Writer), and a viewer (QT4D Player). The suite is available for download at http://worms.zoology.wisc.edu/QT4D.html.

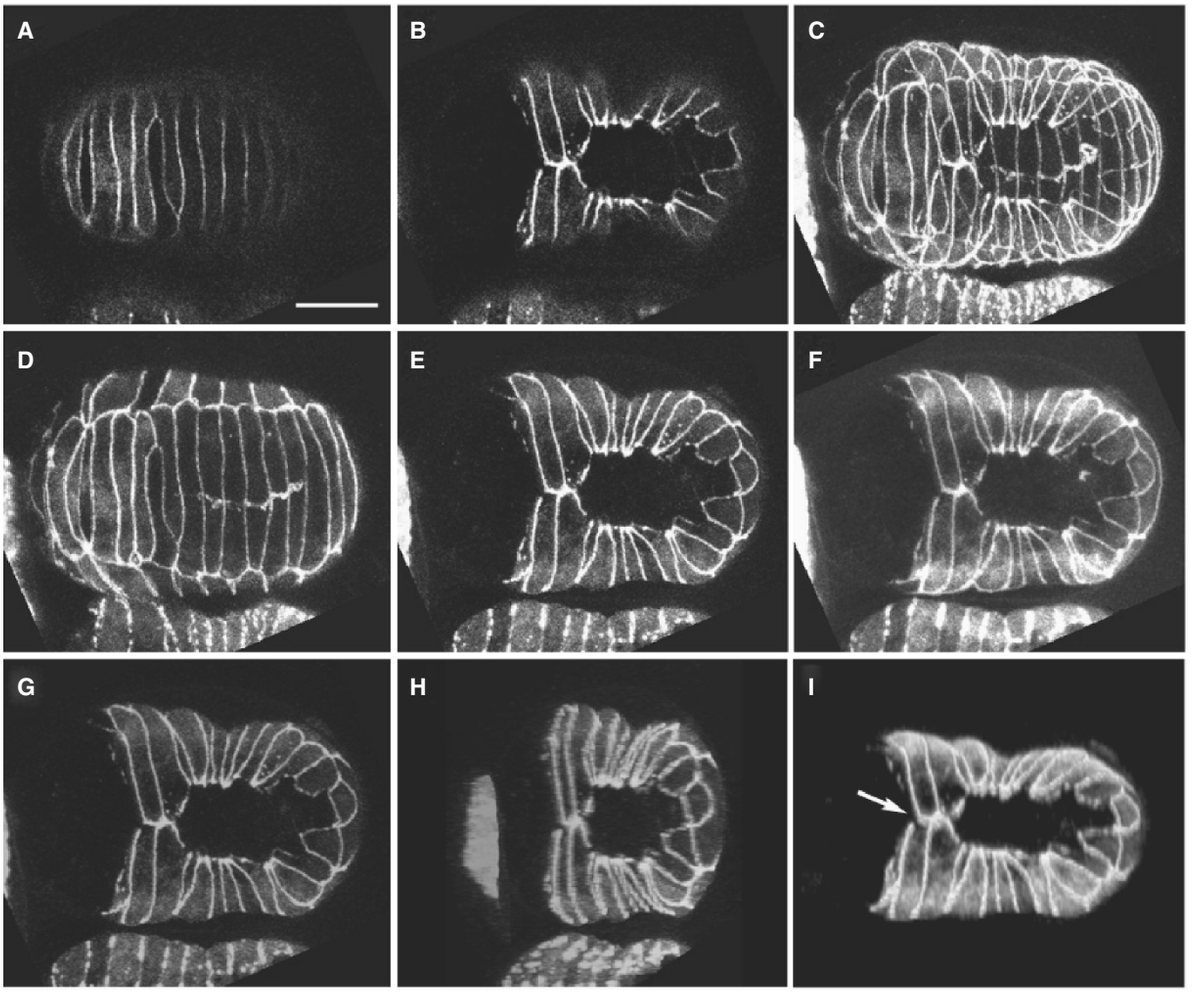


FIGURE 43.11. Using projections can simplify viewing of three-dimensional embryos. (A) Single *C. elegans* embryo expressing DLG-1:GFP (a protein that localizes to epithelial junctions) imaged using MPLSM. Thirty focal planes spaced at 1 µm were acquired. (A) A focal plane deep within the specimen (focal plane 27), showing the dorsal epidermis. (B) A focal plane near the coverslip (focal plane 5), showing the ventral epidermis from the same embryo. (C) A maximum intensity, 2D projection of all 30 focal planes allows visualization of most structures, but material from the ventral surface obscures dorsal structures. (D) A maximum intensity, 2D projection of focal planes 17 to 29, effectively visualizing dorsal structures. (E) A corresponding ventral-only projection (focal planes 3–10). (F) Focal planes 3 to 10 projected using an average intensity projection, followed by contrast enhancement. (G) A 3D projection of focal planes 3 to 10 performed using ImageJ, using the brightest point method, with 0° of rotation. (H) Same data set rotated 50° around the *y*-axis. I. Same dataset visualized as a voxel-based projection using Volocity. The arrows point to the ventral midline, where it is clear that epidermal cells lay down a midline septum of some thickness. Bar = 10 µm.

4D datasets, however. To image the entire embryo or a spatial subset of the 4D dataset, the embryo must be rendered at each time point in such a way that information from multiple focal planes is displayed over time.

There are two common strategies for displaying typical 4D datasets. The multiple optical sections from an image stack can be projected along the *z*-axis to form a 2D dataset, thereby flattening the 3D data (2D + time). Alternatively, the voxels of each original 3D volume can be rendered using a number of different algorithms (3D + time) and then these renderings can be linked to form a movie. In the 2D + time approach, the 3D spatial information in the specimen is lost, but the predominant features of the 3D volume are represented in a format that is computationally less demanding. 2D + time strategies are particularly effective for displaying information from a volume that is relatively thin along the *z*-axis [Fig. 43.11(D–F)]. If most cellular movement occurs in a plane or within a few optical sections, this approach is often the best for qualitative visualization of important details in the dataset.

Some software packages, such as the UltraView software provided with PerkinElmer disk-scanning microscopes, allow adjustable selection of a specific subset of focal planes for projection over time. This provides an animated movie of the equivalent of a thick optical slab over a specific range of *z*-positions within the dataset, but with an important difference: unlike an actual optical thick section, particular features within the slab are still seen distinctly. Many other software packages, including ImageJ, allow projection of single *z*-series, and permit the writing of plug-ins or macros that provide semi-automated production of projected 2D + time datasets.

Various algorithms can be used to project a stack of optical sections (see Chapters 14 and 15, *this volume*). Developmental biologists typically wish to view the readout of the prominent fluorescent details within a volume more directly. To do this, two

sorts of projection strategies are employed: maximum-intensity and average-intensity projections. The maximum-intensity algorithm queries the intensity of a pixel (or neighborhood of pixels) at a given *x*,*y*-position in the projected image, and selects the brightest pixel for display at that position along the line of projection within the image stack.

Maximum-intensity projections [Fig. 43.11(C–E)] are typically the favorite of developmental biologists, because they emphasize the brightest details in the volume, and these are often the most interesting (see Chapter 14, *this volume*). One weakness of maximum-intensity projections is that they are susceptible to artifacts from noise in individual optical sections within the stack. We have found that in such cases, applying standard Gaussian filters can significantly improve the starting image. In general, however, the best projections begin with images that have high intrinsic signals. Another drawback of maximum-intensity projections is that, because they deliberately emphasize small but bright fluorescent structures, they are not really suitable for quantification and they also tend to make near features obscure other features inside the data volume.

The average-intensity projection algorithm sums all of the pixel intensity values along a projection through the stack, calculates the average pixel value, and displays that value at the corresponding position in the projected image. Average intensity projections are less noisy, and are typically considered to produce a more quantitatively accurate representation of the data. Because calculating an average along a projection line that contains many zero intensity pixels reduces the visible contrast of such projections, the results should be viewed using a high contrast look-up table to yield results that are similar to those of maximum intensity projections [Fig. 43.11(F)].

Three-dimensional representations of 4D live embryo data (i.e., 3D + time) can be produced in one of two ways. In the first, less computationally demanding method, rotated 3D projections of image stacks are first produced using a variety of algorithms [Fig. 43.11(G,H)]. Such simple renderings can be extremely useful for identifying the 3D relationships between structures within embryos.[6] The second method, real-time, voxel-based rendering, is much more computationally demanding; for large datasets, current computing hardware accessible to the average laboratory does not permit on-demand, true real-time manipulation of the raw 4D dataset. However, once datasets are rendered, various rendering software suites permit rotation, contrast and brightness adjustment, etc., of the dataset, thereby permitting some direct manipulation of the dataset by the user [Fig. 43.11(I)]. Rendered datasets can provide striking three-dimensional views of structures within embryos (see Chapter 14, *this volume*, for further details).[7] Figures 43.1(A), 43.6(B–D), 43.7(A), 43.8(A), and 43.10(D–G) all used Volocity (Improvision, Coventry, UK) for 4D rendering. 3D + time approaches are well suited to situations in which a specimen is thick relative to its other dimensions. If the process being studied involves extensive movements of cells or relevant features along the *z*-dimension, 3D + time rendering is the method of choice.

The decision to use 2D + time versus 3D + time strategies to depict living embryos depends on several considerations. If the original raw 4D dataset does not need to be retained, 2D + time datasets require much less storage space than true 4D datasets, because they compress the data to 1/*n* its original size, where *n* is the number of focal planes in each stack. As DVD optical drives become ubiquitous, however, saving storage space is becoming less important. A second, more important practical consideration is the time required to render 3D + time datasets. For the typical end user in a developmental biology laboratory, the processing power require for ultrafast rendering of voxel-based data is financially difficult. For more typical hardware configurations, rendering of volumes from 4D datasets can take a few minutes to hours, depending on the method of rendering, the software used and the size of the original 4D dataset.

OTHER USES FOR CONFOCAL AND MULTI-PHOTON MICROSCOPY IN IMAGING AND MANIPULATING EMBRYOS

Multi-Photon–Based Ablation

Galbraith and Terasaki (2003) showed that the Ti : Sa laser in typical multi-photon microscopes can be used to cause localized damage within unlabeled cells of a sea urchin embryo via a multi-photon process (see Chapter 38, *this volume*). To intentionally generate damage, laser power was increased 10-fold, and pixel dwell time was increased 70×, that is, there was a 700× increase in total exposure. Because the multi-photon absorption events are so localized, and because the longer IR wavelengths involved penetrate more deeply into a specimen, they can produce tissue disruption at depths not possible with standard ablation laser systems. Multi-photon–induced damage is characterized by an autofluorescent scar, which allows monitoring of damage and identification of the wound site as development proceeds (see Chapter 38, *this volume*) [Fig. 43.12(A–D)].

Fluorescence Resonance Energy Transfer

The use of fluorescence resonance energy transfer (FRET) in embryos has not been reported in published journal articles, but this will likely change in the near future. FRET is becoming

[6] In addition to the built-in functions within ImageJ, which perform maximum-brightness, nearest-point, and average intensity-based 3D projections, several freeware solutions exist for rendering single time points as rotational projections within ImageJ. These include VolumeJ, by M. Abramoff (http://bij.isi.uu.nl/vr.htm), and the Volume Browser plug-in, by K. U. Barthel, which allows volumes to be manipulated in 3D (http://rsb.info.nih.gov/ij/plugins/volume-viewer.html). I have written a series of ImageJ plug-ins for batch rendering of rotational projections of embryos, available at http://worms.zoology.wisc.edu/QT4D.html. As currently written, these plug-ins support various kinds of 4D datasets, including .PIC, .AVI and .TIF image stacks, and output rotated datasets as sequential TIFF images suitable for compression using QT4DWriter.

[7] Several commercial solutions exist for 4D visualization. These include (1) Volocity from Improvision (http://improvision.com); (2) Imaris, from Bit-Plane AG (http://www.bitplane.com/); and (3) FluVR, from Scientific Volume Imaging B.V. (http://www.svi.nl/products/software/). The latter offers a free program for single-time-point surface rendering, FreeSFP, which can yield excellent rendered views of certain kinds of fluorescent signals within embryos. Freeware programs include (1) Voxx (Clendenon *et al*., 2002; http://www.nephrology.iupui.edu/imaging/voxx/), which allows freehand manipulation of rendered 3D + time data, manipulation of multi-channel data, the ability to render data as anaglyph stereo projections, and export of animations to several file formats that can be easily converted to QuickTime movies. (2) VisBio (Rueden *et al*., 2004; http://www.loci.wisc.edu/visbio/), a Java-based biological visualization tool that emphasizes data discovery and analysis, which can perform slices within 3D datasets and can perform various measurements on the data as well. VisBio's visualization capabilities are more limited in some senses than those of Voxx, but VisBio has superior slicing and interactive measurements capabilities. Because both load datasets into RAM, their memory requirements are demanding.

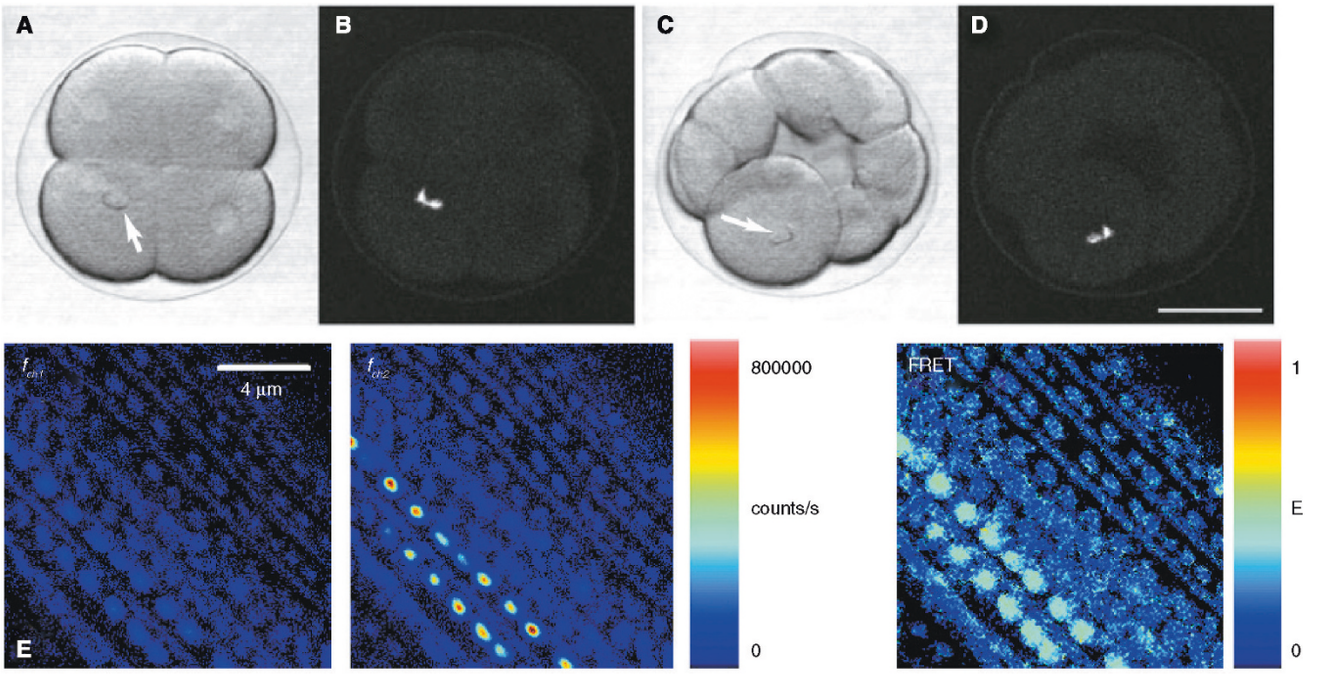


FIGURE 43.12. Multi-photon microscopy can be used to produce controlled damage and to detect protein interactions. (A–D) Damage to a mitotic pole in a sea urchin embryo. (A) Multi-photon damage was made in a two-cell stage sea urchin embryo, using a Zeiss LSM 510 MPLSM (Ti : Sa laser; *arrow*); subsequent development was observed using a Bio-Rad MRC-600 CLSM. Scanning transmission images (A, C) were obtained simultaneously with fluorescence images (B, D; 488 nm excitation) to visualize the fluorescent scar. The daughter cell that inherited the damage did not divide (C), whereas the undamaged daughter cell divided. Bar = 50 µm. (E) Two-photon excitation steady-state intensity (left, middle) and FRET efficiency (E; right) images of dense bodies in a muscle quadrant from a *C. elegans* embryo expressing PAT-4 : CFP and PAT-4 : YFP. f_{ch1}, fluorescence intensity in the CFP channel; f_{ch2}, fluorescence intensity in the YFP channel. FRET efficiency is on the order of ~30%, indicating that PAT-4 protein can self-associate in muscle dense bodies. For details of the procedure, please consult. Breusegem (2002). [A–D are from Galbraith and Terasaki (2003); (E) is from Breusegem (2002), Used by permission.]

increasingly accepted as a method for determining when two subunits of the same proteins interact with one another (intramolecular FRET) or where and when two different proteins physically interact *in vivo* (intermolecular FRET; see Chapter 45, *this volume*). Given their optical-sectioning capabilities, CLSM and MPLSM are potentially well suited to performing and imaging the results of FRET in embryos, especially because currently, the most popular donor/acceptor pair is ECFP/EYFP (Sekar and Periasamy, 2003; Wallrabe and Periasamy, 2005). One issue common to both intra- and intermolecular FRET is the contribution to acceptor excitation by autofluorescence. Embryos often display significant amounts of autofluorescence at the one-photon excitation wavelengths used for FRET, creating additional non-FRET signal that can complicate the analysis of acceptor fluorophore signals. This problem can be overcome by using two-photon excitation, which has the added advantages of increased depth of penetration mentioned previously. Breusegem (2002) reported that excitation at 850 to 870 nm reduces autofluorescence in *C. elegans* embryos.

At the time this chapter was written, no published studies had reported the use of intramolecular FRET in living embryos. However, the use of such intramolecular FRET reporters, which now includes a variety of reporters for signaling events, such as the chameleons for assessing calcium dynamics (Miyawaki *et al.*, 1999) and various reporters for small GTPase activity (Pertz and Hahn, 2004), will likely become more widespread in living embryos as the technology becomes less expensive and more widely available. One published example of intramolecular FRET using chameleons measured calcium dynamics in living *C. elegans* adults (Kerr *et al.*, 2000), suggests it has tremendous promise. Because chameleons are fusion proteins containing CFP and YFP in the same protein, the donor : acceptor ratio is always 1 : 1, so many of the complications that plague intermolecular FRET are largely obviated. This successful use of an intramolecular FRET reporter suggests that in the near future similar experiments will be performed on living embryos.

Performing intermolecular FRET in living embryos presents several additional challenges beyond those associated with intramolecular FRET. In the simplest cases, intermolecular FRET may simply be used qualitatively to show that there is an interaction between two molecules *in vivo*, after suitable correction for spectral bleed-through, but without additional computation (Wallrabe and Periasamy, 2005). In such cases, the stoichiometry of the acceptor and donor fluorophores is usually known, and FRET is reflected in changes in the ratio of both acceptor and donor emission.

However, the power of intermolecular FRET lies in the ability to use the percent energy transfer efficiency (*E%*) as a measure of intermolecular distance, that is, as a spectroscopic ruler. Quantitative FRET is much more complicated in practice than qualitative FRET, and this complication is exacerbated in living embryos. First, it is important to carefully control the concentrations of the donor and acceptor molecules for any quantitative assessment of *E%*. In transgenic animals into which fluorescent-protein-tagged molecules have been introduced, careful measurement of fluorophore concentration is difficult at best. However, in some genetic

systems, it is possible to replace the endogenous gene with a fluorescent-protein-tagged version, ensuring that virtually all of the protein under consideration is tagged. If the replacement gene is integrated as a single copy, it will typically preserve the normal level of expression of the labeled protein. A second problem with intermolecular FRET is that photobleaching of the donor or acceptor fluorophore is often used as a separate demonstration that FRET has occurred. However, photobleaching may not be suitable for embryos, many of which are especially sensitive to photodamage. An alternative is to use fluorescence lifetime imaging (FLIM) to measure FRET efficiency (Clegg *et al*., 2003; see also Chapter 27, *this volume*). FLIM has the advantage that it can be used independent of a measurement of fluorophore concentration, because the donor fluorescence lifetime decreases in the presence of FRET irrespective of fluorophore concentration. This solution introduces a third complication, however. In addition to the substantial complexities of instrumentation, quantitative determination of FRET efficiency using FLIM usually requires the acquisition of several images, which can increase the likelihood of photodamage to the embryo. For thorough quantitative FRET analysis, FLIM is often performed on a pixel-by-pixel basis throughout the field of view, increasing this risk.

Despite these caveats, recent work by Breusegem and colleagues has shown that quantitative FRET can be successfully adapted for use in *C. elegans* embryos (Breusegem, 2002). They showed that that the integrin-linked kinase (ILK), PAT-4, will engage in FRET with itself, and with both PAT-3/β-integrin and PAT-6/actopaxin at muscle dense bodies [structures associated with the attachment of muscles to the epidermis in *C. elegans*; Fig. 43.12(E)]. FRET was confirmed in several different ways, including sensitized YFP emission, and *E%* was measured using both the acceptor and donor photobleaching techniques and by performing FLIM in the time and frequency domains. In the time domain, photons were accumulated by repeated imaging of the same field at 100 µs/pixel, which required 25 to 30 frames to collect >100 photons/pixel. Although such photon-counting methods place severe limits on acquisition speed, because dense bodies are stable structures and, hence, essentially motionless, sampling of discrete points is an adequate substitute for full-field sampling, and this reduces the likelihood of phototoxicity (Breusegem, 2002). Although the use of FRET in embryos is in its infancy, these results suggest that in the near future this imaging tool, the use of which was once exclusive to cell biologists working on flat cells in tissue culture, will soon be available to developmental biologists.

CONCLUSIONS: A BRIGHT FUTURE FOR 3D IMAGING OF LIVING EMBRYOS

Few disciplines within biology have benefited more from improvements in confocal, multi-photon, and related technologies than developmental biology. As more exotic probes are developed for use in living cells, particularly those that can be genetically encoded, the imaging of embryos will continue to become more sophisticated. As each new probe is developed, there may be new challenges for developmental biologists, but based on current imaging modalities, several generalizations will probably continue to hold true.

First, although there are times when more expensive equipment, such as multi-photon microscopes, 4D deconvolution microscopes, or high-speed imaging approaches are necessary, empirical tests of viability using off-the-shelf confocal equipment should be performed first before such equipment is assumed to be necessary. While similar experiments are now being performed using multi-photon microscopy, numerous published experiments indicate that both standard single-beam confocal microscopes and disk-scanning microscopes can often be used to image living embryos in four dimensions without the need for additional equipment.

Second, as computer processing speed continues to increase, deconvolution and 3D projection of 4D datasets will become more routine. This can only improve the ability of the developmental biologist to visualize complex processes in four dimensions. The more routine use of multi-wavelength probes will likewise improve the ability of the developmental biologist to perceive and comprehend the complex beauty of embryogenesis.

Finally, although there has typically been a lag between the application of new imaging modalities in cultured cells and their subsequent use in embryos, the history of the field suggests that eventually many of the approaches first worked out in cultured cells will be adapted for use in embryos. Extension of the successful combination of microsurgical methods and confocal and multi-photon methods presented in this chapter, which effectively make the embryo flatter, will likely allow techniques such as FRET to be used routinely in embryos in the near future. Ultimately, 4D live imaging of fluorescent probes in embryos will cease to be the preserve of the specialist, and will become a part of the standard repertoire of the developmental biologist.

ACKNOWLEDGMENTS

I thank the editor of this volume and my wife, Susie, for their remarkable patience as this work was completed. I am grateful to Brian Burkel and Bill Bement for sharing unpublished data regarding PA-GFP, and to Sophie Breusegem and Bob Clegg for sharing unpublished results regarding FRET in *C. elegans*. Tim Walston, Mark Sheffield, and Chris Lockwood provided movies and images used in this work, and other members of the Hardin laboratory provided moral support. This work was supported by NIH grant GM058038 and NSF grant IBN-0112803, awarded to the author. CLSM footage was generated using a Bio-Rad 1024 confocal microscope originally purchased by NSF grant 9724515 awarded to J. Pawley. Movies associated with this chapter will be available on the Web site associated with this publication. http://www.springer.com/0-387-25921-X.

REFERENCES

Beck, J.C., Murray, J.A., Willows, A.O., and Cooper, M.S., 2000, Computer-assisted visualizations of neural networks: Expanding the field of view using seamless confocal montaging. *J. Neurosci. Methods* 98:155–163.

Bement, W.M., Sokac, A.M., and Mandato, C.A., 2003, Four-dimensional imaging of cytoskeletal dynamics in *Xenopus* oocytes and eggs, *Differentiation* 71:518–527.

Benink, H.A., and Bement, W.M., 2005, Concentric zones of active RhoA and Cdc42 around single cell wounds, *J. Cell Biol.* 168:429–439.

Benink, H.A., Mandato, C.A., and Bement, W.M., 2000. Analysis of cortical flow models *in vivo*, *Mol. Biol.1 Cell* 11:2553–2563.

Bloor, J.W., and Kiehart, D.P., 2002, *Drosophila* RhoA regulates the cytoskeleton and cell-cell adhesion in the developing epidermis, *Development* 129:3173–3183.

Breusegem, S.Y., 2002, *In vivo* investigation of protein interactions in *C. elegans* by Forster resonance energy transfer microscopy, Ph. D. dissertation, University of Illinois, Urbana-Champaign.

Campbell, R.E., Tour, O., Palmer, A.E., Steinbach, P.A., Baird, G.S., Zacharias, D.A., and Tsien, R.Y., 2002, A monomeric red fluorescent protein, *Proc. Natl. Acad. Sci. USA* 99:7877–7882.

Centonze, V.E., and White, J.G., 1998, Multiphoton excitation provides optical sections from deeper within scattering specimens than confocal imaging, *Biophys. J.* 75:2015–2024.

Chalfie, M., Tu, Y., Euskirchen, G., Ward, W.W., and Prasher, D.C., 1994, Green fluorescent protein as a marker for gene expression, *Science* 263:802–805.

Chapman, S.C., Collignon, J., Schoenwolf, G.C., and Lumsden, A., 2001, Improved method for chick whole-embryo culture using a filter paper carrier, *Dev. Dyn.* 220:284–289.

Chong, F.K., Coates, C.G., Denvir, D.J., McHale, N.G., Thornbury, K.D., and Hollywood, M.A., 2004, Optimization of spinning disk confocal microscopy: Synchronization with the ultra-sensitive EMCCD, *Proc. SPIE* 5324:65–76.

Chudakov, D.M., Belousov, V.V., Zaraisky, A.G., Novoselov, V.V., Staroverov, D.B., Zorov, D.B., Lukyanov, S., and Lukyanov, K.A., 2003, Kindling fluorescent proteins for precise *in vivo* photolabeling, *Nat. Biotechnol.* 21:191–194.

Clegg, R.M., Holub, O., and Gohlke, C., 2003, Fluorescence lifetime-resolved imaging: Measuring lifetimes in an image, *Methods Enzymol.* 360:509–542.

Clendenon, J.L., Phillips, C.L., Sandoval, R.M., Fang, S., and Dunn, K.W., 2002, Voxx: A PC-based, near real-time volume rendering system for biological microscopy, *Am. J. Physiol. Cell Physiol.* 282:C213–C218.

Cockell, M.M., Baumer, K., and Gonczy, P., 2004, lis-1 is required for dynein-dependent cell division processes in *C. elegans* embryos, *J. Cell Sci.* 117:4571–4582.

Concha, M.L., and Adams, R.J., 1998, Oriented cell divisions and cellular morphogenesis in the zebrafish gastrula and neurula: A time-lapse analysis, *Development* 125:983–994.

Cooper, M.S., D'Amico, L.A., and Henry, C.A., 1999, Confocal microscopic analysis of morphogenetic movements, *Methods Cell Biol.* 59:179–204.

Cooper, M.S., Szeto, D.P., Sommers-Herivel, G., Topczewski, J., Solnica-Krezel, L., Kang, H. C., Johnson, I., and Kimelman, D., 2005, Visualizing morphogenesis in transgenic zebrafish embryos using BODIPY TR methyl ester dye as a vital counterstain for GFP, *Dev. Dyn.* 232:359–368.

Czirok, A., Rongish, B.J., and Little, C.D., 2004, Extracellular matrix dynamics during vertebrate axis formation, *Dev. Biol.* 268:111–122.

Czirok, A., Rupp, P.A., Rongish, B.J., and Little, C.D., 2002, Multi-field 3D scanning light microscopy of early embryogenesis, *J. Microsc.* 206:209–217.

DeGrauw, C.J., Frederix, P.L.T.M., and Gerritsen, H.C., 2002, Aberrations and penetration in in-depth confocal and two-photon-excitation microscopy, In: *Confocal and Two-Photon Microscopy: Foundations*, *Applications*, *and Advances* (A. Diaspro, ed.), Wiley-Liss, New York, pp. 153–169.

Dubertret, B., Skourides, P., Norris, D.J., Noireaux, V., Brivanlou, A.H., and Libchaber, A., 2002, *In vivo* imaging of quantum dots encapsulated in phospholipid micelles, *Science* 298: 1759–1762.

Edwards, K.A., Demsky, M., Montague, R.A., Weymouth, N., and Kiehart, D.P., 1997, GFP-moesin illuminates actin cytoskeleton dynamics in living tissue and demonstrates cell shape changes during morphogenesis in *Drosophila*, *Dev. Biol.* 191:103–117.

Galbraith, J.A., and Terasaki, M., 2003, Controlled damage in thick specimens by multiphoton excitation, *Mol. Biol. Cell* 14:1808–1817.

Gao, X., Yang, L., Petros, J.A., Marshall, F.F., Simons, J.W., and Nie, S., 2005, *In vivo* molecular and cellular imaging with quantum dots, *Curr. Opin. Biotechnol.* 16:63–72.

Gimlich, R.L., 1991, Fluorescent dextran clonal markers, *Methods Cell Biol.* 36:285–297.

Girdham, C.H., and O'Farrell, P.H., 1994, The use of photoactivatable reagents for the study of cell lineage in *Drosophila* embryogenesis, *Methods Cell Biol.* 44:533–543.

Gomez, T.M., and Spitzer, N.C., 1999, *In vivo* regulation of axon extension and pathfinding by growth-cone calcium transients, *Nature* 397:350–355.

Grevengoed, E.E., Loureiro, J.J., Jesse, T.L., and Peifer, M., 2001, Abelson kinase regulates epithelial morphogenesis in *Drosophila*, *J. Cell Biol.* 155:1185–1198.

Hadjantonakis, A.K., Dickinson, M.E., Fraser, S.E., and Papaioannou, V.E., 2003, Technicolour transgenics: Imaging tools for functional genomics in the mouse, *Nat. Rev. Genet.* 4:613–625.

Hammond, A.T., and Glick, B.S., 2000, Raising the speed limits for 4D fluorescence microscopy, *Traffic* 1:935–940.

Heid, P.J., Raich, W.B., Smith, R., Mohler, W.A., Simokat, K., Gendreau, S.B., Rothman, J.H., and Hardin, J., 2001, The zinc finger protein DIE-1 is required for late events during epithelial cell rearrangement in *C. elegans*, *Dev. Biol.* 236:165–180.

Heid, P.J., Voss, E., and Soll, D.R., 2002, 3D-DIASemb: A computer-assisted system for reconstructing and motion analyzing in 4D every cell and nucleus in a developing embryo, *Dev. Biol.* 245:329–347.

Hell, S., Reiner, G., Cremer, C., and Stelzer, E.H.K., 1993, Aberrations in confocal fluorescence microscopy induced by mismatches in refractive index, *J. Microsc.* 169:391–405.

Henry, C.A., Hall, L.A., Burr Hille, M., Solnica-Krezel, L., and Cooper, M.S., 2000, Somites in zebrafish doubly mutant for knypek and trilobite form without internal mesenchymal cells or compaction, *Curr. Biol.* 10:1063–1066.

Huisken, J., Swoger, J., Del Bene, F., Wittbrodt, J., and Stelzer, E.H., 2004, Optical sectioning deep inside live embryos by selective plane illumination microscopy, *Science* 305:1007–1009.

Jacinto, A., Wood, W., Balayo, T., Turmaine, M., Martinez-Arias, A., and Martin, P., 2000, Dynamic actin-based epithelial adhesion and cell matching during *Drosophila* dorsal closure, *Curr. Biol.* 10:1420–1426.

Jaffe, L.A., and Terasaki, M., 2004, Quantitative microinjection of oocytes, eggs, and embryos, *Methods Cell Biol.* 74:219–242.

Jonkman, J.E.N., and Stelzer, E.H.K., 2002, Resolution and contrast in confocal and two-photon microscopy, In: *Confocal and Two-Photon Microscopy: Foundations*, *Applications*, *and Advances* (A. Diaspro, ed.), Wiley-Liss, New York, pp. 101–125.

Keller, R., 2002, Shaping the vertebrate body plan by polarized embryonic cell movements, *Science* 298:1950–1954.

Kerr, R., Lev-Ram, V., Baird, G., Vincent, P., Tsien, R.Y., and Schafer, W.R., 2000, Optical imaging of calcium transients in neurons and pharyngeal muscle of *C. elegans*, *Neuron* 26:583–594.

Kilian, B., Mansukoski, H., Barbosa, F.C., Ulrich, F., Tada, M., and Heisenberg, C.P., 2003, The role of Ppt/Wnt5 in regulating cell shape and movement during zebrafish gastrulation, *Mech. Dev.* 120:467–476.

Köppen, M., Simske, J.S., Sims, P.A., Firestein, B.L., Hall, D.H., Radice, A.D., Rongo, C., and Hardin, J.D., 2001, Cooperative regulation of AJM-1 controls junctional integrity in *Caenorhabditis elegans* epithelia, *Nat. Cell Biol.* 3:983–991.

Kozlowski, D.J., Murakami, T., Ho, R.K., and Weinberg, E.S., 1997, Regional cell movement and tissue patterning in the zebrafish embryo revealed by fate mapping with caged fluorescein, *Biochem. Cell Biol.* 75:551–562.

Labbe, J.C., McCarthy, E.K., and Goldstein, B., 2004, The forces that position a mitotic spindle asymmetrically are tethered until after the time of spindle assembly, *J. Cell Biol.* 167:245–256.

Langenberg, T., Brand, M., and Cooper, M.S., 2003, Imaging brain development and organogenesis in zebrafish using immobilized embryonic explants, *Dev. Dyn.* 228:464–474.

Lippincott-Schwartz, J., and Patterson, G.H., 2003, Development and use of fluorescent protein markers in living cells, *Science* 300:87–91.

Lippincott-Schwartz, J., Altan-Bonnet, N., and Patterson, G.H., 2003, Photobleaching and photoactivation: Following protein dynamics in living cells, *Nat. Cell Biol.* (Suppl.):S7–S14.

Megason, S.G., and Fraser, S.E., 2003, Digitizing life at the level of the cell: High-performance laser-scanning microscopy and image analysis for *in toto* imaging of development, *Mech. Dev.* 120:1407–1420.

Michalet, X., Pinaud, F.F., Bentolila, L.A., Tsay, J.M., Doose, S., Li, J.J., Sundaresan, G., Wu, A.M., Gambhir, S.S., and Weiss, S., 2005, Quantum dots for live cells, in vivo imaging, and diagnostics, *Science* 307:538–544.

Miyawaki, A., Griesbeck, O., Heim, R., and Tsien, R.Y., 1999, Dynamic and quantitative Ca2+ measurements using improved cameleons, *Proc. Natl. Acad. Sci. USA* 96:2135–2140.

Miyawaki, A., Sawano, A., and Kogure, T., 2003, Lighting up cells: Labelling proteins with fluorophores, *Nat. Cell Biol.* (Suppl.):S1–S7.

Mohler, W.A., 1999, Visual reality: using computer reconstruction and animation to magnify the microscopist's perception, *Mol. Biol. Cell* 10:3061–3065.

Mohler, W.A., Simske, J.S., Williams-Masson, E.M., Hardin, J.D., and White, J.G., 1998, Dynamics and ultrastructure of developmental cell fusions in the *Caenorhabditis elegans* hypodermis, *Curr. Biol.* 8:1087–1090.

Molecular Probes, 2004, *The Handbook — A Guide to Fluorescent Probes and Labeling Technologies*. Carlsbad, CA: Invitrogen Corp.

Molyneaux, K.A., Zinszner, H., Kunwar, P.S., Schaible, K., Stebler, J., Sunshine, M.J., O'Brien, W., Raz, E., Littman, D., Wylie, C., and Lehmann, R., 2003, The chemokine SDF1/CXCL12 and its receptor CXCR4 regulate mouse germ cell migration and survival, *Development* 130:4279–4786.

Oegema, K., Desai, A., Rybina, S., Kirkham, M., and Hyman, A.A., 2001, Functional analysis of kinetochore assembly in *Caenorhabditis elegans*, *J. Cell Biol.* 153:1209–1226.

Paddy, M.R., Saumweber, H., Agard, D.A., and Sedat, J.W., 1996, Time-resolved, *in vivo* studies of mitotic spindle formation and nuclear lamina breakdown in *Drosophila* early embryos, *J. Cell Sci.* 109:591–607.

Patterson, G.H., and Lippincott-Schwartz, J., 2002, A photoactivatable GFP for selective photolabeling of proteins and cells, *Science* 297:1873–1877.

Periasamy, A., Skoglund, P., Noakes, C., and Keller, R., 1999, An evaluation of two-photon excitation versus confocal and digital deconvolution fluorescence microscopy imaging in *Xenopus* morphogenesis, *Microsc. Res. Tech.* 47:172–181.

Pertz, O., and Hahn, K.M., 2004, Designing biosensors for Rho family proteins — Deciphering the dynamics of Rho family GTPase activation in living cells, *J. Cell Sci.* 117:1313–1318.

Poteryaev, D., Squirrell, J.M., Campbell, J.M., White, J.G., and Spang, A., 2005, Involvement of the actin cytoskeleton and homotypic membrane fusion in ER dynamics in *C. elegans*, *Mol. Biol. Cell*. 16:2139–2153.

Rueden, C., Eliceiri, K.W., and White, J.G., 2004, VisBio: A computational tool for visualization of multidimensional biological image data, *Traffic* 5:411–417.

Sekar, R.B., and Periasamy, A., 2003, Fluorescence resonance energy transfer (FRET) microscopy imaging of live cell protein localizations, *J. Cell Biol.* 160:629–633.

Shaner, N.C., Campbell, R.E., Steinbach, P.A., Giepmans, B.N., Palmer, A.E., and Tsien, R.Y., 2004, Improved monomeric red, orange and yellow fluorescent proteins derived from Discosoma sp. red fluorescent protein, *Nat. Biotechnol.* 22:1567–1572.

Skop, A.R., Bergmann, D., Mohler, W.A., and White, J. G., 2001, Completion of cytokinesis in *C. elegans* requires a brefeldin A-sensitive membrane accumulation at the cleavage furrow apex, *Curr. Biol.* 11:735–746.

Squirrell, J.M., Wokosin, D.L., White, J.G., and Bavister, B.D., 1999, Long-term two-photon fluorescence imaging of mammalian embryos without compromising viability, *Nat. Biotechnol.* 17:763–767.

Strickland, L., von Dassow, G., Ellenberg, J., Foe, V., Lenart, P., and Burgess, D., 2004, Light microscopy of echinoderm embryos, *Methods Cell Biol.* 74:371–409.

Strome, S., Powers, J., Dunn, M., Reese, K., Malone, C. J., White, J., Seydoux, G., and Saxton, W., 2001, Spindle dynamics and the role of gamma-tubulin in early *Caenorhabditis elegans* embryos, *Mol. Biol. Cell* 12:1751–1764.

Terasaki, M., 1998, Imaging of echinoderm fertilization, *Mol. Biol. Cell* 9:1609–1612.

Terasaki, M., and Jaffe, L.A., 2004, Labeling of cell membranes and compartments for live cell fluorescence microscopy, *Methods Cell Biol.* 74:469–489.

Thomas, C., DeVries, P., Hardin, J., and White, J., 1996, Four-dimensional imaging: Computer visualization of 3D movements in living specimens, *Science* 273:603–607.

Thomas, C.F., and White, J.G., 2000, Acquisition, display, and analysis of digital three-dimensional time-lapse (four-dimensional) data sets using free software applications, *Methods Mol. Biol.* 135:263–276.

Ulrich, F., Concha, M.L., Heid, P.J., Voss, E., Witzel, S., Roehl, H., Tada, M., Wilson, S.W., Adams, R.J., Soll, D.R., and Heisenberg, C.P., 2003, Slb/Wnt11 controls hypoblast cell migration and morphogenesis at the onset of zebrafish gastrulation. *Development* 130:5375–5384.

Voie, A.H., Burns, D.H., and Spelman, F.A., 1993, Orthogonal-plane fluorescence optical sectioning: three-dimensional imaging of macroscopic biological specimens. *J. Microsc.* 170:229–236.

Wallrabe, H., and Periasamy, A., 2005, Imaging protein molecules using FRET and FLIM microscopy, *Curr. Opin. Biotechnol.* 16:19–27.

Wilson, P., and Keller, R., 1991, Cell rearrangement during gastrulation of *Xenopus*: Direct observation of cultured explants, *Development* 112:289–300.

Wood, W., and Jacinto, A., 2004, Imaging cell movement during dorsal closure in *Drosophila* embryos, *Methods Mol. Biol.* 294:203–210.

44

Imaging Plant Cells

Nuno Moreno, Susan Bougourd, Jim Haseloff, and José A. Feijó

INTRODUCTION

The history of imaging plant cells is intimately related to the very development of microscopes and microscopical techniques. Some of the early microscopists made extensive use of plant specimens, and Hooke's description of cork microstructure (Fig. 44.1) will stand in the imagination of many as the structural foundation for the cell theory. There are several reasons for this to have happened: in many respects plant tissues are easier to deal with, easier to slice and peel to the necessary thickness for observation, they have more water, and consequently are less optically dense than many other tissues, often they are naturally pigmented and the cells are usually larger. Above all, the existence of a skeletal cell wall composed of cellulose and other molecules makes plant cells extraordinarily geometric and highly regulated in their structural features. In many instances, these structural components of the plant cell form the basis of its function, making microscopical analysis a recurrent method for cell and developmental biology research.

Since the 17th century, many gifted microscopists have given cumulative accounts of the different levels of plant cell structure. Perhaps the first truly specialized plant microscopist was Grew (1673), who initiated the first systematic study of plant micro-anatomy. Robert Brown, Amici, Schleiden, and Nawaschin are among the many notables who contributed to the description of some of the fundamental biological features of plants, such as their reproductive cycles, mostly using microscopes as tools. More recently, the seminal textbooks of Esau (1977a,b) and Fahn (1990) systematized definitively the histological and cellular features of higher plants. Plant cell ultrastructure has subsequently been described and systematized in detail in many textbooks and atlases, such as the ones produced by Gunning and Steer (1996). This effort was recently complemented by an extensive review on CD-ROM that stands, and probably will stand for a long time, as a central reference for anyone seeking information on microscopical data concerning plant cells (Gunning, 2003; http://www.plantcellbiologyoncd.com).

The developments in technology and reagents that brought fluorescence-based methods to microscopy have also become prevalent in plant cell biology (Lloyd, 1987). However, plant cells do present a challenge to fluorescence microscopy because they often contain pigments and complex excitable molecules in subcellular structures that generate copious autofluorescence. In many circumstances this is a nuisance in terms of signal-to-noise ratio: the autofluorescence can swamp signal from other fluorescent probes being studied. Furthermore, without the optical sectioning of the confocal microscope, autofluorescence glaring from all planes may obscure the signal from any in-focus structural information. Naturally, confocal imaging has made a strong impact in the area of plant-cell imaging. All these problems have been addressed in extensive reviews about applications of confocal microscopy to plant cell biology (Hepler and Gunning, 1998), imaging ions and other advanced methods (Blancaflor and Gilroy, 2000), and in hand- and textbooks on methods and applications (Galbraith *et al.*, 1995; Hawes and Satiat-Jeunemaitre, 2001).

Green fluorescent protein (GFP) and other genetically encoded fluorescent probes have made a substantial impact on the field (Haseloff and Amos, 1995; Haseloff *et al.* 1997), and extensive lists of references of different applications, spectral conditions, and transient expression systems are available (Brandizzi *et al.* 2002). Detailed comparisons of the relative merits between conventional and widefield (Shaw, 2001) and between two-photon excitation and confocal (Feijó and Moreno, 2004) have shown that there are specific niches for all methods, and probably none should be considered universal, irrespective of their price and sophistication. Previous reviews also included detailed protocols for image acquisition using these different methods. A very useful collection of practical criteria for probe choice, empirical methods, and many tricks for immobilization, perfusion, and loading protocols are described by Fricker and colleagues (2001).

Specific methods for some of the most-used cell and tissue types have also been described (e.g., Kodama and Komamine, 1995; Raghavan, 1995; Sheen, 1995). Various fixation and other histological methods specific for plant cells are extensively described in many references (e.g., Spence, 2001), including complex and sophisticated freeze-fixation and freeze-substitution methods (Galway *et al.*, 1995; Parthasarathy, 1995).

However, recent years have been marked by the introduction of less invasive methods and vital probes, with a strong emphasis on those that are genetically encoded. The focus now is on keeping cells and tissues intact and alive, and this offers the added value of enabling one to study the true dynamics of vital processes. Vesicle trafficking (Bolte *et al.*, 2004), individual gene expression (Shav-tal *et al.*, 2004), and cytoplasmic streaming dynamics (Shimen and Yokota, 2004) are just a few examples of the living processes now reachable using state-of-the-art microscopy in combination with genetic and molecular techniques. We will thus focus this chapter on recent developments that might affect plant biological research beyond the topics covered in the earlier reviews.

Nuno Moreno • Instituto Gulbenkian de Ciência, PT-2780-156 Oeiras, Portugal
Susan Bougourd • University of York, York YO10 5DD, United Kingdom
Jim Haseloff • University of Cambridge, Cambridge CB2 3EA, United Kingdom
José A. Feijó • Instituto Gulbenkian de Ciência, PT-2780-156 Oeiras, Portugal, and Universidade de Lisboa, PT-1749-016 Lisboa, Portugal

Handbook of Biological Confocal Microscopy, Third Edition, edited by James B. Pawley, Springer Science+Business Media, LLC, New York, 2006.

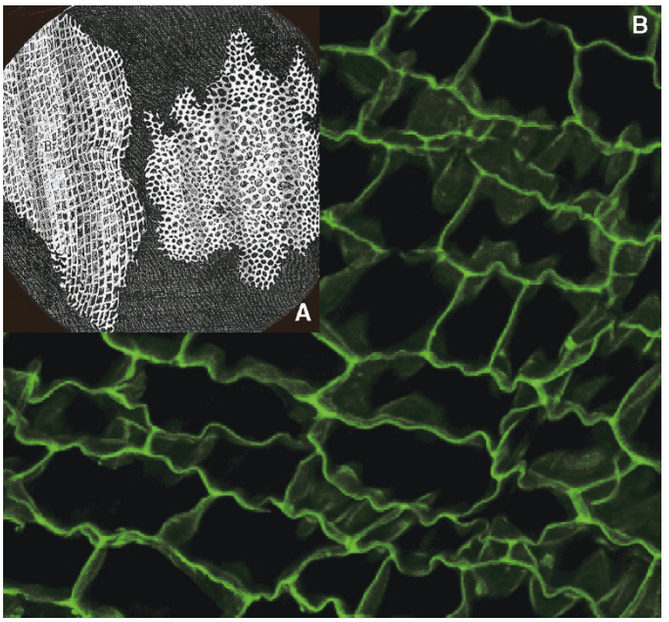


FIGURE 44.1. Cork now and then! Comparison of Robert Hooke's picture (A) and state-of-the-art laser-scanning microscopy (B) of a cork slice, having a time difference of almost 350 years. It was in the book *Micrographia* published in 1665 that Hooke used the term "cells" for the first time to describe the element of this regularity. Despite the obvious differences (one drawn by hand, the other based on digital acquisition of optical slices and software enhancement by using maximum-intensity projection), the evidence of the highly regular structure of plant cells is clearly evident in Hooke's image, and underlies the close relationship between form and function in plant cells. However, the confocal image also shows one of the most prevalent features of plant cells: the almost ubiquitous existence of autofluorescence in various subcellular structures, a factor that can be both informative and a problem to deal with when imaging probes with overlapping fluorescence spectra.

THE EVER PRESENT PROBLEM OF AUTOFLUORESCENCE

Light is potentially damaging to cells, yet plants live in the fast lane. In order for photosynthesis to proceed, leaves and other aerial parts are often exposed to high levels of light radiation, and evolution has resulted in a number of mechanisms for filtering photons before they reach sensitive parts inside the cell. In addition, many plant cell walls accumulate complex hydrophobic molecules that regulate apoplastic water loss and movement (e.g., suberin in cork; Fig. 44.1), and a plethora of secondary metabolites, many working as pigments, have evolved for ecological or allelopathic reasons. Many of these molecules use varied pathways to dissipate photoexcitation, namely, non-radiative decay or relaxation, energy transfer, photosynthesis, and fluorescence. Unfortunately, the latter is common and autofluorescence is a natural feature of almost every plant cell (see Chapter 21, *this volume*, for detailed spectra).

This autofluorescence is a nightmare for many fluorescence applications. On fixed, sectioned, and stained specimens, protocols using strong oxidizing agents such as chlorine bleach, chloral hydrate, or sodium-borohydride have long been used to reduce autofluorescence (Shaw, 2001; Chapter 18, *this volume*). Efficient as they are, these techniques cannot be used when imaging living cells, and the molecular degradation they produce can even destroy the specificity of immunostaining. Many fixation reagents, such as glutaraldehyde, also add to the problem by generating autofluorescent Schiff bases and delocalized electron resonance transfer when they react with cellular components.

The problem is illustrated in Figures 44.1 and 44.2. In Figure 44.1(A), the same cork that Hooke could describe because of its opacity to photon transmission is also shown by state-of-the-art confocal microscopy because the walls of dead cells are impregnated with suberin, a complex lipid with strong autofluorescence. As the cells are empty, after extended focus stacking, the cell walls can be seen with great detail and the confocal capacity of rejecting out-of-focus light renders images with great visual depth.

Figure 44.2 shows what is probably the most common source of imaging problems: the green tissues. Chlorophyll accumulates inside plastids that occur in great numbers in green tissue (the round red organelles in this image). Although in the shoot meristem region, depicted in Figure 44.2, the cell wall is still relatively immature and thus has less autofluorescence (shown in blue), these two signals render the observation of other fluorophores (in this case GFP in the endoplasmic reticulum (ER), shown in green) almost impossible unless the out-of-focus light can be rejected and strong spectral separation is available.

Cell wall autofluorescence swamps the signal from added probes and the absorption and scattering of both the excitation and the signal severely limits the distance that one can image into the tissue. The common way of dealing with spectral mixing is to use selective dichroic/emission filters, with the excitation peak as narrow as sensitivity allows. In a relatively young organ such as that shown in Figure 44.2, good results are obtainable with standard confocal settings (in this case, using a Zeiss Pascal). The importance of being able to produce stringent optical sections is illustrated in Figure 44.2(B), which shows a two-photon image of the GFP in the central section of the same plantlet. The image is almost clear of the other sources of signal.

On a more physical basis, absorption in green tissues usually involves both excitation of a first excited singlet state (responsible for red absorption) and excitation of a second excited singlet state (responsible for blue absorption). In both cases, emission is mainly in the near-infrared because the blue-excited state relaxes to the first singlet [Malkin and Niyogi 2001; Figure 44.2(C)]. This complex response can be either a drawback or a bonus. Chloroplasts emit farther into the red [Fig. 44.2(D) in false blue], but other emissions in the visible spectrum can superimpose important information. Overall, they usually have a broad emission spectrum, and it is not a trivial matter to discriminate it from labeling, even in a spectral microscope.

Many recent confocal microscopes come equipped with the capacity for spectral analysis, and this facility is becoming a useful tool for discriminating against autofluorescence. There are two ways of using the new spectral tools. In the first, one is only concerned with the emission from a single dye, and chooses the narrowest, most selective emission window for the dye involved. This is a one-step method, and only a single reference spectrum is needed for each series of observations. In the second method, one uses linear spectral unmixing to separate the emission of different dyes. Although speed is usually not an issue with the first method, it may be with the second, especially if the signal in the different channels must be acquired sequentially. However, parallel acquisition often implies channels only 10 nm wide and, when an already weak signal is distributed among several narrow spectral windows, there is even less signal in each one. As a result, low signal level can be a problem and no commercial system is devoid of limitations in that respect. Although low signal can be overcome to some extent by more laser power, this can lead to other sorts of physical limitations, particularly singlet-state saturation of the dye and photodamage to the specimen.

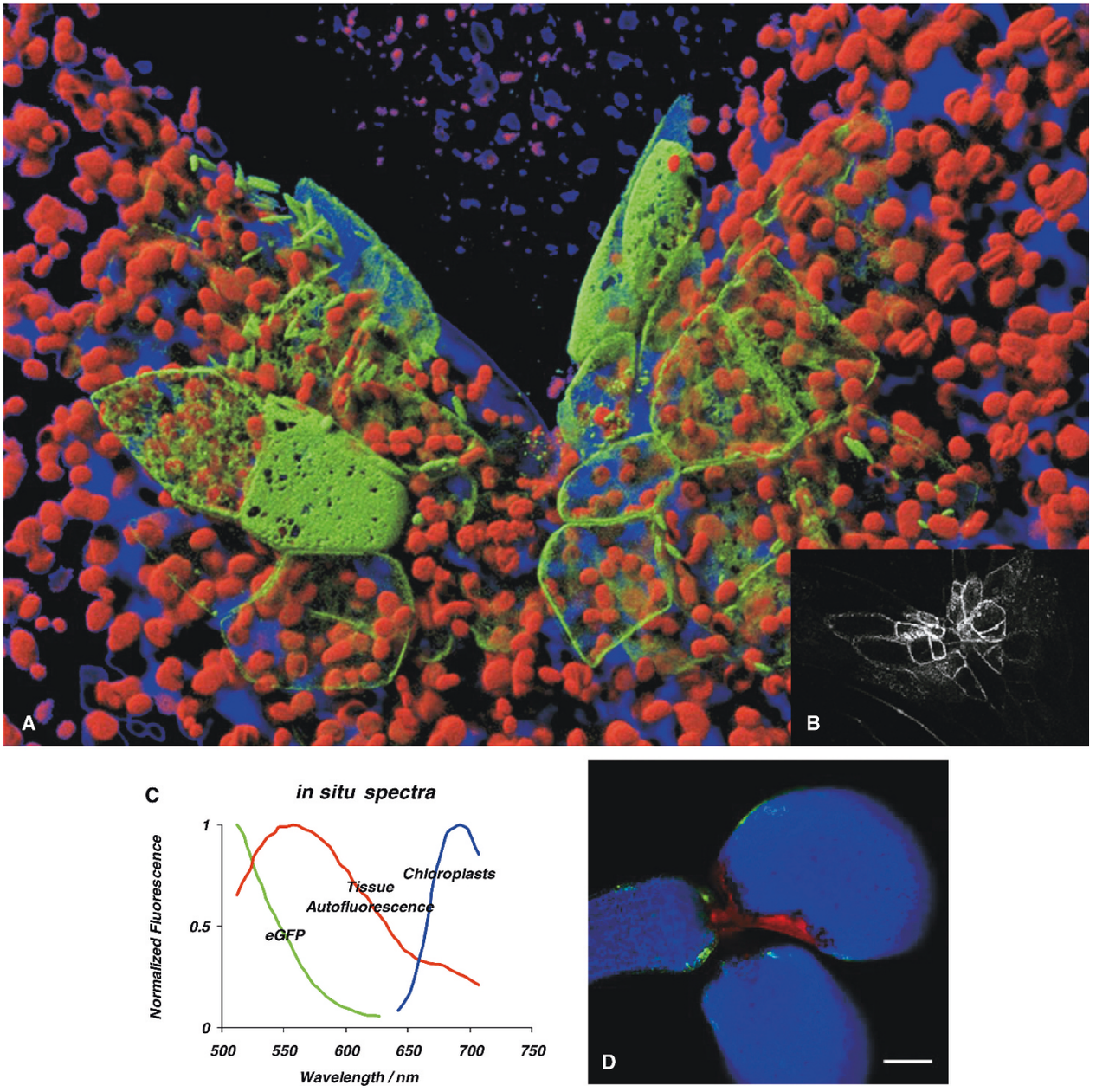


FIGURE 44.2. Three-dimensional reconstruction of an *Arabidopsis* hypocotyl/cotyledon imaged using a Zeiss Pascal with three emission channels and three laser lines (405, 488, and 633 nm) using a 63× Plan Apochromat NA 1.4 oil-immersion objective. This is an enhancer trap line with GFP linked to an ER domain protein, which in this case was activated on the meristematic primordial cells. Using the normal dichroic/emission filters, GFP (green) is well resolved from the chloroplasts (red) because their emission shows up mainly in the near infrared. The immature (thus dimmer in terms of autofluorescence) cell wall appears as shown in false blue. Insert (B) shows a different way of resolving the GFP signal, by two-photon excitation (TPE) at 870 nm. Because the excitation wavelength is not as optimal for the chlorophyll as it is for GFP, the red plastids seen in (A) are much dimmer or invisible. (C) *Arabidopsis* seedling spectra traced *in situ* with a Leica SP2 AOBS. After making a lambda scan from 500 to 700 nm with a spectral gate width of 30 nm, using a 488 laser line and a 10× Plan Apochromat NA 0.4, a spectrum from each part of the tissue was traced for eGFP, cell wall and chloroplast autofluorescence. With these emission spectra, it becomes possible to unmix the lambda stack (D). This software tool comes with all the spectral confocal systems (Leica SP2 AOBS and Zeiss 510 Meta) and works in a similar way to spatial deconvolution but in this case the bleed-through is not caused by out-of-focus signal, but from overlapping fluorescence emission. Bar = 200 µm.

Figure 44.2 shows an *Arabidopsis* seedling with GFP expression in the ER. Reference spectra were generated for the different pigments [Figure 44.2(C)] and the respective signals extracted from the raw xyzλ-image data (a so-called lambda stack), and then merged again with false colors [Fig. 44.2(D)]. It is clear that the channels have been sharply separated. While the principle works, there are limitations, and when several fluorescent proteins are present, it can be more difficult to separate colors, especially if more than one of them occurs in the same voxel. In any case, one needs a specimen capable of producing lots of signal.

As usual there are several engineering solutions to the problem of spectral detection. Leica uses a prism and a set of moveable mirrors to break the spectrum of emitted light into three or four segments, each going to a separate photomultiplier tube (PMT).

Zeiss uses a grating to disperse the emission spectrum over an array of 32 mini-PMTs, and has facilities to digitize as many as 8 channels from any combination of the 32 outputs (Nikon and Olympus are also launching their own solutions). There are pros and cons to each method: generally speaking one can say that the latter gains in terms of temporal resolution during live imaging, but perhaps at the cost of some sensitivity, especially in the red extreme of the spectrum.

Once the spectral data have been obtained, they must be deconvolved (or unmixed) using programs similar to those used to deconvolve widefield structural data (see Chapters 23, 24, and 25, *this volume*), except that, instead of starting with a point-spread function, one starts with stored spectra of each of the dyes present. Least-squares algorithms are used to fit the spectral data measured in each voxel or region to a linear sum of the spectra of the dyes expected to be present. As all the light used by the spectral detector comes through a single pinhole, one cannot use pinhole size to balance the signal intensities from different dyes. Consequently, the procedure works best when the signals from all the various dyes are approximately equal in strength.

SINGLE-PHOTON CONFOCAL MICROSCOPY

Because plant tissue generally consists of deep layers of highly refractile cell walls and aqueous cytosol and contains various autofluorescent and light-scattering components, intact tissue proves a difficult subject for fluorescence microscopy. However, direct imaging of living tissue is possible using suitably corrected microscope optics. Plant seedlings or excised tissues can simply be mounted in water for microscopy and examined using a long-working-distance water-immersion objective to minimize the effects of spherical aberration when focusing deep into an aqueous sample. Even with the use of such specialized objectives, using single-photon excitation, image quality degrades rapidly for optical sections deeper than 60 to 80 µM within the tissue. However, the small size of seedlings, such as those of the model plant *Arabidopsis thaliana*, allows very useful imaging despite this limitation. For example, median longitudinal optical sections can be obtained from intact roots. This direct approach to imaging plant materials has been reviewed elsewhere (Haseloff, 2003).

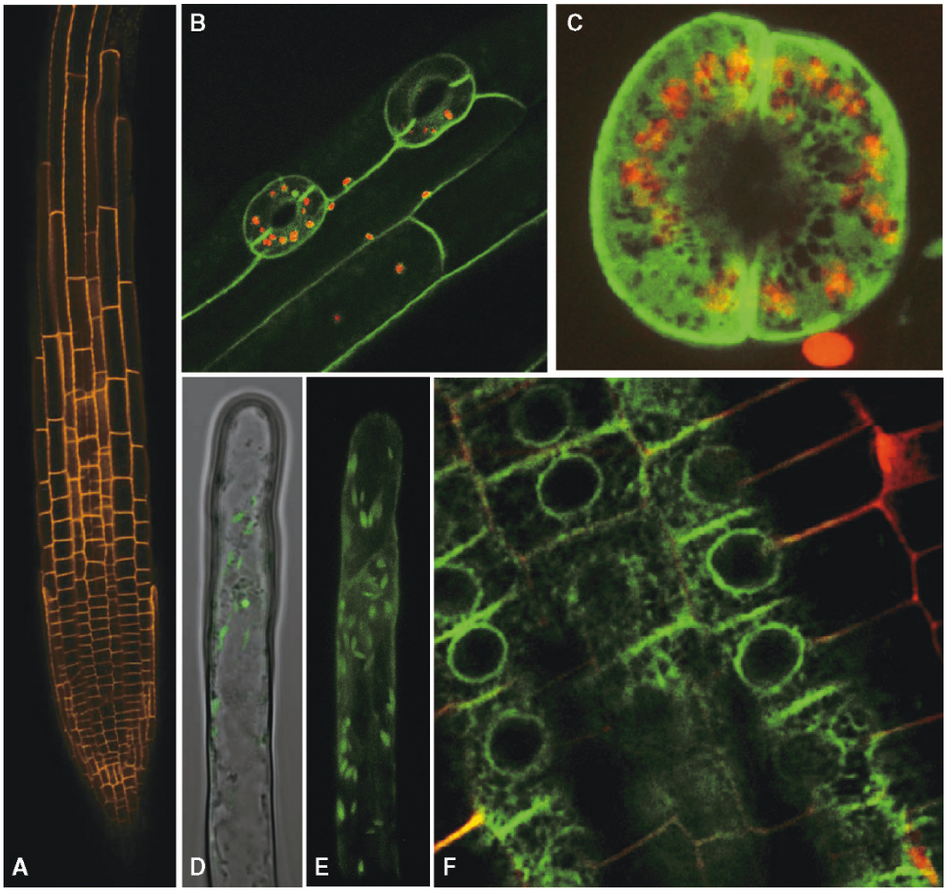


FIGURE 44.3. (A) Optical section of an *Arabidopsis* root with a random insertion (Cuttler *et al.*, 2000) of Clontech-YFP targeted to the plasma membrane (confocal image excited at 525 nm using a Leica SP2 AOBS). (B) Seedling shoot epidermis from a line similar to that shown in (A), but with the Clontech-GFP imaged with TPE at 930 nm. Despite the non-optimal optical response to this wavelength, the beam has enough power to produce the desired excitation and yields outstanding results in terms of tissue penetration and signal-to-noise ratio. (C) Dual-emission confocal imaging from a stoma in which the ER is stained with mGFP5 (enhancer trap line) and the chloroplasts are emitting auto-fluorescence. Mixed widefield and fluorescence (D) and confocal fluorescence (E) of mGFP5 enhancer-trap transformed *Arabidopsis* root hair. GFP is fused to an ER motif, and the dynamics of the big ER inclusions are clearly visible. (F) Double-emission of ER-targeted mGFP5 (Siemering *et al.*, 1996) fusion product with the SCARECROW gene (Wysocka-Diller *et al.*, 2000). Despite the low expression level, the ER and nuclear envelope are clearly resolved in the endodermis, four cell layers deep into the root. The cell wall is stained with vital PI. The optical-sectioning properties of TPE are well illustrated in the sharp fading pattern of the cell wall tangential section.

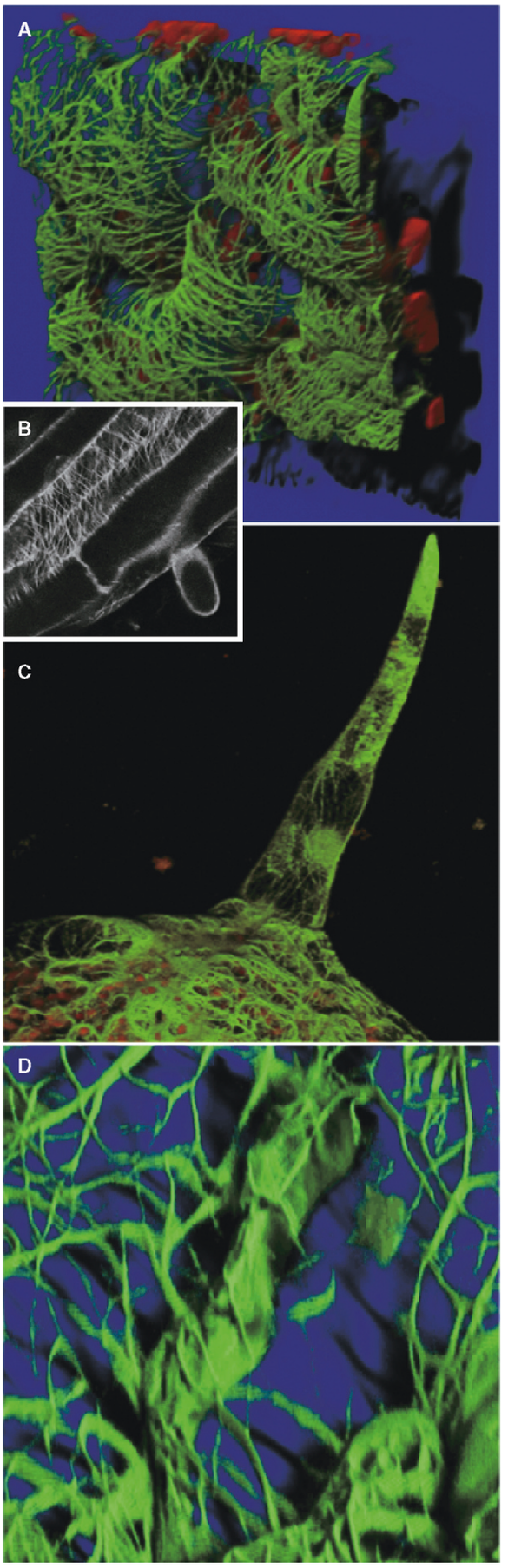


FIGURE 44.4. Leaf epidermal cell of a transgenic *Arabidopsis* with a microtubule-associated protein (MAP4) GFP fusion, imaged with a Zeiss Pascal confocal. *z*-stacks were acquired (B) and 3D volume-rendered. Red organelles are plastids. The subcortical distribution of the microtubules is clearly visible due to the depth created by the rendering algorithm. This construct, while producing excellent results for epidermal microtubules, seems useless for labeling microtubules in other cells. (C, D) Leaf trichome of a transgenic *Arabidopsis* with the actin-bundling protein talin fused with GFP, imaged with a Zeiss Pascal confocal and processed as in (A). Amplification in (D) is particularly noticeable by the details of the actin bundles inside these cells. However, great care must be used in interpreting this result, because under a constitutive strong promoter, talin is prone to creating "artificial" cables of actin, which are not supported by other means of visualization (Ketelaar *et al.*, 2004).

Direct visualization of GFP fluorescence in living tissues is not prone to fixation or staining artifacts, and can provide images of exceptional clarity. Moreover, the activities of living cells, such as cytoplasmic streaming, are clearly evident during microscopy. Ordinarily, movement within a sample is a nuisance, placing constraints on the use of sometimes protracted techniques for noise reduction during confocal microscopy, such as frame averaging. However, it is also possible to monitor dynamic events by time-lapse confocal microscopy, and this combination of a vital fluorescent reporter with high-resolution optical techniques has proven valuable in cell biological and physiological experiments. We have also found that autofluorescent chloroplasts, normally present in the upper parts of the plant, and certain red fluorescent dyes can provide useful counterfluors for GFP. For example, propidium iodide can be applied to live seedlings in water, to specifically label root cell walls, and allow accurate identification of GFP expressing cells [Fig. 44.3(F)].

It is now possible to genetically mark cells or subcellular compartments within a living organism using GFP and to visualize these directly during development. A number of collections of transgenic lines have been developed where GFP gene expression has been targeted to particular cell types or where GFP protein fusions have been used to decorate cell compartments in *Arabidopsis*. For example, Cutler and colleagues (2000) have produced a library of transgenic *Arabidopsis* lines that express random cDNA-GFP fusions. The fluorescent protein is targeted to various subcellular compartments in these lines, and they provide a useful source of dynamic markers for nuclei, plastids, different membranes, and other compartments [Fig. 44.3(A,B)]. In addition, enhancer trap strategies have been used to direct the expression of a foreign transcription activator, GAL4, in different cell types in *Arabidopsis* (Haseloff, 1999a,b). The GAL4 gene was inserted into the *Arabidopsis* genome, using *Agrobacterium tumefaciens*–mediated transformation. Expression of the GAL4 gene is dependent upon the presence of adjacent genomic enhancer sequences, and so different patterns of expression were generated. The inserted DNA also contains a GAL4-responsive GFP gene, and patterns of GAL4 gene expression are immediately detectable, with each GAL4-expressing cell marked by green fluorescence. These lines provide a valuable set of markers, where particular cell types are tagged and can be visualized with unprecedented ease and clarity in living plants [Figs. 44.2 and 44.3(C–E)]. The collections of cDNA fusions and GAL4 enhancer trap lines are available through the *Arabidopsis* stock centers.

A particularly exciting field has also emerged with the successful development of GFP-fusion products with cytoskeleton associated proteins, which enable high resolution imaging of both microtubules (Fig. 44.4) and actin microfilaments

[Figs. 44.4(C,D)]; see also Chen *et al.*, (2003); and Shaw *et al.*, (2003). Use of over-expressing constructs of cytoskeleton binding proteins can, however, disrupt the delicate balance of the dynamic instability that usually takes place during the polymerization of the cytoskeleton under physiological conditions, as recently demonstrated for talin (Ketelaar *et al.*, 2004). Despite their obvious beauty and apparent information, these images and their spatial and temporal kinetics should be interpreted with great care.

Staining Plant Tissues

As an alternative to direct imaging of live specimens, it is possible to fix and stain intact plant tissues and then to clear the material using a high-refractive-index mounting medium. It is then possible to obtain high-resolution optical sections from deep within intact tissues using objectives corrected for oil immersion.

A wide variety of staining techniques have been adopted for plant specimens over the last 150 years. Perhaps the most widely used general tissue stains are Safranin O and Haematoxylin. These are often accompanied by the use of counterstains such as Fast Green, Orange G, or Alcian Blue. In addition, there are a large variety of more specific staining techniques that have been developed for particular plant materials and organelles. For example, Feulgen staining has been used for specifically labeling DNA, the periodic acid–Schiff reaction can be used to label carbohydrates, Aniline Blue for labeling callose, Nile Red for oil bodies, and Phloroglucinol for lignin. A multitude of published protocols are available. An excellent, recently published source of procedures can be found in Ruzin (1999).

Interestingly, many of the synthetic dyes used for plant microtechnique are highly fluorescent. This is particularly so for the red, orange, and yellow dyes in the azine (e.g., Safranin O), acridine (e.g., Acridine Orange), and xanthene (e.g., Rhodamine) families. Thus, many classic histological techniques unintentionally produce specimens that are intensely fluorescent. In addition, aldehyde fixation, certain mountants, and long-term storage of stained preparations can result in tissue fluorescence, and the high concentration of stains deposited in the sections can lead to metachromasia (Mason, 2000). In our hands, it is rare to find stained and sectioned botanical material that is not highly fluorescent. Current confocal microscopes can sometimes allow the clean separation of different fluorescent emission signals and the balancing of signal levels in different channels. Thus, fluorescent images of exceptional clarity and vivid color can be easily obtained (Fig. 44.5). In addition, the optical sectioning properties of the confocal microscope can be used to collect clear images from within thick sections and whole mounts.

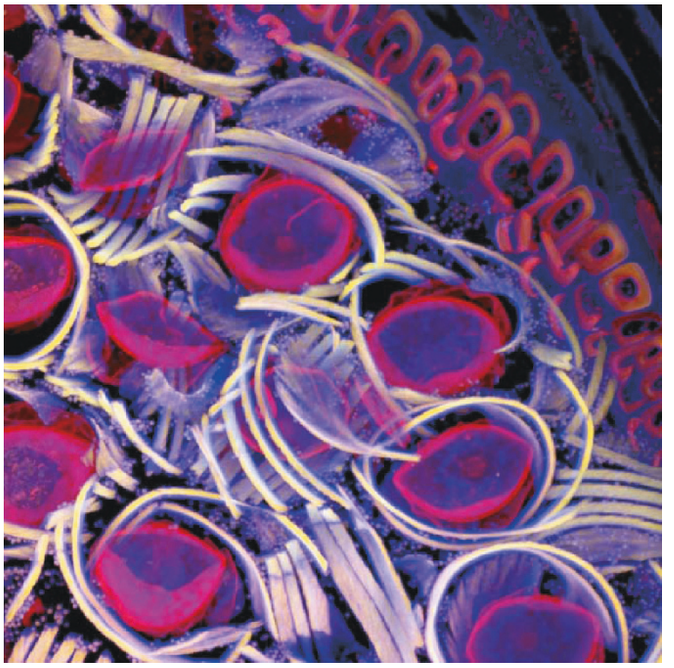


FIGURE 44.5. Confocal microscopy of *Equisetum arvense* spores. *Equisetum* sporangiophore tissue was fixed, cleared in xylene, embedded in paraffin, sectioned using a microtome, and stained with Safranin O and Fast Green FCF. A *z*-series of three-channel color images were collected using a Leica SP confocal microscope with laser excitation at 488 nm, 568 nm, and 633 nm. These were visualized using a maximum intensity projection algorithm. Spores can be seen within the sporangiophore. The spores are surrounded by exosporial elaters, and lignified cells involved in sporangial dehiscence are seen (top right).

Clearing Intact Plant Material

The three-dimensional (3D) anatomical arrangements of plant cells have conventionally been observed using microtomy techniques. However, the laborious nature of thin sectioning, the problem of obtaining the desired plane of section, and difficulty of obtaining a complete series of sections has limited its use to the skilled and patient. Optical sectioning has many advantages from the point of view of speed and simplicity, and it allows software reconstruction of whole mount specimens, assembled from a series of *z*-axis images. However, it is difficult to observe cellular details deep in living plant tissue. Any light penetrating the tissue must pass through many layers of cytoplasm, watery vacuoles, and highly refractile cell walls. The different refractive indices of the material contribute to spherical aberration, and particulate subcellular matter also causes light scattering. Various techniques have been developed in order to produce samples with glass-like optical properties and to maximize image quality. Clearing agents, such as xylene, clove oil, cedar oil, and chloral hydrate have been adopted and combined with compatible mountants such as Canada balsam and Hoyer's solution. All of these reagents have a high refractive index similar to that of glass (~1.55). As a result of these clearing treatments, tissue sections become more transparent, greatly reducing problems with light scattering and spherical aberration as long as oil-immersion lenses are used. This allows high-resolution imaging of thin sections. When the same techniques are applied to thick sections or whole mounts, the results of clearing are even more startling. However, the stain or fluorochrome is generally distributed throughout the cleared tissue and details deep in the sample are still obscured by overlying signal. Here the confocal laser-scanning microscope proves its worth. High-resolution optical sections can be collected to distances of greater than 200 µm in such cleared samples. The depth of image collection is limited mainly by the working distance of available high numerical-aperture objectives. The application of classic, highly fluorescent stains and clearing techniques creates a new field of opportunities for modern confocal microscopy and computerized display methods.

Recently, classic botanical methods have been modified to allow intense and specific staining of plant cells and clearing for 3D microscopy. For example, Aniline Blue has been used as a stain for the cell contents of *Arabidopsis* embryos subjected to 3D imaging (Bougourd *et al.*, 2000). More recently, plant carbohydrates have been labeled by treatment with periodic acid to

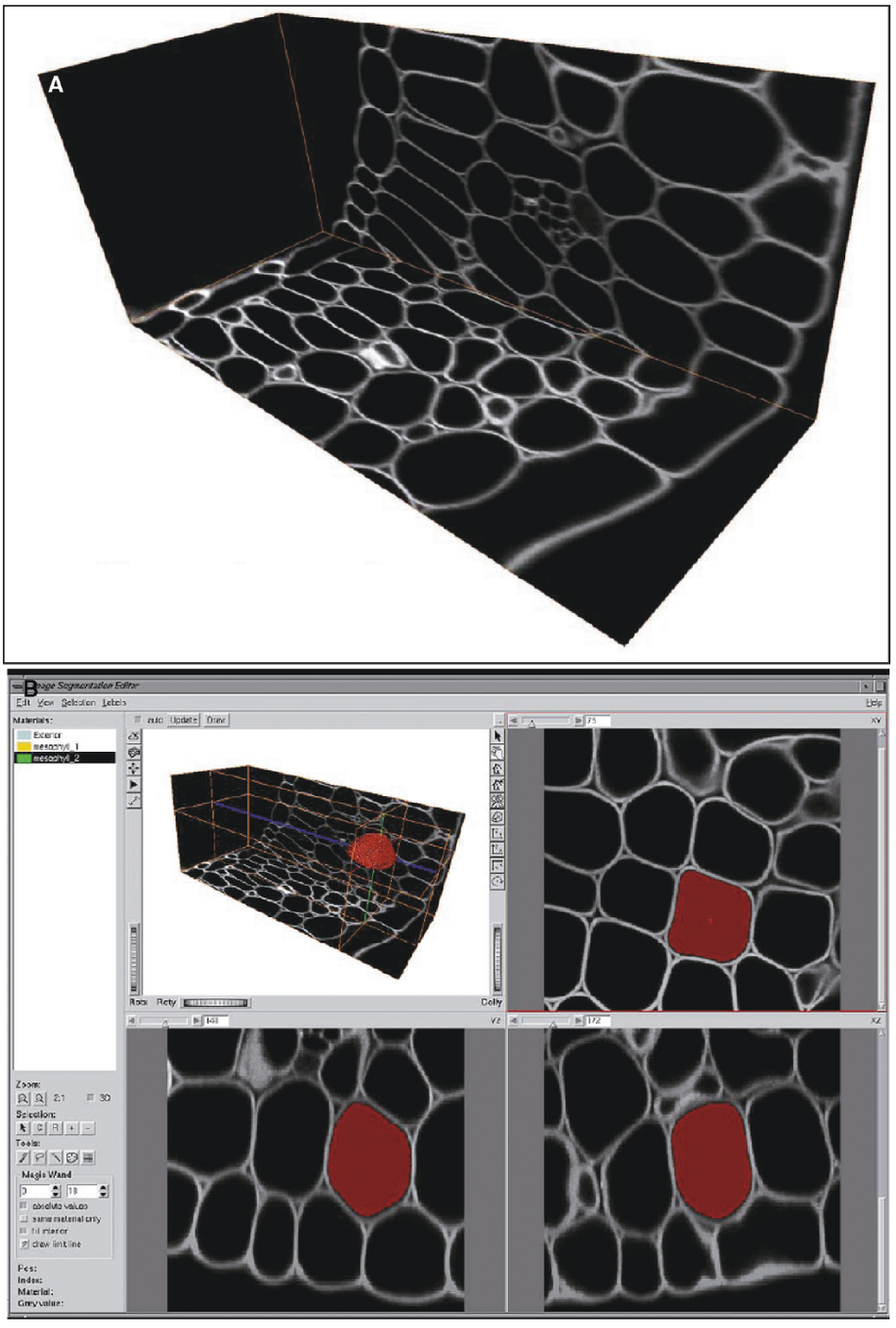


FIGURE 44.6. (A) Deep optical sectioning of cleared *Arabidopsis thaliana* root tissues. Mature *Arabidopsis* embryos were treated with periodic acid to produce aldehyde groups within carbohydrates, and stained using a pseudo-Schiff reaction to specifically label the cell walls. The tissues were mounted in a chloral-hydrate-based clearing agent for microscopy. The combination of clearing and intense staining allows deep optical sectioning of an entire embryo cotyledon. A series of 736 optical sections were obtained to span the cotyledon, producing a dataset with a depth of 147 µ*M*. (B) 3D segmentation of plant cells. A series of confocal optical sections, corresponding to a segment of cotyledon from an *Arabidopsis* embryo, is visualized using the AMIRA orthogonal slicing routines. The AMIRA 3D segmentation editor was used to seed and label particular voxels that correspond to chosen plant cells within the confocal dataset. The use of a specific cell wall stain allows easy selection of the internal volumes of individual cells. A closed, triangulated surface could then be formed over the selected group of voxels, using a marching-cubes algorithm. Rendered cells are displayed at the correct position and scale within the dataset, to build an accurate representation of the shapes, arrangement, and connectivity of cells within the tissue.

produce aldehyde groups that are reacted with fluorescent pseudo-Schiff reagents. If fixed plant tissue is treated in this way, cell walls (and starch-containing plastids, if present) become intensely and covalently labeled with the fluorophore. The labeling of wall material produces a complete outline of each cell. The tissue can then be directly cleared in a high-refractive-index agent containing chloral hydrate, and mounted in Hoyer's solution for microscopy [Haseloff and Bougourd, unpublished results; Fig. 44.6(A)]. The combination of high levels of fluorescence and high refractive index mountant allows the collection of extended *z*-series images at very fine resolution (0.1–0.5 µM steps), using a confocal aperture close to 1 Airy unit, and without fear of photobleaching or signal and resolution loss due to spherical aberration. Imaging to a depth of around 200 µm allows simple optical sectioning throughout an entire *Arabidopsis* root at high resolution. In fact, every cell within a mature *Arabidopsis* embryo can be clearly visualized (Fig. 44.6).

3D Reconstruction

The basic features of a plant's body plan are established during embryogenesis, but its final form results from the continued growth of meristems and the formation of organs throughout its life, often in a modular and indeterminate fashion. Because plant

cells are constrained by rigid cell walls and are generally non-motile, there is the clear possibility that cell fates within a meristem are determined by lineage. However, evidence from plant chimera and wounding studies have demonstrated a more important role for cell–cell interactions during fate determination. It is likely that, during plant development, positional information is exchanged between cells, and that the fate of cells within a developing tissue is determined by a network of local cellular interactions. In order to dissect such a network, it is crucial that we can clearly map individual cells and their neighbors inside intact meristems — and have means to manipulate them. Thus, the cellular anatomy of plants is of particular relevance to the understanding of development and morphogenesis.

Three-dimensional visualization techniques similar to those used in medical imaging can be applied to confocal datasets. This involves the selection and labeling of particular voxels that correspond to a 3D object of interest. Various techniques are available for selecting volumetric objects, which range from the fully manual to automatic tools that detect volume boundaries through differences in local intensity or texture (see Chapters 14 and 15, *this volume*). The use of specific staining techniques can aid the labeling process. For example, cell wall staining produces an outline of every cell in the tissue. This is very helpful as it allows the use of automatic segmentation tools to determine the interior volume of a chosen cell. We routinely use AMIRA, a general-purpose physical modeling and data visualization program (Mercury Computer Systems, www.tgs.com), for our 3D visualization and segmentation [Fig. 44.6(B)]. The software provides an interface for visualizing large multi-dimensional confocal microscopy datasets. AMIRA provides a very useful set of input/output, data handling and visualization modules, and allows software routines to be combined in a modular fashion. This allows specialized 3D reconstruction and visualization techniques to be applied in a flexible way to different types of data, including confocal datasets. In addition, a developer's version, AMIRADev, allows the incorporation of custom visualization techniques. The program provides a simple interface, sophisticated, fast visualization routines, is affordable and robust, and is suitable for both high-end PC and UNIX hardware.

3D Segmentation

High-resolution confocal datasets can be rapidly segmented to allow direct visualization of cell arrangements within intact plant embryos and meristems. The large data files, up to 250 MB in size, can be directly rendered to allow excavation of the data, production of sections in arbitrary planes, and rendering of surface features. In practice, cells are generally chosen by placing a "seed point" manually within the center of a cell in the confocal dataset. This seed is then inflated in three dimensions to find the cell boundaries that are marked by a high staining intensity (Fig. 44.7). The program provides a segmentation editor for this purpose [Fig. 44.6(B)]. The exterior geometry of a segmented cell can then be described using a "marching cubes" algorithm, which if needed can be converted to a solid geometry for the computer-assisted milling of 3D models or for finite element analysis [Fig 44.8]. We can now routinely reconstruct the cellular structure of entire meristems for various experiments.

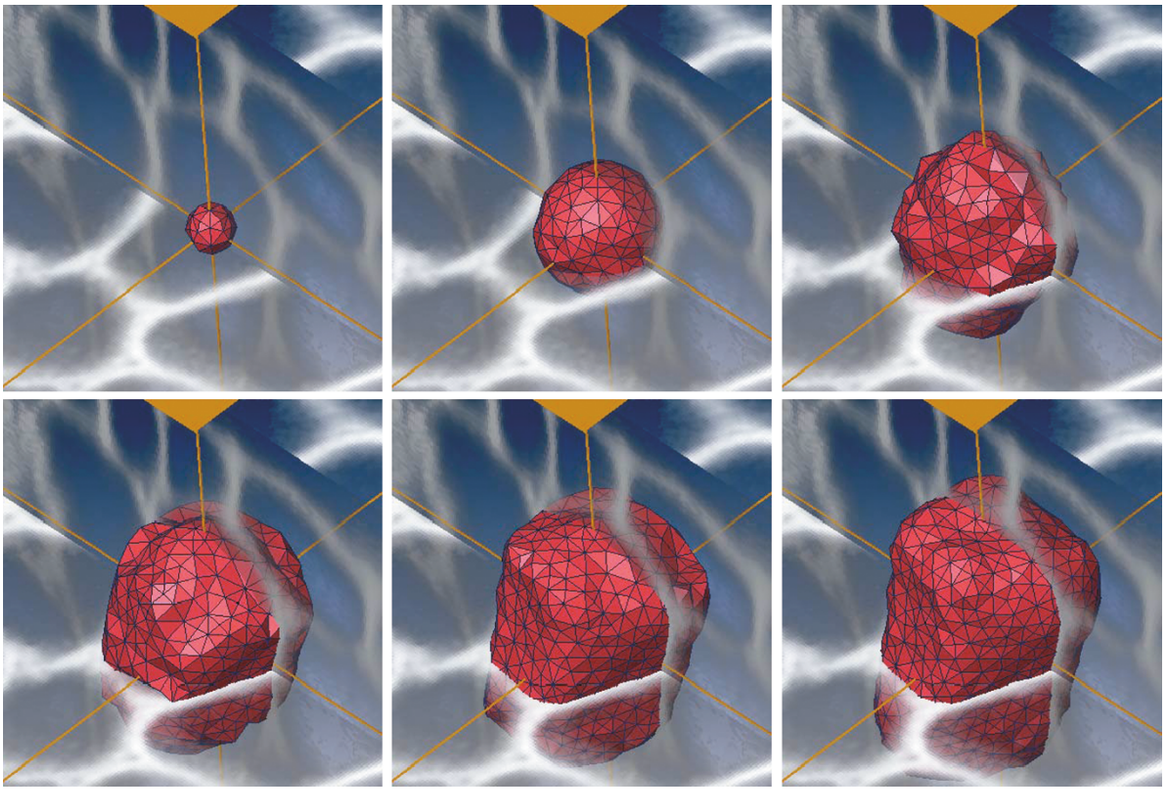
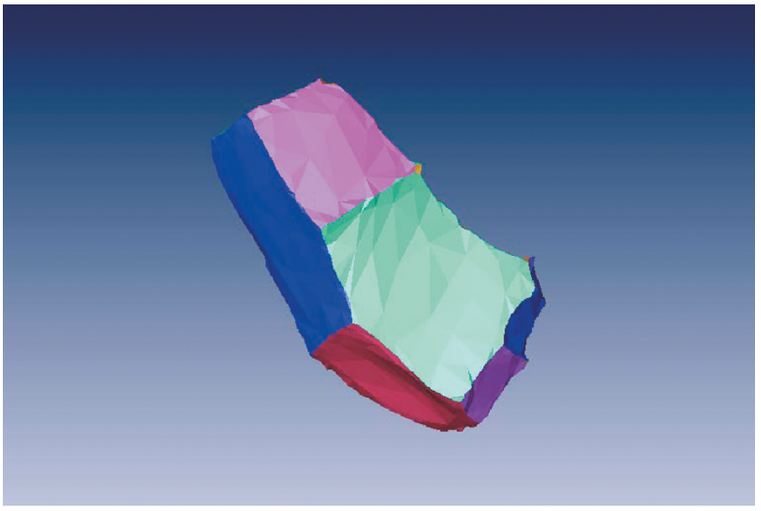


FIGURE 44.7. Balloon model-based segmentation of plant cells. A deformable-mesh algorithm for segmentation was implemented in C++ as a software module inside AMIRA. The module allowed the interactive placement of a seed mesh within the dataset (top left panel). The surface was then inflated using a discrete-time physical model. Expansion was accompanied by adaptive subdivision of the surface during inflation, and ultimately was constrained by a "force" based on the image intensity gradient vector. Vertices on the surface are attracted to intensity maxima in the data, which correspond to the stained boundaries of the cell.



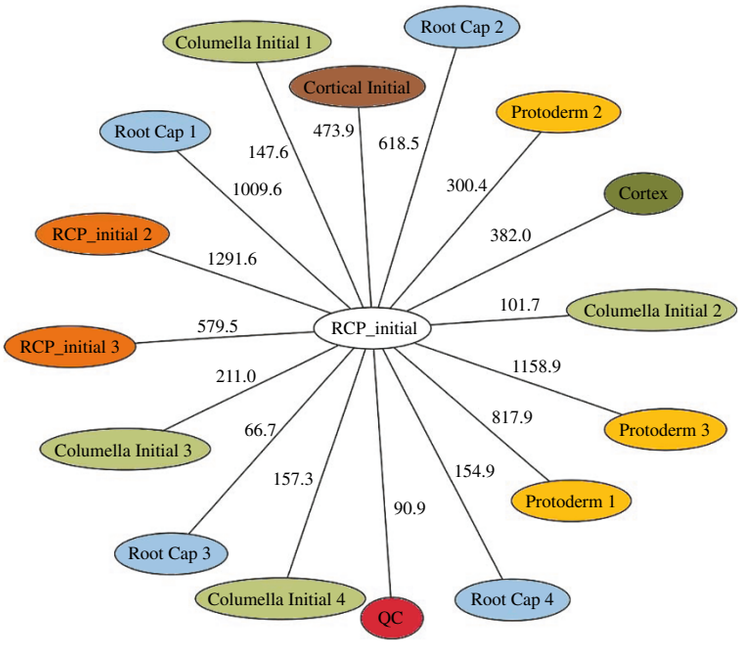


FIGURE 44.8. (A) Watershed algorithm for segmentation. Code from the National Library of Medicine Insight Toolkit (www.itk.org) was adapted to provide a watershed algorithm for the AMIRA visualization platform. The algorithm was applied to a 3D dataset derived from the root primordium of an *Arabidopsis thaliana* embryo. A single, root-cap protodermal initial cell from the segmented dataset is displayed, and its different shared walls are shown color-coded. Each colored segment corresponds to a connection with a different neighboring cell within the meristem. (B) Graph of 3D connections between cells. Using the dataset shown in (A), an adjacency network was computed and cell–cell contact measured. This data was represented using graph-generation software (AT&T Graphvis). The 16 cells making contact with the root cap–protodermal initial (RCP_initial) are shown on the diagram, with measurements of the area of each cell–cell contact.

There are many opportunities for improved analysis of this kind of 3D dataset. For example, plant cells are generally convex and simple in shape, and this allows the use of a more robust model-based segmentation approach: a deformable mesh can be placed within a 3D dataset at chosen seed points and inflated (McInerney and Terzopoulous, 1996). The mesh simulates an elastic surface expanding from the interior of a cell. The surface evolves through a discrete-time physical model and adaptively subdivides to fit the object boundary (Fig. 44.7; Rudge and Haseloff, unpublished results). This type of model-based segmentation is much less sensitive to noise in the experimental data and produces a compact description of plant cell shapes directly. Other techniques produce an intermediate segmented volume, from which a surface must be generated and smoothed.

In addition, it is possible to automatically obtain a measurement of the number and area of shared walls between cells and their neighbors. These values are highly relevant biologically as they correspond to shared walls that contain plasmodesmata, provide conduits for informational molecules that regulate cell behavior, and are an important parameter for modeling approaches. The watershed algorithm is based on the metaphor of water catchment basins in a landscape. First, an initial classification of all points into catchment-basin regions is done by tracing each point down its path of steepest descent to a local minima. The confocal image intensity is used as the landscape height. This process gives ridges between cells and shows slightly uneven terrain in the cell interiors. Next, neighboring regions and the boundaries between them are analyzed according to minimum-boundary height to produce a tree of merges among adjacent regions. By changing the "flood level," we can interactively traverse the merge tree and thus finely tune the segmentation. The technique produces a single boundary between cells with no empty, unclassified intervening space. We can use this property to compute an adjacency network for the cells and measure cell–cell contact areas. This can then be represented diagrammatically using graph-generation software (Fig. 44.8; Rudge and Haseloff, unpublished results).

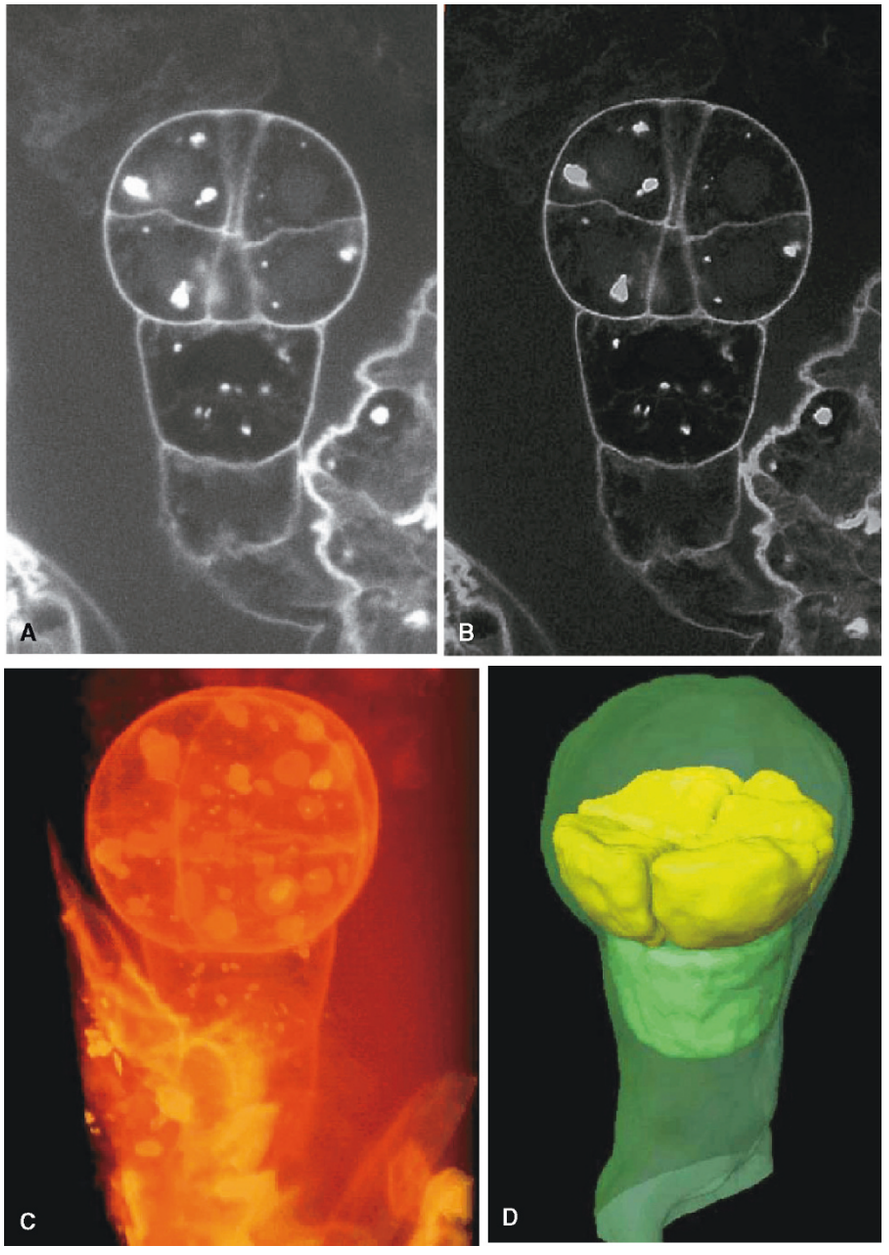


FIGURE 44.9. Three-dimensional reconstruction of cell arrangements within an *Arabidopsis thaliana* embryo. (A) An 8-cell *Arabidopsis* embryo was treated with periodic acid and stained, using propidium iodide as a pseudo-Schiff reagent. The sample was cleared with chloral hydrate and mounted in Hoyer's Solution. A *z*-series of confocal optical sections was collected, and a single optical section from near the middle of the 3D dataset is shown. (B) The 3D image was then processed using a deconvolution algorithm (Huygens Essential, Scientific Volume Imaging). A single optical section is shown from the processed volume. Deconvolution results in improved image detail and S/N. (C) Visualization of the deconvolved 3D dataset, using the Voltex module in AMIRA, provides direct volume rendering. The stalk-like embryo and some surrounding maternal tissues can be seen. (D) Cells in the lower tier of the embryo (yellow) and upper cell of the suspensor (green) have been segmented, converted to new geometrical surfaces, and visualized within the dataset. The cells are shown within a semi-transparent outline of the embryo. Extracted cell geometries can be used to define regions of interest, or co-visualized with the original microscopy data.

These computer visualization methods, which are adapted from the medical imaging field, reduce large datasets to a much more compact and simple description of the 3D shapes and relative arrangement of cells in a meristem or embryo (Fig. 44.9). Because cell–cell signaling plays such an important role in plant development, these techniques show much promise for the analysis of genetically perturbed plants, and as a basis for modeling the cellular interactions themselves.

TWO-PHOTON EXCITATION: ARE TWO BETTER THAN ONE?

Recently, two-photon excitation (TPE) fluorescence microscopy has become a common tool in many advanced cell biology laboratories. A growing body of literature points to several advantages of TPE over other fluorescence imaging methods, with improved signal-to-noise ratios, deep penetration, and benefits for living-cell imaging (Feijó and Moreno, 2004). TPE microscopy is still in an early stage of development and reproducible protocols, probes, and applications remain relatively scarce. However, botanical techniques already in use provide clear advantages. In particular, TPE is relatively immune to the presence of out-of-focus absorbing structures. This section covers some of the aspects of imaging plant cells using TPE.

Improved Signal-to-Noise Ratio and Dynamic Range

Of all the possible advantages of TPE microscopy, the one we feel most confident to stress is the high signal-to-noise ratio (S/N) and dynamic range of the final signal. Generally speaking, once conditions have been sufficiently optimized to produce a good image, TPE provides better contrast, crispness, and image quality. Numer-

ous examples of this rule have been shown elsewhere (Feijó and Moreno, 2004, and references therein; see also Chapter 21, *this volume*). Comparison of images collected using single- and two-photon excitation showed much better detail and signal-to-noise ratio for the TPE data, especially for tangential sections at the extremes of a deep *z*-stack. On such sections, TPE resolves without loss of dynamic range, whereas confocal microscopy gives blurry and ill-defined images (Fig. 44.10). Consequences of this increase in S/N ratio and dynamic range become even more evident on deep/thick or whole-organ imaging. In a quantitative comparison with confocal and widefield epi-fluorescence, TPE was recently shown to outperform the other methods in terms of effective resolution (Cox and Sheppard, 2004).

Imaging Thick/Opaque Specimens

The second generally accepted TPE advantage is its capacity to image deep into tissues that usually allow poor or no penetration in confocal microscopy. This trend is well reflected in the literature and in our own studies on whole-organ imaging of *Arabidopsis* (Feijó and Moreno, 2004). However, it should be pointed out that the ability to image whole organs or thick tissues varies tremendously, especially in plants. Although people have been able to image >500 µm into living brain (M. Vaz Afonso and T. Bonhoeffer, personal communication), brain tissue is far less opaque than most plant tissues. As a result, penetration values this large are very uncommon for botanical specimens unless they have first been fixed and cleared.

On some tissues, we could not penetrate through more than the epidermis (e.g., *Arabidopsis* living styles), apparently because it is covered with an outer cuticle that is so opaque that deeper penetration requires laser power levels that damage the tissue (they can literally boil the epidermal cells). Other tissues (e.g., immature anthers of *Agapanthus*) are reasonably transparent and allow live imaging up to the full working-distance of a high-resolution oil-immersion lens (ca. 200 µm). Roots usually allow much deeper imaging than leaves or other green tissues [Fig. 44.10(A,B)]. Add a low level of stain to these absorption problems, with the frame averaging and the extra excitation/fading this implies, and one can see that any estimate on how deep one can go must be assessed on a case-by-case basis.

Several direct comparisons of confocal and TPE microscopy are offered in the literature. Vroom and colleagues (1999), working on microbial biofilms, made a quantitative comparison of signal intensity, and concluded that, compared to confocal, they were able to record images four times deeper and that these deep images did not lose contrast. In fixed material embedded in Nanoplast resin, TPE showed improvements both in penetration, contrast, and fade resistance (Decho and Kawaguchi, 1999). A practical example in which this improvement led to novel information was documented by Meyer and Fricker (2000). While studying glutathione distribution in different tissues, TPE provided more detail from optical sections deep in the tissue with less signal attenuation, and this ability was pivotal in being able to distinguish vacuoles from cytosol and to get a better separation of the sequestered signal.

On a more technical level, Sun and colleagues (2001) showed that the attenuation of the excitation signal in plant tissues is reduced with TPE. More significantly, Cheng and colleagues (2001b) made probably the most thorough analysis of signal attenuation as a function of the excitation wavelength (see Chapter 21, *this volume*). They determined that in mesophyll cells and whole leaf, while major attenuation of the signal occurs only below 700 nm (the major peak of attenuation at ca. 690 nm, attributable to chlorophyll absorption), the attenuation decreases continuously up until about 1000 nm, which makes it clear that the longer the wavelength, the less appreciable will be the attenuation of the excitation signal.

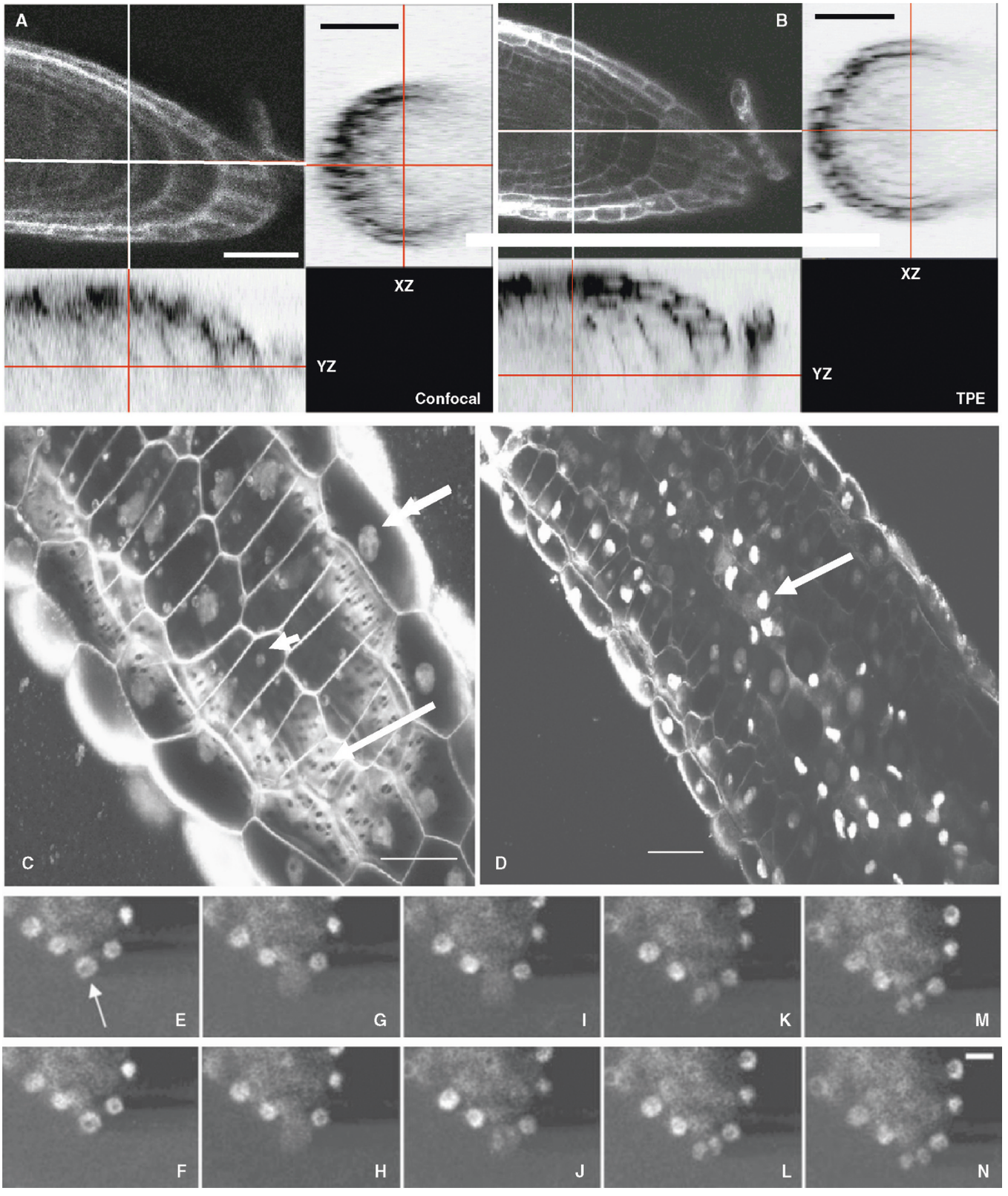
Better dynamic resolution and improved penetration are easy to demonstrate in a number of *Arabidopsis* organs. Figure 44.10 (A,B) shows an application to whole, living roots, in which the cell walls have been stained with propidium iodide (PI) at a vital concentration. Comparison of Figure 44.10(A) (confocal) with Figure 44.10(B) (TPE) makes it clear: TPE provides high contrast and resolution to the mid-sagittal level of the root, in both *yz*- and *xz*-projections, and up to the 10th cell layer (the red lines indicate the relative position of the *zz′*-projections). This comparison is especially noteworthy as exactly the same specimen, optics, and acquisition protocol were used to obtain both images, and the only changes were the excitation source and the pinhole aperture (1 Airy unit for confocal and wide open for TPE). Because roots are cylindrical, this level of performance makes it reasonable to speak of the high-resolution characterization of an entire living root. In contrast, under the very same imaging conditions, confocal resolves no better than five cell layers (note that the red line indicating the projection plane is not even over the central stellar tissues), and the contrast and definition shown on the negative-contrast projection shows a clear deterioration of the signal as the image plane goes deeper.

In other organs, such as living leaves of *Arabidopsis*, penetration is much more limited (Feijó and Moreno, 2004). While one can appreciate improved dynamic range and better structural accuracy (specially with external, non-descanned PMTs), compared to confocal, TPE penetration was still barely more than 50 µm (see also Chapter 21, *this volume*). The conspicuous presence of abundant chloroplasts explains this result. Not only is penetration impaired, but specimen damage also becomes an issue. Complex interactions among all the pigments present can generate a number of potentially harmful products that may make TPE even more damaging than confocal in green tissues (see next section).

We have imaged living anthers at power levels consistent with structural recording of dynamic processes (Feijó and Cox, 2001). Both DNA stained with 4′-6-diamidino-2-phenylindole (DAPI) and autofluorescence from the cell walls contribute to the observed fluorescence at 780 nm [Fig. 44.10(C,D)]. Under TPE, DAPI fades very little and produces a strong signal over an excitation bandwidth of more than 100 nm (720–850 nm). In confocal microscopy, the autofluorescence of the inner cell layers makes it difficult to image deeper than two to three cells, leaving the important *tapetum* and the sporogenic/meiotic cells occluded. However, under TPE, anthers show more transparency, allowing sections close to 200 µm [Fig. 44.10(B); 6–7 cell layers deep], which is the working distance limit of a high-NA immersion lens (in this case, a Nikon PlanApo, 60×, NA 1.4, oil). Remarkably, the same level of laser excitation was used to acquire the entire *z*-stack from the surface epidermis to the central sporogenic tissue [Fig. 44.10(A.B)]. With these improvements, an exquisite degree of contrast and detail is obtained in images of the pit fields and wall stress fibers in tangential/oblique optical sections of intermediary cell walls [Fig. 44.10(A), arrow]. The ability to image the mid-sagittal section of an anther allows direct viewing of the activities of meiotic cells (Feijó and Cox, 2001).

Fading, Vital Imaging, and Cell Viability

Two-photon excitation is effectively confined to a sub-femtoliter volume at the point of focus within the sample, and although it is


A
XZ
YZ
Confocal
B
XZ
YZ
TPE
C
D
E
G
I
K
M
F
H
J
L
N

generally agreed that TPE can minimize phototoxicity and fading during microscopy (Potter, 1996), a word of caution is due in many situations. As both damage and signal is proportional to (at least) the square of the power, power control is often a critical issue. Fragile tissues or those that dissipate heat poorly may pose a problem. For example, thin, fixed, sectioned materials (e.g., specimens used for immunolabeling) are sometimes much more difficult to image with two-photon than using widefield or confocal microscopy, because, in the focus plane, fading occurs more strongly with TPE. Clearly, TPE is not a cure-all.

It takes some effort to determine the best experimental conditions for vital TPE imaging, and it is particularly important to find the best balance between power, excitation wavelength, and probe concentration (when controllable). It usually implies a careful search for the best wavelength (one that maximizes S/N while minimizing photodamage) and then setting the power level so that there is just enough signal to form an image. The tuneability of titanium : sapphire (Ti : Sa) laser sources allows one to search for the optimum excitation wavelength, and this often leads to the choice of a wavelength away from the peak in the excitation spectrum. Continuous wave laser sources used for confocal microscopy are generally restricted to a small number of discrete excitation wavelengths, which makes this sort of optimization impossible. As a rule of thumb, the longer the wavelength the less the damage. Even at low power, using wavelengths less than 800 nm often causes much more damage in the form of fading, arrest of streaming or even slowing growth. A second rule of thumb is that wavelengths longer than 870 nm are almost always more suitable for imaging plant cells. Finally, dye molecules that are more asymmetrical (e.g., DAPI) tend to show better results than symmetrical ones [e.g., fluoroscein isothiocyanate (FITC)]. In symmetrical molecules, usually more than one excitation peak is obtained, and using the longer wavelength tends to produce much better results in terms of less fading, even though it may also show less emission.

An exhaustive analysis and comparison of metabolic imaging led Fricker and Meyer (2001) to conclude that TPE might be the best means to study primary metabolism *in vivo*, if and when the relevant probes are produced and optimized. Because pollen tubes show easily observable signs of vitality in the form of streaming and growth, we have used them to assay comparative phototoxicity. Being relatively resistant to radiation, they can also be used to studying fading (Feijó and Moreno, 2004). When viewing sensitive features such as actin dynamics, streaming, growth rate, pump activity, etc., TPE always seems to produce superior results when operated above 870 nm. For example, expression of an ADF : GFP construct that labels actin microfilaments in pollen tubes, combined with TPE allowed the collection of up to 600 sequential frames without interval, without producing noticeable fading, and with minimal effect on cell growth rates.

Figure 44.10(E–N) illustrates another example of a result difficult to achieve using confocal microscopy. Phil Benfey's laboratory produced lines of *Arabidopsis* with GFP (von Arnim *et al.*, 1998) fused to the putative transcription factor *Shortroot* (*SHR*) under the control of its own promoter and these were then imaged using TPE in our laboratory. Again, better contrast, dynamic range, penetration, and sensitivity were obtained, and the whole root was imaged down to the distal side of the central stele using TPE at 920 nm. Despite the weak signal, a diffuse cytosol labeling was discernible in the central stele cells and labeling in the nuclei of the endodermis shows a perfectly resolved and exclusive perinuclear location of *SHR*. Many of these features are not easily resolved in the equivalent confocal images. The TPE images helped to support the exciting finding that transcription factors may move between cell layers (Hake, 2001; Nakajima *et al.*, 2001), and *SHR* was assigned a role in defining cell fate in the root (Nakajima *et al.*, 2001). The sequence in Figure 44.10(E–N) shows frames of a division of a root meristematic cell (arrow), in which the putative transcription factor diffuses out during nuclear envelope breakdown and later re-aggregates in the two daughter nuclei. Using standard confocal, the signal faded before all the data could be collected because the extremely low fluorescence levels required a number of frames to be averaged to produce each high-definition optical section (G. Senna, 2002, personal communication). In the TPE results shown here, not only was fading reduced to a manageable level, but the radiation seems not to have affected either the division cycle or root growth to any measurable extent.

FIGURE 44.10. Imaging of a whole, living root of *Arabidopsis*, vitally stained with PI (10 µg/mL; wild-type root at ca. 8–12 days after germination) with confocal (A) and TPE (B) microscopy. In healthy cells, the membrane is impermeable to PI, rendering the cell wall fluorescent and clearly defining the cell boundaries. (A) The central confocal image shows an optical section 30 µm deep. The right and bottom panels show negative images of *xz* and *yz* reconstructions of the whole *zz*-stack acquired (confocal excitation using the three visible-light lines of the Kr : Ar-ion laser, emission filter HQ 598/40; the stack was acquired with 0.5 µm steps). The lines mark the relative position of the reconstructions on the central image, or the depth of the specific plane shown on the side panels. Wall boundaries, although visible, are diffuse, despite generous use of Kalman averaging. Three-dimensional projections accentuate that feature, and the *xz*-image shows little contrast and resolution beyond 4 to 5 cell layers. Thus, it is only possible to image the half-diameter of the whole root up to about 100 µm from the tip and the important context of the central stele is lost. Bar = 50 µm. Plan Fluo 40×, oil-immersion objective (NA 1.3). However, under TPE (B), anthers show more transparency, allowing sections close to 200 µm [Fig. 44.5(B); 6–7 cell layers deep], the working distance limit of a high-NA immersion lens. (Reproduced from Moreno and Feijó, 2004, with permission from Springer-Wien.) (C) Image of a living *Agapanthus umbelatus* anther, stained with DAPI. This organ is very translucent, permitting imaging up to the working-distance limit of a high-NA objective (ca. 200 µm, montage from surface to ca. 200 µm is shown from a to f). Nuclei (C, *double arrow*), cell walls (*arrow*), and plastids (*arrowhead*) all show some autofluorescence. (D) A tangential optical section through the cell wall of the third to the fourth cell layer reveals pit fields and cellulose stress directions with exquisite detail. Detailed nuclear structure is clearly visible up to the seventh cell layer, eventually reaching the central meiocyte tissue (B, *arrow*). Imaged with a Plan Apo 60×, oil-immersion objective (NA 1.4); excitation, 780 nm; no barrier emission filter, internal PMT. Bars: (C) 20 µm; (D) 50 µm. (Reproduced from Feijo and Cox, 2001, with permission from Elsevier.) (E–N) Time-lapse sequence of the division of a meristematic cell in the apex of a lateral root of *A. thaliana* that is expressing a fusion protein constructed of SHR and GFP. The montage was extracted from a sequence acquired with a rate of 1 frame/5 min over almost 3 h. During that period the root grew unaffected, and several meristematic and endodermal cells divided. In this sequence, a meristematic cell is shown throughout the cell cycle: the SHR : GFP fusion protein is first located at the periphery of the nucleus (E, *arrow*), but diffuses to the cytosol as soon as the nuclear membrane disappears (G). At this stage, the fluorescence seems continuous with the central stele cells (G–I). Following division and by the onset of cytokinesis (J–L) the nuclei are again discrete and SHR : GFP is again visible in the two daughter nuclei (K–N). (Excitation, 920 nm; emission, 530 nm; external PMT.) Bar = 10 µm. (Reproduced from Feijó and Moreno, 2004, with permission from Springer-Wien.)

Again, a word of caution should be issued. Potential pitfalls will remain until the right conditions to image specific probes in particular tissues are better defined. Until then, any study should be undertaken systematically, with time allowed for long sessions in which the procedures can be optimized for a particular experimental condition.

There are also cases where confocal provides the faster and more reliable path. In a recent case reported by Reddy and colleagues (2004), the shoot apical meristem (SAM) was imaged in an attempt to resolve a number of cell and organ-fate issues (Running, *et al.* 1995). A number of transgenic lines with markers of cell division and cell fate were created, and methods were developed for imaging the shoot growth on the same confocal plane for over a week. The workers were able to image deep stacks encompassing the whole meristem down to the first primordia every 4 h (Reddy *et al.*, 2004). Using Zeiss optics and confocal scanner, they made extensive comparisons with TPE and concluded that confocal significantly outperformed TPE in terms of keeping the SAM growing and dividing (Reddy, personal communication). Being a green tissue, these results come as no great surprise because, as we discussed in the autofluorescence section, the complex interaction between pigments and the high levels of near-infrared radiation makes it predictable that green tissues will always pose a problem for TPE imaging. This example should definitely be kept in mind when deciding on the amount of time and effort one might need to develop a viable protocol with a new method.

Two-Photon Imaging of Plant Cells and Organelles

To date there is a growing body of literature showing the application to TPE of practically all of the common dyes and labels used for visible, one-photon fluorescence. Here we restrict ourselves to plant applications, plus our own experience managing a multi-user facility (see also Table II in Feijó and Moreno, 2004; Chapter 17, *this volume*). Again, most information regarding the use of different dyes with TPE should be considered preliminary and dependent on the specific experimental context (dye, vital/fixed samples, microscope, etc.). The available information should be used as a starting point for the process of fine-tuning. Implicit in this statement is the recognition that it is difficult to obtain clear reproducible spectra for TPE excitation. In contrast to confocal microscopes and spectrofluorimeters, in which power can be kept within close tolerances and the average level has little variation, TPE depends critically on the peak power, which changes dramatically (i) along the tuning range of most ultrafast lasers, (ii) with position inside the focal volume, and even more so (iii) with the pulse width. Generally speaking, longer wavelengths provide shorter pulses, hence higher peak powers. To complicate matters, the average output power of a Ti : Sa laser peaks at around 800 nm, but falls off rapidly at the extremes of the tuning range. As most biology laboratories do not possess (or want to!) the very complex analytical instruments necessary to measure TPE cross-sections properly, wavelength-optimization routines are more likely to be based on somewhat crude empirical experiments. Data are often hard to reproduce directly on another system with different optics and design, but the experimental parameters are often close enough to indicate a range for optimization. One important reference that should be kept in mind is the classic work of Xu and Webb (1996) listing spectra for most of the commonly used dyes. [For updates, check the largest library of TPE spectra at www.drbio.cornell.edu; a small list of commonly used dyes is also given in Diaspro and Robello (2000).]

The ultraviolet (UV)-excited DNA dyes DAPI and Hoechst 33342 are TPE dyes *par excellence* and it is of no surprise that one or the other has been used in every paper published so far to illustrate the TPE principle (e.g., Denk *et al.*, 1990; König, 2000; Tirlapur and König, 2002). In plant tissues other than the classic onion root system, these dyes have been used to image live meiotic nuclei in anthers (Feijó and Cox, 2001), nuclear distribution during arbuscular mycorhization of *Aspergillus nidans* and tomato (Bago *et al.*, 1999) and deep imaging in nanoplast-embedded tissues (Decho and Kawaguchi, 1999). The popularity of these dyes is due to the fact that they are extremely bright and fade resistant under TPE, and that they can be excited over a wide range of wavelengths (720–850 nm for DAPI in our system), a feature that facilitates double- and triple-labeling as well as searches for the best vital imaging conditions.

TPE of Nile Red has been used to follow the mobilization of lipid globules in fungal hyphae (Bago *et al.*, 2002). Autofluorescence was used for high-resolution dynamic analysis of chloroplast division (Tirlapur and König, 2001) and to study the cell wall (König, 2000).

Perhaps one of the most interesting and informative trends relates to TPE visualization of glutathione (GSH). The method was introduced to plants by Fricker and colleagues (2000), and it uses the dyes monochlorobimane (MCB) and monobromobinane (MBB), which complex with GSH to produce glutathione-S-bimane (GSB). Under normal confocal, these workers determined the concentration of GSH to be 2 to 3 m*M* in most cell types. However, using TPE, they were able to obtain more detail with less signal attenuation deep in the tissue and this was pivotal in distinguishing vacuoles from cytosol to get a better separation of the sequestered signal (Meyer and Fricker, 2000). Only under TPE was it possible to measure that GSH concentration in trichoblasts (2.7 ± 0.5 m*M*) was significantly different from that in atrichoblasts (5.5 ± 0.8 m*M*). More recently, trichomes were shown to have 300× more GSH than cells from the basement layer and the epidermis (Gutierrez-Alcalá *et al.*, 2000). These, and other results, support the conclusion that TPE is currently the best approach to studying primary metabolism *in vivo* (Fricker and Meyer, 2001; Meyer *et al.*, 2001).

Two-Photon Excitation Imaging of Green Fluorescent Protein

TPE is well suited for viewing GFP in plants (Xia *et al.*, 1999, Volkmer *et al.*, 2000), and indeed GFP is easily excitable at a wide range of wavelengths and in combination with other dyes, such as propidium iodide [Fig. 44.3(F)]. Special manipulation of the GFP levels have been used to raise signals above the wild-type chlorophyll autofluorescence by using "super" promoters, such as 35S35SAMV, driving especially bright GFPs, such as S65T, a combination successfully used to visualize mitochondria using TPE with good S/N even in green tissues (Köhler *et al.*, 1997). This example points to the need to consider the different kinds of GFP currently available.

The first one introduced was the wild-type GFP which, while excitable at about 800 nm, faded rapidly, perhaps even more so than with confocal. This and other problems led to the development of several enhanced forms of GFP. Here we offer data about some of the commonly used forms: Clontech's EGFP, Jim Haseloff's mGFP forms (Siemering *et al.* 1996; Haseloff *et al.*, 1997) and also the forms engineered by Chiu and colleagues (1996) and by von Arnim and co-workers (1998).

Clontech's version is perhaps currently the most popular. It shows a relatively broad TPE excitation peak from 920 to 940 nm, but can hardly be visualized below 900, unless under very strong

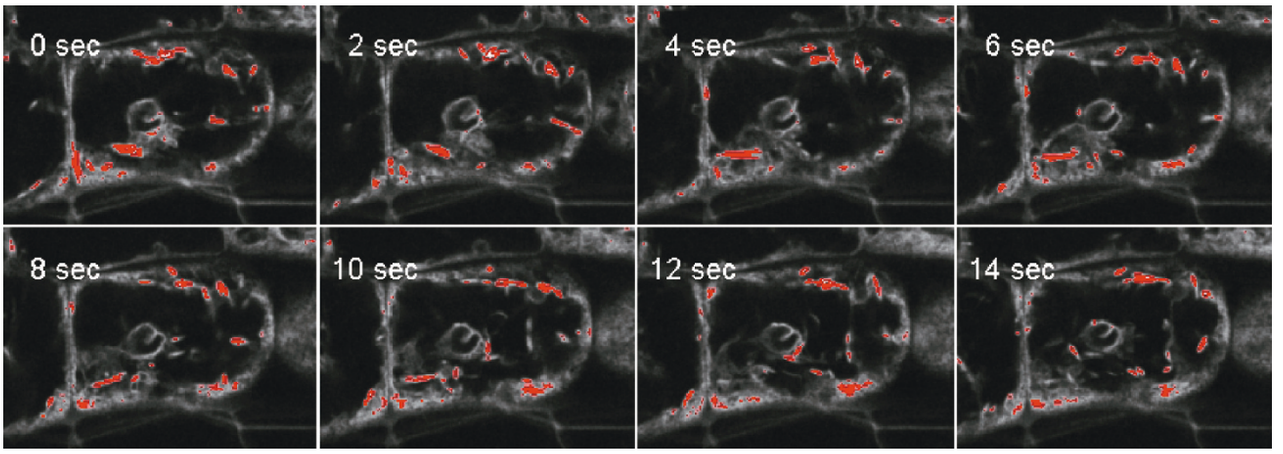


FIGURE 44.11. Fast dynamics in plant cells is illustrated by the movement of the protein inclusion on the ER of the hypocotyl epidermis on enhancer trap lines with GFP fused to an ER motif. In this specific sequence, TPE at 870 nm was used to stretch the limits of viability of this kind of imaging. The images shown were extracted from a time series of a consecutive (no interval) sequence of acquisitions, which was extended up to 650 frames. Despite the amount of exposure, we observed no effect on fading or streaming rates.

promoters or when fused to abundant and stable proteins. Although these wavelengths are near the edge of the tuning range of the Ti : Sa laser and produce some dye fading, they still produce better images than with confocal microscopy [Fig. 44.3(B)], and even very faint markers such as membrane transporters can be imaged in living cells. The same result was obtained for the S65T mutation described by von Arnim and colleagues (1998) [Fig. 44.10(E–N)].

Nevertheless, we have found that the two other enhanced-GFP versions (Chiu *et al.*, 1996; Siemering *et al.*, 1996) are even better for our purposes. First, they seem to behave best at 870 to 890 nm, a much more convenient wavelength range for the Ti : Sa laser, and one that any user can mode-lock. Second, if reasonably expressed, they seem to experience no quantifiable fading, even when sequentially imaged (Fig. 44.11). They provide high-resolution signals, and the mGFP5-ER, expressed in enhancer trap lines, provides superb material for structural characterization, either alone [Fig. 44.3(D,E)] or in combination with PI [Fig. 44.3(F)]. Fine details of the nuclear envelope and of the ER-derived system are resolved, and the exclusive location of the tag in the endodermis is evident from the cell-edge fading that can be seen in tangential optical sections of the root. In streaming movements of the cortical ER, large particles have been followed in mGFP5-ER enhancer trap lines during many hundred consecutive frames, without any visible fading or quantifiable effect on the streaming rates and patterns (Hawes *et al.*, 2001; Fig. 44.11). These two engineered forms of GFP have proven to be exceptional tools for TPE in plants, and can be expected to become the source of many important advances in our understanding of dynamic cell and developmental processes.

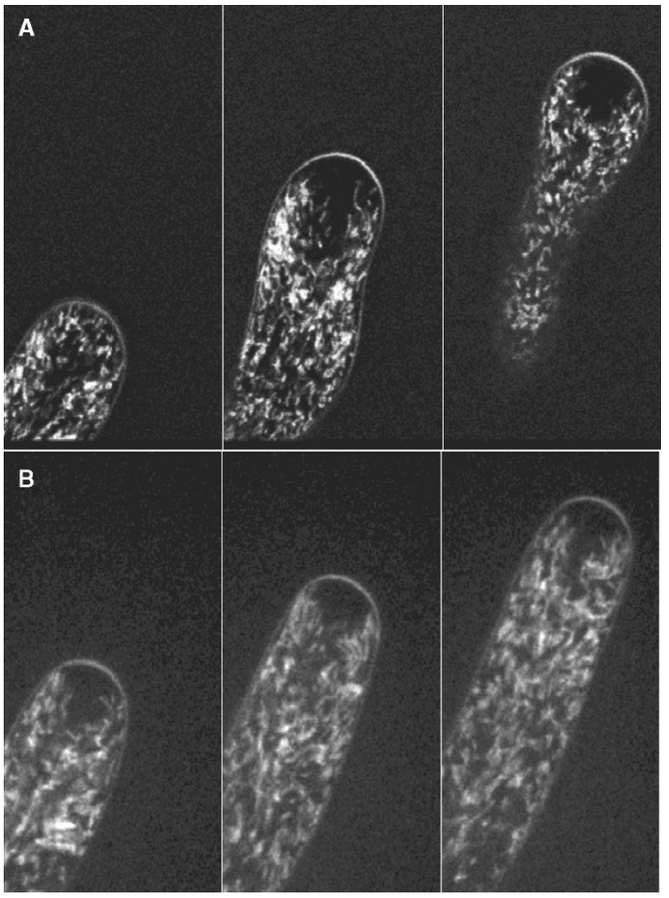


FIGURE 44.12. Comparison of spinning-disk and TPE imaging effects on pollen tube growth, Rhodamine 123–labeled mitochondria in *Lilium longiflorum* pollen tubes after 600 consecutive acquisitions. Frames were taken consecutively without any interval (1 frame/2 s) in the case of the TPE (820 nm excitation with an emission at 598/40 nm) at a speed of 5/s in a scanning disk (488 nm excitation with a triple dichroic). Unlike laser-scanning confocal (Feijó and Moreno, 2004), both systems show a very low phototoxicity. However, in the case of the TPE we should point out the low noise picture, and, in the case of the spinning-disk, the fast image acquisition. With TPE, the growth rate decreases by 30% compared to 10% with the NSDC.

DYNAMIC IMAGING

While cell mobility in plants is strongly limited by the presence of a semi-rigid extracellular matrix, plant cells can display impressive spatial dynamics at the subcellular level. Generally speaking, cytoplasmic streaming is much faster than mechanical movements in animal cells, with organelles moving up to 2 µm/s [e.g., ER inclusions on *Arabidopsis* hypocotyl epidermis (Fig. 44.11) or mitochondria in pollen tubes [(Fig. 44.12)]. The easiest way to

image such a fast process is to use a widefield microscope with a scientific-grade charge-coupled device (CCD) camera, and apply a cost-effective algorithm to the two-dimensional (2D) data, such as no-neighbors 2D filtering (Monck *et al.*, 1992; McNally *et al.*, 1999). This method is a similar to one developed by Castelman (1979), in which three planes are acquired and the information of the outer planes subtracted to produce an improved image of structures present in the central plane.

However, more stringent applications do need optical sectioning. In many cases, deconvolution is not fast enough to provide enough temporal resolution on a moving sample, and other methods, such as single-beam laser-scanning microscope (LSM), TPE, or Nipkow spinning-disk confocal (NSDC), or even video-rate confocal (VRC) must be used.

Frame size is the next critical choice. In a LSM/TPE, one can go up to a few frames per second by choosing a box of only ~10 kilopixels, usually at the cost of proper sampling and, therefore, resolution. For many applications, as long as one does not need to go faster than 2 to 3 frames per second (fps), it is possible to find a compromise between speed and resolution. On the other hand, if speed and resolution are needed simultaneously, a different approach is needed.

NSDC and VRC use detectors that need time to integrate: thus, the dimmer the sample, the more time needed to record a decent picture. As most spinning-disk confocals use cooled CCD cameras [or the new intensified CCDs or even an electron multiplier (EM)-CCDs], one can adjust the exposure time and the binning independently. The first parameter affects acquisition speed and the second, resolution. Sensitivity is an issue, and exposures as long as several seconds are not unusual for lightly stained specimens. Binning 2×2 in a megapixel, cooled CCD improves this parameter dramatically. Although it will bring the effective pixel size close to the Nyquist sampling criteria, either the exposure time can be reduced to roughly one quarter or the S/N increased by a factor of 2.

Though common sense suggests that plant cells should be able to handle lots of light, this is not always true. Because their growth rate is quite sensitive to light, pollen tubes can be used to quantify phototoxicity. As previously mentioned, as long as a reasonable amount of signal is present, TPE above 870 nm produces almost no effects on the growth and streaming rates of pollen tubes [Fig. 44.12(A)]. However, even when imaging continuously, without interval, good resolution still implies a 2s frame-scan time. At this speed, much of the dynamics of fast-moving organelles, such as ER (Fig. 44.11) or especially streaming mitochondria (Fig. 44.12) will be lost.

Provided that there is enough signal to allow use of a fast CCD (the case in Fig. 44.12, stained with the very bright Rhodamine 123), Nipkow-disk–based systems, such as the PerkinElmer/Yokogawa, definitely show a much more informative view [Fig. 44.12(B)]. In this case, it was easy to achieve an increase of one order of magnitude in the time resolution (2 s/frame on TPE and 200 ms/frame with the NSDC) and this allows one to clearly visualize different cytoplasmic domains in which mitochondria move faster or slower. We were unable to record similar data with any single-beam scanning method. As can be appreciated by comparing Figure 44.12(A,B), although the optical thickness is lower, the more accurate dynamic picture clearly outweighs the information lost by lower z-resolution. The ability to record a z-stack of a large, intact specimen in a fraction of the time also makes the technique suitable for time-lapse studies of fast-moving or growing organs.

We expect that NSDC microscopes will be crucial to being able to resolve fine temporal dynamics with minimal fading. The sensitivity issue does exist, and lightly stained samples such as many GFP-fusion lines could either not be imaged at all, or required an integration time so long that the system performance was less than that of TPE. Intensified CCDs or EM-CCDs may soon change this picture quite dramatically, and bring sensitivity to the level of TPE and LSM. Although the new generation of VRCs use high-speed computer interfaces with a bandwidth of 100 MB/s that permit high frame rates, problems with singlet-state saturation prevents single-beam confocal scanners from providing useful information about biological specimens except at low spatial resolution. On the other hand, high-speed line-scanners such as the Zeiss 5-Live avoid this trap by scanning many points at one time (see Chapter 10, *this volume*).

DECONVOLUTION

In the last two decades there has been a boom in the use of 3D microscopy in biology, and botanical samples are no exception (Hepler and Gunning, 1998). Although this trend has been driven largely by the emergence of the confocal microscope, widefield microscopes can also generate raw 3D data, and software that can run on any modern personal computer is now available to extract sharp, 3D reconstructions from these data.

If one considers a microscope to be a "convolution machine," its transfer function can be determined by measuring its response to a subresolution fluorescent bead: namely, its point spread function (PSF). To the extent that one knows the PSF and records the widefield 3D data stack accurately,[1] one should be able to invert the convolution process (deconvolution) to obtain a 3D image of the object imaged. The details of both convolution and deconvolution are covered in detail in Chapters 23, 24, and 25.

Because of the difficulties encountered when trying to measure the PSF, we usually make an average PSF from the 3D images of several beads (Holmes *et al.*, 1995). Although the biggest drawback of this approach is the requirement that the sample must not move or change during data acquisition (restricting the technique to fixed cells or structures moving very slowly), even minimal problems with the optics, such as misalignment, spherical aberration, and dirtiness, will affect the final image to a much greater extent than in confocal and TPE. To some degree, it may be possible to compensate for the degradation of the PSF brought about by spherical aberration (Boutet de Monvel *et al.*, 2001) or by the heterogeneous refraction index of a living cell (Kam *et al.*, 1998). As these techniques improve, they may be important when deconvolution techniques are applied to images of plant cells in which, for example, spheroidal central vacuoles can act as miniature lenses. Despite these limitations, deconvolution retains some substantial advantages for living-cell microscopy: phototoxicity, photobleaching, and price are all often lower.

It is also important to note that **deconvolution protocols not only can, but should, be applied to all 3D confocal and TPE datasets**. Doing so not only substantially reduces the "single-pixel noise features" produced by the statistical uncertainty attendant on measuring small numbers of photons, but it also substantially improves the statistical accuracy of the image data by effectively averaging the signal over many voxels (see Chapter 25, *this volume*).

[1] The main practical limitation to doing this is the presence of both Poisson and read noise in the final data.

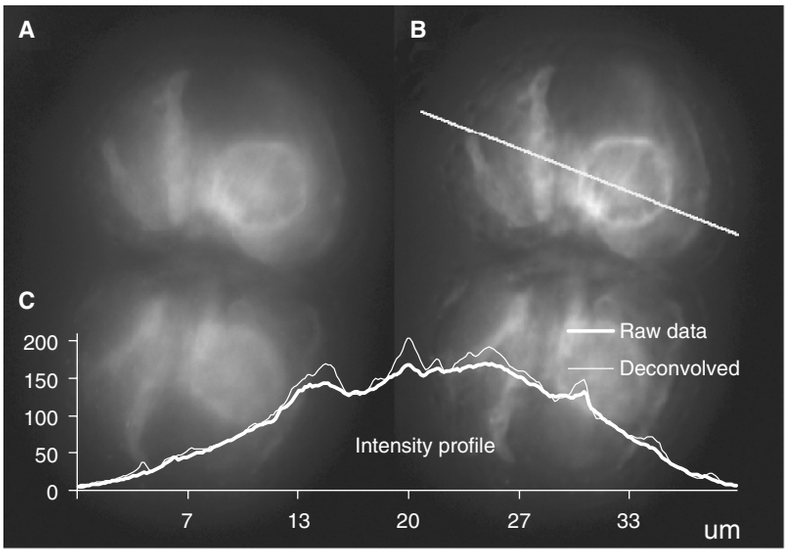


FIGURE 44.13. The effect of deconvolution on a widefield stack. (A) A plane from a stack of a unicellular green algae. (B) A deconvolved version of the same plane using a measured PSF and a glycerol immersion objective (PlanApo 63× NA 1.3). The whole projection was about 30 µm deep (autofluorescence). The improvement in contrast is obvious, and is highlighted in the line scan. The PSF was generated using orange beads from Molecular probes (PS-Speck) with 170 nm diameter.

Figure 44.13(A) shows an autofluorescence image of a unicellular green alga. In this specific sample, several attempts with both confocal and multi-photon microscopes failed to produce a sharp image over extended focus stacks of the entire depth of the cell. The main problem was that the high intensity illumination caused the signal to get dimmer and the autofluorescence to shift from red to green (Cheng *et al.*, 2001). Deconvolution of data stacks collected using a much lower intensity of excitation light made a considerable improvement [Fig. 44.13(B)].

CONCLUSION

Ever since the time of Hooke, plant cells have been the foundation of many of the fundamental discoveries that have shaped cell biology. Underlying all these findings were significant advances in microscopy that have helped to push forward our conceptual thinking, for example, supporting the acceptance of the cell theory. In this chapter we have highlighted what is now the leading edge of this technological effort.

Imaging is now more than lenses and microscopes. Computers are also essential, both to accumulate and display research images, and to extract and analyze enormous amounts of quantitative information from them.

Recent advances range from major hardware (e.g., two-photon equipment) to the development of computer software that now enables us to derive fresh insights from old histological techniques.

We have tried to emphasize that all these techniques are only of value when they enable us to describe previously-unknown biological features, and indeed many of the most important technical developments were developed only as part of specific research projects.

The ever-growing field of genetically encoded probes, such as GFP, seems likely to trigger more new and important technical adaptations that will enable us to obtain more and better dynamic information from living systems. Plant cell biology continues to bloom, and much of this growth is supported by modern imaging methods.

ACKNOWLEDGMENTS

The JAF laboratory is supported by FCT grants POCTI/BCI/46453/2002, POCTI/BIA-BCM/60046/2004, and POCTI/BIA-BCM/61270/2004. Some GFP lines from the Haseloff laboratory were imaged during the 2nd and 3rd Gulbenkian Biology Course on Plant Development (Oeiras, Portugal, 2003) by groups involving the students Niko Geldner, Vaiva Kazanaviciute, Jirina Prochazkova, Kasia Olczak, Martha Alvarado (a very special thanks for the MAP4 and talin lines), Lisa Gao, Martin Potocky, and Chris Nichols. The SB laboratory is supported by grants from BBSRC.

REFERENCES

Bago, B., Zipfel, W., Williams, R.M., Cahmberland, J.G., Lafontaine, J.G., Webb, W.W., and Piche, Y., 1998, *In vivo* studies on the nuclear behavior of the arbuscular mycorrhizal fungus *Gigaspora rosea* grown under axenic conditions, *Protoplasma* 203:1–15

Bago, B., Zipfel, W., Williams, R.M., Jun, J., Arreola, R., Lammers, P.J., Pfeffer, P.E., and Shachar-Hill, Y. 2002, Translocation and utilization of fungal storage lipids in the arbuscular mycorrhizal symbiosis, *Plant Physiol.* 128:108–124

Bago, B., Zipfel, W., Williams, R.M., and Piche, Y., 1999, Nuclei of symbiotic arbuscular mycorrhizal fungi as revealed by in vivo two-photon microscopy, *Protoplasma* 209:77–89.

Blancaflor, E.B., and Gilroy, S., 2000, Plant cell biology in the new millennium: New tools and new insights, *Am. J. Botany* 87:1547–1560.

Bolte, S., Talbot, C., Boutte, Y., Catrice O., Read, N., and Satiat-Jeunemaitre, B., 2004, FM-dyes as experimental probes for dissecting vesicle trafficking in living plant cells, *J. Microsc.* 214:159–173.

Bougourd, S., Marrison, J., and Haseloff, J., 2000, Technical advance: an aniline blue staining procedure for confocal microscopy and 3D imaging of normal and perturbed cellular phenotypes in mature *Arabidopsis* embryos, *Plant J.* 24:543–550.

Boutet de Monvel, J., Le Calvez, S., and Ulfendahl, M., 2001, Image restoration for confocal microscopy: Improving the limits of deconvolution, with application to the visualization of the mammalian hearing organ, *Biophys. J.* 80:2455–2470.

Brandizzi, F., Fricker, M., and Hawes, C., 2002, A greener world: The revolution in plant bio-imaging, *Nat. Rev. Mol. Cell Biol.* 3:520–530.

Castleman, K.R., 1979, *Digital Imaging Processing*, Prentice Hall, Englewood Cliffs, New Jersey.

Chen, C.Y., Cheung, A.Y., and Wu, H.M., 2003, Actin-depolymerizing factor mediates Rac/Rop GTPase-regulated pollen tube growth, *Plant Cell* 15:237–249.

Cheng, P.-C., Lin, B.-L., Kao, F.-J., Gu, M., Xu, M.-G., Gan, X., Huang, M.-K., and Wang, Y.-S., 2001a, Multi-photon fluorescence microscopy — The response of plant cells to high intensity illumination, *Micron* 32:661–670.

Cheng, P.C, Sun, C.K., Lin, B.L., Kao, F.J., and Chu, S.W., 2001b, Nonlinear multimodality spectromicroscopy: Multiphoton fluorescence, SHG and THG of biological specimen, *Proc. SPIE* 4262:98–103.

Chiu, W.-L., Niwa, Y., Zeng, W., Hirano, T., Kobayashi, H., and Sheen, J., 1996, Engineered GFP as a vital reporter in plants, *Curr. Biol.* 6:325–330.

Chu, S.W., Chen, I.-H., Liu, T.-M., Sun, C.-K., Lee, S.-P., Lin, B.-L., Cheng, P.-C., Kuo, M.-X., Lin, D.-J., and Liu, H.-L., 2002, Nonlinear bio-photonics crystal effects revealed with multimodal nonlinear microscopy, *J. Microsc.* 208:190–200.

Cox, G., and Sheppard, C., 2004, Practical limits of resolution in confocal and nonlinear microscopy, *Microsc. Res. Tech.* 62:18–22.

Cutler, S.R., Ehrhardt, D.W., Griffitts, J.S., and Somerville, C.R., 2000, Random GFP::cDNA fusions enable visualization of subcellular structures in cells of Arabidopsis at a high frequency, *Proc. Natl. Acad. Sci. USA* 97:3718–3723.

Decho, A.W., and Kawaguchi, T., 1999, Confocal imaging of in situ natural microfibril communities and extracellular polymeric secretions using nanoplast resin, *Biotechniques* 27:1246–1252.

Denk, W., Strickler, J.H., and Webb, W.W., 1990, Two-photon laser scanning fluorescence microscopy, *Science* 248:73–76.

Diaspro, A., and Robello, M., 2000, Two-photon excitation of fluorescence for three-dimensional optical imaging of biological structures, *J. Photochem. Photobiol.* B 55:1–8.

Esau, K., 1977a, *Anatomy of Seed Plants*, John Wiley and Sons, New York.

Esau, K., 1977b, *Plant Anatomy*, 2nd ed., John Wiley and Sons, New York.

Fahn, A., 1990, *Plant Anatomy*, 4th ed., Pergamon, London.

Feijó, J.A., and Cox, G., 2001, Visualization of meiotic events in intact living anthers by means of two-photon microscopy, *Micron* 32:679–684.

Feijó, J.A., and Moreno, N., 2004, Imaging plant cells by two-photon excitation, *Protoplasma* 223:1–23.

Fricker, M., Parsons, A., Tlalka, M., Blancaflor, E., Gilroy, S., Meyer, A., and Plieth, C., 2001, Fluorescent probes for living plant cells, In: *Plant Cell Biology, A Practical Approach* (C. Hawes and B. Satiat-Jeunemaitre, eds.), Oxford University Press, Oxford, United Kingdom, pp. 35–83.

Fricker, M.D., and Meyer, A.J., 2001, Confocal imaging of metabolism *in vivo*: Pitfalls and possibilities, *J. Exp. Botany* 52:631–640.

Fricker, M.D., May, M., Meyer, A.J., Sheard, J., and White, N.S., 2000, Measurement of glutathione levels in intact roots of *Arabidopsis, J. Microsc.* 198:162–173.

Galbraith, D.W., Bohnert, H.J., and Bourque, D.P., eds., 1995, *Methods in Cell Biology*, Academic Press, New York.

Galway, M.E., Heckman, J.W. Jr., Hyde, G.J., and Fowke, L.C., 1995, Advances in high-pressure and plunge-freeze fixation, In: *Methods in Plant Cell Biology* (D.W. Galbraith, H.J. Bohnert, and D.P. Bourque, eds.), Academic Press, New York, pp. 4–20.

Grew, N., 1673, An idea of a phytological history propounded. Together with a continuation of the anatomy of vegetables, particularly prosecuted upon roots. With an account of the vegetation of roots grounded chiefly thereupon. Published by Nehemiah Grew.

Gunning, B., 2002, Plant cell biology on CD, Author edition, www.plantcellbiologyoncd.com.

Gunning, B.S., and Steer, M.W., 1996, *Plant Cell Biology: Structure and Function*, Jones and Bartlettt Publishers, Boston.

Gutiérrez-Alcalá, G., Gotor, C., Meyer, A.J., Fricker, M., Vega, J.M., and Romero, L.C., 2000, Glutathione biosynthesis in *Arabidopsis* trichome cells, *Proc. Natl. Acad. Sci. USA* 97:11108–11113.

Hake, S., 2001, Mobile proteins signals cell fate, *Nature* 413:261–263.

Haseloff, J., 1999a, GFP variants for multispectral imaging of living cells, *Methods Cell Biol.*, 58:139–151.

Haseloff, J., 1999b, Imaging green fluorescent protein in transgenic plants, In: *Imaging Living Cell* (R. Rizzuto and C. Fasolato, eds.), Springer-Verlag, Berlin, pp. 40–94.

Haseloff, J., 2003, Old botanical techniques for new microscopes, *Biotechniques* 34:1174–1178.

Haseloff, J., and Amos, B., 1995, GFP in plants, *Trends Genet.* 11:328–329.

Haseloff, J., Siemering, K.R., Prasher, D.C., and Hodge, S., 1997, Removal of a cryptic intron and subcellular localization of green fluorescent protein are required to mark transgenic *Arabidopsis* plants brightly, *Proc. Natl. Acad. Sci. USA* 94:2122–2127.

Hawes, C., and Satiat-Jeunemaitre, B., eds., 2001, *Plant Cell Biology, A Practical Approach*, Oxford University Press, Oxford, United Kingdom.

Hepler, P.K., and Gunning, B.E.S., 1998, Confocal fluorescence microscopy of living cells, *Protoplasma* 201:121–157.

Holmes, T.J., Bhattacharyya, S., Cooper, J.A., Hanzel, D., Krishnamurthi, V., Lin, W., Roysam, B., Szarowski, D., and Turner, J., 1995, Light microscopic images reconstructed by maximum likelihood deconvolution, In: *Handbook of Biological Confocal Microscopy* (J.B. Pawley, ed.), Plenum Press, New York, pp. 389–402.

Kam, Z., Hanser, B., Gustafsson, M.G.L., Agard, D.A., and Sedat, J.W., 2001, Computational adaptive optics for live three-dimensional biological imaging, *Proc. Natl. Acad. Sci. USA* 98:3790–3795.

Ketelaar, T., Anthony, R.G., and Hussey, P.J., 2004, Green fluorescent protein-mTalin causes defects in actin organization and cell expansion in *Arabidopsis* and inhibits actin de-polymerizing factor's actin depolymerizing activity *in vitro, Plant Physiol.* 136:3990–3998.

Kodama, H., and Komamine, A., 1995, Synchronization of cell cultures of higher plants, In: *Methods in Plant Cell Biology* (D.W. Galbraith, H.J. Bohnert, and D.P. Bourque, eds.), Academic Press, New York, pp. 315–330.

Köhler, R.H., Zipfel, W.R., Webb, W.W., and Hanson, M.R., 1997, The green fluorescent protein as a marker to visualize plant mitochondria *in vivo, Plant J.* 11:613–621.

König, K., 2000, Multiphoton microscopy in life sciences, *J. Microsc.* 200:83–104.

Lloyd, C.W., 1987, The plant cytoskeleton: The impact of fluorescence microscopy, *Annu. Rev. Plant Physiol.* 38:119–139.

Malkin, R., and Niyogi, K., 2001, Photosynthesis, In: *Biochemistry & Molecular Biology of Plants* (B.B. Buchanan, W. Gruissem, and R.L. Jones, eds.), American Society of Plant Biologists, New York, pp. 568–628.

Mason, W.T., 1993, Fluorescent and luminescent probes for biological activity, Academic Press, London.

McInerney, T., and Terzopoulos, D., 1996, Deformable models in medical image analysis: a survey, *Med. Image Anal.* 2:91–108.

McNally, J.G., Karpova, T., Cooper, J., and Conchello, J.A., 1999, Three-dimensional imaging by deconvolution, *Microsc. Methods* 19:373–385.

Meyer, A.J., and Fricker, M.D., 2000, Direct measurement of glutathione in epidermal cells of intact *Arabidopsis* roots by two-photon laser scanning microscopy, *J. Microsc.* 198:174–181.

Meyer, A.J., May, M.J., and Fricker, M., 2001, Quantitative *in vivo* measurement of glutathione in *Arabidopsis* cells, *Plant J.* 27:67–78.

Monck, J.R., Oberhauser, A.F., Keating, T.J., and Fernandez, J.M., 1992, Thin-section ratiometric Ca2+ images obtained by optical sectioning of fura-2 loaded mast cells, *J. Cell Biol.* 116:745–759.

Nakajima, K., Sena, G., Nawy, T., and Benfey, P.N., 2001, Intracellular movement of the putative transcription factor SHR in root patterning, *Nature* 413:307–311.

Parthasarathy, M.V., 1995, Freeze-substitution, In: *Methods in Plant Cell Biology* (D.W. Galbraith, H.J. Bohnert, and D.P. Bourque, eds.), Academic Press, New York, pp. 57–70.

Potter, S., 1996, Vital imaging: Two photons are better than one, *Curr. Biol.* 6:1595–1598.

Raghavan, V., 1995, Manipulation of pollen grains for gametophytic amd sporophytic types of growth, In: *Methods in Plant Cell Biology* (D.W. Galbraith, H.J. Bohnert, and D.P. Bourque, eds.), Academic Press, New York, pp. 367–377.

Reddy, G.V., Heisler, M.G., Ehrhardt, D.W., and Meyerowitz, E.M., 2004, Real-time lineage analysis reveals oriented cell divisions associated with morphogenesis at the shoot apex of *Arabidopsis thaliana, Development* 131:4225–4237.

Ruzin, S.E., 1999, Plant microtechnique and microscopy, Oxford University Press, Oxford.

Running, M.P, Clark, S.E., and Meyerowitz, E.M., 1995, Confocal microscopy of the shoot apex, In: *Methods in Plant Cell Biology* (D.W. Galbraith, H.J. Bohnert, and D.P. Bourque, eds.), Academic Press, New York, pp. 217–230.

Shav-Tal, Y., Singer, R.H., and Darzacq, X., 2004, Imaging gene expression in single living cells, *Nat. Rev. Mol. Cell Biol.* 5:856–862.

Shaw, P.J., 2001, Introduction to optical microscopy for plant cell biology, In: *Plant Cell Biology, A Practical Approach* (C. Hawes and B. Satiat-Jeunemaitre, eds.), Oxford University Press, Oxford, United Kingdom, pp. 1–33.

Shaw, S.L., Kamyar, R., and Ehrhardt, D.W., 2003, Sustained microtubule treadmilling in *Arabidopsis* cortical arrays, *Science* 300:1715–1718.

Sheen, J., 1995, Methods for mesophyll and bundle sheath cell separation, In: *Methods in Plant Cell Biology* (D.W. Galbraith, H.J. Bohnert, and D.P. Bourque, eds.), Academic Press, New York, pp. 305–314.

Shimmen, T., and Yokota, E., 2004, Cytoplasmic streaming in plants, *Curr. Biol.* 16:68–72.

Siemering, K.R., Golbik, R., Sever, R., and Haseloff, J., 1996, Mutations that suppress the thermosensitivity of green fluorescent protein, *Curr. Biol.* 6:1653–1663.

Spence, J., 2001, Plant histology, In: *Plant Cell Biology, A Practical Approach* (C. Hawes and B. Satait-Jeunemaitre, eds.), Oxford University Press, Oxford, United Kingdom, pp.189–206.

Sun, C.-K., Chu, S.-W., Chen, I.-S., Liu, T.-M., Cheng, P.-C., and Lin, B.-L., 2001, Multi-modality nonlinear microscopy, *Conf. Lasers Electro Opt. Eur. Tech. Dig.* 2001:222–227.

Tirlapur, U., and König, K., 2001, Femtosecond near-infrared lasers as a novel tool for non-invasive real-time high-resolution time-lapse imaging of chloroplast division in living bundle sheat cells of *Arabidopsis, Planta* 214:1–10.

Tirlapur, U., and König, K., 2002, Two-photon near-infrared femtosecond laser scanning microscopy in plant biology, *In: Confocal and Two-Photon Microscopy: Foundations, Applications and Advances* (A. Diaspro, ed.), Wiley-Liss, New York, pp. 449–468.

Volkmer, A., Subramaniam, V., Birch, D.J.S., and Jovin, T.M., 2000, One and two-photon excited fluorescence lifetimes and anisotropy decays of GFPs, *Biophys. J.* 78:1859–1898.

von Arnim, A.G., Deng, X.M., and Stacey, M.G., 1998, Cloning vectors for the expression of green fluorescent protein fusion proteins in transgenic plants, *Gene* 221:35–43.

Vroom, J.M., de Grauw, K.J., Gerritsen, H.C., Bradshaw, D.J., Marsh, P.D., Watson, J.J., Birmingham, C., and Allison, C., 1999, Depth penetration and detection of pH gradients in biofilms by two-photon excitation microscopy, *Appl. Environ. Microbiol.* 65:3502–3511.

Wysocka-Diller, J.W., Helariutta, Y., Fukaki, H., Malamy, J.E., and Benfey, P.N., 2000, Molecular analysis of SCARECROW function reveals a radial patterning mechanism common to root and shoot, *Development*, 127:595–603.

Xia, A.D., Wada, S., Tashiro, H., and Wuang, W.H., 1999, One and two-photon fluorescence from recombinant GFP, *Arch. Biochem. Biophys.* 372:280–284.

Xu, C., and Webb, W., 1996, Measurement of two-photon excitation cross sections of molecular fluorophores with data from 690 to 1050 nm, *J. Opt. Soc. Am. B* 13:481–491.

45

Practical Fluorescence Resonance Energy Transfer or Molecular Nanobioscopy of Living Cells

Irina Majoul, Yiwei Jia, and Rainer Duden

INTRODUCTION

How to make a good science

La luna densa — The moon is dense,
Ogni densa e grave — Everything dense is substantial.
Come sta la luna? — How, moon, do you exist?
Leonardo da Vinci (1452–1519).[1]

For the purpose of this chapter, a free paraphrasing of Leonardo's point might be:

Living cells are moving.
Movement reflects their functional activity.
How, cells, do you function?

After formulating this philosophic question in a poetic form, Leonardo the Scientist, provides us with a real experimental (optical) setup. "As I propose to treat the nature of the moon, it is necessary that I first describe the perspective of mirrors, whether plane, concave, or convex," (B.M.94r — Arundel MS in British Museum). Next, in the pages of Codex Atlanticus (C.A.190r), Leonardo invites us to "Construct the glasses to see the moon magnified" and half a millennium later we are still following him for, as Bulgakov famously said, "Manuscripts do not burn!"

As a master of light and shadow, he knew how the uneven surface of the ocean reflects light in all directions, breaking it into myriad beams. Analyzing the brightness of the light reflected from the moon, Leonardo suggests that its outer surface might be covered with a rippled liquid.

As a scientist he was able to understand how the images of the moon's phases would appear to an observer on the Earth [Fig. 45.2(A), arrow]. In its monthly cycle the moon always exposes the same side towards the Earth. Only when it is opposite to the Sun (with respect to an Earth observer) is the moon fully illuminated by sunlight. Leonardo follows his interest further to conclude that when the moon is on the same side of the Earth as the Sun, it will be illuminated by brilliant daylight reflected from the watery surface of the Earth. This situation, known in astronomy as *lumen cínerium* or "new moon in the old moon's arms," was described and drawn by Leonardo (see Fig. 45.1). Perhaps it was this understanding that later led him to question whether the Sun really does circle around the Earth. Much later, Johannes Kepler reached similar conclusions in "Astronomiae pars optica."

The scientific prediction of Leonardo (based on optics) may have met "real life" when Amerigo Vespucci described the New World to him, possibly during the painting of a portrait by Leonardo that is mentioned in *Lives of Artists* by Giorgio Vasari: "sketch of Amerigo Vespucci shows head of a very handsome old man drawn in charcoal."

For us here, what Leonardo discovered is less important than the approach he used to experience nature and to obtain new knowledge. His further research in optics led him to conclude that perspective images would be closer to reality if they are projected not onto a flat paper but onto a concave spherical surface, as happens in the human eye. In Figure 45.2(B) we see a painter, that might be Leonardo himself, working with perspectrograph (from Codex Atlanticus, folie 5r). Next, Leonardo concludes, that "the gradation of light but not of the colors is what defines the depth in space" (Manuscript G, 8r). Today, in modern microscopy we still use these ideas: DIC images code shape and brightness, color information is used to draw attention to the locations of transfected fluorescent proteins and our best 3D rendering algorithms are

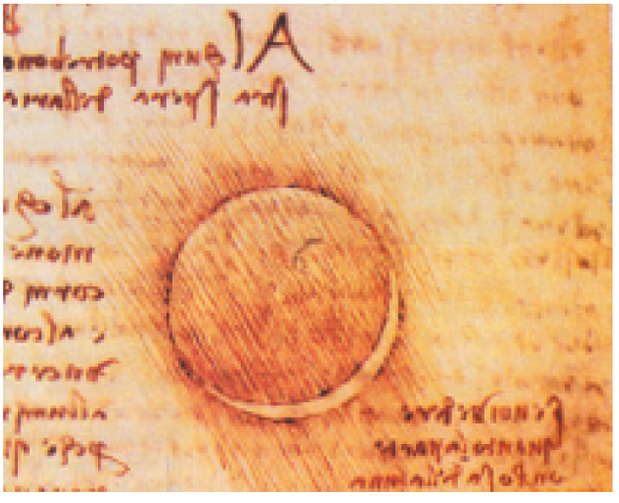


FIGURE 45.1. Leonardo da Vinci, image of a moon phase from the Codex Leicester: 35v, 2r (2A).

[1] Leonardo — Art and Science, 2000, Crispino, ed., Giunti Editore S.p.A. a, Florence Milan.

Irina Majoul and Rainer Duden • Royal Holloway University of London, Egham TW20 0EX, United Kingdom
Yiwei Jia • Olympus America Inc., Melville, New York 11747

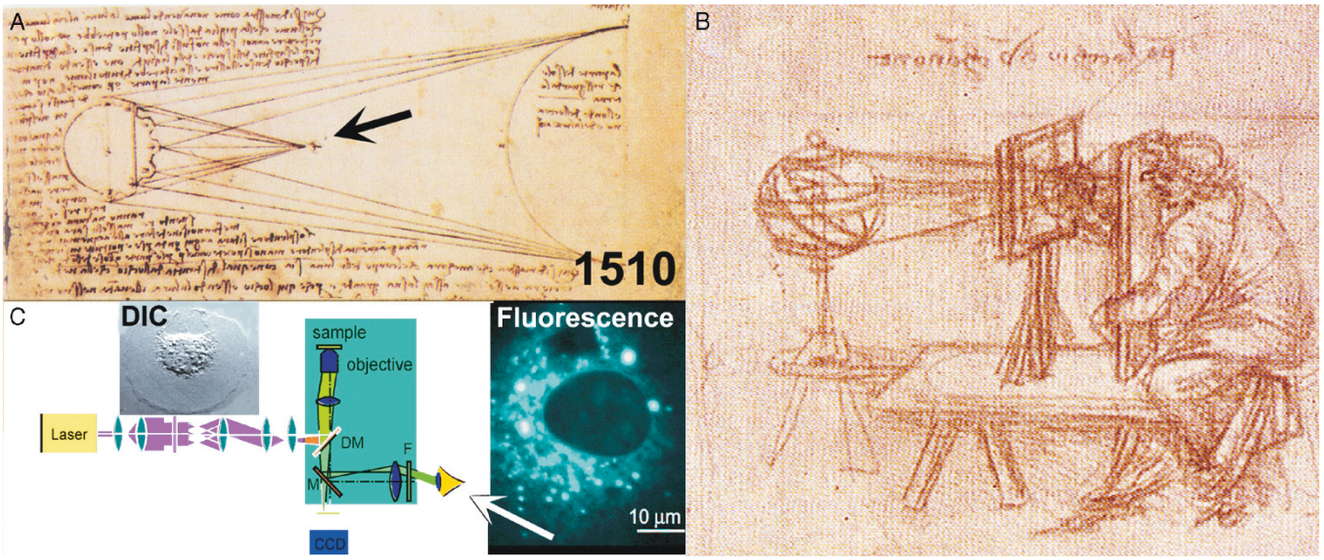


FIGURE 45.2. Leonardo da Vinci. (A) Schematic drawing of the light reflected from the moon that can be analyzed by an observer on the Earth: Codex Leicester [drawn between 1508–1510, 35v, 2r (2A)]. (B) Painter working with perspectrograph, Codex Atlanticus, folie 5r (fragment). (C) Schematic drawing of the laser light path used to illuminate the object in an inverted microscope. (Right) Fluorescence image of a living cell obtained by this setup, inserted DIC image (for details, see text). Both arrows indicate positions of the observer's eye.

designed to code objects that are farther away so that they appear less bright, less distinct and sometimes even bluish [Fig. 45.2(C)].

Although Leonardo had never seen a microscope, his mind worked with the precision of this useful device: starting from a general overview, dissecting and moving to higher magnifications where he captured the smallest details necessary to finally understand the essence of the entire object under investigation.

In a sense, Leonardo's habit of portraying biological structures in 3D foreshadows our modern interest in 3D microscopy. Not yet trapped in the 2D world of the standard light microscope, his view was inherently three-dimensional. He knew instinctively that 3D insight was necessary to understand how biological surfaces must interdigitate to maximize the surface area of the adjoining regions. Figure 45.3(A), shows the interface between contacting surfaces in a womb wall (RL manuscript, 19102r, detail). His 3D image of these surfaces is impressively correct and in agreement with our modern understanding of cellular contacts on a much smaller scale: that of synapses [Fig.45.3(B)] and cell-cell contacts [Fig. 45.3(C)], resolved by modern microscopes almost 500 years later.

His way of following "functionality" and performing "preliminary studies" (that might take him many years) was so correct that, even in the 21st century, his approach remains as important for us as it was for him. Leonardo was a great philosopher and the first one to integrate the four most productive aspects of scientific

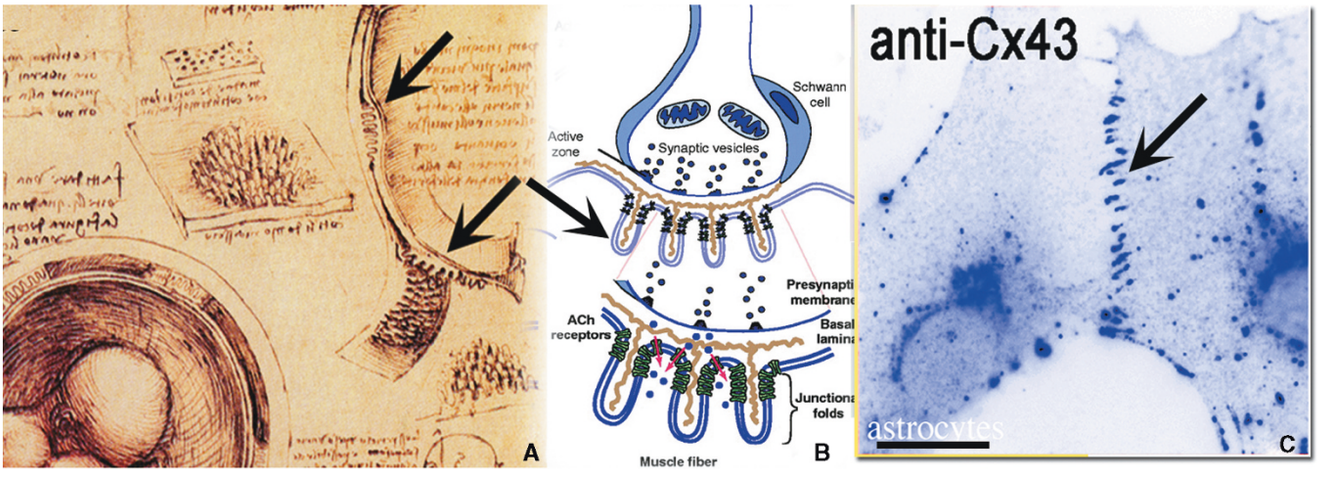


FIGURE 45.3. (A) Taken from an anatomical study of Leonardo da Vinci 1508–1510 (Manuscript RL, 19102r, Windsor Library, UK). The left panel shows the interface between dissected tissues (wall of a womb) where Leonardo used the tools available to him to analyze how two biological surfaces create an adhesive junctional interface. (B) An insert representing junctional folds of a synaptic terminal that creates integrity of the structure (reproduced with permission from Cohen-Cory, 2002). (C) Junctional cell-cell inerface between two cultured primary astrocytes revealed with antibodies against a gap junction protein, Connexin-43 (Butkevich *et al.*, 2004).

thinking: (1) Follow your naive interest; (2) Open your mind, get new ideas and try to understand how things work; (3) Have the patience to develop new and versatile experimental approaches to get new information; (4) Test the new knowledge against your wider experience.

We too are at the beginning of a new era in biology and biotechnology, with neurobiology and stem cell research leading to prominence. Although our tools are now molecular imaging, 3D fluorescence microscopy, proteomics, genetic screens, spectroscopy, nanobiophysics, animal models, and cellular physiology, the overall process remains much the same.

Beauty, Functionality, Cell Cycle, and Living-Cell Imaging

Rule 1: Get To Know Your Cells

Before moving on to the methods of fluorescence resonance energy transfer (FRET) analyses, it is important to include a reminder about the main object of our investigations: living cells. Living cells imaged in the microscope allow one to obtain insight into the complexity of dynamic processes in real time, whereas fixed cells maintain only the last steady state distribution (at the moment of death) for the molecules of interest. For live-cell FRET analyses, it is crucial to keep cells in good condition during the time course of an experiment. This includes temperature and CO_2 control of the medium, proper transfection of the cells with fluorescent proteins tested for functional activity, minimal level of laser illumination throughout the experiment, etc.

The beauty of transfected cells may often serve as an indicator of their biological functionality, and thus can be used as an (almost) scientific criterion. In a sense, beauty is a biological functionality. For example, in cells transfected with yellow fluorescent protein (YFP)-tubulin to highlight the microtubule network, microtubules are impressively beautiful when the cells are taken straight from the incubator and recorded at 37°C. Cells forgotten on the table without temperature control or adequate CO_2 will show partially depolymerized, ugly microtubules. In such cells, transport of proteins in the secretory and endocytic pathways is impaired, and the cells are dying. Investing hard work into badly transfected cells or attempting functional studies on dying cells is a wasted effort (except, of course, when studying apoptosis). In contrast, beautifully transfected cells are a source of a great happiness to the researcher, stimulating him/her to acquire the best possible images.

Figure 45.4 shows two examples of cells after transfection: Figure 45.4(A) shows a cell expressing a physiological level of the transmembrane KDEL receptor (ERD2) that is recognized by cholera toxin to enable toxin transport through the Golgi complex (Majoul *et al.*, 1996, 2001). Figure 45.4(B) shows a cell imaged at longer times after transfection and that is now over-expressing KDEL receptor, which aggregates around the Golgi. Cholera toxin recognizes and binds to functional KDEL receptor molecules [Fig. 45.4(A)], but does not enter the over-expressing structures [Fig. 45.4(B)]. Instead, cholera toxin recognizes native, still functional receptors between the aggregates and thus enters the Golgi [Fig. 45.4(B), arrow]. Clearly, the cells in Figure 45.4(B) should not be used for experiments. The transfection setup, transfection reagents, cells, and possibly even the chimeric proteins must be further optimized to prepare a better experiment.

Because many biological processes are cell cycle–dependent, the cell cycle stage should be considered for FRET experiments. Figure 45.4(C) shows different degrees of surface expression for a glycosylphosphatidylinositol (GPI). GPI-anchored protein is detected with antibodies that make FRET under the plasma membrane. Acceptor bleach revealed different degrees of FRET, showing that the level of GPI-anchored protein expression varies with the stage of the cell cycle.

We have also shown that the appearance of lipid receptors (glycosphingolipids) on the cell surface, and thus the lipid composition of the plasma membrane as well as the distribution of certain lipid-binding proteins under the plasma membrane, is strongly cell cycle–dependent (Majoul *et al.*, 2002a). Surface expression of lipid receptors can be mapped to a specific cell cycle stage using incorporation of BrDU to mark S phase [Fig. 45.4(D)] or by monitoring the expression of cyclins, for example, cyclin B (mitotic marker). To map different lipid microdomains on the plasma membrane, we used fluorescently labeled AB5 toxins (cholera toxin and shiga toxin) and found a strong cell cycle–dependent heterogeneity of binding to cell surfaces [Fig. 45.4(E)]. The molecular basis of this mechanism is an intracellular lipid modification that involves modification of a common lipid precursor (e.g., lactosyl ceramide) with sugar moieties by galactosyl- and glucosyltransferases and the expression of these enzymes turned out to be cell cycle–dependent [Fig. 45.4(F); Majoul *et al.*, 2002a]. Thus, the behavior of many analyzed proteins will be different in the G1, S, G2, or M phases of the cell cycle. The take-home message here is: if a strong FRET heterogeneity is observed in a cell population, it may be useful to synchronize cells and to test directly whether this heterogeneity is cell cycle-dependent.

FLUORESCENCE RESONANCE ENERGY TRANSFER THEORY

More than 50 years ago, the German scientist Förster discovered that close proximity of two chromophores changes their spectral properties in predictable ways (Förster, 1948a). If two biological molecules in a living cell interact functionally, the interaction will bring into close proximity any chromophores attached to these molecules. After collecting spectral data and deciphering this information based on Förster's theory, we can understand changes that occurred in the near-vicinity microenvironment of two chromophores and thus draw biologically meaningful conclusions about the specificity of protein–protein interactions.

The idea of non-radiative dipole–dipole interactions was first formulated by Förster in 1948 (Förster, 1948a,b). Further development of this idea, biological application, and introduction of spectrally distinct fluorescent molecules came later (Stryer and Haugland, 1967; Clegg, 1992; Tsien, 1998; Lacowicz, 1999). Förster's theory explains FRET as a dipole–dipole interaction between neighboring molecules (Fig. 45.5). Förster showed that the presence of an appropriate acceptor in FRET proximity will decrease the time a donor spends in the excited state due to non-radiative energy transfer to the acceptor in close proximity:

$$\begin{array}{ccccc} & & & & k_t \\ D + A + h\nu_E & \Rightarrow & D^* + A & \Rightarrow & D + A^* \\ & & k_D & & k_A \\ & & D & & A \end{array} \qquad (1)$$

Here, k_t is the rate of energy transfer from the donor to the acceptor, $k_D = k_{Df} + k_{Di}$ and $k_A = k_A + k_{Ai}$, k_D and k_A correspond, respectively, to the rate of the radiative decay of the donor and the acceptor (for us here, fluorescence emission), and k_{Di} and k_{Ai} to the rates of the non-radiative decay constant of the donor (D) and the acceptor (A). The ratio between the number of photons emitted

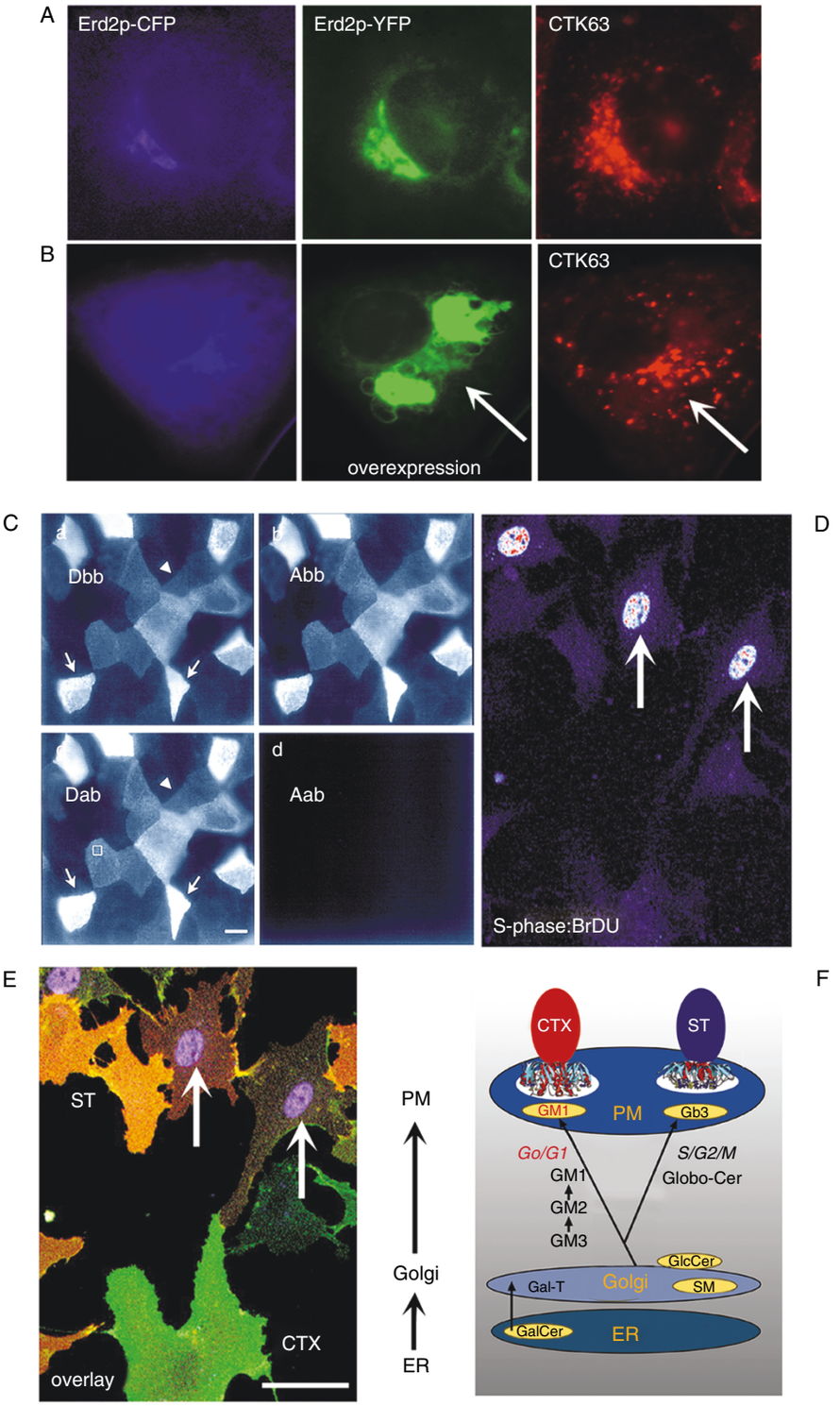


FIGURE 45.4. (A) Cells transfected with a transmembrane Golgi receptor (ERD2-CFP/ERD2-YFP). At near-physiological expression levels, it is localized in the Golgi where it binds to cholera toxin (red). (B) When over-expressed, the receptor aggregates and is excluded from the Golgi. In this case, cholera toxin still recognizes a portion of the native receptor (*shown by arrows*) and can thus enter the Golgi compartment. (C) FRET demonstrated by acceptor bleach on the surface of a cell monolayer labeled with antibodies against GPI-anchored proteins and 5′ NT. The cell-to-cell variation in FRET (E_{eff}) distribution of 5′ NT molecules on the cell surface may have deep biological roots. (Taken from Kenworthy and Edidin, 1998.) (D) Incorporation of BrDU can be used to determine the stage of the cell cycle in individual cells in a non-synchronized cell monolayer. Only cells carrying out DNA synthesis (S phase) will be labeled. (E) Overlay of the same monolayer with labeled CTX (cholera toxin, used as a lipid raft marker) and ST (Shiga toxin) revealed that cells in S phase have weak binding of both toxins. Cells in G1 phase express more GM1 on the cell surface and bind CTX more strongly (shown in green). Gb3-bound ST is shown in red. (F) Cartoon representing cell cycle–specific modifications of a common lipid precursor lactosyl ceramide that can be modified by glycosyl and galactosyltransferases to produce more branched GM1 (G1 phase) or Gb3 (around M phase). Thus, differential expression of lipid receptors on the plasma membrane can be a marker for the phase of the cell cycle.

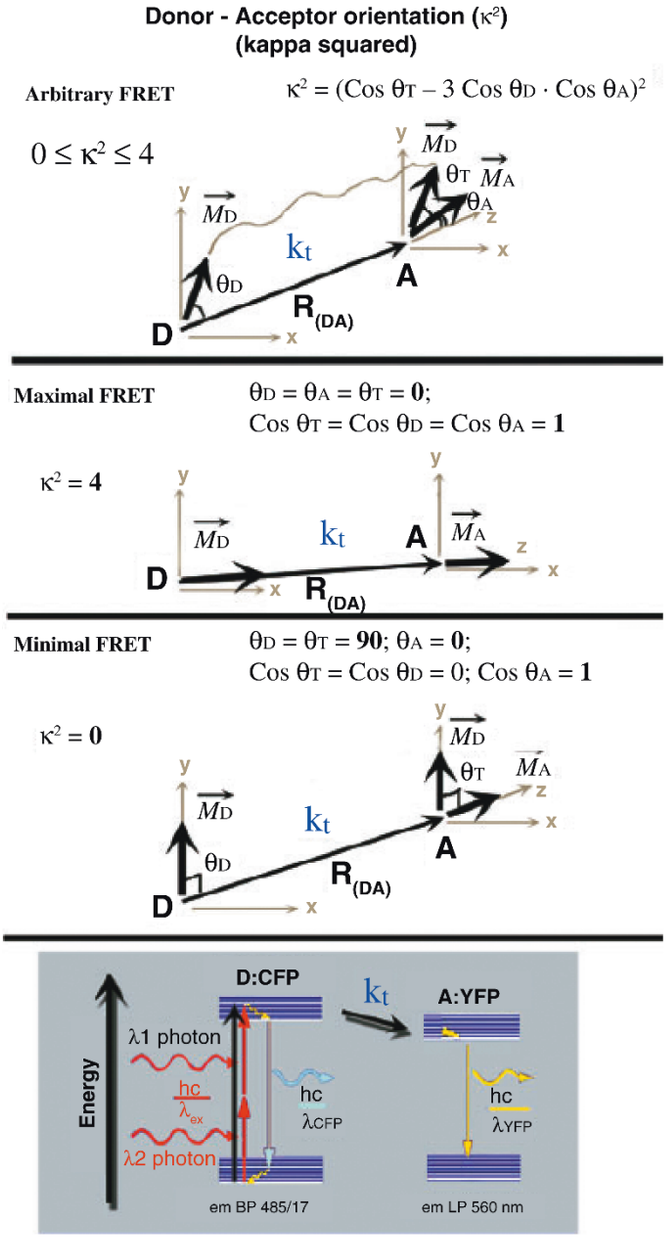


FIGURE 45.5. FRET theory. (Upper panel) Proximity and spatial orientation between the donor (D) and the acceptor (A) pair. An increase in the Förster radius between donor and acceptor (R_{DA}) will lead to a decrease in efficiency of energy transfer. Mutual orientation (angles θ_D, θ_A, θ_T) between the donor and acceptor molecules influence the transfer efficiency E_{eff}. (Lower panel) Jablonski diagram for single- and two-photon excitations of the donor may result either in the emission of the donor (CFP $\lambda_{em} = 474$ nm) or (in case of a close proximity) to the non-radiative dipole–dipole transfer of energy (k_t) to the acceptor molecule followed by the Stokes shift and the emission of fluorescence by the acceptor molecule at a longer wavelength (YFP, $\lambda_{em} = 526$ nm).

to the number of photons absorbed by the donor or the acceptor is known as quantum yield of the donor (Q_D) or of the acceptor (Q_A). The lower the quantum yield of the donor (Q_D), the more photon energy will undergo either non-radiative decay k_{Di} compared to the radiative k_D fluorescence emission of the donor or possible FRET (with k_t, the rate of FRET transfer). The quantum yield of the donor in the absence of an acceptor is represented as:

$$Q_D = k_D/(k_D + k_{Di}) \quad \textbf{(2)}$$

Thus, the quantum yield of the donor in the presence of the acceptor will be:

$$Q_{DA} = k_D/(k_t + k_D + k_{Di}) \quad \textbf{(3)}$$

The fraction of the photon energy absorbed by the donor that can be transferred without radiation to an acceptor represents the efficiency of energy transfer, E_{eff}. The relationship between E_{eff} and the quantum yield of the donor in the presence and absence of acceptor can be described as:

$$Q_{DA}/Q_D + E_{eff} = 1 \quad \textbf{(4)}$$

where Q_{DA}/Q_D is the efficiency of the radiative process that, added to the efficiency of the non-radiative energy transfer (FRET) equals 1. E_{eff} can be also described in terms of k_t, k_D, k_{Di} by substituting of Eqs. 2 and 3 into Eq. 4:

$$E_{eff} = 1 - Q_{DA}/Q_D = 1 - (k_D + k_{Di})/(k_t + k_D + k_{Di}) \quad \textbf{(5)}$$

$$k_t / k_t + k_D + k_{Di} \quad \textbf{(5a)}$$

To perform practical FRET measurements, one needs to keep in mind that the efficiency of energy transfer (E_{eff}) to the acceptor will be strongly decreased by an increase in both radiative (k_D) and non-radiative (k_{Di}) decay of the donor. FRET efficiency is a direct measure of the photon energy absorbed by the donor and transferred to an acceptor (Figs. 45.5 and 45.6). E_{eff} depends strongly on the actual proximity R between the donor (D) and the acceptor (A) molecules and on their mutual orientation (Fig. 45.5). For efficient FRET to occur, the distance (R) between the excited donor and the fluorescent acceptor needs to be typically 2 to 7 nm (Förster, 1948a,b; Stryer, 1978; Lakowicz, 1999; Patterson *et al.*, 2000). The dependence of E_{eff} on R was described by Förster as:

$$E_{eff} = 1/[1 + (R/R_o)^6] \quad \textbf{(6)}$$

The distance between the donor and the acceptor for which $E_{eff} = 0.5$ is called R_o and reflects the properties of a particular *D/A* pair. It is a function of the quantum yield of the donor (Q_D), integral spectral overlap between the donor emission and the acceptor excitation, J_{DA} and a factor reflecting their relative spatial orientation (κ^2) (Figs. 45.5 and 45.6).

If κ is known and fixed, then the FRET efficiency between two chromophores can be taken as a direct measure of R, using Förster's conversion formulae (Eq. 6). Quantitative FRET analyses of different subcellular compartments in a living cell requires that we know the real value of the spatial orientation factor (κ^2). Figure 45.5 describes the common arbitrary case and two extreme cases: maximal FRET to no FRET based on orientation factor (κ^2). A Jablonsky diagram for single- and two-photon excitation in FRET [cyan fluorescent protein (CFP) donor, YFP acceptor] is shown below (Fig. 45.5). Our preliminary data revealed that the same chromophores, CFP and YFP, measured with the identical microscope will display different levels of FRET when attached to proteins from the different subcellular compartments. Two transmembrane Golgi donor and acceptor proteins (i.e., donor and acceptor that can oligomerize only by diffusing laterally in the plane of the Golgi membrane) display less FRET than the combination of the transmembrane acceptor-YFP and a free cytosolic donor-CFP that interact with each other (as shown in Fig. 45.8). It is clear that the rotational mobility, and thus relative spatial orientation factor (κ^2), can be higher for the cytosolic proteins than for the laterally fixed transmembrane fluorescent proteins.

Because in most experiments the actual orientation is difficult to determine, it is common to assume a random orientation of the

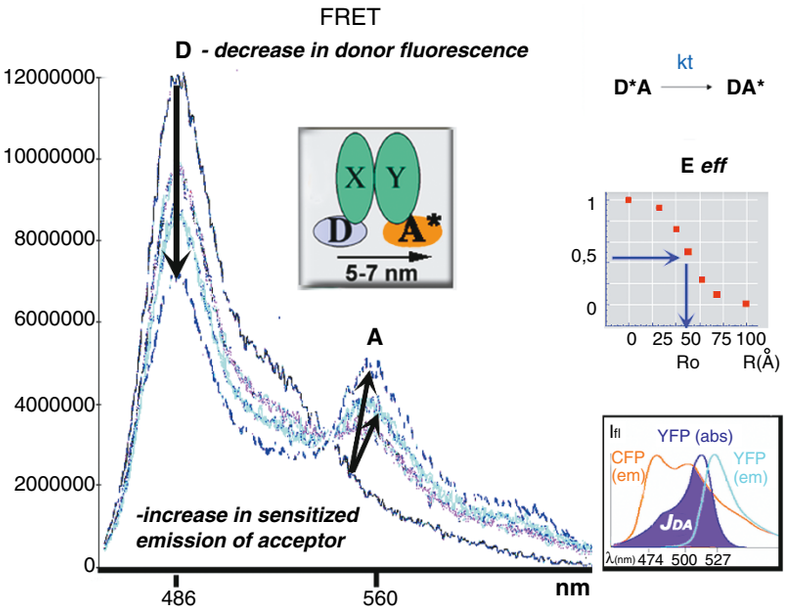


FIGURE 45.6. Spectra illustrating the FRET effect. Spectrofluorimetry allows one to follow the time-dependent appearance of FRET (left). The decrease in donor fluorescence (*long arrow*) correlates with the increase in sensitized emission of the acceptor (*short arrows*). Spectral overlap (J_{DA}) between the emission spectrum of the donor (CFP) and the excitation spectrum of the acceptor (YFP) ensures that FRET can potentially occur between a selected pair of biological molecules (e.g., proteins X and Y of interest), if they functionally interact in living cells (upper right corner). Formulae used for R_o calculations (R_o corresponds to E_{eff} = 50% of a maximal). For a detailed description see the FRET Theory section in the text.

green fluorescent proteins (GFPs) even when they are fused to macromolecules. This uncertainty, plus the uncertainty in chromophore location within the entire chimeric protein, means that FRET with GFP variants is more suited to detecting changes in conformation or percentages of association than to quantifying the absolute value of R.

The dominant uncertainty causing R_o or E_{FRET} fluctuations is the relative orientation of dipoles, as is described for three particular cases in Figure 45.5. When the labeled proteins are not known to be attached to a larger structure, it is common to assume that the two dyes are freely rotating on a time scale comparable to, or faster, than the fluorescence lifetime and that κ^2 can be dynamically averaged to a fixed value of $\kappa^2 = 2/3$. To test whether this assumption holds true for new constructs under investigation, ensemble polarization anisotropy measurements can be performed on selected constructs (Lacowicz, 1999; Mattheyses *et al.*, 2004). For free cytosolic proteins, or a combination of a cytosolic and a membrane-attached protein, it has been found that both free and attached GFP have large anisotropy values (around $r = 0.20$), indicating obstructed rotational diffusion.

In this chapter, calculated values of R_o are based on the assumption that $\kappa^2 = 2/3$, even though we recognize that it is possible that in some subcellular compartments κ^2 can be as high as 2 or even 4 (Fig. 45.5). If the wavelength is measured in centimeters and the molar absorption in $M^{-1}\,cm^{-1}$, and the J_{DA} value is given in $M^{-1}\,cm^{-3}$, then the following formula results:

$$R_o^6 = 8.79 \times 10^{-25}\ \{QD\ \kappa^2 \cdot n^{-4}\ J_{DA}\}\ cm^6 \qquad (7)$$

However, if the wavelength is depicted in nanometers and the molar absorption in $M^{-1}\,cm^{-1}$, and the J_{DA} value is given in $M^{-1}\,cm^{-1}\,nm^{-4}$, the Eq. is the following (see also Fig. 45.6):

$$\mathbf{R_o^6 = 8.79 \times 10^{-5}\ \{QD\ \kappa^2 \cdot n^{-4}\ J_{DA}\}}\ Å^6\ \text{(in Ångströms)} \qquad (8)$$

A number of experimental data have confirmed the linear dependence of E_{eff} on the value of J in the range of distances used to measure FRET. It is important to mention here that, as the GFP variants exhibit relatively small Stokes shifts, R_o values calculated between selected GFP variants can be used for FRET calculations (Patterson *et al.*, 2000).

As the energy absorbed by the single dipole will induce this dipole (e.g., donor) to oscillate along *x*-, *y*-, and *z*-oriented directions (Fig. 45.5), this energy will be in the reverse proportion to the radius R^3. With the appearance of the second oscillating dipole in resonance proximity (acceptor), their common energy will be calculated in reverse proportion to the R^6. E_{eff} is highly and inversely dependent on the distance (R) between the donor and the acceptor chromophores, and can be obtained in the experiment. The Förster equation can in principle be used to calculate the intermolecular distances on a nanometer scale (i.e., FRET = nanobioscopy):

$$E_{eff} = R_o^6/(R_o^6 + R^6) \qquad (9)$$

The actual distance between a particular pair of donor and acceptor molecules can be calculated if their Förster radius (R_o) is known from previous experiments. Calculations of R_o, based on the spectral properties of some donor–acceptor pairs of fluorescent proteins are given in Table 45.1. From Eq. 9, it follows that an increase in the distance between acceptor and donor from $R = R_o$ to $R = 2R_o$ will decrease E_{eff} from 50% to 1.5%. R_o is determined experimentally as the distance in Ångströms (1 nm = 10 Å). E_{eff} can be obtained directly from the experiment:

$$E_{eff} = 1 - F_{DA}/F_D \qquad (10)$$

TABLE 45.1. Calculated Donor–Acceptor Distance (Ro) in Nanometers (Patterson *et al.*, 2000)

	Acceptor (GFP Variant or DsRed)		
Donor	Green	Yellow	Red
Cyan	4.82	4.92	4.17
Green	4.65	5.64	4.73
Yellow	3.25	5.11	4.94

where F is the fluorescence intensity measured in the experiment. F_{DA} is the fluorescence intensity of the donor in the presence of acceptor and F_D is the fluorescence intensity of the donor alone. FRET efficiency E_{eff} can also be measured as the relative fluorescence of the donor in the presence (Dbb) and absence (Dab) of the acceptor (i.e., after photobleaching of the acceptor). As it is usually difficult to achieve complete photoinactivation of the acceptor in living cells, an image of the acceptor is acquired both before bleach (Abb) and after bleach (Aab). The ratio of Aab/Abb then reflects the percentage of non-bleached acceptor that needs to be included in calculations of FRET efficiencies. Acceptor photobleaching allows one to obtain the experimental parameters Dbb and Dab, used for FRET calculations.

$$E_{eff} = 1 - \text{Dbb/Dab} \quad \textbf{(11)}$$

Anisotropy analysis of chimeric fusion proteins can also provide a solid basis for structural analysis (Velez and Axelrod, 1988). Different experimental variations of FRET measurements have been developed for biological applications within the last two decades and continue to be improved in a growing number of laboratories around the world. Nevertheless, it is still useful to perform spectral analyses for any new chromophores selected for FRET to control for their exact properties once they are inside the cell line selected for experiments. Alternatively, one can calculate FRET efficiency from fluorescence lifetime data [τ from a fluorescence lifetime imaging microscope (FLIM) (Lakowicz, 1999; and Chapter 27, *this volume*]. Using the previous equations, we can describe lifetime as:

$$\tau = Q/k$$

where Q is the quantum yield of the fluorophore and k_f the number of photons emitted. The lifetime of the donor in the presence of the acceptor is described as:

$$\tau_{DA} = Q_{DA}/k_D = 1/(k_t + k_D + k_{Di}) \text{ or } k_T + k_D + k_{Di} = 1/\tau_{DA} \quad \textbf{(12)}$$

The lifetime of the donor in the absence of the acceptor will be

$$\tau_D = Q_D/k_D = 1/(k_D + k_{Di}) \quad k_D + k_{Di} = 1/\tau_D \quad \textbf{(13)}$$

Substituting Eq. 12 and Eq. 13 into Eq. 5, FRET efficiency can be calculated directly from the experimental measurements of the lifetime of the donor in the presence (τ_{DA}) and in the absence of the acceptor (τ_D):

$$E_{eff} = 1 - \tau_{DA}/\tau_D \quad \textbf{(14)}$$

FLUORESCENT PROTEINS AND FLUORESCENCE RESONANCE ENERGY TRANSFER

Considering all the non-fluorescent proteins in living organisms, the discovery and, ultimately, cloning of a naturally fluorescent one, GFP, from the marine organism *Aequoria victoria* came as a lucky surprise (Ward *et al.*, 1982; Prasher *et al.*, 1992; Chalfie *et al.*, 1994; Chalfie, 1995; Tsien, 1998). What drove evolution to create a fluorescent protein? One reasonable theory suggests that GFP molecules appeared as a byproduct in the development of antioxidant systems that evolved into the pocket of an excitable chromophore (Heim *et al.*, 1994; Labas *et al.*, 2002). The story is made more interesting by the fact that the native GFP chromophore is excitable with blue light (at a peak of 395 nm) that is internally transferred by a FRET mechanism, resulting in emission at 508 nm (Heim and Tsien, 1996). Thus, FRET already exists as an intrinsic property of native GFP (Ward *et al.*, 1982; Heim *et al.*, 1995).

It took about 20 years after the discovery of GFP before it was put to practical use in the field of cell biology, but then it produced a scientific revolution (Ward *et al.*, 1982; Prasher *et al.*, 1992; Chalfie *et al.*, 1994; Tsien, 1998, 2004; Lippincott-Schwartz and Patterson, 2003). GFP-based methodologies and live-cell imaging, combined with FRET and other biophysical approaches, yielded a vast amount of information, allowing one to study and dissect biochemical pathways at the single cell level (Hirose *et al.*, 1999; Miyawaki *et al.*, 1999; Janetopoulos *et al.*, 2001; Lippincott-Schwartz and Patterson, 2003; Jones *et al.*, 2004; Kusumi *et al.*, 2005).

GFP, and its spectrally shifted variants, CFP and YFP (Heim and Tsien, 1996; Tsien, 1998; Patterson *et al.*, 2001) are particularly useful, either for colocalization studies or as partners for FRET-proximity imaging experiments (Mochizuki *et al.*, 2001). CFP was created by introduction of the S65A, Y66W, S72A, N146I, M153T, and V163A mutations into GFP, resulting in an excitation peak of 434 nm and an emission maximum at 474 nm. YFP differs from GFP by the S65G, V68L, S72A, and T203Y mutations and has an excitation peak of 514 nm and an emission maximum at 527 nm (Heim and Tsien, 1996; Tsien, 1998). Good spectral overlap between CFP and YFP currently favors these two chromophores as the best pair for analyzing protein–protein interactions.

GFP provides the great advantage of allowing us to follow in a living cell any cellular protein for which the coding sequence is known. GFP-based chimeric proteins have been expressed in an almost unlimited range of different cell types, including neurons, in tissue slices, and even in whole living organisms (transgenic mice, rats, rabbits, fish, etc.).

Often GFP chimeras are placed under tissue-specific promoters. The spectral variants of GFP that represent donor–acceptor pairs allow us not only to map intracellular protein localization, but also to analyze their interactions in different cells and subcellular compartments. GFP chimeras can be targeted to different cellular localizations. As GFP itself is a relatively small protein (~27 kDa) with a chromophore inside a cylinder of 2.4 nm in diameter, the centers of the two chromophores cannot get closer to each other than their diameter. Maximal FRET between CFP and YFP was measured at a distance of 4.9 to 5.2 nm, demonstrating FRET (proximity) in a size range of protein–protein complexes (Tsien, 1998). Stryer's dream of FRET as a "Spectroscopic Ruler" started to become a reality.

FRET between fluoroscein and rhodamine molecules was first measured a long time ago and R_o values of 4.9 to 5.4 nm have been known and used for the FITC (fluorescein isothiocyanate) and TRITC (tetramethyl rhodamine) pair as chromophores with high energy transfer efficiency (Johnson *et al.*, 1984).

DsRed, derived from the *Discosoma* coral, is genetically different from GFP (Matz *et al.*, 1999). An intrinsic tendency of DsRed to tetramerize and its slow maturation compared to GFP prevented its broad application for colocalization or FRET studies. However, DsRed has recently been "re-evolved" by extensive mutagenesis, resulting in bright monomeric versions, called mRFP1 or mCherry, which show improved fluorescence and maturation times (Campbell *et al.*, 2002; Shaner *et al.*, 2004). Using GFP as a donor, these mRFPs can now be used for FRET analyses.

Small fluorescent molecules (e.g., Cy2, Cy3, Cy5, Alexa-488, Alexa-543) can be easily attached to bacterial toxin molecules without changing their activity and can then be used for monitor-

ing toxin actions in living cells. These dyes can either form FRET pairs by themselves (e.g., Cy3 and Cy5) or can be combined with GFPs in a FRET pair (e.g., CFP and Cy3, or potentially GFP and Cy5).

Qualitative Analysis

Because in many cases it is difficult either to estimate the level of cellular expression to determine the donor–acceptor ratio or to correct for non-transfer energy loss pathways[1] in a system as complicated as a living cell, many researchers settle for qualitative data. Additionally, lack of precise filters, suboptimal laser excitation wavelengths, and the limited speed of data readout are common sources of errors in FRET analysis.

The spectroscopic properties required for successful FRET measurements in live cells (both for GFP-like chromophores and for organic dyes) include:

- A suitable spectral integral overlap between donor emission and acceptor excitation.
- High donor molar extinction coefficient.
- High fluorescence quantum yield of the donor.
- Comparable rates for donor and acceptor photobleaching.
- Comparable maturation times and intensity of chromophores during FRET records.
- Known ratio of donor:acceptor molecules.

To avoid common mistakes when choosing either a single probe or a FRET donor/acceptor pair, the most important first step is a literature search. For example, the strong pH dependence of YFP makes it unsuitable for fusions on the luminal side of transmembrane proteins of acidic membranous organelles, such as lysosomes. However, when YFP is attached to such proteins on the cytosolic side it will work well and give bright fluorescence (Elsliger *et al.*, 1999; Griesbeck *et al.*, 2001). For each chromophore, it is useful to know whether the fluorescent signal obtained derives from the intrinsic concentration of the chromophore, or if it also reflects properties of the microenvironment (e.g., pH dependence).

Preparation

Preparations for live cell experiments thus should include:

1. Selection of appropriate fluorescent probes and cell lines.
2. Correct design of experiments (strategy) to answer the question.
3. Proper labeling or correct cloning of chimeric fluorescent proteins.
4. Finding a suitable method for introducing fluorescent molecules into cells: transfection/electroporation/microinjection.
5. Proper microscope setup for FRET analyses [lasers, filters, charge-coupled devices (CCDs), photomultiplier tubes (PMTs)].
6. Best conditions for data acquisition from live cells (ensure good cell condition during the experiment, e.g., temperature, CO_2, isotonicity, illumination levels).
7. Appropriate image analysis (e.g., using programs such as MetaMorph 4–6, Imaris, NIH ImageJ, Photoshop, or custom-made software programs) based on controls in which only the donor or only the acceptor is expressed.

[1] For example, a normal cellular protein may act as a non-fluorescent acceptor, partially depleting energy of the donor.

NANOBIOSCOPY OF PROTEIN–PROTEIN INTERACTIONS WITH FLUORESCENCE RESONANCE ENERGY TRANSFER

Methods of Fluorescence Resonance Energy Transfer Measurement

FRET is never observed directly but can only be monitored immediately after the actual act of energy transfer from donor to acceptor. Therefore, all methods discussed here determine FRET indirectly. Changes in the degree of donor–acceptor interactions result in changes in FRET efficiency which is measured by comparing two states: (1) donor signal in the presence of acceptor F_{DA}, compared to (2) donor signal without the acceptor F_D (i.e., after bleach). Several experimental FRET setups are described below.

Sensitized Emission of Acceptor

FRET by sensitized (i.e., increased) emission of the acceptor relies on measurements of acceptor emission resulting from excitation of a donor (Bastiaens and Jovin, 1998; Lakowicz, 1999; Periasamy *et al.*, 2001). Sensitized emission of the acceptor occurs when it is in close enough proximity to an excited donor that it can accept energy non-radiatively from the donor and then emit its own fluorescence without direct excitation. This method is simple but always requires a subsequent correction for cross-talk of the donor fluorescence into the acceptor channel, something that is especially difficult to measure for chromophores with closely related spectra.

The concentration ratio of donor/acceptor molecules present in living cells will also influence FRET results. FRET data on molecular interactions are easier to obtain if the donor/acceptor ratio is in the region of 1 : 1 to 1 : 10 (Gordon *et al.*, 1998; Herman *et al.*, 2001; Hoppe *et al.*, 2002). The optimal D/A pair must be chosen for each particular experiment. Donor–acceptor pairs that are far away in wavelength allow one to avoid significant spectral overlap but usually have poor FRET efficiencies. Alternatively, although D/A pairs that share a large spectral overlap are often difficult to separate and to use reliably in experiments, they almost always show high FRET efficiencies.

The sensitized emission (FRET signal) can also be easily detected by spectrofluorimetry (Fig. 45.6). However, in this case, the FRET signal will be averaged over the entire cell population. Only microscopes equipped with the appropriate filters allow one to resolve both FRET signals together with spatial information at cellular or subcellular level. A FRET signal from a corresponding cellular image obtained with a microscope will thus uniquely provide an additional magnification of the process, surpassing the optical resolution needed to visualize the Golgi, endoplasmic reticulum (ER), lysosomes, mitochondria, and other cellular subcompartments. Often, FRET efficiency (E_{eff}) can be directly visualized under the microscope throughout the entire cell and even resolved at the level of subcellular compartments, for example, the differential increase in FRET at the Golgi/cytosol interface shown in Figure 45.8.

Currently, a typical living-cell FRET experiment involves usually capturing the emitted fluorescence from both the donor CFP and the acceptor YFP after excitation of only the donor (CFP). The increase in sensitized emission corresponds to the degree of physical association between the two fusion proteins. In addition, spectral measurement or ratiometric imaging of the emission profile can be performed. This should include recording (a) emission of a sample expressing donor alone as a control, and (b) recording the interacting FRET pair. Comparison between the

emission spectra of these two samples allows one to assess the degree of FRET (see Fig. 45.6).

Sensitized emission of the acceptor is a quick method for monitoring FRET in living cells, and perhaps the most promising approach for analyzing protein–protein interactions that have fast kinetics. It is also useful for recording neuronal activities and for studying the effects of drugs on specific cellular targets. These experiments require that the detection of the acceptor emission is not significantly contaminated with a non-FRET contribution from the donor. The only way to observe FRET in a dynamic situation is to have filters that effectively eliminate cross-talk between the emitted light from the two fluorophores. The underlying assumption is that the ratiometric analysis of donor and acceptor signals will allow one to monitor and to calibrate the kinetics of the biological responses. Precalibration of the expected effect in the correct time frame and the correct range of fluorescence intensities, laser sources, and filters is required to create an intensity-dependent lookup table, which can then be used during an experiment.

Using sensitized emission, we were able to monitor the time-dependent effect of a bacterial toxin, cholera toxin, on the oligomerization of a transmembrane Golgi receptor over a period of 2 h [Fig. 45.7(A)].

Donor Fluorescence

Acquisition of a clean donor image, that is, non-contaminated with acceptor fluorescence, is the most critical step in this type of FRET analyses. This is especially true for CFP because the CFP/YFP emission spectra are closely overlapping and CFP chimeras are usually less bright than YFP chimeras. The main requirements for acquiring a correct donor image are proper donor excitation wavelength, laser power adjusted to be appropriate for living-cell experiments, and a correct detector gain in the acquisition channel**.** The microscope must be precalibrated to ensure that the detector gains are linear within the working range of the experiment, and, therefore, that each channel is tuned separately for a maximal signal. For each set of experiments, we used a donor-only sample (CFP) to set the gain in the donor channel and to determine the minimum

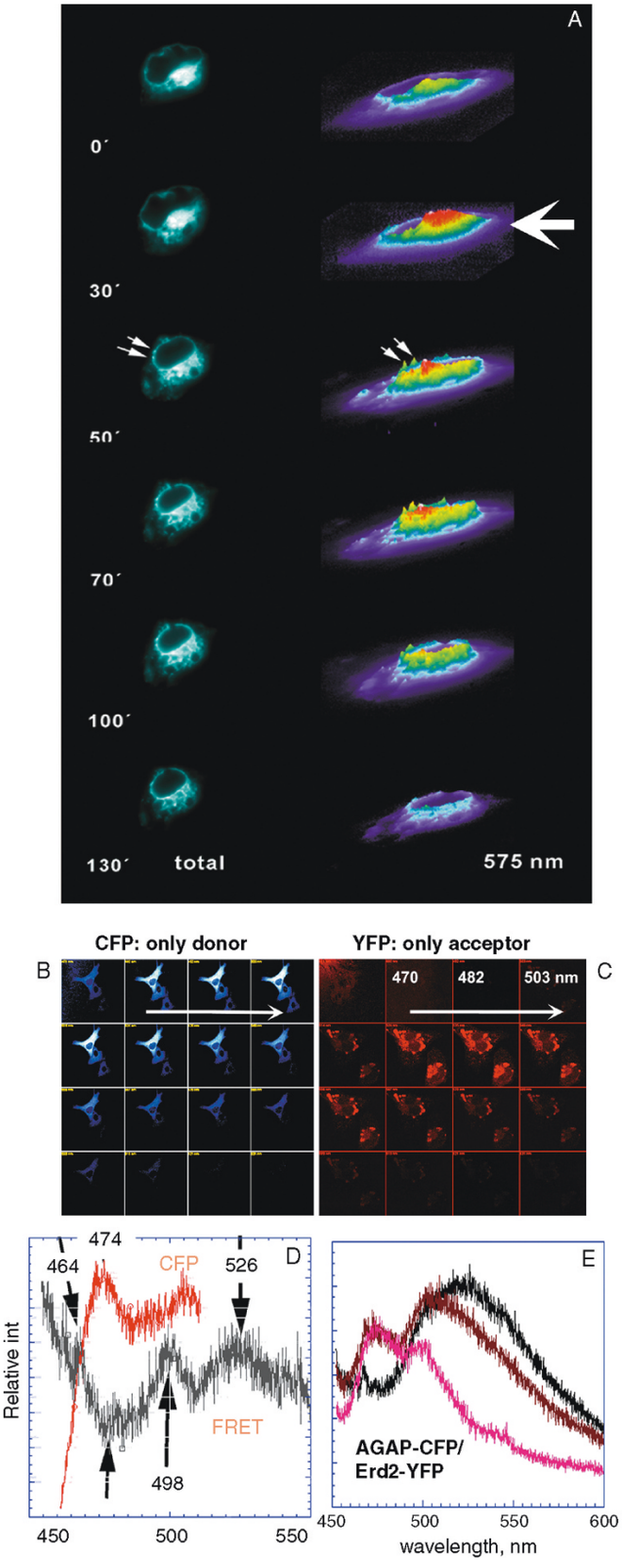


FIGURE 45.7. (A) FRET monitored by sensitized emission of acceptor revealed the time-dependent state of oligomerization at the single cell level. Vero cells were double transfected with CFP and YFP versions of ERD2. During its intracellular transport, cholera toxin binds to the KDEL receptor and induces receptor oligomerization, revealed here by FRET as an increase in sensitized emission of acceptor (*large arrow*). (For details, see Majoul *et al.*, 2001.) (B) The distribution of a CFP signal in 11 nm lambda windows using the LSM-510 META, single transfection with a CFP chimera. (C) The distribution of a YFP signal in 11 nm lambda windows using the LSM-510 META, single transfection with a YFP chimera. Note that the upper four spectral windows contain the CFP signal non-contaminated by YFP, whereas a YFP signal is best detected in the middle windows. The spectral windows are very important for monitoring the FRET-induced increase in the CFP signal after acceptor photobleaching. (D) Spectral characterization of FRET induced between CFP and YFP chimeras; FRET proximity leads to the disappearance of the donor emission peak (λ_{em} = 474 nm) and appearance of the sensitized emission of acceptor (λ_{em} = 526 nm) (gray curve). (E) Time-dependent FRET induced by cholera toxin transport between cytosolic ARFGAP-CFP and transmembrane ERD2-YFP revealed by spectrofluorimetry. Disappearance of CFP (474 nm) peak and the appearance of YFP (526 nm) sensitized emission peak can be followed during these records. Red curve shows typical CFP emission at 474 nm at the beginning of toxin transport, indicating no or low FRET, whereas a later time point (black curve) shows strong FRET. For details, see Majoul *et al.* (2001).

laser power necessary to acquire a donor signal at maximum detector gain. The same process was repeated for the acceptor channel using an acceptor-only (YFP) sample. To acquire a FRET image the same laser power and wavelength was used as for CFP alone.

If FRET occurs, it should result in a decrease in donor fluorescence, and this can be measured by different methods, including fluorescence lifetime. Usually it is done by acquiring sequential sets of donor images and comparing donor intensities, I_D, with I_{DA} (donor in the presence of acceptor) after different ($t + \tau$) and after different amounts of donor photobleaching. The advantage of this approach is the ability to follow FRET-induced changes in the donor fluorescence. The disadvantage is the absence of proper controls for acceptor and other non-FRET ways of donor deactivation.

Acceptor Bleach

The best way to prove that an observed FRET signal reflects a true interaction between two molecules is to remove (photo-inactivate) the acceptor (Bastiaens *et al.*, 1996; Bastiaens and Jovin, 1998). In the case of true FRET, an increase in donor fluorescence will result; from the portion of the donor fluorescence that was recovered after accepter inactivation. The ratio of the donor fluorescence intensities before and after acceptor photobleaching (Dbb/Dab) reports the FRET efficiency. FRET efficiency (E_{eff}) is calculated as the ratio of two intensities generated in the same detection channel but from the same sample before and after acceptor bleach. Depending on how much FRET occurred in a particular region of interest, the ratio of the two intensities measured on the same cell in two different regions of interest (e.g., a bleached and an unbleached region of the same cell treated with bacterial toxin) often varies (Bastiaens *et al.*, 1996).

The application of the acceptor bleach method is often delicate in living biological samples because of the long bleaching times involved and the associated phototoxicity. We used a special built-in laser emitting at 532 nm for acceptor photo-inactivation, and calculated FRET from the percentage of acceptor bleach instead of performing a total inactivation of the acceptor. The degree of acceptor bleach can be calculated from the ratio of acceptor after and before bleach (Aab/Abb), images. In this type of experiment, one needs to ensure also that the process of acceptor photobleaching does not affect the donor intensity, otherwise the experimentally measured FRET value will be lowered.

An example of a strong increase in donor fluorescence after acceptor bleach (Dab), detectable even by eye, at the Golgi/cytosol interface is shown in Figure 45.8. This figure represents data from two different setups used for measuring FRET: a Leica-based, two-photon multi-focal, multi-photon microscopy (MMM) FRET setup (described in detail in Majoul *et al.*, 2001, 2002b) and a single-photon Olympus FV500 setup. Here we compare FRET results measured on the same type of biological samples consisting of interacting CFP and YFP fusions (Fig. 45.8).

In both cases, the fluorescent donor was a CFP chimera of the cellular protein ARFGAP. This normally predominantly cytosolic protein becomes associated with membranes of the Golgi complex in a biologically meaningful way upon its interaction with the acceptor, the YFP-tagged transmembrane Golgi KDEL-receptor (Majoul *et al.*, 2001). We analyzed fluorescence of the donor ARFGAP-CFP before (Dbb) and after acceptor photo-inactivation (Dab) (Fig. 45.8).

The FRET-MMM setup included an 100× oil objective and a cooled back-illuminated CCD camera. For the Olympus setup, a PL APO 60× oil NA 1.4 objective lens was used at λ_{ex} = 458 nm

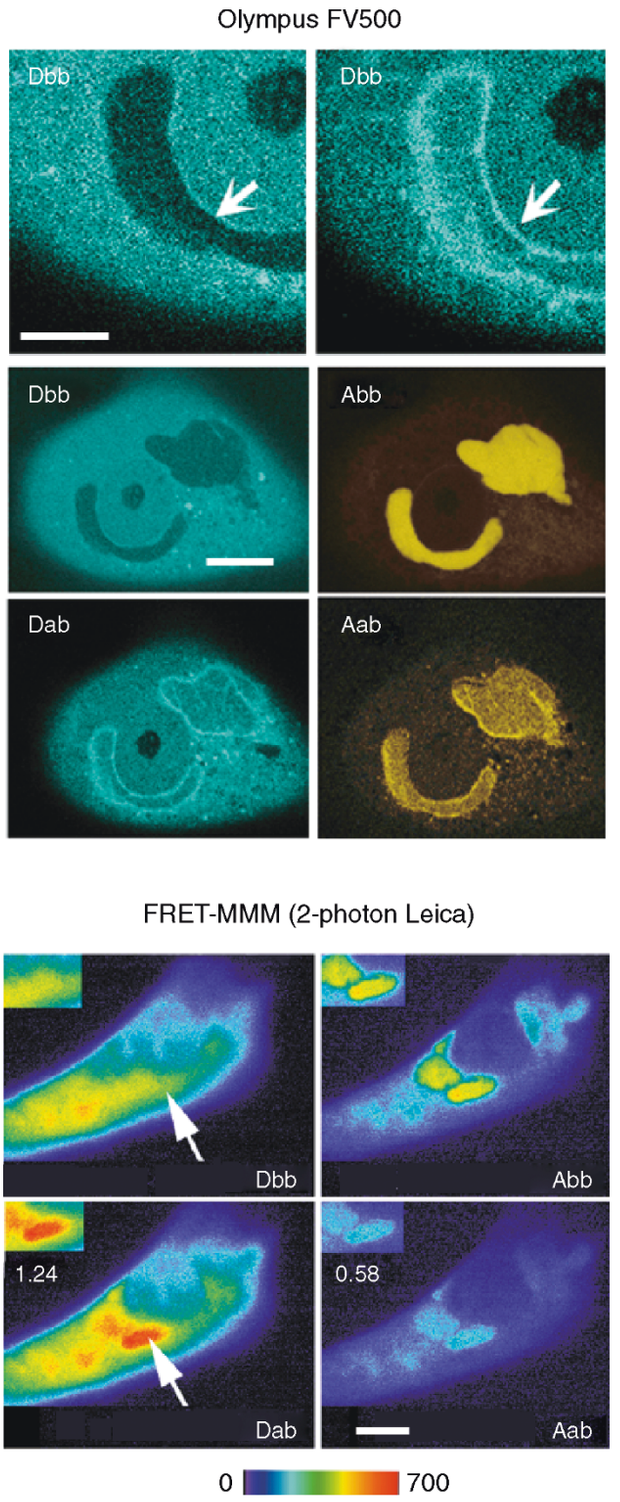


FIGURE 45.8. An example of FRET induced by cholera toxin transport between cytosolic ARFGAP-CFP and transmembrane ERD2-YFP recorded under the microscope. It is obvious that a cytosolic donor can only efficiently interact with the transmembrane Golgi acceptor at the Golgi/cytosol interface. (Upper panel) The Olympus FV 500 setup allowed us to resolve the increase in CFP (donor) fluorescence at the Golgi/cytosol interface even after partial photoinactivation of acceptor (compare Dbb and Dab). (Lower panel) The same combination of cytosolic donor ARFGAP-CFP and the transmembrane acceptor ERD2-YFP was used for FRET-MMM analyses. Although we were able to see an increase in donor fluorescence after acceptor bleach, the fine resolution of FRET at Golgi/cytosol interface was not achieved in this experimental setup. (For more details see text.)

(argon laser, 10% power) and the PMT voltages set to 729 V for the CFP channel and 653 V for the YFP channel. Acceptor emission was detected within a narrow 15 nm wavelength window between 480 and 495 nm. The YFP acceptor was photobleached at λ_{ex} = 532 nm and emission was sensed between 535 and 565 nm. The FRET-MMM two-photon excitation wavelength for the donor (CFP) was λ_{ex} = 820 nm. Acceptor bleaching was done using a Nd:YAG laser at 532 nm and CFP donor fluorescence was detected with the a BP485/17 nm emission filter (Zeiss) in front of a back-illuminated CCD camera. Up to >90% of acceptor (YFP) was photobleached within 72 s. After the irradiation of the acceptor was completed, the de-quenched donor fluorescence was analyzed (Dab) and compared to the initial state of the donor (Dbb) to estimate the degree of donor-acceptor interactions in FRET.

Using FRET-MMM, we were able to see the increase in donor fluorescence (Fig. 45.8, lower panel, big arrows) but were not able to distinguish the Golgi/cytosol interface. We expected to see more FRET at the Golgi membrane/cytosol interface because the cytosolic donor (ARFGAP-CFP) can interact with the transmembrane Golgi acceptor (ERD2-YFP) only in this location, that is, the multiple cytosolic donor molecules accumulating on the Golgi membrane interact with the transmembrane acceptor. Remarkably, using the Olympus setup we could discriminate between outer (looking into the cytosol) and inner surfaces of the Golgi complex (Fig. 45.8, upper panel). The Olympus setup revealed a much stronger de-quenching of the donor at the Golgi/cytosol interface after the acceptor photoinactivation (Fig. 45.8, left panel, see small arrows).

FLUORESCENT PROTEINS AS FLUORESCENCE RESONANCE ENERGY TRANSFER PAIRS

Cyan Fluorescent Protein and Yellow Fluorescent Protein — The Commonly Used Fluorescence Resonance Energy Transfer Pair

As native CFP and YFP molecules normally do not interact, ideally only a biologically meaningful interaction between the non-GFP part of chimeras will bring these chromophores into FRET proximity. However, in over-expressing cells, unspecific stochastic interactions induced by a very high local density of CFP-YFP chimeras can also generate an artificial FRET signal. Such cells should not be used. Normally the interaction time of an unspecific pair of CFP and YFP chimeras should be significantly shorter than that displayed by a pair of CFP and YFP chimeras undergoing a biologically meaningful interaction.[2]

To measure sensitized emission complementary to the FRET microscope data, we used Fluoromax-2 and Fluoromax-3 spectrofluorimeters (ISA, Jobin-Yvon Instruments, Edison, NJ) as a control in the same transfected cell population in bulk cell experiments. CFP was excited at λ_{ex} = 425 nm, and fluorescence emission was detected between 450 to 600 nm. For comparison, YFP was excited separately at λ_{ex} = 498 nm, and its fluorescence was measured between 510 and 600 nm. For a time-dependent analysis of the interactions between CFP and YFP fusion proteins, the culture plate was divided into segments and the cells from different segments were examined by spectrofluorimetry before and after toxin application (Majoul *et al.*, 2001, 2002b).

The ability to detect meaningful signals clearly depends on the signal/noise ratio. For example, although trying to detect GFP fluorescence in the presence of the intrinsically strong autofluorescent background signal found in transfected primary hepatocytes often results in a signal/noise ratio of ~1, the same GFP expressed in primary fibroblast-like cell cultures will produce a signal/noise ratio of ~10 : 1. Compared to fibroblasts, hepatocyte cultures will always present much bigger problems with photobleaching and phototoxicity. An understanding of cell physiology and the photophysics of the dye used in the microenvironment of each cell type is essential for evaluating FRET data obtained with the fluorescence microscope.

Cyan Fluorescent Protein or Green Fluorescent Protein Forms a Fluorescence Resonance Energy Transfer Pair with mRFP1

The development of monomeric forms of DsRed (Campbell *et al.*, 2002; Shaner *et al.*, 2004) provided a new partner for FRET analyses. The current leading FRET pair CFP/YFP usually requires donor excitation at a wavelength (λ_{ex} peak = 430 nm) not found on many confocals. Although confocal microscopes equipped with argon-ion laser lines at 458 nm, 488 nm, and 514 nm, a green helium:neon (He-Ne) laser λ_{ex} = 543 nm or a red He-Ne lasers λ_{ex} = 633 nm can be used,[3] those employing dual-gas krypton/argon-ion lasers with lines at λ_{ex} = 488 nm, 568 nm, and 657 nm are not suitable for exciting either CFP or YFP (excitation peak λ_{ex} = 514 nm). Although CFP can be efficient excited by a krypton-ion laser at λ_{ex} = 413 nm or violet laser diodes at λ_{ex} = 405 nm, both of these are close to the ultraviolet (UV) and potentially cytotoxic, making them unsuitable for long, time-dependent experiments.

As the 488 nm line is common on most confocals and is optimal for exciting GFP, the introduction of mRFP provides us with a new FRET pair that will be highly appreciated by many cell biologists.

Whereas the large spectral overlap between CFP and YFP emission spectra necessitates the use of expensive, narrow band-pass filters and sensitive CCDs, mRFP, and other members of a growing family of red-shifted sea coral fluorophores, emits in the red. This favors their use as FRET acceptors with either GFP or CFP (Galperin *et al.*, 2004). Integral spectral overlaps (J_{DA}) between CFP/mRFP1 and GFP/mRFP1 are critical for FRET measurements (see also Fig. 45.6).

The R_0 values typical of GFP and DsRed are ~5 nm (Patterson *et al.*, 2000). Emission maxima of the donor (CFP or GFP) and the acceptor (mRFP1) measured on a Fluoromax-3 are shown in Figure 45.9, together with integral spectral overlaps. One remaining problem is that mRFP matures slowly in the cytoplasm; mCherry seems to be an improvement in this respect (Shaner *et al.*, 2004). This is a disadvantage for both comparative and quantitative FRET measurements with GFP or CFP, but it may be partially overcome by using a FRET detection algorithm, recently developed to compensate for the slow acceptor maturation in CFP/DsRed or GFP/DsRed pairs (Erickson *et al.*, 2003). Combinations of laser excitation and specific filter sets suitable for different FRET pairs of chimeric fluorescent proteins as well as fluorescent dyes are depicted in Table 45.2.

Fluorescence Resonance Energy Transfer-Based Sensors

Many biological processes are successfully analyzed with fluorescent biosensors where FRET between CFP and YFP reflects a wide variety of events such as phosphorylation of specific sequences, activity of cellular kinases or small GTPases, oscillations of intra-

[2] Except when these fusions may co-aggregate in over-expressing cells.
[3] The 458 nm laser line can be used for CFP excitation but is *not* optimal. A line at ~420 to 430 nm would be better, but these are relatively rare.

cellular Ca^{++}, pH, or binding of specific molecules that increase or abolish FRET (Miyawaki *et al.*, 1997; Miesenböck *et al.*, 1998; Kraynov *et al.*, 2000; Ting *et al.*, 2001; Del Pozo *et al.*, 2002; Wouters *et al.*, 2001; Bunt and Wouters, 2004). Quite often, a fluorescent biosensor is a fusion protein comprising three main components, a functional or targeting domain fused to the C- or N-terminus of enhanced cyan and yellow fluorescent proteins. FRET measurable with the biosensor will change in a predictable way in response to changes in the intracellular environment [pH, Ca^{++}, cyclic adenosine monophosphate (cAMP) levels, redox potential, adenosine triphosphate (ATP) levels, glucose levels, etc.] or the binding of a protein or peptide to the biosensor (reviewed in Hahn, 2003; Meyer and Teruel, 2003; Bunt and Wouters, 2004). GFP-based biosensors have been successfully applied to analyze compartmentalization of many cellular dynamic processes, notably the spatio-temporal analysis of cellular transport, signaling, and development.

Phosphoinositide signaling can be studied using GFP-tagged pleckstrin homology (PH) domain constructs. Different reporters for serine, threonine, and tyrosine protein kinase activities have been reported. Such GFP-based phosphorylation substrates are designed for precise subcellular targeting and to not impair phosphorylation of endogenous substrates. As a result, they allow spatio-temporal resolution of phosphorylation processes in live cells. For example, imaging of FRET-based reporters for protein-kinase C (PKC) translocation (with CFP and YFP fused to the N- and C-terminus of PKC), phosphoinositide bisphosphate conversion to IP3, and diacylglycerol has shown that in HeLa cells PKC-mediated oscillatory phosphorylations correlate with Ca^{2+}-controlled translocation of conventional PKC to the membrane without oscillations of phospholypase-C (PLC) activity or diacylglycerol (Violin *et al.*, 2003). Time-resolved visualization of growth factor–induced activation of Ras and Rap1 in living cells is yet another example of dissecting cellular signaling events using microscopic techniques and FRET sensors (Mochizuki *et al.*, 2001).

A fluorescent biosensor that is useful for temporal measurements of the mitotic clock has been recently described (Jones *et al.*, 2004). High throughput methods of FRET screening using biosensors will likely be useful in pharmaceutical and clinical screens for modulators of tyrosine kinases and phosphatases, and many other cellular activities. The list of useful biosensors is growing by the day. Previously based mostly on biochemical data, real-time observations with FRET in living cells are now becoming major sources for our knowledge of how cells move, divide, and are activated for coordinated cellular actions in signaling and intracellular transport.

TABLE 45.2. Lasers and Filter Configurations for Selected Fluorophores Used

	Laser, λ_{Ex}	λ_{Em} Filters (nm)
CFP	Argon, 457	485/30 or 485/17 (Zeiss)
YFP	Argon, 514	530/50
Alexa488 or GFP	Argon, 488 nm	515/30 or 535/50
Cy3 or Rhod-2 Green	He-Ne, 543 nm	590/70
DsRED/mRFP1	He-Ne, 543	590/70
Cy5	He-Ne 633 or	660LP
	He-Ne 594	660LP

FRET: Acceptor (YFP) bleach: external laser of 530 nm

Filters for the Widefield FRET: Donor/Acceptor λ_{Ex}/BP(nm); λ_{Em}(nm); Dichroic (nm)			
	Donor/Acceptor		
BFP/GFP	365/15 460/50	535/50	390
BFP YFP	365/15 460/50	535/26	390
BFP/mRFP1	365/15 460/50	610/60	390
CFP/mRFP1	436/20 485/17	610/60	455
CFP/YFP	436/20 485/17	535/20	455
GFP/Rhod-2 Green	488/20 535/50	595/60	505
FITC/Rhod-2 Green	488/20 535/45	595/60	505
FITC/Cy3	488/20 535/45	595/60	505
Cy3/Cy5	525/45 595/60	695/55	560
Alexa488/Cy3	488/20 535/45	595/60	505

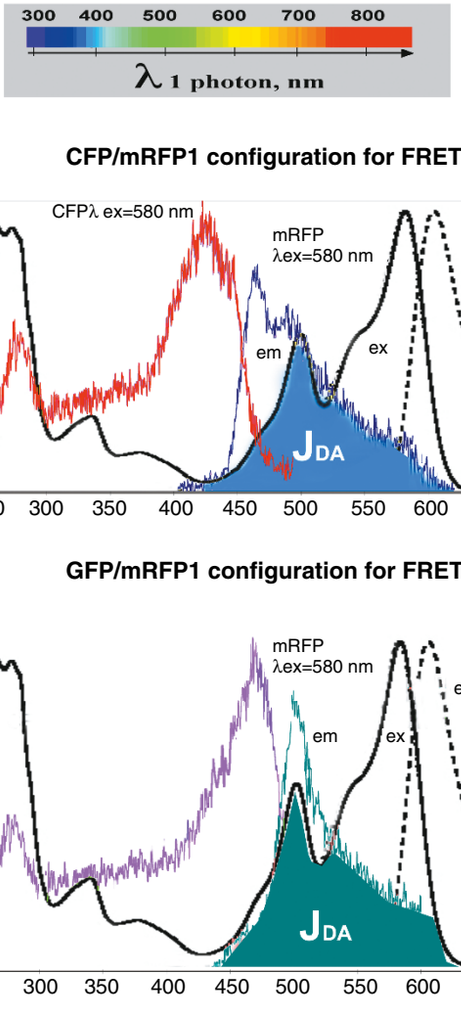


FIGURE 45.9. Monomeric red fluorescent protein (mRFP) is potentially a good FRET acceptor for both CFP and GFP chromophores. Excitation and emission spectra of CFP, GFP, and mRFP together with their integral spectral overlaps (J_{DA}) for CFP/DsRed and GFP/DsRed are given for comparison. Different filter sets used to separate CFP, GFP, and DsRed signals are indicated.

FLUORESCENCE RESONANCE ENERGY TRANSFER AND OTHER COMPLEMENTARY METHODS

Fluorescence Resonance Energy Transfer and Fluorescence Lifetime Imaging Microscope

FLIM is a neat tool for detecting multiple fluorophores in living cells, particularly spectrally overlapping molecules such as GFP

variants, which have different fluorescence lifetimes despite their overlapping spectra (Bastiaens and Squire, 1999). The detection of fluorescence is typically achieved by counting the number of photons emitted by the excited state of a fluorophore. Alternatively, the lifetime of the excited state can be measured by FLIM (Lakowicz, 1999; Chapter 27, *this volume*). FLIM is an excellent tool to measure FRET because the lifetime of the excited state decreases strongly when FRET provides an additional means for decay from the excited state.

FLIM can also be used to monitor FRET-based protein–protein interactions. The lifetime of the donor is the time spent in the excited state (τ) before returning to the ground state (Lakowicz, 1999). Analyses of donor–acceptor interactions thus relies on measurements of the length of time (typically less than 4 ns for GFP molecules) that the donor remains fluorescent after being excited with a fast pulsed laser. FRET can be calculated in such an experiment according to the following Eq. (Lakowicz, 1999):

$$E_{\text{eff}} = 1 - \tau_{DA}/\tau_{D} \qquad \textbf{(14)}$$

Because the change in the fluorescence lifetime of the donor can be analyzed independently of acceptor emission, this technique can be used to detect FRET between GFPs with nearly identical emission spectra but different τ (Bastiaens and Squire, 1999). FLIM measurements are also of advantage for those donor molecules that are prone to quick photobleaching.

Changes in τ can easily be detected by advanced modern technology using the frequency or time domain, or direct photon counting (see Chapter 27, *this volume*). A FLIM setup, suitable for measuring FRET, as well as some results from living cells are shown in Figure 45.10. Comparison between the life time of the donor alone (τ_D) and the donor life time in the presence of the acceptor (τ_{DA}) will provide information on *R*.

The biggest advantage of FLIM analyses is the independence of donor lifetime τ_D on the concentration of the dye (except in some cases of homo-FRET). Nevertheless, the complex calibration procedure for each particular FLIM setup will require professional support. The FLIM approach has a number of limitations:

- Each microscope must be calibrated.
- Spatial resolution may be limited if multiple images must be acquired.
- More photons must be detected to determine τ for a pixel than are required to merely detect presence or absence.

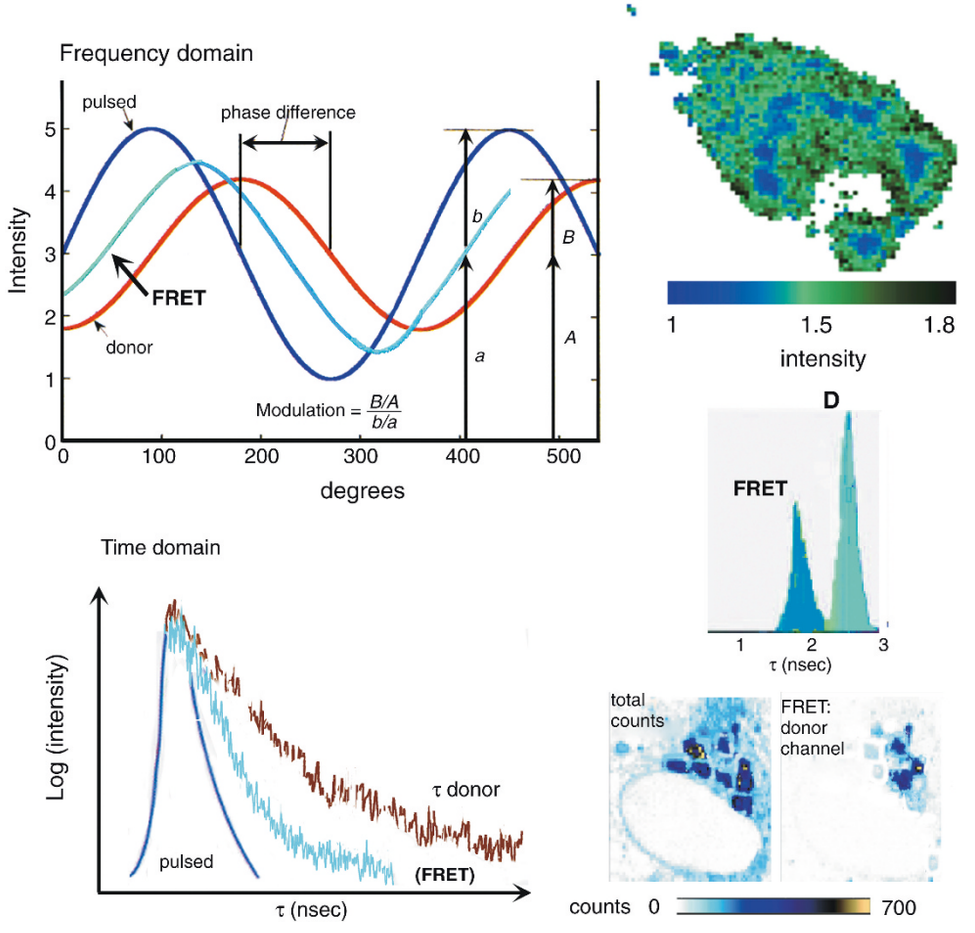


FIGURE 45.10. FRET resolution by FLIM. Upper panel, left: Schematic presentation of FRET in the frequency domain: the pulsed excitation frequency (dark blue); the delayed signal of the CFP-donor (red curve); and the less-delayed signal of the donor when FRET is occurring (light blue) because FRET decreases the donor lifetime. Right: The intensity of the signal having the CFP, (donor) time constant collected under the same conditions, and showing that FRET causes the donor (CFP) intensity to decrease when both CFP- and YFP-tagged connexin molecules are oligomerized in a perinuclear Golgi region of this cell. Middle right: Alternative representation of the data in image above. Histograms represent the shorter donor lifetime when FRET to an acceptor is occurring (T_{FRET}), compared to when only the donor is present (T_D). Lower panel, left: Schematic presentation of the individual parameters in the time domain: Log (intensities) versus lifetime: (T_D) is longer than (T_{FRET}). Left: Images of FRET in the Golgi region of a cell: comparison between total counts and counts sampled only from the donor channel reveals the portion of the donor molecules that are not transferring energy to the acceptor, and thus still emitting in the donor channel.

Despite the existence of commercial hardware and software programs for the task, FLIM data will generally require more complex (global) mathematical analysis of acquired results (Bastiaens and Jovin, 1998; Bastiaens and Squire, 1999; Bastiaens and Pepperkok, 2000; Gerritsen *et al.*, 2001; Herman *et al.*, 2001; and the overview of FLIM given in Chapter 27, *this volume*).

Fluorescence Recovery After Photobleaching and Fluorescence Loss in Photobleaching

Fluorescence recovery after photobleaching (FRAP) is a technique in which a region of interest is selectively photobleached with a high-intensity laser and the recovery that occurs as molecules move back into the bleached region is monitored over time with lower-intensity laser light. Depending on the protein studied, fluorescence recovery can result from protein diffusion, binding/dissociation, or transport processes. FRAP experiments can thus determine the kinetic parameters of a protein, including its diffusion constant, mobile fraction, transport rate, or binding/dissociation rate from other proteins in living cells (Lippincott-Schwartz *et al.*, 2001, 2003). Fluorescence recovery is usually quantitatively monitored by a microscope-mounted CCD camera that is calibrated to the fluorescence signal before photobleaching.

Fluorescence loss in photobleaching (FLIP) is a photobleaching technique complementary to FRAP. In a FLIP experiment, a region of interest in a cell is repeatedly photobleached while fluorescence in the whole cell is continuously monitored. Any cellular regions with connections to the area being bleached will lose fluorescence due to lateral movement of mobile proteins into the bleached area. On the other hand, the fluorescence in unconnected cellular regions will be unaffected (Cole *et al.*, 1996). FRAP and FLIP techniques have been extensively used for studying the trafficking within the secretory pathway in animal cells, especially ER-to-Golgi trafficking (Cole *et al.*, 1996; Lippincott-Schwartz *et al.*, 2001; Presley *et al.*, 2002; Lippincott-Schwartz and Patterson, 2003). In principle, FRET techniques can be nicely combined with both FRAP and FLIP to obtain supplementary information on protein–protein interactions together with kinetic parameters of protein localization, for example, about mobility of plasma membrane receptors and lipids.

Fluorescence Resonance Energy Transfer and Fluorescence Correlation Spectroscopy

Confocal fluorescence correlation spectroscopy (FCS) is a unique tool to analyze processes that can be recorded from a very small area of illumination in a selected region of less than 1 µm (Magde *et al.*, 1972). FCS is thus suitable for quantitative measurements of the local concentrations and diffusional mobility of fluorophores through a small volume of a living cell, for example, in endocytic membrane-bound carriers or other compartments (Bacia *et al.*, 2002; Kim and Schwille, 2003). Diffusion coefficients measured by FCS can be used to calculate the approximate sizes of protein complexes in living cells, and based on quantification of the fluorescence intensity of the diffusing complex the number of molecules can be estimated, as has, for example, been done for the Gag complex during retrovirus assembly (Larson *et al.*, 2004). FRET and FCS can be considered as complementary techniques, where FRET is used to estimate the distance between the donor and acceptor molecules, and FCS to provide information on dynamic properties and the sizes of the protein complexes analyzed.

Fluorescence Resonance Energy Transfer and Total Internal Reflection Fluorescence

In total internal reflection fluorescence (TIRF) microscopy, excitation light approaches an aqueous specimen as a coherent beam of light that strikes the coverslip/water interface at an angle greater than the critical angle. As a result, only an evanescent excitation field penetrates into the water to excite dye molecules, such as transfected GFP chimeras, that are within a few tens of nanometers of the interface. The thickness of the excitation band depends on the wavelength and the approach angle. Images are recorded in widefield using intensified- or electron muliplier (EM)-CCDs.

As this technique excites and visualizes only fluorophores in close proximity to the plasma membrane, it has the obvious advantage of strongly reducing photobleaching and phototoxicity compared to other microscopy techniques. It also reduces background light from out-of-focus planes essentially to zero. Therefore, the parts of living cells near the coverslip can be imaged over longer time periods and with high contrast and improved temporal resolution.

TIRF is the method of choice for those who want to resolve processes occurring close to the plasma membrane. Such processes include endocytosis and exocytosis, cell–cell signaling, formation of cell–cell contacts, and release of neuromediators.

If the biological process under study allows photobleached GFP chimeras to be quickly exchanged from the non-bleached pool of chimeras in deeper regions of the cell, this results in a very stable fluorescent signal for long-term observations. TIRF can be combined with conventional widefield fluorescence or DIC microscopy for localized analyses of cellular processes and/or FRET measurements (Bezzi *et al.*, 2004; Jones *et al.*, 2004).

Quantum Dots and Fluorescence Resonance Energy Transfer

Semiconductor quantum dots were introduced recently into microscopy for applications in cell biology (Michalet *et al.*, 2005). Although they seem to be very promising (Lidke *et al.*, 2004), their application for FRET will be limited. Quantum dots exhibit broad absorption profiles: as both quantum dots at 565 nm and 655 nm can be excited with a single excitation filter 435/70, long-pass emission filters must be used to separate the signals. These parameters will prevent simultaneous use of quantum dots with CFP- or GFP-like live chromophores that could otherwise be complementary donors for live-cell FRET analyses. Nevertheless, double-labeling with quantum dot conjugates is a powerful tool in immunohistochemistry and immunocytochemistry applications (Wu, 2003).

CLONING AND EXPRESSION OF FLUORESCENT CONSTRUCTS FOR FLUORESCENCE RESONANCE ENERGY TRANSFER

Cloning of Fluorescent Chimeras

After deciding to use a FRET approach to study a protein of interest, fluorescent donor–acceptor pairs need to be generated. The most common approach is to obtain the coding regions for the chosen proteins and use commercially available vectors with multiple cloning sites (e.g., BD Biosciences Clontech, Stratagene, Qbiogene, and other companies) to generate in-frame fusions with the CFP, YFP, GFP, or mRFP1 genes. GFP fusions can be gener-

ated at the N- or C-terminus of proteins of interest, or even internally, with GFP being interspaced between domains of a protein coding sequence. It is generally a good idea to simultaneously prepare both N- and C-terminal fusions, hoping that at least one of these chimeras retains functional activity.

One fairly common problem is that the linker between the protein of interest and GFP may be recognized as a nuclear import signal (NLS) by the cellular machinery and the chimera may thus unexpectedly be detected in the nucleus instead of its proper cellular location. This chance is particularly high if the linker contains NLS-like motifs such as repeats of lysines (K) or arginines (R). Such common biological mistakes in linker generation should be avoided. Combinations of other amino acids, especially secondary structure breakers such as glycine (G) or proline (P) or small amino acids such as serine (S), alanine (A), or threonine (T) are less likely to create problems. However, there are no dead-sure recipes for generating functional GFP chimeras, beyond following standard protocols for the cloning itself (Sambrook *et al.*, 1989). Therefore, performing functional tests is critical.

After DNA sequencing to verify the constructs, DNA for mammalian cell transfections needs to be prepared with great care. In general, commercial kits (e.g., Qiagen Maxiprep) work well. For some cell lines (e.g., our favorite cell line, Vero cells) removal of endotoxins (bacterial lipopolysaccharides) is important and easily accomplished with commercial kits. Many transfection reagents routinely used to introduce plasmid DNA into living cells are lipophilic agents that penetrate biological membranes but may also induce unwanted side effects, such as aggregation or fusion of intracellular membranes (see below). This makes cells transfected with these reagents often look clumpy and non-beautiful, and the appearance of intracellular membranous organelles may also be abnormal. As a word of caution, any strong overproduction of a transfected protein (10- to 100-fold above normal cellular levels) may impair cell function, an effect that needs to be controlled by appropriate functional assays. (For useful www links see Table 45.4).

TABLE 45.3. Transfection Buffer for Electroporation, Internal Medium

IM, Transfection Buffer
120 m*M* final MW: 74.56 g/mol Stock solution 1.2*M* ⇒ for 50 mL 4.48 g
KH_2PO_4 10 m*M* final MW: 136.09 g/mol Stock solution 100 m*M* ⇒ for 50 mL 680.45 mg
EGTA 2 m*M* final MW: 380.4 g/mol Stock solution 20 m*M* ⇒ for 50 mL 380 mg
$MgCl_2$ 5 m*M* final MW: 203.31 g/mol Stock solution 50 m*M* ⇒ for 50 mL 508.3 mg
HEPES 25 m*M* final MW: 238.3 g/mol Stock solution 250 m*M* ⇒ for 50 mL 2.98 g
$CaCl_2$ 0.5 m*M* final MW: 147.2 g/mol Stock solution 15 m*M* ⇒ for 50 mL 110 mg
To prepare 50 mL of **cytomix**: Mix 5 mL of each stock solution, except for $CaCl_2$, only 500 µL Add **H_2O** until 50 mL, adjust pH = 7.5–7.6
For **complete cytomix**: Add **GSSG** 5 m*M* final MW: 656.6 g/mol Stock solution 100 m*M* ⇒ for 10 mL 660 mg Add 50 µL/mL **ATP** 2 m*M* final MW: 550 g/mol Stock solution 100 m*M* ⇒ for 10 mL 550 mg Add 20 µL/mL

Modified from Majoul *et al.* (2001).
10^7–10^8 cells washed in PBS are transferred into 400 µL of total Internal Medium Mix for electroporation in Bio-Rad (green cuvette) Cat. #165–20086.
Add 20–40 µL of endo-free plasmid DNA (from stock of 1 µg/µL).
Bio-Rad electroporator: 0.7 kV, main position 50/capacitance extension 200 µF (see on the panel of electroporator). Resulting time constant for this combination should be 1.44–1.64 to get 50%–80% of finally transfected cells.

Functional Activity of Expressed Constructs

Successfully cloned chimeras will be introduced into the cells selected for initial test experiments. First, the expression levels and protein stability of the donor and acceptor needs to be tested in a time course, and the spectral properties of the chimera established. Often, a newly generated chimera may be brightly fluorescent but has lost functional activity, displays the wrong localization, and/or has lost the ability to interact with its normal partners in a protein complex. Therefore, it is most important to check the functional activity of chimeras before attempting to draw any conclusions from their use. Such checks require extreme delicacy because one can only attribute aberrant behavior to the construct if one is sure that the behavior is not being caused by your method of observation. If an antibody against the protein under study is available, the GFP chimera should display the same or a very similar intracellular distribution as the endogenous protein. If normal interactions between the chimera with known cellular partner proteins can be established by co-immunoprecipitation, this is a good sign!

Expression and Over-Expression

Proper expression levels of chimeras are crucial. In the case of many of our CFP/YFP chimeras that have functions in the secretory pathway, we use the intracellular transport of cholera toxin (CTX) as a good functional test. We learned that in cells overexpressing fluorescent chimeras, transport of the toxin from the plasma membrane to the ER, or even to Golgi compartments, was blocked. Extending the time after transfection (in our case using electroporation) to 16 to 20 h for the transmembrane protein ERD2-YFP, which is the receptor for cholera toxin in the Golgi complex, led to severe disturbances not only in the intracellular localization of the chimeras but also resulted in impaired toxin transport. Although cholera toxin was able to recognize the CFP or YFP-fused ERD2 protein 6 to 8 h after transfection [Fig. 45.4(A)], after 16 h of expression, it was no longer able to enter the structures labeled by ERD2 fusions [compare Figs. 45.4(A,B)]. However, even in these damaged cells, CTX still bound to the areas of Golgi containing functional endogenous receptor and exhibited only low labeling with the chimeric receptor [Fig. 45.4(B), long arrows].

Conventional fluorescence microscopy can be used to establish the time course of expression and to select the time when the expression is sufficient to measure FRET, when the chimeras are still localized in the same areas as in their endogenous wild-type counterparts, where their functional activity can be established. In our hands, using CMV promoter constructs, this was usually ~6 to 12 h after electroporation, depending on the construct. In general, the physiological validity of FRET measurements in living cells expressing a given pair of CFP/YFP fusion proteins is strengthened if the observed FRET signals are obtained in response to a known, meaningful physiological trigger, especially when compared with other pairs of CFP/YFP fusion proteins that remain unchanged.

TABLE 45.4 Links Useful for the Design of FRET Experiments

Proteins	
Collection of useful links related to microscopy around the world:	http://www.ou.edu/research/electron/www-vl/long.shtml
Molecular Expressions: The Microscopy Primer. A comprehensive Tutorial Site that includes fascinating "Virtual Microscopy"	http://micro.magnet.fsu.edu/primer/index.html
BIND: Protein–protein interaction database	http://bind.ca/
Fluorophores & other probes: Proteins	http://www.probes.com/
MoBiTec: Tools for Cell and Molecular Biology	http://www.mobitec.de/
Invitrogen: Cloning & expression	http://www.invitrogen.com/
BD Biosciences Clontech: GFP news	http://www.bdbiosciences.com/clontech/gfp/
Protein sequence and classification database	http://pir.georgetown.edu/
Society for Molecular Imaging	http://www.molecularimaging.org
Optics	
Fluorescent Spectra Database	http://www.mcb.arizona.edu/IPC/spectra_page.htm
Chroma Technology: Optical filters for biological applications	http://www.chroma.com/
Omega: Optical filters for biological applications	http://www.omegafilters.com/
Semrock: New generation of filters	http://semrock.com
AHF analysentechnik AG Optical filters including GFPs	http://www.ahf.de
Sutter: Filter changer and light sources for microscopes	http://www.sutter.com/
Bioimage: Biological images for scientific research	http://www.bioimage.org/pub/collaborators.jsp
Semrock: FRET filters	http://www.laser2000.co.uk/semrock/brightline.htm

METHODS FOR INTRODUCING CHROMOPHORES INTO LIVING CELLS

Electroporation

We have described an efficient electroporation technique (Majoul *et al.*, 2001) that has been routinely used during the Vancouver 3D microscopy courses (2002–2005) for multiple transfections with different plasmids. With slight modifications (see Table 45.3), this protocol is now successfully used in many laboratories for transfection of a large variety of cell lines, including primary cultured neurons, to study GFP-highlighted organelles in living cells and for FRET analyses. Instead of using PBS (phosphate-buffered saline), which is not very physiological, we use a high potassium "internal media" buffer condition for the electroporation step (K-glutamate; up to 140 m*M*, pH 7.6). Other essential components are fresh ATP and GSSG (see Table 45.3 for details). We prefer to use a Bio-Rad electroporator, green Gene Pulser cuvette (BioRad Cat. No. 165–2086; gap 0.2 cm) and use plasmid DNA in a total volume of up to 300 µL "internal media" per transfection reaction. In Vero cells (a Green monkey kidney fibroblast cell line), we routinely obtain 90% or more of successfully transfected cells with this method. The advantage of electroporation for transfer of DNA for FRET analyses is the total absence of the unspecific fluorescence background produced by other transfection reagents.

Transfection Reagents

For transfecting cells with foreign DNA, scientists commonly use different commercially available agents with lipid-like properties, able to form micellae around the DNA: for example, Lipofectamine, Lipofectin, Metafecten, FUGENE 6, etc. Transient transfections are usually performed on routine cell lines, such as HEK 297, COS-5, COS-7, NRK (normal rat kidney), 3T3 fibroblast-like cultures, BHK-21 (hamster kidney cell line), or the Vero cells used for the experiments described in this chapter. Cells prepared for transfection are typically grown in media such as Dulbecco's modified Eagle medium (DMEM), supplemented with 10% fetal calf serum (FCS), glutamine, and antibiotics such as penicillin and streptomycin. Exact transfection protocols are often supplied by the manufacturer of the transfection reagents. Many of them work well, although certain cell types, especially neurons, may require different transfection procedures. Ballistic methods to introduce neuronal tracers, plasmid DNA or intracellular calcium indicators into neurons have also been reported, are now in common use (Grutzendler *et al.*, 2003).

Although usually the commercial reagents do not create problems for biochemical experiments, for microscopic, single-cell analyses, remnants of precipitated DNA or aggregates of transfection reagents may cause a strong fluorescent background, especially when two-photon excitation is used. Tetracyclin-regulated promoters cannot be used in combination with two-photon excitation of CFP, as even traces of tetracyclin create a strong fluorescent background in the cell. Expression systems induced by agents such as ecdysone or hygromycine may be more suitable in such cases. We routinely express our fusion proteins of interest under the control of the widely used, strong CMV promotor. Again, selection of the appropriate time window after transfection, with regard to obtaining good fluorescence signals for imaging without having vast over-expression, is crucial for best results.

Microinjection

Microinjection is an elegant way to deliver biological material into living cells, for example, DNA, RNA, and proteins (e.g., fluorophore-labeled or unlabeled recombinant proteins or inhibitory antibodies). Microinjection was used as early as the 1960s (Kohen *et al.*, 1966). One of the first attempts to measure intracellular Ca^{++} with aequorin also was based on microinjection techniques (Blinks *et al.*, 1978). In the 1970s and 1980s microinjection was applied for the transfer of dye between neighboring cells and used to study the permeability of gap junctions (Conn, 1991) (see Fig. 45.11). With the development of antibodies against specific proteins or protein domains, microinjection of antibodies to inhibit the function of the protein under study became popular. Microinjection of antibodies against COPI vesicular transport machinery (anti-β-COP antibodies raised against the EAGE sequence of this subunit) prevented the transport of cholera toxin through the Golgi apparatus (Majoul *et al.*, 1998).

The construction of plasmids encoding specific proteins and the development of anti-sense RNA and RNAi provided another

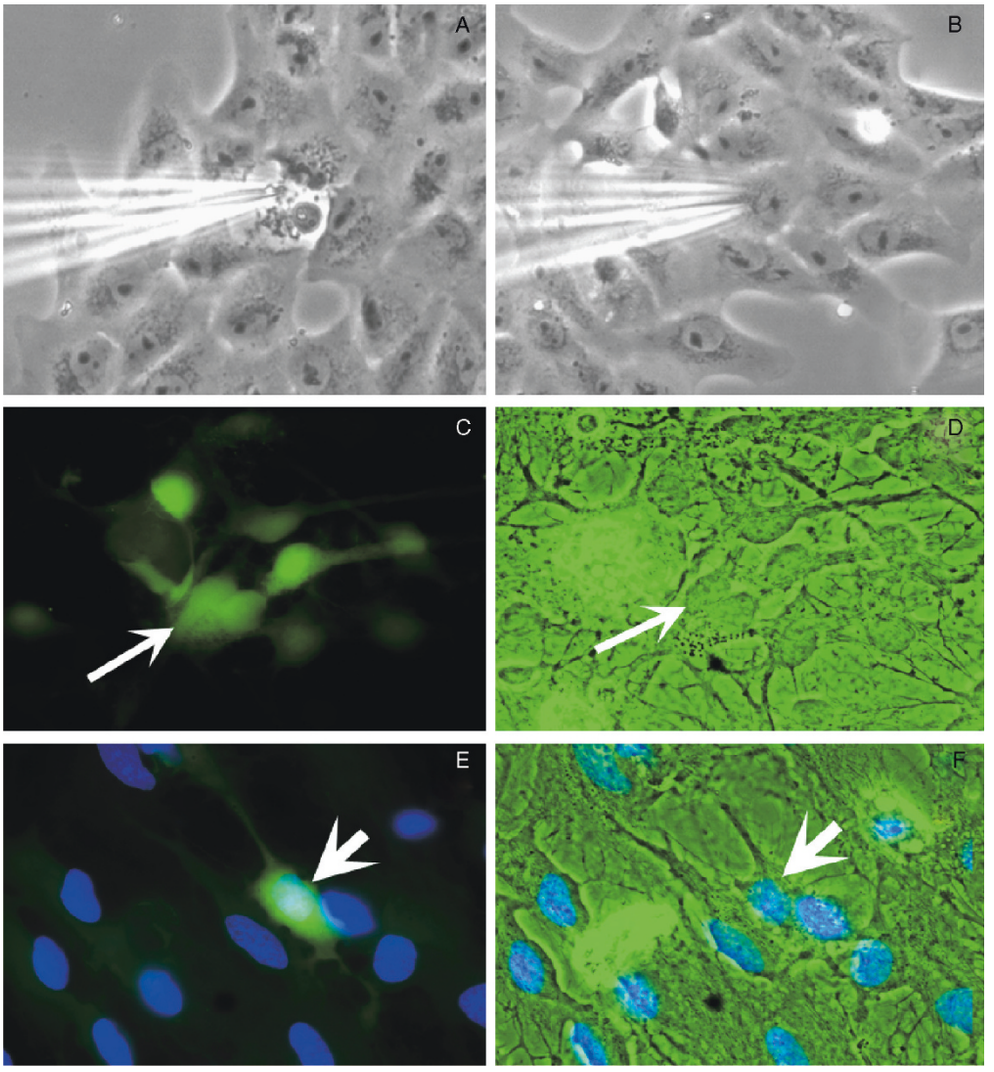


FIGURE 45.11. (A, B) Two examples of microinjection: (A) a dying cell after being impaled by the needle, with collapsed cellular membranes, and (B) successful microinjection into the cytosol of a cell. (C) Dye transfer between astrocytes after microinjection of calcein into a single cell (*indicated by arrow*); (D) The same field viewed in transmission light. (E, F) A decrease in dye transfer from a microinjected cell upon lowering of the extracellular free Ca^{++} concentration. Living-cell nuclei stained with DAPI; (F) the same field viewed in transmission light.

area for rapid development of microinjection techniques. The discovery of GFP and its color variants has led to the use of microinjection for inducing expression of fluorescent chimeras in many different types of cells, including cultured neurons and even live organisms by injecting DNA into *Xenopus* oocytes, embryos, developing zebrafish, *Drosophila,* and other species. In microinjection experiments, Alexa-350 or Cascade blue conjugated to BSA can be co-injected to easily identify the injected cells. In experienced hands and with availability of good equipment, microinjection into cells and micromanipulation of cells and nuclei with glass pipettes, sometimes combined with electrophysiology, can address many complicated biological questions (for an example, see Wakayama *et al.*, 2003).

In short, microinjection can be suitable for:

1. **Introduction of plasmid DNA**: Mostly for cell imaging, while for a macroscale biochemical analysis electroporation is more advisable.
2. **Introduction of RNA**: si-RNA, labeled oligonucleotides, antisense RNA.
3. **Introduction of proteins**: Dominant-negative functionally active molecules (e.g., dynamin) or microinjection of Fab fragments of antibodies because whole divalent antibody molecules may produce unspecific effects by cross-linking the proteins of interest.
4. **Introduction of dyes and other fragments**: Fluorescent markers (e.g., labeled phalloidin to visualize actin), membrane-permeable dyes (e.g., calcein) to study cell–cell contacts, or impermeable agents (e.g., GTP-γ-S).

FUTURE PERSPECTIVES: 3D MICROSCOPY, BIOLOGICAL COMPLEXITY, AND *IN VIVO* MOLECULAR IMAGING

The 21st century should see a huge wave of novel microanalytical techniques. It is now becoming obvious that the major goals of the "post-genomics" and proteomics era will be to analyze protein function and protein-protein interactions at the single-cell level. We now realize that structural anatomy provides only limited

information about pathophysiological consequences, and that the future will involve a struggle to visualize complexes of single molecules (Ha *et al.*, 1999; Kusumi *et al.*, 2005), biochemical events (Hirose *et al.*, 1999; Weijer, 2003) and activities of signaling networks (Hurtley and Helmuth, 2003). Many of these scientific questions are well-suited to molecular proximity methods such as FRET, FCS, FRAP. Eventually, these types of analysis will lead us to a new branch of cell biology — functional cell physiology. Imaging applied not only to living cells, but also to living organisms, should keep us occupied for the next few decades! (Fig. 45.12).

Today, in addition to having a wide variety of fluorescent markers for subcellular compartments (Lippincott-Schwartz and Patterson, 2003), we also have a broad palette of established fluorescent biosensors (Ting *et al.*, 2001) and reporter molecules that can be used to measure cellular activities (Miyawaki *et al.*, 1997; Miyawaki *et al.*, 1999; Zhang *et al.*, 2001; Sato *et al.*, 2002; Sato *et al.*, 2003; Violin *et al.*, 2003; Umezawa, 2005, see also Chapters 16 and 17, *this volume*).

The importance of using FRET to probe the functional assembly of multi-subunit protein complexes, such as the neuronal receptors AMPA, NMDR, the hexameric connexins in the plasma membrane or the immuno-recognition complexes, will drive the development of new FRET partners with custom-designed spectral properties (Tsien, 2004; Galperin *et al.*, 2004). New high-speed/high-resolution microscopes with improved sensitivity are under constant development (Stephens and Allan, 2003; Goldman and Spector, 2005), and will provide new tools transforming the single-molecule analyses of "cellular imaging" into "molecular imaging."

Cellular processes in the plasma membrane, the nucleus and other cellular compartments such as Golgi, ER, etc., will be resolved in real-time and at high spatial resolution. The resulting improvements in the understanding of the cellular physiology of both healthy and diseased organisms (including tumors), will support new frontiers in drug discovery. These are fields in which FRET can be applied to elucidate the core of many of the biological processes that must be understood before we move on to clinical diagnostics and drug screening.

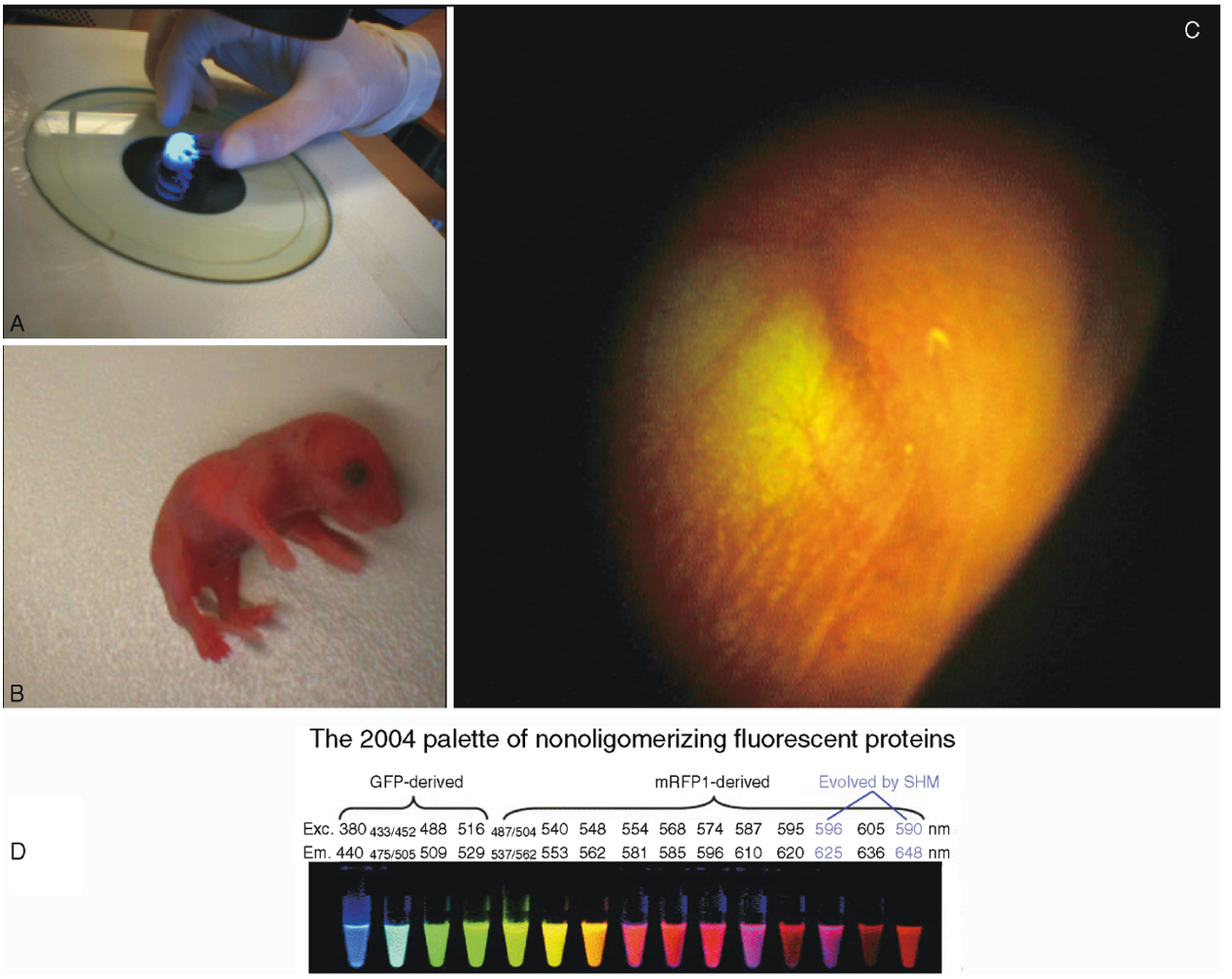


FIGURE 45.12. Experiment performed during the UBC 3D microscopy course, 2004. A simple experimental setup for whole-organism imaging of a transgenic GFP mouse is shown in (A, B). (C) Fluorescence of GFP-expressing neuronal cells in cerebellum can be seen under the microscope even with 5× magnification, and this allows preparation of tissue slices for high-resolution microscopy; (D) the insert shows the new "2004 palette of non-oligomerizing fluorescent proteins" (taken from Tsien, 2004), illustrating the future of live-cell imaging.

IN VIVO MOLECULAR IMAGING

The field of molecular imaging is developing rapidly. Two relatively mature disciplines — molecular biology and radiology are coming together to create an interdisciplinary approach to the biology of tissues and cells and the interactions of molecules. Molecular imaging will add a new dimension to anatomical imaging and the evaluation of histological slides, providing us with the detailed information on the distribution and function of reporters and marker molecules needed to deepen our insight into physiological differences between normal and diseased tissues.

The equipment required to provide this information is now becoming available. A new generation of "stick lens" objectives (Fig. 45.13) was recently introduced by Olympus to permit one to image planes inside the living animal without resorting to the fiber-optical confocal endoscopes described in Chapter 26 (*this volume*). Exciting developments in high-content screening are described in the next chapter.

Many other initiatives are currently focused on the development of high-specificity/high-sensitivity probes designed to improve the detection sensitivity of molecular imaging by 10- to 100-fold. A feature of this new generation of probes will be the development of "Molecular Libraries" that will help to overcome current limitations in our ability to detect and image specific molecular events in animal models and humans. Methods, such as microSpect imaging, as recently described by Choi *et al. (*2005), demonstrate the potential for the pre-clinical application of *in vivo* molecular imaging, a topic also discussed in Chapters 26 and 38. The outlook looks both bright and multi-colored!

ACKNOWLEDGEMENTS

We are grateful to Prof. Natalia Butkevich for extensive discussions of aspects of quantum mechanics and spectroscopy, to Dr. Alexander Goroshkov for his useful suggestions in modern microscopy and image acquisition, Dr. Clemens Kaminski and L.K. Bert van Geest for imaging and discussions about FLIM, to Professor Alberto Luini for help in reading Leonardo da Vinci's original Italian "cryptic" text. We also want to thank Tom Jovin, Bob Clegg Philippe Bastiaens and many others for guiding our initial steps into FRET-science. Finally, we are deeply grateful to Professor James Pawley for his patience, generous interest and continuous support of our often "unconventional" performance. Some of the experimental data presented in this chapter (as indicated in the text) were acquired during the practical course "International 3-D Microscopy of Living Cells," held annually at the University of British Columbia, Vancouver, Canada during the years 2002, 2003, 2004 and 2005.

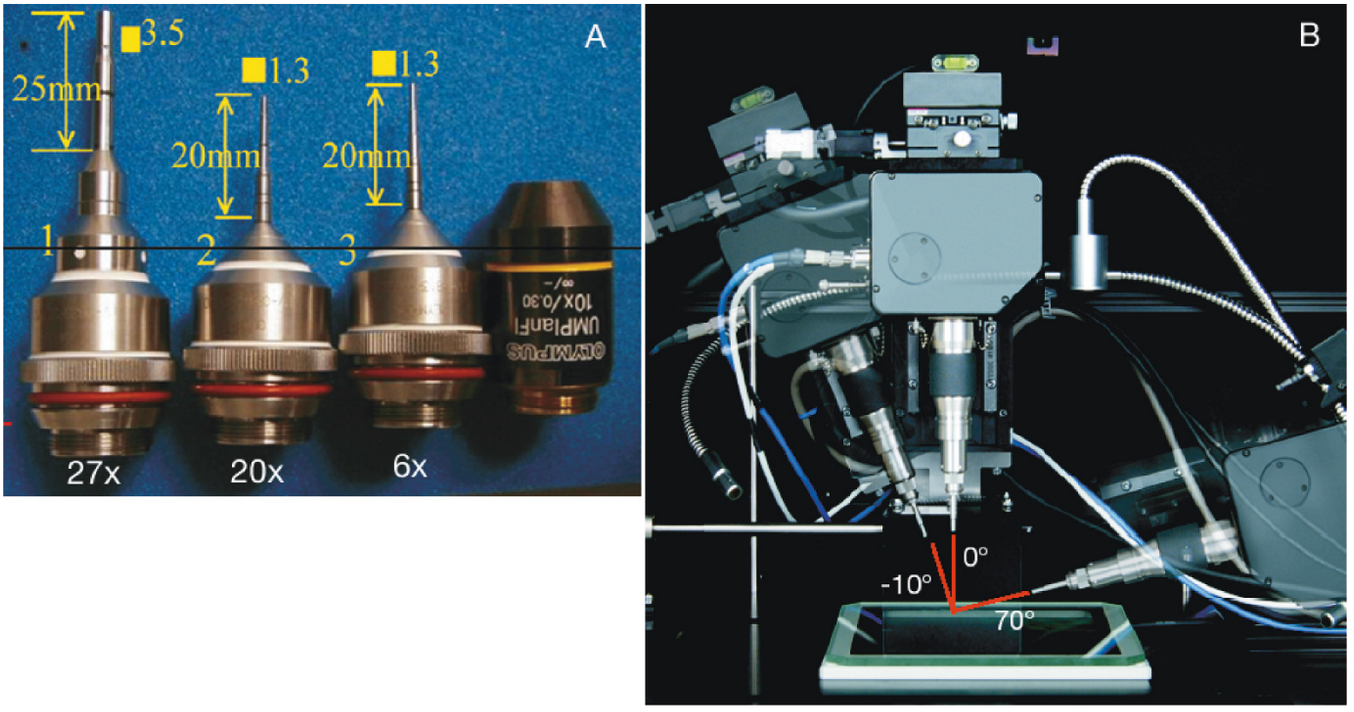


FIGURE 45.13. (A) Three, new "stick lens" objectives have been developed by Olympus especially for *in vivo* imaging of fluorescent signals in whole animals. These objectives were designed to be used with a new, miniaturized, tiltable confocal scan-head, the Olympus IV100 Intravital LSM (B). The system uses an AOTF to select between 488, 561, 633 and 748 nm lasers. Three different stick objectives: 27×/NA 0.7 (3.5 mm diameter, FOV: 200 µm), 20×/NA 0.5 and (1.3 mm diameter, FOV: 200 µm), 6×/NA 0.14 (1.3 mm diameter, FOV: 670 µm) and a comprehensive double-galvanometer scanner provided flexible raster scanning over a wide magnification range. A fixed, 4-channel dichroic beamsplitter and 3 turrets, each with 6 emission filters, provides wavelength selection for 3 PMT detector channels. To minimize the effect of invasive microscopy on living animals, the angle at which the objective and the scanning head approached the animal is adjustable (B) and the whole apparatus is enclosed in a light shield that can also serve as means of administering anesthetic gases.

REFERENCES

Bacia, K., Majoul, I.V., and Schwille, P., 2002, Probing the endocytic pathway in live cells using dual-color fluorescence cross-correlation analysis, *Biophys. J.* 83:1184–1193.

Bastiaens, P.I.H., and Jovin, T.M., 1998, Fluorescence resonance energy transfer (FRET) microscopy, In: *Cell Biology: A Laboratory Handbook* (J.E. Celis, ed.), Academic Press, New York, pp. 136–146.

Bastiaens, P.I.H., and Pepperkok, R., 2000, Observing proteins in their natural habitat: The living cell, *Trends Biochem. Sci.* 25:631–637.

Bastiaens, P.I., and Squire, A., 1999, Fluorescence lifetime imaging microscopy: Spatial resolution of biochemical processes in the cell, *Trends Cell Biol.* 9:48–52.

Bastiaens, P.I.H., Majoul, I.V., Verveer, P.J., Soling. H.D., and Jovin, T.M., 1996, Imaging the intracellular trafficking and state of the AB5 quaternary structure of cholera toxin, *EMBO J.* 15:4246–4253.

Bezzi, P., Gundersen, V., Galbete, J.L., Seifert, G., Steinhauser, C., Pilati, E., and Volterra, A., 2004, Astrocytes contain a vesicular compartment that is competent for regulated exocytosis of glutamate, *Nat. Neurosci.* 7:613–620.

Blackman, S.M., Piston, D.W., and Beth, A.H., 1998, Oligomeric state of human erythrocyte band 3 measured by fluorescence resonance energy homotransfer, *Biophys. J.* 75:1117–1130.

Blinks, J.R., Mattingly, P.H., Jewell, B.R., van Leeuwen, M., Harrer, G.C., and Allen, D.G., 1978, Practical aspects of the use of aequorin as a calcium indicator: Assay, preparation, microinjection, and interpretation of signals, *Methods Enzymol.* 57:292–328.

Bunt, G., and Wouters, F.S., 2004, Visualization of molecular activities inside living cells with fluorescent labels, *Int. Rev. Cytol.* 237:205–277.

Butkevich, E., Hulsmann, S., Wenzel, D., Shirao, T., Duden, R., and Majoul, I., 2004, Drebrin stabilizes connexin-43 and links gap junctions to the submembrane cytoskeleton, *Curr. Biol.* 14:650–658.

Campbell, R.E., Tour, R., Palmer, A.E., Steinbach, P.A., Baird, G.S., Zacharias, D.A., and Tsien, R.Y., 2002, A monomeric red fluorescent protein, *Proc. Natl. Acad. Sci. USA* 99:7877–7882.

Chalfie, M., 1995, Green fluorescent protein, *Photochem. Photobiol.* 62:651–656.

Chalfie, M., Tu, Y., Euskirchen, G., Ward, W.W., and Prasher, D.C., 1994, Green fluorescent protein as a marker for gene expression, *Science* 263:802–805.

Choi, S.R., Zhuang, Z.P., Chacko, A.M, Acton, P.D., Tjuvajer-Gelovani, J., Doubrovin, M., Chu, D.C., and Kung, H.F., 2005, SPECT imaging of herpes simplex virus Type1 thymidine kinase gene expression by [(123)I]FIAU(1). *Acad. Radiol.* 12:798–805.

Clegg, R.M., 1992, Fluorescence resonance energy transfer and nucleic acids, *Methods Enzymol.* 211:353–388.

Cohen-Cory, S., 2002, The developing synapse: Construction and modulation of synaptic structures and circuits, *Science* 298:770–776.

Cole, N.B., Smith, C.L., Sciaky, N., Terasaki, M., Edidin, M., and Lippincott-Schwartz, J., 1996, Diffusional mobility of Golgi proteins in membranes of living cells, *Science* 273:797–801.

Conn, P.M., ed., 1991, *Electrophysiology and Microinjection*, Academic Press, London.

Del Pozo, M.A., Kiosses, W.B., Alderson, N.B., Meller, N., Hahn, K.M., and Schwartz, M.A., 2002, Integrins regulate GTP-Rac localized effector interactions through dissociation of Rho-GDI, *Nat. Cell Biol.* 4:232–239.

Elsliger, M.A., Wachter, R.M., Hanson, G.T., Kallio, K., and Remington, S.J., 1999, Structural and spectral response of green fluorescent protein variants to changes in pH, *Biochemistry* 38:5296–5301.

Erickson, M.G., Moon, D.L., and Yue, D.T., 2003, DsRed as a potential FRET partner with CFP and GFP, *Biophys. J.* 85:599–611.

Förster, V.T., 1948a, Zwischenmolekulare Energiewanderung und Fluoreszenz, *Ann. Phys.* 6:54–75.

Förster, T.H., 1948b, Versuche zum zwischenmolekularen Ubergang von Elektronenanregungsenergie, *Naturwissenschaften* 33:93–100.

Galperin, E., Verkhusha, V.V., and Sorkin, A., 2004, Three-chromophore FRET microscopy to analyze multiprotein interactions in living cells, *Nat. Methods* 1:209–217.

Gerritsen, H.C., and de Grauw, K., 2001, One- and two-photon confocal fluorescence lifetime imaging and its applications, In: *Methods in Cellular Imaging* (A. Periasamy, ed.), Oxford University Press, New York, pp. 309–323.

Gordon, G.W., Berry, G., Liang, X.H., Levine, B., and Herman, B., 1998, Quantitative fluorescence resonance energy transfer measurements using fluorescence microscopy, *Biophys. J.* 74:2702–2713.

Griesbeck, O., Baird, G.S., Campbell, R.E., Zacharias, D.A., and Tsien, R.Y., 2001, Reducing the environmental sensitivity of yellow fluorescent protein. Mechanism and applications, *J. Biol. Chem.* 276:29188–29194.

Grutzendler, J., Tsai, J., and Gan, W.B., 2003, Rapid labeling of neuronal populations by ballistic delivery of fluorescent dyes, *Methods* 30:79–85.

Ha, T., Ting, A.Y., Liang, J., Caldwell, B., Deniz, A.A., Chemla, D.S., Schultz, P.G., and Weiss, S., 1999, Single molecule fluorescence spectroscopy of enzyme conformational dynamics and cleavage mechanism, *Proc. Natl. Acad. Sci. USA* 96:893–898.

Hahn, K., 2003, Monitoring signaling processes in living cells using biosensors, *Sci. STKE* 205:tr5. [DOI: 10.1126/stke.2003.205.tr5]

Heim, R., Cubitt, A.B., and Tsien, R.Y., 1995, Improved green fluorescence, *Nature*, 373(6516):663–664.

Heim, R., and Tsien, R.Y., 1996, Engineering green fluorescent protein for improved brightness, longer wavelengths and fluorescence resonance energy transfer, *Curr. Biol.* 6:178–182.

Heim, R., Prasher, D.C., and Tsien, R.Y., 1994, Wavelength mutations and post-translational autooxidation of green fluorescent protein, *Proc. Natl. Acad. Sci. USA* 91:12501–12504.

Hell, S.W., 2003, Toward fluorescence nanoscopy, *Nat. Biotechnol.* 21:1347–1355.

Herman, B., Gordon, G., Mahajan, N., and Centonze, V.E., 2001, Measurement of fluorescence resonance energy transfer in the optical microscope, In: *Methods in Cellular Imaging*, (A. Periasamy, ed.), Oxford University Press, New York, pp. 257–272.

Hirose, S.K., Kadowaki, M., Tanabe, H., Takeshima, and Iino, M., 1999, Spatiotemporal dynamics of inositol 1,4,5-triphosphate that underlines complex Ca2+ mobilization patterns, *Science* 248:1527–1530.

Hoppe, A., Christensen, K., and Swanson, J.A., 2002, Fluorescence resonance energy transfer-based stoichiometry in living cells, *Biophys. J.* 83:3652–3664.

Hurtley, S.M., and Helmuth, L., 2003, The future looks bright, *Science* 300:75.

Janetopoulos, C., Jin, T., and Devreotes, P., 2001, Receptor-mediated activation of heterotrimeric G-proteins in living cells, *Science* 291:2408–2411.

Jones, J.T., Myers, J.W., Ferrell, J.E., and Meyer, T., 2004, Probing the precision of the mitotic clock with a live-cell fluorescent biosensor, *Nat. Biotech.* 22:306–312.

Johnson, D.A., Voet, J.G., and Taylor, P., 1984, Fluorescence energy transfer between cobra a-toxin molecules bound to the acetylcholine receptor, *J. Biol. Chem.* 259:5717–5725.

Kohen, E., Legallais, V., and Kohen, C., 1966, An introduction to microelectrophoresis and microinjection techniques in microfluorimetry, *Exp. Cell Res.* 41:223–226.

Kenworthy, A.K., and Edidin, M., 1998, Distribution of a glycosyl phosphatidyl inositol-anchored protein at the apical surface of MDCK cells examined at a resolution of <100 Å using imaging fluorescence resonance energy transfer, *J. Cell Biol.* 142:69–84.

Kim, S.A., and Schwille, P., 2003, Intracellular applications of fluorescence correlation spectroscopy: prospects for neuroscience, *Curr. Opin. Neurobiol.* 13:583–590.

Kraynov, V.S., Chamberlain, C., Bokoch, G.M., Schwartz, M.A., Slabaugh, S., and Hahn, K.M., 2000, Localized Rac activation dynamics visualized in living cells, *Science* 290:333–337.

Kusumi, A., Ike, H., Nakada, C., Murase, K., and Fujiwara, T., 2005, Single-molecule tracking of membrane molecules: Plasma membrane compartmentalization and dynamic assembly of raft-philic signaling molecules, *Semin. Immunol.* 17:3–21.

Labas, Y.A., Gurskaya, N.G., Yanushevich, Y.G., Fradkov, A.F., Lukyanov, K.A., Lukyanov, S.A., and Matz, M.V., 2002, Diversity and evolution of the green fluorescent protein family, *Proc. Natl. Acad. Sci. USA* 99:4256–4261.

Lakowicz, J.R., 1999, *Principles of Fluorescence Spectroscopy*, 2nd ed., Kluwer Academic/Plenum Publishers, New York, pp. 367–394.

Larson, D.R., Ma, Y.M., Vogt, V.M., and Webb, W.W., 2004, Direct measurement of Gag–Gag interaction retrovirus assembly with FRET and fluorescence correlation spectroscopy, *J. Cell Biol.* 162:1233–1244.

Lippincott-Schwartz, J., and Patterson, G.H., 2003, Development and use of fluorescent protein markers in living cells, *Science* 300:87–91.

Lippincott-Schwartz, J., Altan-Bonnet, N., and Patterson, G.H., 2003, Photobleaching and photoactivation: following protein dynamics in living cells, *Nat. Cell Biol.* (Suppl.):S7–S14.

Lippincott-Schwartz, J., Snapp, E., and Kenworthy, A., 2001, Studying protein dynamics in living cells, *Nat. Rev. Mol. Cell Biol.* 2:444–456.

Lidke, D.S., Nagy, P., Heintzmann, R., Arndt-Jovin, D.J., Post, J.N., Grecco, H., Jares-Erijman, E.A., and Jovin, T.M., 2004, Quantum dot ligands provide new insights into erbB/HER receptor-mediated signal transduction, *Nat. Biotechnol.* 22:198–203.

Magde, D., Elson, E., and Webb, W.W., 1972, Thermodynamic fluctuations in a reacting system. Measurement by fluorescence correlation spectroscopy, *Phys. Rev Lett.* 29:705–708.

Majoul, I., Schmidt, T., Pomasanova, M., Boutkevich, E., Kozlov, Y., and Söling, H.D., 2002a, Differential expression of receptors for Shiga and Cholera toxin is regulated by the cell cycle, *J. Cell Sci.* 115:817–826.

Majoul, I., Sohn, K., Wieland, F.T., Pepperkok, R., Pizza, M., Hillemann, J., and Söling, H.D., 1998, KDEL receptor (Erd2p)-mediated retrograde transport of the cholera toxin A subunit from the Golgi involves COPI, p23, and the COOH terminus of Erd2p, *J. Cell Biol.* 143:601–612.

Majoul, I., Straub, M., Hell, S.W., Duden, R., and Söling, H.D., 2001, KDEL-cargo regulates interactions between proteins involved in COPI vesicle traffic: Measurements in living cells using FRET, *Dev. Cell* 1:139–153.

Majoul, I., Straub, M., Duden, R., Hell, S.W., and Söling, H.D., 2002b, Fluorescence resonance energy transfer analysis of protein-protein interactions in single living cells by multifocal multiphoton microscopy, *J. Biotechnol.* 82:267–277.

Majoul, I.V., Bastiaens, P.I., and Söling, H.D., 1996, Transport of an external Lys-Asp-Glu-Leu (KDEL) protein from the plasma membrane to the endoplasmic reticulum: Studies with cholera toxin in Vero cells, *J. Cell Biol.* 133:777–789.

Mattheyses, A.L., Hoppe, A.D., and Axelrod, D., 2004, Polarized fluorescence resonance energy transfer microscopy, *Biophy. J.* 87:2787–2797.

Matz, M.V., Fradkov, A.F., Labas, Y.A., Savitsky, A.P., Markelov, M.L., and Lukyanov, S.A., 1999, Fluorescent proteins from nonbioluminescent *Anthozoa* species, *Nat. Biotechnol.* 17:969–973.

Meyer, T., and Teruel, M.N., 2003, Fluorescence imaging of signaling networks, *Trends Cell Biol.* 13:101–106.

Michalet, X., Pinaud, F.F., Bentolila, L.A., Tsay, J.M., Doose, S., Li, J.J., Sundaresan, G., Wu, A.M., Gambhir, S.S., and Weiss, S., 2005, Quantum dots for live cells, *in vivo* imaging, and diagnostics, *Science* 307:538–544.

Miesenbock, G., De Angelis, D.A., and Rothman, J.E., 1998, Visualizing secretion and synaptic transmission with pH-sensitive green fluorescent proteins, *Nature* 394:192–195.

Miyawaki, A., Griesbeck, O., Heim, R., and Tsien, R.Y., 1999, Dynamic and quantitative Ca2+ measurements using improved chameleons, *Proc. Natl. Acad. Sci. USA* 96:2135–2140.

Miyawaki, A., Llopis, J., Heim, R., McCaffery, J.M., Adams, J.A., Ikura, M., and Tsien, R.Y., 1997, Fluorescent indicators for Ca2+ based on green fluorescent proteins and calmodulin, *Nature* 388:882–887.

Mochizuki, N., Yamashita, S., Kurokawa, K., Ohba, Y., Nagai, T., Miyawaki, A., and Matsuda, M., 2001, Spatio-temporal images of growth-factor-induced activation of Ras and Rap1, *Nature* 411:1065–1068.

Nicholl, C., 2004, *Leonardo da Vinci — The flights of the mind*, Allen Lane, Penguin Books Ltd., London.

Patterson, G., Day, R., and Piston, D., 2001, Fluorescent protein spectra, *J. Cell Sci.* 114:837–838.

Patterson, G.H., Knobel, S.M., Sharif, W.D., Kain, S.R., and Piston, D.W., 1997, Use of the green fluorescent protein and its mutants in quantitative fluorescence microscopy, *Biophys. J.* 73:2782–2790.

Patterson, G.H., Piston, D.W., and Barisas, B.G., 2000, Forster distances between green fluorescent protein pairs, *Anal. Biochem.* 284:438–440.

Periasamy, A., Elangovan, M., Wallrabe, H., Demas, J.N., Barroso, M., Brautigan, D.L., and Day, R.N., 2001, Widefield, confocal, two-photon and lifetime resonance energy transfer imaging microscopy, In: *Methods in Cellular Imaging*, (A. Periasamy, ed.), Oxford University Press, New York, pp. 295–308.

Prasher, D.C., Eckenrode, V.K., Ward, W.W., Prendergast, F.G., and Cormier, M.J., 1992, Primary structure of the *Aequorea victoria* green-fluorescent protein, *Gene* 111:229–233.

Presley, J.F., Ward, T.H., Pfeifer, A.C., Siggia, E.D, Phair, R.D., and Lippincott-Schwartz, J., 2002, Dissection of COPI and Arf1 dynamics *in vivo* and role in Golgi membrane transport, *Nature* 417:187–193.

Sambrook, J., Fritsch, E.F., and Maniatis, T., 1989, *Molecular Cloning: A Laboratory Manual*, Cold Spring Harbor Laboratory, Cold Spring Harbor, New York.

Sato, M., Ozawa, T., Inukai, K., Asano, T., and Umezawa, Y., 2002, Fluorescent indicators for imaging protein phosphorylation in single living cells, *Nat. Biotechnol.* 20:287–294.

Sato, M., Ueda, Y., Takagi, T., and Umezawa, Y., 2003, Production of PtdInsP3 at endomembranes is triggered by receptor endocytosis, *Nat. Cell Biol.* 5:1016–1022.

Shaner, N.C., Campbell, R.E., Steinbach, P.A., Giepmans, B.N., Palmer, A.E., and Tsien, R.Y., 2004, Improved monomeric red, orange and yellow fluorescent proteins derived from Discosoma sp. red fluorescent protein, *Nat. Biotechnol.* 22:1567–1572.

Stephens, D.J., and Allan, V.J., 2003, Light microscopy techniques for live cell imaging, *Science* 300:82–86.

Stryer, L., 1978, Fluorescence energy transfer as a spectroscopic ruler, *Annu. Rev. Biochem.* 47:819–846.

Stryer, L., and Haugland, R.P., 1967, Energy transfer: A spectroscopic ruler, *Proc. Natl. Acad. Sci. USA* 58:719–726.

Ting, A.Y., Kain, K.H., Klemke, R.L., and Tsien, R.Y., 2001, Genetically encoded fluorescent reporters of protein tyrosine kinase activities in living cells, *Proc. Natl. Acad. Sci. USA* 98:15003–15008.

Tron, L., Szollosi, J., Damjanovich, S., Helliwell, S.H., Arndt-Jovin, D.J., and Jovin, T.M., 1984, Flow cytometric measurement of fluorescence resonance energy transfer on cell surfaces. Quantitative evaluation of the transfer efficiency on a cell-by-cell basis, *Biophys. J.* 45:939–946.

Tsien, R.Y., 1998, The green fluorescent protein, *Annu. Rev. Biochem.* 67:509–544.

Tsien, R.Y., 2004, Building and breeding molecules to spy on cells and tumors, *FEBS Lett.* 579:927–932.

Umezawa, Y., 2005, Genetically encoded optical probes for imaging cellular signalling pathways, *Biosens. Bioelectron.* 20:2504–2511.

Velez, M., and Axelrod, D., 1988, Polarized fluorescence photobleaching recovery for measuring rotational diffusion in solutions and membranes, *Biophys J.* 53:575–591.

Violin, J.D., Zhang, J., Tsien, R.Y., and Newton, A.C., 2003, A genetically encoded fluorescent reporter reveals oscillatory phosphorylation by protein kinase C, *J. Cell Biol.* 161:899–909.

Wakayama, S., Cibelli, J.B., and Wakayama, T., 2003, Effect of timing of the removal of oocyte chromosomes before or after injection of somatic nucleus on development of NT embryos, *Cloning Stem Cells* 5:181–189.

Ward, W.W., Prentice, H.J., Roth, A.F., Cody, C.W., and Reeves, S.C., 1982, Spectral perturbations of the *Aequorea* green fluorescent protein, *Photochem. Photobiol.* 35:803–808.

Weijer, C.J., 2003, Visualizing signals moving in cells, *Science* 300:96–100.

Wouters, F.S., Verveer, P.J., and Bastiaens, P.I., 2001, Imaging biochemistry inside cells, *Trends Cell Biol.* 11:203–211.

Wu, X., 2003, Multicolor labeling of cells using Qdot™ streptavidin conjugates, *Quantum Dot Vision* 1:10–11.

Zal, T., and Gascoigne, N.R.J., 2004, Photobleaching-corrected FRET efficiency imaging of live cells, *Biophys. J.* 86:3923–3939.

Zhang, J., Ma, Y., Taylor, S.S., and Tsien, R.Y., 2001, Genetically encoded reporters of protein kinase A activity reveal impact of substrate tethering, *Proc. Natl. Acad. Sci. USA* 98:14997–15002.

46

Automated Confocal Imaging and High-Content Screening for Cytomics

Maria A. DeBernardi, Stephen M. Hewitt, and Andres Kriete

INTRODUCTION

The vast amount of biological information emerging from large-scale high-volume genomics and proteomics has significantly changed biological research. The problem is, however, that we currently do not have the methods to analyze the enormous complexity of cells or cellular systems within reasonable time intervals using the traditional approach of hypothesis formulation followed by experimental verification. One challenge is that the data gained from observing a few cells is rarely suited for statistical evaluation. This limitation has stimulated development of new approaches to the comprehensive collection of information with more immediate biological importance at the cellular level (cytomics). This effort spans both basic biomedical research and drug development.

Recent advances in combinatorial chemistry, genomics, and **high throughput** screening (HTS), as they apply to drug discovery, have produced a deluge of potential therapeutic "hits." Conventional cell-based HTS assays rely on measuring single parameters from lysates of cell populations grown in multi-well high-density plates (whole-well average measurement), at single time points (end-point format) with very limited temporal resolution and no spatial resolution. Using standard or more advanced plate readers it is possible to reach the speed requirement of HT primary campaigns for drug discovery. Unfortunately, although advances in automation offer increasing rates of HTS throughput, the past few years have witnessed a dearth of newly approved drugs. At the same time, slowness in the identification and validation of cellular targets potentially affected by leads originally identified by HTS has created a bottleneck in the drug discovery process. Many promising compounds have failed in costly animal studies and in even costlier clinical trials farther down the drug discovery pipeline.

In response, new screening approaches have recently been proposed that are referred to as **high-content** screening (HCS). HCS relies on more sophisticated assays where the higher **quality** (as opposed to higher **quantity** in HTS) of the data being generated is believed both to increase the likelihood of discovery and to accelerate the profiling of successful drugs (Taylor *et al*., 2001; Dove, 2003).

HCS readouts can include simultaneous measurements of several physiological parameters from individual cells living within a population. HCS provides more complex but also more informative data than single, simpler HTS "presence-or-absence" readouts. Importantly, high-content data allow for a faster, comprehensive, mechanistic understanding of all the cellular functions that are affected by the signaling molecules/drug candidates under test and permit us to understand their physiological relevance, in the context of an intact biological system.

In recent years, single-cell imaging has been recognized as a revolutionary way to look at biology (Comley, 2005; Cole *et al*., 2003). As a result, imaging holds a great potential in HCS because of the dynamic and multi-dimensional (multiple targets over time and space) aspect of the data generated.

HTS technologies fail because they look at cell populations, averaging results over the entire well and wrongly assuming the cells to be homogeneous. Although such techniques have provided valuable cell biological insights, they necessarily miss or downplay subtle or rare cellular responses. As an example, if a small subset within a cell population exhibits a cytotoxic reaction to a test compound, such unwanted effect may go undetected if only the overall population response is considered. This could cause the compound not to pass the more stringent screenings in costly animal models later in the drug discovery process. Single-cell imaging on the other hand, allows one to appreciate the heterogeneous behavior of cells (presence/absence of response, magnitude of response, temporal/spatial dynamics) and to characterize it in the context of the cells' innate biological variability (e.g., different stages in the cell cycle, receptor expression, genetic makeup). Consequently, drug profiling can take place in a physiological background that is more representative of an *in vivo* scenario and, therefore, more likely to reflect the true individual global response.

To fulfill their purpose, HCS assays must be able to perform multiplexed analyses (preferably simultaneously and in real time) in the same cell population or, in a higher resolution imaging mode, within spatially distinct domains inside the same cells. A wealth of non-invasive fluorescent probes have been developed and are now available for monitoring cellular/subcellular targets in living specimens. In particular, fluorescence imaging of signalling pathways is a powerful new tool for understanding signal transduction cross-talks (DeBernardi and Brooker, 1998; Meyer and Truel, 2003), as well as the molecular architecture and functionality of cell systems conceived as integrated biological entities or cytomes (Valet, 2003). Rather than dissecting cellular pathways in order to study single components *in vitro,* it is becoming possible to watch

Maria A. DeBernardi • Bioimaging Systems BD Biosciences, Rockville, Maryland; Department of Biology, The Johns Hopkin University, Baltimore, Maryland 20850
Stephen M. Hewitt • National Cancer Institute, National Institutes of Health, Bethesda, Maryland 20886
Andres Kriete • Coriell Institute for Medical Research and Drexel University, Philadelphia, Pennsylvania 19104

Handbook of Biological Confocal Microscopy, Third Edition, edited by James B. Pawley, Springer Science+Business Media, LLC, New York, 2006.

important biochemical events unfold at the cellular and even organismal level. Confocal microscopy, with its high-content information yield, is the tool of choice that provides the required spatial and temporal imaging resolution. As is well documented in the other chapters of this book, confocal imaging techniques have the potential to generate phenotypic, functional, and molecular information via quantitative assessments of subcellular, cellular, and tissue constructs that have long proved capable of elucidating molecular mechanisms. Contextual biology (where/when/how it happens/what happens then) is indeed the current frontier of the life sciences.

PLATFORMS USED FOR AUTOMATED CONFOCAL IMAGING

With their larger pinhole size, lamp-based, spinning-disk confocal systems provide greater scanning speed and light transmission, but thicker optical sections than their laser-based, line-scanning, single-beam relatives. However, for researchers who must balance the need for thin sectioning against the requirement for full-frame, high-speed, real-time confocal imaging, spinning-disk–based confocal systems (see Chapter 10, *this volume*) are the tool of choice. They provide the ability to monitor rapidly occurring events within living cells without compromising *xy*-resolution, and record events that would be missed during the time required to perform a single-beam laser scan.

Besides reduced maintenance cost, other important advantages offered by spinning-disk–based systems include using white light sources rather than lasers permitting full spectrum excitation capability [from ultraviolet (UV) to near-infrared (IR)], and, because of the lower light intensity delivered to the sample (in photons/s/μm^2), reduced photobleaching of the probes and less phototoxicity to the specimen (see Chapters 38 and 39, *this volume*).

These features are of crucial importance for high-content imaging where multiple fluorescent probes (whose absorption peaks often do not match laser lines) can be efficiently excited throughout the spectrum or where prolonged monitoring of fluorescently labeled living cells is needed to follow real-time translocation events.

A number of automated imaging platforms have been introduced to the market. Each instrument solves the problems related to imaging and specimen handling, fluidics/kinetics capabilities, sample throughput, and data analysis in different ways to accomplish HCS. Some of these imaging workstations are confocal (either laser line based or spinning disk based) while some are not (see Table 46.1). It is clear this is a growing new segment of the imaging community that will evolve extensively over the next decade.

One class of commercially available confocal imaging workstations is represented by an automated bioimager that combines full spectrum, Nipkow-based confocal microscopy with kinetic and end-point single-cell imaging capabilities in a compact, flexible benchtop unit (PathwayHT, Bioimaging Systems, BD Bioscience, Rockville, MD). The system is suitable for both academic basic research and pharmaceutical applications in assay development and secondary screening (Vanek and Tunon, 2002).

When the goal of the experiment is to measure multiple cellular events at once, it is advantageous to employ multiple filter sets and multiple light sources. For example, two mercury arcs allow full-spectrum illumination, from 350 nm to near IR, while 16 excitation filters, 10 dichroic mirrors, and 8 emission filters (housed in software-controlled filter wheels) enable the use of most available dyes, both single wavelength [e.g., green fluorescent protein (GFP), Fluo4, rhodamine, Alexa dyes) and ratiometric (e.g., fura-2 and JC-1). Multiple filter sets provide flexibility both in assay development, where fluorescent probes with a wide range of excitation requirements must be tested, and in secondary screening, where multiple cellular events must be measured in a single assay to provide improved speed and more relevant biological information.

The spinning-disk confocal module (readily interchangeable with widefield mode) provides real-time confocal imaging of fast events in live cells with high signal-to-noise ratio and minimal photobleaching and phototoxicity. High-resolution multi-color confocal *z*-stacks and three-dimensional (3D) analysis capabilities are available for localization/redistribution studies of multiple fluorescently tagged biomolecules within subcellular compartments.

Real-time confocal imaging requires sensitive cameras, such as high quantum efficiency charge-coupled device (CCD) cameras that provide high resolution and optimal signal-to-noise ratio. Once the new electron multiplier (EM)-CCD cameras (with exceptional sensitivity, greater speed, and minimal readout noise) become more widely available, it is expected that automated imaging platforms will greatly benefit from their use (see Chapters 2 and 12).

Other required features include integrated temperature and CO_2 control to ensure the consistency of physiological data. On-stage liquid handling for automated drug delivery to living cells provides an image-while-you-add capability and allows one to follow fast-onset kinetic responses (Fig. 46.1).

To permit imaging of adjacent fields while the stage and the sample remain stationary, proprietary optical designs allow objectives mounted below the specimen to move in x-y-z directions while both the stage and the sample remain stationary. This enables suspended or poorly adherent cells to be imaged without mechanical disruption. Motorized *x*-, *y*- , and *z*-positioning of the objective with 100 nm (*xy*) and 50 nm (*z*) precision permits revisiting previously imaged fields. This feature allows (a) prolonged time-lapse experiments to be carried out simultaneously on multiple fields by imaging each field sequentially at different time points, and (b) capture of montaged images of samples larger than the microscopic field of view. Montaging is useful when imaging tissue arrays or whole organisms, such as embryos of *Caenorhabditis elegans*, *Arabidopsis,* zebrafish, and *Drosophila*, and also when dealing with highly heterogeneous populations with rare responders, where a larger sample size is needed to improve statistical significance.

Depending upon the resolution required by a specific application, the type of imaging substrate used (glass/plastic) and the throughput desired, different magnification objectives (2×, 4×, 10×, 20×, 40× dry and 60× oil) can be employed. These optics can be optimized for the demands of the assay. Low power, low NA dry lenses are used for high speed in non-confocal applications. High NA immersion lenses matched to the dish in which the cells are cultured are used for slower studies where higher spatial resolution is needed.

As with other automated bioimagers, the system is amenable to robotic integration with industry standard plate handling and batch processing devices and can be operated in a fully automated mode under software control. A Windows-based software system seamlessly integrates image capture, sample navigation (for multi-well plates; chamber slides, standard microscope slides, culture dishes, etc.), liquid addition, and on-the-fly image analysis (see Chapter 14, *this volume*). A key requirement of the system software is the ability to drive a broad range of endpoints (biomarker identification, localization, translocation, redistribution) and kinetics (ion/second messenger real-time measurements).

TABLE 46.1. Non-Confocal HCS Systems

	Amersham IN Cell Analyzer 1000	Axon ImageXpress	Beckmann-Coulter/Q3DM	Cellomics Arrayscan Vti	Cellomics KineticScan	Universal Imaging Discovery 1
URL		www.axon.com	www.beckmann.com	www.cellomics.com		www.universal-imaging.com
Imaging system	CCD camera–based Non-confocal Nikon objectives	CCD camera–based Non-confocal Nikon objectives	CCD camera–based Non-confocal system	CCD camera–based Non-confocal ZeissApotome Grating optional Zeiss objectives	CCD camera–based Non-confocal Zeiss objectives	CCD camera–based Non-confocal Nikon objectives
Light source	Xenon lamp and filter wheel	Xenon lamp and filter wheel	Mercury lamp	Mercury lamp and filter wheel	Mercury-xenon lamp	Lamp-based and filter wheels
Excitation/ emmission filter #	6/6	10/10	10/10	10/8	8/8	10/10
Binocular eyepiece	No	No	No	No	No	No
Objective choices	4×, 10×, 20×, 40×	4×, 10×, 20×, 40×	4× to 40×	5×, 10×, 20×, 40× & 60×	5×, 10×, 20×, 40×	2×, 4×, 10, 20×, 40×
Plates	96, 384 well	96, 384, 1536 well	96–1536 well & slides	96–384 well	96–384 well	96, 384, 1536 well
Environmental controls	Temp 37 or ambient	Temp CO_2	No	No	Temp CO_2 Humidity	No
Liquid dispensing	Yes	Yes	No	No	Yes	No

Confocal HCS Systems

	Amersham IN Cell Analyzer 3000	BD Pathway HT	Evotec. Opera
URL	www.amersham.com	www.bdbiosciences.com	www.evotec-technologies.com
Imaging system	CCD camera–based confocal line scanning Nikon objectives	CCD camera–based confocal system Nipkow spinning disk Olympus objectives	CCD camera–based confocal spinning disk (Yokogawa)
Light source	2 lasers Krypton and argon 3 lines	Mercury lamp and filter wheel	4 lasers and xenon lamp for UV (non confocal)
Excitation/emmission filter #	3/8	16/8	4/6
Binocular eyepiece	No	Yes	No
Objective choices	40×	2×, 4×, 10×, 20×, 40×, 60×,	10×, 20×, 40×, 60×
Plates	96–384 well	96–384 well & slides; slide holder provided	96, 384, 1536 well
Environmental controls	Temp CO_2 Humidity	Temp CO_2	Temp CO_2
Liquid dispensing	Yes, limited	Yes	Yes, optional

TYPES OF ASSAYS

Selected automated confocal imaging platforms support current kinetics (e.g., calcium and sodium fluxes, mitochondria and plasma membrane potential changes, etc.) and endpoint cell assays (e.g., cytotoxicity, apoptosis, cell cycle, translocations) using common commercially available fluorescent probes (Table 46.2) Multiplexed assays are only limited by the optical compatibility of the fluorescent probes used. In particular, selected applications amenable to automated high-content imaging will benefit from the advantages provided by confocal microscopy including, but not limited to, the following:

- Live/fixed cell assay where fluorescent probes photobleach rapidly, either because of the chemical nature of the fluorophore or because of high sampling frequency (fast kinetics imaging with no or minimal delay between two illumination cycles) [Fig. 46.2(A), left panel].
- Live-cell assays where the fluorescent probes used to label cells are not removed during the imaging phase. This might happen for several reasons:

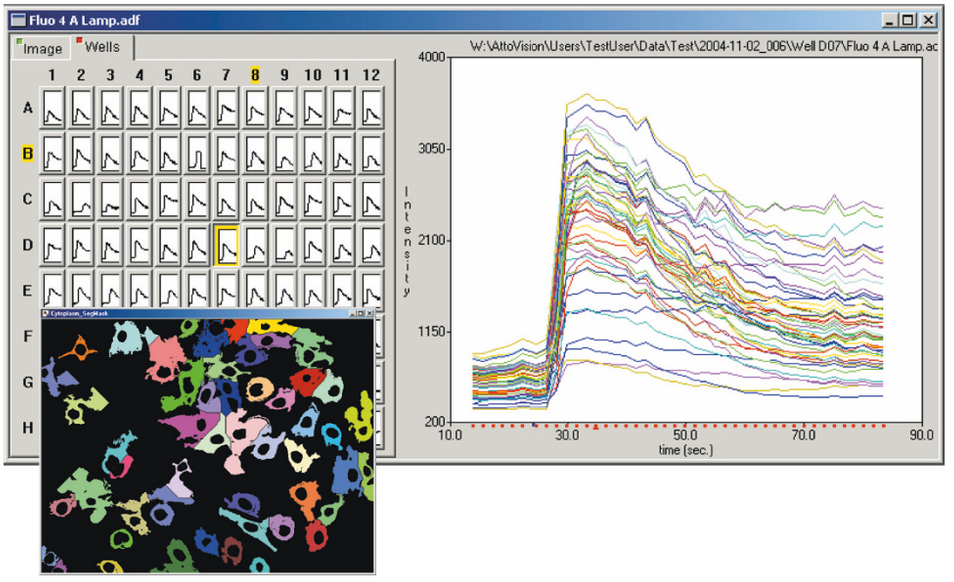


FIGURE 46.1. Automated single-cell kinetic calcium imaging. Screenshot from PathwayHT showing single-cell, real-time calcium fluxes in HeLa cells. Cells were grown on a 96-well plastic plate overnight, labeled with 2 u*M* Fluo-4 and imaged (20×, 0.75NA, at 37°C and 5% CO_2) in resting conditions and during/after automated addition of ATP (50 u*M*), a purinergic receptor agonist that mobilizes intracellular Ca^{2+}. On-the-fly visualization of single-cell-derived kinetic traces reveals profound heterogeneity in the magnitude/dynamic of cell responses to ATP. After completing a user-defined time-lapse, average responses are plotted in each well enabling ready visualization of overall cells' responsiveness. Color-coded single-cell traces identify corresponding cells (cell segmentation mask shown) allowing ready comparison of cell morphological and biochemical patterns.

TABLE 46.2. Methods Suitable for HCS Fluorescence Analysis of Cells

Application	Parameter Measured	Dyes	Information	Areas of Study
Cytotoxicity	Cell viability Cell proliferation	Calcein AM — Live cells Propidium Iodide — Dead cells Hoechst/DAPI nuclear dyes	Number/percentage of live/dead cells over a population	ADME/Tox Cancer biology
Apoptosis	Mitochondria potential changes Phosphatidylserine externalization Caspase activation Chromatin condensation/ fragmentation DNA strand breaks	JC-1, TMRE Annexin V Caspase sensors (cytoplasmic and nuclear) Hoechst/DAPI TUNEL	Early/intermediate/late apoptosis stage Apoptosis/Necrosis DNA damages	Pharmacology Toxicology Cell/cancer biology Genotoxicity
Translocation	Stimulus-induced target redistribution, e.g.: NF-kB (cytoplasm to nucleus) PKCα (cytosol to membrane) STATs (cytosol to nucleus) MAPKAk2 (nucleus to cytoplasm) Receptor internalization and fate	Detection is provided by antibody-based reagents for endogenously expressed targets. Alternatively, targets are expressed in cells as fusion protein with GFP, its variants or other fluorescent protein (biosensors). GFP-βarrestin, CypHer[a]	Organelle changes in fluorescence intensity/ patterns are indicators of specific target activation	Cell signalling Pathway cross-talk Immunology Receptor activation and desensitization
Kinetics	Calcium Sodium Membrane potential (MP) Mitochondria potential Multiplexed cAMP	Fluo-4, fura-2 SBFI Various MP Dyes JC-1 See below[b] ACT:One[c]	Kinetic changes in fluorescence intensity (or ratio) report live cells ion/second messengers response to stimuli. Multiplexing reveals real-time signaling cross-talk	Cell signaling Pharmacology Receptor/ion channel Activation Signaling, (cross-talk)
Cell cycle	DNA content and replication status Stage-specific target expression and/or phosphorylation	Hoechst/DAPI/Anti-nucleotide (e.g., BrdU) antibodies Anti-Histone/cyclins/cyclin-dependent kinase antibodies Cyclin-fusion protein	DNA content (2n/4n) in G1, G2, M phase. Cell cycle stages (e.g., phosphoH3 histone indicates M phase)	Cancer biology Genomics
Neurite outgrowth	Neurite extensions	Neuron specific antibody-based reagents	Number/length/branching upon neurite inducing stimuli	Neuroscience Regeneration Differentiation

Examples of cell-based assays suitable for automated imaging workstations. Listed are representative assays and fluorescent probes; more specifics on dyes can be found in Table 16.1, *this volume*. Kits, cell lines, and fluorescent agents are available from independent suppliers or imaging platform vendors that offer a variety of protocols. Examples include [a]GFP-βarrestin = Transfluor technology (by Norak Biosciences Inc); CypHer, pH sensitive dye (Amersham GE Healthcare); [b]calcium and sodium (Fluo-4 and SBFI); calcium and membrane potential (fura-2 and various MP probes); calcium and mitochondria membrane potential (Fura-2 and JC-1) [c]ACT:One cell lines and dyes for real-time cAMP measurement in live cells (Bioimaging Systems, BD Bioscience).

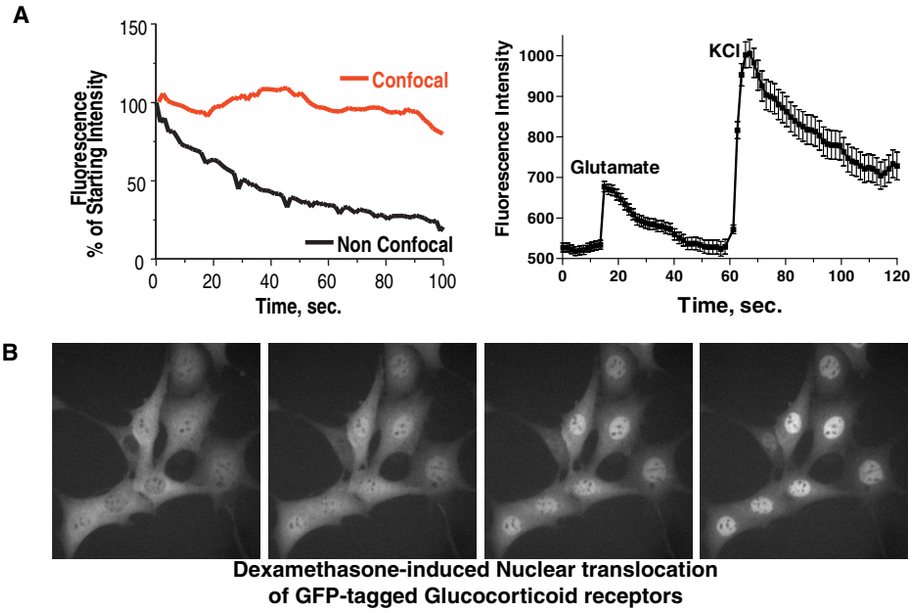


FIGURE 46.2. Confocal imaging of living cells. (A) Confocal imaging of primary rat cerebellar granule neurons. Cells were labeled with a membrane-potential dye and imaged confocally on PathwayHT (20×, 0.75NA) at 37°C and 5% CO_2 without dye removal. Left panel: cells were imaged under continuous illumination either in widefield or confocal mode. By 100 sec, a 75% loss in the probe-generated fluorescence signal was detected in cells imaged in widefield mode while in confocal mode, only ~25% of loss was detected. The reduced photobleaching provided by lamp-based confocal imaging platforms allows monitoring responses whose fast onset might require high-frequency sample illumination. Right panel: Membrane-potential depolarization induced by glutamate (10 u*M*) and KCl (50 m*M*) in primary neurons. Trace represents mean ± SD. (B) Real-time glucocorticoid receptor-nuclear translocation. Living MMTV mouse cells stably expressing GFP-tagged glucocorticoid receptors (GR) were imaged confocally on PathwayHT (40×, 0.9NA) at 37°C and 5% CO_2. GR nuclear translocation was induced by dexamethasone (1 n*M*) and followed over time; images were captured every 20 sec. From left to right: images at 0, 5, 10, 15 min after dexamethasone addition. Cells were kindly provided by Dr. G. Hager, NCI, NIH, Bethesda, MD.

  - — the probe needs to be in contact with the cells for functional measurements to be made (e.g., membrane potential dye) [Fig. 46.2(A), right panel];
  - — a homogeneous assay format with no washing steps is needed to optimize cell responsiveness and improve speed;
  - — active, postloading dye leakage from cells. Drug-resistant cancer cells are notorious for their active extrusion of small fluorescent probes because they over-expressed drug efflux pumps. The ability of the confocal microscope to image a single plane reduces the effect of the background generated by this excess probe, increasing signal-to-noise ratio and assay sensitivity.
- Live-cell assays in which phototoxicity might interfere with biological functions (e.g., prolonged time courses where small organisms expressing GFP or other fluorescent fusion proteins are followed through multiple cellular divisions or where cell lineage is being investigated) [Fig. 46.2(B)].
- Assays employing *in vitro* systems consisting of two-dimensional (2D), mixed-cell populations (e.g., primary neuron cultures with supporting glial cells, or special-purpose feeder layers for differentiating embryonic stem cells). Confocal microscopy will allow imaging at specified focal planes to emphasize the response of the desired cell population.
- Assays where high-resolution spatial discrimination is required for localizing fluorescent markers to specific subcellular compartments. This process could be as simple as assigning a given probe to a given structure (target identification or confirmation of organelle specificity for novel biomarkers) or as sophisticated as generating complete confocal image database towards a systematics for protein subcellular localization (Boland *et al.*, 2001).
- Cell surface targeting assays such as those aimed at identifying biomolecules that either are constitutively present on the outside of the plasma membrane (e.g., surface antigens and receptors) [Fig. 46.3(A)] or become newly exposed on cell surfaces in response to a stimulus (e.g., phosphatidylserine, normally found on the inner side of the plasma membrane, gets externalized during drug-induced apoptosis and its identification by fluorescent annexin V provides a robust assay for early apoptosis classification).
- Multi-color applications where different cell types within a tissue or different organelles or proteins within a cell are labeled with specific probes whose spatial localization or colocalization requires the high spatial resolution provided by confocal imaging [Fig. 46.3(B)]. This scenario might include fixed samples fluorescently labeled with multiple antibodies conjugated to either conventional organic dyes or recently developed semiconductor nanocrystals (quantum dots; Watson *et al.*, 2003; see Chapters 16 and 17, *this volume*) as wells as live/fixed cells expressing multiple GFPs, or other fluorescent fusion proteins, and targeting different subcellular compartments. Phenotypic profiling of either tissues or cell populations labeled with multiple, organelle-specific probes represents a recently developed approach to screen molecules that alter specific cellular parameters, allowing the identification of compounds (or siRNAs) that interact with different systems in the cell such as the cytoskeleton or various signal transduction pathways (Yarrow *et al.*, 2003).
- Pharmacological screening of the hepatoxic potential of compounds in primary liver cells or liver cells lines, using confocal imaging, was reported to provide visual discrimination

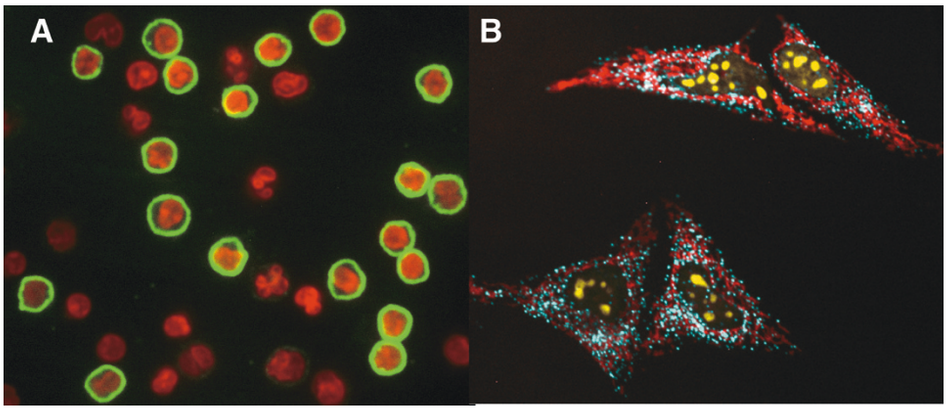


FIGURE 46.3. High resolution confocal imaging of surface and intracellular target. (A) Peripheral Blood Mononuclear Cells (PBMC) labeled with an APC-tagged, anti-CD4 monoclonal antibody (BD Biosciences) (pseudocolored in green) and counterstained with the nuclear dye, Hoechst 33324 (pseudocolored in red). Confocal imaging (60× oil, 1.4NA) clearly shows plasma-membrane-specific localization of cell surface CD4 receptors on a selected subset of PBMC. (B) HeLa cells expressing three organelle-targeted fluorescent fusion proteins: AmCyan-peroxisomes, ZsYellow-nucleus, HcRed-Mitochondria (Clontech, BD Biosciences) were fixed and imaged on PathwayHT (40×, 0.9NA) in confocal mode.

of compound-specific intracellular fat deposition patterns (McMillian *et al*., 2001).

- Endpoint translocation/redistribution assays where, following a relevant stimulus, the labeled target moves from one subcellular compartment to another (e.g., cytoplasm-to-nucleus translocation of NF-kB transcription factor or cytoplasm-to plasma-membrane translocation of protein kinase Cα) or undergoes changes in fluorescence pattern [e.g., redistribution assays where the fluorescence pattern of receptor-bound GFP-β arrestin changes from an evenly diffuse cytosolic pattern to a more punctate one (pits/vesicles formation) upon agonist-induced internalization of the receptor] (Fig. 46.4). Confocal microscopy provides high-resolution images of the fluorescence redistribution patterns that allow more sophisticated image analysis algorithms (such as granularity) to be optimally applied. These in turn lead to greater assay sensitivity.
- Assays based on 3D biological structures (micro-organs) where confocal *z*-stacks captured over time can provide physiologically relevant insights on cell proliferation, differentiation, drug responsiveness within a miniaturized *ex vivo* environment.
- Assays using quantum dots *in vivo* or on fixed cells (Chapters 16 and 17, *this volume*), which, because of their narrow emission bands, allow one to monitor the dynamics and location of several different proteins at once.

An automatic confocal imaging workstation that provides control of temperature and CO_2, precise *xy*-position field revisiting, and automated multiple color *z*-sectioning capabilities with minimal photobleaching and phototoxicity will be the tool of choice for 3D model imaging with applications in cancer biology, toxicology, therapeutics, and regeneration.

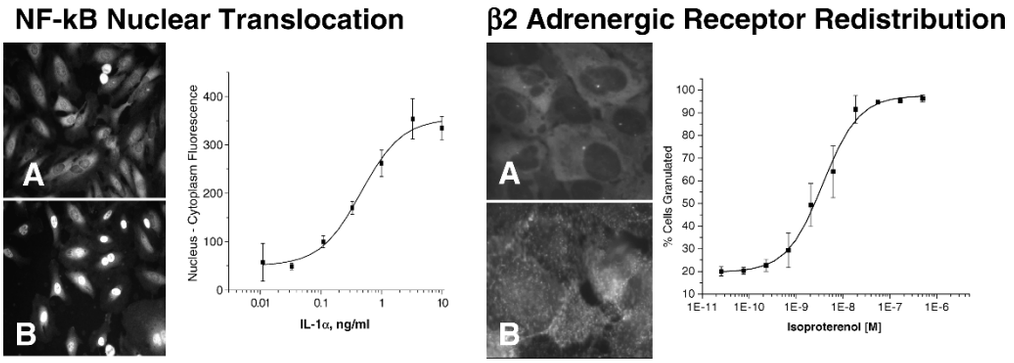


FIGURE 46.4. Automated fluorescence imaging applied to endpoint translocation assays. Left panel: Nuclear translocation of the transcription factor, NF-kB. HeLa cells were grown overnight on 96-well plastic plates and treated with increasing concentrations of IL-1α for 30 min. Cells were fixed, permeabilized and labeled with an anti-NF-kB Alexa488-IgG and the nuclear dye Hoechst 33342. Cells were imaged on PathwayHT in an automated mode (20×, 0.75NA) with fluorescence intensity being measured in the nucleus and the cytoplasm. Images show basal fluorescence signal (A) and IL-1-stimulated increase in nuclear NF-kB fluorescence (B). Cell-by-cell data analysis was performed and a dose-response curve generated using BD Image Data Explorer. Right panel: γ2-adrenergic receptor trafficking visualized by GFP-arrestin fluorescence redistribution. Human osteosarcoma cells (Transfluor technology, Xsira Bioscience, Research Triangle, NC) stably expressing GFP-arrestin were challenged with increasing concentrations of isoproterenol, a γ-adrenergic receptor agonist, fixed and nuclei counterstained with DAPI. Cells were imaged on Pathway HT (40×, 0.9NA) and GFP-β arrestin fluorescence measurements were taken in cytoplasmic regions. (A) basal fluorescence, (B) after isoproterenol. Granularity algorithms (variation in pixel intensity and distribution) were applied for image analysis and data were expressed as % of cells exhibiting a granularity value above a user-set threshold. Dose response curves were generated using BD Image Data Explorer.

3D CELL MICROARRAY ASSAYS

The cell microarray (CMA) is one embodiment of the tissue microarray (TMA) that is a particularly useful type of prepared specimen for confocal high-content screening.

A cell or tissue microarray is a microscope slide containing between 10 and 1000 individual samples arranged in a grid fashion (Braunschweig *et al*., 2004) (Fig. 46.5). This approach converts imaging from a descriptive endeavor to a high-throughput methodology producing databases and requiring statistical analysis. The cell-line array can be an array of different cell lines, or an array of cells grown under different conditions (or both) that can be used to address a variety of questions. At the simplest level, a cell microarray can be considered a "Western blot on a slide," but such a characterization covers only a small portion of the information that can be obtained from such specimens.

CMA can be used with confocal microscopy as a tool to understand the human cytome. Utilizing the 60 cell lines the NCI employs in drug testing, the Tissue Array Research Program (TARP Lab), at the National Cancer Institute, has developed a unique platform, the NC160 CMA, which is studied with a HCS instrument for protein expression, localization, and interaction.

Most CMA cells are obtained from cell-line cultures of transformed cells, however, primary cultures are also sometimes adequate. Current protocols require less than 500,000 cells as starting material. The cells can be from clinical samples such as leukophoresis or flow-sorted specimens. Cells grown *in vitro* must be harvested by scraping. The cells are then embedded in a low melt agarose plug, which is then fixed and processed as if it were tissue to produce a paraffin-embedded block (Hewitt, 2004). Unlike most tissue specimens, formalin is not the only choice of fixation (see Chapter 18, *this volume*). Ten percent formalin, although an excellent fixative for tissue, cross-links the proteins and nicks nucleic acids, as well as producing a significant amount of background autofluorescence. As an alternative, 70% ethanol combines coagulative fixation with dehydration, and does so without cross-linking proteins or nicking nucleic acids (Gillespie *et al*., 2002). An additional advantage of using 70% ethanol as a fixative is that it is significantly easier to translate an antibody used in Western blots or for the immunostaining of frozen tissue to ethanol fixed material. Tissues (and cell–agarose plugs) can be fixed in 70% ethanol exactly as if fixed in formalin, using the same times and volumes. When it is time to process the tissue (dehydration and replacement by paraffin), only the first stage on the processor (10% formalin) need be skipped, as the second stage is 70% ethanol. Although other alcohols and different concentrations are associated with excessive shrinkage and distortion of cellular morphology, 70% ethanol results in shrinkage comparable with 10% formalin (Gillespie *et al*., 2002; Chapter 18, *this volume*).

After processing and embedding, a 3D cell pellet is obtained. This can both be sectioned and viewed as such, or the cell pellet blocks can be utilized for the construction of a CMA. The methods of arraying are straightforward, and can be fabricated manually or using different levels of automatic instrumentation (Braunschweig *et al*., 2004). The recipient array block (CMA block) can then be sectioned into slides for staining (Fig. 46.4). Unlike tissue sections where 4 or 5 µm sections are preferred, CMAs are optimally cut at between 7 and 10 µm to allow more complete 3D representation of the cells on the array.

For confocal imaging of the arrays, appropriate staining protocols must be worked out. It is essential that one use an excellent deparaffinization routine as residual paraffin will reduce the affinity of the antibodies, and will produce increased autofluorescence. Most normal staining protocols are inadequate, and three changes in xylene for 5 min each should be considered a starting point for deparaffinization. Depending on the targets and their cellular localization, the use of 4′,6-diamidino-2-phenylindole (DAPI) may or may not aid in imaging.

In its first embodiment, the NCI60 CMA consisted of 58 cell lines arrayed with 1.00 mm diameter cores of agarose plugs in triplicate cut as 7 µm sections on tape slides from Instrumedics [Fig. 46.5(A)]. The array was designed to present ~300 cells/core for analysis [Fig. 46.5(B)]. Cells were prepared at low density in an agarose plug, and cut as thick sections (7 µm) so that they would have a more homogeneous shape distribution in three dimensions, and had only a few artificial cell–cell contacts. This CMA is optimized for the investigation of cell signaling and protein localization, and their translocation. It is not designed for, and should not

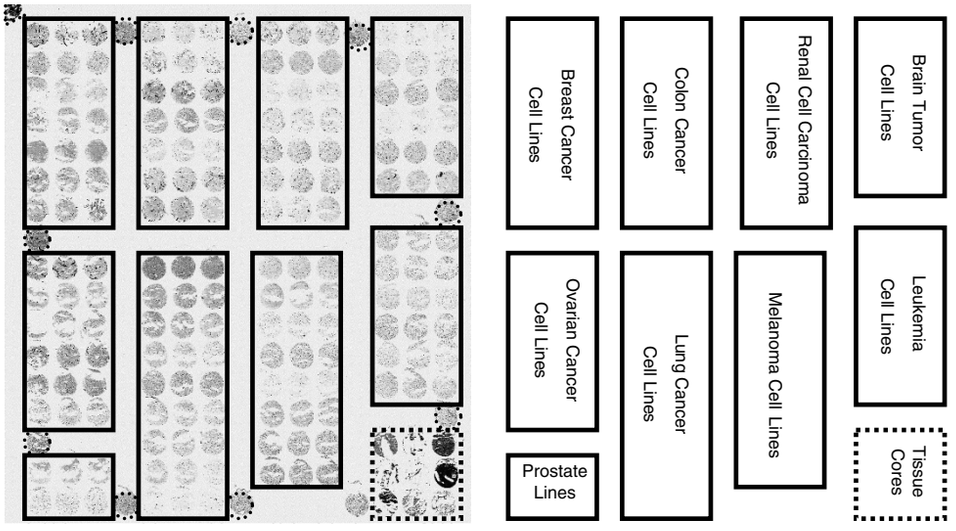


FIGURE 46.5. Cell microassays (Such as NCI160) exhibit different cell lines that allow rapid screening of cellular responses.

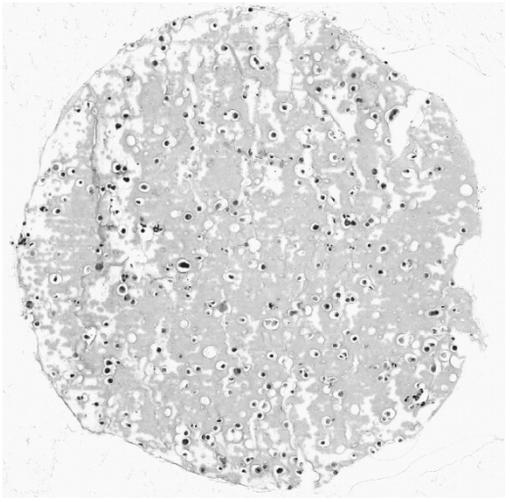


FIGURE 46.6. A single, 1.00 mm core of *in vitro* cultured cells embedded in agarose present on the NC160 CMA. This is a core of NCI-H23 cells, a cell line derived from human lung cancer.

be used for, studies of cell adhesion, communication, or most cytoskeletal studies. The dispersion of the cells within the cores is designed to make analysis simpler. This array is available on a limited basis from through the Developmental Therapeutics Program (DTP) of the NCI.

Confocal imaging of a complete CMA slide with 58 individual cell lines (in triplicate) requires an almost heroic effort and is impractical without an automated stage. Identification of the individual cores requires a "scout image" of the slide. Depending on the method being applied, a low-magnification image of the slide can be made to identify and locate the cores. Alternatively, a high-magnification, low-resolution image of the slide can be made for the same purpose. After the cores have been identified and located, the instrument is then programmed to image the cores individually based on the low-magnification map.

DATA MANAGEMENT AND IMAGE INFORMATICS

High-content imaging generates a vast amount of data that must be analyzed using software analysis programs, either those provided with the commercial instrumentation or custom written for very specific applications. For example, if two proteins are stained, and DAPI is used (especially useful for the low-resolution imaging to locate individual cells) on an NCI160 slide, the imaging demands on the platform are significant. One could anticipate requiring $58 \times 10 \times 3 = 1740$ images (58 cell lines $\times$ 10 z-steps $\times$ 3 fluorophores) for a first-pass imaging run. Assuming that the field imaged approximately 30 cells per core and did not take advantage of the triplicate over-sampling on the array, this experimental design would require $58 \times 10 \times 3 \times 3 \times 5 = 26{,}100$ images even if it attempted to analyze only half of cells presented. Although this approach sounds overwhelming, it is what must be done to deliver useful information.

Automated high-content imaging offers the ability to interrogate thousands of cells, often for multiple responses, to collect a significant volume of data about them, and finally to derive meaning from this biological information The data generated by this class of microscopical scanners and applications, is in the terabyte (TB) range for many industrial applications and is stored in image databases, along with the resulting analytical data. Oracle/Web-object-based relational databases management systems (ORDMS) are the preferred solution for image data management, search, and analysis. Secondary image representations, made by subsampling or data compression, mainly serve Web-based viewing or control purposes and have been developed as part of solutions for the adequate handling and mining of such large datasets. The goal is automated analysis of assays without user intervention. Given the variations in staining and morphology inherent in cell populations, this is a more challenging task for HCS than for more simple endpoint assays in HTS.

The first step in automated imaging is to physically find the specimen, as well as the appropriate image planes for the sample, to identify targets of interest (tissue, cells, subcellular structures). No single slide (or plate) is absolutely flat and it should be expected that some adjustment will be required core to core/plate to plate to determine the imaging planes. This is followed by image capture in one/multiple fluorescence channels. The next step involves using a number of computational algorithms to segment the image into user-defined regions of interest (ROIs) such that each ROI represents a single cell or a compartment (e.g., nucleus, cytoplasm) within a cell from which the relevant biological information (changes in fluorescence intensity/pattern or spatial redistribution) can be extracted and quantified, either on-the-fly or offline. Real-time feedback provides information on the quality of the results, especially in kinetics assays.

Because individual cells are viewed, it is possible to separate (or gate) cells into different response categories (Boolean classification). Cells are grouped (cell classification) based on a number of cellular features (from one or multiple probes) such as overall fluorescence intensity, rate of rise/fall (for kinetics), area, object pixel statistics (average intensity, minimum, and maximum), and variation of pixel intensity within ROIs (e.g., granulation algorithm). Class of cells can be color-coded for easy visualization, and average measurements over a subset of cells can be taken. A well classification is then applied based on the number of cells that, in each well, meet a user-defined threshold. In turn, a response heat plate map that readily highlights cellular trends or hit compounds can be generated. This process enables to identify features that best reflect specific biological responses and, therefore, are good screenable parameters.

Typically, high-content, automated image analysis involves several user-defined, software-driven steps that are compiled into a template (or protocol) that is specific for each assay type (e.g., kinetics or endpoint, single dye or multiple dyes). Easy access to the templates allows users to modify preset parameters that might need day-to-day adjustment, such as camera exposure time, number/volume of drugs being delivered, time-course duration, image capture frequency, number/position of wells to be tested, and type of plates (96-, 384-well plate). Optimized imaging protocols and assay templates are stored (always in a re-settable format) for use in larger volume screening applications. Such protocols can be transferred to other imaging workstations ensuring coherent, standardization of image capture and analysis processes among multiple instruments. Robust analysis procedures that rely on the topology or pattern of cell organelles (see Chapters 15 and 47) and cells, and new object-oriented approaches are preferred solutions that have distinct advantageous over the prevailing pixel-oriented methods.

The kinetics and endpoint data generated by automated bioimagers are typically analyzed with proprietary software packages

that are either integrated with the system or are third-party analysis packages (e.g., ImagePro and Metamorph). Some packages, such as the BD Image Data Explorer (BD Bioscience) use customized database engines to store and access large, multi-dimensional data sets and apply sophisticated statistical routines to allow data visualization and analysis. Analysis programs allow one to quickly import raw data files from imaging workstations and associate them with drug treatment plate maps, containing information on the drug treatment that each well has received. In order to uncover artifacts or highlight rare events, software must be able to provide true **cell-by-cell** analysis rather than averaging cell response characteristics up front using **well-by-well** data.

Powerful data analysis programs can reduce large kinetics or endpoint image datasets into relevant pharmacological data. Data can then be compiled into informative reports that are archived with all the analysis steps included to maintain data integrity. Bar/line graphs, dose-response curves, EC_{50} , signal-to-noise ratio, *z*-scores, and other analysis tools useful to the assay developer and the cellular biologist/pharmacologist can be derived.

CONCLUSION

Automated HCS imaging instruments are hybrid instruments that bridge between low-throughput manual microscopes and high-throughput plate readers. At present, automated confocal imaging technologies mainly find their niche in target identification/validation and secondary drug screenings where the higher information content provided by single-cell imaging balances the limited volume throughput (relatively to HTS biochemical assay). Further refinement in hardware and software is expected to narrow the gap to produce an HTS imaging system capable to deal with primary screening efficiently.

The high-content, high-speed cytomics information yield of the disk-scanning confocal microscope makes it the imaging tool of choice to resolve multiple, distinctly labeled molecular targets in space and time, as they undergo quantitative (e.g., concentration) as well as qualitative changes (redistribution within cellular compartments) in single cells. With new automation, liquid handling, real-time capabilities, and the ability to manage multiple-well plates or cell-line–based tissue microarrays, confocal HCS systems are finding uses not only within the domain of the individual microscopist but in higher throughput (automated) imaging environments where thousands of cells are being quantitatively interrogated for multiple functional responses (Price *et al*., 2002; Giuliano *et al*., 2004; Perlman *et al*., 2004). As such, advanced confocal imaging technologies, amenable to scaling and automation, are opening new avenues in drug discovery and development, toxicology, and also in functional genomics and proteomics.

REFERENCES

Boland, M.V., and Murphy, R.F., 2001, A neural network classifier capable of recognizing the patterns of all major subcellular strauctures in fluorescence microscope images of HeLa cells, *Bioinformatics* 17:1231–1223.

Braunschweig, T., Chung, J.-Y., and Hewitt, S.M., 2004, Perspectives in tissue microarrays, *Comb. Chem. High Throughput Screen.* 7:575–586.

Cole, M.J., Pirity, M., and Hadjantonakis, A.-K., 2003, Shedding light on bioscience, *EMBO Rep*. **4:**838–843.

Comley, J., 2005, High content screening, emerging importance of novel reagents/probes and pathways analysis, *Drug Discovery World* 6(3): 31–53.

DeBernardi, M.A., and Brooker, G., 1998, Simultaneous fluorescence ratio imaging of cyclic AMP and calcium kinetics in single living cells, In: *Advances in Second Messenger and Protein Phosphorylation Research* (E.M.F. Cooper, ed.), Lippincott-Raven, Philadelphia, pp. 195–213.

Dove, A., 2003, Screening for content — The evolution of high throughput, *Nat. Biotechnol*. 21:859–864.

Gillespie, J.W., Best, C.J., Bichsel, V.E., Cole, K.A., Greenhut, S.F., Hewitt, S.M., Ahram, M., Gathright, Y.B., Merino, M.J., Strausberg, R.L., Epstein, J.I., Hamilton, S.R., Gannot, G., Baibakova, G.V., Calvert, V.S., Flaig, M.J., Chuaqui, R.F., Herring, J.C., Pfeifer, J., Petricoin, E.F., Linehan, W.M., Duray, P.H., Bova, G.S., and Emmert-Buck, M.R., 2002, Evaluation of non-formalin tissue fixation for molecular profiling studies, *Am. J. Pathol*. 160:449–457.

Giuliano, K.A., Chen, Y.-T., and Taylor, D.L., 2004, High content screening with siRNA optimizes a cell biological approach to drug discovery: Defining the role of p53 activation in the cellular response to anticancer drugs, *J. Biomol. Screen*. 9:557–568.

Hewitt, S.M., 2004, *Protein Microarrays: Methods and Protocols.* In: *Design, Construction and Use of Tissue Microarrays* (E. Fung, ed.), Humana Press, Totowa, New Jersey.

McMillian, M., Grant, E.R., Zhong, Z., Parker, J.B., Li, L., Zivin, R.A., Burczynski, M.E., and Johnson, M.D., 2001, Nile Red binding to HepG2 cells: An improved assay for *in vitro* studies of hepatosteatosis, *In Vitro Mol. Toxicol*. 14:177–190.

Perlman, Z.E., Slack, M.D., Feng, Y., Mitchison, T.J., Wu, L.F., and Altschuler, S.J., 2004, Multidimensional drug profiling by automated microscopy, *Science* 306:1194–1198.

Price, J.H., Goodacre, A., Hahn, K., Hodgson, L., Hunter, E.A., Krajewski, S., Murphy, R.F., Rbinovich, A., Redd, J.C., and Heynen, S., 2002, Advances in molecular labeling, high throughput imaging and machine intelligence portend powerful functional cellular biochemistry tools, *J. Cell Biol.* 39(Suppl.):194–210.

Taylor, D.L., Woo, E.S., and Giuliano, K.A., 2001, Real-time molecular and cellular analysis: The new frontier of drug discovery, *Curr. Opin. Biotechnol*. 12:75–81.

Valet, G., Leary, J.F., and Tarnok, A., 2004, Cytomics-new technologies: Towards a human cytome project, *Cytometry* 59A:167–171.

Vanek, P.G., and Tunon, P., 2002, High-throughput single-cell tracking in real time, *Genet. Eng. News* 22:34–38.

Watson, A., Wu, X., and Bruchez, M., 2003, Lighting up cells with quantum dots, *Biotechniques* 34:296–300.

Yarrow, J.C., Feng, Y., Perlman, Z.E., Kirchhausen, T., and Mitchison, T.J., 2003, Phenotypic screening of small molecules libraries by high throughput cell imaging, *Comb. Chem. High Throughput Screen.* 6:79–99.

47

Automated Interpretation of Subcellular Location Patterns from Three-Dimensional Confocal Microscopy

Ting Zhao and Robert F. Murphy

INTRODUCTION

Confocal microscopy has been widely used for biological studies because of its unique ability to acquire images free of most out-of-focus light. This property is critical for the acquisition of high-quality three-dimensional (3D) images of cells. Automated image analysis and data mining methods can be used to extract rich information contained in such images. In this chapter, we focus on describing effective methods for automatically interpreting 3D images of protein subcellular location patterns.

Protein Subcellular Location

Proteomics, the large-scale study of proteins, is the next big step in decoding genomes and achieving a thorough understanding of how living systems work. An important aspect of protein behavior is subcellular localization, and the field of *location proteomics* is concerned with systematically analyzing the complex processes by which proteins are localized within cells (Chen *et al*., 2003). Context provided by the location of a protein can help biologists infer possible functions. For example, a protein located exclusively in the plasma membrane may serve as a transporter or ion channel, while a cytoplasmic protein may act as a catalyst. Recent projects have described systematic approaches to the determination of protein location (Kumar *et al*., 2002; Dreger, 2003). However, objectively and quantitatively describing subcellular location patterns in cells using computational methods has not been emphasized.

Most computational studies on protein subcellular location are focused on prediction of locations from the protein sequence (Chou and Elrod, 1999; Chou and Cai, 2002; Park and Kanehisa, 2003; Bhasin and Raghava, 2004). These prediction methods became popular because of the rapid increase in the number of available protein sequences. However, a significant problem with using any prediction system is that none of the methods can give perfect accuracy. This creates the risk that the unverified predicted results may be misleading when they are relied upon by biologists. Furthermore, the low resolution of current prediction schemes prevents them from distinguishing proteins in the same organelle. They can only classify proteins at the predefined organelle level, that is, only 12 categories were used in a recent study to describe the organelles and compartments in an animal or plant cell (Chou and Elrod, 1999). Not only can two proteins that reside in different subcompartments of the same organelle not be distinguished, but minor (or previously unrecognized) patterns cannot be recognized and proteins that show mixed patterns (e.g., residing in more than one organelle or moving from one to another) may not be recognized correctly.

Combining the rapid developments of microscope imaging techniques in biology with advances in image analysis and machine learning, we have over the past few years developed automated systems to analyze the subcellular distributions of proteins quantitatively and precisely at high resolution (Boland *et al*., 1997, 1998; Boland and Murphy, 2001; Huang *et al*., 2003; Murphy *et al*., 2003; Huang and Murphy, 2004b). Fluorescence microscopy is the most common method to experimentally determine subcellular location because it has much higher resolution than subcellular fractionation, and because, unlike electron microscopy, it permits rapid imaging of living cells.

Overview of 2D Dataset Analysis

From 2DCHO to 2DHeLa

Our work on automatic analysis of subcellular location patterns started with two-dimensional (2D) images, initially of five patterns in Chinese hamster ovary cells (the *2DCHO* dataset) and subsequently of 10 patterns in HeLa cells (the *2DHeLa* dataset). The quantitative description and classification of the *2DCHO* dataset opened up the area of systematic analysis of protein subcellular location (Boland *et al*., 1997, 1998). By using four primary antibodies, directed against the Golgi protein giantin, the lysosome protein LAMP2, the yeast nucleolar protein NOP4, tubulin, and a DNA stain, five classes of subcellular location patterns were created. After preprocessing steps including deconvolution, segmentation, and background subtraction, 49 Zernike moments and 13 Haralick texture features were calculated as features for each image. The Zernike moments represent the decomposition of an image into 2D polynomials and the Haralick features capture statistical properties of intensity distribution in neighboring pixels. Using these two sets of features, both global information and local information of an image will be captured. Ten of the 62 features were selected by stepwise discriminant analysis (SDA) and input into a single hidden-layer back-propagation neural network (BPNN). An average classification accuracy of 88% was obtained, demonstrating the initial feasibility of the application of image analysis and pattern recognition methods to subcellular location patterns.

Encouraged by the good results, a more thorough study was carried out on the *2DHeLa* dataset (Boland and Murphy, 2001). This covered most major organelles in animal cells (Fig. 47.1). In this dataset, HeLa cells were labeled for one of nine proteins and in parallel labeled with the DNA intercalating dye 4′,6-diamidino-2

Ting Zhao and Robert F. Murphy • Carnegie Mellon University, Pittsburgh, Pennsylvania 15213

 Handbook of Biological Confocal Microscopy, Third Edition, edited by James B. Pawley, Springer Science+Business Media, LLC, New York, 2006.

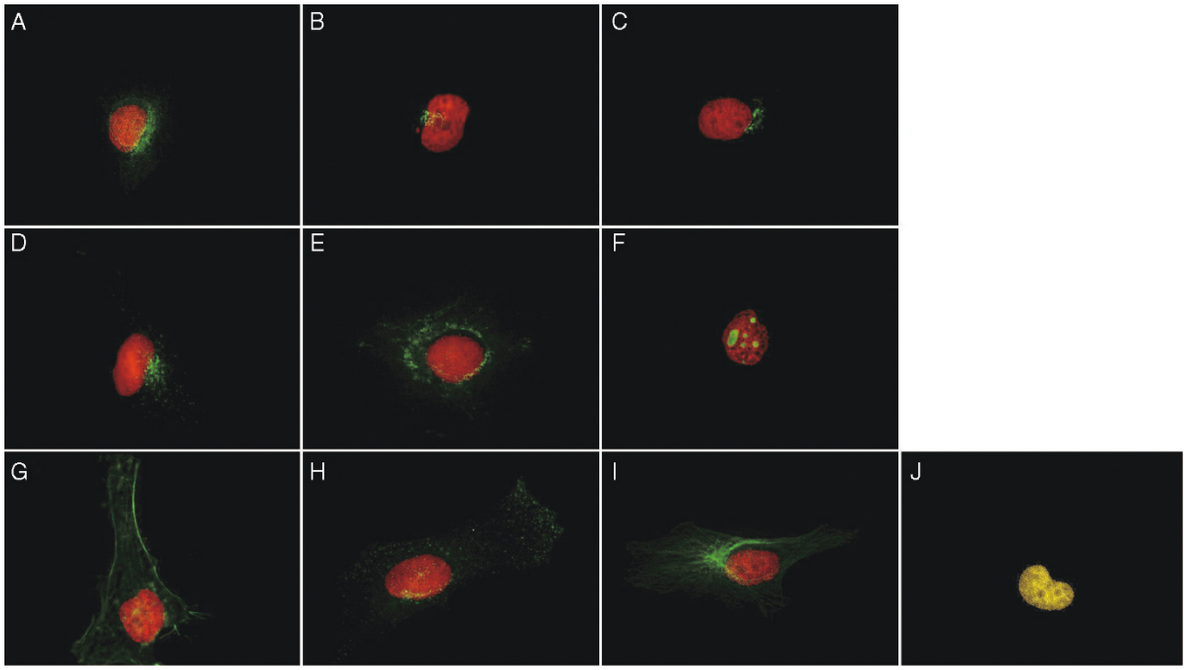


FIGURE 47.1. Typical images from the *2DHeLa* dataset (Boland and Murphy, 2001). The 10 classes are an ER protein (A), the Golgi protein giantin (B), the Golgi protein GPP130 (C), the lysosomal protein LAMP2 (D), a mitochondrial protein (E), the nucleolar protein nucleolin (F), the endosomal protein transferrin receptor (H), the cytoskeletal proteins filamentous actin (G) and tubulin (I), and DNA (J).

phenylindole dihydrochloride (DAPI). Seven of the proteins are located in organelles (endoplasmic reticulum, Golgi complex, lysosome, mitochondria, nucleolus, and endosome), with two of them in the same organelle, the Golgi complex. These two patterns were included to test whether automated methods could distinguish them. The other two proteins are found in cytoskeletal structures (filamentous actin and tubulin). A tenth class was created by considering the parallel DNA images as a class.

2D Subcellular Location Features

The Zernike moment features and Haralick texture features were found to be insufficient to describe all of the patterns in the *2DHeLa* dataset, and other types of measures were therefore implemented. We also implemented a standard nomenclature for referring to features and sets of features so that each result could be associated with the features used to create it (Boland and Murphy, 2001). Each set was referred to by the prefix SLF (for subcellular location features) followed by a number (e.g., SLF1) and each feature within a set was referred to by the set number and an index within it (e.g., SLF1.7).

The subcellular location features (SLF) can be divided into different subsets according to their properties (Table 47.1). SLF1 consists of eight morphological features, five edge-related features, and three convex hull features. These correspond roughly to attributes of patterns typically recognized by cell biologists. SLF2 is formed by adding six DNA-related features to SLF1. The DNA-related features provide the ability to distinguish similar patterns that differ in their proximity to the nucleus. For example, nucleolin can be easily distinguished from other proteins using these DNA-related features. SLF3 is the union of SLF1 with the 49 Zernike moment features and 13 Haralick texture features. SLF4 is the union of SLF3 and the six DNA related features.

TABLE 47.1. Brief Description of 2D Subcellular Location Features

Set	Size	SLF Index	Feature Description
SLF1	16	SLF1.1–1.8	Morphological features
		SLF1.9–1.13	Edge-related features
		SLF1.14–1.16	Convex hull features
SLF2	22	SLF2.1–2.16	SLF1.1–1.16
		SLF2.17–2.22	DNA-related features
SLF3	78	SLF3.1–3.16	SLF1.1–1.16
		SLF3.17–3.65	Zernike moment features
		SLF3.66–3.78	Haralick texture features
SLF4	84	SLF4.17–4.22	SLF2.17–2.22
		SLF4.1–4.16, 4.23–4.84	SLF3.23–3.78
SLF5	37	SLF5.1–5.37	Selected from SLF4 using SDA
SLF6	65	SLF6.1–6.65	SLF3.1–3.65
SLF7	84	SLF7.1–7.9	SLF3.1–3.9
		SLF7.10–7.13	Minor corrections to SLF3.10–3.13
		SLF7.14–7.65	SLF3.14–3.65
		SLF7.66–7.78	Modified Haralick texture features
		SLF7.79	The fraction of cellular fluorescence not included in objects
		SLF7.80–7.84	Skeleton feature
SLF8	32	SLF8.1–8.32	Selected from SLF7 using SDA
SLF12	8	SLF12.1–2.8	SLF8.1–8.8
SLF13	31	SLF13.1–13.31	Selected from SLF7 and SLF2.17–2.22 using SDA
SLF15	44	SLF15.1–15.44	Selected from SLF7 and 90 Gabor and wavelet features
SLF16	47	SLF16.1–16.47	Selected from SLF7, 90 Gabor and wavelet features and SLF2.17–2.22

It is often the case that features anticipated to be valuable for a given classification problem turn out to have little or no useful information. In this case, their presence can actually hinder the performance of a classifier. One approach to this problem is to select an informative subset of all available features, and we have found that the stepwise discriminant analysis (SDA) method performs very well for our purposes (Huang *et al*., 2003). Thus, some SLF sets have been created by selecting informative features from one of the larger sets (e.g., SLF5 was selected from SLF4).

The 13 Haralick texture features are sensitive to image pixel resolution and number of gray levels. To permit the features to be compared for images at different resolutions, a set of improved texture features were defined by first downsampling each image to 1.15 µm/pixel and 256 gray levels. This resulted in a new feature set, SLF7, that consists of SLF3 (with the 13 improved texture features) and six new features that capture the fraction of cellular fluorescence not included in objects and object morphology as reflected in object skeletons.

To provide further information, a set of 90 features calculated by transforming an image into the frequency domain was added. These features were calculated based on the Gabor transformation and the wavelet transformation. Subsets of these features (either with or without the DNA features) were also selected (SLF15 and SLF16).

Classification Results for 2*DHeLa* Dataset

The effectiveness of the SLF for describing subcellular patterns can be evaluated by training and testing classifiers. With good features, different patterns should be distinguished reasonably by a well-trained classifier. A feature set that gives better classification performance is more suitable for describing location patterns.

Since the introduction of the first SLF sets, we have explored additional feature sets and various classification approaches for the *2DHeLa* images. The most common classifier we have used was a BPNN with one hidden layer and 20 hidden nodes (the same architecture used for the *2DCHO* data). Table 47.2 shows that classification accuracy increased when more features were added (SLF2, SLF3, SLF4). However, fewer features can give higher accuracy if they are carefully selected (Huang *et al*., 2003; Murphy *et al*., 2003). SLF5 selected from SLF4 by SDA has fewer features than SLF4, but the classification accuracy is higher. Similarly, SLF8 and SLF13 gave better performance than SLF7.

Another way to increase the classification accuracies is to improve the classifiers. We have therefore compared the performance of eight different classification methods on the *2DHeLa* dataset (Huang and Murphy, 2004b). The results showed that ensemble methods increased the classification accuracy significantly. The best classification accuracy on SLF8 was achieved by Adaboost (88%), a method that keeps modifying the training set based on how well they can be classified by a base classifier. For SLF13, Mixture-of-Experts was the most suitable one among the eight classifiers (90%). This classifier can improve performance by separating the training set into many partitions. The eight classifiers can further be combined to organize optimal majority-voting ensembles. The highest accuracy on *2DHeLa* to date was achieved by such an ensemble on SLF16 (92%).

TABLE 47.2. Average Classification Accuracy of Different SLF Sets and Classifiers on the *2DHeLa* Dataset

Set	DNA	SDA from	Classifier	Accuracy
SLF2	Yes	—	BPNN	76%
SLF3	No	—	BPNN	79%
SLF4	Yes	—	BPNN	81%
SLF5	Yes	SLF4	BPNN	83%
SLF7	No	—	BPNN	74%
SLF8	No	SLF7	BPNN	86%
SLF8	No	SLF7	AdaBoost	88%
SLF13	Yes	SLF7	BPNN	88%
SLF13	Yes	SLF7	MOE	90%
SLF16	Yes	SLF7 + Gabor + wavelet	MVE	92%

The classifiers used included back-propagation neural network (BPNN), mixture-of-experts (MOE), and majority voting ensemble (MVE).

HIGH-RESOLUTION 3D DATASETS

Since the automated interpretation of the 2D images was shown to be successful, the next step was to extend the analysis to 3D images.

3DHeLa

The *3DHeLa* dataset was used to demonstrate the advantages of 3D images. Therefore all patterns used in *2DHeLa* are included in *3DHeLa* to make the results from two datasets comparable (Fig. 47.2).

HeLa cells were stained and imaged by a three-laser confocal scanning microscope. The dataset includes the same nine proteins as in *2DHeLa* and there are 50 to 52 3D images in each class. In addition to a DNA channel for each image, a channel measuring total protein was acquired at the same time (by adding reactive Cy5 dye to label all proteins non-specifically). This resulted in three-color 3D images. The benefits of acquiring the two additional channels are that (1) the two channels can be used to automatically isolate individual cells, (2) the DNA channel can be used for calculating additional features, and (3) a tenth and eleventh class could be created by adding images from the DNA channel (class *DNA*) and images from the total protein channel (class *Cytoplasmic*) to the nine classes of proteins.

For each 3D image, 14 to 24 2D slices were acquired at a *z*- (axial) interval of 0.203 µm. The in-plane intervals between neighboring voxels were 0.049 µm.

3D3T3

An additional source of 3D images is the CD-tagging project, which has created a demonstration database for a number of randomly tagged proteins in NIH 3T3 cells (http://cdtag.bio.cmu.edu/www/public/). By randomly inserting a green fluorescent protein (GFP)-encoding exon into the genome of a cell using a retroviral vector, a different protein can be tagged in many different cells. For the demonstration project, 90 different clones were isolated and the identity of the tagged gene was determined by real-time polymerase chain reaction (RT-PCR) sequencing and genome database searches. For each clone, a number of 3D images were acquired from living cells by spinning-disk confocal microscopy (no parallel channels for DNA and total protein were acquired). Eight to 33 images were collected for each clone, with each image consisting of 1024 × 1024 × 31 voxels and each voxel corresponding to a 0.11 µm × 0.11 µm × 0.5 µm region of the sample. (See Fig. 47.3.)

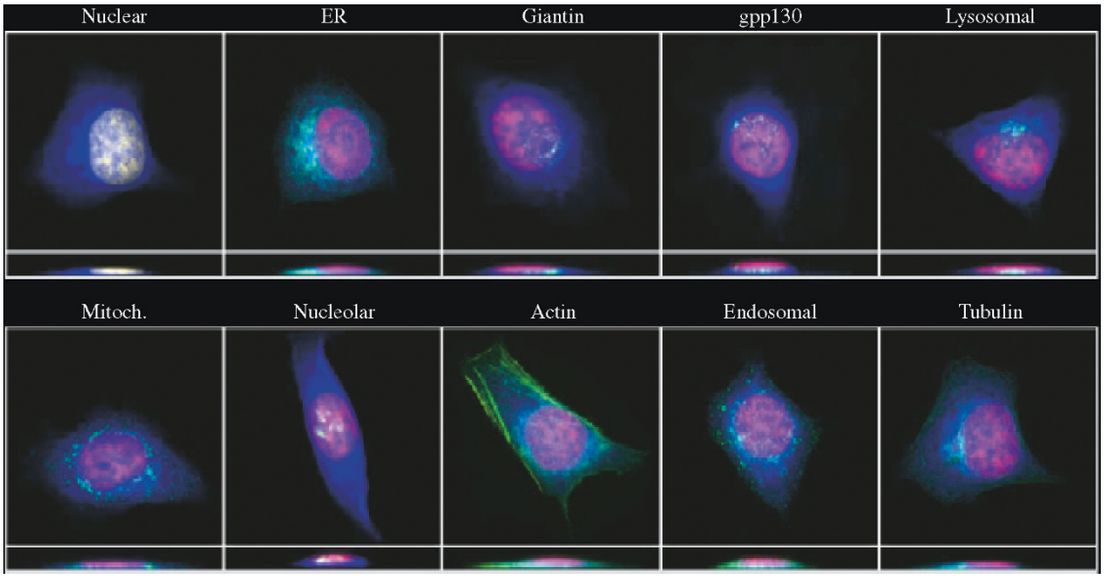


FIGURE 47.2. Typical three-color images from the *3DHeLa* dataset. Red, DNA channel; blue, total protein channel; green, protein channel. (Reprinted by permission of Carnegie Mellon University.)

Image Acquisition Considerations When Using Automated Analysis

Although the whole analysis procedure can be automated, the performance is influenced by how images are acquired. Some important points must be considered in image acquisition to get valid results.

1. In each image there should be at least one whole cell. The SLF are defined to capture information on whole, individual cells, and features from a partial cell might be very different from the features of the expected pattern. For 3D images, the slices should cover the top and bottom of the cell. Some microscopes provide axial range scanning to help decide the range of scanning. For those that don't, ensuring that the number and position of the slices are appropriate is critical.

2. If possible, cells being imaged should be well separated from each other to facilitate automated segmentation. As for a partial cell, the features of a region containing more than one cell are expected to be different from those of single cells.

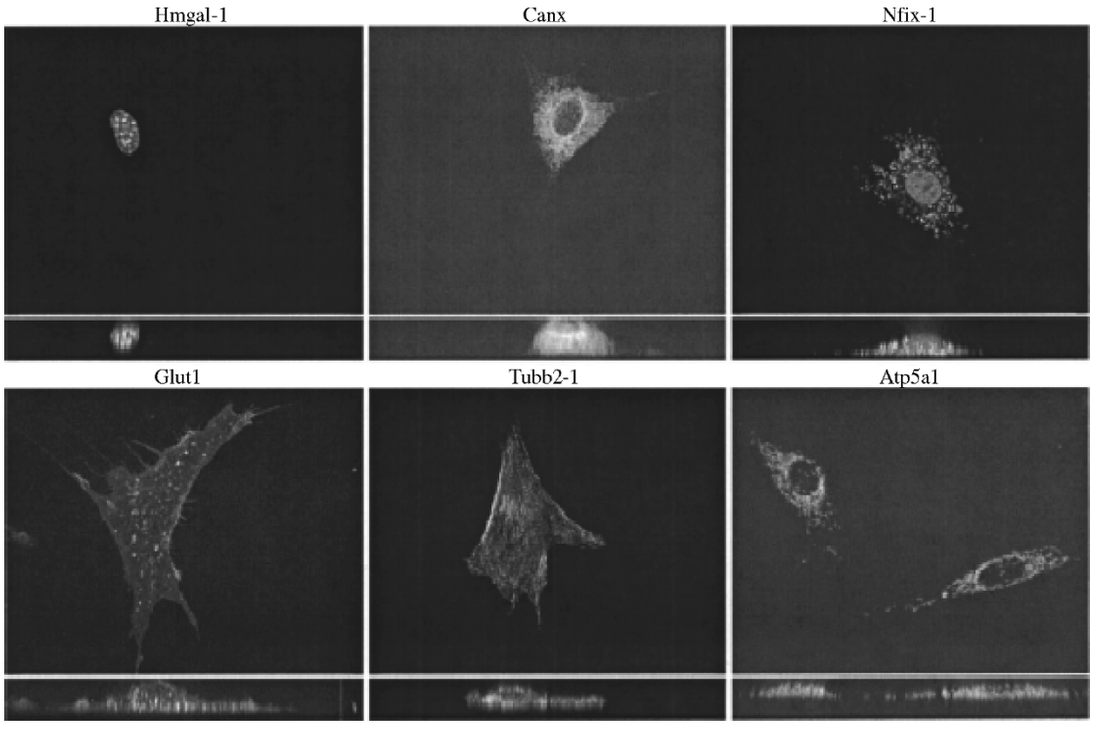


FIGURE 47.3. Example images from the *3D3T3* dataset. (Reprinted by permission of Carnegie Mellon University.)

3. Higher resolution is more desirable. An obvious reason of using higher resolution is that more information can be acquired. The Rayleigh criterion indicates that the resolution is decided by the transmitted wavelength and the numerical aperture of the objective that is used. Because the range of wavelengths is limited, the major consideration is to use an objective with a numerical aperture as large as possible. This is especially important for increasing the axial resolution because it is inversely proportional to the square of numerical aperture.

4. Sampling should be sufficient to capture as much information as possible. The two factors are the voxel dimensions and the number of gray levels in an image. The voxel size in the sample plane is determined by the total magnification and the spacing between pixels on the camera. An image with smaller physical size of each pixel shows finer structure of a location pattern and thus its feature values are more informative. However, the amount of information that can be obtained is limited. A common criterion is to use Nyquist sampling, or sampling at one half of the resolution from the Rayleigh criterion. For 520 nm light and a numerical aperture of 1.3, the Rayleigh limit is 0.244 μm. Additional magnification before the camera may be required to sample at half this value. Given the large dynamic range found in the distribution of many proteins, using a detector with greater than 8-bit image depth is also very valuable.

5. The number of images in each class should be sufficient to describe the variation of the pattern. The details of images in the same pattern are all different because of variations in size, shape, and cellular environment of each individual cell. The ability of numerical features to describe location patterns depends on how well the range of variations is covered. Because essentially all classification and clustering methods are statistical approaches, sufficient data are required to get significant results.

6. Imaging conditions should be kept as unchanging as possible. Most subcellular location features are sensitive to imaging conditions such as the objective used and exposure time. Although normalization steps can decrease such sensitivities, it is always more desirable to avoid such problems at the data acquisition step.

7. It is desirable to acquire parallel channels measuring DNA and total protein. These channels can facilitate isolating individual cells. They can also be used to develop location features because they carry information of cell morphology.

IMAGE PROCESSING AND ANALYSIS

The most critical step of automatic interpretation is the extraction of features from images. These features should be insensitive to cell rotation and translation. If images from more than one source (e.g., different microscopes) are to be analyzed together, the features should also be defined in such a way as to compensate for these differences. The procedure for moving from images to features is described in Figure 47.4.

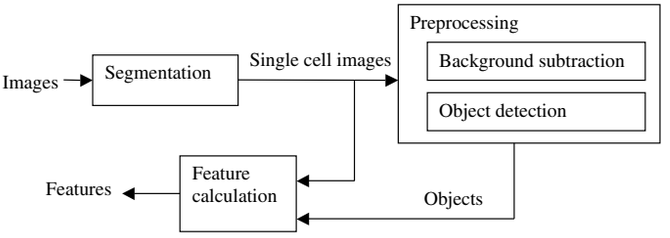


FIGURE 47.4. Feature calculation process.

Segmentation of Multi-Cell Images and Preprocessing

After acquiring images, preprocessing steps are necessary before feature calculation. The most important step is image segmentation, which is used to isolate individual cells from a multi-cell image. Without this step, features defined on individual cells cannot be extracted correctly. It is hard to work on the targeted protein image directly to isolate cells because we do not know how many cells there are in a particular image, and the locations of the cell boundaries relative to the targeted protein depend on which pattern the image contains. A segmentation method that is suitable for one pattern may fail for another. Fortunately, acquiring two more channels, DNA and total protein, make this problem much easier. Nuclei can easily be detected in the DNA channel by thresholding. Small, non-nuclear objects resulting from this thresholding can be easily removed by setting a second threshold on size or integrated intensity. Knowing how many cells are present and where their nuclei are greatly simplifies the problem.

With this information, a seeded watershed method (Lotufo and Falcao, 2000) can be applied. The nuclei are used as seeds and the total protein image is used to find cell boundaries. In our case, the seeded watershed algorithm was implemented by the *mmcwatershed* function from the SDC Morphology Toolbox for MATLAB (SDC Information Systems, Naperville, IL). The output from the function is a set of masks (binary images showing each separated region), each of which corresponds to one cell (and one original seed). It is possible that partial cells will be included, and therefore a criterion based on the distance to the image edge is used to remove partial cells.

By watershed segmentation, 50 to 58 individual cell images per class were obtained from the 50 to 52 original images per class acquired for the *3DHeLa* dataset. However, this segmentation method cannot be applied to the *3D3T3* dataset because there are no available images for the DNA or the total protein channel. Instead, manual segmentation was used.

After finding masks for segmentation, the following steps of preprocessing are the same for both *3DHeLa* and *3D3T3*:

1. Background fluorescence is subtracted from each image. This is done by subtracting the most common pixel value for each image from the values of all pixels and then setting any negative values in the subtracted image to 0. Some type of background correction is needed so that integrated fluorescence intensities properly reflect the fraction of cell fluorescence occupied by each object. The background correction is done before masking the image to isolate individual cells so that it can better reflect the global background (some masked regions may have no background pixels in them).

2. The segmentation masks are applied to each slice in the same 3D image.

3. An automated thresholding method (Ridler and Calvard, 1978) is used.

3D Subcellular Location Features

Subcellular location features (SLF) sets have been shown to be successful for describing 2D images, therefore, a set of 3D SLF were defined on 3D images by extending the 2D SLF. Each 3D

image is composed of several 2D slices with the same size. The extension from 2D SLF to 3D SLF relies on the differences between a voxel and a pixel. First, a voxel is located in a 3D space and has three coordinates, two for the lateral plane and one for the vertical axis. Second, each voxel has 26 adjacent voxels while a pixel has only 8 neighbors. This is especially important for detecting an object.

Three categories of 2D SLF have been extended. They are morphological features, edge features, and texture features.

Morphological Features

These features compose the first set, SLF9, that was used for classifying 3D location patterns (Velliste and Murphy, 2002). SLF9.1–14 are morphological features extended from 2D SLF1.1–8 and SLF2.17–22. For this purpose, objects were defined as a contiguous set of above-threshold pixels (using 26-neighbor connectivity). The features were defined as:

SLF9.1: The number of fluorescent objects in the image.
SLF9.2: The Euler number of the image. This is the difference between number of objects and number of holes in the image.
SLF9.3: The average object size. The size of an object is defined as the number of voxels in the object.
SLF9.4: The standard deviation of the object size.
SLF9.5: The ratio of size of the largest object to the smallest.
Note: SLF9.3–9.5 describe the statistical distribution of object size in a cell.
SLF9.6: The average object distance to the center of fluorescence (COF).
SLF9.7: The standard deviation of object distances from the COF.
SLF9.8: The ratio of the largest to the smallest object to COF distance.
Note: SLF9.6–9.7 describe the spatial distribution of objects in a cell.
SLF9.9: The average object distance from the COF of the DNA image.
SLF9.10: The standard deviation of object distances from the DNA COF.
SLF9.11: The ratio of the largest to the smallest object to DNA COF distance.
Note: SLF9.9–9.11 describe the spatial distribution of objects relative to the nucleus in a cell.
SLF9.12: The distance between the protein COF and the DNA COF.
SLF9.13: The ratio of the volume occupied by protein to that occupied by DNA.
SLF9.14: The fraction of the protein fluorescence that colocalizes with DNA.

SLF9.15 to SLF9.28 were designed to describe the in-plane and axial distribution of the protein. This is especially useful for polarized cells. The membranes of these cells are divided into sides, apical, and basolateral domains. They contact different environments and some proteins must be localized to one of the two domains to carry out their function. For example, the physiologic properties of transporting epithelia are determined by the polarized distributions of ion transporters (Muth and Caplan, 2003). For non-polarized cells, the vertical distribution is also significant because they can become polarized when attaching to a surface to grow.

SLF9.15: The average horizontal distance of objects to the protein COF.
SLF9.16: The standard deviation of object horizontal distances from the protein COF.
SLF9.17: The ratio of the largest to the smallest object to protein COF horizontal distance.
SLF9.18: The average vertical distance of objects to the protein COF.
SLF9.19: The standard deviation of object vertical distances from the protein COF.
SLF9.20: The ratio of the largest to the smallest object to protein COF vertical distance.
SLF9.21: The average object horizontal distance from the DNA COF.
SLF9.22: The standard deviation of object horizontal distances from the DNA COF.
SLF9.23 The ratio of the largest to the smallest object to DNA COF horizontal distance.
SLF9.24: The average object vertical distance from the DNA COF.
SLF9.25: The standard deviation of object vertical distances from the DNA COF.
SLF9.26: The ratio of the largest to the smallest object to DNA COF vertical distance.
SLF9.27: The horizontal distance between the protein COF and the DNA COF.
SLF9.28: The signed vertical distance between the protein COF and the DNA COF.

Edge Features

Edge features were originally developed for the *2DHeLa* dataset to distinguish proteins distributed along long and thin edges from other proteins. For convenience, two edge features were added to 3D SLF by a small modification. Edge detection was performed in each of the 2D slices instead of using a 3D edge-detection method (so that the different resolution of the lateral plane and axial axis does not have to be considered). The Canny method (Canny, 1986) was used for edge detection because it is less sensitive to noise than some other methods.

The two edge features were added to SLF9.1–9.8 and SLF9.15–9.20 to create SLF11:

3D-SLF11.15 The fraction of above-threshold pixels that are along an edge.
3D-SLF11.16 The fraction of fluorescence in above-threshold pixels that are along an edge.

Texture Features

The extension of texture features to 3D requires calculating a co-occurrence matrix in 13 directions because each pixel has 26 neighbors. The mean and range over all 13 directions were calculated for each statistical property of the co-occurrence matrix. This resulted in 26 texture features for each image:

SLF11.17/30 Average/range of angular second moment.
SLF11.18/31 Average/range of contrast.
SLF11.19/32 Average/range of correlation.
SLF11.20/33 Average/range of sum of squares of variance.
SLF11.21/34 Average/range of inverse difference moment.
SLF11.22/35 Average/range of sum average.
SLF11.23/36 Average/range of sum variance.
SLF11.24/37 Average/range of sum entropy.
SLF11.25/38 Average/range of entropy.
SLF11.26/39 Average/range of difference variance.
SLF11.27/40 Average/range of difference entropy.
SLF11.28/41 Average/range of info measure of correlation 1.
SLF11.29/42 Average/range of info measure of correlation 2.

AUTOMATED CLASSIFICATION OF LOCATION PATTERNS

The task of classification is to automatically recognize the pattern of an image. The SLF of images whose pattern is known can be used to train a classifier to recognize an image whose pattern is not known (a service called Subcellular Localization Image Classifier, or SLIC, is available on our Web site at http://murphylab.web.cmu.edu/services/PSLID/). The output of the classifier can only be one of the predefined patterns. So, if we want a classifier to recognize a new pattern, the classifier must be fed with a training set corresponding to the new pattern.

Classification of 3DHeLa Dataset

Feature Normalization

Normalization was performed for all features before feeding them into a classifier. This was done by translation and scaling so that each feature has the mean 0 and variance 1. Otherwise, some features will dominate others during calculation. For example, the number of objects in an image (SLF9.1) can be thousands, but the two edge features are all between 0 and 1. Although no additional information was generated after feature normalization, this step is helpful for training the classifier. Some classifiers like a neural network tend to look for borders in the subspace of dominant features even if these are not good for distinguishing classes. Because the features were divided into a training set and a test set, the normalization factors should be calculated on the training set and then the same factors are used to normalize the test set.

Feature Selection

As discussed above, a very useful procedure at the feature level is feature selection. As shown in 2D classification, more features do not necessarily mean higher classification accuracy. Besides requiring a longer time for training, a classifier may overfit with some noisy features. SDA can be used to deal with this problem by finding a feature subspace in which different classes are well separated while, at the same time, samples from the same class are close to each other. The measurement of this property is defined as the ratio of the within-group covariance matrix to the among-group covariance matrix. The SDA was implemented by the stepdisc function of SAS (SAS Institute, Cary, NC) with default parameter values. The feature set SLF10 is composed of 14 features selected from SLF9 by SDA.

Classification Results

As was done for the *2DHeLa* dataset, we have evaluated different feature sets and classifiers. At first SLF9 and a BPNN with one hidden layer and 20 hidden nodes was compared with classification results from SLF2. This resulted in 91% accuracy, which is higher than the counterpart of 2D classification (76%) and close to the best 2D results (92%). When an eleventh cytoplasmic pattern was added, the classification on the 11 classes was also 91%.

As expected, higher accuracy was obtained when SLF10, selected by SDA from SLF9, was used. This feature set gave 95% accuracy averaged over 10-fold cross-validation (Huang and Murphy, 2004b) using the same classifier. The best classification accuracy (96%, Table 47.3) on the feature set was achieved using an optimal majority-voting ensemble classifier, in which the eight base classifiers were the same as those used on *2DHeLa*.

Downsampled Images with Different Gray Scales

There are two motivations for exploring downsampling and gray-scale binning before calculating texture features. The first is that this is a step to normalize images from different sources. The second is that this may improve the texture features by focusing on the most appropriate spatial frequencies. Texture features calculated at three different pixel resolutions (0.2, 0.4, 1.0 μm) and three different numbers of gray levels (16, 64, 256) have been explored (Chen and Murphy, 2004). To evaluate the contribution of texture features under different conditions, results from different features were compared. We found that higher resolution and more gray levels tend to give better performance (Table 47.4). Figure 47.5 shows the changes of classification accuracy with number of features. Each curve corresponds to a specific feature set. Surprisingly, one of the best classification accuracies was achieved by only seven features (Table 47.5), that were then defined as SLF17. The average accuracy was 98% (Table 47.6), which is the most accurate classification that has ever been obtained. This means that the 10 patterns can be well described in a 7D space, which even has fewer degrees of freedom than the number of the patterns.

TABLE 47.3. Confusion Matrix for Classification of 11 Classes of *3DHeLa* Images Using the Feature Set SLF10

	Output of the Classifier (%)										
True Class	Cyt	DNA	ER	Gia	GPP	LAM	Mit	Nuc	Act	TfR	Tub
Cytoplasmic	**100**	0	0	0	0	0	0	0	0	0	0
DNA	0	**98**	0	0	0	0	0	2	0	0	0
ER	0	0	**97**	0	0	0	0	0	2	0	2
Giantin	0	0	0	**98**	0	2	0	0	0	0	0
GPP130	0	0	0	4	**96**	0	0	0	0	0	0
LAMP2	0	0	0	2	2	**96**	0	0	0	0	0
Mitochondria	0	0	0	4	0	0	**95**	0	2	0	0
Nucleolin	0	0	0	0	0	0	0	**100**	0	0	0
Actin	0	0	2	0	0	0	2	0	**95**	2	0
TfR	0	0	0	0	0	6	4	0	2	**85**	4
Tubulin	0	0	4	0	0	0	0	0	0	2	**94**

The results are averages over 10-fold cross-validation trials on an optimal majority-voting ensemble classifier. The overall average accuracy was 96%. (Data from Huang and Murphy, 2004b.)

TABLE 47.4. The Contents of Each Cell in the Table Are the Net Increase in Percentage Accuracy Over a Classifier Using No Texture Features

Pixel resolution	Number of gray levels		
	256	64	16
0.2 µm	7.7 (16)	5.5 (22)	4.7 (15)
0.4 µm	7.5 (7)	5.3 (18)	3.8 (34)
1.0 µm	3.8 (28)	2.6 (23)	0.1 (10)

The number included in each parenthesis is the number of features selected by SDA. [Data from Chen and Murphy (2004).]

TABLE 47.5. The Seven Features in SLF17 that Give 98% Classification Accuracy on the *3DHeLa* Dataset

SLF9.4	The standard deviation of object volumes
SLF11.16	The fraction of fluorescence in above threshold pixels that are along an edge
SLF11.21	The average inverse difference moment
SLF11.27	The average difference entropy
SLF11.28	The first average information measure of correlation
SLF11.40	The range of the first information measure of correlation
SLF11.42	The range of the second information measure of correlation

CLUSTERING OF LOCATION PATTERNS: LOCATION PROTEOMICS

One goal of proteomics is to study the relations between proteins and group them into meaningful categories. This has been done at the sequence level by sequencing all proteins and clustering them hierarchically according to their sequence similarity. For location proteomics, the clustering should be done by their localization similarity. Our work on automated interpretation of confocal microscope images of cellular proteins allows us to do this, given sets of images for large numbers of proteins. The approaches we have used are described below for the images in the *3D3T3* dataset. We refer to a cluster tree representing a set of subcellular location patterns as a subcellular location tree (SLT).

Exclusion of Outliers

To measure the similarity between the locations of two proteins, their images must be acquired under similar conditions. These conditions include not only the parameters of the imaging conditions, but also the state of the cells. To describe the typical location pattern of a protein, images of normal interphase cells are usually preferred. But biologists may want to randomly choose cells for imaging to avoid observer bias. So some unusual examples of a pattern were included in the *3D3T3* dataset. Cells in these images include dead cells, dying cells, cells just before mitosis, and cells just after cytokinesis. The influence of the outliers increases with their fraction in the whole dataset. Because of the small size of the *3D3T3* dataset (8–33 images per class), there is high risk that the outliers will bias the clustering results. Therefore, the outliers were removed by a stringent procedure discussed below.

Determination of Optimal Clustering

A number of algorithms and distance functions have been used for clustering. Because different feature sets and distance functions result in different clusters or trees, it is necessary to determine which one is the best. A simple way is to visually inspect the tree and determine how consistent it is with biological knowledge and the visual interpretation of the images. However, empirical evaluation is impractical while there are so many classes in the data (or when not all of the protein patterns are known!). Some measurement of goodness should be defined to automate the process. The basic criterion is having enough partitions to separate all distinguishable patterns while at the same time keeping indistinguishable patterns in the same group. The trade-off implies the existence of an optimal partitioning.

As a starting point, all of the *3D3T3* images were clustered by the unsupervised *k*-means method with varying cluster numbers. The optimal cluster number was decided using the Akaike Information Criterion (AIC), which balances the fitness and simplicity of the model represented by the clusters. The results showed that the optimal number of clusters was 17. They also showed that three of the 3T3 clones had their images spread over a number of clusters. We interpreted this as evidence that these clones were either not pure cell lines or that the tagged protein varied extensively in location (perhaps as a function of cell cycle). These 3 clones were therefore removed and all further studies were based on the 87 clones. These initial clustering results were also used to remove outliers: images that were not contained in the major cluster of each clone were removed from consideration.

When all data are used to build a cluster tree, the tree structure can be very dependent on which particular examples from a

TABLE 47.6. Confusion Matrix for Classification of 11 Classes of *3DHeLa* Images Using the Feature Set SLF17

True Classification	Output of the Classifier (%)									
	DNA	ER	Gia	GPP	LAM	Mit	Nuc	Act	TfR	Tub
DNA	**98**	2	0	0	0	0	0	0	0	0
ER	0	**100**	0	0	0	0	0	0	0	0
Giantin	0	0	**100**	0	0	0	0	0	0	0
GPP130	0	0	0	**96**	4	0	0	0	0	0
LAMP2	0	0	0	4	**95**	0	0	0	0	2
Mitochondria	0	0	2	0	0	**96**	0	2	0	0
Nucleolin	0	0	0	0	0	0	**100**	0	0	0
Actin	0	0	0	0	0	0	0	**100**	0	0
TfR	0	0	0	0	2	0	0	0	**96**	2
Tubulin	0	2	0	0	0	0	0	0	0	**98**

The results are averages over 10-fold cross-validation trials on a BPNN classifier with one hidden layer and 20 hidden nodes. The overall average accuracy was 98%. [Data from Chen and Murphy (2004).]

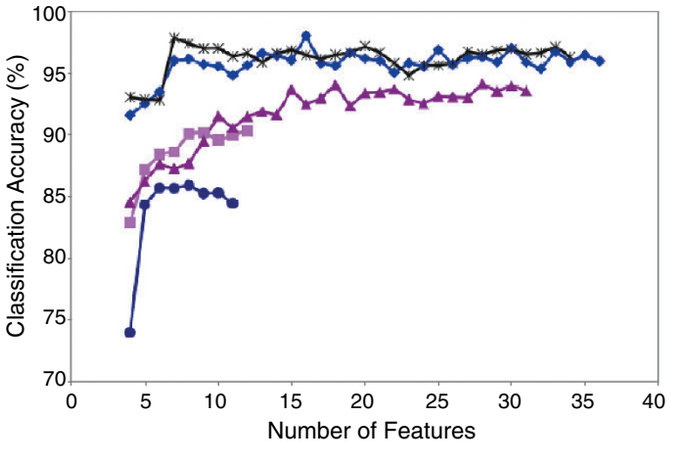


FIGURE 47.5. Classification accuracy over 10 major classes in *3DHeLa* dataset. Each curve represents one of five subsets of SLF11, morphological features only (*closed circle*), morphological and edge features (*closed square*), and morphological, edge, and texture features computed at 256 gray levels and different pixel resolutions: 0.2 μm (*closed diamond*), 0.4 μm (*), and 1.0 μm (*closed triangle*). [Data from Chen and Murphy (2004).]

cluster are present. Therefore, rather than building one tree, we have constructed many trees from random subsets of the images for each clone. The common properties of these trees were extracted to form a consensus tree (Chen and Murphy, 2005). In order to convert the tree into a specific number of clusters, we assumed that the number of clusters obtained by *k*-means/AIC analysis, 17, was correct and cut the consensus tree accordingly.

Many clustering methods use some distance function to measure which observations are similar to each other and should be grouped. As a criterion to choose an optimal distance function, we reason that a good distance function should give consistent results from different clustering methods (Chen and Murphy, 2005). Two other clustering methods independent of the distance function were also applied on the data. One is implemented based on the confusion matrix from a classifier to group easily confused clones together. The other was done by visual inspection. Finally, we had results from four clustering methods, consensus tree, *k*-means/AIC, confusion matrix based method (ConfMat), and visual inspection. Then we need a numerical value to measure the agreement between clusters from any two methods. This value was described by Cohen's κ statistic (Cook, 1998),

$$\kappa = \frac{\text{Observed agreement} - \text{expected agreement}}{1 - \text{expected agreement}}.$$

TABLE 47.7. Evaluation of Consistency of Clustering Methods Based on Different Distance Functions

	z-Scored Euclidean Distribution (κ)	Mahalanobis Distribution (κ)
k-means/AIC vs. consensus	1	0.5397
k-means/AIC vs. ConfMat	0.4171	0.3634
Consensus Vs. ConfMat	0.4171	0.1977
k-means/AIC vs. visual	0.2055	0.1854
Consensus vs. visual	0.2055	0.1156

Data from Chen and Murphy (2005).

Observed agreement is defined as the portion of protein pairs where the two clustering results agree and expected agreement is defined as the agreement between two random clusterings with the same distribution frequencies as the two clusterings being compared (these are obtained by simulation). Two distance functions, *z*-scored Euclidean and Mahalanobis, were tried for building the consensus tree and applying *k*-means/AIC. The results showed that Euclidean distance always results in better agreement (Table 47.7).

The results above allowed us to choose the free parameters to build a consensus tree that is optimal according to the criteria discussed above. Figure 47.6 shows the consensus tree built using these optimal parameters. Visual inspection suggests that this tree is consistent with available biological information. For example, it was found that all nucleolar proteins, including Rpl32, Unknown-25, and Unknown-32, are grouped together. The two groups representing nucleus only and nucleus–cytoplasm mixture were also well separated.

STATISTICAL COMPARISON OF LOCATION PATTERNS

Besides classification and clustering, another interesting task for biologists is to determine whether two patterns are different. A pair of patterns for comparison could be either patterns from different proteins or patterns for the same protein under different experimental conditions. Because the difference between two location patterns implies different functions of the protein, comparing two protein location patterns can help distinguish diseased cells from healthy ones, evaluate drug effects, and find similarities between two proteins.

Although we can tell something about whether two patterns are different or not from a confusion matrix or a cluster tree, it is hard to tell how confident we are in any conclusion. A better way to compare two location patterns is to use a hypothesis test, in which the null hypothesis is that the location patterns are the same. Because we can calculate a feature matrix for each pattern, the null hypothesis becomes that the two feature matrices are from the same population. The hypothesis test generates a value called a test statistic to measure the difference between two groups of location patterns. Usually the test statistic has a known statistical distribution under the null hypothesis. So we can calculate a p value, which is the probability that the test statistic is as much or more extreme than the observed one if the null hypothesis is true. Thus, the two location patterns are considered to be different if the p value calculated from their feature matrices is smaller than some chosen criterion, such as 0.05.

There are many ways to define a test statistic and then calculate the p value. A widely used method is the Hotelling T^2 test, which is the multivariate extension of the t test. This test results in a test statistic or F value measuring the difference between the means of the two feature matrices by considering the correlation of the features. For this test, the total number of images must be greater than the features. This is reasonable because sufficient data is needed to describe the correlation and variance of the features.

This test has been applied on the *2DHeLa* data (Roques and Murphy, 2002). It can be easily applied to the 3D images because after feature calculation both 2D images and 3D images are represented by a feature vector. The Hotelling T^2 test on *3DHeLa* showed that the p values for any pair is almost 0 (unpublished data), which means that all patterns are statistically different. The smallest F value (96.8; $p < 0.01$) was from the gpp130-giantin pair, which is consistent with the results of *2DHeLa*.

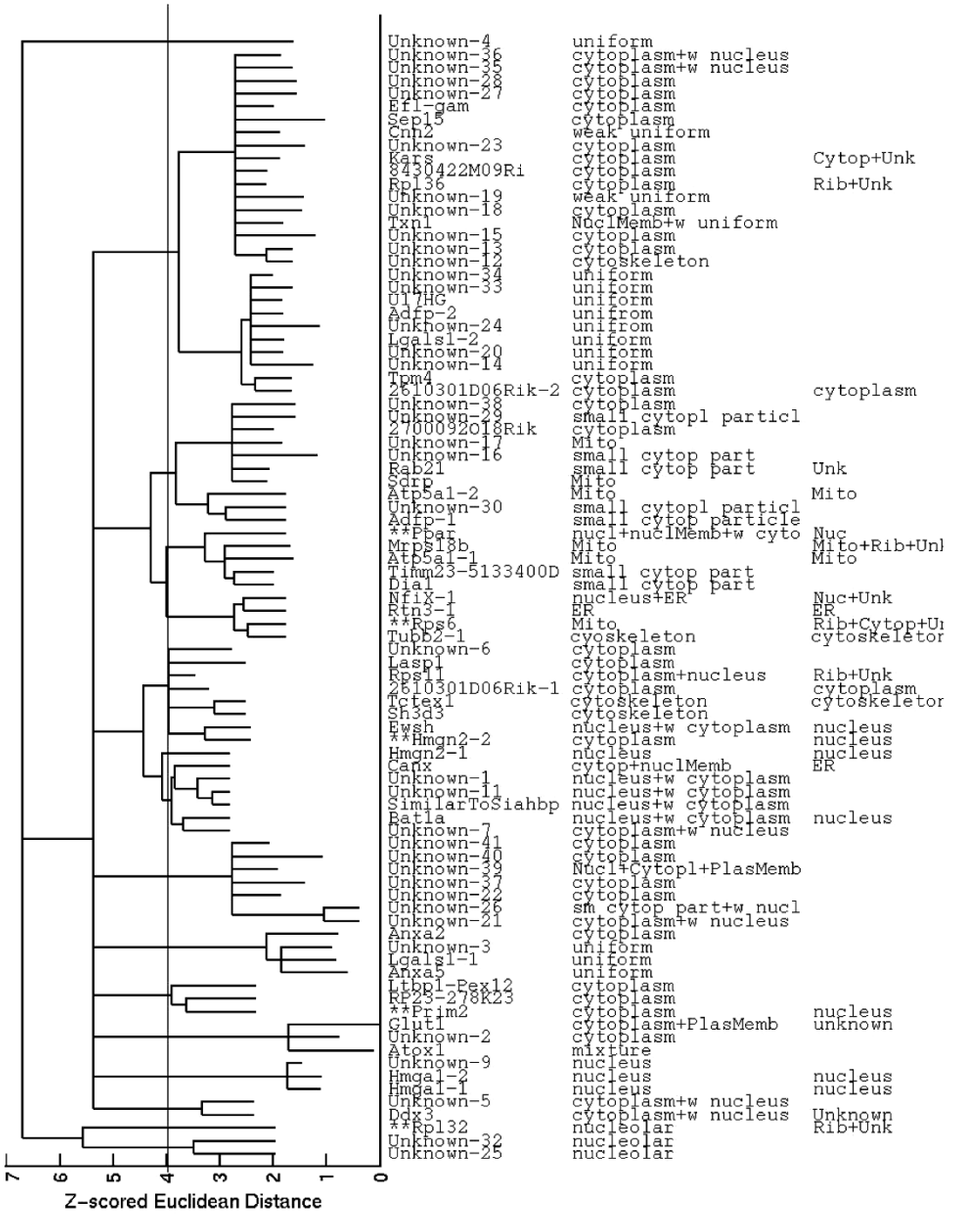


FIGURE 47.6. An optimal consensus tree for the 87 *3D3T3* clones. The text columns show protein names (if any), location description assigned by visual examination, and location description from protein data bases. The tree is also available in a Web page that can display representative images for any branch (http://murphylab.web.cmu.edu/services/PSLID/). From Chen and Murphy (2005).

A Web service for comparison of two location patterns, Statistical Image Experiment Comparator (SimEC) is also available through http://murphylab.web.cmu.edu/services/PSLID/.

IMAGE DATABASE SYSTEMS

The methods described in this chapter are all designed to be carried out in an automated fashion on large numbers of images. Indeed, all of them perform significantly better when the number of available images increases. They also rely on knowledge of the conditions under which an experiment was done and each image was acquired. It is therefore natural to consider an image database system as the most appropriate framework to utilize these tools. We have described such a system (PSLID, for Protein Subcellular Location Image Database) for storing images and their annotations with a focus on providing tools for analyzing subcellular patterns as an integral part of the database (Huang *et al*., 2002). Other image database systems have been described with a focus on cataloguing published images from both fluorescence and electron microscopy (Bioimage) (Carazo and Stelzer, 1999) or on supporting images from many fluorescence microscope systems and biological applications (OME) (Swedlow *et al*., 2003). A number of efforts to improve and expand the capabilities of databases for microscope images are ongoing, and it is anticipated and hoped that a consensus on standards for such systems will emerge to minimize duplication of effort (see Chapter 50, *this volume*).

FUTURE DIRECTIONS

In this chapter we have introduced how automated image analysis methods can be used to interpret 3D confocal microscope images. The core of the whole process is to convert an image to a numer-

ical feature vector. The conversion allows us to apply any available multivariate analysis method to the data. As we have shown, we can perform classification, clustering and comparison on these images automatically. The whole procedure provides a high throughput tool for analyzing data from 3D confocal microscopy. Given these past successes, it is worth considering directions for future work in this area.

The images in the *3D3T3* dataset were segmented manually into single cell images because of the difficulty of automated segmentation without parallel DNA or total-protein channels. The problem becomes more difficult for tissue images in which cells are not well separated. Segmentation of tissue images has been accomplished by collecting parallel DNA and membrane protein images and using active contour methods (De Solorzano *et al*., 2001). An alternative that does not require the parallel images is to develop SLF that are insensitive to the number of cells in the image. We can calculate such features directly from multicell images without segmentation. This approach has shown to be successful for 2D images containing multiple cells (Huang and Murphy, 2004a).

The SLT shown in Figure 47.6 was obtained only for location patterns in interphase cells. To build such a tree, the images of cells under unusual states such as mitosis were removed as outliers. But this does not mean that these outliers do not contain useful information. When adequate images are acquired for each state, a bigger database containing location patterns for different cell states can be created. This is another advantage of determination methods over prediction.

Protein localization is a dynamic process. For example, some proteins are localized to ER or ER membrane after synthesis, and are then sorted to different compartments. The characteristics of such a sorting procedure cannot be described unless we do the analysis on the images of a 3D time series. We are currently extending our methods from 3D to 4D (space and time). Similarly, we can extract features describing movement of proteins and define a new set of SLF that will highlight these features.

Because we have shown that SLF is useful for both *3DHeLa* and *3D3T3*, one interesting question is whether the analysis would be valid if the datasets were mixed, for example, building a SLT for all the patterns in the two datasets. This suggests an even more challenging task: to develop a feature set insensitive to cell type, tagging method, or imaging method. This is an important goal given the number of different confocal microscopes being used and the number of different cell types being studied. Nonetheless, when applied under controlled conditions, the methods described here have been proven to be more objective, reproducible, and sensitive for characterizing the proteome of a particular cell type or comparing protein distribution patterns in the presence and absence of a drug than were visual examination methods.

REFERENCES

Bhasin, M., and Raghava, G.P.S., 2004, ESLpred: SVM-based method for subcellular localization of eukaryotic proteins using dipeptide composition and PSI-BLAST, *Nucleic Acids Res.* 32:W414–W419.

Boland, M.V., and Murphy, R.F., 2001, A neural network classifier capable of recognizing the patterns of all major subcellular structures in fluorescence microscope images of HeLa cells, *Bioinformatics* 17:1213–1223.

Boland, M.V., Markey, M.K., and Murphy, R.F., 1997, Classification of protein localization patterns obtained via fluorescence light microscopy, In: *19th Annual International Conference of the IEEE Engineering in Medicine and Biology Society*, IEEE, Chicago, pp. 594–597.

Boland, M.V., Markey, M.K., and Murphy, R.F., 1998, Automated recognition of patterns characteristic of subcellular structures in fluorescence microscopy images, *Cytometry* 33:366–375.

Canny, J., 1986, A computational approach to edge detection, *IEEE Trans. Pattern Anal. Machine Intell.* 8:679–698.

Carazo, J.M., and Stelzer, E.H.K., 1999, The BioImage database project: Organizing multidimensional biological images in an object-relational database, *J. Struct. Biol.* 126:97–102.

Chen, X., and Murphy, R.F., 2004, Robust classification of subcellular location patterns in high resolution 3D fluorescence microscope images, In: *26th Annual International Conference of the IEEE Engineering in Medicine and Biology Society*, IEEE, San Francisco, pp. 1632–1635.

Chen, X., and Murphy, R.F., 2005, Objective clustering of proteins based on subcellular location patterns, *J. Biomed. Biotechnol.* 2:87–95.

Chen, X., Velliste, M., Weinstein, S., Jarvik, J.W., and Murphy, R.F., 2003, Location proteomics — Building subcellular location trees from high resolution 3D fluorescence microscope images of randomly-tagged proteins, *Proc. SPIE* 4962:298–306.

Chou, K., and Cai, Y., 2002, Using function domain composition and support vector machines for prediction of protein subcellular location, *J. Biol. Chem.* 277:45765–45769.

Chou, K.-C., and Elrod, D.W., 1999, Protein subcellular location prediction, *Protein Eng.* 12:107–118.

Cook, R., 1998, Kappa, In: *The Encyclopedia of Biostatistics* (P. Armitage and T. Colton, eds.), John Wiley and Sons, New York, pp. 2160–2166.

De Solorzano, C.O., Malladi, R., Lelievre, S.A., and Lockett, S.J., 2001, Segmentation of nuclei and cells using membrane related protein markers, *J. Microsc.* 201:404–415.

Dreger, M., 2003, Proteome analysis at the level of subcellular structures, *Eur. J. Biochem.* 270:589–599.

Huang, K., Lin, J., Gajnak, J.A., and Murphy, R.F., 2002, Image content-based retrieval and automated interpretation of fluorescence microscope images via the protein subcellular location image database, In: *2002 IEEE International Symposium on Biomedical Imaging (ISBI-2002)*, IEEE, Chicago, pp. 325–328.

Huang, K., and Murphy, R.F., 2004a, Automated classification of subcellular patterns in multicell images without segmentation into single cells, In: *2004 IEEE International Symposium on Biomedical Imaging (ISBI-2004)*, IEEE, Chicago, pp. 1139–1142.

Huang, K., and Murphy, R.F., 2004b, Boosting accuracy of automated classification of fluorescence microscope images for location proteomics, *BMC Bioinformatics* 5:78.

Huang, K., Velliste, M., and Murphy, R.F., 2003, Feature reduction for improved recognition of subcellular location patterns in fluorescence microscope images, *Proc. SPIE* 4962:307–318.

Kumar, A., Agarwal, S., Heyman, J.A., Matson, S., Heidtman, M., Piccirillo, S., Umansky, L., Drawid, A., Jansen, R., Liu, Y., et al., 2002, Subcellular localization of the yeast proteome, *Genes Dev.* 16:707–719.

Lotufo, R., and Falcao, A., 2000, The ordered queue and the optimality of the watershed approaches, In: *Mathematical Morphology and Its Application to Image and Signal Processing*, (J. Goutsias, L. Vincent, and D.S. Bloomberg, eds.), Kluwer Academic Publishers, New York.

Murphy, R.F., Velliste, M., and Porreca, G., 2003, Robust numerical features for description and classification of subcellular location patterns in fluorescence microscope images, *J VLSI Sig. Proc.* 35:311–321.

Muth, T.R., and Caplan, M.J., 2003, Transport protein trafficking in polarized cells, *Annu. Rev. Cell Dev. Biol.* 19:333–366.

Park, K.J., and Kanehisa, M., 2003, Prediction of protein subcellular locations by support vector machines using compositions of amino acids and amino acid pairs, *Bioinformatics* 19:1656–1663.

Ridler, T.W., and Calvard, S., 1978, Picture thresholding using an iterative selection method, *IEEE Trans. Syst. Man. Cybernet.* 8:630–632.

Roques, E.J.S., and Murphy, R.F., 2002, Objective evaluation of differences in protein subcellular distribution, *Traffic* 3:61–65.

Swedlow, J.R., Goldberg, I., Brauner, E., and Sorger, P.K., 2003, Informatics and quantitative analysis in biological imaging, *Science* 300:100–102.

Velliste, M., and Murphy, R.F., 2002, Automated determination of protein subcellular locations from 3D fluorescence microscope images, In: *2002 IEEE International Symposium on Biomedical Imaging (ISBI-2002)*, IEEE, Bethesda, Maryland, pp. 867–870.

48

Display and Presentation Software

Felix Margadant

INTRODUCTION

The final destination of much of the data you coax out of your microscope is the screen in front of a digital projector. Demonstration software such as PowerPoint, Keynote, QuickTime, and MediaPlayer will convert your digital micrographs and movies into a format suitable for projection. What effect does this conversion have on the data you plan to present? We have endeavored to assess what can be properly presented and identify the most notorious pitfalls of two-dimensional (2D) display software.

This chapter supplements information in Chapter 32 about the performance of the display itself. The final result any viewer sees depends both on the display software output and the quality of the projector. Unfortunately, it is impossible to separate the quality of the result from the nature of the images or animations to be displayed. Some image data will lose more quality and look inferior on some displays using some software than others. Therefore, we will first categorize the images into classes. In this chapter, we concentrate on the output the software generates rather than the visible result on the screen. This way we have a logical separation between the rendering of images and the viewer's visual impression.

We will start by considering the display of still images in terms of the resolution reproduced, artifacts, intensity dynamics, and spectral reliability (i.e., color changes introduced). Later, for the dynamic case (i.e., movies), we will assess the frame rate artifacts, frame drops, and format issues. As we shall see, the choice of data format is a much more critical issue for motion pictures than for static images.

In short, this chapter is a list of shortcomings of display tools and display file formats. In contrast to a few years ago, we found no serious flaws in the way that static images were handled by any of the viewing software inspected. The rendering artifacts that at one time were created solely by naive programming are now gone. The pool of cryptic and incoherent graphics formats has shrunk to a manageable number of common formats. And even for the animation formats, Darwinian selection has preferred those that actually work.

As a result, it makes sense to focus on a few encoder techniques and file formats and thereby provide a decent coverage of the fundamentals. Because all the common tools grew from the few surviving concepts, the file formats used actually do work on many computer systems and will probably remain accessible for several years. We cannot cover the myriad software add-ons used to tune the basic display software.

The display errors of particular interest are those made when images are resized to fit into the slide windows of the presentation software. Most of our measurements relate to Microsoft PowerPoint and MediaPlayer, Apple Keynote, and QuickTime.

Although we usually create a new presentation using a computer system with a screen resolution that is likely to be better than 1024×768 (XGA) pixels, projection systems rarely exceed XGA resolution. All the software we investigated kept the presentation freely scalable. When you import a 1024×1024 image of any format, PowerPoint, Windows Viewer, or QuickTime decodes it by means of a software tool specific to the image format and then resizes it by means of the native viewer to fit the window that the presentation uses. If this window or the screen resolution is resized again, then the software re-applies the same scaling mechanism to the first result and this degrades the image in the ways described later in this chapter. None of these viewers modify the original data, which remains unaffected by these tools. However, the image displayed is still the result of the universal decoding mechanism and the universal resizing mechanism we investigate next.

As we shall describe in more detail, the resizing method performs an interpolation between the original pixel intensities. The values are treated as if they linearly evolve between the actual image pixels, and if several pixels have to be downsized into one, their intensities get averaged in such a way that the "old" pixels located closer to the location of the "new" pixel is contribute more. The term used for this method is **smart bilinear resampling**. The claim to be "smart" comes from its ability to stretch an image as well as average it down to a lower resolution. The averaging is crucial to prevent loss of brightness information. It is called bilinear as it works in two dimensions simultaneously. Bilinear resampling is popular as it is very fast. It is also available in hardware, and rescaling introduces almost no distortions to the images. Hence, it is applicable to a vast class of different images such as all photographs. For micrographs, however, better methods are known. Therefore, if you know that resizing will be necessary, it is wise to resample your images before inserting them into the presentation.

The most common error in using presentation software is not using enough pixels. One cannot squeeze all of the information of a 1024×1024 confocal image into a small patch of a 1024×768 PowerPoint model page. Even if the image array does match the screen resolution, it will nevertheless very likely be scaled because the presentation software will try to achieve a perfect match of the geometry (i.e., the shape and aspect ratio of the presentation window) at the expense of matching the image data pixel-for-pixel to the resolution of the screen. Movie players do this too when operated in full-screen mode, and hence it is important to investigate the effects of minor scale changes as well.

These matters lead to a list of precautions:

- Never use under-sampled image material, because it will not properly scale — not even by 5% — and cannot be processed properly.

Felix Margadant • Zurich, Switzerland

Handbook of Biological Confocal Microscopy, Third Edition, edited by James B. Pawley, Springer Science+Business Media, LLC, New York, 2006.

- If you have to use such material, force it into a consistent form. Use a smoothing filter such as a Gaussian with a radius of larger than 0.5 (i.e., 0.7) to make the image consistent for further operations. This will not give you back a proper image but transformations won't further harm that image to the same extent. Deconvolution of confocal and two-photon data, as is recommended elsewhere in this book, will also ensure a properly sampled image.
- Even when correctly sampled, do not scale down the image any more than absolutely necessary. Reducing image size by 50% or more will likely show aliasing artifacts. As the original image noise worsens those effects, try never to scale down by more than 25%.
- If you are really short of space, it is better to crop the image, and cut away the bits that are not absolutely essential, than to simply rescale.
- Scale the contrast so that it looks acceptable in a bright room. If you cannot see the feature of interest on your screen under these conditions, the projection system is unlikely to do better (see Chapter 32, *this volume*).
- When using contrasting colors, keep in mind that your monitor and the projector do not have the same calibration and the latter may not preserve hues. Macintosh users are often surprised when the color consistency of their system does not transpose to the projector.
- If planning to use compression, test the results by zooming in to enlarge details first. If compression artifacts do emerge, lower the compression ratio.

When we show movies, the presentation program does even more work in the background. In particular, because movies are such big files, compression becomes necessary but serious compression requires many computer cycles, impairs the visual quality, and, as we will demonstrate, can slow the presentation.

When you play your presentation, the software renders all the files that go into each slide to make a 1024 × 768 video stream that is passed from the CPU to the graphics board and from there to the monitor or projector.

TESTING

To quantify the impact of display software or imaging algorithms in general, we use a feedback mechanism based on simple artificial images, called *the reference* that are fed to the displaying software (also referred to as the *viewer*) and a screen capturing program (named the *grabber* or *screen capture*) that reads the content of the display memory at a specified time and hence obtains an unfalsified copy of what will actually be displayed. The difference between the reference and the grabbed result allows us to assess the quality. Metrics for the quality are a matter of taste and we use the maximum norm and the Gaussian norm for reasons of economy and broad acceptance; that is, we measure the maximum deviation and the root mean square of the reference, if and only if a norm can be used. If the images cannot be matched geometrically, we only measure the distortions. The reason for not assessing the quality of any resized image is that to do so one would have to decide how to resample the reference, and this would introduce errors specific to the resampling algorithm chosen.

Resampling to change size can either be thought of as changing the pixel dimensions of the display raster or as changing the amount of the original image data that will displayed as a single pixel. The choice of the algorithm used to generate a pleasant-looking new image is driven by speed requirements, and by a fair bit of superstition about the efficacy of different mechanisms of resampling. The dominant paradigm in computer graphics is that a pixel is a point measurement that is sampled at its center coordinate (this is the official notion for the MPEG movie standards), whereas for a microscopic image, this is the light distribution in the specimen, convolved with the point spread function (PSF) and either sampled from the time-data stream from the photomultiplier tube (PMT), or integrated over the area of a charge-coupled device (CCD) pixel. Nyquist sampling implies that the signal from a point object will be spread over 12 to 16 2D pixels at the detector plane (see Fig. 24.A6, *this volume*), and therefore that the signal in each of these pixels represents only part of the image of a point. Because optical systems can be thought of as working in reverse, we turn this situation around to see that, if a single pixel on the CCD is imaged back onto the object, the image of the pixel will cover an area about 12 to 16 pixels in size. This means that the data recorded in each pixel basically represents signal generated from a volume in the object that is the size and shape of the PSF, an area significantly broader than the physical dimension of that pixel. This feature ("fuzzy edges") allows a variety of linear image-processing procedures to be carried out without seriously damaging the image data. However, if the image is downsampled (i.e., compressed into a smaller number of pixels so that the smallest features becomes <3 pixels wide), this relative immunity from harm is lost.

To assess timing errors in motion displays, we used a simple optical probe: a photodiode in a tube mounted to the display (Fig. 48.1). By intentionally encoding specific brightness fluctuations into the test movie (a blinking beacon and a sinusoidal flash) we can observe timing errors. If the computer time source is accurate, however, almost everything observed with the diode could also have been measured with the grabber.

One notable exception relates to the hardware-accelerated movie players that employ modern, built-in *digital rights management* (DRM). DRM basically is a copy protection mechanism for digital movie material and it is designed to prevent movie displays from being captured. As we wish to assess the performance by doing exactly this and as the DRM mechanism is active not only when playing copyrighted material but is also incorporated into some presentation software, it can prevent us from grabbing the output from the test material.

DRM works by taking over some features of the graphics hardware so that the rendered movie never gets copied into the video

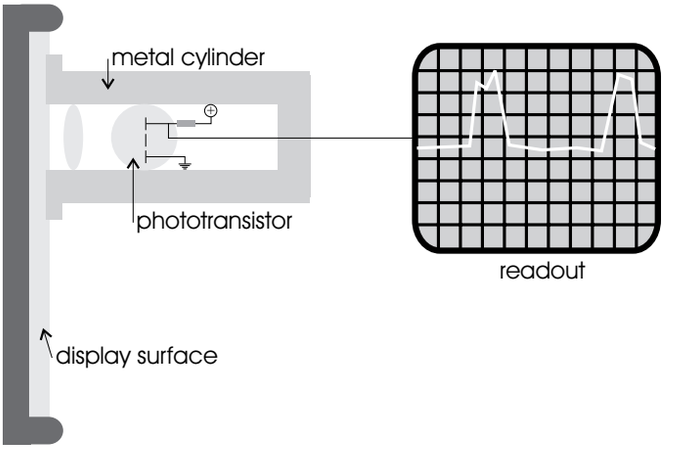


FIGURE 48.1. Test setup for display speed and sensitivity.

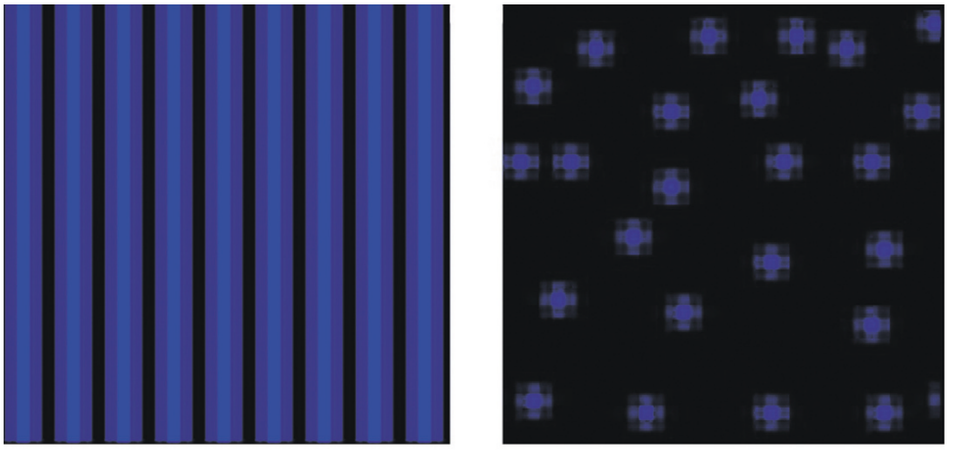


FIGURE 48.2. Sinusoidal grid and sparse dot reference images used to test image reproduction quality.

memory (the method is referred to as overlaying). To gain quantitative insight into the movie playback, we must first disable this hardware feature. However, to assess playback speed and continuity, we must use overlaying, as it improves the rendering performance of the player software, something that we assess using the external timing signal.

During testing, it became obvious that performance limitations usually had less to do with the viewer software than with the underlying universal graphics library that is part of the operating system and hence is shared among all or almost all the graphics programs running on a given computer. If the display module is provided by the operating system, we refer to it as a native viewer in Windows terminology. Furthermore, an image or movie file format is interpreted by dedicated, shared software. This software program is referred to as "codec" (abridged for coder/decoder).

Although these universal software modules keep quality high and independent of the viewer used, they also make it very difficult to assess errors because both the test image generator and the viewer that is being tested likely rely on the same basic software codec.

Codecs are always paired with native viewers: the native image viewer uses a universal codec to handle JPEG images, the native movie player will use codecs for the movie formats used. This layered concept is not new (introduced in 1970), but recently its usage has become far more pervasive. In the end, many presentation packages make use of the underlying graphics subsystem. On a Windows machine, this consists of the Direct X and Direct 3D system; Unix platforms mostly use X Windows; and Macs offer the QuickDraw3D system (see Apple developer site). The graphics subsystem in turn tries to engage the particular hardware features of the particular graphics card that is part of each individual computer, frequently referred to as graphics engine or just the engine. For recent technology of graphics subsystems, see http://developer.nvidia.com/page/home or http://www.ati.com/developer/index.html.

Use of a fast graphics card can have a very positive impact on the rendering speed of the system but it also decouples the performance of the graphics almost entirely from the overall system performance. As a result, we were unable to relate processor power directly to the frame rate of embedded movies. Even worse, there seemed to be no immediate link between the performance of the graphics engine and the movie frame rate, as the entire chain of devices — disk, memory, processor, graphics bus, graphics engine — multi-linearly controls the actual performance.

One result is that the quality of the image displayed on the screen may depend more on the hardware installed on the computer driving the projector and on how this hardware is configured than it does on the program you use. Because Apple specifies minimum quality standards for the graphics engine (http://developer.apple.com/), there seemed to be no (noticeable) difference between software and hardware rendering.

"Static" Image Performance

The setup for testing the ability of the program to display static images is trivial because the resulting image can be grabbed anywhere. The resolution reference test image is a sinusoidal grid at various spatial frequencies and all quantities of interest can be directly extracted from the grabbed image. Another reference used to illustrate under-sampling is an image of sparse dots [Fig. 48.2(B)]. Because it is more difficult to interpret results related to the latter pattern most of the figures below concentrate on the grid [Fig 48.2(A)].

To obtain meaningful results, it is of utmost importance to use properly sampled images with finite line width (i.e., lines at least 4 pixels wide) (Bracewell, 1995), as all modern compression and coding algorithms will fail when applied to images with single-pixel shot noise or steep pixel-to-pixel transitions as we shall illustrate.

The native viewer for Windows XP is the Windows and Fax Viewer; for OS X it is QuickTime. The first finding is that, not surprisingly, when image data is displayed without data reduction, the native viewer does not change the image intensity content at all as long as the image has exactly the same raster size as the graphic window in the slide. Any image with three or fewer channels and 8 or less bits per channel, is displayed as is. This also means that the output of different viewers is indistinguishable, and as all PowerPoint versions later than the 1997 edition use the same underlying graphics library for viewing static images, images that have not been scaled in any way are reproduced accurately; that is, the image grabbed at the output of the computer is identical to the source.

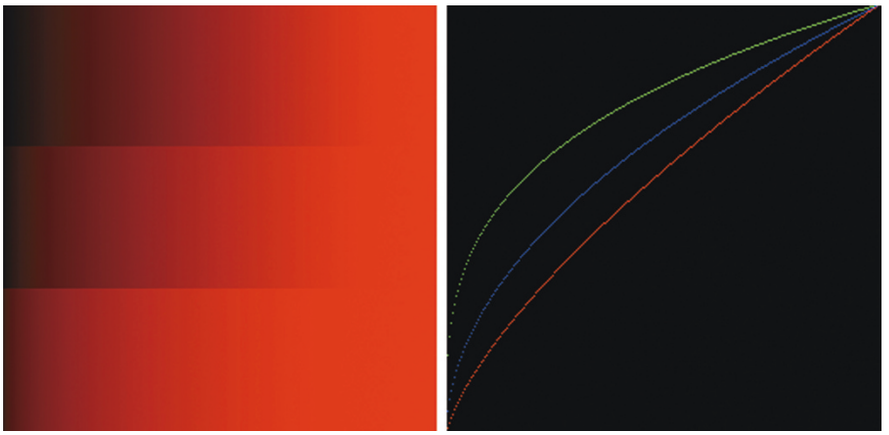


FIGURE 48.3. Strong photometric gamma switched off (left) and on (right) for a linear ramp. The visual brightness is red; the absolute value plotted in green.

Brightness

This equality does not extend to the brightness correction information that is stored with each image. Such information is a feature supported by both the JPEG and TIFF formats.[1] This photometric information (also termed **photometric interpolation**) is intended to standardize the actual brightness of a digital value stored with the image. This is not done as an absolute physical value — which would be difficult to display and print — but as a ratio to the peak brightness displayed. Hence, all packages make adventurous assumptions about the dynamic range and linearity between the darkest and the brightest values displayed. These assumptions range from assuming that everything is fine (i.e., completely ignoring the photometric information as the Windows native viewer does) to properly scaling the image to the photometric ramp (as in Photoshop). When the display contains a stored profile describing its color response, these editing tools will scale the output to take this profile into account.

For example, when Windows 2000 is used with modern graphics cards, the Direct X library includes built-in correction for the display. This has always been an intrinsic part of the system for Apple machines and hence is never an issue.

The Nvidia and ATI graphics drivers refer to this feature as monitor gamma, gamma being the inverse of the brightness response of the display. Fortunately for the user, these values are transparent and can be read by the software. If a monitor contains a gamma specification file, Photoshop and Paintshop image editors will use these preset display values and not add their own correction system. In the end, the results can vary considerably if this feature is used (see Fig. 48.3).

For the user, all of this hidden activity has a very limited impact. Micrographs represent a quantity related to photon counts and hence do not carry any photometric correction information. There is no photometric meaning to microscopic images other than that the brightness scale should be as linear as possible and this is close to the case where no photometric scaling is used.[2]

Conclusion: do not actively adjust the photometric information until one has finalized the image editing for printing. To do otherwise may contaminate your results without adding anything to your image quality. Faulty calibration ramps (or ramps that are considered faulty by an editing program) can sometimes reset your rich, beautiful image to black.

Once the layout is ready for publishing, any photometric information available assures that the results stay constant as long as the images are used with the same set of programs (i.e., an image saved in Photoshop will look much the same on different displays with known profiles). To test this claim, we started with an image that was the inverse of the gamma ramp shown in Figure 48.3(B) and processed it through the same gamma-correction photometric ramp so that the output should mimic the linear ramp. The original data is shown in Figure 48.4 (top) and the reconstructed ramp is seen at the bottom. It looks as expected, except that, because the computation is done in integer numbers, the ramp looks coarser because of round-off errors The colored bars mark lines of identical brightness. These marks are shifted but the effect is quite mild and hard to spot by eye.

Resolution: Changing the Display Size of Your Images

Desktop and notebook displays are now available at decent resolutions. XGA (1024 × 768 pixels) represents the very low end, SXGA (1280 × 1024), SWXGA (1400 × 1050), UXGA (1600 × 1200), UWXGA (1900 × 1200), and Apple's 1200 × 800, 1280 × 854, and 1440 × 900 can be found in low- to medium-priced devices. Desktop screens come in these and higher resolutions. Projection systems, however, feature SVGA (800 × 600) or, more commonly, XGA (see Chapter 32, *this volume*). Higher resolutions are still rare even though SXGA projectors do exist. Briefly: a beautiful micrograph that is 1024 square will simply not fit on today's projector. PowerPoint and the native viewers "solve" this issue by down-sampling the image if needed, using the graphics library and the graphics hardware. Using the test setup to compare different resampling algorithms (Nikolaidis and Pitas, 2000), it is obvious that presentation software uses bi-linear interpolation, as illustrated in Figure 48.5 It is a fast resampling method with the only disadvantage that it does not correspond to any physical system, that is, it cannot be simulated by building an optical system that changes the resolution in the same way.

Although the inherent and unavoidable danger of all down-sampling is the loss in resolution, a fine feature, correctly sampled at the resolution limit, will no longer be correctly sampled when

[1] http://www.jpeg.org/ and http://www.digitalpreservation.gov/formats/fdd/fdd000022.shtml.

[2] The linearity (or not!) of both the display and the visual system is discussed at greater length in Chapters 4 and 32.



FIGURE 48.4. A linear ramp and a gamma ramp with inverse correction.

scaled down. This can be visualized by observing the effect of the process on the line grid image that originally was properly sampled.

To illustrate the damage done by down-sampling in PowerPoint — or linear interpolation in general — we force a 25%, 50%, and 75% scaling of the line grid reference image in Figure 48.6.

Reducing the resolution of the line grid by 25% to 50% hurts the resolution but it does not totally destroy the image content as the undulation between high and low persists through the scaling even though the peak values of the resulting images are less than they were in the reference. This is because, while the 50% scaled image is no longer properly sampled, it is not yet *aliased*: it is the smallest scale at which all details of the original image will still be present. When new structures, such as patterns, appear during the manipulation of a raw image, the phenomenon is referred to as aliasing. When a Nyquist-sampled image is down-sampled to 25% of the original size, it will suffer from severe aliasing even if the down-sampling is performed correctly through the interpolation. As the intensity of four neighboring pixels is averaged, the image becomes homogeneous. This (correct) algorithm for reducing image content to fit it into a smaller window is built into the modern libraries; however, on systems using older software, the interpolation can still go wrong, as Figure 48.7(D) shows.

The ability to sample over more than just the nearest-neighboring pixels when scaling down is called anisotropy (http://www.opengl.org). Because the fast preview modes of Photoshop or Paintshop are often used without anisotropy to increase speed, this phenomenon can still be observed, but it is not an issue for presentation software.

All these cases were "well behaved" in the sense that down-sampling them did not introduce any structure but merely lowered the image quality. However, even with properly sampled images, it is easy to commit true mistakes. Figure 48.6(B) illustrates the common failures of digital image operations. Scaled to 40% of its original resolution, the image content breaks down regardless of the interpolation method chosen. Even though the down-sampling was done correctly, the original structure simply cannot be displayed anymore.

Although the 50% image still conveys the original information [Fig. 48.6(C)], it cannot be manipulated any further. Any rotation or shifting more complex than a 90° rotation or shifting an integer number of pixels will then destroy content, as Figure 48.7(B) proves.

Far stronger under-sampling pattern artifacts (for regular structures, these are called moiré patterns) can occur, as Figure 48.7(C) shows for the 30% scale image. Instead of displaying fine lines, the image exhibits slow undulations. Although similar errors occur from non-regular patterns — such as micrographs — they are harder to recognize. Except when the scanning process itself creates some regular pattern, excessive down-sampling is more likely to break up structures or attach them to neighbors than to create a large-scale pattern (see Fig. 48.8).

How can we prevent such things from going wrong? As XGA can safely be regarded as the low-end display for computers and is the dominant display for projection systems, if scaling your Nyquist-sampled original image down to an XGA display does not force you below the 50% threshold, then details should remain visible. So a 1024 × 1024 Nyquist-sampled micrograph can be

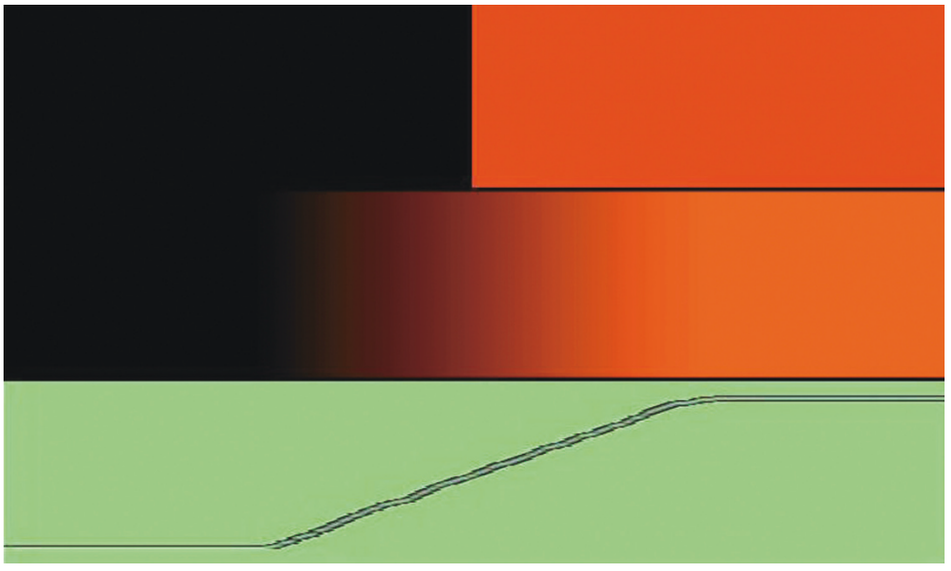


FIGURE 48.5. When a step image (top) is zoomed by PowerPoint, it results in a ramp (center). The intensity plot (bottom) shows a ramp consisting of three linear segments.

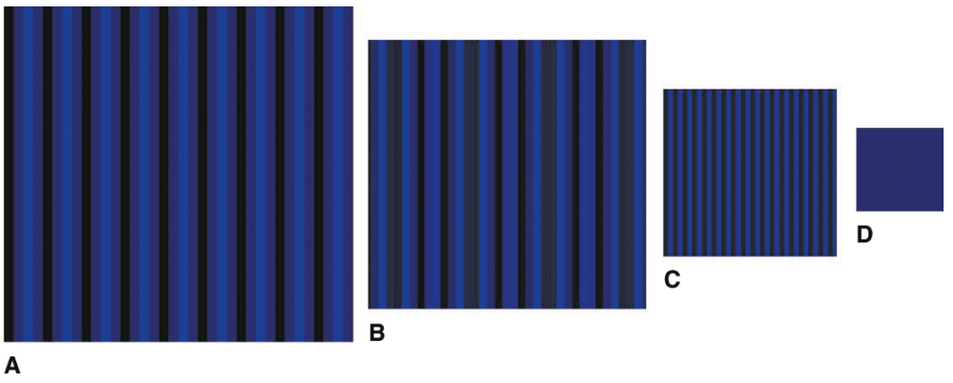


FIGURE 48.6. Down-sampling in PowerPoint. From the left: original image, 25% smaller, 50% smaller, and 75% smaller.

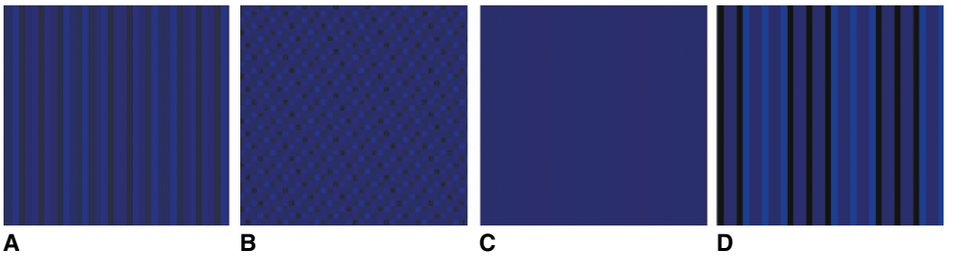


FIGURE 48.7. Classical aliasing gallery: (A) The reference image sampled at 40% of its original resolution; (B) the 50% size image, rotated by 30°; (C) the reference image reduced to 28% of its size; (D) the image at 70% if its resolution with nearest-neighbor interpolation instead of linear interpolation.

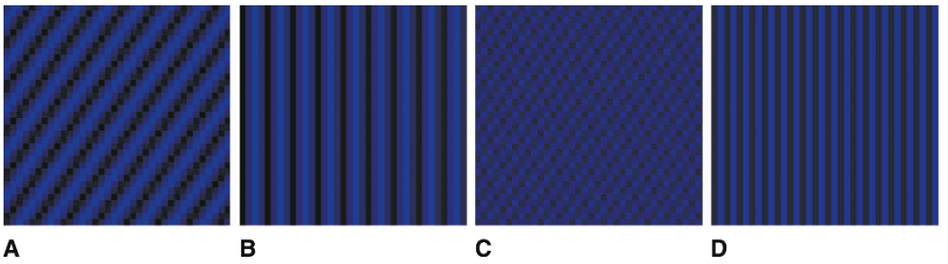


FIGURE 48.8. Operations that do not produce aliasing in properly sampled image data. If you subject your beautiful micrograph to any of these operations, keep the worst case in mind and do not allow it to be scaled down by more than a factor of $\sqrt{2}$.

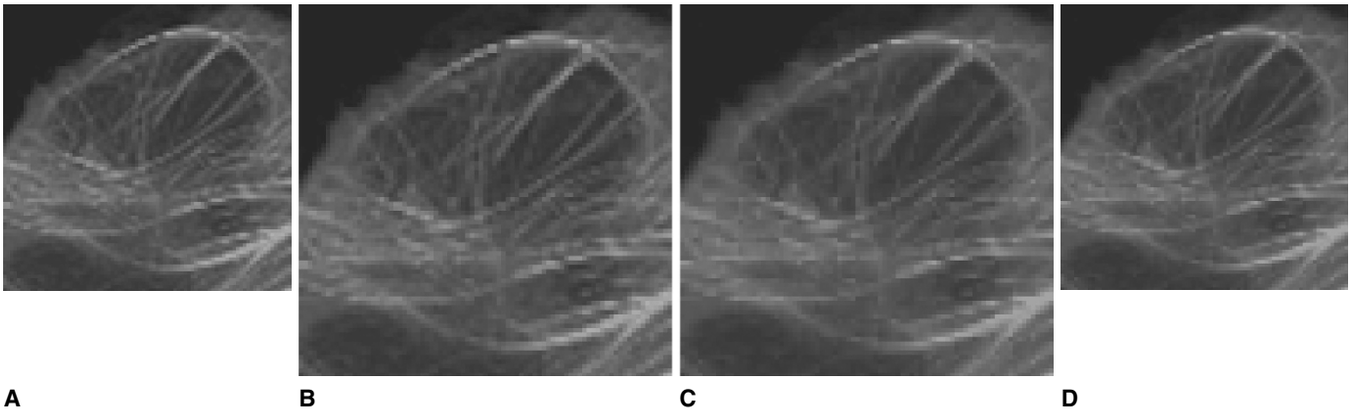


FIGURE 48.9. Up-sampling: (A) a slightly under-sampled image gets up-sampled by 30% with either full anisotropy (B) or basic linear interpolation (C), as used by PowerPoint. For comparison, the pixel resolution in (D) is reduced by 30% to see the similarity of the processes.

shown in a presentation as long as it occupies at least two thirds of the display's height. However, you can only put two such (now 512×512) images side to side for comparison if you utilize the entire width of the screen. If you want borders, you must *crop* the images to cut away all but a *region of interest* (ROI). This is often a good idea anyway as those at the back of the hall can usually not see the finest details on the screen.

The process of scaling, rotating, removing distortion, and aligning images all lower the effective resolution of the digital image, but the order can be important. If you shrink your image into fewer pixels, first, and then rotate or distort it, you will now be working on an under-sampled image and the damage will be more severe: Shrink last!

Digital images have a $\sqrt{2}\times$ coarser resolution in the diagonal direction than along the axes because of the rectangular grid, a property not shared with analog media. If an image is turned by an angle $-45° \le \alpha \le 45°$ away from the axis, the values along the grid will be mapped onto a raster of $\cos(\alpha)$ times the resolution with the $1/\sqrt{2}$ worst case for 45°.

Translating a digital image a fractional number of pixels can also blur the image. Fortunately, the effect is less pronounced on properly sampled data [Fig. 48.8(D)] than is the effect of scaling and rotation [Fig. 48.7(A,B)], but the resulting images lose resolution, as the half-sized images of the rotated reference [Fig. 48.8(C)] and the shifted image [Fig. 48.8(D)] show. The latter shows no loss at all but the shift is no longer noticeable, except for a mild change in intensities.

Even if the damage done in Figure 48.8(C) appears minor, you need to remember that here the operation was done in a single step with maximum care and had the same result been reached as the result of a number of separate steps, errors would have accumulated at each step (Fig. 48.9).

Other types of operations, such as changes in histogram, linear filters, convolution, and deconvolution, do not impair the resolution and little care has to be taken when using them. Median filters, anisotropic filters, and image editing **do** harm image resolution and, as the images may no longer be properly sampled after these steps, caution has to be applied. Even minor changes of a page setup — without any intention to rescale a picture[3] — can result in changing the resolution of the image.

Compared to down-sampling, up-sampling is relatively harmless. Therefore, the safe approach is to keep the image near the target system's resolution and assume that small changes in scale will not harm the content.

Figure 48.10 shows that this happy outcome cannot be fully achieved if the image itself is not properly sampled. This means that even if we can make sure that the images never get reduced in size during a presentation, proper sampling of the original image is still essential to obtain a consistent outcome.

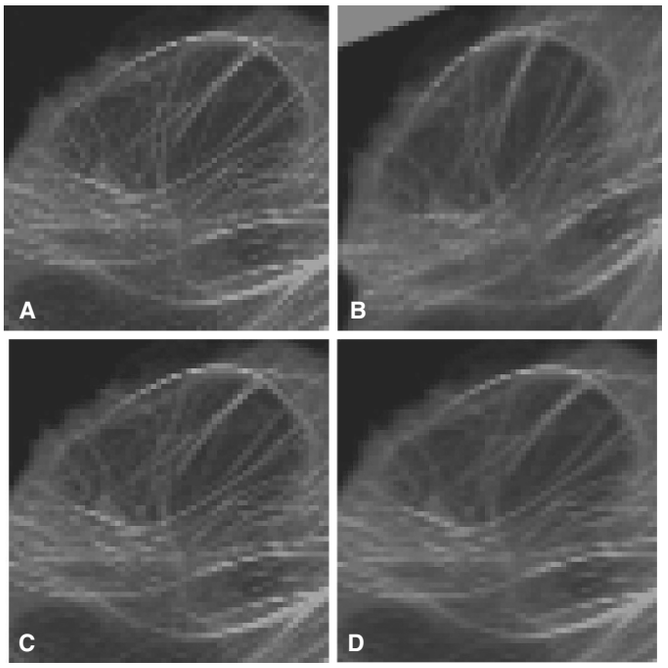


FIGURE 48.10. Manipulation of the slightly under-sampled image. From the original (A), a 30° rotation (B) and a half-pixel shift were performed with sinc interpolation (C) and with linear interpolation (D). The artifacts arising are least pronounced in (C), but all result in some loss of resolution.

Compression

Although compression is often unnecessary for still image presentations, it also has some significance for storing large datasets and hence we briefly touch it here. Classically, compression algorithms are split into two groups. The first type are pure compression methods (so-called no loss methods) that try to exploit redundancies such as homogeneous regions in the image to use less information to encode the image. The second type are data-reduction algorithms that try to identify and remove image information that is not needed for conveying the essential information. As such a compressor cannot really know what it is that you want in an image, using such a procedure is a common source of artifacts.

As light microscope images are inherently noisy and noise has no redundancy, it is important to ALWAYS deconvolve[4] your 3D confocal data before trying to display it. Doing so not only suppresses single-pixel noise, but also effectively averages the signal from many voxels to reduce Poisson noise. Noisy images cannot be compressed noticeably by means of pure compressors (Castleman, 1995). Exceptions to this rule are images with many "black" pixels, as dark regions exhibit little noise. It is trivial to test if your images actually can be compressed. Start with a format such as TIFF that offers pure compressors to squeeze the image and then compare the size of compressed image to the original.

What is lost when compressing microscope images using lossy methods? All modern compressors rely on psycho-visual perception compression (Watkinson, 2001), that is, they try to obliterate any image information that the human eye is bad at reliably picking up. The most famous such reduction is the "spectral coding" which relies on the observation that the spatial resolution of the human eye for color changes is much lower than for intensity changes. How well the compressors take advantage of this fact is shown in Figure 48.11.

Most compressors exploit the connectivity of neighboring pixels. If the image is noisy or not properly sampled and hence does not exhibit this connectivity, the effort to compress will either fail to achieve high compression or — much more likely — introduce errors to the image. It will also often NOT produce a smaller image file.

How does compression affect the display of micrographs that not only should look pretty but must also convey correct bright-

[3] For example, changing the printer reproduction ratio.

[4] Or at least Gaussian filter for 2D data.

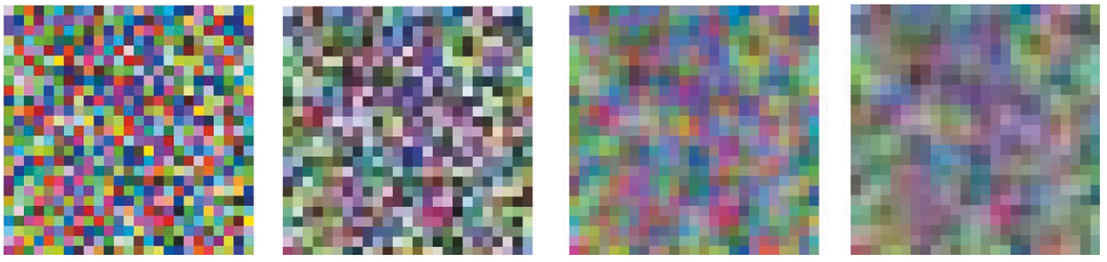


FIGURE 48.11. A random color dot image (A) gets mildly compressed (B). Although the overall hue is preserved (for a display of unity gamma), the individual colors get completely washed out. If, however, the original image is properly lowpass filtered to remove the single-pixel noise (C), the compressed image (D) looks very comparable.

ness information? We focus on a small 200 pixel square subsection of a properly sampled micrograph (with some noise) and assess what compression is doing (Fig. 48.12). First, because the image contains a large black background with relatively low noise, the image can be compressed with little loss by a factor of 3.97.[5]

Even though we get very small error values even for the strongest compression, the visual result is poor as the fine details are lost and this is what we perceive as quality. For image processing, this has substantial consequences: even mildly compressed images are no longer suitable for deconvolution, segmentation, or quantification. However, for presentations, compressed versions of properly sampled images will usually leave a good visual impression.

MOTION PICTURES

Athough motion pictures inherit all the artifacts that plague still pictures, the image changes so fast that the flaws are usually less noticeable. On the other hand, they add timing flaws. The dominant problems are non-steadiness in the picture flow (jittering) and dropped frames because of lack of computer power. In addition, there are implementation mistakes that can create incorrect frame rates or random intervals between frames. The latter are easy to detect and usually require the movie file to be re-created.

As for image-viewer programs, the movie player software is only responsible for a fraction of the possible problems. Once a movie is created, certain flaws can no longer be compensated for by the player software. Because movies that exhibit aliasing in resolution or timing cannot be resurrected by better player tools, correctly coding the movie will be our first focus. The second case of interest is when player and data are set up correctly but do not match the hardware systems they run on.

Movies also add another entire dimension to the problem: that of computing resources. Movies use large amounts of both storage and computing power, and playing a movie at the required frame rate can push a computer over its limits. Also, unless the player software is dedicated to playback-from-disk mode, discontinuities in playback are likely if the entire movie cannot be held in computer memory. These considerations restrict the number of formats that can be used for playing very long time series.

[5] Such compression is possible, at least in part, because all the "black pixels" can be specified as black using fewer bytes than recording a row of zeros. However, the process still entails a "little loss" because setting the "almost black" pixels to zero is a small loss. If the data has been 3D deconvolved before being compressed, few pixels will actually be zero, and one must set a threshold, a process that may also entail some small loss of data.

Of the plethora of animation formats available, we investigate only the most popular ones. There are also the *metaformats* QuickTime and Microsoft's AVI that are really just descriptions of the parameters of the movie such as frame-rate, resolution, color matching, etc., but that do not decode the movie data itself. Within these formats, there is also a parameter that refers to the codec to be used to interpret the movie data. Hence, these metaformats can be reduced to the understanding of the codecs involved. To keep things nice and complex, the word QuickTime is used both as the name of a codec and also as the name of a metaformat. Below, we talk about the basic problems of the codecs rather than the convenience of the player software (i.e., MediaPlayer and QuickTime player).

The codecs investigated are QuickTime, Cinepac, MPEG 1, 2, and 4 (Ebrahimi and Pereira, 2002) [including the new MPEG-4 offspring, H.264 (Richardson, 2003)], and the image-series format. The last mentioned features no movie compression at all but simply consists of a series of frames. The frames themselves can still be compressed but there is no link between the frames other than enumeration. The format comes in a few popular forms, including TIFF series (which simply uses the TIFF image standard for frame handling), Motion-JPEG that uses the JPEG standard (which is incorporated in the mini-DV, digital camcorder format) and the Digital Betacam (broadcasting) formats. These compression standards will now be discussed in more detail.

As we shall see, the following considerations have to be respected:

- Shrinking movies results in the same artifacts as shrinking stills. If scaling down is required, it is wiser to shrink the frames by proper down-sampling before they are encoded into the movie format. However, cropping movie formats should also be considered (Fig. 48.13).
- Movies can also be under-sampled temporally. Depending on the recording device, this can be much harder to prevent than spatial under-sampling. It becomes obvious when structures move enough between frames that they cannot be properly associated in the individual frames. Our vision system compensates a substantial amount of temporal aliasing by utilizing other criteria such as shape, hue, and texture to label moving objects, but this skill is limited to a few objects per scene. Temporal aliasing can be reduced either by increasing the recording frame rate or by reducing the complexity of the scene with proper color staining or labeling.
- If none of these are possible, the best remedy is to play the animation at a very low frame rate so that the visual cortex gains time to understand the scene in each frame. The result resembles a slide show more than an animation.

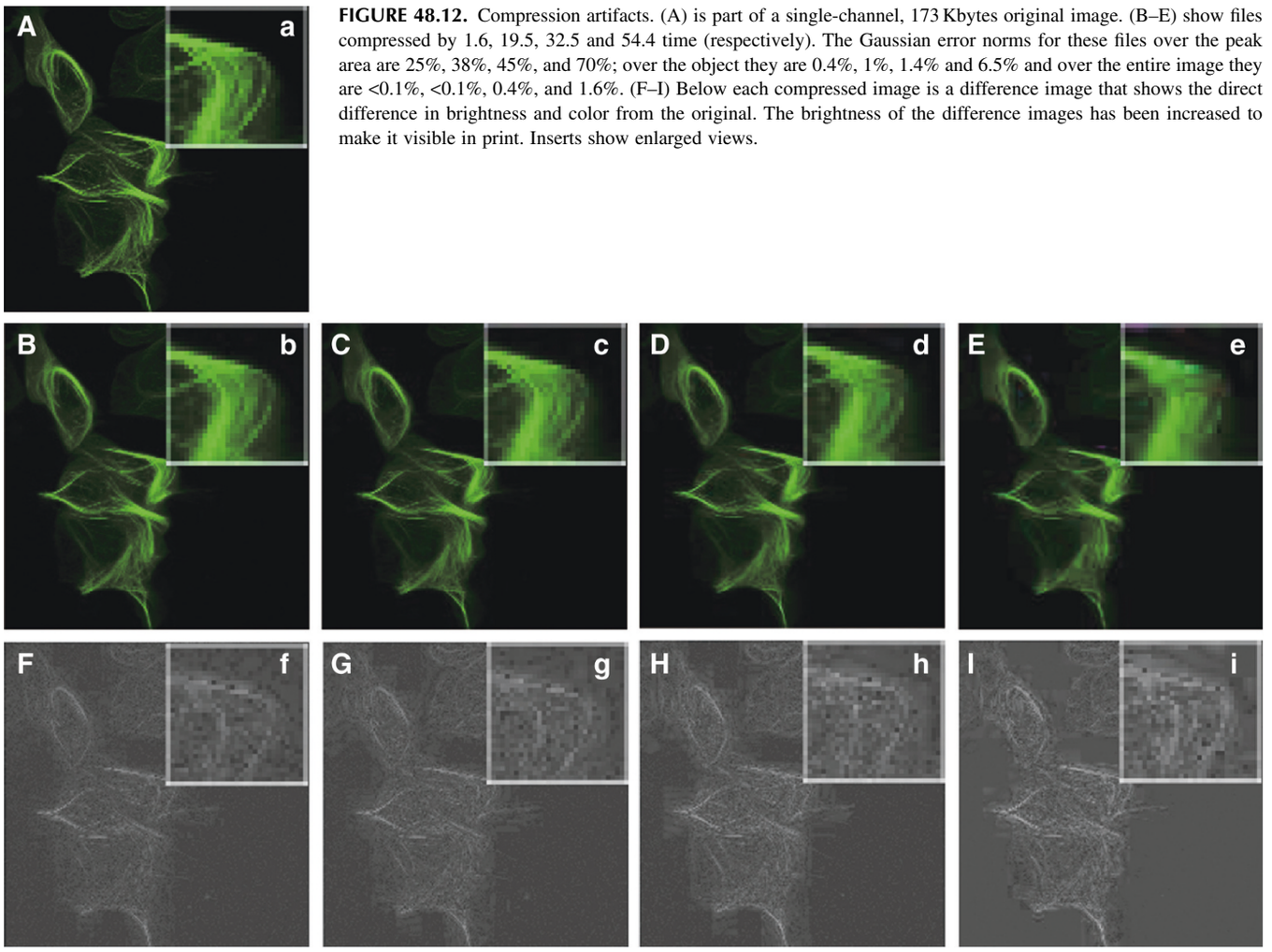


FIGURE 48.12. Compression artifacts. (A) is part of a single-channel, 173 Kbytes original image. (B–E) show files compressed by 1.6, 19.5, 32.5 and 54.4 time (respectively). The Gaussian error norms for these files over the peak area are 25%, 38%, 45%, and 70%; over the object they are 0.4%, 1%, 1.4% and 6.5% and over the entire image they are <0.1%, <0.1%, 0.4%, and 1.6%. (F–I) Below each compressed image is a difference image that shows the direct difference in brightness and color from the original. The brightness of the difference images has been increased to make it visible in print. Inserts show enlarged views.

- The temporal/spatial aliasing dualism of movies also works in the opposite direction. If a movie is sampled properly in time, it conveys an impression of having higher spatial resolution than a still image of the same pixel dimension. This is obvious if you digitize the TV signal. A single frame will appear much coarser than the equivalent animated picture. This means that for movies at high frame rates, the resolution can actually be lowered without seriously reducing the apparent image quality.
- There are only a few universal movie formats. If you stick with the widespread MPEG family of animations, frame rates and resolutions are specified and your movie will have to be trimmed to fit both. The reward for doing so is that you obtain a document that will play reliably on almost all platforms.
- If it is compressed, movie performance depends on the complexity of the movie, as both decoding effort and memory requirements increase with complexity. The exceptions are the MPEG-1 and MPEG-2 formats that offer complexity-independent performance.
- Movies may easily exceed the memory resources of the computer and even when they don't, they may take long to time load. As a result, it can be hard to tell whether the movie is just slow in loading or if it will not play at all because the presentation machine is not sufficiently equipped. The MPEG and QuickTime formats start playing after loading only a small part of the presentation, but only MPEG guarantees proper playback performance if played from the disk.

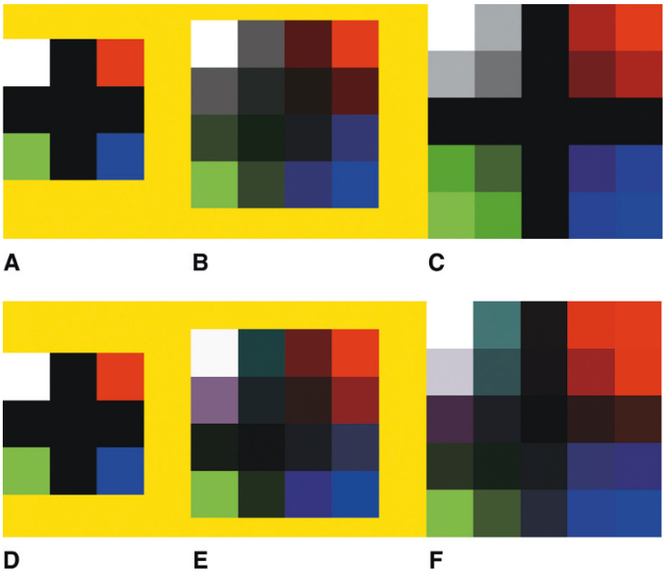


FIGURE 48.13. A 3 × 3 color sample is zoomed to 4 × 4 and 5 × 5 pixels. Linear interpolation (A–C) as it is offered by movie playing hardware versus high order interpolation (D–F). The main advantage of high order interpolation is that the borders stay sharper, even though the image looks no more convincing on such a strongly zoomed scale. (Try looking at it from across the room.)

As with static images, the output of motion players can be grabbed by software grabbers unless the player has the rights-management software installed (as mentioned above). The grabbing setup is synchronized to the refresh rate of the display and during each displayed frame, a small, constant region of the screen is captured as a static image that then can then be compared to the content of the original movie file. To allow for exact matching, frame numbers were written into the test movie file. These can be read by the grabbing software, permitting a one-to-one comparison to reveal when a frame is displayed or not displayed because it was dropped. This simple setup allows analysis of rendering artifacts, jittering, and frame drops all at once. It is important to recognize that the frame rate must not be higher than the refresh rate of the display. This is not entirely an academic problem, as NTSC videocams can record at 60 Hz and some LC displays, especially the very high resolution ones, are limited to a lower refresh. In addition, many projectors use 30 Hz displays, assuming that this is sufficient for rendering full-frame PAL or NTSC at 25 Hz and 30 Hz, respectively.

It is expected that the frame-by-frame (2D) quality of movie players will be worse than in viewers, because movie players rely on fast codecs, supported by the graphics hardware. There is only a problem if the movie is scaled down during the presentation. As a result, it is even more important to avoid downsizing movies than it is for stills. Besides the speed penalties, shrinking movies can result in coding and playback artifacts, some of which we show below.

Coding Limitations

It is trivial but crucial to keep in mind that the same fundamental restrictions hold for movies as for stills. You cannot safely display a movie with a higher format resolution than your display window. All the players are armed with down-sampling algorithms that — due to the strict timing requirements — are texture based (resorting to the Direct X or QuickDraw library) and use linear interpolation. The price is high: uncontrollable loss of image detail even at constant (or increased, for the sake of down-sampling) computing power. Both QuickDraw and DirectX use the texture hardware to zoom images up and down and this will result in sampling errors, if the hardware anti-aliasing has been switched off. Figure 48.6(D) shows a 4-pixel sinusoidal pattern that has been down-sampled by a factor of 4. Although the proper outcome for this pattern is a homogeneous average intensity, the hardware sampling on the Windows machine used is set to only handle interpolation between neighboring pixels and, hence, the result ends up as shown. To show the same outcome on Apple hardware, the down-sizing has to be more severe, exceeding a shrink factor of 4. Although this might happen if many proper 512 square movies are laid out on a single PowerPoint or Keynote slide, it seems rather unlikely.

Most movie formats do not cover really high resolutions properly so users are saved from that mistake by system restrictions.[6] The only way to keep control over your movie details is to limit its resolution to the worst display you are likely to use.

Apart from resolution, movies face a frame rate limit. Most projectors are capable of handling full frames at full resolution at 30 to 60 Hz, except for the very high resolution models. Cathode ray tubes (CRTs) and liquid-crystal displays (LCDs) offer even higher refresh rates, likewise high-speed cameras. However, as human vision cannot resolve these higher frame rates, it is safe to down-sample them to 60 Hz if real time is required or use slow motion if every frame counts. It should be obvious that, when building a movie, one must respect the computational power of the display system. Not doing so results in jerky image motion and the unpredictable behavior of a player running at an arbitrary frame rate and trying to reduce image contents using the fastest (i.e., lowest quality) method available.

Up-Sampling or Frame Rate Matching

Assuming now that we have a healthy movie file designed to run at frame rate f with a horizontal resolution X that the display can accommodate. We then face a temporal scenario that is similar to the spatial scenario we encountered for stills: the display not only exhibits a constant resolution, its frame rate is also fixed. Although both can be changed, doing so requires setup effort and cannot be done on the fly. Given a fixed refresh rate, the player software behaves in the most canonical way possible: that is, at a 60 Hz refresh, frames start ~16.67 ms apart. On the other hand, an 8 Hz movie that issues a new frame every 125 ms produces a display table that looks like Table 48.1, and this is what one obtains from a sequence of grabbed images — each 7 to 8 cycles, the frame counter increases.

Although the player and movie files are both perfectly correct, the images of the movie cannot be displayed for 125 ms each as designed. The first picture (no. 0) is displayed for 133 ms; the next one gets swapped at 250 ms and hence stays for 117 ms, the third one for 133 ms, etc.

In many cases, the 16 ms difference in display time will be hardly noticeable, a feature exploited by low-end conversion between TV standards, where 25 Hz get mapped onto 30 Hz or vice versa.

If however, you encode two labels in alternating frames and display them in red and blue, then one of the channels will appear $\frac{133\,\text{ms}}{117\,\text{ms}} \approx 1.137$ almost 14% brighter than the other one. Not a disaster, but definitely not what one intended to convey. Worse still, each time the sequence is played, randomly, either the red or the blue feature will appear brighter.

There are two lessons to be learned from this: Do not use the compressed movie formats for anything but their designed purpose. If you need to add stereo or highlighting effects, either the movie format has to support them, or you have to code them into the frames, and cannot rely on the interframe time lapse as it is unstable.

A more important message is to only use frame rates that are literally in-sync with your display. So for a 60 Hz display, use any

TABLE 48.1. Synchronization Between Frame Count and Display Cycles

Time	0 ms	16.7 ms	33.3 ms	50 ms	66.7 ms	83.3 ms
Refresh	0	1	2	3	4	5
Frame	0	0	0	0	0	0
. . .						
Time	100 ms	116.7 ms	133 ms	150 ms	166.7 ms	183.3 ms
Frame	0	0	1	1	1	1

[6] However, this situation is in great flux, as Apple recently moved up its H.264 codes to cover the two MPEG high levels, these formats can now actually be created in a high-definition standard. Of course, they cannot yet be played on common consumer hardware or XGA projectors.

integer fraction of 60 Hz, such as 6 Hz or 10 Hz. Because, even in countries with 50 Hz TV standards, projection systems support and prefer 60 Hz modes when connected to a computer, it is much easier to trim your movie for a digital presentation than for your home television. As some CRTs use high and exotic refresh rates such as 85 Hz, 92 Hz, or 120 Hz, it is futile to trim a movie to their needs.

If you cannot match the refresh rate of the display, you can compute the variance of the frame display time: with t_R the refresh time (i.e., the inverse of the refresh rate) and $t_F \geq t_R$ the frame display time and the refresh cycles per frame q: = t_F/t_R, the time mismatch will be $t_M = (q - \lceil q \rceil)t_R$ (Eq. 1). If $t_M > 0$, then the maximum timing error is $\lceil t_R/t_M \rceil \cdot t_M$ (Eq. 2). From Table 48.1, one would expect that the theoretical maximum error would be near $2 \cdot t_R$ and that this would be worse at the start and the end of a movie clip. However, when we captured a series of out-of-register frames it became clear that the movie player had assigned each frame to its closest refresh period rather than to the next one in sequence, that is, they use a *centric* update that reduces the worst frame timing error by half.

Despite this smart feature, Equation 1 has two noteworthy consequences. If there is any timing error whatsoever, the maximum error will always be larger than half a refresh cycle. Even more unexpectedly, any apparently rational ratio between frame rate and refresh rate will result in a largest possible timing error of one entire refresh cycle! So it is not wise to somewhat align the frame rate; they need to be identical.

Practically, this means that if you cannot align your movie frame rate to the refresh rate of the display (something that you might not know) then a timing error of up to one refresh cycle is nearly unavoidable. This timing error is less dramatic if the refresh rate is significantly higher than the movie frame rate. A 7 Hz movie will look OK on all types of displays, whereas the 50 Hz animation noticeably varies in playback speed when viewed on a 60 Hz device (often referred to as *breathing*).

We keep hammering this issue because, very often, one has a choice as to how fast your animation plays back, and slowing it down might actually improve the visual impression. Also, some advanced movie formats (such as MPEG-2 and MPEG-4) do not encode individual movie frames but evolve one frame from the previous one. These formats can produce frames at any desired point in time, not just at the original frame rate. This feature is called *pull down* and is used for standards conversion between television formats. In the case of MPEG-2, it actually can be performed in real time on the very fastest single-CPU machines available. It does not yet offer the quality of offline pull down but will definitely become a method of choice in the future. The MPEG-2 player from Philips already offers this feature. So far no MPEG-4 player can do online pull down. As an intermediate solution, one could create the same movie for each of the refresh rates one is likely to face, one for your native display speed and one for 60 Hz projectors.

Motion Picture Artifacts

Besides the patch and pixelation artifacts inherited from still images, movies face timing subsampling artifacts (temporal artifacts). If a scene evolves too much from one frame to another, the movie will be plagued with temporal aliasing. As in the case of an image with insufficient resolution, this has absolutely nothing to do with the encoding of the movie or technical restrictions and depends solely on the mismatch between movie acquisition and human perception. Fortunately, because human vision is outstandingly tolerant with temporal artifacts and can compensate for it, temporal aliasing catches much less attention than subsampling images spatially. In addition, automated software that can be applied to time sequences is still much less widespread than image-processing algorithms for still images. Finally, because movie formats are seldom used for image-processing applications, we have limited the issue of temporal artifacts to coding errors.

A movie with a fixed data rate cannot always perfectly encode the amount of change between two frames. The different formats cope with this problem in very different ways. The MPEG formats have switches to handle this scenario. MPEG-4 can be set to "scene change detection" that will cue restarting encoding at steep scene changes. MPEG-2 can be allowed to arbitrarily increase its data rate (called *variable bitrate encoding*) when a scene change requires this. Both solutions come at the expense of higher storage requirements. The other movie compressors also invest more in coding data to handle changes but they do so much less consciously, to the extent that image noise can drive their coding effort to the same level as real scene changes. Conversely, limiting their noise encoding restricts their scene update accuracy.

Naturally, none of this holds if one uses a coding format that does not include any compression. TIFF series are lossless as they offer no data reduction either within the frame or over a sequence of frames. For today's large micrographs of one or more channels and megapixel resolution per frame, these formats have little relevance except for programs that allow us to pan and zoom small windows in these datasets.

The second type of artifact comes not from the information encoded in the file but from insufficient machine performance for decoding the animation or from the limited capabilities of the decoder. This can be a very serious restriction when playing back large frames at high rates, especially if one must use an unknown computer. All MPEG-4 formats, independent of resolution, are computationally expensive. Do not expect an aged computer to perform seamless MPEG-4 playback.

At rigid timing, the player will drop frames, causing motion under-sampling to become even worse. In addition, when forced to play all frames, the player may not decode all the image information and may play coarse images with ripples in them. The results look very similar to badly encoded movie formats in general.

As outlined above, decoders usually do an excellent job of squeezing the best possible result from the movie format and computer resources available.

The same cannot be said about encoders (also referred to as compressors) because the task of the compressor is infinitely complex and as long as the compressors do not understand what they are encoding, they have to rely on heuristics to decide what image information they can throw away without visible harm to the movie quality. After all, this is the only way to reduce the data.

The criteria for useless information are unique to each compressor but all are optimized to handle cinema movies or TV shows, a condition that sets clear limits on the color space they must handle and how well they replay motion. Unfortunately, cinema-optimized encoders are notoriously bad at displaying small moving objects against a large constant background, that is, images that look like a fluorescent object on a black background. This is why some encoders have a special setting to encode sports shows, a setting that can be useful to process time sequences of micrographs. Without this optimization, small moving objects drag strong ripple artifacts around with them. On the other hand, fast motion compensation comes at the price of a generally higher noise level. MPEG-2 encoders can achieve both low noise and

small object motion at once but only by requiring higher data throughput. It is usually worthwhile pay the price of a large data file as it usually costs less than more computing power.

The MPEG Formats

A notable feature of movie formats is that the more advanced formats can arbitrate between performance and quality, and are able to sacrifice resolution and sharpness, in order to maintain the frame rate. Depending on the data to be displayed, this can be either useful or noxious. Two major approaches exist to implement this so-called *rigid timing*. MPEG-1 (as it is implemented in the Video For Windows format, also known as H.261) and MPEG-2 (also named H.262) limit the complexity of the movie format (also referred to as *bitrate* capping) upon coding the movie. If content changes too much between frames, capping can only be achieved by jettisoning some of the resolution. MPEG-2 can encode two different bitrates at once, called the *basic* and the *helper* stream. If performance allows for it, the helper stream is decoded as well and this helps to improve the quality. If the resources are insufficient, the basic stream supplies the output. The concept is not very flexible and it can only either boost resolution or lower noise. The unique feature of MPEG-2 is that because the helper stream neither has to be decoded nor read, playback performance is assured.

Because of this, frame-rate tests for MPEG-1 and MPEG-2 yield trivial results — independent of the scene complexity, the frame rate stays constant and frame dropping will only occur when CPU power is very limited and any sort of movie playback is not really possible anyway. On current low-end 2 GHz systems, the CPU load is below 25% of the CPU resources even for very complex movies (see description of entropy) and hence not worth investigating.

MPEG-4 incorporates MPEG-2 modes but adds the capability of limiting the format complexity during playback. Therefore, an MPEG-4 file can be generated at a high bitrate and then be played back at a much lower one (Ebrahimi and Pereira, 2002). In contrast to the MPEG-2 helper stream, however, all data must be read to decode an MPEG-4 stream and this can impede playback performance. Consequently, the player software has a substantial influence on MPEG-4 performance (Walsh and Bourges-Sévenier, 2002).

Many custom players such as the QuickTime or DivX players use the settings of the MPEG-4 codec and the movie format and do not curtail the bitrate. If playback content is too complex to be mastered at full frame rate, the players drop frames. The DivX player incurs a significant jitter because it only notices the timing loss after the frame has been rendered, and CPU cycles that could have been used to render the next frame have just been wasted. However, both players can be performance-tuned by changing the codec settings while leaving the movie file untouched. The Windows Media Player reduces the content complexity within a few frames, so that jitter and frame loss occur only briefly (adaptive bitrate adjustment sometimes called *elastic* bitrate). As useful as these procedures are, they make it hard for the user to tune the trade-off between the available performance and the image.

The long startup time and the huge computing requirements require one to justify when to use MPEG-4. A small 6 MB MPEG-4 file included into PowerPoint did consume an initial startup delay of 2.5 s, allocate 28 MB of system memory, and cause 78% CPU load while playing. Due to the serial coding of the format, however, memory allocation will not exceed some 40 MB, even for long movies. Also startup times will not vary with file size. However, the decoding effort prior to anything being displayed can be cumbersome during a presentation, as can the high CPU load.

The use of MPEG-4 in microscopy should therefore be restricted to what it does best: playing long, highly compressed movies at guaranteed video rates. Like MPEG-2, MPEG-4 can play back an unlimited number of frames from the disk without interruption. Unlike MPEG-2 however, it eats many more CPU cycles and the number depends strongly on the movie content. The complexity of the MPEG-4 resource requirement is touched in the benchmarks listed below. Of more concern, one cannot be sure that an MPEG-4 file that runs smoothly on one system will perform well or even acceptably on a slightly less-powerful system. The only recommendation we can give here is to play the movie on your test system at maximum quality and run the CPU meter (in the TaskManager in Windows systems). Check that the CPU load does not exceed that of the presentation system. Be sure to leave plenty of margins when planning to play an MPEG-4 file this way. In contrast to MPEG-2 hardware, MPEG-4 accelerators are still scarce and — to make things worse — depend on the player software.

MPEG-4 exists in two completely different levels of operation: the more widespread H.263 level, referred to as MPEG-4 part 2, and the widely hailed H.264 (MPEG-4 part 10) (Richardson, 2003). H.263 achieves its very high compression rate by using a plethora of different compression techniques that all rely on certain assumptions about the movie content. For example, H.263 can encode 2D scene rotation, panning, dimming, and even object rotation without storing any image information whatsoever. Sadly, few of these abilities matter for micrographs.

On the other hand, H.264 deploys a new psycho-visual coding technique that is more effective than MPEG-2 but abandons the scene understanding of H.263. Therefore, it compresses less than H.263 but is also less prone for artifact creation. As a consequence, H.263 only works well in microscopy in sparse scenes and when the moving objects are not too small. When maximum compression is not essential there will be no serious use for H.263 in microscopy.

Because modern Apple systems support the H.264 decoders as standard,[7] one cannot use such a system to assure your movie will play well on an inferior machine.

For PCs, the situation is less encouraging but easier to control. Although later Radeon or X-series cards from ATI support the decoding of MPEG-4, they do so to a lesser degree than the Apple H.264 decoders but still boost performance. To get a better estimate, the hardware support for the MPEG-4 codec can be switched off and hence one can get a more reproducible performance estimate.

MPEG Display Formats

The most critical drawback of the MPEG formats is that they come in very few display raster sizes. MPEG-1 is available only in 352 × 288 resolution and hence limited to coarse VHS quality movies only. The upside is that it can be universally played and is not very computing power hungry (decoding effort about one third of main format MPEG-2, that is also well within modest computer limits). The so-called *main profile* of MPEG-2 is defined for the resolutions (called *levels*) 352 × 288 (low), 720 × 576 (main), 1440 ×

[7] H264 offers the same seamless playback and guaranteed frame rates as MPEG-2 does but at roughly half the bandwidth.

1152 (high 1440), and 1920 ×1152 (high) and for two frame rates 30 Hz (NTSC) or 25 Hz (PAL). There are three more MPEG-2 profiles but they offer no additional resolutions or frame rates. The hardware installed on most new graphics boards decodes the main profile but does not go beyond the 720 × 576 resolution. If your movie can be played back at one of these two frequencies or an integer fraction of it, then MPEG-2 offers low load for the computer, universal playback, and color calibration for many systems, and can be written to a DVD. In a presentation, it still may not be wise to play a 2 frame/s (fps) movie as an NTSC MPEG-2 because doing so may inflate a single frame to 15 frames. Also, as the jitter measurement in Table 48.1 shows, it can be cumbersome to encode a 27 fps movie to either PAL or NTSC. For the same reasons that most projectors offer a 30 Hz refresh rate, the NTSC format in a presentation will often play more fluently than the PAL format. If the movie is played full screen, then this limitation does not apply as the refresh will be switched to the 25 Hz needed for PAL.

The MPEG-4 format allows for arbitrary formats but playback software will not support deviations from the MPEG-2 levels. The codecs we tested would work on the main and the low MPEG-2 level for both MPEG-2 and MPEG-4. None would support the two high levels, and one MPEG-4 codec even crashed when using alternate resolutions.

The MPEG standard (Watkinson, 2000, pp. 9–16, 47) assumes that the analog image data is filtered in such a way that it cannot change more rapidly than the resolution that the digital movie contains.

In micrographs, this can be assured by not under-sampling the images. Only those digital micrographs that are properly sampled and not too noisy constitute suitable targets for either JPEG or movie compression algorithms. Unlike JPEG series, high-quality MPEG compression also requires proper temporal sampling to avoid compression artifacts. Consequently, MPEG compressors incorporate digital smoothing filters to handle noisy source images and, when an MPEG-compressed animation appears unnaturally sharp or hard edged with weak ripples and creases, this is a limitation of the standard and not of the player software.

Very High Resolutions

Except for the new H.264 standard, there is no widespread standard for playing movies at 1000 pixel square or higher resolution as is needed by microscopists. The other MPEG formats are practically limited to the MPEG-2 main level, the DVD's resolution. Although QuickTime can assemble single frames of any resolution in use today into movies (there is a filesize limit and a 2^{14} total pixels resolution limit) apart from the dated QuickTime compressor, it does not interface to any advanced movie standard to compress and store the result.

Microsoft's AVI format offers some of the same capabilities but with the even worse restriction that they provide no compressor at all and merely accommodate playback. Movie authoring software such as Adobe Premiere, Final Cut Pro, or Jasc AnimationShop can write megapixel movies, and so do the tools of most microscopy software. When it comes to compression ratios, QuickTime performs better than the antique Sorensen or Cinepak coders used to support the high resolutions for AVI. Apple Final-cut Pro can now create HDTV MPEG-4 (H.264) and H.262 movies.

Movie Compression and Entropy

To obtain some generally valid results and establish a concept of movie performance and quality, it is necessary to focus on the complexity of the movie. The more information a movie conveys (not necessarily the same as **useful** information!) the harder it is to compress, to decompress, and to play back in real time. Complex movies will both suffer from lower frame rates and more compression artifacts. In addition, they will not compress as well. Therefore, the compression factor can be used as a scale for the movie complexity. The compression depends on the entropy of the movie information — the more random the images and animation are, the less it can be compressed without apparent degradation. To get "clean" measurements, we have used an image generator that yields image sequences in which the randomness is controlled. As a result, the image or movie content will be perfectly random to test the movie format but the local changes in the image and the fluctuations in time will be more rapid with higher entropy. In information theory, one can either use this "channel entropy" when talking about compression or when assessing it by taking the autocorrelation of the image sequence. This measure can be scaled to 1 for a completely constant image sequence and 0 for one where neighboring pixels have no relationship to each other in space and time. To benchmark the players and the formats, we devise three movies, one with autocorrelation 0, that is, completely random signal (Format A). One with the highest useful complexity, that is, a movie that is Nyquist sampled in space and time but is as random as possible within these restraints (Format B). And finally, a sparse movie as they are popular in fluorescence labeling, with a real two-channel sequence forced to proper sampling in space and time (Format D). Very often, temporal and spatial sampling is not performed properly. Because, despite all efforts to preach the ultimate importance of proper sampling, under-sampled material still enjoys popularity, we also include an under-sampled version of Format D as Format C.

For the compressor, A is harder to handle than B, B harder than C, and C harder than D. Instead of some meaningless autocorrelation factor, we give the compression ratio (q) as a percentage, that is, the size of the compressed movie file divided by the size of the uncompressed image series. Unfortunately, decompression mostly behaves inversely and a well-compressed movie (low q) will take more computer cycles to play than a more complex one that is compressed less. The exceptions are the MPEG-2 and H.264 formats with a variable bitrate, as here compression and playback effort is symmetric. Because they all guarantee 25 to 30 frames per second, we do not include playback speed in the benchmarks.

Performance Benchmark

Speed benchmarks give you a very coarse idea of what is doable in movie animation. We intentionally do not use the latest Nvidia GeForce6 series or the ATI X600 and X800 engines that are common in G5 Apple machines because we need to get the presentation running on an average system available today. Hence, we test a notebook with a 2-year-old GeForce4MX mobile engine and a desktop with a GeForce 5600. Both cards do not support hardware movie features for non-MPEG playback and hence we should obtain movie performance that is somewhat related to system power.

Compression Ratios for TV-Sized MPEG Movies

VBR is variable bitrate, that is, a compression that adapts to the movie content. CBR stands for constant bitrate, meaning that the compression ratio is held constant, independent of the content.

TABLE 48.2. Compression of TV-Sized Movies (720 × 576)

Format/Type	A	B	C	D
MPEG-2 CBR	2.3%	2.3%	2.3%	2.3%
MPEG-4 CBR	0.8%	0.8%	0.8%	0.8%
MPEG-2 VBR	2.5%	2.5%	2.1%	2.1%
MPEG-4 VBR	2.0%	2.0%	1.7%	1.7%

TABLE 48.4. Playback Frames per Second for PAL TV-Sized Movies (30-s Window)

Format/Type	720 × 576 A	720 × 576 B	720 × 576 C	720 × 576 D
QuickTime NC	27 fps	27 fps	27 fps	27 fps
QuickTime JPG	22 fps	22 fps	24 fps	24 fps
QuickTime QT	32 fps	34 fps	34 fps	34 fps
AVI Cinepac	60 fps	60 fps	60 fps	60 fps

Please note that the two modes cannot be compared to each other as they serve completely different quality needs. CBR is used when there is only a limited bandwidth that can be transferred. VBR is used when one needs at least a certain quality level. The settings used here are default settings for 2-h DVDs (M2 settings), resulting in a 5000 to 6000 kbit/s bitrate. The CBR ratios are trivial as the movie size is given via the bitrate. A high-quality DVD movie would use around 6000 kbit/s. The limit of the MPEG-2 standard (even for VBR movies) is 15,000 kbit/s, including all soundtracks. The MPEG-2 compressors one can buy generally cap at 9200 kbit/s. Commercial DVD movies will not go below 4000 kbit/s.

The raw movie material assumed in developing Table 48.2 would consume a datarate of 30 Hz × 720 width × 576 height × 8 bits per sample, that is, 298,500 kbits/s.

MPEG-4 goes far below this mark. Movies are often encoded at 600 to 700 kbit/s and 1500 kbit/s is considered high quality.

These numbers (Tables 48.3–48.6) list file size and frames per second of different formats. Determining quality involves examining the artifacts introduced and for most rich micrographs, the uncompressed and motion JPG formats may very well be the methods of choice, despite their lack of speed and high memory requirements. Cinepac may be a good and universal choice for a Web page but hardly ever lives up to the needs of displaying micrographs.

Important note: the numbers for QuickTime are QT 6.5 benchmarks, QT 5 actually has higher frame rates for the uncompressed case (17.5 fps) and identical rates for motion JPEG. Because QT 6 (and higher) is more efficient while compressing and supports MPEG-4, we use the latest version.

As in the case of displaying static images, one must realize that the presentation system may have a different screen resolution from the system you tuned the movie on. In this case, the content must either be zoomed or — much more likely — downsized to match the projection system. Respect the restrictions on down-sampling given early in this chapter and also keep in mind that down-sampling will cost CPU power, though less than 5% on a 2 GHz system. If you must run your animation on an unknown computer, make sure that you have plenty of leeway.

TABLE 48.3. Compression Ratios for PAL TV-Sized Movies (720 × 576)

Format/Type	*q* of A	*q* of B	*q* of C	*q* of D
QuickTime NC	100%	100%	100%	100%
QuickTime JPG	27%	18%	3.5%	3.5%
QuickTime QT	17%	18%	3.5%	3.5%
AVI Cinepac	7%	7%	5%	4.5%

Storing Your Presentation for Remote Use

Besides texts and drawings, Keynote and PowerPoint presentations can include image and animation data as well as the complex scripts needed to present them. Images and animations can either be stored within the presentation or they can be linked to the latter by reference. In the latter case, PowerPoint or Keynote will retrieve the original image or movie by a path and file name (the link), and then display it by rules stored within the presentation. The display rules at a minimum consist of dimensions and positions but can also contain timing and movement, triggers that react to certain other events or scripts.

Due to the native viewer concept, PowerPoint hosts images in their original format and hence does not compress or reformat the image data for storage. Any resizing and resampling is done only when the image or movie is displayed. This means that any image included in a PowerPoint presentation will increase the PPT file by the size of the original image (plus a base overhead of about 4 kB for the displaying rules) and will have to be decompressed and resized each time it is displayed in a slide. The data of each image is then cached by PowerPoint so that, the display is faster, the second time it is shown, even though the image must still be decompressed each time. As a result, it is better to only use images that have no more resolution than is actually needed.[8]

There are several reasons for only storing references within a presentation. The premier one is that only a single copy of an image or a movie has to be stored no matter how many different presentations may use it. This also assures update consistency, as changes to a file will be available in all the presentations that include it.

The main drawback is that keeping the references consistent when transporting a presentation to a different computer is not trivial because the path referenced in the document must also function properly on the presentation computer.

There is no perfect solution to this situation and all approaches are plagued with obvious shortcomings:

1. PowerPoint offers a ***pack-and-go*** mode. The file made using this command includes the images and animations (obtained from their references). This is the fastest (and fairly safe) way to complete the task but it leaves one with a single-use presentation. Should you perform changes and add material to the presentation, it will be cumbersome to revert it back into a presentation with links again. The inclusions have to be deleted manually and replaced by new, valid links. So if there is the chance that you will want to update

[8] An exception might be if one is using Keynote or PowerPoint not primarily for a presentation but instead as a way of storing a number of figures for a printed publication. This can be a convenient means of accumulating and annotating the figures and in this case, you can store the images at the resolution appropriate for their final use in the article.

TABLE 48.5. Compression Ratios for Large Movies (1024 Square)

Player/Format	*q* of A	*q* of B	*q* of C	*q* of D
QuickTime NC	100%	100%	100%	100%
QuickTime JPG	24.2%	15.1%	2.75%	2.75%
QuickTime QT	16.6 %	16.7%	2.9%	2.9%
AVI Cincepac	5.2%	5.2%	4.1%	4.0%

your presentation after packing, this approach will not work well.

Also, failures of this procedure have been reported. It works flawlessly for images and PowerPoint animation software but large movies that may be processed by codecs not originally shipped with Windows, sometimes do not play. This is particularly common with movies formats that contain references in themselves such as do MPEG-4 movie streams. Even under OSX, non-standard codecs can lead to incomplete wrapping of the presentation.

The danger here lies in the fact that this situation cannot be avoided by packing then testing the presentation, as the references on the machine the packing is performed on are still valid and failure will only occur once the presentation is loaded onto the target computer. A safe way to force a valid test is to unlink the references — if all your included data is distributed in a path (that would be a directory name in Windows or a folder in OSX) say "all," rename "all" as "former_all." Then running the packed presentation will actually invalidate improper links and the error will show when the presentation is run.

2. ***Moving the entire filesystem*** (or file tree) is a very flexible option for people who try to avoid version conflicts between presentations. If you keep all the data you work with and intend to present in a certain path (a drive and directory tree under Windows or a mounted folder under OSX), then you will be able to move this file system between different computers and keep all references in your presentations valid. For Mac users, this goal can be achieved almost trivially by having a portable disk with a name that does not occur on any of the target computers. So when the disk with the cryptic name is plugged to an alien Mac, it will appear as a folder accessible from the desktop. All presentations can then be moved without any changes.

PCs have an unpleasant restriction that the drive name assigned to such a disk must be free on the target computer. So it is not wise to use any disk drive letter either between A and E, as they tend to be occupied by disks, optical drives, and memory sticks, or using the last characters V through Z as they may also be used for images of network drives. Other than that, the more remote letters work reliably and using a drive letter far from these zones of confusion usually works well.

Newer operating systems, such as Windows 2000 and XP, allow the use of "soft links" similar to the folder concept of the Apple operating system. You can link your portable drive with a soft link from the desktop and when transporting presentations simply re-create that soft link on the target machine. This approach will not work reliably with dated PowerPoint versions as soft links are often resolved to their absolute paths. Given that you use a drive X: with all your presentations, hence using the basic path X:\all_my_presentations, you could soft link it from the desktop, say as "all_my_presentations." PowerPoint 97 may still store the references with the drive name though and hence limit portability. However, as long as this link name is not in use on the target system, this provides a very reliable transportation mechanism for newer PowerPoint versions.

3. Approach 2 won't work if either you cannot use your own disk or want to hand out a presentation. Sharing a presentation is made much easier if the sharing is planned in from the start. If all images and animations for a presentations are made available in a single directory — or folder — from the beginning, then simply copying that folder will make the presentation mobile. This approach is referred to as a ***flat file structure,*** in contrast to the directory tree which is hierarchical. For older PowerPoint versions (especially the still-popular 95 and 97 releases), this can lead to a soft error the first time the presentation is run and PowerPoint will feel obliged to ask each reference for an updated location. The newer versions, however, will deal with the flat file structure smoothly.

Note, however, that with this approach, the person who receives the presentation has copies of the images and movies available in native format. Whether or not you want to give them away, PowerPoint itself does not prevent your data from being extracted. PowerPoint files are documented and even a pack-and-go presentation can be disassembled into its components again.

To obtain more sophisticated protection of your images and animations, make sure to incorporate a copyright watermark into the scans and the movies. Adobe PhotoShop and Premiere, as well as some plug-ins for QuickTime, will perform this task. Watermarks are very difficult to remove with current tools. Another strong protection measure is to lower the resolution of the image material. Scans reduced to half their size, say 512 square will look fine on a projector but will look inferior when printed. Animations in MPEG-1 format can even look great despite the fact that they are of far lower resolution (352×288 pixels at native resolution) than the time series from which they were obtained (usually of megapixel resolution). Both measures, watermarks and lowered resolution, provide the best available protection of your data at this stage. More advanced protection algorithms, such as steganography, which encodes additional information into file formats, is sometimes removed when "saved again" on some tools. Field marks or any other watermarks that cover the entire image are very safe but do impair the image quality. They imprint a noise pattern on the image that is unique to a password you choose and the pattern is chosen in a way that standard filters, such as smoothing or noise reduction, will not remove. In contrast to normal watermarks, however, it is not visible to the eye and hence has no meaning for daily copyright issues. It also does not survive reliably in print and so will not stop others from using it.

In Apple Keynote 2, the Save As command yields a window that asks if you want to copy theme images, audio, or movies into

TABLE 48.6. Playback Frames per Second for Large Movies (30-s Window)

Player/Format	1024 × 1024 A	1024 × 1024 B	1024 × 1024 D	1024 × 1024 D
QuickTime NC	11.5 fps	Same	Same	Same
QuickTime JPG	7.0 fps	8.0 fps	8.0 fps	8.0 fps
QuickTime QT	16.0 fps	15.5 fps	17 fps	17 fps
AVI Cinepac	26.5 fps	27.0 fps	25 fps	25 fps

the document and this seems likely to produce a file similar to the PowerPoint pack-and-go file.

Taking Your Presentation on the Road: Digital Rights Management and Overlaying

When playing animation formats, some advanced features of the native player software can cause substantial inconsistencies. All players are optimized to provide high performance and will exploit hardware features if the drawing libraries (DirectX and QuickDraw) allow this. One of the very popular features shared by the two main players in the field — literally, for once — is dubbed overlaying. For this, the content of the movie frames is not drawn directly into the video memory but into a secondary buffer named the overlay. When the graphics engine refreshes the display, it reads the contents of the overlay, if one is present, rather than the contents of the main image buffer. Overlays must be of rectangular shape and the hardware places strict limits on how many overlays there can be in a display frame. The limit can actually be as low as 1 or 0. The advantage of doing this is that the display does not have to be redrawn when the movie plays. This permits a much more naturally integrated movie window that will respond to scaling and moving much like any other application, and that hides its thirst for computing power.

However, on some hardware, overlaying becomes a problem when a projector is added in parallel to the primary display (i.e., on a laptop, the number of overlays for desktop machines is often more than 1 and hence the problem may not arise — repeat "may"). Under these conditions, sometimes the overlay only works for the primary display and the movie output on the projector is blank (actually, black).

Overlaying can be turned off in MediaPlayer: choose Tools → Options, switch to the Performance tab and choose Advanced, and there, under Video Acceleration, you can disable Use Overlays. There is a second overlay switch for DVD playback below the first one that you might have to deactivate if you play your movie from a DVD.

And in QuickTime: go to Edit → Preferences → QuickTime Preferences, toggle to Video Settings, and deactivate Enable DirectDraw.

As this will disable all acceleration via the graphics library and hence impair performance, it is not the generic setting to be used all the time. It is just a possible solution to the blank-movie window problem described above.

A much more general problem that seems to be dramatically increasing over time is the Digital Rights Management mechanism built into the standard players. This is a protection mechanism intended to uphold copyrights and inhibit duplication of copyrighted material and is capable of preventing you from grabbing screen shots and sequences (clips) from DVDs or other restricted movies.

The problem is that, as there is no open publication of what DRM does and how it affects your system, the normal user can have problems when the player interprets your movie as being copyrighted even when it isn't. This type of error can happen when using advanced formats[9] in QuickTime and MPEG2 and the results can vary from not being able to play the movie in PowerPoint to just not being able to display it on a projector.

A lesser nuisance is that movie startup may be delayed while the player tries to check to see if it is authorized to play the format involved.

The safest way to prevent problems of this kind is to keep your movies in the original format when playing them. Even playing a DVD as part of a presentation may lock the player to a fixed frame rate and format. If the movie files are present in the original, simple format (MPEG files or AVIs that you wrote yourself), it is very unlikely that you will encounter these problems.

Finally, resist the temptation to update the version of your native players just before a presentation. Continuously escalating DRM requirements may make unplayable a movie that had been playable on an earlier version. Although the chances that this will happen are small, they are fatal for a presentation. In general, it is inherently risky to update your player as some of your movie formats may no longer be supported or the new player may insist that your formats must comply with certain rules and will not play them unless they do. This applies particularly to QuickTime files and MPEG-2 or MPEG-4 formats.

At present, most player software still behaves benignly. They will play all formats to the projector if the overlaying is switched off, and when they cannot retrieve a license, they search for a movie file, and then play this format. One notable exception involves movies on DVDs, and these come with severe restrictions and may not even be able to be played at the frame rate of your projector. However, the topic of DRM continues to evolve quickly and, at present, the only way to retain control over your animations is to keep them in the original formats that you can edit (i.e., the production format). In other words, you can use the QuickTime, MPEG-4, and MPEG-2 formats, but you must keep them original (i.e., after writing them, do not package them or write them onto a DVD or VCD), unless you are sure that you have not included or activated an any copyrights when producing the movie.

If you do have to resort to DVDs, make sure that you do not create a *Region Code* that will prevent the DVD from playing on another continent than the one on which the DVD was created. This problem can be a particular nuisance when assembling presentations for use at international conferences. The DVD feature to avoid at all costs is *User Prohibitions*, that is, locking the way the DVD has to be played and accessed. These constraints will prevent the player from playing even an excerpt from the movie and they will also lock down the frame rate of the playback. Unless you can make sure that these features are switched off when creating your DVD, you run the risk that others may not be able to play your presentation and you, yourself, may not be able to play it on any other system or, at least not in the sequence you intend to. To be prepared, it is always wise to carry a copy of your production files with you.

Good Luck!

HELPFUL URLS

The TIFF Standard Archives

http://www.digitalpreservation.gov/formats/fdd/fdd000022.shtml

Nvidia Graphics Cards Technical Details

http://developer.nvidia.com/page/home

[9] If you use an animation editing tool such as Premiere, you can copyright the output material which gives you a different file format from the original data. Editing lingo is production format for the original file and consumer format for the distributed, that is, the copyrighted file. These latter files are susceptible of being handled more strictly by DRM mechanisms.

ATI Graphics Card Technical Details

http://www.ati.com/developer/index.html

Video and Image Compression Lingo Site

http://streaming.wisconsin.edu/terms.html

Wikipedia Encyclopedia

http://en.wikipedia.org

The OpenGL Committee and Graphics Language Reference

http://www.opengl.org

General

http://developer.apple.com/
http://www.vitecmm.com/
http://www.jpeg.org/

ACKNOWLEDGMENTS

Thanks are owed to Valentin Guggiana, ETH Zurich, for his help with setting up benchmarks on systems I do not comprehend; to Dr. Chris Pudney of Focal Technologies for his recommendation and advice on software tools and standards; to Dr. Urs Moser and Felix Gattiker of Sulzer Innotec for providing image material, image-processing software, and numerous hardware platforms to test our assumptions; to Dr. Guy Cox, University of Sydney, for advice on the chapter and providing material from his own chapter; and, finally, to Dr. James Pawley, University of Wisconsin, as the concept and the structure of the chapter and most of its final outcome were conceived by him.

REFERENCES

Castleman, K.R., 1995, *Digital Image Processing*, Prentice Hall, Englewood Cliffs, New Jersey, pp. 247–248.

Bracewell, R., 1995, *Two Dimensional Imaging*, Prentice Hall, Englewood Cliffs, New Jersey.

Ebrahimi, T., and Pereira, F., 2002, *The MPEG-4 Book*, Prentice Hall, Englewood Cliffs, New Jersey.

Nikolaidis, N., and Pitas, I., 2000, *3-D Image Processing Algorithms*, John Wiley and Sons, Inc., New York, pp. 20–24.

Richardson, I.E.G., 2003, *H.264 and MPEG-4 Video Compression: Video Coding for Next Generation Multimedia*, John Wiley and Sons, Hoboken, New Jersey.

Watkinson, J., 2001, *MPEG Handbook*, Focal Press; Linacre House, Oxford, UK.

Walsh, A.E., and Bourges-Sévenier, M., 2002, *MPEG-4 Jump-Start*, Prentice Hall, Englewood Cliffs, New Jersey.

Woo, M., Neider, J., and Davis, T., 2000, Texture mapping, in *OpenGL(R) Programming Guide*, Addison Wesley, pp. 351–466.

49

When Light Microscope Resolution Is Not Enough: Correlational Light Microscopy and Electron Microscopy

Paul Sims, Ralph Albrecht, James B. Pawley, Victoria Centonze, Thomas Deerinck, and Jeff Hardin

INTRODUCTION

Early Correlative Microscopy

Notwithstanding the many ways, amply documented elsewhere in this book, in which fluorescent light microscopy can elucidate biological structure and function, there are times when the available spatial resolution is just not sufficient to answer the biological question. Consequently, there is a need to follow up the initial light microscope (LM) findings by subsequently viewing the LM specimens in the transmission or scanning electron microscope (TEM or SEM). Correlative microscopy of this type has a long history. In 1973, shortly after LM stains had been developed that identified T- and B-lymphocytes, Wetzel viewed the same exact cells, first in the LM and then in the SEM to show that being a T or a B cell bears no relation to whether the cells appeared to be "rough" or "smooth" when viewed in the SEM (Wetzel *et al*., 1973).

Somewhat later, Sepsenwol used time-lapse studies in the LM followed by high-voltage electron microscopy (HVEM) and SEM to study the unusual protein on which *Ascaris* sperm motility is based (Pawley *et al*., 1986; Sepsenwol *et al*., 1989; Sepsenwol and Taft, 1990).

Early 4D Microscopy

Albrecht and his group tracked the motion of colloidal gold–labeled proteins on the surface of activated platelets, using time-lapse, rectified, differential interference contrast (DIC), LM (Fig. 49.1), before determining the final position of the gold particles using both low-voltage SEM (LVSEM; Figs. 49.2, 49.3, and 49.4; Pawley, 1990, 1992) and HVEM (Figs. 49.5 and 49.6; Albrecht *et al*., 1989, 1992; Loftus *et al*., 1984).

This pioneering work did much to elucidate the mechanism of clot formation. It was possible in part because the platelet is small enough to be viewed in the HVEM as a critical-point-dried (CPD) whole mount and in part because the colloidal gold used to label the surface receptors of interest could be seen in the LM, the SEM and the HVEM. The LM allowed one to watch the movement of the Au-labeled, fibrinogen receptors; the LVSEM at 1 and 5 kV allowed one to see how these markers were bound to the surface (Pawley and Albrecht, 1988); and stereo views from the HVEM allowed one to correlate these surface changes with changes in the location and orientation of the cytoskeleton. The details of these early studies are found in the captions of Figures 49.1 through 49.9.

More recently, this group extended the technique by adding an additional, sensitive charge-coupled device (CCD) camera and an ingenious system of dichroic filters to permit them to image living cells using ultraviolet (UV) fluorescence at the same time that they were being viewed using rectified DIC. This has allowed them to follow the motion of the 20 nm gold particles in the DIC image while monitoring the intracellular Ca^{++} concentration using fura-2. As shown in the previous images, the binding of fibrinogen to the receptor (and associated receptor cross-linking) triggers a centripetal movement (edge to center) of the receptor–ligand complexes over the platelet surface. The new instrumentation has allowed them to determine that the movement of the receptors across the platelet surface coincides with a Ca^{++} transient (Fig. 49.10) and to do this on a platelet that they can view subsequently by LVSEM.

CORRELATIVE LIGHT MICROSCOPE/ELECTRON MICROSCOPE TODAY

Light Microscope and Electron Microscope Have Different Requirements

Because the structural details of electron microscope (EM) samples must be preserved in much greater detail and because almost all EM specimens must be viewed *in vacuo*, procedures for preparing them differ markedly from those used in the LM. Correlative studies can be segregated in several ways. The first way is based on the order in which observations are made:

1. The LM observations are made first, on fixed or living cells, and these are then prepared for EM.[1]
2. The preparation is fixed and stained before LM observation.
3. Cells incorporating fluorescent markers are prepared for thin-section TEM, but these are viewed in the LM just before being viewed in the EM.

[1] Because the act of observing a biological specimen in an EM subjects it to a flux of radiation so high that virtually all the organic molecules present (such as dyes or stains) are irretrievably damaged, there is seldom much point in viewing a specimen in an LM after it has been viewed in an EM. The exception to this rule is the quantum dot, a fluorescent label that, as discussed below, is not destroyed by being observed in the TEM.

Paul Sims, Ralph Albrecht, James B. Pawley, and Jeff Hardin • University of Wisconsin, Madison, Wisconsin 53706
Victoria Centonze • University of Texas Health Science Center, San Antonio, Texas 78229
Thomas Deerinck • University of California, La Jolla, California 92093

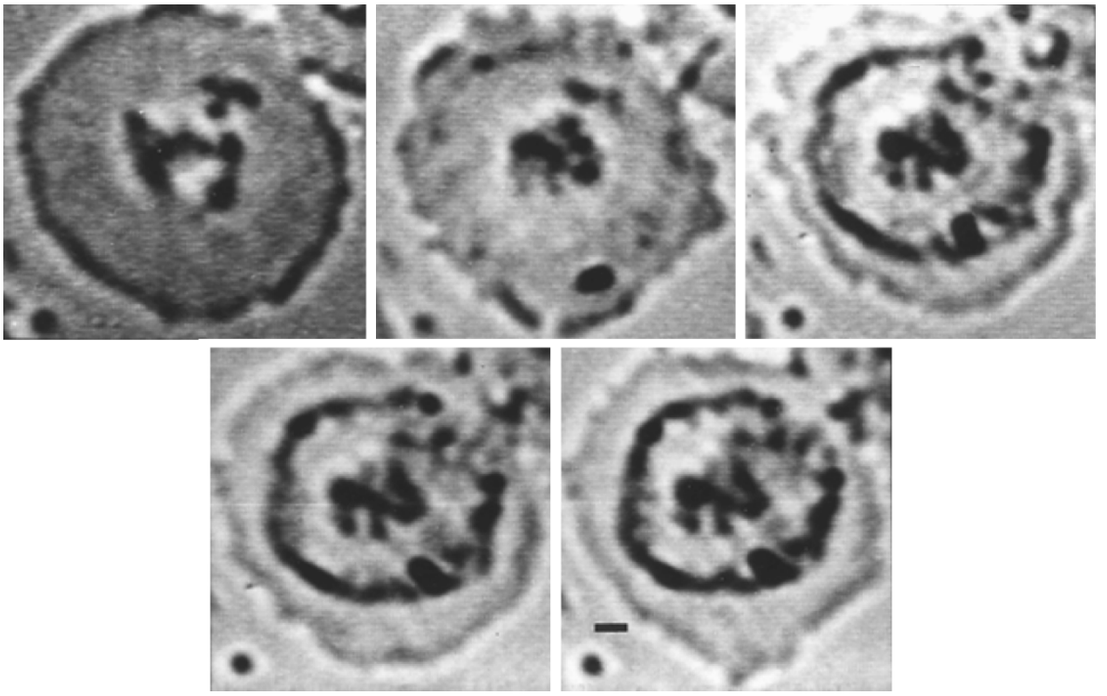


FIGURE 49.1. Time-series of DIC images showing initial binding of Au-conjugated fibrinogen (black) to the platelet surface membrane over the subjacent peripheral web and outer-filamentous zone of the cytoskeleton of a fully spread, substrate-adherent platelet. This label binds to the integrin receptor for fibrinogen on platelets. Over several minutes, bound labels are transported over the surface, towards the platelet center coming to rest, still on the membrane surface, but now overlying the inner filamentous zone. The platelet is then fixed, stained with osmium and uranyl-actetate, and dried by the critical-point procedure for subsequent LVSEM and HVEM. Bar = 1 μm.

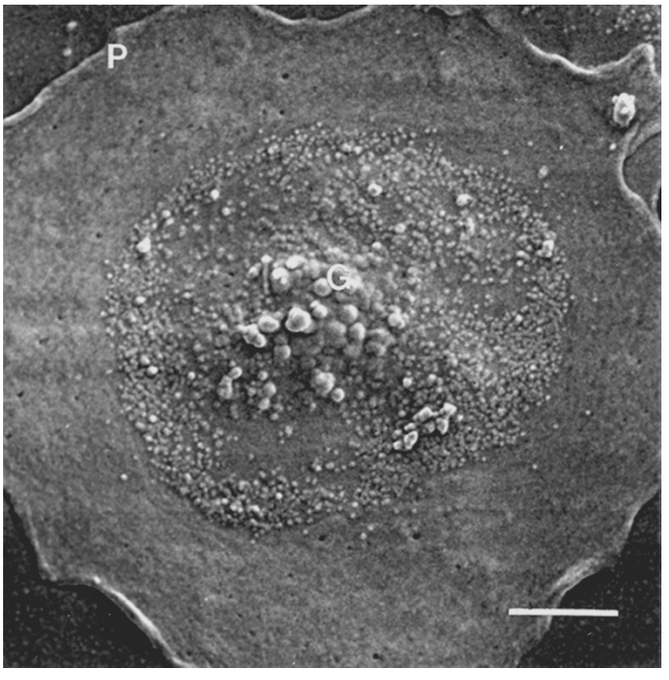


FIGURE 49.2. Surface image of the same uncoated platelet as Figure 49.1 viewed in LM at 1 kV accelerating voltage in a modified Hitachi S-900 SEM. It shows the platelet surface and labels in detail. What is actually seen is the platelet surface and the fibrinogen-covered individual gold particles. Bar = 1 μm.

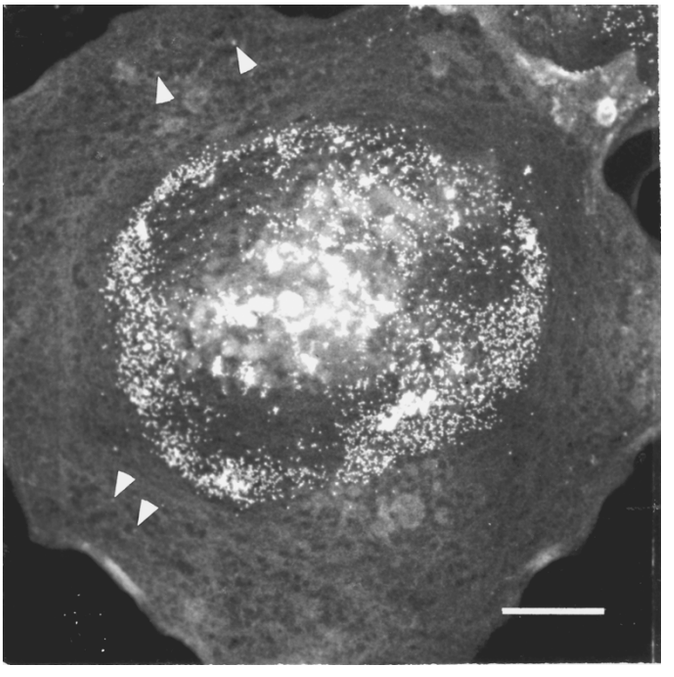


FIGURE 49.3. SEM at 5 kV, still in the SE mode. The increased beam penetration clearly demonstrates the location of the gold particles, bright spots, relative to stained internal cytoskeletal structures. However, surface structure is less apparent. Bar = 1 μm.

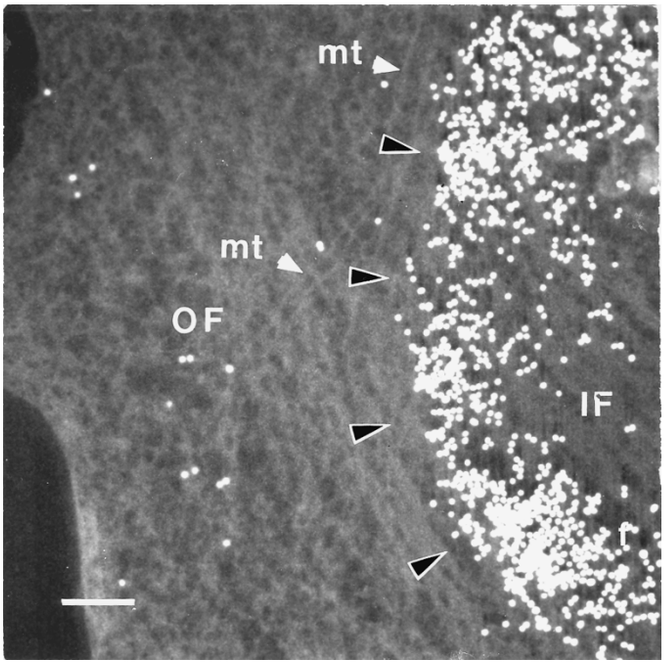


FIGURE 49.4. SEM at 20 kV and somewhat higher magnification. This demonstrates the relationship of the labels on the membrane surface to the underlying cytoskeletal organization. Bar = 0.25 µm.

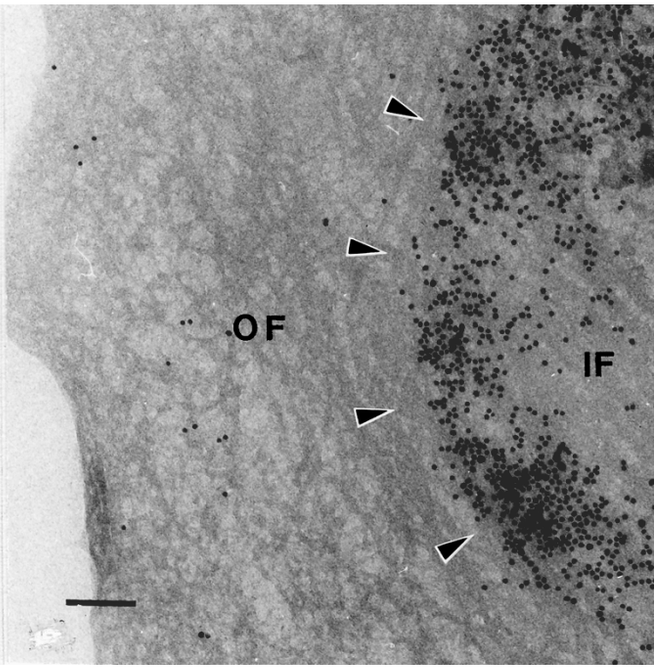


FIGURE 49.6. A higher magnification HVEM of the same area of the platelet as seen in Figure 49.4. P, peripheral web; OF, outer filamentous zone; IF, inner filamentous zone; G, granulomere; mt, microtubules; dark arrowheads, margin of inner filamentous zone; white arrowheads in Figure 49.3 point to labels trapped under the platelet. Bar = 0.25 µm.

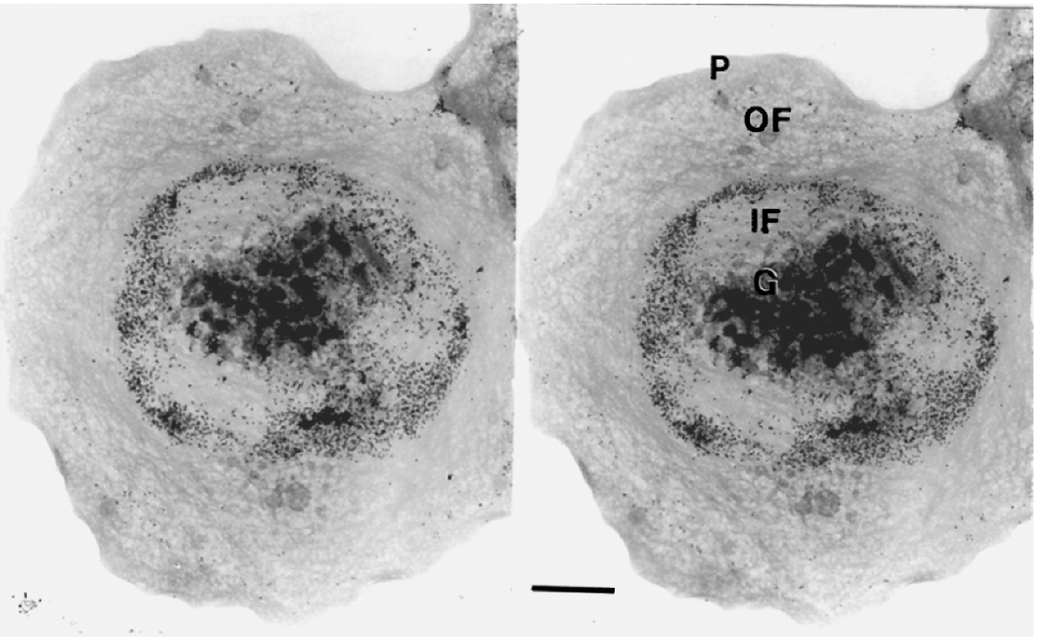


FIGURE 49.5. HVEM stereo-pair whole mount of the same platelet, which offers a clear view of the platelet cytoskeleton. The gold labels, black spots, are clearly seen in relationship to the subjacent platelet cytoskeleton. Bar = 1 µm.

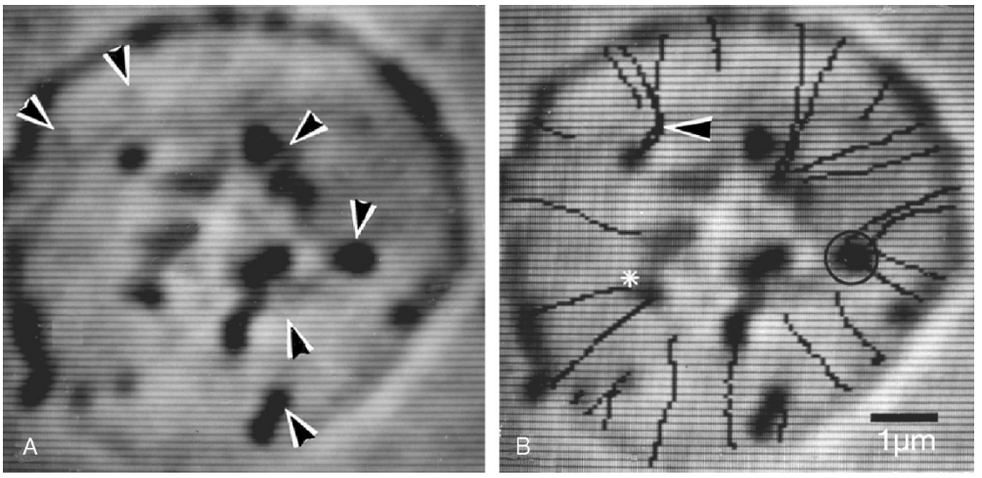


FIGURE 49.7. DIC imaging tracking of movement of individual label particles across the surface of a fully spread platelet.

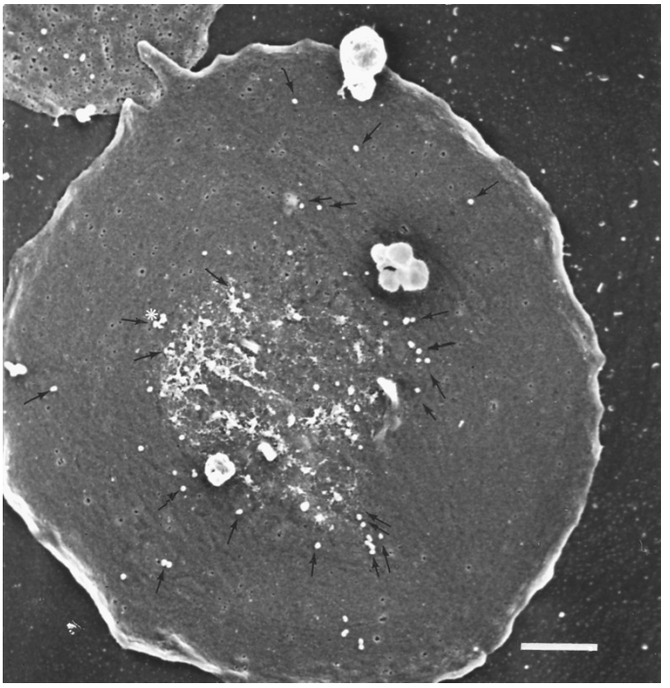


FIGURE 49.8. The same platelet, following fixation, staining, and dehydration, is seen via LVSEM at 1.5 kV accelerating voltage. The position of the individual tracked particles at the time of fixation relative to the platelet surface can be seen.

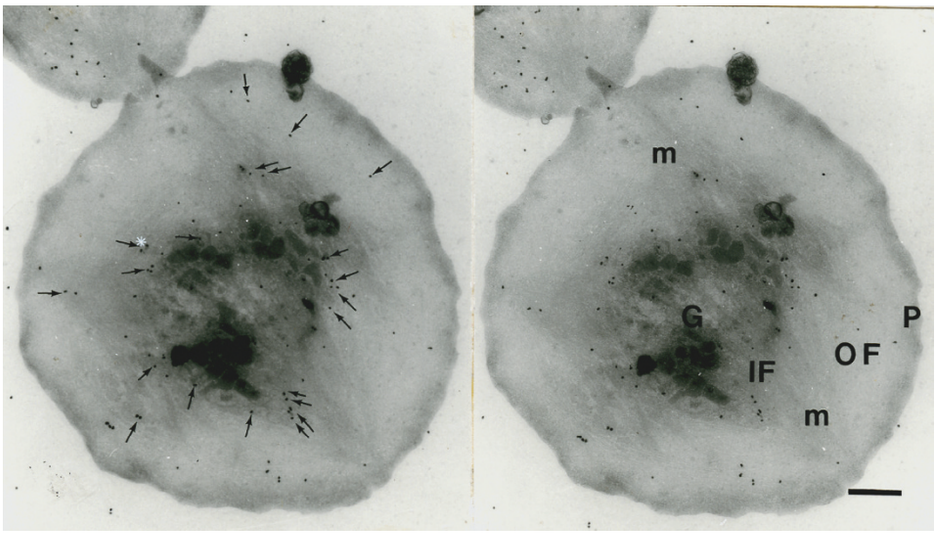


FIGURE 49.9. The same platelet, HVEM stereo-pair, demonstrating the position of the particle labels relative to internal structure. P, peripheral web; OF, outer filamentous zone; IF, inner filamentous zone; G, granulomere zone; m, microfilament bundles. Arrows point to individual labels also seen in Figure 49.8, asterisk indicates particle tracked in Figure 49.7 and seen in Figures 49.8 and 49.9. Labels fixed in transit generally still appear over the outer filamentous zone while labels that have completed their movement are generally seen over the inner filamentous zone. Bar = 1.0 μm.

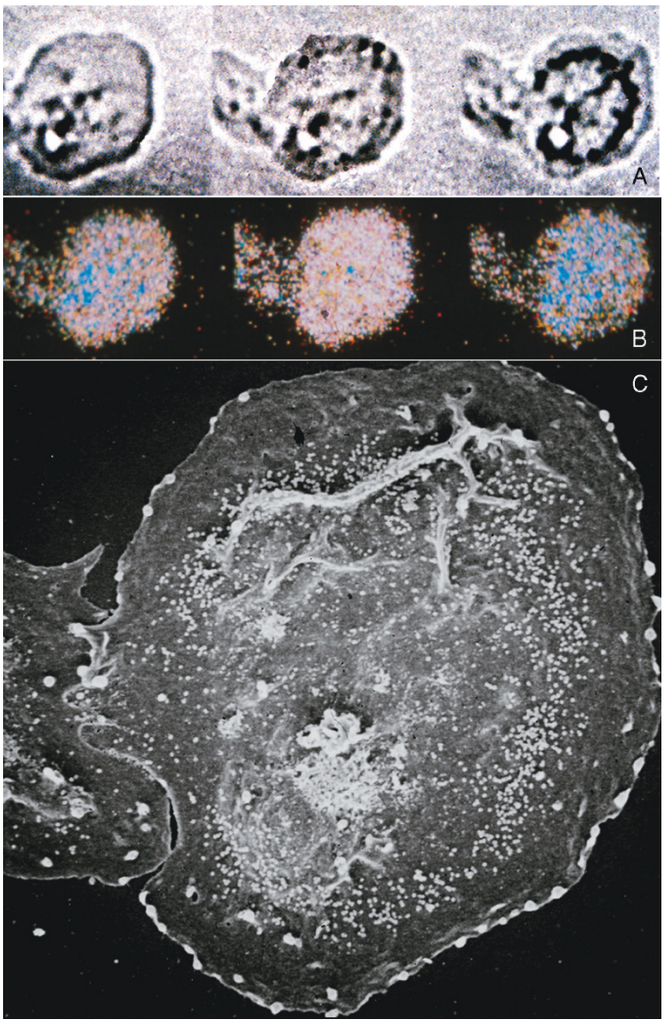


FIGURE 49.10. (A) and (B) show a platelet imaged simultaneously via DIC and UV fluorescence. In (A), the diffraction images of colloidal gold–fibrinogen particles can be followed over time as they move across the platelet surface. (B) Fura-2 340 nm/380 nm ratio images that provide a measure of the free internal [Ca^{++}] as the process proceeds (blue represents resting [Ca^{++}] levels while red and white show increasing [Ca^{++}]). Although the initial fibrinogen-binding produces no increase in free [Ca^{++}] (left panels), once the movement of the fibrinogen-receptor complexes is initiated, [Ca^{++}] is seen to increase (middle panels) until the movement is complete (right panels). (C) An LVSEM image of the same platelet shows the final position of the gold-fibrinogen-receptor complexes (bright spots) relative to platelet surface structure.

Another way of dividing correlative methods is between those using the TEM and those using the SEM. A final criterion that might be used to characterize correlative LM/EM studies is whether it is essential to view exactly the same cell using all methods or if it is sufficient to use the EM image merely to find out the general type of structures being labeled in the LM preparation. The following sections will include a brief review of recent studies illustrating all of these approaches.

Finding the Same Cell Structure in Two Different Types of Microscope: Light Microscope/Scanning Electron Microscope

Because both the LM and the SEM permit one to view quite large specimens, it is often easier to find the exact cell previously viewed in an LM using an SEM rather than a TEM. Centonze and coworkers used this combination to investigate the effect of fluorescence recovery after photobleaching (FRAP) on the molecular structure of the labeled structures. In FRAP, a structure or volume that has been labeled with fluorescent dye in a living cell is intentionally bleached and one then measures the rate at which fluorescence returns to the bleached area (see Chapters 5, 8, 9, 17, and 45, *this volume*). Alternatively, one may wish to derive inferences from the motion of the bleached area. One well-studied example is the motion of a band bleached across a mitotic apparatus made of fluorescent tubulin. In this case, the band did not move even though mitosis proceeded (Gorbsky *et al*., 1987). Centonze used the SEM to investigate this further.

To do this, gold was evaporated through an EM finder grid onto the surface of a glass coverslip to create a fiduciary pattern that could be seen in both the LM and the SEM. These coverslips were then mounted into a hole in the bottom of a plastic Petri dish using silicone grease and isolated, fluorescent microtubules were allowed to adhere to the glass. After obtaining reference transmission and fluorescence LM images, some of the microtubules not located over the gold were bleached, using 546 nm light from an argon-ion laser, for a measured period of time at a known power level. The preparation was then fixed, critical-point dried, coated with ion-beam-sputtered Pt, and viewed in a high-resolution, low-voltage SEM at 1.5 kV. Figure 49.11 shows the results. While a 10 ms pulse caused little visible damage, 30 ms caused total destruction. Fortunately, as is shown in Figure 49.12(A), it is possible to produce significant bleaching using a pulse only 1 ms in duration, a period thought unlikely to cause severe structural damage. It should also be noted that dissolution or disruption of microtubules could also be induced by repeated illumination under conditions used for normal fluorescence observations.

Figure 49.13 shows this system applied to bleaching microtubules in a living cell grown on a marked coverslip. In this case,

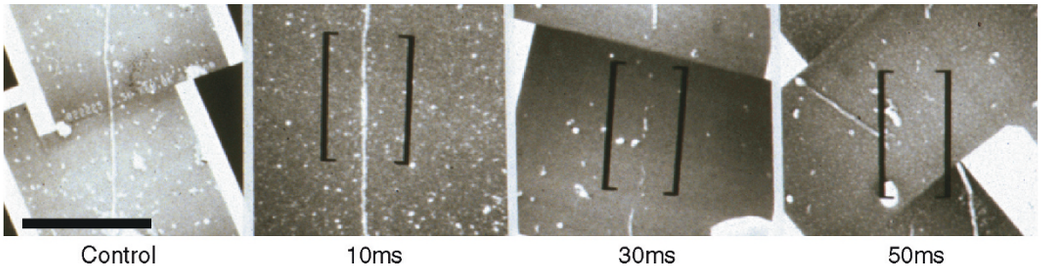


FIGURE 49.11. Low-voltage scanning electron micrographs of single fluorescent microtubules that had earlier been subjected to irradiation by a 546 nm bleaching beam for the times listed. Any exposure above 10 ms destroyed the microtubule.

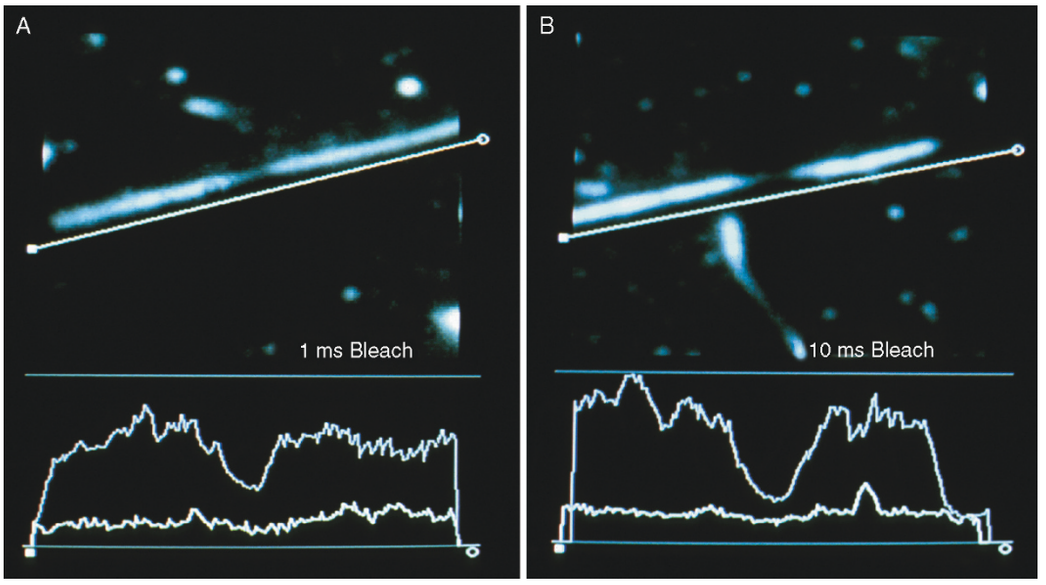


FIGURE 49.12. Fluorescence micrographs showing single microtubules, composed of *in vitro* polymerized microtubules made from rhodamine-conjugated tubulin, across which a bar has been bleached by exposure to a 546 nm laser beam for the noted times. (A) shows that substantial bleaching is produced by a 1 ms exposure, a level 10× lower (B) than that shown to produce structural damage in Figure 49.11. The plots below each image show the intensity along a line down the center of the microtubule (upper trace) and along the straight white line, showing the background signal (lower trace).

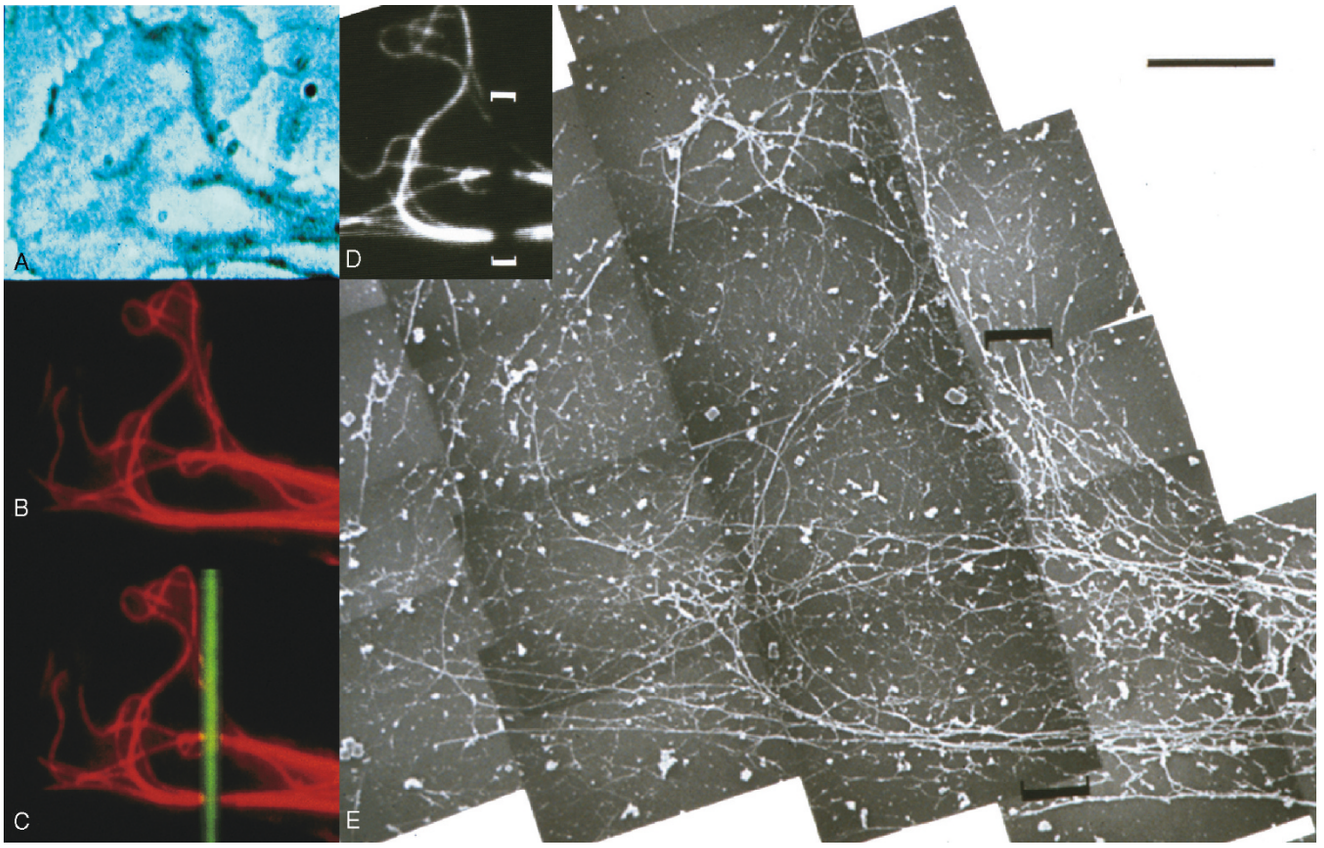


FIGURE 49.13. (A) Phase-contrast image of a spread cell containing microtubles made out of rhodamine-conjugate tubulin. (B) Fluorescence image of the same field. (C) Bleached bar and (D) fluorescence image of the same areas of the specimen after it has been prepared for SEM. (E) Tiled montage of low-voltage SEM images in which one can see that all the microtubules visible in the LM images, even those in the bleached zone (brackets), remain physically intact after the bleaching event.

fibroblast cells were grown on gold-sputtered, locator coverslips and injected with fluorescent derivatized tubulin. After the injected tubulin was allowed to incorporate into the microtubule cytoskeleton for at least 1 h, the injected cells were relocated using phase-contrast microscopy. Fluorescent microtubules were imaged both before and after photobleaching a discrete region [Fig. 49.13(D)]. Because the fixation protocol involved lysing the cells in Triton X-100 detergent before fixation in 2% glutaraldehyde in a cyto skeletal-stabilizing buffer containing, Pipes, Hepes, EGTA and Mg^{++} (PHEM) buffer, the montage of SEM images shows the cytoskeleton, rather than the cell membrane. In this case, bleach levels were low enough to create a photobleach mark without disrupting the microtubules so that all of the microtubules visible in the fluorescence image are visible in the SEM montage. LVSEM images of specimens bleached with higher power, or for a longer time, showed that the affected microtubules could be completely ablated. The ablation was documented in three ways: (1) the fluorescence recovery rates were observed to be different in the bleached region; (2) treatment with fluorescent anti-tubulin produced no staining in the photobleached region because the structures were destroyed; and (3) SEM images clearly show no microtubule structures in the photobleached region (data not shown). This correlational study should give pause to anyone convinced that the ONLY possible effect of photobleaching is that the dye in the irradiated volume becomes non-fluorescent. More insight into photodamage mechanisms is provided in Chapters 38 and 39.

Finding the Same Cell Structure in Two Different Types of Microscope: Light Microscope/Transmission Electron Microscope

Although correlative microscopy uses both light and electron microscopy to examine the same sample, each microscopic method produces contrast in a very different way. When viewing living biological specimens in the LM, one commonly uses phase, DIC, or more recently, fluorescence imaging. However, in the TEM, none of these factors produces significant contrast, and, in addition, the TEM specimen must be considerably thinner than most cells. To produce enough mass-thickness contrast to make biological structures visible in the TEM, one must somehow decorate them with heavy metal stains, such as uranyl–acetate and lead compounds. As a result, LM/TEM correlative methods generally depend on the use of some technique that will deposit heavy metals at or near the site of the fluorescent dye. Possibilities include double labeling with both fluorescent and Au-conjugated antibodies and using light captured by the fluorescent dye to initiate a chemical reaction that later results in the deposition of a heavy metal. Finally, quantum dots are particularly useful because they are both fluorescent and directly visible in the TEM (Niesman *et al*., 2004).

Correlative LM/TEM techniques are also complicated by the fact that the visible area of a TEM grid is usually less than 2 mm in diameter and quite a lot of this area is obscured by grid bars. Moreover, it is in general hard to keep track of changes in the orientation of specific structures in the LM specimen as the sample passes the many steps needed to prepare it for thin-section TEM. This can make it very difficult to find exactly the same feature using both methods, especially if the handedness of the image has been changed by the section having been mounted upside-down.

Making LM Labels Visible in the Transmission Electron Microscope

There are a few techniques that allow the same stained sample to be used for both light and electron microscopy. One of the most successful methods for doing this, called fluorescence photo-oxidation, was developed by Maranto (1982) and later extended to immunolabeling and *in situ* hydridization by Ellisman (Deerinck *et al*., 1994). It relies on the fact that, when certain fluorescent dyes, such as eosin, are excited in the presence of diaminobenzidine (DAB), the reactive oxygen produced by the triplet-excited fluorescent compound causes the DAB to form a deposit very close to the reaction site. This deposit can then be stained with considerable specificity with osmium tetroxide (Fig. 49.14), rendering it visible by both transmitted light and electron microscopy. Because the reaction is limited to only the region near the excited fluorescent dye, the precise area can be located in the epoxy-embedded specimen by light microscopy and then prepared for thin section electron microscopy.

More recently, this group has adapted the tetracysteine genetic marking technique to produce the reactive oxygen needed to deposit the DAB in labeled cells (Griffin *et al*., 1998; see Chapter 16, *this volume*). In this technique, a tetracysteine tag sequence is

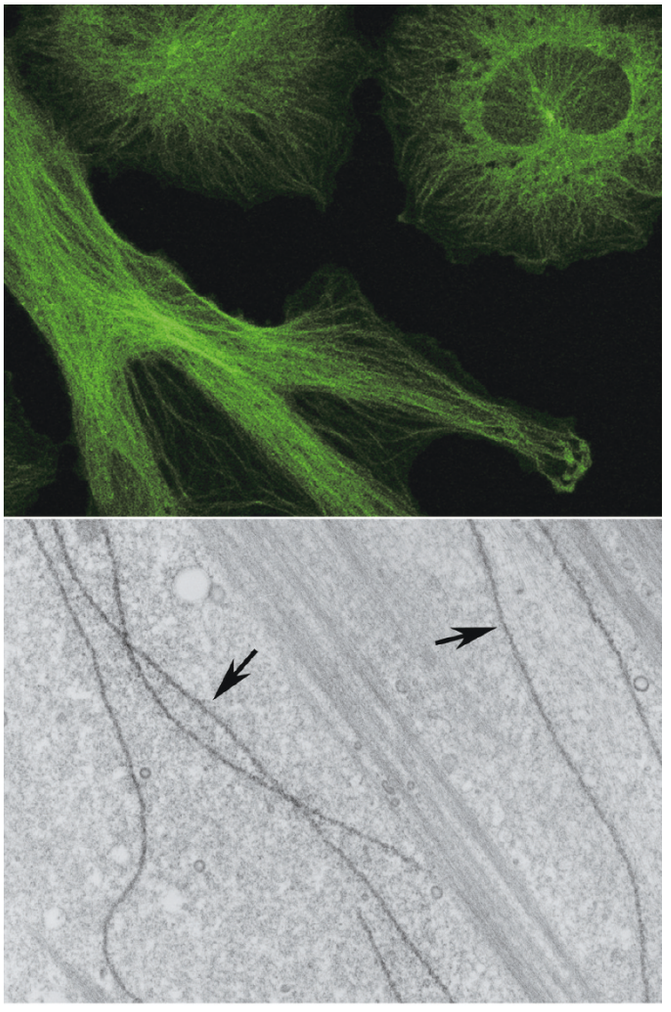


FIGURE 49.14. (A) Using immunofluorescently stained bovine aortic epithelial cells for both light and electron microscopy, cultured cells were labeled with an antibody to beta-tubulin followed by a secondary antibody-eosin conjugate. Following confocal imaging of the eosin fluorescence, the specimen is intensely illuminated in the presence of diaminobenzidine. The resulting reactive oxygen creates a reaction product that can be subsequently visualized by electron microscopy (B). (Image kindly provided by the laboratory of Mark Ellisman at the National Center for Microscopy and Imaging Research, University of California, San Diego.)

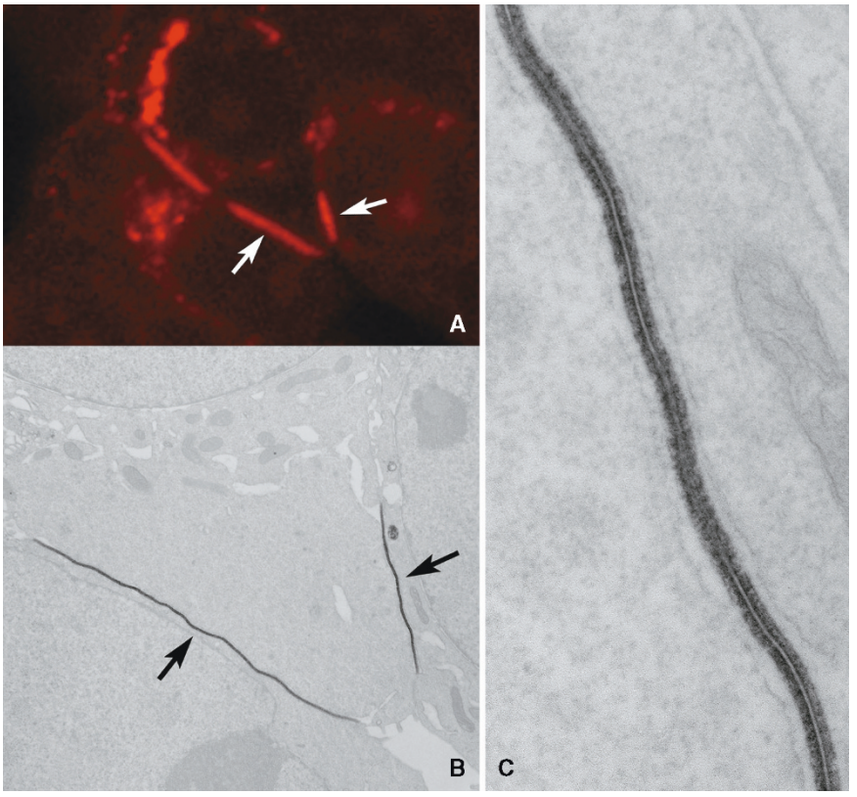


FIGURE 49.15. Using a genetically encoded tetracysteine tag for labeling proteins for light and electron microscopy, cultured cells expressing a recombinant version of the major gap junction protein Cx43 that contains a small tetracysteine tag. Living cells are stained with the biarsenical red fluorescent compound ReAsH (A). Following imaging, the cells are fixed and the specimen is intensely illuminated in the presence of diaminobenzidine. The resulting reactive oxygen creates a reaction product that can be subsequently visualized by electron microscopy (B). (C) is a higher magnification view of (B). (Images kindly provided by the laboratory of Mark Ellisman at the National Center for Microscopy and Imaging Research, University of California, San Diego.)

introduced into the gene of the protein of interest in such a way that the four cysteines can bind to a bi-arsenical derivative of fluorescein (green fluorescence) or resorufin (red fluorescence). Living cells can be bathed in a solution of these membrane-permeant dyes without damage as long as the arsenicals are neutralized with small vicinal dithiols such as 2,3-dimercaptopropanol or 1,2-ethanedithiol. The dye becomes fluorescent only when it bonds specifically to the tetracysteine moiety. Like eosin, the red-fluorescent version of this dye (called ReAsH), is capable of producing reactive oxygen and depositing DAB. The result is a genetically encoded marker that can be seen in both LM (by fluorescence) and TEM (by specific staining) (Gaietta *et al*., 2002; Fig. 49.15). LM/EM correlation can be obtained by embedding the cells still attached to the coverslip and making high- and low-magnification images of them with a confocal microscope before the coverslip is removed. These fluorescent images can them be correlated with low-magnification TEM images of serial-section ribbons made starting from what had been the plastic/coverglass interface.

This same group has also had success labeling structures in such a way that the label can be seen in both LM and EM using quantum dots. These nanocrystals are both fluorescent (Nisman *et al*., 2004) and directly visible in thin-section TEM (Giepmans, 2005; Fig. 49.16). One of the major advantages of using quantum-dot fluorophores is that different colors of quantum dots can be

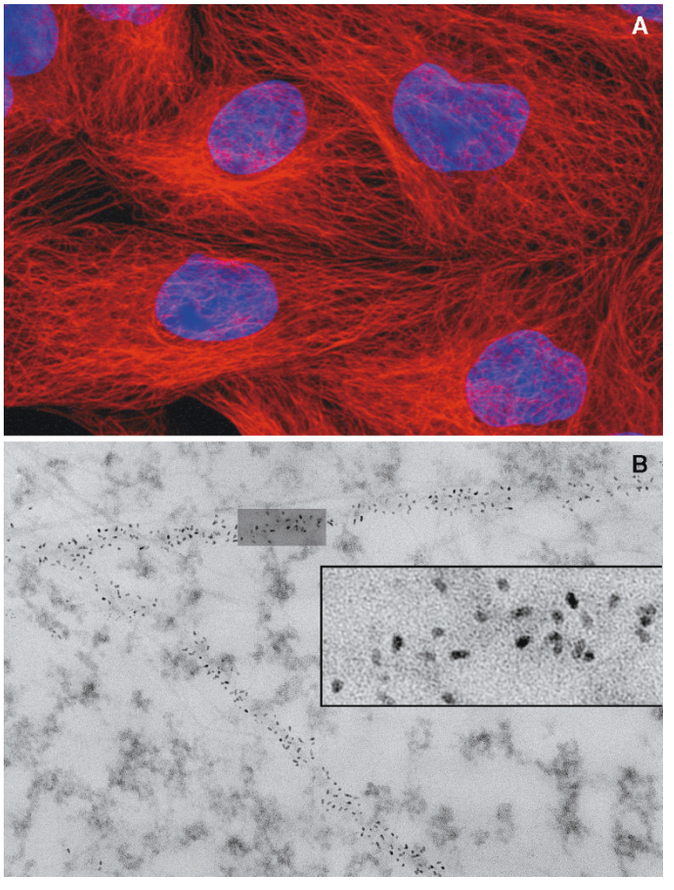


FIGURE 49.16. Using quantum dots as labels for light and electron microscopy, cultured cells were labeled with an antibody to beta-tubulin followed by a secondary antibody-quantum dot 655 conjugate (cell nuclei were counterstained with Hoechst 33342). Following confocal imaging (A), the specimen is prepared for electron microscopy (B). The crystalline core of the quantum dots are readily visible by electron microscopy. (Image kindly provided by the laboratory of Mark Ellisman at the National Center for Microscopy and Imaging Research, University of California, San Diego.)

discriminated by both light and electron microscopy (via size and shape differences), making double or even triple labeling possible. Furthermore, they are not so readily destroyed by electron irradiation as are organic dyes. As a result, it is possible to obtain fluorescent images from the sections after they have been viewed in the TEM. On the other hand, the fluorescence of quantum dots is destroyed if heavy metal stains are used to produce contrast.

Both of these techniques allow one to test and optimize antibody-labeling parameters first by LM before continuing the more laborious processing for electron microscopy.

Marrying Fluorescence with TEM Replicas to Analyze the Cytoskeleton

Phase-contrast and fluorescence microscopy have been used to visualize actin dynamics at the leading edge of living cells in which various cytoskeletal proteins have been labeled with GFP. Svitkina and colleagues followed up such studies by removing the membranes with an extracting buffer, and then shadowing the preparation with Pt after it had been critical-point dried to visualize actin filament structure in the TEM. This led them to propose a filopodial initiation model (Svitkina *et al*., 2003). Such studies provide additional insights into the detailed topology of cytoskeletal assemblies in cells. Because processing for EM is performed on cells with a known history based on LM and potential shrinkage artifacts are carefully monitored during fixation, this approach provides greater confidence that the more highly resolved EM images directly reflect events imaged using LM.

FluoroNanoGold for Cryosections to be Viewed by LM, then TEM

In addition to its utility in analyzing living, migrating cells, viewing specimens first using LM followed by TEM also has other uses. In some cases (e.g., immunostaining), it is far easier to label the structures of interest in fixed and sectioned specimens using LM techniques. Knowing that a given specimen contains the features of interest provides more confidence that subsequent processing for TEM will yield a specimen worth analyzing in detail.

Although it has long been clear that, compared to chemical fixation, cryopreparative techniques both arrest cellular processes faster (milliseconds vs. seconds) and preserve biological structure down to the molecular level better, the complexity of the equipment and procedures needed to freeze even modest-sized specimens without creating ice-crystal artifacts has delayed its widespread use in light microcopy (Biel *et al*., 2003). However, because cryotechniqes are unsurpassed when it comes to preserving antigenicity, in 1998 Takizawa and colleagues stained thin, cryosections with FluoroNanoGold (FNG) antibodies for correlative LM and TEM on the same thin section (Takizawa *et al*., 1998). Ultrathin cryosections were cut from a frozen suspension of fixed cells embedded in gelatin/sucrose. The sections were picked up on finder grids, stained with FNG, and viewed first by fluorescence LM and then by TEM. FluoroNanoGold labels consist of ondeca gold conjugated with a fluorescent dye. As the ondeca gold contains only 11 gold atoms, it often penetrates better than the large colloidal-Au labels. On the other hand, it is difficult to see even in TEM unless it has been decorated by enhancement using silver or gold salts.

Several examples of this technique have been reported. To determine the diameter of transcription sites in the nuclei of HeLa cell, Pombo and colleagues made cryosections 100 to 200 nm thick, stained them with fluorescent antibodies for imaging in the LSCM, and then re-embedded them in Epon to image the same structures by TEM (Pombo *et al*., 1999). In 2001, Robinson reviewed the techniques then used for correlative LM and TEM in cryosections and the advantages of viewing thin sections by LM (Robinson *et al*., 2001).

Any selective staining protocol must face the problem of how to see structure **not** stained with the selective agent. One solution is to use an energy-filtering TEM (EFTEM) to maximize the contrast between unstained protein and embedding resin. Ren and coworkers used this technique to image Quetol-embedded cells in which promyelocytic leukemia (PML)-bodies had been antibody-labeled with Cy-3. They found cyanine and Alexa dyes to be stable in this resin (Ren *et al*., 2003) and also used quantum dots for correlative fluorescence and EFTEM (Nisman *et al*., 2004).

Green Fluorescent Protein Methods

The introduction of the genetically based marker, green fluorescent protein (GFP), has revolutionized the study of cell biology (see Chapter 16, *this volume*). In 2003, Luby-Phelps showed that GFP fluorescence, which was destroyed by most TEM embedding techniques, survived embedding in LR White (Luby-Phelps *et al*., 2003). Adjacent thin and 1 μm sections were cut from preparations of zebrafish eyes and viewed using the TEM and LM, respectively.

Recently, we have extended this approach to thin sections. Specifically, we were interested in the relationship between two junction proteins, HMP-1 [*Caenorhabditis elegans (Ce)* alpha-catenin] and DLG-1 (*Cediscs* large). Confocal fluorescence LM had shown that DLG localizes near HMP-1. To find out if these molecules colocalized at the EM level, we imaged HMP-1::GFP in a thin section by LSCM and immuno-gold-labeled DLG-1 in the same section. EM localization of DLG-1 gold particles with HMP-1::GFP expression is consistent with LM data and confirms the gold labeling parameters needed to label DLG. Thin sections, adhered to EM finder grids and floating on coverslips, were first imaged in an LSCM using both fluorescence and backscattered light (BSL), to reveal the section surface [Fig. 49.17(A)], and fluorescence, to show HMP-1::GFP [Fig. 49.17(B)]. The combination of BSL (displayed in red) and GFP, in green [Fig. 49.17(C)], shows the location of GFP within each embryo and is useful for locating a specific embryo in the TEM [Fig. 49.17(D)]. At higher magnification, the boxed area shows the 20 nm gold labeling due to DLG-1 [Fig. 49.17(F)].

We have also imaged AJM-1::GFP (a novel *Ce* junction molecule) in the pharynx with 20 nm-gold anti-GFP in LR-Gold thin sections after chemical fixation [Fig. 49.18(A)]. Although colloidal gold particles have been shown to quench the fluorescence of molecules in close proximity to them (Kandela *et al.*, 2004), we have found that rhodamine-linked secondary antibodies, not actually conjugated to the gold-label [Fig. 49.18(B)] still fluoresce [Fig. 49.18(C)] (Sims and Hardin, 2004). Like the ReAsH system mentioned above, this procedure also allows one to visualize a genetic marker in a thin section, using both fluorescence LM and a specific stain visible in TEM.

Using Phalloidin as a Correlative Marker

As GFP fluorescence had been shown to survive dehydration and embedding in methacrylate resin, we were curious if rhodamine–phalloidin might also survive this process. *C. elegans* embryos that had been bleached to remove the eggshell, were fixed and incubated in buffer containing saponin and rhodamine–phalloidin. After low-temperature embedding in LR-Gold, 100 nm sections were cut and imaged by confocal laser scanning

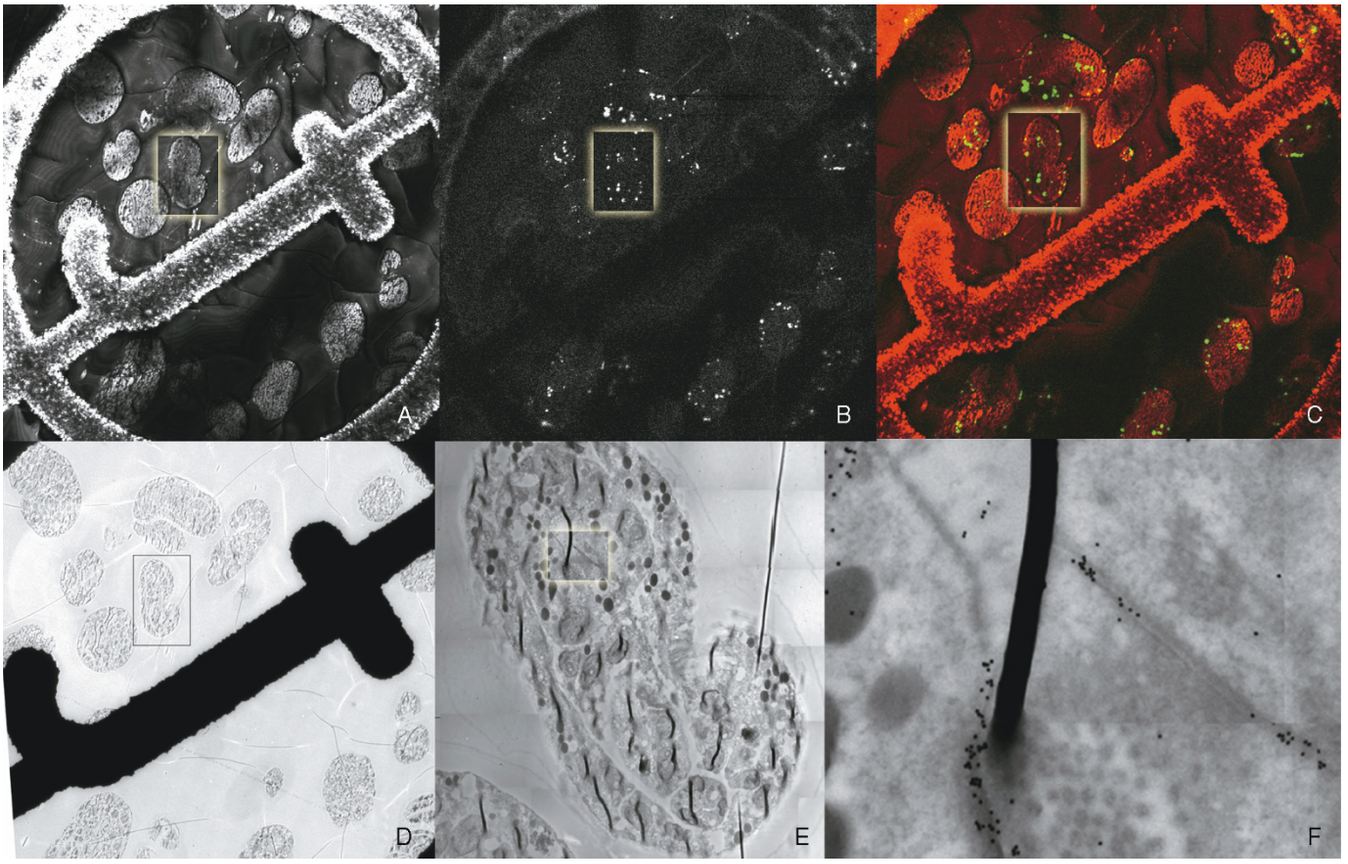


FIGURE 49.17. (A) BSL image of a thin section on an EM finder grid. (B) HMP-1::GFP from the same thin section. (C) A red-green merge of BSL and GFP images which is useful to orient fluorescence to specific embryos. (D) TEM of the same area imaged in (A–C) with the same embryo highlighted by the boxed area. (E) Higher magnification TEM montage of the comma-staged embryo also observed in all previous figures. (F) Boxed area in (E) with 20 nm gold labeling DLG-1, a junctional protein that colocalizes with AJM-1.

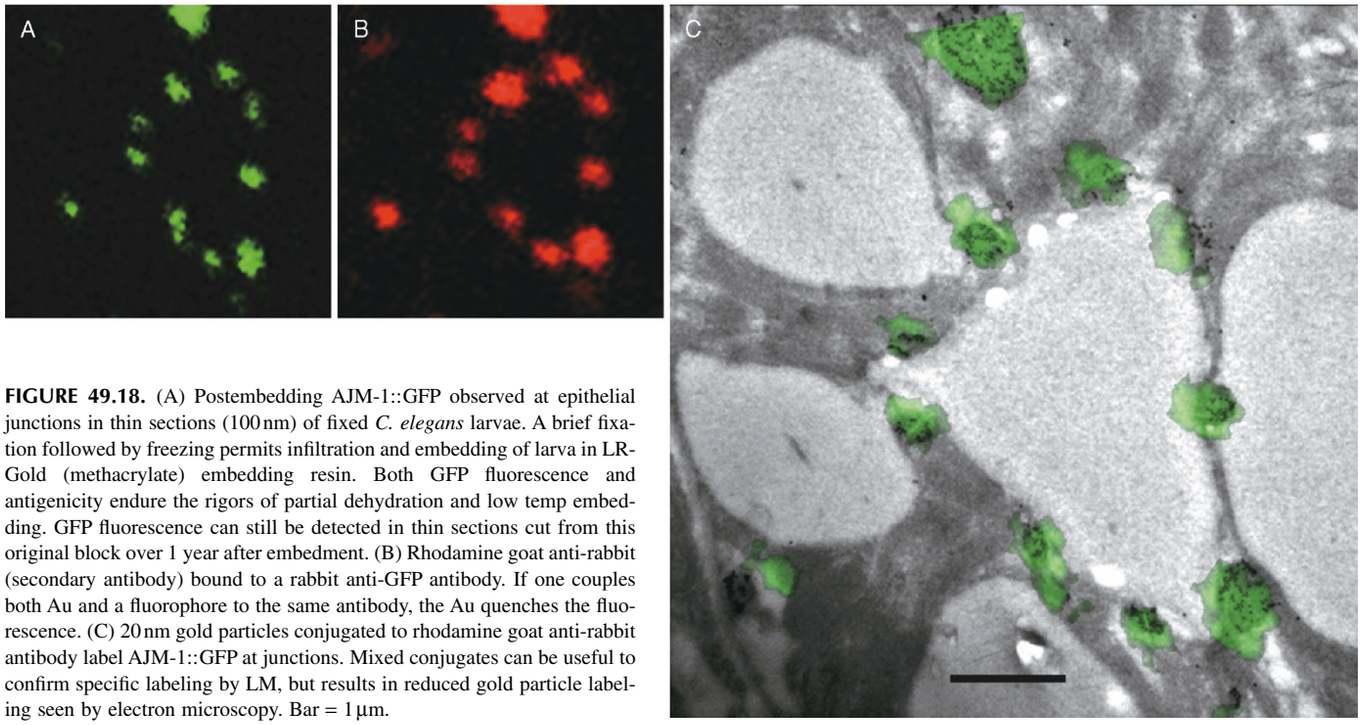


FIGURE 49.18. (A) Postembedding AJM-1::GFP observed at epithelial junctions in thin sections (100 nm) of fixed *C. elegans* larvae. A brief fixation followed by freezing permits infiltration and embedding of larva in LR-Gold (methacrylate) embedding resin. Both GFP fluorescence and antigenicity endure the rigors of partial dehydration and low temp embedding. GFP fluorescence can still be detected in thin sections cut from this original block over 1 year after embedment. (B) Rhodamine goat anti-rabbit (secondary antibody) bound to a rabbit anti-GFP antibody. If one couples both Au and a fluorophore to the same antibody, the Au quenches the fluorescence. (C) 20 nm gold particles conjugated to rhodamine goat anti-rabbit antibody label AJM-1::GFP at junctions. Mixed conjugates can be useful to confirm specific labeling by LM, but results in reduced gold particle labeling seen by electron microscopy. Bar = 1 μm.

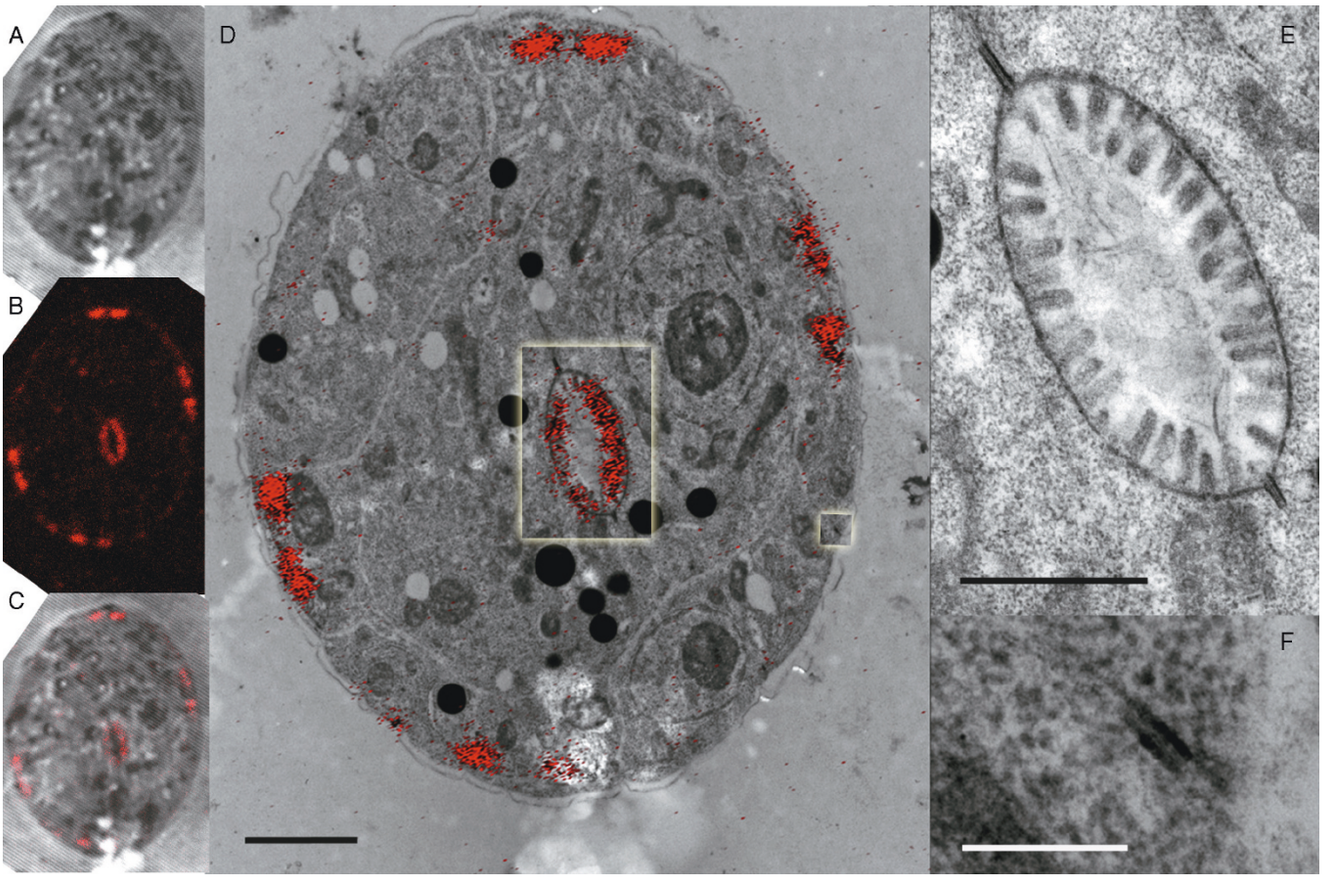


FIGURE 49.19. TEM cross-section of a *C. elegans* larva, *en bloc*-stained with rhodamine-phalloidin and viewed simultaneously in backscattered (A) and fluorescent (B) light on a confocal microscope. (C) Overlay of (A) and (B). (D) A low-magnification TEM (bar = 2 µm). The two boxed areas are seen at higher magnification in (E), a close-up of the intestine (bar = 1 µm) and (F) a hypodermal adherens junction (bar = 0.5 µm). Phalloidin staining is seen decorating the intestinal microvilli and the four muscle quadrants on the sides of the worm.

microscopy (CLSM). A BSL image [Fig. 49.19(A)] and a fluorescent image [Fig. 49.19(B)] were merged together [Fig. 49.19(C)] showing actin-rich, phalloidin-stained muscle quadrants and intestinal microvilli in red. The contrast from the rhodamine signal was increased and overlayed on a low-magnification TEM image [Fig. 49.19(D)]. The boxed regions in Figure 49.19(D) are shown at higher magnification in Figure 49.19(E), covering the intestinal microvilli, and Figure 49.19(F), showing an adherens junction. Overall, this study demonstrates that, at least for proteins as concentrated as actin in muscle and microvilli, one can assess which structures are labeled by analyzing only the fluorescent LM images.

Cryo-Immobilization Followed by Post-Embedding Confocal Laser Scanning Microscopy on Thin Sections

Chemical fixation is known to be slow and to introduce a wide variety of artifacts. Unfortunately, the only alternative is cryopreservation, a technique that depends for its success on freezing the important part of the specimen without forming detectable ice-crystal artifacts. At atmospheric pressure, ice crystals can only be avoided by using cryoprotectants, such as sucrose and polyethylene glycol, or by freezing the tissue very fast indeed (>10^5 K/s; Studer *et al*., 1989; McDonald *et al*., 1993). As using a cryoprotectant requires at least some prefixation, it is not a great improvement on other types of chemical fixation. However, fast freezing is also complex; largely because of the high heat-of-fusion of water and the low thermal conductivity of ice, even cryogens as efficient as liquid-He–cooled copper are unable to extract the heat from the specimen fast enough to prevent ice-crystal artifacts from more than the outer 10 to 15 µm of the specimen.

Objects the size of *C. elegans* (60 µm diameter) can only be successfully frozen using a high-pressure freezer (Studer *et al*. 1989; McDonald *et al*., 1993). In this device, pressurized LN_2 is used to cool a specimen about 2 mm in diameter and 200 µm thick from ambient temperature to 77 K in about 20 ms, under a transient pressure spike of about 2000 bar. Under these conditions, water freezes at a lower temperature (~253 K rather than 273 K), and ice crystals propagate more slowly for various reasons, including the fact that the viscosity of the water increases with ambient pressure. The result is that a relatively high fraction of such specimens are frozen without noticeable artifact.

For TEM observation, freezing is followed by either freeze fracture/metal shadowing/carbon replication, or freeze substitution with ethanol or acetone followed by "normal" epoxy embedment in Lowicryl HM-20. With the latter approach, the plastic-

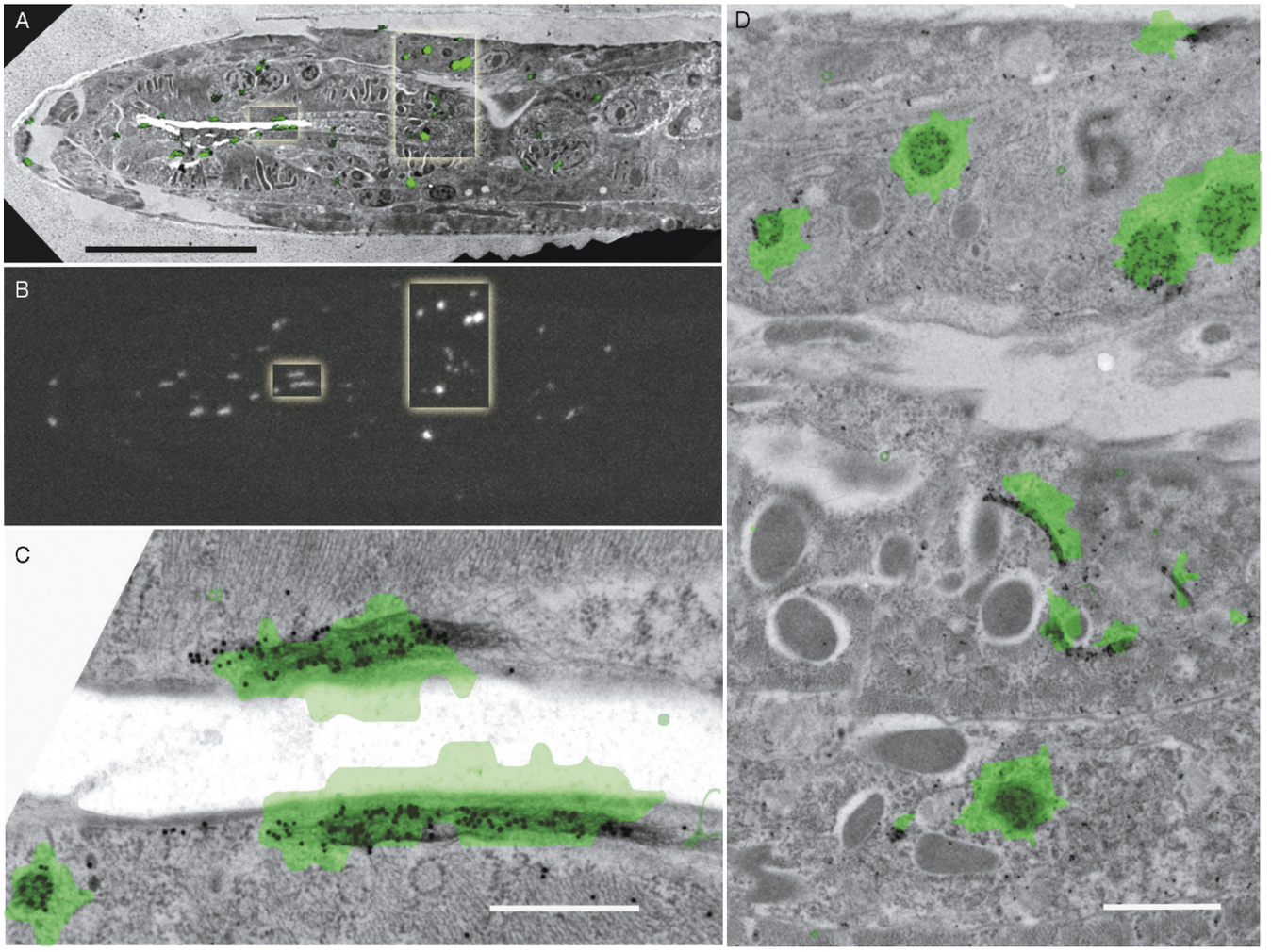


FIGURE 49.20. (A) TEM longitudinal section of an adult *C. elegans*. (B) The same section viewed by fluorescent confocal microscopy showing that the fluorescence of AJM-1::GFP has not been eliminated by embedding in LR-Gold. Boxed areas in (A) and (B) are shown at higher magnification in (C) and (D), where the fluorescence image has been overlaid in green over the TEM image. As the section was also labeled with anti-GFP-gold, these insets show good agreement between the distribution of these two markers in pharynx (C) and around the gut (D). Bar = (A, B) 10 µm; (C) 0.5 µm; (D) 1 µm.

embedded specimen can be viewed directly using CLSM, and this image can be used to choose the best area of the block to be sectioned for TEM (Biel *et al*., 2003).

Cryopreparation of *C. elegans*

Because the eggshell and the vitelline membrane reduce penetration by chemical fixatives, *C. elegans* embryos are difficult to fix chemically. As a result, we have adapted the freeze-substitution protocol to prevent it from damaging frozen GFP specimens. Although Ward observed that GFP fluorescence was completely extinguished if specimens were placed in absolute ethanol (Ward, 1998), Walther and Ziegler (2002) found that adding 1% to 5% water to the freeze-substitution medium increased the visibility of membranes, and we reasoned that a similar approach might preserve GFP structure. We found that freeze substitution in 95% ethanol/5% water, followed by low-temperature embedding in LR Gold, preserves AJM-1::GFP in thin sections (Fig. 49.20). Figure 49.20(B) shows a thin section of a specimen containing AJM-1::GFP and also stained with Au-conjugated anti-GFP, imaged with a disk-scanning confocal microscope. In Figure 49.20(A), an image of GFP fluorescence is overlaid on a low-magnification TEM image. Higher magnification TEMs of the two areas highlighted in Figure 49.20(B) are shown in Figure 49.20(C,D). The green overlays roughly colocalize with the 20 nm gold label.

This technique allows one to combine the ability of fluorescence LM to search large areas of the section rapidly to identify rare stained structures and then find and view these rare structures in the TEM. The result confirms that this HPF protocol preserves GFP fluorescence and specimen immunoreactivity and also allows one to correlate AJM-1::GFP with specific cellular structures visible only at the ultrastructural level.

Another application of GFP and cryopreservation involves identification of wild-type and mutant embryos prior to cryopreservation and processing with immunogold. Although *C. elegans* embryos containing mutant copies of the *ajm*-1 gene arrest soon after the 2-fold stage, an average 60% of them can be rescued to viability if the hermaphrodite (parent) is microinjected with an extrachromosomal array that includes a functional copy of the

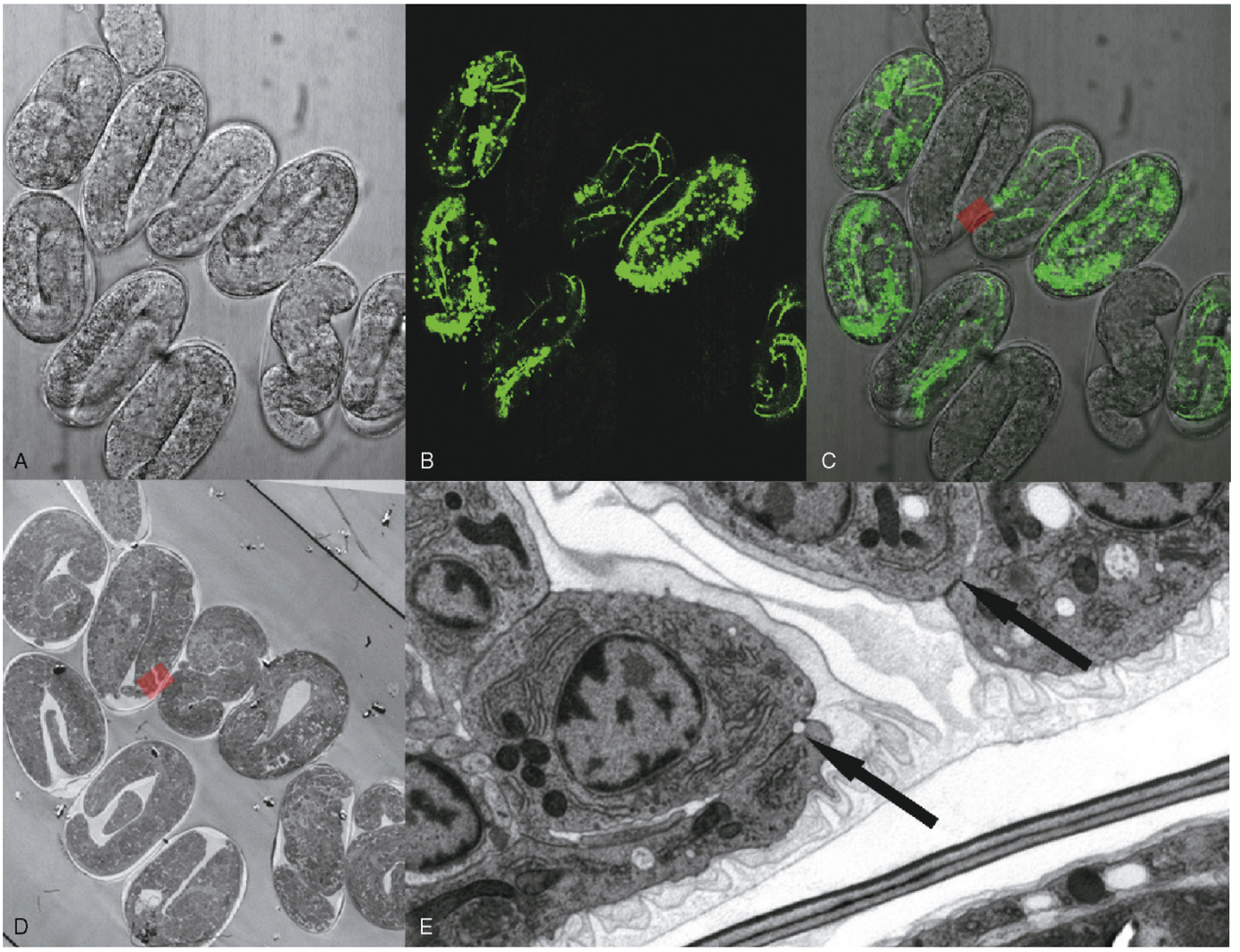


FIGURE 49.21. (A) A transmitted light image of living embryos embedded in agar. (B) A brightest-pixel projection (ImageJ) of AJM-1::GFP expression in the same embryos in (A). Transmitted light and fluorescence images were obtained simultaneously on a Bio-Rad 1024 confocal using 488 nm excitation. Embryos older than comma stage which do not express GFP, lack the *ajm*-1 gene. (C) Overlay of the fluorescent projection over the transmitted light image. Red-shaded area is a 2-fold embryo which lacks *ajm*-1. (D) A TEM image of the same embryos after HPF and embedding in Epon. Same area red-highlighted in (C) and (D) is shown in (E), where arrows point to epithelial cell membrane separations associated with the loss of *ajm*-1.

ajm-1 gene, in this case *ajm*-1 fused to the GFP-coding region. The GFP label allows the observer to determine which of the living embryos carry the *ajm*-1 gene and which do not. Although one could make a similar discrimination by applying Au-conjugated, anti-GFP antibodies to the thin sections, optimal fixation and staining could be compromised by the need to preserve the antigenicity of the GFP. Correlating the LM fluorescence image of a living embryo with the TEM image of a section from this embryo avoids this problem, particularly if rescued and non-rescued embyos are next to one another on the same TEM grid. Any observable differences are more likely to be real when one knows that the high-pressure freezing, fixation, and staining are identical.

Figure 49.21(A) shows a transmitted light image of a group of 10 embryos, 6 of which have been rescued (Koppen *et al*., 2001; Simske *et al*., 2003). Although the non-rescued embryos look normal in transmitted light, they are clearly marked by the absence of GFP fluorescence [Fig. 49.21(B,C)]. Following high-pressure freezing, freeze substitution, embedding in Epon, and sectioning, the same group of embryos can be visualized at low magnification by TEM [Fig. 49.21(D)]. The small red-shaded boxes in Figure 49.21(C,D) indicate the area shown at higher magnification in Figure 49.21(E). Arrows point to separations at epithelial cell junctions believed to be associated with the loss of *ajm*-1.

Tiled Montage Transmission Electron Microscope Images Aid Correlation

Many modern TEMs incorporate both electronic image recording and motor-driven stage motion. This combination of features greatly facilitates LM/TEM correlational studies by making it much easier to obtain high-resolution images over a wide area of the specimen. Figure 49.22 shows such a tiled montage of a specimen prepared in the same way as that shown in Figure 49.21. This image covers an area $30 \times 50\,\mu m$ in size and consists of 36 images recorded at an original magnification of 3.5×. The green overlay represents AJM-1::GFP fluorescence recorded on a Bio-Rad 1024 confocal microscope.

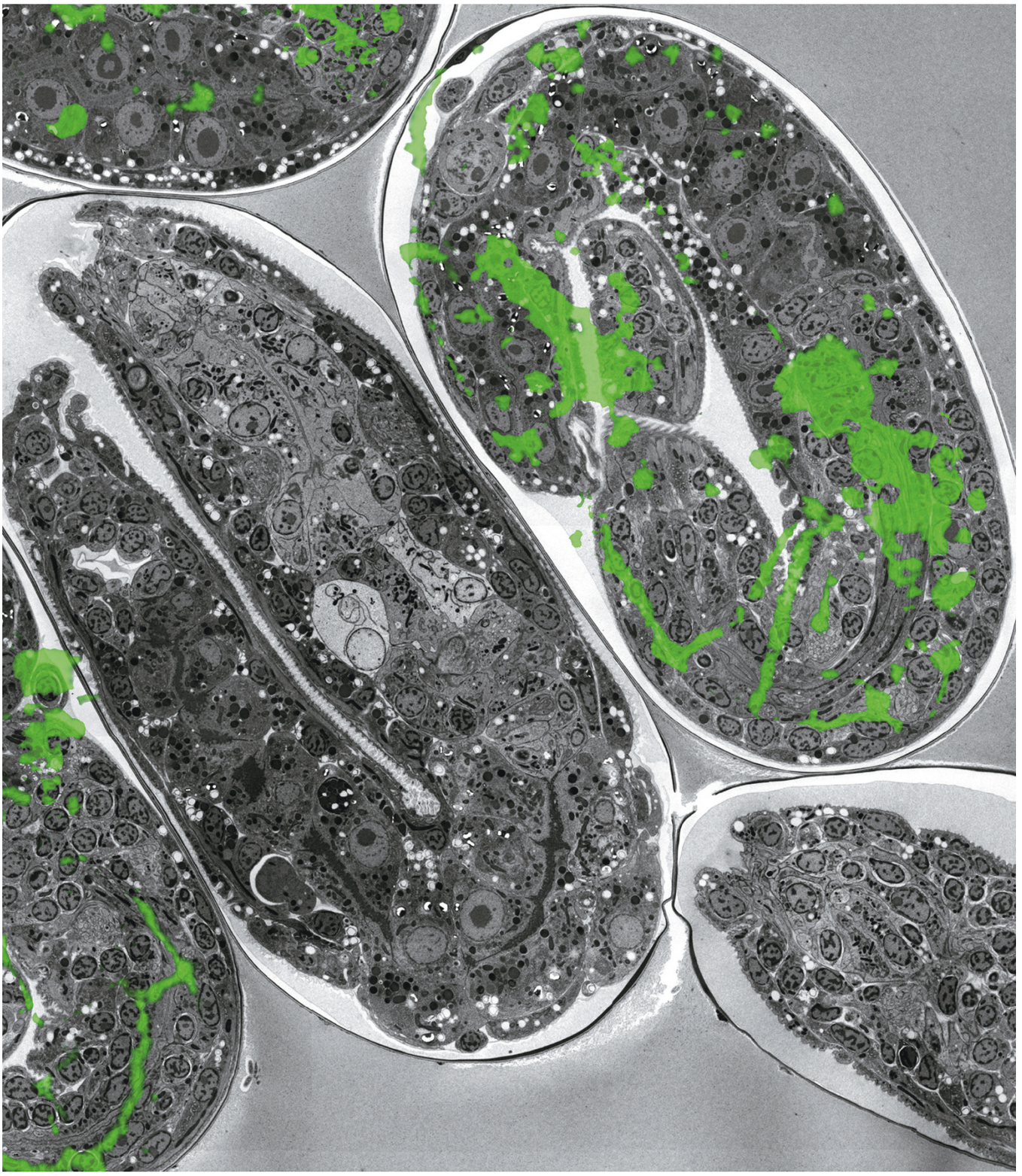


FIGURE 49.22. A tiled montage TEM image of a specimen prepared in the same way as that shown in Figure 49.11. The original montage covered an area of the specimen 50 × 32 µm in size and consisted of 36 images recorded at 80 kV using an original magnification of 3400× on a Phillips 120 using a Soft Imaging Systems, Keenview, CCD camera coupled to the phosphor by a 3.4× fiber-optic taper. The green overlay represents AJM-1::GFP fluorescence recorded on a Bio-Rad 1024 confocal microscope.

CONCLUSION

Although during the 1950s and 1960s light microscopy languished beneath the high-resolution shadow of the electron microscope, starting in the early 1970s, it flowered as a variety of new technical improvements were introduced: video-enhanced DIC, video-intensified fluorescence, improved CCD cameras, and myriad new fluorescent probes. Suddenly, the fact that one could observe function in wholly new ways seemed to more than offset the ability to image the internal features of intracellular organelles. These LM developments were soon followed in the 1980s and 1990s by the widespread use of a variety of confocal microscopes, and more recently by the advent of GFP and its many relations. This entire book is a testament to the fact that live-cell fluorescent light microscopy is blossoming as never before.

On the other hand, we lose nothing by admitting that much of the business of cells occurs at a size scale that is much smaller than that which can be imaged with the light microscope. When this occurs, it is useful to remember that help is at hand; given the effort needed to boost LM spatial resolution by a factor of 2, it is salutary to acknowledge how much more clearly one can see when it is increased by a factor of 40.

ACKNOWLEDGMENTS

This work was supported by grants from the National Institutes of Health: GM-058038 (Hardin), RR-04050 (Ellisman), and NIGMS-63001 (Albrecht); and from the National Science Foundation IBN-0712803 (Hardin).

REFERENCES

Albrecht, R.M., Goodman, S.L., and Simmons, S.R., 1989, Distribution and movement of membrane-associated platelet glycoproteins: Use of colloidal gold with correlative video-enhanced light microscopy, low-voltage high-resolution scanning electron microscopy, and high-voltage transmission electron microscopy, *Am. J. Anat.* 185:149–164.

Albrecht, R.M., Olorundare, O.E., Simmons, S.R., Loftus, J.C., and Mosher, D.F., 1992, Use of correlative microscopy with colloidal gold labeling to demonstrate platelet receptor distribution and movement, *Methods Enzymol.* 215:456–479.

Biel, S.S., Kawaschinski, K., Wittern, K.P., Hintze, U., and Wepf, R., 2003, From tissue to cellular ultrastructure: Closing the gap between micro- and nanostructural imaging, *J. Microsc.* 212:91–99.

Deerinck, T.J., Martone, M.E., Lev-Ram, V., Green, D.P., Tsien, R.Y., Spector, D.L., Huang, S., and Ellisman, M.H., 1994, Fluorescence photooxidation with eosin: A method for high resolution immunolocalization and *in situ* hybridization detection for light and electron microscopy, *J. Cell Biol.* 126:901–910.

Gaietta, G., Deerinck, T.J., Adams, S.R., Bouwer, J., Tour, O., Laird, D.W., Sosinsky, G.E., Tsien, R.Y., and Ellisman, M.H., 2002, Multicolor and electron microscopic imaging of connexin trafficking, *Science* 296: 503–507.

Giepmans, B.N., Deerinck, T.J., Smarr, B.L., Jones, Y.Z., and Ellisman, M.H., 2005, Correlated light and electron microscopic imaging of multiple endogenous proteins using Quantum dots, *Nature Methods* 2(10):743–749.

Gorbsky G.J., Sammak, P.J., and Borisy, G.G., 1987, Chromosomes move poleward in anaphase along stationary microtubules that coordinately disassemble from their kinetochore ends, J. *Cell Biol*. 104:9–18.

Griffin, B.A., Adams, S.R., and Tsien, R.Y., 1998, Specific covalent labeling of recombinant protein molecules inside live cells, *Science* 281:269–272.

Kandela, I.K., Bleher, R., and Albrecht, R.M., 2004, Correlative labeling studies in light and electron microscopy, *Microsc. Microanal*. 10(Suppl, 2):1212–1213.

Koppen, M., Simske, J.S., Sims, P.A., Firestein, B.L., Hall, D.H., Radice, A.D., Rongo, C., and Hardin, JD., 2001, Cooperative regulation of AJM-1 controls junctional integrity in *Caenorhabditis elegans* epithelia, *Nat. Cell Biol.* 3:983–991.

Loftus, J.C., Choate, J., and Albrecht, R.M., 1984, Platelet activation and cytoskeletal reorganization: High voltage electron microscopic examination of intact and Triton-extracted whole mounts, *J. Cell Biol.* 98:2019–2025.

Luby-Phelps, K., Ning, G., Fogerty, J., and Besharse, J.C., 2003, Visualization of identified GFP-expressing cells by light and electron microscopy, *J. Histochem. Cytochem.* 51:271–274.

Maranto, A.R., 1982, Neuronal mapping: A photooxidation reaction makes Lucifer yellow useful for electron microscopy, *Science* 217:953–955.

McDonald, K., and Morphew, M.K., 1993, Improved preservation of ultrastructure in difficult-to-fix organisms by high-pressure freezing and freeze-substitution: I. *Drosophila melanogaster* and *Strongylocentrotus purpuratus* embryos, *Microsc. Res. Tech*. 24:465–473.

Nisman, R., Dellaire, G., Ren, Y., Li, R., and Bazett-Jones, D.P., 2004, Application of quantum dots as probes for correlative fluorescence, conventional, and energy-filtered transmission electron microscopy, *J. Histochem. Cytochem.* 52:13–18.

Pawley, J.B., 1990, Practical aspects of high resolution LVSEM, *Scanning* 12:247–252.

Pawley, J.B., 1992, LVSEM for high resolution topographic and density contrast imaging, *Adv. Electron. Electron Phys*. 83:203–274.

Pawley, J.B., and Albrecht, R., 1988, Imaging colloidal gold labels in LVSEM, *Scanning* 10:184–189.

Pawley, J.B., Sepsenwol, S., and Ris, H., 1986, Four-dimensional microscopy of *Ascaris* sperm motility, *Ann. N Y Acad. Sci.* 483:171–180.

Pombo, A., Hollinshead, M., and Cook, P.R., 1999, Bridging the resolution gap: Imaging the same transcription factories in cryosections by light and electron microscopy, *J. Histochem. Cytochem.* 47:471–480.

Ren, Y., Kruhlak, M.J., and Bazett-Jones, D.P., 2003, Same serial section correlative light and energy-filtered transmission electron microscopy, *J. Histochem. Cytochem.* 51:605–612.

Robinson, J.M., Takizawa, T., Pombo, A., and Cook, P.R., 2001, Correlative fluorescence and electron microscopy on ultrathin cryosections: Bridging the resolution gap, *J. Histochem. Cytochem.* 49:803–808.

Sepsenwol, S., Ris, H., and Roberts, T.M., 1989, A unique cytoskeleton associated with crawling in the amoeboid sperm of the nematode, *Ascaris suum*, *J. Cell Biol.* 108:55–66.

Sepsenwol, S., and Taft, S.J., 1990, *In vitro* induction of crawling in the amoeboid sperm of the nematode parasite, *Ascaris suum*, *Cell Motil. Cytoskeleton* 15:99–110.

Sims, P.A., and Hardin, J.D., 2004, Visualizing green fluorescent protein and fluorescence associated with a gold conjugate in thin sections with correlative confocal and electron microscopy, *Microsc. Microanal*. 10(Suppl. 2):156–157.

Simske, J.S., Koppen, M., Sims, P., Hodgkin, J., Yonkof, A., and Hardin, J., 2003, The cell junction protein VAB-9 regulates adhesion and epidermal morphology in *C. elegans* [comment], *Nat. Cell Biol.* 5:619–625.

Studer, D., Michel, M., and Muller, M., 1989, High-pressure freezing comes of age, *Scanning* 11(Suppl. 3):253–269.

Svitkina, T.M., Bulanova, E.A., Chaga, O.Y., Vignjevic, D.M., Kojima, S., Vasiliev, J.M., and Borisy, G.G., 2003, Mechanism of filopodia initiation by reorganization of a dendritic network, *J. Cell Biol*. 160:409–421.

Takizawa, T., Arai, S., Osumi, M., and Saito, T., 1998, Ultrastructure of human scalp hair shafts as revealed by freeze-substitution fixation, *Anat. Rec.* 251:406–413.

Walther, P., and Ziegler, A., 2002, Freeze substitution of high-pressure frozen samples: The visibility of biological membranes is improved when the substitution medium contains water, *J. Microsc*. 208:3–10.

Ward, W.W., 1998, *Green Fluorescent Proteins: Proteins, Applications and Protocols*, John Wiley and Sons, New York.

Wetzel, B., Erickson, B.W., and Levis, W.R., 1973, The need for positive identification of leukocytes examined by SEM, Part III:535–541.

50

Databases for Two- and Three-Dimensional Microscopical Images in Biology

Steffen Lindek, Nicholas J. Salmon, and Ernst H.K. Stelzer

INTRODUCTION

Modern computerized and automated microscope technology enables researchers, technicians, and quality-assurance personnel to collect large numbers of high-quality images. However, despite the addition of digital storage (see Chapter 32, *this volume*) and networking, microscopes are still generally used in a stand-alone manner insofar as the output is simply a huge number of image files. There is little attempt at proper cataloguing, and little metadata beyond the filename to identify and describe the contents of each image (Gonzalez-Couto *et al*., 2001).

This is not only a problem for the individual scientist who wants to document his or her work and master the flood of data that accumulates over the years, or for the manager of a microscopy facility, who has to maintain the huge amounts of data generated by different users on different instruments. It also concerns the scientific community on a global scale: in contrast to textual documents such as journal articles, microscopy data is difficult to discover (usually based only on keyword searches in literature databases, rather than on image-specific information). In addition, getting copies of the data usually relies on a personal correspondence with the author, in which he/she is asked to send the data and any relevant information regarding the experiment (Anonymous, 2004).

The first steps towards a better archive infrastructure are the networking of instruments so that data can be easily transferred from one point to the other, and the introduction of databases both at the individual microscope level and at the large-scale level to hold the metadata that allows others to manage and use the data. The latter two developments go hand in hand: Having local solutions does not solve the global problem of data access, and having a universal database for microscopy data requires local solutions to develop an efficient data submission procedure.

This chapter outlines the developments made in both areas. It discusses the benefits of integrating a database into a microscope to store information about both the instrument and the image data generated by it, and it presents preliminary efforts made to develop a database infrastructure at the global level.

DATA AND METADATA MANAGEMENT IN MICROSCOPES

In early confocal microscope systems, information about the machine configuration was contained within a single text file that could be read and written at any time during data acquisition or processing. Such a flat file format avoided the need for recompilation of the entire microscope program, but as its length increased, it rapidly became unsuitable for human viewing.

Online configuration of a number of system parameters was possible, often by running a setup file containing a subset of the information required to obtain the image. However, the information was intended as an aid to simply getting an image, rather than adjusting the large number of machine variables. Indeed, storage of some component settings was impossible or useless because these were machine settings that did not provide information about what was actually happening to the specimen. Moreover, if a hardware component were replaced, then apparently identical machine settings could result in different image data, for example, because filter selection was implemented by reference to filter wheel positions, rather than to actual filters.

Image intensity data was saved as a stream of bytes, and information about a particular image was mostly limited to saving pixel spacing information in an adjacent text file. Thus, reading such data into image processing programs often required some programming effort and, in most cases, manual intervention. Currently, most light microscopes generate a small metadata set that helps retrieve the image data and refers mainly to storage related issues (i.e., format, number of lines/pixels, date, etc.). Traditionally, developers have not offered the possibility of storing much extra information because they could see only limited opportunities for its later use.

Standard file systems permitted restricted searches of the text files, often using laboriously constructed string searches where the results were returned in a similarly user-unfriendly manner.

Recent Developments

More recently, it has become standard practice to store image data in more sophisticated, generic file formats that may also hold a number of parameters, for example, in an expanded TIFF format. This offers the advantage of being automatically readable by a large number of image-processing programs, where simple measurements can be performed.

TIFF is actually an excellent example because one can add as many tags as one wants and could add a lot of metadata. Whatever is not recognized by the program reading the file is ignored. The increasing number of proprietary raw image formats created by camera manufacturers has recently prompted Adobe (http://www.adobe.com) to release a unified TIFF-based file format (DNG, Digital Negative) that supports a wide range of metadata declared by manufacturers.

Steffen Lindek and Ernst H.K. Stelzer • European Molecular Biology Laboratory (EMBL), Heidelberg, Germany
Nicholas J. Salmon • SLS Software Technologies GmbH, Heidelberg, Germany

Handbook of Biological Confocal Microscopy, Third Edition, edited by James B. Pawley, Springer Science+Business Media, LLC, New York, 2006.

Recent initiatives to remedy these problems led to the development of MPEG-7 (Pereira and Koenen, 2001) as the new standard for content description of multi-media files. MPEG-7 provides descriptive elements ranging from basic features, such as colors, textures, and shapes, to complex information about motion. However, its complexity, and its lack of clarity for those illiterate in metadata management, are an impediment to its implementation.

Although standard database technology has been available for many years, it is only recently that commercial relational database management systems (RDBMS) have ventured from mainframe and workstation systems to systems suitable for use on the desktop. Improvements in the quality of such systems and in the range of interfaces now available for development environments now offer microscopists the chance to store data in personalized databases. Moreover, there are now more data processing programs, such AVS Express (http://www.avs.com), available to access such database stores.

Even the ubiquitous MS-Office package can access databases from within Word, Access, and Excel. Nevertheless, currently available systems are far from providing seamless integration of image data acquisition and analysis (Andrews *et al*., 2002).

Most recently, microscopes with integrated RDBMS have been developed (Salmon *et al*., 1999) and some of these are incorporated into systems such as the LSM510 (Carl Zeiss Jena), and the compact confocal camera (CCC), the microscope used for research at the European Molecular Biology Laboratory (EMBL). These machines use an RDBMS to describe and store their hardware configurations to an unprecedented level of accuracy and completeness. Parts can be changed without affecting performance, and the machine is automatically configured, which requires tagging the components such that they can be recognized by the software. Image data and associated metadata are all managed via databases, and common software such as Word, Access, and Excel can be used to access the databases.

IMAGE INFORMATION MANAGEMENT

Image information has to be managed both at the local level, at the scientist's desk, and at the global level, for example, at scientific journals. With the advent of digital microscopy, many scientists have replaced their folders of glossy prints or slides by shelves with hundreds of CDs/DVDs and drawers full of tapes. Some may have adopted desktop-based image management systems, either using software coming with their instrument (e.g., Zeiss' LSM Image Browser or Leica's IM1000) or commercial packages which are becoming more widespread due to the increased usage of digital photography (see Appendix). Alternatively, they may use an image archiving system tailored to microscopy such as DDL's Aequitas or RVC's Research Assistant (see Appendix).

At the other end, journals have started to make the image data submitted by authors available electronically (Anonymous, 2004). Initially this was done as an annual CD containing supplementary data, now as files for download from the publishers' Web sites (e.g., in *Science*'s Supporting Online Material or *Nature*'s Supplementary Information). This also enabled publishers to provide data that could not be published in the printed journals due to its dimensionality or its huge volume. However, almost none of this image data is managed in a database, and — at least for the external user of the Web site — there is no way to bypass the individual articles and any relevant keywords appearing in the text body and directly access all images on one publisher's site relating to a particular topic, such as fluorescence microscopy of GFP-labeled proteins in the Golgi apparatus. It is also not possible to search for a particular topic across the Web sites of different publishers (in case of the two leading journals mentioned above, a link to the image section is shown only together with the individual article).

Increased usage of laboratory information management systems (LIMS) (Nakagawa, 1994) that typically use a database format to store information demonstrates how the continual improvement of data collection and processing operations is also vital for running many types of laboratory procedures, such as screening assays. As legal demands increase, LIMS may become mandatory for demonstrating conformance to stringent quality requirements. Potential benefits for LIMS users include smoother work flow, better access to information, improved quality of results, better control of costs, and increased processing speed. And, last but not least, these systems replace the traditional laboratory books in which scientists keep their handwritten notes.

THE AIMS OF MODERN MICROSCOPE SYSTEM DESIGN

We have pointed out two important aspects to microscope design: On one side of the system there should be a networked microscope that functions within database structures. On the other side there should be an image database that provides easy querying and access to both data and metadata.

That the database system plays a key role as the mediating component between data acquisition, image processing, and data analysis software has been recognized by the Open Microscopy Environment (OME, http://www.openmicroscopy.org), a project that seeks to improve networking of biological microscopy data and to transfer the data from the instrument to image processing and analysis software for quantitative analysis (Andrews *et al*., 2002; Swedlow *et al*., 2003). There is actually an additional element in this data flow: the software must maintain contact between the acquisition parameter and the processed result so that the chain from data acquisition to the global database remains unbroken.

The complete infrastructure envisaged for the management of information is shown in Figure 50.1. With computer-controlled microscopes, information about the operational state of the instrument can be stored automatically. A single program should control a family of instruments and organize the interaction between them and the user. The details of this interaction are retrieved from a database that describes the hardware as completely as possible, storing at least all variable parameters and periodically accessing results to see if benchmarks of resolution and stability are met. Changes in the microscope hardware are reflected in changes to database entries and affect the user interface. To this end, the components of the microscope should be labeled such that the software can recognize them automatically, as it is now done in Zeiss AxioImager.

Further information concerning the specimen and the experiment being performed can be gathered from the user in a non-intrusive manner by fully integrating the data collection process with the microscope control program. This information is saved in a database, together with a pointer to the image data such that the user can always be offered seamless navigation from the acquisition parameters to the image data.

Figure 50.1 doesn't make any statement regarding the nature of the archive. It may be a central file server or a network of distributed servers. As the major concern with modern digital microscopy is the size of the data and the required bandwidth, a

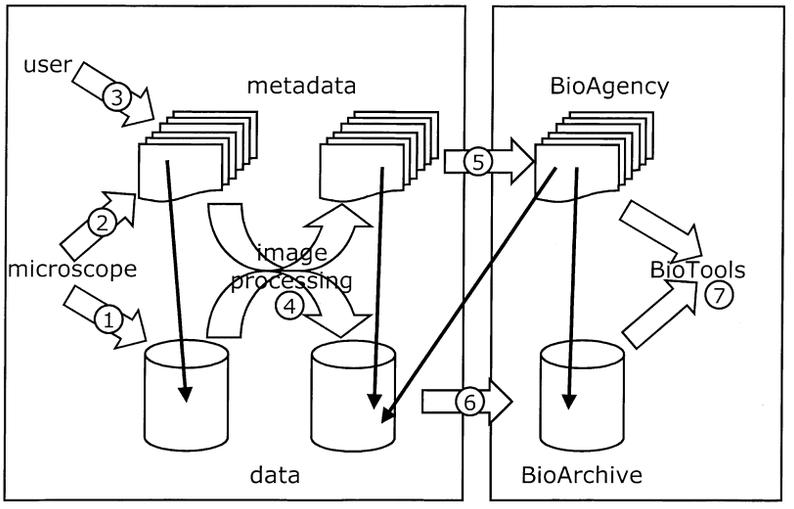


FIGURE 50.1. The life cycle of microscopy data and metadata. Data from one or more microscopes is stored on a file server (1). Technical information is automatically written into a database (2). The user adds details on the biology of the experiment (3). Metadata and data are reused by image processing software, resulting data is saved on the file server, and the metadata database is updated (4). Metadata is transferred to a global database, such as BioImage (5), while the image data stays on the author's server or is archived somewhere else (6). Third parties access the metadata in the BioImage database, which directs them to the data. The BioImage user can use tools that access the metadata to get and process the data (7). Note that the microscope can be considered as a tool in the sense of the diagram: using the metadata saved with the original data, it can reconfigure itself and repeat the experiment. The black arrows symbolize pointers to the data. The left-hand side is a local computer system, while the right-hand side is a global system. The three-components concept for databases of biologically relevant data (BioAgency, BioArchive, and BioTools) was introduced in Carazo and Stelzer (1999).

distributed storage system will be preferable for a large project with global focus.

Use of an integrated microscope and database system can provide the following benefits (Salmon *et al.*, 1999):

- **Fast, simple, and automatic machine configuration** can be achieved by associating a complete set of configuration parameters with each dataset. The microscope can then be adjusted and optimized by repeatedly changing the parameters, rescanning the same sample area into a new scan window, and analyzing the effect of these changes. The best image can then be quickly selected by the user and the associated parameters reused as a start point for all subsequent scans. Moreover, functions to reuse subsets of parameters can also be created. Thus, preselected areas can be quickly scanned with the same illumination and detector sensitivity parameters, or the same area can be scanned with different detector sensitivity parameters. Loops can also be inserted to check that the data flow has not changed so much as to imply a hardware malfunction requiring operator intervention.
- **Configuration of different machines to the same state** is possible if the microscope configuration interface uses real-world physical units rather than arbitrary units, for example, the actual laser power at some location close to the microscope objective rather than the voltage used to set the laser power output. Also, the microscope magnification should be calibrated rather than relying on the magnification value engraved into the side of the objective lens. Finally, storing the detected signal data in units of photons or photoelectrons would permit one to make a close estimate of its statistical accuracy. With parameters properly handled as physical values, users are no longer tied to finishing an experiment within a single session or using a particular machine, and collaborating scientists can compare images acquired under conditions that are strictly comparable.
- **Improved analysis of results** can be achieved by storing more information about the system and using more sophisticated models. Although this is often assumed, many properties of a light microscope are not described by a constant relationship (e.g., resolution is not constant over the entire field of view and often changes with focus plane). Saving such information allows for a better calibration, and makes room for the subsequent development of algorithms to compensate for this variance. For example, because of aberrations induced by refractive index mismatch (Hell *et al.*, 1993), image signal intensity is reduced the deeper the focus plane moves into the sample. Image processing programs such as AVS can improve image data using information about the immersion medium, the optical system, and the position of data samples relative to optical boundaries, such as the coverslip. Although the corrected image data has a more uniform contrast, making images easier to view and giving a considerable improvement in the results of three-dimensional (3D) rendering techniques such as ray tracing, it is not reasonable to imagine that such programs can correct for all the vagaries that beset fluorescence microscopy (Pawley, 2000).
- **Improved access to data** is possible when more information is stored in a modern RDBMS. Such programs are not only optimized to perform fast queries on the data they contain, but typically also offer an array of tools and interfaces that serve both novice and expert programmers in the task of data processing. RDBMS also offer presentation interfaces to many commonly used office programs, as well as dynamically generated HTML files. Users can perform sort, select, retrieve, and compare operations on image archives, querying not only the filenames, but also the entire spectrum of information associated with the image.
- **Semi-automatic submissions to other databases** becomes possible when more information is stored in a database. In the past, users were satisfied if they could import the image files

into image-processing programs. However, now that more details can be stored with the source microscope images, users can make more useful, semi-automatic submissions to data warehouses. For example, for biological applications, it is highly valuable to export data to databases that also store biology-related information, such as in the BioImage Database described below.

- **Remote monitoring and maintenance** is possible if the actual state of the instrument is stored and made available via a computer network. A system administrator can examine the information online, and users can benefit from fast fault diagnosis, rectification, or advice on the microscope configuration.
- **Repetition of experiments** is a key requirement in science that is much easier to satisfy if the experimental process can be automated. By saving data and constructing systems that use this information to repeat the experiment automatically, the potential for error is reduced.
- **Performance and development**: A well-defined database structure enables not only faster runtime performance, but also simplifies programming and program structure, speeding development time of the overall machine control program.

INSTRUMENT DATABASE MODEL

The database must contain sufficient information to enable the microscope control program to facilitate the communication between the user and the instrument. This technical information can be divided into four types (Fig. 50.2). Additional information describing the biological specimen is required to meet the fundamentals of solid scientific work.

- The first group of tables describing the microscope comprises essentially datasheet-like descriptions of items that could *potentially* be used within the instrument. This information is general, and therefore valid for any machine within a family of instruments that is served by the database. The collection of tables describing all possible components is like a library for machine construction. Typically, entries provide information on how to control a part, how to incorporate it into the system, and indicate its expected performance.
- Each particular machine contains either 0, 1, or many instances of a specific component. Each of these *available* parts requires a unique database entry through which it can be referenced and controlled. Because many parts require calibration, separate *calibration* details must also be included. Available parts and their calibration form the second and third groups.
- Every time a sample is scanned and data is collected, parameters of some parts such as the photomultiplier tube (PMT) voltage or the laser power are set to values that may be different from those used for other scans. To record these temporally changing values, a fourth group of tables is required. These can exist in a separate database because they do not relate to a particular machine.
- Any specimen examined under a microscope has been subjected to processing steps prior to observation. It may also be subject to processing steps, such as the addition of chemicals, between observations. In addition, different features or areas of interest may be imaged. Finally, information obtained by the microscope may be subject to one of a number of postprocessing steps such as deconvolution. Therefore, backward references to other instruments that looked at or manipulated the sample before, and forward references to what will or might happen next, complete the information network.

The design of the model to hold this metadata is a time-consuming task, but it has to be done carefully if the model is to remain optimal over the long term. Recently, ontologies have been developed that describe the knowledge in many scientific areas in a systematic computer-processable form (for a review, see Bard and Rhee, 2004). Such a framework enables consistent indexing of experimental data and allows systems in different domains to communicate with each other: Without it, one cannot exchange information without loss. The development of ontologies for the different expertise areas of microscopy is **the** major milestone that must be passed before the integration of databases for different individual instruments can work seamlessly (Pouchard and Walker, 2001).

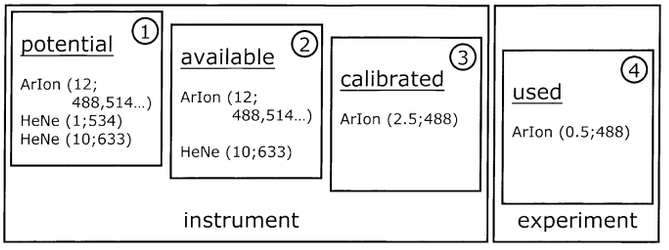


FIGURE 50.2. The four instrument metadata levels. The most generic level (1) holds datasheet-like information on potential components that may be used in a certain microscope (e.g., three different lasers: a 12 mW argon-ion laser with several wavelengths, a 534 nm 1-mW He-Ne laser, and a 633 nm 10 mW He-Ne laser). The next level (2) is for the documentation of the parts actually available in the microscope (only two of the lasers). These parts are associated with an entry at the third level (3), that holds calibration details (these will be different for each instance of a part). In our example, the actual maximum laser power of the 488 nm line is only 2.5 mW (25% of the calibrated value of 10 mW, which is the sum of the power of all laser lines). Thus, a setting of 20% in an experiment means that a power of 0.5 mW was used, which is documented at the fourth level (4). While the first three levels are instrument specific, the fourth level is experiment specific and does not need to be stored in the instrument database.

SYSTEM REQUIREMENTS

The complete description of a confocal microscope such as EMBL's CCC contains about ninety tables. Fortunately, component specifications and part descriptions do not change during the lifetime of the microscope, and take up only a few megabytes of disk space. On the other hand, the user's metadata database increases in size by a few kilobytes every time an image is saved, so even with thousands of experiments, the amount of data stored in the tables will remain relatively small.

Users should be able to back up their archives on a networked computer, and then view them on any computer they choose. Thus, the database program should be separate from the archive files, easy to install, and preferably either available on a number of different computing platforms or accessible via an HTML interface that can be accessed with any Web browser.

IMAGE DATABASE MODEL

The model of any database for biological microscopy data has to accommodate metadata from the following five areas (Lindek *et al.*, 1999):

- Organizational/administrative metadata, such as people, institutes, manufacturers and suppliers, etc.
- Data and file metadata, such as number of pixels, image location pointers, etc.
- Technical/instrumentation metadata, such as information about the microscope, its components, and their settings during data acquisition.
- Biological metadata, such as sample taxonomy (general information) and age (sample specific information).
- Experiment metadata, such as preparation steps and their physical, chemical, and biological parameters.

Because the emphasis of these databases is on the (biological) content of the images, not as many technical details would be available as on an individual microscope. In addition, images from a wide spectrum of microscope techniques have to be stored and collated. Component parameters therefore have to be restricted to those that are characteristic of a large set of instrument types and that are necessary to accurately document the image acquisition process and to subsequently evaluate the data. On the other hand, general databases may store considerably more information about the specimen, sample preparation techniques, and the features visible in individual images.

The improved analysis of results and the better access to data that are regarded as the benefits for microscope/database integration are also advantages of global image databases. Furthermore, if they are multi-specimen and multi-technique, they allow the comparison of complementary information obtained from similar samples observed with different techniques, providing different levels of resolution and visualizing different types of interaction.

To be efficient, image repositories at the desktop, in the laboratory, or at the global level cannot stand in isolation. First, as discussed above, they need to be connected to the instruments that produce the data; second, they need to be associated with other databases (Martone *et al*., 2002); and third, they need to be incorporated into a network of scientific resources. Such a network is being set up for the life sciences by E-BioSci (http://www.e-biosci.org). It aims to bring together the various databases used in the laboratories on a daily basis: literature, sequences, structures, images, etc. (Grivell, 2001).

SELECTED PROJECTS

While there is no global microscopy database available at the time of writing this chapter, there are some projects that are more or less mature and have the potential of playing that role (Table 50.1). One major example is the BioImage Database, now managed by a team in Oxford, United Kingdom. Initially designed as a database for all kinds of biological microscopy data, it has recently been expanded to include other types of biological image data. However, while less ambitious because more restricted in scope, other projects also deserve mention in this section.

BioImage

BioImage is a database of multi-dimensional digital images for the life sciences that at the time of writing is being restructured but will soon accept image data from a variety of instruments (from microscopy to satellite remote sensing) relating to all aspects of biology (from ultrastructural biology to wildlife conservation). In its first phase (1996–1999), six European research groups and two industrial partners collaborated on a publicly funded project investigating the possibility of storing, in a single database, data generated from very different specimens (ranging in size from whole biological organisms down to macromolecules) using very different microscopes (light, electron, and atomic force microscopes, etc.). The aim was to design a database system providing hitherto unprecedented levels of comparison and data access to emphasize different, and complementary structural aspects of similar objects.

During the transitional period that followed (2000–2001), the consortium partners looked for a new orientation of the database that might lead to a sustainable business model. This led to the integration of BioImage into the ORIEL project (2002–2004): Online Research Information Environment for the Life Sciences (http://www.oriel.org), an EC-funded E-BioSci research project to integrate Internet-based biological information resources for the scientific community. Because E-BioSci embraces all life sciences topics, this meant expanding the scope of the BioImage Database to cover non-microscopical image data such as wild-life photography, behavioral biology, ecology, etc. At the same time, the ability to store detailed technical information was reduced.

TABLE 50.1. Image Management Software

Project	URL	Reference
BioImage	www.bioimage.org	Carazo and Stelzer, 1999
Biomedical Image Library	ted.hul.harvard.edu:8080/ted/deliver/home?_collection=bil	
Scientific Image DataBase	sidb.sourceforge.net	
Quartz Imaging	www.quartzimaging.com	
ARKive	www.ARKive.org	
Bristol BioMed Image Archive	www.brisbio.ac.uk	
Wellcome Trust Medical Photographic Library	medphoto.wellcome.ac.uk	
IWF Contentport / Digiclip	www.iwf.de	
Getty Images	www.gettyimages.com	
Corbis	www.corbis.com	
FlyBase	www.flybase.org	The FlyBase Consortium, 2003
FlyView/FlyMove	flyview.uni-muenster.de; flymove.uni-muenster.de	Janning, 1997; Weigmann *et al*., 2003
Mouse Databases at Jackson Lab	www.jax.org	Bult *et al*., 2004
Mouse Atlas	genex.hgu.mrc.ac.uk	Burger *et al*., 2004
Open Microscopy Environment	www.openmicroscopy.org	Goldberg *et al*., 2000

One of the most critical issues for the BioImage Database (and for all global image databases) is data harvesting. Because it is designed as a global database, data entry requires significant curation, even though large parts can either be automated or delegated to submitters. The process is simplified if submitters are not solely individual scientists, as initially foreseen, but also organizations entering lots of data in well-defined formats. BioImage therefore focuses on three types of data source: The first type consists of corporate submitters, such as scientific journals or learned societies, that send their image data to the BioImage Database on a regular basis. The second type contains individuals, research groups, and museums with large image collections who wish to make these collections widely available. The third type contains other databases which would provide their metadata and links to their own image data.

Biomedical Image Library

Harvard University's Biomedical Image Library (BIL) took a completely different approach from the top-down approach chosen by BioImage. BIL focused on local data in a standard format (TIFF) and started with a few microscopy techniques (light, fluorescent, or confocal microscopy). This is an approach that a lot of smaller projects are likely to take. The big risk in doing so is that the data model designed for a restricted set of data will not be able to cope effectively with the wide variety of metadata in the outside world. At the time of writing this chapter, BIL is accepting data from any Harvard researcher and has a publicly accessible Web interface.

Scientific Image DataBase

One of the most recent initiatives at the interface between academia and industry is the Scientific Image DataBase (SIDB), a Web-based archive for microscopy data initiated by Scientific Volume Imaging B.V. (www.svi.nl) and developed at the Universities of Utrecht and Leiden. The current version, 0.4, released in June 2005, is available from SourceForge: http://sourceforge.net/projects/sidb. SIDB has the merit of being an open source and based on free tools for processing and archiving images.

Other Projects

In electron microscopy (EM), the basic problems are the same as for other microscopy techniques, though some companies now provide software packages for EM instrumentation and image management at the laboratory level (e.g., Quartz Imaging has compiled a well-designed suite of software tools for digital image management). Recently, a couple of papers were published which described the efforts to set up databases for EM data (Metoz *et al*., 2001; Fellmann *et al*., 2002; Martone *et al*., 2002).

Image databases are also set up in many fields related to biological microscopy. Topical image archives, such as ARKive, provide well-documented still images and videos of endangered species, and intends to ultimately cover the more than 12,000 species on IUCN's Red List. Among purpose-oriented image databases, there is an increasing number of projects aiming at providing teaching materials, such as the Bristol BioMed Image Archive, a password-protected collection of about 8000 medical, dental, and veterinary images or the Wellcome Trust Medical Photographic Library, a resource of images on the history of medicine and modern biomedical sciences. At the other end of the spectrum, there are commercial databases marketing videos and photographs, such as IWF's Contentport (also known under its former name, Digiclip) or the general-purpose photography collections at Getty Images or Corbis. In addition, there are many subject- and species-specific biological databases such as FlyBase, FlyView/FlyMove, the Mouse Databases at Jackson Laboratory, or the Mouse Atlas, that integrate image data with other types of information related to the subject.

Finally, there are projects that aim at the integration of microscopy data such as the Open Microscopy Environment (OME) that is developing an open format for preserving much of the metadata that is usually lost when the images are transferred from one system to the other, for example, from the microscope to the data-analysis software package.

CRITERIA AND REQUIREMENTS FOR MICROSCOPY DATABASES

User Interface

The users of local microscopy databases are different from those that use global databases, primarily because the former are involved in the research and know what is in the database, while the latter are exploring an unknown universe. Another factor is that the former are mainly data producers and therefore likely to be more interested in technical parameters, while the others are mainly consumers who are more interested in the scientific content of the data. Despite these differences, there are some commonalities in their approach to using an image database.

Most users browse a database by microscopy technique, specimen type, biological process, or taxonomical name. This can be facilitated by providing appropriate metadata fields for these categories. A single description field that provides a place for a full-text narrative description of the object is not appropriate.

Any database software has to provide a search interface that enables quick iterative searching (i.e., one that returns rapid results and allows easy revision), and optimally provides two different types: a simple search interface and an advanced one where fields can be specified and controlled vocabularies can be used.

The results have to be as informative as possible. All important parameters have to be displayed (e.g., the names *and* initials of *all* the authors, not just of the first one; the number of other images associated with the one found, etc.).

Groupings of images should not be based only on key metadata (same data acquisition date, same instrument, same author, same sample, etc.) — there has to be a mechanism to associate one image with others to form a project (i.e., images that share a common grant number).

Query by Content

While the storage of the images and their associated metadata in a database opens up a wide range of search options, the biggest advantage of such systems lies in the possibility of querying by content. Query by content is the search for image feature based on what is visible in the image (e.g., for all images showing round objects of 0.1 mm diameter; de Alarcón *et al*., 1999). In some cases, the system could rely on metadata that has been extracted *a priori*. In other cases (where the processing of the images is less time consuming or where too much data would be generated for storage) it would compute such information on the fly. Chapter 47 discusses how such data might be extracted.

Metadata Structure

Support for controlled vocabularies has to be provided, especially for multi-user databases. One of the most frequent reasons for missing hits when entering a specific keyword is that of using a synonym or a different spelling of the word that was stored. To remedy this, controlled vocabularies must be created for fields such as the microscopy technique, the taxonomic name, etc. Note that the development of a hierarchical vocabulary allows for the easy extension of queries (searching for "confocal fluorescence microscopy" if "confocal two-photon fluorescence microscopy" does not give enough hits, and that would also include "confocal three-photon microscopy").

It is also very important that the database knows that "confocal two-photon fluorescence microscopy" is both a type of "confocal microscopy" and a type of "fluorescence microscopy." Otherwise it would not be able to return a complete set of hits to a query for "confocal microscopy" data.

Another reason for beginning to use controlled vocabularies as early as possible is to reduce the effort required to maintain the database. Many large, scientific databases started years ago as small one-man or one-laboratory projects and, as they grew, they had to be migrated from one DBMS to another or their model had to be re-engineered. This is often when curators realize how messy and uncontrolled the fields have become due to ignorance or lack of diligence.

Digital Rights Management

The usage of microscopy image data from a database (e.g., for teaching purposes) is only possible for a third party if the rights for such usage have been granted. Because greater attention is now being paid to correct observation of image copyright, this means that any database needs to be aware of digital rights, facilitate their management, and provide a clear permitted-use policy.

FUTURE PROSPECTS

In this chapter, we have pointed out the benefits of integrating image databases with digital microscopes and provided the basic information required for achieving this integration. Similar benefits could clearly be gained by applying the same principles to any data acquisition system, and indeed the coverage of the prototype CCC confocal system at EMBL has already been extended to include a wider range of scientific instruments.

This task is ultimately one for microscope manufacturers. They should aim at providing a unified user environment in which the user does not need to know anything about the microscope, not even its brand, to carry out his experiments. This would not only be an advantage to the scientist who can now concentrate on the experiment instead of worrying about the technology; it is also a plus for the manufacturers, who could increase the compatibility of their instruments. Systems with a large number of control parameters would clearly benefit and allow better online control of the machine. Other parties involved include software manufacturers, who currently provide inadequate database connectivity (Goldberg *et al*., 2000). Instead, they should reuse the parameters provided by the instruments and encourage the addition of further information that can be used by their analysis packages. There is still a need for BioTools (Fig. 50.1), tools for data access and manipulation (Boudier and Shotton, 2000), data analysis (Machtynger and Shotton, 2002) and visualization (Pittet *et al*., 1999), data interchange (Boudier and Shotton, 1999), and database connectivity.

The path that BioImage has paved shows quite clearly that microscopy data is only one piece of the puzzle. In line with developments in completely different areas such as proteomics, where the structure and sequence databases have recently been brought closer together, there is a broader perspective which comprises both microscopy data and macroscopical photographs via images generated by medical instrumentation, and which spans the gamut from structural to behavioral biology.

BioImage shows another way to go: as there is no way to put all data into a single central database, it is essential to share metadata among all specialized databases, with topical databases, with educational projects, with commercial scientific image data providers, and, of course, with companies generating image data of general scientific interest in the course of their work.

In view of all the concrete advice that has been given, it may seem surprising that image databases are still in their infancy (Martone *et al*., 2002). But compared with the historical past of textual databases and taking into account that visual information represents 70% of all life science data generated (Gonzalez-Couto *et al*., 2001), this is probably as it should be.

ACKNOWLEDGMENTS

SL is grateful to David Shotton (BioImage, Oxford) for helpful comments on the manuscript, and to Paul Bain (BIL, Harvard) for valuable discussions on image databases.

REFERENCES

Andrews, P.D., Harper I.S., and Swedlow, J.R., 2002, To 5D and beyond: Quantitative fluorescence microscopy in the postgenomic era, *Traffic* 3:29–36.

Anonymous, 2004, Images to reveal all? *Nat. Cell Biol.* 6:909.

Bard, J.B., and Rhee, S.Y., 2004, Ontologies in biology: Design, applications and future challenges, *Nat. Rev. Genet.* 5:213–222.

Boudier, T., and Shotton, D.M., 1999, Video on the Internet: An introduction to the digital encoding, compression, and transmission of moving image data, *J. Struct. Biol*. 125:133–155.

Boudier, T., and Shotton, D.M., 2000, VIDOS, a system for video editing and format conversion over the Internet, *Computer Networks* 34:931–944.

Bult, C.J., Blake, J.A., Richardson, J.E., Eppig, J.T., and the Mouse Genome Group, 2004, The Mouse Genome Database (MGD): Integrating biology with the genome, *Nucleic Acids Res.* 32:D476–D481.

Burger, A., Davidson, D., and Baldock, R., 2004, Formalization of mouse embryo anatomy, *Bioinformatics* 20:259–267.

Carazo, J.M., and Stelzer, E.H.K., 1999,. The BioImage Database Project: Organizing multidimensional biological images in an object-relational database, *J. Struct. Biol.* 125:97–102.

de Alarcón, P.A., Gupta, A., and Carazo, J.M., 1999, A framework for querying a database for structural information on 3D images of macromolecules: A Web-based query-by-content prototype on the BioImage macromolecular server, *J. Struct. Biol.* 125:112–122.

Fellmann, D., Pulokas, J., Milligan, R.A., Carragher, B., and Potter, C. S., 2002, A relational database for cryoEM: Experience at one year and 50000 images, *J. Struct. Biol.* 137:273–282.

Goldberg, I., So, P., and Sorger, P.K., 2000, *The Open Microscopy Environment (OME),* Massachusetts Institute of Technology, Cambridge, Massachusetts (white paper available at http://ome1-sorger.mit.edu/OMEWhitePaper.pdf).

Gonzalez-Couto, E., Hayes, B., and Danckaert, A., 2001, The life sciences Global Image Database (GID), *Nucleic Acids Res.* 29:336–339.

Grivell, L., 2001, E-BioSci, *FEBS Lett.* 498:123.

Hell, S., Reiner, G., Cremer, C., and Stelzer, E., 1993, Aberrations in confocal fluorescence microscopy introduced by mismatches in refractive index, *J. Microsc.* 169:391–405.

Janning, W., 1997, FlyView, a *Drosophila* image database, and other *Drosophila* databases, *Semin. Cell. Dev. Biol.* 8:469–475.

Lindek, S., Fritsch, R., Machtynger, J., de Alarcón, P.A., and Chagoyen, M., 1999, Design and realization of an on-line database for multidimensional microscopic images of biological specimens, *J. Struct. Biol.* 125:103–111.

Machtynger, J., and Shotton, D.M., 2002, VANQUIS, a system for the interactive semantic content analysis and spatio-temporal query by content of videos, *J. Microsc.* 205:43–52.

Martone, M.E., Gupta, A., Wong, M., Qian, X., Sosinsky, G., Ludäscher, B., and Ellisman, M.H., 2002, A cell-centered database for electron tomographic data, *J. Struct. Biol.* 138:145–155.

Metoz, F., Sherman, M.B., and Schmid, M.F., 2001, Adopting a database as a solution to managing electron image data, *J. Struct. Biol.* 137:273–282.

Nakagawa, A.S., 1994, *LIMS: Implementation and Management,* The Royal Chemistry Society, Cambridge, United Kingdom.

Pawley, J.B., 2000, The 39 steps: A cautionary tale of quantitative 3-D fluorescence microscopy, *Biotechniques* 28:884–888.

Pereira, F., and Koenen, R., 2001, MPEG-7: A standard for multimedia content description, *Int. J. Image Graphics* 1:527–546.

Pittet, J.J., Henn, C., Engel, A., and Heymann, J.B., 1999, Visualizing 3D data obtained from microscopy on the Internet, *J. Struct. Biol.* 125:123–132.

Pouchard, L., and Walker, D.W., 2001, A community of agents for user support in a problem-solving environment, In: *Lecture Notes in Computer Science*, Vol. 1887, (T. Wagner and O.F. Rana, eds.), Springer-Verlag, Heidelberg, Germany, pp. 192–198.

Salmon, N.J., Lindek, S., and Stelzer, E.H.K., 1999, Databases for microscopes and microscopical images, In: *Handbook of Computer Vision and Applications* (B. Jähne, H. Haußecker, and P. Geißler, eds.), Vol. 2, Academic Press, San Diego, California, pp. 907–926.

Swedlow, J.R., Goldberg, I., Brauner, E., and Sorger, P.K., 2003, Informatics and quantitative analysis in biological imaging, *Science* 300:100–102.

The FlyBase Consortium, 2003, The FlyBase Database of the *Drosophila* genome projects and community literature, *Nucleic Acids Res.* 31:172–175.

Trinkwalder, A., 2002, Ordnungshüter — Neun Möglichkeiten, Bilder, Movies und MP3s zu bändigen, *c't* 1:98–107.

Trinkwalder, A., 2004, Sortiermaschinen — Professionelle Mediendatenbanken für Windows und Mac OS, *c't* 9:156–163.

Weigmann, K., Klapper, R., Strasser, T., Rickert, C., Technau, G., Jäckle, H., Janning, W., and Klambt, C., 2003, FlyMove — A new way to look at development of *Drosophila*, *Trends Genet.* 19:310–311.

APPENDIX

The increased popularity of digital photography has boosted the development of software packages for managing and archiving digital photographs. These systems, which range between $40 and $800 in price, are affordable for every scientist — the question is whether they are able to fulfill the needs of the microscopist who wants to manage his image files. In this area the photo management software has to compete with tools offered by microscope manufacturers (e.g., Zeiss' LSM Image Browser or Leica's IM1000) and more expensive scientific image and data management systems such as Dynamic Data Links' Aequitas[1] or RVC's Research Assistant.[2]

This Appendix intends to give a short overview of the features of the latter software tools (Table 50.A1) because a scientist who doesn't own a microscope and who is faced with the decision to choose an image management system will more likely opt for one of these systems rather than a microscope manufacturer's solution. Many of the impressions are based on recent comprehensive reviews in the magazine *c't* (Trinkwalder, 2002; Trinkwalder, 2004). A detailed account of the software is, however, beyond the scope of this Appendix, as new versions and updates are released almost every year and many additional features will have been incorporated during the first year this book is released. For example, communication with other programs to import or export data and metadata currently seems to be a general shortcoming, but it is expected that this will soon be overcome. The same probably holds for platform dependence: currently, iView is only available for Macintosh; IMatch, ThumbsPlus, Aequitas, and Research Assistant are Windows-only programs. Cumulus has even a server version that runs on Unix systems.

The programs all work according to the same principle. They do not store the image data itself, but just hold a thumbnail picture of the image and a link to the original file in the file system (in this respect they work similarly to the BioAgency–BioArchive tandem, the first of which stores the metadata and a pointer to the data stored in the second system). They provide a means to map the file system onto one or more independent structures that the user creates himself, based on categories.

Most important for microscopy data management are tools to create additional categories and keywords, and to organize them in a hierarchy rather than merely in an alphabetical list. Here, the solutions offered by the software range from poor to excellent. While ACDSee does not even allow one to create user-defined fields, IMatch, for example, provides means to build property sets, which are actually database entities that are independent of the image itself (e.g., a person or an experiment) and which can be related to the image, thereby offering one the possibility of setting up a relational database to get away from an image-centric model.

Image formats are a big issue, and development is partly focused on importing data directly from imaging hardware. In this respect, Aequitas and Research Assistant promise to offer connectivity to equipment used in microscopy. Some software, on the other hand, does not even provide video-handling capabilities (IMatch and ThumbsPlus do not even provide the full range of .avi, .mpeg and .mov file handling).

Query features are important to find and retrieve images efficiently. Here again, the solutions range from too simple to more complex, the best marks being for programs like Cumulus and Portfolio that are very database-near. Aequitas even offers support

[1] The software hasn't been updated for 5 years and it is not clear if further releases can be expected.

[2] This software is often updated and the most recent release is from October 2004.

TABLE 50.A1. Image Management Software

	Cumulus	Portfolio	Imatch	ThumbsPlus	iView	ACDSee	Aequitas	Research Assistant
URL	www.canto.com	www.extensis.com	www.photools.com	www.cerious.com	www.iview-multimedia.com	www.acdsystems.com	www.ddlinks.co.uk	www.rvc.nl
Pros	Good video handling Good metadata management Good user interface	Good metadata management	Good metadata management Good user interface			Good video handling Good user interface	Good video handling Good metadata management Support of hardware typical for microscopy	Microscopy-tailored Good metadata management Support of hardware typical for microscopy
Cons		Upper price range for photo software	Only available for Windows	Only available for Windows Unusual user interface	Only available for Macintosh	Poor metadata management Poor search capabilities	Only available for Windows Quite expensive	Only available for Windows

for SQL searches and IMatch allows sophisticated regular expressions. A plus in some programs (IMatch, ThumbsPlus, iView, Aequitas) is the ability to query by example, which provides a quick way to find visually similar images. However, with fluorescence images being false colored, preferably in green and red, and with scientists having collections of dozens of almost identical images, this feature is not very helpful in fluorescence microscopy. Another extra seems to be more useful: Some programs have a macro editor, which allows scripting more complex applications.

Finally, the most recent article by Trinkwalder (2004) also has some benchmarks for the cataloguing of Photoshop, TIFF, and JPEG files. The differences are sometimes considerable, both depending on the file type and the software, but apparently they only rule out the usage of IMatch for Photoshop files.

51

Confocal Microscopy of Biofilms — Spatiotemporal Approaches

R.J. Palmer, Jr., Janus A.J. Haagensen, Thomas R. Neu, and Claus Sternberg

INTRODUCTION

Biofilms consist of microbial cells (bacteria, fungi, and algae) that are fixed in a spatially defined relationship to one another, typically involving attachment to a substratum by means of extracellular polymeric substances (EPS). A few real-world examples of biofilms include dental plaque, slimes on rocks, slimes occurring in liquid distribution systems (e.g., drinking water supplies and sewers), and natural bacterial populations on plant and animal surfaces (e.g., skin microflora, epiphytic and rhizosphere microorganisms). In nature, the vast majority of microbial biomass is attached to a substratum. The most complex biofilms are mixtures of phylogenetically and physiologically different organisms. These mixed populations can be investigated from the community perspective, that is, in their totality as the sum of their parts, or at the level of their component members, that is, as collections of single cells. Even a pure-culture biofilm formed from a population of clonal bacterial cells can have qualities that are worthy of examination at the single-cell level (Rainey and Travisano, 1998; Singh *et al*., 2002; Boles *et al*., 2005). Because bacterial cells typically measure at most 5 µm in the longest dimension, observation of biofilms using a microscope can range over several orders-of-magnitude: from a few micrometers (single cell) to several millimeters (the extent of many biofilms in *in vitro* and in natural systems).

While biofilm microscopy owes much to biological microscopy, it is a unique field for which general biological and microbiological techniques have been adapted. We present here a collection of approaches and methodologies, many of which originated in eukaryotic cell biological investigations but which have been adapted to studies of microorganisms on substrata.

SAMPLE PRESENTATION

Flowcells and Other Perfusion Chambers

To obtain single-cell resolution in bacterial biofilms, one must use lenses with high numerical aperture (NA): oil- or water-immersion lenses, or the highest NA (0.9) water-immersible lenses (dipping lenses, no coverslip required). Also, sample preparation techniques which are routine for other biological material and which include fixation and embedding/sectioning are less frequently employed for *in vitro* biofilm research because the biofilms are generally thin enough (≤50 µm) that the optical sectioning provided by confocal microscopy is sufficient to examine much of the sample's *z*-dimension. Together, these factors have resulted in a preference for the examination of hydrated, living biofilms grown in perfusion chambers known as flowcells or flow chambers. The basic flowcell design is very simple: grooves are cut into a plastic block and, using silicone sealant, a microscopy coverglass is attached covering the grooves. The coverglass thus constitutes one wall of the perfusion chamber while also providing an optically correct substratum through which the developing biofilm is viewed. It is useful to design the flowcell so that a standard commercially available coverslip (e.g., 24 × 50 mm) can be used, although many coverglass suppliers are willing to prepare custom sizes. Autoclaveable homemade designs exist (Palmer and Caldwell, 1995; Kolenbrander *et al*., 1999) and some commercially available systems are autoclaveable (see, e.g., http://cu.imt.net/~mitbst/Flow_Cells.html). However, many plastics warp after repeated autoclaving and therefore the simplest designs are sterilized using ethylene oxide gas or are simply disinfected with bleach or ethanol. After the assembled flowcell is disinfected, the experimental bacteria are introduced into the chamber, after which sterile medium is pumped through the chamber to remove unattached bacteria while providing nutrients for growth of the developing biofilm. Growth directly on the coverslip means that high-NA immersion lenses can be used to maximum advantage. After microscopic examination and termination of the experiment, the coverglass is removed, the flowcell is cleaned, and a new coverglass is attached. Historically, these chambers have been used on upright microscopes, although many designs work just as well on inverted platforms. Various flowcell designs are shown in Figure 51.1. Many commercially available perfusion chambers can be used for biofilm work, the most important criterion being the ability to pump liquids through the chamber under conditions of laminar flow (no mixing through turbulence). Equations important for these calculations are available in the literature (Zinn *et al*., 1999). A disadvantage of the basic design is that transmitted light microscopy is difficult or impossible. However, other approaches exist (different flowcell designs, use of glass capillaries) that can make use of transmitted light to varying degrees (Bos *et al*., 1994; Palmer and Caldwell, 1995; Stoodley *et al*., 1999).

Once a flow chamber design is chosen, the chamber must be integrated into a setup that will move liquid through the chamber. The typical approach is to feed the medium from a reservoir to the

R.J. Palmer, Jr. • National Institute of Dental and Craniofacial Research, National Institutes of Health, Bethesda, Maryland 20886
Janus A.J. Haagensen and Claus Sternberg • Center for Biomedical Microbiology Biocentrum-DTU, Technical University of Denmark, 2800 Lyngby, Denmark
Thomas R. Neu • UFZ Center for Environmental Research Leipzig-Halle, 39114 Magdeburg, Germany

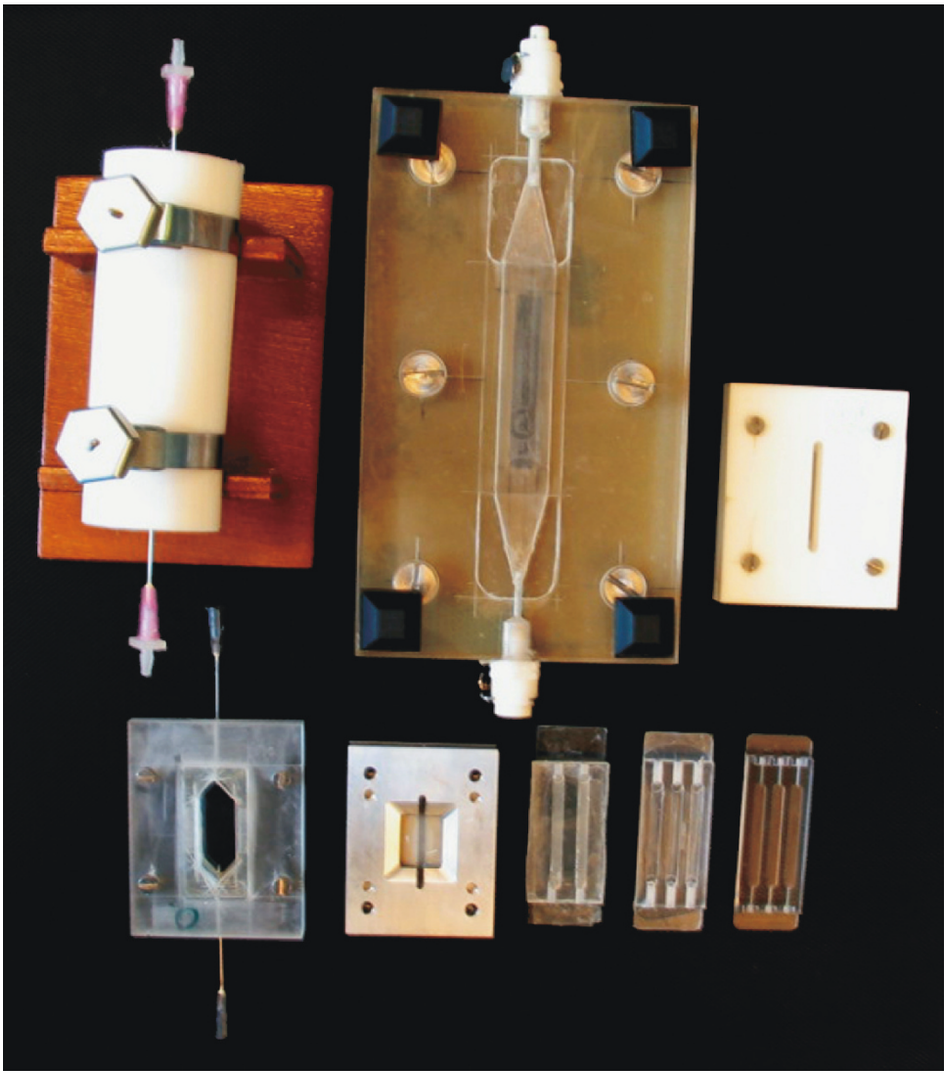


FIGURE 51.1. Flow cells as they have developed over the last 15 years at the Center for Biomedical Microbiology, BioCentrum-DTU, Denmark. The design at the lower left is currently in use.

chamber with a peristaltic pump placed between the reservoir and chamber. Everything on the upstream side of the chamber (including the chamber itself) must be disinfected or sterilized. The element most likely to fail in such a setup is the tubing on which the peristaltic pump acts. Repeated autoclaving of this tubing invariably leads to degradation in the tubing's mechanical properties and thus to altered flow rates or even tubing failure (leaks). Furthermore, the peristaltic action encourages bubble formation within the tubing; bubble-trap designs exist to prevent passage of bubbles into the flow chamber — a detailed description of this type of system is presented below. Finally, should an obstruction occur, the high-pressure capability of the pump can cause the chamber to leak, a happenstance not always well tolerated by the optical components.

As an alternative, if the pump is placed downstream of the flow chamber and the medium reservoir is slightly elevated above the height of the flowcells and downstream tubing, a siphon can be started prior to inoculation by using a syringe to pull the medium through the line space ahead of the pump; the primed tubing is then attached the to the pump, which acts more as a metering device than as the driving force for liquid transport. In the most extreme example, the pump can be eliminated entirely by using a set of hanging flasks on either end of the system (Bos *et al*., 1994).

Pumps are selected on four criteria: stability, flow rate, number of channels, and number of rollers. Stability is quite important; the pump should be able to run unattended for extended periods of time. Required flow rates will depend on flowcell dimensions (laminar flow, see previous), and the best pumps accommodate tubing of different bore diameters within the pump head thus providing, through a combination of pump speed and bore diameter, as much as a five order-of-magnitude range in flow rate. Versatile pumps have multiple channels (multiple tubes through which liquid is pumped); the cheaper pumps have two to three channels while the more expensive pumps have as many as 32 channels. Multiple channels are required to simultaneously run flow chambers with different medium compositions, and even to run multiple chambers with the same medium. Chambers connected in series are subject to changes in the medium induced by bacterial metabolism in upstream chambers, and chambers connected in parallel (but to the same main feed via splitters inserted downstream of the pump) are subject to variation in flow rate from chamber to chamber. Another feature of precision pumps is a high number of

rollers (e.g., 8–10) in the pump head. The greater the number of rollers, the smoother the flow (peristalsis is less vigorous). Although syringe pumps are alternatives to peristaltic pumps, single-syringe pumps must be refilled. Dual-syringe pumps such as are used in high-pressure liquid chromatography require no refilling, but have the major disadvantage of providing only a single output channel.

Water-Immersible Lenses

Bacteria grow under almost any condition presented by nature, and retrievable substrata can greatly simplify the examination of biofilms grown under complex experimental regimes. To examine biofilms produced under a particular set of conditions within a fermenter or within a natural environment (e.g., a stream, a lake, or the oral cavity), one need only insert a "coupon" that can be retrieved at a later time for microscopic examination. Two problems exist in such an approach. First, the coupon invariably passes through the air–liquid interface at least once in its route to the microscope, and is thereby subject to shear stress that may remove biomass. Second, the sample must be either investigated with a water-immersible lens (dipping lens, no coverslip required), or the sample must have a coverslip placed on it with resultant pressure distortion. If the biofilms are very thin, that is, essentially monolayers of bacterial cells, then distortion arising during careful addition of a coverslip can be minimal; such is the case in recent experimental work on epiphytic biofilms (Monier and Lindow, 2003, 2004). A gasket can be used to hold the coverslip at a fixed distance from the slide to eliminate pressure directly on the biofilm; however, a gap between the biofilm surface and the underside of the coverslip is thereby created which typically precludes use of low-working-distance (high-NA, immersion) lenses. Biofilms therefore represent exactly the sort of sample for which all major microscope suppliers offer high-resolution (ca. 60×0.9 NA) water-immersible lenses that also have working distances of several millimeters. These lenses can resolve fluorescently labeled single bacterial cells and can be used to examine very irregular or tilted substrata, such as human tooth enamel (Palmer *et al*., 2003). They can also be used to directly examine biofilms on particles such as sand grains or chromatographic supports; as with other substrata, the difficulty is not so much in the microscopy, but rather in bringing the substratum to the microscope without altering the biofilm (or scratching the lens!).

Upright Versus Inverted Microscopes

Throughout the preceding text, it should be clear that an upright microscope is the most versatile platform for biofilm microscopy, primarily because it can easily accommodate water-immersible lenses. Biofilms can be grown *in vitro* under stagnant conditions if nutrients are provided by replenishing the medium. Thus, multi-well plates (e.g., Whatman catalog no. 7716–2375) and chamber slides (e.g., Nunc LabTek coverslip chambers) designed for inverted microscopy can be used for biofilm research provided that the plates/slides incorporate a substratum that is amenable to high-NA immersion objectives. On the other hand, as small-well-format multi-well plates (e.g., ≥96 wells/plate) cannot be viewed with immersible lenses on upright microscopes because the lens tip diameter is typically larger than the well diameter, these must be examined using an inverted microscope. However, a dipping lens can be used on an inverted platform to examine non-coverslipped samples by building up a ring of wax or some other easily removable material (certain types of gaskets can be useful) around the lens tip. A convex puddle of water can be formed on top of the lens face and contained within the ring. The lens is then moved up towards the substratum to be imaged (which is placed with the biofilm on the underside or facing downwards towards the objective) until the water contacts the substratum.

Setup of a Flow Chamber System Setup — A Practical Example

The flow chambers are produced in translucent technical polycarbonate. Each channel has a depth of 1 mm and the base has a size similar to a standard microscope slide. Such designs are compatible with typical microscope slide-mounting hardware, and the biofilm can be examined using either reflected light or epifluorescence confocal modes. The flowcell is assembled by using a single-use syringe to apply threads of silicone glue (e.g., Super Silicone Sealant, 3M, St. Paul, MN) to the top of the polycarbonate base. Long, continuous threads of glue should be applied to cover the area between and around the channels, and the syringe should not touch the base, otherwise the silicone glue will smear. The coverslip is placed on top of the silicone and pushed carefully until the silicone spreads over the whole area of the base between the channels [Fig. 51.2(A)]. Allow the silicone to solidify before use, preferably overnight.

Silicone tubing with dimensions of 1 mm inner and 3 mm outer diameter is used throughout the system except at the pump, where the stronger Marprene tubing (Watson-Marlow, Wilmington, MA) is required to withstand the extensive wear of the pump rollers. The complete system with all the tubing is diagrammed in Figure 51.2(C).

Bubble traps [Fig. 51.2(B)] are constructed using 5 mL syringes mounted on top of a piece of polycarbonate with inlet and outlet (the inlet holes are situated higher than the outlet holes) inside the syringe. The syringes are closed at the top with a Luer-lock stopper (not shown in Fig. 51.2), during normal operation. The system effluent is collected in bottles that must be placed at or above the level of the flow channels so that any leak in a flow channel will not result in the entrance of air. Also, the ends of the effluent tubes must be well above the surface of the waste liquid to prevent reverse siphons out of the effluent collection bottle.

The fully assembled system is disinfected with 0.5% hypochlorite because ethanol dissolves 3M Super Silicone Sealant. The system is first filled up to the bubble traps. The stoppers should be off and stored in 70% ethanol. When the traps are filled, continue flow for approximately 5 to 10 min at a high flow rate, during which the feed liquid pours out of the top of the bubble traps, leaving the downstream part of the system dry. Once the stoppers are inserted into the bubble traps, the rest of the system is filled. Bubbles are removed from the system by carefully tapping the flow cells while the pump is running (5–10 min). Continue sterilization for 2 to 4 h with low or no flow.

The flow system is washed to remove the hypochlorite by filling and emptying the system two to three times, as described above, with a total of 1 to 2 L of autoclaved double-distilled water. To ensure removal of all disinfectant, the system is purged with air between the disinfectant and sterile water runs. Water is then run through the system overnight at a low flow rate, after which the system is filled with medium and the laminar flow rate is set to approximately 0.2 mm/s (approximately 3 mL/h/channel). If the carbon source is very hydrophobic, then medium is run in the

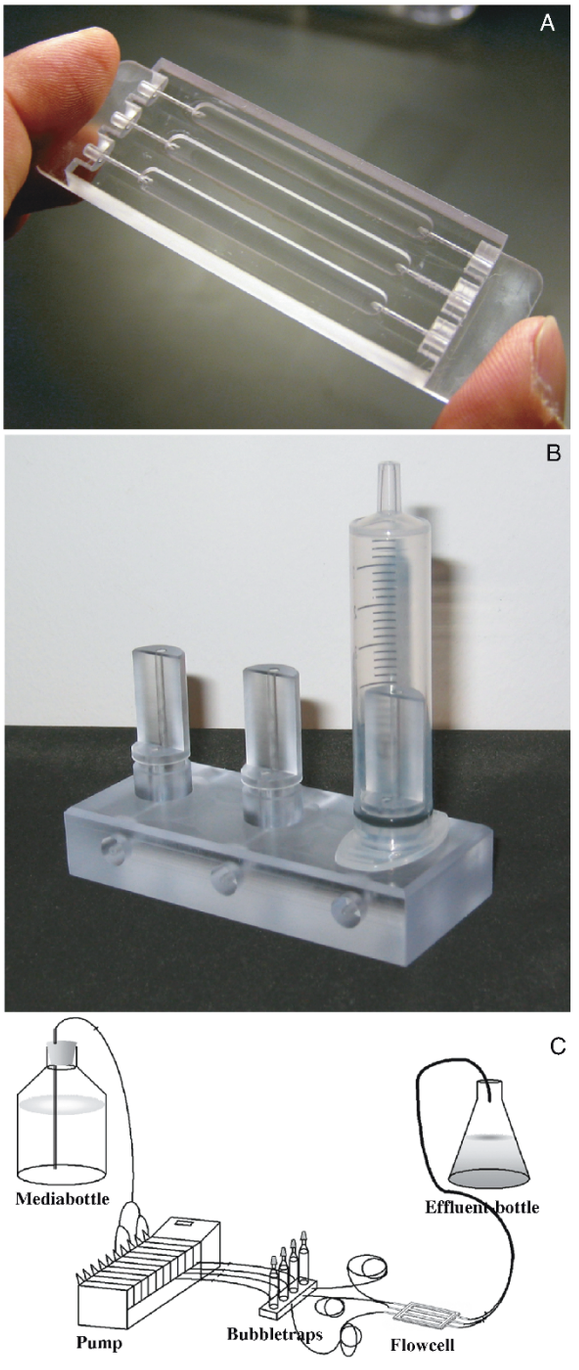


FIGURE 51.2. Flow chamber (A) and bubble trap (B) design. Complete system (C). This system was designed at BioCentrum-DTU, but many variations exist. (C) was drawn by J.A.J. Haagensen and K.B. Barken.

system overnight to saturate the silicone tubing. If the experimental temperature is above ambient, the medium supply must be equilibrated to that temperature or bubbles may appear in the system. Because autoclaving removes dissolved gases from the medium, the medium supply can be placed at the experimental temperature without prior cooling. Sterilization of the flow system can also be done by autoclaving at 121°C. Polycarbonate flow chambers will not warp in the autoclave, but other materials may.

After sterilization and filling, the flowcells can be inoculated with microorganisms. Before inoculation, flow is stopped and the tubing between the flow chamber and the bubble trap is clamped off. The outer surface of the tubing at the injection site is disinfected with 70% ethanol. A 0.5 mL syringe is filled with 250 µL of an appropriately diluted overnight culture of the cells. The needle is inserted into the tubing as near as possible to the flow channel inlet and the bacteria are carefully injected. After inoculation, the tubing surface is again disinfected, and silicone is used to seal the injection site. The flowcell is placed with the glass surface facing downward to encourage contact between the bacteria and the coverglass. After 1 h, the chamber is turned upright, the clamps are removed, and medium flow is started.

MAKING BACTERIA FLUORESCENT

Fluorescent Proteins

Classic methods for labeling bacteria involve the addition of staining reagents to the cells. Fluorescent proteins (FP) have eliminated the need for the addition of any external component. The properties of FP are described in depth elsewhere in this volume, and we will list here only the key features important for bacterial biofilm work.

Green fluorescent protein (GFP) from the jellyfish *Aequorea victoria* has been studied from the early 1960s and has been used as a tool in biology since its cloning (Chalfie *et al*., 1994). GFP is a small protein (238 amino acids; 27 kDa) which is excited by ultraviolet (UV) to blue light and which can be expressed in many bacteria. The excitation maximum of the protein is 395 nm with a minor peak at 470 nm. Emission maximum is 507 nm with a shoulder at 540 nm (Shimomura *et al*., 1962; Morin and Hastings, 1971). Small amounts of oxygen are needed for the newly synthesized protein to become fluorescent in a maturation process that requires several hours, after which it remains largely stable for days (Tombolini *et al*., 1997). However, it is this very stability that precludes use of wild-type GFP for dynamic gene expression studies. In response to these various problems, mutations in the GFP gene sequence were developed that resulted in altered spectral properties (Table 51.1). Shorter maturation times were noted with these variants.

Although green or blue fluorescence may suffice for many applications, FP that emit in the red or orange were desired. Red fluorescence can be seen from GFP when it is synthesized anaerobically (Heim *et al.*, 1994), but any exposure to oxygen results in rearrangement and change to wild-type green fluorescence. Although *Aequorea* GFP could not be mutagenized to emit outside of a relatively limited range of wavelengths, other organisms (corals in particular), provided FP with interesting spectral properties (Table 51.2).

TABLE 51.1. Spectral Variants of *Aequorea victoria* Green Fluorescent Protein

Name	Ecitation (nm)	Emission (nm)	Color
BFP (Blue FP)	380 (UV)	440	Pale blue
CFP (Cyan FP)	433/453	475/501	Cyan
YFP (Yellow FP)	513	527	Greenish-yellow

*Data from Heim and Tsien (1996), Heim *et al.* (1995), Ormö *et al.* (1996), and Siemering *et al.* (1996).

TABLE 51.2. Fluorescent Proteins from Organisms Other than *Aequorea Victoria*

Name	Organism of origin	Excitation (nm)	Emission (nm)	Color	Reference
Am Cyan	*Anemonea majano*	458	489	Cyan	Matz *et al*., 1999
ZsGreen	*Zoanthus* sp.	493	505	Green	Matz *et al*., 1999
ZsYellow	*Zoanthus* sp.	529	539	Yellow	Matz *et al*., 1999
DsRed	*Discomonas* sp.	558	583	Red	Matz *et al*., 1999
AsRed2	*Anemonia sulcata*	576	592	Red	Lukayanov *et al*., 2000
HcRed	*Heterectis crispa*	588	618	Far Red	Gurskaya *et al*., 2001

In addition to excitation/emission wavelength, maturation times and stability are properties that determine if a particular protein can be used for dynamic studies. Maturation times are generally shortened by random mutagenesis, while other methods are used to make the proteins less stable. Unstable variants have been constructed by the addition of short oligopeptides to the C-terminal end of the protein, thereby making the mutant protein a target of indigenous proteases and shortening its lifetime to several minutes (Andersen *et al*., 1998; Li *et al*., 1998). In biofilm experiments, such degradable FP have been used to demonstrate differential gene expression in *Pseudomonas* bacterial microcolonies (Sternberg *et al*., 1999; Christensen *et al*., 2002).

Most fluorescent molecules will bleach under intense or lengthy illumination. In FRAP (fluorescence recovery after photobleaching), an area of the biofilm is bleached and then observed over time for fluorescence recovery as unbleached fluorophore diffuses or is transported into the dark area. Cell or solute movements in defined regions can thus be studied. An example using two isogenic strains of *P. aeruginosa* demonstrates the role of pili. The wild-type strain has pilus-dependent motility (the *pilA* gene) and is expressing YFP. The *pilA* mutant is non-motile and is expressing CFP. Figure 51.3 shows the cell migration following a bleaching of a small area in the biofilm: the *pil*A mutant stays and the wt moves into the bleached area, indicating a *pil*A-dependent active relocation of cells in a biofilm (Haagensen *et al*., submitted). Because the relocating cells originate outside of the bleached area, photodamage to cells during bleaching is considered irrelevant in this experiment.

STAINS

Nucleic Acid Stains

The traditional nucleic acid stains 4′,6-diamidino-2-phenylindole (DAPI) and Acridine Orange stain bacteria well when used alone or in sequential scanning modes; however, they have some disadvantages for confocal work. Excitation of DAPI requires expensive ultraviolet or two-photon lasers; the UV excitation wavelength can result in high autofluorescence and therefore can make simultaneous multi-channel imaging difficult. Simultaneous imaging is also difficult with Acridine Orange because the stain is extremely bright and has a long, red emission tail. In fact, Acridine Orange displays red emission when bound to RNA and green emission when bound to DNA, a trait that can be advantageous when used as the single dye in a sample (see Fig. 39.1, *this volume*).

SYTO stains (cyanine dyes produced by Molecular Probes, Inc., Eugene, OR) bind to nucleic acids in the cells, but the different SYTO stains differ in penetration efficiency, binding affinity and spectral properties. In particular, bacterial strain-dependent differences exist. For example, the red fluorescent nucleic acid stain SYTO 62 works well in combination with GFP or other fluorescent proteins. SYTO 62 stains *Pseudomonas* spp. weakly, but strong staining occurs with *Acinetobacter* C6 and with polymorphonuclear leucocytes (PMN). This difference was used in investigation of interactions between *Acinetobacter* C6 and KT2440, as well as in experiments on the influence of PMN on *P. aeruginosa* (Fig. 51.4).

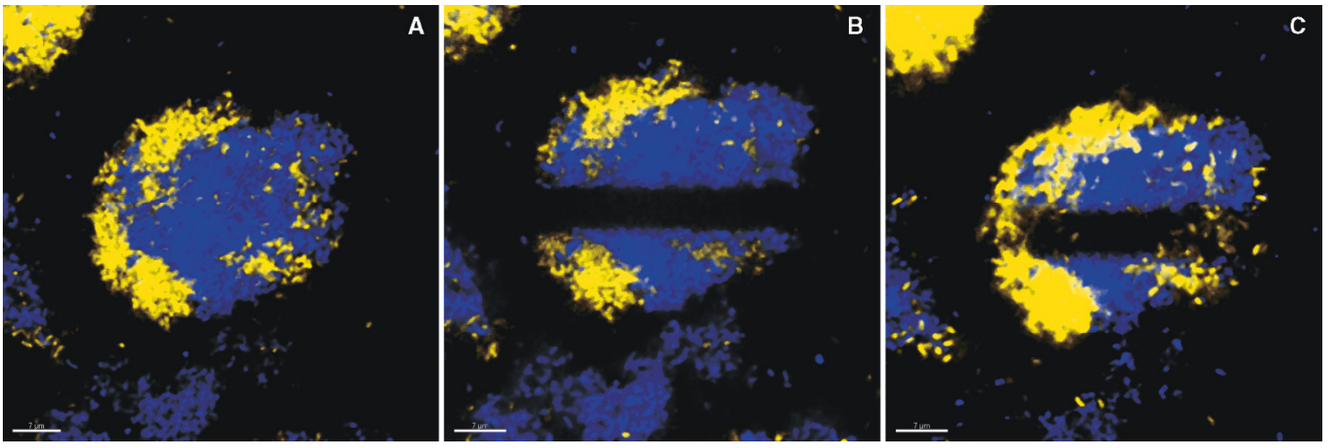


FIGURE 51.3. FRAP in biofilms. One-day-old biofilm established using a 1:1 mixture of YFP-tagged *P. aeruginosa* PAO1 wild type and CFP-tagged non-motile *pilA* mutant PAO1. (A) *xy*-image of the biofilm structure before bleaching. (B) The bleached microcolony. (C) The microcolony 40 min after bleaching.

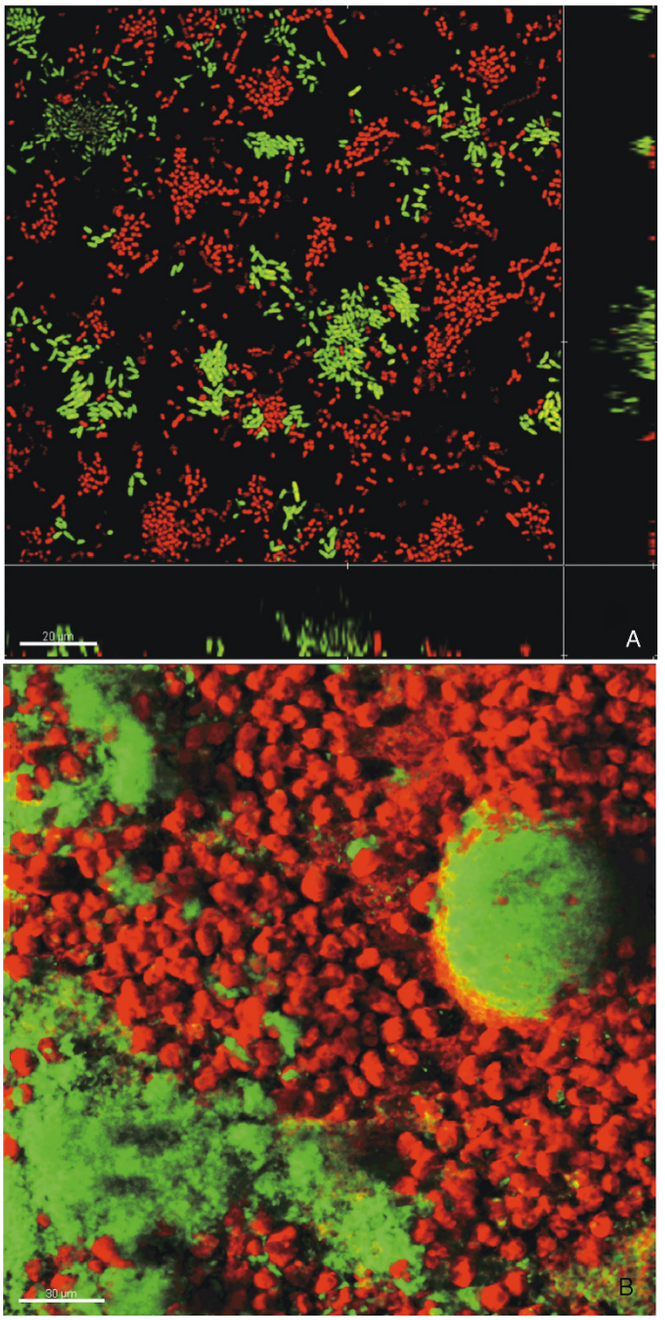


FIGURE 51.4. Differential staining of bacteria and eukaryotic cells using SYTO 62 (excitation, 633 nm; emission, 676 nm) and GFP. SYTO 62 (1 µL of a 5m*M* stock in DMSO) is dissolved in 1 mL of medium or 0.9% NaCl. Five to 15 min prior to microscopy, 0.5 mL of the diluted SYTO 62 is injected into the flow chamber. (A) Spatial distribution of cells in a biofilm containing *Acinetobacter* C6, stained with SYTO 62, and *P. putida* KT2440, tagged with GFP. Image acquired after 1 day of flow-chamber growth (S.K. Hansen, unpublished). (B) *P. aeruginosa* expressing GFP in interaction with SYTO 62-stained polymorph nuclear neutrophils (red) (Bjarnsholt *et al*., 2005).

Live/Dead Stain

The BacLight Live/Dead Bacterial Viability Kits (Molecular Probes) provide a rapid assay of bacterial viability based on membrane integrity. The kits contain two nucleic acid stains: SYTO 9, a proprietary formula; and propidium iodide (PI), a stain with an extensive history in eukaryotic viability determination. PI, a charged molecule, does not go across polarized cell membranes, whereas SYTO 9 crosses all cell membranes. The basis of the viability determination rests in the combined application of the dyes. Cells that have intact polarized membranes are permeable only to SYTO 9, whereas cells lacking sufficient polarization are permeable to both stains. PI has a higher binding affinity than does SYTO 9 and therefore preferentially stains the nucleic acid of those cells in which both stains penetrate (dead or inactive cells). It is possible to use a single laser line (488 nm) or, to use multiple laser lines from an argon laser (488, 514 nm) to excite both dyes (SYTO 9 excitation maximum, 480 nm; PI excitation maximum, 530 nm). The emission wavelengths are well separated (SYTO 9 maximum, 500 nm; PI maximum, 635). In this way, even single-laser confocal microscopes or epi-fluorescence microscopes (480 nm LP filter) can be used for detecting both stains. However, if a green helium-neon laser (543 nm) is used together with the 488 nm line and sequential excitation, then spectral overlap can be greatly reduced.

Under conditions unfavorable to bacterial growth, cells can display an intermediate staining in which PI and SYTO 9 fluorescence occur simultaneously and single cells appear yellow-green to yellow when examined through the oculars with a fluorescein long-pass filter. Yellow cells are rare in flowcell experiments because growth conditions are generally good (see Hansen *et al*., 2000, for an exception), but they are frequently seen with bacteria stained directly from soil or other natural habitats. Figure 51.5 shows examples of typical Live/Dead staining and of yellow cells. Molecular Probes provides information on the precise protocols by which the Live/Dead kit is calibrated, as well as on the bacteria for which these protocols have been tested. Investigators are recommended to calibrate staining for their strain-of-interest because the ratio of SYTO 9 to propidium iodide which provides optimal results varies with strain. Because of this, it is difficult to interpret staining in natural mixed-species populations.

Combination of FP-tagged bacteria with PI staining makes possible discrimination of live (FP-containing) from dead (PI-positive) cells. FP fluorescence is not detectable when PI is present (Fig. 51.6). It is also possible to add PI directly to the medium feed (a smaller reservoir of medium is used to limit the cost of the staining). The biofilm will be continuously stained and viewing can take place directly over time without additional sample handling.

Fluorescence *In Situ* Hybridization

In situ hybridization techniques allow for identity and/or activity measurements of individual cells. Fluorescence *in situ* Hybridization (FISH) is typically used in biofilm research to provide spatially resolved taxonomic information and is normally based on small subunit (16S) ribosomal RNA (rRNA) gene sequences. These sequences consist of regions that are either highly conserved between species or highly variable. In most cases, one can design probes that hybridize with rRNA from only a single species or even subspecies, as well as probes that target a broader taxonomic unit (genus, kingdom). In this way, it is possible not only to identify the organisms but also to reveal their precise location within the three-dimensional (3D) community. FISH has been used extensively in environmental microbiology, enabling investigators to map complex biofilm communities (Daims *et al*., 2001; Thurnheer *et al*., 2004). Assuming quantitative labeling (i.e., all ribosomal rRNA molecules are labeled), it is possible to assess the growth rate of a cell because the amount of rRNA is correlated with overall protein synthesis rate. However, because not all

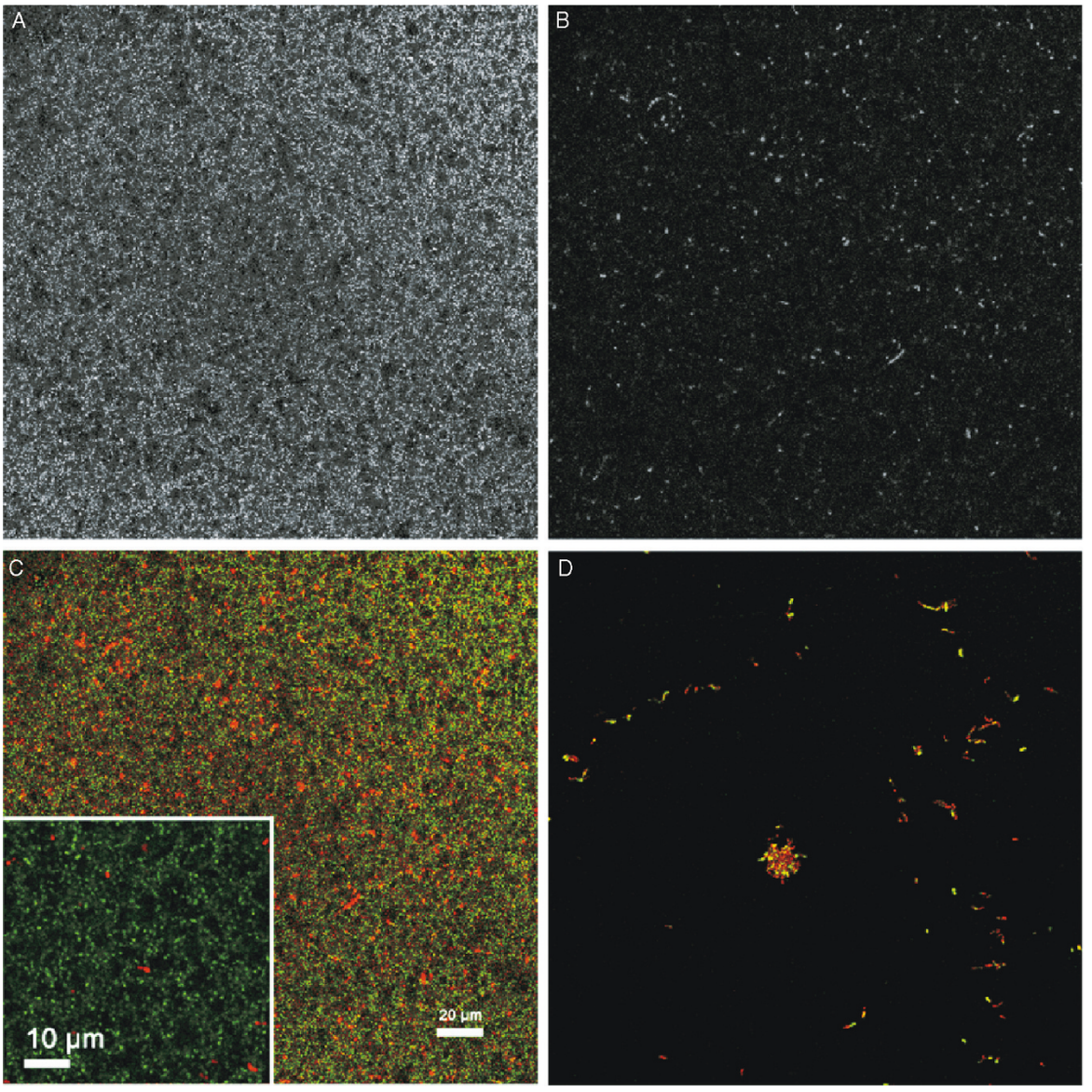


FIGURE 51.5. Live/Dead (Molecular Probes, Eugene, OR; catalog no. L7012) staining of a *Streptococcus gordonii* biofilm after typical overnight growth in a flowcell and of a *S. mutans* biofilm after overnight growth under starvation conditions. Molecular Probes protocol "Staining of bacteria in suspension" was followed. Maximum projection images of confocally acquired image stacks. (A) SYTO 9 channel; *S. gordonii*. (B) PI channel; *S. gordonii*. (C) Overlay of (A) and (B). Inset shows 3× zoom of center of sample for single-cell resolution. (D) Overlay of SYTO 9 and PI channels for *S. mutans* biofilm showing intermediate staining of poorly growing cells. Scale bar in (C) applies to all images except the inset.

ribosomes are actively synthesizing protein, actual growth rate may be lower than the theoretical maximum rate as determined by this assay.

The use of FISH in confocal microscopy requires not only that the sample be labeled, but also that its 3D properties are retained. Microbial biofilms grown in flowcells presented a problem because the multiple washing steps involved in FISH might change the 3D structure of the biofilm. Embedding and physical sectioning as applied in eukaryotic systems were not useful because they generated samples that were not transparent, were autofluorescent, or were too hard. A simple and effective method employing acrylamide as the embedding agent is described below. After polymerization of the acrylamide, biofilm samples could be removed from the flowcells as intact slabs and then subjected to FISH outside the flowcell with subsequent confocal microscopy (Fig. 51.7).

General Procedure for Embedding of Flowcell-Grown Biofilms for Fluorescence *In Situ* Hybridizatioin

Details of this procedure have been published (Christensen *et al.*, 1999). Briefly, the biofilm is first fixed using an 4% aqueous solution of paraformaldehyde. A solution of standard sequencing grade acrylamide (20%, 200 : 1 acrylamide : *bis*-acrylamide) is used, to which the TEMED (*N*,*N*,*N*′,*N*′-tetramethylethylenediamine) and the ammonium persulfate catalyst are added just prior to intro-

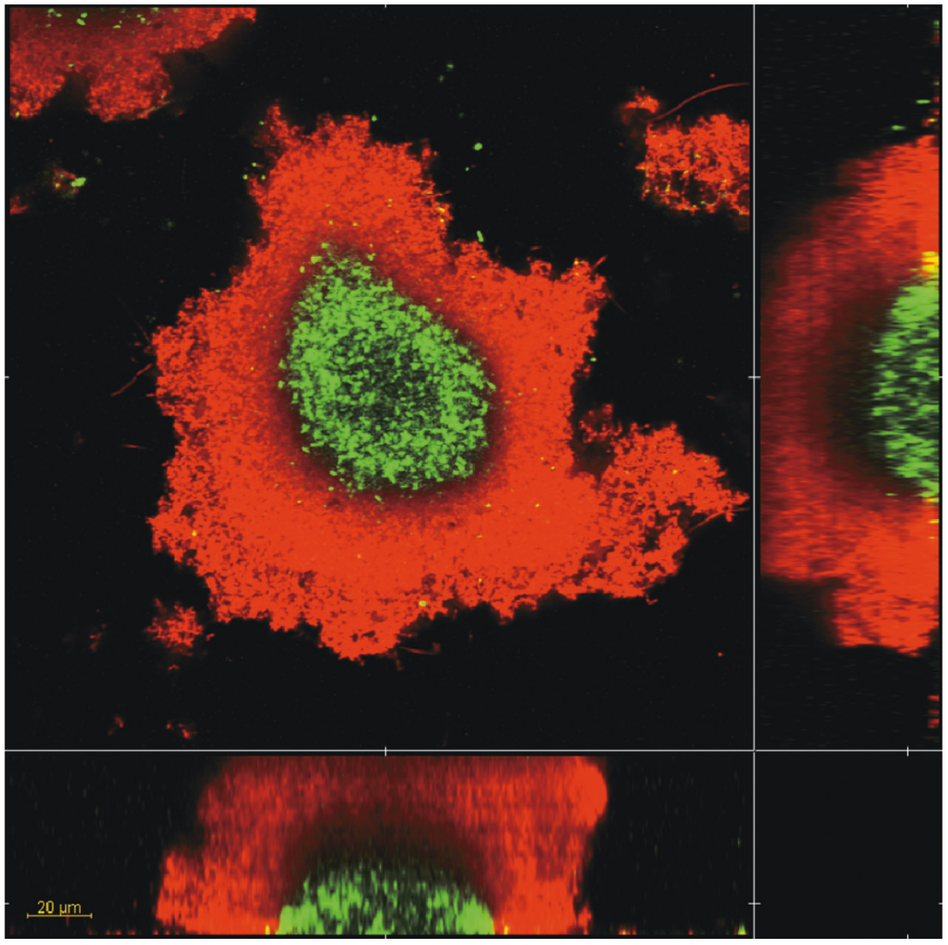


FIGURE 51.6. Effect of antibiotic (colistin) treatment on *Escherichia coli* F+ biofilm. GFP expressing *E. coli* cells were grown in a flowcell for 2 days. Propidium iodide (used at 10 µ*M* final concentration) stains dead cells red (J.A.J. Haagensen, unpublished results).

duction into the flowcell. Catalyst concentration must be calibrated such that solidification commences just after the flow chamber becomes filled with embedding solution. Also, introduction of the solution must occur slowly enough that the biofilm is not damaged by the shear force. Bubbles must not be introduced because they can both destroy the biofilm's 3D structure and hinder solidification. Once solidified, the polyacrylamide gel containing the embedded biofilm is reasonably robust and the coverglass can be removed. Hybridization can be done on several samples at a time using standard hybridization slides in a humidified chamber. Once hybridized, samples are stable for up to several months. FISH can also be performed on samples containing GFP or other fluorescent proteins. The fixation procedure kills the cells but *Aequorea* GFP and derivatives have very long half lives, and the FISH procedure will allow the GFP to be preserved. However, as SDS (a permeableizing agent) will reduce GFP lifetime (unpublished results), it should be reduced or omitted from the hybridization in FP-containing samples. FISH efficiency may suffer, but the FPs will better retain their fluorescence.

Antibodies

Antibody-labeled cells can be detected microscopically by two routes. In primary immunofluorescence, also known as direct immunofluorescence, fluorophore molecules are directly conjugated to the antigen-targeting IgG molecules. When enough of these labeled IgG molecules bind to a cell, fluorescence is detectable. Typically, as a single IgG molecule can only be coupled to between one and four fluorophore molecules, many labeled IgG molecules must bind to the target to reach the fluorophore concentration required for easy detection by cameras or PMTs.

In secondary or indirect immunofluorescence, the unlabeled IgG is detected by using a second fluorescently labeled antibody made against the animal in which the primary antibody was made. Thus, a primary antibody made in a rabbit would be detected using anti-rabbit secondary antibody made in, for example, a goat. One advantage of this approach is that several secondary antibodies, each bearing several fluorophores, react with each primary antibody. Typically at least a 3-fold amplification of the signal is achieved in comparison with that obtained through primary immunofluorescence. Another advantage is that a wide range of secondary antibodies (different fluorophores, different production animals) is commercially available. A third advantage is that commercially prepared secondary antibodies are available as Fab fragments, that is, they lack the Fc region that is recognized by Fc receptors present on certain bacteria.

One major disadvantage of secondary immunofluorescence is that the use of more than one primary antibody in an experiment

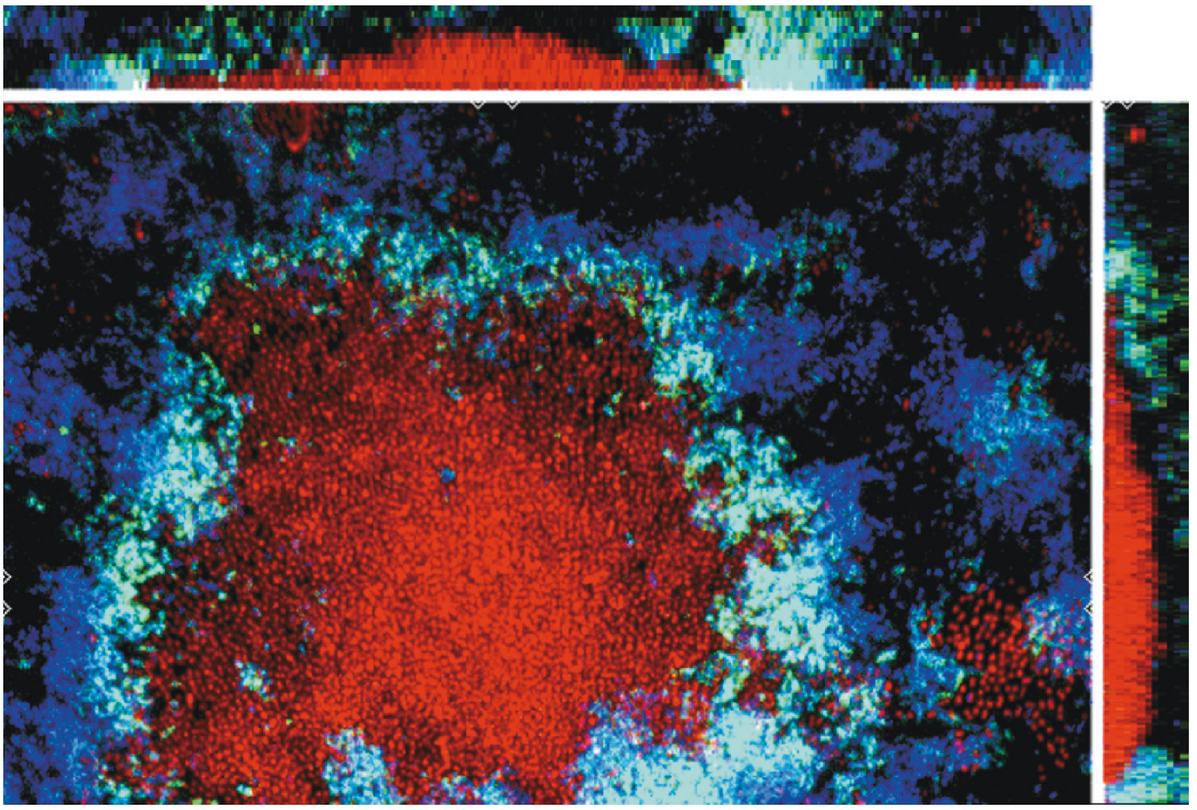


FIGURE 51.7. Fluorescence *in situ* hybridization (FISH) in combination with expression of fluorescent protein. CLSM micrographs showing the structural relationships between *Acinetobacter* C6 and *P. putida* R1, with different activity, in a mixed biofilm consortium. Three days after inoculation, the biofilm was embedded and hybridized. *P. putida* R1 was targeted with a CY5-labeled FISH probe (blue), and *Acinetobacter* C6 with a CY3-labeled FISH probe (red). *P. putida* R1 cells actively making ribosomes were monitored via a degradable GFP expressed from the *rrnB*P1 promoter. These cells are cyan (combination of green GFP and blue FISH probe). *xy*-images are extended focus projections. To the right and above the *xy*-images are virtual vertical sections through the biofilm collected at the positions indicated by the white triangles. (Reproduced with permission from Christensen *et al*., 2002.)

is made difficult. Either each primary antibody must be made in a different animal (rabbit, mouse, chicken) with each primary antibody being detected with a different secondary antibody, or the sample must be subjected to time-consuming exhaustive washing and blocking between sequential application of each primary/secondary antibody pair to assure that each individual primary antibody is detected with fidelity. Even meticulous washing and blocking cannot absolutely exclude migration of previously applied secondary antibodies to other binding sites.

Preparation of Labeled Primary Antibodies

For studies of the interactions between different bacterial species in oral biofilms at the National Institute of Dental and Craniofacial Research (NIDCR), primary immunofluorescence is used because the goal is to identify multiple organisms in a single sample: frequently a complicated undefined natural sample such as dental plaque. Polyclonal antibodies are produced commercially in rabbits from bacterial suspensions we provide. The suspensions are phosphate-buffered-saline-washed cells from overnight culture and are standardized at 10^{10} cells/mL. The suspension is mixed with Freund's incomplete adjuvant and injected subcutaneously. A booster injection is given every week until a total of three injections have been made. The animal is exsanguinated after about 2 months and the serum is shipped to us frozen. The IgG fraction is prepared using a commercially available protein A column (Pierce); typical yields range from 1 to 3 mg IgG/mL serum. The unlabeled antibody is then tested for cross-reactivity using secondary immunofluorescence. Washed cells (about 5×10^8) of the antigen strain are used to determine the minimum concentration of primary antibody at which the cells are easily visible in the epi-fluorescence microscope. This concentration is then used to check for cross-reactivity with other bacterial strains. If cross-reactivity is a problem, absorption against a cross-reactive strain is performed overnight at 8°C in the presence of protease inhibitors, then the IgG is repurified over a protein A column. The final antibody is then labeled with Alexa Fluor protein labeling kits (Molecular Probes). Twice the recommended amount of reactive dye is used in each conjugation because we have not often achieved a satisfactory degree of labeling using the standard dye concentration. In our conjugations, typically 1 to 3 moles of Alexa Fluor are conjugated per mole IgG. Unlabeled dye is removed using the column supplied in the kit, and typical recovery of labeled IgG is 90%. The labeled primary antibody is then titrated to determine the minimum concentration necessary for easy detection of the antigen strain. With these Alexa Fluor polyclonal conjugates, effective concentrations typically range between 1 and 5 µg/mL. Bovine albumin (0.1%) is used as a blocking agent and we have yet to observe non-specific binding of antibody, even in natural samples from the oral cavity (Palmer *et al*., 2003).

In certain experimental situations, cross-reactivity can be advantageous. If one wishes to distinguish between two cell types

in a dual-species *in vitro* experiment, then it is only important that the antibodies employed show this difference. An antibody we have prepared to *Streptococcus gordonii* that cross-reacts with *Streptococcus oralis* can in fact be made specific for *S. gordonii* through absorption against *S. oralis*. However, we would not use the specific (absorbed) antibody in an *in vitro* experiment containing *S. gordonii* and another bacterium that is unreactive with the *S. gordonii* antibody because the less specific antibody is sufficient under these circumstances.

In contrast, when one examines a natural population such as dental plaque, then the use of a less selective antibody will temper claims on the identity of antibody-reactive organisms. Nucleic acid stains can be used to reveal cells that are not antibody reactive (Fig. 51.8).

Imaging Bacteria Without Fluorescence

In certain cases it may be necessary to image unstained bacteria on the confocal microscope. Many instruments are equipped for transmitted light differential interference contrast (DIC) imaging using laser light and, despite the fact that this is a non-confocal technique and the fact that many flowcells have thick bases, good transmitted light images can often still be obtained [Fig. 51.9(A)]. Another possibility is reflected light confocal imaging, more properly known as backscattered light (BSL) imaging. In this approach, the primary dichroic mirror is replaced with a neutral beamsplitter that transmits the laser light scattered by the specimen back to the detector. Typically the 488 nm laser line is used but other lines work equally well. Figure 51.9(B) shows a maximum projection of a 30 µm thick confocal stack through a two-species biofilm containing streptococci (round cells) and fusobacteria (long thin rods). The inset shows a single section taken 20 µm away from the coverslip. BSL imaging is an approach with confocal resolution applicable to thick non-fluorescent samples.

IMAGING EXTRACELLULAR POLYMERIC SUBSTANCES IN BIOFILMS

Microbial biofilms are composed not only of cells but also of the extracellular polymeric substances (EPS) produced by the microorganisms (Wingender, 1999). The major constituents of EPS are proteins, polysaccharides, nucleic acids, and amphiphilic polymeric compounds such as lipopolysaccharides and emulsants. A multitude of structural and functional roles have been ascribed to EPS (Wolfaardt *et al*., 1999) but its characterization is difficult; nevertheless two major approaches have been taken. The first approach involves extraction and isolation of polymers with subsequent chemical analysis (Nielsen and Jahn, 1999). Several variations of this destructive approach exist but they are applicable only in pure culture studies where one or a few extracellular polymers are present. However, as environmental biofilm systems contain numerous types of different bacteria and therefore also contain numerous types of polymers (Staudt *et al*., 2003), chemical analyses are often presented as a sum parameter (e.g., percentage carbohydrate, protein, etc.) and detailed information on a single polymer class or individual polymers is often difficult to assess.

The second approach is an *in situ* staining technique employing specific fluorescently labeled probes in combination with laser-scanning microscopy (Lawrence and Neu, 1999; Neu and Lawrence, 2002). The approach takes advantage of the carbohydrate specificity of lectins that bind to the glycoconjugates found in the biofilm (Neu and Lawrence, 1999a, 1999b). Lectin-binding analysis of biofilms has been critically assessed (Neu *et al*., 2001) and 70 commercially available lectins have been tested on certain types of biofilms (Staudt *et al*., 2003). Lectin staining may be combined with other stains such as general nucleic acid stains, specific gene probes (Böckelmann *et al*., 2002) or probes characterizing the microhabitats in biofilms (Lawrence *et al*., submitted).

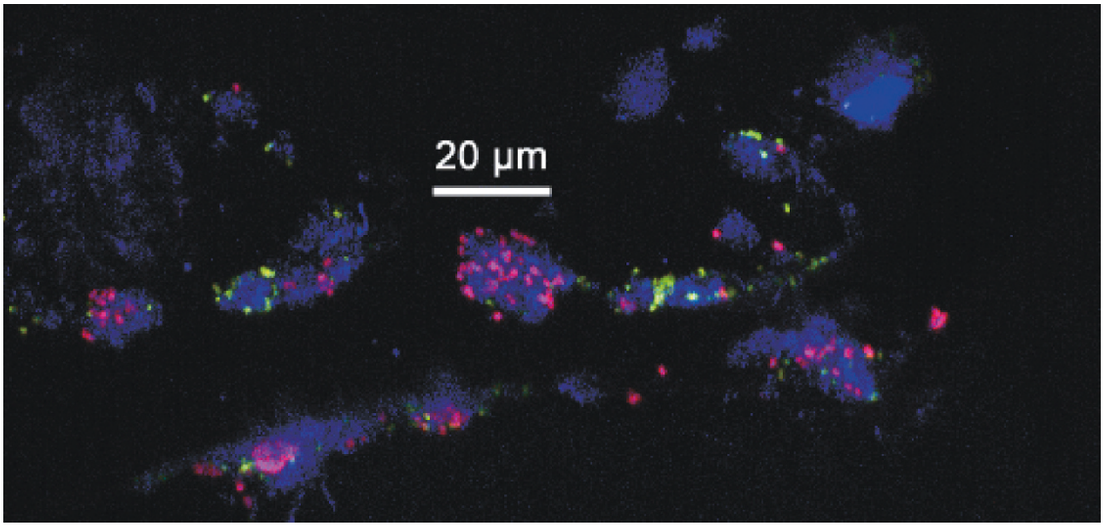


FIGURE 51.8. Eight-hour-old oral biofilm community on a human tooth enamel chip retrieved from the human mouth. Combination of primary immunofluorescence and nucleic acid staining demonstrate interactions between members of this undefined natural community. Green cells are reactive with AlexaFluor 488-conjugated anti-*Streptococcus gordonii*. Red cells are reactive with AlexaFluor 546-conjugated anti-streptococcal-receptor-polysaccharide. Blue cells are stained with the nucleic-acid-binding SYTO 59.

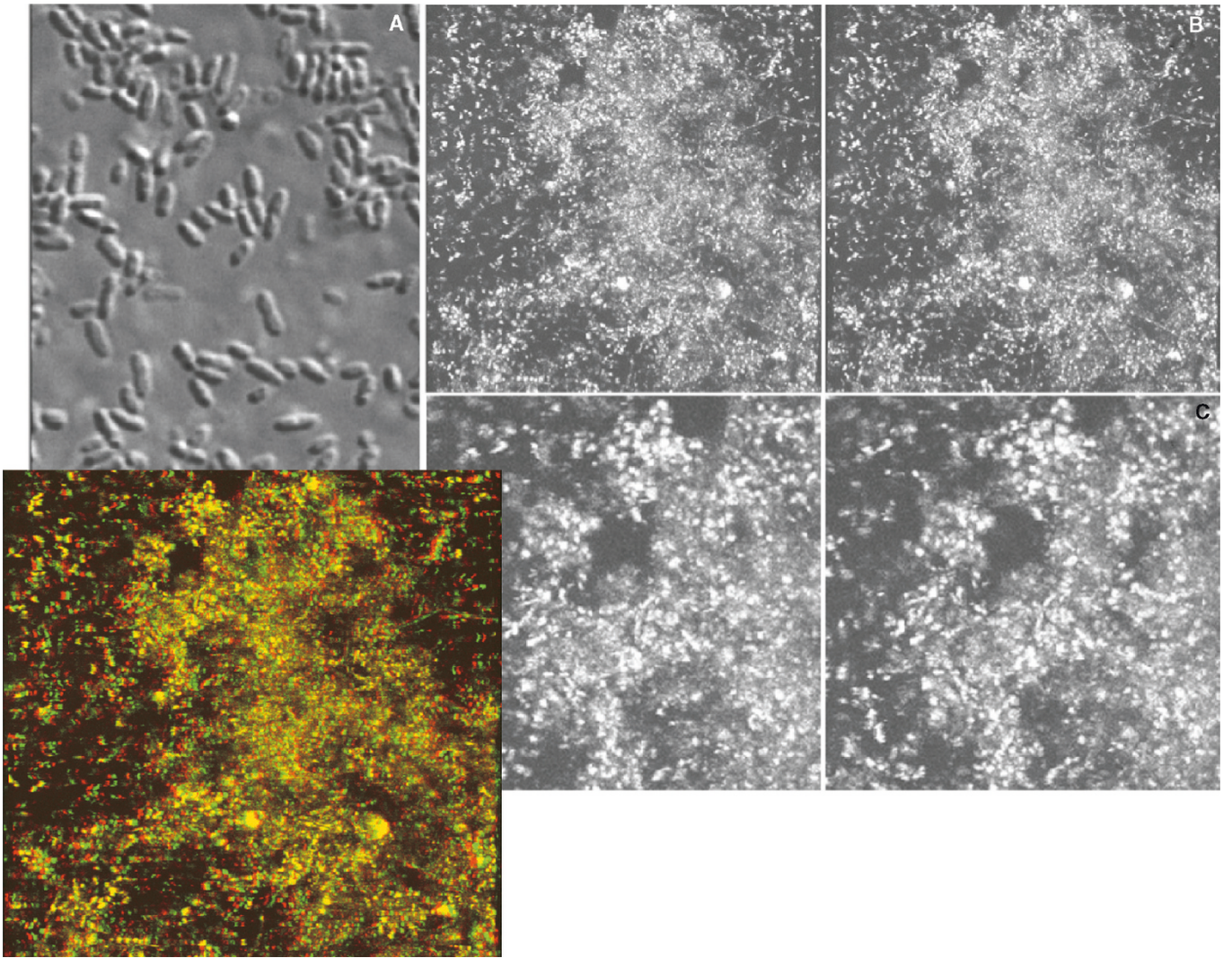


FIGURE 51.9. (A) Transmitted laser light image collected through the flow chamber shown in Figure 51.2. (B) Stereo-pair maximum projection image of a 30 µm thick confocal stack collected using backscattered light. The biofilm is composed of streptococci (round cells) and fusobacteria (long thin rods). (C) shows a magnified image from the upper central part of (B). The color panel is an anaglyph stereo-pair of (B). Use red-green glasses to view.

Using digital image analysis, the glycoconjugate signal can be quantified (Staudt *et al*., 2004) and, after object definition, the signals of cells and polymers can be related to each other (Neu *et al*., submitted). In contrast to immunological techniques requiring the isolation of polymers and subsequent production of specific antibodies, lectin-binding analysis can be applied immediately to environmental biofilm samples. In summary, lectin-binding analysis allows (1) *in situ* visualization and quantification of glycoconjugates within biofilms, (2) detection of cell-surface-bound, microcolony-related, and cell-free glycoconjugates, and (3) differentiation of various types of glycoconjugates in microbial biofilms. Clearly, lectin-binding analysis serves as a valuable tool for examining the polymer matrix of microbial biofilm systems.

Examples of lectin-binding analysis in biofilms developed from activated sludge are shown in Figure 51.10. The first images (A–C) show the principle of lectin-binding analysis in a chemoautotrophic biofilm. The biofilm was first stained with *Aleuria aurantia* — AlexaFluor 488-conjugated lectin and then counterstained with SYTO 60. The gray scale images (A,B) show the single-channel signal of each stain; however, the color overlay (C) reveals the true architecture of the biofilm consisting not only of cellular signals but to a large degree of glycoconjugates. The sensitivity of lectin-binding analysis is also shown in a series of three images made by zooming into the biofilm, starting with an overview (D), via the microcolony towards the single bacterial cell (E,F). In the overview, it is obvious how the microbial biofilm developed in the direction of flow (top to bottom in the figure) and how it is embedded in a thick layer of glycoconjugates (D). This sample was stained with two different lectins (*Solanum tuberosum* — CY5, *Arachis hypogaea* — TRITC) and counterstained with SYTO 9. The next image (E) shows a microcolony with a group of bacteria embedded in extracellular glycoconjugates forming a capsular sheath around the cells. The biofilm microcolony was stained with AlexaFluor 488-conjugated *Solanum tuberosum* lectin and with SYTO 60. At the cellular level, it is possible to use lectins to distinguish between various regions on the bacterial cell surface

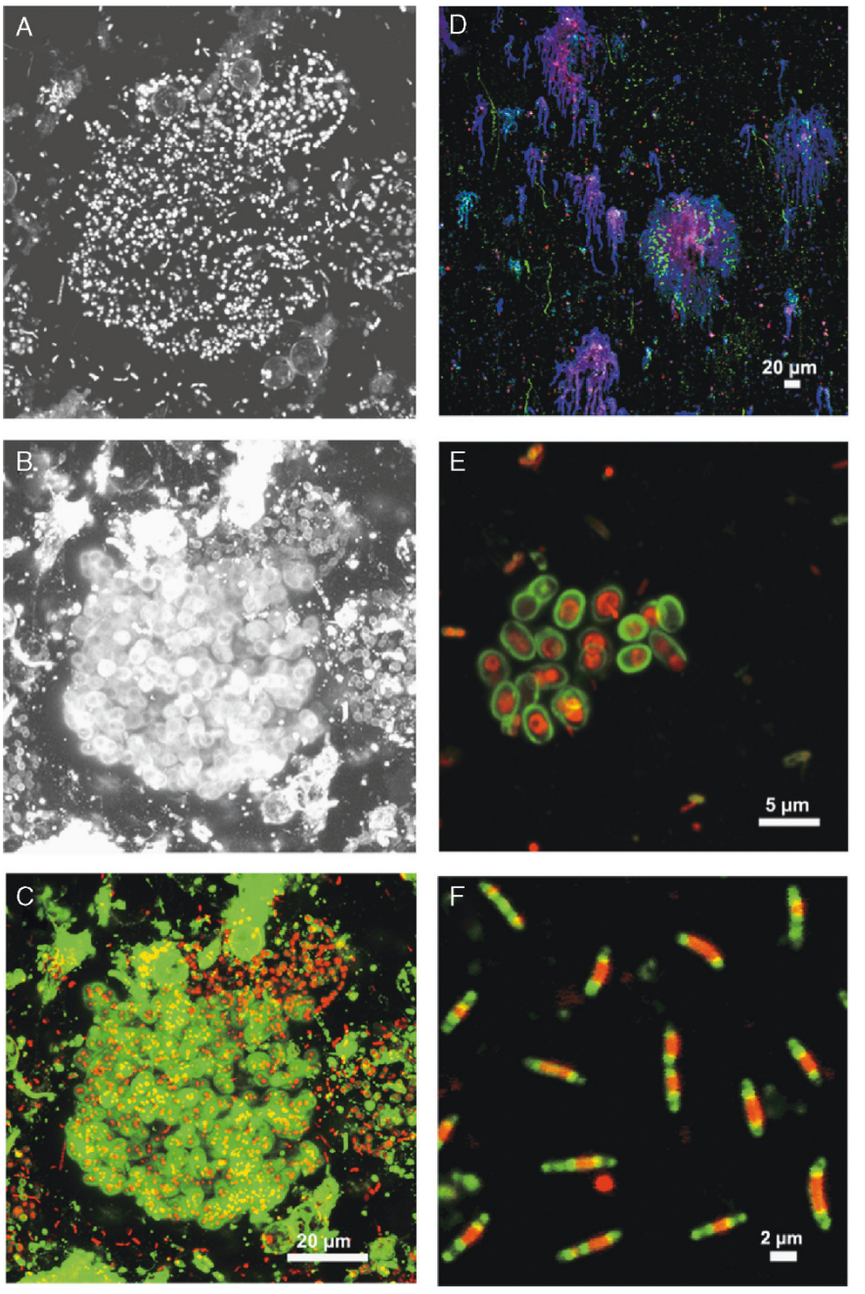


FIGURE 51.10. Lectin-binding analysis in bacterial biofilms. (A–C) Principle of glycoconjugate (lectin) staining in combination with nucleic acid staining. (A) Maximum intensity projection of a biofilm showing nucleic acid staining (SYTO 60, red). (B) AlexaFluor 488-conjugated *Aleuria* lectin staining (green) and (C) the resulting overlay. Single-photon excitation/emission: 488/500–550 nm and 633/650–800 nm. (D–F) Zooming into a biofilm sample showing different patterns of lectin staining. (D) Maximum intensity projection as an overview with two lectins (Cy5-conjugated *Solanum tuberosum*, blue; TRITC-conjugated *Arachis hypogaea*, red) and nucleic acid staining (SYTO 9, green). Colocalization of the two lectins appears pink. Single-photon excitation/emission: 488/500–550 nm, 568/590–625, and 633/650–800 nm. (E) Microcolony stained with AlexaFluor 488-conjugated *Solanum* lectin (green) and SYTO 60 (red). Single-photon excitation/emission: 488/500–550 nm and 633/650–800 nm. Single bacterial cells showing a specific glycoconjugate banding pattern after lectin staining (green) and nucleic acid staining (SYTO 60, red). Excitation/emission as in (D).

having a different glycoconjugate makeup (F). In this case, the biofilm sample was stained with AlexaFluor 488-conjugated *Aleuria aurantia* and SYTO 60.

In the natural environment, most biofilms are routinely exposed to light. These phototrophic biofilms consist of heterotrophic and chemo-autotrophic bacteria as well as algae and cyanobacteria. The latter two organisms show autofluorescence due to their photosynthetic pigments. In the example shown as an isosurface projection [Fig. 51.11(A)], the bacteria are stained with SYTO 44 and imaged simultaneously with the autofluorescence in the red and far red emission channel. The different makeup of the pigments allows a separation of cyanobacterial signal (phycoerythrins/phycocyanins as well as chlorophyll a) from algal signal (chlorophyll a only) by colocalization (Neu *et al.*, 2004b). Lectin-binding analysis may also be applied to phototrophic biofilms. Lectin-staining using AlexaFluor 488-conjugated *Aleuria aurantia* lectin in combination with autofluorescence is demonstrated in a three-channel shadow projection [Fig. 51.11(B)]. The image shows the distribution of algal cells (mainly diatoms) and cyanobacterial cells. Lectin is present as a surface coating on diatoms as well as in separate glycoconjugate clusters in between the phototrophic cells. The *xyz*-projection [Fig. 51.11(C)] demonstrates a four-channel projection of reflection, cyanobacterial, and algal autofluorescences in the red and far red, as well as lectin staining (AlexaFluor 488-conjugated *Iberis amara* lectin). Using colocalization, the cyanobacterial signal in the red channel and far red channel can be separated from the algal signal that is found only in the far red channel. The strong lectin signal of

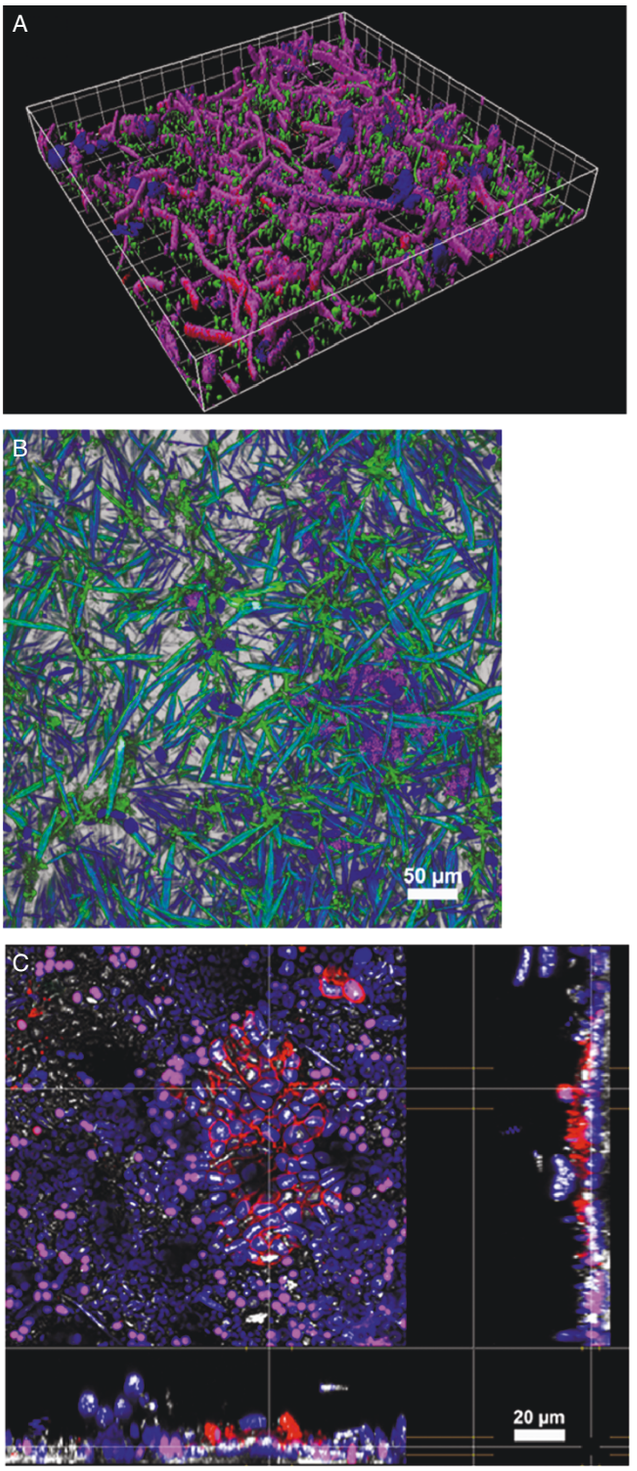


FIGURE 51.11. Lectin-binding analysis in phototrophic biofilms. (A) Isosurface projection of a thin biofilm (22 µm) showing algal autofluorescence (blue), cyanobacterial autofluorescence (pink), and SYTO 44 (green). Grid size = 10 µm. Single-photon excitation/emission: 458/470–540 nm, 568/590–625, and 633/650–800 nm. (B) Shadow projection of a thick biofilm (220 µm) after lectin staining. Cyanobacterial autofluorescence (pink), algal autofluorescence (blue), AlexaFluor 488-conjugated *Aleuria* lectin (green). Single-photon excitation/emission: 488/500–550 nm, 568/585–625, and 633/650–800 nm. (C) Extended *xyz*-projection of reflection and fluorescence signals, biofilm thickness = ~45 µm. Color allocation: cyanobacteria, pink; algae, blue; *Iberis* lectin, red. Single-photon excitation/emission: 488/480–495 nm, 568/590–625, and 633/650–800 nm.

glycoconjugates is also present in the red channel due to the cross-talk between the green and red channels.

APPLICATION OF TWO-PHOTON LASER-SCANNING MICROSCOPY FOR BIOFILM ANALYSIS

Since the first experimental proof of two-photon laser-scanning microscopy (2PLSM) by Denk and colleagues (Denk *et al*., 1990) (see also Chapter 28, *this volume*) and the many applications in cell biology (König, 2000), 2PLSM has found its way into several microbiological laboratories. Nevertheless, few published examples of 2PLSM biofilm research exist. Benefits of 2PLSM for the examination of biofilm structures are obvious as microbial biofilms form extended 3D structures that can be up to several hundred micrometers in thickness. As a result of microbial activity, biofilms show gradients of, for example, oxygen and pH, and they form layered structures in which different cellular and polymeric constituents are organized in three dimensions.

As the highly complex structure of environmental biofilms makes them prone to scattering (excitation light as well as emission light), the longer wavelengths used in 2PLSM should make this technique ideal for collecting highly resolved images at deeper levels within microbial biofilms. The first application of 2PLSM in microbiology (Vroom *et al*., 1999) demonstrated this capability deep within model oral biofilms.

One technical issue in 2PLSM is the applicability of common fluorochromes and whether multiple fluors can be excited individually, as in one-photon laser-scanning microscopy. Neu *et al.* (2002) addressed 2P excitation of fluorochromes specific for cellular and polymeric biofilm constituents and reported the optimal IR excitation wavelengths, as well as providing the first multichannel 2P images of microbial biofilm systems. In this study, fluorochromes and/or autofluorescence was excited at one wavelength and the emission signals detected in two or three different channels. This approach has been taken one step further in a methodological report on the differentiation of photo-autotrophic biofilm constituents, such as cyanobacteria and algae, using two-photon excitation (Neu *et al*., 2004b). Due to the strong autofluorescence signals of such phototrophic biofilms, it is relatively easy to collect multi-channel signals from deep levels within them.

A comparison of single-photon and two-photon laser-scanning microscopy of biofilms is presented in Figure 51.12. EDTA-degrading biofilms were grown on carrier material (sand and pumice) in a fluidized-bed reactor under shear force. The extremely dense biofilm was stained with the SYTO 40. The *xz*-scan [Fig. 51.12(A)] shows blurred signal in the single-photon image, whereas the two-photon image [Fig. 51.12(B)] yields higher resolution of the cells. The EDTA biofilm was also examined using the nucleic acid stain SYBR Green (Molecular Probes). The *xy*-images at a depth of 14 µm from the coverglass side of the biofilm also demonstrate the lower intensity and lower resolution of the single-photon image [Fig. 51.12(C)] compared to the two-photon image [Fig. 51.12(D)]. The frame indicates the cropped section which was used for 3D projection. The 3D images are shown as a comparison of single-photon [Fig. 51.12(E)] and two-photon excitation [Fig. 51.12(F)], and again demonstrate the higher resolution using two-photon excitation. The higher signal intensity and higher resolution using two-photon excitation may be due to the higher excitation photon flux resulting in increased signal from the fluorochrome,

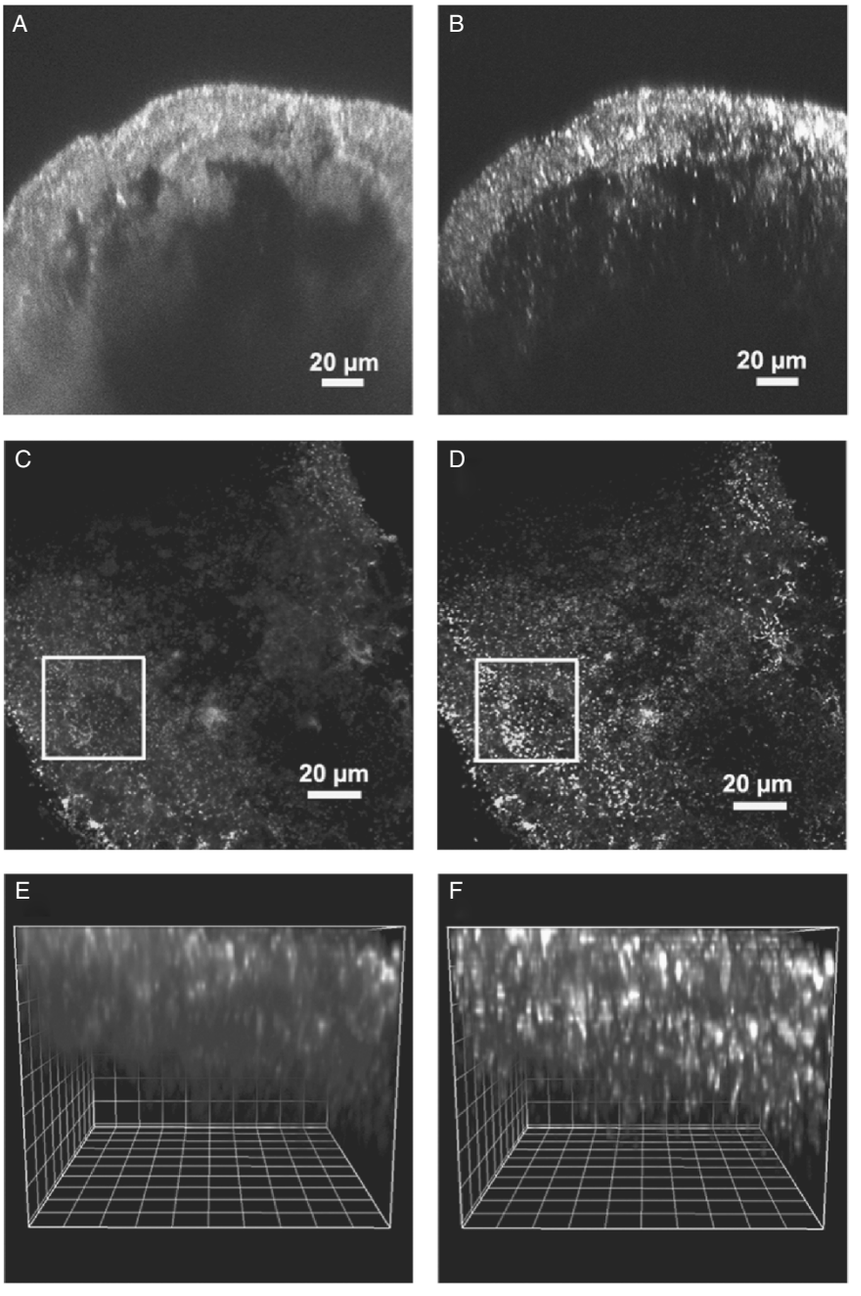


FIGURE 51.12. Comparison of single-photon and two-photon imaging in dense biofilms stained with SYTO 40. (A) *xz*-scan with single-photon excitation/emission: 488/500–550 nm. (B) Two-photon excitation/emission: 840/400–750 nm. (C,D) *xy*-scans after staining with SYBR Green at the same depth (14 µm). (C) Single-photon excitation/emission: 488/500–630 nm (D) two-photon excitation/emission: 860/400–750 nm. (E,F) Three-dimensional projections of the framed area in C and D. (E) Single-photon excitation/emission: 488/500–630 nm. (F) Two-photon excitation/emission: 860/400–750 nm. Grid size is 5 µm. See also 3D reconstructions on Handbook http://www.springer.com/0-387-25921-X.

reduced non-specific signal from autofluorescence away from the focal plane and reduced scattering.

Due to the wide excitation cross-section of most fluorochromes for two-photon excitation, it is possible to use a single wavelength to excite two fluorochromes and subsequently record the emission in two channels. Two examples showing biofilms stained with a lectin and with a nucleic-acid stain are presented. The first example shows a biofilm stained with TRITC-conjugated *Canavalia ensiformis* lectin and SYTO 9 [Fig. 51.13(A)]. The glycoconjugates in this image are mainly located in large clusters. The second example shows a biofilm stained with AlexaFluor 488-conjugated *Aleuria aurantia* lectin and SYTO 40 [Fig. 51.13(B)]. Here the lectins are mainly staining the cell surface of protozoa and the capsule of certain bacteria. The third example is a phototrophic biofilm in which the autofluorescence of the phototrophic pigments from algae and cyanobacteria were collected in the red and far red channel [Fig. 51.13(C)]. One advantage of using a single beam for exciting two fluorophores is that one can be sure that, regardless of any possible effects of chromatic aberration, the signal detected in both channels at a given instant, originated from the same location in the cell.

Because it uses a pulsed laser, 2PLSM can also be employed to measure fluorescence lifetimes (see Chapter 27, *this volume*). Two-photon intensity imaging and two-photon lifetime imaging were discussed recently as a useful tool for studying the microbial ecology of biofilm systems (Neu, 2004a). One example of fluorescence lifetime imaging (FLIM) is the measurement of pH gradients in biofilms made possible because the fluorescence lifetime of some dyes varies with pH (Vroom *et al.*, 1999). Another example is the differentiation of starving, slow-growing, and fast-

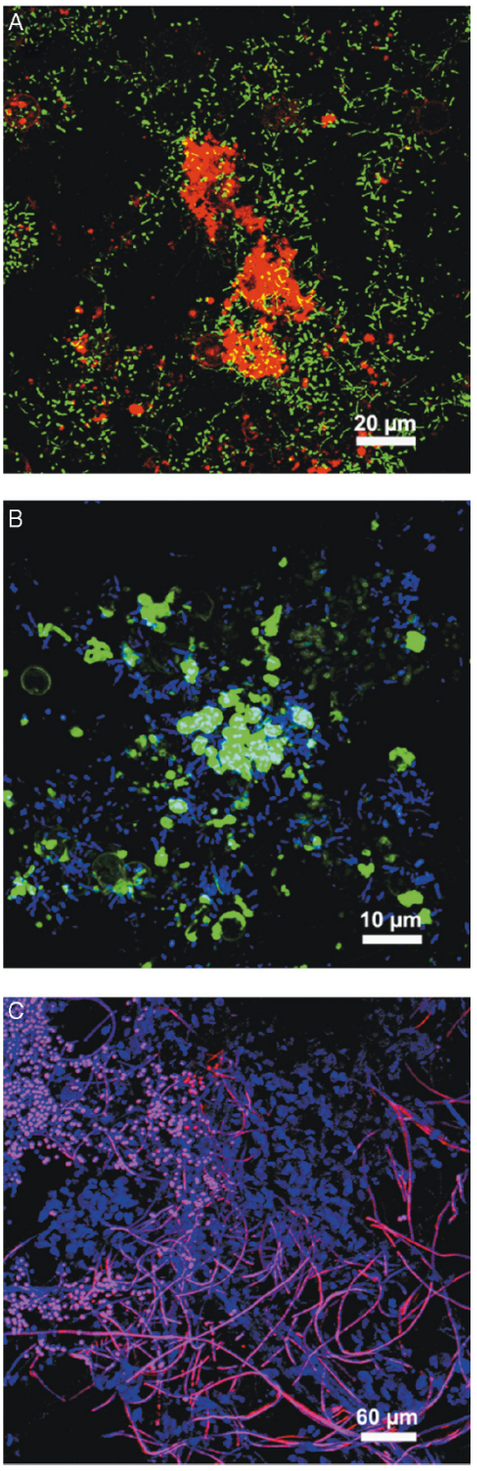


FIGURE 51.13. Dual-channel imaging of biofilms after two-photon excitation, presented as maximum intensity projection. (A) Staining with TRITC-conjugated *Canavalia ensiformis* lectin (red) and SYTO 9 (green). Two-photon excitation/emission: 800/480–550 and 600–700 nm. (B) Staining with Alexa-Fluor 488-conjugated *Aleuria aurantia* lectin (green) and SYTO 40 (blue). Two-photon excitation/emission: 800/425–500 and 500–600 nm. (C) Phototrophic biofilm showing autofluorescence of pigments. Cyanobacterial pigments (pink), algal pigments (blue). Two-photon excitation/emission: 800/580–640 and 650–800 nm.

growing bacteria in microbial biofilms. By using the nucleic-acid stain SYTO 13, bacterial activity can be assessed (Neu, 2004a). Although FLIM is still a new technique in biofilms (Neu and Lawrence, 2004), two-photon lifetime imaging, in combination with advanced digital image analysis, seems about to open up new ways of studying them.

Limitations of Confocal Laser Scanning Microscopy and Two-Photon Laser-Scanning Microscopy in Biofilm Analysis

Some of the limitations of LSM for biofilm examination should be discussed. Microbial biofilms in environmental habitats can be several millimeters in thickness and may incorporate non-cellular matter such as detritus and sand or clay. An extreme example are microbial mats that can be centimeters thick (Stal, 2000). Examination of biofilms with such scattering properties and spatial dimensions are a challenge for both CLSM and 2PLSM. In fact, penetration of the excitation beam becomes the limiting factor (Barranguet *et al*., 2004) and even the deeper penetration of infrared (2PLSM) does not help for scattering samples. Consequently, thick biofilms must be embedded, physically sectioned, stained, and then examined (Yu *et al*., 1994). If this approach is used, specific software routines must be developed in order to analyze the distribution of the fluorescence signals across all the sections from the base to the top of the biofilm. If biofilms are reasonably solid or developed under high shear force, they can be easily embedded in OCT medium (Tissue-Tek, Miles Inc., USA) frozen, and subsequently cryosectioned into relatively thick slices (50 or 100 µm). After sectioning, the biofilm slices are stained and may be mounted on slides and examined as coverslipped preparations. The same procedure is applicable to mobile biofilm systems such as solid sludge granules or fungal pellets.

Examples of sectioned biofilms appear in Figure 51.14. In the first example, the biofilm was grown on pumice in a fluidized bed reactor under high shear force. The dense biofilm was directly sectioned and a section was stained with AlexaFluor 488-conjugated *Aleuria aurantia* lectin and SYTO 60. Due to the thickness of the original sample, the section was so large that five slightly overlapping, tiled, 3D data stacks were collected by laser-scanning microscopy and assembled in Photoshop to show the full thickness of the biofilm [Fig. 51.14(A)]. The second example of a phototrophic biofilm was prepared by cryosectioning and staining with FITC-conjugated *Triticum vulgaris* lectin. As the brightness of five image stacks was adjusted to view the bright autofluorescence signal of cyanobacteria, the weaker signal of the green algae could not be visualized [Fig. 51.14(B)]. Nevertheless, the distribution of the glyconjugates forming the polymeric matrix of the phototrophic biofilm is obvious in both images.

Another two-photon limitation is the strong absorption of infrared (IR) light by some plastic materials. As discussed elsewhere in this chapter, *in vitro* biofilm research frequently uses plastic materials as a substratum for bacterial attachment and growth. The materials include polystyrene, polycarbonate, Teflon, and silicone rubber. Regardless of the reason for using plastics, if biofilms developed on plastic materials are examined close to the substratum, then the strong IR absorption results in local heating effects with subsequent melting of the plastic material and destruction of the biofilm (Neu and Lawrence, 2004). Using substrates that do not absorb in the IR, such as glass, solves the problem.

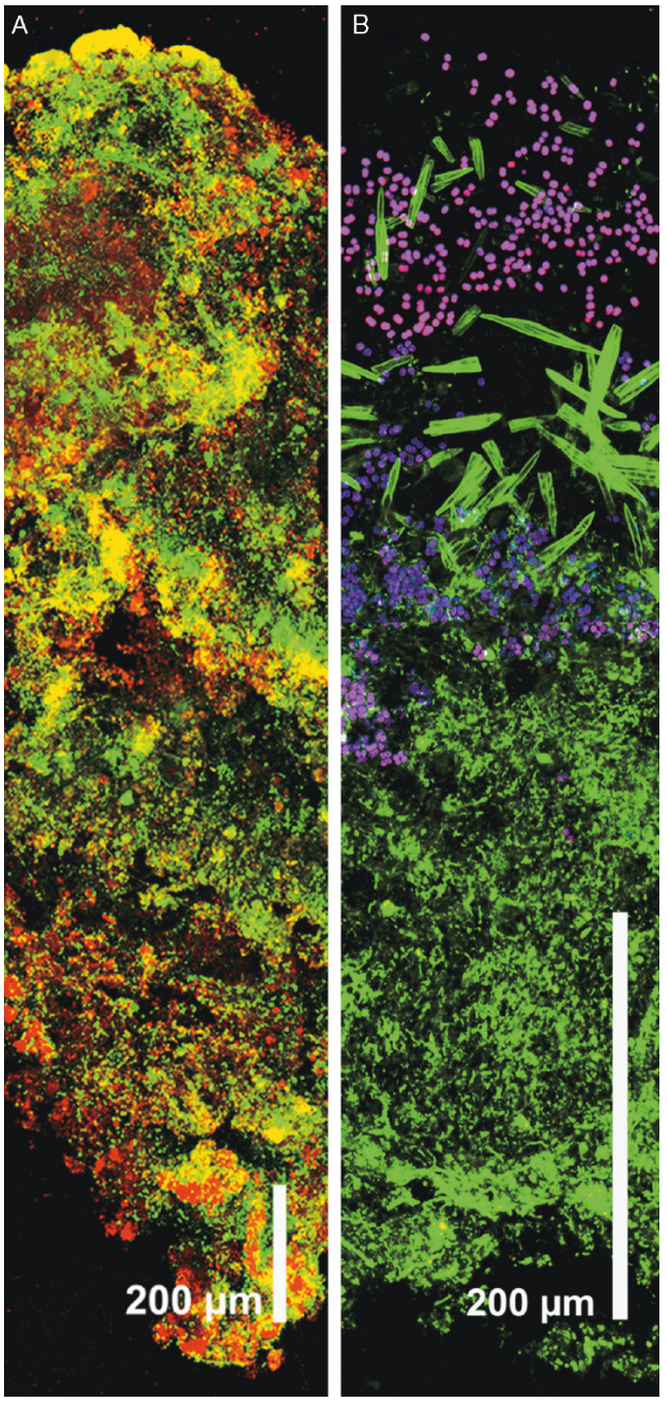


FIGURE 51.14. Thick environmental biofilms imaged after sectioning. (A) Bacterial biofilms, developed on carrier material and stained with AlexaFluor 488-conjugated *Aleuria aurantia* lectin (green) and SYTO 60 (red) were manually sectioned with a scalpel. The side of the biofilm attached to the substratum is at the bottom, the interface of the biofilm with the bulk liquid is at the top. Five tiled 3D stacks were recorded using single-photon excitation/emission: 488/500–550 nm and 633/650–800 nm, then projected, and assembled in Photoshop. (B) Phototrophic biofilm sectioned on a cryotome. Differences in autofluorescence intensity allowed the detector to be adjusted to image cyanobacteria only; algal signal is not visible. The side of the biofilm attached to the substratum is at the bottom of the image, the biofilm water/medium interface is at the top of the image. Cyanobacterial autofluorescence (pink), FITC-conjugated *Triticum vulgaris* lectin (green). Single-photon excitation/emission: 488/500–550 nm, 568/585–625 and 633/650–800 nm.

TEMPORAL EXPERIMENTS

Because biofilms are not static entities, imaging approaches that maintain a temporal perspective are preferred to those that deliver only single-timepoint data. In temporal studies, one can see single cells attach to the substratum, develop into microcolonies, and then into mature biofilms. Even in so-called mature biofilms, a dynamic turnover occurs.

Although experimental biofilm biology does not yet emphasize measurements of rapid processes, that is, those operating on time scales of milliseconds or seconds; high-speed, point-scanning and disk-scanning confocal microscopy have yet to be appropriately applied to biofilm research. The most rapid events typically measured in a biofilm occur over the course of minutes and thus are well within the range measurable using even the slowest single-beam confocal microscope. The most commonly measured temporal parameters are changes in overall architecture and changes in the positioning of cells relative to one another. Two strategies are used to address these temporal measurements. One strategy is to align flow chambers in series and then to remove them sequentially for examination. In this strategy, it is crucial that all the chambers in a series receive the identical inoculum at the same time; this is accomplished simply by introducing a volume that is twice that of the chambers plus any intervening tubing. Also, one must be confident that the metabolic activity in downstream chambers is similar to that in upstream chambers, that is, that the quantity and quality of nutrients in the most downstream chamber is equivalent to that in the upstream chamber.

A series approach is normally employed when the staining methods employ chemicals, such as Acridine Orange or DAPI, thought of as toxic to the cells. Prior to staining with such chemicals, the flowcell is removed from the system because the biofilm is not expected to continue normal growth.

A second strategy is to use non-toxic biological macromolecules produced by the bacterial cells as fluorescent labels; molecules such as fluorescent proteins. In this approach, it is assumed that imaging of, for example, GFP-labeled bacteria does not harm the cells to the extent that they no longer grow normally. In this case, a single flow chamber can be imaged repeatedly over the course of an experiment and can even be left connected to the pump and medium reservoir while being imaged. Imaging conducted in this manner is truly temporal, whereas the series approach relies on replicate samples being sacrificed at different timepoints. Another truly temporal imaging approach is video microscopy; a technique that has been used in a time-lapse and in a real-time approach to record rapid processes such as cell migration along the substratum and motion of biofilm streamers (Klapper *et al.*, 2002). Heretofore, video techniques have been dependent upon transmitted light microscopy and therefore compatible only with some flowcell designs. It remains to be seen what can be learned when biofilms growing in flow chambers are viewed in real-time with the emerging generation of high-frame-rate confocal microscopes.

Time-Lapse Confocal Imaging

Modern confocal microscopes have the ability to automatically take images or stacks of images at set time intervals. The most advanced systems include a motorized computer-controlled *xy*-stage to position the sample. In a complex setup, a time-lapse experiment can collect 3D data at several *xy*-positions, using varied settings of light sources, filter sets, number of slices, and time interval between samplings. Some systems even have soft-

ware auto-focus. Special features such as regional bleaching can typically also be controlled from the software while performing time-lapse experiments. During lengthy time-lapse experiments, temperature control is an important consideration and microscopes can be fitted with thermostat-controlled sample holders and objective heaters to avoid temperature-variation-induced focus shifts as well as deleterious biological effects.

Confocal time-lapse recordings were used to investigate the spatiotemporal development of flowcell-grown, monospecies biofilms as well as of communities that contain mutants introduced to investigate single-gene influences on structure over time. In one example, structural development and organization of a *P. aeruginosa* biofilm was followed using time-lapse recording. The end-stage biofilm is shown in Figure 51.15, and the development stages are shown in Figure 51.16. A movie made from this data will be available on the Handbook http://www.springer.com/0-387-25921-X. After inoculation, the flow cell was mounted on the *xy*-table on the confocal microscope. The focus plane at the substratum, where the cells had attached to the glass surface, was determined and read into the software. Care was taken to allow for mechanical drift over the duration of the experiment by setting the "near" endpoint a bit outside below the substratum plane. The far endpoint is set to allow for the growth of the sample (this point can sometimes be adjusted during the time series). Finally the number of image slices of the defined area is set, together with number of repetitions and time intervals for the time-lapse recording.

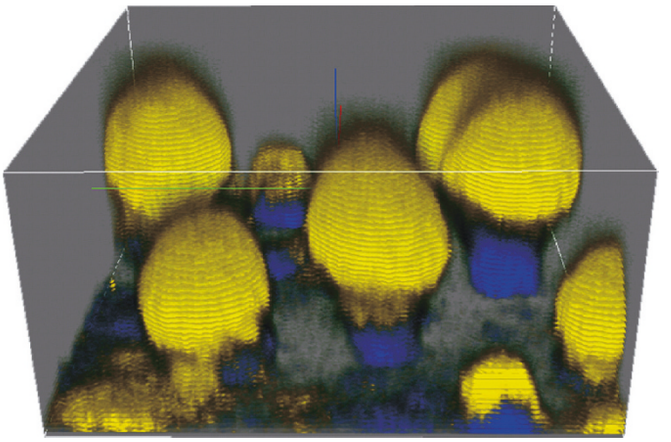


FIGURE 51.15. Mushroom-shaped multi-cellular biofilm structures with yellow caps and cyan stalks after 4 days of development. (Reproduced with permission from Klausen *et al*., 2003.)

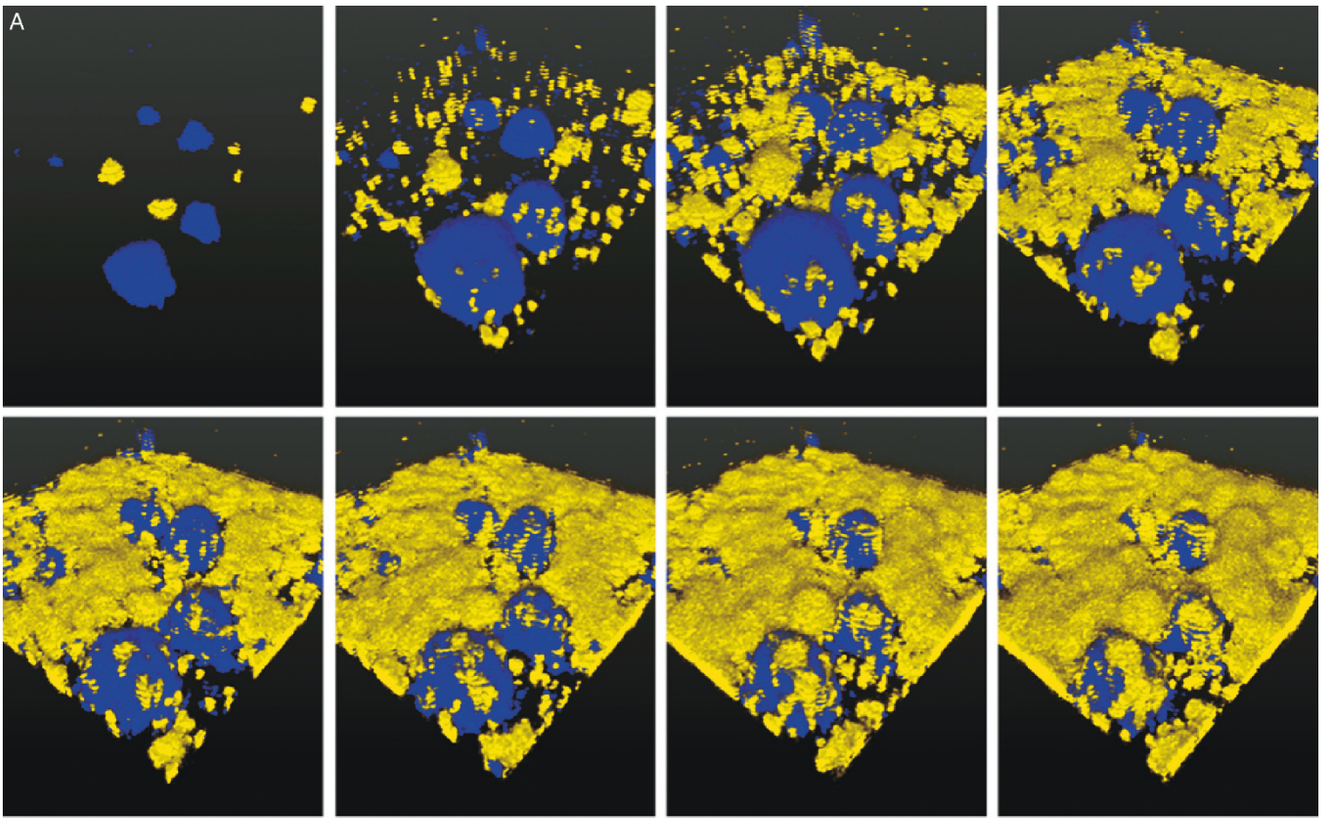


FIGURE 51.16. Time-lapse recording of microcolony formation. (A) Confocal micrographs showing biofilm development initiated with a 1:1 mixture of YFP-expressing *P. aeruginosa* PAO1 wild-type and a non-motile *pilA* mutant of PAO1 expressing CFP. See Klausen and colleagues (2003) for experimental details. Images are 3D projections from a time-lapse recording during the first 64 h after inoculation. The *pilA* mutant (blue) was preferentially located in the stalk of the characteristic mushroom-shaped structures formed by this *Pseudomonas* strain. Over time, the motile wild-type mounted the *pilA* mutant structure, forming a cap composed of the migratory wild-type cells. Timepoints measured in hours from inoculation. Top, left to right: 10, 14, 17, and 27 h. Bottom: 35, 42, 59, and 64 hours.

SUMMARY AND FUTURE DIRECTIONS

- Laser-scanning microscopy is the only way to obtain spatiotemporally resolved information on community structure and interactions in complex microbial communities.
- Fluorescence *in situ* hybridization (FISH) and variations such as FISH-MAR, CARD-FISH, or combined mRNA/rRNA FISH (Pernthaler and Amann, 2004) provide new directions for examination of bacterial identity and activity within microbial communities.
- A variety of reporter systems exist, especially fluorescent proteins and their degradable variants, which are useful for studies of gene expression under controlled conditions.
- Lectin-binding analysis represents the only *in situ* approach that allows simultaneous visualization, quantification, and especially differentiation of EPS glycoconjugates in microbial biofilms.
- Two-photon laser-scanning microscopy is an emerging technique in biofilm research with potential for intensity and lifetime imaging.
- Limitations of laser-scanning microscopy (single- or multiphoton) for biofilm examination relate only to the sample parameters (size, thickness, density). These are the most common limitations encountered when examining natural biofilms.
- New strategies in probing biofilm systems may allow us to examine matrix components in greater detail, and to measure biofilm metabolic processes in real time. While much has been accomplished in this regard, much remains to be done. A few pioneers are needed to begin these explorations. Advanced microscopic approaches will be crucial tools in advancing our understanding of bacterial biofilm biology.

ACKNOWLEDGMENTS

TRN appreciates the excellent technical support by Ute Kuhlicke, and thanks Matthias Boessmann, Christian Staudt, and Barbara Zippel for images. RJP thanks Owen Schwartz (NIAID/NIH) for assistance with backscattered light imaging.

REFERENCES

Andersen, J.B., Sternberg, C., Poulsen, L.K., Bjørn, S.B., Givskov, M., and Molin, S., 1998, New unstable variants of green fluorescent protein for studies of transient gene expression in bacteria, *Appl. Environ. Microbiol.* 64:2240–2246.

Bjarnsholt, T., Jensen, P.O., Burmølle, M., Hentzer, M., Haagensen, J.A.J., Hougen, H.P., Calum, H., Madsen, K.G., Moser, C., Molin, S., Høiby, N., and Givskov, M., 2005, Pseudomonas aeruginosa tolerance to tobramycin, hydrogen peroxide and polymorphonuclear leukocytes is quorum-sensing dependent, *Microbiology* 151:373–388.

Barranguet, C., van Beusekom, S.A.M., Veuger, B., Neu, T.R., Maanders, E.M.M., Sinke, J.J., and Admiraal, W., 2004, Studying undisturbed autotrophic biofilms: Still a technical challenge, *Aquat. Microbial Ecol.* 34:1–9.

Böckelmann, U., Manz, W., Neu, T.R., and Szewzyk, U., 2002, A new combined technique of fluorescent *in situ* hybridization and lectin-binding-analysis (FISH-LBA) for the investigation of lotic microbial aggregates, *J. Microbiol. Methods* 49:75–87.

Boles, B.R., Thoendel, M., and Singh, P.K., 2005, Self-generated diversity produces "insurance effects" in biofilm communities (Vol 101, Pg 16630, 2004), *Proc. Natl. Acad. Sci. USA* 102: 955–955.

Bos, R., Vandermei, H.C., Meinders, J.M., and Busscher, H.J., 1994, Quantitative method to study co-adhesion of microorganisms in a parallel-plate flow chamber — Basic principles of the analysis, *J. Microbiol. Methods* 20:289–305.

Chalfie, M., Tu, Y., Euskirchen, G., Ward, W.W., and Prasher, D.C., 1994, Green fluorescent protein as a marker for gene-expression, *Science* 263:802–805.

Christensen, B.B., Sternberg, C., Andersen, J.B., Palmer, R.J. Jr., Toftgaard-Nielsen, A., Givskov, M., and Molin, S., 1999, Molecular tools for study of biofilm physiology, *Methods Enzymol*. 310:20–42.

Christensen, B.B., Haagensen, J.A.J., Heydorn, A., and Molin, S., 2002, Metabolic commensalism and competition in a two-species microbial consortium, *Appl. Environ. Microbiol.* 68:2495–2502.

Daims, H., Nielsen, J.L., Nielsen, P.H., Schleifer, K.H., and Wagner, M., 2001, *In situ* characterization of Nitrospira-like nitrite oxidizing bacteria active in wastewater treatment plants, *Appl. Environ. Microbiol.* 67: 5273–5284.

Denk, W., Strickler, J.H., and Webb, W.W., 1990, Two-photon laser scanning fluorescence microscopy, *Science* 248:73–76.

Gurskaya, N.G., Fradkov, A.F., Terskikh, A., Matz, M.V., Labas, Y.A., Martynov, V.I., Yanushevich, Y.G., Lukyanov, K.A., and Lukyanov, S.A., 2001, GFP-like chromoproteins as a source of far-red fluorescent proteins, *FEBS Lett*. 507:16–20.

Hansen, M.C., Palmer, R.J. Jr., and White, D.C., 2000, Flowcell culture of *Porphyromonas gingivalis* biofilms under anaerobic conditions, *J. Microbiol. Methods* 40:233–239.

Heim, R., and Tsien, R.Y., 1996, Engeneering green fluorescent protein for improved brightness, longer wavelengths and fluorescence resonance energy transfer, *Curr. Biol*. 6:178–182.

Heim, R., Cubitt, A.B., and Tsien, R.Y., 1995, Improved green fluorescence, *Nature* 373:663–664.

Heim, R., Prasher, D.C., and Tsien, R.Y., 1994, Wavelength mutations and post-translational autooxidation of green fluorescent protein, *Proc. Natl. Acad. Sci. USA* 91:12501–12504.

Klapper, I., Rupp, C.J., Cargo, R., Purvedorj, B., and Stoodley, P., 2002, Viscoelastic fluid description of bacterial biofilm material properties. *Biotechnol. Bioeng*. 80:289–296.

Klausen M., Aaes-Jørgensen, A., Molin, S., and Tolker-Nielsen, T., 2003, Involvement of bacterial migration in the development of complex multicellular structures in *Pseudomonas aeruginosa* biofilms, *Mol. Microbiol.* 50:61–68.

Kolenbrander, P.E., Andersen, R.N., Kazmerzak, K., Wu, R., and Palmer, R.J. Jr., 1999, Spatial organization of oral bacteria in biofilms. *Methods Enzymol.* 310:322–332.

König, K., 2000, Multiphoton microscopy in life sciences, *J. Microsc.* 200:83–104.

Lawrence, J.R., and Neu, T.R., 1999, Confocal laser scanning microscopy for analysis of microbial biofilms, *Methods Enzymol.* 310:131–144.

Li, X., Xiao, X.N., Fang, Y., Jiang, X., Doung, T., Fan, C., Huang, C.C., and Kain, S.R., 1998, Generation of destabilized green fluorescent protein transcription reporter, *J. Biol. Chem*. 273:34970–34975.

Lukayanov, K.A., Fradkov, A.F., Gurskaya, N.G., Matz, M.V., Labas, Y.A., Savitsky, A.P., Markelov, M.L., Zaraisky, A.G., Zhao, X., Fang, Y., Tan, W., and Lukyanov, S.A., 2000, Natural animal coloration can be determined by a nonfluorescent green fluorescent protein homolog, *J. Biol. Chem*. 275:25879–25882.

Matz, M.V., Fradkov, A.F., Labas, Y.A., Savitsky, A.P., Zaraisky, A.G., Markelov, M.L., and Lukyanov, S.A., 1999, Fluorescent proteins from nonbioluminescent Anthozoa species, *Nat. Biotechnol*. 17:969–973.

Monier, J.M., and Lindow, S.E., 2003, Differential survival of solitary and aggregated bacterial cells promotes aggregate formation on leaf surfaces, *Proc. Natl. Acad. Sci. USA* 100:15977–15982.

Monier, J.M., and Lindow, S.E., 2004, Frequency, size, and localization of bacterial aggregates on bean leaf surfaces, *Appl. Environ. Microbiol.* 70:346–355.

Morin, J.G., and Hastings, J.W., 1971, Energy transfer in a bioluminescent system, *J. Cell. Physiol*. 77:313–318.

Neu, T.R., and Lawrence, J.R., 1999a, *In situ* characterization of extracellular polymeric substances (EPS) in biofilm systems, In: *Microbial Extracellular Polymeric Substances* (J. Wingender, T.R. Neu, and H.-C. Flemming, eds.), Springer, Heidelberg, Germany, pp. 21–47.

Neu, T.R., and Lawrence, J.R., 1999b, Lectin-binding-analysis in biofilm systems, *Methods Enzymol.* 310:145–152.

Neu, T.R., and Lawrence, J.R., 2002, Laser scanning microscopy in combination with fluorescence techniques for biofilm study, In: The *Encyclopedia of Environmental Microbiology* (G. Bitton, ed.), John Wiley and Sons, New York, pp. 1772–1788.

Neu, T.R., and Lawrence, J.R., 2004., One-photon versus two-photon laser scanning microscopy and digital image analysis of microbial biofilms, *Methods Microbiol.* 34:87–134.

Neu, T.R., Kuhlicke, U., and Lawrence, J.R., 2002, Assessment of fluorochromes for two-photon laser scanning microscopy of biofilms, *Appl. Environ. Microbiol.* 68:901–909.

Neu, T.R., Swerhone, G.D.W., and Lawrence, J.R., 2001, Assessment of lectin-binding analysis for *in situ* detection of glycoconjugates in biofilm systems, *Microbiology* 147:299–313.

Neu, T.R., Walczysko, P., and Lawrence, J.R., 2004a, Two-photon imaging for studying the microbial ecology of biofilm systems, *Microbes Environ.* 19:1–6.

Neu, T.R., Woelfl, S., and Lawrence, J.R., 2004b, Three-dimensional differentiation of photo-autotrophic biofilm constituents by multi-channel laser scanning microscopy (single-photon and two-photon excitation), *J. Microbiol. Methods* 56:161–172.

Nielsen, P.H., and Jahn, A., 1999, Extraction of EPS, In: *Microbial Extracellular Polymeric Substances* (J. Wingender, T.R. Neu, and H.-C. Flemming, eds.), Springer, Berlin, pp. 49–72.

Ormö, M., Cubitt, A.B., Kallio, K., Gross, L.A., Tsien, R.Y., and Remington, S.J., 1996, Crystal structure of the *Aequorea victoria* green fluorescent protein, *Science* 273:1392–1395.

Palmer, R.J. Jr., and Caldwell, D.E., 1995, A flowcell for the study of plaque removal and regrowth, *J. Microbiol. Methods* 24:171–182.

Palmer, R.J. Jr., Gordon, S.M., Cisar, J.O., and Kolenbrander, P.E., 2003, Coaggregation-mediated interactions of Streptococci and Actinomyces detected in initial human dental plaque, *J. Bacteriol.* 185:3400–3409.

Pernthaler, A., and Amann, R., 2004, Simultaneous fluorescence *in situ* hybridization of mRNA and rRNA in environmental bacteria, *Appl. Environ. Microbiol*. 70:5426–5433.

Rainey, P.B., and Travisano, M., 1998, Adaptive radiation in a heterogeneous environment. *Nature* 394:69–72.

Shimomura, O., Johnson, F.H., and Saiga, Y., 1962, Extraction, purification and properties of Aequorin, a bioluminescent protein from the luminous hydromedusan *Aequorea*, *J. Cell. Comp. Physiol*. 59:223–239.

Siemering, K.R., Golbik, R., Sever, R., and Haselhoff, J., 1996, Mutants that suppress the thermosensitivity of green fluorescent protein, *Curr. Biol.* 6:1653–1663.

Singh, P.K., Parsek, M.R., Greenberg, E.P., and Welsh, M.J., 2002, A component of innate immunity prevents bacterial biofilm development, *Nature* 417:552–555.

Stal, L.J., 2000, Cyanobacterial mats and stromatolites, In: *The Ecology of Cyanobacteria* (B.A.Whitton and M. Potts, eds.), Kluwer Academic Publishers, New York, pp. 61–120.

Staudt, C., Horn, H., Hempel, D.C., and Neu, T.R., 2003, Screening of lectins for staining lectin-specific glycoconjugates in the EPS of biofilms, In: *Biofilms in Medicine, Industry and Environmental Technology* (P. Lens, A.P. Moran, T. Mahony, P. Stoodley, and V. O'Flaherty, eds.), IWA Publishing, United Kingdom, pp. 308–327.

Staudt, C., Horn, H., Hempel, D.C., and Neu, T.R., 2004, Volumetric measurements of bacterial cells and extracellular polymeric substance glycoconjugates in biofilms, *Biotechnol. Bioeng.* 88:585–592.

Sternberg, C., Christensen, B.B., Johansen, T., Toftegaard-Nielsen, A., Andersen, J.B., Givskov, M., and Molin, S., 1999, Distribution of bacterial growth activity in flow-chamber biofilms, *Appl. Environ. Microbiol*. 65:4108–4117.

Stoodley, P., Lewandowski, Z., Boyle, J.D., and Lappin-Scott, H.M., 1999, Structural deformation of bacterial biofilms caused by short-term fluctuations in fluid shear: An *in situ* investigation of biofilm rheology, *Biotechnol. Bioeng.* 65:83–92.

Thurnheer, T., Gmur, R., and Guggenheim, B., 2004, Multiplex fish analysis of a six-species bacterial biofilm. *J. Microbiol. Methods* 56:37–47.

Tombolini, R., Unge, A., Davey, M.E., de Bruijn, F.J., and Jannson, J.K., 1997, Flow cytometric and microscopic analysis of *Pseudomonas fluorescens* bacteria, *FEMS Microb. Ecol.* 22:17–28.

Vroom, J.M., Grauw, d.C.J., Gerritsen, H.C., Bradshaw, A.M., Marsh, P.D., Watson, G.K., Birmingham, J.J., and Allison, C., 1999, Depth penetration and detection of pH gradients in biofilms by two-photon excitation microscopy, *Appl. Environ. Microbiol.* 65:3502–3511.

Wingender, J., Neu, T.R., and Flemming, H.-C., (eds.), 1999, *Microbial Extracellular Polymeric Substances*, Springer, Heidelberg, Germany.

Wolfaardt, G.M., Lawrence, J.R., and Korber, D.R., 1999, Function of EPS in microbial biofilms, In: *Microbial Extracellular Polymeric Substances* (J. Wingender and T.R. Neu, eds.), Springer, Berlin, pp. 171–200.

Yu, F.P., Callis, G.M., Stewart, P.S., Griebe, T., and McFeters, G.A., 1994, Cryosectioning of biofilms for microscopic examination, *Biofouling* 8:85–91.

Zinn, M.S., Kirkegaard, R.D., Palmer, R. J. Jr., and White, D.C., 1999, Laminar flow chamber for continuous monitoring of biofilm formation and succession, *Methods Enzymol.* 310:224–232.

52

Bibliography of Confocal Microscopy

Robert H. Webb

This is an update of the selected bibliography, as of early 1994, of accessible papers on confocal microscopy. In the 10 years since, the number of papers has exploded, in part because many of us publish in little increments rather than a single summarizing paper. So some of the papers listed are nibbles at the archive, and will have to lead you to other papers on almost the same topic by the same author. Not included are conference reports and other documents not likely to be available in most technical libraries. I have tried to include a note as to the content — often taken from the abstract.

I have done some sorting into categories, but there is a lot of overlap. CM is my abbreviation for confocal microscope.

A. BOOKS AND REVIEW ARTICLES

Some summaries and general work.

Baxes, G.A., 1984, *Digital Image Processing: A Practical Primer*, Prentice Hall, Englewood Cliffs, New Jersey. Also (1988) from Cascade Press, PO Box 27631, Denver, CO 80227. Truly a "practical primer."

Brelje, T.C., Wessendorf, M.W., and Sorenson, R.L., 1993, Multi-color laser scanning confocal immunofluorescence microscopy: Practical application and limitations, *Methods Cell Biol*. 38:98–182. A review of the dyes and the techniques for using them. Very specific. Complete.

Cagnet, M., Françon, M., and Thrierr, J.C., 1962, *Atlas of Optical Phenomena*, Springer Verlag, Berlin. See page 23 for a beautiful through-focus display.

Castleman, K.R., 1979, *Digital Image Processing*, Prentice Hall, Englewood Cliffs, New Jersey. A standard reference on this subject.

Inoué, S., 1986, *Video Microscopy*, Plenum Press, New York. A very complete basic book.

Inoué, S., and Oldenbourg, R., 1994, Optical instruments: Microscopes, In: *Handbook of Optics* (M. Bass, ed.), Vol. 2, 2nd ed., McGraw-Hill, New York, Chapter 17.1–17.52.

Kino, G.S., and Corle, T.R., 1989, Confocal scanning optical microscopy, *Phys. Today* 42:55–62. A review article for non-specialist physicists.

Maddox, P.S., Moree, B., Canman, J.C., and Salmon, E.D., 2003, Spinning disk confocal microscope system for rapid high-resolution, multimode, fluorescence speckle microscopy and green fluorescent protein imaging in living cells, *Methods Enzymol*. 360:597–617. A review for biologists.

Oppenheim, A.V., Willsky, A.S., and Young, I.T., 1983, *Signals and Systems*, Prentice Hall, Englewood Cliffs, New Jersey. Chapter 8 describes sampling theory very well.

Pawley, J.B., 1991, Fundamental and practical limits in confocal light microscopy, *Scanning* 13:184–198. A general review of some of the choices we all make, with attention to photobleaching problems, optimization of optics, and pinholes.

Petran, M., Hadravsky, M., and Boyde, A., 1985, The tandem scanning reflected light microscope, *Scanning* 7:97–108. Summarizes the tandem scanning microscope.

Pratt, W.K., 1978, *Digital Image Processing*, John Wiley and Sons, pg. 309 ff. A standard reference in this field.

Shotton, D., ed., 1993, *Electronic Light Microscopy — Techniques in Modern Biomedical Microscopy*, Wiley-Liss, New York, 351 pp. Many of the usual suspects have contributed chapters, with some further chapters on display, video, and sample preparation. A good companion to this volume.

Slater, E.M., and Slater, H.S., 1993, *Light and Electron Microscopy*, Cambridge University Press, New York. A fine general book on microscopes.

Squier, J., and Muller, M., 2001, High resolution nonlinear microscopy: A review of sources and methods for achieving optimal imaging, *Rev. Sci. Instrum*. 72:2855–2867. Reviews instrumentation used in high resolution nonlinear microscopy and techniques for temporal and spatial calibration.

Webb, R.H., 1991, Confocal microscopes, *Optics Photonics News* 2:8–13. A review for optical scientists who do not specialize in microscopes.

Webb, R.H., 1996, Confocal optical microscopy, *Rep. Prog. Physics* 59:427–471. My version for physicists, with some (then) new material mixed in.

Webb, R.H., 1999, Theoretical basis of confocal microscopy, *Methods Enzymol. Confocal Microsc*. 307:3–20. My version for biologists.

White, J.G., and Amos, W.B., 1987, Confocal microscopy comes of age, *Nature* 328:183. General article by two of the early users of the CM.

Wilson, T., 1980, Imaging properties and applications of scanning optical microscopes, *Appl. Phys (Germany)* 22:19–128. A review paper, with 57 references.

Wilson, T., 1985, Scanning optical microscopy, *Scanning* 7:79–87. Summary article.

Wilson, T., ed., 1990, *Confocal Microscopy*, Academic Press, London. Chapters by many of the usual folk. Much of the thinking of the 1980s summarized and updated.

Wilson, T., and Sheppard, C.J.R., 1984, *Theory and Practice of Scanning Optical Microscopy*, Academic Press, London. Reprints some of their early papers.

B. HISTORICAL INTEREST

Some of the original articles, mostly now superseded by later work — often of the same authors. I have tried to avoid the "gee whiz!" articles.

Amos, W.B., White, J.G., and Fordham, M., Use of confocal imaging in the study of biological structures, *Appl. Opt*. 26:3239–3243. A good general review, and an early description of the MRC (Bio-Rad) microscope.

Åslund, N., Liljeborg, A., Forsgren, P.-O., and Wahlsten, S., 1987, Three-dimensional digital microscopy using the PHOIBOS scanner, *Scanning* 9:227–235. Consecutive optical sections to generate digital three-dimensional microscopy.

Baer, S.C., 1970, Optical apparatus providing focal-plane specific information, US Patent No. 3,547,512. An early CM idea, largely ignored for 17 years.

Brakenhoff, G.J., Blom, P., and Barends, P., 1979, Confocal scanning light microscopy with high aperture immersion lenses, *J. Microsc*. 117:219–232. For point objects the theoretically expected factor of 1.4 can be realized. A further improvement by a factor of 1.25 after apodization with an annular aperture.

Robert H. Webb • Schepens Eye Research Institute and Wellman Center for Photomedicine, Boston, Massachusetts 02114

Brakenhoff, G.J., van der Voort, H.T.M., van Spronsen, E.A., Linnemans, W.A.M., and Nanninga, N., 1985, Three-dimensional chromatin distribution in neuroblastoma nuclei shown by confocal scanning laser microscopy, *Nature* 317:748–749. An early use of optical sectioning and higher resolution for studying the three-dimensional morphology of biological structures.

Chou, C.-H., and Kino, G.S., 1987, The evaluation of V(z) in a type II reflection microscope, *IEEE Trans. Ultrason. Ferroelectr. Freq. Control*. 34:341–345. Theory: V(z) of an acoustic microscope, non-paraxial and finite pinhole and the asymmetry of the V(z) curve for a perfect reflector. This is about the acoustic microscope, but it set the stage for a lot of early CM work.

Davidovits, P., and Egger, M.D., 1971, Scanning laser microscope for biological investigations, *Appl. Opt.* 10:1615–1619. Also: Davidovits, P., and Egger, M.D., 1969, Scanning laser microscope, *Nature* 223:831. Two seminal papers of historical interest.

Egger, M.D., and Petran, M., 1967, New reflected-light microscope for viewing unstained brain and ganglion cells, *Science* 157:305–307. A largely unnoticed description of the tandem scanning microscope, but it was all there!

Hamilton, D.K., Wilson, T., and Sheppard, C.J.R., 1981, Experimental observations of the depth-discrimination properties of scanning microscopes, *Opt. Lett*. 6:625–626. Optical sectioning.

Maurice, D.M., 1973, A scanning slit optical microscope, *Invest. Ophthalmol*. 13:1033–1037. A pioneer paper describing an early form of confocal microscopy for imaging layers in the cornea of the eye. This system used a scanning slit 3 µm wide to give depth definition, and scanning was carried out by moving a photographic film and the specimen in opposite directions. High-quality images of the cornea were obtained, which took about 20 min to form.

Minsky, M., 1988, Memoir on inventing the CSM, *Scanning* 10:128–138. A valuable historical document, and enjoyable reading. Minsky's patent ran out before the world was ready for the idea, but his early ideas have all proved out well. See Minsky, M., 1961, Microscopy apparatus, US Patent No. 3,013,467.

Petran, M., and Hadravsky, M., 1967, Method and arrangement for improving the resolving power and contrast, US Patent No. 3,517,980, filed 4–12–67, granted 30–6-70.

Petran, M., and Hadravsky, M., 1968, Tandem-scanning reflected-light microscope, *J. Opt. Soc. Am.* 58:661–664. Source paper on TSM. See also 79. Petran, M., Hadravsky, M., Benes, J., Kucera, R., and Boyde, A., 1985, The tandem scanning reflected light microscope. Part 1 — The principle, and its design, *Proc. Roy. Microsc. Soc*. 20:125–129.

Ploem, J.S., 1987, Laser scanning fluorescence microscopy, *Appl. Opt*. 26:3226–3231. Another general description of CM.

Sheppard, C.J.R., and Choudhury, A., 1997, Image formation in the scanning microscope, *Opt. Acta* 24:1051–1073. Fourier imaging in microscopes of type 1 (conventional) and type 2 (confocal). Single- and two-point resolution, response to a straight edge, annular pupil functions.

Sheppard, C.J.R., and Wilson, T., 1978, Depth of field in the scanning microscope, *Opt. Lett*. 3:115–117. Various definitions of depth of field in the microscope are discussed.

Toraldo di Francia, G., 1955, Resolving power and information, *J. Opt. Soc. Am*. 45:497–501. Two-point resolution is impossible unless the observer has *a priori* an infinite amount of information about the object.

Welford, W.T., 1972, On the relationship between the modes of image formation in scanning microscopy and conventional microscopy, *J. Microsc*. 96:105–107.

White, J.G., Amos, W.B., and Fordham, M., 1987, An evaluation of confocal versus conventional imaging of biological structures by fluorescence light microscopy, *J. Cell Biol*. 105:1–48. An early general article which helped introduce the technique.

Wilke, V., 1985, Optical scanning microscopy — The laser scan microscope, *Scanning* 7:88–96. The Zeiss CM.

C. THEORY (MOSTLY)

Confocal microscopes do as predicted, so there has been a lot of prediction. The separation between theory and its implementation is not always urgent, so this and the next section overlap a good deal.

Bertero, B., De Mol, C., and Pike, E.R., 1987, Analytic inversion formula for confocal scanning microscopy, *J. Opt. Soc. Am. A* 4:1748–1750. A simple analytic expression for the inverse problem in CMs.

Carlsson, K., 1991, The influence of specimen refractive index, detector signal integration, and non-uniform scan speed on the imaging properties in confocal microscopy, *J. Microsc*. 163:167–178. Index mismatch causes spherical aberrations that affect axial resolution most.

Cogswell, C.J., and Sheppard, C.J.R., 1992, Confocal differential interference contrast (DIC) microscopy: including a theoretical analysis of conventional and confocal DIC imaging, *J. Microsc*. 165:81–101. DIC with a CM is compared to existing confocal differential phase contrast (DPC) techniques and to conventional Nomarski differential interference contrast (DIC). A theoretical treatment of DIC imaging is presented, which takes into account vignetting by the lens pupils.

Corle, T.R., and Kino, G.S., 1990, Differential interference contrast imaging on a real time confocal scanning optical microscope, *Appl. Opt*. 29: 3769–3774. The advantage of DIC in a CM is that both the height and width of an edge can be measured without ambiguity, even if the edge is taller than half a wavelength.

Cox, I.J., Sheppard, C.J.R., and Wilson, T., 1981, Improvement in resolution by nearly confocal microscopy: The theory of the direct-view confocal microscope, *J. Microsc*. 124:107–117. Resolution increased by offsetting the pinhole. Dark-field conditions are produced with the pinhole over the first dark ring in the Airy disk. Theory for conventional and scanning microscopes, partial coherence, and TSMs.

Cox, I.J., and Sheppard, C.J.R., 1986, Information capacity and resolution in an optical system, *J. Opt. Soc. Am*. 3:1152–1158. A non-standard approach giving useful general results without major math.

Gu, M., and Sheppard, C.J.R., 1992, Confocal fluorescent microscopy with a finite-sized circular detector, *J. Opt. Soc. Am. A* 9:151–153. The OTF has negative values when the detector radius exceeds certain magnitudes.

Gu, M., and Sheppard, C.J.R., 1992, Three-dimensional optical transfer function in a fiber-optical confocal fluorescence microscope using annular lenses, *J. Opt. Soc. Am. A* 9:1991–1999. Annular lenses in a system with optical fibers can result in improved resolution in both transverse and axial directions.

Gu, M., and Sheppard, C.J.R., 1992, Effects of defocus and primary spherical aberration on three-dimensional coherent transfer functions in confocal microscopes, *Appl. Opt*. 31:2541–2549. Three-dimensional confocal imaging is strongly degraded if the amount of aberration is larger than a quarter wavelength. Spherical aberration compensated by defocus.

Hamilton, D.K., and Wilson, T., 1984, Two-dimensional phase imaging in the scanning optical microscope, *Appl. Opt*. 23:348–352. Early spilt-detector phase imaging.

Hegedus, Z.S., 1985, Annular pupil arrays. Application to confocal scanning, *Opt. Acta* 32:815–826. Radically symmetrical pupil masks with a continuously varying transmittance can be made by vacuum deposition or photographic integration, or a binary mask of a concentric array of annuli.

Hell, S., Reiner, G., Cremer, C., and Stelzer, E.H.K., 1993, Aberrations in confocal fluorescence microscopy induced by mismatches in refractive index, *J. Microsc*. 169:391–405. An extensive and readable analysis of this frequent topic. Scaling factors for correction.

Hobbs, P.C.D., and Kino, G.S., 1990, Generalizing the confocal microscope via heterodyne interferometry and digital filtering, *J. Microsc*. 160: 245–264. A true heterodyne CM, yielding both phase and amplitude.

Kino's papers on acoustic microscopes were an important precursor of many of the CM theory papers.

Inoué, S., 1989, Imaging of unresolved objects, superresolution, and precision of distance measurement with video microscopy, *Methods Cell Biol*. 30:85–112.

Mendez, E.R., 1986, Speckle contrast variation in the CM. Hard-edged apertures, *Opt. Acta* 33:269–278. Speckle contrast variation as a function of defocus, and the statistical properties of random diffusing objects.

Sandison, D.R., and Webb, W.W., 1994, Background rejection and signal-to-noise optimization in the confocal and alternative fluorescence microscopes, *Appl. Opt*. 33:603. A complete analysis of signal, background, and noise in the family of confocal microscopes.

Sandison, D.R., Piston, D.W., Williams, R.M., and Webb, W.W., 1995, Quantitative comparison of background rejection, signal-to-noise ratio, and resolution in confocal and full-field laser-scanning microscopes, *Appl. Opt*. 34:3576–3588. See previous entry.

Schmitt, J.M., Knuttel, A., and Yadlowsky, M., 1994, Confocal microscopy in turbid media, *J. Opt. Soc. Am. A* 11:2226–2235. ". . . [T]rade-off between signal level and background scattered-light rejection places a fundamental limit on the sectioning capability of the microscope."

Sheppard, C.J.R., 1988, Aberrations in high aperture conventional and confocal imaging systems, *Appl. Opt*. 27:4782–4786. In an aberration function for high numerical aperture the effects on the defocus signal of a confocal imaging system of aberrations, high aperture, finite Fresnel number, system configuration, and surface tilt are discussed.

Sheppard, C.J.R., and Wilson, T., 1981, The theory of the direct-view confocal microscope, *J. Microsc*. 124:107–117. Theory embracing conventional microscopes with partially coherent source and scanning microscopes with partially coherent effective source and detector, including confocal microscopes and the TSM of Petran.

Sheppard, C.J.R., and Wilson, T., 1986, Reciprocity and equivalence in scanning microscopes, *J. Opt. Soc. Am. A* 3:755–756. The principle of reciprocity and methods of Fourier optics in conventional and scanning microscopes: their behavior is identical even for objects thick enough for multiple scattering to occur, provided that there is no inelastic scattering or birefringence present.

Sheppard, C.J.R., Cogswell, C.J., and Gu, M., 1991, Signal strength and noise in confocal microscopy: factors influencing selection of an optimum detector aperture, *Scanning* 13:233–240.

Van Der Voort, H.T.M., and Brakenhoff, G.J., 1990, 3-D image formation in high-aperture fluorescence confocal microscopy: A numerical analysis, *J. Microsc*. 158:43–54. Electromagnetic diffraction theory of the field near focus as developed by Richards and Wolf is used to compute the optical properties of the model.

Visser, T.D., Groen, F.C.A., and Brakenhoff, G.J., 1991, Absorption and scattering correction in fluorescence confocal microscopy, *J. Microsc*. 163:189–200. With one space-dependent extinction coefficient, the total attenuation process can be calculated to the deeper layers.

Wilson, T., 1991, Comment on "Image formation in a superresolution phase conjugate scanning microscope," *Appl. Phys. Lett*. 58:314. Johnson, Cathey, and Mao [1989, *Appl. Phys. Lett*. 55:1707] proposed using a phase conjugate mirror to exhibit superresolution. A phase conjugate mirror is not strictly necessary and a similar, or even enhanced, effect may be obtained by processing the image from a standard confocal microscope in an extremely simple way.

Wilson, T., and Carlini, A.R., 1987, Size of the detector in confocal imaging systems, *Opt. Lett*. 12:227–229. Original of many familiar figures.

Wilson, T., and Carlini, A.R., 1989, The effect of aberrations on the axial response of confocal imaging systems, *J. Microsc*. 154:243–256. Aberrations are diminished by smaller pinholes.

Wilson, T., and Tan, J.B., 1996, Finite sized coherent and incoherent detectors in confocal microscopy, *J. Microsc*. 182:61–66. Not just pinhole size, this paper includes high numerical aperture (NA), polarization, and aberration matters.

D. TECHNICAL

This is the group of "how-to" papers that brought us confocal microscopy. Not all need be read to understand the instrument. This is now divided into (pretty arbitrary) subsections:

E. GENERAL

The historic how-to papers on confocal microscopes.

Aikens, R.S., Agard, D.A., and Sedat, J.W., 1989, Solid state imagers for microscopy, *Methods Cell Biol*. 29:291–313. A complete discussion of the detector of choice in many disk-scanning and widefield microscopes.

Entwistle, A., and Noble, M., 1992, The quantification of fluorescent emission from biological samples using analysis of polarization, *J. Microsc*. 165:347–365. Analysis of fluorescence depolarization can identify regions in which fluorophore concentration exceeds the range of linear fluorescent emission.

Fricker, M.D., and White, N.S., 1992, Wavelength considerations in confocal microscopy of botanical specimens, *J. Microsc*. 166:29–42. Some of the problems associated with multiple wavelengths. CMs make severe demands on achromatized optics.

Glass, M., and Dabbs, T., 1991, The experimental effect of detector size on confocal lateral resolution, *J. Microsc*. 164:153–158. The discrepancy between data and theory attributed to apodization from multi-element thick lenses and a non-ideal, truncated Gaussian beam profile.

Hong, Q., and Elson, E.L., 1991, Analysis of confocal laser-microscope optics for 3-D fluorescence correlation spectroscopy, *Appl. Opt*. 30:1185–1195. Quantitative fluorescence correlation spectroscopy and fluorescence photobleaching recovery measurements.

Janssen, G.C.A.M., Rousseeuw, B.A.C., and Van Der Voort, H.T.M., 1987, Test pattern for fluorescence microscopy, *Rev. Sci. Instrum*. 58:598–599. Fluorescent test pattern with submicron dimensions. An electron beam writes on (in?) PMMA impregnated with rhodamine dye.

Marsman, H.J.B., Stricker, R., Wijnaendts van Resandt, R.W., Brakenhoff, G.J., and Blom, P., 1983, Mechanical scan system for microscopic applications, *Rev. Sci. Instrum*. 54:1047–1052. A high-speed mechanical scanning stage for high-resolution confocal ultraviolet (UV) microscopy.

Oldenbourg, R., Terada, H., Tiberio, R., and Inoué, S., 1993, Image sharpness and contrast transfer in coherent confocal microscopy, *J. Microsc*. 172:31–39. How to measure the resolution of your CM.

Shack, R.V., Bartels, P.H., Buchroeder, R.A., Shoemaker, R.L., Hillman, D.W., and Vukobratovich, D., 1987, Design for a fast fluorescence laser scanning microscope, *Anal. Quant. Cytol. Histol*. 9:509–520. Discussion of the design consideration of the principal components, including the optical elements.

Tsien, R.Y., and Poenie, M., 1986, Fluorescence ratio imaging: a new window into intracellular ionic signaling, *Trends Biochem. Sci*. 11:450–455. Describes one of the major tools used in CM.

Tsien, R.Y., 1989, Fluorescent probes of cell signaling, *Ann. Rev. Neurosci*. 12:227–253. A general review of the dyes CM uses.

Webb, R.H., and Hughes, G.W., 1993, Detectors for scanning video imagers, *Appl. Opt*. 32:6227–6235. Avalanche photodiodes are superior to photomultiplier tubes when scan rates are in the video range.

Wilson, T., 1990, The role of detector geometry in confocal imaging, *J. Microsc.* 158:133–144. Point detectors, slit detectors, detector arrays, and finite-sized detectors.

Wilson, T., and Hewlett, S.J., 1990, Imaging in scanning microscopes with slit-shaped detectors, *J. Microsc*. 160:115–139. An important addition to Wilson's opera, spelling out the variations for slits. Not particularly reader-friendly.

Wilson, T., Hewlett, S.J., and Sheppard, C.J.R., 1990, Use of objective lenses with slit pupil functions in the imaging of line structures, *Appl. Opt*. 29:4705–4714. The gradient of the image of a straightedge is 17.8% sharper if one of the lenses has a slit pupil function.

F. ADAPTIVE OPTICS

Aberration correction by adaptive optics modification of the wavefront at the pupil. This is new since 1994.

Booth, M.J., Neil, M.A.A., Juskaitis, R., and Wilson, T., 2002, Adaptive aberration correction in a confocal microscope, *Proc. Natl. Acad. Sci*. 99:5788–5792. A later addition to a series by these authors. Also Booth, M.J., Neil, M.A.A., and Wilson, T., 2002, New modal wave-front sensor: Application to adaptive confocal fluorescence microscopy and two-photon excitation fluorescence microscopy, *J. Opt. Soc. Am*. A 19:2112–2120. And a few other reports. This is actual image improvement by adaptive optics, some of it for widefield microscopes that then exhibit optical sectioning of a sort. Different wavefront sensors are used, and a deformable mirror is the corrector.

Marsh, P.N., Burns, D., and Girkin, J.M., 2003, Practical implementation of adaptive optics in multiphoton microscopy, *Opt. Express* 11:1123–1130. Built on a Bio-Rad MRC-600, the system uses the brightness of the return as "wavefront sensor," and corrects for index mismatching (spherical aberration). The depth at which the point spread function (PSF) is good is increased from 3 to 46 µm. The corrector is a deformable mirror.

Neil, M.A.A., Juskaitis, R., Booth, M.J., Wilson, T., Tanaka, T., and Kawata, S., 2000, Adaptive aberration correction in a two-photon microscope, *J. Microsc*. 200:105–108. Both wavefront sensor and corrector are a ferroelectric liquid-crystal spatial light modulator.

Sherman, L., Ye, J.Y., Albert, O., and Norris, T.B., 2002, Adaptive correction of depth-induced aberrations in multiphoton scanning microscopy using a deformable mirror. *J. Microsc*. 206:65–71. Intensity provides the wavefront sensing, and a deformable mirror the correction.

G. DIFFERENTIAL

Including DIC (Nomarski) and interferometric and heterodyne.

Amos, W.B., Reichelt, S., Cattermole, D.M., and Laufer, J., 2003, Re-evaluation of differential phase contrast (DPC) in a scanning laser microscope using a split detector as an alternative to differential interference contrast (DIC) optics, *J. Microsc*. 210:166–175. DPC detects the intensity difference between opposite halves or quadrants of a split photodiode detector placed in an aperture plane. It seems to allow a greater depth of field, as well as its freedom from polarization sensitivity and to be more flexible in many ways. It needs only 5% of the power that DIC needs.

Atkinson, M.R., and Dixon, A.E., 1994, Single-pinhole confocal differential phase-contrast microscopy, *Appl. Opt*. 33:641–653. DPC with a split detector is compared to that with two pinholes and two detectors. This is much easier and accomplishes the same.

Boyer, G., and Sarafis, V., 2001, Two pinhole superresolution using spatial filters, *Optik* 112:177–179. Subtractive coherent imaging.

Brakenhoff, G.J., and Muller, M., 1996, Improved axial resolution by point-spread autocorrelation function imaging, *Opt. Lett*. 21:1721–1723. Interferometric spatial autocorrelation of two shifted PSF combined with confocal detection provides improved axial resolution compared with conventional confocal imaging.

Garside, J.R., Somekh, M.G., and See, C.W., 1997, Biological imaging using fast laser scanning heterodyne differential phase confocal microscopes, *J. Microsc*. 185:385–395. An application paper.

Hamilton, D.K., and Sheppard, C.J.R., 1986, Interferometric measurements of the complex amplitude of the defocus signal V(z) in the confocal scanning optical microscope, *J. Appl. Phys*. 60:2708–2712. A confocal interference microscope with electro-optic phase modulator makes simultaneous measurements of the in-phase and quadrature components of the confocal signal as a reflecting surface is scanned axially, the so-called V(z) response.

Horikawa, Y., Yamamoto, M., and Dosaka, S., 1987, Laser scanning microscope: Differential phase images, *J. Microsc*. 148:1–10. A TV-rate acousto-optic deflector laser-scanning microscope for DPC images using the split-detector technique.

Kempe, M., Genack, A.Z., Rudolph, W., and Dorn, P., 1997, Ballistic and diffuse light detection in confocal and heterodyne imaging systems, *J. Opt. Soc. Am*. A 14:216–223. In typical samples for biomedical imaging, the limits of ballistic light detection in confocal imaging are close to the noise limits of standard detectors. Heterodyne detection with narrow-bandwidth light extends these limits.

Kempe, M., Rudolph, W., and Welsch, E., 1996, Comparative study of confocal and heterodyne microscopy for imaging through scattering media, *J. Opt. Soc. Am*. A 13:46–52. Applied primarily to turbid media.

See, C.W., and Iravani, M.V., 1988, Differential amplitude scanning optical microscope: Theory and applications, *Appl. Opt*. 27:2786–2792. Differential means two adjacent spots to catch small changes of height or index. This is a dynamic range stretcher for those quantities.

Stelzer, E.H.K., Marsman, H.J.B., and Wijnaendts van Resandt, R.W. 1986, A setup for a confocal scanning laser interference microscope, *Optik* 73:30–33. The interference mode installed on a CM is compared with that on a conventional microscope and high-quality images are presented.

Torok, P., Laczik, Z., and Sheppard, C.J.R., 1996, Effect of half-stop lateral misalignment on imaging of dark-field and stereoscopic confocal microscopes, *Appl. Opt*. 35:6732–6739. A way to make a CM yield dark-field and/or stereoscopic imaging. Extended to DPC in the same year: *Optik* 103:101–106. As usual, there are a few other papers on the same topic at the same time, by the same authors.

Wilson, T., and Carlini, A.R., 1988, Effect of detector displacement in confocal imaging systems, *Appl. Opt*. 27:3791–3799. In certain cases a degree of detector offset may be used to advantage in determining the position of an edge.

Wilson, T., Carlini, A.R., and Sheppard, C.J.R., 1985, Phase contrast microscopy by nearly full illumination, *Optik* 70:166–169. A simple phase-contrast technique where the two lenses in a scanning microscope are not equal is equally applicable to conventional and CMs and is demonstrated experimentally.

Wilson, T., Juskaitis, R., and Tan, J.B., 1994, Differential imaging in confocal microscopy, *J. Microsc.* 175:1–9. Uses a two-mode optical fiber for differential amplitude and phase contrast.

H. DISPLAY

The literature on three-dimensional image display is far larger than that on confocal microscopy. These are some of the specialized papers.

Carlsson, K., Danielsson, P.E., Lenz, R., Liljeborg, A., Majlof, L., and Åslund, N., 1985, Three-dimensional microscopy using a confocal laser scanning microscope, *Opt. Lett*. 10:53–55. Visualizes in stereo and rotation by making look-through projections of the digital data in different directions. Contrast enhanced by generating gradient volume to display the border surfaces between regions in opposing senses for the two images.

Conchello, J.A., and Hansen, E.W., 1990, Enhanced 3-D reconstruction from CM images. I. Deterministic and maximum likelihood reconstructions, *Appl. Opt*. 29:3795–3804. The feasibility of obtaining longitudinal resolution comparable to the lateral diffraction limit by posterior processing of confocal sections.

Dilworth, D.S., Leith, E.N., and Lopez, J.L., 1991, Three-dimensional confocal imaging of objects embedded within thick diffusing media, *Appl. Opt*. 30:1796–1803. Exfoliative deconvolution to sharpen a volume image in which the blur is depth variant.

Hiraoka, Y., Sedat, J.W., and Agard, D.A., 1990, Determination of three-dimensional imaging properties of a light microscope system. Partial confocal behavior in epifluorescence microscopy, *Biophys. J*. 57:325–333. Through-focus series of a point object were recorded on a charge-coupled

device image detector. From these images, the three-dimensional PSF and its Fourier transform, the optical transfer function, were derived for use in processing a CM image.

Oldmixon, E.H., and Carlsson, K., 1993, Methods for large data volumes from confocal scanning laser microscopy of lung, *J. Microsc*. 170:221–228. How to stitch together adjacent small fields to achieve high resolution over a large area (500 resels per diameter). Intensity variations are adjusted for uniformity of measurement.

Schormann, T., and Jovin, T.M., 1992, Contrast enhancement and depth perception in three-dimensional representations of DIC and CM images, *J. Microsc*. 166:155–168. A new contrast enhancement transformation based upon local statistics and a gray-level probability density function provides improved depth perception, increasing the number of usable optical sections by up to five.

I. FIBER-OPTIC CONFOCAL MICROSCOPES

In this variant, the fiber is an essential component for confocality, or a fiber bundle carries the object plane to inaccessible places.

Balaji, J., Garai, K., Chakrabarti, S., and Maiti, S., 2003, Axial resolution limit of a fiber-optic fluorescence probe, *Appl. Opt.* 42:3780–3784. This mostly theoretical paper has no scanning.

Dabbs, T., and Glass, M., 1992, Single-mode fibers used as confocal microscope pinholes, *Appl. Opt*. 31:705–706. And, Dabbs, T., and Glass, M., 1992, Fiber-optic confocal microscope: FOCON, *Appl. Opt*. 31:3030–3035. The beam-splitter is replaced by a fiber-optic splitter, and the core of a single-mode fiber takes the place of both the source and detector pinholes. Scanning in the *x*-, *y*-, and *z*-directions is by moving the end of the optical fiber.

Gan, X., Gu, M., and Sheppard, C.J.R., 1992, Fluorescent image formation in the fibre-optical confocal scanning microscope, *J. Mod. Opt*. 39:825–834. Unlike a finite circular pinhole, there is no missing cone of spatial frequencies, and no negative tail in the transfer function.

Ghiggino, K.P., Harris, M.R., and Spizzirri, P.G., 1992, Fluorescence lifetime measurements using a novel fibre-optic laser scanning confocal microscope, *Rev. Sci. Instrum*. 63:2999–3002. A fiber-optic CM with a mode-locked dye laser excitation source, avalanche photodiode detector, and time-correlated photon-counting electronics allows spatially resolved fluorescence decay profiles from fluorescent dyes in solution and polymer films.

Giniunas, L., Juskaitis, R., and Shatalin, S.V., 1991, Scanning fiber-optic microscope, *Electron. Lett*. 27:724–726. A phase-sensitive scanning fiber-optic microscope designed to be used as an endoscope. Confocal operation with single-mode fiber yields 0.8 mm lateral resolution.

Gobel, W., Kerr J.N.D., Nimmerjahn, A., and Helmchen, F., 2004, Miniaturized two-photon microscope based on a flexible coherent fiber bundle and a gradient-index lens objective, *Opt. Lett*. 29:2521–2523. Typical of the fiber bundle relay microscopes.

Gu, M., and Bird, D., 2003, Three-dimensional optical-transfer-function analysis of fiber-optical two-photon fluorescence microscopy, *J. Opt. Soc. Am. A* 20:941–947. The latest in a series of papers, mostly theory, no scanning.

Gu, M., and Sheppard, C.J.R., 1991, Signal level of the fiber-optical CM, *J. Mod. Opt*. 38:1621–1630. The efficiency of total power transformation and signal level of the fiber-optical CM, including defocus effects.

Gu, M., Sheppard, C.J.R., and Gan, X., 1991, Image formation in a fiber-optical confocal scanning microscope, *J. Opt. Soc. Am. A* 8:1755–1761. Coherent transfer functions in both in-focus and defocused cases are derived and calculated.

Jung J.C., and Schnitzer, M.J., 2003, Multiphoton endoscopy, *Opt. Lett*. 28:902–904. This is not strictly a fiber, but a long rigid GRIN lens. Pulse degradation is less a problem than in a fiber bundle.

Juskaitis, R., and Wilson, T., Differential CM with a two-mode optical fiber, *Appl. Opt*. 31:898–902. Both the differential amplitude and the differential phase images can be obtained by adjusting the differential phase delay between the fiber modes.

Juskaitis, R., and Wilson, T., 1992, Imaging in reciprocal fiber-optic based CMs, *Opt. Commun*. 92:315–325. Single- and two-mode fibers in a reciprocal scheme. Confocal, differential amplitude, or phase contrast imaging and surface profilometry with reduced alignment tolerances.

Juskaitis, R., and Wilson, T., 1994, Direct-view fiberoptic confocal microscope, *Opt. Lett*. 19:1906–1908. A moving fiber is the scan, and the direct view comes from a synchronously scanned out-coupled fiber.

Juskaitis, R., Reinholz, F., and Wilson, T., 1992, Fiber-optic based confocal scanning microscopy with semiconductor laser excitation and detection, *Electron. Lett*. 28:986–988. Collected light reenters the laser and the image is detected as a modulation of the laser power.

Juskaitis, R., Wilson, T., and Watson, T.F., 1997, Real-time white light reflection confocal microscopy using a fiber-optic bundle, *Scanning* 19:15–19. White light to avoid speckle.

Kimura, S., and Wilson, T., Confocal scanning optical microscope using single-mode fiber for signal detection, *Appl. Opt*. 30:2143–2150. Always coherent, which is fundamentally different from a finite-sized pinhole.

Liang, C., Sung, K.B., Richards-Kortum, R.R., and Descour, M.R., 2002, Design of a high-numerical-aperture miniature microscope objective for an endoscopic fiber confocal reflectance microscope, *Appl. Opt*. 41:4603–4610. Another fiber bundle relay, this one with specialized optics and real images. See also: Sung, K.B., Liang, C., Descour, M., Collier, T., Follen, M., Malpica, A., and Richards-Kortum, R., 2002, Near real time *in vivo* fiber optic confocal microscopy: Sub-cellular structure resolved, *J. Microsc*. 207:137–145.

Lin, C.P., and Webb, R.H., 2000, Fiber-coupled multiplexed confocal microscope, *Opt. Lett.* 25:954–956. An incoherent fiber bundle with a line-scanning CM. Like most *Optics Letters* papers, this one hasn't gone anywhere yet.

Rouse, A.R., Kano, A., Udovich, J.A., Kroto, S.M., and Gmitro, A.F., 2004, Design and demonstration of a miniature catheter for a confocal microendoscope, *Appl. Opt.* 43:5763–5771. Used in real situations, this coherent fiber bundle relays a line-scanned CM. The first paper from this group was in 1999, so reality is tough!

Zhou, H., Sheppard, C.J.R., and Gu, M., 1996, A compact confocal interference microscope based on a four-port single-mode fiber coupler, *Optik* 103:45–48. Uses a four-port coupler and heterodynes against an internal reflection.

J. INDEX MISMATCH

Aberrations due to index differences are primarily spherical.

Arimoto, R., and Murray, J.M., 2004, A common aberration with water-immersion objective lenses, *J. Microsc*. 216:49–51. A tilted cover slip introduces off axis aberrations with a water immersion objective.

Booth, M.J., Neil, M.A.A., and Wilson, T., 1998, Aberration correction for confocal imaging in refractive-index-mismatched media, *J. Microsc*. 192:90–98. A general paper on the subject of oil-immersion objectives and thick "water" samples.

Diaspro, A., Federici, F., and Robello, M., 2002, Influence of refractive-index mismatch in high-resolution three-dimensional confocal microscopy, *Appl. Opt.* 41:685–690. A detailed look at the problem.

Egner, A., and Hell, S.W., 1999, Equivalence of the Huygens-Fresnel and Debye approach for the calculation of high aperture point-spread functions in the presence of refractive index mismatch, *J. Microsc.* 193:244–249. Many reference to earlier work.

Gu, M., Day, D., Nakamura, O., and Kawata, S., 2001, Three-dimensional coherent transfer function for reflection confocal microscopy in the presence of refractive-index mismatch. *J. Opt. Soc. Am. A* 18:2002–2008. Gu and Sheppard and Torok have written more on this, some of which is found in the PSF category.

Haeberle, O., Ammar, M., Furukawa, H., Tenjimbayashi, K., and Torok, P., 2003, Point spread function of optical microscopes imaging through stratified media, *Opt. Express* 11:2964–2969. Stratified media exacerbate the mismatch problem.

Jacobsen, H., Hanninen, P., Soini, E., and Hell, S.W., 1994, Refractive-index-induced aberrations in 2-photon confocal fluorescence microscopy, *J. Microsc*. 176:226–230. The mismatch-induced aberrations make multiphoton microscopy more difficult.

Kawata, Y., Fujita, K., Nakamura, O., and Kawata, S., 1996, 4Pi confocal optical system with phase conjugation, *Opt. Lett*. 21:1415–1417. Phase conjugation is said to relieve the mismatch aberrations in 4PI.

Pawley, J.B., 2002, Limitations on optical sectioning in live-cell confocal microscopy, *Scanning* 24:241–246. The "optical section" surface can be profoundly distorted by the index irregularities associated with the presence of nuclei and other subcellular structures.

Sheppard, C.J.R., Connolly, T.J., Lee, J., and Cogswell, C.J., 1994, Confocal imaging of a stratified medium, *Appl. Opt*. 33:631–640.

Sieracki, C.K., Levey, C.G., and Hansen, E.W., 1995, Simple binary optical-elements for aberration correction in confocal microscopy, *Opt. Lett*. 20:1213–1215. Pupil engineering to alleviate the aberrations.

Smithpeter, C.L., Dunn, A.K., Welch, A.J., and Richards-Kortum, R., 1998, Penetration depth limits of *in vivo* confocal reflectance imaging, *Appl. Opt*. 37:2749–2754. Index mismatches in real samples limit penetration depth.

Visser, T.D., and Oud, J.L., 1994, Volume measurements in 3-dimensional microscopy, *Scanning* 16:198–200. The refractive index mismatch between oil immersion and object leads to a severe over-estimation of the object's size.

Wan, D.S., Rajadhyaksha, M., and Webb, R.H., 2000, Analysis of spherical aberration of a water immersion objective: Application to specimens with refractive indices 1.33–1.40, *J. Microsc*. 197:274–284. Spherical aberration is measured by an interferometer converted from a confocal microscope for samples with different refractive indices.

K. MULTIPLEX

Including tandem-scanning (disk, direct view) and array microscopes.

Andresen, V., Egner, A., and Hell, S.W., 2001, Time-multiplexed multifocal multiphoton microscope, *Opt. Lett*. 26:75–77. Adjacent foci illuminate the sample at different time points. More details appear in an earlier version: Bewersdorf, J., Pick, R., and Hell, S.W., 1998, Multifocal multiphoton microscopy, *Opt. Lett*. 23:655–657.

Boyde, A., Xiao, G.Q., Corle, T., Watson, T.F., and Kino, G.S., 1990, An evaluation of unilateral TSM for biological applications, *Scanning* 12:273–279. Two designs of tandem scanning reflected light microscopes, due to Petran and to Kino.

Brakenhoff, G.J., and Visscher, K., 1992, Confocal imaging with bilateral scanning and array detectors, *J. Microsc*. 165:139–146. A hybrid CM/TSM using an array detector such as a CCD for confocal image collection and a double-sided scanning mirror to scan and collect data. This is the scheme implemented by Meridian.

Brakenhoff, G.J., and Visscher, K., 1993, Imaging modes for bilateral confocal scanning microscopy, *J. Microsc*. 171:17–26. Details of the double-sided mirror rescanning system. The remitted light traverses the confocal pinhole to yet another scanning mirror (the second side of the original one) to be spread again into an image viewable by eye or camera. See Maurice and Koester for earlier implementations. This is the scheme implemented by Meridian.

Fewer, D.T., Hewlett, S.J., McCabe, E.M., and Hegarty, J., 1997, Direct-view microscopy: Experimental investigation of the dependence of the optical sectioning characteristics on pinhole-array configuration, *J. Microsc*. 187:54–61. And Fewer, D.T., Hewlett, S.J., and McCabe, E.M, 1998, Laser sources in direct-view-scanning, tandem-scanning, or Nipkow-disk-scanning confocal microscopy, *Appl. Opt.* 37:380–385. Results for practical systems as regards pinhole-array design and fabrication.

Juskaitis, R., Wilson, T., Neil, M.A.A., and Kozubek, M., 1996, Efficient real-time confocal microscopy with white light sources, *Nature* 383:804–806. A white-light, multiple-point-source method which can in principle produce images in real time, with light efficiencies as high as 50%.

Neil, M.A.A., Wilson, T., and Juskaitis, R., 1998, A light efficient optically sectioning microscope, *J. Microsc*. 189:114–117. A one-dimensional grid pattern, on a spinning disk, produces an optically sectioned image superimposed on a conventional image. A blank sector on the disc provides the widefield image, which is then subtracted to yield the optically sectioned image in real time. See also Wilson, T., Juskaitis, R., Neil, M.A.A., and Kozubek, M., 1996, Confocal microscopy by aperture correlation, *Opt. Lett*. 21:1879–1881.

Tanaami, T., Otsuki, S., Tomosada, N., Kosugi, Y., Shimizu, M., and Ishida, H., 2002, High-speed 1-frame/ms scanning confocal microscope with a microlens and Nipkow disks, *Appl. Opt.* 41:4704–4708.

Watson, T.F., Juskaitis, R., and Wilson. T., 2002, New imaging modes for lenslet-array tandem scanning microscopes, *J. Microsc*. 205:209–212. A later addition to this series, describing the now common disk scanner with microlenses.

Xiao, G.Q., Corle, T.R., and Kino, G.S., 1988, Real-time confocal scanning optical microscope, *Appl. Phys. Lett*. 53:716–718. This describes the one-sided tandem scanning microscope from Kino's lab.

L. NONLINEAR

Including multi-photon and third harmonic microscopes.

Barad, Y., Eisenberg, H., Horowitz, M., and Silberberg, Y., 1997, Nonlinear scanning laser microscopy by third harmonic generation, *Appl. Phys. Lett*. 70:922–924. This method can resolve interfaces and inhomogeneities with axial resolution comparable to the confocal length of the beam.

Booth, M.J., and Hell, S.W., 1998, Continuous wave excitation two-photon fluorescence microscopy exemplified with the 647-nm ArKr laser line, *J. Microsc*. 190:298–304. NA = 1.4 and 210 mW.

Brakenhoff, G.J., Muller, M., and Ghauharali, R.I., 1996, Analysis of efficiency of two-photon versus single-photon absorption for fluorescence generation in biological objects, *J. Microsc.* 183:140–144. Total exposure for equivalent fluorescence by single-photon absorption is an order of magnitude lower than by two-photon absorption.

Brakenhoff, G.J., Squier, J., Norris, T., Bliton, A.C., Wade, M.H., and Athey, B., 1996, Real-time two-photon confocal microscopy using a femtosecond, amplified Ti : sapphire system, *J. Microsc.* 181:253–259. With the bilateral line scanning approach and a Ti : Sa laser.

Egner, A., Andresen, V., and Hell, S.W., 2002, Comparison of the axial resolution of practical Nipkow-disk confocal fluorescence microscopy with that of multifocal multiphoton microscopy: Theory and experiment, *J. Microsc*. 206:24–32. Multi-photon is better.

Schrader, M., and Hell, S.W., 1996, 4Pi-confocal images with axial superresolution, *J. Microsc*. 183:189–193. A suitable combination of aperture enlargement, two-photon excitation, confocalization, and three-point deconvolution yields axial resolution of 145 nm.

Schrader, M., Bahlmann, K., and Hell, S.W., 1997, Three-photon-excitation microscopy: Theory, experiment and applications, *Optik* 104:116–124. Theory and experimental results.

Squier, J., and Muller, M., 2001, High resolution nonlinear microscopy: A review of sources and methods for achieving optimal imaging, *Rev. Sci. Instrum*. 72:2855–2867. Reviews instrumentation used in high resolution nonlinear microscopy and techniques for temporal and spatial calibration.

M. POLARIZATION

Polarization always matters but only a few papers deal with it as a separate topic.

Hansen, E.W., Allen, R.D., Strohbehn, J.W., Chaffee, MA., Farrington, D.L., Murray, W.J., Pillsbury, T.A., and Riley, MF., 1985, Laser scanning phase modulation microscope, *J. Microsc.* 140:371–381. Quantitative polarized light imaging with a phase-modulation feedback loop for precise measurement of birefringence.

Massoumian, F., Juskaitis, R., Neil, M.A.A., and Wilson, T., 2003, Quantitative polarized light microscopy, *J. Microsc*. 209:13–22. A rotating analyzer lock-in detection.

Nielsen, P.M.F., Reinholz, F.N., and Charette, P.G., 1996, Polarization-sensitive scanned fiber confocal microscope, *Opt. Eng.* 35:3084–3091. A single-mode fiber with polarization rotator.

Wilson, T., and Juskaitis, R., 1995, On the extinction coefficient in confocal polarization microscopy, *J. Microsc.* 179:238–240. You never get complete extinction in a CM.

N. PROFILOMETRY

Many profilometers are confocal microscopes, and a few confocal microscopes are profilometers.

Corle, T.R., Fanton, J.T., and Kino, G.S., 1987, Distance measurements by differential confocal optical ranging, *Appl. Opt.* 26:2416–2420. Dithering generates a differential measurement, placing a zero-crossing at the peak of the depth response. Sensitivities to surface vibrations of 0.01 nm and thin film measurements to 0.04 mm.

Hamilton, D.K., and Matthews, H.J., 1985, The confocal interference microscope as a surface profilometer, *Optik* 71:31–34. A non-contacting high-resolution surface profiling technique, with feedback to maintain a constant phase relationship between the signal and the reference beams of a confocal interference microscope.

Hamilton, D.K., and Wilson, T., 1982, Three-dimensional surface measurement using the confocal scanning microscope, *Appl. Phys*. B27:211–213. 0.1 mm axial resolution on a semiconductor.

Lee, B.S., and Strand, T.C., 1990, Profilometry with a coherence scanning microscope, *Appl. Opt*. 29:3784–3788. Uses coherence effects rather than physical apertures. Longitudinal resolution is decoupled from lateral.

Matthews, H.J., Hamilton, D.K., and Sheppard, C.J.R., 1986, Surface profiling by phase-locked interferometry, *Appl. Opt*. 25:2372–2374. 1-nm height resolution. A feedback arrangement keeps in quadrature the two arms of a confocal interference microscope by modulating the reference beam using an electrooptic phase modulator.

Toy, D.A., 1990, Confocal microscopy: The ups and downs of 3-D profiling, *Semicond. Int*. 13:120–123. Confocal techniques can solve the problems of depth of field versus resolution.

O. POINT SPREAD FUNCTION

Including pupillary masking, adaptive optics, problems with index mismatching, and modifications of the PSF by selective bleaching, 4PI, and theta microscopes and angled objectives.

Bahlmann, K., and Hell, S.W., 2000, Polarization effects in 4Pi confocal microscopy studied with water-immersion lenses, *Appl. Opt*. 39: 1652–1658. Refinements of the 4Pi microscope.

Barth, M., and Stelzer, E.H.K., 1994, Boosting the optical transfer-function with a spatially resolving detector in a high numerical aperture confocal reflection microscope, *Optik* 96:53–58. A CCD view of the PSF at the "pinhole" position allows careful analysis.

Gu, M., 1998, Image of a sharp edge in type-3 laser scanning microscopy, *Optik* 107:115–117. A way to measure the PSF.

Haeberle, O., Xu, C., Dieterlen, A., and Jacquey, S., 2001, Multiple-objective microscopy with three-dimensional resolution near 100 nm and a long working distance, *Opt. Lett*. 26:1684–1686. Confocal, theta, and 4Pi microscopes.

Heintzmann, R., Jovin, T.M., and Cremer, C., 2002, Saturated patterned excitation microscopy — A concept for optical resolution improvement, *J. Opt. Soc. Am. A* 19:1599–1609. The post-acquisition manipulation of the acquired data is computationally more complex than in STED or ground-state depletion, but the experimental requirements are simple.

Hell, S.W., Lindek, S., Cremer, C., and Stelzer, E.H.K., 1994, Measurement of the 4pi-confocal point-spread function proves 75 nm axial resolution, *Appl. Phys. Lett*. 64:1335–1337. The ultimate in theta or angled CMs. Here the two objectives look at each other and thus accept light from 4 pi steradians. See also: Hell, S.W., and Stelzer, E.H.K., 1992, *J. Opt. Soc. Am. A* 9:2159; Hell, S.W., Stelzer, E.H.K., Lindek, S., and Cremer, C., 1994, Confocal Microscopy with an increased detection aperture — type-b 4pi confocal microscopy, *Opt. Lett*. 19:222–224. Hell (and many others) have written extensively on the 4Pi microscope with many variations.

Juskaitis, R., and Wilson, T., 1998, The measurement of the amplitude point spread function of microscope objective lenses, *J. Microsc*. 189:8–11. Using an optical fiber interferometer.

Klar, T.A., Dyba, M., and Hell, S.W., 2001, Stimulated emission depletion microscopy with an offset depleting beam, *Appl. Phys. Lett*. 78:393–395. Stimulated emission depletion (STED) reduces the axial extent of a confocal spot from 490 to 175 nm, and simultaneously from 183 to 70 nm along the direction of the offset.

Klar, T.A., Engel, E., and Hell, S.W., 2001, Breaking Abbe's diffraction resolution limit in fluorescence microscopy with stimulated emission depletion beams of various shapes, *Phys. Rev. E* 64:6. Particles that are only 65-nm apart are resolved with focused light.

Kuypers, L.C., Dorckx, J.J.J., and Decraemer, W.F., 2004, A simple method for checking the illumination profile in a laser scanning microscope and the dependence of resolution on the profile, *Scanning* 26:256–258. Pointing out that most real CMs are somewhat apodized by a Gaussian profile at the pupil.

Lindek, S., Stefany, T., and Stelzer, E.H.K., 1997, Single-lens theta microscopy — A new implementation of confocal theta microscopy, *J. Microsc*. 188:280–284. A somewhat randomly chosen member of a series on theta microscopy by some of its originators.

Matthews, H.J., Hamilton, D.K., and Sheppard, C.J.R., 1989, Aberration measurement by confocal interferometry, *J. Mod. Opt*. 36:233–280. Aberrations and apodization of microscope objectives measured from the defocus signal in a confocal interference microscope system. Phase distortions can be measured to approximately l/100, and quantitative information is given about the imaging performance of the lenses *in situ* in the optical system.

Nagorni, M., and Hell, S.W., 2001, Coherent use of opposing lenses for axial resolution increase in fluorescence microscopy. I. Comparative study of concepts, *J. Opt. Soc. Am. A* 18:36–48. and II. Power and limitation of nonlinear image restoration, *J. Opt. Soc. Am. A* 18:49–54. Comparison of PSF and OTF for many variants, including the standing wave microscope, the incoherent illumination interference image interference microscope [(IM)-M-5], and the 4Pi confocal microscope for one and two photons.

Nieman, L., Myakov, A., Aaron, J., and Sokolov, K., 2004, Optical sectioning using a fiber probe with an angled illumination-collection geometry: Evaluation in engineered tissue phantoms, *Appl. Opt*. 43:1308–1319. I have my doubts about how real any phantoms are compared to skin. They also used oral mucosa, and that's real and easy.

Schrader, M., and Hell, S.W., 1996, Wavefronts in the focus of a light microscope, *J. Microsc*. 184:143–148. Scanning a scattering probe through the focal region of a lens illuminated by plane waves.

Schrader, M., Hofmann, U.G., and Hell, S.W., 1998, Ultrathin fluorescent layers for monitoring the axial resolution in confocal and two-photon fluorescence microscopy, *J. Microsc*. 191:135–140. A how-to paper.

Shaw, P.J., and Rawlins, D.J., 1991, The point-spread function of a confocal microscope: Its measurement and use in deconvolution of 3-D data, *J. Microsc*. 163:151–165. PSF for an MRC-500 CM using subresolution fluorescent beads. The resulting optical transfer functions were used in an iterative, constrained deconvolution procedure to get three-dimensional confocal data sets from a biological specimen.

Sheppard, C.J.R., and Choudhury, A., 2004, Annular pupils, radial polarization, and superresolution, *Appl. Opt*. 43:4322–4327. Bessel beam and radial polarization gets to 100 nm PSF.

Sheppard, C.J.R., and Gu, M., 1991, Aberration compensation in confocal microscopy, *Appl. Opt*. 30:3563–3568. Spherical aberration due to focusing deep within the specimen can be compensated by altering the effective tube length. Sheppard and Gu have contributed many papers on the general theme of pupil masking to improve the PSF. This is an early one. A recent member of the class is:

Sheppard, C.J.R., and Gu, M., 1992, Axial imaging through an aberrating layer of water in confocal microscopy, *Opt. Commun*. 88:180–190. The axial response modeled by a series of signals reflected from different interfaces. Altering the effective tube length for an optimum axial response, experimental results are well in agreement with theoretical predictions.

Sheppard, C.J.R., Hamilton, D.K., and Cox, I.J., 1982, Optical microscopy with extended depth of field observation of optical signatures of materials, *Appl.*

Phys. Lett. 41:604–606. Depth of field may be extended while high-resolution, diffraction-limited imaging is retained. The technique is similar to one already used in acoustic microscopy.

Stark, P.R.H., Rinko, L.J., and Larson, D.N., 2003, Fluorescent resolution target for super-resolution microscopy, *J. Microsc*. 212:307–310. The authors claim this is a better resolution probe than beads.

Stelzer, E.H.K., 1998, Contrast, resolution, pixelation, dynamic range and signal-to-noise ratio: Fundamental limits to resolution in fluorescence light microscopy, *J. Microsc*. 189:15–24. "In conclusion: (a) real optical systems will never be able to achieve the theoretical resolution, (b) wide-field fluorescence microscopy will often provide a better resolution than confocal fluorescence microscopy, (c) decreasing the observed volume does not necessarily increase the resolution and (d) using multiple fluorophores can improve the accuracy with which distances are measured."

Stelzer, E.H.K., Lindek, S., Albrecht, S., Pick, R., Ritter, G., Salmon, N.J., and Stricker, R., 1995, A new tool for the observation of embryos and other large specimens — Confocal theta-fluorescence microscopy, *J. Microsc*. 179:1–10. Details with real samples (and with phantoms).

Tapang, G., and Saloma, C., 2002, Behavior of the point-spread function in photon-limited confocal microscopy, *Appl. Opt*. 41:1534–1540.

Wang, T.D., Contag, C.H., Mandella, M.J., Chan, N.Y., and Kino, G.S., 2003, Dual-axes confocal microscopy with post-objective scanning and low-coherence heterodyne detection, *Opt. Lett*. 28:1915–1917. This architecture can be scaled down to millimeter dimensions with micro-electromechanical systems.

Young, M.R., Jiang, S.H., Davies, R.E., Walker, J.G., Pike, E.R., and Bertero, M., 1992, Experimental confirmation of super-resolution in coherent confocal scanning microscopy using optical masks, *J. Microsc*. 165:131–138. Super-resolution in a coherent scanning microscope with a special optical mask, a Fourier lens, and detector pin-hole to carry out optical processing of the image. The form of the special mask was calculated using the theory of singular systems.

P. PUPIL ENGINEERING

Pupil masks and modifications to improve the PSF.

Boyer, G., 2002, New class of axially apodizing filters for confocal scanning microscopy, *J. Opt. Soc. Am. A* 19:584–589. Typical of a large group of papers on pupil engineering to enhance the PSF.

Davis, B.J., Karl, W.C., Swan, A.K., Unlu, M.S., and Goldberg, B.B., 2004, Capabilities and limitations of pupil-plane filters for superresolution and image enhancement, *Opt. Express* 12:4150–4156. Resolution cannot be improved solely by adding pupil-plane filters but signal-to-noise can be.

de Juana, D.M, Oti, J.E., Canales, V.F., and Cagigal, M.P., 2003, Transverse or axial superresolution in a 4Pi-confocal microscope by phase-only filters, *J. Opt. Soc. Am. A* 20:2172–2178. Resolution-improving phase functions differ for transverse and axial.

Grochmalicki, J., and Pike, R., 2000, Superresolution for digital versatile discs (DVD's), *Appl. Opt*. 39:6341–6349. It's good to be reminded that most of the CMs in the world are in a consumer product.

Gu, M., and Sheppard, C.J.R., 1994, 3-Dimensional transfer-functions in 4pi confocal microscopes, *J. Opt. Soc. Am A* 11:1619–1627. The effects of apodization are taken into account.

Gu, M. 1996, Effect of apodization on axial resolution in confocal microscopy of high aperture, *Optik* 102:120–124. Gu and Sheppard have a series of papers on pupil engineering.

Gustafsson, M.G.L., 2000, Surpassing the lateral resolution limit by a factor of two using structured illumination microscopy, *J. Microsc*. 198:82–87. A very complex system.

Lin, L., Wang, X.H., Wang, Z.Q., and Mu, G.G., 2003, Binary phase-only pupil filters application to high-aperture confocal microscopy, *Optik* 114: 329–332.

Lindek, S., Cremer, C., and Stelzer, E.H.K., 1996, Confocal theta fluorescence microscopy with annular apertures, *Appl. Opt.* 35:126–130. An annular aperture is the simplest pupil mask.

Liu, L., Deng, X.Q., Yang, L.S., Wang, G.Y., and Xu, Z.Z., 2000, Effect of an annular pupil filter on differential confocal microscopy, *Opt. Lett*. 25:1711–1713. Extends the axial dynamic range and improves transverse resolution by sacrificing axial resolution.

Martinez-Corral, M., Kowalczyk, M., Zapata-Rodriguez, C.J., and Andres, P., 1998, Tunable optical sectioning in confocal microscopy by use of symmetrical defocusing and apodization, *Appl. Opt.* 37:6914–6921. Very simple to implement.

Martinez-Corral, M., Pons, A., and Caballero, M.T., 2002, Axial apodization in 4Pi-confocal microscopy by annular binary filters, *J. Opt. Soc. Am. A* 19:1532–1536. Proper pupil engineering (masking) improves the PSF, even in 4Pi.

Neil, M.A.A., Juskaitis, R., Wilson, T., Laczik, Z.J., and Sarafis, V., 2000, Optimized pupil-plane filters for confocal microscope point-spread function engineering, *Opt. Lett*. 25:245–247. Using reconfigurable binary optical elements.

Schilders, S.P., Gan, X.S., and Gu, M., 1998, Microscopic imaging through a turbid medium by use of annular objectives for angle gating, *Appl. Opt.* 37:5320–5326. To exclude multiply scattered photons.

Sheppard, C.J.R., Sharma, M.D., and Arbouet, A., 2000, Axial apodizing filters for confocal imaging, *Optik* 111:347–354. A more recent contribution to the series.

Q. THICKNESS

Distinguishing between index and thickness allows measurement of both.

Fukano, T., and Yamaguchi, I., 1996, Simultaneous measurement of thicknesses and refractive indices of multiple layers by a low-coherence confocal interference microscope, *Opt. Lett.* 21:1942–1944. Combining with OCT, multiple layers can be sorted out.

Fukano, T., and Yamaguchi, I., 1999, Separation of measurement of the refractive index and the geometrical thickness by use of a wavelength-scanning interferometer with a confocal microscope, *Appl. Opt.* 38:4065–4073. A wavelength-scanning heterodyne interferometer works better. Later papers, *Appl. Opt*. 41:4497–4502 and *Appl. Opt*. 41:2414–2419, elaborate on this.

Ilev, I.K., Waynant, R.W., Byrnes, K.R., and Anders, J.J., 2002, Dual-confocal fiber-optic method for absolute measurement of refractive index and thickness of optically transparent media, *Opt. Lett.* 27:1693–1695. Two independent identical apertureless fiber-optic CMs with a single 2×2 fiber coupler.

Jester, J.V., Petroll, W.M., and Cavanagh, H.D., 1999, Measurement of tissue thickness using confocal microscopy, *Methods Enzymol*. 307:230–245. A review for biologists. The tissue in question is the cornea, and the CM a tandem-scanning microscope.

R. TURBIDITY

Thick biological samples introduce so much scattering that they are a special problem.

Bertrand, C., and Corcuff, P., 1994, In vivo spatiotemporal visualization of the human skin by real-time confocal microscopy, *Scanning* 16:150–154. Tandem scanning microscope and much processing to remove noise.

Booth, M.J., and Wilson, T., 2000, Strategies for the compensation of specimen-induced spherical aberration in confocal microscopy of skin, *J. Microsc*. 200:68–74. See also the category of index mismatch.

Corcuff, P., Gonnord, G., Pierard, G.E., and Leveque, J.L., 1996, *In vivo* confocal microscopy of human skin: A new design for cosmetology and dermatology, *Scanning* 18:351–355. Limitations of the tandem scanning microscope in this usage, but real results.

Gan, X., Schilders, S.P., and Gu, M., 1999, Image enhancement through turbid media under a microscope by use of polarization gating methods, *J. Opt. Soc. Am. A* 16:2177–2184. Polarization gating methods are superior to the pinhole gating method when signal strength is weak. One in a series of compensation methods.

Gan, X.S., and Gu, M., 1999, Effective point-spread function for fast image modeling and processing in microscopic imaging through turbid media, *Opt. Lett*. 24:741–743. Monte Carlo modeling.

Gu, M., Tannous, T., and Sheppard, J.R., 1996, Effect of an annular pupil on confocal imaging through highly scattering media. *Opt. Lett*. 21:312–314.

Rajadhyaksha, M., Anderson, R.R., and Webb, R.H., 1999, Video-rate confocal scanning laser microscope for imaging human tissues *in vivo*, *Appl. Opt*. 38:2105–2115. Details of the instrument reported in *J. Invest. Dermatol*. 1995:946–952.

Schmitt, J.M., Knuttel, A., and Yadlowsky, M., 1994, Confocal microscopy in turbid media, *J. Opt. Soc. Am. A* 11:2226–2235. "The major conclusion of the paper is that the trade-off between signal level and background scattered-light rejection places a fundamental limit on the sectioning capability of the microscope."

S. VARIANTS ON THE MAIN THEME

Confocal microscopes that are not used as bench microscopes, or that have some other unusual wrinkle.

Bailey, B., Farkas, D.L., Taylor, D.L., and Lanni, F., 1993, Enhancement of axial resolution in fluorescence microscopy by standing-wave excitation, *Nature* 366:44–48. A means of increasing axial sectioning resolution at the expense of an uncertainty in choice of which standing wave plane is addressed. Combined with CSLM, an improvement to 0.05 µm is claimed, although the standing waves are $\lambda/2\eta$ apart (0.15 µm).

Benedetti, P.A., Evangelista, V., Guidarini, D., and Vestri, S., 1992, Confocal-line microscopy, *J. Microsc*. 165:119–129. Confocal in one dimension, no moving parts. Linear imagers permit transmission, reflection, and emission images simultaneously.

Benschop, J., and van Rosmalen, G., 1991, Confocal compact scanning optical microscope based on compact disc technology. *Appl. Opt*. 30:1179–1184. A compact CM based on the optics and mechanics of a compact disc (CD) player is equipped with automatic focusing. The laser in the CD player is replaced by the endface of a single-mode fiber which acts both as the emitting source and as a point detector.

Burns, D.H., Hatanagadi, R.B., and Spelman, F.A., 1990, Scanning slit aperture confocal microscopy for three-dimensional imaging, *Scanning* 12:156–160. A CM using stationary slit apertures of variable width employing an oscillating mirror at 150 frames/s.

Buurman, E.P., Sanders, R., Draaijer, A., Gervitsen, H.C., Van Veen, J.J.F., Houpt, P.M., and Levine, Y.K., 1992, Fluorescence lifetime imaging using a confocal laser scanning microscope, *Scanning* 14:155–159. Fluorescence lifetime imaging method in a CM uses a low-power CW argon laser chopped to 25 MHz nanosecond pulses. Time-gated detection measures the lifetime of a pixel in 40 µs.

Callamaras, N., and Parker, I, 1999, Construction of line-scan confocal microscope for physiological recording, *Methods Enzymol*. 307:152–169. A review for biologists.

Carter, K.C., Bowman, D., Carrington, W., Fogarty, K., McNeil, J.A., Fay, F.S., and Lawrence, J.B., 1993, A three-dimensional view of precursor messenger RNA metabolism within the mammalian nucleus, *Science* 259:1330–1335. A demonstration of the alternative (software) approach of Carrington and Fay, in real use.

Chim, S.S.C., and Kino, G.S., 1990, Correlation microscope, *Opt. Lett*. 15:579–581. A Mirau interferometer used with Kino's disk-scanning confocal microscope allows collection of both amplitude and phase information.

Ching, B.J., Finzi, L., and Bustamante, C.J. , 1988, Design and application of a computer-controlled confocal scanning differential polarization microscope, *Rev. Sci. Instrum.* 59:2399–2408. Basic theory and design. Anisotropy 10^{-5}, typical CSLM resolutions

Cohen-Sabban, J., Rodier, J.C., Roussel, A., and Simon, J., 1984, Scanning ophthalmoscope, *Innov. Tech. Biol. Med.* 5:24. A scanning laser ophthalmoscope with two galvo mirrors.

Curley, P.F., Ferguson, A.I., White, J.G., and Amos, W.B., 1992, Application of a femtosecond self-sustaining mode-locked Ti: sapphire laser to the field of laser scanning confocal microscopy, *Opt. Quant. Electron*. 24:851–859. With a femtosecond Ti : Sa laser in a CM, spectra are given for various fluorescent stains under two-photon excitation.

Denk, W., Strickler, J.H., and Webb, W.W., 1990, Two-photon laser scanning fluorescence in microscopy, *Science* 248:73–76. Two infrared photons excite the same fluorescence as one UV photon, but there must be a lot of IR in one small volume. No confocal pinhole is necessary because the requisite convolution of two $J_1(r)^2/r^2$ functions comes from the two illuminations.

Dickensheets, D.L., and Kino, G.S., 1996, Micromachined scanning confocal optical microscope, *Opt. Lett*. 21:764–766. Single-mode fiber and a two-phase off-axis zone plate objective lens. One µm resolution over a 100 µm field.

Dixon, A.E., Damaskinos, S., and Atkinson, M.R., 1991, Transmission and double-reflection scanning stage confocal microscope, *Scanning* 13:299–306. A stage-scanning transmitted- and reflected-light laser microscope is described.

Dobson, S.L., Sun, P.C., and Fainman, Y., 1997, Diffractive lenses for chromatic confocal imaging, *Appl. Opt.* 36:4744–4748. Zone plate for wavelength-to-depth coding.

Draaijer, A., and Houpt, P.M., 1988, A standard video-rate confocal laser-scanning reflection and fluorescence microscope, *Scanning* 10:139–145. The CM developed at TNO has standard video-rate imaging, and is capable of working in reflection and in fluorescence mode simultaneously.

Freimann, R., Pentz, S., and Horler, H., 1997, Development of a standing-wave fluorescence microscope with high nodal plane flatness, *J. Microsc*. 187:193–200. A standing-wave pattern of laser light with alternating planar nodes and antinodes. Along the axis different fluorescent structures can be distinguished. A SWFM is most powerful when the axial extension of the specimen is comparable to the wavelength of light, otherwise several planes are illuminated simultaneously and their separation is hardly feasible.

Gimitri, A.F., and Aziz, D., 1993, Confocal microscopy through a fiber-optic imaging bundle, *Opt. Lett*. 18:565–567. A coherent fiber bundle relays the scan between objectives, presently with low power objectives.

Goldstein, S.R., Hubin, T., Rosenthal, S., and Washburn, C.A., 1990, Confocal video-rate laser-beam scanning reflected-light microscope with no moving parts, *J. Microsc*. 157:29–38. Acousto-optic scanners for the incident beam, and confocal descanning and detection by an image dissector tube.

Gustafsson, M.G.L., Agard, D.A., and Sedat, J.W., 1999, (IM)-M-5: 3D wide-field light microscopy with better than 100 nm axial resolution, *J. Microsc*. 195:10–16. Sample is observed and/or illuminated from both sides simultaneously using two opposing objective lenses. Separate interference effects in the excitation light and the emitted light give access to higher resolution axial information.

Hanley, Q.S., Verveer, P.J., Gemkow, M.J., Arndt-Jovin, D., and Jovin, T.M., 1999, An optical sectioning programmable array microscope implemented with a digital micromirror device, *J. Microsc*. 196:317–331. A PAM (programmable array microscope) is a form of tandem-scanning microscope using a spatial light modulator instead of a spinning disk. This one uses the Texas Instruments digital micromirror device.

Heintzmann, R., Hanley, Q.S., Arndt-Jovin, D., and Jovin, T.M., 2001, A dual path programmable array microscope (PAM): Simultaneous acquisition of conjugate and non-conjugate images, *J. Microsc*. 204:119–135. The PAM of the previous citation can give both confocal and anti-confocal images.

Hell, S., and Stelzer, E.H.K., 1992, Fundamental improvement of resolution with a 4Pi-confocal fluorescence microscope using two-photon excitation, *Opt. Commun*. 93:277–282. An implementation of Watt Webb's microscope is proposed. Calculations demonstrate that an axial resolution on the order of 100 nm can be achieved in a confocal microscope with enlarged aperture when two-photon excitation is applied. The proposed microscope yields the highest point resolution ever achieved in far-field microscopy.

Hell, S., Witting, S., Schickfus, M.V., and Neiger, M.A., 1991, Confocal beam scanning white-light microscope, *J. Microsc*. 163:179–187. CM with a continuous Xe short-arc lamp operating in the visible spectrum. Resolution of the white- light microscope is equivalent to that of the scanning laser microscope, without artifacts caused by interference.

Hiraoka, Y., Minden, J.S., Swedlow, J.R., Sedat, J.W., and Agard, D.A., 1898, Focal points for chromosome condensation and decondensation from

three-dimensional *in vivo* time-lapse microscopy, *Nature* 342:293–296. Chromosomes can now be studied in the transitions to and from interphase. Demonstrates 3D analysis, time-lapse display, and the (software) emulation of confocal microscopy.

Jungerman, R.L., Hobbs, P.C., and Kino, G.S., 1984, Phase sensitive scanning optical microscope, *Appl. Phys. Lett*. 45:846–848. An electronically scanned optical microscope measuring amplitude and phase and insensitive to mechanical vibrations. Phase information gives an axial accuracy of 10 nm and can improve the lateral resolution.

Juskaitis, R., and Wilson, T., 1994, Scanning interference and confocal microscopy, *J. Microsc*. 176:188–194. "The interference term in confocal and conventional scanning interference microscopes is identical in all respects including optical sectioning. This observation is used to obtain confocal images and surface profiles from conventional scanning interference microscope images."

Juskaitis, R., Wilson, T., and Reinholtz, F., 1993, Spatial filtering by laser detection in confocal microscopy, *Opt. Lett*. 18:1135–1137. The laser itself is the confocal pinhole, and is modulated by the remitted light.

Kang, D.K., Seo, J.W., and Gweon, D.G., 2004, Improvement of detected intensity in confocal microscopy by using reflecting optical system, *Rev. Sci. Instrum.* 75:550v552. A 37% increase in detected intensity.

Koester, C.J., 1980, Scanning mirror microscope with optical sectioning characteristics: Applications in ophthalmology, *Appl. Opt*. 19:1749–1757. The original paper on Koester's real-time slit scanner.

Koester, C.J., Auran, J.D., Rosskothen, H.D., Florakis, G.J., and Tackaberry, R.B., 1993, Clinical microscopy of the cornea utilizing optical sectioning and a high-numerical-aperture objective, *J. Opt. Soc. Am. A* 10: 1670–1679. Use of the specular microscope with a dipping cone and film recording.

Kwon, S., and Lee, L.P., 2004, Micromachined transmissive scanning confocal microscope, *Opt. Lett.* 29:706–708. Electrostatically actuated microlenses focus and scan. Objective lenses, scanners, pupil, and pinhole are microfabricated in $<2\,mm^3$. Objective lenses are two vertically cascaded polymer microlenses integrated into micromachined comb actuators. Raster scanning by actuating in orthogonal directions.

Lichtman, J.W., Sunderland, W.J., and Wilkinson, R.S., 1989, High-resolutuion imaging of synaptic structure with a simple confocal microscope, *The New Biologist* 1:75–82. An oscillating slit at a relayed image plane turns a conventional microscope into a TSM variant. Origin of the Newport CM.

Mansfield, S.M., and Kino, G.S., 1990, Solid immersion microscope, *Appl. Phys. Lett*. 57:2615–2616. A real-time optical microscope with the liquid replaced by a solid lens of high refractive index material.

McLaren, J.W., and Brubaker, R.F., 1988, A scanning ocular spectrofluorophotometer, *Invest. Ophthalmol. Vis. Sci*. 29:1285–1293. Measures fluorescence in a two-dimensional cross-section through the anterior chamber and cornea of the eye.

Morgan, C.G., Mitchell, A.C., and Murray, J.G., 1992, Prospects for confocal imaging based on nanosecond fluorescence decay time, *J. Microsc*. 165:49–60. Two detection schemes: one based on an imaging single-photon detector equipped with an external photon correlator and the other using an RF-modulated intensified charge-coupled device (CCD) camera. Possible routes to development of a confocal version of the microscope.

Ooki, H., and Iwasaki, J., 1991, A novel type of laser scanning microscope: Theoretical considerations, *Opt. Commun*. 85:177–182. Differential interference contrast by means of mode interference in a waveguide device. Phase and amplitude separately.

Piston, D.W., Kirby, M.S., Cheng, H., Lederer, W.J., et al., 1994, Two-photon-excitation fluorescence imaging of three-dimensional calcium-ion activity. *Appl. Opt*. 33:662. Actual imaging with the two-photon microscope. Some 50 mW of near IR in 100 fs pulses into an MRC 600.

Pitris, C., Bouma, B.E., Shiskov, M., and Tearney, G.J., 2003, A GRISM-based probe for spectrally encoded confocal microscopy, *Opt. Exp.* 11:120–124. A single-optical-axis element based on high index-of-refraction prisms and a transmission holographic grating for the design of narrow diameter SECM.

Podoleanu, A.G., Dobre, G.M, Cucu, R.G., and Rosen, R.B., 2004, Sequential optical coherence tomography and confocal imaging, *Opt. Lett*. 29: 364–366. A lower-depth-resolution image for target positioning before collection of stacks of en-face OCT images.

Puppels, G.J., Colier, W., Olminkhof, J.H.F., Otto, C., de Mul, F.F.M., and Greve, J., 1991, Description and performance of a highly sensitive confocal Raman microspectrometer. J. *Raman Spectrosc.* 22:217–225. Lateral resolution 0.45 μm and 1.3 μm axial, for single living cells and metaphase and polytene chromosomes. Excitation 660 nm to avoid sample degradation. $1000\,cm^{-1}$ Raman shift. For signal detection a liquid nitrogen-cooled slow-scan CCD camera is used. Laser powers of 5 to 10 mW suffice to obtain high-quality Raman spectra, with signal integration times of the order of minutes. As an example, spectra obtained from the nucleus and the cytoplasm of an intact human lymphocyte are shown.

Ruckstuhl, T., and Seeger, S., 2003, Confocal total-internal-reflection fluorescence microscopy with a high-aperture parabolic mirror lens, *Appl. Opt*. 42:3277–3283. For confocal imaging and spectroscopy of nanoparticles and single molecules. The large aperture excites fluorescence within the evanescent field.

Sawatari, T., Optical heterodyne scanning microscope, *Appl. Opt*. 12:2768–2772. Image similar to CM because the same self-convolution of the diffraction pattern is required. Ambient light effects eliminated. High-contrast images from low-contrast objects.

Sawyer, N.B.E., Morgan, S.P., Somekh, M.G., See, C.W., Cao, X.F., Shekunov, B.Y., and Astrakharchik, E., 2001, Wide field amplitude and phase confocal microscope with parallel phase stepping, *Rev. Sci. Instrum.* 72:3793–3801. A widefield phase-sensitive CM based on correlation between speckles.

Sheppard, C.J.R., and Cogswell, C.J., 1990, Confocal microscopy with detector arrays, *J. Mod. Opt.* 37:267–279. Imaging in a scanning optical microscope with a detector consisting of an array of rings is considered. It is found that both transverse and axial resolution can be increased simultaneously.

Sheppard, C.J.R., Roy, M., and Sharma, M.D., 2004, Image formation in low-coherence and confocal interference microscopes, *Appl. Opt.* 43:1493–1502. OCT is a confocal interference microscope, but cannot compensate aberrations. The coherence probe microscope is not confocal, so provides no optical sectioning.

Shoemaker, R.L., Bartels, P.H., Hillman, D.W., Jonas, J., Kessler, D., Shack, R.V., and Vukobratovich, D., 1982, An ultrafast laser scanner microscope for digital image analysis (cytology application). *IEEE Trans. Biomed. Eng*. 29:82–91. An ultrafast laser scanner microscope to make high-resolution cell analysis practical at data rates comparable to flow cytometry.

Smith, P.J., Taylor, C.M, Shaw, A.J., and McCabe, E.M., 2000, Programmable array microscopy with a ferroelectric liquid-crystal spatial light modulator, *Appl. Opt.* 39:2664–2669. A PAM with a spatial light modulator that is somewhat more friendly than the TI device.

Somekh, M.G., Valera, M.S., and Appel, R.K., 1995, Scanning heterodyne confocal differential phase and intensity microscope, *Appl. Opt.* 34:4857–4868. "Interfering the two signal beams with a common reference beam (indirect interference) permits an optimum differential phase and intensity performance to be obtained simultaneously."

Stimson, M.J., Haralampus-Grynaviski, N., and Simon, J.D., 1999, A unique optical arrangement for obtaining spectrally resolved confocal images, *Rev. Sci. Instrum.* 70:3351–3354. The detection device is placed in an intermediate position between fully descanned detection and nondescanned detection (direct projection).

Sun, C.K., Chen, C.C., Chu, S.W., Tsai, T.H., Chen, Y.C., and Lin, B.L., 2003, Multiharmonic-generation biopsy of skin, *Opt. Lett*. 28:2488–2490. To avoid the in-focus photodamage and phototoxicity problem of two-photon-fluorescence excitation. 1200 nm multi-harmonic generation biopsy of fixed mouse skin.

Tearney, G.J., Webb, R.H., and Bouma, B.E., 1998, Spectrally encoded confocal microscopy, *Opt. Lett*. 23:1152–1154. A scanning CM that uses a quasi-monochromatic light source and a transmission diffraction grating to detect the reflectivity simultaneously at multiple points along a transverse line within the sample. Because this method does not require fast spatial scanning within the probe, the equipment can be miniaturized and incorporated into a catheter or endoscope.

Uhlendorf, K., Notni, G., and Kowarschik, R., 1999, Resolution enhancement in a reflection-type confocal microscope with a phase-conjugate mirror, *Appl. Opt*. 38:869–873. One of a series on CMs with phase-conjugate mirrors.

van der Oord, C.J.R., Gerritsen, H.C., Levine, Y.K., Myring, W.J., Jones, G.R., and Munro, I.H., 1992, Synchrotron radiation as a light source in confocal microscopy, *Rev. Sci. Instrum*. 63:632–633. A CM using a synchrotron as light source from 200 nm up to 700 nm. Using 325-nm laser light, it is shown that the lateral resolution is about 125 nm, and the axial resolution better than 250 nm.

van Norren, D., and van de Kraats, J., 1989, Imaging retinal densitometry with a confocal scanning laser ophthalmoscope, *Vis. Res*. 29:1825–1830. Use of the scanning laser ophthalmoscope (SLO) as an imaging retinal densitometer.

VanKempen, G.M.P., vanVliet, L.J., Verveer, P.J., and vanderVoort, H.T.M., 1997, A quantitative comparison of image restoration methods for confocal microscopy, *J. Microsc*. 185:354–365. Comparison of three methods.

Verveer, P.J., Hanley, Q.S., Verbeek, P.W., Van Vliet, L.J., and Jovin, T.M., 1998, Theory of confocal fluorescence imaging in the programmable array microscope (PAM), *J. Microsc*. 189:192–198. A good review of the PAM the Jovin group uses.

Visscher, K., Brakenhoff, G.J., and Visser, T.D., 1994, Fluorescence saturation in confocal microscopy, *J. Microsc*. 175:162–165. An early precursor to some saturation-based manipulations.

Webb R.H., 1984, Optics for laser rasters, *Appl. Opt*. 23:3680–3683. Optics for shaping and manipulating laser beams in a video-scanning system, including an awkward but usable solution to the problem of chromaticity in diffraction scanners.

Webb, R.H., and Rogomentich, F.J., 1995, Microlaser microscope using self-detection for confocality, *Opt. Lett*. 20:533–535. Uses its own source lasers as detectors to provide a matched array of confocal apertures. Detection of the laser light by a single avalanche photodiode makes the electronics simple.

Webb, R.H., Hughes, G.W., and Delori, F.C., 1987, Confocal scanning laser ophthalmoscope, *Appl. Opt.* 26:1492–1499. The SLO sold by Rodenstock. Works in real time, using an avalanche photodiode as detector. Last in a series on this instrument.

Appendix 1

Practical Tips for Two-Photon Microscopy

Mark B. Cannell, Angus McMorland, and Christian Soeller

INTRODUCTION

As is clear from a number of the chapters in this volume, 2-photon microscopy offers many advantages, especially for living-cell studies of thick specimens such as brain slices and embryos. However, these advantages must be balanced against the fact that commercial multiphoton instrumentation is much more costly than the equipment used for confocal or widefield/deconvolution. Given these two facts, it is not surprising that, to an extent much greater than is true of confocal, many researchers have decided to add a femtosecond (fs) pulsed near-IR laser to a scanner and a microscope to make their own system (Soeller and Cannell, 1996; Tsai *et al.*, 2002; Potter, 2005). Even those who purchase a commercial multiphoton system find that it helps to understand a bit more about how to optimize the performance of the fs laser system.[1] This Appendix has been added to the Handbook to provide the basic alignment and operating information that such people need.

First, the safety announcement . . .

LASER SAFETY

Light sources for multiphoton microscopy are almost without exception very powerful pulsed lasers (laser class *IV*). It is vital that any personnel who perform alignment or other operations that carry a risk of beam exposure are familiar with and follow laser safety regulations. During routine operation one **MUST** ensure that accidental exposure to the pulsed laser beam is prevented by providing proper shielding and interlocks.

During alignment, protective eyewear is not an option — it is essential!

See http://www.osha.gov/SLTC/laserhazards/ for US guidelines.

LASER ALIGNMENT

Just as in any other type of microscopy, correct optical alignment is crucial for achieving optimal, diffraction-limited performance in 2-photon microscopy. The alignment of external lasers such as the Ti : S or similar 2-photon sources into a laser scanning microscope can be simplified if a well-aligned "internal" or reference laser is available. In commercial confocal microscopes, typical candidate lasers include Argon-ion or green HeNe lasers or, more recently, blue and green diode lasers. To provide an alignment beam to which the external laser can be aligned, light from this reference laser needs to be bounced back through the microscope optical train and out through the external coupling port:

CAUTION: Before you switch on the reference laser in this configuration make sure that all PMTs are protected and/or turned off.

Place a front-surface mirror on the stage of the microscope and focus onto the reflective surface using an air objective for convenience (at sharp focus, you should be able to see scratches or other mirror defects through the eyepieces). The idea of this method is to cause the reference laser beam to bounce back through the optical train and emerge from the other laser port. To do this, select filter settings that will allow some of the light from the internal laser to exit the chosen coupling port. In order to bring two laser beams to co-linearity, a beam-steering device is essential. A single-mirror beam steerer provides angular control while changing the separation between the mirrors of a 2-mirror steerer provides beam translation (Fig. A1.1).

It is also possible to achieve beam translation with a second angular control mirror. After adjusting the incoming near-IR beam to an intensity where it can be viewed without totally overwhelming the reference beam,[2] adjust one mirror to make both laser spots merge at the surface of the other (angle-adjustable) mirror. Then that mirror is adjusted to bring the beams to co-linearity. We find it useful to use a piece of light-blue paper as this shows the dimmed infrared beam well. If the laser has been tuned to the far part of the spectrum, you may have to use an IR viewer or viewer card to visualize the beam.

TESTING ALIGNMENT AND SYSTEM PERFORMANCE

On a regular basis and particularly subsequent to laser alignment, the performance of the multiphoton microscope should be tested. The prime indicator of proper alignment of an imaging system is its point-spread function, as measured by using a sample containing sub-resolution fluorescent beads. A test slide can be prepared by letting a drop of diluted beads dry onto a coverslip. The beads are then embedded in a drop of Sylgard elastomer (Dow Corning, USA) with a microscope slide placed on top. We usually use 0.2 µm beads from Molecular Probes (Eugene, OR). These are available in a range of colors suitable for 2-photon microscopy. It

[1] The Multiphoton Users Group e-mail network at ⟨mplsm-users@yahoogroups.com⟩, operated by Steve Potter at Georgia Tech, enrolled its 500th member in 2003.

[2] As is explained below, this can be achieved by over-closing the slit and/or reducing pump power, because mode-locking is not required. We typically use <20 mw @ 800 nm and <10 mW at 720 nm.

Mark B. Cannell, Angus McMorland, and Christian Soeller • Department of Physiology, FMHS, University of Auckland, New Zealand

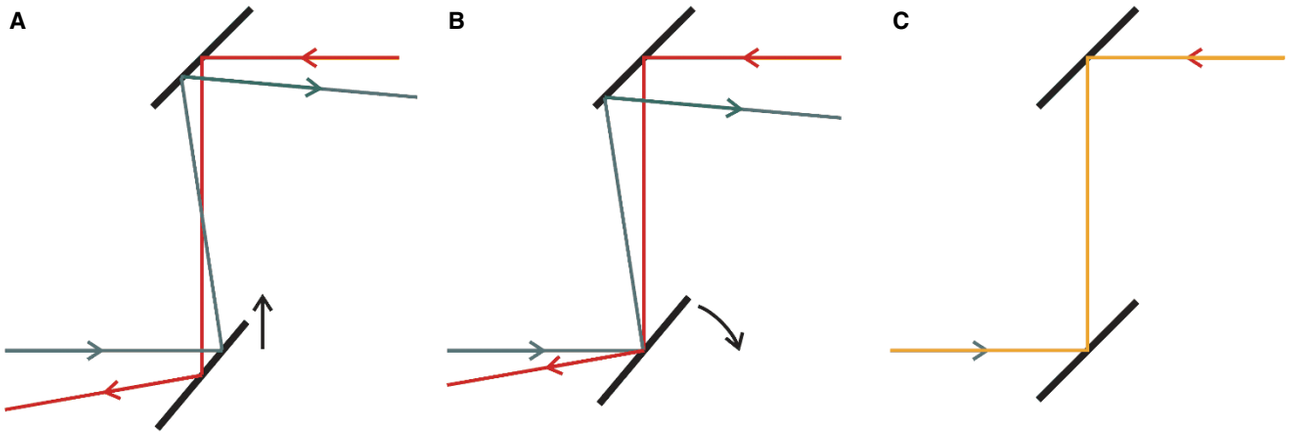


FIGURE A1.1. (A) 2D simplification of the beam alignment process using a conventional beam-steerer. A vertical translation of a tilted mirror is used to bring the two beams to a common point on a second, tiltable mirror. (B) Rotation of the second mirror at the point of the common spot makes the two beams co-linear. (C) The co-linear beams after alignment.

takes only about 30 minutes to prepare 10 slides in this way. Once the elastomer has set, these slides will last for months if kept in a dark drawer. As a result, they provide a good standard to check the microscope sensitivity and resolution provided you have recorded microscope and laser settings (including center wavelength, laser power and bandwidth/pulse length) with each reference image.

With proper alignment, the beads should blur approximately evenly as you focus above and below them. Asymmetric blurring above-and-below best focus indicates spherical aberration while motion of the centroid of intensity means that the objective aperture is filled asymmetrically. The spatial resolution (without a pinhole) should be similar to confocal performance, values between 0.2–0.4 µm in plane, full-width at half maximum (FWHM) and 0.5–0.8 µm out of plane (in the z direction) should be attainable when using a high-numerical-aperture (NA ~1.3) objective.

A very weak and noisy signal can have a number of causes. If there is no problem with the detectors or emission filters (most of which would also be apparent when operating the microscope with conventional [1-photon] laser excitation), check that the laser beam fills the objective rear aperture fully and evenly by rotating the objective turret to an empty position, placing a lens tissue over the opening and inspecting the pattern of illumination (using an IR viewer if necessary). The beam should be accurately centered in the empty socket and should form a uniform circle of light that will cover the rear aperture (~8–10 mm wide) of a typical objective lens. If the light intensity at the rear aperture is low (<10 mW) make sure that no IR-opaque optical items are obstructing the illumination path.[3] It is also possible that the beam is so badly misaligned that only scattered light is being observed. You can check for this by ensuring that adjustments of the alignment mirrors have the expected effects on the spot in the BFP.

If the microscope is a combined confocal/multiphoton system, the bead slide is also a useful tool to disclose alignment offsets between the 2-photon laser system and any other lasers. In particular you should check for any axial offsets (i.e., focus shifts), particularly if the system is to be used for 2-photon flash photolysis or combined confocal and multiphoton co-localization studies.

In our laboratory we perform a basic system test with a prepared bead sample on a daily basis. This check (usually conducted following system startup) is well worth the ~5 minutes it takes, especially if it helps avoid debugging signal problems later when a precious biological sample is on the stage.

LASER SETTINGS AND OPERATION

Historically, the mode-locked lasers used for 2-photon imaging could be quite temperamental and ensuring that proper laser operation was a large part of the challenge of running a multiphoton microscope. With the advent of fully computer-controlled turn-key laser systems, this has become less of an issue. In any case, as the most versatile source for 2-photon imaging is still the tunable Ti:S laser in the femtosecond configuration, we will focus on it here. Regardless of whether you are using a fully automated or a manually adjusted Ti:S system, it is important to monitor and optimize the laser output before imaging.

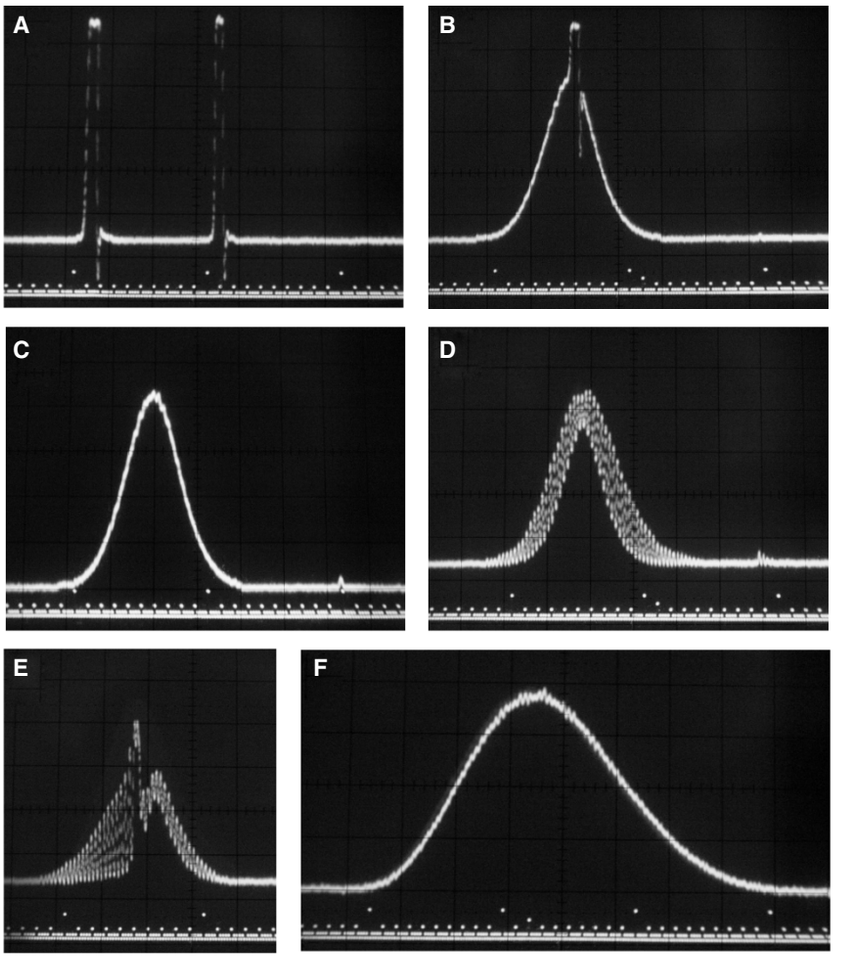
The choice of center wavelength is generally determined by the fluorochromes to be excited. As a general rule of thumb you should try to use the longest wavelength compatible with the dyes in your sample as this will help minimize photodamage and also reduce scattering of the excitation light. Data on excitation spectra is now available from many sources in the literature and, if in doubt, there are mailing lists where one can ask other researchers for advice (see http://groups.yahoo.com/group/mplsm-users/ and http://listserv.acsu.buffalo.edu/archives/confocal.html).

MONITORING LASER PERFORMANCE

During tuning and imaging, laser operation can be very conveniently monitored using a spectrum analyzer. We use a system made by Rees Instruments (currently available models include the Rees E200 series laser spectrum analyzers by Imaging and Sensing Technology Ltd., Alton, UK) to monitor a secondary beam containing only a small fraction of the total output power. During laser tuning, this device allows one to measure the center wavelength and, more importantly, the width of the spectrum. The spectral

[3] If little light is coming out of the objective, it may be the anti-reflection coatings that are at fault. Coatings used to reduce reflection losses in the visible may become mirrors in the near-IR. See the transmission tables in Chapter 7 and its Appendix.

width of the beam, as displayed by the analyzer, provides the feedback for optimizing the slit width and position to obtain mode-locked operation (with manually tuned laser systems). The start of mode-locked operation is indicated by the change of the spectral shape from one or a small number of sharply defined lines which indicate continuous wave (CW) operation, see Figure A1.2A, to an approximately Gaussian-shaped output spectrum which may have a spike (Fig. A1.2B) indicating CW breakthrough. Optimal closure of the slit leads to a smooth Gaussian-like spectrum (Fig. A1.2C) which, in this case, is ~5nm wide (FWHM). At 750 nm this spectral width implies a 120 fs pulse. Closing the slit further can lead to an oscillation of pulse amplitude (Q-switching), which is shown



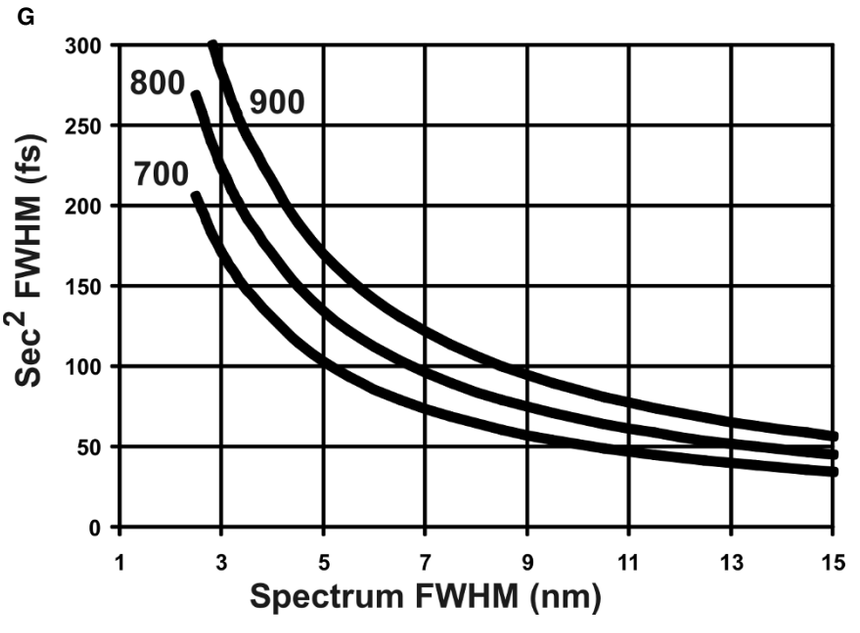


FIGURE A1.2. (A–F) show spectrum analyzer output during Ti : S tuning. The small gradations at the bottom indicate 1nm. (A) Before mode-locking, the spectrum consists of a few narrow spikes. (B) With mode-locking underway, the spectrum increases in width, but the spike indicates CW breakthrough. To cure this, the slit needs to be closed more. (C) Optimal operation, the slit has been closed just enough to stop CW but at the same time not so closed that Q-switching starts, a mode of behavior shown in (D,E). To stop Q switching, more prism must be inserted into the beam path (which will increase system bandwidth) and/or the slit needs to be opened (or even a reduction in pump power). (F) shows the shortest pulse that can be readily achieved with our Coherent MIRA 900F system. The FWHM of the spectrum is ~14 nm at a center wavelength of ~750 nm. (G) shows the relationship between the FWHM of the spectrum and the pulse width for a transform-limited sec^2 pulse, with center wavelength indicated next to each curve. In this case, a 14 nm bandwidth from our laser (F) implies a very short pulse width of 40 fs. Generally, we use longer pulses (~120fs e.g., C) than this in imaging experiments.

in the spectrum as oscillations (Figs. A1.2D, A1.2E) and should be removed by re-opening the slit or increasing the intra-cavity group velocity dispersion by moving the intra-cavity prism further in. By suitable adjustment of the slit and the intra-cavity group velocity dispersion, the pulse may be shortened and this will be reflected in an increase the width of the output spectrum (Fig. A1.2F). With our laser, a 14 nm FWHM bandwidth can be achieved corresponding to a ~40 fs pulse at 750 nm. During imaging, Q-switching manifests itself as a sudden increase in image noise due to aliasing between laser excitation and the pixel clock. A quick look at the spectrum should indicate if the laser needs tuning to remove this source of image noise.

Typically, pulses leaving a commercial Ti : S laser, as used for 2-photon microscopy, are ~100 fs long. Pulse length is an important variable that is most accurately determined with an optical autocorrelator. However, from a practical point of view, a spectrum analyzer is easier to use than an autocorrelator and gives sufficient information on laser performance. The length of the laser pulse is inversely proportional to the spectral FWHM during mode-locked operation. Figure A1.2G shows this relationship for various center wavelengths.

POWER LEVELS AND TROUBLE-SHOOTING

In our experience illumination power levels at the sample should be kept <20 mW in living cells to minimize the risk of cell damage, although that figure is dependent on the nature of the experiment, the 2-photon absorber, the objective NA, and sample scattering.

Problems with mode-locked lasers in 3D microscopic imaging most often arise from:

1. Pump laser noise (amplitude noise or beam-pointing instability).
2. Pump laser alignment.
3. Dirt on mirrors.
4. Poor alignment within the cavity.
5. Stray reflections from surfaces that reflect energy back into the cavity.
6. Poorly trained personnel changing the alignment between the pump and the prisms of the Ti : S cavity over time.
7. UFM (unidentified fingerprints on mirrors!).
8. Air currents that affect beam-pointing stability.
9. Loss of alignment of laser to microscope.
10. Poor matching of laser beam profile to microscope aperture.

To address problems 1–4, the manufacturer generally provides troubleshooting advice that should be consulted. Problem 5 can be avoided by using an optical isolator, i.e., a device which allows light to pass only in the forward direction but blocks back reflections. A simpler workaround (that has worked well in our hands) involves slightly tilting strongly reflecting surfaces (e.g., neutral density filters — see below) with respect to the optical axis. For laser safety you should provide an appropriate beam dump for any strong reflections off the optical axis. Problems 6 and 7 should be resolved by the system manager. Problem 8 can be reduced by surrounding all beams with plastic tubes. Problem 9 can be ascertained using a reference laser, especially a laser built into the microscope itself. Problem 10 arises from the laser beam being too small to fully fill the objective rear aperture (so a loss of resolution occurs) or too large, in which case there is a loss of intensity at the sample. In both cases, the problem can be fixed using laser beam expansion (or compression) with a telescope (Galilean beam expander). In our microscope we use ~4x expansion of the Ti : S laser beam as a reasonable compromise between filling the real aperture adequately and throughput. (We built a simple expander from a plano-convex and a plano-concave lens which were single-layer antireflection coated.) In addition, by focusing the beam expander carefully, it is possible to minimize the axial shift of focal plane between visible light and the IR.

CHOICE OF PULSE LENGTH

The dispersion of the pulse by the microscope optics is typically >2000 fs^2 at 800 nm. This suggests that the shortest pulse width that can be delivered to the sample would be >100 fs unless group velocity dispersion compensation is performed to "prechirp" the pulse (Soeller and Cannell, 1996). Shorter pulses increase the ratio of 3- to 2-photon excitation and, since 3-photon excitation at 800 nm would correspond to hard UV, such excitation is generally undesirable. We therefore suggest that for routine operation ~120 fs pulses are probably optimal. Perhaps paradoxically, in the absence of GVD compensation, a shorter pulse at the laser is translated to a much longer pulse at the sample. As it is hard to run a conventional Ti : S laser with pulses longer than ~150 fs, longer pulses at the sample may be produced by making very short pulses (e.g., 40 fs) at the laser. See Chapters 5 and 28 for further discussion on pulse broadening.

CONTROLLING LASER POWER

Being able to control laser power electronically is useful because it permits rapid suppression of the beam at the end of each scan line where the beam slows and stops before retracing its path. This slow movement subjects the parts of the specimen at either side of the raster to very high integrated excitation which is very damaging. Unfortunately, the acousto-optic modulators (AOM), which are commonly used for this purpose in visible light microscopes, are less suitable for 2-photon because heating and birefringent effects in the crystal reduce beam intensity stability. The square-law dependence of 2-photon excitation on input power amplifies this instability at the sample. Additionally, because the mode-locked laser beam has significant bandwidth (compared to a CW laser) the beam will be dispersed if it is diffracted in the AOM. As the rear aperture of the objective must be overfilled, this dispersion results in a loss of bandwidth and therefore a longer and misshapen pulse. This effect can be avoided if one uses the zero-order (i.e., undiffracted) beam of the AOM for microscopy and the first order beam is used simply to extract energy from it. However, as only about 75% of the beam can be diffracted out, this approach only reduces the beam to 25% of the input power.

A better alternative is to use a Pockels cell. While more expensive, these devices are much faster and more controllable than an AOM, but they also suffer from some problems:

1. The Pockels cell has a limited lifetime that is dependent on the time spent in the energized state.
2. Alignment is critical: the full power of the beam must pass cleanly through the free aperture and not touch the interior of the cell under any circumstance or damage will result.
3. High voltages are present.

It should be noted that, for ~120 fs pulses, dispersive broadening by the Pockels is generally small and should therefore be of no concern when it is used in a 2-photon imaging setup.

If rapid beam modulation is not needed, laser power can be controlled by neutral density filters or a polarizer. Such neutral

density filters need to be of the reflecting type as high powers destroy absorbing filters. The beam reflected from the filter needs to be absorbed by something for safety and we use a "beam dump" made of black anodized aluminum with a machined recess so it is hard to see the dumped beam. Since the output beam of the laser is polarized, beam intensity may be modulated by rotating a polarizer in front of it. Glass Glan-Thompson polarizers can be used but plastic polarizers are quite unsuitable for typical power levels as they melt (see also Attenuation of Laser beams in Chapter 5, *this volume.*)!

AM I SEEING TWO-PHOTON EXCITED FLUORESCENCE OR . . .

Sometimes it is unclear if a detected signal is due to multiphoton-excited fluorescence or if it is due to optical bleed-through of the (much more intense) near-IR excitation light. Such bleed-through can occur, for example, if one uses filters with an unknown response in the near-IR region. A simple test to distinguish between these possibilities can be made by taking a control image with the multiphoton laser source running in CW mode (at similar power). When using a mode-locked Ti : S laser with manually operated slit this can easily be achieved by over-closing the slit until mode-locking is lost and then reopening the slit with the starter mechanism disabled. If the signal in question disappears when using CW illumination, it must be due to some sort of multiphoton excitation (2- or 3-photon fluorescence, or second- or third-harmonic generation). However, this simple test does not replace the more complex illumination-power vs. signal-intensity measurements needed to fully characterize each of these high-order excitation processes.

STRAY LIGHT AND NON-DESCANNED DETECTION

One of the attractions of 2-photon microscopy resides in the improved penetration depth obtained when imaging in strongly scattering biological samples such as brain slices (see Soeller and Cannell, 1999). Central to this advantage is the need to collect emitted photons that are also scattered and so may not be focused by the microscope optics and are therefore lost at intermediate apertures. This problem can be overcome by using a photomultiplier tube that is mounted close to the sample (so that the emitted light does not pass through the scanning system) to create a "non-descanned detector." Such detectors are arranged so that any photons of the right color, regardless of where they originate, are directed onto the photocathode. As a result, non-descanned detection is also far more likely to pick up stray light from the microscope surroundings than conventional confocal optics. For example, in a normal laboratory, light from computer screens and equipment LEDs can cause a strong background signal even when the room lights are turned off. To shield your setup from this stray light, you may need to fabricate suitable shields around the sample from black material. Alternatively, you may shield the whole microscope from the surroundings by enclosing it in a completely light tight box. This can be conveniently combined with electrical shielding by providing a Faraday cage around 3 sides and the top of the instrument and fully closing it during imaging by drawing a black curtain or blind across the fourth side. For safety reasons, this cage and any blinds or curtain should be made from fire-proof materials.

LASER POWER ADJUSTMENT FOR IMAGING AT DEPTH

Although 2-photon excitation penetrates deeper into scattering samples (such as brain), the loss of peak excitation power at the focus caused by scattering and spherical aberration still leads to a loss of signal at depth. The solution to this problem is to alter the illumination power as a function of depth and this is where the intensity modulation provided by the Pockels cell may be used to advantage. There are alternative ways to achieve changes in illumination power but all assume that the maximum power available from the 2-photon laser is higher than is needed for normal operation. Thus, a wheel of reflective neutral density (ND) filters may be placed in the beam path, providing intensity control to quantized levels appropriate for different imaging depths. A second option is to use a continuously variable reflective neutral density filter, which allows more precise control over laser power, but requires either manual rotation during imaging or a motorized filter wheel. We suggest that the ideal solution is to automatically attenuate the laser beam. using a Pockels cell supplied with a varying drive voltage controlled by the focus position.

In our experience, the laser power needs to increase (roughly) exponentially with depth (e.g., see Fig. A1.4 in Soeller and Cannell, 1999) but the exponential factor is highly dependent on the sample. Thus a control experiment may be needed where a similar sample is labeled with fluorescent beads (~2 µm in diameter). For brain slices, or other tissues which can be perfused, this can be achieved by injecting the beads into a blood vessel before slicing. By imaging the beads at different depths, the depth dependence of the excitation may be determined and used in subsequent experiments. (Using beads will give more reliable results than simply staining the entire specimen with a dye as this avoids problems arising from non-uniform staining.) It is important to note that not all the signal loss is due to reduced excitation as emitted light is also lost by scattering and adsorption. Thus, even if complete compensation of signal loss with depth can be achieved by raising excitation power, it is better to err on the side of caution as delivering too much power into the preparation at any depth may lead to other concerns — for example, heating and other higher-order effects (see Chapter 38, *this volume*). If 100 mW were delivered and (eventually) absorbed within $10 mm^3$ of tissue, the *average* rate of rise of temperature would be 2.5°C/s. Although this power is close to the maximum that may be achieved by typical 2-photon microscopes, it is clearly in the range where heating effects could become a serious problem.

SIMULTANEOUS IMAGING OF MULTIPLE LABELS

Another advantage of 2-photon excitation is that the 2-photon excitation spectra of fluorochromes are wider than their 1-photon counterparts. Multiple labels may therefore be imaged simultaneously by using a single excitation wavelength and multiple detectors with appropriate optics to isolate each different emitted wavelength. This approach has several benefits: (1) Removal of offset problems caused by non-confocality of different lasers; (2) reduction in imaging time (which may be important for imaging of live-cell processes); (3) reduction in the total amount of laser exposure to the tissue and (4) avoidance of chromatic aberrations. Care must be taken to ensure that bleed-through from one channel to another

is minimized by the use of the optimal beam-splitters (see also Chapter 3, *this volume*). If some bleed-through is unavoidable then an accurate measurement of the amount of bleed-through can be made by imaging, in all channels, control slides that contain the individual fluorochromes. From these measurements, contributions from bleed-through from one channel to another can be estimated and removed by subtraction during post-imaging analysis (so-called "spectral unmixing").

MINIMIZE EXPOSURE DURING ORIENTATION AND PARAMETER SETTING

In most applications, imaging parameters need to be established by trial and observation prior to the commencement of image acquisition. Common examples are scanning across tissue looking for "that cover image" and then establishing the upper and lower limits of a volume of interest. While the use of 2-photon excitation prevents photobleaching above and below the focal plane, in-plane photobleaching can be severe and care must be taken to avoid over-exposure of samples to illumination light during these adjustment procedures.

The key is to think before imaging. For example, if the sample needs to be located in focus, is full power really necessary or will the detection of just a few photons be sufficient? It follows that during setup, the detector gain should always be set high and laser power as low as possible. Single scans should be used in preference to continuous scanning. Can the sample be moved to an unexposed region once the acquisition parameters are set? Once the correct settings have been determined, then laser power can be increased for actual imaging and focal-plane bleaching indicates that the maximum amount of information available has been extracted from the dye in the sample.

ULTRAVIOLET-EXCITED FLUOROCHROMES

The use of ultraviolet (UV) excited dyes in 1-photon imaging is restricted by the opacity of conventional optical components at UV wavelengths as well as by chromatic aberrations and by the cost and size of UV lasers. 2-photon excitation of UV dyes does not suffer from these problems because the excitation wavelengths are near-infrared, in a range that is compatible with normal optics. The ability to use UV dyes allows more labels, and colors, to be used in multiple-labeling experiments. In addition, combining a UV-excited probe emitting in the blue part of the spectrum allows greater spectral separation from a yellow-red label. UV dyes, in general, may be excited by 2-photons at wavelengths ≤750 nm. For example, the AlexaFluor 350 fluorochromes (Molecular Probes, Eugene, OR) come in a range of forms. The near-UV-excited nucleic-acid probes DAPI and Hoechst are often so well excited using 2-photon illumination that it is necessary to use very low concentrations to prevent bleed-through into other channels.

ACKNOWLEDGEMENTS

We would like to thank Tim Murphy (University of British Columbia, Vancouver, CA) for helpful comments on the manuscript.

REFERENCES

Potter, S.M., 2005, Two-photon microscopy for 4D imaging of living neurons. In: *Imaging in Neuroscience and Development. A Laboratory Manual*, (R. Yuste, and A. Konnerth, eds.), pp. 59–70, Cold Spring Harbor Laboratory Press.

Soeller, C., and Cannell, M.B., 1996, Construction of a two-photon microscope and optimisation of illumination pulse width. *Pflugers. Archiv.* 432: 555–561.

Soeller, C., and Cannell, M.B., 1999, Two-photon microscopy: Imaging in scattering samples and three-dimensionally resolved flash photolysis. *Microsc. Res. Tech.* 47:182–195.

Taal, P.S., Nishimura, N., Yoder, E.J., White, A., Doluick, E., and Kleinfeld, D., 2002, Principles, design and construction of a two-photon scanning microscope for *in vitro* and *in vivo* studies, In: *Method for* in vivo *Optical Imaging*, (R. Frostig, ed), CRC Press, pp. 113–171.

Appendix 2

Light Paths of the Current Commercial Confocal Light Microscopes Used in Biology

James B. Pawley

INTRODUCTION

Since biologists became aware of the confocal microscope in the late 1980s, numerous optical designs have been introduced by manufacturers to try to meet the often-contradictory requirements of the biological microscopist. Although many of these designs are discussed at greater length in other chapters of the Handbook, it was thought that it might be both useful to the reader, and fairer to those designs not discussed elsewhere, to provide the reader with a concise compilation of all the designs now available.

To that end I requested optical diagrams and tabular information from all of the major suppliers of the instruments used by biologists for 3D microscopy[1] and the items that they provided make up the bulk of this Appendix. Often manufacturers were hesitant to provide specific information about details such as PMTs or scanning speeds etc., because they realized that there was a good chance that such data would go out of date with their next product announcement. However, I tried to apply the same criteria to all the contributors and this is as good a place as any to thank the manufacturers for their splendid cooperation.

To assist the reader, some of the optical information considered most relevant to the optical performance of these instruments has been collected in Table A2.1. Although such a table cannot contain all of the relevant information about such complex instruments, the headings have been chosen to reflect those specifications indicated to be of prime importance in the other chapters of the Handbook. Abbreviations are explained in the footnote.

Of course, the manufacturers are correct about this information going out of date. Fortunately the WWW is now there to bring you up to date. Even when the models are all different, we hope that the you find the column headings in the table of optical parameters useful as the basis of questions you might ask about future models.

There has been no effort to compare the computer operating systems used to control these instruments. I wish to emphasize that this is not because I think such details unimportant, but rather because software systems tend to change with great speed and, in addition, operating systems are probably best assessed in person.

[1] We have neglected to include any information on the systems for widefield/deconvolution only because the optical paths of such systems are fairly straightforward, and not in need of explanation.

James B. Pawley • University of Wisconsin, Madison, Wisconsin, 53706

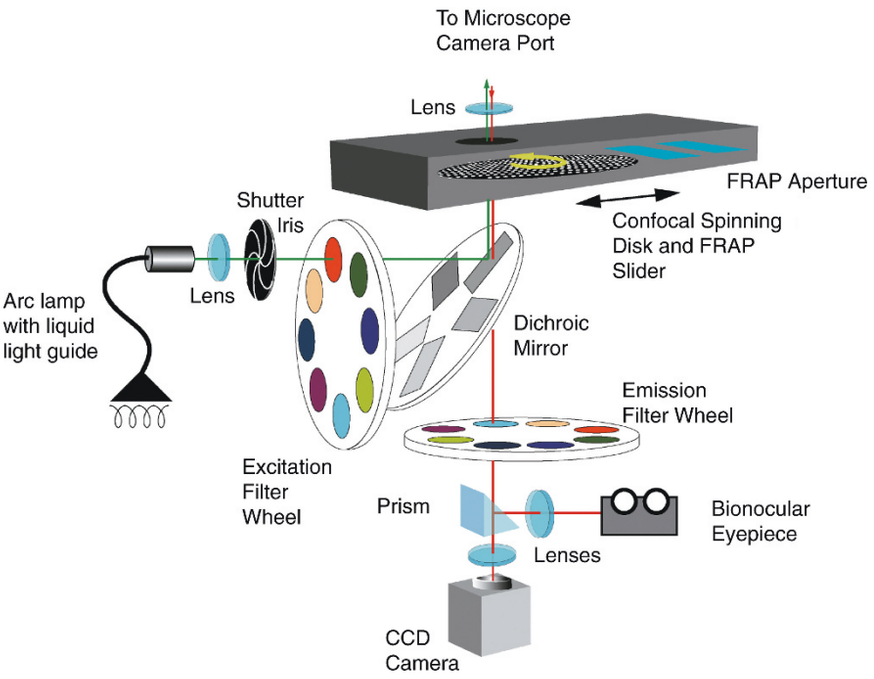


FIGURE A2.1. Schematic of the BD-CARV II light path. The variable intensity light from a Hg/metal halide light source passes through an excitation filter before being defleted by a dichroic mirror towards the sample. The excitation light passes through a Nipkow spinning-disk containing multiple sets of spirally-arranged pinholes placed in the intermediate-image plane of the objective lens. The column of excitation light is projected through 1000 pinholes to simultaneously scan the entire field once every millisecond, thereby creating a full image of the focal plane in real-time. The emitted light passes through the dichroic mirror and the emission filter before either entering the CCD camera or the binocular eye-piece. The pinhole disk can be moved in and out of the light path to produce a confocal or a widefield fluorescence image. A variable slit at the image plane can be used to selectively illuminate an area of the sample allowing Fluorescence Recovery After Photobleaching (FRAP) to be performed. All movable parts including the filter wheels, spinning-disk shutters, and mirrors are automated and are controlled via touchpad or third-party software. Figure kindly provided by BD-Biosciences, (Rockville, MS).

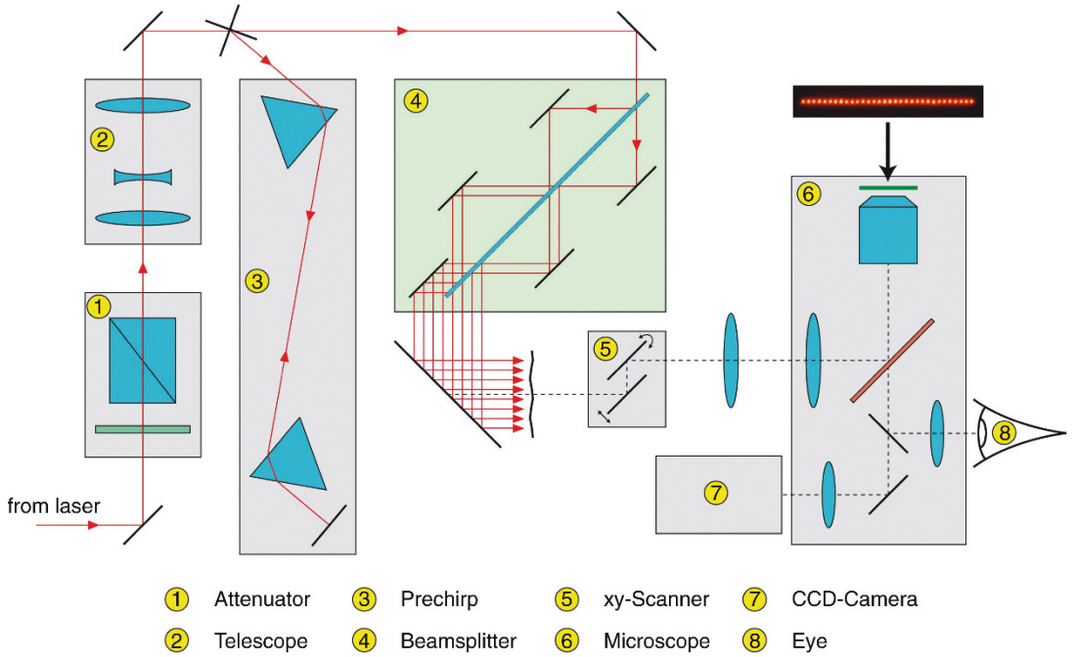


FIGURE A2.2. Schematic of the LaVision-BioTec TriM-Scope light path. Multifocal multiphoton microscopy using a beamsplitter built with flat optics**.** Light from a fs, near-IR, pulsed laser first passes a polarizing attenuator and a beam-expander before entering a pre-chirp compensator. It is then formed into as many as 64 beams of equal intensity and spacing by being reflected from an array of sliding, planar, optical elements. The linear array of beams is then deflected by 2, closely-spaced galvanometer mirrors and fed into the microscope by being reflected off a high-pass beam-splitter. Two-photon-excited fluorescence from any dye located at the focus plane of the objective passes through the short-pass dichroic, and barrier filters to a CCD camera or other photodetector.[2] Because of the large number of parallel beams and the high-QE of the CCD camera, it is possible to obtain useful, optical-section images at up to 3.5 k frames/second and, because the system relies on 2-photon excitation, bleaching is restricted to the focal plane. For more discussion see Chapter 29, *this volume*.

[2] T. Nielsen, M. Fricke, D. Hellweg, P. Andresen, (2001), High efficiency beam splitter for multifocal multiphoton microscopy, *J. Microsc.*, **201**:368–376.

Table A2.1. Optical Parameters of Current Commercial Confocal Microscopes

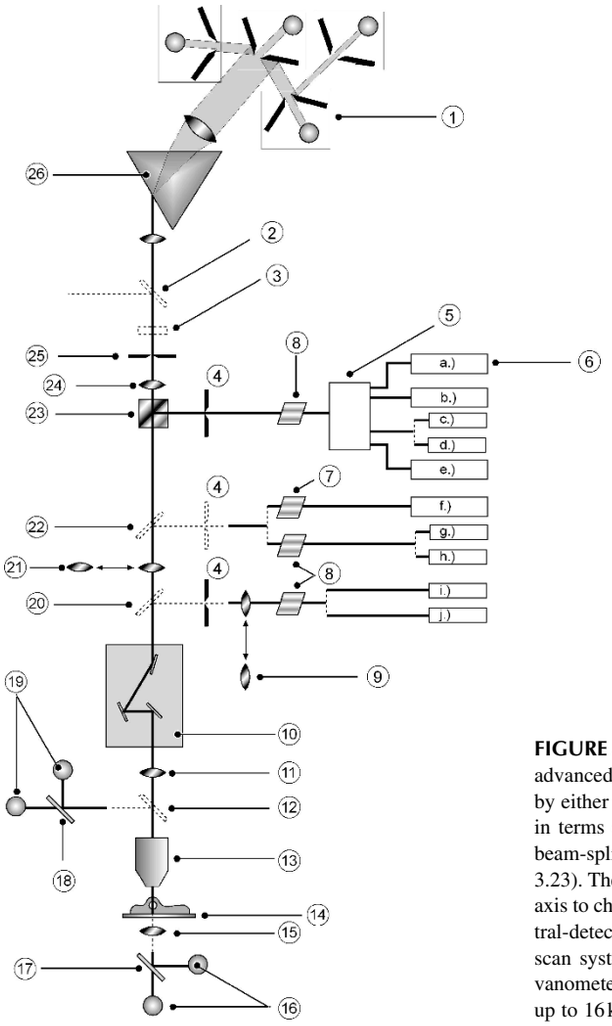
Company	Model	Lasers/Arc	Retrace protect/Laser atten	Fiber optics	Pre-optics	Beam expander	Scanner	Fastest line scan, Hz	Pixel times	Scanned field, diam. int im. plane	Largest Raster Pixel
BD-Biosciences	CARV II	X-Cite 120 Hg/halide arc, 8-place filter wheel	NA/intensity controlled by aperture	Liquid-filled light guide	NA	NA	Single-sided Petran disk	1 k fps 5 k rpm	~1 µs	21 mm	CCD
Lavision-Biotech	TriMScope[2]	Ti-sapph 750–100 nm, 100 fs pulse	NA/ Attenuator 0.1–100%	Laser is coupled directly	NA	Yes	1–64 beams scanned by 2 galvos	3.5 k fps	> 500 ns	20 mm, adapted to CCD used	CCD
Leica	TCS SP2 AOBS	Many, 351–633 nm	Yes/3 AOTFs	SM-PP	Laser-merge	Adjustable	Rotatable k-scan	1.4 k or 2.8 k in bi-direct	>500 ns	22 mm	4096 × 4096
	MP RS	Ti-Sapph	Yes, EOM	SM-PP	Laser-merge	Adjustable	Rotatable k-scan	4 k, or 8 k in bi-direct	>500 ns	22 mm	4096 × 4096
Nikon	C1-plus	Up to 3, 408–638 nm	AOM (opt)	SM-PP	Laser-merge	Fixed	2 close galvos	500, 1k in bi-direct	>1.68us @512 × 512	17 mm	2048 × 2048
	C1si	Up to 3, 408–638 nm	AOM	SM-PP laser input fiber. MM emission fiber	Laser-merge	Fixed	2 close galvos	500, 1k in bi-direct	From 4.08us at 512 × 512 in spectral mode	17 mm w/scan rotation	Up to 512 × 512 in spectral mode
Olympus	FV 300	Many, 405–633 nm IR port	Yes, AOTF	SM-PP	Laser-merge	Fixed	2 close galvos	1 k or 2 k bi-direct	>2 µs	20 mm	2048 × 2048
	FV 1000	Many, active stabilizer, 351–633 nm, IR port	Yes, AOTF	SM-PP	Laser-merge	Fixed	2 pair of close galvos, separate image/bleach scanners, circular bleach	2 k or 4 k bi-direct	>2 µs	18 mm	4096 × 4096
	DSU	Hg arc	NA/intensity controlled by aperture	NA	NA	NA	Interchangeable single-sided slit-pattern disk, 3 k rpm	3 k rpm, 15 fps	>1 µs	18 mm	CCD
Visitech	VT-infinity	Many, 405–647 njm	Yes, AOTF	SM-PP	Laser-merge (opt)	NA	Single galvo scans an array of point sources	2 kHz	2 µs	17	CCD
	VT-Eye	Many, 351–647 nm	Yes, AOTF	SM-PP	Laser-merge (opt)	Fixed	1 galvo, 1 AOD	50 kHz	20–125 ns		1024 × 1024
Yokogawa[5]	CSU 10	2 or 3 lines[6]	NA/AOTF	SM 3.5 µm core	Laser-merge	Fixed	Double Petran Disk w/micro-lenses	1800 rpm, 360 fps	~1 µs	13 × 9.5 mm	CCD
	CSU 22	3 or 4 laser lines	NA/AOTF	SM 3.5 µm core	Laser-merge	Fixed	Double Petran Disk w/micro-lenses	Variable, to 5 k rpm, 1 k fps	~1 µs	13 × 9.5 mm	CCD
Zeiss	LSM510META	Many, 351–633 nm (Ti : Sapph)	Yes, AOTF 0.05–100% (AOM)	SM-PP	Laser-merge	Adjustable	2 close galvos	1.3 k or 2.6 k in bi-direct	640 ns–2.3 ms	18 mm	2048 × 2048
	LSM 5 Pascal	Many, 405–633 nm	No/ Mechanical attenuator 0.05–100%	SM-PP	Laser-merge	Adjustable	2 close galvos	1.3 k or 2.6 k in bi-direct	640 ns–2.3 ms	18 mm	2048 × 2048
	LSM5-LIVE	Many, 405–635 nm	Yes, AOTF 0.05–100%	SM-PP	Laser-merge	Adjustable Cylindrical	1 galvo line-scan	(>60 k) 120 fps, 512 × 512, 1010 fps, 512 × 50	16 µs–20 ms	18 mm	1024 × 1024

[1] Record transmitted light through disk.
[2] As the TriMScope is actually a multi-focus multiphoton fluorescence illuminator with widefield detection onto a CCD, its performance depends a great deal on the performance of this device.
[3] These numbers assume that the tube mag is 1×.

Table A2.1. (*Continued*)

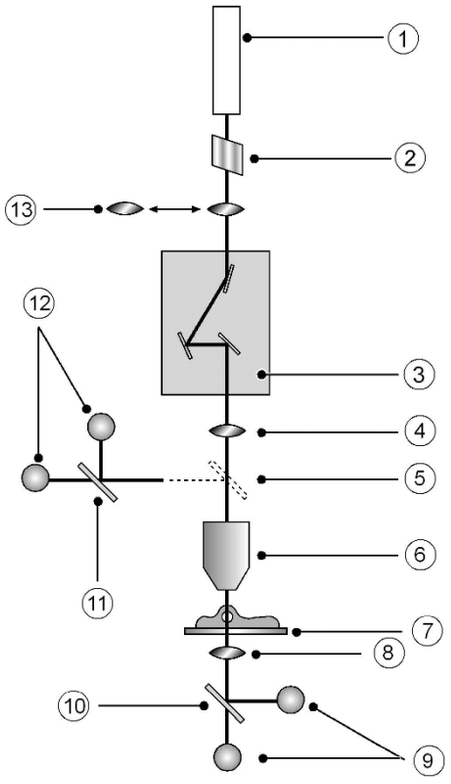
Zoom range	Tube mag	Beam dump	Beam-splitter	Pinhole alignment	Pinhole range	Spectral selection	Photodetector	Channels	Reflected/ transmitted	Digitizer	*z*-motion
NA	1.1×	NA	5-place dichroic wheel	Self-aligning	Fixed 70 µm, 180 µ spacing	8-place filter wheel	CCD or EM-CCD	2-camera port	No/yes[1]	CCD	Piezo ±100 nm (opt)
ROI for CCD mode	1×	NA	Short-pass dichroic	NA (multiphoton excited only)		8-place filter wheel, spectrometer (opt)	CCD or EM-CCD, 1–32 PMT array	3-camera port	Yes/no	CCD, (opt ion, PMT, 12-bit)	Stepper motor, (peizo opt)
32 : 1		Yes	Acousto-Optic	Preset	Common pinhole, adjust 20–800 µm	Prism, motorized mirrors	4 PMT, cooling option, APD option	8	Yes/yes	12-bit	Galvo, ±40 nm
32 : 1		Yes	Acousto-optic	Fixed	Common pinhole, adjust 20–800 µm	Prism, motorized mirrors	4 PMT, cooling option, +2 non-descanned	8	Yes/yes	12-bit	Galvo, ±40 nm
infinite	3.8	Yes	Dichroic, changes with cube	Fixed w/focusable, alignable pinhole lens	Common pinhole, 30, 60, 100, 150 µm[3]	Replaceable filter cubes	3 side-window fiber-coupled PMTs	4	Yes/yes	12-bit	Stepper, ±50 nm
infinite			Dichroic, changes with cube	Fixed w/focusable, alignable pinhole lens	Common pinhole, 30, 60, 100, 150 µm[4]	3 diffraction gratings for 2.5 nm, 5 nm, and 10 nm channel width	32 element multianode PMT	32 acquired simultaneously	Yes/yes	12-bit	Stepper, 50 nm increments
10 : 1 (infinity)	3.42×	Yes	Dichroic, cubes, 2 positions	Common pinhole, alignable	5 sizes	Dichroic filter cube	3 PMTs, 2 fluor, 1 trans	3, 2 fl, 1 trans	Yes/yes	12-bit	Stepper, ±10 nm
50 : 1 (infinity)	3.82×	Yes	Dichroic wheel, 6 positions	Common pinhole, alignable	adjust 50–800 or 50–300 on spectral	2 diff-grating channels, motorized slits	5 PMTs, 2 spectral, 1 trans, Photon counting mode	5, 4 fl, 1 trans	Yes/yes	12-bit	Stepper, ±10 nm
NA	1×	No	Filter cube	Self-aligning	Vert & horiz slits, 5 sizes	Dichroic filter cube	CCD or EM-CCD	1	No/yes	CCD	Stepper, ±10 nm
NA		No	Dichroic, 4 positions	preset, rect. array adjustable	~1 k fixed, 50 µm	Dichroics/ filters	CCD	CCD	Yes/no	CCD	Piezo, ±100 nm
50 : 1		No	Dichroic, 6 positions	preset/ adjustable	5 slits, 10–100 µm	Dichroics/ filters	4 hi-QE PMTs	4	Yes/yes	10 bits	Piezo, ±100 nm
NA	1×	NA	1 dichroic, exchangeable by user	Self-aligning	50 µm, 20 k on disk, ~1 k /FOV	Dichroics/ Filters, 3 emisson, 3 barrier	CCD or EM-CCD	2-camera port	No/no*	CCD	
NA	1×	NA	Dichroic, 3 positions	Self-aligning	50 µm, 20 k on disk, ~1 k /FOV	Dichroics/ Filters, 3 emisson, 3 barrier	CCD or EM-CCD	2-camera port	No/no*	CCD	
0.7–40×	0.84×	Yes	Dichroic, 4 positions	4 *x*,*y*,(*z*), diameter adjustable	3, 200 steps, 0.1–13 Airy Units 10–1 k µm	3 dichroics, 6 positions, + spectral detector, 10 nm /channel	3/4 filtered PMTs;&/or diff. Grating w/32 µPMTs array,[7]	8	Yes/yes	8–12-bit	Microscope 10 nm, Piezo, ±5 nm
0.7–40×	0.84×	Yes	Dichroic, 2 positions	2 *x*,*y*, diameter adjustable	1, 200 steps, 0.1–13 Airy Units 10–1 k µm	2 dichroics, 6 positions	2 filtered PMTs, trans PMT	4	No/yes	8–12-bit	Microscope 10 nm, Piezo, ±5 nm
0.5–2×	1.18×	Yes	Achrogate, line-mirror on clear blank	2 adjustable	17 slits, 0.5–10 Airy units	detector dichroic, 12 positions, 8 position barriers	512 × 1 linear CCD	2	No/no	8–12-bit	Microscope 10 nm, Piezo, ±5 nm

[4] These numbers assume that the tube mag is 1×.
[5] Yokogawa scanners are manufactured by Yokogawa Electric (Tokyo, Japan), but retailed by a number of companies including, Andor Technologies (Belfast, UK), Solamere Technology (Salt Lake City, UT), PerkinElmer (Downer Grove, Il), Visitech (Sunderland, UK).
[6] It is possible to use 4 lasers with a quad, dichroic beamsplitter.
[7] Transmission PMT and 4-channel non-descanned PMT detector also available.



1. Detection channels with stepless tunable bandpass and PMT
2. Beam splitter or mirror for auxiliary emission outlet (optional)
3. Emission filter and polarization filter (rotatable) (optional)
4. Excitation pinholes (excpt. IR)
5. Merge module. Combination of up to 4 visible lasers
6. a) Multiline Ar-Laser (457 – 476 – 488 - 496 – 514) b) HeNe Laser 543
   c) HeNe Laser 594 d) Kr Laser 568
   e) HeNe Laser 633 f) IR Laser TiS for Multiphoton excitation
   g) HeCd Laser 442 h) Solid state Laser 430
   i) Ar Laser 351 – 364 j) Diode Laser 405
7. EOM for intensity control of IR Laser
8. AOTF for intensity control on VIS and UV Lasers
9. Variable adaptation optics for UV / 405nm illumination
10. K-Scanning module for optically correct scanning method and field rotation
11. Scan lens
12. Beam splitter for non-descanned reflected light mode (optional)
13. Objective optics
14. Sample
15. Condensor optics
16. Detectors for non-descanned transmitted light (optional)
17. Secondary beam splitter for NDD transmitted light (optional)
18. Secondary beam splitter for NDD reflected light (optional)
19. Detectors for non-descanned reflected light (optional)
20. Beam splitter for UV illumination (optional)
21. Variable beam expander optics
22. Beam splitter for IR or violet illumination (optional)
23. Acousto Optical Beam Splitter (AOBS™)
24. Pinhole optics
25. Detection pinhole
26. Spectral detector prism

FIGURE A2.3. Schematic diagram of Leica TCS SP2 AOBS. The Leica TCS SP2 AOBS is an advanced confocal microscope in which all filtering and beam-splitting functions are performed by either liquid-crystal or acousto-optical components. This makes the system extremely flexible in terms of being able to add new lasers or adapt to new emission bands. The acousto-optical beam-splitter (AOBS) is essentially transparent except at exactly the laser wavelengths (see Fig. 3.23). The K-scan galvanometer mirror arrangement is capable of being rotated around the optical axis to change scan directions. There is one adjustable pinhole for all 4 prism/moving-mirror spectral-detection channels. Leica also makes the TCS SP5, which is similar but employes a tandem scan system which permits one to switch between a scanner employing a normal, analog galvanometer and one employing resonant galvanometer for high-speed, bi-directional scanning at up to 16k lines/s.



1. TiS Laser (pulsed IR)
2. EOM for intensity control of IR Laser
3. K-Scanning Module for optically correct scanning method and field rotation
4. Scan optics
5. Beam splitter for non-descanned reflected light mode (optional)
6. Objective lens
7. Sample
8. Condensor optics
9. Detectors for non-descanned transmitted light
10. Secondary beam splitter for NDD transmitted light
11. Secondary beam splitter for NDD reflected light (optional)
12. Detectors for non-descanned reflected light (optional)
13. Variable Beam expander optics

FIGURE A2.4. Schematic of the Leica MP RS Multiphoton Fluorescence Microscope. The Leica MP RS is a single-beam scanning fluorescence microscope that uses a ps near-IR laser light source to produce optical-section images of suitable specimens. It is designed for viewing living cells and incorporates a variety of non-descanned detectors to record both transmitted and backscattered fluorescence signal. This instrument uses a fs-pulsed, near-IR laser multiphoton excitation and a high speed galvanometer to provide fast imaging. Figures kindly provided by Leica Inc. (Heidelberg, Germany).

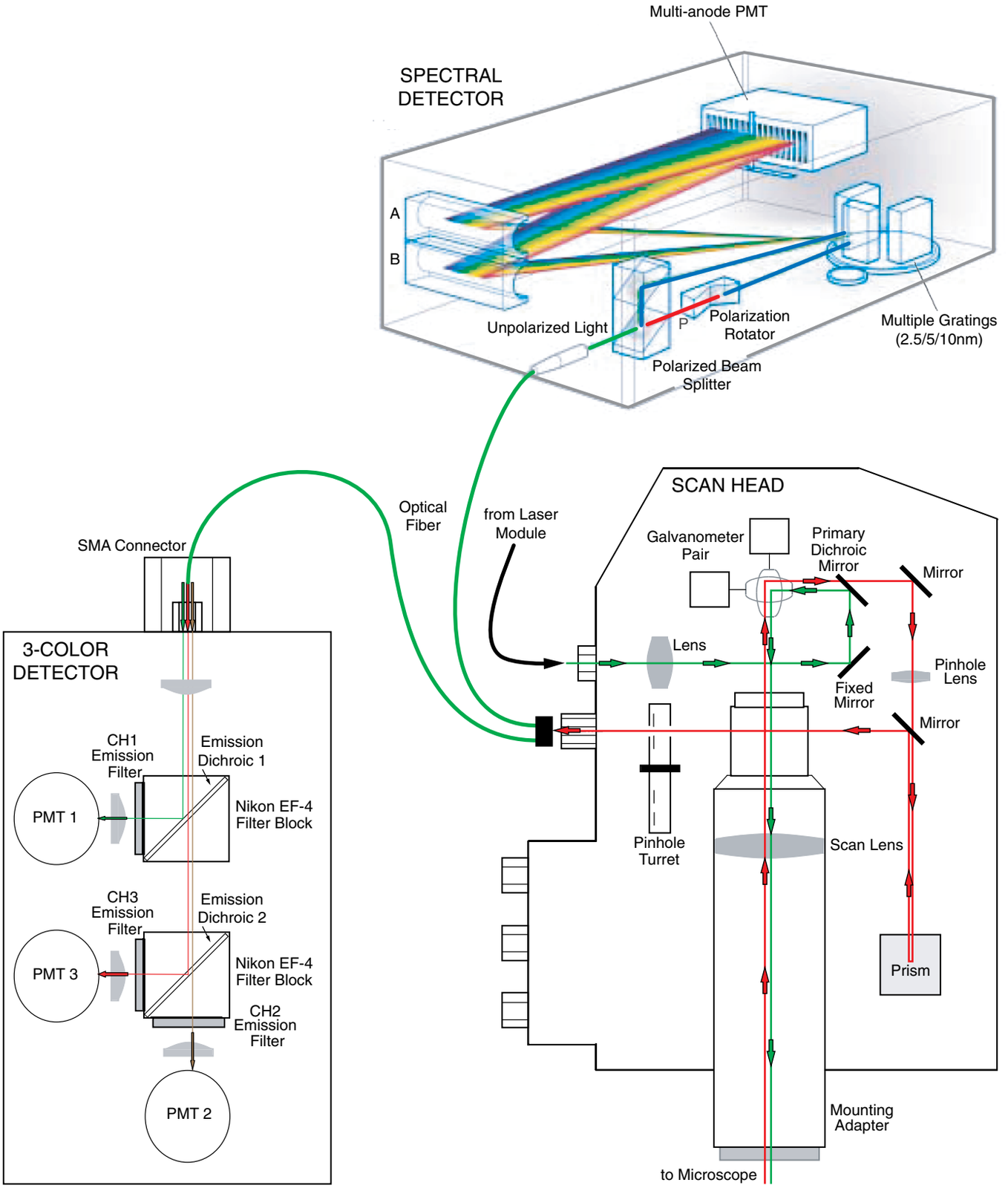


FIGURE A2.5. Schematic of the Nikon C1si light path. The C1-Plus is a 3-channel fluorescence plus transmission, single-beam, galvanometer-scanned, confocal microscope. Because both the lasers and the PMTs are located externally and coupled through fibers, the C1 scan head is extremely compact and is very easy to move from one microscope to another. The standard unit includes laser module, in which a wide variety of gas and solid-state lasers can be installed. a scan-head and a DU-3 three-PMT detector module containing the collimating and focusing lenses, and photomultiplier tubes. The "si" version includes an additional sophisticated spectral detector that is also coupled to the scan head through a multi-mode fiber. The detector itself incorporates a Diffraction Efficiency Enhancement System (DEES) in which a polarized beam splitter separates the unpolarized signal beam into two parts (red and blue lines). One part passes through a prism polarization rotator so that all the light strikes the diffraction grating with the optimal (s-plane) polarization to be diffracted with maximum efficiency by one of 3 gratings (2.5, 5 and 10 nm/channel). Both ray bundles are then focused onto a 32 channel micro PMT by a pair of reflecting lenses (A and B). Simultaneous readout is possible from all channels. The digitization system uses 2 sample-and-hold circuits to optimize signal integration. Figures kindly provided by Nikon Inc. (Tokyo, Japan).

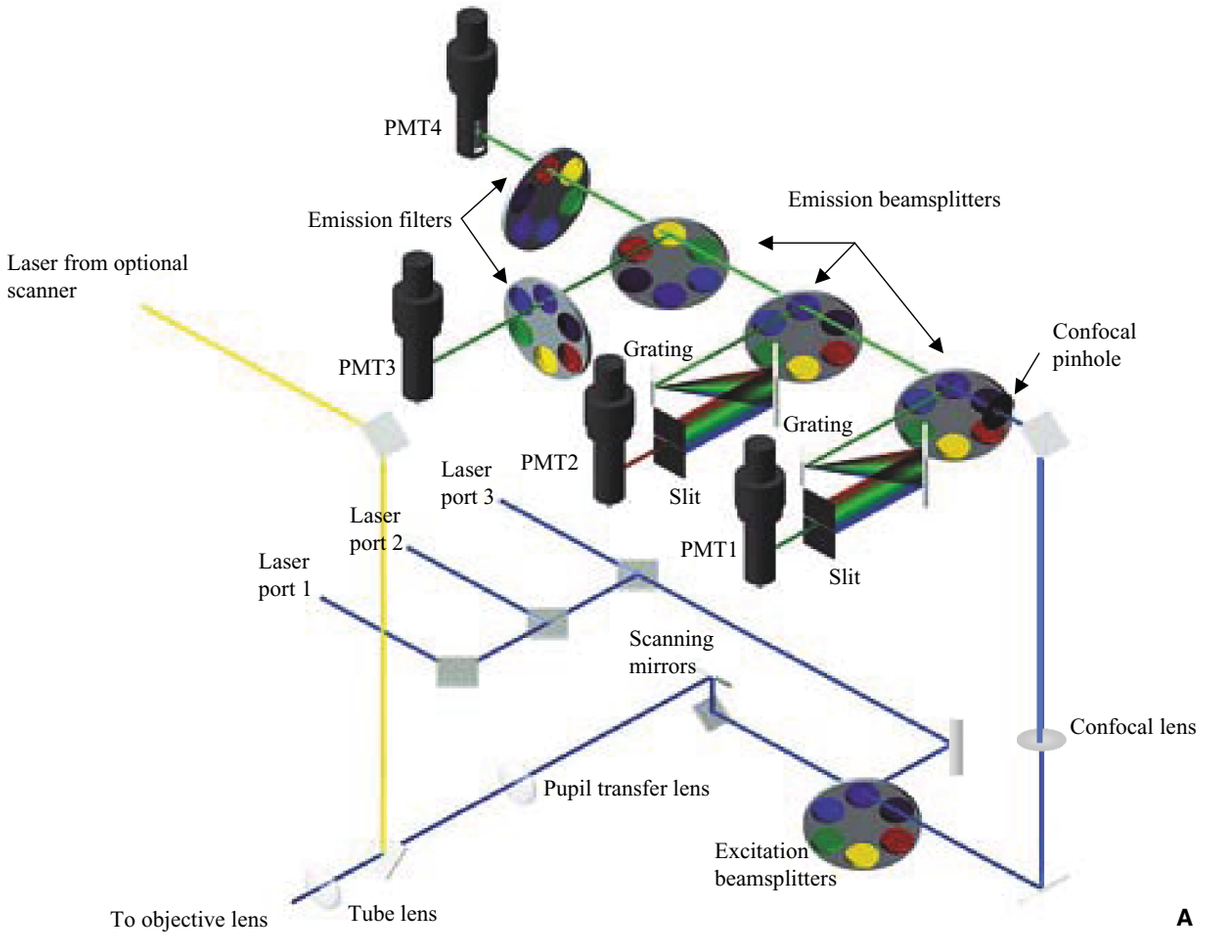
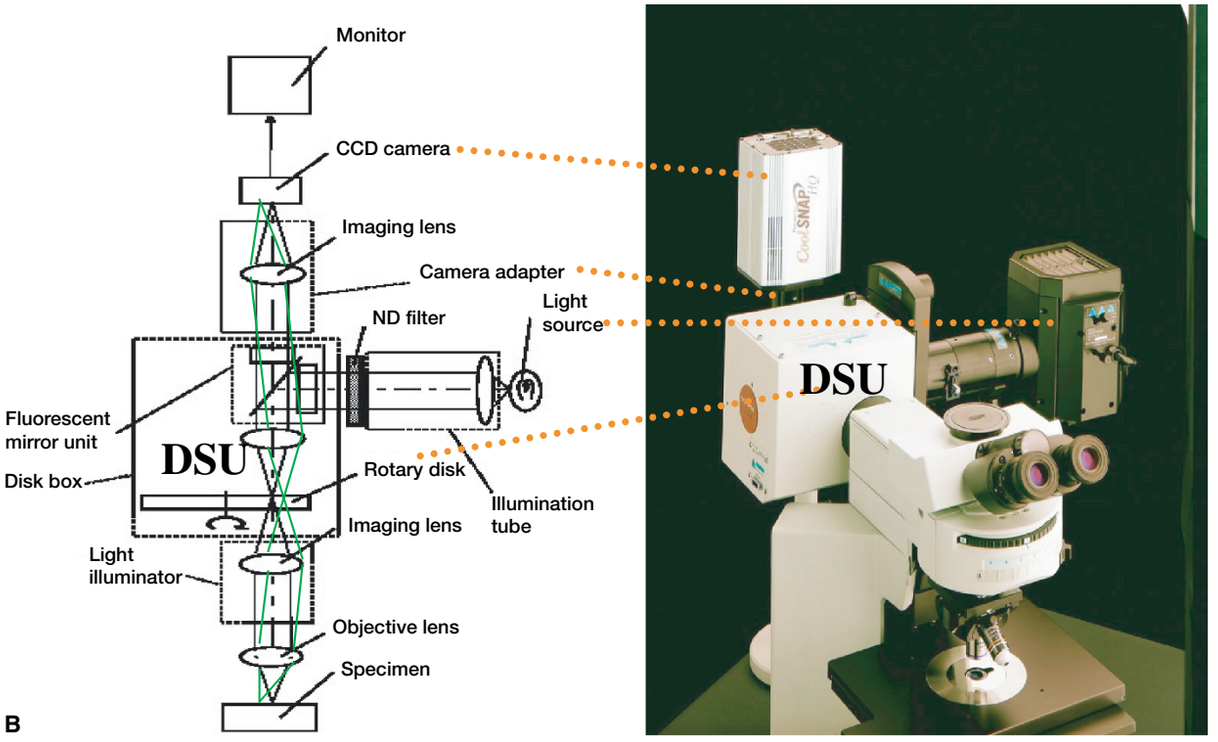


FIGURE A2.6. (A) Schematic of the Olympus Fluoview 1000. The Fluoview 1000 is the most recent single-beam laser-scanning confocal fluorescence microscope introduced by Olympus. It offers 4 separate fluorescence detection channels, two of which incorporate diffraction gratings and adjustable slits to tune the passband. Besides the normal scanning mirrors there is a second independent SIM-scanning arrangement (not shown in the figure) to control lasers used for photo-uncaging or for intentionally bleaching the specimen. To keep the signal up when the light dose to the specimen must be kept low, this new scanner not only incorporates dichroic elements employing "hard' coatings to ensure the highest transmission, it also offers a photon-counting option to reduce PMT multiplicative noise. Figures kindly provided by Olympus Corp. (Tokyo, Japan).



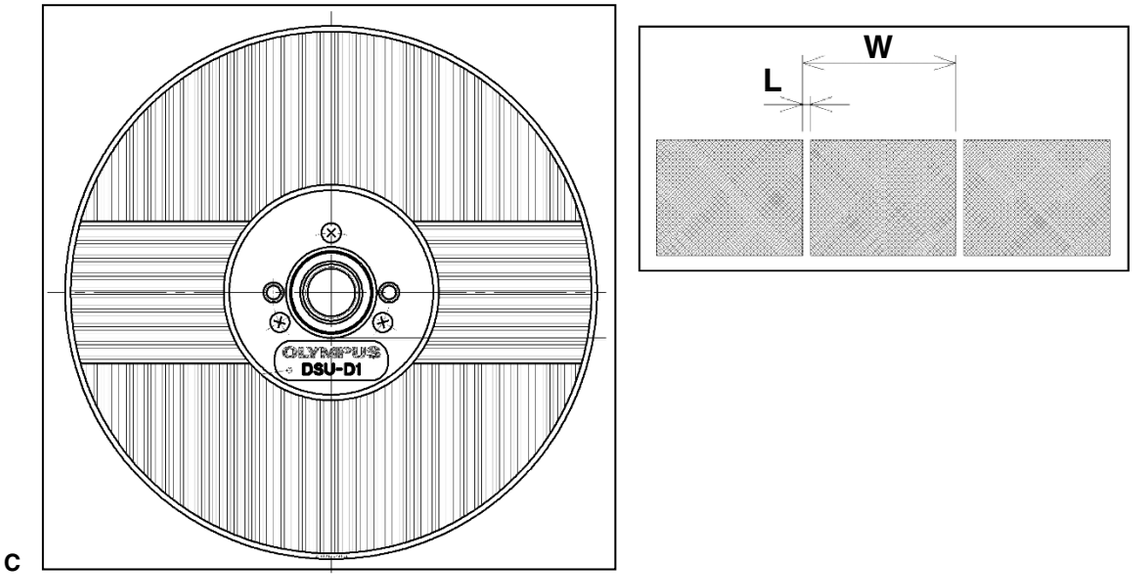


FIGURE A2.6. (*Continued*) **(B, C) Schematic of the Olympus DSU disk-scanner.** The Olympus DSU is a disk-scanning confocal fluorescence microscope that uses a mercury arc for excitation. The optical system is identical to that used for normal epi-fluorescence with the exception that an opaque disk is located in the intermediate image plane. Slits in this coating on this disk allow light to reach the focus plane and prevents light from this plane from reaching the CCD camera. To keep the light dose to the specimen low, this new scanner not only incorporates "hard" coatings to ensure the highest transmission of the dichroic elements, it also offers a photon-counting option to reduce PMT multiplicative noise. (C) Layout of one of several interchangeable scanning disks used in the Olympus DSU disk-scanner. The thickness and spacing of the slits varies on the 5 available disks have each been optimized for use with a particular objective. Figures kindly provided by Olympus Corp. (Tokyo, Japan).

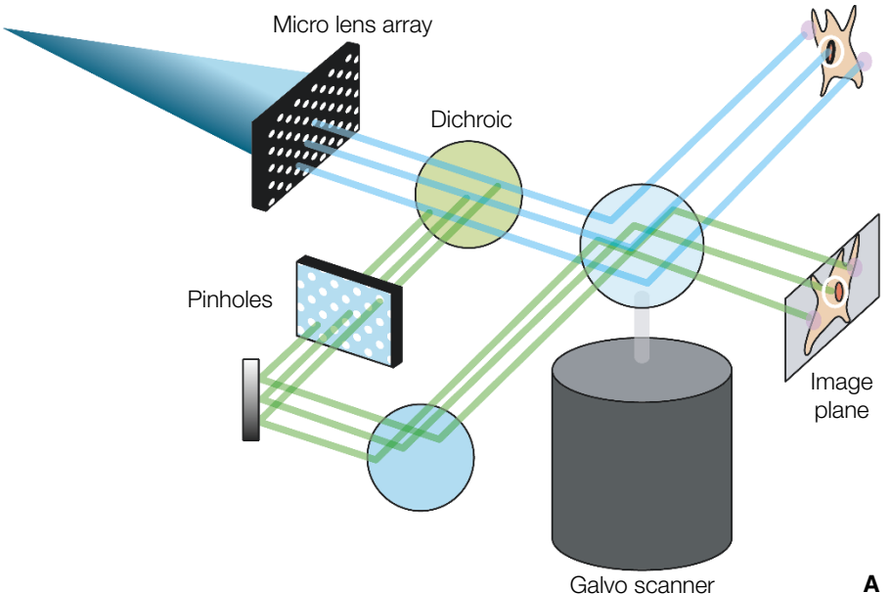


FIGURE A2.7A. Schematic diagram of Visitech VT Infinity. The optical path starts with a stationary micro-lens array illuminated by an expanded laser beam. A galvanometer mirror (*x*) incorporating a piezoelectric micro-deflector (*y*) scans the array to cover the sample and then de-scans the returning fluorescence signal. This light is separated from the illuminating beam by a dichroic mirror, and passes through a stationary pinhole array to create confocal data. This data is re-scanned, in perfect synchronization, by being reflected off the reverse side of the galvanometer mirror onto a sensitive CCD camera. The galvanometer scanner is readily synchronized to the camera capture parameters, both exposure time and frame capture rate. Either multiple-line lasers or multiple lasers in any combination can be coupled through an AOTF that provides high speed (~µs) laser-line selection and intensity control. Laser excitation can be coupled in either by optical fiber or by direct coupling. Motor-driven filters change dichroic and detection bandpass. This system couples the advantages of high-brightness, laser illumination with multipoint scanning to keep the instantaneous intensity down while providing a data rate high enough for fast image detection, using a high-quantum-efficiency CCD camera. Figure kindly provided by Visitech Inc. (Sunderland, UK).

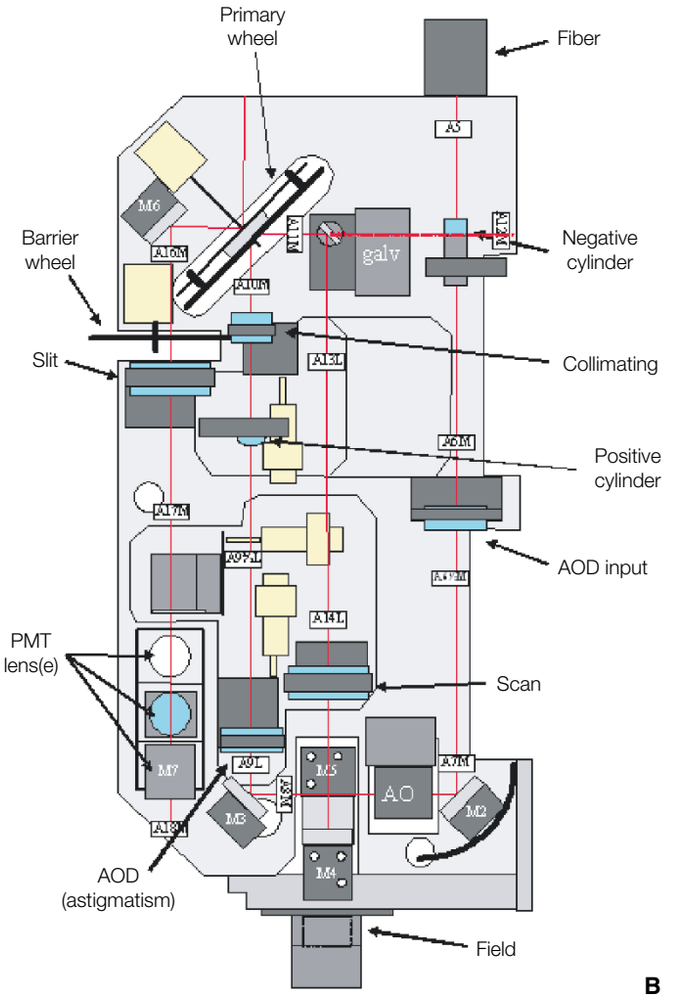


FIGURE A2.7B. Schematic diagram of Visitech VT-eye. The VT-eye incorporates a novel acousto-optical deflector (AOD) scanner, that combines ultra-fast horizontal scanning to provide high-resolution confocal imaging for real-time, living-cell confocal microscopy. The AOD scans the X axis at up to 50,000 lines/s or 400 frames/s, fast enough to capture clear images of dynamic events such as Ca^{++} puffs, sparks and waves. Multi-wavelength imaging for multi-labeled specimens from UV through the visible to the near infrared is achieved by using a selection of motorized, primary multi-band dichroics. The system operates with almost any laser, or combination of lasers, and uses AOTF technology to provide fast laser-line selection. The VTeye comes with up to 4 high-QE PMTs. The piezoelectric focusing system is capable of changing focus positions at up to 100 slices per second. Although high-speed acquisition creates vast quantities of data in a very short time, hours of experiments may be recorded at the maximum capture rates on a range of parallel, hard-disk modules. Figure kindly provided by Visitech Inc. (Sunderland, UK).

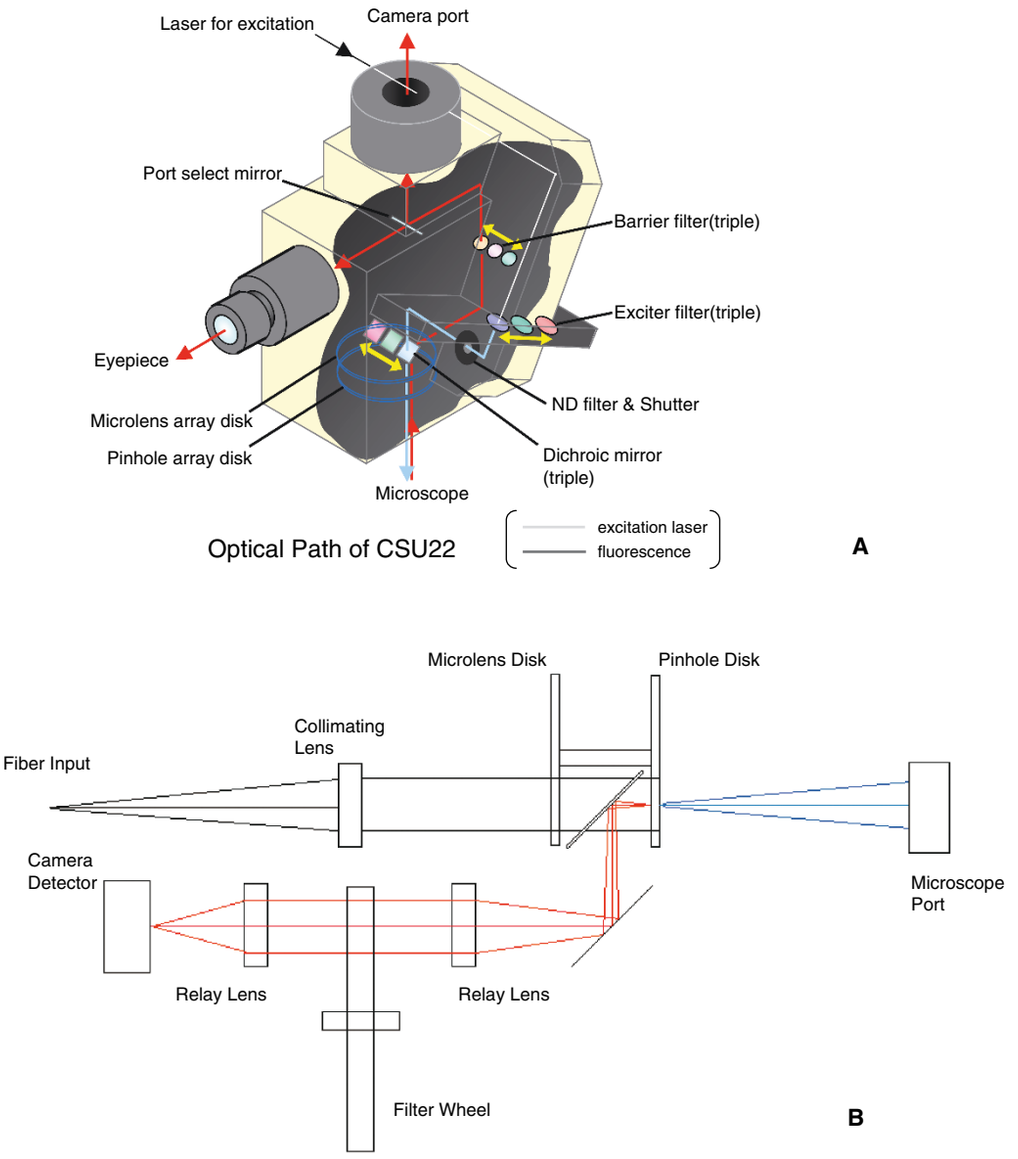
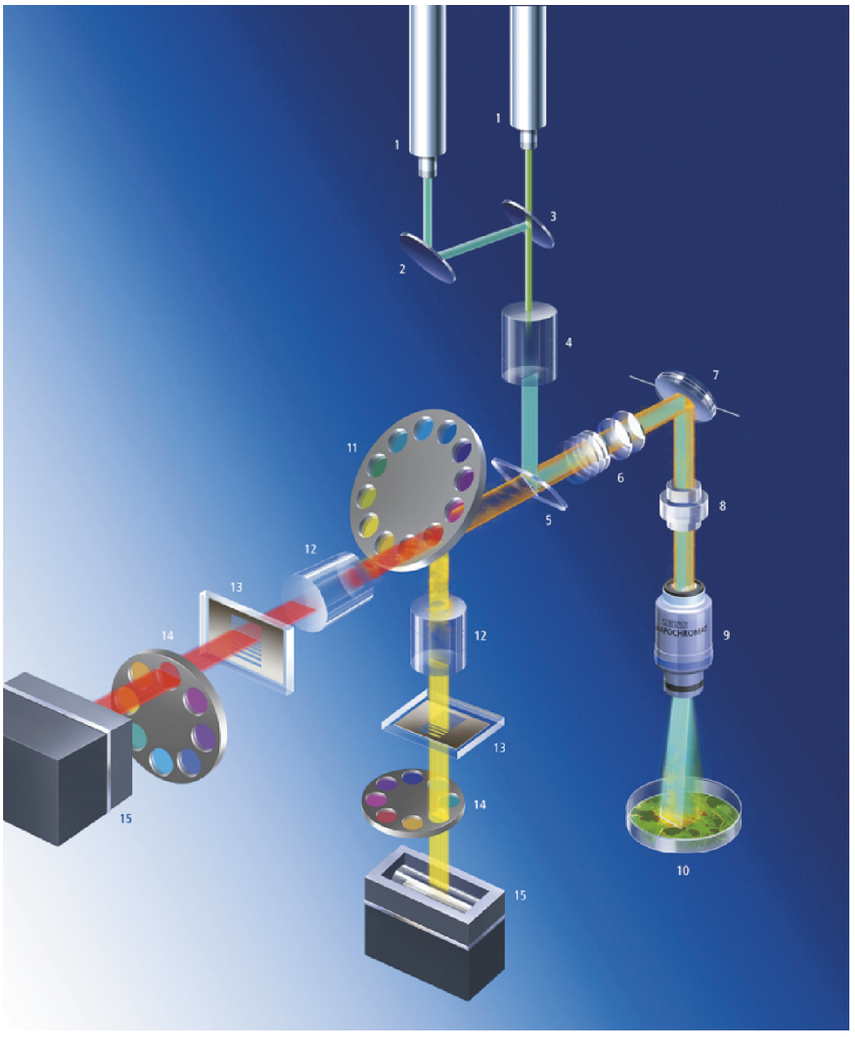
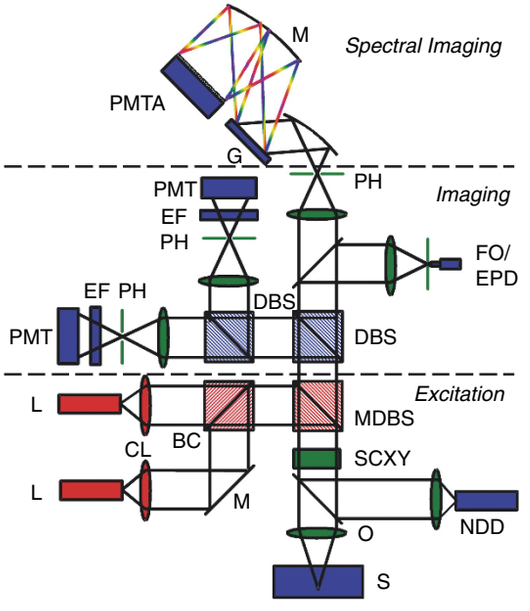


FIGURE A2.8. Schematic of the Yokogawa CSU 22. The Yokogawa scanner was the first disk scanner to offer both laser illumination and multibeam excitation. The mircolenses increase the efficiency of the illumination path from the 2–10% common to ordinary disks to almost 60%. (A) Laser light enters the scan head through a single-mode optical fiber, reflects off a mirror and through one of 3 exciter filters. After passing through an ND filter, and a beam expander, it illuminates the microlens array on the top disk of the rotating scanning assembly. The lenses focus the light through a short-pass dichroic and onto the array of pinholes in the lower disk. As this disk is in an image plane, the light passing each pinhole is focused into a point at the focus plane of the objective. Fluorescent light returning from the focus plane passes up through the pinholes, and reflects off one of 3 dichroic mirrors located between the two disks and into the detection path. After passing through one of 3 barrier filters, a selection mirror sends this light either to the camera port or to the eyepiece. (B) Simplified ray optical diagram of the CSU-22. The pinhole disk resides in an image plane and the signal passing the pinholes is first made parallel by a relay lens, then passed through the emission filter before being focused onto the CCD chip by a second relay lens. Other details shown in Figure 10.9. Figures kindly provided by PerkinElmer Corp. (Shelton, CT).



A

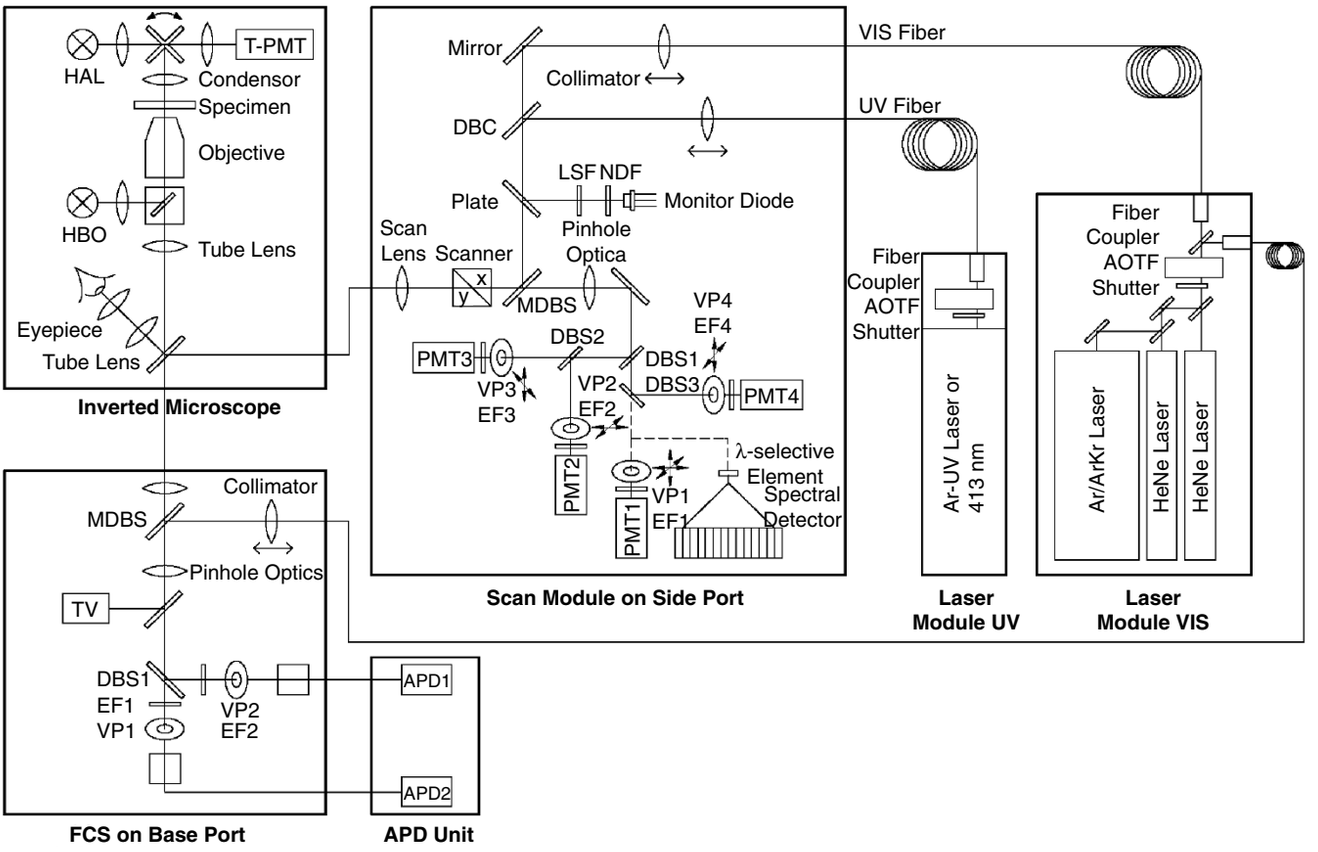
FIGURE A2.9A. Schematic diagram of Zeiss LSM-5-LIVE Fast Slit Scanner. The LSM-5-Live is a line-scanning confocal microscope using line illumination and a linear detector. Because it illuminates about 100x more points than does a single-beam instrument, the LSM-5 Live can acquire data at a much higher speed while still keeping the peak light intensity low enough to avoid singlet-state saturation. In addition, the quantum efficiency of the linear CCD is about 10x greater than that of most PMTs. Laser light enters the scan head through optical fibers (1) where it is combined by a series of mirrors (2, 3) and then passes to beam shaper (an expander and a cylindrical lens that converts the collimated Gaussian beam into laser light with a rectangular cross-section) (4) and also focuses it precisely onto the **AchroGate** beam splitter (5), reflects all wavelengths but only along a reflective line across its center. As a result, no matter what the wavelength, it reflects 100% of the laser light but passes >95% of the signal light to the detectors. The size of the raster on the specimen is controlled by a 0.5–2x zoom optic (6), that feeds the light to the *y*-scanning mirror (7), through the scan lens (8), the objective lens (9) and on to the specimen, (10). Returning signal follows the same path but mostly misses the reflective strip in the Achrogate and proceeds through a wheel of secondary dichroic beam-splitters (11) to one of 2 tube-lenses (12) that each focuses the line illuminated in the specimen onto a 17-position, slit aperture plate (13). Light passing the slits is first filtered by emission filters (14) and then detected by a 1 × 512 linear CCD detector (15) (see also Fig. 9.6).



L	laser
CL	collimator lens
M	mirror
BC	beam combiner
MDBS	main dichroic beam splitter
SCXY	scanner X/Y
O	objective
S	sample
PH	variable pinhole
DBS	dichroic beam splitter
EF	emission filter
PMT	photo multiplier tube
G	grating
PMTA	PMT array (META)
NDD	non-descanned detector
FO	fiber out
EPD	external photodetector

B

FIGURE A2.9B. Optical beam path of the Zeiss LSM 510 META. A unique scanning module is the core of the **LSM 510 META**. It contains motorized dichroic mirrors and barrier filters, adjustable collimators, individually adjustable and alignable pinholes for each of 3 (or even 4) detection channels, as well as scanning mirrors, and highly sensitive PMT detectors including the 32 micro-PMTs of the META spectral detector. All these components are arranged to ensure optimum specimen illumination and efficient collection of reflected or emitted light. The highly optimized optical diffraction grating in the META detector provides an innovative way of separating the fluorescence emission spectrum to strike 32 separate, micro-PMTs, each of which covers a bandwidth of ~10 nm. Thus, a spectral signature is acquired at each pixel of the scanned image. Such a dataset can subsequently be digitally "unmixed" to separate signals from dyes with overlapping emission spectra. **The Beam Path:** (1) Optical Fibers, (2) Motorized collimators, (3) Beam combiner, (4) Main dichroic beamsplitter, (5) Scanning mirrors, (6) Scanning lens, (7) Objective lens, (8) Specimen, (9) Secondary dichroic beamsplitter, (10) Confocal pinhole, (11) Emission filters, (12) Photomultiplier, (13) META detector, (14) Neutral density filter, (15) Monitor diode, (16) Fiber out.



C

FIGURE A2.9C. (*Continued*) **Schematic diagram of Zeiss LSM FCS** showing how the fluorescence-correlation spectroscopy (FCS) unit is attached via the base port of the Axiovert 200M microscope while the LSM 510 META is attached to the side camera port. All figures kindly provided by Carl Zeiss Inc. (Jena, Germany).

Appendix 3

More Than You Ever Really Wanted to Know About Charge-Coupled Devices

James B. Pawley

INTRODUCTION

The electronic structure of crystalline Si is such that electromagnetic waves having the energy of light photons (1.75–3.0 electron volts) can be absorbed to produce one free or "conduction" electron. If an image is focused onto a Si surface, the number of the photoelectrons (PE) produced at each location over the surface is proportional to the local light intensity. Clearly, all that is needed to create an image sensor is a method for rapidly converting the local PE concentration into an electronic signal. After almost 40 years of NASA and DOD funding, the slow-scan, scientific-grade, charge-coupled device (CCD) camera is now an almost perfect solution to this problem.

Success in modern biological light microscopy depends to an ever-increasing extent on the performance of CCD cameras. Because such cameras differ widely in their capabilities and are also items that most biologists buy separately, rather than as part of a system, some knowledge of their operation may be useful to those practicing biologists who have not yet found it necessary to be particularly interested in "electronics." Although the basics of CCD operation are described in many other chapters (particularly, Chapters 4, 10 and 12) this Appendix describes the operating principles of these devices in greater detail and also discusses the ways that they "don't work as planned." It then covers the operation of the electron-multiplier CCD (EM-CCD), a new variant that reduces the read noise almost to zero, although at the cost of reduced effective quantum efficiency (QE_{eff}).[1] The second section, *How to choose a CCD*, is a review of CCD specifications with comments on the relevance of each in fluorescence microscopy.

PART I: HOW CHARGE-COUPLED DEVICES WORK

The first step is to imagine a rectangular area of the Si surface as being divided into rows and columns, or more usually, lines and pixels. Each pixel is between $4 \times 4\,\mu m$ and about $24 \times 24\,\mu m$ in size and the location of any pixel of the surface can be defined in terms of it being x pixels from the left side, on line *y*.

To construct an actual system like this, start with a smooth Si surface; cover it with a thin, transparent, insulating layer of SiO_2; deposit onto the SiO_2, a pattern of horizontal strips, made out of a transparent conductor called amorphous silicon (or poly-silicon), so that the strips cover the entire image sensor area. Although, viewed from the top, these strips partially overlap each other, they are kept electrically separate from their neighbors by additional layers of SiO_2. Every third stripe is connected together to form three sets of interdigitating strips that we will refer to as Phases 1, 2 and 3 (ϕ_1, ϕ_2, ϕ_3, Fig. A3.1). Taken together, all these phases constitute the vertical register (VR) and, after the assembly has been exposed to a pattern of light, they are used to transfer the photo-induced charge pattern downwards, one line at a time. The pixels along each line are separated from each other by vertical strips of positively doped material injected into the Si. These positive "channel blocks" create fields that prevent charge from diffusing sideways without reducing the active area of the sensor.

Any photon that passes through the stripes and the SiO_2, is absorbed in the Si, producing a PE. If a small positive voltage (~15 volts) is applied to the ϕ_1 electrodes, any PE produced nearby will be attracted to a location just below the nearest ϕ_1 strip (Fig. A3.2). As additional PEs are produced, they form a small cloud of PEs referred to as a charge packet. The number of PEs in the packet is proportional to the local light intensity times the exposure period and the problem now is to convey this packet to some location where its size can be measured, and to do this without changing it or losing track of the location from which it was collected. This will be achieved by using the overlying electrodes to drag the charge packet around in an orderly way until it is deposited at the readout node of the charge amplifier.

Charge Coupling

The dragging mechanism operates in the following way: First ϕ_2 is also made positive so that the cloud diffuses to fill the area underneath both ϕ_1 and ϕ_2. Then ϕ_1 is made zero, forcing the packet to concentrate under ϕ_2 alone (Fig A3.2).

So far, these 3 steps have succeeded in moving the charge packets that were originally under each of the ϕ_1 electrodes downwards by one phase or 1/3 of a "line" in the *x-y* raster. If this sequence is now repeated, but between ϕ_2 and ϕ_3 and then again between ϕ_3 and the ϕ_1 belonging to the next triplet of strips, packets will have moved down by the one entire raster line. PEs created within a particular pixel of each horizontal stripe remain confined by the channel stops as they are transferred to the next line below.

A pixel of the image is therefore defined as the area under a triplet of overlying, vertical charge-transfer electrodes and between two neighboring channel blocks. The pixels on scientific CCDs, are usually square, 4 to $30\,\mu m$ on a side while those on commercial, video CCDs are likely to be wider than they are high, to conform with the reduced horizontal resolution of commercial video standards. Only square pixels can be conveniently displayed in a truly digital manner. Larger pixels have more leakage current (dark-current), but are also able to store more charge per pixel (see Blooming, below).

[1] This loss can be avoided if the system is used in photon-conting mode.

James B. Pawley • University of Wisconsin, Madison, Wisconsin 53706

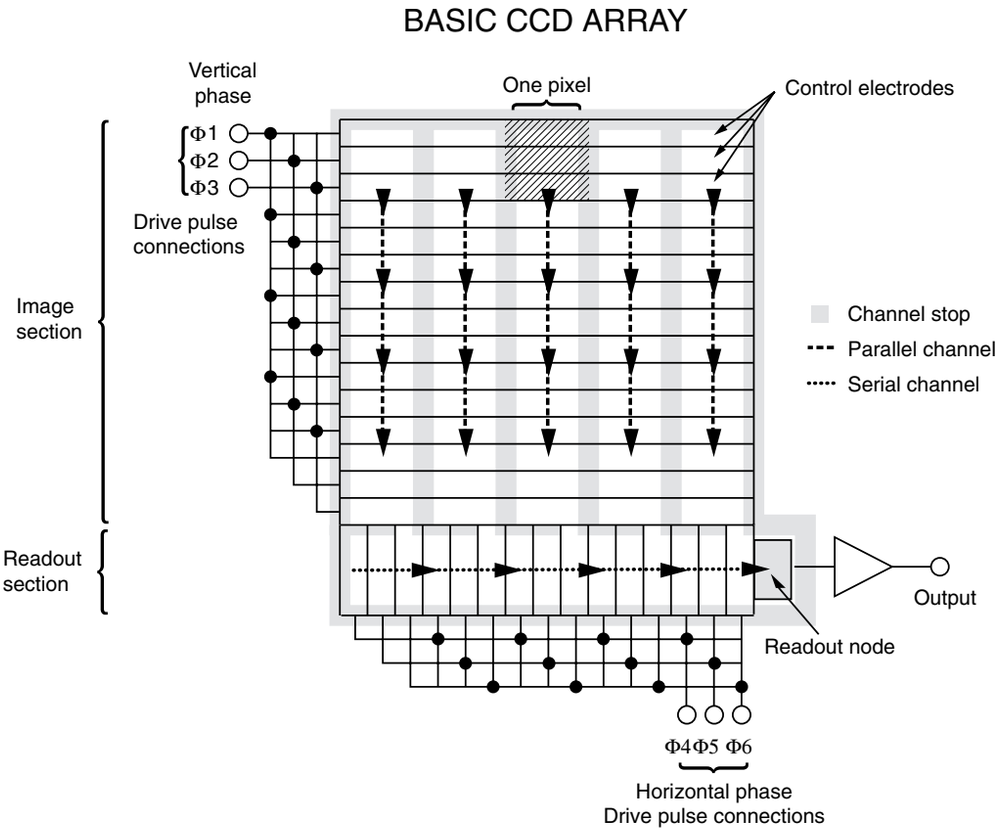


FIGURE A3.1. Layout of CCD array, viewed *en face*.

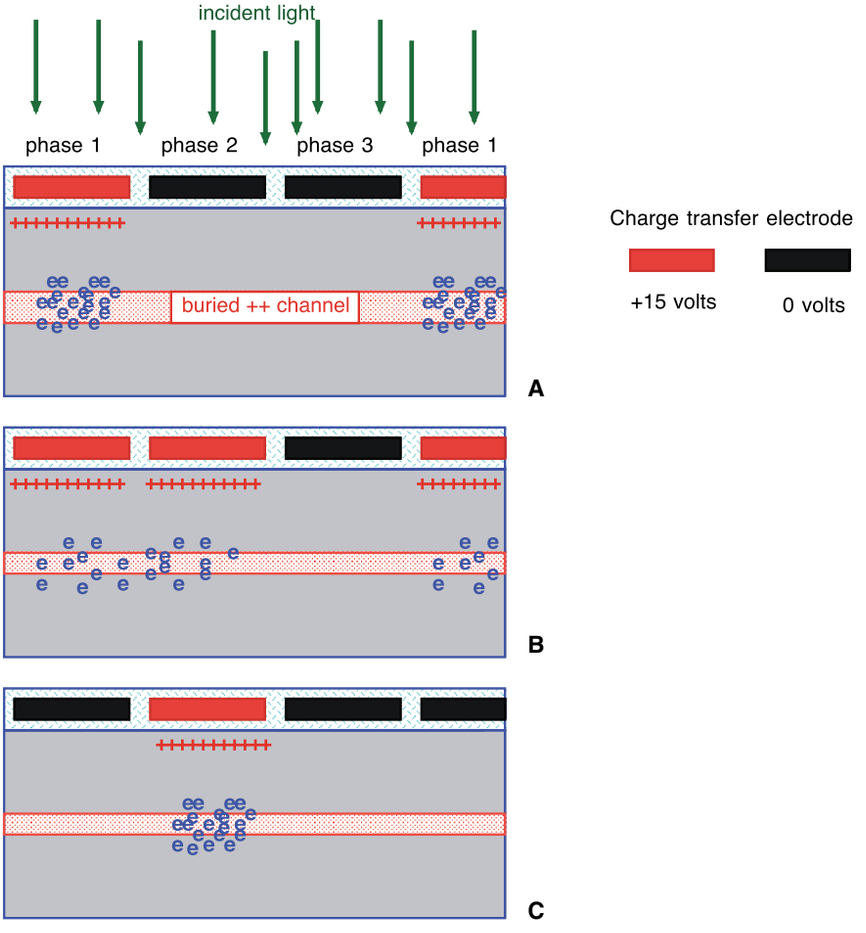


FIGURE A3.2. Charge coupling: Three stages in the process of moving a charge packet initially beneath phase 1 (A), so that it first spreads to be also under phase 2 (B) and finally is confined to entirely under phase 2 (C). These 3 steps must be repeated 3 times before the charge packet has been moved downwards (or in the diagram, to the right) by one line of the CCD array.

At the bottom of the sensor, an entire line of charge packets is simultaneously transferred to the adjacent pixels of the horizontal register (HR, also sometimes called a shift register). Like the VR, the HR is composed of a system of overlying poly-Si electrodes and channel stops. Each column of pixels in the VR is eventually transferred directly into the same specific pixel on the HR. The three phases of the HR (ϕ_4, ϕ_5, ϕ_6) work exactly like those in the VR, except that they must cycle at a much faster rate because the entire HR must be emptied before the next line of packets is transferred down from the bottom line of the VR. In other words, in the time between one complete line-transfer cycle of the VR and the next, the horizontal register must cycle as many times as there are pixels in each line.

At the right-hand end of the HR is a charge amplifier that measures the charge in each packet as it is transferred into it from the last pixel of the HR. The first pixel to be read out is that on the extreme right-hand side of the bottom line. The last pixel will be that on the left side of the top line.[2]

The entire charge-transfer process has the effect of coding position as time. If we digitize the signals from the charge amplifier, and store the resulting numbers in a video memory, we will be able to see a representation of the light intensity pattern striking the sensor on any monitor attached to this video memory. Alternatively, as long as the dimensions of the CCD array match those of some video standard, such as NTSC or PAL, the time sequence of charge-packet readout voltages can be smoothed and, with the addition of synch pulses, turned into an analog video signal. While this latter process is often convenient, it is a poor plan if the analog signal must then be re-digitized. The necessity to digitize twice can reduce the effective horizontal resolution of the CCD sensor by about a factor of 2 and because the process is AC coupled, photometric accuracy is severely compromised.

It is important to understand the relationship between the charge-transfer electrodes and the charge packet. The electrodes do not somehow "connect to" the charge packet, and "conduct" it to the amplifier. Such a process would be subject to resistive losses, charge would be lost and a lot of "wires" would be needed. The charge-coupling process is better thought of in terms of a ball bearing "dragged" over the surface of a loose blanket by moving a cooking pot around underneath the blanket. The weight of the ball and the lip of the pot create a dimple and gravity keeps the ball in the dimple as the pot is moved. The voltage on the charge-transfer electrode creates an electronic "dimple." Changing the voltages on nearby electrodes moves the dimple. In this way, groups of charged particles (electrons) can be pushed around without actually "touching" or losing them.

Readout Methods

There are three distinct methods for reading out the charge pattern of a CCD: full-frame, full-frame transfer and interline transfer (Fig. A3.4). Most early scientific CCDs used the first method, which operates as has just been described. Although **full-frame** readout provides the largest sensitive area for a given area of silicon, the lowest level of readout noise and the greatest photometric accuracy, it also has some disadvantages. One cannot both collect and read out signal at the same time. Unless some sort of shutter is used to prevent light from striking the sensor during vertical transfer, signal will be added to any packets that are transferred past bright features in the image, producing vertical streaking. This problem is more important when the exposure time is short relative to the readout time.

In **frame transfer** readout, at the end of the exposure, the entire charge pattern is rapidly (0.1–3 ms) transferred by charge-coupling to a second 2D **storage** array. The storage array is the same size as the **sensor** array and is located next to it but it is physically masked with evaporated metal to shield it from light. The charge pattern is then read out from the storage array while the sensor array collects a new image. Because vertical transfer can be much faster if the charge packets do not have to be read out, this system reduces streaking by up to 1000× but does not eliminate it and the need for a storage register reduces the fraction of the Si surface area that can be used for sensing by 50%.

In **interline transfer**, the masked storage cells are interlaced between the sensor cells (i.e., each pixel is divided into sense and read areas). After exposure, all charge packets can be moved to the readout array in less than a microsecond. This ability can be used as an electronic shutter to eliminate vertical smearing but, because at least half of the area of each sensor must be masked, and any light striking a masked area is lost, the "fill factor" of the sensor is reduced, proportionately decreasing QE_{eff}. A solution to the "fill-factor" dilemma is to incorporate an array of microlenses, aligned so that there is one above every pixel. With such a system, most of the light striking any pixel will be focused onto the unmasked area.[3] Although microlenses restore the QE_{eff} somewhat, the full-well signal possible is still limited by the smaller sensitive area.

WHAT COULD GO WRONG?

When I first heard the CCD story, it struck me as pretty preposterous! How could you get all the correct voltages (9 different voltage combinations per pixel shift, ~3.6 million for each TV frame, 108 million/s for video rate!) to the right charge-transfer electrodes at the correct times? How could you get all of the charge in a packet to stay together during a transfer? Wouldn't Poisson statistics apply, making even one transfer imprecise and the 2000 transfers needed to read out the top, right pixel of a 1000 × 1000 pixel array impossibly inaccurate? How long would the PEs stay free to be dragged around the lattice? Wouldn't the charge packets decay with time?

In fact, many of these problems did occur, but remedies to most have now been devised. The difference between a $300 commercial CCD camera and a $65,000, top-of-the-line scientific CCD can often be measured in terms of how many of these remedies have been implemented. Therefore, it is worthwhile trying to understand some of them so that one can buy what one needs. The following discussion will define and discuss some of the more important CCD technical specifications.

Quantum Efficiency

Quantum efficiency is the ratio of the number of impinging photons to the number of PEs produced.[4] Any photon with energy in the range of 1–100 eV striking crystalline Si has a very high probability of producing a PE. However, reflections and absorption by the overlying polysilicon electrodes,[5] reduce the QE of

[2] This may seem backwards until one remembers that any image of the real world is usually focused onto the CCD by a single, converging lens, a process that always inverts the image.

[3] This occurs only as long as the initial angle of incidence is near to normal, a condition met when CCDs are used for light microscopy.

[4] In the visible range, each absorbed photon makes only one PE.

[5] Kodak had pioneered the use of charge transfer electrodes made out of In and Sn oxides that scatter less light than do those made of poly-Si.

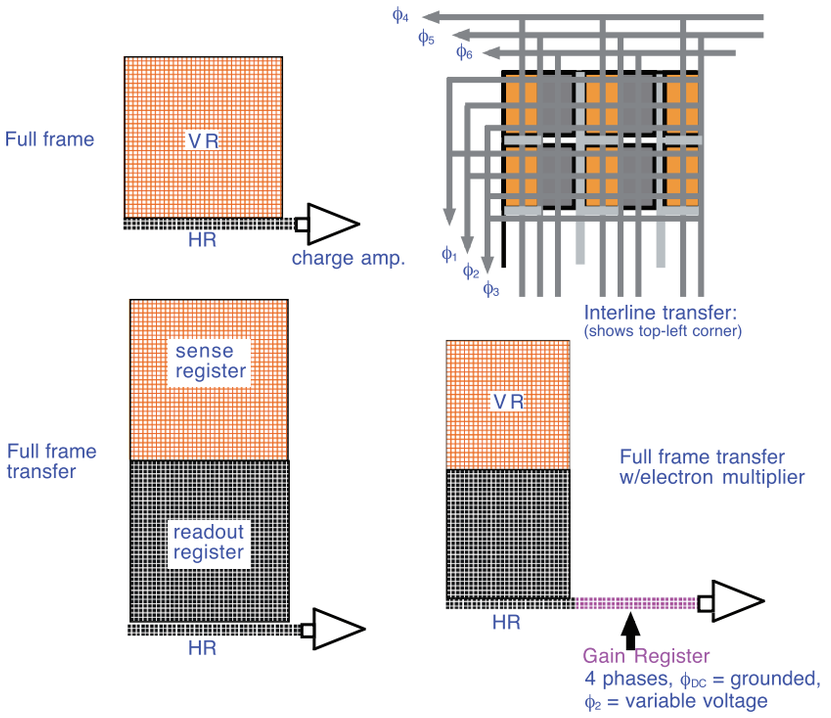


FIGURE A3.3. Four CCD readout patterns: Full-frame, frame-transfer, interline transfer and gain register (EM-CCD).

front-illuminated CCDs especially in the blue end of the spectrum. To reduce this effect, some UV-enhanced sensors are coated with fluorescent plastics, which absorb in the blue and emit at longer wavelengths. Others have their backs etched away and are turned over to permit the illumination to reach the light-sensitive area from the back side.[6] Figure A3.4 shows the intrinsic QE of different types of CCD (not Q_{eff}, which would take into account the light lost if some of the sensor is covered by charge storage areas). The effective QE can usually only be determined by actual measurement or by very careful evaluation of the published specifications ($QE_{effective} = QE_{intrinsic} \times$ fill factor).

Edge Effects

In early CCDs, PEs were often "lost" in the crystalline imperfections that are always present at the Si/SiO_2 junction. To avoid this, ion implantation is now used to make an N-doped, sub-surface layer called the buried channel about 1 µm below this surface (Fig. A3.2). This channel attracts the free PEs, keeping them away from the edge of the Si crystal. Any serious CCDs will have a buried channel but the need for ion-implantation keeps CCD chip prices high! Figure A3.5 shows the readout noise, in root-mean squared (RMS) electrons/pixel, for surface and buried-channel CCDs having two different pixel sizes. From this you can see that small pixels (here ~5.5 × 5.5 µm) have lower read noise than larger ones (~17 × 17 µm), mostly because the larger ones have higher capacitance and capacitance is the most important parameter of read-amplifier noise. One can also see that at readout speeds higher than 1 MHz (or 1 second to read out a 1024 × 1024 CCD), the read noise increases with the square root of the read speed.

Charge Loss

The lifetime of a PE (before it drops back into the ground state) depends on the purity and crystalline perfection of the Si and on other factors such as temperature. Generally it is long enough that little charge is lost during the exposure times commonly used in fluorescence microscopy. If necessary, it can be increased by cooling the detector, something often done to reduce dark charge.

Leakage or "Dark Charge"

Dark charge is the charge that leaks into a pixel during the exposure time in the absence of light. It can be thought of as the **dark current**[7] deposited into one pixel. Many processes other than photon absorption can add PE to the charge packet. The magnitude of this dark charge depends on the length of the exposure, and is substantially reduced by cooling. The rule of thumb is that for every 8°C of cooling, the dark charge is halved. As noted above, dark charge is principally a problem because it produces Poisson noise equal to the square root of its magnitude, and if this is left unchecked, it can significantly increase the noise floor of the CCD.

Since ~1987, a process called multipinned phasing (MPP) has been available to reduce dark charge build-up by about a factor of 1000, making it immeasurable in exposures up to a minute or so. This feature should be specified if one expects to use exposures longer than a few seconds without deep-cooling.

[6] Back-illuminated CCDs have to be thinned to 7–10 µm so that conduction electrons created near what would have been the back surface can respond to the fields created by the buried channel and the CC electrodes. Thinning increases cost and also reduces QE at longer wavelength where the absorption distance of the photons becomes comparable with the actual thickness. Back-illuminated CCDs are also more expensive because it is difficult to create electrical contacts with electrodes, etc., that are now on the bottom side of the chip.

[7] A current is a flow of charge measured in charge/time. The unit of charge is the Coulomb (c). The unit of current is the Ampere (A). One Amp represents a flow of one Coulomb/s or 6.16×10^{18} electrons/s.

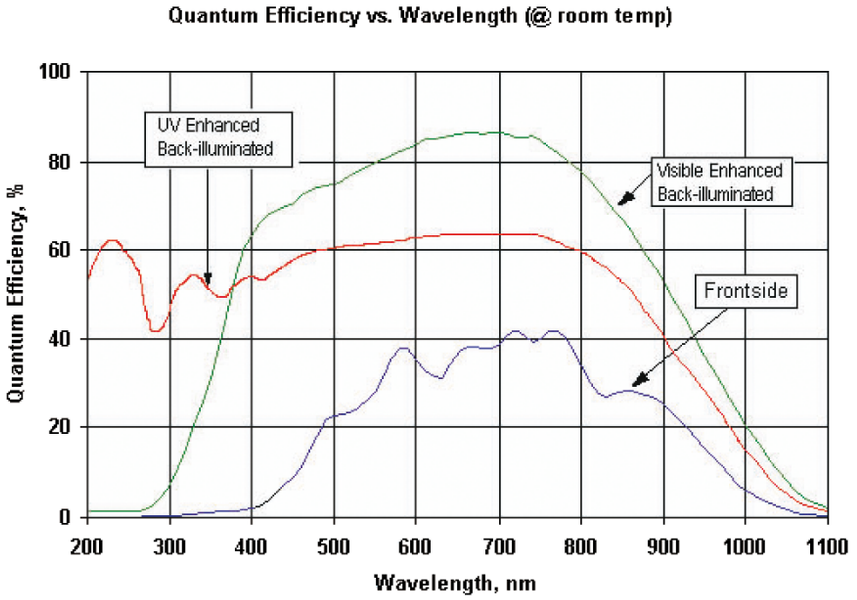


FIGURE A3.4. Intrinsic QE as a function of wavelength for a front-illuminated CCD (blue), a visible-enhanced, back-illuminated CCD (green) and a UV-enhanced CCD (red).

It should also be remembered that, while dark charge is never good, its average value can be measured and subtracted on a pixel-by-pixel basis, by subtracting a "dark image" from each recorded image as part of flat-fielding. However, because, by definition "dark" images contain very few photons/pixel, they have relatively high Poisson noise and low S/N. Therefore, a number of such images must be averaged to produce a correction mask that is statistically defined well enough that subtracting it from the data does not substantially increase the noise present in the final, corrected image.

This is not a problem when there are many counts in each pixel because the subtractive process of dark-charge normalization involves a change that is small compared with the intrinsic noise present in a large signal. It can be a problem when the black mask image is subtracted from a faint image that also contains only a few counts/pixel.

What cannot be removed by flat-fielding is the Poisson noise associated with the dark charge. This is equal to the square root of the number of electrons/pixel it represents. CCDs should always be operated such that the noise on the dark charge is less than the readout noise. On conventional CCDs this condition can usually be met quite easily by slightly cooling the sensor (0°C or about –20°C from ambient). The use of lower temperatures is complicated by the risk of condensing atmospheric water, a process that can be avoided only by enclosing the sensor in a vacuum chamber. Generally, a vacuum-hermetic enclosure, combined with good outgassing prevention, carries with it the significant benefits of more effective cooling, long-term protection of the sensor from moisture and other degrading organic condensates as well as the prevention of front-window fogging. At video rate, where exposures are short, dark charge is only a problem when the readout noise is reduced to <1 e/pixel, as it is when an "electron-multiplier" (EM) charge amplifier is used (see below and also Chapters 4 and 10). In EM-CCDs the read noise is so low that dark current becomes the main source of noise and cooling to –80°C becomes necessary.

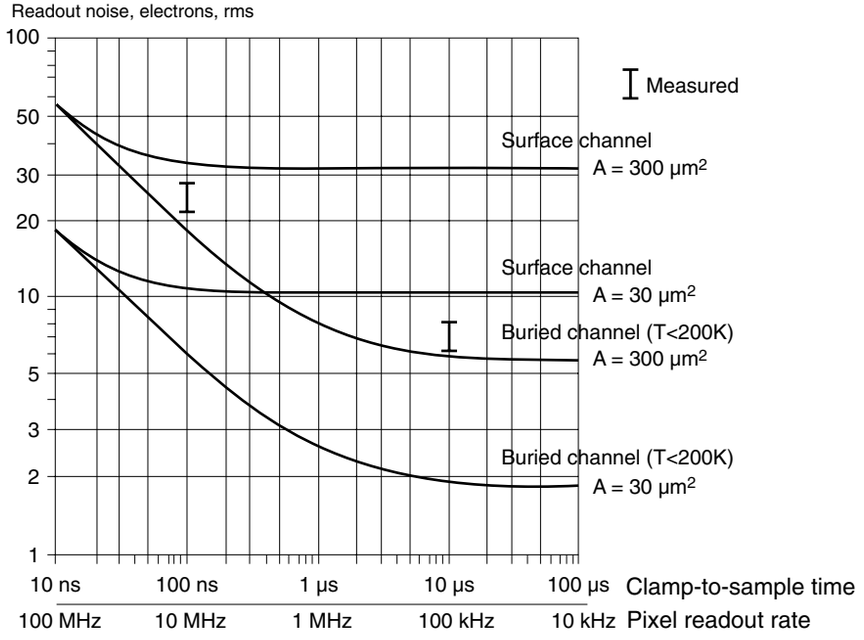


FIGURE A3.5. CCD field effect transistor (FET) noise as a function of pixel dwell time for large and small pixels and when using buried channel vs. surface channels. Smaller pixels have less read noise because they have less capacitance. Buried channels have almost 10× less read noise than surface channels.

TABLE A3.1. Typical Performance of Various Types of CCD Cameras. The "Sensitivity" Column Is a Reasonable Estimate of the Relative Suitability of the Camera for Detecting Very Faint Signals. It Spans a Very Large Range of Performance!

All CCDs are not equal						
Type	Grade	QE % (effective)	Noise (e/pix)	Sensitivity (relative)	Bit depth	Dynamic Range
Video	commercial color	10	200	1	10	1,000
	monochrome	20	200	2	10	1,000
Digital	1 Mhz, color	15	50	12	12	4,000
	1 Mhz, mono	30	50	24	12	4,000
	Back. Illum/ slow-scan	90	5	720	15	40,000
	LLL-CCD (EMCCD)	45	0.1	(18,000)*	?*	200,000

*Because the gain of the electron multiplier amplifier is unknown and large, it is not simple to measure, or even define, the sensitivity and bit depth of the EM-CCDs.

Blooming

As more photons are absorbed, the charge packet clustered around the buried channel grows and mutual repulsion between these electrons renders the field imposed by the charge-transfer electrode ever less successful in keeping the packet together. The maximum charge packet that can be stored without it overflowing into nearby pixels can be estimated by multiplying the pixel area (in square micrometers) by 600 PE/pixel (i.e., 27 k PEs for a 6.7 × 6.7 µm pixel, 540 k PEs for a 30 × 30 µm pixel). This overflow problem is referred to as "blooming" and, in CCDs for the home-video market it is limited by the presence of an *n*-layer, deeper in the Si. When the charge packet gets too big, mutual repulsion between the PEs forces some of them into this overflow layer, through which they are conducted to ground.

While this anti-blooming feature is convenient for removing the effects of the specular reflections found in images from everyday life,[8] it is not incorporated into many full-frame or frame-transfer scientific CCDs because it reduces QE for long-wavelength light. As this light penetrates farther into the Si crystal before being absorbed, much of it reaches the overflow layer where any PEs produced are lost.

Incomplete Charge Transfer

Sometimes, an imperfection in the Si will produce a pixel that "leaks" charge. Charge deposited into, or transferred through, this pixel will be lost, producing a dark vertical line above it. In addition, if one pushes the pixel clock too fast, some PE in the packet will not move fast enough and they will be left behind. In general however, on a slow-scanned, scientific CCD, fewer than 5 PEs out of a million are lost (or gained) in each, slower, vertical transfer and only 50 (0.005%) are lost during each, faster horizontal transfer. In such devices, the main noise term is Poisson noise for any signal level above ~20 PE/pixel,[9] and it seems hard to imagine doing much better than this except for signal levels <16 PE/pixel.

On the other hand, it is also true that the vast majority of CCDs made (those for camcorders, surveillance cameras and even many scientific applications), operate with much (100×?) less perfection. In microscopy today, we find CCDs that span this range of performance (Table A3.1).

All CCDs are not equal!!

CHARGE AMPLIFIERS

So far, I have described an image sensor in which up to 90% of the impinging photons make free PEs and explained how the charge packets that result from many photons hitting a given pixel can be conveyed to the **charge amplifier**, in a time-labeled manner and almost without change. Clearly the performance of the entire image detector will depend crucially on the capabilities of this amplifier.

What Is a Charge Amplifier?

Although most scientists have had some exposure to electronic circuits that amplify an input voltage or current, they may be less familiar with the operation of the type of charge amplifier found in a CCD. The following outline is presented to enable the reader to understand enough about the process to appreciate some of the important differences between the various types of CCD.

Because of the pulsatile nature of the CCD charge delivery system, the optimal way to measure charge packet size is to deposit it into a (very) small capacitor (the "read node") and then measure the voltage on this capacitor with a high impedance amplifier. As a field-effect transistor (FET) has an almost-infinite input impedance, it is ideal for this purpose and in fact, its existence makes charge-amplification possible.

There are two basic types of conventional CCD readout amplifier, non-destructive and destructive.[10] Both employ FET amplifiers.

Non-destructive ("skipper") amplifiers use an FET with a "floating gate" to sense the size of a charge packet by responding to the moving field that is produced as the packet is transferred along a charge-coupled register. Because the charge packet itself is not affected by this process, the process can be repeated hundreds or even thousands of times. If the results of all these measurements are averaged, very low readout noise levels (>±1 electron/pixel) can be obtained, but at the cost of a substantial

[8] Features such as the image of the sun reflecting off a shiny automobile can be over 1,000× brighter than the rest of the scene. Fortunately, such extremely bright features are seldom found in microscopic images unless a crystal of fluorescent dye occurs in the field of view.

[9] This calculation assumes that the read noise is 4 e/pixel, and this will be less than the Poisson Noise for any signal >16 PE. However, as many CCDs used in microscopy have >4 e/pixel of noise, this cut-off point should not be considered inflexible.

[10] The "electron-multiplier" amplifiers mentioned previously, act essentially as pre-amps to the conventional FET amps described here. They will be covered later in this Appendix.

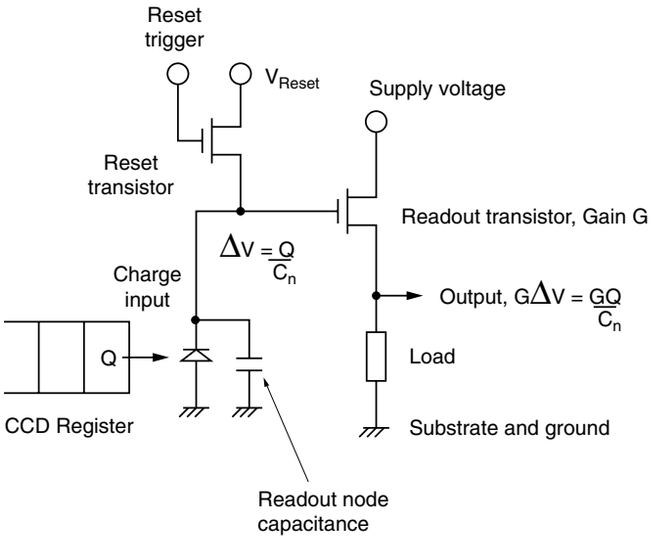


FIGURE A3.6. Destructive read-out amplifier for a CCD chip.

(×100 or ×1,000) increase in readout time and logical complexity. This approach might make sense on a Mars probe but it has not been used in microscopy to my knowledge.

Destructive readout amplifiers are more common, probably because they can operate more rapidly (Fig. A3.6). As implemented in a scientific CCD, the charge amplifier consists of the following components:

- overlying charge transfer electrodes to drag the next charge packet into the "read node"
- the read node itself: a 0.03–0.1 picofarad capacitor
- the sense FET
- the reset FET

In operation, fields from the overlying charge-coupling electrodes force a charge packet into the read-node capacitor, creating a voltage, V_c, that is proportional to the amount of charge in the packet. This voltage is sensed by the sense FET and the output is passed, via additional amplifiers, to the analog-to-digital converter (ADC) where the signal is converted into a digital number. Finally, just before the next charge packet is coupled into the read node, a reset FET discharges the capacitor, forcing V_c to zero, and allowing the read-FET to sense it again.

FET Amplifier Performance

The signal current (signal charge/s) coming from a CCD sensor is very small. Suppose that there were, on average, 400 PE in every pixel of a 512 × 512 pixel sensor.[11] Reading this out in one second would constitute a current of only 10^{-11} Amps. The current through the bulb in a home flashlight is 10^{10} times more. A very good conventional electronic amplifier designed to amplify this current would, itself, produce a random electronic noise signal larger than this, and electronic noise increases with readout speed, read-node capacitance and, to a lesser extent, temperature.

The success of the CCD in overcoming this limitation depends on two factors:

- The extremely small capacitance of the read node compared to that of any other photosensor such as a photodiode.
- Special measurement techniques such as correlated double-sampling

Clearly there are a lot of tricks to making the perfect CCD amplifier and not all CCDs employ them. Table A3.1 lists typical performance for a variety of common camera types.

NOISE SOURCES IN THE CHARGE-COUPLED DEVICE

Fixed Pattern Noise

When exposed to a uniform level of illumination, some pixels in a CCD array will collect more charge than others because of small differences in their geometry or their electrical properties. Consequently, it can be necessary to use stored measurements of the relative sensitivity of each pixel to normalize, or "**flat field**," the final dataset on a pixel-by-pixel basis. This is accomplished by first recording an image of a featureless "white" field. This is often approximated by a brightfield transmission image with no specimen, a process that will also record "inhomogeneity," or mottle, in the optical system. Differences in gain between pixels are evident as visible as nonuniformities in the digital signal stored in the memory and these are used to derive multiplicative correction coefficients.[12]

Unfortunately, one can only preserve the high precision of the CCD output if the coefficient used to normalize each pixel is equally precise. In any event, these correction coefficients vary with both the photon wavelength and the angle at which the light passes through the polysilicon electrodes on its way to the buried channel. This, in turn, depends on the details of the precise optical path in operation when an image is recorded and may even change with microscope focus! As the intrinsic noise of a pixel holding 360 k, PEs is only ±600 electrons or 0.16%, pixel-to-pixel normalization for changes in sensor gain is seldom perfectly effective and consequently there is usually some level of "Fixed-pattern noise" superimposed on the final data.

In addition, the "white" image that must be used for pixel-level sensitivity normalization is itself subject to intrinsic noise (±600 electrons for a signal from a pixel with a full well charge of 360 k electrons) and so multiplicative normalization may actually add some noise to the raw, uncorrected signal! Fortunately, if the white image can be defined by a multi-frame averages of several, nearly full-well "white" images, this normalization noise should only be noticeable when the image data to be corrected is similarly noise free. Without details of the signal levels present or the optical system in use, it is difficult to estimate the magnitude of normalization noise but it will be comparatively less important for images of faint objects containing few counts/pixel because these measurements are themselves less precise.

[11] Although this number may seem small, it is actually quite high compared to some uses in biological confocal microscopy. Many authors have found that in normal" use, a single-beam confocal microscope used to image a fairly faint stain will count 4–8 PE/pixel in bright areas of the image. Allowing that the effective QR of a good CCD will be ~10× higher than that of the photomultiplier tube used in the confocal microscope, this makes the expected peak CCD signal in an image from a disk-scanning confocal microscope only 40–80 PE/pixel.

[12] These correction coefficients are small and only needed when operating on images involving large numbers of photons (and consequently having relatively low Poisson noise and good S/N).

It should be also noted that the vignetting and "mottle" visible in images characteristic of video-enhanced contrast microscopy will produce small intensity errors in the data obtained by both widefield and confocal. However, this noise term will be more noticeable in widefield where more photons are used and hence the precision of the data is greater. Mottle is produced by dirt and surface imperfections on any optical components that are not located exactly at aperture planes, as well as by non-uniformities in the image sensor. Fortunately, to the extent that it is stable with time, mottle will be removed by the flat-field correction for CCD sensitivity just discussed.

What will not be removed is any change in signal caused by stray light (room light, light that goes through filters designed to remove it, etc.). The simplest test of any CCD set-up is to record an image of "nothing" (i.e., room dark, no excitation, no specimen etc.). Then do the same with 100× longer exposure time with the room lights at your normal operating level. Now adjust the display look-up tables so that you can "see the noise" in both the images on the screen. Although the only difference between the two images should be increased dark noise in the image with the longer exposure, this is seldom the case.

Noise from the Charge Amplifier

Noise is generated by both the readout and the reset FETs in the charge amplifier. Noise generated in the readout FET reaches the ADC directly. If thermal noise in the reset FET prevents it from completely discharging the read-node capacitance, it produces a random offset at each pixel (i.e., the read-node voltage is not reset exactly to zero). This is referred to as Reset Noise and has the effect that the dark charge seems to vary from pixel to pixel. Fortunately, Reset noise can be almost eliminated by employing the technique of Correlated Double-sampling (CDS) in the readout amplifier. In CDS, the circuitry of the charge-to-voltage amplifier is modified so that the output is proportional to the difference between the value of V_c just after the reset pulse and its value after the next charge packet has been inserted.

Although CDS essentially eliminates the effect of reset noise, it also distorts the noise spectrum. On the one hand, this distortion has the beneficial effect of converting the low frequency, 1/F noise from the FET into broadband noise which is more easily treated theoretically and which is less visually distracting than the short, horizontal flashes characteristic of 1/F noise.[13] On the other hand, it means that the input to the ADC must be carefully frequency-filtered. This filtering can be implemented either by employing RC circuits or by using dual-slope integration (DSI) in the ADC itself. If there are large intensity variations between neighboring pixels, the use of RC circuits will effectively compromise the large dynamic range of the CCD. Therefore, ADCs using DSI are employed on most slow-scan scientific, cooled-CCDs.

The fact that CDS and, in particular, DSI work best at low readout speeds is a final reason why most scientific CCDs operate best at relatively low readout speeds (Fig. A3.5). The other two reasons are improved charge transfer efficiency and the reduction in broadband electronic noise from the FETs (noted above.)

[13] In a CCD without CDS, noise features will seem to be smeared sideways, while in one with CDS, they will appear as one-pixel-wide stipple with no directionality.

Where Is Zero?

A final important feature of the CCD readout is that, compared to the photomultiplier tube (PMT), it is relatively difficult to determine the exact output signal level that corresponds to a zero-light signal. A properly operated PMT never records negative counts. However, as the electronic readout noise of a cooled-CCD is an RMS function with both positive and negative excursions, there will be some pixels that measure lower than the mean value of the zero-light pixel intensity distribution.

To ensure that no data is "lost," scientific CCDs are usually set up so that the zero-light signal is stored to be a few tens of digital units (ADU) above zero. A histogram of numbers stored from a "black" image will show a Gaussian-like peak centered at the offset and with a half-width equal to 2× the RMS read noise (see Fig. 4.20). This offset makes it more difficult to apply the gain and offset normalization procedures to images that record only a few detected photons in each pixel, a factor that will become more important as CCDs are increasingly used to image living cells that cannot tolerate intense illumination and which therefore produce substantially lower signal levels.

A NEW IDEA: THE GAIN REGISTER AMPLIFIER!!

Early in 2002, a new type of readout amplifier was introduced by Texas Instruments (Houston, TX) and E2V Technologies (Chelmsford, UK). As only E2V makes back-illuminated sensors, I will describe their system but both work along similar lines. E2V originally referred to their device as the "gain register" and its purpose is to amplify the size of the charge packet before it arrives at the read node. Although the term gain register has recently been replaced by the term "electron multiplier", it is important to remember that these new detectors work on a completely different principle from that employed in intensified-CCDs.

The gain register superficially resembles an additional HR, with two important differences:

- There are 4 phases rather than the usual 3 and the new phase consists of a grounded electrode located between ϕ_1 and ϕ_2.
- The charge transfer voltage on ϕ_2, is now variable, between +35 and +40 volts rather than the usual +15 volts.

As a result, when ϕ_2 is excited, there exists a high electric field between it and the grounded electrode. The high field accelerates the electrons in the charge packets more rapidly as they pass from ϕ_1 to ϕ_2 with the result that each PE has a small (but finite; usually in the range of 0.5% to 1.5%) chance of colliding with a lattice electron and knocking it into the conduction band (Fig. A3.7). Assuming the 1% gain figure, this means that for every 100 PE in the packet, on average one of these will become two electrons before it reaches the space under ϕ_2. Although this seems like a trivial improvement, after it has been repeated as part of the 400 to 590 transfers in the gain register, a total average gain of hundreds or even thousands is possible. If the voltage on ϕ_2 is reduced to normal levels, the sensor operates as a normal CCD.

As a result, a single PE can be amplified sufficiently to be safely above the noise of the FET amplifier, even when it is operating at speeds considerably higher than video rate (35–50 MHz, vs. 13 MHz for video). As the amount of gain depends exponentially on the exact voltage on ϕ_2, it is possible to "dial in" the amount of gain needed to keep the signal level well above the noise of the FET amplifier. However, it is important to remember that

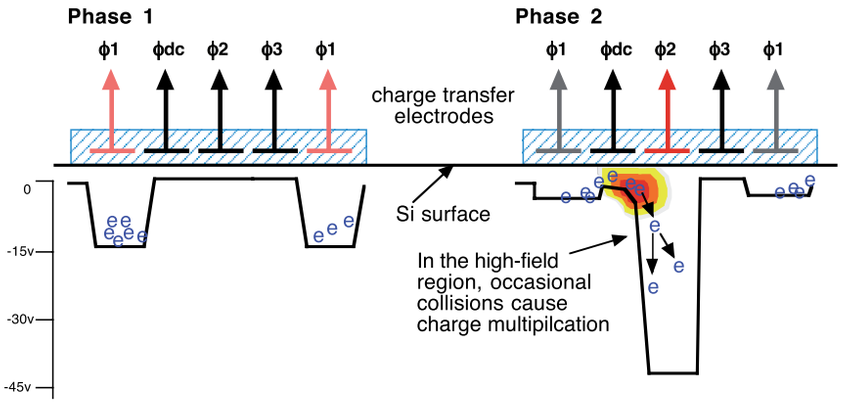


FIGURE A3.7. Energy diagram of an electron-multiplier CCD amplifier. The high field region that occurs between ϕ_2 and ϕ_{DC} when ϕ_2 goes strongly positive (right) causes about 1% of the electrons passing this region to collide with a lattice electron with sufficient energy to boost it to the conduction band. Repeated over hundreds of transfers, this process is capable of providing an average amplification of hundreds or even thousands of times.

the use of high EM gain will tend to saturate the "full-well" capacity of later pixels in the gain register, reducing intra-scene dynamic range.[14] Although this effect can be reduced to some extent by making each pixel in the gain register (and the read node) larger, this approach is limited by the fact that one triplet of electrodes can control a band of silicon only ~18 µm wide and because a larger read-node capacitance increases the read noise of the FET amplifier.

In sum, the gain-register CCD works like a normal fast-scan CCD with no read noise. The high scan speed makes focusing and sample scanning quick and easy and the device preserves the full spatial resolution of the CCD because the charge packet from one pixel is always handled as a discrete entity (unlike in an intensified-CCD). Of course, with fast readout, there is less time to accumulate much signal and the resulting image may have considerable Poisson noise. But this is not the camera's fault!

Alternatively, the output of many frames can be summed to reduce Poisson noise or, if the signal is bright, one can turn off the EM gain and have a fully functional scientific CCD.[15]

If the gain-register CCD is read out fast, there is so little time for dark charge to accumulate that cooling would seem unnecessary until one remembers that one can now "see" even one PE of dark-charge above the read noise. Because multi-pinned phasing (MPP) is less effective during the readout clockings, significant dark charge can be generated during readout. If the exposures are short, this source of dark charge becomes significant, and in an EM-CCD, even one electron is significant! In practice, the best performance is obtained when the EM-CCD is cooled to between −80° and −100°C.

EM-CCDs have one other important form of "dark noise" called Clock Induced Charge (CIC, also known as spurious noise). CIC typically consists of the single-electron events that are present in any CCD, and are generated by the vertical clocking of charge during the sensor readout. The process involved is actually the same impact ionization that produces multiplication in the gain register; however, levels are much lower because lower voltages are involved. In conventional CCDs, CIC is rarely an issue as single-electron events are lost in the read noise. However, in EM-CCDs where the read noise is essentially zero and dark charge has been eliminated through effective cooling, CIC is the remaining source of single-electron, EM-amplified noise. If left unchecked, it can be as high as 1 event in every 7 pixels. Fortunately, it can be minimized by careful control of clocking voltages and by optimizing the readout process to cope with faster vertical clock speeds (down to 0.4 µs/shift). This leaves a detector with less than one noise pulse in every 250 pixels: a detector extremely well adapted for measuring zero!

Of Course, There Is One Snag!

The charge amplification process is not quite noise free because the exact amount by which each electron in the packet is amplified varies in a stochastic manner (i.e., some electrons are "more equal" than others.). The statistical arguments are discussed in a paper found at the URL listed below and in Chapter 4. In summary: as the multiplicative noise inherent in the charge multiplication process creates noise that has a form very similar to that produced by Poisson statistics, the easiest way to think of its effect is to assume that the amplifier has no noise at all but that the signal being fed into it is half as big as it really is. In other words, the camera will work perfectly but it will work as though it has a QE that is only half of what it really is. Back-illuminated sensors are now available with an intrinsic QE of about ~90% or ~45% when used in the gain-register mode. This is 5–10× better than the performance available from most PMTs especially in the red end of the spectrum.

It is worth noting that one can use electron multiplication and still maintain the full QE by using the detector in photon-counting mode, as is now being done by many astronomers. Photon counting is only possible when one is able to confidently see a single-

[14] If a register designed with enough pixel area to hold a normal full-well charge of 30,000 electrons, is used with a gain of 100×, then the pixels near the end of the gain register will become full whenever the original charge packet has >300 electrons.

[15] Because, as noted above, the read node of the FET amplifier at the end of the gain register in an EM-CCD has a relatively large capacitance, E2V offers two separate FET readout amps. The one mounted at the end of the gain register is optimized for fast readout. The other is mounted at the end of the HR not connected to the gain-register, has low input capacitance and is optimized to read out slowly with low noise. Signal is sent to the latter by reversing the charge transfer sequence applied to the HR.

photon event as different from any dark event and when the number of photons collected during an exposure is so low that there is little probability of >2 photons falling into a pixel. To implement photon-counting, one records a sequence of short exposures containing "binary"-type single-photon data, and combines them to generate an image that is free of multiplication noise.[16] To be useful for recording dynamic events in living cells, an extremely fast frame rate would be needed. This may be more possible with some future EMCCD sensors.

(More info on EM-CCDs at http://www.emccd.com and http://www.marconitech.com/ccds/lllccd/technology.html)

PART II: EVALUATING A CHARGE-COUPLED DEVICE

A. Important Charge-Coupled Device Specs for Live-Cell Stuff!

Although in Part I, much time was spent discussing cooled, slow-scan, scientific CCDs, in fact, these have not been much used in biological microscopy since Sony introduced the ICX085, 1 k × 1.3 k, micro-lens-coupled, interline-transfer chip in the late 1990s. Although initially developed not for the scientific market but to meet the needs of the Japanese high-definition TV standard, these chips offered a set of practical advantages that biologists found very appealing:

— As an interline transfer chip, it needed no mechanical shutter and could be run so as to produce a continuous stream of images.
— The high readout speed (up to 20 Mhz) allowed real-time imaging compared with the 5–10 s/frame readout then common.
— The 6.45 × 6.45 µm pixels were small enough to sample the image produced with high-NA 40× and 60× objectives.
— The 1 k × 1.3 k raster size was both sufficient for most biological microscopy and significantly higher than that of the other scientific chips then available.
— Mass production allowed the development of a micro-lens array that increased the QE_{eff} to an acceptable level for a front-illuminated, interline chip and did so at a price biologists could afford.

As a result, the majority of CCDs sold for use in biological microscopy today use this chip or its higher-QE cousin, the ICX285. Although mass production made quality CCDs available to many who formerly could not have obtained one, it is important to remember that the read noise of ±8–24 electrons/pixel (depending on read speed) is substantially higher than ±2–3 electrons/pixel that characterized the best, slow-scan, scientific CCDs. Although, as noted below, the difference is only important if the dimmest pixel records fewer than ~50 electrons, and this seldom occurs in widefield fluorescence microscopy, the disk-scanning confocal fluorescence microscopes now available do provide an image in which this difference is significant (Chapter 10).

1. Quantum Efficiency (QE):

QE is the ratio of photons striking the chip to electrons kicked into the conduction band in the sensor. It should be at least 40% and on back-illuminated chips, it can reach 90% (with somewhat higher fixed-pattern noise).

The **fill-factor** is the fraction of the sensor surface actually sensitive to light. On the best frame-transfer CCDs, it can be almost 100%. On interline transfer CCDs it may be only 40%. Light not absorbed in a sensitive area is lost, reducing the QE_{eff} of the sensor proportionally.

Factors affecting QE:

Front-illuminated chips

- Light is scattered by the transparent, polysilicon charge-transfer electrodes that overlie the photosensitive silicon surface.
- This scattering is more severe at shorter wavelengths. Light that is scattered is not detected.
- As blue light is absorbed nearer to the surface than red light, and "deep electrons" may go to the wrong pixel, CCD resolution may be a bit lower than the pixel count at longer wavelengths, especially on chips with small pixels.
- Best QE: ~20% blue, ~35% red/green
- Two efforts to improve the QE of front-illuminated chips include "Virtual Phase" (one phase "open," Texas Instruments, Houston, TX) and the use of indium oxides for the transfer electrodes (Kodak, Rochester, NY). These have increased peak QE to the range of 55%.

Micro-lens array chips

- Sony has pioneered a process in which a micro-lens is mounted above each pixel of a front-illuminated, interline-transfer CCD. The lenses focus most of the impinging light onto a part of the CCD where reflection losses are least, pushing the QE to 65% in the green, less in the red (because of losses to the overflow drain) and purple.

Back-illuminated chips

- Made by thinning the silicon and then turning it over so that the light approaches the pixel from what would have been the back side. This avoids scattering in the transfer electrodes and increases the QE to about 90% in the green and >70% over the visible range.
- More expensive because of the extra fabrication.
- Slightly less resolution and more fixed-pattern noise, caused by imperfections in the thinning operation, and the presence of two sets of surface states.

Color Chips

- One-chip color sensors employ a pattern of colored filters, one over each pixel. Light stopped by any such filter cannot be detected and is therefore lost. The QE of such sensors is therefore at least 3× lower than for an otherwise comparable monochrome chip.
- 3-chip color sensors use dichroic mirrors to separate the "white" light into three color bands, each of which is directed to a separate monochrome CCD sensor. While this would seem to ensure that "all photons were counted somewhere," because such systems seldom employ microlenses, their effective QE is not much better than the 1-chip color sensors and alignment of the signal light is important.[17]

[16] There is no multiplicative noise because any spike above the FET noise floor counts as one electron, no matter how much it has been amplified.

[17] While the QE is not much better, the resolution of the 3-chip camera is the same as that of each chip, without the interpolation needed to disentangle the 3 colored images from the output of a 1-chip color sensor.

- Color can be detected by making sequential exposures of a monochrome chip through colored glass or LCD filters. This produces the same QE losses as the patterned filter but has the advantage that it can be removed when higher sensitivity is needed. This design is not suited for imaging moving objects.

2. Readout Noise:

This spec is a measure of the size of the pixels and the quality of the circuitry used for measuring the charge packet in each pixel. It is measured in "±RMS electrons of noise" (i.e., 67% of a series of "dark" readings will be ± this much).

- A good scientific CCD camera should have a noise level of <±5 electrons at a readout speed of 1 M pixels/second.
- The readout noise increases with the square root of the **readout speed** (see Table A3.2).
- **NO Free Lunch!** A chip that has ±5 e RMS of noise when readout at 100 k pixels/sec (or 10 seconds to read out a 1024 × 1024 chip), should produce ±50 e RMS of noise if read out at 10 M pixels/sec (or 0.1 sec to read the same chip).

What Is "Good Enough"?

Very low readout noise is only essential when viewing very dim specimens: luminescence, or low level fluorescence. Read noise is only a limitation when it is more than the statistical noise on the photon signal in the dimmest pixel (i.e., >sqrt of the number of detected photons = sqrt # electrons).

Consider the signal levels that you plan to use. Will the darkest important part of your image have zero signal or do you expect some background signal from diffuse staining or out of focus light? If the dimmest pixel in your image represents ~100 electrons, then the Poisson or statistical noise on this background signal will be ±10 electrons. "Adding" an additional ±10 electrons of readout noise will not make much difference to a measurement of this background signal and it will be even less significant when added to the even greater Poisson noise present in pixels where the stained parts of the image are recorded.

This is especially true because RMS noise signals add as the "sqrt of the sum of the squares" (i.e., the total noise from ±10 electrons of readout noise and ±10 electrons of Poisson noise is only sqrt (100 + 100) = ±14 electrons).

On the other hand, if you are really trying to keep those cells alive and you find that 2,000 electrons in the bright areas is enough, the dark areas may now be only 50 electrons. As the sqrt of 50 is about ±7, an additional ±10 electrons of readout noise may no longer be acceptable, but only if you have to make measurements in the dark areas on your image. In this case, the obvious choice is a slower, quieter CCD or an EM-CCD.

While in widefield fluoresecence, the background stain level is seldom so low that the sqrt of the signal recorded is lower than the read noise, the disk-scanner does provide such an image (Chapter 10). As one of the main advantages of disk-scanning is that one can scan an entire image plane very rapidly, the fact that one can read out the EM-CCD very rapidly without increasing the read noise makes it the ideal detector for this type of scanner (or, indeed for high-speed line scanning confocal microscopes).

3. Pixel Size:

- **Nyquist sampling:** The size of a pixel on the CCD is, in itself, not very important **BUT** one must satisfy the Nyquist criterion: The pixels on the chip must be **~4+** smaller than the smallest **features** focused onto it[18] (see Chapter 4): **Pixel size on the chip determines the total specimen-to-chip magnification needed!**

TABLE A3.2. Dynamic Range and Pixel Size

	12-bit camera w/small pixels	14-bit camera w/large pixels
Pixel Size	6.7 × 6.7 µm	24 × 24
Full Well	27,000	345,000
Least significant bit =	**6.5 electrons**	**21 electrons**
Implied noise level	**±13 electrons**	**±42 electrons**

Two examples:

a. 1.4 NA 100× objective and a 1× phototube.
   - The Abbe Criterion resolution @ 400 nm is about 0.22 µm. Magnified by a total magnification of 100×, this becomes 22 µm at the CCD.
   - A CCD having 8 × 8 µm pixels samples such an image adequately (~2.8 pixels/resolution element).

b. 1.3 NA 40× objective and a 1× phototube.
   - The Abbe Criterion resolution @ 400 nm is now 0.25 µm. Magnified 40× this becomes, 10 µm.
   - A CCD having 8 × 8 µm pixels is inadequate to sample this lower-mag, high-resolution image.

If you must use this objective, you need either a higher mag phototube (2.5×) or a chip with 3 × 3 µm pixels or (as CCD pixels are seldom this small), some combination.

- **Saturation signal level:** The maximum amount of signal that can be stored in a pixel is fixed by its area. The proportion is 600 electrons/square µm, so a 10 µm × 10 µm pixel can store a maximum of 60,000 electrons before they start to bleed into neighboring pixels. In practice, as fluorescent micrographs of living cells seldom produce signals this large, large pixels are usually unnecessary.

  However, the saturation level also represents the top end of another spec, the **dynamic range**. This is usually quoted as 12-bit (4000 : 1) or 14-bit (16,000 : 1) etc., and represents the ratio between the full-well saturation level and the readout noise. **Therefore**, a camera with relatively high readout noise can still look good in terms of dynamic range if it has large pixels and hence a high full-well capacity. Conversely, a 12-bit camera with small pixels can have less actual noise-per-pixel intensity measurement than a 14-bit camera with large pixels.

  In this case, the noise level of the 14-bit camera is >3× that of the 12-bit camera. Your signal/pixel would have to be 3× larger in order to be "seen" when using this particular 14-camera.

4. Array Size:[19] The argument for small

- Assuming 0.1 µm pixels (referred to the object plane), a 512 × 512 pixel chip will image an area of the specimen that is about 51 × 51 microns. If this is enough to cover the objects you need to see, this small chip has a lot of advantages over chips that are 1024 × 1024, or larger.
- Lower cost

[18] Of two times smaller than the "resolution," as defined by Rayleigh, or Abbe.
[19] The array size refers to the number of lines and pixels in the sensor, not to its total area.

- 4× fewer pixels to read out, meaning either:
  - — 4× slower readout clock, giving 2× lower readout noise.
  - — Same clock speed and noise level but 4× faster frame time. (Easier to scan specimen to find the interesting part! Time is money!)
- 4× less storage space needed to record data.

The argument for big:

- Manufacturing improvements are reducing readout noise levels at all readout speeds, and CCDs with more pixels often also have smaller pixels which can lead to lower read noise. If your labels are bright, having a larger chip allows you to see more cells in one image (as long as they are confluent!). Assuming that Nyquist is met in both cases, a large print of an image recorded from a larger sensor always looks sharper than one from a smaller array.
- **Binning:** Binning refers to the process of summing the charge from neighboring pixels before it is read out. This increases the size of each charge packet read (making it look brighter) and reduces the number of pixels. For example: 2 × 2 binning allows the owner of a 1024 × 1024 chip to obtain the speed/noise performance similar to the smaller chip (512 × 512) and to do so in a reversible manner. However, the optical magnification may need to be increased to preserve Nyquist sampling.

Before deciding that you need a larger chip, compare what you would get if the same money were spent on another scope/CCD/graduate student!

Bottom line:

- If more pixels means smaller pixels, they will each catch fewer photons unless the magnification is reduced proportionally. More pixels at the same frame[20] rate mean somewhat higher read noise because the pixel clock must go faster.

5. Readout Speed:

Although readout speed has been discussed above, we haven't mentioned that some good CCD cameras have variable speed readouts and the new EM-CCDs impose no high read speed penalty (Table A3.3).

It is convenient to be able to read out the chip faster when searching and focusing as long as one can then slow things down to obtain a lower read noise in the image that is finally recorded. However, the read speed is only one limitation on the frame rate:

TABLE A3.3. CCD Specifications

Array size	Pixel Clock Rate	Noise level*	Frame time	Frame rate/s
640 × 480	13 MHz (video rate)	200 e/pixel**	0.033	30
512 × 512	100 kHz	5 e/pixel	2.5 sec	0.4
	1 MHz	15 e/pixel	0.25 sec	4
	5 MHz	35 e/pixel	0.05 sec	20
1024 × 1024	100 kHz	5 e/pixel	10 sec	0.1
	1 MHz	15 e/pixel	1 sec	1
	5 MHz	35 e/pixel	0.2 sec	5

*Assumes conventional FET circuits. **The readout noise is relatively higher at video rate because the higher speed often precludes the use of various techniques, such as correlated double sampling, that reduce readout noise.

if the signal level is so low that 1 s/frame is required to accumulate enough signal to be worth reading out, then reducing the read time much below 0.1 s loses some of its appeal.

Faster readout speeds are particularly important for moving specimens, especially when doing widefield/deconvolution or when following rapid intracellular processes, such as vesicle tracking or ion fluxes.

6. Shutter Stability:

Though not strictly a CCD spec, electronic (LCD) or mechanical shutters are often built into modern CCD cameras.[21] The latter have the disadvantages of producing vibration and having a limited lifetime but the advantage that they transmit all of the light when they are open (even an "open" LCD can absorb >50% of the light, other electronic shutters may be better).

There seems little point in having a camera capable of recording (say) 40,000 electrons/pixel with an accuracy of ±200 e (or 0.5%!) if the shutter opening time is only accurate, or even reproducible, to ±10%. If one shutters the light source instead of the camera, similar limitations apply.

7. User-friendliness:

State-of-the-art cameras often seem to have been designed to make sure that no one unwilling to become a devotee of "CCD Operation" can possibly use them efficiently! Start off by asking to see an image on the screen, updated and flat-fielded at the frame-scan rate and showing as "white" on the display screen, a recorded intensity that is only ~5% of the full-well signal. This is where you should do most living-cell work. Then ask the salesman **to help you to save time-series of this image**. Increase the display contrast until you see the noise level of the image, both before and after "flat-fielding." Put a cursor on one pixel in the top frame of the stack and plot its intensity over the series.

8. "The Clincher" (Well, at least sometimes . . .):

Ask him/her what the intensity number stored in the computer for some specific pixel means, in terms of the number of **photons** that were recorded at that location, while the shutter was open. To answer, the salesperson will have to know the QE, the fill factor and the conversion factor between the number of electrons in a pixel and the number stored in the computer memory (sometimes called the gain-setting). To help them out, any "real" scientific CCD camera has the latter number written, by hand, in the front of the certification document (usually a number between 3 and 6). If the salesman doesn't understand the importance of this fundamental number, what hope is there for you? (Hint: It is important because the Poisson noise is the sqrt of the number of electrons in the well, not the sqrt of some arbitrarily proportional number stored in your computer.)

B. Things That Are (Almost!) Irrelevant When Choosing a Charge-Coupled Device for Live-Cell Microscopy

1. Dynamic Range:

This is the ratio of the "noise level" to the "full-well" (or maximum) signal. Although 16-bit may sound a lot better than 12-bit, you need to think before you are impressed.

The noise level should not be more than 5 electrons/measurement. Period!

[20] The readout speed of a 2 × 2 binned 1024 × 1024 is a bit slower than an actual 512 × 512 because twice as many vertical clock cycles are needed, and one still needs to read out pixel by pixel in the horizontal direction.

[21] Often the same advantage can be gained by shuttering the light source. This may become more common as pulsed laser or light-emitting-diode light sources are introduced (see Chapters 5 and 6).

Twelve bits is 4,000 levels. If the first level represents 5 electrons (in fact, it should represent half the noise or 2.5 e), then the 4,000th represents 20,000 electrons or (assuming a QE of 50%), about 40,000 photons/pixel/measurement.

How often do you expect to be able to collect this much signal from an area of a living cell only 100 × 100 nm in size? You should be able to get a good, 8-bit image using only 6% of the dynamic range of a 12-bit CCD (Fig. A3.8).[22]

As the "full-well" signal is only proportional to the area of the pixel on the chip (area in sq. µm × 600), the dynamic range is only really impressive if it is high **AND** a chip has small pixels. Then it means that the readout noise is low. A test for actual dynamic range is described below.

Bottom line: For disk-scanning confocal microscopy, a large dynamic range is only important if it reflects a low readout noise level.

Easier to just check the readout noise!

2. High Maximum Signal (high, full-well number, because of large pixels):

On living cells, you will probably never have enough light to reach a full-well limit of even 20,000 electrons. Even if you do, there are better ways to use it (more lower-dose images to show time course?).

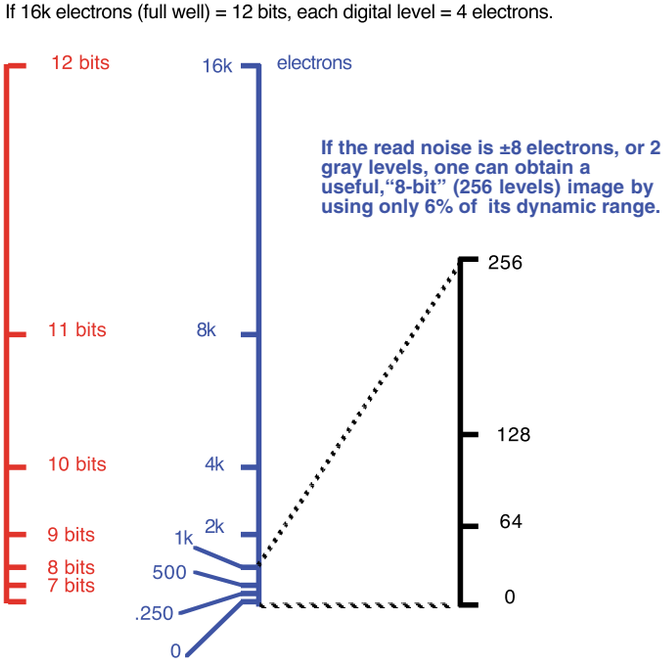


FIGURE A3.8. Not using the full dynamic range of a CCD. As most scientific CCDs have more dynamic range than one "needs" in live-cell fluorescence microscopy, the excitation dose to the specimen can be reduced if one sets up the CCD control program to display an 8-bit image using only the bottom 1,024 levels of a 12-bit image. Such an image is more than adequate for many functions in live-cell biological microscopy (particularly when other factors such as dye-loading etc., may cause larger errors) and will require only 6% as much signal as would a "full-well" image.

[22] Remember, given optical and geometrical losses, you can collect no more than about 3–10% of the photons produced, and, each fluoroscein molecule will only produce perhaps 30,000 excitations before "dying."

3. "Imaging Range" "Sensitivity" (or anything measured in LUX):

Stick to something you (and I?) understand: Photons/pixel or electrons/pixel. The other conversions are not straightforward.

4. "Neat Results":

Unless you know how well stained the specimen is, **you cannot evaluate an image of it in a quantitative manner**. (Though you may not want to admit this!) By all means, view your own specimens, but viewing "test specimens" that are not expected to fade and have a known structure (fluorescent beads in some stable mounting medium?) facilitates A/B comparison. If you do use your own test specimens to compare cameras, be sure to view them on the same scope, and with the same conditions of pixel size and readout time etc.

Better still . . .

C. A Test You Can Do Yourself!!!

Set up each camera that you want to evaluate on a tripod, add a C-mount lens, and an ND 3 or ND 4 filter. Hook up a monitor or computer and view some scene in your laboratory under ordinary illumination (avoid light from windows which may vary from day to day).

Close the lens aperture down until you can no longer discern the image (see Fig. 4.20). This is the "noise-equivalent light level": the signal level at which the electron signal (i.e., photons/pixel × QE) just equals the total noise level. Your measure is the aperture at which the image disappears.[23] Because it is sensitive to both QE and readout noise level, this is a very useful measure of what we all think of as the "sensitivity." Of course, the signal level depends not only on the light intensity but also on the exposure time and the pixel area, so make sure to keep the former constant and make allowances for the latter.

If you do not have even these meager facilities (a C-mount lens, an ND filter, a tripod and some time), take an image of nothing. Look at "no light" for one second, and for 100 seconds. Ask to see a short line profile that plots intensity vs. position along a line short enough that one can see the intensity of each individual pixel. The difference in the average intensity between the short and long exposure is a measure of the leakage.[24] With a little calibration from the published full-well specs (a spec less open to "interpretation" than "noise"), you can even get a direct measure of the read noise level from these dark images. (It should be the standard deviation of the values as long as they are counted in electrons, not "magic computer units" and as long as fixed-pattern noise is not a factor.) And just trying to work it all out will give you some idea if the salesman knows anything . . .

D. Intensified Charge-Coupled Devices

Intensified CCDs (ICCDs) are just that: the mating of an "image intensifier" to a CCD. The idea is that the photon gain of the intensifier (can be 200–2000×) will increase the signal from even a

[23] If the lens doesn't have a calibrated aperture ring, you can open the aperture all the way and reach the "threshold" exposure level by reducing the **exposure time** and adding ND filters. Remember to also correct for pixel area. Larger pixels intercept more photons.

[24] With a good EM-CCD, this measurement can be done using a short exposure and high EM gain, then counting the number of amplified dark charge/CIC spikes across a typical line of the raster.

single photoelectron above the read noise of the CCD. This occurs, and can be particularly useful where fast readout is needed such as when measuring ion transients. Finally, pulsing the voltage on the intensifier section makes it possible to shutter ("gate") the camera on the ns time scale, making the ICCD useful for making fluorescence lifetime measurements (Chapter 27, *this volume*).

However, ICCDs do not have the photometric accuracy of normal CCDs for a number of reasons:

- The relationship between number stored in memory and the number of photons detected is generally unknown and variable.
- The intensifier photocathode has low QE[25] (compared to that of a back-illuminated CCD).
- The "resolution" is generally only dimly related to CCD array size because of blooming in the intensifier. To check this, reduce light intensity until you can see the individual flashes produced by single photoelectrons. See how many lines wide they are. (They should be one line wide.)
- They have additional noise sources: phosphor noise, ions in intensifier section create flashes, high multiplicative noise in the intensifier section greatly decreases QE_{eff}, etc.
- Photocathode resistivity can produce "dose-rate" effects: nonlinearities in which the recorded intensity of the brightest areas may depend on (and affect) the brightness of nearby features.

Because I expect that EM-CCDs such as those mentioned above will soon supplant ICCDs except where fast gating is needed, I have not gone into more detail here. For more info, go to: http://www.stanfordphotonics.com/

[25] And the GaAsP photocathode with better QE, have to be cooled, making the assembly very expensive.

ACKNOWLEDGEMENTS

The author would like to thank Dr. J. Janesick, formerly of the Jet Propulsion Lab (California Institute of Technology, Pasadena, CA), for many conversations about CCD operation and for the original sketches for Figures A3.1, A3.4, and A3.5 and to Colin Coates, (Andor Technologies, Belfast, UK) for his helpful comments on the manuscript and for Figure A3.6.

REFERENCES

Inoue and Spring, 1997, Video Microscopy, Second Edition, Plenum, New York, 1-741, particularly Chapters 5–9.

Pawley, J.B., 1994, The sources of noise in three-dimensional microscopical data sets, *Three Dimensional Confocal Microscopy: Volume Investigation of Biological Specimens*, (J. Stevens, ed.), Academic Press. New York, 47-94.

Index

I suppose it is inevitable that indexes are compromises: If one includes every mention of every entry, the index becomes as long as the book. There is also the time dimension: As one cannot start writing the index until the book has been paginated, every day spent on the index directly delays the publication date. For the Second Edition, I prepared the index somewhat in parallel with the page proofs and it took most of a semester. For this Third Edition, a professional indexer was used to compile the initial index. We then expanded the level of cross-referencing through a series of digital searches. The final result may show its mixed parentage.

As you use this index, please consider the following. I confess that many entries contain far fewer referents when they appear as sub- or sub-sub-heads than when they appear as capitalized headings. In addition, some See alsomarkers use acronyms and it is also true that these can get confused with the real title of the entry. In compensation, have tried to put in bold type those page numbers on which I one would find the more comprehensive discussions of the topic we have added a period at the end of the major heads to distinguish them from sub-heads. My apologies for any errors.

My thanks to Helen Noeldner for her calm and competent assistance during this long and laborious process. Please use the Feedback page at http://www.springer.com/387-25921-X to bring errors to our attention so that they can be corrected in future printings. Remember that this Handbook has always been a community project. Good hunting!

JP, 2/21/06

Numbers

2D imaging, blind deconvolution approach, 476–477.
2D-time *vs.* 3D-time, embryo, 762–764.
2D pixel display space, 291.
2DCHO dataset, 818.
2DHeLa dataset, 818.
2-photon, (2PE). *See* Two-photon excitation.
3D Constructor, 282.
3D imaging, alternative approaches, 475–476, 607–624. *See also,* Confocal topics; Multidimensional microscopy topics.
  episcopic fluorescence image capture (EFIC), 607–608
  light sheet microscopy (SPIM), 613
  magnetic resonance microscopy (MRM), 618–624
    amplitude modulation of RF carrier, 620
    applications, 623–624
    basic principles, 618–619
    botanical imaging, 624
    developmental biology, 624
    Fourier transform, image formation, 620
    future developments, 624
    hardware configuration, 621, 622
    histology, 623, 624
    image contrast, 622–623
    image formation, 619–621
    Larmor frequency, 620
    phenotyping, 623
    schematic, 619
    strengths/limitations, 622
  micro-computerized tomography (Micro-CT), 614–618
    contrast/dose, 614–615
    CT scanning systems, 615–618
    dose *vs.* resolution, 616
    layout, 614
    living mouse, 615, 617
    mouse femur, 616
    operating principle, 614
    tumor-bearing mouse image, 617
  optical coherence tomography (OCT), 609–610
    human retina 609
    schematic, 610
    Xenopus laevis embryo, 610
  objectives on a tandem scanner, 154, 304
  optical projection tomography (OPT), 610–613
    lamprey larva, 612
    mouse embryo, 612
    plants, 774–775
    setup, 611
    real-time stereo imaging using LLCD
  related methods, 607–625
  selective plane illumination microscopy (SPIM), 613
    Medaka heart, 614
  surface imaging microscopy (SIM), 607–608
3D Scanning Light Macrography, 672.
3D for LSM, 282.
3D methods compared, **448–451**, **644–647**.
  table, 647
3D multi-channel time-lapse imaging (4D/5D). *See also,* Time-lapse imaging.
  table, 384.
3D3T3 high-content screening dataset, 820, 821.
3DHeLa high-content screening dataset, 820, 821.
3PE. *See* Three-photon excitation.
4D imaging. *See* Four dimensional imaging.
4Pi microscopy, 561–570.
  4Pi-PSF, 570
  axial resolution, 563
  I^5M, 561, 569–570
    OTF, 569–570
  living mammalian cell imaging, 564–565
    Golgi apparatus, image, 566
  lobe-suppression techniques, 561
    interference of excitation and detection, 561
    confocal detection, 561
    two-photon excitation (2PE), 561
  MMM-4Pi microscopy, 554, 556, 563–564
    basics, 565
    scheme, 563
  optical transfer function (OTF), 562, 563
  outlook, 568–569
  point spread function (PSF), 562–563
  signal-to-noise ratio, 561
  space invariance of PSF, 457, 490, 564
  theoretical background, 562–563
  type C, with Leica TCS, 4Pi, 565–568
    imaging of living cells, 568
    lateral scanning, 567
    mitochondrial network, image, 568
    optical transfer function (OTF), 567
    resolution, 567
    sketch, 566
    thermal fluctuations minimized, 567
  z-response, 563
5D image space, display, 291–294.
  2D pixel display space, 291
  animations, 292–293
  color display space, 291
  efficient use, 292
  image/view display options overview, table, 293

5D image space, display (*cont.*)
multiple channel color display, 292
optimal use, 293–294
pseudo-color, 173–175, 190, 291
stereoscopic display, 293
true color, 291

A
Abbe, Ernst, 1, 5.
Abbe refractometer, 377.
Abbe resolution criterion, 36, 37, 60, 61, 65–68, 574, 575, 631–636, 928. *See also,* Rayleigh criterion.
breaking the Abbe limit, 573
calculation, 65–66
individual point features separated by, 68
pixel size, 62, 65, 634–635, 784, 928
Abbe sine condition, 151, 239.
Abbreviations, list, 125.
Aberrations, 109, **146–156**, 241, 411–412, 471, 480–481, 542, 629, **640–641**, 654, 655, 657–659, 747. *See also,* Chromatic aberrations; Refractive index mismatch; Spherical aberration.
astigmatism, 145, **151–152**, 245–247, 249, 483,
axial, 242, 505, 542, 630
chromatic, 152–156, 160, 177–178, 209, 242–243, 641, 659
in 2-photon disk scanning, 542, 550, 554
of AODs, 56
axial chromatic registration, 287, 658
chromatic registration, 657–658
of collector lenses, 657–658
intentional, for height measurement, 224
magnification error, 155, 287, 331, 493, 542, 641, 657, 883, 904
measurement of, 243–244, 654, 659
multi-photon microscopy, 542
of optical fibers, 504, 507
signal loss, in confocal, 156, 178, 542, 641
standards, table, 157
coma, 145, **151**–152, 245–246, 249, 483, 630
detecting, 241
monochromatic, 147–152, 542. *See also,* Spherical aberration
optical, avoiding with thin disk lasers, 109
of refractive systems, 146–156
signal loss, 156, 178, 542, 641
spherical, 15, 34, **147–149**, 151, 160, 192, 208, 241, 244, 247, 330, 395, 404–413, 454–455, 463, 466, 480, 542, 629, 640, 654–655, 657, 658, 728, 772, 774. *See also,* Spherical aberration; Mismatch, refractive index
blind deconvolution to remove, 480–481
cause of signal loss, 330, 389, 395, 413, 457, 542, 661
chapter, 404–413
correction for refractive index mismatch, 192, 287, 411–412, 542
corrections for, 145, 411–412, 654–655
corrector optics, 192, 395, 398, 411, 477, 640, 655, 657
deconvolution, 463, 466, 468, 469, 471, 480, 498–499, 784
generated by specimen, 192, 418, 454–455, 654, 658, 747, 772, 775
of GRIN lens, 108
for IR wavelengths, 160
measurement using small pinholes, 145, 407
monochromatic, 147–151
multi-photon excitation, 542, 407–410
PSF, 148, 407, 455, 471, 481, 492, 657
secondary, 247, 249
in thick embryo imaging, 747
Zernicke coefficients, 247, 248
wave-front, measuring performance, 145
Ablation, 2-photon, 107, **764–765**.
Absorber, saturable-crystal, 107, 111, 112.
to cover gap in titanium:sapphire lasers, 112
indium-gallium arsenide, InGaAs, 111
Absorption, 25, 163, **309–312**, 338–339, 341, 514–518, 542, 550, 613, 704.
2-photon, 405, 535–536, 541, 545, 550, 552, 705, 719, 764, 884
caged compounds, 543, 544
CARS, 595–596, 599
contrast, **162–165**, 211, 595, 610, 613, 770, 779
cross-section, 189, 426
energy levels, 514, 517, 682, 697, 705, 792
excited state, 544, 692
fiber optics, 501, 502
filters, 552
of fluorescent dyes, table, 345
fluorescent excitation, 45, 88
FRET, 184
and heating, 21, 218, 252, 539, 685
of incident light, 163, 177, 427
by ink, 73
and laser operation, 82, 108, 110, 116
light lost by, 25, 166, **414–418**, 457, 654
lighting models, 283, 285, 309–312
molar extinction, 80–81, 343, 353, 357, 793
nonlinear, 188, 416, 427, 680, 704, 709–710
of optical materials, 158
and photodamage, 22, **685–686**, 690, 750
in photodetectors, 253
photon, 550, 749
quantum dots, 221, 343, 357–358, 696, 759, 801
RESOLFT/STED, 573
self-absorption, 490
spectra, 217, 267, 338–339, 345, 355, 390, 415–416, 421, 538–539, 681–682, 706
in UV, 195
Absorption coefficient, complex specimen, 164.
Absorption contrast, 164–167, 195, 427.
equations, 164, 539
heating, 539, 685
Accuracy.
biological *vs.* statistical, 24, 36–37, 68, 312
position, 39–41
Acetoxymethyl ester indicators, 726.
deposits formaldehyde, 738
derivatization, 738
formula/reaction, 359, 738
loading method (AM ester), 358–359, 361, 726, 738–739, 744
painting brain slices with, 726–737
Achrogate beam-splitter/scan mirror, 50, 212, 231–232, 916.
operation, 50, 232, 916
Zeiss LSM5 line scanner, 212, 231–232, 916
Achromat, 152, 153, 244.
chromatic correction of, 153
flatness of field and astigmatism, 152
longitudinal chromatic correction, 153
measurement, 244
Acousto-optical beam splitters (AOBS), 45, 55–**57**, 88, 102, 211, 218, 395.
to select wavelength and intensity, 88, 102
to separate illumination and emission, 45, 218
Acousto-optical components, 43, **54–57**.
tellurium oxide crystal, 55
thermal stability, 56, 57, 219
Acousto-optical deflectors (AOD), 25, 33, 54–**56**, 88, 447, 519, 543, 664, 762, **908**.
as beam-splitters, to reduce loss, 33
to gate light source, 25. *See also,* AOM
group velocity dispersion due to, 88, 540, 646
multi-photon excitation, 88, 540, 543, 646
multi-tracking, 664performance, 55
problem descanning fluorescent light, 56, 447
Acousto-optical modulators (AOM), 11, **55–57**, **88**, 231, 519, 540, 543.
FRAP experiments, for controlling laser, 56
group velocity dispersion, 88
Acousto-optical tunable filters (AOTF), 43, **55–56**, 88, 102, 219, 237, 346, 543, 651, 660, 673, 806, **908**.
for selecting CW laser lines, 88, 102
blanking, 54, 55, 237, 389, 543, 628, 651

leakage, 660
to regulate light intensity, 43
to spectrally filter light, 55
thermal sensitivity, 56–57, 219
Acridine Orange, 23, 344, 531, 665–667, 691, 774, 874.
bleaching, 693–694
Acronyms, list, 125.
Actin filament, 7, 236, 372, 378, 383, 692, 696, 714, 719, 748–749, 753, 756, 759–760, 773, 781, 804, 819, 824–825, 854, 856.
widefield source suitability, 142
Active laser medium, defined, 81.
Active mode-locked, pulsed laser, 111.
Actual focal position (AFP) defined, 405.
Actuator, galvanometer, 52.
Acute neocortical slice protocol, 723.
Adams, Ansel, zone system, 71–72.
Adaptive optics, 892.
ADC. *See* Analog-to-digital converter.
Adipocyte cells, CARS imaging, 604.
Adjacent fields, automated confocal imaging, 810.
ADU, analog digital units, 74–77, 630, 925.
Advanced Visual System. *See* AVS.
Aequorea victoria, biofilms, 348, 356, 736, 794, 873–874, 877.
variants, table, 873, 874
Aequorin, Ca^{2+} reporter,736–737, 739, 741, 802.
developmental cellular application, 736
ion binding triggers light emission, 737
Ca^{++} signal detection, 737
AFP. *See* Actual focal position.
AIC. *See* Akaike Information Criterion.
Airy aperture, optimum for NA, 28.
Airy disks, 4, 24, 65, 131, **145–146**, 151, 156, 210, 443, **444–449**, 454–456, 463–465, 474, 485, 492–493, 562, 567, 630, 655–657.
Abbe criterion resolution, 65–66, 225
defined, 146, 444
diameter in image plane, 210, 225
four-lobed, from astigmatism, 151
image, 38, 146, 225
intensity ratios, 28, 145–146
inverse, 11
and line spacing, 24
radius and pixel size, 4, 24, 38, 39, 60, 65–67, 227, 485
vs. NA and wavelength, 1, 4, 146
Airy figure image, 38, 75, 79, 146, 147, 225, 479, 486–487, 562.
FWHM as optimal pinhole/slit size, 28, 36, 225, 232, 443, 454, 463–465, 564, 567–568, 630–631, 633, 655–657
and resolution, 65–67
size, and Nyquist criterion, 38, 39, 60
Airy unit, 28, 36, 41, 210, 222, 227, 232, 274, 443–451, 632, 775, 779.
Akaike Information Criterion (AIC), 825.
AlexaFluor dyes, 81, 103, 184–185, 190, 192, 236, 330, 342–344, 353–357, 360, 363, 393, 395, 416, 533, 540, 694, 726, 731, 749, 794, 799, 804, 810, 814, 854, 878, 880, 905.
fluorescence excitation, 355
living cells rapid assessment, table, 360
structure, 356
Alexandrite (Cr^{3+} in $BeAl_2O_4$), tunable laser, 109.
Alga.
autofluorescence, 357
autofluorescent image, 173, 175, 192, 194–195, 438–439, 528, 585, 785, 870, 881–885
biofilm, 870, 881–885
cell chamber for, 429
in laser cooling water, 116
Aliasing, 38–39, 271, 291, 293, 448, 588, 590–592, 640, 830, 833–834, 836–839, 903.
and Nyquist criterion, 38–39, 448
temporal, 39, 41, 391, 836–837, 839
Alignment, 25, 85, 134–135, 157, 505, **629–631**, 651.
of laser systems, to reduce instability, 85
of optical coherence tomography, 610
of optical system, thermal stress, 85
importance, 25, 630
and PSF, 646
of source, 134–135, 629–631
Alkali vapor lasers, diode-pumped, 103–105.
Allium cepa. *See also*, Onion epithelium.
Alpha blending, 302, 304.
Alumina (Al_2O_3) ceramic tubes for lasers, 102.
Amira, 282–283, 286, 296, 302, 308, 312, 775–778.
Amoeba pseudopod, detail, 168.
Amplifier rods, maintenance, 116.
Analog digitization, for photon counting, 29, **33–37**, 41, 65, 74, 78, 251, 254, **258–261**, 263–264, 404, 460, 495, 522, 525–526, 542, 634, 766.
Analog-digital unit (ADU), to calibrate CCDs, 74, 77, 630, 925.
Analog-to-digital converter (ADC), 31–34, 64–66, 70, 72, 74–75, 258–259, 261, 263, 286, 521, 630–632, 924–925.
Analyze (software), 281–282, 288, 290, 301–304, 312, 651.
Analyzer, in pol-microscopy, 25, 157, 229.
Analyzer, spectrum, 901–902.
Anemonea majano, sulcata, 874.
Angular deflection, distortion, 211.
Aniline Blue stain, 430–432, 435, 438, 774.
Animations, 281, 283–285, 289–290, 292–293, 295, 299, 308, 312, 764, 829, 835–839, 841–844.
Anisotropic crystals, 114.
Anisotropic sampling, 287–288.
when resampling, 833–835
Anisotropic specimens, 163, 286, 320, 329, 420, 623, 675, 678, 690, 710, 793.
Anisotropy analysis, chimeric proteins, 794.
Anisotropy of fluorescence, 742, 794.
Anisotropy of interference filters, 49.
Annular aperture, 4, 9, 20, 211, 889.
3D pattern of point-source from lens, 4–20
in specimen-scanning confocal microscope, 9
Anti-bleaching agents, 36, 340, 363, 368, 375, 499, 694.
Antibody stains, 292, 339, **342–343**, 348, 357–360, 375, 528, 576–578, 582, 610, 612, 664, 696, 731, 748, 760, 789, 802–804, 812, 852–855, **877–880**.
artifacts, 664
biofilms, 877–880
FRET, 790–791
high-content screening, 812–815, 818
in situ, 612
penetration, 387
preparation, 369, 371–372, **375–377**, 878
and TEM, 852–855
Antifade agent, 36, 340, 363, 368, 375, 499, 694. *See also,* Antioxidants.
Antiflex optics, to reduce reflections, 158, 171, 507, 513.
Antioxidants, living cell imaging, 341–342, 363, 389, 390, 729, 794.
Anti-reflection (AR) coatings, 1, 8–9, 25, 49, 117, 139, 145, 151, 158–159, 212, 505–506, 901.
color effect, 139
of optical fibers, 506
AOBS. *See* Acousto-optic beam-splitter.
AOTF. *See* Acousto-optic tuning filter.
APD. *See* Avalanche photodiode.
Apochromat, 15, 147–148, 151, 153–155, 158, 240–245, 409–410, 454–455, 655, 659, 771.
chromatic correction, 153
compared with fluorite objective, 154
longitudinal chromatic correction, 153
Apodization, high-NA objective lenses, 240, 243, **249–250**, 272, 567, 889.
Applied Precision Instruments (API), 131, 137, 282, 388, 651.
APSS up-converting dye, saturation, 165.
AR. *See* Anti-reflection.
A. thaliana, 169, 173, 174, 175, 193, 196, 202, 416, 420–421, 423, 425, 426, 427, 431, 771, 772, 773, 775, 778, 779, 780.
attenuation spectra, 416
birefringent structures in cells, 420–421. *See also,* Anisotropic specimens
bleaching, 203
double imaging, 169
fluorescence spectra, 421, 423, 425

A. thaliana (*cont.*)
GFP protein fusion, 773
limitations for imaging, 772
mesophyll protoplasts, 196, 426
optical sectioning, 772, 775
protoplasts, 195–196, 203, 416, 421, 425–427, 429–430 438–439, 693
root tip fluorescence spectra, 173–175
seedling, autofluorescent image, 202
three-dimensional reconstruction, 190, 193, 771, 775, 777–778, 781
two-channel confocal images, 169, 175, 193, 196, 203, 427, 431, 772
two-photon excitation, advantages, 779, 780
two-photon fluorescence image, 427, 780
two-photon fluorescence spectra, 425, 426
Arc lamps, 132, 136–138.
current/stability of plasma, 138–139
monitoring during exposure, 137
radiance, 137–138
sensitivity to environmental variation, 136
shape of discharge, 132
shift of wavelength with temperature, 137
stability of, *vs.* filament lamps, 137
Area of interest. *See also,* Region of interest.
identifying, 201–202
Argon-ion laser, 85–86, 90–102, 107, 109–110, 112, 119, 124, 203, 338, 341, 346, 353, 355, 375, 540–541, 655, 657.
CW, 90–103, 107, 109–110, 112, 119, 124
emission stability, 86, 102
references, 124
Argon-krypton mixed-gas laser, 90, 92, 93, 102, 108, 119, 203, 343, 375, 748, 798, 811.
Artificial contrast, vibration and ambient light, 201–204.
Artificial lighting, image display, 306–312
Astigmatism, 145, **151–152**, 245, 247, 249, 483, 505, 542, 630.
of AOD, 914
and flatness of field, 152
and intensity distribution, 152, 246, 630
laser optics, 89, 106–107, 505
measuring subresolution pinholes, 145
at off-axis points, 151, 245, 247, 249
ATP-binding cassette, 362.
ATP-buffer, 802–803, 812.
ATP-caged, 544.
ATP-gated cation channels, 359.
Attenuation of light.
by specimen, 164, 287, 298, 304, 320, 321, **414–418**, 428, 439, 538, 558, 706, 779, 782
plots, 415, 706
of laser beams, 85, 87, 354, 415, 904
modeling, 309, 311, 320–321, 330
of PSF, 456, 462–463, 466, 494
x-ray, 614–615
Atto Bioscience CARV confocal microscope, 215, 229, 230, 907.
Autofluorescence, 44, 81, 90, 173, 175, 195, 202, **339–340**, 360–361, 369–370, 387, 414, 416, **421–434**, 442–445, 447–449, 451, 509–510, 528, 530, 545, 607, 612, 663, 667–670, 678, 682, 690, 698, 706, 710–711, 713, 729, 742–743, 745, 764–765, 769–773, 779, 781–782, 785, 798, 815, 874, 876, 881–885.
of alga chloroplast, 168, 172–176, 202, 429–435, 556, 785
A. thaliana seedling, 202, 303, 307, 772
bleaching, 202, 698, 729
cell wall, 303, 431, 438, 770
emission spectra in plants, 176, 421–423
extracellular matrix, 311
fixation, as a cause, 358, 369–370
fluorescent probes, 339–340, 360–361
harmonic signals. *See* Harmonic signals
lamprey larvae, 612
multi-photon microscopy (MPM) *See also,* harmonic signals, 545
optical materials, 45, 158
plants, 190, 193–195, 421–428, 770–772
plots, 176, 421–423
removal using spectral unmixing, 192, 382, 664–667
examples, 665–666
removal on basis of fluorescence lifetime, 345–346, 348, 349, 528
UV excitation, 347
Automated 3D image analysis methods, 316–335. *See also,* Automated interpretation of subcellular patterns.
biological objects, 319
blob segmentation example, 322–324
gradient-weighted distance transform, 323
model-based object merging, 323–325
watershed algorithm, 322–325, 777, 822
combined blob/tube segmentation, 328–330
data collection guidelines, 319–320
defined, 316, 328
future directions, 334
hypothesis testing, 318
illustrations, 317
image preprocessing, 320–321
background subtraction, 320
morphological filters, 320
signal attenuation-correction, 320–321
vs. manual, 316–317
montage synthesis, 282, 293, 312, **328–332**, 748, 753, 851–852, 855, 858–859
defined, 329–330
examples, 330–332, 780–781
neuron, 330
scanning electron micrographs, 851–852, 855
TEM implementation, 858–859
neurobiology example, 320
quantitative morphometry, 331
rationale, 316
registration synthesis, 328–331
defined, 328
landmark-based, 328–329
multi-view deconvolution, 291, 330, 675–677
segmentation methods, 321–322
bottom-up, 321
hybrid, bottom-up/top-down, 322
integrated, 322
intensity threshold-based, 321
region-based, 321–322
top-down, 322
segmentation testing methods, 333–334
manual editing, 333–334
specimen preparation, 319–321
imaging artifacts, 320
stereology, 316
time series *in vivo* images, 319
tube-like object segmentation example, 324–328
mean/median template response, 328
skeletonization methods, 324–325
vectorization methods, 324, 326, 327
types, 318–319
Automated fluorescence imaging, 814.
endpoint translocation assays, 814
Automated interpretation of subcellular patterns, 818–828. *See also,* Automated 3D image analysis methods 2D dataset analysis.
automated 2D analysis methods, 818
2D subcellular location features, 819–820
2DHeLa dataset images, 819
CHO cell dataset, 818, table, 820
Haralick features, 818–820
HeLa cells 2DHeLa dataset, 818
Zernike moments, 818–820
automated 3D analysis methods, 824
classification results, 824
feature normalization, 824
feature selection, 824
automated classification of location patterns, 824–825
classification accuracy, 826
confusion matrix for 3DHeLa images using SLF10, table, 824
confusion matrix for 3DHeLa images using SLF17, table, 825
features in SLF17, table, 825
measured classification accuracy, table, 825
clustering of location patterns with clustering consistency, table, 826
exclusion of outliers, 825
methods, 826

optimal clustering determination, 825–826
optimal consensus tree, 827
clustering of location patterns, 825–826
downsampled images, different gray scales, 824–825
future directions, 827–828
high-resolution 3D datasets, 820–822
3D3T3, 820
3DHeLa, 820
color images from 3DHeLa, 821
image acquisition requirements, 821–822
images from 3D3T3, 821
image database systems, 827
image processing/analysis, 822–823
3D SLF, 822–823
edge features, 823
feature calculation process, 822
morphological features, 823
segmentation of multi-cell images, 822
texture features, 823
protein subcellular location, 818
statistical comparison of patterns, 826–827
AutoMontage software, 282, 293, 304.
Avalanche photodiode (APD), 77, 233, **252–255**, 404, 527, 542, 558, 567, 698.
array, for multi-beam sensing, 558
noise currents, 256
pulse pileup, 253, 527
unsuitability for non-descanned detection, 542
vacuum ADP, 254–255
Average intensity, 66, 110, 516, 556, 668, 684, 695, 747, 763–764, 816, 838, 930.
equation, 302, 309, 668
AVS (Advanced Visual System), 282–283, 286, 300, 311–311, 862, 863.
Axial chromatic aberration, 155, 658–659.
Axial chromatic registration, 154, 658.
Axial contrast. *See* z-contrast.
Axial edge response, 409–410, 654.
calculations for glycerol, table, 409
calculations for water, table, 409
Axial illumination, 60–61, 134.
Axial laser modes, 82, 110.
Axial minimum, 3D diffraction pattern, 4, 147.
Axial rays, spherical aberration, 148.
Axial resolution, **3–4**, 6, 172, 182, 209, 211, **225–228**, 230, 240–241, 243–244, 320, 370, 395, 407–411, 413, 444–446, 489, 493, 499, 511, 513, 551–553, 559, 561–568, 571–577, 610–611, 613, 649, 651, 654, 656–657, 659, 674, 704, 747, 750–751, 822.
4Pi microscopy, 561–568
coding, display, 305
defined, 3–4, 240, 444–446
focus shift, 243, 407–410
as function of pinhole diameter, 656
magnification, 215
measurement, 194, 656–657, 659
multi-photon, 750
multiview, 678
near focal plane, slit-/point-scan confocal microscopes, 225–228
SHG, 704
SPIM, 614, 674, 751
STED, 571–577
tandem-scanning confocal microscope, 6, 225
tomography, 610–611
using mirror, 656–657

B

Back-focal plane (BFP), 34, 50–51, 58, 61–62, 84, 126–128, 166, 208–210, 225, 239, 268, 487, 509, 627, 629, 708.
Background light, from transmission illuminator, 201–202.
Background noise, 260–262, 275.
Background signal, 12, 26, 28, 37, 68–69, 71–72, 88, 90, 112, 115, 158, **162**, 168, 172–173, 175, 184, 188, 201–202, 221–225, 227, 232, 235, 248, 251, 257, 266–275, **278–279**, 283, 287,-288, 290, 301–302, 305, 312, 321, 326, 339–340, 343, 345, 348, 360–362, 375, 421, 423, 428–429, 432–433, **442–451**, 462, 465, 472–477, 486, 493, 497, 506, 509–510, 518–519, 535, 541, 543, 553, 559, 582, 584–585, 595, 598–600, 602, 604, 621, 633, **656**, 663–370, 676, 694, 697, 698, 707, 713, 727, 733–734, 736, 747, 755–757, 760, 798, 801, 803, 809, 813, 815, 818, 822, 830, 836, 839, 851.
Background subtraction, 284, 301, **320**, 473, 510.
Back-illuminated CCD, 31, 77, 222, 232, 234, 754.
Back-propagation neural network (BPNN), 818.
Backscattered light (BSL), 22–23, 57, 83–84, 130, 141, 145, 165, 169–170, 180–182, 191, 196, 202, 212, 221, 228, 240, 376, 378, 416, 430, 436, 442, 631, 879.
access to, antiflex optics, 6, 57, 141, 212, 229, 507, 513, 609, **631**, 704, 707, 854, 879, 990
biofilm, image, 880
contrast, effect of specimen absorption, 165
effect of coherence on, 130–131, 170
images made using, 22–23, 154, 436–438, 513, 638, 855, 880
Amoeba pseudopod, 168–170, 191
cheek cells, 22, 23
diatom, 145, 438, 638–640, 881
latex bead, 182, 196, 197, 653
transparent ciliate protozoa, 141
LLLCD objectives/3D color-coded BSL
as a noise signal, 663
optical coherence tomography, 609
practical confocal microscopy, 631
from specimen, 202
unmixing, 192, 382, 664–667
Back-thinned CCD, 31, 77, 222, 232, 234, 754.
QE plot, 29
Bacteria. *See* Biofilms.
Ballistic microprojectile delivery, 360, 726, 803.
Ballistic photons, 418, 427, 538.
Ballistic scans, 40, 41.
Balloon model segmentation methods, 776.
Bandpass, optical filters, **43–44**, 46, 48, 49, 51, 76, 87, 132, 141, 173, 204, 341, 528, 708, 798.
for CARS, 598–599
coupling short and long-pass filters, 46
excitation and emission, 48, 141, 217, 341, 708, 757, 798
laser, 106–107
liquid crystal, 425
to select range of wavelengths, 43–44
spectral detector, 203–204, 662–663, 666–667
Bandwidth, 32, 64, 69.
3 dB point, definition, 59, 65
of AOBS, 57
electronic/optical, digitization, 32, 34, 70, 238
head amplifier, 251
limiting, to improve reconstruction, 69
Nyquist reconstruction, output, 64, 69, 70, 238
Bead, fluorescence emission, 181, 182, 196.
fluorescent, 454, 477, 493, 499, 527, 652, 653, 656, 659, 784, 900, 904, 930
image, 656
table, 653
glass, in water, 181, 198–199
latex, fluorescence image, 196, 407, 455–457, 463, 471, 656
in water, confocal serial sections, 182
Beam blanking, 54, 55, 237, 389, 543, 628, 651.
Beam collimation, 728.
for fiber delivery, 506
Beam delivery, with fiber optic coupling, 85–88, 107, 216, 503, 506–508.
Beam deviation, unintentional, 15–16.
Beam expander, 8, 84, 124, 208, 212–214, 231, 650, 682, 708, 728, 907.
advantages, 213
Beam pointing, lasers, 85, 103, 107, 201, 250.
active cavity stabilization, 87
Beam quality, of diode lasers, 107.

Beam shift, vignetting due to, 211.
Beam-splitter, 33, 46–48, 50–51. *See* Dichroic mirrors.
  Achrogate, 50, 212, 231–232, 916
  AOBS, 56–57
  broadband, 346
  dichroic, 25, 33, 35, 43–51, 56–57, 83–84, 88, 139, 132, 135, 143, 151, 162, 203–204, 207–208, 211–214, 217–218, 229, 231–232, 266, 339, 341, 346, 375, 386, 424, 469, 503–504, 552, 563–564, 599, 630–632, 647, 650, 657–658, 664, 667, 691, 707–708, 747, 771–772, 810, 846, 879, 910, 907
    table, 799
  fiber-optic, 503–504
  forty-five degree, performance, 47
  fused-biconic coupler, 503–504
  long-pass cut-off, 43, 46, 51, 175, 204, 564, 801, 875
  multi-photon, 540–541
  polarizing, 13, 50, 57, 85, 87, 100, 217, 513, 631
  spectral problems, 50–51
  triple dichroic, 33, 46, 48, 217–218, 658, 783
    losses due to, 33
    performance, 46–48
Beam scanning, along optical axis, 215, 555.
Beam-scanning confocal microscope. *See* Confocal entries; Flying spot ultraviolet (UV) microscope.
  chromatic correction, 177
Beam-scanning systems, 6, 7, 16, 132, 146, 151, 156, 166, 177, 214–215, 218, 381, 554, 562, 564, 567, 568, 599.
  coma in, 151
  off-axis aberrations affecting, 156
Before-bleach/after-bleach ratio, FRET, 794.
Benchtop fiber-optic scanning confocal microscopes, 507–508.
Bertrand lens, 61, 157, 412, 643.
Beryllium oxide (BeO), for laser tubes, 102.
Beta barium borate (BBO), non-linear crystal for frequency doubling, 100, 109, 114–115, 125.
BFP. *See* Back-focal plane.
Bibliography, annotated, 889–899.
  adaptive optics, 892
  books on 3D light microscopy, 889
  differential phase contrast, 892
  display methods, 892–883
  fiber-optic confocal microscopes, 883
  general interests, 891
  historical interests, 889–890
  index mismatch, 893–894
  multiplex, 894
  non-linear, 894
  point spread function, 895–896
  polarization, 894–895
  profilometry, 895
  pupil engineering, 896
  review articles, 889
  technical interests, 891–892
  theory, 890–891
  thickness, 896
  turbidity, 896–897
  variants on main theme, 897–899
Binding equation, for fluorescent indicators, **740**.
Biocytin, 730, 731.
  EM imaging of brain cells labeled, 731
  protocol, 730
Biofilms, 287, 688, 529, 530, 624, 779, **870–887**.
  2-photon imaging, 530, 882–885
    dual-channel imaging, 884
    limitations of CLSM and 2-photon, 884
    single-photon/2 photon comparison, 883
    thick environmental biofilms image, 885
  autofluorescence, 545
  backscattered light, 880
  fluorescent proteins for, table, 874
  future directions, 887
  GFP variants for, table, 873
  imaging extracellular polymeric substances (EPS), 879–882
    lectin-binding analysis, figures, 881, 882
  lifetime imaging, 530
  magnetic resonance microscopy, 624
  making bacteria fluorescent, 873–874
  pH imaging, 530, **739–745**
  sample mounting, 870–873
    flow chamber system setup, 872–873
    perfusion chambers, 870–872
    pump selection, 871
    upright *vs.* inverted microscopes, 870, 872
    water-immersible lenses 149. 161, 209, 411, 429, 568, 613, 727, 737, 870, 872.
  stains for, 874–879, 875
    Acridine Orange, 23, 344, 531, 665–667, 691, 774, 874
    antibodies, 877–878
    biofilm community on tooth, 879
    DAPI, 874. *See also*, DAPI
    effect of antibiotic treatment, 877
    embedding for FISH, 876–877
    FISH with fluorescent protein, 875–876, 878
    imaging bacteria, backscattered light, 879
    live/dead stain, *Streptococcus gordonii*, 876
    nucleic acid, 874–875
    preparing labeled primary antibodies, 878
    SYTO, 874–875
  temporal experiments, 885–886
    multi-cellular biofilm structures, 886
    time-lapse confocal imaging, 885–886
    transmitted laser light image, 880
Bioimagers, kinetics, endpoint analysis, 816–817.
Biolistic transfection, 360, 724–726, 803.
Biological accuracy, *vs.* statistical accuracy, 24, 36–37, 68, 73, 312.
Biological reliability, of measurements, 24, 36–37, 68, 73, 312.
Biological specimens, 6, 11, 12–13. *See also,* Plant cell imaging, Biofilms, Specimen preparation, and entries under specific equipment and cell/tissue type.
  backscattered light images, 22–23, 25, 167–168, 170, 880
  CARS imaging, 603–604
    adipocyte cells, 604
    epithelial cells, 603
    erythrocyte ghosts, 603
  distortions caused refractive index
  inhomogeneity, 40–41, 181, 182, 198–199, 419
  tandem scanning systems for, 6, 11
  Yokogawa CU-10, 12–13
Biophotonic crystals, 188, 428.
Bio-Rad, 25, 33, 35–36, 70, 113, 214, 260, 630, 638–640, 657, 748–752, 757, 759–762, 858, 889.
  1024ES, 710–711, 714, 718–719
    data storage, 585
    using white light source, 113
  MRC 1024, photon counting, 33
    photon efficiency, 25, 32, 261, 748–752
  MRC-600 scanner, full-integration digitizer, 70
  PMT, 260–261
  Radiance-2100, 23, 185
  resolution, 657
Biosensors, fluorescent, **33–8348**, 799, 805. *See also,* Dyes, Fluorophores, and Chapters 16 and 17.
  future, 805
  mitotic clock measurements, 799
Birefringence, 6, 15, 54, 83, 103, 109, 113, 116, 162–164, 188, 189, 414, 420–421, 431, 434, 436, 438, 479, 503, 710–711, 714, 717, 894.
  acousto-optics, 54, 55
  collagen fibers, 164, 188, 717
  contrast, 15, 162–164, **188**, 414–428, 431–438, 710–711, 714, 717, 719, 894
  deconvolution, 479–480
  defined, 163, 188
  in fiber-optics, 503
  harmonic generation from, **428**, 431–438
  images of *Cymbopetalum baillonii*, 189
  in laser components, 85, 103, 109, 113, 116
  quarter-waveplate, 6
  table, 715

Birefringent crystals, 188, 420–421.
optical effects of acoustic fields on, 54, 55
Black-body radiation, 44, 135–136.
from incandescent lamps, 44, 126, 135–136
spectrum, 136
Bleaching, 10, 12–13, 20, 24, 44, 63–64, 90, 142, 186–187, 194, 202–203, 210, 218, 220, 222, 340, 382–387, 442, 539–540, 690–702, 797, 905, 907.
2-photon excitation, 539–540, **680–689**, 905
acceleration, 341
of acceptor in FRET, 184–187
anti-bleaching agents, 36. *See also,* Anti-bleaching agents
bleach patterns, 3D, 538, 628, 693
beam blanking, to reduce, 53–54
before/after ratio, for donor/acceptor pair, 794
chapter, 690–702
combining fluorescence with other, 383–386
in dye lasers, 103
dynamics, 202–203
fluorescence correlation spectroscopy, 383, 801
fluorescence lifetime, 382–383
fluorescence recovery after photobleaching, 51, 54, 56, 80, 90, 187, 210, 218, 224, 229, 237, 362, **382**, 684, 390, 691, 759, 801, 805, 850
FRET, 186, 382, **794–798**, 800
fluorescence speckle microscopy, 383
in four-dimensional imaging, 222
improvement, recent, 36
laser trapping, 383
linear unmixing, 192, 382, 664–667
of living cells, 212, 220, 382, 797. *See also,* FRAP, FLIP
intensity dependence, 341, 363
mechanism, 222–223
of non-specific fluorescence, 27, 44, 74
optical tweezers, 383, 385
performance limitations, 221, 224, 232, 381, 448–450, 556, 693. *See* Chapter 39
photoactivation, 187, 224, 383, 385, 541, 544–545, 693, 759
photo-uncaging, 383. *See also*, Photo-uncaging and signal per pixel, 63–64
spectral unmixing, 192, 382, 664–667
table, 384–385
techniques, 125
temperature as a variable, 696–698
time-lapse fluorescence, 382
Bleedthrough fluorescence, 185, 203, 664, 904.
multi-tracking, reduces bleed-through, 664
Blind deconvolution, 190, **468–487**. *See also*, Deconvolution.
2D approach, 476–477
3D approach, 475–476
advantages/limitations, 468–472
algorithms, 472–474
of *A. thaliana* seedling image, 190
confocal stack, 470
data collection model, 472
data corrections, 477
defined, 469
DIC schematic, 475
DIC stack example, 470
different approaches, 475–477
deblurring algorithm, 476
Gold's ratio method, 476
inverse filter algorithm, 476
iterative constrained algorithms, 475–476
Jansson-van Cittert algorithm, 476
nearest-neighbor algorithm, 476
no-neighbor algorithm, 476–477
processing times/memory table, 476
Richardson-Lucy, 497, 568
TIRF microscopy, 477
differential interference contrast (DIC), 473–475
examples, 469, 470, 481, 482, 483
flowcharts, 473, 474
future directions, 483
Gerchberg-Saxton approach, 472
hourglass widefield PSF, 474
light source/optics alignment, 478
maximum likelihood estimation (MLE), 472–477, 669–670
new developments, 478–480
live imaging, 480
polarized light microscopy, 479
subpixel imaging, 478–479
optical sectioning schematic, 469
OTF frequency band, 474
simulated example, 481, 482
speed, 482–483
spherical aberration correction, 480–481, 471
spinning-disk confocal example, 481, 482, 482
transmitted light, bright-field (TLB), 472, 477
two photon example, 481, 483
widefield simulated example, 481, 469
WWF stack example, 469
Blind spots, due to sampling with large pixels, 38.
Blue Sky Research, ChromaLase 488, 107.
Boar sperm cells, 557.
BODIPY dye, 142, 342–343, 353–356, 389, 692, 749, 760–762.
BODIPY TR, methyl ester dyes, 760–762.
Bolus injection protocol, 360, 726, 728, 731.
Bone, reflectance, 167.
Books on 3D LM, listing, 889.
Borohydride, to reduce glutaraldehyde autofluorescence, 374, 770.
Botanical specimens, **414–439**, 624, **784–785**. *See also*, Plant cell imaging, and Chapters 21 and 44.
birefringent structures, 420–421. *See also*, Birefringence
deconvolution, 784–785
effect of fixation on, 195, 428
Equisetum, 774
fluorescence properties, 421–428
emission spectra, 421–423
microspectroscopy, 421–426
fluorescence resonance energy transfer, 425.
See FRET, 425
harmonic generation properties, 428, 711–715
light attenuation in plant tissue, 414–418
absorption spectrum, 415
A. thaliana example, 416
maize stem attenuation spectra, 417, 418
M. quadrifolia attenuation spectra, 416
M. quadrifolia optical sections, 419
Mie scattering, 162–163, 167, 417–418
nonlinear absorption in, 416–417
Rayleigh scattering, 162–163, 167, 417, 703
light-specimen interaction, 425–428
living plant cell, 429–439
calcofluor staining procedure, 424, 438
callus, 429
cell walls, 168–169, 188–189, 303, 306, 416–417, 420–421, 428–431, 435–136, **438**, 439, 710–711, 713–715, 769–776, 779–781
chamber slides, use, 429
culture chamber, 429
cuticle, 434–437, 715, 717, 779
fungi, 438–439, 624, 782, 870
hairs, 431, 434–436, 772
meristem, 168, 420, **430**, 770, 776–778, 783
microsporogenesis, 431–432
mineral deposits, 163, 420, **436–438**, 703
pollen germination, 420, 433–434, 781, 783
pollen grains, 202, 305, 313, 420, **431–433**, 553, 558, 781, 783
protoplasts, 195–196, 203, 416, 421, **423–427**, 429–431, 438–439, 693
root, 172, 174, 303, 307, 421, 429, **430–431**, 438, 464–465, 556, 772–773, 775, 777, 779–783
starch granules, 202, 420–421, 428, **432–433**, 435, 703, 710–712, 715, 719
stem, 168, 172, 180, 417–419, 421, 424, **429**, 556, 707, 710–711, 713–714
storage structures, 435–436

Botanical specimens (*cont.*)
suspension-cultured cells, 189, 429–430
tapetum, 433–434, 779
waxes, 420, 428, 434–435, 714–715
point spread function in, 784
refractive index heterogeneity, 192, 418–420
maize stem, 419
Bovine embryo, 750.
Boyde, Alan, 2, 6, 141, 154, 224. *See also*, Stereoscopic images.
BPNN. *See* Backpropagation neural network.
Bragg grating, tuning diode, 107.
Brain slices, 392–398, 722–734. 686.
beam collimation, 728
choice of objectives, 395, 727–728
future directions, 929
image processing for, 732–734
algorithms, 733
alignment, center of mass in, 732–733
alignment, based on image overlap, 732
automatic detection of neurons, 733–734
drift/vibration compensation, 396, 732
image de-noising using wavelets, 734
image processing/analysis, 330–331, 395–396, 730–732
biocytin protocol, 730
classified using cluster analysis, 731–732
correlated electron microscopy, 731
montaging, 331
neuron reconstruction, 330–331, 730
protocol for PCA/CA, 731–732
spectral imaging, 382
two-photon/neurolucida system, 316
image production, 729
2-photon excitation, 727
deep imaging, 395
living neurons, 725
maintaining focus, 395, 732
microglia, 397–398
neuronal ensembles, 726
objective lenses, choice of, 727–728
second harmonic imaging, 729–730
in vivo observations, 387
preparation, 387
labeling cells, 394–396, 724–727
biolistic transfection, 724–725
bolus injection, 726
calistics, 726
choice of dyes, 729
diolistics, 726
dye injection/patch clamp, 726
genetic manipulation, 725–726
GFP transgenic mice, 726
Helios Gene Gun, 724
live-dead staining, 393
painting with AM-ester indicators, 726–737
photoactivation, 383
slice loading, 726
linear unmixing, 192, 382, 664–667
making brain slices, 393, 722–724
acute slices, 722–723
autofluorescence, 383
cultured slices, 724
mouse visual cortex, 723
primary visual cortex, 724
protocols, 731
thalamocortical slice, 724
photodamage, 729
pulse broadening, 728
reducing excitation light, 390–391
resolution, 729
second harmonic imaging (SHG), 729–730
silicon-intensified target (SIT) camera use, 730
slice chamber, 394
protocol, 727
speckle microscopy, 383
useful techniques, table, 384–385
time-lapse, 382
two-photon imaging, 727
calcium imaging, 729
z-sectioning, 729
Breakdown.
electrical, in PMTs, 263, 660
optical, high power density, 198, 680, 682, **685**, 687, 703, 705
Brewster surfaces, 83.
Brewster windows, 83, 102–103, 115.
Bright-field microscopy, 6, 127, 130, 201, 224, 229, 448, 468, 649, 728.
CCD for, 127, 483
deconvolution, 468, 472–473
depth of field, 4
low coherence light for, 130, 134–135, 139–140
optical projection tomography, 610–612
Brightness, source, 21, 26, **126–127**, 129–130, 141–142, 215.
and exposure time, 141–142
gray levels, 71–73
as limitation of disk-scanners, 21, 215
of non-laser light sources, 126–127
of sun, 127, 135
Brillouin background, in glass fibers, 88.
Brillouin effect, reduction, 110.
Brownian motion, microtubules, 11.
BSL. *See* Backscattered light.
Buffering, fluorescent ion measurement, 740.
Bulk labeling, in living embryos, 761.

C

C. elegans, 746, 748, 766, 856, 857–858.
cryopreparation, 857–858
FRET imaging, 766
as model system, 746, 748
TEM images, 856, 857
Ca^{2+} imaging, *see* Calcium imaging.
Ca^{2+} indicators, 346–347, 738, 742–743. *See also*, Ca^{2+} sparks, 737–738, 742.
discovery, 737, 738
Caenorhabditis elegans. see C. elegans.
Caged compounds, 759–760.
multi-photon excitation, 543–544
Calcein AM dye, 355, 360, 362–363, 426–427, 430, 685, 804, 812.
Calcium imaging, 529, 545, 584, 736–737, 812.
calibration, 742–743
data compression, 584
intensity image, 529
introduction, 736
multi-photon excitation, 545
ratiometric, 189
signal-to-noise ratio, 737
single-cell kinetic, 812
TIRF for measuring, 180
very fast imaging, 237
Calcium ion dyes, 183, 189, 237, 736, 737, 741–743. *See also*, fura-2, Fluo-3 and Indo-1.
Fluo-3 and Fura Red indicator system for determining, 183
Fluo-3 indicator system for determining, 737
fura-2 reactions, 741–742
Indo-1 and Fura-2 indicator system for
Calcofluor, 424, 438.
staining procedure, 438
Calibration, 34, 75–76, 742–745.
Ca^{2+} sparks, 742
of CCD to measure ISF, 75–76
confocal microscopy, 742
errors in, 744
of ion concentrations, 742–745
ion interference, 745
of effective pinhole size, 34
in vitro, 742
Calistics, 726.
Callus, 429.
Cambridge Technology, galvanometers, 54.
cAMP indicators, 347.
Canna, 422, 710.
fluorescence spectra, 422
as function of excitation intensity, 165
nonlinear absorption, 710
Carbon arc lamps, 136.
CARS. *See* Coherent anti-stokes Raman scattering.
CARS correlation spectroscopy (CS-CARS), **602**.
Raman spectra, 602
CARV disk-scanning confocal microscope, 215, 226, 229, 230, 907–908.
diagram, 230, 907
CAT. *See* Computed axial tomography.
Cathode-ray tube (CRT), 5–6, 53, 67, 72–73, 291, 293, **588–589**.
gamma, compensation, 73
Cavities, of dielectric coatings, 46, 47.

Cavity-dumped lasers, 111, 114.
  for FLIM imaging, 114
CCD. *See* Charge-coupled devices.
CD. *See* Compact disks.
cDNA-GFP fusion, in plants, 773.
Cedara, **281–282**, 288, 302, 308.
Cell adhesion imaging with TIRF, 90.
Cell autofluorescence, 742.
Cell chambers, 11, 22, 191, 219, 370–371, **386–387**, **394**, 429–430, 564, 610–611.
  for 4Pi confocal, 564
  for biofilms, 870–873, 875, 877, 880, 885
  brain slice, 394, 723, 727, 729
  for epithelial cells, 370–371, 377, 386
  finder chamber, 683
  flow chamber, 870–873, 875, 877, 880, 885
  for high-content screening, 810
  for optical projection tomography, 610–611
  perfusion, 394
  for plant cells, 191, 429–430
  simple, 22, 394
  for SPIM, 613, 625, 673
  table of required functions, 380
  table of suppliers, 388–389
  test chamber/dye, 654, 661
Cell cycle, 790, 791.
Cell damage, 2-photonmicroscopy, 680–688 *See also*, Bleaching; Photodamage.
  absorption spectra of cellular absorbers, 681
  intracellular chromosome dissection, 688
  mitochondria, 686
  nanosurgery, 219, 686–687
  one-photon *vs.* multi-photon, **680–689**
  by optical breakdown, 198, 680, 682, **685**, 687, 703, 705
  photochemical, 682–685
    absorbers/targets, 682
    beam power sensor, 683
    impact on reproduction, 686, 685
    laser exposure parameters, 682–683
    NIR-induced DNA strand breaks, 683–684
    NIR-induced ROS formation, 683
    photodynamic-induced, 684
    spectral characteristics, table, 682
  photothermal, 685
  reproductive effect, short NIR pulses, 682, 686
  ultrastructure modifications, 685–686
Cell microarray (CMA), 815–816.
Cell motility, 757.
Cell nuclei, optical effects, 23.
Cell pellet, three dimensional, 815.
Cell surface targeting assays, 813.
Cell walls of plants, 168–169, 188–189, 303, 306, 416–417, 420–421, 428–431, 435–436, **438**, 439, 710–711, 713–715, 719, 769–776, 779–782.
  labeling, 775
  viability, 780
Cell-by-cell analysis, 817.
Cell-cell signaling, 778.
Cellular structures, optical effects, 22–23.
Center-of-mass alignment protocol, 733.
Center pivot/off-axis pivot mirrors, 1, 214.
Cerium, doping of quartz lamp envelope, 116.
CFP and YFP molecules, in FRET pair, **798–800**.
Chambers for living cell imaging, 388–389.
  commercial suppliers, table, 388–389
Charge amplifiers, 923–924.
  defined, 923
  destructive readout, 923
  FET amplifier performance, 923
  non-destructive (skipper), 923
Charge-coupled device (CCD), 26–28, 30–31, 39, 61–62, 65, 70, 74–78, 88, 127, 137, 142, 215, 233, 254, 458–459, 460–461, 482, 552, 558, 644, 754–755, 784, **918–931**. *See also*, Electron-multiplier
CCD.
  bit depth, 75
  camera, 918–931
    advances in, for speed, 754–755
    bright-field imaging, 127
    for disk scanner systems, 78, 205, 215, 220, **233–235**, 349, 459, 754–755
    pixel size, 62, 65, 634–635, 784
    specifications, table, 929
    time for sampling, 70
  choosing,
  color, 927
  computer-assisted pulse shaper, 88
  confocal imaging, 458–459
  cooled, advantages and limitations, 30–31
    quantum efficiency, 26–28
    spatial quantization of signal, 39
  digital camera, 75
  digital *vs.* video camera, 61–62
  electron multiplier-CCD, 30–31, 76–77, 233–**235**, **262**, 459–461, 482, 925–926
    multiplicative noise, 77, **234**, **257**, 262, 926
    result, 205, 234, 755
    table, 233, 459
  evaluating, 927–931
    array size, 928–929
    "the clincher," 929
    comparison, CCD/EM-CCD, table, 233, 459
    dynamic range *vs.* pixel size, table, 928
    maximum signal, 930
    quantum efficiency, 927–928
    readout noise, 928
    readout speed, 928–929
    self test, 930
    sensitivity, 930
    shutter stability, 929
    specifications, 927, table, 233, 929
    user-friendliness, 929
  gain-register, 76–78, 460–461
  intensified, 930–931. *See also*, Intensified CCD
  monitoring during exposure, 137
  multi-focal multi-photon microscopy, 552, 558
  noise sources, **256**, **924–925**
    charge amplifier, 925
    clock-induced charge (CIC), 234, 926
    fixed pattern noise, 924–925
    multiplicative noise, 77, **234**, **257**, 262
    noise *vs.* pixel dwell time, 922
    table, 256
  operation, 254, 918–927
    blooming, 923
    charge amplifiers, 923–924
    charge coupling, 918–920
    charge loss, 921
    dark charge, 921–922
    destructive readout amplifiers, 924
    edge effects, 921
    electron multiplier, 926–927
    FET amplifier performance, 253, 922, 924
    frame transfer readout, 920
    full-frame readout, 920
    gain register amplifier, 925–926
    incomplete charge transfer, 923
    interline transfer readout, 920
    leakage, 921–922
    non-destructive (skipper) amplifiers, 923–924
    possible problems, 920
    quantum efficiency *vs.* wavelength, 922
    quantum efficiency, 920–921
    readout methods, 920
    signal level representing zero photons, 925
    storage array, 920
  performance, table, 256, 459, 923
  piezoelectric dithering, increases resolution, 70
  pixel size, 62, 65, 634–635, 784, 928
  quantum efficiency and noise, 29, 644, 920, 922
    measuring, 74–76, **926**
  sensors size, parallel data collection, 142
  snapshot camera, 65
  specifications, described, 927–930
  testing, 930
Cheek cells, backscattered light image, 22–23.
Chemical environment probe, 517.
Chimeric fusion proteins, 794, 801–802.
  anisotropy analysis, 794
  cloning for FRET, 801–802
  overexpression, 802
Chinese hamster ovary cell, 197, 556. 684^{+}, 818.
Chirp, pre-compensation, 88, 111, 602, 907.

Chlorophylls, autofluorescence, *A. thaliana,* 175, 194, 203, **425–426**, 528, 711, 714, 779, 782, 881.
bleaching, 203
FLIM, **528**
Cholera toxin transport, 790–791, 796–797, 802.
FRET, 796–797, 802–803
Chromatic aberrations, 134, 152–156, 178, 242–245, 657–658, 659.
apparatus for measuring, 243
axial chromatic registration, 243–345, 658, 657–659
of incandescent and arc lamps, 134
intentional, for color/height encoding, 154
lateral chromatic registration, 657–658
fluorescent latex bead labeled, 178
linear longitudinal chromatic dispersion, 154, 659, 664
measuring, 242–245
Chromatic corrections, 157, 177.
excitation/emission wavelength, 177
tube length, table, 157
Chromatic magnification difference. *See* Lateral chromatic aberration.
Chromatin, 385, **390**, 684, 693–695, 812.
Chromophores, **338–348**, **543–544**, 803–804. *See also*, Dyes; Fluorophors; Fluorescent probes etc.
cellular introduction methods
electroporation, 359–360, 803
microinjection, 360–361, 388, 739, 748, 755, 795, 803–804
table, 344–345, 803
transfection reagents, 358, 360, 362, 556, 682, 790–791, 795, 803
multi-photon excitation, 543–544
CIC, clock-induced charge, EM-CCDs, 234, 926.
Circular exit pinhole, 9.
Circular laser beam, corrective optics, 106.
Classification, pattern. *See* Automated interpretation of subcellular patterns.
Clathrin-GFP dynamics, 236.
Clearing agents. *See also*, Mounting media.
optical projection tomography, (OPT) 610, 624
plant material, 166, 417–420, 439, 774–775
Clock, role in digitizing and reconstructing analog signal, 64.
Clock-induced charge, in EM-CCDs, 234, 926.
Closterium, 192–194.
chloroplast autofluorescence, 192–195
signal variation with depth, 194
CLSM. *See* Confocal laser-scanning microscopy.
Cluster analysis (CA), 731–732, 826.
neurons classified using, 731–732
protocol with PCA and, 731–732
subcellular patterns, 826
CMA. *See* Cell microarray.
CNS, (central nervous system), 392–393, 395. *See also*, Chapters 19 and 41.
Codecs, image processing, 831, **836**, 840–841.
Coefficient of variation, 660, 661.
Cohen's k statistic, 826.
Coherence length, 7–8, 84.
defined, 7–8, 84, 130–131
reducing, for laser light, 84
Coherence surface, 84.
Coherence volume, 84.
Coherent anti-stokes Raman scattering (CARS), 90, 204, 550, 595–605.
advantages, 204, 596
correlation spectroscopy, 602–603
defined, 595
energy diagram, 596
epi-detected, 597–599
forward/backward detected, 597–599
Hertzian dipole radiation pattern, 598
history, 595–596
imaging of biological samples, 603–604
adipocyte cells, 604
artificial myelin, 204
epithelial cells, 603
erythrocyte ghosts, 603
intensity distribution, 597
mapping intracellular water, 90
microscope schematic, 599
multiplex CARS microspectroscopy, 601–602
non-resonant background suppression, 600–601
energy diagram for multiplex CARS, 601
epi-detection, 600
phase control of excitation pulses, 600
picosecond *vs.* femtosecond pulses, 600
polarization-sensitive detection, 600
time-resolved CARS detection, 600
optimal laser sources, 599–600
pumped optical parametric oscillator (OPO)
systems, 600
perspectives on, 604–605
unique features under tight-focusing, 596–597
Coherent illumination, 1, 83–84.
properties of laser light, 83–84
and resolution, 1
Collagen fibers, 164, 188, 313, 361, 393, 514, 703–704, 715.
autofluorescence, 545
birefringence, 164, 188, 717
gels, 393
polarization microscopy, 164, 188
second harmonic image (SHG), 703–704, 715
Collector optics, elliptical and parabolic, 129.
Colliding-pulse, mode-locked laser (CPM), 540.
Colloidal gold labels, 167, 241, **846–859**.
contrast, 167
electron microscope markers, 846–857
correlative, 850, 852, 855
SEM, 850
TEM
FluoroNanoGold, 854
GFP related, 854–855, 857–858
measuring resolution, 241
quenches fluorescence, 854
Rayleigh scattering, 167
Colocalization, 517, 650, **667–670**, 794, 813, 881.
FRET, FRET, 519
erroneous, 581
Color display, 291, 292.
display space, 291
multiple channel display, 292
palette, 291
pseudo, 173–175, 190, 291
resolution, 291
true, 291
Color centers, in optics, avoidance, 116.
Color filters, **43–52**. *See also*, Filters.
long-pass, **43–46**, 175, 203–204, 212
short-pass, 45, 46
bandpass, 44, 45
Color print images, 592.
Color reassignment, 173–175, 190, 291.
Coma, 145, 151, 245, 247, 249, 483, 630.
distortion away from optical axis, 151
observation using point objects, 145, 246
Commelina communis, images, 712.
Commercial confocal light microscopes, 906–917.
BD-CARV II, 230, 907
La Vision-BioTec TriM-Scope, 907
Leica, TCS SP2 AOBS, 910
Leica MP RS Multi-photon, 910
Nikon C1si, 911
Olympus DSU, 913
Olympus Fluoview-1000, 912
optical parameters of current, table, 908–909
Visitech VT Infinity, 914
Visitech VT-eye, 914
Yokogawa CSU 22, 231, 915
Zeiss LSM 510 META optical, 916–917
Zeiss LSM-5-LIVE Fast Slit Scanner schematic, 232, 916
Compact disks (CD) for data storage, 499, **586–587**, 588, 731.
Compact flash cards, 588.
Components, of confocal fluorescence microscopes, 43–58, 207–208.
acousto-optical devices, 54–57
chapter, 43–58
electroptical modulators, (Pockels cells), 25, 54, 57, **87**, 116, 543, 701, **903–904**
filters/beam-splitters, 44–51

mechanical scanners (galvanometers), 51–54
polarizing elements, 58
Computed axial tomography (CAT), 610–611.
Compression, data see, Data compression.
Condenser lens, size, 129.
magnification, 128–129
Configuration of pixels in image plane, 62.
ConfMat. *See* Confusion matrix based method.
Confocal disk-scanning microscope. *See also*, Disk-scanning confocal microscopy.
Confocal fluorescence microscope, 73, 207, 404–413. *See also*, Confocal microscopy; Confocal laser-scanning microscopy.
basic optical layout, 207
limitations due few photons, 73, 459
refractive index mismatch, 404–413 *See also*, Refractive index
Confocal imaging, 4–5, 232, 235–236, 737, 738, 746–766, 809–817. *See also*, next major head and Chapters 35 and 36.
4Pi. *See* 4Pi microscopy
automated
for cytomics chapter, 809–817
of microarray slide, 816
platforms used for, 810
real-time, 810
temperature control, 810
types of assays for, 811, 813–814
workstations, 814
of biofilms, Chapter 50
deconvolution, 753. *See* Deconvolution
by disk-scanning confocals, 232
fast, 235–236
of fluo-3 loaded cardiac myocyte, 737
fluorescent indicators for, 738
high-resolution datasets, cell arrangements, 776
of living cells, 813
of living embryos, chapter, 746–766
methods compared, 459, **644–647**. *See* Chapters, 22, 23, and 24
of plants, 773. *See also*, Chapters 21and 43
vs. non-confocal, 746
time-lapse. *See* Time-lapse imaging
Confocal laser-scanning microscopy (CLSM), 9–15, 32, 38, 81, 89, 118, 222–224, 408, 518, 678, 690, 697, 750–751, 754, 884–885. *See also*, next major head
advantages and limitations, 11–12, 222–223, **644–647**, 884–885
alternatives to, **644–647**, 754
comparisons, **644–647**
disk-scanning and scanned slit, table, 224
digitizer employing full integration for, 32
edge response, 408
fluorescence lifetime imaging, chapter, 518
laser power required, 81
laser requirements for, 89
vs. multi-photon laser-scanning microscopy, 750–751. *See* Chapters 22, 23, 24
photobleaching, 690, 697
vs. selective plane illumination microscopy, (SPIM), 678
stage-or object-scanning, 13–15
TEM mode, 118
zoom magnification and number of pixels, 38
Confocal microscopy, 90, 141, 265, 381–399, 444–447, 453–467, 650–670, 742, 770, 774, 779, 810, 811, 815, 870–887. *See also*, preceding major head and Chapters 35 and 36.
art of imaging by, 650
automated, platforms used for, 810
balancing multiple parameters for, 650
of biofilms, 870–887
calibration of, 742
cell microarray and, 815
colocalization, 667–670
effect of MLE and threshold, table, 669
fluorogram analysis, 669
image collection, 667–668
nerve fiber, 669
quantifying, 668
setting thresholds, 668
spatial deconvolution in studies, 668–670
vs. deconvolution, **644–647**, 453–467. *See also*, Chapters 22, 23, 24
CCD/confocal imaging combination, 458–459
deconvolving confocal data, 461–464, 466, **488–500**
fluorescence excitation, 459
fluorescent light detection, 459–460
gain register CCDs, 460–461
image sections, figures, 455, 456, 462
imaging as convolution, 453–457
integration of fluorescence intensity, 459
limits to linearity, 457
model specimens, 461
noise, 459–463
out-of-focus light, 461
point spread function, 453–457
practical differences, 458, 463–466
resolution, 459–463
same specimen comparison, 465
sensitivity, 459–463
shift invariance, 457, 490, 564
single point imaged, 454
summary of pros/cons, table, 459
temporal resolution, 458
focus positioning, 651–652
getting a good confocal image, 629–631
alignment of optics, 629–630
back-focal plane (BFP), 210, 509, 629, 633
focus, 629
low signal, 631
mirror test specimen, 630
no signal, 631, 660
simultaneous BSL/fluorescence, 631
high-content screening systems, table, 811
illumination sources, **126–144**, 650–651 *See also*, Lasers; Non-laser sources
acousto-optic tuning filter (AOTF), 651.
laser sources, chapter, **80–125**
laser stability, 651
power measurement, 650–651
living cells, 381–399. *See also*, Living cells
Minsky first confocal design, 2, 4–6, 11, 141, 216, 890
monitoring instrument performance, 650–663
illumination source, 650–651
optical performance, 652–660
photon efficiency, 14–15, 24
scan raster/focus positioning, 651–652
signal detection, 660–663
with non-laser light, 141
objective lens, 652–660. *See* Chapter 7
optical performance, 652–660. *See also* Chapters 7, 11
axial chromatic registration, 658–659
axial resolution *vs.* pinhole, 656–657. *See also*, Axial resolution
contrast transfer function, 656. *See* CTF
coverslip thickness and RI, table, 654
field illumination, 658
flatness of field, 659
Focal Check™ beads, 657–659
lateral chromatic registration, 657–658
lateral resolution, 655
refractive index, 654. *See* Chapter 20
resolution test slides, 656
self-lensing artifacts, 659
spherical aberration, correction, 654, 655
subresolution beads, 655–656
x-y and z resolution using beads, 656
optimizing multi-labeling, 663–667
bleed-through between channels, 663
control samples, establishing limits, 663
measuring autofluorescence, 663
multi-tracking, reduces bleed-through, 664
positively labeled sample, 664
reflected light contribution, 663
secondary conjugate contribution, 664
photon efficiency, 24, 26, 28, 30 33–34, 36
polarizing elements, 57
scan raster, 651–652

Confocal microscopy (*cont.*)
malfunctioning system, 653
phototoxicity from uneven scan speed, 651
sources of fluorescent beads, table, 653
well-calibrated system, 652
x and y galvanometers, 651–652
z-drive mechanism, 652
z-positioning calibration, 654
z-positioning stability, 652
separating signal by spectral regions for, 664
sequential collection reduces bleed-trough, 664
signal detection for, 660–663
coefficient of variation, 660–661
instrument dark noise, 660
PMT linearity, 661–662
signal-to-noise ratio, 660
spectral accuracy, 662
spectral detector systems, 662
spectral resolution, 662–663
wavelength response, 663
signal level, 444–445
signal-to-noise ratio, 444–447
spectral analysis, of plants, 770
spectral unmixing, 192, 382, 664–667
limitations to, 667
overlapping fluorophores separation, 664–667
removing autofluorescence, 667
stage-scanning, 9
staining plant cells, 774
vs. structured-illumination methods, 265
vs. two-photon excitation, 779
Confusion matrix based method (ConfMat), 826.
Constant output power laser stabilization, 86.
Continuous wave (CW) laser, 87, 88, **90–118**.
beam intensity stabilization, 86–87
diode (semiconductor), 105–110
output power/cooling, 108
pumped solid-state, table, 94, 95
dye lasers, 86, 103, 112, 114, 124, 540–541
fiber up-conversion, 109–110
gas lasers
Argon-ion, 90, 102
Krypton-ion, 102
HeNe, 102
HeCd, 103
cesium and rubidium vapor, 103–105
table, 92–93
titanium-sapphire, 109
Contrast, 7, 11, 16, 37, 39, 49, **59–62**, 68, 159, **162–204**, 248, 421, 473, 488, 542, 599–600, 607, 622, 656, 657, 675. *See also*, Rose criterion and CTF.
absorption, equations, 164
chapter, 162–206
defined, 162
flare, 649
formation of, chapter, **162–206**
fluorescence. *See* Dyes, and Fluorophores
as function of feature size, 16, 61–62, 37, 634
intrinsic, 633
measuring, 16, 59
polarization. *See* Polarization microscopy
second harmonic generation. *See* SHG
and statistics, 633
third harmonic generation. *See* THG
Contrast medium, and laser power, 80–81.
Contrast method, defines signal required, 126.
Contrast transfer function (CTF), 16, 35, 37–39, 59–62, 656, 747.
in confocal *vs.* non-confocal microscopy, 16.
See Chapter 11
as function of grating period, 16
of microscope optical system, 35
relationship with objective BFP, 61
and spatial frequencies, 16, 37
and stages of imaging, 62
Control, of non-laser light sources, 138–139.
Convalaria majalis, 425, 556.
fluorescence microscopy of rhizome, 425
multi-focal multi-photon imaging, 556
Conversion techniques, 259–260.
analog-to-digital, 259
digital-to-analog, 259–260
Convolution, a primer, 485–487.
3D blurring function, 486
Fourier transforms, 487
geometrical optics, 487
out-of-focus light, 486–487
Cooling water, checking/maintaining, 116–117.
Cork microstructure, 770.
Correction collar, (spherical aberration), 15, **145–149**, 158, 160–161, 178, **241–242**, 247, 377, 407, **410–412**, 471, **654–655**, **657**.
adjustment, 377, 407, 471, 499, **654–655**
dry objectives, 410
multimedia, 640
Correctors, 70, 147.
spherical aberration, 15, 151, 147, 192, 411–412
Intelligent imaging innovations, 78–79, 151, 192, 395, 411, 654
to stored data, second Nyquist constraint, 70
Corrective optics, for diode lasers, 107–108.
Correlational light microscopy/electron microscopy, 731, 434, 436–437, 846–860.
BSL image, 855
brain slices, 731then CLSM, 856–857
cryopreparation of *C. elegans*, 857–858
DIC image tracking, 849
DIC image/UV fluorescence image, 850
different requirement of LM/EM, 846–850
early 4D microscopy, 846
fluorescence/TEM to analyze cytoskeleton, 854
fluorescent micrographs, 851
FluoroNanoGold for cryosections, 854
GFP, 854. *See also*, Green fluorescent protein
HVEM stereo-pair, 848–849
immuno-stained bovine aorta, 852
LVSEM of FRAPed microtubules, 849, 850
phalloidin as correlative marker, 235–236, 344, 376, 378, 694, 696, 756, 804, **854–856**
phase-contrast imaging, 851
postembedding, 855
quantum dot labeling, 853
same cell structure LM/SEM, 850–852
same cell structure LM/TEM, 852–856
SEM images at 5kV and 20kV, 847, 848
TEM cross-section of *C. elegans,* 856
TEM longitudinal section of *C. elegans,* 857
tetracysteine tag labeling, 221, 348, 357, 853
tiled montage TEM images, 858
time-series DIC images, 847
Correlative LM/EM. *See* Correlational light microscopy/electron microscopy.
Coumarin dye, 114, 339, 344–345, 353, 355, 654–655, 661, 693.
Counting statistics, 20, 30. *See* Poisson statistics.
Cover glass. *See* Coverslip.
Coverslip, and spherical aberration, 15, 147–150, 201. *See also*, Spherical aberration.
CPM laser. *See* Colliding pulse mode-locked laser.
Crane fly spermatocyte, metaphase spindle, 15.
Creep, in piezoelectric scanners, 57.
Cr:Fosterite, femtosecond pulsed laser, 109, 114, 415, 541, 706–709, 712–714.
Critical angle, for reflection of incident light surface of refracting medium, 167, 502.
Critical illumination of the specimen, 128–129.
Crosslinking fixatives, 369.
Crosstalk.
between fluorescence channels, 203, 424, 882
between disk pinholes, 227
between excitation foci, **553–556**, 558–559, 564
CRT. *See* Cathode-ray tube.
Crystal Fiber A/S, HC-800-01 bandgap fiber, 88.
CSU. *See* Confocal scanning unit.
CTF. *See* Contrast transfer function.

Curtains, laser, safety, 118, 904.
Cuticles, plant, 434–437, 715, 717, 779.
  insect, 166
  maize, 436
CW. *See* Lasers, continuous wave.
Cyan fluorescent protein (Cyan), 221–222.
Cyanine dyes, 339, 342, 344, **353–355**, **362–363**, 374, 443, 540, 587, 760, 854, 874.
Cytomics, 810, 811.
  automated confocal imaging, 810
  automated confocal imaging, table, 811
Cytoskeletal structures, 24, 188, 190, 328–329, 368, 370, 372, 378, 383, 461–462, 577, 703, 715, 719, 773–774, 813, 846–848, 852, 854.
  LM-TEM analysis, 846, 854
  stabilizing buffer, 852
Cytosolic markers, 757.
Cytotoxicity, reducing, 36–37. *See also,* Bleaching; Phototoxicity.

D

DAC. *See* Digital-to-analog converter.
Damage threshold, LED sources, 139.
DAPI, 140, 344–345, 355, 358, 376, 431.
  plants, 431
  use of, 376
Dark current, 29, 76, 234.
  fixed-pattern noise due to, 76
  of photomultiplier tube, 29, 660
  reducing, 234
Dark noise, defined, 232.
Darkfield microscopy, 5, 7, 172, 474, 672.
  depth of field, 4
Data, 11–12, 33, 64, 76, 237.
  conversion from ADU to electron data, 76
  degradation by multiplicative noise and digitization, 33
  reconstructing, 64
  speed of acquisition, 11–12
  storage of volume of data, 237
Data collection guidelines, 319–320.
Data collection model, blind deconvolution, 472.
Data compression, 288–289, 292–293, 295, 319, 499, **580–585**, 762, 764, 819, **835–836**.
  algorithms, 580
    discrete cosine transform (DCT), 581
    Huffman encoding, 580
    Lempel-Ziv-Welch (LZW), 580
    run-length encoding (RLE), 580
  archiving systems, 580
    gzip, 580
    PKzip, 580
    WinZip, 580
  calcium imaging, 584
  color images, 581
  different techniques, table, 581
  Dinophysis image, 585
  effects on confocal image, 583
  examples, 583–585, 592, 834–837
  file formats for, 580–588
    fractal compression, 581–582
    GIF (graphics interchange format), 580
    JPEG (Joint Photographic Experts Group), 581–584
    MPEG, 836–839, **840–841**
    PNG (portable network graphic), 581, 584
    QuickTime, 829, 831, 836–837, 840–844
    TIFF (tagged image file format), 580
    wavelet compression, 581–584, 819
  movies, 836–842
    artifacts, 839
    compression ratios, 842–843
    entrope, 841
    MPEG formats, 840–841
    Up-sampling, 838
  pixel intensity histograms, 584
  testing, 830, 835
  time required, table, 581for WWW use, 816
  useful websites, 844–845
Data projectors, 590.
Data storage, 106. *See also*, Mass storage.
Data storage systems, 287, 395. **580**, **594**, 764.
  chapter, 580–594
  characteristics of 3D microscopical data, 287
  databases, **861–869**. *See* Databases
  random access
    CDR, CDRW, 586–587
    DVD, 587
    Magnetic disks, 586
    semiconductor, FLASH memory, 588
  for remote presentation, 842
  role for STED, 577
Databases, 2D/3D biology images, 827, 861–869.
  benefits, 863–864
    fast, simple machine configuration, 863
    improved analysis and access, 863
    performance, 863
    remote monitoring, 863
    repeatability of experiments, 863
    submissions to other databases, 863
  criteria/requirements, 866–867
    digital rights management, 867
    metadata structure, 867
    query by content, 866–867
    user interface, 866
  data/metadata management, 861–862
  future prospects, 867
  image database model, 864–865
  image information management, 862
  image management software, table, 865, 868
  instrument database model, 864
  laboratory information management systems (LIMS), 862
  microscopy data/metadata life cycle, 863
  modern microscopes design aims, 862–865
  projects, 865–866
    BioImage, 865–866
    Biomedical Image Library (BIL), 866
    Scientific Image DataBase (SIDB), 866
  recent developments, 861–862
    MPEG-7 format, 862
    relational database management systems (RDBMS), 862
    TIFF format, 861
  software for, 868–869
    ACDSee, 868
    Aequitas, 868, 869
    Cumulus, 868
    Imatch, 868, 869
    iView, 868, 869
    Portfolio, 868
    price, 868
    Research Assistant, 868
    ThumbsPlus, 868, 869
  system requirements, 864
DBR. *See* Distributed Bragg reflector.
DCT. *See* Discrete cosine transform.
Deblurring algorithm, 476.
Deconvolution, 7, 26–28, 39, 40, 66, **189–190**, 222–223, 278, 456–458, 464, 468, **488–500**, 542, 564, 736, 746, **751–753**, 778, **784–785**, 828, 864, 900, 929. *See also*, Blind deconvolution.
  of 2-photon images, 498
  and 3D Gaussian filtering, 70, 281, 285, 323, 392, 395, 667. *See also*, Gaussian
  4Pi lobe removal, 562, 565
  advantages and limitations, 458, 475
  algorithms, **472–476**, 490, **495–497**, 751, 778
    comparison, 497–498
    iterative constrained Tikhonov-Miller, 497
    Jansson-van Cittert, 496
    nearest neighbor, 495–496
    non-linear constrained iterative, 496–497
    Richardson-Lucy, **497**, 568
    Weiner filtering, 496
  background history, 488–490
    blurring process contributions, 488
    equation showing restoration possible, 489
    image formation, 489–490
    schematic diagram of convolution, 489
  blind, 189–190, 431, 463, 469, 472–473, 478, 486, 492, 496–497, 646
    chapter, 468–487
    maximum likelihood estimation, 472–477, 483, 669–670
  blurring process contributions, 488
  confocal data, 39, 40, **453–467**, **488–500**, 753, 778. *See also*, Confocal microscopy, *vs.* deconvolution.

Deconvolution (*cont.*)
of simulated confocal data, 40
CARS data cannot be deconvolved, 397, 399
chapter, 453–467
colocalization, 668–670 comparison of methods, 66, 453, 467, 475–477, **497–499**, **644–648**
convolution primer, 485–478
convolution and imaging, 490–491
Fourier transform of PSF, 489, 490
linearity, 490
optical transfer function, 490–491
shift invariance, 457, 490, 564
and data compression, 584–585
test results, 401, 461, 464–466, 481–482, 483
defined, 189–190, 468
display of data, 301, 830, 835–836
examples, **40**, 190, 392, 411, 462, 466, 471, 488–498, 510
4Pi, 468, 565
botanical specimens, 784–785
brightfield, 411, 475, 478
cardiac t-system, 498
confocal, 470
DIC, 470
polarized, 479
of simulated confocal data, 40
STED, 574–576
flatfielding the data, 477
black reference, 76
white-reference, 76
fluorescence lifetime imaging, 521
four dimensional deconvolution, **391–392**, 752
Fourier transform of PSF, 489, 490
future directions, 483, 766
and image formation, 490–492
linearity and shift-invariance, 457, 564
live imaging, 480, 564, 751–754
missing cone problem, 494
model specimens, 461, 464–466, 481–482, 483
multi-photon, **488–500**, 542
multi-view montaging, 330, 677
ion imaging, 736
noise, 495, 635
and Nyquist reconstruction, 59, 65, 67, **68**, 222–223, 635
suppressing Poisson noise, 39
optical sectioning, 752
out-of-focus light, 26–28, 431, **487**, 644
and pinhole, 26, 487
point-spread function (PSF), 223, 241, 247, 453, 463, 471, 489–492, 635, 655
approximations, 493
measuring PSF, 492–494
and Poisson noise reduction, 320
pre-filtering, 281, 497, 581
problem with specimen heterogeneity, 22, 648
purpose, 468
requirements and limitations, 489–494
diagram demonstrating convolution, 489
linearity, 490
missing cone problem, 494
noise, 495
optical transfer function, 490–491
point spread function, 489, 492–494
shift invariance, 457, 490, 564
sampling frequency, 635
spherical aberration, 471, 480–481
stain sparsity, 28
structured illumination, comparison, 265–279
subpixel refinement, 478–479
temporal/spatial, 392, 458, 753
transmitted light imaging, 472, 475, 478
of wavelength spectra, 382, 663–667, 771–772
limitations, 667
Deconvolution lite, 68–70.
Deflector, acousto-optical. *See* Acousto-optical deflector.
Defocusing, size and intensity distribution, 146.
Degree of modulation, 268–270.
locally calculated, 268–270
absolute magnitude computation, 268–269
equations, 269
homodyne detection scheme, 268–269
max/min measured intensity difference, 268
scaled subtraction approach, 269–270
square-law detection, 268–269
synthetic pinholes, 268
Delamination, and interference fringes, 168–170.
Delivery, dye, 355, 357–360, 810.
Deltavision, 132, 282.
Demagnification, and numerical aperture, 127.
Depth discrimination, in LSCM. *See* Axial resolution.
Depth of field, 4, 9, 13.
extended-focus images, 9
fluorescence microscopy, 4
phase-dependent imaging, 13
Depth-weighting, projection images, 304, 306.
exponential, 304
linear or recursive, 304
Derived contrast (synthetic contrast), 188–201.
Descanned detection, 166, 208, 212, 537, **540–542**, 754, **904**.
Design of confocal microscopes, 43, 145, 166, 207–211, 237. *See also*, Commercial confocal light microscopes.
4Pi, 563, 566
of confocal fluorescence microscope, 208
efficiency in, 43
fast-scanning confocal instruments, 237
intermediate optical system, 207–209
of microscope optics, 145
MMM, 552, 555
practical requirements, 210–211
of transmitted confocal microscope, 166
Detection efficiency, 34, 35, 210–211.
measurement, 34–35
practical requirements, 210–211
Detection method, multi-photon, 541, 542.
descanned, 542
Detectors, 9, 11, 25, 28, 251–264. *See also,* Photomultiplier tube; Charge-coupled device, etc.
area detectors. *See* Image detectors
assessment of devices, 260–262
CCD, 254
noise *vs.* pixel dwell time, 922
comparison, table, 255–256
conversion techniques, 259–260
descanned, 208, 212, 537, **540–542**, 774, **904**
direct effects, 252
errors, 211–212
evaluation, 211–217
future developments, 262–264
history, 262–264
image dissector, 254–255
image intensifier, 13, **232–233**, 519–520, 524, 555–556
gated, 233, 519–522, 524, 555–556
intensified. *See* Intensified CCD
MCP-PMT. *See* Microchannel plate
microchannel plate, 232–233, **255**, 262
MCP-CCD, 262
gated, 519, 523–524, **527**, 532
noise internal, 256–259
internal detection, 256
noise currents, table, 256
photoemissive devices, 256–257
photon flux, 257–258
pixel value represented, 258–259
non-descanned, 185, 201, 218, 381, 447, 456, 507, **542**, 552, 559, 643, 646, 727, 750, 779, 904, 909–910
phase-sensitive, 518–520, 619
photoconductivity effects, 252, 253
photoemissive, 254
photography. *See* Photographic systems
photomultiplier tube, 9, 11. *See also*, PMT
photovoltaic effect, 252–253
photon interactions in, 252–256
point detectors, 260–261
quantal nature of light, 251–252
quantum efficiency (QE) *vs.* wavelength, 25
for second harmonic detection, table, 707
silicon-intensified target (SIT) vidicon, 730
spectral, 203–204, 662–663, 666–667

TCPSC, 518, 520–523, 526
time-gated, 522
thermal effects, 252
work functions, table, 252–253
vacuum avalanche photodiode, 254, 255
Developmental biology, 545, 624.
multi-photon microscopy (MPM), 545
Dextran labeling, 173–174, 292, 512, 757.
DFB. *See* Distributed feedback.
4′,6-diamidino-2-phenylindole, 140, 344–345, 355, 358, 376, 431. *See* DAPI.
plants, 431
use of, 376
Diatom, 438, 638–640, 881.
as standard for measuring objectives, 145
test specimen, 638–640
DIC. *See* Differential interference contrast.
Dichroic filters, 212.
intensity loss, 212
transmission, 212
Dichroic mirrors (beam-splitters), 44, 45, 50–51, 129, 211, 217–218.
coating for collection mirrors, 129
double and triple, 217–218
effect of deflection angle, 211
separating emission/excitation, 44–45, 50–51
Die, of light-emitting diode, 133, 134.
Dielectric butterfly, galvo feedback, 54.
Differential interference contrast (DIC) imaging, 10, 14, 76, 127, 146, 171, 453, 468, 473–475, 846.
blind deconvolution, 473–475
converting phase shifts to amplitude, 171
narrow bandpass filter use, 76
Nomarski DIC contrast, 2, 268, 746, 892
photon flux reduction, 127
schematic for, 475
three dimensional, 470
Wollaston prism, 156, 468, 473, 475
Diffraction, 61, 65.
contrast transfer function, 16, 35, 37–39, 59–62, 656, 747
and sharpness of recorded data, 65
Diffraction limit, 210–211. *See also*, Rayleigh criterion.
defined, 210
point-spread function, 146
practical requirements for, 210–211
Digital light processor (DLP), projectors, 590.
Digital memory system, 64.
Digital microscopy, optics/statistics/digitizing, 79.
Nyquist sampling, 146
Digital printers, 591–593.
Digital processing, in disk-scanning confocal, 12.
Digital projectors, 590.
Digital rights management (DRM), 830, 844.
Digital video disks (DVD), 587–588.
Digital-to-analog converter (DAC), 64, 259–260.
operation, 64
Digitization, 25, 31–32, 36, 38–39, 59, 62–63, 66, 72, 75, 79, 259, 261, 286, 460, 495, 639, 911.
aliasing. *See* Aliasing
blind spots, 38
and Nyquist criterion, 38–39
precision, 25
and pixels, 62–63
of voltage output of photomultiplier rube, 31–32
DiI derivatives, 760.
Dimethylsulfoxide (DMSO), 697, 726–727, 760, 875.
handling, 739
DIN standard, microscopes, 156.
Dinophysis image, 585.
Diode injection lasers, 105–108.
Diode lasers, 86, 87, 107, 112, 116.
distributed feedback, 107
emission stability, 86
intensity, 87
maintenance, 116
modulated, 112
noise sources, 86
physical dimensions, 106
violet and deep blue, 107
visible and red, 107
wavelength stabilization, 87
Diode-pumped alkali lasers (DPAL), 103–105.
Diode-pumped lamp (DPL), 108–109.
Diode-pumped solid-state lasers (DPSS), 108–109, 111, 112.
kits, companies offering, 109
passively mode-locked, 111
ultrafast, 112
Diolistics, ballistic gene transfer, 726.
Dipping objective, 149. 161, 209, 411, 429, 568, 613, 727, 737, 870, 872.
Direct permeability, 358–359.
Discrete cosine transform (DCT), 581.
Disk-scanning confocal microscopy, 215–216, 224, 225, 228–229, 234–235 754, 755.
advantages and limitations, 223–224
for backscattered light imaging, 228–229
chapter, 221–238
commercial instruments, 907, 913, 915
comparing single- *vs.* multi-beam, 224
table, 226
and electron multiplier CCDs, 78, 205, 215, 220, **233–235**, 349, 459, 754–755
embryo, 754
high-speed image acquisition, 216, 222–224, 754
image contrast in, 168–171
microscopes, table, 224
optical sectioning, 235
types, 228–232
Dispersion, optical, 56, 88, 152, 154, 242, 411, 542–543, 609, 683.
in acousto-optical devices, 3, 15, 55–56, 88
CARS signal generation, 728
compensation, 566–567
defined, 152
in fiber lasers, ultra-fast pulses, 88, 110, 113
by filter blank material, 211
generates third harmonic signal, 704–705
group delay dispersion, 537–538, 543
group velocity dispersion, 88, 111, 210, **537**, 609, 903
in optical coherence tomography, (OCT), 609
in optical fibers, 502, 504, **507**
and temperature, 15, 411
for multi-channel detection, 51
using to correct for chromatic aberration, 153
Display software. *See* Presentation software.
Displays, 580, **588–590**, 594, 892.
cathode ray tube (CRT), 5–6, 53, 67, 72–73, 291, 293, **588–589**
data projectors, 590
digital light processor (DLP), 590
halftoning *vs.* dithering, 589
international television standards, 589
liquid crystal (LCD), 589–590
supertwisted nematic (STN), 589
thin-film transistor (TFT), 589
monitors, 588–589
Distortion, 39–41, 152.
and resolution, practical, 39–41
Distributed Bragg reflector (DBR) diode laser, 107.
Distributed feedback (DFB) diode laser, 107, 113.
ultrafast, 113
Dithering *vs.* halftoning display, 589.
DLP. *See* Digital light processor.
DMSO, 697, 726–727, 760, 875.
handling, 739
DNA damage, **390**, 517, 539, 680, **682–684**, 812.
DNA probes, 273, 317, 339, 343, 354, 358, 360, 362, 369, 393, 396, 459, 520, 531–532, 539–540, 691–695, 774, 779, 782, 812, **818–825**, 828, 874.
DAPI, 140, 344–345, 355, 358, 376, 431
DRAQ5, 343
Hoechst, DNA dye, 136, 339, **344**, 360, 362, 520, 565–566, 683, 782
DNA sequencing, constructs for, 801–802.
DNA transfer, 724, 756, 760, 773, 790, 802–804.
Dominant-negative effects, 755.
Donor/acceptor pair (FRET), 790, 792–794, 796–797. *See also*, FRET.
before bleach/after bleach ratio, 794
equations, 790, 792–794

Donor/acceptor pair (FRET) (*cont.*)
fluorescence, 796–797
fluorophores, 794
separation in nm, table, 793
Double-image, diagram and example, 169.
Double-label, 375.
Down-conversion, parametric, 114.
DPAL. *See* Diode-pumped alkali lasers.
DPL. *See* Diode-pumped lamp.
DPSS. *See* Diode-pumped solid-state lasers.
Drift, **386–387**, 652, 655, 732.
CCD read amplifier, 76
compensation for, 392–393, 732–733, 886
focus, 16, 40, 115, 190, **219**, 386, 489, 567, 652, 720, 729, 886
compensating, 396, 732
lasers, 85–86, 115
DRM. *See* Digital rights management.
Drosophila, 273, **675–676**, **747–748**, 751–752, 754, 756, 759, **804**, 810.
living embryo, 675–676, 752
salivary chromosomes, 273
SPIM, image, 675–676
Duty cycle, laser, defined, 110.
DVD, 587–588.
Dye lasers, 86, 103, 112, 114, 124, 540–541
in cancer treatment, 112
colliding-pulse mode-locked, 112
with intra-cavity absorbers, 112
noise and drift, 86
references, 124
as wavelength shifters, 103
Dye-filling, studying micro-cavities, 173–174.
Dyes, 22–23, 36, 44, 90–102, 109, 116, 118, 165, 173, 183, 212, 222, **342–346**, 353–358, 360, 430, 461, 462, 527, 528, 575, 726, 736–738, 740–745, 748, 749, 755, 759–760, 774, 775, 782, 804. *See also*, Green fluorescent protein (GFP); Rhodamine dyes; Fluorescein.
affect on living cells, 391, 748
AlexaFluor, 353–355
Aniline Blue, 430–432, 435, 438, 774
APSS and *Canna* yellow, non-linearity, 165
bandwidth of emission, 44
BODIPY TR, methyl ester, 760
BOPIDY, 142, **342–343**, **353–355**, 389, 692, 749, 760–762
Calcein AM, 355, 360, 362–363, 426–427, 430, 685, 804, 812
calcium dyes, **346–347**
cAMP, 347
characteristics of probes/specimen, table, 344–345, 354–355
coumarin, 114, 339, 344–345, 353, 355, 654–655, 661, 693
cyanine, 339, **342**, **344**, **354–355**, 362–363, 374, 443, 540, 587, 760, 854, 874
diI derivatives, 355, 362, 389, 726, **760**
donor acceptor pair, 794. *See also*, FRET
DNA probes, **343–344**, 531–532, **818–825**, *See also*, DNA probes
DRAQ5, 343
dyes *vs.* probes, 353, for embryos, 748, 761
exciting efficiently, 44
fade-resistant, 36 *See also*, Antifade; Bleaching
for fatty acid, 347. *See also*, FM4–64, below
Feulgen-stained DNA, 166, 200, 298, 433, 437
Fluo-3 and Fura Red, for calcium, 180, **183**, 345, 434
Fluo-3 for calcium, 737
fluorescein, 353, 355. See Fluorescein; FITC
fluorescence lifetime, 517, 527–528
FluoroNanoGold, 854
FM4–64, FM1–43, lipophilic dyes, 236, 355, 359–360, 389, 556, 755, **760–761**
fura-2, 103, 189, 234, 257, 345, **346**, 348, 358–359, 361, 529, 531, 726–727, 730, 733, 741–743, 810, 812, 846, 850
Fura Red, 180, 183, 345, 454
future developments, 348–349
genetically expressed, 348
Glutathione, 342, 358, 545, 694, 779, 782
hazards in using, 116, 118
for ion concentration, 346–347
ion-sensitive probes, table, 531
kinetics, 741–742
lanthanum chelates, 345–346
laser/filter configuration, table, 799
lineage tracers, 461
lipid dyes, 236, 355, **359–360**, 389, 556, 755, **760–761**
living cells, rapid assessment, table, 360
loading, uniformity, 749. *See also*, Loading
LysoTracker Red DND-99, 360
membrane labels, 344–345
membrane potential, 205, 346
microinjection, 360–361, 388, 739, 748, 755, 795, **803–804**
MitoTracker Red , 142, 170, 353, 358, 360, 430–431, 692, 750
multi-photon excitation, 543–544
nano-crystals, 343, 345. *See also*, Quantum dots
Nile Red, 435, 528, 575, 774, 782
organic, 342–343, 353–356
oxygen sensor, 347
patch clamp loading, 360, **726**, 734, 738–740
pH indicator, **346**, **739–745**. *See also*, pH
imaging
photoactivatable, 187, 210, 224, **383**, 385, 541, 544–545, 693, 729, 759–760, 912
Kaede, 187, 383, 385
Kindling, 574, 760
PA-GFP, 187, 383, 385, 752, 759–760
photodestruction, 340–341. *See also*, Bleaching
and Chapter 39
photophysical problems, 338–340
absorption spectra, 339
autofluorescence, 339–340
contaminating background, 339–340
optimal intensity, 340
Rayleigh/Raman scattering, 339
singlet state saturation, 338–339. *See* saturation, below
triplet state saturation, 339
phycobiliproteins, 338, 341, **343**, 355–357, 693
for plants, 774–775. See Chapters 21 and 44
two-photon, 782
propidium iodide, 344, 355, 360, 426, 651, 693–695, 773, 778–779, 782, 812, 875, 877
quantum yield, 172, 180, 184, **338–845**, 347, 353–354, 360, 363, 383, 421, 543–544, 574, 661, 683, 690–692, 710, 737, 792, 794–795
ratio methods, 346–348, 742–743
rhodamine, 353, 355. *See also*, Rhodamine
excitation, 109
saturation , 21–22, 41, 142, 222, 265, 276, 338–340, 448, 643, 647, 899
Schiff-reagent, 262, 369, 770, 774–775, 778
selection criteria for, 353–358
signal optimization strategies for, 341–342
SNARF, **345–346**, 531, 739, 744–745
specimen damage, 340–341
spectral properties, 212, 342, 344–345
spectral unmixing, 192, 382, 664–667
for STED, table, 575
Dynamic Image Analysis System (DIAS), 396–397, 783–784.
living cells of rodent brain, 396
of plant cells, 783–784
Dynamic range, 929–930.

E

e2v Technologies, EM-CCDs, 76–77, 233–234, 237, 262, 460, **925–926**.
E-CARS. *See* Epi-detected CARS.
ECL. *See* Emitter-coupled logic.
Edge detector (software), 309, 322, 327, 396, 823–826.
Edge effect, self-shadowing, 172.
Edge-emitting diode laser, 89, 106.
corrective optics for, 89
cross-section through, 106

Efficiency, laser, 102, 105–106. *See also,* Quantum efficiency (QE); Photon efficiency.
of diode injection lasers, 105–106
wall-plug, of argon-ion lasers, 102
EFIC. *See* Episcopic fluorescence image capture.
EGS. *See* Ethylene glycol-*bis*-succinimidyl.
E-h. *See* Electron-hole.
Electro-magnetic interference, in electro-optical modulators, 57.
Electron microscopy, 167.
brain slices, 730–731
chapter, 846–860
cryo-techniques, 854
fixation, 167, 368–369
immuno-stained, 371–372, 852
micrographs, 479, 847–853, 855–858
tomography (EMT), 610–611
Electron-multiplier CCD (EM-CCD), **30–31**, 74–75, 78, 142, **233–235**, 262, 466–467, 482, 647, 678, 737, 753–754, 784, **923–926**.
advantages and disadvantages, 30–31, 220, 228, 233–235, 237, 459–460, 647, 737, 909, 923–926
CIC, clock-induced charge, 234, 926
and disk-scanners, 76, 205, 215, 220, 270
frame-transfer, 262, 234
gain-register amplifier, 76–77, 258, **753**, **925**
interline-transfer, 233–234
mean-variance curves, 78
multiplicative noise, **77**
noise currents, 256
parameters, *vs.* normal CCD, table, 233
QE(effective), 78, 927
readout amplifier, 76–77, 258, 753–754, **925**
results, 235, 237, 755
Electron-beam-scanning television, 6–7.
Electron-hole (e-h) pairs and photon counting, 29.
Electronic bandwidth, 64–65. *See also,* Bandwidth.
Electronic noise, defined, 232.
Electronik Laser Systems GmbH, VersaDisc, 109.
Electrons, interaction with light, 129–130.
Electro-optical modulators (EOM), 25, 54, 57, **87**, 116, 543, 701, **903–904**.
Electroporation, 359–360, 795, **803**.
for chromophores, 803
Ellis, Gordon, 2, 3, 7, 8, 13, 14, 84, 129, 131, 478, 507.
Embryo imaging. *See* Living embryo imaging.
Embryos, 761–766.
bulk labeling, with dyes, 761
depiction, in time and space, 762–764
dyes, for multi-wavelength analysis, 756
FRET, 764–766
labeled proteins, 756
photobleaching, 759
transcriptional reporters, 756
EM-CCD. *See* Electron-multiplier CCD.
Emission filter. *See* Filters.
Emission spectra, of arc sources, 136, 176.
Emission spectra, fluorophores, 1- *vs.* 2-photon excitation, 421.
Emitter-coupled logic (ECL), 259.
EMT. *See* Electron microscopy tomography.
Endomicroscopy, 511, 513, 514.
distal tip for, 514
fiber-optics, 513
human cervix image, 513
human gastrointestinal track image, 514
miniaturized scanning confocal, 511
Endoplasmic reticulum, 374, 770, 819.
and DiOC6, 390
FLIP, 382
FRET, 795
genetic fluorescent probes, 771, 783
and harmonic signal generation, 703
in ion-imaging, 738
and phototoxicity, 685
table, 363
Endpoint data analysis, 816–817.
Endpoint translocation/redistribution assays, 814.
Energy diagram, lasers, 102, 105, 106.
argon-ion laser, 102
helium-cadmium laser, 105
helium-neon laser, 105
semiconductor laser, 106
titanium:sapphire four-level vibronic laser, 109
Energy, of single photon, 35, 127.
Energy transfer rate, for FRET, 790, 792.
Entrance aperture. *See* Back-focal plane.
EOM. *See* Electro-optical modulators.
Epi-detected CARS (E-CARS), 597–599.
erythrocyte ghosts, 603
Epi-fluorescence microscopy. *See* Fluorescence microscopy, 44, 166, 172–173, 195, 202, 235.
Epi-illuminating confocal microscope, 9, 166. *See also*, Confocal laser scanning microscopy; Confocal microscopy.
Episcopic fluorescence image capture (EFIC), 607–608.
mouse embryo image, 608
Epithelial cells, 14–15, 603.
CARS image, 603
oral, optical sections, surface ridges, 14–15
EPS. *See* Extracellular polymeric substances.
Erythrocyte ghosts, CARS imaging, 603.
Ester-loading technique. *See* Acetoxymethyl esters loading method.
Ethylene glycol-*bis*-succinimidyl (EGS), 369.
Euphorbia pulcherrima, spectrum, 710.
European Molecular Biology Laboratory (EMBL), 53, 212.
compact confocal camera, 212
Evanescent waves, 90, **177**, 180, 245, 503, 801.
defined, 90, 180
optical fibers, 503
resolution measurement, 245
Excess light. *See* Stray light.
Excimer lasers, 112, 116.
maintenance, 116
for tissue ablation, 112
Excitation efficiency, multi-focal multi-photon microscopy, 552.
Excitation filter, requirements, 44. *See also,* Filters.
Excitation source, laser. *See* Lasers; Non-laser sources.
Excitation wavelength change, contrast, 173.
Explants, for imaging living embryo, 748–749.
Exposure time, 62, 65, 71–76, 81, 127, 137, **141–142**, 176, 212, 219, 224, 226, **231–236**, 267, 270, 276, 346, 363, 392–393, 423, 427, 459–460, 477, 495, 556, 613, 627–628, 651, 655, 681–686, 692–697, 708, 746–747, 753–755, 760–764, 783–784, 816, 822, 850–851, 873.
for CCDs and EM-CCDs, 127, 137, 141–142, 231–236, 267
disk scanners, 231–235
laser, safety, **117–118**, **839**, 900, 903–904
reducing, 753–755
and source brightness, 141–142
total, comparison of methods, 442, 449
UV, 116
x-ray, 614–616
External laser optics, maintenance, 117.
External photoeffect. *See* Photoemissive effect.
External Pockels cell, 25, 54, **87**, 116, 543, 701, **903–904**.
External-beam prism method, laser control, 90.
Extracellular polymeric substances (EPS), 183, 311, 358, 376, 703–704, 717, 760, 783, 870, **879–880**. *See also*, Collagen.
bleaching, 693
damage, 685
dye, 361
lectin-binding in biofilms, 870, 879–880
matrix, 760
negative contrast, 173
in optical projection tomography, 612
plants, 438, 783
preparation, 376
Extrinsic noise, reduction, 21.

F

Fabry-Perot interferometer, optical cavity, 81–82.

Fast Fourier transform, 487.
to identify interference fringes, 202
Fast line scanner, 231–232.
Fatty acid indicator, 347.
FBG. *See* Fiber Bragg Grating.
FBR. *See* Fiber Bragg Reflector.
FBTC. *See* Fused biconical taper couplers.
F-CARS. *See* Forward-detected CARS.
FCS. *See* Fluorescence correlation spectroscopy.
Feedback, 136, 139.
for control of light-emitting diode, 139
to increase source stability, 136
Femtosecond pulsed lasers. *See* Ultrafast lasers.
Feulgen-staining, DNA, 166, 200, 298, 433, 437
Fianium-New Optics, Ltd., FemtoMaster-1060
fiber laser, 113–114.
Fiber Bragg Grating (FBG), laser stabilization, 87.
Fiber Bragg Reflector (FBR), stabilizes laser, 87.
Fiber lasers, 85, 101, 109–110, 113–114, 124.
defined, 109–110
temperature sensitivity, 85
tutorial reference, 124
ultrafast, 101, 113–114
Fiber optics. *See* Chapter 26.
beam-splitters, 503–504
Bow-tie, pol-preserving fiber, 503
cable, for delivering ultrafast pulses, 88
laser output, 106
pigtail, 106
Fiber optics used in microscopy, 501–507.
evanescent waves in optical fibers, 503
fiber image transfer bundles, 504–505
fiber-optic beam-splitters, 503–504
fused biconical taper couplers, 503–504
glass made from gas, 501
gradient-index optical fibers, 501–502
key functions of fibers, 505–507
delivering light, 505–506
detection aperture, 506
diffuse illumination, 507
for femtosecond laser pulses, 507
large-area detection, 507
large-core fibers, as source/detection apertures, 507
same fiber for source and detection, 506
single-mode fiber launch, 505
SMPP optical arrangement, 216
managing insertion losses, 506
angle polishing of fiber tips, 506
anti-reflection coating of fiber tips, 506
index matching of fiber tips, 506
microstructure fibers, 504
modes in optical fibers, 502
polarization effects in optical fibers, 503
polarization-maintaining fibers, 503
step-index *vs.* gradient index, 502
step-index optical fibers, 501–502
transmission losses in silica glass, 502
Fiber-optic confocal microscopy, **501–515**, 893.
benchtop scanning microscopes, 507–508
clinical endomicroscopy, 513
distal tip, 514
human cervix image, 513
human gastrointestinal track image, 514
image transfer bundles, 504–505
managing insertion losses, 506
miniaturized scanning confocal, 508–512
bundle imagers for *in vivo* studies, 509
with coherent imaging bundles, 508–509
imaging heads, 508–512
objective lens systems, 509
optical efficiency, 509
optical schema, 508
resolution, 509
rigid endoscope, 511
vibrating lens and fiber, 510–511
in vivo imaging in animals, 510–514
Fiber-optic interferometer, 240–241, 504, 609.
diagram, 241
for measuring point spread function, 240–241
Fiber-optic light scrambler, 8, 13, **131–132**, 143.
Fibroblasts, 292, 361, 691, 798, 803, 852.
Field diaphragm, 34–35, **127–128**, 139, 461, 627, **648–649**.
Field effect transistor (FET) CCD amplifier, 30–31, 77, **922–927**, 929.
noise *vs.* pixel dwell time, 922
Filament-based lamps, 34, 44, **126–132**, **135–138**, 346, 507, 648, 663.
fiber optic, 507
image, 100 W halogen bulb, 135
size, 126–127
spectrum, 44, 136
stability, 34, 137
File formats, multi-dimensional images, 288–289.
Fill factor.
of CCD, 920–921, 927, 929
disk-scanning microscopes, 224–228, 233, 552
Filtering, digital, 281, 810. *See also,* Deconvolution.
Gaussian, 41, 65. *See also*, Gaussian filters
multi-dimensional microscopy display, 281
nonlinear, deconvolution, 190
sets, for automated confocal imaging, 810
smoothing, effect on contrast, 59
to reduce “noise” features, 70
Filters, optical, **43–51**, 70, 89, 162, 190, 212, 753. *See also*, Heat filters.
conventional, 45
hard *vs.* soft coatings, 45–49
intensity loss, 212
interference, 45–51
conventional and hard coatings, 46
multi-channel detection, 51
ND filters, 43, 89
notch and edge, 50
tuning with angular dependence, 50
to select image contrast features, 162
short-pass, interference type, 46
transmission *vs.* laser line, 212
types, 46
wavelength selective, 43–51
FiRender, 281–282.
First or front intensity, projection rule, 302, 304.
FITC. *See* Fluorescein isothiocyanate.
Fixation, specimen, 368, 378, 428, 852, 854, 856.
antibody screening with glutaraldehyde fix, 377
artifacts, 195, 369–373, 428, 624, 815, 854, 857
autofluorescence, 358, 663
borohydride to reduce autofluorescence, 374, 770
chapter 368–378
characteristics, 368–370
chemical fixatives, 369
crosslinking fixatives, 369
freeze substitution, 369, 769, **854–856**
microwave fixation, 369
protein coagulation, 369
cryo-fixation, 854
dehydration, 166, 368, 417–418, 481, 611, 623–624, 815, 849, 854–855
effect on plants, 428
for electron microscopy, 167, 368–369, 372, 479, 731, **851–860**
ethylene glycol-*bis*-succinimidyl, 369
evaluation, 371–374
cell height to measure shrinkage, 371–373
MDCK cell example, 372, 373
formaldehyde, 369–370, 373
general notes, 374–378
geometrical distortion, 372–373, 815
GFP, 854, *See also*, Green fluorescent protein
arsenical derivatives, 348
glutaraldehyde, 369, 370
high-content screening, 815
immunofluorescence staining, 371, 372, 852
improper mounting, 376
microwave, 377–378
mounting methods, 370–374
critical evaluation, 371–374
media refractive index, table, 377
technique, 371
optical properties of plants, 428
pH shift/formaldehyde, 370–371, 373

plants. *See also*, Botanical specimens, Plant cells, 428, 769–770, 773–774
refractive index of mounting media, table, 377
optical effects, 428
refractive index of tissue/organs, table, 377
shrinkage, 369–373, 624, 815, 854
staining, 370–371
tissue preparation, 376
Fixed wavelength lasers, table, 119–120.
Fixed-pattern noise, 74–76, 278, 924, 927, 931.
Flare, out-of-focus light, 6, 132, 157–158, 172, 395, 456, 465–466, 469, 471, 481, 649, 731.
Flatness of field, 145, 151, 154, 418, 457, 639.
measurement/ small pinholes, 145, 457, 639
objectives, to improve, 151–152
Flat-fielding CCD data, 76, 477.
black reference, 76
white-reference, 76
Flexible scanning, 51–52.
FLIM. *See* Fluorescence lifetime imaging microscopy.
FLIP. *See* Fluorescence loss in photobleaching.
Flip mirrors, to control laser, 58.
Floppy disks, 586.
Fluorescein,48, 80–81, 88, 203, 261, **353–355**, 375, 443, 582, 697, 781, 794, 930.
arsenical derivatives, 348
calculating laser power needed, 80–81, 443
derivatization, diagram, 354
double-labeling, 375
filters for, 48
photobleaching quantum yield, 363
rhodamine and, FRET between, 794
Fluorescein isothiocyanate, 88, 198, 203, 261, 263, 335, 375, 394, 397–398, 511–512, 527–528, 582–583, 693–694, 781, 794, 799, 884, 885. *See also*, Fluorescein.
2-photon, 781
biofilms, 884–885
dextran, 292, 512
filter sets, 48–49
FRET, 794, 799
lifetime, 527–528, 532
photobleaching quantum yield, 363
toxicity, 391, 693–694
Fluorescence anisotropy measurements, 742.
Fluorescence contrast, 172–173.
Fluorescence correlation spectroscopy (FCS), 5, 363, **383**, 385, 602, 801, 803, 805, 917.
and CARS, 602
FRET, 801
laser requirements, 81
table, 385
Fluorescence emission, botanical specimens, 425–428.
1- *vs.* 2-photon excitation, 421
Fluorescence imaging, deconvolution *vs.* confocal, 459–460, **644–648**.
Fluorescence *in situ* hybridization (FISH), 316–317, 319, 323, 331, 333–334, 343, 875–878.
biofilms stains, 875–878
with fluorescent protein, 878
Fluorescence ion measurement, 736–738, 740–745. *See also*, Calcium imaging, pH, etc.
calcium imaging, 736–737
concentration calibration, 742–745
indicator choice, 738
interpretation, 740–741
pH imaging, 346, **739–745**
water-immersion objectives, 737
Fluorescence lifetime imaging microscopy (FLIM), 108, 111, 114, 139, 204, 233, 382–383, 385, 516–533, 799–801.
advantages, 766, 800
alternatives to, 766
analysis, 251
applications, 516–518, 527–532
calcium imaging, 529
chemical environment probe, 517
FRET, 517–518
ion concentration, 517, 528–530
multi-labeling with dyes, 517, 527–528
pH imaging, 529–530
probes, 517
table, 530–532
comparison of methods, 523–527
acquisition time, 525–526
bleaching, 524
cost, 526
detector properties, 526–527
multi-exponential lifetime, 523–524
photon economy, 524–525
pile-up effect on detection efficiency, 526
shortest lifetime, 523
table, 526
decay process of excited molecule, table, 518
frequency domain methods, 518–520
disk-scanning implementations, 520
phase fluorometry method, 518–519
point-scanning implementations, 520
widefield, spinning-disk, 519–520
frequency-domain, 108
reducing repetition rate, 111
FRET, 799–801
history, 516
Jablonski diagram, 516, 517, 697, 792
with light-emitting diode sources, 139
limitations, 800
living cell images, 204
methods, 518–527
comparison, 523–527
frequency domain, 518–520
time domain, 520–523
multi-focal multi-photon microscopy, 555–556
quantitative fluorescence, 517–518
quantum efficiency, 516
spectroscopy, 516
table, 385
time domain detection methods, 520–523
point-scanning, 522
streak camera, 520
TCSPC FLIM, 522–523
time-gated FLIM, 523
use of intensified CCDs for, 233
Fluorescence loss in photobleaching (FLIP), 187, 382, 384, 801.
FRET, affected by, 801
table, 384
Fluorescence microscopy, 4, 9. 13, 43–44, 154, 166, 172–173, 195, 202, 235, 251, 448–451, 809–810 *See also*, Widefield (WF) fluorescence microscopy.
chromatic correction, 154
compared to disk-scanning microscopes, 235
vs. confocal imaging, 13
depth of field, 4
filters for selecting wavelengths for, 43–44
folded optical path, 166
increase contrast with less intensity, 172–173
signal-to-noise ratio comparative, 448–451
bleaching-limited performance, 448–450
configurations of microscope, 448, 449
disk-scanning microscope, 449
line illumination microscope, 449
saturation-limited performance, 450
scanning speed effects, 450–451
S/N ratios, table, 450
wide field (WF) microscope, 450
spectral problems, 44
Fluorescence, quenched by colloidal gold, 854.
Fluorescence recovery after photobleaching (FRAP), 51, 54, 56, 90, 187, 210, 218, 224, 229, 237, 362, 382, 384, 390, 691, 759, 801, 805, 850.
in biofilms, 874
damage to cellular structure, 341, 859–851
damage to microtubules, 341, 850–851
efficiency of illumination light path, 210
related to TEM of same specimen, 850–851
setups for, 218, 907
table, 384
using CARV2 disk-scanner, 229, 907

Fluorescence resonance energy transfer (FRET), 26–28, 34, 184–187, 204, 218, 221–222, 382, 384, 425, 517–518, 556, 650, 691, 741–742, 764–766, **788–806**, 796–797.
  based on protein-protein interactions, 800
  based sensors, 798–799
  botanical specimens, 425
  C. elegans, 766
  chapter, 778–806
    cloning and expression of fluorescent constructs for, 801–804
  donor/acceptor pair, 790, 792–794
    donor, 796–797
  efficiency, 792
  experimental preparation, 795
  FCS and, 801
  FLIM and, 799–801
  between fluorescein and rhodamine, 794
  fluorescence lifetime imaging, 517–518
  fluorescent proteins, 794–795
  FRAP and, 801. *See also*, Fluorescence recovery after photobleaching future perspectives, 805
  induced by cholera toxin transport, 797
  intramolecular, 765
  kinetics, 741–742
  in living cells, 195–186, 204
    chapter, 788–806
  in living embryos, 764–766
  MMM, 797–798
  nanobioscopy of protein-protein interactions
    acceptor bleach for, 797–798
    donor fluorescence for, 796–797
    measurement methods for, 795
    sensitized emission of acceptor, 795–796
  photobleaching, 691
  practical measurements, 792
  probes, 221–222
  quantum dots, 801
  setups, 218
  small molecules, 794–795
  spatial orientation factor, 792–793
  spectrofluorimetry, 793
  spectroscopic properties used for, 795
  standards for, 34
  table, 384
  theory, **790–794**
  TIRF and, 801
  total, measured with widefield, 26–28
  in transgenic animals, 765
  wavelength depiction, 793
Fluorescence saturation, singlet-state, 21–22, 41, 142, 265, 276, 339, 448, 643, 647, 899.
Fluorescence speckle microscopy (FSM), 13, **383**, 385, 889.
  table, 385
Fluorescent biosensor, 799, 805.
  future, 805
  mitotic clock measurements, 799
Fluorescent constructs for FRET, 801–802.
  cloning of fluorescent chimeras, 801–802
  expression and over-expression, 802
  functional activity of expressed, 802
Fluorescent dyes. *See* Dyes; Fluorescent indicators; Fluorescent probes.
Fluorescent efficiency, 34.
Fluorescent emission, incoherence, 130.
Fluorescent indicators, 346–348, 736–743. *See also*, Fluorescent probes, and particular ions.
  binding equation, 740–741
  buffering, 740
  calcium imaging, 736–737
    calibration, 742–743
    indicators, 738
  cellular introduction, 738–739. *See also*, Loading
  cellular trapping, 738
  choice, 738
  concentration, 741–742
  dialysis, 740
  free diffusion, 741
  genetically expressed intracellular, 348
    green fluorescent protein, 348
    ion indicators, 348
    ligand-binding modules, 348
  handling, 739–740
  inaccurate measurements, 740–741
  intracellular parameters imaged, 346–348
    Ca^{2+}, 346–347
    cAMP, 347
    fatty acid, 347
    ion concentrations, 346–347
    membrane potentials, 346
    other ratioing forms, 347–348
    oxygen, 347
    pH, 346, **739–745**
    wavelength ratioing, 346
  positive pressure, 740
  selectivity, 743
Fluorescent intensity (IF), TIRF, 180.
Fluorescent labels, 342–346, 530–532, 761, 775. *See also*, Dyes; Fluorescent probes; Chapters 16–17, and by name of dye.
Fluorescent probes. 353–364, 387–389, 517, 530–532, 736–737, 739–740, 755, 769, 771, 773, 783, 806, 810, 811. *See also*, Dyes, Fluorescence indicators and by name of dye, Chapters 16, 17.
  automatic living cell assays, 811
  bound, 737
  care, 739–740
  characteristics, table, 344–345, 354
  development, 736
  dye criteria for, 353–358
    AlexaFluor dyes, 353–355
    BOPIDY dyes, 353–355, 749, 760–762
    coumarin dyes, 353, 355
    cyanine dyes, **353**, 374, 587, 760, 854, 874
    dye classes, table, 355
    dye *vs*. probes, 353
    fluorescein, 353, 355. *See also*, Fluorescein fluorescent proteins, 355–357
    GFP, 355–357. *See*, Green fluorescent protein indicators of intracellular sate, 346–348
    Ca^{2+} indicators, 346–347
    protein
    multi-photon excitation, 357–358
    phycobiliproteins, 355–357
    probes/specimen characteristics, table, 354
    quantum dots, 357
    rhodamine, **342–345**. *See also*, Rhodamine
  excitation, 737, 344–345
  for fluorescence lifetime imaging, 517, 530–532
  genetically encoded, for plant imaging, 769, 771, 773, 783. *See also*, Transcriptional reporters; Transfection agents for high-content screening, 810
  high specificity/high sensitivity, 806
  living cell imaging, 387–389
    rapid assessment by, table, 360
  loading methods, 358–360. *See also*, Loading
    acetoxymethyl esters, 359
    ATP-gated cation channels, 359
    ballistic microprojectile delivery, 360, 724–725, **802–803**
    direct permeability, 358–359
    electroporation, 359–360, 795, **803**
    microinjection, 360–361, 388, 739, 748, 755, 795, **803–804**
    osmotic permeabilization, 359
    peptide-mediated uptake, 359
    transient permeabilization, 359
    whole-cell patch pipet delivery, 360, 726–727, 734, 738–740
  photoactivatable, 210, 224, **383**, 385, 541, 544–545, 693, 759–760, 912
    Kaede, 187, 383, 385
    Kindling, 574, 760
    PA-GFP, 187, 383, 385, 752, 759–760
  photobleaching, 362–363. *See also*, Bleaching
  phototoxicity, 363–364 *See also*, Phototoxicity factors influencing, table, 363
  specimen interactions, 361–362
    cytotoxicity, 362
    localization, 361–362
    metabolism, 361–362
    perturbation, 362
  target abundance/autofluorescence, 360–361
  tissues, 360
Fluorescent proteins, 187, 355–357, 739, 794–795.

emission change after photodamage, 187
FRET, 794–795
genetically engineered variants, 739
ion binding regions, 739
Fluorescent lights, stray signal, 201, 632, 904.
Fluorescent staining, 371, 393, 438, 774. *See also*, Dyes; Staining.
immunofluorescence, 371, 372, 852
living cells, 393
microglia, 319–320, **393–398**
nuclei of living or dead cells, 393
Fluorite (CaF2), optical to reduce chromatic aberration, 153.
FluoroNanoGold, cryosections, 854.
Fluorophores, 44, 338–349, 543–544, 664–667, 748, 794, 799. *See also*, Dyes, Fluorescent labels.
Flying spot detector for measuring photon efficiency, 34–35.
Flying spot ultraviolet (UV) microscope, 6–7.
Fly's-eye lenses, for diode lasers, 107–108.
FM4-64, FM1-43, and other lipophilic membrane dyes, 236, 355, 359, 360, 389, 556, 775, **760–761**.
Focal Check™ beads, 657–659.
Focal-plane array detection, 2-photon, 542.
Focal shift for mismatched RI, 405, 407–410, 553.
defined, 405
dependence, 410
for glycerol, table, 409
for water, table, 409
Focus, 3–4, 13, 36, 197.
for confocal microscope, 36
displacement, by living cell specimen, 22–23
effect of coverslip, 197
extended, 9
in phase-dependent imaging, 13–14
planes, diagram, 27
position, confocal microscopy, 651–652
Focused spot. *See* Point spread function.
Folded optics, for trans-illuminated confocal microscopy, 166.
Formaldehyde, 369–370, **373–377**, 428, 738.
AM-loading releases formaldehyde, 738
fixation protocol, 371
permeabilization agents for, 375
pH shift method, 370–371, 373
for plants, 428
stock solutions, 370–371
Förster distance, defined, 184, 790, 792, 793.
Förster equation, 184, 790, 793.
Förster resonance energy transfer. *See* also, Fluorescence resonance energy transfer.
Forsterite laser (Cr_4^+ in $MgSiO_4$), 109, 114, 415, 541, **706**, 707–709, 712–713.
second/third harmonic generation, 114
tunable, 109
Forward-detected CARS(F-CARS), 597–599, 603.
erythrocyte ghosts, 603
Foundations of confocal LM, chapter, 1–19.
Four-dimensional images, 746–749, 752, 761–764.
advantageous techniques, 746–747
automatic image analysis, 321
deconvolution, 495
embryogenesis visualization strategies, 761–764
living cells, 393
of living embryos
cellular viability, 747–748
challenges, 762
dataset display strategies, 393, 763–764
deconvolution, 752
for large thick specimen, 746–747
photobleaching during, 747–748
photodamage during, 746
required datasets for, 746–747
multi-photon, 535
structured illumination, 482
SPIM, 676
Fourier analysis.
4Pi microscope, 563, 576
analogy with image reconstruction, 69
of blind deconvolution, 472–476, 478
and convolution, **485–487**
of image formation, 446, 454, 456–457
MRM, 618–620
of periodic test specimen, 638–639
of short laser pulses, 88, 728
SPIM multiview processing, 675–677
STED, 574
of structured-illumination images, 268, **270–273**
and wavelet processing, 734
Fourier plane. *See* Back-focal plane, 201, 245, 509.
Fourier space, 270–271.
Fourier transform, 201, 202, **271**, 487, 489, 490–492, 620.
of AC interference in image, 201–202, 651
and convolution, 487
and deconvolution, 487, **490–492**
for detecting stray light into detector, 201
identifying interference fringes, 202
of microtubule TIRF image, 183
missing cone problem, 494
MRM image formation, 620
of point spread function, 489, 490
Fractal compression, 581–582.
Frame rate. *See also*, Speed
in confocal microscopy, 11
matching, 838–839
FRAP. *See* Fluorescence recovery after photobleaching.
Free diffusion, of fluorescent indicators, 741.
Free-ion concentration, 742.
Freeze thawing, 731, 739.
Frequency, 52, 65, 82.
laser *vs*. pumping power, 82
of resonant galvanometer, 52
of sampling clock, 64
Frequency doubling. *See* Second harmonic generation.
Frequency-resolved optical gating (FROG) for pulse length measurement, 115.
FRET. *See* Fluorescence resonance energy transfer.
Frustrated total internal reflection, defined, 177.
FSM. *See* Fluorescence speckle microscopy.
Full-well of CCD pixel, defined, 75.
Full-width half maximum (FWHM) resolution.
4Pi, 562, 567
of beams in scanning disk, 554
of CARS, 597, 599
of confocal performance, 656–657, 661–662
of emission wavelength
LED, 136
quantum dots, 343
of interference filters, 44
laser bandwidth, 93, 95, 100, 101
laser pulse length, 109, 112, 507, 537, 538, **902**
micro-surgery precision, 219, 687
multi-photon, 682–683, 901–902
objective resolution (PSF), 149, 209, 225, 444–445, 456, 492, 509, 552, 571
PMT rise time, 225
resolution, with spherical aberration, 407
table, 409
SPIM, 675
STED, 572, 576–578
z-resolution, measured, 194
Fundamental limits, chapter, 20–42.
Fungi, 438–439, 624, 782, 870.
Fura-2 [calcium ion] indicator dye, 103, 189, 234, 257, 345, **346**, 348, 358–359, 361, 529, 531, 726–727, 730, 733, 741–743, 810, 812, 846, 850.
Fused bi-conical taper couplers (FBTC), 503–504.
Future, 143–144, 160, 192, 219–220, 234.
of EM-CCD with interline transfer, 234
of laser-scanning confocal microscopes, **219**
of non-laser light sources, 143–144
spherical-aberration corrector, 15, 147, 151, 192
of tunable objective, 160
FWHM. *See* Full-width half maximum.

G
Gain, 31, 232.
  of image intensifier, 232
  photomultiplier tube, from collisions at first
  dynode, diagram, 31
Gain register, (EM-CCD) 76–78, 233–234.
  CCD (CCD), 76–78
  of electron multiplier-CCD, 233–234
Gain setting, 75, 115.
  defined, 75
  effect of bandwidth on, 115
GAL4 genes, 773.
Gallium arsenide (GaAs).
  diode laser, 107, 111
  InGaAs photodiode, 707–708
  LEDs, 133, 138, 143
  PMT photocathode, 4, 28–29, 232, 252, 255, 263, 464, 527, 931
Galvanometer, 11, 25, 36, 40, **51–54**, 56, 57, 63, 211, 215, 223, **231–232**, 513, 543, 552, 558, 599, 651–652, 753, 806, 907, 910–911, 914, 931. *See also*, Linear galvanometers.
  defined, 52–54
  distortion, 211
  electromechanical properties, 40
  errors, 40
  in fiber-optic micro-confocal, 513
  figure, 63
  line-scanner, 231–232
  linear, 52, 53, 223
  measurement, 651–656
  multi-focal, 554
  multi-photon, 543
  resonant, 25, **52–54**, 56–57, 223, 447, 510, 539, 543, 552, 558, 910
  specifications for, 214, 543
  ultra-precise, 211
  x-y scanners, **213–215**, 223, **651–654**, 806, 907, 910–911, 914
Gamma, brightness non-linearity, 72–73, 287, **832–833**.
  data projector, 590
  display, 582–583, 589, 832–833
Gas lasers, 86, 90–105. *See also*, CW lasers; Pulsed lasers.
  continuous wave, 90–105
  maintenance, 116
  noise sources, 86
  pressure, 102
Gating, intensified CCD, 25, 233, 262, 522, 555.
Gaussian beam profile, lasers, 80–81, 83–84, 108–109, 111, 113, 116, 231, 269, 338, 456, 496, 502, 538–539, 554, 891.
  in CARS, 597
  converted into line, 231, 916
  fiber optic, 502, 505, 506
  filling back-focal plane, 210, 509, 629, 633
  "Gaussian-to-flat-wavefront" converter, 554
  Kerr effect produces self-focusing, 111
  laser beam profile, 538–539, 554, 597, 635–636
  noise, 473, 497, 925
  from optical fiber, 502, 505–506
  optical tweezers, 89. *See also*, Laser trapping spatial filter, 89, 729
Gaussian filters, digital, 39, 41, 65, 70, 89, 281, 285, **301**, 323, 338, **391–392**, 399, 497, 499, 510, 650, 667–668, 676, 729, 734, 753, 764, **830**.
  of 3D data to reduce Poisson noise, 39, 41, 65, 69–70, 269, 281, 285, 323, 391–392, 399, 499, 510, **635–636**, 650, 667–668, 676, 764, 830
  "Gaussian blob," 635–636
  and Nyquist reconstruction, 65
  in presentation displays, 830
  results, 285, 676, 733, 835–837
Gaussian laser pulses, 536–536, 902.
Gaussian noise, 473, 497, 925.
Gaussian norm statistical tests, 830, 835, 837.
GDD. *See* Group delay dispersion.
Gene gun, 360, 724–724, 730.
Geometric contrast, 180–187.
Geometric distortion, 6, 23, 36, 39–41, 53, **152**, **211**, 215–216, 265, 297, 329, 372–373, 448, 480, 590, 641, 653–654, 741, 835.
  kinetic, 741
  measurement, 651–656
  projector, 590
  of specimen preparation, 372–373, 815, 872
Gerchberg-Saxton algorithm, deconvolution, 472.
GFP. *See* Green fluorescent protein.
Ghost images, from transmission illuminator, 201–202.
GIF (Graphics interchange format), 580.
Gires-Tournois interferometer (GTI), to reduce GVD, 88.
Glan-Taylor polarizer, 85, 87, 100, 171.
  in single-sided confocal microscope, 171
Glan-Thompson polarizer, attenuator, 85, 904.
Glutaraldehyde, fixative, 369, **369–374**, 377–378, 428, 438, 731, 852.
  antibody screening with, 377
  autofluorescence of, 374, 428, 770
  fixation protocol, 370
  stock solutions for, 370
Glutathione (GSH), 342, 358, 545, 694, 779.
  visualization, in plant cells, 782
Glycerol, immersion/mounting medium, 404, 407, 409–410, 435, 563, 654, 698, 785.
  clearing, 198, 200
  diffusion in, 698
  immersion objective lenses, 412, **563**, **567**
    example, 785
  mounting media, 371, 373, 375, 377–**378**, 420
  RI-mismatch, table, 409, 410
Goggles, laser, for eye protection, 118.
Gold's ratio method, 476.
Golgi receptor, 374, 389, 556, 564–566, 791.
Golgi stain, 107, 283, 298.
Gourard shading, **308**, 309, 311.
Gouy phase shift, 597.
Graded index (GRIN) lenses, 84.
  in diode lasers, 108
Gradient index optical fibers, 501–502.
Gradient-weighted distance transform, 323.
Graphics interchange format. *See* GIF.
Grating, periodic.
  GVD compensator, 88, 504, 538, 686
  laser tuning, 90, 103, 106–107, 111
  minimum spacing, 1, 16, 652
  OCT phase-delay, 609
  pulse compressor, 113
  spectral detector, 87, 346, 422, 664, 772
  structured illumination, 266–267, 273
Gray levels, 71–76.
  intensity spread function, 74–76
  printer, 592
Green fluorescent protein (GFP), 90, 174, 221–222, 348, 355–357, 429, 478–479, 556, 568, 571, 612, 614, 625, 675–676, 690, 692, 698–699, 724–725, 727, 731, 741, 747–752, 755, **756–763**, 766, 769–773, 781–785, **798–806**, 812–815, 820, 854–859, 862, 873–875, 877–879, 885. *See also*, Transfection reagents; Transcriptional reporters.
  biofilms labeling, 873
  or CFP molecules, as FRET pair, 798
  constructs, in embryos, 756
  EM imaging, brain cells, 731, 854–859
  FRET, 793–795, 798–803
  image contrast, 174
  limitations, 760
  membrane localized, 749
  methods with Correlative LM/EM, 854
  mice, 727
  photoactivatable, 187, 383, 385, 752, 759–760
  photobleaching, 690, 692, 698
  for plant imaging, 424, 429–430, 769–773, 781–785
    direct visualization, 773
    genetic fusions, 773, 783
    genetic marking, 773
    two-photon excitation, 782–783
  protein fusions/cytoskeleton, 773–774, 801
  tagged proteins, 758
  TIRF, 90

FRET, 794
Grey levels, 71–76.
printer, 592
GRIN. *See* Graded index.
Ground state depletion (GSD), 573.
Group delay dispersion (GDD), 537–538, 543.
Group velocity dispersion (GVD), 88, 111, 210, **537**, 606, 609, 903.
in optical coherence tomography, 609
pulse broadening due to, 88, 111, 210, 537–538, 543, 606, 609, 728, 903
GSD. *See* Ground state depletion.
GTI. *See* Gires-Tournois interferometer.
Guinea-pig bladder, calcium sparks, image, 237.
GVD. *See* Group velocity dispersion.
Gzip, 580.

H

Hairs, plant, 431, 434–436, 772.
Halftoning *vs*. dithering, 589.
Halogen lamps, **126–127**, 132, 136–139, 143, 159, 663.
brightness *vs*. temperature, 136
filaments, 132
image, 135
lifespan, 136
power available, 126–127
stability plot, 137
Haralick features, 818–820.
Hard coatings, for interference filters, 45, 48.
Hard copy, 580, 590–594.
photographic systems for, 590–591
printers, 591–593
aliasing, 592
color images, 592
digital, 591–593
grey levels, 592
ink jet, 593
laser, 593
posterizing, 591
scaling techniques, 592
Harmonic signals, 2, 49, 80, 90, 100, 109, **113–114**, 162–163, 174, **179–180**, 188, 243, 361, 414, 428, 535, 545, 550, 556, 577, 596–597, 682, **703–704**, **708–719**, 722, 729, 734, 894 *See also*, Second harmonic generation; Third harmonic generation *see* Structured illumination.
chapter, 703–721
contrast, 179–180, 188
descanned detection, 56
in lasers, 109, 113, **114**, 115
plants, 428
second and higher, 114
Haze, from out-of-focus light, 227.
HBO-50 mercury-arc bulb, 126.
HCS. *See* High content screening.
Heat, 84–85, 89–90, 109, 129, 133.
filtering, dichroic filters, 43–44, 129, 132
heat sink for LED light source, 133
from laser cooling, 84–85, 109
of optical trap, 89–90
placing system components, 129
Heat filters, to exclude IR light, 43–44, 129, 132.
liquid, 132
Heating. *See also*, Thermal variables.
detectors, 252
microwave fixation, 377
in magnetic resonance imaging, 621–622
multi-focal, multi-photon, 551, 556, 685, 903
specimen, by the chamber, 387–389, 394, 732
specimen, by the illumination, 43, 89, 132, 211, 218, 341, 536, **539**, 544, 556, 621–622, 681, 685, 884, 903
calculation, 89, 685, 904
stability, 652
HeLa cells, 391–392, 693, 799, 812, 814, 820, 828, 854.
Helios Gene Gun System, 724.
Helium-cadmium (He-Cd) laser, 83, 86, 90, 93, **103**, 105, 115.
operational lifetime, 115
output variation, 86
transverse electromagnetic mode, 83
Helium-neon (He-Ne) laser, 82, 84, 88–90, 93, **102–103**, 105, 107, 240, 241, 376, 673, 680, 798, 799, 864, 875.
four state, 82, 105
Heterectis crispa, 874.
Hidden-object removal, 304–305.
High content screening (HCS), 809–817.
for cytomics chapter, 809–817
data management/image informatics, 816–817
fluorescence analysis of cells, table, 812
multiple fluorescent probes, 810
High resolution spatial discrimination, 813.
High throughput screening (HTS), 809.
High voltage electron microscope (HVEM), 846.
stereo images of platelets, 848–849
Hippocampal brain slices, 268, 316–317, 393, 556–557, 722, 724–725, 727.
calcium imaging, 556–557
culture protocol, 724–725
damage, 341
at neurons, 205, 268, 316–317, 393
Histology, 623, 624.
Historic overview of biological LM, table, 2–3.
Hoechst, DNA dye, 136, 339, **344**, 360, 362, 520, 565–566, 683, 782, 812.
4Pi, image, 565–566
FLIM image, 521
high-content screening, 812, 814
Holey optical fiber/non-linear effects, 88.
Holographic diffusers, to reduce coherence, 84.
Holography, holomicrography, 7–8.
Hooke, Robert, image of cork, 769–770, 785.
HTS. *See* High throughput screening.
Huffman encoding, 580–581.
Human endomicroscopy, confocal.
cervix, 513
gastrointestinal track, 514
Human retina, viewed with OCT, 609.
Huygens, 3D software, 104, 413, 669, 778.
Huygens-Fresnel wavefront construction, 406.
HVEM. *See* High-voltage electron microscope.
Hybrid mode-locked dye laser, 540–541.
Hymenocallis speciosa, fluorescence spectra, 422.
Hysteresis.
in Piezoelectric scanners, 57, 754
temperature cycling of lenses, 249

I

I^5M, (Incoherent Illumination Image Interference Imaging), 275, 561, **569–570**, 672.
optical transfer function (OTF), 569–570
ICNIRP. *See* International Commission of Non-Ionizing Radiation Protection.
ICTM. *See* Iterative constrained Tikhonov-Miller algorithm.
IEC. *See* International Electrotechnical Commission.
IF. *See* Fluorescent intensity.
Illumination, 44, 210. *See also*, Structured-illumination microscopy, and Chapter 6.
brightness, table, 140
errors, 211–212
evaluating, 211–217
goal in confocal microscopy, 210
path, 211–212
types of lamps, 44
vignetting caused by beam shift, 211–212
Image(s), 9, 11–12, 30–31, 38–39, 59, 145, 192, 210, 219, 280, 286–290. *See also*, Multidimensional microscopy images.
contrast, 7, 11, 16, 39, 49, **60**–62, 68, 159, **162**, 165, 167, 173–175, 180, 189–190, 192, 201–204, 248, 421, 473, 488, 542, 599–600, 607, 622, 656, 657, 675
chapter, 162
flare, 649
definition, 280
degradation of, measuring, 145
extended-focus, 9
motion between specimen and objective, 39
multi-dimensional microscopy, 286–290
anisotropic sampling, 287

Image(s) (*cont.*)
calibrating image data, 286–288
contrast transfer function (CTF), 61. *See* CTF
data type/precision in computations, 288–289
digitization, defined, 62
dimensions, 286–288
display devices, non-linearity of, 72–73
file formats, table, 288–289
processor performance, 289–290
Voxel rendering speed, 290
real, disk- and line-scanners, 30–31
reconstructing, and noise reduction, 38–39. *See also*, Reconstruction; Nyquist reconstruction sharpness of *vs*. signal intensity, 192
of source and detector pinholes, 210
speed of acquisition, 11–12. *See also*, Speed as sum of point images, 59
thermal distortion, 219. *See also*, Thermal variables
Image analysis. *See* Automated 3D image analysis methods; Automated interpretation of subcellular location pattern.
Image dissector, 254–255.
in trans-illumination mode, 10
Image enhancement. *See* Deconvolution, 488–499.
Image iconoscope, for television, 6–7.
Image intensifiers, 13, 232–233, 235, 255, 460, 477, 519–520, 522, 524, 555–556, 730, 737, 784, 801, 930.
Image Pro Plus, 282, 290.
Image processing. *See also*, Automated 3D analysis methods, and Multi-dimensional microscopy display.
for display, Chapter 14
for measurement, Chapter 15
Image resolution, 8, 9. *See also*, Resolution.
Image substrate, automated confocal, 810.
ImageJ, free software, 282, 290, 395, 732–733, 762–764, 795, 858.
Imaging system, optics characterized by CTF, 61.
Imaging techniques, 382–386, 394–395.
combining fluorescence with other, 383–386
fluorescence correlation spectroscopy, 383
fluorescence lifetime (FLIM), **382**, **516–532**
fluorescence loss in photobleaching (FLIP), 382
fluorescence recovery after photobleaching, 382
fluorescence resonance energy transfer, 382
fluorescence speckle microscopy (FSM), 383
laser trapping, 383
linear unmixing, 192, 382, 664–667
multi-channel time-lapse fluorescence, 382
optical tweezers, 383
photoactivation, 187, 224, **383**, 385, 541, 544–545, 693, 759
photo-uncaging, 383. *See also*, Photo-uncaging physiological fluorescence, 383
spectral, 382
table, 384–385
time-lapse fluorescence, 382
Imaris, software, 193, 281–282, 284, 287–288, 290–291, 299, 301–303, 308, 311–312, 764, 795.
In vitro fertilization, mitotic apparatus, 188.
In vitro preparations.
2D mixed-cell, assays, 813
antifade agents. *See also*, Antifade, 342
automated analysis, 318–320
backscattered light image, 513
biofilms, 870, 872, 879, 884
bleaching, 551, 851
brain slices. *See* Brain slices, 392–393, 725
cell maintenance, **387**
cytoskeleton, 368
fertilization, 188
GFP, 357
high content screening, 809, 813–816
high speed imaging, 11, 237, 809, 813, 815–816
ion imaging, calibration, 742
living cell imaging, 387
micro-CT, 614, 617
micro-MRI, 618, 621, 623–625
multi-photon, 535
optical coherence tomography image, 609
photodamage, 684
In vivo (intact animal) imaging, 112, 368–377, 512, 545, 806.
2-photon microscopy (MPM), 535, 543, 545
cell preparations, **387**
comparison with fixed material, 368–377
FLIM calibration, 517
labeling, 372–373
miniaturized confocal, 504, 508, 511–513
micro-CT, 614, 617
micro MRI, 618, 621, 623–625
molecular imaging, 806
photodamage, 684, 693–694, 698
"stick" lenses, 806
Incandescent lamps, 34, 126, 133–137, 477, 499 *See also*, Halogen lamps.
black-body radiation emitted by, 135–136
spectrum *vs*. temperature, 137
stability, 137, 477
Incidence angle, 49, 50.
efficiency, 143
interference filters/transmission, 49
reflectivity, diagram, 50
Incident light beam, sample interaction, 162–163.
Indo-1, calcium indicator, 103, 189, 257, 345, **346**, 348, **529**, 531, 544, 693, 697, 742–743.
Infinity corrected optics, 155–157, 166, 239, 405.
advantages, 156–157, 166, 239, 405
Infinity PhotoOptical, InFocus spherical aberration corrector, 15, 151.
Infinity space, generating, 157.
Information, 27, 60, 64, 73–74, 179, 235, 241, 243, 268, 270–275, 278, 330, 334, 353, 369, 382–383, 396, 398, **443**, 448, 459, 468, 475–476, 481, 487, 488–490, 494, 496–499, 506, 512–513, 517, 519, 522–524, 543–544, 556, 559, 570, 580–587, 596, 643, 650, 732, 715, 769, 774, 776, 779, 782, 790, 794, 800.
3-dimensional, 321, 378, 396, 747
4Pi, 570
and bleaching, 222, 690–692, 705
CARS, 597–598, 602
colocalization, 668
confocal, 461, 462
contrast, *see* Chapter 8 and Contrast
crystal orientation, 179, 188
display of, 280–281, 288–291, 293, 295–297, 299–301, 304–305, 311
efficiency, 336, 628, 631
of electronic signal, limitations on, 64
genetic, 756, 762–763
lost signal, 25–28
matching gray levels to, 73–74
micro-CT, 615
micro MRI, 618
and Nyquist sampling. *See* Nyquist sampling, 38, 39, 634–637
chapter, 59–79
optical projection tomography, 612
out-of-focus light, 27, 368, 458, **461**, 746, 784
parallel *vs*. serial acquisition, 223–224
PSF, 245, 247, 250
from second harmonic generation signal, 179
Shannon theory, 443
on source brightness, 137
spectral, 665–667
SPIM, 614, 675–378
storage, 106
chapter, 580–594
theory, 4, 64, 443
transmission, contrast transfer function, 37, 60
Index mismatch. *See* Spherical aberration.
Infrared (IR) lasers, 89, 383, 385. *See also*, Ultrashort lasers; Laser tweezers.
solid state lasers, 108–109
Infrared paper, to identify infrared beams for safety purposes, 118.
Ink jet printers, 593.
Innova Sabre/frequency-doubling crystal, 102.

Insect cuticle, transparency to NIR light, 166.
Installation requirements, for laser sources, 85.
Instrument dark noise, 660. *See also*, Noise
Integrated circuit (IC) chip, 9.
Intelligent imaging innovations, (III), 3D imaging system supplier, 78–79, 151, 192, 395, 411, 654.
Intensified CCD, 13, **232–233**, 460, 477, **519–522**, 524, 555, 556, 737, 784, **930**.
Intensity, light, 26, 37, 43, 58, 59, 61, 71–72, 86, 87, 133, 136, 163, 165, 180, 189, 192, 208, 217, 222, 228, **258**, 270, 391, 413, 426, 459, 461, 487, 536, 538, 571–573, 633, 681, 693, 705, 810, 901.
of excitation light, 80, 222, 680–682
laser beam, stability, 86
losses
detection path, table, 217
illumination path, table, 217
minimum needed, 392
on optical response of specimen, 165
in photons/second, 80
regulating, 43, 88
singlet-state saturation, *See* Saturation
and visibility, 37
Intensity control.
continuous wave laser, 88
non-laser, 128
Intensity distribution, 146–154.
of Airy disk, 65, 146. *See also*, Airy disks
changes with focus, 147, 407, 455, 463, 471
effect of coverslip thickness, 149
effect of RI mismatch, 148. *See also*, Spherical aberration
in focal spot, plots, 147–154
nonsymmetrical change with focus, 148
unit image, 147
with astigmatism, 152
with coma present, 151
with spherical aberration, 148–150, 212
Intensity loss, with spherical aberration in detection path, 148–150, 212. *See* Spherical aberration.
Intensity spread function (ISF), 74–78.
CCDs and PMTs compared, table, 78
defined, 75
estimating intensity measurement error, 76
and gray levels, 74–75
measuring, 75
Interference contrast.
differential interference contrast, (DIC), 10, 14, 76, 127, 146, 171, 453, 468, 473–475, 846, *See also*, Differential interference contrast.
deconvolution of, 473–475
phase-contrast, 9, **171**, 368, 372, 453, 506, 643, 649, 731, 851, 854, 890, 892. *See also*, Phase contrast
centering the phase rings, 643. *See also*, Bertrand lens scanning, 9, 13
using fiber optics, 506
RI inhomomogeneity and contrast, 22–23, 41
Interference filters, **45–51**, 102, 136, 212.
in argon-ion laser systems, 102
continuously-graded, 137
destructive and constructive reflections, 45
transmission, 212
types, 46–49
Interference fringes, coverslip surface, 168, 170.
Amoeba plasma membrane/coverslip, 170
in close proximity, 168
Interference mirrors, 46.
Interference mode, coherent light, 130.
Interference, speckle pattern, 8, 13, 84, 90, **130–132**, 144.
in backscattered light images, 448
fluorescence speckle microscopy (FSM), 13, 383, 385, 889
Interferometer.
4Pi microscopy, 561
Fabry-Perot (laser), 81–82
fiber-optic, for testing objectives, 240–241
Gires-Tournois, 88
Mach-Zender, to measure pupil function, 245
optical coherence tomography, (OCT), 504, 609
Twyman-Green, 239
Inter-fluorophore distance, measurement, 184. *See also*, Fluorescence resonance energy transfer.
Interfocal crosstalk, **227–228**.
disk scanners, **227–228**, 444, 449
time multiplexing as solution to, 553–554
Interlocks, laser safety, 118.
Intermediate optical systems, LSCMs, chapter, 207–220.
Internal focusing elements, in objective, 157, 511.
International Commission of Non-Ionizing Radiation Protection (ICNIRP), 117.
International Electrotechnical Commission (IEC), 117.
International television standards, 589.
Internet sources. *See* Links.
lasers, 123, 124
Intrinsic noise, 21. *See also*, Poisson noise.
Inverse filter algorithm, 476, 477.
Ion-binding in *Aequorin* emits light, 737.
Ion concentrations, 346–347, 517, 528–530, 741.
chapter, 736–745
determination, 517, 528–530
Ion-concentration imaging, 736–738, 740–745. *See also*, Calcium imaging, pH, etc.
calcium imaging, 736–737
concentration calibration, 742–745
indicator choice, 738
interpretation, 740–741
pH imaging, 739–745
water-immersion objectives, 737
Ion sensitive probes, optical, **348**, **737**.
table, 531–532
IR. *See* Infrared; Near infrared.
Irradiance, arc and halogen light sources, 130.
table comparing, 130
ISO standard, microscope dimensions, 156.
Iso-intensity surface, or arc sources, 304.
Iterative constrained algorithms, 475–476. *See also*, Deconvolution; Nonlinear constrained iterative deconvolution algorithms.
Iterative constrained Tikhonov-Miller algorithm (ICTM), 497.

J

Jablonski energy diagrams, 516, 517, 697, 792.
Jansson-van Cittert algorithm, 476, 496.
Jitter, defined, for scanners, 54.
JND. *See* Just noticeable difference.
Joint Photographic Experts Group. *See* JPEG.
JPEG (Joint Photographic Experts Group), 581–584.
Just noticeable difference (JND), ocular response, 72–73.

K

Kaede, photoactivatable fluorescent protein, emission change after photodamage, 187, 383, 385.
example image, 187
Kalman averaging, 21, 39, 53, **304**, 306, 627, 638, 655, 750, 754, 781.
comparison with deconvolution, in reducing
intensity, 39
Kepler, Johannes, 788.
Kerr cell, 516.
mode-locking (KLM), 111, 133
of titanium:sapphire lasing rod, 113
Kerr effect, defined, 111, 179.
self-focusing of pulsed laser light, 111
Kindling proteins, 574, 760.
Kinetics, 691, 694–698, 741–742, 774, 796, 810–812, 816–817.
bleaching, 691, 694–698
and endpoint data analysis, 816–817
fluorescence, 262–263, 348, 383, 385, 571, 578, 741–742. *See also*, FLIM
FRET, 796
high content screening, 810–812, 816–817

Kinetics (*cont.*)
ion concentration dyes, 741
and STED, 571, 578
Kino, Gordon, confocal design, 6.
KLM. *See* Kerr lens mode-locking.
Köhler illumination, 34, 127–128, 131, 229, 251, 627, **648–649**.
coherence of light, 131
in disk scanner, 229
field diaphragm, 35, **127–129**, 139, 461, 627, 645, **648–649**
to limit non-uniformity of illumination, 127–128
to measure photon efficiency, 34
Krypton laser, 102, 119, 346, 355.
comparison with argon-ion laser, 102
wavelength, 102
Krypton/argon (Kr/Ar) laser, 90, 92, 93, **102**, 108, 119, 203–204, 343, 375, 748, 798, 811.
stabilization, 88
KTP. *See* Potassium titanium oxide phosphate.

L

Labeled structures, plants, 757, 761, 775.
bulk labeling, living embryos, 761
cell walls, 775
selective labeling, 757
Label-free microscopy, noise, 114.
Lamp housing, 134.
Lamprey.
labeled axons, 235, 236
larva, optical projection tomography image, 612
Landmark-based registration synthesis method, 328–329.
Lanthanide chelates, 345–346.
Large mode area photonic crystal fiber (LMAPCF), 110.
Larmor frequency, MRM imaging, 618–622.
Laser(s), 7–9, 44, 80–83, 88, 90, 94, 112–114, 119–120, 131, 540–543, 599–600. *See also*, Fiber lasers; Mode-locked lasers; Multi-photon ultrafast lasers; Up-conversion fiber lasers; Ultrafast lasers.
Alexandrite, 109
amplifier rods, 116
attenuation of, 85, 87–88, 354, 415, 904
axial or longitudinal modes, 83
basic operation, 81–83, 116
CARS microscopy requirements, 599–600
chapter, 80–125, table, 119–120
coherence, spatial and temporal, 83–84
colliding-pulse mode-locked (CPM), 540
for confocal, 7, 9–10, 77–78, 280, 535–545
continuous-wave, **90–110**
control of power, 543
Cr:Forsterite, 109, 114, 415, 541, 706–709, 712–714
excitation wavelength choice, 540–542. *See also*, Acousto-optical devices, filters
femtosecond pulsed laser, 44. *See also*, Ultrafast lasers
fiber-based lasers, 109–111, 113–118
table, 94
ultrafast, 113–114
up-conversion fiber lasers, 109–110
fiber light delivery, 107,*See also*, Fiber-optics
GaAs, 107, 111
gas, 90, **91–10**. *See also*, lasers by gas.
alkali-vapor, 103
Ar-ion, 90, 101–102
Kr-ion, 102
HeNe, 102–103
HeCd, 103
heat removal, 84
hybrid mode-locked dye laser, 540–541
important properties for confocal, 80
light delivery, 87–89
fiber-optic, 106
mirrors, 88
longitudinal modes, 82–83
maintenance, 115–116
active media replacement, 115
cooling components, 116–117
optical resonator, 116
metal vapor, 112
microscopical uses
nonlinear: 2- 3-photon, 90
Raman and CARS, 90
TIRF, 90
tweezers, 89. *See* Laser trapping
multi-photon. *See* Multi-photon microscopy
Nd:glass, 706–708
Nd:YAG, lasers, 88–89, 91, 95, 97, 103, 107–109, 111, 113–115, 117, 218, 245, 514, 680, 798
Nd:YLF, lasers, 89, 98, 100, 103, 109, 112–114, 750, 760–761
Nd:YVO_4, lasers, 89, 95, 100, 103, 107–109, 111, 113–114, 541
NO SMOKING, 116
performance tables, **91–101**
phase randomization, 8, 13, **131–132**, 143
pointing error, 87
active cavity stabilization, 87
polarization, 83, 88–89
power control, 543
pulse broadening/compensation, 88, 901–904
pulsed, **110–115**. *See also*, Titanium-sapphire, Cr:Forsterite, Nd:glass,YAG/YLF/YVO_4, etc.
cavity dumped, 111
Kerr lens mode-locked, 111
modulated diode lasers, 112
pulse-length measurement, 115, **901–903**
purpose, 110
saturable Bragg reflector, 111
ultrafast, DPSS lasers, 112
ultrafast, fiber lasers, 113
white-light continuum lasers, 113
why are they useful?, 110
pumping power requirements, 82
safety, **117–118**, **839**, 900. *See also*, Safety
goggles, 118
screens and curtains,118, 904
solid state, 103. *See also*, Solid-state lasers
semi-conductor, 105–107
thin-disk lasers, 109
spectrum of light, 44
stabilization, 85–87
active, 87
titanium:sapphire laser, 82, 84–86, 88–91, 94, 100–103, 105, 107, **109**, 111–112, 114, 123–124, 165, 346, 358, 415, 423–424, 459, **541**, 550, 551, 645–647, 688, 706–708, 713, 727, 750, 756, 759
4Pi, 563–564, 567
brain slices, 731
CARS, 599
compared to other fast lasers, 82–83, 85, 110, 112–113
embryos, 731, 750, 756, 759, 764
maintenance, 116
and OPO, 114–115
plants, 415, 423–424, 706–708, 713–714, 717, 781–783
popular models, specs, table, 120
STED, 575
transverse modes, 82–83, 85, 110
tweezers, 89. *See* Laser trapping
types, 90
ultrafast fiber, 113–114, *See also*, Ultrafast lasers
wavelength expansion by sum-and-difference mixing, 114
optical parametric oscillators, 114–115
second/third harmonic generation, 114
white light continuum lasers, 88, 109, 113
continuum, 88, 109
He:Cd, 113.
Laser cavity stabilization, active, 87.
Laser cutters, 686–687.
integration, 218–219
Laser illumination, conditions for, 8.
Laser lines, using acousto-optical tunable filters, 56.
Laser media, maintenance, 115–116.
Laser printers, 593.
Laser rods, maintenance, 116.
Laser Safety Officer, 117.
Laser sources, 9, 80–125. *See also*, Lasers.
Laser speckle, 84, 90, 130–132, 448.
removing, 84. *See also*, Scramblers
source, 130
Laser trapping, 80, **89**, 110, 218–219, 383, 385, 539, 646, 680.

Laser tubes, operational lifetime, 102, 115.
components likely to fail, 115
Laser tweezers. *See* Laser trapping.
LaserPix, 282.
Laser flying-spot microscope, 7.
Lasersharp, confocal microscopes, 282, 284, 285, 288, 292, 296, 302–306.
LaserVox, 281–282.
Lateral chromatic aberration (LCA), 14, **155–156**, 239, **242–243**, 287, **640**, 657–658.
correction in conventional optics, 155
measured, 657–658
Lateral coherence, 8, 84, 267.
Lateral resolution, 1–4, 9, 11–13, 28, 207, 209, 222, **225**, 230, 238, 270, 320, 409, 453, 511, 513, 542, 552, 554, 563, 568, 651, 654–656, 747. *See also*, Resolution.
4Pi, 568
CARS, 596–597, 599
confocal endoscopy, 511, 513
confocal optics, improvement, 9, 651, 654–656
of display, 292
light microscopy, 1–3
optical coherence tomography, 609–610
with pinhole and slit disks, 225
and spherical aberration, 409
SPIM, 613, 674
STED, 573–575, 578
table, 209, 409
Laterally-modulated excitation microscopy, *see* Stuctured-illumination.
LCA. *See* Lateral chromatic aberration.
LCD. *See* Liquid crystal display.
LCOS. *See* Liquid-crystal-on-silicon.
LCS (Leica Microsystems AG), 282, 312, 910.
Lecithin myelin figures, CARS image, 204.
LED. *See* Light-emitting diode.
Leica, confocal manufacturer, 51–53, 56–57, 160, 218, 797, 910.
acousto-optical beam-splitter, 160, 218
objective lens transmission, 160
RS Scanner, 52–53
spectral confocal, TCS SP2, 51, 56–57, 910
tube length conventions, 157, 239
Leica Microsystems AG, 282, 910.
Leica TCS 4Pi, 119–120, 565–568.
4Pi microscopy type C, 565–568
imaging of living cells, 568
lateral scanning, 567, 910
mitochondrial network image, 568
optical transfer function (OTF), 567
sketch, 566, 910
thermal fluctuations minimized, 567
Lempel-Ziv-Welch (LZW), 580–582, 584.
Lens aberrations, 13–15. *See also*, Aberrations.
Lens focal length, change, with wavelength, 152.
Leonardo da Vinci, early optical studies, 788–790.
Leukocytes, 347, 387, 520, 815, 854.
automatic analysis, 815
multi-photon, phase-based FLIM, 521
Lifetime. *See* Fluorescence lifetime imaging microscopy.
Ligand-binding modules, 256, 348, 741, 846.
Light detection, general, **28–33**, **251–264**. *See also*, Detectors; specific detectors: CCDs, PMTs, etc.
assessment of devices, 260–262
charge-coupled device (CCD), 254
comparison, table, 233, 255–256, 647
conversion techniques, 259–260
direct effects, 252
future developments, 262–264
history, 262–264
image dissector, 254–255
microchannel plate, 232–233, **255**, 262
gated, 519, 523–524, **527**, 532
MCP-CCD, 262
noise internal to, 256–259
internal detection, 256
noise currents table, 256
photoemissive devices, 256–257
photon flux, 257–258
pixel value representation, 258–259
photoconductivity, 252, 253
photoemissive, 254
photon interactions, 252–256
work functions, table, 252–253
photovoltaic effect, 252–253
point detectors, 260–261. *See also*, PMT
quantal nature of light, 251–252
thermal effects, 252
vacuum avalanche photodiode, 254, 255
Light dose, related to pixel/raster size, 64.
Light, effects, on plant cells, 770. *See also*, Bleaching, Phototoxicity.
Light-emitting diode (LED), 34, 54, 132–133, 135–139, 143, 237.
aligning, 135
control by current-stabilized supply, 138–139
definition, 105
to detect galvanometer rotor position, 54
excitation wavelength for fluorophores, 136
expected cost reduction, 237
fluorescence image, 142
galvanometer position feedback, 53
lifespan, 137
to measure photon efficiency, 34
microscope illumination, **131–139**, 141, 143
organic, projected development, 143
radiance, 138
spectra, 133
stability, 136
temperature effects, 137
wavelength *vs*. current change, 137
Light flux, light-emitting diode temperature, 133.
Light intensity, 71, 163.
Light microscopy history, 1–4.
Light paths. *See also*, Commercial confocal light microscopes.
separating excitation/emission, 44–45
Light piping by specimen *vs*. depth, 182.
Light-sheet illumination, 672–673.
Light sheet microscopy, 613.
chapter, 672–679
optical setup for, 613
white-light continuum lasers, 113
Light sources, widefield, 132–139, 143. *See also*, Chapters 5 and 6, Arc lamps, LEDs, Lasers; Nonlaser light sources; Filaments; Halogen.
commercial sources, 143
solar, 126–127, 131, **135**
stand-alone, 143
table, comparative performance, 140
types, 132–139
Light transmission, 11, 139, 160–161, 223–229.
cummulative loss along optical path, 139
of Nipkow disk system, 11, 223–229
specifications for objectives, table, 160–161
Lighting models, 3D image display, 306–312.
absorption, 309–312
advanced reflection models, 309
artificial lighting, 309–312
Gourard shading, 308
gradient reflection models for voxel objects, 309
Phong shading, 308–309
Phong/Blinn models, 308
simulated fluorescence process, 310
surface shading, 310
transparency, 280, 284, 287, 300, 304, **309**, 311–312
Lilium longiflorum, image, 783.
Limitations, confocal microscopy, chapter, 20–42.
fundamental, 20–42
table, 41, **647**
typical problem, 21, 24
Linear galvanometers, 54.
Linear longitudinal chromatic dispersion (LLCD), stereoscopic confocal image, 154.
Linear unmixing. *See* Spectral unmixing.
Line-scanning confocal microscope, 50, 51, **231–232**, 237, 784, 908, 916.
Linearity, 72, 490.
deconvolution for image enhancement, 490
display advantages and disadvantages, 72
Links (Internet addresses).
2 photon excitation spectra, 546, 727, 729, 782
brain slices, 727

Links (Internet addresses) (*cont.*)
CCDs, 76, 234, 927, 931
components, 58
confocal Listserve, 390, 901
deconvolution, 495
dyes, 221, 343–344, 782
fluorescent beads, 653
FRET technique, 185, 803
high-content screening systems, **811**
image management, 865
lasers, 104, 115, 120, 123–125
live-cell chambers, 388–389, 870
movies related to book, 235, 392
muscles, 237
non-laser light sources, 138, 143
plants, 769
safety, 900
software, 282, 376, 594, 734, 762, 764, 776, 777, 820, 824, 827, 831–833, 844, 845, 864–862, 865–867, **869**
SPIM, 672
Lipid dyes, 236, 355, **359–360**, 389, 556, 755, **760**–761.
Lipid receptors, 790.
Liquid crystal-on-silicon (LCOS), 266.
Liquid crystal display (LCD), 39, 67, 73, 291, 293, **589–590**.
digital projectors, 590
filters, 928
non-linearities, 73
shutters, 299, 929
supertwisted nematic (STN), 589
thin-film transistor (TFT), 589
Liquid crystal technology/dynamic polarization microscopy, 188. *See also*, Pol-scope.
Lissajous pattern, circular scanning. 554.
"tornado" mode, SIM scanner, 52
List servers, 125.
Lithium triborate (LBO), as non-linear crystal for multiplying infrared output, 109, 115.
Living cells, 80, 90, 114, 136, 145–161, 167, 219, 221–222, **381–399**, 429–439, 480, 564–566, 568, 746–766, 770, 772–773, 788–806, 811, 813. *See also*, Brain slices, Plants cell imaging, and by cell/organism name.
2-photon, penetration, 749–751
2D plus time, 753–754, 762–764
3D projection, 763
4D data, 746–747, 764
4Pi microscopy, 564–565, 568
acquisition speed, 222, 753–754
algorithms, 763–764
assays, 811
beauty and functionality, 790
bleaching of, 797. *See* Bleaching; Photodamage
cell-chamber, 11, 22, 191, 219, 370–371, **386–387**, **394**, 429–430, 564, 610–611
for 4Pi confocal, 564
for biofilms, 870–873, 875, 877, 880, 885
for brain slices, 394, 723, 727, 729
for epithelial cells, 370–371, 377, 386
finder chamber, 683
flow chamber, 870–873, 875, 877, 880, 885
for high-content screening, 810
for optical projection tomography, 610–611
perfusion, 394
for plant cells, 191, 429–430
simple, 22, 394
for SPIM, 613, 625, 673
table of required functions, 380
table of suppliers, 388–389
test chamber/dye, 654, 661
cell-cycle effects, 790
chromatin, 385, 390–392, 684, 693–695, 812
chromatin dynamics, 390–392
CNS tissue slice preparation, 393
confocal microscopy, 381–399, 746, 813
difficulties, 381
future directions, 398–399
considerations, 386–390
antioxidants, 390
experimental variables, table, 386
fluorescent probes, 387–389
maintenance of cells/tissues, 387
minimizing photodynamic damage, 136, 389
photon efficiency, 141–161, 389–390
in vitro preparations, *see In Vitro*
in vivo preparations, *see In Vivo*
contrast, 747
dyes, 748. *See also*, Dyes; Fluorophors etc.
for rapid assessment, table, 360
embryos, imaging, 746–766. *See also*, Living embryo imaging
external membranes, SHC image, 90
fluorescent staining, 393
microglia, 393
nuclei, living/dead cell, 393
fluorophore effects, 748
FRET imaging, chapter, 788–806
future, 221–222
handling data, 395–396
imaging techniques, 382–386, 394–395
low-dose imaging, 391–392
microglial cell behavior example, 392–398
no damage from SHG imaging, 114
online confocal community, 390
photon efficiency, 141–161, 389–390
phototoxicity, 390–391
assays for, 813
plant, 429–439. *See also*, Plant cell imaging reflectance imaging, 167
second harmonic generation. *See also*, SHG
of external membranes, 90
no damage, 114
test specimen for, 390
widefield, 646–647, 751–753
working distance, 5, 9, 129, 145, 154, **157**, 198, 249, 511, 568, 598, 634, 673, 678, 727–728, 747, 774, 779, 781, 872
table, 158
Living embryo imaging, 749–751, 762–764.
aberrations caused by, 747
apparatus, 748
C. elegans, 746, 748
deconvolution helps confocal, 751–753
developmental changes, 746
Drosophila, 273, **675–676**, **747–748**, 751–752, 754, 756, 759, **804**, 810
dyes, 748
introduction of, 755
embryo size *vs.* speed acquisition, 753–754
explants, 748–749
future developments, 766
fluorescent probe
four dimensional, 746–747, 749
cellular viability, 747–748
challenges, 762
dataset display strategies, 761–764
photodamage during, 746–748
high speed acquisition
disk-scanning confocal microscopy, 754
hardware, 754–755
light scattering, 747
optimal acquisition, parameters, 753–754
refractile specimens, 747
superficial optical sections, 748
thick specimens
effective strategies, 748–753, 755–761
inherent trade-offs, 747–748
selective plane illumination (SPIM), 751
"Test drives," for living embryo imaging, 752.
widefield/deconvolution, 751–752
LLCD. *See* Longitudinal chromatic dispersion.
LMA-PCF. *See* Large mode area photonic crystal fiber.
Loading methods, fluorescent probe, 347, **358–360**, 430, 732–734, 738, 739.
acetoxymethyl esters, 359, 360. *See also*, Acetoxymethyl esters
ATP-gated cation channels, 359
ballistic microprojectile delivery, 360, 726, 803
direct permeability, 358–359
electroporation, **359–360**, 795, **803**
ion indicators, 738–739, 742
low level, 430
membrane permeant esters, 359–360
microinjection, **360**, 361, 388, 739, 748, 755, 795, **803–804**

neurons, 722, 726, 730, 732–734
osmotic permeabilization, 359
peptide-mediated uptake, 359
plant cells, 769
stabilizing chemicals, 341–342, 362
transient permeabilization, 359
whole-cell patch pipet, 360
Local projections, display, 305–306, 307.
Location proteomics, 818.
Longitudinal chromatic aberration, 152–155.
Longitudinal coherence length, 7, 8, 84, 130, 131.
Longitudinal linear chromatic dispersion (LLCD) objectives for 3D color-coded BSL confocal, 154.
Long-pass filters, 43–44.
Low-voltage scanning electron microscope (LVSEM), 846–847, 849–850, 852.
LSM. *See* Laser-scanning confocal microscopes; Laser-scanning flying-spot microscope. 6–7
Lucoszs formulation, 273.
Luminescent nanocrystals, 343, 345.
Luminous intensity vs, color, dye molecule, 138.
LVSEM, 846–847, 849–850, 852.
LysoTracker Red DND-99, 359–360, 709–710.
rapid assessment table, 360
spectra, 710
LZW compression. *See* Lempel-Ziv-Welch.

M

Mach-Zehnder interferometry, 245.
Machine learning. *See* Automated interpretation of subcellular patterns.
Macrography, 3D light scanning, 672.
Magnesium fluoride (MgF2).
for anti-reflection coating, 158
Magnetic disks, 586.
Magnetic resonance imaging (MRI), 618.
Magnetic resonance microscopy (MRM), 618–624.
amplitude modulation for RF carrier, 620
applications, 623–624
botanical imaging, 624
developmental biology, 624
histology, 623
phenotyping, 623
basic principles, 618–619
Fourier transform/image formation, 620
future development, 624
hardware configuration, 621–622
image contrast, 622–623
image formation, 619–621
Larmor frequency, 620
Schematic diagram, 618–619
strengths/limitations, 622
Magnification, 24, 35–41, 62, 131, 215, 443. *See also*, Nyquist sampling; Over-sampling; Undersampling.
calibrating, 653, 658
and CCD pixel-size, 62, 70
confocal, 52–53, 62–64
effect on pixel size, 24, 928
factor, 24, 28
and lateral chromatic aberration, 278
for line-scanner, 232
over-sampling, 68–70, 493, 509, **635**, 729
high-content screening, 816
and pinhole size, 28
under-sampling, 68
zoom magnification, 11, 24, 37, 63–34, 66, 70, 79, 317, 389, 493, 627, 634–636, 731
Maintenance.
cell viability, 387
dye lasers, 114
lasers, **115–117**, 124
remote logging of, 864
troubleshooting reference, 124
Maize *(Zea mays)*, 167–168, 172, 179, 202, 417–424, 428, 438, 710–711, 713–714.
2-photon, time-lapse microspectroscopy, 423
abnormal vasculature, 437
anther, 420, 433
attenuation spectrum, leaf, 418
cross-sections, stem, 172, 707
emission spectrum, 710, 711, 713
fluorescence spectra, 422–424
leaf,
attenuation spectrum, 418
optical section, 172, 179
reflectance, 167
surface, 436
meristem, 420, 430–432, 707
multi-photon excited signals, 422–424
polarization microscopy, 707, 711
pollen grain, 202, 433–434
protoplast, 424
root, 432
second harmonic imaging, 707, 711
silica cells, 428, 437, 707
spectrum, 422, 423, 710
starch, 420, 435–436, 707, 711
stem
attenuation spectra, 417, 418, 713
optical sections, 419, 714
storage structures, 420, 435–436, 707, 711
Manufacturers. *See also*, Commercial confocal light microscopes; Appendix 2.
listing with web addresses, table, 104–105.
Mapping conventions, in image processing, 294–296, 300–304.
data values, 300–304
choosing data objects, 300–301
object segmentation, 301–302
projection rules, 302–304
scan conversion, 301–302
table, 300
visualization, 300
multi-dimensional image display, 294–296
G function, 294
image/space view, 296
orthoscopic view, 294
reducing geometric dimensions, 294
rotations, 294–296
visualization process, 294
MAR. *See* Mark/area ratio.
Marching cubes algorithm, 301–302, 304, 776.
Marconi, CAM-65 electron multiplier CCD camera, 76. *See also*, EM-CCD.
Mark/area ratio (MAR), 279.
Marsilea quadrifolia, 416, 419.
attenuation spectra, 416
optical section, 419
Mass balancing, to reduce scanner vibration, 54.
Mass storage, 580–588, 593–594.
data compression for, 288–289, 292–293, 295, 319, 499, **580–585**. *See also*, Data compression
algorithms, 319, 580
archiving systems, 580
color images, 581
file formats, 580–588
removable storage media, 585–588. *See also*, Removable storage media
random-access devices, 586–588
sequential devices, 585–586
solid state devices, 588
time required, table, 581
Materials, silicon, fused quartz, beryllium, 52.
Mathematical formulas, for confocal microscope performance, table, 209.
Maximum intensity projection, 180, 284–285, 292, **294**, 298, **302–304**, 307, 313–314, 319, 325–326, 330–331, 585, 755, 763–764, 770, 774, 881, 884.
local, 305
Maximum likelihood estimation (MLE), **472–475**, 495, 497–498, 669.
blind deconvolution, 472–475, 498, 784
effect on colocalization, table, 669
M-CARS. *See* Multiplex CARS microspectroscopy.
MCP. *See* Microchannel plate, 232–233, **255**, 262.
MCP-CCD, 262
Gated intensified, 519, 523–524, **527**, 532
MCP-PMT. *See* Microchannel plate photomultiplier.
MDCK cell, 372–374.
actin cytoskeleton, 374
Golgi apparatus, image, 374
morphologic changes, 374
stereo image, 373, 374
vertical sections, image, 372

Measurements, 20, 33–36, 76, 139–141, 159.
achromat performance, 194
buffering of, ion measurement, 738, 740
field flatness, 26–28
geometric distortion, 653–654
laser pulse length, 109, 112, 115, 507, 537, 538, 902–903
light throughput, 139–141
limits on confocal intensity, accuracy, 20
photon efficiency, 33–36
pinhole, effective size, 34
intensity spread function histogram, 74–78
resolution, 241–245, 657, 658
shrinkage, specimen preparation, 371–373
spectral transmission of objective, 159
spherical aberration, 145, 407
surface height, using LLCD BSL confocal, 224
z-resolution, 194
Mechanical scanners, 51–54.
Melles Griot catalog, real lens, performance, 210.
Membrane permeant esters, 361, **358–359**, 361, 726, 738–739, 744.
Membrane potentials, 179, 188, 204–205, **346**, 353, 383, 517, 743, 811–813.
Memory stick, 588.
Mercury arc lamp, 37, 44, 132, 135–138.
fluorophores matching excitation, 135–136, 139
iso-intensity plots of discharges, 132
and pinhole size, 37
radiance, improvements, 137–138
wavelengths, 44
Mercury-halide arc source, 136, 138, 143–144.
spectrum, 144
Mercury-iodine (Hg-I) arc lamp, radiance, 138.
Mercury-xenon arc lamps, 136–138.
spectral lines, 136
Meristem, 168, 420, 430, 432, 770, 776–778, 782.
maize, 168, 432
Merit functions, confocal scanners, 217.
object-dependent, defined, 217
object-independent, defined, 217
Mesophyll cells, 169, 193, 195, 417–418, 423, 428, 430, 711–712, 714, 779.
A. thaliana, 193, 196
photodamage, 203
protoplasts, 196, 203, 424, 425–426, 430, 439
harmonic images, 711–712, 714
image, 424
spectra
attenuation, 416, 418
change with 1- *vs.* 2-photon, 421, 423
emission, 423
Metal-halide light source, 136, 143–144, 907, 908.
Metal vapor lasers, 112.
Metamorph, **281–282**, 290, 311, 817.
Microchannel plate (MCP) image intensifier, 233, 255, 519, 532.
multiplicative noise, 233
photocathodes, 262
PMT, 255, 523, 532
Microchannel plate PMT (MCP-PMT), 255.
Micro-computerized tomography (Micro-CT), 614–618.
contrast/dose, 614–615
dose *vs.* resolution, graph, 616
layout, 614
mouse images, 615–617
tumor-bearing, 617
operating principle, 614
Micro-CT. *See* Micro-computerized tomography.
Microdissection.
with multi-photon IR light, 686–687
with nitrogen lasers, 112
Microelectrodes, for introducing indicator, 738.
Microglial cell behavior, 392–398.
Microinjection, **360–361**, 388, 739, 748, 755, 795, **803–804**.
of chromophores, 803–804
Microlens array, 12, 134, 135, 216, 225, 231, 235.
for 4Pi confocal, 563–565
for CCD, 237
for disk scanners, 6, 12, **216**, 224, 226, 231, 458
for light-emitting diode source, 134–135
for multi-focal, multi-photon, (MMM), 537, **551–555**, 558
principle, 135
in Yokogawa disk-scanning confocal, 12, 224–226, 231, 235
Microscopes, 217, 226. *See also*, particular types.
attachment of confocal scanner, 217
specification comparisons, table, 226
Microscopy laboratory URLs, 125. *See also*, Links.
Microspectroscopy, 421–425, 426, 516.
CARS, 601–602
fluorescence properties of plants, 421–425
lifetime, 516
of maize, 424
multi-photon setup, 424
Microspores, birefringence images, 189, **431–432**.
Microsporogenesis, 431–432.
Microstructure fibers, 504.
Microsurgery, 112, 219, 686–687, **764–765**.
Microtubule, 11, 68, 80, 188, 222, 292, 432, 582, 703, 714, 752–753, 759, 773, 790, 852. *See also*, Cytoskeleton.
birefringence, 714–715
Brownian motion of, 11
electron microscopy, 848, 850
fixation, 369, 372–375
fluorescence correlation spectroscopy, 383
GFP, 12. *See also*, Green fluorescent protein
in mitosis, 759. *See also*, Mitotic apparatus
polarization microscopy, 15, 173, 188, 420–421
photodamage of, 341, 850–851
stabilizing buffers, 852
STED, 576–577
stereo image, 752
TIRF, 180, 183
second harmonic generation, for tracking, 90
Microwave fixation, 377–378.
Microwire polarizer (Moxtec Inc.), 85.
Mie scattering, 162–163, 167, 417–418.
clearing with index-matched liquid, 167
comparison with Rayleigh scattering, 163
light attenuation in plant tissue, 417
by refractive structures, 162–163
MII. *See* Multi-photon intrapulse interference, 88.
Mineral deposits, plant, 163–420, **436–437**, 703.
Miniaturized fiber-optic confocal microscope, 508–512.
bundle imagers for *in vivo* studies, 509
clinical endoscope, 514
objective lens system, 509
optical efficiency, 509
optical schema, 508
resolution, 509
rigid endoscope, 511
single fiber designs, 510
vibrating lens and fiber, 510–511
in vivo imaging in animals, 512
Minolta, CS-100 radiospectrometer, 139.
Minsky, Marvin, 2, 4–6, 11, 141, 216, 890.
Mirror coupling, pulse width and pulse shape, 88.
Mirrors, 26, 48, 54, 63, 209–210, 214.
galvanometer, 54. *See also*, Galvanometers
internal, testing reflectance losses, 26
laser-line, 48
performance, 54, 63.
scan angle and magnification, 63
size calculation for LSCM, 209
x-y scanning mirror orientations, 214
Mismatch, 893.
probe shape/pixel, 39, 466
caused by chromatic aberration, 243
refractive index, **377**, **404–412**, 411, 654, 658, 747, 863, 893
4Pi, 568
causing signal loss, **148–150**, 408–409, 654
chapter, 404–412
corrections, 411–412
embryos, 747
film *vs.* CCD, 590
harmonic signal generation, 704–705
less, at long wavelength, 416

measurement, **148–150**, 655–656
of movie frame rate, 839
MRM, contrast agent *vs.* imaging time
mylar flakes, 198
resolution loss measured, 192–194
vector mismatch in CARS, 596–597, 600
z-distortion, 287
Mitotic apparatus, 15, 173, 373–374, 377, 386, 421, 431, 693, 749, 752, 799. *See also*, Microtubules.
damage, 693
fixation, 373–374, 377
FRET, 765
marker, cyclin-B, 790
Pol-scope, 13, 188, 432, 468, 479–480.
deconvolved, 479
images, 15, 188, 479, 717
SHG imaging, 702, 718–719
in vitro fertilization, 188
Mitotracker stain, 142, 170, 353, 358, 360, 430–431, 692, 750.
living cells rapid assessment, table, 360
Mixing, sum or difference, to generate laser wavelengths, 114.
MLE. *See* Maximum likelihood estimation.
MMM. *See* Multi-focal, multi-photon microscopy.
MMM-4Pi microscopy, 556.
MO (magneto-optical) disks, 586.
Model-based object merging, 323–325.
Mode-locked lasers, 87, 101, **111–114**, 118, 124, 358, 520, 646, 728–729, 749, **901–904**.
active, pulsed laser class, 111
adjustment of, **901–904**
for CARS, 599–600
colliding pulse, 112
fiber, ytterbium and neodymium, 113–114
fiber/diode, ultrafast, 113–114
FLIM, 520
interference with, by specimen, 171
Kerr lens, 111
modulator, fiber lasers, 111
multi-photon, 535–536, **540–541**, 550–551, 563–564, 567, 646, 728–729, 749
passive, 111, 113–114
saturable Bragg reflector, 111
SHG, THG, 706–707
Mode-locked oscillators. *See also*, Mode-locked lasers.
nanojoule pulse energies, 111
Moiré effects, 270–271, 755.
ambient fluorescent room lighting, 201
banding patterns, 755
disk-scanners and CCDs, 231, 754–755
structured-illumination methods, 268–271, 273
Molecular imaging, *in vivo*, 387, 618, 624, 790, **803–806**.
FRET, 790, **803–806**
micro-CT, 618
MRM, 624
Monitors, computer display, 588–589.
Monkey cells, 693, 803.
Monomeric red fluorescent protein (mRFP) constructs, 756, 760, 798.
with CFP or GFP molecules, as FRET pair, 798
Montage synthesis method, 281, 312, 318, **328–331**, 748, 753, 851–852, 855, 858–859.
defined, 329–330
examples, 330–332, 780–781
scanning electron micrographs, 851–852, 855
TEM methods, 858–859
Moon, early phase measurements, 788, 789.
Morphological filters, 285, 300–301, 316–317, **320–322**, **730–734**, 817, 826.
high-content screening, 812, 819, 826
Morphometry, 145, 316, 319, **331**, 726, 728.
group properties, 331
intensity/spectral measures, 331
interest points, 331
invariants, 331
location/pose, 331
shape measures, 331
size measures, 331
texture measures, 331
topological measures, 331
Mosaicing. *See* Montage synthesis method.
Mounting medium, 166, 198, 342, 370–371, **373–377**, **404–413**, 418, 454, 457, 473, 493–794, 499, 564, 631, 642, 652, 655, 696, 730, 774 *See also*, Clearing agents.
brain slices, 730
chapter, 404–413
clearing solutions, 166, **417–418**, **420**, 439, 610, 624, 774–775
effect of glass bead, 199
plant specimens, 418, 431, 774
refractive index, tables, 377
selection, 198, 631
Mouse, 192, 376, 393, 608, 612, **615**$^{+}$, 723, 726.
confocal colonoscopy, 509, 512
embryo
optical projection tomography image, 612
SIM/EFIC image, 608
GFP transgenic, 726
hippocampus, 393
micro-CT image, 614–615, 617
femur, 616
tumor, 617
spectral unmixing image, 192, 382, 664–667
examples, 665–666
visual cortex brain slices image, 723
Movement contrast, 190.
Movie compression, 836–840.
Moving-coil actuators, galvanometer, 52.
Moxtec Inc., Microwire polarizer, 85.
MPA. *See* Multi-photon absorption.
MPE. *See* Multi-photon excitation.
MPEG display formats, 836–841.
MPEM. *See* Multi-photon microscopes.
MPLSM. *See* Multi-photon laser-scanning microscopy.
MPM. *See* Multi-photon microscopy.
MQW. *See* Multiple quantum wells.
mRFP. *See* Monomeric red fluorescent protein.
MRI. *See* Magnetic resonance imaging.
MRM. *See* Magnetic resonance microscopy.
Multi-channel experiments, 813.
filters and dispersive elements, 51
time-lapse fluorescence imaging, 382, 384
toxicity, 755
Multi-dimensional microscopy, display, **280–314**. *See also*, Automated 3D image analysis methods.
2D pixel display space, 291
efficient use, 292
animations, 292–293
artificial lighting, 306–308
CLSM images, 286–290
anisotropic sampling, 287
calibrating image data, 286
data type/computational precision, 288–289
dimensions available, 286–287
file formats for calibration/interpretation, 288–289
image data, 286
image size available, 287
image space calibration, 287–288
image/view dimension parameters, table, 288
processor performance, 289–290
storing image data, 286
voxel rendering speed, 290
color display space, 291–292
commercial systems, tables
available systems, 282–283
desirable features, 288–289
display options, 293
geometric transformations, 295
projection options, 300
realistic visualization techniques, 307
criteria for choosing visualization, 281
data values, definition, 222, 280
dimensions, 280, 323
degrees of freedom, optical image, 8–9
depth-weighting, 304, 306
exponential, 304
linear, 304
recursive, 304
display view, definition, 280
hidden-object removal, 304–305
local projections, 305–307
z-buffering, 304–305
highlighting previously defined structures, 284
image, definition, 280

Multi-dimensional microscopy, display (*cont.*)
image/view display options, table, 293
geometric transformations, table, 295
intensity calibration, 304
iso-intensity surface, 304
laser-scanning microscopy, 280
lighting models, 306–312
absorption, 309–312
advanced reflection models, 309
artificial lighting, 309–312
Gourard shading, 308–309
gradient reflection models/voxel objects, 309
Phong shading, 308–309
Phong/Blinn models, 308
simulated fluorescence process, 310
surface shading, 310
transparency, 309–312
living cells of rodent brain, 392–398
mapping data values, 300–304
choosing data objects, 300–301
object segmentation, 302
projection rules, 302–304
scan conversion, 301–302
segmenting data objects, 301
visualization model, 300
mapping into display space, 294–296
G function, 294
image/space view, 296
orthoscopic view, 294
reducing geometric dimensions, 294
rotations, 294–296
visualization process, 294
measurement capabilities *See also*, Chapter 15
reconstructed views, 312–313
results, 284–285
objective *vs.* subjective visualization, 281
prefiltering, 281
principle uses, 281–285
projection/compositing rules, 302–304
alpha blend, 302, 304
average intensity, 302
first or front intensity, 302
Kalman average, 304
maximum intensity, 302
pseudo color, 173–175, 190, 291
purpose, 281–285, 293–295
realism added to view, 306–308
techniques for, table, 307
reconstructed view generation, 290–312
5D image display space, 291–294. *See also*, 5D image display space
choosing image view, 291–294
subregion loading, 290–291
reconstruction, definition, 280
reflection models, 306–308
rendering, definition for, 280
software packages, table, 282–283
stereoscopic display, 293, 296–299
color space partitioning, 297
interlaced fields of frame, 297
pixel-shift/rotation stereo, 297
stereo images example, 298
synchronizing display, 297
true color, 291
unknown structure identification, 281–284
viewing data from, 283
visualization parameters, table, 285
z-coordinate rules, 304
z-information retained by, 296–300
non-orthoscopic views, 299
stereoscopic views, 296–299
temporal coding, 299–300
z-depth, 299–300
Multi-fluorescence, systems for utilizing, **217**⁺.
Multi-focal, multi-photon microscopy (MMM), 221, 276, **550–559**, 797.
4Pi-MMM, 563–564
basics, 565
scheme, 563
alternative realizations, 554–555
background, 550
beam subdivision approaches, table, 558
current developments, 558–559
experimental realization, 551–555
FRET, 797
imaging applications, 556
boar sperm cells, 557
Convallaria, 556
FRET, 556
hippocampal brain slices, 557
pollen grains, 556
Prionium, 556
interfocal crosstalk, 553–554, 556
time-multiplexing, 553–555
limitations, 556–558
localization, 538
Lissajous pattern of scanning foci, 554
"tornado" mode, SIM scanner, 52
Nipkow-type microlens array, 551–552
optimum degree of parallelization, 550–551
resolution, 552–553
schematic diagram, 552
time multiplexing, 553–554
variants, 555–556
FLIM, 555–556
MMM-4Pi, 556
SHG, 556
space multiplexing, 555
Multi-length fiber scrambler, 8. *See also*, Scramblers, light.
Multi-photon absorption (MPA), 535.
Multi-photon excitation (MPE), **356–358**, **535–545**, 894. *See also*, Multi-focal multi-photon microscopy.
absorption, 705–707
advantages/disadvantages, 644–647, 749–751
autofluorescence, plants, 424, 427
background from SHG/THG, 361, 708–709, 728
backscattered light imaging, 429
bleaching, 218, 338, 539–540, **680–689**, 692–693, 905. *See also*, Bleaching; Chapter 38
caged compounds, 187, 383, 543–544, 692, 729, 912
cell viability during imaging, 544–545
chromophores for, 543–544
detection, 538
duty cycle, 644
excitation localization, 538
excitation spectra, 125
FLIM, 576
fluorophores for, 543–544
FRET, 797
heating, 539–540
history, 535
image formation, 535–540
instrumentation, 540–543, 900–905. *See also*, lasers for. *See also*, Ultrafast lasers
Alexandrite, 109
Cr:Forsterite, 109, 114, 415, 541, 706–709, 712–714
Nd:glass, 706–708
Nd:YAG, 88–89, 107–109, 514, 680, 798
Nd:YLF, 89, 112–114, 750, 760–761
Nd:YVO_4, 89, 95, 107–109, 113–114, 541
Ti:Sapph. *See* Laser, titanium-sapphire laser
multi-focal, multi-photon microscopy
alignment, 900–901
beam delivery requirements, 541
control of laser power, 543
CPM laser, 540
descanned detection, 166, 208, 212, 428, 537, 540–542
excitation wavelengths, 541
focal plane array detection, 542
hybrid mode-locked dye laser, 540–541
lasers/excitation wavelength choice, 540–542
non-descanned detection, 185, 201, 218, 381, 447, 456, 507, **542**, 552, 559, 643, 646, 727, 750, 779, 904, 909, 910
non-mechanical scanning, 543
optical aberrations, 542
power requirements, 541, 903, 904
pulse spreading due to GDD, 547, 538, 543
resonant scanning, 543
whole-area and external detection, 541–542
optical pulse length, 537–538
group delay dispersion, 537–538, 543
group velocity dispersion, 88, 111, 210, **537**, 606, 903
measurement, 115, 901–903
penetration, 749–750
photodamage, 539–540, **680–688**, 692–693

physical principles, 535–540
refractive index mismatch, 404–413
resolution, 539
SHG and THG background, 361, 708–709, 728
two-photon absorption cross-sections, 125 (URL) 543–544
wavelengths, 538–539
Multi-photon intrapulse interference (MII), 88.
Multi-photon microscopy (MPM), 10–11, 56, 172–177, 210, **535–545**, 681, 682, 685–688, 746–766, 894, **900–905**.
advantages/disadvantages, 644–647, 749–751
alignment, 901–902
autofluorescence, 425–427, 545
SHG, THG, 361, 708–709, 728
calcium imaging, 545
cell damage during, 544–545, 682, 685
1-photon *vs.* 2-photon excitation, 681
absorption spectra of cellular absorbers, 681
intracellular chromosome dissection, 688
mitochondria, 686
nanosurgery, human chromosomes, 686–687
by optical breakdown, 198, 680, 682, **685**, 687, 703, 705
photochemical, 682–685
photothermal, 539, 545, 681, 685, 904
reproduction affected by ultrashort NIR pulses, 686
ultrastructural modifications, 685–686
cell viability, 544–545
compared with other 3D methods, 644–647, 748–751
deconvolution, 495–498
developmental biology, 545, 746–754, 757, 759–760, 764
dispersion as problem, 56. *See also*, GVD; GDD
fluorescence, contrast, 172–177
for living embryo imaging, chapter, 746–766
need for efficient illumination light path, 210
optical layout, 540
photobleaching, 545, **680–688**, 692–693
practical operation, 900–905
protein damage/interactions, 765
resolution, 552
setup/operation, 540, 900–905
schematic diagram, 540, 901–902
in vivo (intact animal) imaging, 545
ultrafast lasers, 88, 90, 109. *See also*, Ultrafast lasers
Alexandrite, 109
Cr:Forsterite, 109, 114, 415, 541, 706–709, 712–714
Nd:glass, 706–708
Nd:YAG, 88–89, 107–109, 514, 680, 798
Nd:YLF, 89, 112–114, 750, 760–761
Nd:YVO4, 89, 95, 107–109, 113–114, 541
Ti:Sapph. *See* Laser, titanium-sapphire laser
uncaging, 545
Multi-photon-based photo-ablation, 764.
Multi-slit design, for disk-scanning confocal, 229.
Multi-view deconvolution, 330, 675–677.
Multiple quantum wells (MQW), diode injection lasers, 106.
Multiplex CARS microspectroscopy (M-CARS), 601, 602.
Multiplicative noise, **28**–33, 51, **77–78**, 224, 234, 256–258, 262, 275, 443, 460, 633, 661, 667.
of EM-CCD, **30–31**, 77–78, 264, 256, 262
losses in effective QE from, 33, 234, 443
from PMT, 29, 51, 77–78, 233, 256–258, 460, 633, 661, 667
and quantum efficiency, 33, 234, 443
photon counting, 32–33, 78
pulse pile-up, **32–33**, 35, 78, 521, 523, **526–527**
table, 256
why it is usually unnoticed in LSCM, 633, 661
Muscle, 737, 739–742.
fatigue, 739–740

N

NA. *See* Numerical aperture.
Nanobioscopy, protein/protein interactions, 795–798.
acceptor bleach, 797–798
donor fluorescence, 796–797
FRET measurement, 795
sensitized acceptor emission, 795–796
Nanoscale resolution with focused light, 571–578. *See also*, Stimulated emission depletion (STED) microscopy.
breaking the diffraction barrier, 571–573
different approaches, 573–574
ground state depletion (GSD), 573
STED, 573–574
outlook, 577
RESOLFT concept, 571–573
resolution, new limiting equation, 571
measured, 578
stimulated emission depletion (STED), 573–578
axial resolution increase, 576
compared to confocal microscopy, 576
dyes, suitable, table, 575
OTF comparison, 578
PSF comparison, 578
Nanosurgery, 219.
with multi-photon systems, 90
NCI60 CMA, standard encapsulation, 816.
NCPM. *See* Non-critical phase matching.
ND. *See* Neutral-density filters.
Near infrared (NIR) lasers, 10, 90, 106. *See also*, Lasers: titanium-sapphire; Nd:; Cr:Forsterite.
Near infrared (NIR), 10, 90, 106.
diode injection lasers, 106
for laser tweezers, 90
objective lenses designed, 174
Nearest-neighbor deconvolution algorithm, 476.
image enhancement, 495–496
Negative contrast, for fluorescence microscopy, 173–174.
Negative feedback, to correct mirror motion, 53.
Neodymium glass laser, 706–708.
Neodymium-yttrium aluminum garnet (Nd:YAG) lasers, 88–89, 91, 95, 97, 103, 107–109, 111, 113–115, 117, 245, 514, 680, 798.
infrared range, 108
pumping non-linear crystal/green light, 114–115
Neodymium-yttrium lithium fluoride (Nd:YLF) laser, 89, 98, 100, 103, 109, 112–114, 750, 760–761.
Neodymium-yttrium orthovanadate ($Nd:YVO_4$) laser, 89, 95, 100, 103, 107–109, 111, 113–114, 541.
kits utilizing, 113
Nerve cells, images.
Alexa stained, 330
backscattered light images, 167
eye, optic nerve, 481
Golghi-stained, 298
Lucifer-yellow, 314
microglia, 396–398
rat-brain neurons, 398
transmitted light, 475
Neutral-density filters (ND), 43, 76, 126.
in fixed-pattern noise measurements, 76
to reduce source brightness, 43, 126
NFP. *See* Nominal focal position.
Nikon, confocal manufacturer, 13, 15, 119–120, 161, 199, 201, 507, 638–640, 657, 750, 910.
C1 confocal microscope, 119–120, 507
C1si spectral confocal microscope, 908, 910
CF objectives, 154–156, 217, 669, 779
confocal *x-z*, BSL image, 22
Plan Apo objective, 13, 15, 638
resolution, measured, 16, 638–640, 657
water-immersion lenses, 15
high-content screening, 810
tube length conventions, 157, 239
Nile Red, dye, 435, 528, 575, 774, 782

Nipkow disk scanning, 2, **5–6**, 11, 12, 41, 215, 223, **231**, 276, 551, 754, 783–784, 810, 894. *See also*, Yokogawa; Disk-scanning confocal microscopy.
commercial systems, 907, 913, 915
compared to single-beam scanning, 458
for high-content screening, 810
micro-lens system, 6, 12, 216, 224–226, 231, 234, 237, 551–552
multi-photon, 537, 551–558, 563–565. *See also*, Multi-focal, multi-photon microscopy rotation, 754
for single-sided confocal, 6, 141, 223, 229
source brightness, 141
speed of image acquisition, 11, 220, **222–226**, 227, 231
for tandem-scanning, 141, 215
visualization, of cells, 458, 667, 754, 784
Nipkow, Paul, 5–6, 109
NIR. *See* Near infrared.
Nitrogen lasers, 112.
nanosurgery using, 219
NLO. *See* Non-linear optical effects.
NMR. *See* Nuclear magnetic resonance.
Noise, 21, 28, 74–77, 83, 87, 114, 190, 232, 256–259, 442–444, 495. *See also*, Signal-to-noise ratio; Poisson noise; Quantum noise.
background, 443–444
of CCD detectors, 30–31, 77–78, 232–233, 256, 262
equations, 256
table, 256
vs. photomultiplier tube detectors, 74, 77
CIC, clock-induced charge, EM-CCDs, 234, 926
in counting quantum-mechanical events, 21
deconvolution reduced noise, 39–40, 114, 392, 495, 498, 667, 783, 835–836
detector, 28
fixed-pattern, 74, **76**, 278, 924, 927, 931
in fluorescence microscopy, defining, 74–75
in lasers, sources, 85–86
reducing, 87
limits grey levels, 443
measurement, 74–75
multiplicative, **28–33**, 51, **77–78**, 224, 234, 256–258, 262, 275, 443, 460, 633, 661, 667
in photon detectors, 256–259
noise currents table, 256
photo flux, 257–258
photoemissive devices, 256–257
pixel value represented, 258–259
Poisson. *See* Poisson noise
polarization, in laser systems, 83
read, and readout speed, 77
shot, 442–443. *See also*, Poisson noise
single-pixel, 65, 67, 190, 635, 832, 835–836
deconvolving, to reduce, 39–40, 392, 498, 667, 784, 835–836
reducing, 39, 40, 190, 41, 65, 392, 498
sources of, 442–444
wavelet transform to reduce, 733–734, 819–820
Nomarski DIC contrast, 2, 368, 746, 892. *See also*, Differential interference contrast.
Nominal focal position (NFP), 405, 408, 409.
calculations for glycerol, 409
calculations for water, 409
z-responses, diagram, 408
Non-confocal microscopy *vs.* confocal, 746.
high content screening, table, 811
Non-critical phase matching (NCPM), 114–115.
Non-descanned detection, for MPM, 185, 201, 218, 381, 447, 456, 507, **542**, 552, 559, 643, 646, 727, 750, 779, **904**, 909, 910.
for CARS, 559
No-neighbor algorithm, 476–477, 496.
Non-laser light sources, chapter, **126–144**.
arc sources, 130, 132, 140
commercial systems, table, 143
comparative performance, table, 140
control, 138
for disk-scanning confocal, 141
filament sources, 135–136
LEDs, 132–133, 135, 138–139, 143
light scramblers, 131–132
measured performance, 139–141
results, 142
solar, 126–127, 131, **135**
stability, 136–137
Nonlinear constrained iterative deconvolution, 68, 458, 475–476, 496–497, 499, 520, 568.
Nonlinear conversion, tunable laser, 114.
Nonlinear crystals, frequency multiplying, 109.
Nonlinear optical (NLO) effects, in microscopy, 90, 114, 163, 165, 177, 179, 188, 190, 195, **416–417**, 426–427, 430, 442, 504, 535, 507, 703–720, 728, 741, 751. *See also*, Multiphoton/microscopy; Harmonic signals; SHG, THG.
absorption, 188, **415–418**, 426–427, 430, 705
bleaching, 536, 550, 558, 645, 680–685, 693, 697, 707, 729. *See also*, Bleaching; Photodamage
CARS, 595–598, 600
DIC, 473–474. *See also*, Differential interference contrast
fluorescence, 172, 179
focus shift with spherical aberration, 409
harmonic generation, **704–705**
emission, 710–711
energy state diagram, 705
multi-photon absorption/fluorescence, 705
second harmonic generation (SHG), 704–705
setup, 708–709
third harmonic generation (THG), 705
light sources/detectors, 706–708
light attenuation spectra in plants, 706
photodetector characteristics, 707
pulsed-laser, table, 706. *See also*, Ultrafast lasers
in optical fiber, 504–508
optically active animal structures, 714–717
man-made collagen matrix, 717
signal-producing structures, table, 715
spindle apparatus, 717–718
zebrafish embryo, 716, 718
optically active plant structures, 710–714
Canna, 710
Commelina communis, 712
emission spectrum of maize, 710, 711
maize stem, 711, 714
potato, 712
rice leaf, 712, 715
polarization dependence of SHG, 717, 719
setup for, 708–710
spectra, 415, 417, 435
Euphorbia pulcherrima, 710
maize leaf, 710
Pyrus serotina, 711
STED microscopy, 571–579. *See also*, STED microscopy.
structured illumination, 270, 276
Non-radiative dipole-dipole interactions, 790.
Non-specific staining, 27, 44, 74, 303, 345, 357–358, 442, 467, 472, 617, 660, 667–668, 760, 820, 878, 882. *See also*, Background.
Non-tunable solid-state laser, 103.
Normal, free-running, pulsed laser, 111.
Northern Eclipse, software, 282.
Notch filter, to transmit laser line, 49.
Novalux Inc., Protera 488 laser system, 107.
NSDC. *See* Nipkow spinning-disk confocal.
Nuclear import analysis, 802.
Nuclear magnetic resonance (NMR), 618.
Numerical aperture (NA), 1, 4, 24, 28, 61, 126, **141**, 145, 148, 168, 180, 195, 198, **239–250**.
affects surface reflection contrast, 180
defined, 1
determining axial resolution, 4, 241–242, 657
determining lateral resolution, 1, 241–242, 656
diffraction orders accepted by, 61
effect on self-shadowing, 168, 198

in fiber-based mini-confocal endoscopes, 509
image brightness, 126
matching to CCD pixel size, 62, **928**
objective lenses with high, 145, 239–250
empty aperture, 248
with oil-immersion *vs.* water objective, 148
pinhole size as function, 28
and refractive index mismatch, 147–148. *See also*, Spherical aberration in tandem scanning confocal microscopy, 141
vertical shadowing, 195
and zoom setting optimal, 24
Nyquist criterion, and digitization, 38–39, 64–68.
Nyquist digitizing, 65, 67.
Nyquist filtering, 70–79, 281.
Nyquist frequency, 64, 301. *See also*, Shannon sampling frequency.
Nyquist, Harry, 64.
Nyquist noise, 256.
Nyquist reconstruction, limit output bandwidth, 59, **66–67**, 69, 70, 173, 235–236, **280–315**, 458, **468–469**, 474–475, 496–497, 563, 585, 603, 607, 610, 615, **635**, 672, 675, 677–678, 690, 772, 730–731, 762, 77, 774–776, 778, 784, 883.
Nyquist sampling, 24, 37, 39, 40, 53, **60**, **64–70**, 73, 75–76, 78–79, 142, 146, 152, 205, 222, 258, 271, 273, 289, 386, 391, 448, 635–636.
blind spots, 38
for CCD camera, 70, 233, 273, 928
and deconvolution, 59, 65, **67–68**, 222–223, 635
diagram, 60
optimal, results of deviating from, 24
practical confocal microscopy, 448, 635–636
reconstruction, *see* Nyquist reconstruction.
relationship with Rayleigh-criterion and PSF, 39, 60, 64, 66
signal-to-noise ratio, 67, 448
subpixel, resampling, 478–479

O

Object scanners, image quality, 216.
Objective lenses, 13, 15, 25–26, 34, 49, 145, 152, 156, 239–250, 652–660. *See also*, Aberrations.
apodization, 250
axial chromatic registration, 287, 658
axial resolution measurement, 656–657
vs. pinhole size, 656
chromatic aberrations 14, **145**, 152–156, 160, 177–178, 209, 242–243, 641, 659
apparatus in measuring, 243–244, 654, 659
axial shift, 243–245, 657–658
chromatic registration, 657–658
cleaning, 642
confocal performance, 145–161, 652–660
contrast transfer function (CTF), 16, 35, 37–39, 59–62, 656, 747
coverslip thickness, table, 654
dipping lenses, 161, 209, 411, 429, 568, 613, 727, 737, 870, 872
dry, high-NA, aberrations, 15
field illumination, 34–35, 127–128, 139, 461, 627, 658
flatness of field, 145, **151–152**, 154, 418, 457, 639, 659
Focal Check™ beads, 657
high-NA planapochromat, 13, 145, 239–250
infinity correction, **155–157**, 166, 239, 405
advantages, 49
lateral chromatic registration, 657–658
lateral resolution. *See* CTF
light, vector nature, 267
mounting media. *See* Mounting media
photon efficiency losses, 25–26
plan objectives, table, 152
point spread function of high NA, 239–250
measuring, 240–242, 455, 462, 471, 656
polarization effects, 249–250
pupil function, measured, 245–248
3D point spread function restored, 247–248
empty aperture, 248
Mach-Zehnder interferometry, 245
phase-shifting interferometry, 245
Zernike polynomial fit, 245–247
table, 247
resolution test slide, 169, 656
spherical aberration. *See* Spherical aberration
correction, 654–655
sub-resolution beads, 181–182, 196, 454, 477, 493, 499, 527, 652–656, 784, 900, 904, 930
images, 656
table of suppliers, 653
temperature variations, 248–249
transmission, optical, 154, 158, 159–161. *See* Transmission, objective
table of objective lenses, 159–161
water-immersion, 145, 149–150
dipping objectives, 161, 209, 411, 429, 568, 613, 727, 737, 870, 872
use and limitations, 15
working distance, 5, 9, 129, 145, 154, **157**, 198, 249, 511, 568, 598, 643, 673, 678, 727–728, 747, 774, 779, 781, 872
x-y and z resolution using beads, 656
OCT. *See* Optical coherence tomography.
OLED. *See* Organic light-emitting diodes.
Olympus, confocal manufacturer, 52–53, 54, 119–120, 161, 184, 187, 204, 229, 230, 234–236, 419, 421, 427, 557, 708–709, 727–730, 797, 908, 912.
Fluoview-1000, 119–120, 184, 187, 204, 908, 912
DSU disk-scanning confocal microscope, 229–230, 234–235, 908, 913
FRAP system, 210
FRET, 797
high content screening, 811
objectives, 557, 727–730
stick, *in vivo* objectives, 806
TIRF objectives, 183
transmission, table, 159, 161
SIM scanner, 52–54
tube-length conventions, 157, 239
On-axis reflections, artifact, 171.
Onion epithelium *(Allium cepa)*, 390.
Online confocal community, Listserv, 390.
OPA. *See* Optical parametric amplifiers.
OpenLab, 282.
Operational lifetime, of laser tubes, 102.
OPFOS, Orthogonal-plane fluorescence sectioning, 672–673.
OPO. *See* Optical parametric oscillators.
OPT. *See* Optical projection tomography.
Optical aberrations, 109, 542. *See also*, Aberrations.
thin-disk laser optics, 109
Optical layout of confocal microscopes, 212–213. *See also*, Optical paths
by class, 213
evaluation, 212–213
class 1 systems, 212
class 2 systems, 212–213
class 3 systems, 213
Optical bandwidth/electronic bandwidth, 32. *See also*, Bandwidth.
Optical breakdown, 198, 680, 682, **685**, 687, 703, 705.
Optical coatings, maintenance, 116.
Optical coherence tomography (OCT), 609–610.
of human retina, 609
schematic, 610
Xenopus laevis embryo, 610
Optical components, chapter, 43–59.
Optical density (OD), **71**, 81, 416.
filters, 43, 49–50
Optical disks, 586.
Optical efficiency, improvements, 143–144, 216. *See also*, Photon efficiency.
of disk scanners, 216
of light-emitting diodes, 143–144
Optical elements, 43–58, 128, 211.
confocal light beam affected by, 211
of Köhler illumination components, 128
light beam characteristics affected by, 211
chapter, 43–58

Optical excitation, diagram, 82.
Optical fiber. *See* Fiber optics.
Optical fiber, for scanning by moving fiber tip, 213–214.
Optical heterogeneity, specimen, **22–23**.
  reflection, refraction, scattering, 192–197
Optical images, electronic transmission, 5–6.
Optical materials, 158, 501.
  thermal properties, 158, 248–249
Optical parametric amplifiers (OPA), 100–101, 112, **114–115**, 118, 124.
  components, 115
  table, 101
Optical parametric oscillators (OPO), 100–102, 111–112, **114–115**, 118, 541, 600.
  for CARS microscopy, 600
  cavity dumped, to increase white light, 113
    tunable, 114–115
  table, 101
Optical path. of.
  4Pi, confocal, 563
    commercial, 566
  acousto-optical device, 55
  compound light microscope, 156–157
  CARS, 599, 601, 907
  CARV-2 disk scanner, 230
  confocal, 10, 208–209, 212, 632, 681
    beam-splitter, 213
    disk-scanner, 12, 216
    folded, 166
    scanning systems, 214
  fiber-optic confocal, 508
  interferometers, 243, 245
  Kino single-sided disk scanner, 229
  LaVision-Biotec, Trimscope, 907
  Leica, TCS AOBS, 910
  magnetic resonance imaging, 621
  Minsky confocal, 5, 25
  for measuring photon efficiency, 34
  multi-photon, 540, 681, 708–709
    multi-focal, 552, 555
    spectrometer, 424
  Nikon C1si, 911
  Olympus DSU disk-scanner, 230
  Olympus Fluoview-1000, 912
  optical coherence tomography, 610
  optical projection tomography (OPT), 611
  Petran tandem scanner, 228
  selective plane illumination (SPIM), 613, 673
  or simultaneous BSL and fluorescence, 128
  surface 3D imaging, SIM/EFIC, 608
  surface spherical aberration, 405–406
  STED, 573
  structured-illumination, 266
  Visitech VT-Infinity and VT-eye, 914
  Yokogwawa dual-disk-scanner, 231, 915
  Zeiss LSM-510, META, 916–917
  Zeiss LSM-5-Live, 50, 232, 916
Optical performance, practical tests, 652–660.
  axial chromatic registration, 658
  axial resolution using mirror, 656–657
  chromatic aberration, 659
  chromatic registration, 657–658
  contrast transfer function (CTF), 656
  coverslip thickness *vs.* RI, table, 654
  field illumination, 658
  flatness of field, 659
  Focal Check™ beads, 657, 658
  lateral resolution, 655
  resolution test slides, 655–656
  specimen self-lensing artifacts, 659
  spherical aberration correction, 654–655
Optical power, specimen plane, table, 140, 644.
Optical probes, 737. *See also*, Dyes; Fluorescent indicators; Fluorophors; Fluorescent labels.
Optical projection tomography (OPT), 610–613.
  lamprey larva, 612
  mouse embryo, 612
  refractive index, 613
  setup, 611
Optical pulse length, 537–538. *See also*, Pulse broadening.
  group delay dispersion, 537–538
  group velocity dispersion, 537
  measurement, 115, 901–903
Optical resonator in laser, 81–82, 116.
  laser, 81–82
  maintenance, 116
Optical sectioning, 9–10, 13, 180, 182, 222, 223, 236, 268–270, 469, 748, 763–764, 772, 774, 775, 784. *See also*, Deconvolution, Confocal, etc.
  algorithms for widefield, 763–764
  of *A. Thaliana* root, 772, 775
  with confocal laser-scanning microscope, 9–10
    example, 182, 463, 471, 492, 656
  dynamic imaging, 784
  improvement, with deconvolution, 752
  latex bead, 3D image, 196
  limiting excitation, 223
  near surface of living embryo, 748
  near to refractive index interface, 180
  selective plane illumination, 748
  structured illumination, 268–270
  with widefield phase-dependent imaging, 13
Optical system, losses, 25–32, **217**.
Optical transfer function (OTF), 164–165, 490–491, 562, 563, 567, 569–570, 578. *See also*, Point-spread function; Contrast transfer function.
  4Pi microscopy, 562, 563, 567
  contrast, 164–165
  deconvolution for image enhancement, 490–491
  I^5M, 569–570
  point spread function, 490–491. *See also*, Point-spread function
  STED comparison, 578
Optical tweezers, 89–90, 110, 218, 383, 385.
  setups for integrating, 218
  table, 385
  trapping wavelength, 89–90
Optics, general, 12, 125, 156–157.
  finite *vs.* infinity, 156–157
Optiscan confocal endoscope, 213–214.
Organic dyes, 109, 203, 342–343, 353–356. *See also*, Dyes; Fluorophores; Fluorescent labels; Fluorescent probes.
  AlexaFluor, 353–355
  BOPIDY, 353–355
  classes, table, 355
  coumarin, 353, 355
  cyanine, 353–355
  fluorescein, 353–355
  rhodamine, 109, 203, 353, 355
Organic light-emitting diodes (OLED), 143.
Orthogonal-plane fluorescence sectioning (OPFOS), 672–673.
Oryza sativa. See Rice.
Oscillating-fiber scrambler, 8.
Osmotic permeabilization, 359.
OTF. *See* Optical transfer function.
Out-of-focus light.
  deconvolution *vs.* confocal microscopy, 461.
  information, 26, 32, 487, 644–646.
Output amplifier, reconstructing analog signal, 64.
Output modulation, of semiconductor lasers, 108.
Overheating, of filters, 43. *See also*, Thermal variables.
Overlap alignment protocol, montaging, 732.
Over-sampling, 60, 70, 728.
  vs. duplicate-and-smooth process, 70
  reasons for, 68
  subpixel, resampling, 478–479
Oxygen sensor, 45, 347.

P

Pack-and-go mode, Power Point, 842, 844.
Paeonia suffruticosa, 421.
Panda pattern, polarization-preserving fiber, 88.
PAS. *See* Periodic-acid Schiff.
Passively mode-locked lasers, 111.
Patch clamp, for loading dye, 360, 726–727, 734, 738–740.
Patch pipette, 738.
Pattern analysis. *See* Automated interpretation of subcellular patterns.
Patterned-illumination microscopy, *see* Structured illumination microscopy
PC. *See* Personal computer.
PCA. *See* Principal component analysis.
P-CARS, Polarization-sensitive detection CARS.

PCF. *See* Photonic crystal fiber.
PE. *See* Photoelectrons.
Pear (*Pyrus serotina*), spectrum, image, 711.
Pearson's correlation coefficient, 668.
Pellicle beam-splitter, 216, 228–229, 231, 346.
Peltier cooling.
  CCDs, 234, 447
  cell chamber, 387–389
  lasers, 85, 106–108, 111, 117
Penetration depth, 177, 343, 643, 672, 731, 765.
  of dyes, 360, 387, 731, 739, 882, 874
  of fixative, 369–370, 376, 857
  FRET sensors, 798–799
  long laser wavelengths, 109, 416, 418, 427–428
  multi-photon, 381, 418, 433, 435, 439, 543, 545, 558, 646, 684, 708, 714, 728, 749, 904
  in plant imaging, 779
  in scanning electron microscopy, 847
  in SPIM, 613, 675–678
  TIRF, 177–178
Peony flower, autofluorescent petals, 173–174, 176, 421, 423.
Peptide-mediated uptake, 359.
Perfusion.
  chambers, 381, **386–389**, 394, 726, 729, 769, 870–873
  fixation, 376
Periodic grating. *See* Grating.
Periodic-acid Schiff (PAS) reagent, 262, 369, 770, 774–775, 778.
  maize pollen grain, 202
Periodically poled (PP) waveguides, 114–115.
Perrin-Jablonski diagram, 516, 517, 697, 792.
  photobleaching, 697
Personal computer (PC), performance needed for image processing, 289–290.
Perspectograph, early studies, 789.
Petrán disk, 2, 6, 11, 135, 141, 215, 223–224, 228, 251, 265, 381, 387, 447, 458, 554.
Petrán, Mojmir, 2, 6, 11, 215, 223, 228.
pH imaging, 188–189, 221, **346**, 348, 359, 386, 421, 517, 529–530, 664, 739–740, **743**, 744.
  calibration, 421, 530, 745
  display, 287
  intensity image, **529**, 530, 739, 740, 744
  lifetime image, 530
pH indicators, 346, 739–742.
pH shift/formaldehyde fixation, 370–371, 373.
Phalloidin, as correlative marker, 235–236, 344, 376, 378, 694, 696, 756, 804, **854–856**.
Pharmacological screening, 813–814.
Phase and intensity determination from correlation and spectrum only (PICASO), 115.
Phase contrast, 9, **171**, 368, 372, 453, 506, 643, 649, 731, 851, 854, 890, 892.
  coherent light for, 130
  depth of field, 13
  and holography, 7
  scanning, 9, 13, 386
Phase fluorometry, 518–519, 526.
  comparison of FLIM methods, table, 526
  excitation/emission signals, 519
  fluorescence lifetime imaging, 518–519
Phase randomization, to scramble light, 8, 13, 84, 131–132, 143, 507.
Phase-dependent imaging, depth of field, 13.
Phase-shifting interferometry, 245.
Phenotyping, 623–624.
Phong shading, 308–309.
Phong/Blinn models, 308.
Phosphoinositide signaling, 799.
Photo efficiency. *See* Photon efficiency.
Photoactivatable dyes. *See* Photoactivation.
Photoactivation, 187, 224, **383**, 385, 541, 543–545, 693, 759.
  example, 759
  genetically encoded
    Kaede, 187, 383, 385
    Kindling, 574, 760
    PA-GFP, 187, 383, 385, 752, 759–760
  table, 385
Photobleaching, 174, 218, 224, 275, **341–342**, 362–363, 545, **690–700**, 729, 747–748, 759. *See also*, Bleaching, and Chapter 39.
  autofluorescence, 698
  defined, 218, 691
  dynamics, as a source of contrast, 202–203
  effect on contrast, 174
  fluorescence intensity loss, 691, 694, 696, **698**$^{+}$
  fluorescent image of single protein, 699
  fluorescent probes, 362–363
  fluorescent recovery *vs.* irradiation time, 699
  fluorophores signal optimization, 341–342
    choice of fluorophore, 342
    fluorophore concentration, 342
    light collection efficiency, 217, 341
    protective agents, 36, 341–342, 363, 368, 375, 499, 694
    spatial resolution, 341
  in four-dimensional imaging, 747–748
  green fluorescent protein (GFP), 690, 692, 698
  intentional *See* Fluorescence recovery after photobleaching (FRAP)
  kinetics, 695
  mechanisms, 340, 691–693
    FRET, 691
  multi-exponential fluorescent bleaching, 697
  multi-photon microscopy (MPM), 545
  Perrin-Jablonski diagram of bleaching, 697
  photocycling, fluorescent proteins, 698
  propidium bound to DNA, plot, 695
  reactive oxygen species, 341–342, 362–363, 390, 544, **682–684**, 691, 693–694, 852–853
  reduction in, 693–696
    antifade agents, 36, 341, 368, 375, 499, 694
    disk-scanning microscopy, 224
    quantum dots, 694
  results, in living embryos, 759
  of single molecules, 696–698
  structured-illumination methods, 275
  two-photon excitation microscopy (TPEM), 690, 697
Photocathode, PMT, 28–29, 232–233.
  quantum efficiency, 232–233
  to reduce transmission losses, 28–29
Photoconductivity, in photodetectors, 252, 253.
Photocycling, fluorescent protein molecules, 698.
Photodamage. *See* Phototoxicity.
Photodetector. *See* Detectors; Light detectors;
CCD; EM-CCD; PMT etc.
Photodiode, 134–135, 253–255, 610, 707–708.
  feedback, to stabilize laser, 87, 682
  feedback, to stabilize arc/filament, 134–135, 137
  in hybrid PMT, 29, 30
  infrared sensitive for IR lasers, 707
  photometer sensor, air space, 26
  quadrant, for alignment, 87, 134
  of self-aligning source, 134–135
  for testing display software response, 830
  vacuum avalanche, 254, 255
Photoelectric effect, and LED operation, 137.
Photoelectrons (PE), 29, 30, 62–63, 77, 232–234, **254–255**, 257, 259–264, 339, 633, 863.
  amplification of, 62–63
  in the CCD, 232–234, 495, 918, 931
  production in PMT, 30
    single-PE pulse-height spectrum, 29, 77
  secondary electrons, as source of PMT multiplicative noise, 77
Photoemissive devices, 256–257.
Photoemissive effect, 254.
Photographic recording systems, 6–7, 11–12, 20, 22, 30, **71–72**, 132, 139, 141, 162, 207, 217, 263, 280, 488, **581**$^{+}$, 588, 590–591, 593–594, 607, 613, 628–629, 633, 640, 643, 712, 829, 862, 865–867.
  "toe" response, quadratic, 71
Photometer paddle, to measure light beam, 26, 35, 139–140, 159, 391, 650–651, 665.

Photometric response, and HD curves, 71.
Photomicrography (Loveland), 139.
Photomultiplier tube (PMT), 9, 28–31, 35–36, 51, 62–63, 74–75, 222, 232, 251, 254, 255, 258–261, 443, 527, 661–662.
  after pulsing, 257
  Bio-Rad, 260–261
  as confocal detectors, pros/cons, 222
  for epi-fluorescence confocal microscope, 9
  functioning, 62–63
  GaAs photocathode, 28–29, 232, 252, 255, 263, 527, 931
  gain from collisions at first dynode, 31
  grey levels, 443
  hybrid, single-pixel signal levels, 31, 254–255
  linearity, 661–662
  microchannel plate, 232–233, **255**, 262
  mini-PMT arrays, 51, 667
  multiplicative noise, **28–30**, 77, 633, 677, 926. *See also*, Multiplicative noise
  in multi-channel detection systems, 51
  noise and gain, 74–75
  number of photons striking per unit time, 35–36
  optical enhancer to increase QE, 28–30
  photon counting, 21, **29–30**, 32–35, **258–259**, 260–263, 542
  quantum efficiency, 527
    vs. cooled CCD, 26–28
  signal variation with time, 232
  transit time spreads, 527
Photon(s), 20–21, 30, 33–36, 63–64, 132.
  counting precision, 20–21
    uncertainty, 63–64
  interactions with photomultiplier tube, 30
  lost, 33–36
Photon counting, 21, **29–30**, 32–35, **258–259**, 260–263, 542.
  circuits, 33–34, 258, 521
  digital representation of optical data, 32–33
  effects, 34–35
  examples, 35, 263
  hybrid PMT, 29–30
  pile-up losses, **32–33**, 35, 78, 521, 523, **526–527**
  with PMT, 29–30, 32–35, 258–259, 260, 263
Photon detector types. *See* Detectors and entries by each detector type.
  CCD, 254
  direct effects, 252
  image dissector, 254–255
  microchannel plate, 232–233, **255**, 262
    MCP-CCD, 262
    gated, 519, 523–524, **527**, 532
  photoconductivity effects, 252, 253
  photoemissive, 254
  photovoltaic, 252–253
  thermal effects, 252
  vacuum avalanche photodiode, 254, 255
  work functions, table, 252–253
Photon efficiency, 24–36, 215, 217, 341, 631.
  defined, 24
  as a limitation of confocal systems, 24, 223
  measuring, 26, 33–36, 217
  practical confocal microscopy, 631
  of scanners, 215
  table listing photon losses, 217
Photon flux, statistics, 256–258.
Photon interactions, 252–256.
Photon (shot) noise, 660–661. *See also*, Poisson noise.
Photonic crystal fiber (PCF), laser delivery, 1, 88, 109–110, 113, 504, 541.
  for white light source, 113
Phototoxicity, 112, 363–364, 390–391, 651, 729, 746, 770.
  chapter, 680–689
  in brain slices, 729
  damage is higher to either side of raster, 54
  factors influencing, table, 363
  fluorescent probes, 363–364
  live cells, 390–391
  reduction, 391
  from uneven scan speed, 651
Photo-uncaging, 187, 210, **383**, 385, 541, 544–545, 692, 729, 760, 912. *See also*, Photoactivation.
Photovoltaic effect, 252–253.
Phycobiliproteins, 338, 341, 343, 355–357, 693.
Physical limitations, 20, 24, 63–64.
  on accuracy and completeness of data, 20
  Poisson noise, 63–64. *See also*, Poisson noise
Physiological fluorescence imaging, 383, 385.
PICASO. *See* Phase and intensity determination from correlation and spectrum only.
Piezoelectric effect, defined, 57.
Piezoelectric focus controls, 166, 215, 219, 222, 231, 241, 245, 268, 468, 754, 909.
Piezoelectric scanning systems, 57, 215, 238, 510, 555, 610.
Piezoelectric devices.
  AOD driver, 54–55, 57
  acousto-optical components, 54–55, 57
  to align objective, 166
  dithering to increase CCD resolution, 70
  effect described, 57
  to focus objective, 166, 215, 219, 222, 231, 241, 245, 268, 468, 754, 909
  laser alignment, 87
  light scrambler, 84
  to move optical fiber, 84
  to move scanning mirror, 57, 215, 238, 510, 555, 610
  to move stage, 215, 567
  phase-shifter
    in 4Pi confocal, 609
    in structured illumination, 268
    optical coherence tomography, 609–610
  stretching optical fiber, 609
Pile-up, of pulses.
  in avalanche photodiode, 253
  in photomultiplier tube output, 32–35
  measuring risk of, 34–35
p-i-n diode, 253.
Pinhole, 26–28, 33–35, 149, 150, 154, 201, 210, 213, 215, 224–228, 395, 631–632.
  advantages and disadvantages, 26–28
  calibrating diameter, 33–34
  confocal, proper use, 28
  disk-scanning, 224–228
  mini-image detection, 32
  optical fiber as, 506–507
  optimal size, 226–227, Chapter 22
    Fraunhofer formula, 225
  position in confocal microscope, 210
  practical, in confocal, 631–632
  radius, effective, 35
  ray paths, different sizes, 226–227
  single-mode polarization preserving fiber, 213
  small pinholes, effect, 225
  of tandem scanners, 215
  vibration shifts relative positions, 201
Pinhole disks, critical parameters, 224–228.
Pinhole energy, with spherical aberration, 149, 150, 154, 631–632.
  penetration into water, 149, 150
  defocus and NA, 150
  defocus and wavelength planapochromat, 154
Pixel clock, digitization, 62, 64–65, 201, 234–235, 258, 903, 923, 929.
  CCD, table, 929
Pixels, 38–39, 60, 62–63, 65, 258–259.
  defining, 60
  digitization, 62–63
  optimal, 63–64, 66
  representing intensity, 258–259
  and resolution, 38–39
  and Abbe criterion resolution, 38–39, 65
PKzip, 580.
Plan objectives, Zeiss, field diameter, table, 152.
Planapochromat, 152, 155. *See also*, Objectives.
  flatness of field and astigmatism, 152
  lateral chromatic aberration, 155
Plancks law, energy of photon, 35, 137, 252, 424.
Planar illumination, SPIM, optical sectioning, 751.

Plane of focus, distortion, 16, 23.
by beam deviations, 16
by refractile cellular structures, 23
Plant cell imaging, 769–785.
autofluorescence, 770–772
birefringent structures, 162–164. 420–421. *See also*, Birefringence
chamber slides for plants, 429
clearing intact plant material, 166, **417–418**, **420**, 439, 610, 624, 774–775
computer visualization methods, 778
deconvolution, 784–785
direct imaging, 772–773
dynamic imaging, 783–784
effect of fixation, 195, 428
Equisetum, *774*
fluorescence properties, 421–428
emission spectra, 421–423
microspectroscopy, 421–426
fluorescence resonance energy transfer, 425. *See also*, FRET
harmonic generation *See* Harmonic signals fungi, 438–439
genetically encoded probes, 769, 773, 783
green fluorescent protein fusions, 773, 783
of green tissues, 770
hairs, 434–435
history, 769
light attenuation in plant tissue, 414–418
A. thaliana, example, 416
absorption spectrum, 415
effect of fixation, 428
maize stem spectra, 417, 418
M. quadrifolia spectra, 416
M. quadrifolia optical sections, 419
Mie scattering, 162–163, 167, 417–418
nonlinear absorption, 416–417
Rayleigh scattering, 162–163, 167, 417, 703
light effects on, 770
light-specimen interaction, **425–428**
living plant cell specimens, 429–439
calcofluor staining procedure, 424, 438
callus, 429
cell walls, 168–169, 188–189, 303, 306, 416–417, 420–421, 428–431, 435–136, **438**, 439, 710–711, 713–715, 769–776, 779–781
chamber slides, use, 429
cuticle, 434–437, 715, 717, 779
fungi, 438–439, 624, 782, 870
hairs, 431, 434–436, 772
meristem, 168, 420, **430**, 770, 776–778, 783
microsporogenesis, 431–432
mineral deposits, 163, 420, **436–438**, 703
pollen germination, 420, 433–434, 781, 783
pollen grains, 202, 305, 313, 420, **431–433**, 553, 558, 781, 783
protoplasts, 195–196, 203, 416, 421, **423–427**, 429–431, 438–439, 693
root, 172, 174, 303, 307, 421, 429, **430**$^{+}$, 438, 464–465, 556, 772–773, 775, 777, 779–783
culture chamber, 429
starch granules, 202, 420–421, 428, **432–433**, 435, 703, 710–712, 715, 719
stem, 168, 172, 180, 417–419, 421, 424, **429**, 556, 707, 710–711, 713–714
storage structures, 435–436
suspension-cultured cells, 189, 429–430
tapetum, 433–434, 779
waxes, 420, 428, 434–435, 714–715
new spectral tools, 770
obtaining spectral data, methods, 772
penetration values, 779
photodamage, 770
point spread function, 722, 784
refractive index heterogeneity, 192, 418–420
single-photon confocal excitation, 772–778
specific methods, 769
spectral unmixing, 770
examples, 665–666
staining, 774
technological developments, 769
textbooks, 769
three dimensional, 771
clearing agents, 166, **417–418**, **420**, 439, 610, 624, 774–775
deconvolution protocols, 784
reconstruction, 775–776
segmentation, 776–778
two-photon excitation, 415–419, 421, 423
advantages, 778–779
best conditions, 781
compared with one photon, 421
cell viability, 779–782
deconvolution protocols, 784
dyes, 782
green fluorescent protein, 782–783
light-specimen interaction, 425–427
microspectrometer, 424
pitfalls, 782
thick specimens, 779
in vivo, 781
Plasma membrane, microscopy. *See* Total internal reflection microscopy (TIRF).
Plasma light sources, spectra, 44.
Plasmid DNA, nick-damage, 684, 724, 802–804. *See also*, Microinjection; Electroporation; Biolistic transfection.
Plasmodesmata, 777.
Plumbago auriculata, fluorescence spectra, 422.
PMT. *See* Photomultiplier tube.
p-n diode, 253. *See also*, Photodiode.
PNG (Portable network graphic), 581, 584.
Pockels cell, variable beam attenuator, 25, 54, 57, **87**, 116, 543, 701, **903–904**.
Pockels effect, in crystals, 57.
Point-spread function (PSF), 4, 10, 23, 27, 39, 68–70, 145–146, 189–190, 208, 223, **239–250**, 271, 275, 330, 378, 405, 407, 409, 446, 448, **453–457**, 485–486, 489–494, 536, **562–564**, 570, 574, 578, 635, 656, 674, 750, 784, 830, **895**.
3D, 68–70, 247–248
4Pi microscopy, 562–563
additional information from, 570
space invariance of PSF for, 564
apodization, 240, 243, 249, **250**, 272, 567, 889
blind deconvolution, 468, 485
in botanical specimens, 772, 784
in brain slices, 729
calculations, RI-mismatch, 407
for glycerol, table, 409
for water, table, 409
CARS, 596
comparing widefield with confocal, 27, 453–457, 493, 644–647
confocal, 10, 12, **208**$^{+}$, 212, 216, 405, 632, 681
vs. deconvolution, 27, 453–457, 493, 644–647
deconvolution, 189–190, 223, 489, 490–494, 784. *See also*, Deconvolution
quantifying PSF, 492–494
deformation caused by RI anomalies, 22–23
Fourier transform, 489, 490
lateral resolution. *See* Lateral resolution measuring, **240–242**, 455, 462, 471, 656
amplitude/phase, 242
fiber-optic interferometer, 240–241
images, 246–248
high-NA objectives, **239–250**, 492, 656
pupil function, 240
for 3D deconvolution, 145–146
non-linear, 552, 750
and Nyquist, 635, 636, 751, 752
optical transfer function, related to, 490–491
polarization effects, 249–250
pupil function, 245–248. *See also*, Pupil function
Rayleigh-criterion and Nyquist sampling, 39
refractive index mismatch, 405, 407
spherically aberrated, 148–150, 407, 492
shape in telecentric systems, 208
SPIM, 674

Point-spread function (PSF) (*cont.*)
STED, diagram, 574, 578
structured illumination see Structured illumination microscopy
temperature effects, 25, 85, 248–249, 630
terminology, 405
Wiener filtering, 494
Points, defined, 59.
Point-source, for measuring photon efficiency, 33.
Poisson noise, **20–21**, 29, 37, 63–64, 67, 69, 74–75, 81, 164–165, 211, 232, 234, **442**, 456, 460–463, 468, 487, 495, 497, 633–636, 647, 651, 655, 660, 693, 784, 835, 923–924, 926. *See also*, Quantum noise, Shot noise.
bleaching, 693
of CCD
charge transfer, 920
dark charges, 921–922
CT imaging, 615
and display linearity, 72–73, 588
digitization, as part of signal, 65, 69, 633–636
of EM-CCD, 233–235, 262, 927–928
and FLIM, 524–525
and gray levels, 74
importance of deconvolution, **38–41**, 60, 69, 189–190, 222–223, 320, 399, 471–472, 481, 495, 751–753, 835
intensity spread function, 75–78
photomultiplier tube, 74–75
affects effective QE, 31
multiplicative noise, 29, 647, 660
in photon detection, 63–64
and pixel size, 64, 68, 633–636, 928
practical effects, 67
single-pixel noise, 65, 67, 190, 635, 832, 835–836
spectral unmixing, 667, 770
examples, 665–666
structured illumination, 278
uncertainty in contrast, 74, 164–165
and visibility, 37, 667
Polarization, 13, 49, 57, 83, 88, 89, 211–212.
attenuator, 43, 543, 907
beam-splitter, 13, 50–51, 57, 85, 87, 100, 171, 217, 513, 631, 904
to avoid spectral distortion, 49
circular or phase randomized, 211–212, 229
effect on AODs, 55
effect, of dichroic beam-splitters, 34, 49–50
Kerr cell, 111, 113, 516
of laser light, 8, 83, 88–89, 113, 478, 558
optical components, 57, 155, 211
optical fibers, 213
Pockels cell, 25, 54, 57, 87, 116, 543, 701, **903**$^{+}$
rectified DIC optics, 846
to reduce reflections, 6, 25, 141, 158, 171, 516, 229. *See also*, Antiflex system
scramblers, 8, 84, 132, 143
Polarization effects, 211, **249–250**, 503.
birefringence, 188, 420–421, 431, 434, 436, 438, 480, 503. *See also*, Birefringence
blind deconvolution, 479
and CARS microscopy, 595, 600–604
high-NA objective lenses, 249–250, **267**
interaction with nucleus, 23
optical fibers, 503, 507
stereo image displays, 299, 589
Polarization microscopy, 43, 50–51, 154, 156, 162, **188**, 288, 348, 438, 479–480, 513, 555, 711, 714–715, **717**, 719, 891, 894.
centrifuge microscope, 8
of collagen fibers, 164, 188, 717
DIC, 10, 14, 127, 146, 468, 473
and FRET, 793
and harmonic generation, 179, 428, 704–706, **717**, 719
MFMP, 555
mitotic apparatus, 15, 717
p- and s-, and incidence angle, 50–51
Pol-scope, 13, 188, 432, 468, 480
PSF, 406–407
to regulate light intensity, 43
STED, 578
Polarization noise, in lasers, 83.
Polarization-preserving fiber, 49, 87, **503**, 505, 507.
as a pinhole, 213
Polarization-sensitive detection CARS (P-CARS), 600, 601, 604.
adipocyte cells, 604
Polarized light, 7, 14, 83–85, 146, 158, 162, 171, 229, 406–407, 420, 479, **894**.
deconvolution, 479
image formation, 406–407
PSF, 479
Polarizer, 83, 128, 188, 249, 268, 275, 420, 479, 711, 903–904.
for antiflex, 6, 84, 141, 158, 229
for attenuation, 43, 85, 87–88, 543, 903–904
for CARS, 601
Glan-Taylor, 85, 87, 100, 171
Glan-Thompson, 85, 904
LCD, 589, 715
micro-wire, 85
structured illumination, 264
tunable, 715
Pollen germination, 433–434.
Pollen grains, 202, 305, **431–433**, 438, 553, 556, 558, 678, 781, 783.
germination, 433–435, 783–784
multi-focal multi-photon imaging, 556
Pol-scope, 13, 188, 432, 468, 479–480
test specimen, 195, 269, 313, 553, 556, 678
Pol-scope, 13, 188, 432, 468, 479–480.
deconvolved, 479
images, 15, 188, 479, 717
Portable network graphic. *See* PNG.
Position, accuracy in CLSM, 40.
Position sensors, galvanometer, 53–54.
Posterizing, 591.
Potassium titanium oxide phosphate (KTP) crystal
for non-linear optical frequency conversion, 107.
Potato (*Solanum tuberosum*) SHG signal, 712.
Power requirements, for lasers, 65, 80–81.
Power spectrum. *See* Contrast transfer function.
Power supply, laser as noise source, 86.
PP, Periodically poled waveguide, 114–115.
Practical confocal, 2-photon microscopy, tutorial. *See also*, each topic as a major entry.
2-photon
excitation duty cycle, 644
peak power level, 644
photodamage *vs.* penetration, 645
power *vs.* penetration, 646
3D microscopy methods compared, table, **647**$^{+}$
best 3D method for, 644–647
biological reliability, 631
bleaching pattern, 627–628
quantum efficiency, 628
chapter, 627–649
confocal images with few photons, 634
deconvolution, factors, 646
filling back-focal plane, 210, 509, 629, 633
focus, compensating drift, 395, 732
getting a good confocal image, 629–631
alignment of optics, 629–630
back-focal plane (BFP), 210, 509, 629, 633
focus, 629
low signal, 631
mirror test specimen, 630
no signal, 631, 660
simultaneous BSL/fluorescence, 631
getting started, 627
Köhler illumination for transmission, 34, 127–**128**, 131, 229, 627, **648–649**
multi-photon *vs.* single-photon, 646
new controls, 631–636
biological reliability, 631
pinhole size, 631–632
pixel size, 62, 634–635, 784, 928
Nyquist reconstruction/deconvolution, 635–636
over-sampling, 635
photon efficiency, 24–26, 215, 217, 341, 631
pinhole summary for, 26–28, 633

pixel size, 62, 634–635, 784, 928
measuring, 635
summary for, 636
poor performance, reasons, 640–643
air bubbles, 643
curvature of field, 641
dirty objective, 642–643
imaging depth, 643
under filling objective pupil, 642
optical problems, 640–641
sampling problems, 640
singlet-state saturation, 643
under-sampling, 635
schematic diagram, 632
statistical considerations, 633–634
stray light, 201, 632, 904
test specimen, 636–640
description, 636–637
diatom, 638–640
figures, 637–640
reasons for, 636
widefield *vs.* beam scanning, 647
Prairie Technologies, LiveScan Swept Field design, 237.
Pre-amplifier, in digitizing analog signal, 64.
Precompensation, in fiber optic cables, 88.
Presentation software, 829–845.
helpful URLS, 844–845
movies, 837–844
artifacts, 839–840
coding limitations, 838
compression of large movies, graph, 843
compression of PAL TV movies, table, 842
digital rights management, 844
entropy, 841
frame count matching display cycle, 838–839
MPEG display formats, 840–841
overlaying, 844
Pack-and-go mode, 842, 844
performance benchmarks, 841–842
region code, 844
remote use, 842–844
rules 837–838, 844
up-sampling, 838–839
very high resolutions, 841
precautions, 829–830
testing, 830–836
aliasing gallery, 834
aligning images, 835
brightness, 832
changing display size, 832–835
codecs, 831
compression, 835–836
compression artifacts, 837
cropping, 835
digital rights management (DRM), 830
down-sampling in PowerPoint, 834
fast graphics cards, 831, 832
gamma, 832–833
measuring display speed/sensitivity, 830
random color dot image, 836
reference images, 830–831
removing distortion, 835
resolution, 832–835
rotating, 835
scaling, 835
screen capture, 830
static image performance, 831
step image, 833
under-sampled image, 835
up-sampling, example, 834
viewer, 830
Preventive maintenance, lasers, 115–116.
Principal component analysis (PCA), 731–732.
Printers, 591–593.
aliasing, 592
color images, 592
grey levels, 592
ink jet, 593
laser, 593
posterizing, 591
scaling techniques for, 592
Prionium, MMM image, 556.
Probe, mismatch with pixel shape, 39.
Processor performance, 3D-image display, **289**+.
Projection/compositing rules, 3D-image display, 302–304, 763–764.
alpha blend, 302, 304
average intensity, 302
first or front intensity, 302
Kalman average, 304
maximum intensity, 302
Propidium iodide, 344, 355, 360, 426, 651, 693–695, 773, 778–779, 782, 812.
dead cell indicator, 426, 651, 875, 877
Proteins, 195, 756, 760, 794–795, 804. *See also*, Green fluorescent protein, etc.
chimeric fusion, 794
fluorescent, FRET, 794–795
Kaede, 187, 383, 385
Kindling, 760
microinjection, 804
PA-GFP, 187, 383, 385, 752, 759–760
tagged, 756, 758
translational fusions, 756
UV absorption, 195
Proteomics, 237, 790, 804, 809, **818**, 867.
location, 825
Protoplasts, 195, 416, 429, 430, 431.
A. thaliana, 195–196, 203, 416, 421, **423–427**, 429–431, 438–439, 693
Proximal tubule, labeled, 744.
Pseudo color display, 173–175, 190, 291.
PSF. *See* Point spread function.
Pulse broadening, 88, 111, 210, 537–538, 543, 606, 609, 728, 903.
Pulse length measurement, 115, 901–903.
Pulse spreading. *See* Pulse broadening.
Pulsed lasers, 81, **96–100**, 110–114, 120, 137. *See also*, Lasers; Ultrafast lasers.
broadband tunable, table, 120
diode, table, 96–97
DPSS, table, 98
dye, table, 96
excimer, table, 96
for FLIM, 537
kits, table, 98, 100
nitrogen, table, 96
scanning only region of interest, 237
for 2-photon excitation, 81
ultrafast, table, 99–100
vapor, table, 97
Pulse-counting mode, 21, **29–30**, 32–35, **258–259**, 260, 263.
Pump sources, for dye lasers, 103.
Pumping media, maintenance, 116.
Pumping power *vs.* frequency cubed, 65, 82.
Pupil function, 211, **245–248**.
3D point spread function restored, 247–248
4Pi, 566–567
AOD, 56
empty aperture, 248
of human eye, 72, 128
intermediate optics, 211, 222, 225, 250
Köhler illumination, 34, 127–128, 131, 229, 251, 627, **648–649**
Mach-Zehnder interferometry, 245
measurement, 246–248
images, 246–248
objective, 24, 155, 158–159, 211, 239–240, 242, 492, 551–552, 554, 566–567, 650
orthonormal Zernike polynomial for, table, 247
phase-shifting interferometry measuring, 245
polarizing effects, 249
pupil plane, 50 *See also*, Back-focal plane transfer lens, 728
view of pupil image, 629
Zernike polynomial fit, 245–247
Purkinje cells, Golgi-stained, 167–168.
Pyrus serotina. See Pear.

Q

QE. *See* Quantum efficiency.
Q-switched pulsed laser systems, 111, 114–115.
Quantitative analysis, flying-spot microscope, 6–7.
Quantization, limitations imposed by, 37–39. *See also*, Chapter 4.
Quantum dots, 221, 343, **357**–358, 360–361, 656, 694, 696, 757, **801**, 814, 846, 853. *See also*, Semiconductor nanocrystals.
assays for, 814
in electron microscope, 852–854
FRET, 801

Quantum dots (*cont.*)
labeling, 853
toxicity, 357, 694
Quantum efficiency (QE), 25–30, 74–78, 222, 232–234, 238, 251, 254–255, 349, 355, 375, 383, 390, 442–443, 459, 516, 527, 575, 628, 646, 556, 703, 751, 793, 920–922.
of back-illuminated CCD, 77–78
charge-coupled device (CCD), **26–28**, 74–76, 142, 215, 232, 234, 257–258, 261, 644, 707, 751, 754, 810, **920–921**
comparative among CCD cameras, 76
effect on Poisson noise, 74–75
effective QE, of photon detectors, 28, 29
of electron-multiplier CCD, 4, 30, 59, 234, 920
FLIM, 516–517, 520, 523, 526–527, 529, 530
FRET, 792
of human eye, 251
and intensity spread function, 74–75
and multiplicative noise, 77
optical enhancer, to increase QE, 28–30
optimal 3D microscopy, 644
photomultiplier tube (PMT), 26–28, 51, 77, 222, 257, 262, 527, 707
graph, 29
table, 707
signal-to-noise ratio, 263, 442–443
variation with wavelength, 29
vs. wavelength, 922
Quantum noise, 21 63–64, 69–70, 468, 472. *See also*, Poisson noise.
and approximation, for reconstruction, 69–70
Quantum wells, as absorbers, 111.
Quantum yield, of fluorescent dyes, 172, 180, **338–345**, 353, 360, 363, 383, 421, 543–544, 574, 661, 683, 690, 710, 737, 792, 794–795.
Quartz-halogen lamp, control, 138–139. *See also*, Halogen lamps.

R

Rabbit, 237, 744.
antibodies, 855, 877–878
kidney proximal tubule, pH, 744
Radiance, of non-laser light sources, 126, 132, **137–139**, 141.
measuring with radiospectrometer, 139
Table, 1140
Radiospectrometer, radiance *vs.* wavelength, 139.
Raman background, in glass fibers, 88, 90, 162, 506–507.
lower in large-mode-area, fiber, 110
Raman scattering, 162–163, 167, 339–340, 348, 506–507, 545, 697.
and bleaching, 697
defined, 162
Raman spectroscopy, 48–49, 90, 167, 254, 339–340, 507, 545, 697. *See also*, CARS.
CARS, 204, 550, 577, **595–605**
chemical imaging, 90
hard-coating on interference filters used, 48–49
image contrast, 167
Ramp-up, for light sources, 136, 137.
and long-term stability, 137
and short-time stability, 136
Rare earths, for doping fiber lasers, 110.
Raster, 62–64.
convolution, 485–486
dimensions, in specimen, 63
retrace, 25, 33, 53–54, 219, 338, 389, 543, 628, 651, **908**. *See also*, Retrace, raster scanning shape, 63
size, *vs.* pixel size and light dose, 64
temporal limitations, 141
Raster scanning, 5–6, 25, 141–142, 223, 540, 596.
alignment, 629–630, 651
assymmetrical sampling, 38–40
bleach pattern, 3D, 538, 628, 693
chromatic aberration limitations, 156, 640–641
damage is higher to either side of raster, 54
display, 830–831, 835
distortion, 40
and electronic bandwidth, 70, 238
for fast confocal imaging, 223
fiber-scanning, 214, 508
galvanometer limits, **52–54**, 223, 651
limitations imposed by AODs, 56
MPEG formats, 840
Nyquist sampling, 38, 41, 59–60, 62, 634–635
off-axis aberrations, 151, 640–641, 659–662
pattern on Nipkow disk, 5–6, 223–225. *See also*, Nipkow disk scanning
retrace gating, 25, 54, 56, 219, 389, 543, 628, 651, 908
scan angles, 209, 214
stability, 708
sampling in time and space, 141–142
timing, 33, 53, 753
zoom, raster size and magnification, 11, 24, 37, 63–64, 66, 70, 79, 317, 389, 493, 627, **634–636**, 655–658, 683, 731
Rat, cells and tissues, 205, 320, 323, 330, 398, 739, 813.
brain slices, 393, 398, 686
CA1 region, 323
cardiac muscle, 498, 529, 556
cerebellar granule neurons, 813
EDL muscle, calcium, 740
fixation, 370, 372, 393
hippocampus, 268, 317, 341
interossi muscles, SNARF-1, pH image, 739
intervertebral disk, 310–311
kidney, 511, 803
leukemia cells, 347, 520–521
FLIM image, 521
neuron, membrane potential, 205
tooth, 667
Rate, imaging, limited by signal level, 73.
Ratiometric imaging, 189, 346–347. *See also*, Calcium imaging, pH, etc.
bleach ratio, 697–698
calcium, 736–737, 850. *See also*, Calcium imaging
CARS, 600, 602, 604. *See also*, CARS
concentration calibration, 742–745
to detect colloidal gold labels, 167
to determine ionic concentration, 36
FLIM, 516–532. *See also*, FLIM
FRET, 174, 184, 790, 794–795, 797–798. *See also*, FRET
glutaraldehyde autofluorescence assay, 369
HCS, high-content screening, 813, 823–824.
indicator choice, 738
interpretation, 740–741
live/dead assay, 875
pH, 739–744. *See also*, pH imaging
structured illumination. *See* Structured illumination microscopy
water-immersion objectives, 737
Rayleigh criterion (Abbe criterion), **1–3**, 9, 37–39, 60–61, 66, 129, 146, 486, 703, 822, 928.
breaking the Abbe/Rayleigh barrier, 571–573
Nyquist sampling, 39, 60, 66
of two point images, 1–3, 146
Rayleigh scattering, 162–163, 166, 167, **339**, 342, **417**, 703, 747.
compared to Mie scattering, 163
in embryos, 747
by colloidal gold labels, 167
light attenuation in plant tissue, 417
wavelength dependency, 162–163
Rayleigh unit, 147.
Reactive oxygen species (ROS), 341–343, 362–363, 390, 544, **682–684**, 691, 693–694, 852–853. *See also*, Bleaching; Phototoxicity.
as basis of correlative TEM staining, 852–853
Readout noise, 74–75, 77, 232. *See also*, Noise.
and readout speed, 77
Real image, disk-scanners, 224.
Real-time 2D imaging, 12–13, 167–168, 215, 222–224, 232, 235, 307, 496, 542.
Real-time 3D imaging, 154.
Receptors.
cholera toxin, 790–791, 796–797, 802

deconvolution, 495
EGF, 533
ERD2, 791, 796
fibrinogen, 846–847, 850
high-content screening, 809, 812–814
KDEL, 790, 797
ligands, 354
lipid, 790, 791
proteins, 357
Streptococcus, 879
transferin, 819
uncaging, 545
Reconstruction, 3D.
definition, 280.
Nyquist and filtering/deconvolution, 59, **66–67**, 69, 70, 173, 235–236, **280–315**, 458, **468–469**, 474–475, 496–497, 563, 585, 603, 607, 610, 615, **635**, 672, 675, 677–678, 690, 772, 730, 731, 762, 77, 774–776, 778, 784, 883
Recording times, 141–142.
in widefield microscopy, 141–142
using LED source systems, 141–142
Recovery curve, after bleaching, 187.
Red fluorescent protein (RFP), 221–222.
Reference list.
historic, 889–899
lasers, 123–125
Reflected-light images, 180, 181. *See also*, Backscattered light.
confocal, of integrated circuit, 180
of glass bead, in water, 181
Reflecting objectives, constraints, 156.
Reflection contrast technique, Antiflex, 159.
Reflection mode, low coherence light, 130.
Reflectivity, optical surfaces, 159, 163, 167–171.
anti-reflection coatings, 158
on-axis, artifact, 168–171
refractive index, 159, 163, 167
Refracting regions affect imaging beam, 15–16.
Refractive index, (RI), 14–15, 23, 45, 148, 152, 163, 198, 377, **404–413**, 418–420, 613, 654. *See also*, Spherical aberration; Dispersion.
anomalies in, effect on PSF, 23, 418–420
of biological structures, 163, 377
table, 277
of botanical specimens, 418–420
coverslip thickness, importance, table, 654
of immersion medium, 277, 411
effect on PDF, 23, 418–420
effect on sharpness, 14–15
effect of wavelength and temperature on, 148, 248–249, 411
and intensity, and spectral broadening, 111
of layers in interference filters, 45
of mounting media, table, 198, 342, 370–371, **373–377**
of optical glass *vs.* wavelength, 152
optical projection tomography (OPT), 613
self-shadowing, 198
temperature, 148, 248–249, 411
of tissue/organs, table, 377
Refractive index mismatch, effects, **404–413**. *See also*, Spherical aberration.
table for glycerol, 409
table for water, 409
calculation, 404–407
dependence of focal shift, 410
diagram, 404
dry objectives, 410–411
experiments, 409–410
water/glycerol results, table, 410
field strength calculation, 405
other considerations, 410–413
spherical aberration correctors, 15, 151, 147, 192, 411–412
terminology, 405
actual focal position (AFP), 405
focal shift, 405
nominal focal position (NFP), 405
theory, 404–407
Region code, for MPEG-encoded movies, 844.
Region-of-interest (ROI), 835.
brain slice, 726, 733
diagonal, 658
display presentation, 835
embryos, 747, 759
FRAP, 51, 187
FRET, 797, 801
in image processing, 289, 300, 323, 330, 676
labeling, 353
must be smaller at high resolution, 577
nanosurgery, 219, 686
photobleaching, 690
preprocessing, 676
rapid acquisition, 236–237
structured illumination, example, 272
viability studies, 683
Registration synthesis method, 328–331.
defined, 328
landmark-based, 328–329
multi-view deconvolution, 330
Relationships, in fluorescence microscopy, 80.
energy per photon, 80
flux per pixel, 80
photons/s *vs.* wavelength, 80
Relative motion, objective *vs.* specimen, 39–40.
Relaxation, in laser energetics, 82.
Relay optics (telan lenses), 145, 157, 214, 455.
Reliability.
of 3D image, 461, 517
biological, *vs.* damage, 24, 68, 631, 633
lasers, 80, 102, 115
living cell work, 387
mirror position, 40
photometric, 312
spectral detectors, 662
Removable storage media, 585–588.
random-access devices, 586–588
compact disks (CD), 586–587
digital video disks (DVD), 587–588
floppy disks, 586
magnetic disks, 586
MO (magneto-optical) disks, 586
optical disks, 586
WORM (write once, read many) disks, 586
Rendering, of 3D views, 280, 285, 290, 301, 307, 309, 311, 377, 749, 762, 764.
definition, 280
voxel speed, 290
RESOLFT microscopy, 571–574, 577. *See also*, STED.
breaking diffraction barrier, 571–573
concept, 571–573
different approaches, 573–574
ground state depletion (GSD), 573
STED, 573–574
outlook for, 577
resolution, new limiting equation, 571
triplet-state saturation, 573
Resolution, 1, 4, 13, 16, 24, 36–41, 59, 61, 65–67, 210. *See also*, PSF; FWHM.
adequate levels, 36–41
axial, 13
axial-to-lateral ratio *vs.* NA, 4
back-focal plane diameter, table, 210
confocal *vs.* non-confocal, 16
and contrast transfer function, 37, 59, 61
estimating, 65–67
measured, widefield, 16
minimum resolvable lateral spacing, 1, 16
spatial and temporal, 24
sufficient, 36–37
Resolution, structured illumination.
Fourier-space, 270–271
linear image reconstruction, 271
Lucosz's formulation, 273
methods, 270–276
Moiré effects, 270–271
photobleaching, 275
reconstruction results, 272
standing-wavefield microscope, 275
thick samples, 274, 275, 278–279
Resolution scaling, STED comparison, 578.
Resolution test slides, 16, 656.
Resonant cavity, laser, **81–82**, 111, 115.
Resonant scanners, 52–54, 56–57, 223, 447, 543.
acceleration distorts mirror shape, 53
blanking, 25, 218, 338, 389, 543, 628, 651, **908**
compared to acousto-optical deflector, 56
duty cycle, 52
galvanometer, 52
multi-photon excitation, 543
raster-scanning, 33, 53–54, 56

Resonant scanners (*cont.*)
retrace, 54, 56. *See also*, Retrace, below.
scan speed, 54
Retrace, raster scanning shape, 25, 54, 56, 219, 389, 543, 628, 651, 908.
acousto-optical deflector, 56
blanking, 25, 219, 338, 389, 543, 628, 651, **908**
raster-scanning, 33, 53–54, 56
Review articles, listing, 889.
RFP. *See* Red fluorescent protein.
Rhodamine, dyes, 81, 109, 116, 136, 140, 203, 264, 292, 339, **342–345**, 353, 355, 362–363, 375–378, 409, 538, 553, 592, 693, 697–698, 762, 783–784, 794, 851, 854–856.
arsenical derivatives, 348
bleaching, 697, 698
calibration plot, 661, 851
excitation of, 181, 109
fluorescence correlation spectroscopy, 693
FRET, 347
photobleaching quantum yield, 363
planar test specimen, 538
power for 1-, 2-photon excitation, 81, 3 41
Rhodamine-123, 374, 389
resolution measurement, 409
stability and cost, 116
Rice (*Oryza sativa*), 168, 171, 414, 415, 712, 715.
absorption spectrum, 415, 706
backscattered light image, 168, 171
emissions spectra, autofluorescence, 713
leaf fluorescence images, 714–715
light attenuation in plant tissue, 414
silica deposits, 714–715, 717
Richardson-Lucy, deconvolution, 497, 568.
Richardson Test Slide Gen III, 652, 656.
RLE. *See* Run-length encoding.
RNA, microinjection of, 803, 804.
RNA labels, 344, 369, 465, 531–532, 612, 691, 758, 874–875.
ROI. *See* Region of interest.
Room light, as stray signal, 201, 632, 904.
Roots, plants, 172, 174, 303, 307, 421, **430–432**, 438, 464–465, 556, 772–773, 775, 777, **779–783**.
maize, image, 432
mounting, 429, 431
ROS. *See* Reactive oxygen species.
Rose Criterion, 37–38, 68, **164**, 633.
relationship with signal-to-noise ratio, 164
for visibility, 37
Rotating, specimen, 188, 568, 835.
micro-CT, 615
optical projection tomography, 610–611
SPIM, 672–673, 676, 751
Rotor, galvanometer, detecting position, 53–54.
Run-length encoding (RLE), 580.

S

Safety, 83, 85, 90, 115, **117–118**, **124**, 132–139, **900**, 903, 904.
arc sources, 132–139
beam-stop design and use, 118. **903–904**
classification of laser systems by hazard, 117
cleaning objectives, 642
display geometry, 297
equipment needed, 900
eye protection
against Brewster surface reflections, 83
goggles, 118
with external-beam prism method, 90
fiber optics for transporting laser light, 88
hazardous materials
fluorescent laser dyes, 85, 103, 116
used beryllium oxide tubes, 115
high pressure Xe lamps, 136
monitor power to avoid explosions, 138–139
in disk-scanning confocal microscope, 231
laser, **117–118**, **839**, 900, 903–904
installation requirements, 85
monitor power to avoid explosions, 138–139
references, list, 123
safety curtains, 117, 904
training, 118
SAM, saturable absorber mirror, 111.
Sampling. *See* Digitization, 20, 63–64.
non-periodic data, 38
optimal, 63
Saponin, formaldehyde fixation, 359, 375, 856.
Saturable absorber mirror, pulsed lasers, 111.
Saturable Bragg reflector (SBR), 111.
Saturable output coupler (SOC), 107, 111.
Saturation, singlet-state fluorescence, 21–22, 41, 142, 265, 276, 339, 442, 448, 450, 643, 647, 899.
performance limitations, 81, 450, 928
SBR, saturable Bragg reflector, 111.
SBT. *See* Spectral bleedthrough.
Scaling techniques, 592, 835.
Scan angle, and position in image plane, 209–210.
Scan instability, detecting, 40–41.
Scan raster, testing, 651–654.
malfunctioning system, 653
phototoxicity from uneven scan speed, 651
sources of fluorescent beads, table, 653
well-calibrated system, 652–653
x and y galvanometers, 651–652
z-positioning calibration, 652, 654
stability, 652
Scanned-slit microscopes, table, 224.
Scanner arrangements, evaluation, 213–215.
Scanners, 51–55, 57, 214–216.
acousto-optical deflectors, 55. *See also*, AODs
mirror arrangements, 214
evaluating, 215–216
mechanical, 51–54. *See also*, Galvanometers
piezo-electric, 57, 215, 238, 510, 555, 610
single mirror/double tilt, 215
sinusoidal, "tornado" mode, SIM scanner, 52
Scanning electron micrographs, 428, 434, 437, 846–848, 850–852.
Scanning laser ophthalmoscope (SLO), 480.
Scanning fiber-optical microscopy. See Fiberoptic confocal microscope.
Scatter labeling for tracing lineage, 461, 462.
Scanning systems for confocal light microscopes. *See also*, Galvanometers; Disk-scanning confocal microscopy; Acousto-optical deflectors; Linescanning confocal microscopes; Raster.
Lissajous pattern, circular scanning. 554
"tornado" mode, SIM scanner, 52
Scattering, 162–163, 167–171, 550.
coherent anti-Stokes Raman (CARS), 550
elastic, Rayleigh, 162–163, 166–167, **339**, 342, 417, 703–747
Raman, 162, 167, 339–340, 348, 506–507, 545 and reflection contrast, 167–171
Scattering object, viewed by TIRM 177. *See also*, Backscattered light.
Schiff reagents, 262, 369, 770, 774–775, 778.
Schottky diode, photodetector, 253.
Scientific thought, four aspects, 789–790.
Scion Image, 281–282, 395, 730.
Scramblers, light, 8, 13, 84, 131–132, 143, 507.
Screen capture, 830.
Screens, to enclose laser beams, 118.
SD. *See* Static discharges.
SDA. *See* Stepwise discriminant analysis.
Sea urchin, *S. purpuratus*, 173, 198, 200.
Second harmonic generation (SHG), 90, 114–115, 166–167, **179**, 188, 550, 552, 556, **703–719**, **729–730**. *See also*, Harmonic signals.
as autofluorescence, 361
cell chambers, 166, 429, 552
detectors, 706–708, 728
disk-scanning, 552, 556
double-pass detection, 166–167
table, 706–708
crystals for SHG, 103, 107, 114–115, 188, 703
energy relations, 705
in lasers, 103, 107, 114–115
layout, 166, 191, 552, 708–709, 712

light attenuation spectra, 706
light sources, 706–708
brain slices, 729–730
non-linear optical microscopy, 704–705
optically active animal structures in, 714–717
brain slice, 729–730
collagen structure, 703, 717
sarcomeres, 716
spindle in mouse zygote, 717
spindle in zebrafish embryo, 718
structures producing SHG, table, 715
table of structures, 715
zebrafish embryo, 716, 718
optically active plant structures, **428**, 710–714
Canna, nonlinear absorption, 710
cell wall, 428, 711, 714
Commelina communis, 712
emission spectrum of maize, 710, 711
Euphorbia pulcherrima, spectrum, 710
mineral deposits, 436
Pyrus serotina, spectrum, 711
rice leaf, 712, 715
starch granules, 433
maize, 710–711, 713–714
emission spectrum, 710–711
leaf spectrum, 710
pol-microscopy, 711
stem, optical section, 714
stem, spectrum, 710, 713
chloroplasts, tumbling, 713
membranes of living cells, 90
mineral, deposits, 436
photodetector suitability, table, 706–707
polarization dependence, 71, 717–720
potato, as SHG detector, 712
pulsed laser suitablity, table, 706
signal generation, 179, 552, 597, 704–705
spectra, 706
spectral discrimination, 421
starch granules, 433
Segmentation, FLIM image, 527–528.
Segmentation methods, 281, 283–285, 290, 300–302, 304–306, 309, 311–312, 316–319, **321–330**, **333–334**, 527–528, 776–778, 812.
3D, 776, 822, 828
automated, 818, 821–822, 828
background, 321
blob segmentation example, 322–324
gradient-weighted distance transform, 323
model-based object merging, 323–325
watershed algorithm, 323–324
bottom-up, 321
combined blob/tube segmentation, 328–330
foreground, 321
hybrid bottom-up/top-down, 322
integrated, 322
intensity threshold-based, 321
object, 321
for plant cells, 774–777
balloon model, 776
watershed algorithm, **322–325**, 777, 822
region-based, 321–322
top-down, 322
tube-like object segmentation, 324–328
mean/median template response, 328
skeletonization methods, 324–325
vectorization methods, 324–327
validation/correction, 333–334
manual editing, 333–334
Selective plane illumination microscopy (SPIM), 613, 614, 672–679, 751.
3D scanning light macrography, 672
anisotropic resolution, 678
applications, 675
axial resolution, 674–675
vs. CLSM, 678
Drosophila embryogenesis, **675–676**, **747–748**, 751–752, 754, 756, 759, **804**, 810
and FLIM, 527
images processing, 675–678
image fusion, 676–677
pre-processing, 676
registration, 676
lateral resolution, 674
light-sheet illumination, 672–674
light sheet thickness, 674–675
Medaka, 614–615
heart image, 614
embryo image, 675
multi-view reconstruction, 675–678
point spread functions (PSF), 674
schematic setup, 613, 673
thin, laser light-sheet microscope,TLLSM, 672
Self-aligning arc source, 135.
Self-shadowing, 165, 174, 194, 195.
in confocal optical sections, 174
spherical structure, 195
in epi-fluorescent mode, 165, 194
SEM. *See* Scanning electron microscope.
Semi-apochromat, pros and cons, 158.
Semiconductor lasers, 86, 105–108.
noise sources, 86
Semiconductor nanocrystals (quantum dots), 221, 343, **357–358**, 360–361, 656, 694, 696, 757, 759, **801**, 814, 846, 853.
as probes, 221, 757, 759
Semiconductor saturable absorber mirror (SESAM), 107, 111.
for self-starting intense optical pulse trains, 111
Sensitivity, video photodetectors, 6–7.
Sensitized emissions, of acceptor, 795–796. *See also*, FRET.
Sequential devices, 585–586.
Serial sampling, single-beam confocal, 20.
SESAM, Semiconductor saturable absorber mirror, 107, 111.
SFP. *See* Simulated fluorescence process.
Shannon, Claude, 64–65.
Shannon sampling frequency, defined, 64, 443.
SHG. *See* Second harmonic generation.
Shift invariance, deconvolution, 457, 490, 564.
Short-pass filters, 43–44.
Shot noise, 232, 256–257, 286, **442**, 460–461, 495, 558, 660–661, 831. *See also*, Poisson noise, Quantum noise.
Signal, 27, 62. *See also* Speed relationship to magnification, 62
Signal attenuation-correction, 320–321.
Signal detection, basics, 660–663, 918–931. *See also*, Detectors.
coefficient of variation, 660
instrument dark noise, 660
photon (shot) noise, 660–661
PMT linearity, 661–662
signal-to-noise ratio, 660
spectral accuracy, 662
spectral resolution, 662–663
wavelength response, 663
Signal levels, 16-photon peak signal, 73–74.
Signal-to-background ratio, of titanium-sapphire laser, 112.
Signal-to-noise (S/N) ratio, 37, 53–54, 67, 81, **164**, 251, 257, 265, **330**, 340, 386, 391, **442–451**, 470, 481, 495, 498–499, 528, 542, 562, 567, 582, 599, 621–622, **660**, 690, 696, 699, 707, 736–737, 740, 753, 769, 772, **778–780**, 810, 813.
3D imaging, 448–451
4Pi microscopy, 562–567
bleaching, 391, 442, 690, 696
in calcium imaging, 737
chapter, **442–451**
comparative performance, 256, 448–451
bleaching-limited performance, 448–450
configurations of microscope, 448, 449
disk-scanning microscope, 449
line illumination microscope, 449
saturation-limited performance, 450
scanning speed effects, 53, 450–451
structured illumination, 265–266, 270, 275–276, 279–280
S/N ratios for, table, 450
widefield (WF) microscope for, 450
confocal microscope, 444–447, 660
calculations, 444
detectability, 446–447
methods compared, 450
noise model N1, 444–445
noise model N2, 446–447
deconvolution, 470, 481, 495, 498–499
designs, confocal, 212–216, 447–448, 450
disk-scanners, 221
dynamic range, 2-photon, 644, 778–780
high-content screening, 810

Signal-to-noise (S/N), ratio (*cont.*)
improvements, 736
micro-CT, 615
magnetic resonance microscopy, 621–622
multi-photon fluorescence microscope, 112, 427, 447, 542, **779**
Nyquist sampling, 67, 448
optimal excitation power, 81, 340
Rose criterion, visibility, 37–38, 68, **164**, 633
saturation, 442
vs. scan rate, 53
signal level, 67, 75, 528
sources of noise
background noise, 443–444
grey levels, 443
quantum efficiency, 442–443
shot noise, 442–443
sources of noise, 442–444
STED, 574
and visibility, 37
Silica glass, transmission losses, 502.
Silicon diodes, near infrared emission, 132.
Silicon-intensified target (SIT) camera, 730.
brain slices, 730
SIM. *See* Surface imaging microscopy.
Simplicity, as design goal, 43, 66, 220, 229, 387, 508, 647.
Simulated fluorescence process (SFP), 310.
Single-cell automatic imaging, 809, 812.
Single-cell calcium imaging, 812.
Single-longitudinal-mode fiber laser, 110.
Single-mirror/double tilt scanner, 215.
Single-molecule, 80.
biochemistry, 221–222, 575, 690, 693, 696
bleaching, 690, 693, 696, **697–698**, 699
Single-photoelectron pulse heights, 30.
Single-photon, energy, equation, 35.
Single-photon counting avalanche photodiodes (SPAD), 527.
Single-photon excitation, plant imaging, 772–778.
Single-photon pulses. *See* Photon counting.
Single-scan images measure scan stability, 40–41.
Single-sided disk scanning, confocal microscopy, 132, 141–142, **168**, 171, 175, 215–216, **229**, 231, 907, 913. *See also*, Disk-scanning confocal microscopy.
advantages and disadvantages, 215–216
basic description, 141
commercial, 907, 913
light source, 132, 141–142
Singlet state saturation, **21–22**, 41, 81, 142, 265, 276, **338–339**, 442, 448, 450, 643, 647, 899, 928.
Sinusoidal bidirectional scanning, 25, 52–54. *See also*, Resonant scanners.
duty cycle, 53, 260
Sinusoidal image, 831, 838.
fiber-optic confocal, 510
Sinusoidal modulation, in FLIM, 524–526.
SIT. *See* Silicon-intensified target camera imaging.
SLF. *See* Subcellular location features.
Slice AM-dye-painting protocol, 726–727.
Slice chamber protocol, 727.
Slit scanning confocal, 12, 25, 37, 50, 51, 56, **221–226**, **231**$^{+}$, 235, 238, 519, 522, 664, 741, 914, 916.
Achrogate, 50, 212, **231–232**, 916
with AOD scanning, 56, 914
commercial, 913–914, 916
critical parameters, 224–228
optical sectioning, 228, **444–449**
optimal slit size, 225
point excitation, slit detection, 914
SLM. *See* Spatial light modulator.
SLT. *See* Subcellular location tree.
Smart media, digital storage, 588.
SMD. *See* Surface mount device.
SNARF-1, 345, 346, 531, 739, **744–745**.
ratiometric pH label, 744–745
stained rat *interossi* muscles, 739
table of variants, 531
Snell's law of refraction, 167, 654.
SOC. *See* Saturable output coupler.
Software packages, visualization, table, 282–283.
SoftWorx, 3D display software, 282.
Solanum tuberosum, potato, 712.
Solid state memory devices, 588.
compact flash cards, 588
memory stick, 588
smart media, 588
Solid-state photodetector, 30–31, **918–931**. *See also*, CCD; EM-CCD.
Solid-state lasers, 86, 103–118, 236–237.
cooling, 108
noise sources, 86
thin-disk lasers, 109
tunability, 109
use, 236–237
Source brightness, measure, radiance units, 126.
Source optics, reflecting and collecting light, 134.
Space invariance, telecentric systems, 207–208.
Space multiplexing, in MMM, 555.
Spacer, material in interference filters, 46.
SPAD, single-photon counting APD, 527.
Spatial coherence, 84.
Spatial filter, 89, 107, 391, 542, 708, 729.
optical devices for, 89, 222–223, 729
digital, 391–392. *See also*, Gaussian filtering
Spatial frequency, 37, 60, 65, 66. *See also*, CTF.
and contrast transfer function, 37
and geometry, 66
response of microscope, and pixel size, 65
zero, as measure of brightness, 60
Spatial laser beam, characteristics, 89.
Spatial light modulator (SLM), 266.
Spatial orientation factor, for FRET, 792–793.
Spatial resolution, in confocal microscopy, 24. *See also*, Resolution, PSF, CTF.
Special setups, for CLSM, 218–219.
Specifications, general, for scanner, 54.
Specimen, general considerations, 192–197, 228, 361–362, 779. *See also*, Living cells, Living embryo imaging.
fluorescent probes interactions, 361–362
cytotoxicity, 362
localization, 361–362
metabolism, 361–362
perturbation, 362
optical heterogeneity, 22, 23
plants. *See* Plant cell imaging; Botanical specimens
Specimen chambers. *See* Living cell chambers.
Specimen heating, in 2-photon, 539.
Specimen holder, for scanning specimen, 9.
Specimen preparation, for automatic 3D image analysis, 319–321.
image analysis, 319–321
imaging artifacts, 320
Specimen preservation, general, 368–378.
antibody screening on glutaraldehyde-fixed specimens, 377
evaluation, 371–374
cell height to measure shrinkage, 371–373
defined structures, distortion, 373–374
MDCK cell, stereo image, 373
MDCK cell, vertical sections, 372
fixation/staining, 370–371
fixative characteristics, 368–370
chemical fixatives, 369
cross-linking fixatives, 369
freeze substitution, 369
microwave fixation, 369
protein coagulation, 369
formaldehyde, 369–370, 373
general notes, 374–378
glutaraldehyde, 369, 370
immunofluorescence staining, 371
improper mounting, 376
labeling thick sections, 376–377
microwave fixation, 377–378
mounting methods, 370–374
critical evaluation, 371–374
mounting media, table, 377
pH shift/formaldehyde fixation, 370–371, 373
refractive index mismatch, 377
mounting media, table, 377
refractive index of tissue/organs, table, 377
tissue preparation, 376
triple labeling, 375–376
Specimen-scanning confocal microscope, 9.

Speckle, from high-coherence sources, 8, 84, 90, **130–132**, 448.
Speckle microscopy, 13, **383**, 385, 889.
Spectra, emission.
  arcs, 130
  black body, 136
  LEDs, 133
  solar, 127
  tungsten source, 153
Spectral accuracy, 662.
Spectral bleedthrough (SBT), 185, 203–204, 664.
  in intensity-based FRET, 185
Spectral confocal image *A. thaliana* seedling, 175.
Spectral detector, 203–204, 662–663, 666–667.
  testing, 662
Spectral discrimination, filter bandwidths, 44.
Spectral imaging, 175, 382, 384.
  table, 384
Spectral leakage, inter-channel signal imbalance, 185, 203–204.
Spectral phase interferometry, for direct electric field reconstruction (SPIDER), 115.
  for pulse length measurement, 115, 901–903
Spectral properties, of filters *vs.* angle, 49.
Spectral resolution, of detection system, 203–204, 662–663, 666–667.
Spectral response.
  of CCD chips, 29, 234, 922
  of eye, 153
  PMT photocathodes, 29
Spectral transmission, objectives, plots, 159–161.
Spectral unmixing, **190–192**, 319, 361, 382, 384, 386, 423–425, 431, **664–667**, 770, 905.
  detectors for, 51, 667
  examples, 665–666
  limitations, 51, 382, 667
  overlapping fluorophore emission, 190, 319, 423–425, 664–667
  removing autofluorescence using, 667
Spectrofluorimetry, for FRET, 793, 795.
Spectroscopic ruler, 765.
Speed, in confocal imaging, 7, 11–12, 36, 41, 53, 142, 222–224, 235–236, 434, 447, 450, 458, 460, **482**, 526, 536, 563–564, 748, **753–755**, 784. *See also*, Temporal resolution.
  4Pi-MMM, 563–564
  AOD, 55–56
  calcium imaging, 741
  CARS, 599–600, 604
  charge-coupled device cameras, 77–78, 142, 229, **231–235**, 259, 647, 651, 754–755, 885
  data compression, 581–582, 586–588
  detector, in FLIM, 523, 558
  disk-scanning confocal, 141, 216, 224, 754
  for display, processing, 803, 839, **841-842**, 862
  factors affecting, 235–236, 482, 496, 753–754
  of fixation, 370
  FRET, 795, 805
  galvanometer, 52–54, 211, 214
  high-content screening, 809–810, 813
  MMM, 551–555, 563–564
  need for, in living cell imaging, 222, 753–754
  rendering, 3D display, 831
  SPIM, 613, 678
Spermatocyte, crane fly, 15.
Spherical aberration, 15, 34, **147–149**, 151, 160, 192–197, 208, 241, 244, 247, 330, 395, **404–413**, 454–455, 463, 466, 471, 480–481, 542, 629, 640, 654–655, 657–658, 728, 772, 774, 893, 903–904. *See also*, Aberrations, spherical.
  blind deconvolution, 471, 480–481
  chapter, 404–413
  confocal microscopy performance, 654
  correction of RI mismatch, 192, 287, 411, 542
  correction of, figure, 145, 411–412, 654–655
  corrector, 92, 395, 398, 411, 477, 640, 654
  deconvolution, 463, 466, 468–469, 471, 480, 498–499, 658, 728, 784
  effect of specimen, 192–197, 418, 454, 747
  index mismatch. *See* Index mismatch
  measurement, 145, 407, 455, 471, 481, 492, 657
  signal loss, 330, 389, 395, 413, 457, 661
SPIDER, Spectral phase interferometry for direct electric field reconstruction, 115, 901–903.
Spill-over, between detection channels. *See* Bleedthrough.
SPIM. *See* Selective plane illumination microscopy.
Spinning disk, 3, 5–6, 11, 40, 141, 176, 216, 223–224, **231–232**, **235–236**, 260–265, 459–460, 464, 468, 481–483, 783–784, 810–811. *See also*, Diskscanning confocal microscopy.
  commercial, 907, 913, 915
  FLIM, 519–520, 522
  high-content screening, 810–811, 820
  MMM, 554, 558
  performance, 449–450
  systems for, cytomic imaging, 810
  vs. TPE imaging, in plant cells, 783
  Yokogawa CSU-10/22, 231. 915
Spinning-disk light scrambler, ground glass, 8.
Spinning filter disk, digital projector, 590.
Spirogyra, and depth of optical sections, 195.
Spot scanning, to avoid coherence effects, 84.
Spot size, full-width at half-maximum. *See* Pointspread function, Full-width half-maximum.
Square pixels, advantage of using, 62.
Stability, 86, 102, **103**, **136–139**, 826.
  algorithmic, 473
  arc sources, 136–137, 477
  argon-ion laser *vs.* krypton laser, 102
  disk scanners, 215
  of DVDs, 587
  dye. *See* Dyes; Bleaching from fiber-optic coupler, 505–506
  galvanometer, 54
  halogen sources, 136–139, 346
  interferometer, 240–241, 267
  laser, 81, **85–89**, 704
    diode, 106, 108–109
    fiber output, 505
    helium-cadmium, (low), 103
    intensity, 85–87, 113, 116, 136, 477, 903
    measurement, 650–651
    pointing, 87, 903
    results, 86, 103
    structure, 82–85, 103
    thermal, 111
    wavelength, 106–108, 115, 118
  mechanical, 39, 82, 85, 201, 267, 512, 652
  objectives, 146
  photostability, 363, 369, 690–702, 802. *See also*, Dyes; Bleaching
  scan, 40, 638–639, 651
  shutter, CCD camera, 929
  thermal, 111, **219**, 387, 389, 394, 539. *See also*, Thermal variables
Stage-scanning confocal microscope, 11.
  piezoelectric scanners, 57, 708
Staining, plants, 438, 774. *See also*, Dyes; Livingcells; Botanical specimens; Plant cell imaging; Fluorophors.
  calcofluor procedure, 438
  of plant tissues, 774
Standards, ISO (DIN) microscope design, **156**$^{+}$.
Standing-wavefield microscope, 275.
Starch granules, plant, 202, 420–421, 428, 432–**433**, 435, 703, 710–712, 715, 719.
Static discharges, destroy semiconductors, 109.
Statistical noise, in counting quantum-mechanical. *See* Poisson noise.
STED. *See* Stimulated emission depletion.
Stem-cells, 623, 678, 762, 790, 813.
Stem, plant, 168, 172, 180, 417–419, 421, 424, 430, 556, 707, 710–711, 713–714.

Stentor coeruleus, backscattered light image, 168.
Step index optical fibers, 501–503.
Stepwise discriminant analysis (SDA), 818, 820.
Stereo Investigator, software, 282.
Stereology, 316, 319.
Stereoscopic image, about, 6–7, 9, 11, 154, 224, 298–299, 317, 396.
biofilms, 880
cheek-cell specimen, 23
diatom, 640
Drysophila, microtubules, 752
embryo, 200
fat crystal, polarization, 479
neurons, 298, 314
Alexa stained, 330
backscattered light images, 167
eye, optic nerve, 481
Golghi-stained, 298
Lucifer-yellow, 314
microglia, 396–398
rat-brain neurons, 398
transmitted light, 475
lung, 292
MDCK cells, 373–374, 378
Milium chromosomes, Fuelgen-stained, 298
Paramecium, chromosomes, 298
pea root, RNA transcript, 465
platelet, high-voltage, EM, 848–849
sea urchin, *S. Purpuratus*, 173, 198, 200
skin, 298
Spirogyra, 195
tandem-scanning confocal microscope, 6
Stereoscopic views, image processing and display, 290, 292, **293**, **295–299**, 451, 764.
color space partitioning, 297
display, **293**, 299
interlaced fields of frame, 297
movie projection, 838
pixel-shift/rotation stereo, 297
stereo images example, 298
synchronizing display, 297
Stick objective, for *in vivo* confocal, 806.
Stimulated emission depletion (STED) microscopy, 3, 539, 561, 568, **571–578**.
axial resolution increase, 576
breaking the diffraction barrier, 571–573
challenges, 577
compared to confocal, 575–576
diagram, 573
different approaches, 573
dyes used successfully, table, 575
OTF compared to confocal, 578
outlook, 577
PSF compared to confocal, 578
RESOLFT, the general case, 572–573
results, 576, 578
triplet-state, 573
Stimulated emission of radiation, defined, 82–83, 124.
Raman scattering, 167
semiconductor, 106
and stimulated-emission depletion, 573, 577
STN, supertwisted nematic, 589.
Stochiometry, ion kinetics, 741.
Stokes field intensity, 595, 597.
Stokes laser, in CARS microscopy, 595, 597–604.
Stokes shift, 44–45, 268, **338**, **341**, **343**, 443–447, 539, 542, 690, 759, 792–793.
anti-Stokes,
CARS, 550, 595–604
defined, 44–45
in fluorescence resonance energy transfer, **792**$^{+}$
large, in 2-photon, 539, 646
of quantum dots, 694, 759
size of fluorophores, 45
Storage, digital. *See* Data storage.
Storage structures, plant, 435–436.
maize, image, 436
Stray light, 58, 632, 904.
laser light, 632
non-descanned detection, 904
practical confocal microscopy, 632
room light, 201, 632
Streak camera, FLIM detector, 520.
Strehl ratio, measure of image sharpness, 247.
S. purpuratus (Sea urchin), 173, 198, 200.
embryo, 173, 198, 200
first mitotic division, 173
image degradation, from top and bottom, 198
stereo-pairs of embryo, 200
Structural contrast, 188. *See also*, Harmonic signals.
Structure, optical, 59, 68, 132–135.
of light-emitting diodes (LED), 133
of microscope sources, 132–135
recognizing features in noisy images, 68
chapter, 265–279
Structured illumination microscopy, 265–279.
advantages/disadvantages, 265
computing optical sections, 268–270
vs. confocal microscopy, 265
degree of spatial excitation modulation, 268–270
absolute magnitude computation, 268–269
homodyne detection scheme, 268–269
max/min intensity difference, 268
scaled subtraction, 269–270
square-law detection, 268–269
synthetic pinholes, 268, 269
experimental considerations, 265–268
illumination masks for, 266
light source for, 267
pattern generation, 266–268
schematic setup, 266
nonlinear, 276
resolution improvement, 270–276
Fourier-space, 270–271
linear image reconstruction, 271
Lucosz's formulation, 273
Moiré effects, 270–271
photobleaching, 275
reconstruction steps/results, 272
standing-wavefield microscope, 275
test results, 274
thick samples, 274, 275, 278–279
Subcellular location features (SLF) in automatic image analysis, 819–820, 822–824, 828.
2D, 819–820
2D SLF feature descriptions table, 819
3D SLF, 822–823
test results, table, 824
Subcellular location tree (SLT), 825.
Subpixel deconvolution, 478–479.
Subresolution beads, 655–656. *See also*, Beads.
Sun, microscope light source, 126–127, 131, **135**.
spectrum, 127
Superficial optical sections, living embryo, 748.
Supertwisted nematic (STN), 589.
Surface imaging microscopy (SIM), 607–608.
mouse embryo, 608
setup, 608
Surface mount device (SMD), for LED, 133.
Surface orientation, affects reflected light, 181.
Surface structures, distortion, 197.
Surface topography, maximum intensity, 180.
Surfaces, of interference filters, 47.
Suspension-cultured cells, 189, 429–430.
bacteria, 876, 878
image, 430
frozen, 854
Swept-field confocal microscope, 238.
Synchrotron, wide-spectrum light source, **135**$^{+}$.
Synthetic pinholes, in structured-illumination
microscopy, 268, 269.
images, 269
SYTO, 396, 874–876, **879–885**.

T

Tagged image file format. *See* TIFF.
Tandem-scanning confocal microscope (TSM), 2–6, 11, 13–15, 39–40, 141, 167, 215–216, 223–224, **228–229**, 447.
comparison with other confocals, 13–15

description, 6, 141, 215–216, 228–229
development, 5–6
evaluation, 215, 216
observing ciliate protozoa, 141
rate of data acquisition, 11
real-time imaging of tooth, 167
sources of vibration, 39–40
viewing color/depth-coded, real-time, stereo
images, 154, 304
Tapetum, plant, 433, 434, 779.
TEC, Thermo-electrically cooled, *see* Peltier cooling.
Telan systems, 129, 157.
Telecentric plane, 208–209, 211.
conjugate, 208–209
effect of angular deflection in, 211
Telecentricity, 207, 214.
of closely-spaced scan mirrors, 214
defined, 207
Tellurium oxide (TeO_2), for use in AODs, 55
TEM. *See* Transmission electron microscope.
TEM. *See* Transverse electromagnetic modes.
Temperature, 29, 56, 133, 135–136, 856, 885. *See also*, Thermal variables.
Temperature tuning, of diode lasers, 108.
Temperature effects on high NA objectives, **248**$^{+}$.
Temporal aliasing, 39, 41, 391, 836–837, 839.
Temporal coding, 299–300.
Temporal coherence, 7–8, 82–85, 131.
defined, 84
Temporal dispersion, 502. *See also*, Pulse broadening.
Temporal displays, 292–293, 297, 836.
Temporal experiments, biofilms, 885–886.
Temporal pulse behavior, pulsed laser, 111. *See also*, Pulse length measurement; Pulse broadening.
Temporal resolution, 12, 24, 36–38, 41, 221–222, 322, 334, 386, 391, 399, **458**, 558, 577, 618, 620, 622, 651, 667, 730, 737, 746, 772, 784, 801, 809. *See also*, Fluorescence lifetime imaging (FLIM).
of photodetectors, 263
Temporal signals, 162, 286, 331, 383.
"Test drives," for living embryo imaging, 752.
TFT. *See* Thin-film transistor.
Tetracysteine, labels, 221, 348, 359, 853.
Thalamocortical slice protocol, 724.
Thermal lensing, pulsed lasers, 109, 113, 543.
Thermal variables, 219, 856.
active medium, lasers, 81
of AODs, 56–57
arcs, peak emission wavelengths, 129
automated confocal imaging, 810
cell chambers, 117, 386–389, 394, 727, 790, 810, 814, 885–886. *See also*, Cell chambers cooling, 108, 133
cryo preparation for EM, 856–857
on detectors, 29, 252, 256–257, 495
drift, 16, 115, **219**, 386, 567, 489, 652
compensating, 396, 732
on dye labeling, 359, 361, 738–739
effects of anti-bleaching agents, 694
effect on bleach rate, 696–689
effect fiber pinhole size, 506
fiber-optic, pol-preserving fiber, 503
filament spectra, 135–136
fixation, 369–372, 375, 377
incandescent lamp emission, 135–136
laser cavity, 34, 82, 85–88, 107, 109, 111, 541
of LED, 133, 136–138
brightness, 133
lensing, in pulsed lasers, 109, 113, 543
and light-source output, 136, 138, 650
noise signal, 254, 257, 232–234, 261–262, 495, 660, 734, 921, 924, 925
on objective lenses, 248–249
in photography, 71
properties of ice, 856
properties of optical materials, 158, 248–249
and photomultiplier tube, (PMT), 29
on refractive index, 15, 56, 145, 411
immersion oil, 148–149, 248–249, 411
retinal exposure, 117–118
sensors, 255–256, 727
solid-state laser, 86, 108
specimen damage, 84–85, 139, **685**
specimen heating, 539, 545, 681, 685, 904
temperature tuning, laser, 108, 115
thermomechanical effects, 685
time constant, 38
Thermo-electrically-cooled, *see* Peltier-cooled.
diode lasers, 85, 107–108, 111, 117
THG. *See* Third harmonic generation.
Thick samples, 274, 275, 278–279. *See also*, Living embryo imaging; Brain slices; Biofilms.
background, 278
structured illumination, 274, 275, 278–279
close focus region, 279
distant focus region, 279
in focus region, 278
number of collected photons, 279
Thin disk lasers, 109–110.
Thin Laser Light Sheet Microscope (TLLSM), 672. *See also*, SPIM.
Thin-film transistor (TFT), 589.
Third harmonic generation (THG), 90, **166–167**, 179–180, 188, **428**, 435, 550, **705–718**.
CARS, 596–597
contrast mechanism, **166–167**
deposits no energy, 361
detectors for, 421, 706–708
table, 707
double-pass detection method, 166–167
intracellular inhomogeneities tracked, 90
light attenuation spectra, 706
light sources, 706–708
to make more laser lines, 109, 114
mechanism, 705
microspectroscopy, 421
MMM, 551, 559
non-linear optical microscopy, 705
optical sectioning, 704
optically active animal structures, 714–717
collagen mat, polarization microscopy, 717
mouse zygote spindle, 717
structures producing THG, table, 715
zebrafish embryo, 716, 718
optically active plant structures, 710–714
cell walls, 438
Commelina communis, 712
Euphorbia pulcherrima spectrum, 710
maize, emission spectrum, 710, 711, 713
maize, polarization microscopy, 711
maize, stem section, 714
phytoliths, polarization microscopy, 720
potato, 712
Pyrus serotina spectrum, 711
rice leaf, image, 712, 715, 719
photon interactions, 179
pulsed lasers suitable, table, 706
STED, 577
structural contrast, 188
Three-decibel point (3dB), for bandwidth, 59, 65.
Three dimensional cell pellet, 815.
Three dimensional microscopy, 766, 771, **804**$^{+}$.
future perspectives, 804–805
living embryos, 766
of plant cells, 771
Three dimensional projections, embryo, 763.
Three dimensional segmentation, plant, 776–778.
Three-channel confocal microscopy.
with 4 recombinant proteins, 190
assays for, 814
Three-dimensional diffraction image, 4, 147, 407, 455, 463, 471, 491.
Three-dimensional micro-array assays, 815–816.
Three-dimensional reconstruction, 775–776, 778, and Chapters 14 and 15.
plant imaging, 775–776
A. thaliana, 778
Equisetum, 774

Three-photon excitation (3PE), 88, 415, 447, 535, 550–552, 555, 558, 647, 680, 709, 876.
absorption cross-section, 680
damage, 682, 686
fiber-optics, 507
resolution, 447
setup, 708–709
TIFF (Tagged image file format), 580.
Tiled montage, 851, 858.
Tiger, ECDL laser system, 90.
Time correlated single-photon counting (TCSPC), 518, **520–523**, 526.
for lifetime imaging, table, 526
FLIM, 520–523
FRET-FLIM, 186
schematic diagram, 521
Time multiplexing, of adjacent excitation spots, to reduce flare in MMM, 553–554.
Time-gated detection, FLIM, **522–524**, 526, **528**$^{+}$.
diagram, 522
FLIM methods compared, table, 526
FLIM, image, 528–529
Time-lapse imaging, 136, 222, 354, **382**–384, **392–399**, 652, 773, 885–886.
Amoeba pseudopod, 191
confocal of plant cells, 773
high-content screening, 812
illumination stability, 136
image analysis, 286, 320, 333, 732–733
mechanical stability, 219
microspectrometry, maize damage, 424–426
rectified-DIC, of platelets, 846
SPIM, 613
table, 384
three-dimensional plus time, 222
two-dimensional plus time, 222
Time-lapse recordings.
Amoeba pseudopod, 191
Ascaris sperm, 846
biofilms, 885
brain slices, 725, 727, 729, 732–733
embryos, 676, 749, 752, 759, 761
meristem growth, 430
plant roots, 781, 784
rectified-DIC, of platelets, 846
two-photon microscopy, 10
TIRF. *See* Total internal reflection fluorescence.
TIRM, 177–179, 477.
Tissue specimens, introducing the probe, 360.
Titanium:sapphire laser (Ti : Sa), 82, 84–86, 88–91, 94, 100–103, 105, 107, 109, 111–112, 114, 123–124, 165, 346, 358, 415, 423–424, 459, 541, 550, 551, 645–647, 688, 706–708, 713, 727, 750, 756, 759. *See also*, Lasers, titanium : sapphire and Ultrafast lasers.
4Pi, 563–564, 567
brain slices, 731
CARS, 599
compare to other fast lasers, 112–113
Cr : Fosterite, femtosecond pulsed laser, 109, 114, 415, 541, 706–709, 712–714
embryos, 750, 756, 759, 731, 764
emission stability, 86
four-level vibronic model, 82, 109
maintenance, 116
multi-photon excitation, 541
and OPOs, 114–115
plants, 415, 423–424, 706–708, 713–714, 717, 781–783
popular models, specs, table, 120
STED, 575
ultrafast, 112–113
URLs, 124
TLB. *See* Transmitted light bright-field.
TLLSM. *See* Thin Laser Light Sheet Microscope.
Tobacco, 116, 189–190, 430, 693.
smoke, not around lasers!, 116
suspension-cells,
birefringence, 189–190
GFP expressing cells, 430
photo-bleaching, 693
"Toe" photographic response, defined, 71.
Tornado mode, SIM scanner, 54.
Total fluorescence signal, 742.
Total internal reflection fluorescence microscopy (TIRF), 90, 160, **180–184**, 223, 477, **801**.
blind deconvolution, 477
vs. confocal image, 184
contrast, 180–184
cytoskeleton, image, 183
FRET, 801
limits excitation to single plane, 223
objectives, for epi-TIRF, 161
Total internal reflection microscopy (TIRM), 177–179, 477.
blind deconvolution, 477
evanescent wave generation, 178
TPE. *See* Two-photon excitation.
TPEM. *See* Two-photon excitation microscopy.
Trade-offs, 36, 68, 78–79, 221, 224, **644–648**, **747–748**, 825.
beam power, visibility/damage, 693
blind deconvolution, 483, 488, 499
compression algorithms, 581, 840
confocal endoscopes, 508
when digitizing, 68, 78–79
embryo specimens, **747–748**
high-content screening, optimal clustering, 825
living cells, 381, 693
micro-CT, dose/resolution, 616
MRM, time/resolution, 622
and pinhole size, 265, 267
processing speed/segmentation, 301
speed, S/N, sensitivity and damage, 221, 224, 232, 556, **644–648**
SPIM, resolution and number of views, 613
Transcriptional reporters, embryo analysis and, 748, **755–756**.
FluoroNanoGold, 854
mRNA, 316–317, 465
plants, 773, **781**
NF-kB, 814
Transfection buffer, electroporation, table, 802.
Transfection, cellular, 756–758, 790, 791.
brain slices, 722, **724–725**, 730–731
Transfection reagents, for chromophores, 358, 360, 362, 556, 682, 790–791, 795, **803**.
2-OST-EGFP, 566
COS7, 693
EB3-GFP, 183
for FRET, CFP/YFP, 795–796, 798, 801–802
GaIT-EGFP, 566
GFP-MusculoTRIM, 184
ligand binding, 348
Transfer function, implications for image contrast, 164–165. *See also*, CTF.
Transient permeabilization, **359**, 373, 375.
Trans-illumination, absorption contrast, 166.
Transistor-transistor logic (TTL), 259.
Transit time spreads (TTS), 527.
Translational fusions, 756, 757. *See also*, Transfection agents.
subcellular specific protein distribution, 756
Transmission, 33, 49, 159, 225, 231, 804.
AOBS, 57
contrast, 163–164
disk-scanning micro-lens array, 223–226, 227–229, 231, 235
dispersion, 683
of filters. *See* Filters
linear *vs.* log plots, 44–49
of glass fibers, 501–505
illuminator, 201, 127–128
losses due to refractive optics, 33, 217
table, 217
of objectives, 154, 158, 159–161, 641
relative, measurement, 26, 34, 36
table, transmission, 158, 159–161
of plant tissue, spectra, 416, 422
of Polaroid materials, 85
SHG signal detection, 707–709, 729–730
by small pinholes or slits, 225
Transmission electron microscope (TEM), 846.
correlated LM-TEM images, 852–855, 857–859
stereo images of platelets, 848–849
Transmission illuminator, ghost images, 201–202.
Transmission intensity, specimen thickness, 164.

Transmittance, optical system, measured, 25–26.
table, 217
Transmitted light brightfield, 468, 472–473, 477.
blind deconvolution, 472–473, 477
Transparency, lighting models, 309–312.
Transverse electromagnetic modes (TEM) laser, 83.
Trends, in laser design, 118.
Triple-dichroic, 33, 46, 48, 217–218, 678, 783.
light loss due to, 33
performance, 46–48
Triplet state, 103, 338, **339–342**, 348, 362–363, 390, 516–518, 573, 646, 684, 691–693, 697, 698, 704, 852.
saturation, 339, 573
as a RESOLFT mechanism, 573
Triton X-100, 730, 852.
formaldehyde fixation, 370–372, 375–377
True color, 291.
TSM. *See* Tandem-scanning confocal microscope.
TTL. *See* Transistor-transistor logic.
Tube length/chromatic corrections, table, 157.
Tunable lasers, 91, 103, 107, 109, 120.
broadband, table, 120
continuous wave dye, table, 91
diode, emerging techniques, 107
solid-state, 106, 109
solid-state ultrafast, 103
Tungsten carbide electrodes, radiance, 137–138.
Tungsten halogen source, 132, 137, 153.
Turnkey ultrafast laser systems, 118.
Tutorials, lasers by level, 124.
Tweezers, optical, 89–90, 110, 218, 383, 385.
setups for integration, 218
single-longitudinal-mode fiber laser for, 110
trapping wavelength, 89–90
Two-channel confocal images, 175–177, 177, 193, 425, 522.
A.thaliana, epidermal/mesophyll cells, 193, 425, 431–432, 434–436
Amoeba pseudopod, 169
colocalization, 667
display, 311, 841
FLIM, 522
harmonic images, 714–716
mouse muscles, 716
montaging, 331
neurons, 332
microglia, 396–398
eye, optic nerve, 481
Golghi-stained, 298
Lucifer-yellow, 314
rat-brain neurons, 398
transmitted light, 475
of peony petal, cytoplasmic, 175–176
rat intervertebral disk, 310–311
of zebrafish embryo, 177
Two-dimensional imaging, 60, 222, 397–398.
time lapse, 222, 397–398
Two-photon fluorescence excitation (2PE), 156, 160, 218, 535, 536, 750, 778–783.
chapter, **535–549**
chromatic correction for, 156
for plant cells
advantages of, 778–779
cell viability, 779–781
vs. confocal microscopy, 779
dyes, 782
of green fluorescent protein, 782–783
pitfalls, 782
of thick specimens, 779
in vivo, 781
special objectives for, 160
visible and ultraviolet dyes, 218
Two-photon microscopy, 10–12, 195, 357, **535–549**, 690, 697, 900–905. *See also*, Multi-photon excitation; Multi-photon microscopy
autofluorescence, 545
basic principles, 535
of biofilms, 882–885
bleach planes, in fluorescent plastic, 193, 194
caged compounds, 544
calcium imaging, 545
chromophores, 543
2-photon absorption, 543
diagram, 540
detection, 538, 541
descanned, 542
non-descanned (whole area) detector, 541
stray light, 904
fluorescence, shadowing, 195
group delay dispersion, 5443
laser. 540–541
alignment, 900–904
monitoring, 901–903
mounting, 541
power level, 903–904
safety, **117–118**, **839**, 900, 903–904
living cell studies, review, 544–545
living animal studies, 545
minimize exposure during orientation, 905
mirror scanning, 543
optical aberrations, 542
photobleaching, 690, 697
practical tips, 900–905
beam alignment, 901
bleed-through, 904
choice of pulse length, 537, 903
pulse length, 109, 112, 115, 507, **537**, 538, **902–903**
specific specimens, *see* specimens by name imaging multiple labels, 904–905
neurolucida protocol, 731
resolution, 539
and speed, 12
vs. spinning disk imaging. in plant cells, 783
stray light and non-descanned detection, 904
theory, 535, 537
wavelengths, 538–541, *See also*, Botanical specimens

U

UBC 3D living-cell, microscopy course, 174, 183, 184, 190, 205, 364, 430, 435, 439, 805–806.
Ulbricht sphere, for measuring light, 140.
Ultrafast imaging, two dimensional, 222.
3D, 235
Ultrafast lasers, 88, 101, 103, 112–114.
Cr : Fosterite. 109, 114, 415, 541, **706**, 707–709, 712–713
diode-pumped solid-state (DPSS), 112
distributed feedback (DFB) diode laser, 113
fiber, 113–114
table, 101
fiber-diode, mode-locked, 113
Nd : YAG, 88–89, 91, 95, 97, 103, 107–109, 111, 113–115, 117, 218, 245, 514, 680, 798
Nd : YLF, 89, 98, 100, 103, 109, 112–114, 750, 760–761
Nd : YVO_4, 89, 95, 100, 103, 107–109, 111, 113–114, 541
solid-state, tunable, 103
spectrum, 44
titanium : sapphire, 112–113. *See also*, Laser, titanium : sapphire; Titanium-sapphire laser
Ultrafast pulses, delivery by fiber optics, 88, **507**.
dispersion losses, 502
Ultraviolet (UV), argon-ion laser lines, 85, 87, 90, **102**, 339, 346.
other UV lasers, 111–117
use for micro-surgery, 218–219
Ultraviolet (UV) confocal microscopy, 109, 174, 195, 571.
absorption, 707, 713
autofluorescence, 431–432, 434, 544
CCD response, 29, 255, 459, 921–922
correct imaging with planapochromats, 14, 154
damage, 212, 290, 439, 544, 680, 686, 903
disk-scanners, 229
DNA-dyes, 782, 874. *See also*, DAPI; Dyes GFP excitation, 798, 873
high-content screening, 811
ion-imaging, 346, 383, 529, 738, 742

Ultraviolet (UV) confocal microscopy (*cont.*)
multi-photon excitation, 535, 538, 544, 559, 646, 706, **905**
photoactivation, 759
safety, **117–118**, **839**, 900, 903–904
simultaneous with DIC imaging, 846, 850
as source of stray signal in PMT envelopes, 257
Ultraviolet performance of objective lenses, 154, 159–161, 706.
Ultraviolet widefield light sources, 132, 136, 139, 143, 226, 542.
table, 226
Ultraviolet transmission of optical fibers, 88.
Ultraviolet (UV) light, effects produced by multiphoton intrapulse interference, 88.
Ultraviolet scanning light microscope, 6–7.
Uncaging, multi-photon microscopy, 383, 385, 545, 693, 760–764. *See also*, Photoactivation.
Unconjugated bodipy/ceramide dyes, 760.
Under-sampling, 79, 635, 640, 652, 662, 831, 833, 836, 839, 841.
example, 640
uses, 68
Uniformity, of light source, 127–129.
Unit image body, 3D Airy figure, 147.
Upright *vs.* inverted microscope, 140, 157, 217, 230, 413, 722, 727, **870–872**.
Unmixing. *See* Spectral unmixing; structured illumination.
Up-conversion, fiber lasers, 110.
doped ZBLAN, 110
dual-ion doped, 110
UV. *See* Ultraviolet.

V

Vacuum avalanche photodiode (VAPD), 31, 254, 255.
definition, 254
schematic, 31, 255
VAPD. *See* Vacuum avalanche photodiode.
Vertical-cavity semiconductor diode laser (VCSEL), 108.
Vibration.
compensation, 732
from cooling water, 84, 102, 499
of disk scanner, 753
causing distortion, 16, 39–41, 166, 201
of galvanometer mirrors, 40, 201
high-frequency, of acousto-optic devices, 55, 84
isolation, 85, **201**, **219**, 541
measurement, 30–41, 652
of mechanical shutters, 929
of objective lens motion, 754
optical fiber isolation, 505, 507
of optical fiber scrambler, 8, 84, 131
Vibronic laser, Ti : Sa four-level, 109.
Video, 2, 4, 5–7, 11–14, 17, 37, 52–53, 61–62, 88, 219, 237, 261, 263, 346, 372, 430, 451, 505, 539, 554, 556, 589–590, 593, 604, 860, 885.
confocal, 25, 237, **914**
impact on light microscopy, 5–7, 14
results, 14
signal, 258–259
Video-enhanced contrast microscopy, imaging small features, 14, 68.
Vignetting, 210–211, 229, 245–247, 492, 541.
objective, off-axis performance, 245–247
Visibility, and signal-to-noise ratio, 37–38, 68. *See also*, Rose Criterion.
Visilog/Kheops, software, 282, 301–302, 312.
Visitech, confocal manufacturer, descriptions, 88, 119–120, 226, 237, 908.
VT eye, 119–120, 908, 914
VT Infinity, 119–120, 908, 914
Visual cortex, identification of primary, 724.
Visual observation, magnification for, 146.
non-linearity, 72–73
Visualization, 280, 282–283. *See also*, Multidimensional microscopy images; Rendering.
definition, 280, 292
software packages for, table, 282–283
Vitrea2/Voxel View, software, 282, 335.
Volocity (software), 281, 236, 282, 295, 299, 312, 757, 762–764.
VolumeJ, software, 282, 304, 764.
VolVis, 281–282.
VoxBlast, 283, 301–302, 309, 312.
Voxel, defined, 20.
Voxel rendering, speed, 290.
Voxx, software, 283, 377, 764.

W

WAD. *See* Whole-area; Non-descanned detection.
Water, as immersion medium, 409, 410.
refractive index mismatch, table, 409, 410
two-edge response curves, 410
Water-coverslip interface, spherical aberration generated at, 147.
Water-immersion objectives, 15, 23, 36, 141, **148–149**, 154, 190, 235, **241–242**, 247, 261, 377, 386–387, 389, 395, **411–412**, 513, 542, 552, 556, 562, 567–568, 584, 654–656, 708, 727–728, 737, 747, 772. *See also*, Spherical aberration.
4Pi, 562, 567–568
advantages, 149
biofilms, 870, 872
brain slices, 727–728, 730, 737
chapter, 404–413
correction-color/flatness/transmission, 154
deep imaging, 395
dipping objectives, 161, 209, 411, 429, 568, 613, 727, 737, 870, 872
in fluorescence ion measurement, 737
ion measurement, 737
living cells, 386–387, 389, 395, 398
performance measured, 47, 655–656
plant cells, 429, 433, 772
STED, 576
transmission curves, 159–161
use and limitations, 15
Watershed algorithm, **322–325**, 777, 822.
for segmentation, plant cell images, 777
Wave optics, 4, 10.
for calculating axial resolution, 4, 146, 154
Wavefront error, 217.
lower, with hard coatings on filters, 45
Wavelength, 24, 28, 43–51, 62, 88, 107, 114–115, 118, 129–130, 135–139, 165–166.
calculation of Forster radius, FRET, 793
and CCD coupling tube magnification, 62
filters for selecting, 43, 44, 88
in multi-photon lasers, 165–166. 415, 750
multiple, dynamic embryo analysis, 756
of non-laser light sources, 129–130, 135–136
and optimal zoom setting, 24
vs. pinhole size, 28
selecting, with interference filter, 88, 165–166
stability, in non-laser light sources, 137–139
tunability, of lasers, 107, 109.
Wavelength expansion, non-linear, 114–115.
Wavelength ratioing, 346. *See also*, FRET; FLIM.
Wavelength response, chromatic aberration, 663.
Wavelength-selective filters, 43–51, 88.
Wavelength-tunable lasers, summary, 107, 113, 116, 118, 550.
Wavelet compression, 581–584.
Wavelet de-noising protocol, 733–734, 819–820.
Waxes, plant, 420, 428, **434–435**, 714–715.
Website references, 123.
2 photon excitation spectra, 546, 727, 729, 782
brain slices, 727
CCDs, 76, 234, 927, 931
components, 58
confocal Listserve, 390, 901
deconvolution, 495
dyes, 221, 343–344, 782
fluorescent beads, 653
FRET technique, 185, 803
high-content screening systems, 811
image management, 865
lasers, 104, 115, 120, 123–125
live-cell chambers, 388–389, 870
movies related to book, 235, 392
muscles, 237

non-laser light sources, 138, 143
plants, 769
safety, **117–118**, **839**, 900, 903–904
software, 282, 376, 594, 734, 762, 764, 776, 777, 820, 824, 827, 831–833, 844, 845, 864–862, 865–867, 869
SPIM, 672
Wedge, compensator, 566–567.
Wedge, rotating, for light scrambling, 84, 131.
Wedge error, in interference filters, 45–46, 151, 211–212, 630.
in traditional filters, 45
Wedged fiber-optics, reduce reflections, 85.
Well-by-well data, 817.
WF. *See* Widefield.
WFF. *See* Widefield fluorescence microscopy.
White light continuum lasers, 88, 109, 113
continuum, 88, 109
He:Cd, 113.
Whole-area and external detection, 541–542. *See also*, Non-descanned detectors.
Whole-cell patch pipet delivery, 360, 726–727.
Widefield deconvolution, 751–753, 785. *See also*, Deconvolution.
botanical specimens, 785
for living imaging, 751–753
Widefield (WF) fluorescence microscopy, 3, 22–23, 26, 172–173, 219, 453–467, 518. *See also*, Epifluorescence microscopy, Deconvolution.
compared to confocal, 453–467, **644–647**
CCD/confocal comparison, 458–459, 465
same specimen, 465, 482
compared to structured illumination, 274
deconvolution, imaging living cells, 23, 392
deconvolving confocal data, 461–464, 466
fluorescence detection, 459–460
fluorescence excitation, 459
fluorescence lifetime imaging, 518
gain-register CCDs, 460–461
images utilizing out-of-focus light, 26
imaging as convolution, 453–457
imaging thin specimens, 172–173
integration of fluorescence intensity, 459
interaction of photons with specimen, 22–23
light-emitting diode sources, 136
limits, linearity/shift-invariance, 457, 490, 564
model specimens, 461
noise, 459–463
optical sectioning schematic, 469
optical tweezers/cutters, 219, 89, 383, 385
out-of-focus light, 461
point-spread function, 453–457, 459–463
resolution, 3
sensitivity, 459–463
single point images, 454
pros/cons, **644–648**
table, 459
temporal resolution, 458
Wiener filtering, 494, 496. *See also*, Gaussian filtering.
image enhancement, 496
image restoration by, image, 494
Windows software, for automated confocal, 810.
WinZip, 580.
Wollaston prisms, DIC, 156, 468, 473, 475. *See also*, Nomarski; DIC contrast.
Working distance (WD) of objective lenses, 5, 9, 129, 145, 154, **157**, 198, 249, 511, 568, 598, 634, 673, 678, 727–728, 747, 774, 779, 781, 872.
table, 157–158
WORM disks (write once, read many), 586.

X

Xenon arc lamps, 44, 132, 137–138, 144.
iso-intensity plot of discharge, 132
pulsed-operation, 137–138
shapes of electrodes, 132
spectral distribution, 144
super-pressure, spectrum, 44, 136
explosion hazard, 136
wavelengths available for detection, 44
Xenon/iodine fill arc, radiance, 137–138.
Xenopus laevis, 13, 610, 746, 748–753.
blastomere, 757
confocal/multi-photon comparison, 750
embryo
viewed with confocal, **748–753**
viewed with OCT, 610, 749
embryo viewed with MRM, 623–264
in situ imaging, 746, 748
oocyte wound closure, 749
X-Y resolution, confocal/widefield compared, 36.

Y

Yellow fluorescent protein (YFP), 221–222, 429.
FRET pair with CFP, **791–803**
YFP, 221–222, 429
Yokogawa disk-scanning confocal system, 6, **12–13**, 16, 216, 224–226, **231**, 234–237, 458, 754.
CSU-10/22 model, 223, 231, 236, 915
with EM-CCD, 234, 237, 755
high speed acquisition, 11, 220, **222–226**, 229, 231, 458, 667, 754, 784
results, 236–237, 755, 783
vibration, 16
Ytterbium tungstate (Yb:KGW) laser, 108.

Z

ZBLAN up-conversion glass fiber, 110.
Z-buffering, 304–305.
Z-contrast, in confocal microscopy, 180.
Zea mays. See Maize.
Zebrafish, 174, 176, 761.
GFP image, 176, 176
autofluorescence, 174
pancreas expressing DsRed, 176
scatter labeling/lineage tracers, 761
Zeiss, confocal manufacturer, 212, 214, 217, 226, 231–232, 655, 771, 916–917.
510 META confocal microscope, 655, 908, 916
Achrogate beam-splitter/LSM 5-Live, 50, 119–120, 212, **231–232**, 916
Axioimager system, 217
fluorescence correlation spectrometer (FCS), **383**, 385, 602, 801, 803, 805, 917
HBO-100 source, self-aligning, 134–135
high-content screening, 811
LSM 5-Live line-scanning confocal microscope, 50, 51, 231–232, 237, 784, 908, 916
META confocal spectral detector, 51, 119–120, 161, 202, 660, 663, 796, 916.
mini-PMT arrays, 51, 667FRET, 706
tests, 663
objectives, advantages of, 155–156
Infinity Color-corrected System, 155, 217
plan objectives, table, 152
transmission specifications, 161
tube length conventions, 157, 239
working distance of objectives, table, 158
Zernike moments, 247–249, 818–820.
Zernike polynomial fit, 245–247.
table, 247
wavefront aberration function, 247
Zinc selenide (ZnSe) diode lasers, 106.
Zirconium arc lamps, 136, 141.
spectrum, 136
Zone System (Ansel Adams), 71–72.
Zoom magnification, 11, 24, 37, 63–64, 66, 70. *See also* Magnification
optimal, 24
optical *vs.* electronic bandwidths, 70
relationship to area scanned, 63
Z-position and pinhole/slit size, 227.
Z-resolution, **3–4**, 22, 36, 149–150, 224, **225–228**, 563, 752. *See also*, Axial resolution.
4Pi microscopy, 563
in confocal fluorescence microscopy, 36
effect, of fluorescence saturation, 22
improvement, 752
of pinhole disks, 224
in STED, 576
Z-scanners, evaluating, 215.
Z-sectioning, imaging brain slices, 729.
Z-stack, 23, 754.
of images of cheek-cell specimen, 23
speed acquisition constraint, 754